UNIVERSITY TURBINE SYSTEMS RESEARCH PROGRAM

ANNUAL REPORT

Reporting Period Start Date: January 1, 2006
Reporting Period End Date: December 31, 2006

Principal Authors: Nicholas Rigas
Richard A. Wenglarz
Robert Leitner
William H. Day

March, 2007

DOE Award: DE-FC26-02NT41431

Submitted by: Clemson University Research Foundation
South Carolina Institute for Energy Studies
P.O. Box 946, 386-2 College Avenue, Clemson, SC 29633-0946

DISCLAIMER

ABSTRACT

The US Department of Energy (DOE) initiated a cooperative agreement in 1992 with the South Carolina Institute for Energy Studies (SCIES) for the Advanced Gas Turbine Systems Research (AGTSR) program. In 2002, the DOE established a follow-up cooperative agreement for a program now designated as the University Turbine Systems Research (UTSR) Program. As stated in the cooperative agreement, the objective of the program is to support and facilitate development of advanced energy systems incorporating turbines through a university research environment.

This document is the fifth annual, technical progress report for the UTSR Program. The Executive Summary describes activities for the year by the South Carolina Institute for Energy Studies (SCIES), which administers the UTSR Program. Included are descriptions of:

- Outline of program administrative activities
- Request for university proposals (UTSR RFP)
- Selection of projects for award in 2007
- UTSR Peer Review Workshop
- UTSR Fellowships awards to higher level university students
- Increased number of Performing Member Universities
- Summary of Outreach activities
- Summary table describing the active UTSR research projects during 2006

The remainder of this report describes in detail the technical approach, results, and conclusions to date for the UTSR university projects.

TABLE OF CONTENTS

Spectroscopic In-Situ Non-Destructive Evaluation to Monitor the Health of Thermal Barrier Coatings, Cleveland State University

Superior Thermal Barrier Coatings for Industrial Gas Turbines Using a Novel Solution Plasma Spray, University of Connecticut

An Advanced Diagnostic and Prognostic System for Gas Turbine Generator Sets with Experimental Validation, Clemson University

The Effects of Fuel distribution, Velocity Distribution, and Fuel Composition on Static and Dynamic Instabilities and NOx, Penn State University

Improved Film Cooling Performance for Turbine Vanes and Endwalls with Realistic Surface Conditions, Virginia Tech

Combustion Instability and Blowout Characteristics of Fuel Flexible Combustors, Georgia Tech

Correlation of Ignition Delay with IGCC Type Fuels, University of California, Irvine

Heat Transfer from Rotating Blade Platforms With and Without Film Cooling, Texas A&M University

Combustion Characterization and Modeling of Fuel Blends for Power Generation Gas Turbines, University of Central Florida

Effects of Coating Blockage and Deposits on Film Cooling Effectiveness and Heat Transfer, University of Pittsburgh

Investigation of Materials Performance in High Moisture Environments Including Corrosive Contaminants Typical of Those Arising by Using Alternate Fuels in Gas Turbines, University of Pittsburgh

Autoignition Studies of Syngas and Hydrogen (SGH) Fuels, Penn State University

Degradation of Thermal Barrier Coatings with Syngas Combustion, University of Central Florida

Aero Losses, Heat Transfer, Discharge Coefficients for Different Vane Trailing Edge Configurations for Syn Gas Fired Turbines, University of North Dakota

Deposition of Alternative (Syngas) Fuels on Turbine Blades with Film Cooling, Brigham Young University

Fundamental Studies in Syngas Premixed Combustion Dynamics, Massachusetts Institute of Technology

INTRODUCTION

Cooperative agreement DE-FC26-02NT41431 for the Advanced Gas Turbine Systems Research (AGTSR) program was established on March 20, 2002 between the U.S. Department of Energy/National Energy Technology Laboratory and the Clemson University Research Foundation/South Carolina Institute for Energy Studies (SCIES). This cooperative agreement established a five-year basic and fundamental research program that is a conduit for university support of the DOE's Fossil Energy Turbine Program. To emphasize the university role, the program was renamed the University Turbine Systems Research Program (UTSR) in late 2002.

One of the requirements of the Cooperative Agreement is a yearly technical progress report. This document provides the technical progress report for the year 2006.

The major activities specified in the Scope of Work for the UTSR Program are related to the establishment and oversight of university research projects and outreach activities. The research is to be of high importance to long-term health of the U.S. energy (especially gas turbine) industry. The outreach is to aid in transfer of university research technology and entice growth of the number of industry and university participants in the program.

Major Program Plan elements identified in the Scope of Work implemented by SCIES for the UTSR Program are:

- Identification and selection of university research topics
- Request for proposals (RFP)
- Proposal selection
- Technology transfer
- Outreach

SCIES activities for 2006 in these areas are described in the Executive Summary of this report. The remainder of this report describes the ongoing university research projects that are being administered by SCIES in the UTSR Program and recently completed projects.

EXECUTIVE SUMMARY

In the UTSR Program, the DOE and Industrial Review Board (IRB) provide input to define needed energy systems (particularly gas turbine systems) research and Performing Member universities conduct the research. Under DOE direction, new activities were added to the UTSR Program beyond those of the previous AGTSR Program. These include:

- Outreach activities
- Emphasis on coal derived syngas and hydrogen fuels for turbines, rather than natural gas
- Broadened university research areas (e.g., instrumentation, sensors and life)
- New and expanded reporting requirements for SCIES and the universities.

UTSR Activities For 2006

Research Related Activities

UNIVERSITY PROJECT ADMINISTRATION

SCIES administration activities for the UTSR university projects included:

- UTSR request for proposals (RFP) from universities
- Project selection for award in 2007
- New project awards/subcontracts
- University project administrative and technical oversight
- Processing requested subcontract modifications
- Sending semi-annual reports with evaluation forms to the IRB for review
- Informing university principal investigators of the most significant IRB comments from review of their semi-annual reports
- Coordinating IRB reviews for sensitive information in university technical papers submitted for publication by the ASME and other technical societies

REQUEST FOR UNIVERSITY PROPOSALS (RFP) – Inputs from several sources were used by SCIES to determine the 2006 RFP research topics. The DOE solicited research needs from turbine manufacturers that produce large turbines for power plants. The DOE provided the resulting responses to SCIES. The Academic Advisory Board (AAB) for the UTSR also recommended appropriate university technical studies to achieve DOE Turbine Program goals. Mani Manivannan of the DOE also suggested materials related research. The EPRI representative on the UTSR IRB (Industrial Review Board) recommended university research topics. In addition, SCIES reviewed literature describing the technical progress and issues for the turbine systems being advanced through the DOE Turbine Program.

From the extensive list of candidate research topics identified by the above sources, SCIES determined the most important topics for the RFP based on in-house experience previously developed over many years in the gas turbine industry. These topics were incorporated into a draft RFP sent to the DOE for approval. After minor modifications resulting from DOE comments, the RFP was released to more than 100 UTSR Member Universities in May. The proposal due date was July 17, 2006.

UNIVERSITY PROJECT SELECTION FOR AWARD IN 2007 – SCIES received 38 university proposals (14 in Aero/Heat Transfer, 14 in Combustion, and 10 in Materials) in response to the 2006 UTSR RFP. The proposals, along with scoring forms, were sent to the 17 UTSR IRB organizations for evaluation. The evaluations were received by SCIES in late August and early September. SCIES compiled the proposal rankings by the IRB organizations to obtain a composite ranking order within each of the three technology areas of Aero/Heat Transfer, Combustion, and Materials. The composite rankings were sent to the IRB organizations well in advance of the IRB Meeting at Clemson on October 16. At that meeting, SCIES coordinated the selection of a short list of six projects (two in each of the three technology areas) for award in 2007, subject to available DOE funding for the UTSR program.

UNIVERSITY PROJECT AWARDS FOR 2006 – Because of funding limitations, no new university projects were awarded in 2006. The available UTSR budget over the five-year cooperative agreement supports a fixed number of multi-year university project awards. The much higher than average yearly number of projects that were awarded in the first two years of the program (10 in the first year and 9 in the second year) resulted in fewer projects than average that could be awarded in later years. Budget evaluations in the first quarter of 2005 showed insufficient funding for new project awards in 2006 due to funding requirements for the UTSR projects awarded to date and a decrease in the UTSR budget from the DOE. In agreement with the DOE Contracting Officer's Representative, SCIES notified contact persons at the Performing Member Universities that a UTSR RFP would not be released in 2005. Consequently, there were no new university project awards in 2006.

WORKSHOP – SCIES organized UTSR Peer Review Workshop IV which was conducted at the Clemson University Madren Conference Center and Inn on October 17-19, 2006. The workshop included twenty peer review presentations describing on-going UTSR university research projects; seven in areo/heat transfer, six in combustion, five in materials, and two in instrumentation, sensors and life. The UTSR Academic Advisory Board (AAB) Chairman presented AAB activities. Posters from six UTSR fellows and nine non-UTSR research efforts were presented at an evening reception. Rich Dennis, the DOE Manager of Turbine Technology, described "The DOE Turbine Program" in a presentation. Presentations on needed university gas turbine research were provided by four gas turbine companies on the Industrial Review Board. Eighty-seven persons from academia, industry, and government attended the workshop.

IRB MEETING – The annual UTSR IRB meeting was held on October 16, 2006, the day before the start of the Workshop. As described above, six short-listed projects were selected for possible award in 2007. The meeting also addressed a summary of UTSR finances, UTSR personnel/staffing, UTSR Continuation Request, and other administrative activities.

UTSR FELLOWSHIP PROGRAM – During 2006, 14 student Fellows from 10 US universities were placed at 13 IRB companies for periods of 10-12 weeks. Siemens funded one student on their own from among those that applied for UTSR Fellowships. This benefited the UTSR Program, since an additional Fellowship applicant received placement.

TECHNOLOGY INTERACTIONS WITH OTHER ORGANIZATIONS

In order to determine beneficial university research, SCIES interacted with several organizations to identify and exchange information on research needs and experience for turbines operating with syngas and high hydrogen fuels:

ORNL: SCIES continued to interact with Oak Ridge National Labs (ORNL) in areas mutually beneficial to their DOE materials project and the UTSR project. ORNL will be conducting thermo-chemical analyses to calculate the composition of species (including trace ash compounds) in the flow path of turbines operating with syngas and high hydrogen fuels. This information will be useful input to UTSR materials and aero/heat transfer projects. SCIES suggested analyses at ORNL that will be beneficial to both programs (effects of turbine inlet temperature and variations in syngas ash chemistry). SCIES previously obtained input information (e.g., fuel, air and diluent flows into a syngas turbine combustor along with trace impurity data for syngas) needed for ORNL to conduct the thermo-chemical analyses. Additional suggestions were also provided on analyses scenarios to explore.

CINERGY: SCIES previously visited the CINERGY Wabash River IGCC plant and obtained a third stage blade from the same Wabash River turbine row that had experienced a blade failure. SCIES facilitated the analyses of the blade by SouthWest Research Institute to determine if operation with syngas contributed to the failure. The analysis, completed in 2006, did not implicate the syngas fuel in the failure.

UK-US Collaboration: Resulting from a recommendation by SCIES, one of several US-UK collaborative projects being developed involves using an existing Cranfield University (UK) facility to simulate turbine flow path conditions for tests of materials and turbine protection approaches for syngas turbines. SCIES was assigned as the lead for the US portion of this collaborative project. Of particular importance will be tests at the higher gas temperatures being considered for next generation syngas turbines to meet the DOE IGCC efficiency objectives. Information and data on turbine flow path environments and materials degradation resulting from this test program are intended to be useful as input to UTSR projects. In 2006, materials specimens were prepared and SCIES interacted with EPRI concerning the remaining incremental funding needed for the tests at Cranfield.

TECHNICAL PUBLICATIONS/PRESENTATIONS

A paper, “Erosion and Deposition in Turbomachinery”, with coauthors from the University of Cincinnati and SCIES was published in a special section of the March-April 2006 AIAA Journal of Propulsion and Power.

The SCIES contribution to the above AIAA publication was expanded and submitted for a chapter in the book, “Turbine Science and Technology” to be published in 2007 as an AIAA Progress in Astronautics and Aeronautics series volume.

A Paper, “Gas Turbine Issues in Advanced Gasification Systems,” by R. A. Wenglarz (SCIES) and J. Oakey (Cranfield University) was invited for the Materials for Advanced Power

Engineering Conference 2006, in Liege, Belgium. The paper reviewed the status of materials experience for current syngas turbines and issues for higher temperature future syngas turbines, such as being considered for DOE programs. It was presented and published in the three volume bound books of proceedings for the conference.

R. A. Wenglarz was invited to provide one of the two keynote presentations at the GEN 5 2006 Conference in Long Island, NY, in September. The paper titled "Coating/Materials Experience and Issues for Alternate Fuel Turbines" discussed thermal barrier coating needs for turbines operating with coal-derived syngas/hydrogen and other alternate fuels.

Outreach Activities

The major outreach activities for 2006 were in the areas of:

- UTSR program support
- Related Turbine Program support
- UTSR program publications

UTSR PROGRAM SUPPORT

MEMBERSHIP – The US Naval Academy joined as a Performing Member University in June 2006. There are now 111 Performing Member Universities in 42 states. No new companies joined the Industrial Review Board (IRB) during 2006. One IRB member, Capstone, withdrew because of funding limitations.

FELLOWSHIP PROGRAM – The fellowship program, funded by IRB membership fees, offers students valuable work experience and the opportunity to practice the "art" of engineering in an industrial setting. Discipline areas related to land-based gas turbine power generation systems include mechanical design and manufacturing, heat transfer, aerodynamics, combustion, thermodynamic analyses, materials and coatings, and testing and evaluation.

Emphasis is placed on gas turbine component design and manufacturing techniques, using state-of-the-art experimental and computational facilities. UTSR professors and industry engineering staff serve as mentors and advisors for the fellows. Students are exposed to gas turbine design techniques, analysis and system optimization methods, design limitations and practical problems encountered in the industry.

In the past 11 years, 174 students have participated in and completed the program. In 2004, a study was conducted to determine the placement of these students after graduation. It was determined that approximately 80% of the interns had taken positions in gas turbine or gas turbine-related organizations.

During 2006, 14 students from 11 Performing Member Universities were placed at 13 IRB companies through this SCIES administered program.

INTERNATIONAL GAS TURBINE INSTITUTE (IGTI) SUPPORT – The cooperative agreement with IGTI that was signed in 2005 was continued in 2006. SCIES coordinated with IGTI to obtain promotional support to the Fellowship Program on their website and with ASME, of which IGTI is a part, who published a promotional segment on the Fellowship Program in their student e-newsletter. SCIES also assisted the IGTI with the review of 4 ASME papers on turbine R&D that were submitted for publication at Turbo Expo 2006. SCIES arranged for the Director of IGTI to attend the UTSR Peer Review Workshop to promote awareness of the UTSR program technical accomplishments.

RELATED TURBINE PROGRAM SUPPORT

SCIES provided program materials to the AAB in support of their efforts to assist Turbine Program management in defining and justifying the overall Turbine Program and the contribution of UTSR to the overall program goals and objectives.

SCIES developed a plan and cost estimate for conducting a Peer Review Workshop, similar to the workshop SCIES manages for UTSR, for the Turbine Program.

SCIES performed technical reviews and ranking of 7 Small Business Innovation Research (SBIR) program proposals for turbine research.

SCIES provided input to several articles and e-news items by Gas Turbine World on the merits of IGCC.

SCIES provided NETL program management with information on IGCC in support of turbine program planning and justification.

OUTREACH RELATED PUBLICATIONS

SCIES wrote ASME Paper #GT2006-90060 "University Turbine Systems Research Program" and also provided presentation charts. The paper was presented at Turbo Expo 2006.

SCIES provided a draft for "UTSR Focus Shifts To Syngas And Hydrogen Turbine Design Issues", published in Gas Turbine World, May-June, 2006. SCIES produced the input to the article, including interviews with stakeholders and write-ups on the interviews.

SCIES wrote "University Turbine Systems Research Program", a section of the DOE Turbine Handbook.

SCIES assisted the DOE in preparing ASME Paper GT2007-28228, "Turbine Program of the US Department of Energy: Risk and Benefit Analysis."

SCIES provided input to the DOE on the UTSR Program overview paper for Turbo Expo 2007.

UTSR UNIVERSITY PROJECT SUMMARIES

Table 1 summarizes projects active in 2006 and identifies the principal investigator, university, project title and project objectives. Experimental and analyses approaches, results to date, and conclusions to date from these projects are discussed in the next section.

Table 1. Active UTSR Projects in 2006

Contract No ; Applicant; Award Date	**Principal Investigator**	**City/State & Business Contact**	**Area of Research (Materials, AHT: Aero-Heat Transfer, Combustion, ISL: Instrumentation, Sensors, and Life): Project Title, Goal-Accomplishment**
02-01-SR095; Georgia Institute of Technology; 5/1/02	Ben Zinn 404.894.3033 ben.zinn@aerospace.gatech.edu	Atlanta, GA	C: "*Understanding and Control of Combustion Dynamics in Gas Turbine Combustors*." Experimentally evaluate factors that cause and sustain combustion instabilities and develop models to analytically predict the occurrence and amplitude of oscillations.
02-01-SR096; University of Minnesota; 5/1/02	Terrence Simon 612.625.5831 tsimon@mc.umn.edu	Minneapolis, MN	AHT: "*Aerothermal Effects of Interfacial Leakage and Film Cooling Schemes with Endwall and Leading Edge Contouring*." Evaluate the use of cooling flows, cavity flows, and endwall contouring to reduce aerodynamic losses and improve heat transfer for turbine flow passages.
02-01-SR097; University of Connecticut; 5/1/02	Eric Jordan 860.486.2371 jordan@engr.uconn.edu	Storrs, CT	M: "*Measurement of Three Critical Parameters as a Basis for a Simple Life Prediction Method*." Develop a TBC life prediction method using measurements of i) bond coat surface defects/irregularities, ii) stress in the thermal grown oxide (TGO), and iii) TGO thickness.
02-01-SR098; Louisiana State University; 5/1/02	Sumanta Acharya 225.578.5809 acharya@alpha2.eng.LSU.edu	Baton Rouge, LA	AHT: "*Experiments and Computations on Film-Cooled End Walls with Contouring*." Evaluate a strategy of end-wall contouring and leading edge fillet design to suppress passage aerodynamic losses due to secondary flows and explore coolant injection upstream of blades for effective end-wall cooling.
02-01-SR099; Virginia Polytechnic Institute; 5/1/02	Uri Vandsburger 540.231.4459 uri@shakti.me.vt.edu	Blacksburg, VA	C: "*Modeling and Control of Ultra-Lean Premixed Combustion Dynamics for Gas Turbines*." Develop and use design-oriented modeling capabilities for determining passive energy absorption strategies or active control approaches that reduce the occurrence and level of instabilities and extend lean blowout limits for combustors.

02-01-SR100; Virginia Polytechnic Institute; 5/1/02	Danesh Tafti 540.231.9975 dtafti@vt.edu	Blacksburg, VA	AHT: "*Enhanced Prediction Techniques Based on Time-Accurate Simulations for Turbine Blade Internal Cooling*." Evaluate alternate techniques for predicting flows in internal cooling passages of turbine blades and then validate those techniques in an experimental facility.
02-01-SR101; University of Pittsburgh; 5/1/02	Gerald Meier 412.624.9741 ghmeier@engrng.pitt.edu	Pittsburgh, PA	M: "*Mechanism-Based Testing Methodology for Improving the Oxidation, Hot Corrosion and Impact Resistance of High-Temperature Coatings for Advanced Gas Turbines*." Develop a mechanism-based non-destructive testing methodology to assess metallic coating and TBC degradation resulting from cyclic oxidation, hot corrosion, and foreign object impact damage.
02-01-SR102; Georgia Institute of Technology; 5/1/02	Jerry Seitzman 404.894.0013 jerry.seitzman@ae.gatech.edu	Atlanta, GA	ISL: "*Advanced Sensor Approaches for Monitoring and Control of Gas Turbine Combustors*." Develop sensing strategies to monitor turbine combustor health and performance and also enable control systems to actively manage engine status to compensate for changes in ambient conditions and system degradation (e.g., wear).
02-01-SR103; University of Central Florida; 5/1/02	Yong-ho Sohn 407.882.1181 ysohn@mail.ucf.edu	Orlando, FL	M: "*Assessment of Failure Mechanisms for Thermal Barrier Coatings by Photoluminescence, Electrochemical Impedance and Focused Ion Beam*." Use multiple types of measurement methods to determine causes of TBC failures and refine non-destructive evaluation techniques for TBC coatings.
02-01-SR104; Brigham Young University; 6/1/02	Jeffrey Bons 801.422.8036 jbons@byu.edu	Provo, UT	AHT: "*Turbine Surface Degradation With Service and Its Effects on Performance*." Establish the groundwork for a model to assess the effect of turbine service time on engine performance degradation due to factors such as erosion, deposition and coating spallation from airfoils.
03-01-SR105; University of Wisconsin; 7/1/03	Scott Sanders 608.262.3540 sanders@engr.wisc.edu	Madison, WI	ISL/SYN: "*Advanced Optical Sensor for Monitoring and Control of Multiple Gas and Turbine Blade Properties*", Evaluate the potential of fiber optic sensors for monitoring and active control input for gas turbines. Sensed parameters include strain and temperature of gas turbine components and gas temperature and composition. Directly contributes to the advancement of SGH turbines through monitoring capabilities for measuring water vapor and alkalis, in addition to gas and surface temperatures.

03-01-SR106; Cleveland State University; 7/1/03	Kang Lee 216.433.5634 kang.n.lee@lerc.nasa.gov	Cleveland, OH	M/SYN: "*Spectroscopic In-Situ Non-Destructive Evaluation to Monitor the Health of Thermal Barrier Coatings",* Evaluate an approach based on optically monitoring turbine exhaust composition for detection of thermal barrier coating degradation and impending failure. Directly contributes to the development of SGH turbines because premature spallation of TBC has been an issue in current coal IGCC plants.
03-01-SR107; University of Connecticut; 7/1/03	Nitin Padture 860.486.4206 nitin.padture@uconn.edu	Storrs, CT	M/SYN: "*Superior Thermal Barrier Coatings for Industrial Gas turbines Using a Novel Solution Plasma Spray",* Evaluate a new Solution Plasma Spray (SPS) process to produce improved thermal barrier coatings. At representative syngas turbine conditions, determine the hot corrosion performance of SPS TBCs compared to conventional TBCs. Directly contributes to the advancement of SGH turbines by producing thicker TBC to improve component protection for increased temperature SGH turbines and evaluating the corrosion resistance of the unique SPS microstructure.
03-01-SR108; Clemson University; 7/1/03	John Wagner 864.656.7376 jwagner@clemson.edu	Clemson, SC	ISL/SYN: "*An Advanced Diagnostic and Prognostic System for Gas Turbine Generator Sets with experimental Validation",* Develop a real-time conditioning monitoring and prediction program for gas turbine engines to diagnose and predict short term health and readiness. Use behavior models, sensor fusion strategies, neural networks, and extensive statistical analyses in the program along with a prognostic model to predict onset of faults, degraded operation, and to facilitate maintenance scheduling. Indirectly contributes to the advancement of SGH turbines by improving turbine system diagnostic and prognostic methods concerning systems degradations for operation with both conventional and SGH fuels.
03-01-SR109; Pennsylvania State University; 7/1/03	Domenic Santavicca 814.863.1863 das8@psu.edu	University Park, PA	C/SYN: "*The Effects of Fuel distribution, Velocity Distribution, and Fuel Composition on Static and Dynamic Instabilities and NOx",* Investigate the effects of fuel-air profile and velocity profile on lean blowout, combustion dynamics, and NOx emissions under conditions representative of lean premixed combustors operating with coal syngas and natural gas. Directly contributes to the advancement of SGH turbines by

			addressing SGH fuel effects on combustor performance.
03-01-SR110; Virginia Polytechnic Institute; 7/1/03	Karen Thole 540.231.7192 thole@vt.edu	Blacksburg, VA	AHT/SYN: "*Improved Film Cooling Performance for Turbine Vanes and Endwalls with Realistic Surface Conditions*", Investigate the effects on airfoil cooling performance of surface roughness and cooling hole partial blockage, such as caused by deposits in syngas turbines. Evaluate cooling hole traverse slots to improve cooling effectiveness and alleviate effects of partial blockage of cooling holes by deposits. Directly contributes to the development of SGH turbines by evaluating deposition effects on cooling related to SGH fuels.
03-01-SR111; Georgia Institute of Technology; 7/1/03	Timothy Lieuwen 404.894.3041 tim.lieuwen@aerospace.gatech.edu	Atlanta, GA	C/SYN: "*Combustion Instability and Blowout Characteristics of Fuel Flexible Combustors",* Use experiments and analyses to improve understanding and develop modeling capabilities for effects of fuel variability on a combustor's static (lean blowout) and dynamic stability characteristics. Tests and analyses are expected to use fuels and gas compositions representative of coal syngas. Directly contributes to the development of SGH turbines by considering SGH fuel composition effects on combustor stability.
03-01-SR112; University of California, Irvine; 7/1/03	Scott Samuelsen 949.824.5468 gss@uci.edu	Irvine, CA	C/SYN: "*Correlation of Ignition Delay with IGCC Type Fuels",* Using simulated coal synfuels, conduct ignition delay experiments to identify design rules for avoiding autoignition in lean premixed combustion systems. Directly contributes to the development of SGH turbines by evaluating SGH fuel effects on combustor flashback and autoignition.
03-01-SR113; Texas A&M University; 7/1/03	J. C. Han 979.845.3738 jchan@mengr.tamu.edu	College Station, TX	AHT: "*Heat Transfer from Rotating Blade Platforms With and Without Film Cooling",* Obtain experimental data and numerical predictions to enable turbine designers to improve the cooling efficiency of rotating blades and thereby increase turbine power and efficiency. Indirectly contributes to the development of SGH turbines by developing information for the cooling design of increased temperature turbines planned for SGH fuels.

04-01-SR114; University of Central Florida; 8/1/04	E. Petersen, 407.823.6123 Petersen@mail.ucf.edu	Orlando, FL	C: "*Combustion Characterization and Modeling of Fuel Blends for Power Generation Gas Turbines*", Measure combustion characteristics (flame speed, autoignition, kinetics, NOx) over a wide range of fuel compositions and conditions representative of syngas turbines. Directly contributes to the development of SGH turbines by exploring fuel variability effects related to SGH fuels.
04-01-SR115; University of Pittsburgh; 8/1/04	M. Chyu 412.624.9783 mkchyu@engr.pitt.edu	Pittsburgh, PA	AHT: "*Effects of Coating Blockage and Deposits on Film Cooling effectiveness and Heat Transfer*", Experiments and computations to explore transport processes and effects on cooling performance associated with film cooling hole blockage and surface deposits. Directly contributes to the development of SGH turbines by evaluating deposition effects on cooling related to SGH fuels.
04-01-SR116; University of Pittsburgh; 8/1/04	F. S. Pettit 412.624.9730 pettit@engrng.pitt.edu	Pittsburgh, PA	M: "*Investigation of Materials Performance in High Moisture Environments Including Corrosive Contaminants Typical of Those Arising by Using Alternate Fuels in Gas Turbines*", Experiments and data analyses to develop a fundamental understanding of corrosion of typical turbine alloys and coatings due to deposits and moisture environments under conditions representative of operation with alternate fuels. Directly contributes to development of SGH turbines by evaluating effects on materials from conditions associated with SGH turbines.
05-01-SR117; Penn State University; 8/1/05	Robert Santoro 814.863.1285 rjs2@psu.edu	University Park, PA	C: *"Autoignition Studies of Syngas and Hydrogen (SGH) Fuels",* Experiments to characterize the autoignition of syngas and hydrogen (SGH) fuels at high pressures and temperatures typical of lean premixed gas turbine engine conditions. Autoignition delay times determined in the first two years for CO/H2 mixtures representing syngas (CO+3H2) to pure hydrogen (H2). For the third year, autoignition characteristics of CO/H2/H20 mixtures are evaluated. Directly contributes to the development of SGH turbines by evaluating combustion characteristics for SGH compositions and conditions.
05-01-SR118; University of Central Florida; 8/1/05	Yongho Sohn 407.882.1181 ysohn@mail.ucf.edu	Orlando, FL	M: *"Degradation of Thermal Barrier Coatings with Syngas Combustion",* Advanced microstructural analyses techniques (such as advanced electron microscopy) used for

			the first time to evaluate degradation mechanisms of TBCs under SGH conditions. Directly contributes to the development of SGH turbines by evaluating turbine materials in realistic syngas combustion environments produced at test facility located at the Dakota Gasification Company site.
05-01-SR119; University of North Dakota; 8/1/05	Forrest Ames 701.777.2095 forrest_ames@mail.und.nodak.edu	Grand Forks, ND	AHT: "*Aero Losses, Heat Transfer, Discharge Coefficients for Different Vane Trailing Edge Configurations for Syn Gas Fired Turbines*", Performance characteristics of five different approaches for cooling trailing edges of turbine airfoils experimentally evaluated in this project. Directly contributes to the development of SGH turbines through experiments that include representation of the effects of airfoil surface roughness caused by deposition in syngas turbines.
05-01-SR120; Brigham Young University; 8/1/05	Jeffrey Bons 801.422.8036 jbons@byu.edu	Provo, UT	AHT: "*Deposition of Alternative (Syngas) Fuels on Turbine Blades with Film Cooling*", A natural gas combustion stream seeded with coal and biomass products of combustion particulate and accelerated to turbine flow velocities in a simulator where specimens of turbine materials are exposed. Phase 1 of the project explores the possibility of increased cooling of specimens (and turbine surfaces) to mitigate deposition. Phase 2 evaluates the influence of deposit formation on film cooling. Directly contributes to the development of SGH turbines by evaluating deposition issues for ash bearing fuels such as SGH fuels.
05-01-SR121; Massachusetts Institute of Technology; 8/1/05	Ahmed Ghoniem 617.253.2295 ghoniem@MIT.EDU	Cambridge, MA	C: "*Fundamental Studies in Syngas Premixed Combustion Dynamics*", Data on flammability limits, stability characteristics, laminar and turbulent flame propagation, flame anchoring mechanisms, burning conditions, and syngas composition are collected experimentally and synthesized into models. Directly contributes to the development of SGH turbines by experimentally evaluating the fundamental characteristics of syngas combustion over a wide range of conditions representative of SGH turbines.

UTSR UNIVERSITY PROJECTS

COPIES OF THE MOST RECENT REPORTS FROM UTSR UNIVERSITY PROJECTS ACTIVE IN 2006 ARE IN THIS SECTION

Understanding and Control of Combustion Dynamics in Gas Turbine Combustors

Final Report

Reporting Period Start Date: May 1, 2002

Reporting Period End Date: November 30, 2005

Principal Investigators: Ben Zinn, Yedidia Neumeier, Tim Lieuwen

Date Report was issued June 30, 2005

DOE Award Number DE-FC26-02NT41431

UTSR Project Number 02-01-SR095

School of Aerospace Engineering

Georgia Institute of Technology

Atlanta, GA 30332-0150

DISCLAIMER:

"This report was prepared as an account of work sponsored by an agency of the United States Government. Neither the United States Government nor any agency thereof, nor any of their employees, makes any warranty, express or implied, or assumes any legal liability or responsibility for the accuracy, completeness, or usefulness of any information, apparatus, product, or process disclosed, or represents that its use would not infringe privately owned rights. Reference herein to any specific commercial product, process, or service by trade name, trademark, manufacturer, or otherwise does not necessarily constitute or imply its endorsement, recommendation, or favoring by the United States Government or any agency thereof. The views and opinions of authors expressed herein do not necessarily state or reflect those of the United States Government or any agency thereof."

1. ABSTRACT

This program investigates the causes and active control of combustion driven oscillations in low emissions gas turbines. These oscillations are a critical problem encountered in the development of new systems and the availability and maintainability of fielded systems. This document is the final report under this contract . During the duration of the contract, substantial progress has been made in improving the understanding of the dynamics of unstable combustors. Both experimental and theoretical efforts have been pursued and completed over the period of the contract.

This report describes all of the experimental and theoretical work undertaken during the last 3-1/2 years. Specifically, this report describes experimental studies which investigated the mechanisms responsible for saturation of the flame transfer function and therefore control the limit cycle amplitude of unstable gas turbine combustors. In addition, theoretical studies were performed to investigate nonlinear flame response behavior. Significantly, these studies were able to capture and explain many phenomenon observed in experiments.

Furthermore, experiments on unstable combustors including open loop active control studies and nonlinear frequency interaction investigations were performed to improve the understanding of the underlying physics which control combustion instabilities.

2. TABLE OF CONTENTS

3. LIST OF FIGURES

4. EXECUTIVE SUMMARY

Under the High Efficiency Engines and Turbines-University Turbine Research (HEET-UTSR) program, Georgia Institute of Technology is investigating the mechanisms and control of detrimental oscillations in gas turbine combustors. This program consists of two main tasks. The first task is investigating the dynamics of uncontrolled combustors. These results are improving capabilities to predict the occurrence and amplitudes of instabilities. The second task is investigating active control of combustion dynamics. This work is developing methods for suppressing these instabilities in the highly turbulent, harsh combustor environment and improving understanding of the factors that effect active control authority. Currently, combustion dynamics severely reduce the reliability and availability of gas turbines by damaging parts and substantially reducing time between overhauls, both of which ultimately affect the consumer by increasing the cost of electricity.

This program investigates the causes and active control of combustion driven oscillations in low emissions gas turbines. These oscillations are a critical problem encountered in the development of new systems and the availability and maintainability of fielded systems. This document is the final report under this contract . During the duration of the contract, substantial progress has been made in improving the understanding of the dynamics of unstable combustors. Both experimental and theoretical efforts have been pursued and completed over the period of the contract.

This report describes all of the experimental and theoretical work undertaken during the last 3-1/2 years. Specifically, this report describes experimental studies which investigated the mechanisms responsible for saturation of the flame transfer function and therefore control the limit cycle amplitude of unstable gas turbine combustors. In addition, theoretical studies utilizing one possible mechanism were performed to investigate nonlinear flame response behavior.

Furthermore, experiments on unstable combustors including active control studies and nonlinear frequency interaction investigations were performed to improve the understanding of the underlying physics which control combustion instabilities.

Interactions with industrial partners was also a priority during this contract. We have initiated a program with an OEM to incorporate and validate the modeling work performed under this program into their in-house prediction codes. We also maintain regular discussions with combustion engineers at many of the OEM's.

5. PROJECT DESCRIPTION

Under the High Efficiency Engines and Turbines-University Turbine Research (HEET-UTSR) program, Georgia Institute of Technology is investigating the mechanisms and control of detrimental oscillations in gas turbine combustors. This program consists of two main tasks. The first task is investigating the dynamics of uncontrolled combustors. These results are improving capabilities to predict the occurrence and amplitudes of instabilities. The second task is investigating active control of combustion dynamics. This work is developing methods for suppressing these instabilities in the highly turbulent, harsh combustor environment and improving understanding of the factors that effect active control authority.

Currently, combustion dynamics severely reduces the reliability and availability of gas turbines by damaging parts and substantially reducing time between overhauls, both of which ultimately affect the consumer by increasing the cost of electricity. This work will result in improved understanding of the processes that cause these oscillations and strategies to eliminate them. Successful completion of this project will benefit the gas turbine and energy industry in several ways. First, through its improvement of turbine reliability and availability, it will reduce maintenance needs and costly downtime. In addition, it will broaden the operating envelope of gas turbines, so that they will be able to operate at higher power as well as at idle without worry of damaging oscillations. For example, many fielded turbines are not able to operate at full power because of the enormous dynamics problems encountered there. Elimination of the dynamics problem will allow them to increase their maximum power, thereby improving their capabilities to respond to peak power demands.

6. NONLINEAR FLAME TRANSFER FUNCTION CHARACTERISTICS

This section describes an experimental investigation of the relationship between flow disturbances and heat release oscillations in a lean, premixed combustor. This work is motivated by the fact that combustion instabilities continue to be one of the most serious issues hindering the development and operation of industrial gas turbines[1-4]. These instabilities generally occur when the unsteady combustion process couples with one or more of the natural acoustic modes of the combustion chamber, resulting in self-excited oscillations. These oscillations adversely affect engine performance and emissions, and can be destructive to engine hardware.

Our focus here is on the amplitude response of the heat release at some frequency, f, to a harmonic disturbance of amplitude, A, at that same frequency. The heat release response, H(A), generally exhibits a linear dependence upon the disturbance amplitude at small values of A. At high amplitudes, however, they are related nonlinearly. This is significant because the dynamics of an unstable combustor are controlled by both linear and nonlinear processes. This can be seen from Figure 1, which plots the amplitude dependence of hypothetical driving, H(A), and damping, D(A), processes. Note that the disturbance amplitude stays the same, decreases, or increases depending upon whether H(A)=D(A), H(A)<D(A), or H(A)>D(A), respectively. Linear combustor processes generally control the balance between driving and damping processes at low amplitudes of oscillation, H(A)-D(A), and, thus, determine the frequency and growth rate, $A \sim e^{\alpha t}$, of inherent disturbances in the combustor. Note that the initial growth rate of the instability, α, is proportional to the difference between the driving and damping processes in the linear regime. Nonlinear combustor processes control the finite amplitude dynamics of the oscillations. For example, predicting the limit cycle amplitude of self-excited oscillations requires an understanding of the nonlinear characteristics of H(A) and D(A). To illustrate, Figure 1 depicts a situation where H(A) saturates and D(A) remains linear, so that the two curves cross at the limit cycle amplitude, A_{LC}.

Understanding of a combustor's linear dynamics is needed to predict the frequency and conditions under which inherent disturbances in the combustor grow or decay. As a result of extensive work in this area, capabilities for modeling the acoustics of the combustor system are reasonably well developed (e.g., see Refs. [5,6]). Also, capabilities for modeling the interactions of flow and mixture disturbances with flames, needed to predict the conditions under which instabilities occur, are improving rapidly[7,8]. Much of this work is being transitioned to industry and being incorporated into dynamics predictions codes. In fact, most gas turbine manufacturers have reported model development efforts for predicting instability frequencies, mode shapes, and conditions of occurrence[9-11].

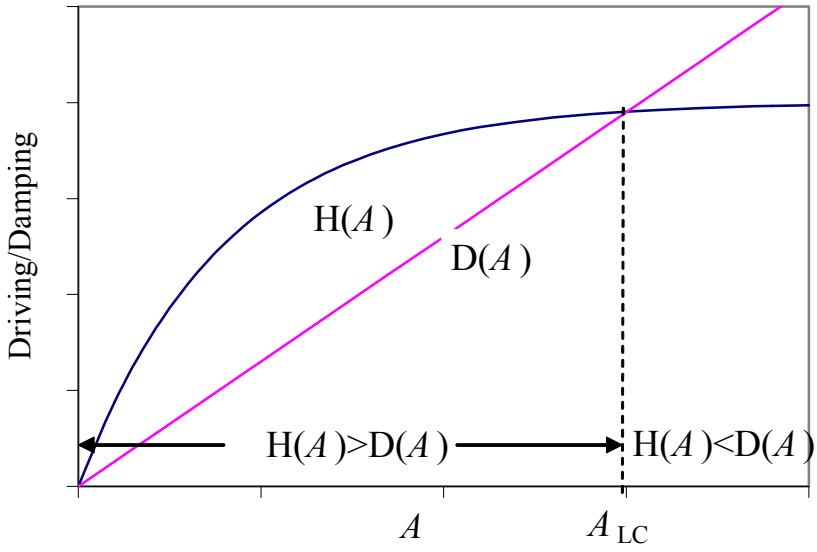

Figure 1: Qualitative description of the dependence of acoustic driving, H(*A*), and damping, D(*A*), processes upon amplitude of oscillation, *A*

As noted above, understanding of a combustor's linear dynamics is not sufficient to describe the finite amplitude dynamics of self-excited oscillations; e.g., for predicting the limit cycle amplitude. The need to predict instability amplitudes and observations of "triggered" instabilities in rockets that were linearly stable motivated past workers to consider these nonlinear effects; e.g., see Refs. [5, [12-14]]. Much of this work focuses on the role of nonlinear gas dynamics in combustors, however. As such, it is likely more relevant to instabilities in combustion systems where fluctuating pressure amplitudes achieve significant percentages of the mean (e.g., p'/p_o ~20-50%, such as is observed in rockets), than lean premixed gas turbine combustors where reported instability pressure amplitudes are typically on the order of 1-5% of the mean pressure[2, 15].

Recent studies[15-18] suggest that acoustic processes essentially remain in the linear regime, even under limit cycle operation, and that it is the nonlinear relationship between flow and heat release oscillations that causes saturation of the instability amplitude. As such, the flame's nonlinear response to harmonic disturbances may play a critical role in the overall dynamics of an unstable combustor. For example, Dowling[16] introduced a phenomenological model for the finite amplitude response of a flame to velocity perturbations. The model is dynamic in nature, but the essential nonlinearity consists of a quasi-steady relation between flow velocity and heat release rate. It assumes a linear relation between the heat release, Q, and velocity perturbation when the total velocity ($u(t) = u_o + u'(t)$) lies between 0 and $2u_o$. When $u(t)<0$, the heat release goes to zero and when it is greater than $2u_o$ it saturates at $2Q_o$. Thus, the essential mechanism of nonlinearity lies in the fact that the lowest amplitude of heat release oscillation cannot indefinitely decrease with perturbation amplitude because it cannot achieve negative values. A similar mechanism was proposed in an experimental study of Poinsot *et al.*[19]. In another study, Dowling[20] introduced a nonlinear boundary condition at the flame anchoring point. She assumed that the instantaneous flame anchoring point was fixed when the total gas velocity exceeded the flame speed. When the gas velocity fell below the flame speed, the former condition was replaced by one that allowed the flame to propagate upstream. Peracchio & Proscia[17] developed a quasi-steady nonlinear model to describe the response of the flame to

equivalence ratio perturbations. They assumed the following relationship for the response of the instantaneous mixture composition leaving the nozzle exit to velocity perturbations:

$$\phi(t) = \frac{\bar{\phi}}{1 + ku'(t)/\bar{u}} \tag{1}$$

where k is a constant with a value near unity. They also utilized a nonlinear relationship relating the heat release per unit mass of mixture to the instantaneous equivalence ratio. Wu *et al.*[18] developed a more general asymptotic analysis which focuses on the nonlinear interaction/coupling among acoustic, vortical, and Darrieus-Landau instability modes at the flame. This theory is found to agree well with the experimental work presented in Searby[21].

Several of the above analyses suggest that the ratio of fluctuating and mean velocity, u'/u_o, is an important non-dimensional parameter that controls the amplitude of the limit cycle oscillations through its effect upon the nonlinear relationship between flow disturbances and heat release oscillations. A similar conclusion was reached empirically in an experimental study of Lieuwen[15], who found that combustion instability amplitudes had a strong dependence upon a mean combustor velocity scale, u_o.

In an effort to understand the mechanisms controlling the growth rates and limit cycle amplitudes of combustion instabilities, the response of the flame under external forcing of the flow field has been analyzed by several researchers (e.g., see Refs.[[22]-[26]]). Külsheimer & Büchner[22] measured the effect of driving frequency and amplitude on premixed swirled and unswirled flames. They characterized the conditions under which large-scale coherent ring-vortex structure were evident, a key mechanism for self-excited oscillations, as well as the resulting flame response, on driving amplitude and frequency. They found that vortex formation occurred at lower driving amplitudes as the driving frequency was increased. Furthermore, the peak flame response in swirl flames shifted to higher frequencies for larger flow perturbations. No explicit characterization of the nonlinear interaction between the flame's heat release and the flow perturbations were reported, however.

The potentially significant nonlinear relationship between acoustic perturbations and heat release perturbations suggested by the theoretical studies above, are also supported by recent measurements of Lieuwen & Neumeier[23], Lee & Santavicca[24], and Balachandran *et al.*[26] who characterized the pressure-heat release relationship as a function of oscillation amplitude. The former study found that this relationship was linear for pressure amplitudes below about 1% of the mean pressure. At higher forcing levels, they found that the heat release oscillation amplitude began to saturate. In contrast to the assumed model of Dowling[16], however, Lieuwen & Neumeier found saturation to occur at $CH^{*\prime}/CH^*_o$ values of ~25%, in contrast to the 100% value assumed in her model. Data were only obtained at one operating condition and two driving frequencies, however, so the manner in which these saturation characteristics depend upon operating conditions and frequency is unclear.

Durox *et al.*[27] and Bourehla & Baillot[25] appear to have performed the only systematic study characterizing the response of a non-swirling flame to large amplitude perturbations. Their study was performed on a laminar Bunsen flame and primarily focused on its qualitative characteristics. No measurements of the dependence of unsteady heat release or chemiluminescence emissions were reported. They found that at low frequencies (f < 200 Hz) and velocity amplitudes (u'/u_o<0.3), the flame front wrinkles symmetrically about the burner axis due to a

convected wave traveling from the burner base to its tip. With increasing amplitude of low frequency velocity perturbations, they found that the flame exhibited a variety of transient flame holding behavior, such as flashback, asymmetric blowoff, and unsteady lifting and re-anchoring of the flame. In addition, they noted that its response was asymmetric and disordered. Finally, at high frequencies and forcing amplitudes (u'/u_o>1), they found that the flame tip collapses to a hemispherical shape.

As can be seen from the above review, there is a need for systematic measurements of the flame's nonlinear response to flow perturbations, i.e. saturation of the curve *H(A)* in Figure 1. Such characteristics must be understood in order to, for example, predict instability amplitudes or model the transient response of a combustor to active control. As such, we obtained measurements of the pressure/ velocity/ chemiluminescence amplitude and phase relationships in a swirling flame over a range of driving amplitudes. These results were obtained by externally driving oscillations in the combustor with varying amplitudes. Measurements were obtained at several driving frequencies and fuel/air ratio.

Gas Turbine Combustor Simulator

The data presented in this paper were measured in a lean, premixed gas turbine combustor simulator, shown in Figure 2, which has been previously described in Lieuwen *et al.*[28]. Tests were performed at a mean pressure of 1.7 atmospheres and mean equivalence ratios ranging from 0.83 to 1.0. All tests were performed at a total flow rate of 5.5 g/s which corresponds to a premixer velocity of 11.5 m/s. Inlet temperatures were kept constant at room temperature.

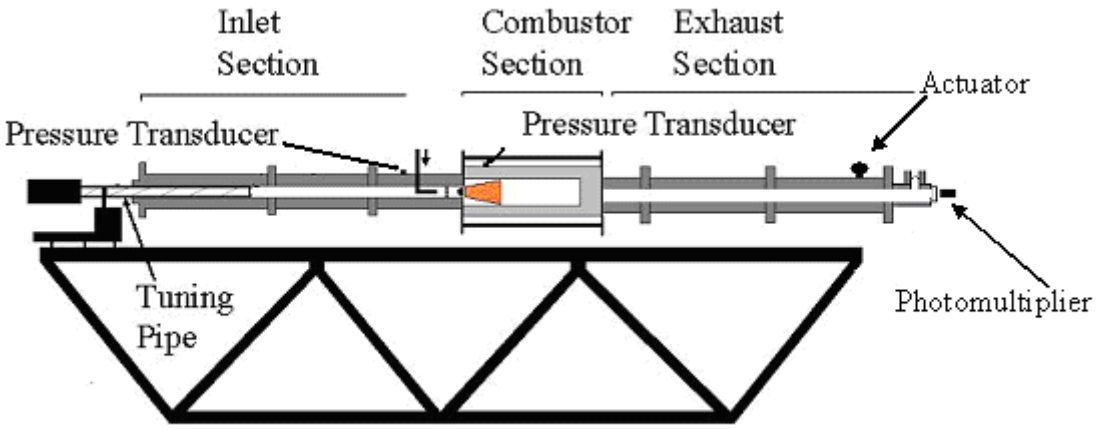

Figure 2: Schematic of Georgia Tech lean, premixed combustor facility

The facility consists of inlet, combustor and exhaust sections. High-pressure natural gas and air are supplied from building facilities, whose flow rates are measured with calibrated critical orifices. In order to ensure that acoustic oscillations do not affect fuel/air mixing processes, the air and fuel are introduced upstream of a second choke point, well upstream of the swirler. Thus, the equivalence ratio of the reactive mixture entering the flame is

essentially constant. This was done because of the sensitivity of the flame chemiluminescence levels to both heat release rate and equivalence ratio. If the equivalence ratio and heat release rate simultaneously vary, monitoring the flame chemiluminescence alone would not be sufficient to infer information about heat release fluctuations[24]. Note that the fuel/air mixing processes were not acoustically isolated in the previous study of Lieuwen & Neumeier[23].

The fuel-air mixture enters the circular 4.75cm diameter, 60cm long inlet section and passes through a 45° swirler prior to entering the combustor, see Figure 3. Combustion occurs in the 5x5x51cm square combustor downstream of the conical flame holder, and the combustion products then flow through a circular 7.6cm diameter, 195cm long exhaust section before leaving the system. A separate high-pressure air stream cools the combustor walls, and mixes with the combustion products in the exhaust section. The flow leaves the setup through an exhaust nozzle.

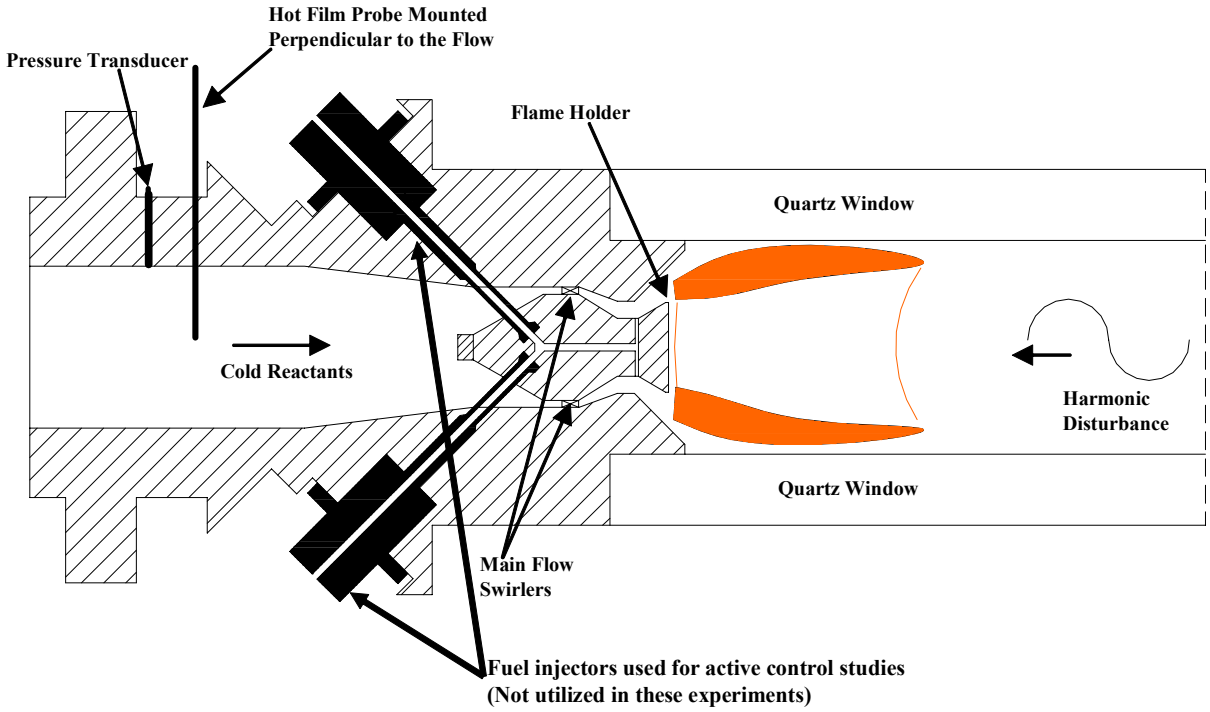

Figure 3: Detail of mixing and combustion section

Instrumentation

Pressure oscillations were measured with two Model 211B5 Kistler pressure transducers mounted in the inlet section and combustor. These transducers are mounted 33.2 cm upstream and 5.1 cm downstream of the conical flame holder, respectively. The latter transducer was flush mounted and water-cooled. The instantaneous velocity was measured with a TSI model hot-film probe mounted 23 cm upstream of the swirler and oriented perpendicular to the inlet flow in the radial center of the inlet pipe, as shown in Figure 3. The fluctuating velocity at the premixer exit, used to define the flame transfer function, was determined by measuring the transfer function between the velocity oscillations at the hot-wire location and the premixer exit in off-line experiments. This transfer function was also calculated with a quasi-one dimensional analysis by discretizing the premixer domain into a series

of regions characterized by their lengths and cross-sectional areas, and applying momentum and energy conservation at the interfaces (see Ref. [6]). The swirler was modeled as a resistance that was determined from the flow velocity and measured mean pressure drop. The model and measurements agreed very well over the 10-550 Hz frequency range, except in transfer function magnitude in the vicinity of 80 and 420 Hz. At these frequencies, the transfer function has large values (on the order of 5) and the model and measurements disagree by 100% in the peak magnitude; however, they agree quite well in predicting the frequencies at which these occur. At all other frequencies, the transfer function magnitude is essentially constant and equal to the cross sectional area ratio between the two points, as expected from quasi-steady considerations. Because of the sensitive frequency dependence of the velocity transfer function between the measurement location and premixer exit plane at 80 and 420 Hz, no nonlinear forced response studies were performed at these frequencies.

Global CH* and OH* chemiluminescence measurements were obtained with a photomultiplier tube (PMT) fitted with 10 nm bandwidth filters centered at 430 and 310 nm, respectively. The PMT was installed downstream of a quartz window at the rear end of the setup, see Figure 2. This arrangement permitted it to view the entire combustion zone. The linearity of the PMT output was verified over the entire range of instantaneous light intensity levels seen in these experiments. Data were obtained with a National Instruments DAQ controlled by Labview software at a sampling rate of 10 kHz. A total of 16,384 data points were taken during each test.

Oscillations were driven in the combustor with an actuator developed at Georgia Tech for active combustion control applications[29]. The actuator was mounted 5m downstream of the flame zone. It is capable of driving oscillations over a frequency range of approximately 0-1500Hz. The actuator modulates a constant secondary supply of air that is introduced near the combustor exit by periodically varying the degree of constriction of a valve. Maximum amplitude of driving occurs when the flow passage is completely blocked for a portion of the cycle and, thus, the actuator modulates 100% of the flow through the valve. The amplitude of forcing can be controlled via the supply pressure of air to the actuator.

Forced Flame Characteristics

The basic experimental procedure consists of externally driving oscillations in the combustor with varying amplitude at a fixed frequency or fixed amplitude at varying frequencies while obtaining simultaneous measurements of pressure, velocity, and chemiluminescence. For all cases, the combustor was quite stable in the absence of driving. The flame length ranged from 5-15cm between the equivalence ratios of 1.0-0.83, respectively.

Driving Effects on Average Flame and Coherence Characteristics

In addition to exciting oscillations, the imposed driving altered the mean flame characteristics, similar to prior observations (e.g., see Ref. [[30]]). With increased driving levels, the flame's time-averaged length increased by up to 100%. In addition, its global intensity generally decreased very slightly, but not always in a monotonic manner. Typical results are shown in Figure 4. In general, OH* and CH* levels were found to exhibit similar dependence upon disturbance amplitude.

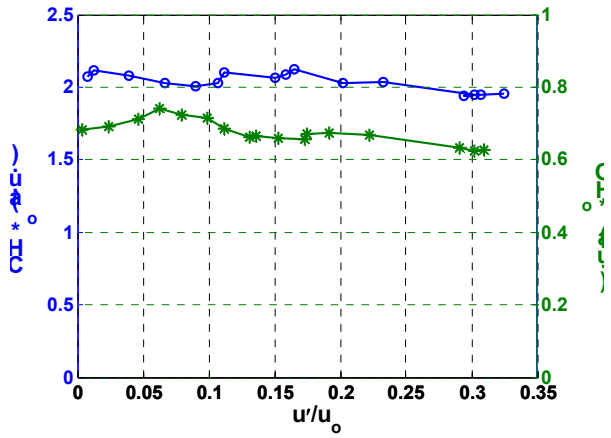

Figure 4: Dependence of mean CH* and OH* signals upon velocity oscillation amplitude (f_{drive} = 280 Hz, ϕ = 0.95)

In order to obtain accurate transfer function data, it is important to have good coherence between the pressure, velocity and chemiluminescence oscillations at the frequency of interest. This was always achieved except at the lowest driving amplitudes; typical coherence values were greater than 0.95. The effect of nonlinearities is to also decrease the coherence value, so we would not expect perfect coherence values, even if the input-output variables were perfectly correlated.

The amplitudes of the oscillations were determined by integrating the area under the power spectrum in the vicinity of the driving frequency. The RMS levels of the oscillations were determined from these values via Parseval's relation and then multiplied by $\sqrt{2}$ to obtain the fluctuating amplitude. This procedure is equivalent to determining the fluctuating amplitude after bandpass filtering the signal about the driving frequency. The phases of the fluctuating parameters were determined from their Fourier transforms at the driving frequency.

Linear Flame Response

Baseline measurements of the linear flame response were obtained by driving oscillations at low amplitudes over the 10-550 Hz frequency range. The amplitude of the velocity-CH* transfer function is plotted in Figure 5(a). The uncertainties were determined using formulae from Ref. [31].

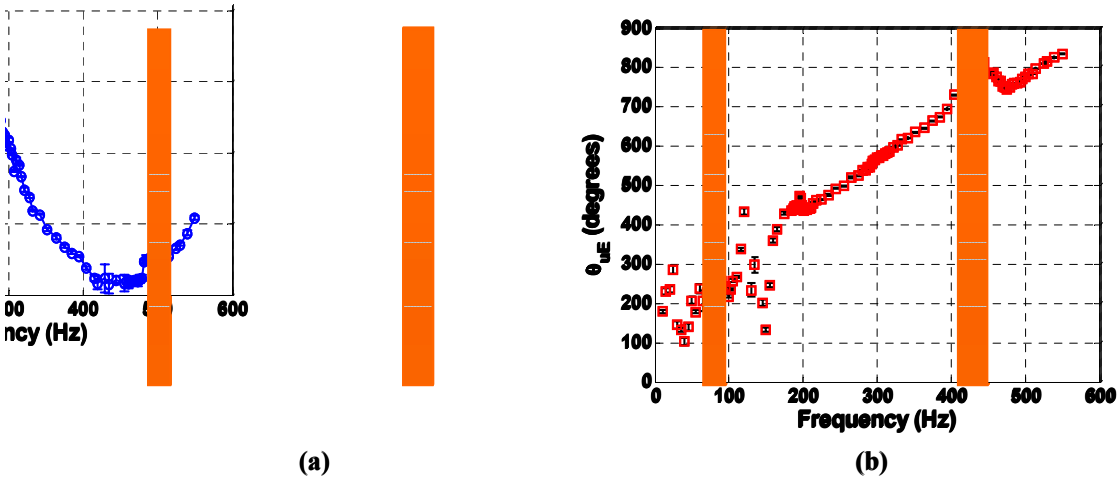

Figure 5: Dependence of (a) linear velocity-CH* transfer function and (b) velocity-CH* phase angle upon driving frequency

This transfer function apparently has local maxima at 90 and 240 Hz and monotonically decays in the 250-400 Hz region. Similar peaks at intermediate frequencies were reported experimentally by Külsheimer and Büchner[22]. The corresponding phase of the transfer function is plotted in Figure 5(b). The phase results exhibit a linear increase with frequency up to approximately 400 Hz. This phase dependence suggests a roughly constant time delay relationship between the pressure/velocity and chemiluminescence; i.e., $CH^*(t) \sim u'(t-\tau)$. This time delay can be estimated from the slope of this phase dependence to yield a value of approximately 3.5 ms. For reference, the time required for a disturbance to convect the length of the approximately 8 cm flame at the premixer exit velocity is $\tau_{flame} \sim$ 7 ms. This linear phase dependence ceases at frequencies above 400 Hz as the phase dips then rises again. Recall, however, that the transfer function between the velocity oscillations at the measurement point and flame base changes rapidly in the vicinity of 80 and 420 Hz. Thus the results at these frequencies should be interpreted with caution.

It is interesting to note the similarities between these gain and phase results and the measured and predicted transfer functions reported by Schuller *et al.*[32]. This is interesting because they obtained their results for a laminar flame while our data are obtained from a swirling, turbulent flame. Apparently, the average "V" shapes of the two flames are the primary thing they have in common. This observation indicates that the theoretical result used to describe laminar flame dynamics can be fit to our data very satisfactorily.

Nonlinear Flame Response

Next, we consider the amplitude dependence of this transfer function. For brevity, only velocity results are presented since the pressure-velocity relationship is linear over the entire driving amplitude range, e.g., see Figure 6. Therefore, the p'-CH* transfer function has an identical form (although the results are "cleaner" due to the larger p'-CH* coherence values). Figure 7(a) presents typical results showing the dependence of the normalized CH* and OH* chemiluminescence amplitudes upon the normalized velocity amplitudes over a range of driving amplitudes.

The departure of this transfer function from linearity is illustrated by comparing the data with the solid line that is drawn in (the reason for the gap in the data is discussed in the "Nonlinear Heat Release-Linear Acoustics Interaction" section). Note also in Figure 6 and Figure 7 that the normalized amplitudes of the pressure and velocity oscillations at the point where nonlinear effects become obvious are roughly 3% and 30% while the normalized chemiluminescence is approximately 40%. These relatively low pressure fluctuations and significant chemiluminescence oscillations are consistent with speculations that heat release nonlinearities, as opposed to gas dynamic ones, control the nonlinear dynamics of premixed combustion systems. It should be pointed out that these pressure amplitudes where nonlinearities in the p'-CH* relationship are observed (p'/p_o~2-3%) are of similar magnitude as typical instability amplitudes (p'/p_o~0.5-2%) which were measured in other tests on this combustor[28]. Also, the amplitude of the normalized CH* oscillations are on the order of 30-40% of the mean, consistent with previous experiments[23].

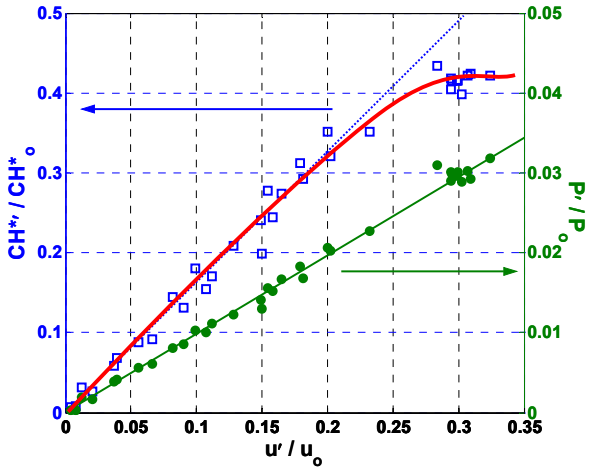

Figure 6: Dependence of CH* chemiluminescence and pressure oscillation amplitude on velocity fluctuation amplitude (f_{drive} = 280 Hz, ϕ= 0.95).

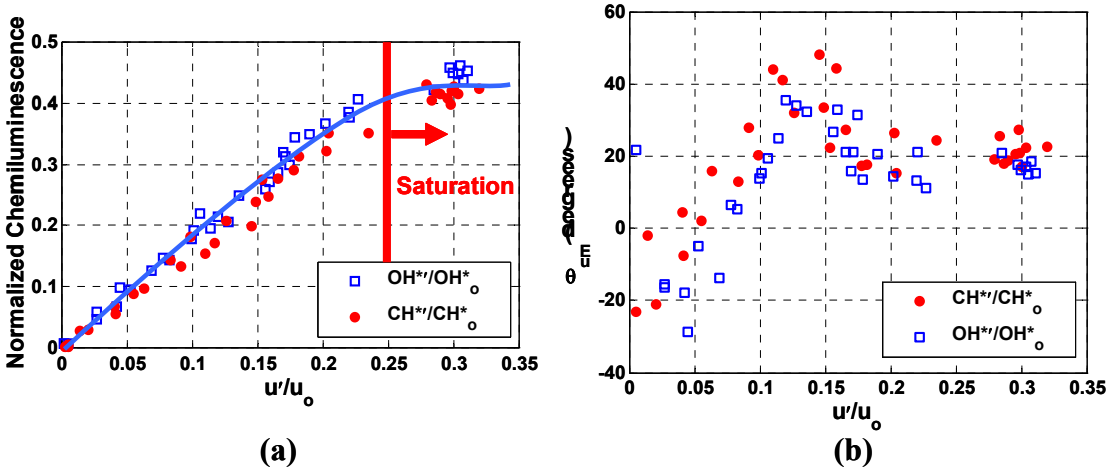

Figure 7: Dependence of CH* and OH* chemiluminescence (a) amplitude and (b) phase angle on velocity oscillation amplitude. Chemiluminescence saturation occurs in (a) at $u'/u_o > 0.25$. Uncertainty in phase angle for $u'/u_o < 0.05$, $\Delta\theta \sim 30°$; for $u'/u_o > 0.05$, $\Delta\theta \sim 2°$. (f_{drive} = 283 Hz)

Figure 7(b) presents the phase relationship between the velocity oscillations and the normalized chemiluminescence. The figures indicate that the phase angle has a complex dependence on the amplitude of oscillations. It increases monotonically by about 40 degrees from $0.05 < u'/u_o < 0.15$. At larger disturbance amplitude, the phase decreases somewhat, then levels off. Note that the phase exhibits amplitude dependence at disturbance levels significantly lower than the gain. It is likely that the monotonic phase increase in the $0.05 < u'/u_o < 0.15$ region is due to the lengthening of the flame with increased disturbance amplitudes. Due to the strong similarity in both the CH* and OH* results, only CH* results are presented in the remainder of the paper.

Equivalence Ratio Dependence

Figure 8(a) presents the dependence of CH*' upon u' for equivalence ratios ranging from 0.83 to 0.90. It is important to note that the maximum driving amplitude point is not due to actuator limitations, but flame blowoff. It is clearly seen that the slope in the linear regime as well as the CH* saturation amplitude decreases as the equivalence ratio is decreased. The results also show that the blowoff velocity oscillation amplitude for the majority of tests is approximately constant except for the leanest case investigated, $\phi = 0.83$. This result clearly shows that the saturation amplitude is a function of the equivalence ratio. For equivalence ratios between 0.87 and 0.9, the velocity-CH* relationship is highly nonlinear while the richest (ϕ=0.95, not shown) and leanest cases investigated show little nonlinearity, presumably because blowoff occurs before saturation. Figure 8(b) presents the corresponding phase relationship between u' and CH*'. In most cases, the phase angle initially increases to a maximum and then decreases or stays roughly constant with increase in velocity oscillation amplitude.

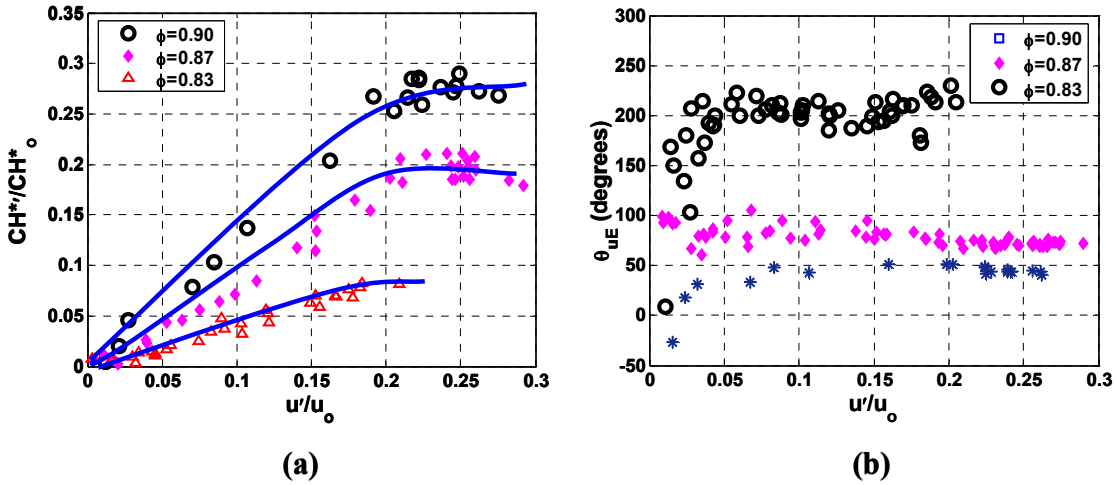

Figure 8: Dependence of (a) CH* chemiluminescence amplitude and (b) velocity-CH* chemiluminescence phase angle on amplitude of velocity oscillations at several equivalence ratios. Uncertainty in phase angle for $u'/u_o < 0.05$, $\Delta\theta \sim 30°$; for $u'/u_o > 0.05$, $\Delta\theta \sim 2°$. (f_{drive} = 300 Hz)

Driving Frequency Effects

In addition to varying the equivalence ratio, the effect of driving frequency between 260 and 320 Hz was extensively analyzed. This range was chosen because of the high quality data that could be obtained at these frequencies due to the large flame response, see Figure 5 and its proximity to a 310 Hz combustor resonance (discussed further below). Figure 9 presents the dependence of the CH* amplitude and phase upon u'/u_o over the 260 to 320 Hz frequency range. Note that the slopes of these curves in the linear region are equal to the transfer function values plotted in Figure 5. Nonlinearities in the CH*-u' gain relationship are prominent in the 280 and 290 Hz driving cases, while the transfer function is substantially more linear at the other frequencies. The near linearity of the transfer function in some cases all the way to flame blowoff strongly suggest that nonlinearity is not due to flame holding; if flame holding were a key nonlinear mechanism, one would expect the transfer function at all frequencies and equivalence ratios to become nonlinear near the blowoff point. The normalized CH* fluctuations at the point where nonlinearity is evident have similar values for 280 and 290 Hz, but the corresponding velocity amplitudes appear to vary slightly with driving frequency. Figure 9(b) shows that the phase exhibits similar amplitude dependence as in the equivalence ratio results. Again, note that nonlinearity is evident in the phase behavior at very low amplitudes, e.g., $u'/u_o \sim 0.05$, where the gain is still very linear.

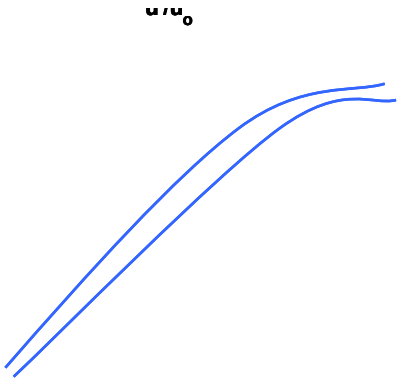

(a) (b)

Figure 9: Dependence of CH* chemiluminescence (a) amplitude and (b) phase upon velocity amplitude at several driving frequencies. Uncertainty in phase angle for $u'/u_o < 0.05$, $\Delta\theta \sim 30°$; for $u'/u_o > 0.05$, $\Delta\theta \sim 2°$. ($\phi = 0.95$)

Harmonic and Subharmonic Characteristics

In addition to characterizing the dependence of the flame transfer function on the fundamental driving frequency, extensive analysis of the higher and sub-harmonics of the dynamic signals was performed. Prior studies suggest that such data are needed to obtain a comprehensive understanding of the nonlinear combustion process. For example, it is well established from forced response studies in various mixing layers, jets, and wakes that such understanding is key to the system's nonlinear dynamics (e.g., see Ref. [33]). These amplitudes are substantially smaller than those of the fundamental, however, resulting in reduced coherence between the fundamental and first harmonic, $\gamma_{i=f,j=2f}$. As such, only a single subharmonic and harmonic of the chemiluminescence signal ($CH^{*\prime}_{f=fdrive/2}$ and $CH^{*\prime}_{f=2fdrive}$) could be accurately quantified. The first subharmonic as well as the first and second harmonics of the pressure signal could be quantified due to much higher coherence values. While the presence of higher harmonics in the data could be either to actuator or combustion process nonlinearities, analysis of our data indicates that the dominant source of harmonic generation can be attributed to the nonlinear combustion process.

First harmonic characteristics of the CH* oscillations are presented in Figure 10 for two equivalence ratios, $\phi = 0.95$ and $\phi = 0.90$ at a driving frequency of 300 Hz. These two cases present examples where the flame transfer function remained linear throughout the range of disturbance amplitudes as well as where the flame transfer function saturated at large amplitudes of velocity oscillations. Figure 10 illustrates that the first harmonic behavior can change markedly between linear and nonlinear cases. For the linear case, $\phi = 0.95$, the first harmonic of the chemiluminescence exhibits a quadratic behavior on the fundamental throughout. This result is indicative of the other cases where the transfer function remains linear. For nonlinear cases, however, the functional relationship between the first harmonic and the fundamental changes. At low disturbance amplitudes, the general quadratic behavior is followed for $\phi = 0.90$. At forcing amplitudes above the saturation point of the fundamental, however, the first harmonic has been found to exhibit a variety of behaviors. For $\phi = 0.90$, the first harmonic deviates from the quadratic dependence, by increasing much more rapidly. In other cases, the first harmonic increases more

slowly than the quadratic dependence, such as can be seen in the pressure in Figure 11. The quadratic dependence between the fundamental and first harmonic is more clearly evident in the pressure data which has a much higher signal to noise ratio. We have also found that the amplitude of the second harmonic of the pressure (due to its higher coherence values) is essentially proportional to the third power of the fundamental, as might be expected, see Figure 11. Figure 12 presents the phase angle between the CH* chemiluminescence fundamental and first harmonic. While the overall phase dependence upon disturbance amplitude is approximately linear at each driving frequency, the amplitude dependence of the phase angle slope switches signs between 290 and 300 Hz. Furthermore, there is substantial amplitude dependence of this phase angle, as it changes by over 800 degrees.

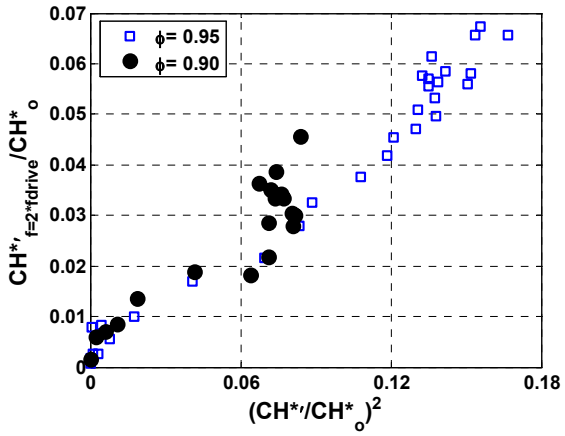

Figure 10: Dependence of CH* 1st harmonic on the square of CH* fundamental at two equivalence ratios (f_{drive} = 300 Hz)

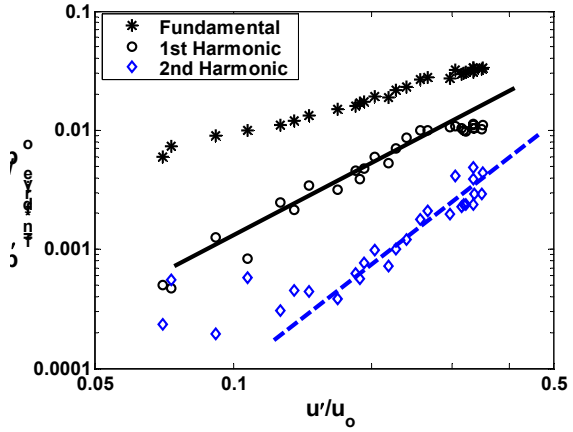

Figure 11: Dependence of pressure harmonic amplitude on velocity oscillation amplitude (f_{drive} = 290 Hz, ϕ = 0.95). Quadratic trend indicated by the solid line, cubic trend indicated by dashed line.

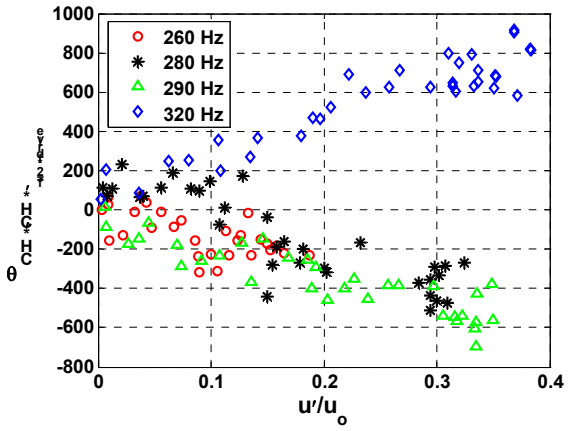

Figure 12: Dependence of CH* chemiluminescence fundamental-1st harmonic phase angle on velocity oscillation amplitude at several driving frequencies (ϕ = 0.95). Uncertainty in phase angle for u'/u_o < 0.05, $\Delta\theta \sim 30°$; for u'/u_o > 0.05, $\Delta\theta \sim 3°$.

Consider next the CH* subharmonic characteristics; i.e. $CH^*_{f=fdrive/2}$. In contrast to the higher harmonic characteristics, the subharmonic amplitudes do not exhibit a power law dependence upon the fundamental at low or high disturbance amplitudes. Its amplitude jumps up, however, in the vicinity of the point where the fundamental saturates, as shown in Figure 13. Figure 13 illustrates the dependence of the CH* chemiluminescence subharmonic on the amplitude of velocity oscillations for one case where the flame transfer function saturates, 280 Hz. In addition to the subharmonic, this figure also illustrates the gain of the flame transfer function over the entire range of disturbance amplitudes.

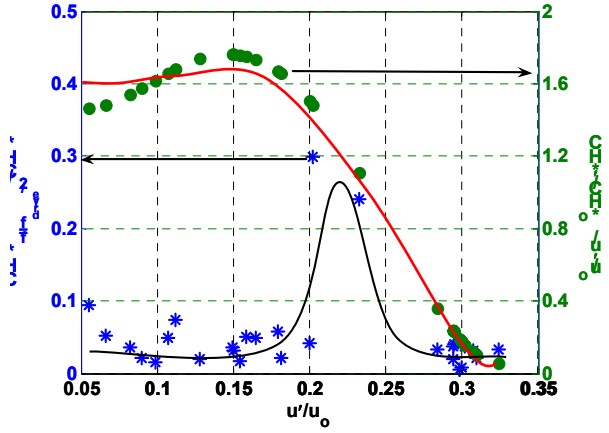

Figure 13: Dependence of CH* subharmonic and transfer function gain on velocity oscillation amplitude (f_{drive}=280 Hz, ϕ = 0.95)

For this case, the subharmonic amplitudes are very low and incoherent with respect to the fundamental when the corresponding transfer function is in the linear regime (u'/u_o < 0.2). Coherence values around 0.6-0.7 for these low values will create uncertainties which are as large as or larger than the values themselves. As the transfer function approaches the saturation point (approximately, u'/u_o ~ 0.2 for the case illustrated), the subharmonic

exhibits a sharp increase in amplitude. At this point, the coherence between the subharmonic and fundamental has values of ~ 0.99. Corresponding plots of the velocity and pressure subharmonics show no such increase and remain incoherent. After this sharp increase, the subharmonic amplitude decreases sharply and is again quite incoherent with the fundamental. This discontinuous dependence of the subharmonic on the fundamental is exhibited for all cases where saturation of the transfer function occurs. It should be noted, however, that the presence of subharmonic oscillations does not always accompany saturation. There were some cases where a peak in the CH* subharmonic occurred when the flame transfer function remained linear. This peak in the chemiluminescence subharmonic was accompanied by similar peaks in the velocity and pressure subharmonics, in contrast to the cases described above.

The subharmonic's dependence upon amplitude is very similar to the measurements of Bourehla and Baillot[25] in a laminar, Bunsen flame. At intermediate forcing amplitudes, they observed, in some cases, a subharmonic flame response. Analysis of this response showed that the subharmonic amplitude increased and the fundamental amplitude decreased as one went downstream from the burner lip. That is, the flame base responded more to the fundamental frequency and the flame tip responded more to the subharmonic. In all cases, the subharmonic response disappeared at the highest forcing amplitudes, and the flame exhibited the hemispherical behavior noted earlier. This phenomenon appears to be manifestation of the so-called "parametric instability", where pulsating cellular structures appear on the flame, which oscillate at half the instability frequency[34-37]. Analogous to Bourehla and Baillot's result, these studies in nominally flat flames found the subharmonic response only at intermediate amplitudes; at very high amplitudes the flame response was highly chaotic and disordered.

This instability is produced by the unsteady acceleration of the flame front by the velocity field, which separates two regions of differing densities, coupling with the three-dimensional flame dynamics. With increased amplitudes, the structures lose their well-defined nature and break up into disordered, turbulent wrinkles. This period doubling was recognized by Markstein[38] as indicative of a parametrically pumped oscillator that can be described by an equation of the form:

$$A\frac{d^2y(k,y)}{dt^2} + B\frac{dy(k,y)}{dt} + \left[C_o - C_1 cos(\omega t)\right]y(k,t) = 0 \qquad (2)$$

where A, B, C are coefficients defined by Markstein, k is the wave number of the perturbation, and ω is the frequency of the imposed oscillations. The damping coefficient, B, is always positive, but the coefficient C_o is negative if the nominal planar flame front is unstable. Such an equation has the well known property that sub-harmonic oscillations (i.e., $\omega/2$) are excited for large enough disturbance amplitudes, C_1.

This is the first observation, to the authors' knowledge, of the presence of the parametric instability in a swirl-stabilized turbulent flame. Vaezi and Aldredge[37] have performed the only experimental work analyzing the parametric instability during turbulent flame propagation. They found substantial enhancement of axial and circumferential velocity fluctuations as a result of the parametric instability was found for all levels of pre-ignition turbulence. Also, the magnitude of amplification decreased with increasing Reynolds number. In our experiments,

the Reynolds number defined by the premixer exit diameter was substantially larger than those investigated by Vaezi & Aldredge[37]. Analogous to their results, no sudden visible changes in the flame position, length, or shape were noted before saturation of the transfer function occurred which indicate that turbulent flame speed enhancement was minimal. However, it appears highly probable that nonlinear interactions between the flow forcing and parametric instability (possibly through its impact on the fluctuating flame position) are responsible for saturation of the flame response. This is evidenced by the fact that 1) the jump in subharmonic amplitude occurs at essentially the same value as that at which saturation occurs, and 2) subharmonic oscillations are always present in cases where saturation of the fundamental occur.

Atmospheric Swirl Stabilized Burner

INSTRUMENTATION AND EXPERIMENTAL FACILITY

This section describes the continuation of the nonlinear flame response experiments described in the previous section. Instead of performing the experiments on the gas turbine combustor simulator (described in Figure 2), experiments were performed on an atmospheric, swirl-stabilized burner, schematically shown in Figure 14, which can be operated up to 100 KW. All tests were performed at a fixed equivalence ratio of 0.8. Unlike the previous test, we investigated more thoroughly the effect of driving frequency. In addition, we performed a parametric study on the effect of Reynolds number on the nonlinear flame response. The flow rate regime investigated ranged from Reynolds numbers of Re_D=21,000-43,000 (based on premixer exit diameter) corresponding to average premixer exit plane velocities of 22-44 m/s. Reactant inlet temperatures were kept constant at room temperature.

Natural gas and air are supplied from building facilities, whose flow rates are measured with rotameters. In order to ensure that acoustic oscillations do not affect fuel/air mixing processes, the air and fuel are introduced upstream of a choke point. Thus, the equivalence ratio of the reactive mixture entering the flame is essentially constant. This was done because of the sensitivity of the flame chemiluminescence levels to both heat release rate and equivalence ratio [24].

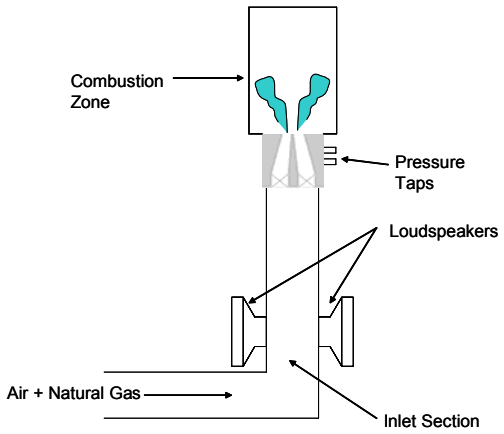

Figure 14. Schematic of swirl-stabilized combustor

The mixture goes through the premixer, consisting of a 40° swirler and an annular passage, see Figure 15. The flow expands into a cylindrical 70mm i.d. and 190 mm long quartz tube combustion chamber. Pressure oscillations are measured with Model 211B5 Kistler pressure transducers mounted downstream of the swirl vanes, located 5.85cm and 7cm upstream of the flame holder, respectively. Velocity oscillations are calculated using the two microphone method, outlined in, e.g. Ref. [39]. These results were checked with direct velocity measurements using a hot-wire anemometer in cold-flow conditions.

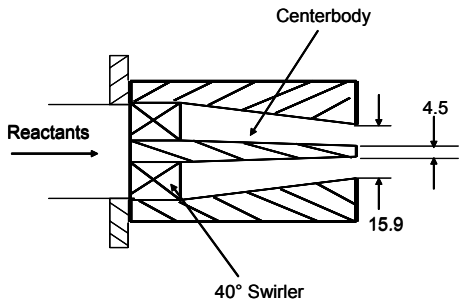

Figure 15. Schematic of burner premixer. All dimensions are in mm (not to scale).

The relative magnitude of the combustion heat release oscillations are obtained by measuring the global CH* and OH* chemiluminescence with photomultipliers fitted with a 10 nm bandwidth filter centered at 430 nm and 310 nm, respectively. The fiber optic is installed downstream of the flame zone at an angle such that it is allowed to "view" the entire combustion zone. For the results presented in this paper, the normalized chemiluminescence measured by the photomultipliers is nearly identical. Thus CH* chemiluminescence results will be shown for the remainder of the paper. Oscillations are driven in the combustor by two loudspeakers mounted into the 5.5 cm diameter inlet section.

In order to observe the flame, OH planar laser-induced fluorescence (PLIF) was utilized to obtain a two-dimensional image of the flame. Figure 16 shows the layout of the laser diagnostic facility used in the present study. The laser system consists of a cluster of an Nd:YAG laser, 1 dye laser, and high-resolution ICCD cameras. For OH

PLIF, the frequency-doubled output from the dye laser was tuned near 281.4 nm to pump the $R_1(9)$ transition of the $A^1\Sigma - X^2\Pi$ *(1, 0)* band. OH fluorescence integrated over a wavenumber range of 300-380 nm is captured by the ICCD camera through both a WG-305 and UG-11 Schott glass filter. The OH PLIF intensity images were corrected for background noise and also for beam profile inhomogeneities.

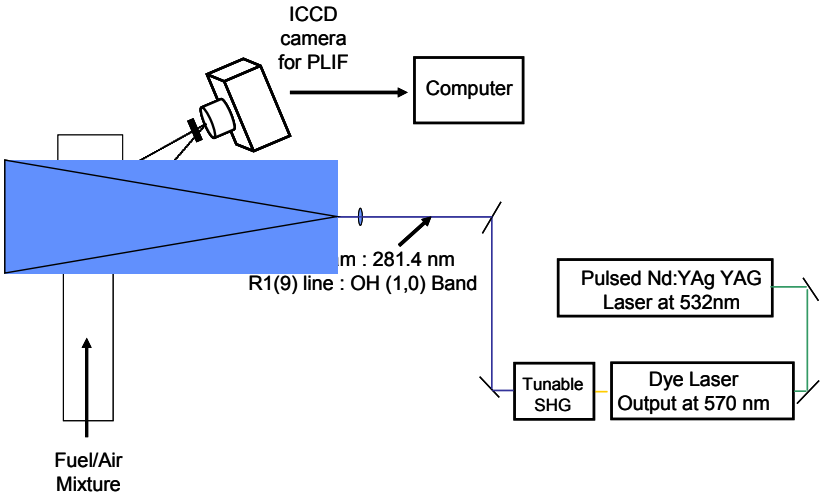

Figure 16. Schematic of laser setup for OH PLIF imaging

The laser imaging was phase locked with the driving signal input to the loudspeakers. The frequency of image acquisition is limited by the frequency of the Nd:YAG laser which operates at 10 Hz. Therefore, since the frequencies of interest in this study are much greater than this value, successive phase-locked images were actually obtained several cycles apart from each other. Then, the flame response over a sequence of phase angles is reconstructed over different phases and different cycles. The acoustic cycle was divided into 8 phases, with 200 images taken at each phase angle. The OH PLIF intensity images were corrected for background noise and also for beam profile inhomogeneities. These images were then filtered with a 3 pixel width Gaussian filter.

RESULTS AND DISCUSSION

PARAMETRIC CHARACTERIZATION OF NONLINEAR FLAME TRANSFER FUNCTION

Results were obtained by externally driving oscillations in the combustor with varying amplitude at a fixed frequency. Simultaneous measurements of pressure, velocity, and chemiluminescence were taken. For all cases, the combustor was quite stable in the absence of driving.

A typical transfer function between simultaneously measured CH* chemiluminescence and velocity oscillations is shown in Figure 17(a) at a Reynolds number of 21000 and equivalence ratio of 0.8. For low forcing amplitudes, Figure 17 shows that the CH* chemiluminescence increases with perturbation amplitude in a linear manner. At large velocity amplitudes, the CH* chemiluminescence saturates at values of $CH^{*\prime}/CH^*_o$ of ~0.45. These velocity and CH* values where saturation occurs are consistent with the results in the previous section. This result indicates that global extinction where oscillating heat release amplitudes reach 100% of the mean, proposed

theoretically by Dowling [16], is not an important mechanism at this condition. Figure 17(b) presents the corresponding u'-CH*' phase relationship. The phase relationship exhibits a complex amplitude dependence on the amplitude of velocity oscillations. The phase angle changes by nearly 50 degrees while the transfer function remains linear. The sharp decrease in phase angle at u'/u_o ~0.45 occurs after the $CH^{*\prime}/CH^*_o$ value saturates.

Figure 18(a) presents transfer function results for driving frequencies between 130-150 Hz at a Reynolds number of 21000. Figure 18 illustrates that the transfer function at 130 Hz and 140 Hz remains linear up to $CH^{*\prime}/CH^*_o$ values near 0.95 before saturating. Thus, the saturation amplitude here is substantially higher than that in Figure 17, illustrating the substantial dependence of saturation amplitude upon flow conditions and disturbance frequency. Note that the saturation amplitude here is quite close to 100%, suggesting a global extinction type mechanism as proposed by Dowling [16]. Figure 18(b) presents the corresponding u'-CH*' phase. Similar to the comparison between the saturation amplitudes between the cases at 210 and 130 Hz, the phase angle shapes for these two frequencies are also quite different. The phase angle at these frequencies exhibits significant amplitude dependence at velocity oscillation amplitudes where the gain of the transfer function remains in the linear regime. This effect is again consistent with the results in the previous section. The phase angle is seen to almost saturate as well and remain relatively constant around 85-90 degrees over nearly 50% of the velocity amplitude range.

Both Figure 17 and Figure 18 illustrate typical shapes of transfer functions that have been observed experimentally and proposed theoretically. For low velocity amplitudes, the corresponding heat release oscillations increase linearly. At the largest velocity amplitudes, the heat release fluctuations saturate. However, more complex amplitude dependencies were observed at other conditions. Figure 19 shows two such cases, obtained at 340 and 410 Hz, respectively. Both curves show that the CH* chemiluminescence increases linearly with increasing velocity oscillation amplitudes at low values of driving. At 340 Hz, the CH* oscillation amplitude begins to saturate at values around 0.65-0.7 of the mean value. However, instead of remaining nearly constant, with further increases in excitation amplitude the response increases again. In a similar manner, for 410 Hz, Figure 19 shows that the transfer function begins to saturate at a $CH^{*\prime}/CH^*_o$ value of 0.35. Similar to the 340 Hz case, the flame response begins to increase again before saturating again at $CH^{*\prime}/CH^*_o$ value of nearly 0.6. This trend is similar to the experimental results of Balachandran *et al.* for a bluff-body stabilized flame without swirl [26].

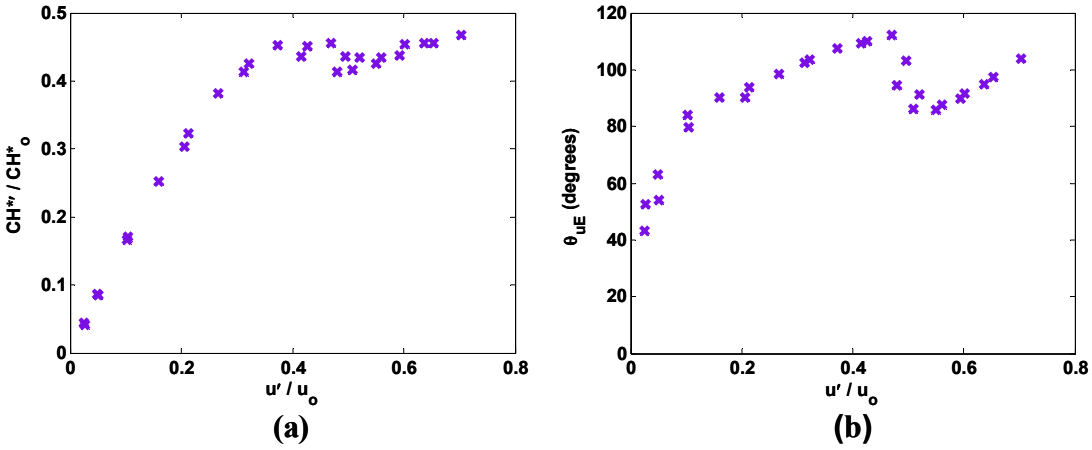

Figure 17. Dependence of (a) CH* oscillation amplitude and (b) u'-CH*' phase angle upon velocity oscillation amplitude (f_{drive} = 210 Hz, ϕ=0.80, Re_D = 21000). CH* saturation amplitude = 0.45. Uncertainty in phase angle < 5°.

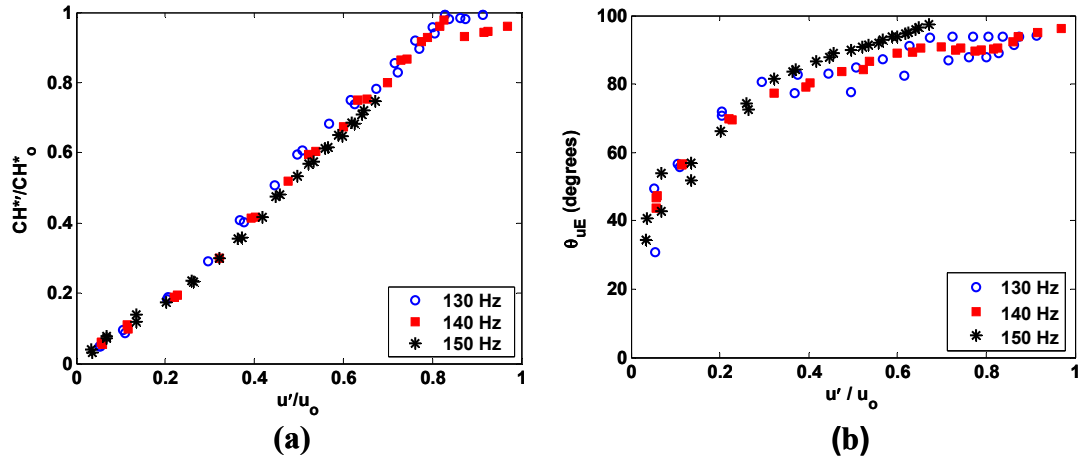

Figure 18: Dependence of (a) CH* oscillation amplitude and (b) u'-CH*' phase angle upon velocity oscillation amplitude, ϕ = 0.80, Re_D = 21000. CH* saturation amplitude ~ 0.98. Uncertainty in phase angle < 5°.

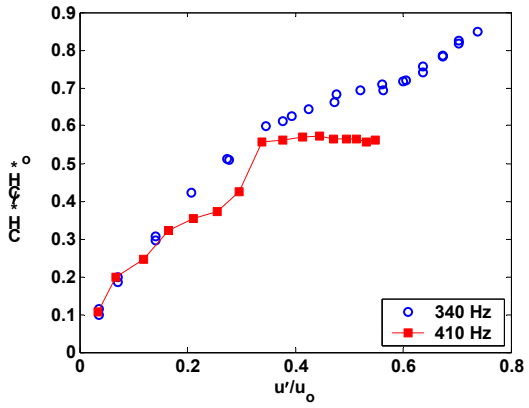

Figure 19. Dependence of CH* oscillation amplitude upon amplitude of velocity oscillations for two driving frequencies (Re_D = 21000, ϕ = 0.80)

Even more complex behavior was observed at other conditions. Figure 20 presents the u'-CH*' transfer function for 160-180 Hz at a Reynolds number of 30000 and equivalence ratio = 0.8. For these three cases, after an initial linear increase in heat release oscillations, there is a sharp decrease in these values, followed by an increase. This sharp decrease in the gain of the transfer function is also manifested in the corresponding phase between the velocity and chemiluminescence oscillations. Figure 20(b) shows the phase angle at f_{drive}= 170 Hz drops considerably (over 100 degrees) between normalized velocity oscillation amplitudes of 0.1 and 0.2. After this drop, the phase angle remains constant around 80 degrees, at similar values as the 130-150 Hz cases shown in Figure 18.

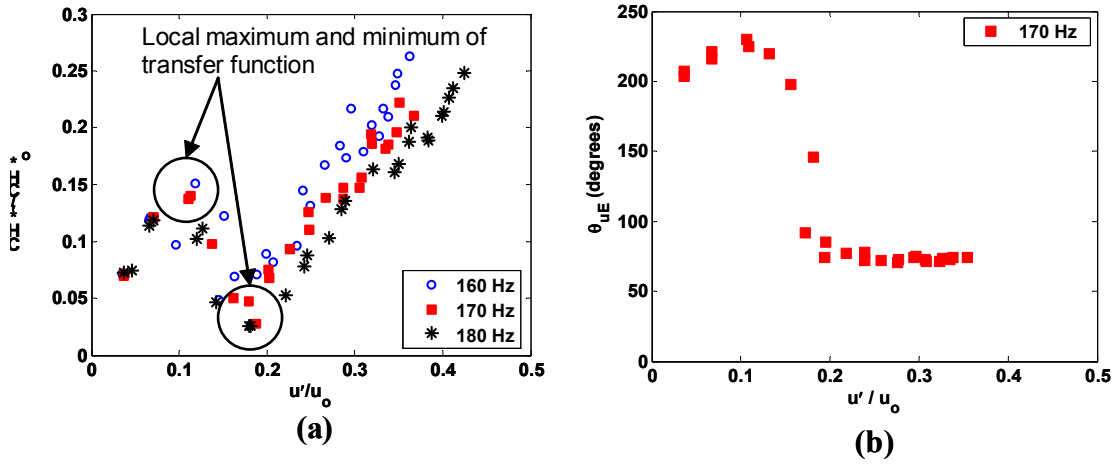

Figure 20. (a) Dependence of CH* oscillation amplitude upon amplitude of velocity oscillations for f_{drive} = 160-180 Hz. (b) Dependence of u'-CH*' phase angle upon velocity oscillation amplitude for f_{drive} = 170 Hz. (Re_D = 30000, ϕ = 0.80).

Figure 21 presents the Fourier transform of the chemiluminescence and one pressure transducer for two cases: at the local maximum in the transfer function and the local minimum in the transfer function (circled in Figure 20). Comparing the two chemiluminescence spectra, it is clear that the flame response shifts from the fundamental frequency to the 1st harmonic with an increase in driving from 10% velocity oscillation to 20% velocity oscillation.

The pressure FFT, on the other hand (and thus the velocity) always responds to the fundamental, however, and increases with increased driving. Similar behavior has also been reported in bluff-body flames by Balachandran *et al*.[26]. We are currently investigating the cause of this behavior to better understand the underlying mechanism.

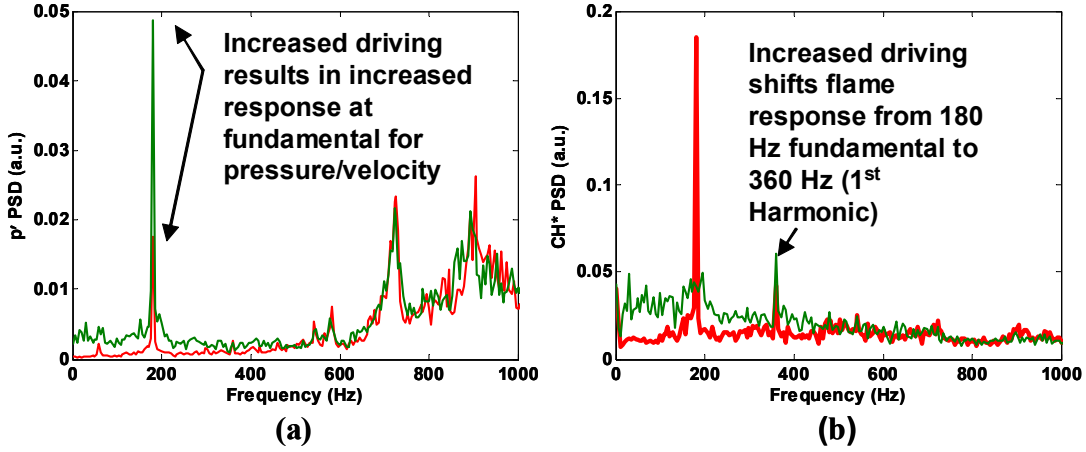

Figure 21. Fourier transforms of (a) pressure and (b) CH* chemiluminescence signals at local maximum of transfer function (red) and local minimum of transfer function (green) for f_{drive} = 180 Hz (Re_D = 30000, ϕ = 0.80).

One of the key conclusions we drew from this parametric study was that the flame response characteristics are more varied and complex than a simple linear response regime followed by a saturation regime. However, one of our goals for the study was to parameterize the dependence of saturation amplitude upon operating conditions, frequencies, etc. In order to compile all the results into one graph, we determined the chemiluminescence amplitude at which nonlinearity in the flame response becomes evident, see Figure 22. This amplitude was defined as the point where the transfer function deviates from its linear value by more than 10-20%. The lower limit is set for cases such as those in Figure 18, where saturation occurs at nearly 100% of the mean chemiluminescence value. The upper limit is set for saturation/nonlinear behaviors that occur at values much less than 100% of the mean, e.g., Figure 19 and Figure 20. At the lowest flow rate, Figure 22 indicates that the saturation amplitude varies with frequency by a factor of almost five. This frequency sensitivity is diminished at the higher flow rates. At the highest Reynolds number, the saturation amplitude is nearly constant over the frequency range investigated. Saturation at 100% chemiluminescence is only seen for the lowest flow rate. The results presented indicate that a variety of behaviors can exist in a single combustor. We should emphasize, however, that determination of the "amplitude at which nonlinearity becomes evident" is somewhat subjective. Thus, while these curves certainly have the form shown here, they could vary in detail somewhat based upon the method of parameterizing nonlinearity.

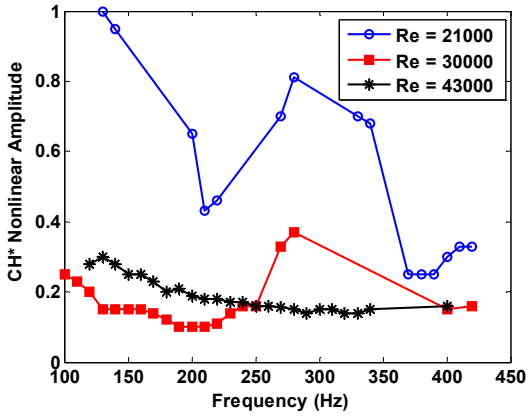

Figure 22. Dependence of CH* nonlinear amplitude on driving frequency as a function of Reynolds number (ϕ = 0.80).

IMAGING OF FLAME UNDER LARGE AMPLITUDE FORCING

During this parametric study it was observed that the flame visibly changed in structure at the point where the transfer function saturates when significant saturation occurred (e.g., f_{drive} = 210 Hz and 410 Hz); however, this was not necessarily the case in all situations (e.g., f_{drive} = 130 Hz). High speed line of sight images of the flame confirmed this observation as shown in Figure 23 which shows images of the flame at two different driving amplitudes at a driving frequency of 410 Hz. These sequences of images were obtained by phase locking an ICCD high speed camera to the input driving signal. A BG-38 Schott glass filter was placed in front of the ICCD camera to effectively eliminate wavelengths of light above ~700nm.

Figure 23(a) shows the line-of-sight view of the flame at low velocity amplitude where the transfer function remains linear in Figure 19. At this low amplitude of oscillation, the flame is easily observed to have a well-defined shape and stabilization point throughout the cycle. The flame responds to forcing by increasing and decreasing in length. No visible change in the shape is seen over the cycle. In contrast, Figure 23(b) shows the line-of-sight view of the flame at a velocity amplitude where the flame transfer function has saturated. From these images, it appears that the flame is not stabilized by the centerbody as shown in Figure 23(a). Instead the flame appears to have "lost" its structure and has become more chaotic in nature. This behavior begins to occur exactly at the point of saturation (e.g., $u'/u_o \sim 0.35$ in Figure 19).

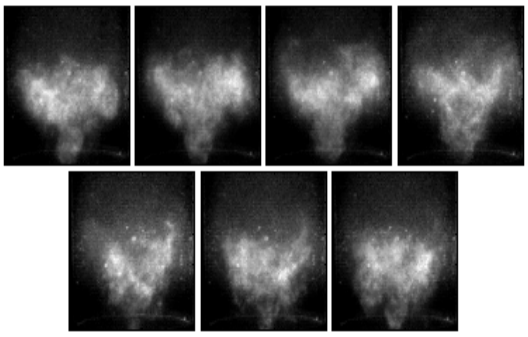

(a)

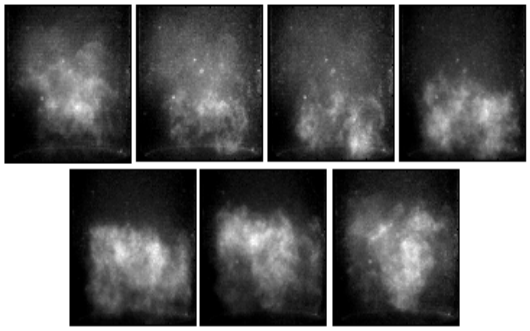

(b)

Figure 23: Phase-locked instantaneous line-of-sight images of flame over 1 cycle of acoustic forcing for (a) low (linear) and (b) high (nonlinear) amplitude of oscillation (f_{drive} = 410 Hz, Re_D = 21000, ϕ = 0.80).

Since similar flame behavior seen in Figure 23 for 410 Hz was not observed for 130 Hz, we will concentrate on these two results for the remainder of the paper. In an effort to further investigate some of the potential mechanisms controlling the nonlinear flame dynamics, we performed extensive OH-PLIF studies at these two driving frequencies. We should emphasize two key limitations of these images. First, the flow is highly three-dimensional, so that flame structures come in and out of the images. Thus, one cannot estimate the instantaneous flame area, of interest because of its relationship to heat release. Second, "consecutive" images are not truly consecutive, as they were taken several cycles apart – thus, one should only attempt to infer global flow features, and not try to track the evolution of a particular flow feature from image to image.

Figure 24(a) presents instantaneous OH PLIF images for the 130 Hz case at a low velocity oscillation amplitude. Here the heat release is in the linear response regime. The images obtained are phase-locked to the driving signal, but the phase angles presented in these figures are with respect to the velocity oscillations calculated from the two microphone method. These figures indicate that the flame is anchored on the centerbody throughout the cycle. The oscillating velocity is evident, as the flame moves back and forth throughout the cycle; in some images, the presence of convecting flow structures are perhaps evident. Figure 24(b) shows the corresponding flame response for high velocity oscillations; at this level of driving, the instantaneous flow velocity oscillates between 2-42 m/s through out the cycle. Thus it oscillates between nearly reversing itself to a very high speed jet. At the velocity minimum the turbulent flame speed is on the same order as the local velocity value and the flame is propagating towards the premixer. The flame, however, never flashes back into the premixer, but remains just at the

premixer exit. Thus there is a lower limit to the flame response. At the point of highest flow velocity and maximum flame length, the clear rollup of the flame into the central recirculation zone is evident, see 45 and 90 degrees.

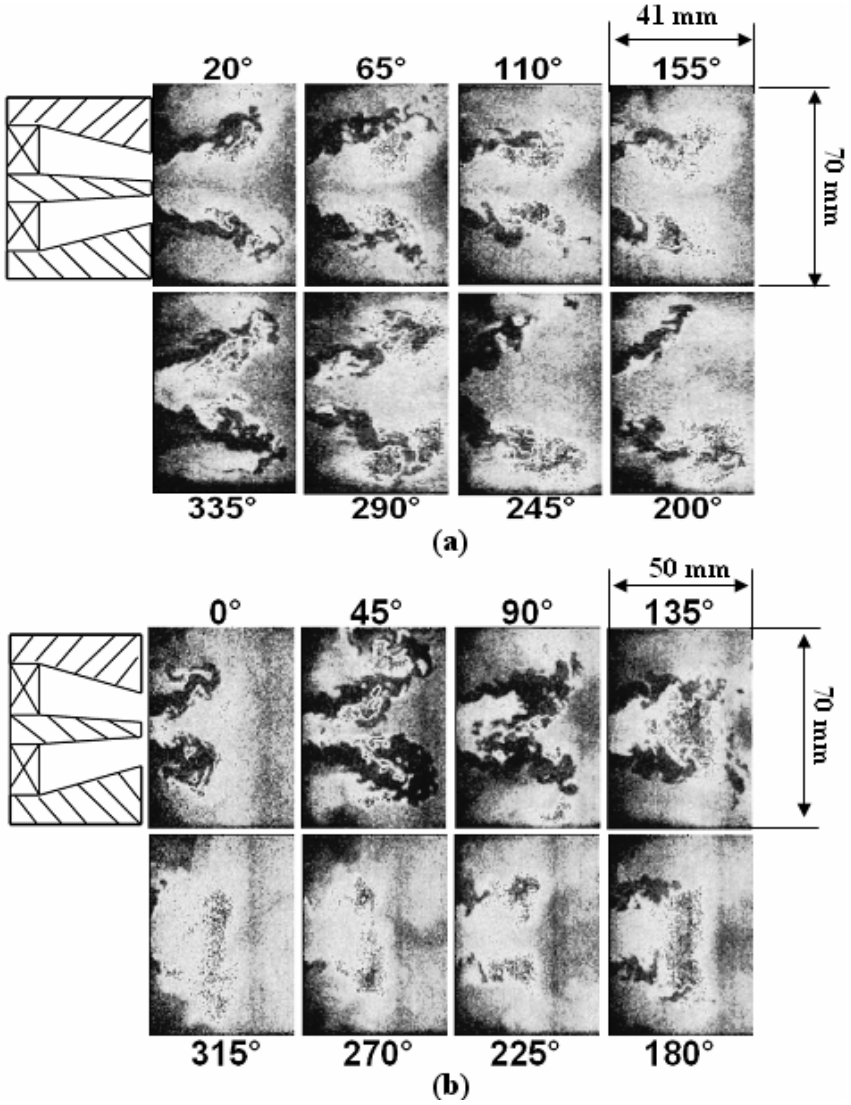

Figure 24. Instantaneous OH PLIF images showing evolution of flame response over 1 cycle of acoustic forcing for (a) low (linear) and (b) high (nonlinear) velocity oscillation amplitudes (f_{drive} = 130 Hz, Re_D = 21000, ϕ = 0.80)

This rollup of the flame into the central recirculation zone causes occasional merging of the two flamefronts. The rapid reduction in flame area associated with this rollup, and the subsequent flame propagation and rapid reduction in flame area, is believed to be the mechanism causing saturation of the flame response since this behavior is observed in most of the 200 images obtained at these phases. This assertion is also supported by the fact that rollup is first observed roughly at the point where the CH* chemiluminescence saturates at $u'/u_o \sim 0.8$ in Figure 18. This is the same observation of Balachandran *et al.* in a non-swirling flame [26]. At this point, the flame area is very rapidly reduced, due to flame propagation normal to itself. Also, note that the flame remains attached throughout the cycle, even at the highest amplitudes, in contrast to the 410 Hz result shown next. Several other

features can also be noted. First, note the substantially more corrugated nature of the flame front at the point of highest jet velocity, 90 degrees, relative to lower velocity points. These images suggest that the turbulent flame speed is modulated through the cycle. .

At the point of highest flow velocity and maximum flame length, the clear rollup of the flame into the central recirculation zone is evident, see 45 and 90 degrees. In some images, this rollup of the flame into the central recirculation zone causes occasional merging of the two flame branches. As will be shown next, the rapid reduction in flame area associated with this rollup causes saturation of the flame response. This point can be seen from ensemble averages images of the flame, see Figure 25. The average flame edge shown in these images were obtained by averaging the PLIF images, and extracting the flame edge (roughly corresponding to a line of constant progress variable of 0.3) using a gradient method. In Figure 25(a), for low amplitude forcing, the flame is stabilized off of the bluff body at the exit of the premixer and confirms the observations made from the instantaneous images in Figure 24. Figure 25(b) shows the phase averaged flame fronts for high amplitude forcing, after the point where the *u'-CH*'* transfer function has saturated. This figure clearly shows the reactants on average are consistently rolled up towards the centerline of the burner at the point of peak response in the cycle, see 90 degrees. This roll-up of the flame causes a very rapid reduction in its certain area and, therefore, heat release rate. As such, the flame heat release response does not increase proportionately with the perturbation, and saturation occurs.

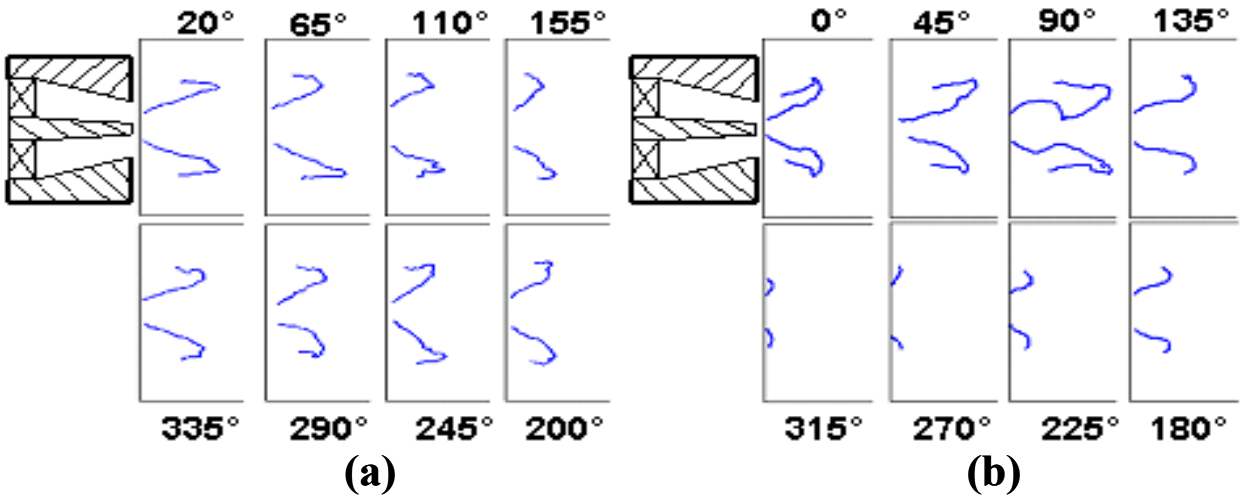

Figure 25. Phase-averaged flame edges showing evolution of flame response over 1 cycle of acoustic forcing for (a) low (linear, u'/u_o = 0.3) and (b) high (nonlinear, u'/u_o = 0.9) velocity oscillation amplitudes (f_{drive} = 130 Hz)

This flame rollup can be further seen in Figure 26 which illustrates the manner in which the flame response at the point of its maximum downstream displacement varies with disturbance amplitude. The dashed lines indicate the average flame front location (obtained by averaging all the images at this particular phase and using a gradient method to extract an edge) at excitation amplitudes where the transfer function remains linear, u'/u_o= 0.3 and 0.6. These curves show that the downstream flame displacement increases with perturbation amplitude, but with a

similar shape. In contrast, the solid lines show average flame front locations at excitation amplitudes near and beyond the point where saturation in flame response occurs, u'/u_o= 0.83, and 0.9. Here the downstream displacement of the flame position clearly stops growing with perturbation amplitude. Instead, the reactants roll up into the central recirculation zone, causing a more rapid reduction in flame surface area relative to the lower amplitude cases due to flame propagation normal to itself.

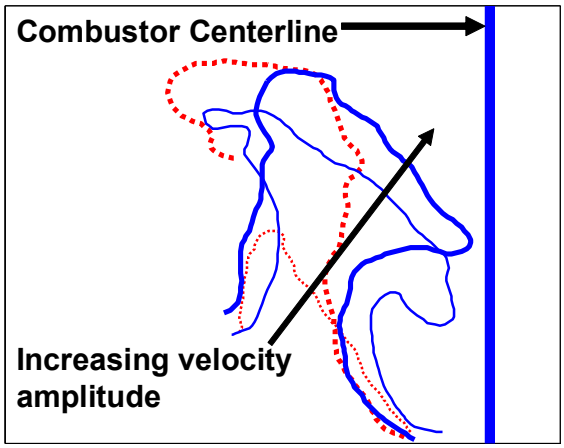

Figure 26. Averaged flame edges at 65-110 degrees phase angle at four velocity oscillation amplitudes (f_{drive} = 130 Hz, u'/u_o = 0.3, 0.6, 0.83, 0.90). Dashed (- - -)/ solid (—) lines indicate peak flame response when transfer function is linear/saturated, respectively.

Consider next the 410 Hz results. Recall from Figure 19 that saturation occurred well below 100% CH* chemiluminescence amplitude. Figure 27(a) shows the flame response at a low velocity amplitude (u'/u_o = 0.2) for 410 Hz. Similar to the 130 Hz in Figure 27(a) and inferred from Figure 23, the flame is stabilized at the centerbody of the premixer. The flame increases in length and shows increased wrinkling at the peak of the cycle. Figure 27(b) illustrates the flame response at a high velocity oscillation amplitude (u'/u_o = 0.6), where the flame exhibits a very different behavior from the 130 Hz results. First, at all 8 phases, the flame is clearly lifted off the centerbody and appears to be stabilized near the stagnation point in a low velocity region, as also shown in the direct flame images in Figure 23. Only at one small part of the cycle, 45-90 degrees, can the flame be seen attempting to stabilize itself on the centerbody.

The liftoff of the flame from the centerbody with increasing excitation amplitude can be seen from Figure 28. Similar to Figure 26, dashed lines indicate the flame front where the transfer function is linear (u'/u_o = 0.2, 0.3) and the solid lines indicates peak response flame edges near and beyond the saturation point of the transfer function (u'/u_o = 0.53, 0.6). The plot clearly shows the transition of the stabilization point of the flame from the centerbody to a point downstream with increasing disturbance amplitude. Since the flame is lifted off, the two flames that are present in the linear regime are merged together into one flame- it can be seen that the flame area is lower than it would be if the flame were attached. This unsteady liftoff, and consequent reduction in flame area, is the mechanism of nonlinearity for this case. It is first observed in the images at u'/u_o amplitudes around 0.35; i.e., where the transfer function begins to saturate

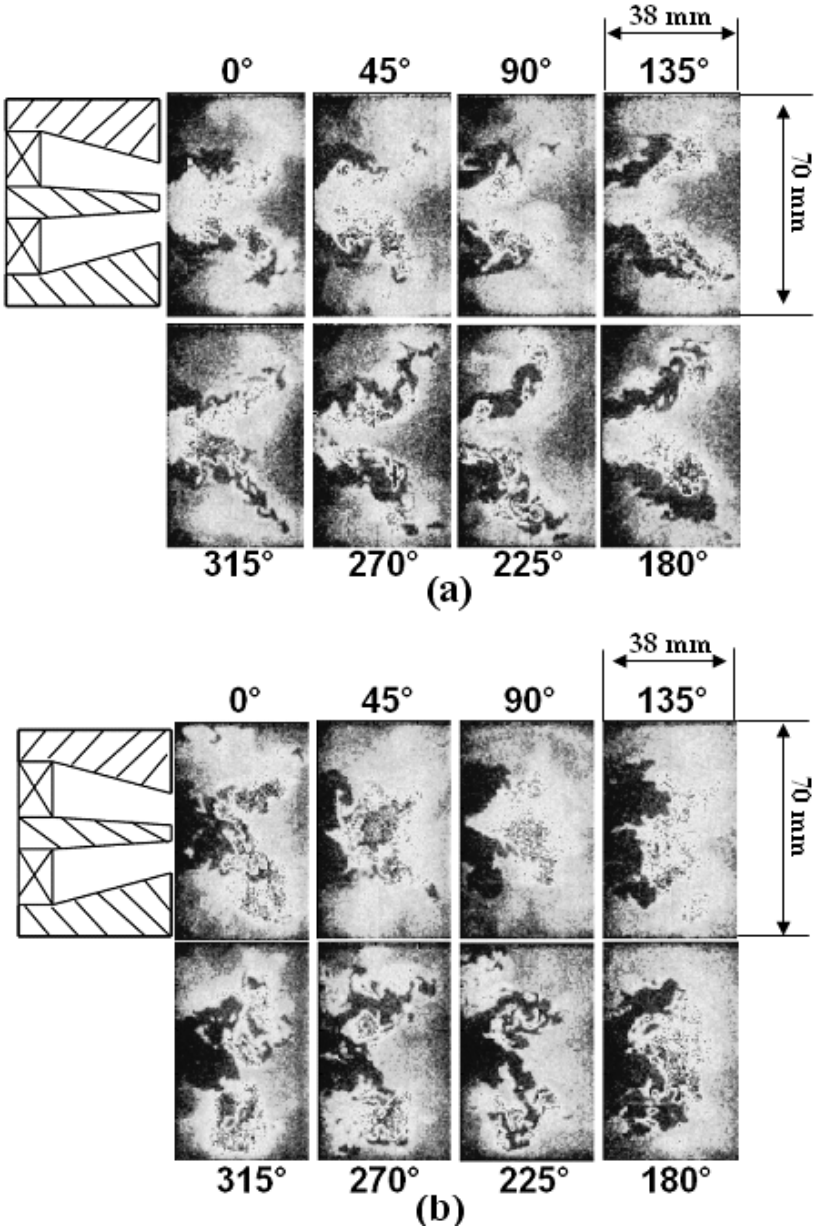

Figure 27. Instantaneous OH PLIF images showing evolution of flame response over 1 cycle of acoustic forcing for (a) low (linear, u'/u_o = 0.2) and (b) high (nonlinear, u'/u_o = 0.6) velocity oscillation amplitudes (f_{drive} = 410 Hz, Re_D = 21000, ϕ = 0.80)

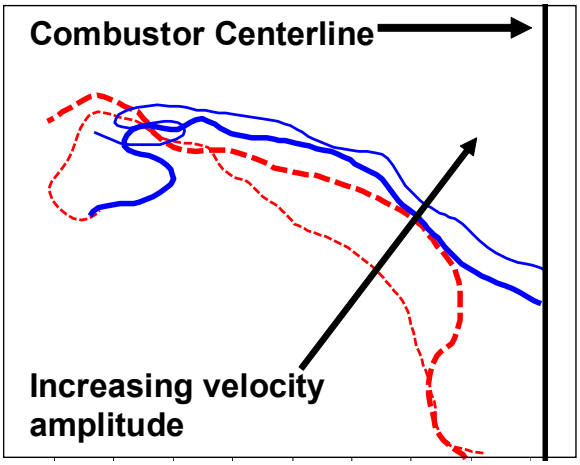

Figure 28. Average flame edges at 180-225 degree phase angle at four velocity oscillation amplitudes (f_{drive} = 410 Hz, u'/u_o = 0.2, 0.3, 0.53, 0.6). Dashed (- - -)/ solid (—) lines indicate peak flame response when transfer function is linear/saturated, respectively.

7. THEORETICAL NONLINEAR FLAME RESPONSE CHARACTERISTICS

This paper describes the dynamics of premixed flames responding to harmonic velocity disturbances. Results are derived from analytical and computational solutions of the nonlinear *G*-equation and used to interpret a number of experimental observations. It is shown that the linear and nonlinear characteristics of the flame dynamics are controlled by the superposition of two sources of flame disturbances: those originating at the flame anchoring point due to boundary conditions and from flow non-uniformities along the flame. These disturbances do not necessarily propagate along the flame at the same speed. Consequently, they may either constructively or destructively superpose with each other, so that the overall linear flame response depends upon two Strouhal numbers, St_2 and St_c, related to the amount of time taken for a flow (St_c) and flame front (St_2) disturbance to propagate the flame length, normalized by the acoustic period. Unsteady stretch effects, responsible for the reduction in the flame front wrinkle size in the flow direction (referred to as "filtering" by Bouehla & Baillot[25], become significant when $\sigma^* St_2 \sim O(1)$, where σ^* is a non-dimensionalized Markstein length. The nonlinear flame response is driven by flame propagation normal to itself ("kinematic restoration"), which smoothens out the wrinkles induced by the forcing. Because the overall flame response is a superposition of the two flame disturbance contributions, the flame's nonlinear response can exhibit two qualitatively different behaviors. For parameter values where these disturbances constructively interfere, the nonlinear flame transfer function gain saturates and is, therefore, always less than its linear value. When the flame disturbances destructively interfere, the nonlinear transfer function may actually exceed its linear value before saturating. This result explains Durox *et al's*[27] experimentally observed variation of the nonlinear flame response with frequency. One interesting prediction of this analysis concerns the impact of flow forcing on average flame length. We show that in most cases, the flame length decreases with increasing perturbation amplitude, as has been experimentally observed by Bourehla & Baillot[25] and Durox *et al*[40]. However, the analysis also predicts that the flame can lengthen under certain conditions, a result that has apparently not yet been experimentally observed.

This paper describes an analysis of the linear and nonlinear dynamics of laminar premixed flames responding to harmonic velocity disturbances. The key objective of this work is to predict the heat release response of the flame, and to isolate the key non-dimensional parameters which characterize these interactions. While this problem is of great interest from a fundamental standpoint, it is also motivated by pressing practical problems. This paper's focus on premixed flames is motivated by the fact that low emissions combustion systems for land-based gas turbines, future aircraft engines, industrial heaters and boilers rely on a premixed or partially premixed combustion process. Furthermore, its focus upon harmonically oscillating flow disturbances stems from the fact that these combustion systems are exceptionally prone to combustion instabilities[3,8, 41-44] which generally occur when the unsteady combustion process couples with the natural acoustic modes of the combustion chamber, resulting in self-excited oscillations. These oscillations are destructive to hardware and adversely affect performance and emissions.

While clearly the ultimate goal is to develop a general theory that describes the dynamics of harmonically perturbed, fully turbulent flames, our focus here upon laminar flames is motivated by the lack of understanding of their dynamics even in very simple situations.

An unstable combustor's dynamics are controlled by a complex interplay of linear and nonlinear processes. To illustrate, consider an acoustic disturbance with amplitude, ε. Referring to **Figure 29**, note that this disturbance amplitude stays the same, decreases, or increases depending upon the relative magnitudes of the driving, $H(\varepsilon)$, and damping, $D(\varepsilon)$, processes; i.e., whether $H(\varepsilon)=D(\varepsilon)$, $H(\varepsilon)<D(\varepsilon)$, or $H(\varepsilon)>D(\varepsilon)$, respectively. Linear combustor processes generally control the balance between driving and damping processes at low amplitudes of oscillation and, thus, determine the growth rate of inherent disturbances in the combustor. Nonlinear combustor processes control the finite amplitude dynamics of the oscillations. Predicting the limit cycle amplitude of self-excited oscillations requires an understanding of the nonlinear characteristics of $H(\varepsilon)$ and $D(\varepsilon)$. To illustrate, **Figure 29** depicts a situation where $H(\varepsilon)$ saturates and the two curves cross at the limit cycle amplitude, ε_{LC}.

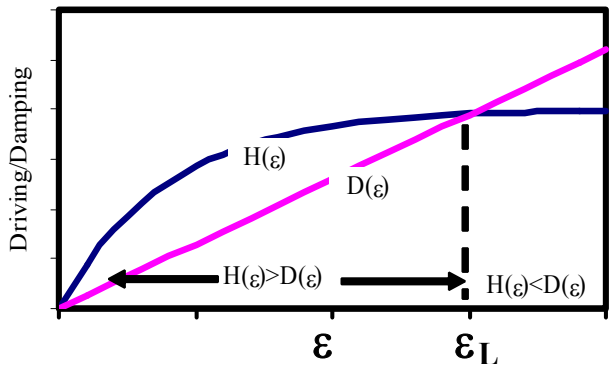

Figure 29. Qualitative description of the dependence of acoustic driving, H(ε) and damping, D(ε), processes upon amplitude, ε

The focus of this paper is on the heat release dynamics, i.e., to understand the characteristics of $H(\varepsilon)$ in both the linear and nonlinear regime. This focus on heat release dynamics is motivated by observations that the nonlinear gas dynamical processes are less significant in many premixed combustors. For example, Dowling[16] suggests that gas dynamic processes essentially remain in the linear regime, even under limit cycle operation, and that it is the relationship between flow and heat release oscillations that provides the dominant nonlinear dynamics in premixed combustors, i.e., $H(\varepsilon)$. The primary point of these observations have been confirmed by several experimental studies[45-47], which show that substantial nonlinearities in the heat release response to acoustic disturbances occur, even at amplitudes as low as $p'/p_o \sim 1\%$ and $u'/u_o \sim 20\%$.

A variety of mechanisms exist for causing nonlinearities in heat release dynamics; e.g., local or global flame extinction[16,19,48], pressure sensitivity of the mass burning rate[49-52], flame holding and/or nonlinear boundary

conditions[2,20] (e.g., the point where the flame anchors depending upon amplitude) equivalence ratio oscillations[15,17] and flame kinematics[53,54]. It is this latter kinematic mechanism, i.e., the response of the flame front position as it adjusts to perturbations in flow velocity that is the focus of this study. Because the flame's position and orientation depends upon the local burning rate and flow characteristics, velocity perturbations cause wrinkling and movement of the flame front. In turn, this modifies its local position and curvature, as well as its overall area or volume. These velocity disturbances can be acoustic or vortical in nature and, thus, propagate at the sound speed or with the flow, respectively. To illustrate the excitation of a flame by a velocity disturbance, Figure 30 shows a photograph from Durox *et al.* (2005)[40] of a Bunsen flame disturbed by flow oscillations generated by a loudspeaker placed upstream of the flame. The figure clearly shows the large distortion of the flame front. This flame disturbance is convected downstream by the mean flow, so that it varies spatially over a convective wavelength.

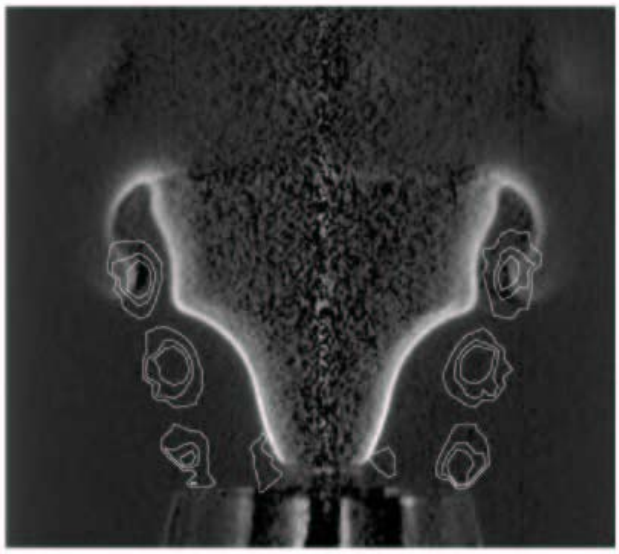

Figure 30. Vorticity field superposed with the flame front. Image reproduced with permission from Ref. [[40]].

A variety of experimental observations have been made of similar flames which will be reviewed next. Baillot and co-workers performed a systematic experimental and theoretical study of the response of laminar Bunsen flame to velocity perturbations of varying amplitude and frequency[25,27,55]. While their principal observations are quite similar to those previously observed by Blackshear[56], they appear to be the first systematic characterization of the flame response as a function of perturbation amplitude. Similar to the illustration in Figure 30, they found that at low frequencies (f<200 Hz) and velocity amplitudes (u'/u_o<0.3), the flame front wrinkles symmetrically about the burner axis due to a convected wave traveling from the burner base to its tip. At higher frequencies, but similar low amplitudes, they observed a phenomenon which they refer to as "filtering" wherein the flame wrinkles are only evident at the flame base and decay with axial location downstream. This high frequency behavior is due to the increased importance of the flame's curvature dependent burning velocity and the very short convective wavelengths of the imposed disturbances at these higher frequencies.

Bourehla & Baillot[25] also found that laminar, conical Bunsen flames subjected to high amplitude, low

frequency velocity perturbations exhibited a variety of transient flame holding behavior, such as flashback, asymmetric blowoff, unsteady lifting and re-anchoring of the flame. In addition, they note that its response is asymmetric and extremely disordered. However, at high frequencies and forcing amplitudes, the flame remains firmly attached, but its overall shape dramatically changes. They found that the flame becomes "collapsed" with a rounded off tip region, and for sufficiently high forcing intensities ($u'/u_o>1$), the flame's mean shape becomes hemispherical[25]. Baillot et al.[55] also reported a theoretical study, where they solved the *G*-equation and showed good agreement between predicted and measured flame shapes, even at larger amplitudes of forcing where the flame front becomes strongly cusped. The so-called *G*-equation is a front tracking equation for the flame position, given by:

$$\frac{\partial G}{\partial t} + \vec{u}\nabla G - S_L \left|\nabla G\right| = 0 \quad (1)$$

where $G(x,t)=0$ is an implicit expression defining the instantaneous flame position, $\vec{u}'$ is the velocity field and S_L is the laminar burning velocity.

Recent work complements the studies of Baillot and co-workers discussed above, by quantifying the *global* heat release response, Q', of the flame[8,32,40]. These workers obtained high speed images and transfer functions, $(Q'/Q_o)/(u'/u_o)$, of acoustically forced Bunsen and inverted wedge flames. Significantly, they showed that most of the key flame response characteristics could be quantitatively predicted by assuming that the flame's heat release was directly proportional to its instantaneous area. The flame area was calculated using the *G*-equation, where measured velocity fields were used as inputs.

Solution of the *G*-equation is a key analytical approach used in this paper, as well as the above cited studies, for quantitative analysis of this problem. This approach for treating unsteady flame problems was apparently first introduced by Markstein[57] and, in the context of acoustically forced flames, by Marble & Candel[58]. It has subsequently been extensively developed[59] and is used in a variety of flame dynamic studies. The key assumption behind its application is the separation of acoustic/hydrodynamic scales of the flow field, and the flame thickness. Given the disparity between flame and acoustic length scales, the flame front essentially appears as a discontinuity to the flow. As such, the fluid dynamics of the flows up and downstream of the flame can often be treated separately from that of the flame structure. However, we should emphasize that there is not necessarily a *corresponding disparity in time scales*; e.g. forming a flame response time scale, τ_M, from the ratio of the laminar flame thickness and flame speed leads to values of τ_M~0.002 - .07 s for methane/air flames. These are of similar magnitude of perturbations with frequencies between 20-500 Hz. Thus, the interior flame structure and, consequently, quantities such as the flame speed, do not respond in a quasi-steady manner to flow perturbations.

Because of the mutual interaction between the flame position and the flow field, free boundary problems such as this are extremely difficult to handle analytically. Initial studies used an integral technique[58,60-63] to make it analytically tractable. Further progress has been made in more recent studies[7,8,53,60,] which circumvented the analytical difficulties encountered in the fully coupled flame-flow problem by neglecting the coupling of flow perturbations across the flame, as will also be done in this study. As such, they calculated the response of the flame from an imposed velocity disturbance of given amplitude and phase upstream of the flame. In essence, this

approximation neglects the density change across the flame front. Nonetheless, the substantially reduced complexity of the approach facilitates a much more transparent analysis; moreover, their results give excellent agreement with experiments in many instances. We will discuss the conditions under which this approximation is appropriate, and not appropriate, at length below.

In closing, we should draw the readers attention to several additional analyses which, though not directly aimed at the acoustic flame interaction problem, did analyze the kinematics of a nominally flat flame front in an unsteady and/or periodic, prescribed, flow field; e.g., see Refs. [64-67].

The key contribution of the present work is to provide a systematic treatment of linear and nonlinear flame dynamics – including unsteady stretch effects - in response to harmonically oscillating flow disturbances. The rest of the paper is organized in the following manner: Section 0 describes the key processes impacting the flame dynamics and the disturbance field. In particular, the principle assumptions of the analysis are identified and the phenomena which can and cannot be captured by the analysis are discussed. Section 0 presents the modeling approach and analysis procedure. Section 0 presents results that quantify the effects of flame geometry, disturbance field characteristics, perturbation frequency and stretch sensitivity upon the flames linear (Section 0) and nonlinear (Section 0) characteristics. The response of the flame at the perturbation frequency and its harmonics are discussed as well as changes in the mean flame length.

Basic Considerations

Flame Dynamics

The basic problem of interest is this: Given a disturbance velocity field, $u'\left(\vec{x},t\right)$, determine the response of the flame position, $\zeta\left(\vec{x},t\right)$, and in particular, the total heat release rate of the flame. The global heat release rate of the flame is given by:

$$Q(t) = \int_s \rho_l S_L \Delta h_R dA_{FL} \quad (2)$$

where the integral is performed over the flame surface, A_{FL}, and Δh_R is the heat release per unit mass of reactant. Equation (2) shows the three fundamentally different ways of generating heat release disturbances in a premixed flame: fluctuations in mass burning rate ($\rho_l S_L$), heat of reaction, or flame area. As noted by Clanet *et al.*[68], they can be classified based upon either their modification of the local internal structure of the flame (such as the local burning rate) or its global geometry (such as its area).

As we are focused upon the flame response to flow perturbations, we assume constant Δh_R and mixture density, ρ_l; analysis of the effects of these perturbations are given in Refs. [49,69]. Of course, if the flow perturbation is acoustic in origin, a density disturbance will accompany the velocity fluctuation. However, their relative impacts differ greatly, on the order of the flame speed Mach number. As such, our subsequent calculations focus upon the quantity:

$$\frac{Q'}{\overline{Q}} = \frac{\int S_L' d\overline{A}_{FL}}{\int \overline{S}_L d\overline{A}_{FL}} + \frac{A_{FL}'}{\overline{A}_{FL}} \quad (3)$$

Flame speed perturbations are generated by the oscillating stretch rate, proportional to $\nabla^2 G$, and are discussed in Section 0. Flame area fluctuations are directly related to perturbations in the flame position through the relation:

$$A_{FL}(t) = \int \delta\left(G - G_o\right)\left|\nabla G\right| dS \quad (4)$$

where G_o denotes the flame surface. This equation shows that the quantity of interest is not G itself, but its gradient ∇G - a very important observation. Another key observation is that only the velocity component normal to the flame, $u' \cdot n' = u_n$, a scalar quantity, impacts the flame dynamics. This can be seen by rewriting Eq. (1) as:

$$\frac{\partial G}{\partial t} + \left(u_n - S_L\right)\left|\nabla G\right| = 0 \quad (5)$$

This necessarily implies that the full three dimensional details of the velocity field are not significant; it is only the component that is normal to the flame. As such a detailed specification of the velocity field is not necessary for an understanding of the flame dynamics and, furthermore, a variety of different velocity fields can give an essentially identical flame response. This is the reason why we assume a relatively simple form of the disturbance velocity field, as will be detailed in Sec. 0. However, for large amplitude oscillations, this point must be conditioned with the fact that the flame normal exhibits large fluctuations, so the relative contribution of each vector component of the velocity field varies throughout the cycle.

Several general comments can be made regarding the dynamics of the flame position gradient, which is directly related to its surface area through Eq (4); these will provide a great deal of insight into the flame dynamics. From a mathematical point of view, the linear solution to the equation for flame surface area can be decomposed into two canonical components: the homogeneous solution and the particular solution. The linearized version of Eq. (1) can be written in a coordinate system aligned normal to the mean flame position as (see Figure 31)

$$\frac{\partial \xi}{\partial t} + U_o \frac{\partial \xi}{\partial X} = U'\left(X,t\right) \quad (6)$$

where X denotes the coordinate along the mean flame position, U_o is the mean velocity component along the X axis and $\xi\left(X,t\right)$ is the perturbed flame position normal to this coordinate. The dynamics of $\partial\xi / \partial X$, which is directly related to that of the flame area itself, is described by the following solution*:

* In Eq (7), after evaluating the velocity gradient $\partial U'/\partial X$, the integration has to be performed with respect to dx'after replacing the variable X by x' and t by t-(X-x')/U_o

$$\frac{\partial \xi(X,t)}{\partial X} = \frac{1}{U_o}\int_0^X \underbrace{\left(\frac{\partial U'(X,t)}{\partial X}\right)_{X\to x',t\to\left(t-\frac{X-x'}{U_o}\right)}}_{\text{Flow non-uniformity (particular solution)}} dx' + \underbrace{\frac{1}{U_o}\left(U'(X=0,t-\frac{X}{U_o}) - U'_{base}(t)\right)}_{\text{Boundary condition (homogeneous solution)}} \quad (7)$$

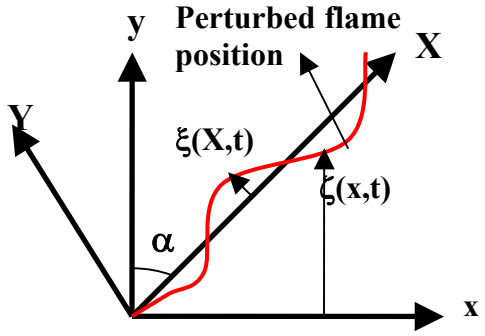

Figure 31. Coordinate system illustrating the perturbed flame shape

The homogeneous and particular solutions have a clear physical significance which can be understood as follows. A spatially uniform disturbance velocity disturbance only excites the homogeneous solution (second term in Eq (7)). This can be understood by first assuming that the flame edge moves exactly in step with the particle velocity, i.e., $U'_{base} = U'(X=0, t-\frac{X}{U_o})$. In this case, the entire flame simply moves up and down in a bulk motion without a change in shape or area[70]. However, if a flame anchoring boundary condition is imposed ($U'_{base} = 0$), such that the flame remains fixed, the flow disturbance excites a flame front disturbance that originates at the boundary and propagates along the flame front at a speed that is proportional to the mean flow velocity. These "homogeneous solution" flame dynamics were extensively analyzed by Fleifil *et al.*[7]. If the disturbance flow field is spatially non-uniform, i.e., $\partial U'/\partial X \neq 0$, the particular solution is excited (first term in Eq (7)). This results in waves originating at the spatial location(s) of flow non-uniformity that also propagate along the flame at roughly the mean flow velocity.

Because the *G*-equation is first order in time, the flame acts as a low pass filter to flow disturbances, so that the amplitude of the two canonical solutions individually decay with increases in frequency as *1/f*. As such, the transfer function relating the response of the flame area to a spatially uniform velocity disturbance (where only the homogeneous solution is excited), $(A'/A_o)/(u'/u_o)$ has a value of unity at zero frequency, decays monotonically with frequency, but generally is not identically zero[†]. In contrast, when the flame is perturbed by a spatially non-uniform disturbance (so that both the homogeneous and particular solution are excited), the flame area consists of a

[†]An exception occurs in two-dimensional flames at frequencies where the flame tip motion is zero. In this case, the flame's linear area response is also zero.

superposition of the two solutions. As such, though each solution decreases with frequency, their sum has oscillatory behavior and, in cases where they constructively interfere can even cause the transfer function, $(A'/A_o)/(u'/u_o)$ to exceed unity. This result was first predicted by Schuller *et al.*[32] and experimentally observed by Durox *et al.*[40]. In addition, the two solutions can destructively interfere, and in certain cases, exactly cancel each other so that the resulting transfer function $(A'/A_o)/(u'/u_o)$ identically equals zero.

Consider next several basic features of the nonlinear flame dynamics. The key mechanism of nonlinearity is illustrated in Figure 32. In this illustration, a flame is perturbed by a transient disturbance so that it has a corrugated shape, but then allowed to relax back to its steady state, planar position. Flame propagation normal to itself smoothens out the wrinkle, so that its area eventually returns to being constant in time. As such, kinematic processes work to destroy flame area, as shown by the dashed lines in the bottom sketch. The rate of these area destruction processes depends nonlinearly upon the amplitude and length scale of the flame front disturbance. Large amplitude corrugations are smoothed out at a relatively faster rate than small amplitude perturbations. In the same way, short length scale corrugations are smoothed out faster than long length scales of the same disturbance magnitude. As discussed further below, this is the reason that nonlinearity is enhanced at higher disturbance frequencies, which generate shorter length scale flame corrugations.

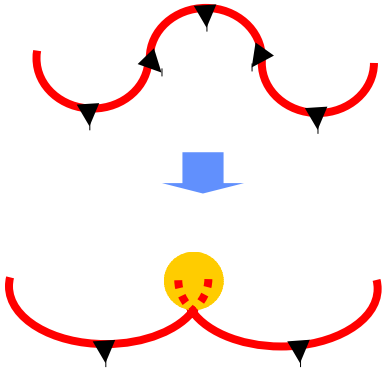

Figure 32. Sketch of a flame that is initially wrinkled (top), showing the destruction of flame area by kinematic restoration processes (bottom)

If the disturbance velocity field is spatially uniform (so that only the homogeneous solution is excited), nonlinear effects cause the nonlinear transfer function relating flame area and velocity perturbations, $(A'/A_o)/(u'/u_o)$, to monotonically decrease with disturbance amplitude[54]. In other words, the linear transfer function is larger than the nonlinear transfer function. Since the scale of flame wrinkling is inversely proportional to frequency (scaling roughly as u_o/f), this reduction in finite amplitude transfer function relative to its linear value grows with frequency. As such, the flame area response to a velocity disturbance exhibits saturation characteristics, quite similar to the $H(\varepsilon)$ curve plotted in **Figure 29**.

In the general nonlinear case, as in the linear case, the effect of the superposition of the homogeneous and particular solutions upon the overall flame response depends upon whether the two solutions lie in a region of constructive or destructive interference. In particular, it can be anticipated that if the two solutions lie in a region of destructive interference and are affected unequally by nonlinearity, their superposition may cause the nonlinear

transfer function to actually exceed its linear value. We will show that this occurs in some cases and, furthermore, has been experimentally observed.

Finally, the flame curvature introduced by the flow perturbations introduces perturbations in flame speed. In flames that are thermo-diffusively stable (as assumed in this analysis), these unsteady stretch effects act to smooth out the flame front corrugation. This causes the amplitude of the flame wrinkle to diminish as it propagates along the flame. As the radius of flame wrinkling is approximately proportional to the inverse of the squared frequency, it can be anticipated that this effect grows in significance with frequency. This axial decay in flame wrinkling amplitude has been observed by Bourhela & Baillot[25], which was referred to as "filtering".

Disturbance Field

The prior section touched upon the influence of the velocity field upon the flame dynamics. It showed that it is the normal component of the velocity, and not the velocity itself, that is significant in determining the flame response. Also implicit in Eq. (7) is that the detailed structure of these flow non-uniformities at each axial location is less significant than their integrated effect from the flame attachment point to that axial location. This section considers in more detail the character of the velocity field.

The velocity field can be decomposed into an irrotational, compressional component (the acoustic field) and a solenoidal, rotational component (vorticity field). Acoustic disturbances propagate with a characteristic velocity equal to the speed of sound. In a uniform flow, vorticity disturbances are convected at the bulk flow velocity, u_o. Acoustic properties vary over an acoustic length scale, given by $\lambda_a=c/f$, while vortical disturbances vary over a convective length scale, given by $\lambda_c=u_o/f$. Consequently, in low Mach number flows, these disturbances have substantially different length scales. The vortical mode "wavelength" is shorter than the acoustic wavelength by a factor equal to the mean flow Mach number, $\lambda_c/\lambda_a=u_o/c=M$.

Vorticity disturbances propagate with the mean flow and diffuse from regions of high to low concentration. In contrast, acoustic disturbances, being true waves, reflect off boundaries, are refracted at property changes, and diffract around obstacles. The reflection of acoustic waves from multi-dimensional flame fronts generally results in a complex, multi-dimensional acoustic field in the vicinity of the flame.

Experiments have highlighted the significance of both acoustic and vorticity wave interactions with the flame front. These vorticity oscillations are generally manifested as large scale, coherent structures that arise from the growth of intrinsic flow instabilities. The phase velocity and growth rate of the flow instabilities is strongly affected by the amplitude of forcing and the relationship between the acoustic forcing frequency and the intrinsic flow instability. Acoustic excitation often causes their shedding rate to "lock-in" to the forcing frequency or one of its harmonics. For example, visualizations from the study of Durox *et al.*[40], clearly indicate that these convected vortical disturbance are excited at the shear layer of the burner exit by the imposed acoustic oscillations. Figure 30 obtained from this study superposes an image of the instantaneous wrinkled flame front and the convected vorticity field. By incorporating the convective phase variation into the disturbance velocity field, they show that the modeled flame area response agrees quite well with their data.

The characteristics of the instability waves that grow and merge to form these large scale structures are a function of the specific characteristics of the burner exit shear layer, such as co-flow velocity, and specifically upon the receptivity of this shear layer to external disturbances. In addition, the phase speed of the convected vortical instability waves are not equal to the flow velocity, but vary with frequency and shear layer characteristics. The instability wave growth rate similarly varies with frequency and the shear layer characteristics. To illustrate, Figure 33 plots Michalke's[73] theoretical curves of the dependence of the phase speed, u_c, of shear layer instability waves in a jet flow upon Strouhal number, $S_\theta = f\theta/u_o$, for several values of the momentum thickness, θ, to jet radius, R, ratio, R/θ. The figure shows that, for all R/θ values, the ratio of u_c/u_o equals unity and 0.5 for low and high Strouhal numbers. For thin boundary layers, e.g., R/θ =100, the phase velocity actually exceeds the maximum axial flow velocity in a certain S_θ range. This ultra-fast phase velocity prediction has been experimentally verified by Bechert & Pfizenmaier[71] and may explain a similar measurement in a Bunsen flame by Ferguson *et al.*[72]. The dispersive character of the instability wave convection velocity has been confirmed by a variety of measurements in acoustically forced flames. For example, Baillot *et al.*[53] measured u_c/u_o values of 1.13 and 1.02 at 35 and 70 Hz, respectively, on a conical Bunsen flame. Durox *et al.*[40] measured u_c/u_o =0.5 values at 150 Hz in an axisymmetric wedge flame.

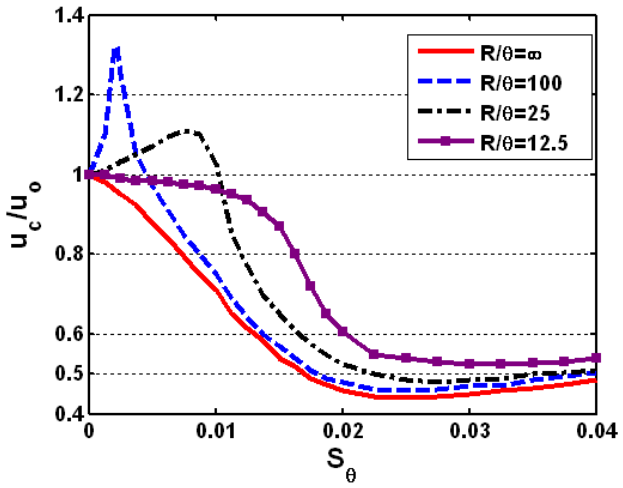

Figure 33. Dependence of shear wave convection velocity and growth rate in a jet flow upon Strouhal number and ratio of jet radius to momentum thickness. Figure reproduced from Michalke[73] (1971).

In general, the disturbance field may have both acoustic and vortical components, whose relative magnitude depends strongly upon the vortex shedding dynamics at the burner shear layer. For example, Ferguson *et al.*[72] found that the disturbance field transitioned from a convected character to one with an acoustic character at "low" and "high" frequencies, respectively. This behavior may be due to the corresponding dependence of vorticity wave growth rate upon frequency. These points show that the character of the disturbance field can vary significantly between its relative acoustic and vortical components, as well as their spatial structure (such as phase speed) – these characteristics will change with experimental configuration, frequency, and amplitude of

perturbation. This point is a key motivator for our development of a general theory for arbitrary phase speed velocity disturbances.

The amplitude dependence of the disturbance field characteristics should be noted. Even in the absence of convected vorticity waves, the impact of the fluctuating flame position upon the acoustic field should cause the acoustic disturbance field to have a "convected" character. This is due to the fact that the flame response to the acoustic field and the acoustic field disturbing the flame are coupled. For large amplitude disturbances, the flame develops large corrugations, such as can be seen in Figure 30, that convect with a phase speed proportional to the axial flow velocity. These convecting flame wrinkles impact the character of the interior acoustic field. It can be anticipated that this mechanism causes the acoustic field structure to revert from being nearly uniform (assuming a compact flame) to having some convected charactereristics at low and high amplitude disturbances, respectively. This issue requires further clarification, as the effects of amplitude and frequency on the acoustic field structure have not been measured or calculated in the large amplitude case.

In this analysis, we prescribe, rather than solve for, the velocity field as done in most recent studies of the problem. In general, it should be emphasized that the thermal expansion of gases at the flame front causes the flame to influence the velocity field upstream of it; this coupling is responsible for the Darrius-Landau flame instability. We next turn attention to the very important issue of the manner in which these mutual interactions impact the results, the conditions under which the present analysis is appropriate, and the conditions where additional physics qualitatively influences the flame dynamics.

First it should be noted that imposing the velocity field is a rigorously valid approximation in the limit of low dilatation flames; i.e., in the limit where $T_b/T_u \rightarrow 1$. This is also the limit considered by other authors for studies of the thermal-diffusive instability and is the basis of the Sivashinsky-Kuramoto equation[74,75]. Besides being of academic interest in allowing one to analytically handle the problem, this is actually a useful limit for many practical devices. It is often pointed out in the combustion literature that practical flames have temperature ratios on the order of 6-10. This is true for flame's consuming reactants at *room temperature* but not, however, for the conditions encountered in most practical devices. Due to the need for high efficiencies (e.g., devices utilizing regenerative heating or high compression ratios such as industrial boilers or gas turbines) or because the devices are using vitiated air (duct burners or jet engine augmentors), unburned gas temperatures are substantially higher. Correspondingly, the requirement for low NOx emissions implies lower burned gas temperatures. As such, typical temperature ratios for practical premixed combustion devices are in the range of 2-3, and even as low as 1.5 in certain industrial applications with large amounts of regenerative pre-heating.

Clearly, however, as T_b/T_u deviates from unity, there will be an impact upon the approach flow characteristics. It can readily be shown that the impact of the flame on the acoustic field scales as $(T_b/T_u)^{1/2}$, which is the ratio of the gas impedances across the flame. Based upon the discussion in the prior section it can be anticipated that, at least for low amplitude perturbations, the alteration of the local acoustic field by the flame does not introduce qualitative changes into the flame dynamics, although it may certainly exert quantitative impacts that increase as $(T_b/T_u)^{1/2}$. This assertion has been previously confirmed by Lee & Lieuwen[70], who computationally determined the

flame's acoustic nearfield for various T_b/T_u values, determined the flame area response, and compared the results to the constant density analyses of Fleifil *et al.*[7] and Ducruix *et al.*[8].

Similarly, it is known that the effect of a stable flame on the vortical approach flow velocity scales approximately as T_b/T_u[76] As in the acoustic case, there is clearly also a frequency-wavenumber dependence, as well as an inverse dependency upon proximity to flame stability boundaries.

The qualitative similarities between fully coupled flame dynamics and that determined using an imposed velocity field break down when both T_b/T_u and perturbation velocity amplitudes are large; i.e., new dynamics appear that cannot be captured with this analysis. This is due to the appearance of a parametric flame instability[35,36,77], manifested by cellular structures that oscillate at half the period of the disturbance. This parametric acoustic instability is due to the periodic acceleration of the flame front by the unsteady velocity field, which separates two regions of differing densities. With increased amplitudes, these organized cellular structures break down into a highly disordered, turbulent front. The regimes in T_b/T_u vs u'/S_L space where this instability occurs can be determined from from Eq. (1) in Bychkov's analysis for a given dimensionless frequency, defined as $w = \dfrac{\omega \delta_f}{S_L}$ where ω is the forcing frequency and δ_f is the flame thickness[35]. The results are plotted in Figure 34. This graph illustrates the regions (above the curve) where application of a prescribed velocity theory is inappropriate. As could be anticipated, it shows that the range of disturbance amplitudes diminishes with increasing temperature ratio across the flame.

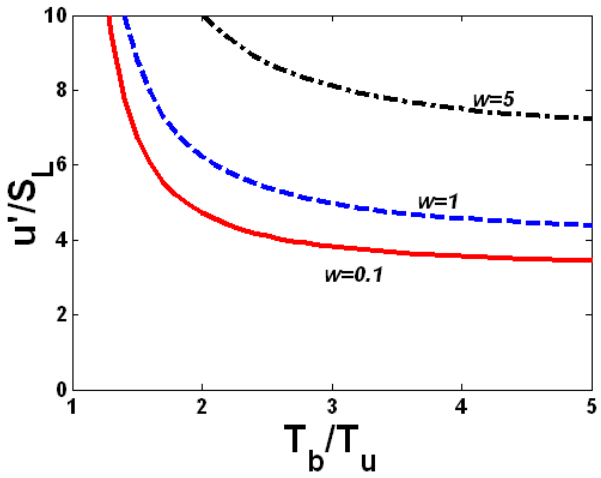

Figure 34. Parametric stability limits of flat flame (unity Lewis and Prandlt number, no gravity).

As such, we conclude that the qualitative linear dynamics of the flame are captured by this analysis for all T_b/T_u values, although the quantitative accuracy of the results deteriorates as T_b/T_u increases. Calculations that quantify these effects are given in Lee & Lieuwen[70]. In contrast, the nonlinear dynamics of the flame are only correctly described by this analysis for low T_b/T_u values. This is the reason for the restriction to low heat release flames indicated in the title of this paper.

Modeling Approach

Figure 35 illustrates the two basic geometries considered. On the left is a conical flame stabilized on a tube, such as a Bunsen flame. On the right is a wedge flame, stabilized on a bluff body. The flame's have axial and radial dimensions given by the flame length, L_f, and radius, R. The instantaneous flame sheet location at the radial location, r, is given by $\zeta(r,t)$, assumed to be a single-valued function of r. This assumption necessarily limits the range of amplitudes which can be treated with this formulation.

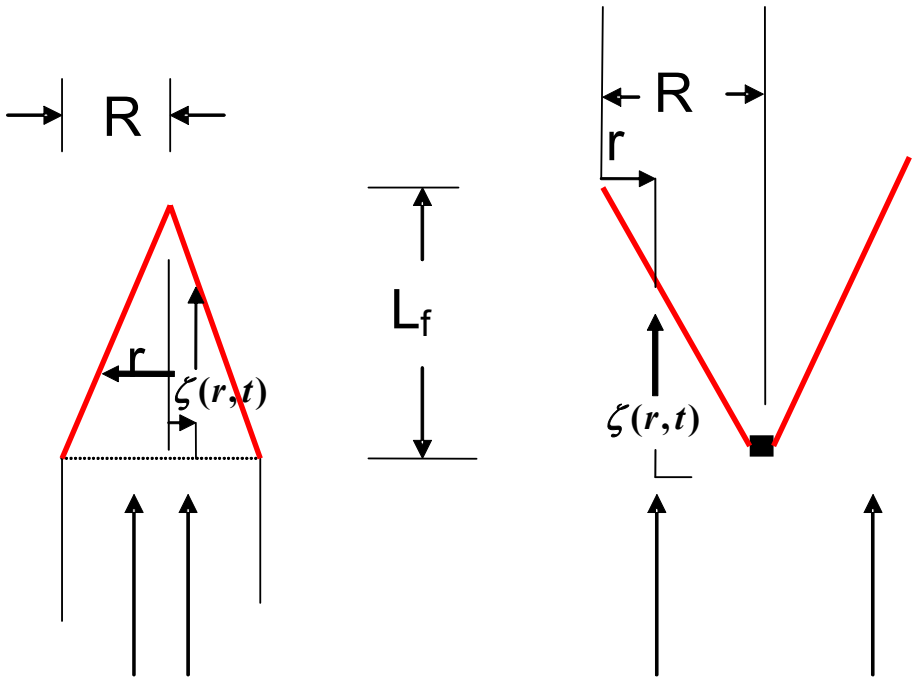

Figure 35. Illustration of conical (left) and wedge shaped (right) flame geometries.

Formulation

The analytical approach used here closely follows Refs. [7,8,53]. The flame's dynamics are modeled with the front tracking equation[59]:

$$\frac{\partial \zeta}{\partial t} = u - v\frac{\partial \zeta}{\partial r} - S_L\sqrt{\left(\frac{\partial \zeta}{\partial r}\right)^2 + 1} \quad (8)$$

where u and v denote the axial and radial velocity components, and S_L the flame speed.

Assuming that the flame speed is only a function of the local curvature of the flame front, it can be expressed as[57]:

$$S_L = S_{L,o}\left(1 - M_l \Phi\right) \quad (9)$$

where M_l is the Markstein length (a function of frequency) and the curvature Φ is given by:

$$\Phi = \frac{\dfrac{\partial^2 \zeta}{\partial r^2}}{\left(1+\left(\dfrac{\partial \zeta}{\partial r}\right)^2\right)^{\frac{3}{2}}} \quad (10)$$

The variables t, r, a, u and ζ are non-dimensionalized by u_o/L_f, R, R, u_o and L_f. (note that the value of L_f and R refer to their nominal values without imposed oscillations), where u_o is the mean axial velocity. They are related to the nominal flame speed and average flow velocity by:

$$\frac{u_o}{S_{L,o}} = \sqrt{\left(\frac{L_f}{R}\right)^2 + 1} \quad (11)$$

The ratio of the flame length to radius plays an important role in the flame's dynamics and is denoted by β.

$$\beta = \frac{L_f}{R} \quad (12)$$

Given these assumptions, the flame dynamics are given by (from this point on we use the same symbol for the dimensionless variable):

$$\frac{\partial \zeta}{\partial t} + \sqrt{\frac{1+\beta^2 \zeta_r^2}{1+\beta^2}}\left(1 - \frac{\sigma \beta \zeta_{rr}}{\left(1+\beta^2 \zeta_r^2\right)^{\frac{3}{2}}}\right) = u(\zeta,t) - \beta\, v(\zeta,t)\zeta_r \quad (13)$$

where $\sigma = M_l/R$ is the ratio of Markstein length to duct radius.

Following prior studies[7,53] we assume that the flame remains anchored at the base; i.e.,

$$\zeta(r=1,t) = 0 \quad (14)$$

For conical flames, the second boundary condition comes from the fact that the flame is symmetric about the axis (see Figure 35) i.e.

$$\frac{\partial \zeta(r=0,t)}{\partial r} = 0 \quad (15)$$

For wedge flames, the boundary condition is:

$$\frac{\partial^2 \zeta(r=0,t)}{\partial r^2} = 0 \quad (16)$$

It turns out that both of these boundary conditions introduce terms which are exponentially small functions of σ, terms which are neglected in the ensuing analytical treatments (but not in the computations). As such, although formally required to solve the problem, neither boundary condition exerts any influence on the leading order analytical solutions.

Specification of velocity field

The velocity field is specified as:

$$u(\zeta,t) = u_o + u' \, Cos[k\zeta - \omega_o t] \quad (17)$$

Here the convective wave number k is defined as:

$$k = \frac{\omega_o}{u_c} = \left(\frac{\omega_o}{u_o}\right)\left(\frac{u_o}{u_c}\right) = K\left(\frac{\omega_o}{u_o}\right) \qquad (18)$$

where u_c is defined as the phase velocity of the disturbance and ω_o denotes the angular frequency of the velocity disturbance. K is a parameter which denotes the ratio of the mean flow velocity to the phase velocity of the disturbances. The two key impacts of the flow field on the flame front given by the term $\partial u'/\partial X$ in Eq (7) are captured here by the perturbation amplitude ε and the velocity length scale, u_c/ω_o.

The non-dimensionalized velocity field is then given by:

$$u(\zeta,t) = 1 + \varepsilon Cos\left[St\left(K\zeta - t\right)\right] \quad (19)$$

where

Strouhal number, $St = \dfrac{\omega_o L_f}{u_o}$

Velocity perturbation: $\varepsilon = \dfrac{u'}{u_o}$

The velocity is assumed to be purely axial. It should be emphasized that our goal here is not to simulate the exact disturbance field of any particular experimental setup, but rather to elucidate the key physical processes and non-dimensional parameters that influence the flame's dynamics. However, assuming a two dimensional velocity field does not introduce substantial analytical difficulties, but does reduce the generality of the results, as its characteristics are strongly influenced by geometric details.

Note that the boundary condition given by Eq (14) cannot be used for disturbance velocity magnitudes where the instantaneous flow velocity is lower than the flame speed. In this case, the flame will flash back and Eq. (14) must be replaced by a different condition[20]. In this study, calculations are performed for velocity magnitudes up to this critical value, which will be referred to as ε_f, where:

$$\varepsilon_f = 1 - \frac{1}{\sqrt{1+\beta^2}} \quad (20)$$

Analysis Procedure

Two approaches were used to analyze the properties of Eqs (13) and (3). Analytical expressions for the linear and nonlinear flame response were obtained from a perturbation analysis carried out to third order in ε. Terms of $O(\varepsilon^3)$ are required to determine the leading order nonlinear correction to the flame transfer function at the forcing frequency. Nonlinear corrections to the average flame length and the flame response at the first harmonic, $2\omega_0$, are obtained at $O(\varepsilon^2)$. Exponentially small terms of σ, e.g., $\exp(-1/\sigma)$, are also neglected as these are smaller than all

powers of σ, i.e., $\lim_{\sigma \to 0} e^{-\frac{1}{\sigma}} < \sigma^n$, where n is any integer.

For the fully nonlinear case, Eq.(13) is solved numerically. A robust numerical scheme is necessary which can accurately capture the formation of sharp gradients and cusps in the distorted flame front. Spatial derivatives are discretized using a Weighted Essentially Non-Oscillatory (WENO) scheme designed specifically for Hamilton-Jacobi equations[79]. This scheme is uniformly fifth order accurate in regions wherein the spatial gradients are smooth and third order accurate in discontinuous regions. Derivatives at the boundary nodes are calculated using fifth order accurate upwind-differencing schemes so that only the nodes inside the computational domain are utilized. A Total Variation Diminishing (TVD) Runge-Kutta scheme[80], up to third order accurate, is used for time integration. The flame front perturbation is tracked and the corresponding change in the flame surface area is calculated as a function of time for a given upstream flow velocity perturbation. The transfer function relating the flame area to the convective velocity perturbation is then evaluated. The flame response at a given frequency was determined from the Fourier transform of the flame area at that frequency.

Results and Discussion

Linear Flame Dynamics

In this section, we derive expressions for the flame area-velocity transfer function that generalize the result of Schuller *et al.*[32], by determining the response of a flame to a disturbance with an arbitrary phase velocity and curvature dependent flame speed.

Flame shape

The flame position is expanded as[53]:

$$\zeta(r,t) = \zeta_o(r) + \zeta_1(r,t)\ \varepsilon\ +\ \zeta_2(r,t)\ \varepsilon^2 + \zeta_3(r,t)\ \varepsilon^3 + O(\varepsilon^4) \quad (21)$$

The evolution equation for $\zeta_1(r,t)$ is computed here and the $\zeta_2(r,t)$, $\zeta_3(r,t)$ terms are computed in Section 0. The mean flame shape in the absence of perturbations is given by

$$\zeta_o(r) = 1 - r + O\left(e^{-\frac{1}{\sigma}}\right) \quad (22)$$

Stretch effects at the flame tip provide an exponentially small correction to $\zeta_o(r)$. An exact expression for $\zeta_o(r)$ is given in Appendix A. Substituting Eqs (21) and (22) into Eq (13), the evolution equation for ζ_1 is:

$$\frac{\partial \zeta_1}{\partial t} - \frac{\beta^2}{1+\beta^2}\frac{\partial \zeta_1}{\partial r} - \frac{\sigma\beta}{\left(1+\beta^2\right)^{3/2}}\frac{\partial^2 \zeta_1}{\partial r^2} - Cos\left[St\left\{K(1-r)-t\right\}\right] = 0 \quad (23)$$

The solution of Eq. (23), given the boundary condition in Eq. (14) and Eq. (15) (for conical flames) or Eq. (16) (for wedge flames) (only terms of $O(\sigma^*)$ are shown below for brevity, full solutions are in Appendix B) is

$$\zeta_1 = \zeta_{1,BC} + \zeta_{1,Flow}$$

$$= \left(\frac{\left(\alpha^2 + (r-1)\sigma^* St^2\right) Sin\left[\left(\frac{St\ \ (r-1+\alpha t)}{\alpha}\right)\right]}{\alpha^2(\eta-1)\ \ St} - \frac{\sigma^* \eta^2 Cos\left[\left(\frac{St\ \ (r-1+\alpha t)}{\alpha}\right)\right]}{\alpha(\eta-1)^2} \right) \quad (24)$$

$$+ \left(\frac{\sigma^* \eta^2 Cos\left[St\left\{K(r-1)+t\right\}\right]}{\alpha(\eta-1)^2} - \frac{Sin\left[St\left\{K(r-1)+t\right\}\right]}{(\eta-1)\ \ St} \right)$$

where

$$\alpha = \frac{\beta^2}{\beta^2+1} \quad (25)$$

$$\sigma* = \frac{\sigma}{\beta\sqrt{\beta^2+1}} = \frac{\sigma(1-\alpha)}{\sqrt{\alpha}} \quad (26)$$

$$\eta = K\alpha \quad (27)$$

This equation explicitly decomposes the solution into contributions from boundary conditions and flow forcing non-uniformities. Note that this expression is valid for both conical and wedge flames (i.e. the second boundary condition is satisfied by the exponentially small terms which have been neglected in the above expressions.). The flame front position is controlled by the superposition of the flame disturbances created at each point due to flow non-uniformity and disturbances originating from the flame base that are convected along the flame front. The stretch contribution is controlled by the parameter σ^* and becomes prominent when $\sigma^* St$ ~O(1).

The limit where $\eta \to 1$ (corresponding to instances where the two disturbances propagate along the flame at the same speed), requires special care and is given by:

$$\lim_{\eta \to 1} \zeta_1 = (r-1)\left(\frac{\left(2\alpha^2 + \sigma^* St^2 (r-1)\right) Cos[\, St\left\{\frac{(r-1)}{\alpha} + t\right\}] + 4\sigma^* \alpha St\ Sin[\, St\left\{\frac{(r-1)}{\alpha} + t\right\}]}{2\alpha^3} \right) \quad (28)$$

Note that for this case stretch effects have a stronger impact at high Strouhal numbers ($\sigma^* St^2$ ~O(1)).

In order to illustrate the effect of stretch on the flame shape, the deviation of the flame front from its average position is shown in Figure 36. The point X=0 in Figure 36corresponds to the point of attachment at the flame base. In the absence of stretch (σ^*=0), it is well known that the flame front exhibits sinusoidal wrinkling with a constant amplitude[60]. However, in the presence of stretch, the amplitude of the flame front perturbation decays continuously from the flame base to the tip, see Figure 36. This feature wherein the oscillations on the flame front are only evident at the flame base and become strongly damped at axial locations downstream has been experimentally observed and referred to as "filtering" by Bourhela & Baillot[25]. They observed this phenomenon for a conical flame under conditions corresponding to St>38, β=2 and σ^*~0.005, the same conditions simulated in the figure. The strong damping in the flame front oscillations away from the flame base at the same conditions is clearly

captured in Figure 36.

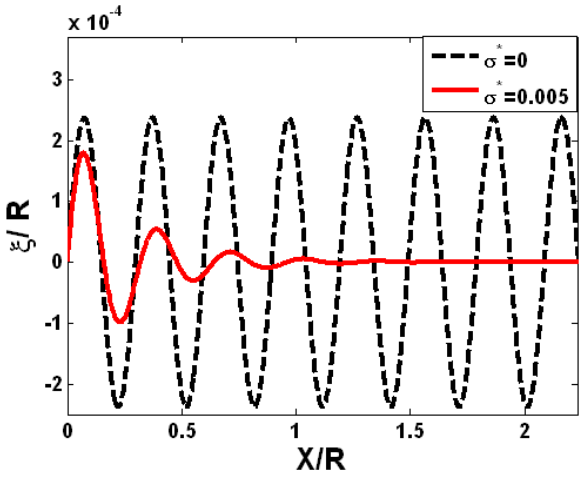

Figure 36. Instantaneous conical flame shape with X axis along the flame front. β=2, ε=0.01, St = 39, K=0

Flame area-velocity transfer function: relative contribution of different sources

Consider the total heat release of the flame, obtained using Eq (3). The first term is entirely due to stretch effects on the flame speed and for conical flames can be expressed as:

$$\frac{\int S_L' d\bar{A}_c}{\int \bar{S}_L d\bar{A}_c} = -2\varepsilon\sigma^* \alpha \int_0^1 r \frac{\partial^2 \zeta_1}{\partial r^2} dr = -2\varepsilon\sigma^* \alpha \left(\zeta_1(r=0,t) - \zeta_1(r=1,t) + \frac{\partial \zeta_1(r=1,t)}{\partial r} \right) \quad (29)$$

To evaluate the second term in Eq (3), note that the non-dimensionalized surface area for a conical flame is given by:

$$\frac{A_c(t)}{\bar{A}_c} = 2 \frac{\int_0^1 r \sqrt{1+\beta^2 \left(\frac{\partial \zeta}{\partial r} \right)^2}\, dr}{\sqrt{1+\beta^2}} \quad (30)$$

Substituting Eqs. (21), (22) and (24) in Eq. (30) and defining

$G_c = \dfrac{Q'/\bar{Q}}{u'/u_o}$ yields (only terms of O(σ^*) are shown below for brevity, full solutions are in Appendix B):

$$G_c(St_2, \eta, \sigma^*) = \overbrace{G_{c,S_L}}^{S_L \text{ Fluctuation}} + \overbrace{G_{c,Area}}^{\text{Area Fluctuation}} \quad (31)$$

where the contribution due to curvature induced S_L fluctuations is:

$$G_{c,S_L} = 2\sigma^* \left(1 + i \frac{e^{i\eta St_2} - e^{iSt_2}}{(\eta - 1)\ St_2} \right)$$

$G_{c,Area}$ can be written in the following form that explicitly separates the contributions from the boundary conditions and flow non-uniformity:

$$G_{c,Area} = G_{c,Area,BC} + G_{c,Area,Flow}$$

$$= \underbrace{2\left(\frac{e^{iSt_2} - 1 - iSt_2}{(\eta-1)\,St_2^2} + \sigma^* \frac{i(e^{iSt_2}-1)(1-\eta+\eta^2) + St_2\left(e^{iSt_2}(1-\eta)+\eta^2\right)}{(\eta-1)^2 St_2}\right)}_{\text{Boundary Condition}} + \underbrace{2\left(\frac{1-e^{i\eta St_2} + i\eta St_2}{\eta(\eta-1)St_2^2} - \sigma^*\eta\frac{ie^{i\eta St_2} - i + \eta St_2}{(\eta-1)^2 St_2}\right)}_{\text{Flow non-uniformity}}$$

Alternatively, it can be written in a form which separates out the stretch effects:

$$G_{c,Area} = 2\left(\frac{\eta\left(1-e^{iSt_2}\right) + e^{i\eta St_2} - 1}{\eta(1-\eta)St_2^2}\right) + 2\sigma^*\underbrace{\left(i\frac{\left(e^{i\,St_2}\left(\eta^2-\eta+1\right) - \eta e^{i\,\eta St_2} - (\eta-1)^2\right)}{(\eta-1)^2 St_2} + \frac{e^{i\,St_2}}{(1-\eta)}\right)}_{\text{Stretch Contribution to Area Fluctuation}}$$

where

$$St_2 = \frac{St}{\alpha} = \frac{St\left(1+\beta^2\right)}{\beta^2} \quad (32)$$

Following a similar procedure, the following result can be obtained for wedge flames:

$$\frac{A_w(t)}{\bar{A}_w} = 2\frac{\int_0^1 (1-r)\sqrt{1+\beta^2\left(\frac{\partial\zeta}{\partial r}\right)^2}\,dr}{\sqrt{1+\beta^2}} \quad (33)$$

$$G_w(St_2,\eta,\sigma^*) = \underbrace{G_{w,S_L}}_{S_L\ \text{Fluctuation}} + \underbrace{G_{w,Area}}_{\text{Area Fluctuation}}$$

$$G_{w,S_L} = 2\sigma^*\left(\frac{(i+St_2)e^{iSt_2} - (i+\eta St_2)e^{i\eta St_2}}{(\eta-1)\,St_2}\right)$$

$$G_{w,Area} = \underbrace{2\left(\frac{1+i(i+St_2)e^{iSt_2}}{(\eta-1)\,St_2^2} - \sigma^*\frac{\left(i(e^{iSt_2}-1) + St_2e^{iSt_2}\right)(1-\eta+\eta^2) + i(\eta-1)St_2^2e^{iSt_2}}{(\eta-1)^2 St_2}\right)}_{\text{Boundary Condition}}$$

$$+ \underbrace{2\left(\frac{(1-i\eta St_2)e^{i\eta St_2} - 1}{\eta(\eta-1)St_2^2} + \sigma^*\eta\frac{e^{i\eta St_2}(i+\eta St_2) - i}{(\eta-1)^2 St_2}\right)}_{\text{Flow non-uniformity}}$$

$$= 2\left(\frac{\eta - 1 + i(i+St_2)\eta e^{iSt_2} + (1-i\eta St_2)e^{i\eta St_2}}{\eta(\eta-1)St_2^2}\right)$$

$$- \underbrace{2\sigma^*\left(i\frac{\left(e^{i\,St_2}\left(\eta^2-\eta+1\right) - \eta e^{i\,\eta St_2} - (\eta-1)^2\right)}{(\eta-1)^2 St_2} - \frac{(\eta^2-\eta+1)e^{i\,St_2} - \eta^2 e^{i\,\eta St_2}}{(\eta-1)^2} + \frac{iSt_2e^{i\,St_2}}{(\eta-1)}\right)}_{\text{Stretch Contribution to Area fluctuation}}$$

(34)

The above results reduce to those previously developed by Schuller *et al.*[32] when σ^*=0 and the phase speed of the disturbances is equal to that of the mean flow (i.e. K=1) (note that they refer to St_2 as ω_* and α as $\mathrm{Cos}^2\alpha$).

Thus, the linear flame transfer functions for both the conical and wedge flames, Eqs. (31) and (34), depend upon three parameters: St_2 ,η and σ^*. It is useful to define a Strouhal number based upon the convective velocity (u_c) of the flow disturbances, St_c, which naturally arises in the two transfer functions (Eqs. (31) and (34)) and equals ηSt_2:

$$\eta St_2 = KSt = \left(\frac{u_o}{u_c}\right)\left(\frac{\omega_o L_F}{u_o}\right) = \frac{\omega_o L_F}{u_c} = St_c \quad (35)$$

These two Strouhal numbers are related to the amount of time taken for a flow (St_c) and flame front (St_2) disturbance (which is ultimately created by a flow disturbance) to propagate the flame length, normalized by the acoustic period. Before looking at the total flame transfer functions, it is useful to understand the relative contributions of the two sources: Area fluctuations (G_{Area}) and flame speed fluctuations (G_{SL}). The contribution of the area fluctuations can in turn be broken down into contributions from the boundary condition and flow forcing non-uniformities. Their ratio is given by:

$$\frac{G_{c,Area,Flow}}{G_{c,Area,BC}} = \frac{1-e^{i\eta St_2}+i\eta St_2}{\eta\left(e^{iSt_2}-1-iSt_2\right)} + \sigma^* St_2 \frac{\left(1-e^{i\eta St_2}+i\eta St_2\right)\left(e^{iSt_2}(i+St_2)-i\right)}{\eta\left(e^{iSt_2}-1-iSt_2\right)^2}$$

$$\frac{G_{w,Area,Flow}}{G_{w,Area,BC}} = \frac{(1-i\,\eta\,St_2)e^{i\eta St_2}-1}{\eta\,\left(1-(1-i\,St_2)e^{iSt_2}\right)} - i\sigma^* St_2 \frac{\left((1-i\,\eta\,St_2)e^{i\eta St_2}-1\right)\left(1+e^{iSt_2}(-1+iSt_2+St_2^2)\right)}{\eta\left(-i+(i+St_2)e^{iSt_2}\right)^2}$$

When σ^*=0, the magnitude of this ratio is identical for both wedge and conical flames, see Figure 37. The phase of this ratio is different for conical and wedge flames and plotted in Figure 38 and Figure 39, respectively.

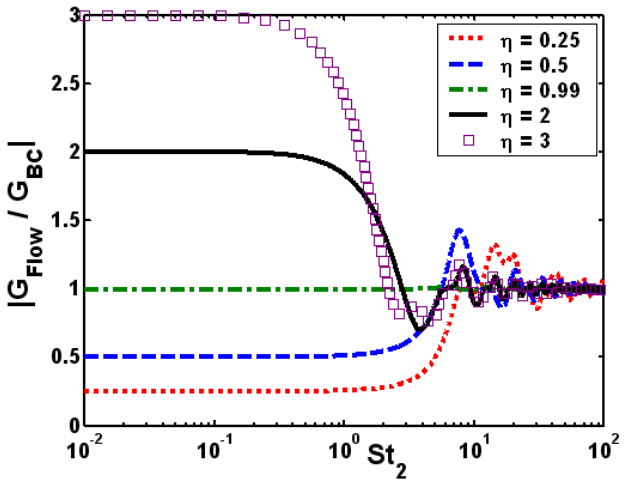

Figure 37. Strouhal number dependence of the magnitude of the ratio of the transfer functions due to the flow non-uniformity and boundary condition terms for different values of η, σ*=0

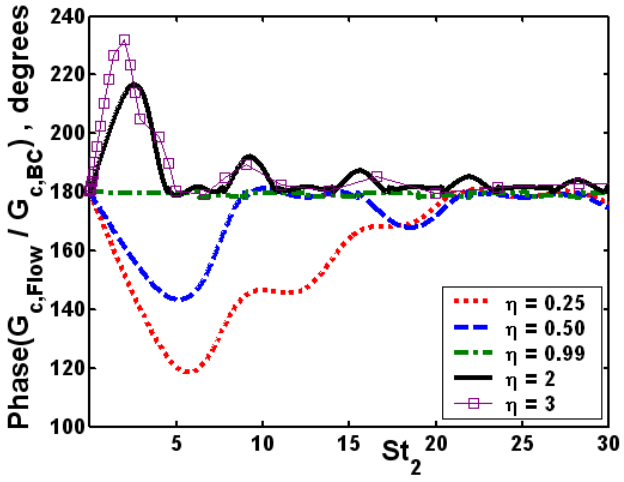

Figure 38. Strouhal number dependence of the phase of the ratio of the transfer functions due to the flow non-uniformity and boundary condition terms for conical flames for different values of η, σ^*=0

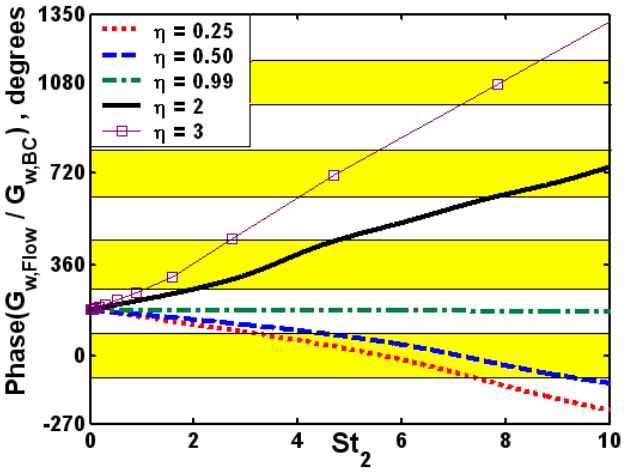

Figure 39. Strouhal number dependence of the phase of the ratio of the transfer functions due to the flow forcing and boundary condition terms for wedge flames. Shaded regions indicate points where boundary condition and flow non-uniformity terms are in phase, σ^*=0

It is instructive to analyze the characteristics of this ratio for limiting values of the parameters η and St_2. First, note that in the $\eta \to 0$ limit (i.e., a spatially uniform disturbance), the flame dynamics for both the wedge and conical flames is controlled exclusively by the boundary condition term, irrespective of the Strouhal number.

$$\lim_{\eta->0}\left(\frac{G_{c,Flow}}{G_{c,BC}}\right) = \lim_{\eta->0}\left(\frac{G_{w,Flow}}{G_{w,BC}}\right) = 0 \qquad (36)$$

This result can be anticipated from the discussion in the Introduction section and reflects the fact that only the homogeneous solution is excited when the flow disturbance is uniform.

In the $St_2 \to 0$ limit, the relative contribution of the two terms is determined by the value of the parameter η:

$$\lim_{St_2->0}\left(\frac{G_{c,Flow}}{G_{c,BC}}\right)=\left(\frac{G_{w,Flow}}{G_{w,BC}}\right)=-\eta \quad (37)$$

The boundary condition and flow forcing terms dominate when η<1 and η>1, respectively. For long flames (β>>1), this physically corresponds to situations where the disturbance phase velocity is greater than and less than the mean flow velocity, respectively. The two terms tend toward equal magnitudes when $\eta = 1$[‡]. These points can be clearly observed in Figure 37. Note also that the flow disturbance and boundary condition terms are 180º out of phase for low St_2 values see Figure 38 and Figure 39. In the intermediate Strouhal number range, say 1<St_2<10, either the flow forcing or the boundary condition may dominate depending upon η and St_2.

To understand the St_2>>1 limit, we need to consider stretch effects. The influence of stretch for wedge flames is illustrated quantitatively in Figure 40 wherein the transfer functions due to flow forcing and boundary conditions, normalized by their values in the absence of stretch (σ^*=0), are plotted as a function of the Strouhal number. As the Strouhal number increases, the length scale of wrinkling decreases, leading to curvature effects becoming prominent. The trends in Figure 40 indicate that contributions from the boundary condition term, $G_{w,Area,BC}$, are much more strongly affected than those due to flow non-uniformities, $G_{w,Area,Flow}$. Hence, stretch affects the flame response primarily through disturbances created at the anchoring point. This is also evident in Eq. (24) wherein the stretch effect on flame position is dominated by the term $\sigma^* St$ in $\zeta_{1,BC}$ whereas the contribution to the $\zeta_{1,Flow}$ is O~σ^*. A similar result holds for conical flames, although it should be noted that the conical flame transfer function is significantly less stretch sensitive than the wedge flame. This is due to the fact that stretch effects are more prominent at the flame tip, a region which contributes to the majority and negligible amount of the flame area for wedge and conical flames respectively.

In the limit of St_2>>1 (and σ^*=0), the contribution from both the boundary conditions and flow forcing term are equal, as shown in Figure 37:

$$\lim_{St_2->\infty}\left(\frac{G_{c,Area,Flow}}{G_{c,Area,BC}}\right)=-1-i\sigma^* St_2 e^{iSt_2}$$

$$\lim_{St_2->\infty}\left(\frac{G_{w,Area,Flow}}{G_{w,Area,BC}}\right)=-(1+\sigma^* St_2^2)e^{i(\eta-1)St_2} \quad (38)$$

[‡] Some care is required in analyzing this η=1 result, as the two terms tend to have equal magnitudes and are 180 degrees out of phase. The overall response is not zero, however, as the common denominator (η-1) in Eqs. (31) and (34), which has been cancelled out when taking their ratio, causes their sum to have a non-zero value.

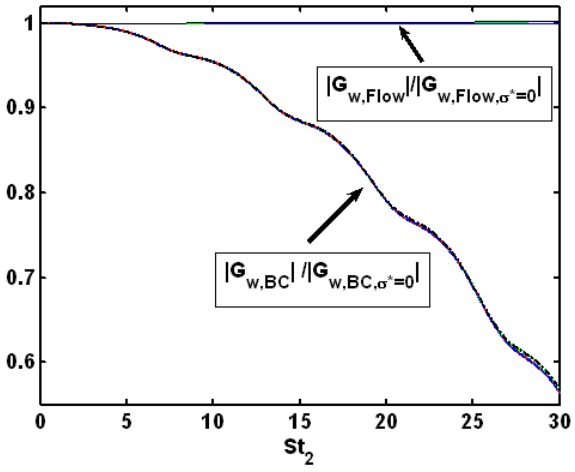

Figure 40. Effect of Stretch on the Strouhal number dependence of transfer functions due to flow non-uniformity and boundary condition terms for wedge flames, σ^*=0.0005

Equation (38) also shows that, in this limit, the relative magnitude contribution of these two terms is independent of η (assuming that the ηSt_2 product does not simultaneously go to zero). *Furthermore in the limit of* St_2>>1 and σ^*=0*, the two terms are always out of phase for conical flames irrespective of the Strouhal number and* η*,* as shown in Figure 38. In contrast, for wedge flames the phase difference between the two contributions monotonically increases with St_2, as shown in Figure 39 (the shaded bands in the figure indicate regions of constructive interference). Note that the above conclusion is modified in the presence of stretch. As discussed before in the case of wedge flames, stretch causes the contribution from the BC term to decrease with increasing Strouhal number. *Hence for wedge flames (which has an O~*$\sigma^* St_2^2$ *correction), in contrast to the* σ^**=0 case, the flow forcing term dominates over the contribution from the boundary condition at high Strouhal numbers*. Conical flames have a smaller stretch correction O~$\sigma^* St_2$ (see Eq (38)) and the response increases/decreases depending upon the Strouhal number.

To this point, the discussion has focused on contribution of the area fluctuations to the flame transfer function. Moving on to the contribution from the flame speed fluctuations (see Eqs. (31) and (34)), it can be shown that at low Strouhal numbers (where curvature effects are less), $G_{w,SL}$ and $G_{c,SL}$ tends to zero. The contribution reaches a maximum in the intermediate Strouhal number range (3<St_2<50) for a given η. Overall, the contribution from G_{SL} is insignificant in comparison to G_A for both conical and wedge flames for typical σ values (0.002-0.02), and is not considered further.

Flame area-velocity transfer function: overall features

The dependence of the magnitude and phase of the total conical flame transfer function $G_c(St_2,\eta,\sigma^*)$ upon St2 at several η values is plotted in Figure 41 and Figure 42, respectively. Consider the magnitude results first. As previously noted by Schuller et al.[32], at low Strouhal numbers the transfer function gain is identical in the cases

where η = 0 or 1 (this is not true at higher Strouhal numbers where stretch effects come into play). Physically, this corresponds to cases where the disturbance velocity is uniform, η=0 or its phase speed matches the flame front disturbance velocity, η=1. The gain transfer function differs for all other disturbance phase velocity cases. Note also that the gain value is always less than one and generally decreases monotonically with St_2, although there is some ripple at higher St_2 values due to constructive and destructive interference between $G_{c,Flow}$ and $G_{c,BC}$. The transfer function phase starts at zero degrees at low St_2 and initially increases monotonically with St_2. For the η=0 case, the phase tends to a limiting value of 90º for large St_2 (see Figure 42). In all other cases, the phase monotonically increases and for high values of η and St_2 the phase curves collapse into a single line.

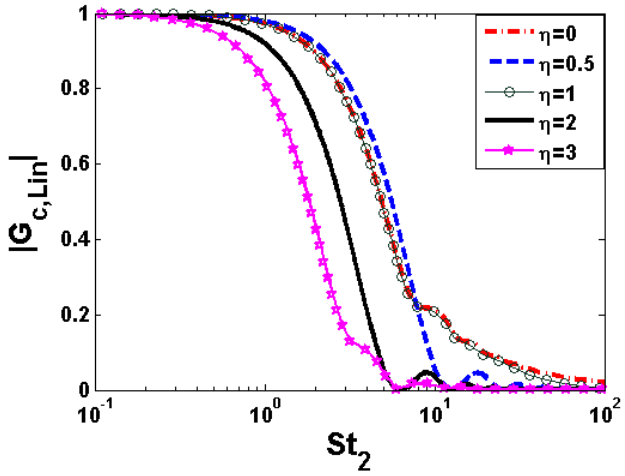

Figure 41. Axisymmetric conical linear transfer function $G_c(St_2,\eta)$ magnitude dependence upon the reduced Strouhal number (St_2) for different values of η, σ*=0.0005

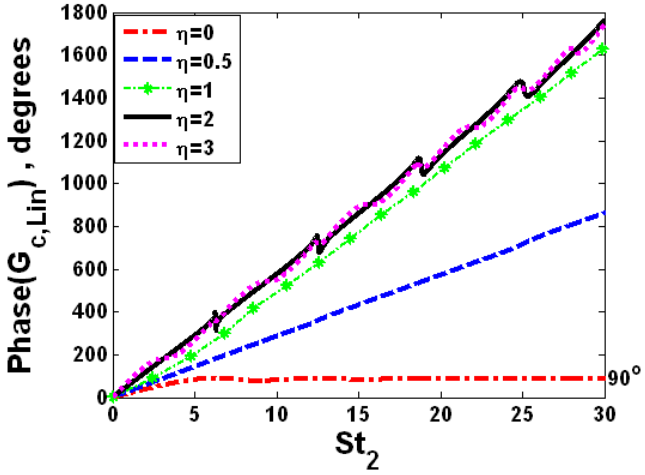

Figure 42. Axisymmetric conical linear transfer function $G_c(St_2,\eta)$ phase dependence upon the reduced Strouhal number (St_2) for different values of η, σ*=0.0005

For wedge flames, the gain and phase of the flame transfer function $G_w(St_2,\eta)$ are shown in Figure 43 and Figure 44 respectively. Note that, similar to conical flames, all gain values tend toward values of unity at low St_2. However, only in the uniform velocity case, η=0, does the gain then decrease with increases in St_2, as might be expected. In all other cases, the gain increases to values of greater than unity, due to the constructive superposition of $G_{w,Flow}$ and $G_{w,Bc}$. This amplification of the flame response over its quasi-steady value was previously predicted by Schuller *et al.*[32] and confirmed in measurements by Durox *et al.*[40]. The magnitude and St_2 value of the peak value of this amplification region is controlled by η. As shown in Figure 43, the magnitude of the peak value of G_w initially increases from unity as η increases with zero, reaches a maximum at η=1, and then decreases back to unity with further η increases. Note also from Figure 43 that the secondary maxima in the transfer functions appear at a lower St_2 values with increases in η. This behavior can be understood by noting that increases in η at a fixed St_2 is equivalent to an increase in the convective Strouhal number, $St_c=\eta St_2$. *In contrast to conical flames, stretch effects in wedge flames have a significant impact upon the high Strouhal number results,* $\lim_{St_2\to\infty} G_w = \frac{2i\sigma^* St_2 e^{iSt_2}}{1-\eta}$. Turning to the phase in Figure 44, note that the phase increases with St_2 with similar characteristics for all η values.

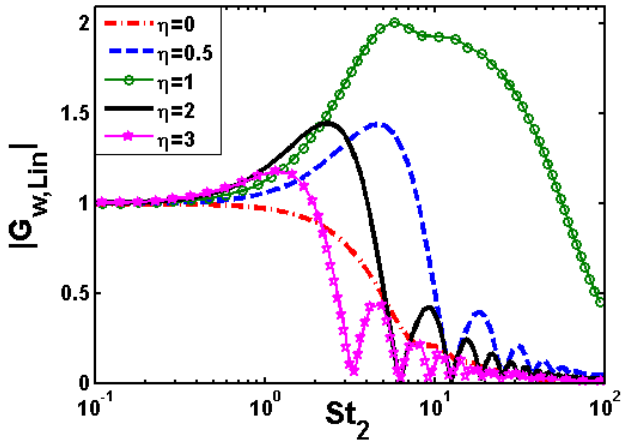

Figure 43. Axisymmetric wedge linear transfer function $G_w(St_2,\eta)$ amplitude dependence upon the reduced Strouhal number (St_2) for different values of η, σ^*=0.0005

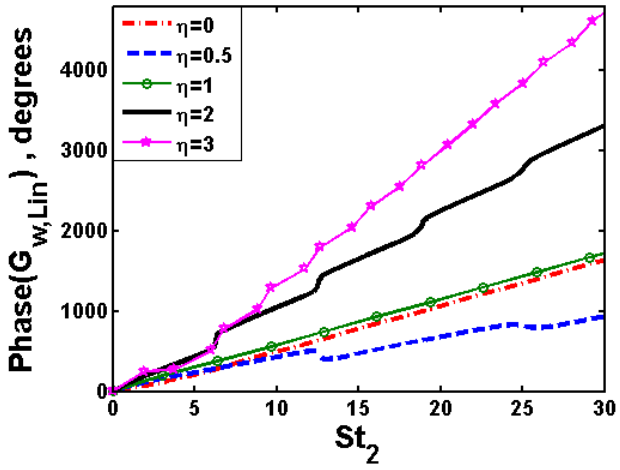

Figure 44 Axisymmetric wedge linear transfer function $G_w(St_2, \eta)$ phase dependence upon the reduced Strouhal number (St_2) for different values of η, σ^*=0.0005

As can be observed from Figure 41 and Figure 43, η (along with St_2) plays a significant role in determining the outcome of the competition between flow disturbance non-uniformity effects and boundary conditions. This fact is further highlighted in Figure 45 which shows, for a given Strouhal number, the value of the parameter η at which the maximum possible response occurs for conical and wedge flames. For conical flames in the range $0<St_2<8$, the maximum gain occurs at η=0.5 (see Figure 41 and Figure 45). For $St_2>8$, the maximum response occurs at two η values (η~0 and η~1) as shown in Figure 45. For wedge flames, the maximum possible gain for $St_2>5$ occurs at η=1 (see Figure 45). Note that for the η=1 case, the wedge flame acts as an amplifier for a wide range of St_2 values as shown in Figure 43. *It is interesting to note that, for any Strouhal number, the peak response for wedge flames always occurs for* $\eta \geq 1$; i.e. for cases wherein the phase speed of the disturbances is less than the mean flow speed. In contrast the *maximum gain for conical flames, at any Strouhal number, always occurs for* $\eta \leq 1$*;* i.e. for cases wherein the disturbances propagate faster than the mean flow speed.

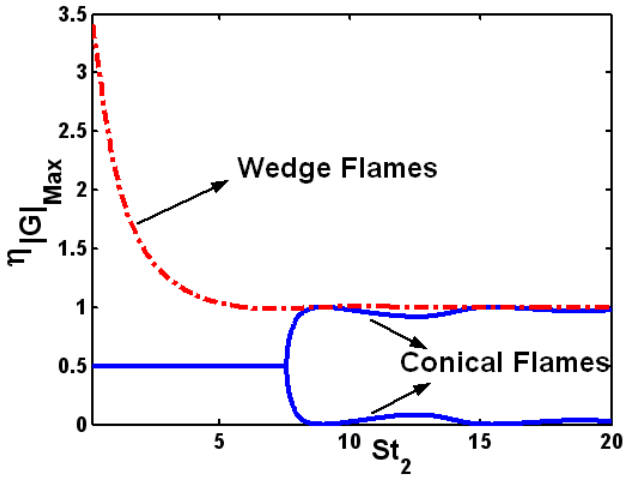

Figure 45. Strouhal number dependence of the parameter η at which the maximum possible linear response occurs for axisymmetric conical and wedge flames, σ*=0

Nonlinear Flame Dynamics

We turn our attention next to the large amplitude flame response. Before considering specific results in the nonlinear case, several general conclusions which can be obtained from analysis of the equations should be considered. Note that nonlinearities in the flame area response arise from three sources. The first is the nonlinear flame dynamics, through the term $\sqrt{1+\beta^2\left(\partial\zeta/\partial r\right)^2}$ in Eq. (13). The second is the static nonlinearity introduced through the dependence of the flame area upon flame position gradient through a term with the same form, $\sqrt{1+\beta^2\left(\partial\zeta/\partial r\right)^2}$, see Eqs. (30) and (33). In both of these cases, the nonlinearity is purely geometric in origin and is introduced by the relationship between the instantaneous flame front normal and flame position gradient. The third nonlinearity is due to the flow forcing itself, and is due to the dependence of the disturbance velocity at the flame front upon the flame position, *u(ζ,t)*.

The fact that the first two sources of nonlinearity are identical can be used to write the final expressions for the flame area, Eqs. (30) and (33), in a revealing form. By substituting Eq. (13) into Eqs. (30) and (33), the term $\sqrt{\left(1+\beta^2\left(\partial\zeta/\partial r\right)^2\right)/\left(1+\beta^2\right)}$ which appears in both the area integrals can be written as:

$$\sqrt{\frac{1+\beta^2\left(\dfrac{\partial\zeta}{\partial r}\right)^2}{1+\beta^2}}=u(\zeta,t)-\frac{\partial\zeta}{\partial t} \qquad (39)$$

Thus, *the explicit form of the nonlinearity disappears*. Nonlinearities in flame front dynamics are included in the $\partial\zeta/\partial t$ term (note that the flow forcing nonlinearities also effect $\partial\zeta/\partial t$, as shown in Eq. (13)), while those due to the flow forcing nonlinearity noted above are included in the *u(ζ,t)* term. Based upon Eq. (39), the following

observations can be made regarding the effects of various parameters upon nonlinearity in the flame's response to flow perturbations.

Strouhal Number: At low Strouhal numbers, *St*, the unsteady term in Eq. (39) is negligible. Moreover, the ζ dependence of the velocity field, $u(\zeta,t)$, is weak, at least for the velocity fields considered here. Thus, the flame area's velocity response remains linear for low Strouhal numbers, as *St* is the dimensionless ratio of the flame response time to perturbation period. This point shows that the flame's *nonlinear area response is an intrinsically dynamic phenomenon; its quasi-steady response is linear*.

Flow Uniformity: Nonlinearities in the $u(\zeta,t)$ term are directly due to non-uniformity in flow disturbances. Thus, the contribution of this term to flame area nonlinearities is suppressed in the $\eta\rightarrow 0$ limit.

Boundary conditions: If the flame remains anchored at the attachment point, as it is in this study, then $\partial\zeta/\partial t$ is identically zero at this point for all time. As such, the flame area perturbations in the vicinity of the attachment point (where $\zeta\approx 0 \Rightarrow u\approx u(0,t)$) exhibit a linear dependence upon velocity amplitude. Nonlinearities only arise at points of the flame that are spatially removed from the attachment point. As such, the axisymmetric conical flame exhibits a more linear response than the axisymmetric wedge flame for comparable values of ε, since most and very little, respectively, of the flame area is concentrated near the attachment point. This discussion also shows the potential coupling between the flame kinematic and flame holding sources of nonlinearity.

Flame Aspect Ratio: The flame dynamics tend to linearity when $\beta>>1$; i.e., when the flame is very long. This can be seen by noting that the left side of Eq. (13) becomes linear in this case: $\sqrt{1+\beta^2\left(\partial\zeta/\partial r\right)^2}=\pm\beta\,\partial\zeta/\partial r$. As such, the flame dynamics is approximately described by the equation $\frac{\partial\zeta}{\partial t}\pm\frac{\partial\zeta}{\partial r}=u(\zeta,t)$. In this case, the flame dynamics are linear, although the flow forcing term need not be. This discussion shows that β is an important nonlinearity parameter for this problem; i.e., the flame's area response can be anticipated to exhibit a linear dependence upon the perturbation velocity for much larger ε values at large β values.

Next, we derive an expression for the lowest order nonlinear correction to the flame area-velocity transfer function by determining the response of a flame to a disturbance with an arbitrary phase velocity. Stretch effects are not included here, but retained in the computations. Returning to the perturbation expansion for the flame position in Eq. (21), the following equations describe the dynamics of the second and third order correction terms, ζ_2 and ζ_3:

$$\frac{\partial\zeta_2}{\partial t}-\alpha\frac{\partial\zeta_2}{\partial r}+\frac{\alpha(1-\alpha)}{2}\left(\frac{\partial\zeta_1}{\partial r}\right)^2+\zeta_1 KSt\;\; Sin[\,St\{K(1-r)-t\}]=0$$

$$\frac{\partial\zeta_3}{\partial t}-\alpha\frac{\partial\zeta_3}{\partial r}+\frac{\alpha^2(1-\alpha)}{2}\left(\frac{\partial\zeta_1}{\partial r}\right)^3+\alpha(1-\alpha)\left(\frac{\partial\zeta_1}{\partial r}\right)\left(\frac{\partial\zeta_2}{\partial r}\right)+\frac{\zeta_1^{\,2}K^2St^2}{2}\;\; Cos[\,St\{K(1-r)-t\}] \qquad (40)$$
$$+\zeta_2 KSt\; Sin[\,St\{K(1-r)-t\}]=0$$

The solution of Eq. (40), subject to the boundary condition in Eq. (14), is given in Appendix C. In the ensuing discussion, we focus upon the total heat release response. Defining the conical flame area-velocity transfer

function at the fundamental frequency as $G_{c,\omega_o} = \dfrac{A_c'(\omega_o)/A_{c,o}}{u'(\omega_o)/u_o}$ yields:

$$G_{c,\omega_o} = G_{c,Lin} + \varepsilon^2 \left(\frac{\tilde{A}_{c,\omega_o}\, e^{i K\alpha St_2}}{8\ K\alpha^3\ (K\alpha-1)^5 St_2^2} + \frac{\tilde{B}_{c,\omega_o}\, e^{i St_2}}{8\ \alpha^2\ (K\alpha-1)^5 St_2^2} + \right.$$
$$\left. \frac{\tilde{C}_{c,\omega_o}\ K\ (\alpha-1)\ e^{i(2-K\alpha)St_2}}{8\ (K\alpha-2)^3\ (K\alpha-1)^5 St_2^2} + \frac{\tilde{D}_{c,\omega_o}\ K^2 e^{i(2K\alpha-1)St_2}}{8\ (2K\alpha-1)^2\ (K\alpha-1)^5 St_2^2} + \frac{\tilde{E}_{c,\omega_o}}{2K\alpha^3(K\alpha-2)^3(2K\alpha-1)^2\ St_2^2} \right)$$

(41)

where $G_{c,Lin}$ refers to the linear transfer function, Eq. (31) with σ^*=0. The coefficients $\tilde{A}_{c,\omega o}$ - $\tilde{E}_{c,\omega o}$ in this expression are defined in Appendix C.

Similarly, the wedge flame area transfer function is:

$$G_{w,\omega_o} = G_{w,Lin} + \varepsilon^2 \left(\frac{\tilde{A}_{w,\omega_o}\, e^{i K\alpha St_2}}{8\ K\alpha^3\ (K\alpha-1)^5 St_2^2} + \frac{\tilde{B}_{w,\omega_o}\, e^{i St_2}}{8\ \alpha^2\ (K\alpha-1)^5 St_2^2} + \right.$$
$$\left. \frac{\tilde{C}_{w,\omega_o}\ K\ (\alpha-1)\ e^{i(2-K\alpha)St_2}}{8\ (K\alpha-2)^3\ (K\alpha-1)^5 St_2^2} + \frac{\tilde{D}_{w,\omega_o}\ K^2 e^{i(2K\alpha-1)St_2}}{8\ (2K\alpha-1)^2\ (K\alpha-1)^5 St_2^2} + \frac{\tilde{E}_{w,\omega_o}}{2K\alpha^3(K\alpha-2)^3(2K\alpha-1)^2\ St_2^2} \right) \quad (42)$$

The coefficients $\tilde{A}_{w,\omega o}$ - $\tilde{E}_{w,\omega o}$ in Eq. (42) are defined in Appendix C.

The conical transfer functions evaluated using Eq. (41) are compared with numerical simulations (details of the numerical approach are given in Section 0) for a representative case in Figure 46. Although not shown, comparable results are obtained for wedge flames using Eq. (42). Non-linearity is enhanced as the velocity amplitude or the Strouhal number increases. As expected, the perturbation analysis is accurate at higher velocity amplitude when the Strouhal number is low.

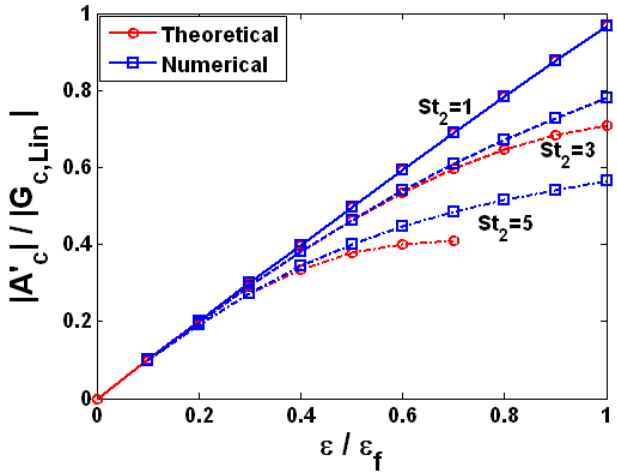

Figure 46. Dependence of flame area fluctuations upon disturbance velocity amplitude for axisymmetric conical flames at η=1

Note that, in the absence of stretch, the linear component of the transfer function in Eq. (41) and (42) is

described by only two parameters; i.e. $G_{Lin} = G(St_2, \eta)$. For the general nonlinear case, the gain G is also dependent on ε and β; i.e. , $G = G(St, K, \varepsilon, \beta)$. Also, as can be seen from the contribution of the non-linear terms to the transfer function in Eqs. (41) and (42), two new characteristic time scales arise which are represented by the non-dimensional terms: $(2\text{-}K\alpha)St_2 = 2St_2\text{-}St_c$ and $(2K\alpha\text{-}1)St_2 = 2St_c\text{-}St_2$. As discussed in the previous section, the linear transfer function can be explicitly decomposed into contributions from boundary conditions and flow forcing non-uniformities. The boundary conditions and flow non-uniformities give rise to the characteristic times represented by the terms containing St_2 and St_c, respectively. When the analysis is extended to the non-linear regime, the same conclusions can be reached regarding the origin of the time scales represented by the terms St_2 and St_c (the terms with the coefficients $\overset{\%}{B}_{\omega_o}$ and $\overset{\%}{A}_{\omega_o}$ in Eqs. (41) and (42)). In addition, the time scale represented by the terms $(2K\alpha\text{-}1)St_2$ and $(2\text{-}K\alpha)St_2$ arises as a result of the nonlinear interaction between these two sources of flame disturbance. Hence, to the order of approximation considered here, the nonlinear characteristics of the flame dynamics are controlled by the superposition of the flame disturbances represented by the terms: St_2, St_c, $2St_2\text{-}St_c$ and $2St_c\text{-}St_2$.

It is worth considering two limits: $K\to 0$ and $\eta = K\alpha \to 1$. In both the limiting cases, albeit for different reasons, there is a single characteristic time scale represented by the term St_2. Recall from the prior discussion that the flame dynamics in the uniform velocity case (K=0) are exclusively controlled by the boundary condition. In this case, the transfer function expressions reduce to:

$$\lim_{K\to 0} G_{c,\omega_o} = \frac{2\left(1 - e^{i\,St_2} + iSt_2\right)}{St_2^{\,2}} - \varepsilon^2\left(1-\alpha\right)\left(\frac{6\alpha + iSt_2 + 2i\alpha St_2 + e^{i\,St_2}\left(-6\alpha - iSt_2 + 4i\alpha St_2 + \left(\alpha - 1\right)St_2^2\right)}{4St_2^2\alpha^2}\right)$$

(43)

$$\lim_{K\to 0} G_{w,\omega_o} = \frac{2\left(-1 + e^{i\,St_2}\left(1 - iSt_2\right)\right)}{St_2^2} - \varepsilon^2\left(1-\alpha\right)\left(\frac{6\alpha\left(-1 + e^{i\,St_2} - iSt_2 e^{i\,St_2}\right) - 3\alpha St_2^2 e^{i\,St_2} + i\left(\alpha - 1\right)St_2^3 e^{i\,St_2}}{4St_2^2\alpha^2}\right)$$

(44)

Note that in the limit of long flames ($\alpha\to 1$), the non-linear contribution to the transfer function disappears for both conical and wedge flames. This result was anticipated in the discussion in the beginning of this section.

The limit of $K\alpha\to 1$, corresponds to exact coincidence of flame front and flow disturbance velocity leading to a case wherein all the previously discussed dimensionless time scales, $(2\text{-}K\alpha)St_2$, $(2K\alpha\text{-}1)St_2$ and $K\alpha St_2$, reduce to a single one represented by the term St_2. Figure 47 shows the variation of the non-linear part of the transfer function for wedge flames as a function of the Strouhal number when $K\alpha\to 1$ for different values of α. Expectedly, for low Strouhal numbers ($St\to 0$), the contribution from the non-linearities goes to zero. The presence of a single characteristic frequency St_2 implies the absence of any destructive interference effect leading to a monotonic increase in the nonlinear contribution with increasing Strouhal number. Moreover, the contribution to the gain is substantially enhanced as the flame gets shorter (i.e. lower values of α) consistent with the *Flame Aspect Ratio* argument in the introduction of this section.

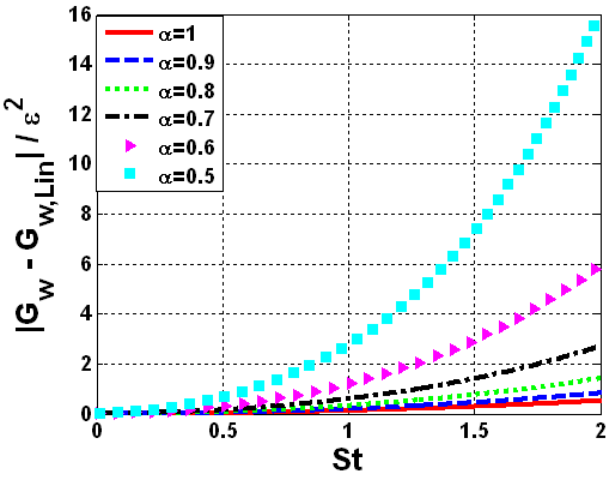

Figure 47. Dependence of non-linear part of the transfer function for axisymmetric wedge flames at η=1

Hence the presence of a single characteristic time scale, for the uniform velocity (K=0) and the $\eta=K\alpha\rightarrow 1$ case, causes the nonlinear contribution to monotonically increase with increasing Strouhal number and/or decreasing flame aspect ratio. As discussed further below, *it is only for these two cases that the non-linearities always lead to a reduction in the magnitude of the total transfer function*. These conclusions are valid even at higher velocity amplitudes as shown by numerical simulations in Figure 48-Figure 51 which plot the St_2 dependence of the gain and phase of the nonlinear transfer function upon St_2 at several η values. The gain transfer functions are normalized by their linear values, G/G_{Lin}. Results are shown for two convective wave speeds, η=0 and η=1, but the same β=1 value. Thus, these results allow for a convenient comparison of the effects of nonlinearities from boundary conditions alone, and the combined effect of boundary conditions and flow disturbance non-uniformity. Consider the gain curves first, Figure 48 and Figure 50. As predicted earlier, the response tends to its linear value in all cases at low St_2. In the η=0 case, nonlinear effects are more apparent at high St_2. For the wedge flame in Figure 50 the response is considerably nonlinear even at moderate values of Strouhal number. The enhanced nonlinear response of wedge over cone flames is explained by the *Boundary Conditions* argument discussed earlier.

Turning to the η=1 case, note the substantial reduction in flame area relative to its linear value; i.e., there is a substantial degree of gain saturation. Although plotted in a different form, the resulting gain curves look quite similar to the qualitative plot of $H_n(A)$ in **Figure 29**. In agreement with the *Strouhal Number* argument discussed earlier, the degree of nonlinearity increases with St_2. As shown in Figure 48 and Figure 50, the gain for the conical and wedge flames decreases by about 60% and 70% respectively (at $\varepsilon=\varepsilon_f$ in the St_2= 20 and η= 1 case). In contrast, the gain never drops below 5% of its linear value for conical flames and 35% of its linear value for wedge flames in the η=0 case. Moreover, unlike the η=0 case, the phase of the area response for both the conical and wedge flames exhibits a strong amplitude dependence, as shown in Figure 49 and Figure 51 respectively. These results indicate the extent to which flow non-uniformities can significantly modify the nonlinear flame response.

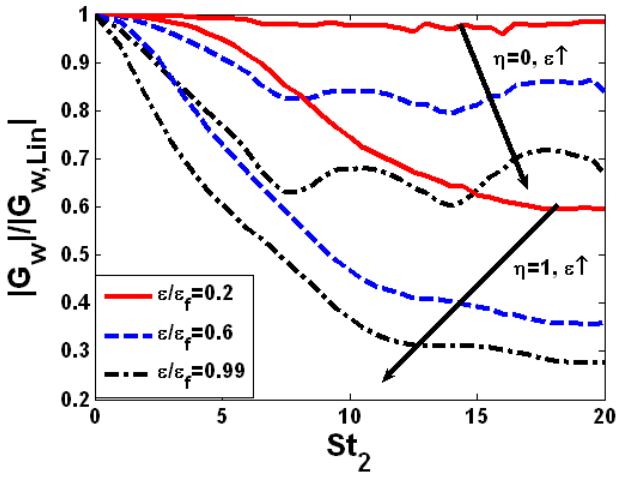

Figure 48. Strouhal number dependence of the ratio of the magnitude of the flame area-velocity transfer function to its linear value for the axisymmetric wedge flame, β=1, σ^*=0.005

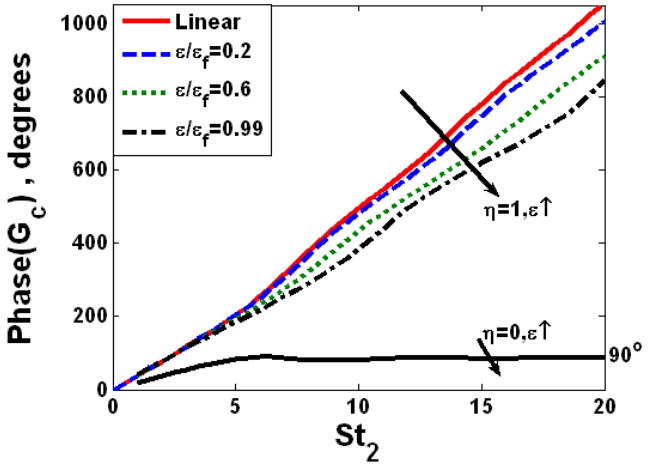

Figure 49. Strouhal number dependence of the phase of the flame area-velocity transfer function for the axisymmetric conical flame, β=1, σ^*=0.005

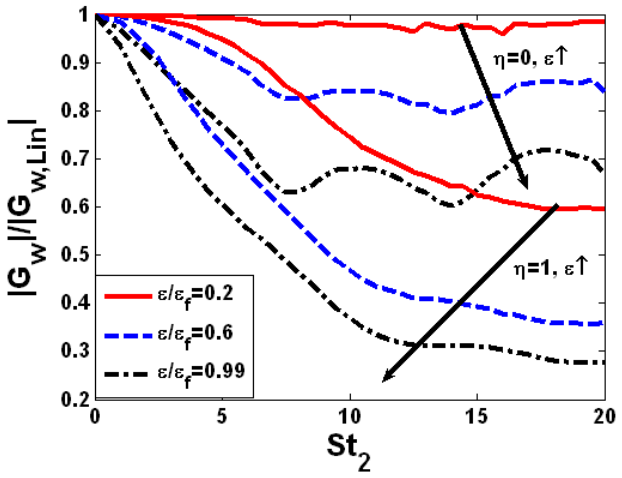

Figure 50. Strouhal number dependence of the ratio of the magnitude of the flame area-velocity transfer function to its linear value for the axisymmetric wedge flame, β=1, σ*=0.005

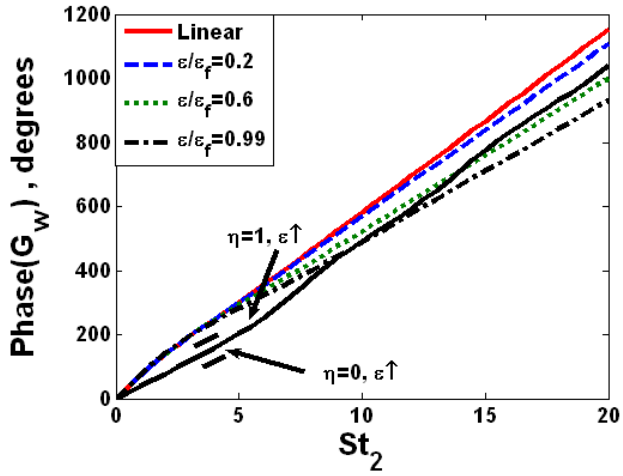

Figure 51. Strouhal number dependence of the phase of the flame area-velocity transfer function for the axisymmetric wedge flame, β=1 , σ*=0.005

In the more general case of $\eta \neq 0$, 1, the nonlinear flame dynamics is controlled by the superposition of flame disturbances with the four different characteristic time scales discussed earlier. In contrast to the above results, interactions between the boundary condition and flow forcing non-uniformity solutions causes a non-monotonic variation in the transfer function gain with disturbance amplitude. To illustrate, Figure 52 shows the flame response for a wedge flame when $\eta=2$ (i.e. $\alpha=0.8$ and disturbances are traveling at $0.4u_o$). Note that the gain results are not normalized by their linear value here. The gain result indicates that in the $5<St_2<8$ range, the nonlinear transfer function actually *exceeds* its linear value. This result can be understood by noting that this behavior occurs in the vicinity of the regions where the linear transfer function achieves a minimum. At these St_2 values, the contributions from the boundary conditions and the flow forcing terms destructively interfere, leading to low linear gains. As the velocity amplitude is increased, nonlinearities cause the gain due to both the boundary conditions and the flow

forcing terms to decrease. However, since the relative "ages" of the two disturbances are unequal, the discussion in the context of Figure 32 shows that the magnitude of their gain reductions is different. Since the individual gain decreases by different amounts, the total gain does not go to zero at the St_2 value at which the linear gain is zero, but actually shifts to a higher St_2 value in the ε=0.2ε_f case. At higher disturbance levels, the two terms never exactly cancel and the gain does not go to zero. Rather, there is a monotonic decrease in the gain of the transfer function with increase in velocity amplitude. Analogous behavior also occurs in conical flames, although less dramatically.

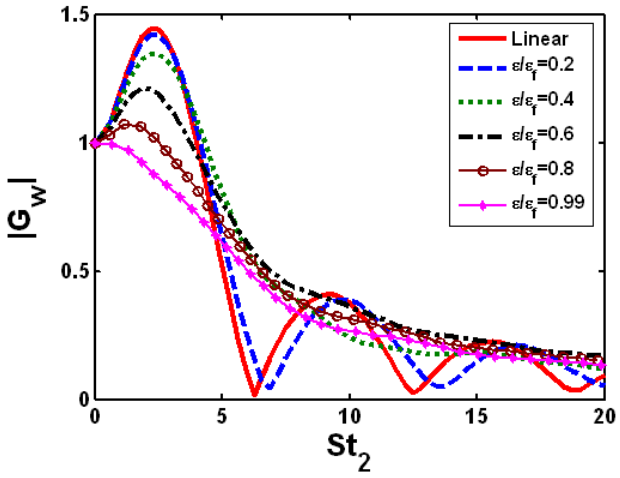

Figure 52. Strouhal number dependence of the magnitude of the flame area-velocity transfer function for the axisymmetric wedge flame, α=0.8,K=2.5, σ*=0.005

These predictions can be compared to related measurements on wedge flames, where the phase speed of the disturbances was half the mean flow speed40. They obtained measurements at four forcing amplitudes ε~0.05-0.2 and β~5.6. Interestingly, they found both increases and decreases in the transfer function gain with changes in disturbance amplitude, depending upon Strouhal number. Their results are reproduced in Figure 53. The transfer functions plotted here equals the ratio of the fluctuating CH^* emission intensity to the velocity disturbance amplitude slightly above the burner exit. Note the strong similarities between their measurement and the predictions from Figure 52. In the $2<St_2<5$ regions where the transfer function exceeds unity, the nonlinear gain monotonically decreases with disturbance amplitude. In the $5<St_2<8$ range, the nonlinear transfer function first increases with disturbance amplitude, then decreases. This trend is completely consistent with the predictions of this study.

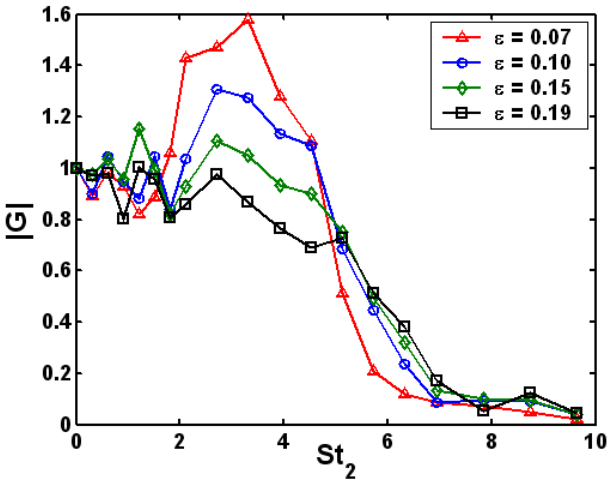

Figure 53. Experimentally measured gain for an inverted conical flame for a mean velocity u_o= 2.05 m/s, ϕ = 0.92. Data reproduced from Durox *et al.*[40].

Using the perturbation analysis, the non-linear contribution to the wedge flame transfer function is shown for varying phase speeds at unity Strouhal number in Figure 54. *It shows that the non-linear contribution is higher when the phase speed of the disturbances is less than the mean flow speed (i.e. K>1)* in comparison to the case wherein 0<*K*<1. This is a direct manifestation of the *Flow Uniformity* argument discussed earlier. As noted earlier, non-linearity decreases with increase in the flame aspect ratio (i.e. increasing α), consistent with the *Flame Aspect Ratio* argument. Note that this result is valid for a low Strouhal number case wherein the interaction between the disturbances of different characteristic time scales is weak. The results for a general case are shown in Figure 55 which plots the gain dependence upon η at different St_2 values for conical flames. For the St_2=1 case, the linear gain does not go to zero for both the conical and wedge flames (not shown here). Hence, the gain monotonically decreases with increasing disturbance amplitude. However in the St_2 = 5 and 10 cases, the linear gain goes to zero at certain η values. It is only in the vicinity of this η that we find the corresponding increase in nonlinear flame transfer function. This result prominently highlights the sensitivity of the flame response to the phase speed of the disturbances. Moreover, it demonstrates how the competition between boundary condition and flow nonuniformity terms can significantly impact the flame response behavior.

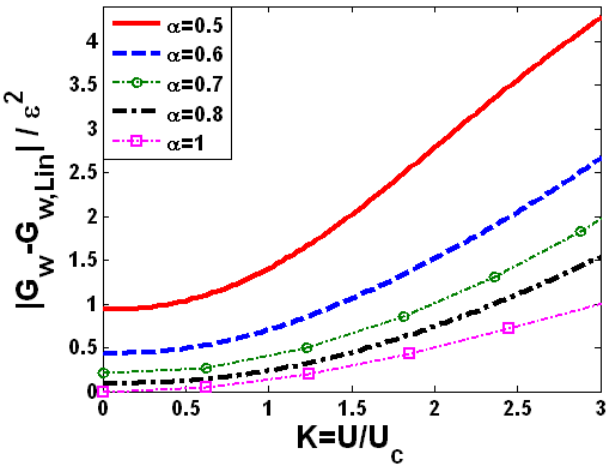

Figure 54. Dependence of non-linear part of the transfer function on the phase speed of the disturbances (K) for axisymmetric wedge flames, St=1, σ=0

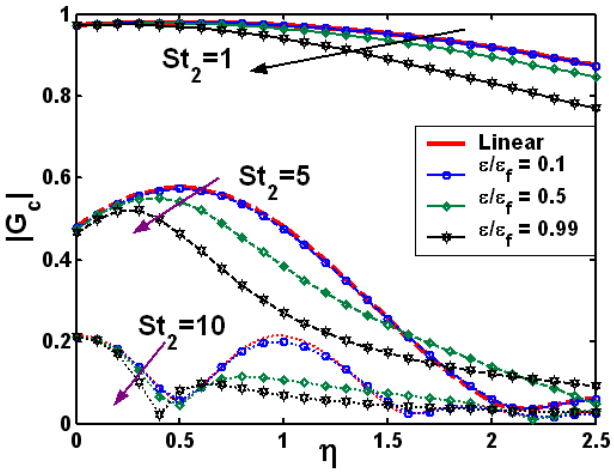

Figure 55. Dependence of the magnitude of the flame area-velocity transfer function on η for the axisymmetric conical flame for different Strouhal numbers, β=8, σ=0. Arrow points towards increasing velocity amplitude ε.

These results have important applications in the type of bifurcations which may be observed in unstable combustors. In situations where the gain curves resemble that qualitatively shown in **Figure 29**, only supercritical bifurcations will occur and a single stable limit cycle amplitude, ε_{LC} is possible. In situations where the gain exceeds, then is less than, the linear gain (see Figure 52); i.e., it exhibits an inflection point, multiple stable solutions for the instability amplitude may exist, and sub-critical bifurcations are possible. This can be seen from Figure 56, which plots the dependence of $A_w'/A_{w,o}$ vs ε for St_2=6.25, K=2.5, α=0.8. This curve represents $H(\varepsilon)$. A hypothetical damping curve, $D(\varepsilon)$ is also drawn in Figure 56. Note the 3 intersection points, two of which are stable, ε=0 and $\varepsilon=\varepsilon_{LC}$, and one of which is unstable, $\varepsilon=\varepsilon_T$. In this case two equally valid solutions are possible, ε=0 or $\varepsilon=\varepsilon_{LC}$, which one the system is actually at depends upon initial conditions. Such a system will manifest characteristics such as hysteresis and triggering (i.e., the destabilization of a linearly stable system by a sufficiently large disturbance[81]).

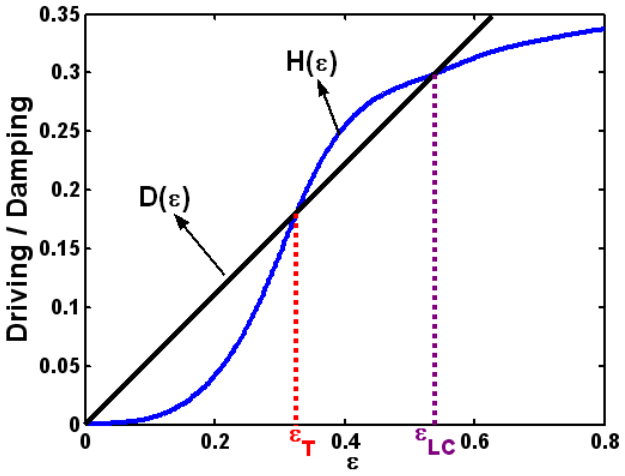

Figure 56. Dependence of acoustic driving, H(ε) (where H(ε) is equated for this example to $A_w'/A_{w,o}$) and damping, D(ε), processes upon velocity amplitude ε, for wedge flames at St_2=6.25 with K=2, α =0.8, σ^*=0.005

The regions in parameter space (defined by K and St_2), where the nonlinear transfer function has an inflection point can be determined from the analytical solutions and is shown in Figure 57. The plot shown is for a wedge flame with an aspect ratio α=0.8, ε=0.1. *Note that an inflection point is more likely to exist when the phase speed of the disturbances is less than the mean flow speed (K>1) in comparison to the case wherein 0<K<1.* This is in accordance with the earlier discussion which showed that non-linear effects were enhanced for K>1. *For the uniform velocity, K=0, and the Kα=1 case, the presence of a single characteristic time scale causes a monotonic decrease in the transfer function with increasing velocity amplitude, implying that it will always exhibit a supercritical type of bifurcation (see* Figure 57*).*

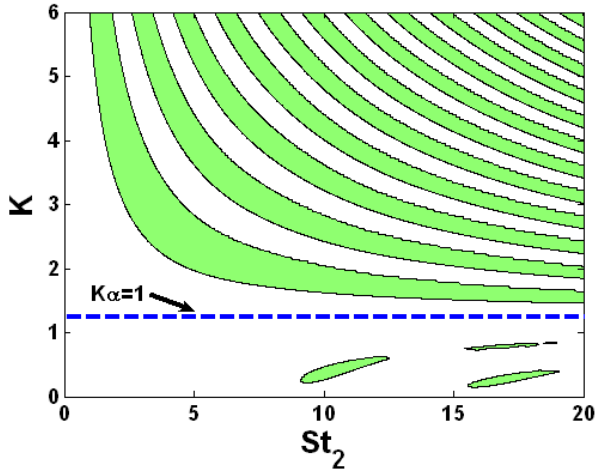

Figure 57. Qualitative representation of regions where nonlinear flame transfer exceeds (shaded) or is less than (white) linear transfer function, α=0.8,ε=0.1, σ=0

We next consider the combined effects of nonlinearity and stretch. Figure 58 plots the amplitude dependence of the wedge flame transfer function for cases with and without stretch. While the qualitative

dependence of the transfer function upon amplitude remains the same with or without stretch, note that the combined effects of stretch and nonlinearity draw the two curves closer together with increasing ε. Thus, stretch effects upon the *global* flame area dynamics become *less* significant with increasing amplitude. The reason for this is the following: stretch is most significant in the high curvature, concave regions of the flame with respect to the reactants. As the perturbation amplitudes increases, these regions become highly cusped, and have a progressively smaller influence upon the total flame area. Thus, while the effect of stretch becomes more significant in certain regions of the flame with increasing ε, these regions of the flame also occupy a progressively smaller fraction of its total flame area.

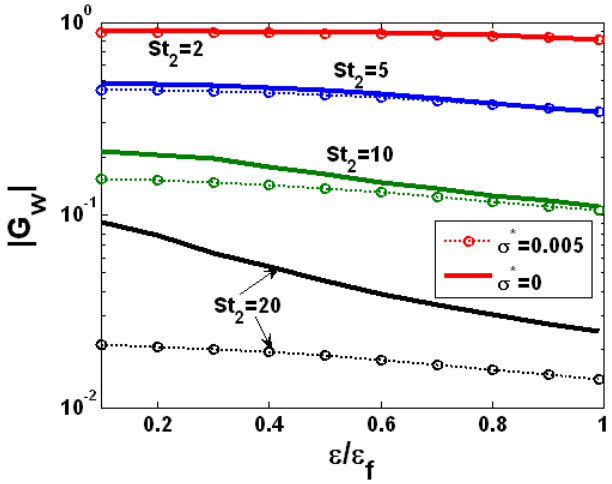

Figure 58. Amplitude dependence of the magnitude of the flame area-velocity transfer function for an axisymmetric wedge flame: Comparison between models with and without Stretch effects. β=1, K=0

Finally, a brief comment on the response of the flame at the first harmonic of the forcing frequency. The previous discussion about the role played by the phase speed of the disturbances, Strouhal number and the flame aspect ratio upon nonlinearity in flame response is directly applicable here as well, since excitation of harmonics is another manifestation of nonlinearity. These results are not discussed here, but analytical expressions for the flame response at $\omega = 2\omega_o$ are provided in Appendix E.

Flame Length

The changes in the average flame characteristics (such as its location and length) with increasing disturbance amplitude have been reported in many experimental studies[27,42,45]. These changes are indicative of non-linear effects and have potentially important effects upon the flame transfer function phase because they change the time delay between when a disturbance is created and when it encounters the flame. For example, Bellows *et al.*[45] observed a monotonic increase in the velocity-CH* chemiluminescence transfer function phase with disturbance amplitude and suggested it was due to the corresponding increase in flame length (however, note that this study was for a swirling flame).

Using the perturbation analysis, the average flame length normalized by its steady state value, L_f can be

expressed as:

$$L_{avg} = 1 + \varepsilon^2 \frac{\left(\alpha\left(K\alpha - 1\right)\left(-1 + \alpha + 2K\alpha + (\alpha - 3)K^2\alpha^2\right)St_2 + 2\alpha^3 K\left(K - 1\right)Sin[\left(K\alpha - 1\right)St_2]\right)}{4\alpha^3 (K\alpha - 1)^3 St_2} \quad (45)$$

As shown in Eq. (45), the contribution of the non-linearities to the flame length is a function of the velocity amplitude, flame aspect ratio, Strouhal number and the phase speed of disturbances i.e. $L_{avg}=L_{avg}(\varepsilon,\alpha,St,K)$. In order to highlight the effect of each of these terms, we consider various limits. In the limit of $K\alpha\rightarrow 1$, Eq. (45) reduces to:

$$\lim_{K\alpha->1} L_{avg} = 1 - \varepsilon^2 \frac{(1-\alpha)(3+St_2^{\,2})}{12\alpha^2} \quad (46)$$

Eq. (46) predicts that L_f decreases with increasing Strouhal number (note that $\alpha<1$) and velocity amplitude. Moreover this effect is amplified with decreasing flame aspect ratio, α.

In the limit of low Strouhal numbers, the average flame length can be expressed as:

$$\lim_{St->0} L_{avg} = 1 - \varepsilon^2 \frac{(1-\alpha)}{4\alpha^2} \quad (47)$$

Equation (47) indicates that, at low Strouhal numbers, the average flame length is a function of only ε and flame aspect ratio and *is independent of the phase speed of the disturbances (K) and frequency (St)*. Moreover if the flame is long (i.e. $\alpha\rightarrow 1$), the effect of non-linearities disappear (see Eq. (47)) and the average flame length remains constant.

Another interesting feature is that for uniform disturbance velocity (K=0), or when the phase speed and mean flow speed are equal (K=1), *the average flame length is independent of the Strouhal number*, i.e.:

$$\lim_{K->0} L_{avg} = \lim_{K->1} L_{avg} = \lim_{St->0} L_{avg} \quad (48)$$

Next we consider the case of long flames (i.e. $\alpha\rightarrow 1$). For this case, the flame length expression can be simplified to:

$$\lim_{\alpha->1} L_{avg} = 1 - \varepsilon^2 K\left(\frac{\left(K-1\right)St_2 - Sin[\left(K-1\right)St_2]}{2(K-1)^2 St_2}\right) \quad (49)$$

Figure 59 plots the normalized flame length (Lavg) as a function of the phase speeds at different Strouhal numbers when $\alpha\rightarrow 1$. It can be inferred from Figure 59 that the flame length decreases with increased disturbance amplitudes when the phase speed of the disturbances is smaller than the mean flow speed (K>1). This conclusion is true in general (i.e. is not limited to long flames only) as shown in Figure 60, which plots the contours of constant Lavg as a function of St2 and K for a range of α. For a given flame aspect ratio α, the arrows in Figure 60 indicate regions in the parametric space (defined by St2 and K) wherein the average flame length increases. Note that it is only for fast phase speed disturbances (0<K<1) that the flame length actually increases for certain values of St2 (see Figure 60) and this effect is amplified at higher α. When the phase speed of the disturbances is smaller than the mean flow speed (K>1), the average flame length always decreases.

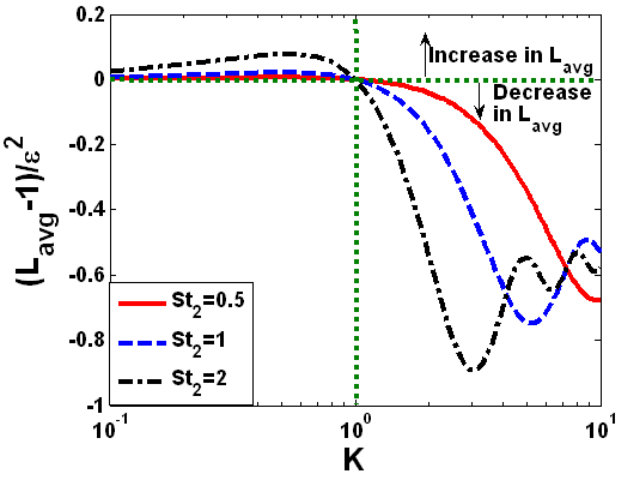

Figure 59. Dependence of flame area fluctuations upon disturbance velocity amplitude for axisymmetric conical flames at η=1

The discussion above is in conformity with experiments reported by Durox et al.[27], wherein a reduction in the average flame length was observed with increased velocity amplitudes. Their experiments were conducted at a frequency of 1000 Hz, α ~0.5 and a range of velocity amplitudes. The present analysis indicates (see Figure 60 which shows that α~0.57 is the lowest value for which the flame length may increase) that for α~0.5, the average flame length always decreases irrespective of the frequency and phase speed of the disturbances. Similar agreement is obtained with the results of Bourehla & Baillot[25] under conditions where their measured velocity profiles are similar to those considered here. These conditions correspond to K~1-2, St2~8-12 and K=0, St2>23.

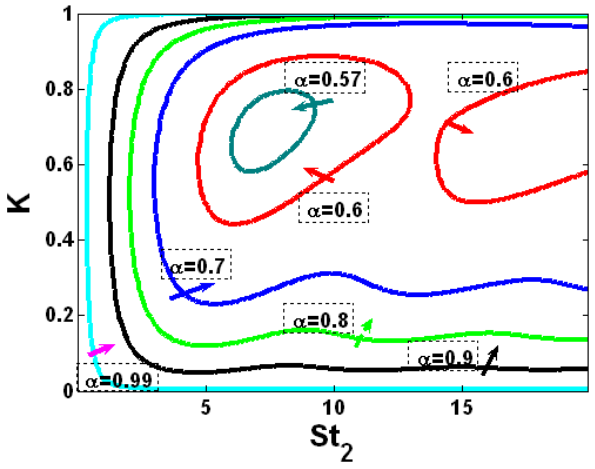

Figure 60. Contours of constant L_{avg} (average flame length) as a function of K and St_2 for different values of α. Arrows indicate regions of increasing flame length.

8. Nonlinear Interactions in Gas Turbine Combustors

Nonlinear Heat-Release/Linear Acoustic Interactions

It has been argued that the dynamics of an unstable combustor are dominated by heat release nonlinearities which interact with linear acoustic processes. Because the combustor is a reverberant acoustic environment, it possesses a number of acoustic modes. Many researchers (e.g., see Culick[14], Zinn & Powell[12], Culick & Yang[82]) have shown that the dynamics of each mode may be described by an oscillator equation of the form:

$$\ddot{\eta}_i + 2\zeta\omega_o\dot{\eta}_i + \omega_o{}^2\eta_i = F(\eta_i, \dot{\eta}_i) + E(t) \tag{1}$$

where ω_o is the linear natural frequency, ζ is the damping coefficient, $F(\eta_i, \dot{\eta}_i)$ refers to the system nonlinearities, and $E(t)$ is the external excitation.

Before presenting further data, we briefly summarize several classical results for a nonlinear system that is externally forced at a frequency near resonance, i.e. $E(t) = A\cos\omega t$, where $\omega \approx \omega_o$. Consider first nonlinearities in "stiffness", i.e. $F = F(\eta_i)$. It is well known that such a system exhibits "bending" in the frequency response curve, such as shown in Figure 61(a). As such, the frequency of the maximum oscillator response shifts with frequency; e.g., increases/decreases in the effective stiffness with increasing disturbance amplitude cause the curve to bend toward higher/lower frequencies. As the frequency of the large amplitude excitation is swept, the response of the nonlinear system follows one branch of the curves to a bifurcation point where the system jumps discontinuously to the other branch. This manifests itself in hysteresis in frequency and amplitude where this jump occurs.

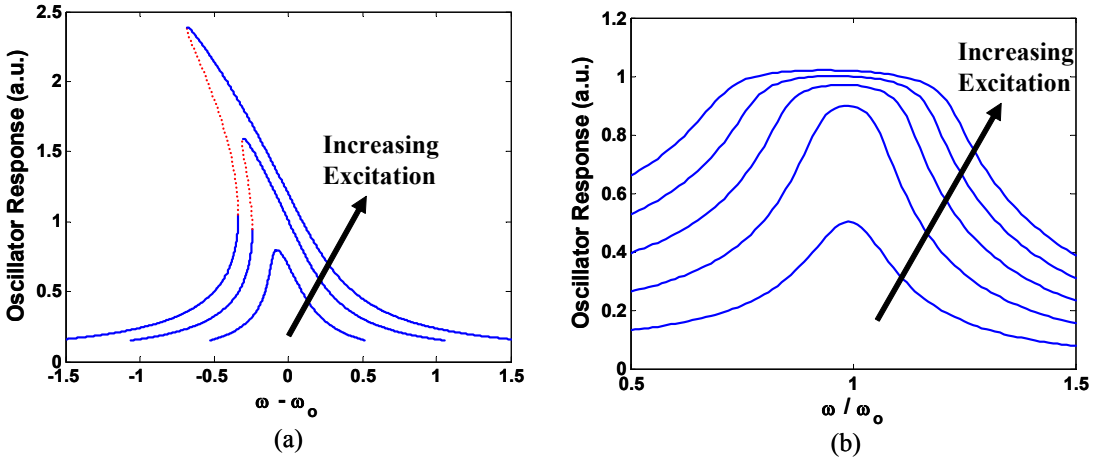

Figure 61: Frequency–response curves at several excitation amplitudes for a second order oscillator with nonlinearities in (a) stiffness and (b) damping

Consider next nonlinearities in damping, i.e., $F=F(\dot{\eta}_i)$. The peak amplitude of this type of nonlinear

system will not increase proportionally to the disturbance amplitude. If damping grows nonlinearly, amplitude saturation causes a flattening of the response curve around the resonant frequency. Therefore, the maximum response is distributed over a broader range of frequencies than a linear damped oscillator, e.g, see the example in Figure 61(b). Further details are in Nayfeh & Mook[83].

Both types of behavior illustrated in Figure 61 were observed in our data. These data were obtained in the gas turbine combustor simulator discussed previously and shown in Figure 2. A representative result is shown in Figure 62(a), which plots the frequency dependence of the pressure amplitude at a large disturbance amplitude. This data is obtained by keeping the driving amplitude constant and varying the driving frequency. Figure 62(a) shows that the pressure amplitude response bends over to the left indicative of a "softening" spring. Second, the pressure amplitude jumps in the 285-290 Hz range, with hysteresis in the frequency value where this jump occurs. Third, the peak response of the pressure remains relatively constant over a range of driving frequencies, indicating nonlinearity in damping. This behavior can be seen more clearly in Figure 62(b), which plots similar results at several driving amplitudes. The plot clearly shows the progressive trend away from a classical forced-resonant linear system at low disturbance amplitudes to a response that bends over toward lower frequencies and "flattens" in response.

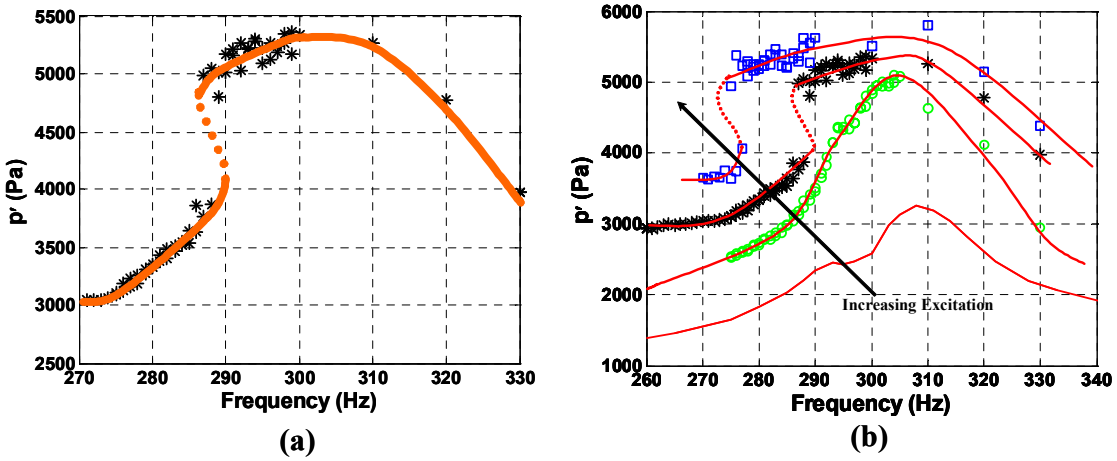

Figure 62: Dependence of pressure amplitude upon frequency at (a) a single disturbance amplitude, 2.8A and (b) several disturbance amplitudes, 1.8-3.0A (ϕ = 0.95).

If the forcing frequency is held constant, while the excitation amplitude is varied, a similar bifurcation occurs as shown in Figure 63. Figure 63 shows that the pressure oscillation data have a similar dependence on frequency. As noted above, the linear natural frequency is approximately 310 Hz. At 280 Hz there is a noticeable jump in the pressure response. At frequencies below and above 310 Hz, the pressure response exhibits a "quadratic" and "square root" dependence upon excitation amplitude.

Referring back to Figure 9(a), note the clear saturation of the CH*-velocity transfer function at 280 Hz. Referring to the specific data points, note that a clear "gap" in the velocity amplitude is observed at a point coinciding with that where saturation is observed. It should be noted that the driving levels were increased in a regular, stepwise fashion over the whole range of amplitudes. This jump in the velocity coincides with the jump in

pressure amplitude illustrated in Figure 64(a); i.e. the jump in pressure and velocity coincides with the point where the heat release response exhibits nonlinearity.

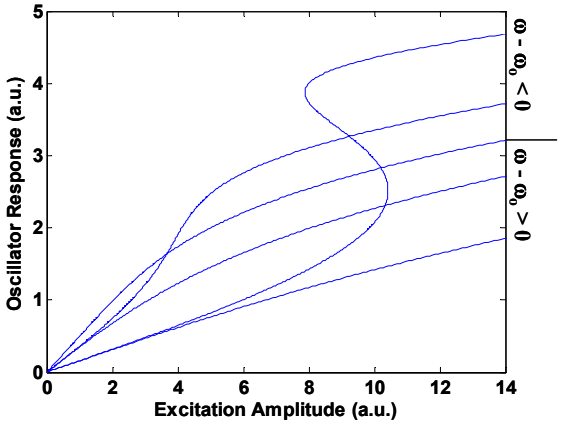

Figure 63: Excitation–response curves for softening spring oscillator at several excitation frequencies.

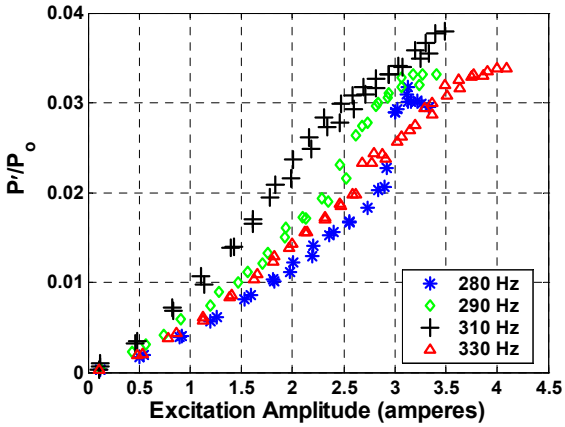

Figure 64: Dependence of pressure oscillation amplitude on excitation amplitude for varying driving frequencies ($\phi = 0.95$)

A detailed study of this bifurcation and the associated hysteresis was performed in the 280-290 Hz frequency range. Figure 65 summarizes the amplitude-frequency parameter regions where single and multi-valued behaviors occur. Hysteresis occurs at driving amplitudes larger than about 2.6 Amperes (A) and extends all the way to 3.1A, where blowout occurred. The corresponding frequencies range from 292 to 276 Hz at the low and high amplitude driving ranges.

Figure 66 provides a further visualization of this bifurcation by quantifying the CH* - pressure transfer function as a function of frequency at fixed driving amplitudes (we illustrate the CH*-pressure relationship here due to the fact that the uncertainty values are smaller than those for the velocity measurements; the trends, however, are identical). The figure plots these dependencies at both a low and high driving amplitude of 2.4 and 3.0 Amperes.

For low driving amplitudes, the transfer function exhibits a smooth, monotonically decreasing dependence upon frequency, as would be anticipated by the results shown in Figure 5. However, when the driving amplitude is increased beyond the cutoff point of 2.6 amperes, the transfer function changes markedly. This result is illustrated in Figure 66(b) where a clear jump in the transfer function values occurs (~14% for the CH*-pressure transfer function value) for the 3.0 Amperes driving case. Note that the frequency dependence of the transfer function is much "flatter" in the high driving case. The frequency where the jump occurs depends upon the direction of frequency change (increasing/decreasing) with a total hysteresis of about 3 Hz. Note that the transfer function itself does not exhibit a discontinuous dependence upon amplitude; rather the pressure amplitude exhibits a discontinuity in the region where the transfer function changes. This transfer function change is responsible for the bifurcation in pressure amplitude. As such, it is not possible to measure a monotonic change in the transfer function at these frequencies because of the discontinuous jumps that occur in acoustic amplitude. A similar result is found in the corresponding phase relationships.

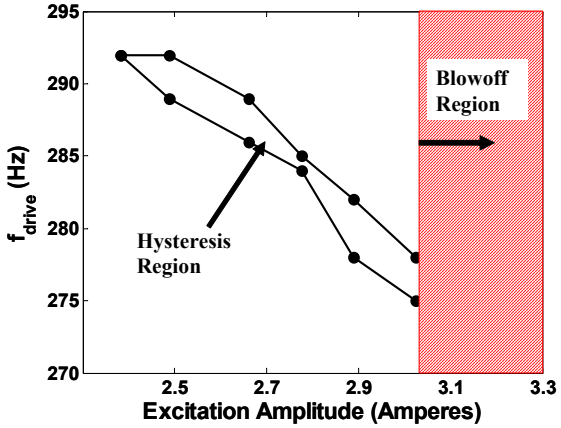

Figure 65: Amplitude-frequency ranges over which the chemiluminescence-pressure-velocity relationship exhibited single and multi-valued behavior

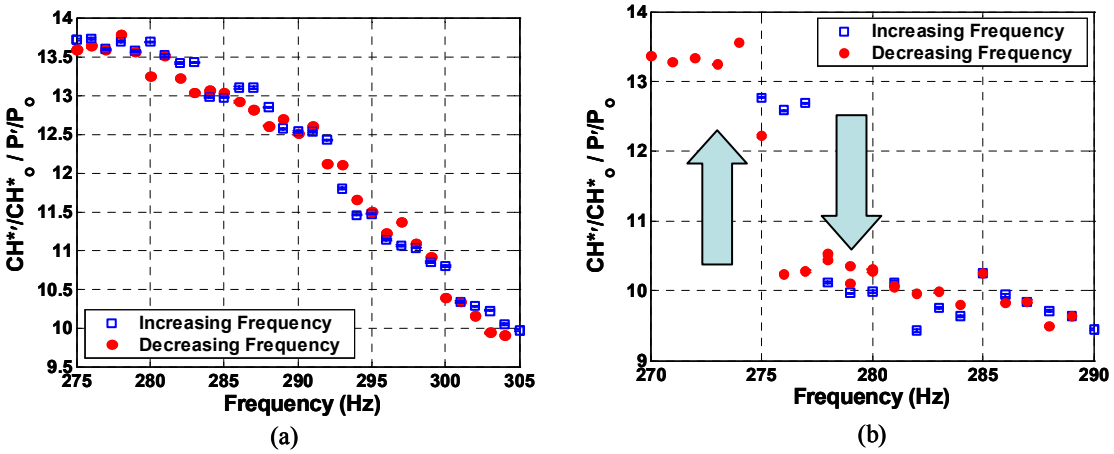

Figure 66: Dependence of pressure-CH* transfer function on driving frequency (excitation amplitude = 2.4 amperes (a), excitation amplitude = 3.0 amperes (b), $\phi = 0.95$)

NONLINEAR FREQUENCY INTERACTIONS

This section describes an ongoing investigation into the nonlinear interactions between natural acoustic modes and driven oscillations in a lean, premixed swirl stabilized combustor. This work is motivated by the fact that combustion instabilities continue to hinder gas turbine combustor development and operation[84-88]. These instabilities occur when the unsteady combustion process couples with one or more of the combustor's acoustic modes, resulting in self-excited oscillations. The objective of this work is to improve the understanding of the nonlinear dynamics associated with these oscillations. Improved understanding of the nonlinear combustion process is needed to further development of methods to predict limit cycle amplitudes.

In addition to improved understanding of nonlinear combustor dynamics, this work also has implications on active instability control[89]. In many cases, active control is implemented by closed loop control of fuel flow oscillations that are out of phase with the instability. However, the use of open loop, non-resonant frequency, forcing has also been demonstrated by many researchers[90-94]. The present study provides some insight into the underlying combustor processes which impact the effectiveness of these open loop control strategies.

This work is motivated by a previous study focusing on the nonlinear flame transfer function between driven pressure oscillations and heat release fluctuations in a high-pressure, gas turbine combustor simulator**Error! Bookmark not defined.**. During these tests, nonlinear interactions between a natural combustor mode and those due to acoustic forcing were observed. Specifically, the amplitude of the unstable mode monotonically decreased, before it disappeared completely, with increases in amplitude of the driven mode. This behavior was attributed to frequency-locking, a well-known nonlinear oscillator phenomenon. Frequency locking is due to nonlinear interactions between oscillations that are closely spaced in frequency. It is manifested as a decrease in amplitude of the self-excited or natural mode oscillations as the amplitude of the driven oscillations increases.

Lieuwen & Neumeier[23] performed a limited investigation of the effect of forcing frequency upon this frequency locking phenomenon by considering two forcing frequencies. Their data did not indicate a significant change in the entrainment amplitude at the two driving frequencies. This was contrary to expectation, however, as we had anticipated the entrainment amplitude to be proportional to the frequency spacing between the forced and self-excited frequency. These considerations motivated this study, which more systematically investigates these frequency spacing effects on entrainment amplitude.

Experiments were performed on a 100 KW swirl stabilized burner, which was previously shown schematically in Figure 14. The reported tests were performed at a nominally unstable condition, with an instability frequency of 461 Hz. The forcing frequencies investigated ranged from 150 to 430 Hz and for all cases, the overall acoustic power was substantially reduced by the presence of acoustic forcing.

A typical result is shown in Figure 67. The nominal amplitude of the 461 Hz instability is about 1.5-2% of the mean pressure in the combustor. In this particular case, forced oscillations are excited at 200 Hz over a range of amplitudes. As shown in Figure 67, increased forcing levels cause the 461 Hz mode amplitude to monotonically decrease, and to nearly disappear when the driving amplitude reaches approximately 25% of the mean velocity. Thus, the entrainment amplitude for this case is $u'/u_o=0.25$. It is also seen that the harmonic associated with the instability at 922 Hz disappears. Also shown in the figure is the overall RMS amplitude in the 0-1000 Hz range, which has a minimum near the entrainment amplitude and then begins to rise with increased forcing levels, due to the growing amplitude of the imposed oscillations. The acoustic power in the spectra between 0 and 1000 Hz is reduced by 90% for this case.

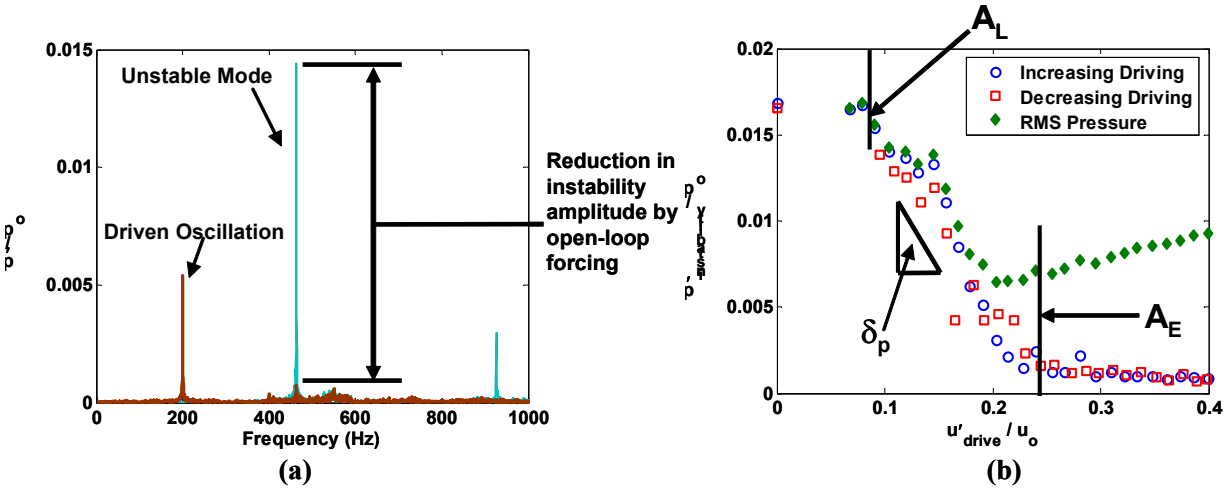

Figure 67: (a) Spectrum of combustor pressure at two driving amplitudes showing decrease in combustor instability mode as driving amplitude is increased (instability frequency = 461 Hz, driving frequency = 200 Hz). (b) Dependence of instability amplitude on driving velocity amplitude at 200 Hz driving frequency.

The typical dependence of the natural instability amplitude on the driving amplitude is shown in Figure

67(b). At the highest driving amplitudes, the instability has essentially disappeared at the cost of the increase in amplitude of the driven pressure. There are several basic features of the instability amplitude dependence upon driving amplitude that can be discerned from Figure 67(b). First, the instability amplitude is independent of the forcing amplitude for some amplitude range before decreasing; we have referred to the driving amplitude at which this decrease begins as A_L. Second, the instability amplitude decreases with some slope, δ_p, for further driving amplitude increases. Third, the instability amplitude essentially goes to zero, or to near zero values above some driving amplitude, referred to here as the entrainment amplitude, A_e. For example, in Figure 67(b) the entrainment amplitude is ~25% of the mean velocity at the premixer exit. Finally, the dependence of the unstable mode amplitude upon the driving amplitude exhibits some hysteresis. In this study, hysteresis occurred at only at select frequencies in the 150-430 range we have tested so far at this instability condition. No significant trend was found that was dependent on driving frequency. This hysteresis behavior is shown in Figure 68. Typical hysteresis levels are found to be between 3-5% of the mean velocity value.

These characteristics depend significantly upon driving frequency. We consider first the entrainment amplitude dependence upon driving frequency, which is plotted in Figure 69(a). The entrainment amplitude, A_E, grows as the forcing frequency is moved away from the instability frequency of 461 Hz, except very close to the instability (f_{drive} = 400-430 Hz). The trend in Figure 69 was expected although we do not have any specific theory our intuition was based upon. Figure 69 also reinforces the fact that the velocity oscillation amplitude in unstable combustors is a major controlling factor which affects the nonlinear combustion process. It should be noted that a different trend is observed if the perturbation pressure[§] (see Figure 69b), rather than velocity were used to quantify the forcing amplitude. This is due to the frequency dependence of the pressure-velocity relation. This result explains the confusion over this issue raised in our prior study, which used the perturbation pressure as a measure of disturbance amplitude.

[§] In this combustor, the entrainment pressure amplitude increases monotonically with decreasing frequency up to about 230 Hz. It then decreases for lower frequencies.

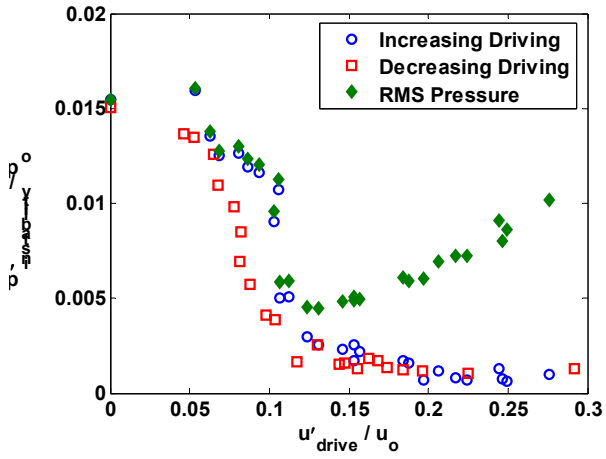

Figure 68: Dependence of instability amplitude on driving amplitude for driving frequency = 410 Hz (instability frequency = 461 Hz).

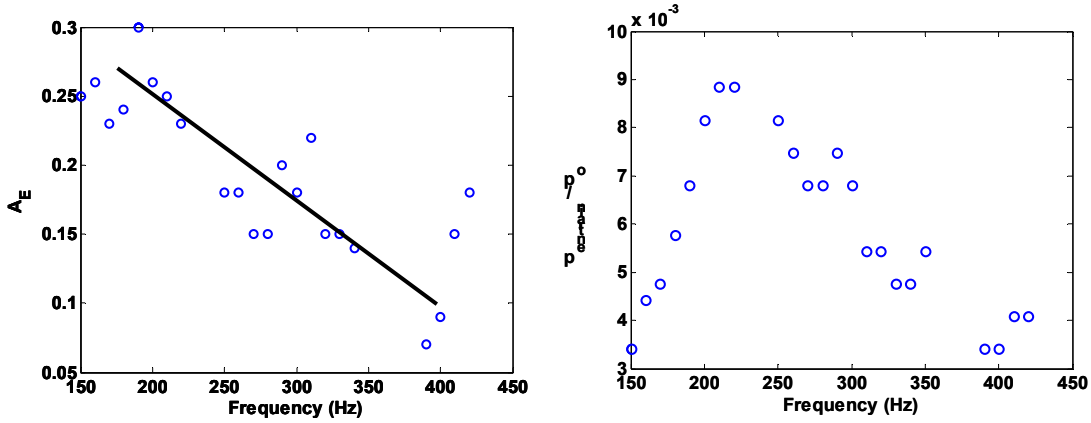

Figure 69: Dependence of (a) velocity entrainment amplitude, AE, and (b) corresponding pressure amplitude values upon driving frequency (instability frequency = 461 Hz).

We next consider the slope of the instability amplitude rolloff, δ_p, shown in Figure 70. In contrast to the entrainment amplitude, the instability rolloff has a complex dependence on frequency which is not understood. The highest slopes, and therefore the most rapid rolloff of the instability amplitude, occur at 250 and 400 Hz. Local minima are seen at 160 Hz and 310 Hz. Similarly, the parameter A_L's frequency dependence is shown in Figure 71. In general, A_L is found to be largest at frequencies which are far away from the instability and smallest at frequencies closer to the instability. The values of A_L range from u'/u_o= 0.02-0.10. At 240 Hz, this value decreases linearly from it maximum value, near where the instability rolloff hits its maximum, and flattens out after 310 Hz, where the instability rolloff hits a minimum. In general, the parameter A_L is seen to change values near local

minima and maxima in the instability rolloff value.

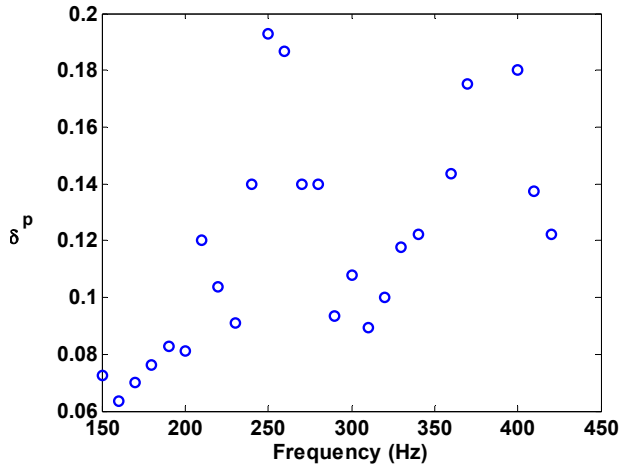

Figure 70: Dependence of instability rolloff, δp on driving frequency (instability frequency = 461 Hz)

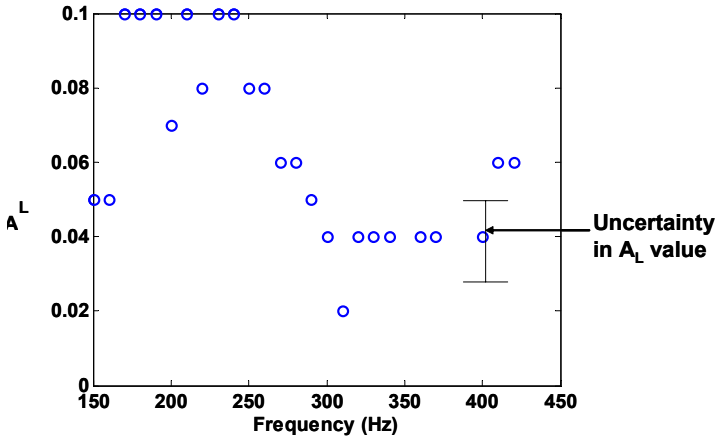

Figure 71: Dependence of AL parameter (velocity oscillation amplitude range which is independent of forcing) on driving frequency (instability frequency = 461 Hz)

As these results have direct implication on open loop forcing as an active control methodology, it is of interest to analyze the total acoustic power reduction in the 0-1000 Hz range where power is defined as:

$$Power = \int |p'|^2 df \qquad (1)$$

Figure 72 plots the frequency dependence of the maximum reduction in acoustic power due to open-loop forcing observed at each frequency over the whole forcing amplitude range. We have found that we can reduce the acoustic power by at least 70% of its original value at optimized driving amplitudes at this operating condition. The best results occur at frequencies where the entrainment *pressure* amplitude is smallest and the worst results are where the entrainment pressure amplitude is highest, as may be expected. For larger entrainment amplitudes, more

acoustic power is being added into the system at the point of entrainment. Therefore, the reduction in instability amplitude comes at the cost of larger driven amplitudes.

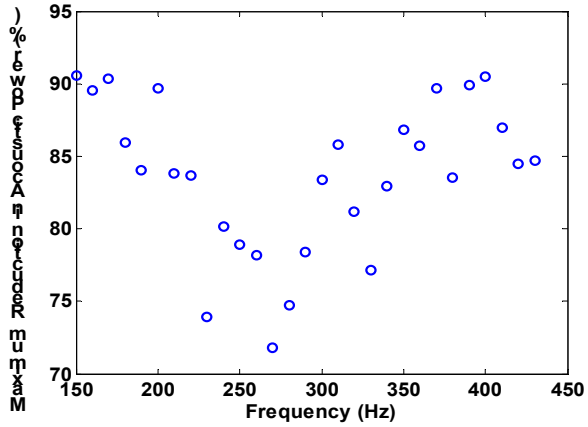

Figure 72: Dependence of maximum acoustic power reduction on driving frequency (instability frequency = 461 Hz).

9. Active Control of Combustion Instabilities

This note describes an experimental investigation of active control of instabilities in a high pressure, liquid fueled combustor. Active control has been widely demonstrated as a technically viable method for suppressing combustion instabilities (e.g., see Refs. [95, 96,97]). For example, it has been shown that instabilities can be suppressed by measuring the pressure or heat release in the combustor, suitably phase shifting and amplifying the measured signal, then driving a secondary fuel injector with this signal. While significant progress has been made, a number of problems are still in need of investigation. Active controllers are often found to work well at certain operating conditions, while their effectiveness is significantly reduced at others. Results in the literature quantifying the degree of suppression of the instability amplitude vary substantially, from factors of under 2 to over 50. Experiments have shown that the same methodology performs very differently on different combustors and at different operating conditions. Thus, although at this point it is well established that *some degree* of suppression of combustion instabilities is possible, more research is needed to understand the dynamics of actively controlled combustors and the factors that limit control effectiveness.

A variety of factors determine the impact of an active control system upon an instability. First, the uncontrolled combustor dynamics play a significant role on the effect active control has upon the oscillations. Control effectiveness will clearly depend upon such issues as instability amplitude, instability frequency and background noise levels. In addition, nonlinear characteristics of the combustor, such as hysteresis and saturation, play important roles in control effectiveness.

Next, the issues of observability and controllability are significant; i.e., the extent to which the state of the system can be sensed and affected by actuation, respectively. Observability does not appear to be a significant issue limiting control effectiveness, unless, for example, a pressure sensor is located in a node. Controllability issues are more significant due to the challenges of actuating coherent fuel pulses at high frequencies. In many cases, liquid fuel is actuated using on-off, pulse-width modulations which causes spectral broadening of the excited heat release oscillations about the carrier wave frequency. This broadening is partially responsible for the peak splitting phenomenon discussed by Cohen and Banaszuk [1]. Cohen and Banaszuk [1] and Lee and Santavicca [24] have also emphasized the importance of fuel placement and/or mixedness upon control effectiveness.

Turning to the controller itself, the poorly understood nonlinear and stochastic nature of crucial combustor processes renders classical model based approaches difficult for implementation on actual hardware. Prior experimental controllers have either filtered the pressure/ chemiluminescence signal about the instability frequency (which must be known *a priori*) or used observers to extract the amplitude and frequency of the instability. The optimal control phase is typically determined using either off-line testing or adaptive schemes.

Probably one of the most significant factors determining the effectiveness of the combined controller-actuation system is the overall controller time delay. As might be expected, several studies have shown that the combined effects of background noise and time delays substantially impair control effectiveness. For example, it has been observed that the combustor appears to “run away” from the control when sufficient control actuation is

applied; e.g., the phase of the oscillations rapidly moves around or even seems to jump [96]. In addition, time delays are partially responsible for the peak-splitting phenomenon encountered with high controller gains [1]. Many of these factors are reviewed in detail by Cohen and Banaszuk [1].

The above discussion emphasized a number of issues in need of investigation to better understand the factors determining control effectiveness. In this note, we focus on the effects of uncontrolled combustor dynamics and, in particular, the effect of the level to which the controller attempts to drive the instability amplitude toward. A systematic study of these effects requires capabilities to alter the nature of the investigated combustor. In order to accomplish this *in a known and controllable manner*, self-excited oscillations were created by feeding back the measured pressure through a phase-shifter to an air actuator mounted in the rear of the combustor. This air actuator drove oscillations by pulsing a high pressure air flow. The linear and nonlinear characteristics of the self-excited feedback loop were then varied by changing the gain and phase of the pressure signal that was used to drive the air actuator. Control of the induced oscillations was achieved by pulsing the combustor fuel flow rate with a second fuel actuator.

Facility and Instrumentation

Experiments were performed in the gas turbine combustor shown schematically in Figure 2 operating at 4.4 atm, 430 K inlet air temperature at an overall equivalence ratio of 0.9. The combustor operated under liquid fuel which was supplied through the fuel injectors outlined in Figure 3, which has not been used in our nonlinear flame response studies. As the facility has been described previously in Ref. [28] for gaseous operation and in Ref. [98] for liquid fueled operation, only its key features are summarized here. The fuel is injected into the swirling air stream at the end of a conical bluff body, where it is atomized by the shearing action of the high velocity, swirling air. Oscillations were driven in the combustor with a magneto-restrictive air actuator described earlier. The air actuator modulates a constant secondary supply of air that is introduced near the combustor exit by periodically varying the degree of constriction of a valve. In order to generate self-excited oscillations, whose linear and nonlinear characteristics could be varied in a *known and systematic manner*, the pressure signal was fed back to this air actuator through a gain and phase shifter; see Figure 73. Note that simply driving oscillations with a function generator does not emulate the critical features of combustion instabilities because the phase and amplitude of the oscillations remains fixed, regardless of the control action.

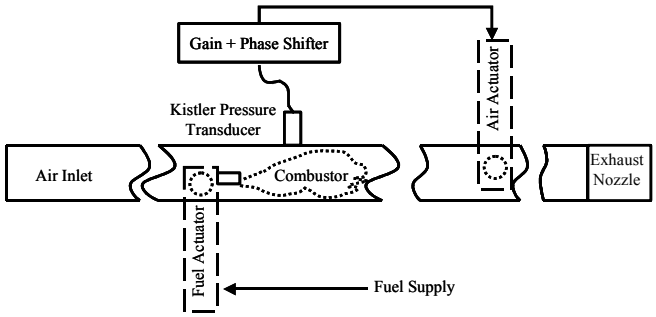

Figure 73. Block diagram of gain/phase shifter between pressure transducer and air actuator used to generate self-excited oscillations.

The combustor was operated under conditions under which it was nominally stable. By setting an appropriate gain and phase shift, the air actuator excited oscillations. The linear and nonlinear (e.g., saturation amplitude) characteristics of the oscillations could be systematically varied by changing the gain/saturation amplitude of this feedback loop. The amplitude dependence of the acoustic forcing provided by the air actuator closely resembles the saturating characteristic of heat release oscillations[16,99].

Fuel for active control is modulated using a second magnetostrictive fuel actuator. A controller is used to maintain the mean flow rate constant around the specified value, regardless of amplitude of the oscillating component.

Control Implementation

The details of the frequency observer and controller used here are described elsewhere [98], so only the key features are summarized here. The main components in the active controller are a pressure transducer, software comprising a real-time observer, a controller, and the magnetostrictive fuel actuator. During operation, the sensor continuously measures the combustor pressure which is bandpass filtered between 20 and 1000 Hz, digitized, and read in by the computer. The digitized signal is processed by the observer that extracts the amplitudes and frequencies of the largest amplitude combustor modes. The observed amplitude is compared to the desired amplitude and the difference between the two serves as the input to a PI type controller. The "desired" amplitude is the value which the controller attempts to drive the actual amplitude toward *and in general, is not zero*. It is important to note that if the desired amplitude is set to a level that the controller cannot satisfy, particularly zero, the integrator will increase until saturation. As shown in prior studies [1] and below, in such a case, the resulting large control signal that is applied to the fuel injector may result in reduced controller performance. However, if the desired amplitude is set to an attainable value, the integrator stabilizes at some non-saturated value and automatically set the control amplitude to the necessary value. The phase of the control signal relative to the measured pressure signal is set manually by determining the optimum value that maximizes instability amplitude suppression.

Results

As noted earlier, instabilities were generated by feeding back the pressure signal with a phase shift to the air actuator. A typical result showing the combustor pressure during a 0.31 psi, 92 Hz instability with and without control is shown in Figure 74. In these data, control was turned on at the indicated point, with the desired amplitude set to 0.18 psi. Once actuated, the control requires a little over one second to bring the amplitude to the desired level, due to integrator windup. Note that the control successfully brings the instability amplitude to the desired level; however, there is substantial "breathing" in amplitude of the oscillatory pressure both before and after control is implemented. At any instant in time, the actual instability amplitude varies about the indicated value by about 0.06 psi. The indicated fluctuating pressure amplitude was determined by low pass filtering the envelope of the pressure oscillations at 0.5 Hz.

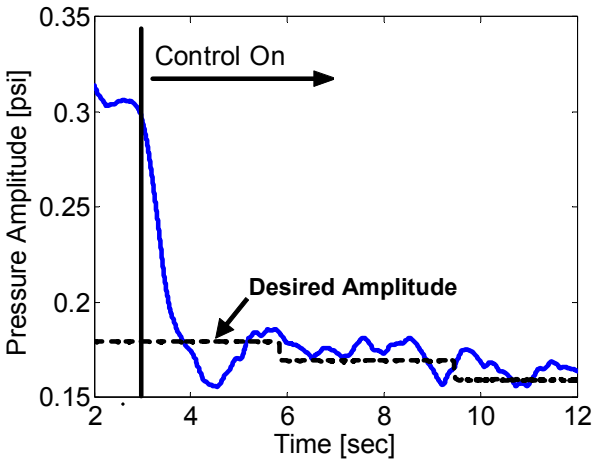

Figure 74 Low pass filtered time dependence of oscillatory combustor pressure amplitude with and without control.

Effect of Desired Amplitude

In order to elucidate the factors limiting control effectiveness, a series of experiments were performed where the "desired" instability amplitude was successively reduced. Recall that the "desired" amplitude refers to the amplitude the controller attempts to drive the oscillation level to, even if it is capable of reducing the instability amplitude further. Control performance was investigated as the desired amplitude level was monotonically decreased from 100 - 0% of its nominal value without control. Results quantifying the dependence of the actual oscillation amplitude upon the "desired" level are shown in Figure 75. The figure indicates that the nominal instability amplitude (without control) is 0.35 psi. Once the desired amplitude level drops below this value, the controller turns on to reduce the instability amplitude. The figure shows that the controller precisely drives the average instability amplitude to the desired levels down to about 0.14 psi, a 60% reduction in amplitude.

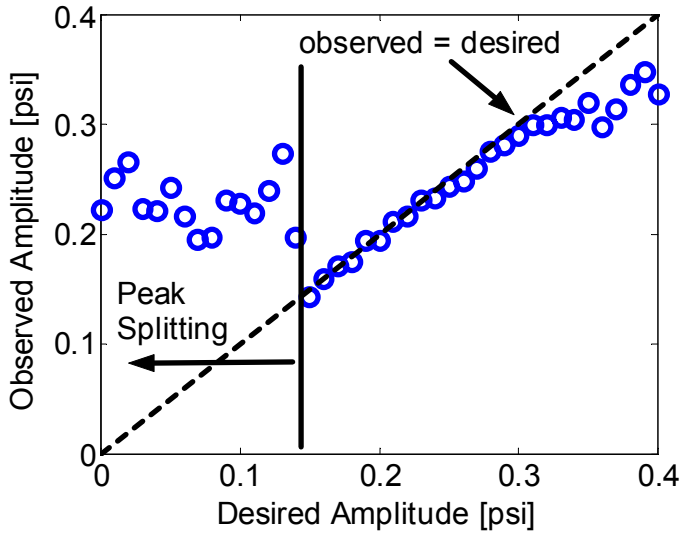

Figure 75. Dependence of mean and fluctuating instability amplitude upon desired level.

Returning to Figure 75, note the jump in instability amplitude for desired amplitude levels below 0.14 psi. This result clearly shows that *optimal control performance is not necessarily achieved by attempting to drive the instability amplitude to zero*. Rather, the best performance occurs at an intermediate value. This reduction in performance is due to imposing too large a gain on the system that introduces undesired dynamics in the combustor response. This can be seen from Figure 76 and Figure 77, which plot the Fourier transform of the combustor pressure at several desired amplitudes. Note the monotonic reduction in instability amplitudes at 92 Hz in Figure 75. Figure 76 and Figure 77 show that the 92 Hz oscillations are nearly absent and are replaced by two larger amplitude sidebands at 77 and 115 Hz. In this same region, the fuel injector command signal saturates.

This behavior is analogous to the "peak-splitting" phenomenon that has been previously explained by Cohen and Banaszuk [1]. The key processes responsible for this behavior is the fact that oscillations are excited over some spectral bandwidth centered about that of the instability frequency. If the controller phase is optimized to suppress oscillations at the center frequency, because of system time delays, they will necessarily not be optimized at higher and lower frequencies. In fact, the phase of the control at the excited sideband frequencies is 180º relative to the center frequency, resulting in the excitation of oscillations.

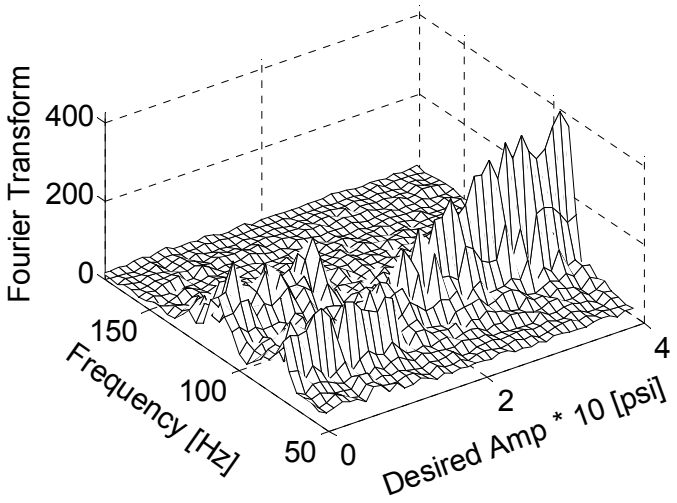

Figure 76. Fourier transform of combustor pressure at desired amplitude levels of 0-0.4 psi.

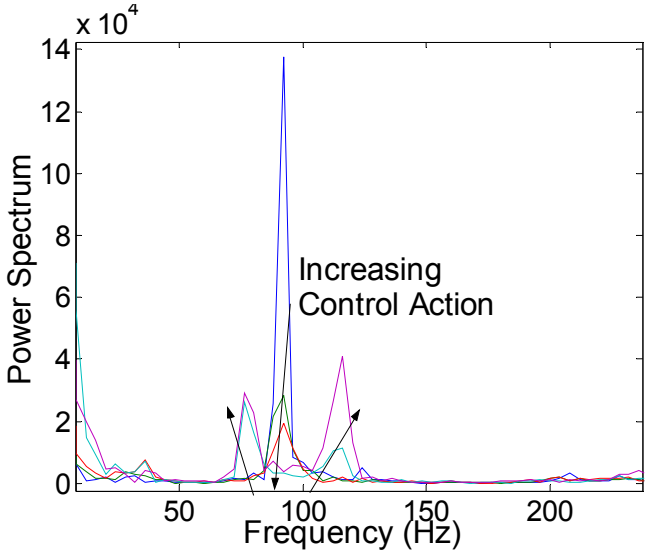

Figure 77. Fourier transform of combustor pressure at desired amplitude levels of 0.4, 0.2, 0.16, 0.14, and 0.13 psi (nominal instability amplitude = 0.35 psi).

Effect of Air Actuator Gain and Saturation

Control experiments were performed at two values of the gain between the unsteady pressure and the air actuator. The purpose of this experiment was to emulate the affects of different heat release dynamics (linear gain as well as saturation characteristics) and the resultant impact upon control effectiveness. As shown in Figure 78 the air actuator command signal and pressure amplitudes are linearly related at low amplitudes. At higher levels the air actuator amplitude driving signal is saturated, regardless of the pressure amplitude.

The effect of active control upon instability amplitude for these two air actuator gains is plotted in **Figure 79**. These data were taken by slowly sweeping the phase of the control signal relative to that of the pressure at a desired amplitude of zero. The horizontal line indicates the nominal instability amplitude. As expected, the instability amplitude is reinforced or damped, depending upon the phase. Comparing the two gain results, note the similarity and difference, respectively, in the amount the pressure amplitude is reinforced or damped. That is, the pressure amplitude is increased by nearly the same factor (two) in both gain results. The amplitude minima, however, are approximately 0.22 and 0.16 psi, a difference of 40% and a difference in reduction of 15%.

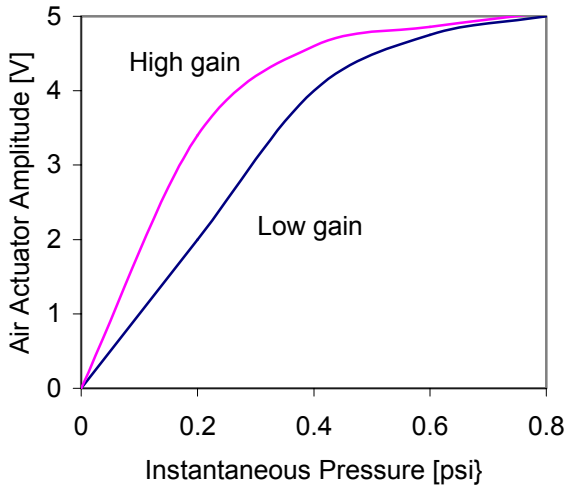

Figure 78 Instability driving characteristic visualized by plotting the dependence of the instantaneous air actuator driving signal upon pressure.

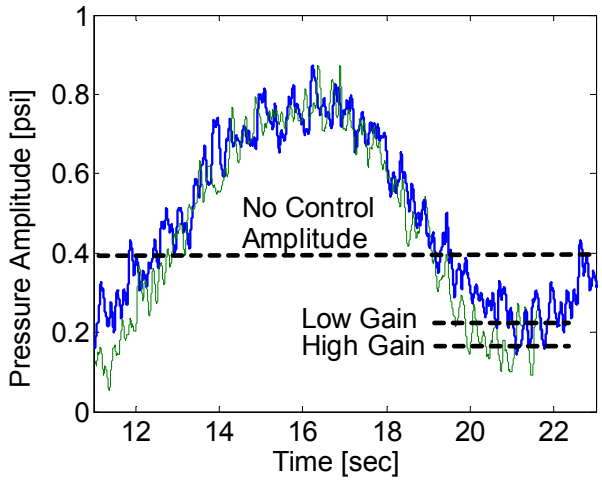

Figure 79. Dependence of instantaneous pressure amplitude upon time as phase of control signal is swept relative to that of the instability.

The same maximum amplitude is achieved because the air actuator driving command signal is saturated; i.e., there is no difference in driving characteristics above a pressure amplitude of about 0.6 psi. The difference in minima is apparently due to the effect that the combustor's nominal dynamics (i.e., without control) has upon its response to too large a gain of the fuel injector control signal, resulting in peak splitting. This over-gaining of the control signal is due to the fact that the desired amplitude was always set to zero. Analysis of the moving average of the Fourier transform shows the peak splitting phenomenon in the pressure over approximately 1/8 of the phase sweep cycle in the low gain case. In contrast, the peak splitting phenomenon just barely appears in the higher gain case, occurring only at the pressure minimum over about 1/32 of the phase sweep cycle.

10. CONCLUSIONS

This final report describes many important experimental and theoretical advances on the study of unstable gas turbine combustors. In particular, much emphasis was placed on the mechanisms which can control the limit cycle amplitudes of unstable combustors, as well as active control and interactions between natural and driven oscillations. The important conclusions from each aspect of this study are described below.

Nonlinear Flame Response – Gas Turbine Combustor Simulator

From these data, several conclusions can be drawn regarding the nonlinear response of the unsteady heat release to flow perturbations. The amplitude relationship between the pressure/velocity and heat release saturates at sufficiently high forcing levels at certain frequencies and equivalence ratios, but remains linear at others all the way to flame blowout. Also, substantial amplitude dependence of the CH* phase was found at all driving frequencies and equivalence ratios, clarifying the questions raised by Lieuwen & Neumeier[23]. These results suggest that heat release-acoustic nonlinearities in both gain and phase may play comparable roles in swirling, premixed combustors. While the measured flame transfer functions themselves are independent of the system's acoustics, a saddle-node bifurcation in pressure amplitude occurs around the natural frequency that is introduced by the nonlinear combustion process.

One of the key conclusions of this study is that nonlinear interactions between the flow forcing and parametric instability (possibly through its impact on the fluctuating flame position) may be responsible for saturation of the flame response. The presence of the parametric instability is manifested by the jump in amplitude of oscillations at half the driving frequency at certain disturbance amplitude values. This jump in subharmonic amplitude occurs at essentially the same value as that at which saturation occurs. Furthermore, subharmonic oscillations are always present in cases where saturation of the fundamental occurs. To our knowledge, this observation of the parametric instability is the first in a turbulent, swirl-stabilized flame.

In addition, however, there are other potential mechanisms which may also be present. These include local extinction of the flame and flame sheet kinematics. For example, increasing amplitudes of oscillation lead to increased flame strain which could cause local flame extinction events. Increased extinction could, in turn, result in decreased heat release response. This mechanism could be responsible for the decreasing mean chemiluminescence levels upon perturbation amplitude seen in some test cases. Additionally, flame sheet kinematics also may be important. While their significance was alluded to above in the context of the parametric flame instability (i.e., fluctuating flame position effects), they may play additional roles through nonlinear dependencies of flame area destruction with disturbance amplitude. For example, large amplitude corrugations of the flame may be consumed by flame propagation faster than small amplitude perturbations, as emphasized by Preetham and Lieuwen[100] based on theoretical considerations and very recently, by Balachandran *et al.*[26] , based on experimental imaging studies.

While it is not possible to conclusively determine the relative roles of all potential mechanisms of nonlinearity, we can eliminate some mechanisms which have been suggested as potentially significant:

Global" Extinction – This is the mechanism proposed by Dowling[16] and Poinsot *et al.*[19] which follows from the simple observation that the instantaneous heat release cannot go negative, thus limiting the chemiluminescence fluctuations to 100% of the mean value. Our data indicate saturation at substantially lower amplitudes, however, implying that this mechanism is not significant in this combustor.

Chemical Kinetics – Reaction rates depend upon pressure and temperature in a nonlinear manner. These nonlinearities will apparently become significant when the fluctuating pressure and temperature achieve amplitudes on the order of their mean values. This mechanism does not appear likely here, however, as nonlinearity occurs at p'/p_o values of ~2%.

Equivalence ratio oscillations – The nonlinear dependence of the equivalence ratio amplitude and heat release response discussed by Peracchio & Proscia[17] and Lieuwen[15] is not important here, as the fuel/air mixture had a constant composition. As such, though we cannot comment on the magnitude of these types of nonlinearities in situations where they are present, the data presented here indicate that other flame processes also cause nonlinearities in flame response.

Flame holding – The many data indicating a linear CH* response all the way to blowoff indicate that nonlinearities due to marginal flame holding are probably not important

Nonlinear Flame Response – Atmospheric Burner

From the results presented, we can make the following conclusions. First, substantial nonlinearities in the flame response to forced velocity oscillations have been shown. The phase between the flow oscillation and heat release is also seen to have substantial amplitude dependence. Various mechanisms appear to be important in different frequency and flowrate regimes. For instance, at low flow rates, the saturation amplitude of CH* can vary greatly with driving frequency and range from 25-100% of the mean value. In contrast, for higher flow rates, it is observed that the nonlinear amplitude of CH* is roughly independent of driving frequency. In addition, the shape of the transfer function can change markedly for different driving frequencies and flow rates. Therefore, there are a variety of behaviors which are present in a single combustor. Thus, one single theory is not adequate to describe the nonlinear dynamics of a forced or unstable combustor.

OH PLIF imaging of the flame was performed at two frequencies where two mechanisms potentially controlled the saturation amplitude of the global heat release from the flame. Two phenomena, vortex rollup and flame liftoff, are found to be the likely mechanisms which govern saturation of the flame transfer function from these images. The latter mechanism visibly changes the flame structure when comparing these results with line-of-sight images. Both mechanisms act to reduce the flame area.

No sub-harmonic flame response was observed in any of these studies, as opposed to the earlier study in the combustor simulator as mentioned above. This result is not understood, as it is well known that parametric flame instabilities occur at high forcing amplitudes, resulting in a subharmonic response. Future work will attempt to

reconcile these differing observations

Theoretical Nonlinear Flame Response

One of the key points made here is that the linear and nonlinear characteristics of the flame dynamics are controlled by the interaction between flame disturbances due to boundaries and flow non-uniformities. A constructive superposition of the two flame disturbance contributions can cause the flame to act as an "amplifier" at certain frequencies whereas a destructive superposition can cause the flame response to be identically zero. The theory also captures the effect of flame stretch and shows that it is responsible for the experimentally observed phenomenon of "filtering".

In the nonlinear regime, the flame response is critically dependent on whether the solution lies in a region of constructive or destructive interference of the flame disturbances. In regions of constructive interference, the nonlinear flame transfer function gain is always less than its linear value whereas in regions of destructive interference the nonlinear transfer function may exceed its linear value. These characteristics can cause the same combustor to exhibit sub-or supercritical type of bifurcation depending on the operating condition. The analysis shows that nonlinearity is enhanced and that there is a greater tendency for the nonlinear transfer function to have an inflection point when the phase speed of the disturbances is less than the mean flow speed. Moreover, the average flame length decreases with increasing perturbation amplitude for most conditions which is consistent with the available experimental data.

Several additional studies are motivated by this work. First is an analysis of the nonlinear flame response in cases where the flame is being simultaneously disturbed by deterministic harmonic fluctuations as well as random fluctuations. The latter fluctuations simulate the impact of background turbulent fluctuations. As such, the analysis would allow for a rudimentary comparison of the nonlinear dynamics of laminar and turbulent flames. Second there is a need to couple the flow field and flame dynamics so that the effect of gas expansion can be captured. This would introduce a new parameter into the results, the ratio T_b/T_u.

Nonlinear Interactions in Unstable Combustors

These results have implications of the type of bifurcations which may be observed in unstable combustors. This study clarifies a number of issues related to the nonlinear interactions between driven and natural unstable combustor modes but also raises new questions. It has been shown that the entrainment velocity amplitude monotonically grows with driving-instability frequency separation. We have found that the instability rolloff and velocity oscillation range which is independent of forcing amplitude both have complex dependencies on driving frequency. Changes in the parameter, A_L, are seen to accompany local minima and maxima in instability rolloff. Further work is being performed to analyze the effect on these parameters of driving frequencies greater than the instability frequency.

In addition, open loop forcing of the combustor, at frequencies different from the instability frequency, was

found to significantly reduce the acoustic power in the 0-1000 Hz range by as much as 90%. The performance of this open loop control scheme is dependent on the entrainment amplitude. The best results were obtained for frequencies which had the lowest entrainment pressure amplitudes, as might be expected.

The generality of this methodology is an open question, however, as we found some operating conditions where entrainment did not occur in the same fashion and the instability amplitude is marginally reduced. For example, in one situation, the addition of forcing caused a shift in instability frequency to a value 40 Hz higher than its unforced value (from 510 Hz to 550 Hz). For driving frequencies whose harmonics do not fall around this new frequency, this value is relatively constant. The acoustic power in the 0-1000 Hz range is only slight reduced (~20%) before increasing rapidly, unlike the conditions presented in this paper. An investigation on this behavior is also ongoing.

The theoretical study has further highlighted the importance of the interactions between the contributions from flame disturbances due to boundaries and flow non-uniformities. The present investigation extends the analytical solutions for the flame response from the linear to the non-linear regime.

Active Control Studies of Unstable Combustors

A variety of factors determine the impact of an active control system upon an instability. First, the uncontrolled combustor dynamics play a significant role on the effect active control has upon the oscillations. Control effectiveness will clearly depend upon such issues as instability amplitude, instability frequency and background noise levels. In addition, nonlinear characteristics of the combustor, such as hysteresis and saturation, play important roles in control effectiveness.

.

Appendix A

This section solves for the steady state flame shape $\zeta_o(r)$. The governing equation for the steady state case (see Eq (13)), is

$$\sqrt{\frac{1+\beta^2\zeta_{o,r}^2}{1+\beta^2}}\left(1-\frac{\sigma\beta\zeta_{o,rr}}{\left(1+\beta^2\zeta_{o,r}^2\right)^{\frac{3}{2}}}\right)=1 \quad (50)$$

Integrating Eq. (50) and applying the boundary condition for conical flames, Eq. (15), the exact implicit solution for $\zeta_o(r)$ can be expressed as:

$$\left(\frac{1+\zeta_{o,r}}{1-\zeta_{o,r}}\right)\left(\frac{\sqrt{1+\beta^2\zeta_{o,r}^2}+\sqrt{1+\beta^2}\ \zeta_{o,r}}{\sqrt{1+\beta^2\zeta_{o,r}^2}-\sqrt{1+\beta^2}\ \zeta_{o,r}}\right)=e^{\left(-\frac{2\beta\sqrt{1+\beta^2}}{\sigma}r-2\beta\,Tan^{-1}(\beta\zeta_{o,r})\right)} \quad (51)$$

The flame position gradient can be expanded in powers of $\exp(-r/\sigma^*)$ as:

$$\zeta_{o,r}=-1+\frac{2}{\sqrt{1-\alpha}}e^{-\frac{1}{\sigma^*}r}+O[e^{-\frac{1}{\sigma^*}r}]^2$$

Hence the lowest order correction, for stretch effects, to the conical flame position gradient is an exponentially small function of σ^*.

Also note that for wedge flames, the solution given by $\zeta_{o,r}=-1$ satisfies the governing Eq (50) and the boundary conditions given by Eqs (14) and (16) .

Appendix B

Defining $\Lambda=\sqrt{1-4i\sigma^*\,St_2}$, the solution for $\zeta_1(r,t)$ in Eq (23) is:

$$\zeta_1(r,t)=Re\left(\frac{e^{-iSt\,t}\left(e^{i\eta St_2(1-r)}-e^{\frac{(1-r)(1-\Lambda)}{2\sigma^*}}\right)}{St\left(i(\eta-1)+\sigma^*\eta^2St_2\right)}\right)$$

The conical and wedge flame transfer functions in the linear regime can be expressed as:

$$G_c(St_2,\eta,\sigma^*) = 2\underbrace{\frac{\left((1+\Lambda)(\eta-1)-2i\sigma^*\eta St_2-2\Lambda\eta e^{\frac{1-\Lambda}{2\sigma^*}}+e^{i\eta St_2}\left(1+\Lambda-i\sigma^*(1-\Lambda)\eta^2St_2\right)\right)}{\eta St_2^2\left(1+\Lambda\right)\left(1-\eta+i\sigma^*\eta^2St_2\right)}}_{\text{Area Fluctuation}}$$

$$+2\sigma^*\underbrace{\left(\frac{\left(\Lambda\eta+\eta-2\right)St_2-2i\Lambda e^{\frac{1-\Lambda}{2\sigma^*}}+ie^{i\eta St_2}\left(1+\Lambda-2i\sigma^*\eta St_2\right)}{St_2\left(1+\Lambda\right)\left(-1+\eta-i\sigma^*\eta^2St_2\right)}\right)}_{S_L\text{Fluctuation}}$$

$$G_w(St_2,\eta,\sigma^*) = 2\underbrace{\frac{\left(\begin{array}{l}e^{i\eta St_2}\left((1+\Lambda)(1-i\eta St_2)-2i\sigma^*St_2+\sigma^*\eta St_2^2(-2+\sigma^*(1-\Lambda)\eta^2)-2i\sigma^{*2}\eta^3St_2^3\right)\\+2i\Lambda\eta e^{\frac{1-\Lambda}{2\sigma^*}}\left(\sigma^*St_2+(i+St_2)\right)+\left((1+\Lambda)(\eta-1)-i\sigma^*St_2(\Lambda\eta-2+3\eta)\right)\end{array}\right)}{\eta St_2^2\left((\eta-1)-i\eta^2St_2\sigma^*\right)\left(1+\Lambda-2iSt_2\sigma^*\right)}}_{\text{Area Fluctuation}}$$

$$+2\sigma^*\underbrace{\left(\frac{e^{\frac{1-\Lambda}{2\sigma^*}}2\Lambda(1-iSt_2)+e^{i\eta St_2}\left(-1+i\eta St_2-2\sigma^{*2}\eta^2St_2^2+\Lambda\left(-1+i\eta St_2+\sigma^*\eta^2St_2^2\right)+\sigma^*St_2\left(2i+2\eta St_2+\eta^2St_2\right)\right)}{St_2\left(i+i\Lambda+2\sigma^*St_2\right)\left(1-\eta+i\sigma^*\eta^2St_2\right)}\right)}_{S_L\text{Fluctuation}}$$

Note that the term $\exp((1-\Lambda)/2\sigma^*)$ is not exponentially small and hence is retained in the analysis.

Appendix C

The solutions for the flame position are:

$$\zeta_o(r,t) = 1-r$$

$$\zeta_1(r,t) = \left(\frac{2Sin[\left(\frac{St(K\alpha-1)(1-r)}{2\alpha}\right)]}{(K\alpha-1)\ St}\right)Cos[\,St\left\{\frac{(K\alpha\ +1)(r-1)}{2\alpha}+t\right\}]$$

$$\zeta_2(r,t) = \left(\frac{r+\alpha-r\alpha-1}{4(K\alpha-1)^2\alpha^2}\right)Cos[\,2\ St\left\{\frac{r-1+\alpha t}{\alpha}\right\}] + \left(\frac{6K-4K\alpha-3K^2\alpha+K^2\alpha^2}{8\ St(K\alpha-1)^3}\right)Sin[\,2\ St\left\{\frac{r-1+\alpha t}{\alpha}\right\}] +$$

$$\left(\frac{K\alpha(K-1)}{2(K\alpha-1)^3\ St}\right)Sin[\,St\,\frac{(1-r)(K\alpha-1)}{\alpha}] + \left(\frac{2K-K^2\alpha-K^2\alpha^2}{8\ St(K\alpha-1)^3}\right)Sin[\,2\ St(K(r-1)+t)] +$$

$$\left(\frac{-2K+K\alpha+K^2\alpha}{2(K\alpha-1)^3\ St}\right)Sin[\,St\left\{\frac{(K\alpha+1)(r-1)+2\alpha t}{\alpha}\right\}] + \left(\frac{(r-1)(-1+\alpha+2K\alpha-3K^2\alpha^2+K^2\alpha^3)}{4\alpha^2(K\alpha-1)^2}\right)$$

$$\zeta_3(r,t)=\left(\frac{(r-1)(1-\alpha)(-3+13K\alpha-4K\alpha^2-13K^2\alpha^2-3K^2\alpha^3+10K^3\alpha^3)}{8(K\alpha-1)^4\alpha^3}\right)Cos[St\left\{\frac{r-1+\alpha t}{\alpha}\right\}]-$$

$$\left(\frac{2(r-1)^2(1-\alpha)^2(K\alpha-1)^2St^2+K\alpha^4(4-4\alpha-8K-5K\alpha+9K\alpha^2+27K^2\alpha-15K^2\alpha^2-4K^2\alpha^3-18K^3\alpha^2+14K^3\alpha^3)}{16(K\alpha-1)^5\alpha^4\ St}\right)$$

$$\times Sin[St\left\{\frac{r-1+\alpha t}{\alpha}\right\}]-\left(\frac{K(r-1)(-1+\alpha+2\alpha K-3K^2\alpha^2+K^2\alpha^3)}{4\alpha^2(K\alpha-1)^3}\right)Cos[\ St(K(r-1)+t)]$$

$$-\left(\frac{K(\alpha-1)(-8+16K-21\alpha K^2-2K^2\alpha^2+15K^3\alpha^2)}{16(K\alpha-1)^5St}\right)Sin[\ St(K(r-1)+t)]$$

$$+\left(\frac{K(r-1)(1-\alpha)(1-2\alpha+K\alpha)}{8\alpha^2(K\alpha-1)^4}\right)Cos[St\frac{(1-r)(K\alpha-2)+\alpha t}{\alpha}]$$

$$+\left(\frac{K(\alpha-1)(4-8K+8K\alpha-3\alpha K^2-2K^2\alpha^2+K^3\alpha^2)}{16(K\alpha-1)^5St}\right)Sin[St\frac{(1-r)(K\alpha-2)+\alpha t}{\alpha}]+$$

$$\left(\frac{K^2\alpha(5-\alpha-3K-5K\alpha+2K^2\alpha+2K^2\alpha^2)}{16(K\alpha-1)^5St}\right)Sin[St\frac{(1-r)(2K\alpha-1)+\alpha t}{\alpha}]$$

$$+\left(\frac{(1-\alpha)(r-1)(-1+7K\alpha-4K\alpha^2-3K^2\alpha^2+K^2\alpha^3)}{8\alpha^3(K\alpha-1)^4}\right)Cos[3St\left\{\frac{r-1+\alpha t}{\alpha}\right\}]$$

$$+\left(\frac{K\alpha^4(-12+12\alpha+52K-57K\alpha+9K\alpha^2-45K^2\alpha+41K^2\alpha^2-4K^2\alpha^3+10K^3\alpha^2-6K^3\alpha^3)-6(r-1)^2(1-\alpha)^2(K\alpha-1)^2St^2}{48(K\alpha-1)^5\alpha^4\ St}\right)$$

$$\times Sin[3St\left\{\frac{r-1+\alpha t}{\alpha}\right\}]+\left(\frac{K(r-1)(1-\alpha)(-3+2\alpha+K\alpha)}{8\alpha^2(K\alpha-1)^4}\right)Cos[St\frac{(1-r)(K\alpha+2)-3\alpha t}{\alpha}]$$

$$+\left(\frac{K(\alpha-1)(-4+4\alpha+28K-32\alpha K+8K\alpha^2-23K^2\alpha+17K^2\alpha^2-2K^2\alpha^3+5K^3\alpha^2-K^3\alpha^3)}{16(K\alpha-1)^5St}\right)Sin[St\frac{(1-r)(K\alpha+2)-3\alpha t}{\alpha}]$$

$$-\left(\frac{K^2(4-3\alpha K-7\alpha^2K+2K\alpha^3+K^2\alpha^2+3K^2\alpha^3)}{48(K\alpha-1)^5St}\right)Sin[\ 3St(K(r-1)+t)]$$

$$+\left(\frac{K^2(12-13\alpha+5\alpha^2-9K\alpha+\alpha^2K+2\alpha^2K^2+2\alpha^3K^2)}{16(K\alpha-1)^5St}\right)Sin[St\frac{(r-1)(2K\alpha+1)+3\alpha t}{\alpha}]$$

Appendix D

The transfer function coefficients referred to in Eq. (41) are:

$$\%A_{c,\omega_o} = -8\ (\alpha-1)^2 + 4K\alpha\{2 - i(\alpha-1)St_2\} - 2K^2\alpha^2\{10+\alpha+\alpha^2 + i8St_2 - i4\alpha St_2\}$$
$$+K^3\alpha^3\{\ 27 - \alpha(3 + i8St_2) + i32St_2\} + K^4\alpha^4\{-17 + 9\alpha - i32St_2 + i8St_2\alpha\} - i4K^5\alpha^5 St_2\{\alpha - 3\ \}$$

$$\%B_{c,\omega_o} = 2(\alpha-1)\{6\alpha + iSt_2 - i4\alpha St - (\alpha-1)St^2\} + 4K\alpha(\alpha-1)\{-10 + i4St_2 - St_2{}^2 + \alpha(i + St_2)^2\}$$
$$+K^2\alpha^2\{-76 + 81\alpha - \alpha^2 - i44(\alpha-1)St_2 - i6(\alpha-1)St_2\alpha - 2St_2{}^2(\alpha-1)^2\}$$
$$+K^3\alpha^3\{-8\alpha^2 + i(\alpha-1)(i49 + 46St_2 + 6\alpha St_2)\} + 2K^4\alpha^4\{-7 + 9\alpha - i10St_2(\alpha-1)\}$$

$$\%C_{c,\omega_o} = \{8(iSt_2 - 2)\} + 4K\{5 - \alpha - i3St_2(1+\alpha)\} + 2K^2\alpha\{2 + 6\alpha + i11St_2 + i2St_2\alpha\}$$
$$-2K^3\alpha^2\{11 + \alpha + i6St_2\} + K^4\alpha^3\{9 + i2St_2\} - K^5\alpha^4$$

$$\%D_{c,\omega_o} = 4 - \alpha + \alpha^2 - K\alpha(13 + 3\alpha) + 2K^2\alpha^2(9+\alpha) - 8K^3\alpha^3$$

$$\%E_{c,\omega_o} = \ \ 16(\alpha-1)^2 + 4K\alpha\{-6 + 10\alpha - 8\alpha^2 + iSt_2(3 - 5\alpha + 2\alpha^2)\}$$
$$+2K^2\alpha^2\{2(-15 + 31\alpha - 2\alpha^2) - iSt_2(19 - 28\alpha + 9\alpha^2)\}$$
$$+3K^3\alpha^3\{29 - 44\alpha - 5\alpha^2 + i2St_2(12 - 13\alpha + \alpha^2)\}$$
$$+K^4\alpha^4\{-59 + 77\alpha + 8\alpha^2 + i2St_2\{-9 + 8\alpha + \alpha^2)\} + 2K^5\alpha^5\{7 - 9\alpha - i2St_2(\alpha-1)\}$$

The transfer function coefficients referred to in Eq. (42) are

$$\%A_{w,\omega_o} = 8(\alpha-1)^2 - i8K\alpha\{-i + (\alpha-1)^2 St_2\} + 2K^2\alpha^2\{10 + \alpha + \alpha^2 + i4St_2 + 2(\alpha-1)St_2{}^2\}$$
$$+K^3\alpha^3\{\ -27 - i20St_2 - i2St_2\alpha^2 + 16\ \ St_2{}^2 + \ \alpha(3 - i2St_2 - 8St_2{}^2)\}$$
$$+K^4\alpha^4\{17 + i27St_2 - 32St_2{}^2 + \alpha(-9 - i3St_2 + 8St_2{}^2)\} - K^5\alpha^5 St_2\{i17 - 32St_2 + \alpha(8St_2 - i9)\ \}$$
$$+4\ \ K^6\alpha^6(\alpha-3)St_2{}^2$$

$$\%B_{w,\omega_o} = 2(\alpha-1)\{3\alpha St^2 - 6\alpha(1 - iSt_2) - i(\alpha-1)St^3\ \} + i4K\alpha(\alpha-1)\{(\alpha+10)(1 - iSt_2) - (5+\alpha)St_2{}^2 + i\ \ (\alpha-1)St_2{}^3)\}$$
$$+K^2\alpha^2\{(1 - iSt_2)(76 - 81\alpha + \alpha^2) + 2St_2{}^2(\alpha-1)(23 + 2\alpha + iSt_2 - i\alpha St_2)\}$$
$$+K^3\alpha^3\{8\alpha^2(1 - iSt_2) - (\alpha-1)(-49 + i49St_2 + 46St_2{}^2 + 6\alpha St_2{}^2)\}$$

$$\%C_{w,\omega_o} = \{-16(i + St_2)^2\} + 4K\{-5 + \alpha + i10St_2 + \ i2\alpha St_2\ \ + \ 6St_2{}^2 + 8\alpha St_2{}^2\} - 4K^2\alpha\{1 + i3St_2 + 14St_2{}^2$$
$$+\alpha(3 - i7St_2 + 5St_2{}^2)\} + 2K^3\alpha^2\{11 + \alpha - i24St_2 - i8\alpha St_2 + 23St_2{}^2 + 2\alpha St_2{}^2\}$$
$$+K^4\alpha^3\{-9 + i2(20+\alpha)St_2 - 16St_2{}^2\} + K^5\alpha^4\{1 - i11St_2 + 2St_2{}^2\} + iK^6\alpha^5 St_2$$

$$\%D_{w,\omega_o} = \{(1 + iSt_2(1 - 2K\alpha))\ \ (-4 + \alpha - \alpha^2 + K\alpha(13 + 3\alpha) - 2K^2\alpha^2(9+\alpha) + 8K^3\alpha^3)\}$$

$$\%E_{w,\omega_o} = -16(\alpha-1)^2 + 8K\alpha\{3 - 5\alpha + 4\alpha^2\} + 4K^2\alpha^2\{15 - 31\alpha + 2\alpha^2\} + 3K^3\alpha^3\{-29 + 44\alpha + 5\alpha^2\}$$
$$+K^4\alpha^4\{59 - 77\alpha - 8\alpha^2\} + 2K^5\alpha^5\{-7 + 9\alpha\}$$

The transfer function expressions in the limit of $K\alpha \rightarrow 1$ are given by:

$$\lim_{K\alpha\to 1} G_{c,\omega_o} = \frac{2\left(-1+e^{i\,St_2}(1-iSt_2)\right)}{St_2^{\,2}} + \varepsilon^2\left(\frac{26-59\alpha+31\alpha^2+iSt_2(\alpha-1)(5\alpha-4)}{2St_2^2\alpha^2}+\right.$$

$$\left. e^{i\,St_2}\frac{-30(26-59\alpha+31\alpha^2)+60iSt_2(11-25\alpha+13\alpha^2)+15St_2^2(3\alpha-2)(7\alpha-9)+5iSt_2^3\left(13-31\alpha+16\alpha^2\right)-(15St_2^4-2iSt_2^5)(\alpha-1)^2}{60St_2^2\alpha^2}\right)$$

$$\lim_{K\alpha\to 1} G_{w,\omega_o} = \frac{2\left(1+e^{i\,St_2}(-1+iSt_2+St_2^2)\right)}{St_2^{\,2}} + \varepsilon^2\left(\frac{-26+59\alpha-31\alpha^2}{2St_2^2\alpha^2}+\right.$$

$$\left. e^{i\,St_2}\frac{30(1-iSt_2-\frac{St_2^2}{2})(26-59\alpha+31\alpha^2)+5iSt_2^3\left(28-61\alpha+31\alpha^2\right)+5St_2^4\left(4-13\alpha+7\alpha^2\right)-(7iSt_2^5+2St_2^6)(\alpha-1)^2}{60St_2^2\alpha^2}\right)$$

Appendix E

The transfer function at the first harmonic, defined as $G_{2\omega_o} = \dfrac{A'(2\omega_o)/A_o}{u(\omega_o)'/u_o}$, is:

$$G_{2\omega_o} = \varepsilon\left(\frac{\tilde{A}_{2\omega_o}e^{i\,2K\alpha\,St_2}}{8\alpha(K\alpha-1)^3St_2^2}+\frac{\tilde{B}_{2\omega_o}e^{i\,2\,St_2}}{8\alpha(K\alpha-1)^3St_2^2}+\frac{\tilde{C}_{2\omega_o}\;K\,e^{i\,(K\alpha+1)\,St_2}}{(K\alpha+1)^2(K\alpha-1)^3St_2^2}+\frac{\tilde{D}_{2\omega_o}}{8\alpha(K\alpha+1)^2St_2^2}\right) \quad (52)$$

where the coefficients $\tilde{A}_{2\omega o}$ to $\tilde{D}_{2\omega_o}$ for conical flames are given as

$$\tilde{A}_{c,2\omega_o} = (3-\alpha-2K\alpha)$$
$$\tilde{B}_{c,2\omega_o} = (\alpha-3)\alpha^2K^2+(4-2\alpha(1+iSt_2)+2iSt_2)\alpha K+i2(\alpha-1)(i+St_2)$$
$$\tilde{C}_{c,2\omega_o} = (-3+2\alpha+\alpha^2K^2)$$
$$\tilde{D}_{c,2\omega_o} = 5-\alpha(3+i2St_2)+i2St_2+K\alpha(3-\alpha(1+i2St_2)+i2St_2)$$

The coefficients for wedge flames reduce to:

$$\tilde{A}_{w,\omega_o} = (-3+\alpha+2K\alpha)(1-i2\alpha KSt_2)$$
$$\tilde{B}_{w,\omega_o} = i(\alpha-3)(i+2St_2)\alpha^2K^2-2(\alpha-1)(-1+i2St_2+2St_2^2)+2\alpha K(-2+\alpha+i4St_2-i2\alpha St_2+2(\alpha-1)St_2^2)$$
$$\tilde{C}_{w,\omega_o} = i(-3+2\alpha+\alpha^2K^2)(i+St_2(1+\alpha K))$$
$$\tilde{D}_{w,\omega_o} = -5-3\alpha(K-1)+\alpha^2K$$

Note that the response at the first harmonic has three characteristic time scales represented by the terms $2St_2$, $2St_c$ and $(K\alpha+1)St_2 = St_2+St_c$. As discussed in the previous section, boundary conditions are solely responsible for St_2 while flow non-uniformities account for St_c. The new characteristic time scale represented by the term $(K\alpha+1)St_2$ arises from coupling between non-linearities due to boundary conditions and flow non-uniformities. Similar to the response at the fundamental frequency, there is a single characteristic time scale in the limit of $(K\alpha\to 1)$ represented by the term $2St_2$. In the limit of $(K\alpha\to 1)$, Eq. (52) reduces to:

$$\lim_{K\alpha\to 1} G_{c,2\omega_o} = \varepsilon\left(\frac{3(\alpha-2)(e^{i2St_2}-1)-3i(\alpha-1+(\alpha-3)e^{i2St_2})St_2+6e^{i2St_2}St_2^2+i2(\alpha-1)e^{i2St_2}St_2^3}{24\alpha St_2^2}\right)$$

$$\lim_{K\alpha\to 1} G_{w,2\omega_o} = \varepsilon\left(\frac{-3(\alpha-2)(e^{i2St_2}-1)+6(\alpha-2)(i+St_2)e^{i2St_2}St_2+4St_2^3e^{i2St_2}(i(\alpha+2)-(\alpha-1)St_2^4)}{24\alpha St_2^2}\right)$$

For the uniform velocity case (K=0), the transfer functions for conical and wedge flames can be simplified to:

$$\lim_{K\to 0} G_{c,2\omega_o} = \varepsilon(\alpha-1)\left(\frac{e^{2i\,St_2}(1-iSt_2)-1-iSt_2}{4St_2^2\alpha}\right) \quad (53)$$

$$\lim_{K\to 0} G_{w,2\omega_o} = \varepsilon(\alpha-1)\left(\frac{1+e^{2i\,St_2}(-1+2St_2(i+St_2))}{4St_2^2\alpha}\right) \quad (54)$$

As the flame becomes long (i.e. increase in α), the gain drops considerably.

11. REFERENCES

[1] Cohen, J., Banaszuk, A., *J. Prop. Power*, Vol. 19 (5), 2003.
[2] Straub, D.L., Richards, G.A., Effect of Fuel Nozzle Configuration on Premix Combustion Dynamics, *ASME paper # 98-GT-492*, 1998.
[3] Paschereit, C.O., Gutmark, E., Weisenstein, W., Control of Thermo-Acoustic Instabilities and Emissions in an Industrial Type Gas Turbine Combustor, *Proc. Comb. Inst.*, 1998.
[4] Hsiao, G.C., Pandalai, R.P., Hura, H.S., Mongia, H.C., Combustion Dynamic Modeling for Gas Turbine Engines, *AIAA paper # 98-3380*.
[5] Crocco, L., Cheng, S., *Theory of Combustion Instability in Liquid Propellant Rocket Motors*, Butterworths Scientific Publications, London, 1956.
[6] Munjal, M., *Acoustics of Ducts and Mufflers*, John Wiley & Sons: New York, 1987.
[7] Fleifil, M., Annaswamy, A.M., Ghoniem, Z.A., Ghoniem, A.F., Response of a Laminar Premixed Flame to Flow Oscillations: A Kinematic Model and Thermoacoustic Instability Results, *Comb. and Flame*, Vol. 106, 1996, pp. 487-510.
[8] Ducruix, S., Durox, D., Candel, S., Theoretical and Experimental Determinations of the Transfer Function of a Laminar Premixed Flame, *Proc. Comb. Inst*, Vol. 28, 2000.
[9] Kruger, U., Hüren, J., Hoffman, S., Krebs, W., Bohn, D., Prediction of Thermoacoustic Instabilities with Focus on the Dynamic Flame Behavior for the 3A-Series Gas Turbine of Siemens KWU, *ASME Paper #99-GT-111*.
[10] Walz, G., Krebs, W., Hoffman, S., Judith, H., Detailed Analysis of the Acoustic Mode Shapes of an Annular Combustion Chamber, *ASME Paper #99-GT-113*.
[11] Schuermans, B.H., Polifke, W., Paschereit, C.O., Modeling Transfer Matrices of Premixed Flames and Comparison with Experimental Results *ASME Paper #99-GT-132*.
[12] Zinn, B.T., Powell, E.A., Nonlinear Combustion Instability in Liquid- Propellant Rocket Engines, *Proc. Comb. Inst*, Vol. 13, 1970.
[13] Culick, F.E.C., Burnley, V., Swenson, G., Pulsed Instabilities in Solid-Propellant Rockets, *J. Prop. Power*, Vol. 11(4), 1995.
[14] Culick, F.E.C., Non-Linear Growth and Limiting Amplitude of Acoustic Oscillations in Combustion Chambers, *Comb. Sci. Tech.,* Vol. 3(1), 1971.
[15] Lieuwen, T., Experimental Investigation of Limit Cycle Oscillations in an Unstable Gas Turbine Combustor, *J. Prop. Power*, Vol. 18 (1), 2002.

[16] Dowling, A.P., Nonlinear Self-Excited Oscillations of a Ducted Flame, *J. Fluid Mech*. Vol. 346, pp. 271-290, 1997.
[17] Peracchio, A.A., Proscia, W.M., Nonlinear Heat Release/Acoustic Model for Thermo-Acoustic Instability in Lean Premixed Combustors, *Journal of Engineering for Gas Turbines and Power*, Vol. 121, 1999.
[18] Wu, X., Wang, M., Moin, P. Peters, N., Combustion Instability due to the Nonlinear Interaction Between Sound and Flame, *J. Fluid Mech.*, Vol. 497, 2003, pp.23-53.
[19] Poinsot, T., Veynante, D., Bourienne, F., Candel, S., Esposito, E., Surget, J., Initiation and Suppression of Combustion Instabilities by Active Control, *Proc. Comb. Inst*., Vol. 22, 1988.
[20] Dowling, A.P., A Kinematic Model of a Ducted Flame, *J. Fluid Mech*., Vol. 394, pp. 51-72, 1999.
[21] Searby, G., Acoustic Instability in Premixed Flames, *Comb. Sci. Tech.*, Vol. 81, 1992, pp.221-231
[22] Kulsheimer, C., Buchner, H. Combustion Dynamics of Turbulent, Swirling Flows, *Comb. and Flame*, Vol. 131, 2002, pp.70-84.
[23] Lieuwen, T., Neumeier, Y., Nonlinear Pressure-Heat Release Transfer Function Measurements in a Premixed Combustor, *Proc. Comb. Inst.*, Vol. 29, 2002.
[24] Lee, J.G., Santavicca, D. Experimental Diagnostics for the Study of Combustion Instabilities in Lean, Premixed Gas Turbine Combustors, *J. Prop. Power*, Sept. 2003.
[25] Bourehla, A., Baillot, F., Appearance and Stability of a Laminar Conical Premixed Flame Subjected to an Acoustic Perturbation, *Comb. and Flame*, Vol. 114, pp. 303-318, 1998.
[26] Balachandran, R., Ayoola, B.O., Kaminski, C.F., Dowling, A.P., Mastorakos, E., Experimental Investigation of the Nonlinear Response of Turbulent Premixed Flames to Imposed Velocity Oscillations, *Comb. And Flame*, Vol. 143, 2005, pp. 37-55.
[27] Durox, D., Baillot, F., Searby, G., Boyer, L., On the Shape of Flames Under Strong Acoustic Forcing: A Mean Flow Controlled by an Oscillating Flow, *J. Fluid Mech*., Vol. 350, pp. 295-310, 1997.
[28] Lieuwen, T., Torres, H., Johnson, C., Daniel, B.R., Zinn, B.T., A Mechanism for Combustion Instabilities in Premixed Gas Turbine Combustors, *Journal of Engineering for Gas Turbines and* Power, Vol. 123(1), 2001, pp. 182-190.
[29] Neumeier, Y., Nabi, A., Zinn, B.T., Investigation Of The Open Loop Performance Of An Active Control System Utilizing A Fuel Injector Actuator, *AIAA paper # 96-2757,* 1996
[30] Broda, J.C., Seo, S., Santoro, R.J., Shirhattikar, G., Yang, V., An Experimental Investigation of Combustion Dynamics of a Lean, Premixed Swirl Injector, *Proc. Comb. Inst.,* Vol. 27, 1998, pp. 1849-1856
[31] Bendat, J., Piersol, A., *Random Data: Analysis and Measurement Procedures*, John Wiley and Sons: New York, 1986
[32] Schuller, T., Durox, D., Candel, S., A Unified Model For The Prediction of Laminar Flame Transfer Functions: Comparisons Between Conical and V-Flame Dynamics, *Comb. Flame*, Vol. 134, pp. 21-34, 2003.
[33] Coats, C., Coherent Structures in Combustion, *Prog. Energy Combust. Sci*., Vol. 22, 1996, pp. 427-509
[34] Clavin, P., Pelce, P., He, L., One-Dimensional Vibratory Instability of Planar Flames Propagating in Tubes, *J. Fluid Mech.*, Vol. 216, 1990, pp. 299-322
[35] Searby, G., Rochwerger, D., A Parametric Acoustic Instability in Premixed Flames, *J. Fluid Mech.*, Vol. 231, 1991, pp. 529-543
[36] Vaezi, V., Aldredge, R.C., Laminar Flame Instabilities in a Taylor-Couette Combustor, *Comb. and Flame,* Vol. 121, 2000a, pp. 356-366
[37] Vaezi, V., Aldredge, R.C., Influences of Acoustic Instabilities on Turbulent-Flame Propagation, *Experimental Thermal and Fluid Science*, Vol. 20, 2000b, pp.162-169.
[38] Markstein, G., "Flames as Amplifiers of Fluid Mechanical Disturbances", *Proceedings of the Sixth National Congress on Applied Mechanics*, 1970, pp. 11-33.
[39] Abom, M., Boden H., Error Analysis of Two-Microphone Measurements in Ducts with Flow. *J. Acoust. Soc. Am.*, **83**(6), pp.2429–2438, 1988.
[40] Durox, D., Schuller, T. & Candel, S. 2005. *Proc. Comb. Inst* **30**: 1717-1724
[41] Candel, S. 2002. *Proc. Comb. Inst* **29**: 1-28
[42] Broda, J. C., Seo, S., Santoro, R. J., Shirhattikar, G. & Yang, V. 1998. *Proc. Comb. Inst.* **27**: 1849-1856
[43] Dowling, A. P. & Stow, S. R. 2003. *J. Prop. Power* **19**(5): 751-764
[44] Ducruix, S., Schuller, T., Durox, D. & Candel, S. M. 2003. *J. Prop. Power* **19**(5): 722-734
[45] Bellows, B., Zhang, Q., Neumeier, Y., Lieuwen, T. & Zinn, B. T. (2003-0824). AIAA

[46] Lee, J. G. & Santavicca, D. A. 2003. *J. Prop. Power* **19**(5): 735-750
[47] Lieuwen, T. & Neumeier, Y. 2002. *Proc. Comb. Inst.* **Vol. 29**(1): 99-105
[48] Poinsot, T., Veynante, D., Bourienne, F., Candel, S., Esposito, E. & Surget, J. 1988. *Proc. Comb. Inst.* **22**: 1363-1370
[49] McIntosh, A. C. 1999. *Phil. Trans. R. Soc. Lond. A.* **357**: 3523-3538
[50] Keller, D. & Peters, N. 1994. *Theoret. Comput. Fluid Dynamics* **6**: 141-159
[51] Peters, N. & Ludford, G. S. S. 1983. *Comb. Sci. Tech.* **34**: 331-344
[52] Van Harten, A., Kapila, A. & Matkowsky, B. J. 1984. *SIAM J. Appl. Math.* **44**(5): 982-995
[53] Baillot, F., Durox, D. & Prud'homme, R. 1992. *Comb. Flame* **88**(2): 149-168
[54] Lieuwen, T. 2005. *Proc. Comb. Inst.* **30**(2): 1725-1732
[55] Baillot, F., Bourehla, A. & Durox, D. 1996. *Comb. Sci Tech.* **112**: 327-350
[56] Blackshear, P. 1953. *Proc. Comb. Symp.* **4**: 553-566
[57] Markstein, G. H. (1964). Nonsteady flame Propagation, Pergamon
[58] Marble, F. E. & Candel, S. M. 1978. *Proc. Comb. Inst.* **17**: 761-769
[59] Matalon, M. & Matkowsky, B. 1982. *J. Fluid Mech.* **124**: 239-260
[60] Boyer, L. & Quinard, J. 1990. *Comb. Flame* **82**(1): 51-65
[61] Poinsot, T. & Candel, S. M. 1988. *Comb. Sci. Tech.* **61**
[62] Subbaiah, M. V. 1983. *AIAA* **21**(11): 1557-1564
[63] Yang, V. & Culick, F. E. C. 1986. *Comb. Sci. Tech.* **45**: 1-25
[64] Aldredge, R. 1992. *Comb. Flame* **90**(2): 121-133
[65] Ashurst, W. & Sivashinsky, G. 1991. *Comb. Sci Tech.* **80**(1-3): 159-164
[66] Ashurst, W., Sivashinsky, G. & Yakhot, V. 1988. *Comb. Sci Tech.* **62**(4-6): 273-284
[67] Joulin, G. & Sivashinsky, G. 1991. *Comb. Sci Tech.* **77**: 329-335
[68] Clanet, C., Searby, G. & Clavin, P. 1999. *J. Fluid Mech.* **385**: 157-197
[69] Cho, J. H. & Lieuwen, T. 2005. *Comb. Flame* **140**(1): 116-129
[70] Lee, D. H. & Lieuwen, T. 2003. *J. Prop. Power* **19**(5): 837-846
[71] Bechert, D. & Pfizenmaier, E. 1975. *J. Fluid Mech.* **72**: 341-352
[72] Ferguson, D., Richards, G., Woodruff, S., Bernal, S. & Gautam, M. 2001. *Proc. 2nd Joint Meeting U.S. Sections Comb. Inst.*
[73] Michalke, A. 1971. *Z. Flugwiss.(in German)* **19**
[74] Kuramoto, Y. & Tsuzuki, T. 1975. *Prog. Theo. Phys* **54**(3): 687-699
[75] Sivashinsky, G. I. 1983. *Ann. Rev. Fluid Mech* **15**: 179-199
[76] Searby, G. & Clavin, P. 1986. *Comb. Sci. Tech.* **46**(3-6): 167-193
[77] Bychkov, V. 1999. *Phys. Fluids* **11**(10): 3168-3173
[78] Searby, G. & Rochwerger, D. 1991. *J. Fluid Mech.* **231**: 529-543
[79] Jiang, G. & Peng, D. 2000. *SIAM J. Sci. Comput.* **21**: 2126-2143
[80] Gottlieb, S. & Shu, C. 1998. *Math. Comput.* **67**: 73-85
[81] Wicker, J. M., Greene, W. D., Kim, S. & Yang, V. J. 1996. *J. Prop. Power* **12**(6)
[82] Culick, F.E.C., Yang, V. "Overview of Combustion Instabilities in Liquid-Propellant Rocket Engines" *Liquid Rocket Engine Combustion Instability* Chapter 1, Progress in Astronautics and Aeronautics vol. 169, eds., V. Yang and W.E. Anderson, pp. 3-37, 1995.
[83] Nayfeh, A.H., Mook, D.T., *Nonlinear Oscillations*, John Wiley & Sons: New York, 1995.
[84] Cohen, J., Wake, B.E., Choi, D., Investigation of Instabilities in a Lean, Premixed Step Combustor*, J. Prop. Power*, Vol. 19(1), pp.81-88, 2003.
[85] Straub, D.L., Richards, G.A., Effect of Fuel Nozzle Configuration on Premix Combustion Dynamics, *ASME paper # 98-GT-492*, 1998..
[86] Paschereit, C.O., Gutmark, E., Weisenstein, W., Control of Thermo-Acoustic Instabilities and Emissions in an Industrial Type Gas Turbine Combustor, *Proc. Comb. Inst.*, 1998.
[87] Mongia, H.C., Held, T.J., Hsiao, G.C., Pandalai, R.P., Challenges and Progress in Controlling Combustion Dynamics in Gas Turbine Combustors, *J. Prop. Power*, Vol. 19(5), pp.822-829, 2003.
[88] Cowell, L.H., Experience at Solar Turbines with Combustion Oscillations in Lean Premixed Combustion, Proceedings of AGTSR Combustion Workshop, Penn. State, Sept. 10-11, 1995.

[89] McManus, K.R., Poinsot, T., Candel, S.M., Review of Active Control of Combustion Instabilities, *Prog. Energy Combust. Sci.*, **19**(1), 1993, pp.1-29.
[90] Neumeier, Y., Zinn, B.T., "Experimental Demonstration of Active Control of Combustion Instabilities Using Real Time Modes Observation and Secondary Fuel Injection", *Proc. Comb. Inst.,* **26**, 1996.
[91] Sattinger, S.S., Neumeier, Y., Nabi, A., Zinn, B.T., Amos, D.J., Darling, D.D., "Sub-scale Demonstration of Active Feedback Control of Gas-Turbine Combustion Instabilities", *Proc. Int. Gas Turbine and AeroEngine Congress and Exhibition,* 1998.
[92] Johnson, C.E., Neumeier, Y., Darling, D.D., Sattinger, D.D., Neumaier, M., Zinn, B.T., "Demonstration of Active Control of Combustion Instabilities on a Full Scale Gas Turbine Combustor", *36th AIAA/ASME/SAE/ASEE Joint Propulsion Conference,* 2000.
[93] Neumeier, Y., Cohen, J., Shcherbik, D., Lubarsky, E., Zinn, B.T., "Suppression of Combustion Instabilities in Gaseous Fuel Combustor Using Fast Adaptive Control, Part 1: Controllability Tests", *AIAA paper 2002-4076*, 2002.
[94] Lubarsky, E., Shcherbik, D., Zinn, B.T., "Active Control of Instabilities in High-Pressure Combustor by Non-Coherent Oscillatory Fuel Injection", *AIAA paper 2003-4519*, 2003
[95] McManus, K., Poinsot, T., Candel, S.M., *Prog. Energy Combust. Sci*., Vol. 19, pp. 1-29, 1993.
[96] Johnson, C., Neumeier, Y., Lubarsky, E., Lee, J., Zinn, B.T., *AIAA Paper # 2000-0476*.
[97] Sattinger, S.S., Neumeier, Y., Nabi, A., Zinn, B.T., Amos, D.J., Darling, D.D., *J. Engr. Gas Turbines Power*, Vol. 122, 2000, pp 262-268.
[98] Coker, A., Neumeier, Y., Lieuwen, T., Zinn, B.T., Menon, S., *AIAA Paper #2003-1009*.
99 Lieuwen, T., "Modeling Premixed Combustion-Acoustic Wave Interactions: A Review", Journal of Propulsion and Power., Vol. 19 (5), 2003, pp. 765-781.

[100] Preetham, Lieuwen, T., Nonlinear Flame-Flow Transfer Function Calculations: Flow Disturbance Celerity Effects Part 2, *AIAA paper 2005-0543*, 2005.

Aerothermal Effects of Interfacial Leakage and Film Cooling Schemes with Endwall and Leading Edge Contouring

Final Report
May 2002 -October 2005

by T.W. Simon (tsimon@me.umn.edu) and R.J. Goldstein (rjg@me.umn.edu), PIs
J.D. Piggush (jpiggush@me.umn.edu) and Marco Papa (marco.papa@me.umn.edu), RAs

Date Report was issued (December 2005)
DOE Award Number (Clemson U/02-01-SR096/DOE PR)
UTSR Project Number (02-01-SR096)

Heat Transfer Laboratory
Department of Mechanical Engineering
University of Minnesota
111 Church St. S.E.
Minneapolis, Minnesota
55455

Administrative Office: Sponsored Projects Administration, University of Minnesota
450 Gateway Building, 200 Oak Street S.E., Minneapolis, MN 55455-2070
c/o Shannon Lovelace <slovelac@umn.edu>

Disclaimer

Abstract

In this report, significant results from the University of Minnesota endwall study conducted over a three-year contract period are presented. During this period, the test sections were modified and qualified then used to take detailed flow, heat (mass) transfer and adiabatic effectiveness measurements in both a vane cascade and a rotor cascade.

In the vane cascade, a series of experiments was completed where the effects on heat transfer coefficients and adiabatic effectiveness values were documented for various geometries and injection rates. The results show the effects of introducing gaps at the transition between the combustor and the first stage vane endwall or in the platform of the endwall. Shown is how the endwall convective heat transfer coefficients and adiabatic effectiveness values are changed by the gaps, gap leakage and steps at the gaps.

In the rotor cascade, direct comparisons of heat and mass transfer measurements on the blade and endwall surfaces show the validity of the heat and mass transfer analogy. The effects of leading edge modifications are investigated through heat and mass transfer measurements on the endwall of the cascade. The effects of simulated wheelspace coolant injection upstream of the cascade are quantified through mass transfer measurements, deriving maps of adiabatic cooling effectiveness on the blade and endwall surfaces. Finally, the use of mass transfer data to validate a numerical heat/mass transfer code is demonstrated, comparing mass transfer measurements on the blade and endwall surfaces to values predicted by a RANS simulation using the SST k-ω model for turbulence closure.

Table of Contents

Introduction

The first stage turbine is directly downstream of the combustor and is thus subject to extremely high temperatures. Adding to the severity, recent combustor development in gas turbine engines has resulted in a more uniform temperature distribution across the first stage turbine inlet passage than in earlier designs. Thus, the endwall regions of the first stage turbine must support higher thermal loading than in earlier generations and efficient cooling schemes that focus on the endwall region must be developed. Cooling the endwall region of the turbine is made more difficult by complex secondary flows that result from interactions between passage and horseshoe vortices, leakage flows from component interfaces and emerging film-cooling flows. In support of the development of more efficient endwall cooling schemes, experiments are conducted to document the effectiveness of leakage through the combustor-to-turbine transition slot or through the endwall slashface gap within the turbine using various injection methods. To address real problems associated with assembly misalignment and in-use thermal growth, several flow path geometries that replicate less than ideal alignment of components are considered. Documentation is by way of endwall and airfoil heat or mass transfer rates and flow measurements within the passage, with focus on the near endwall regions. Heat transfer data are obtained under a nearly constant temperature boundary condition, which is equivalent to a constant mass concentration in the cases of mass transfer measurements. This is the best choice for thermal boundary condition of the traditional, well-defined, test-type boundary conditions for it is the best simulation of engine conditions. The measurements are taken at sufficiently high chord Reynolds number values that the test flows are similar to those in operating turbines.

The highest thermal loading is in the vane section. This region is studied experimentally via a vane cascade. Measurements focus on reduction of the effects of secondary flows in the endwall region via endwall contouring and on the effects of gaps in the endwall surface and leakage through those gaps. Aerodynamic measurements are with pitot and hotwire probes. The thermal measurement method uses a thermocouple probe to document the temperature field within the passage, including very near-wall temperature distributions that can be used to obtain local heat transfer coefficient values when the wall is heated. The same probe is employed to measure adiabatic effectiveness values when the wall is adiabatic. These boundary conditions are applied to the pressure surface, the suction surface and the endwall of the passage under study. Using near-wall temperature profiles, gradients in the thermal boundary layer are measured and used to calculate local heat flux values by Fourier's law. The near-wall temperature measurements are extrapolated to the wall to determine the wall temperature. Gaps either without steps or with forward- or backward-facing steps are introduced to the test geometry to allow measuring heat transfer coefficients and adiabatic effectiveness values on the endwall as affected by such non-ideal geometries. Also, aerodynamic losses within the passage are measured under such non-ideal passage geometries as described by the gaps and steps at the gaps. These gaps are ahead of the airfoil row and between airfoils on the endwall (gutters or slashfaces). The effects of leakage flow through the gaps are documented.

Though in a lower temperature region, the rotor has additional strength considerations associated with rotation. Thermal loading is, thus, equally as important as in the vane section. In the rotor study, local heat transfer coefficients are measured using a thermal boundary layer probe. A digital power supply is used to control heaters embedded in the

blade and endwall and maintain their surfaces at a constant set temperature. Concurrently, local mass transfer measurements are made in the same flow to provide higher resolution of the heat (mass) transfer coefficient distributions. This high resolution has been previously shown to be of great value toward describing how the complex near-endwall flow field affects the heat transfer. These data are used also to further describe the analogy between heat and mass transfer in complex flows. A better understanding of the analogy would allow a more complete utilization of the extensive mass transfer database that now resides in the literature. The effects of gaps and steps ahead of the airfoil row on heat (mass) transfer are documented, as well as the effects of leakage flow issuing out the gaps. In a gas turbine engine cooling air is generally bled from the compressor, fed to the wheelspace and then discharged into the mainstream through a `peripheral rim seal,' ideally preventing ingestion of hot gases into the wheelspace. While a number of studies have investigated the mechanisms that govern ingestion, very few have looked at the cooling potential of wheelspace coolant injection on the rotor blade and hubwall surfaces. In order to address this issue, the rotor cascade has been modified to include an injection system that simulates the wheelspace coolant injection upstream of the rotor blades.

Executive Summary

In the vane cascade, measurements of heat transfer performance with the various geometric changes quantify the effects of real passage geometry changes and real leakage flow injection rates on passage heat transfer. Once the thermal conditions are established, the measurements are taken by detailed surveys with a simple thermocouple probe. Computed are the wall heat flux, the wall temperature, the flow temperature distribution, the convective heat transfer coefficient distribution on the endwall and the adiabatic effectiveness of the leakage flow for endwall cooling. The vane cascade has on axially contoured endwall and one straight endwall. Sensitivities of heat transfer behavior to the presence of a gap in the contoured endwall, the amount of gap flow or the degree of misalignment at the gap are documented. One gap is at the junction between the turbine and the combustor-to-turbine transition section. Also presented are studies of the effects of having vane section gaps (slashface gaps). With the slashface gap are the slashface gap flow rate and the misalignment of vane sections on either side of the slashface. These results have been documented in five papers [1 though 5] which have been presented at gas turbine heat transfer sessions. The data indicate a large effect of the slashface gap.

In the rotor cascade study, heat and mass transfer measurements are taken on the blade and endwall surfaces and compared to verify the heat and mass transfer analogy, assessing sensitivity to Reynolds number, freestream turbulence and boundary layer thickness. The effects of a blade leading edge modification have been documented through heat and mass transfer measurements on the endwall surface. The effects of a simulated wheelspace coolant injection are documented through mass transfer measurements on the blade and endwall surfaces. The mass transfer data are reduced to derive maps of adiabatic cooling effectiveness.

I. Project Description

Thermal loading of the endwall region is of concern in the design of the first stage of a gas turbine engine for it is immediately downstream of the combustor and is therefore in a severe thermal environment. As a result, active cooling is needed. However, efficient cooling of the endwall region is difficult because of the complex secondary flows in that region, revealed as passage and horseshoe vortices, leakages from component interfaces and flow from film cooling jets. So far, designers' understanding of transport in this region is not complete and, as a result, cooling schemes are less than optimum. To achieve performance goals, the next generation of engines must have improved thermal management in this region.

The objective of this DOE AGTSR (Advanced Gas Turbine System Research) project is to use an experimental and computational approach to understand transport in the endwall region of a gas turbine and to use the understanding gained to support the design of cooling strategies for this region.

More specific objectives are to:

1. Describe the flow features more completely and document their effects on aerodynamic losses and heat transfer in the endwall region. This is done via detailed measurements of flow and surface heat transfer.

2. Investigate the effects of changes in design variables under simulated engine conditions. This is done via experiments. Variables include airfoil leading edge configurations near the endwall, endwall contouring shapes and degree of component (endwall segments and combustor–to-turbine transition duct joint) misalignment.

3. Document the performance of leakage flow in support of advanced cooling concepts which more efficiently utilize the available leakage flow as coolant.

4. Improve the analogy factor for converting mass transfer data to heat transfer values for flows such as turbine endwall flows.

5. Evaluate computational tools used for gas turbine thermal design.

II. The Experiments

2.1 Measurements in the Linear Vane Cascade

2.1.1 The Vane Cascade Test Facility

The test facility is designed to simulate the geometry and flow inside a first stage vane passage of a modern, mid-sized gas turbine engine. The test section, consisting of three airfoils with two passages, simulates the nozzle guide vanes and endwalls. A detailed description of the test facility is provided in references [1] through [6]. A schematic of the facility is shown in Figures 1 through 3. Contouring provides acceleration of the flow ahead of, and entirely through, the airfoil passage. This has a major influence on the strength of the secondary flow in the passage near each endwall. The freestream turbulence intensity for all cases in this facility is 12% at the vane row inlet plane.

2.1.2 Total Pressure Measurements

Total pressure measurements are made using a 0.7 mm (0.028in) diameter, square tipped total pressure probe. Diaphragm-type pressure transducers with carrier demodulators (Validyne DP-45 and Validyne CD15) produce voltages which are then digitized over a period of 20 seconds using an IOTech ADC488/8SA. These measurements are used to characterize the passage aerodynamic losses. Results were previously documented and are summarized in references [1] and [3]. An example is given in Figure 4.

2.1.3 Heat Transfer Measurements

Thermal measurements within the test section were made by thermocouples. The thermocouples used in this experiment were E-type formed from Constantan and Chromel wires. The wires used for measurement within uniform temperature flow and solids were made using thermocouples of 24 gage wires with junctions electrically welded. Traversing thermocouples used for in-flow measurement, including boundary layer traverses, were also E-type. However, they were formed of 76μm (3 mil) diameter wire and were butt-welded. A total of 117 temperature profiles are taken over the endwall surface for each test run. Measurements are more heavily clustered near the slashface gap and in the downstream portion of the passage (see Figure 5). The method produces accurate heat transfer coefficient distribution measurements over the passage endwall. The probe geometry prevents taking measurements very close to casting fillets at the junction of the vane and endwall and very close to the slashface gap. The heat transfer data were calculated from detailed and direct measurements of the thermal boundary layer at each of the measurement locations. Details can be found in [2], [4] and [6]. An example is shown in Figure 6. Dotted contour lines are included using intervals of 0.5 for Stanton numbers under $7x10^{-3}$. Heat transfer measurements were taken in the upper passage (of the two passages of this test section). These data are replotted, without contour lines, in the adjacent passages. This method of obtaining heat transfer coefficients is particularly suitable for application to this vane passage experiment. First, it does not require the surface to be isothermal or of a uniform heat flux. With an aluminum wall and embedded heaters, the thermal boundary condition is nearer to a constant temperature condition, rather than to a constant heat flux condition. The constant temperature condition more

closely reproduces the passage thermal boundary conditions in the actual engine. For test cases similar to a turbine endwall, the calculated single-sample Stanton numbers were found to agree with those taken through traditional methods to within 11% [6]. To establish the repeatability of the method, the nominal case was repeated a total of four times. In order to more easily compare the cases, the passage is split into 6 regions and the heat transfer coefficients are averaged over each region. The standard deviation ranges from 2 to 7% of the average heat transfer coefficient, which is acceptable considering the difficulty in obtaining accurate heat transfer measurements in this geometry.

2.1.4 Adiabatic Wall Thermal Measurements

Adiabatic wall temperature measurements were made with the adiabatic contoured endwall and airfoil sections in place. For this series of runs, the leakage flow was heated to nominally10K above the freestream temperature. Extrapolation to the endwall of the data taken in the passage gives the surface temperature of the endwall and the adiabatic wall temperature. An example is shown in Figure 7. These data can be used to compute the adiabatic effectiveness. The flow passage data identify where the leakage fluid migrates and how it mixes. An example is shown in Figure 8. The same probe used in the heat transfer measurement is used for the adiabatic wall measurements, with a slight modification. A small detector switch is mounted on the stem of the probe so the switch is activated when the probe contacts the wall. The probe for the heated wall study could use an electrical continuity circuit to determine when the probe touches the wall.

2.1.5 Net Heat Flux Change

Calculation of the net heat flux reduction combines the information gathered from the heat transfer and adiabatic wall temperature studies to give an indication of how much area on the endwall is affected by a change in the blowing parameters. The comparison made in this study is designed to show the change between the heat flux at the nominal case and the heat flux found with some other set of parameters. This computed change distribution gives an indication of how changes in the leakage flow, or geometry of the endwall, may affect the heat flux into the vane endwall. An example is shown in Figure 9. A positive NHFC indicates a reduction of heat flux of the perturbation case over the nominal case.

2.2 Measurements in the Linear Rotor Cascade

2.2.1 The Rotor Cascade Test Facility

Investigations of the rotor flow field and heat/mass transfer are conducted in a blowing type wind tunnel with a five bladed linear cascade in a blade-centered configuration. The blades are large-scale models of a first stage rotor blade of a high-pressure turbine. Details of the facility can be found in Jin and Goldstein [7]. The test section, shown in Figures 10 and 11, has been modified to accommodate endwall plates for heat and mass transfer experiments (Figure 12). The main parameters of the turbine cascade are reported in Table 1.

Table 1. Turbine cascade parameters

Number of blades	5
Chord length of blade – C	18.4 cm
Axial chord length of blade – C_x	13.0 cm
Pitch of cascade – P	13.8 cm
Height of cascade – H	45.7 cm
Aspect ratio (Span/Chord) – H/C	2.48
Solidity (Pitch/Chord) – P/C	0.75
Blade inlet angle – β_1	35^o
Blade outlet angle – β_2	-72.5^o
Inlet/Exit area ratio of the cascade (AR)	2.72
Area ratio of the contraction	6.25
Exit Reynolds number – $Re_{ex}x10^{-5}$ range	4.5-6.9

2.2.2 Mass Transfer Measurements

The heat transfer measurements are performed using an indirect technique that makes use of the analogy between heat and mass transfer [8]. The simulated blade and endwall surfaces are coated with naphthalene through a casting procedure and exposed to the wind tunnel flow. Photographs of the endwall and blade are reported in Figure 12b and 13b. The profiles of the two surfaces are measured with an LVDT (Linear Variable Differential Transformer) probe before and after the wind tunnel test to determine the sublimation of the naphthalene layer. Schematic diagrams of the measurement systems used for the naphthalene surface measurement are reported in Figure 11. The data are then reduced to derive non-dimensional mass transfer coefficients in the form of Sherwood numbers, *Sh*.

2.2.3 Heat Transfer Measurements

Direct heat transfer measurements are performed by measuring the temperature profiles within the conductive region of the thermal boundary layer. Three temperature probes with E-type thermocouples of a diameter of 76μm have been fabricated and calibrated for measurements on the bottom endwall and on the blade pressure and suction surfaces. Each probe consists of three parts: the bare thermocouple wire, the hypodermic needle holding the wire and the stem of the probe. A photograph is shown in Figure 15. The probes are traversed within the thermal boundary layer by a 5-axis measurement system, programmed to automatically find the wall position and move the probes normally to the surface.

A heat transfer endwall plate and a heat transfer blade have been designed to produce uniform surface temperature that would match the boundary conditions of the mass transfer experiments. The blade has fourteen holes for cartridge heaters and one slot near the trailing edge for a strip heater. Thermocouples are installed near the blade surface on both the suction and pressure. An insulating section made of ultra high molecular weight polypropylene with low conductivity (~ 0.4 W/mK) reduces heat conduction losses. This insulating section is hollow to facilitate passage of heater and thermocouple wires. The outputs of the fifteen heaters are individually adjusted to obtain uniform temperature. The heat transfer endwall plate consists of a balsa wood plate, an aluminum plate, a bottom

insulating plate, one hundred 25.4 mm x 25.4 mm strip heaters and thermocouples. Balsa wood is used to provide an unheated region in front of the aluminum plate. Thermocouples are installed close to the surface of the aluminum plate at the center of each heater. An insulating wall made of ultra high molecular weight polypropylene is placed underneath the heaters to reduce heat loss to the bottom wall. The heaters are individually controlled to obtain a uniform surface boundary condition. Photographs of the heat transfer endwall and blade are reported in Figures 12a and 12b, respectively.

A multiple-output digital power supply has been designed to control the 115 heaters (15 in the blade and 100 on the endwall). A PID control algorithm reads the temperatures measured by the thermocouples embedded in the blade and endwall and adjusts the power supplied to each heater to maintain uniform surface temperatures. A photograph of the power supply is reported in Figure 14. Its specifications are summarized in Table 2.

Table 2. Specification of multiple-output digital power supply

Total power	1200 watts
Power at each output	10 watts
Number of output	128
Voltage range	0-10, 20, 30 and 40 with 256 steps
Control method	Parallel port in Linux

2.2.4 Injection System

An injection system has been added to the facility to simulate the effects fo the wheelspace coolant injection upstream of the rotor blades. Compressed air taken from the building supply enters a plenum located below the wind tunnel test section before being injected into the mainstream. Schematic diagrams of the injections system are reported in Figure 16. The flow is injected at a 45º angle to the bottom endwall and has no component in the pitchwise direction of the cascade. This corresponds to an idealized situation in which the wheelspace coolant rotates with the disk onto which the rotor blades are mounted. This assumption allows the investigation of a limiting case and has the advantage of yielding the same injection direction for all blowing ratios.

Before entering the plenum, the injection air flows through a valve, a pressure regulator, a heat exchanger and a calibrated orifice meter. The heat exchanger, located in the wind tunnel upstream of the contraction, helps bring the temperature of the injection air close to the mainstream flow temperature. Finer adjustment of the temperature of the injection air is obtained using a tape heater controlled with a variable power supply, located shortly upstream of the plenum. The temperature of the injected flow is measured with an E-type thermocouple located in the upper portion of the plenum. Five E-type thermocouples embedded in the naphthalene with their beads close to the surface measure the naphthalene temperature at the interface with air. During the experiments, these two temperatures are kept to within 0.2 ºC of each other. Their variation in time during the run, which lasts for approximately one hour, does not exceed 0.2 ºC. Accurate measurement and control of the temperature is important, as the value of naphthalene vapor pressure is strongly dependent on temperature (roughly 10% variation per ºC).

In studying the effect of upstream component misalignment on fluid flow and mass transfer three configurations are used: a step up (forward facing step), a step down

(backward facing step) and no step. Schematic diagrams for the three configurations are reported in Figure 17. The step height and the slot width measure 3.1% of the axial chord, and the slot is located at a distance of 10% of the axial chord upstream of the cascade.

2.2.5 Adiabatic Cooling Effectiveness Measurements

Results of film cooling studies are usually presented in terms of the adiabatic cooling effectiveness, η_f, that can be calculated directly from temperature measurements on a nominally adiabatic surface. This parameter can also be derived from experiments with a constant wall temperature boundary condition [9], which can be conveniently performed using the heat/mass transfer analogy with naphthalene sublimation. The technique consists in coating the specimen with naphthalene and measuring the profiles before and after exposure to the flow to determine the local sublimation depth. The data are reduced to derive non-dimensional mass transfer coefficients in the form of Sherwood numbers, Sh. Two sets of experiments are needed to derive η_f. In the first case naphthalene-free air is injected upstream of the surface being studied, while naphthalene-saturated air is injected in the second set of experiments. In an equivalent heat transfer experiment these two conditions would correspond to injecting fluid at the freestream temperature and at the endwall temperature, respectively. The mass transfer coefficients obtained injecting naphthalene-saturated air are denoted using a prime in this report. The local adiabatic cooling effectiveness is calculated as $\eta_f = (Sh - Sh')/ Sh$.

III. Results and Discussion

3.1 Measurements of Flow and Heat Transfer from the Linear First-Stage-Vane Cascade Experiment

The cases studied may be generally grouped into eight configurations:

- Smooth passage: No steps, gaps or leakage flows
- Nominal configuration: No steps, 0.5% MFR through the slashface and transition section gaps
- Increased transition section gap leakage: No steps, 0.5% MFR through the slashface gap and 1.0% MFR through the transition section gap
- Increased slashface gap leakage: No steps, 1.0% MFR through the slashface gap and 0.5% MFR through the transition section gap
- Transition section forward facing step: 1.5% step at the transition section gap, 0.5% MFR through the slashface and transition section gaps
- Transition section backward facing step: -1.5% step at the transition section gap, 0.5% MFR through the slashface and transition section gaps
- Slashface forward facing step: 1.5% step at the slashface gap, 0.5% MFR through the slashface and transition section gaps
- Slashface backward facing step: -1.5% step at the slashface gap, 0.5% MFR through the slashface and transition section gaps

Five methods used to produce the data which document each of these configurations:

- Factorial study of experiment parameters on exit total pressure loss
- Single parameter perturbation study of exit total pressure loss
- Heat transfer coefficient study
- Adiabatic effectiveness distribution study
- Net heat flux change study

The conclusions for each of these cases based on the studies outline above are:

Smooth passage: No steps, gaps or leakage flows.

The smooth passage case has losses typical of other contoured vane passages studied in the literature. Contouring of one endwall (while keeping the second endwall straight) and the streamwise acceleration associated with contouring, was shown to strongly decrease endwall secondary flows on both the straight and the contoured endwalls. The effects of endwall curvature on the loss distribution are noted as added losses on the contoured endwall surface relative to the losses on the straight endwall surface. Heat transfer coefficients for this configuration are similar to those found in other studies with endwall contouring: inlet plane coefficients are characteristic of an inlet boundary layer development. Heat transfer coefficients increase as the flow accelerates in the passage and a zone of high heat transfer is observed in the vane wake. The substantial influence of the pressure side leg of the horseshoe vortex noted in cascades which had no endwall contouring was not observed in this case due to the contouring.

Nominal configuration: No steps, 0.5% MFR through the slashface and transition section gaps

The nominal configuration had a large increase in loss, as compared with the smooth passage case. This was due to the low-momentum leakage fluid being introduced at the slashface. Details of the flow measurements are in [1] and [3]. A comparison of pressure coefficient distributions is shown in Figure 18. Heat transfer coefficients are increased over those of the smooth case. This is mainly the result of the slashface gap which experiences a sink flow in the upstream portion of the gap. In the downstream portion of the passage, flow is ejected from the gap to the passage, pushing the thermal boundary layer off the endwall and creating blockage. This is shown in Figure 19. Details of the heat transfer measurements are in [2] and [4]. Adiabatic effectiveness values for the nominal case show good leakage coverage near the suction side of the transition section gap, but little coverage in downstream portions of the passage. This is shown in Figure 20. Details of the adiabatic effectiveness measurements are in [5].

Increased transition section gap leakage: No steps, 0.5% MFR through the slashface gap and 1.0% MFR through the transition section gap

The factorial study did not indicate a significant influence of the increased transition section flow on losses. However, the single parameter perturbation study indicates somewhat larger losses with high injection momentum flux ratios. Losses associated with transition section gap leakage appear to scale with momentum flux. The heat transfer is mainly affected by the higher mass of fluid in the boundary layer in the upstream portion of the cascade. Downstream portions of the endwall experience an increase in heat transfer coefficients due to the added turbulence. Adiabatic effectiveness measurements indicate much more uniformity with increased transition section leakage flow. The net heat flux is substantially reduced upstream of the throat. Downstream of the throat, some regions show a slight increase in heat flux with the increase in transition section gap leakage.

Increased slashface gap leakage: No steps, 1.0% MFR through the slashface gap an 0.5% MFR through the transition section gap

The factorial study indicates a large rise in loss with increased slashface blowing. Perturbation studies confirm that losses increase with increased slashface leakage. Heat transfer data indicate similar inlet plane heat transfer coefficients to those of the nominal case. Heat transfer coefficients downstream of the slot are depressed by the added mass of fluid in the boundary layer. Adiabatic effectiveness measurements indicate improved coverage downstream of the slashface gap; however, adiabatic effectiveness values remain small. The net heat flux is slightly reduced over much of the passage, with a greater reduction in the portion of the passage downstream of the slashface gap. This is shown in Figure 9.

Transition section forward facing step: 1.5% step at the transition section gap, 0.5% MFR through the slashface and transition section gaps

The forward facing step imposes acceleration on the flow just ahead of the inlet plane. This is shown by the factorial study to reduce losses. Heat transfer rates in the downstream portion of the passage are increased slightly. The leakage flow from the transition section gap is distributed more uniformly from the slot due to the imposed acceleration over the

gap. Heat flux is little changed over much of the endwall surface, except for the portion of the endwall between the suction side of the vane and the forward portion of the slashface gap. The heat flux is increased as a result of the forward-facing step at the transition section.

Transition section backward facing step: -1.5% step at the transition section gap, 0.5% MFR through the slashface and transition section gaps

The backward facing step is shown by the factorial study to increase losses. This may be due to the increase in boundary layer thickness produced by the low momentum fluid behind the step. Heat transfer data indicate lower heat transfer rates downstream of the slashface gap, as compared to values for the nominal case (Figure 21). This is the result of the thickened boundary layer. The value of adiabatic effectiveness over much of the passage is increased in this case and a corresponding reduction in the net heat flux is seen in some portions of the passage.

Slashface forward facing step: 1.5% step at the slashface gap, 0.5% MFR through the slashface and transition section gaps

The influence of the slashface step on passage losses is shown to not be significant in the factorial study; although a slight reduction in losses is observed in the single parameter perturbation study. Heat transfer rates are shown to be slightly decreased from those of the nominal study. The net heat flux in the forward of the passage is increased near the suction surface of the vane and decreased on the pressure side portion of the endwall. Heat flux rates in the portion of the passage downstream of the gap show a slight reduction, as compared to the nominal values.

Slashface backward facing step: -1.5% step at the slashface gap, 0.5% MFR through the slashface and transition section gaps

A slight reduction in losses is shown in the single-parameter perturbation study for this configuration. Heat transfer rates for this configuration are similar to those found in the nominal configuration. The net change in heat flux shows a slight reduction from nominal values over much of the endwall surface.

The study indicates that passage leakage flows have an impact on passage loss and heat transfer. The influence of misalignment appears to often change the distribution of heat flux. Some areas show an increase while others indicate a reduction. From an aerodynamic standpoint, the forward facing transition section step appears to be desirable. From a heat transfer perspective, the backward facing step is more beneficial. The slashface step appears to have an effect on passage heat flux, causing a slight reduction in the downstream portion for both the case of a forward facing step and a backward facing step. Similarly, a slight reduction in losses is observed for both of the slashface step heights.

3.2 Measurements of Flow and Mass/Heat Transfer from a Linear First-Stage-Rotor Cascade

3.2.1 Mass and Heat Transfer Measurements on the Endwall

Mass transfer experiments have been conducted for six different cases of varying

Reynolds numbers, turbulence intensity values and trip wire diameters. The conditions for each run are listed in Table 3.

Table 3. Mass transfer conditions on an endwall

No	Name	Trip wire diam. (mm)	Re_{ex}	U_{ex} (m/s)	Tu(%)
1	MT-B-Run1	0.5	4.5×10^5	39.2	0.2
2	MT-B-Run2	0.5	5.82×10^5	50.6	0.2
3	MT-B-Run3	1.0	4.38×10^5	38.5	0.2
4	MT-B-Run4	1.0	5.77×10^5	50.6	0.2
5	MT-B-Run5	1.0	4.27×10^5	37.4	8.5
6	MT-B-Run6	1.0	5.67×10^5	49.9	8.5

Some inferences can be made on the effects of the individual parameters. Results show that the boundary layer thickness does not play an important role. The larger diameter tip wire, which generates a thicker boundary layer, was therefore chosen for most of the runs. Sherwood number contours allow a clear identification of a number of secondary flow features associated with the complicated secondary flow system that exists in the near-wall region. The horseshoe vortices form close to the leading edge and merge with the leading edge corner vortices. The passage vortex develops from the pressure leg of the horseshoe vortex. The high turbulence intensity acts to suppress the passage vortex.

Heat transfer experiments have been conducted matching the experimental conditions used for the mass transfer tests. The boundary layer thickness was once again found to play a minor role. The 1*mm* diameter trip wire was used to trip the boundary layer for all three reported heat transfer runs. The Reynolds numbers were lower than those investigated in the mass transfer experiments, since higher Reynolds numbers were found to cause excessive vibration of the thermal probe. The detailed conditions for each run are listed in Table 4.

Table 4. Heat transfer conditions on an endwall

No	Name	Trip wire diam. (mm)	Re_{ex}	U_{ex} (m/s)	Tu(%)
1	HT-B-Run1	1.0	2.56×10^5	21.6	0.2
2	HT-B-Run2	1.0	1.95×10^5	16.2	0.2
3	HT-B-Run3	1.0	2.29×10^5	19.6	8.5

While the mass transfer experiment can measure more than 5000 points in an hour, the heat transfer experiment can only measure 140 points in six hours. The lower spatial resolution does not allow a detailed thermal field description as in the case of the local mass transfer measurements. A region of high heat transfer coefficients upstream of the leading edge is clearly identified but it is not possible to clearly distinguish the effects of the passage vortex, as was possible with the mass transfer measurements.

Comparison of the normalized Nusselt and Sherwood number distribution shows very good agreement when using an analogy factor, F, of 0.557 (corresponding to n=0.5, n being the exponent of the Pr (Sc) number dependency of the heat (mass) transfer coefficients).

3.2.2 Mass and Heat Transfer Measurements on the Blade

Mass transfer experiments are performed for one nominal set of experimental conditions. A single experiment provides data for both the pressure and suction sides at several spanwise locations. The detailed conditions for the reported run are described in Table 5.

Table 5. Mass transfer conditions on the blade

No	Name	Location	Re_{ex}	U_{ex} (m/s)	Tu(%)
1	MT-PS-Run1	3D	2.29×10^5	19.9	0.2

Mass transfer coefficients are measured on 53 locations on the suction side and 47 locations on the pressure side of the airfoil. In the spanwise direction, 55 locations are selected ranging from z/C=0.01 to 1.0.

Heat transfer experiments are conducted matching the experimental conditions used for the mass transfer tests. In this case, however, each run provides data for only one spanwise location. The data reported for different spanwise locations are therefore obtained from different experiments (e.g. cases 1 through 4). Table 6 describes the conditions used for each test.

Table 6. Heat transfer conditions on an endwall

No	Name	Location	Re_{ex}	U_{ex} (m/s)	Z/C	Tu (%)
1	HT-P-Run1	3-D-P	2.48×10^5	21.9	0.09	0.2
2	HT-P-Run2	3-D-P	2.49×10^5	21.9	0.18	0.2
3	HT-P-Run3	3-D-P	2.38×10^5	21.3	0.28	0.2
4	HT-P-Run4	3-D-P	2.38×10^5	21.2	0.66	0.2
5	HT-S-Run5	3-D-S	2.41×10^5	21.4	0.09	0.2
6	HT-S-Run6	3-D-S	2.41×10^5	21.4	0.18	0.2
7	HT-S-Run7	3-D-S	2.41×10^5	21.4	0.28	0.2
8	HT-S-Run8	3-D-S	2.42×10^5	21.4	0.66	0.2

Measurements are performed at 37 locations on the pressure side, ranging from $S_p/C=0.0$ to 1.0, and 43 locations on the suction side, ranging from $S_s/C=0.07$ to 1.26. Measurements on the suction side over the range from $S_s/C=0.0$ to 0.07 could not be performed due to physical restrictions imposed by the size of the access window.

The data at z/C=0.09 from MT-PS-Run1 and HT-P-Run1 are plotted for the pressure side in Figure 22. The data are normalized and compared to the normalized heat transfer results. The mass transfer coefficient is expressed as $Sh/(\mathrm{Re}^{1/2} Sc^n)$ and the heat transfer coefficient is expressed as $Nu/(\mathrm{Re}^{1/2} \mathrm{Pr}^n)$. The normalized Nusselt numbers agree well with the normalized Sherwood numbers on the pressure side when a value of n=0.5 is adopted.

The data at z/C=0.09 from MT-PS-Run1 and HT-S-Run1 are plotted for the suction side in Figure 23. Heat and mass transfer data are normalized in the same manner as described for Figure 22. On the suction side, normalized Nusselt numbers agree well with the normalized Sherwood numbers using n=0.5 up to $S_s/C=0.6$. Beyond $S_s/C=0.6$, the use

of n=0.7 allows better matching of the two data sets. The different behavior after the specified chord coordinate could be due to the different flow regimes. However, heat transfer measurements downstream of $S_s/C=0.6$ are extremely difficult to take due to the limited size of the linear conduction region near the wall compared to the probe size. Further investigations are needed to draw final conclusions on the interpretation of the results for this region.

3.2.3 Mass and Heat Transfer Measurements on the Endwall with a blade leading edge modification

A leading edge fillet was designed following the guidelines reported in Zess and Thole [10], having a height and length of seven times the boundary layer displacement thickness (~30 mm in the present apparatus). Mass transfer measurements were conducted with an active (mass transfer) endwall and an inactive blade. Two Reynolds numbers and two turbulence intensity values were used for the plain (no contouring) blade and for the modified leading edge blade to check the benefits of installing the fillet. Mass transfer measurements, which include 5000 points, are taken to show the development of secondary flows and the effects of these on endwall mass transfer.

In the case with 0.2% freestream turbulence, the fillet eliminates the horseshoes vortex and reduces the passage vortex significantly. However, the passage vortex still exists even though it is appears to be reduced and displaced downstream to x/C=0.4. With a higher turbulence intensity of 8.5%, the horseshoe vortex is not clearly observed, either with or without fillets.

For heat transfer measurements 130 positions on the endwall have been selected. Since the heat transfer measurement technique is sensitive to vibration, the Reynolds number was reduced to $Re=2.5 \times 10^5$. The heat transfer experiments do not show the fine detail given by the mass transfer technique, due to the smaller number of measurement locations.

Comparisons of heat and mass transfer measurements were made to validate the heat/mass transfer analogy in the cascade geometry on the endwall with the modified leading edge blades. Figure 24 compares the Nusselt and Sherwood number with n=0.5, Pr=0.707, and Sc=2.28. Each plot shows comparisons at different streamwise positions between blades. The rectangular bars represent the cross section of the blades and the numbers indicate the blade number. The letter 'P' indicates the blade pressure side and 'S' indicates the suction side. In the passage between blade 3 and blade 4, heat and mass transfer results with fillets show good agreement with n=0.5, as suggested by Eckert et al. [11].

3.2.4 Adiabatic cooling effectiveness on the blade and endwall surfaces

Measurements have been performed with no turbulence-generating grids at the exit Reynolds number of Re=600,000 based on true chord and cascade exit velocity. The injected flow is introduced at an effective blowing rate of unity, calculated as the ratio between the average velocity out of the slot and the freestream velocity. The density of the injected flow is equal to that of the freestream, yielding a density ratio of unity.

The boundary layer on the bottom wall of the tunnel is tripped with a 1*mm* wire placed 828*mm* upstream of the leading edge of the central blade of the cascade, producing a

turbulent boundary layer with close to zero freestream turbulence (<0.2%). Hot wire measurements performed at four locations upstream of the cascade show that the boundary layer profile follows a power law with exponent 1/6.45 and that the projected momentum thickness at the location of the central blade leading edge is 2.2*mm*.

Results show that the injection significantly alters the flow field and mass/heat transfer in the upstream portion of the passage. The coolant exiting from the slot is drawn to the suction side of the blade and climbs up the suction surface of the airfoil, being pushed up by the action of the passage vortex system and leaving a well defined streak of cooling effectiveness on the blade surface, as shown in Figures 25 and 26. For a blowing rate of unity, very little coolant reaches the pressure side of the blade.

For the step-up configuration, the coolant penetrates further downstream in the pressure side of the passage. When the endwall is brought down to create a step-down configuration, the coolant penetrates less on the pressure side of the passage and more on the suction side of the passage and on the airfoil suction surface, providing a higher overall cooling effectiveness.

IV. Numerical Predictions

4.1 Numerical Heat/Mass Transfer Predictions in the Linear Rotor Cascade

In recent years designers have been increasingly relying on numerical simulations to predict the temperature and flow fields within the turbine. While computationally intensive technique such as LES (Large Eddy Simulation) and DES (Detached Eddy simulation) are becoming more attractive, RANS (Reynolds Averaged Navier-Stokes) simulations still constitute the most common industrial practice as a result of the lower computational cost. In the development of codes, validation with experimental results remains a most important tasks.

Mass transfer measurements using naphthalene sublimation can be conveniently used for the validation of numerical codes. They can generally be performed with a high spatial resolution, they are free from conduction and radiation errors typical of heat transfer measurements and they allow the imposition of well-defined boundary conditions. In an equivalent heat transfer experiment, naphthalene coated surfaces would in fact correspond to isothermal boundaries while the non-coated surfaces would correspond to adiabatic boundaries.

The flow and heat/mass transfer in the rotor linear cascade in its baseline configuration (without injected flow and without leading edge modifications) are numerically predicted with a RANS code using the software "Fluent." The SST k-ω model is used for turbulence closure [12]. The flow and thermal boundary conditions are carefully matched to the ones measured in the experiments, providing guidelines for using mass transfer data for validation of numerical heat transfer codes.

Results show that the code generally performs well in predicting the main features of the secondary flows in the near-wall region. The numerical simulation captures the formation of the horseshoe vortex system upstream of the blade leading edge, and the migration of the pressure side leg of the horseshoe vortex towards the suction side of the neighboring blade, where it meets the suction side leg of neighboring horseshoe vortex system. The heat (mass) transfer rates on the endwall are very well predicted in the first portion of the passage, but downstream of the merge-point the code underpredicts the effect of the corner vortex and overpredicts the heat (mass) transfer rates associated with the cross-flow within the passage. On the airfoil surface, the simulation captures the enhancement of the heat transfer coefficients on the suction side of the blade due to the action of the passage vortex system. The agreement in the two-dimensional region of the airfoil is excellent, but the code predicts an early transition to turbulence on the blade suction side.

Figure 27 shows the predicted Sherwood number contour plots on the blade and endwall surfaces. Detailed results of the numerical simulation are reported in reference [13].

Conclusions

Test facilities have been constructed with the necessary features to carry out this experimental program with its various geometry changes and flow injection schemes. These facilities have been qualified, a major milestone in any test program. Measurements have been taken, as follows: 1). Aerodynamic losses have been measured within a passage with a contoured endwall. 2). Endwall heat and mass transfer measurements have been taken to document effects that the passage secondary flows have on the local transfer rates. 3). On-airfoil measurements of heat and mass transfer rates have been taken and the analogy between the two was described. Noted was the change in the analogy factor between upstream measurements and downstream measurements. This change is considered to be attributable to a change in flow regime.

In the vane cascade, the effects of gaps, gap flow and component misalignments on aerodynamic losses, heat transfer coefficients and adiabatic effectiveness values are presented.

In the rotor cascade, heat and mass transfer measurement are conducted with modified leading edge blades. The modified leading edge delays the development of the passage vortex and reduces the strength of the passage vortex in mass transfer measurements. The comparison between heat and mass transfer is in good agreement with the theory suggested by Eckert at el. [11]. The effect of the wheelspace coolant injection on the secondary flows and on the mass (heat) transfer in the wall and near-wall region has been documented. Misalignment between the endwall and the upstream platform was considered.

A numerical RANS code that uses the SST k-ω model has been developed to predict the flow and heat/mass transfer in the rotor cascade. Results are compared with mass transfer measurements taken on the blade and endwall surfaces with equivalent boundary conditions. The numerical simulation is able to capture most of the secondary flow features that have been experimentally observed.

References

[1] Piggush, J and Simon, T.W., 2005, :Flow Measurements in a First Stage Nozzle Cascade having Endwall Contouring, GT2005-68340, 2005 International Gas Turbine Conference, Reno, NV, Recommended for the J. of Turbomachinery.

[2] Piggush, J. D. and Simon, T. W., 2005. "Heat Transfer Measurements in a First Stage Nozzle Cascade having Endwall Contouring, Leakage and Assembly Features, HT2005-72573, 2005 National Heat Transfer Conference San Francisco, CA.

[3] Piggush, J. D. and Simon, T. W., 2005. "Flow Measurements in a First Stage Nozzle Cascade having Leakage and Assembly Features: Effects of Endwall Steps and Leakage on Aerodynamic Losses," IMECE2005-83032, 2005 IMECE, Orlando, FL.

[4] Piggush, J. D. and Simon, T. W., 2006. "Heat Transfer Measurements in a First Stage Nozzle Cascade having Endwall Contouring: Misalignment and Leakage Studies," GT2006-90575, 2006 International Gas Turbine Conference, Barcelona, Spain.

[5] Piggush, J. D. and Simon, T. W., 2006. "Adiabatic Effectiveness Measurements in a First Stage Nozzle Cascade having Endwall Contouring, Leakage and Assembly Features," GT2006-90576, 2006 International Gas Turbine Conference, Barcelona, Spain.

[6] Piggush, J., D., 2005. An experimental investigation of endwall leakage flows and misalignment in a gas turbine nozzle guide vane cascade. Master's thesis, Mechanical Engineering Department, University of Minnesota.

[7] Jin, P., and Goldstein, R. J., 2003. "Local mass/heat transfer on a turbine blade tip. international journal of rotating machinery," International Journal of Rotating Machinery, 9(2), pp. 81–95.

[8] Goldstein, R. J., and Cho, H. H., 1995. "A review of mass transfer measurements using naphthalene sublimation," Experimental Thermal and Fluid Science, 10, pp. 416–434.

[9] Eckert, E. R. G., 1984. "Analysis of film cooling and full coverage film cooling of gas turbine blades," Journal of Engineering for Power, 106, pp. 206–213.

[10] Zess G. A. and Thole K. A., "Computational Design and Experimental Evaluation of Using a Leading Edge Fillet on a Gas Turbine Vane," Journal of Turbomachinery, Vol. 124, 2002, p167-175.

[11] Eckert, E.R.G., Sakamoto, H., and Simon, T.W., "The Heat/Mass Transfer Analogy Factor, Nu/Sh, for Boundary Layers on Turbine Blade Profiles," International Journal of Heat and Mass Transfer, Vol. 44, 2001, p1223-1233.

[12] Menter, F. R., 1994. "Two-equation Eddy-Viscosity Turbulence Models for Engineering Applications." AIAA Journal, vol. 32, pp. 1598–1605.

[13] Papa, M., Goldstein, R.J., Gori, F., 2006, "Numerical heat transfer predictions and mass/heat transfer measurements in a linear turbine cascade," submitted to the 2006 ASME-ATI Conference, Milan, Italy.

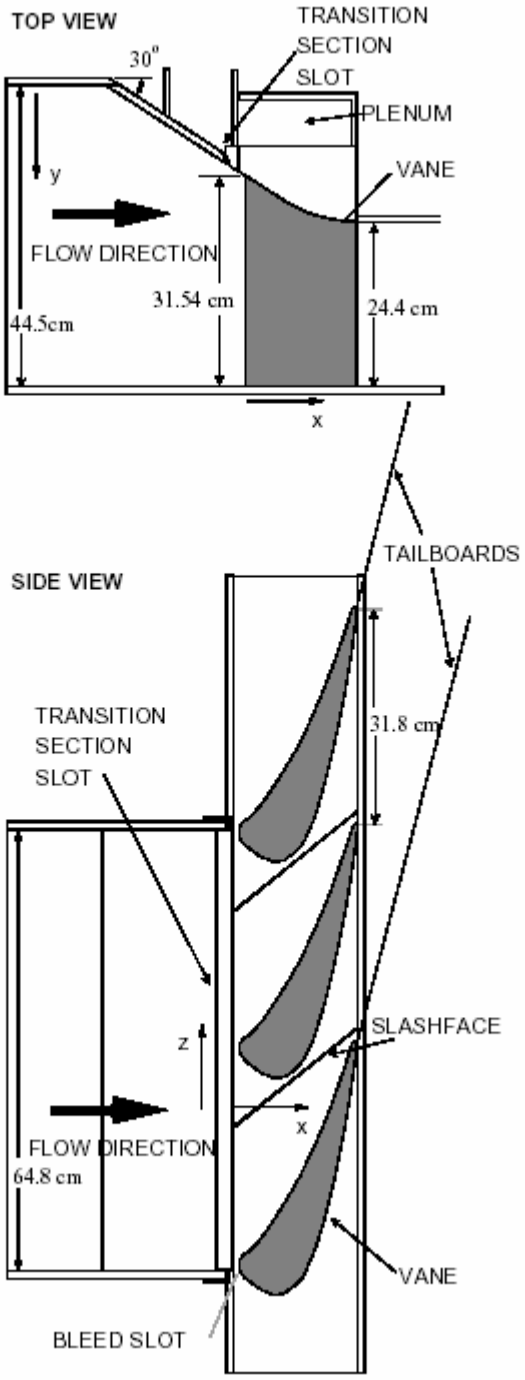

Figure 1: Schematic of the test facility.

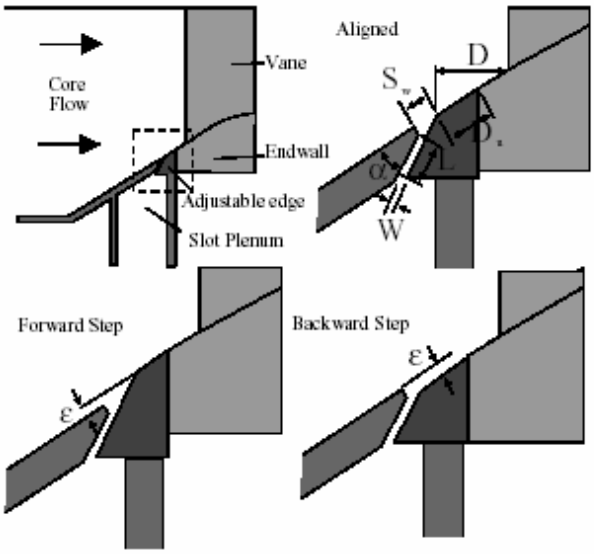

Figure 2: Schematic of the transition section slot geometry. Details are of the portion enclosed in the dashed square. Note that the light gray portion indicates the heated sections of the endwall and vane. The dark gray piece was moved to create steps at the transition section slot.

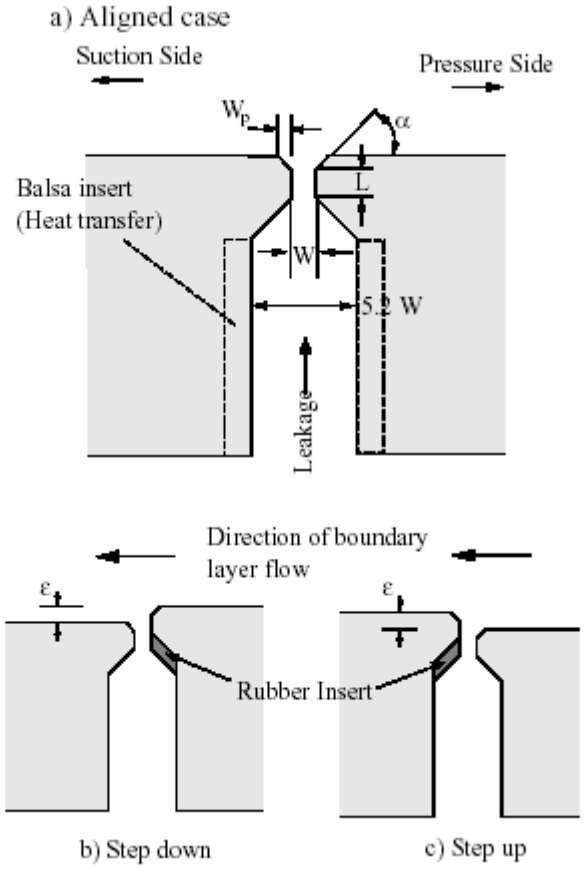

Figure 3: Schematic of the slashface slot geometry. The balsa and rubber insulation sections are included for the heat transfer studies.

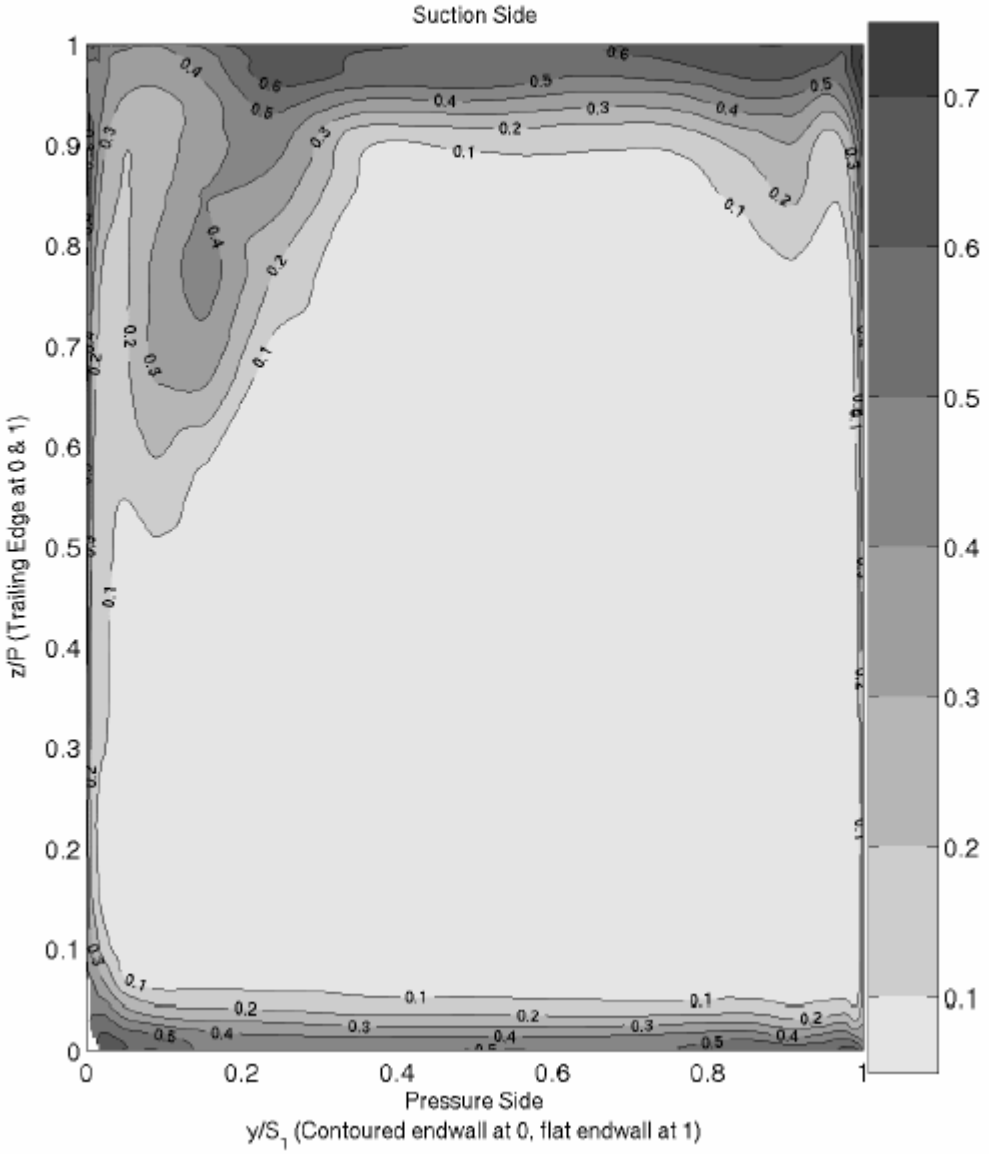

Figure 4: Exit pressure loss contours for the nominal case, where the gaps are open and are blowing at 5% of the passage mass flow rate. There are no steps.

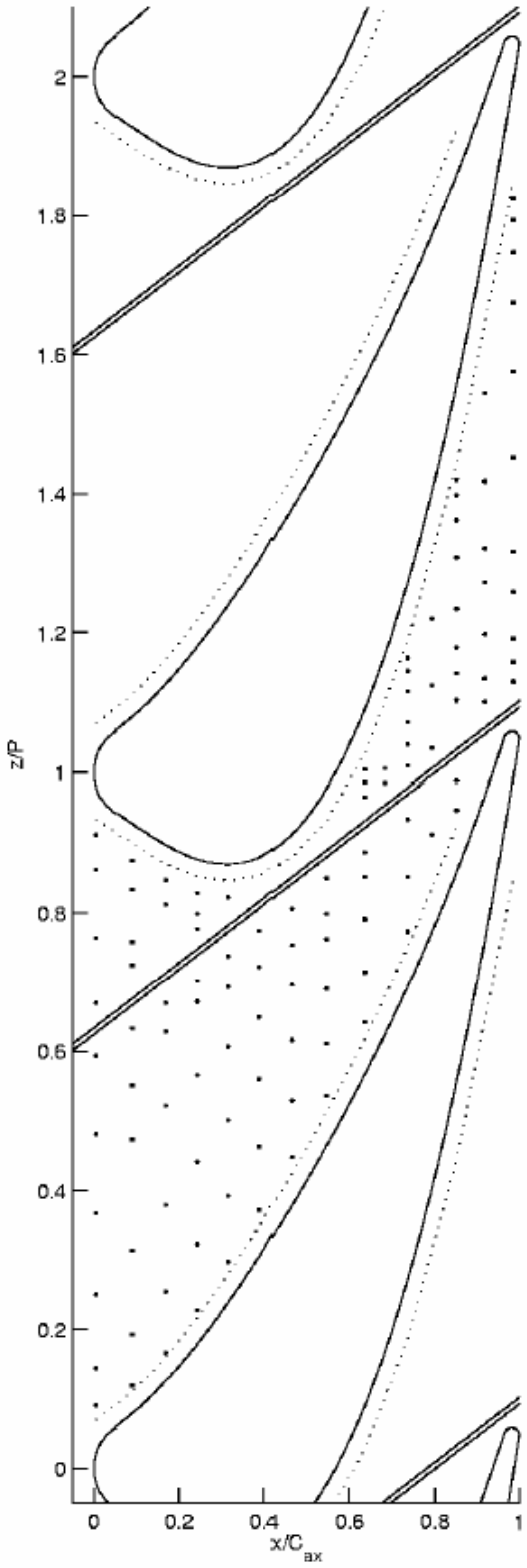

Figure 5: Locations of measurements points for temperature profile measurements.

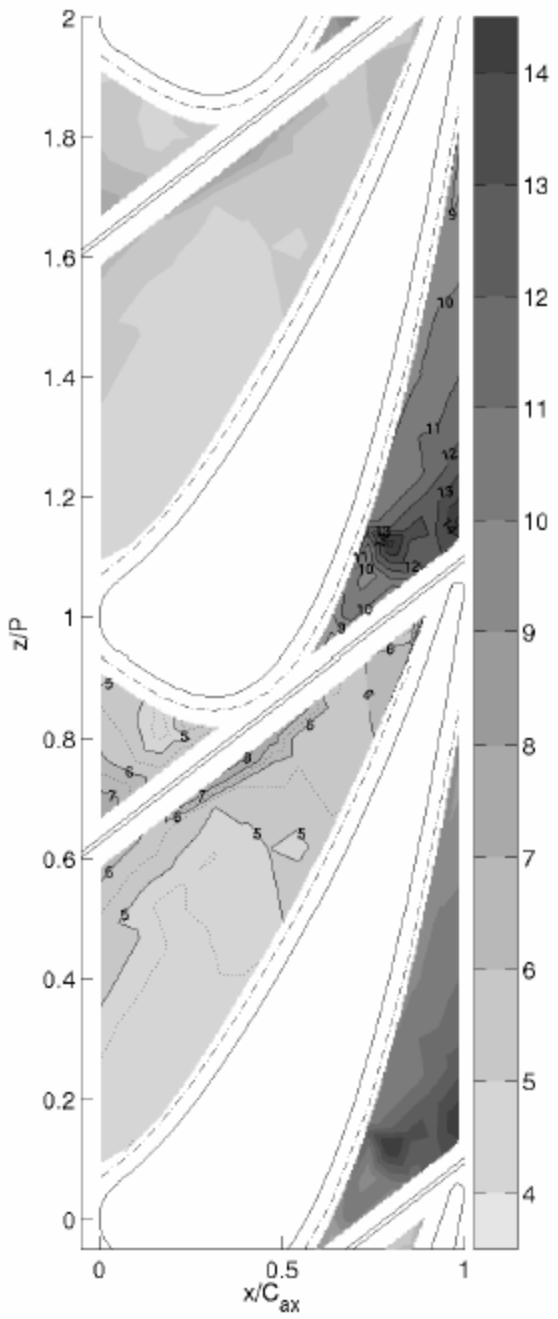

Figure 6: Stanton number (x1000). The nominal case, where the gaps are open and are blowing at 5% of the passage mass flow rate. There are no steps.

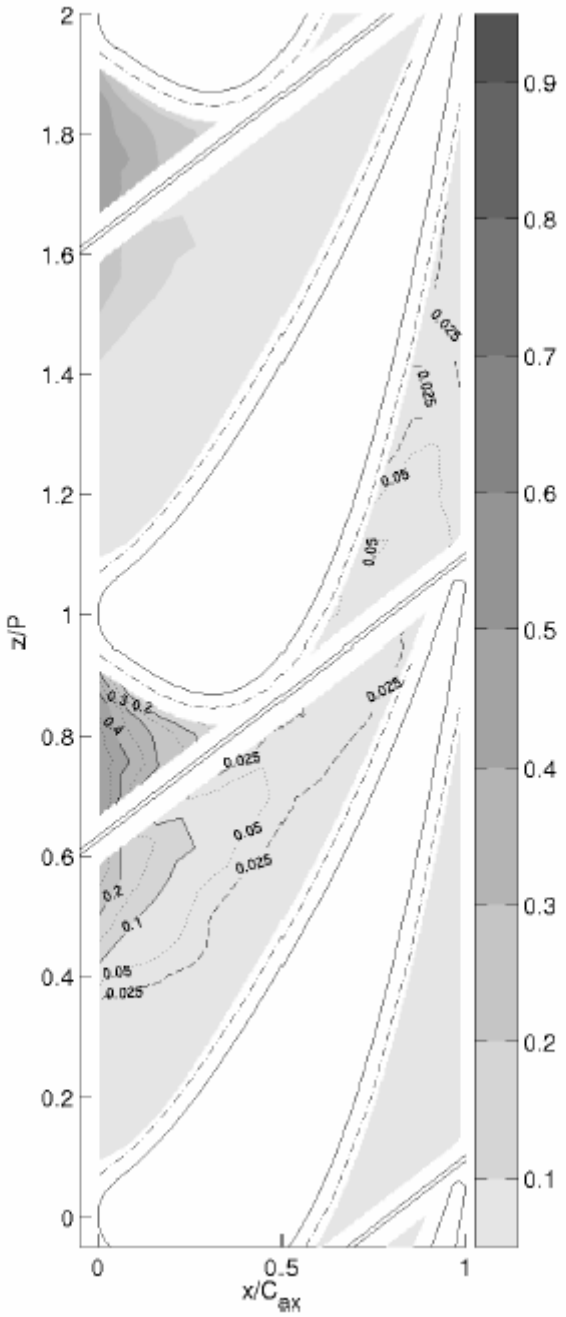

Figure 7: Adiabatic wall temperatures for the nominal case, where the gaps are open and are blowing at 5% of the passage mass flow rate. There are no steps.

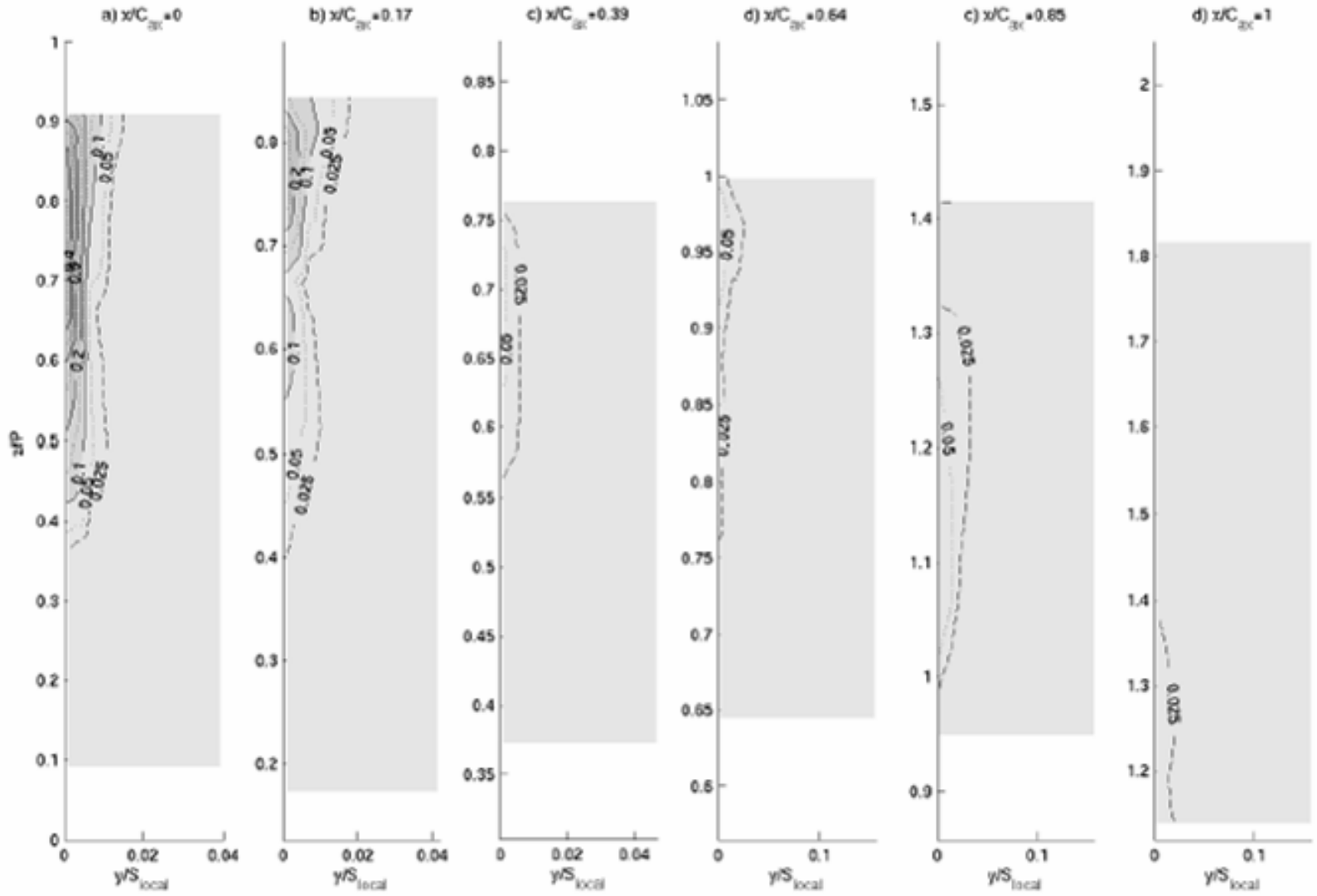

Figure 8: Adiabatic effectiveness distribution for the nominal case, where the gaps are open and are blowing at 5% of the passage mass flow rate. There are no steps.

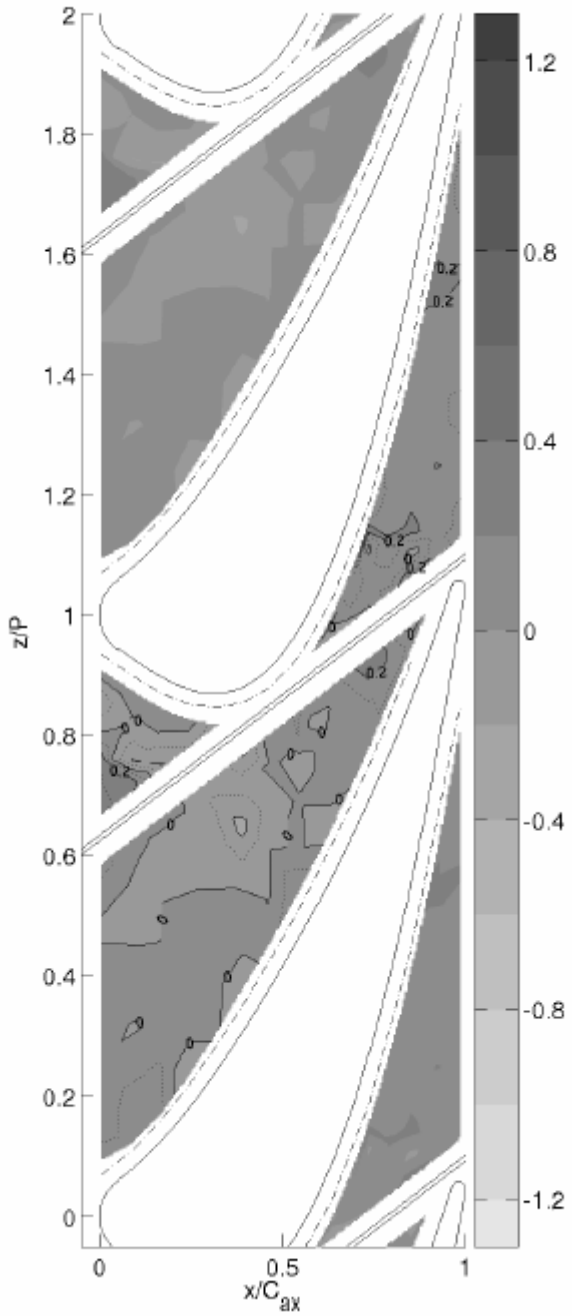

Figure 9: Net heat flux reduction, elevated slashface blowing of 1% of the passage mass flow rate vs. the nominal case, where the gaps are open and are blowing at 5% of the passage mass flow rate. There are no steps in either of the two comparison cases.

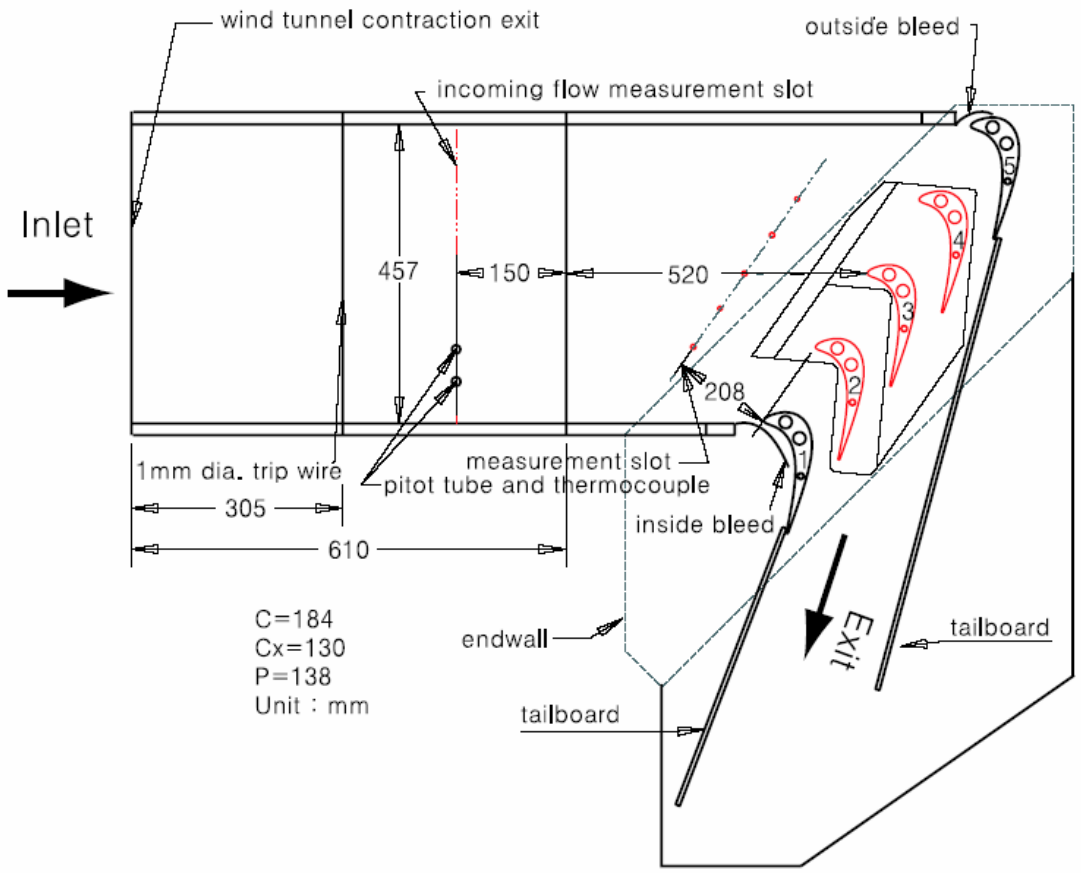

Figure 10: Linear rotor cascade facility

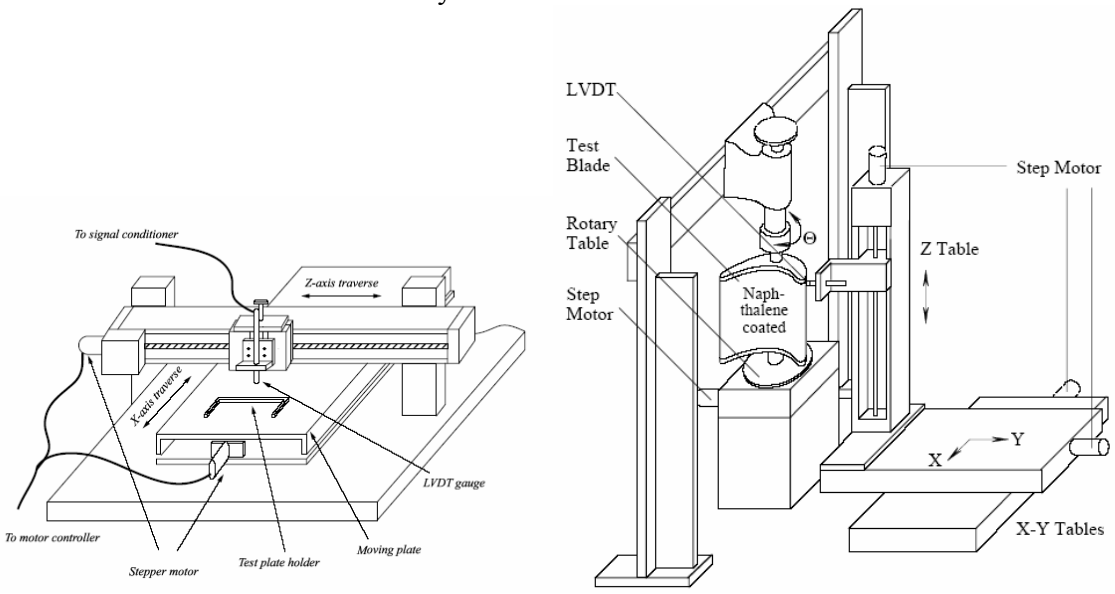

(a) 2-axis table (b) 4-axis table

Figure 11: Endwall and blade measurements systems for the acquisition of naphthalene surfaces profiles before and after exposure to the wind tunnel flow

(a) heat transfer plate

(b) mass transfer plate

Figure 12: Endwall plates for heat and mass transfer experiments

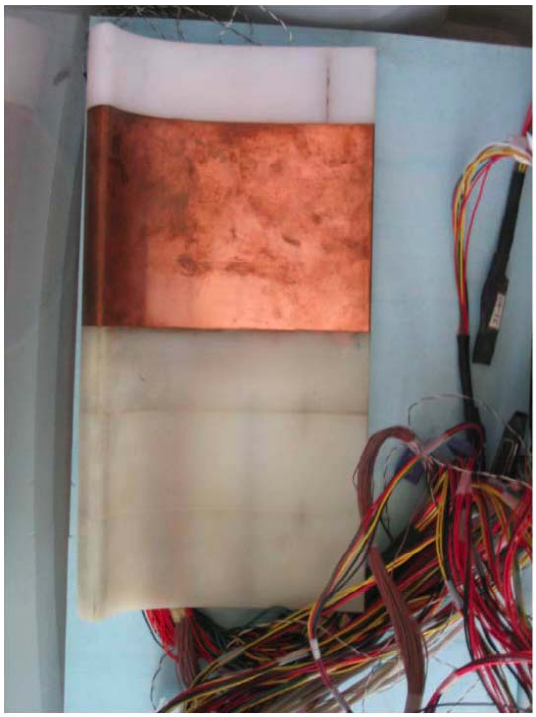

(a) heat transfer blade

(b) mass transfer blade

Figure 13: Blades for heat and mass transfer experiments

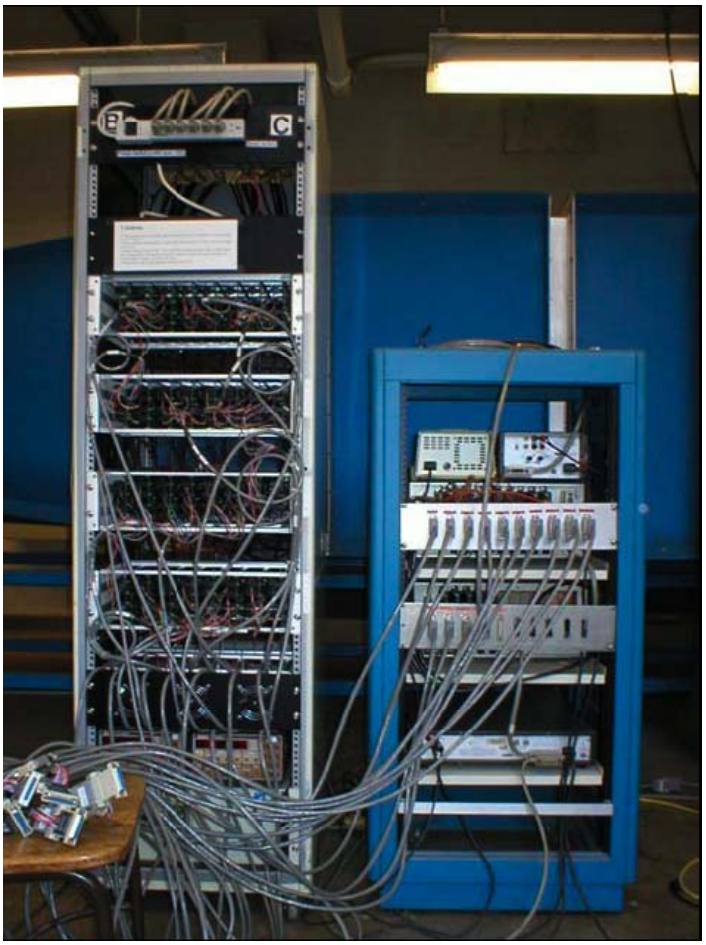

Figure 14 Digital power supply and measurement unit

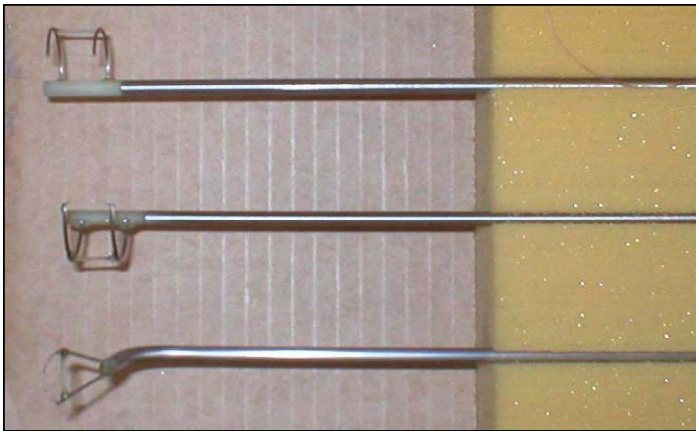

Figure 15 Photograph of temperature boundary layer probes used in the rotor cascade study

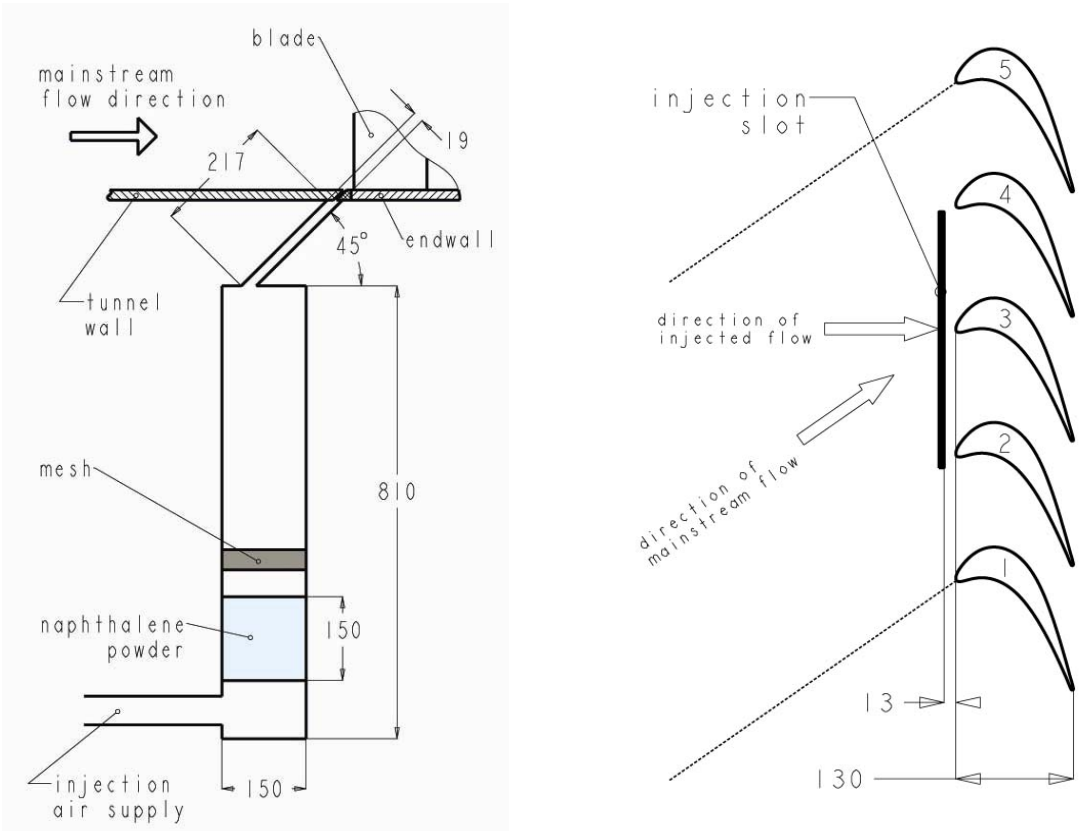

Figure 16: Schematic diagrams of injection system to simulate the wheelspace coolant injection upstream of the row of rotor blades

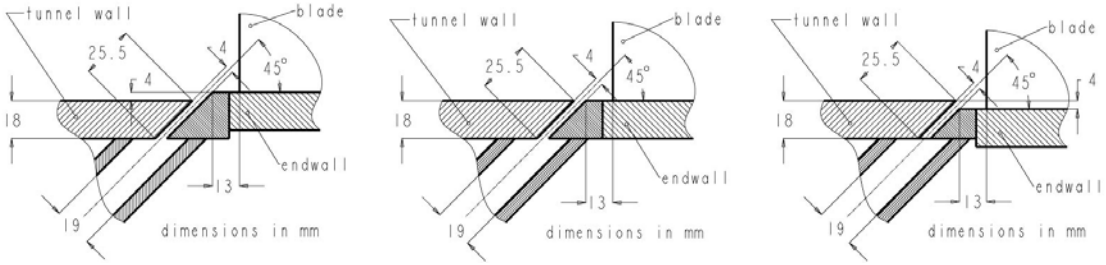

(a) step up (b) no step (c) step down

Figure 17: Gap configurations for the injection upstream of the rotor cascade

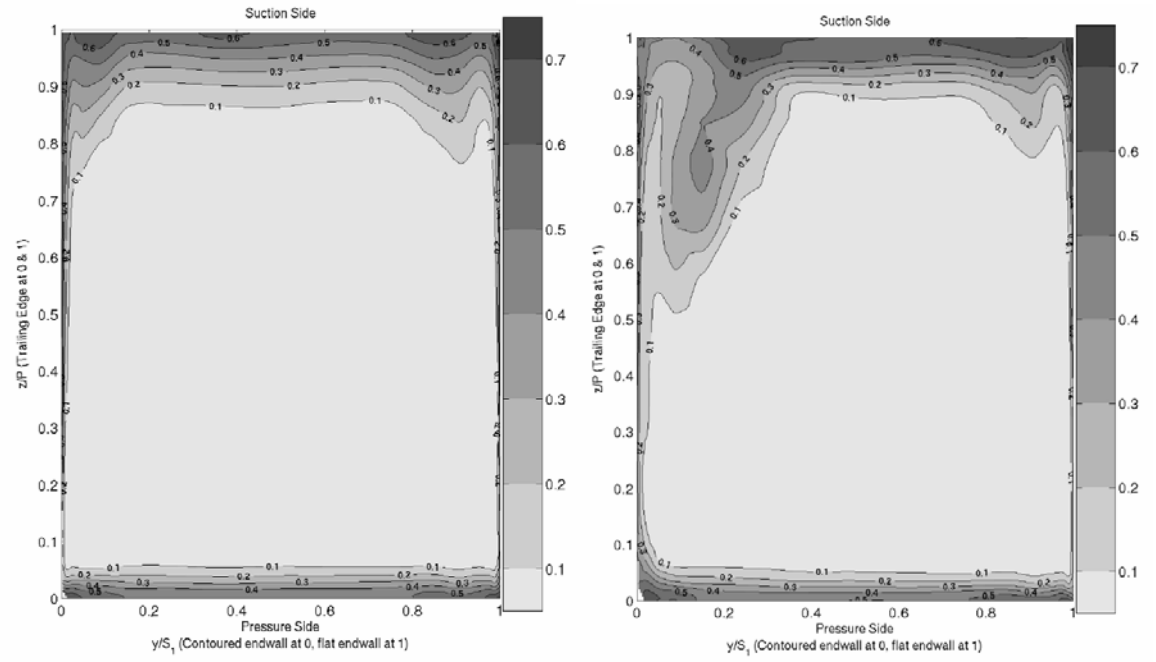

Figure 18. Exit pressure loss contours, $\frac{p_{0,1}(x,y)-p_{0,0}}{p_{0,0}-p_1}$. Smooth case (no steps, gaps or blowing), left, vs. nominal case (no steps, gaps open with 0.5% MFR through the transition section and slashface gaps), right. The main effect is due to flow into the upstream portions of the slashface gap, with ejection of that flow from the downstream portions of that gap.

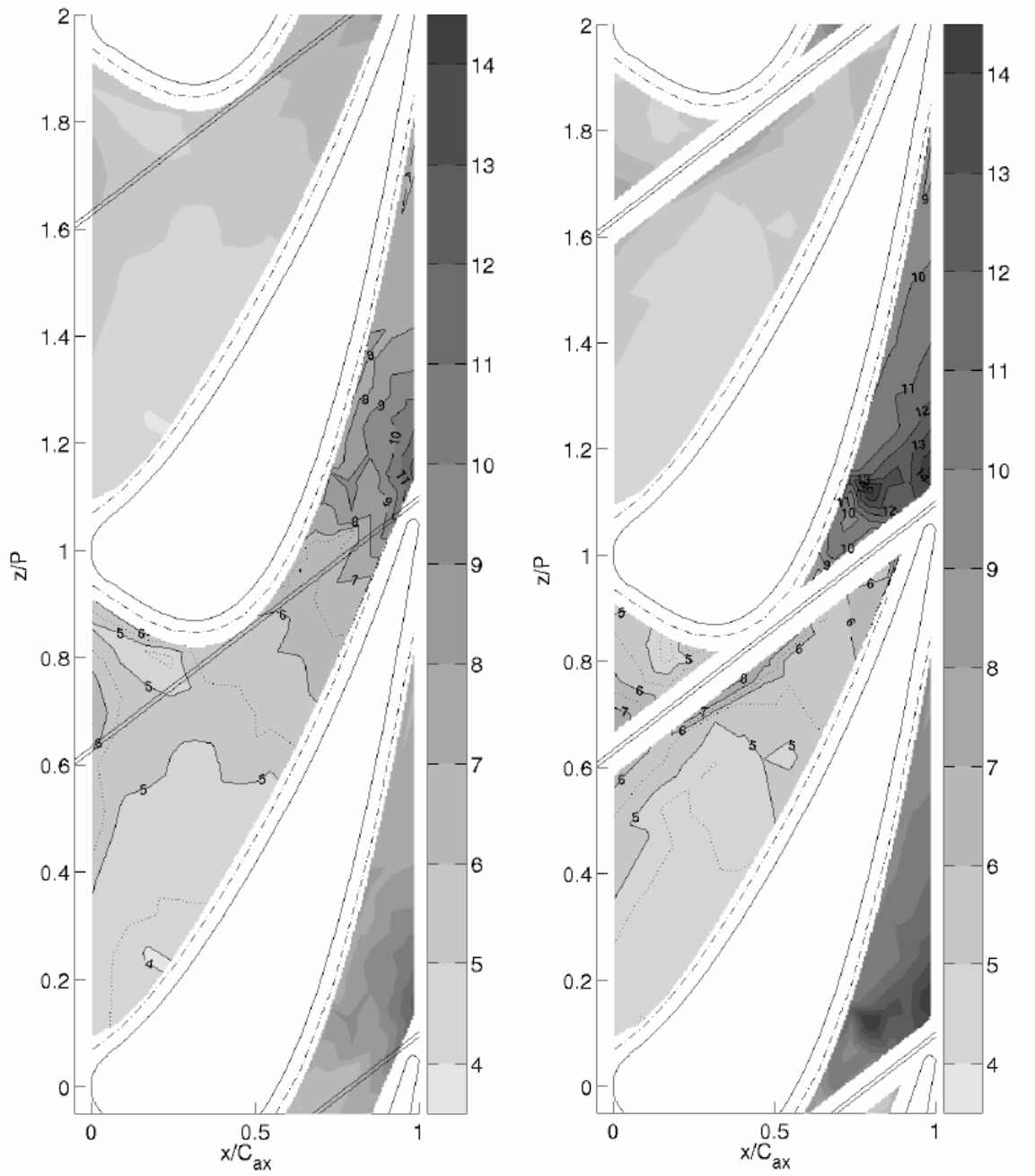

Figure 19 Endwall Stanton number distributions (x1000). Smooth case (no steps, gaps or blowing), left, vs. nominal case (no steps, gaps open with 0.5% MFR through the transition section and slashface gaps), right. The main effect on the heat transfer coefficient distribution is due to flow into the upstream portions of the slashface gap, with ejection of that flow from the downstream portions of that gap.

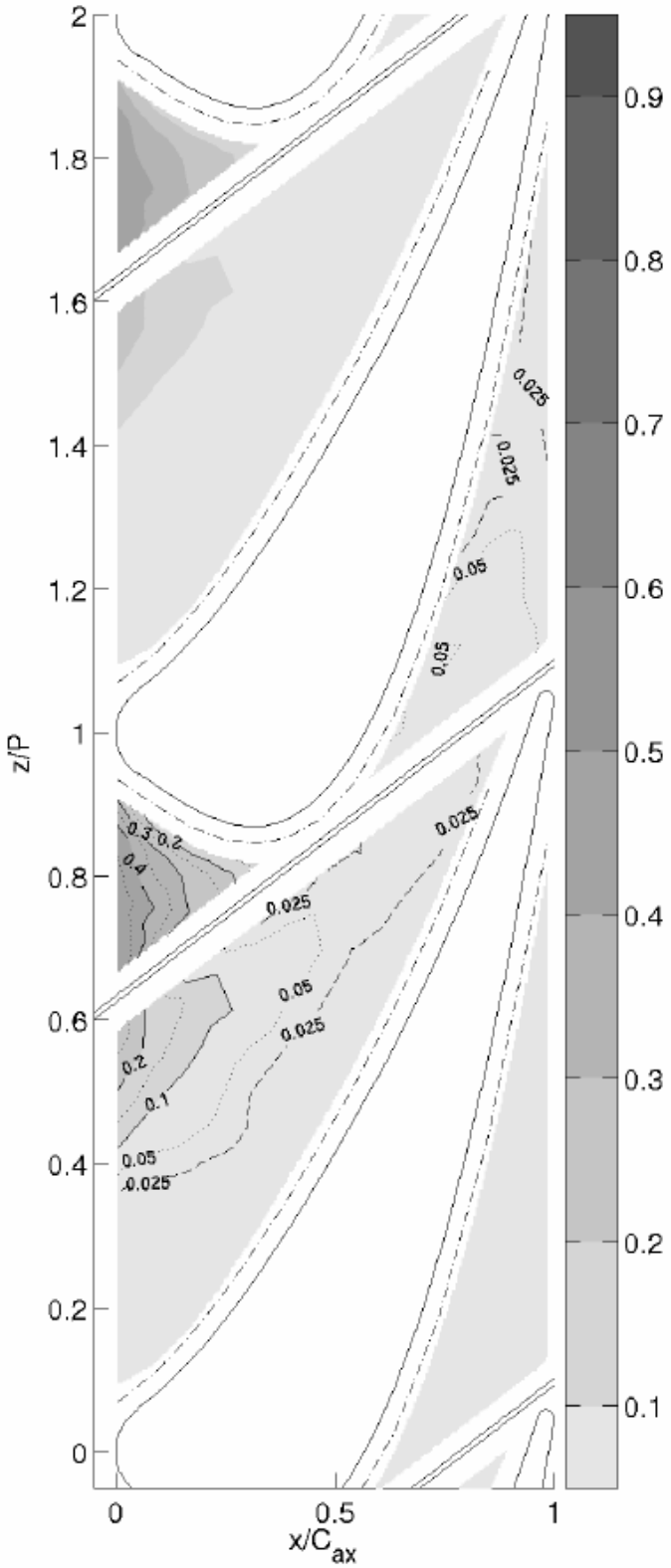

Figure 20 Adiabatic effectiveness value distribution for the nominal case (no steps, gaps open with 0.5% MFR through the transition section and slashface gaps).

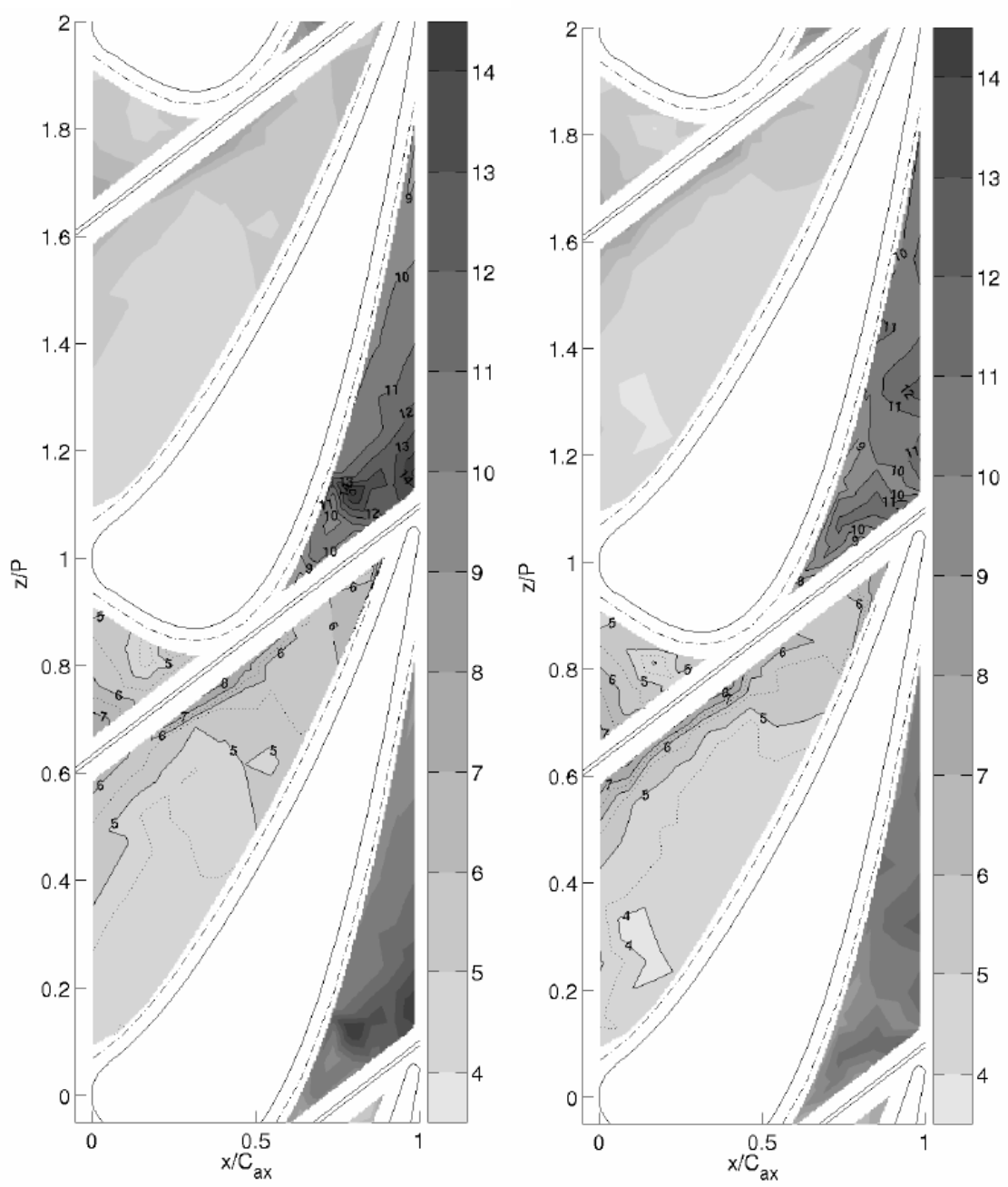

Figure 21 Stanton number (x1000) distributions for the nominal case (left) and the case with a backstep at the transition section gap (right).

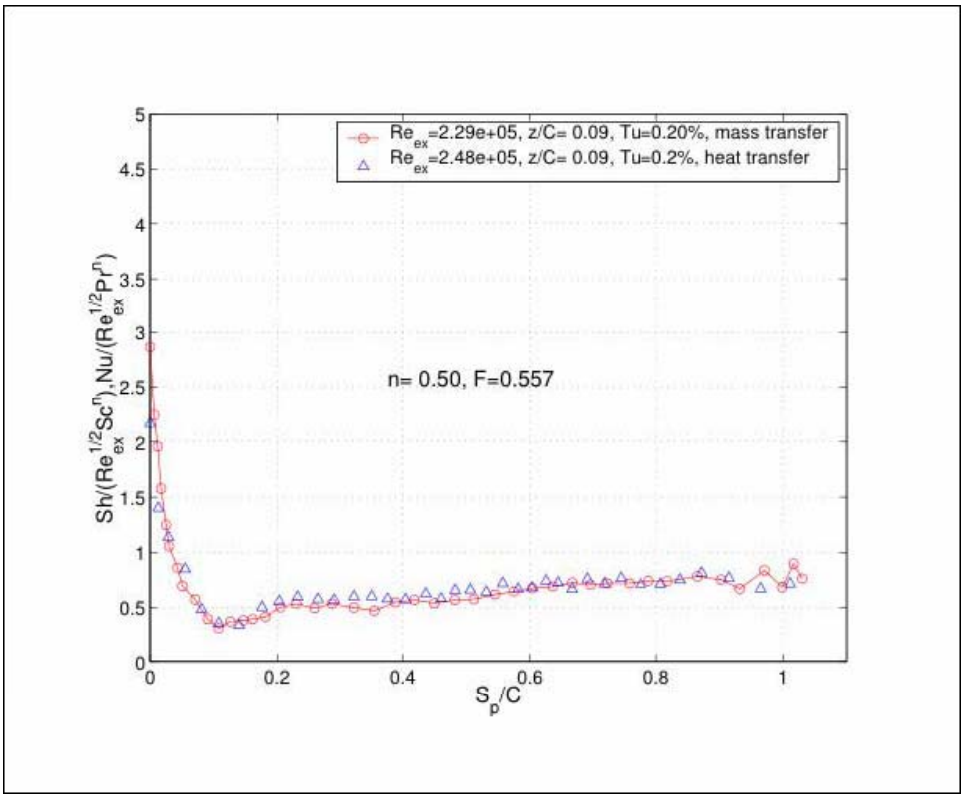

Figure 22 Heat and mass transfer comparison on the pressure side

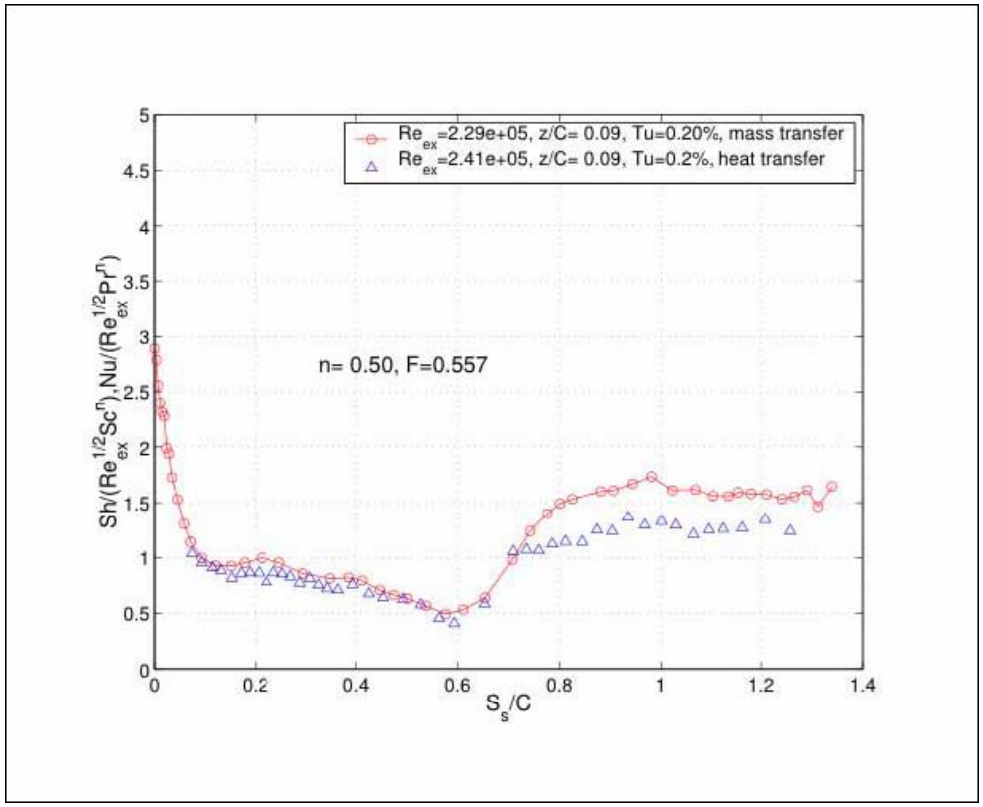

Figure 23 Heat and mass transfer comparison on the suction side

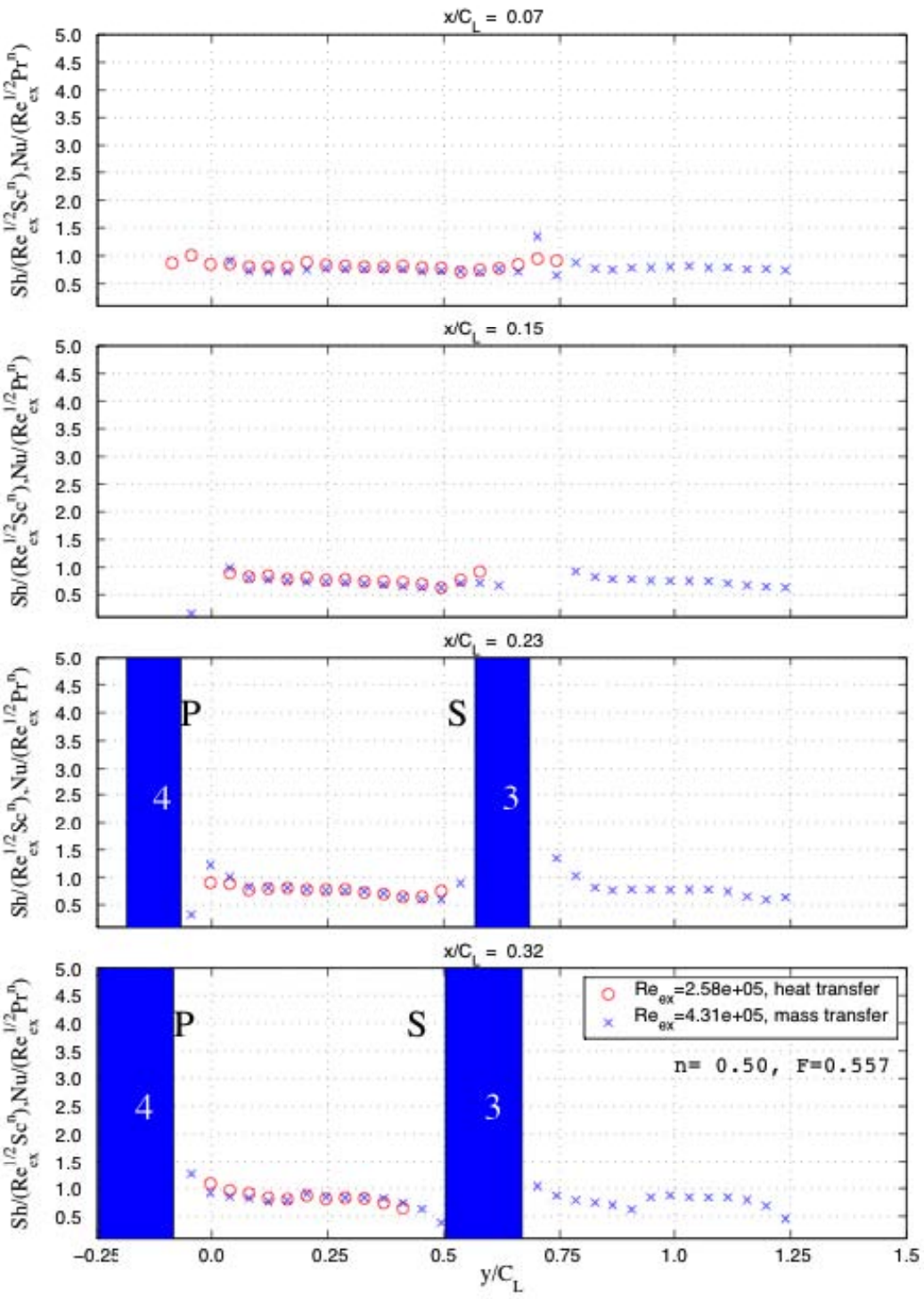

Figure 24 Nusselt and Sherwood number comparisons, with fillets

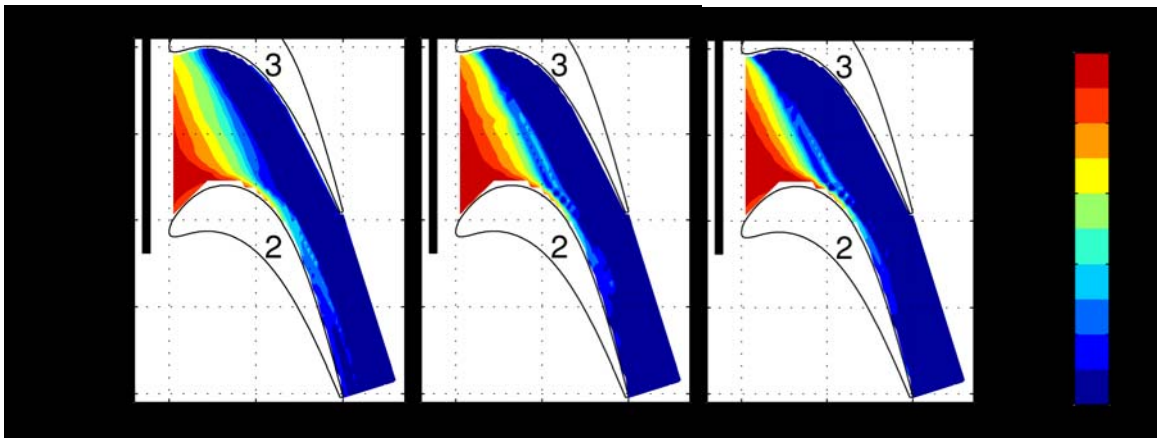

(a) step up (b) no step (c) step down

Figure 25 Adiabatic cooling effectiveness on bottom endwall in the rotor linear cascade with an effective blowing rate of unity

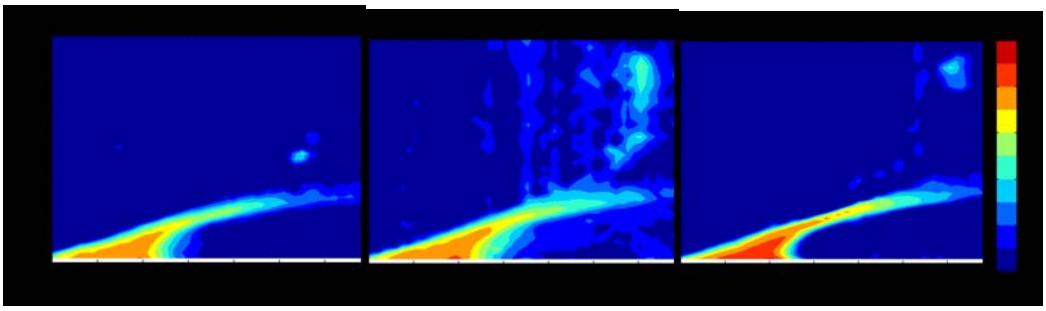

(a) step up (b) no step (c) step down

Figure 26 Adiabatic cooling effectiveness on blade suction side in the rotor linear cascade with an effective blowing rate of unity

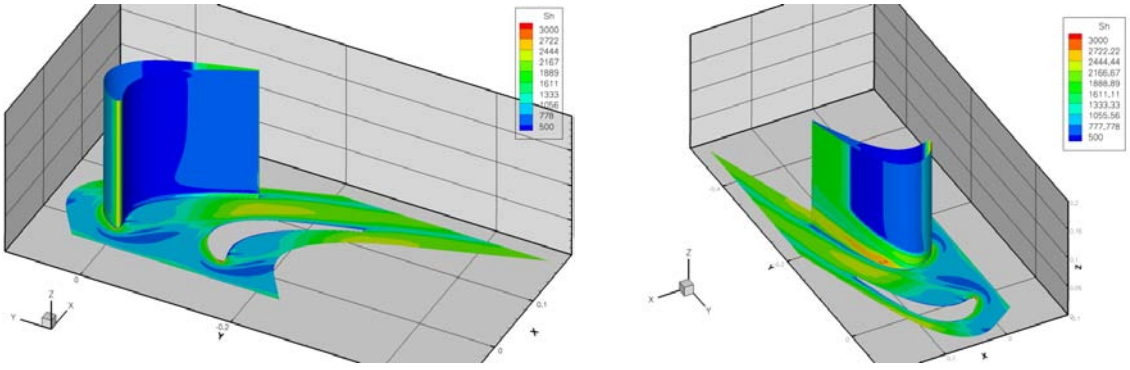

Figure 27 Sherwood number contour plots obtained from numerical simulations

Final Report

Measurement of Three Critical Parameters As A Basis For A Simple Life Prediction Method

Reporting period 5/1/02-10/31/05

Eric Jordan and Maurice Gell
University of Connecticut, Storrs, CT
Report Issued November 30, 2005
DOE Subcontract No. 02-01-SR097

University of Connecticut
191 Auditorium Road
Storrs, CT 06268

DISCLAIMER* -- The Disclaimer must follow the title page, and must contain the following paragraph:

ABSTRACT- This report describes a project designed to investigate the use of three measured parameters for assessment of remaining life of thermal barrier coatings in gas turbine hot section environments. The parameters investigated were, the stress in the thermally grown oxide (TGO) measure optically, the TGO thickness measured by advanced eddy current methods and the initial bond coat surface geometry measured ty interferometry. It was shown for samples with diffusion aluminide bond coats TGO stress was a single valued function of life fraction independent of temperature and this allowed accurate remaining life predictions for this type of system and this is now being implemented on industrial parts under an industrial contract. MCrAlY bond coated systems required the use of all three measured parameters. It was shown that the surface metric based on surface curvature the arise naturally from the failure mode expected is much more predictive of cyclic coating life than other traditional measures like RMS roughness and that the three parameter approach is also predictive of remaining life.

Table of Contents

List of Figures

List of Tables

1. INTRODUCTION

Executive Summary

The current program was based on the premise that the remaining life of thermal barrier coatings (TBCs) could be predicted based on the non-destructive measurement of three physical parameters. The three parameters are: (a) the stress in the thermally grown oxide (TGO) measured by a spectroscopic technique, (b) the thickness of the TGO measured by an advanced AC potential drop method and (c) the geometry of the bond coat surface measured using an interferometric surface profilometer.

To investigate this premise, five different TBC systems were tested; three with Pt modified beta NiAl bond coats and two with MCrAlY bond coats, all of which were supplied by industrial engine and coating manufacturers. The TBCs were tested in a cyclic furnace rig at three temperatures 1100 ^{o}C, 1121 ^{o}C, and 1151 ^{o}C for two different cycle durations: 1 hour and 24 hours per cycle. Periodic non-destructive measurements were made as a function of thermal cycing. Predictive ability was then tested using the experimentally determined cyclic spallation lives and the non destructively measured parameters.

The lives of the Pt modified NiAl bond coated samples was well-predicted using just the measured TGO stresses. The remaining life of the samples was predicted within 10% in temperature blind tests. These accurate predictions were deemed sufficiently exciting that an engine manufacturer is funding a substantial program to evaluate the technique on service turbine blades.

It was discovered that the stress trends as function of thermal cycles and the spallation mode changed with cycle duration (1 hour compared to 24 hour cycle tests) as did the failure mode.

The prediction of the remaining lives of the MCrAlY samples required the use of all three parameters. To do this, it was necessary to extract maps of the mean surface curvature from the measured shapes. This measure of surface roughness proved to be much more predictive of behavior than traditional measures like RMS roughness. The resulting life prediction for specimens with differing surface geometries were predicted within 10% at a single temperature.

In addition, tests in which the cycle temperature and/or the cycle time were changed in a step wise fashion during the tests were carried out for the first time. It was found that the linear damage rule worked very well for step changes in temperature, but not for changes in cycle duration. The change in cycle duration changed the failure mode, so it is not surprising that the linear damage rule was not obeyed.

Surface rumpling was a very important failure mode in these TBCs It was discovered that for the Pt modified NiAl bond coated samples that quantitative measures of rumpling were a single valued function of TGO thickness, independent of temperature and cycle duration. This finding provides an experimental challenge to models of rumpling and was an important, unexpected result.

Some samples showed bimodal spectra. Robust deconvolution software was developed for analyzing such spectra. It was shown that the zero-stress component of the bi-modal spectra corresponded to cracked regions in the TGO.

In summary, the three parameter approach proved highly useful in making remaining life predictions in 5 TBCs. Predictions based on TGO stress alone proved sufficiently useful that industrial evaluation on turbine blades is underway. Interesting new results concerning rumpling and the linear damage rule were also obtained.

BACKGROUND

The efficiency of gas turbine engines, whether for industrial power generation, marine applications, or aircraft propulsion, increases with increasing firing temperature or turbine inlet temperature and has steadily improved for years. The need for greater performance from advanced turbine engines will continue, requiring even higher operating efficiencies, longer operating lifetimes and reduced emissions. Improved structural design and airfoil cooling technology applied to high temperature alloys, cast by increasingly complex methods, and coated with improved coating systems, have led to remarkably efficient turbine engines for aircraft propulsion and power generation. From 1940 to 1970, numerous superalloy compositions and cooled turbine blades were developed and the fuel consumption of gas turbines was reduced by more than half, while thrust-to-weight ratios were tripled [Jones; 1996].

A large share of the improved operating efficiencies has resulted from higher operating temperatures. The ongoing quest for higher temperatures in gas turbine engines is one of the major driving forces for the development of insulating ceramic coatings, called thermal barrier coatings (TBCs). The reason for this recent approach is that the temperature capability of superalloys is ultimately limited by their melting point. Superalloys in today's high thrust engines operate at 90 percent of their melting point in some applications [Schulz; 2003], as shown in Figure 1.1. Thus, achieving even higher

temperatures requires the use of surface insulation to allow superalloys to operate at temperatures below their melting point. For this reason, TBCs were developed and applied to hot section gas turbine components more 30 years ago, and are seeing greatly increased application today.

1.1. Review of Thermal Barrier Coatings

Thermal barrier coatings are ceramic coatings applied to high-temperature gas turbine components to insulate the substrate from the heat of the gas path [Nicholls *et al*; 2002, Wigren *et al*; 1998]. Depending on the heat flux and the thickness of the coating, the temperature difference across the thermal barrier coating can reach 175°C [Beele *et al*; 1999].

Thermal barrier coatings are multi-layer coatings, consisting of a low thermal conductivity ceramic topcoat and an intermediate oxidation and corrosion resistant bond coat, typically rich in aluminum, deposited on a superalloy substrate, as shown in Figure 1.2. On exposure to high temperatures either during service or during heat treatment, oxygen easily penetrates the topcoat and reacts with the bond coat, which oxidizes to produce a protective thermally grown oxide (TGO) at the interface between the topcoat and the bond coat. The role of the bond coat is also to ensure proper adherence of the ceramic coating and to provide an aluminum reservoir for growing the protective oxide layer.

TBCs reduce the severity of thermal transients and lower the substrate temperature, enhancing the thermal fatigue and creep capabilities of coated components. In addition, although TBCs do not provide significant reduction in oxygen transport to

the substrate, the lower component temperature can lead to a reduction in oxidation and hot corrosion. Finally by increasing the allowable surface temperature total heat flux is reduced and therefore cooling air requirements are reduced. As a result, TBCs are finding increased application in overall component design. The benefits of TBC in terms of engine efficiency are comparable to those brought by the replacement of directionally solidified alloys with single crystal superalloys (Strangman; 1985). In addition to the cost savings due to increased lifetimes of parts, other benefits include reduced maintenance, lower fuel consumption and reduced emissions.

The application of TBCs makes it possible to: (1) increase the hot gas temperature without increasing the substrate temperature (increased efficiency), (2) reduce the cooling airflow while keeping the hot gas temperature unchanged (increased efficiency), (3) reduce the substrate temperature while keeping the cooling airflow unchanged (increased component lifetime) and (4) reduce the transient stresses (increased component lifetime).

1.1.1. Ceramic Top Coat

The concept of applying an insulating ceramic layer to the surface of high temperature components requires materials that meet fundamental requirements and development of associated processing technologies. Some fundamental requirements for a TBC include: (a) high melting point; (b) low density; (c) high thermal shock resistance; (d) resistance to oxidation and corrosion; (e) high surface emissivity; (f) low vapor pressure; (g) resistance to mechanical erosion; (h) low thermal conductivity; (i) high coefficient of thermal expansion [Jones; 1996]. There are only a few ceramics known today which meet those criteria, and zirconia has been the optimum choice for the last 30

years, especially because of its extremely low thermal conductivity and its high thermal expansion coefficient.

Zirconia needs to be stabilized, because pure zirconia shows a phase transformation from the monoclinic to the tetragonal phase at 1180°C and from the tetragonal to the cubic phase at 2370°C and both these transformations are connected with a change in volume. For state-of-the-art TBCs, zirconia is stabilized with 6 - 8 wt. % Y_2O_3 [YSZ], and consists completely of non-transformable tetragonal t' phase [Schulz *et al*; 1996]. Several other oxides, like CaO, MgO, CeO_2, InO_2 and Sc_2O_3, show similar phase stabilizing effects [Jones; 1996].

The stabilization of zirconia with yttria has been found suitable as it hinders the transformation from tetragonal to monoclinic zirconia, which is associated with a 4% volume change and hence large residual stresses. The stabilization of zirconia with yttria is dependent on the amount of yttria being added, as shown in Figure 1.3. It has been found that zirconia possesses the highest fracture toughness when it has the metastable tetragonal (t) phase [Bengtsson; 1997], which is allowed to form during rapid cooling following deposition of the coating. The maximum content of metastable t phase is obtained when the Y_2O_3 content is around 8 wt. %. Though this t-phase has very high strength and toughness, it is susceptible to stress-induced solid-state transformation of the metastable tetragonal to monoclinic phase [Bengtsson; 1997, Olsson; 1994]. Hence, a mixture of zirconia with 6-8 wt. % yttria is heated and cooled at appropriate rates to obtain a different tetragonal phase called the t′-phase. Since this phase does not transform to monoclinic and cubic phases under stress, it is referred to as the non-transformable tetragonal phase. Thermal cycling tests have also shown that maximum thermal cycle life

is obtained for zirconia partially stabilized with 6-8 wt. % [Stecura; 1985]. The superior cyclic life of this composition has been attributed to the maximum stability of the non-transformable t′-phase of YSZ.

The TBC itself must be "strain tolerant" to avoid rapid delamination. This is achieved by incorporating either porosity or through-thickness microcracks [Hillery; 1996, Rigney *et al*; 1995]. Thermal barrier coating layers are produced by the following methods: Air plasma spray (APS), Low-pressure plasma spray (LPPS)/Vacuum plasma spray (VPS), Shrouded plasma spray (SPS), High velocity oxygen fuel (HVOF), Pack or Chemical Vapor Deposition (CVD) aluminizing of an electroplated platinum layer and Electron beam physical vapor deposition (EB-PVD). All these methods can be used to apply the bond coat, but APS and EB-PVD are the only methods that are suitable for deposition of the ceramic topcoat. LPPS/VPS, CVD and SPS are exclusively used for depositing bond coats.

The EB-PVD process uses an electron beam to evaporate the oxide from a ceramic YSZ ingot and directs the vapor onto the preheated component [Rigney *et al*; 1995]. The vapor then deposits on to the substrate surface, which can be rotated above the vapor source. Figure 1.4 is a schematic of an EB-PVD coater. The deposition conditions are designed to create a columnar grain structure with both intra- and inter-columnar porosities that, respectively, enhance the thermal resistance and control the strain tolerance. The columnar microstructure of the EB-PVD TBCs exhibits very high levels of stress compliance, where the individual columns prevent the build-up of tensile stresses and accommodate the CTE differences between the TBC and the base metal [Morrel *et al*; 1998].

In the APS process, YSZ powder is injected into a plasma gas and melts rapidly. The molten spherical particles hit the surface of the substrate and form splats. A successive deposition of splats, along side and on top of one another, forms a coating that consists of relatively high-density intra-splat regions and relatively low-density planar splat boundaries. Figure 1.5 is a schematic of the plasma spray process.

Figure 1.6 illustrates the microstructures of the topcoat applied using both the APS and the EB-PVD processes. The APS structure is lamellar with horizontally deformed splats, which are formed when the molten particles hit the surface and form splat boundaries that are highly porous and partially cracked. The EB-PVD structure, on the other hand, is highly columnar. The columnar structure offers improved strain tolerance due to inter columnar porosity acting as stress reliving crack like structures, and, because the individual columns are harder, offers improved erosion resistance compared to APS.

Key reasons to use zirconia for TBCs are its low thermal conductivity, which is 2.5 W/mK in the sintered and dense condition [Bengtsson; 1997] and its high coefficient of thermal expansion (CTE-11 ppm/C). Because of the defected splat boundaries and porosity, the thermal conductivity of APS YSZ TBCs can be reduced to about 1 W/mK [Bengtsson; 1997], with minimal temperature sensitivity [Kingrey *et al*; 1976]. The higher thermal conductivity in EB-PVD zirconia TBCs, compared to APS TBCs, is due to the improved heat conduction path provided by the columnar microstructure.

For a ceramic, zirconia has a relatively high thermal expansion coefficient. The difference in thermal expansion between the substrate and topcoat induces detrimental thermally generated stresses during operational temperature changes. However, the

porous APS and columnar EB-PVD microstructures give a reduced elastic modulus and an enhanced strain tolerance. The best strain tolerance has been obtained in the columnar structured EB-PVD coating,

1.1.1.1. Coating Deposition Methods

Electron-beam physical vapor deposition is often favored over plasma deposition for TBCs on turbine airfoils of high-pressure turbine vanes and blades. Using this deposition process, the shape and diameter of the cooling holes remain relatively unaffected and the resulting surface roughness is low compared with APS coatings (0.5 to 1 µm average roughness R_a for EB-PVD coatings compared with 4 to 10 µm R_a for APS coatings). The main drawbacks of the EB PVD process are the high capital and coating costs. EB-PVD TBCs are deposited at rates of 10-20 µm per minute and complex rotating and tilting of the substrate within the coating chamber are necessary in order to ensure uniform coating coverage [Terry; 1998]. The substrate needs to be heated to 900–1100°C during deposition.

The widely used plasma-spray process has its own benefits, including simplicity, faster coating rates, the possibility of easily controlling and changing process parameters, and better thermal insulation due to the aligned splat boundaries, a lower application cost, an ability to coat a greater diversity of components with a wider composition range, and a large installed equipment base. The coating composition in the APS process is determined by the powder composition and does not have to take into account different constituent vapor pressures, as is the case of the EB-PVD process. Although EB-PVD coatings have a somewhat higher thermal conductivity than APS coatings, they generally

exhibit longer life and are increasingly used in the hottest gas turbine component applications, such as first stage turbine blades and vanes. [Fairbanks *et al*; 1987].

The microstructure of APS TBCs is significantly influenced by process parameters such as flame temperature and feed rates, gas velocities and grain size distribution of the ceramic powder [Funke *et al*; 1997]. In general, more porosity is found in coatings applied at lower velocities.

The microstructure of EB- PVD TBC coating is mainly affected by the following deposition parameters [Rigney *et al*; 1995, Novak; 1995]:

- Substrate temperature
- Surface roughness of the bond coating: A smooth surface promotes parallel growth of lamellar zirconia. With increasing surface roughness, the width of the lamellae increases, as well as the deviation from ideal orientation. [Rigney *et al*; 1995]
- Rotation rate of the component and vapor flux from the evaporator: To coat complex shaped parts uniformly, rotation and tilting of the components has to be performed during the coating process. Increasing vapor flux at constant rotation rate results in coarser substructures due to higher condensation rates. Decreasing rotation rates, at constant vapor flux also promotes coarser substructures.

1.1.2. Bond Coat

Since the ceramic top coat is not an oxygen barrier, an oxidation resistant coating, referred to as the bond coat, is applied to TBC coated parts. Typically, the bond coat is a MCrAlY overlay or a diffusion coating with a thickness of 50-150 μm and its most

important functional part is aluminum. Its purpose is to allow for the growth of an oxidation-resistant oxide layer. Of all possible oxides, a-Al_2O_3 is known to offer excellent protection and very low growth rates (in a minority of cases, Cr oxides are preferred). The composition of the bond coat must therefore be chosen carefully so as to ensure growth of a uniform and continuous layer of a-Al_2O_3.

A wide variety of processes are used to apply bond coats, although they rely on one of three general methods: physical vapor deposition, chemical vapor deposition, and thermal spray. Diffusion coatings are well bonded to the substrate but have limited compositional flexibility and hence their usefulness is strongly dependent on substrate chemistry. Overlay coatings are typically well bonded and have broad compositional flexibility; however, they are more expensive and thicker than diffusion coatings.

The two most widely used types of high-temperature coatings are aluminides (Ni Al or Ni_2Al_3) and MCrAlY coatings. While the aluminides are obtained by surface enrichment by diffusion, the MCrAlY overlay coatings are obtained by plasma spray or electron beam physical vapor deposition (EB-PVD) processes [Nicholls *et al*; 2002].

MCrAlY coatings are often used because they offer the excellent combinations of oxidation and corrosion protection [Nicholls *et al*; 2002]. The diffusion type of bond coat is more suitable for lower temperature applications, is less expensive and provides better adherence.

1.1.2.1. Aluminides

Diffusion coatings protect the turbine components against the environment by promoting an oxide scale. These coatings can be produced by enriching the component

surface through diffusion by an oxide-forming element, usually Al, Cr or Si [Angenete; 1999]. The most common diffusion coating is an aluminide coating since alumina has low oxygen diffusivity and superior adherence. Diffusion aluminide coatings are based on the intermetallic compound ß-NiAl. This can be understood from Figure 1.7, which is the Al-Ni phase diagram. Aluminum in the coating reacts with oxygen in the environment resulting in the formation of a protective alumina scale. The protective ability of the coating decreases with time as the aluminum reservoir in the coating is consumed.

Diffusion coatings can be applied by using techniques such as pack cementation, slurry-fusion and chemical vapor deposition (CVD). Pack cementation and slurry fusion were the first methods introduced. The CVD method came later, and is advantageous for coating cooling passages. The pack cementation is the traditional way and the most widely used method to apply diffusion coatings, as it is inexpensive and well adapted to coating of small parts. It has been used since the late 1950s for protecting turbine blades under aero, industrial and marine service [Goward; 1998].

1.1.2.2. Platinum Aluminides

NiAl coatings tend to suffer strongly from interdiffusion with the substrate, which results in formation of ?' at the expense of ß. The idea of introducing a diffusion barrier led to the invention of the Pt-aluminide coatings, which are obtained by similar methods as conventional aluminide, but after electroplating the component with Pt. The Pt layer is typically of 5-10 µm [Schultz; 2000]. Because Pt electroplating can increase the life of the blades by up to three times [Sivakumar *et al*; 1989], its use is cost-effective.

Interestingly, it was found that Pt additions did not only provide a diffusion barrier, but also enhanced Al diffusion [Chen; 1997]. When applied on the second-generation superalloy CMSX-4, Pt formed TCP (topologically close-packed) phases with some elements of the substrate (Re, W, Mo, and Cr). The exact reasons for the beneficial effect of Pt are not fully understood, but it was found that Pt improves oxide adherence and also contributes to better hot corrosion resistance. Pt also delays transformation of ß-NiAl to ?'-Ni_3Al in aluminides, which improves the high temperature oxidation resistance. Pt appears to partially substitute for Ni in ß-NiAl, and also to form $PtAl_2$, which is believed to act as an Al reservoir.

1.1.2.2.A. Pack Cementation Process

Pack cementation falls in the category of chemical vapor deposition. In this process, the components to be coated are sealed in a chamber containing a pack [Nicholls *et al*; 2002] consisting of Al powder, ~ 1-2 wt.% halide activator (e.g. 1% NaF or NH_4Cl) that supports the transport of solute to the material to be coated, and an inert filler that prevents sintering of the pack. By heating the chamber to reactive temperatures of 800-1000°C, in argon or H_2 atmosphere, the activator and aluminum powder form a high activity aluminum vapor (in the form of aluminum halide) that reacts with the surface, which has a low chemical activity of aluminum. Interdiffusion between the substrate and the gas results in the formation of the intermetallic NiAl coating. After the aluminization process, the component is heat treated in different steps in order to optimize the coating microstructure and to restore the initial microstructure of the substrate. Two variants of NiAl coatings can be produced with pack aluminization [Buhl; 1992]: high activity aluminum (inward diffusing) and low activity aluminum (outward diffusing).

1.1.2.2.B. Inward Diffusing Aluminide

In packs where the activity of aluminum is high with respect to nickel, aluminum diffuses inwards faster than nickel can diffuse outwards. Hence the coating forms mainly by inward diffusion of aluminium and results in formation of a brittle surface layer consisting of ß-NiAl + d - Ni_2Al_3. This occurs when a high activity powder of Al or Cr-30Al and a process temperature of 700-950°C are used. A subsequent heat treatment at 1050-1200°C is usually required to transform the brittle d-Ni_2Al_3 to ß-NiAl.

1.1.2.2.C. Outward Diffusing Aluminide

In packs with low aluminum contents, where the activity of aluminium is lower than that of nickel, nickel diffuses outwards. The formation of the coating thus occurs mainly by Ni diffusion, and results in the direct formation of a nickel rich NiAl layer. The process requires high temperature (1000-1100°C). In service, the interdiffusion with the substrate is very limited and the gradient of Al in ß- NiAl is low. This occurs when a low activity powder, for example Cr-15Al, and a process temperature of 1000-1200°C is used. In this case, a ß-NiAl coating is obtained in one stage, but has a lower Al content than the high activity coating.

Figures 1.8 and 1.9 show the typical microstructures for the inward and outward type coatings. Typically, both types of coating have an interdiffusion zone between the coating and the substrate [Goward; 1970]. The interdiffusion zone is a Ni-depleted zone formed during the outward diffusion of Ni and consists of elongated precipitates based on heavy elements such as Cr, Co, W, etc [Goward; 1970, Angenete; 1999, Das *et al*; 1998]. Since the inward type of coating is exposed to a second heat treatment at 1050-1200°C

[Goward; 1970, Angenete; 1999, Das *et al*; 1998], this type also contains an intermediate layer of outward type and an interdiffusion zone between the outer coating region and the substrate, as shown in Figure 1.8.

Unlike the outward diffusion process, which produces a relatively pure NiAl composition, the inward diffusion process gives a coating that contains other alloying elements than nickel, either in solution or as secondary phases. Also, the outward diffusion generates fewer grain boundaries and a thicker region of interdiffusion zone [Goward; 1970]. The main matrix phase in NiAl coatings is ß-NiAl, but ?'-Ni_3Al may also be present [Angenete; 1999]. NiAl is a highly ordered intermetallic compound, which is stable up to very high temperatures but it has a low ductility [Noebe *et al*; 1999]. Especially in the case of the inward type of coating, different precipitate phases such as TCP-phases (µ and s), bcc-phases (a- Cr and a-W) and carbides are present [Angenete; 1999]. The microstructure of diffusion aluminides depends on substrate composition, as well as, the coating process and post-coating heat treatment. .

1.1.2.3. Inward and Outward Diffusing TBC Bond Coats

The main difference between the inward and outward grown bond coats used in this study is that the inward grown bond coat is made by the traditional pack cementation method while the outward grown bond coat is made by a CVD process. Basta *et al* (1997, US Patent # 5658614) have compared the cyclic oxidation resistance of these two bond coats at 1100°C. They reported that the platinum modified outward aluminide coating produced under CVD conditions has superior oxidation resistance compared to the platinum modified inward aluminide bond coat produced by pack cementation. The improved oxidation resistance of the outward grown bond coat has been attributed to the

CVD conditions associated with making the outward grown, single phase platinum modified aluminide bond coats. The CVD method of depositing the outward grown bond coats has two beneficial factors compared to the inward grown platinum modified aluminide coating that is formed at a lower temperature by the pack cementation process: A purification effect on the as-formed bond coat from the standpoint of substantially reducing (1) the concentration of one or more substrate substitutional alloying elements, such as W, Mo, etc., and/or (2) one or more surface active tramp elements, such as B, P, and S, in the coating. While the substitutional impurities (particularly, the substrate refractory alloying elements) produce doping effects resulting in significant increases in the growth rate of the protective alumina scale, the surface active tramp elements adversely affect the adherence of the protective scale. The purification effect of the CVD aluminizing process has also been demonstrated by Basta *et al* (1997, US Patent # 5658614) using composition profiles across the outward grown bond coated foil. The outward grown CVD platinum modified aluminide coating has been shown to have about 40% longer life than the inward grown pack cemented platinum modified aluminide coating, the superior oxidation resistance being attributed to a slower growing more adherent protective alumina scale [Basta *et al*; 1997, US Patent # 5658614].

Angenete and Stiller (2002) have also compared the oxidation behavior of the inward grown and outward grown platinum modified aluminide bond coats produced by pack cementation and CVD methods respectively, at 1050°C under isothermal conditions. They have reported [Angenete and Stiller; 2002] that the outward grown coating made by a CVD process produces a slower growing oxide that was more spallation resistant than the inward grown platinum aluminide bond coat produced by

pack cementation process. The main mechanism behind the higher oxide growth of the inward grown bond coat was reported to be the larger effective surface area (because of its smaller bond coat grain size and hence a greater number of grain boundaries) and the apparently smaller grain size of the oxide on the inward grown bond coat. Other possible reasons were also identified: bond coat purity, bond coat surface topography and ductile to brittle transition temperature. Figure 1.10 compares the cross-section microstructures of the two bond coats in the as-coated condition [Angenete and Stiller; 2002].

1.1.2.4. MCrAlY Bond Coat

MCrAlY overlay coatings were first developed at Pratt & Whitney in the late 1960s [Goward; 1998] and offer two main capabilities:

- The coating composition can be made independent of the substrate composition.
- Coating compositions can be varied over a wide range, thus the best compromise of oxidation resistance, hot corrosion resistance and mechanical properties can be obtained.

Typical MCrAlY bond coats (M=Fe, Co, Ni or Ni/Co) contain at least 4 elements. The presence of a significant amount of Cr gives these coatings excellent combinations of corrosion and oxidation resistance Diffusion coating methods cannot be used to form McrAlYs because it is impossible to control the activity of each element in the pack to obtain the desired composition. Alternative methods are therefore preferred, such as air plasma spray (APS), low-pressure plasma spray (LPPS), or electron beam physical vapor deposition (EB-PVD). Deposition is followed by a high-temperature heat-treatment in vacuum to allow interdiffusion and therefore improve adhesion [Richard *et al*; 1996].

The M of MCrAlY stands for either Ni or Co, or a combination of both, depending on the type of superalloy. It was first found that reactive elements additions such as yttrium of about 1 wt% improve oxide adherence. It was initially thought that yttrium helped in the formation of oxide pegs that helped anchor the oxide layer to the coating. However, it has been shown [Smeggil; 1987], that the main role of Y is to combine with sulfur and prevent its segregation to the oxide layer, which is detrimental to its adhesion. Additions of hafnium (Hf) play a similar role. The effects of other additions have also been investigated [Nicoll *et al*; 1992].

CoCrAlY coatings have favorable combinations of hot corrosion and oxidation resistance, but limited ductility, and NiCrAlY coatings exhibit good ductility, but poor corrosion resistance. As a compromise, this has led to the development of the NiCoCrAlY type of coatings, which have been satisfactorily used for many years in gas turbine applications. An often-used composition is the Ni-23%Co-15%Cr-12%Al-0.5%Y. Co-based coatings appear to have superior corrosion resistance and Cr provides hot-corrosion resistance, but the amount that can be added is limited by the effect it is expected to have on the substrate, and the formation of Cr-rich phases in the coating. Al content is typically around 8-12 wt. %. Since oxidation life is essentially controlled by the availability of Al, it would be expected that higher aluminum contents are desirable. However, this results in significant reductions in ductility [Sivakumar *et al*; 1989]. It was found that silicon (Si) significantly improved cyclic oxidation resistance; however it also decreased the melting point of the coating - 5 wt. % being sufficient to lower the melting temperature to about 1140°C. There is also evidence that it affects phase stability. For cyclic oxidation at 1000°C, 2.5 wt% was found to be the optimum content. Additions of

rhenium (Re) have been shown to improve isothermal and cyclic oxidation resistance and thermal cycle fatigue resistance [Czech *et al.*; 1994]. Additions of tantalum (Ta) were also found to increase the oxidation resistance. Figure 1.11 is a schematic describing the optimum bond coat composition in relation to its oxidation and hot-corrosion resistance [Schulz; 2003].

MCrAlY coatings typically exhibit a two-phase microstructure of ß+?. The presence of ? increases the ductility of the coating thereby improving its thermal fatigue resistance. As in the case of ß-NiAl coatings, high temperature exposure results in depletion of the Al from the bond coat both to the TGO and to the substrate by interdiffusion. As the amount of Al decreases, the ß phase tends to dissolve. For this reason, it is often described as an aluminum reservoir, and coating life is often measure in terms of ß depletion. Figure 1.12 shows a typical microstructure of APS NiCoCrAlY coatings. The main phases in these coatings are: the ß-NiAl phase which is a B2 type ordered superlattice compound with bcc derivative structure, the ?'-Ni_3Al phase which is a L12 type ordered superlattice compound with a fcc-derivative structure and a continuously ?-NiCoCr phase of fcc structure. As shown in Figure 1.12, the APS microstructure contains splat boundaries, pores and oxide stringers and has an anisotropic microstructure, the latter being a result of the flattening of the splats when they hit the surface.

1.1.3. Thermally Grown Oxide

The protective layer in a TBC is the highly stable aluminum oxide that forms on the bond coat during heat treatment and engine service. The thickness of the TGO, prior to engine service, is typically less than 0.5 µm. It prevents oxidation of the bond coat and

provides a strong bonding of alumina ceramic to YSZ ceramic [Terry; 1998]. The growth of the TGO is essentially parabolic indicating that it is controlled by oxygen diffusion through the TGO layer, requiring both inward diffusion of oxygen anions and outward diffusion of Al cations for its formation [Evans et al; 2000].

EB-PVD TBCs generally fail at the bond coat/TGO interface; whereas, APS TBCs normally fail in the TBC itself [Clarke *at al*; 1997]. Failure of EB-PVD TBCs typically initiates by fracture and delamination of the brittle Al_2O_3 scale along the TGO/bond coat interface, which results in spallation of the ceramic top coat [Meier *et al*; 1991, Meier *et al*; 1992, Maricocchi *et al*; 1995, Parks *et al*; 1997] and the concomitant loss of thermal protection. From this perspective, development of bond coats with significantly improved alumina scale adherence is a critical step in improving the performance of state-of-the-art TBCs. The reasons for failure in EB-PVD TBCs being localized in the region of the TGO are the high compressive oxide growth stresses which arise in the TGO during heat treatment, especially as the TGO keeps growing during high temperature service and the progressive increase of the TGO undulations, as explained in Section 2.4. A thin, dense layer of YSZ deposited on the TGO enhances its resistance to buckling and rumpling.

In some cases, other metastable forms of Al_2O_3 (δ, γ, θ) are formed prior to formation of the most stable α-Al_2O_3. The θ-phase has a needle-like appearance, suggestive of outward diffusion of Al. The metastable θ–phase transforms to α-Al_2O_3 on exposure to high temperatures [Lipkin *et al*; 1997a]. This transformation is followed by a significant volume contraction [Lipkin *et al*; 1997b], which is said to cause tensile

cracking of the TGO. Hence the occurrence of non-α alumina phases, prior to deposition of TBC, is believed to cause separation at the TGO/TBC interface [Clarke *et al*; 1999].

1.2. Durability of EB-PVD TBC's

The major challenge for the development of improved TBCs is coating durability, particularly the resistance of the coating to spalling. There are a number of degradation modes which can limit the life of a TBC - TBCs fail as a result of erosion, impact damage, interfacial oxidation of the bond coat, or thermo mechanical strain at the ceramic/metal interface. The durability of EB-PVD TBCs in oxidizing environments is determined by the interplay of the stored elastic energy driving spallation versus the interfacial toughness of the TGO/bond coat interface, since failure often occurs at this interface. A number of studies of TBC degradation have indicated that the fabrication methods of the YSZ and bond coat can in?uence the crack path and the time to failure [Bose *et al*; 1995]. The composition of the bond coat and that of the substrate alloy are other factors that affect TBC durability [Miller; 1995]. Other factors include: the stress state in the zirconia layer, the bond coat microstructure, TGO stress and TGO thickness. It was pointed out by Miller [Miller; 1984] that the bond coat oxidation is a critical factor in governing EB-PVD TBC lives.

The failure modes of a given TBC can vary with temperature, hold time, and severity of thermal transients. Accordingly, there is a compelling need to understand how the dominant spallation failure mechanisms are modi?ed when the test conditions are changed. A substantial research effort has been devoted to the investigation of mechanisms that dictate the durability of thermal barrier systems [Miller; 1984,

Strangman; 1985, Hillery; 1996, Miller; 1995, Wright and Evans; 1999, Maricocchi *et al*; 1995, Evans *et al*; 2001, Stiger *et al*; 1999, Gell *et* al; 1999, Vaidyanthan *et al*; 2000, Sohn *et* al; 2001, Xie *et al*; 2003, Sridharan *et al*; 2004, Vaidyanthan *et al*; 2004, Sridharan *et al*; 2005, Wen; 2005], with a focus on the analysis of disc-shaped specimens that undergo thermal cycling in a furnace.

Furnace cyclic tests are typically designed to simulate engine service conditions. The performance and durability of TBCs are strongly dependent on the operating conditions and the environment in which they operate. TBCs operate within the following two principal domains with vastly different thermal histories: (1) Thermo-mechanical loadings, typical of those applicable to "power generation", with long high temperature exposures and minimal thermal cycling and (2) Loadings representative of aero-engines comprising extensive thermal cycling [Evans *et al*; 2001]. This cycle frequency affects TBC durability. In the first case, cracking is dominated by a combination of the TGO growth stresses and those from the thermal expansion mismatch. TBC failure in the second case is more likely to be affected by cyclic phenomena like rumpling; wherein, cyclic displacements of the TGO into the bond coat result in delamination strains in the TBC. In addition, the TBC service conditions for aircraft engines also differ from those of the land based gas turbine engines, as shown in Table 2.1.

1.2.1. Effect of Cycle Temperature on Spallation Life

The number of cycles to failure has been observed to increase with decreased test temperatures [Mutasim *et al*; 1999, Kim *et al*; 2002, Evans *et al*; 2001]. The lower testing temperature decreases the rate of bond coat oxidation, and; therefore, lowers the thickness of the oxide layer, thus increasing the number of cycles to failure.

The strong effect of oxidation temperature on failure time indicates that TGO growth rate, i.e. oxide thickness, is a key factor in determining TBC failure. Tolpygo and Clarke [Tolpygo and Clarke; 2001] argue that there is critical oxide thickness (5–7 μm for Pt–aluminide bond coats) beyond which the coating will fail. Wright [Wright; 1998] questions the validity of the ‘‘critical oxide thickness’’. The effect of temperature and similar hot times to failure for isothermal and one-hour cycling tests observed in a study by Kim *et al* [Kim *et al*; 2002] and [Tolpygo and Clarke; 2001] support the concept of a critical oxide thickness for failure. However, coatings can fail at smaller oxide thicknesses if other processes intervene.

1.2.2. Effect of Cycle Duration on Spallation Life

The results obtained from recent numerical and analytical models [Karlsson *et al*; 2002, Xu *et al*; 2003, Karlsson *et al*; 2003, Yu *et al*; 2001, He *et al*; 2003] indicate that the rate of cracking at the TBC/TGO interface is dictated by the magnitude of the TGO displacement instabilities. Basic analysis [Karlsson *et al*; 2003] has indicated that these TGO displacements are strongly influenced by the hold time, t_{hold}, at high temperature, because of the limit on the growth stress established by plastic relaxation mechanisms operating in the TGO, with consequent effect on the cycle-by-cycle extension of cracks in the TBC.

The number of cycles to failure has been observed to increase, while the total hot time to failure has been found to decrease with decrease in cycle time [Mutasim *et al*; 1999, Kim *et al*; 2002, Evans *et al*; 2001]. Mechanical stresses are generated between the metallic and ceramic interface, at or above the TGO, during heat-up and cool-down of

each thermal cycle, due to the thermal expansion mismatch between the various layers. The total hot time to failure decreases with decrease in cycle hold time due to the increased mechanical stresses on the specimens from thermal cycling. The number of cycles increases because bond coat oxidation is lowered with shorter hot times. In a study conducted by Kim *et al*, the type of thermal exposure (cycle hold time and cycle temperature) not only affected the time to failure but also the fracture path when the specimens failed.

The peak cycling temperature and hold time have also been found to be major factors for inducing delamination in the TGO resulting from oxidation and CTE misfit. In a study conducted by Chaudhury *et al* [Chaudhury *et al*; 1997], a 60-minute hold time was found to be more severe than tests with 45-minute hold time, with extensive separation at the TBC/TGO interface occurring in the 60-minute hold-time tests.

1.3. Photoluminescence Piezospectroscopy (PLPS)

Premature spallation of TBC's during service is a major concern and has slowed the pace of TBC applications. The current approach is to estimate the service life from extensive laboratory and engine testing and apply a large safety factor. Thus, there is a great need for a non-destructive technique to assess the extent of accumulated damage and to predict the useful residual lifetime of the coatings in service. The photoluminescence piezospectroscopy (PLPS) technique provides for the measurement of TGO stress and for the determination of TGO type (a, ?, ? alumina) and distribution.

This PLPS technique, invented by Paton, Murphy, and Clarke for TBCs (US Patent #6, 072, 568), and further developed by Clarke *et al*, [Lipkin and Clarke; 1995, Christensen et al; 1996, Lipkin et al; 1997, Clarke et al; 1997, Peng and Clarke; 2000] and Gell, Jordan, *et al*, Gell *et al*; 1999, Schlichting *et al*; 2000, Sohn *et al*; 2001, Xie *et al*; 2003, Sridharan *et al;* 2004; Gell *et al*; 2004] has been successful in non-destructively measuring the stress in the TGO under the ceramic. This was applied for the first time, to measure stress in the TGO in a commercial EB-PVD TBC by Christensen *et al*; 1996.

1.3.1. Basic Principles

When a TBC is illuminated with a green or blue laser beam, the colors that correspond to the principal absorption bands of Cr^{3+} in α-alumina, a red luminescence is produced. This photo-stimulated luminescence originates from the TGO formed by high-temperature oxidation beneath the TBC and is characterized by an intense, spectral doublet, R_1 and R_2, that occur at 14,402 cm^{-1} and 14,432 cm^{-1} respectively. This is illustrated in Figure 1.13.

The R_1 and R_2 doublet photoluminescence frequency is known to be dependent on three factors: the hydrostatic component of the applied stress, ambient temperature and local Cr concentration [Lipkin and Clarke; 1995]. The effect of temperature on the R_1 and R_2 frequencies has been studied by He and Clarke (1995) and the frequencies have been found to decrease with increasing temperature by 0.134 cm^{-1} °C and 0.144 cm^{-1} °C, respectively, for the R_2 and R_1 lines.

The effect of chromium concentration on R_1 and R_2 lines has been studied by Kaplyanskii *et al* (1969). But since it is extremely difficult to determine the chromium

concentration independently, the measured luminescence frequency is typically compared to that recorded from a spalled fragment of the oxide to obtain the 'stress-free' frequency. Since the chromium concentration will not have changed significantly when the oxide fails, it is assumed that the only change in frequency is due to release of the stress in the spalled fragment. In the event that failure has not yet occurred, a sapphire standard is used to obtain an estimate of the stress-free frequency.

The effect of uniaxial stresses along different crystallographic directions and the effect of hydrostatic pressure have also been systematically studied on sapphire crystals (single crystal alumina) containing chromium and the values of the piezospectroscopic coefficients have been determined [He and Clarke; 1995]. The frequency shift measured using PLPS is related to the biaxial stress in the TGO, assuming a random orientation of the grains in the TGO [He and Clarke; 1995] by the following equation:

$$\Delta\nu = \frac{2}{3}(\Pi_{11} + \Pi_{22} + \Pi_{33})\,\sigma_B$$

where the sums of the coefficients have been found to be 7.61 and 7.59 cm^{-1} GPa for R_2 and R_1, respectively. Experiments under hydrostatic pressure have indicated that the separation between the R_1 and R_2 peaks is 30.0 cm^{-1} at room temperature and that it does not change with pressure. However, when the stress state is not hydrostatic, the peak separation does depend on stress and the stress state.

1.3.2. PLPS Data from EB-PVD TBC's

The PLPS technique has been applied to both EB-PVD and APS coatings [Gell *et al*; 1999, Schlichting *et al*; 2000, Sohn *et al*; 2001, Xie *et al*; 2003, Sridharan *et al;* 2004, Gell *et al*; 2004, Wen *et al*; 2005]. The columnar microstructure of EB-PVD coatings act

as optical wave-guides for the laser and ensure that the optical signals are not attenuated, The presence of microstructural defects, such as porosity, splat boundaries, and micro cracks in APS coatings results in an attenuation of the optical signal. PLPS can hence be used for full-thickness EB-PVD coatings (=300 µm), [Gell *et al*; 1999, Sohn *et al*; 2001, Xie *et al*; 2003, Sridharan *et al;* 2004] but, at present, can be used for APS coatings of only =75 µm [Schlichting *et al*; 2000, Sohn *et al*; 2000]. Thicker APS TBCs can be examined if the pores and splat boundaries are filled with a liquid whose refractive index more closely matches that of the YSZ [Schlichting *et al*; 2000, Sohn *et al*; 2000]. Thus, attempts at using this technique for the examination of full thickness plasma-sprayed TBCs have been, for the most part, unsuccessful.

1.3.2.1. Types of Spectral Characteristics

In order to obtain information about the stress and damage in a TBC, the collected PLPS spectra are analyzed using commercially available software. Several spectral characteristics can be extracted, some of which are shown in Figure 1.14. They are R_1 and R_2 peak positions, R_1 and R_2 peak separation, which depends on the stress state in the alumina, R_1 and R_2 peak intensities, R_1 and R_2 peak intensity ratio, the shape of the R_1 and R_2 peaks as defined by the fraction of Lorentzian to Gaussian character, the full width at half maximum (FWHM) of each R line and finally, the ratio of the FWHM (peak broadening) of the R_2 peak relative to that of the R_1 peak. For the most part, all these characteristics have been previously calibrated in their response to stress [Grabner *et al*; 1978, He and Clarke; 1995], temperature [Munro et al; 1985, Lipkin and Clarke; 1996] and chromium concentration [Schawlow *et al*; 1959].

1.3.2.2. Origin of Spectral Characteristics

This section details the origin and source of some of the spectral characteristics listed in the previous section. Based on a study by Lipkin et al [Lipkin *et al*; 1997], the broadening of the peaks or the peak width is indicative of the existence of stress variation within the probed volume. In the same study, it was suggested that the value of the intensity ratio depended on the crystallographic orientation with respect to the polarization of the laser used to stimulate the luminescence. However, an experiment conducted by Xie et al [Xie *et al*; 2003] using a quarter wave plate proved this assumption to be incorrect. The R_1 and R_2 lines can be modeled as a mixture of Lorentzian and Gaussian functions [Lipkin and Clarke; 1996, Peng and Clarke; 2000, Munro *et al*; 1985] and the L: G ratio was found to decrease for the stressed TGO in comparison to the stress-free sapphire. This was considered to be concomitant with peak broadening due to crystal misorientation and strain gradients in the film.

1.3.2.3. Effect of Bond Coat on PLPS Data

For PLPS spectral characteristics to be useful in detecting early damage, they should exhibit a monotonic change with thermal cycling. It has been found that the particular spectral characteristic that shows a monotonic change may vary from TBC to TBC, consistent with the damage mechanism. The operative TBC damage mechanism and the associated spectral trends are hence a function of bond coat composition and processing, and service history variables that include time, temperature, and thermal transient effects.

1.3.2.3.A. Pt-Aluminide Bond Coat

Most EB-PVD TBCs on grit-blasted platinum-aluminide bond coats have shown a consistent and monotonic decline in TGO stress with thermal cycling, as illustrated in Figure 1.15 [Selcuk and Atkinson; 2003, Clarke, Xie *et al*; 2003, Sridharan *et al*; 2004, Wen *et al*; 2005]. However, other spectral characteristics have not shown any systematic trend with thermal cycling. While some systems with platinum aluminide bond coats resulted in bimodal PLPS spectra with two stress contributions [Selcuk and Atkinson; 2003, Wen *et al*; 2005], a high and a low stress contribution to the residual stress sampled at a single analysis point, other systems produce unimodal stress values [Xie *et al*; 2003, Sridharan *et al*; 2004]. The mean compressive residual stress has been shown to increase during the first 5-10 % of the TBC life, due to in-plane growth of the non-planar TGO as it thickens and becomes more resistant to bending. In the remaining part of the TBC life, the mean stress has been shown to decrease due to relaxation by a number of local damage events. The observed stress change for the platinum aluminide bond coated systems is due to TGO rumpling and localized separations at the TBC/TGO interface.

However, platinum aluminide bond coat systems that are not grit-blasted have not shown any significant stress decrease with thermal cycles. This difference between the grit-blasted and the non grit-blasted platinum aluminide bond coats is presumably due to the greater extent of rumpling in the grit blasted bond coats [Sridharan *et al*; 2005], which have a rougher initial bond coat surface than the non-grit blasted bond coats [Xie *et al*; 2003].

1.3.2.3.B. MCrAlY Bond Coat

PLPS measurements on EB-PVD TBCs with MCrAlY bond coats [Sohn *et al*; 2001] have shown a very different behavior; a monotonic increase in TGO stress with

cycling followed by a sharp decline just prior to failure. Most MCrAlY bond coats produce bimodal spectra and the observed stress increase for this system is due to an increase in the bimodal stress states, associated with both intact TBC and locally damaged regions where the TBC has detached from the substrate. The bimodal fraction (stress-free component) for MCrAlY bond coat systems is seen to initially increase sharply, then gradually decrease and increase again close to TBC failure [Sohn *et al*; 2001]. This initial increase of bimodal sprectra is attributed to the initial formation of θ-alumina and its subsequent transformation to α-alumina on thermal cycling. For another MCrAlY system, only a slight decline in the TGO stress was observed just prior to failure [Shen, 2004]. The TGO stress evolution with cycles for MCrAlY bond coated TBCs did not provide any useful means of detecting early TBC damage and its impending failure.

1.4. Failure Modes in EB-PVD TBC's

This section reviews the different failure modes observed in EB-PVD TBCs when subjected to high temperature thermal cycling. Degradation mechanisms for TBCs are a function of the engine operating conditions, engine mechanical design, and the component base materials. Engine operating conditions determine operating temperature and structural loads, while engine design determines the amount of air made available to cool the hot structure. The various failure modes that pertain to TBCs include:

- High-Temperature Oxidation: The rate of oxidation increases exponentially with temperature;

- Hot Corrosion: Electrochemical reaction between metal and molten salts, typically sodium and potassium sulfates. Two forms of hot corrosion are generally recognized: Type I (high-temperature), which typically occurs between the temperatures of 820 and 920°C (1500°F and 1700°F), with a maximum at about 870°C (1600°F); and Type II (low-temperature), which typically occurs between 590 and 820°C (1100 and 1500°F), with a maximum at about 700°C (1300°F);
- Mechanical Distress: Erosion and impact damage caused by the ingestion of particles in the air stream;
- Solid-State Diffusion: Reduction of the aluminum content of the coating because of interdiffusion with the base metal;
- Spallation: Loss of protective oxide at the coating/oxide interface;
- Thermo mechanical Fatigue (TMF) Cracking: Long-term (i.e., over many cycles) formation and propagation of cracks because of external mechanical stresses and residual stresses from lack of thermal expansion compatibility between the substrate and the coating;

Spallation of TBCs is an important failure mode and rapidly degrades the insulating properties of the coating and accelerates attack of the underlying metallic bond coat or substrate. TBC spallation is a mechanical event that results in the removal of the ceramic layer by delamination from the bond coat. Numerous processes may trigger this, but the two main reasons are bond coat oxidation and the strain generated by a thermal expansion mismatch between the ceramic top coat and the metallic components of the

system [Miller and Lowell; 1982, Strangman; 1985, Hillery *et al*; 1988, Demasi-Marcin *et al;* 1989].

Data in the literature indicate that these two factors have a synergistic effect on TBC failure. Under realistic conditions, the action of either alone cannot cause failure of plasma-sprayed [Miller and Lowell; 1982] or EB-PVD TBCs [Manning-Meier *et al*; 1991]. This generality may not hold for conditions of extreme thermal transients, however [Brindley and Nesbitt; 1988]. Since oxidation and thermal-cycle strains must both be present to cause TBC failure, reducing either could dramatically improve TBC life. However, the details of degradation differ substantially for EB-PVD and plasma-sprayed TBCs because of their substantially different ceramic layer and interface structures.

The main degradation modes for EB-PVD coatings include:

- Cracking within the TBC leading to spallation of a part of the TBC
- Cracking along the interface between the TGO and the bond coat resulting in spallation of the entire TBC
- Sintering of the TBC at the outer surface, which increases the thermal conductivity of the TBC and the total elastic strain energy stored in the coating, which provides additional driving force for cracking and spallation of the TBC

The three overarching principles that govern TBC failure are [Evans *et al*; 2001], as shown in Figure 1.16:

i. The TGO experiences large in-plane compressions, especially upon rapid cooling from high temperatures. It attempts to alleviate the stress and the elastic strain energy by lengthening itself through out-of-plane displacements. This can happen by buckling, ratcheting or rumpling and by visco-plastic deformation of the bond coat. These displacements induce tensile stresses normal to the TGO/bond coat interface.

ii. When imperfections exist around the TGO or near the TGO/bond coat interface, tensile stresses are induced normal to the TGO/bond coat interface and within the TBC. These cause cracks to nucleate and grown in the vicinity of the imperfections. The coalescence of these cracks causes ultimate failure.

iii. The TBC has sufficient stiffness to resist small scale buckling, so failure occurs by large scale bucking after a sufficiently large separation has developed near the interface.

The durability of the TBC is thus governed by the number of cycles needed to form such large-scale separations by a sequence of nucleation, propagation and coalescence, involving the strain energy density in the TGO and the size and spacing of the imperfections.

1.4.1. Damage Initiation at Imperfections at TGO/Bond Coat Interface

Imperfections are important because of the tensile stresses that develop around them as the TGO grows and the TBC is thermally cycled. In the presence of imperfections, local tensile stresses are created normal to the interface, large enough and

over sufficient spatial extent to cause the formation of well-defined interfacial separations. The principal focus is on the out-of plane tensile stresses, because these are the stresses governing crack growth parallel to the interface, near the TGO. At this stage, the energy release rate G associated with the separation increases to a peak [Hutchinson *et al*; 2000] and then decreases as it extends, causing it to be stable and self arresting. However, when the separation becomes large enough to satisfy buckling requirements, opening of the crack occurs, substantially increasing G and resulting in a minimum [Hutchinson *et al*; 2000]. These stresses, in turn, initiate cracks along trajectories having lowest toughness [Stiger *et al*; 1999, He *et al*; 2000]. Often, the important imperfections grow with exposure/cycling [He *et al*; 2000], thereby increasing the nucleation probability while also extending previously formed cracks.

In specimens subject to minimal thermal cycling, these stresses in the TBC are dominated by TGO growth [Evans *et al*; 2000] and amplified by thermal expansion misfit. Extensive thermal cycling introduces other stresses by ratcheting of the TGO into the bond coat [He *et al*; 2000].

In a study conducted by Vaidyanathan *et al* (2001), damage initiation was observed at surface imperfections, which manifest themselves as a geometric network of ridges. In the same study, TBC failure was observed to occur by separation at these ridge tops at the TGO/bond coat interface, at a fairly constant value of out-of-plane tensile stress. Also, reducing the initial size of these imperfections by grit blasting was found to improve the mean life of these coatings.

1.4.2. Bond Coat Surface Rumpling

Cyclic morphological instabilities in the TGO represent a source of failure in some TBCs. Observations and simulations [Ambrico *et al*; 2001, Brindley and Whittenberger; 1993, Mumm *et al*; 2001, Karlsson *et al*; 2002a, Karlsson *et al*; 2002b, Karlsson *et al*; 2002c, Karlsson *et al*; 2003] have indicated that several factors interact to cause these instabilities to propagate: (i) thermal cycling; (ii) thermal expansion misfit; (iii) oxidation strain; (iv) yielding in the TGO and the bond coat; and (v) initial geometric imperfections. Spallation is a failure mode dominated by the strain energy density in the TGO, and its interaction with imperfections in and around the TGO. The TGO develops large compressive stress upon cooling from operating temperatures, due to the substantial thermal expansion misfit with the underlying superalloy component. These large compressive stresses, being present within a thin layer of the TGO, cause the TGO to be morphologically unstable. The thin TGO seeks mechanisms to relieve the compression, by means of out-of-plane displacements. The sign and magnitude of the displacements are dictated by the mechanical properties of the bond coat and the TBC, as explained by Mumm, *et al* (2001). In practice, at high temperature, the bond coat is relatively soft, while the TBC layer remains elastic. Thus, the displacements occur preferentially into the bond coat, as shown in Figure 1.17. Failure then occurs as a sequence of crack nucleation, propagation and coalescence events [Wright and Evans; 1999, Evans *et al*; 2001, Choi *et al*; 1999]. The thermo-mechanical response in this failure mode comprises an out-of-plane displacement instability in the TGO, with ensuing crack evolution in the TBC overlayer, as shown in Figure 1.17.

The literature indicates the possibility of two such instabilities. One is manifest as the formation of regular, long wavelength undulations, referred to as "rumpling" [Tolpygo and Clarke; 2000, Deb *et al*; 1987, Holmes and McClintock; 1990, Pennefather and Boone; 1994]. The second comprises a localized penetration of the TGO into the bond coat, in the presence of a TBC layer. It has been referred to as "ratcheting" [He *et al*; 2000].

Aspects of the rumpling phenomenon have previously been explored through experimental studies on bond-coated specimens without the TBC [Deb *et al*; 1987, Holmes and McClintock; 1990, Pennefather and Boone; 1995, Tolpygo and Clarke; 2000, Zhang *et al*; 1999]. Platinum aluminide, nickel aluminide and NiCoCrAlY bond coats deposited on superalloy substrates rumple to wavelengths ranging from ~ 40 μm [Tolpygo and Clarke; 2000] to ~ 300 μm [Pennefather and Boone; 1995] upon thermal cycling to temperatures up to 1200°C. The amplitude of the rumpled surfaces in these experiments was up to 15 μm. Under isothermal experiments at 1100°C [Deb *et al*; 1987, Panat and Hsia; 2004] and at 1150°C [Tolpygo and Clarke; 2000], no rumpling was observed, while at 1175°C and at 1200°C, the bond coat was seen to rumple [Panat and Hsia; 2004]. Suo *et al* (2003) found extensive void formation below the TGO after 300 h isothermal exposure in air at 1150°C. Under very fast heating and cooling rates (1050°C to 300°C temperature change in less than a minute) along with mechanical loading of the superalloy substrate, the bond coats did [Holmes and McClintock; 1990, Zhang *et al*; 1999] or did not [Busso and McClintock; 1993] show rumpling.

This rumpling instability is shown to be suppressed when the TGO–ceramic interface remains intact [Tolpygo and Clarke; 2001]. The suppression of rumpling can,

however, give rise to residual stresses at the BC–TGO interface and contribute to other TBC failure processes (e.g. BC–TGO separation). In order to understand the bond coat rumpling phenomenon, the driving force for rumpling needs to be determined. According to He *et al* (2000) and Karlsson and Evans (2001), plastic ratcheting of the bond coat due to the thermal mismatch stresses in the developing TGO during thermal cycling can cause rumpling. Suo (1995), on the other hand, has suggested that the highly compressive growth stresses in the TGO (of the order of 2-4 GPa) would provide the driving force necessary for the metal atoms to diffuse along the TGO–metal interface, leading to a wavy metal surface. In a recent model, Balint and Hutchinson (2003) have shown that the compressive stresses in the TGO, along with the stresses in the bond coat, can lead to rumpling under the conditions of the bond coat undergoing power-law creep (dislocation creep). The above models are generic to metal–oxide systems and require the existence of a highly stressed TGO for rumpling to occur. Tolpygo and Clarke (2000) have speculated that the rumpling in bond coat–superalloy systems occurs as a result of differential diffusion of various constituents such as Ni and Al, perpendicular to the bond coat surface. The model of Panat *et al* (2003) is based on the assumption that the stresses in the bond coat provide the necessary driving force for rumpling. A balance between the strain energy density at the bond coat surface and the bond coat surface energy would then determine the characteristic rumple wavelength. The mechanism that Panat *et al*.; 2003 proposed is that of the surface diffusion of bond coat atoms. It was concluded that the TGO played a limited role in BC surface rumpling behavior, since rumpling was observed to occur even in the absence of oxidation when experiments are conducted in vacuum and in the absence of a significant oxide layer, the driving force for rumpling

formation was suggested to be the thermal expansion mismatch stress in the bond coat [Panat *et al*; 2003].

Thus, the possible deformation mechanisms of rumpling include: (1) cyclic plastic ratcheting of the BC driven by the stresses in the TGO; (2) dislocation creep in the BC driven by the stresses in the TGO and the BC; and (3) diffusive processes in the BC driven by the material concentration gradients in the BC cross-section, influenced by the stresses in the BC and/or in the TGO. The sources of the stresses in the TGO include its thermal expansion mismatch with the bond coat [He *et al*; 2000, Tolpygo and Clarke; 2000] and its own growth at high temperatures [Suo; 1995], while those in the bond coat include its thermal mismatch with the superalloy substrate [Karlsson and Evans; 2001, Watanabe *et al*; 2002, Panat *et al*; 2003], the martensitic phase transformation occurring in the bond coat at 650–700°C [Chen *et al*; 2003], or as a response to a highly stressed TGO. The diffusive processes contributing to the deformation in the bond coat, either near the bond coat surface or in the bond coat itself, driven by bond coat stresses, include surface diffusion, bulk diffusion, grain boundary diffusion, and interdiffusion between the bond coat and the superalloy substrate.

Despite several efforts being carried out to understand rumpling in several TBC systems, it remains to be explained why the (Ni, Pt) Al bond coats are susceptible to this failure mode, whereas others (such as the ß/?' materials in the NiCoCrAlY category) appear to fail by other mechanisms [Mumm and Evans; 2000].

1.5. Remaining Life Assessment And Life Prediction Models

The availability of accurate models for predicting the life of TBCs is essential to realize the full potential of component performance and durability. TBC modeling is important for life prediction, for understanding TBC behavior, and for design of new coatings. In spite of the use of TBCs for over 35 years, there has been relatively little activity in modeling their durability and reliability. In the past 15 years, there have been several large studies sponsored by NASA. This section discusses models of TBC life prediction and directions for future development.

The current models for life prediction, based on high-temperature oxidation, hot corrosion of coatings and mechanical strain, are not well developed and are largely empirical or semi-empirical. Existing approaches test coatings in furnaces or burner rigs to determine their life and use thermal history and other known data to relate the life in the furnace or burner rig to the life in the engine. These approaches are largely unsatisfactory because they predict life to no better than a factor of 2X. Limitations of these approaches include:

- Burner-rig tests typically exhibit a large amount of scatter and are often useful only for comparison with other laboratory reference materials.
- Furnace testing does not simulate the high-velocity gases and high heat fluxes to which coatings are exposed and which can be important to their behavior.
- Hot-corrosion life depends on the deposition of the corrodants on the surface. The composition of the corrodent and rate of this deposition are

not truly represented in the burner rig or other methods used to test hot-corrosion resistance.

- The actual environments, including the erosive species, to which the coatings are exposed, vary widely, especially for industrial engines. These conditions are difficult, if not impossible, to simulate in the laboratory.

1.5.1. Review of TBC Life Prediction Models

Lacking detailed knowledge of failure mechanisms and microstructure-level mechanics, designers have relied on so-called 'engineering models'. These models are generally physically based, but take a remote view of the failure process, relying on overall system responses guided by empirical observations. To do this, each model incorporated information known about the active degradation mechanisms for the specific coating and its operational regime. In addition, the models were heavily dependent on calibration to experimental data to predict the correct absolute lifetimes.

Most of the modeling has been for high-temperature oxidation combined with thermal cycling. Hot corrosion of TBCs is not well understood, and there has been only a limited effort in modeling the hot-corrosion life of TBCs. Early TBC studies combined modeling and experimental work to define some of the important factors in TBC durability [Sevcik and Stoner; 1978, Cassenti *et al*; 1981], viz., the effect of residual stress generated during processing on coating spallation, the correlation of in-plane compressive stresses on ceramic layer spallation, the importance of maximum operating temperatures on TBC life.

Many of the engineering life models now in use for TBCs stem from NASA-sponsored research in the 1980s. Miller [Miller; 1984] formulated a cumulative damage-based model, based on both oxidation and mechanical cycling, which combined a thermally activated law for oxide thickness with mechanical damage from a basic fatigue law. This approach was subsequently modified [Meier *et al*; 1991] to better correlate the data obtained under combinations of oxidation and thermal cycling. Since that time, less has been published. The most notable recent publication [Wright; 1998] has described a thermo mechanical fatigue (TMF) testing approach, used to quantify the mechanical strain dependence of spalling, where TBC life was demonstrated to depend on the combined strain in a simple power law form. The following sections discuss some of these models in greater detail.

1.5.2. Oxidation and Mechanical Strain Based Models

An oxidation-based failure model was proposed by Miller (1984) assuming that the strains imposed on the ceramic layer were caused by thermal-cycle effects and that time at temperature effects acted to increase the effective thermal-cycle strains caused by oxidation. The model was used to calculate cycles-to-failure as a function of heating cycle duration. It was based on the assumption that oxidation is the single important time-dependent factor which limits the life of these coatings, and that oxidation-induced strains combine with cyclic strains to promote slow crack growth in the ceramic layer.

$$N_f = \left(\frac{e_f}{e_r} \right)^{-b}$$

$$e_e = (e_f - e_r)\left(\frac{W}{W_c}\right)^m + e_f$$

where N_f is the number of cycles to failure, ε_f is the failure strain in one cycle with no oxidation, ε_r is the thermal expansion mismatch strain, W is the weight gain by oxidation, and W_c is the weight gain that should cause failure in one cycle, b and m are material constants determined from the experimental data. Miller's model correlated the cyclic life of a specific coating system tested at 1100°C for different thermal cycle times.

DeMasi *et al* (1989) used a model similar to Miller's for plasma-sprayed TBCs, except that the thermal-cycle strains were included using a finite-element analysis that incorporated a Walker constitutive model [Walker; 1981] for inelastic deformation of the ceramic during thermal cycling, and the strain to failure in one cycle, ε_f, changed with oxidation. Thus, this model incorporated cyclic inelastic strain and interfacial oxidation as the primary degradation modes.

$$N_f = A\left(\frac{\Delta e_p}{e_f}\right)^{-b}$$

$$e_f = e_c\left(1 - \frac{W}{W_c}\right) + \Delta e_p\left(\frac{W}{W_c}\right)$$

where $\Delta\varepsilon_p$ is the inelastic strain range, ε_c is ε_f at W = 0, and the other terms are as in Miller's model. This model was shown to correlate cyclic thermal spallation life results within a factor of $\pm 3X$ over a broad range of relative mechanical and oxidative exposure severities.

This model by DeMasi *et al* (1989) was also used for life predictions of EB-PVD coatings [Manning-Meier *et al*, 1991], except that the EB-PVD YSZ layer was assumed

elastic, the bond coat was assumed to have inelastic behavior, and the thermal strain of the alumina scale was included. Since the out-of-plane stresses were a small fraction of that required to fail the TGO, the EB-PVD TBC spallation was attributed to the interfacial cracking caused by in-plane TGO strains. Therefore, the important cyclic strain for the EB-PVD ceramic was between the alumina layer and the substrate. This model based on maximum in-plane TGO tensile mechanical strain and TGO thickness correlated with burner rig specimen spallation lives within a factor of ± 2X.

A high-temperature oxidation model has also been developed by Probst and Lowell (1988), based on isothermal oxidation and thermal cycling.

$$x \cdot W_{ox} Or \frac{\Delta m}{A} \propto \sqrt{(k_p \cdot t)}$$

where ? is the scale thickness, W_{0X} is the weight of the oxide scale, ?m/A is the mass gain per unit area, k_p is the parabolic rate constant, and t is time. k_p is related to temperature by an Arrhenius rate law:

$$k_p = k_{p0} \cdot \exp\left(\frac{-Q}{R \cdot T}\right)$$

where k_{po} is a material constant, Q is the activation energy, R is the universal gas constant, and T is the absolute temperature in K or °R. k_{po} is a function of oxygen partial pressure. The model tracks the formation of the oxide by a parabolic growth law (although other growth kinetics can be used), and the spallation of the oxide due to thermal cycling.

$$W_{spall} = Q_0 \cdot W^2{}_{oxide}$$

where W_{spall} is the weight per unit area of the oxide spalled, Q_0 is an experimentally derived material constant, and W_{oxide} is the weight per unit area of the oxide prior to spalling. The spallation equations are empirical and are based on careful experimental measurement of the weight of the spalled oxide. Barrett and Lowell (1975) have also developed a mathematical expression to fit cyclic oxidation data. Both of these approaches rely heavily on empirical methods, are based on experimental calibrations of the amount of oxide spalled instead of a more fundamental, predictive model.

Wright *et al* (1991) have developed models for erosion-modified oxidation, based on an erosion rate assumed to increase with the thickness of the oxide.

$$x = act - \frac{x_1\left(1 - x_1^{\,k}\right)}{k+1}$$

where *?* is the scale thickness as a function of time, t is the time between erosion events, *a* is an oxidation rate term, *c* is the Pilling-Bedworth ratio, which is the ratio of the volume of the oxide formed to the volume of the metal consumed, $?_1$ is the scale thickness after the last erosion event ($?_1 = 0$ at t = 0), and *k* is a term describing the oxidation kinetics (k = 0 for linear kinetics and k = 1 for parabolic kinetics). A numerical solution method is used to determine the degradation of the coating. Chang *et al* (1990) have also studied the interaction of erosion and oxidation and have defined the various regimes of erosion and oxidation. These two models were developed for coal gasification and fluidized bed applications.

An example of the approach to modeling based on correlation with engine service experience was given by Strangman (1990). For high-temperature oxidation, Strangman computed the oxidation rate as the product of an engine experience factor, a burner-rig

calibration constant, and a term for the temperature dependence of oxidation. Two expressions were thus calculated for hot-corrosion rate and oxidation rate and the total environmental attack was the sum of the hot-corrosion rate and the oxidation rate. These equations were solved by means of a computer program.

Nesbitt (1984, 1989) developed a diffusion-based approach to determine the oxidation life of coatings and bulk NiAl. For bulk materials, the model computed the flux of aluminum to the surface and the removal of aluminum by oxidation. The model was based on the fact that when the aluminum flux became less than the aluminum consumption by formation of Al_20_3, $NiAl_20_4$ became the stable oxide. Since this spinel was not protective, the bulk metal was attacked at this point. For coatings, the flux of aluminum in the coating to the surface and the interdiffusion of the coating with the base metal were computed. This interdiffusion reduced the aluminum concentration in the coating, shortening the life of the coating.

Fracture mechanics approaches to modeling coating spallation have been and are continuing to be developed [Evans; 1994]. They usually predict a dependence on the square of the temperature change, ?T

$$W_{spall} \propto (\Delta T)^2$$

One of the principal difficulties in modeling high-temperature oxidation for actual service components is the ability to accurately predict the surface temperature of the blades and this is a barrier that limits the ability of any coating degradation model to accurately determine the life of the coating.

1.5.3. Mechanical Strain Based Models

A thermal mechanical fatigue (TMF) test developed by Wright (1998) has permitted a direct measurement of the effect of strain on TBC life. Testing on EB–PVD YSZ coated single crystal superalloy samples was performed under a variety of imposed strain cycles, to vary the imposed strain range on the coating and thus separate strain dependence of life from oxidation effects. A dependence of coating life on applied strain was seen, for which the governing factor appeared to be the extent of compression at minimum cycle temperature. Results showed that as the compression on the coating at minimum temperature was increased, the cycles to spall decreased. The results were evaluated in terms of the maximum total mechanical (thermal mismatch + applied) strain on the oxide scale and a power law life dependence on total mechanical strain with an exponent of about -3 was found to describe the life capability

Hillery *et al* (1988) focused on the edges of TBCs as failure initiation sites for some TBC applications. Edge failures were driven by shear stresses in addition to normal stresses and oxidation. Oxidation was included through changes in the time-dependent material behavior and the stress state. This model was found to give within ± 3 X agreement with experiment.

Strangman *et al* (1987) used a linear damage rule, which included damage from thermal cycling, oxidation, and hot corrosion, to reduce the strain-to-failure of the ceramic, instead of increasing the effective strain per cycle. This model reduced to a Coffin-Manson relation and the agreement to the experimentally measured lives was within ± 3 X.

The vast majority of TBC modeling, including those models cited above, has been for current aircraft applications, which have a much different operational profile than land-based or marine gas turbines. Thus, for non-aircraft applications, it may be expected that the relative contributions and importance of different mechanisms to TBC failure would be different. These mechanisms include oxidation of the bond coat, topcoat creep, sintering of the topcoat, and the mechanical behavior of the alumina scale.

A few models have addressed long-term oxidation behavior and loss of alumina-forming capability of overlay coatings [Nesbitt and Heckel; 1984] and bond coats for TBCs [Lee and Sisson; 1994]. In these models, TBC life was determined by the life of the bond coat.

1.5.4. Computer Models for TBC Life Prediction

Comprehensive models that can predict TBC life from first principles are necessary to be able to account for the wide range of conditions to which TBCs are exposed. Computer modeling has been used to investigate TBC behavior by isolating and investigating issues not easily amenable to experimental study. Chang *et al* (1987) and Phucharoen (1990) developed a finite-element model that examined the effect of the rough interface between the bond coat and ceramic layer, the mechanical effects of oxidation on the stresses in ceramic layers, and the effect of bond coat properties on TBC life. The most important of these issues are the effect of interface geometry and oxidation on TBC stress levels. Another computer model examining failure mechanisms, instead of life prediction, used the observed bond coat creep response [Brindley and Whittenberger; 1993] to show that bond coat creep can result in substantial increases in the ceramic layer delamination stresses [Brindley; 1995], which should result in decreased TBC cyclic lives. Ferguson *et*

al (1994) included bond coat and topcoat creep along with a rough interface to provide a clearer picture of the role of these factors increasing the stresses generated in a TBC during thermal cycling. Apart from failure mechanisms, theoretical modeling may also shed light on heat transfer through TBCs, which in turn may guide design of more-insulating coatings.

1.5.5. Scope For Future Work

Studies of a fundamental nature, as opposed to an engineering evaluation, are needed to determine how coatings are exposed and how they perform in the field, particularly for industrial gas turbines. The understanding of the degradation and failure mechanisms of high-temperature coatings in the field need to be improved, particularly with respect to the effects of engine operation and environment on the coating performance (e.g., thermal cycling).

Qualitative and quantitative models need to be developed that predict coating life based on mechanisms observed in operational engines. These models need to be applied to optimize coating development and to estimate more accurately the remaining coating life for in-service engines. However, property measurements using reliable test methods are required before modeling.

The models discussed above have been used to guide TBC development and design over the last few decades. However, most of these models have been based on an aggregate of parts operating under nominal conditions. In reality, individual parts operate under different operating conditions and hence exhibit varied spallation mechanisms. Hence, a more "design capable" model for TBCs is necessary to facilitate more rapid

development and implementation of TBCs, which would need to incorporate operating conditions, life prediction from first principles, and thermal modeling from first principles. In this context, this study deals with studying individual specimen behavior, specifically their TGO stress using PLPS. The TGO stress data collected non-destructively will be used to develop a TGO stress versus TBC life database under various thermal cycling conditions that match or approximate those of actual engine service, for use as a non-destructive inspection tool in assessing remaining life of TBCs. These stress measurements will be coupled with TBC failure mechanism evaluations to perform mechanisms-based remaining life predictions.

Table 1.1: Typical Duty Cycles for Various Gas-Turbine Engines [Hillery *et al*; 1996].

	Typical Mission Time per Engine Start (hours)		
Duty Cycle	Minimum	Average	Maximum
Airline/Transport	1	2	8
Military/Fighter[a]	1	2	4
Mechanical Drive	40	2,000	8,000
Base Power Generators	500	2,000	8,000
Peak Power Generators	2	4	12

[a] The mission profile for military aircraft has greater thermal transient and low-cycle fatigue because of periods of supersonic

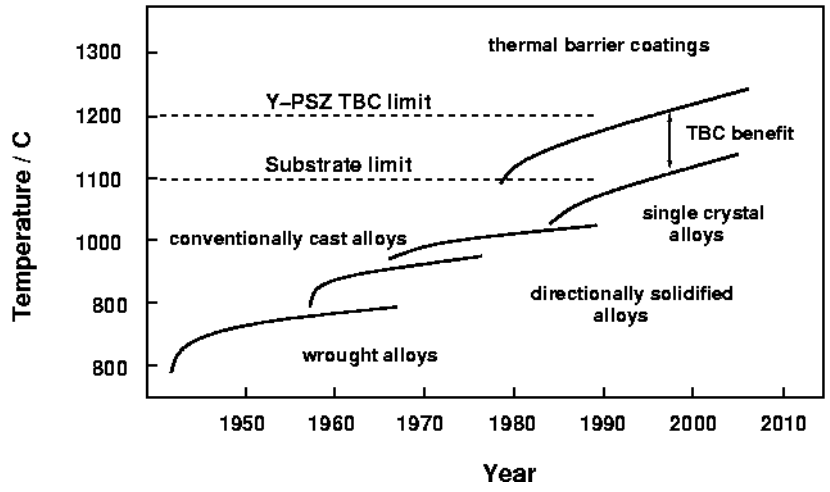

Figure 1.1: Increase in operational temperature of turbine components [Schulz; 2003].

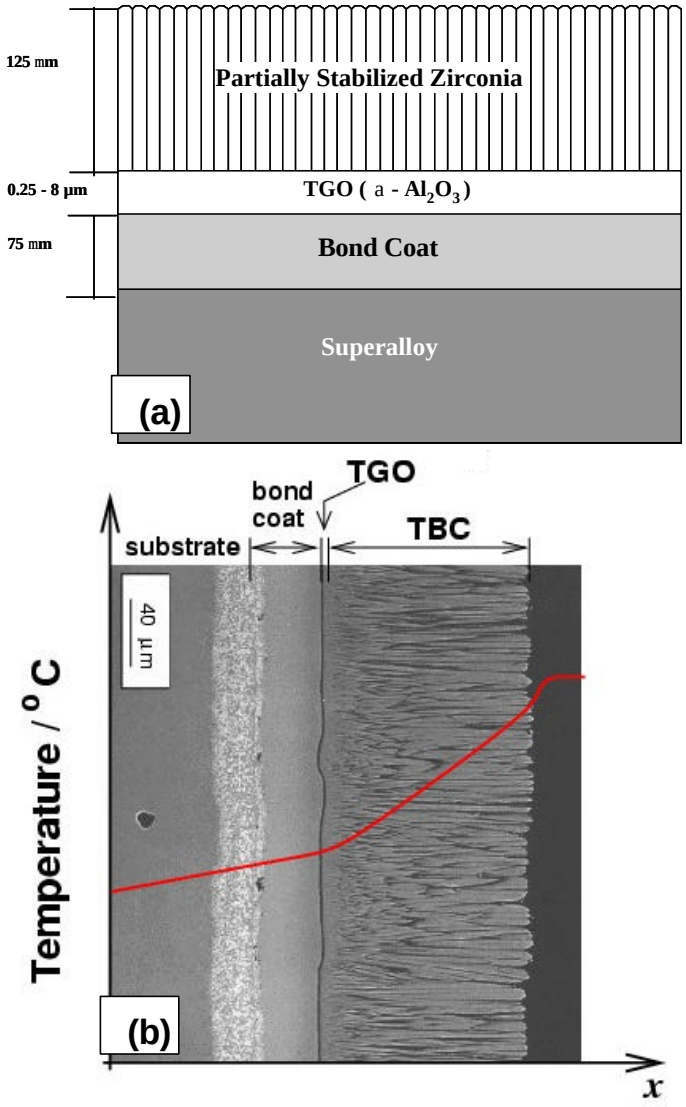

Figure 1.2: (a) Schematic showing the four layers in a thermal barrier coating system and (b) cross-sectional micrograph of a TBC.

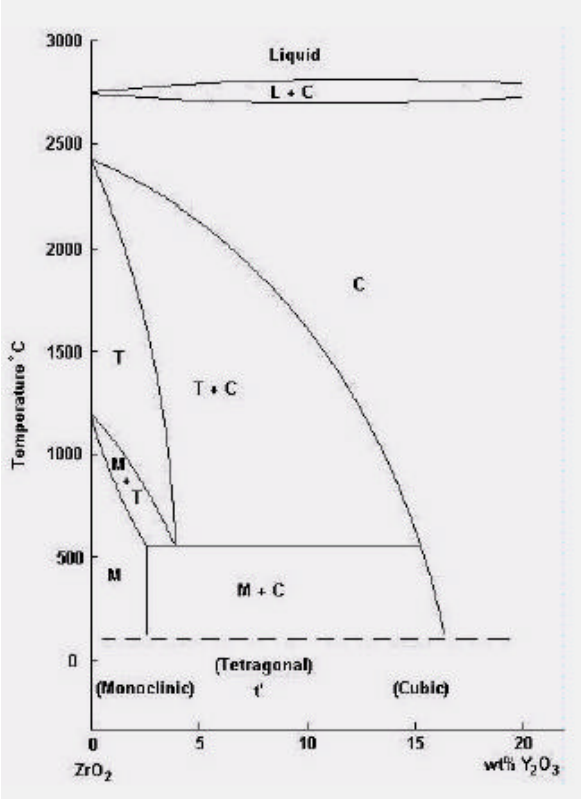

Figure 1.3: Phase diagram of ZrO_2 - Y_2O_3 system [Schulz et al; 1996].

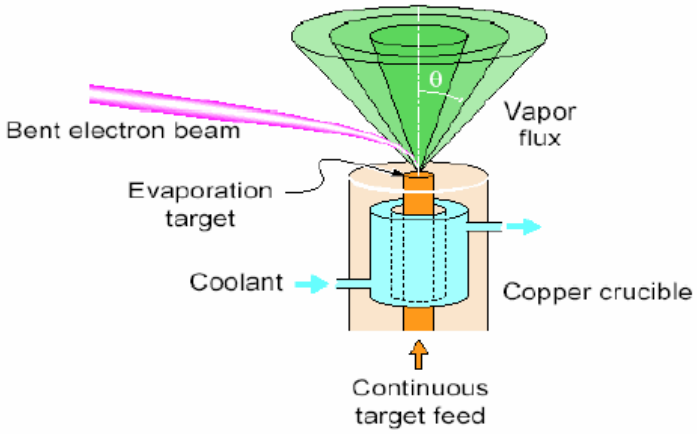

Figure 1.4: Schematic of the conventional EB-PVD coater [Goodge; 1997].

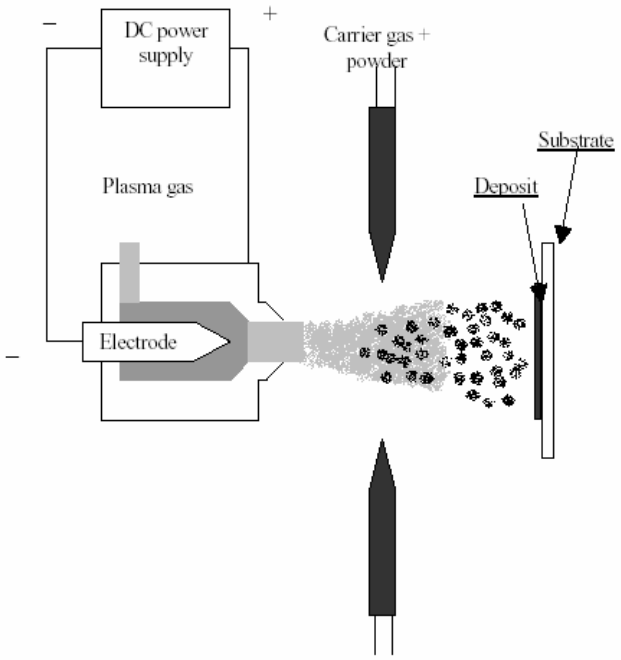

Figure 1.5: Schematic of the plasma spray process [Hillery; 1996].

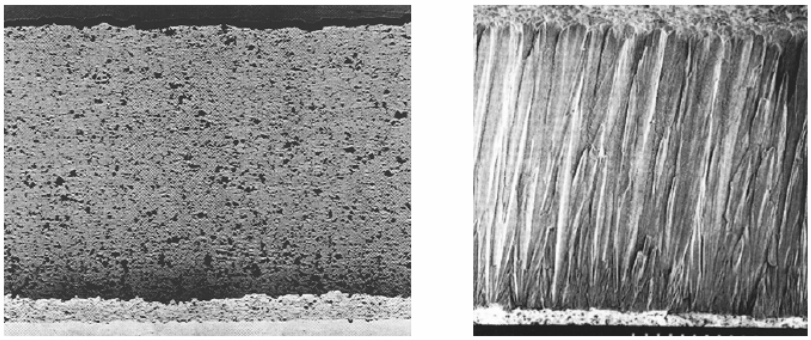

Figure 1.6: Comparison of the microstructures of APS and EB-PVD TBCs [Nicholls *et al*; 2002].

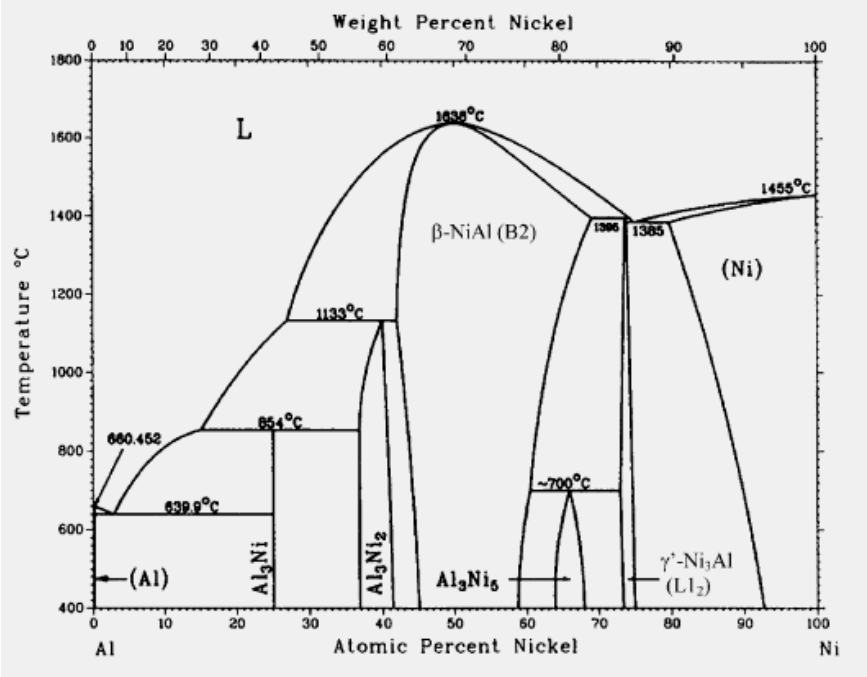

Figure 1.7: Binary phase diagram of Al-Ni system [Massalski; 1986].

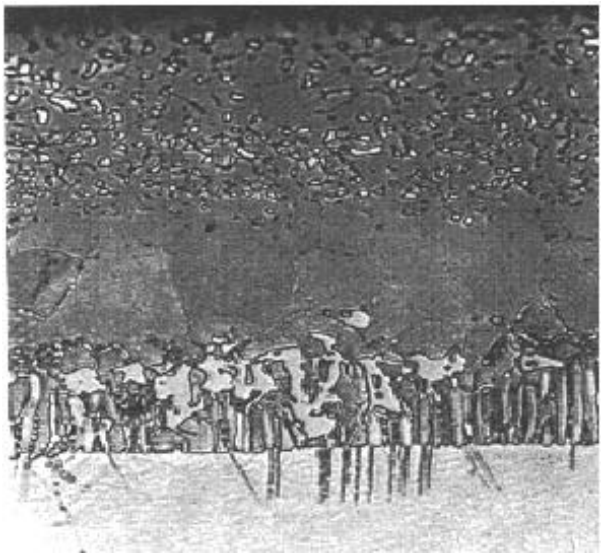

Figure 1.8: Microstructure of an inward diffusing (high activity) type of NiAl coating applied on a Ni-base alloy [Goward; 1970].

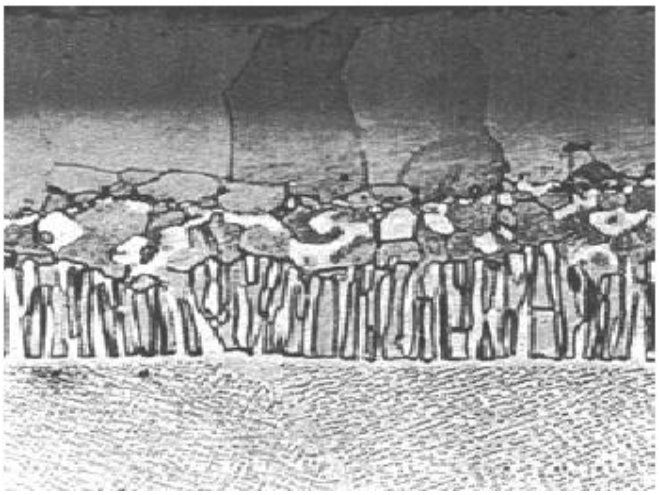

Figure 1.9: Microstructure of an outward diffusing (low activity) type of NiAl coating applied on a Ni-base alloy [Goward; 1970].

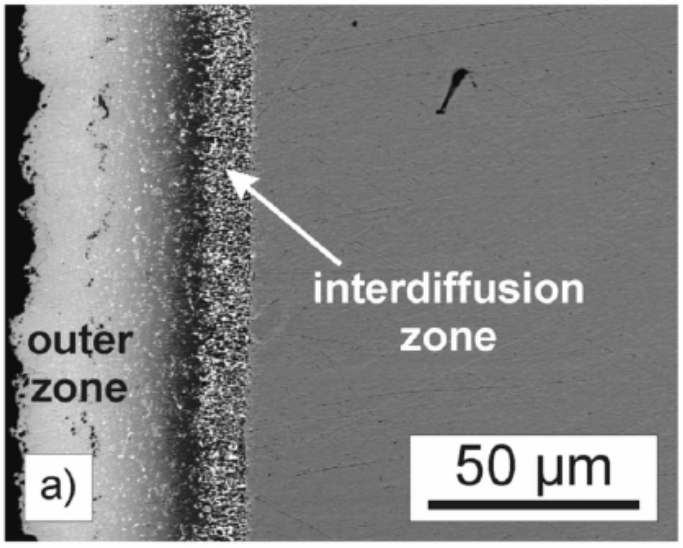

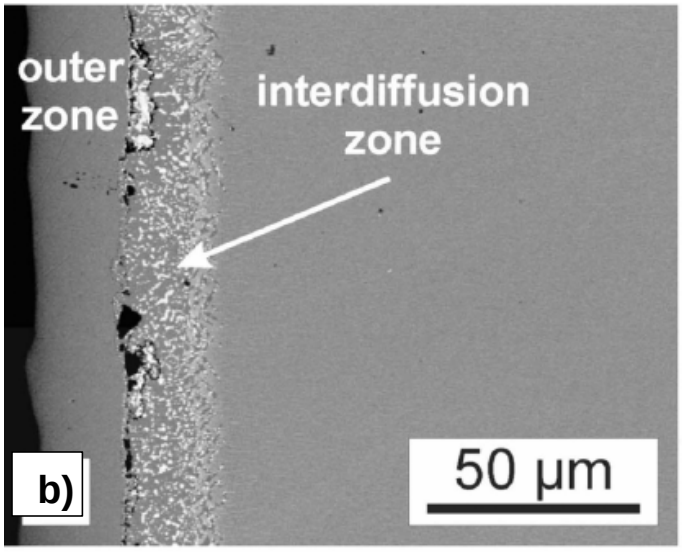

Figure 1.10: Cross-section back-scatter micrograph of the (a) inward grown and (b) outward grown platinum modified nickel aluminide bond coat in the as-coated condition.

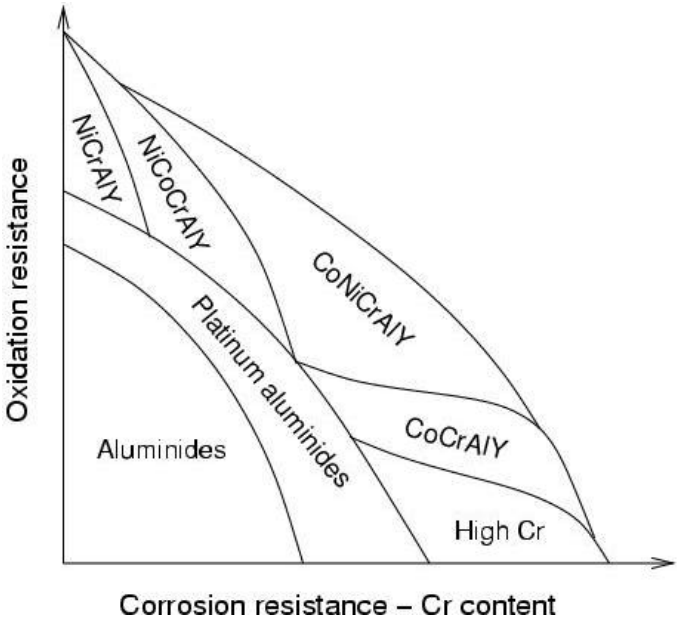

Figure 1.11: Coating compositions as related to oxidation and corrosion resistance [Novak; 1994].

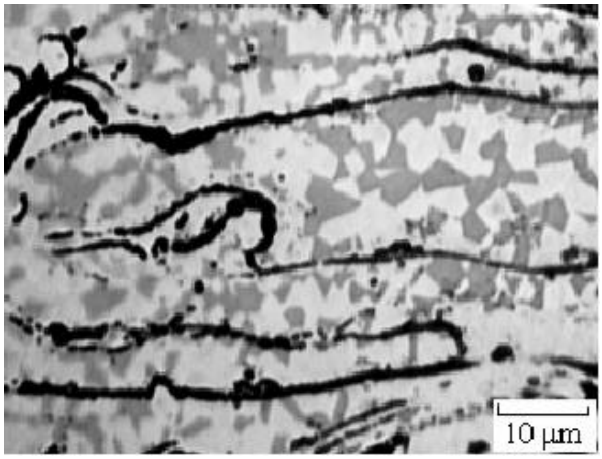

Figure 1.12: Microstructure of APS NiCoCrAlY coating; the black area represents oxide, the grey area the ß-NiAl phase and the light area the ?-Ni-base phase [Hebsur and Miner; 1986].

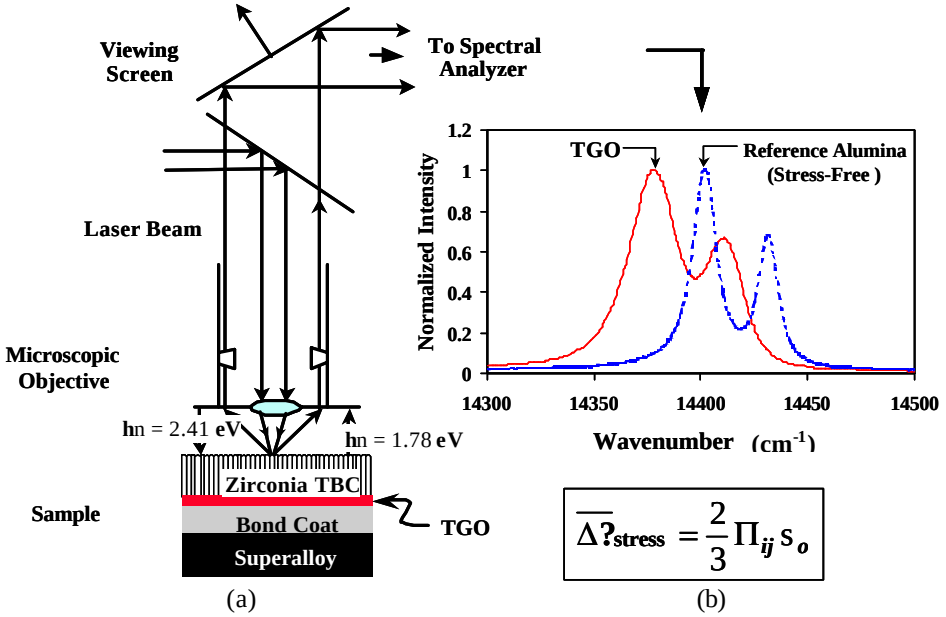

Figure 1.13: (a) Schematic illustration of the photo-stimulated luminescence piezospectroscopy technique; (b) Typical R1/R2 fluorescence spectra for chromium-containing stress-free and stressed ? -Al2O3.

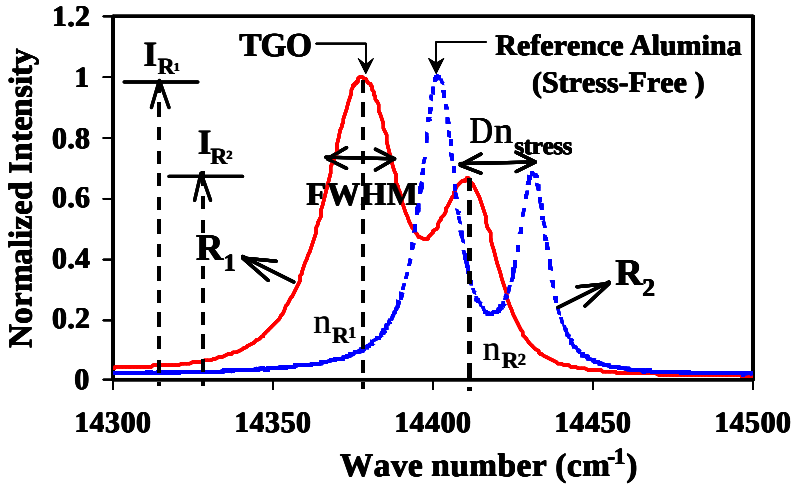

Figure 1.14: R_1 and R_2 spectral characteristics evaluated for the spectra obtained from alumina and from TGO formed on a bond-coated sample.

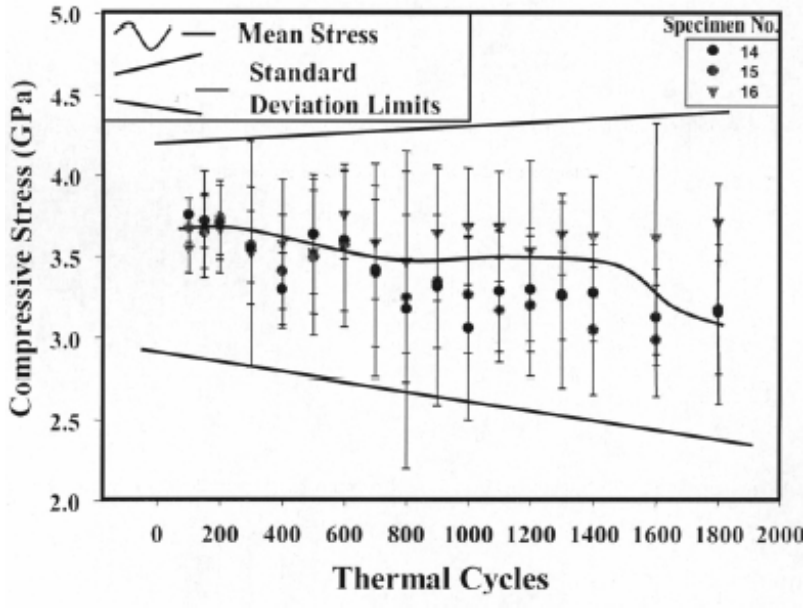

Figure 1.15: Evolution of TGO stress as a function of thermal cycling for a TBC with grit blasted [(Ni, Pt) Al] bond coat [Gell *et al*; 1999]. Note the monotonic decrease in TGO stress with cycling.

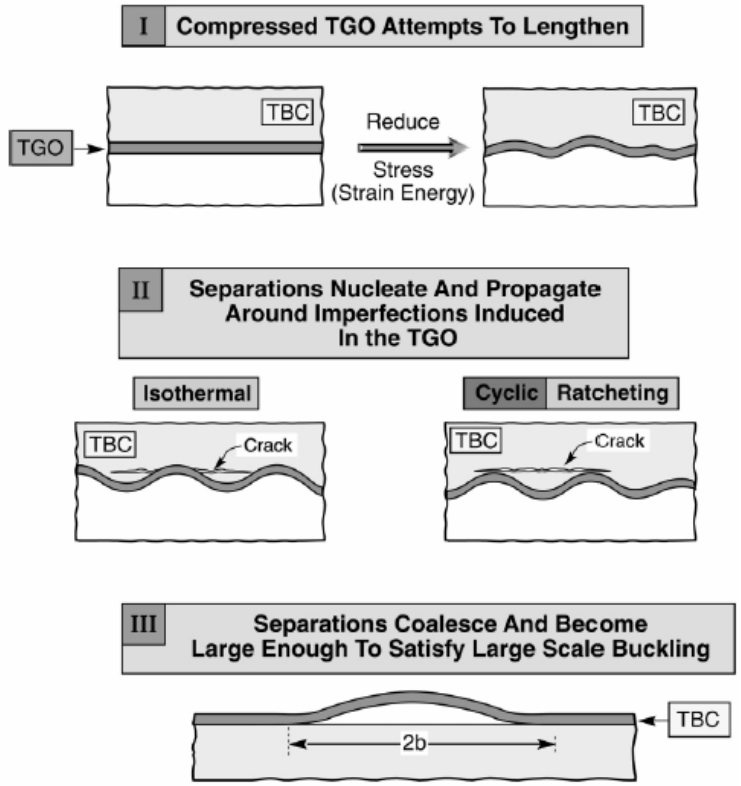

Figure 1.16: Schematic illustrating the three overarching principles that govern TBC failure [Evans et al; 2001].

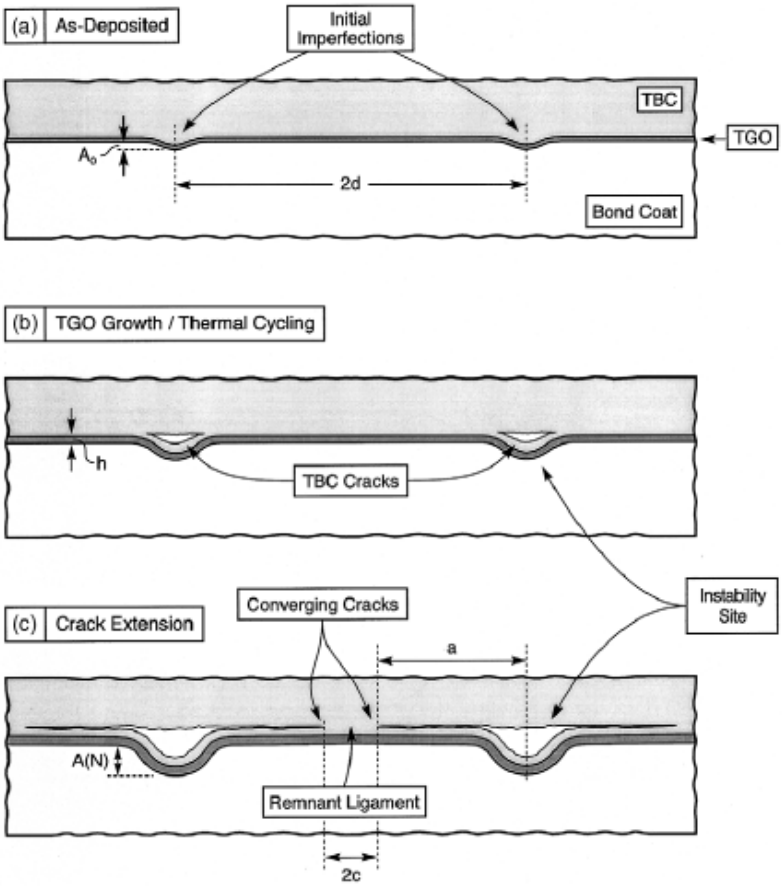

Figure 1.17: Schematic showing the thermo-mechanical response of a (Ni, Pt) Al-based TBC: (a) the development of a displacement instability, (b) the associated crack nucleation and growth in the TBC, and (c) crack coalescence leading to coating spallation [Mumm *et al*; 2001].

2. Experimental Procedure

2.1. TBC Specimens

Disk-shaped coupons, 25.4 mm in diameter and 3.2 mm in thickness, coated with four production TBCs, Types I, II, III and IV, have been evaluated in this work. A schematic describing the specimen geometry is shown in Figure 2.1. The composition and thickness of the layers of the TBCs are given in Table 2.1, Table 2.5 and Table 2.6. Both types I, II, and III TBCs have platinum aluminide bond coats, the bond coats being grit blasted prior to deposition of the ceramic layer. Type I TBC has an outward diffusing single phase β platinum modified nickel aluminide bond coat produced by CVD process, referred to as MDC-150 L, while Type II TBC has an inward diffusing single phase [(Ni, Pt) Al] platinum aluminide bond coat produced by pack cementation process, referred to as LDC-2E. Both TBCs were supplied by Howmet Corporation. These two TBCs which have been supplied by the same coating supplier with the same TBC top coat and on the same superalloy substrate will facilitate a comprehensive comparative study of two very similar TBCs on an outward and an inward diffusing single-phase platinum-modified aluminide bond coats, with minimal processing variability between them. Type III TBC has the single phase (Ni,Pt)Al bond coat supplied by another coating supplier. Type IV TBC has the two phase (Ni,Co)CrAlY bond coat.

2.1.1. Outward Diffusing Platinum Aluminide Coating – Type I

Type I TBCs consisted of a 150μm 7 wt. %Y_2O_3 stabilized ZrO_2 (7YSZ) coating, 75 μm grit blasted platinum-modified nickel-aluminide bond coat [(Ni, Pt) Al] and a single crystal CMSX-4 Ni-base superalloy substrate. The bond coat [(Ni, Pt) Al] was

produced by a two-step process on the single crystal superalloy CMSX-4. The superalloy substrate was first electroplated with 9 - 11 mg/cm^2 platinum, after which a CVD process aluminized the surface.

The outwardly grown CVD single phase platinum aluminide coating was formed at a substrate temperature of 1080°C using coating gas mixture comprising 5.5 volume % aluminum trichloride, 94.5 volume % hydrogen [U.S. Patent 5,658,614]. In the as coated condition, the MDC-150L coating exhibits a single phase (Ni, Pt) Al layer and the diffusion zone is about one third of the total bond coat thickness.

These platinum aluminide coatings have then been heat treated in vacuum, to form a homogeneous (Ni, Pt) Al bond coat and a thin adherent alumina layer (TGO). The specimens were bond coated on both sides and the bond coats were grit blasted (grit blasting parameters: # 220 Al_2O_3 grit at ~ 0.2 MPa suction) prior to coating deposition by an electron beam physical vapor deposition process, which produces a strain tolerant columnar microstructure.

2.1.2. Inward Diffusing Platinum Aluminide Coating – Type II

Disk-shaped (2.54 cm in diameter and 0.32 cm in thickness) TBC specimens investigated in this study were supplied by engine and coatings manufacturers. The configuration of the specimens is shown in Fig. 3.1. The specimens consist of a nominal thickness 140 ? m electron beam physical vapor deposited (EB-PVD) 7 wt.% Y2O3 stabilized ZrO2 (YSZ) coating, a nominally 50 ? m thick platinum-modified nickel-aluminide bond coat (Ni, Pt)Al and a single crystal CMSX-4 superalloy substrate. The typical compositions of the coating and the superalloy used in this study are shown in

Table 3.1. The specimens were bond coated on both sides to allow study of the oxidation behavior of the bare bond coat using the back side of specimens. Consistent with standard industry practice, the bond coats were grit blasted prior to TBC deposition by the EB-PVD process.

2.1.3. (Ni, Pt)Al Bond Coated TBC – Type III

Disk-shaped (2.54 cm in diameter and 0.32 cm in thickness) TBC specimens investigated in this study were supplied by engine and coatings manufacturers. The configuration of the specimens is shown in Fig. 2.1. The specimens consist of a nominal thickness 140 ? m electron beam physical vapor deposited (EB-PVD) 7 wt.% Y2O3 stabilized ZrO2 (YSZ) coating, a nominally 50 ? m thick platinum-modified nickel-aluminide bond coat (Ni, Pt)Al and a single crystal CMSX-4 superalloy substrate. The typical compositions of the coating and the superalloy used in this study are shown in Table 2.5. The specimens were bond coated on both sides to allow study of the oxidation behavior of the bare bond coat using the back side of specimens. Consistent with standard industry practice, the bond coats were grit blasted prior to TBC deposition by the EB-PVD process.

2.1.4. (Ni,Co)CrAlY Bond Coated TBC – Type IV

Disk-shaped specimens (2.54 cm in diameter and 0.32 cm in thickness) with the same configurations in Fig. 2.1 were used. The substrate was a nickel based single crystal superalloy CMSX-4. The bond coat was the vacuum plasma sprayed (VPS) MCrAlY (NiCoCrAlY with additions of Si and Hf) consolidated by a shot-peening process. Different surface finishing processes were carried out before TBC deposition in order to study the effects of surface roughness on the durability of the TBCs.

Two surface finishing processes include: (1) as-received (vacuum plasma sprayed bond coat followed by shot-peening); (2) 90 minutes' centrifugal barrel finishing. The barrel finishing was done by USF Surface Preparation Group and is suitable for industrial processing of gas turbine blades. The centrifugal barrel finishing process is identical to conventional barrel finishing except the device is rotated in such away to create a force approximately 20 times that of gravity. Relatively coarse media (nuggets) were used in this study, but much smoother finishes are possible using multistage finishing. The surface morphology and roughness of the specimens were evaluated using scanning electron microscopy and ZYGOTM surface interferometry (see section 3.4). After bond coat surface processing, the bond coat was pre-oxidized in Ar-H2 (PO2 ? 10-8) at 1100? C for 2 hours. Then the coupons were sent to our industry partner for EB-PVD deposition of the 7 YSZ coating. The TBC consists of a nominally 145 ? m thick electron beam physical vapor deposited (EB-PVD) 7 wt.% Y2O3 stabilized ZrO2 (YSZ) coating, a nominally 100 ? m thick NiCoCrAlY bond coat and a single crystal CMSX-4 superalloy substrate. The typical compositions of the coating and the superalloy used in this study are shown in Table 2.6.

2.2. Furnace Cycling Tests

In an effort to study the effect of hold time on TBC durability in the laboratory, two specific cycling regimes have been adopted - a 1-hour thermal cycle and a 24-hour thermal cycle. In addition, the effect of temperature has also been studied by carrying out the 1-hour cycles at three different peak temperatures of 1100°C, 1121°C and 1151°C.

Cyclic oxidation tests in air at three temperatures and using two hold times have been conducted in a bottom-loading thermal cycling furnace made by CM furnaces Inc., Bloomfield, NJ. Figure 2.2 is a photograph of the furnaces used in this study. Three S-type thermocouples, welded to superalloy disks, were placed in slots of the multi-specimen holder to monitor temperature across the holder. The TBC specimens were systematically rotated within the stage to ensure uniformity of exposure temperature. The temperature variation across the specimen holder was found to be less than ± 5°C.

2.2.1. 1-hour Furnace Cycling Tests

The 1-hour cycles consisted of a 10-minute heat-up to the peak temperature followed by a 40-minute hold at the peak temperature and then a 10-minute forced-air-quench. The 1-hour thermal cycles at were carried out on type I, II and III TBCs at three temperatures – 1121°C, 1100°C and 1151°C. Type IV TBCs were subject to 1-hour test at 1121°C. Figure 2.3 shows a schematic describing the temperature profile during these 1-hour cyclic tests. These cyclic tests were designed to simulate loadings representative of aero-engines comprising extensive thermal cycling.

2.2.2. 24-hour Furnace Cycling Tests

The 24-hour cycles were carried out at 1121°C and consisted of a 10-minute heat-up to 1121°C followed by a 1430-minute hold at 1121°C (2050°F) and a 10-minute forced-air-quench. These cyclic tests were designed to simulate thermo-mechanical loadings, typical of those applicable to "power generation", with long high temperature

exposures and minimal thermal cycling. Figure 2.4 shows a schematic describing the temperature profile during these 24-hour cyclic tests.

2.2.3. Type I Specimen Test Matrix

Specimens were removed at specific intervals to measure the oxide stress using PLPS and to observe the micro structural evolution by using Environmental Scanning Electron Microscopy (ESEM). A total of 60 Type I specimens were cycled at three temperatures and using the two hold times, of which 38 were cycled to failure. Failure of the TBC's was defined by spallation greater than 50 % of the specimen area. Table 2.2 gives a list of Type I specimens tested.

2.2.4. Type II Specimen Test Matrix

A total of 31 Type II specimens were cycled at three temperatures and using the two hold times, of which 15 were cycled to failure. Failure of the TBC's was defined by spallation greater than 50 % of the specimen area. Table 2.3 gives a list of Type II specimens tested.

2.2.5. Non-Constant Amplitude Tests

Commercial engines often are subjected to operational cycles that differ from the previous cycles. In order to address such situations where the actual engine parts do not have repeated operational cycles, the first ever two-stage cyclic tests consisting of one test condition, A, followed by a second test condition B have been adopted. These two-stage cyclic tests included both multi- temperature and multiple hold time conditions and

were carried out in the same bottom-loading furnace as for the 1-hour and 24-hour cyclic tests. Figures 2.5 and 2.6 show the temperature and the hold time profile during these variable amplitude tests.

Types I and II TBCs have been subjected to two multiple history cycling tests, one consisting of two different temperatures and the other consisting two different hold times. These additional experiments have been designed to assess the cumulative damage and estimate TBC life, when parts are subjected to multiple temperatures and cycle times. PLPS measurements have been made throughout the TBC cyclic life and the effect of peak temperature/hold time on TGO stress state has been monitored. In addition, the linear damage rule has been verified and the possibility of any synergistic damage accumulation effects has been investigated for the very first time in TBCs.

In all, six Type I TBC and 4 Type II specimens were cycled to failure under each cycling condition. The TBC life fraction at each exposure temperature and hold time was evaluated and this was used in estimating the linear damage rule for this TBC.

2.2.5.1. Multiple Temperature Tests

The multi-temperature tests were designed such that two Type I specimens, LD 73 and LD 74, and one Type II specimen, LV 37, were cycled each to approximately half their cyclic life at 1121°C using 1-hour cycles (known from furnace cyclic tests previously conducted at 1121°C) and were then subsequently cycled to failure at 1151°C. Similarly, two more Type I specimens, LD 82 and LD 84, and one Type II specimen, LV 48, were cycled each to approximately half their cyclic life at 1151°C using 1-hour cycles

(known from furnace cyclic tests previously conducted at 1151°C) and then cycled to failure at 1121°C.

In addition, one Type II specimen, LV 49, was cycled to approximately half its cyclic life at 1121°C using 1-hour cycles (known from furnace cyclic tests previously conducted at 1121°C) and then cycled to failure at 1100°C. Similarly, one more Type II specimen, LV 30, was cycled to approximately half its cyclic life at 1100°C using 1-hour cycles (known from furnace cyclic tests previously conducted at 1100°C) and was then cycled to failure at 1121°C.

2.2.5.2. Multiple Hold Time Tests

Multiple history tests consisting of one hold time followed by a second hold time were also conducted. One specimen, LE 33, was cycled to roughly half its cyclic life at 1121°C using 1-hour cycles (known from furnace cyclic tests previously conducted using 1-hour cycles at 1121°C) and was then cycled to failure using 24-hour cycles at 1121°C. Similarly, a second specimen, LE 04, was cycled to roughly half its cyclic life at 1121°C using 24-hour cycles (known from furnace cyclic tests previously conducted using 24-hour cycles at 1121°C) and was then cycled to failure using 1-hour cycles at 1121°C.

2.3. Photoluminescence Piezospectroscopy

Photoluminescence Piezospectroscopy is one of three techniques that are presently under development as an NDI tool for EB-PVD TBCs. This technique has the potential to support a number of EB-PVD TBC applications including (a) quality control,

(b) NDI, (c) assessment of life-remaining and (4) input to simplified, accurate lifetime prediction methodologies.

The PLPS technique, invented by Paton, Murphy and Clarke for TBCs [Paton et al., US Patent # 6, 072, 568], and further developed by Clarke et al. and Gell, Jordan et al., has been successful in non-destructively measuring the stress in the TGO under the ceramic. This technique is based on the frequency shift in the Cr^{3+} (present in the TGO) photo stimulated R-luminescence (Figure 2.7). The PLPS technique also provides for the determination of TGO type (α, θ, γ alumina) and its distribution.

The capability of PLPS as an NDI tool to detect damage and assess remaining life of EB-PVD TBCs has been demonstrated and validated in this study, based on specimen and engine component measurements.

2.3.1. Instrumental Design and Set-up

Stress measurements were made using a Renishaw™ Ramascope™ 2000 (Renishaw, Glouchestershire, UK) system in conjunction with a Leica™ DM/LM light microscope. The schematic of the setup is shown in Figure 2.7. The setup utilizes an Argon ion 514 nm wavelength laser beam operating at 35 mW for exciting the chromium impurity (Cr^{3+}) in the α - alumina. At a magnification of 20 X, the spot size for these stress measurements, which determines the spatial resolution of this technique, is typically 5 µm –7 µm at the TGO, in the absence of the YSZ. Due to scattering within the YSZ, the effective spot size for these samples is reduced to ~ 20 µm.

The specimen surface is first observed under white light using a Leica™ light microscope and is brought to focus using a 20× objective lens. The laser beam is then passed through the same objective lens that enables the focusing of the laser to the area of interest. Parameters such as the power of the incident laser beam, the collection time and the number of accumulations were adjusted to ensure that a minimum of 100, 000 cumulative counts/spectrum were collected. These set-up parameters were recorded for every measurement. The instrument was initially calibrated by collecting spectral data from a standard Al_2O_3 disc chosen as the reference. Two distinct fluorescence transitions corresponding to the R_1 and R_2 fluorescence doublets occur at frequencies of 14402 cm^{-1} and 14432 cm^{-1} respectively for the stress-free sapphire disk (Figure 2.7). This data was deconvoluted and a positive or negative offset was applied until the R_2 peak position for this alumina disc was at 14432.2 cm^{-1}. Five measurements were made randomly along the alumina disk surface and the average peak positions were calculated. This process was then repeated on the specimen of interest. A systematic shift in the position of the R_1 and R_2 peaks collected from the TBC coated sample was used to calculate the bi-axial compressive stress in the TGO.

2.3.2. Measurements on TBC Specimens

As a part of this doctoral work, a testing scheme has been designed to thermally cycle forty specimens each of two different TBCs at three temperatures and two hold times. PLPS measurements made on these samples at specific cycling intervals will provide us with a large PLPS versus cycles database.

At specific cycling intervals, thirty measurements were made randomly on the YSZ coated top surface of each sample. About ten measurements were also made along the edge of every specimen and on the bond coated backside of the specimens, which allowed us to study the evolution of oxide stress in the absence of a TBC top coat. Figure 2.8 is a schematic illustration of the PLPS measurements made on the TBC coated specimens. The collected spectra were then curve-fit using Grams 32™ Spectral Notebase software. The mean stress, standard deviation of 30 stress measurements, R_1 and R_2 peak widths and their area ratios were extracted and studied as a function of cycles.

The measured TGO stress, standard deviation, peak widths and area ratios were plotted as a function of cycles to failure, hot time and as a function of TBC life fraction (on a relative basis, normalized to TBC lives).

PLPS measurements were also carried out on cross-section TBC specimens as a function of thermal cycling and compared to results obtained from measurements made through the TBC. The purpose of this study was to correlate the observed TGO stress trends with the evolution of the TGO/bond coat interface due to cycling. The stress measurements were specifically carried out on areas of the TGO with thickness imperfections, at TGO displacement instabilities (rumpled regions) and on cracked areas where there is cracking at the TGO/YSZ interface or within the TGO. Thus, a systematic decrease in the TGO stress with cycling could possibly be related to the cycling-induced microstructural degradation of the TGO. Standard metallographic procedures were adopted to ensure that there is minimal damage due to polishing and grinding, to ensure

that all damage correlations made using stress measurements in cross-section were indeed from thermal cycling and not polishing-related.

2.3.2.1. Area Mapping

In addition to the 30 random measurements made on the specimens, PLPS spectral data were sometimes also collected over a much larger area. This was done using the motorized stage set-up in the PLPS instrument and by defining the initial and final coordinates and the step sizes. Two types of mapping grids were chosen – a coarse grid and a fine grid. The step sizes and the number of spectra collected for each of these are shown in Table 2.4. Collecting spectral data over such a large area provided a means to detect damage initiation and propagation, since intact areas gave high stresses while locally damaged or separated areas gave low stresses.

The TGO stresses obtained using these coarse and fine area maps were plotted as a function of their x and y coordinates and represented by a two dimensional contour plot. These stress contour plots were obtained for Type II TBCs at different life fractions and compared. This helped track the sequential evolution of damaged areas in specimens as a function of thermal cycling.

2.4. Sample Preparation for Metallography

The metallographic specimen preparation techniques used to prepare samples for microstructural observation using optical and scanning electron microscopy are described in this section. Standard metallographic preparation techniques were used to grind and polish the mounted samples.

2.4.1. Sectioning and Mounting of Specimens

All the Type I and Type II specimens that were removed from cycling at various life fractions were sectioned using a Buehler's ISOMET™ low speed diamond saw. In addition to these specimens, failed specimens were also mounted, sectioned and polished after observation of their spallation surface under the scanning electron microscope. The ceramic side of the specimen was kept facing down on the diamond saw and the rotational speed of the saw was set at 150-200 rpm, to prevent compressive stresses on the ceramic which could lead to spallation of the top coat. Samples with more than 60 % cyclic life were mounted in Buehler's EpoThin® low viscosity epoxy before sectioning, to prevent any separation between the TGO and the TBC during sectioning.

100 parts of Buehler's EpoThin® epoxy resin and 36 parts of the hardener were weighed out and blended thoroughly for at least a minute. This epoxy blend is known to be fluid enough at 80°F to allow good penetration of voids/cracks during curing and good adherence to the specimen. The mounted sample was then cured at room temperature for eight to ten hours. This procedure not only ensures coating integrity, but also helps in identifying artifacts that could be introduced during sectioning and mechanical polishing. Any cracks or separations that are impregnated with epoxy can be safely assumed to have been present prior to sectioning and polishing.

2.4.2. Grinding and Polishing of Mounted Samples

After mounting, the specimens were first ground in order with 180, 300, 600 grit SiC polishing papers. The mounted specimens were thoroughly rinsed between each

stage of grinding. After rough grinding, the specimens were ultrasonically cleaned, first in distilled water and then in acetone and dried.

Fine polishing of the specimens was done on Struers RotoPolish semi-automatic polisher using 30 µm, 6µm, and 1µm diamond paste and 0.05µm alumina suspension on a new polishing disk (Buehler's DP-Dac). The semi-automatic polisher was set up for the following parameters: an applied force of 10 N with progressive force reduction during the 2½ minutes of each polishing step; the specimen holder was set in counter rotation mode at a speed of 150 rpm. A mineral oil-based lubricant was also used during polishing.

2.5. TBC Characterization

Microstructural characterization was carried out on the sectioned, mounted and polished cross-section samples, both in the as-received condition and in the thermally cycled state (at specific life fractions), to examine the evolution of the TBC/TGO interface and that of the bond coat with thermal cycling. Characterization was also done on the failed samples to identify the failure interface.

2.5.1. Optical Microscopy

Low magnification images of the polished cross-section samples in the range of 200 X – 800 X were obtained using a Nikon Metaphot Optical Microscope. This unit was equipped with Normaski Interference capability which was useful in enhancing subtle topographical contrasts and thus helped in identifying the bond coat grain boundaries and the network of ridges, which cannot be observed using conventional SEM technique,

without the need for etching. Optical microscopy was particularly useful during the final stages of grinding and polishing to determine the quality of polishing. The localized bumps seen on the top coat of the specimen surface in cycled specimens were also photographed by using multiple light sources at an oblique angle.

2.5.2. Surface Interferometry

Surface interferometry measurements were made using a Zygo™ New View 5000 interferometer system. This instrument is equipped with a microscope, an automated sample stage, and a computer for data acquisition, data processing and analysis. The three-dimensional surface topographic information of the bond coat surface was obtained using this method. The data obtained using this technique has been presented as three-dimensional filled plots.

The height of the bond coat ridges (peak-to-valley distance – PV) and the average roughness (R_a, obtained from the surface roughness profile) of the bond coat surface were measured from the back side of the bond-coated specimens, in both the as-received condition and in the failed condition and compared, to understand the morphological evolution of the bond coat surface on thermal cycling.

2.5.3. Scanning Electron Microscopy

The mounted and polished specimens, in the as-received and cycled condition, and the failed specimens were carbon coated prior to observing them in the Philips ESEM and the Jeol SEM to make the surface conductive. Carbon tape and copper tape were used to connect the specimen surface to the specimen stub. Additionally, silver paint was also applied on the sample surface to prevent charging inside the ESEM. EDX measurements

using the ESEM were also carried out on the failed surfaces to identify the elemental composition of the failed surfaces. This information was then used to determine the final failure interface.

2.5.4. Energy Dispersive Spectroscopy (EDS)

Localized chemical analyses of specimens were performed using an AMRAY 1000A equipped with EDAX 9100/60 energy dispersive x-ray spectrometer (JEOL, Tokyo, Japan) that is capable of analyzing elements of atomic number down to sodium. Carbon coating is preferred over a gold coating in the EDS analysis since it provides minimum interference. Point analysis and area mapping (X-ray elemental maps) were performed.

2.5.5. X-ray Diffraction (XRD)

XRD was carried out to determine the phase structure of the TBC specimens, and the types of oxide found on spalled surfaces. All XRD analysis was done in the Bruker AXS, D5005 X-ray diffractometer (Bruker Analytical X-ray Systems, Inc., Madison, WI) with Cu K? radiation (? =0.154 nm). The determination of phases was performed by comparison of obtained spectral patterns with the standard PDF data base.

2.5.6. Image Analysis

The image analysis in this study was performed using a UNIX-based application software (microGOP 2000, ContextVision, Linkoping, Sweden). Different image processing and analyzing procedures were used for different purposes; the detailed procedures will be described below.

2.5.6.1 Characterization of Rumpling

To study the morphological evolution of the metal-oxide interface during thermal cycling, a series of cross-sectional SEM micrographs were first taken at the same magnification for about 800 ? m along the interface. Then, the morphological evolution of interface was characterized using image analysis of cross-sectional SEM micrographs. For roughness analysis, the coordinates of the metal-oxide interface were extracted from a series of SEM micrographs. The root mean square roughness parameter (RMS) was calculated from the resulting interface profiles.

$$RMS = \sqrt{\frac{1}{n}\sum_{i=1}^{n} y_i^2} \qquad (2.1)$$

where n is the number of data points along the interface and yi is the current coordinate (height) of the interface relative to the mid-section (the height of mid-section is defined equal to 0). Tortuosity was determined by the ratio of the interface length to the lateral straight-line length L/L0. The spacing between inward displacements was characterized using a power spectrum plot and the Fast Fourier Transform (FFT) method.

2.5.6.2 Measurement of TGO Thickness

TGO thickness was studied as a function of thermal cycles at three temperatures. Cross-sectional SEM micrographs were taken and fifty measurements of TGO thickness were performed along each cross section. The average TGO thickness and its standard deviation were calculated.

2.5.6.3 Measurement of Crack Density

SEM micrographs were converted into binary images in which black represents cracks and white represents uncracked regions. The length for every crack was measured

from each image. The crack density was calculated as the total length of cracks divided by the total image area.

2.5.6.4 Measurement of Area Fraction of Fracture Surface

SEM micrographs were input into the image analysis software. By choosing suitable threshold values, the gray image can be converted into a binary image in which the black represents the exposed bond coat surface and the white represents the rest of the fracture surface. The area fraction was calculated as the area of the exposed bond coat surface divided by the total area of surface.

2.6. Quantitative Analysis of Bond Coat Rumpling and TGO Tortuosity

Quantitative measurements of the amplitude of TGO displacements were made for Types I and II TBCs using image analysis from cross-section micrographs obtained at various cyclic life fractions.

2.6.1. Estimating Amplitude of Bond Coat Rumpling

The inward displacements of the TGO were located on the micrograph and their peak-to-valley distances, PV (depth) were obtained. The depth of these displacements was measured as the distance through which the TGO had bowed into the bond coat, starting from the region where the YSZ was attached to the TGO (Figure 2.9). These values were then divided by the total number of such displacements found in the micrograph to obtain the average PV amplitude for that micrograph. A minimum of 10

such micrographs obtained along the entire diameter of the sample was used for any given specimen. This guaranteed that a minimum of forty measurements per sample were used in computing the average. The bond coat thicknesses in each of these samples were measured prior to making the PV measurements to ensure that any change in the amplitude of these displacements was not as a result of the sample-to-sample variation in the bond coat thickness.

These amplitude measurements were obtained for Type I and Type II specimens at specific life fractions and were plotted as a function of cycles to failure, hot time and TBC life. The rumpling amplitudes, A, were also plotted as a function of the square root of the number of thermal cycles, $\sqrt{N}$ and these plots were then fit to a straight line, of the form $A = x\sqrt{N} + y$. This equation was differentiated to determine the rumpling rate, given by dA / dN.

2.6.2. Calculating TGO Tortuosity

Tortuosity is the ratio of the length of the interface to its straight-line length. Tortuosity of the TGO/bond coat interface was determined using SEM cross-section images. For each average tortuosity value reported, a minimum of 10 cross-section images were used. Since the surface distortion was confined to specific regions involving the downward displacements of the bond coat (Figure 2.9), tortuosity was calculated only from these locations and these high distortion regions were not averaged with regions that showed no change. The active area was roughly half of the total interface.

The tortuosity measurements have also been used to calculate the fraction of the total in-plane growth strain of the TGO that ends up as lengthening of the bond coat

surface. If the surface length at N number of cycles as measured by tortuosity is L (N), the in-plane oxide growth strain was estimated as follows:

$$e_g = [L (N+ 1)-L (N)] /L (N)$$

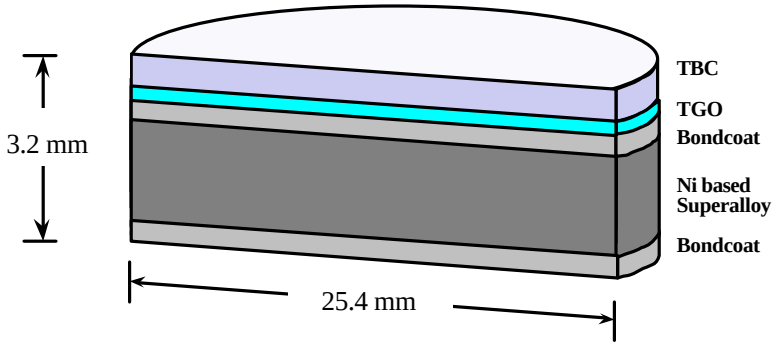

Figure 2.1: Schematic describing the specimen geometry of the TBCs used in this study.

Figure 2.2: A photograph of the furnaces used in this study.

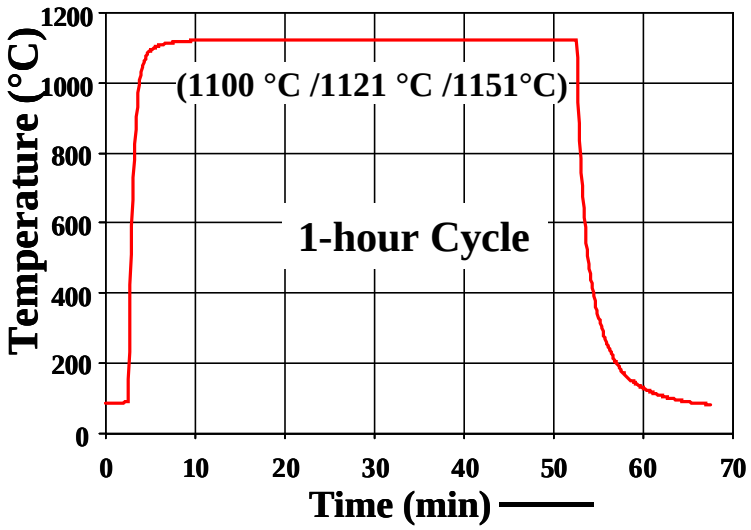

Figure 2.3: Schematic describing the temperature profile during the 1-hour cyclic tests.

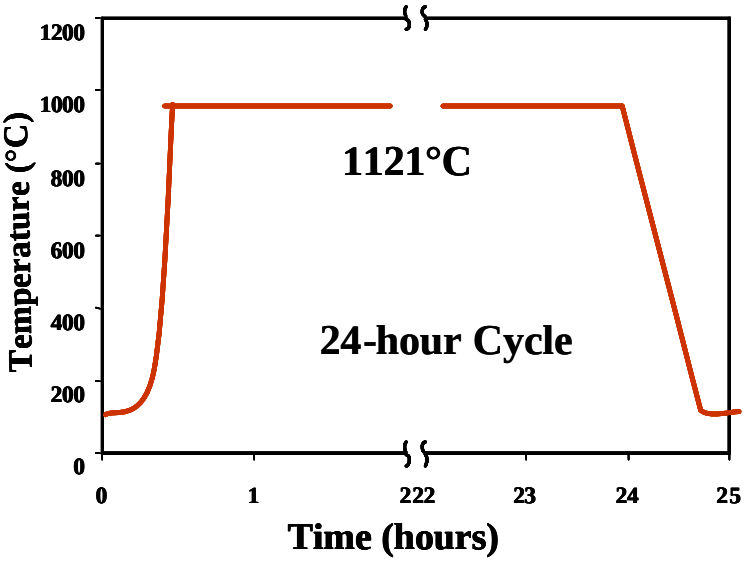

Figure 2.4: Schematic describing the temperature profile during the 24-hour cyclic tests.

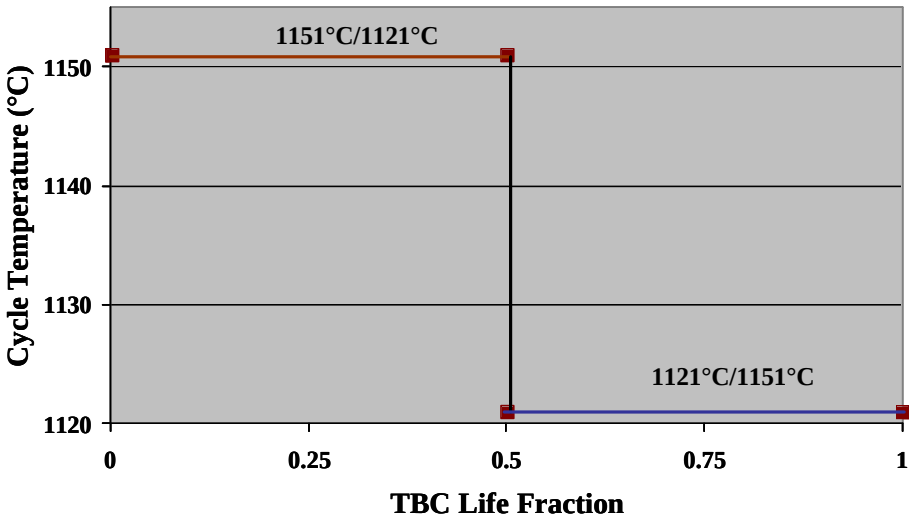

Figure 2.5: Schematic showing the temperature profile during the multi-temperature tests.

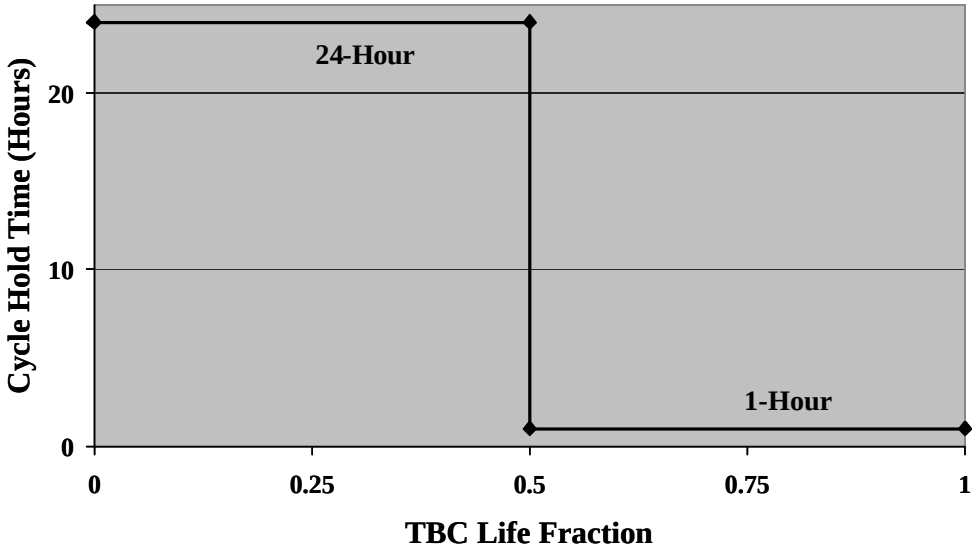

Figure 2.6: Schematic showing the hold-time profile during the multiple hold time tests.

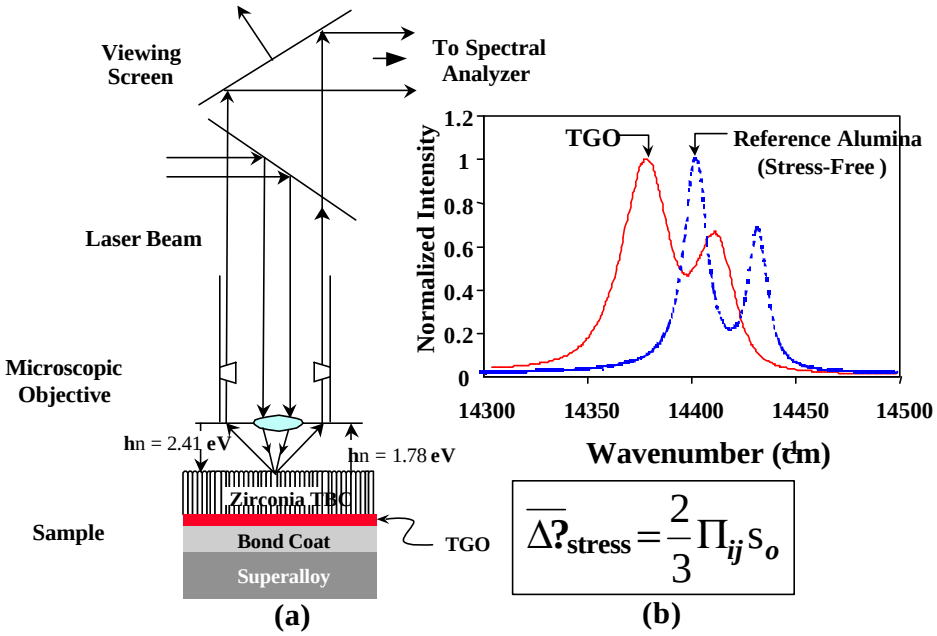

Figure 2.7: Schematic illustration of the photo-stimulated luminescence piezo spectroscopy technique; (b) Typical R_1/R_2 fluorescence spectra for Cr-containing stress-free and stressed α -Al_2O_3.

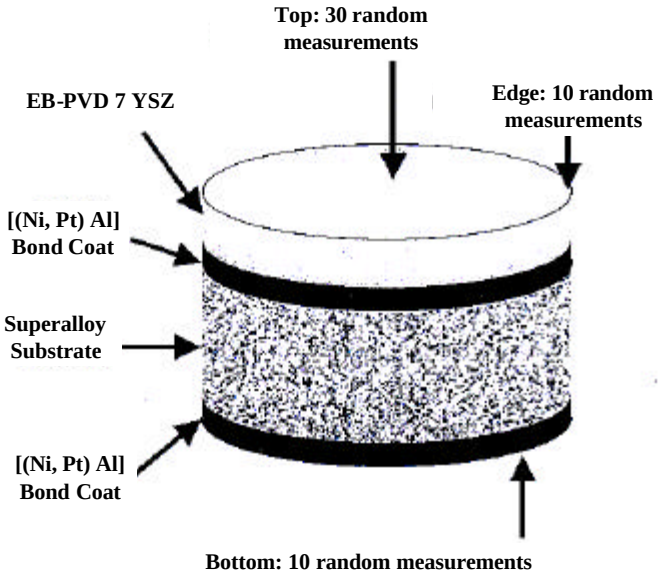

Figure 2.8: A schematic illustration of PLPS measurements made on TBC coated specimens.

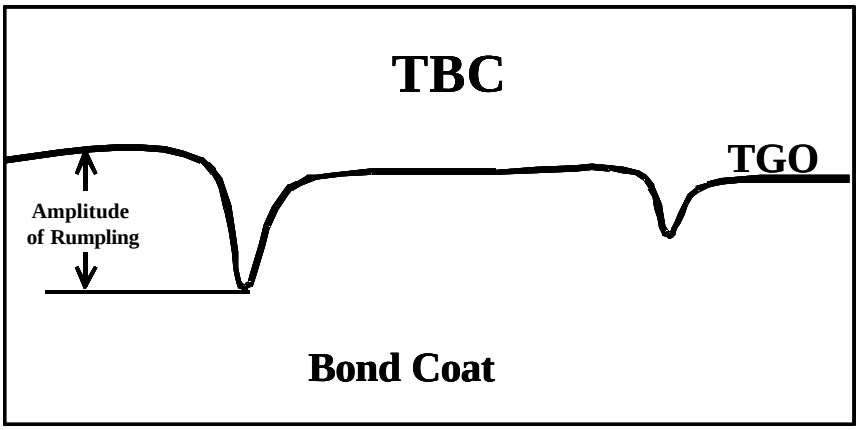

Figure 2.9: Schematic describing the procedure used for measuring the amplitude of rumpling and tortuosity in the cycled Type I TBC specimens.

Table 2.1: Composition and thicknesses of the two TBCs studied.

Type	Superalloy Substrate	Bond Coat		Ceramic (7 YSZ)	
		Type	Thickness (μm)	Type	Thickness (μm)
I	Single Crystal CMSX-4	Grit Blasted on Ouward Diffusing Single Phase Platinum Modified Nickel Aluminide	75	EB-PVD	150
II	Single Crystal CMSX-4	Grit Blasted on Inward Diffusing Type Single Phase Platinum Modified Nickel Aluminide	55-60	EB-PVD	175

Table 2.2: List of Type I TBC specimens tested.

Cyclic Test Condition	Total # Specimens Cycled	# Specimens Cycled To Failure	Cyclic Intervals At which Microstructural Characterization Was Done	Cyclic Intervals At which PLPS Measurements Were Made
1- hour at 1100°C	16	9	100, 300, 400, 600, 800, 1000, 1200	Every 150 Cycles
1 – hour at 1121°C	16	7	10, 50, 100, 200, 300, 400, 500, 600, 650	Every 75 Cycles
24 - hour at 1121°C	16	7	0, 1, 4, 8, 12, 17, 25, 32, 40	Every 4 Cycles
1 – hour at 1151°C	13	7	50, 100, 150, 200, 250, 300	Every 40 Cycles

Table 2.3: List of Type II TBC specimens tested.

Cyclic Test Condition	Total # Specimens Cycled	# Specimens Cycled To Failure	Cyclic Intervals At which Microstructural Characterization Was Done	Cyclic Intervals At which PLPS Measurements Were Made
1- hour at 1100°C	8	3	50, 200, 425, 625, 811	Every 150 Cycles
1 – hour at 1121°C 24 - hour at 1121°C	10 5	6 2	50, 150, 400, 500 0, 8, 20, 33	Every 50 Cycles Every 8 Cycles
1 – hour at 1151°C	8	4	50, 100, 200, 300	Every 40 Cycles

Table 2.4: The step sizes and the number of spectra collected for the coarse and fine area mapping measurements done using PLPS.

Mapping Type	Step Size (mm)	# Spectra
Coarse Mapping	1500	100
Fine Mapping	500	350

Table 2.5. Typical composition of various layers of TBC III

Layer	Material	Composition (wt.%)
Substrate	Single crystal superalloy CMSX-4	9 Co, 6.5 Cr, 6.5 Ta, 5.6 Al, 6.0 W, 3.0 Re, 0.6 Mo, 0.1 Hf, 1.0 Ti, balance Ni
Bond Coat	Ni-rich Pt-Al	20 Pt, 21 Al, balance Ni
Ceramic TBC	Yttria stabilized Zirconia	7 Y_2O_3 in ZrO_2

Deleted: the

Deleted: system

Deleted: ¶
¶
¶

Page Break

Table 2.6. Typical composition of various layers of TBC IV

Deleted: the

Deleted: system

Layer	Material	Composition (wt.%)
Substrate	Single crystal superalloy CMSX-4	9 Co, 6.5 Cr, 6.5 Ta, 5.6 Al, 6.0 W, 3.0 Re, 0.6 Mo, 0.1 Hf, 1.0 Ti, balance Ni
Bond Coat	NiCoCrAlY with addition of Si, Hf	20 Co, 18 Cr, 12.5Al, 0.6 Y, 0.4 Si , 0.25 Hf, balance Ni
Ceramic TBC	Yttria stabilized Zirconia	7 Y_2O_3 in ZrO_2

3. Experimental Results

Four EB-PVD TBCs, Type I with an outward diffusing platinum modified nickel aluminide bond coat produced by CVD and Type II with an inward diffusing platinum aluminide bond coat produced by pack cementation, Type III with (Ni,Pt)Al bond coat and Type IV with (Ni,Co)CrAlY bond coat were studied as a part of this research. The results for the Type I and II TBC are presented first, followed by the results for the Type III and IV TBC.

3.1. As-Received TBC Characterization

3.1.1. Optical Microscopy

The typical cross-section microstructure of the Type I TBC in the as-received condition is shown in Figure 3.1. The specimen was characterized using an optical microscope in combination with Normaski interference illumination. The specimens in the as-received condition have a very thin TGO layer (~ 0.5 μm) and a 75 μm thick single phase β, Pt-modified NiAl bond coat. As seen in Figure 3.1, the EB-PVD 7 YSZ has a columnar structure and a thickness of 150μm. The presence of bond coat ridges is evident from these Normaski Interference micrographs (indicated by arrows in Figure 3.1). It can also be seen that every ridge is associated with a bond coat grain boundary. These ridges are formed during the CVD aluminizing of the bond coat.

3.1.2. Surface Interferometry

The as-received samples were also characterized using surface interferometry. Using this technique, three-dimensional (3D) plots, filled plots and contour plots, were obtained, which provide details about the height of the ridges on the bond coat surface. Such information cannot be obtained either using the optical or the scanning electron microscope, since these techniques only provide pictures in planar, two-dimensional (2D) view.

The ridges found on the bare bond coat surface were found to be about 3.5 μm high, as shown in Figure 3.2. The samples used in this study were grit blasted prior to TBC deposition, which is known to reduce the height of these ridges and make them flatter. However, it has been reported [Xie *et al*; 2003] that this grit blasting procedure does not completely remove the ridges. Also, grit blasting produces a much rougher bond coat surface, as shown in Figure 3.3.

3.1.3. Scanning Electron Microscopy

The bond coat ridges were also seen in the cross-section scanning electron microscope (SEM) pictures of the as-received samples, as shown in Figure 3.4. The TGO was found to be thin and uniform, with an average thickness of ~ 0.5 μm. As mentioned before, the grit blasted bond coat surface was found to be rougher than the as-deposited bond coat (Figure 3.3). This roughness manifests itself as imperfections at the TGO/bond coat interface. These imperfections are in the form of undulations of the TGO at the TGO/TBC interface (shown by white arrow in Figure 3.4). These features have been

observed in many EB-PVD TBCs having platinum aluminide bond coats [Mumm *et al*; 2001, Karlsson and Evans; 2001, Selcuk and Atkinson; 2003].

As can be seen in Figure 3.4, these inward undulations almost always coincide with regions in the ceramic where the YSZ converges at a certain distance from the YSZ/TGO interface (as indicated by the black arrow in Figure 3.4), thereby distorting the columnar grain structure of the EB-PVD TBC. This has been previously reported by [Mumm *et al*; 2001]. The initial amplitude of these interface undulations was measured from the electron micrographs using image analysis (see Experimental Procedure). The average peak-to-valley amplitude of these inward undulations was found to be ~ 1 μm in the majority of samples. Alumina grits left over from the bond coat grit blasting can also be seen at the TGO/bond coat interface, as shown by white circles in Figure 3.4.

3.2. Failure Lives of Thermally Cycled TBC's

A minimum of eight samples were cycled to failure for every thermal exposure studied. A list of these samples and their failure lives are tabulated in the following sections. Two or three samples were chosen as the baseline specimens for every cycle time and cycle temperature tested and these were cycled to failure, without any periodic inspection for PLPS measurements or SEM characterization. The failure lives of these baseline specimens provided a rough estimate of the average TBC spallation lives for the thermal exposures studied.

3.2.1. Spallation Criterion

After every twenty thermal cycles, the TBC samples were examined for the appearance of cracks, buckling or separations. As the number of thermal cycles approached the average failure lives calculated using the baseline samples, the specimens were inspected more often, every 5-10 cycles. Final failure was defined as separation over more than 50% of the YSZ surface or buckling of 50% or more of the YSZ topcoat from the substrate.

3.2.2. One Hour Cycles

Ten samples were cycled to failure during the 1-hour cycling tests conducted at 1100°C. A list of these specimens and their spallation lives are listed in Table 3.1. The failure lives of the thermally cycled samples are plotted and shown in Figure 3.5. The average spallation life of the 1-hour samples at 1100°C was 1388 cycles. The standard deviation of the spallation lives is found to be within ± 9 %. This suggests that there is not a big variation in spallation lives from sample to sample.

Eleven samples were cycled to failure during the 1-hour cycling tests conducted at 1121°C. A list of these specimens and their spallation lives are listed in Table 3.2. The failure lives of the thermally cycled samples are plotted and shown in Figure 3.6. The average spallation life of the 1-hour samples at 1121°C was 677 cycles.

Nine samples were cycled to failure during the 1-hour cycling tests conducted at 1151°C. A list of these specimens and their spallation lives are listed in Table 3.3. The failure lives of the thermally cycled samples are plotted and shown in Figure 3.7. The average spallation life of the 1-hour samples at 1151°C was 358 cycles.

Eight samples were cycled to failure during 24-hour cycling tests conducted at 1121°C. A list of these specimens and their spallation lives are listed in Table 3.4 and plotted in Figure 3.8. The average spallation life of the samples subjected to 24-hour cycles at 1121°C was 45 cycles.

3.2.3. Spallation Life Summary

1-hour thermal cycling was carried out at 1100°C, 1121°C and 1151C° and 24-hour cycling at 1121°C. The average times to failure for the various thermal exposures are shown in Figure 3.9. The standard deviation of failure lives was found to be within 15 % of the average spallation lives, indicative of small sample-to-sample variations. The average number of cycles to failure was found to decrease by a factor of sixteen on changing the cycle frequency from 1-hour to 24-hour; and to decrease by a factor of four on increasing the cycling temperature from 1100°C to 1151°C. It is worth mentioning here that despite the decreased number of cycles to failure for the 24-hour tests compared to the 1-hour tests, the total time to failure for the 24-hour tests was twice as long as that for the 1-hour tests. These results are consistent with results obtained by Kimmel *et al* (1999) and Kim *et al* (2002) on a similar TBC.

3.2.4. Multiple History Tests

A total of six samples were cycled to failure during the multiple-hold time and multi-temperature tests. Table 3.5 shows the spallation lives for the multiple temperature tests and Table 3.6 lists the failure lives for the multiple hold time tests. For the samples subjected to multi-temperature tests and the sample subjected to 24-hour test followed by the 1-hour test, there was no observed loss or gain in TBC life based on linear damage

summation, which indicated the absence of accelerated or decelerated failure modes. This is shown in Figure 3.10, which is a plot of the TBC cyclic life fractions for each stage of the two-level variable amplitude tests. However, for the sample, LE 33, which was cycled to approximately half its expected life using the 1-hour tests followed by the 24-hour tests, the 24-hour cyclic life was found to be half its expected life. This could imply possible synergistic damage accumulation effects on changing from the 1-hour to the 24-hour test conditions.

3.3. PLPS Measurements

PLPS measurements were conducted on the thermally cycled TBC specimens at periodic intervals, as described in Table 2.2. The residual compressive stress in the TGO, determined from the frequency shift of the R_2 peak, was then studied as a function of thermal cycles for the different cycle times and temperatures. The PLPS measurements were carried out for at least six specimens for each exposure condition. The plots of stress versus cycles for these samples are presented in this section. The stress evolution for the 1-hour tests carried out at the three temperatures of 1100°C, 1121°C and 1151°C are discussed first, followed by the results for the 24-hour tests.

3.3.1. TGO Stress Measurements for 1-hour Cycles

The TGO stress values for the 1-hour cycled samples were plotted as a function of thermal cycles and as a function of the TBC life fraction normalized with respect to cycles for these TBC specimens.

3.3.1.1. Evolution of TGO Stress as a Function of Cycles

The TGO stress was found to evolve with cycles as shown in Figures 3.11 and 3.12. In these and subsequent figures, the error bars represent one standard deviation of the 30 measurements made on the sample, whose mean value is plotted. It is worth mentioning here that bimodal spectra, consisting of two sets of peaks, were not seen for these specimens at any measurement interval. The compressive stress in these specimens was seen to increase from about 1.3 GPa in the as-received condition to about 2.9 GPa during the first 50 cycles, 100 cycles and 200 cycles respectively for the tests conducted at 1100°C, 1121°C and 1151°C, as shown in Figure 3.11 and then gradually decreased to 1.2 GPa at failure, as shown in Figure 3.11. Also, the slope of stress versus cycles was similar for the tests conducted at the different temperatures, as seen in Figures 3.11 and 3.12.

3.3.1.2. Evolution of TGO Stress as a Function of Cyclic Life Fraction

The furnace cyclic tests conducted at three temperatures and two hold times provided us with stress versus cycles plots at multiple temperatures and multiple hold times. This allowed us to study the evolution of TGO stress as a function of TBC life fraction normalized with respect to cycles, which would shed light on the effect of temperature and hold time on the TGO stress evolution. This was the first time that such a study has been carried out. The TBC life fraction was calculated as the number of cycles at each measurement interval divided by the number of cycles to failure for the sample.

TGO stress values were then plotted as a function of the TBC cyclic life fraction, as shown in Figure 3.13. The TGO stress increases during the first 10 -15 % of the cyclic life followed by a monotonic decrease with TBC cyclic life fraction, for all three cycle temperatures. As can be seen in these figures, the TGO stress evolution is insensitive to the cycling temperature and the TGO stress versus TBC life has a nearly single valued relation.

3.3.2. TGO Stress Measurements for 24-hour Cycles

The TGO stress values for the 24-hour cycled samples were also plotted as a function of thermal cycles and as a function of the TBC cyclic life fraction. Some similarities and differences were observed between the 24-hour stress plots and those of the 1-hour tests conducted at 1121°C.

3.3.2.1. Evolution of TGO Stress as a Function of Cycles

The TGO stress for the 24-hour cycled samples was plotted as a function of cycles and total hot time. This was then compared with the stress plots obtained for the 1-hour cycled samples. While Figures 3.14 and 3.15 are plots of stress versus cycles for the 1-hour and 24-hour tests, Figure 3.16 is a plot of TGO stress versus hot time for the 1-hour and 24-hour tests.

The similarities between the TGO stress evolution for the 24-hour and the 1-hour cycled specimens are that the TGO stress increases from about 1.3 GPa in the as-received condition to about 2.9 GPa within the first 5 cycles (Figure 3.14) and then gradually decrease to 1.2 GPa at failure (Figure 3.15). However, the rate of stress evolution was substantially different for the 1-hour and the 24-hour tests conducted at the same

temperature (Figure 3.16). But, this difference in the rate of TGO stress evolution is not clearly evident from Figure 3.16, since the 1-hour cycled samples have failure lives 16 X that of the 24-hour cycled samples. So the TGO stress values have been plotted as a function of TBC cyclic life fraction to compare them on a similar scale. This is discussed in the next section.

3.3.2.2.Evolution of TGO Stress as a Function of Cyclic Life Fraction

When plotted as a function of the cyclic life fraction, the difference in the rates of the TGO stress evolution between the 1-hour and the 24-hour tests becomes more evident. This is shown in Figure 3.17. The stress evolution is found to be slightly slower for the 24-hour tests than that for the 1-hour tests, indicating that the stress evolution changes to a limited extent with hold time changes.

3.3.3. TGO Stress Measurements for Multiple History Tests

In order to evaluate the effects of cyclic temperatures and hold times on the photoluminescence response of these TBCs, the TGO stress evolution was studied as a function of thermal cycles and as a function of TBC cyclic life fraction during each stage of the two-level furnace cyclic tests. These two-stage variable amplitude tests consisted of cycling a sample to approximately half its expected cyclic life either at the first temperature or using the first hold time, followed by cycling it to failure at the second temperature or using the second hold time. This study was conducted to determine the feasibility of using PLPS as a viable NDI technique. PLPS measurements were made at shorter intervals of one to five cycles following transition to each new test temperature.

3.3.3.1. Evolution of TGO Stress as a Function of Cycles

Figure 3.18 is a plot of the TGO stress versus cycles for the four samples that were subjected to multiple-temperature tests. For the multi-temperature tests where the samples were cycled each to approximately half their cyclic life at 1121°C using 1-hour cycles and then subsequently cycled to failure at 1151°C, there was a slight increase in the TGO stress during the first twenty cycles of transition to the higher test temperature, following which the original slope of the stress versus cycles curve was restored. However, for the tests carried out at 1151°C followed by 1121°C, the slope of the stress versus cycles remained fairly constant during the first twenty cycles of transition to the higher test temperature and the original slope of the stress versus cycles curve remained unchanged at the high and low test temperatures. This indicates that the test temperatures do not affect the stress response of the system.

Multiple hold time tests consisted of cycling the sample to 50 % of its expected cyclic life using the first hold time followed by cycling it to failure using the second hold time. Figure 3.19 is a plot of the TGO stress versus hot time for the two samples that were subjected to the multiple hold time tests, which consisted of cycling the sample using 1-hour hold time at 1121°C followed by 24-hour hold time at 1121°C. The stress values for the 24-hour test results are also included in this plot for better clarity in comparing the trends. For the case where the 1-hour tests were followed by the 24-hour tests, there was a significant drop in the slope of the stress versus hot time curve on transition to the 24-hour hold time and the original rate of stress reduction typical of the 1-hour tests, was not restored at any point during the 24-hour hold time tests that followed. However, for the samples that were cycled using the 24-hour hold time

followed by the 1-hour hold time at 1121°C, the slope of the stress versus cycles became steeper on changing to the 24-hour hold time and the original rate of stress reduction, typical of the 24-hour tests, was not restored at any point during the 1-hour hold time tests that followed. This indicates that the cycle time irreversibly affects the stress response.

3.3.3.2. Evolution of TGO Stress as a Function of Cyclic Life Fraction

Figure 3.20 is a plot of the TGO stress versus TBC life for the four samples that were subjected to the multiple-temperature tests. The stress versus TBC cyclic life fraction relation does not change on changing the test temperatures. The stress versus life curves for the 1-hour tests conducted at 1121°C and 1151°C are also included in this plot for comparison. As seen in Figure 3.20, the stress versus TBC life curves for the constant amplitude tests resemble those obtained for the variable amplitude tests. This indicates that a change in the cyclic temperature amplitude does not affect the normalized stress response of the system. This result is consistent with identical spallation mechanisms for all the 1-hour tests conducted at the three temperatures.

Figure 3.21 is a plot of the TGO stress versus cyclic life fraction for the samples that were subjected to the multiple hold time tests. The stress versus TBC life fraction relation does change to a limited extent on changing the hold times. The stress versus life curves for the 24-hour tests conducted at 1121°C are also included in this plot for comparison. As seen in Figure 3.21, the stress versus TBC life curves for the constant amplitude tests resemble those obtained for the variable amplitude tests, except for a slight change in the slope of the stress evolution on changing the hold time. This indicates that the change in the hold time does affect the stress response of the system. This result

is consistent with a change in the spallation mechanism on varying the hold time from 1-hour to 24-hours.

3.3.4. TGO Stress at Failure

PLPS measurements were also carried out on all the fracture surfaces of the failed specimens. These measurements were made on the bare bond coat surfaces that were exposed on spallation of the TBC. No bimodal spectra were seen for these failed specimens. The TGO stress at failure in these specimens was found to be constant (~ 1.2 GPa), as shown in Figure 3.22, irrespective of the cycling temperature and cycle time.

3.3.5. Evolution of Other Spectral Characteristics with Thermal Cycling

Besides the TGO stress, other characteristics of the photoluminescence spectra were determined and studied as a function of thermal cycling, for the different thermal exposures.

3.3.5.1. Change of Standard Deviation for the Peak Positions

The standard deviation of the 30 stress measurements made on the TBC coated top surface was determined and plotted as a function of cyclic life fraction. Similarly, the standard deviation was also determined for the measurements made using the coarse and fine area maps. Figure 3.23 shows the standard deviation of measured TGO stress as a function of TBC life fraction, normalized with respect to cycles. The standard deviation increases gradually with cycling. Also, this trend was nearly constant for the different cycle times and temperatures studied.

3.3.5.2. Change of Peak Width and Peak Shape

Figure 3.24 shows the full width at half maximum (FWHM) for the R_2 peak as a function of TBC life fraction and Figure 3.25 shows the Lorentzian/Gaussian ratio as a function of TBC life. The R_2 peak width shows a fairly monotonic decreasing trend with TBC life. There is no systematic trend observed for the L/G ratio as a function of TBC life. The peak widths were fairly constant for the three cycling temperatures and two cycle times studied.

3.3.5.3. Change of Intensity Ratio of R1 and R2 Peaks

Figure 3.26 shows the ratio of R_1 and R_2 peak intensities as a function of TBC life fraction. No systematic trend of the area ratio intensities versus TBC life was observed. The area ratio intensities were found to be constant for the various exposure conditions examined.

3.3.5.4. Change of Relative Intensity of N2 and R2 Photoluminescence

In addition to the R_1-R_2 luminescence from α-Al_2O_3, N-luminescence, N_1, N_2 and N_3, were also observed for all as-received and thermally cycled TBCs. The presence of N-luminescence indicates the presence of Cr^{3+} concentration in the Al_2O_3 scale [Schawlow *et al*; 1959]. A doublet characterizes the N-Line spectrum at ≈ 14225cm^{-1} and 14300cm^{-1} at 77 K. This doublet is attributed to chromium ions in octahedral coordination. The fluorescence spectrum of Ruby, single crystal alumina, with different chromium concentrations has been studied by Wood *et al* (1959). This paper has been used as a reference to arrive at a relation between the chromium ion (Cr^{3+}) concentration

and the N-line intensity ratio for the given spectra. A relation between the N-line intensity ratio and the chromium ion concentration was obtained:

$$C_{Cr} = 0.08(I_r) - 0.005(I_r)^2 + 0.0001(I_r)^3$$

An increase in the concentration of Cr^{3+} in the α-Al_2O_3 scale causes a frequency shift in the R-luminescence [Kaplyanski *et al*; 1969] and hence decreases the calculated magnitude of compressive residual stress.

The relative intensities of the N_2 and R_2 photoluminescence were determined and studied as a function of thermal cycling, in order to determine if the presence of the N-luminescence in these TBC samples caused a shift in the R luminescence and hence in the measured value of the TGO stress.

Figure 3.27 shows the ratio of the N-line intensity to that of the R_2 peak. The corresponding Cr^{3+} concentration in the α-Al_2O_3 scale was estimated from these intensity ratios [Schawlow *et al*; 1959]. Figure 3.28 shows the estimated Cr^{3+} concentration versus cycles. As shown in Figure 3.27, the intensity of N-luminescence increases initially during the thermal cycling, indicating an increase in the concentration of Cr^{3+} ions in α-Al_2O_3. However, after 100 thermal cycles, the intensity of the N-luminescence decreases and then disappears after 250 cycles. The maximum concentration of Cr^{3+} in the α-Al_2O_3 scale was calculated to be around 0.3 wt% after 100 thermal cycles as shown in Figure 3.28. This value of Cr^{3+} concentration was found to be too low to significantly affect the measured value of the TGO stress, since 0.3 wt% Cr_2O_3 corresponds to approximately 0.3 cm^{-1} shifts in absolute wave number, and would decrease the magnitude of compressive residual stress by less than 0.1 GPa [Kaplyanski *et al*; 1969].

3.3.6. Determining TGO Thickness Using the Normalized Area Under the R2 Fluorescence Peak

Besides the TGO stress, the TGO thicknesses were also measured for these specimens at various life fractions. As a part of this research, the possibility of a new to measure the TGO thickness non-destructively was examined. The TGO thicknesses were plotted as a function of the fluorescence intensity (normalized area under the R_2 fluorescence peak) as shown in Figure 3.29. A linear relationship between the normalized intensity and the TGO thickness was found. This is consistent with previous results [Vaidyanathan; 2001] which indicated that the fluorescence signal comes from the entire thickness of the TGO. Figure 3.29 shows that there is a possibility of determining the TGO thickness, non-destructively, using the photoluminescence intensity. However, this trend was found to be true only for samples cycled to up to 50 % cyclic life. Beyond 45% cyclic life, the normalized intensity was found to decrease with cycles monotonically as shown in Figure 3.30. The reason for this is not clear at this point. Also such a measurement requires a means of accounting for any changes in the attenuation of the signal due to sintering or surface deposits of soot or ingested minerals on the overlying TBC, and this is yet to be demonstrated. Since the TGO thickness is not a single valued function of spectral intensity for the entire TBC life, it is unlikely this method can be used to non-destructively determine TGO thickness.

3.4. Microstructure of 1-hour Cycled Specimens

The microstructural evolution of the thermally cycled specimens was observed using a scanning electron microscope. In addition to the TGO evolution, two interfaces, the YSZ/TGO interface and the TGO/bond coat interface were examined and studied as a function of cycles.

3.4.1. Changes of the YSZ/TGO Interface With Cycling

The evolution of the morphology of the YSZ/TGO interface with thermal cycling, typical of all the TBC's tested for 1-hour cycles, is well-represented by Figure 3.31, which is for the tests run at 1121°C. The microstructural evolution was found to be qualitatively similar for the 1-hour tests conducted at all three temperatures, despite the 4-fold variation in spallation lives. Progressively with cycling, the TGO is seen to thicken and cracking is seen at the YSZ/TGO interface above the valleys in the bond coat, as indicated by arrows in Figure 3.31. This cracking is due to changes in the bond coat surface shape with cycles; wherein, the valleys become deeper and cause separation of the TBC above these valleys, as the TGO is pulled away from the ceramic coating layer. This cracking at the TBC/TGO interface was observed to start at ~ 15 % to 20 % of TBC cyclic life for all temperatures. Eventually, these cracks extend along this interface and, also sometimes into the TGO, (Figure 3.31) and the cracks from the adjacent regions coalesce resulting in the complete separation of the TBC from the TGO.

3.4.2. Bond Coat Surface Rumpling

The TGO/bond coat interface was also found to change with cycling, specifically, the inward displacements of the TGO into the bond coat were found to progressively

increase. This is often referred to as rumpling [Tolpygo and Clarke; 2000, Deb et al; 1987, Holmes and McClintock; 1990, Pennefather and Boone; 1994]. As a part of this research, the rumpling behavior of this system has been quantified. The details of the procedure used in the quantitative analysis of rumpling are mentioned in the Experimental Procedure section. .

3.4.2.1. Measurement of TGO Instabilities

Quantitative measurements of the amplitude of TGO displacements were made using image analysis from cross-section micrographs obtained at various cyclic life fractions. The inward displacements of the TGO were located on the micrograph and their peak-to-valley distances, PV (depth) were obtained. The depth of these displacements was measured as the distance through which the TGO had bowed into the bond coat, starting from the region where the YSZ was attached to the TGO (Figure 2.9). To obtain the average PV amplitude, these values were divided by the total number of such displacements found in each micrograph. A minimum of 10 such micrographs, obtained along the entire diameter of the sample, were used for each specimen. This guaranteed that a minimum of forty measurements per sample were used in computing the average. The bond coat thicknesses in each of these samples were measured prior to making the PV measurements to ensure that any change in the amplitude of these displacements was not as a result of the sample-to-sample variation in bond coat thickness.

3.4.2.2. Evolution of TGO Displacement Amplitude with Cycles

These amplitude measurements were plotted as a function of cycles to failure, hot time and TBC life. Figures 3.32 and 3.33 show the rumpling amplitude plotted as a function of hot time and the square root of hot time, respectively, for all the 1-hour tests conducted. The rumpling amplitudes increase parabolically as a function of hot time. It can also be seen that the rate of increase of the rumpling amplitudes increases with temperature.

3.4.2.3. Effect of Temperature on Rumpling Rate

Figure 3.33 is a plot of the rumpling amplitudes as a function of the square root of total hot time for the 1-hour tests. These amplitude data were fitted to the square root of time both linearly and parabolically and the best fits were obtained for the linear case. Although there is considerable scatter, the fit is most similar to that used for parabolic oxidation. This parabolic increase in the rumpling amplitude is very similar to that of the TGO thickness shown in Figure 3.34. The rumpling amplitudes, A, were also plotted as a function of the square root of the number of thermal cycles, $\sqrt{N}$ and these plots were then fit to a straight line, of the form $A = x\sqrt{N} + y$. This equation was differentiated to determine the rumpling rate, given by dA / dN. The rumpling rates have also been plotted as a function of cycles for the different tests conducted, as shown in Figure 3.34. For the 1-hour tests, the rate of increase of the rumpling amplitudes increases with the exposure temperature.

3.4.2.4. Rumpling Amplitude at Failure

The amplitude of rumpling was also determined for the failed samples. The rumpling amplitude values at failure for the 1-hour cycled samples are shown in Figure 3.35. Failure in this TBC occurs at a constant amplitude of rumpling, in the range of 10.1 to 10.4μm.

3.4.3. Evolution of TGO Thickness With Thermal Cycling

3.4.3.1. Parabolic Growth Constants

The TGO thicknesses were measured from cross-sectional micrographs of specimens at various life fractions and were plotted as a function of the square root of total hot time for the three cycle temperatures and two hold times. This is shown in Figure 3.36. An average of ten measurements was made along the length of the mounted specimen and four such micrographs at a magnification of 1000X were used to make these thickness measurements. As seen in Figure 3.36, the oxidation kinetics conforms to a parabolic rate law. The parabolic growth constants have been evaluated at the three cycle temperatures. The TGO growth rate equations for the tests conducted at 1100°C, 1121°C and 1151°C are, respectively:

$$h = 0.50 + 0.25 \cdot \sqrt{t(hours)}$$
$$h = 0.50 + 0.27 \cdot \sqrt{t(hours}$$
$$h = 0.50 + 0.48 \cdot \sqrt{t(hours)}$$

where, h is the TGO thickness in microns and t is the total hot time in hours. As expected, the oxidation rate increases with temperature.

3.4.3.2. Activation Energy Measurements

The parabolic growth constants for the three cycle temperatures were determined as described in the previous section and were plotted as a function of the reciprocal of the test temperature. This Arrenhius type plot is shown in Figure 3.37. The data was fit to a straight line and the activation energy for TGO growth was calculated. The activation energy was found to be 139 KJ/mole. Assuming that oxygen transport is the rate-limiting step, the corresponding activation energy for oxygen transport is doubled to 278 KJ/mole, which is in the same range for this activation energy found in the literature [Dorre and Hubner; 1984], 220 KJ/ mole - 420 KJ/ mole.

3.4.3.3. TGO Thickness at Failure

It has often been suggested that failure occurs at a certain critical TGO thickness [Evans *et* al; 2001a, Evans *et* al; 2001b]. Figure 3.38 shows that for the current experiments, failure occurs at TGO thicknesses varying from 6.6 μm to 8.6 μm and, thus, a critical TGO thickness at failure is not observed for this TBC.

3.5. Fracture Surface Analysis of 1-hour Cycled Samples

The failed samples from the 1-hour tests conducted at the three temperatures were analyzed using optical and scanning electron microscopy. The macro failure mode was observed, following which a more elaborate failure analysis was carried out to determine the final failure interface. Damage critical parameters were also identified and quantified.

3.5.1. Macro Photographs of Failed TBC Specimens

Figures 3.39 and 3.40 show the macro failure photographs of specimens that failed after 1350 1-hour thermal cycles at 1100°C and 300 1-hour thermal cycles at 1151°C. The TBC spalled in one large piece in a single cycle.

3.5.2. Failed Bond Coat Surface

Figures 3.41 and 3.42 are secondary electron micrographs showing the failed bond coat surfaces in plan view for samples that failed after 1350 1-hour thermal cycles at 1100°C and 300 1-hour thermal cycles at 1151°C, respectively. The failure occurs within the YSZ ceramic, except at each grain boundary ridge, where the fracture is along the TGO/TBC interface. The bond coat side of the spalled sample, as seen in Figures 3.41 and 3.42 shows large areas of retained YSZ, that appear as shiny white speckles, interrupted by failure occurring at the bond coat/TGO interface along the bond coat ridge tops. It is worth mentioning here that the fracture surfaces for all 1-hour cycled samples are similar, irrespective of cycle temperature, despite a 4-fold variation in spallation lives.

3.5.3. Spalled YSZ TBC

Figures 3.43 and 3.44 are secondary electron micrographs showing the bottom surface of the spalled YSZ in plan view for samples that failed after 1350 1-hour thermal cycles at 1100°C and 300 1-hour thermal cycles at 1151°C respectively. The bottom surfaces of the spalled YSZ appear to be a mirror image of the failed bond coat side shown in Figures 3.41 and 3.42, consisting of retained YSZ except at the bond coat ridges, where the failure has occurred at the bond coat/TGO interface, as seen by the

remnant TGO. The spalled YSZ surfaces for all 1-hour cycled samples are similar, irrespective of cycle temperature, despite a 4-fold variation in spallation lives.

3.5.4. Area Fraction Analysis

The final failure interface was determined using the failure micrographs obtained at a fairly low magnification of 300X. Image analysis was then used to quantify the extent of damage occurring at each of the two interfaces: the YSZ/TGO and the TGO/bond coat interfaces, in terms of the area fraction of the spalled area that failed at the TGO/BC interface. These measurements were made to understand the operating failure mechanism for this TBC under each cycling condition.

Figure 3.45 shows the area fraction of the failure surface corresponding to failure at the TGO/BC interface for the 1-hour tests conducted at the three temperatures. Much of the fracture occurs at the TBC/TGO interface and there seems to be no appreciable effect of the cycle temperature on the failure mode or the final failure interface.

3.6. Microstructure of 24-hour Cycled Specimens

A very important observation made in the 1-hour cyclic tests was that for all three test temperatures, TBC failure was predominantly rumpling driven. It is expected that the cyclic plasticity of the bond coat plays a significant role in bond coat rumpling. In order to isolate the cyclic plasticity effect, 24-hour tests and associated microstructural characterizations were conducted. It should be noted here that the 1-hour tests conducted at 1121°C experience 24 times the number of cycles for a given hot time as do the 24-hour cycles at 1121°C.

3.6.1. Evolution of YSZ/TGO Interface With Cycling

The evolution of the morphology of the YSZ/TGO interface with thermal cycling, typical of all the TBC's tested in the 24-hour cycles, is well represented by Figure 3.46. Some similarities and dissimilarities can be observed between the 1-hour and 24-hour tests conducted at 1121°C. The thickening of the TGO with cycles and the increasing amplitude of rumpling, as seen in the bowing down of the TGO into the bond coat, are qualitatively similar to that seen in the 1-hour tests conducted at 1121°C, as shown in Figure 3.47.

The primary difference between the 24-hour cycled and the 1-hour cycled samples; however, is the relative absence of separation at the TGO/YSZ interface in the 24-hour tests, as seen in Figure 3.47. Some cracking at the YSZ/TGO interface was observed to start at ~ 15 % to 20 % of the TBC life for the 24-hour tests, but no crack extension was observed, as indicated by arrows in Figure 3.46. The final failure for these samples occurs at the bond coat/TGO interface.

3.6.2. Bond Coat Surface Rumpling

Bond coat rumpling was observed for the 24-hour cycled samples and the inward displacements of the TGO into the bond coat were found to progressively increase with cycling.

3.6.2.1. Evolution of TGO Displacement Amplitude with Cycles

Figures 3.48 and 3.49 show the rumpling amplitude, A, plotted as a function of hot time and as a function of square root of hot time respectively, for the 1-hour and 24-hour tests conducted at 1121°C. The rumpling amplitudes increase parabolically as a

function of hot time. It can also be seen that the rate of increase of the rumpling amplitudes increases only slightly with increase in hold time, despite the much reduced number of cycles per unit time.

3.6.2.2. Effect of Hold Time on Rumpling Rate

Figure 3.49 is a plot of the rumpling amplitudes as a function of the square root of total hot time for the 1-hour and 24-hour tests. The best fit for this data is a straight line. The parabolic increase in the rumpling amplitudes is very similar to that of the TGO thickness shown in Figure 3.52.

The rumpling rates were determined as described previously and were plotted as a function of cycles for the 1-hour and 24-hour tests conducted at 1121°C, as shown in Figure 3.50. Here again, the rumpling rate for the 24-hour tests at 1121°C is found to be only slightly higher than for the 1-hour tests, which experience 24 times the number of cycles for a given hot time.

3.6.2.3. Rumpling Amplitude at Failure

The rumpling amplitude values at failure for the 24-hour and the 1-hour tests at 1121°C are shown in Figure 3.51. Failure for the 24-hour tests occurs at a rumpling amplitude of 12.8μm while that for the 1-hour tests carried out at 1121°C is found to occur at 10.2μm. Hence, the critical rumpling amplitude for the 24-hour tests occurs at a higher value than that for the 1-hour tests. This difference can be explained on the basis that the spallation mechanism for the 24-hour tests is different from that for the 1-hour tests. Also, since the total time to failure for the 24-hour tests is twice as long as that for the 1-hour tests at 1121°C, given the very similar rumpling rates for the 1-hour and the

24-hour tests, it is expected that the rumpling amplitude at failure would be greater for the 24-hour tests than for the 1-hour tests.

3.6.3. Evolution of TGO Thickness With Cycling

3.6.3.1. Parabolic Growth Constants

Figure 3.52 is a plot of the TGO thickness versus square root of hot time for the 1-hour and 24-hour tests conducted at 1121°C. The oxidation kinetics for the 24-hour tests also conforms to a parabolic rate law. The TGO growth rate equations for the 1-hour and 24- hour tests, respectively, conducted at 1121°C are:

$$h = 0.50 + 0.27 \cdot \sqrt{t(hours)}$$
$$h = 0.50 + 0.28 \cdot \sqrt{t(hours)}$$

where, h is the TGO thickness in microns and t is the total hot time in hours. It can be seen from these equations that the oxide tends to grow slightly faster for the 24-hour tests as compared to the 1-hour tests. This finding is consistent with previous results reported where the oxidation rate was found to be greater for isothermal conditions as compared to cyclic tests carried out at the same temperature [Vaidyanathan; 2001].

3.6.3.2. TGO Thickness at Failure of TBC specimens

Figure 3.53 shows the TGO thicknesses at failure for the 1-hour and 24-hour cycled samples. It can be seen that for the current experiments, failure occurs at TGO thicknesses varying from 6.6 μm for the 1-hour tests at 1121°C and at 9.7 μm for the 24-hour tests at 1121°C. This indicates that the critical TGO thickness for the 24-hour tests is at a much higher value than that for the 1-hour tests. This difference can be explained

on the basis that the spallation mechanism for the 24-hour tests is different from that for the 1-hour tests. Also, since the total time to failure for the 24-hour tests is twice as long as that for the 1-hour tests at 1121°C, it is expected that the TGO thickness at failure would be greater for the 24-hour tests than for the 1-hour tests.

For the same hot times in the 1-hour and 24-hour tests, very similar oxide growth rates and rumpling rates are observed (See Figures 3.49 and 3.52).

3.7. Fracture Surface Analysis of 24-hour Cycled Samples

The failed samples from the 24-hour tests were analyzed using optical and scanning electron microscopy.

3.7.1. Macro Photographs of Failed TBC Specimens

Figure 3.54 shows the typical spallation morphology of a specimen that failed after 41 24-hour thermal cycles at 1121°C. The 24-hour cycled samples failed into many pieces and failure occurred over a period of three to four cycles. Thus, a marked difference can be observed in the macro failure modes of the 24-hour cycled samples and that of the 1-hour cycled samples, as shown in Figure 3.55.

3.7.2. Failed Bond Coat Surface

Figure 3.56 is a secondary electron micrograph showing the failed bond coat surface in plan view of a sample that failed after 41 24-hour thermal cycles at 1121°C. The presence of extensive bright bare bond coat regions that appear light grey in Figure 3.56 indicates that the failure in the 24-hour cycled samples has occurred predominantly

at the TGO/bond coat interface. Additionally, a few regions that appear dark are also seen which indicate the areas where the failure has occurred at the YSZ/TGO interface. This is in direct contrast with the failure mode observed in the 1-hour cycled samples shown in Figures 3.41 and 3.42, which had a shiny white appearance (YSZ) and where failure had occurred predominantly at the YSZ/TGO interface. In Figure 3.56 which is the bond coat side of the failed sample, occasional retained TGO (dark phase) and YSZ (white phase) can be seen along with an occasional oxide free pore such, as seen near the center of Figure 3.56.

3.7.3. Spalled YSZ TBC

Figure 3.57 is a secondary electron micrograph showing the bottom surface of the spalled YSZ in plan view for a sample that failed after 41 24-hour thermal cycles at 1121°C. The micrograph in Figure 3.57 shows the ceramic side and consists mostly of YSZ that appears as shiny white areas. The TGO is absent from most regions, except along the grain boundary ridges, where the TGO is virtually always retained. The absence of TGO from both the bond coat and the ceramic sides of this failed sample indicates that the remaining TGO separated from both sides at failure and has been lost in the furnace.

3.7.4. Area Fraction Analysis

Figure 3.58 shows the area fraction of the failure surface corresponding to failure at the TGO/BC interface for the 1-hour and the 24-hour tests conducted at 1121°C. For the 24-hour tests, failure occurs predominantly at the TGO/BC interface, while for the 1-hour tests, much of the fracture occurs at the TBC/TGO interface. Thus, there is an obvious change in the failure mode between the 1-hour and the 24-hour tests.

3.8. Remaining Life Calculations Using TGO Stress Measurements

As a part of this research, the single valued relationship between TGO stress and TBC life has been used to make quantitative predictions of remaining life. The motivation for remaining life predictions is for use in making retirement-for-cause decisions of individual parts in gas turbines. Such predictions have been made for two TBCs tested at a single temperature [Jordan *et al*; 2001]. In that study, remaining life was predicted to within ± 7% for EB-PVD TBCs with Pt modified nickel aluminide bond coats and to within ± 2 % for EB-PVD TBCs with MCrAlY bond coats, using simple regression methods and neural network methods. Neural network based predictions were found to be substantially better than those based on simple regression for the MCrAlY bond coated TBCs, while for the Pt aluminide bond coated system, the simple regression based results were found to be better than those obtained using neural networks.

These initial results are promising, but cannot easily be used in actual turbine component assessment, because such components experience a wide variety of temperatures at different locations even on a single part. As a result, it is important to obtain results over a range of temperatures. With such results, it would be possible to use these PLPS results versus remaining life, choosing reference data appropriately for the location and the associated temperature in question. The present work was carried out to obtain the required data. As shown in the previous sections, it was discovered that the remaining life fraction as a function of measured stress turned out to be essentially independent of temperature, potentially simplifying the use of such data in the non-destructive assessment of turbine components subject to non-uniform temperatures. In this study, an attempt is made to assess the remaining life of TBCs based on the stress

versus TBC life plots obtained for both the 1-hour tests and the 24-hour tests at both constant and variable amplitude.

The prediction task at hand is to be able to make remaining life predictions based on stress measurements made up to, but not after the inspection interval, in order to simulate a situation where a part replacement decision has to be made.

3.8.1. Regression Method

For the Type I TBC, the spectral characteristics that showed a monotonic trend as a function of TBC life were the TGO stress, the standard deviation of TGO stress and the R_2 peak width. The results based on the TGO stress plots are presented first followed by those using the peak width and the standard deviation values. Since the stress versus TBC life behavior was different for the 1-hour and the 24-hour tests, the remaining life assessments were performed separately for these two test conditions.

The stress data obtained from the 1-hour tests carried out in the constant amplitude and the variable amplitude situations was fit to a quadratic function using a simple regression technique, as shown in Figure 3.59. Using the quadratic equations obtained, the threshold stress levels were evaluated for three possible inspection intervals: 25 % TBC life, 50 % TBC life and 75 % TBC life. Then each individual data set was fit to a quadratic function using the same regression method and the actual remaining life fraction corresponding to these threshold stress values were determined and compared to the ideal value of a remaining life fractions of 25%, 50 % and 75%. Figure 3.60 illustrates this procedure for a Type I sample cycled at 1151°C using the 1-hour cycles. The error in making this remaining life prediction was then calculated as the difference

between the actual remaining life estimated and the ideal expected remaining life at the inspection interval, taking into account the sign of the error. These results are presented in Table 3.7. The errors in making these remaining life predictions have been estimated in two ways: the maximum absolute error and the root mean square value or the RMS error. The maximum absolute errors have been reported in this section.

The above procedure was repeated for the 24-hour tests carried out in the constant amplitude and the variable amplitude situations. The maximum absolute error in assessing the remaining life of Type I TBCs for the 1-hour tests and the 24-hour tests, in both the constant amplitude and the variable amplitude situations are shown in Figure 3.61. The maximum absolute error has been evaluated for three different inspection intervals of 25 %, 50 % and 75 % TBC life, as shown in Table 3.8. As seen in Figure 3.61, the maximum absolute error in assessing the remaining life of Type I TBCs at half-life inspection is 10% for the 1-hour tests and the 24-hour tests. As seen in Figure 3.61, the maximum absolute error is also found to decrease as the inspection intervals approach TBC failure lives.

The above procedure was repeated to assess TBC remaining life based on the peak width data obtained for the 1-hour and 24-hour tests. The peak width data obtained was fit to a quadratic function using simple regression technique, as shown in Figure 3.62. The threshold peak width levels were evaluated for three possible inspection intervals: 25 % TBC life, 50 % TBC life and 75 % TBC life, as described previously and these values were used to determine the remaining life of each sample tested. Figure 3.63 illustrates this procedure for a Type I sample cycled at 1151°C using the 1-hour cycles. The maximum absolute error in making this remaining life prediction is shown in Figure

3.64. The standard deviation of the TGO stress was also used to assess TBC remaining life using the procedure described above. The maximum absolute error in making this remaining life prediction is shown in Figure 3.65. One interesting observation as seen in Figures 3.64 and 3.65 is that the error in predicting remaining life for the 24-hour tests is smaller than that for the 1-hour tests. This is contrary to the trends seen in Figure 3.61. It is also seen in Figure 3.64 that the maximum absolute error in predicting remaining life using peak width values decreases as the inspection intervals get closer to the TBC failure lives. However the error in predicting the remaining life using the standard deviation data increases to its maximum value during the 50 % TBC life inspection interval and decreases at the 75 % life inspection interval (Figure 3.65).

3.9. Type II TBCs

The results presented in the preceding sections have established a clear relationship between the measured TGO stress and TBC life, which can serve as a basis for nondestructive TBC remaining life assessment. However, the elastic strain in the TGO, and consequently the TGO stress, depend on many factors like TBC processing methods, bond coat composition and processing, cycle time and temperature, etc. Hence, it is important from a practical standpoint, to determine whether and to what extent these factors affect the temperature independent stress versus life relationship, which was obtained for the Type I TBC. In this context, this research was extended to a second TBC, Type II, with different processing, bond coat composition and heat treatment compared to the Type I TBC. Table 3.9 lists these differences between the two TBCs.

The effects of hold time and peak temperature on the spallation mechanisms of Type II TBCs were examined and their roles on the TGO stress versus TBC life information were determined. The results for Type II TBCs will be compared and contrasted with the results for Type I TBCs.

3.9.1. As-Received Microstructure

A cross-section secondary electron image of Type II TBC in the as-received condition is shown in Figure 3.66. The bond coat thickness varies between 55 and 60 µm on different parts of the same sample. Three distinctly different zones were seen: (1) a 17-µm thick outer zone (OZ), (2) a 26 µm zone below the OZ marked by alumina grits (left over from bond coat grit blasting) on its outer edge, consisting of β - NiAl enriched with Pt and precipitates rich in heavy elements and (3) a 17µm thick intermediate inter-diffusion Zone (IZ) consisting of larger precipitates rich in heavy elements. The TGO was found to be thin and uniform, with an average thickness of ~ 0.6 µm. As with Type I TBC, the grit blasted bond coat surface for Type II TBC was found to have imperfections in the form of displacements of the TGO at the TGO/TBC interface (Figure 3.66). The average peak-to-valley amplitude of these inward TGO displacements was found to be ~ 2.1 µm, compared to 1µm for Type I. Thus, the Type II TBC has a much rougher bond coat than the Type I TBC.

3.9.2. Failure Lives

Furnace cyclic tests were conducted on Type II TBC specimens at 1100°C, 1121°C and 1151°C using 1-hour hold time and at 1121°C using a 24-hour hold time.

Three samples were cycled to failure during the 1-hour cycling tests conducted at 1100°C. A list of these specimens and their spallation lives are listed in Table 3.10. The failure lives of the thermally cycled samples are plotted and shown in Figure 3.67. The average spallation life of the samples during the 1-hour tests at 1100°C was 1098 cycles.

Six samples were cycled to failure during the 1-hour cycling tests conducted at 1121°C. A list of these specimens and their spallation lives are listed in Table 3.11. The failure lives of the thermally cycled samples are plotted and shown in Figure 3.68. The average spallation life of the samples subjected to 1-hour tests at 1121°C was 563 cycles.

Four samples were cycled to failure during the 1-hour cycling tests conducted at 1151°C. A list of these specimens and their spallation lives are listed in Table 3.12. The failure lives of the thermally cycled samples are plotted and shown in Figure 3.69. The average spallation life of the samples subjected to 1-hour tests at 1121°C was 363 cycles.

Two samples were cycled to failure during the 24-hour cycling tests conducted at 1121°C. A list of these specimens and their spallation lives are listed in Table 3.13 and plotted in Figure 3.70. The average spallation life of the samples subjected to 24-hour cycles at 1121°C was 67 cycles.

In summary, the average times to failure for the 1-hour tests are shown in Figure 3.71. The average number of cycles to failure was found to decrease by a factor of eight on changing the cycle frequency from 1-hour to 24-hour; and decrease by a factor of three on increasing the cycling temperature from 1100°C to 1151°C. As also seen for the Type I TBC specimens, the total time to failure for the 24-hour tests was 4 X as much as that for the 1-hour tests. It is worth mentioning here that while the 1-hour cyclic lives for Type II TBC specimens at 1100°C and 1121°C were 0.77 X shorter than that for Type I

TBC specimens, the 1151°C failure lives were comparable for the two TBCs. Also, the 24-hour cyclic lives for the Type II TBCs were 1.5 X longer than that for the Type I TBCs.

In addition to the 1-hour and the 24-hour cyclic tests, multi-temperature variable amplitude tests were also conducted using two Type II TBC samples. A list of these specimens and their spallation lives are listed in Table 3.14.

3.9.3. TGO Stress Versus TBC Life

PLPS measurements were made on Type II TBC samples at specific cycling intervals for the 1-hour and 24-hour tests as shown in Table 2.3. In addition to the TGO stress and the standard deviation of the TGO stress, other spectral characteristics including the peak width, peak area ratio, and peak shape were evaluated and studied as a function of cycles.

The TGO stress in the Type II TBC specimens was seen to increase from about 1.8 GPa in the as-received condition to about 3.3 GPa during the first 10 % of the TBC cyclic life, as shown in Figure 3.72 and then monotonically decreased to ~ 1.2 GPa at failure, as shown in Figures 3.72 and 3.73. The slope of stress versus cycles was similar for the 1-hour tests conducted at the different temperatures, as seen in Figures 3.72 and 3.73. Two important observations from Figures 3.72 and 3.73 are that the TGO stress evolution for Type II TBC is insensitive to the cycling temperature and that the TGO stress versus TBC life fraction has a single valued relationship. It should be noted here that bimodal spectra, consisting of two sets of peaks, were not seen for these specimens at any measurement interval.

Figure 3.74 is a plot of TGO stress as a function of hot time at 1121°C and Figure 3.75 is a plot of TGO stress versus TBC life fraction for the 1-hour and 24-hour cycled samples. The similarities between the TGO stress evolution for the 24-hour and the 1-hour cycled specimens were that the TGO stress values increased from about 1.8 GPa in the as-received condition to about 3.2 GPa during the first 10% of the cyclic life (Figures 3.74 and 3.75) and then gradually decreased to ~ 1.2 GPa at failure. However, the rate of stress evolution was slightly different for the 1-hour and the 24-hour tests conducted at the same temperature, as seen in Figure 3.75. The stress evolution is found to be slightly slower for the 24-hour tests than that for the 1-hour tests.

Figure 3.76 is a plot of TGO stress versus cycles and Figure 3.77 is a plot of TGO stress versus TBC life fraction for two Type II TBC samples that were subjected to the multiple-temperature tests. For the tests carried out at 1121°C followed by 1151°C, there was a slight deviation in the TGO stress versus cycles trend during the first 25 cycles on transition to the higher test temperature, following which the slope of the stress versus cycles curve changes from that at the lower test temperature. Similar changes were observed for the tests carried out at 1151°C followed by 1121°C, as shown in Figures 3.76 and 3.77. However, the change in the slopes of the stress versus cycles and stress versus life curves were not as substantial as that for the tests carried out at 1121°C followed by 1151°C. These results indicate that test temperatures variations do have an effect on the stress response of this TBC.

3.9.4. TGO Stress At Failure

Stress measurements made on the fracture surfaces of the failed Type II TBC specimens are presented in Figure 3.78. The TGO stress at failure for the Type II TBC

specimens was found to be fairly constant in the range of 1.1 GPa to 1.3 GPa, as shown in Figure 3.78, irrespective of the peak temperature and cycle time.

3.9.5. Evolution of Other Spectral Characteristics with Thermal Cycling

Figure 3.79 shows the standard deviation of measured TGO stress as a function of TBC life fraction for Type II TBC specimens. As seen in Figure 3.79, the standard deviation increases slightly with cycling and has a sharp increase just prior to failure. Also, this trend did not vary much for the different cycle times and temperatures studied.

Figure 3.80 shows the full width at half maximum (FWHM) for the R_2 peak as a function of TBC life fraction. There is a decreasing trend with cycling. Figure 3.81 shows the ratio of R_1 and R_2 peak intensities as a function of TBC life fraction for Type II TBCs. As seen in Figure 3.81, no systematic trend of the area ratio versus TBC life was observed. The area ratio values were found to be constant for the various exposure conditions examined. Figure 3.82 shows the Lorentzian/Gaussian ratio as a function of TBC life. As seen in Figure 3.82, there is no systematic trend observed for the L/G ratio as a function of TBC life.

3.9.6. Summary of PLPS Results on Type I and Type II TBCs

Many similarities were observed between the PLPS results obtained on Type I and Type II TBC specimens. This section will highlight the similarities and differences between the PLPS trends observed for the two TBCs. The maximum TGO stress for Type II TBC specimens was found to be lower than that for Type I TBCs, as shown in Figure 3.83. The TGO stress versus life relation was found to be single valued, independent of the cycle temperature for both TBCs. Additionally, changing the hold time was found to

change the stress versus life relation for both TBCs. The measured TGO stress at failure was found to be lower for the Type II TBC as compared to that for the Type I TBC, as seen in Figures 3.22 and 3.76. The R_2 peak width, R_1 and R_2 peak area ratio and the peak shape for both TBCs were found to be very similar as can be seen in Figures 3.24 to 3.26 and Figures 3.80 to 3.82.

3.9.7. Microstructural Evolution

The microstructural evolution of the thermally cycled Type II TBC specimens was observed using a scanning electron microscope. The results for the 1-hour tests will be presented first followed by the 24-hour test results.

3.9.7.1. One hour Tests

The microstructural evolution for Type II TBCs was found to be qualitatively similar for the 1-hour tests irrespective of the test temperature, despite the 3-fold variation in spallation lives. The evolution of the YSZ/TGO interface with thermal cycling, typical of all Type II TBC's tested in the 1-hour cycles, is well represented by Figure 3.84, which is for the tests run at 1121°C. As in the case of the Type I TBCs, three important features were observed for Type II TBCs with 1-hour cycling, as seen in Figure 3.84: (a) progressive thickening of the TGO, (b) increase in rumpling of the TGO/bond coat interface, and consequently, (c) increased cracking at the YSZ/TGO interface above the valleys in the bond coat.

One notable difference between the microstructural evolution during the 1-hour tests for the two TBCs studied is that the extent of rumpling observed in Type II TBCs is much larger than that for Type I TBCs, as can be seen in Figure 3.85. This can be

explained based on the observation that the initial bond coat roughness for the Type II TBCs was almost twice as much as that for the Type I TBCs, as shown in Figure 3.86. Hence, a rougher, initial bond coat in Type II TBCs would be expected to rumple faster with cycling than a smoother bond coat in Type I TBC [Vaidyanathan *et al*; 2000, Tolpygo and Clarke; 2000].

The TGO growth rate equations for Type II TBCs for the 1-hour tests conducted at 1121°C and 1151°C are:

$$h = 0.56 + 0.46 \cdot \sqrt{t(hours)}$$
$$h = 0.56 + 0.73 \cdot \sqrt{t(hours}$$

where, h is the TGO thickness in microns and t is the total hot time in hours. As expected, the oxidation rate increased with increase in cycle temperature, as shown in Figure 3.87. The parabolic growth constants for the two cycle temperatures were plotted as a function of the reciprocal of the test temperature. This Arrenhius type plot is shown in Figure 3.88. The data was fit to a straight line and the activation energy for TGO growth was calculated. The activation energy was found to be 112 KJ/mole. Assuming that oxygen transport is the rate-limiting step, the corresponding activation energy for oxygen transport is obtained by doubling the activation energy for TGO growth, which is 224 KJ/mole, which is in the same range for this activation energy found in the literature [Dorre and Hubner; 1984], 220 KJ/ mole - 420 KJ/ mole. It should be noted here that the TGO growth rates for the Type II TBCs are higher than that for Type I TBCs, which is consistent with the results obtained by Angenete and Stiller (2002) on two similar TBCs.

3.9.7.2. 24-hour Tests

The evolution of the YSZ/TGO interface with thermal cycling, typical of all Type II TBC's tested in the 24-hour cycles, is well-represented by Figure 3.89. As with the Type I TBCs, some similarities and dissimilarities were observed between the 1-hour and 24-hour tests conducted at 1121°C. The TGO growth rate for the 24-hour tests was found to be greater than that for the 1-hour tests, as shown in Figure 3.90. The amplitude of rumpling, as seen in the bowing down of the TGO into the bond coat, was qualitatively similar to that seen in the 1-hour tests conducted at 1121°C, as seen in Figure 3.91. The primary difference between the 24-hour cycled and the 1-hour cycled Type II TBC samples was the relative absence of cracking and separation at the TGO/YSZ interface in the 24-hour tests, compared to the 1-hour tests, as seen in Figure 3.91.

Figure 3.90 is a plot of the TGO thickness versus square root of hot time for the 1-hour and 24-hour tests conducted at 1121°C. As seen in Figure 3.90, the TGO growth rate equations for the 1-hour and 24- hour tests conducted at 1121°C are:

$$h = 0.56 + 0.46 \cdot \sqrt{t(hours)}$$
$$h = 0.56 + 0.58 \cdot \sqrt{t(hours)}$$

where, h is the TGO thickness in microns and t is the total hot time in hours. It can be seen from these equations that the oxide tends to grow faster for the 24-hour tests as compared to the 1-hour tests. An important difference between the 1-hour and 24-hour growth rates for the two TBCs studied is that while the difference in the growth rates is fairly small for Type I TBCs, the difference is quite significant for Type II TBCs.

3.9.8. Fracture Surface Analysis

The results from the failure analysis of the failed Type II TBC samples from the 1-hour and 24-hour tests are presented in this section.

3.9.8.1. One hour Tests

Figure 3.92 shows the macro failure photographs of Type II TBC specimens that failed after 1103 1-hour thermal cycles at 1100°C and 413 1-hour thermal cycles at 1151°C. The 1-hour cycled Type II samples failed on cooling to room temperature in a single cycle by large-scale buckling and fracture propagation across the entire specimen surface.

A typical failure surface for the samples subjected to 1-hour cycles is shown in Figure 3.93, which is a secondary electron micrograph showing the failed bond coat surface in plan view for a sample that failed after 450 1-hour thermal cycles at 1121°C. The bond coat side of the spalled sample, as seen in Figure 3.93, shows large areas of retained YSZ, that appear as shiny white speckles, interrupted by failure occurring at the bond coat/TGO interface along one or two bond coat ridgetops. The failure occurs predominantly within the TBC, except at a few grain boundary ridges, where the fracture is along the TGO/TBC interface. It is worth mentioning here that the fracture surfaces for all 1-hour cycled samples looked similar, irrespective of cycle temperature, despite a 3-fold variation in spallation lives.

3.9.8.2. 24-hour Tests

A typical macro photo of the failed 24-hour samples is shown in Figure 3.94, which shows the spallation morphology of a specimen that failed after 65 24-hour

thermal cycles at 1121°C. As seen in Figure 3.94 the 24-hour cycled Type II TBC samples failed into many pieces, largely by buckling in localized areas and failure occurred over a period of three to four cycles. The failure surface of the 24-hour cycled samples showed some intact regions in addition to the spalled areas, indicating that failure did not occur across the entire specimen. Thus, the macro failure modes of the 24-hour cycled samples, shown in Figure 3.94, differed from that of the 1-hour cycled samples, shown in Figure 3.92.

Figure 3.95 is a secondary electron micrograph showing the failed bond coat surface in plan view of a sample that failed after 69 24-hour thermal cycles at 1121°C. The presence of extensive bright bare bond coat regions that appear light grey in Figure 3.95 indicates that the failure in the 24-hour cycled samples has occurred predominantly at the TGO/bond coat interface. Additionally, a few regions that appear as white speckles and some dark areas are also seen, which indicate the areas where the failure has occurred within the YSZ or at the YSZ/TGO interface. This is in direct contrast with the failure mode observed in the 1-hour cycled samples shown in Figure 3.93, which had a shiny white appearance (YSZ) and where failure had occurred predominantly within the YSZ. In Figure 3.95, cavities (shown by white arrow) and oxide-free pores (shown by double arrows) are also seen.

Several similarities and some differences are observed between the failed Type I and Type II TBC samples. Both TBCs were shown to fail in the TBC, near the TBC/TGO interface for the 1-hour tests irrespective of the test temperature. The spallation mechanism was shown to change on varying the hold time for both the TBCs. The macro

failure modes for the 1-hour tests differed for the Type I and Type II TBCs, as seen in Figures 3.96.

3.10. Results of (Ni,Pt)Al Bond Coated Type III TBCs

3.10.1. **Microstructure and Failure Analysis**

3.10.1.1. Microstructure of As-Coated TBCs

X-ray diffraction of the as-coated YSZ shows the coating is made of the desirable, non-equilibrium tetragonal (t') phase (Fig. 3.97). It was observed that only parts of the peaks (400 and 200) were visible, indicating that the coating has a preferred orientation, which probably is due to its columnar structure. The top surface morphology of the as-coated YSZ coating is shown in Fig. 3.98 and the "cauliflower" like morphology is clear with a grain diameter about 2-3 μm.

The cross-sectional micrograph of the as-coated TBC is shown in Fig.3.99. The YSZ topcoat has a nominal thickness of 140 μm with a columnar structure. The platinum-modified nickel-aluminide bond coat (Ni, Pt)Al is nominally 50 μm thick. The bond coat closest to the TGO is single phase (Ni, Pt)Al, confirmed by XRD (Fig. 3.100). Further from the TGO and near the substrate, there is an inter-diffusion zone with the substrate. Alumina inclusions entrapped from the grit blasting procedure are present in the bond coat. A thin, continuous TGO layer (~0.5 μm) was observed and undulations of the interface between the ceramic top coat and bond coat were present. These undulations come from grit blasting of the bond coat before depositing the TBC.

Higher magnification micrographs (Fig. 3.101) show the imperfections where the bond coat surface is locally concave and the TBC near the TGO layer above this concave region has some defects or voids. These imperfections have been observed previously in EB-PVD TBC systems with Pt modified aluminide bond coats (88). It has been proposed that these imperfections localize the thermal expansion mismatch stress, causing nucleation of cracks and separations driven by the strain energy stored in the TGO (74).

3.10.1.2. Microstructural Evolution of TBCs During Thermal Cycling

One-hour thermal cycling tests were conducted at 1151ºC, 1121 ºC and 1100 ºC. It was found that the microstructural evolution was similar for specimens tested at all three temperatures. One typical example, well represented by Fig. 3.102, will be used to illustrate the microstructural evolution of TBCs during thermal cycling. Figs. 3.102 shows a cyclic sequence of cross-sectional micrographs for tests at 1151 ºC. The following major changes in the microstructure of specimens were observed with thermal cycling: (1) the interface between the top coat and the bond coat becomes rougher (referred to as either rumpling or ratcheting) and both the amplitude and the number of sites of downward displacement increase with cycles; (2) the TGO thickness increases; (3) β-(Ni, Pt)Al $\rightarrow \gamma$'-Ni3Al transformation occurs in the bond coat led by aluminum depletion due to oxidation and inter-diffusion with the substrate (85); and (4) cracking occurs. The cracks initiate at about 30% of the cyclic life.

A higher magnification image in Fig. 3.103 shows a typical example of crack initiation. As the TGO penetrates into the underlying bond coat, cracking initiates near the TGO/TBC interface above the rumpling-induced valley in the bond coat. This image

also shows that a defective region in the TBC; a “pinched-off” region characterized by columnar grains that converge a small distance from the interface. These regions, also observed by Mumm et al. (88), are often associated with as-fabricated depressions in the bond coat surface. After initiation, cracks extend laterally from these defects with increasing cyclic exposure as shown in Fig. 3.102C.

3.10.1.2.1 Interface Rumpling During Thermal Cycling

The bond coat/oxide interface profiles at various stages of thermal cycling were extracted from the cross-sectional micrographs and the results are shown in Fig. 3.104a (1151°C) and b (1100°C). It is apparent that the roughness of the interface, or the amplitude of rumpling, increases with thermal cycles at both temperatures. The amplitude of largest downward displacements is about 10 μm at both temperatures.

Quantitative analyses of the rumpling were carried out by calculating the RMS parameter and tortuosity from the interface profiles. The values of the interface RMS parameter and the tortuosity as a function of thermal cycles at different temperatures are shown in Fig. 3.105 and Fig. 3.106, respectively. The RMS parameter and the tortuosity increase almost linearly with thermal cycles at different temperatures, although there is some scatter of data. The slopes of the fitting lines represent the rate change of the roughness (characterized by the RMS parameter or tortuosity). The larger the slope the faster the roughness increases. It is clearly shown that the rumpling rate increases with temperature and the specimens with shorter lives have larger rumpling rate. Moreover,

the values of the RMS parameter at failure are similar (~3.0 μm), despite the different test temperatures. This suggests that a critical rumpling value drives spallation for this TBC.

Power spectrum plots were obtained to characterize the spacing of downward displacements as a function of cycles using the Fast Fourier Transform (FFT) method (Only one example of a power spectrum plot for the profile of the specimen after 125 cycles at 1151°C is shown in Fig.3.107). A broad range of frequencies was produced and no dominant wavelength could be determined. However, the most probable wavelength (indicated by the asterisk in Fig. 3.107) seems to decrease with thermal cycles (Fig.3.108), consistent with observations that the number of imperfection sites increases with cycles.

Rumpling was also studied on the backside of specimens (bond coated only without ceramic topcoat) using surface interferometry. It is clearly shown that the surface roughness increases with thermal cycles (Fig. 3.109 and 3.110). Compared to the metal/oxide interface, the rumpling amplitude of the bare bond coat side was found to increase faster, indicating the ceramic top coat partially constrains the roughening of the bond coat surface (Fig. 3.111).

3.10.1.2.2 TGO Thickness

The TGO thickness increases with thermal exposure and the thickness as a function of hot time is shown in Fig. 3.111. The TGO growth is consistent with parabolic growth kinetics. The TGO growth rate increases as the cycling temperature increases. Fig. 3.112 shows the logarithm of the parabolic growth coefficient at three temperatures

as a function of the reciprocal of the temperature (1/T). It was found that the growth coefficient is governed by an Arrhenius equation

(4.1)

where k is parabolic growth coefficient, Ea is the activation energy, T is the temperature. The activation energy for TGO growth was calculated from the slope of the fit line and found to be 282 kJ/mol. This activation energy is close to the value obtained by Sridharan et al. (30) on a similar system, and in the same range for the activation energy for oxygen transport in alumina (238 kJ/mol) (128). The activation energy values for TGO growth on (Ni, Pt)Al bond coat here and in ref. (30) are also comparable to that on NiCoCrAlY bond coat in ref. (31) after using the consistent parabolic law equation

(4.2)

where h is the TGO thickness, t is the time and k is the rate constant. This indicates that TGO growth is controlled by oxygen transport. The average TGO thickness at failure is 4.6-5.3 μm and it is approximately constant at the three temperatures.

Fig. 3.113 shows interface roughness as a function of TGO thickness. It was found that both the RMS parameter and tortuosity increase as TGO thickness increases, relatively independent of temperature and with surprisingly small data scatter.

3.10.1.3. Microstructural Analysis Near and After Spallation

The spallation life at the three temperature tests is shown in Table. 4.1. One specimen showed abnormally short life (202 cycles) at 1121°C, otherwise the samples

showed relatively consistent spallation lives. The average spallation life and its standard deviation for tests at various temperatures are shown in Fig. 3.114. The average life of specimens are 928 cycles at 1100°C, 458 cycles at 1121°C, 178 cycles at 1151°C, respectively. The average spallation life decreases by a factor of five on increasing the cycling temperature from 1100°C to 1151°C. These results are consistent with the results obtained by Kim et al. (129) and Sridharan et al. (30) on similar systems, where a temperature increase of 100°C decreases the hot time to failure by a factor of 10.

Fig. 3.115 shows macrophotographs taken at various stages of TBC life. The general observations are that the top surface of specimens showed no signs of damage until final spallation and only limited spallation occurs at the free edge of specimens during cycling (Fig. 3.115a). The final spallation was catastrophic and large scale buckling occurred with fracture propagation across the entire specimen surface (Fig. 3.115 b and Fig. 3.116). Spallation failure of the ceramic is into many small pieces.

The spalled surface of the bond coat side is shown in Fig. 3.117. The spallation surface of the bond coat side of specimens consists of exposed regions of bond coat, TGO and TBC. Fig. 4.3.117 shows a typical higher magnification image of spalled surfaces and associated EDS spectra at different regions. It was found that the bond coat forms a continuous region containing islands of TGO and TBC. The TBC that remains on the spalled surface is almost always at the center of these TGO islands. The exposed bond coat surface shows the imprinted TGO grain morphology. The oxide contains cleavage facets indicating that they were mechanically detached from the TGO. The bond coat comprises 52 to 68% of the spalled surface.

Fig. 3.118 shows the spallation surface of the bottom side of the ceramic top coat. It consists of regions of TGO and TBC. The exposed TGO surface has the granular morphology that mirrors the imprint in the bond coat side. The root of the exposed TBC columns is porous and equiaxed.

It is apparent that specimens exhibit a mixed failure pathway, with cracking occurring at the TGO/TBC and TGO/BC interfaces and even through the TGO. Fig. 3.119 shows the cross-sectional images near the failure in which cracks go through the TGO and along the TGO/BC interface. The fracture surfaces and the failure pathways are similar for specimens tested at all three temperatures. This indicates that, for this TBC, although the cracks initiate near the TGO/TBC interface (Fig. 3.103) and may extend laterally along this interface (Fig. 3.103c), they can also divert into the TGO and extend along the TGO/BC interface when the specimen is close to failure. Similar results have been reported by Spitsberg et al. (89).

In some cases, structural imperfections such as cavities form as shown in Fig. 3.120. Almost all cavities occur at locations having depressions due to rumpling, indicating that these cavities are strongly associated with rumpling induced depressions.

Fig. 3.121 shows the XRD patterns of the spalled surface on the bond coat side. The phase constituents include the β-NiAl, γ′- Ni3Al and α-Al2O3. γ′- Ni3Al comes from the phase transformation of β-NiAl and α-Al2O3 is the residual TGO on the spalled surface. Chen et al. (85) reported that a reversible β-M martensitic transformation accompanies thermal cycling in a platinum modified diffusion aluminide bond coated TBC and the strains caused by the martensitic transformation contributes to the rumpling.

In contrast, no L10 martensite phase is detectable, indicating there is no martensitic transformation in this TBC.

3.10.1.4. Phase Stability and Sintering of YSZ Coating

Fig. 3.122 shows the comparison of the XRD patterns of as-coated and failed YSZ coatings. No significant phase changes were observed during thermal cycling.

The sintering behavior of the YSZ coating was examined using SEM. The top surface morphologies of the as-coated and failed coatings are shown in Fig. 3.123. "Mud-flat cracking" of the coating is seen in the failed specimens. A comparison of images at higher magnification, for both the as-coated and failed specimens, shows that the columns have sintered during thermal cycling. In addition, the surface of the failed specimen is smoother and the crystallographic facet structure of the individual columns becomes much less distinctive compared to the as-coated specimens.

Fig. 3.124 shows that the comparison of cross-sectional images for as-coated and failed specimens. Consistent with the surface morphologies, the serrations on the column edges become smoother with thermal cycling. In some cases, a neck is formed between adjacent columns (see Fig. 3.124e).

Raman spectroscopy was also used to detect coating phases with thermal cycling. As shown in Fig. 3.125, the coating remains t' phase during thermal cycling. Although there is no phase change, the peak width changes and the characteristic peaks become sharper with thermal cycling. The reason for this change is not clear; it may be due to the decrease in site disorder resulting from yttrium and oxygen vacancy ordering (130).

3.10.2. TGO Stress Evolution

3.10.2.1. Typical Luminescence Spectra during Thermal Cycling

PLPS measurements were carried out for as-coated TBC specimens and for thermally cycled specimens at specified life-fractions at three temperatures (1151°C, 1121°C and 1100°C). All spectra were analyzed using the automated deconvolution procedure. This procedure was developed for the first time under this research and the details are described in Appendix I. The spectral characteristics (frequency shift, peak area ratio, peak width, and Lorenztian fraction) were extracted and analyzed as a function of thermal cycling. Typically, two types of spectra were observed in the specimens during thermal cycling. The first type is the spectra showing only one set of R1-R2 luminescence peaks and, correspondingly, exhibiting one major stress level (i.e. unimodal luminescence). The second type is the spectra showing two sets of R1 and R2 luminescence peaks exhibiting two stress components, with one of them being close to zero (i.e. bimodal luminescence). Examples of each type of spectra and the corresponding fitted peaks are shown in Fig. 3.126.

3.10.2.2. TGO Stress and Its Standard Deviation

The evolution of the residual stress in the TGO under the YSZ coating as a function of thermal cycles at 1151°C, 1121°C and 1100°C is shown in Fig. 3.127. In these and subsequent figures, the data points and error bars are the average values and associated standard deviations of multiple measurements on a single sample, respectively. At all three temperatures, the compressive stress increases to its maximum in the first few

cycles and then decreases monotonically with thermal cycles until failure. The average compressive stress in the TGO increases from approximately 1.5 GPa to about 2.3 GPa in 5 cycles at 1151°C; whereas the maximum stress value is reached in 50 cycles at 1121°C and 1100°C. In contrast, the specimen showing abnormally short life (202 cycles) at 1121°C starts with a higher stress and fails at an abnormally high stress (~2.4 GPa). This specimen is being studied in detail now and the explanation about its abnormal behavior needs further investigation. Since this specimen is the only specimen having such abnormal behavior, for the sake of clarity, this specimen will be eliminated from the following discussions.

The figures of average stress vs. thermal cycling are re-plotted after removing data points from the initial, transient stage (Fig. 3.128). As shown, the change of average stress vs. thermal cycles can be fit as a linear function. The slope of the linear function can be obtained and represents the rate of change of stress with cycling. There is a consistent relationship between the slope and the actual lives of specimens; the shallower the slope, the longer the spallation life.

Fig. 3.129 shows the standard deviation of the TGO stress as a function of thermal cycles. The standard deviation increases from the as-received condition to about 0.16 GPa and then decreases a little within a very short time. After the first 15% of cyclic life at all three temperatures, the standard deviation increases continuously until failure.

The average TGO stress values have also been plotted as a function of life fraction of the specimens, as shown in Fig. 3.130. The TGO stress decreases monotonically with life fraction after the initial stage (about 10% of the cyclic life). This result also shows that the TGO stress evolution with life fraction is quite insensitive to

the cycling temperature, consistent with the result obtained by Sridharan et al. (30) on another 7YSZ EB-PVD/ (Ni, Pt)Al/CMSX-4 TBC.

3.10.3. Relationships among Rumpling, TGO Stress Evolution and Specimen Life

As shown in section 4.1.2.2, after an initial transient period, the TGO stress decreases monotonically with thermal cycles until failure at all three temperatures. Fig. 3.131 shows the TGO stress as a function of thermal cycles for one specimen at each temperature after removing the data points for the transient period. The stress decreases faster with increasing cycling temperature. The stress relaxation rates (GPa/cycle) of specimens were found to be 0.0053 at 1151°C, 0.0025 at 1121°C and 0.0011 at 1100°C. Comparisons of quantitative results of rumpling rate and TGO stress relaxation rate at various temperatures show that TGO stress relaxation rate increases with increasing rumpling rate. If we further combine TGO stress relaxation rate and rumpling rate with specimen life, it is found that both rumpling rate and TGO stress relaxation rate increase, while spallation life decreases as the cyclic temperature increases (Fig. 3.132).

3.10.4. PLPS Spectral Characteristics Evolution

PLPS data consists of the fluorescence spectra coming from the thermally grown oxide layer (TGO). For a homogeneous stress state, two peaks designated R1 and R2 are recorded and these peaks shift linearly with the magnitude of the hydrostatic stress in the TGO (Fig. 3.6). Because damage to the oxide can result in a non-uniform stress, various features of the spectra can change, including: the peak position related to stress, the

standard deviation of the stress from multiple measurements at different locations on a given sample, peak width related to stress homogeneity, the R1/R2 peak area ratio and the Gaussian/Lorentzian fraction used to fit the peaks. For this TBC, in addition to the TGO stress, all spectral characteristics changed in a similar manner with thermal cycling, independent of temperature. For the sake of brevity, spectral characteristics with cycling will be only described at two temperatures (1151°C and 1121°C) below.

3.10.4.1. Change of R2 and R1 Peak Area Ratio with Thermal Cycling

Fig. 3.133 shows the ratio of the integrated area of peak R2 divided by the area of peak R1 as a function of thermal cycles. Similar to the relationship of stress vs. thermal cycling, the area ratio increases initially and then decreases monotonically until failure. The change of area ratio vs. thermal cycles can also be fit using a linear function, excluding the initial transient stage, as shown in Fig. 3.134. Again, the rate of change can be related to specimen life, the shallower the slope, the higher the spallation life. This is the first time that a systematic change of area ratio with thermal cycling has been reported. The magnitude of area ratio for samples falls in the range of 0.35-0.45 which is close to the value of stress–free, randomly oriented polycrystalline α-Al2O3 (reference disk). This indicates that the TGO layer is randomly oriented and does not have preferential orientation.

3.10.4.2. Change of Peak Width and Shape with Thermal Cycling

Peak broadening is a measure of the TGO stress variation within a probed volume (112, 118). Fig. 3.135 shows the peak broadening (full width at half maximum (FWHM) height for the R2 and R1 peak) as a function of thermal cycles at 1151°C and 1121°C. No significant change in peak width was observed with thermal cycling.

There was no significant change of peak shape (as measured by Gaussian or Lorentzian fractions) with thermal cycling. The Lorentzian fractions were found to remain relatively unchanged with thermal cycling and have values of about 0.11 for the R2 peak and 0.58 for the R1 peak.

3.10.4.3. Change of Bimodal Spectra With Thermal Cycling

Bimodal luminescence spectra were observed during thermal cycling. For the bimodal spectra, the low stress component was usually close to zero (below 0.5 GPa in compression), but occasionally the low stress component reached a maximum tension level of 0.8 GPa. The high stress component ranged from 1.6 to 3.0 GPa in compression. The evolution of the fraction of bimodal spectra with thermal cycling at 1151°C for the TGO under the ceramic top coat, using the fine mapping technique, is shown in Fig. 3.136. The fraction of bimodal spectra shows systematic changes with thermal cycling. The fraction increases initially up to 5 cycles, gradually decreases and then increases again when close to failure. The evolution from coarse mapping shows the same trend as fine mapping.

3.10.4.4. Stress Distribution

Stress mapping was carried out with thermal cycling at both 1151°C and 1121°C. Stress distribution maps based on the bimodal luminescence contribution were obtained. Fig. 3.137 shows one example of a stress distribution map for a specimen cycled at 1121°C. The black regions represent the regions exhibiting bimodal spectra; whereas, the white regions represent the regions showing unimodal spectra. The maps show that the number and size of regions having bimodal spectra increase with thermal cycling. The increase is more pronounced when the sample is close to failure. It is noted that the fraction of bimodal spectra extracted from these maps does not decrease after the initial increase, which is different from the evolution of the fraction of bimodal spectra at 1151°C shown before. The possible reason is that we did not catch the correct time in the early stage to make measurements and missed the data points showing the initial increase and then decrease. However, we did observe that the number and size of regions having bimodal spectra increased when the sample was close to failure for tests at both 1151°C and 1121°C.

3.10.4.5. Relationship of TGO Cracking and Bimodal Luminescence

The back-sides of specimens which were bond coated but not ceramic coated were polished to remove the original thin oxide layer and then heated at 1151°C to form a new alumina scale.

Fig. 3.138 shows an optical image of the alumina morphology after 10 minutes oxidation and the corresponding PLPS spectra. Both unimodal spectra (one set of peak pairs) (Fig. 3.138b) and bimodal spectra (two set of peak pairs) (Fig. 3.138c and d) of α-

Al2O3 were observed. The stress value for the low stress component of bimodal spectra was close to zero. The regions producing bimodal spectra corresponded consistently to microcracked regions (Fig. 3.138a, point 2 and 3); whereas, all regions without visible cracks gave unimodal spectra (Fig. 3.138a, point 1). The fraction of bimodal spectra for the oxide layer without a ceramic top coat as a function of cyclic oxidation time is shown in Fig. 3.139. The fraction increases sharply up to 10 minutes (point a), gradually decreases (points a to c), and then increases (points c to d) again after 100 hours until spallation. The fraction of bimodal spectra for the oxide layer without a ceramic top coat shows the same trend with cyclic oxidation as that for TGO under the ceramic top coat with the initial increase, a subsequent decrease and a final increase before failure.

Fig. 3.140 shows the microstructure of the aluminum oxide surface after different exposure times. The alumina layer, formed on the surface of the bond coat after oxidation for 10 minutes at 1151°C, has a large number of microcracks. With increasing oxidation time, the microcracks start to heal and this result in a decrease in the number of microcracks. In some places, microcracks form outward protrusions (see arrows in the Fig. 3.140b). The density of microcracks reaches a minimum at 100 hours and the grain structure becomes evident. With increasing oxidation time, the alumina scale spalls, accompanied by the appearance of large cracks (Fig. 3.140d). The crack density as a function of time is shown in Fig. 3.141. The density of cracks as a function of oxidation time increases initially, decreases and then increases again after 100 hours. The change of the fraction of bimodal spectra as function of oxidation time is consistent with the change of the density of cracks (compare Figs 3.139 and 3.141). The fraction of bimodal spectra

and the density of cracks exhibit a qualitative relationship and change in a similar manner with thermal cycling.

θ-Al2O3 can be detected by the PLPS method due to the fact that θ-Al2O3 has characteristic luminescence peaks easily distinguished from those of α-Al2O3 (35). Quite fortuitously, two small regions in which a-Al2O3 and a-Al2O3 coexisted were observed to confirm the transformation after the initial oxidation stage. Fig.3.142a shows an optical image of one region in which α-Al2O3 and θ-Al2O3 coexist after oxidation of 10 minutes at 1151°C. The small island of θ-Al2O3 was surrounded by the α-Al2O3 matrix. The existence of α-Al2O3 (R2 = 14420 cm-1) and θ-Al2O3 (R2 = 14613 cm-1) was identified by the different frequencies of the characteristic peaks in PLPS (Fig. 3.142b). Similar results were also obtained after oxidation for 2 minutes. With increasing oxidation time, the relative amount of α-alumina increases by the transformation of θ to αalumina. Fig. 3.142c is an oxide-type distribution area map indicating the distribution of alumina (alpha and non-alpha). The figure shows the initial presence of an island of θ-alumina surrounded by α-alumina. The island is reduced in size, by the transformation of θ to αalumina, after 1-hour exposure, and then disappears after 5 hours.

The aluminum oxide layer formed on the bare bond coat surface starts to become wavy or rumpled after oxidation for 5 hours. The amplitude of rumpling increases with increasing oxidation time (Fig. 3.143). Measurements of the local residual stress in the oxide scale were made using PLPS. Since the oxide rumpling wavelength (the distance between the ridges and the valleys) is sufficiently large, the local stress in the vicinity of

the ridges and the valleys can be resolved with a probe whose size, (about 2 ? m), is smaller than the rumpling wavelength. Figs. 3.144a and b show a typical morphology of rumpled α-Al2O3 scale after oxidation for 100 hr and the frequency shift of this oxide layer from a series of PLPS measurements, respectively. It is clear that the frequency shift is smaller at the ridges than at the valleys. Although the exact stress value cannot be obtained due to the wavy surface, the corresponding hydrostatic compressive stress is smaller at the ridges than at the valleys. This is consistent with finite element calculations (21, 71, 74) and from the expectation that a wrinkled scale produces tensile stress across the coating-metal interface at ridges and compressive stress in the valleys.

The oxide stress measured by PLPS is the overall stress in the small probed volume. The in-plane stress for the oxide is in compression at both the ridges and valleys; whereas, the out-of-plane stress is tensile at the ridges and compressive at the valleys. Thus, the overall hydrostatic compressive stress for the oxide scale at the ridges should be smaller than that at the valleys due to the normal stress contribution. The experimental results which were obtained from PLPS (Fig.3.144) show the frequency shift is indeed smaller at ridges than at valleys.

3.10.5. TBC Life Prediction

Before describing the detailed procedure of remaining life prediction, we want to point out that, different approaches were used to make temperature-blind remaining life predictions based on the TGO stress for specimens tested at two temperatures (1151°C and 1121°C). Here, “temperature-blind” means that all data was

placed together and the methodology did not know which specimen was tested at which temperature. After the prediction accuracy of different approaches were compared, then the best approaches were applied and the predictions were extended for specimens tested at three temperatures.

3.10.5.1. Analysis Procedure

3.10.5.1.1. Description of Data Set and Prediction Methods

The data set consists of 7 samples tested to failure: 5 samples were tested at 1151°C and 2 samples were tested at 1121°C. The lifespan of each sample is known (Table 3.15).

For this TBC, the measured stress and its standard deviation and the R1/R2 peak area ratio are the only spectral characteristics that change systematically with cycles. By dividing the corresponding cycles at which measurements were made by the lifespan of each sample, the corresponding life fraction at which the measurements were taken was obtained. Thus, the original data set has several features: TGO stress, standard deviation of stress, R1 and R2 peak area ratio and the corresponding life fraction at which measurements were taken. In addition, we can extract other features from the original data set such as the first derivative and second derivative of stress with respect to life fraction.

There are, in principle, many ways in which the features can be combined or used separately to make predictions. Two methods were used to estimate the remaining life. First, a straightforward regression approach was used. Second, a method based on

training a neural network was examined. The basic information about neural networks can be found in Appendix II.

3.10.5.1.2. Leave-one-out cross-validation

Leave-one-out cross-validation (131) was adopted as a means of assessing the predictive capabilities of the neural network approaches. In this approach, all data sets except one are used to train the neural network, and the predictive capacity of the network is tested by making a prediction of the data set left out. By repeating the procedure, leaving out each data set in turn, prediction accuracy measures such as average error, root mean square (RMS) error and maximum error of prediction can be determined in an unbiased way. The hypothetical prediction task provides a basis for making a decision whether to re-use or replace a given part during a regular inspection. The PLPS measurements are used to make the life prediction. Accordingly, the data for each test sample must be based on the PLPS measurements up to but not after the chosen inspection time.

3.10.5.2. Remaining Life Predictions Based on Regression

3.10.5.2.1. Prediction Using Stress vs. Life Fraction

The assessment of the predictive ability of the simple regression approach was based on a retirement for cause task in which a part replacement opportunity is available at half the expected life. We will use life prediction at an inspection around half life as an example to illustrate the proposed prediction method in the following. The data set has a total 7 samples at two temperatures 1151ºC and 1121ºC. For each sample, there is

stress vs. life fraction data, as shown in Fig. 3.145. The whole data set was fit using a quadratic polynomial function to get the master curve (solid line in Fig. 3.145). To make a prediction for an individual sample, the sample's stress vs. cycle data up to the last inspection at roughly half-life is fit to a quadratic function. The intersection of the quadratic line with the stress from the master curve corresponding to 50% life fraction (S=1.79 GPa) yields the number of cycles corresponding to half life for the individual sample and its predicted life is exactly twice the life at the point where the extrapolated stress curve reaches the stress on the master curve corresponding to half life. The prediction accuracy can be calculated from the difference between the actual and predicted lives.

The prediction results are shown in Table 3.15. The average value of absolute error is 11.2%. The root mean square (RMS) error of prediction is 12.4% and the maximum absolute error is 19.4%. It is worth noting that the above results are only an example showing the prediction at around half-life. In fact, depending on the stress level obtained from inspection (one stress measurement is the extreme case), corresponding life fractions predicted from the master curve can be obtained and the total life can be calculated from this life fraction and the number of cycles at which the sample is inspected.

There is inevitably uncertainty in prediction using the regression mean curve. In an engineering context, one is interested in how much reduction in expected usable life is required to achieve reduced probability of an unexpected failure. Statistical methods were used to study this uncertainty on the limited specimens available. It was found that two-parameter Weibull distribution represented life data pretty well (Fig. 3.146). The

resulting cumulative distribution from this Weibull distribution is shown in Fig.3.147. Using this distribution function, it is possible to estimate the reduction in expected remaining life fraction that is required to have various levels of increased reliability against having a failure before the end of the expected remaining life fraction. This for example could be used to determine when the next inspection should be done or in making a decision to remove a part or continue running it. Table 3.16 shows results for PLPS inspections running at life fraction 25%, 50% and 75 % from the master curve. The values in the table show the allowable remaining life if the chance for a part reaching that life is to be 50%, 90% or 95% according to the Weibull analysis. For example, at the measurement at 50% of life, there is 50% of reliability that the remaining life is equal to or more than 49.6% while the reliability that the remaining life is equal to or more than 31.4% is 90%. We note that for a sample set as small as the present one, these are just engineering estimation that will be increasing questionable for tail ends of the distributions such as for prediction of very high reliabilities.

3.10.5.2.2. Prediction Using Peak Area Ratio and Standard Deviation of Stress vs. Life Fraction

Figures 3.148 and 3.149 show the peak area ratio and standard deviation of stress, respectively, as a function of life fraction for all samples. Following the same procedure of section 4.1.5.2.1, life predictions can be separately made using R1 and R2 peak area ratio vs. life fraction and standard deviation of stress vs. life fraction. The corresponding results are shown in Tables 3.17 and 3.18. It is shown that the predictions using the peak area ratio (RMS error 23.9%), and standard deviation of stress (RMS error 30.3%), vs.

life fraction were worse than those using the stress vs. life fraction (RMS error 12.4%). This is probably due to the fact that the change of area ratio and standard deviation of stress as a function of life fraction are relatively temperature sensitive, which makes the data more scattered. In contrast, the change of stress as a function of life fraction is nearly temperature independent, which leads to a master curve representing all sample behavior fairly well; thus, the predicted results are better.

3.10.5.2.3. Prediction Using The Weighted Average of Three Features

The regression approach was used to make remaining life predictions based on all three features: TGO stress, peak area ratio, and standard deviation of stress vs. life fraction. A simple weighted average method was used to combine the three features and the results are shown in Table 3.19. The weighting factors for a given data feature were selected to be inversely proportional to the root mean square error found in regression predictions using that particular feature alone. As would be expected, the results were better than those based on the area ratio and standard deviation of stress vs. life fraction, but worse than those based on the stress vs. life fraction. The RMS error of the prediction was 19.3%. Therefore, predictions based on combination of multiple features by simple weighted average were inferior to those made using stress alone.

3.10.5.3. Remaining Life Predictions Based on Neural Network

3.10.5.3.1. First Neural Network Method

The input features into the training network are:

– Stress (smoothed, Fig. 3.150a)

– First derivatives of stresses (smoothed, Fig. 3.150b)

– Standard deviation of stresses

– R1 and R2 peak area ratio

– Second derivatives of stresses (smoothed, Fig. 3.150c)

The output is the predicted remaining life fraction at certain time points of measurements.

The results are shown in Table 3.20. It was found that the prediction is better for reduced measurements (three measurements) than for full measurements (five measurements). One possible reason for this is that the measurements prior to failure are noisier than those at the beginning of test. The comparison of the radial basis function network and generalized regression neural network (GRNN) did not show a significant difference in performance. Compared with the simple regression method or weighted average method, some accuracy has been gained by using neural networks, which allow simultaneously use of multiple features. For the data containing three measurements, the RMS error is 10.0% for the radial basis function network and 8.2% for the GRNN, respectively. However, the benefit of using neural network with this method is modest. As mentioned before, we think it is probably due to the fact that the change of area ratio and standard deviation of stress as a function of life fraction is relatively temperature sensitive, which makes the data more scattered. This increases the difficulty of pattern recognition by neural network and decreases the accuracy of prediction.

3.10.5.3.2. Second Neural Network Method

Recognizing that there is temperature sensitivity for the area ratio and standard deviation of stress, a second neural network method was developed. First, the stress vs. life fraction data was fit with a quadratic polynomial function to get the master curve (dashed line in Fig. 3.151), as was done before in the regression method. Second, the stress and the pseudo life fraction (pseudo LF) derived from the master curve were used in training neural networks and fit to the actual life fraction of samples at various times of measurement. So the input features used in training the network are:

– TGO Stress

– Pseudo life fraction (pseudo LF) at which the stress was measured that we derived from the master curve

The output is the predicted remaining life fraction at certain points in time.

The results are shown in Table 3.21. The prediction again is better for reduced measurements (three measurements) than for the full measurements (five measurements). Compared to the first method, it is shown that the accuracy of prediction is significantly better. We conclude that with the reduced measurements of current data, the radial basis function network combined with the master curve gives the best prediction results. The RMS error is 6.1% and the maximum absolute error is 8.2%, both of which are encouraging.

3.10.5.4. Remaining Life Predictions for Specimens Tested at Three Temperatures

Based on the above results, two approaches were chosen to predict remaining life for specimens tested at the three temperatures. One is the regression method based on stress alone (Fig. 3.152), the other is the radial basis function network combined with the master curve. The prediction accuracy is shown in Table 3.22 and 3.23. Finally, the performance of predictions was compared with the inherent variation in spallation lives of all samples tested at three temperatures and the results are shown in Fig. 3.153. The standard deviations of predictions using training neural network and regression method are 6.6% and 14.7%, respectively, which are much improved compared to the inherent variation of spallation lives of 34.6%.

3.11. Results of NiCoCrAlY Bond Coated TBCs

3.11.1. Characterization of Bond Coat Surface Before YSZ Deposition

As described in section 3.1.2, different surface finishing processes were carried out before TBC deposition in order to study the effect of surface roughness on the durability of NiCoCrAlY bond coated TBCs. Two surface finishing processes include: (1) as-received; (2) 90 minutes' centrifugal barrel finishing. Figure 3.154 shows one example of as received bond coat surface. It is shown that the surface of this specimen is very rough and has very large ridges. The height between peaks and valleys within sample (PV) is 18.6 μm.

Figure 3.155 shows one example of barrel finished bond coat surface. The surface roughness of specimen after centrifugal barrel finishing decreases significantly compare

to the as-received specimen. The PV value is 5.6 μm. The change of surface roughness proves that centrifugal barrel finishing is very successful in removing large ridges.

The summary of surface roughness data after various surface finishing treatments is shown in Fig. 3.156. It is apparent that surface roughness of specimens decreases dramatically after barrel finishing. The average surface roughness (Ra) of as-received specimens is 2.6 μm. The surface of specimens after barrel finishing is smoother and the average surface roughness (Ra) of specimens after barrel finishing is 0.4 ? m.

As described in section 2.2.2, a parameter more directly related to the failure mechanism is the localized radius of curvature of the bond coat surface, rather than Ra or Pv. The surface geometry of specimens is characterized using a surface curvature map, a novel method developed in this study. The detailed procedure of developing the surface curvature mapping software is described in Appendix III. Fig. 3.157 shows one example of the original surface and the corresponding curvature maps for as-received and barrel finish bond coat surfaces. As shown in Fig. 3.157, the average roughness of the bond coat surface before barrel finishing is higher than that after finishing by a factor of three, but the curvature before finishing is smaller than that after finishing, which indicates that the asperity of the barrel finished surface is sharper and more severe.

Fig. 3.158 shows the surface morphology of a bond coat. Cavities were found on the as-received bond coat surface. After barrel finishing for 90 minutes, there is bond coat loss and the size and depth of both ridges and cavities decreases. On the other hand, some scratches were introduced.

The TGO layer formed after pre-oxidation and before YSZ deposition was studied using PLPS. From observation of PLPS, no θ-Al2O3 is shown (Fig. 3.159) in any of the specimens regardless of surface conditions. All specimens contain stable α-Al2O3.

3.11.2. Microstructure of As-Coated TBCs

After bond coat processing and characterization, all specimens were sent for deposition of YSZ coating. The as-coated EB-PVD YSZ coating consists of a non-equilibrium tetragonal (t') phase. The cross-sectional micrograph of the as-coated TBC is shown in Fig.3.160. The YSZ topcoat has a nominal thickness of 145 μm with a columnar structure. The NiCoCrAlY bond coat is nominally 100 μm thick. The bond coat has a characteristic two-phase structure. The dark region is β-NiAl phase, and the light region is γ-Ni solid solution. A thin, continuous TGO layer (~ 0.5 μm) was observed for the as-coated TBCs. Below the relatively uniform TGO layer, TGO protrusions or embedded oxides were also found (see arrows in Fig. 3.160b and c). These imperfections originate from the shot-peening and heating treatment of the NiCoCrAlY bond coat prior to the deposition of the YSZ coating.

3.11.3. Spallation Life and Microstructural Evolution

One-hour thermal cycling tests were conducted at 1121°C and the spallation lifetime for specimens is shown in Fig. 3.161. The average spallation life for specimens with the as-received bond coat surface is 102 cycles and the average spallation life for specimens after barrel finishing is 98 cycles. Both types of specimens show fairly short

lives compared to the typical lifetime for EB-PVD MCrAlY TBCs, which is around 500-700 cycles (39). The reasons why all the specimens have short spallation lives have been studied and the detailed explanation can be found in ref. (132).

No significant changes in the surface morphology or the phase constituents of the YSZ coating were observed during thermal cycling. Microstructural evolution of TBCs is shown in Fig. 3.162. During thermal cycling, TGO thickness increases and recession of the two-phase ($\beta + \gamma$) region occurs. β- to γ- phase transformation occurs in the bond coat and the γ-phase grows at the expense of the β-phase. The quantitative results of TGO growth and recession of the two-phase region will be described in section 4.2.5. Formation of oxide-filled cavities containing non-α-Al_2O_3 oxide was found in the embedded oxides as shown in Fig. 3.163. The non-α-Al_2O_3 oxide in the cavities contained Cr-rich oxide and Y-rich oxide identified by EDS analysis (Figs. 3.164 and 3.164). The XRD pattern of the bond coat surface after spallation indicates that the phase constituent of the Y-rich oxide is $Al_5Y_3O_{12}$ (Fig. 3.166). Fig. 3.167 shows example of the TGO/bond coat interface rumpling during thermal cycling. TGO penetrates into the underlying NiCoCrAlY bond coat, similar to that in (Ni,Pt)Al bond coated TBC. However, contrast to (Ni,Pt)Al bond coated TBC, the rumpling is more limited and the amplitude of the largest displacement is only about 2 μm. No cracking or apparent damage were observed at TGO/TBC interface due to rumpling, even after separation of the TGO/BC interface due to increased strain energy.

Fig. 3.168 shows the macrographs of the failed specimens. The specimens spalled catastrophically into many small pieces. Prior to failure, limited spallation was observed originating from specimen edges (Fig. 3.168b). The top view of the spalled

surface on the bond coat side is shown in Fig. 3.169. The spalled surface consists primarily of bond coat, indicating that the failure occurs predominantly at the TGO/bond coat interface. The cross-sectional SEM image of the failed specimen is shown in Fig. 3.170. Consistent with the top view, the failure interface is predominantly at the TGO/bond coat interface. The area fraction of exposed bond coat surface is around 90%.

3.11.4. TGO Stress Evolution

The TGO stress was measured as a function of thermal cycles using PLPS. One typical example of PLPS spectra during thermal cycling is shown in Fig. 3.171. No evidence for θ-Al2O3 was found at any point of cyclic life. The TGO stress evolution is shown in Fig. 3.172. The average TGO stress in the as-coated condition ranges from 2.8 to 3.5 GPa. The compressive stress increases to the maximum stress (about 4.0 GPa) in the first 25 cycles and then remains relatively unchanged until failure. The fact that the TGO stress remains constant until failure makes it impossible to use this PLPS spectral characteristic to predict the TBC life.

Fig. 3.173 shows the standard deviation of stress as a function of thermal cycles. The standard deviation in stress has a tendency to increase with thermal cycles, which indicates that progressive TGO damage is occurring. However, the large data scatter within different samples precludes the possible use of the standard deviation of stress in life prediction. In previous study (39) on another EB-PVD MCrAlY bond coated TBC with life around 500-700 cycles, the TGO stress increases initially, remains relatively unchanged, and then sharply decreases prior to the final spallation failure. In addition, the final decrease in the stress is accompanied by a sharp increase in the standard

deviation of the stress. The systematic change of the TGO stress and its standard deviation has been used in life predictions (127). We think that the specimens in the present study did not show such behavior in stress, probably because the specimens failed prematurely.

3.11.5. TGO Thickness and β-depletion

The TGO grows with thermal cycling as shown in Fig. 3.174. TGO growth satisfies parabolic growth kinetics. The average TGO thickness at failure was around 4 μm. Along with the growth of the TGO, the β- to γ- phase transformation occurs in the bond coat and the γ-phase grows at the expense of the β-phase.

The thicknesses of both the lower and upper β-depletion zones were measured as a function of thermal cycles (Fig. 3.175). The recession of the two-phase (β + γ) region satisfies the parabolic growth law and the recession coefficient for the lower depletion zone was larger than for the upper depletion zone. The rates of TGO growth and two-phase recession were both parabolic, suggesting that both processes are controlled by diffusion.

As an attempt to non-destructively measure TGO thickness, TGO thickness was also measured using AC impedance by Jentek Sensors Inc.. The information about AC impedance measurement is described in Appendix IV. The thickness measured by AC impedance was compared to that measured by metallography. As shown in Fig. 4.80, the lift-off change measured by AC impedance matched the TGO thickness measured by metallography fairly well, except for specimen 1 at high cycles.

4.2.6 Life Prediction Based on TGO Stress, TGO Thickness and Curvature of Bond Coat Surface

The failure of this NiCoCrAlY bond coated TBC is predominantly at the TGO/bond coat interface. The high strain energy stored in the TGO layer plays an important role in driving the failure. Based on microstructural observations and the results of a previous study (75), the proposed failure scenario is as follows: first debonding occurs at ridge tops at a critical value of the tensile normal stress (? n (critical)) at the bond coat/TGO interface (Fig. 3.177) and then several ridge top debonds of sufficient size results in unstable fracture driven by the strain energy in the TGO. Therefore, a preliminary life prediction approach was proposed based on the measurement of initial bond coat surface geometry, TGO stress and TGO thickness, and correlating these properties by fracture mechanics as described below.

As described in section 2.2.2, the tensile normal stress at the ridge tops can be expressed as

(2.2)

where σN is normal (out-of-plane) stress in the TGO/bond coat interface, σ0 is the biaxial stress in the TGO layer, R1 and R2 are the principal radii of curvature at the asperities, hTGO is the oxide thickness. TBC failure occurs at a critical value of σN (75). Thus for specimens with the ridges with smallest radii of curvature, the TGO is relatively thin at spallation; whereas for the ridges with largest radii of curvature, the TGO has to grow considerably thicker before the same σN (critical) is reached.

Conversely, for a given hTGO, the regions having smaller radii of curvature than a minimum will debond according to equation (2.2) and size of the local debonding regions can be obtained if σN, σ0 and (1/R1+1/R2) are known. As shown in the above sections, σ0 was measured by PLPS, (1/R1+1/R2) was extracted from the surface curvature map. For an EB-PVD/(Ni,Pt)Al TBC in the previous study, σN (critical) was found to be 0.3 GPa (75). However, it is reasonable to say that this critical value is different for different TBC. In the present approach, the critical stress value for debonding was derived from the known life data for specien with barrel finish. Then we used this critical stress value as a known input value to predict the life of specimen with as-received surface condition. The critical normal stress value was found to be 2.0 GPa for this TBC.

With thermal cycling, TGO thickness, TGO strain energy and the size of debonded regions increase. When the debonded regions reach sufficient size and the strain energy release rate exceeds the interface toughness, final failure will occur. The TGO thickness required for final failure at this sufficient large debond region can be calculated based on fracture mechanics. Finally, the spallation life is predicted according to this thickness value at failure and the oxide growth rate which can be extracted from the measured data of TGO thickness vs. exposure time.

Based on the above analysis, the flowchart of the life prediction procedure is shown in the Fig. 3.178. First, the surface curvature map is obtained. Second, a specific TGO thickness is proposed as an initial starting point. The continuous debond region at this thickness will be determined based on the equation (2.2). The size of every continuous debond region will be obtained using image analysis. In the third step, whether the largest continuous debond region size reaches the critical size for bulk

spallation or not is determined by fracture mechanics. If it is, then the proposed thickness is the minimum thickness to spallation. If not, then TGO thickness will be increased and then the steps 2 and 3 will be iterated until the minimum TGO thickness to spallation will be found. Finally, the spallation life is predicted based on this minimum thickness to spallation and the TGO growth rate.

Fig. 3.179 shows one example of surface curvature and the corresponding debond region at different TGO thickness. Table 4.11 shows the largest continuous debond region size at different TGO thickness. If we assume this debonded region has the shape as idealized in Fig. 3.180 (133) and near or parallel to the free edge of the specimen, the flaw at TGO thickness h = 4 μm has the shape with W = 8.45 μm and d = 3.45 μm. According to the result from Ambrico and Begley (133) done for such flaw shape (Fig. 3.181), in the present case, d/W = 0.41 and d/h = 0.86 gives a normalized strain energy release rate of G/G0 = 0.37. The available strain energy G0 ( ) is calculated using the TGO thickness and stress measured from PLPS and found to be 65 J/m2. Thus the strain energy release to drive the crack is 24 J/m2, which is greater than 10 J/m2, the fracture toughness of TGO/bond coat interface (134). So the debond region when TGO thickness reaches 4 μm is sufficient to cause unstable fracture of the entire interface.

Fig. 3.182 shows that the prediction results for specimens with two surface conditions: as-received and barrel finish. The predicted and actual lives agree within 15%. It is worth noting that the spallation lives for as-received and barrel finished specimens are comparable, although there are large differences in surface roughness. As shown before, the surface curvature does not vary much although the average roughness

(Ra) does, which indicates that surface curvature is more directly related to TBC life than average roughness.

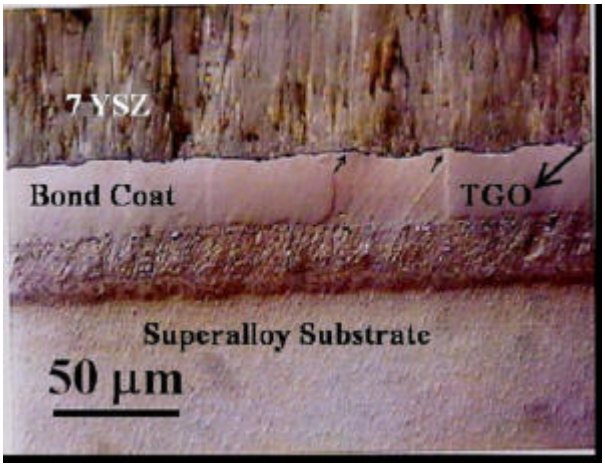

Figure 3.1: Normaski interference optical micrograph showing the as-received microstructure of Type I TBC in cross-section. Small arrows indicate the ridges.

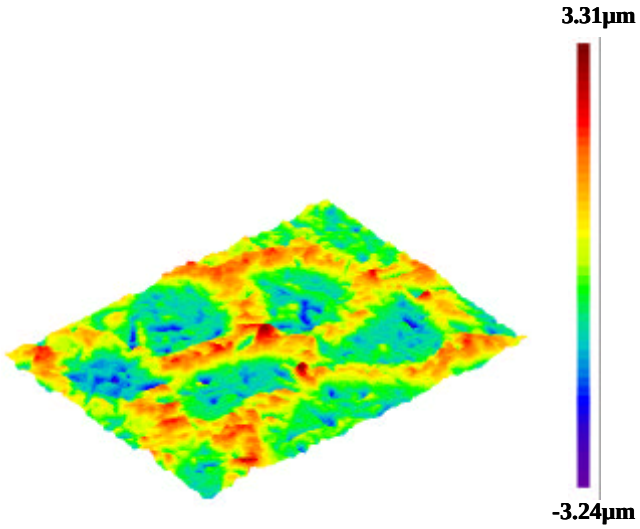

Figure 3.2: A 3-D filled plot of the bare bond coat surface of Type I TBC in plan view obtained using surface interferometry.

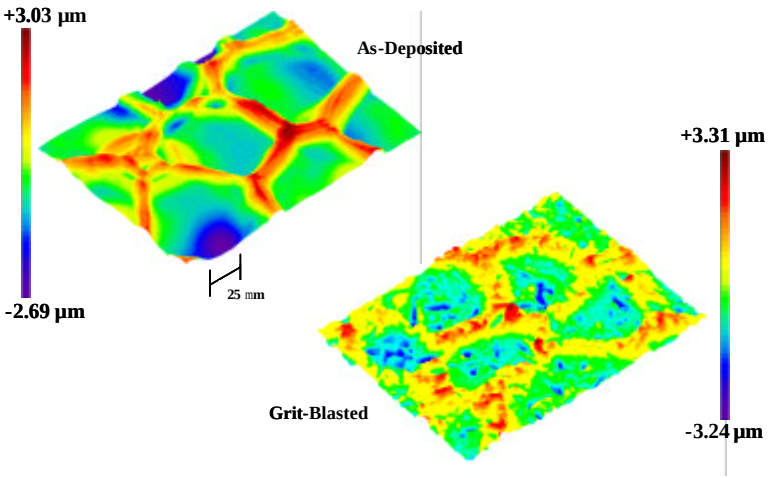

Figure 3.3: 3-D plots of the bare bond coat surfaces of Type I TBC in plan view obtained using surface interferometer showing the bond coat surface morphologies before and grit blasting.

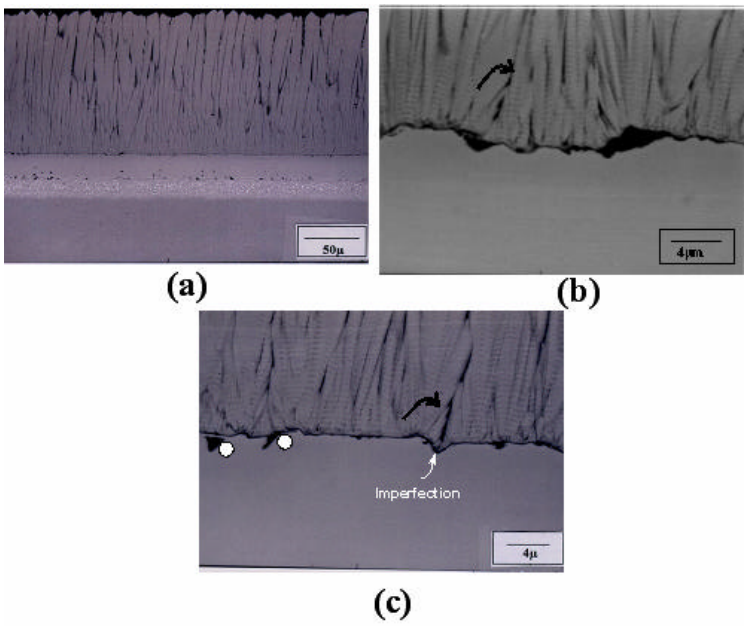

Figure 3.4: Cross-sectional secondary electron micrographs of Type I TBC system in the as-received condition. White arrow points to the TGO displacement into the bond coat and away from the TBC. Black arrow points to the YSZ converging above the region of the TGO displacement. White circle point to the alumina grits.

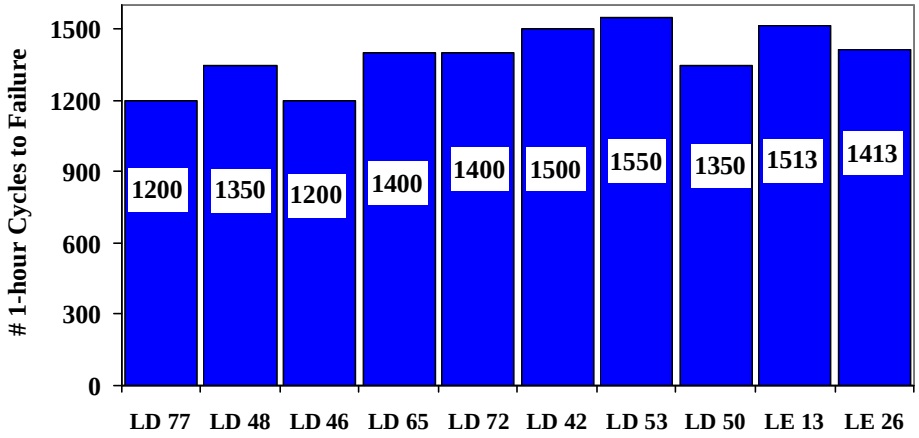

Figure 3.5: Spallation Lives for Type I TBC samples cycled at 1100°C using 1-hour cycles.

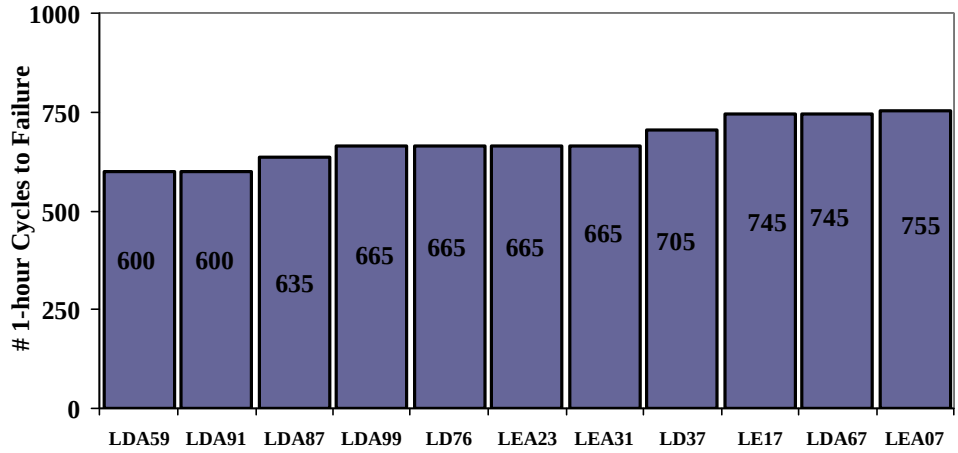

Figure 3.6**:** Spallation Lives for Type I TBC samples cycled at 1121°C using 1-hour cycles.

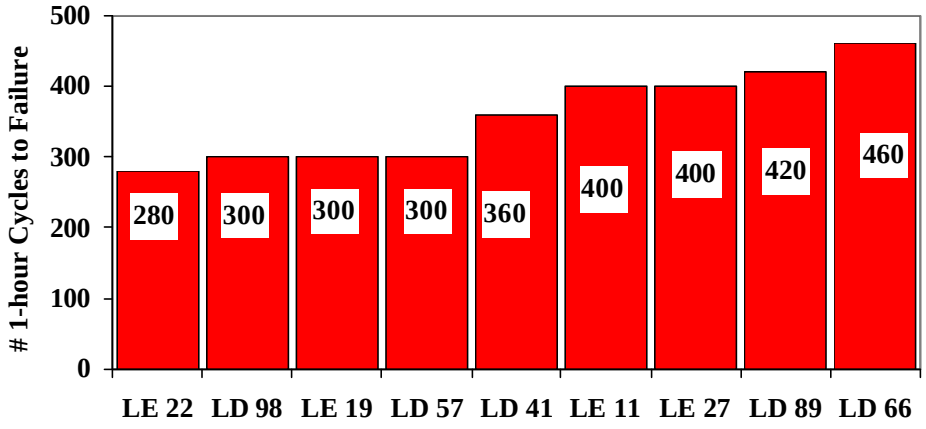

Figure 3.7: Spallation Lives for Type I TBC samples cycled at 1151°C using 1-hour cycles.

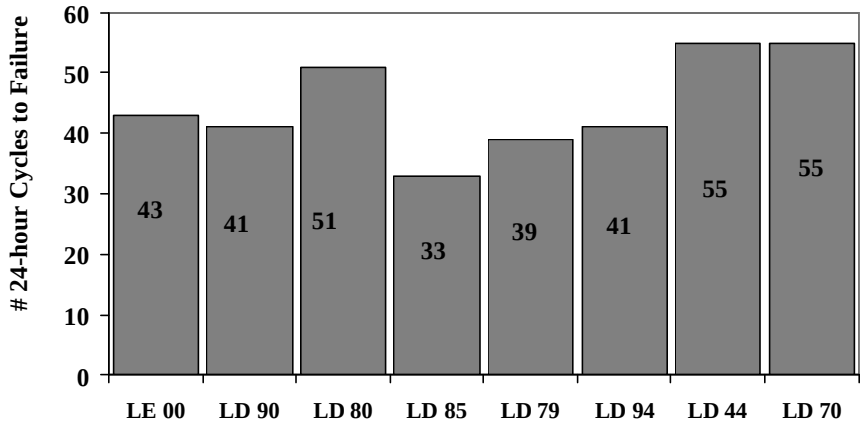

Figure 3.8: Spallation Lives for Type I TBC samples cycled at 1121°C using 24-hour cycles.

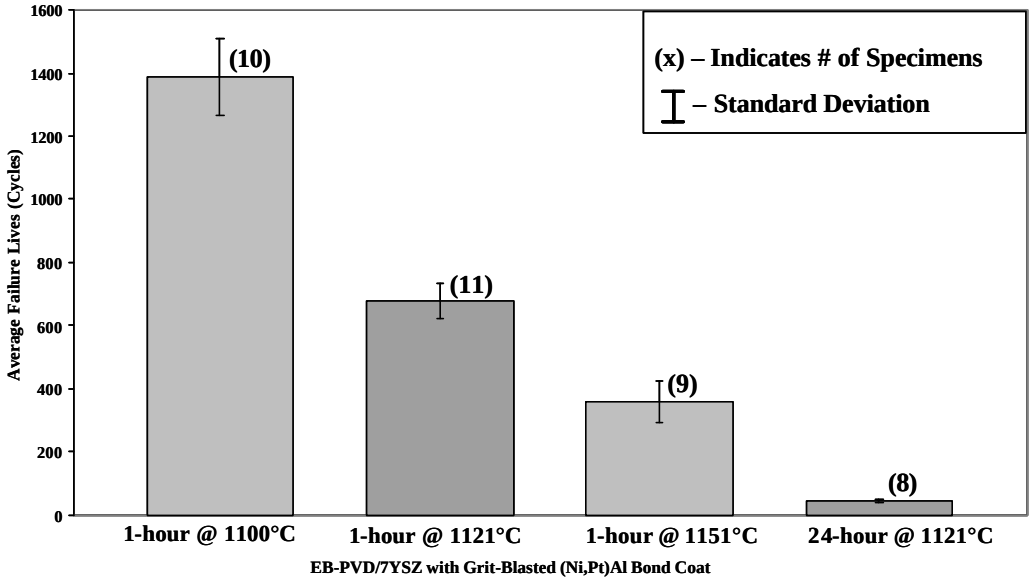

Figure 3.9: Average thermal cyclic lifetime of Type I TBC specimens for various thermal exposures.

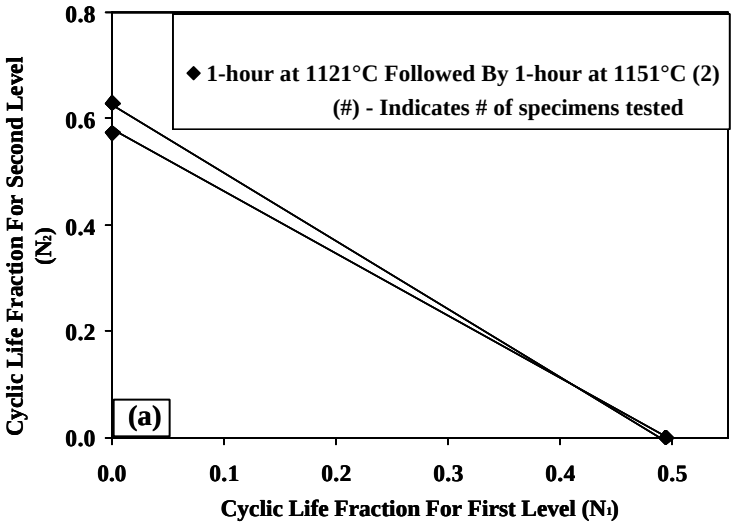

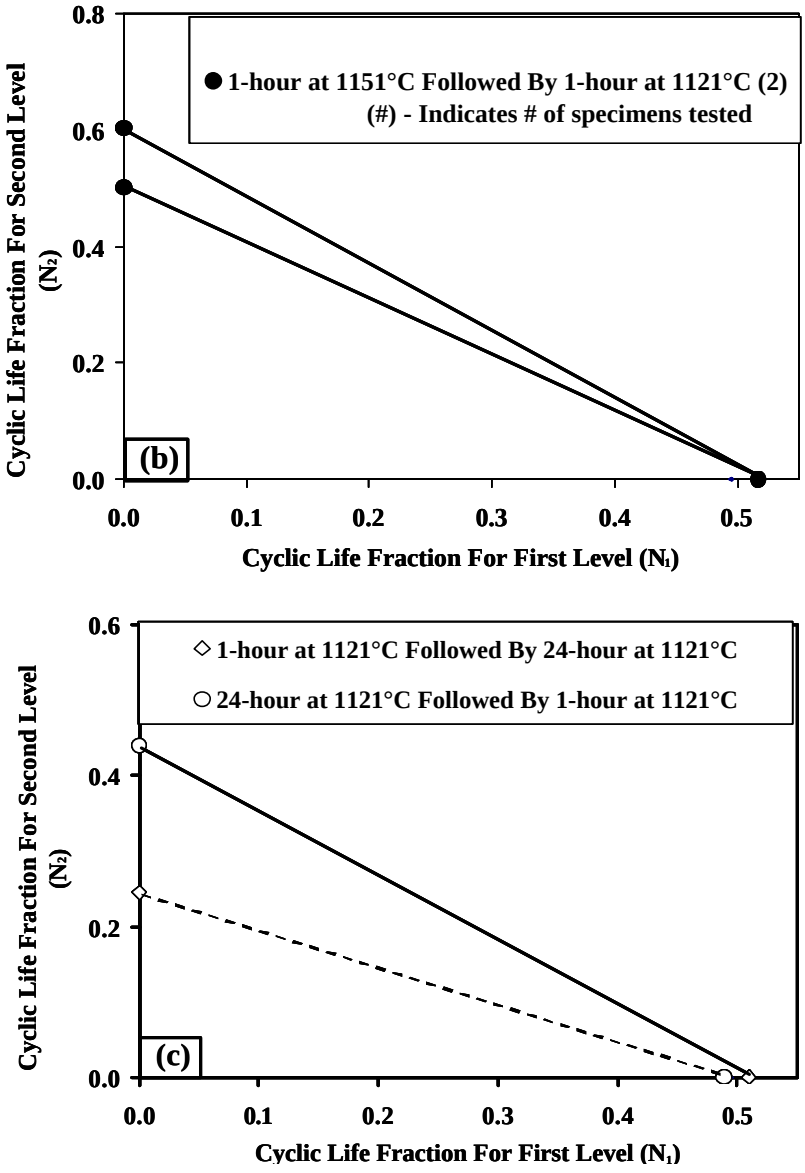

Figure 3.10: Plot of linear damage fractions for Type I TBC during (a) and (b) multi-temperature variable amplitude tests and (c) multiple hold time tests.

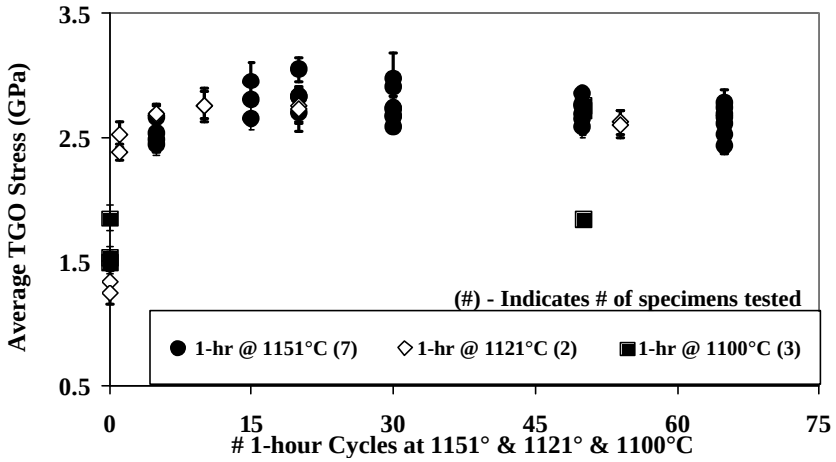

Figure 3.11: Evolution of TGO stress as a function of cycles for Type I TBC, during the first 75 cycles, for the three different cycling temperatures.

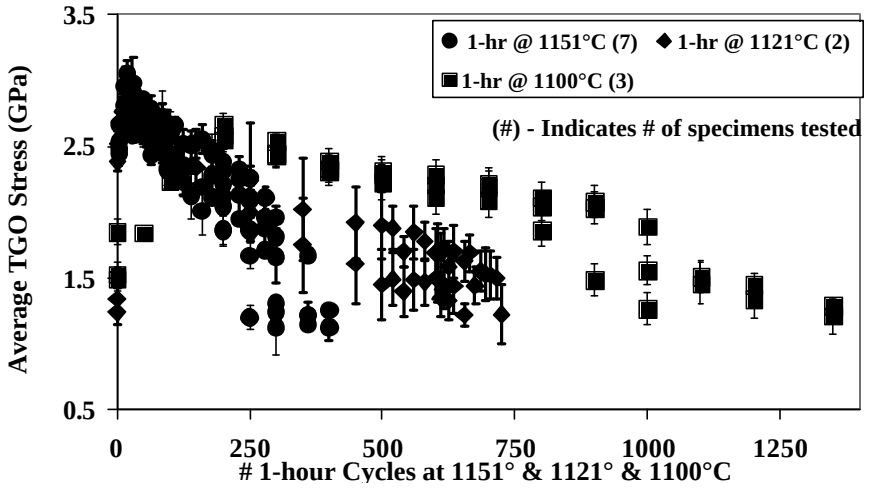

Figure 3.12: Evolution of TGO stress for Type I TBC as a function of cycles for the three different cycling temperatures.

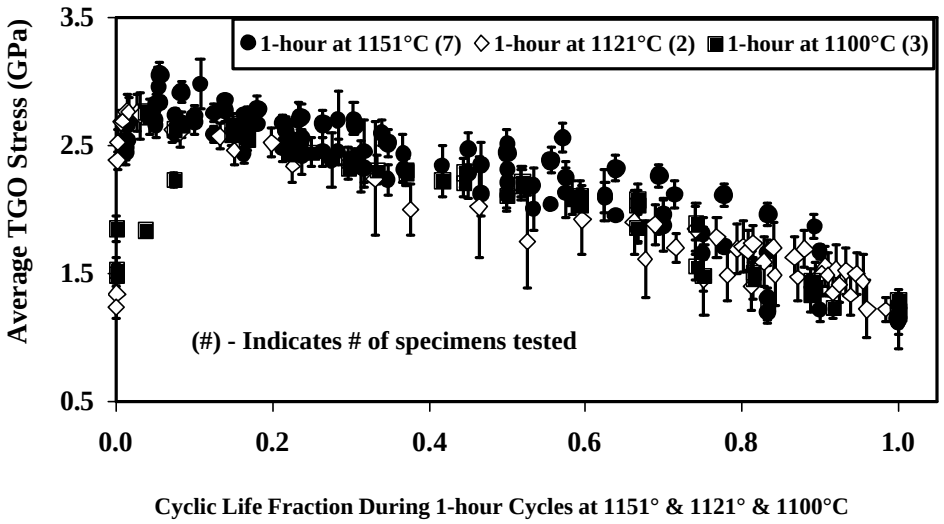

Figure 3.13: Evolution of TGO stress as a function of TBC life fraction for Type I TBC for the three cycling temperatures.

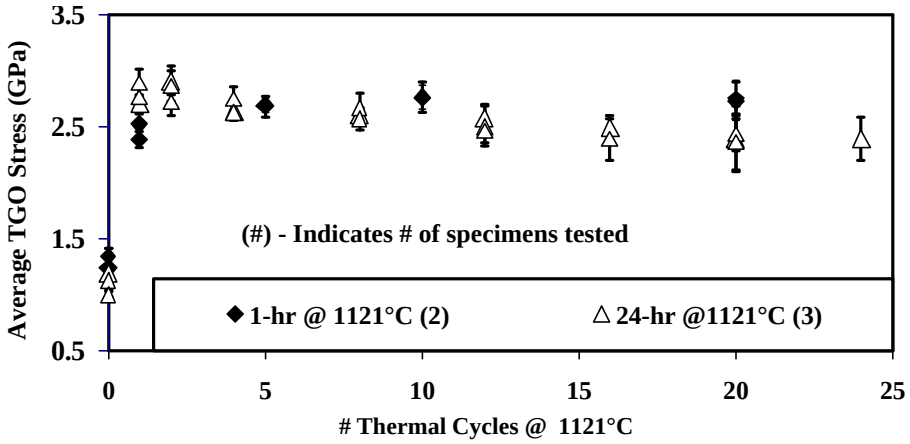

Figure 3.14: Evolution of TGO stress as a function of cycles for Type I TBC during the first 25 cycles for the 1-hour and 24-hour tests.

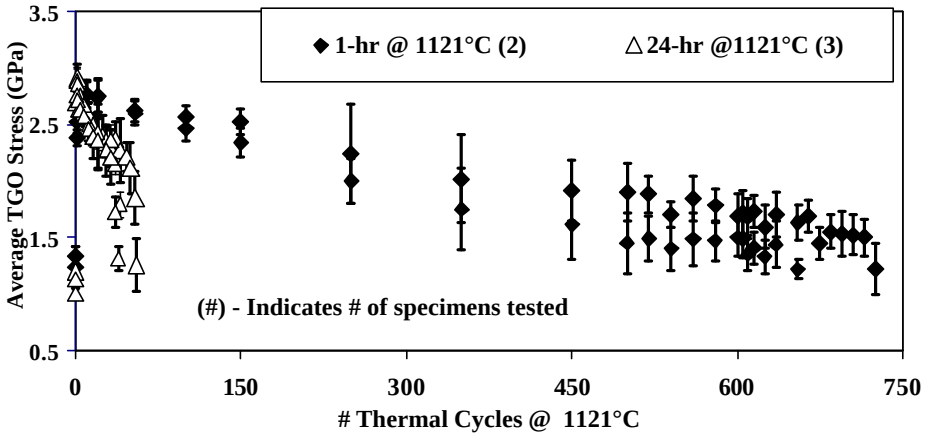

Figure 3.15: Evolution of TGO stress as a function of cycles for Type I TBC for the 1-hour and 24-hour tests.

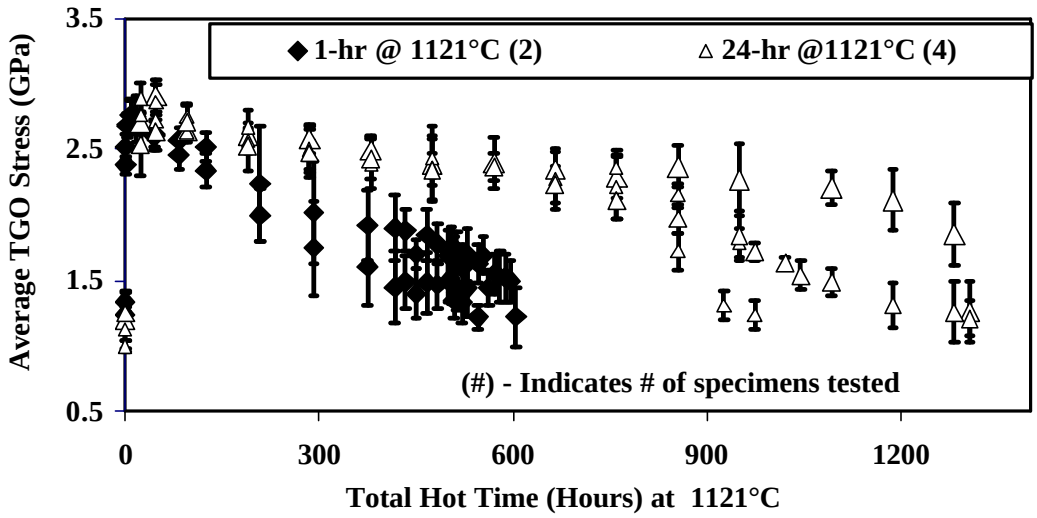

Figure 3.16: Evolution of TGO stress as a function of total hot time at 1121°C for Type I TBC for the 1-hour and 24-hour tests.

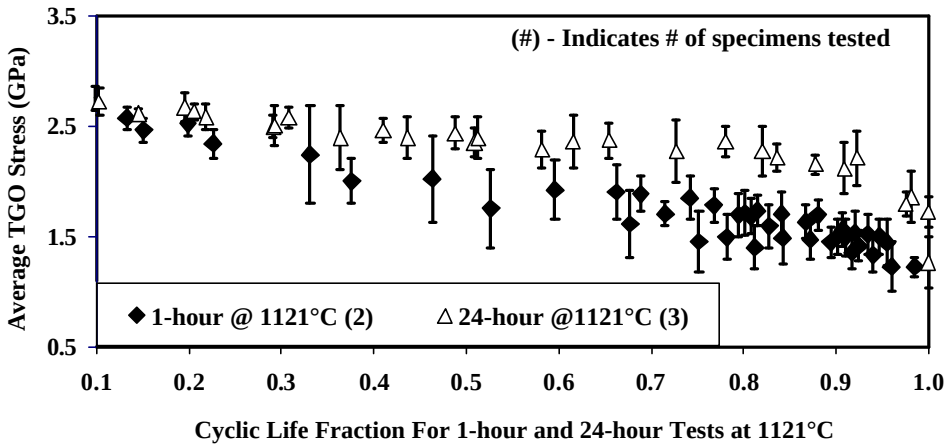

Figure 3.17: Evolution of TGO stress as a function of cyclic life fraction for Type I TBC for the 1-hour and 24-hour tests.

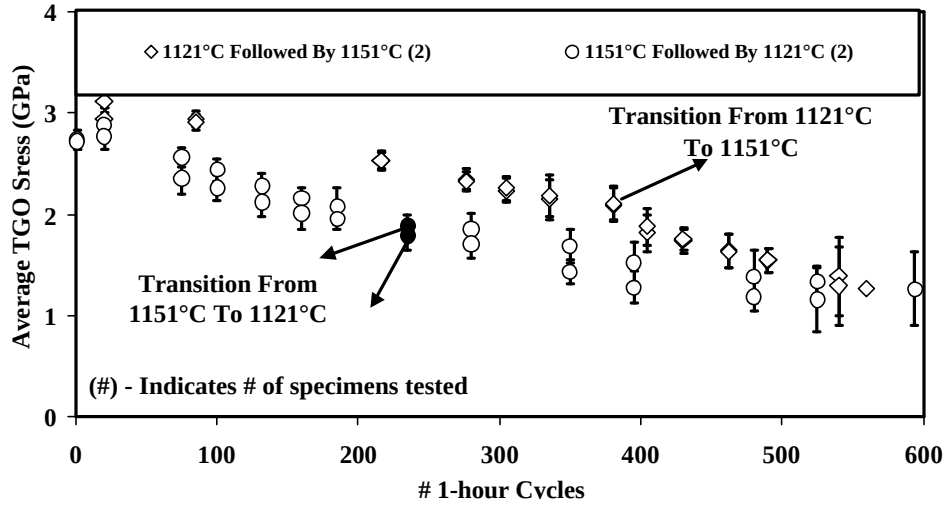

Figure 3.18: Evolution of TGO stress as a function of cycles to failure for Type I TBC for the multi-temperature variable amplitude tests. The filled data points indicate the transition to the high and low temperatures.

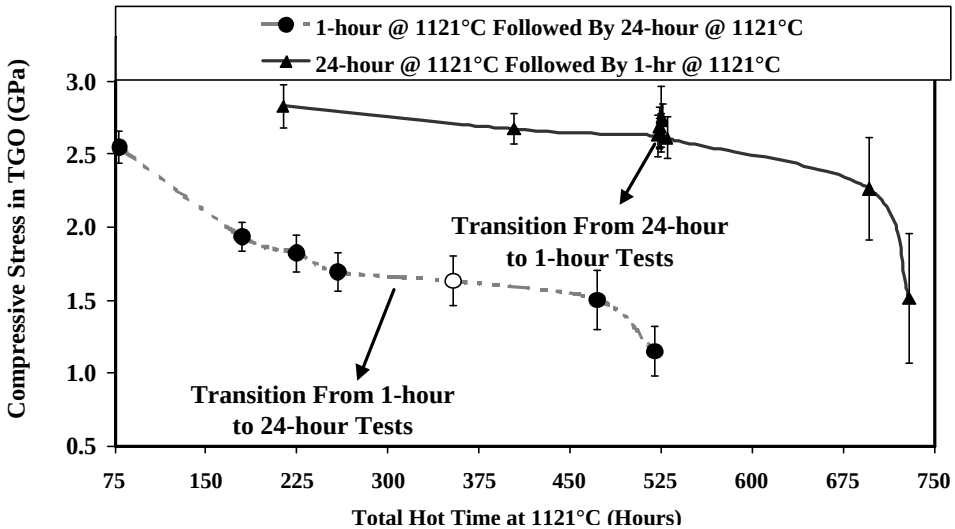

Figure 3.19: Evolution of stress versus hot time at 1121°C for Type I TBC for the multiple hold-time tests.

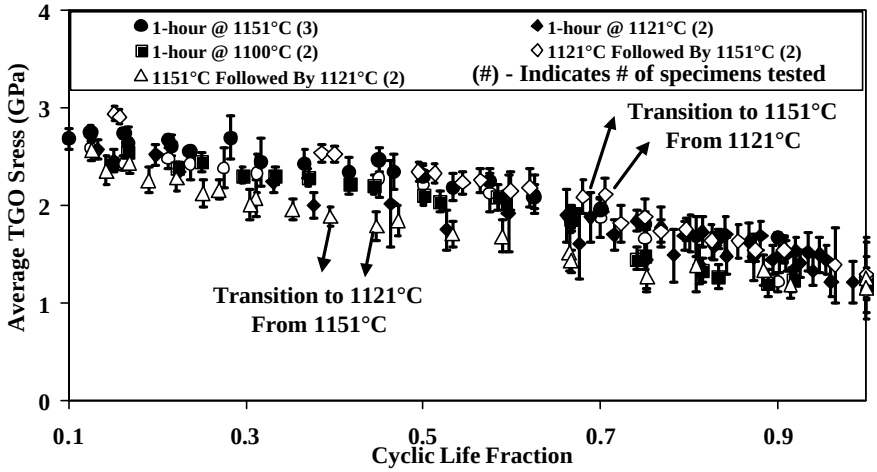

Figure 3.20: Evolution of TGO stress as a function of cyclic life fraction for Type I TBC for the multi-temperature variable amplitude tests. The unfilled data points indicate the transition to the high and low temperatures.

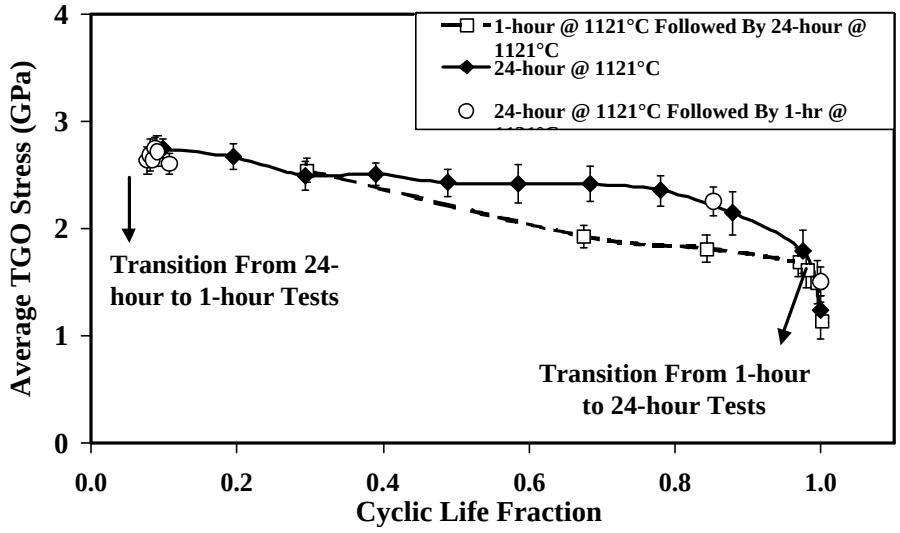

Figure 3.21: Evolution of stress versus TBC life fraction for Type I TBC for the multiple hold-time tests conducted at 1121°C.

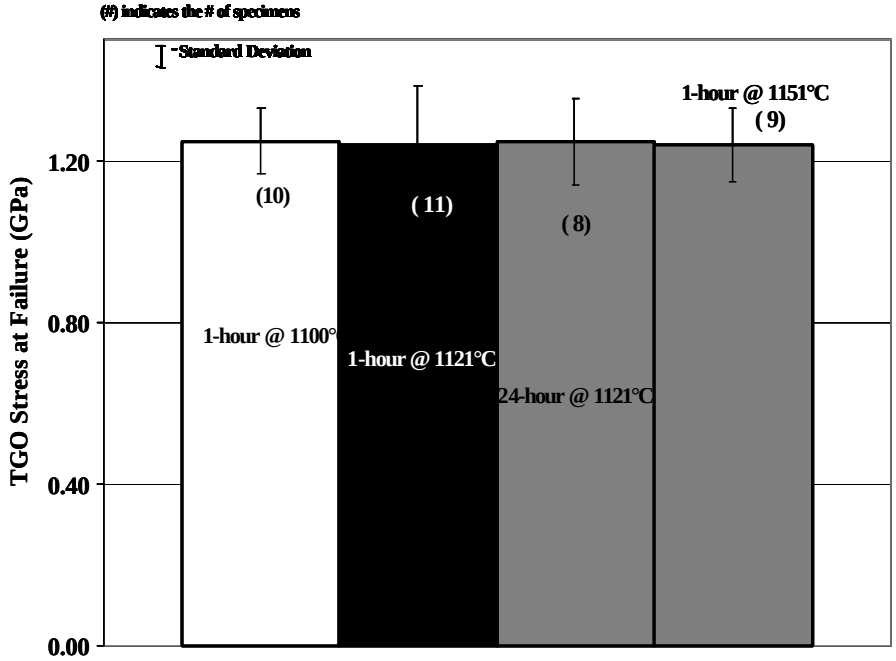

Figure 3.22: Average TGO stress at failure for Type I TBC specimens.

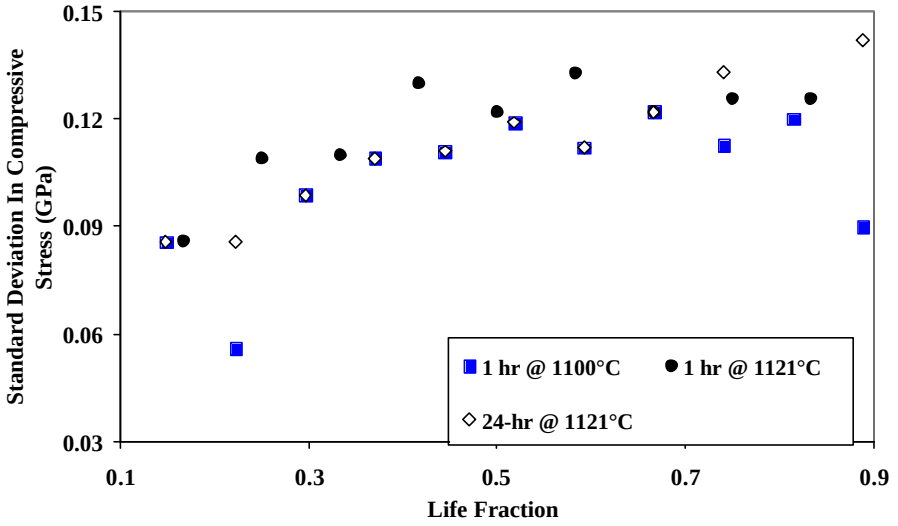

Figure 3.23: Change of standard deviation of the measured TGO stress versus TBC life fraction for Type I TBC the 1-hour and 24-hour tests.

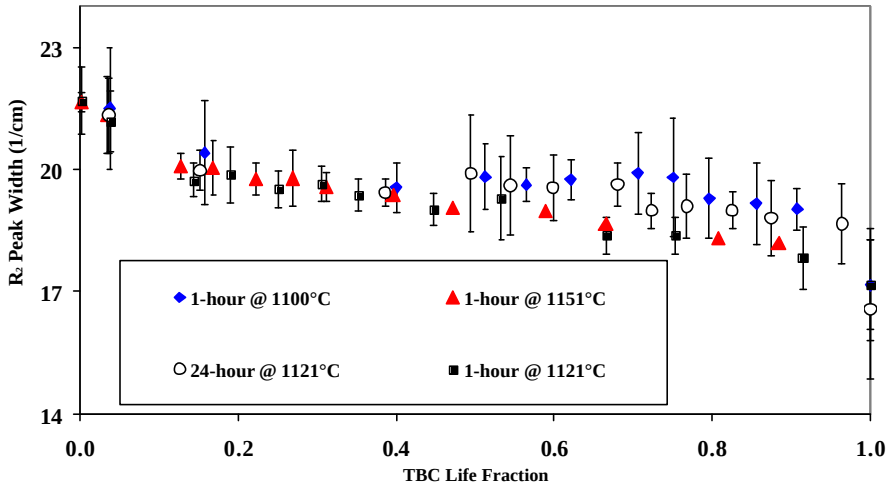

Figure 3.24: Change of R_2 peak width versus TBC life fraction for Type I TBC for the 1-hour and 24-hour tests.

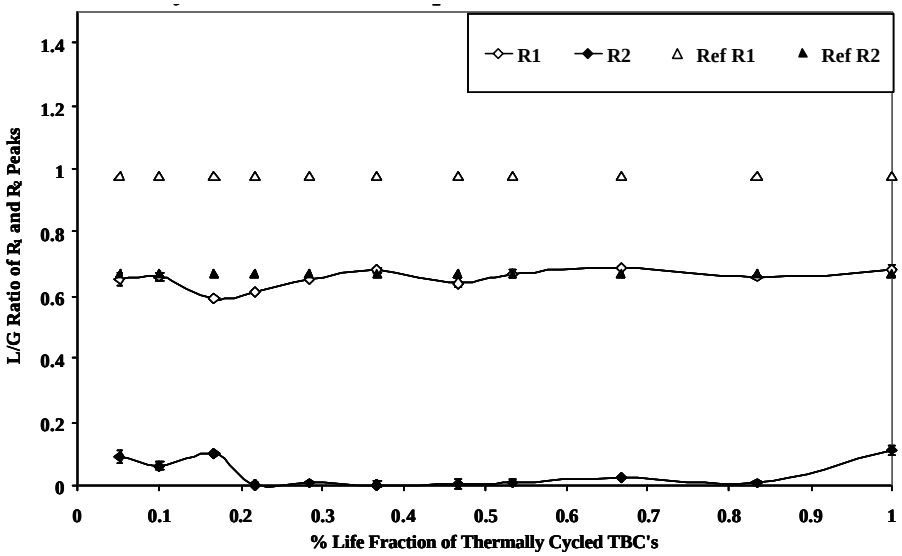

Figure 3.25: Change of the Lorentzian to Gaussian ration of the R_2 peaks versus TBC life fraction for Type I TBC for the 1-hour and 24-hour tests.

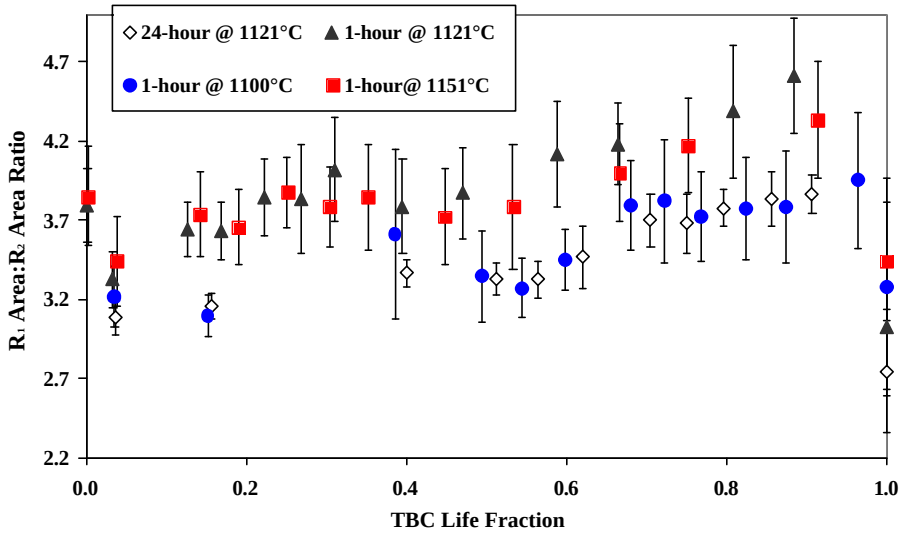

Figure 3.26: Change of the R_1 to R_2 peak area ratio versus TBC life fraction for Type I TBC for the 1-hour and 24-hour tests.

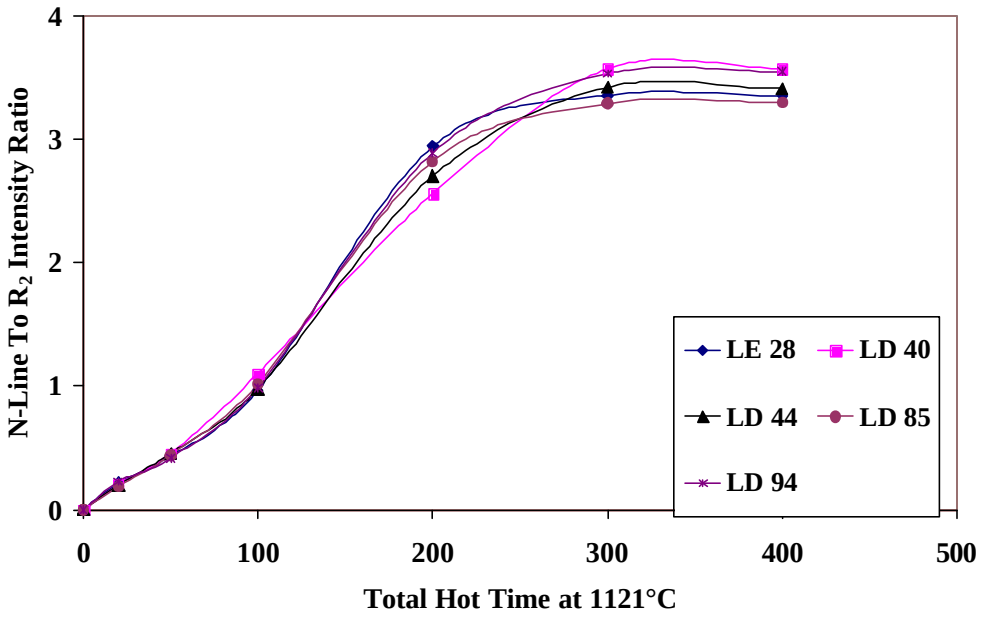

Figure 3.27: Variation of N-line to R2 intensity ratio with 24-hour thermal cycling at 1121°C for Type I TBC.

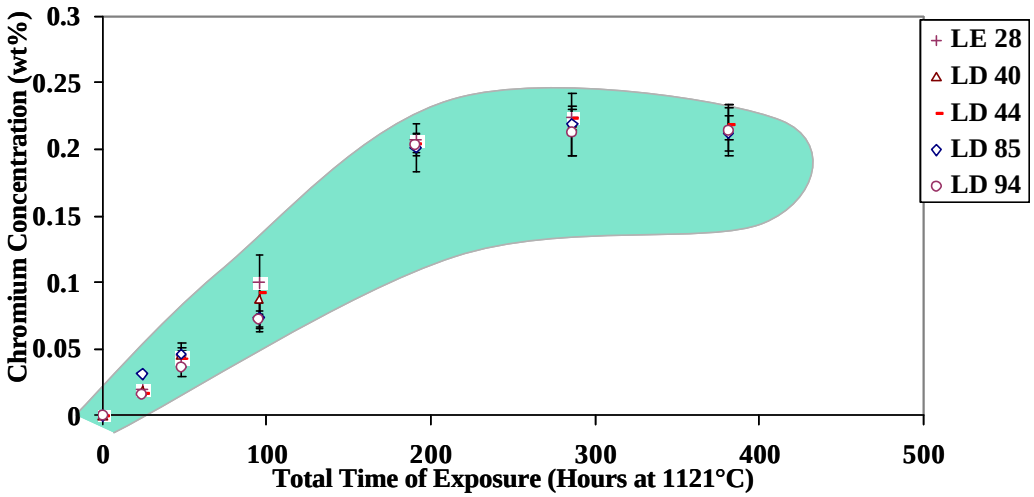

Figure 3.28: Variation of Chromium concentration with 24-hour thermal cycling at 1121°C for Type I TBC.

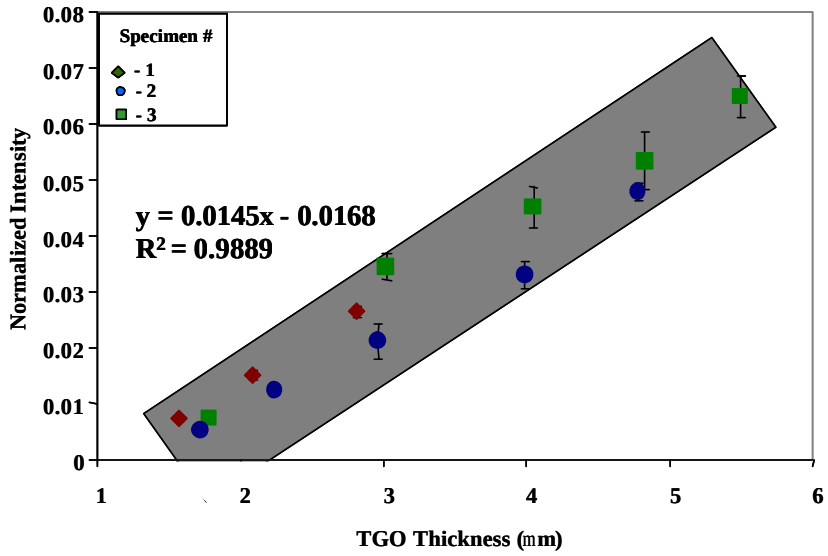

Figure 3.29: Plot of TGO Thickness versus Normalized PLPS Intensity for Type I TBC.

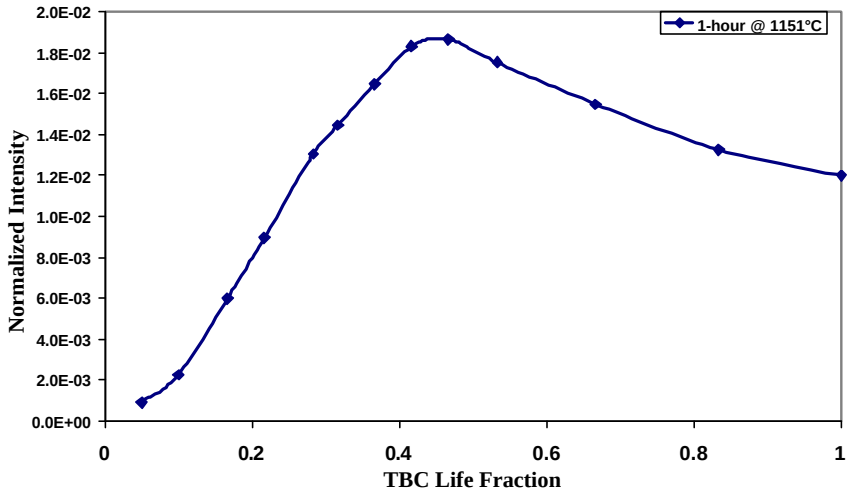

Figure 3.30: Plot of Normalized PLPS Intensity versus TBC life fraction for Type I TBC cycled at 1151°C using 1-hour cycles. Figure shows a drop in the normalized intensity after 45 % TBC life.

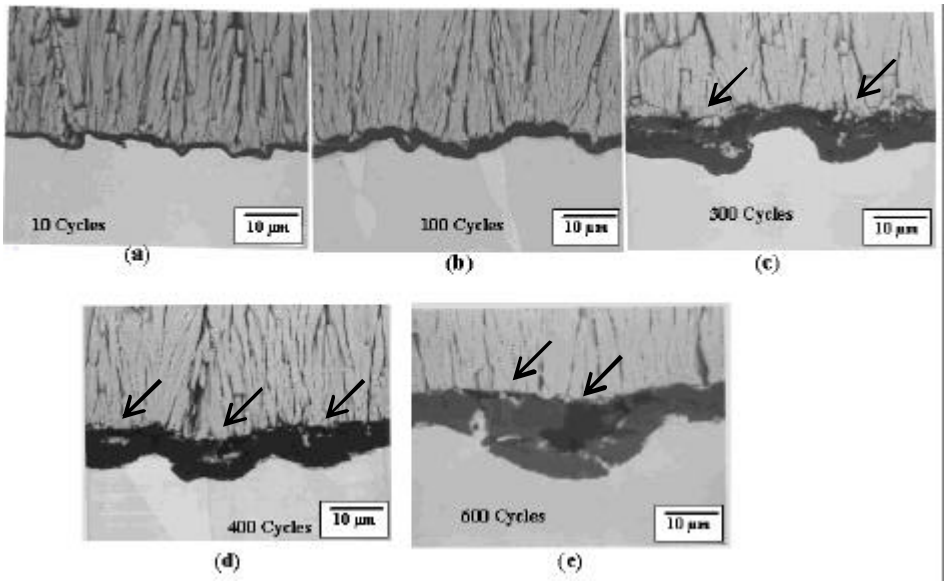

Figure 3.31: Cross-sectional secondary electron micrographs showing the continuous increase in the amplitude of rumpling and cracking at the TBC/TGO interface for Type I TBC during the 1-hour thermal cycling at 1121°C after (a) 10 cycles (b) 100 cycles (c) 300 cycles (d) 400 cycles and (e) 600 cycles. Arrows point to the cracking at the YSZ/TGO interface.

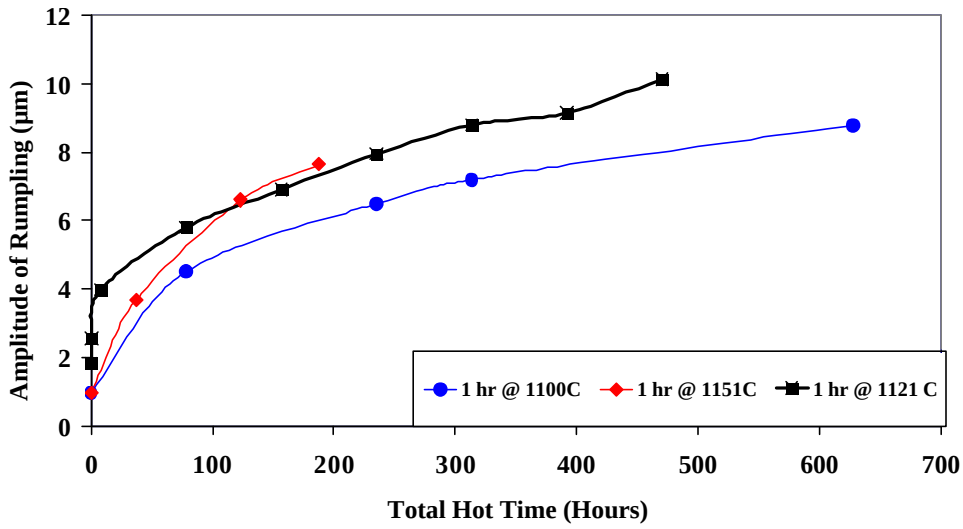

Figure 3.32: Evolution of the amplitude of rumpling as a function of hot time for Type I TBC for the 1-hour tests.

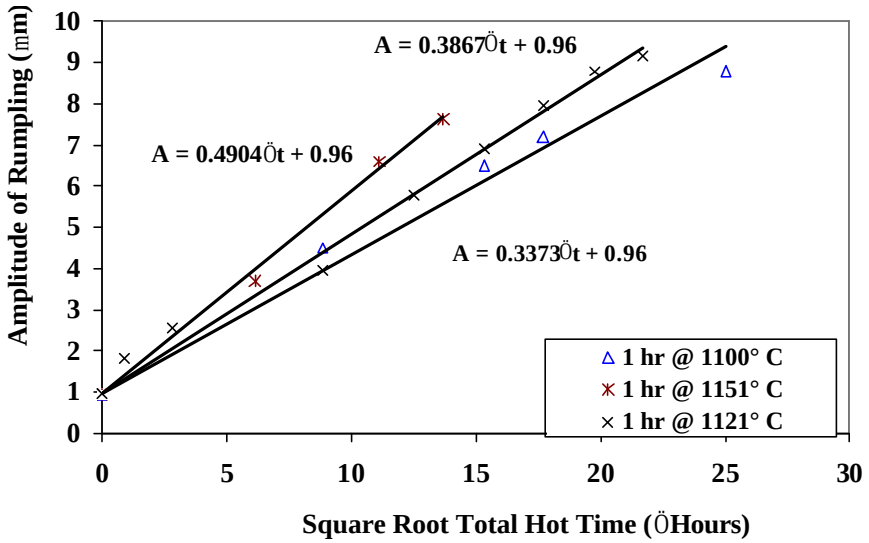

Figure 3.33: Evolution of the amplitude of rumpling as a function of square root of hot time for Type I TBC for the 1-hour tests.

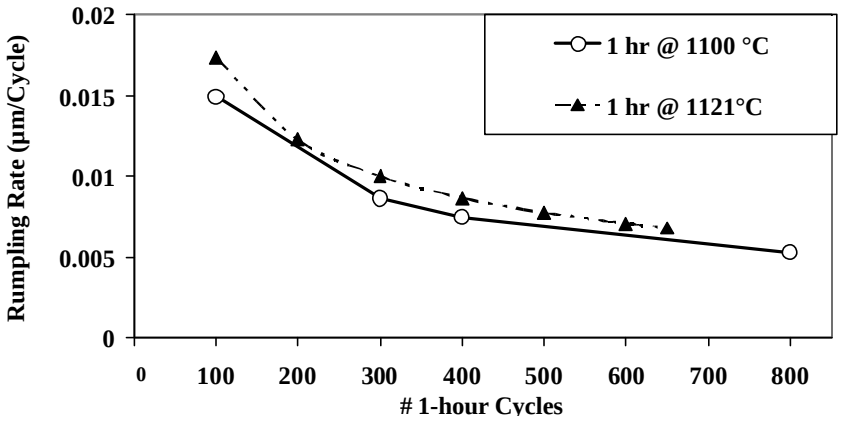

Figure 3.34: Evolution of the rate of rumpling as a function of cycles for Type I TBC for the 1-hour tests.

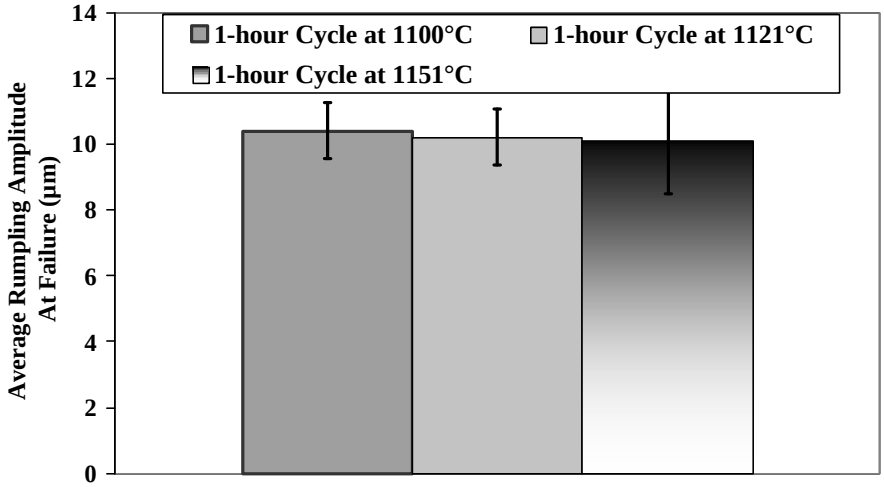

Figure 3.35: Rumpling amplitudes at failure for Type I TBC for the 1-hour tests.

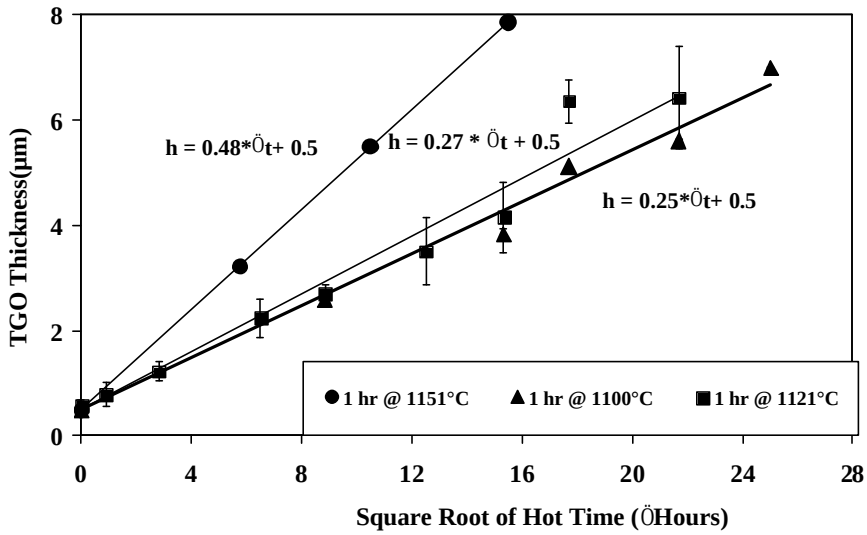

Figure 3.36: Plot of TGO thickness as a function of square root of total hot time for Type I TBC at the three different cycling temperatures.

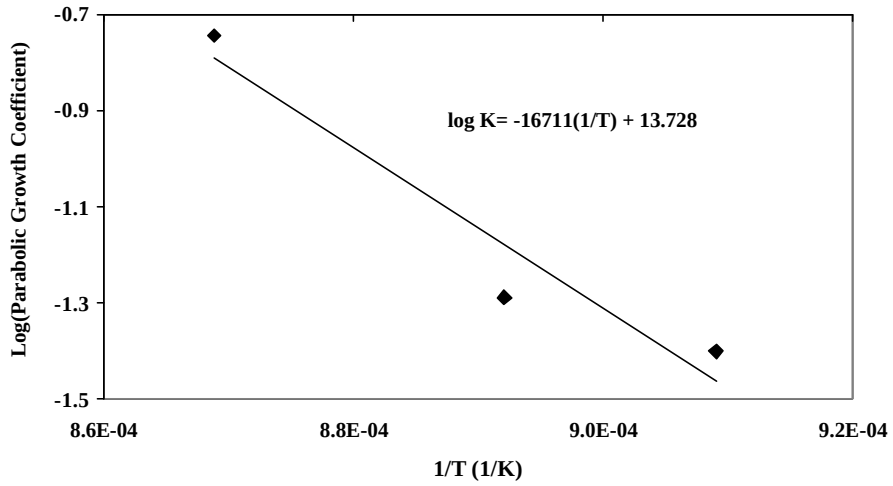

Figure 3.37: Arrenhius plot of the parabolic growth coefficients for Type I TBC as a function of reciprocal of the absolute cycling temperatures (1/T) on a logarithmic scale.

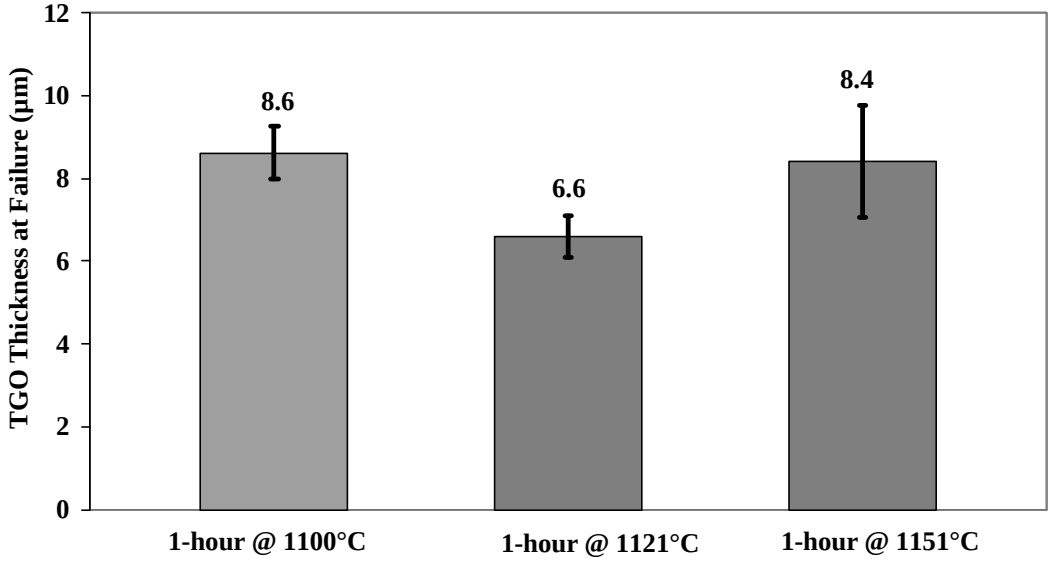

Figure 3.38: TGO thicknesses at failure for Type I TBC for the 1-hour tests.

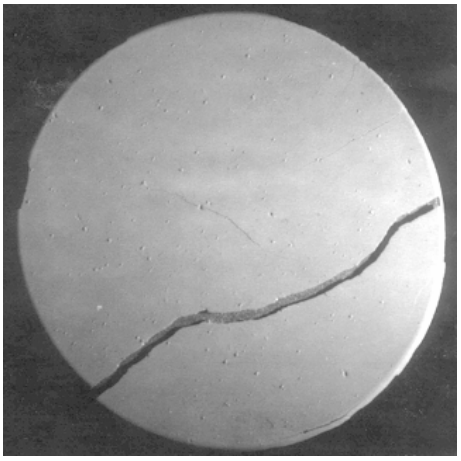

Figure 3.39: Macro photograph of a Type I TBC specimen that failed after 1350 1-hour cycles at 1100°C.

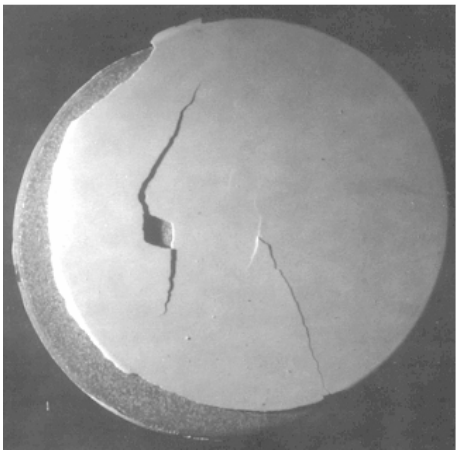

Figure 3.40: Macro photograph of a Type I TBC specimen that failed after 300 1-hour thermal cycles at 1151°C.

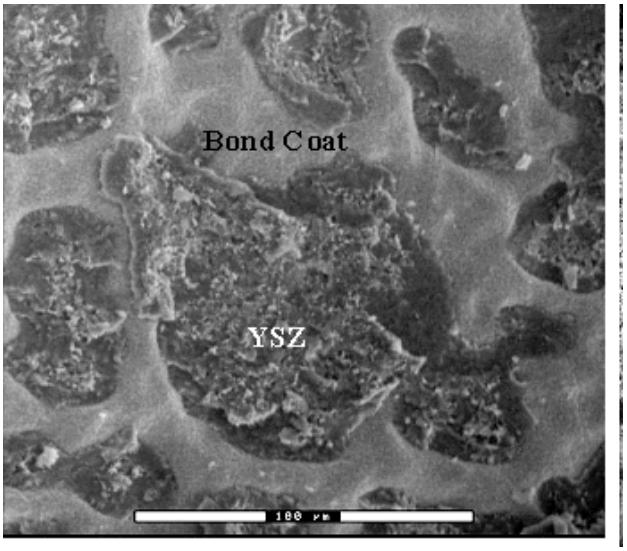

Figure 3.41: Secondary electron micrograph showing the failed bond coat surface in plan view for a Type I TBC that failed after 1350 1-hour thermal cycles at 1100°C.

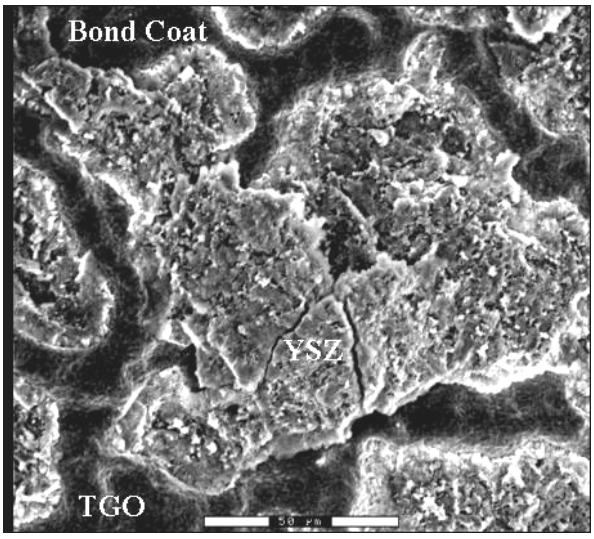

Figure 3.42: Secondary electron micrograph showing the failed bond coat surface in plan view for a Type I TBC that failed after 300 1-hour thermal cycles at 1151°C.

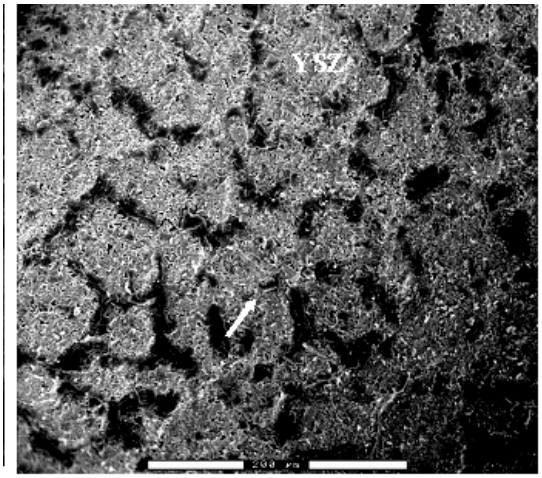

Figure 3.43: Secondary electron micrograph showing the bottom surface of the spalled YSZ in plan view for a Type I TBC that failed after 1350 1-hour thermal cycles at 1100°C. Arrow indicates TGO retained at the bond coat ridges.

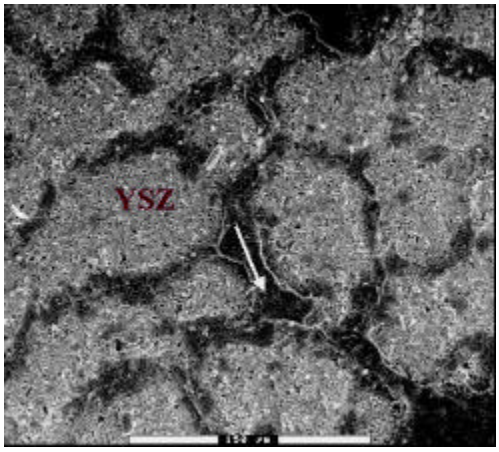

Figure 3.44: Secondary electron micrograph showing the bottom surface of the spalled YSZ in plan view for a Type I TBC that failed after 300 1-hour thermal cycles at 1151°C. Arrow indicates TGO retained at the bond coat ridges.

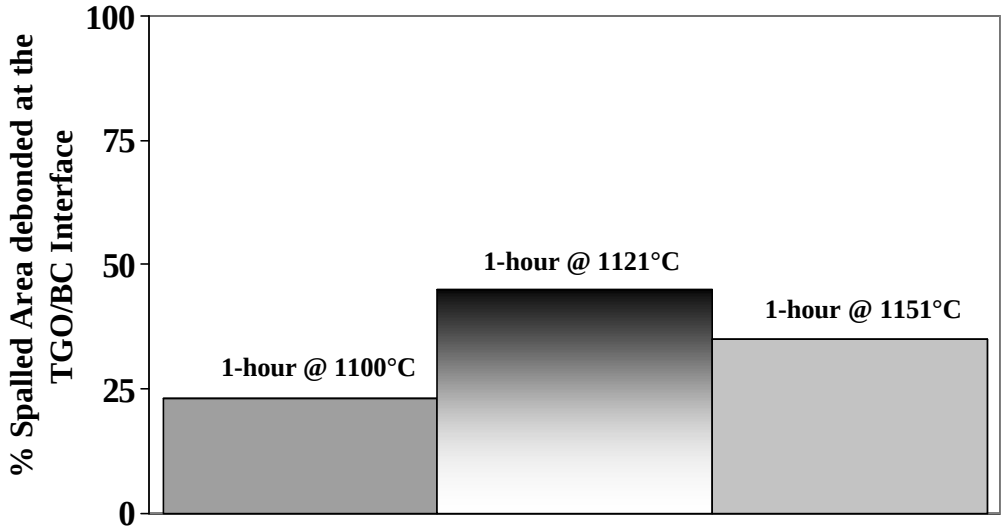

Figure 3.45: Area fraction of the spalled area that failed at the TGO/BC interface for Type I TBC for the 1-hour tests.

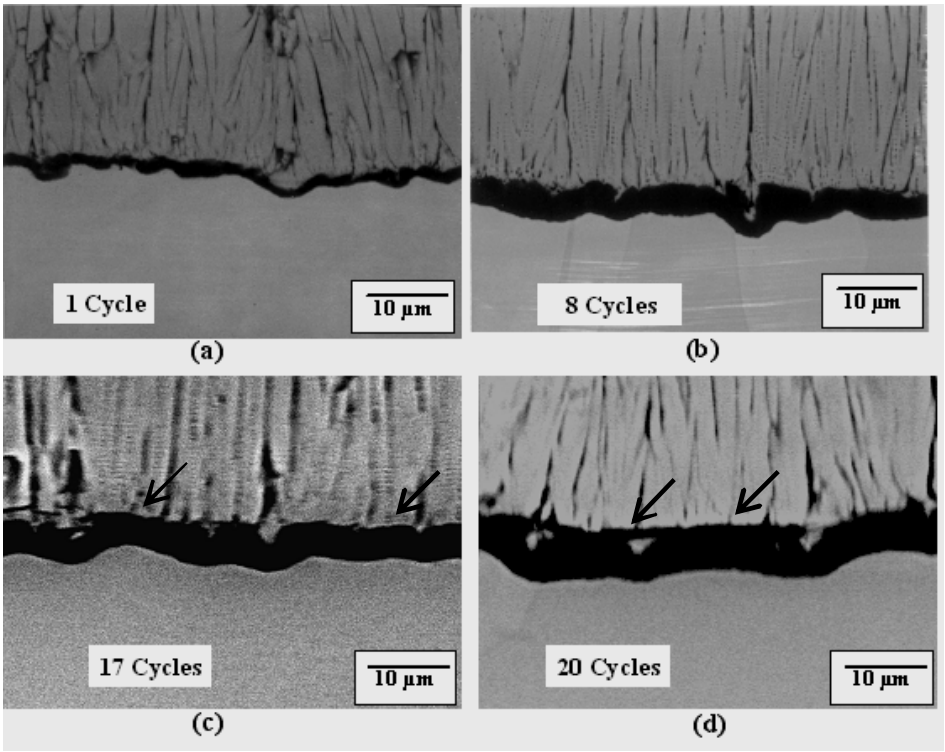

Figure 3.46: Cross-sectional secondary electron micrographs showing the continuous increase in the amplitude of the rumpling and cracking at the TBC/TGO interface for Type I TBC during the 24-hour thermal cycling at 1121°C after (a) 1 cycle (b) 8 cycles (c) 17 cycles and (d) 20 cycles. Arrows point to the cracking at the YSZ/TGO interface.

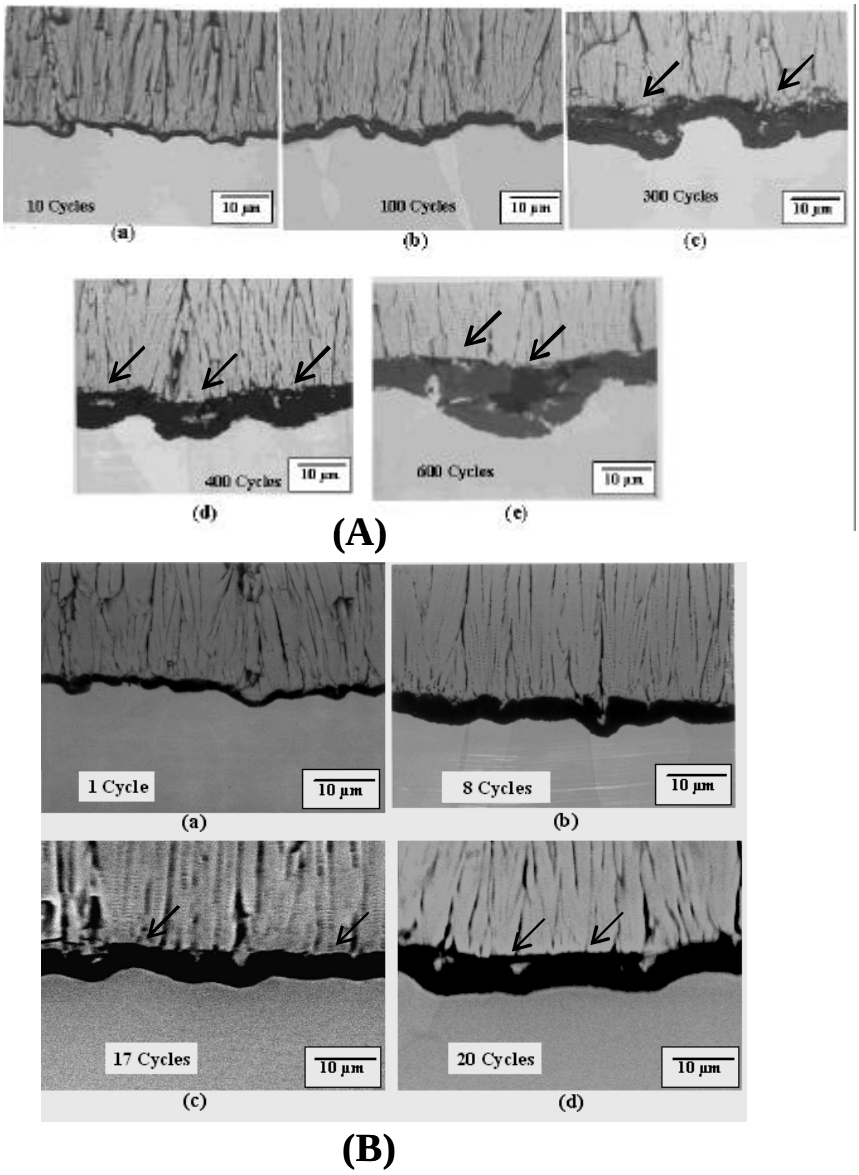

Figure 3.47: Comparison of cross-sectional secondary electron micrographs showing the continuous the TGO growth, increase in the amplitude of rumpling and cracking at the TBC/TGO interface for Type I TBC during (A) 1-hour and (B) 24-hour thermal cycling at 1121°C.

.

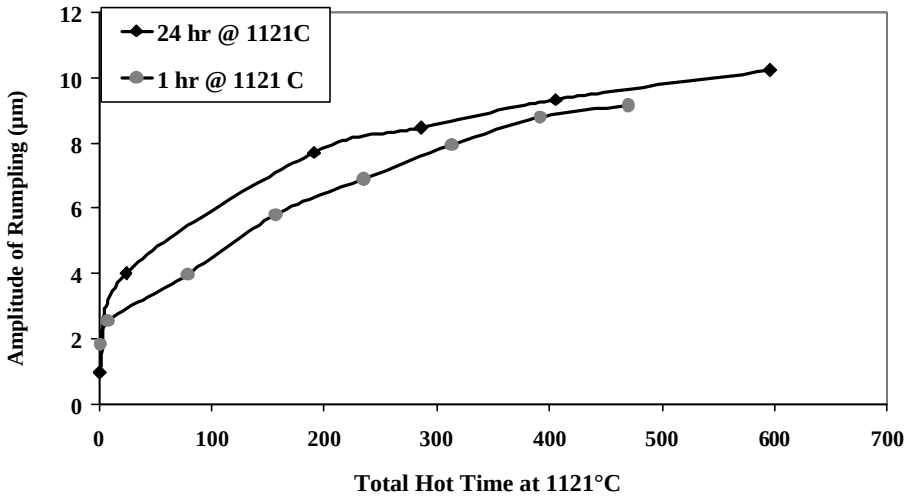

Figure 3.48: Evolution of the amplitude of rumpling as a function of total hot time for Type I TBC at 1121°C for the 1-hour and 24-hour tests.

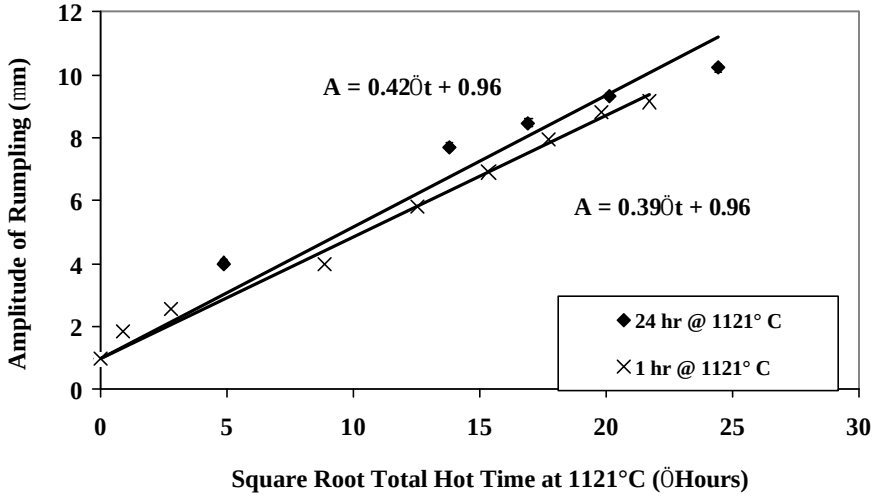

Figure 3.49: Evolution of the amplitude of rumpling as a function of the square root of total hot time for Type I TBC at 1121°C for the 1-hour and 24-hour tests.

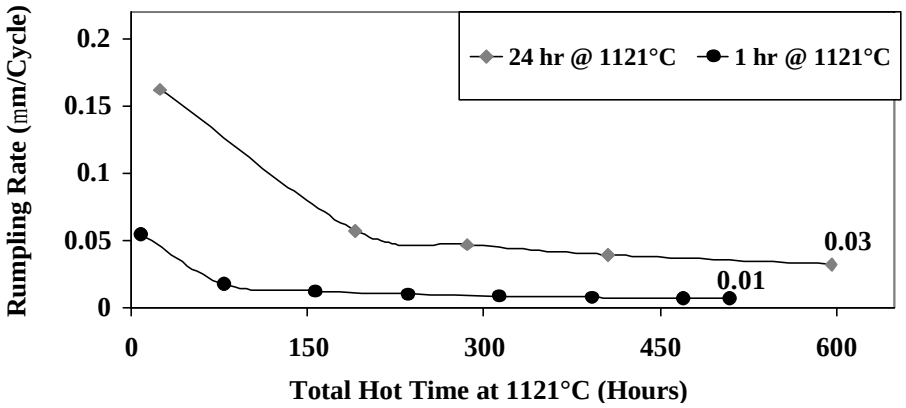

Figure 3.50: Evolution of the rate of rumpling as a function of total hot time at 1121°C for Type I TBC for the 1-hour and 24-hour tests.

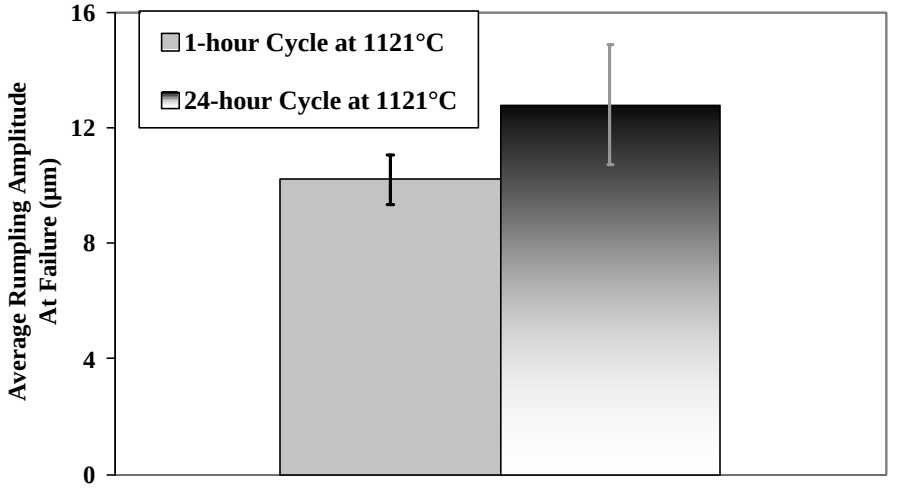

Figure 3.51: Rumpling amplitudes at failure for Type I TBC for the 1-hour and the 24-hour tests conducted at 1121°C.

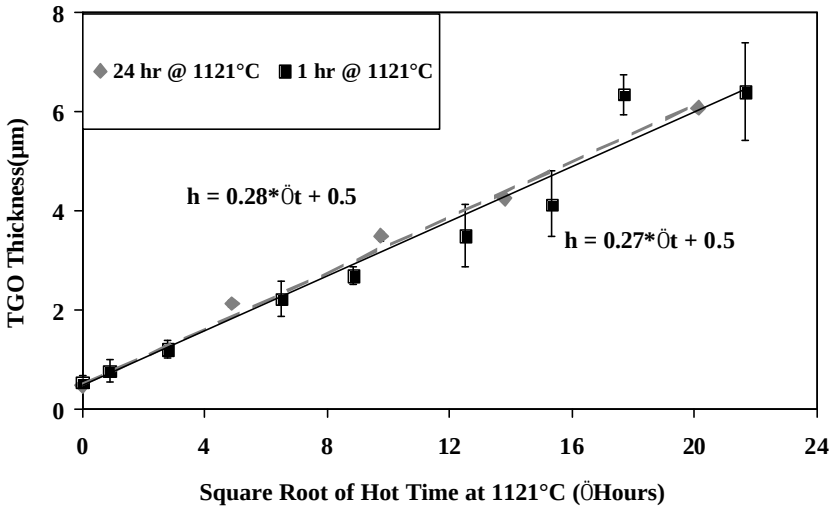

Figure 3.52: Plot of TGO thickness as a function of square root of total hot time at 1121°C for Type I TBC for the 1-hour and the 24-hour tests.

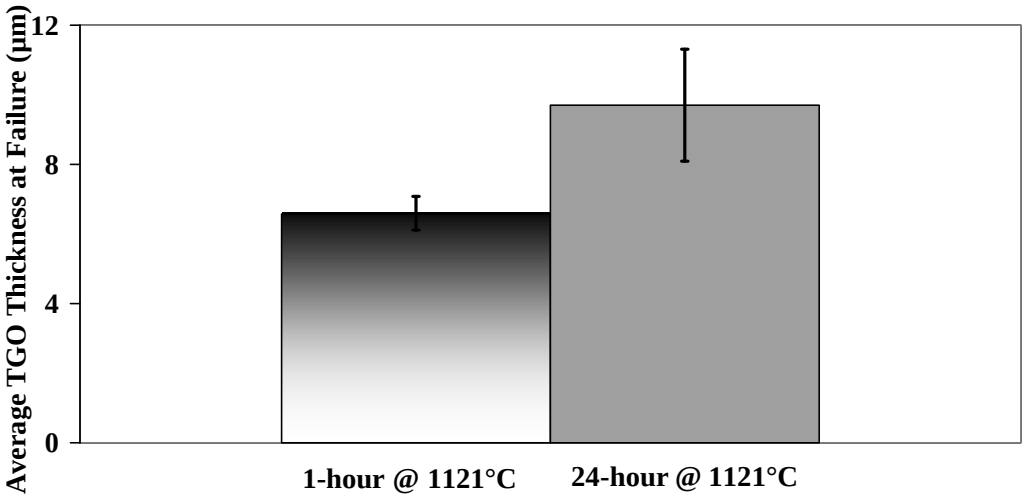

Figure 3.53: Average TGO thickness at failure for Type I TBC for the 1-hour and the 24-hour tests conducted at 1121°C.

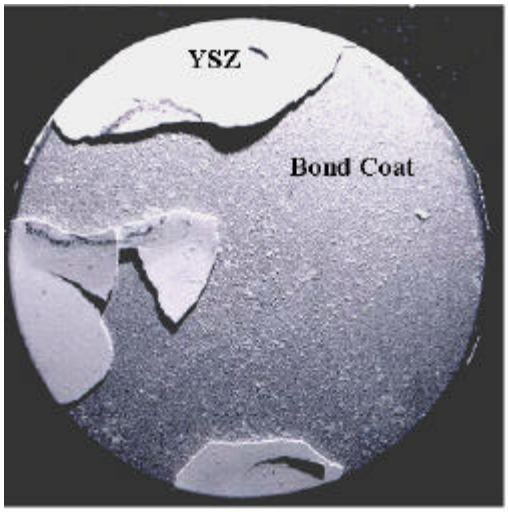

Figure 3.54: Macro photograph of a Type I TBC that failed after 41 24-hour cycles at 1121°C.

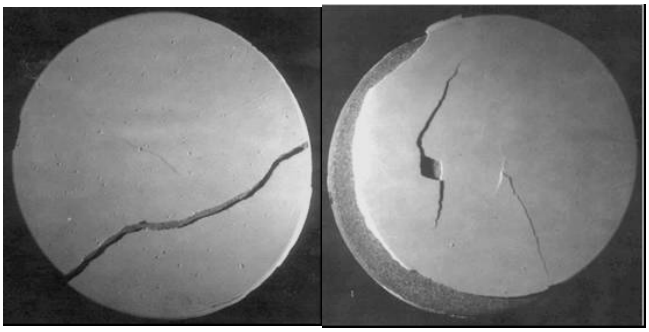

(A)

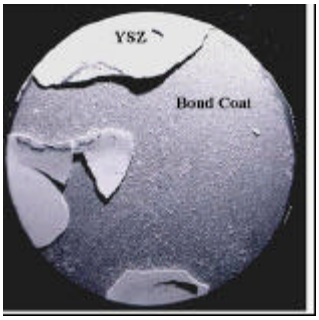

(B)

Figure 3.55: Comparison of macro failure modes of Type I TBC during the (A) 1-hour and (B) 24-hour cycles at 1121°C.

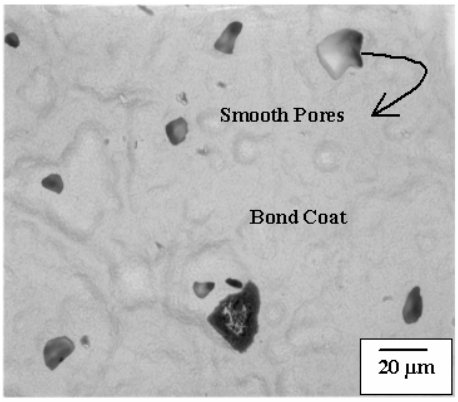

Figure 3.56: Secondary electron micrograph showing the failed bond coat surface in plan view of a Type I TBC that failed after 41 24-hour thermal cycles at 1121°C.

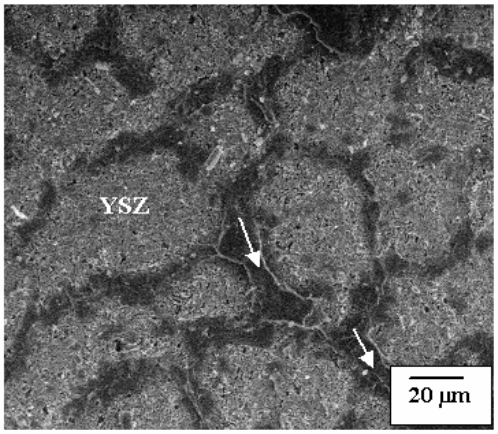

Figure 3.57: Secondary electron micrograph showing the bottom surface of the spalled YSZ in plan view of a Type I TBC that failed after 41 24-hour thermal cycles at 1121°C. Arrow indicates TGO retained at the bond coat ridges.

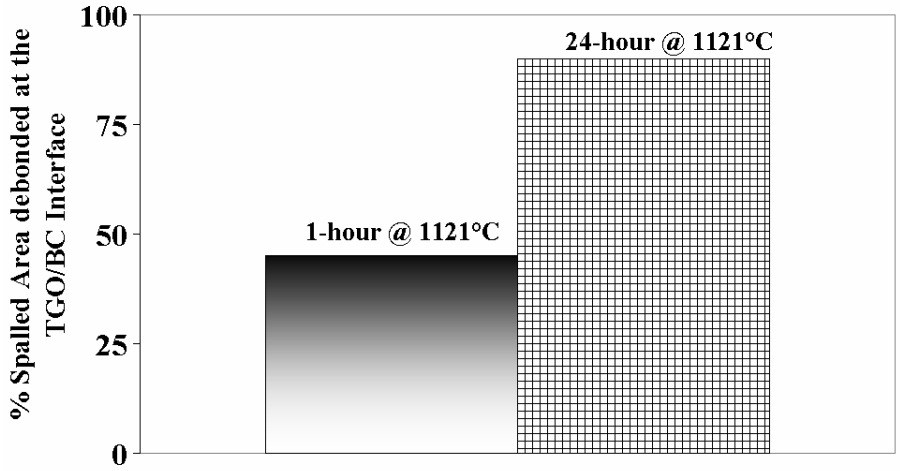

Figure 3.58: Area fraction of the spalled area that failed at the TGO/BC interface for Type I TBC for the 1-hour and 24-hour tests conducted at 1121°C.

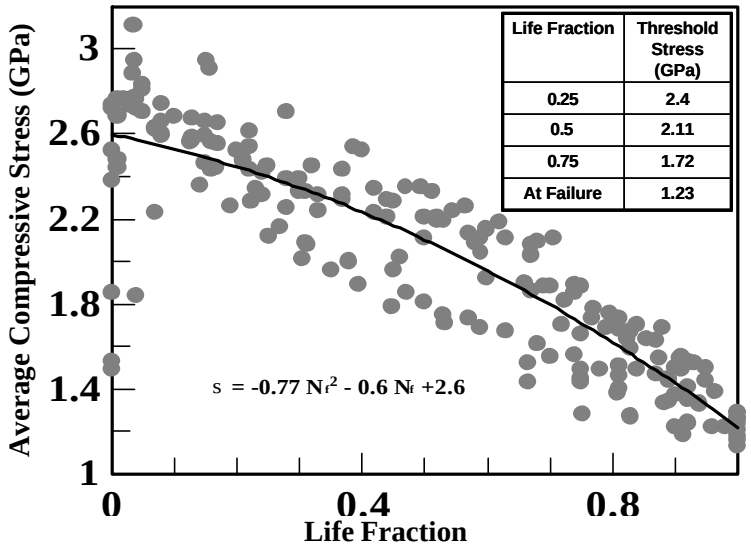

Figure 3.59: TGO stress versus TBC life fraction for Type I specimens cycled using the 1-hour constant and variable amplitude tests fit to a quadratic curve using regression. The table on the top right hand corner shows the estimated stress threshold values at 25%, 50% and 75% TBC life intervals.

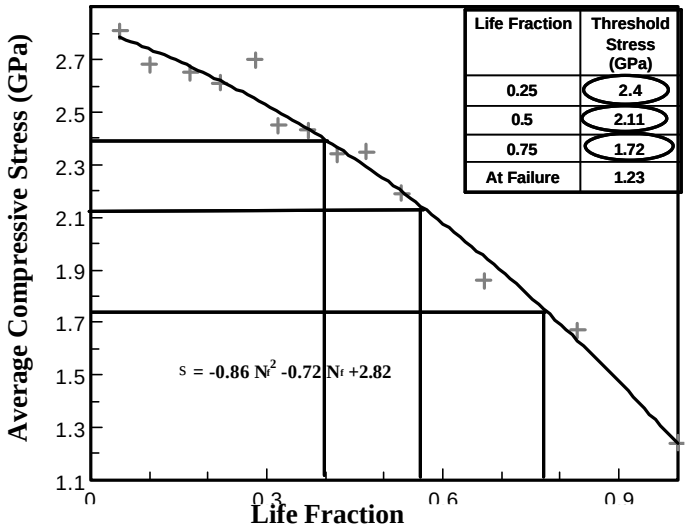

Figure 3.60: Procedure used to determine the actual remaining life of a Type I specimen cycled at 1151°C from the stress threshold values determined using the master curve.

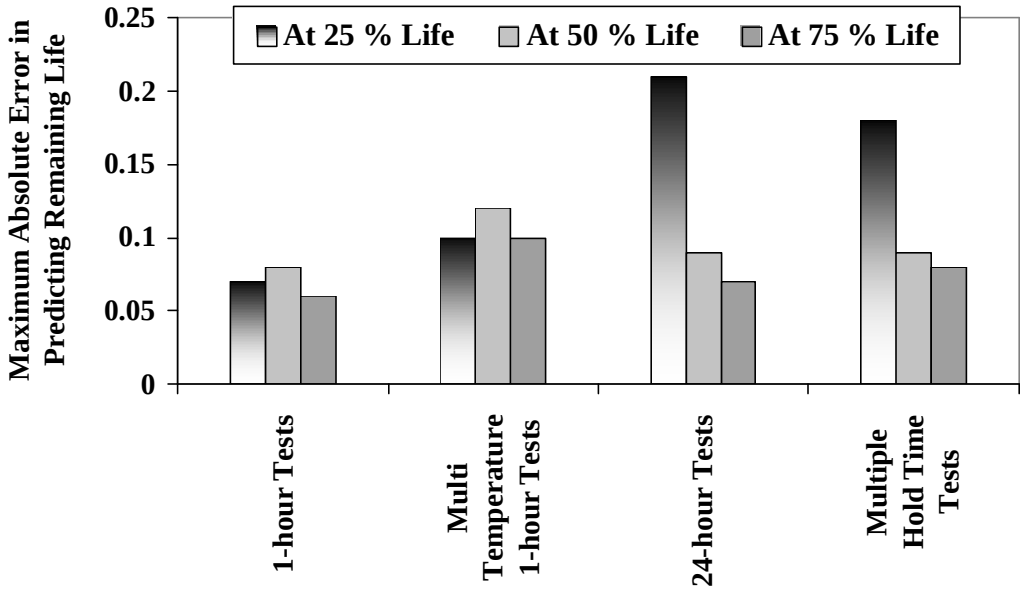

Figure 3.61: Comparison of the maximum absolute error in assessing remaining life of Type I TBCs for the 1-hour and 24-hour constant and non-constant amplitude test conditions, during three different inspection intervals of 25%, 50% and 75% TBC life.

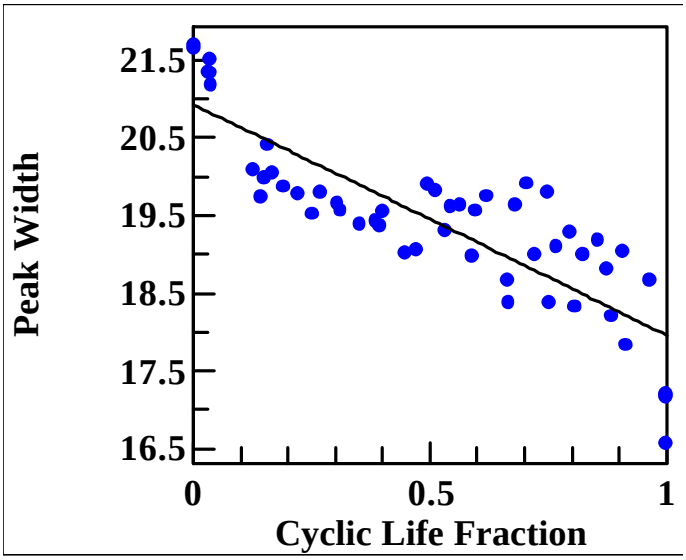

Figure 3.62: R_2 peak width versus TBC life fraction for Type I specimens cycled using the 1-hour constant and variable amplitude tests fit to a quadratic curve using regression.

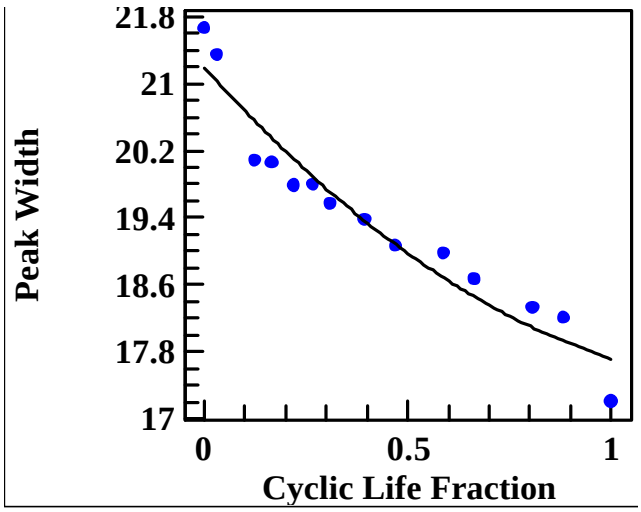

Figure 3.63: Procedure used to determine the actual remaining life of a Type I specimen cycled at 1151°C from the peak width threshold values determined using the master curve.

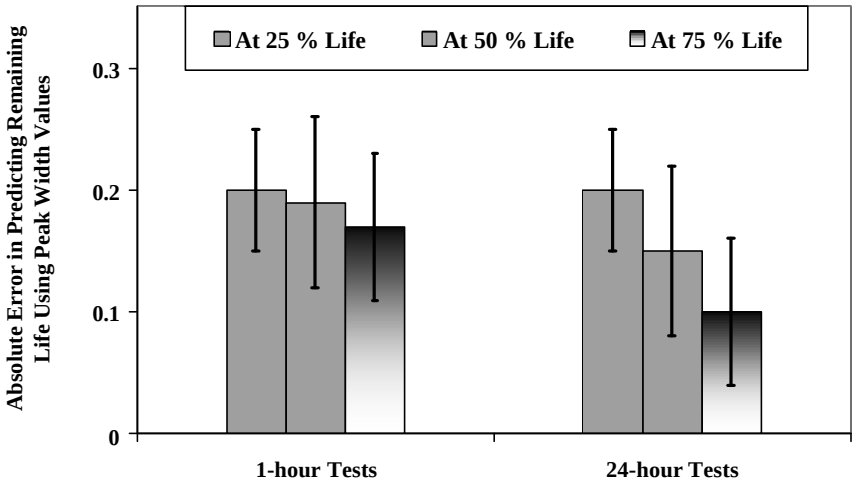

Figure 3.64: Comparison of the maximum absolute error in assessing remaining life of Type I TBCs using peak width values for the 1-hour and 24-hour constant and non-constant amplitude test conditions, during three different inspection intervals of 25%, 50% and 75% TBC life.

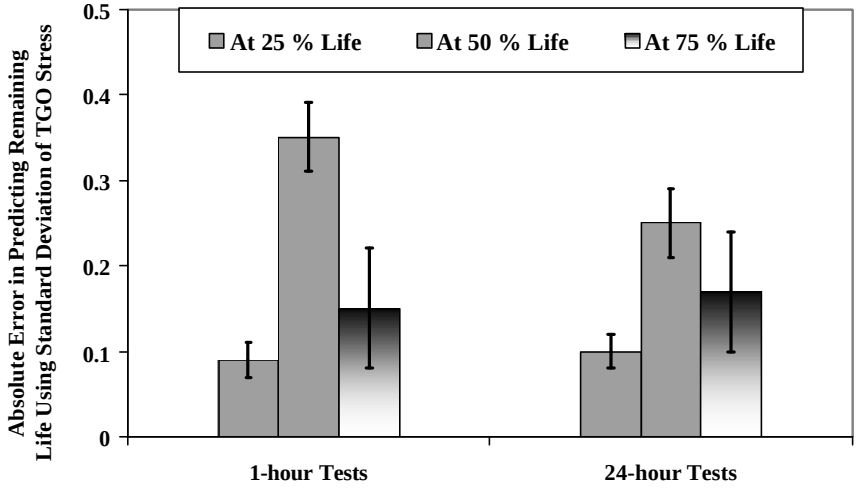

Figure 3.65: Comparison of the maximum absolute error in assessing remaining life of Type I TBCs using the standard deviation of TGO stress for the 1-hour and 24-hour constant and non-constant amplitude tests, during three different inspection intervals of 25%, 50% and 75% TBC life.

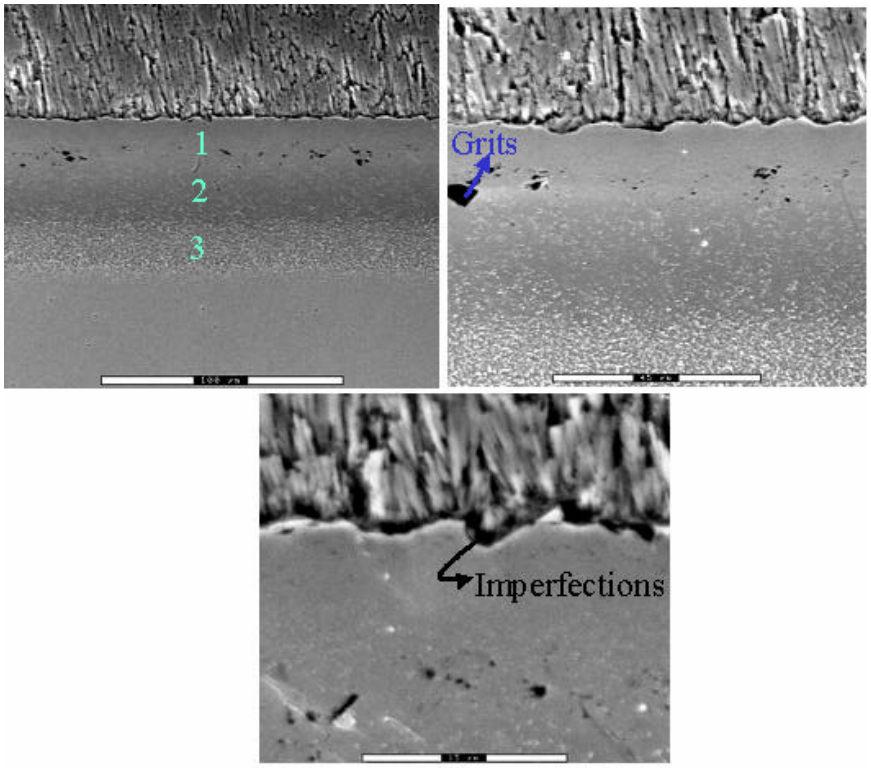

Figure 3.66: Cross-sectional secondary electron micrographs of Type II TBC system in the as-received condition. 1, 2 and 3 indicate the three zones found in the bond coat.

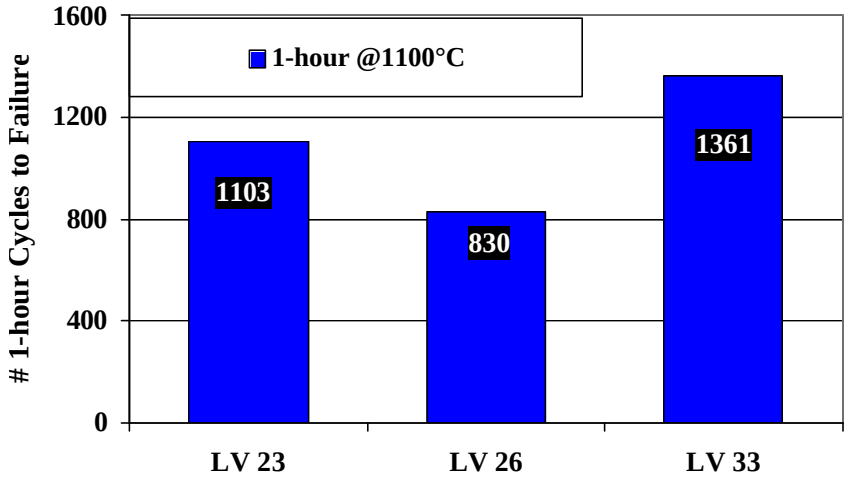

Figure 3.67: Spallation Lives for Type II TBC samples cycled at 1100°C using 1-hour cycles.

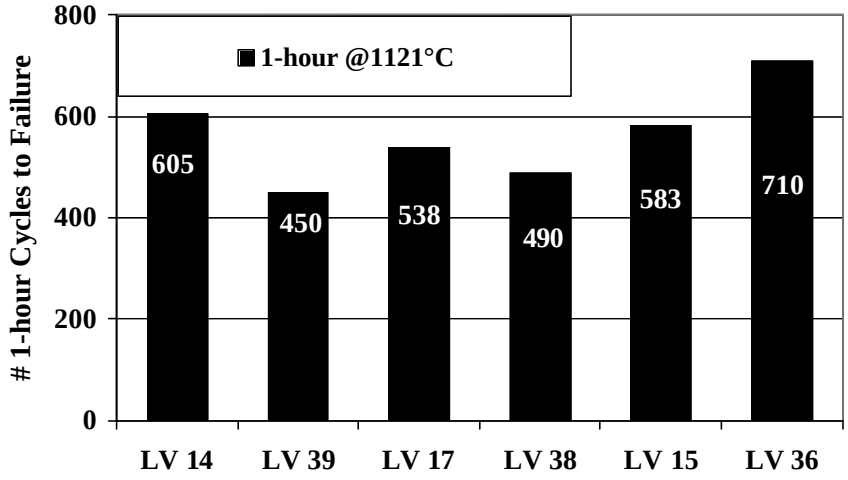

Figure 3.68: Spallation Lives for Type II TBC samples cycled at 1121°C using 1-hour cycles.

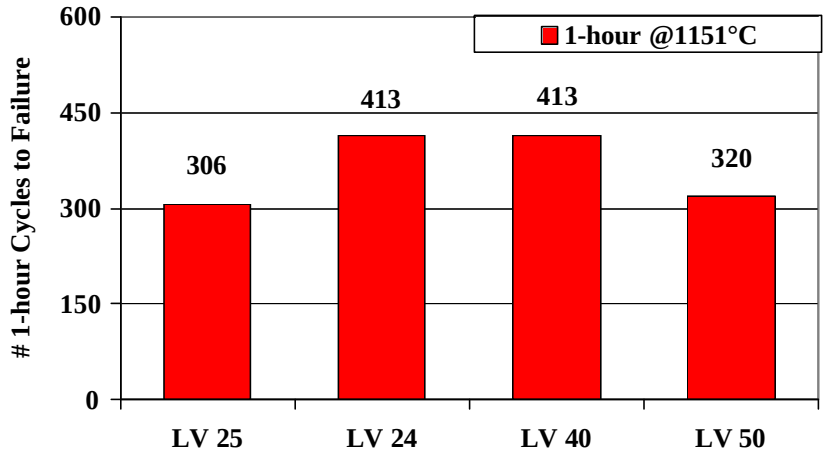

Figure 3.69: Spallation Lives for Type II TBC samples cycled at 1151°C using 1-hour cycles.

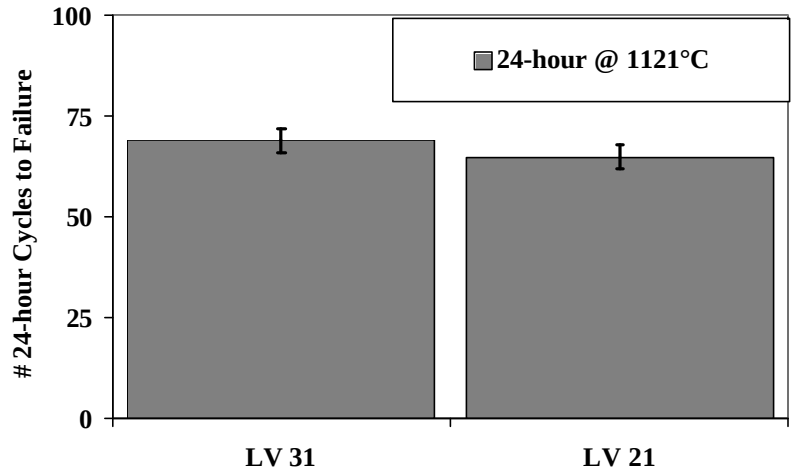

Figure 3.70: Spallation Lives for Type II TBC samples cycled at 1121°C using 24-hour cycles.

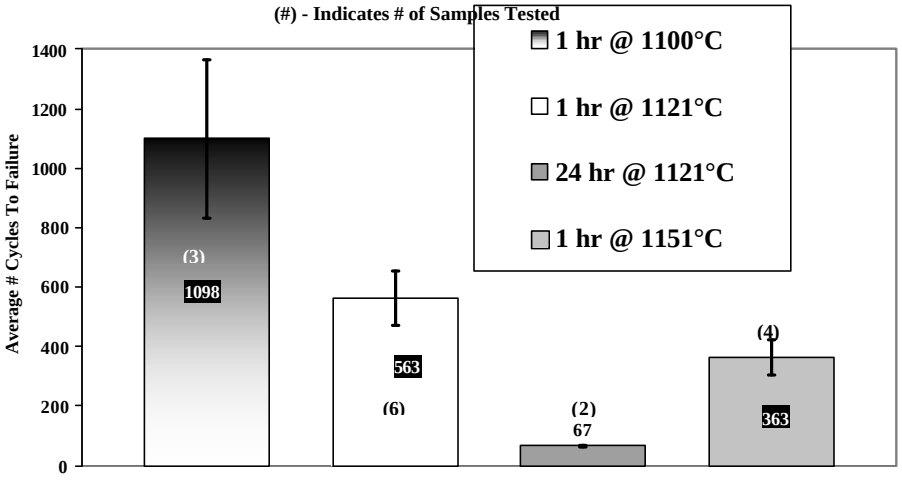

Figure 3.71: Average thermal cyclic lifetime of Type II TBC specimens for various thermal exposures.

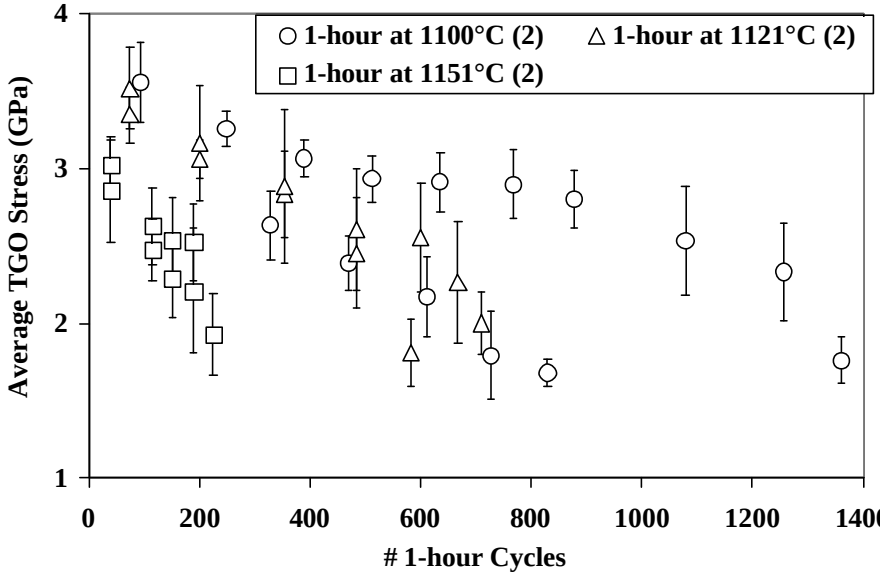

Figure 3.72: Evolution of TGO stress as a function of cycles for Type II TBCs for the 1-hour tests at three different cycling temperatures. The numbers in the parentheses indicate the number of samples whose data is reported.

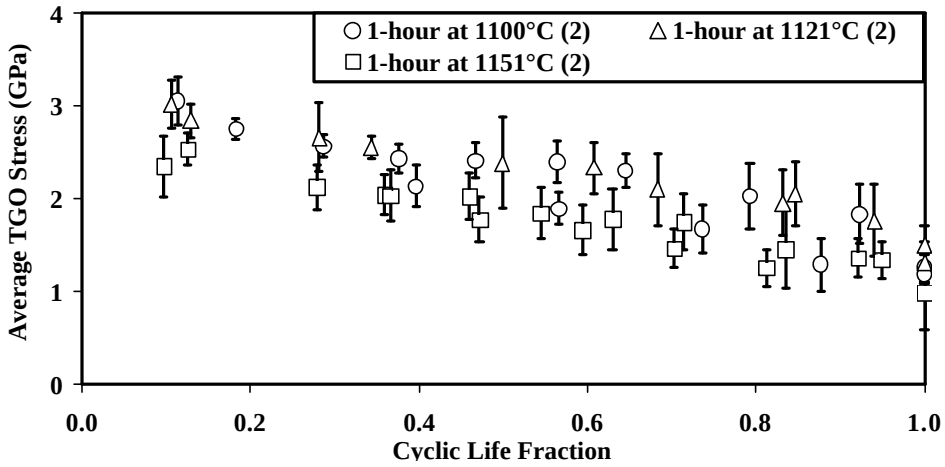

Figure 3.73: Evolution of TGO stress as a function of TBC life fraction for Type II TBCs for the 1-hour tests at the three cycling temperatures. The numbers in the parentheses indicate the number of samples whose data is reported.

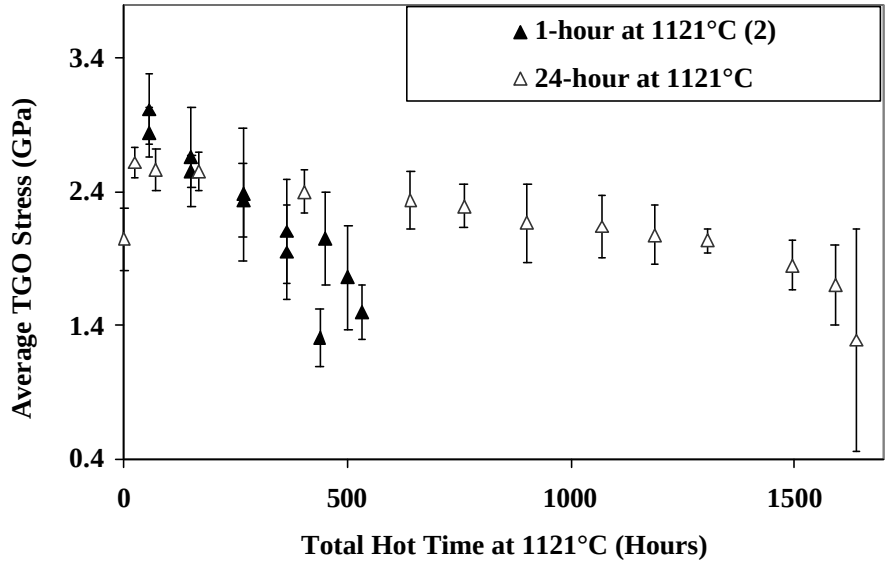

Figure 3.74: Evolution of TGO stress as a function of hot time at 1121°C for Type II TBCs for the 1-hour and 24-hour tests conducted at 1121°C. The numbers in the parentheses indicate the number of samples whose data is reported.

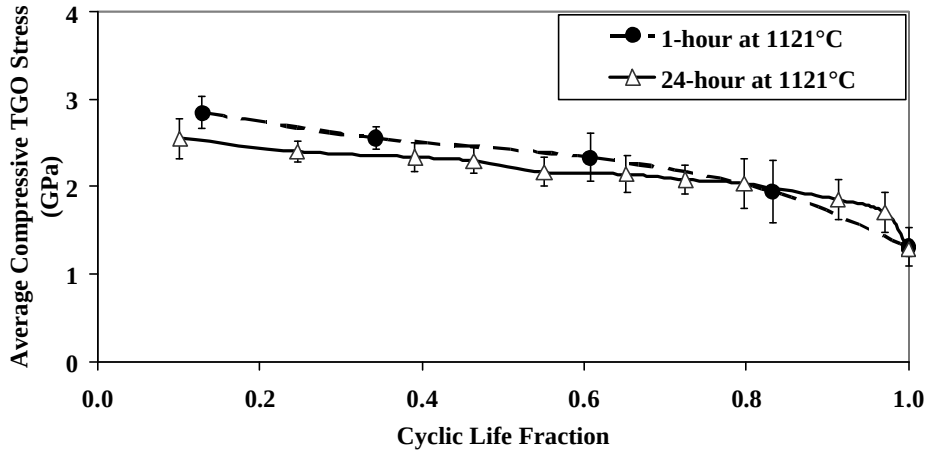

Figure 3.75: Evolution of TGO stress as a function of TBC life fraction for Type II TBCs for the 1-hour and 24-hour tests at 1121°C.

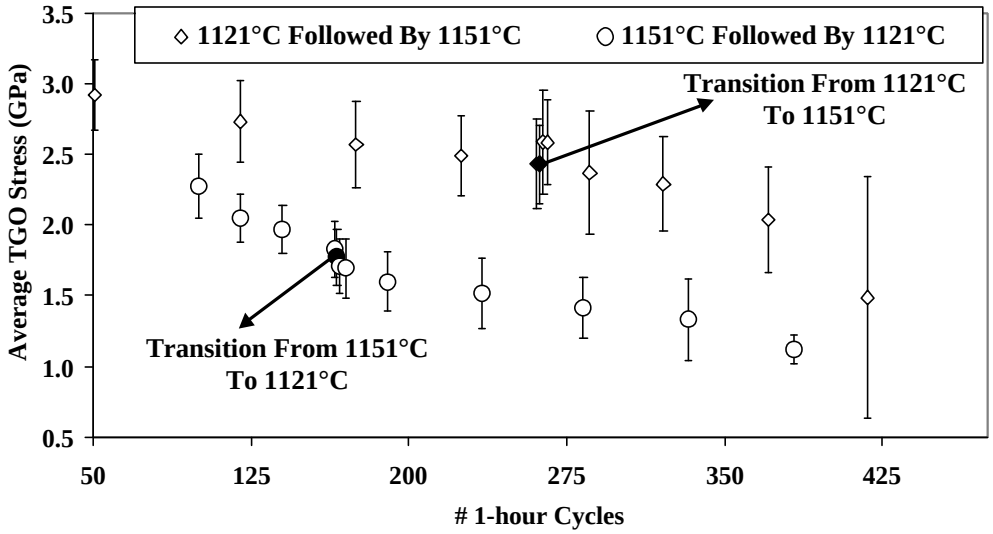

Figure 3.76: Evolution of TGO stress as a function of cycles to failure for the multi-temperature variable amplitude tests for Type II TBCs. The filled data points indicate the transition to the high and low temperatures.

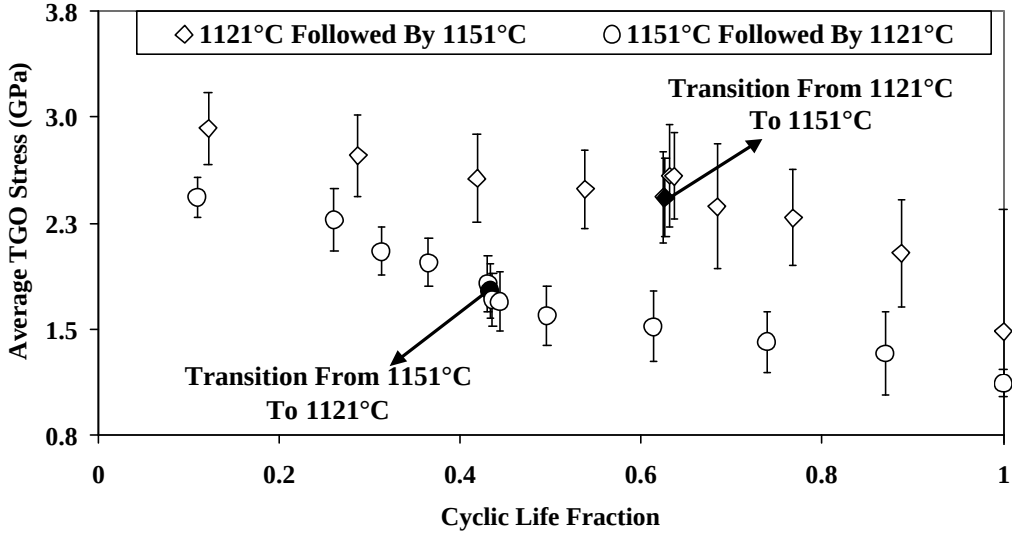

Figure 3.77: Evolution of TGO stress as a function of TBC life fraction for the multi-temperature variable amplitude tests for Type II TBCs. The filled data points indicate the transition to the high and low temperatures.

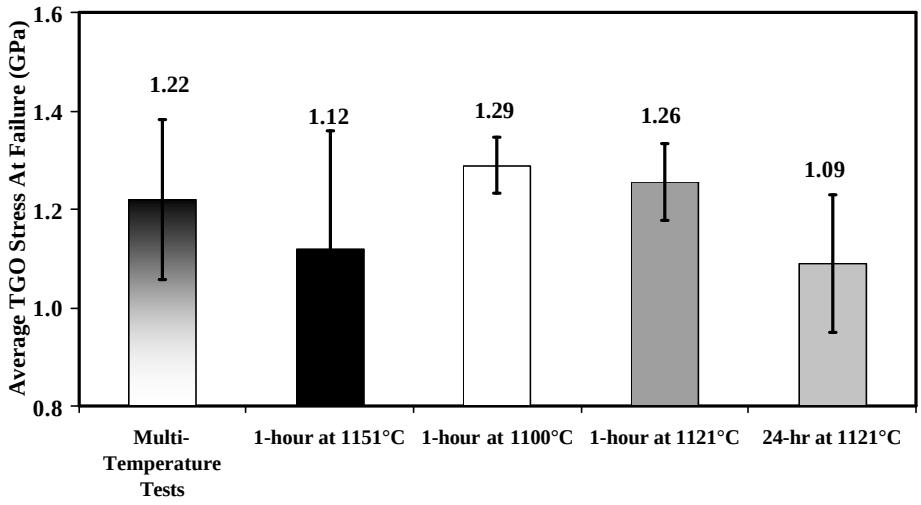

Figure 3.78: Average TGO stress at failure for Type II TBC specimens.

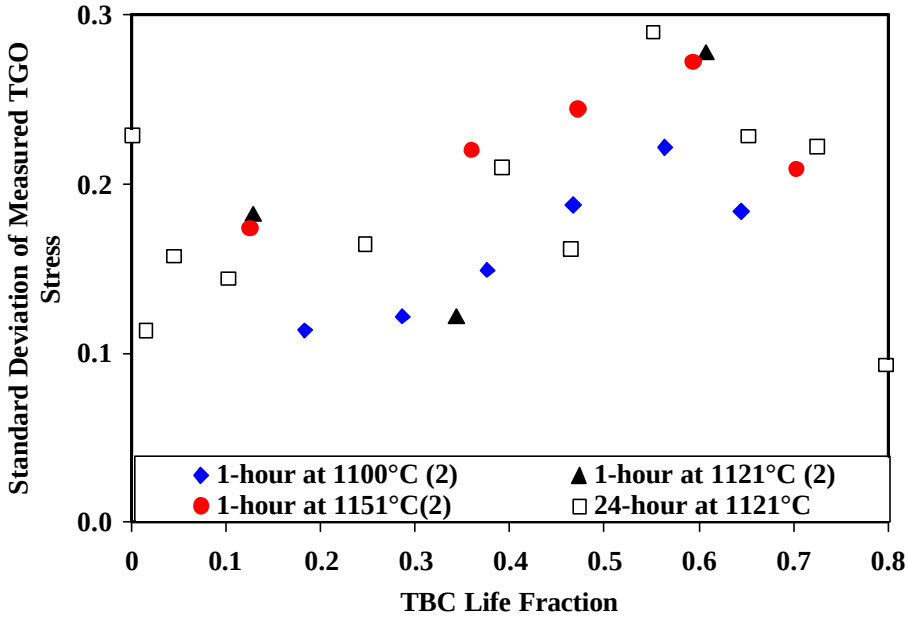

Figure 3.79: Change of standard deviation of the measured TGO stress versus TBC life fraction for the Type II TBCs for the 1-hour and 24-hour tests.

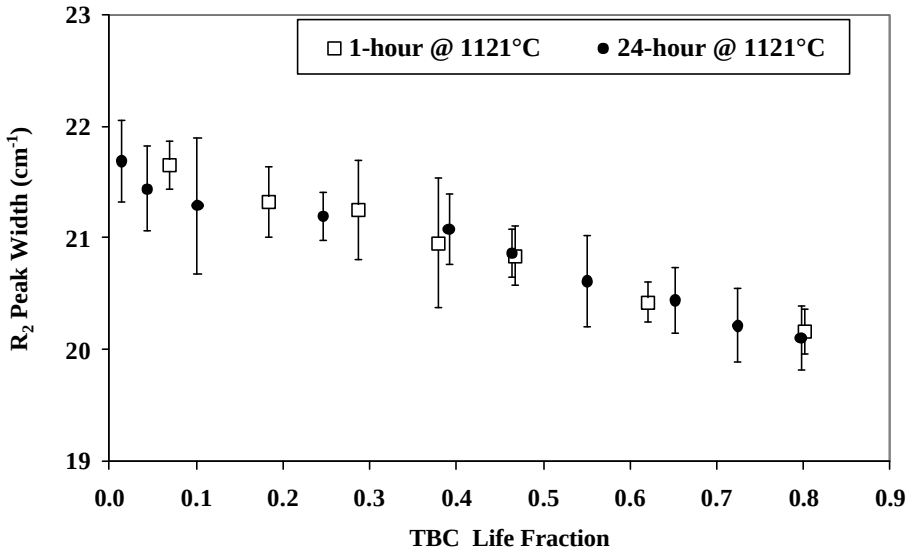

Figure 3.80: Change of R_2 peak width versus TBC life fraction for the Type II TBCs for the 1-hour and 24-hour tests.

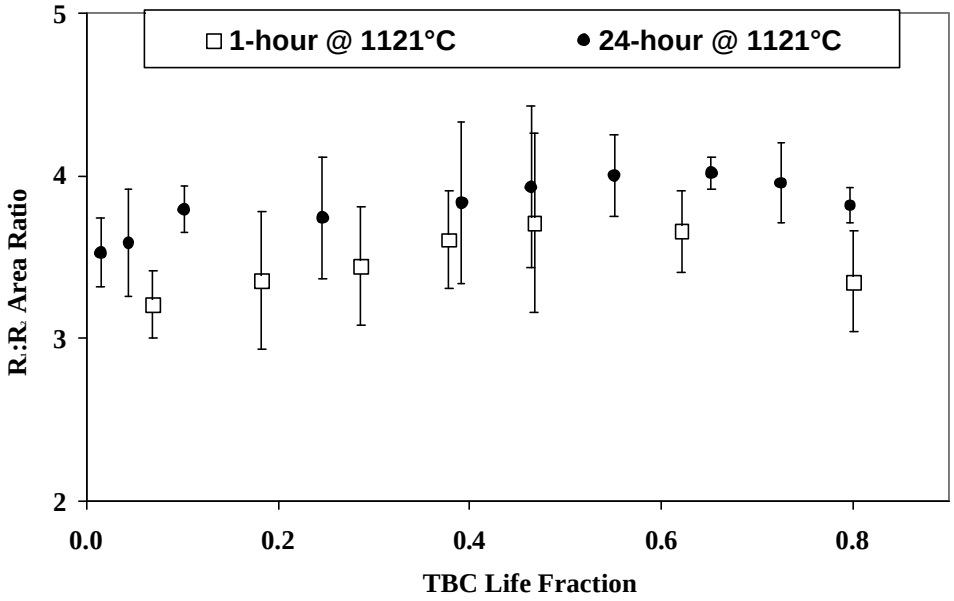

Figure 3.81: Change of R_1 to R_2 peak area ratio versus TBC life fraction for the Type II TBCs for the 1-hour and 24-hour tests.

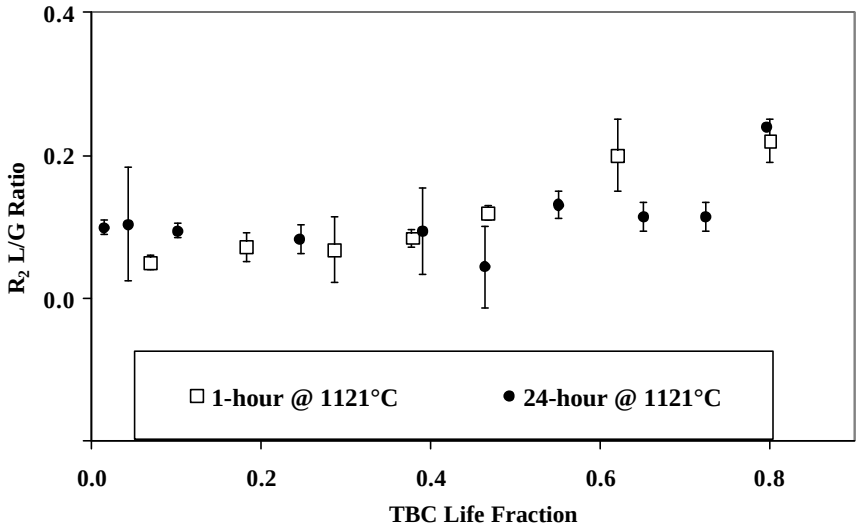

Figure 3.82: Change of R_2 peak shape, given by the Lorentzian to Gaussian ratio, versus TBC life fraction for the Type II TBCs for the 1-hour and 24-hour tests.

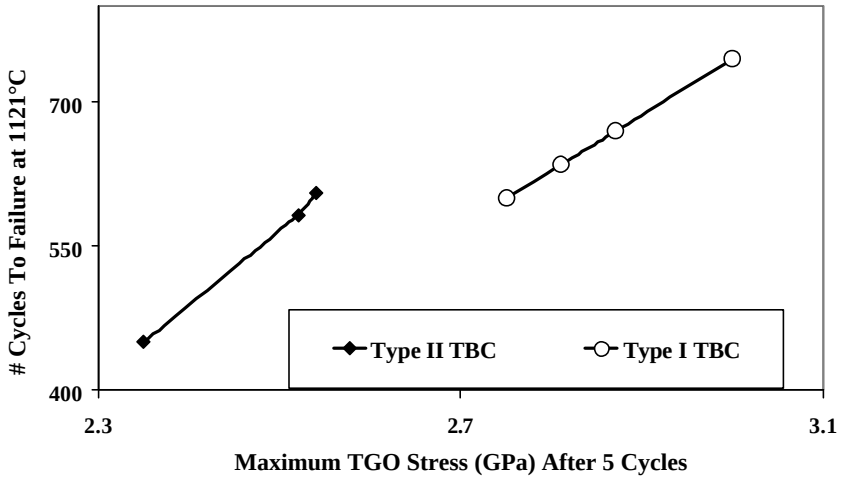

Figure 3.83: Plot of maximum TGO stress versus cycles to failure for Type I and Type II TBCs for the 1-hour tests at 1121°C.

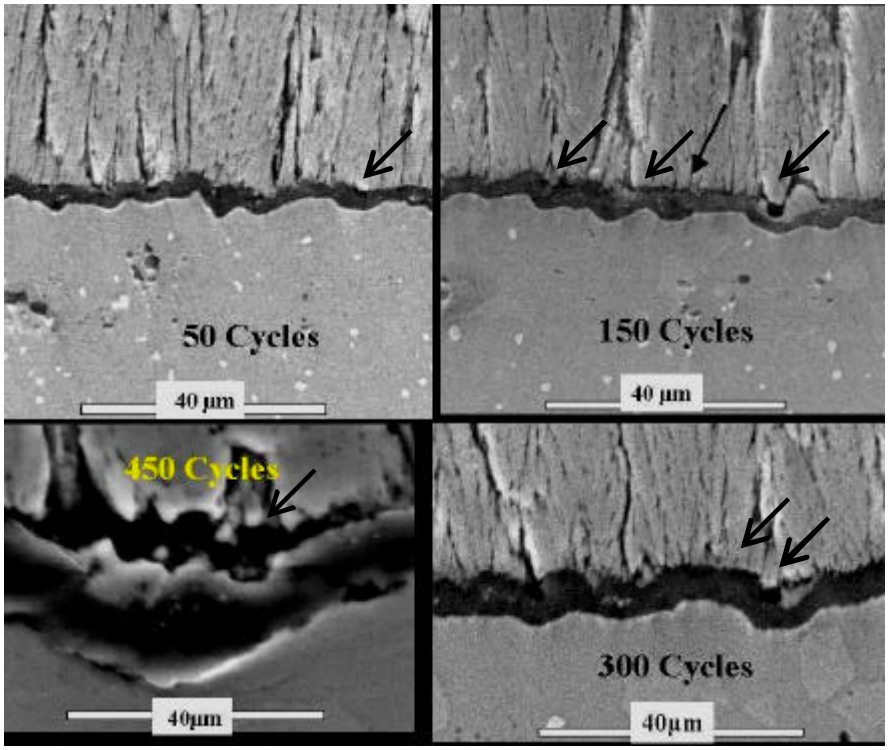

Figure 3.84: Cross-sectional secondary electron micrographs showing the continuous increase in rumpling and cracking at the TBC/TGO interface for Type II TBCs during the 1-hour thermal cycling at 1121°C after (a) 50 cycles (b) 150 cycles (c) 300 cycles and (d) 450 cycles. Arrows point to the cracking at the YSZ/TGO interface.

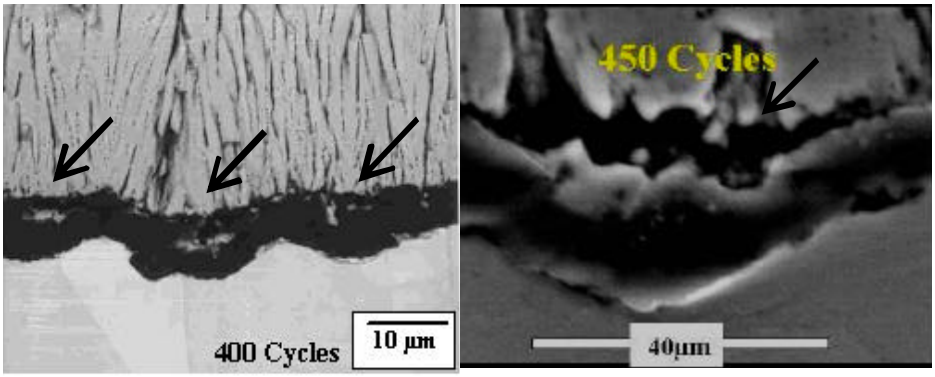

Figure 3.85: Comparison of cross-sectional secondary electron micrographs showing the continuous increase in rumpling and cracking at the TBC/TGO interface for (A) Type I after 400 cycles and (B) Type II TBCs after 450 cycles during the 1-hour thermal cycling at 1121°C. Arrows point to the cracking at the YSZ/TGO interface.

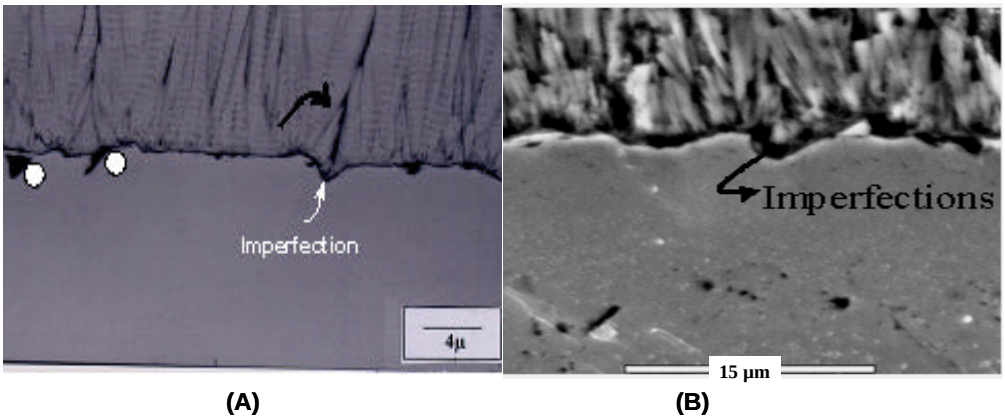

Figure 3.86: Comparison of cross-sectional secondary electron micrographs of (A) Type I TBC and (B) Type II TBC in the as-received condition.

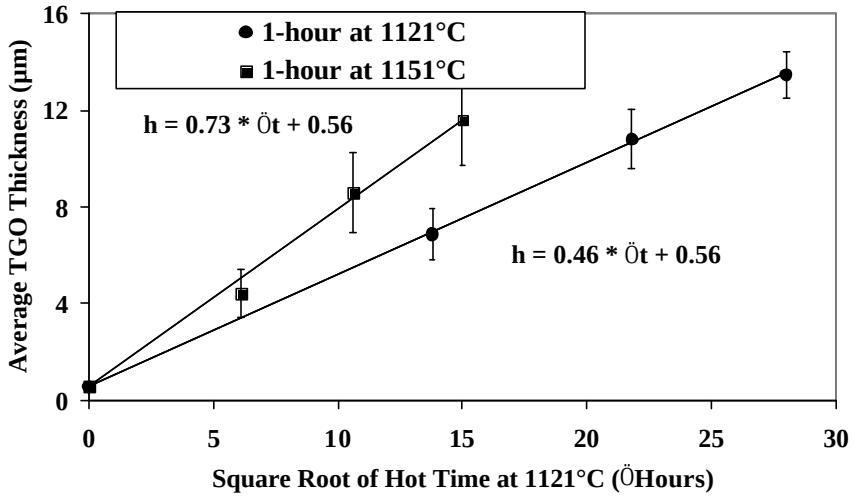

Figure 3.87: Plot of TGO thickness as a function of square root of total hot time at two cycling temperatures for Type II TBCs.

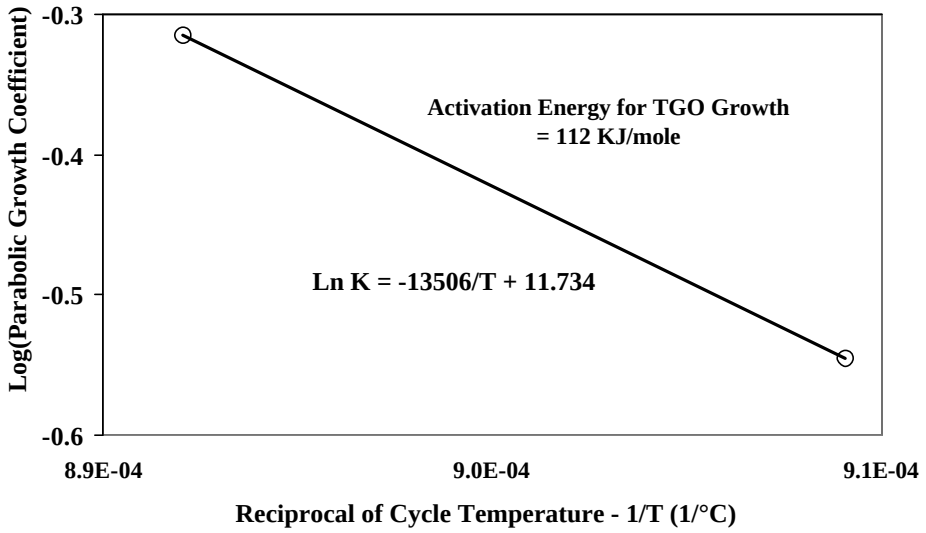

Figure 3.88: Arrenhius plot of the parabolic growth coefficients as a function of reciprocal of the absolute cycling temperatures (1/T) on a logarithmic scale for Type II TBCs.

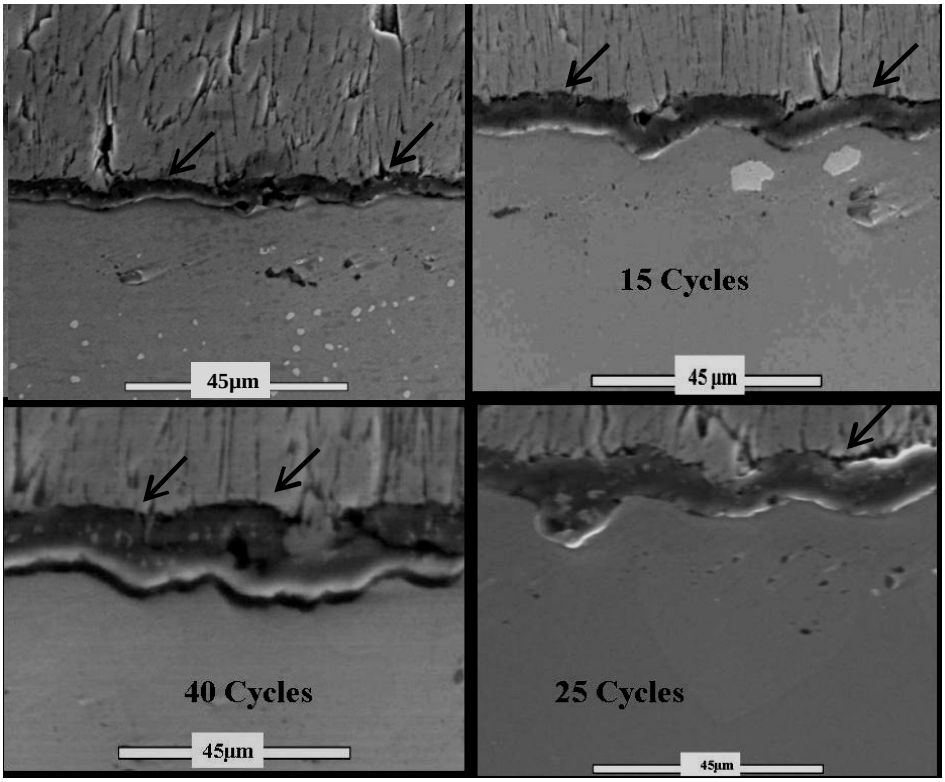

Figure 3.89: Cross-sectional secondary electron micrographs for Type II TBCs during the 24-hour thermal cycling at 1121°C after (a) 8 cycles (b) 15 cycles (c) 25 cycles and (d) 40 cycles. Arrows indicate cracking at the YSZ/TGO interface.

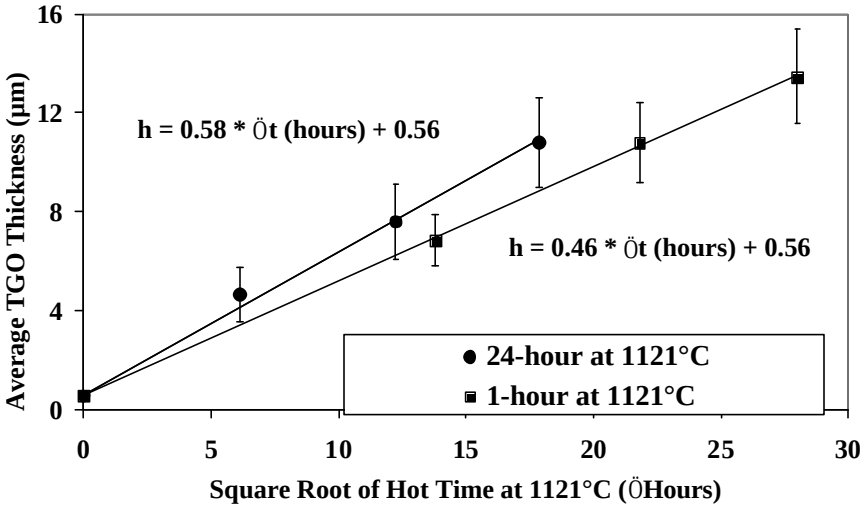

Figure 3.90: Plot of TGO thickness as a function of square root of total hot time at 1121°C for Type II TBCs °C for the 1-hour and the 24-hour tests.

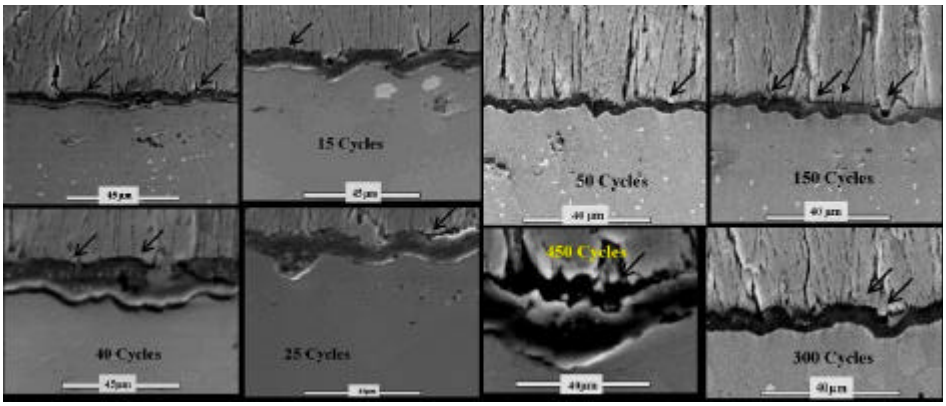

Figure 3.91: Comparison of cross-sectional secondary electron micrographs showing the increase in TGO growth, the continuous increase in the amplitude of rumpling and cracking at the YSZ/TGO interface for Type II TBCs during (A) 24-hour and (B) 1-hour tests at 1121°C.

Figure 3.92: Macro photograph of a Type II TBC specimen that failed after 450 1-hour cycles at 1121°C.

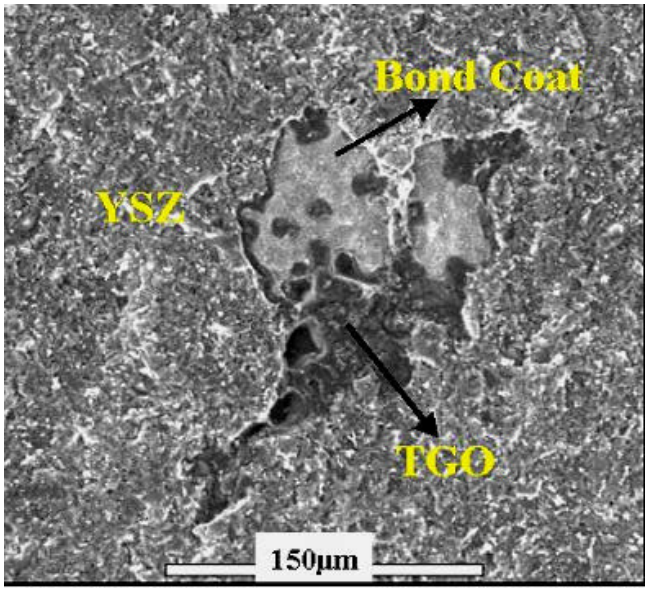

Figure 3.93: Secondary electron micrograph showing the failed bond coat surface in plan view for a Type II TBC that failed after 450 1-hour thermal cycles at 1121°C.

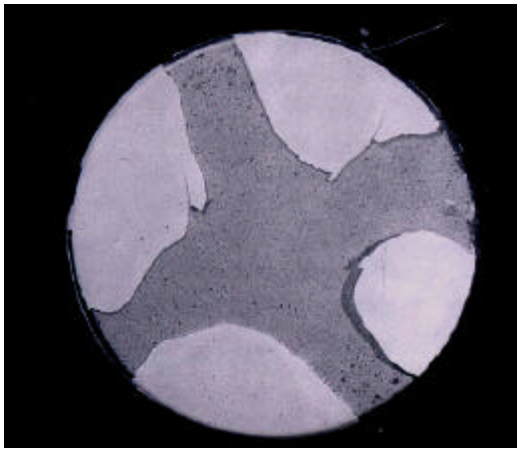

Figure 3.94: Macro photograph of a Type II TBC specimen that failed after 65 24-hour cycles at 1121°C.

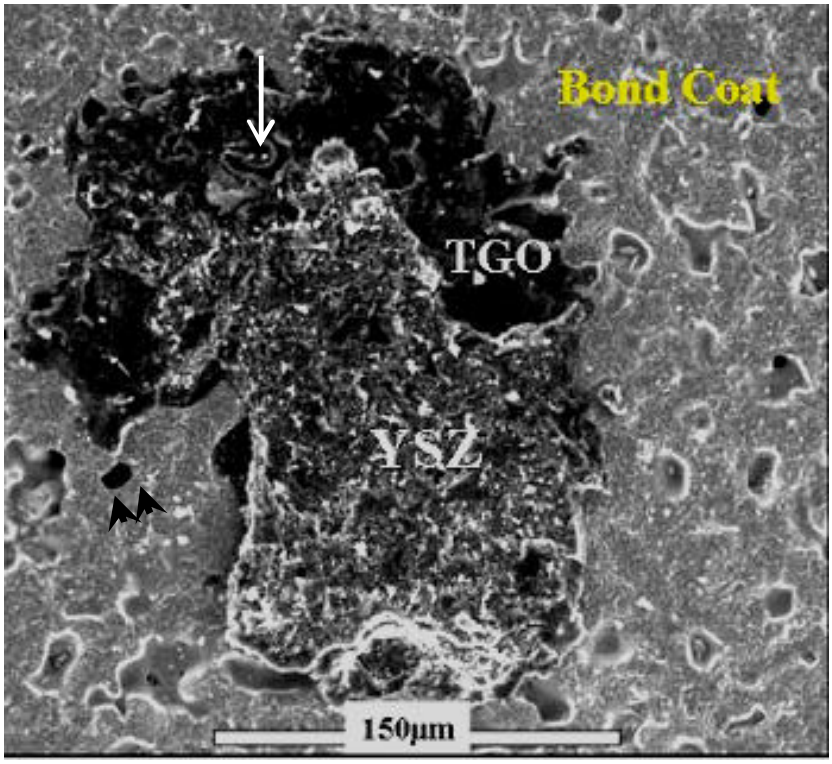

Figure 3.95: Secondary electron micrograph showing the failed bond coat surface in plan view for a Type II TBC that failed after 65 24-hour thermal cycles at 1121°C. Double arrows indicate oxide free pores and white arrow points to a cavity.

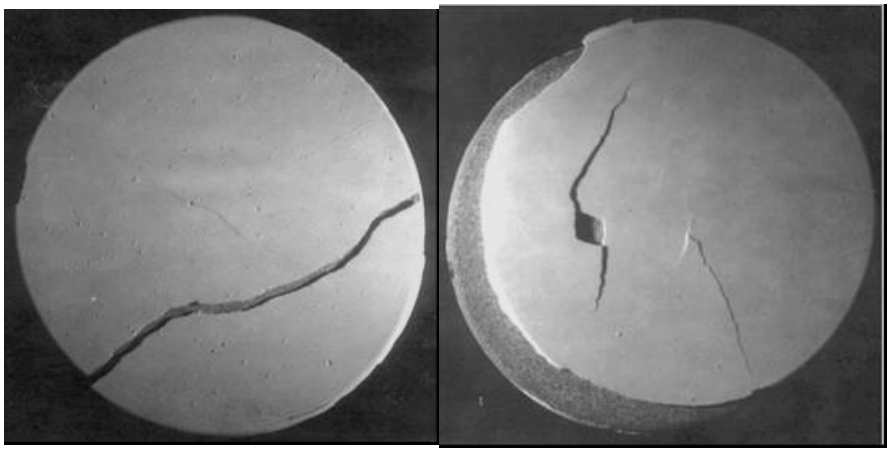

(A)

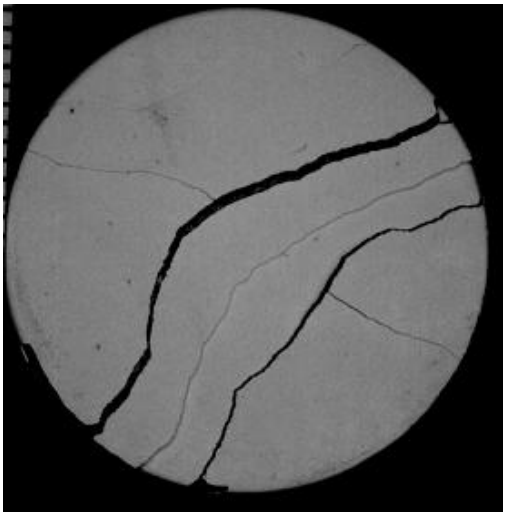

(B)

Figure 3.96: Comparison of macro failure modes of (A) Type I TBCs and (B) Type II TBCs during the 1-hour cycles at 1121°C.

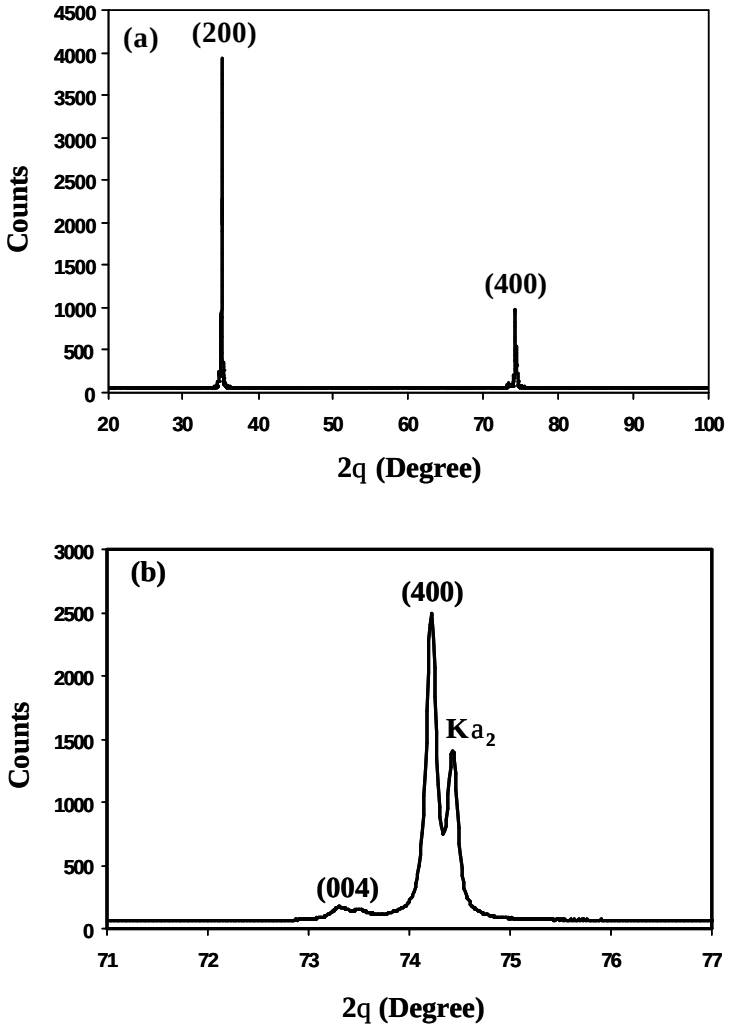

Fig. 3.97. XRD patterns of As-coated (Ni,Pt)Al bond coated TBC

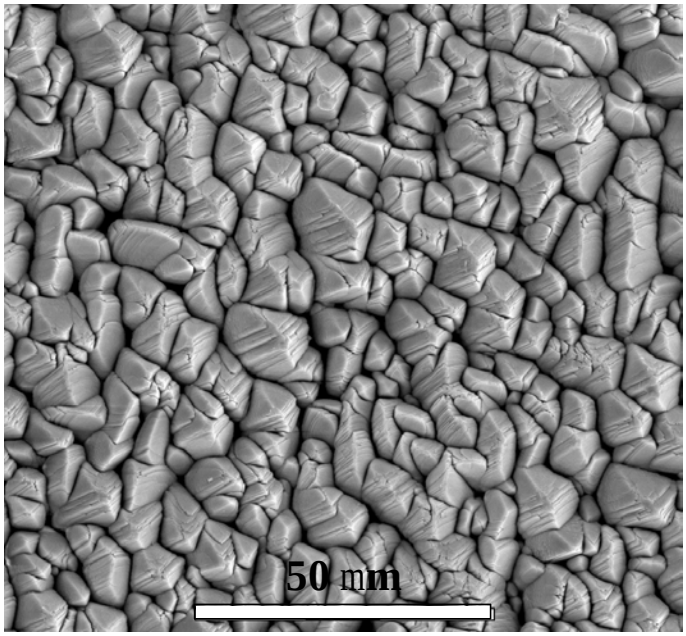

Fig. 3.98. Top surface morphology of as-coated TBC specimen with (Ni,Pt)Al bond coat

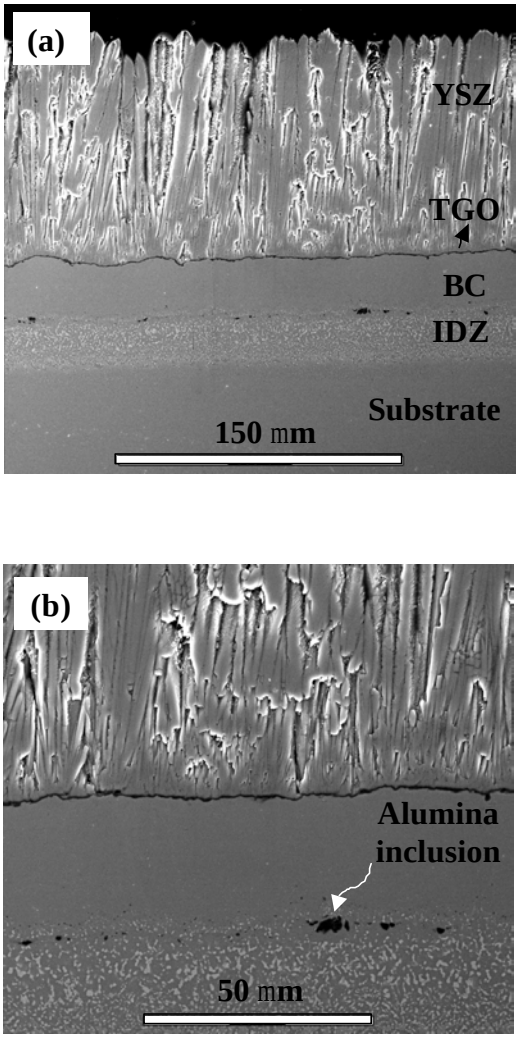

Fig. 3.99. As coated microstructure of (Ni,Pt)Al bond coated TBC

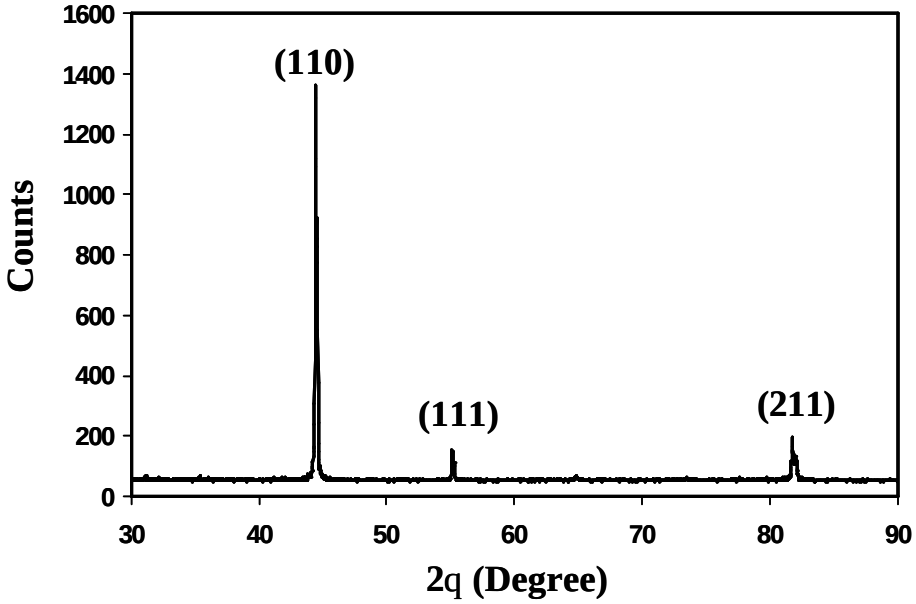

Fig. 3.100. XRD pattern of bond coat for as-coated (Ni,Pt)Al bond coated TBC

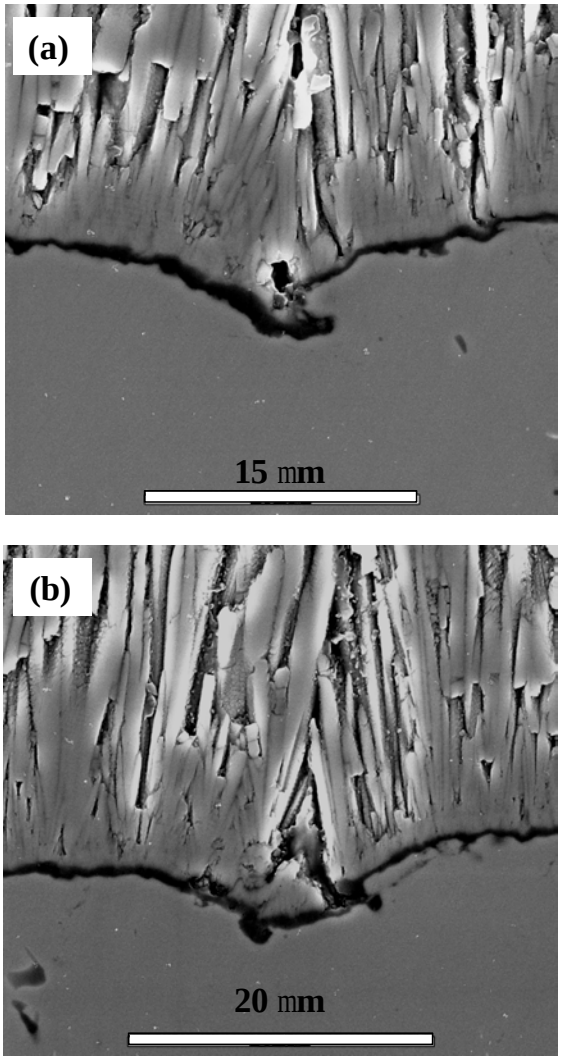

Fig. 3.101 Imperfections in the vicinity of TGO in the as-coated microstructure

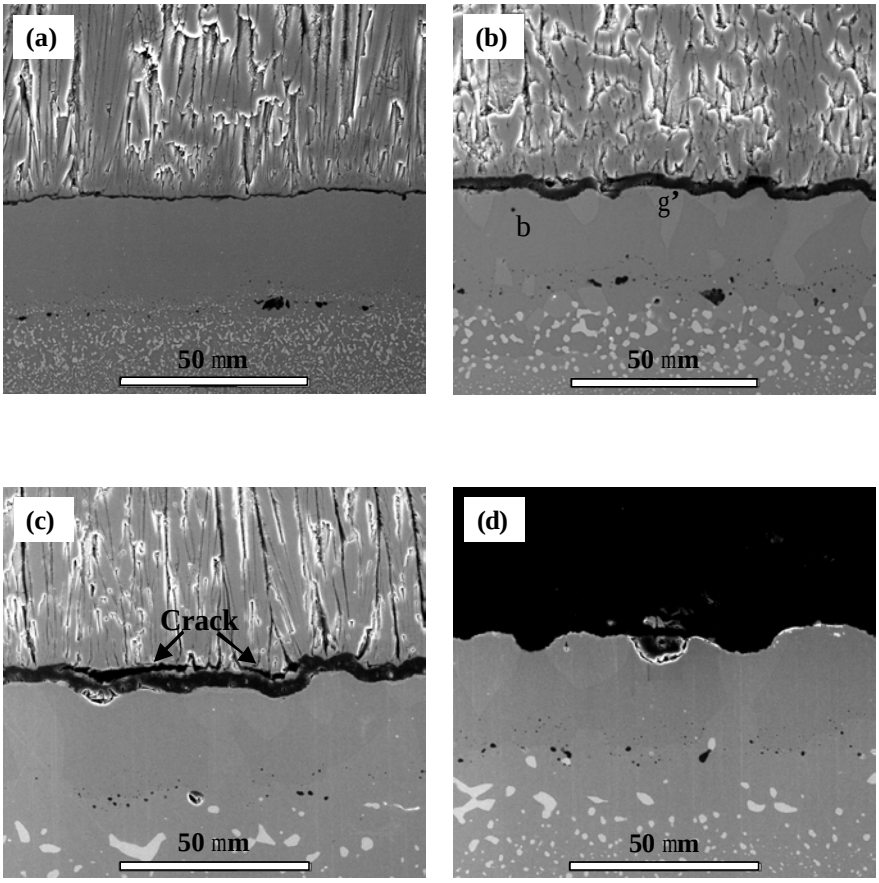

Fig. 3.102. Microstructural evolution at (a) 0 cycles, (b) 60 cycles, (c) 125 cycles and (d) 190 cycles at 1151°C

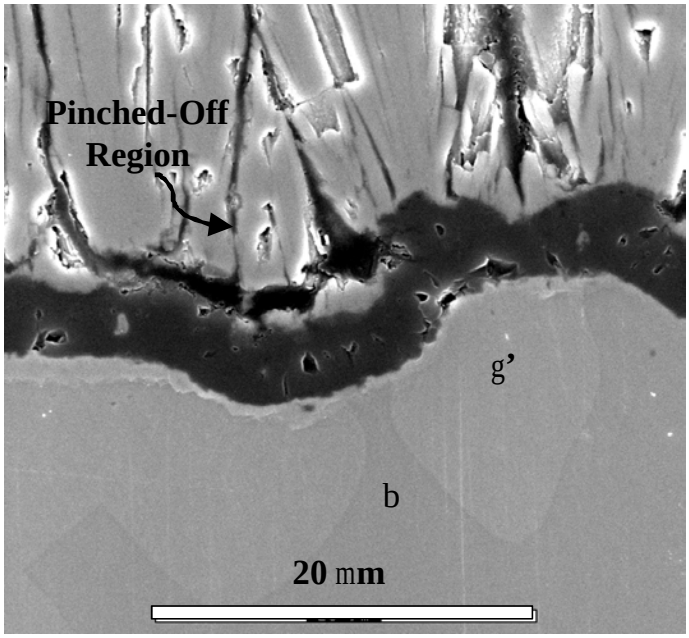

Fig. 3.103. Higher magnification image showing a typical example of crack initiation

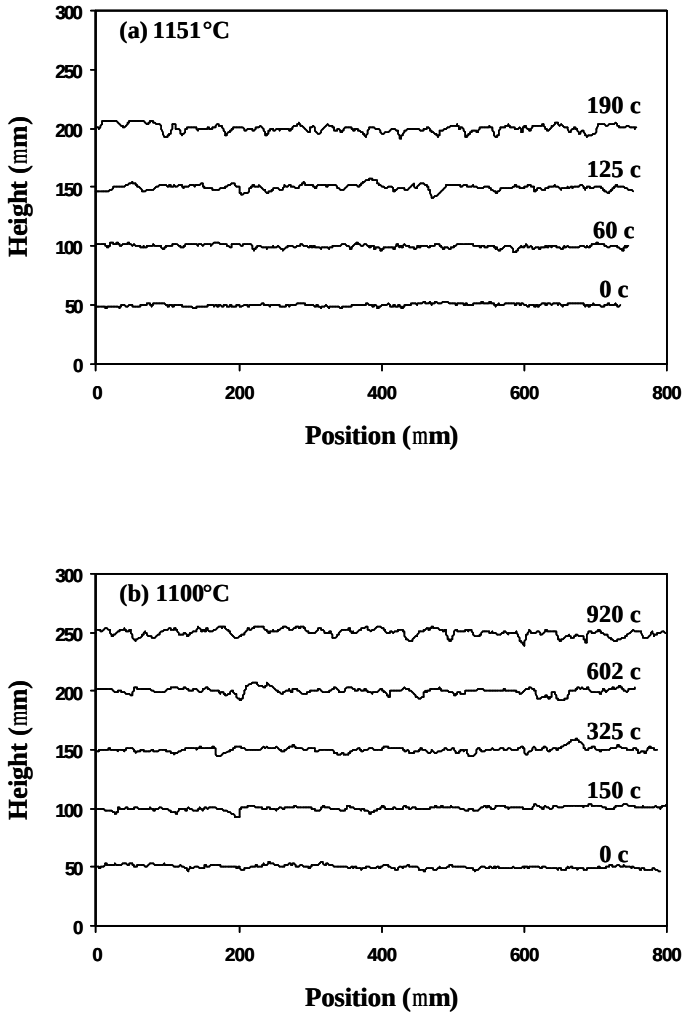

Fig. 3.104. Profiles of metal/oxide interface at various stages of thermal cycling at (a) 1151°C and (b) 1100°C

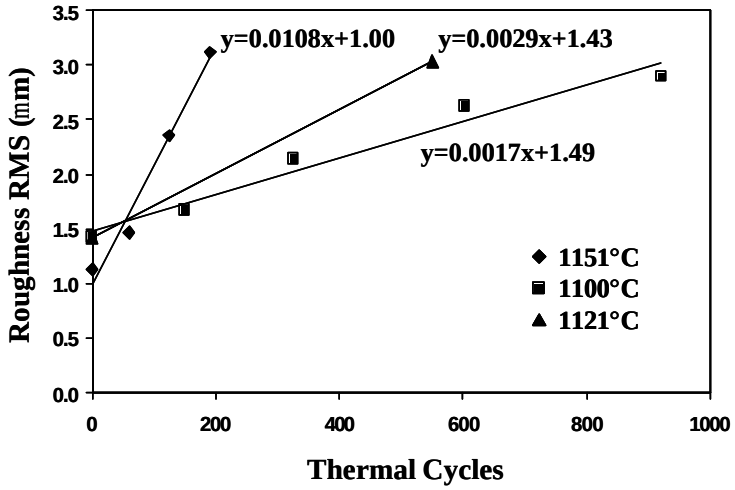

Fig. 3.105. Root-mean-square roughness (RMS) of metal/oxide interface as a function of thermal cycles at various temperatures

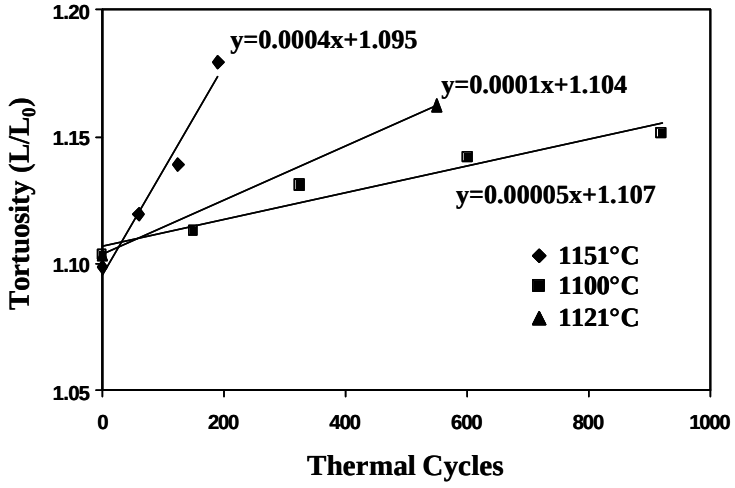

Fig. 3.106. Tortuosity of metal/oxide interface as a function of thermal cycles at various temperatures

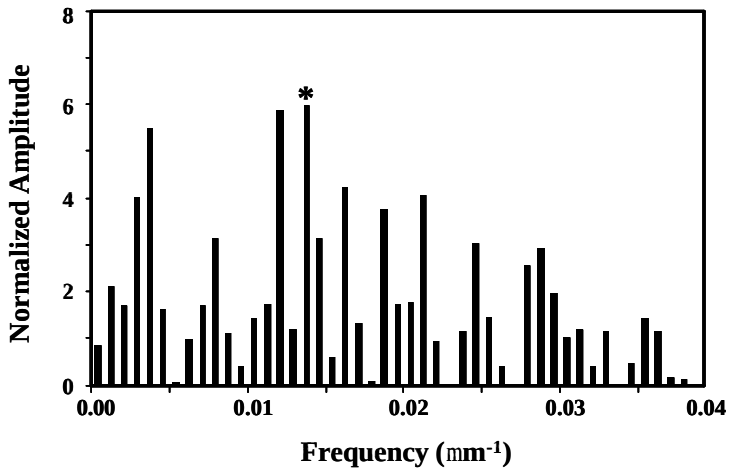

Fig. 3.107. Power spectrum plot for profile of specimen after 125 cycles at 1151°C in Fig. 4.8

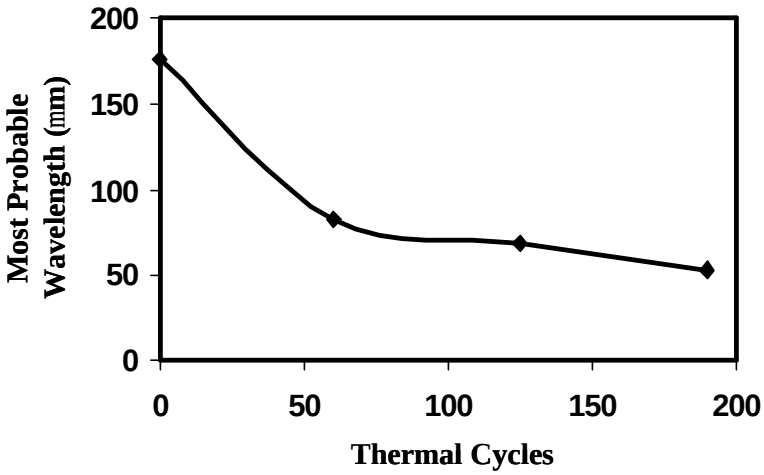

Fig. 3.108. Probable wavelength as a function of thermal cycles for specimens tested at 1151°C

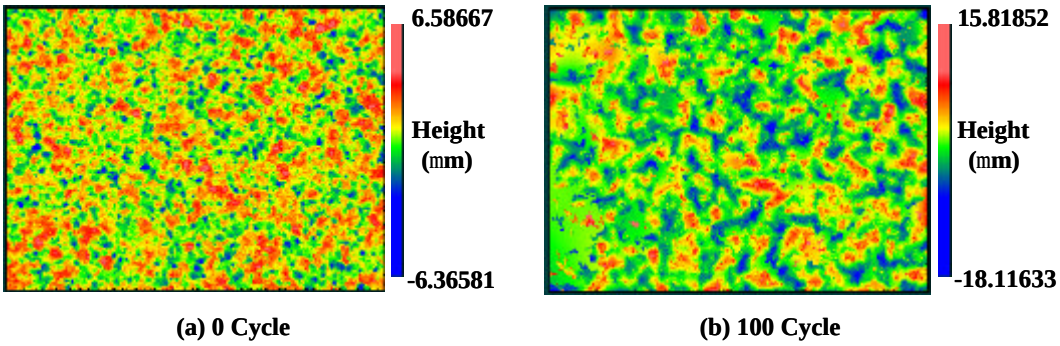

Fig. 3.109. Filled plot of back side of TBC specimen after (a) 0 and (b) 100 cycles at 1151°C

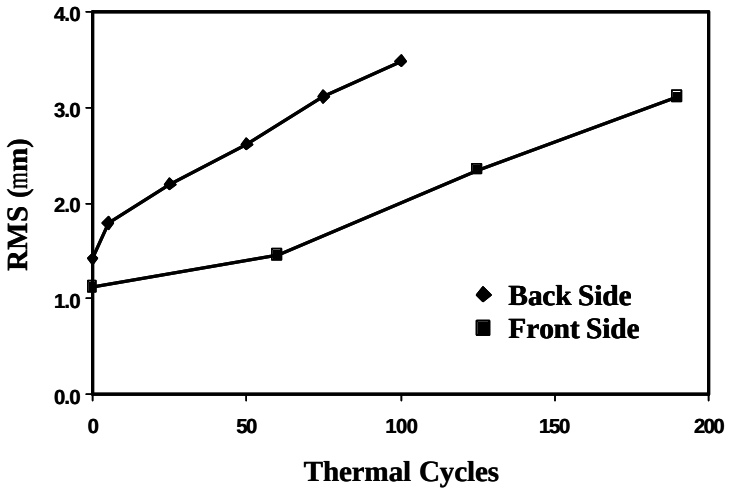

Fig. 3.110. RMS value of back side (bare bond coat) and front side (under ceramic top coat) of bond coat surface as a function of thermal cycles at 1151°C.

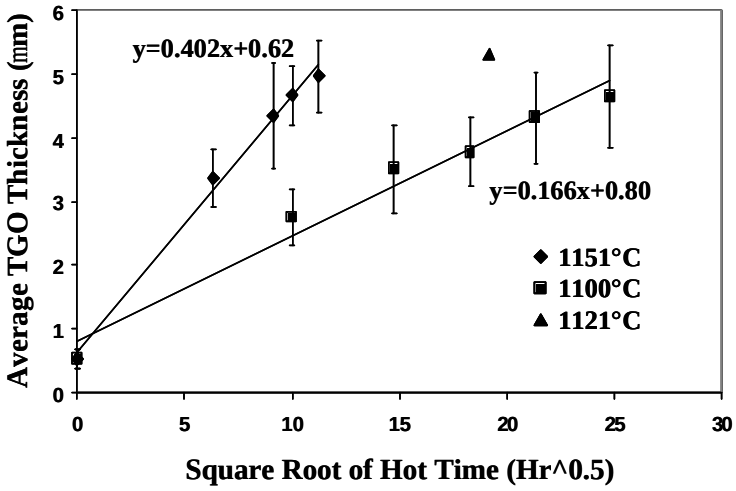

Fig. 3.111. TGO Thickness as a function of square root of hot time at various temperatures

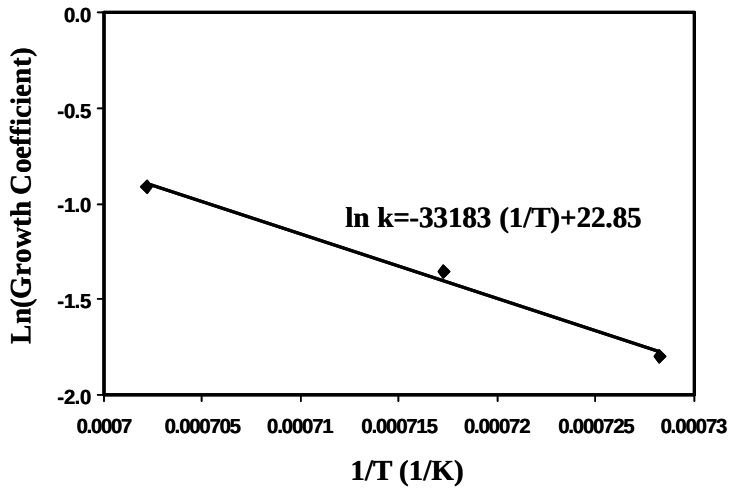

Fig. 3.112. Logarithm of parabolic growth coefficient (ln k) as a function of the reciprocal of the temperature (1/T)

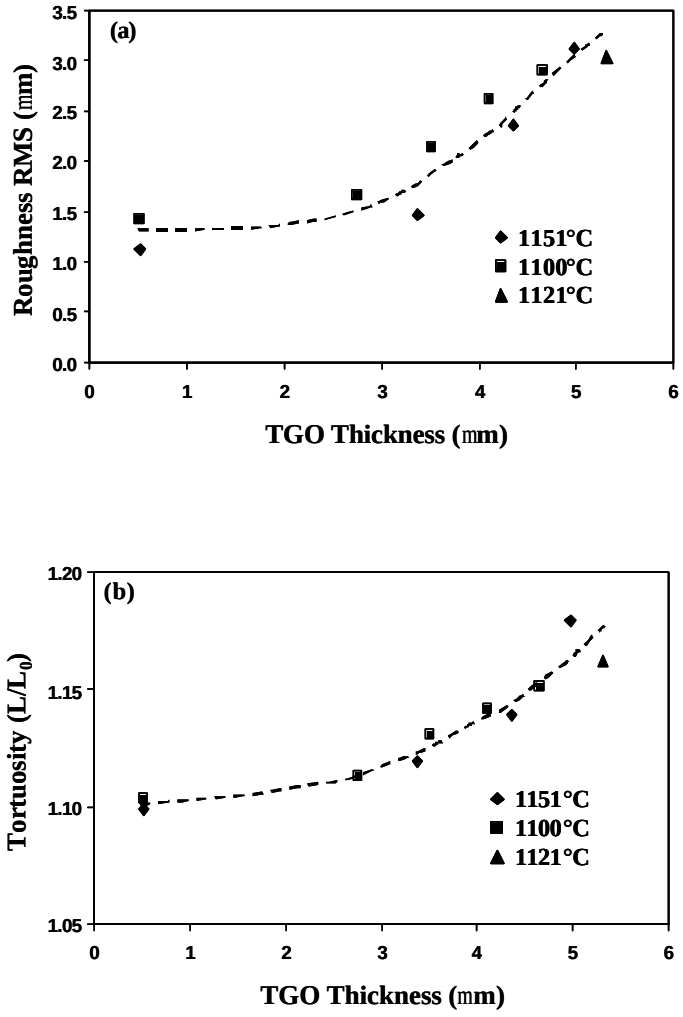

Fig. 3.113. (a) RMS roughness and (b) tortuosity as a function of TGO thickness

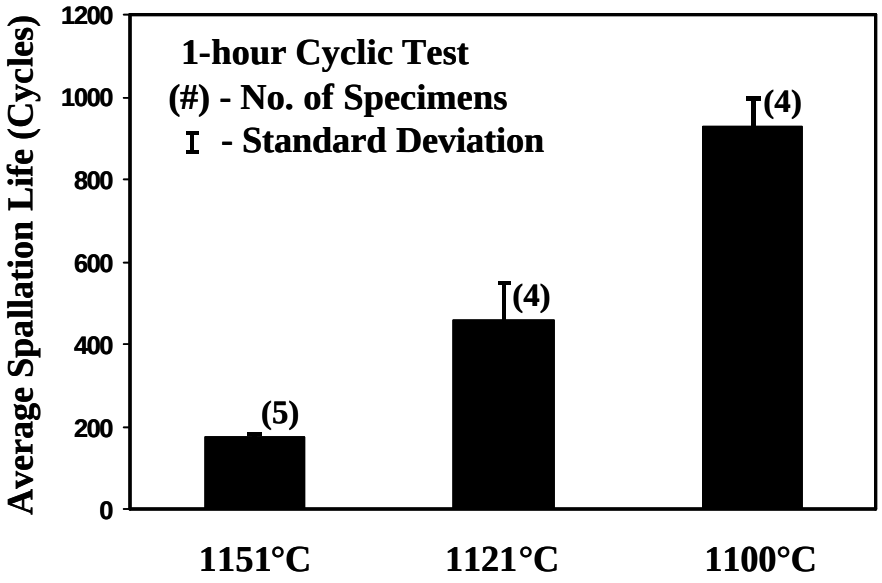

Fig. 3.114. Spallation lives of TBC specimens at various temperatures

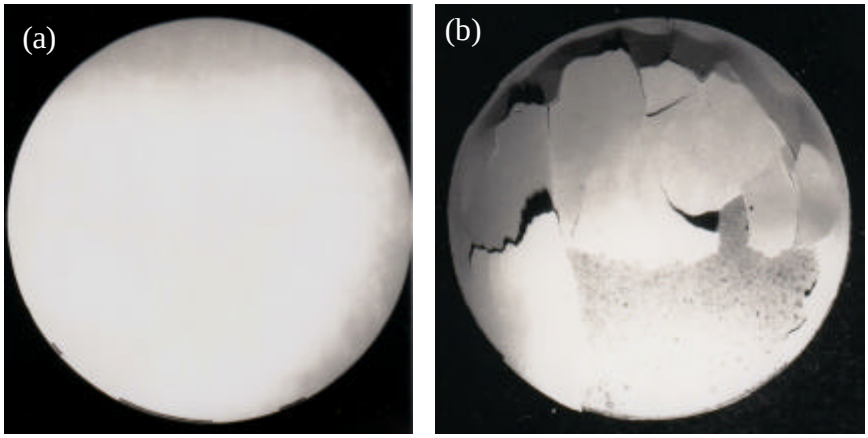

Fig. 3.115. Macrographs of specimens at (a) about 20% and (b) 100% of life

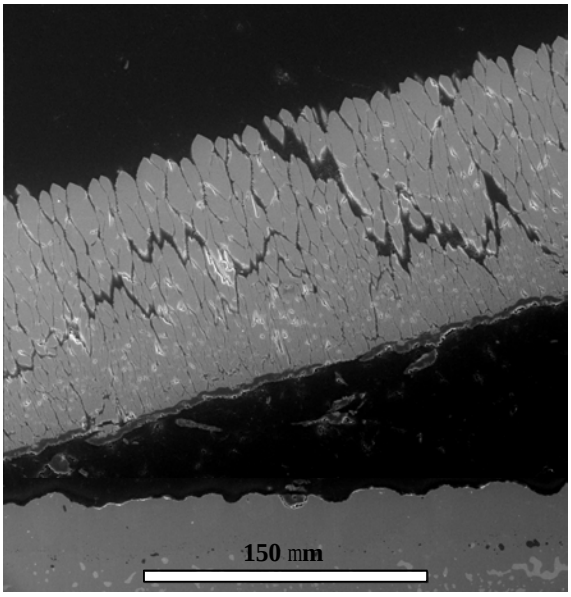

Fig. 3.116. Cross-sectional Micrograph of failed specimen showing buckling

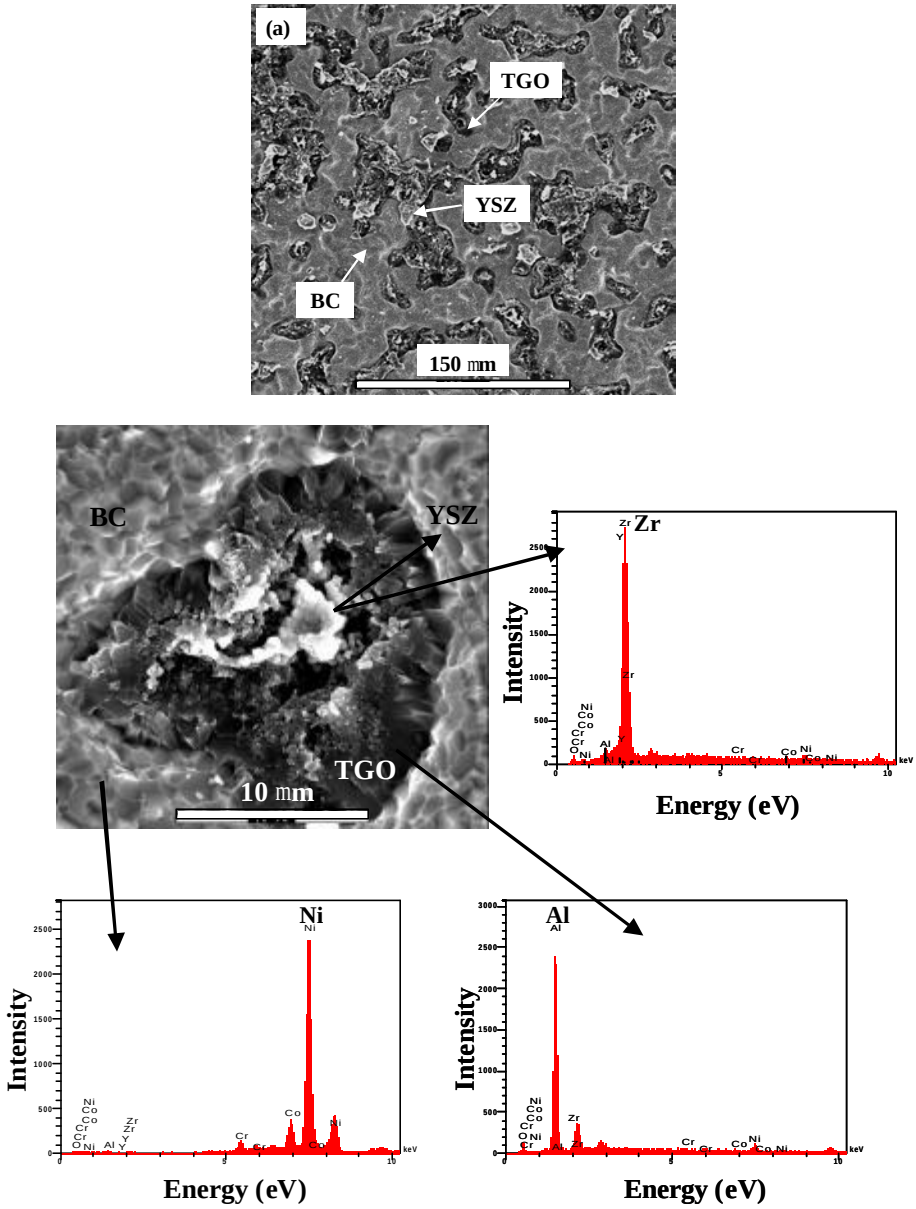

(b)

Fig. 3.117. Images of spalled surface of substrate side at (a) lower magnification and (b) higher magnification and associated EDS spectra after 190 cycles at 1151°C

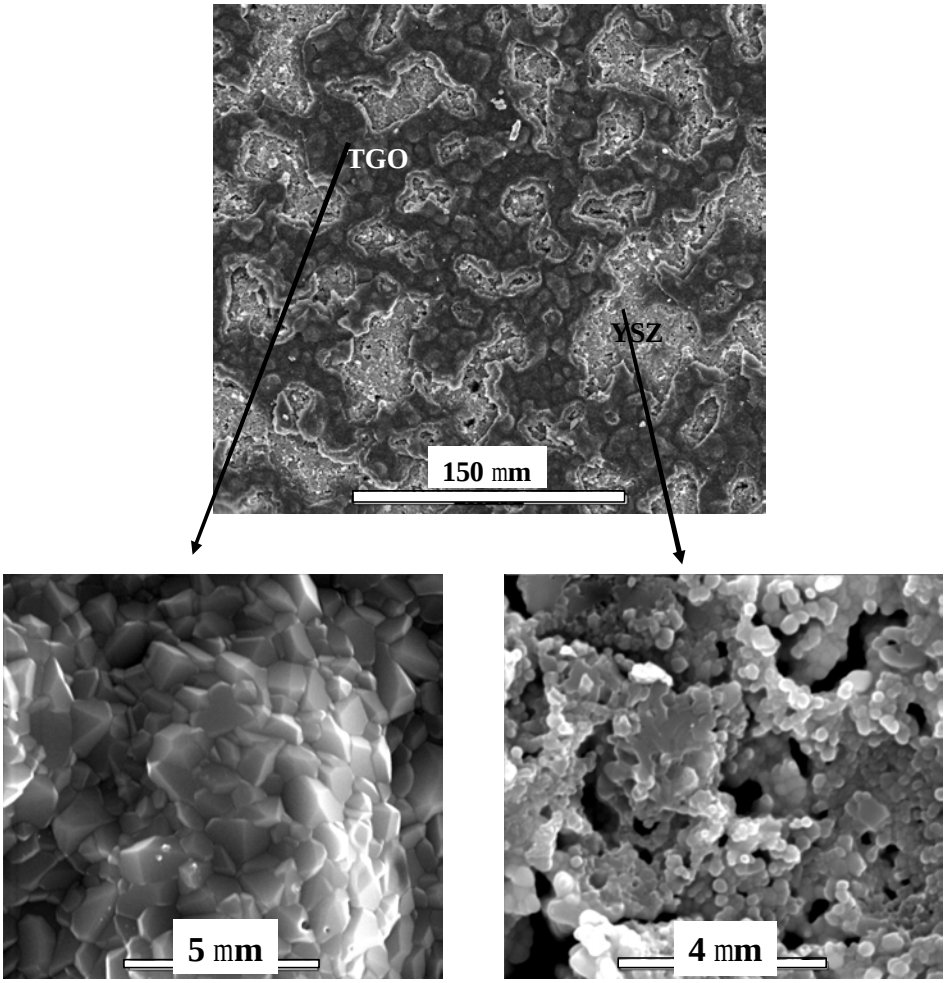

Fig. 3.118. Spalled surface of bottom side of YSZ after 190 cycles at 1151°C

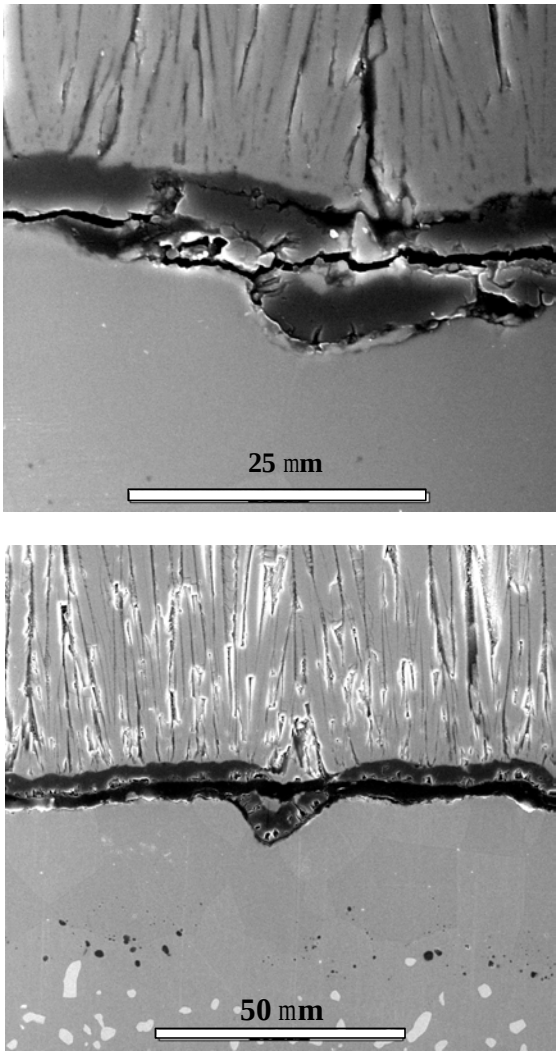

Fig. 3.119. Cross section images showing crack go through TGO and along TGO/BC interface

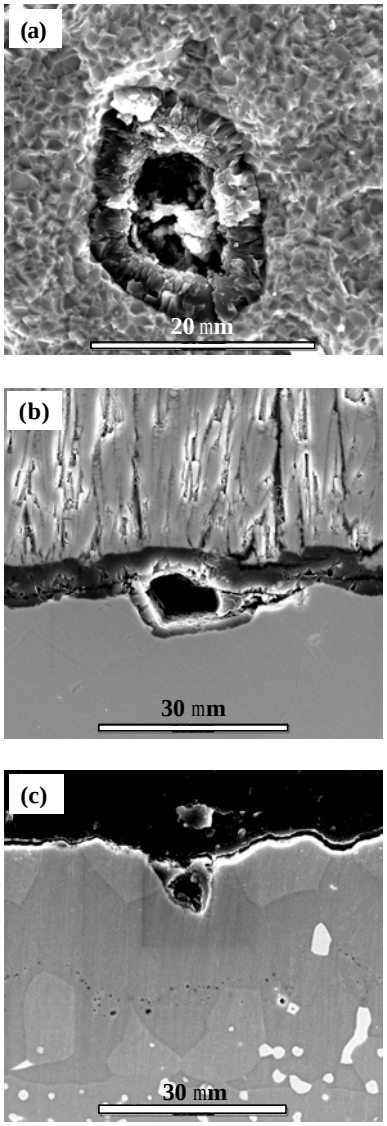

Fig. 3. 120. Higher magnification images of spalled surface on substrate side (a) and cross-sectional images (b, c) showing cavity

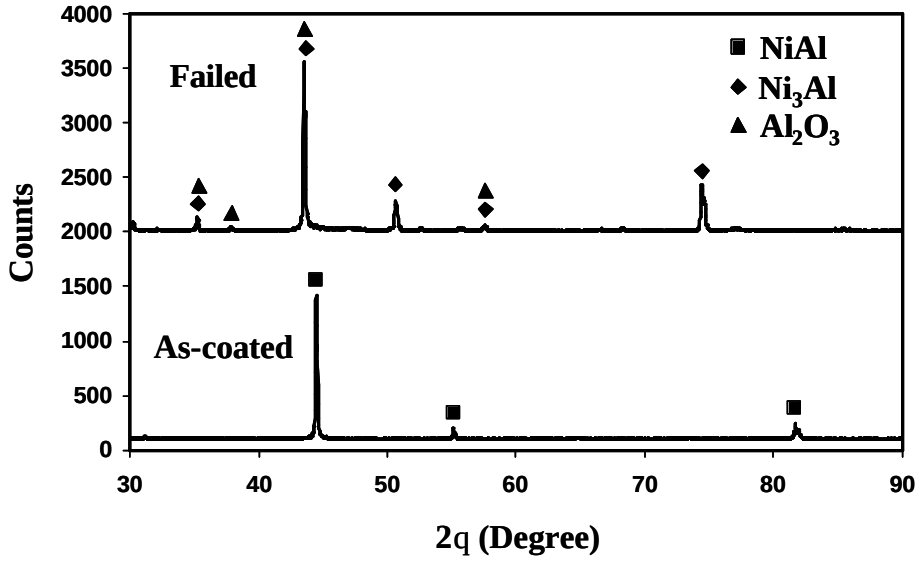

Fig. 3.121. XRD patterns of bond coat for as-coated and failed specimens

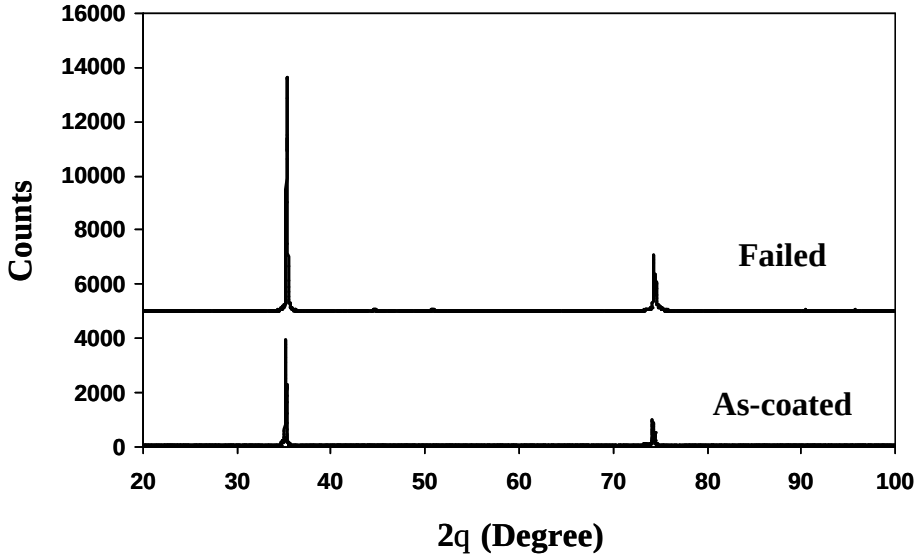

Fig. 3.122. XRD patterns of YSZ top surface for as-coated and failed specimens

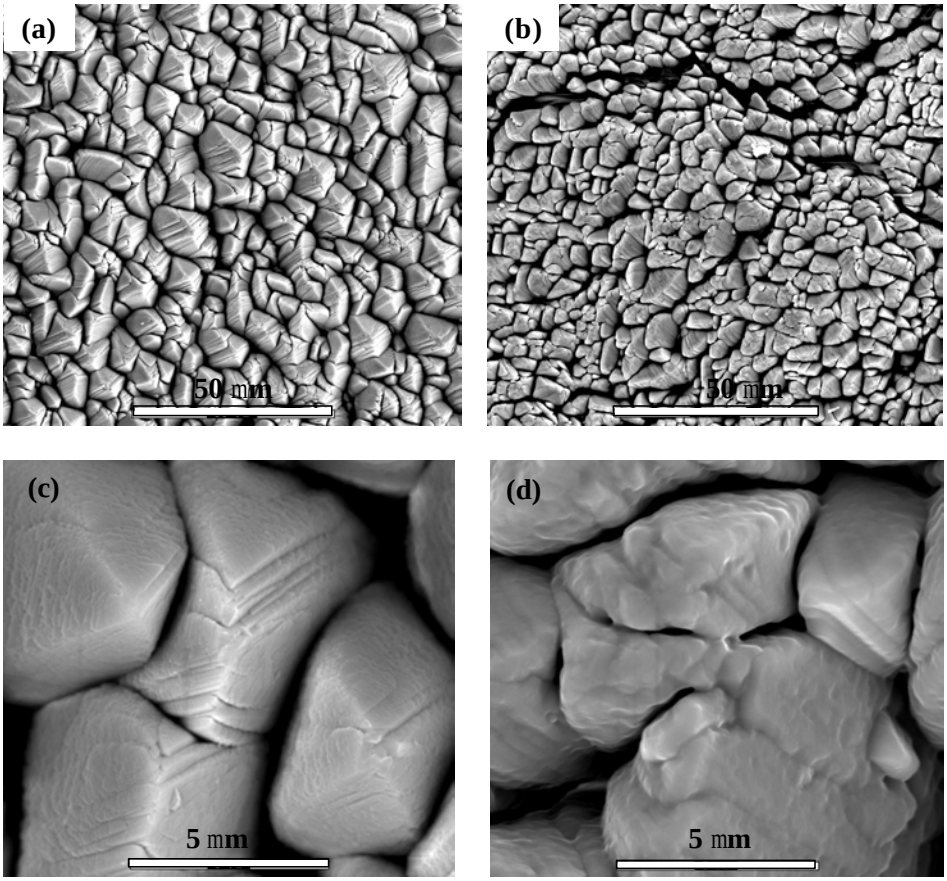

Fig. 3.123. Top surface morphology of as-coated (a, c) and failed (b, d) specimens

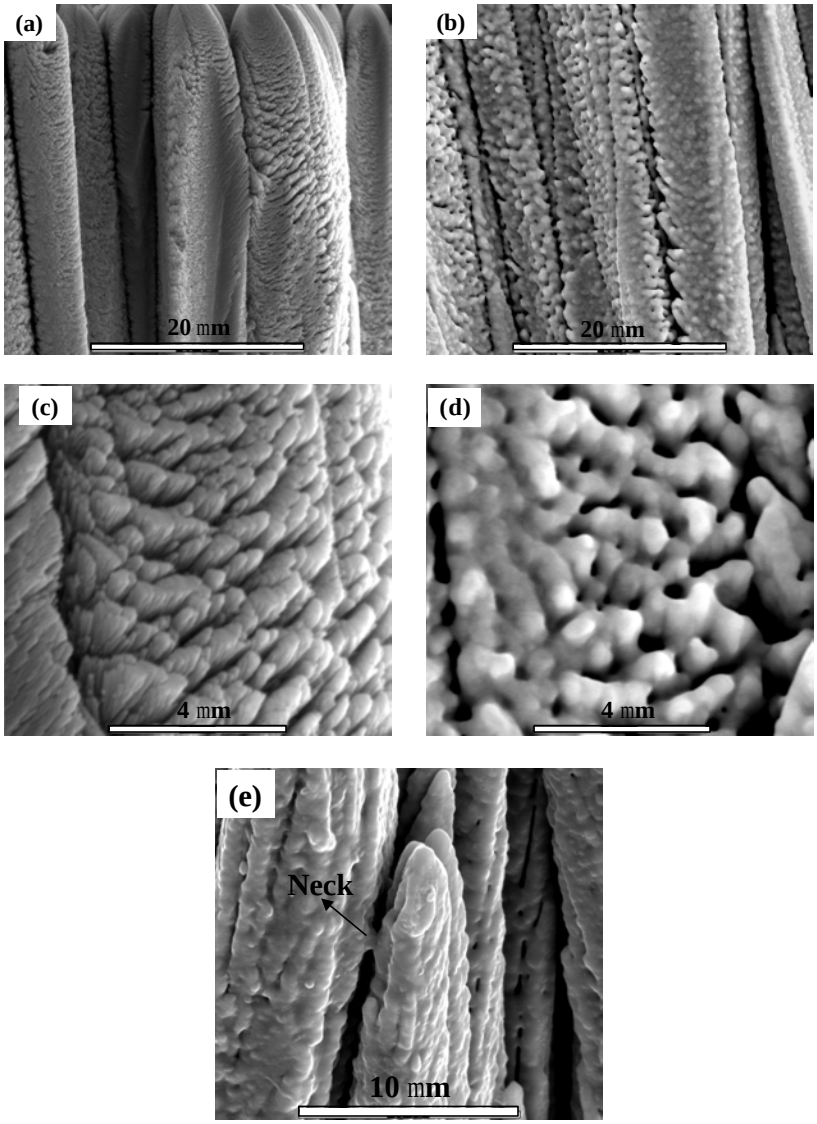

Fig. 3.124. Cross section images of YSZ columns of as-coated (a, c) and failed (b, d, e) specimens

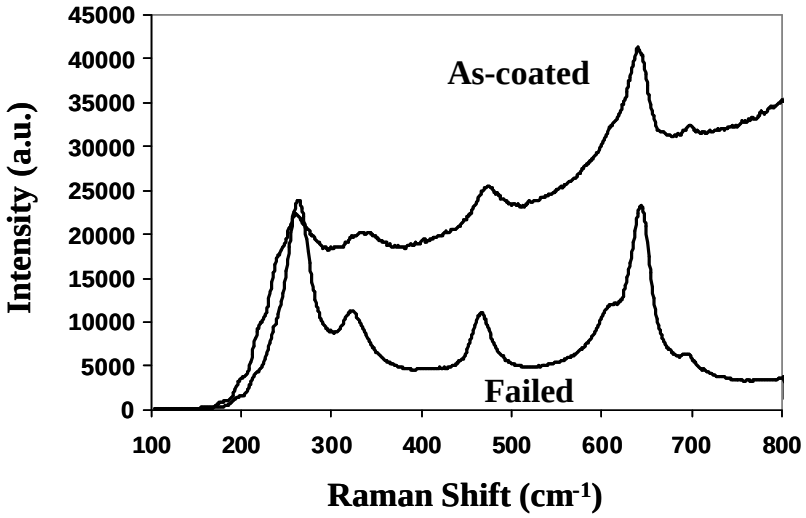

Fig. 3.125. Raman spectra of YSZ coating for as-coated and failed specimens both showing t' phase characteristic peaks

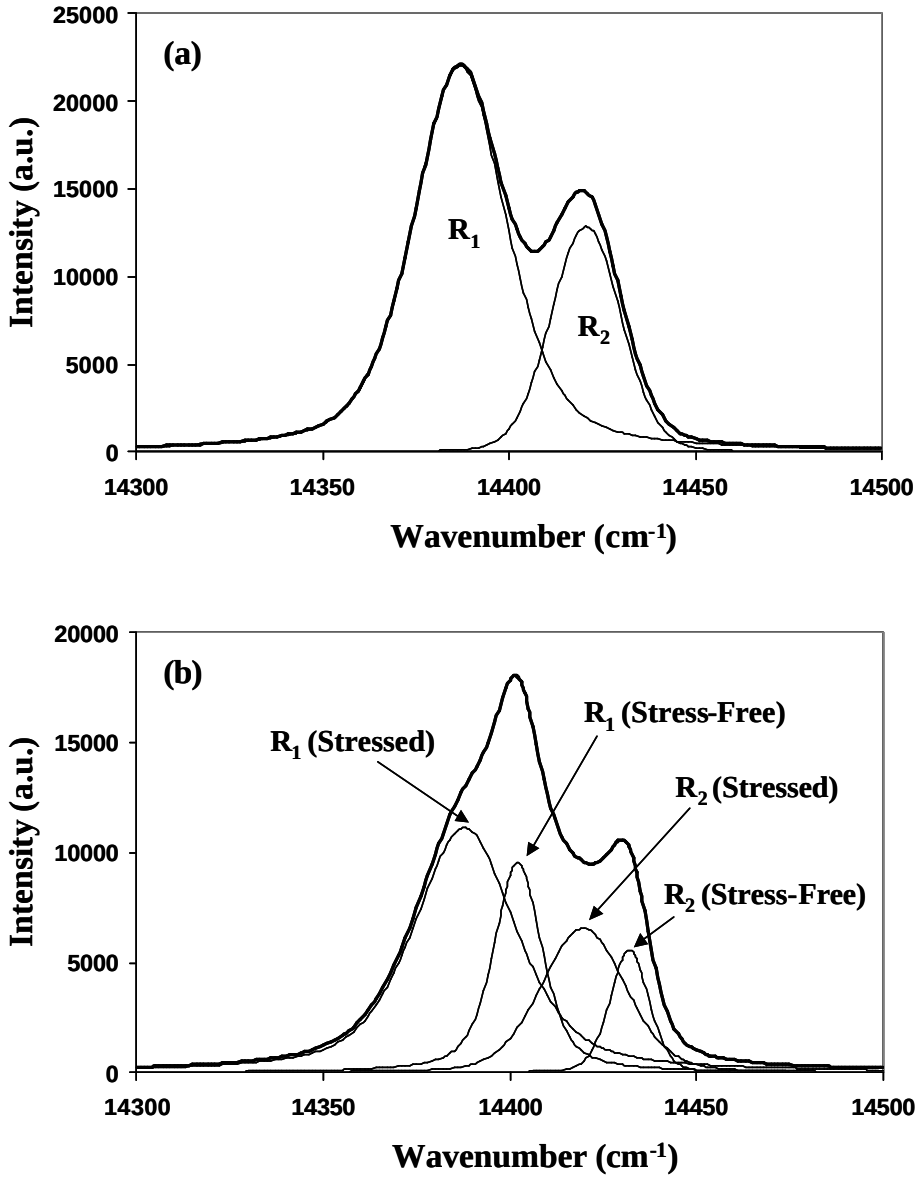

Fig. 3.126. Typical photoluminescence spectra showing (a) one set of peak pairs and (b) two sets of peak pairs

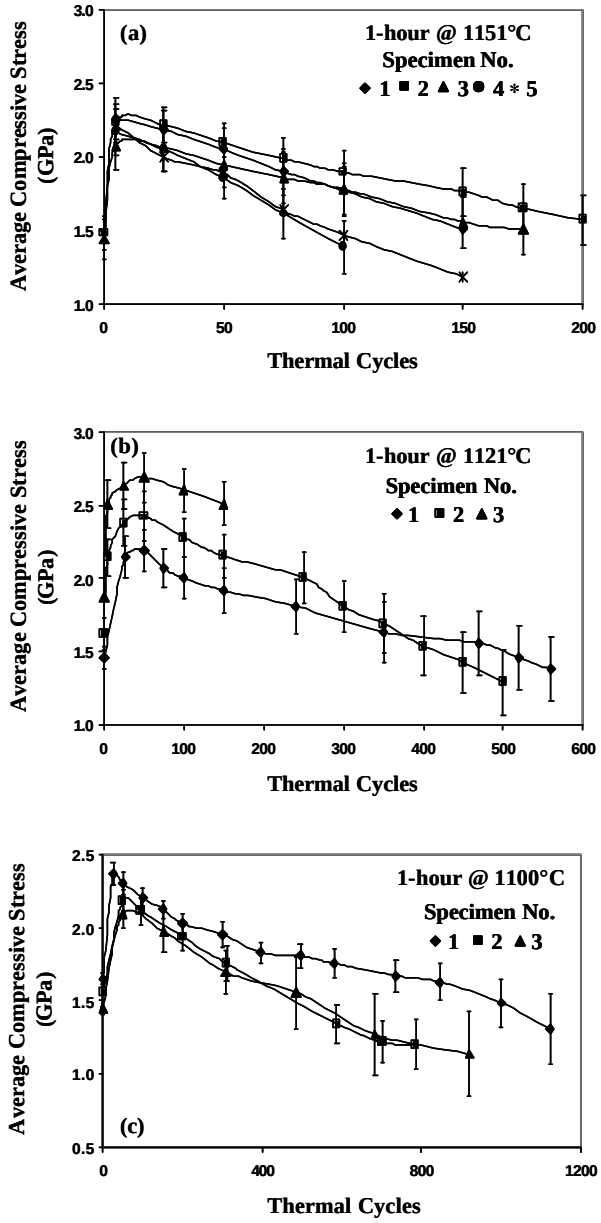

Fig. 3.127. Evolution of TGO stress as a function of thermal cycles at (a) 1151°C, (b) 1121°C and (c) 1100°C

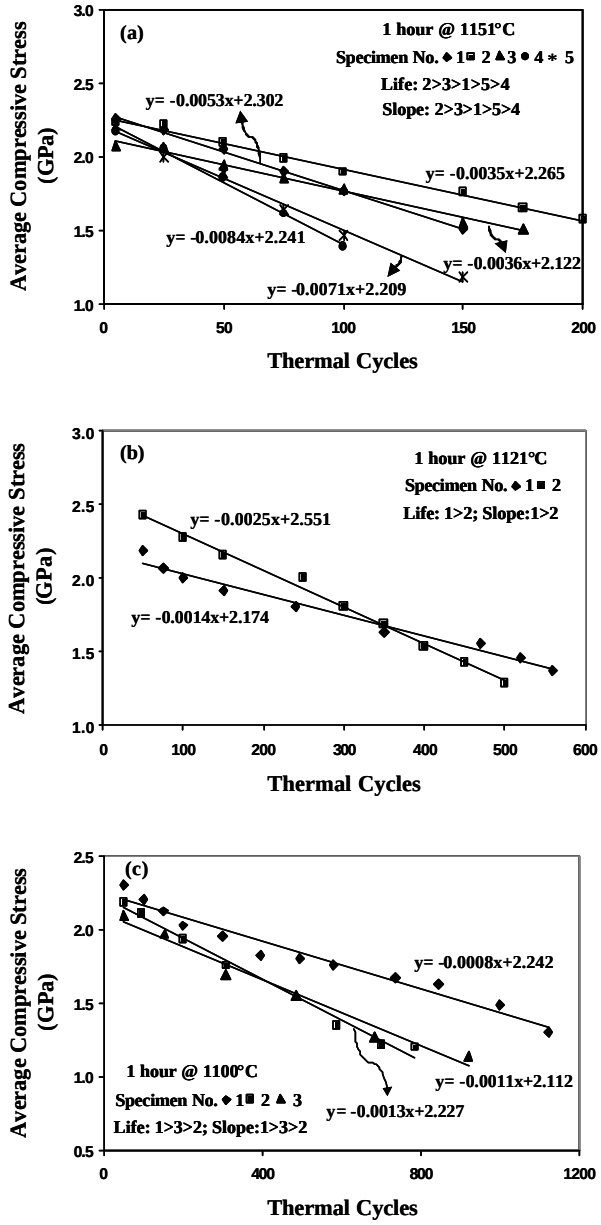

Fig. 3.128. Average stress vs. thermal cycles showing the relationship of slope and lives

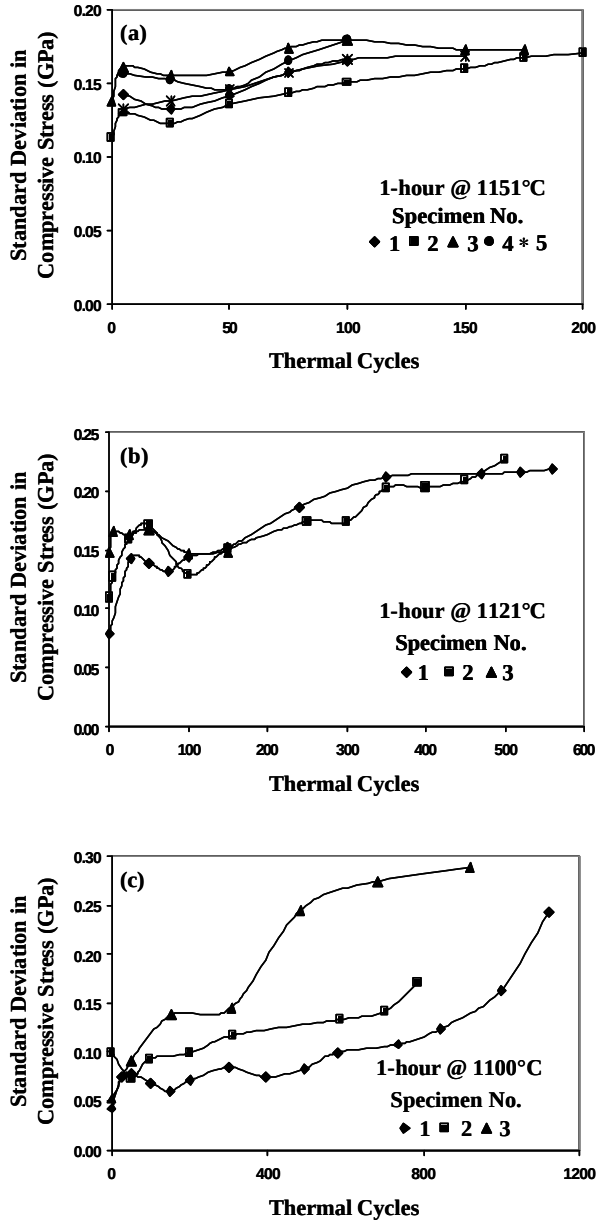

Fig. 3.129. Standard deviation in TGO stress as a function of thermal cycles at (a) 1151°C, (b) 1121°C and (c) 1100°C

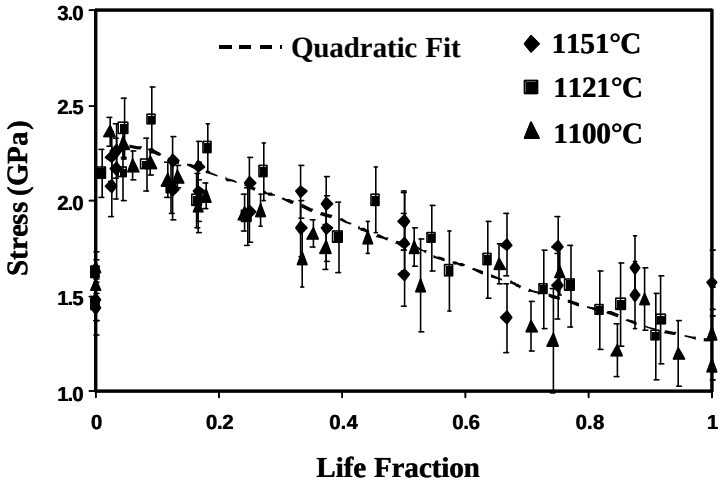

Fig. 3.130. Evolution of TGO stress as a function of life fraction at 1151°C and 1121°C

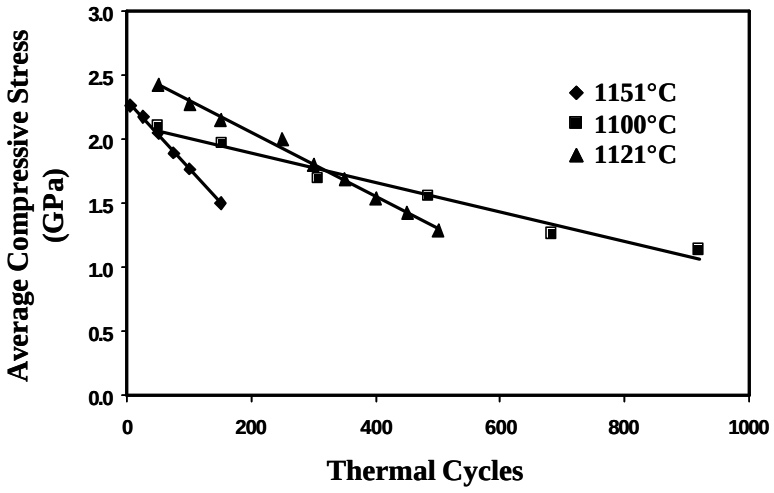

Fig. 3.131. Average TGO stress as a function of thermal cycles at various temperatures

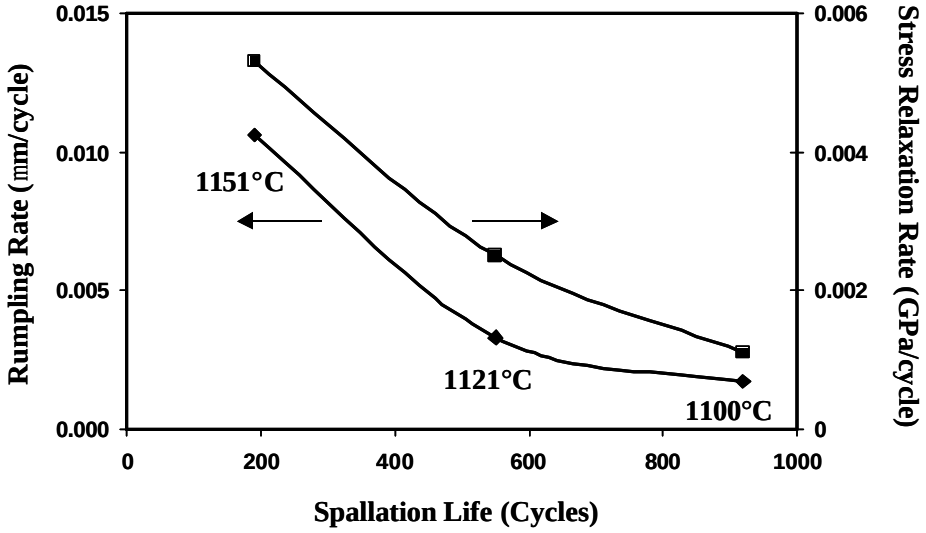

Fig. 3.132. Relationships among rumpling, TGO stress relaxation and specimen life

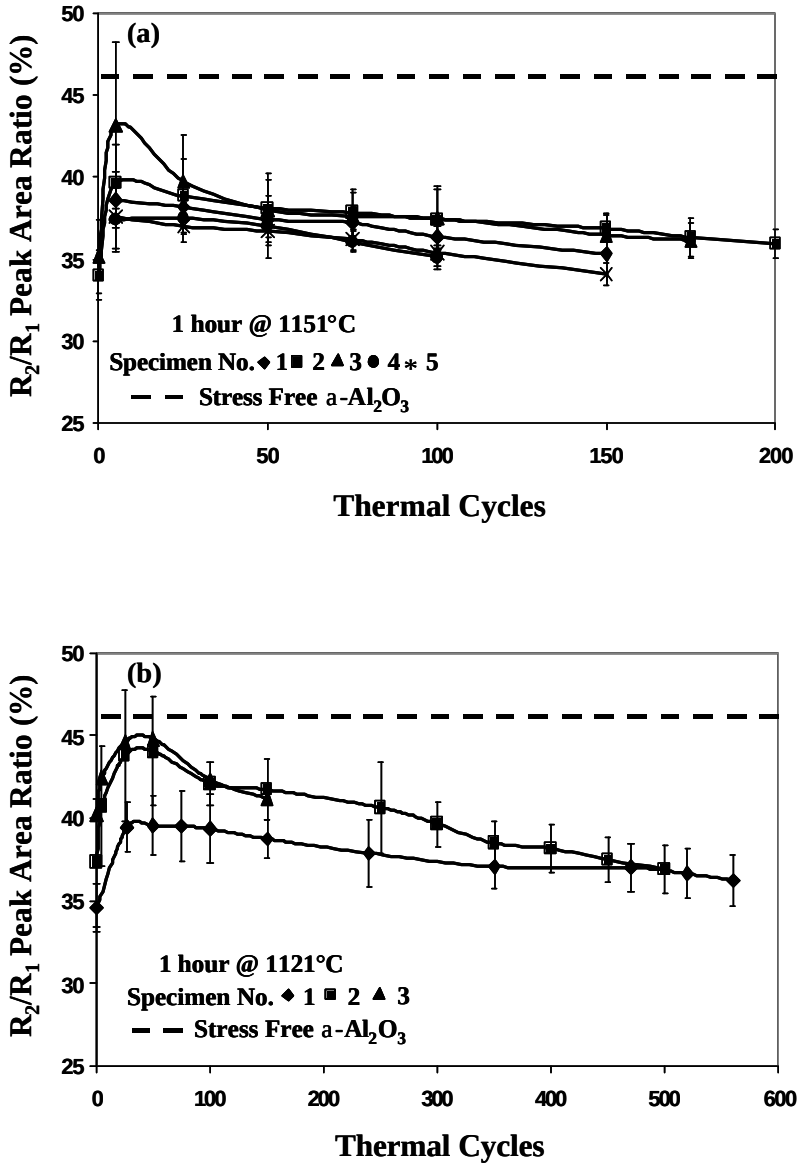

Fig. 3. 133. Change of area ratio of R_1 and R_2 peak with thermal cycling at (a) 1151°C and (b) 1121°C

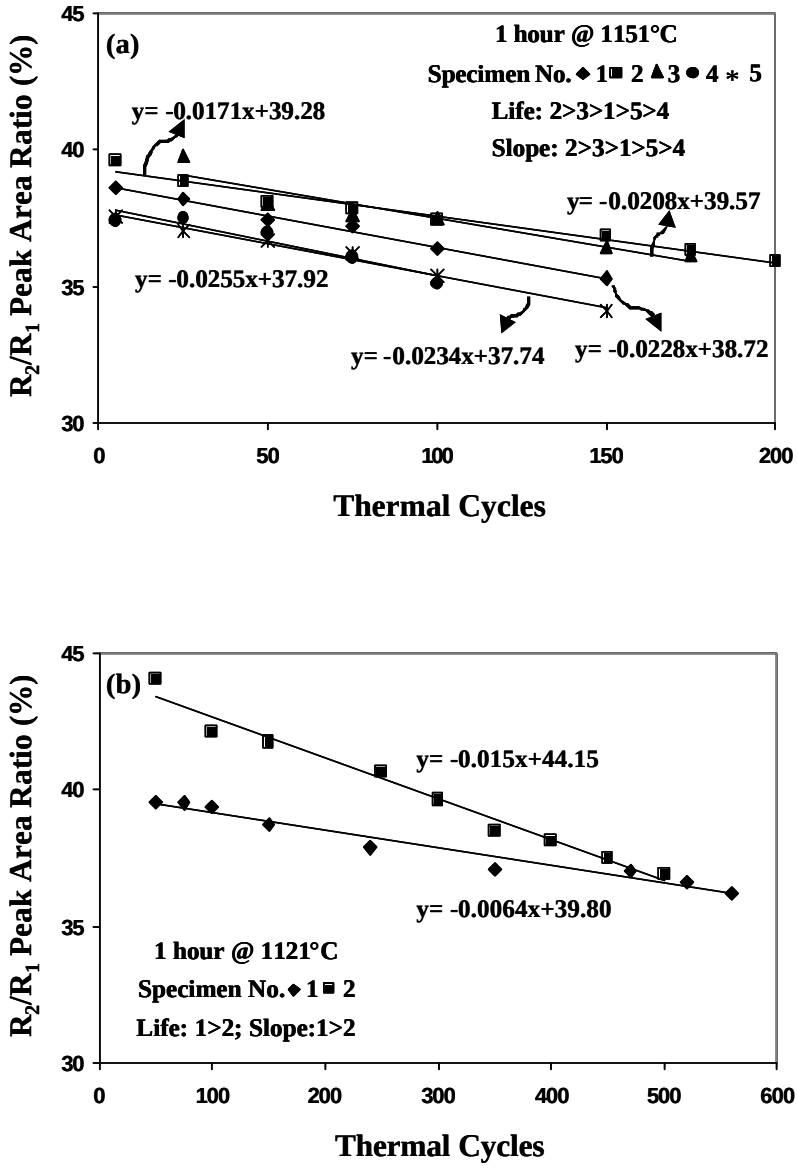

Fig. 3.134. Change of peak area ratio showing the relationship of slope and lives

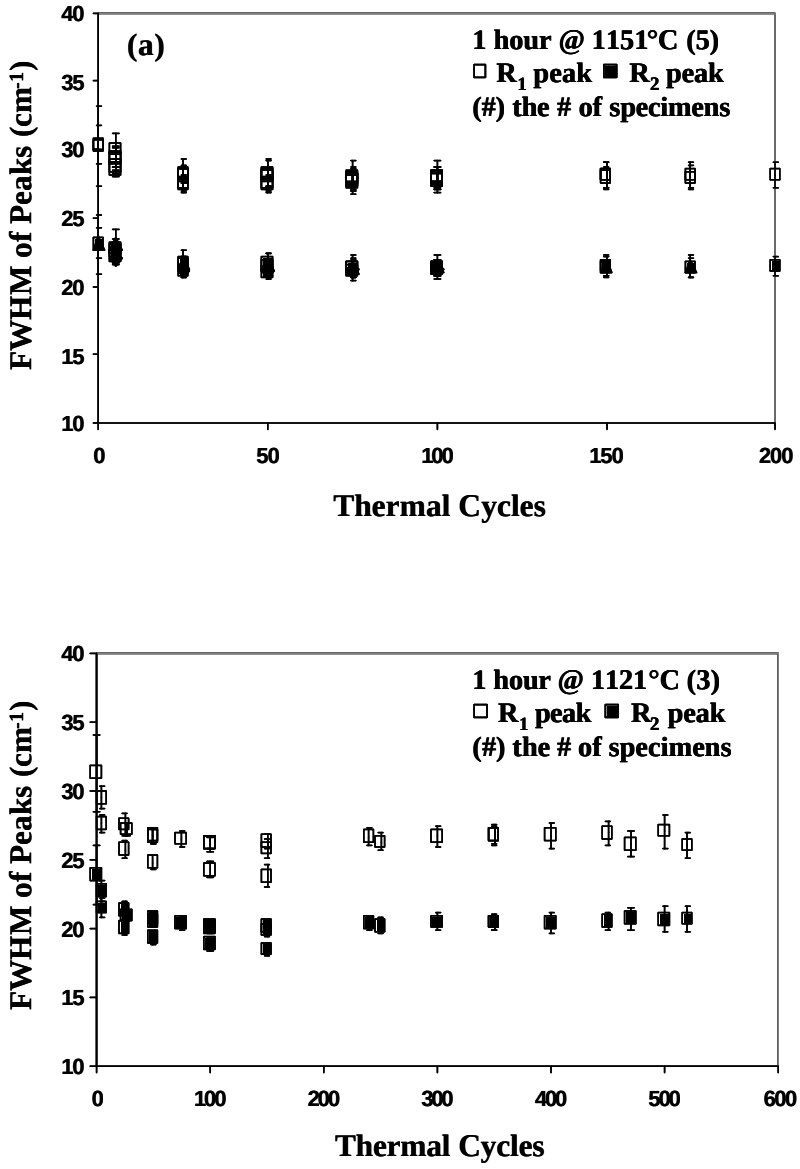

Fig. 3.135. Change of R_1 and R_2 peak width with thermal cycling at (a) 1151°C and (b) 1121°C

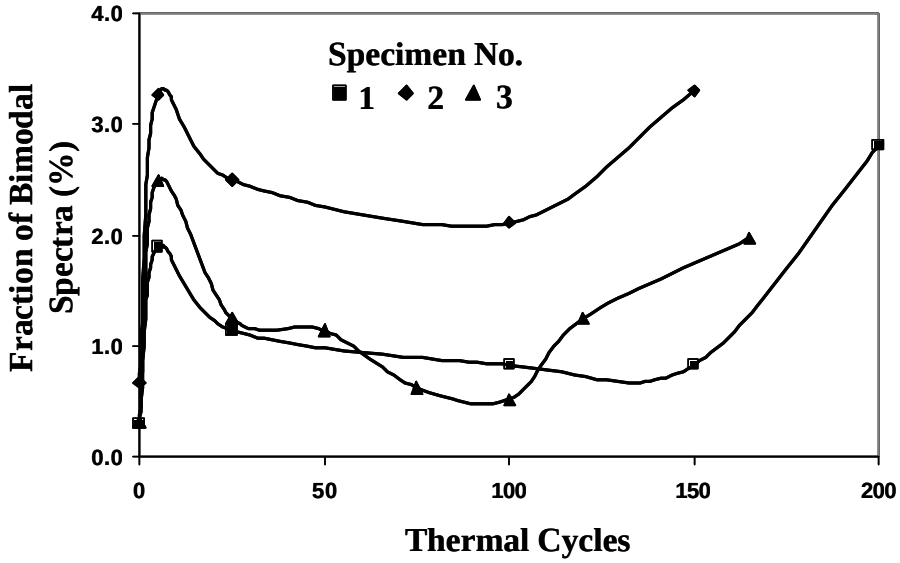

Fig. 3.136. Fraction of bimodal spectra of TBC specimens as a function of thermal cycles at 1151°C

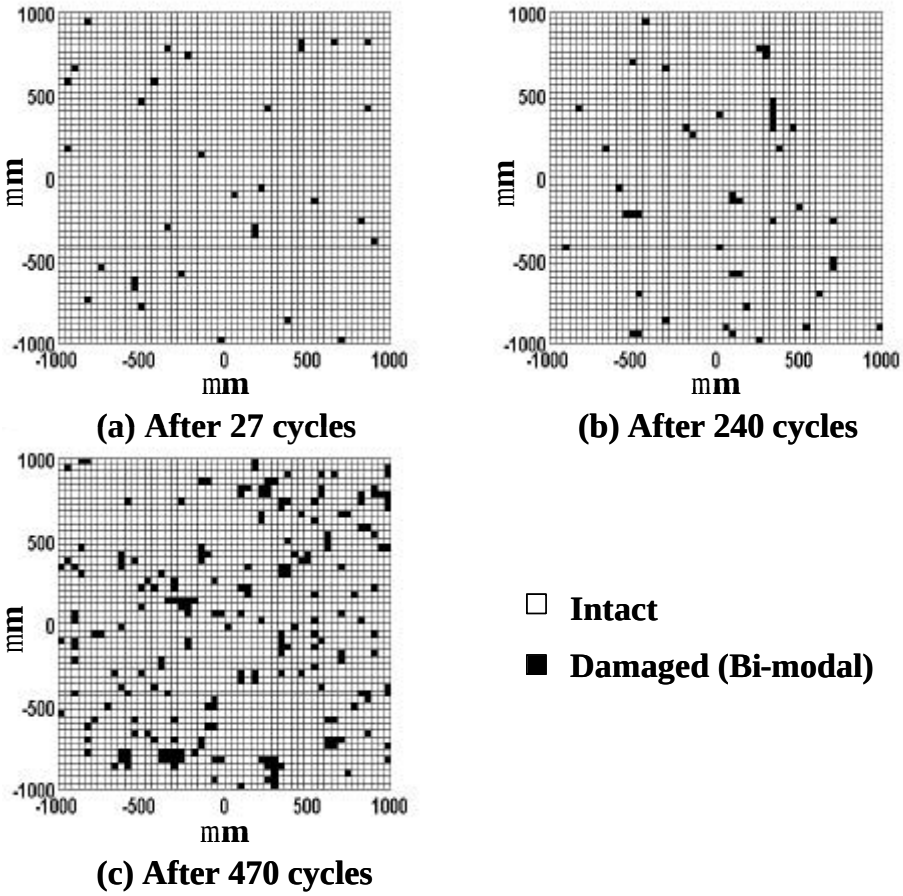

Fig. 3.137. TGO stress mapping distribution of TBC specimens after (a) 27 cycles, (b) 240 cycles and (c) 470 cycles at 1121°C

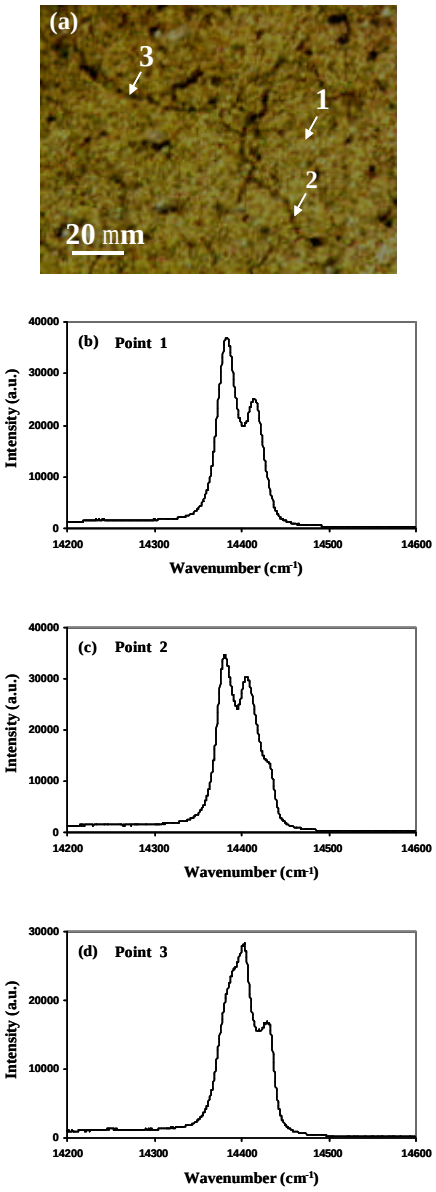

Fig. 3.138. Optical image (a) and corresponding luminescence spectra of alumina scale formed on different location of bare bond coat after oxidation 10 minutes at 1151°C showing: (b) unimodal, (c) bimodal, and (d) bimodal

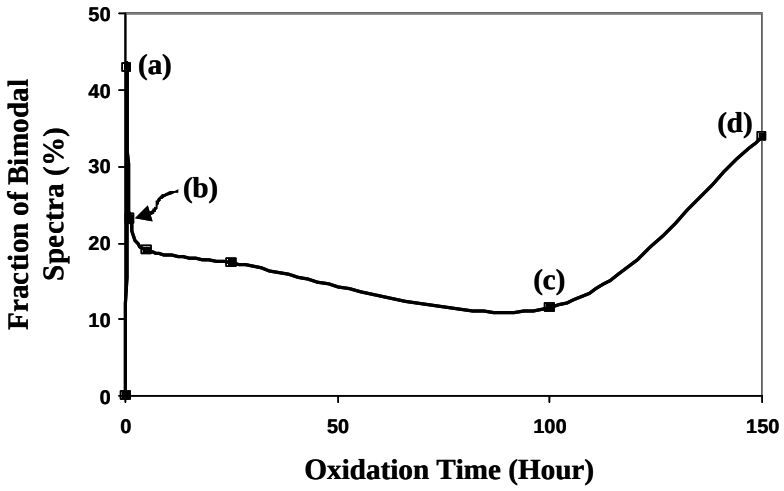

Fig. 3.139. Evolution of fraction of bimodal spectra on bare bond coated sample after oxidation at 1151°C for (a) 10 minutes, (b) 1 hour, (c) 100 hours, and (d) 150 hours

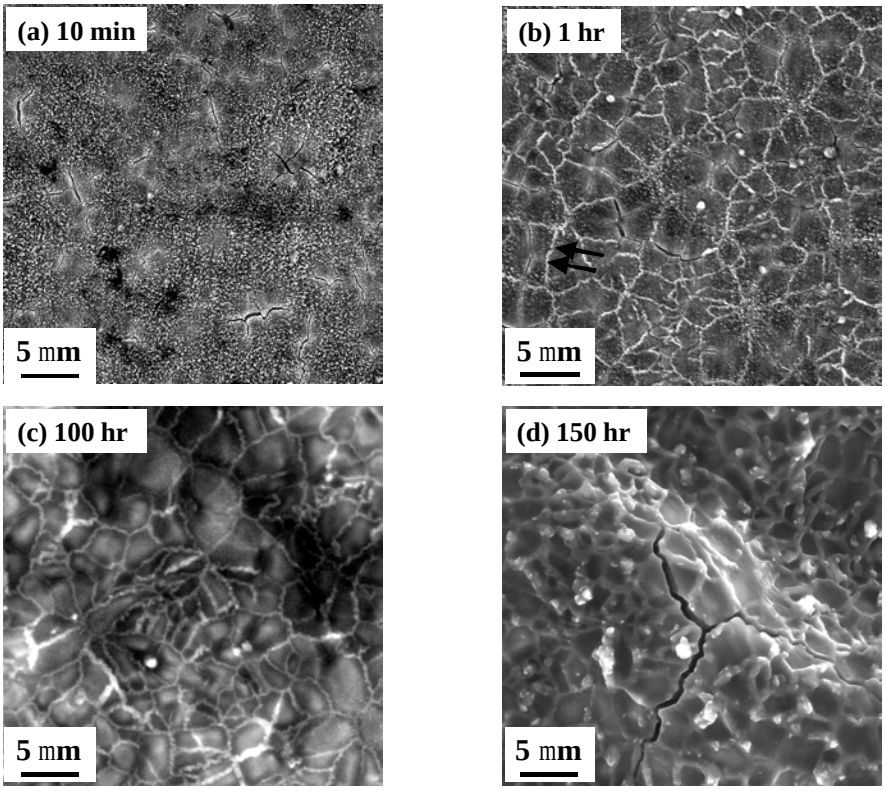

Fig. 3.140. Oxide morphology on bare bond coated sample after oxidation at 1151°C for (a) 10 minutes, (b) 1 hour, (c) 100 hours, and (d) 150 hours

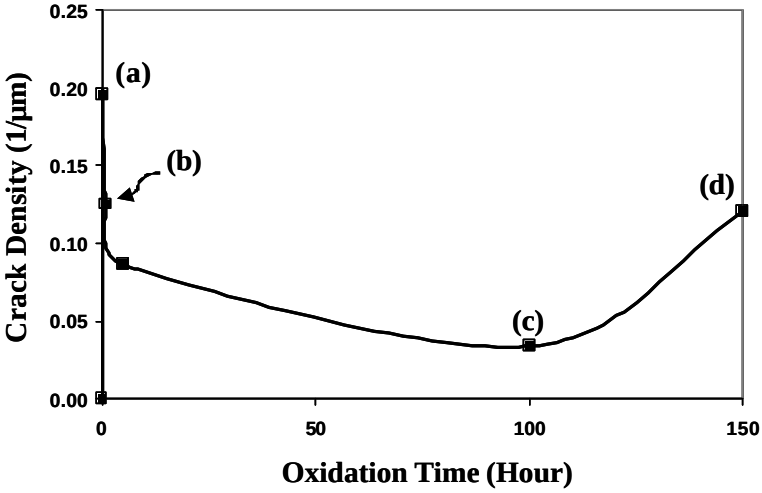

Fig. 3.141. Evolution of crack density on bare bond coated sample after oxidation at 1151°C for (a) 10 minutes, (b) 1 hour, (c) 100 hours, and (d) 150 hours

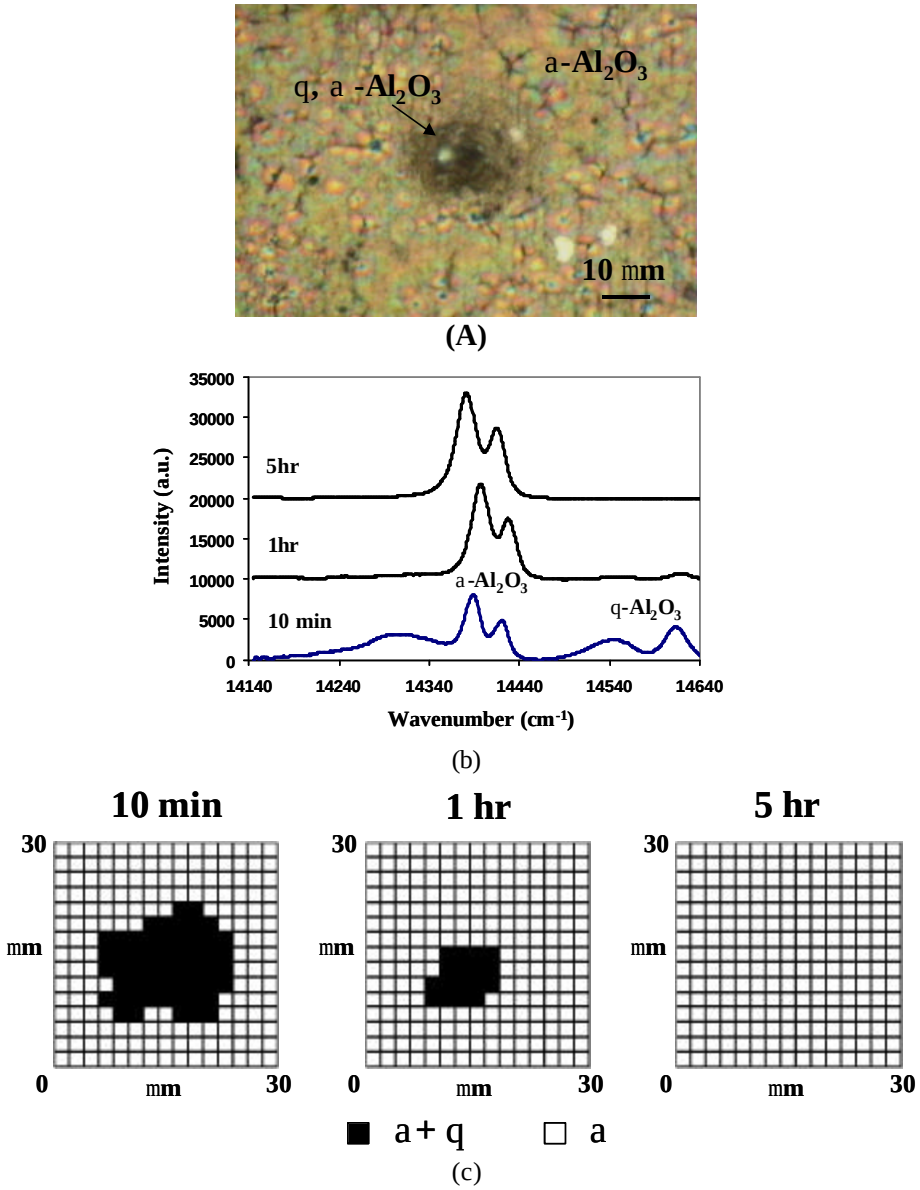

Fig. 3.142. Optical image (a), PLPS spectra (b) and oxide type distribution maps (c) of alumina scale on bare bond coated sample showing the distribution of α and θ alumina after oxidation different time at 1151°C

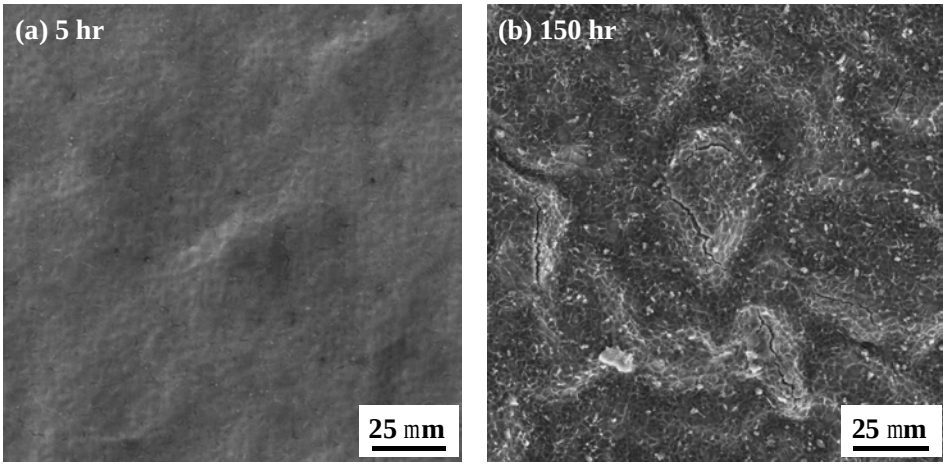

Fig. 3.143. Top surface of bare bond coated sample showing rumpling after oxidation (a) 5 hours and (b) 150 hours at 1151°C

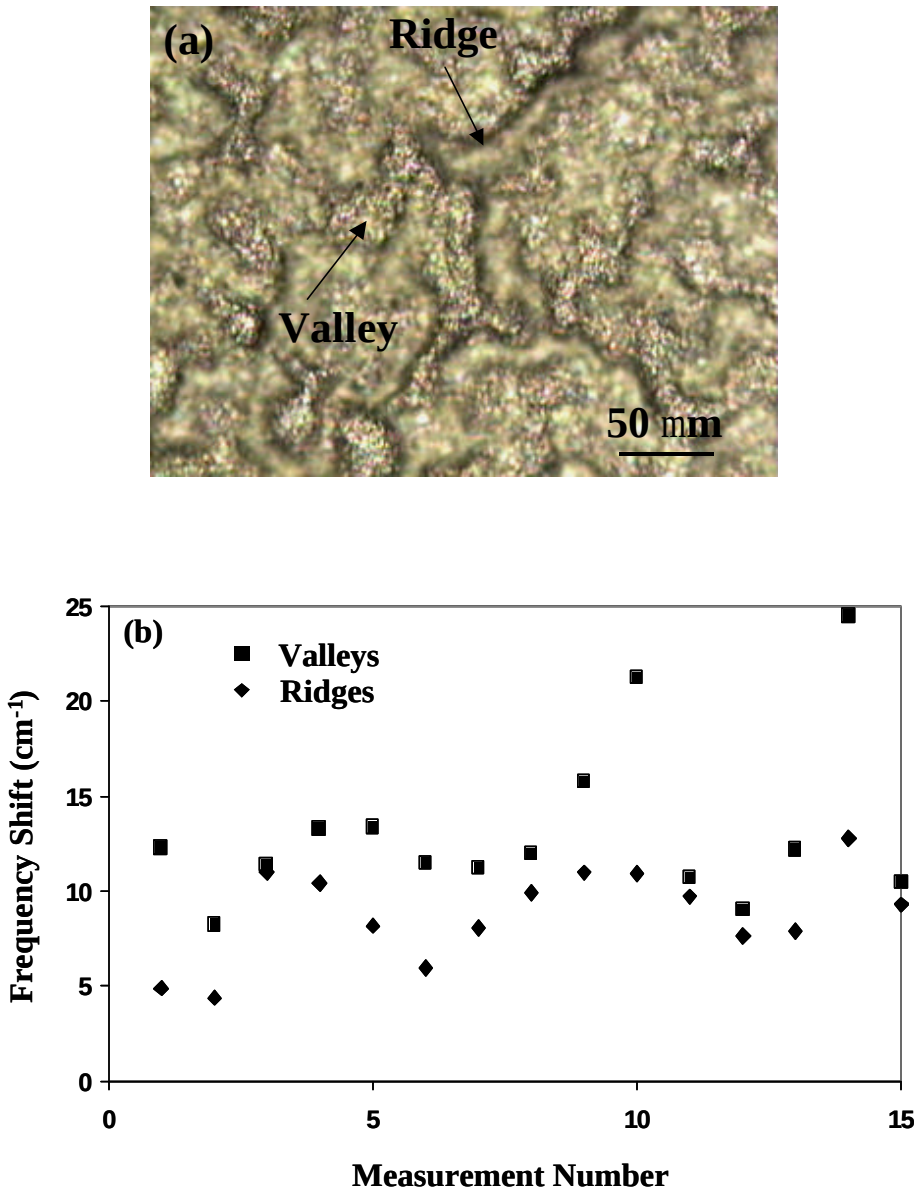

Fig. 3.144. Optical image (a) and luminescence results (b) of a series of measurements of the rumpled alumina scale after oxidation 100 hours at 1151°C

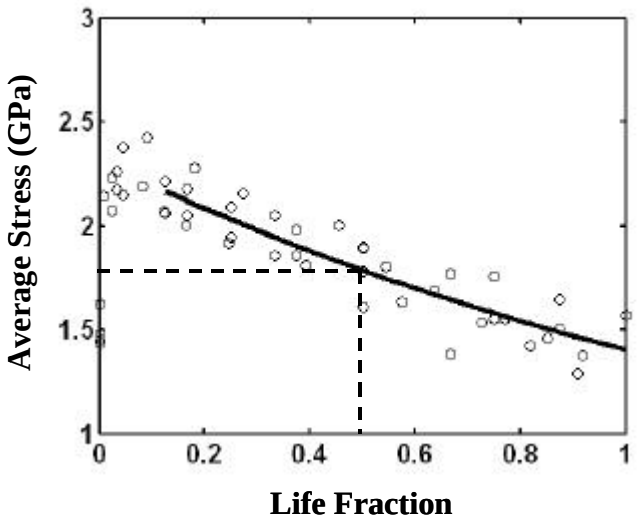

Fig. 3.145. Quadratic fit for stress vs. life fraction for samples tested at 2 temperatures

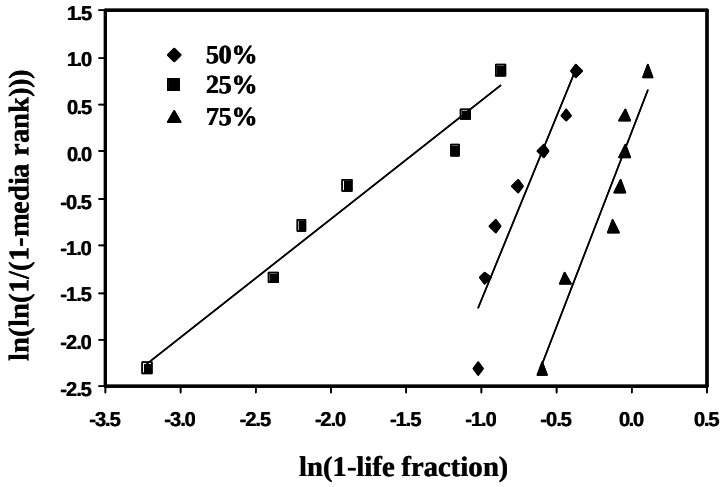

Fig. 3.146. Weibull plot of life fraction data for PLPS inspections at life fraction 25%, 50% and 75% from master curve.

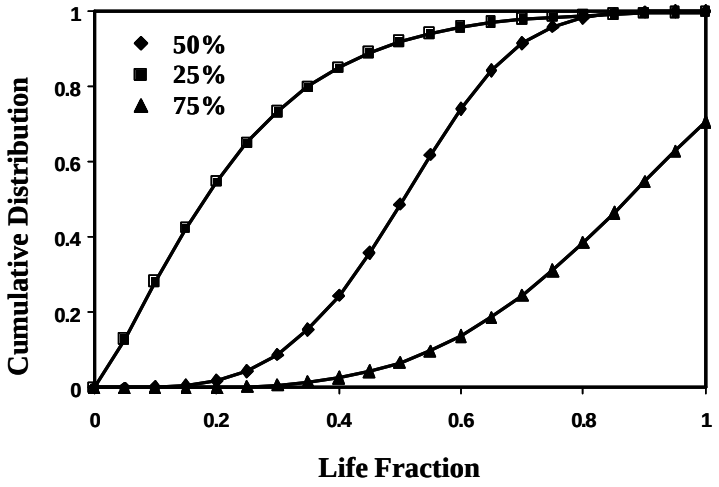

Fig. 3.147. Cumulative distribution of life fraction data for PLPS inspections at life fraction 25%, 50% and 75% from master curve

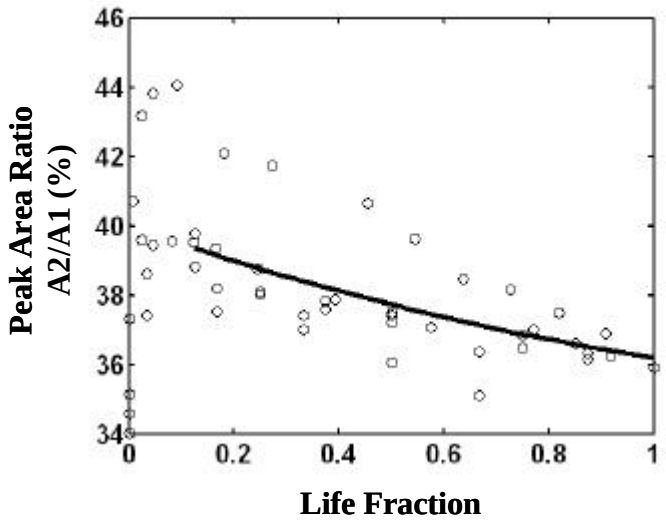

Fig. 3.148. Quadratic fit for peak area ratio vs. life fraction for samples tested at 2 temperatures

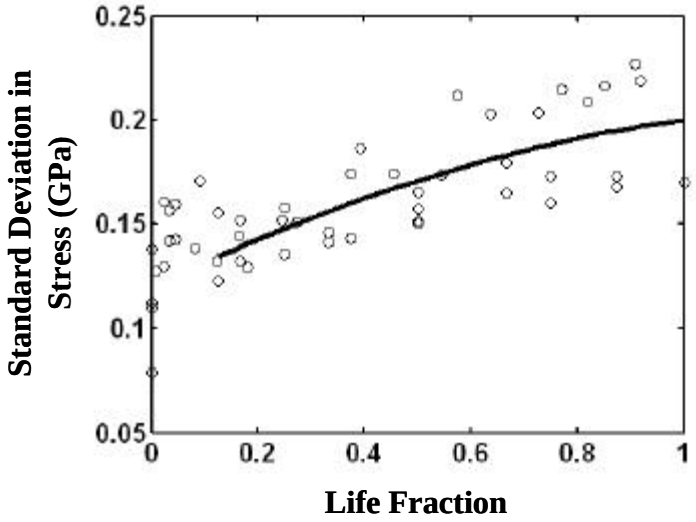

Fig. 3.149. Quadratic fit for standard deviation of stress vs. life fraction for samples tested at 2 temperatures

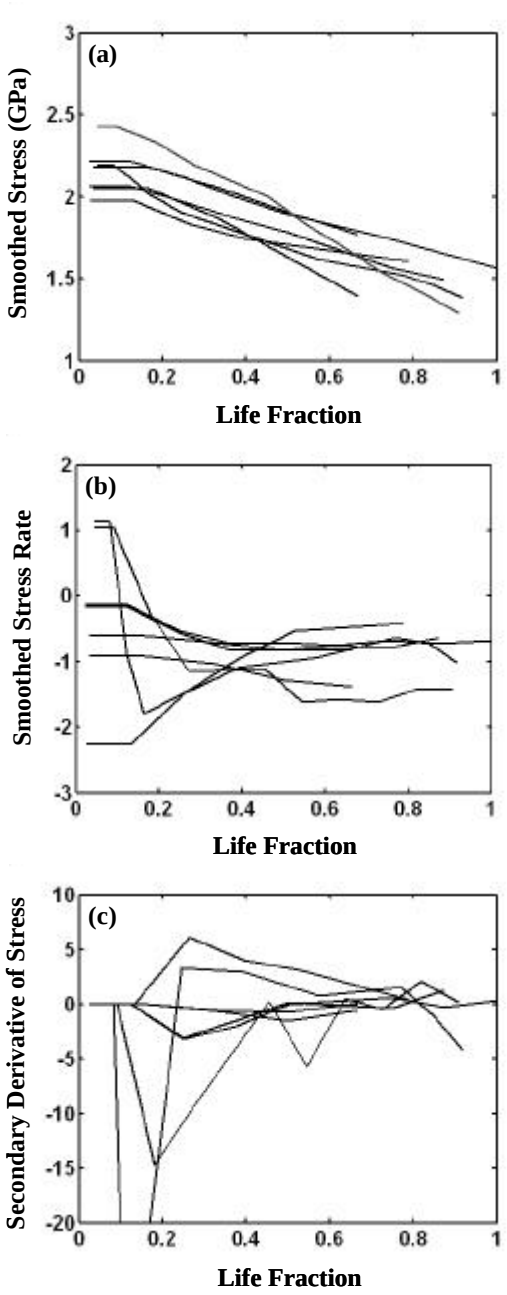

Fig. 3.150. (a) Smoothed stress, (b) first derivative and (c) second derivative of stress

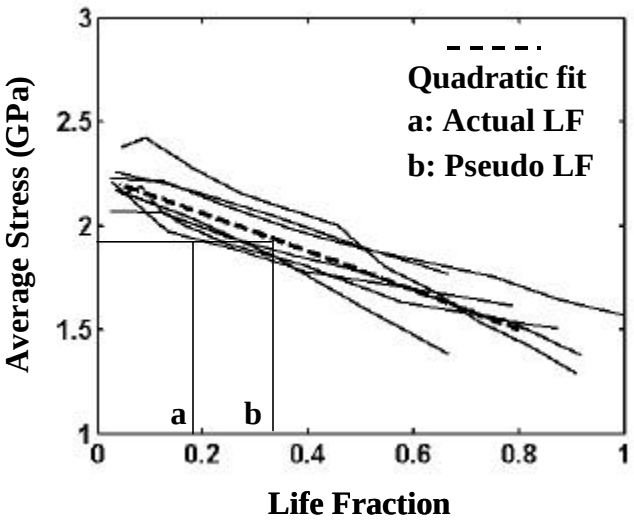

Fig. 3.151. Stress vs. life fraction for neural network method 2

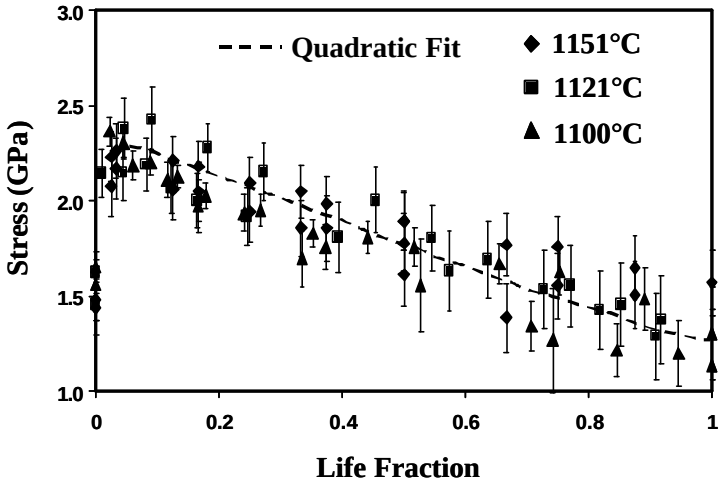

Fig. 3.152. Quadratic fit for specimens at three temperatures

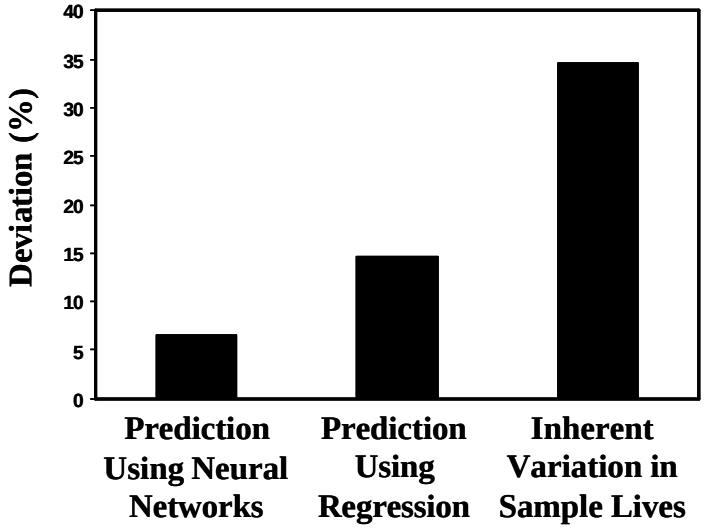

Fig. 3.153. Comparison of prediction accuracy and inherent variation of lives

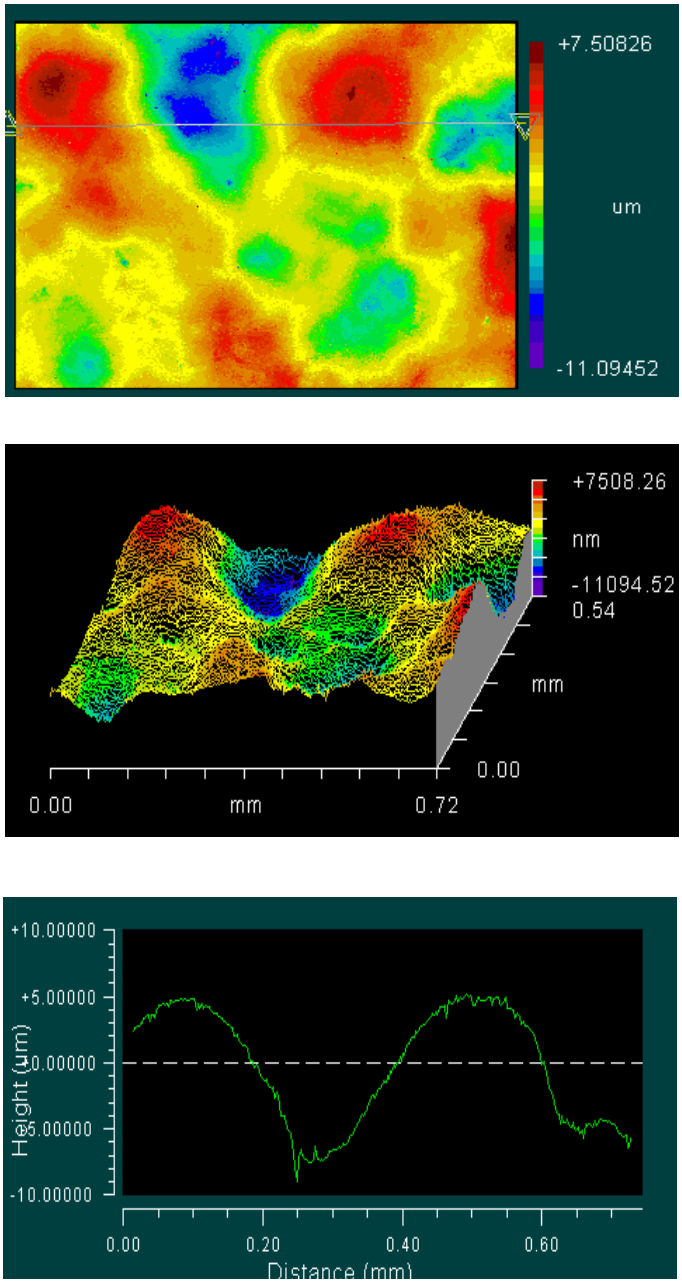

Fig. 3.154: Surface geometry of as-received specimen

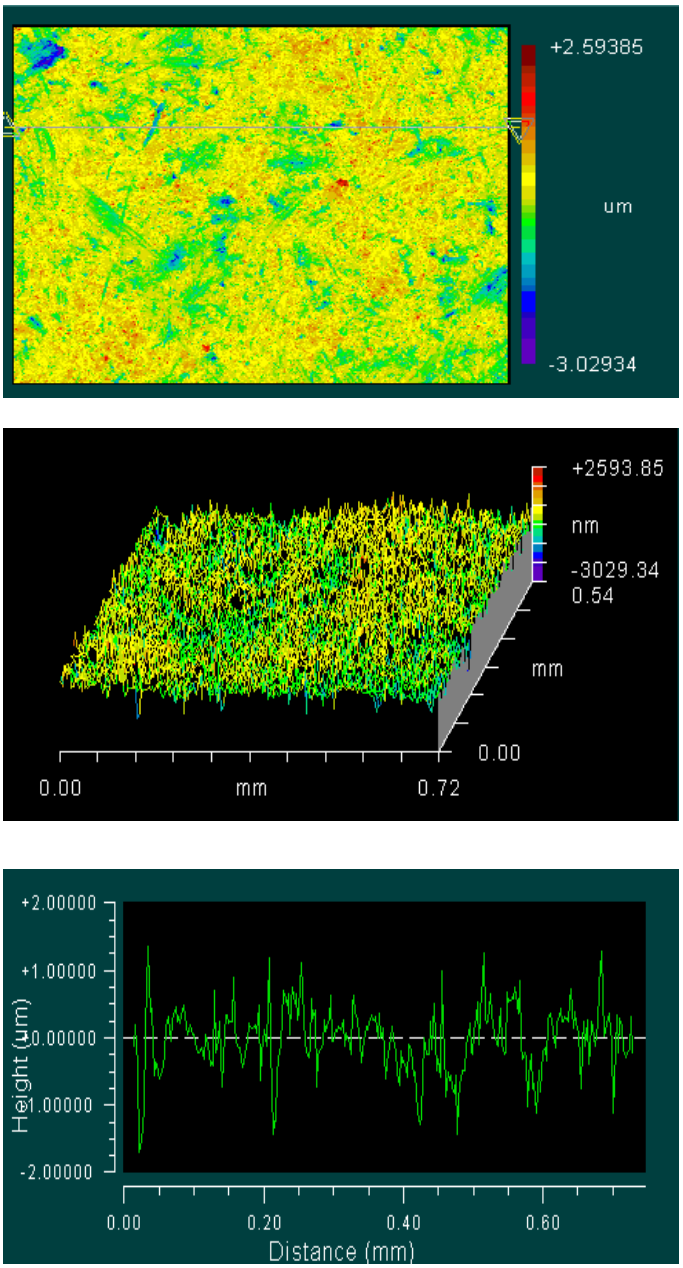

Fig. 3.155: Surface geometry of barrel finished specimen

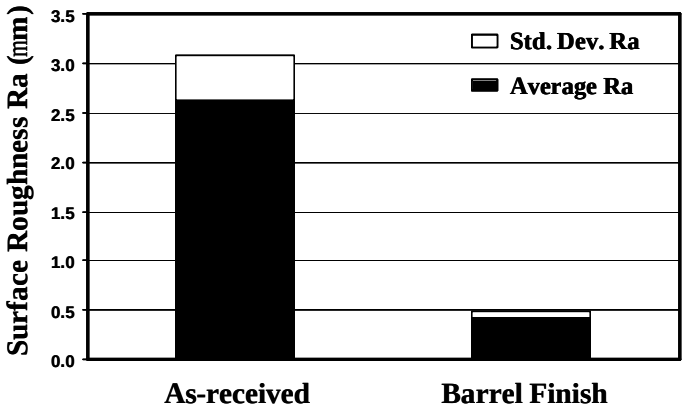

Fig. 3.156. Summary of surface roughness for specimens after different finishing

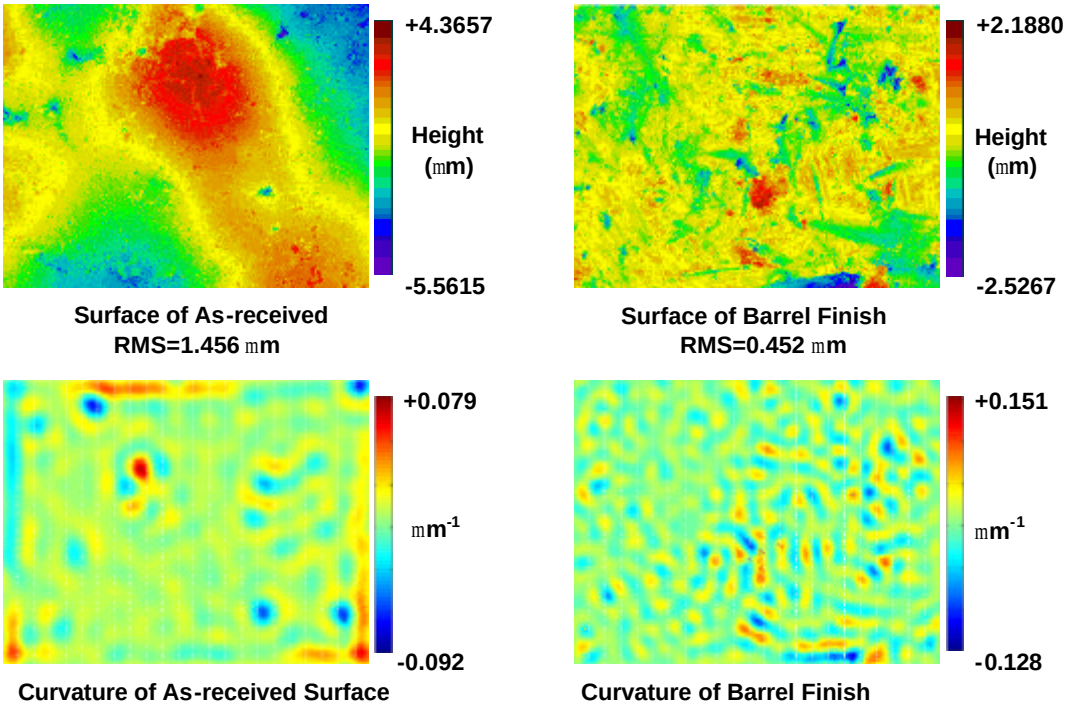

Fig. 3.157. Bond coat surface geometry and curvature map before and after barrel finishing

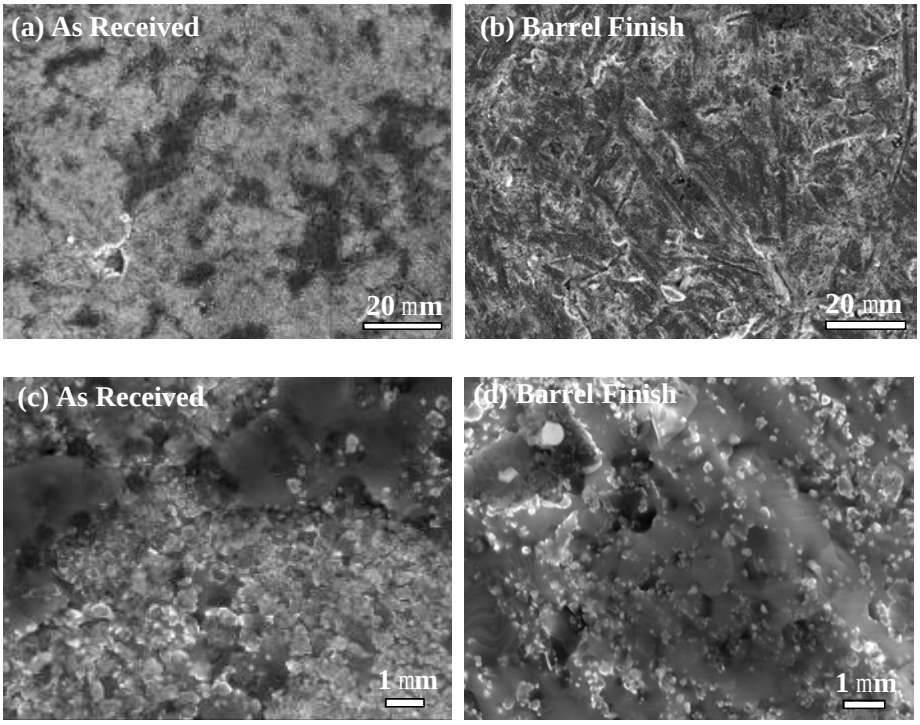

Fig. 3.158. SEM of as-received and barrel finished bond coat surface

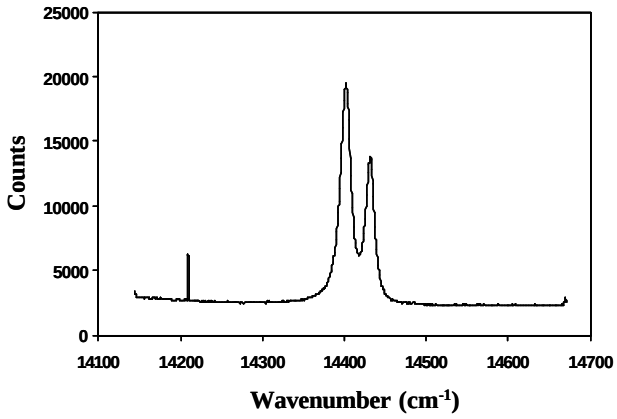

Fig. 3.159. PLPS spectra of bond coat surface showing α-Al_2O_3

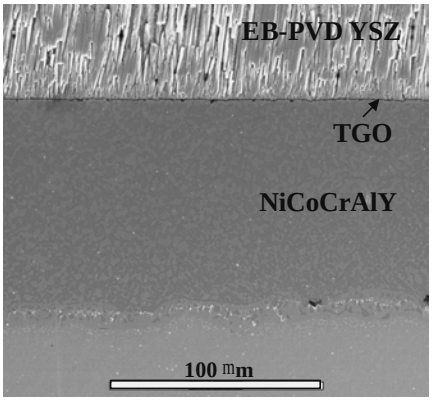

(a)

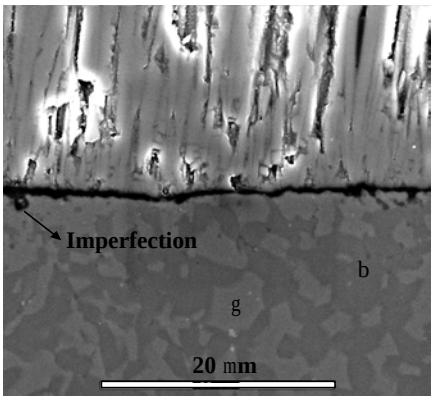

(b)

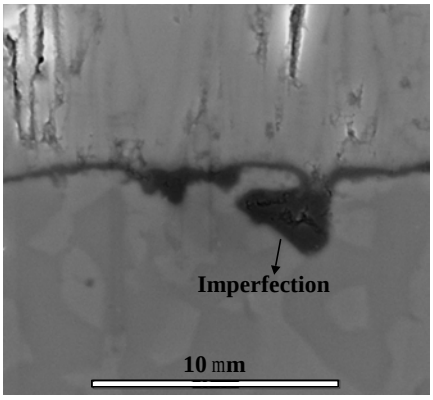

(c)

Fig. 3.160. SEM micrographs of as-coated TBC

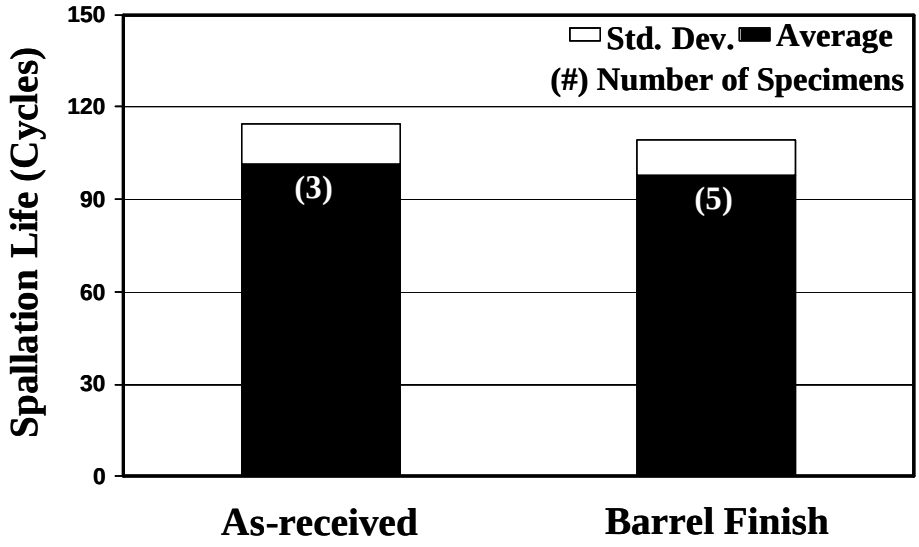

Fig. 3.161. Spallation life of specimens

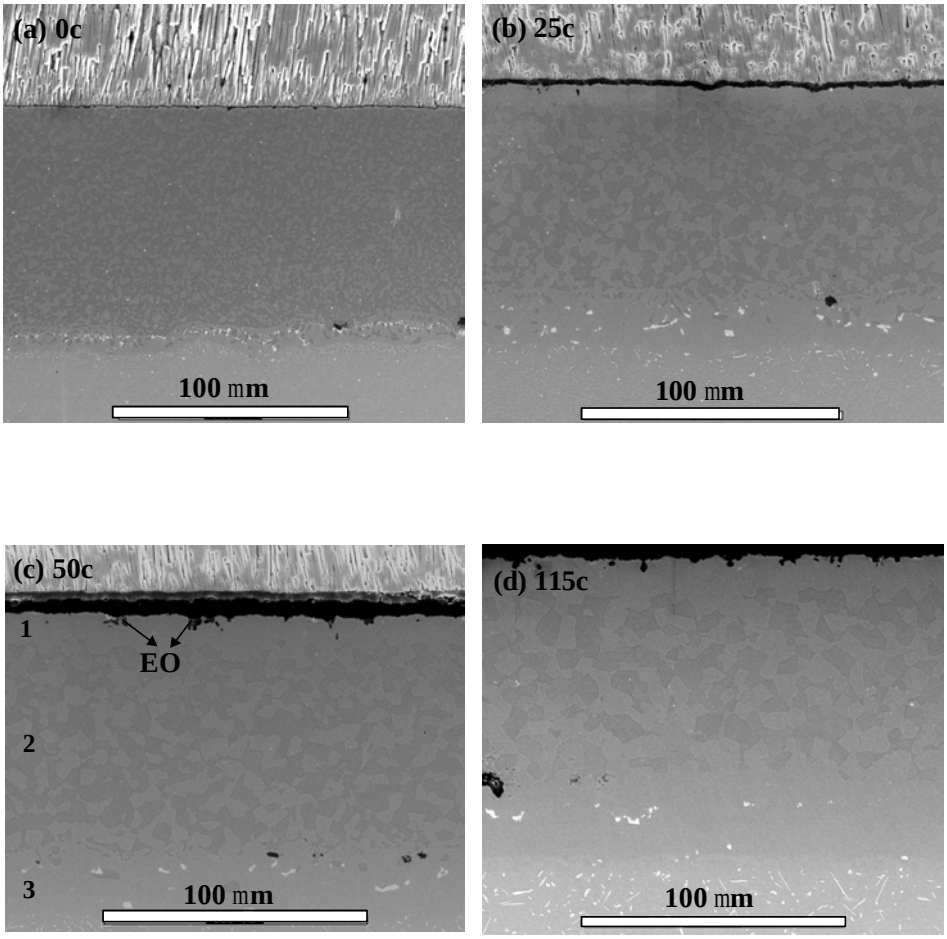

Fig. 3.162. SEM micrographs of specimens at various stages of thermal cycling showing: 1. upper depletion zone; 2. two-phase (β + γ) region; 3. lower depletion zone; and embedded oxides (EO).

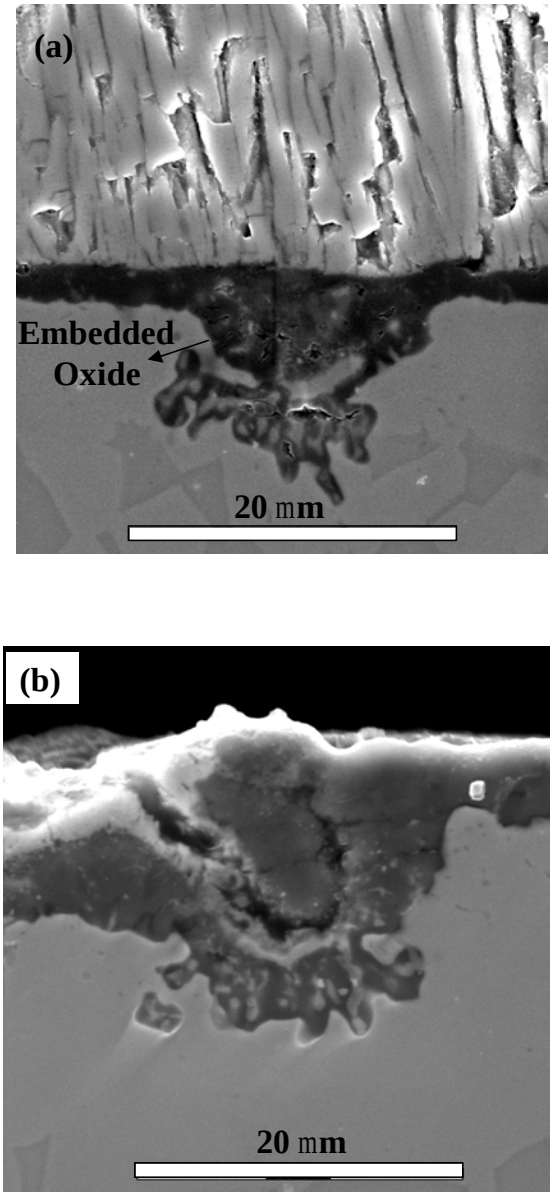

Fig. 3.163. SEM micrographs showing embedded oxides

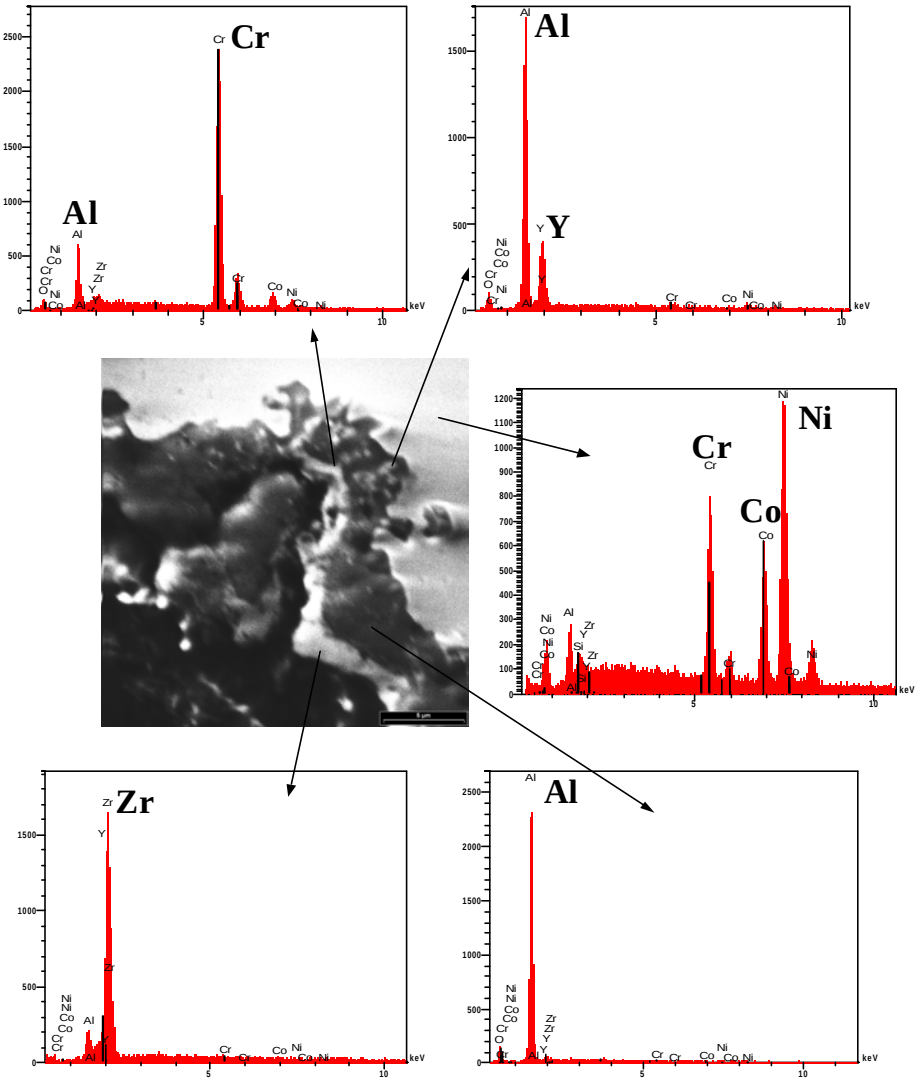

Fig. 3.164. Back scattered image of embedded oxide and EDS spectra at different regions

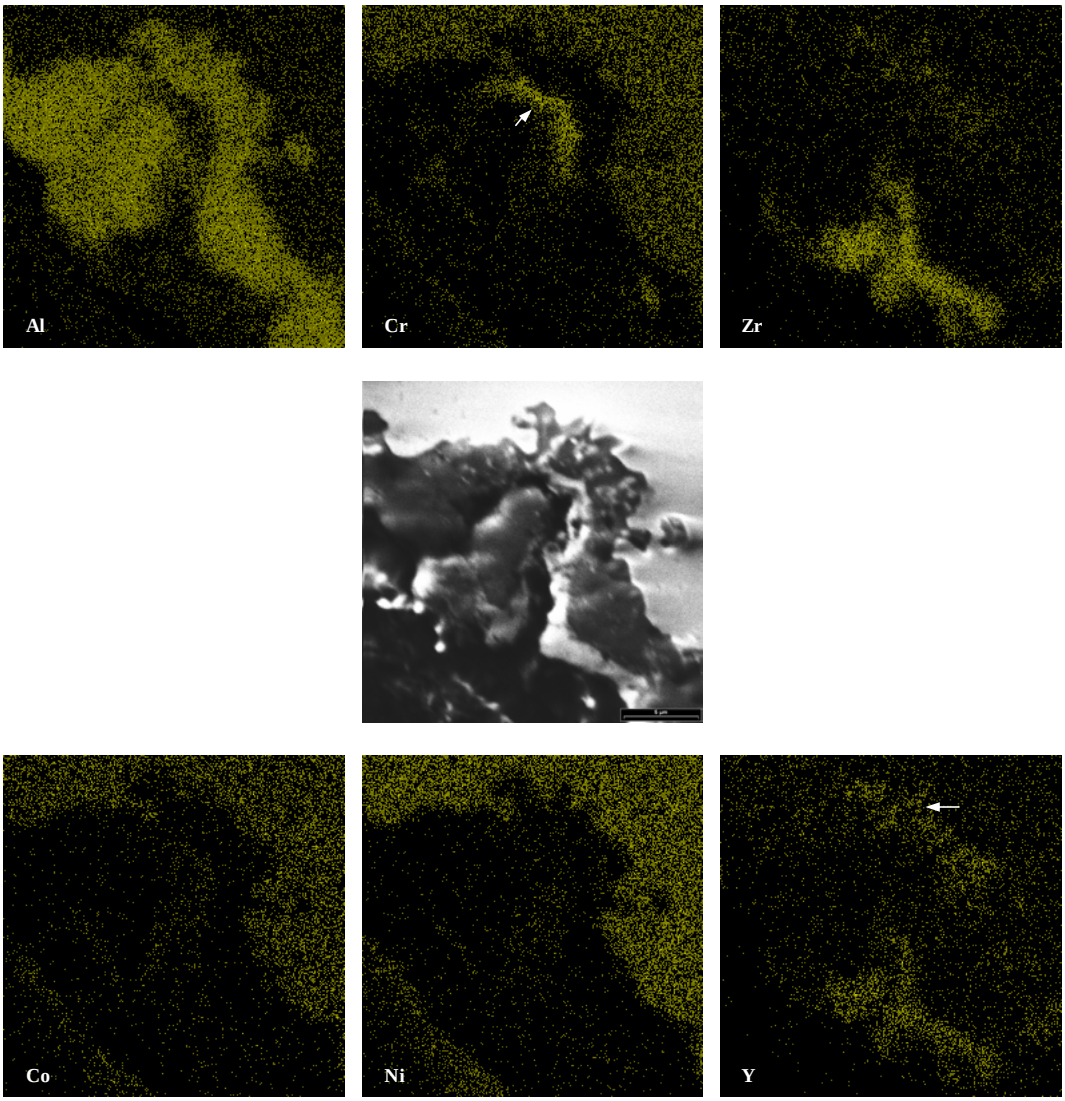

Fig. 3.165. Back scattered image of embedded oxide and x-ray mapping

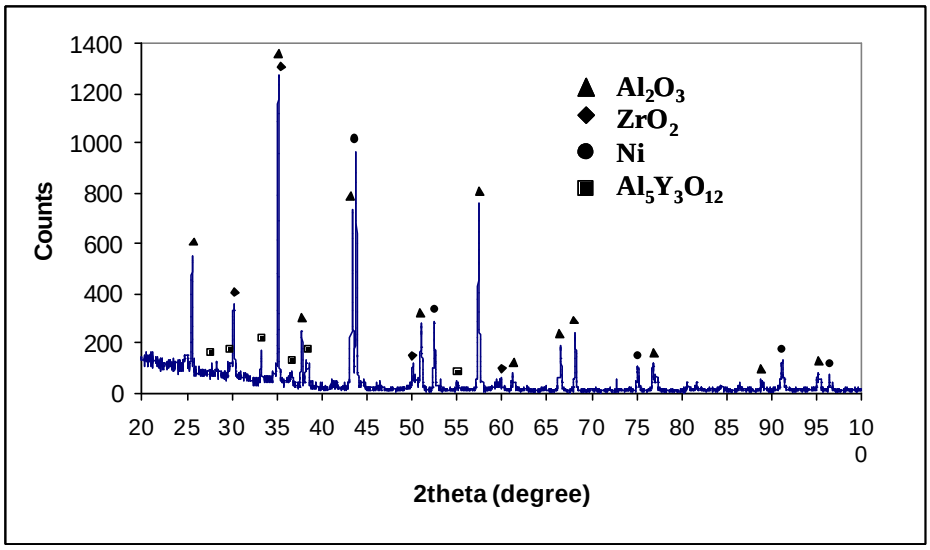

Fig. 3.166. XRD pattern of bond coat surface after spallation

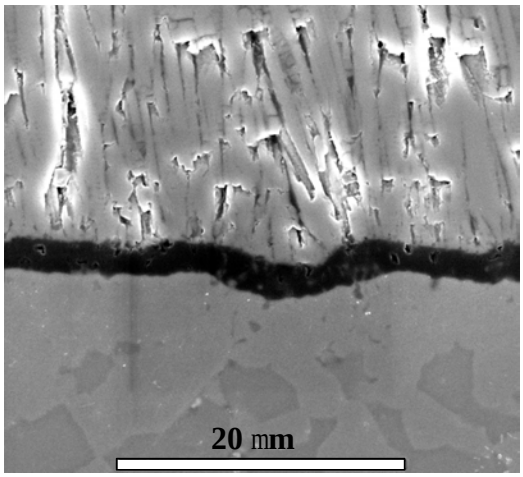

Fig. 3.167. SEM micrograph showing rumpling without damage

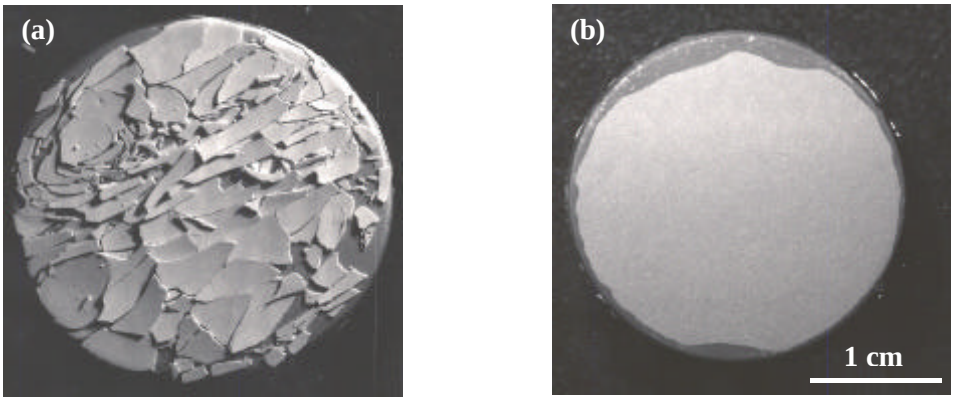

Fig. 3.168. Macrographs of failed specimens

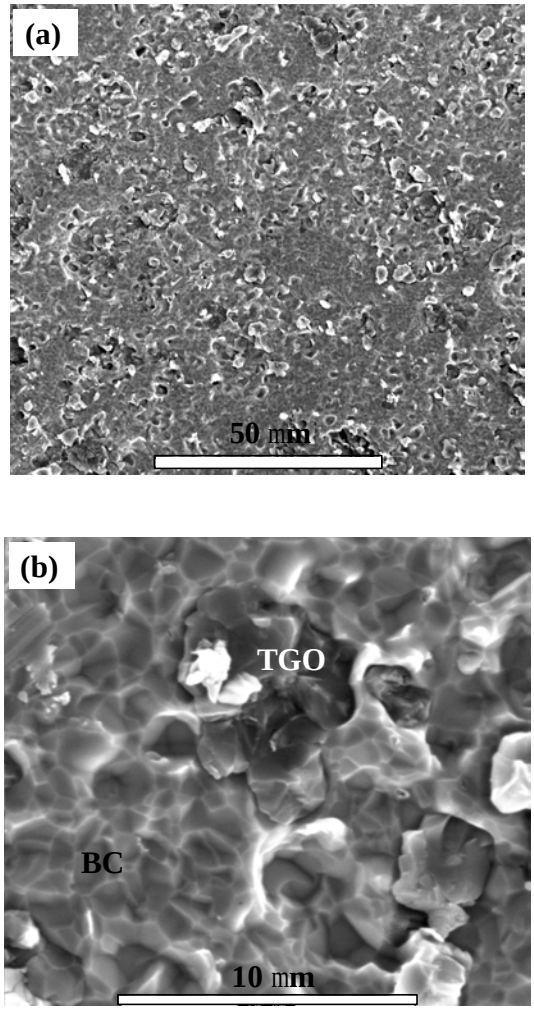

Fig. 3.169. SEM micrographs of spalled surface on the bond coat side

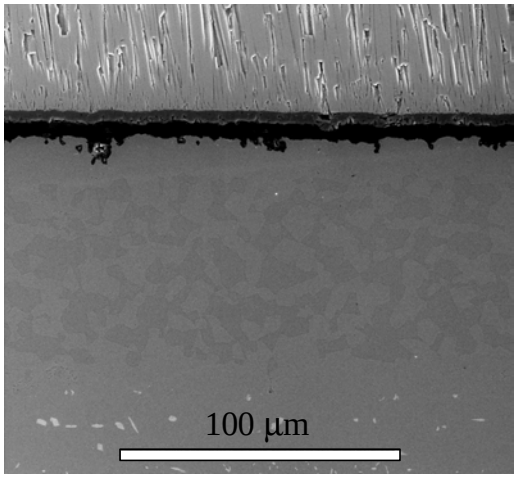

Fig. 3.170. Cross-section of failed specimen

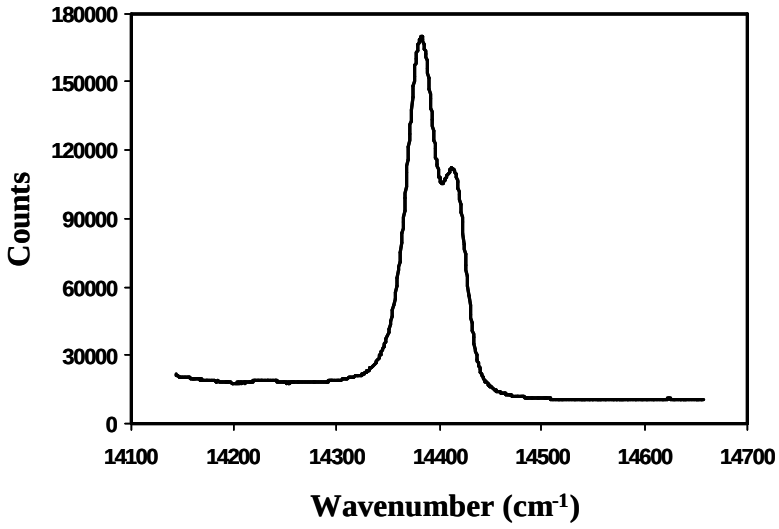

Fig. 3.171. Typical example of PLPS spectra during thermal cycling

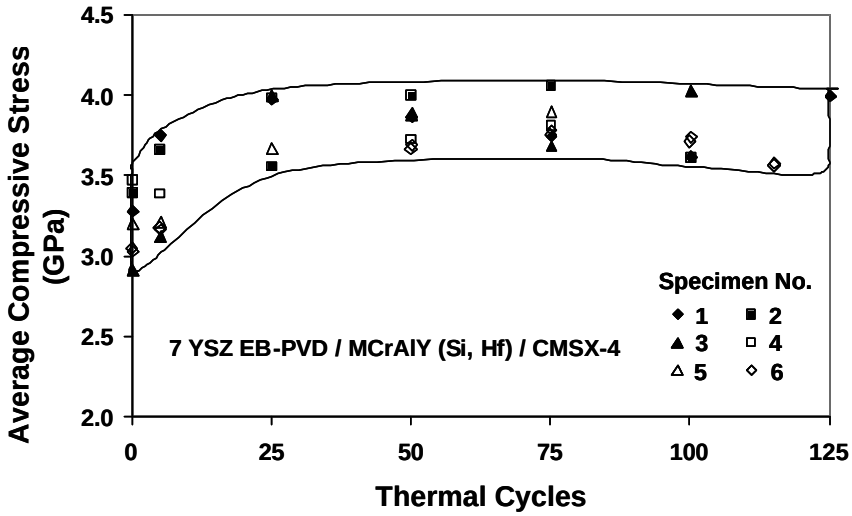

Fig. 3.172. Evolution of TGO compressive stress as a function of thermal cycling

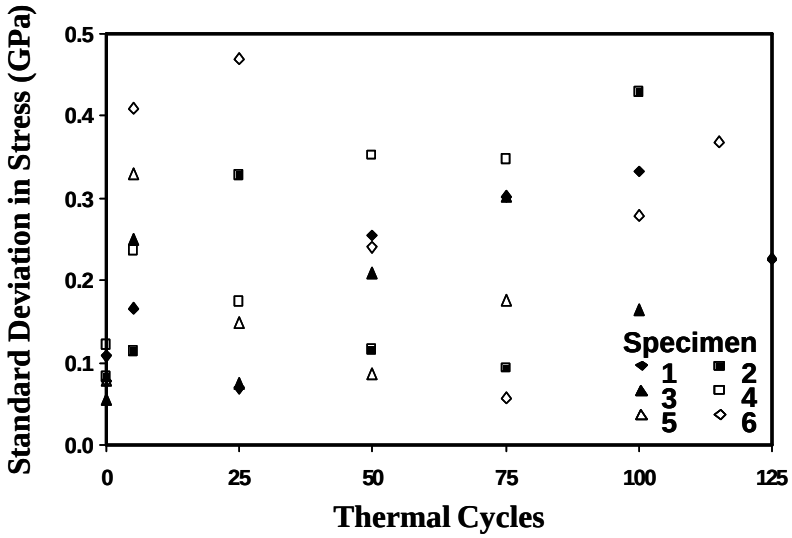

Fig. 3.173. Standard deviation in stress as a function of thermal cycles

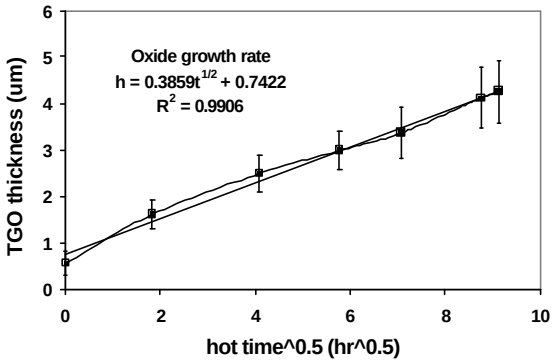

Fig. 3.174. TGO thickness as a function of square root of hot time

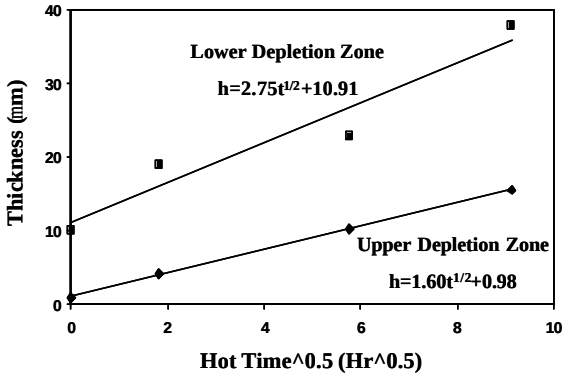

Fig. 3.175. Thickness of depletion zones as a function of square root of hot time

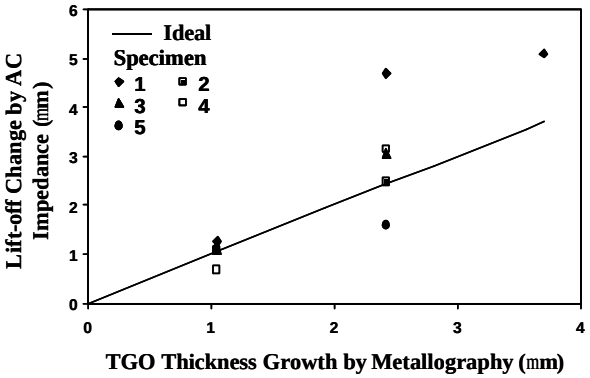

Fig. 3.176. Comparison of TGO thickness measured by metallography and AC impedance

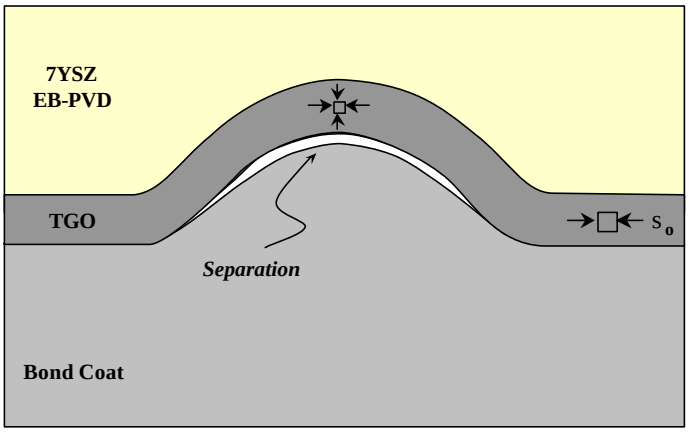

Fig. 3.177. Failure governed by debonding at ridge tops due to normal tensile stress that increase with TGO thickness (*75*).

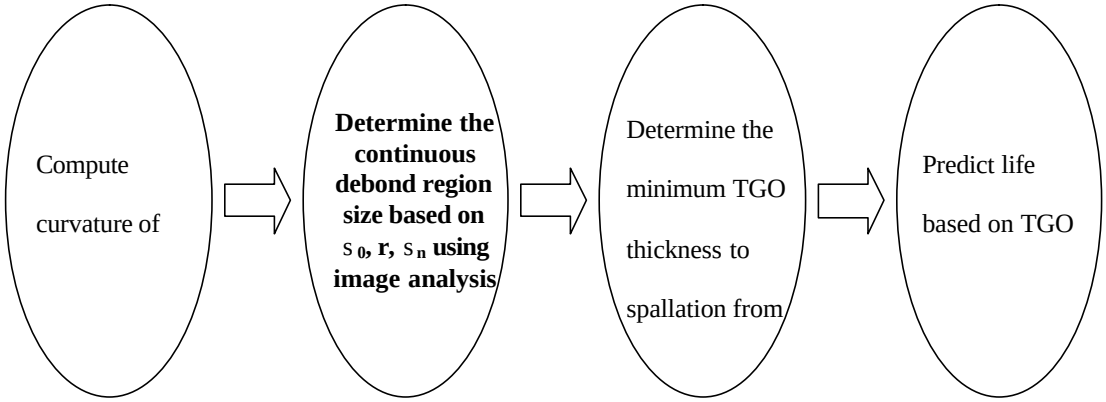

Fig. 3.178. Flow chart showing the procedure of life prediction

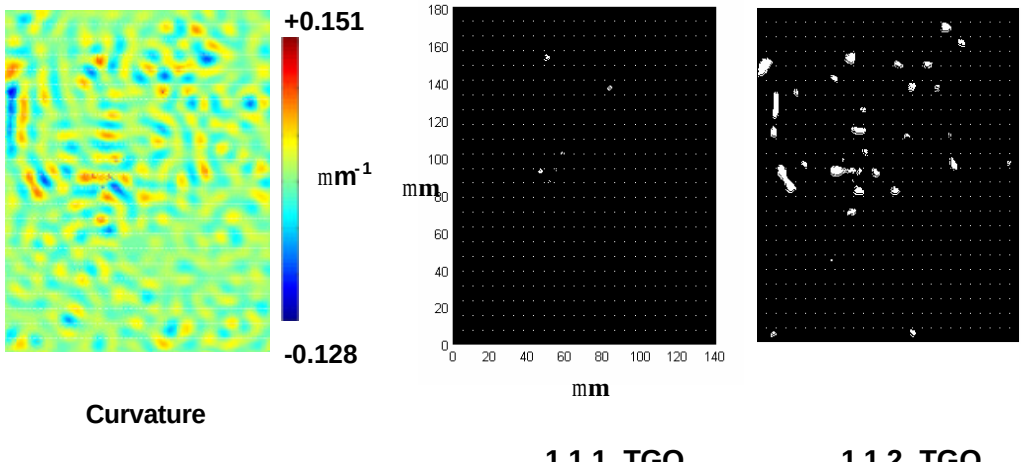

Fig. 3.179. Example showing the debonding region based on curvature map

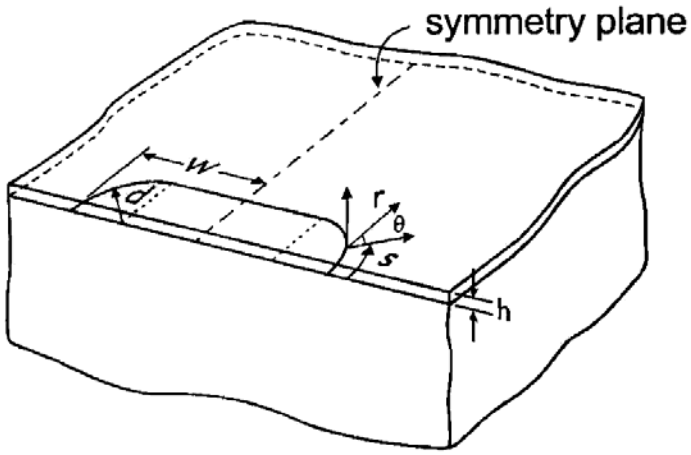

Fig. 3.180. General configuration of a flaw existing at the TGO/bond coat interface, along the free edge of the specimen (133)

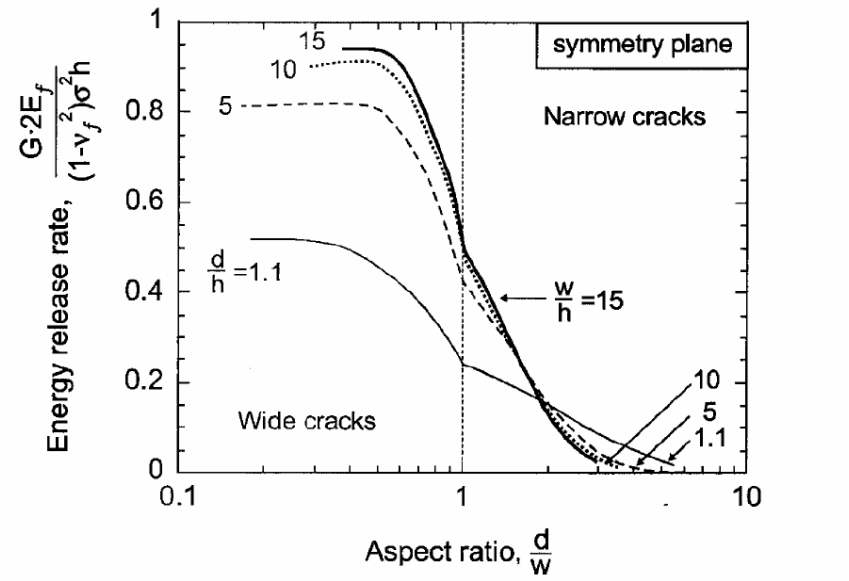

Fig. 3.181. Stored strain energy release rate (G_0) for different geometries of debonds (*133*)

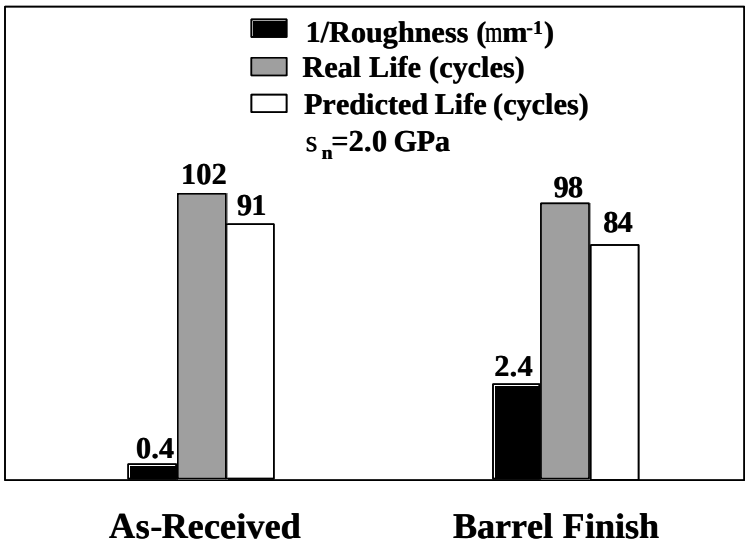

Fig. 3.182. Comparison of predicted and real lives

Table 3.1: List of Type I TBC specimens used in 1-hour thermal cycling tests at 1100°C and their failure lives.

Specimen	# Of Cycles To Failure
LD 77	1200
LD 48	1350
LD 46	1200
LD 65	1400
LD 72	1400
LD 42	1500
LD 53	1550
LD 50	1350
LE 13	1513
LE 26	1413

Table 3.2: List of Type I TBC specimens used in 1-hour thermal cycling tests at 1121°C and their failure lives.

Specimen	# Of Cycles To Failure
LDA 59	600
LDA 91	600
LDA 87	635
LDA 99	665
LD 76	665
LEA 23	665
LEA 31	665
LD 37	705
LDA 67	745
LEA 07	755
LE 17	745

Table 3.3: List of Type I TBC specimens used in 1-hour thermal cycling tests at 1151°C and their failure lives.

Specimen	# Of Cycles To Failure
LE 22	280
LD 98	300
LE 19	300
LD 57	300
LD 41	360
LE 11	400
LE 27	400
LD 89	420
LD 66	460

Table 3.4: List of Type I TBC specimens used in 24-hour thermal cycling tests at 1121°C and their failure lives.

Specimen	# Of Cycles To Failure
LE 00	43
LD 90	41
LD 80	51
LD 85	33
LD 79	39
LD 94	41
LD 44	55
LD 70	55

Table 3.5: List of Type I TBC specimens used in multi-temperature variable amplitude tests and their failure lives.

Sample	First Exposure Temperature, T_1 (°C)	Second Exposure Temperature, T_2 (°C)
LD 73	1121	1151
# Cycles at each Temperature	335	205 (Failed)
LD 74	1121	1151
# Cycles at each Temperature	335	225(Failed)
LD 82	1151	1121
# Cycles at each Temperature	185	340(Failed)
LD 84	1151	1121
# Cycles at each Temperature	185	409(Failed)

Table 3.6: List of Type I TBC specimens used in multiple hold time variable amplitude tests and their failure lives.

Sample	First Hold Time, t_1 (minutes)	Second Hold Time, t_2 (minutes)
LE 33	45	1425
# Cycles at each Hold Time	345	11 (Failed)
LE 04	1425	45
# Cycles at each Hold Time	22	298(Failed)

Table 3.7: Maximum absolute error in determining the remaining life of Type I TBCs for the 1-hour constant and non-constant amplitude tests, during three inspection intervals of 25%, 50% and 75% TBC life.

	Threshold Stress At 25 % Life $S_{0.25}$ = 2.4 GPa	**Threshold Stress At 50 % Life $S_{0.5}$ = 2.11 GPa**	**Threshold Stress At 75 % Life $S_{0.75}$ = 1.72 GPa**
Sample	**Error in Predicting Remaining Life Fraction**	**Error in Predicting Remaining Life Fraction**	**Error in Predicting Remaining Life Fraction**
1-hr @ 1100°C	**+ 0.11**	**- 0.09**	**- 0.02**
1-hr @ 1100°C	**+ 0.04**	**- 0.02**	**+ 0.02**
1-hr @ 1121°C	**+ 0.09**	**+ 0.18**	**+ 0.15**
1-hr @ 1121°C	**- 0.02**	**+ 0.01**	**- 0.03**
1-hr @ 1151°C	**- 0.14**	**-0.08**	**- 0.04**
1-hr @ 1151°C	**- 0.07**	**- 0.05**	**0**
1-hr @ 1151°C	**+ 0.05**	**+ 0.15**	**+ 0.16**
ABSOLUTE AVERAGE ERROR	**+ 0.07**	**+ 0.08**	**+ 0.06**
NET AVERAGE ERROR	**+ 0.01**	**+ 0.01**	**+ 0.03**

Multiple Temperature History Tests Sample	**Threshold Stress At 25 % TBC Life $S_{0.25}$ = 2.4 GPa Error in Predicting Remaining Life Fraction**	**Threshold Stress At 50 % TBC Life $S_{0.5}$ = 2.11 GPa Error in Predicting Remaining Life Fraction**	**Threshold Stress At 75 % TBC Life $S_{0.75}$ = 1.72 GPa Error in Predicting Remaining Life Fraction**
1121°C To 1151°C	- 0.21	**- 0.12**	**- 0.05**
1121°C To 1151°C	- 0.24	**- 0.15**	**- 0.08**
1151°C To 1121°C	+ 0.07	**+ 0.19**	**+ 0.22**
1151°C To 1121°C	+ 0.10	**+ 0.23**	**+ 0.28**
ABSOLUTE AVERAGE ERROR	**+ 0.10**	**+ 0.12**	**+ 0.10**
NET AVERAGE ERROR	**+ 0.02**	**+ 0.02**	**+ 0.06**

Table 3.8: Maximum absolute error in determining the remaining life of Type I TBCs for the 24-hour and the multiple hold time tests, during three inspection intervals of 25%, 50% and 75% TBC life.

	Threshold Stress At 25 % TBC Life $S_{0.25}$ = 2.51 GPa	**Threshold Stress At 50 % TBC Life $S_{0.5}$ = 2.45 GPa**	**Threshold Stress At 75 % TBC Life $S_{0.75}$ = 2.08 GPa**
Sample	**Error in Predicting Remaining Life Fraction**	**Error in Predicting Remaining Life Fraction**	**Error in Predicting Remaining Life Fraction**
# 1	**- 0.13**	**+ 0.01**	**+ 0.02**
# 2	**- 0.30**	**- 0.10**	**- 0.04**
# 3	**+ 0.15**	**- 0.14**	**- 0.08**
# 4	**- 0.27**	**- 0.09**	**- 0.09**
ABSOLUTE AVERAGE ERROR	**+ 0.21**	**+ 0.09**	**+ 0.07**
NET AVERAGE ERROR	**- 0.14**	**- 0.08**	**- 0.06**
1 H – 24 H Multiple Hold Time	**- 0.07**	**+ 0.13**	**+ 0.11**
ABSOLUTE AVERAGE ERROR	**+ 0.18**	**+ 0.09**	**+ 0.08**
NET AVERAGE ERROR	**- 0.12**	**- 0.04**	**- 0.07**

Table 3.9: Bond coat processing methods, heat treatment conditions, compositions and thicknesses for the two TBCs studied.

Type	Bond Coat Single Phase Platinum Modified Nickel Aluminide – [(Ni, Pt) Al]							
	Type	Grit Blasted	Processing Method				Thickness (㎜)	Composition (wt. %)
			Pt Deposition	Aluminizing	Substrate Temperature	Heat Treatment		
I	Outward Diffusing Type	Yes	Electroplating	CVD	1080°C	No pre-diffusion heat treatment prior to CVD aluminizing	75 µm	19 Pt, 20 Al, balance Ni
II	Inward Diffusing Type	Yes	Electroplating	High Activity Low Temperature Pack Cementation	982°C	1052°C + 1 hour prior to pack cementation	55 – 60 µm	30.6 Pt, 26 Al, balance Ni

Table 3.10: List of Type II TBC specimens used in 1-hour thermal cycling tests at 1100°C and their failure lives.

Specimen	# Of Cycles To Failure
LV 23	1103
LV 26	830
LV 33	1361

Table 3.11: List of Type II TBC specimens used in 1-hour thermal cycling tests at 1121°C and their failure lives.

Specimen	# Of Cycles To Failure
LV 14	605
LV 39	450
LV 17	538
LV 38	490
LV 15	583
LV 36	710

Table 3.12: List of Type II TBC specimens used in 1-hour thermal cycling tests at 1151°C and their failure lives.

Specimen	# Of Cycles To Failure
LV 24	413
LV 25	306
LV 50	320
LV 40	413

Table 3.13: List of Type II TBC specimens used in 24-hour thermal cycling tests at 1121°C and their failure lives.

Specimen	# Of Cycles To Failure
LV 31	69
LV 21	65

Table 3.14: List of Type II TBC specimens used in multi-temperature variable amplitude tests and their failure lives.

Sample	First Exposure Temperature, T_1 (°C)	Second Exposure Temperature, T_2 (°C)
LV 37	1121	1151
# Cycles at each Temperature	261	157 (Failed)
LV 48	1151	1121
# Cycles at each Temperature	165	218 (Failed)

Table 3.15. Remaining life prediction based on average stress vs. life fraction

Temperature (°C)	Sample	Life (Cycles)	Actual Life Fraction at Stress S=1.79GPa[a]	Actual Remaining Life Fraction[b]	Error In Remaining Life Prediction
1151	1	190	0.648	0.352	-0.148
	2	200	0.694	0.306	-0.194
	3	200	0.469	0.531	+0.031
	4	150	0.361	0.639	+0.139
	5	150	0.378	0.622	+0.122
1121	1	610	0.404	0.596	+0.096
	2	550	0.556	0.444	-0.056
Average					0.112
RMS					0.124
Maximum					0.194

[a] Life fraction from master curve at S=1.79GPa, LF=0.50.
[b] Predicted remaining life fraction from master curve, RLF=0.50.

Table 3.16. Remaining life prediction based on peak area ratio vs. life fraction

Temperature (°C)	Sample	Actual Life Fraction at Area Ratio A2/A1=37.7%[a]	Actual Remaining Life Fraction[b]	Error In Remaining Life Prediction
1151	1	0.341	0.659	0.159
	2	0.445	0.555	0.055
	3	0.411	0.589	0.089
	4	0.156	0.844	0.344
	5	0.013	0.987	0.487
1121	1	0.477	0.523	0.023
	2	0.584	0.416	-0.084
Average				0.177
RMS				0.239
Maximum				0.487

[a] Life fraction from master curve at peak area ratio A2/A1=37.7%, LF=0.50.
[b] Predicted remaining life fraction from master curve, RLF=0.50.

Table 3.17. Remaining life prediction based on standard deviation of stress vs. life fraction

Temperature (°C)	Sample	Actual Life Fraction at Deviation in Stress DS=0.171GPa[a]	Actual Remaining Life Fraction[b]	Error In Remaining Life Prediction
1151	1	0.669	0.331	-0.169
	2	0.985	0.015	-0.485
	3	0.142	0.858	0.358
	4	0.426	0.574	0.074
	5	0.878	0.122	-0.378
1121	1	0.214	0.786	0.286
	2	0.354	0.646	0.146
Average				0.271
RMS				0.303
Maximum				0.485

[a] Life fraction from master curve at deviation in stress DS=0.171GPa, LF=0.50.
[b] Predicted remaining life fraction from master curve, RLF=0.50.

Table 3.18. Remaining life fraction using weighted average method

Error (%)	Stress vs. Life Fraction	Peak Area Ratio vs. Life Fraction	Deviation in Stress vs. Life Fraction	Weighted Average of 3 Attributes
3.9.8.3.Average	11.2	17.7	27.1	16.3
RMS	12.4	23.9	30.3	19.3
Maximum	19.4	48.7	48.5	33.4

Table 3.19. Prediction results using neural network method 1

Error (%)	Using Three Measurements		Using Five Measurements	
	Radial Basis Network	Generalized Regression Neural Network	Radial Basis Network	Generalized Regression Neural Network
3.9.8.4.Average	7.2	7.2	14.3	13.1
RMS	10.0	8.2	16.0	15.1
Maximum	22.1	13.3	22.7	21.4

Table 3.20. Prediction results using neural network method 2

Error (%)	Using Three Measurements		Using Five Measurements	
	Radial Basis Network	Generalized Regression Neural Network	Radial Basis Network	Generalized Regression Neural Network
3.9.8.5.Average	5.5	7.2	6.5	12.2
RMS	6.1	8.8	7.4	13.1
Maximum	8.2	18.6	10.9	20.5

Table 3.21. Remaining life prediction based on average stress vs. life fraction for specimens tested at three temperatures

Temperature (°C)	Sample	Life (Cycles)	Actual Life Fraction at Stress S=1.76GPa[a]	Actual Remaining Life Fraction[b]	Error In Remaining Life Prediction
1151	1	190	0.672	0.328	-0.172
	2	200	0.722	0.278	-0.222
	3	200	0.521	0.479	-0.021
	4	150	0.376	0.624	0.124
	5	150	0.434	0.566	0.066
1121	1	610	0.462	0.538	0.038
	2	550	0.56	0.44	-0.060
1100	1	1122	0.302	0.698	0.198
	2	830	0.352	0.648	0.148
	3	920	0.276	0.724	0.224
Average					0.127
RMS					0.147
Maximum					0.224

[a] Life fraction from master curve at S=1.76GPa, LF=0.50.
[b] Predicted remaining life fraction from master curve, RLF=0.50.

Table. 3.22. Prediction accuracy made by regression and neural network for specimens tested at three temperatures

Error (%)	Radial Basis Network	Regression
3.9.8.6.Average	5.3	12.7
RMS	6.6	14.7
Maximum	13.4	22.4

Table 3.23. Size of debonding region at different TGO thickness

TGO Thickness (mm)	**Size of Largest Debonding Region (mm)**	**Spallation**
2	0	No
3	Length = 1.3; Width =1	No
4	Length = 16.9; Width =6.9	Yes

4. Discussion

Four different TBCs were studied as a part of this research. Furnace cyclic tests were carried out at three different exposure temperatures and two hold times. At least five specimens were cycled to failure for each TBC under each thermal cycling condition. The standard deviation of failure lives was found to be very small, indicative of small sample-to-sample variations. This is expected since all the samples used in this study were coated at the same time; thus, reducing processing variability. The results from the thermal cyclic tests indicate a 4-fold increase in spallation lives for the Type I TBCs and a 3-fold increase for the Type II TBCs on decreasing the peak temperature from 1151°C to 1100°C. Additionally, the cycles to failure showed a 16-fold decrease for the Type I TBCs and an 8-fold decrease for the Type II TBCs on increasing the hold time from 1-hour to 24-hours. However, changing the hold time from 1-hour to 24-hours also roughly doubled and quadrupled the allowable hot time for Types I & II TBCs, respectively. These results indicate that cycling, as well as hot time, induces TBC damage.

The results for Type I and II TBCs will be discussed first, followed by the results for Type III and IV TBCs. The main findings for these four TBCs will then be compared and the reasons for the similarities and differences in the observed behavior of these four TBCs will be explained.

The results presented for the 1-hour and the 24-hour tests for the Type I TBCs have four notable features: (1) the linear relation between TGO stress and TBC life fraction, which is independent of temperature, but changes moderately with hold time, (2) a failure mode that is independent of cycle temperature, but changes dramatically with

cycle hold time, (3) a linear relation between rumpling of the TGO/bond coat interface and the TGO thickness, indicating that rumpling is controlled directly by the TGO growth independent of cycle duration or temperature and (4) TBC spallation occurs at a constant value of rumpling amplitude and TGO stress.

It should be mentioned here that this is the first time that the effects of hold-time on TGO stress behavior have been studied. These results indicate that there is a physical basis for the observed TGO stress relaxation with TBC life. Hence, a mechanisms-based life prediction approach is adopted to determine the nature of TBC spallation and to correlate spallation mechanisms with TGO stress behavior.

All samples tested using 1-hour cycles, regardless of temperature, failed in the TBC, near the TBC/TGO interface, due to progressive cracking beginning at ~ 20% life fraction. In contrast, the 24-hour samples failed almost exclusively at the TGO/bond coat interface, with little or no cracking at the YSZ/TGO interface. This indicates a mechanism change on changing the hold time and; hence, any multi-hold time mechanistic damage model will need to include two types of damage and failure can be predicted on the basis of whichever spallation mechanism occurs first.

Bond coat rumpling is the cause of crack initiation, since the cracking at the YSZ/TGO interface, prior to failure, was consistently observed over regions where the bond coat has pulled away from the TBC or where the TGO/bond coat interface has rumpled (Figures 3.31 and 3.46). The amplitude of rumpling and the rate of rumpling were determined and studied as a function of cycling for these TBCs. It was found for Type I TBCs that the rumpling rate for the 24-hour tests at 1121°C was only slightly higher than for the 1-hour tests, which experienced 24 times the number of cycles for a

given hot time. Additionally, though the 24-hour samples experienced greater total rumpling, they tolerated more rumpling with little or no cracking. Thus, in spite of similar oxide growth rates and fairly similar rumpling rates for the 1-hour and the 24-hour tests, different failure modes were observed. In order to understand the reasons for these observations, it is important to understand the underlying mechanisms responsible for rumpling and the effect of cycling on rumpling and its role in TBC failure for the 1-hour and 24-hour tests.

4.1. Spallation Mechanisms

The mechanisms responsible for TBC spallation during the 1-hour and the 24-hour tests are discussed in this section, based on the physical evidence provided by cross-section micrographs of specimens at different life fractions and the appearance of the final failure surface.

4.1.1. One hour Tests

Spallation failure in Type I TBCs during the 1-hour tests is shown to be greatly influenced by the presence of initial imperfections, oriented into the bond coat, at the TGO/bond coat interface, referred to as inward TGO displacements (Figures 2.9 and 3.4). Failure in the 1-hour cycled samples occurs by crack-initiation at the YSZ/TGO interface, starting at ~ 20 % of the cyclic life, as shown by the arrows in Figure 3.31, followed by crack extension along the YSZ/TGO interface and sometimes into the TGO (Figure 3.31), resulting in complete separation of the YSZ from the TGO. This is consistent with the fracture surfaces for all the 1-hour cycled samples shown in Figures 3.41 and 3.42, which

show large areas of retained YSZ, along with some retained TGO only at the bond coat ridges. Thus, the final failure for the 1-hour cycled samples is shown to occur within the TBC, except at grain boundary ridges, where failure occurs at the TGO/YSZ interface along the bond coat ridge tops (Figures 3.41 and 3.42). Area fraction analysis indicates that separation at the TGO/YSZ interface occurs at 77 % of the total area for the 1-hour tests at 1100°C, at 55 % of the total area for the tests at 1121°C, and at 65 % of the total area for tests at 1151°C Figure 3. 45).

The cracking at the YSZ/TGO interface is shown to be due to the progressive increase in the size of the TGO displacements, referred to as rumpling, as shown in Figure 3.32. The rate of increase of the rumpling amplitude increases with temperature for the 1-hour cycle tests, Figure 3.34. This is also illustrated in Figure 4.1, which compares the amplitudes of rumpling after 300 and 400 1-hour cycles at 1100°C and 1121°C. The amplitude of rumpling is greater after the same number of cycles at the higher temperature than at the lower temperature. This is consistent with rumpling being the cause for reduced failure lives with temperature for 1-hour cycling in this TBC.

Figure 4.2 is a plot of rumpling amplitude versus the TGO thickness for the 1-hour tests. This plot indicates that the rumpling amplitude is nearly a single-valued function of the TGO thickness for all three temperatures. This implies that rumpling is directly related to oxide growth and that the oxide growth kinetics governs the rumpling rate for this TBC. The implications of these results will be further discussed in subsequent sections.

4.1.2. 24-hour Tests

Several differences and a few similarities were observed between the 1-hour and the 24-hour tests conducted at 1121°C. The TGO growth rate per hour for the 24-hour cycles is the same as that for the 1-hour cycles, as shown in Figure 3.52. This is expected since the oxide growth is a function of the total time at temperature and does not depend on the number of thermal cycles.

One notable difference between the microstructural evolution for the 1-hour cycles and the 24-hour cycles is the lesser extent of cracking at the YSZ/TGO interface in 24-hour cycled samples compared to the 1-hour cycled samples. For the 24-hour cycles, even after 45 % of the cyclic life, cracking is less common and there is almost no marked separation of the YSZ from the TGO, as seen in Figure 3.46. The absence of cracking and separation at the YSZ/TGO interface in the 24-hour cycled sample is consistent with the failure surface shown in Figure 3.56. Figure 3.56 shows occasional retained TGO (dark phase) and YSZ (white phase) suggesting that final failure for the 24-hour cycled samples occurs predominantly at the TGO/bond coat interface. Area fraction analysis indicates that separation at the TGO/bond interface occurs at 90 % of the total area for the 24-hour tests at 1121°C, as compared to 45 % of the total area for the 1-hour tests at 1121°C (Figure 3.58). Though final failure in the 24-hour cycled samples occurs predominantly at the TGO/bond coat interface, rumpling of the bond coat/TGO interface was observed as shown in Figure 3.46. Before discussing the role of rumpling in the 1-hour and 24-hour failures, it is important to note that the rumpling amplitudes for the 24-hour cycled samples were also shown to be a single valued function of TGO thickness (Figure 4.3). This plot indicates that the rumpling amplitude is nearly a single-valued function of TGO

thickness, irrespective of hold time or test temperature, which suggests that rumpling is directly related to the oxide growth and that the oxide growth kinetics govern the rumpling rate for this TBC for both 1- hour and 24-hour tests.

As seen in Figure 3.50, the rate of increase of the rumpling amplitudes increases only slightly with the increase in hold time from 1-hour to 24-hours. This is illustrated in Figure 4.4, which compares the amplitudes of rumpling after 200 and 400 hours at 1121° C during the 1-hour and 24-hour cycles. The amplitude of rumpling is greater after the same number of 24-hour cycles than after the 1-hour cycles. This strongly indicates that rumpling is not solely cycle driven, but is also dependent on total hot time. The increase in the rate of rumpling is also shown to slow down with time (Figure 3.50), showing indications of an asymptotic behavior after the first 100 hours at 1121°C.

The 24-hour tests last longer and because of their slightly higher rumpling rates, the 24-hour samples experience greater total rumpling (Figure 3.48). Despite, the slightly higher rumpling rates for the 24-hour cycled samples compared to the 1-hour cycled samples, there was little or no cracking at the YSZ/TGO interface for the 24-hour cycled samples. Thus, though the 24-hour cycled samples showed slightly greater rumpling than the 1-hour cycled samples (Figure 4.4), the 24-hour cycled samples apparently have tolerated rumpling better in the YSZ and hence the rumpling in the 24-hour cycled samples did not cause cracks to form in the YSZ or at the YSZ/TGO interface.

The proposed explanation for the greater tolerance of rumpling distortion in the 24-hour tests is based on three assertions. First, rumpling distortion occurs primarily at elevated temperature. Second, the TBC can accommodate rumpling distortion at the maximum temperature by its ability to creep [DeMasi-Marcin *et al*; 1990, Rejda *et al*;

1999, Xie *et al*; 2003]. Third, rumpling distortion significantly damages the TBC only upon cooling. The 24-hour cycle tests lack a sufficient number of cooling events to damage the TBC before the TGO separates from the bond coat due to increasing strain energy related to high TGO stress [Vaidyanathan *et al*; 2000, Sridharan *et al*; 2004, Vaidyanathan *et al*; 2004] and steadily increasing TGO thickness. The evidence for the fact that strain energy release can account for spallation in the 24-hour tests is presented in the following paragraph. Cracks can be initiated by tensile normal stresses at grain boundary ridge tops as described in [Vaidyanathan *et al*; 2004]. The evidence for the idea that the 24-hour TBC failure at the BC/TGO interface is associated with release of strain energy and not rumpling induced, despite their higher rumpling amplitudes, is presented in Figure 4.5. The stored elastic strain energy in the TGO is proportional to the TGO thickness and the square of the TGO stress and is given by:

$$G_o = \frac{(1-\nu_{TGO}^2)\cdot h_{TGO}\cdot \sigma_o^2}{2\cdot E_{TGO}} \qquad (5.1)$$

Figure 4.5 is a plot of TGO strain energy calculated using Equation 5.1 for the 1-hour and 24-hour cycled Type I TBCs. Figure 4.5 clearly shows that the TBC failure for 1-hour tests occurs when the strain energy in the TGO is at a much lower value than that for the 24-hour tests. This suggests that 1-hour TBC failure is ultimately driven by rumpling, long before the TGO strain energy reaches a critical value, whereas the 24-hour TBC failure is not affected by rumpling but instead occurs when the TGO strain energy reaches a critical value.

A key finding of this research is that the 1-hour cycled TBCs fail in the YSZ by rumpling induced damage (cycling dependent), while the 24-hour cycled TBCs fail at the

TGO/bond coat interface by release of a large amount of stored elastic strain energy in the TGO (hot time dependent). This result suggests that the relative ratio of hot time to cycles is an important factor that governs the operating TBC spallation mechanism and spallation life.

TBC systems typically operate within two principal domains depending on their proposed applications. The failure mechanisms may differ for the two predominant areas of application – propulsion and power generation, because of their vastly different thermal histories. Systems used for propulsion and for power peaking experience multiple thermal cycles, whereas most power systems operate largely in an isothermal mode with few cycles. Let us consider two extreme case scenarios:

1. A typical duty cycle for base power generators consists of 2000 hours per cycle. In this case, TBCs experience minimal thermal cycling with long high temperature exposures (large hot time to cycles ratio). Longer hot times in this case translate into higher TGO thicknesses and failure is driven by release of stored elastic strain energy in the TGO, which in turn is a function of the TGO stress and its thickness. Failure, in this case is not based on cycling or rumpling driven but is on a hot time basis.

2. In the case of peak power generators, a typical duty cycle consists of 4 hours per cycle. Here, TBCs experience extensive thermal cycling with short high temperature exposures (small hot time to cycles ratio). Failure, in this case is thus strictly based on cycling and on rumpling driven by cycling. Thus, final failure is likely to be rumpling – induced and is likely to occur in the TBC.

The occurrence of rumpling distortion at the maximum temperature, as proposed above, is also consistent with the following experimental findings from the present study:

1. The similar rumpling rates in the 1-hour cycle and 24-hour cycle experiments, despite the much larger number of cycles experienced in the 1-hour cycle tests.
2. The very low measured flow stress (< 26 MPa at 1000°C) in Pt-Al bond coats [Pan *et al*; 2003].
3. The absence of rumpling related failure in the 24-hour TBC; and 1-hour TBC failure occurring in the YSZ, associated with rumpling-induced cyclic failure.
4. The singled value of rumpling amplitude vs. TGO thickness.

The evidence for the fact that 1-hour TBC failure in the YSZ is associated with rumpling-induced cyclic failure is presented in Figures 4.6a, b and c. Figure 4.6a shows cross-section and plan view secondary electron micrographs of Type I TBC after 200 1-hour cycles at 1121°C. The TGO in the Type I TBC with 200 cycles in the plan view picture was exposed by dissolving the YSZ. It is seen from Figure 4.6a that the YSZ/TGO interface starts to separate at the concave areas (relative to the bond coat), but remains intact at the convex areas. Similar observations can also be made from plan view fracture surfaces shown in Figures 4.41 to 4.44. Figures 4.6b and c show cross-section secondary electron micrographs of Type I TBC that failed after 600 and 635 1-hour cycles at 1121°C. As seen in Figures 4.6b and c, failure has occurred at the YSZ/TGO interface and this separation is consistently associated with regions where the bond coat has pulled away from the TBC and into the bond coat, as seen from the epoxy resin that has filled up in the region of separation between the YSZ and TGO (indicated by white arrows in Figures 4.6b and c).

4.2. Failure Map

Two key factors have been shown to compete to cause final failure in the two TBCs tested: (1) the release of elastic strain energy of TGO due to debonding at the TGO/bond coat interface and (2) rumpling induced cracking and separation at the YSZ/TGO interface. The stored elastic strain energy in the TGO is proportional to the TGO thickness and the square of the TGO stress and is given by:

$$G_o = \frac{(1-\nu_{TGO}^2)\cdot h_{TGO}\cdot \sigma_o^2}{2\cdot E_{TGO}} \qquad (5.1)$$

and the rumpling amplitude has been shown to be dependent on the TGO thickness (Figures 4.2 and 4.3).

Figure 4.7 shows a schematic failure map, which represents the basic elements of this competition and also illustrates the effect of cycle rate on the occurrence of the two failure modes. In the upper left of Figure 4.7, for relatively smaller hot time to cycles values, where the TBCs experience a greater number of cycles for a given hot time, failure occurs predominantly in the YSZ by rumpling. In the lower right, for relatively larger hot time to cycles values, where the TBCs experience a much smaller number of cycles for a given hot time, failure occurs due to high stored elastic strain energy in the TGO, which provides a strong driving force for debonding at the TGO/bond coat interface. For intermediate values of hot time to cycles ratios, TBC spallation is likely to occur by a combination of these two spallation modes. This failure map provides an preliminary experimental framework for addressing TBC spallation within the two principal domains: (1) long high temperature exposures with minimal thermal cycling, (such as the 24-hour tests in the present study) which have a larger hot time to cycles

ratio; and (2) loadings comprising extensive thermal cycling, (such as the 1-hour tests in the present study) which have a much smaller hot time to cycles ratio. A failure map such as shown in Figure 4.7, can be used when more data is available to determine damage critical parameters, to predict failure and to eventually improve TBC durability, for all TBC applications operating within these domains.

4.3. Rumpling Mechanism

Based on the results and data found in the literature and based on the findings of this study, a mechanism for rumpling is proposed. Before describing the proposed mechanism, some of the critical observations and analytical and numerical models for rumpling will be reviewed.

Previous experiments at 1121°C on a similar bond coat have shown that rumpling does not occur for isothermal exposures [Gell *et al*; 1999, Tolpygo and Clarke; 2000] and, consequently the rumpling phenomena has been associated with cyclic plasticity [Gell *et al*; 1999, Tolpygo and Clarke; 2000] and modeled as such [Karlsson *et al*; 2002 a, Karlsson *et al*; 2002 b, Karlsson *et al*; 2002 c; Karlsson *et al*; 2003, Ambrico *et al*; 2001, Brindley and Whittenberger; 1993]. Other experiments [Tolpygo and Clarke; 2000] have shown that rumpling after 100 1-hour cycles is much greater than after 100 6-minute cycles showing that, although cycling is necessary for rumpling, cycling is not the sole factor. This study by Tolpygo and Clarke (2000) also suggested that it is the oxidation time, rather than the number of cycles per se, that determines rumpling, implying that rumpling may be occurring at the peak temperature and not during heating or cooling.

In the present study, test data on two TBCs are available at three temperatures and two hold times; thus, providing more information than previously available, and excellent input for a more definitive description of the nature of rumpling.

Figure 4.8 compares the rumpling amplitude per unit time for the 1-hour and the 24-hour tests conducted at 1121°C. The increase in rumpling amplitude per unit time is nearly the same for these two tests with vastly differing hold times.

In the present experiments, consistent with some of the earlier results [Tolpygo and Clarke; 2001, Gell *et al*; 1999], it is shown that hot time alone correlates with rumpling rates suggesting that rumpling is driven by oxide growth. Two other aspects of the data reinforce this idea. First, the rate of rumpling growth follows the square root of time kinetics (Figure 3.33), as does the TGO thickness increase (Figure 3.36). Secondly, and most stunning, the rumpling amplitude is nearly a single valued linear function of TGO thickness independent of temperature (Figures 4.2 and 4.3). These findings can be reconciled with earlier results, if it is assumed that TGO growth is rate controlling for rumpling.

The implications of the present experimental findings can be understood by reviewing the results in the context of the rumpling models found in the literature. Modeling results have shown that rumpling only occurs when the TGO lengthens via the Rhines and Wolf mechanism, in addition to the expected thickening [Ambrico *et al*; 2001, Mumm *et al*; 2001, Karlsson and Evans; 2001], where the lengthening is conveniently measured in terms of in-plane growth strain per cycle or per unit time. Rhines and Wolf [Rhines and Wolf; 1970], after describing a series of experiments in which they characterized the plastic extension of nickel rods and sheets on oxidation,

introduced a conceptual model for the origin of the growth strain and stress. They pointed out that if the oxide grows by inward diffusion of oxygen at the oxide / alloy interface, no lateral strains would be created. Likewise, if the oxide grows by outward diffusion of the metal, the new oxide would form at the top of the oxide scale and again no lateral strain would be created. They also pointed out that if new oxide were to form at grain boundaries lying parallel to the oxide / alloy interface, no lateral growth would occur. In all these three instances, the volume change accompanying the oxidation reaction can be accommodated by a rigid body displacement of the oxide perpendicular to the oxide / alloy interface. Rhines and Wolf argued that only when new oxide formed along grain boundaries lying perpendicular to the oxide / alloy interface, would a lateral strain be generated and this requires concurrent inward diffusion of oxygen and outward diffusion of metal ions. These features constitute what is now known as the Rhines–Wolf model.

The response of TGO rumpling to different hot times has been explained on the basis of TGO yielding [Karlsson *et al*; 2002 a, Karlsson *et al*; 2003]. It has been shown [Karlsson *et al*; 2002 a, Karlsson *et al*; 2003] that the extent of rumpling has a maximum value set by in-plane oxide growth, but that the actual growth is less than or equal to this maximum value due to the conversion of lengthening strains to thickening strains, when the oxide layer yields at high temperature. These modeling results have shown that the rumpling rate will directly depend on the in-plane growth of the TGO until the growth increment becomes sufficiently large to produce TGO yielding. Yielding in the TGO becomes increasingly likely in two cases: first, as the in-plane growth increment for a given hold time increases, and second, as the ratio of the TGO yield stress to bond coat yield stress decreases. When TGO yielding occurs, the compressive in-plane growth

strain is converted into increased TGO thickness. Thus, once TGO yielding occurs, the elongation rate becomes less that the maximum rate allowed by the in-plane elongation of the TGO.

Calculations made by Karlsson *et al* (2003) have also shown that for sufficiently small in-plane growth increments and sufficiently strong oxide and sufficiently low-strength bond coat, the entire compressive growth strain increment shows up as increased interface length (toruosity), otherwise, yielding converts some of the compressive in-plane growth to thickness increase.

Thus, based on the modeling results discussed, the possible explanation for the 24-hour tests in the present study, with their larger in-plane growth increment not experiencing quite as much rumpling per unit time as the 1-hour tests (Figure 4.8) is that a slightly larger fraction of the in-plane growth is converted to thickness increase due to TGO yielding.

In contradiction to this argument, the bond coat properties evaluated for a very similar TBC by Pan *et al* (2003) indicates that the Pt-Al bond coat has a very low yield strength at elevated temperatures. This leads to the possibility, that for this TBC, the yield strength of the bond coat at temperature is much lower than that of the TGO and therefore the bond coat does all the yielding and no TGO yielding occurs during cycling. Thus the in-plane TGO growth occurs at the peak temperature and directly appears as rumpling displacements of the TGO.

Thus, in order to determine the possibility of TGO yielding in this TBC and explain the rumpling behavior, the minimum in-plane growth strain necessary to produce the observed rumpling change has been estimated. The in-plane growth strains necessary

to explain the oxide surface lengthening have been estimated as shown in Figure 4.9. The in-plane growth strain, e_g, is estimated based on an assumption that all such strain appears as increased surface length, which will underestimate the growth strain, if TGO yielding occurs. If L is the surface length of the TGO/bond coat interface at N number of cycles be denoted as L (N), the in-plane oxide growth strain was estimated as follows:

$$e_g = \frac{[L(N+1) - L(N)]}{L(N)}$$

Using the above equation, in-plane TGO growth strains for the 1-hour and the 24-hour tests at 1121°C are shown in Figure 4.9.

Examination of the modeling results by Karlsson *et al*, as shown in Figure 15 from [Karlsson *et al*; 2003] (Figure 4.10), show that maximum rumpling occurs for in-plane growth strains between 1 x 10^{-3} and 5 x 10^{-3}, corresponding to values of growth strain values between 2 t_0 and 10 t_0 in Figure 4.10. Maximum rumpling can be identified from Figure 4.10 as those locations, in the range of growth strain values between 5 x 10^{-3} and 1 x 10^{-2}, corresponding to values of growth strain values between 10 t_0 and 20 t_0 in Figure 4.10, where the rumpling increases linearly with the imposed in-plane growth strain. Thus, qualitatively there is a regime where cyclic plasticity based models [Karlsson *et al*; 2002 a, Karlsson *et al*; 2002 b, Karlsson *et al*; 2002 c; Karlsson *et al*; 2003, Ambrico *et al*; 2001, Brindley and Whittenberger; 1993] predict behavior consistent with the present study.

We note in the present experiments that the in-plane growth strain, as shown in Figure 4.9, is between 2 x 10^{-4} and 9 x 10^{-4} and is, therefore, in the necessary range for TGO growth rate limited behavior, according to the modeling results by Karlsson *et al*

(2003). The present results have also shown that rumpling is proportional to the TGO growth rate (Figures 4.2 and 4.3) and these are also consistent with the model by Karlsson *et al* (Karlsson *et al*; 2003), where the rumpling rate increases linearly with the in-plane growth increment up to the point where the in-plane strain per cycle is between 1 x 10^{-3} and 5 x 10^{-3}. The one caveat is that the lateral growth strain estimated in Figure 4.9 is a lower bound in that any strain relieved by TGO yielding would not be included in the strain estimated from the rumpling rate. In spite of this caution, the idea that the full in-plane growth strain appears as rumpling is consistent with the low bond coat yield stress, the estimated range from modeling and is the simplest explanation of the observed single valued rumpling rate versus TGO thickness.

Thus, the findings from the present experiments, where longer hold times (24-hour tests) produced only slightly larger rumpling than shorter hold times (1-hour tests), as shown in Figure 4.4, can be reconciled with the finite element and analytical modeling results reported [Karlsson *et al*; 2002 a, 2002 b, 2002 c; 2003] if it is assumed that there were no significant TGO yielding and all of the elongation strain occurring in the oxide showed up as a length increase.

4.4. PLPS Measurements

A goal of this research has been to develop a method for determining remaining life of TBCs using PLPS. As seen in the previous section, the stress in the TGO plays a vital role in dictating the failure mechanisms of TBCs. Hence, it is valuable to non-destructively measure the TGO stress as a function of cycles for different exposure

conditions and correlate the measured value of the TGO stress to TBC damage and TBC life. The results, thus obtained, can be used in developing a mechanisms-based life prediction model to assess the remaining life of the TBCs. To this end, the PLPS technique and associated spallation mechanisms were evaluated, for the first time, for two TBCs as a function of cycles at three temperatures and two hold times. The evolution of TGO stress versus TBC life for the 1-hour tests at the three temperatures is discussed first. The TGO stress behavior for the 1-hour and the 24-hour tests are then compared and contrasted. Reasons for the observed initial increase and the subsequent monotonic decrease in the TGO stress with cycles are presented. A correlation is then made between the microstructural evolution, the stress relaxation and the final TBC spallation mechanism. Additionally, reasons are also presented for the lack of a systematic change in some of the spectral features like the peak area ratio and the peak shape.

4.4.1. Effect of Cycle Temperature on the TGO Stress Evolution

The present experiments were carried out as part of a program designed to examine the viability of using PLPS data as a non-destructive inspection (NDI) technique for turbine coatings and most specifically to use this technique for making retirement for cause decisions. The financial incentive to carry out such measurements is large because of the high cost of unplanned shutdowns and the need to replace components based on statistically minimum performance. The inability to identify those individual components that will be the lowest performers results in low utilization of the potential service life of the majority of parts.

The PLPS spectral characteristics have been evaluated and examined as a function of 1-hour thermal cycles at a single temperature (1121°C) for several EB-PVD TBCs

[Gell *et al*; 1999, Vaidyanathan; 2001, Sohn *et al*; 2001, Xie *et al*; 2003, Wen *et al*; 2005]. The systematic changes in the TGO stress levels with cycles in these TBCs have allowed PLPS to be used as an NDI technique to detect damage and to make reliable remaining life predictions in these TBCs to within ± 7% error [Jordan *et al*; 2001] using either a simple statistical regression based approach or though training a neural network. None of these studies, however, have addressed the very serious potential complication presented by the fact that different locations on a given part are exposed to different temperatures or that different operators may have different temperatures and exposure times. Hence, it is important to obtain stress versus cycles data over a range of temperatures.

It was found that the measured stress as a function of TBC life fraction shows a monotonic decline and is independent of temperature, as shown in Figure 3.13, simplifying the use of such data in the non-destructive assessment of turbine components subject to non-uniform temperatures. This finding suggests that the TBC remaining life can be uniquely estimated from the measured stress level and the number of exposure cycles experienced to date by the component. However, it is important to note that the temperature range used in this study is small compared to that experienced by engine components.

The TGO stress was shown to increase to its maximum value during the first fifty cycles and then decrease monotonically with cycling until failure. The initial increase in the TGO stress may be due to growth stresses in the TGO [Lipkin *et al*; 1997, Tolpygo and Clarke; 1998 a, Tolpygo and Clarke; 1998 b, Tolpygo *et al*; 1998], which partly may be attributed to the transformation of the ?-Al_2O_3 to a -Al_2O_3 during the early stages of

TBC deposition and oxidation [Lipkin *et al*; 1997]. However, no θ peaks were recorded from the spectral data obtained on these specimens. In earlier work done on the same TBC [Xie *et al*; 2003], the initial rise in TGO stress was attributed to the conversion of a discontinuous to a continuous TGO film.

In the present study, the initial TGO did not form a continuous layer until after the first 5-10 thermal cycles, as seen from the SEM micrographs of the bare bond coated bottom of the specimens. Thus, the result of the conversion of this TGO film from discontinuous to continuous is the likely reason for the increasing TGO stress during the first 5-10 cycles. The presence of non-continuous TGO in the SEM plan view pictures is shown in Figure 4.11.

The monotonic decrease in the TGO stress with further cycling can arise from several causes. The surface geometry of the bond coat generally gets rougher with cycling due to rumpling [Gell *et al*; 1999, Tolpygo and Clarke; 2000, Mumm *et al*; 2001, Panat and Zhang; 2003] which in turn allows the TGO to get longer, potentially relieving the compressive stresses in the TGO. There is also an effect of oxide geometry on the stress that leads to decreasing average stresses with increasing TGO thickness on rough surfaces [Gong and Clarke; 1998]. In addition, this effect is further aggravated if the surface roughness increases due to rumpling.

4.4.2. Effect of Cycle Hold Time on the TGO Stress Evolution

As shown in Figure 3.17, the TGO stress evolution for the 24-hour tests is found to be slightly slower than that for the 1-hour tests, indicating that the stress evolution changes distinctly with hold time changes. The 24-hour tests essentially show no decline

of TGO stress with cycles until close to failure. It is also seen that final failure occurs in the YSZ at or near the YSZ/TGO interface for the 1-hour tests at all three temperatures (Figures 3.41 and 3.42). However, the failure mode changes to that occurring predominantly at the TGO/bond coat interface for the 24-hour tests, as shown in Figure 3.56. It is consistent with the above observations that the TGO stress evolution with cycles remains unchanged for a given TBC, as long as the failure mode remains the same; and changes when the failure mode is different. Also, since the decrease in the TGO stress is associated with rumpling [Xie *et al*; 2003, Tolpygo and Clarke; 2003, Wen *et al*; 2005], the same fractional decline of the stress in the 1-hour cycled specimens is indicative of the same extent of rumpling for the 1-hour cycled samples, which implies the same failure mode in these specimens.

The above finding also suggests that differences due to cycle period will necessitate generation of databases specific to a given engine's temperature-time operational pattern. These results indicate that the trends observed for any particular spectral characteristic with cycling may vary for a given TBC consistent with its damage mechanism. Hence, the operative TBC damage mechanism and the associated spectral changes with thermal cycling should be determined for each TBC of interest, under thermal cycling conditions that match or approximate those of engine service. Table 4.1 lists the differences in the PLPS behavior and the failure modes during the 1-hour and the 24-hour tests for Type I and Type II TBCs used in this study.

The change in failure mode with cycle duration means that life prediction for this TBC will ultimately require the use of two independent damage measures and failure must be predicted on the basis of whichever spallation mechanism comes first. Finally,

the temperature independence of the stress versus life fraction curve, as seen in Figure 3.13, will greatly simplify the use of TGO stress values for non-destructive inspection for TBCs where rumpling is the dominant failure mode.

4.4.3. TGO Stress Relaxation Mechanisms

As mentioned before, rumpling of the TGO/bond coat interface has been identified as a possible stress relaxation mechanism for Type I and Type II TBCs. In order to verify this statement, the TGO stress relaxation rate and the rumpling rate were plotted as a function of TBC life. As shown in Figure 4.12, similar trends were observed between rumpling rate versus life and stress relaxation rate versus life for all the test conditions evaluated. Also, both the rumpling amplitude (Figure 3.35) and the measured TGO stress (Figure 3.22) reach a fairly constant value at failure, independent of the exposure condition. Also, as shown in Figure 4.13, the tortuosity of the TGO/bond coat interface is shown to increase from 1.05 in the as-received state to 1.29 at 45 % life. This indicates that rumpling allows the TGO to get longer, thus potentially relieving the compressive stresses in the TGO. It can be concluded based on these observations that rumpling is indeed the reason for the observed TGO stress relaxation in this system.

PLPS measurements were also carried out on cross-sectional TBC specimens as a function of cycles. The measured TGO stress values obtained from the measurements carried out on the cross-section were then compared to results obtained from measurements made through the TBC to identify the possible reasons for the observed stress reduction with cycling. As shown in Figure 4.14, lower stress levels are observed for areas of the TGO with thickness imperfections and for areas where the TGO has

rumpled, indicating that a systematic decrease in the TGO stress with cycling is related to the rumpling-induced microstructural degradation of the TGO.

4.4.4. Change of Other Spectral Characteristics with Cycling

Six spectral characteristics that can be related to damage have been identified in the literature: peak position (indicating TGO stress) [Christensen et al; 1996 a, Lipkin and Clarke; 1996, Vaidyanathan; 2001, Sohn *et al*; 2001, Xie *et al*; 2003] peak width as measured by FWHM [Clarke et al; 1997, Vaidyanathan; 2001, Sohn *et al*; 2001, Xie *et al*; 2003], peak shape as indicated by Gaussian/ Lorentzian mix [Clarke et al; 1997], R_1/R_2 peak intensity ratio [Clarke et al; 1997], the standard deviation of measured stress location to location [Vaidyanathan; 2001, Sohn *et al*; 2001, Xie *et al*; 2003] and finally the fraction of measured peaks that can be fit by two sets of R_1-R_2 peak pairs (also referred to as bimodal fraction) [Sohn *et al*; 2001, Wen *et al*; 2005]. In the present study and earlier ones [Vaidyanathan; 2001, Sohn *et al*; 2001, Xie *et al*; 2003], the peak position, standard deviation of the measured TGO stress and the R_2 peak width have shown systematic change with cycles. [Sohn *et al*; 2001] and [Wen *et al*; 2005] showed the bi-modal fraction changing systematically with cycles and [Wen *et al*; 2005] also showed the peak area ratio declining monotonically with cycles. Though all spectral attributes should continue to be studied for possible use in NDI, it appears that the TGO stress level is the single most consistently promising measure of TBC damage.

The peak position observed for an interrogated volume of the TGO is created by the superposition of peaks from each infinitesimal sub volume. Thus, if there were heterogeneity on a size scale larger than the probe volume, it would be expected that the variations between individual separated probe volumes would change in a systematic

manner with damage. The standard deviation of the measured TGO stress is a measure of this stress heterogeneity. As shown in Figure 3.23, the standard deviation for the measured TGO stress is shown to increase with cycling, which suggests damage accumulation and an increasing proportion of locally damaged areas with cycling.

As explained by Lipkin *et al* (1997), peak broadening indicates the existence of stress variation within the probed volume. The rough grit blasted bond coat surface found in Types I and II TBCs results in strain variations in the TGO from place to place and through the thickness [Cheng *et al*; 1998]. Additionally, since the peak position observed for an interrogated volume of oxide is created by the superposition of peaks from each infinitesimal sub volume, the peak width is determined by stress heterogeneity. Damage, hence, in general, would be expected to affect stress heterogeneity and peak width has been proposed as a measure of detecting damage [Lipkin and Clarke; 1995]. In addition, the difference in the peak width between the stressed TGO in the cycled samples and the stress free α-alumina is considered an approximate measure of the range of stress gradient within the TGO. However, the monotonic decrease in the peak width of the spectra from the investigated specimens, as shown in Figure 3.24 and the linear increase in the difference in the peak width between the stressed TGO in the cycled samples and the stress free α-alumina with the average stress level in the TGO, as shown in Figure 4.15, is not consistent with this notion. Hence, the peak narrowing seen in Type I and Type II TBCs do not appear to be driven by damage accumulation in the TGO. A possible explanation for the peak narrowing seen in Figures 3.24 and 3.80 can be explained on the basis of inhomogeneity (through the TGO thickness) in the injection of alumina at the TGO/ bond coat interface by the Rhines and Wolf mechanism [Rhines and

Wolf; 1970] eventually resulting in a lateral growth strain, and the monotonic decrease in the R_2 peak width with cycling would hence suggest a decrease in this through-thickness inhomogeneity.

This linear increase in the stress gradient in the TGO with the average TGO stress level is consistent with the results of Lipkin *et al* (1997a), who have reported that the stress gradient decreases by 6-7 times while the average stress itself decreases by 50% with cycling for stressed oxides, assuming pure Lorentzian peak shapes for unstressed oxides.

No systematic changes were seen in the peak shape or the peak area ratios with cycling, as shown in Figures 3.25 and 3.26. Thus, it appears that the existence of trends in the 6 spectral attributes is highly system specific and need to be studied on a case-by-case basis.

4.4.5. Photoluminescence Response for Multiple History Tests

TBC coated turbine blades typically experience different temperatures during an engine cycle. In order to simulate such situations, two-level furnace cyclic tests consisting of multiple temperatures and multiple hold times were carried out and the photoluminescence response of the specimens from each stage of the two-level tests was compared.

Results from the PLPS measurements on Type I TBC specimens subjected to changing peak temperatures during thermal cycling are shown in Figures 3.18 and 3.20. The overall TGO stress response of Type I TBCs remains unchanged on changing the

peak temperature amplitude, establishing and validating the possibility of using this type of data for TBC remaining life assessment.

The TGO stresses on these Type I TBC specimens were measured only after 40-50 cycles following the transition to the new test temperature. In order to better understand the effect of the change in the test temperature on the stress response, the PLPS measurements for the Type II TBC samples were made after every cycle on transition to the new temperature. Since the TGO stress measurements for the multi-temperature tests on the Type I TBC specimens were not conducted in shorter measurement intervals of 1-5 cycles on changing the peak temperature, it is difficult to understand the time taken for the TGO stress to redistribute and stabilize at each new peak temperature. For this reason, the results from the multi-temperature tests for Type II TBCs are discussed here.

Figure 3.76 is a plot of the TGO stress versus cycles for the two Type II TBC samples that were subjected to the multiple-temperature tests. For the tests carried out at 1121°C followed by 1151°C, there was a slight deviation in the TGO stress versus cycles trend during the first 25 cycles on transition to the higher test temperature, following which the original slope of the stress versus cycles curve was restored. The TGO stress measured after the first 2 cycles at the higher test temperature of 1151°C shows a value of 2.59 GPa from a measured TGO stress of 2.43 GPa at the previous lower test temperature of 1121°C, which is a ratio of 1.06. The ratio of stress values between these two temperature amplitudes (2.59 GPa / 2.43 GPa = 1.06) corresponds well with the ratios of temperature drops, ΔT, ((1151°C-21°C)/ (1121°C-21°C) = 1.03), suggesting that the TGO stress value accurately reflects the thermal history of the specimen. Similarly, for

the tests conducted at 1151°C followed by 1121°C, the ratio of stress values between these two temperature amplitudes (1.83 GPa / 1.77 GPa = 1.03) corresponds well with the ratios of temperature drops, ΔT, ((1151°C-21°C)/ (1121°C-21°C) = 1.03), again confirming the previous notion that the TGO stress values truly represent the thermal history of the sample.

It is also worth noting here (Figure 3.76) that the time taken for the TGO stress to stabilize and for the slope of the TGO stress versus cycles trend to return to its original value is 25 cycles for the tests run at 1121°C followed by 1151°C and 50 cycles for the tests run at 1151°C followed by 1121°C. The longer time taken for the stress to stabilize on lowering the temperature to 1121°C from 1151°C suggest the roles of TGO and bond coat creep, both of which are thermally activated processes. These observations are consistent with results obtained on another TBC by Vaidyanathan (2001).

For the Type I TBC samples subjected to a change in cyclic hold time, the TGO stress measurements were made after every cycle at the new hold time, which allows us to understand the time taken for the TGO stress to stabilize and start following the previous monotonic trend. First, we consider the sample subjected to 24-hour cycles followed by 1-hour cycles at 1121°C Figure 3.19. The TGO stress increased from 2.63 GPa to 2.69 GPa after the first two cycles and to 2.76 GPa after the first four 1-hour cycles at 1121°C Figure 4.16. It can also be seen from these figures that the TGO stress stabilized and the TGO stress versus cycles returned to its previous slope after 10 1-hour cycles at 1121°C. The slope of the stress versus cycles increases slightly on changing to the 1-hour hold time and the original rate of stress reduction, typical of the 24-hour tests, was not restored at any point during the 1-hour hold time tests that followed. This

indicates that the cycle time affects the stress response irreversibly, as seen in Figure 3.21.

For the sample subjected to the 1-hour tests followed by the 24-hour tests at 1121°C, there was a slight drop in the slope of the stress versus hot time curve on transition to the 24-hour hold time, and the original rate of stress reduction, typical of the 1-hour tests, was not restored at any point during the 24-hour hold time tests (Figure 3.19). In order to understand how the TGO stress changes in the first few cycles on transition to the new hold time, the transitional portion of Figure 3.19 is presented in Figure 4.17. The TGO stress decreases from 1.69 GPa to 1.63 GPa during the first four 1-hour cycles at 1121°C. The reasons for this drop in TGO stress on changing the hold time are not clear at this time. Thus, while the 24-hour tests followed by the 1-hour tests shows an increase in the TGO stress by 0.06 GPa after the first four cycles at the new hold time and a subsequent increase in the slope of the stress versus life curve, the 1-hour tests followed by the 24-hour tests shows a decrease in the TGO stress by 0.06 GPa after the first two cycles at the new hold time and a subsequent decrease in the slope of the stress versus life curve.

Thus, the effects of changes in cyclic temperature and hold time on TGO stress behavior has been studied and documented. It can be concluded that a change in the cyclic temperature amplitude does not affect the normalized stress response of the system, while a change in the hold time does affect the stress response of the system. Hence, PLPS can be used as a viable NDI technique for the repeated duty cycles with non-uniform temperature exposures. However, the effect of changing the hold time on the stress behavior seems significant and hence the TGO stress versus cycles or TBC life

trends should be generated and studied separately for every cycle with a different hold time.

4.5. Relationship Between Maximum TGO Stress and Spallation Life

If there is a relationship between the maximum, initial TGO stress and the ultimate spallation life, it would then be possible to use PLPS as a quality control instrument immediately following coating deposition. Figure 4.18 shows the maximum TGO stress value for five Type I TBC samples cycled at 1121°C using 1-hour cycles as a function of their failure lives and Figure 4.19 shows the maximum TGO stress value for three Type I TBC samples cycled at 1121°C using 24-hour cycles as a function of their failure lives. The higher the initial TGO stress, the longer the spallation life for the seven specimens. Hence, these preliminary results indicate that the maximum TGO stress can be used for quality control purposes. These results together with the finding that the TGO stress at failure for Types I and II TBCs was fairly constant for all exposure conditions (Figures 3.22 and 3.78) have allowed us to make very accurate remaining life assessments.

4.6. Mechanism - Based Remaining Life Assessments Using PLPS

As mentioned in Section 4.8, the single valued linear relation between the TGO stress and the TBC life, which was found to be independent of the peak temperature, and the critical TGO stress value were used to make reliable remaining life assessments using

a simplistic regression approach. It has previously been reported in work done on a similar TBC system [Wen *et al*; 2005, Jordan *et al*; 2001], that when multiple spectral features showed systematic trends with cycling, a more complex neural network approach had to be adopted. However, for both Types I and II TBC systems, the TGO stress and the peak width were the only spectral features that changed monotonically with TBC life. So, a simplistic regression approach was used in this study to assess the remaining life of Types I and II TBCs using these two spectral features.

In actual turbine components, there is typically a variation of temperature from part to part and from location to location on a given part. These temperature variations are the most common cause for variation in part lives. It is thus important in practice to have a prediction method that does not require the precise knowledge of the exposure temperature. In order to address such situations in the present study, the TGO stress versus TBC life data obtained for the constant and variable amplitude test conditions have been used to make temperature-blind remaining life predictions. Being the first attempt of its kind at making remaining life predictions without using the knowledge of the temperatures, these predictions have significant meaning for engine use.

In order to evaluate the performance of this prediction method the maximum error in making the predictions, as shown in Tables 3.7 and 3.8 were compared with the inherent variation in the Type I TBC spallation lives of all samples tested at the three temperatures and the two hold times, in the constant and variable amplitude conditions. These results are shown in Figure 4.20. While the maximum error in assessing the remaining life for the 1-hour test conditions at half-life inspection is 9 %, the actual scatter in the TBC spallation lives for these exposure conditions is 55 %. Similarly, for

the 24-hour tests and the multiple hold time tests, while the maximum error in assessing the remaining life at half life inspection is 10 %, the actual scatter in the TBC spallation lives for these exposure conditions is 75 %. These comparisons indicate that this method is truly predictive. Thus, using a simplistic regression method, the TGO stress measurements on the Type I TBCs have been useful in making remaining life predictions to within 10 % accuracy. This prediction accuracy is very significant considering the simplicity of the regression method and the fact that the knowledge of the test temperature or the hold time was not used in making these predictions.

In addition, the remaining life assessments made using TGO stress values were compared to those made using peak width values and standard deviation of TGO stress. Figure 4.21 compares the maximum absolute error in calculating remaining life using TGO stress and peak width values for Type I TBCs during the 1-hour and 24-hour tests at 50 % inspection intervals. Figure 4.22 compares the maximum absolute error in calculating remaining life using TGO stress, peak width and standard deviation of TGO stress values for Type I TBCs during the 1-hour and 24-hour tests at 50 % inspection intervals. It can be concluded based on Figures 4.21 and 4.22 that the remaining life assessments made using the peak width and the standard deviation of stress are much less accurate than those made using the TGO stress.

4.7. Linear Damage Rule

Two stage block-loading tests were completed for the first time on TBCs. The average failure lives for the multi-temperature and multiple hold time tests for the Type I

TBCs are presented in Tables 3.4 and 3.5. The TBC life fractions for the Type I TBC samples for each stage of these two-stage cyclic tests and the total calculated TBC life fraction at failure are listed in Table 4.2. The linear damage fractions, denoted as LDF in, have been evaluated for this TBC. Besides the average value of the linear damage fraction, the minimum and the maximum values (denoted as LDF-Min and LDF-Max in Table 4.2) and their standard deviations have also been determined. Several observations can be made from these results. First, for the multi-temperature tests, the linear damage rule is reasonably satisfied. Second, for the multiple hold time tests, where the 24-hour tests were followed by the 1-hour tests, the linear damage rule is also verified. However, for the case where the 1-hour tests were followed by the 24-hour tests, the total TBC life fraction is calculated to be 0.75. Thus, for the sample that was cycled to approximately half its expected life using the 1-hour tests at 1121°C and then subjected to the 24-hour tests at 1121°C, the 24-hour cyclic life was found to be half its expected life. This could suggest possible synergistic damage accumulation effects on changing from the 1-hour to the 24-hour test conditions. The previous finding from this work, which has shown a change in the failure mode between the 1-hour and 24-hour tests, may be an explanation for this observation.

The average value of the linear damage fraction (LDF), the minimum and the maximum values (denoted as LDF-Min and LDF-Max) and their standard deviations for the Type II TBCs for each stage of the two-stage variable amplitude tests are listed in Table 4.3. It can be seen that for Type II TBCs, the linear damage rule is satisfied for the test run which included only temperature shift tests and no hold time shift test. The results for Type II TBCs are similar to that for Type I TBCs.

4.8. Differences Between Type I and Type II TBCs

The average failure lives for Type II TBCs during the 1-hour tests at 1100 and 1121^{o}C is shown to be 0.7 X that for Type I TBCs, as shown in Figure 4.23.

A two-sample t test assuming unequal variances was performed to verify whether the difference in the average failure lives of Type I and Type II TBCs is statistically significant [http://www.physics.csbsju.edu/stats/t-test.html]. The t value for 95% con?dence interval was calculated for all the four exposure conditions (1-hour at 1100°C, 1121°C and 1151°C and 24-hour at 1121°C). This calculated t-value was then compared with the critical t-value obtained from the t-tables. The calculated t-value being significantly greater than the critical t-value would indicate that the difference in the failure lives of the two TBCs is statistically significant. The t-test results indicate that the difference in the average failure lives of the two TBCs is statistically significant for the 1-hour tests at 1100°C and 1121°C and the 24-hour tests at 1121°C, while the difference for the 1-hour tests at 1151°C is not. The data is presented in Table 4.4. This suggests that the average failure lives of the two TBCs for the 1-hour tests at 1151°C are comparable.

The results presented in Figure 4.23 are consistent with results obtained in the comparative studies of similar inward and outward grown platinum modified aluminide bond coats by Angenete and Stiller (2002) and by Basta *et al* [U.S. Patent # 5658614; 1997]. Basta *et al* [U.S. Patent # 5658614; 1997] have attributed the improved cyclic oxidation resistance of the outward grown bond coat to a slower growing and more adherent protective alumina scale. Angenete and Stiller (2002) have reported the inward grown bond coat to have a higher oxide growth rate and a reduced oxidation resistance

compared to the outward grown bond coat. These results are true in the present study as well.

Reduced cyclic durability for Type II TBCs in the 1-hour tests (Figure 4.23), in which the predominant failure mode is by rumpling (Figure 3.84), would be consistent with (1) a higher TGO growth rate and (2) faster rumpling in Type II TBCs as compared to Type I TBCs. The oxide growth rate for the Type II TBC with the inward grown bond coat are shown to be twice that for the Type I TBC with an outward grown bond coat, as seen in Figure 4.24. The extent of rumpling in Type II TBCs during the 1-hour tests is shown to be qualitatively larger than that for Type I TBCs, as seen in Figure 3.85. This is likely due to the higher amplitude of the TGO displacements (2μm) for Type II TBCs in the as-received condition compared to (1μm) for Type I TBCs as seen in Figure 3.86 and the hypothesis that rougher bond coats rumple faster than smoother bond coats [Tolpygo and Clarke; 2000, Vaidyanathan *et al*; 2000]. Thus, a higher TGO growth rate (Figure 4.24) and faster rumpling (Figure 3.86) in Type II TBCs is consistent with the average 1-hour cyclic lives of Type II TBCs being 20-25% smaller than that for Type I TBCs (Figure 4.23).

The TGO growth rate is influenced by several factors, such as: effective bond coat surface area, which is inversely proportional to the bond coat grain size (for grain boundary diffusion in the bond coat]; surface roughness; oxide grain size (since the main transport across the TGO occurs along the oxide grain boundaries [Felten and Pettit; 1976, Sheasby and Jory; 1978]); high Al content in the bond coat surface, which decreases the growth rate by formation of a purer oxide [Pettit; 1967]; high Pt content in

the bond coat which affects the purity of the oxide [Niu *et al*; 1993, Tawancy *et al*; 1995], thereby lowering the growth rate.

It is known that the outward diffusion process generates fewer grain boundaries and a larger bond coat grain size [Goward; 1970]. Thus, the lower TGO growth rate for the outward grown bond coat in Type I TBC can be attributed to the larger bond coat grain size, lower bond coat surface roughness and hence a smaller effective bond coat surface area.

It has been shown both in the present study and studies in the past [Angenete and Stiller; 2002, Basta *et al* - U.S. Patent # 5658614; 1997] that the outward grown bond coat has a better resistance to oxide spallation than the inward grown bond coat. The spallation behavior of the TGO during cooling is influenced by several factors, such as: (1) the build-up of thermal stresses and their distribution; (2) the adherence of the TGO to the bond coat; and (3) the ductile to brittle transition temperature (DBTT) of the bond coat. The relative contribution of these factors to the difference in the oxidation resistance of the two bond coats is discussed below.

1. Thermal stresses: Since the difference in thermal expansion coefficient between the substrate and bond coat can be expected to be very similar for both bond coats, it is not likely that this factor can account for the difference in spallation behavior of the two bond coats. However, due to the rougher surface of the inward grown bond coat in Type II TBCs, larger out-of-plane tensile stresses components will be generated [Tolpygo and Clarke; 2000, Cheng *et al*; 1998], which in turn increases the tendency for spallation.

2. Oxide adherence: It has often been proposed that the oxide adherence is strongly affected by impurities, among which sulfur has been thoroughly investigated

[Lee *et al*; 1998, Haynes *et al*; 1999, Smialek; 1991, Smialek and Tubbs; 1995; Zhang *et al*; 1999]. Since CVD processes for the outward grown bond coat will introduce less S than pack aluminizing for the inward grown bond coat [Basta *et al* - U.S. Patent # 5658614; 1997], this is a possible reason for the improved oxidation resistance of the outward grown bond coat. It is also known that the presence of substrate substitutional alloying elements, such as Ti, V, W and Mo in the coating reduces the oxidation resistance [Wood and Goldman; 1987]. The CVD aluminizing process used for the outward grown bond coat in Type I TBC is known to substantially reduce the concentration of these alloying elements and surface active tramp elements, such as B, P and S in the bond coat, thus providing them improved oxidation and spallation resistance than the inward grown bond coat [Basta *et al* - U.S. Patent # 5658614; 1997],.

3. Ductile to Brittle Transition Temperature (DBTT): The DBTT was defined by Lowrie and Boone (1997) as the temperature above which the coating can withstand a total strain of 0.6% without cracking. A low DBTT would mean that larger differences in thermal expansion could be accommodated by deformation of the bond coat thus resulting in lower thermal stresses in the bond coat and more plastic deformation. Previous studies have shown that for simple aluminide coatings, the DBTT decreases with decreasing bond coat thickness [Hancock *et al*; 1990] and decreasing Al content [Bernard and Remy; 1990]. It is also known that the addition of Pt increases the DBTT, especially if continuous $PtAl_2$ layers are allowed to form [Vogel *et al*; 1987]. It has been shown that for otherwise similar Pt modified nickel aluminide bond coats, the inward growth (high activity) coating processes result in a higher DBTT than the outward growth process [Vogel *et al*; 1987]. Thus, since the outward grown bond coat in Type I TBC is

thinner and has a lower Al content (since the inward grown bond coat is processed by a high aluminum activity low temperature diffusion method) compared to the inward grown bond coat in Type II TBC, these factors suggest a lower DBTT for the outward grown bond coat in Type I TBC than for the inward grown bond coat in Type II TBC. The lower DBTT for the outward grown bond coat in Type I TBC suggests that Type I TBC is likely to rumple more than Type II TBCs and hence have lower cyclic life, which is contrary to the results seen in Figure 4.23.

Despite the reduced 1-hour cyclic lives, the 24-hour cyclic lives for Type II TBCs were found to be 1.5 X higher than that for Type I TBCs, as shown in Figure 4.23. The damage critical parameters, viz., the TGO thickness, the TGO stress and the rumpling amplitudes were examined in order to account for this result. As illustrated in Figure 4.5, the release of elastic strain energy of the TGO due to debonding at the TGO/bond coat interface is the driving force for failure during the 24-hour tests for Type I TBCs. The stored elastic strain energy in the TGO, as mentioned previously, is proportional to the TGO thickness and the square of the TGO stress and is given by:

$$G_o = \frac{(1-\nu_{TGO}^2)\cdot h_{TGO}\cdot \sigma_o^2}{2\cdot E_{TGO}} \qquad (5.1)$$

Though the initial TGO thickness (Figure 3.86) and the TGO growth rates (Figure 4.24) for Type II TBCs are higher than that for Type I TBCs, the maximum value of TGO stress (Figure 3.83) and the TGO stress at failure (Figure 3.78) for Type II TBCs are lower than that for Type I TBCs. Thus, the stored strain energy in the TGO for Type II TBCs based on Equation 5.1 can be expected to be higher for Type I TBCs than for Type II TBCs. Thus, the 24-hour cycled samples, which fail by the release of stored

strain energy, are likely to fail earlier for Type I TBCs than for Type II TBCs. This is consistent with the results shown in Figure 4.23.

While Type I TBCs have a maximum TGO stress of 2.8 - 3.0 GPa after 5 cycles, the Type II TBC have a stress of 2.2 – 2.5 GPa. This is consistent with the concept that the higher the maximum TGO stress; the longer are the TBC spallation lives.

The TGO stress at failure is shown to be lower for Type II TBCs, in the range of 1.1 to 1.3 GPa (Figure 3.78), compared to 1.2 to 1.4 GPa for Type I TBCs (Figure 3.22). This is consistent with rumpling being the cause for TGO stress relaxation in Type I and Type II TBCs and the larger initial rumpling amplitudes together with the greater extent of rumpling observed in Type II TBCs (Figure 3.85), which would result in a lower TGO stress at failure for Type II TBCs.

The slopes of the TGO stress versus cycles curves were also evaluated for Types I and II TBCs for the three test temperatures and two hold times. Figures 4.25 to 4.28 compare the slopes of the TGO stress versus cycles data for the two TBCs for the1-hour and 24-hour tests. As seen in Figures 4.25 to 4.27, Type II TBCs have a higher slope of TGO stress versus cycles data for the 1-hour tests, while Type I TBCs have a higher TGO stress versus cycles slope for the 24-hour tests as seen in Figure 4.28. Figures 4.25 to 4.28 suggest that there is a correlation between the slope of the TGO stress versus cycles data and the spallation life. The smaller the slope, the longer the spallation life, Hence, the slope of the TGO stress versus cycles data for Types I and II TBCs can be used to explain the lower 1-hour cyclic lives of Type II TBCs compared to those of Type I TBCs and the higher 24-hour cyclic lives of Type II TBCs compared to those of Type I TBCs (Figure

4.23). In Figure 4.23, the lives for Types I and II are the same at 1151°C, which would also be consistent with the similar slopes in Figure 4.27.

The macro failure mode was also shown to be different for the two TBCs, as seen in Figure 3.96. The differences in the macro failure modes of the two TBCs are also listed in Table 4.1. While the Type II TBCs spalled on cooling by large scale buckling and fracture propagating across the entire specimen (Figure 3.96), the Type I TBCs spalled in a single piece (Figure 3.96).

4.9. Similarities Between Type I and Type II TBCs

The TGO growth followed parabolic kinetics for both systems. The activation energies for TGO growth were consistent with the activation energy for oxygen diffusion in α-alumina. The 1-hour cycled samples for both systems were found to fail in the YSZ near the YSZ/TGO interface due to rumpling induced cracking at the YSZ/TGO interface. In contrast, the 24-hour cycled samples failed almost exclusively at the TGO/bond coat interface, with little or no cracking at the YSZ/TGO interface.

The PLPS characteristics evaluated for the two systems evolved in a similar manner with cycles. As seen in Figures 3.13 and 3.73, the TGO stress versus TBC life relation was shown to be single valued and independent of temperature for both TBCs, indicating that the bond coat composition, its processing method and the starting microstructure did not have an effect on the stress versus life relation. This is shown in Figure 4.29, which shows the TGO stress data for all the 1-hour tests for both Type I and Type II TBCs plotted together as a function of TBC life fraction. Figure 4.29 shows that

the TGO stress versus TBC life data for the two TBCs overlap suggesting that the TGO stress versus TBC life behavior for the two TBCs is identical. Also, as seen in Figures 3.17 and 3.75, the 24-hour hold time was shown to change the TGO stress versus life relation for both systems.

The other spectral characteristics, such as, standard deviation of the measured stress, peak width, peak area ratio and peak shape, and their evolution as a function of cycles were found to be comparable for the two TBCs (Figures 3.23 to 3.26 and Figures 3.79 to 3.82).

Thus, it has been shown that while the bond coat composition and processing methods for the two platinum modified aluminide bond coats studied have a substantial effect on the TBC durability, they do not have an effect on the trends in PLPS characteristics as a function of cycles. This is consistent with the notion that the PLPS trends depend on the operative TBC damage mechanism, which is shown to be the same for the two systems used in this study, which were processed differently and had a different composition.

4.10. Type III - (Ni,Pt)Al Bond Coated TBCs

4.10.1. Rumpling-TGO Stress-Spallation Life Analysis

4.10.1.1. Effect of Rumpling on Spallation Life

Rumpling has been frequently observed in Pt-modified aluminide bond coated TBCs (8, 43, 49, 50, 64, 76-89). The observations (Fig. 4.7) in the present study clearly show that rumpling can initiate the separation and cracking near the TGO/TBC interface

above rumpling sites. As the TGO penetrates into the underlying bond coat, the displacement can induce the out-of-plane tensile strains in the TBC. The strains initiate localized cracking near the TGO/TBC interface. After initiation, cracks may extend laterally along the TGO/TBC interface (Fig. 4.6c), or they may go through the TGO or along the TGO/BC interface (Fig. 4.23). Eventually, these mixed mode cracks lead to spallation of the TBC (Fig. 4.21-23). In addition to cracking initiation, formation of other structural imperfections (cavities) is also associated with rumpling.

An intriguing result is that the roughness values at failure are similar (~3.0 μm) at the three test temperatures with lives variation of 5X. A critical rumpling value seems to exist beyond which the coating will fail. TBC durability would be dominated by the rate of rumpling if there is a critical rumpling value. The spallation life would be shorter if the rate of rumpling is faster. It was found that the rate of rumpling increases as cycling temperature increases, whereas the spallation life decreases at same time (Figs. 4.9 and 4.10). This fact is consistent with the critical rumpling value observations. Based on the observations that cracks initiate at rumpling sites and there is a critical rumpling value at failure, rumpling is responsible for failure. The RMS parameter and tortuosity as a function of life fraction are shown in Fig. 5.1. The roughness increases monotonically as a function of life fraction relatively independent of temperature, consistent with the idea that rumpling is responsible for the failure and TBC durability is determined by rumpling.

Since rumpling is responsible for failure, decreasing the rate of rumpling will enhance TBC durability. It has been reported that rumpling did not occur and durability was increased for smooth bond coats and when surface imperfections were removed by polishing (67).

4.10.1.2. Oxide Growth and Its Relation to Rumpling

Tolpygo and Clarke (135) argue that there is a critical oxide thickness for failure. Kim et al. (129) support this concept and suggest that the TGO growth rate is a key factor in determining TBC failure. Although a critical TGO thickness at failure was not observed in all cases (26, 64), it seems to be valid for the present TBC, where an approximately constant TGO thickness of 4.6 to 5.3 microns was observed at failure. The strong effect of temperature on TGO growth rate and the existence of a critical oxide thickness at failure indicate TGO growth kinetics plays an important role in determining failure. The strong effect of temperature on rumpling rate and a critical rumpling value at failure were also observed in this TBC, suggesting there is causal effect between rumpling and oxide growth.

As shown in Fig. 4.17, both the RMS parameter and tortuosity increase as TGO thickness increase relatively independent of temperature. The fact that rumpling is a single value function of TGO thickness is an indication that rumpling depends on oxide growth. Evans et al. (76, 83, 88) proposed that rumpling is related to the cyclic strains in the bond coat driven by growth strains in the oxide and the lateral growth of the TGO plays critical role in rumpling. Because lateral oxide growth is generally believed to be correlated to thickness growth, these results are consistent with the critical role of the in-plane growth strain (76, 83, 88) in rumpling, and are consistent with the behavior reported in Ref. (64) for a similar system. This relationship of oxide growth to rumpling is only true if the entire TGO lateral growth shows up as increased interface length as opposed to being absorbed by TGO yielding. Simulations (83) show that for low in-

plane growth rates, TGO yielding will not occur and the resulting TGO rumpling tortuosity change is equal to that needed to accommodate the growth strain. The in-plane growth strain, calculated from the tortuosity change, in the present study is in the range of low strain ($1 \times 10\text{-}3 \sim 5 \times 10\text{-}3$) without TGO yielding obtained from simulations (83).

4.10.1.3. Relationship of Rumpling, TGO Stress and Spallation Life and Its Significance in TBC Life Prediction

The evolution of the TGO stress with thermal cycling for the (Ni,Pt)Al TBC can be separated into two stages. At all three temperatures, the compressive stress increases with cycling to its maximum in the first stage and then decreases monotonically in the second stage. The increase in the stress may be due to the growth stress in the TGO (41, 43, 111), which may be attributed, in part, to the θ to α phase transformation during the early stages of TBC deposition and oxidation (111). The transformation was observed in our studies from the occasional appearance of θ-Al2O3 spectra (R2 = 14613 cm-1), which co-existed with α-Al2O3 (R2 = 14420 cm-1) at very short oxidation time. It was observed that the end of the first stage coincided with the completion of the transformation.

After the initial transient stage, the TGO stress decreases monotonically until failure. The observed stress relaxation can be due to various mechanisms, such as rumpling (88) and the effect of oxide induced geometry changes on the stress with increasing TGO thickness on rough surfaces (71) and creep of the bond coat and the oxide (47). In the present study, rumpling of the bond coat surface occurs. The bond

coat/TGO interface gets rougher and the amplitude of rumpling increases with thermal cycling (Fig. 4.9). Both the compressive growth stress and the compressive stress resulting from the thermal expansion mismatch in the TGO would provide a strain energy driving force for deformation. Conversely, rumpling is certainly a mechanism of strain energy relaxation (71), although there may be other mechanisms. Associated with the observation of progressive rumpling of the oxide and the bond coat interface, the TGO stress was found to decrease monotonically until failure after the initial transient period. More convincing, the rate of stress relaxation increases with increasing rate of rumpling (Fig. 4.36). In addition, a previous study (106) shows that the TGO stress decreases very slowly and remains almost constant with cycling for specimens that do not exhibit rumpling behavior. Based on these observations, and the relationship between rumpling and stress relaxation, it is proposed that the oxide stress relaxation of this TBC is mainly due to rumpling.

Since the durability of this TBC is dominated by rumpling, the TGO stress relaxation and specimen life can be connected using rumpling as a bridge. The rate of stress relaxation relates to the severity of rumpling, and ultimately to spallation life. As the temperature increases, rumpling rate and TGO stress relaxation rate increase, while specimen life decreases (Fig. 4.36). This connection provides a physical basis for use of TGO stress measurements as a non-destructive method for TBC life prediction. In fact, as part of this thesis, successful life predictions have been made for specimens tested at different temperatures based on the measurement of TGO stress as a function of life fraction by PLPS. Most significantly, since the TGO stress can be monitored non-destructively during thermal cycling, TGO stress based TBC life predictions can be

made. Thus, PLPS is an extremely powerful technique compared to other NDI techniques, for detecting early damage initiation, the progression of damage, and use in a mechanisms-based life prediction system.

4.10.2. Remaining Life Prediction of (Ni,Pt)Al TBC

The present study is the first attempt at remaining life predictions for TBC samples at three different temperatures, without using knowledge of the temperatures. We note the temperatures at critical locations in service components can vary within a component and from component to component within a given engine. Component temperature variation is one of the most important features leading to variations in component lives. It is, thus, important to have a life prediction method that doesn't require precise knowledge of temperatures.

The ability to make predictions in a temperature blind manner, over the limited ranges of temperatures that were practical to test in the current work, is promising. Even though test lives of specimens vary by a factor of 5, remaining life predictions (the radial basis network prediction with the RMS error of 6.6%) are still successful. The successful predictions are based on the fact that the TGO stress decreases systematically with life fraction relatively independent of temperature in the studied temperature range. If the temperature independence proves true over a wider range of temperatures, then knowledge of local temperatures will not be needed for good life prediction. To make life predictions of components in service, it is necessary to construct a data base for the exact coating/substrate system to be used and to select component relevant temperature ranges and cycle times. With such a data base and a few stress measurements (one in the extreme case) over time for the engine parts, life predictions can be made.

It is worth noting that the TGO stress based remaining life predictions are based on the experimentally determined failure mechanism of this TBC. In the present predictions, the samples fail due to rumpling that directly influences the stress measured and the present results are expected to be applicable primarily to systems failing in this way. The failure modes of TBCs depend on the specifics of the alloy-bond coat- TBC being tested. Other failure modes can and do occur (8). In such cases, additional information may be needed to make life predictions. For example, for the NiCrCoAlY bond coated TBC, the prediction method was developed based on bond coat surface curvature maps, the TGO stress and thickness measurements (section 4.2.6). In addition, for this and other TBCs, the occurrence of bimodal stress distributions may be predictive (116,117). It is worth noting that a commercial engine manufacturer has issued a contract to UConn to perform remaining life predictions on engine parts based on the results shown in this and a related UConn thesis (136).

4.10.3. Bimodal Luminescence and TGO Cracking

4.10.3.1. Bimodal Spectra Associated with TGO Cracking and Its Implication in NDI Use

In the present work, the bimodal spectra have for the fist time been clearly connected with TGO cracking (localized damage). First, there was a perfect one to one correspondence between the measured bimodal spectra and observed cracks in the bare TGO formed on the bond coat. That is, bimodal spectra were observed only from regions of the TGO in the immediate vicinity of cracks and never detected where cracks were not

seen (Fig. 4.42). Second, the crack density and fraction of bimodal spectra changed in the same manner with thermal cycling.

When the probed regions in the PLPS contain both intact and damaged regions, the probed regions will have stress variations and will produce two sets of peak pairs with the high stress component corresponding to intact regions and the low stress component corresponding to damaged regions. It would be reasonable to assume that the likelihood of getting bimodal spectra increases with increasing localized damage. In fact, there were consistent trends in the fraction of bimodal spectra and the crack density as a function of cycles. The fraction of bimodal spectra increases when the density of cracks increases (compare Fig. 4.43 and 4.45). The correspondence of the trends in the crack density and the fractional presence of bimodal spectra are consistent with the idea that bimodal spectra are caused by small regions of stress free TGO associated with cracking.

Tolpygo and Clarke (35) studied the theta-alpha transformation in alumina scales on platinum-modified nickel aluminides and found that bimodal spectra can originate from the alumina scales containing whiskers. The TGO consisting of continuous and whiskers morphologies is constrained and unconstrained, respectively, under in-plane compression with the underlying metal. The luminescence from regions containing both constrained and unconstrained TGO would give rise to bimodal spectra (35). In the present work, bare alumina scales were also observed containing whiskers (Fig. 5.2) and the whiskers disappeared after oxidation for 25 hours. In contrast with the Tolpygo's study, the bimodal spectra were not observed from the scales containing whiskers, but only from the regions of the TGO in the immediate vicinity of observed cracks. The possible reason for the differing results in the two studies is that, in this study, the volume

of whiskers is too small compared to the continuous and constrained TGO layer, making the low stress peaks from whiskers difficult to detect.

Because the association of bimodal spectra and cracking was directly observed on the bare TGO layer, the fraction of bimodal spectra measured through the ceramic layer also gives an indication of the extent of damage. In the case of measurements made through the ceramic layer, the diameter of the spatial region from which spectra are collected is estimated to be around 70 μm, due to scattering by the columnar structure of the EB-PVD TBC (114). As a result, the presence of bimodal spectra through the TBC has a statistical aspect representing the degree of cracking for a relatively large area of the TGO. The change in the fraction of bimodal spectra seen through the TBC parallels the change observed in the occurrence of bimodal spectra in the bare oxide and also for the crack density observed on the bare oxide (Fig. 4.40, 4.43 and 4.45).

In addition, the stress distribution mapping based on bimodal spectra contribution can provide a visual record of the number and size of the damage sites. The stress distribution maps (Fig. 4.41) show clearly that damage accumulation occurs with thermal cycling. Both the number and the size of continuous damage sites increase with thermal cycling. Therefore, the fraction of bimodal spectra is another powerful tool in assessing damage initiation, damage progression, and assessing remaining life. This is a recommended item for future research.

4.10.3.2. Mechanisms of Crack Formation During Thermal Cycling on the Bare Bond Coat

The early increase in bimodal spectra and associated observed cracking in this work is attributed to the effect of volume change associated with the transformation of θ-Al2O3 to α-Al2O3 (35). Numerous studies of nickel aluminides (32-36,118) have shown that metastable alumina phases such as θ-Al2O3 may form and then transform into stable phase α-Al2O3 in the very early stage of oxidation, which results in a volumetric shrinkage due to the phase change. The present experimental observations are consistent with the idea that transformation of θ-Al2O3 to α-Al2O3 is responsible for the early increase in crack density and associated increase in bimodal spectra. First, the transformation occurs early in oxidation, as confirmed by the occasionally observed regions in which α-Al2O3 and θ-Al2O3 coexist (Fig. 4.46). Second, the appearance of maximum peak crack density occurred just prior the time at which θ-Al2O3 disappeared based on the PLPS spectra. Finally, the θ-Al2O3 island was observed to be surrounded by an α-Al2O3 matrix, as would lead to isolated cracks (Fig. 4.46).

The subsequent decrease in the occurrence of bimodal spectra is associated with crack healing. This crack healing is directly observed as decreasing crack density seen on the bare oxide and indicated by the decrease in the fraction of bimodal spectra for both bare and ceramic coated specimens.

By direct observation, the final increase in the fraction of bimodal spectra is associated with TGO cracking, which occurs almost exclusively near the highest parts of protruding regions of the TGO as shown in Fig. 4.44d and 4.47b. It is worth noting that these cracks are quite open and of the type expected if in-plane tension exists in the TGO. These cracks are therefore different from delamination cracks that result from out-of-

plane tensile stresses (21, 71, 74). Local tensile stresses associated with rumpling and with elemental transport (aluminum depletion from oxide growth and Ni influx from the substrate (85)) seems to be the best candidate explanations for cracking at this time.

4.10.4. Combination of Multiple PLPS Characteristics for NDI Use

In previous studies on EB-PVD TBCs on platinum aluminide bond coats (30, 106), only the peak frequency shift (i.e. stress) has a systematic change with cycles and it seems that the stress level is the single most promising feature for possible use in NDI. In the EB-PVD TBCs on platinum aluminide bond coats studied in this thesis, the most striking result is that (a) the average TGO stress, (b) its standard deviation, and (c) the R1 and R2 peak area ratio all show systematic changes with thermal cycling. Both the average stress and R1 and R2 peak area ratio decrease monotonically with thermal cycling. It is surprising that this system showed a systematic change in R1 and R2 peak area ratio and standard deviation of stress while a highly similar system (30) from a different manufacturer did not show a systematic variation of these two quantities. Since both systems were tested in the same furnace and spectra analyzed using the same apparatus and procedure, the experimental details don't provide an explanation for such a difference. These results also highlight the importance of characterizing each individual TBC before using PLPS as a tool for detecting damage and assessing life remaining.

The intensity ratio of the R1 and R2 peaks is weakly dependent on temperature and pressure. Munro et al. (137) found the intensity ratio of the Ruby R lines (R2/R1) varied by –0.00047°C-1 and –0.013 GPa-1, with temperature and pressure, respectively. In this study, the temperature dependence can be ignored since all the measurements were

taken at room temperature. According to the pressure dependence factor found by Munro et al. (137), the calculated area ratio change attributed to the stress change is about 20% of the observed area ratio change and is in the opposite direction. Therefore, the effect of pressure variation on peak area ratio is not an explanation for the observed changes. It has also been suggested that the peak intensity ratio depends on the crystallographic orientation with respect to the polarization of the laser in Refs. (113, 118). This can be a large effect for a single crystal but not for polycrystalline alumina. The ratio obtained in the present study falls in the range of 0.35-0.45. This is close to the value of an α-Al2O3 reference disk (stress free and randomly oriented polycrystalline) and in good agreement with the value (~0.5) for polycrystalline α-Al2O3 reported in Ref. (118). Also, the sample was randomly rotated and tilted and no change was observed for the area ratio. Therefore, it is reasonable to say that Al2O3 has no preferential orientation and it is un-textured or weakly textured. Thus, crystallographic orientation can be excluded from the cause for the systematic change of area ratio with cycles. At the present time, the cause of the systematic change of the area ratio with cycles is unknown.

The standard deviation of stress is a measure of the stress heterogeneity in the measured volume. In the present case, as damage increases, stress heterogeneity and the standard deviation increase. However if the characteristic dimension of the heterogeneity is much smaller than the probe characteristic dimension (around 70 μm in this case (114)), then averaging would obscure this variation and may be the reason for not seeing this in the other TBC (30). Although the cause of the systematic change of the area ratio and standard deviation in the stress with cycles is unknown, as an engineering approach

they can be used in an attempt to predict life due to a systematic change with cycles (section 4.1.5).

Most importantly, it is clear that behavior of PLPS spectral characteristics with thermal cycling is sensitive to not only composition but also processing. Therefore, all the spectral characteristics need to be studied on a system-by-system basis for possible use in NDI. These complexities make it necessary to construct a PLPS database and continue to study the physical basis for spectral characteristics. For this particular TBC, because of the observed systematic variation with cycles of the three spectral characteristics, they are candidates for use in non-destructive inspection and making remaining life predictions.

4.11. Type IV - NiCoCrAlY Bond Coated TBC

During thermal cycling, several changes in the microstructure related to the failure of the TBC were observed: TGO growth, depletion of β phase in the bond coat, the TGO/BC interface rumpling, and formation of non-α-Al2O3 oxide in the embedded oxide. TGO growth increases the strain energy available for crack propagation. The formation of a non-α-Al2O3 oxide decreases the toughness of the TGO/bond coat interface. Although rumpling has been found to be responsible for the failure of (Ni,Pt)Al bond coated TBC in this study, no apparent damage was observed in the MCrAlY bond coated TBC due to rumpling even though some rumpling occurred. We believe that these samples prevented from failing by rumpling because another failure mode occurred first. This result is consistent with a previous study on MCrAlY bond

coated TBCs (39). Based on the observations that the failure interface is predominantly at the TGO/bond coat interface and the embedded oxides only account for a small fraction of the total failure area, the failure is initiated by debonding at ridge tops and followed by unstable fracture driven by the strain energy in the TGO.

The most surprising feature of this experiment is that the spallation lives for as-received and barrel finished specimens are comparable despite their surface roughnesses (Ra) differing by a factor of about 6. However, the curvature before and after finishing does not vary much, although the average roughness (Ra) does (Fig. 4.61). Therefore, based on equation (2.2), the critical TGO thickness for failure for as-received and barrel finished specimens should not vary much. This is what leads to the equivalent lives for the as-received and barrel finished specimens.

From this experiment, we can clearly see the significance of surface curvature in evaluating TBC life. Compared to Ra values based on averaging height information from the sample surface, the curvature map can give the localized curvature at every location of the sample surface. Curvature is better in evaluating TBC life since the failure of the TBC is not determined by average information from the whole specimen surface but by the size and geometry of localized flaws. Specifically, though as-received specimens contain large ridges and deep cavities, the feature size is large and the surface height changes slowly. Thus, the localized curvature is relatively small. On the other hand, for barrel finished specimens, the height between peaks and valleys is less than that of as-received specimens, but, the feature size is small and the localized surface height changes rapidly. Thus the curvature is comparable to or even larger than in as-received specimens.

The reason that barrel finishing produces this kind of surface is that barrel finishing removes the high ridges, however, at the same time it increases small features such as sharp corners or sharp scratches. At these localized sharp corners or scratches with large localized curvature, the tensile normal stress increases rapidly and debonding occurs preferentially. Thus the standard surface roughness analysis, which uses a single number, such as average surface roughness (Ra) or peak to valley (Pv) to characterize the surface, can give misleading information in evaluating TBC life. Surface curvature maps, developed in this research, appear to be a superior tool in characterizing surface geometry and determining TBC life.

4.12. Comparison of (Ni,Pt)Al and NiCoCrAlY Bond Coated TBCs

(Ni,Pt)Al and NiCoCrAlY bond coats have individually characteristic compositions and microstructures. These differences result in distinct different TGO growth characteristics, as well as differing tendencies for plastic deformation (8). Accordingly, the failure mechanisms are often different. Specifically, the similarities and differences of the two TBCs studied in this research are summarized in Table 5.1. The oxide growth in both TBCs satisfies parabolic growth kinetics, suggesting that oxide growth is diffusion controlled. Aluminum depletion occurs in both bond coats due to oxide formation and interdiffusion.

Most importantly, there are some distinct behaviors between the two TBCs. Failure mechanisms and associated failure modes of the two TBCs are different. In the (Ni,Pt)Al bond coated TBC, rumpling is responsible for the failure and the durability of TBC is determined by rumpling. In the NiCoCrAlY bond coated TBC, limited rumpling

occurs and no apparent damage occurs due to rumpling. Failure is determined by strain energy stored in the TGO layer. In addition, non-α- aluminum oxide forms in the NiCoCrAlY bond coated TBCs, consistent with other studies (31, 39). Formation of non-α-Aluminum oxide is usually observed in the NiCoCrAlY bond coated TBCs, mainly due to aluminum depletion in the bond coat (see section 4.2.3) and exhibits poor adherence to the bond coat (15, 91-94).

In addition to failure mechanisms, the PLPS behavior for the two TBCs is also different. Consistent with other studies, the TGO stress for the EB-PVD TBC on platinum-aluminide bond coats shows a consistent and monotonic decline (30, 106) after the initial transient period. The peak area ratio and standard deviation in the stress also show systematic changes with cycles. These spectral characteristics can be used for NDI and remaining life prediction.

In contrast for the EB-PVD NiCoCrAlY bond coated TBC, the TGO stress remains constant with cycling after the initial period. This is probably associated with the relative absence of bond coat rumpling and other forms of damage progression that the PLPS technique can detect.

Since failure mechanisms and PLPS behavior are different for the two TBCs, the life prediction method selected will also be different. The life prediction for (Ni,Pt)Al bond coated TBC is based on the measurement of the TGO stress. The life prediction for NiCoCrAlY bond coated TBC is based on the measurement of initial bond coat surface geometry, TGO stress and TGO thickness, and correlating these properties by fracture mechanics.

4.13. Use of PLPS For TBC Quality Control, Non- Destructive Inspection and Life Prediction

4.13.1 PLPS for Quality Control

As described in section 4.1.4.5, θ-Al2O3 and α-Al2O3 can be detected by the PLPS method due to the fact that they have characteristic luminescence peaks easily distinguished in the spectra and the oxide distribution can be obtained from the area mapping. It has been proposed that the tra nsformation from θ- to α-Al2O3 is responsible for additional residual stress from the volumetric shrinkage in the TGO and nucleation of tensile cracking (35). The oxidation study of bare (Ni,Pt)Al bond coated TBC in this thesis also shows that the phase transformation of oxide produces microcracks (see section 4.1.4.5). In a previous study (132) of the effects of bond coat surface finish and heat treatment on TBC performance, the presence of a thin layer of continuous TGO comprising α-alumina prior to YSZ deposition was found to be favorable for producing durable TBCs. In addition, some PLPS measurements on as-coated vanes showed that the long-life vanes had a TGO consisting only of α-alumina, while the short life vanes had a TGO consisting of both α- and θ-alumina (102). Based on these results, the formation of a "perfect" oxide that consist only of stable α-Al2O3 prior to deposition of YSZ may lead to improved durability and reliability of both stand-alone metallic coatings and TBC bond coats. Therefore, the ability of PLPS to non-destructively determine the oxide type and its uniformity makes it a very valuable quality control tool.

4.13.2 PLPS for Non-destructive Inspection

For the (Ni,Pt)Al bond coated TBC, the TGO stress and R1 and R2 peak area ratio show a monotonic decline (Fig. 4.31), and the standard deviation in the TGO stress shows a systematic increase (Fig. 4.33) with thermal cycles. These systematic changes of specific spectral characteristics can be used in NDI to detect early damage and damage progression. The most significant result is that TGO stress evolution is relatively independent of temperature as a function of life fraction in the studied temperature range (Fig. 4.34). Thus knowledge of local temperatures is not needed and this greatly simplifies the use of PLPS as a NDI tool for turbine coatings since the temperature can vary with a component and from component to component in engine service.

Bimodal spectra were observed during thermal cycling in the (Ni,Pt)Al bond coated TBC. The occurrence of bimodal spectra has been found to be directly associated with TGO cracking in this research. Early TGO damage such as cracks as small as microns can be detected using PLPS. The fraction of bimodal spectra initially increases sharply, then gradually decreases and increases again close to TBC failure (Fig.4.40). The area maps of stress distribution based on bimodal spectra contribution give the visual record of the number and size of damage sites. Damage progression is apparent with thermal cycles, as shown in Fig. 4.41. Thus both the fraction of bimodal spectra and stress maps can detect damage progression and have the potential to assess TBC life remaining.

4.13.3 PLPS for Remaining Life Prediction

When TBC coated components are examined following field service, it is desirable to evaluate the condition of the coating to determine whether it can be reliably used until the next planned inspection. For (Ni,Pt)Al bond coated TBCs, remaining life predictions cycled at three temperatures were made for the first time based on the PLPS data without knowledge of the test temperature. The predictions using regression methods and neural network methods were compared. It was found that both methods produce accurate life remaining predictions, but the neural network methods were superior. The lowest RMS error for the oxide-based predictions using regression method and neural network method was 14.7% and 6.6% respectively. For a data set with a 34.6% RMS spallation life variation about the mean, the prediction results obtained are highly encouraging. Therefore, satisfactory remaining life predictions in a temperature blind manner are promising for this TBC.

4.13.4 PLPS for Life Prediction

The fact that there was no systematic change of spectral characteristics with thermal cycling for the NiCoCrAlY bond coated TBC makes it impossible to solely use spectral characteristics to predict TBC life. However, the failure of this TBC was shown to relate to the strain energy in the TGO layer which is associated with the TGO stress, thickness and curvature of the bond coat surface. A life prediction method was developed based on the measurement of initial bond coat surface geometry, TGO stress and TGO thickness, and the correlation of these characteristics by fracture mechanics. The predicted lives correlated with experimental results within 15%. PLPS measurements of the TGO stress were used as input in this prediction approach. Since

the TGO stress is highly dependent on specific the TBC system and its thermal history, non-destructive measurement of the TGO stress allows a more accurate calculation of the TGO strain energy than using approximate value calculated from thermal expansion mismatch.

4.13.5 Overall Assessment of The PLPS Technique

This research has shown that PLPS is an extremely powerful technique for TBC quality control, non-destructive inspection, assessment of remaining life and for use in life prediction. The spectral characteristics (frequency shift, i.e. the TGO stress and its standard deviation, peak area ratio, peak width and peak shape, and bimodal spectra fraction) and their change with thermal cycling can give information about damage initiation, progression and can be used in quality control, NDI, assessment of remaining life and life prediction.

A systematic methodology should be employed in using PLPS for a new TBC because it is clear that PLPS spectral characteristics are dependent on both composition and processing. Different spectral characteristics and their change with thermal cycling can be used for different TBCs. The combined use of multiple characteristics may give improved results in some applications. So all spectral characteristics need to be studied for each new TBC for possible use in NDI and life prediction. In addition, determination of TGO spallation mechanisms will aid in the application of the PLPS spectral data.

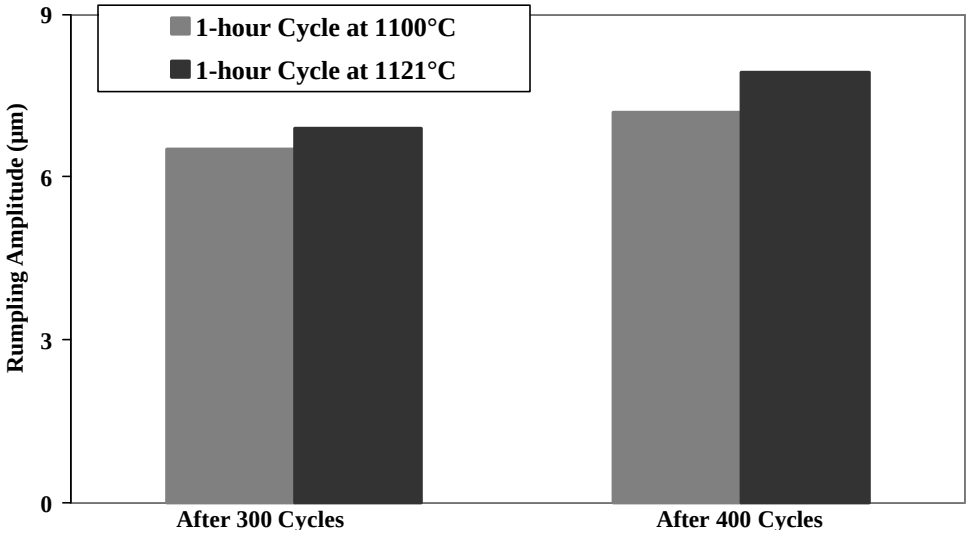

Figure 4.1: Comparison of the amplitudes of rumpling for Type I TBC after 300 and 400 1-hour cycles at 1100°C and 1121°C respectively.

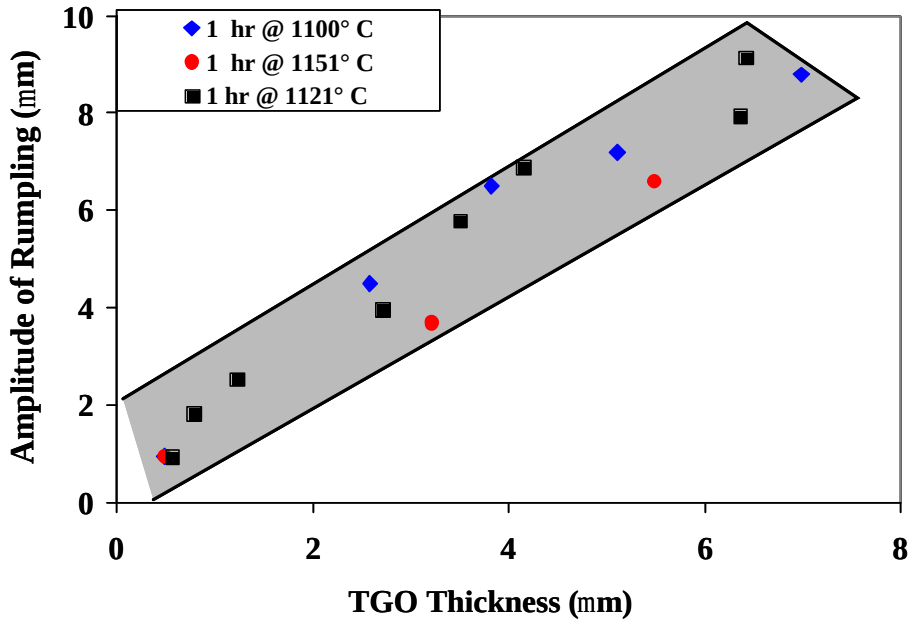

Figure 4.2: Plot of rumpling amplitude versus TGO thickness for Type I TBC for the 1-hour tests.

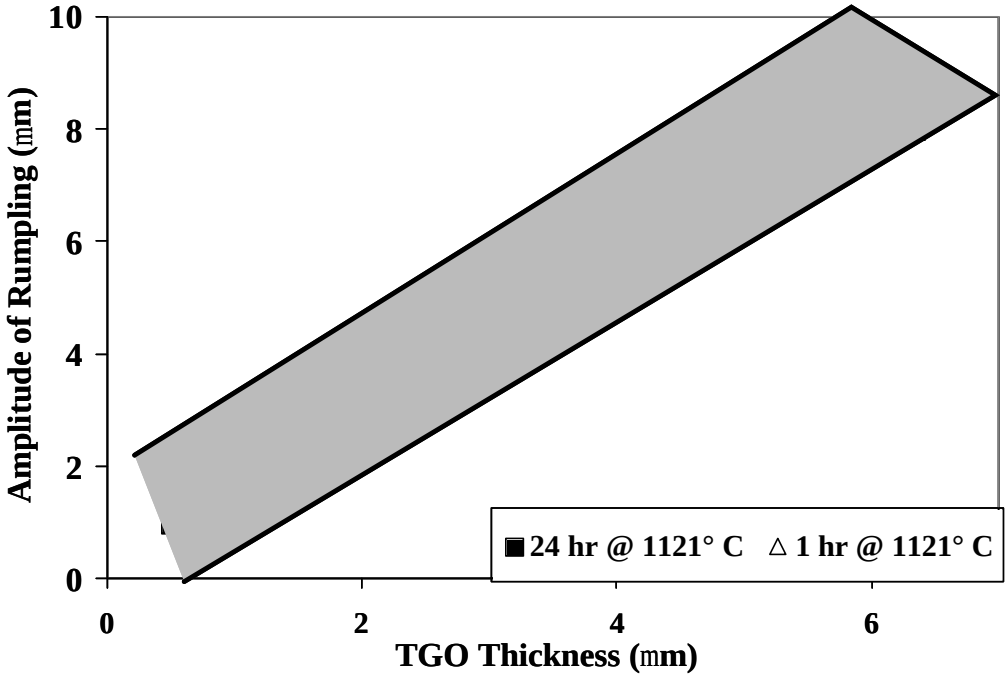

Figure 4.3: Plot of rumpling amplitude versus TGO thickness for Type I TBC for the 24-hour tests.

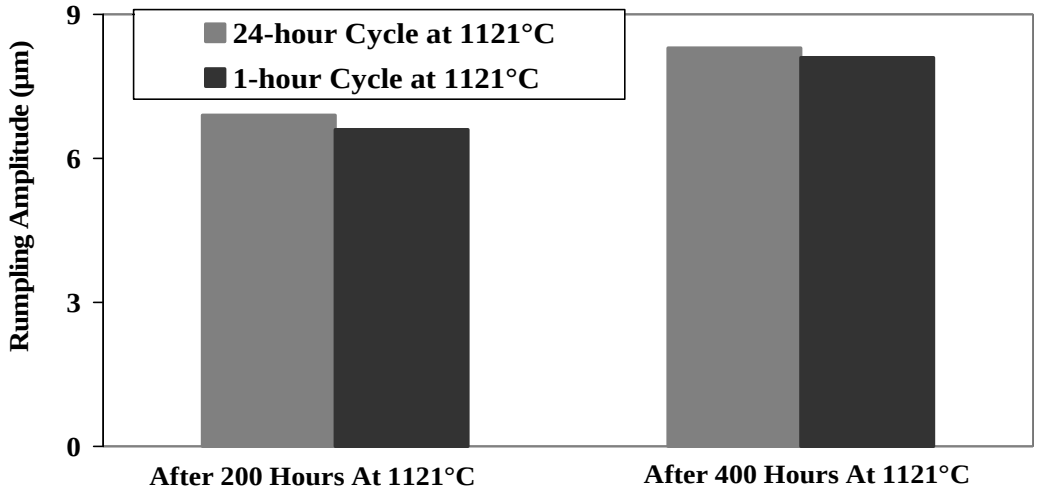

Figure 4.4: Comparison of the amplitudes of rumpling for Type I TBC after 200 and 400 hours during the 1-hour and 24-hour cycles at 1121°C.

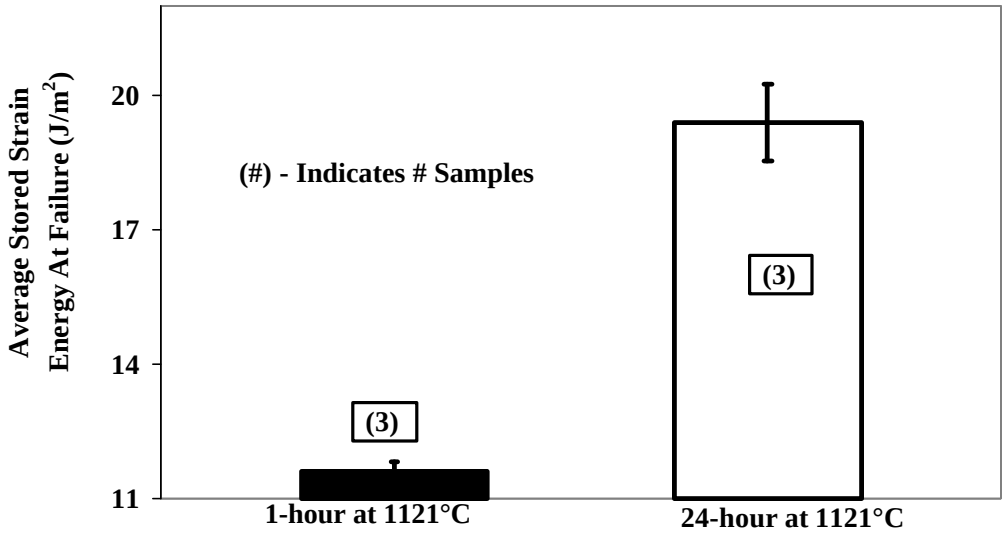

Figure 4.5: Comparison of stored strain energy in the TGO at failure for the Type I TBC samples during the 1-hour and 24-hour tests at 1121°C.

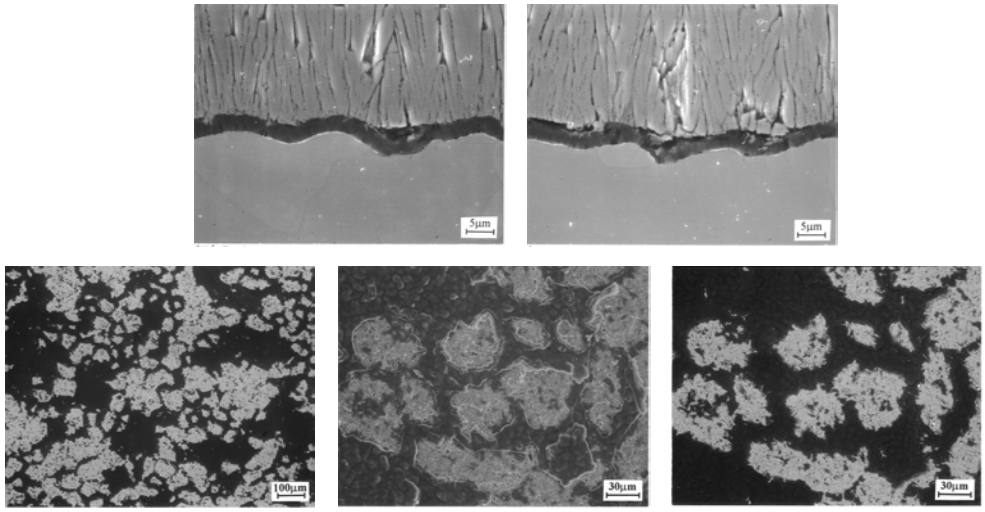

(TGO Surface Exposed by Dissolution of Metals; Bright Region: 7YSZ; Dark Region: TGO)

(a)

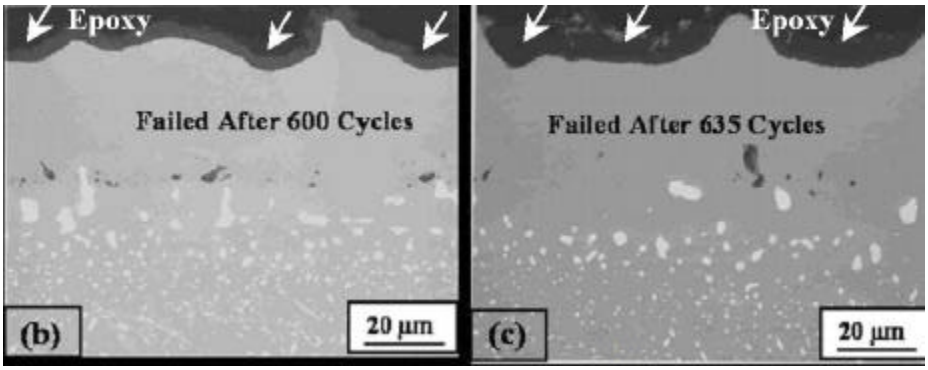

Figure 4.6: (a) (top) Cross-section secondary electron micrographs and (bottom) Plan view micrographs of Type I TBC after 200 1-hour cycles at 1121°C; Cross-section secondary electron micrographs of failed Type I TBC after (b) 600 and (c) 635 1-hour cycles at 1121°C. White arrows point to the separation at the YSZ/TGO interface at places where the TGO/bond coat interface has rumpled, as seen by the epoxy resin that has filled the separation.

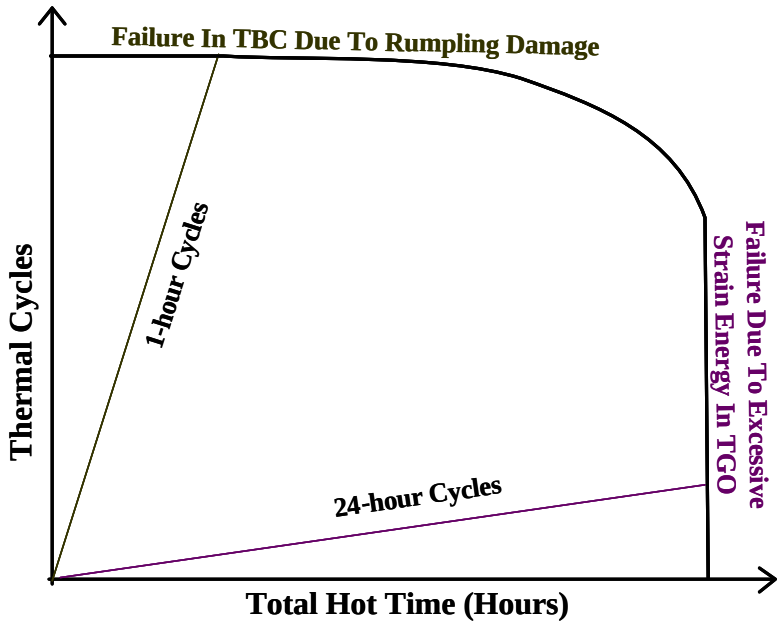

Figure 4.7: The cyclic response of Type I TBC system during the 1-hour and 24-hour tests.

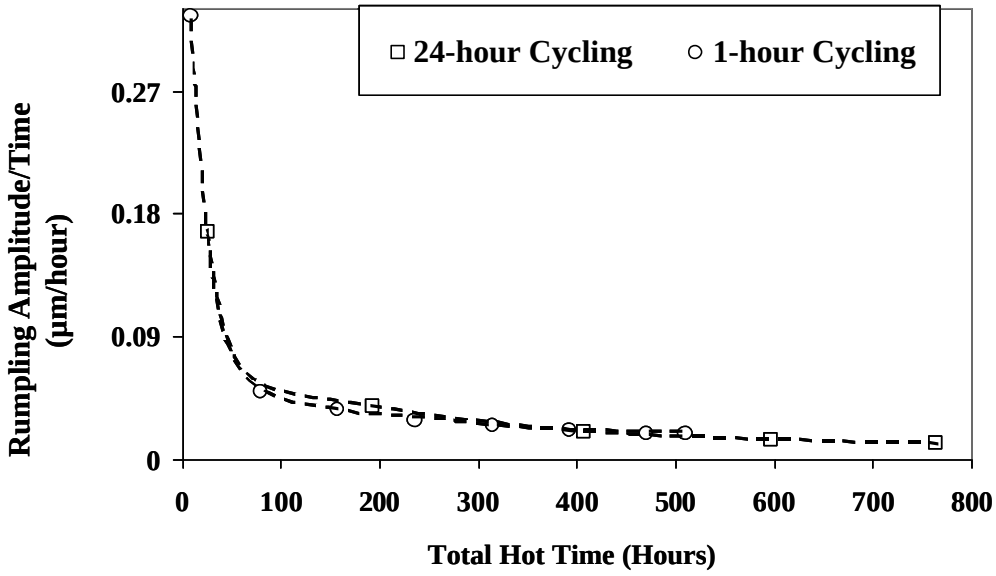

Figure 4.8: Comparison of rumpling amplitude per unit time for the 1-hour and 24-hour tests at 1121°C.

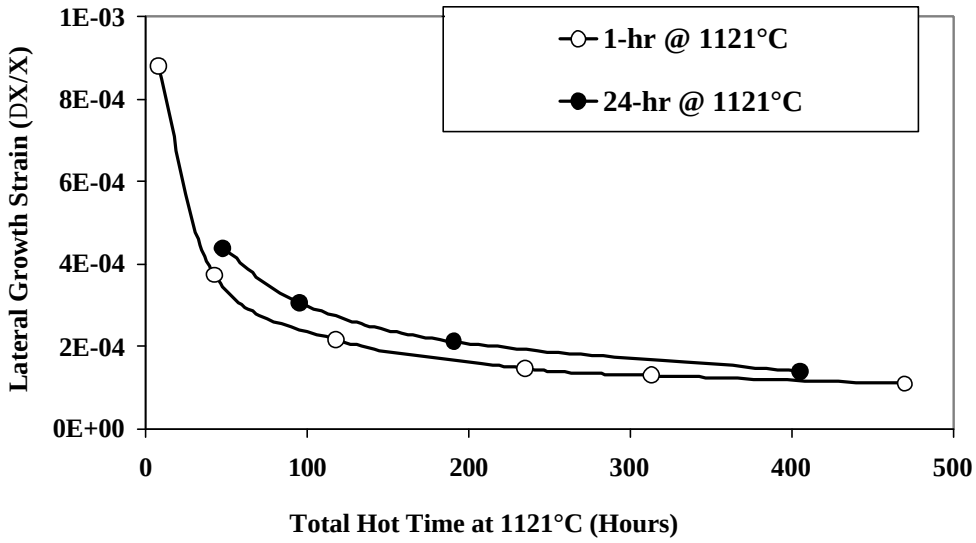

Figure 4.9: Plot of lateral growth strain necessary to explain the oxide surface lengthening in the 1-hour and 24-hour tests conducted at 1121°C for Type I TBC.

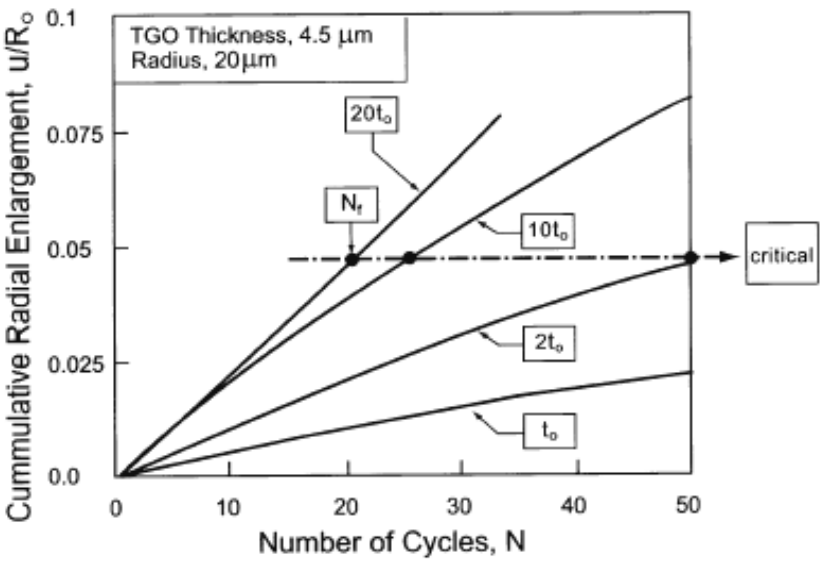

Figure 4.10: Effect of hold time on rumpling amplitude, based on analytical modeling by Karlsson et al [Karlsson et al; 2003]. In the figure, t0 = 5 x 10-4.

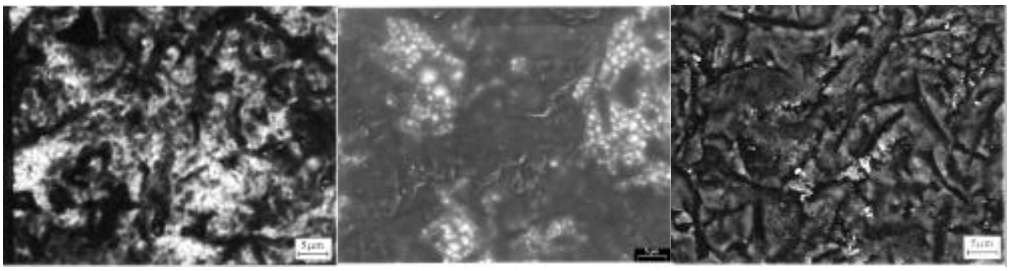

(a) **(b)** **(c)**

Figure 4.11: Back scattered electron image of the bare bond coat surface of Type I TBC after a) 1 cycle b) 10 cycles c) 50 cycles. Figure shows the conversion of discontinuous TGO to a more uniform and continuous TGO.

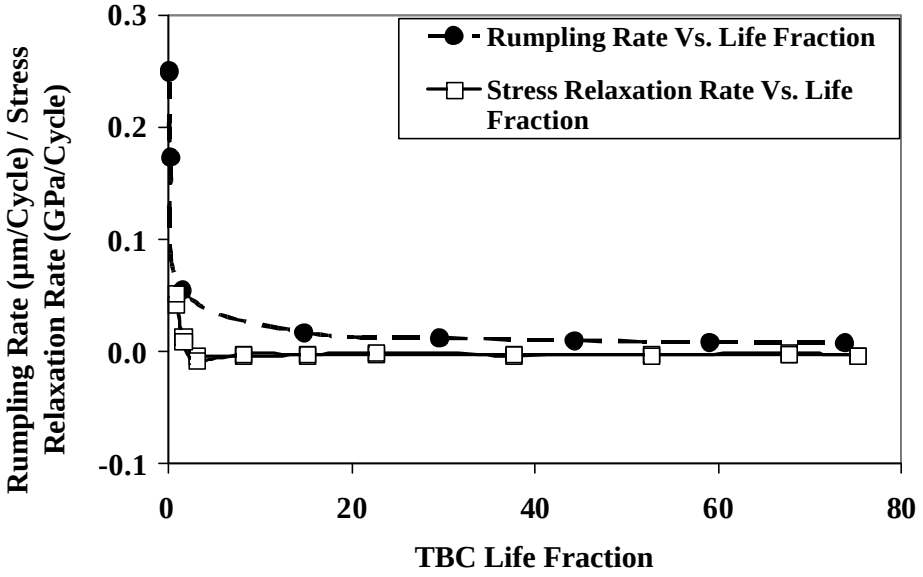

Figure 4.12 (a): Correlation between rumpling rate and stress relaxation rate for Type I TBC for the 1-hour tests at 1121°C.

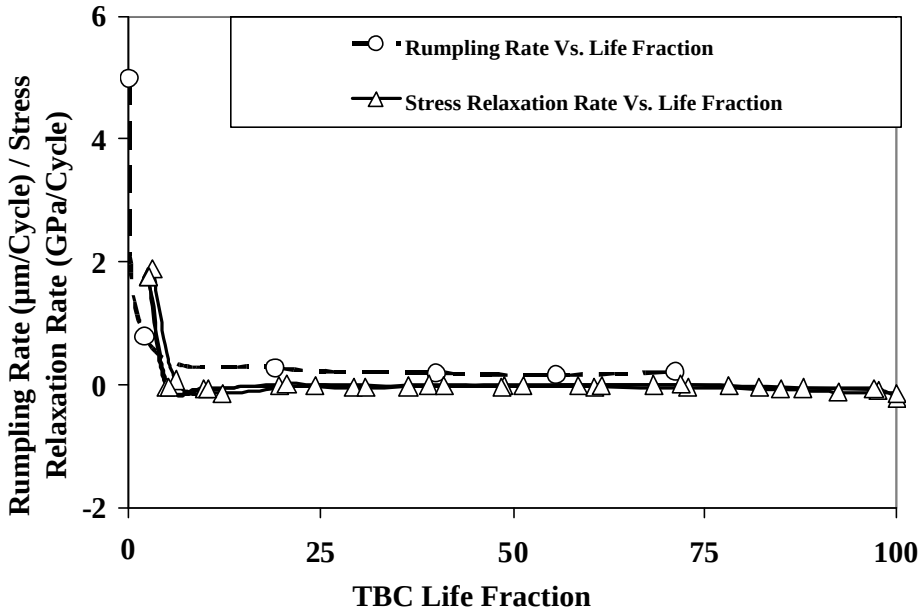

Figure 4.12 (b): Correlation between rumpling rate and stress relaxation rate for Type I TBC for the 24-hour tests at 1121°C.

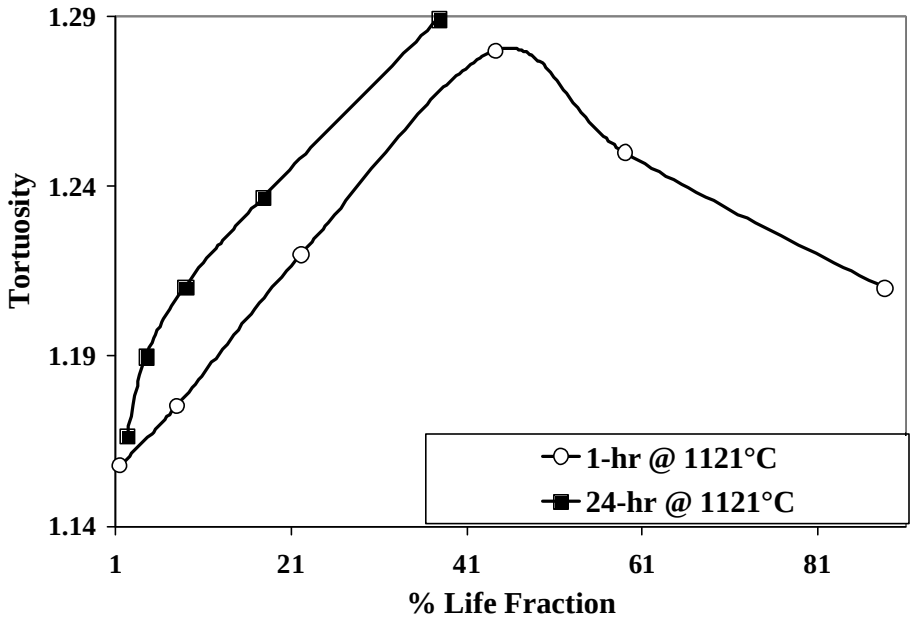

Figure 4.13: A plot of the tortuosity of the YSZ/TGO interface as a function of TBC life fraction for Type I TBC for the 1-hour and the 24-hour tests at 1121°C.

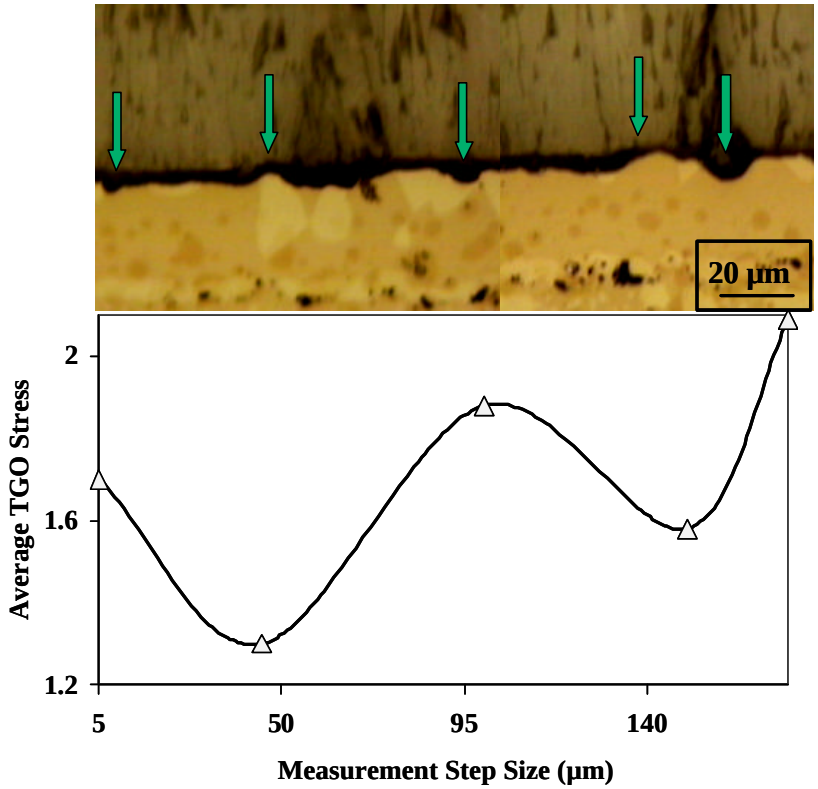

Figure 4.14: Variation of TGO stress in cross-section for a Type I TBC sample having 300 cycles at 1121°C.

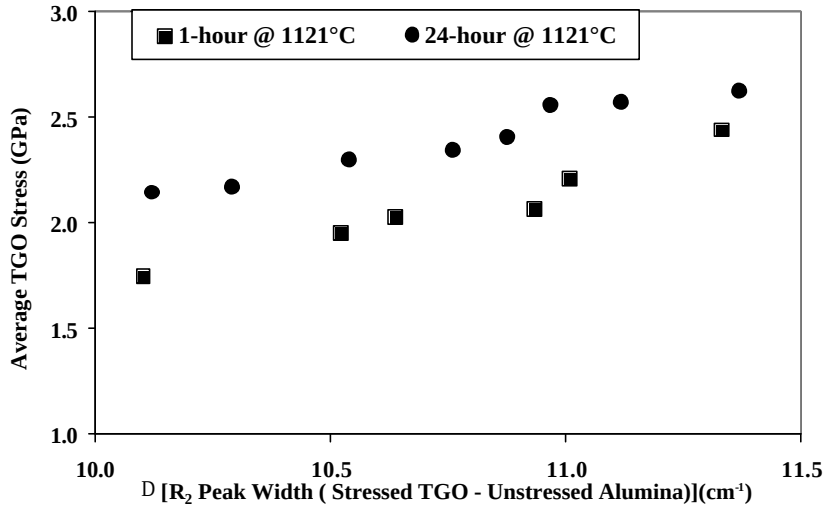

Figure 4.15: Change of the difference in the R2 peak width of the stressed TGO and the unstressed alumina with average TGO stress.

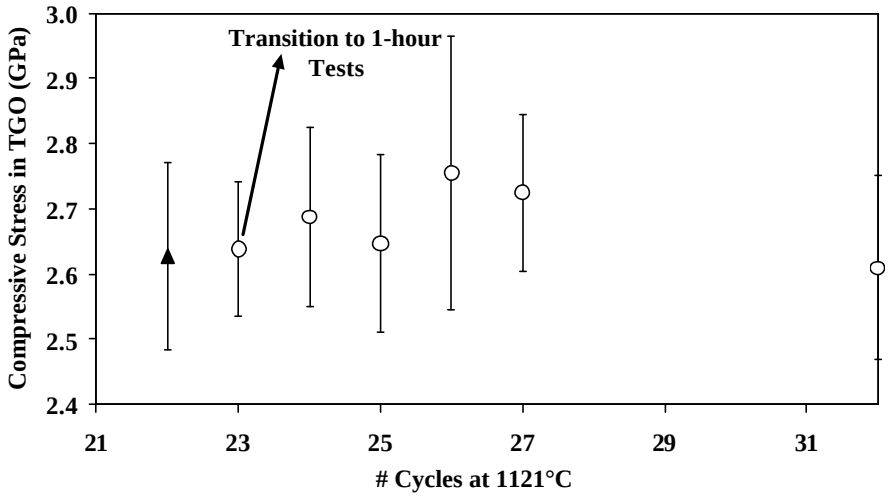

Figure 4.16: Evolution of TGO stress versus cycles for Type I TBC subjected to 1-hour cycles at 1121°C following 24-hour cycles at 1121°C for 50 % of its cyclic life. The figure shows the TGO stress evolution during the second stage of the multiple hold time test. The filled triangle indicates the last measurement made for the 24-hour test condition and the first unfilled circle denotes the first measurement point on transition to the 1-hour test condition.

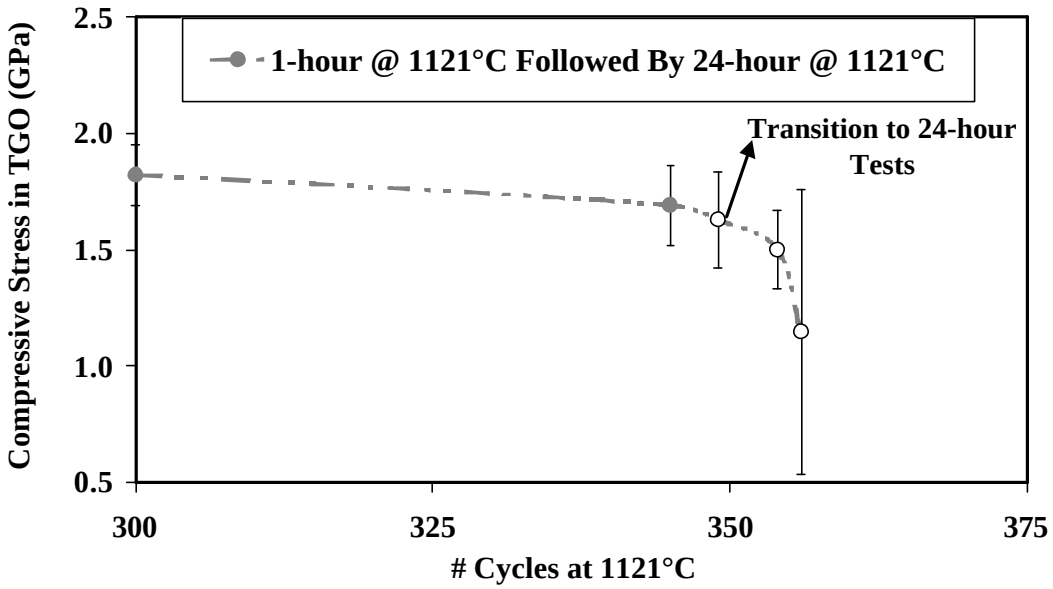

Figure 4.17: Evolution of TGO stress versus cycles for Type I TBC subjected to 24-hour cycles at 1121°C following 1-hour cycles at 1121°C for 50 % of its cyclic life. The figure shows the TGO stress evolution during the second stage of the multiple hold time test. The filled circles indicate the last two measurements made for the 1-hour test condition and the first unfilled circle denotes the first measurement point on transition to the 24-hour test condition.

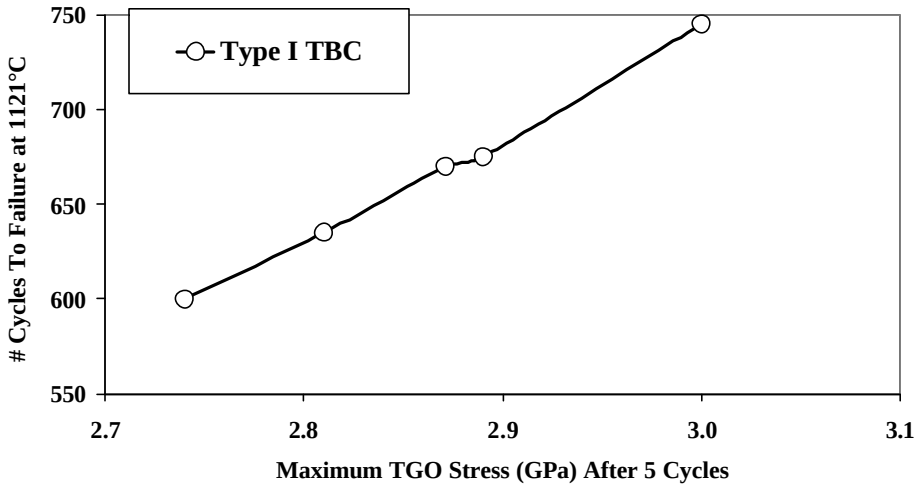

Figure 4.18: Correlation between the maximum TGO stress and spallation lives for five Type I TBC samples cycled at 1121°C using 1-hour cycles.

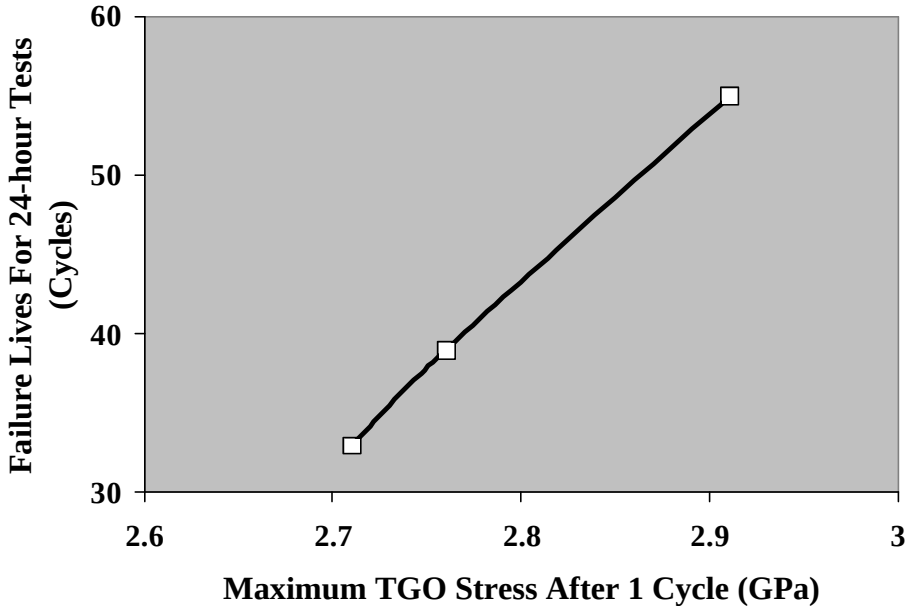

Figure 4.19: Correlation between the maximum TGO stress and spallation lives for three Type I TBC samples cycled at 1121°C using 24-hour cycles.

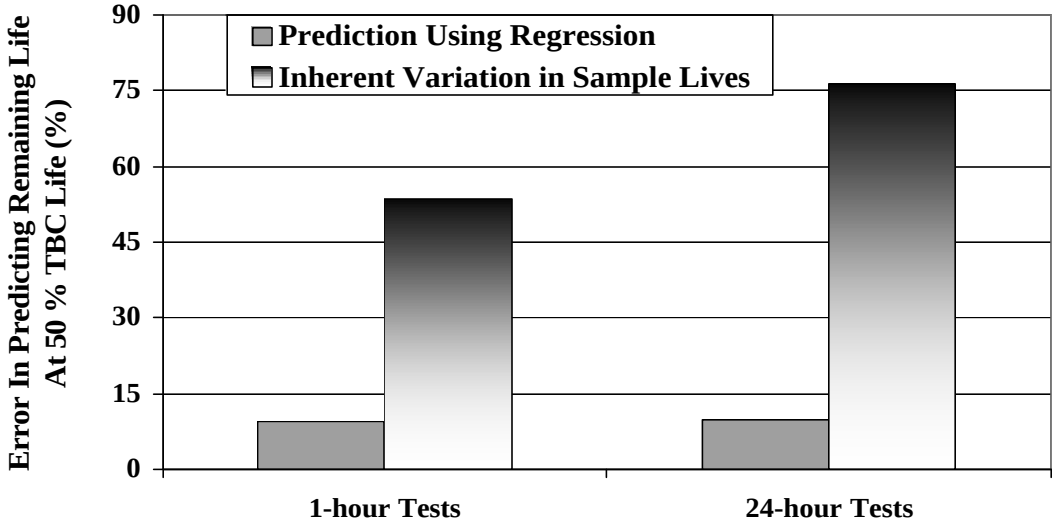

Figure 4.20: Comparison of the maximum error in assessing remaining life of Type I TBCs with the inherent variation in the spallation lives for the 1-hour and 24-hour constant and variable amplitude tests.

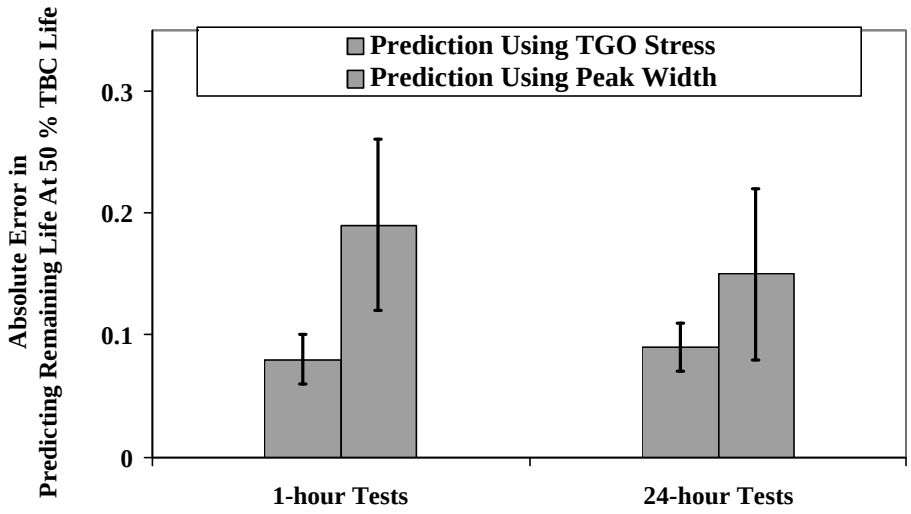

Figure 4.21: Comparison of the maximum absolute error in assessing remaining life of Type I TBCs using TGO stress values and peak width values for the 1-hour and 24-hour tests at 50% inspection interval.

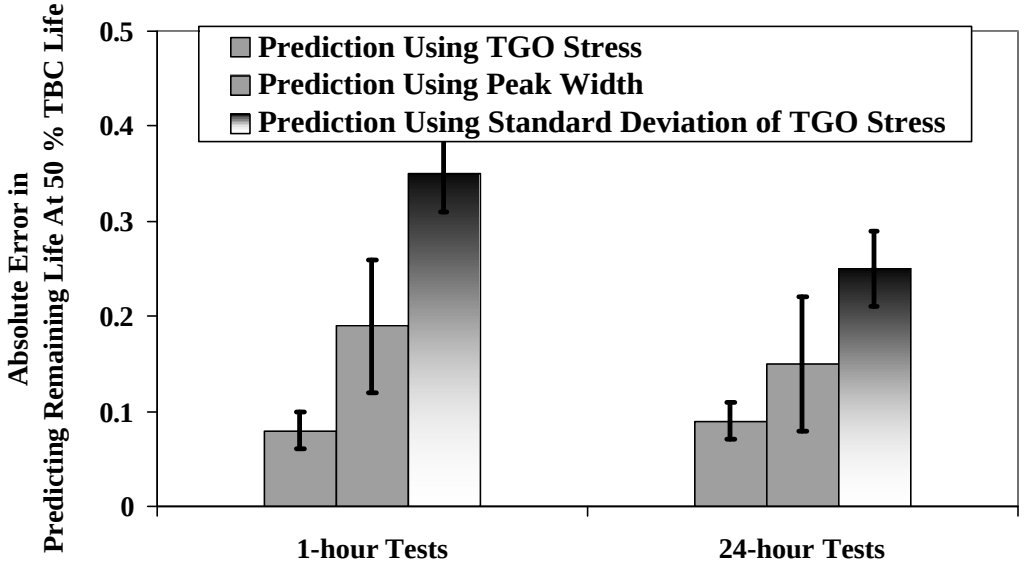

Figure 4.22: Comparison of the maximum absolute error in assessing remaining life of Type I TBCs using TGO stress values, peak width and standard deviation of TGO stress for the 1-hour and 24-hour tests at 50% inspection interval.

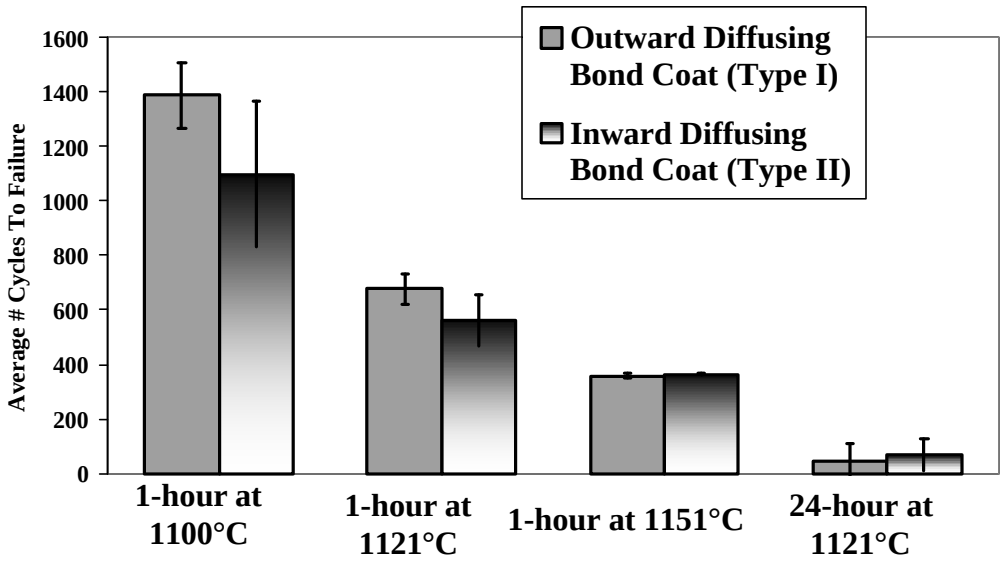

Figure 4.23: Comparison of 1-hour and 24-hour cyclic lives of Types I and II TBCs.

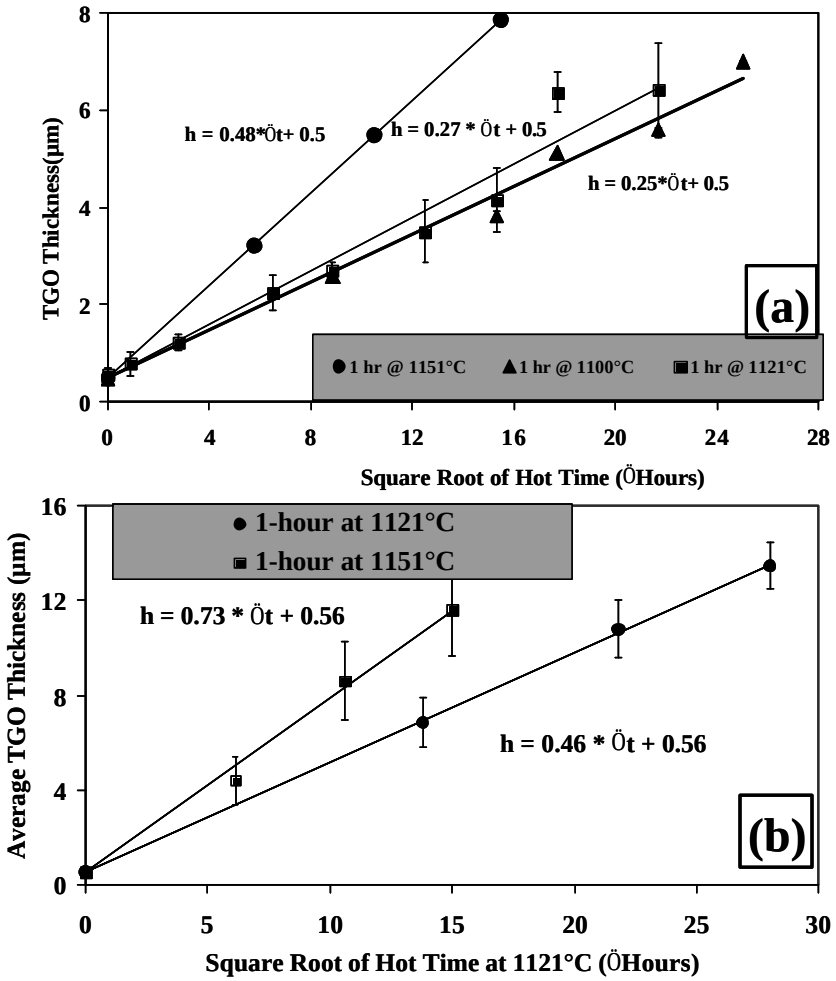

Figure 4.24: Comparison of 1-hour TGO growth rates of (a) Type I and (b) Type II TBCs.

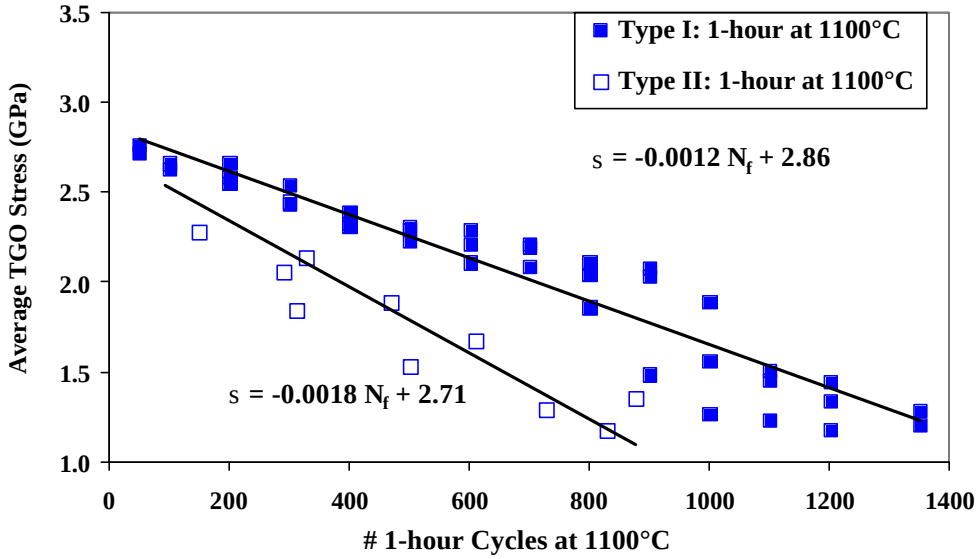

Figure 4.25: Comparison of slopes of TGO stress versus cycles to failure for Type I and Type II TBC samples during the 1-hour tests at 1100°C.

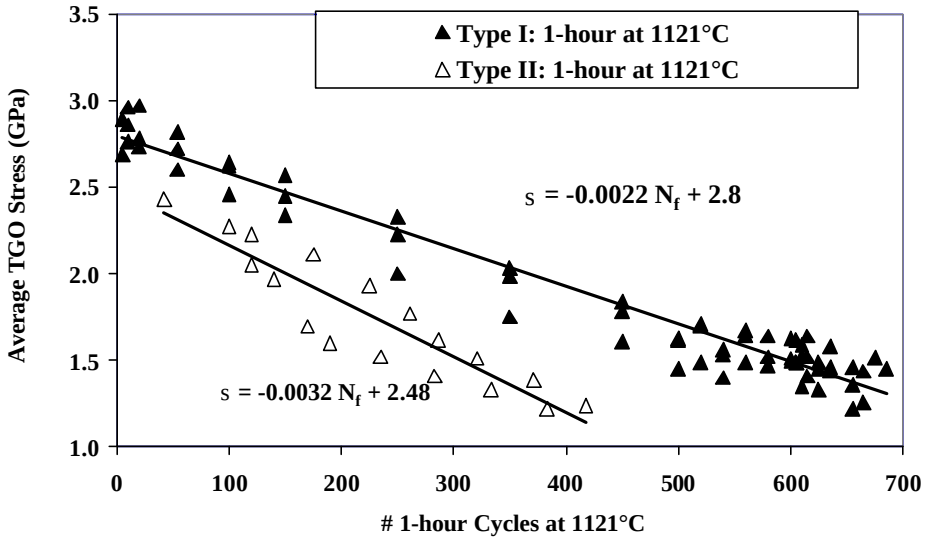

Figure 4.26: Comparison of slopes of TGO stress versus cycles to failure for Type I and Type II TBC samples during the 1-hour tests at 1121°C.

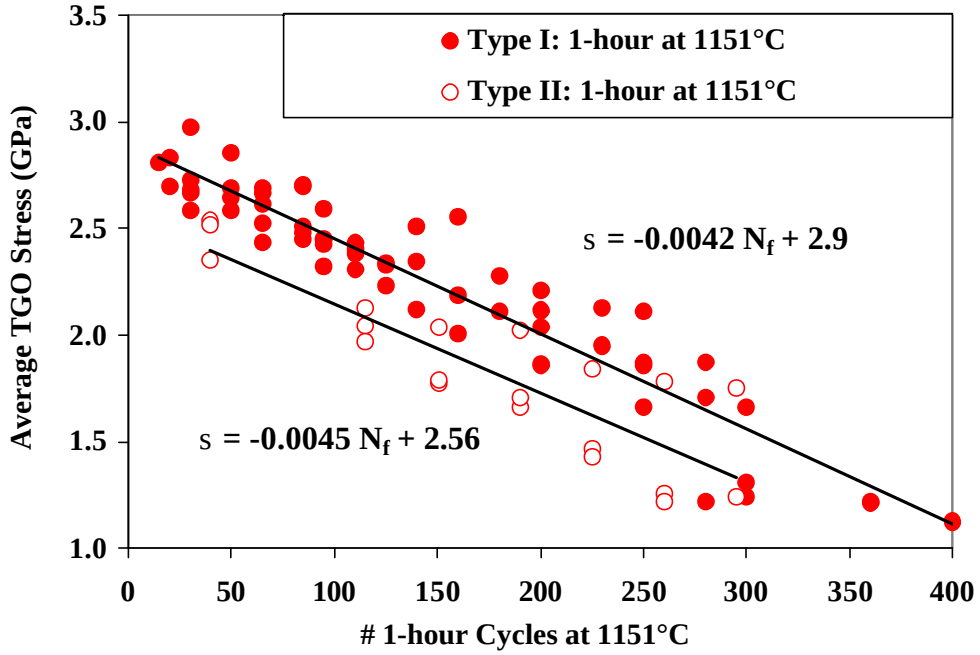

Figure 4.27: Comparison of slopes of TGO stress versus cycles to failure for Type I and Type II TBC samples during the 1-hour tests at 1151°C.

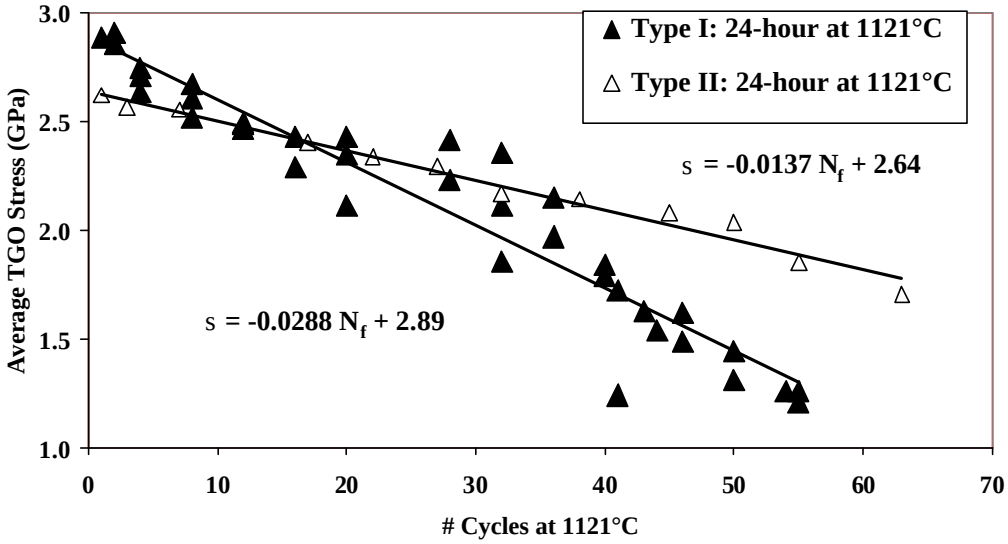

Figure 4.28: Comparison of slopes of TGO stress versus cycles to failure for Type I and Type II TBC samples during the 24-hour tests at 1121°C.

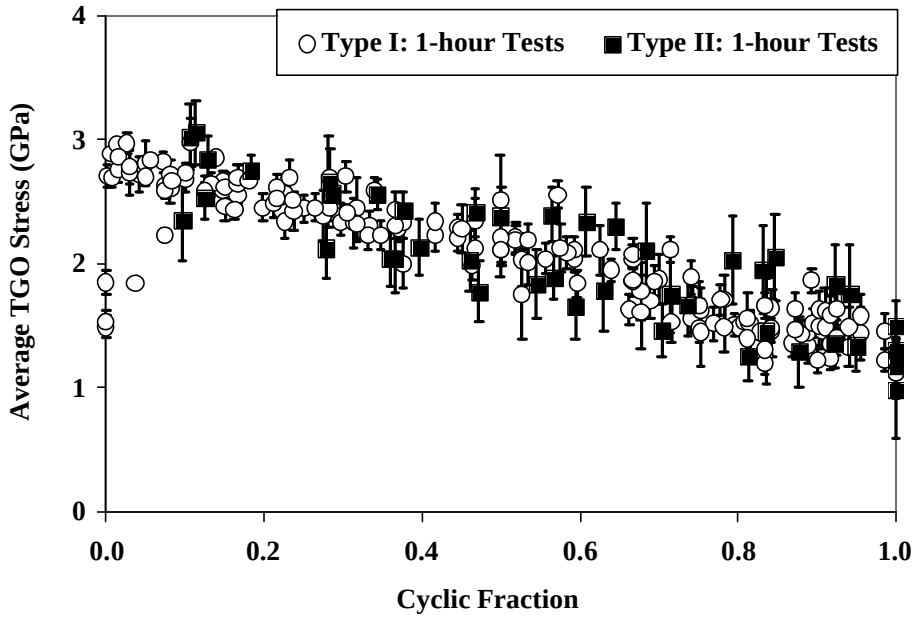

Figure 4.29: Comparison of TGO stress versus TBC life fraction for Type I and Type II TBC samples during the 1-hour tests.

Table 4.1: Differences and similarities in the PLPS behavior and failure modes of Type I and Type II TBCs used in this study.

TBC	**Type I**	**Type II**
Average # Cycles To Failure		
1-hour at 1121°C	677	563
24-hour at 1121°C	45	67
Effect of Temperature on Spallation Life	4 X change on increasing from 1100°C to 1151°C	3 X change on increasing from 1100°C to 1151°C
Effect of Hold Time on Spallation Life	16 X change on increasing from 1-hour to 24-hours	8 X change on increasing from 1-hour to 24-hours
Initial TGO Thickness (µm)	0.5 µm	0.6 µm
Initial Rumpling Amplitude (µm)	1 µm	2.1 µm
TGO Growth Rate (µm/Ö hours)		
1- hour at 1100°C	0.25	-
1- hour at 1121°C	0.27	0.46
24- hour at 1121°C	0.28	0.58

TBC	Type I	Type II
1- hour at 1151°C	0.48	0.73
Activation Energy for O_2 Diffusion in a **-alumina**	278 KJ/mole	224 KJ/mole
Maximum TGO Stress (GPa)	2.8 – 3.0	2.3 – 2.5
Slope of TGO Stress Versus Cycles Data (GPa/Cycle)	**Absolute Value**	**Absolute Value**
1- hour at 1100°C	0.0012	0.0018
1- hour at 1121°C 24- hour at 1121°C	0.0022 0.0289	0.0032 0.0137
1- hour at 1151°C	0.0045	0.0042
TGO Stress At Failure (GPa)	1.2 – 1.4	1.1 – 1.3
PLPS Characteristics That Show Systematic Trends with Cycles	1. TGO Stress 2. Standard Deviation of TGO Stress 3. R_2 Peak Width	1. TGO Stress 2. Standard Deviation of TGO Stress 3. R_2 Peak Width

TBC	Type I	Type II
Macro Failure Mode		
1-hour Tests	YSZ Spallation in one large piece in a single cycle	Failure in single cycle by large scale buckling across the entire specimen surface
24-hour Tests	YSZ Spallation into many pieces over three to four cycles	YSZ failure over three to four cycles into many pieces by buckling in localized areas
Final Failure Interface		
1-hour Tests	Separation in the TBC at or near the YSZ/TGO interface	Separation in the TBC at or near the YSZ/TGO interface
24-hour Tests	At the TGO/bond coat interface	At the TGO/bond coat interface

Table 4.2: Linear Damage Fractions Evaluated for the Multiple Temperatures and Multiple Hold Time Tests for Type I TBCs. LDF-Min and LDF-Max denote the minimum and maximum values of the linear damage fraction while N_1 and N_2 denote the actual TBC life fraction during each stage of the TBC cyclic life at each temperature or for each hold time.

Test Condition	LDF-Min	LDF-Max	LDF Avg	LDF-Stdev	N_1	N_2
1121°C To 1151°C	0.89	1.29	1.07	0.28	0.49	0.57
1121°C To 1151°C	0.93	1.36	1.12	0.30	0.49	0.63
1151°C To 1121°C	0.94	0.99	1.12	0.03	0.52	0.60
1151°C To 1121°C	0.85	0.88	1.02	0.02	0.52	0.50
1-hour To 24-hour at1121°C	0.66	0.91	0.75	N.A	0.51	0.24
24-hour To 1-hour at1121°C	0.79	1.16	0.93	N.A	0.49	0.44

Table 4.3: Linear Damage Fractions Evaluated for the Multiple Temperatures Tests for Type II TBCs. LDF-Min and LDF-Max denote the minimum and maximum values of the linear damage fraction while N_1 and N_2 denote the actual TBC life fraction during each stage of the TBC cyclic life at each temperature or for each hold time.

Test Condition	LDF-Min	LDF-Max	LDF Avg	LDF-Stdev	N_1	N_2
1121°C To 1151°C	0.75	1.09	0.90	0.28	0.49	0.57
1151°C To 1121°C	0.71	1.02	0.84	0.03	0.52	0.60

Table 4.4: Two-sample t-tests assuming unequal variances.

Exposure Condition	$t_{Critical}$ From t-Tables	$t_{Calculated}$ at 95 % Confidence Limit	Conclusion
1-hour at 1100°C	2.201	2.81	Difference in Averages is Significant
1-hour at 1121°C	2.131	3.23	Difference in Averages is Significant
24-hour at 1121°C	2.262	4.6	Difference in Averages is Significant
1-hour at 1151°C	2.201	0.137	Difference in Averages is **NOT** Significant
$t_{calculated} > t_{critical}$ þ Averages of the 2 sample sets are significantly different			

5. Summary And Conclusions

5.1. TGO Stress Measurements Using PLPS

1. Two TBCs, Type I and Type II, have been studied in this research. Type I TBC has an outward diffusing single phase platinum modified nickel aluminide bond coat produced by a CVD process, while Type II TBC has an inward diffusing single phase platinum aluminide bond coat produced by a pack cementation process, referred to as LDC-2E. Both these TBCs, supplied by Howmet Corporation, have a CMSX-4 single crystal superalloy substrate and a 7 YSZ TBC topcoat.
2. For the first time, multi-temperature and multiple hold time TGO stress data as a function of thermal cycles were obtained for the two TBCs.
3. For both TBCs, three spectral features showed monotonic trends with cycling: TGO stress, R_2 peak width and the standard deviation of TGO stress.
    i. The TGO stress and peak width decreased monotonically with thermal cycles for all exposure conditions after a brief transient.
    ii. The standard deviation of TGO stress increased systematically with cycling.
4. The TGO stress versus TBC cyclic life fraction was found to be single valued and independent of cycle temperature, within the range studied for both TBCs.
5. Thermal cycle hold time changed the relation between TGO stress and life fraction to a small extent.
6. The TGO stress at failure was found to be constant (1.2 – 1.4 GPa) for Type I TBC and 1.1 – 1.3 GPa for Type II TBC, independent of cycle temperature and cycle time.

7. It was determined that there was a correlation between the maximum TGO stress and the spallation life: the higher the initial TGO stress, the longer the spallation life.
    i. The maximum TGO stress for Type I TBCs was 2.8 - 3.0 GPa and that for Type II TBC was 2.2 – 2.5 GPa.
8. It is also found that Type I TBC has a smaller slope of the TGO stress versus cycles curve compared to that of Type II TBC, for the 1-hour tests, and a higher slope for the 24-hour tests. This indicates that there is a correlation between the slope of the TGO stress versus cycles curve and the spallation life: the smaller the slope of TGO stress versus cycles, the longer the spallation life.
9. Temperature-blind remaining life predictions were made, for the first time, using three spectral features, the TGO stress, peak width and the standard deviation of TGO stress, using standard regression analyses.
10. Among the 3 spectral characteristics showing a monotonic trend with cycles, the maximum absolute error in making remaining temperature-blind life predictions using TGO stress was found to be superior: 8 % for the 1-hour tests and 9 % for the 24-hour tests and the multiple hold time tests.
11. The error when using the peak width values was found to be 19 % for the 1-hour tests and 15 % for the 24-hour tests, and that when using the standard deviation of TGO stress was found to be 35 % for the 1-hour tests and 25 % for the 24-hour tests.
12. These small errors compare to the high values of the actual scatter in the TBC lives, which were 55% and 77%, respectively.

13. Thus, the remaining life assessments made using the TGO stress values are found to be the most useful and accurate for Type I TBC.

5.2. Non-Constant Amplitude Tests/Linear Damage Rule

1. Two stage block-loading tests were completed for the first time on TBCs. The linear damage rule was valid only in the case of the multiple temperature tests and not for the multiple hold time tests.
2. The TGO stress response, as evaluated from the multi-temperature and multiple hold time tests, was found to have a brief transient on switching to different test conditions.
3. The slope of the stress versus TBC life curve, obtained from the variable temperature tests, was found to be consistent with that from isothermal tests, indicating that a change in the cyclic temperature amplitude does not affect the normalized stress response of the system. This is consistent with a similar spallation mechanism for all 1-hour tests.
4. However, the effect of changing the hold time on the stress behavior was significant, indicating that a change in the hold time does affect the stress response of the system. This is consistent with a change in spallation mechanism on varying the hold time from 1-hour to 24-hours. The same conclusion holds for the linear damage rule done on life alone ignoring TGO stress measurements.
5. This necessitates that TGO stress versus cycles or TBC life trends be generated and studied separately for every cycle with a different hold time.

5.3. Spallation Failure Lives

1. Decreasing the cycle temperature from 1151°C to 1100°C resulted in a 4-fold increase in the number of cycles to failure for Type I TBCs and a 3-fold increase in the number of cycles to failure for Type II TBCs.
2. Increasing the cycle hold time from 1-hour to 24-hours results in a decrease in the number of cycles to failure by a factor of 16 for Type I TBC, but roughly doubles the allowable hot time, indicating that cycling, as well as hot time, are damaging.
3. Increasing the cycle hold time from 1-hour to 24-hours results in a decrease in the number of cycles to failure by a factor of 8 for Type II TBC but increases the allowable hot time by a factor of 4, indicating that cycling as well as hot time are damaging.
4. Type I TBCs show a 20 – 25 % increase in cyclic life compared to Type II TBCs during the 1-hour tests, while Type II TBCs show a 45 - 50 % increase in cyclic life over Type I TBCs during the 24-hour tests.
5. The improved cyclic oxidation resistance of Type I TBC during the 1-hour tests can be attributed to a slower growing and more adherent protective alumina scale.
6. The lower maximum TGO stress and the lower TGO stress at failure values for Type II TBCs compared to those of Type I TBCs and the higher slopes of the TGO stress versus cycles curves for Type II TBCs compared to those of Type I TBCs are all consistent with the concept that the lower the maximum TGO stress and higher the slope of the TGO stress versus cycles curve, the shorter are the TBC spallation lives.

7. The improved 24-hour cyclic performance of Type II TBCs compared to Type I TBCs can be explained on the basis of the lower amount of stored elastic strain energy in Type II 24-hour cycled samples than that for Type I TBCs, which is consistent with the lower maximum value of TGO stress and lower TGO stress at failure for Type II TBCs than for Type I TBCs.

5.4. Spallation Mechanisms

1. All Type I and Type II samples tested in the 1-hour cycles, regardless of temperature, failed in the TBC, near the TBC/TGO interface, due to progressive cracking beginning at ~ 20% life fraction.
2. In contrast, the 24-hour cyclic test samples failed almost exclusively at the TGO/bond coat interface, with little or no cracking at the YSZ/TGO interface beginning at ~ 20% life fraction.
3. This indicates there is a spallation mechanism change on varying the hold time and hence, any multi-hold time mechanistic damage model will need to include two types of damage. Failure can be predicted on the basis of whichever spallation mechanism occurs first.
4. It was determined that for 1- hour cycles that bond coat rumpling is the cause of crack initiation because TBC cracking prior to failure is consistently associated with regions where the bond coat has pulled away from the TBC.
5. The rumpling observed on the bond coated back side of the sample was much greater (2-2.5 times greater amplitude) than under the TBC, clearly showing that the TBC restricts rumpling.

6. The oxidation kinetics in both TBCs conformed to a parabolic rate law.

7. The TGO growth rate in Type II TBCs was found to be greater than that in Type I TBCs for both the 1-hour and 24-hour test conditions.

    i. The reasons for the higher oxide growth of Type II TBCs are the larger effective bond coat surface area (determined the bond coat surface roughness which is found to be higher for Type II TBCs than for Type I TBCs) and the apparently smaller grain size of the oxide on Type II TBCs. Other possible reasons were also identified: bond coat purity, bond coat surface topography and ductile to brittle transition temperature.

    ii. Specifically, the CVD method of producing Type I TBCs has a purification effect, since it substantially reduces the concentration of substrate substitutional alloying elements, such as W, Mo, etc., and surface-active tramp elements, such as B, P, and S, in the coating, which in turn improves the oxidation resistance of Type I TBCs. This is in direct contrast to Type II TBCs, which are formed at a lower temperature by the pack cementation process.

8. The activation energy for TGO growth was found to be 139 KJ/mole for Type I TBCs and 112 KJ/mole for Type II TBCs. The activation energy for oxygen diffusion in ? - alumina, corresponding to these values of 139 KJ/mole and 112 KJ/mole would be 278 KJ/mole and 224 KJ/mole, which are in the same range as the values of 220 KJ/ mole - 320 KJ/ mole reported in the literature.

9. The rumpling rate for Type I TBC for the 24-hour tests at 1121°C was only slightly higher than for the 1-hour tests, which experienced 24 times the number of cycles for a given hot time.

10. Though the 24-hour samples experienced greater total rumpling, they tolerated more rumpling with little or no cracking. Final failure occurred at the TGO/bond coat interface. This is because the 24-hour cycle tests lack a sufficient number of cooling events to damage the TBC before the TGO separates from the bond coat due to increasing strain energy that is related to the high TGO stress and steadily increasing TGO thickness.

11. A mechanism for rumpling in these TBCs, based on the above observations and consistent with present analytical and numerical models, involves plastic deformation at the maximum temperature in the cycle and cracking of the ceramic upon cool down. In other words, the in-plane TGO growth that occurs at the peak temperature directly appears as rumpling displacements of the TGO.

12. The low measured flow stress (< 26 MPa at 1000°C) in Pt-Al bond coats is additional suggestive evidence that all the TBC yielding is confined to the bond coat and little or none occurs in the TGO.

13. The observed single-valued relationship between the TGO thickness and rumpling amplitude, independent of temperature and cycle time, also strongly indicates that rumpling in this system is primarily dependent on TGO growth.

14. This research has established a mechanistic understanding of how durability of TBCs is affected by exposures to different test conditions, likely to be encountered in the

operation of advanced gas turbines. This understanding has been used develop approaches to predict remaining lives of thermally cycled TBCs.

15. These mechanisms-based remaining life assessments performed in this research have shown great promise and have a great potential for use in real gas turbine engines.

5.5. Physical Basis For The Observed Stress Versus Life Trends

1. For cross-section PLPS measurements, lower stress levels were observed on areas of the TGO with thickness imperfections, at areas where the TGO had rumpled and at places where there were cracks at the YSZ/TGO interface, indicating that a decrease in the TGO stress is related to cycling-induced microstructural degradation of the TGO.
2. Several analogies can be drawn between the TGO stress versus life relationship and failure modes for the 2 TBCs, when studied as a function of temperature and hot time:
    i. Both are insensitive to temperature but depend on hold time.
    ii. Similar trends are observed between rumpling rate versus life and stress relaxation rate versus life for all the test conditions evaluated.
    iii. Both the amplitude of rumpling and the measured TGO stress reach a fairly constant value at failure, irrespective of the exposure condition.
3. Rumpling allows the TGO to get longer, as indicated by an increase in the tortuosity of the TGO/bond coat interface, potentially relieving the compressive stresses in the TGO.

4. Thus, the observed monotonic decrease in TGO stress for both TBCs is consistent with that expected due to rumpling of the TGO/bond coat interface.

5. The lower values of TGO stress at failure for Type II TBCs compared to that for Type I TBCs are also consistent with the larger initial rumpling amplitudes together with the greater extent of rumpling observed in Type II TBCs.

References

Ambrico J. M., Begley M. R., Jordan E. H., Acta Materialia 49-9 1577 (2001).

Angenete J., Ph. D. Thesis, Chalmers University, Gothenburg (1999).

Angenete J., Stiller K., Surface & Coatings Technology 150 107-118 (2002).

Balint D. S., Hutchinson, J. W., Acta Materialia 51 3965 (2003).

Barrett C. A., Lowell C. E., Oxidation of Metals 9 307-355 (1975).

Beele W., Marijnissen G., Vvan Lieshout H., Surface & Coatings Technology 120-121 61 (1999).

Bengtsson P., Ph. D. Dissertation, # 509, Inst. of Technol., Linköpings University, (November 1997).

Bernard H., Remy L., Proceedings: "High Temperature Materials for Power Engineering", Kluwer Academic Publications, Doordrecht, The Netherlands 1185–1194 (1990).

Bose S., DeMasi-Marcin J. T., "Thermal barrier coating experience in gas turbine engines at Pratt & Whitney": TBC Workshop, NASA CP 3312 63 (1995).

Brindley W. J., "Properties of plasma sprayed bond coats": Proceedings of the Workshop on Thermal Barrier Coating, NASA-CP-3312 Cleveland, Ohio: National Aeronautics and Space Administration Lewis Research Center 189-202 (1995).

Brindley W. J., Nesbitt J. A., Advanced Earth to Orbit Propulsion Technology, 1 NASA-CP-3012. Washington, D.C.: National Aeronautics and Space Administration (1988).

Brindley W. J., Whittenberger J. D., Materials Science and Engineering A 163-1 33-41 (1993).

Buhl H., MRE-Materials Research and Engineering, Eds. Illschner B., Russel K. C., Springer-Verlag, Heidelberg, (1992).

Busso E. P., McClintock F. A., Materials Science & Engineering A 161-165 (1993).

Cassenti B. N., Brickley A. M., Sinko G. C., "Thermal and stress analysis of thermal barrier coatings" In AIAA/SAE/ASME 17th Joint Propulsion Conference, Colorado Springs, New York: American Institute of Aeronautics and Astronautics, Inc July 27-29 (1981).

Chang G. C., Phucharoen W., Miller R. A., Surface & Coatings Technology 32 307-325 (1987).

Chang S. L., Pettit F. S., Birks N., Oxidation of Metals 34 1-2 23 (1990).

Chaudhury Z. A., Newaz G. M., Nusier S. Q., Ahmed T., Materials Science & Engineering A 231 34-41 (1997).

Chen J. H., Surface & Coatings Technology 92 69-77 (1997)

Cheng J., Jordan E. H., Barber B., Gell M., Acta Materialia 43 5839–5850 (1998).

Choi S. R., Hutchinson J. W., Evans A. G., Mechanics of Materials 31 431 (1999).

Christensen R. J., Lipkin D. M., Clarke D. R., Murphy K. S., Applied Physics Letters 69 [24] 3754-3756 (1996).

Clarke D. R., Christensen R. J., Tolpygo V. K., Surface & Coatings Technology 94-95 89- 93 (1997).

Das D. K., Singh V., Joshi S. V., Metallurgical & Materials Transactions. A 29 2173(1998).

Deb P., Boone D. H., Manley T. F. II., Journal of Vacuum Science & Technology A 5 6 3366 (1987).

DeMasi J. T., Sheffler K. D., Ortiz M., "Thermal Barrier Coating Life Prediction Model Development - Phase I Final Report" NASA-CR-182230, Washington, D.C.: National Aeronautics and Space Administration (1989).

DeMasi-Marcin J. T., Sheffler K. D., Bose S., ASME Paper 89-GT-132. New York: American Society of Mechanical Engineers (1989).

Evans A. G., Materials at High Temperatures 12(2-3) 219-227 (1994).

Evans A. G., He M. Y., Hutchinson J. W., Progress in Materials Science 46 249–71 (2001 a).

Evans A. G., Mumm D. R., Hutchinson J. W., Meier G. H., Pettit F. S., Progress in Materials Science 46-5 505-553 (2001 b).

Fairbanks J. W., Hecht R. J., Materials Science & Engineering A 88 321 (1987).

Fawley R. W.: "Superalloy Progress" In: Sims, C.T, Hagel, W.C. (Hrsg.): The Superalloys, Wiley, New York 3-29 (1972).

Felten E. J., Pettit F. S., Oxid. Met. 10 189–223 (1976).

Ferguson B. L., Petrus G. J., Ordillas M., "A Software Tool to Design Thermal Barrier Coatings - Final Report": NASA Contract NAS3-2728. Washington, D.C.: National Aeronautics and Space Administration (1994).

Funke C., Siebert B., Vaßen R., Stöver D., ICMCTF San Diego, USA (1997).

Goodge A. C., M.S. Thesis, University of Virginia, 1997.

Goward G. W., Journal of Metals 31 (October 1970).

Goward G. W., Surface & Coatings Technology 108-109 73 (1998).

Grunling H. W., Rechtenbacher H., Singheiser L., Materials Science Forum 251-254 483 (1997).

Hancock P., Chien H. H., Nicholls J. R., Stephenson D. J., Surface & Coatings Technology 43–44 359–370 (1990).

Haynes J., Zhang Y., Lee W., Pint B., Wright I., Cooley K., Proceedings: "Elevated Temperature Coatings", Science and Technology III, The Minerals, Metals and Materials Society (1999).

He J., Clarke D. R., Journal of American Ceramic Society 78 5 1347 (1995).

He M. Y., Evans A. G., Hutchinson J. W., Acta Materialia 48 2593–2601 (2000).

Hebsur M. G., Miner R. V., Materials Science Engineering 83 239 (1986).

Hillery R.V., Pilsner B.H., McKnight R.L., Cook T.S., Hartle M.S., "Thermal Barrier Coating Life Prediction Model Development - Final Report": NASA-CR180807. Washington, D.C.: National Aeronautics and Space Administration (1988).

Holmes J. W., McClintock F. A., Metallurgical Transactions A 21 1209 (1990).

Hutchinson J. W., He M. Y., Evans A. G., Journal of Mech. and Phys. of Solids 48 709-734 (2000).

Jones R. L., “Thermal Barrier Coatings” In: Stern, Kurt H. (Hrsg.): Metallurgical and Ceramic Protective Coatings, Chapman & Hall, London 194-235 (1996).

Kaplyanskii A. A., Przhevuskii A. K., Rozenbaum R. B., Soviet Physics Solid State 10 8 1864–1868 (1969).

Karlsson A. M., Hutchinson J. W., Evans A. G., Journal of the Mechanics and Physics of Solids 50-8 1565 (2002 a).

Karlsson A. M., Levi C. G., Evans A. G., Acta Materialia 50-6 1263 (2002 b).

Karlsson A. M., Xu T., Evans A. G., Acta Materialia 50-5 1211 (2002 c).

Karlsson A. M., Hutchinson J. W., Evans A. G., Materials Science & Engineering A 351 244 (2003).

Kim G. M., Yanar N. M., Hewitt E. N., Pettit F. S., Meier G. H., Scripta Materialia 46 489 (2002).

Kimmel J., Mutasim Z., Brentnall W., ASME 99-GT-350 1-9 (1999).

Kingery W. D., Bowen H. K, Uhlmann D. R., Introduction to Ceramics, Wiley and Sons, New York (1976).

Lee E. Y., Sisson R. D., “The effect of bond coat oxidation on the failure of thermal barrier coatings: Thermal spray industrial applications”: In Proceedings of the 7th National Thermal Spray Conference, Boston, Mass., June 20-24, Eds. Berndt C. C., Sampath S., Materials Park, Ohio: ASM International 55-59 (1994).

Lee W. Y., Zhang Y., Wright I. G., Pint B. A., Liaw P. K., Metallurgical & Materials Transactions A 29A 833–841 (1998).

Lipkin D. M., Clarke D. R., Journal of Applied Physics 77 [5] 1855-1863 (1995).

Lipkin D. M., Clarke D. R., Oxidation of Metals 45 267 (1996).

Lipkin D. M., Clarke D. R., Hollatz M., Bobeth M., Pompe W., Corrosion Science 39-2 231-242 (1997 a).

Lipkin D. M., Clarke D. R., Hollatz M., Bobeth M., Pompe W., Corrosion Science 39-2 243 (1997 b).

Manning-Meier S., Nissley D. M., Sheffler K. D., Cruse T. A., "Thermal Barrier Coating Life Prediction Model Development" ASME Paper 91-GT-40. New York: American Society of Mechanical Engineers (1991).

Maricocchi A., Bartz A., Wortman D. J., Proceedings of the 1995 Thermal Barrier Coating Workshop, ed. Brindley W. J., NASA Conference Publication No. 3312, 79-89 (1995).

Meier S. M., Gupta D. K., Sheffler K. D., JOM 43 50-53 (1991).

Meier S. M., Nissley D. M., Sheffler K. D., "Thermal barrier coating life prediction model development - Phase II" NASA CR-18911 (July 1991).

Meier S. M., Nissley D. M., Sheffler K. D., Cruse T. A., Transactions of ASME 114 258-263 (1992).

Miller R. A., Lowell C. E., Thin Solid Films 95-3 265-273 (1982).

Miller R. A., Journal of American Ceramic Society 67 517 (1984).

Miller R. A., In: Proceedings of the Thermal Barrier Coatings Workshop. NASA-CP-3312 17 (1995).

Morrel P., Rickerby D. S., In: AGARD-R-823 20 (1998).

Mumm D. R., Evans A. G., Acta Materialia. 48 8 1815 (2000).

Mumm D. R., Evans A. G., Spitsberg I. T., Acta Materialia 49 2329 (2001).

Munro R. G., Piermarinin G. J., Block S., Holzapfel W. B., Journal of Applied Physics 57 2 165 (1985).

Nesbitt J. A., Heckel R. W., Thin Solid Films 119 281-290 (1984).

Nesbitt J. A., Journal of the Electrochemical Society 136 - 5 1511-1527 (1989).

Nicholls J. R., Rickerby D. S., Materials and Processes for High Temperature Surface Engineering", Proc. Materials Congress 1998 in Cirenchester, in "B278-Materials for High Temperature Power Generation and Process Plant Application", Ed. A. Strang, IOM Communications Ltd. 279 (2002).

Nicoll A. R., Thin Solid Films 95 21-34 (1992).

Niu Y., Wu W. T., Boone D. H., Smith J. S., Zhang J. Q., Zhen C. L., J. Phys. 3 511–519 (1993).

Noebe R. D., Bowman R. R., Nathal M. V., Physical Metallurgy and Processing of Intermetallic Compounds, Eds. Stoloff N. S., Sikka V. S., Chapman & Hall, 212.

Novak R. C., Coating Development and Use: Case Studies: “Presentation to the Committee on Coatings for High-Temperature Structural Materials”, National Materials Advisory Board, National Research Council, Irvine, California, April 18-19 (1994).

Novak R. C., NASA TBC Workshop, Cleveland, Ohio, 153 (1995).

NRC Report (Ed. R. Hillery), “Coatings for High Temperature Structural Materials: Trends and Opportunities”, National Academy Press (1996).

Olsson M., Ph. D. Dissertation “Mechanical Modeling of Ceramics”, Royal Inst. Techn. (1994).

Pan D., Chen M. W., Wright P. K., Hemker K. J., Acta Mater. 51-82205 (2003).

Panat R. P., Zhang S., Hsia K. J., Acta Materialia 51 239–249 (2003).

Panat R. P., Hsia K. J., Proceedings of Royal Society of London, Series A 460 1957 (2004).

Parks W. P., Hoffman E. E., Lee W. Y., Wright I. G., Journal of Thermal Spray Technology 6 - 2 187-192 (1997).

Peng X., Clarke D. R., Journal of American Ceramic Society 83 [5] 1165-1170 (2000).

Pennefather R. C., Boone D. H., Surface & Coatings Technology 76–77 47 (1994).

Pettit F. S., Trans. Met. Soc. AIME 239 1296–1305 (1967).

Phucharoen W., Unpublished Ph.D. dissertation, Cleveland State University (1990).

Probst H. B., Lowell C. E., Journal of Metals 40 - 10 18 (1988).

Rhines F. N., Wolf J. S., Metallurgical Transactions1 1701–1710 (1970).

Richard C. S., Surface & Coatings Technology 82 99-109 (1996).

Rigney D. V., Viguie R., Wortmann D. J., Shelly D. W., Proc. of the Workshop on Thermal Barrier Coatings, NASA-CP-3312, 135-150, NASA Lewis Research Center, Cleveland, Ohio, 135 (1995).

Schlichting K. W., Vaidyanathan K., Sohn Y. H., Jordan E. H., Gell M., Padture N. P., Materials Science and Engineering A, 291 [1-2] 68-77 (2000).

Schultz M., Corrosion and Environmental Degradation II, Wiley-VCH (2000).

Schulz U., Oettel, H., Bunk, W., Zeitschrift fuer Metallkunde 87 488-492 (1996).

Schulz U., Aero. Sci. Technology 7 73-80 (2003).

Selcuk A., Atkinson A., Acta Materialia 51-2 535-549 (2003).

Sevcik W. R., Stoner B. L., "An Analytical Study of Thermal Barrier Coated First Stage Blades in a JT9D Engine" NASA-CR-13560, Washington, D.C.: National Aeronautics and Space Administration (1978).

Sheasby J. S., Jory D. B., Oxidation of Metals 12 527–539 (1978).

Sivakumar R, Surface & Coatings Technology 37 139-160 1989.

Smeggil J. L., Materials Science & Engineering 87 261-265 (1987).

Smialek J. L., Metallurgical Transactions A 22A 739–752 (1991).

Smialek J. L., Tubbs B., Metallurgical Transactions A 26A 427–435 (1995).

Sohn Y. H., Schlichting K., Vaidyanathan K., Jordan E. H., Gell M., Metallurgical & Materials Transactions 31A 2388-2391 (2000).

Sohn Y. H., Krishnakumar Vaidyanathan, Ronski M., Jordan E. H., Gell M., Surface & Coatings Technology 146-147 102-109 (2001).

Stecura S., NASA-TM-86905 (1985).

Stiger M. J., Yanar N. M., Topping M. G., Pettit F. S., Meier G. H.. Z. Metallk 90 1069–1078 (1999).

Stover D., Funke C., J. of Materials Processing Technology 92-93 195 (1999).

Strangman T. E., Thin Solid Films 127 93-105 (1985).

Strangman T. E., Liu A., Neumann J., "Thermal Barrier Coating Life-Prediction Model Development - Final Report": NASA-CR-179648, Washington, D.C.: National Aeronautics and Space Administration (1987).

Strangman T. E., "Turbine coating life prediction model", In 1990 Proceedings of the Workshop on Coatings for Advanced Engines, Washington, D.C.: U.S. Department of Energy (August 1990).

Swetha Sridharan, Xie L. D., Jordan E. H., Gell M., Surface & Coatings Technology 179 [2-3] 286-296 (2004).

Swetha Sridharan, Xie L. D., Jordan E. H., Gell M., Materials Science & Engineering A 3931-2 51-62 (2005).

Tawancy H. M., Sridhar N., Abbas N. M., Rickerby D., Scripta Mat 33 1431–1438 (1995).

Terry, S.: "Microstructural evolution of thermal barrier coatings grown by physical vapor deposition", Dissertation Proposal, UCSB (1998).

Tolpygo V. K., Surface & Coatings Technology 120-121 53-60 (1999).

Tolpygo V. K., Clarke D. R., Acta Materialia 48 3283 (2000).

Tolpygo V. K., Clarke D. R., “Damage induced by thermal cycling of thermal barrier coatings”: In Dahotre N. B., Hampikian J. M., Morral J. E., Eds., Elevated temperature coatings: Science & Technology IV, TMS 94 (2001).

Tolpygo V. K., Clarke D. R., Surface & Coatings Technology 163-1 81-86 (2003).

Vogel D., Newman L., Deb P., Boone D. H., Materials Science & Engineering 88 227–231 (1987).

Vuoristo P., Ahmaniemi S., Tuurna S., Mäntylä T., Cordano E., Fignino F., Gualco G. C., ITSC 2002, Essen, (2002).

Walker K. P., “Research and Development Program for Nonlinear Structural Modeling with Advanced Time-Temperature Dependent Constitutive Relationships”, NASA CR 165533, November 1981.

Watanabe M., Mumm D. R., Chiras S., Evans A. G., Scripta Materialia. 46 67 (2002).

Wigren J., Pejryd L., Proceedings of the 15th International Thermal Spray Conference, 25-29 Nice, France, 1531 (May 1998).

Winkler M. F., Parker D. W., Advanced Materials Processing 5 17 (1992).

Wood J. H., Goldman E. H., In: Sims C., Stoloff N., Hagel W. (Eds.), Superalloys II, Wiley, New York 359–384 (1987).

Wright I. G., Sethis V. K, Nagarajan V., Journal of Engineering for Gas Turbines and Power 113 616 (October 1991).

Wright P. K., Materials Science & Engineering A 245 191–200 (1998).

Wright P. K., Evans A. G., Current Opinion in Solid State and Materials Science 4, 255–265 (1999).

Xie L. D., Sohn Y. H., Jordan E. H., Gell M., Surface & Coatings Technology 176-1 57-66 (2003).

Xu T., He M. Y., Evans A. G., Interface Science 11 349 (2003).

Yu H. H., He M. Y., Hutchinson J. W., Acta Materialia 49 93 (2001).

Zhang Y. H., Withers P. J., Fox M. D., Knowles D. M., Materials Science & Technology 15 1031–1036 (1999 a).

Zhang Y. H., Lee W., Haynes J., Wright I., Pint B., Cooley K., Liaw P., Metallurgical & Materials Transactions A 30A 2679–2687 (1999 b).

Zhao L., Lugscheider E., Surface & Coatings Technology 149 2-3 230 (2002).

http://www.physics.csbsju.edu/stats/t-test.html

1. R. A. Miller, *Surface and Coatings Technology* **30**, 1-11 (1987/1, 1987).

2. W. J. Brindley, R. A. Miller, *Advanced Materials and Processes* **136**, 29 (1989).

3. J. T. DeMasi-Marcin, K. D. Sheffler, S. Bose, *Journal of Engineering for Gas Turbines and Power* **112**, 521-526 (1990).

4. J. T. DeMasi-Marcin, D. K. Gupta, *Surface and Coatings Technology* **68/69**, 1-9 (1994).

5. T. E. Strangman, *Thin Solid Films* **127**, 93-105 (1985).

6. R. L. Jones, in *Metallurgical and Ceramic Protective Coatings* K. H. Stern, Ed. (Chapman & Hall, London, 1996) pp. 194-235.

7. S. M. Meier, D. K. Gupta, *Journal of Engineering for Gas Turbines and Power* **116**, 250-257 (January 1994, 1994).

8. A. G. Evans, D. R. Mumm, J. W. Hutchinson, G. H. Meier, F. S. Pettit, *Progress in Materials Science* **46**, 505-553 (2001).

9. N. P. Padture, M. Gell, E. H. Jordan, *Science* **296**, 280-284 (12 April 2002, 2002).

10. S. Bhattacharjee, U. Syamaprasad, R. K. Galgali, B. C. Mohanty, *Mater. Lett.* **15**, 281-284 (1992).

11. N. P. Padture *et al.*, *Acta Materialia* **49**, 2251-2257 (2001/7/17, 2001).

12. D. Zhu, R. A. Miller, *Surface and Coatings Technology* **108-109**, 114-120 (1998/10/10, 1998).

13. D.-M. Zhu, R. A. Miller, *MRS bulletin* **25**, 43-47 (2000).

14. H. E. Eaton, J. R. Linsey, R. B. Dinwiddie, in *Thermal conductivity 22* T. W. Tong, Ed. (Technomic, Lancaster, PA, 1994) pp. 289.

15. M. J. Stiger, N. M. Yanar, M. G. Topping, F. S. Pettit, G. H. Meier, *Z. Metallk* **90**, 1069-1078 (1999).

16. B. A. Pint *et al.*, *Materials Science and Engineering A* **245**, 201-211 (1998/5/1, 1998).

17. W. J. Brindley, R. A. Miller, *Surface and Coatings Technology* **43-44**, 446-457 (1990).

18. W. Lih, E. Chang, B. C. Wu, C. H. Chao, *Oxidation of Metals* **36**, 221 (1991).

19. W. Lih, E. Chang, C. H. Chao, M. L. Tsai, *Oxidation of Metals* **38**, 99 (1992).

20. A. G. Evans, M. Y. He, J. W. Hutchinson, *Acta Materialia* **45**, 3543-3554 (1997/9, 1997).

21. J. Cheng, E. H. Jordan, B. Barber, M. Gell, *Acta Materialia* **46**, 5839-5850 (1998/10/9, 1998).

22. M. Gell, K. Vaidyanathan, B. Barber, J. Cheng, E. Jordan, *Metallurgical and Materials Transactions A* **30A**, 427-435 (February 1999, 1999).

23. M. Gell *et al.*, *Surface and Coatings Technology* **120-121**, 53-60 (1999/11, 1999).

24. P. Kofstad, *High temperature corrosion* (Elsevier Applied Science, New York, 1988).

25. P. K. Wright, A. G. Evans, *Current Opinion in Solid State and Materials Science* **4**, 255-265 (1999/6, 1999).

26. P. K. Wright, *Materials Science and Engineering A* **245**, 191-200 (1998).

27. T. A. Cruse, S. E. Stewart, M. Ortiz, *Journal of Engineering for Gas Turbines and Power* **110**, 610-616 (October 1988, 1988).

28. S. M. Meier, D. M. Nissley, K. D. Sheffler, T. A. Cruse, *Journal of Engineering for Gas Turbines and Power* **114**, 258-263 (April 1992, 1992).

29. M. Wen, E. Jordan, M. Gell, *Materials Science and Engineering A* (2005).

30. S. Sridharan, L. Xie, E. H. Jordan, M. Gell, *Surface and Coatings Technology* **179**, 286-296 (2004/2/23, 2004).

31. M. Madhwal, E. H. Jordan, M. Gell, *Materials Science and Engineering A* **384**, 151-161 (2004/10/25, 2004).

32. D. Strauss *et al.*, *Surface and Coatings Technology* **135**, 196 (2001).

33. M. R. Brickey, J. L. Lee, *Oxidation of Metals* **54**, 237 (2000).

34. D. Toma, W. Brandl, U. Koster, *Surface and Coatings Technology* **120-121**, 8 (1999).

35. V. Tolpygo, D. R. Clarke, *Materials at High Temperatures* **17**, 59-70 (2000).

36. M. Wen, E. Jordan, M. Gell, *Surface and Coatings Technology* (2005).

37. C. Mennicke, D. R. Mumm, D. R. Clarke, *Z. Metallk* **90**, 1079-1085 (1999).

38. D. R. Clarke, R. J. Christensen, V. Tolpygo, *Surface and Coatings Technology* **94-95**, 89-93 (1997/10, 1997).

39. Y. H. Sohn, J. H. Kim, E. H. Jordan, M. Gell, *Surface and Coatings Technology* **146-147**, 70-78 (2001/0, 2001).

40. D. M. Lipkin, D. R. Clarke, *Oxidation of Metals* **45**, 267-280 (1996).

41. V. K. Tolpygo, J. R. Dryden, D. R. Clarke, *Acta Materialia* **46**, 927-937 (1998/1/23, 1998).

42. V. Sergo, D. R. Clarke, *Journal of the American Ceramic Society* **81**, 3237-3242 (1998).

43. V. K. Tolpygo, D. R. Clarke, *Acta Materialia* **46**, 5153-5166 (1998/9/1, 1998).

44. R. J. Christensen, D. M. Lipkin, D. R. Clarke, *Acta Materialia* **44**, 3813-3821 (1996/9, 1996).

45. C. Sarioglu, J. R. Blachere, F. S. Pettit, G. H. Meier, 1997.

46. E. Schumann, C. Sarioglu, J. R. Blachere, F. S. Pettit, G. H. Meier, *Oxidation of Metals* **53**, 259 (2000).

47. J. Rosler, M. Baker, M. Volgmann, *Acta Materialia* **49**, 3659-3670 (2001/10/26, 2001).

48. J. Cho, M. P. Harmer, H. M. Chan, J. M. Rickman, A. M. Tompson, *Journal of American Ceramic Society* **80**, 1013 (1997).

49. V. K. Tolpygo, D. R. Clarke, *Acta Materialia* **48**, 3283-3293 (2000/8/1, 2000).

50. M. Wen, E. Jordan, M. Gell, *Surface and Coatings Technology* (2005).

51. A. Evans, M. Y. He, J. W. Hutchinson, *Progress in Materials Science* **46**, 249-271 (2001).

52. A. Evans, J. W. Hutchinson, M. Y. He, *Acta Materialia* **47**, 1513-1522 (1999).

53. J. G. Smeggil, *Materials Science and Engineering A* **87**, 261 (1987).

54. D. K. Gupta, D. S. Duvall, *Superalloy 1982*.

55. B. A. Pint, *Oxidation of Metals* **48**, 303 (1997).

56. B. A. Pint, *Surface and Coatings Technology* **188-189**, 71-78 (2004/0, 2004).

57. J. L. Smialek, D. T. Jayne, J. C. Schaffer, W. H. Murphy, *Thin Solid Films* **253**, 285 (1994).

58. M. Gell, D. N. Duhl, D. K. Gupta, K. D. Sheffler, *journal of metals* **39**, 11 (1987).

59. U. Schulz, M. Menzebach, C. Leyens, Y. Q. Yang, *Surface and Coatings Technology* **146-147**, 117-123 (2001/0, 2001).

60. J. E. Schilbe, *Surface and Coatings Technology* **133-134**, 35-39 (2000).

61. U. Kaden, C. Leyens, M. Peters, W. A. Kaysser, paper presented at the TMS, Warrendale, OH 1999.

62. H. Lau, C. Leyens, U. Schulz, C. Friedrich, *Surface and Coatings Technology* **165**, 217-223 (2003/2/17, 2003).

63. D. Zhu, R. A. Miller, *Materials Science and Engineering A* **245**, 212-223 (1998/5/1, 1998).

64. S. Sridharan, L. Xie, E. Jordan, M. Gell, *Materials Science and Engineering A* **393**, 51-62 (2005).

65. D. R. Mumm, M. Watanabe, A. G. Evans, J. A. Pfaendtner, *Acta Materialia* **52**, 1123-1131 (2004).

66. R. A. Miller, C. E. Lowell, *Thin Solid Films* **95**, 265 (1982).

67. K. Vaidyanathan, M. Gell, E. Jordan, *Surface and Coatings Technology* **133-134**, 28-34 (2000/11, 2000).

68. E. P. Busso, J. Lin, S. Sakurai, M. Nakayama, *Acta Materialia* **49**, 1515 (2001).
69. A. Rabiei, A. Evans, *Acta Materialia* **48**, 3963 (2000).

70. K. W. Schlichting, N. P. Padture, E. H. Jordan, M. Gell, *Materials Science and Engineering A* **342**, 120-130 (2003/2/15, 2003).

71. X.-Y. Gong, D. R. Clarke, *Oxidation of Metals* **50**, 355-376 (1998).

72. C.-H. Hsueh, E. R. FullerJr., *Materials Science and Engineering A* **283**, 46-55 (2000/5/15, 2000).

73. A. G. Evans, G. B. Crumley, R. E. Demaray, *Oxidation of Metals* **20**, 193 (1983).

74. M. Y. He, A. G. Evans, J. W. Hutchinson, *Materials Science and Engineering A* **245**, 168-181 (1998).

75. K. Vaidyanathan, E. Jordan, M. Gell, *Acta Materialia* **52**, 1107-1115 (2004).

76. M. Y. He, A. G. Evans, J. W. Hutchinson, *Acta Materialia* **48**, 2593-2601 (2000/6/14, 2000).

77. V. K. Tolpygo, D. R. Clarke, *Acta Materialia* **46**, 5167-5174 (1998/9/1, 1998).

78. V. K. Tolpygo, D. R. Clarke, *Acta Materialia* **52**, 615-621 (2004/2/9, 2004).

79. V. K. Tolpygo, D. R. Clarke, *Acta Materialia* **52**, 5115-5127 (2004/10/4, 2004).

80. V. K. Tolpygo, D. R. Clarke, *Acta Materialia* **52**, 5129-5141 (2004/10/4, 2004).

81. A. M. Karlsson, A. G. Evans, *Acta Materialia* **49**, 1793-1804 (2001/6/13, 2001).

82. A. M. Karlsson, T. Xu, A. G. Evans, *Acta Materialia* **50**, 1211-1218 (2002/3/14, 2002).

83. A. M. Karlsson, J. W. Hutchinson, A. G. Evans, *Materials Science and Engineering A* **351**, 244-257 (2003/6/25, 2003).

84. R. Panat, S. Zhang, K. J. Hsia, *Acta Materialia* **51**, 239-249 (2003/1/8, 2003).

85. M. W. Chen, M. L. Glynn, R. T. Ott, T. C. Hufnagel, K. J. Hemker, *Acta Materialia* **51**, 4279-4294 (2003/8/15, 2003).

86. R. C. Pennefather, D. H. Boone, *Surface and Coatings Technology* **76-77**, 47-52 (1995/11, 1995).

87. D. R. Mumm, A. Evans, *Acta Materialia* **48**, 1815-1827 (2000).

88. D. R. Mumm, A. G. Evans, I. T. Spitsberg, *Acta Materialia* **49**, 2329-2340 (2001/7/17, 2001).

89. I. T. Spitsberg, D. R. Mumm, A. Evans, *Materials Science and Engineering A* **394**, 176-191 (2005).

90. M. Y. He, J. W. Hutchinson, A. Evans, *Acta Materialia* **50**, 1063-1073 (2002).

91. H. E. Evans, M. P. Taylor, *Oxidation of Metals* **55**, 17 (2001).

92. E. A. G. Shillington, D. R. Clarke, *Acta Materialia* **47**, 1297-1305 (1999/3/10, 1999).

93. B. C. Wu, E. Chang, S. F. Chang, D. Tu, *Journal of American Ceramic Society* **72**, 212 (1989).

94. E. Y. Lee, R. R. Biederman, R. D. Sisson, *Materials Science and Engineering A* **121**, 467-473 (1989).

95. J. I. Eldridge, C. M. Spuckler, J. A. Nesbitt, K. W. Street, *Ceramic Eng. Sc. Proc.* **24**, 511-516 (2003).

96. X. Chen, G. Newaz, X. Han, paper presented at the 2001 ASME Int. Mech. Eng. Congress, New York, NY 2001.

97. G. Newaz, X. Chen, *Surface and Coatings Technology* **190**, 7-14 (2005/1/3, 2005).

98. B. Jayaraj, V. H. Desai, C. K. Lee, Y. H. Sohn, *Materials Science and Engineering A* **372**, 278-286 (2004/5/15, 2004).

99. B. Jayaraj, S. Vishweswaraiah, V. H. Desai, Y. H. Sohn, *Surface and Coatings Technology* **177-178**, 140-151 (2004/1/30, 2004).

100. D. R. Clarke, *Current Opinion in Solid State and Materials Science* **6**, 237-244 (2002/6, 2002).

101. Q. Ma, D. R. Clarke, *Journal of the American Ceramic Society* **76**, 1433-1440 (1993).

102. M. Gell, S. Sridharan, M. Wen, E. Jordan, *International Journal of applied ceramic technology* **1**, 316-329 (2004).

103. K. W. Schlichting *et al.*, *Materials Science and Engineering A* **291**, 68-77 (2000/10/31, 2000).

104. R. J. Christensen, D. M. Lipkin, D. R. Clarke, *Applied Physics Letters* **69**, 3754-3756 (9 December 1996, 1996).

105. Y. H. Sohn, K. Vaidyanathan, M. Ronski, E. H. Jordan, M. Gell, *Surface and Coatings Technology* **146-147**, 102-109 (2001/0, 2001).

106. L. Xie, Y. Sohn, E. H. Jordan, M. Gell, *Surface and Coatings Technology* **176**, 57-66 (2003/0, 2003).

107. N. E. Paton, K. S. Murphy, D. R. Clarke, in *United States Patent*. (2000).

108. D. M. Lipkin, D. R. Clarke, *Journal of Applied Physics* **77**, 1855-1863 (1 March 1995, 1995).

109. J. He, D. R. Clarke, *Journal of the American Ceramic Society* **80**, 69-78 (1997).

110. J. He, D. R. Clarke, *Journal of the American Ceramic Society* **78**, 1347-1353 (1995).

111. D. M. Lipkin, H. Schaffer, F. Adar, D. R. Clarke, *Applied Physics Letters* **70**, 2550-2552 (12 May 1997, 1997).

112. X. Peng, D. R. Clarke, *Journal of the American Ceramic Society* **83**, 1165-1170 (2000).

113. J. A. Nychka, D. R. Clarke, *Surface and Coatings Technology* **146-147**, 110-116 (2001/0, 2001).

114. J. A. Nychka *et al.*, *Surface and Coatings Technology* **163-164**, 87-94 (2003/1/30, 2003).

115. Y. H. Sohn, K. Schlichting, K. Vaidyanathan, E. Jordan, M. Gell, *Metallurgical and Materials Transactions A* **31A**, 2388-2391 (September 2000, 2000).

116. A. Selcuk, A. Atkinson, *Materials Science and Engineering A* **335**, 147-156 (2002/9/25, 2002).

117. A. Selcuk, A. Atkinson, *Acta Materialia* **51**, 535-549 (2003/1/22, 2003).

118. D. M. Lipkin, D. R. Clarke, M. Hollatz, M. Bobeth, W. Pompe, *Corrosion Science* **39**, 231-242 (1997).

119. W. J. Moore, *Seven solid states* (W.A.Benjamin, Inc., New York, 1967).

120. J. H. Eggert, K. A. Goettel, I. F. Silvers, *Physical Review B* **40**, 5724-5732 (1989).

121. S. L. Wunder, P. E. Schoen, *Journal of Applied Physics* **52**, 3772-3775 (1981).

122. L. Grabner, *Journal of Applied Physics* **49**, 580-583 (1978).

123. A. A. Kaplayanskii, A. K. Przhevuskii, R. B. Rozenbaum, *Sov. Phys. Sol. State* **10**, 1864 (1969).

124. A. L. Schawlow, D. L. Wood, A. M. Clogston, *Physical Review Letter* **3**, 271-273 (1959).

125. R. A. Miller, *Journal of the American Ceramic Society* **67**, 517-521 (1984).

126. R. A. Miller, *Journal of Engineering for Gas Turbines and Power* **109**, 448-451 (October 1987, 1987).

127. E. H. Jordan *et al.*, paper presented at the Autotestcon, Valley Forge, PA 2001.

128. E.Dorre, H.Hubner, *Alumina-Processing, Properties and Applications*, (Springer-Verlag, New York, 1984)

129. G.M. Kim, N.M. Yanar, E.N. Hewitt, F.S. Pettit, G.H. Meier, *Scripta Mater.* **46,** 489-495 (2002)

130. V. Lughi, V.K. Tolpygo, D.R. Clarke, *Materials Science and Engineering A* **368,** 212-221 (2004)

131. D. Michie, D.J. Spiegelhalter, C.C. Taylor, *Machine Learning, Neural and Statistical Classification*, (Ellis Horwood, 1994), Chap. 7

132. J. Shen, *Thermal Barrier Coatings and Metallic Coatings with Improved Durability*, M.S. Thesis, University of Connecticut, Storrs, CT 2005

133. J.M. Ambrico, M.R. Begley, *Eng. Frac. Mech.* **70**, 1721, (2003)

134. J. W. Hutchinson, Z. Suo, in *Advanced Apply Mechanics,* J. W. Hutchinson, Y.Y. Wu Ed., (1992) pp. 63-191.

135. V.K. Tolpygo, D.R. Clarke, in: *Elevated Temperature Coatings: Science and Technology IV* , N.B. Dahotre, J.M. Hampikian, J.E. Morral (Eds.), (TMS; 2001) pp.93-108

136. S. Sridharan, thesis to be finished

137. R.G. Munro, G.J. Piermarini, S. Block, W.B. Holzapfel, *J. Appl. Phys.* **57**, 165-169, (1985)

138. L.H. Tsoukalas, R.E. Uhrig, *Fuzzy and Neural Approaches in Engineering,* (John Wiley & Sons Inc., New York, 1997)

139. www.mathworks.com

140. Y. Bar-Shalom, X.R. Li, *Estimation and Tracking: Principles, Techniques and Software*, (Artech house, Dedham, MA, 1993)

141. N. Goldfine, D. Schlicker, Y. Sheiretov, in *Monitoring and Diagnostics Applications: ASME Turbo Expo Land, Sea & Air*, pp.1-9, (2001)

ENDWALL COOLING WITH ENDWALL CONTOURING AND LEADING EDGE FILLET

DOE Award Number: DE-FC26-02NT41431

UTSR Project Number: 02-01-SR098

Final Report
March 2007

Principal Investigator
Sumanta Acharya, Professor
acharya@me.lsu.edu

Collaborators
Gazi Mahmood, Ph.D., Research Associate
Arun Saha, Ph. D., Research Associate
Ross Gustafson, M. S student
James Post, M. S student

Turbine Innovation and Energy Research (TIER) Center
Louisiana State University
Baton Rouge
Louisiana 70803

Administrative Office
James Bates, Director
Office of Sponsored Research
Louisiana State University
Baton Rouge, LA 70803

DISCLAIMER

ABSTRACT

The potential of contouring the end wall and/or using a leading edge fillet to control secondary flows and heat transfer in blade passages is being investigated. Secondary vortical flows in blade passages enhance heat transfer to the end wall, and interfere with the film coolant jet. The goal of the ongoing project is to explore specific strategies of reducing in-passage secondary flows (contouring the end wall, placing a leading edge fillet, and strategically locating coolant injection) so that aerodynamic losses and thermal loading on the end wall is minimized.

The results reported here is the work accomplished through December 2006. The work, starting in Fall 2002, was chronologically accomplished by first exploring the role of leading edge fillets, then examining the role of in-passage contouring, and finally adding film cooling. The work with the leading edge fillets is already in the published literature (J. of Turbomachinery, J Heat Transfer and J. of Fluids Engineering). In this report we will focus attention on the results that provide detailed measurements and simulations in the linear blade passage employing a ***3-Dimensional non-axisymmetric contoured endwall with and without the full-coverage film cooling***. This data is obtained from: (i) experimental measurements with no film cooling, (ii) experimental measurements with film cooling, and (iii) computational simulations with no film cooling. Also, included are the numerical results showing optimization of the non-axisymmetric contoured endwall profile. The data with the film cooling reported here are measured with different inlet blowing ratios ranging from 1.0 to 2.4. None of the results reported here have, as yet, appeared in journals except the results with the flat endwall used here for comparison purposes only. However, several ASME Turbo Expo publications in 2006 and 2007 have covered some of these issues. For completeness, we will also present the earlier results with leading edge fillets, re-cast in the form of comparisons with the contoured endwall results. The ongoing efforts toward the end of the study focused on high speed tests.

TABLE OF CONTENTS

LIST OF GRAPHICAL MATERIALS

INTRODUCTION

Lean premixed combustors used in modern industrial gas turbine systems have relatively flat temperature profiles at the combustor exit. Thus, effective cooling strategy for the end walls has become increasingly important. Film cooling of the end walls is commonly employed. However, strong secondary flows in the vane/blade passage interfere with the injected coolant, and make effective cooling of the endwall a difficult problem. The secondary flows in the passage are driven by the development of the horseshoe vortex at the leading edge and the strong pressure gradients in the vane/blade passage. Therefore, for effective cooling of the endwall region, strategies for reducing or eliminating the passage secondary flows must be explored. The goal of the present research was to investigate the strategies of endwall contouring and using leading edge fillets to suppress passage secondary flows. The work explores both uncooled and film-cooled end walls. Experimental and computational results have been obtained for uncooled endwalls (flat end wall, filleted leading edge, and contoured end wall) and for film cooled endwalls (flat end walls, non-axisymmetric 3D-endwall and filleted leading edge). The results convincingly demonstrate significant reductions in aerodynamic loss with the 3D endwall contouring and reductions in the endwall Nusselt numbers with both leading edge and endwall contouring. These favorable results are demonstrated to be a consequence of the reduction in size and strength of the passage secondary flows effected by the contouring.

The end-goal of the project was to provide the turbine designer improved strategies for reducing the heat load to the endwall, and lowering aerodynamic losses. The results from the work provide guidance for improved endwall designs leading to the lower utilization of coolant air, greater aerodynamic efficiency, and greater reliability. Results obtained clearly indicate the potential of realizing the benefits in reducing losses and end wall thermal load, and should provide impetus to turbine designers in pursuing this technology.

EXECUTIVE SUMMARY

The potential of contouring the end wall and/or using a leading edge fillet to control secondary flows and heat transfer in vane/blade passages is being investigated. Secondary vortical flows in vane/blade passages enhance heat transfer to the end wall and interfere with the film coolant jet. The goals of the ongoing project are to explore specific strategies (contouring the end wall, placing a leading edge fillet, strategically locating coolant injection) so that secondary flows are minimized. Specific tasks include:

- Utilization of validated CFD to explore detailed flow physics, and to optimize leading edge fillet and end wall contouring parameters. The results of these parametric investigations are utilized in defining the experimental test matrix.
- Investigation of the effects of end-wall contouring on reducing secondary flows and thermal loading in the blade passage without end-wall cooling.
- Investigation of the effects of full coverage film cooling with strategically located film holes in the flat endwall in the blade passage.
- Investigation of the effects of end-wall contouring on reducing secondary flows in the vane/blade passage with film cooling. For the blade, non-axi-symmetric contouring is being explored, while for the vane, axi-symmetric contouring is being explored.
- To validate selected leading-edge contouring (fillet) configurations in a hot-cascade facility with realistic conditions for temperature ratios, turbulence conditions and pressure ratios.

Extensive measurements and computations have been made in an atmospheric cascade facility with a blade geometry in the passage; more limited studies have been done in a pressurized cascade facility with vane geometry in the passage. Present experimental results include qualitative and quantitative flow structures in the blade passage as well as flow temperature and endwall Nusselt number measurements in the blade passage. The present results include data with no film cooling flow and with full coverage film cooling flow at the non-axisymmetric endwall. The endwall geometry employed is contoured in both the axial and the pitchwise direction forming the non-axisymmetric profile. Numerical results have been obtained for several configurations of the non-axisymmetric contoured endwall. The optimum configuration based on the computational results was selected to be investigated experimentally.

The flow structure with the contoured endwall in the blade passage is determined with smoke flow visualization, and is quantified with five-hole pressure probe, and cross-wire anemometer measurements. Heat transfer coefficients are measured from infrared images in conjunction with thermocouples. Results indicate that the contoured endwall reduces total pressure loss and end wall heat transfer coefficients across the passage compared to the baseline case. Through flow visualization and flow measurements one can conclude that the pressure and suction side leg of the horseshoe vortex and consequently the passage vortex reduce in size and strength with the contoured endwall. The total pressure losses are also reduced significantly compared to the baseline flat endwall case when the full coverage film cooling flow is introduced at the contoured endwall. Also, compared to the case of the contoured endwall without any film flow, the total pressure losses are lower when the inlet blowing ratios are greater than 1.60 at the film cooled contoured endwall. Measurements

with contouring of the leading edge also show significant and comparable benefits in reducing the end wall heat transfer coefficients.

Numerical simulations show that heat transfer coefficients decrease significantly in the leading edge area and in the throat area with the optimized non-axisymmetric endwall contouring compared to the heat transfer at the flat endwall profile. Computations with contoured endwall are consistent with the measurements.

PROJECT DESCRIPTION

Gas Turbine Research Need

Secondary flows in blade passages contribute to increased aerodynamic losses, and increased heat transfer coefficients. These contribute to reduced efficiencies and increased cooling requirements. Therefore there is a clear need in the gas turbine community to reduce secondary flows. The ongoing research addresses this need through strategies aimed at reducing the formation and development of the horseshoe and passage vortices in the flow.

Experimental and Analytical Approach

The research included both the experimental and computational effort. Both approaches are described in detail later. The experimental effort was performed on cascade facilities described below:

- An atmospheric cascade facility, with scaled up E^3 blades, which permits detailed flow measurements and relatively easy modifications to accommodate a variety of end wall and leading edge contours. The detailed flow measurements are necessary for model validation in the computational effort. Measurements made include velocity measurements (using hot-wire anemometry, and five-hole pressure probe), heat transfer measurements (using Infra-red Imaging), flow temperature measurements (using a thermocouple probe), and surface static pressure measurements.
- A pressurized hot-cascade facility, with vanes, which will permit heat transfer and pressure measurements for a contoured end wall section with end wall film cooling. End wall heat transfer data will be collected with IR based techniques.

The computational work primarily involved validated RANS approaches for predicting the in-passage flow and heat transfer. The goal of the computational effort was to make a detailed parametric study with different endwall and leading edge contours that enablde a more limited set of cases to be studied experimentally. Further, the simulations provide additional information to help assess the flow and heat transfer behavior.

Expected Benefits

The goal of the project is to provide the turbine designer improved strategies for reducing the heat load to the end wall, and lowering aerodynamic losses. The strategies to be explored include contouring the end wall, placing a fillet along the leading edge of the blade, and strategically locating film cooling injection holes in the endwall. The results from the work will provide guidance for improved endwall designs leading to the lower utilization of coolant air, greater aerodynamic efficiency, and greater reliability.

Accomplishments

This report documents the results from the work accomplished during the 2003-2006 period. The following major activities were pursued during this time period:

Three Dimensional Non-axisymmetric Endwall Geometry-Atmospheric Cascade

- Flow-visualization of the passage vortex.

- Five hole probe measurements and hot-wire anemometer measurements at different axial chord planes for mapping the flow field with and without film cooling flow.
- Infrared thermal images of the heated endwall to obtain heat transfer coefficients.
- Validation of CFD results that provide optimization of the contoured endwall configuration.
- Setting and modifications of the blade cascade test section to measure the film cooling effectiveness with film injections at the contoured endwall and at the flat endwall with leading edge fillets in blade passage.

Vane Cascade Geometry-Pressurized Cascade

- Construction of the vane cascade test facility with the E^3 first stage vane (scale 1:1) in a blow down high speed flow channel of cross section 8.93 cm by 3.81 cm. The cascade includes two passages with three vanes and is designed for the inlet to exit pressure ratio of about 2:1. The two-dimensional axi-symmetric contour endwall shape from the E^3 design and from computations is located upstream of the cascade inlet.
- A coolant loop that will supply coolant air to the vane test section has been completed. The loop is designed for providing the range of inlet blowing ratios from 1.0 to 2.0 and the coolant to main stream density ratio greater than 1.0.
- Necessary instrumentation (pressure taps, thermocouples, IR window, etc.) have been installed.
- The two passages in the cascade are aerodynamically balanced to simulate a periodic condition of the flow.
- Film cooling effectiveness measurements made in a high speed vane cascade facility.

Hot Vane-Cascade Facility-Pressurized, Hot Cascade

- Lab renovation and installation of the required air handling capability needed for the hot cascade facility has been completed. The renovated labs have capability of 2600 SCFM and 150 psig pressure. In addition, a 200 psig natural gas line, and a 200 psig compressed water line has been installed for the pressurized cascade.
- The various components of the hot cascade facility and associated instrumentation have all been delivered by General Electric and the hot cascade ahs been assembled.
- Preliminary pressure data on the hot cascade has been completed.

Computations

- Numerical gridding and calculations of the selected vane/blade profile with the three dimensional endwall contours using GridPro and Fluent have been completed.
- Parametric explorations were performed with the numerical code for different three-dimensional endwall contours and leading edge contours in the GE-E^3 blade/vane passage. Eight different endwall contour cases were completed with incompressible flows. Several fillet cases were also studied.
- A final recommendation of a three-dimensional endwall contour and a leading edge contour was made for the experimental test program.

EXPERIMENTS & RESULTS

Atmospheric Cascade Facility

The experimental data presented here are obtained in a closed loop cascade facility that operates in a suction mode under atmospheric conditions. A schematic of the test facility is shown in Fig. 1(a). The construction of the facility allows air to flow through a two-dimensional nozzle of contraction ratio 3.4: 1, then through a smooth developing inlet channel of rectangular cross-section of aspect ratio 1.36:1 before entering the test section. The test section accommodates three two dimensional blades forming two blade passages. The two passages are made aerodynamically periodical by balancing the mass flow rate in the two passages by suitably positioning the two tailboards on the side blades with a traverse mechanism. The blade profiles are based on the hub side section of the GE-E^3 cascade geometry. The blade profile and passage configuration used in the study are scaled up ten times the actual blade geometry. The blades are oriented such that their stagnation planes are parallel to the mean flow stream in the inlet channel. Table 1 provides the geometry of the present cascade section and the flow conditions employed for the measurements. In the present arrangement, the data are measured with a flat smooth endwall at the tip side and a non-axisymmetric contoured endwall at the hub side of the blade cascade in the test section.

As shown in Figs.1 (a) and (b), the top wall of the test section has slots parallel to the passage inlet at different axial locations to allow access of the hot-wire probe and five-hole subminiature probe. During the heat transfer measurements on the bottom end-wall, this top wall is replaced by another top wall of the same geometry with cut out sections for infrared image viewing. The bottom end-wall and the blade profiles are instrumented with thermocouples, foil heaters, and static pressures taps. The 0.30 mm diameter pressure taps are drilled in 1.65 mm diameter stainless steel tubes that are mounted flush in the grooves on the blade profile. The boundary layer suction bleeds in the top, bottom, and side walls of the inlet channel are adjusted to provide uniform flow conditions in the channel. A passive turbulence grid system made of cylindrical rods of diameter 1.22 cm is located 0.61 hydraulic diameter downstream of the nozzle exit or 4.12 chord upstream from the center blade stagnation point.

Pressure signals from the tubes and five-hole pressure probe are obtained in a HP3497A and in an Agilent 34970A data acquisition control unit through Validyne and Omega differential transducers. The five-hole subminiature probe, that has a tip diameter of 2.40 mm, is custom fabricated. Data acquisition rate with the five-hole probe is 240 Hz over a period of 60 sec through an Agilent 34970A™ data acquisition control unit. The hot-wire sensors employed in the measurements are TSI™ model constant cross-film anemometers. Signals from the hot-wire probes are obtained in a IFA-300™ acquisition control unit. The data are acquired at the rate of 5.0 kHz over 13.1 sec and processed through the manufacturer supplied software.

Fig. 1(b) shows the locations of the flow measurement planes along with the coordinate systems employed in the cascade facility. The right hand (X_G,Y_G,Z_G) corresponds to the global coordinate system originated at the furthest upstream point on the center blade. The (X,Y,Z) then corresponds to the local coordinate systems inside the blade passages. The local velocity components (U,V,W) follow the local coordinate system (X,Y,Z). The measurement planes inside the passages are normal to the X_G- or X-direction.

Non-axisymmetric 3-Dimensional Contour Endwall

The non-axisymmetric contoured wall profile employed at the bottom endwall for the present measurements and computations in the blade passage is shown in Fig. 2. The top endwall remains always flat without any contouring as mentioned. The profile height varies in the pitchwise direction as well as in the axial direction. The design of the profile is based on the concept proposed in Ref. [1-5]. Several endwall profiles with the pitchwise profile-height and the axial profile-height varied by independent sinusoidal profiles were simulated numerically. The final profile chosen for the experimental study was based on the best numerical results that provide the lowest total pressure loss and endwall heat transfer along the passage.

Fig. 2(a) shows the independent sinusoidal curves chosen separately for the pitchwise and axial variations of the selected endwall profile employed for the experimental measurements. Height=0.0 mm refers to the location of the baseline flat endwall. Pitchwise height in Fig. 2(a) is flattened near the pressure side (for manufacturing ease) and is the lowest near the suction side where the two sine curves coincide. The two profile variations are then simply multiplied to obtain the non-axisymmetric profile heights shown in Fig. 2(b). The maximum height of the complete profile is located slightly downstream of the leading edge. The lowest trough in the profile is located across the maximum height in the pitchwise direction and near the suction side. The entire endwall was fabricated on a stereo-lithography printer in the Mechanical Engineering Department at LSU.

Upstream Flow Conditions of the Test Section

The reference properties for normalizing the measured quantities in the passage are measured across a plane parallel to the passage inlet. Computational data at the same location are used to normalize the numerical results. This reference plane is located 0.33C upstream of the passage inlet. The reference properties are then obtained from the arithmetic mean of the local data in the reference plane and shown in Table 2. In the table, conditions below atmospheric pressure refer to negative gage values.

Surface Static Pressure Coefficeint

Surface static pressures are measured on the blade surface and on the contoured endwall itself. Figure 3 presents the surface static pressure coefficients on the blade surface. The baseline data are included for comparison. Blade surface static pressure coefficients are determined from the equation as follow.

$$C_p = \frac{P_{stat} - P_{stat,o}}{0.5 * \rho_{air} * U_{ref}^2} \tag{1}$$

In the equation, P_{stat} is the measured wall static pressure at Y/S=0.333, $P_{stat,o}$ is the measured wall static pressure on the leading edge at Y/S=0.333, ρ_{air} is air density, and U_{ref} is reference velocity from Table 2. The surface coordinate s/C originates from the blade trailing edge at the suction side and the stagnation point is located at s/C~1.50. Note, that the Y/S=0.0 for the endwall contour data refers to the location of the baseline endwall. The peak and trough locations on the contour endwall are located at Y/S=0.096 and -0.101 relative to the baseline endwall location. The C_p values in Fig. 3 are about the same for the endwall contour case and

the baseline case on the pressure data. The C_p values further downstream on the suction side at s/C<0.90 for the contoured endwall are nearly identical or only slightly higher than for the baseline. This illustrates that the effects of the endwall profile on the flow in the free stream inviscid regions are very weak.

Endwall static pressure coefficients $C_{p,e}$ are presented in Fig. 4 and are determined from the following equation.

$$C_{p,e} = \frac{P_{s,w} - P_{stat,r}}{0.5 * \rho_{air} * U_{ref}^2} \quad (2)$$

Here, $P_{s,w}$ is endwall static pressure and $P_{stat,r}$ is the reference static pressure from Table 2. The difference in $C_{p,e}$ from the pressure side to suction side reduces significantly for the contoured endwall as compared to the baseline. For example, the maximum differences in $C_{p,e}$ at X_G/C_{ax}=0.20 and 0.70 between the pressure side and suction side are 1.60 and 1.40, respectively, for the baseline. At the same locations, the differences are 0.90 and 1.20, respectively, for the contoured endwall. Such differences in $C_{p,e}$ in the pitchwise direction for the contoured endwall significantly decrease upstream of the throat at X_G/C_{ax}<0.70. This can be considered a significant achievement toward weakening the secondary flows near the endwall. The cross-pitch pressure gradient is one of the primary sources for the development and energizing of the passage vortex near the endwall upstream of the throat [6-8].

Instantaneous Flow Visualization

Qualitative comparison of the secondary flow structure i.e., vortex location, size, and shape for the baseline and contoured endwall case are provided in the instantaneous images of flow visualization with smoke in Figs 5 and 6. The smoke in the channel is generated by applying coats of toy train liquid smoke on Nichrome wires (diameter 24 gage, 0.051 cm), which are then heated by passing controlled dc current through them. The wires are located about 1.5C upstream of the passage inlet and span across the width of the inlet channel. When air flows through the channel, plane sheets of white smoke are generated from nine wires that are placed both inside and outside the boundary layer upstream of the blade passage. As the sheets of smoke approach the passage, they contour according to the shape and size of the secondary flows. A plane sheet of light generated with a 2000 watts theatrical lamp shinning through a thin slot over the channel top wall illuminates the smoke patterns inside the passage. The images are captured and recorded by a SONY DFW-V500 digital video camera and image capturing software provided by the camera manufacturer. Images are captured at a frame rate of 60 Hz with 640x480 lines of resolution. The images are then further enhanced in Adobe Photoshop™ v8.10. The relative positions of the camera and light plane where the smoke flow pattern is illuminated are shown in Fig. 5. The camera focuses approximately normal to the light planes. The relative position of the camera changes as the location of the light plane changes. In Figs. 5 and 6, the endwall is located at the bottom, the pressure side is on the right, and the suction side is on the left of the image. Images in the two light planes PS1 and PS4 are presented here. More flow visualization instant images in other light plane locations were presented in the Semi-Annual Report for May 2004-December 2004 of the same project.

Figure 5 shows the secondary vortex patterns in the pitchwise plane PS1 which is located at X_G/C_{ax}=0.167 and slightly downstream the blade stagnation line. In the baseline image, two large vortex structures originating from the pressure side leg of the leading edge horseshoe

vortex can be seen midway between the pressure side and suction side. This vortex pair rotates in the clockwise sense and periodically merge together to form one large vortex with the same sense of rotation. For the contoured endwall, the clockwise rotating vortex structures, also identified as originating from the pressure side leg vortex pair, are located just above the endwall but the individual vortices are separated far apart-one appears near the pressure side and the other is seen near the suction side. Their size is reduced significantly compared to the baseline vortex pair. Unlike the baseline case, this pair remains separated at relatively the same location. The pressure side leg vortex pair for the contour endwall case is smaller because the endwall structure along the leading edge plane displaces the boundary layer fluid reducing the boundary layer thickness and leading edge horseshoe vortex size. This occurs as the flow accelerates along the leading edge plane as the endwall height increases toward the leading edge (refer to Fig. 2(b)) forcing the incompressible fluid to be removed from the boundary layer due to the continuity. The clockwise rotating vortex pair of the pressure side leg remains separated on the contoured endwall in Fig. 5 as one horseshoe vortex forms at the leading edge of the contour endwall and the second one forms far apart at the junction of the blade leading edge and endwall. The smaller pitchwise pressure gradient and consequently the weaker pitchwise cross flow for the contour endwall case than the baseline are not strong enough to bring the vortex pair close together as the vortices advect inside passage along with the cross flow. Also note in Fig. 5, the presence of a small counter-clockwise rotating vortex on the left and adjacent to the large vortex pair for the baseline case. The size of this single vortex is nearly one-third of the large vortex pair for the baseline. This is the suction side leg of the leading edge horseshoe vortex. The suction side leg vortex also appears above the contoured endwall but is located just above pressure side leg vortex near the suction side. The suction side leg vortex is comparable in size for both the endwall cases.

The visualization plane PS4 (nearly perpendicular to both the pressure and suction side) is located near the passage throat region. The baseline case shows two large structures of the passage vortex system rotating clockwise which again periodically merge into one large vortex having the same sense of rotation. Both the vortices are located near the suction side of the passage and little evidence of any smoke is present near the pressure side. This occurs as the strong cross flow and high pressure gradient at the flat endwall region sweep the pressure and suction side leg vortices toward the passage suction side as they travel inside the blade passage [6, 8]. Even at such a far downstream location as PS4, the contoured endwall in the left image of Fig. 6 shows the two pressure side leg vortex structures rotating clockwise are still far apart. One of the legs is situated on the endwall where the flat profile starts to dip down near the pressure side while other is situated just above the lowest location of the endwall near the suction side. This further illustrates that the contoured endwall reduces the pressure gradient and cross flow from the pressure side to suction side. Near the suction surface for the contoured endwall case of Fig. 6, the curling smoke pattern located above the pressure side leg vortex is the suction side leg vortex that rotates counter-clockwise. In comparing the sizes of the clockwise rotating vortices, the vortices above the contour endwall are nearly half of those above the flat baseline endwall.

Time-averaged Secondary Flow Field (No Coolant Flow)

The Time-averaged secondary flow field is measured for the contoured endwall case at four pitchwise planes (Plane 2, 3, 4, 5) located at four axial distances as shown in Fig. 1(b). The

planes are parallel to the inlet and exit planes of the passage. Flow field measurements in the four planes are obtained at a reference velocity of 10.10 m/s. The measured quantities provide axial development of the total pressure loss, axial vorticity, pitchwise cross flow velocity, and streamwise turbulence intensity along the passage. These data are presented in the non-dimensional forms in this section along with the data for the baseline case. Total pressure loss coefficient $C_{pt,loss}$ is determined from the following equation. In this equation, P_t is the measured local total pressure and $P_{tot,r}$ is the reference pressure from Table 2.

$$C_{pt,loss} = \frac{P_{tot,r} - P_t}{0.5 * \rho_{air} * U_{ref}^2} \tag{3}$$

The axial vorticity Ω_x is determined from the derivatives of the spline fits on the local velocity data and from the following equation. V is velocity in spanwise direction and W is velocity in pitchwise direction.

$$\Omega_x = \frac{\partial W}{\partial Y} - \frac{\partial V}{\partial Z} \tag{4}$$

Figure 7 shows streamwise turbulence intensity in the plane at X_G/C_{ax}=0.085 for the baseline and contour endwall. The turbulence intensity values are much higher just above the baseline endwall for Z/P>-0.40 compared to the values at the same location for the contoured endwall. The high turbulence intensity just above the endwall is caused by the pressure and suction side leg vortices at this location. The data in Fig. 7 suggest that the vortices are much weaker and smaller for the contoured endwall. The streamwise turbulence intensity at X_G/C_{ax}=0.916 near the exit plane in Fig. 8 shows that it decreases significantly at 0.10<Y/S<0.22 and -0.65<Z/P<-0.55 with the contoured endwall as compared to the baseline case. The passage vortex at this location near the suction side (Fig. 8) causes the high turbulence intensity. Clearly, the passage vortex is weaker for the contoured endwall as indicated by the smaller magnitudes of the turbulence intensity.

Normalized axial vorticity $\Omega_x C/U_{ref}$ for the baseline and contoured endwall at X_G/C_{ax}=0.085 is compared in Fig. 9. The high negative $\Omega_x C/U_{ref}$ between -0.70<Z/P<-0.55 and positive $\Omega_x C/U_{ref}$ between -0.45<Z/P<-0.33 above the baseline endwall indicate strong suction side leg and pressure side leg vortex regions. Such high negative or positive $\Omega_x C/U_{ref}$ region is absent or much smaller above the contoured endwall in Fig. 9 indicating weaker and smaller vortex structures. Normalized axial vorticity near the trailing edge shown in Fig. 10 indicates that a much larger region and higher magnitude of $+\Omega_x C/U_{ref}$ is present above the baseline endwall than above the contoured endwall near the suction side. The high $\Omega_x C/U_{ref}$>6 region refers to the passage vortex location (contour level arbitrarily selected), and clearly, the contour endwall reduces the size and strength of this vortex significantly. However it should be noted that because of the three dimensional nature of the passage vortex, the center location and magnitude of axial vorticity are dependent upon the axis of rotation of the passage vortex. Thus, a quantitative conclusion on the vortex center or core location based on the results in Fig. 10 should be done with caution. A small negative $\Omega_x C/U_{ref}$ region exists above the passage vortex region near the suction side and represents the suction side leg of the horseshoe vortex. This negative region for the contoured endwall is about half the size of that for the baseline.

Pitchwise velocities indicating the cross flow from the pressure side to suction side are compared in Figs. 11 and 12 with negative magnitudes of W/U_{ref} velocity directed toward the suction side. Near the endwall at X_G/C_{ax}=0.424 in Fig. 11, the baseline case has a larger and

stronger cross flow region with W/U_{ref} of lower negative magnitudes compared to the contoured endwall case. Near the contoured endwall in Fig. 11 the cross flow reduces because of the smaller surface pressure gradient as shown in Fig. 4. Normalized pitchwise velocities at X_G/C_{ax}=0.916, shown in Fig. 12, are much larger in magnitude for the contoured endwall case than for the baseline near the suction side. Pitchwise velocity reduces near the suction side when it encounters the clockwise rotating passage vortex. Stronger pitchwise velocities exists near the suction surface up to Y/S = 0.10. This indicates a larger region of cross-flow. As this cross-flow region approaches the suction surface its spanwise component becomes stronger in the positive Y/S direction, pushing the passage vortex up. The contoured endwall in Fig. 12 also shows a smaller cross flow region with W/U_{ref}<-1.30 between -0.82<Z/P<-0.30 compared to the baseline case. This causes the passage vortex for the contoured endwall to be located lower than that for the baseline case.

Flow yaw angles in Figs. 13 and 14 show the turning of the cross-flow relative to the axial direction. Positive and negative yaw angles indicate the flow turning counter-clockwise and clockwise, respectively, from the +X direction as shown in Fig. 1(b). Thus, the higher yaw angles indicate a stronger cross-flow component in the pitchwise direction. The yaw angles at X_G/C_{ax}=0.424 in Fig. 13 decrease by about 15 deg, and at X_G/C_{ax}=0.916 in Fig. 14 the yaw angles decrease by about 20 deg near the contoured endwall relative to those near the baseline endwall. The pitchwise component of the cross-flow in the endwall boundary layer region funnels fluids into the passage vortex and strengthens it (refer to Figs. 10 to 12). Thus, the results in Figs. 13 and 14 signify that the secondary flows for the contoured endwall must have weakened. Also, note that the yaw angle magnitudes in the inviscid regions of Figs. 13 and 14 are more uniform in the pitch-direction for the contoured endwall than for the baseline. Particularly, the results at X_G/C_{ax}=0.916 in Fig. 14 show a significant improvement with the contoured endwall with more uniform exit flow angles.

Figure 15 compares the total pressure loss coefficients at X_G/C_{ax} = 0.085 for the baseline and contoured endwall. The left side of the figure is the suction side and the right side for the baseline case is located roughly at the pitchwise middle position in the plane. A higher $C_{pt,loss}$ region exists just above the endwall near the suction side between -0.65<Z/P<-0.45 for the baseline than for the contoured endwall. This region indicates the presence of a strong suction side leg of the horseshoe vortex for the baseline. $C_{pt,loss}$ for the contoured endwall are about 29.0% smaller in the region corresponding to the suction side leg vortex. The total pressure loss coefficient $C_{pt,loss}$ contours in Fig. 16 show that the high loss magnitudes representing the passage vortex are elevated from the endwall and shift closer to the suction side. This occurs as the passage vortex is driven by the cross flow. Here also, the contoured endwall reduces the size and magnitudes of the high $C_{pt,loss}$ in the passage vortex. The $C_{pt,loss}$ values are about 37% less in the core of the passage vortex region for the contoured endwall than for the baseline.

Measured flow field downstream of the cascade in the pitchwise plane at X_G/C_{ax}=1.214 is presented in Figs.17 and 18. The plane extends one complete pitch in the pitchwise direction. The complete structure of the passage vortex can be seen in the $\Omega_x C/U_{ref}$ and turbulence intensity contours in the figures between Y/S=0.10 and 0.30. The magnitudes of $\Omega_x C/U_{ref}$ >0.0 region in Fig. 17, which is caused by the passage vortex, is considerably reduced by the contoured endwall. The negative $\Omega_x C/U_{ref}$ regions above the passage vortex and about Z/P=-0.37 above the endwall represent the suction side leg/induced vortex and corner vortex[6]. These vortex structures are also reduced by the contoured endwall. In Fig. 17, the contour region of $-6<\Omega_x C/U_{ref}<-2$ is caused by the trailing edge wake. In Fig. 18, the streamwise

turbulence intensity greater than 9% about Z/P=-0.37 is caused by the passage vortex and wake for the contoured endwall case. The high turbulence intensity just above the endwall is located at the same location where the high axial vorticity for the corner vortex occurs. The highest turbulence intensity between Y/S=0.15 and 0.30 is located at the core of the passage vortex where the total pressure losses are found to be the highest for the contoured endwall.

Non-dimensional Flow Temperature (No Coolant Flow)

Non-dimensional temperature profile of the air stream along the contoured endwall passage is shown in Fig.19. The contour values θ are determined from the following equation where $T_{o,in}$

$$\theta = \frac{T - T_{o,in}}{0.5 * U_{ref}^2 / C_p} \tag{5}$$

is the reference temperature from Table 2, T is local air stream temperature, and C_p is specific heat of air at constant pressure. The air stream in the passage is heated by heating the bottom endwall both upstream and inside the passage with a constant heat flux boundary condition of magnitude 1600 W/m^2. Copper strips of width 5.0 mm soldered in a serpentine pattern are laid on the contoured endwall at 1.0 mm spacing and then are heated by passing controlled DC current. The upstream endwall is heated using commercially available Kapton^{TM} encapsulated air heater. A Chromel-Constant thermocouple (type-E) probe of tip diameter of 0.50 mm is traversed along the pitchwise plane to measure the air stream temperature.

The θ value at X_G/C_{ax}=0.152 in Fig. 19 is high above the endwall at -0.60<Z/P<-0.40 because of the presence of suction side leg vortex. The vortex flow mixes the near wall hot fluid with the cold main stream fluid and raises the mainstream air temperature. As the vortex structures grow downstream of the passage, the region of the heated air stream or high θ values also grow larger which is evidenced at X_G/C_{ax}=0.493. The region of high θ values is about the same size as the passage vortex region near the suction side and endwall junction. The region of high θ grows further at X_G/C_{ax}=0.954 in Fig. 19, and is elevated from the endwall as the passage vortex lifts upwards.

Heat Transfer Coefficient on the Endwall (No Coolant Flow)

Heat transfer measurements on the contoured endwall are obtained with the same heater arrangement as is used for air stream temperature measurements. Nusselt numbers on the endwall are computed from the time averaged infrared images and thermocouple data. Temperature from the thermocouples embedded in the endwall is used for the insitu calibration of the infrared images. One-dimensional energy balances are used to compute the conduction heat loss from the endwall. Infrared images are captured by a Raytheon Radiance HS 2012 camera at a frame rate of 33.3 Hz through a Zinc-Selenide window placed on the channel top wall. The images are recorded in the gray scale form of 12 bit/pixel in 256x256 pixel resolution. The pixel gray scale values then converted to local Nusselt numbers applying the insitu calibration data obtained during the infrared image data acquisition. Nusselt number is computed from the following equation where C is blade actual chord length, T_{wall} is end-wall temperature measured from the infrared images, $T_{o,in}$ is reference temperature from Table 2, and k_{air} is thermal conductivity of air at the temperature $T_{o,in}$.

$$Nu = \frac{q''_{conv} * C}{(T_{wall} - T_{o,in}) * k_{air}} \quad (6)$$

The convective heat flux q''_{conv} from the strip heaters is given by $q''_{conv} = (V * I - Q_{cond}) / A_{heater}$. Here, V is voltage drop across heater, I is current through heater, A_{heater} is heater area, Q_{cond} is one dimensional conduction loss through the end-wall. Radiation losses to the surrounding are assumed to be negligible as the wall temperature varies between 35 ^{o}C and 55 ^{o}C, and hence, is not accounted for in the *Nu* computation. Measured one dimensional conduction loss is small, 1.5% of the total power input for the baseline endwall and 7.0% of the total power input for the contoured endwall case. Thus, a constant heat flux boundary condition is assumed for the Nu calculation. A_{heater} in the above equation is based on the actual area of the contoured endwall. The input heater power level for the contoured endwall case is about twice of that for the baseline case. The convective heat flux q''_{conv} is 900 W/m^2 for the baseline and 1650 W/m^2 for the contoured endwall.

Figure 20 presents Nusselt number distribution along the contoured endwall. For the comparison, the baseline measurement is also included. The effects of the contoured profile of endwall on Nu are clearly distinguishable as the Nu are smaller everywhere upstream of the throat region for the contoured endwall than for the baseline. Nu are significantly smaller at $X_G/C_{ax}<0.50$ for the contoured endwall. This occurs as the suction side leg vortex and passage vortex are considerably reduced in size and strength in this region of the contoured endwall. As evidenced, the legs of high Nu contours starting at the leading edge regions of both pressure and suction side of the baseline endwall are reduced considerably on the contoured endwall. Nusselt numbers are also much smaller at $0.60<X_G/C_{ax}<0.85$, which is the throat region, for the contoured endwall than for the baseline.

Film Cooling Hole Configuration (Contoured Endwall) and Coolant Supply Circuit

The geometric configuration of the film cooling holes is shown in Fig. 21(a) and is adopted based on input from the gas turbine industry. The same configuration is used for the baseline flat endwall and non-axisymmetric contoured endwall. The cylindrical coolant holes are oriented at 30 deg relative to the tangent on the surface profile. The orientation of the hole at the coolant ejection side is directed approximately along the inviscid local streamwise direction. The holes are 5.0 mm in diameter and machined in a 19.0 mm thick acrylic plate for the flat baseline endwall. The non-axisymmetric contoured endwall are fabricated with a stereo-lithography printer at LSU. The coolant holes are integrally fabricated during the lithography process. The same end-wall contour profile as in Fig. 2 is employed for the film cooling measurements. The thickness of the contoured endwall is 19.0 mm in the vertical direction. Therefore, the hole length-to-diameter ratio for baseline endwall is constant and 7.6, while it varies for the contoured endwall depending on the location of the a hole in the endwall. The coolant to the test section is supplied from a plenum located below the end wall.

Results presented in Figs. 22 to 37 include flow field and air stream temperature measurements. Figure 21(a) shows the axial location of the pitchwise planes where the measurements are obtained with the five-hole pressure probe, hot-wire probe, and thermocouple probe. Six inlet blowing ratios between Min=1.0 and 2.4 are employed for the measurements. The following table shows the test matrix which was completed for the film cooling

measurements on the contoured endwall. Presently, the infra-red measurements of the film cooling effectiveness on the contoured endwall are underway. The inlet blowing ratio, M_{in} in the table below (Table 3) is determined based on the definition in [9].

$$M_{in} = \sqrt{\frac{P_{o,plenum} - P_{stat,r}}{P_{tot,r} - P_{stat,r}}} \tag{7}$$

In Eq. (7), $P_{stat,r}$ and $P_{tot,r}$ are the reference quantities from Table 2, and $P_{o,plenum}$ is the measured total pressure in plenum box for film cooling. The temperature difference between the main air stream and the coolant is maintained at about 0.0 ^{o}C and 20.0 ^{o}C during flow structure measurements and air stream temperature measurements, respectively. The endwall is unheated and maintained at the adiabatic condition as the thermal conductivity of the endwall material (which has a commercial name ABS plastic) is very low. The same ambient air as the main channel flow is used for the film cooling flow. As shown in Fig. 21(b), the ambient air is blown with a small blower of capacity 3.0 m^3/min in a secondary supply circuit where the air passes over two heat exchangers cooled by the chiller water. The cold air is then blown in the plenum box and then throug the film cooling holes. Mass flux of the film cooling flow and consequently, the plenum pressure can be controlled by adjusting the blower speed with a dc power supply. The minimum temperature of the coolant flow thus achieved is 10.0 ^{o}C, but the coolant air density ρ_c is nearly the same as the main air stream density ρ_{air} for all the blowing ratios.

Table 3: Measurement Test Matrix for Contoured Endwall with Film Cooling

Measurement location	Five-hole probe measurement (I)	Hot-wire probe measurement (II)	Thermocouple probe measurement (III)
X_G/C_{ax}=0.085 (I, II)	M_{in}=1.0, 1.6, 2.0, 2.4	M_{in}=1.0, 1.6, 2.0	M_{in}=1.0, 1.6, 2.0
X_G/C_{ax}=0.152 (III)	$T_c/T_{o,in}$=1.0	$T_c/T_{o,in}$=1.0	$T_c/T_{o,in}$=0.93
	ρ_c/ρ_{air}=1.0	ρ_c/ρ_{air}=1.0	ρ_c/ρ_{air}=1.0
X_G/C_{ax}=0.424 (I, II)	M_{in}=1.0, 1.6, 2.0	M_{in}=1.0, 1.6, 2.0	M_{in}=1.0, 1.6, 2.0
X_G/C_{ax}=0.493 (III)	$T_c/T_{o,in}$=1.0	$T_c/T_{o,in}$=1.0	$T_c/T_{o,in}$=0.93
	ρ_c/ρ_{air}=1.0	ρ_c/ρ_{air}=1.0	ρ_c/ρ_{air}=1.0
X_G/C_{ax}=0.916 (I, II)	M_{in}=1.0, 1.3, 1.6, 1.8, 2.0,	M_{in}=1.0, 1.3, 1.6,	M_{in}=1.0, 1.6, 2.0
X_G/C_{ax}=0.954 (III)	2.4	1.8, 2.0, 2.4	$T_c/T_{o,in}$=0.93
	$T_c/T_{o,in}$=1.0	$T_c/T_{o,in}$=1.0	ρ_c/ρ_{air}=1.0
	ρ_c/ρ_{air}=1.0	ρ_c/ρ_{air}=1.0	

Time-averaged Secondary Flow Field (With Film Cooling Flow)

Time-averaged flow structure on the contour endwall with film cooling flow is measured for the same upstream conditions and in the same passage as those for the baseline case and the contoured endwall without film cooling case. Also, the same flow measuring probes and measurement techniques are used for all the cases. The film cooling holes are located in the passage between the center blade and the blade on the pressure side of the center blade (see Fig. 21). However, the same contour profile is employed in the two passages of the cascade in Fig. 1. Therefore, flow measurements downstream of the cascade where different fields from the two passages are mixing with each other are not obtained. The contoured endwall has already

shown significant improvement in the flow field. Hence, the results with film cooling flow presented here are compared with those for the contoured endwall without coolant flow to report any further improvements in the flow field.

Figure 22 shows the streamwise turbulence intensity for three blowing ratios, M_{in}=1.0, 1.6, and 2.0 at X_G/C_{ax}=0.085. Compared to the no-coolant flow case on the left of the figure, the turbulence intensity near the endwall increases with the coolant flow. At the same location, turbulence intensity also increases with the blowing ratio. Most of the coolant jets upstream of this measurement plane are ejected at an angle to the approaching boundary layer and increase the turbulence intensity of the boundary layer. At Z/P>-0.30 near the pressure side, distinct traces of the coolant jets become clearly identifiable by the turbulence intensity contours of magnitudes greater than 9% as M_{in} increases. These jets are issued from the four holes located just upstream of this location near the pressure side. Similar pattern of turbulence intensity associated with the coolant jets near the leading edge pressure side are observed by [10]. Also, note the high turbulence intensity adjacent to junction of the suction side and contoured endwall especially for M_{in}=1.6 and 2.0. This is caused by the jets from holes located near the suction side at the leading edge. The momentum of these jets increases with the blowing ratio and the endwall profile dips down at this location near the suction side. Therefore, the coolant jets from the holes located upstream of X_G/C_{ax}=0.085 near the suction side lift above the endwall causing high turbulence intensities adjacent to the suction side.

Figure 23 compares the streamwise turbulence intensity at X_G/C_{ax}=0.424 between the film cooled contoured endwall cases and baseline contoured endwall with no coolant jet flow. Film cooling data are presented for M_{in}=1.0, 1.6, and 2.0. The turbulence intensity contours of magnitudes greater than 10% at the junction of the suction side and baseline contour endwall indicate the passage vortex core. At the same location for the film cooling case in Fig. 23, the turbulence intensity in the passage vortex core decreases for all M_{in}. The turbulence intensity in the passage vortex core is the lowest for M_{in}=1.6. This suggests that the coolant flow jets weaken the passage vortex by opposing the turning of the cross flow near the endwall toward the suction side. However, the turbulence intensities above the endwall and adjacent to the suction side are higher for M_{in}=2.0 than for M_{in}=1.0 and 1.6. This is caused by the higher momentum of the coolant jets located upstream of X_G/C_{ax}=0.424 for the blowing ratio M_{in}=2.0.

The effects of the full coverage film cooling on the flow field are realized when the combined effects from all the coolant jets are measured at a downstream location of the holes. The streamwise turbulence intensities near the passage exit at X_G/C_{ax}=0.916 are presented in Fig. 24 for M_{in}=1.0, 1.6, and 2.0. The turbulence intensity of 11% and higher near the suction side at 0.05<Y/S<0.30 for the baseline contour endwall in the figure is caused by the passage vortex core which is elevated from the endwall at this axial position. Here also, it is clearly evident that the film cooling jets reduce the turbulence intensity in the passage vortex core significantly and thus, weaken the passage vortex. The area of high turbulence intensity in the vortex core is also reduced significantly in the film cooling case compared to the baseline contoured endwall case. The area of high turbulence intensity of 8% and higher at 0.05<Y/S<0.30 appears to be the smallest for M_{in}=2.0. The high magnitudes near the endwall-suction side corner for M_{in}=1.6 and 2.0 are caused by the high momentum coolant jets located near the suction side in the passage.

Figure 25 shows the mass-averaged streamwise turbulence intensities computed along constant pitchlines and plotted in the spanwise direction at X_G/C_{ax}=0.916. Data are presented for all six inlet blowing ratios. M_{in}=0 indicates the data for the baseline contoured endwall case

with no coolant flow. The averaged turbulence intensities decrease from the location Y/S=-0.03 near the dip of the endwall profile to the location Y/S=0.03 near the hump of the endwall profile at X_G/C_{ax}=0.916. This occurs as most of the boundary layer fluid is swept toward the suction side, where the endwall dip is located, by the endwall cross-flow. Turbulence intensity then increase between Y/S=0.03 and Y/S=0.10 because of the passage vortex. Further above the endwall, average turbulence intensity decreases as Y/S increases. Little differences are observed in the data between Y/S=0.05 and Y/S=0.40 in Fig. 25. The pitchwise-averaged data at Y/S<0.05 are slightly higher for M_{in}=1.0, 1.3, and 2.4 than for the rest of the cases. The differences in the data at Y/S>0.40 are caused the coarse resolution of the measurement grids.
Figure 26 shows the overall mass-averaged streamwise turbulence intensity and axial turbulence intensity as varied with M_{in} at X_G/C_{ax}=0.916. The overall average is computed over the area extended from the endwall to the mid-span. Here also, M_{in}=0 is the case for the baseline contoured endwall. Both the streamwise turbulence intensity and axial turbulence intensity in Fig. 26 change little with M_{in}. This is a desirable result for the film cooling jet configuration as the overall turbulence intensity changes little for the film cooled endwall compared to the case for the baseline contoured endwall near the passage exit.

Normalized axial vorticity Ω_x*C/U_{ref} at X_G/C_{ax}=0.085 for blowing ratio M_{in}=1.0 to 2.0 is presented in Fig. 27. The vorticity magnitudes of -6 and lower at the corner of the baseline contour endwall and suction side are caused by the suction side leg vortex. The negative vorticity at the same location is almost absent in the data at X_G/C_{ax}=0.085 with the film cooling. The strong positive vorticity of the coolant jets near the leading edge suction side must have consumed the counter-clockwise rotating suction side leg vortex. The tiny region of positive vorticity with Ω_x*C/U_{ref}>2 near Z/P=-0.4 for the baseline contoured endwall indicates the trace of a very weak and small pressure side leg vortex. However, the Ω_x*C/U_{ref}>5 across entire pitchline above the endwall with the film cooling flow is mostly caused by the coolant jets. As the momentum of the jets increases with M_{in}, the area and magnitudes of these positive vorticity regions also increase.

Figure 28 shows normalized axial vorticity Ω_x*C/U_{ref} at X_G/C_{ax}=0.424 for M_{in}=1.0 to 2.0 and compares the data with the baseline contoured endwall case with no film cooling flow. For the baseline case, the positive vorticity region and the negative vorticity region above it near the suction side-endwall corner indicate the passage vortex and suction side led vortex, respectively. At the same corner for the film cooling case, the area and magnitudes of the positive vorticity are reduced significantly indicating the weakened structure of the passage vortex. The location of the positive vorticity region is also slightly elevated at the corner as the coolant films are injected under the boundary layer. The small region of high vorticity Ω_x*C/U_{ref}>10 adjacent to the suction side for M_{in}=1.6 and 2.0 is caused by the jets ejected near leading edge suction side. The signature of these jets adjacent to the suction side (Ω_x*C/U_{ref}>10) is also evident in Fig. 27. The signature of the suction side vortex (Ω_x*C/U_{ref} <0) above the positive vorticity region near the suction side is completely eliminated for the film cooling case. This is expected as the suction side vortex is also not evident in the film cooling data upstream at X_G/C_{ax}=0.085. However, the negative magnitudes of Ω_x*C/U_{ref} adjacent to the endwall across the pitchline in Fig. 28 indicates the signatures of the cooling jets. These Ω_x*C/U_{ref}<0 contours decrease in magnitudes and increase in area as M_{in} increases. Most of jets located upstream of X_G/C_{ax}=0.424 are ejected in the positive yaw angle direction (see Figs. 1(b) and 21(a)). As the boundary layer cross-flow travels toward the suction side, it tries to rotate the jet fluids counter-clockwise creating the negative vorticities in the coolant jets near X_G/C_{ax}=0.424. This is

opposite to the mechanism observed at X_G/C_{ax}=0.085 where the jets have positive axial vorticities as shown in Fig. 27.

The combined effects of all the coolant jets on the axial vorticity are shown in the results of Fig. 29 for M_{in}=1.0 to 2.0. The contour size of the normalized axial vorticity Ω_x*C/U_{ref}>6 near the suction side at X_G/C_{ax}=0.916 indicating the passage vortex core is much smaller for the film cooling cases than for the baseline contoured endwall. The positive vorticity magnitudes in the passage vortex region at Z/P<-0.60 also reduce slightly as M_{in} increases. Also, note that the location of the Ω_x*C/U_{ref}>6 contour is higher in Y/S direction for the film cooling case than for the baseline contoured endwall case. The small regions of Ω_x*C/U_{ref}>6 near the pressure side for M_{in}=2.0 are the signature of the coolant jets located near the pressure side. At M_{in}=2.0, the momentum of these jets are high enough to remain attached to the endwall down to the location X_G/C_{ax}=0.916. The negative vorticity region about Y/S=0.30 near the suction side for the baseline contoured endwall is the signature of the suction side leg vortex and induced wall vortex [6]. But, the negative vorticity region at the same location and at bottom the corner of the suction side for the film cooling case are caused primarily either by the remnants of the film jets or by the induce vortex structures.

The normalized pitchwise velocity, W/U_{ref} at X_G/C_{ax}=0.424 shown in Fig. 30 near the endwall is increased in magnitudes for the film cooling cases compared that for the baseline contoured endwall case. The magnitudes near the endwall are also increased as the blowing ratio M_{in} increases from 1.0 to 2.0. This suggests that the strength of the cross flow along the pitchline is reduced with the film cooling and is reduced further as M_{in} increases. As a consequence, less amount of boundary layer fluid is funneled into the passage vortex and the secondary flow is weakened and reduced in size as M_{in} increases, which is also observed in Fig. 28. Figure 31 also shows W/U_{ref} at X_G/C_{ax}=0.916 for the M_{in}=1.0 to 2.0. Hers, the negative W/U_{ref} magnitudes in the passage vortex region between Y/S=0.17 and Y/S=0.30 near the suction side increases with the film cooling flow compared to that with the no coolant flow case. However, the negative W/U_{ref} magnitudes near the endwall region at Z/P<-0.40 decreases with the film cooling flow and as M_{in} increases compared to that with the no coolant flow case in Fig. 31. This occurs as the cross-pitch flow is strengthened by the film jets located downstream of X_G/C_{ax}=0.424 which are ejected along the cross flow direction.

Figure 32 shows the total pressure loss coefficients, $C_{pt,loss}$>0.40 at X_G/C_{ax}=0.424 due to the passage vortex is affected little when compared between no coolant flow case and coolant flow case up to M_{in}=1.6. The region of $C_{pt,loss}$>0.40 near the suction side-endwall corner becomes smaller for the higher blowing ratio at M_{in}=2.0. The distinct small region of $C_{pt,loss}$>0.50 adjacent to the suction side for M_{in}=1.6 and 2.0 is caused by the high vorticity of the lifted jet from the holes near the leading edge suction side.

The $C_{pt,loss}$ at X_G/C_{ax}=0.916 for the blowing ratios, M_{in}=1.0 to 2.4 are shown in Fig. 33. The local $C_{pt,loss}$, in fact, increases in the passage vortex region between Y/S=0.17 and Y/S=0.30 near the suction side with the film cooling flows compared to that with no coolant flow case. Since the passage vortex is weakened with the film cooling as evident earlier, the higher $C_{pt,loss}$ must have been caused by the coolant jets as they are lifted from the endwall and mixed with low energy boundary layer flow. However, the higher momentum of the coolant jets at M_{in}>1.6 decreases the $C_{pt,loss}$ above the endwall in Z/P>-0.60 which will be further evident in Fig. 34.

Figure 34 shows the pitchwise mass-averaged $C_{pt,loss}$ plot and overall mass-averaged $C_{pt,loss}$ plot at X_G/C_{ax}=0.916 for the blowing ratio ranging from 1.0 to 2.4. The baseline contoured endwall case is also included as M_{in}=0. The dotted line in the plots refers to the baseline flat

endwall case. The pitchwise mass-averaged data computed the measured data along constant pitchline are plotted against the spanwise Y/S direction. The pitch-averaged $C_{pt,loss}$ data for the baseline flat endwall higher for most of the Y/S than for all the contour endwall cases (with and without film cooling). In comparing pitch-averaged data for the film cooled contour endwall with the baseline contoured endwall (M_{in}=0), the film cooled $C_{pt,loss}$ are higher at location Y/S<0.0. This is probably caused by the losses in the corner vortex which is strengthened by the film jets. At 0.0<Y/S<0.1, the averaged $C_{pt,loss}$ are lower for M_{in}>1.6 than for the other cases. This is caused by the small magnitudes of local $C_{pt,loss}$. Note that the averaged $C_{pt,loss}\leq$0.0 for the cases of M_{in}=2.0 and 2.4 occurs because the high momentum film jets near the pressure side increase the local magnitudes of total pressure P_{tot}.

The overall mass-averaged $C_{pt,loss}$ in Fig. 34 are computed from the local data between the endwall and mid-span. Here, the averaged $C_{pt,loss}$ for all the contoured endwall cases are nearly half of that for the baseline flat endwall case. For contoured endwall cases, the overall-averaged $C_{pt,loss}$ are higher for M_{in}=1.0 to M_{in}=1.6 than for M_{in}=0.0. However, the overall-averaged data decreases as M_{in} increases from 1.0 to 2.4. Note that in defining the $C_{pt,loss}$ the coolant plenum pressure has not been used, and therefore for the film cooling cases, the $C_{pt,loss}$ values represent a dimensionless pressure rather than a total loss coefficient. The $C_{pt,loss}$ values with coolant plenum pressures included will be presented in a later report.

Non-dimensional Flow Temperature (With Film Cooling Flow)

The non-dimensional flow temperature θ_f of the measured air stream temperature for the film cooling case is redefined in Eq. (8) below. The reference temperature in this definition is chosen

$$\theta_f = \frac{T - T_c}{0.5 * U_{ref}^2 / C_p} \tag{8}$$

to be the coolant temperature T_c which is the lowest temperature in the cascade. In Eq. (5), the reference temperature is $T_{o,in}$ as the inlet temperature of the flow is the lowest temperature. In Eq. (8) above, T is the local air temperature measured with the same thermocouple probe that is used for the data measurements on the heated contoured endwall. Thus, higher magnitudes of θ_f indicate the air stream higher above the endwall and lower magnitudes of θ_f indicate the air stream infected by the cold film jets. As mentioned earlier, the endwall is not heated and is maintained at the adiabatic condition for T measurements with the cold film jets. The results are presented in Figs. 35 to 37. The pitchwise Z resolution of the measurement grid is 2.0 mm near the blade surfaces and 4.0 mm at the mid-pitch locations. The spanwise Y resolution is 1.0 near the endwall and 5.0 mm at the mid-span locations.

Figure 35 shows θ_f at X_G/C_{ax}=0.152 for M_{in}=1.0, 1.6, and 2.0. The magnitudes of θ_f <325 are the signature of the cold jet stream above the endwall. The mass flux or volumetric flow rate of the coolant jet increases with M_{in}. Therefore, the region with θ_f <325 near the endwall increases with M_{in}. Note that the cold temperature region is bound well within the velocity boundary layer along most of the pitchline in Fig. 35. The lower θ_f higher above the endwall at the suction side is caused by the lifted jets at this location.

The θ_f contours for the same blowing ratios M_{in}=1.0 to 2.0 at X_G/C_{ax}=0.493 are shown in Fig. 36. Here also, the region of θ_f <325 identifying the coolant jets increases with M_{in}. The magnitudes of θ_f also decrease with increasing M_{in}. Nine distinct regions of θ_f <175 for M_{in}=1.6

and 2.0 identify nine coolant jets located upstream of X_G/C_{ax}=0.493. The θ_f contours near the endwall change little for M_{in}=1.6 and 2.0. The data in Fig. 36 also show that the low temperature fluid remain close to the endwall across the entire pitchline for $M_{in}\geq$1.6.

The θ_f contours at X_G/C_{ax}=0.954 in Fig. 37 show that θ_f magnitudes decrease significantly above the endwall across the pitchline as M_{in} increase from 1.0 to 2.0. Near the suction side, θ_f<325 extends up to Y/S=0.22 as the cross-flow and passage vortex lifts the cold boundary layer fluid and coolant jets higher above the endwall. The low temperature blanket above the endwall with θ_f<275 at Z/P>-0.40 are the thickest for M_{in}=2.0 because of the higher mass flux in the coolant jets ejected from the locations near the pressure side.

Comparison with Filleted Cases

Measurements are obtained for static pressure, pitchwise velocity, flow yaw angle, streamwise vorticity, Nusselt numbers on endwall and blade surface, and air temperature near the endwall for the baseline and modified passages. The endwall contouring information was provided earlier. The pictures of the leading edge modification are shown in Fig. 38. The cascade inlet conditions are measured in a plane at $0.40C_{ax}$ upstream of the passage inlet and presented in Table 4 below. The quantities included in the table are the arithmetic average of the local data in the plane. Pressure inside the wind tunnel is below atmospheric as the air flows under the blower suction. The pressure values in Table 4 are thus negative gage units. The free-stream velocity and turbulence intensity in the table are measured in the streamwise direction which is oriented 55^o from the blade axis. The Reynolds number in the table is based on actual blade chord and inlet free-stream velocity.

Table 4: Inlet conditions to cascade for the filleted caes

U_o (m/s)	Re_{in}	TI%	$P_{s,\infty}$ (Pa)	$P_{t,\infty}$ (Pa)	ρ (kg/m^3)	δ (mm)	θ (mm)
10.10	239,000	4.00	121.90	60.50	1.20	46.0	26.0

(i) Static Pressure

Static pressure is measured along the blade surface and endwall and normalized by the inlet dynamic pressure to present the data in Figs. 39 and 40. Figure 39 shows the static pressure coefficient C_p distributions along the blade surface near the endwall. Data for the baseline and fillet cases are presented. The contour endwall covers the blade pressure side at the *Z/S* locations presented in Fig. 39. Also, the same *Z/S* locations relative to the contour endwall and relative to the flat endwall location are geometrically different positions on the blade surface. Therefore, C_p data for the contour endwall are not included in Fig. 39. The following equation is used to determine C_p from the blade surface pressure.

$$C_p = \frac{P_{s,\infty} - P_s}{0.5\rho U_o^2}$$

Here, P_s is the measured blade-surface static pressure. The C_p value is the highest at the stagnation location (*s/C*~1.50) in Fig. 39. The value decreases away from the stagnation location as the flow accelerates on the blade pressure and suction side along the passage. In *Z/S*=0.044 and 0.087 near the stagnation region (1.40<*s/C*<1.70), filleted data are not presented as the blade locations are covered by the fillet volume. The C_p distributions on the suction side, as indicated in Fig. 39, increases at *s/C*<0.80 in *Z/P*=0.044, and at *s/C*<0.70 in *Z/P*=0.087 and

0.131. This occurs because of the adverse pressure gradients at these *s/C* suction surface locations and the start of the boundary layer separation. The *s/C* location of the separation differs away from the endwall as the laminar to turbulent transition on the suction side occurs nearer the leading edge near the endwall than the transition location away from the endwall. Also, the suction side C_p values are generally lower in Z/S=0.087 and 0.131 than those in Z/S=0.044 because flow speed is higher away from the endwall region. However, there are insignificant differences between the baseline C_p distributions and filleted C_p distributions in Fig. 39 in all location on the blade surface. This indicates that the fillets influence little the flow dynamics and pressure on the blade surface near the endwall.

Figure 40 shows the normalized static pressure differences along the pitch-line just above the endwall. The quantity ΔP_s in the figure is determined from the difference between the blade pressure-side pressure (P_{ps}) and local passage pressure (P_e), both of which are located about 3.0 mm above the endwall and in the same pitch-line or at the same axial distance. The differences are shown along the pitch-lines 3.0 mm above the endwall at three axial locations in Fig. 40. The data for all the four cases i.e., the baseline, contour endwall, and filleted cases are compared here. The data are important as such pressure differences near the endwall drive the cross flow from the pressure side to suction side and consequently, affect the endwall region secondary flows. The normalized pressure differences in Fig. 40 increase generally from the pressure side to suction side as the static pressure decreases near the passage suction side. The differences at X_G/C_{ax}=0.085 (Fig. 40i) are the highest for the contour endwall case compared to the other cases with the flat endwall. As the contour endwall is high near the pressure side at X_G/C_{ax}=0.085, the flow spanwise area decreases increasing the flow velocity in the boundary layer. The flow is also almost parallel to the passage inlet flow at X_G/C_{ax}=0.085. Thus, the static pressure increases near the pressure side for the contour endwall compared to that for the flat endwall cases to divert the flow inside the passage at X_G/C_{ax}=0.085. This causes the normalized ΔP_s distribution to be higher for the contour endwall in Fig. 40(i). The data for the Fillet-1 is slightly smaller than those for the baseline and Fillet-2 in the same figure. For the baseline and filleted cases in Fig. 40(i), the data near the pressure side are not measured as the orientation of the measuring probe (the five-hole probe) has to change at Z/P>-0.30. This changes the axial location of the probe head and the measured data.

At X_G/C_{ax}=0.423 in Fig. 40(ii), the normalized ΔP_s distribution at Z/P<-0.20 away from the pressure side is higher for the baseline than for the other cases. The lowest distribution is observed for the contour endwall in this location. Then, between the filleted cases, the pressure differences are smaller for Fillet-2. As the streamlines in the passage are turned and diverted by ΔP_s, the lower ΔP_s values for the modified passage in Fig. 40(ii) turn the endwall region streamlines less toward the suction side weakening the pitchwise cross flow and the passage vortex. The data suggest that the least turning of the streamlines at X_G/C_{ax}=0.423 occurs for the contour endwall.

The ΔP_s distributions at X_G/C_{ax}=0.92 in Fig. 40(iii) indicate that the pressure differences are also the smallest for the contour endwall in Z/P>-0.40, but still remain smaller than those for the baseline in Z/P<-0.50. The data are the smallest for Fillet-1 in Z/P<-0.40. The baseline data in Fig. 40(ii) are usually higher along the pitchline in X_G/C_{ax}<-0.20 than the data for the modified passages. However, the ΔP_s distributions near the pressure side are about the same for the baseline and fillets. The implication of the ΔP_s distributions here is that the boundary layer streamlines near the exit plane are less diverted toward the suction side for the contour endwall and fillets compared to those for the baseline. The exit flow then becomes more uniform in the

spanwise direction for the modified passages than for the baseline. This is one of the desired exit flow conditions from the blade row.

(ii) Pitchwise Velocity, W/U_o

The pitchwise velocity component in the endwall boundary layer fuels the passage vortex and causes the spanwise non-uniformity in the exit flow. Weakening the pitchwise velocity then reduces such adverse conditions in the blade passage. Figure 41 shows the effects of the passage modifications on the normalized pitchwise velocity, W/U_o in three axial planes. These are the same locations as those in Fig. 40. The local W/U_o data are mass averaged along the constant pitchlines (lines in the pitchwise direction at a constant X_G/C_{ax}) parallel to the Z-axis and then plotted in the spanwise Y/S direction in Fig. 41. The average values increase from the endwall region with Y/S and then, become almost constant at Y/S>0.25 in all axial locations. The dotted lines in the figure indicate the location of the flat endwall. The average W/U_o at X_G/C_{ax}=0.085 in Fig. 41(i) are the largest for the contour endwall in Y/S<0.15. The data for the fillets change little from the baseline and are about the same for all cases in Y/S>0.15. The positive magnitudes of W/U_o at X_G/C_{ax}=0.085 indicate the pitchwise velocity from the suction side to pressure side. The higher positive W/U_o near the endwall then increases the pressure side static pressure and consequently, the higher pitchwise pressure differences for the contour endwall as shown in Fig. 40(i).

The mass averaged W/U_o values at X_G/C_{ax}=0.423 and 0.920 in Fig. 41(ii) and Fig. 41(iii), respectively, are negative indicating the pitchwise velocity from the pressure side to suction side. The higher W/U_o value then translates that the cross flow from the pressure side to suction side is weaker. Also, the pitchwise velocity is more negative near the endwall than that away from the endwall because the streamline turning is higher in the boundary layer than in the inviscid region. The W/U_o values for the contour endwall at X_G/C_{ax}=0.423 thus indicate the weakest pitchwise cross flow in the endwall boundary layer region. The filleted W/U_o values are also higher than the baseline case at X_G/C_{ax}=0.423, but still smaller compared to the contour endwall case in Y/S<0.15. This occurs as the pitchwise pressure differences at this axial location are smaller for the modified passages, which are further smaller for the contour endwall compared to those for the fillets.

The mass-averaged W/U_o values at X_G/C_{ax}=0.92 for the contour endwall and Fillet-2 are about the same as for the baseline in Y/S<0.12. In the same locations, the Fillet-1 data are more negative indicating stronger cross flow compared that for the other cases. The average W/U_o values in Y/S>0.12 are mostly influenced by the fully developed passage vortex system located at the pressure side. The peaks of the W/U_o distributions in Fig. 41(iii) occur at the spanwise location of the passage vortex core. It is apparent therefore that the passage vortex core for the contour endwall is located nearer the endwall.

(iii) Flow Yaw Angle, ψ- ψ_{ms}

The flow yaw angle is the measure of streamline turning toward the suction side. As the inviscid streamlines in the mid-span region are parallel to the passage walls, the yaw angle relative to the mid-span yaw angle shows the level of streamline turning toward the suction side. Figure 42 shows the mass averaged relative yaw angle, ψ- ψ_{ms} as varying along the span, Y/S in three axial planes. The planes are the same as those in the previous two figures. The averages are computed along the pitchlines parallel to the Z-axis. The data for the baseline and all three modified cases are compared in Fig. 42. The positive (ψ- ψ_{ms}) indicates the streamline turning

toward the suction side and the negative (ψ- ψ_{ms}) indicates the streamline turning away from the suction side relative to the inviscid flow direction. The (ψ- ψ_{ms})>0 streamlines near the endwall strengthens to pitchwise cross flow and contribute to the secondary flow evolution. The dotted lines in Fig. 42 show the location of the flat endwall. Note that (ψ- ψ_{ms}) increases as the flat endwall location approaches in Fig. 42 so that the radial force on the streamlines in the boundary layer balances the pitchwise pressure gradient.

The average (ψ- ψ_{ms}) at X_G/C_{ax}=0.085 in Fig. 42(i) decreases for the contour endwall in Y/S<0.0. Because of a large dip in the contour profile at this location, the near endwall flow passes between the dipping wall of the contour profile and the suction side. Thus, the streamlines follow the suction wall profile in this location as Y/S decreases and (ψ- ψ_{ms}) decreases with Y/S. In Fig. 42(i), the (ψ- ψ_{ms}) values in 0.0<Y/S<0.06 are higher for the fillets than for the contour endwall and baseline because the fillet on the pressure side deflects the flow causing more turning in the streamlines toward the suction side.

The average (ψ- ψ_{ms}) at X_G/C_{ax}=0.423 in Fig. 42(ii) for the contour endwall are smaller in Y/S<0.20 than for the baseline and fillets. This occurs as the pitchwise pressure gradients in these locations are the smallest from the contour endwall. The pitchwise cross flow thus is the weakest in these locations for the contour endwall. The (ψ- ψ_{ms}) values are also smaller for the fillets than for the baseline in these locations. The (ψ- ψ_{ms})<0.0 values about Y/S=0.15 are caused by the streamlines that are turned away from the suction side by the motion of the upper side of the secondary vortex flows.

At X_G/C_{ax}=0.92 in Fig. 42(iii), the average (ψ- ψ_{ms}) distributions are smaller in 0.0<Y/S<0.08 for the modified passage than for the baseline as the modified passages try to align the local streamlines with the mid-span flow direction. This reduces the strength of the pitchwise cross flow for the contour endwall and fillets. The negative (ψ- ψ_{ms}) values about Y/S=0.18 here also are caused by the streamlines that are turned away from the suction side by the motion of the upper side of the passage vortex. Note that (ψ- ψ_{ms}) values about Y/S=0.18 are higher for the contour endwall compared to those for the fillets and baseline as the passage vortex motion is weakened for the contour endwall.

(iv) Streamwise Vorticity, $\omega_s C/U_o$

The normalized streamwise vorticity, $\omega_s C/U_o$ in Fig. 43 are shown in the pitchwise plane at X_G/C_{ax}=0.423. All the cases of baseline, contour endwall, Fillet-1 and Fillet-2 are compared to show the effects of the passage modification on the passage vortex. Streamwise vorticity from the measured velocity components are determined as follows.

$$\omega_s = \Omega_x \, Cos\psi_{ms} + \Omega_z \, Cos\psi_{ms}$$

$$\Omega_x = \frac{\partial W}{\partial Y} + \frac{\partial V}{\partial Z}$$

$$\Omega_z = \frac{1}{U}\left[\frac{1}{\rho}\frac{\partial P_t}{\partial Y} + W\,\Omega_x\right]$$

In the above Eq., ψ_{ms} is the mid-span yaw angle at a given pitchwise position. The derivatives are determined by taking derivatives of the spline-curve fits of the measured V, W, and P_t.

The passage vortex in Fig. 43 is shown by the contour level greater than 3 ($\omega_s C/U_o$>5.0). Clearly, the normalized vorticity magnitudes and the region of the passage vortex are the smallest for the contour endwall (Fig. 43ii) indicating the weakest passage vortex. The vorticity

region with $\omega_s C/U_o \geq 10.0$ for the fillets extends between $Z/P < -0.30$ and $Y/S < 0.04$ compared to the region between $Z/P < -0.25$ and $Y/S < 0.05$ for the baseline. This indicates a smaller passage vortex core for the fillets than for the baseline. Such reductions in the size and strength of the passage vortex for the contour endwall and fillets are caused by the weaker pitchwise cross flow in the modified passage at $X_G/C_{ax}=0.423$.

(iv) Endwall Nusselt Number, *Nu*

The effects of the endwall region secondary flows are indicated by the heat transfer on the endwall along the passage as shown in Figs. 44 to 46. The endwall Nusselt numbers in Fig. 44 are determined based on the constant heat flux boundary condition, $\dot{q}_w^{"}$ and free-stream temperature, T_∞ as follows.

$$Nu = \frac{\dot{q}_w^{"} C}{(T_w - T_\infty)k}$$

The large region of *Nu* contours of magnitudes 880 and higher for the baseline in $X_G/C_{ax} < 0.50$ in Fig. 44(i), which extends from the pressure side, is caused by the passage vortex. The small region of $Nu \geq 880$ in $X_G/C_{ax} < 0.50$ around the baseline suction side is caused by the suction side leg vortex. The $Nu \geq 960$ contours in $X_G/C_{ax} > 0.75$ for the baseline are then caused by the flow acceleration through the passage throat area. For the contour endwall case in Fig. 44(ii), the high *Nu* contour region caused by the passage vortex reduces significantly. The high *Nu* contour region near the suction side caused by the suction side leg vortex also reduces for the contour endwall. These are the direct results of the weakened passage vortex and suction side leg vortex in the contour endwall passage.

Nusselt numbers for the filleted passage are obtained without heating the fillet surface. Thus, no data are presented in the filleted region in Figs. 44(iii) and 44(iv). Note that the *Nu* values in the region between the fillets in $X_G/C_{ax} < 0.38$ reduce compared to those for the baseline in the same locations. This occurs as the secondary vortex flows on the endwall are also weakened by fillets. It should also be noted that since the fillet is unheated the region occupied by the fillets is not included in the averaging process, and therefore the passage-endwall area over which the Nu-averaging is performed is not identical for the four cases.

The line plots in Fig. 45 obtained from the data presented in Fig. 44 are shown along constant pitchlines in three axial locations. The *Nu* distribution in $X_G/C_{ax}=0.20$ in Fig. 45(i) for the baseline is significantly high near the pressure side with the maximum *Nu* value reaching about 1100. Near the suction surface the maximum *Nu* for the baseline is about 900. When the *Nu* distributions for the contour endwall and fillets are compared with baseline in Fig. 45(i), the *Nu* values are much lower for the modified passages. The *Nu* distributions for the fillets are even lower than for the contour endwall.

The *Nu* distributions in Figs. 45(ii) and 45(iii) also show that *Nu* values are smaller for the contour endwall and fillets than those for the baseline in the mid-passage and passage throat area. In these locations, the *Nu* values away from the pressure side and suction side are comparable for the contour endwall and fillets. As the passage vortex reduces in size as shown in Fig. 43 for the contour endwall and fillets, the boundary layer separation region along the 3-dimensional separation line reduces. Thus, flow reattachment location moves upstream for the contour endwall and fillets compared to reattachment location for the baseline. Thus, the velocity boundary layer develops thicker along the modified passage downstream of the separation line. The thicker boundary layer acts as the thicker thermal insulation for the

modified passage endwall and the heat transfer or *Nu* decreases in X_G/C_{ax}>0.423 for the contour endwall and fillets compared to those for the baseline. The *Nu* values for the contour endwall in Figs. 45(ii) and 45(iii) near the pressure side increase as the boundary layer velocity increases due to the reduction in the spanwise flow area. Near the suction side in the same plots, the *Nu* values for the contour endwall increase because of the formation of additional corner vortices. When the two fillet cases are compared in Fig. 45, the *Nu* values appear to reduce more for Fillet-2 than for Fillet-1.

Figure 46 presents the area averaged *Nu* for the baseline and modified passages as varying along the axial direction. The *Nu* data in the figure are area averaged over the local data in Fig. 44 along the constant pitchlines. The *Nu* distributions are the lowest for the fillets in Fig. 46. The *Nu* distributions for the contour endwall are also lower than for the baseline, but higher compared to those for the fillets. Between the fillets, Fillet-2 data in Fig. 46 are slightly smaller than the Fillet-1 data.

COMPUTATIONS & RESULTS

Calculations are performed with the commercial code FLUENT. Grid generation is done using GRIDPRO. The number of grid points used is generally over one million with near-wall stretching of the grid points toward the bottom end-wall. Realizable k-ε with two-layer near wall turbulent model is employed to simulate the flow. The grids are made fine enough near the walls so that the y+ values are below unity. The computations are performed for the same GE-E^3 first stage blade passage as in the experiments.

Several endwall contour configurations are simulated. The results presented here are only for the same contoured endwall as in the measurements since this configuration was shown to be the best in the numerical optimization studies. The summary results for the other contour configurations are presented in Table 5 of this report. Inlet flow conditions and cascade geometric parameters employed for the blade passage domain are obtained from Tables 1 and 2.

The results presented here are obtained in the computational domain and pitchwise planes as shown in Fig. 47. The domain spans one pitch distance in the pitchwise direction and $1.361C_{ax}$ upstream of the leading edge and $1.103C_{ax}$ downstream of the trailing edge. The baseline computation results are also included for the comparison. Figure 48 shows the static pressure coefficients $C_{p,e}$ on the endwall. The coefficients are computed from Eq. (2). The $C_{p,e}$ values increase on the suction side at $X/C_{ax}<0.50$ for the contoured endwall compared to baseline case. At this location, the elevation differences from the pressure side to suction side are significantly high on the contoured profile. This reduces the pressure gradient in the pitchwise direction in this location with the contoured endwall. However, $C_{p,e}$ values downstream of $X_G/C_{ax}=0.50$ near the suction side, where passage throat is located, decrease slightly for the contoured endwall compared to the baseline case.

The effects of pressure gradients in the pitchwise direction directly affect the pressure and suction side leg of the leading edge horseshoe vortex as illustrated in Figs. 49 and 50. These results are presented in the pitchwise plane at $X/C_{ax}=0.036$ that is located close to the blade leading edge. In these figures, the blade surface on the right hand side is the pressure side and on the left hand side is the suction side. Streamlines for the baseline case in Fig. 49 show the counter-clockwise rotating pressure side leg vortex structure between $0.0<Z/S<0.025$ and $0.05<Y/P<0.35$. A clear structure of the suction side leg vortex for the baseline case is not evident. The streamlines above the contoured endwall between $0.07<Z/S<0.15$ and

$0.05<Y/P<0.35$ complete only half turn of a vortex structure and indicate weak formation of the pressure side leg vortex. The streamlines on the contoured endwall suction side are curled downwards in contrast to the baseline case. The strength of these vortex structures are shown in the normalized axial vorticity in Fig. 50. The values of $\Omega_x C/U_{ref}>35$ located very close to the endwall are associated with the near-wall boundary layer flow. The normalized vorticity in the pressure side leg vortex region is significantly smaller for the contoured endwall than for the baseline indicating again a very weak pressure side vortex structure. This is consistent with the measured data presented earlier. However, the $\Omega_x C/U_{ref}$ magnitudes on the suction side are higher for the contoured endwall case. As mentioned earlier, the two-dimensional vorticity does not provide a complete structure of the three-dimensional vortex system in the passage.

Figure 51 presents the streamlines superimposed on normalized axial vorticity $\Omega_x C/U_{ref}$ at $X/C_{ax}=0.20$. In the plots, the presence of cross flow from suction to pressure side of the blade is clearly seen for both the baseline case and contoured endwall case. Additionally, the formation of a roll up vortex (counter-clockwise rotation) near the pressure side is due to the pressure side leg vortex in both cases. Comparison of the vortex roll up and the magnitude of the vorticity of the both cases reveal that the contoured endwall reduces the strength and size of the secondary flow significantly near the pressure side. Note that the contoured endwall shows the boundary layer separation at $Y/P\sim0.20$ near the wall; this is clear from the zoomed-out view of the streamlines. This particular phenomenon is absent for the flat endwall.

The streamlines superimposed on normalized axial vorticity contours at $X/C_{ax}=0.80$ are presented in Fig. 52. The magnitude and the size of the secondary vortices indicated by $\Omega_x C/U_{ref}>4.0$ near the suction side decrease in case of the contoured endwall compared with the baseline case. Though the vorticity contours reveal the strong generation of secondary vortices i.e. the passage vortex, the streamlines in the 2-D plane do not clearly exhibit the vortex roll-up as seen at an upstream location (see Fig. 51). This suggests a more 3-dimensional and diffused structure of the vortex. The streamline curvature seen near the baseline endwall-suction side corner is reduced for the contoured endwall case.

The total pressure loss coefficient $C_{pt,loss}$ at $X/C_{ax}=0.80$ plane for the baseline and the contoured endwall is compared in Fig. 53. The region of high $C_{pt,loss}$ at the suction side indicates the location of the passage vortex. The distribution of peak region of the loss coefficient is seen to be altered due to the contoured endwall and its location moves towards the bottom endwall. The magnitude of the peak coefficient is seen to be lower for contoured endwall. However, the overall (area averaged) total pressure loss coefficient for baseline and contoured endwall are computed to be about the same, 0.2164 and 0.2176, respectively. The decrease in the spatial pressure gradient for the contoured case, however, indicates the effectiveness of the three-dimensional endwall in reducing the cross flow locally.

Figure 54 illustrates the non-dimensional turbulent kinetic energy distribution in the pitchwise plane at $X/C_{ax}=1.20$ located downstream of the blade trailing edge. As evident, the drop in turbulent kinetic energy is distinct everywhere for the contoured endwall compared to the baseline case. The kinetic energy about $Y/P=0.0$ near the contoured endwall also decreases relative to the baseline case.

The normalized axial vorticity contours along with the streamlines are plotted at $X/C_{ax}=1.20$ plane in Fig. 55. The vorticity contours show the presence of high vorticity region ($\Omega_x C/U_{ref}>2.0$) at $0.02<Z/S<0.23$ for baseline and at $0.02<Z/S<0.15$ for contoured endwall. The vorticities in the passage vortex for the two cases are further compared in the line plot at $Y/P=-0.1$ in Fig. 55. In this plot, the higher $\Omega_x C/U_{ref}$ between $Z/S=0.10$ and 0.25 for the

baseline indicates that the size of the passage vortex for the contoured case is still smaller far downstream in the blade passage.

The contours of the total pressure loss coefficient at X/C_{ax}=1.20 for the baseline and contoured endwall are compared in Fig. 56. The closed contour lines represent the passage vortex here. Both the cases show almost identical magnitudes of the pressure loss. However, the center of the peak $C_{pt,loss}$ for the contour endwall moves towards the endwall. The magnitude of peak is also lower for the contoured case. The area-averaged $C_{pt,loss}$ are 0.2528 and 0.2474 for the baseline and contoured endwall, respectively, at this plane. It is seen that at the upstream location X/C_{ax}=0.80 the total pressure loss is less for the flat endwall. With the increase in the axial distance, the cross flow weakens by the action of imposed pressure field created by the contouring of the endwall and this results in lower $C_{pt,loss}$.

To get a clear idea about the near wall flow structures, surface streamlines are generated using the two components of shear stresses and shown in Fig. 57 for the baseline and contoured endwall. Because of the formation of horse-shoe vortex ahead of the blade leading edge, the streamlines near the surface shows the separation line and saddle point. However, the position of the saddle moves farther inside the passage and the separating line pattern is different for the contoured endwall. Also, the distinctive separation line along the suction side of the baseline case is not clearly evident on the contoured endwall. Further note that the streamlines inside the passage are directed more toward the axial direction for the contoured endwall case than for the baseline case. This is a clear evidence of the weakened cross flow in the near wall region and is caused by the smaller pitchwise pressure gradient on the endwall for the contoured endwall case.

Figure 58 compares the endwall Nusselt numbers between the baseline and contoured endwall case. It is clearly seen that the flat endwall has larger region of high Nu around the blade leading edge region, particularly on the suction side. The leading edge horse-shoe vortex system is advected by the strong cross flow in the blade passage and forms three-dimensional pressure-side leg vortex and suction-side leg vortex systems. The contour endwall profile weakens the horse-shoe vortex and results in lower Nu at the leading edge region. As the flow accelerates towards the throat area because of the narrowing passage area, the heat transfer is enhanced. However, the region of high Nu found along the baseline throat area is reduced significantly for the contoured endwall. In the throat area itself, the peak Nu value is higher on the contoured endwall than on the baseline endwall. This is due to the fact that the flow accelerates locally in the throat area more for the contoured endwall because of the additional reduction in the flow area. The overall (area-averaged) Nusselt number is calculated to be 736 and 678 for the baseline and contoured endwall, respectively, thus giving a reduction of 8% in the average Nu for the contoured endwall.

Table 5 provides the summary of computed area-averaged Nusselt number and total pressure loss coefficient $C_{pt,loss}$ across the blade passage for several contoured endwall profile. The pitchwise variation for all the contoured profiles is the same as that given in Fig. 2(a). The table shows the axial variation of the contoured profile in each case. X_u is the distance of the peak height in the axial curve from the blade leading edge. X_d is the distance between the peak height in the axial curve and the end of the profile. Z is the height of the final non-axisymmetric endwall profile which is generated by combining the pitchwise profile and the axial profile. As shown in Table 4, case 9 provides the optimum results in terms of average Nu and $C_{pt,loss}$. All the results presented earlier are obtained with this profile.

CONCLUDING REMARKS

A three-dimensional non-axisymmetric endwall has been designed and tested both numerically and experimentally in the atmospheric cascade facility. Measurements are also obtained with the full coverage film cooling with the coolant holes located and oriented strategically in the contoured endwall. The performance of the endwall is compared first with that of a flat endwall with respect to heat transfer and secondary flow structure. The performance of the film cooling-hole configuration is then compared with that of the contoured endwall without film cooling. In addition, studies have been conducted with leading edge modifications and contouring. The following are the main conclusions drawn from the present work.

Contoured endwall without film cooling:

1. The three-dimensional endwall is found to be effective in bringing down the total pressure loss across the blade passage.
2. The strength and size of the secondary vortex flow reduces with the contoured endwall.
3. The heat transfer along the contoured endwall is lower compared with the flat endwall. The reduction in both the total pressure loss and heat transfer is a consequence of the decrease in the near-wall pitchwise pressure gradient.

Contoured endwall with film cooling:

1. The suction side leg vortex is completely eliminated and the passage vortex strength is reduced with the film cooling compared to that with the baseline contoured endwall.
2. Mass averaged total pressure loss is decreased with film cooling when the inlet blowing ratio is greater than 1.60 compared to that with the baseline contoured endwall.
3. Overall total pressure loss at the passage exit for the contoured endwall with and without film cooling is nearly half of that measured for the baseline flat endwall.
4. The cold film cooling jets can blanket the contoured endwall across the entire pitchline better at the higher inlet blowing ratios, $M_{in} \geq 1.60$.

Leading Edge Contouring:

1. The leading edge fillets do not significantly influence the blade surface pressure distributions near the endwall.
2. The pitchwise pressure gradients between the blade pressure side and flow streamlines near the endwall away from cascade inlet are smaller for the contour endwall and fillets compared to those for the baseline. As the pitchwise pressure gradients near the endwall drives the cross flow from the pressure side to suction side, such reductions in the pressure differences weaken the cross flow hindering the development of the passage vortex.
3. The endwall region weakened cross flow reduces the pitchwise velocity for the contour endwall and fillets compared to that for the baseline passage. The pitchwise velocity funnels fluid in the secondary vortex motions and causes it to develop along the passage. The contour endwall and fillets then cause less funneling of the boundary layer fluid in the passage vortex.
4. The endwall region flow turns less toward suction side when the contour endwall and leading edge fillets are employed. This also weakens the pitchwise cross flow in the modified passages.

5. Because of the smaller pitchwise pressure gradients, weaker pitchwise velocity, and less turning of the streamlines toward the suction side, the streamwise vorticity of the passage vortex is reduced and the passage vortex becomes smaller for the contour endwall and fillets.
6. The weaker and smaller passage vortex for the contour endwall and fillets then reduces the endwall heat transfer and the Nusselt numbers along the endwall especially upstream of the mid-passage location. The passage vortex downstream of the mid-passage location lifts up from the endwall and influences little the endwall heat transfer.
7. Pressure losses are reduced to a greater extent by the full-passage three-dimensional end wall contouring. However, end wall Nusselt numbers are lower with the leading edge fillets.

Also, a high speed blow down facility has been completed where two-dimensional section of the GE-E^3 first stage vane has undergone tests. The vanes, with a scaling factor of 1:1, have been fabricated in the stereo-lithography printer at LSU. The experiments being conducted include the axial contouring of upstream bottom endwall and in-passage bottom endwall of the vane cascade test section. In addition, the film cooling effectiveness with film holes located upstream of the vane passage inlet is measured with and without contouring of the endwall. The computational results in the vane passage with axially contoured endwall have already been reported in the previous reports. These results were used in selecting the test profile for the present measurements. In addition to this, a high-pressure, heated cascade facility has been set up and has undergone preliminary tests. This facility was designed and built by General Electric. The intent is to obtain data under realistic conditions of elevated pressures, temperatures and density ratios. Preliminary data from these high speed tests have been obtained, and were presented in the 2006 UTSR Annual Meeting in Clemson.

REFERENCES

[1] Hartland, J.C., Gregory-Smith, D.G., and Rose, M.G., 1998, “Non-axisymmetric endwall profiling in a turbine rotor blade,” ASME 98-GT-525.
[2] Yan, J., Gregory-Smith, D.G., and Walker, P.J., 1999, “Secondary flow reduction in a nozzle guide vane cascade by non-axisymmetric end-wall profiling,” ASME 99-GT-339.
[3] Harvey, N.W., Rose, M.G., Taylor, M.D., Shahpar, S., Hartland, J., and Gregory-Smith, D.G., 2000, “Nonaxisymmetric turbine end wall design: Part I- three-dimensional linear design system,” ASME Tran., J. Turbomachinery, Vol. 122, pp.278-285.
[4] Hartlland, J.C., Gregory-Smith, D.G., Harvey, N.W., and Rose, M.G., 2000, “Nonaxisymmetric turbine end wall design: Part II- experimental validation,” ASME Tran., J. Turbomachinery, Vol. 122, pp.286-293.
[5] Ingram, G., and Gregory-Smith, D., 2002, “The effect of end-wall profiling on secondary flow and loss development in a turbine cascade,” ASME GT-2002-30339.
[6] Wang, H.P., Olson, S.J., Goldstein, R.J., and Eckert, E.R.G., 1997, “Flow Visualization in a Linear Turbine Cascade of High Performance Turbine Blades,” ASME Tran. J. Turbomachinery, Vol. 119, pp. 1-8.
[7] Mahmood, G.I., Gustafson, R., and Acharya, S., 2005, “Experimental Investigation of Flow Structure and Nusselt Number in a Low Speed Linear Blade Passage With and Without Leading Edge Fillets,” ASME Tran. J. Heat Transfer, Vol. 127, pp. 499-512.
[8] Mahmood, G.I. and Acharya, S., 2005, “Experimental Investigation of Secondary Flow Structure in a Blade Passage With and Without Leading Edge Fillets”, accepted, ASME Trans. J. Fluids Engineering.
[9] Friedrichs, S., Hodson, H.P., and Dawes, W.N., 1997, “Aerodynamic Aspects of Endwall Film-Cooling,” ASME Tran., J. Turbomachinery, Vol. 119, pp.786-793.
[10] Kost, F. and Nicklas, F., 2001, “Film-Cooled Turbine Endwall in a Transonic Flow Field: Part I- Aerodynamic Measurements,” ASME Proc. Turbo Expo, 2001-GT-0145.

Table1: Cascade Geometric Parameters

Actual chord length, C (cm)	35.86
Axial chord length, Cax (cm)	30.36
Aspect ratio (true chord length to blade span), C/S	0.77
Solidity ratio (true chord length to blade pitch), C/P	1.23
Flow inlet angle (degrees)	0

Table 2: Upstream reference properties for measurements and computations

Average upstream reference velocity, U_{ref} (m/s)	10.10 (measurements) 10.26 (computations)
Inlet Reynolds number, Re_{in}	2.30×10^6 (measurements) 2.33×10^6 (computations)
Average reference static pressure, $P_{stat,r}$ (Pa, gage)	-138.0 (measurements) -40.0 (computations)
Average reference total pressure, $P_{tot,r}$ (Pa, gage)	-78.0 (measurements) 25.0 (computations)
BL thickness, δ (mm)	44.0 (measurements) 29.0 (computations)
Disp. thichness, $\delta 1$ (mm)	5.5 (measurements)
Mom. Thickness, $\delta 2$ (mm)	4.3 (measurements)
Thermal boundary layer thickness (mm)	28.0 (measurements) 18.0 (computations)
Stagnation temperature, $T_{o,in}$ (K)	302
Stagnation pressure, $P_{o,in}$ (Pa)	1.013×10^3 (measurements)
Upstream streamwise turbulence intensity	4.0%

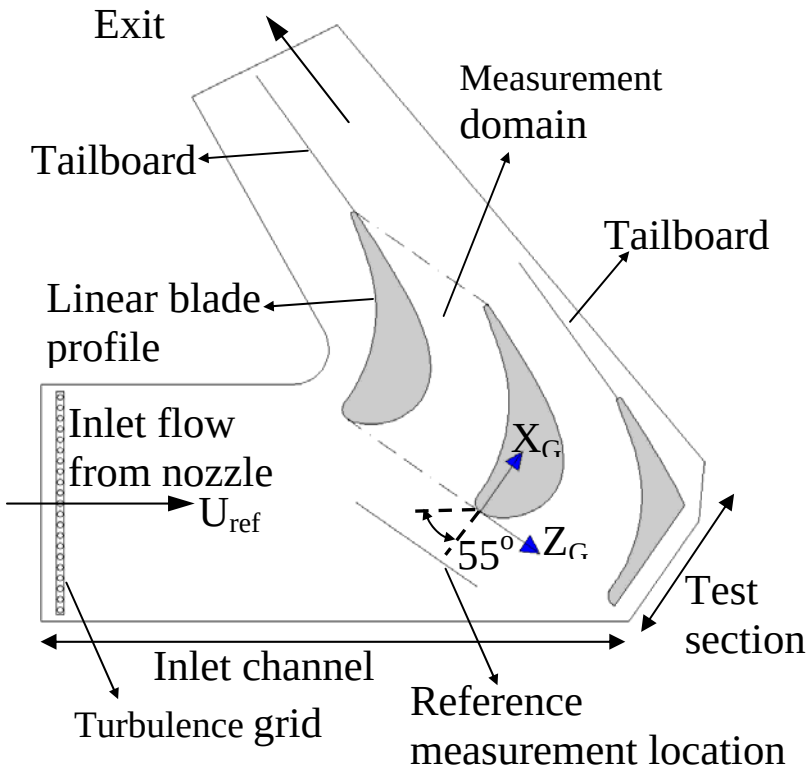

Fig. 1(a): Schematic of the cascade test facility and blade orientation in the test section.

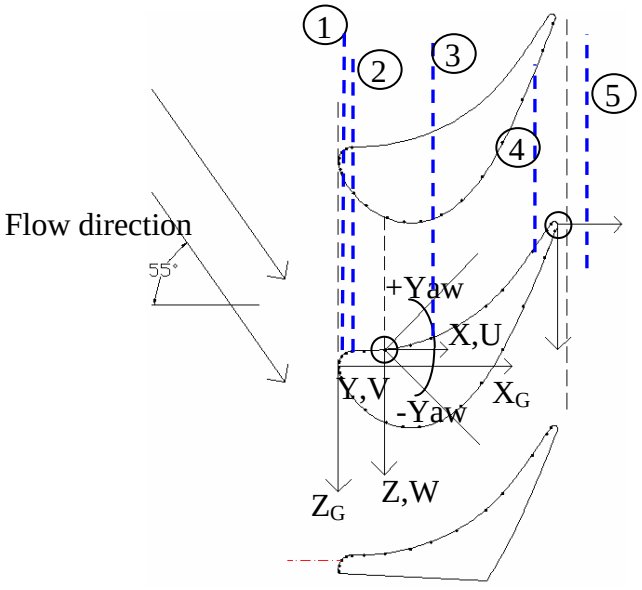

Flow analysis plane	Location, X_G/C_{ax}
1	0.036
2	0.085
3	0.424
4	0.916
5	1.241

Figure 1(b): Coordinate systems and flow analysis plane in the blade passage.

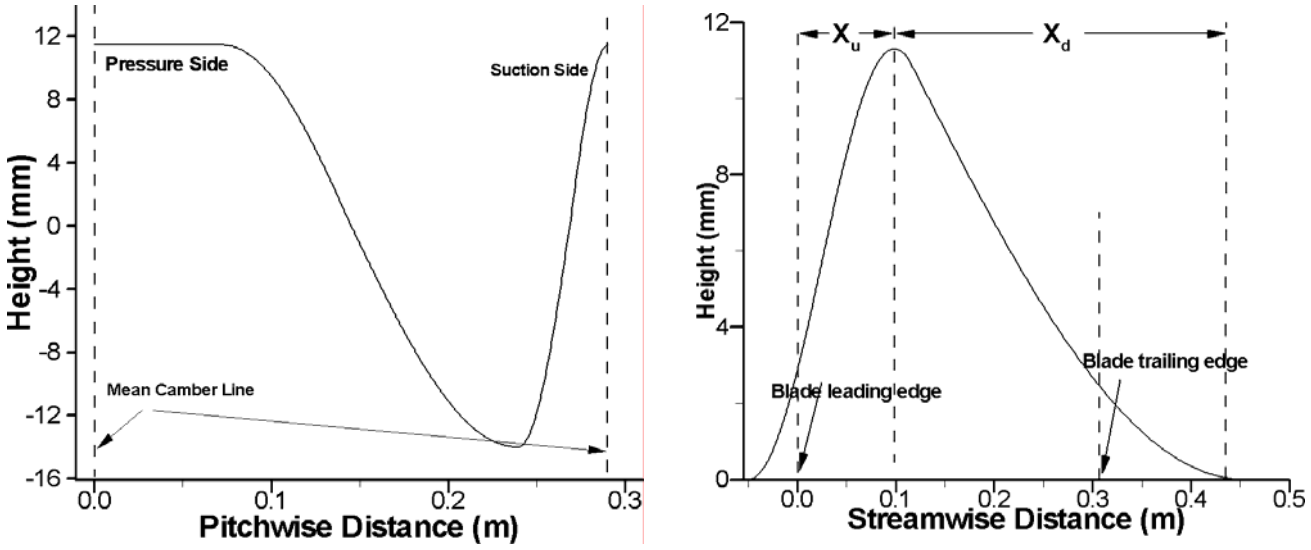

Figure 2(a): Curves employed to vary the pitchwise and streamwise heights of the experimental non-axisymmetric endwall profile.

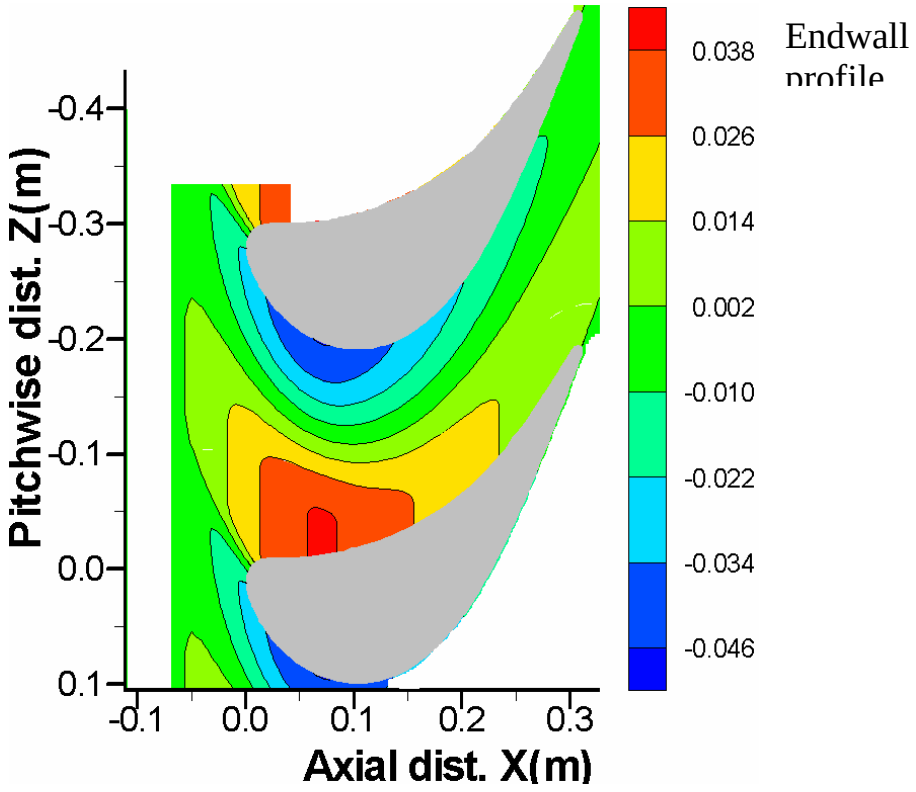

Figure 2(b): Non-axisymmetric endwall profile height obtained from the curves in Fig. 2(a).

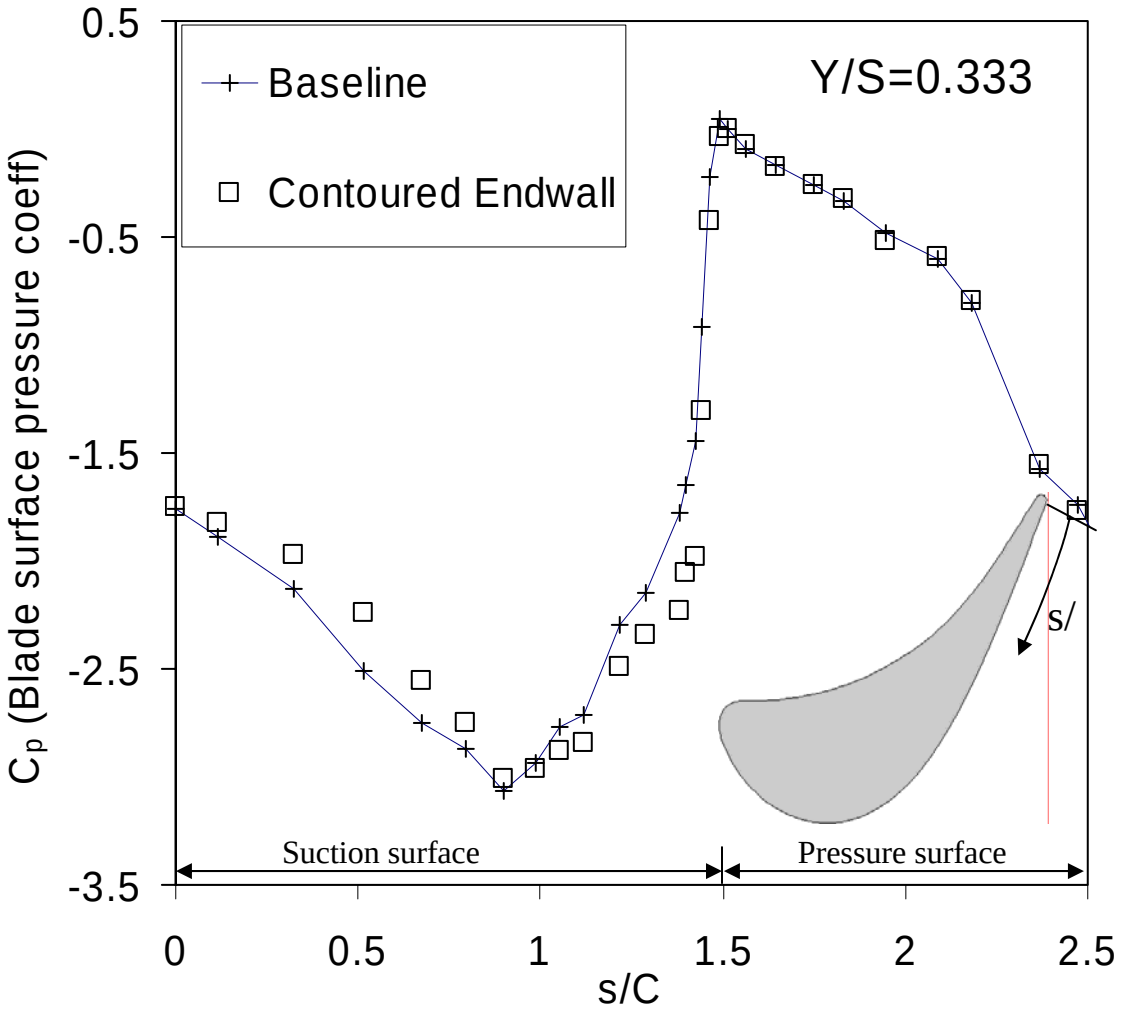

Figure 3: Blade wall static pressure coefficient at spanwise location Y/S=0.333 for the baseline and contoured endwall.

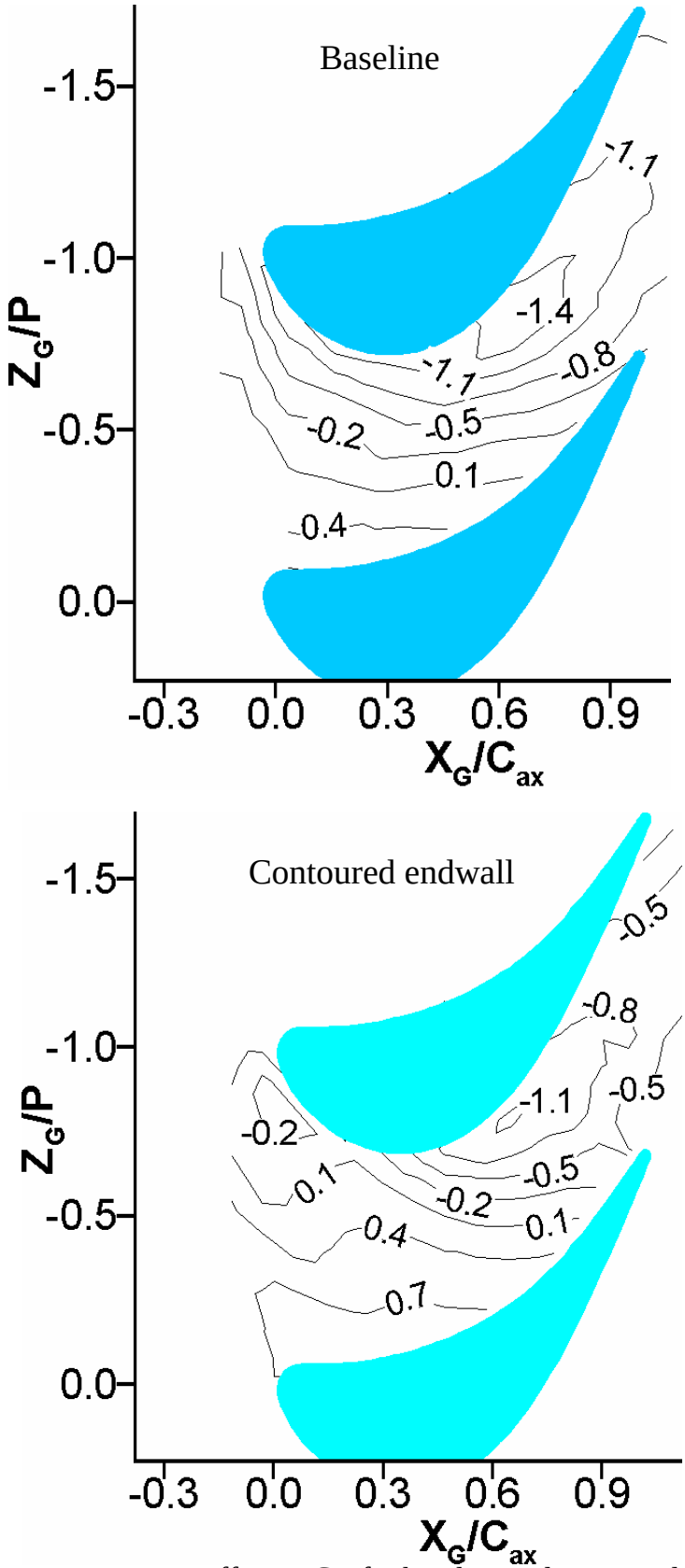

Figure 4: Endwall static pressure coefficient $C_{p,e}$ for baseline and contoured endwall.

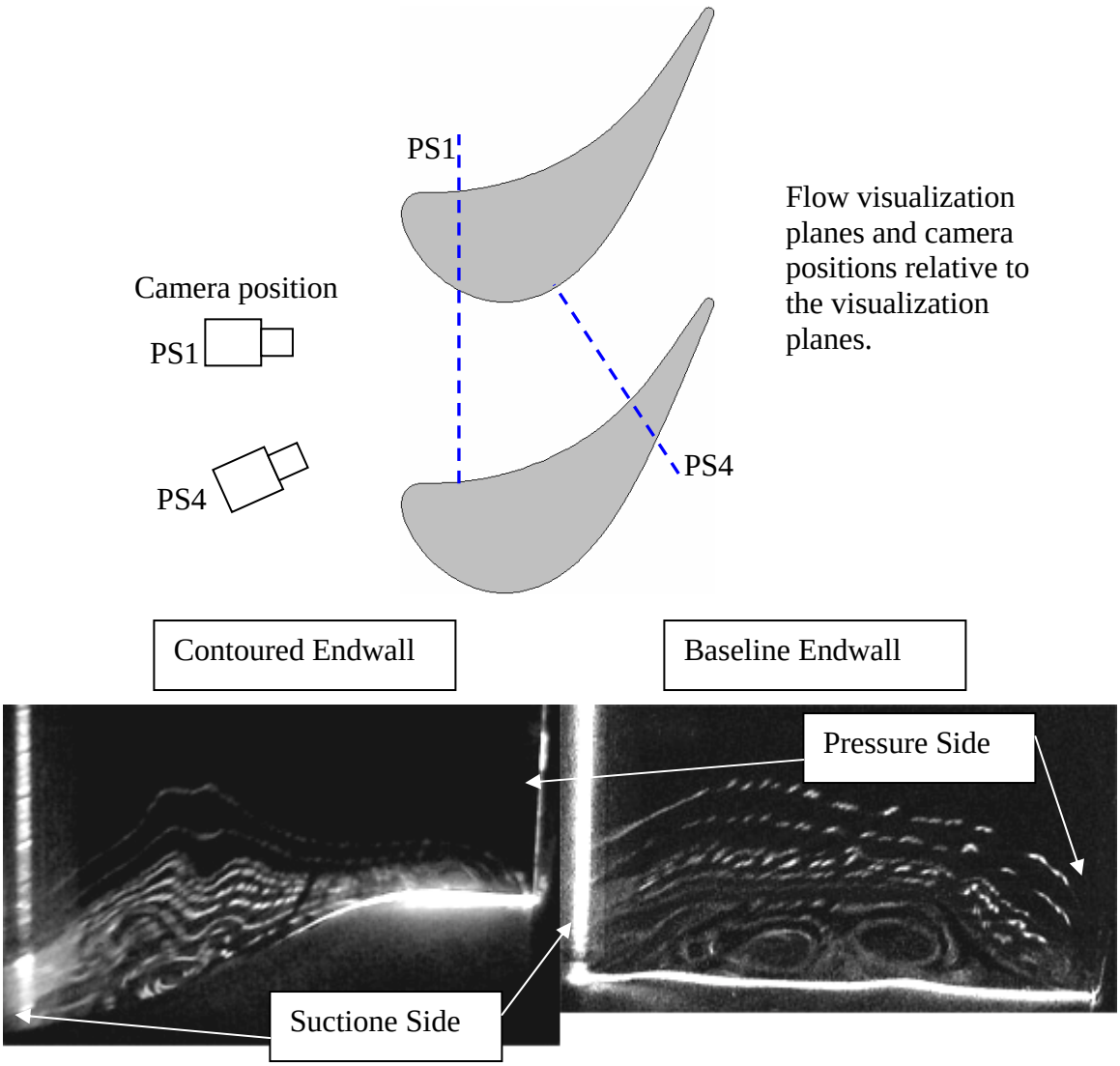

Figure 5. Instantaneous flow visualization images in the plane PS1 for baseline and contoured endwall.

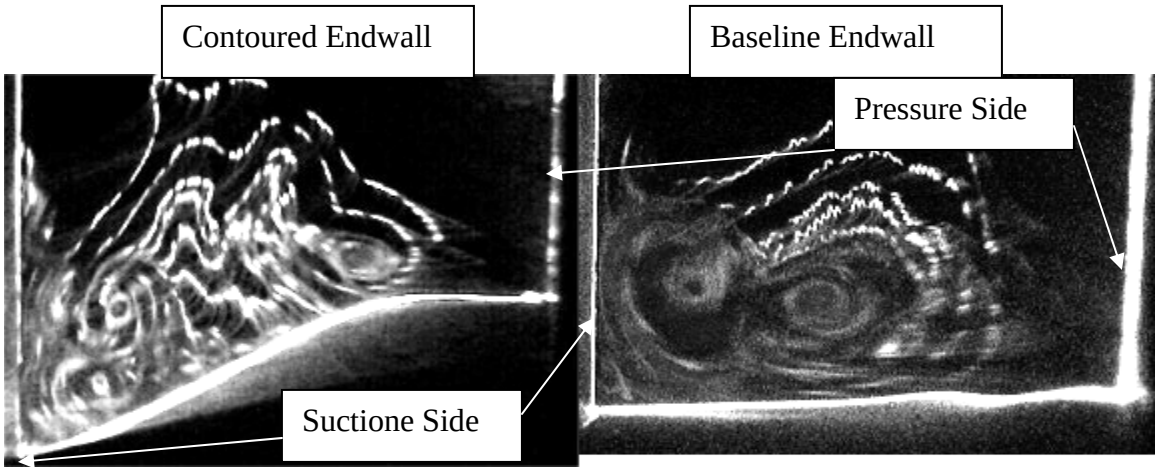

Figure 6. Instantaneous flow visualization images in the plane PS4 for baseline and contoured endwall.

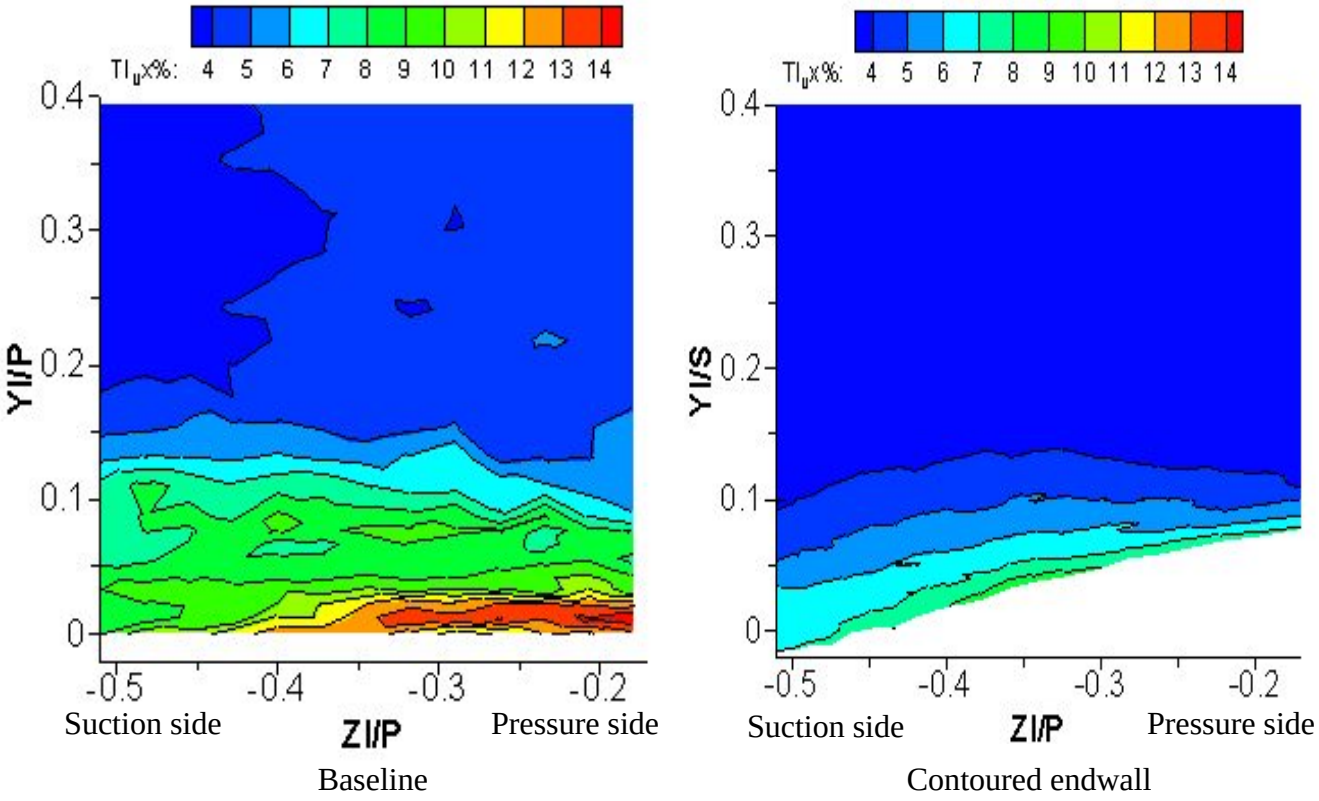

Baseline Contoured endwall

Figure 7: Streamwise turbulence intensity (%) in pitchwise plane at X_G/C_{ax}=0.085 for baseline and contoured endwall.

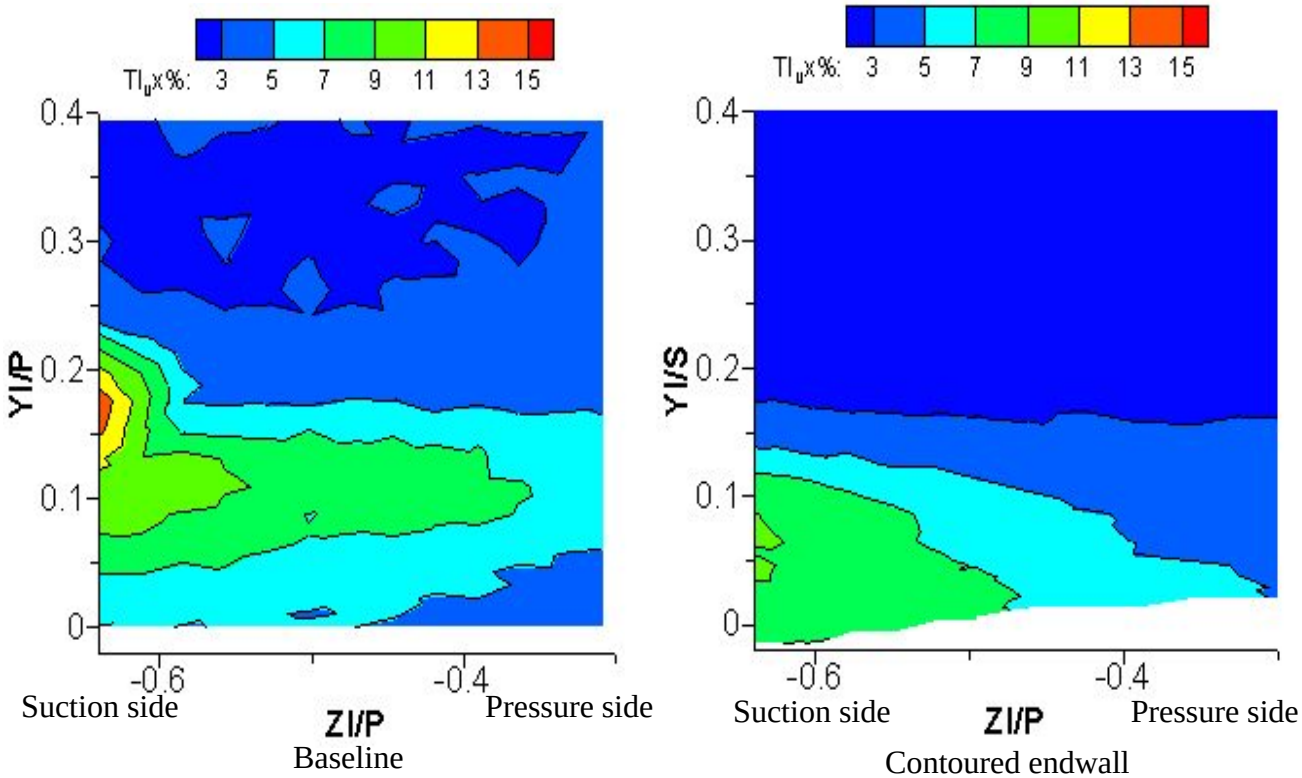

Baseline Contoured endwall

Figure 8: Streamwise turbulence intensity (%) in pitchwise plane at X_G/C_{ax}=0.916 for baseline and contoured endwall.

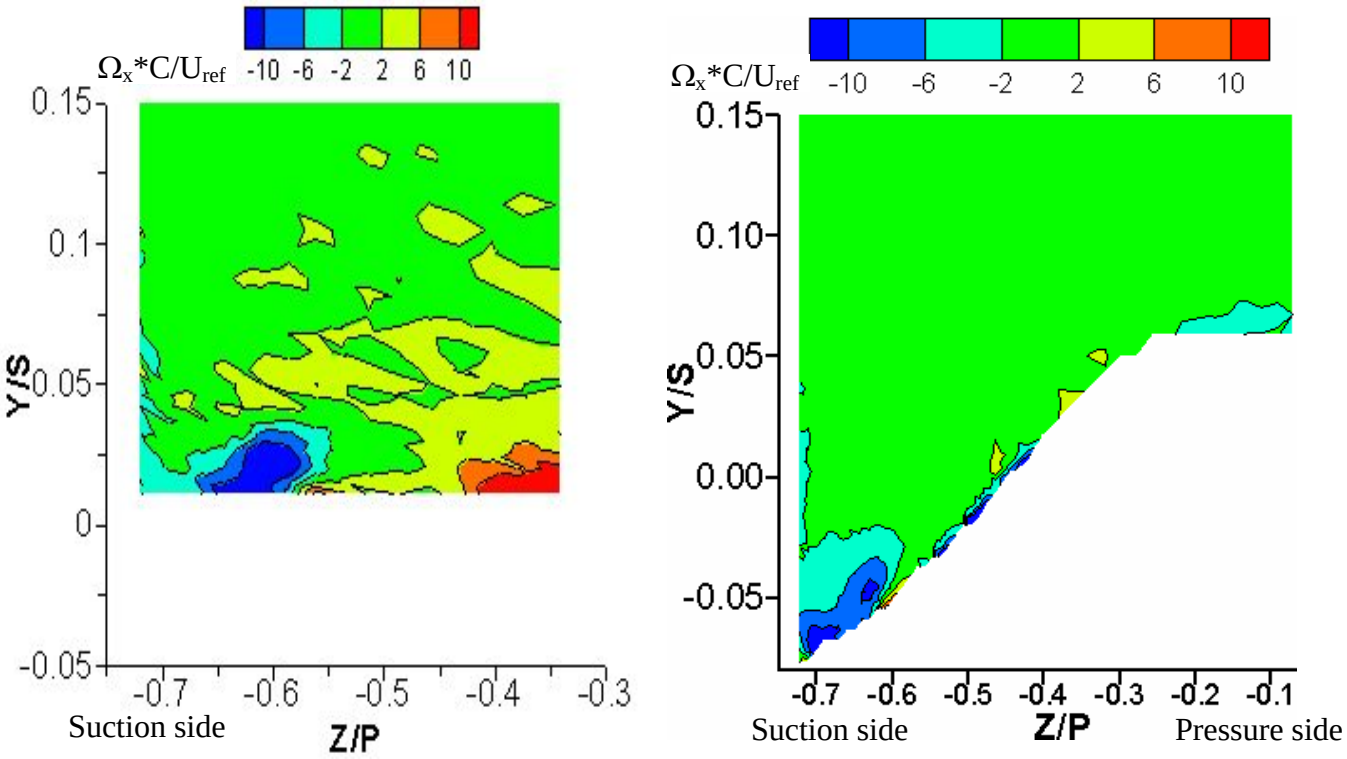

Baseline Contoured endwall

Figure 9: Normalized axial vorticity, $\Omega_x C/U_{ref}$ in pitchwise plane at X_G/C_{ax}=0.085 for baseline and contoured endwall.

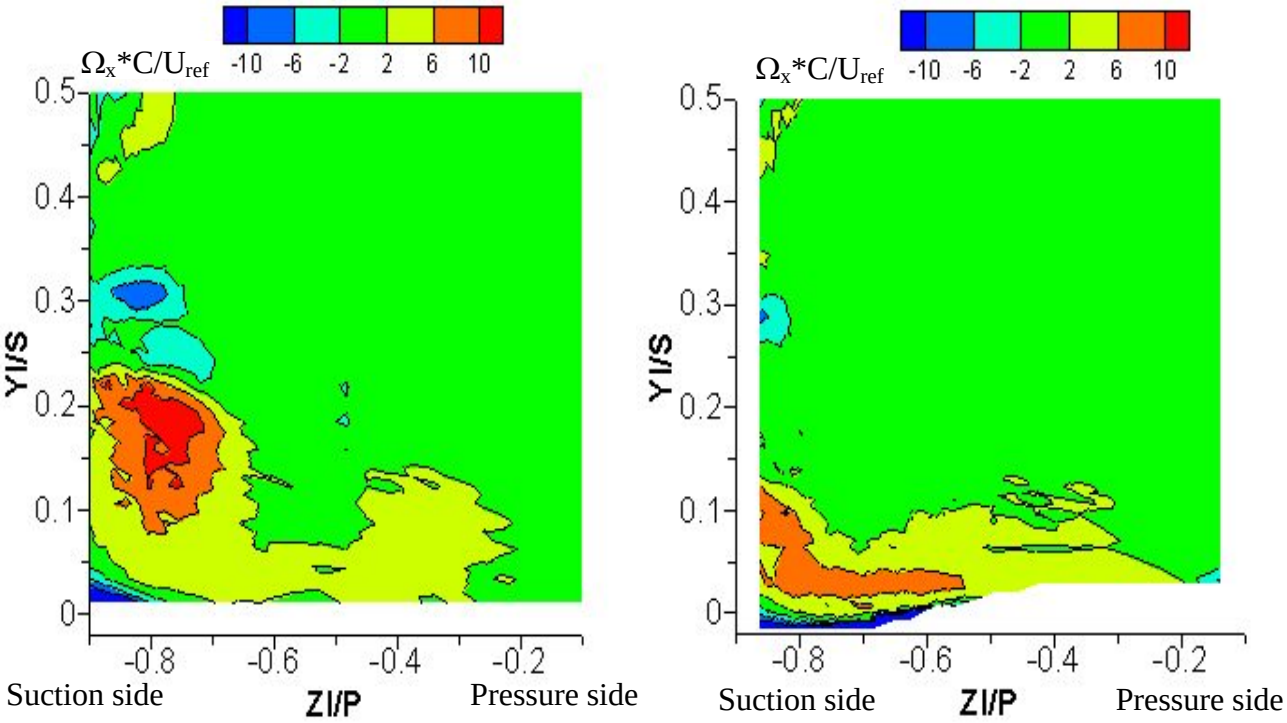

Baseline Contoured endwall

Figure 10: Normalized axial vorticity, $\Omega_x C/U_{ref}$ in pitchwise plane at X_G/C_{ax}=0.916 for baseline and contoured endwall.

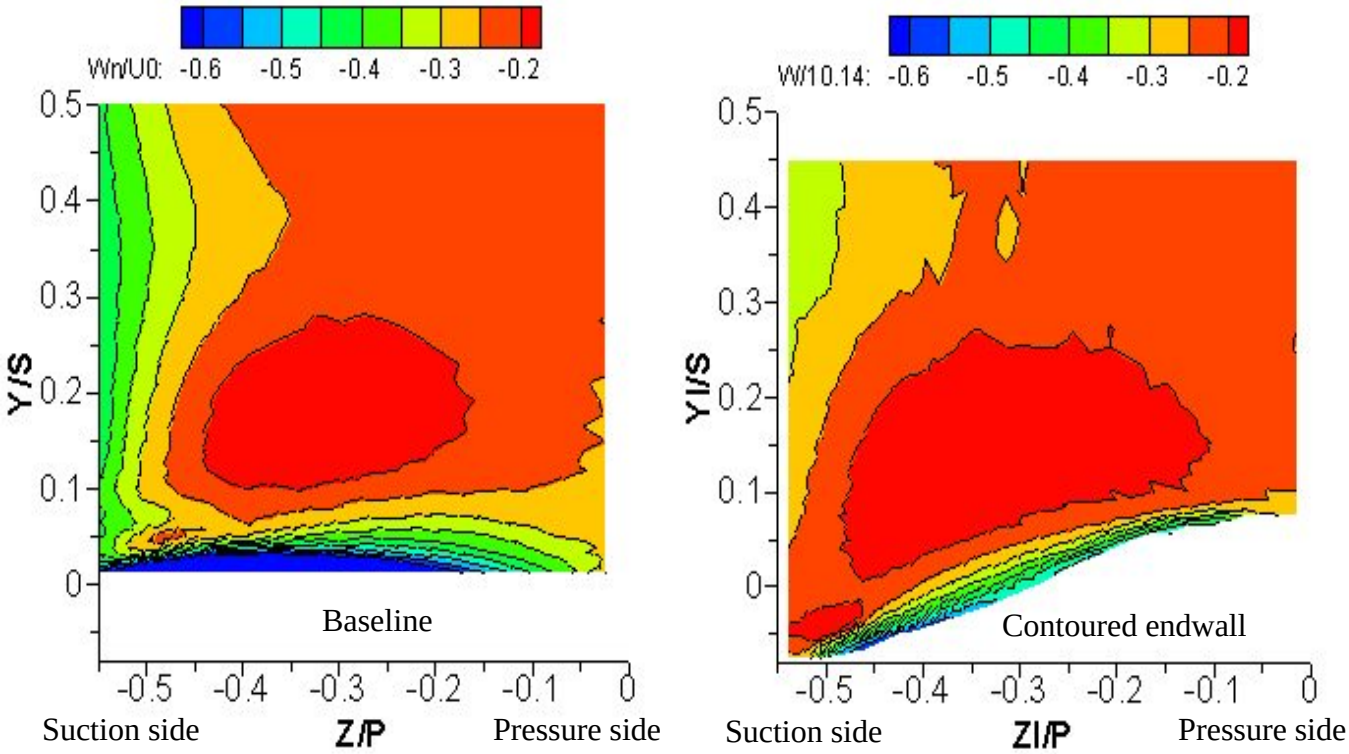

Figure 11: Normalized pitchwise velocity, W/U_{ref} in pitchwise plane at X_G/C_{ax}=0.424 for baseline and contoured endwall.

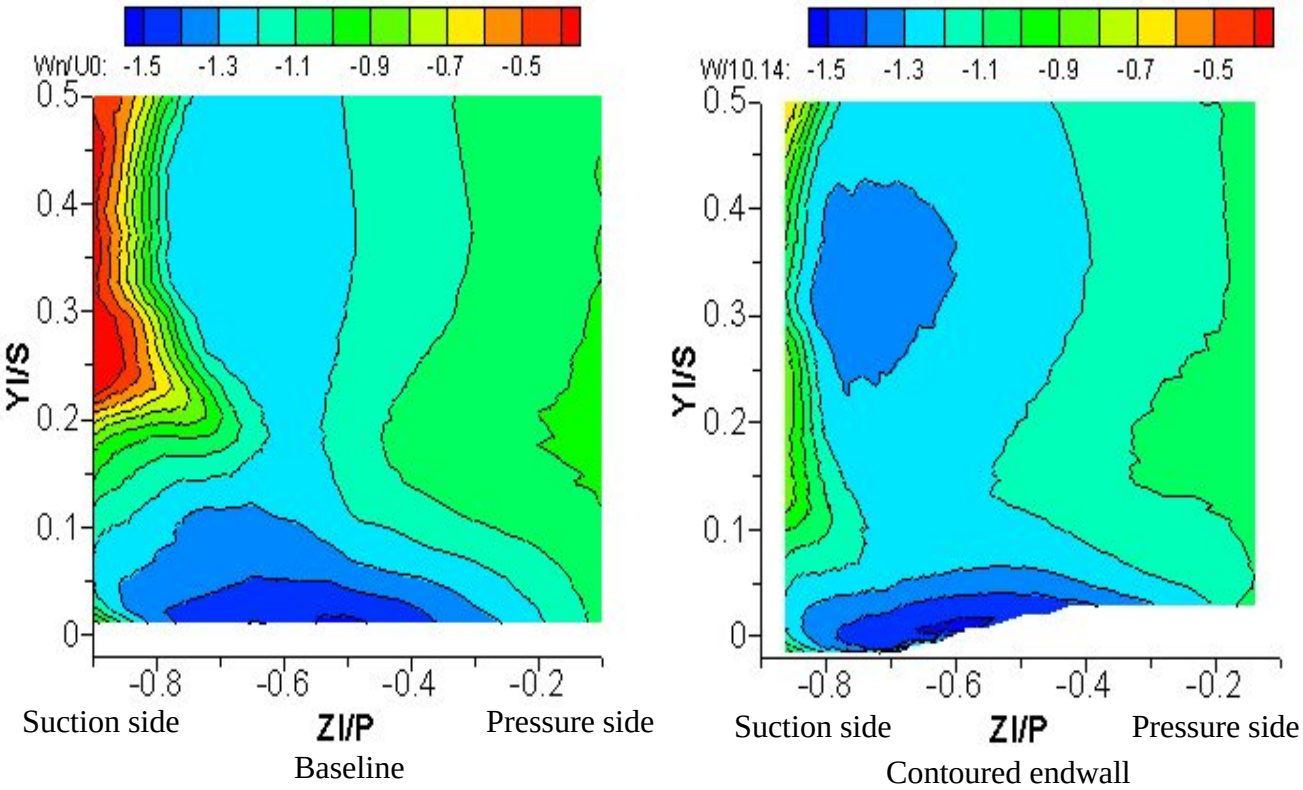

Figure 12: Normalized pitchwise velocity, W/U_{ref} in pitchwise plane at X_G/C_{ax}=0.916 for baseline and contoured endwall.

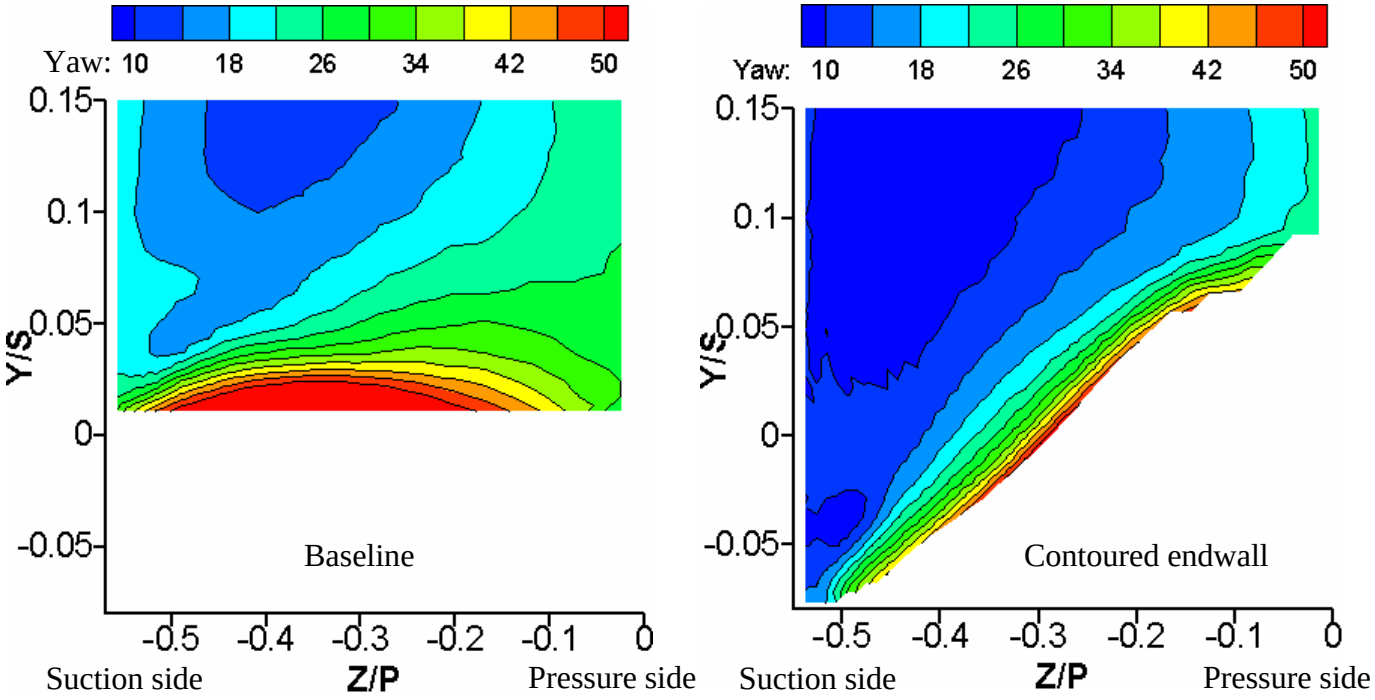

Figure 13: Flow Yaw angle (degree) in pitchwise plane at X_G/C_{ax}=0.424 for baseline and contoured endwall.

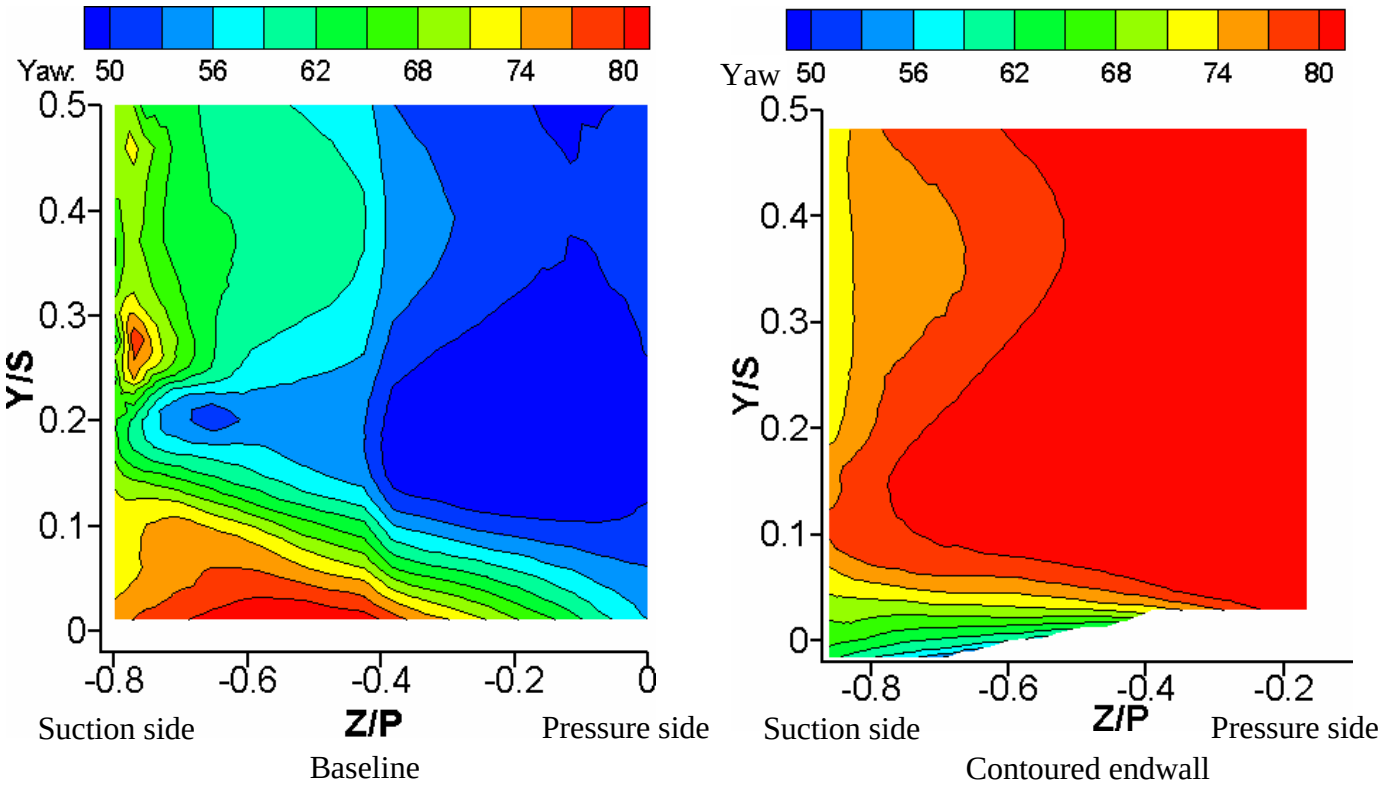

Figure 14: Flow Yaw angle (degree) in pitchwise plane at X_G/C_{ax}=0.916 for baseline and contoured endwall.

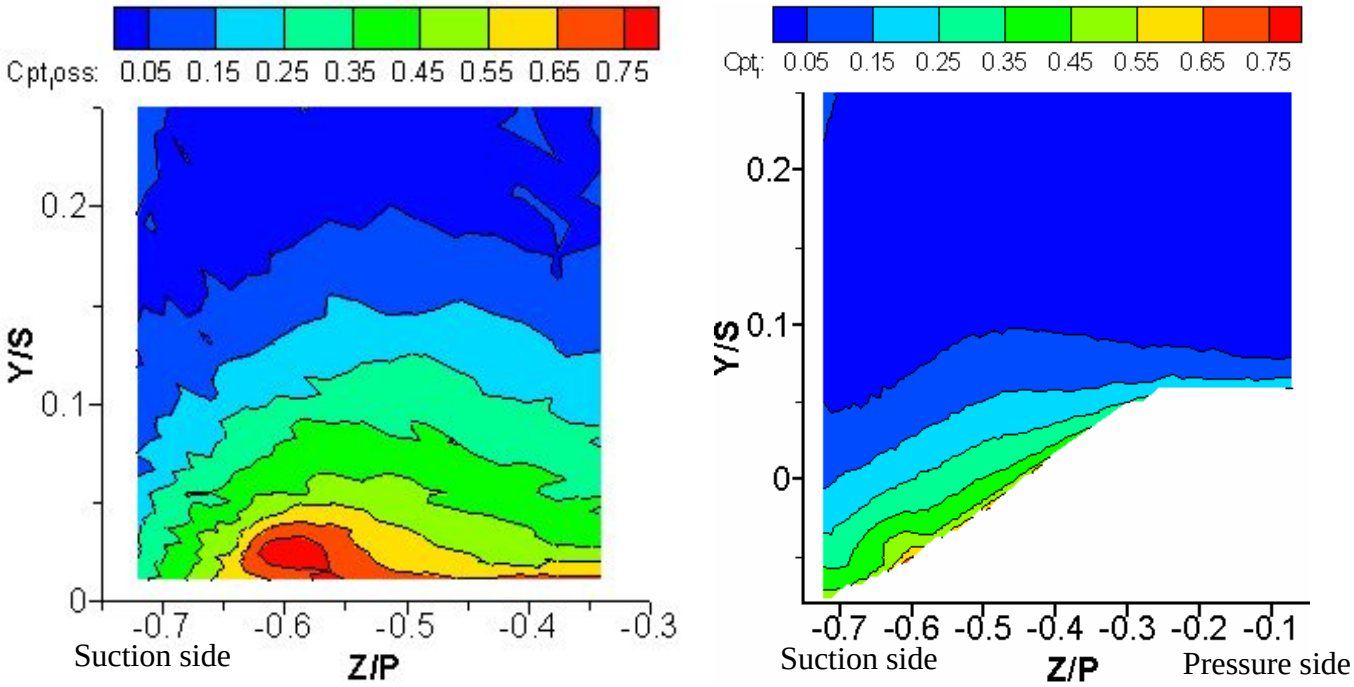

Baseline Contoured endwall

Figure 15: Total pressure loss coefficient, $C_{pt,loss}$ in pitchwise plane at X_G/C_{ax}=0.085 for baseline and contoured endwall.

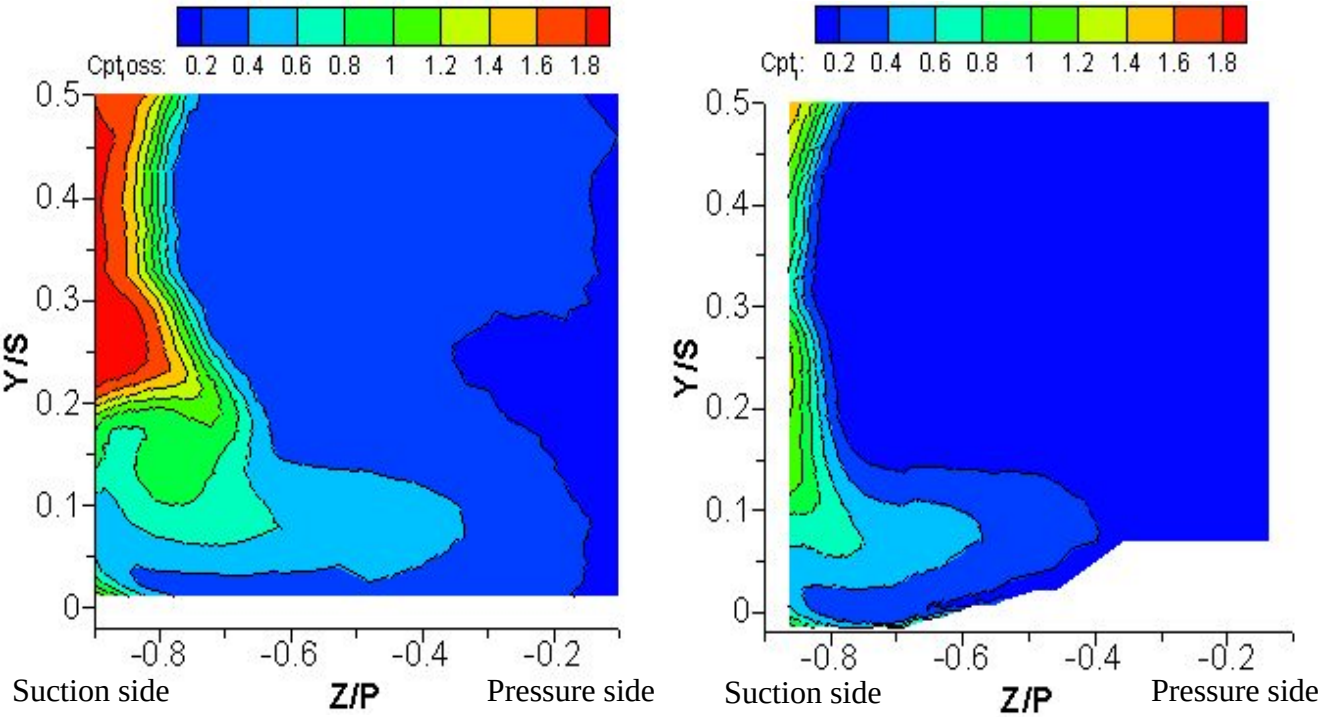

Baseline Contoured endwall

Figure 16: Total pressure loss coefficient $C_{pt,loss}$ in pitchwise plane at X_G/C_{ax}=0.916 for baseline and contoured endwall.

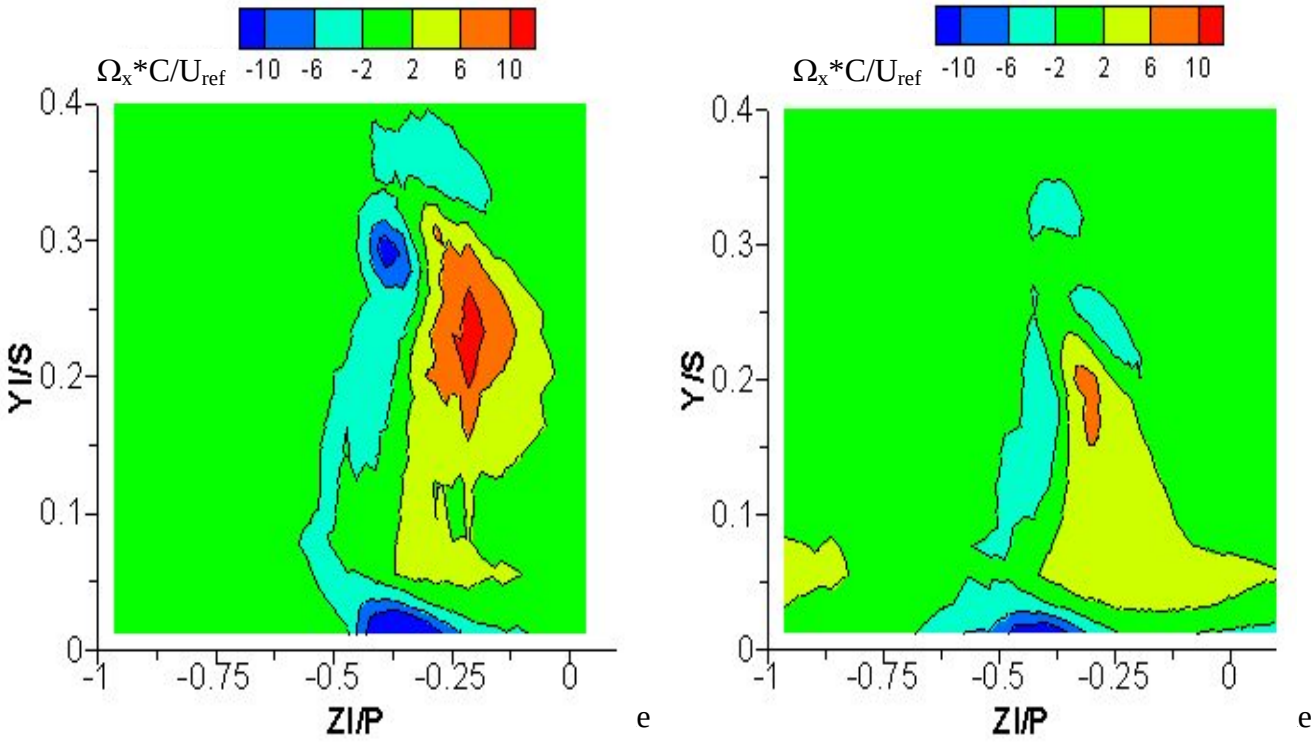

e

Baseline

Contoured endwall

e

Figure 17: Normalized axial vorticity, $\Omega_x C/U_{ref}$ in pitchwise plane at X_G/C_{ax}=1.214 for baseline and contoured endwall.

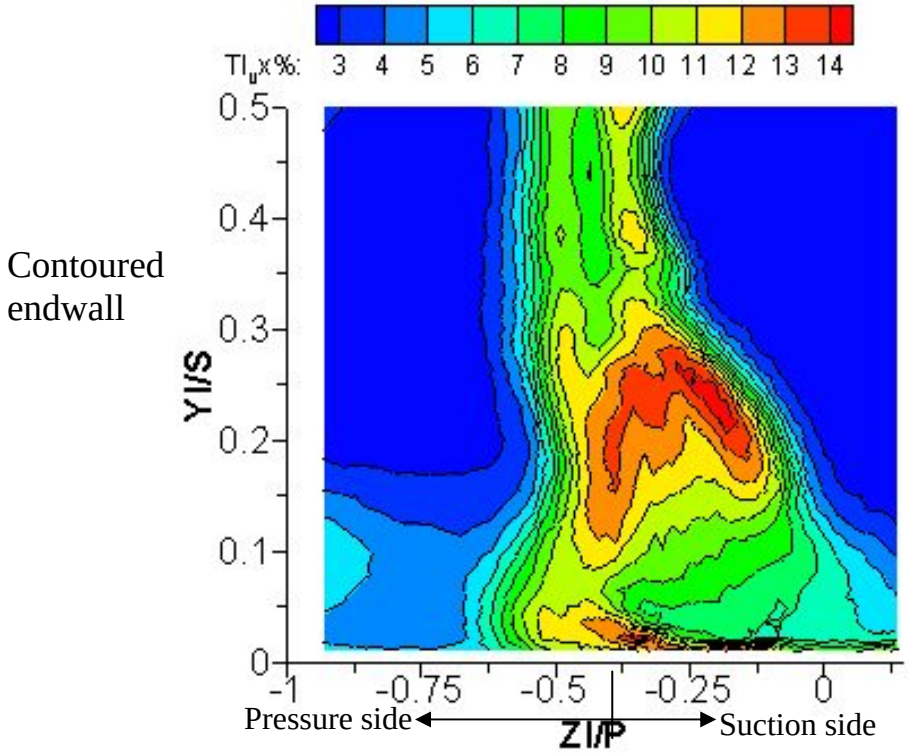

Contoured endwall

Figure 18: Streamwise turbulence intensity (%) in pitchwise plane at X_G/C_{ax}=1.214 for the contoured endwall.

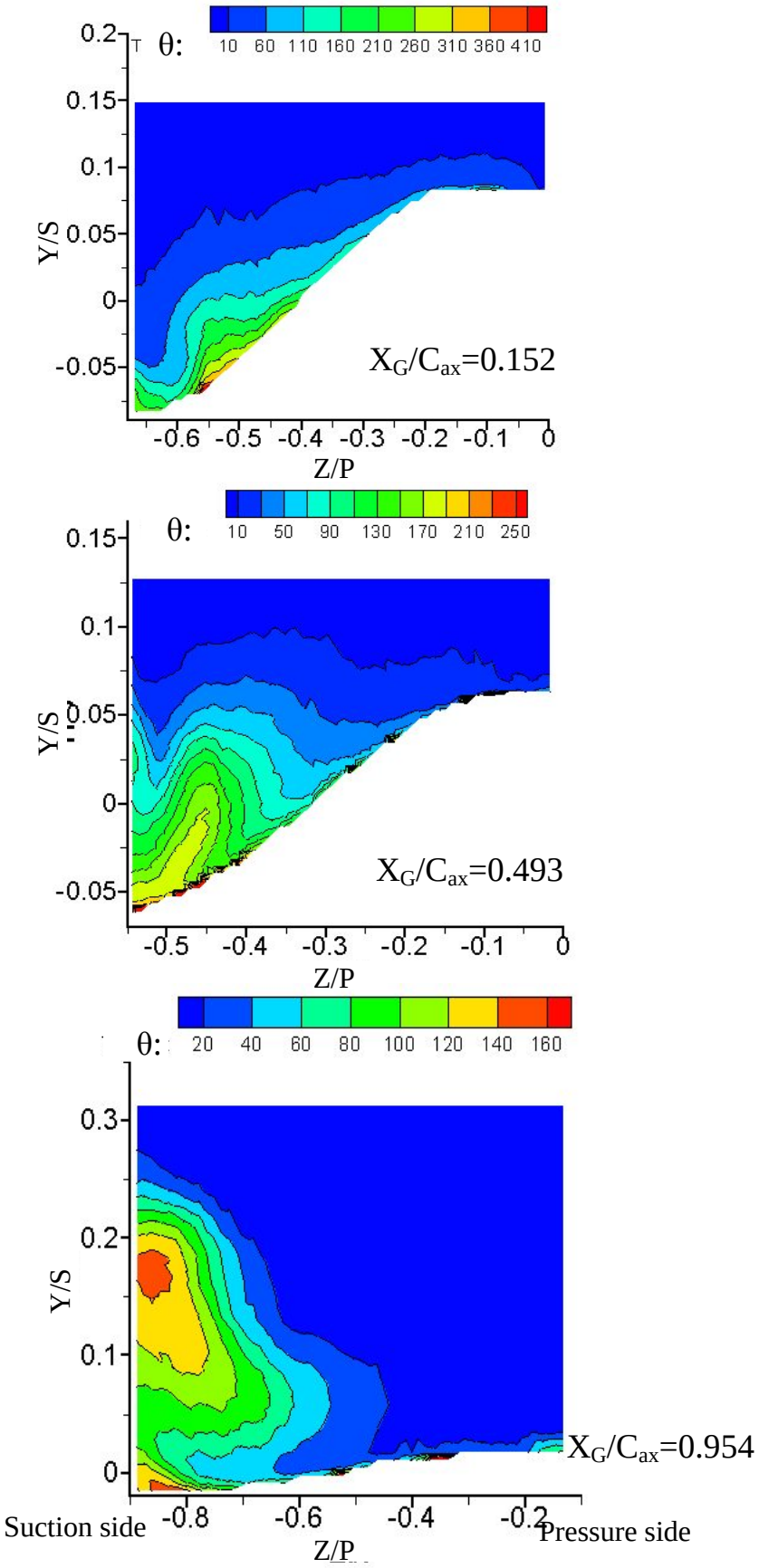

Figure 19: Non-dimensional fluid temperature, θ in pitchwise planes near endwall at different axial locations for the contoured endwall with endwall heating at constant flux.

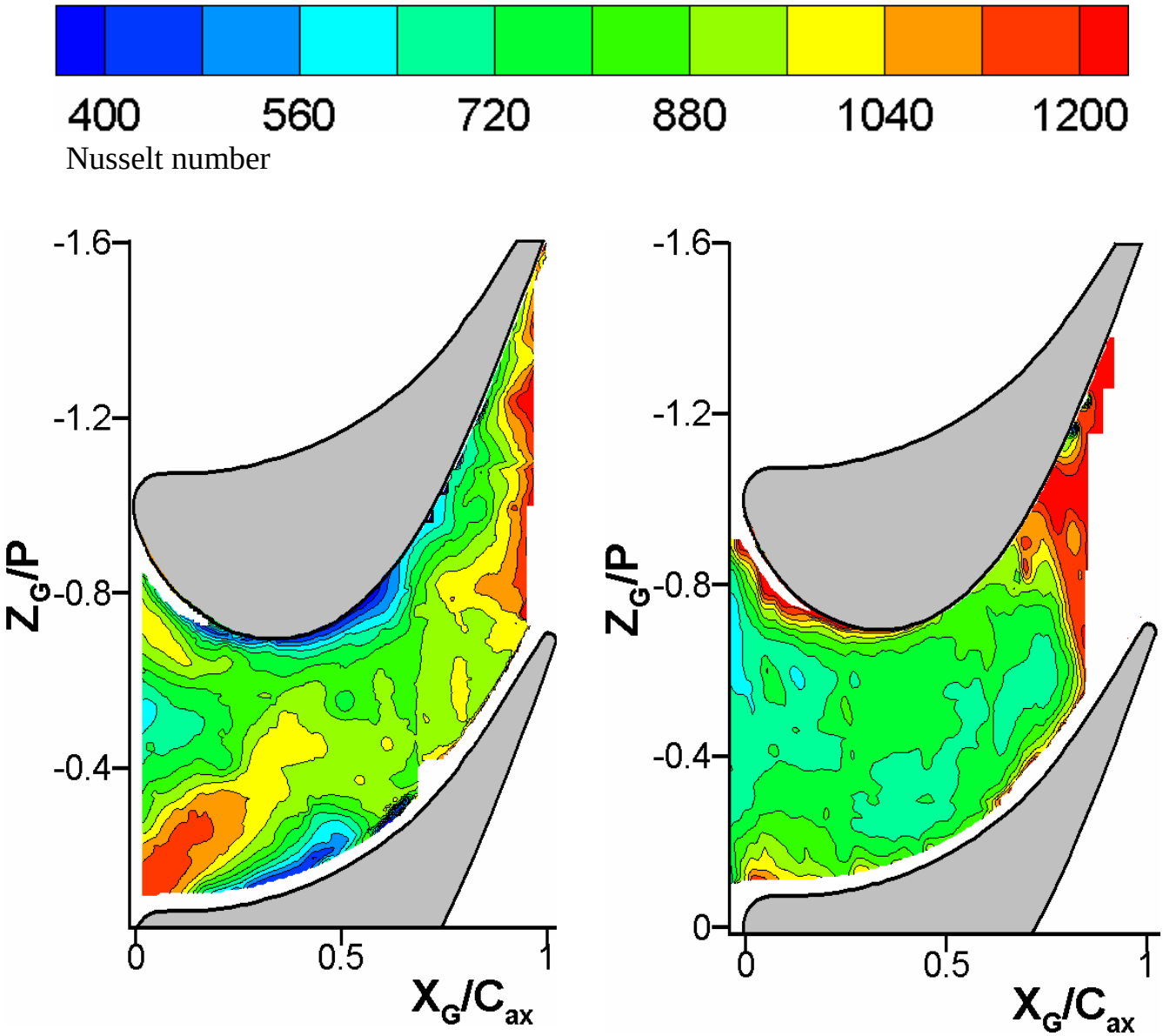

Baseline (flat endwall)

3D non-axisymmetric endwall

Figure 20: Nusselt number distributions on endwall along blade passage for baseline and 3D non-axisymmetric endwall.

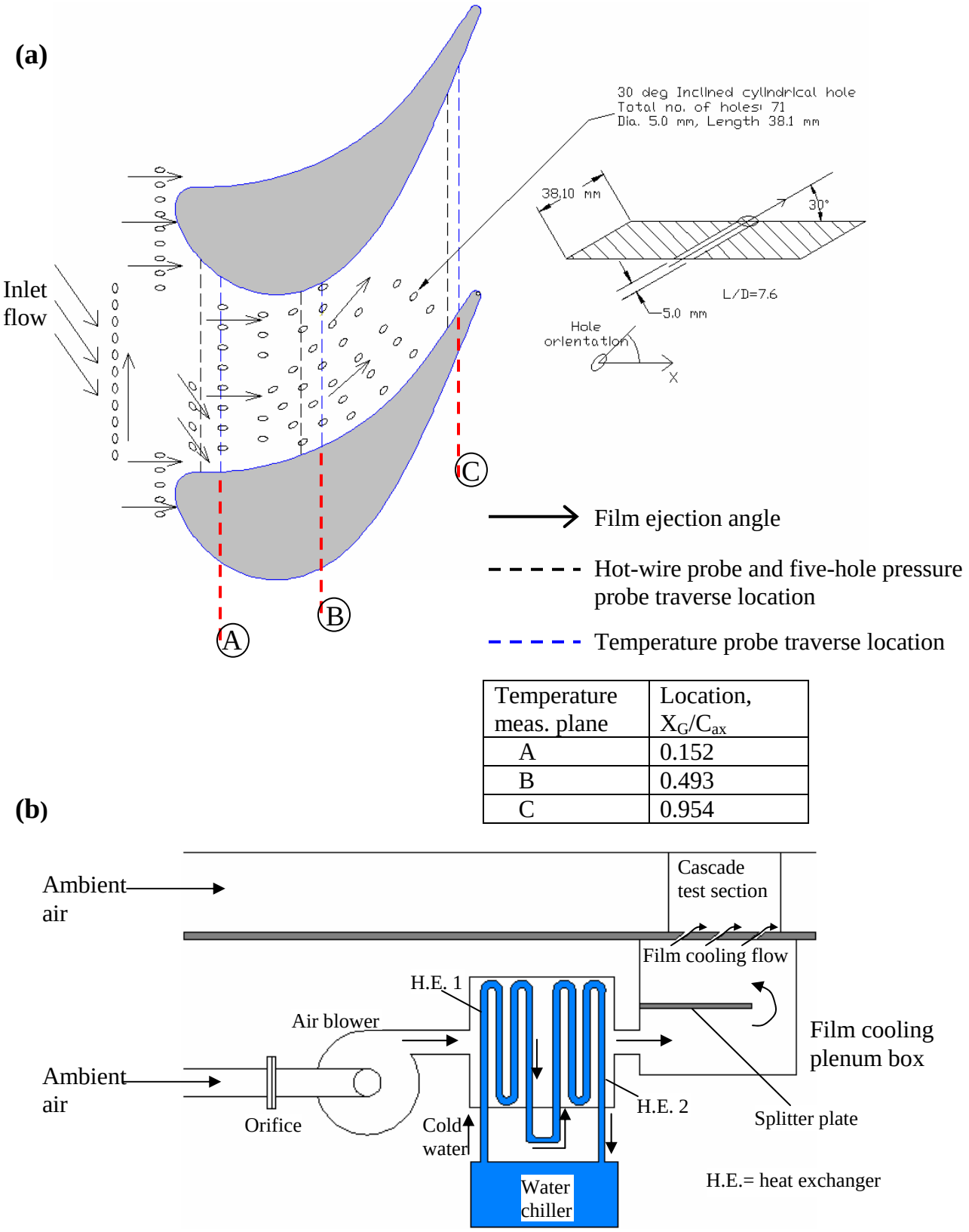

Temperature meas. plane	Location, X_G/C_{ax}
A	0.152
B	0.493
C	0.954

Figure 21: (a) Configuration of film cooling holes in contoured endwall and locations of flow measurement and temperature measurement planes relative to cooling holes.
(b) Schematic of coolant supply circuit to film cooled endwall.

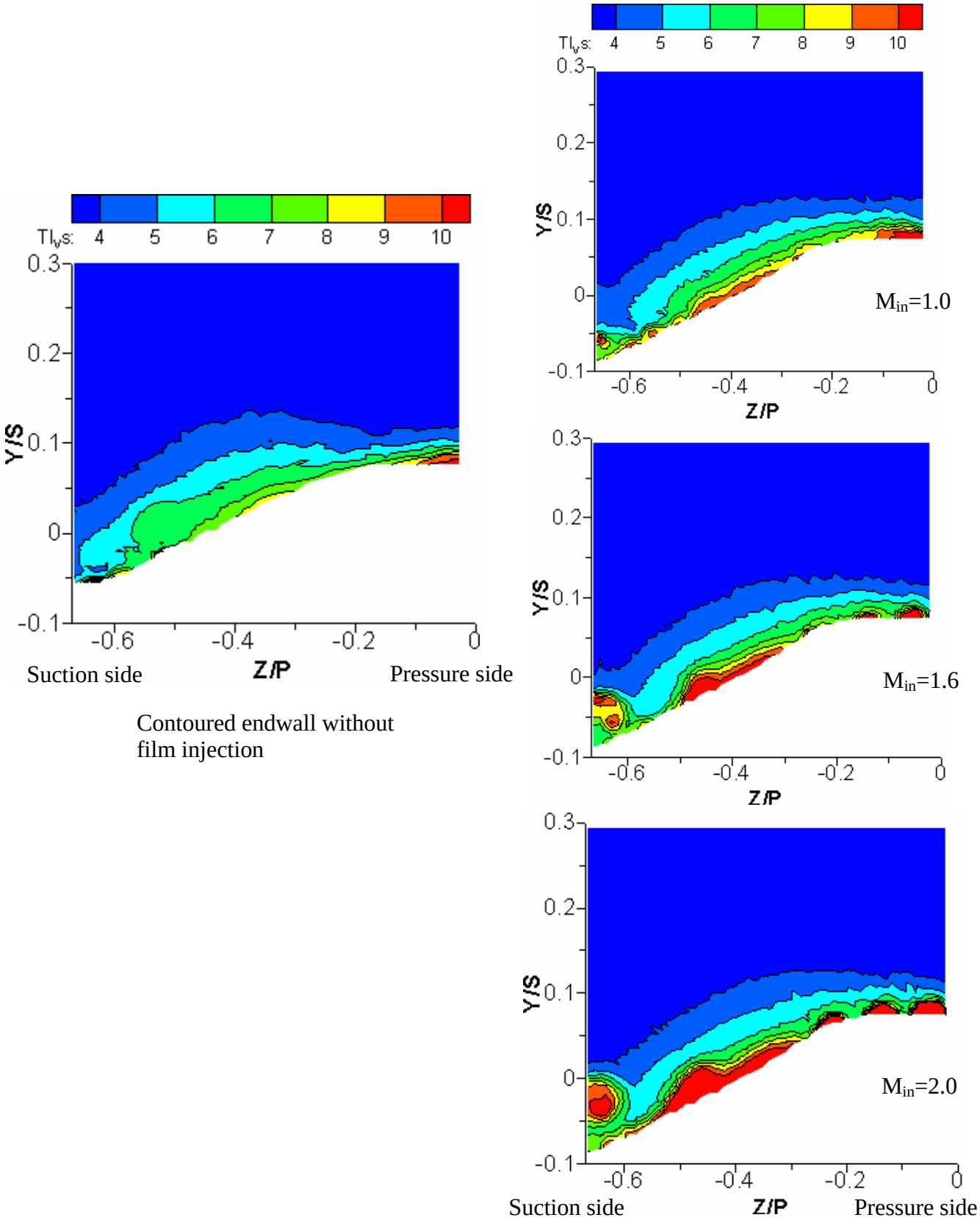

Figure 22: Streamwise turbulence intensity (%) in pitchwise plane at X_G/C_{ax}=0.085 for contoured endwall without and with film injection at inlet blowing ratios M_{in}=1.0 to 2.0.

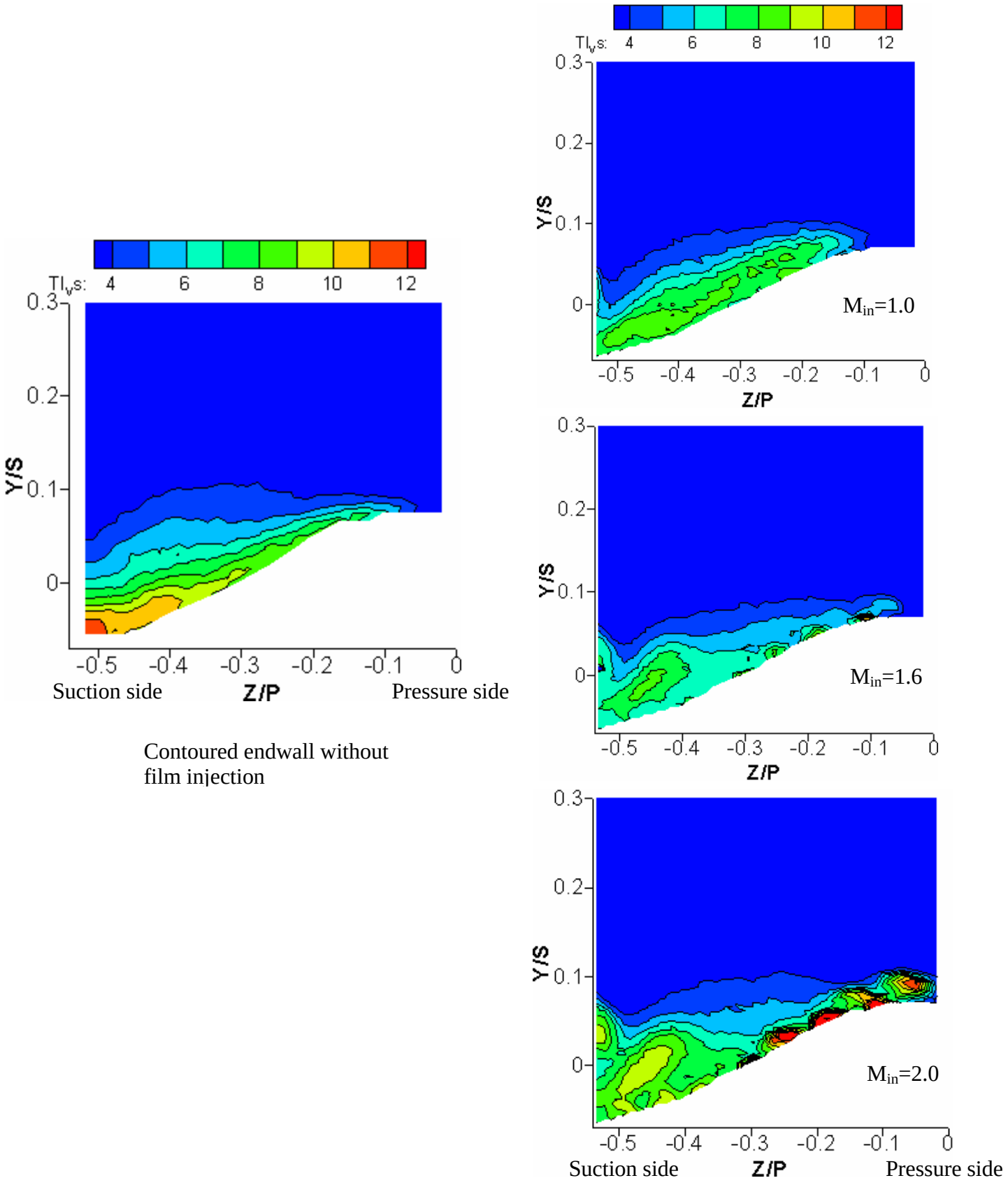

Contoured endwall without film injection

Figure 23: Streamwise turbulence intensity (%) in pitchwise plane at X_G/C_{ax}=0.424 for contoured endwall without and with film injection at inlet blowing ratios M_{in}=1.0 to 2.0.

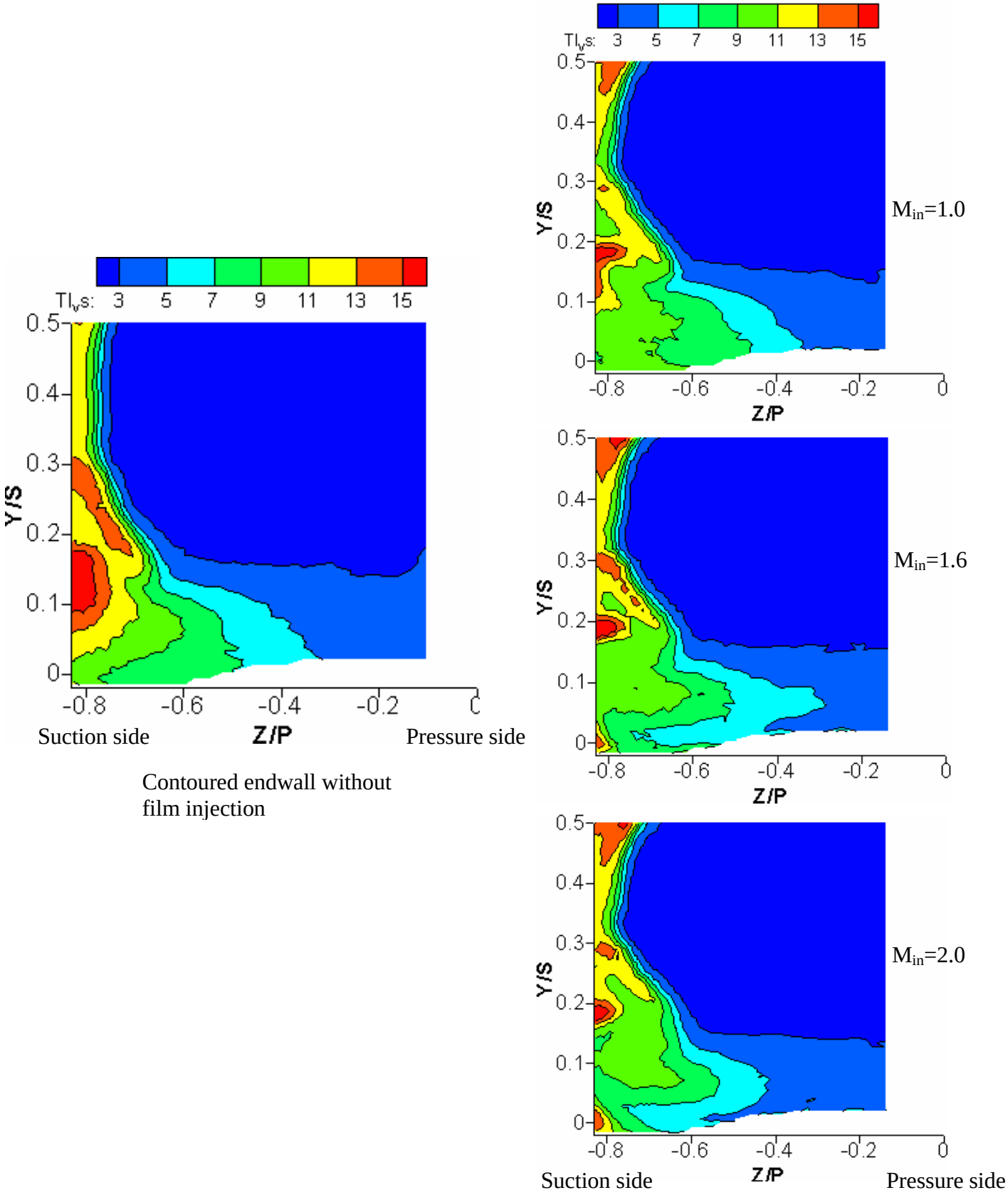

Figure 24: Streamwise turbulence intensity (%) in pitchwise plane at X_G/C_{ax}=0.916 for contoured endwall without and with film injection at inlet blowing ratios M_{in}=1.0 to 2.0.

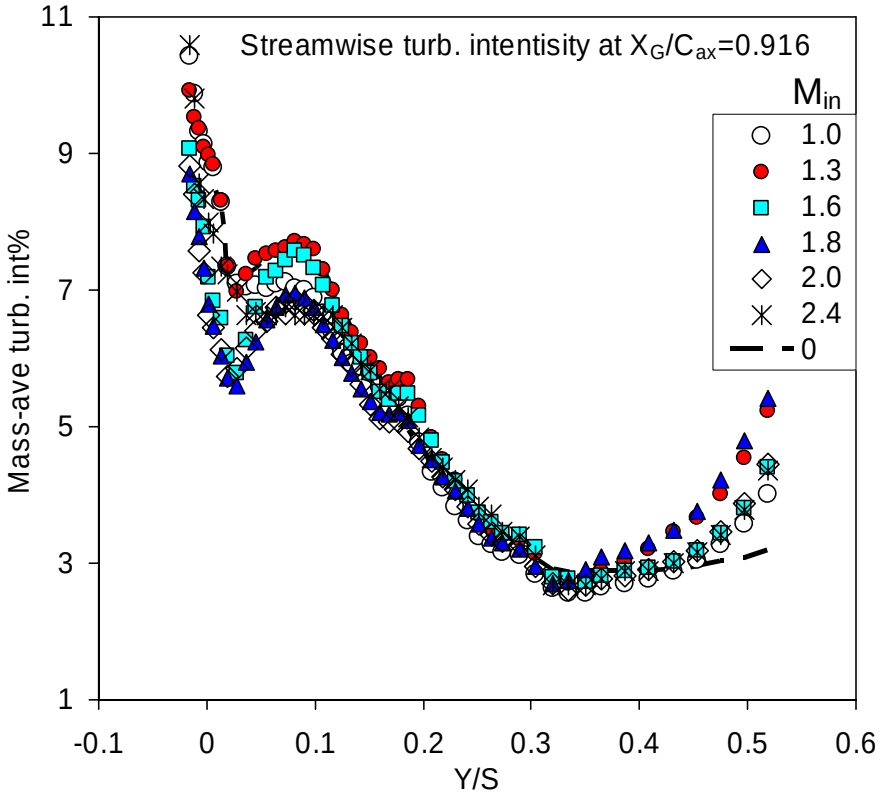

Figure 25: Pitchwise mass-averaged streamwise turbulence intensity at X_G/C_{ax}=0.916 for contoured endwall without and with film injection at inlet blowing ratios M_{in}=1.0 to 2.4.

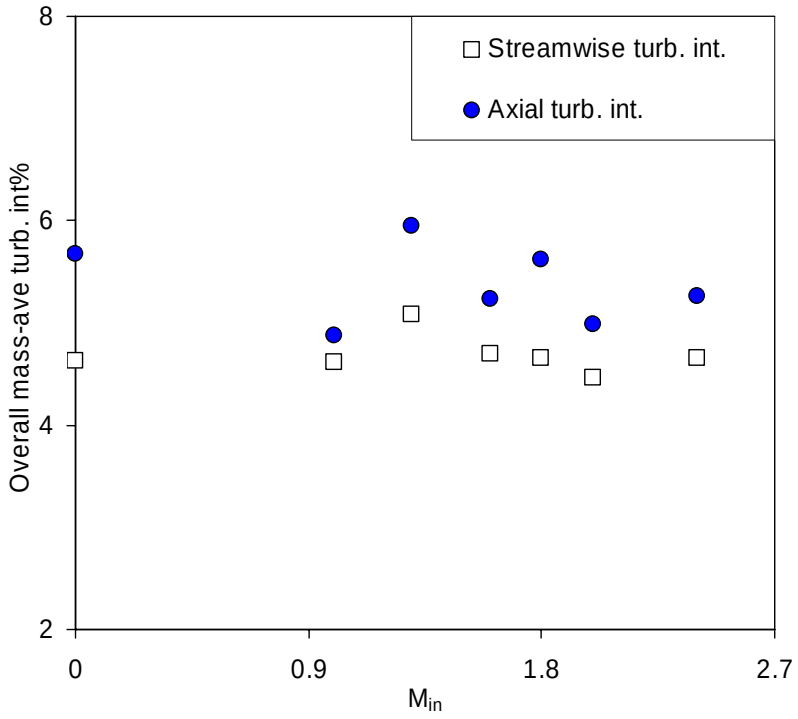

Figure 26: Overall mass-averaged streamwise and axial turbulence intensities as dependent upon inlet blowing ratio, M_{in} at X_G/C_{ax}=0.916 for contoured endwall with film injection.

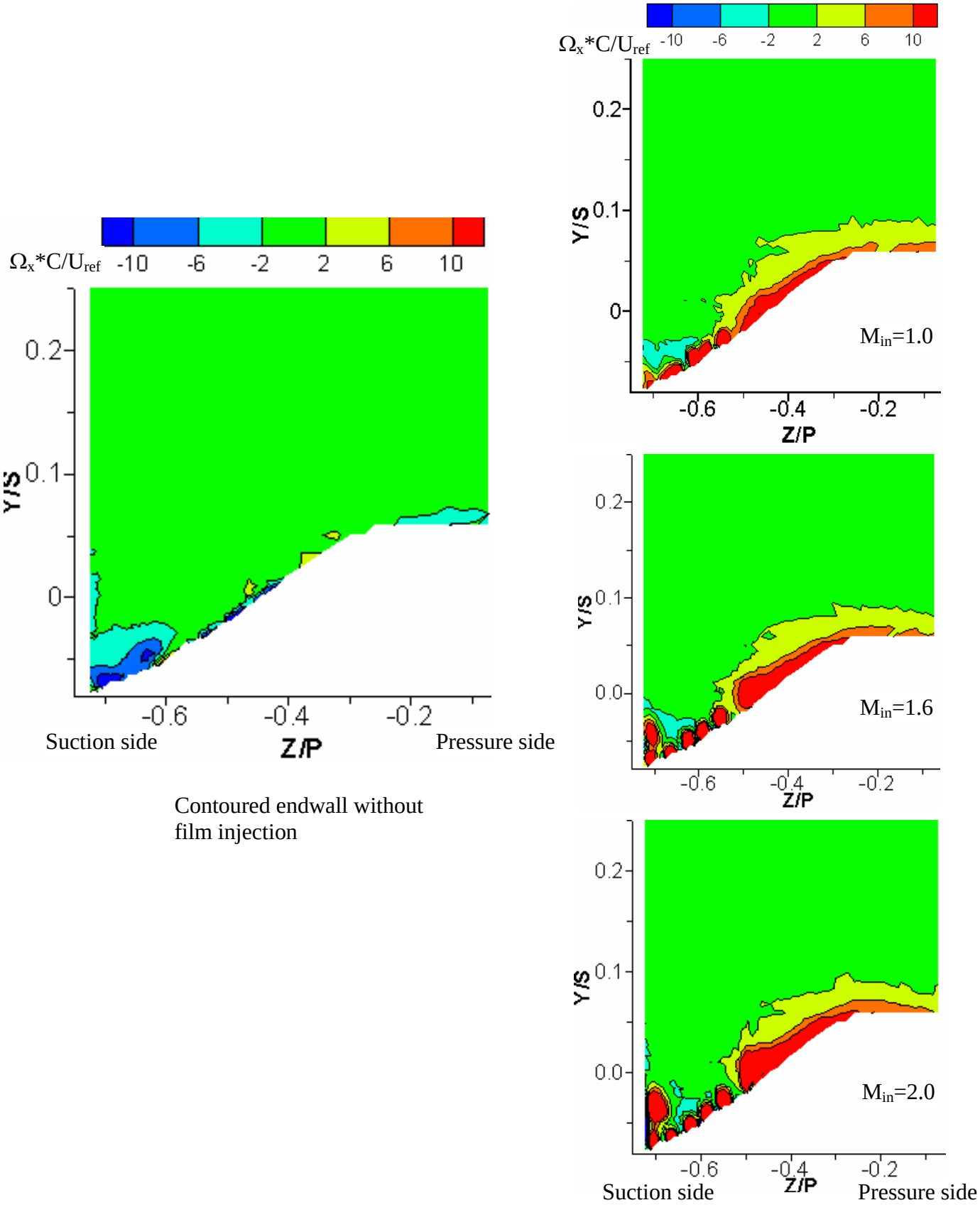

Figure 27: Normalized axial vorticity, Ω_x*C/U_{ref} in pitchwise plane at X_G/C_{ax}=0.085 for contoured endwall without and with film injection at inlet blowing ratios M_{in}=1.0 to 2.0.

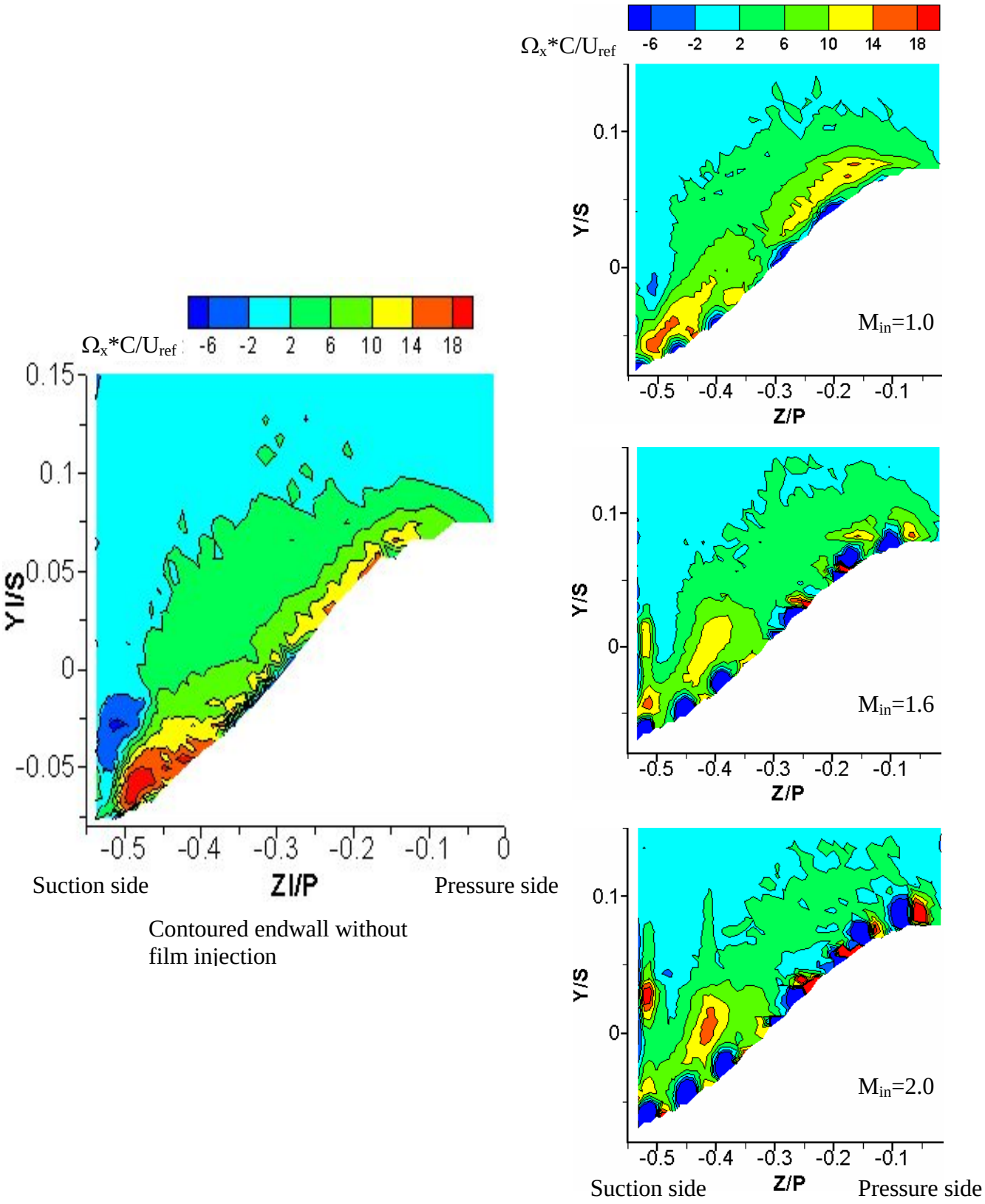

Contoured endwall without film injection

Figure 28: Normalized axial vorticity, Ω_x*C/U_{ref} in pitchwise plane at X_G/C_{ax}=0.424 for contoured endwall without and with film injection at inlet blowing ratios M_{in}=1.0 to 2.0.

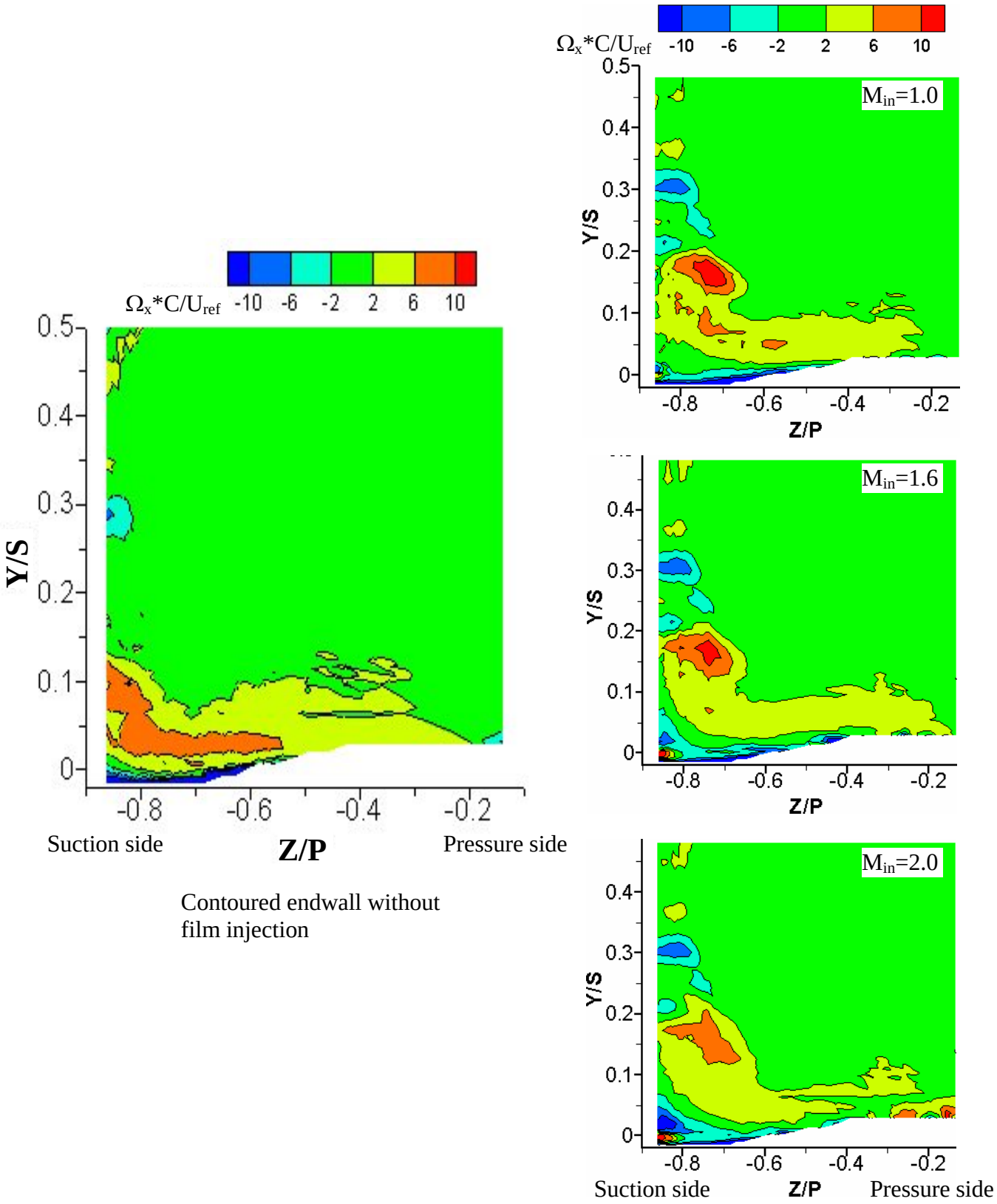

Contoured endwall without film injection

Figure 29: Normalized axial vorticity, Ω_x*C/U_{ref} in pitchwise plane at X_G/C_{ax}=0.916 for contoured endwall without and with film injection at inlet blowing ratios M_{in}=1.0 to 2.0.

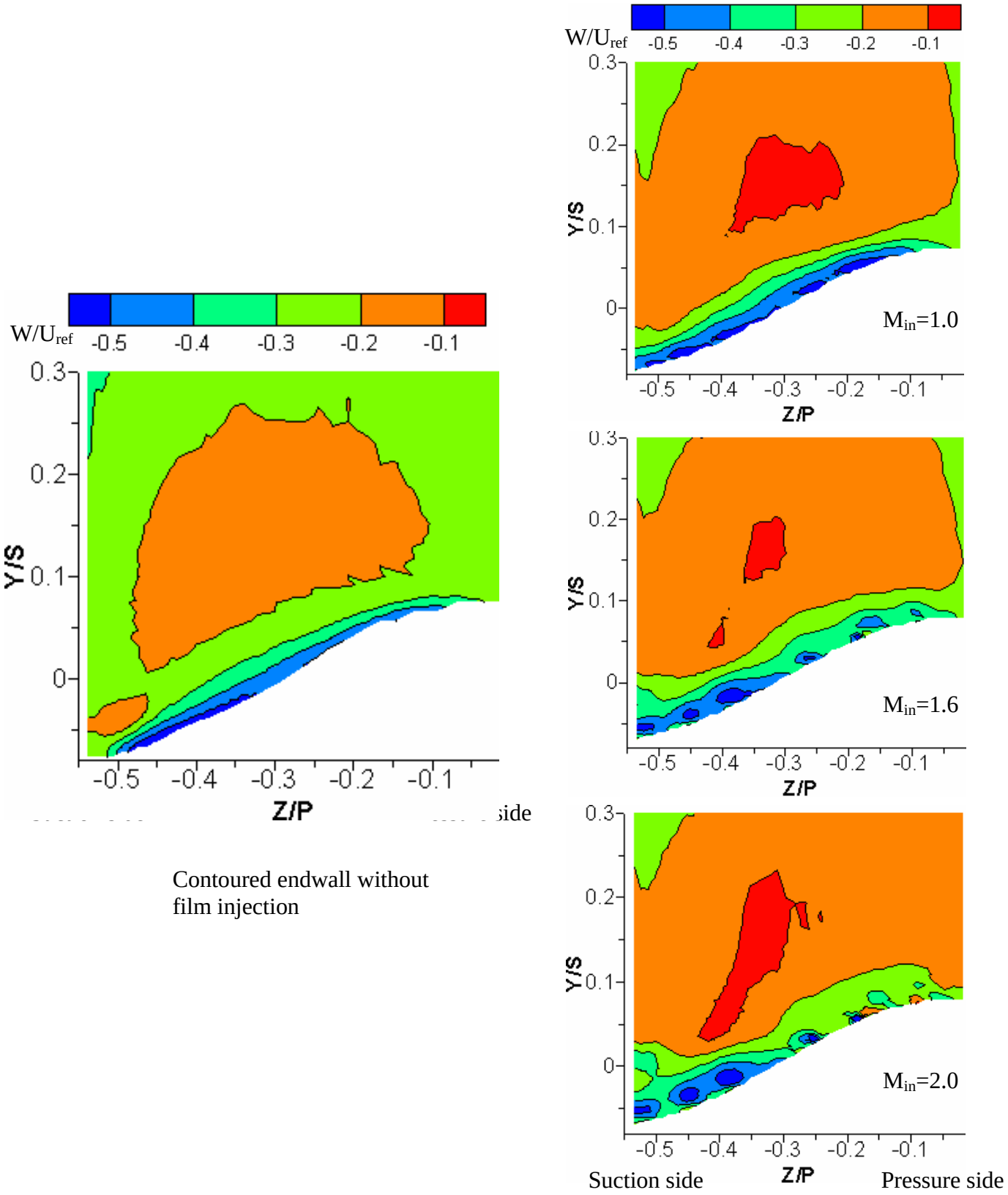

Figure 30: Normalized pitchwise velocity, W/U_{ref} in pitchwise plane at $X_G/C_{ax}=0.424$ for contoured endwall without and with film injection at inlet blowing ratios $M_{in}=1.0$ to 2.0.

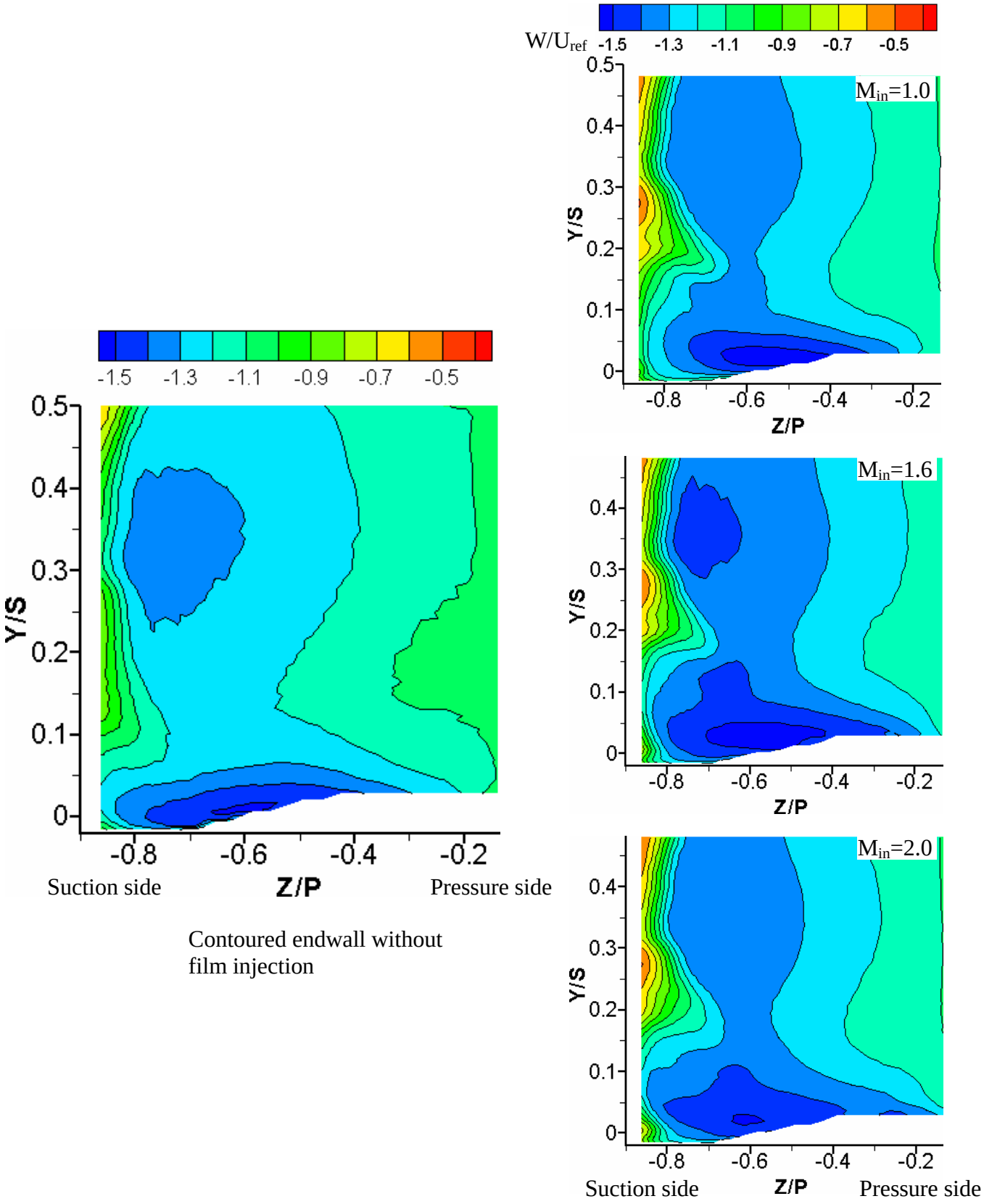

Contoured endwall without film injection

Figure 31: Normalized pitchwise velocity, W/U_{ref} in pitchwise plane at X_G/C_{ax}=0.916 for contoured endwall without and with film injection at inlet blowing ratios M_{in}=1.0 to 2.0.

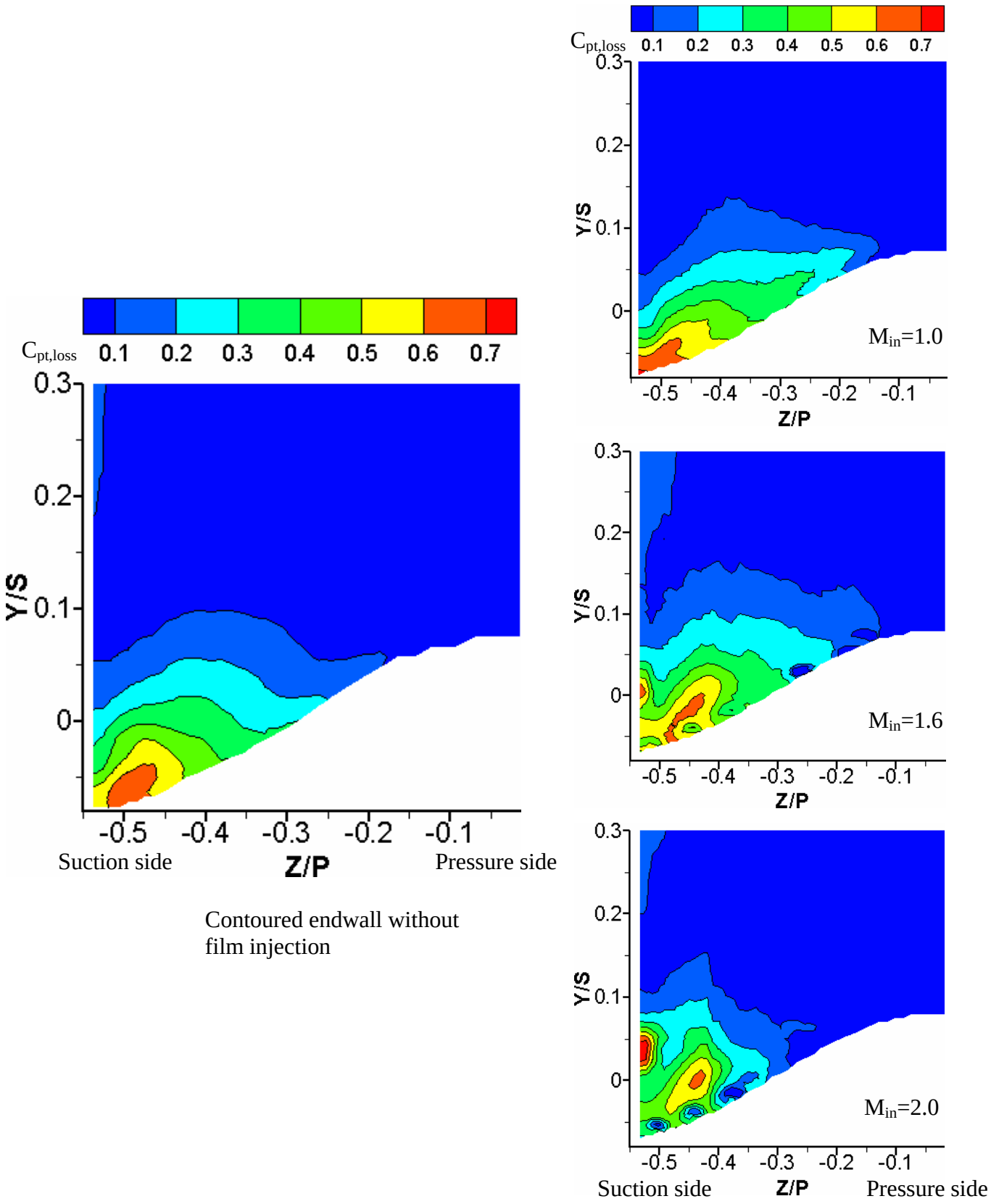

Contoured endwall without film injection

Figure 32: Total pressure loss coefficient, $C_{pt,loss}$ in pitchwise plane at X_G/C_{ax}=0.424 for contoured endwall without and with film injection at inlet blowing ratios M_{in}=1.0 to 2.0.

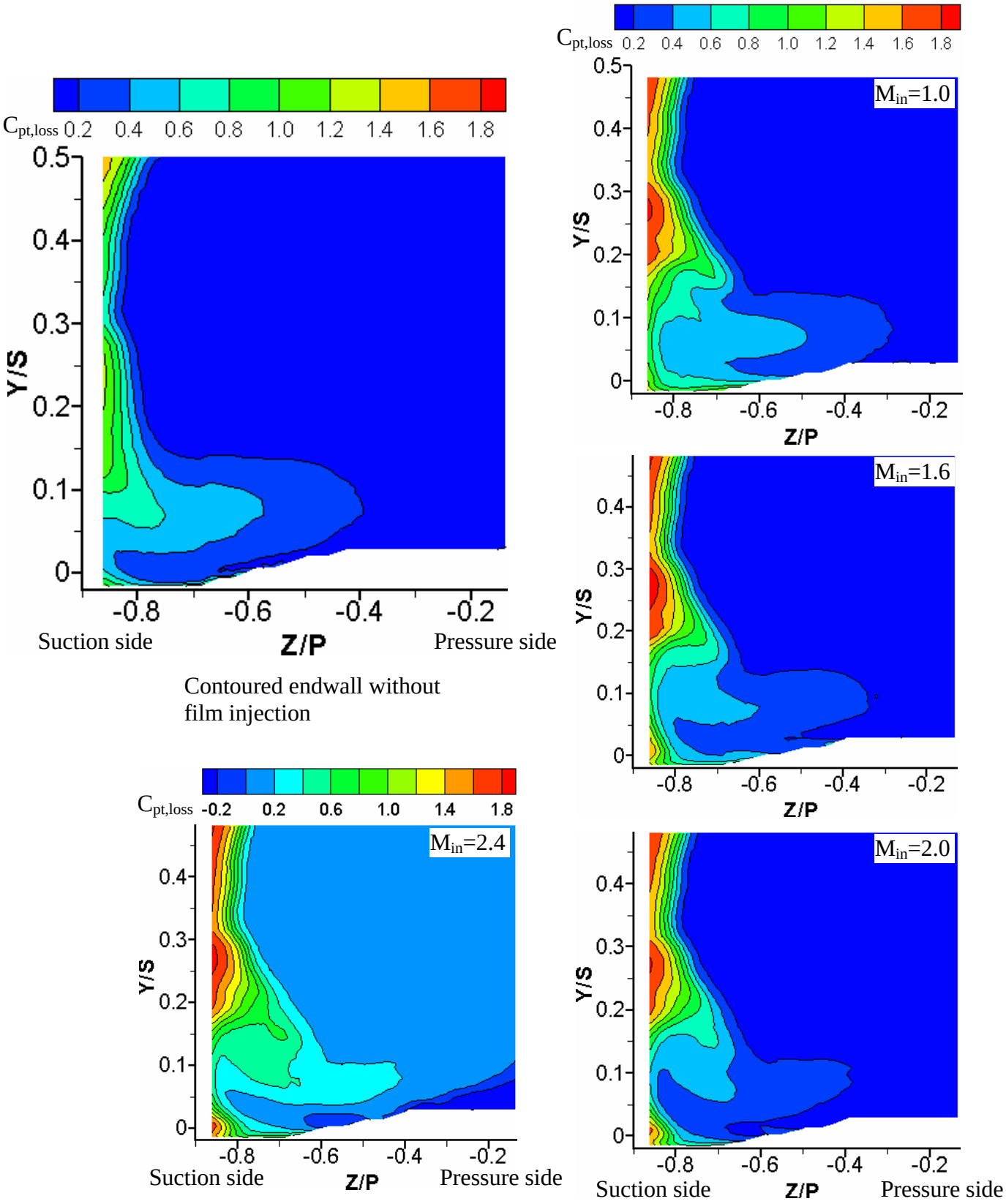

Figure 33: Total pressure loss coefficient, $C_{pt,loss}$ in pitchwise plane at X_G/C_{ax}=0.916 for contoured endwall without and with film injection at inlet blowing ratios M_{in}=1.0 to 2.4.

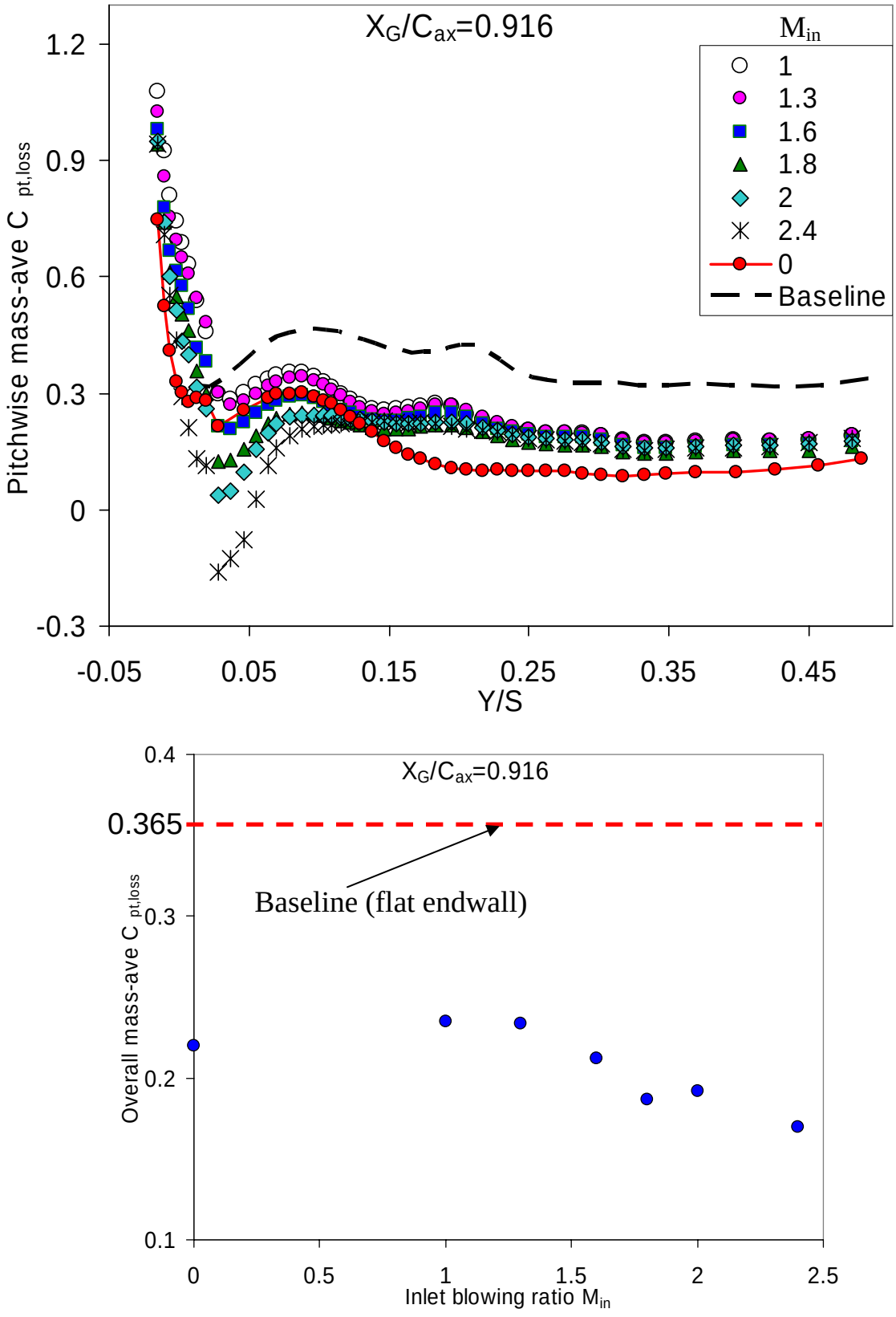

Figure 34: Pitchwise mass-averaged and overall mass averaged total pressure loss coefficient, $C_{pt,loss}$ at X_G/C_{ax}=0.916 for contoured endwall with and without film injection.

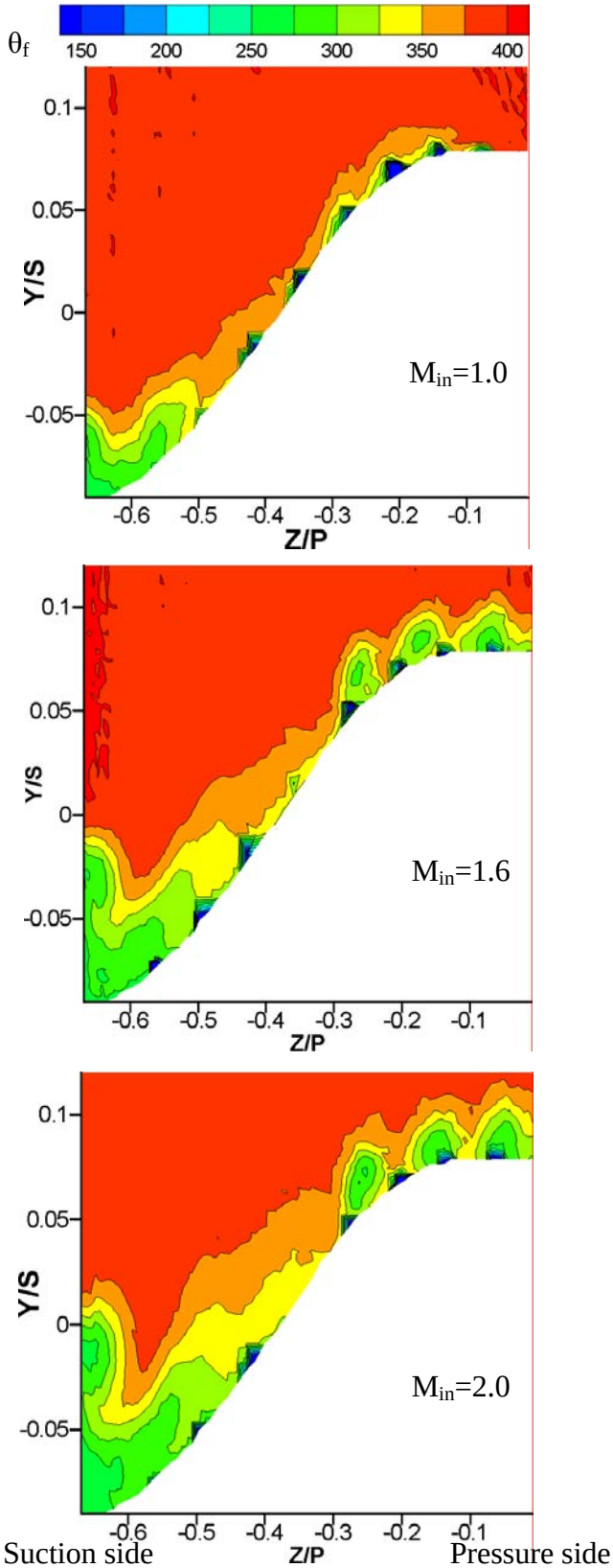

Figure 35: Non-dimensional fluid temperature, θ_f near endwall at X_G/C_{ax}=0.152 for contoured endwall with film injection at inlet blowing ratios M_{in}=1.0 to 2.0.

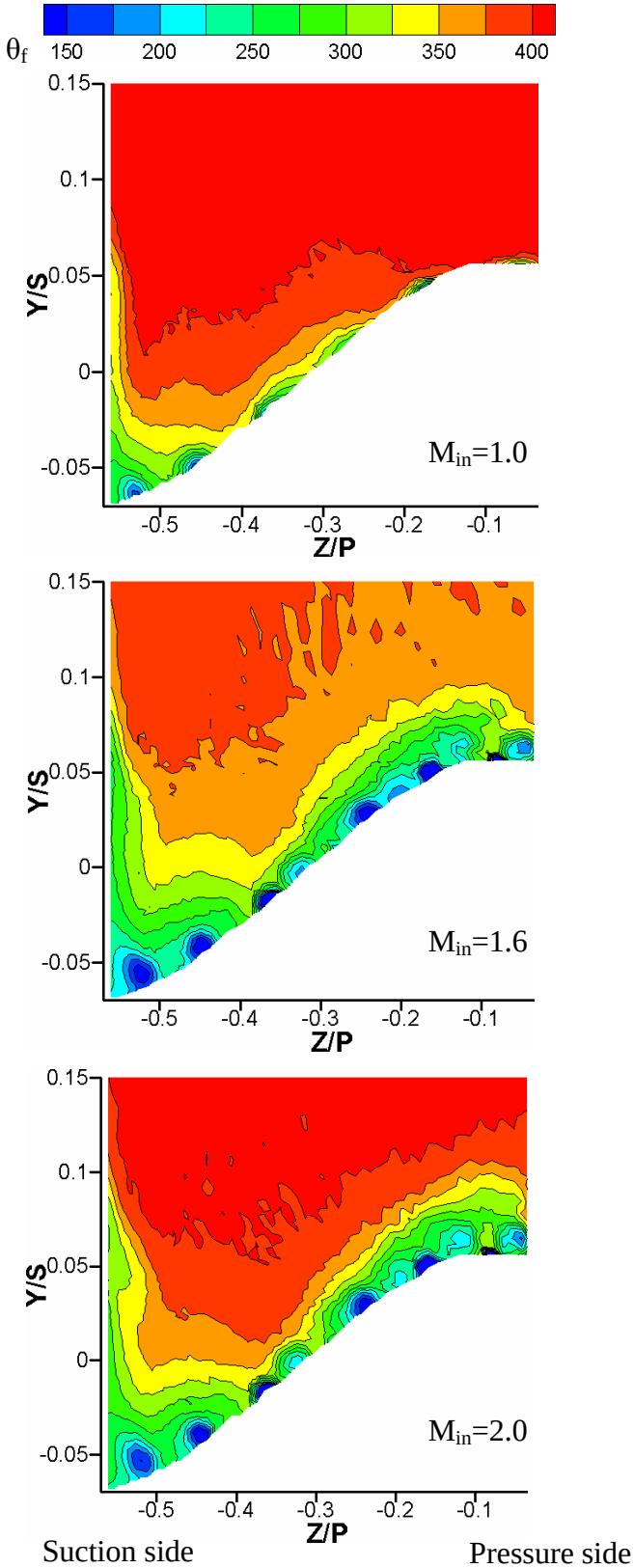

Figure 36: Non-dimensional fluid temperature, θ_f near endwall at X_G/C_{ax}=0.493 for contoured endwall with film injection at inlet blowing ratios M_{in}=1.0 to 2.0.

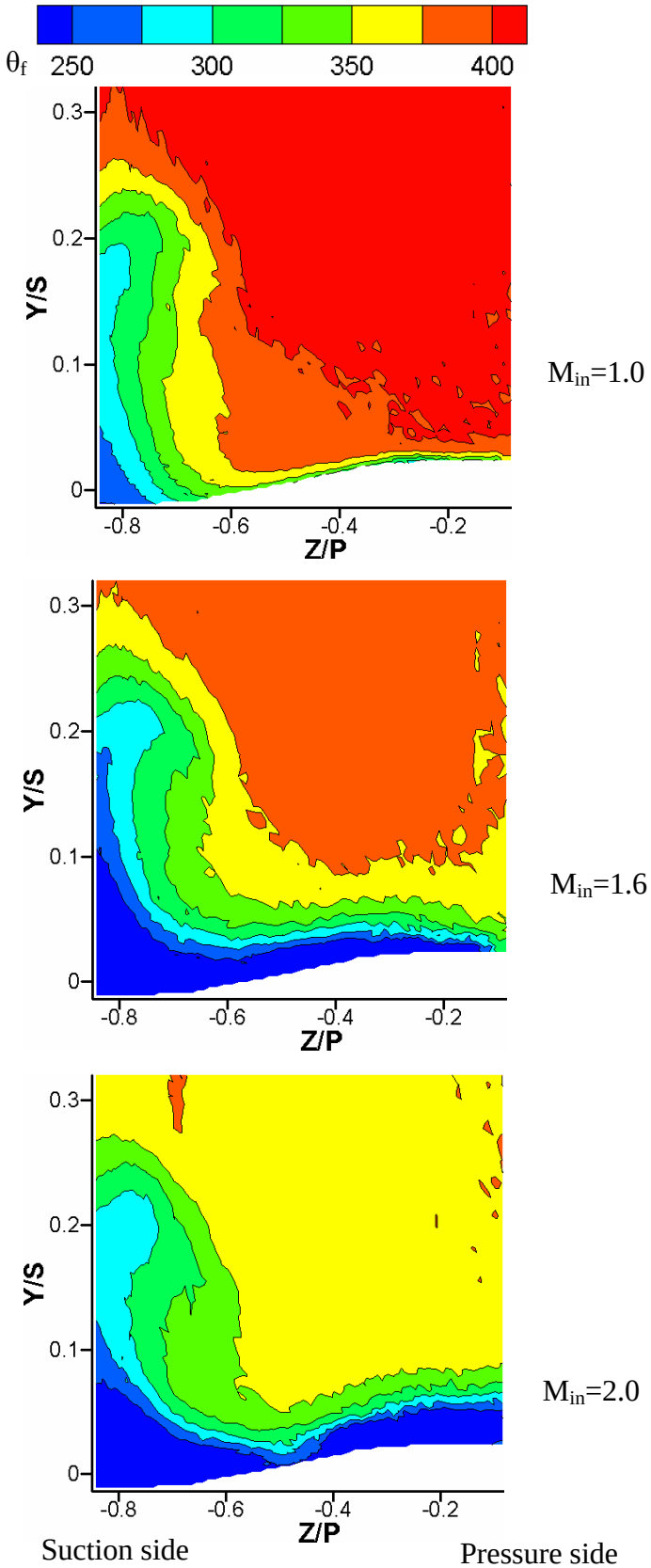

Figure 37: Non-dimensional fluid temperature, θ_f near endwall at X_G/C_{ax}=0.954 for contoured endwall with film injection at inlet blowing ratios M_{in}=1.0 to 2.0.

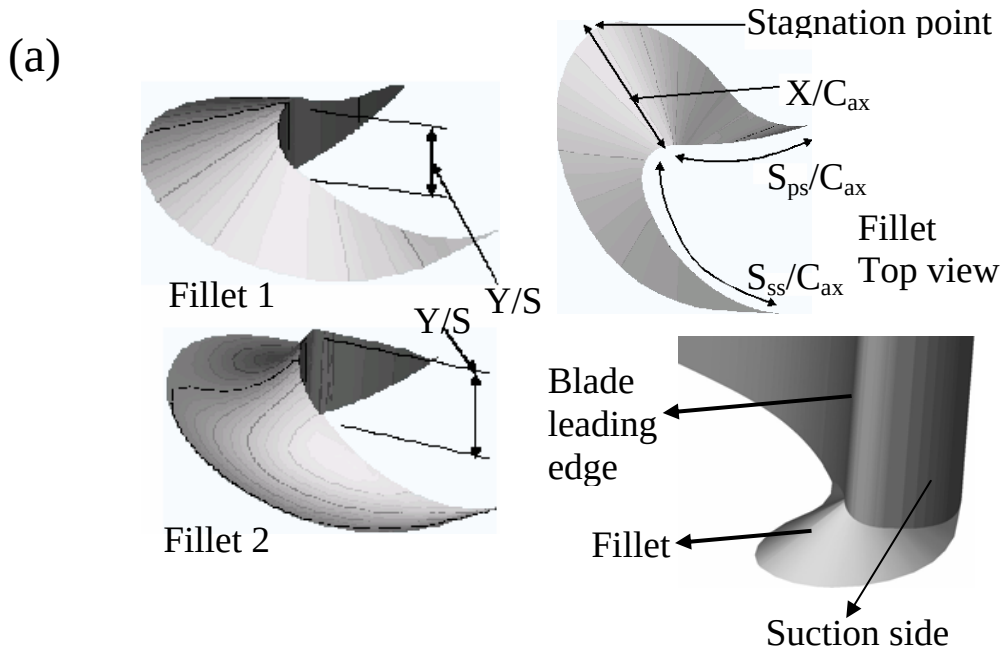

Figure 38: (a) Leading edge fillet geometry

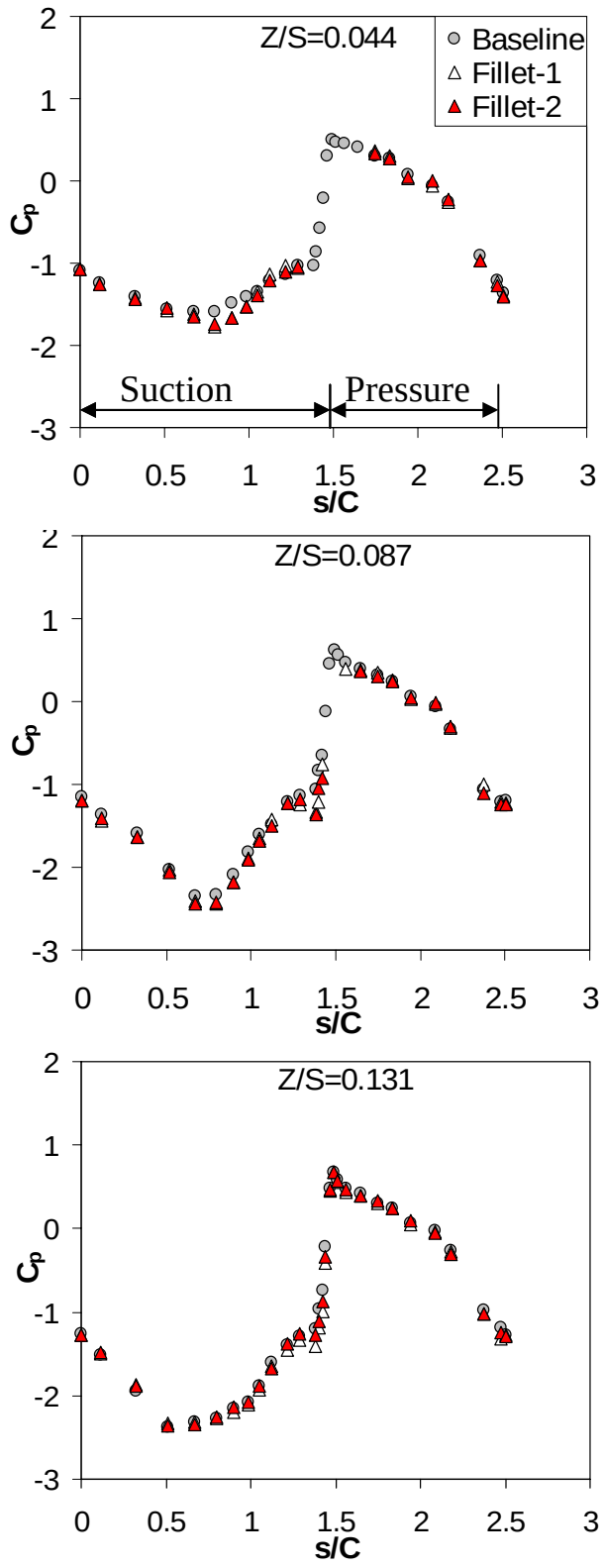

Figure 39: Static pressure coefficients C_p on blade surface near endwall for baseline and filleted cases.

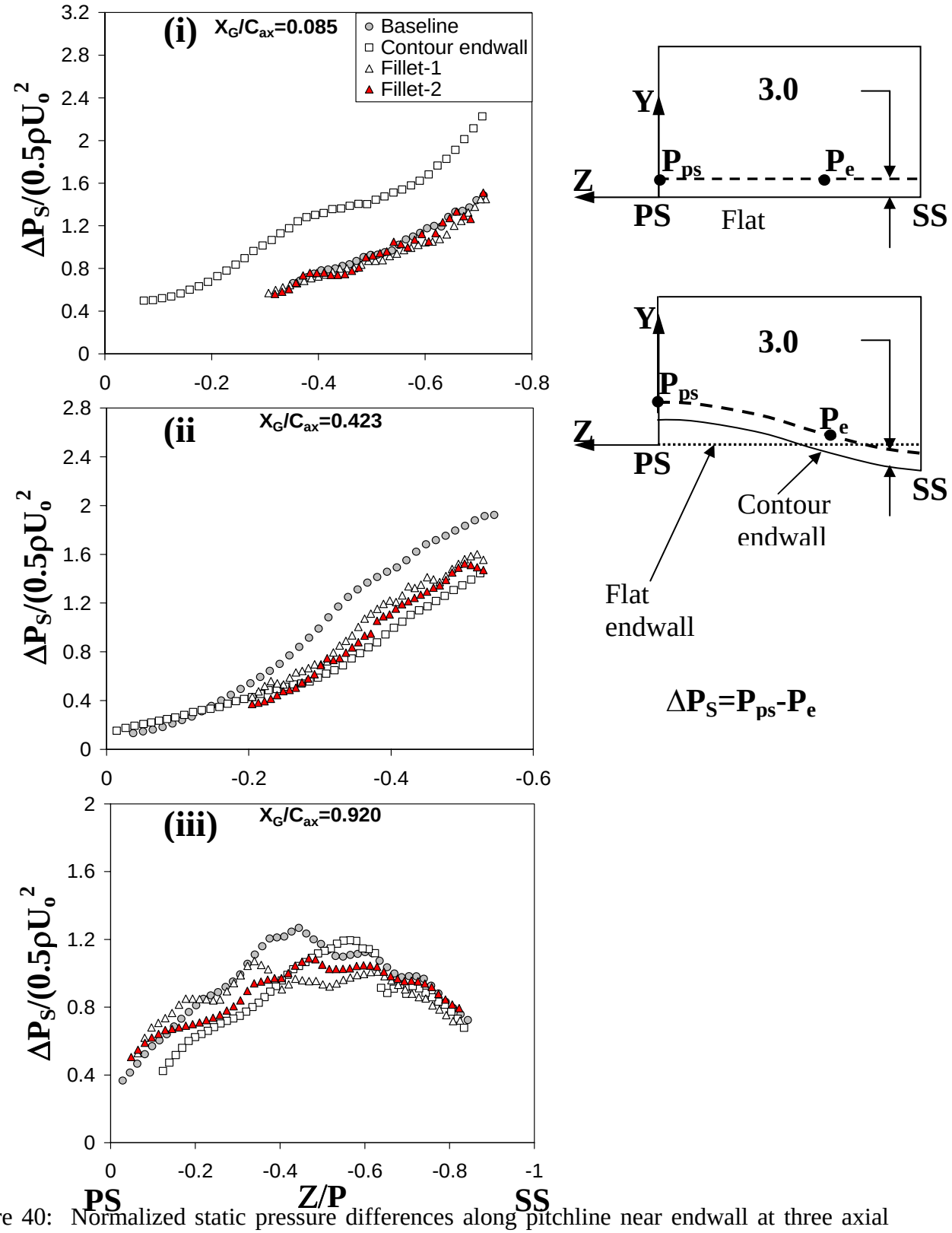

Figure 40: Normalized static pressure differences along pitchline near endwall at three axial distances for baseline and other cases: (i) X_G/C_{ax}=0.085, (ii) X_G/C_{ax}=0.423, (iii) X_G/C_{ax}=0.920.

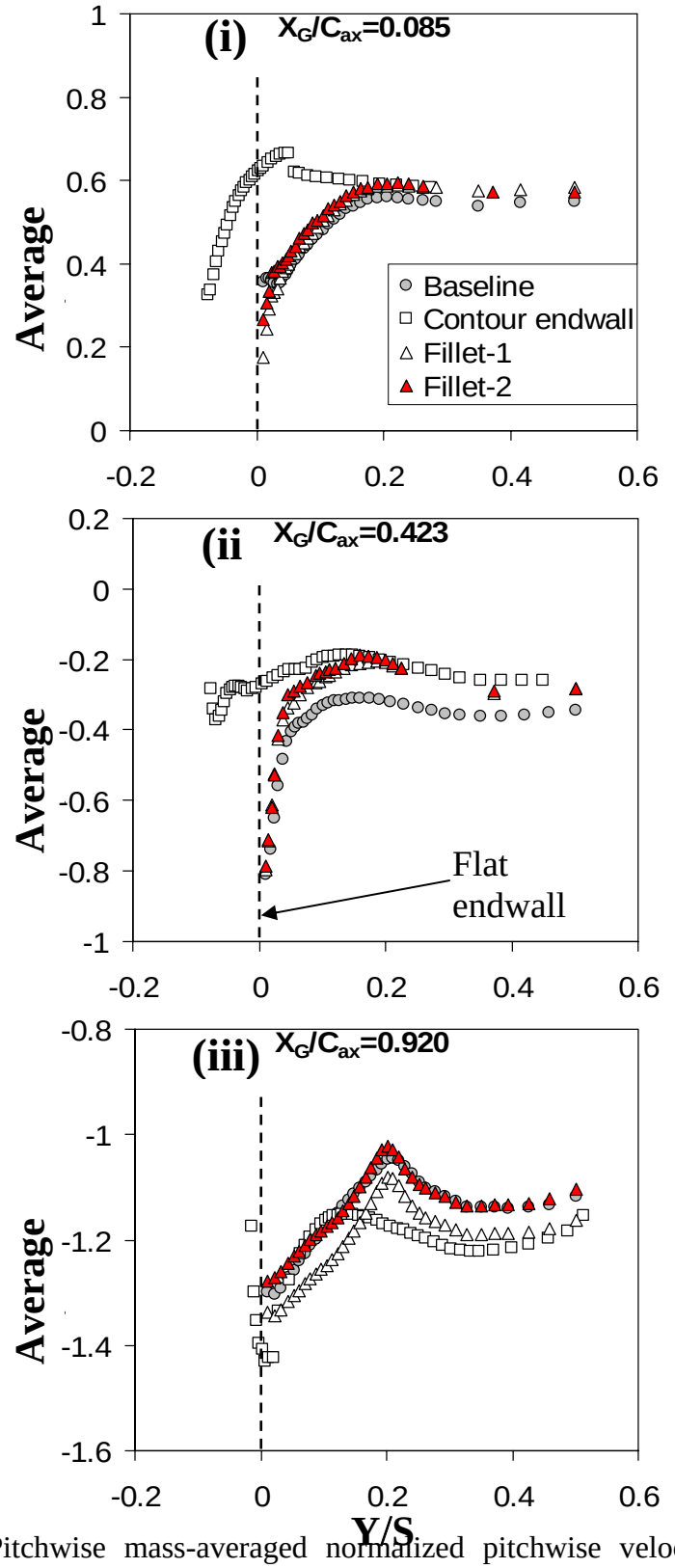

Figure 41: Pitchwise mass-averaged normalized pitchwise velocity W/U_o at three axial distances for baseline and other cases: (i) X_G/C_{ax}=0.085, (ii) X_G/C_{ax}=0.423, (iii) X_G/C_{ax}=0.920.

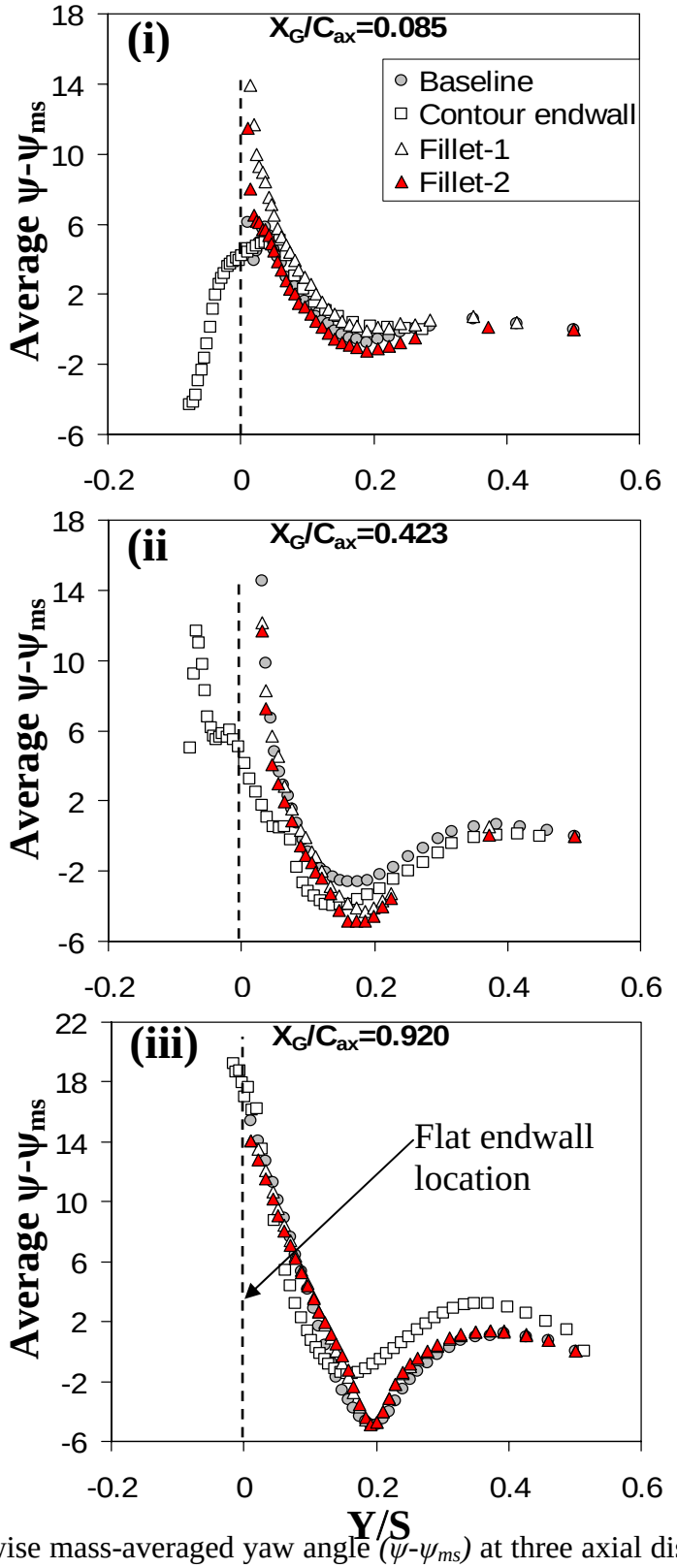

Figure 42: Pitchwise mass-averaged yaw angle (ψ-ψ_{ms}) at three axial distances for baseline and other cases: (i) X_G/C_{ax}=0.085, (ii) X_G/C_{ax}=0.423, (iii) X_G/C_{ax}=0.920.

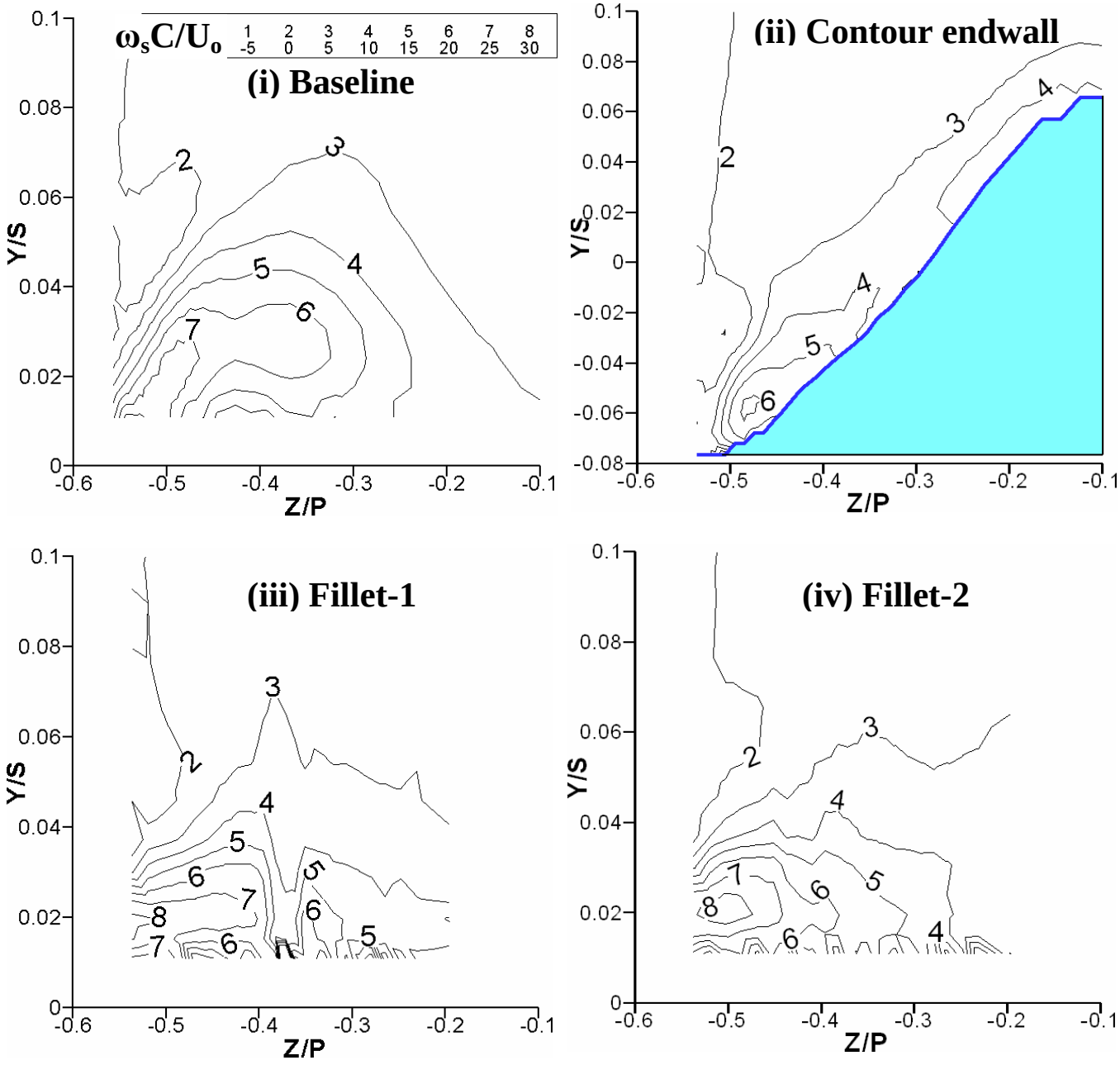

Figure 43: Streamwise normalized vorticity at X_G/C_{ax}=0.423 for baseline and other cases: (i) Baseline, (ii) Contour endwall, (iii) Fillet-1, (iv) Fillet-2.

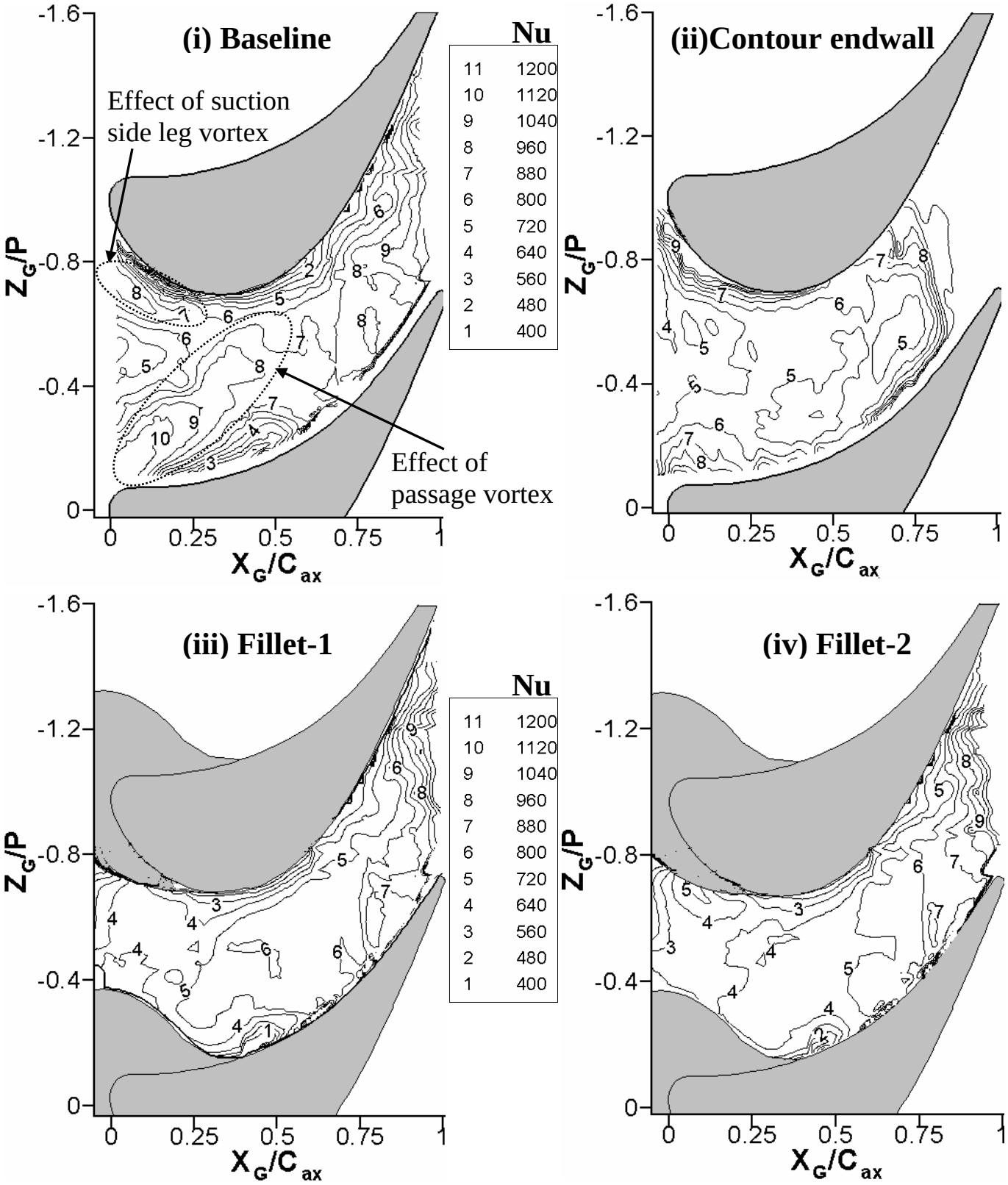

Figure 44: Nusselt number *Nu* along endwall for baseline and other cases: (i) Baseline, (ii) Contour endwall, (iii) Fillet-1, (iv) Fillet-2.

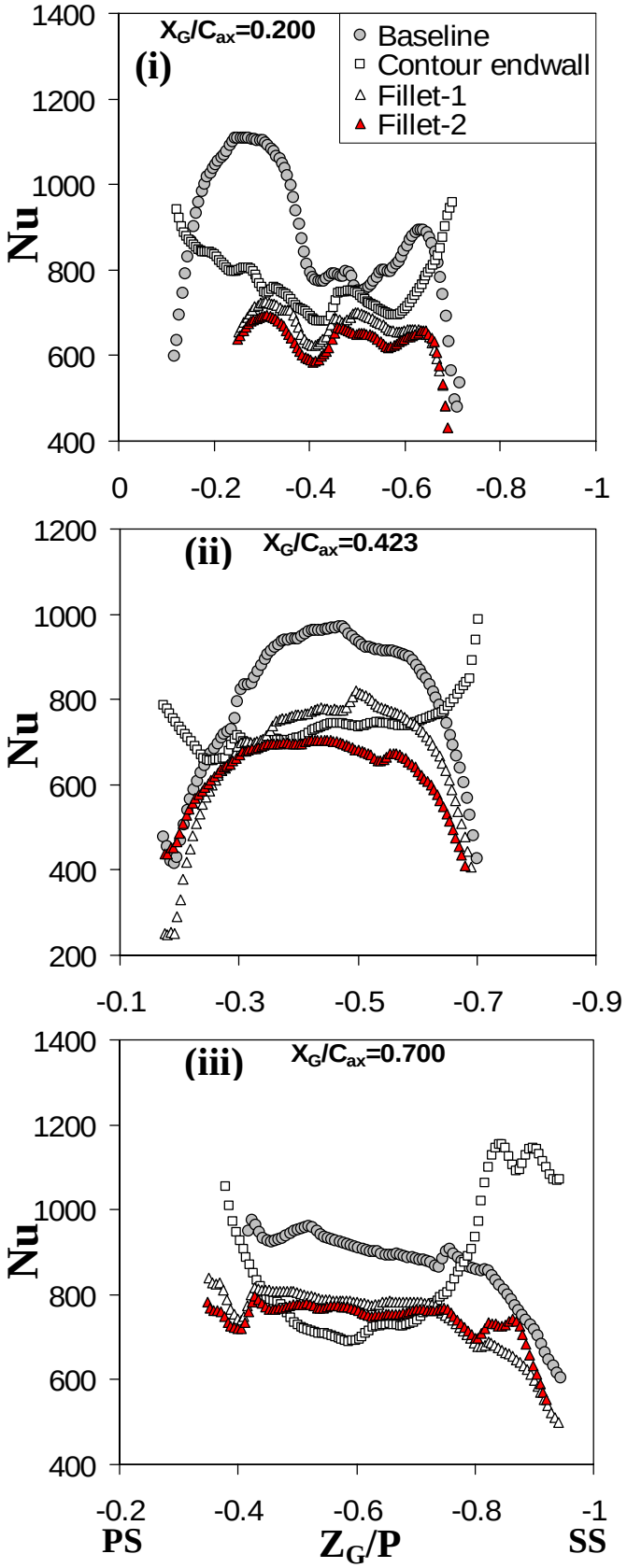

Figure 45: Nusselt number *Nu* along pitchline at three axial distances for baseline and other cases: (i) X_G/C_{ax}=0.200, (ii) X_G/C_{ax}=0.423, (iii) X_G/C_{ax}=0.700.

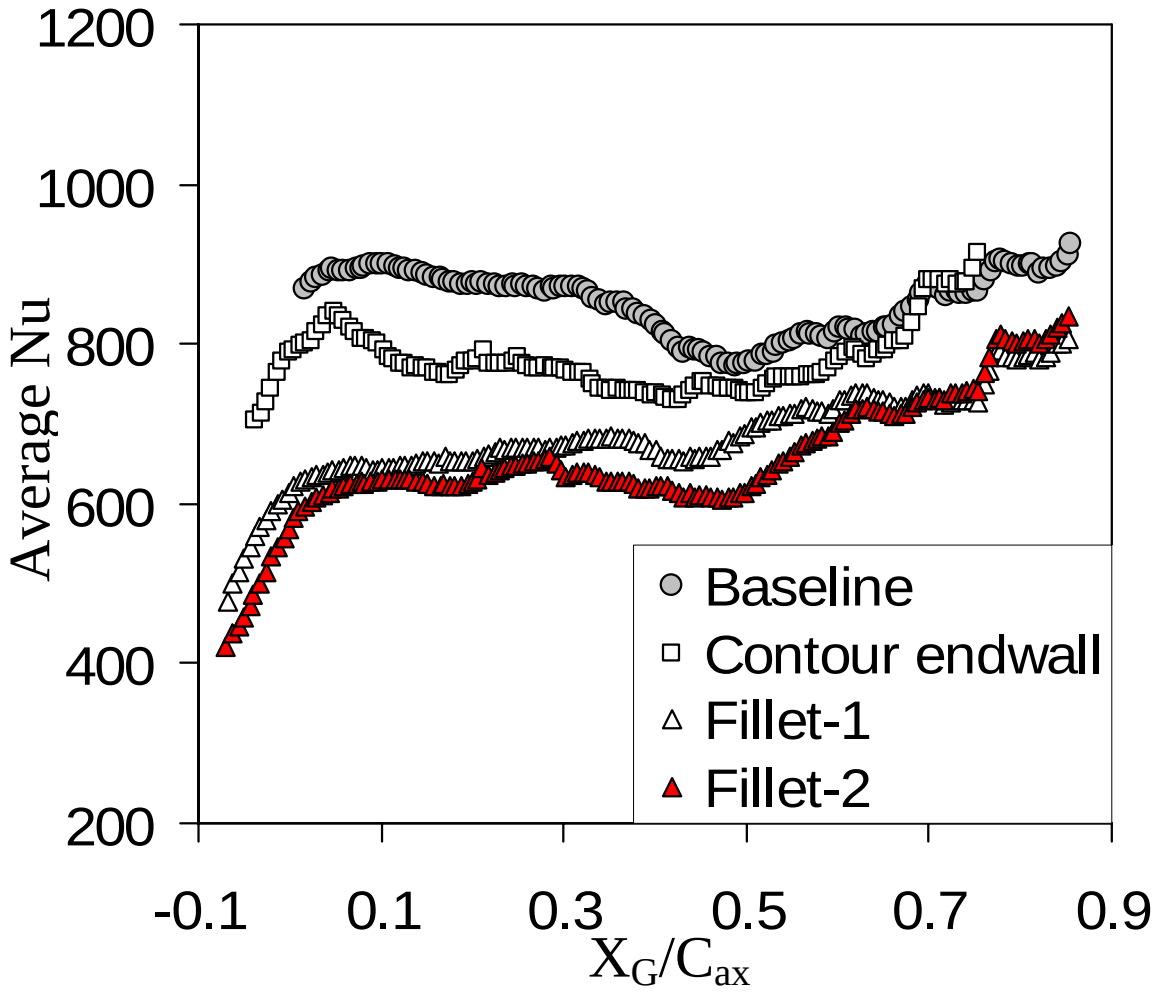

Figure 46: Pitchwise area-averaged Nusselt number *Nu* along endwall for baseline and other cases.

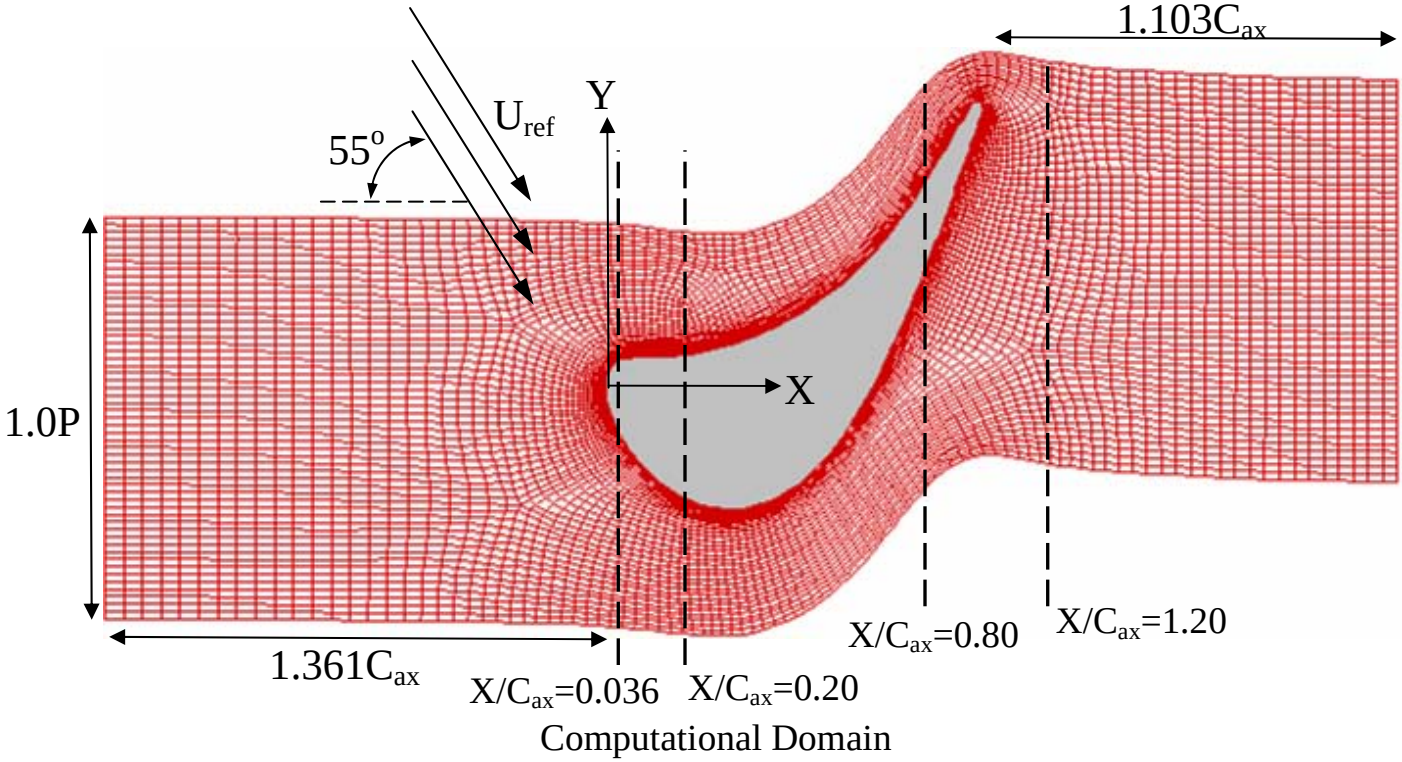

Figure 47: Computational domain and endwall grid geometry for baseline and contoured endwall.

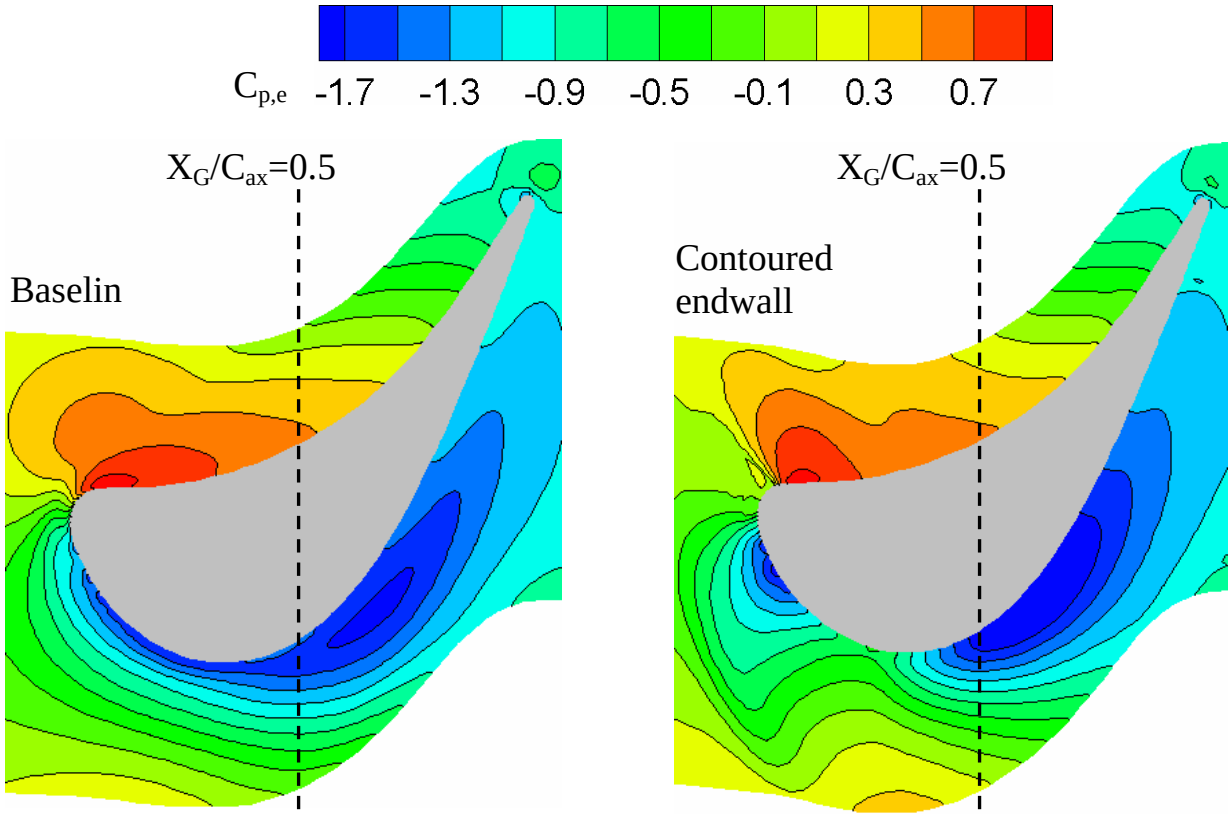

Figure 48: Endwall static pressure coeffis. for baseline and contoured endwall (computations).

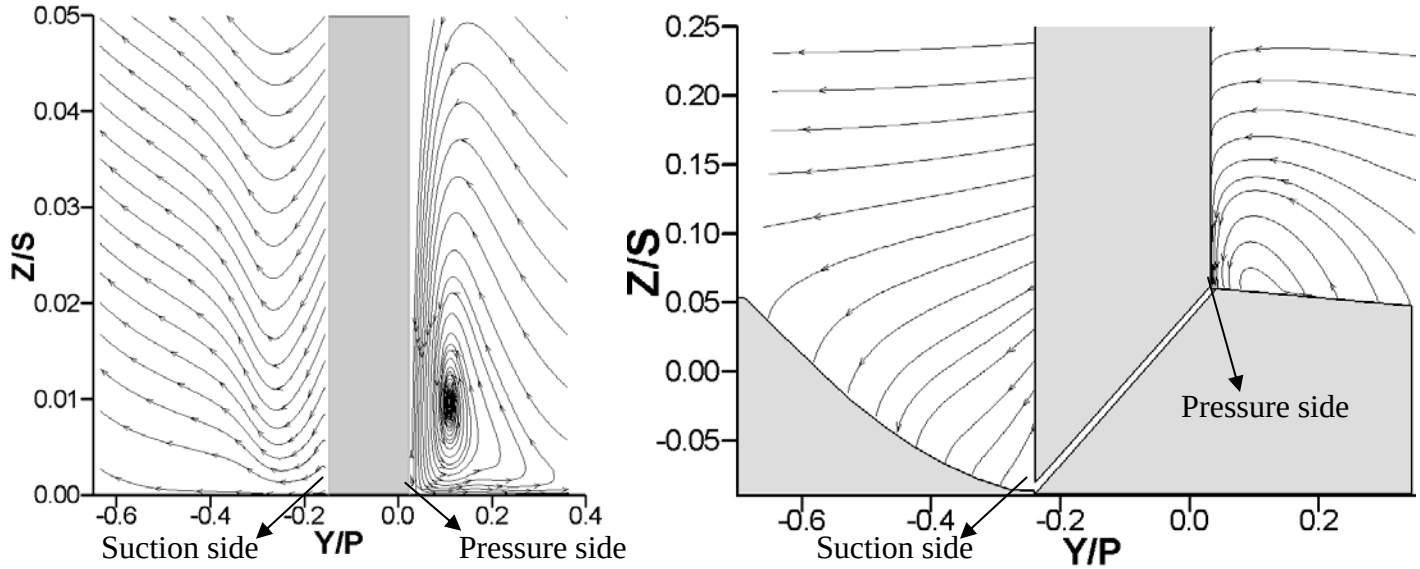

Figure 49: Streamlines in pitchwise plane at X_G/C_{ax}=0.036 for baseline and contoured endwall.

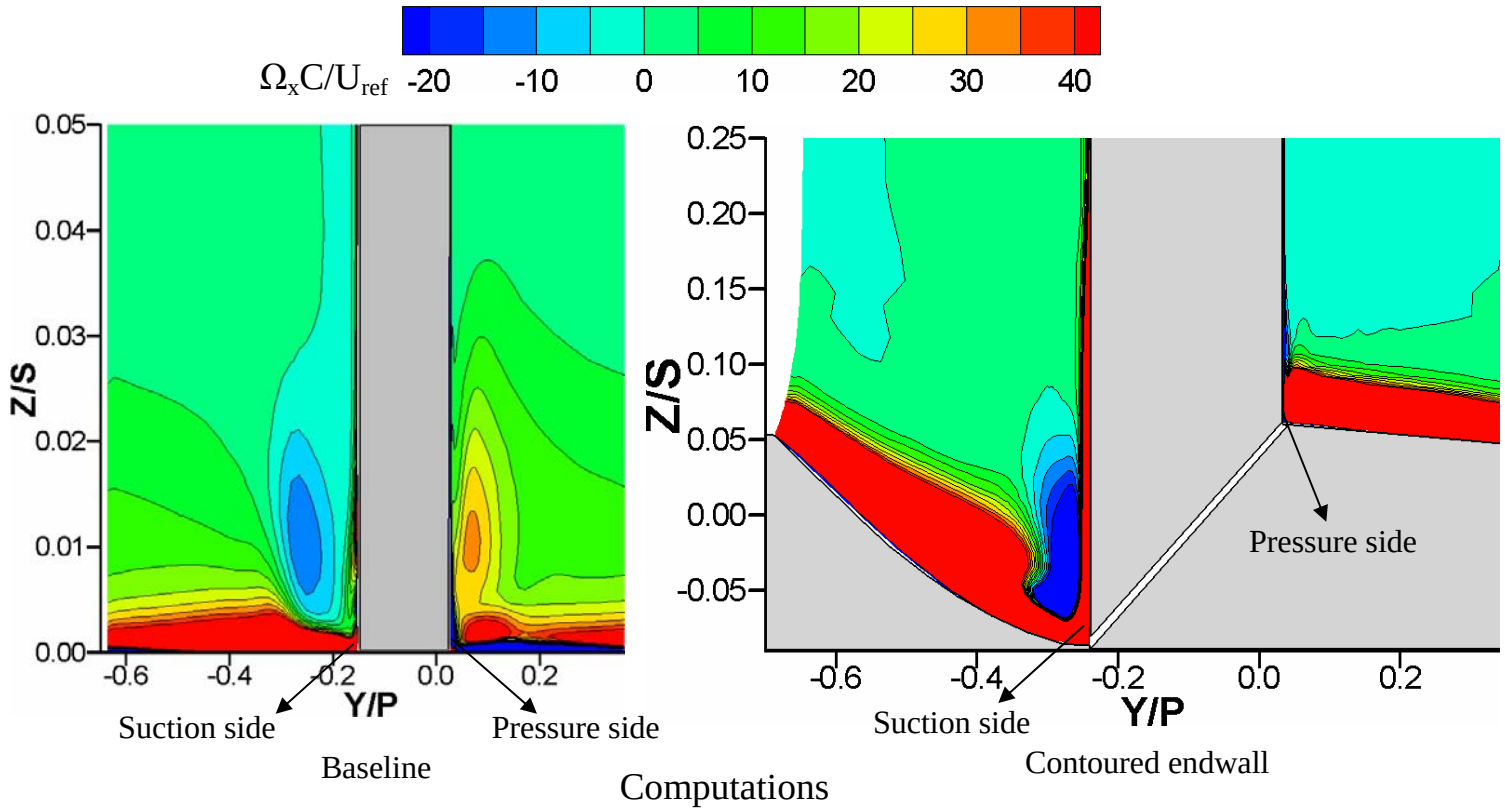

Figure 50: Normalized axial vorticity $\Omega_x C/U_{ref}$ in pitchwise plane at X_G/C_{ax}=0.036 for baseline and contoured endwall.

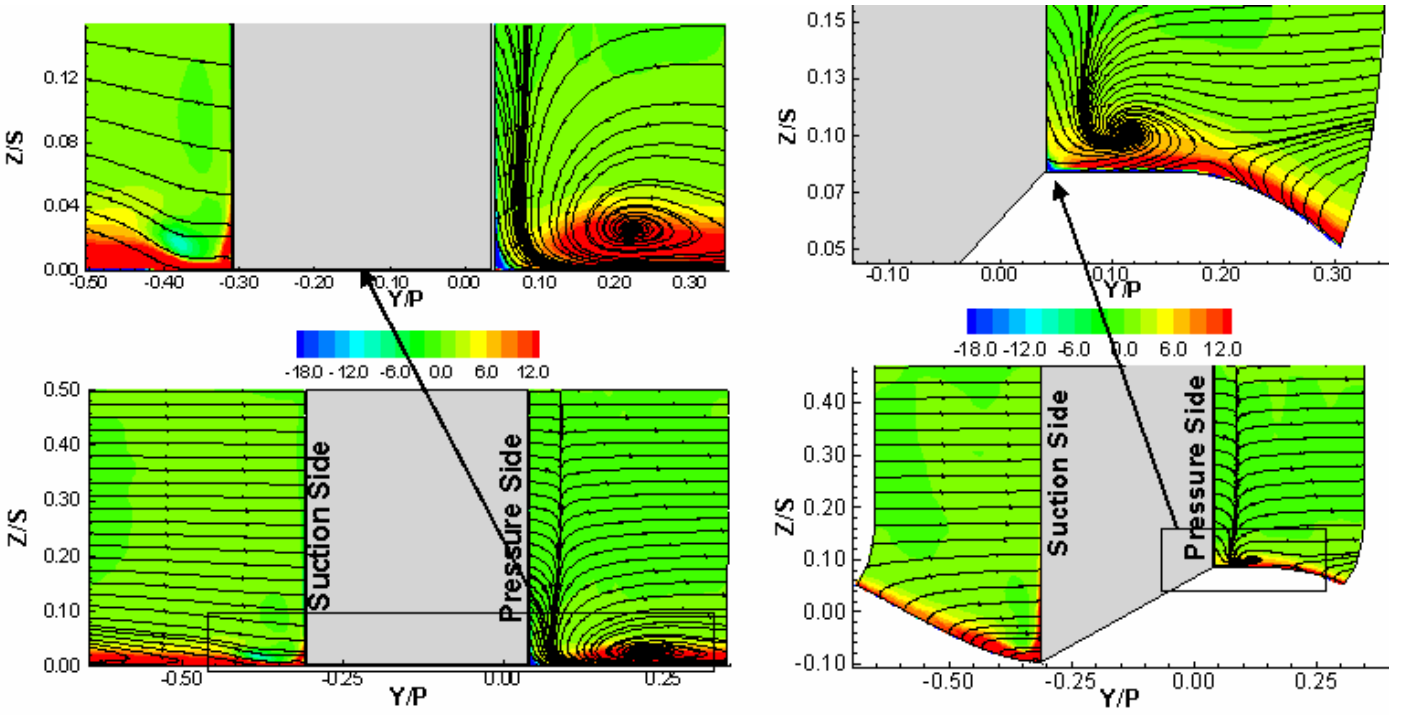

Figure 51: Streamlines superimposed on normalized axial vorticity in pitchwise plane at X_G/C_{ax}=0.20 for baseline and contoured endwall (computations).

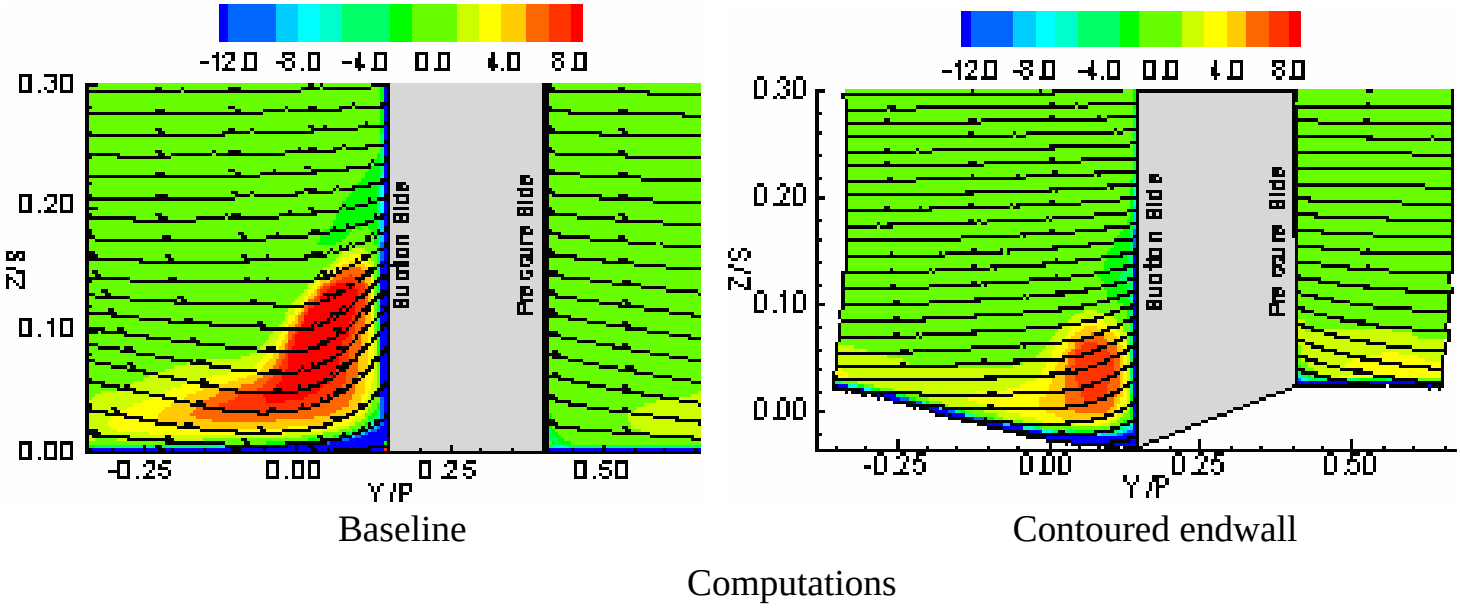

Figure 52: Streamlines superimposed on normalized axial vorticity $\Omega_x C/U_{ref}$ in pitchwise plane at X/C_{ax}=0.80 for baseline and contoured endwall (computations).

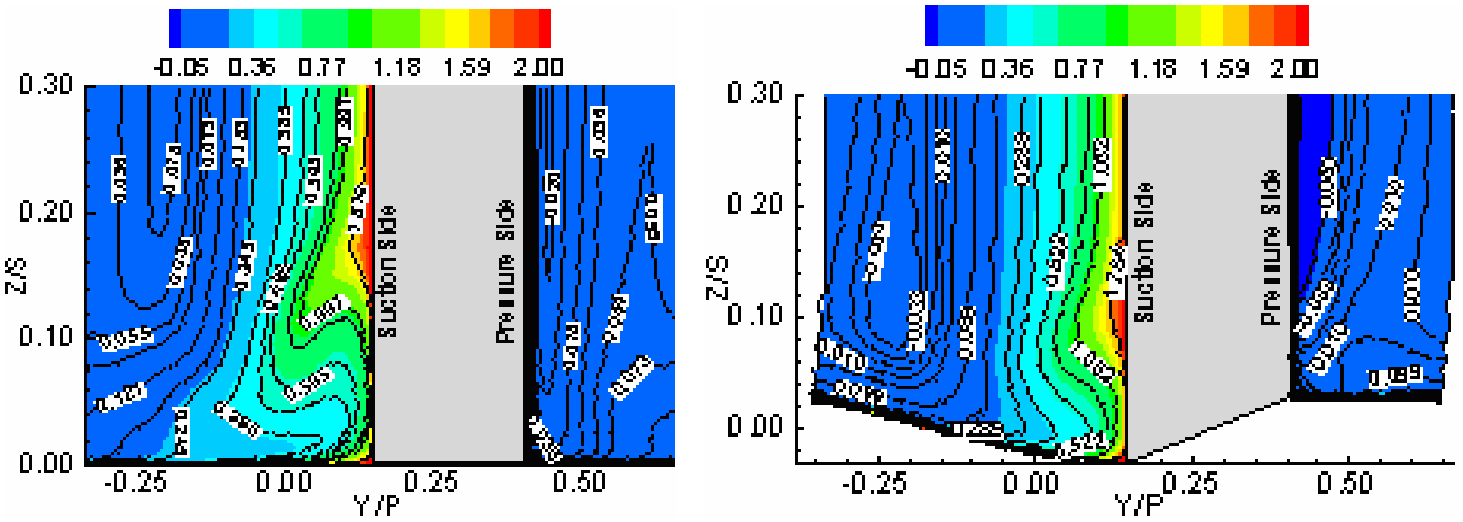

Baseline Contoured endwall

Computations

Figure 53: Total pressure loss coefficient $C_{pt,loss}$ in pitchwise plane at X_G/C_{ax}=0.80 for baseline and contoured endwall (computations).

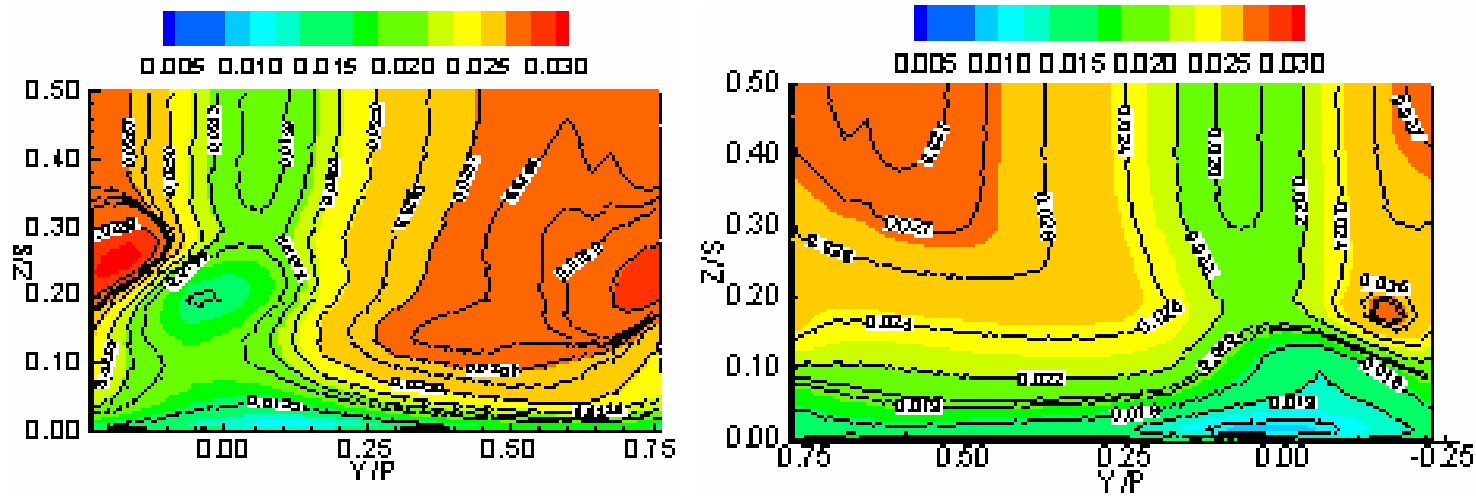

Baseline Contoured endwall

Computations

Figure 54: Non-dimensional turbulent kinetic energy in pitchwise plane at X_G/C_{ax}=1.20 for baseline and contoured endwall (computations).

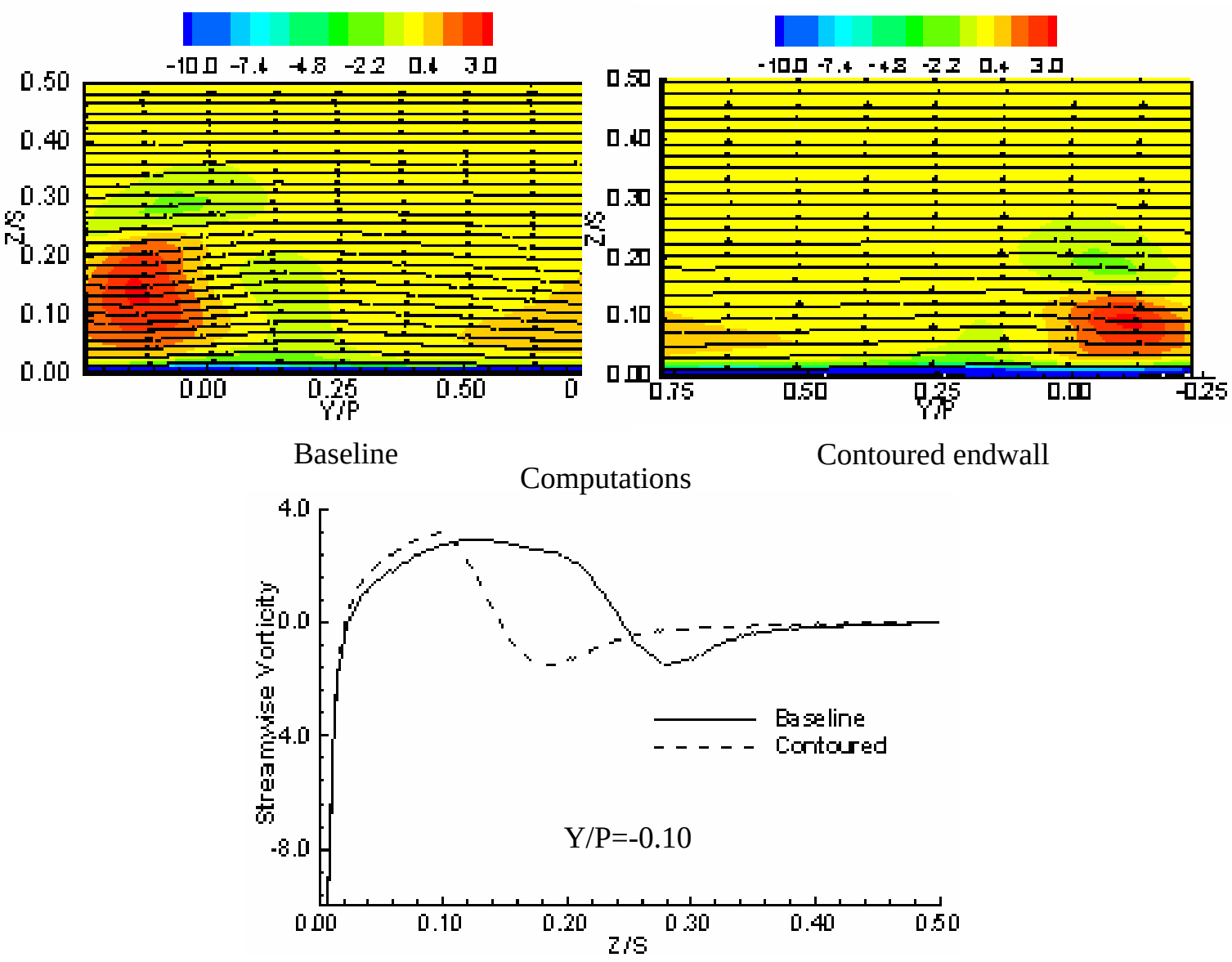

Figure 55: Streamlines and normalized axial vorticity $\Omega_x C/U_{ref}$ in pitchwise plane at X_G/C_{ax}=1.20 for baseline and contoured endwall (computations).

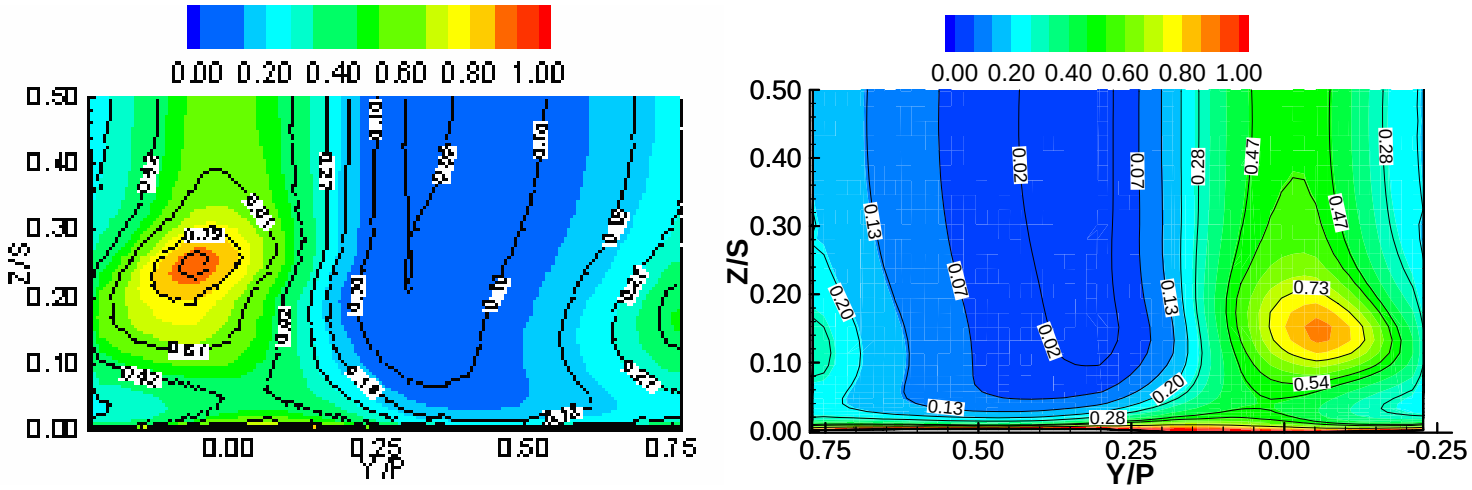

Baseline Contoured endwall

Computations

Figure 56: Total pressure loss coefficient $C_{pt,loss}$ in pitchwise plane at X_G/C_{ax}=1.20 for baseline and contoured endwall (computations).

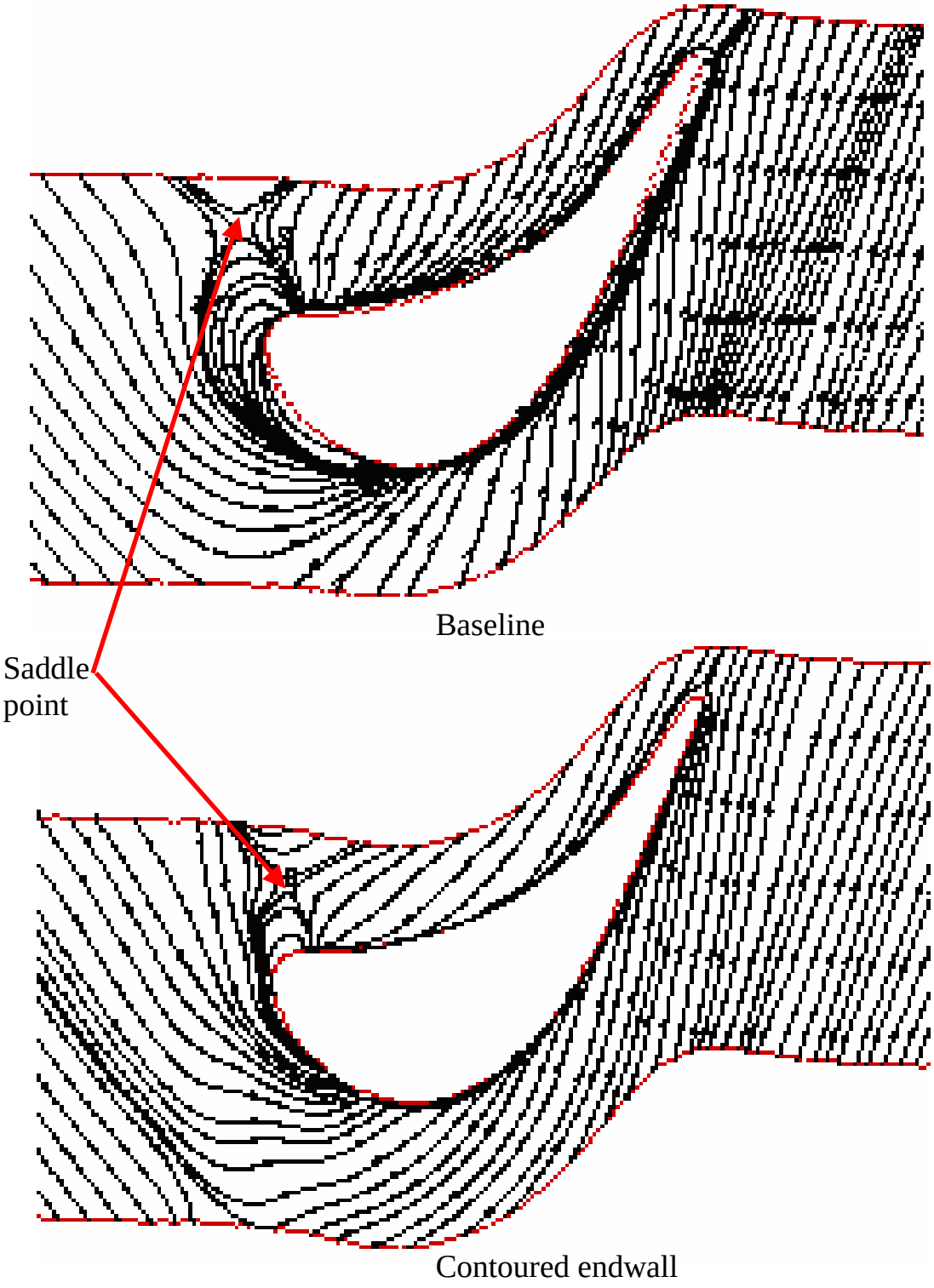

Figure 57: Surface streamlines on the endwall for baseline and contoured endwall (computations).

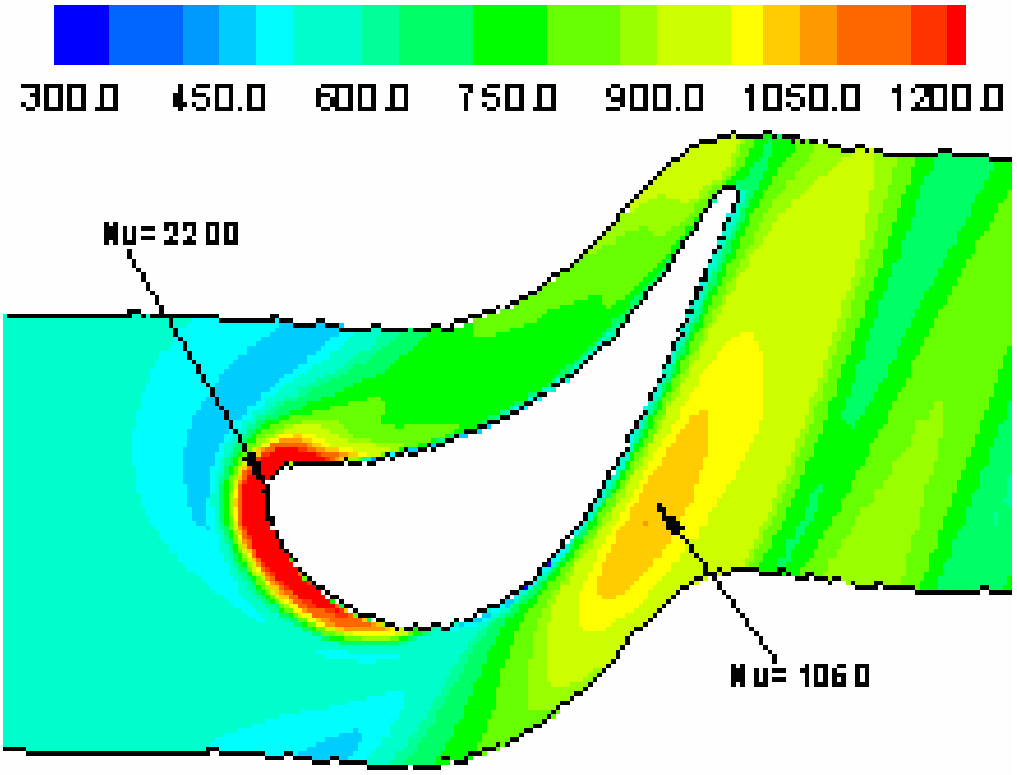

Baseline

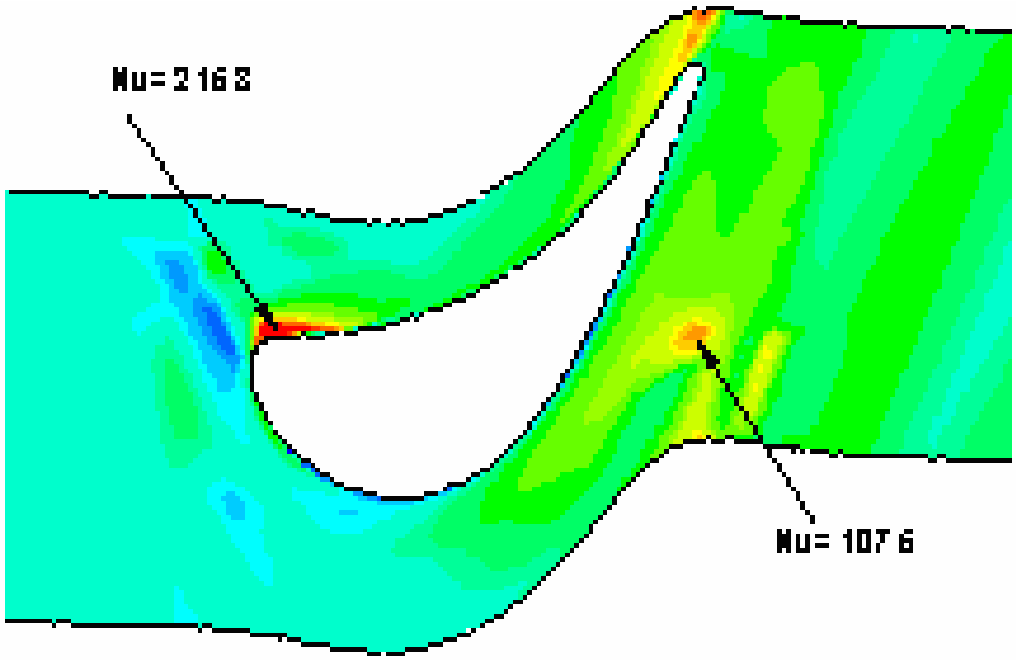

Contoured endwall

Figure 58: Endwall Nusselt number Nu for baseline and contoured endwall (computations).

Table 5: Summary Results (Computational) for Several Contoured Endwall Profile

Cases	Axial variation of contoured endwall	Geometric parameters(m) and Average Results
1	Flat Endwall (Baseline)	Nu= 736, $C_{pt,loss}$ = 0.2592 (exit plane)
2	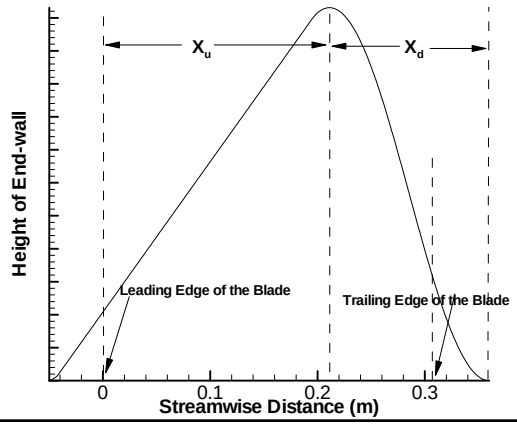	X_u=0.21, X_d=0.15 Endwall height, Z_{max}=0.039m , Z_{min}=-0.047m Nu= 710, $C_{pt,loss}$ = 0.2674 (exit plane)
3		X_u=0.18, X_d= 0.18, Z_{ma}=0.039, Z_{min}=-0.046 Nu= 709, $C_{pt,loss}$ = 0.2641 (exit plane)
4		X_u=0.16, X_d=0.2, Z_{max}=0.039, Z_{min}=-0.045 Nu= 704, $C_{pt,loss}$ = 0.2599 (exit plane)
5		X_u=0.13, X_d=0.23, Z_{max}=0.039, Z_{min}=-0.045 Nu= 697, $C_{pt,loss}$ = 0.2603 (exit plane)
6	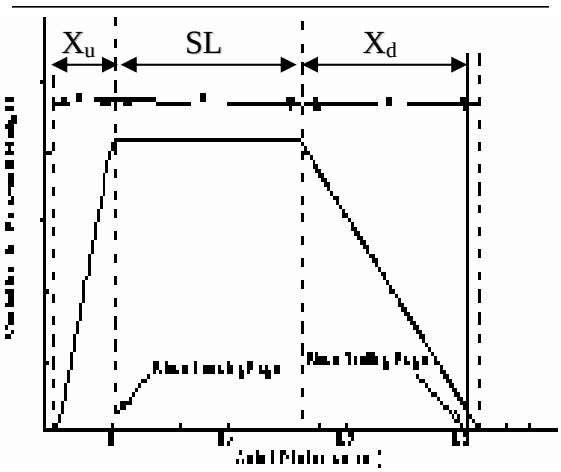	X_u=0.16, X_d=0.16, SL=0.07, Z_{max}=0.019, Z_{min}=-0.023 Nu= 691, $C_{pt,loss}$ = 0.2585 (exit plane)
7		X_u=0.16, X_d=0.16, SL=0.07, Z_{max}=0.029, Z_{min}=-0.035 Nu= 678, $C_{pt,loss}$ = 0.2589 (exit plane)
8	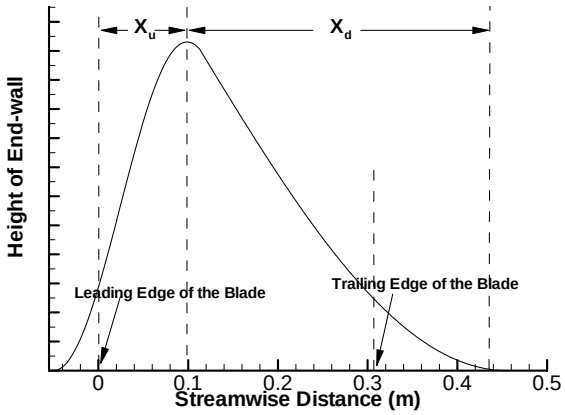	X_u=0.15, X_d=0.21, Z_{max}=0.039, Z_{min}=-0.046 Nu= 689, $C_{pt,loss}$ = 0.2596 (exit plane)
9		X_u=0.10, X_d=0.34, Z_{max}=0.039, Z_{min}=-0.046 Nu= 678, $C_{pt,loss}$ = 0.2548 (exit plane)

Modeling and Control of Ultra-Lean Premixed Combustion Dynamics for Gas Turbines

Semi-Annual Activity Report

Period: May 2005 - November 2005

Dr. William T. Baumann
Dr. William R. Saunders
Dr. Uri Vandsburger
Dr. Robert L. West

DOE Award Number DE-FC26-02NT41431
UTSR Project Number 02-01-SR099

P.O.C: Uri Vandsburger
Department of Mechanical Engineering
Email: uri@vt.edu
Phone: (540) 231-5882/4585

Virginia Active Combustion Control Group
College of Engineering
Mechanical Engineering Department MC0238
Virginia Polytechnic Institute and State University
Blacksburg, VA 24061

Submitted 10 February 2006

Abstract

Under the Advanced Gas Turbine Systems Research – High Efficiency Engines and Turbines (AGTSR-HEET) program, Virginia Tech is developing reduced order models and control methodologies for ultra-lean premixed combustion dynamics. Specifically, the study includes the measurement and modeling of heat release dynamics, equivalence ratio fluctuations, high temperature acoustics, and lean blowout dynamics. Methodologies to control flame stabilization and thermoacoustic instabilities are also being investigated.

This report contains a detailed description of the activities which were executed in May-November 2005. The emphasis of the work was on advancing reduced order models of the various parts of the system, i.e., the combustor/flame, the acoustics, and the mixing process.

The activities follow the original plan as outlined in the proposal. The report also includes a work plan for each task for the period December 2005 through May 2006.

Table of Contents

List of Graphical Material

1 Introduction

For the HEET program, ultra-low emissions (defined in this proposal as single digit NO_x and CO) are one of the strongest driving forces. Under the prior ATS program, this led to the choice of LP combustion, with ever increasing attempts to push the lean limit of operability. Lean operation has in turn led to the occasional occurrence of combustion oscillations. In this situation, a burner that has been designed for "static" operational conditions is being used under dynamic conditions, as manifested by velocity fluctuations, equivalence ratio fluctuations, and unsteady heat and mass transfer. Therefore, reduced order models development for ultra-lean combustion must address both static and dynamic flame stability, as well as combustion oscillations.

There is currently a debate in the combustion community about the efficacy of reduced-order models versus CFD models for combustor design. It is believed that highly complex CFD models will ultimately deliver the most accurate predictions of dynamic behavior in combustors. However, even if one assumes that available transient, reacting CFD codes are accurate; such models are unwieldy and extremely time-consuming when used as an iterative design tool. The proposed project, therefore, focuses on so-called "reduced-order models." The two key reasons for this focus are the natural link between achievable experimental measurements and reduced order models, as well as the easy transformation of reduced order models into linear stability models. Stability prediction is urgently needed by virtually all gas turbine designers, particularly for ultra-lean combustor designs.

Although it is relatively easy to qualitatively "explain" why instabilities might tend to occur under certain conditions and at certain frequencies, the problem of accurate prediction is much more difficult. Our approach to combustor stability predictive tools is based on systems theory and models the instability feedback loop as an interconnected set of subsystems, each corresponding to a relevant physical mechanism. For accurate stability prediction, it is absolutely necessary that all subsystem (dynamic) models accurately characterize the gain and phase versus frequency behavior of the actual subsystem in physical units. For example, it is not enough to show that a model predicts the trends of a voltage observed at the output of a transducer responding to heat release rate – it is necessary to accurately predict the total heat release rate in J/sec. It is obvious, therefore, that the current knowledge in this area needs to be advanced and the work tasks outlined in the following sections describe how this will be accomplished.

Ultra-lean premixed combustor operation is significantly more susceptible to lean-blowout of the flame. Thus, this project seeks to understand better the critical parameters that define both static and dynamic flame stability, with particular emphasis on the dynamic coupling between combustion oscillations and dynamic stability of the flame and the effects of fuel variability on these phenomena. Through a series of experiments dynamic models will be progressively defined in order to predict critical dynamic velocities that must be maintained in the combustors to ensure stable operation.

Several control strategies, including passive, active, and a blend of both, will then be considered in order to demonstrate the feasibility of extending the limits of flame stabilization while simultaneously minimizing the occurrence or severity of combustion oscillations during ultra-lean combustor operations.

The payoff from successful development of the types of models proposed here is enormous for the gas turbine community since such models will lead to predictive capabilities that can rapidly discern whether a specific combustor design is susceptible to unstable operation at any operating conditions. The great attraction of these tools is the potential significant shortening of the development cycle.

2 Executive Summary

The central goal of the proposed project is to develop dynamic models for ultra-lean combustion in gas turbine engines. Ultra-lean combustion is intended to satisfy single-digit NO_x emission goals without degrading CO emissions across a range of operating conditions. The primary obstacles to achieving successful ultra-lean operation for HEET platforms are static and dynamic flame stabilization (i.e. lean blowout), as well as thermoacoustic instabilities. To answer this need, this project will develop design-oriented modeling techniques that describe the flame-holding and thermoacoustic combustion subsystems based on aerodynamic, geometric, and various operating condition data. These models will then be utilized to develop passive energy absorption strategies or active control systems that reduce occurrence and level of instabilities and enhance the lean blowout limits. The proposed effort will encompass a broad range of HEET interests including: flame stabilization, LBO, reduced-order modeling, dynamic effects of fuel variability, and control system design. The project will be executed in combination and with active participation of willing IRB members. A university-sponsored workshop will be held at the conclusion of the project to facilitate the transition of the modeling tools to industry engineers working on ultra-lean combustor design.

As was stated earlier, we promised that the goals of the project will lead to marked improvements in reduced-order modeling capabilities via new investigations of: 1) three-dimensional finite element acoustic models versus duct acoustic models; 2) effects of fuel variability on ultra-lean combustion stability; and 3) system models that illuminate passive and active stabilization strategies for ultra-lean combustor operation.

The specific activities undertaken during the reporting period included:

1. Acquired all data for equivalence ratio fluctuations effect on flame dynamic heat release rate for natural gas.
2. Acquired FRFs for velocity (mass flow rate) fluctuations and equivalence ratio fluctuations for propane.
3. Developed a ROM for flame dynamics using an unsteady WRS (Well stirred reactor) modeling approach.
4. Developed a model for turbulent mixing and time lag of dispersion of f' pulse.
5. Assembled a finite element acoustic code with real boundary conditions for the turbulent, swirl-stabilized laboratory combustor.

   Executed code and compared with measurements.

The work plan for the period Nov 2005-May 2006 includes the following items:

1. Completion of a 3-D finite element model for the hot combustor acoustics.
2. Develop model of coupled combustion – acoustics, i.e., closed loop, based on FRF's obtained for the combustor acoustics and flame dynamics.
3. Acquire dynamics data for fuel variations, hydrocarbons and bydrogen.
4. Based on ROM of combustion dynamics develop control algorithm.

3 Project Description

3.1 Quantifying Heat Release Dynamics for Turbulent Swirled, Premixed, Lean Flames (Task 1).

Objectives: This task focuses on obtaining the frequency-resolved response of the heat release rate, in physical units, to perturbations in mass flow rate and equivalence ratio. Using the experimental frequency response, physics-based, reduced-order models will be derived. The models will then be validated on self-excited combustors in the Virginia Active Combustion Control Group laboratory, the National Energy Technology Laboratory, and in industry.

Methodology: To accurately measure heat release rate, Tunable Diode Laser Absorption Spectroscopy (TDLAS) and chemiluminescence will be used simultaneously. TDLAS methods will be used to measure the unsteady temperature of the products in the immediate post-flame zone. The temperature measurement is based on the ratio of the absorption of water lines at 1392 nm and 1343 nm. In this manner, the sensible part of the change in enthalpy can be obtained. Hydroxyl radical (OH*) chemiluminescence has been shown to be an excellent indicator of chemical heat release rate in premixed flames. Thus, it will be used to determine the chemical reaction contribution to changes in enthalpy. Both measurements will enable true characterization of the acoustic driving source term for thermo-acoustic instabilities.

In practical LP gas turbine combustors the onset of TA instabilities/oscillations involves fluctuations in both mass flow rate $\dot{m}'$ and the equivalence ratio, ϕ'. Therefore the dynamic response of the flame to $\dot{m}'$ and ϕ must be captured. Fluctuations in both will be imparted on the flow. $\dot{m}'$ fluctuations via a large speaker, and ϕ' with a high frequency on/off meso value. The fluctuations are quantified with an acoustic intensity meter and 3.39 μm absorption.

3.2 Modeling Time Lag and Dispersion of Equivalence Ratio Variations (Task 2).

Objectives: This task focuses on investigating the effect of time lag on flame stability and dynamics. The time lag is defined as the time for a perturbation in equivalence ratio to result in a perturbation in heat release rate. The effect of diffusion and turbulent mixing on equivalence ratio variations will also be studied.

Methodology: Methane absorption of an infrared Helium-Neon laser will be used to measure variations in equivalence ratio. The equivalence ratio will be modulated through a system employing high-frequency solenoid valves, rotating valves, voice coils, or loudspeakers. The effect of equivalence ratio variations on heat release rate will be measured via chemiluminescence and TDLAS methods, as described previously. The time lag will be measured as the time from when a perturbation is given to the equivalence ratio to the time a response is observed in heat release rate. Computational Fluid Dynamics (CFD) will be used to model the velocities and flame location in the combustor. This information can then be used to solve for the convective time lag and compare to the experimental values. Using this data, observations can be made on the effects of time lag on flame dynamics and stability. These observations will then be incorporated into reduced-order models. As in other tasks, the experimental methods will be verified on the laminar burner before beginning work on the turbulent burner.

3.3 High Temperature Acoustics Validation (Task 3).

Objectives: Using experimental data acquired from actuator excitations and flow noise, 3D FEA acoustical models for both cold, no-flow and actual operating conditions will be verified.

Methodology: FEA models of combustor acoustics, with ability to handle complex boundary conditions, and combustor CAD models as inputs will be developed. Recent experience in formulating FEA models of industrial combustors will serve as a baseline. Goals include

developing a neutral file format for sharing geometric data, integration with CFD models, and developing guidelines for partitioning models.

3.4 Premixed Flame Stabilization and Lean Blowoff Limits (Task 4).

Objectives: This task will focus on the measurement and modeling of static and dynamic lean blowoff limits over a range of operating conditions.

Methodology: The flame dynamics measurements will be extended to the lean blowoff limits. In addition, a system will be implemented to force fluctuations in equivalence ratio. The impact of equivalence ratio perturbations on flame stability will be investigated.

3.5 Prediction of Combustor Instabilities and Dynamic LBO (Task 5).

Objectives: The entire modeling methodology will be validated through prediction of combustion instabilities and lean blowoff limits on various combustors. Reduced-order models will be applied to VACCG test combustors, the NETL rig, and the Solar Turbines test rig.

Methodology: Using models for combustion system components developed in the preceding tasks, a model of the combustion instability feedback loop will be built for the target combustors. Stability predictions will be compared to experimental data over a wide range of operating conditions.

3.6 Control of Unsteady Combustor Operation (Task 6).

Objectives: Control unsteady combustor performance, i.e., TA instabilities and flame stabilization

Methodology: use developed ROM to design a control methodology for combustor stabilization over the whole equivalence ratio range. Pulsed pilots an main fuel, and staged premixed flames, will be considered.

4 Experimental

4.1 Experimental Apparatus

The experimental apparatus employed in continuing pursuit of quantifying heat release dynamics in turbulent, swirled, premixed, lean flames (task 1) is detailed in the Semi-Annual Activity Report for the period of May 2003-November 2003. A description of this apparatus in brief follows, with a schematic available in Figure 4.1. For the studies of flame dynamic response to velocity perturbations, an acoustic driver is used to generate a perturbation at a single frequency. The perturbation in velocity is measured with a two-microphone probe located around five inches below the flame. The pressure fluctuations measured by this probe are converted into velocity fluctuations according to the one dimensional form of Euler's equation written in the direction of the flow. The response of the flame heat release rate to this excitation is obtained through Hydroxyl radical chemiluminescence, measured via emission from the flame by a photomultiplier tube.

While fuel flow fluctuations were still measured using the methane laser absorption setup, a Matrix solenoid valve was added to the system to provide actuation for two radically opposed fuel injectors which introduced a fuel jet, creating equivalence ratio perturbations. The injectors were located at the same axial location as the two microphone probe, directly upstream of the swirler. The perturbations were introduced with the valve operating at a fixed frequency and a 50% duty cycle. The magnitude of the fuel pulses was approximately 10% of the premixed fuel flow.

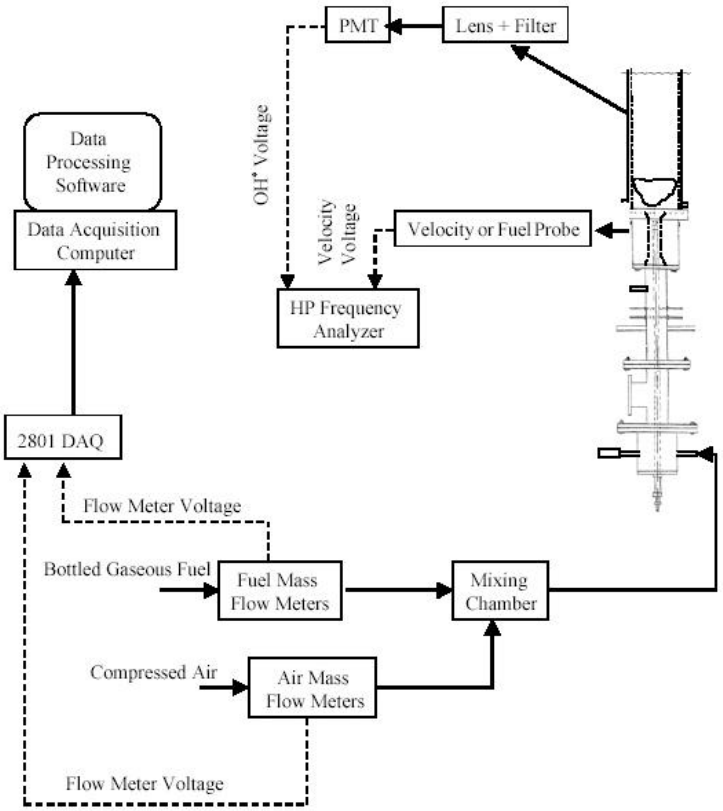

Figure 4.1 - Frequency response function to velocity perturbations for varying equivalence ratio

4.2 Data Acquisition and Observed Results

Tests were performed using LabView data acquisition software to control the speaker and fuel supply valve, which provided the fluctuations. Measurements were taken at several equivalence ratios for each of the perturbation types. Perturbations were introduced at a single frequency, while time-traces were stored for measurement of the perturbation and the flame heat release. The frequency of perturbation was varied from 10 to 400 Hz at a 10 Hz interval and data from the input and output signals experiencing this perturbation were stored. A time trace of 180000 data points on each channel at a sampling frequency of 3600 Hz was taken at each excitation frequency. When the frequency of perturbation was varied, 15 seconds were allowed prior to taking more data to allow transients to die out. The data was then processed at each frequency of excitation, calculating the transfer function by determining individual Fourier coefficients. The Fourier coefficients were then combined to form the full band transfer function.

The trends in this data with changes in frequency were validated through comparison to data obtained from the raw voltage signals by a Hewlett Packard spectrum analyzer. In the case of equivalence ratio perturbation, the HP measured signal had some uncertainty due to the inability to account for changes in the reference intensity, but trends still showed good agreement. Further, tests were carried out to validate the trends across mean equivalence ratio by fixing the frequency of excitation and varying the equivalence ratio. This helped to ensure there was no corruption in the data due to day-to-day variations in ambient environment or other factors. As before, in the case of equivalence ratio fluctuations, the inability to account for variations in reference intensity introduced some uncertainty, but still allowed for an overall increase in measurement confidence.

In the case of velocity perturbations, full transfer functions including coherence were found over the equivalence ratio range of 0.48 through 0.63. The leanest case was the stabilization limit for the flame in this experimental setup. Results for ultra lean conditions showed higher scatter and

lower coherence due to the reduced overall flame heat release and intrinsic fluctuations present as the flame began to flicker. All of the test conditions were checked for repeatability.

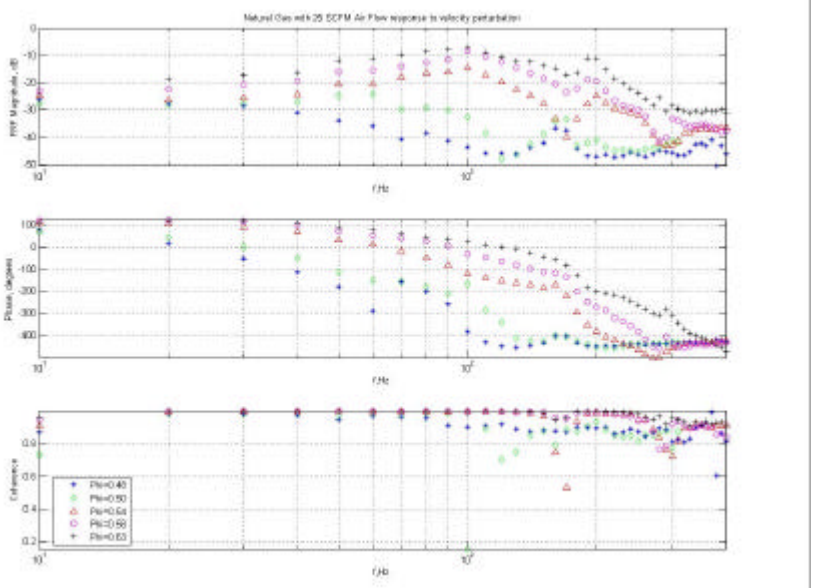

Figure 4.2 Frequency response function to velocity perturbations for varying equivalence ratio

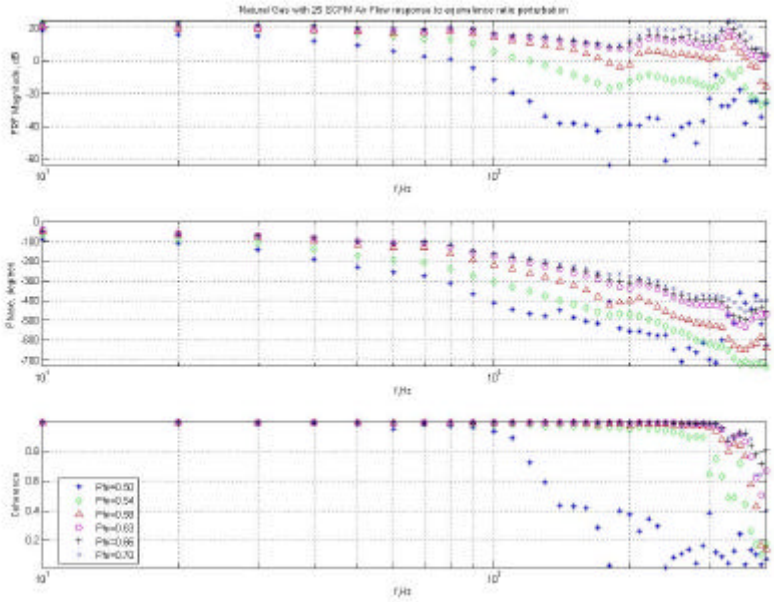

4.3 Frequency response function to equivalence ratio perturbations for varying mean equivalence ratio

The FRF data for the flame has a low pass characteristic. The data for richer equivalence ratios exhibit a slight peak immediately before rolling off around 100 Hz. This peak remains stationary until very lean equivalence ratios are reached. The break frequency and the low frequency magnitude decrease with decreasing equivalence ratio and the falloff becomes steeper. An acoustic

resonance is present in the system around 180 Hz and accounts for the dip in coherence at this point. Higher order dynamics are evidenced near 200 Hz and 300 Hz, especially in the richer cases.

Phi perturbations were introduced with equivalence ratio varying from 0.50 to 0.70. Again, low pass filter behavior was evidenced. In this case the initial band and roll off around 100 Hz appeared to be first order, though as with the velocity data, some higher order dynamics were present, especially at higher frequencies. A very small magnitude drop was observed with the decrease in equivalence ratio, particularly toward the leanest cases. A shortening bandwidth with decreasing equivalence ratio is also clearly evidenced by the data at lean equivalence ratios. The maximum drop for the richest cases was around 20 dB while the drop for leaner cases was significantly greater.

4.3 Planned Activities for Next Six Months

Further work in the direction of this task lies in the quantification of flame dynamics for varying fuels. This has important applications in the area of robust combustor design, with particular interest as a result of attempts to design combustors for medium BTU fuels. While varying blends of hydrocarbons yield one potential experimental area, application of similar techniques to measure dynamics of hydrogen combustion provide another direction of interest.

The most immediate work to be carried out is the investigation of the dynamic response of turbulent, premixed, swirl stabilized propane flames to perturbations in equivalence ratio and velocity. The experimental setup required for this study is identical to that required for natural gas. Blends of natural gas and propane will also be considered to evaluate the effect of fuel variability on the flame dynamics, yielding a beginning at understanding of the generalized effect of fuel composition on flame dynamics.

For reasons of expediency, the tasks dealing with LBO, 4 and 5, will be folded into the present both experimentally and in model development.

5 Turbulent Mixing and Convective Time Delay (Task 2)

5.1 Motivation

Dynamic variations in the fuel-air ratio and the transport delay associated with these variations are important characteristics of the overall combustion system model. In this section we investigate a simple model for turbulent mixing and transport, discuss the experimental measurements of these effects on a test combustor, and show that the model can be used to match the experimental observations.

5.2 An Analytical Model

A simple model of turbulent mixing and transport was proposed by Scarinci and Freeman based on concepts from the atmospheric dispersion of pollutants from a smokestack. The basic idea is that the concentration at a point x at time t is a function of the source concentration and the transition probability density — the probability that a particle at point x' at time t' ends up at point x at time t. For simplicity, only mixing in the axial direction will be considered, although the results can be easily extended to three dimensions. Assuming stationary, homogeneous turbulence, and a constant flow velocity, U, the transition probability Q has the Gaussian form

$$Q(x,t \mid x',t') = \frac{1}{\sqrt{2p}\,s_x(t)} \exp\left(-\frac{(x - x' - U(t-t'))^2}{2s_x^2} \right) \tag{5.2-1}$$

The fuel concentration at point *x* and time *t* can be written as

$$C(x,t) = \int_{-\infty}^{\infty}\int_{0}^{t} Q(x,t \mid x',t')S(x',t')dt'dx' \tag{5.2-2}$$

If the fuel is injected a distance x_o upstream of the point of interest, $x = 0$, then the response to a unit impulse of fuel injection, $S(x,t) = d(x + x_o)d(t)$, is given by

$$h(0,t) = \frac{1}{\sqrt{2p}\, s_x(t)} e^{-\frac{(x_o - Ut)^2}{2 s_x^2(t)}} \tag{5.2-3}$$

By taking the Fourier transform of this impulse response we can obtain the frequency response of the mixing process and by using the convolution integral

$$C(0,t) = \int_0^t h(0,t)S(x_o,t)\, dt \tag{5.2-4}$$

the time response of the concentration at $x = 0$ can be found due to a time-varying source concentration at $x = -x_o$.

To find $s_x(t)$, note that

$$s_x^2(t) = \left\langle X^2(t) \right\rangle = \int_0^t\int_0^t \left\langle v(t')v(t'') \right\rangle dt'dt'' \tag{5.2-5}$$

where *v* is the unsteady part of the *x* velocity and

$$R(t' - t'') = \left\langle v(t')v(t'') \right\rangle \tag{5.2-6}$$

is known as the Lagrangian correlation function. For turbulent diffusion problems, this function has been approximated by the simple exponential function

$$R(t - t') = \overline{v^2} e^{-b|t-t'|} \tag{5.2-7}$$

where *1/b* is the correlation time and $\overline{v^2}$ is proportional to the total turbulent kinetic energy of the flow. Plugging into the previous equations and making a change of variable results in

$$s_x^2(t) = 2\int_0^t (t-x)R(x)\,dx = \frac{2\overline{v^2}}{b^2}[bt-(1-e^{-bt})] \tag{5.2-8}$$

If the correlation time is much less than the convection time, then $bt >> 1$, and the previous expression reduces to

$$s_x^2(t) = \frac{2\overline{v^2}}{b}t \tag{5.2-9}$$

leaving only one unknown parameter.

We should note at this point that the above analysis is for a varying fuel input in a fixed mean velocity flow field. The actual problem in a combustor is for a fixed fuel input in a varying mean velocity flow field. This latter problem is significantly more complicated to set up analytically as it involves a variable time delay. We make the assumption that for small velocity perturbations the two problems will behave similarly.

5.3 Experimental Measurements

Experimental measurements were performed on a premixed, turbulent combustor that is shown diagrammatically in Figure 5.1. The main fuel and air enter the bottom of the combustion section shown already well mixed. A fast solenoid valve was used to inject fuel pulses at a 50% duty cycle into one of two ports below the swirler: position 1 is located slightly below the swirler and position 2 is located significantly below the swirler, as indicated in the figure. The fuel concentration was measured by laser absorption at a port slightly above the swirler position.

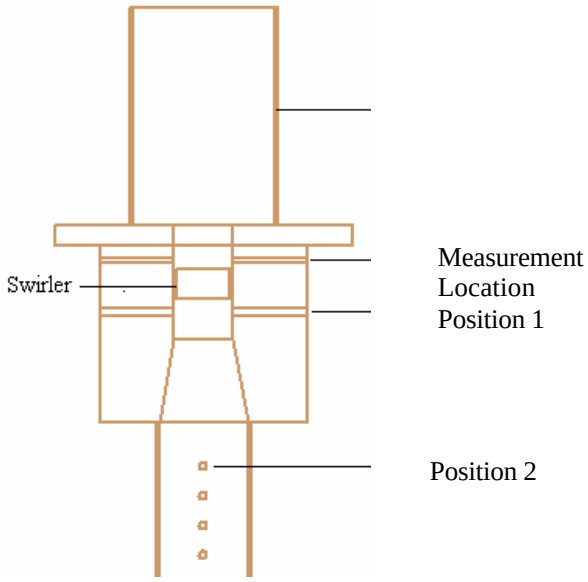

Figure 5.1: Diagram of combustor cross section showing injection and measurement ports.

The transfer functions between the input voltage to the solenoid valve and the fuel concentration fluctuations at the downstream measurement location were measured. The results for

Position 1 are given in Table 5.1 and plotted in Figure 5.2. The convection time delay, estimated based on the flow rate and distance traveled, is given by

$$T_{delay} = \frac{L}{U_{avg}} = \frac{4.445cm}{713.42cm/\sec} = 6.2m\sec$$

Table 5. 1: Frequency Response Data for Position 1

Frequency	Magnitude (dB)	Phase (degrees)
20.	-8.9	-56.8
40.	-10.9	-104.4
60.	-10.6	-149.7
80.	-14.6	-215.1
100.	-11.9	-233.2
120.	-17.9	-274.2
140.	-15.8	-314.2
160.	-18.2	-354.2
180.	-20.9	-419.3
200.	-23.4	-490.8
220.	-30.7	-612.2
240.	-33.9	-669.2
260.	-32.6	-643.0
280.	-30.8	-651.8
300.	-35.6	-637.0
320.	-31.6	-639.8
340.	-30.2	-588.6
360.	-30.1	-590.1

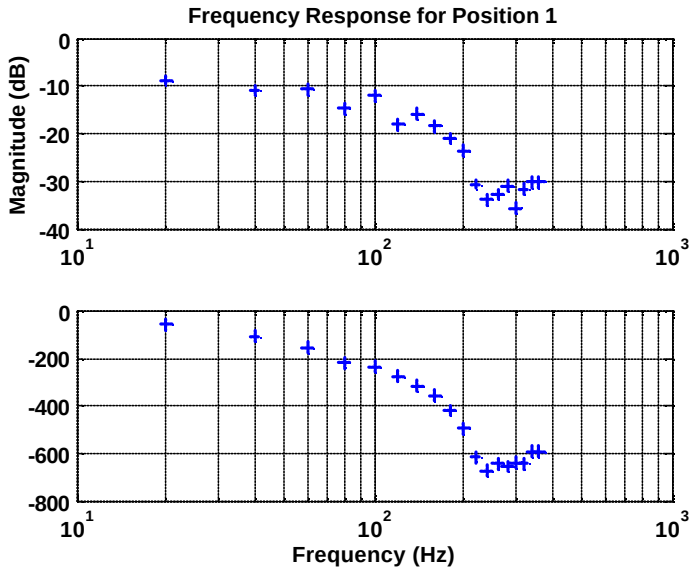

Figure 5.2.: Frequency Response for Position 1

Similarly, the results for Port 2 are given in Table 5.2. and plotted in Figure 5.3. The convection time delay estimated based on the flow rate and distance traveled is given by

$$T_{delay} = \left(\frac{L_1}{U_{avg_1}} + \frac{L_2}{U_{avg_2}} + \frac{L_2}{U_{avg_3}} \right) = \left(\frac{3.98}{253.4} + \frac{6.98}{483.41} + \frac{6.98}{713.42} \right) = 39.94 m \sec$$

where the three distances correspond to lengths having different cross sectional areas, and hence different mean velocities, as shown in the combustor schematic.

Table 5.2.: Frequency Response Data for Position 2

Frequency	Magnitude (dB)	Phase (degrees)
20	-17.9	-282
40	-18.0	-557
60	-20.5	-837
80	-23.7	-1107
100	-28.4	-1401
120	-35.1	-1668
140	-38.3	-1927
160	-46.0	-2243
180	-41.3	-2839
200	-39.1	-3106
220	-51.6	-3421

240	-53.1	-3506
260	-57.8	-3658
280	-47.5	-3838

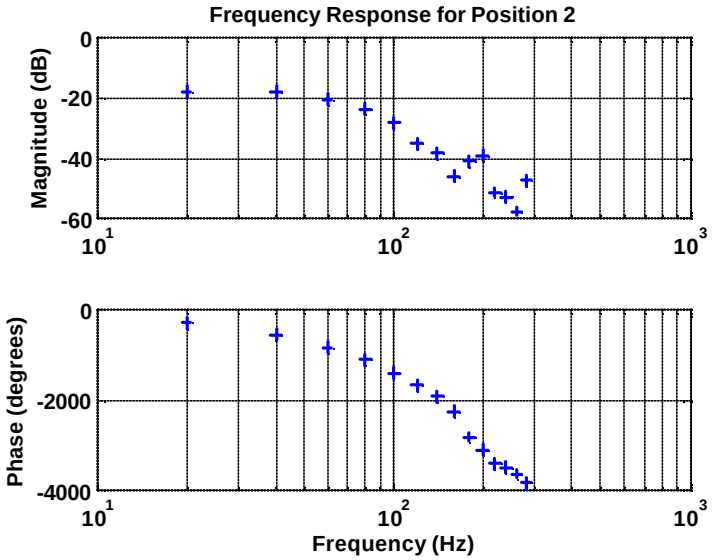

Figure 5.3: Frequency Response for Position 2

5.4 Analysis

The frequency response measurements detailed above are easier to make reliably than pulse measurements because of the higher signal to noise ratio. But our main interest is in how a pulse of fuel is delayed and mixed as it propagates through the mixer. Two different time delays must be distinguished, as shown in Figure 5.2.4: pure time delay and convective time delay. The pure time delay is the delay between when a pulse of fuel is applied and when it is first observed at the measurement location. The convective time delay is the time between when a pulse is applied and when the maximum change is observed at the measurement location. These two delays would be the same for a very narrow pulse if there were no mixing, but turbulent mixing causes the delays to be different.

From a modeling point of view, we are interested in pure time delay so that our overall model consists of the cascade of a delay followed by a causal dynamical system. If we use the convection time for the delay, then our dynamical system model would have to be acausal, which makes the modeling situation more complicated. On the other hand, convection time is easily estimated from the mean velocity and so is the more natural delay to discuss. For our present purposes, we will consider delay to mean convective delay.

To estimate the delay and diffusion of a fuel pulse from our frequency response data, we will fit this data as accurately as possible with a model consisting of a time delay and an a causal dynamical system. This will yield an estimate of the convection delay embodied in the frequency response data and the impulse response of the dynamical system will show how an impulse of fuel at the input position spreads out by the time it reaches the measurement position. This is a very effective way of getting the pulse shape due to a very narrow pulse of fuel. In addition, it is an effective way of estimating delay. Trying to estimate delay from looking at the phase of the system

is problematic since the phase has components from both the time delay and the dynamics, which can be difficult to separate.

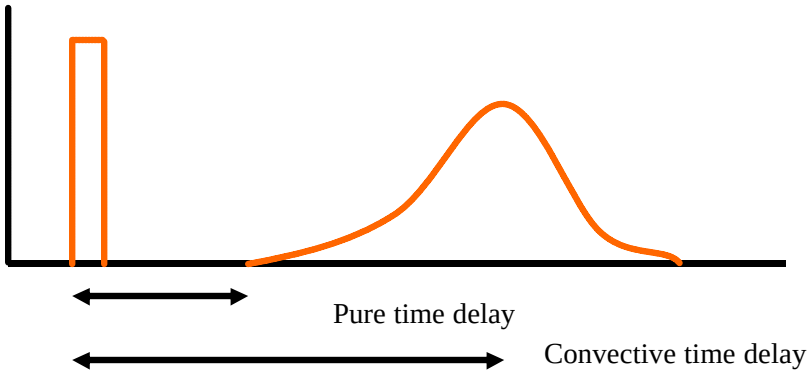

Figure 5.4: Definitions of Different Time Delays.

For position 1, the time delay was estimated to be 6.8msec and the frequency response fit and resulting impulse response are shown in Figures 5.5 and 5.6.

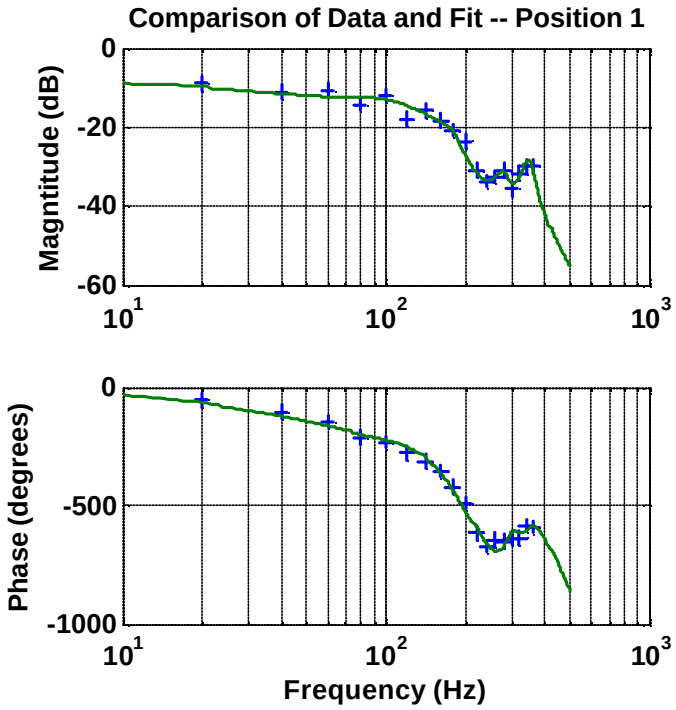

Figure 5.5: Frequency Response Fit for Position 1

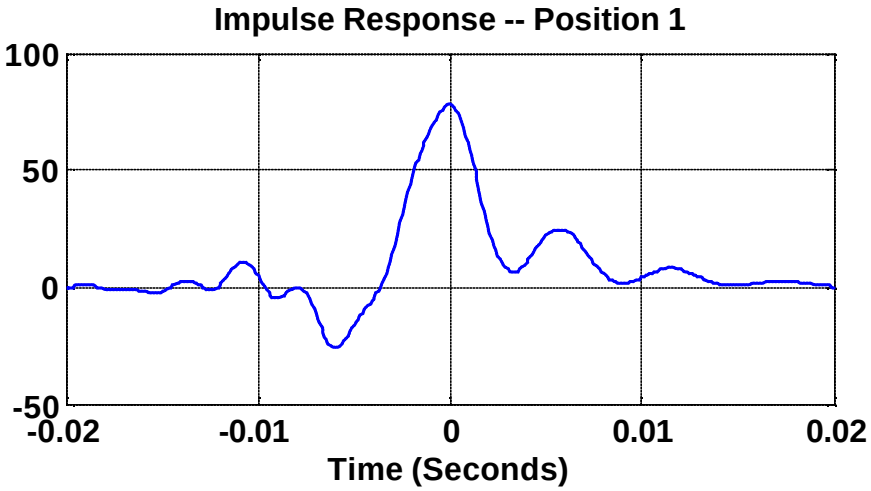

Figure 5.6: Impulse Response from Position 1.

For position 2, the time delay was estimated to be 38.8msec and the frequency response fit and impulse response are shown in Figures 5.7 and 5.8.

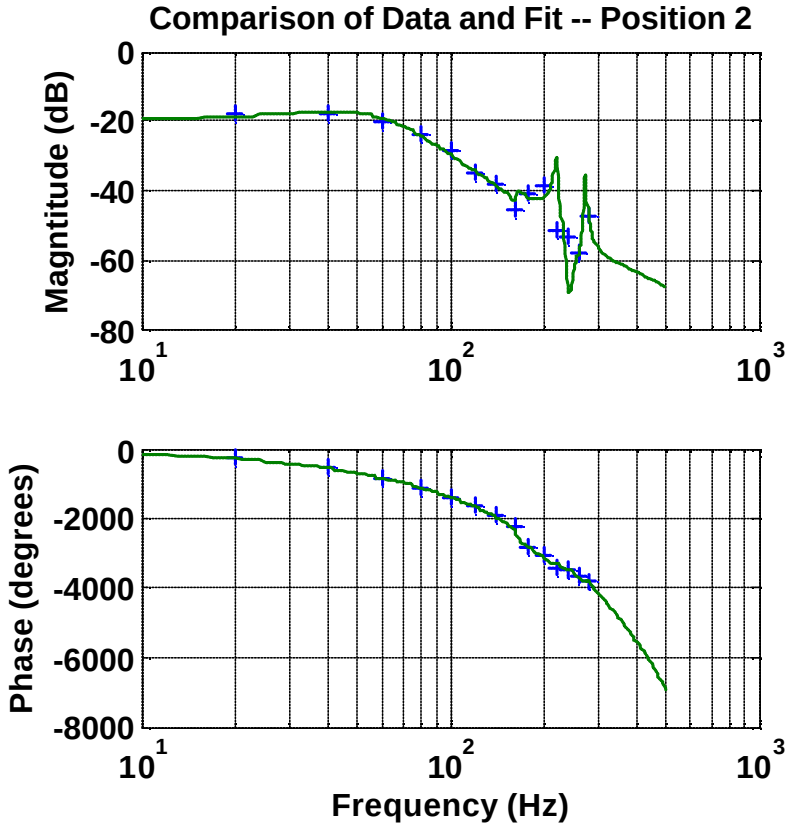

Figure 5.7: Frequency Response Fit for Position 2.

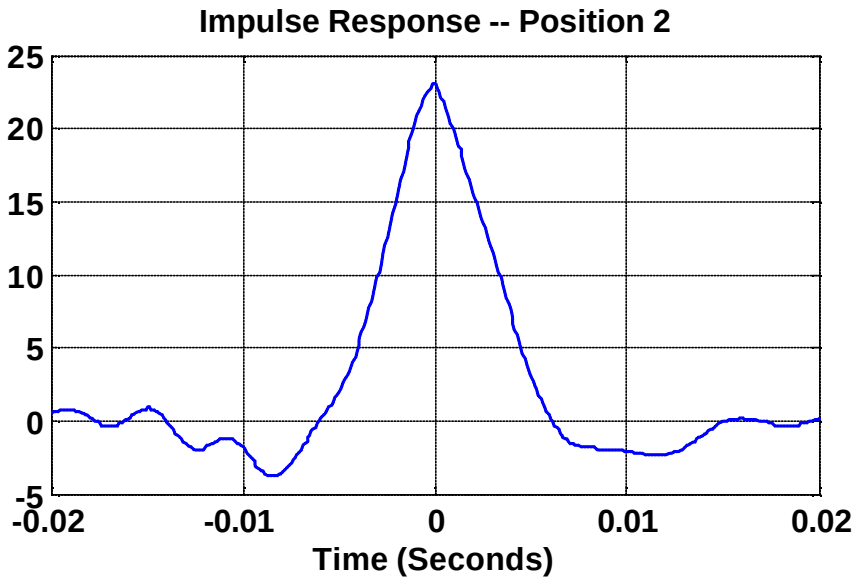

Figure 5.8: Impulse Response from Position 2.

As can be seen from the following table, the convection delay times determined by the frequency response fits compare very well with the simple distance over mean velocity calculations.

Table 5.3: Delay Times

Position	Convection	FRF
1	6.2msec	6.8msec
2	39.9	38.6

In addition, the delay times are different by a factor of about 6 while the pulse widths differ by a factor of about 2. From our analysis, we would expect the widths to be roughly proportional to the standard deviation (5.1.2) evaluated at the convection time. Since the standard deviation goes as $\sqrt{t}$, we would expect the pulse widths to vary as $\sqrt{6} = 2.4$, which is in reasonable agreement with the results of the frequency response analysis.

In its simplest form, the mixing model (5.1.1-2) requires the specification of only one parameter, the mean square turbulent velocity times the correlation time. If we take this to be $50\text{cm}^2/\text{sec}$ and compare the model to the actual data we get the results shown in Figures 5.9-10. The impulse response can be computed directly from (5.1.1), while the frequency response can be computed from the Fourier transform of the impulse response. The frequency responses compare relatively well with the measured responses. At the higher frequencies, the measured data does not keep falling off as predicted by the model but exhibits additional dynamics. This discrepancy might be due to the reduced signal to noise ratio at these points, acoustic or fluid mechanical dynamics excited by the pulsed injection, or dynamics in the solenoid valve at high frequencies. But since these variations occur at a level 20dB below the low frequency response, they will probably be insignificant with regard to the overall loop stability.

The impulse responses for position 2 compare quite favorably, but the reconstructed and model responses for position 1 differ significantly in height, even after normalizing the measured frequency responses, which have arbitrary units, to have a dc gain of $1/U_{avg}$. (At very low frequencies, the amount of fuel injected per unit time at the injection point must pass the measurement point without attenuation). Since narrow pulse reconstruction will depend critically on the high frequency portion of the measured frequency response, the measurements and fit in this region are most critical while at the same time most likely to be in error.

On the whole, this simple model appears to give very reasonable results, especially considering that the flow goes through area/velocity changes and a swirler prior to measurement.

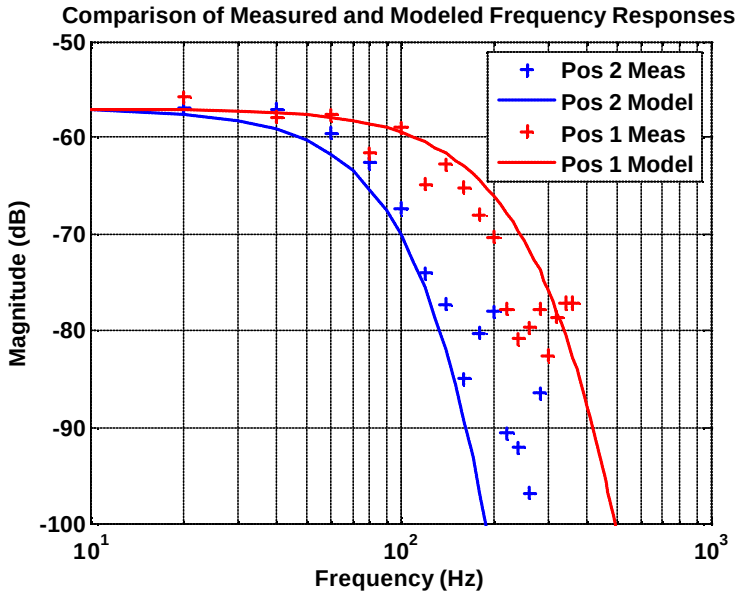

Figure 5. 9: Comparison of Turbulent Mixing Model and Measured Frequency Response for positions 1 and 2.

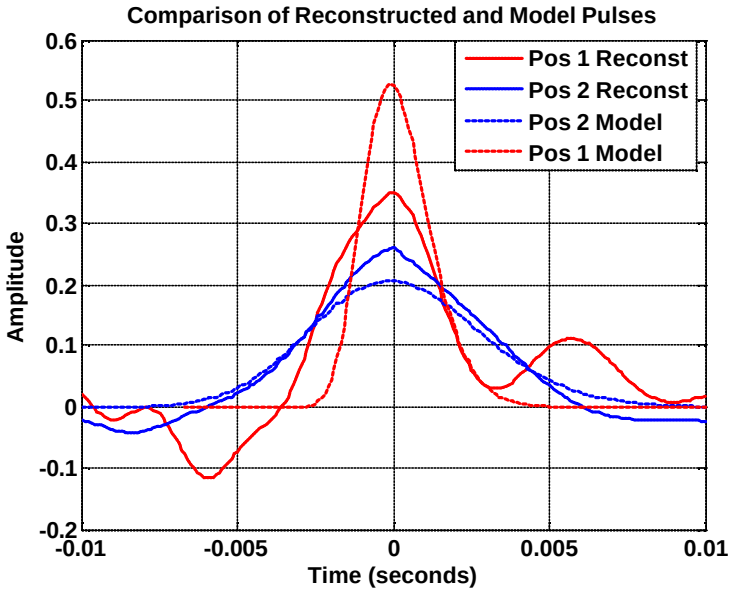

Figure 5.10: Comparison of Impulse Responses from Model and Reconstructed from the Measured Frequency Responses.

6 Combustor Acoustics

6.1 Introduction

Thermoacoustic combustion instabilities are often associated with large pressure amplitudes leading to serious performance degradation and severe structural damage. This problem has been studied for a long time; however, due to the complexity of this phenomenon, it is still not well understood.

The motivation for this project is to develop a process or methodology that industry can use to predict thermoacoustic instabilities for gas turbine combustor design purposes. In previous studies (Bloxsidge, 1988), it has been postulated that instabilities can be understood and predicted from a knowledge of the transfer function of the flame and the acoustic impedance on either side of the flame. This research is taking a similar approach. The flame transfer function is derived from first principles using a reduced order model and is discussed in a different section of this report. The acoustic impedance is discussed in this section and is described with a frequency response function (FRF) between the pressure at the flame to the particle velocity at desired locations.

Since currently the combustor is open at the top, the FRF downstream of the flame is disregarded. Upstream of the flame, two FRFs are required to account for the unsteady velocity approaching the flame and the equivalence ratio fluctuations at the fuel lines. Figure 6.1 shows a simple block diagram of the system. The diagram demonstrates the two ways in which the acoustics couple with the flame model to produce instabilities.

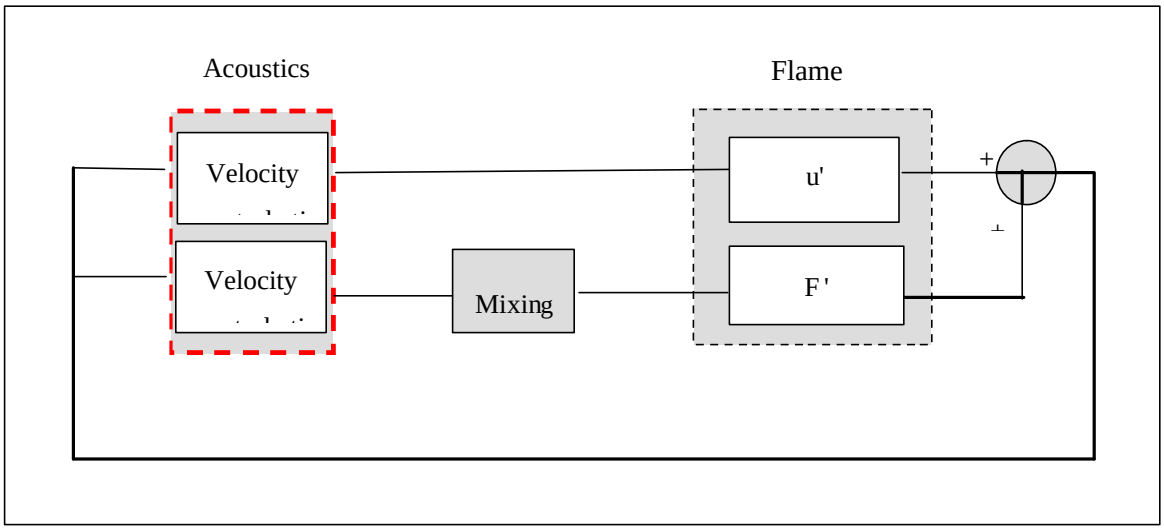

Figure 6.1: Block diagram for combustor model

6.2 Overview

Acquiring the frequency response functions mentioned above is accomplished by using a one dimensional acoustic finite element model. The focus of this section of the report will be devoted to discussing research progress, results, and issues of the acoustic finite element modeling task for this project period. Specifically, the following sections of the report focus on the motives for using "one dimensional" acoustic finite element models, modeling techniques, and a comparison with experimental results. Acoustic mode visualization is discussed and the experimental procedure is described. The frequency response functions for the "cold" combustor are shown and discussed.

Future work in temperature mapping and "hot" combustor modeling is also explained. Lastly, future goals and issues on hot combustor modeling and testing will be discussed.

6.3 One Dimensional Finite Element Modeling

6.3.1 One Dimensional Model

Originally, it was believed that a three dimensional finite element model was requisite to accurately predict the acoustic behavior of combustors. However, due to the decreased degrees of freedom inherent in reduced order modeling, it has become apparent that a one-dimensional acoustic model would be more appropriate.

The basis for a one-dimensional model is the fact that the frequency range of interest is typically very low. The reason for the low frequency range is due to the flame's low pass filter characteristics. In general, frequencies above about 250 Hz do not excite the flame and therefore do not produce significant enough dynamics to be considered important for reduced order modeling.

In the low frequency range of interest, plane wave behavior will be the dominant acoustic response. A plane wave is an acoustic wave that propagates in only one direction, longitudinally along the axis of the combustor and has no variation in properties over its cross-section. The plane wave assumption is valid until the frequency range exceeds the cut off frequency of the first cross mode. The equation for the cutoff frequency for a combustor of circular cross section is given below.

$$f_c = \frac{1.84c}{p\,d} \tag{0.1}$$

Where c is the speed of sound in the medium and d is the largest diameter in the combustor. For the laboratory gaseous combustor under study in this project, the cutoff frequency is about 1,364 Hz. In general, the plane wave assumption works well when the cutoff frequency for the first cross mode is less than the cutoff frequency of the flame (about 250 Hz).

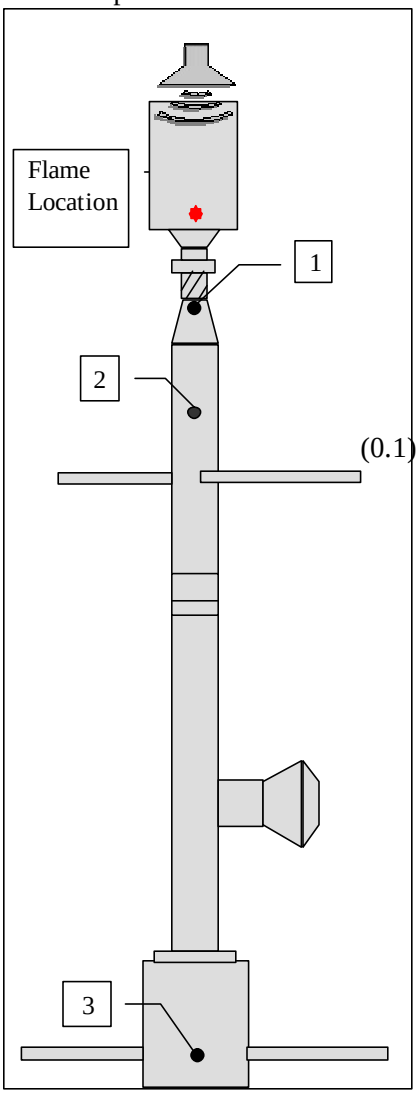

Figure 6.2: Schematic of combustor rig

6.3.2 Finite Element Modeling Techniques

As discussed above, the acoustic response of the combustor consists of plane wave interactions. In order to capture these interactions accurately, two parameters are required: the equivalent cross-sectional area, and the corresponding length of each section.

Once the equivalent geometry is known, it is used to create the structure for the finite element model. The ABAQUS finite element package is used in this research; however, other commercial codes may also be adequate.

In ABAQUS, a one dimensional deformable fluid structure of variable cross-sectional area was utilized. This structure was meshed with one-dimensional quadratic acoustic elements. There are a total of 1,097 elements in the finite element mesh. A higher number of elements produce no change in the results. In fact, it is likely that fewer elements are needed for the finite element solution to converge.

Rigid boundary conditions were enforced everywhere except at the top of the combustor where an open duct impedance condition was specified. Lastly, a constant volumetric drag of $50\ \mathrm{N\cdot s/m^4}$ was specified as material property of the air to make the finite element model lightly damped.

6.4 Experimental Comparison

Figure 6.2 shows a simple schematic of the combustor rig used for experimental validation. The three places numbered on the schematic represent three different locations where the finite element model was compared with experimental results. The results were compared using frequency response functions formed by dividing the pressures at the four different locations in the rig by the pressure at the idealized location of the flame.

Figures 6.3, 6.4, and 6.5 on the following pages show the FRF's predicted by the acoustic finite element model vs. the experimental FRF's at the same locations. It should be noted that the data being compared in the following graphs is only used as a means for validating the accuracy of the finite element model. It is not the actual data that will be input into the reduced order model; that data will be discussed in detail later in the "Velocity/Impedance Measurements" section of the report.

The frequency range displayed in the figures below goes from 25 to 650 Hz. Notice that in all three figures, the peaks in the FRF are approximately at the same frequencies. These frequencies are the first five natural or resonance frequencies of the combustor and each one has a corresponding mode shape that will be discussed in further detail in the "Mode Visualization" section.

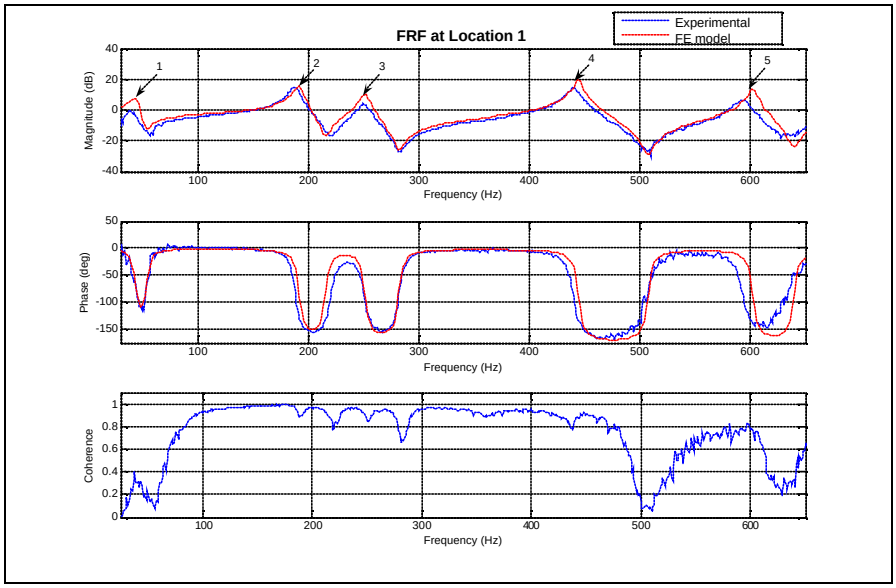

Figure 6.3: Frequency response function between pressure at location 1 and the pressure at the idealized flame location.

The frequency response function shown in Figure 6.3 is taken at location one (referenced in Figure 6.2), about 3.5 inches upstream from the flame. It can be seen from the figure above that both magnitude and phase of the FRF are very accurately predicted from the one-dimensional finite element model. It should also be noted that at the anti-resonance frequencies, the coherence is poor. This occurs because the FRF magnitude is so low at these locations that the inherent noise in the signal shows up and drives the coherence down.

The resonance frequencies are the most critical things to capture in the FRF's. These frequencies have been numbered in Figure 6.3 for convenience and will be referred to by the numbers in the future. Table 1 below compares the experimental and finite element resonance frequencies listing the frequencies, the difference between experimental and finite element, and the percent error. The percent error is calculated from the following equation.

$$\text{Percent Error} = \left|\frac{\text{Measured-Predicted}}{\text{Measured}}\right| \times 100$$

Table 6.1: Resonance Frequency comparison between experimental and finite element model

Number	Measured resonance Frequency (Hz)	Predicted resonance Frequency (Hz)	$\lvert$**Measured - Predicted**$\rvert$ (Hz)	Error (%)
1	39	42	3	7.7
2	190	192	2	1
3	250	250	0	0
4	440	444	4	.9
5	594	602	8	1.3

The table above shows that the first resonance frequency has the largest percent error with a value of 7.7%. However, it should be realized that the percent error calculation is more sensitive to differences at lower frequencies. The other resonance frequencies all have errors of less than two percent. These errors are very low, and fall within the acceptable range error established at the start of the project.

Figures 6.4 and 6.5 below are comparisons made at two other locations in the combustor and have essentially identical resonance frequencies and consequently the same small amount of error.

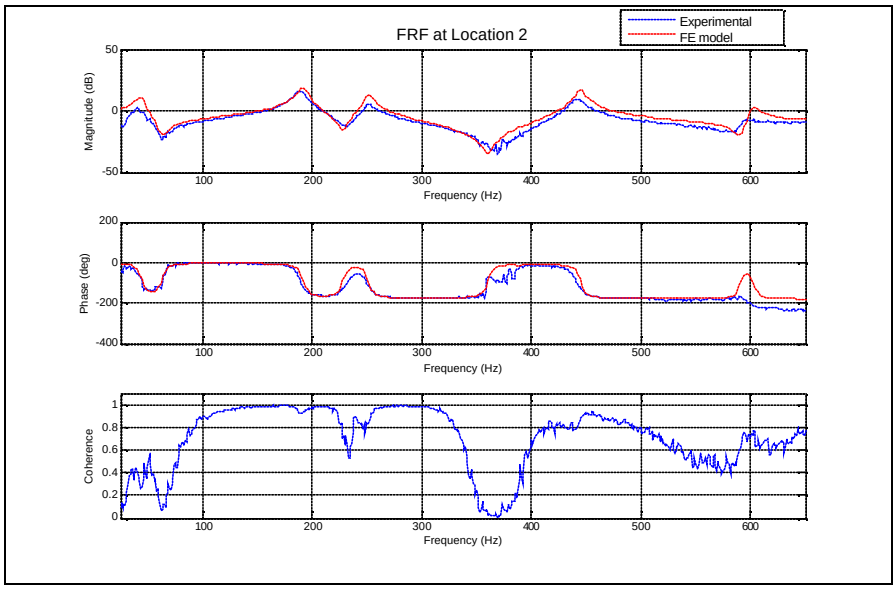

Figure 6.4: FRF between pressure at location 2 and the pressure at the idealized flame location.

The frequency response function shown in Figure 6.4 is taken at location two (refer to Figure 6.2), about 11 inches upstream from the flame. Once again, the finite element model does an accurate job in predicting the magnitude and phase of the FRF. It should be noted that there is some extra noise in the experimental magnitude and phase plots around 360 Hz, as well as a drop in coherence in this region. These affects are attributed to the resonance of a thin aluminum plate used to cap off the middle side branch where a speaker is sometimes placed (see Figure 6.2). To eliminate these affects the thin plate should be replaced with a significantly stiffer plate.

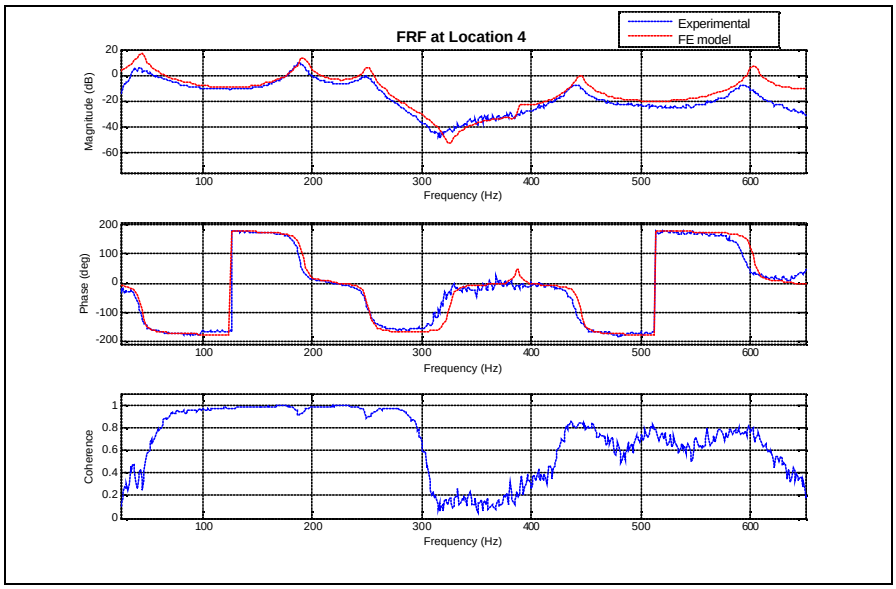

Figure 6.5: FRF between pressure at location 4 and the pressure at the idealized flame location.

The frequency response function shown in Figure 6.5 is taken at location 6.3 in Figure 6.2, about 40 inches upstream from the flame. The finite element model still does an excellent job at predicting magnitude and phase of the FRF. The overall magnitude of the FRF has been significantly reduced compared to the magnitudes in Figures 6.3 and 6.4. A large part of this magnitude reduction is due to a honeycomb and perforated plate section placed in the lower end of the combustor for flow straitening purposes. The result is that only a fraction of the acoustic wave is transmitted through. In the finite element model the honeycomb and perforated plate were modeled simply as an equivalent cross-sectional area reduction. It is evident from the high accuracy in the predicted FRF in Figure 6.5 that the equivalent area reduction works very well when modeling this type of obstruction.

As mentioned previously, there appears to be extra noise in the experimental data near 360 Hz due to the vibration of the thin aluminum plate. This again results in low coherence at these locations.

6.5 Summary of Finite Element Modeling

The accuracy of the one-dimensional finite element model is remarkable. This is especially evident when one looks at some of the geometric complexities in the feed lines, swirler, perforated plate, and cross sectional area changes shown in Figure 6, a picture of the actual combustor. In addition to the one dimensional model having excellent accuracy, it is also substantially easier to create than a three-dimensional model. For example, once the equivalent geometry and boundary conditions are known, it would take an experienced user of ABAQUS roughly two or three hours to create the finite element model. The one dimensional model also requires significantly less computational time to solve. For a three-dimensional finite element model of the combustor, it takes several hours on a super computer to solve. In comparison, it takes about one minute on a desktop computer to solve the one-dimensional combustor finite element model. Because of the very good accuracy and efficiency of the one-dimensional finite element model it is recommended that it be used in place of the three-dimensional model when ever possible.

6.6 Mode Visualization

The five resonance frequencies shown in Figures 6.3 through 6.5 correspond to the first five modes or dominant standing wave patterns of the combustor. These modes can be visualized by spatially plotting the real part of the acoustic pressure at the resonance frequency. The ability to visualize each acoustic mode aids in understanding the contribution and coupling of each geometric subsystem and how it affects the overall acoustics of the combustor. The visualization of modes can also be beneficial for both designing the geometry of the combustor, as well as, for creating passive control devices for controlling the thermoacoustic oscillations. The first three acoustic modes of the laboratory combustor are shown in the figures below.

1) **142 Hz ? First axial mode**, only the overall length of the combustor affects this mode. This mode is approximated as a quarter wave, $\lambda/4$, mode.

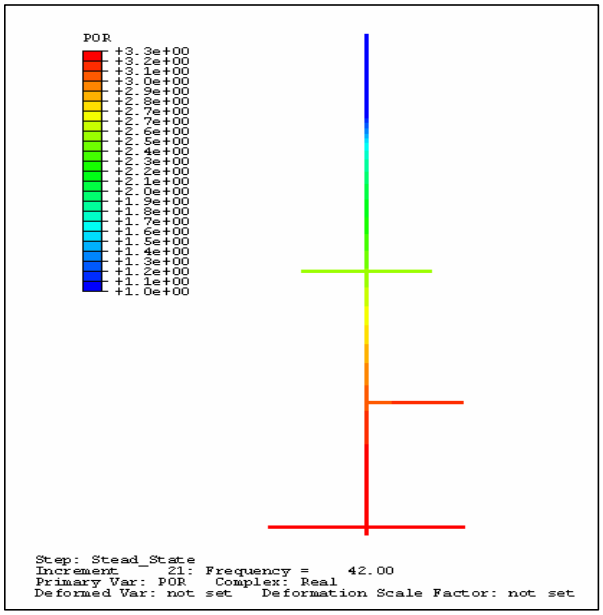

2) **192 Hz ? Second axial mode**, this mode is once again a function of the overall length slightly coupled with the lower side branch. This mode is approximated as a $3\lambda/4$ mode.

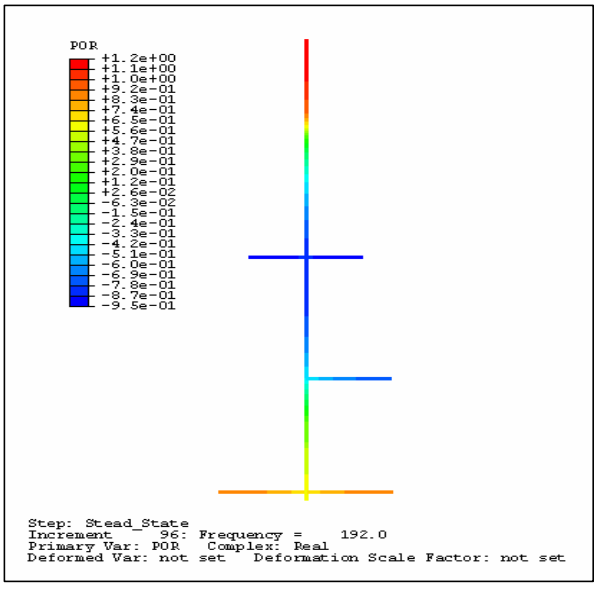

3) 250 Hz ? **Third axial mode**, this mode is also a function of the overall length and is strongly affected by the dimension of the middle side branch. This mode is approximated as a 5λ/4 mode.

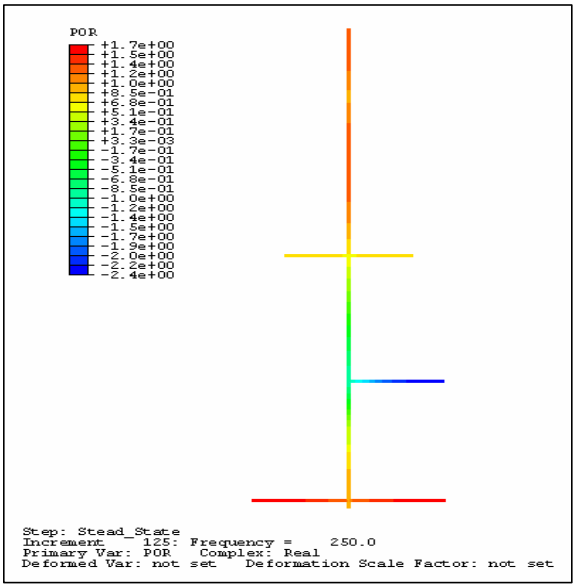

The mode visualization technique shown in the plots above is particularly useful in designing the geometry of the combustor. One can simply modify the geometry that a given acoustic mode is most sensitive to, and consequently modify the resonance frequency and amplitude of the mode. One example of this was observed with the resonance frequency associated with the third axial mode. When the length of the middle side branch was shortened by 1 inch, the third resonant frequency shifted from about 250 Hz to about 260 Hz. Similar results would occur from changing other dimensions in the combustor. As mentioned above, this process can be used as an important tool in the design of combustors.

6.7 Experimental Validation

Figures 6.3 through 6.5 show experimental results that were acquired on the gaseous laboratory combustor at Virginia Tech's Active Combustion and Control laboratory. A picture of the test apparatus has been attached below along with its specifications.

Table 6.2: Specifications for VACCG Laboratory-Scale Combustor

Combustor Type	Swirl and dump & enables turbulent flame stabilization
Air Flow rate	200 SCFM
Power	400 KW
Reynolds Number	100,000 max
Swirl Number	0.4-1.8
Pressure	Atmosphere to 10 bar

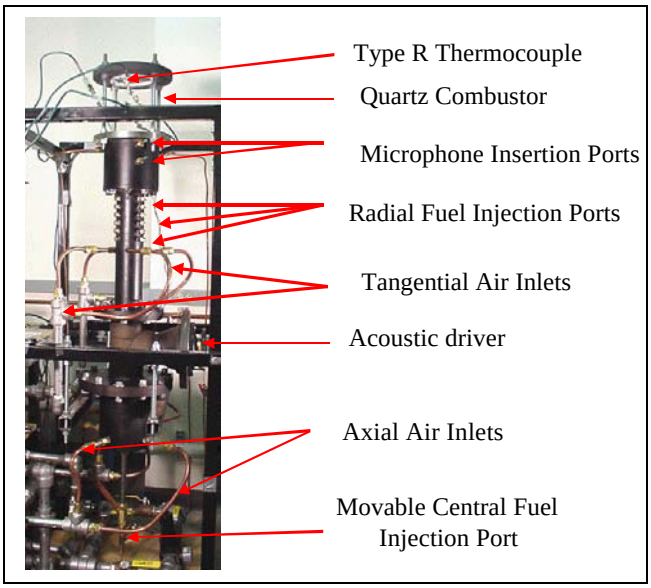

Figure 6.6: The VACCG Laboratory-Scale Combustor.

The purpose of the experiments was to determine the "cold" acoustic behavior of the combustor. A speaker was used to excite the acoustics with white noise at the top of the combustor. The speaker was placed in a location spatially consistent with the flame and can be considered as an acoustic source representing the flame. High precision microphones were used to measure the acoustic pressure at the several spatial locations in the combustor rig including the three locations referred to in Figures 6.3 through 6.6. The data from these experiments was used to reconcile the "cold" acoustic model, explore additional acoustic properties in the combustor, and provide frequency response functions used in the closed-loop reduced-order model.

Plans are currently being made to develop experimental procedures to verify the "hot" acoustic response of the combustor. The main challenge is to find ways to mount microphones so that they will not be damaged by heat.

6.8 Velocity/Impedance Measurements

As mentioned in the introduction, the desired outputs of the finite element model are the frequency response functions between the pressure at the flame to the particle velocity at desired locations. These FRF's are input into the reduced order flame model and play a significant role in predicting the thermoacoustic instabilities.

Two figures are shown below. Figure 6.7 shows the FRF immediately upstream of the flame. Figure 6.8 represents the FRF at the fuel lines.

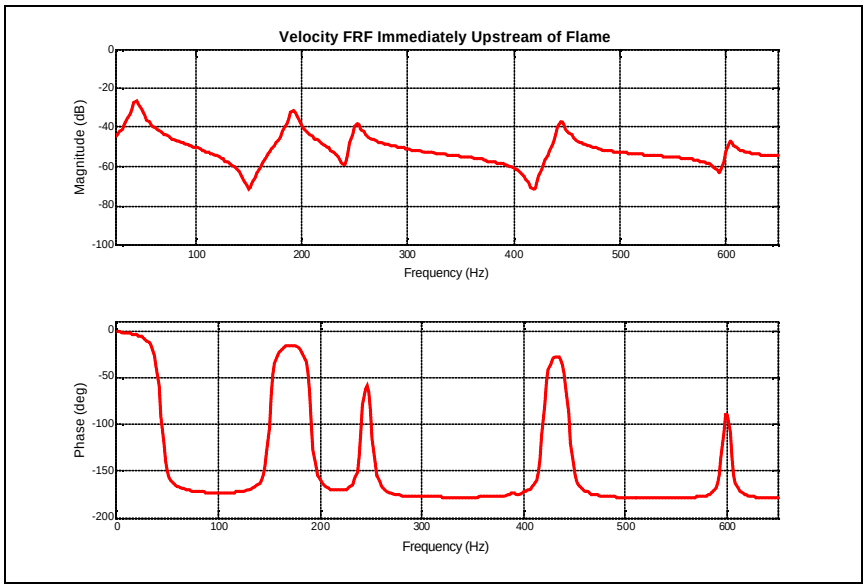

Figure 6.7: Particle velocity frequency response function between the pressure at the flame and the particle velocity directly upstream of the flame.

The above frequency response function describes the relationship between the pressure when the flame acts as an acoustic source and velocity fluctuations that occur in the air fuel mixture being fed to the flame. These velocity fluctuations essentially give the flame an unsteady air-fuel mixture which in turn causes heat release fluctuations. The unsteady heat release becomes the main cause of the thermoacoustic instabilities.

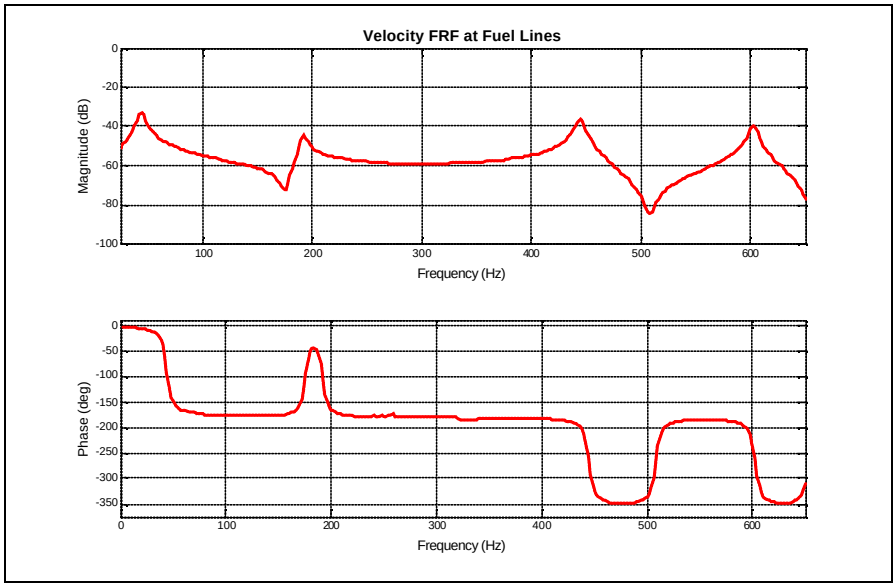

Figure 6. 8: Particle velocity frequency response function between the pressure at the flame and the particle velocity at the fuel lines.

The frequency response function shown above represents the relationship between the pressure when the flame acts as an acoustic source and velocity fluctuations that occur at the fuel lines. These fluctuations cause the equivalence ratio to vary and consequently variations in the heat release rate. Once again the heat release fluctuations are the main cause of thermoacoustic

instabilities. It is also interesting to note that the third resonance frequency at 250 Hz does not show up in this velocity FRF.

As mentioned previously, the FRF's shown in Figures 6.7 and 6.8 are the outputs from the finite element model which are input into the reduced order model.

6.9 Hot Combustor Acoustics Modeling

The current acoustic finite element model of the combustor has been validated to accurately predict the "cold" acoustic response of the combustor. Additionally, the impact of coupling different subsystems attached to the combustor on the overall acoustic behavior has also been explained. The last phase of the study is to incorporate temperature gradients into the acoustic model. Steep temperature gradients associated with combustion can cause both reflection and refraction of incident sound waves. These effects can cause the resonance frequencies to move. To account for this in the finite element model, temperature changes can be represented by changes in the bulk modulus and density of the medium. Both of these quantities are temperature dependent and can be spatially mapped to the finite element model once the spatial temperature distribution is known.

An approximation to the temperature distribution of the gaseous laboratory combustor is shown in Figure 6.9. The temperature distribution is based on experimental data taken on the combustor and from other combustors in the VT Combustion Systems Dynamics Laboratory.

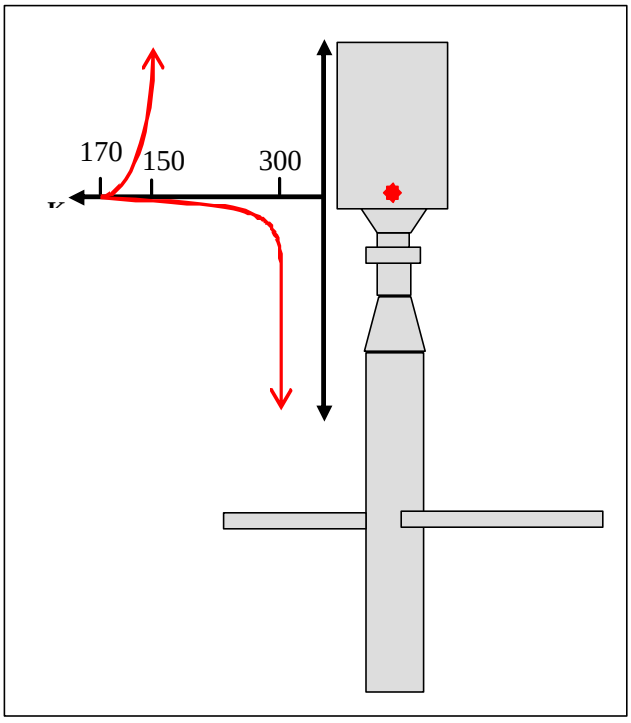

Figure 6.9: Approximate temperature distribution for combustion rig

The temperature profile above is an approximation of the actual temperature profile in the combustor under study. A more accurate distribution will be obtained in this phase of the study through the use of either computational fluid dynamics or actual experimental measurements on the

rig. As mentioned above there will also be a need to validate the "hot" acoustics experimentally. There is still a significant amount of work to be done on characterizing "hot" acoustics. This will become the focus of research in the upcoming months.

6.10 Status and Work Plan

The entire focus of this project is to develop a design-based methodology or process whereby industry can predict instabilities at the design level itself. Developing this process will help in predicting instabilities in both large scale and industrial scale combustors.

Figure 6.10, shown below, indicates the state of the acoustics tasks in the overall project. All the green tasks have been completed which refer to the development of the "cold" finite element model. Currently, work is being done to complete the yellow and red tasks. The task associated with mapping temperatures from either CFD code or experiments is well underway. Code has already been developed and the first significant revision has been made to that code for mapping temperatures onto the nodes of the acoustic finite element model; however, further refinement is planned.

The "hot" acoustic model is to be completed and coupled with the acoustic flame model by the end of April.

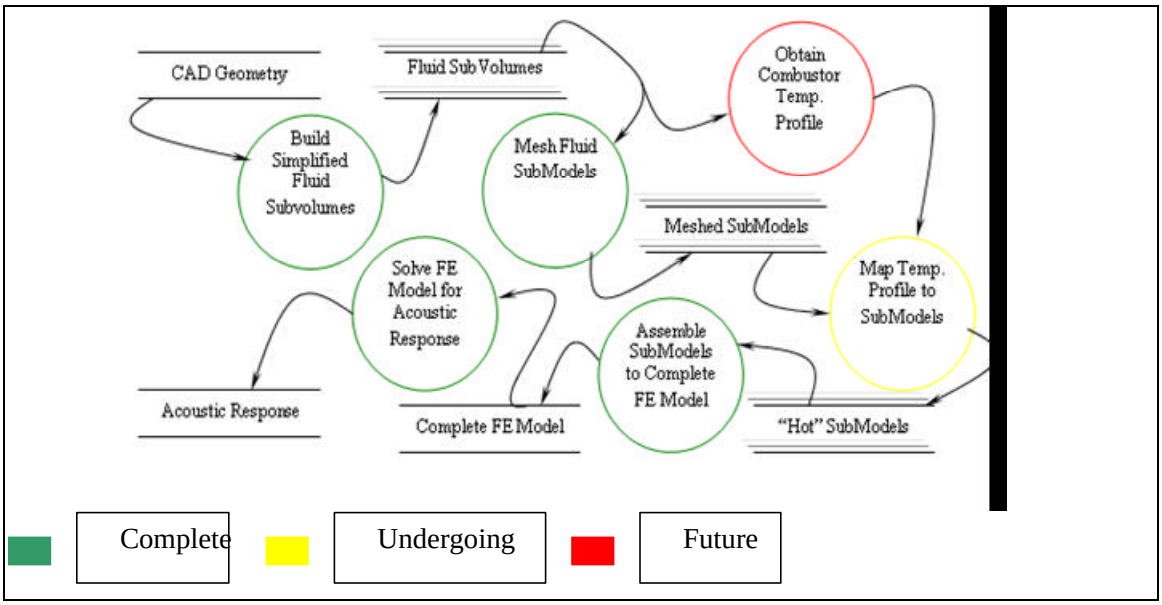

Figure 6.10: Flow diagram for acoustic Finite Element modeling for hot combustors

7 Prediction of Combustion Instabilities

7.1 Introduction

Thermo-acoustic combustion instabilities occur due to a dynamic coupling between a flame and the acoustic response inside the combustion chamber such that the two inherently stable phenomena produce an unstable system. To add to the complexities that are inherent to a reacting flow problem, the manner in which these couplings occur varies with a number of parameters. It is the unfortunate result that much of the work on modeling combustion instabilities in gas turbine engines is either combustor specific or utterly non-physical and only good for qualitative analysis.

This work is targeted to developing simplified equations that capture the significant physical elements of thermo-acoustic instability in a gas turbine combustor such that they may be applied to

numerous geometries in order to predict instability. Such models are of interest to academic and industrial communities since not only do predictive models provide invaluable influence in the design of new products and the modification of existing ones, but, as this discussion will show, can also provide unique insights into the physical phenomena that cause these instabilities.

Dissection of the System into Physical Components

The system can be modeled with general equations, treating spatial variations in species, pressure, temperature, density, etc… with partial differential equations. In additional to being far too cumbersome to hope for any sort of analytical solution, it would be difficult to even extract any meaningful, non-combustor-specific information from the model. It has become a common practice, therefore, to conceptualize thermo-acoustic combustion phenomena as consisting of two separate but interacting physical components – the *flame* and the *acoustics.*

Though this may seem so intuitive as to be obvious, the ability to decouple the two physical dynamic events and model them independently is an important step that presents some unique challenges of its own. The manner in which these components interact is dependent on a number of factors, including but not limited to fuel type (gaseous or liquid), injection method (direct or premixed), flow regime (turbulent or laminar), and numerous complications that can be brought on by the combustor geometry itself.

Works of Note

Works bearing resemblance to this are not uncommon in the literature. Lieuwen[1] et. al. of Georgia Tech have published multiple papers using models similar to ones presented in this document to model a dynamic combustor. Similarly, Gohniem[2] et. al. of MIT have even gone so far as to develop a closed-loop analysis with exactly the flame-acoustic decoupling mentioned above. Despite novel suggestions as to the potential causes for combustion instabilities, the simplified flame models often have difficulty matching the observed frequency response characteristics for physical flames. The MIT group has released papers using more advanced chemical kinetics that demonstrate reasonable bandwidths and that serve as a potential retort to the alleged limitations on the work.

This document treats the detailed development of one particular type of flame model, targeted specifically to the reasonably accurate prediction of dynamic phenomena. First, general governing integral equations are developed for the dynamic flame and later applied specifically to a Well-Stirred Reactor. These equations are developed, however, with the strict intent that they be general enough to be applied to other reactors as well. An appropriate chemical kinetic model is developed for the model. Lastly, various means for constraining the flame geometrically and the potential impacts on the model's dynamic response are investigated and compared with physical measurements.

7.2 Declaration of the Governing Equations

The Well Stirred Reactor's (WSR) governing equations are obtained by neglecting spatial variations in the flame region and integrating the full reacting flow equations to obtain the equations below. Since the only spatial change in properties that is permitted occurs at the inlet, the properties at the outlet are assumed to be identical to those throughout the reactor, leaving only two states that need to be considered – the inlet and the outlet. For ease of notation, any parameter evaluated at the inlet is designated with a zero subscript and all others are taken to be at the outlet. Equations 1 and 2 govern the conservation of species and energy respectively. Conservation of mass is absent since it is implicitly included in both the species and energy equations.

$$\frac{dY_i}{dt} + \frac{\dot{m}_0}{M}\left(Y_i - Y_{i,0}\right) = \frac{\dot{w}_i}{r} \tag{7.2-1}$$

$$\frac{dh}{dt} + \frac{\dot{m}_0}{M}\left(h_i - h_{i,0}\right) = \frac{1}{r}\frac{\partial p}{\partial t} \tag{7.2-2}$$

The mass source per unit mass due to chemical reaction for the i^{th} species in Equation 1 as predicted by global, single-step, Arrhenius chemical kinetics is defined in Equation 3.

$$\dot{w}_i \equiv \left(n_i'' - n_i'\right) MW_i A \exp\left(-\frac{E_a}{R_u \bar{T}}\right)\left(\frac{Y_F}{MW_F}\right)^m \left(\frac{Y_F}{MW_F}\right)^n \tag{7.2-3}$$

Equation 2 is the WSR energy equation for inviscid, adiabatic flow. This can be manipulated to yield Equation 3, which is similar in form to those that typically appear in combustion texts. The reaction rate term naturally appears by substituting Equation 1, leaving us with a term that can intuitively be dubbed the heat release of the flame since it appears as a source term in the energy equation. In addition, with the perfect gas assumption the terms in the summation on the left could be reduced to sensible enthalpy convection. Since enthalpy cannot be assumed to be linear with temperature, however, it is necessary to keep the equation in this form.

$$c_p \frac{dT}{dt} + \frac{\dot{m}_0}{M}\sum_i Y_{i,0}\left(\frac{\partial h}{\partial Y_i} - \frac{\partial h_0}{\partial Y_i}\right) = \frac{1}{r}\frac{\partial p}{\partial t} - \sum_i \frac{\partial h}{\partial Y_i}\frac{\dot{w}_i}{r} \tag{7.2-4}$$

This model includes four species – fuel, oxidizer, products, and diluent. Since diluent does not participate in the chemical reaction and is therefore neither formed nor depleted, nor do changes in diluent mass fraction significantly influence the reaction rate apart from implicit changes in fuel or oxidizer mass fractions, it is sufficient to consider diluent mass fraction constant. Furthermore, at any given time at any given location in space, the sum of the mass fractions must be unity, so one of the remaining three mass fractions may be written explicitly in terms of the other two. Since fuel and oxidizer appear explicitly in the reaction rate equations, it is convenient to eliminate the product mass fraction from the equations.

Varying inlet mass flow, which appears as a coefficient in both Equations 1 and 2, parametrically excites the system, while inlet mass fractions appear as a source term in Equation 1. Since the variations in upstream mass fractions can be expressed explicitly as variations in upstream equivalence ratio, the system can be described as being excited by two inputs – equivalence ratio and mass flow.

7.3 Methods for Constraining the Flame Size

Traditional, steady WSR models assume a constant volume process. This is particularly appropriate for steady reaction processes where the reaction volume is well defined. However, the above equations are written in terms of the mass of materials inside the flame region, M. If this parameter is allowed to vary in time, it is necessary to establish a law that governs its change. It can be shown that regardless of how the flame mass changes in time, these same governing equations still apply, so it is only necessary to add a fourth equation to the system. If the equation is differential, it will simply increase the order of the system. If the equation is an algebraic

relationship, it can be solved for mass and directly substituted into the original equation. In the literature, this has typically been done by arbitrarily obeying the original constraints on WSR models by fixing the flame volume such that

$$M = \forall r \ .$$

(7.3-1)

Since the flame is known to pulsate in time with the various perturbations, this is a non-physical assumption. To specify the mass of materials in the reaction region to be constant in time is equally arbitrary, but affords a study on more intuitive physical parameters. Observe that if *M* is constant, the ratio of inlet mass flow to flame mass as it appears in Equations 1, 2, and 3 is also constant. Therefore, these equations take on a form that appears identical to typical convective control volumes with a well-documented first-order response, possessing a time constant of

$$t = \frac{M}{\dot{m}_0} .$$

(7.3-2)

7.4 Linearization of the Dynamic Equations

It is, therefore, possible to write a state equation on the state variable, *x*, and an input vector, *u*, where

$$x_1 = T \, , x_2 = Y_F \, , x_3 = Y_{Ox}$$

(7.4-1)

and

$$u_1 = \Phi, u_2 = \dot{m}_0$$

(7.4-2)

such that

$$\dot{x}_i = G_i \left(x_j \, , u_k \right)$$

(7.4-3)

where *G* represents the dynamic WSR equations. In order to compute a frequency response using linear system theory, the system must be linearized. By considering a small perturbation from the steady operating conditions, a Taylor expansion of Equation 4 yields the desired linearized model. The steady state operating conditions may be computed by forcing Equation 4 to zero for some steady input vector. Therefore, the inverse of Equation 5 yields the steady operating condition.

$$0 = G_i \left(\bar{x}_j \, , \bar{u}_k \right)$$

(7.4-4)

Using the Einstein index summation convention for ease of notation, the Taylor expansion of a small perturbation about the steady state is given by

$$\dot{\tilde{x}}_i = G_i \big|_{\bar{x},\bar{u}} + \left. \frac{\partial G_i}{\partial x_m} \right|_{\bar{x},\bar{u}} \tilde{x}_m + \left. \frac{\partial G_i}{\partial u_n} \right|_{\bar{x},\bar{u}} \tilde{u}_n + \mathrm{K}$$

(7.4-5)

Since *G* evaluated at the steady conditions has already been said to be zero, and since higher order terms may be neglected due to the small perturbation assumption, this expression can be reduced to Equation 6.

$$\dot{\tilde{x}}_i \approx \left.\frac{\partial G_i}{\partial x_m}\right|_{\bar{x}\,\bar{u}} \tilde{x}_m + \left.\frac{\partial G_i}{\partial u_n}\right|_{\bar{x},\bar{u}} \tilde{u}_n \qquad (7.4\text{-}6)$$

Once in this realization, it is possible to find pole and zero locations and frequency response plots using traditional linear state space analysis.

7.5 Constant Mass WSR Dynamics

The first logical means of testing the validity of the model is to compare the frequency response plot generated from the linear theory of the previous section to the data collected from the physical system. Figures 1 and 2 show the frequency response plots for mass and phi perturbations respectively for various mean phi values. Though the bandwidth trends agree with the physical behaviors, the actual bandwidths are an order of magnitude or more higher than physical data has indicated. This is consistent with the work of Gohniem et al, who used more heavily simplified dynamic WSR models to examine possible explanations for combustion instability.

There is the appearance of low-frequency dynamics in the Φ-response that are absent in the mass-flow-response. These are characterized by a low frequency zero that causes a rising phase and rising amplitude, halted by a pole at a slightly higher frequency that causes a plateau in the amplitude and restores the phase to zero. The low-frequency pole is of great interest since it appears precisely in the frequency range (80 – 200Hz) at which the flame seems to consistently seems to lose response. These dynamics appear absent from the mass perturbations since the zero appears extremely close to the pole, almost exactly canceling the dynamics.

Because there are high frequency dynamics that seem to match crude trends, but that differ vividly in bandwidth and low frequency dynamics that have failed to even appear in most other works, the discussion of these results is divided into the high and low frequency dynamics.

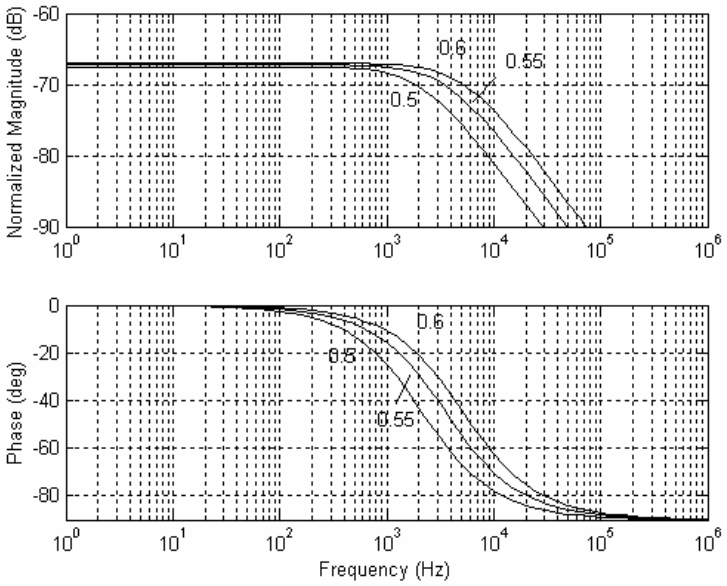

Figure 7.5.1 – Dynamic WSR reaction rate frequency response to mass-flow perturbations. The output is reaction rate, normalized by the mass-flow perturbation.

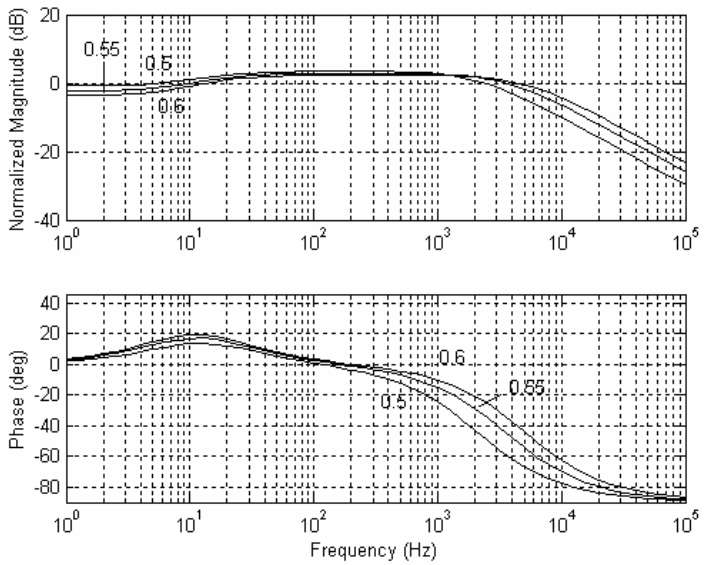

Figure 7.5.2 – Dynamic WSR reaction rate frequency response to upstream Φ perturbations. The output is reaction rate, normalized by the Φ perturbation.

High Frequency Dynamics

The high frequency dynamics are the only part of the results that seem to agree with other published works. The cutoff frequency decreases with falling equivalence ratio, similar to the physical data, but the pole is a full order of magnitude higher in frequency that the cutoffs observed in the physical system.

An investigation into the significant determining factors in the placement of the high frequency pole demonstrated sensitivity to a number of parameters, perhaps the most remarkable being the exponential constant on the fuel mass fraction appearing in Equation 3. Figure 3 shows three

frequency response plots overplotted for various values of *m*. As *m* was varied, a new value for *A* (also appearing in Equation 3) was selected such that the mass-flow limits for blow-off were conserved.

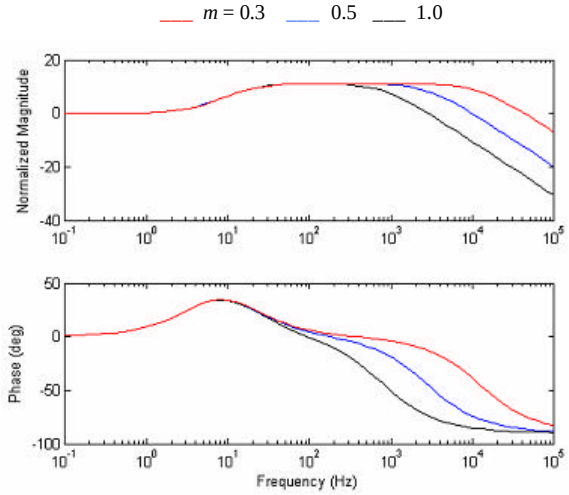

Figure 7.5.3 - Φ excitation response change due to changes in *m*
as it appears in Equation 3 while simultaneously varying *A*
such that the blow-off limits are preserved.

While the low-frequency dynamics showed no change whatsoever, the high frequency pole was clearly heavily influenced by changes in the chemical kinetic properties. Changes that affect the flame temperature had similar effects, though none were as significant as variations in *m*. This tends to indicate that the high-frequency pole is largely influenced by chemical kinetics. This is the school of thought most commonly found in the literature <Lieuwen, Gohniem>, though when using such a simplified chemical kinetic model designed to predict static events such as flammability limits, it is unlikely that accurate frequency response predictions could be reasonably expected.

Low Frequency Dynamics

The only dynamics that agree in bandwidth; the low frequency dynamics appear to differ completely in behavior from the physical system. Figures 1, 2, and 3 all demonstrate that despite changes in the equivalence ratio and chemical kinetics, the low-frequency pole and zero remained utterly unchanged. It is only as the mass flow or reactor mass is varied that the low frequency dynamics change at all. Furthermore the time constant corresponding to that pole is exactly that described as the convective residence time in Equation 5.

The low-frequency zero appears to be non-physical. Despite some hints of rising amplitude in the velocity perturbation data, none of the physical data seems to exhibit such a drastic plateau extending to high frequencies as the model predicts. Worst of all, the model predicts a positive and completely non-physical low frequency phase.

These points are motivation to reinvestigate the constant mass reactor assumption. It has been well documented that as the steady equivalence ratio is changed, the flame size should vary as well <Turns>. Leaner flames have lower flame temperatures, which result in slower reaction rates, requiring more burning time in order to exhaust the fuel. It stands to reason that at the very least the reactor mass should be a function of the steady equivalence ratio. That function may be defined by the reactor size necessary to completely consume the fuel.

If a WSR is forced to react all of its fuel, however, the WSR must also be of infinite size. This can easily be verified by observing that in the limit as fuel mass fraction goes to zero, the reaction rate also goes to zero, forcing *M* in the fuel species equation to infinity for any finite mass flow.

This problem can be solved by arbitrating that the fuel will combust until the fuel mass fraction drops below some critical value, below which the mixture can no longer support a reaction.

Using this scheme, some critical fuel mass fraction was selected and the reactor size was iteratively computed for a variety of steady equivalence ratios while mass flow remained fixed. Once the reactor sizes were computed, the dynamics were recomputed for each operating condition and compared with the physical data. Since the data is quite difficult to visually interpret, any attempt to obtain an empirical transfer function for comparison by curve fitting would be disappointingly arbitrary and could be massaged to demonstrate almost anything. Instead, in order to simply compare movements in the low-frequency dynamics, a simple, first order transfer function of the form

$$\frac{b}{s+a} \tag{7.5-1}$$

was overplotted with the physical data where a was determined by the iteratively computed low-frequency pole. Since the measured frequency response data is not in physical units with an unknown scaling factor, b had to be chosen to match the measured dc-gain rather than relying on the computed gain in order for the results to be directly compared.

The critical mass fraction was iteratively selected such that one of the frequency responses agreed in bandwidth with the equivalence ratio data. Then, the same critical value was used to generate all the other cases. Figure 4 shows the results for six different steady equivalence ratios. Figure 5 shows the predicted pole frequency as a function of equivalence ratio for the six cases.

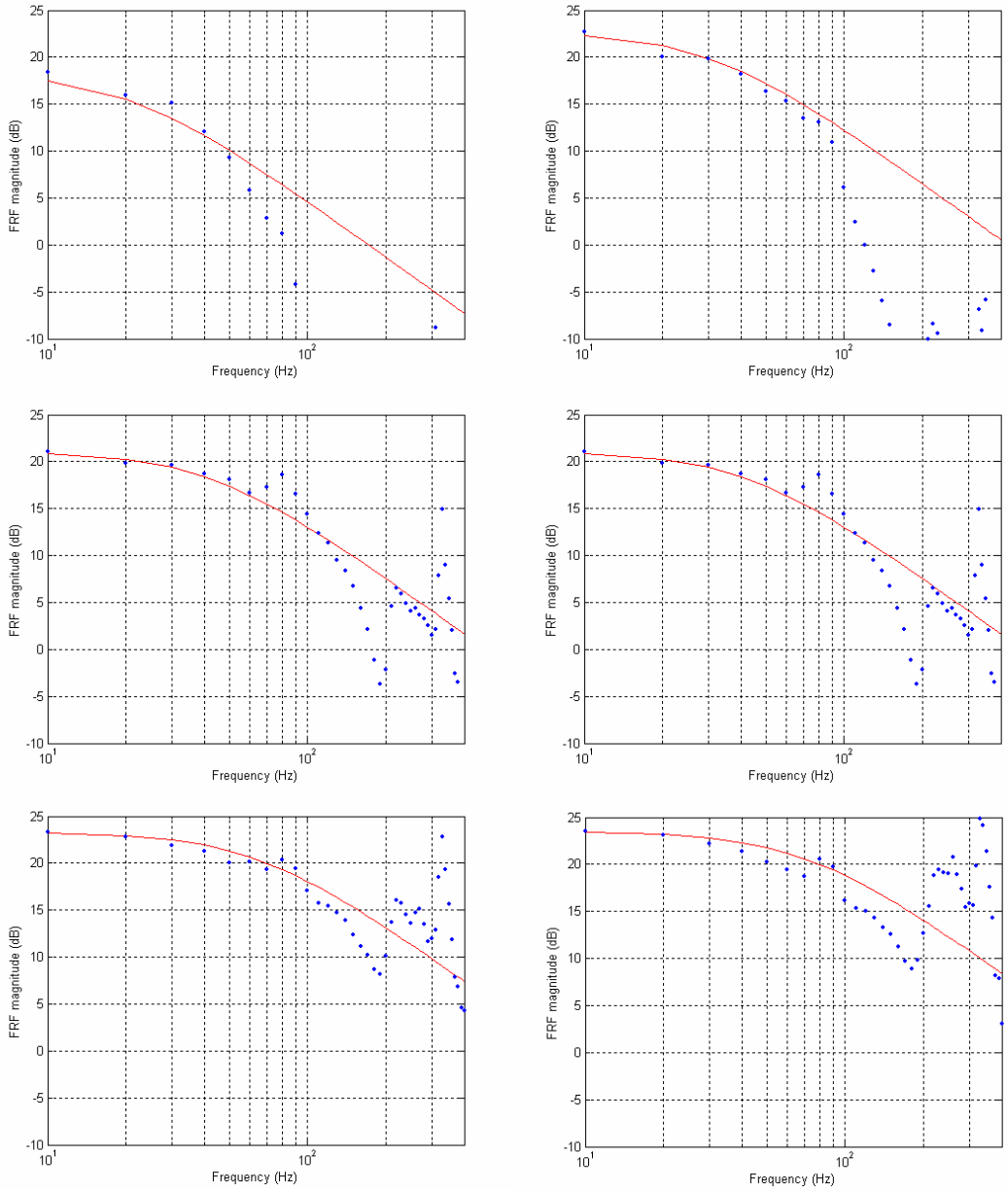

Figure 7.5.4 – The convective residence time was iteratively computed in order to produce a consistent exit fuel mass fraction for equivalence ratios of 0.50, 0.54, 0.58, 0.63, 0.66, and 0.70. The resulting frequency response plots are displayed in order starting from the upper left. The calculated dynamics (red) quite accurately predict the physical behavior (blue dots) for low frequencies.

In all cases, the pole prediction seems to be very accurate. Ultra-lean cases appear to encounter either a second pole or a resonant zero pair, which causes a sharper decline in the amplitude at higher frequencies before reaching a very low-magnitude plateau. At higher equivalence ratios, the magnitude only appears to deviate from the predicted curves with a resonant peak at 80Hz and a resonant zero at 200Hz. Since these phenomena are predicted at precisely these frequencies by the 1-dimensional acoustic model and have been measured in the physical rig, it is safe to suggest that these are small acoustic affects that normalization failed to remove.

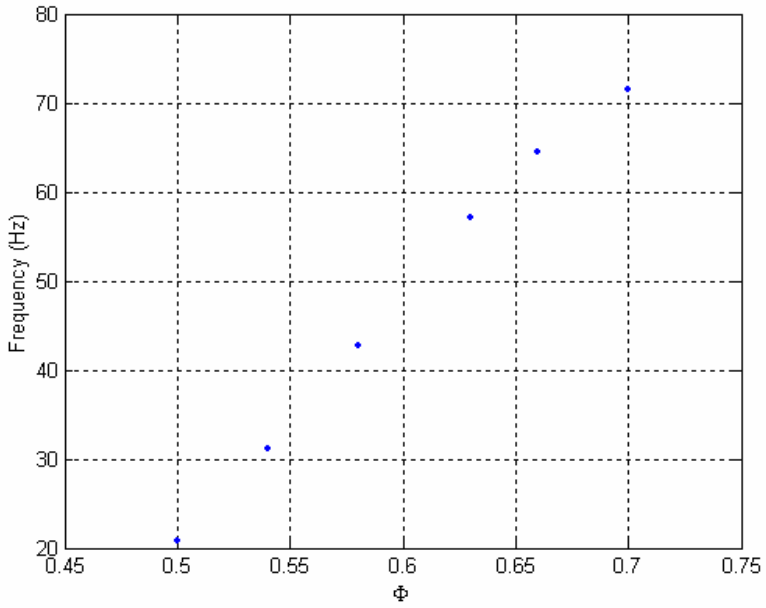

Figure 7.5.5 – Predicted convective pole frequency as a function of mean equivalence ratio. This is the frequency corresponding to a system with the time constant expressed in Equation 5.

7.6 Conclusions and Future Work

The precision to which the low frequency pole predictions match the measurements present a strong argument that it is simple convection and not chemical kinetics that decide the dominant dynamics of the turbulent flame. This conclusion, combined with the marked disagreement between the zeros predicted by the constant-mass reactor and physical data infers that arbitrary constraint of the reactor size is not only statically erroneous, but results in inaccurate dynamic predictions as well. Given the initial success of the work, there are three natural proceeding courses of actions.

1) If chemical kinetics rather than convection decided the dominant dynamics, an arbitrary assumption regarding the flame's size might not have affected the model significantly, but since convection is predominant mechanism limiting the flame's response, it is vital to accurately capture how the flame region oscillates in time. The next step is to derive governing equations for a WSR with new control volume constraints. Given the empirical evidence, it seems likely that the new constraints would follow the data far more closely.
2) The presence of the acoustic peaks in the data must be investigated so that they can be eliminated, ensuring an accurate flame transfer function measurement.
3) Once an accurate flame transfer function can be predicted a closed loop analysis will be used to predict conditions for thermo-acoustic instability. These conditions will be verified by modifying the existing combustor with a chimney to induce instability.

Work Plan for January to May, 2006

These are the goals for the remainder of the project:

January – resolve inconsistencies between these results and results observed in the literature. Investigate other geometric constraints on the flame.

February – Generate coupling equations between the flame and the acoustic transfer function. Is it adequate to model heat release rate as a pressure input to the acoustic equation? Are additional

dynamics present? Reconcile any differences between new conclusions and previous conclusions in the literature.

March – Code and analyze the resulting closed-loop model. Investigate different flame models and the effect of various assumptions on the stability of the model.

April – Conclude the analysis and generate a write-up summarizing the results.

8 Conclusions (Summary)

During the reporting period, May-November 2005 activities were conducted addressing tasks 1, 5, 2, 3, and 4. For tasks 1 and 4, measurements of the flame dynamic response to sine-dwell excitation were done for equivalence ratios from the lean-blowout (LBO) up to $f \approx 0.75$. Flame response was examined for $\dot{m}(m')$ fluctuations, as well as equivalence ratio fluctuation, f'. Flame response was measured via OH* Chemiluminescence. Very generally the turbulent, swirl stabilized flames behaved as first order systems, after it was suspected that higher frequency peaks may have been related to yet uncoupled rig acoustics, in spite of efforts done to that effect. This issue will be investigated with a hot wire probe, placed upstream of the swirler, to measure m' directly instead of using the two-microphone probe.

Follow-up work on task 1, will include, in addition to clarifying and achieving complete decoupling of the rig acoustics from the flame/combustion transfer function, an investigation of various fuels. Specifically dynamics of mixtures of HE fuels, and hydrogen-HC and hydrogen-HC-CO mixtures will be examined, i.e., the flame response to $m'(\dot{m})$ and f'.
A model for the dispersion and axial diffusion of a f' probe was constructed under Task 2. The model which incorporates turbulence characteristics was related to observed f' characteristics.

A model for the prediction of combustion instabilities, and blowout was constructed. The model will have to address the two key phenomena of the acoustics field in the combustor and attached cavities, and the flame/heat source. Initially the two models are developed separately, and after their verification, they are coupled.

Under Task 5a particular type of flame model targeted to provide a reasonably accurate prediction of dynamics. The uses the conservation equations applied to an unsteady Well Stirred Reactor (WSR). The equations were developed strictly so that they can be applied to other reactors too. Appropriate chemical kinetic model was also developed. Various means for constraining flame geometry and the potential impact on the model's dynamic response were investigated and compared with measurements.

The model resulted in good agreement with measured data at low frequencies, however, any acoustic peeks must be uncoupled. The low frequency agreement suggests that it is convection and not chemical kinetics that decide the dominant dynamics. Disagreement between a fixed mass reactor and measured zeros, indicate that size constraints on a reactor (V=const) lead to inaccurate dynamics, on top of erroneous statics.

The work plan for Nov 2005-May 2006 includes, resolution of disagreements with measurements, resolution of conflicts with literature, construct flame- acoustics coupled model to predict closed loop thermoacoustics.

Under Task 3 a very detailed model for the acoustics of the turbulent swirl stabilized combustor is being constructed. The activities, results and work plan are outlined below.

The work tasks for finite element modeling over the last project period were associated with updating cold combustor acoustics models of the laboratory-scale turbulent combustor and reconciling the models with experimental acoustic data. Experimental acoustic work was conducted on the turbulent combustor resulting in the acoustic natural frequencies and frequency response functions for the combustor. A plane-wave or one-dimensional finite element model was developed for the combustor justified on the fact that the frequency range of interest is low due to the flame's low pass filter characteristics and that acoustics above 250 Hz do not appear to excite the flame to produce significant dynamics for reduced order modeling. The accuracy of the one-dimensional finite element model is remarkable. This is especially evident when one looks at s the geometric complexities of the actual combustor. In addition to the one dimensional model having excellent accuracy, it is significantly easier to develop, solve and postprocess results than a three-dimensional model. The plane-wave FE model solves in less than one minute vs. the three-dimensional model which solves in several hours. The significant savings in model development, solution and postprocessing time allow engineering time to be spent on model exploration and design tasks. Because of the very good accuracy and efficiency of the one-dimensional finite element model it is recommended in place of the three-dimensional model when ever possible.

The last phase of this study is to incorporate temperature gradients into the acoustic model. Steep temperature gradients associated with combustion can cause both reflection and refraction of incident sound waves. These effects can cause the resonance frequencies to move. To account for this in the finite element model, temperature changes can be represented by changes in the bulk modulus and density of the medium. Both of these quantities are temperature dependent and can be spatially mapped over the finite element model once the spatial temperature distribution is known. An approximation to the temperature distribution of the gaseous laboratory combustor is based on experimental data taken on the combustor and from other combustors in the VT Combustion Dynamics Laboratory**.** A more accurate distribution will be obtained in this phase of the study through the use of either computational fluid dynamics or additional experimental measurements on the rig. As mentioned above there will also be a need to validate the "hot" acoustics experimentally. This task will become the focus of research in the upcoming months.

9 Bibliography

Bloxsidge, G.J., Dowling, A.P, Langhorne, P.J., "An acoustically coupled combustion instability. II – Theory" Journal of Fluid Mechanics 193, 445-473 (1988).

Park, S., Annasway, A., Ghoniem, A., "Heat release dynamics modeling of kinetically controlled burning," Combustion and Flame 1228:217-231 (2002).

Lieuwen, T. and B.T. Zinn, "The role of equivalence ratio oscillation sin driving combustion instabilities in low Nox turbines," In Proc. of the 27th International Symp. On Combustion, pp. 1809-1816, 1998a.

Liewen, T.Y., Neumeier, and B.T. Zinn, "The role of unmixedness and chemical kinetics in driving combustion instabilities in lean premixed combustors," Combustion Science and Technology, Vol. 135, pp. 193-211, 1998a.

Turns, S., *An Introduction to Combustion,* McGraw-Hill Co., New York, 2000.

10 List of Acronyms and Abbreviations

CAD	Computer-Aided Design
CFD	Computational Fluid Dynamics
FEA	Finite Element Analysis
He-Ne	Helium-Neon
IR	Infra-red
LBO	Lean Blow-Off
NETL	National Energy Technology Laboratory
p’	pressure perturbation
TEC	Thermo-Electric Cooler
TDLAS	Tunable Diode Laser Absorption Spectroscopy
u’	Velocity Perturbation
VACCG	Virginia Action Combustion Control Group
f'	Equivalence Ratio Fluctuation

Enhanced Prediction Techniques Based on Time-Accurate Simulations for Turbine Blade Internal Cooling

Final Report

D. K. Tafti
Mechanical Engineering Department

January 2007

DOE Award Number
DE-FC26-02NT41431

UTSR Project Number
02-01-SR100

Virginia Polytechnic Institute and State University
Blacksburg, VA 24061

Disclaimer

This report was prepared as an account of work sponsored by an agency of the United States Government. Neither the United States Government nor any agency thereof, nor any of their employees, makes any warranty, express or implied, or assumes any legal liability or responsibility for the accuracy, completeness, or usefulness of any information, apparatus, product, or process disclosed, or represents that its use would not infringe privately owned rights. Reference herein to any specific commercial product, process, or service by trade name, trademark, manufacturer, or otherwise does not necessarily constitute or imply its endorsement, recommendation, or favoring by the United States Government or any agency thereof. The views and opinions of authors expressed herein do not necessarily state or reflect those of the United States Government or any agency thereof.

Abstract

The project was successful in highlighting the accuracy of LES over RANS methods in developing flow and in the 180^o bend region of internal cooling ducts. LES was particularly successful in capturing secondary flow effects and extra strains produced by Coriolis forces and centrifugal buoyancy effects. However LES is still computationally intensive and turnaround times are high compared to RANS methods. DES or a hybrid LES-RANS method was implemented and for the first time applied to internal heat transfer problems typical of internal cooling applications. It was established that DES is a good alternative to LES and is able to capture the anisotropies introduced by rotation and centrifugal buoyancy and gives LES like accuracy at roughly one-tenth to one-fifth the cost.

Table of Contents

Executive Summary

Our objective is to evaluate and develop prediction techniques for the internal cooling of turbine blades based on time-accurate methods. The project plan calls for a systematic evaluation of these methods in different flow regimes encountered in the cooling passages, namely fully-developed conditions, developing flow conditions, and flow and heat transfer in 180º bends. The initial geometry chosen for evaluation of different techniques is a square duct with normal ribs of e/D_h=0.1 and P/e = 10 at a nominal bulk Reynolds number of 20,000. This geometry, together with the action of Coriolis and buoyancy forces, contains all the essential elements for testing and evaluation. Other angled ribbed configurations are also being studied.

It was established that LES was able to accurately predict the flow and heat transfer in internal cooling ducts under typical industry operating conditions. It was also established that hybrid RANS-LES (or DES) gave LES like accuracy at one-fifth to one-tenth the cost. The superior prediction capability of DES was established in stationary and rotating ducts under the influence of Coriolis and centrifugal buoyancy

Three graduate students, Samer Abdel-Wahab (M.S.), Evan Sewall (Ph.D) and Aroon Viswanathan (Ph.D) have been supported on this project. Samer Abdel-Wahab graduated with a M.S. degree and is employed at Florida Turbine Technologies. Evan Sewall graduated in Dec 2005 and joined GE Global Research. Aroon Viswanathan graduated in Summer 2006 and joined Modine Mfg. Co.

The project has been particularly successful in disseminating technical results via conference and journal publications and also in collaborating with industry. Since its inception, fifteen conference papers [1-15] and eleven journal publications [16-26] have resulted. Andy Smith at GE Global research has used our LES simulations to benchmark some of his reduced-order calculations. Additional data was also made available to Dr. Jiang Luo at Solar Turbines to aid in benchmarking activities.

Overall the project has accomplished all of its technical objectives and we would like to acknowledge the support provided by the UTSR program and the IAB members which made all this possible.

Project Description

The internal cooling of turbine blades is a critical problem for the gas turbine industry. Prediction of these flows has been complicated by the presence of turbulence generators for heat transfer augmentation, rotational Coriolis and buoyancy forces. The Reynolds number ranges from moderate $O(10^4)$ to very high $O(10^5)$, depending on the application. Rotation numbers can be of O(1), and centrifugal buoyancy driven Rayleigh numbers can be of $O(10^8)$. The turbulent flow is highly anisotropic, and all attempts at predicting the flow and heat transfer have focused on the solution of steady Reynolds–Averaged Navier-Stokes (RANS) and energy equations. Different turbulence closure models have been used with varying degrees of success. Eddy-viscosity-type models, which assume isotropy, do not perform very well, while more complicated models based on the solution of the turbulent stress equations have been found to perform reasonably well. However, in all cases the quality of the solution is dependent on empirical tuning of the models. Furthermore, steady RANS modeling provides minimal insight into the dynamic processes that enhance heat transfer. The validation of these models has been further plagued by the lack of velocity and turbulence data in internal cooling geometries under rotating conditions.

In this study we propose to look at alternative prediction techniques based on solving the time-dependent Navier-Stokes and energy equations. The objectives are two-fold: a) Use high resolution Large-Eddy Simulations (LES) for predicting and understanding the myriad of physical effects which affect heat transfer, and b) Develop and evaluate the prediction capabilities of hybrid unsteady RANS and LES methods via Detached Eddy Simulations (DES). The combined approach will be integrated with experiments from the literature as well as results from previously funded projects through this program for validation. To support the validation of the flow field predictions, three-component mean and turbulence measurements will be made in a large-scale, stationary flow channel with ribs using a laser Doppler velocimeter.

The work plan proposes to systematically apply these techniques to different flow regimes in internal cooling geometries with ribs: a) fully-developed flow regime, b) U-bend or sharp 180º bend, and c) developing flow regime. We will validate our procedures with experimental data from the literature and with experiments in which mean and turbulence velocities will be measured in a ribbed channel with a U-bend or sharp 180º bend. The validated calculations will

then be extended to high rotation and buoyancy numbers, data for which is scarce in the literature. Issues pertaining to subgrid modeling, numerics, and resolution will also be studied. The DES procedure will also be validated against LES calculations. In the final year of the project, we will apply a combined LES/DES procedure to a full two-pass channel with roughness elements.

The computational tools to be used in this research already exist and have been extensively validated in the past in unsteady flow simulations for air-side heat transfer enhancement in compact heat exchangers and other turbulent flows. Hence, code development will be minimal.

Because of the lack of literature documenting the mean and turbulent flow fields in a ribbed channel, the proposed work includes performing these measurements. The channel will be designed to insure that adequate spatial resolution is achieved while maintaining a velocity range that can be accurately measured. The channel will be constructed using plexiglass to allow for optical access since the primary measurement tool will be a three-component laser Doppler velocimeter.

The results of this project will add a large measure of repeatability and reliability in predicting the internal heat transfer coefficient under extreme operating conditions and will eventually lead to better blade designs.

The research tasks and their status as of April 2003 are summarized below:

1. LES

a. Fully-developed regime with ribs
    1. Stationary ribbed duct **(complete)**
    2. Rotating ribbed duct with Coriolis Forces **(complete)**
    3. Rotating ribbed duct with Coriolis forces and centrifugal buoyancy **(complete)**

b. Developing Flow regime with ribs
   The calculations will start a sufficient distance upstream of the first rib in the passage and continue into the passageway until the flow is fully developed.
    1. Auxiliary calculations in smooth fully developed duct to generate time-dependent velocity inlet boundary conditions **(complete)**
    2. Stationary ribbed duct **(complete)**
    3. Rotating ribbed duct with Coriolis forces **(complete)**
    4. Rotating ribbed duct with Coriolis and centrifugal Buoyancy **(complete)**.

c. U-bend with ribs
   These calculations will start upstream of the U-bend such that the inlet plane is outside the domain of influence of the U-bend and will extend downstream of the U-bend into the second-pass including the first few ribs.
    1. Stationary U-bend **(complete)**
    2. Rotating U-bend with Coriolis forces **(complete)**

3. Rotating U-bend with Coriolis and centrifugal Buoyancy **(complete)**

2. DES

   a. Implement suitable RANS model into computer code GenIDLEST under DES framework. **(complete).**
   b. Smooth duct, fully developed. Test model for different mesh resolutions and evaluate accuracy against LES and experiments.
      1. Stationary duct **(complete)**
      2. Rotating duct with Coriolis forces **(NA)**
      3. Rotating duct with Coriolis and centrifugal buoyancy **(NA)**
   c. Ribbed duct, fully developed. Test model for different mesh resolutions and evaluate accuracy against LES and experiments.
      1. Stationary duct **(complete)**
      2. Rotating duct with Coriolis forces **(complete)**
      3. Rotating duct with Coriolis and centrifugal buoyancy **(complete).**

3. LES/DES in full two-pass channel with ribs.

   1. Effects of Coriolis forces **(complete)**
   2. Effect of buoyancy

4. Experimental Measurements **(complete)**

   a. Spatial maps of all the mean and turbulent quantities of all three components in the ribbed duct
      1. Developing region
      2. Fully-developed region
      3. In the 180° bend region

Computational and Experimental Method

Computational Method

GenIDLEST (Generalized Incompressible Direct and Large-Eddy Simulations of Turbulence) is a computer program developed for application to turbulent flows in complex geometries. It utilizes a non-staggered finite-volume mesh with Cartesian velocities and temperature as the primary dependent variables. A fractional-step algorithm, with explicit as well as semi-implicit time advancement, is used. It uses both Message Passing Interface (MPI) and OpenMP for parallel execution. Full details about GenIDLEST are described in Tafti [27]. Here we give a brief overview.

GenIDLEST solves the incompressible Navier-Stokes and energy or temperature equations. The transformed *non-dimensional*, time-dependent, incompressible Navier-Stokes and energy equations are written in conservative form as[1]:

Continuity:

$$\frac{\partial}{\partial \xi_j}\left(\sqrt{g}U^j\right)=0 \tag{1}$$

Momentum:

$$\begin{aligned}\frac{\partial}{\partial t}\left(\sqrt{g}u_i\right)+\frac{\partial}{\partial \xi_j}\left(\sqrt{g}U^j u_i\right)=&-\frac{\partial}{\partial \xi_j}\left(\sqrt{g}(\vec{a}^{\,j})_i P\right)+\frac{\partial}{\partial \xi_j}\left(\left(\frac{1}{\mathrm{Re}}+\frac{1}{\mathrm{Re}_t}\right)\sqrt{g}g^{jk}\frac{\partial u_i}{\partial \xi_k}\right)\\&-2\sqrt{g}\mathrm{Ro_k}\overline{u}_m\in_{ikm}+\sqrt{g}\cdot\in_{ilm}\cdot\in_{jlk}\cdot Ro_j\cdot Ro_m\cdot r_k\frac{(T-T_{ref})}{T_{ref}}+\sqrt{g}S_{u_i}\end{aligned} \tag{2}$$

Energy:

$$\frac{\partial}{\partial t}\left(\sqrt{g}T\right)+\frac{\partial}{\partial \xi_j}\left(\sqrt{g}U^j T\right)=\frac{\partial}{\partial \xi_j}\left(\left(\frac{1}{\mathrm{Pr}\,\mathrm{Re}}+\frac{1}{\mathrm{Pr}_t\,\mathrm{Re}_t}\right)\sqrt{g}g^{jk}\frac{\partial T}{\partial \xi_k}\right)+\sqrt{g}S_T \tag{3}$$

where $\vec{a}^{\,i}$ are the contravariant basis vectors[2], $\sqrt{g}$ is the Jacobian of the transformation, g^{ij} are the elements of the contravariant metric tensor, $\sqrt{g}U^j=\sqrt{g}(\vec{a}^{\,j})_i u_i$ is the contravariant flux vector, u_i is the Cartesian velocity vector, T is the temperature, and S_{u_i} and S_T are the source

[1] Henceforth, all usage is in terms of non-dimensionalized values.

[2] The notation $\left(\vec{a}^{\,j}\right)_i$ is used to denote the *i-th* component of vector $\vec{a}^{\,j}$. $(\vec{a}^{\,j})_i=\partial\xi_j/\partial x_i$

terms in the momentum and energy equations, respectively. Re_t is the turbulent Reynolds number, and Pr_t is the turbulent Prandtl number Ro is the rotation number, and r is the radial component from the axis of rotation. Re_t is calculated based on a subgrid scale stress model in the case of LES and by a RANS model in the case of RANS or DES calculations, the details of which are given in later sections.

In equation (2), both the rotational Coriolis forces and the centrifugal buoyancy forces are included in the formulation when relevant. In a developing flow, the effect of centrifugal buoyancy is strongest at the inlet to the duct and gets weaker as the temperature approaches the wall temperature in the streamwise direction, but is augmented as r, the distance from the axis of rotation increases. The centrifugal buoyancy term uses the Boussinesq approximation to approximate the effect of density differences from the bulk reference density. The mean centrifugal force term (centrifugal pumping) is implicitly included with the pressure gradient term.

Eqns. (1-3) are solved using an overlapping multi-block structured mesh topology. In each block the equations are mapped from physical $(\vec{x})$ to logical/computational space $(\vec{\xi})$ by a boundary conforming transformation $\vec{x} = \vec{x}(\vec{\xi})$, where $\vec{x} = (x, y, z)$ and $\vec{\xi} = (\xi, \eta, \zeta)$. Inter-block connectivity can be structured (ξ+ face adjoining a ξ- face) or unstructured. In an unstructured inter-block topology a ξ- face boundary can adjoin a η or ζ face with arbitrary axes orientations.

GenIDLEST can handle non-matching or non-conformal boundary interfaces, i.e. there does not have to be a one-to-one correspondence between meshes of adjoining block faces. This allows additional flexibility in meshing complex domains and can also be used for local refinement. In such cases dependent variables have to be interpolated between faces. For this purpose, bilinear interpolation functions are used together with integral conservation of mass, momentum, and energy fluxes. The fluxes are conserved globally (over face) versus locally, which would constrain the generality of the non-matching interfaces. Since the gradient of pressure is the driving force, it, instead of pressure, is conserved across non-matching interfaces.

The multiblock framework provides a natural framework for parallelization. Depending on the total number of blocks and processors, each processor is assigned multiple blocks. Further,

within each block "virtual cache blocks" are used. The "virtual" blocks are not explicitly reflected in the data structure but are used only in the solution of linear systems. The motivation to construct much smaller "cache" blocks is to extract performance on cache-based hierarchical memory systems. These small "cache" blocks form the basic computing units for preconditioning linear systems. Hence, underneath the coarse grained parallelism of MPI processes, there exists additional parallelism across multiple blocks, or across the mesh nodes in each block, and across the multiple cache blocks. Hence, GenIDLEST is instrumented for coarse-grained parallelism with MPI and for embedded or fine-grained parallelism with OpenMP.

The governing equations are discretized with a conservative finite-volume formulation. In non-orthogonal coordinate systems, there are a number of choices in the selection of the grid topology and the dependent variable in the momentum equations. In GenIDLEST, we adopt a non-staggered grid topology with Cartesian velocities as dependent variables. The Cartesian velocities, pressure, and temperature are calculated and stored at the cell center, whereas contravariant volume fluxes are stored and calculated at the cell faces. The convection term can be approximated in a number of different ways. Presently, there are two basic approximations, second-order central difference and the third-order upwind biased approximation, to calculate the cell face values. These two approximations can either be used in their basic form or combined with TVD criteria to preserve monotonicity of the convected variable. In addition to the TVD limiter, a multi-dimensional flux limiter [28] is also implemented. The flux limiter is based on the less restrictive universal limiter proposed by Leonard [29]. In this scheme, the intermediate velocities are first calculated with the base approximations and then checked for monotonicity in a multidimensional framework. Two subgrid-scale stress models are available at this time, the Smagorinsky [30] and the dynamic Smagorinsky model [31]. Additionally, several high and low *Re*-number RANS models, based on the k-ω model [32-34] and Menter's [35-37] models are also available.

A variety of boundary conditions are available in GenIDLEST, and they are specified individually for each computational block. With the exception of periodic or inter-block boundaries, each boundary face can have multiple boundary conditions assigned to it.

(a) Periodic or inter-block boundaries: Both of these boundaries precipitate the same action, which involves exchanging boundary information between adjacent faces. For

unstructured block connectivity and/or non-conformal interfaces, the boundary information is filtered by coordinate rotations and interpolations as required. Coordinate rotations and interpolation factors are calculated at the beginning of each run.

(b) Wall boundary: When the velocity normal to the boundary is zero or there is no influx (outflux) of mass, the boundary is specified as a wall. Wall boundaries can have slip velocities imposed on them and temperature or heat flux (gradients) specified.

(c) Inlet boundary: When there is a known net influx (outflux) of mass from the boundary, it is specified as an inlet. Only temperature can be specified at this boundary.

(d) Outflow boundary: Outflow boundaries use a convective boundary condition in which the dependent variable is allowed to convect out of the domain. Both temperature and heat flux can be specified.

(e) Symmetry boundary: At this boundary, the normal velocity and gradients of tangential velocities and temperature are set to zero.

(f) Pressure boundary: Pressure, and not velocity, is specified at this boundary. The velocities are derived from the flow generated by the pressure.

For increased flexibility in meshing, internal blanked zones or solid obstacles can also be specified in each computational block. Boundary conditions on these regions use Dirichlet conditions on velocities, including suction or blowing. Temperature or heat flux can be specified.

The discretized continuity and momentum equations are integrated in time using a projection method. The temporal advancement is performed in two steps, a predictor step, which calculates an intermediate velocity field, and a corrector step, which calculates the updated divergence free velocity at the new time step. The predictor step can be fully explicit in time or semi-implicit, in which the viscous terms are treated implicitly. Both methods are incorporated in GenIDLEST. The semi-implicit method is useful for low Reynolds number flows and in flows with large effective viscosities by allowing larger time steps than what would be allowed by the viscous stability condition. The corrector step uses the continuity equation to formulate the pressure equation. The computed pressure is then used to update the intermediate velocity field.

The linear system generated in the solution of the pressure equation and the implicit treatment of viscous terms is non-symmetric on non-orthogonal meshes. Further, the presence

of non-conformal or non-matching boundaries creates additional strong non-symmetries. In GenIDLEST we use Krylov methods based on the method of Conjugate Gradients (CG) for symmetric systems and BiCGSTAB or GMRES(m) for non-symmetric systems. These are coupled with preconditioners based on a two-level Additive Schwarz domain decomposition (DD) method [38,39,40].

GenIDLEST is very portable between different computer architectures and compilers. It has a front-end Java AWT/SWING interface for the creation of input files. A number of post-processing utilities are present, including the ability to obtain mean and turbulent statistics in a distributed computing environment, time-dependent data dumps for analysis and visualization, and vortex identification techniques based on the $\nabla\vec{u}$ [41] and λ_2 method [42].

Fully-Developed Flow and Heat Transfer Assumption

In a fully-developed flow and heat transfer model, a periodically repeating spatial unit consisting of two ribs (one on either side of the duct) is simulated. An example configuration with normal ribs is shown in Figure 1. The duct walls as well as all six faces of the two ribs exposed to the main flow are heated by imposing a constant heat flux ($q"$) boundary condition. The governing flow and energy equations are non-dimensionalized by a characteristic length scale, which is chosen to be the hydraulic diameter of the channel (D_h), a characteristic velocity scale, given by the friction velocity $u_\tau = \sqrt{\Delta\bar{P}_x / \rho}$, and a characteristic temperature scale, given by $q''D_h / k$. The assumed periodicity of the domain in the streamwise or x-direction requires that the mean gradients of pressure and temperature be isolated from the fluctuating periodic component as follows:

$$\begin{aligned} P(\vec{x},t) &= P_{in} - \beta x + p(\vec{x},t) \\ T(\vec{x},t) &= T_{in} + \gamma x + \theta(\vec{x},t) \end{aligned} \tag{4}$$

On substitution, Eqns. (2-3) take the following form:

Momentum:

$$\begin{aligned} &\frac{\partial}{\partial t}\left(\sqrt{g}u_i\right) + \frac{\partial}{\partial \xi_j}\left(\sqrt{g}U^j u_i\right) = -\frac{\partial}{\partial \xi_j}\left(\sqrt{g}(\vec{a}^j)_i p\right) + \frac{\partial}{\partial \xi_j}\left(\left(\frac{1}{\mathrm{Re}_\tau} + \frac{1}{\mathrm{Re}_t}\right)\sqrt{g}g^{jk}\frac{\partial u_i}{\partial \xi_k}\right) + \sqrt{g}\beta\delta_{i1} \\ &- 2\sqrt{g}(Ro_{\tau_k})\bar{u}_m \in_{ikm} + \sqrt{g}\cdot\in_{ilm}\cdot\in_{jlk}\cdot Ro_{\tau j}\cdot Ro_{\tau m}\cdot r_k\frac{(\theta-\theta_{ref})}{\theta_{ref}} + \sqrt{g}S_{u_i} \end{aligned} \tag{5}$$

Energy:

$$\frac{\partial}{\partial t}\left(\sqrt{g}\theta\right)+\frac{\partial}{\partial \xi_j}\left(\sqrt{g}U^j\theta\right)=\frac{\partial}{\partial \xi_j}\left(\left(\frac{1}{\mathrm{Pr}\,\mathrm{Re}_\tau}+\frac{1}{\mathrm{Pr}_t\,\mathrm{Re}_t}\right)\sqrt{g}g^{jk}\frac{\partial\theta}{\partial \xi_k}\right)-\sqrt{g}\gamma u_1+\sqrt{g}S_T \tag{6}$$

In equation (5), both the rotational Coriolis forces and the centrifugal buoyancy forces are included in the formulation when needed. In the context of a periodic fully-developed flow, buoyancy parameter does not change with the radial or streamwise location ($\vec{r}$ is assumed fixed). The fully-developed calculations assume that the same buoyancy parameter is acting over the periodic pitch and represents one *x*- location (or a pitch surrounding one *x*- location) in a corresponding developing flow. In effect, a fixed Richardson number is defined as:

$$Ri_{\tau i}=\frac{\in_{ilm}\cdot\in_{jlk}\cdot Ro_{\tau j}\cdot Ro_{\tau m}\cdot r_k}{\theta_{ref}}$$

and the buoyancy term in eqn. (5) is represented as:

$$\sqrt{g}\cdot Ri_{\tau_i}\cdot(\theta-\theta_{ref})$$

The Buoyancy number (*Bo*) is commonly used to quantify the effect of centrifugal buoyancy. In the present context, the Buoyancy number (*Bo*) is related to the Richardson number (Ri_τ) by the following expression:

$$Bo=\frac{\Delta\rho}{\rho_o}\frac{r}{D_h}Ro^2\approx\frac{Ri_\tau.\overline{(\theta_s-\theta_{ref})}}{\bar{u}_b^{\,2}}$$

where the quantity under the bar is area averaged over all heat transfer surfaces in the duct.

In the calculations, β is assumed to be unity, whereas γ is calculated from a global energy balance as: $\gamma = q''\Omega / \mathrm{Re}_\tau\,\mathrm{Pr}\,Q_X L_x$. The boundary conditions imposed on the duct walls and ribs are as follows:

$$\begin{aligned}&\vec{u}=0\\&\nabla p\cdot\vec{n}=0\\&\nabla\theta\cdot\vec{n}=1-\gamma\vec{e}_x\cdot\vec{n}\end{aligned} \tag{7}$$

and in the streamwise direction as:

$$\phi(x+L_x)=\phi(x),\ \phi=\vec{u},p,\text{ and }\theta. \tag{8}$$

RANS Modeling for RANS and DES Calculations

The Reynolds stresses are given by $\tau_{ij} = -\overline{u_i' u_j'}$ where $\bar{\phi}$ denotes an ensemble averaged quantity and $\phi = \bar{\phi} + \phi'$, where ϕ' is the fluctuating quantity. Several high and low *Re*-number models based on the *k*-ω model are available and used in GenIDLEST. Here only the basic *k*-ω model of Wilcox [34] is shown. In addition, the Wilcox [32] and Wilcox [33] low-*Re*-number models are also used. Two other models developed by Menter [35-37], the Baseline model (MBSL) and shear stress model (MSST), are also implemented and used. In the basic *k*-ω model, the turbulent Reynolds stresses are modeled by using an eddy viscosity such that

$$\tau_{ij}^{a} = \tau_{ij} + \frac{2}{3}\delta_{ij}k = \frac{2}{\mathrm{Re}_t}\bar{S}_{ij}, \tag{16}$$

where

$$\frac{1}{\mathrm{Re}_t} = \frac{k}{\omega}. \tag{17}$$

The *k*-ω equations are written as:

$$\frac{\partial}{\partial t}\left(\sqrt{g}k\right) + \frac{\partial}{\partial \xi_j}\left(\sqrt{g}U^j k\right) = \tau_{ij}^{a}\left((\vec{a}^m)_j \frac{\partial u_i}{\partial \xi_m}\right) - \beta^* k\omega + \frac{\partial}{\partial \xi_j}\left(\left(\frac{1}{\mathrm{Re}} + \frac{\sigma_k}{\mathrm{Re}_t}\right)\sqrt{g}g^{jk}\frac{\partial k}{\partial \xi_k}\right) + \sqrt{g}S_k \tag{18}$$

$$\frac{\partial}{\partial t}\left(\sqrt{g}\omega\right) + \frac{\partial}{\partial \xi_j}\left(\sqrt{g}U^j \omega\right) = \gamma\frac{\omega}{k}\tau_{ij}^{a}\left((\vec{a}^m)_j \frac{\partial u_i}{\partial \xi_m}\right) - \beta\omega^2 + \frac{\partial}{\partial \xi_j}\left(\left(\frac{1}{\mathrm{Re}} + \frac{\sigma_\omega}{\mathrm{Re}_t}\right)\sqrt{g}g^{jk}\frac{\partial \omega}{\partial \xi_k}\right) + \sqrt{g}S_\omega, \tag{19}$$

where σ_κ=0.5, σ_ω=0.5, β*=0.09, β=0.075, and γ=0.55.

In DES mode, the base model not only functions as a RANS model in the near wall region but also as the LES model in regions where the eddies are resolved by the underlying mesh. The switch from RANS to LES is made by choosing a minimum of the RANS length scale and the length scale associated with the large eddies resolved on the underlying mesh: $l_{DES} = \min(l_{RANS}, l_{LES})$, where $l_{RANS} = \dfrac{\sqrt{k}}{\beta^*\omega}$ and $l_{LES} = C_{DES}\max(\Delta_x, \Delta_y, \Delta_z)$. For two equation models based on *k*, the dissipation term in Eqn. (18) is written in terms of the DES length scale as $k^{3/2}/l_{DES}$. The constant C_{DES} can assume values anywhere from 0.5 to 1.0. Previous studies have shown that the solution accuracy is not sensitive to C_{DES}.

Experimental Method (K. Thole)

A test rig designed for validation of the computations in this project was designed and built by a group of six undergraduate students as part of a senior-level design course. A photograph of the completed test rig is shown in Figure 2. The large-scale, two-pass channel was designed to simulate the developing and fully-developed regions of a two-pass channel as well as the upstream and downstream sides of a 180º bend. Two measurement techniques will be employed in the testing: Laser Doppler Velocimetry (LDV) for producing measurements of the turbulence quantities of the flow, and infrared thermography to provide heat transfer data on the heated surfaces.

The final design consists of a closed-loop, two-pass rig with a 180º bend. The channel includes a ribbed entrance region, a test section designed for studying the thermal development within a hydrodynamically fully-developed flow, and a 180º bend. Figure 3 shows a schematic indicating the entry length, test section and return section. A 2 hp fan, donated by Cincinnati Fan, is capable of producing Reynolds numbers ranging from 10,000 to 100,000. A heat exchanger, donated by Super Radiator Coils, is used initial flow conditioning, and a venturi tube is used for flow measurement through the return loop.

A one-to-one geometric comparison to the computations performed in this project was a primary goal of the rig construction, so the non-dimensional parameters describing the rib size and locations matches the same parameters simulated in the calculations. The duct has a square cross section with square ribs on two walls of size $e/D_h = 0.1$ spaced at a streamwise pitch $P/e = 10$. The hydraulic diameter of the channel is approximately 6 inches.

To study the heat transfer characteristics a separate test section was built. A constant heat flux is imposed on the bottom wall, ribs, and side wall with a series of Inconel strips. A heated rib, with Inconel covering three sides, is compared to an unheated rib, used in the LDV measurements, in Figure 4. A full ANSYS model was created for the rib to insure uniform heating for this heated rib design.

Initial benchmark testing closely matches the fully-developed flow characteristics found in the literature. Figure 5 shows a comparison of local friction factors near the channel entrance for a Reynolds number of 20,000. This graph shows a comparison with experiments reported by Rau, et al. [45] for a fully developed internal turbine channel flow with a similar geometry.

The close comparison seen in the figure suggests hydrodynamically fully-developed flow soon after the third rib with a flat velocity profile at the inlet.

RESULTS AND DISCUSSION

Journal Papers

1. Viswanathan, A.K., Tafti, D.K., Investigation of Detached Eddy Simulations in Capturing the Effects of Coriolis Florces and Centrifugal Buoyancy in Ribbed Ducts, Submitted *ASME J. Heat Transfer*, Sep. 2006., accepted.

The predictive capability of Detached Eddy Simulations (DES) is investigated in stationary as well as rotating ribbed ducts with relevance to the internal cooling of turbine blades. A number of calculations are presented at Re=20,000 and rotation numbers ranging from 0.18 to 0.67 with buoyancy parameters up to 0.29 in a ribbed duct with ribs normal to the main flow direction. The results show that DES by admitting a LES solution in critical regions transcends some of the limitations of the base RANS model on which it is based. This feature of DES is exemplified by its sensitivity to turbulence driven secondary flows at the rib side-wall junction, to the effect of Coriolis forces, and centrifugal buoyancy effects. It is shown that DES responds consistently to these non-canonical effects when RANS and URANS with the same model cannot, at a cost which is about a tenth of that of LES for the geometry and Reynolds number considered in this study.

2. Viswanathan, A.K., Tafti, D.K., Capturing the Effects of Rotation in Sudden Expansion Ducts using Detached Eddy Simulations, submitted AIAA J., Sep 2006.

The capabilities of DES in predicting the turbulent flow downstream of the backward facing step in a rotating sudden expansion channel are validated. Computations have been carried out in a duct with an expansion ratio of 2 for a global Reynolds number of 10000 and global rotation numbers of –0.08 (clockwise rotation) to +0.08 (anti-clockwise rotation). Two different aspect ratios – 5 and 2 are considered. The Reynolds number of the flow is maintained constant for all the cases and so the reattachment length is a function of rotation direction, rotation number (non-dimensional angular velocity) and the aspect ratio of the duct. Rotation augments

or attenuates the turbulence in the separation region downstream of the step and therefore the size of the separation region changes accordingly. Previous studies show the incapability of RANS in accurately capturing the effects of Coriolis forces. DES, on the other hand, treats the separation region in LES mode. This treatment sensitizes the RANS model to grid length scales and thereby allows the natural instabilities of the flow in this region to develop. Thus DES overcomes the shortcoming of the base RANS model and predicts the variation in the reattachment length accurately.

3. Sewall, E.A., Tafti, D.K., Large Eddy Simulation of Flow and Heat Transfer in the Developing Flow Region of a Rotating Gas Turbine Blade Internal Cooling Duct with Coriolis and Buoyancy Forces, *ASME J. Turbomachinery* 129, pp. 1-7, 2007.

The problem of accurately predicting the flow and heat transfer in the ribbed internal cooling duct of a rotating gas turbine blade is addressed with the use of large eddy simulations (LES). Four calculations of the developing flow region of a rotating duct with ribs on opposite walls are used to study changes in the buoyancy parameter at a constant rotation rate. The Reynolds number is 20,000, the rotation number is 0.3, and the buoyancy parameter is varied between 0.00, 0.25, 0.45, and 0.65.

Previous experimental studies have noted that leading wall heat transfer augmentation decreases as the buoyancy parameter increases with low buoyancy, but heat transfer then increases with high buoyancy. However, no consistent physical explanation has been given in the literature. The LES results from this study show that the initial decrease in augmentation with buoyancy is a result of larger separated regions at the leading wall. However, as the separated region spans the full pitch between ribs with an increase in buoyancy parameter, it leads to increased turbulence and increased entrainment of mainstream fluid which is redirected toward the leading wall by the presence of a rib. The impinging mainstream fluid results in heat transfer augmentation in the region immediately upstream of a rib. The results obtained from this study are in very good agreement with previous experimental results.

4. Viswanathan, A.K., Tafti, D.K., A comparative study of DES and URANS for Flow prediction in a Two-pass Internal Cooling Duct, ASME *J. Fluids Engineering*, 128(6), pp. 1336-1345, Nov. 2006.

The capabilities of the detached eddy simulation (DES) and the unsteady Reynolds averaged Navier-Stokes (URANS) versions of the 1988 k-ω model in predicting the turbulent flow field in a two-pass internal cooling duct with normal ribs is presented. The flow is dominated by the separation and reattachment of shear layers; unsteady vorticity induced secondary flows and strong streamline curvature. The techniques are evaluated in predicting the developing flow at the entrance to the duct and downstream of the 180 deg bend, fully developed regime in the first pass, and in the 180 deg bend. Results of mean flow quantities, secondary flows, and the average friction factor are compared to experiments and large-eddy simulations (LES). DES predicts a slower flow development than LES, whereas URANS predicts it much earlier than LES computations and experiments. However, it is observed that as fully developed conditions are established, the capability of the base model in predicting the flow is enhanced by the DES formulation. DES accurately predicts the flow both in the fully developed region as well as the 180 deg bend of the duct. URANS fails to predict the secondary flows in the fully developed region of the duct and is clearly inferior to DES in the 180 deg bend.

5. Viswanathan, A.K., Tafti, D.K., Detached Eddy Simulation of Flow and Heat Transfer in Fully-Developed Rotating Internal Cooling Channel with Normal Ribs, *Int. J. Heat and Fluid Flow* 27(3), pp. 351-370,2006.

Numerical predictions of a hydrodynamic and thermally developed turbulent flow are presented for a rotating duct with square ribs aligned normal to the main flow direction. Three rotation numbers Ro = 0.18, 0.35 and 0.67 are investigated. The rib height to channel hydraulic diameter (e/D_h) is 0.1, the rib pitch to rib height (P/e) is 10 and the calculations have been carried out for a bulk Reynolds number of 20,000. The capability of the detached eddy simulation (DES) in predicting the turbulent flow field and the heat transfer under the effects of rotation has been evaluated against unsteady Reynolds-averaged Navier Stokes (URANS), large-eddy simulations

(LES), and experimental data. It is shown that DES by capturing a large portion of the turbulent energy in the resolved scales is much more capable than URANS in transcending the underlying shortcomings of the RANS model. DES shows much better fidelity in calculating critical components of the turbulent flow field and heat transfer than URANS.

6. Sewall, E.A., Tafti, D.K., Large Eddy Simulation of Flow and Heat Transfer in the 180º Bend Region of a Stationary Ribed Gas Turbine Blade Internal Cooling Duct, *ASME J. Turbomachinery* (128), pp.763-771,2006

Large eddy simulation of the 180 deg bend in a stationary ribbed duct is presented. The domain studied includes three ribs upstream of the bend region and three ribs downstream of the bend with an outflow extension added to the end, using a total of 8.4 million cells. Two cases are compared to each other: one includes a rib in the bend and the other does not. The friction factor, mean flow, turbulence, and heat transfer are compared in the two cases to help explain the benefits and disadvantages of the wide number of flow effects seen in the bend, including flow separation at the tip of the dividing wall, counter-rotating Dean vortices, high heat transfer at areas of flow impingement, and flow separation at the upstream and downstream corners of the bend. Mean flow results show a region of separated flow at the tip of the dividing region in the case with no rib in the bend, but no separation region is observed in the case with a rib. A pair of counter-rotating Dean vortices in the middle of the bend is observed in both cases. Turbulent kinetic energy profiles show a 30% increase in the midplane of the bend when the rib is added. High gradients of heat transfer augmentation are observed on the back wall and downstream outside wall, where mean flow impingement occurs. This heat transfer is increased with the presence of a rib. Including a rib in the bend increases the friction factor in the bend by 80%, and it increases the heat transfer augmentation by approximately 20%, resulting in a trade-off between pressure drop and heat transfer.

7. Viswanathan, A.K., Tafti, D.K., Detached Eddy Simulation of Turbulent Flow and Heat Transfer in a Two-Pass Internal Cooling Duct, *Int. J. Heat and Fluid Flow* 27(1), pp. 1-20, 2006.

Numerical predictions of a hydrodynamic and thermally developed turbulent flow are presented for a stationary duct with square ribs aligned normal to the main flow direction. The rib height to channel hydraulic diameter (e/D_h) is 0.1, the rib pitch to rib height (P/e) is 10 and the calculations have been carried out for a bulk Reynolds number of 20,000. The capability of the detached eddy simulation (DES) version of the 1988 k–ω model has been validated in predicting the turbulent flow field and the heat transfer in a complete two pass channel. Results of mean flow quantities, secondary flows, friction and heat transfer are compared to experiments and large-eddy simulations (LES). It is concluded that in spite of shortcomings in predicting transition correctly at the entrance to the duct, DES surpasses the base capability of the underlying RANS model and predicts flow and heat transfer with good accuracy in a flow which is dominated by separation and reattachment of shear layers, unsteady vortex induced secondary motions, and strong streamline curvature. In all aspects it reproduces the correct physics and shows good quantitative comparisons with LES and experiments while reducing the computational complexity by nearly an order of magnitude.

8. Sewall, E.A., Tafti, D.K., Thole, K.A., Graham, A., Experimental Validation of Large Eddy Simulations of Flow and Heat Transfer in a Stationary Ribbed Duct, ***Int. J. Heat and Fluid Flow*** **27 (2), pp. 243-258, 2006.**

Accurate prediction of ribbed duct flow and heat transfer is of importance to the gas turbine industry. The present study comprehensively validates the use of large eddy simulations (LES) for predicting flow and heat transfer with measured flowfield data in a stationary duct with 90° ribs and elucidates on the detailed physics encountered in the developing flow region, the fully developed region, and the 180° bend region. Among the major flow features predicted with accuracy are flow transition at the entrance of the duct; the distribution of mean and turbulent quantities in the developing, fully developed, and 180° bend; the development of secondary flows in the duct cross-section and the 180° bend; and friction and heat transfer augmentation. At the duct inlet, both the computations and experiments show that the peak turbulence intensities reach values as high as 40% in the streamwise and spanwise directions and 32% in the vertical direction, and a comparison of values along the centerline of the developing flow region shows that the mean flow and turbulent quantities do not become fully developed until

they reach beyond the seventh rib of the duct. Turbulence intensities in the 180° bend are found to reach values as high as 50%, and local heat transfer comparisons show that the heat transfer augmentation shifts towards the outside wall downstream of the bend with little or no shift upstream. In addition to primary flow effects, secondary flow impingement on the smooth walls is found to develop by the third rib, while it continues to evolve downstream of the sixth rib. In all different aspects, it is found that LES produces the correct physics both qualitatively and quantitatively to within 10–15% of experiments.

9. Viswanathan A. and Tafti, D. K., Detached Eddy Simulation of Turbulent Flow and Heat Transfer in a Ribbed Duct, *ASME J. Fluids Engineering* 127(5), pp. 888-896, 2005.

Detached Eddy Simulation (DES) of a hydrodynamic and thermally developed turbulent flow is presented for a stationary duct with square ribs aligned normal to the main flow direction. The rib height to channel hydraulic diameter (e/D_h) is 0.1, the rib pitch to rib height (P/e) is 10 and the calculations have been carried out for a bulk Reynolds number of 20,000. DES calculations are carried out on a 96^3 grid, a 64^3 grid, and a 48^3 grid to study the effect of grid resolution. Based on the agreement with earlier LES computations, the 64^3 grid is observed to be suitable for the DES computation. DES and RANS calculations carried out on the 64^3 grid are compared to LES calculations on $96^3/128^3$ grids and experimental measurements. The flow and heat transfer characteristics for the DES cases compare well with the LES results and the experiments. The average friction and the augmentation ratios are consistent with experimental results, predicting values within 10% of the measured quantities, at a cost lower than the LES calculations. RANS fails to capture some key features of the flow.

10. Tafti, D. K., Evaluating the Role of Subgrid Stress Modeling in a Ribbed Duct for the Internal Cooling of Turbine Blades, *Int. J Heat and Fluid Flow 26(1),* pp. 92-104, 2005.

Time-dependent simulations are performed in a ribbed square duct with rib height to hydraulic diameter ratio of 0.1 and rib pitch to rib height ratio of 10. The calculations are performed for a

nominal bulk Reynolds number of 20,000. Hydrodynamic and thermal fully-developed conditions are assumed. Two mesh resolutions, 96^3 and 128^3 are tested in a quasi-DNS mode and in LES mode with the Dynamic Smagorinsky model. Time evolution, mean, and turbulent quantities are presented, together with friction and heat transfer. It is found that in general, both quasi-DNS and LES resolve the bulk mean features of the flow within 10–15% of each other. These include recirculation patterns and secondary flows which are characteristic of this geometry. However, there are large differences in predicting the friction and heat transfer coefficients, both of which are very sensitive to the predicted turbulent field near the duct surfaces. Both quasi-DNS calculations underpredict the heat transfer and friction coefficient by amounts which range between 20% and 30% on the 96^3 mesh and 15–20% on the 128^3 mesh. However, the LES calculations with the dynamic Smagorinsky model predict these quantities within 5–10% of experimental values for both mesh resolutions. It is concluded that in an average sense, the level of turbulence augmentation provided by the dynamic model is commensurate with the mesh resolution such that the turbulent energy, heat transfer coefficient, and friction are predicted at the right levels independent of the resolution.

11. Abdel-Wahab, S. and Tafti, D. K., Large Eddy Simulations of Flow and Heat Transfer in a 90º Ribbed Duct with Rotation - Effect of Coriolis and Centrifugal Buoyancy Forces, *J. Turbomachinery* 126(4), pp. 627-636, 2004.

Results from large eddy simulations (LES) of fully developed flow in a 90 deg ribbed duct are presented with rib pitch-to-height ratio P/e = 10 and a rib height-to-hydraulic-diameter ratio e/D_h = 0.1. Three rotation numbers Ro = 0.18, 0.36, and 0.68 are studied at a nominal Reynolds number based on bulk velocity of 20 000. Centrifugal buoyancy effects are included at two Richardson numbers of Ri=12, 28 (Buoyancy parameter, Bo = 0.12 and 0.30) for each rotation case. Heat transfer augmentation on the trailing side of the duct due to the action of Coriolis forces alone asymptotes to a value of 3.7±5% by Ro=0.2. On the other hand, augmentation ratios on the leading surface keep decreasing with an increase in rotation number with values ranging from 1.7 at Ro=0.18 to 1.2 at Ro=0.67. Secondary flow cells augment the heat transfer coefficient on the smooth walls by 20% to 30% over a stationary duct. Centrifugal buoyancy further strengthens the secondary flow cells in the duct cross-section which leads to an

additional increase of 10% to 15%. Buoyancy also accentuates the augmentation of turbulence near the trailing wall of the duct and increases the heat transfer augmentation ratio 10% to 20% over the action of Coriolis forces alone. However, it does not have any significant effect at the leading side of the duct. The overall effect of buoyancy on heat transfer augmentation for the ribbed duct is found to be less than 10% over the effect of Coriolis forces alone. Friction on the other hand is augmented 15% to 20% at the highest buoyancy number studied. Comparison with available experiments in the literature show excellent agreement.

Conference Papers

1. Viswanathan, A. K. and Tafti D. K., Large Eddy Simulation of the fully developed flow and heat transfer in a rotating duct with 45° ribs, GT 2006-90229, ASME Turbo Expo 2006, 8- 11 May 2006, Barcelona, Spain.

2. Viswanathan, A. K. and Tafti, D. K., A comparative study of DES and URANS in a Two-pass Internal Cooling Duct with Normal Ribs - IMECE2005-79288, 2005 ASME International Mechanical Engineering Congress and Exposition, November 5-11, 2005, Orlando, Florida.

3. Viswanathan, A.K., Tafti. D.K., Abdel-Wahab, S., Large Eddy Simulation of Flow and Heat Transfer in an Internal Coolingg Duct with High Blockage Ratio 45^{o} staggered Ribs, GT 2005-68086, Proceedings of ASME Turbo Expo 2005, June 6-9, Reno-Tahoe,USA.

4. Viswanathan, A.K., Tafti. D.K., Large Eddy Simulation of Flow and Heat Transfer in a Ribbed Duct With Skewed Ribs of Rounded Cross-section, GT 2005-68117, Proceedings of ASME Turbo Expo 2005, June 6-9, Reno-Tahoe,USA.

5. Viswanathan, A.K., Tafti. D.K., Deatched Eddy Simulation of Flow and Heat Transfer in a Stationary Internal Cooling Duct with Skewed Ribs,GT 2005-68118, Proceedings of ASME Turbo Expo 2005, June 6-9, Reno-Tahoe, USA.

6. Sewall, E.A., Tafti, D.K., Large Eddy Simulation of Flow and Heat Transfer in the 180º Bend Region of a Stationary Ribed Gas Turbine Blade Internal Cooling Duct, Proceedings of the ASME Turbo Expo 2005, Reno-Tahoe, Nevada, ASME Paper No. GT2005-68518.

7. Sewall, E.A., Tafti, D.K., Large Eddy Simulation of Flow and Heat Transfer in the Developing Flow Region of a Rotating Gas Turbine Blade Internal Cooling Duct with Coriolis and Buoyancy Forces, Proceedings of the ASME Turbo Expo 2005, Reno-Tahoe, Nevada, ASME Paper No. GT2005-68519.

8. Graham, E, Sewall, E. and Thole, K. A., 2004, Flowfield Measurements in a Ribbed Channel Relevant to Internal Turbine Blade Cooling, GT2004-53361, ASME Turbo Expo: 2004, Vienna, Austria.

9. Viswanathan A. and Tafti, D. K., Detached Eddy Simulation of Turbulent Flow and Heat Transfer in a Duct, HT-FED2004-56152, 2004 ASME Heat Transfer/Fluids Engineering Summer Conference, July 11-15, Charlotte.

10. Abdel-Wahab, S. and Tafti, D. K., Large Eddy Simulation of Flow and Heat Transfer in a Staggered 45º Ribbed Duct, GT2004-53800, ASME Turbo Expo: 2004, Vienna, Austria.

11. Abdel-Wahab, S. and Tafti, D. K., Large Eddy Simulations of Flow and Heat Transfer in a 90º Ribbed Duct with Rotation – Effect of Coriolis Forces, GT2004-53796, ASME Turbo Expo: 2004, Vienna, Austria.

12. Abdel-Wahab, S. and Tafti, D. K., Large Eddy Simulations of Flow and Heat Transfer in a 90º Ribbed Duct with Rotation - Effect of Coriolis and Centrifugal Buoyancy Forces, GT2004-53799, ASME Turbo Expo: 2004, Vienna, Austria.

13. Sewall, E, and Tafti, D. K., Large Eddy Simulation of the Developing Region of a Stationary Ribbed Internal Turbine Blade Cooling Channel, GT2004-53832, ASME Turbo Expo: 2004, Vienna, Austria.

14. Sewall, E, and Tafti, D. K., Large Eddy Simulation of the Developing Region of a Rotating Ribbed Internal Turbine Blade Cooling Channel, GT2004-53833, ASME Turbo Expo: 2004, Vienna, Austria.

15. Tafti D. K., Large Eddy Simulations of Heat Transfer in A Ribbed Channel for Internal Cooling of Turbine Blades, Paper No. GT2003-38122, Proceedings of ASME/IGTI Turbo Expo., Atlanta, Georgia, June 16-19, 2003.

SUMMARY AND CONCLUSIONS

The project was successful in highlighting the accuracy of LES over RANS methods in developing flow and in the 180^o bend region. LES was particularly successful in capturing secondary flow effects. However LES is still computationally intensive and turnaround times are high compared to RANS methods. DES or a hybrid LES-RANS method was implemented and for the first time applied to internal heat transfer problems typical of internal cooling applications. It was established that DES is a good alternative to LES and is able to capture the anisotropies introduced by rotation and centrifugal buoyancy and gives LES like accuracy at roughly one-tenth to one-fifth the cost.

References

1. Tafti D. K., 2003, Large Eddy Simulations of Heat Transfer in A Ribbed Channel for Internal Cooling of Turbine Blades, Paper No. GT2003-38122, Proceedings of ASME/IGTI Turbo Expo., Atlanta, Georgia, June 16-19, 2003.
2. Abdel-Wahab, S. and Tafti, D. K., 2004a, Large Eddy Simulation of Flow and Heat Transfer in a Staggered 45º Ribbed Duct, GT2004-53800, ASME Turbo Expo: 2004, Vienna, Austria.
3. Abdel-Wahab, S. and Tafti, D. K., 2004b, Large Eddy Simulations of Flow and Heat Transfer in a 90º Ribbed Duct with Rotation – Effect of Coriolis Forces, GT2004-53796, ASME Turbo Expo: 2004, Vienna, Austria.
4. Abdel-Wahab, S. and Tafti, D. K., 2004c, Large Eddy Simulations of Flow and Heat Transfer in a 90º Ribbed Duct with Rotation - Effect of Coriolis and Centrifugal Buoyancy Forces, GT2004-53799, ASME Turbo Expo: 2004, Vienna, Austria.
5. Sewall, E, and Tafti, D. K., 2004a, Large Eddy Simulation of the Developing Region of a Rotating Ribbed Internal Turbine Blade Cooling Channel, GT2004-53833, ASME Turbo Expo: 2004, Vienna, Austria.
6. Sewall, E, and Tafti, D. K., 2004b, Large Eddy Simulation of the Developing Region of a Stationary Ribbed Internal Turbine Blade Cooling Channel, GT2004-53832, ASME Turbo Expo: 2004, Vienna, Austria.
7. Graham, E, Sewall, E. and Thole, K. A., 2004, Flowfield Measurements in a Ribbed Channel Relevant to Internal Turbine Blade Cooling, GT2004-53361, ASME Turbo Expo: 2004, Vienna, Austria.
8. Viswanathan A. and Tafti, D. K., 2004, Detached Eddy Simulation of Turbulent Flow and Heat Transfer in a Duct, HT-FED2004-56152, ASME Heat Transfer/Fluids Engineering Summer Conference, July 11-15, Charlotte.
9. Sewall, E, and Tafti, D. K., 2005a, Large Eddy Simulation of Flow and Heat Transfer in the Developing Flow Region of a Rotating Gas Turbine Internal Cooling Duct with Coriolis and Buoyancy Forces, GT2005-68519, ASME Turbo Expo 2005, June 6-9, Reno-Tahoe, Nevada, USA.

10. Sewall, E, and Tafti, D. K., 2005b, Large Eddy Simulation of Flow and Heat Transfer in the 180^o Bend Region of a Stationary Ribbed Gas Turbine Internal Cooling Duct, GT2005-68518, ASME Turbo Expo 2005, June 6-9, Reno-Tahoe, Nevada, USA.
11. Viswanathan, A. and Tafti, D. K., 2005a, Large Eddy Simulation of Flow and Heat Transfer in a Ribbed Duct with Skewed Ribs of Rounded Cross-Section, GT2005-68117, ASME Turbo Expo 2005, June 6-9, Reno-Tahoe, Nevada, USA.
12. Viswanathan, A. and Tafti, D. K., 2005b, Detached Eddy Simulation of Flow and Heat Transfer in a Stationary Internal Cooling Duct with Skewed Ribs, GT2005-68118, ASME Turbo Expo 2005, June 6-9, Reno-Tahoe, Nevada, USA.
13. Viswanathan, A. and Tafti, D. K., 2005c, Large Eddy Simulation of Flow and Heat Transfer in an Internal Cooling Duct with High Blockage Ratio 45^o Staggered Ribs, GT2005-68086, ASME Turbo Expo 2005, June 6-9, Reno-Tahoe, Nevada, USA.
14. Viswanathan, A. K. and Tafti, D. K., 2005d, A comparative study of DES and URANS in a Two-pass Internal Cooling Duct with Normal Ribs - IMECE2005-79288, 2005 ASME International Mechanical Engineering Congress and Exposition, November 5-11, 2005, Orlando, Florida.
15. Viswanathan, A. K. and Tafti D. K., 2006, Large Eddy Simulation of the fully developed flow and heat transfer in a rotating duct with 45° ribs, GT 2006-90229, ASME Turbo Expo 2006, 8- 11 May 2006, Barcelona, Spain.
16. Abdel-Wahab, S. and Tafti, D. K., 2004d, Large Eddy Simulations of Flow and Heat Transfer in a 90º Ribbed Duct with Rotation - Effect of Coriolis and Centrifugal Buoyancy Forces, *J. Turbomachinery* 126(4), pp. 627-636.
17. Tafti, D.K., 2005. Evaluating the Role of Subgrid Stress Modelling in a Ribbed Duct for the Internal Cooling of Turbine Blades, *Int. J Heat and Fluid Flow* 26(1), pp. 92-104.
18. Viswanathan A. and Tafti, D. K., Detached Eddy Simulation of Turbulent Flow and Heat Transfer in a Ribbed Duct, *ASME J. Fluids Engineering* 127(5), pp. 888-896, 2005.
19. Viswanathan A.K., Tafti, D. K., 2006a, Detached Eddy Simulation of Turbulent Flow and Heat Transfer in a Two-Pass Internal Cooling Duct, *Int. J. of Heat Fluid Flow* 27(1), pp. 1-20.

20. Sewall, E.A., Tafti, D.K., Graham, A., Thole, K.A., 2006. Experimental Validation of Large Eddy Simulation of flow and heat transfer in a Stationary Ribbed Duct. *Int. J. Heat and Fluid Flow* 27 (2), pp. 243-258.
21. Viswanathan A.K., Tafti, D. K., 2006b, Detached Eddy Simulation of Flow and Heat Transfer in Fully Developed Rotating Internal Cooling Channel with Normal Ribs, *Int. J. of Heat Fluid Flow* 27(3), pp. 351-370.
22. Viswanathan, A.K., Tafti, D.K., 2006c, A comparative study of DES and URANS for Flow prediction in a Two-pass Internal Cooling Duct, *ASME J. Fluids Engineering*, 128(6), pp. 1336-1345, Nov. 2006.
23. Sewall, E.A., Tafti, D.K., 2006a, Large Eddy Simulation of Flow and Heat Transfer in the Developing Flow Region of a Rotating Gas Turbine Blade Internal Cooling Duct with Coriolis and Buoyancy Forces, *ASME J. Turbomachinery*, 129, pp. 1-7, 2007.
24. Sewall, E.A., Tafti, D.K., 2006b, Large Eddy Simulation of Flow and Heat Transfer in the 180º Bend Region of a Stationary Ribbed Gas Turbine Blade Internal Cooling Duct, accepted for publication, *ASME J. Turbomachinery* (128), pp.763-771, 2006.
25. Viswanathan, A.K., Tafti, D.K., 2006d, Investigation of Detached Eddy Simulations in Capturing the Effects of Coriolis Florces and Centrifugal Buoyancy in Ribbed Ducts, Submitted *ASME J. Heat Transfer*, accepted for publication.
26. Viswanathan, A.K., Tafti, D.K., Capturing the Effects of Rotation in Sudden Expansion Ducts using Detached Eddy Simulations, submitted AIAA J., Sep 2006.
27. Tafti, D. K., 2001, GenIDLEST - A Scalable Parallel Computational Tool for Simulating Complex Turbulent Flows, Proceedings of the ASME Fluids Engineering Division, FED - vol. 256, pp. 347-356, ASME-IMECE, Nov. 2001, New York.
28. Thuburn, J., 1996, Multidimensional Flux-Limited Advection Schemes, *J. Comput. Phys*., vol. 123, pp. 74-83.
29. Leonard, B. P., 1991, The ULTIMATE conservative difference scheme applied to unsteady one-dimensional advection, *Comp. Methods in App. Mech, and Engineering* 88, pp. 17-74.
30. Smagorinksy, J., 1963, General Circulation Experiments with the Primitive Equations. I. The Basic Experiment, *Monthly Weather Review,* vol. 91, pp. 99-164.
31. Germano, M., Piomelli, U., Moin, P., and Cabot, W. H., 1991, A dynamic subgrid-scale eddy viscosity model, *Physics of Fluids* A. vol. 3, pp. 1760-1765.

32. Wilcox David C. 1994, Simulation of Transition with a Two-Equation Turbulence model, *AIAA Journal*, vol. 32, No. 2, pp. 247-225.
33. Wilcox David C. 1998, Turbulence modeling for CFD, DCW Industries, Inc.
34. Wilcox, D.C., 1988. Reassessment of the Scale-Determining Equation for Advanced Turbulence Models, *AIAA Journal*, Vol 26 (11), pp 1299-1310. Nov 1988.
35. Menter Florian R., 1993, Zonal Two Equation $k-\omega$ Turbulence Models for Aerodynamic Flows, 24th Fluid Dynamics Conference, AIAA paper 93-2906, July 6 – 9, Orlando, Florida.
36. Menter, F.R., 1992. Improved Two-Equation *k-ω* Turbulence Models for Aerodynamic Flows, NASA Technical Memorandum 103975, Oct 1992.
37. Menter, F.R., 1993. Zonal Two Equation *k-ω* Turbulence Models for Aerodynamic Flows, AIAA Paper 93-2906.
38. Wang G., Tafti, D. K., 1998b, Parallel performance of Additive Schwarz preconditioners on Origin 2000. *Advances in Engineering Software*, vol. 29, no. 3-6, pp. 433.
39. Wang, G. and Tafti, D. K., 1999, Performance Enhancement on Microprocessors with Hierarchical Memory Systems for Solving Large Sparse Linear Systems. *The International Journal of Supercomputing Applications and High Performance Computing*, vol. 13, no. 1, pp. 63.
40. Wang, G., Tafti, D. K., 1998a, Uniprocessor performance enhancement by Additive Schwarz preconditioners on Origin 2000. *Advances in Engineering Software*, vol. 29, no. 3-6, pp. 425.
41. Chong, M. S., Perry, A. E., and Cantwell, B. J., 1990, A general classification of three-dimensional flow fields, *Physics of Fluids* A. vol. 2, pp. 765-777.
42. Jeong, J. and Hussain, F., 1995, On the identification of a vortex, *J. Fluid Mech*., vol. 285, pp 69-94.
43. Najjar, F. M. and Tafti, D. K., 1996a, Study of Discrete Test Filters and Finite Difference Approximations for the Dynamic Subgrid-Scale Stress Model, *Phys. Fluids*, vol. 8, pp. 1076-1088.
44. Lilly, D. K., 1992, A proposed modification of the Germano subgrid-scale closure method, *Phys. Fluids A* 4, 633.

45. Rau, G., Çakan, M., Moeller, D. and Arts, T., 1998, The Effect of Periodic Ribs on the Local Aerodynamic and Heat Transfer Performance of a Straight Cooling Channel, *ASME J. Turbomachinery*, 120, pp. 368-375.

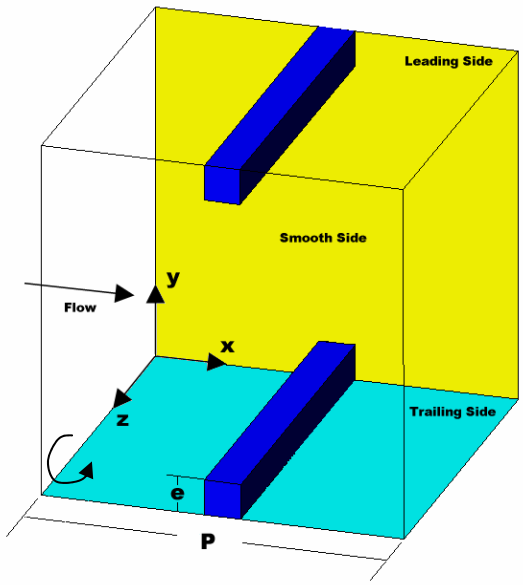

Figure 1: Computational domain for fully-developed flow and heat transfer in ribbed duct with and without rotation. Periodic boundary conditions are applied in the streamwise *x*-direction.

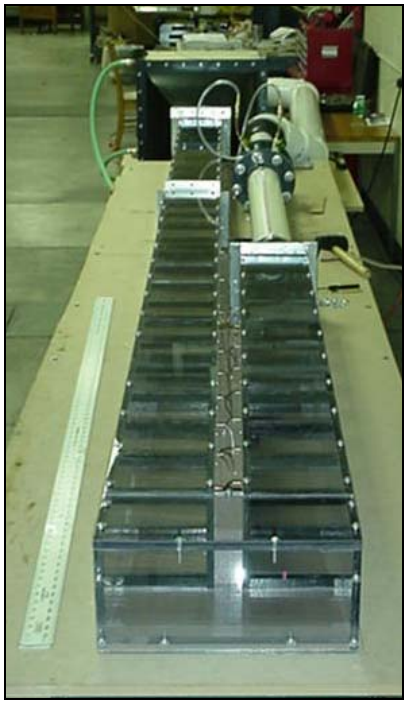

Figure 2: Photograph of the completed test rig. The ruler in the foreground is 6 feet long. The test rig was constructed of Lexan walls and equipped with pressure taps at 6-in. increments.

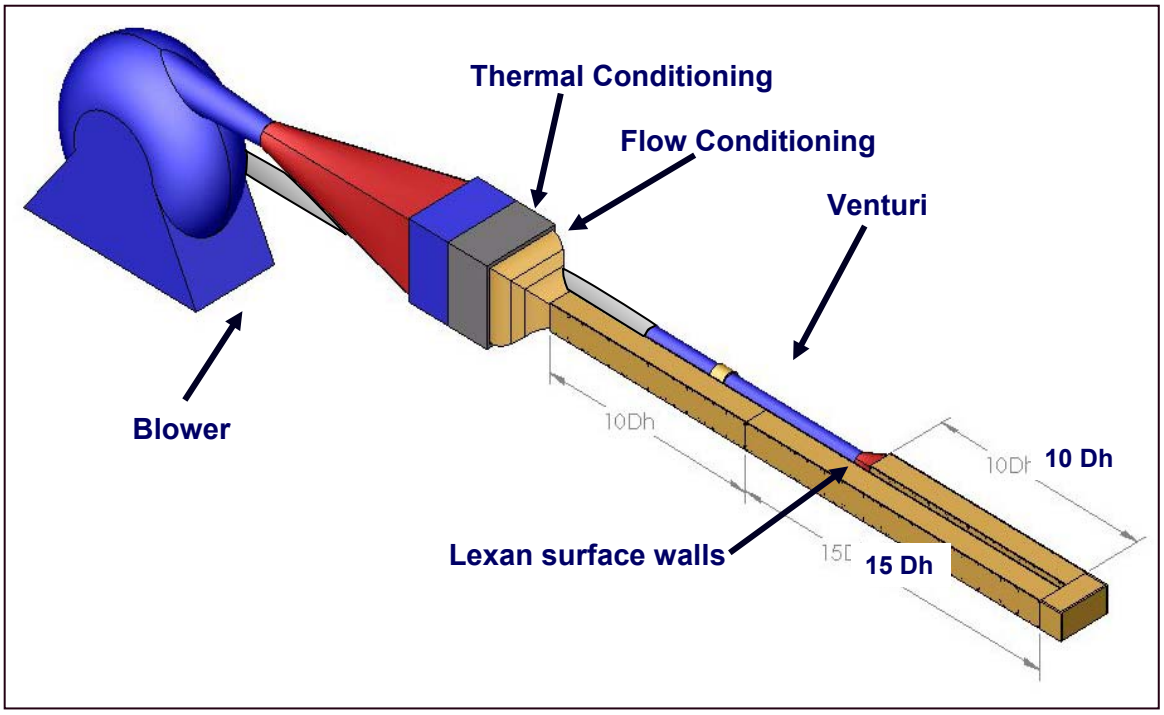

Figure 3: Three dimensional CAD rendering of testing facility for ribbed channel studies.

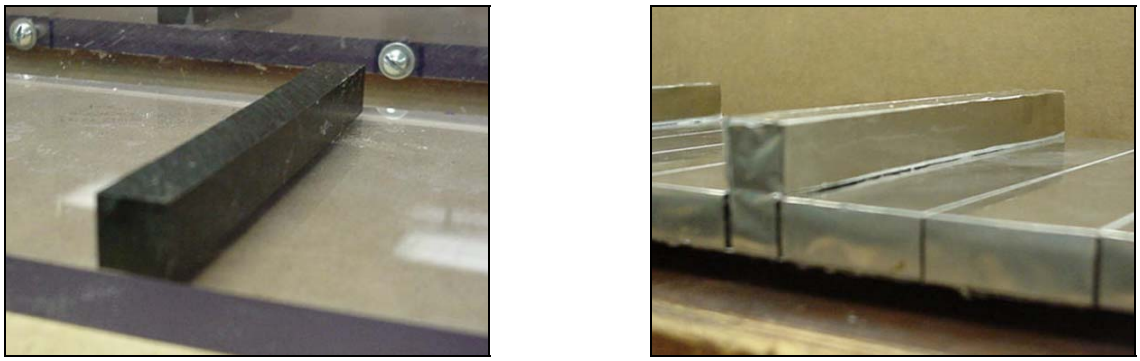

(a) (b)

Figure 4: Detailed photograph of Delrin rib for (a) heated and (b) unheated studies.

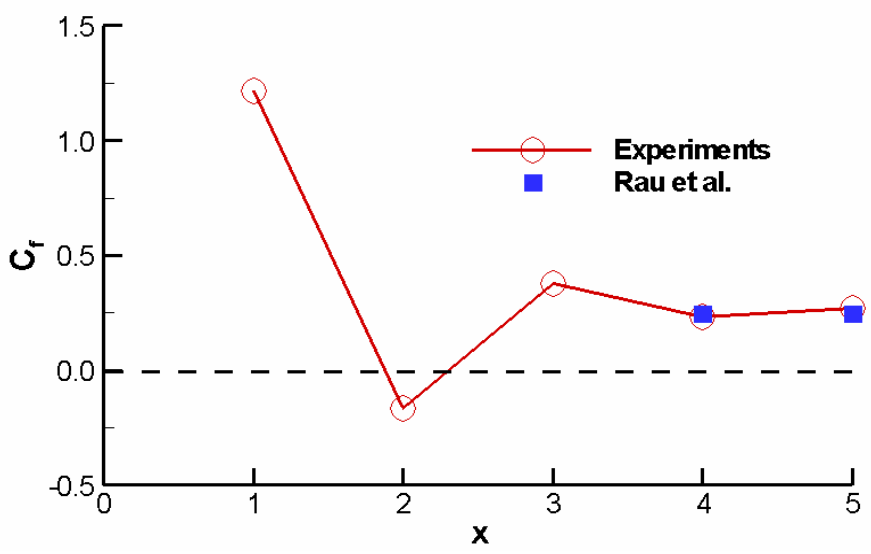

Figure 5: Comparison of experimental friction factors with data from Rau et al. [44].

Mechanism-Based Testing Methodology For Improving the Oxidation, Hot Corrosion and Impact Resistance of High-Temperature Coatings for Advanced Gas Turbines

Final Report
30 November, 2005

Principal Investigators:
Frederick S. Pettit (pettit@engr.pitt.edu)
Gerald H. Meier (ghmeier@engr.pitt.edu)

Report Date: 31 May, 2005

DOE Award: DE-FC26-02NT41431
UTSR Project: 02-01-SR101

Submitted by:
Department of Materials Science & Engineering
848 Benedum Hall
University of Pittsburgh
Pittsburgh, PA 15261

Subcontract Information:
Department of Mechanical Engineering
Carnegie Mellon University
5000 Forbes Avenue
Pittsburgh, PA 15213-3890
Jack L. Beuth (beuth@andrew.cmu.edu)

ABSTRACT
This project comprises a collaborative University/National Laboratory/Industry effort to develop a mechanism-based testing methodology for improving the oxidation resistance of high temperature metallic coatings and TBCs. This testing methodology involves a significant number of nondestructive tests directed at assessing coatings degradation and damage accumulation. The test results are being used in an attempt to develop a life prediction protocol. The work on the project has been detailed in six semi-annual reports. This document is the final report of this effort.

TABLE OF CONTENTS

LIST OF GRAPHICAL MATERIALS

INTRODUCTION

The primary goal of this research is to advance accelerated testing methods for cyclic oxidation and hot corrosion tests of interest to the gas turbine and coating manufacturing industries. Emphasis is on the study of fundamental mechanisms controlling coating degradation and correlating these mechanisms with standard and accelerated tests. The mechanisms of cyclic oxidation are being systematically studied via imaging of oxide and interface structures, mechanics models of interface decohesion, and stress and toughness measurements of coating systems as a function of exposure. The PIs are working closely with National Laboratories in conducting the research and with industrial collaborators to transition their findings to the coating and gas turbine industries, where the current standard is to perform time and cost-intensive burner rig tests to quantify coating durability.

The focus of this project has been on developing techniques for accelerated cyclic oxidation testing and measuring the fundamental properties of coatings systems that control oxide adherence. The systems studied consist of alumina scales grown on nickel-base superalloy substrates, coated superalloys, and analogous thermal barrier coating (TBC) systems that contain an alumina scale. Both types of coating systems typically include an oxidation-resistant bond coat, which is deposited onto the superalloy substrate.

The adherence of protective oxides to the coatings considered in this project is governed by the stored elastic energy in the oxide, which drives delamination, and the fracture resistance of the alloy/oxide interface as illustrated schematically in Figure 1.

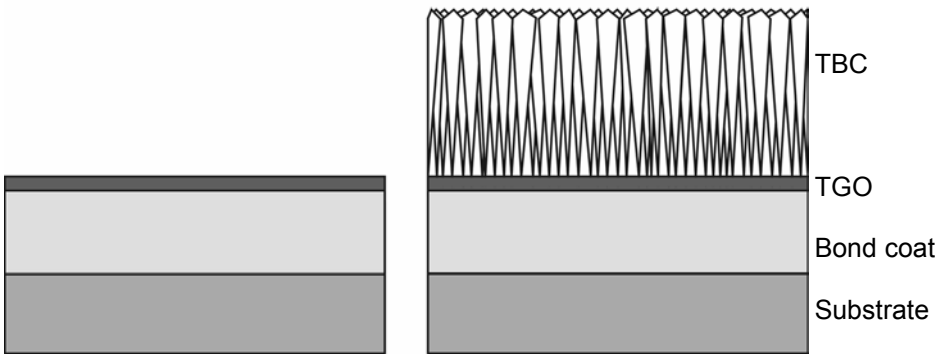

Figure 1. Schematic diagram of oxide only and TBC systems.

Clearly, any modifications to the alloy substrate or the exposure environment which decreases the former or increases the latter will improve the durability of a given system. The stored elastic energy is determined by the stress level in the oxide and the oxide thickness. The stress state in an oxide scale is determined by stresses which arise during the oxide formation (*Growth Stresses*), stresses produced during temperature changes as the result of thermal expansion mismatch between the oxide and the alloy (*Thermal Stresses*), and any stress relaxation which occurs as the result of creep of the scale or alloy. In systems that include a TBC, elastic energy is also stored in the TBC layer. Stresses in the TBC are purely thermal stresses, but their magnitude can be a strong function of the density of the TBC, which can change with high temperature exposure.

The fracture energy of the interface (i.e. TGO/bond coat or TBC/TGO interfaces) is a function of the composition at the interface, the microstructure in the interfacial region, and the composition of the exposure environment.

Previous research by the PIs has included

a. Measurement of Times to Failure of Oxidation-resistant Coatings and Thermal Barrier Coatings as a Function of Temperature

b. Measurement of Interface Fracture Toughness Using an Indentation Test and Arrhenius Analysis of Indent Test Results

This research is described in more detail in the following:

a. <u>Measurement of Times to Failure of Thermal Barrier Coatings as a Function of Temperature</u>

The study of measured times to failure of thermal barrier coatings (TBCs) in cyclic oxidation tests has indicated that the rate of failure follows an exponential dependence on the exposure temperature. Typical results are shown in Figure 2 for TBCs

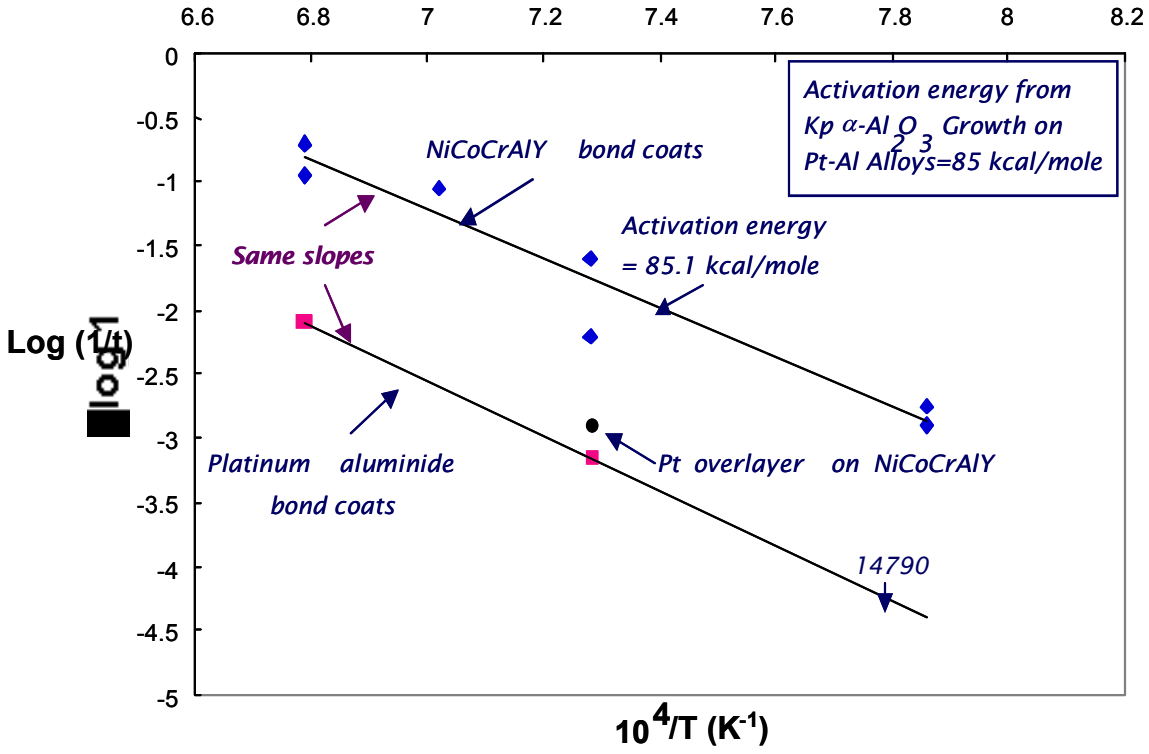

Figure 2. Effect of Temperature on the Failure Time of Two TBC types.

with two different bond coats. This Arrhenius behavior can form the basis for using relatively high temperature tests and extrapolating the results to lower temperatures where the failure times might be too long to reasonably study in the laboratory.

The exponential relationship between failure time and exposure temperature observed by the PIs also suggests that a single set of thermally activated mechanisms may govern TBC failure over a wide range of exposure temperatures. Fracture toughness testing (an indentation test described below), imaging of oxide and interface structures, oxide stress measurements and acoustic emission measurements are being used to search for additional evidence of a dominant failure mechanism for these systems.

b. Measurement of Interface Fracture Toughness using an Indentation Test: Accelerated Testing via Mechanical Loading

In a previous project, the PIs have developed indentation testing methods for quantifying changes in interfacial toughness in TBC systems as a function of thermal exposures. The indentation test produces spallation in oxide and TBC systems at times much shorter than those required for spontaneous failure. *Thus inducing spallation at early times (via indentation) has emerged as one means for accelerating the evaluation of coating system durability due to high temperature exposures.*

The test consists of indenting the TBC system with a Brale type conical indenter (a Rockwell hardness tester or mechanical testing machine can be used for this purpose). The indenter penetrates the TBC and oxide layers and plastically deforms the metallic bond coat and substrate below. As illustrated in Figure 3(as viewed from above), this induces an axisymmetric debond of the TBC and oxide layers. Systems with poor adhesion between the oxide and bond coat show large debond radii. Systems with good adhesion will show small debond radii or no debonding at all.

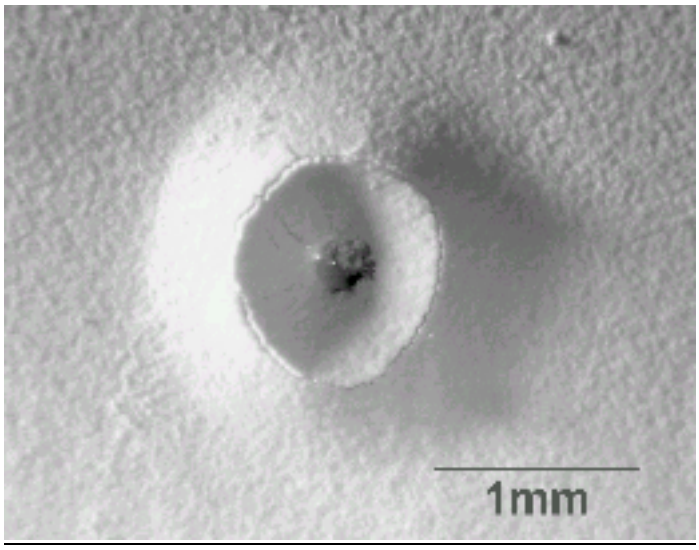

Figure 3. Optical Micrograph of the Debonded Portions of an Indented TBC Specimen, as Viewed from Above.

Fracture mechanics analyses of the indentation test have been performed to allow determination of an interfacial toughness (a value of critical stress intensity factor, K_c, or

critical energy release rate, G_c) for the interface between the oxide and bond coat layers, based on a measured debond radius.

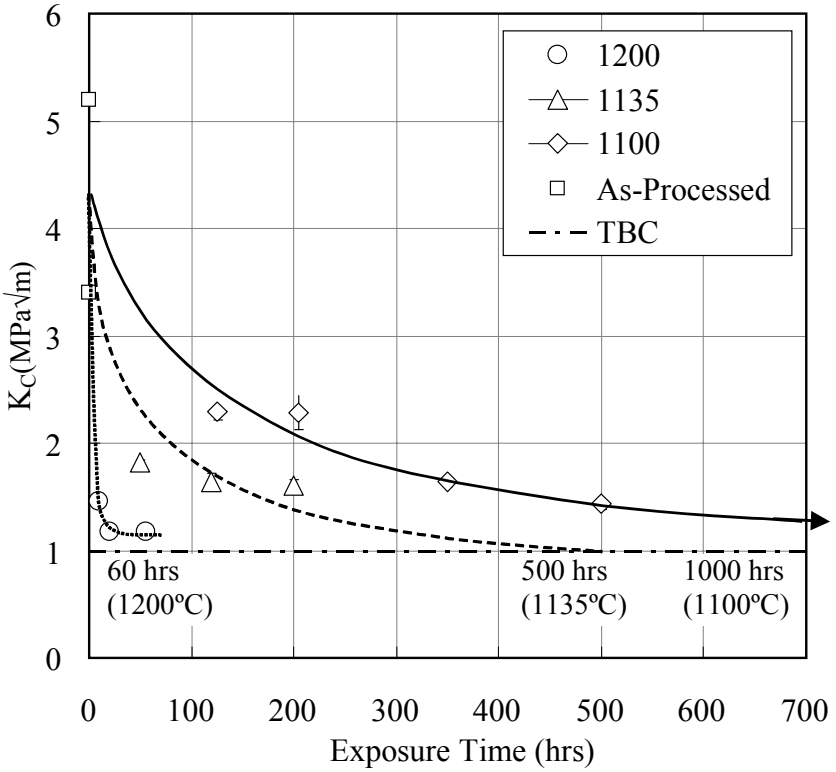

Figure 4. Plot of Apparent Toughness Loss (Assuming no Changes in TBC System Properties) vs. Isothermal Exposure Time.

This test allows tracking of toughness changes in TBC systems as a function of thermal exposures, including the ability to perform many indentations on a single specimen, as its exposure times are increased. For example, Figure 4 shows a plot of "apparent" losses of interfacial toughness for EBPVD TBC/PtAl bond coat systems exposed to 1200°C, 1135°C and 1100°C isothermal exposures in lab air, as determined by room temperature indent tests. (Note that there is some variability in the toughness for as-processed specimens.) The times of 60, 500 and 1000 hrs are approximate times to spontaneous spallation at temperatures of 1200°C, 1135°C and 1100°C, respectively. At such times, the interfacial fracture toughness matches the applied stress intensity factor due to thermal strains alone, which is approximately equal to 1 $MPam^{1/2}$. This is the first data of this type available for TBC systems and it indicates that substantial toughness loss occurs at a fraction of the time needed for spontaneous failure to occur. Because early toughness losses are correlated with TBC system life, measurement of toughness losses for short exposure times can be the basis of accelerated durability tests.

The data plotted in Figure. 4 assumes constant, as-processed properties of the TBC, system, not accounting for the effects of oxide growth, TBC density increases due to sintering or any other adhesion-reducing changes in the TBC system that may be independent of a true degradation of the oxide/bond coat interface. Because non-interfacial changes in the TBC system can result in a measured reduction in toughness, these are referred to as "apparent" losses of toughness.

Arrhenius Analysis of Indent Test Results: Accelerated Testing via Higher Temperatures

To gain further insight into the mechanisms leading to TBC system oxide/bond coat interfacial adhesion loss, the results presented in Figure 4 have been re-cast in the form of an Arrhenius plot. Figure 5 gives a plot of ln(1/time) vs. 1/Temperature, where the "time" variable is the time to reach a specified value of apparent interfacial toughness. In other words, a single line in Figure 5 is determined by drawing a horizontal line across the plot of Figure 4, at values of K_c = 2.5, 2.0, 1.5 or 1.0 MPam$^{1/2}$, and determining intersection points with test data at 1200°C, 1135°C and 1100°C. Data plotted for a K_c value of 1.0 MPam$^{1/2}$ denote times required to experience spontaneous spallation.

It is clear from Figure 5 that the slopes of the plotted lines for each K_c value are approximately the same (the slopes for K_c = 2.5, 2.0, and 1.5 are equal and the slope for K_c = 1.0 is a factor of 0.81 of the slopes for the other K_cs). Thus, the thermally activated mechanisms that lead to apparent toughness loss appear to be the same as those leading to spontaneous spallation (final failure). As a result, as suggested in the previous section, use of an indentation test to obtain measured toughness losses at early exposure times appears to be a valid means of gaining information on TBC system durability without having to perform long-term tests to failure.

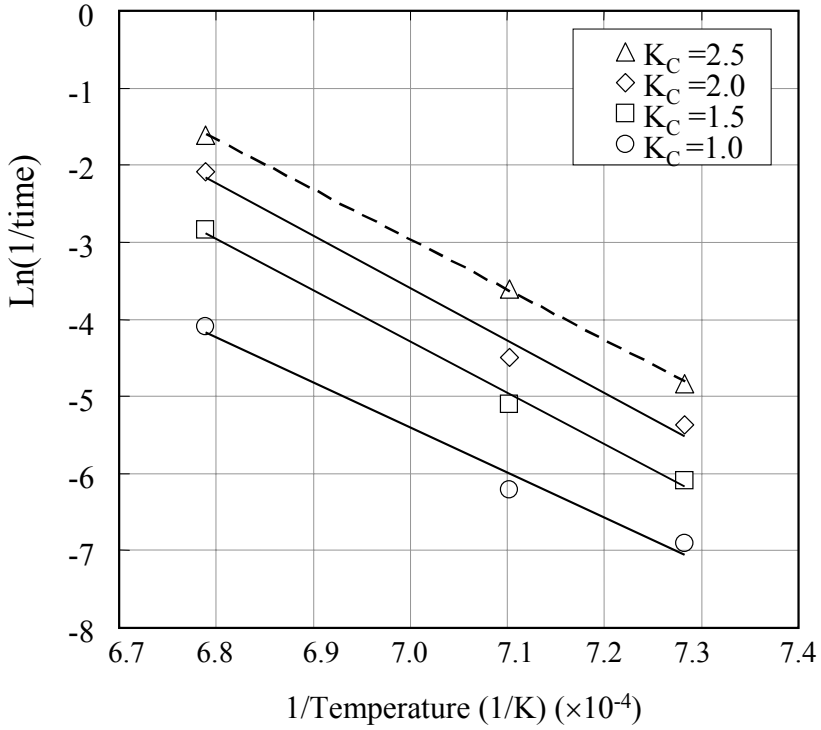

Figure 5 Arrhenius plot for various levels of apparent toughness.

EXECUTIVE SUMMARY

This project comprises a collaborative University/National Laboratory/Industry effort to develop a mechanism-based testing methodology for improving the oxidation resistance of high temperature metallic coatings and TBCs. This testing methodology involves a number of nondestructive tests directed at assessing coating degradation and damage accumulation. The ultimate goal is to use such tests as part of newly developed life prediction protocols.

The project team members and their areas of responsibility were as follows. Professors Pettit and Meier of the University of Pittsburgh led the effort and performed corrosion studies and acoustic emission and x-ray diffraction experiments. Professor Beuth of CMU performed indentation tests of spallation resistance and fracture mechanics analyses. Dr. Michael Lance of ORNL performed piezospectroscopic stress measurements and Dr. William Ellingson of ANL perform optical backscatter experiments. Specimens were prepared by Praxair and Howmet. GE provid input on testing conditions for the various degradation modes.

The specific tasks are summarized in the following.

Task I: Processing Comparisons and Modifications
This Task was concerned with processing comparisons and modifications using state-of-the art-coatings. Specimens of bare René N5, René N5 coated with a straight aluminide and platinum-modified aluminide, and René N5 with an EBPVD TBC over a platinum-modified aluminide bond coat were studied. Specimens with NiCoCrAlY coatings were fabricated by low pressure plasma spraying and Argon-shrouded plasma spraying.

Task II: Compositional Modifications
This Task involveed compositional modifications of state of the-art coatings. Growth of a very pure and adherent alumina scale on these alloys was attempted.

Task III: TBC Selection and Fabrication
This Task consists of selection and preparation of one or more TBC systems for study in this project. Thermal barrier coatings with platinum aluminide and NiCoCrAlY bond coats were studied.

Task IV: Specimen Testing
This Task was concerned with cyclic oxidation and hot corrosion testing of the prepared specimens.

Cyclic oxidation experiments involved testing of a variety of alumina-forming alloys and coatings with and without EBPVD TBCs for times up to that causing failure. Apparatus for hot corrosion testing was constructed but the actual testing is being included as a part of a separate UTSR project begun at the University of Pittsburgh in August, 2004.

Task V: Nondestructive Evaluation of Coating Systems
This Task involved using a number of nondestructive techniques to attempt to determine the amount of degradation of exposed systems. Specimens of René N5 with platinum aluminide coatings were exposed and examined by x-ray diffraction (XRD) and piezospectroscopic measurements of the stress in the alumina scale and by optical backscatter measurements to detect scale damage. Specimens of René N5 with a platinum aluminde coating and a TBC were exposed over a range of cycles and have undergone piezospectroscopic and optical backscatter measurements. Substantial improvements were made in the XRD stress measurement technique . Recent information regarding an error in the published elastic constants for alumina have necessitated recalculation of previously-determined stresses.

Task VI: Destructive Evaluation of Coating Systems
This Task was directed at documenting the amount of degradation present in specimens using destructive techniques. The main technique employed was an indentation test for TBC system interfacial toughness developed under a previous DOE ATS grant. This technique was used to track the toughness of as-received TBCs and TBCs exposed to a wide range of thermal cycles. The use of the nondestructive techniques of SEM charging and optical backscatter to image the debond produced by indentation improved the accuracy of the toughness measurements.

Task VII: Definition of Effective Nondestructive Evaluation Procedures
This Task consisted of selecting those nondestructive techniques, which are most effective in describing degradation. As documented in previous semi-annual reports, for coating systems without TBCs, acoustic emission has proven to be an effective nondestructive test. For coating systems with TBCs subjected to cyclic loading, piezospectroscopy has emerged as an effective nondestructive test for tracking the evolution of mechanical damage below the TBC (leading to loss of TBC adhesion).

Task VIII: Modeling and Prediction of Failures
This Task involved using the data from the nondestructive and destructive tests to develop models of the degradation processes and to attempt to predict coating lives. This effort involved using the COSP Model, developed at NASA, as the basis for the prediction. Acoustic emission measurements were used to obtain critical parameters in the model from short time experiments. As noted in previous semi-annual reports, substantial progress has been made in improving this modeling.

Task IX: Definition of Optimized Coatings for Specific Applications
This Task was directed at specifying coating compositions and processing procedures to optimize performance for specific applications. This task was performed using data from the other tasks.

This project offers the following benefits to the gas turbine industry: a) development and definition of metallic coatings and TBCs for use under specific gas turbine conditions, b) description of nondestructive tests to assess damage in coatings and TBCs, c) development of lifetime prediction models, d) close collaboration between

universities, national laboratories, and industrial coatings manufacturers and users, and e) a strong educational component contributing to the education of two Ph. D students. Two Ph. D degrees have been awarded during this project: Dr. Matthew J. Stiger (UPitt) and Dr. Qin Ma (CMU).

PROJECT DESCRIPTION

In the next generation gas turbine, resistance to thermal cycling damage may be as important as resistance to long isothermal exposures. Moreover, metallic coatings and Thermal Barrier Coatings (TBCs) may encounter attack by deposits arising from combustion of low-grade fuel and air borne impurities. Finally, there is currently a need for nondestructive techniques to assess metallic coating and TBC degradation and damage as a result of exposure to cyclic oxidation and hot corrosion.

The focus of the project is:

- Development of a mechanism-based testing methodology for improving the oxidation and hot corrosion resistance of high temperature metallic coatings and TBCs.
- Incorporation of a significant number of nondestructive tests in this methodology directed at assessing coatings degradation and damage accumulation.

The overall objectives of this program were to establish a mechanistic understanding of how the durability of oxidation resistant coatings and TBCs is affected by exposures to degradation conditions likely to be encountered in the operation of advanced gas turbines and develop approaches for minimizing detrimental effects on component lifetimes and predicting remaining lives of exposed coatings.

More specifically the goals were to use existing testing techniques and develop new techniques, particularly nondestructive ones, to

1.Evaluate the adhesion of alumina to MCrAlY and aluminide coatings.
2.Understand the degradation mechanisms of TBCs under thermal cycling conditions.
3.Evaluate the hot corrosion mechanisms of the coatings and the effect of intermittent exposure to hot corrosion conditions on cyclic oxidation resistance. (The bulk of this work will be completed under a UTSR grant that began at the University of Pittsburgh in August 2004).
4.Use the test data to model the degradation mechanisms of the coatings and extend the experimental results in a predictive manner.
5.Propose a limited number of improvements to existing coatings (compositions and processing) and evaluate their performance.

The University Turbine Systems Research (UTSR) program, the University of Pittsburgh and Carnegie Mellon University partnered with industry and several national laboratories in the development of a mechanism-based testing methodology for improving the oxidation, resistance of high temperature metallic coatings and TBCs. This testing methodology involved a significant number of nondestructive tests directed at assessing coatings degradation and damage accumulation. Metallic coatings on

superalloys were prepared by Praxair Surface Technologies and Howmet Inc. The coatings were tested and microstructurally characterized at the University of Pittsburgh and Carnegie Mellon University. Nondestructive testing of exposed specimens were performed at Oak Ridge National Laboratory (ORNL) and Argonne National Laboratory (ANL) as well as the University of Pittsburgh.

The project involved the following specific tasks. Task I was concerned with processing comparisons and modifications using state-of-the art-coatings. Task II involved compositional modifications of the state of the-art coatings. Task III consisted of selection and preparation of a TBC system. Task IV was concerned with oxidation and hot corrosion testing of the prepared specimens. Task V involved using a number of nondestructive techniques to attempt to determine the amount of degradation of exposed systems. Task VI was directed at documenting the amount of degradation present in specimens using destructive techniques. Task VII consisted of selecting those nondestructive techniques, which are most effective in describing degradation. Task VIII involved using the data from the nondestructive and destructive tests to develop models of the degradation processes and to attempt to predict coating lives. Task IX was directed at specifying coatings compositions and processing procedures to optimize performance for specific applications.

The project team members and their areas of responsibility were as follows. Professors Pettit and Meier of the University of Pittsburgh led the effort and performed corrosion studies and acoustic emission and x-ray diffraction experiments. Professor Beuth of CMU performed indentation and impact tests and fracture mechanics analysis. Dr. Michael Lance of ORNL performed piezospectroscopic stress measurements and Dr. William Ellingson of ANL performed optical backscatter experiments. Specimens were prepared by Praxair and Howmet. GE provided input on testing conditions for the various degradation modes.

This project offers the following benefits to the gas turbine industry: a) development and definition of metallic coatings and TBCs for use under specific gas turbine conditions, b) description of nondestructive tests to assess damage in coatings and TBCs, c) development of lifetime prediction models, d) close collaboration between universities, industrial coatings manufacturers, and e) a strong educational component contributing to the education of graduate and undergraduate students in areas important to gas turbine technology.

EXPERIMENTAL

Materials

A nickel-base single-crystal superalloy substrate, René N5, was studied.

Four coatings on this substrate were studied. These were:

A NiCoCrAlY Overlay Coating
Diffusion Aluminide and Platinum-modified Aluminide Coatings
A TBC with NiCoCrAlY Bond Coat
A TBC with Platinum-modified Aluminide Bond Coat

Evaluation Techniques

Destructive

Cyclic Oxidation Experiments

Cyclic oxidation exposures were performed in two furnaces, a bottom-loading furnace and a vertical tube furnace, in laboratory air. The initial exposures involved one-hour cycles between 1100°C and approximately 35°C. Failure of the TBC-coated specimens was taken as the time at which a significant amount of the TBC has separated from the substrate. Failure of the specimens without TBC coatings was taken as the time at which the mass change of the specimen reaches negative values.

Indentation Tests

Indentation tests [1, 2] were also performed on the specimens. The test, shown schematically in Figure 6, consists of indenting the TBC system with a Brale type conical indenter (a Rockwell hardness tester or mechanical testing machine can be used for this purpose). The indenter penetrates the TBC and oxide layers and plastically deforms the metallic bond coat and substrate below. As illustrated in Figure 3 (as viewed from above), this induces an axisymmetric debond of the TBC and oxide layers.

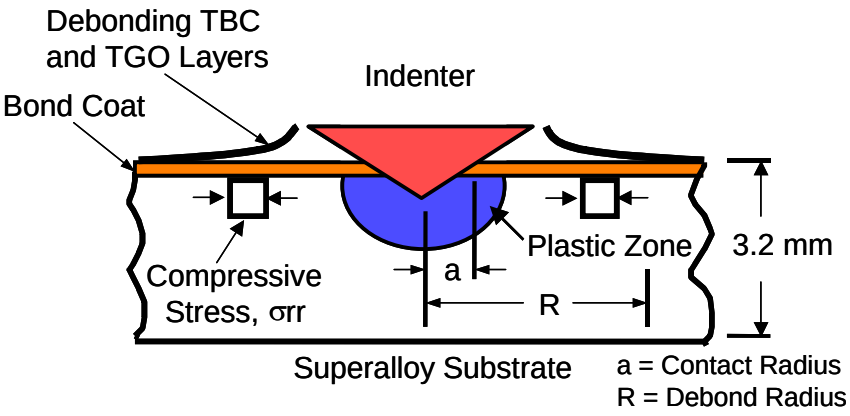

Figure 6. Schematic diagram of the indentation test.

Nondestructive

Stress Measurement by X-ray Diffraction

The stresses in the oxide films grown on specimens without TBCs were measured by x-ray diffraction (XRD). The stress normal to the free surface of a film is usually assumed to be zero. Neglecting shear stresses, the resulting biaxial stress can be expressed quite simply for an isotropic elastic medium, as described by Noyan and Cohen [3]. The quantities measured are strains, which can be measured by XRD as a change in lattice spacing with inclination with respect to the surface of a sample. This strain is usually expressed as:

$$\varepsilon_{\phi\psi} = \frac{d_{\phi\psi} - d_o}{d_o} \tag{1}$$

in which d_o is the stress-free lattice spacing of the selected (hkl) planes and $d_{\phi\psi}$ is the lattice spacing of these (hkl) planes for a given tilt ψ. It can be shown that this strain is expected to be proportional to $\sin^2\psi$. For an equal biaxial stress in the irradiated layer, equation 1 can be expressed as [3]:

$$\frac{d_{\phi\psi} - d_o}{d_o} = \tfrac{1}{2} s_2(hkl)\sigma_o \sin^2\psi + 2s_1(hkl)\sigma_o, \tag{2}$$

where $\frac{1}{2}s_2$ and s_1 are the x-ray elastic constants and σ_o is the biaxial stress in the oxide scale. A number of $d_{\phi\psi}$ are measured over a range of ψs to establish the classical d vs. $\sin^2\psi$ relation. This multipoint relation reduces the error of d_o compared to a single point method. If the $\sin^2\psi$ curve is linear, as is expected from an isotropic surface layer which is polycrystalline and not textured, the stress in any direction ϕ can be calculated from the slope of the measured d vs. $\sin^2\psi$ relation.

Another benefit of using the multipoint method is only one of the x-ray elastic constants is required. Two models have been proposed to average the response of the alumina grains to the average stress. Both models assume a random distribution of crystal orientations. The Voigt model assumes that the all grains are subjected to identical strains and the following relation exists[4] for hexagonal crystals

$$\tfrac{1}{2}s_2 = \frac{15}{7C_{11} + 2C_{33} - 5C_{12} - 4C_{13} + 12C_{44}} \tag{3}$$

where the C_{ij} are the single crystal elastic constants of stiffness for alumina. The other, the Reuss model, assumes a uniform stress in all grains and the $1/2s_2$ is determined from

$$\begin{aligned}\tfrac{1}{2}s_2(hkl) = {} & \tfrac{1}{2}(2S_{11} - S_{12} - S_{13}) - \tfrac{1}{2}(5S_{11} + S_{33} - 3S_{44} - S_{12} - 5S_{13})a_{33}^2 \\ & + \tfrac{3}{2}(S_{11} + S_{33} - S_{44} - 2S_{13})a_{33}^4 + 3S_{14}a_{22}a_{33}(3a_{11}^2 - a_{22}^2)\end{aligned} \tag{4}$$

where S_{ij} are the compliance constants for single crystal alumina. Previous work on this project was used to evaluate the relative accuracy of the Voigt and Reuss models for calculating the x-ray elastic constants. However, we have recently been alerted by colleagues [5] that a recent study [6] has detected a sign error in one of the elastic constants for alumina in the data used in every laboratory [7]. This has necessitated recalculation of all the stress values determined in this study. This work is proceeding.

Capabilities were developed at the University of Pittsburgh in four XRD stress measurement methods. These methods are the classical tilting and rocking techniques, which are equivalent and are based on the determination of the $\sin^2\psi$ curves. In the third method, the tilting method has been extended to thinner films by the use of fixed low incidence techniques. An XRD machine with an open Eulerian cradle provides the tilting of the specimen in symmetrical diffraction ("classical" method) or asymmetric diffraction with fixed low incidence. The rocking technique is performed on a powder machine. The powder machine and the dual arm are also used with a hot stage.

The design of the powder machine and the hot stage make it desirable that the specimen be nearly horizontal during high temperature experiments. For this purpose a new fixed (low) incidence XRD technique, the fixed incidence multiplane method (FIM), using more than one set of (hkl) planes has been developed. Usually for residual stress measurements, one (hkl) plane is tilted (or rocked) in order to measure the strain at various angles to the surface. With fixed incidence and a fixed specimen, diffraction occurs for different sets of (hkl) planes with different inclinations with respect to the surface thus providing the equivalent of the tilting or rocking in other methods.

The four methods were tested at room temperature and shown to give equivalent results. They have already been used for the measurement of residual stresses in chromia and alumina scales. The room temperature data are well behaved i.e. the $\sin^2\psi$ plots are good straight lines with no splitting or oscillation [8-10]. Results for alumina scales on

FeCrAl alloys are in close agreement for the calculated residual stresses with data obtained by piezospectroscopy [9]. The FIM method has been shown capable of application to the measurement of growth stresses at temperatures to 1100°C while still maintaining the advantages of the $\sin^2\psi$ analyses of the diffraction data [9].

Stress Measurement by Piezospectroscopy

Stresses in the alumina scales formed on specimens with and without TBCs were measured by piezospectroscopy by Dr. Michael Lance at ORNL. Aluminum oxide formed by high temperature oxidation invariably contains a minor concentration of chromium, either as a result of it being an alloying addition or as an impurity in the alloy. On oxidation, chromium is incorporated as Cr^{3+} into the aluminum oxide crystal structure, substituting for Al^{3+} and occupying an octahedral site. When appropriately stimulated, for instance with a laser beam or an electron beam, the chromium ion luminesces, emitting two particularly intense, narrow lines, the R_1 and R_2 lines. In the absence of any strain, the R_1 and R_2 lines have energies of 1.790 and 1.794 eV at room temperature.

When aluminum oxide is strained, the oxygen octahedra around the Cr^{3+} are distorted which, in turn, alters the crystal field of the d^3 electrons in the Cr^{3+} ions and thereby the energies of the R_1 and R_2 lines. The shift in energy of the luminescence spectrum with strain is termed the piezospectroscopic effect. For small strains, the shift in the R lines can be written phenomenologically in terms of the stress as:

$$\Delta\nu_{stress} = \Pi_{ijkl}\sigma^{c}_{ij} \tag{5}$$

where $\Delta\nu$ is the shift, expressed as a frequency, σ^{c}_{ij} is the stress and Π_{ijkl} is the piezospectroscopic tensor. When the stress is a hydrostatic pressure, the frequency shift is linearly related to the pressure and the equation reduces to the well-known equation used in the high pressure community to monitor the pressure in high pressure, diamond anvil cells. Since the frequency shift is related through equation 5 to the stress, equation 3 can be inverted so as to determine the stress from a measurement of the frequency shift. This is the basis of the piezospectroscopic measurement of stresses in alumina films proposed in this work.

In the technique pioneered by Prof. D. R. Clarke at UCSB [11], an optical probe is used to excite the R-line luminescence and the luminescence is recorded from all the Cr^{3+} ions within the probed volume. Thus, the measured frequency shift is the integration of the frequency shifts from the individual Cr^{3+} ions and the local stress within the probed volume. In addition, for polycrystalline materials, the probed volume, if it is larger than the grain size, also includes different orientations of the Cr-O octahedra. As a result, it can be shown that the measured frequency shift is related to the average stress within the probed volume as:

$$\overline{\Delta\nu} = \Pi_{ii}\langle\sigma_{ii}\rangle \tag{6}$$

An important feature of equation 6 is that the frequency shift is related to the trace of the stress tensor not simply the hydrostatic pressure. Thus, if the orientation of the stress field is known, for instance, for a thin film on a substrate well away from the edge, the stress field is biaxial, and so equation 6 can be used directly to measure the biaxial stress.

The precision of measurement depends on the accuracy to which the piezospectroscopic coefficients can be determined and the precision to which the frequency shift can be measured. The piezospectroscopic coefficients, including nonlinear terms, have been determined [12]. The accuracy of the frequency measurements depends on the spectral resolution of the spectrometer used as well as the temperature dependence of the spectrometer. It was found that the stress in single crystals of sapphire can be measured to ± 20 MPa and in polycrystalline films to ± 40 MPa. By using a focused optical probe, for instance, using an optical microscope or fiber optic, measurements can be made down to regions a few microns across.

A number of comparisons have been made between measurements of the stress in alumina films, grown by high temperature oxidation, made by X-ray diffraction and piezospectroscopy with good agreement [9].

Optical Backscatter Experiments

Experiments to evaluate thermal cycling damage or as-fabricated damage at the interfaces between the thermally grown oxide, the underlying metallic coating and/or the overlying TBC were performed by Dr. William Ellingson and Mr. Robert Visher at Argonne National Laboratory using an optical backscatter technique.

In this technique, polarized light from a laser is focused on the specimen. Because the materials under study are optically translucent, light from the laser can penetrate below the surface and back scatter out through the surface to a high sensitivity light detector. The backscattered radiation is acquired as the specimen is moved in the x and y directions, which gives the effect of the laser being rastered across the specimen surface. The backscattering process seems to be sensitive to variations in the topography at the interface between the TGO and the substrate, including debonds at the TGO-substrate interface. Now by analyzing the data from the high sensitivity detectors, primarily by looking at the x-y scan data as a two-dimensional statistical array, ANL computes the statistical parameter, C_v, the coefficient of variation , for each data set. By looking at the coefficient of variation as a function of the number of thermal cycles, a relationship can be established between the Cv and number of thermal cycles. Thus, in principle, with a reasonably strong experimental data base, one can predict damage that has been produced by thermal cycling well before specimen failure.

Acoustic Emission Measurements

Cracking caused by cyclic oxidation can be detected in-situ using acoustic emission measurements. The AE equipment used was the commercially available Physical Acoustic Group AEDSP-32/16B acquisition and processing hardware with the

Mistras-2000 data acquisition software. A R15 transducer with the frequency range from 100 to 1000Hz was attached to a stainless steel cone. The cone acts as a transition from the transducer diameter to the Pt-wave guide diameter of 1mm. This 80cm wave-guide was necessary for this application because of the incompatibility of the transducer and the high temperatures in the furnace. The apparatus used is shown schematically in Figure 7.

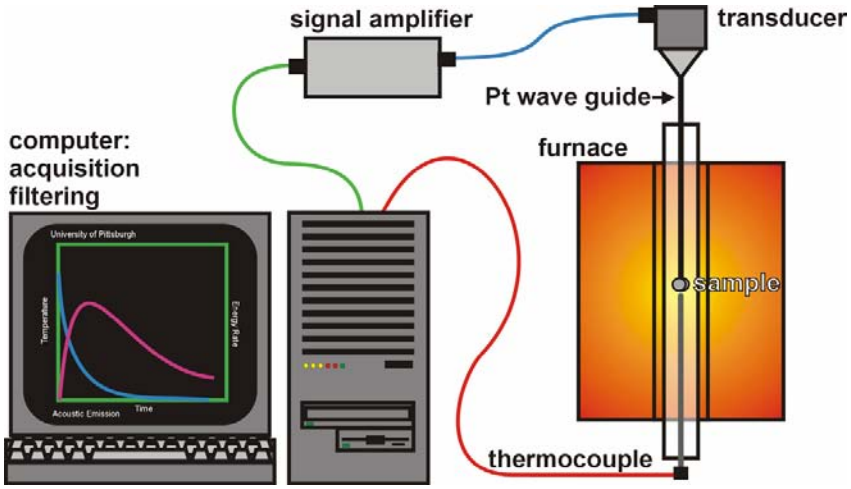

Figure 7. Acoustic Emission Testing Apparatus.

Modeling

A number of models have been created to describe the isothermal growth kinetics of oxide scales, but to describe the cyclic oxidation behavior, Lowell et. al. [13] have developed COSP (Cyclic Oxidation Spall Program). COSP is a statistical model that deals with each cycle as a step in an iterative process of growth and spallation of the scale. Two versions of this model exist as the uniform layer and Monte Carlo versions. The uniform layer version treats spallation of the oxide during cooling as fracture within the oxide and followed by loss of continuous top layer of oxide. The Monte Carlo version effectively divides the surface of the oxide into discrete elements and spallation occurs independently for each element. Although the uniform layer version is mathematically simple, the Monte Carlo version is a better representation of observed oxide spallation as independent areas.

Both versions of the COSP model follow similar steps but a description of the uniform layer method will be described in the following. Oxide growth behavior follows the isothermal growth kinetics to determine the weight of the oxide after the heating portion of the cycle prior to cooling, W'r. During the subsequent cooling step of the cycle, a portion of the oxide will spall with a mass of Ws. After the cycle is complete, the total mass of the oxide retained, Wr, is the starting point for the next cycle as graphically shown in Figure 8a.

In the COSP model, the fraction, F, of the oxide that spalls is proportional the amount of oxide that is present where

$$F = Qo \cdot W'r. \tag{7}$$

Here Qo is introduced as the spall constant and the expression for the weight of the spalled oxide is

$$Ws = F \cdot W'r. \tag{8}$$

With the W'r and Ws for this cycle, the Wr can then be calculated by

$$Wr = W'r - Ws. \tag{9}$$

Monitoring the amount of retained and spalled oxide through the duration of the calculations, mass change curves can then be calculated and the effect of Qo on these curves is shown Figure 8b.

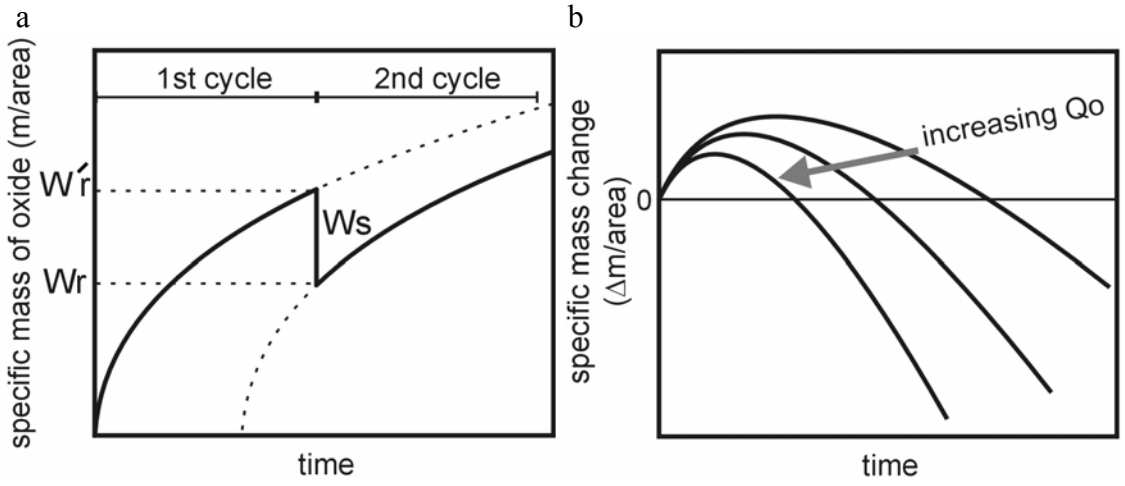

Figure 8. Graphical representation of important parameters in the COSP model.

In the Monte Carlo version, the surface of the sample is divided into separate areas and the growth and spallation of the oxide is treated independently for each area. This treatment allows complete oxide loss to expose the metallic substrate over discrete areas on the specimen. The amount of surface are that exhibits spallation is handled in a probabilistic manner. On a per surface unit basis, Wr' is similar to the UL version, yet the fraction of the spalled oxide will be one only when complete spallation occurs. The probability for complete spallation to the metal-oxide interface to occur is determined by

$$P = Qo \cdot W'r. \tag{10}$$

If the condition is met for complete spallation, Ws would equal Wr' and an oxide free surface would be ready for exposure on the next cycle. If no spallation, the oxide would continue to grow on the following cycle according to isothermal kinetics. Behavior of several area units are averaged to determine the behavior of the complete surface and a plot similar to Fig. 8b can be constructed.

RESULTS AND DISCUSSION

The earlier results from this program were presented in the six semi-annual reports [14-19]. These include:

1. Significant advances in the use of x-ray diffraction (XRD) to measure stresses in oxides grown on superalloys and coatings and correlation between stresses measured by XRD and luminescence (at ORNL).
2. Improvement of an indentation technique for measuring the fracture toughness of interfaces in TBC systems. This has been accomplished, in part, by developing SEM charging and optical backscatter techniques (at ANL) for imaging the debond produced by the indentation and measuring the debond radius. Also, the use of different indenter shapes to optimize the measurements for different types of systems has been accomplished.
3. Use of the indentation technique, coupled with stress measurements to characterize the mechanisms leading to toughness loss in TBC systems during thermal cycling. Results show a strong correlation between toughness loss caused by mechanical damage above, below and within the TGO layer and reductions in stress measured by piezospectroscopy.
4. The indentation test has been used to elucidate the effects of bond coat surface preparation on TBC degradation
5. Use of acoustic emission measurements to detect damage occurring in superalloys and coated superalloys at short times during thermal cycling and combining these measurements with modification of a spalling life model COSP (developed at NASA) to form the basis for a life prediction protocol.
6. For coating systems without TBCs, acoustic emission (coupled with TGA measurements and COSP modeling) has emerged as an effective nondestructive testing technique. For coating systems with TBCs subjected to cyclic loading, piezospectroscopy has emerged as a potentially effective nondestructive test for tracking the evolution of mechanical damage below the TBC (leading to loss of TBC adhesion).

The following section updates results obtained since the previous report.

1. Previous work on this project was used to evaluate the relative accuracy of the Voigt and Reuss models for calculating the x-ray elastic constants. However, we have recently been alerted by colleagues [5] that a recent study [6] has detected a sign error in one of the elastic constants for alumina in the data used in every laboratory [7]. This has necessitated recalculation of all the stress values determined in this study. This work is proceeding and will be submitted as a journal publication.

2. One of the objectives of the present study was to develop improved methods for hot corrosion testing. Hot corrosion testing apparatus has been constructed. However, a UTSR project focusing on hot corrosion degradation was begun at the University of Pittsburgh in August 2004 (UTSR Project 04 01 SR116) and the hot corrosion testing is being performed under the new project.

Technology Transfer

The results of this program have been disseminated in a variety of ways. This includes six Semi-annual UTSR Reports, two journal article articles:

Q. Ma, J. L. Beuth, F. S. Pettit, G. H. Meier, and M. J. Stiger, "Use of Indentation Fracture Tests to Investigate Toughness Loss Mechanisms in Thermal Barrier Coating Systems", Coatings 2005 (Nitin Padture, Lorraine Francis, Janet Hampikian and Narendra Dahotre, eds.) Proc. Materials Science and Technology 2005, Pittsburgh, September 2005, pp. 3-6.

M. J. Stiger, G. H. Meier, F. S. Pettit, Q. Ma, J. L. Beuth, and M. J. Lance "Accelerated Cyclic Oxidation Testing Protocols for Thermal Barrier Coatings and Alumina-Forming Alloys and Coatings" Materials and Corrosion, 27, 1-13 (2006).

and two Ph D theses:

Qin Ma, "Indentation Methods for Adhesion Measurement in Thermal Barrier Coating Systems", Ph D Thesis, Department of Mechanical Engineering, Carnegie Mellon University, 2004.

Mathew J. Stiger, "Correlation of Short-Term to Long-term Oxidation testing for Alumina Forming Alloys and Coatings", Ph D Thesis, Department of Materials Science and Engineering, University of Pittsburgh, 2004.

The results have also been described in over twenty oral presentations. These include UTSR Workshops, Professional Society Meetings and seminars at the laboratories of gas turbine manufacturers and coating vendors.

REFERENCES

1. A. Vasinonta, and J. L. Beuth, Engineering Fracture Mechanics, 68, 843 (2001).
2. R. A. Handoko, J. L. Beuth, G. H. Meier, F. S. Pettit, and M. J. Stiger, "Mechanisms for Interfacial Toughness Loss in Thermal Barrier Coating Systems," Durable Surfaces, D.R. Mumm, M. Walter, O. Popoola and W.O. Soboyejo, eds., Proceedings of the Materials Division Symposium on Durable Surfaces, 2000 ASME International

Mechanical Engineering Congress and Exposition, Orlando, November, 2000, Trans Tech Publications, Switzerland, pp.165-183.
3. I. C. Noyan and J. B. Cohen, Residual Stresses, Springer-Verlag, (1987).
4. P. D. Evenshor, W. Frohlich and V. Hauk, Z. Metallde., 62, 38 (1971).
5. Private Communication, D. Hovis and A. Heuer, Case Western Reserve University, 2005.
6. J. R. Gladden, J. H. So, J. D. Maynard, P. W. Saxe, and Y. LePage, Appl. Phys. Letters, 85, 392 (2004).
7. J. Wachtman, Jr., W. Tefft, D. Lam, and R. Stinchfield, J. Res. Natl. Bur. Stand., Section A, 64, 213 (1960).
8. E. Schumann, C. Sarioglu, J. R. Blachere, F. S. Pettit, and G. H. Meier, Oxid. Metals, 53, 259 (2000).
9. C. Sarioglu, G. H. Meier, F. S. Pettit, J. L. Smialek, J. R. Blachere, and C. Mennicke. "The Effects of Reactive Element Additions, Sulfur Removal, and Specimen Thickness, on the Oxidation Behavior Of Alumina-forming Ni- and Fe-base Alloys", Materials Science Forum, 251-254, 405 (1997).
10. C. Sarioglu, J. R. Blachere, F. S. Pettit, and G. H. Meier, "Room Temperature and In-Situ High Temperature Strain (or Stress) Measurements by XRD Techniques", Microscopy of Oxidation 3 , B. Newcomb and J. A. Little, eds., The Institute of Materials. London, 1997, p. 41.
11. D. M. Lipkin and D. R. Clarke, Oxid. Metals, 45, 267 (1996).
12. J. He and D. R. Clarke, J. Am. Ceram. Soc. 78, 1347 (1995).
13. C. E. Lowell, C. A. Barrett, R. W. Palmer, J. V. Auping, and H. B. Probst, Oxid. Metals, 36, 81 (1991).
14. F. S. Pettit, G. H. Meier, and J. L. Beuth, "Mechanism-Based Testing Methodology For Improving the Oxidation, Hot Corrosion and Impact Resistance of High-Temperature Coatings for Advanced Gas Turbines", First Semi-Annual Report on UTSR Project 02-01-SR101, November, (2002).
15. F. S. Pettit, G. H. Meier, and J. L. Beuth, "Mechanism-Based Testing Methodology For Improving the Oxidation, Hot Corrosion and Impact Resistance of High-Temperature Coatings for Advanced Gas Turbines", Second Semi-Annual Report on UTSR Project 02-01-SR101, May, (2003).
16. F. S. Pettit, G. H. Meier, and J. L. Beuth, "Mechanism-Based Testing Methodology For Improving the Oxidation, Hot Corrosion and Impact Resistance of High-Temperature Coatings for Advanced Gas Turbines", Third Semi-Annual Report on UTSR Project 02-01-SR101, November, (2003).
17. F. S. Pettit, G. H. Meier, and J. L. Beuth, "Mechanism-Based Testing Methodology For Improving the Oxidation, Hot Corrosion and Impact Resistance of High-Temperature Coatings for Advanced Gas Turbines", Fourth Semi-Annual Report on UTSR Project 02-01-SR101, May, (2004).
18. F. S. Pettit, G. H. Meier, and J. L. Beuth, "Mechanism-Based Testing Methodology For Improving the Oxidation, Hot Corrosion and Impact Resistance of High-Temperature Coatings for Advanced Gas Turbines", Fifth Semi-Annual Report on UTSR Project 02-01-SR101, February, (2005).
19. F. S. Pettit, G. H. Meier, and J. L. Beuth, "Mechanism-Based Testing Methodology For Improving the Oxidation, Hot Corrosion and Impact Resistance of High-

Temperature Coatings for Advanced Gas Turbines", Sixth Semi-Annual Report on UTSR Project 02-01-SR101, May, (2005).

ADVANCED SENSOR APPROACHES FOR MONITORING AND CONTROL OF GAS TURBINE COMBUSTORS

FINAL REPORT
FOR THE PERIOD 1 MAY 2002 – 31 OCT 2005

PIS: JERRY SEITZMAN AND TIM LIEUWEN

DEC 2005

DOE AWARD: DE-FC26-02NT41431

UTSR PROJECT: 02-01-SR102

GEORGIA INSTITUTE OF TECHNOLOGY

SCHOOL OF AEROSPACE ENGINEERING

ATLANTA, GA. 30332 – 0150

jerry.seitzman@aerospace.gatech.edu

tim.lieuwen@aerospace.gatech.edu

ABSTRACT

This report describes sensing strategies that were developed for monitoring the health and performance of gas turbine combustors. Sensor systems based on these approaches enable control and monitoring systems that improve combustor reliability and operability, achieve optimal performance (e.g., lower NO_x emissions) over extended periods of time, reduce maintenance, prevent forced outages, and increase engine life. Specifically, we developed methods to: 1) sense imminent loss of static combustor stability, e.g., precursors to flame loss or lean blow out; 2) determine local fuel-air ratio and heat release variations that can arise from mixedness variations; and 3) sense the proximity of the combustor to its dynamic stability margin, i.e., detecting how close the system is to the point where detrimental combustion instabilities would occur. The approaches involve a combination of nonintrusive optical and acoustic sensing, as well as ion concentration probes. The methods were evaluated for their applicability in natural gas and syngas fueled combustors. In addition to tests in our laboratory, field tests of the stability margin sensing were pursued with industrial partners.

TABLE OF CONTENTS

I. EXECUTIVE SUMMARY

This report covers the development of sensing strategies for monitoring gas turbine combustor health and performance. These new sensing capabilities will enable the development of control systems that actively manage engine condition and compensate for changes in ambient conditions or system degradation. Used for monitoring purposes, they will help gas turbine operators more quickly identify potential system problems, before they become serious, and allow them to vary conditions to remove the problem. Used as long term monitors of system operation, they can be used to help schedule required maintenance. Thus the development of these advanced sensor capabilities will improve combustor reliability and operability, achieve optimal performance, lower NOx emissions, reduce maintenance costs, prevent forced outages and increase system life.

Our approach was to develop methods to extract relevant combustor performance and status information from the light and sound naturally produced by the combustion processes. For example, some of the chemical reactions involved in combustion produce molecules in electronically excited states that give off light as they decay to their ground state. This is called chemiluminescence, and one example is the blue light produced by most hydrocarbon flames. Similarly, the turbulence and fluctuations in the heat released by the combustion processes are sources of sound (acoustics) in a gas turbine combustor. These optical and acoustic emissions can easily be monitored without requiring the placement of sensors directly into the most hostile regions of the flow. Furthermore, acoustic and optical sensors are already employed to some extent in currently fielded industrial gas turbines. We also explored ion current sensing that could be added to combustor igniters. We measured the sensor signatures of a number of different types of combustors as a function of operating conditions, such as fuel-air ratio, pressure, temperature, flow velocity, and system stability. We then used physics-based analysis methods to relate these system parameters to changes we observed in the sensor outputs.

Sensor methods were developed and tested for three specific applications: 1) sensing proximity static combustor stability loss (lean blow out); 2) determining local flame zone variables such as fuel-air ratio variations that can arise from unmixedness; and 3) sensing combustor dynamic stability margin, i.e., detecting how close the system is to the point where detrimental combustion instabilities would occur. The static stability sensing was successfully demonstrated for optical, acoustic and ion sensing in various combustors and for both natural gas and syngas fueled systems. The approach relies on capturing precursor events using a simple and robust thresholding method. Flame zone sensors for local fuel-air ratio monitoring were demonstrated for lean natural gas fueled combustors based on properly corrected ratios of CH and OH chemiluminescence. For lean ($\phi<0.7$) syngas systems, similar results can be obtained with the ratio of CO_2 and OH chemiluminescence. In addition, physics-based modeling of the combustion process was used to predict the chemiluminescence, which should allow further improvements in this sensing approach. Finally, dynamic stability margin sensing, based on dynamic pressure measurements, was demonstrated in various combustors by monitoring the decay of the autocorrelation at the known combustor instability frequencies. This method has been field tested in cooperation with industrial partners. The method was also extended to unstable operation conditions to help operators or control systems rapidly recover stable operation should instabilities occur.

II. PROJECT DESCRIPTION

II.A. Overall Needs and Benefits

This project involves the development of sensing strategies for monitoring gas turbine combustor health and performance. These sensing capabilities will enable control systems that actively manage engine condition and compensate for changes in ambient conditions or system degradation. Such monitoring systems will also be useful for isolating system problems and for scheduling engine maintenance. Thus the development of advanced sensor capabilities is expected to lead to: improvements in combustor reliability and operability, optimal performance (e.g., lower NO_x emissions) over extended periods of time, reduced maintenance downtown or forced outages, and increased combustor life.

II.B. General Approach

Combustor health and performance monitoring requires strategies that involve sensing conditions in the combustor, rather than downstream, especially when injector-to-injector variations are important. Given the harsh combustor environment, non-intrusive sensors are the most viable candidates. Since a combustor naturally produces light and sound, both can be monitored without requiring the placement of sensors directly into the most hostile regions of the flow.

While there are a number of sources for electromagnetic radiation from a combustor, the source most directly connected to the combustion reactions is chemiluminescence. This radiation is from (electronically) excited molecules that are produced by the oxidation reactions and which can relax to lower energy states by emitting light. Since the intensity of emission is proportional to the chemical production rate of the particular molecule, the chemiluminescence intensity can be related to chemical reaction rates.[1] For this reason, chemiluminescence has been used previously as a rough measure of reaction rate and heat release rate.[2-5] Chemiluminescence can provide information on the presence and strength of the combustion process in a specific region of the combustor. Also, it inherently has a fast time response providing fast detection of flame instability events. Acoustic radiation can be produced by combustion through temporal fluctuations in volume expansion in the flame zone due to changes in heat release rates. It has been shown by previous researchers that acoustic emissions from turbulent combustion processes are dominated by unsteady heat release processes as opposed to flow noise.[5, 6,7] Thus acoustic sensing can detect events associated with changes in the overall heat release rate and some details of dynamics of combustion at several time scales.

Since the combustor naturally produces light and sound, and they can be monitored without requiring the placement of sensors directly into the most hostile regions of the flow, this program is focused on developing the capability for interpreting the electromagnetic and acoustic waves radiated by the combustion processes. Furthermore, acoustic and optical sensors are already employed to some extent in some currently fielded industrial gas turbines. For example, a number of gas turbines are equipped with ports for measurements of acoustic pressure.

Ion concentration measurements can also provide useful diagnostics into (unsteady) combustion reaction characteristics.[8,9] It is widely accepted that during combustion, radicals from the fuel and oxidizer undergo chemi-ionization reactions[10] (e.g., CH + O =

$HCO^+ + e^-$) to produce ions (like HCO^+) and free electrons e^-, enabling the flow of electrical current through hydrocarbon flames. A typical flame ionization sensing technique consists of at least two electrodes arranged such that a voltage potential can be applied across the flame, or a part of the flame, and the induced current through the flame is measured. The probe therefore responds to the ion emission intensity, which is related to (specific) chemical reaction rates and is a rough measure of the heat release rate in the combustor.[11] Thus, ion probes can provide information on the presence and strength of the combustion process in a specific region of the combustor, making them suited for health monitoring and diagnostics.

II.C. Specific Sensing Issues and Approaches

This research program consists of three main tasks, involving both experimental and analytic efforts.

Task 1. Transient Flame Holding Event Sensors

The first task was development of methods for sensing transient flame holding events, such as imminent blowout. This will allow turbine engines to operate closer to the lean limit and hence, with lower NO_x emissions. The current, standard approach is passive control through combustor design or load scheduling. In this approach, one must ensure that the turbine operates within a conservatively *estimated* safety margin from the lean blowout point because of system uncertainties, fuel composition variability, system wear, or ambient condition changes. With an active control system that employs blowoff precursor detection, the system's operating point can be adjusted to prevent flame blowoff and loss of operability while achieving optimal performance. The approach in this case was to measure acoustic, optical emissions from the flame, and electrical signals from an ion sensor, under various operating conditions (and in multiple combustors), and analyze the results using a physical model of blowout.

This work was motivated by observations that the combustion process exhibits enhanced unsteadiness while transitioning between the static stability and blowout.[12-14] However, the primary focus of the pre-existing literature on the subject was devoted to predicting the blowout limits of a given system as a function of such parameters as equivalence ratio, air temperature, or pressure.[15-19] Little work had been done to characterize the combustion processes as it transitions from static stability to blowout.

Task 2. Flame Zone Sensors

The second task involved development of sensor approaches for monitoring local *reaction zone* equivalence ratio and heat release rate. Because key performance metrics, such as NO_x emissions and pattern factor, are directly related to locally richer packets of fuel or non-uniformity in heat release, the development of these sensing capabilities, combined with a control system, will provide increased hot section life and reduced pollutant emissions. Our approach is to use the light produced by the chemical reactions in the flame (chemiluminescence). First, we characterized the chemiluminescence of high-pressure, preheated natural gas combustion systems as a function of operating conditions. Then, we determined the dependence of the chemiluminescence signature on various combustor conditions, such as equivalence ratio and heat release.

Task 3. Combustor Dynamics Stability Margin Sensors

The third task involved sensing the proximity of the combustor to its dynamic stability margin, i.e., detecting how close the system is to the point where detrimental combustion instabilities would occur. Generally when turbines are being commissioned or during routine operation, the operator has no real-time information on how the relative stability of the system is affected by changes to fuel splits or other operating conditions (unless, of course, the system actually becomes unstable – leading to possible damage or shutdown). Dynamic stability margin sensors provide an online measure of the turbine stability. This diagnostic is achieved by measurement and advanced signal processing of the flame's acoustic signatures. The basic approach is to compute the autocorrelation function (i.e., the inverse Fourier transform of the power spectral density), and determine (primarily) the decay of its envelope.

III. EXPERIMENTAL

III.A.Combustors Overview

A number of combustors were employed in this effort. By studying multiple combustor geometries we increased the likelihood that the sensor methodologies developed here are robust. The first system is an atmospheric pressure, open burner, shown in Figure 1. The burner is supplied with air from compressed air tanks. The supply air passes through a plenum containing lined baffles for reducing flow noise. The duct transitions to a diverging/converging section to change the duct diameter from its supply value to the desired burner diameter. This section is followed by a straight section for flow conditioning. Fuel is introduced either after the baffle section, or near the exit in order to vary the amount of premixing. The figure shows a pilot stabilized configuration, where an array of closely spaced external pilot flames are placed around the burner exit. Besides this current circumferential piloting, several additional flameholding schemes can be examined, including swirl and bluff body approaches.

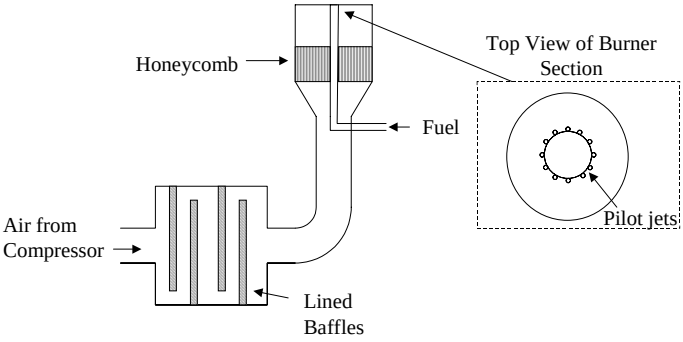

Figure 1. Simplified schematic of open burner assembly.

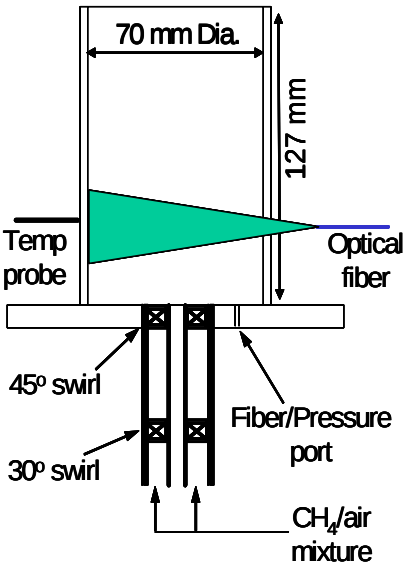

Figure 2. Atmospheric-pressure, swirl-stabilized gas turbine model combustor.

A confined, atmospheric pressure combustion is also being used (see Figure 2). It includes many of the attributes of a lean,

premixed gas turbine combustor, including a swirl inlet and a dump plane. In this design, a combustible mixture of fuel (methane or natural gas) and air flow passes through swirl vanes housed in a 22 mm i.d. tube, producing a swirl number of ~0.4. Upon leaving the swirler, the flow expands into a cylindrical, quartz combustor of 70 mm i.d.. The combustor typically operates with an average (post-combustion) gas velocity of 6-9 m/s.

The third combustor is a small scale, high pressure gas turbine combustor simulator (see Figure 3). This facility is designed to simulate conditions in typical gas turbine combustors, i.e., the air is preheated, the fuel is injected, the two are premixed and pass through a swirler. It can operate at pressures up to 30.4 kPa (30 atm) with air preheated up to 540 °C (1000 °F). The swirlers can be readily swapped out to determine the effect of different design parameters such as blade angle on the flow characteristics. The centerbody can be changed from a single outlet piloting type nozzle to one with multiple radial holes on its surface for active combustion control experiments. Also, the flow area can be varied in order to have different expansion ratios. The combustor is also optically accessible through the two side windows (one of which can be seen in the figure) as well as from the exhaust; i.e., both side and "end on" imaging of the flame is possible. This combustor was operated on both natural gas and synthetic fuel gas.

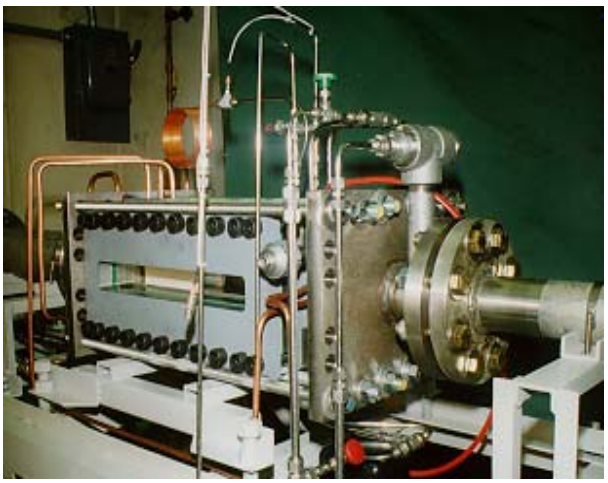

Figure 3. Georgia Tech high pressure gas turbine combustor simulator.

A simpler jet flame apparatus was also used for studying synthetic gas fuels (see Figure 4). The desired fuel composition is first prepared using a bank of calibrated rotameters, one for each gas. After mixing thoroughly, the fuel is split into two flows: the desired flowrate of fuel passes through another rotameter (calibrated for the particular fuel composition), while the remainder is flared in a diffusion flame. Finally, the required quantity of air is added, and the mixture goes to the burner. This arrangement allows simple control over the equivalence ratio (ϕ) and the average velocity through the burner. All the rotameters are calibrated with a bubble flow meter to $\pm$ 1% accuracy, with fuel flows in the range of 0.1 to 5 slpm. The reactants are preheated by electrical resistance tape wrapped around the burner. Once the desired reactant temperature is achieved (as

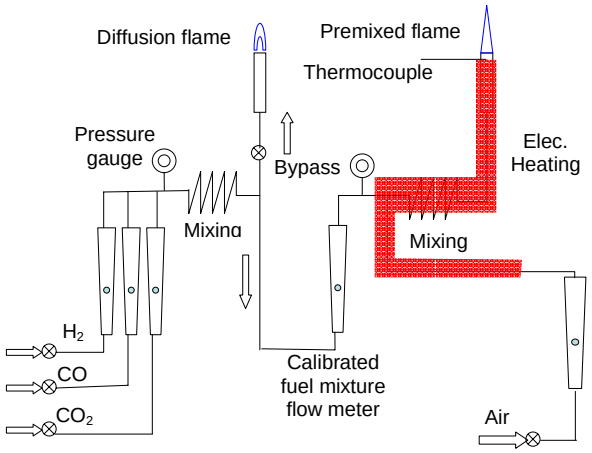

Figure 4. Apparatus for fundamental synthetic gas fuel measurements.

determined by a type-K thermocouple temporarily placed at the burner exit), the surface temperature of the burner is monitored by a second thermocouple and held constant by a temperature controller.

Some experiments were also performed on an atmospheric pressure, single cup swirl combustor (Figure 5)**.** Non-vitiated, preheated air is supplied to the swirl cup from a plenum chamber. Air enters the combustor through counter-rotating swirlers, while the fuel is injected through a centrally located fuel nozzle. This is followed by a small annular passage leading to the test section. Liquid fuel was used for all tests.

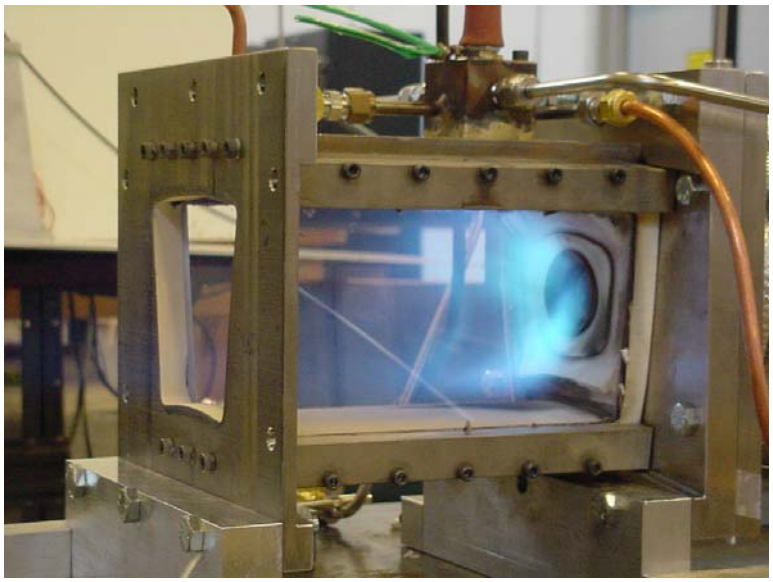

Figure 5. Single swirl-cup combustor.

III.B. Measurement Approaches

As noted above, the sensing approaches are based on measurement of the optical and acoustic radiation from the combustors. The optical signatures were measured using a variety of techniques. For measurement of "complete" optical spectra, we employed an imaging spectrometer. The spectrometer, with a 300 groove per mm grating, is coupled to a 1024×256 multi-element detector (intensified CCD). The system can simultaneously capture emission spectra from ~280–550 nm. The light is captured from the combustors using fiber optic inputs, to resemble more closely the behavior of a practical sensor. With this sensor, flame spectra can be acquired at a range of pressures, inlet air temperatures and equivalence ratios, but with relatively low temporal resolution (~10 Hz). Temporal variations in the spectral signature are measured using a group of miniature photomultipliers, with built-in amplifiers (bandwidth of 20 kHz) to convert the detector current to voltage. In this case, the optical collection also occurs through a fused silica optical fiber. The radiation passes through different interference filters to isolate specific spectral bands, e.g., a filter centered at 308 nm with a full-width-half-maximum of ~10 nm collects ultraviolet emissions from the OH $A^2\Sigma$-$X^2\Pi$ transition.

The acoustic radiation is measured by monitoring the acoustic pressure oscillations. Pressure oscillations are measured with Kistler pressure transducers (Model 211B5). For the flame holding measurements, a single transducer is used. For the dynamic stability sensing, two transducers are used, one in the inlet section and one in the combustor. The transducers are mounted 33.2 cm upstream and 5.1 cm downstream of the conical flame holder, respectively. The latter transducer is flush mounted and water-cooled. More recently, acoustic oscillations for sensing flame stability were measured with calibrated,

Bruel and Kjaer type 4939 condenser microphones that have a flat frequency response up to 40 kHz.

The ion measurement work reported here was performed in a collaborative program with Woodward Industrial Controls, which was partially funded by Woodward.

IV. Results And Discussion

IV.A. Transient Flame Holding (Blowout) Event Sensors

In previous work, we had shown that either optical (chemiluminescence) or pressure signals could be used to detect blowout precursors in swirl combustors. In this work, we first measured simultaneous optical and acoustic signals, or simultaneous acoustic and ion sensor signals from the two atmospheric-pressure, swirl-stabilized combustors. The combustor's proximity to blowout was controlled by varying the fuel and air flowrates (equivalence ratio). A well-defined combustion region was visible for the stable flames. Close to blowout, near flame loss events are occasionally observed.

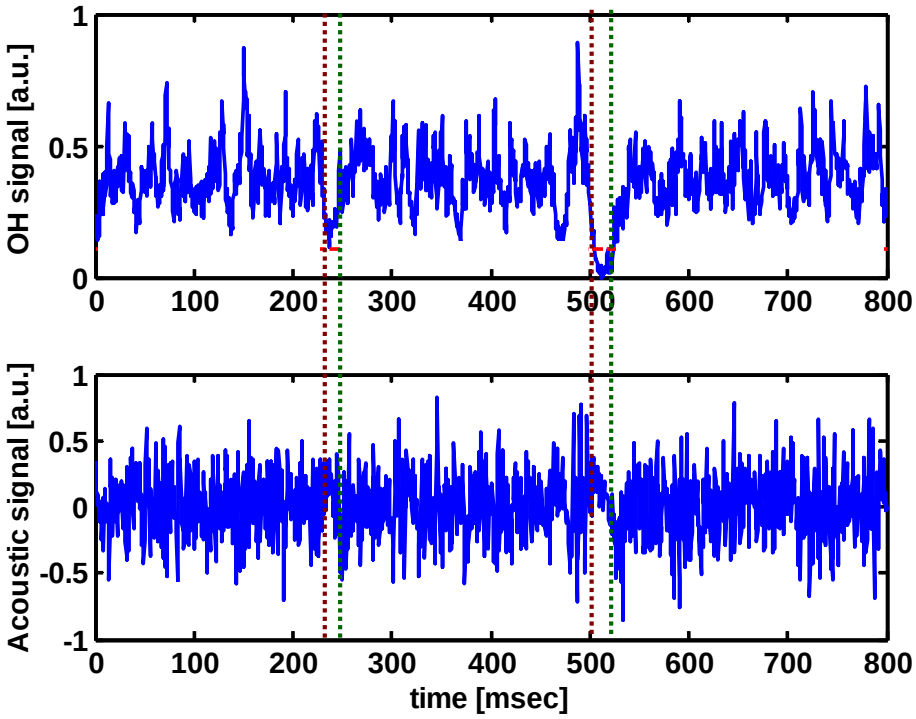

Figure 6. Comparison of optical and acoustic signals near lean blowout in a swirl stabilized combustor operating at atmospheric pressure.

As indicated in Figure 6, strong precursor events are simultaneously can be detected by multiple types of sensors (optical and acoustic in this case). During the precursor events, the flame disappears from part of the combustor. Then, the radiation signal re-appears, suggesting re-ignition of the unburned fuel. These extinction and re-ignition events span a period of several to tens of milliseconds, depending on the combustor and operating conditions. The events are nonperiodic and occur prior to blowout. As the lean blowout limit is approached, the frequency and duration of these events increase.

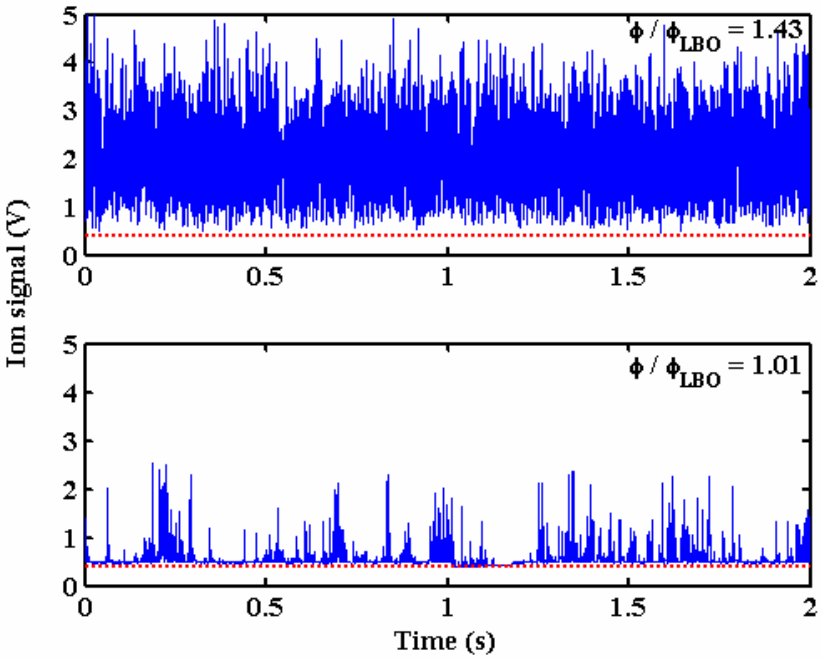

Figure 7. Ion signal from the burner for ϕ/ϕ_{LBO} = 1.43 (stable case) and 1.01 (close to blowout).

This work represents the first use an ion sensor to capture the events previously sensed using optical and acoustic approaches. Figure 7 shows ion signals obtained at two conditions, ϕ/ϕ_{LBO}=1.43 and 1.01, where ϕ_{LBO} is the equivalence ratio at lean blowout. The mean ion concentration decreases with equivalence ratio in this case, as the fuel flow rate is reduced here and therefore decreases heat release. As the combustor was brought closer to its blowout limit, the ion emissions occasionally dropped to its "near" zero value (which corresponded to ~0.4V), indicating the occurrence of the short duration, extinction events. These events increased in duration and number as blowout was approached.

IV.A.1 Signal Analysis

In this work, we evaluated various methods for identifying the precursors in the various sensor signals. The most straightforward approach explored to detect these time-localized surges in the signal is thresholding. The basic idea is to count the number of times the instantaneous signal level crosses a threshold value, usually defined as some multiple of the signal's recent mean or standard deviation. Thresholding the data provides a convenient way of converting a data stream into a quantitative blowout indicator; e.g. an LBO avoidance logic can be invoked when the data exceeds a threshold level a certain number of times.

Thresholding worked quite well when applied to the raw optical and ion sensor outputs. Because the acoustic signal is a spatially integrated measure of the unsteady heat release over the entire flame, very pronounced changes in the heat release in a localized region of the flame may not be very evident in the overall signal. As such, we found thresholding techniques to be most useful when performed after wavelet-based filtering of the acoustic data.[20] The advantage of identifying a "customized" wavelet lies in its ability to accentuate the amplitude of time-localized events whose shape resembles that

of the wavelet. An example is shown in Figure 8; the dashed lines correspond to a threshold of 1.02σ (σ is the variance of the wavelet coefficient for the stable combustion case). Near blowout, many more events (threshold crossings) occur. The effect of threshold upon level crossing frequency of the wavelet filtered acoustic signal can be understood from Figure 9, which plots the PDF of the wavelet coefficients for ϕ/ϕ_{LBO} = 1.8, 1.1 and 1.01 at a wavelet scale of 18.5 Hz. The increased presence of high amplitude outliers close to blowout results in the long tail in the PDF. The figure indicates that the signal from the stable flames rarely exceeds ~1σ.

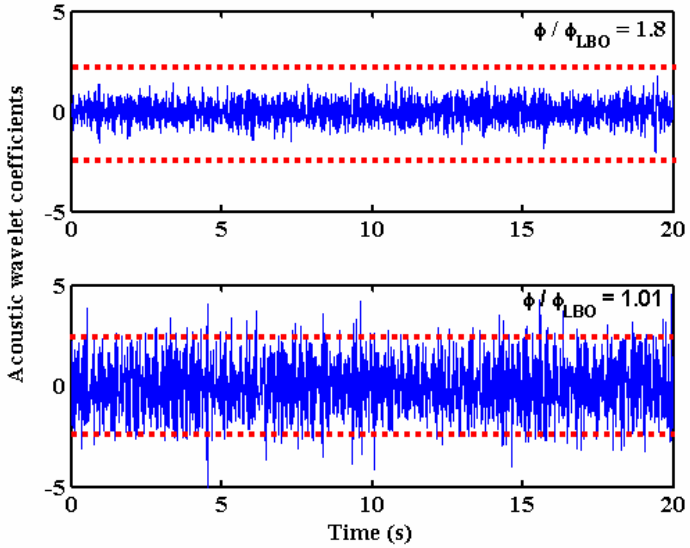

Figure 8. Time dependence of computed $W_2(t)$ wavelet coefficients of acoustic signal at a scale of 18.5 Hz for ϕ/ϕ_{LBO} = 1.8 and 1.01.

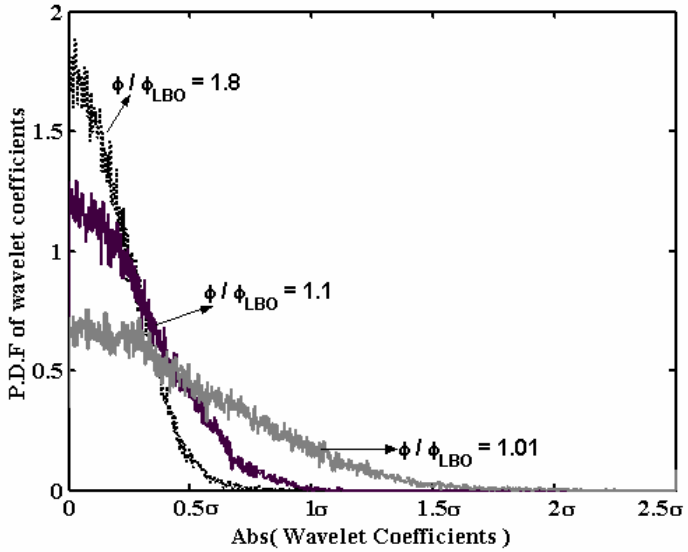

Figure 9. P.D.F of acoustic wavelet coefficients at a scale of 18.5 Hz for of ϕ/ϕ_{LBO} = 1.8, 1.1 and 1.01.

IV.A.1 Results

The ability to determine proximity to LBO is illustrated in Figure 10, which shows the dependence of the number of acoustic events upon ϕ/ϕ_{LBO} at three thresholds: 0.86σ, 1.02σ and 1.21σ. There are two influences of the threshold level: number of events detected and the ϕ/ϕ_{LBO} value where events are first detected. With increasing threshold level, there are fewer events detected. Furthermore, no events are detected until the system is very close to blowout. In contrast, at low thresholding levels, the frequency and duration of the alarms close to blowout is much higher, however, events are detected at equivalence ratios much farther from blowout.

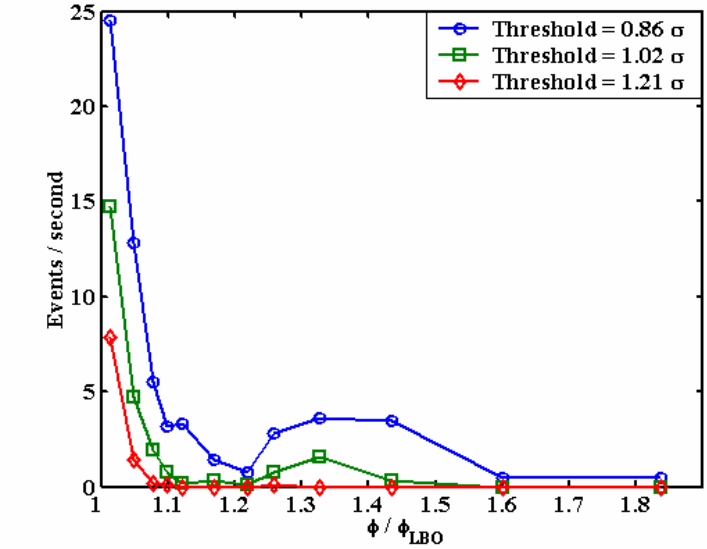

Figure 10. Dependence of the number of acoustic events upon ϕ/ϕ_{LBO} for three thresholding levels of 0.86σ, 1.02σ and 1.21σ.

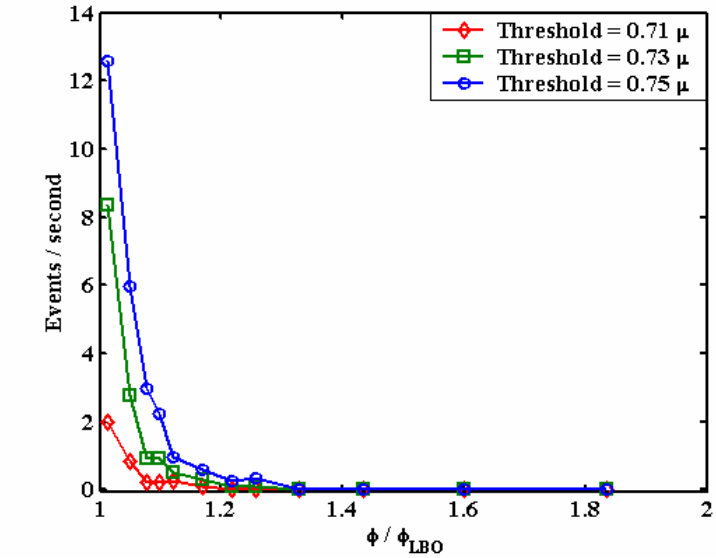

Figure 11. Dependence of the number of ion events upon ϕ/ϕ_{LBO} for three thresholding levels of 0.71μ , 0.73μ and 0.75μ.

Results for thresholding of the raw ion signal are shown in Figure 11 for three (lower) thresholds of 0.71μ, 0.73μ and 0.75μ (where μ is the time-localized mean of the ion signal). The number of events detected clearly increases as LBO is approached. Similar results and tradeoffs as illustrated in the case of the acoustic signal are observed for the ion signal as well.

During the latter part of this effort, our efforts were refocused on extending the blowout precursor sensing to hydrogen-enhanced natural gas combustors and syngas fueled combustors. Experiments were performed in the high pressure, swirl-stabilized gas turbine model combustor with acoustic and optical sensing. Figure 12 shows results obtained for a hydrogen-doped natural gas case. As in the earlier tests, the occurrence of the LBO precursors increases dramatically as the combustor approaches its blowout limit. Figure 13 shows similar result for a syngas mixture. What is dramatically different in the results is the way the precursor rate increase near LBO. For the natural gas case, the rise is relatively gradual, with precursors beginning around $\Delta\phi$=0.02 before the LBO limit. For the syngas case, the rise is much more rapid, with $\Delta\phi$=0.005. While the syngas fuel does produce a more stable combustion, the change in the precursor behavior is primarily limited to the way in which the threshold was chosen for the optical sensor.

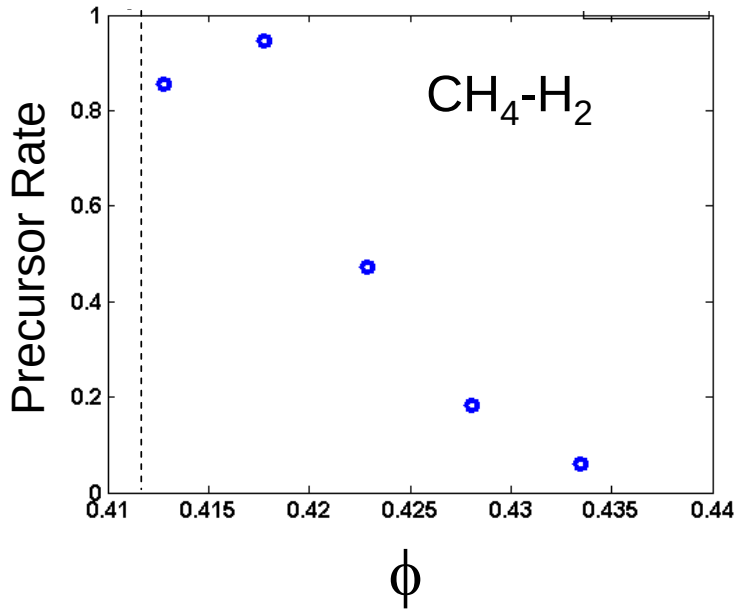

Figure 12. LBO sensor output as a function of operating fuel-air ratio for a natural gas fuel with a small amount of hydrogen added. The combustor was run preheated at a pressure of 1.5 atm. LBO occurs just before an equivalence ratio of 0.41 (as indicated by the dashed line).

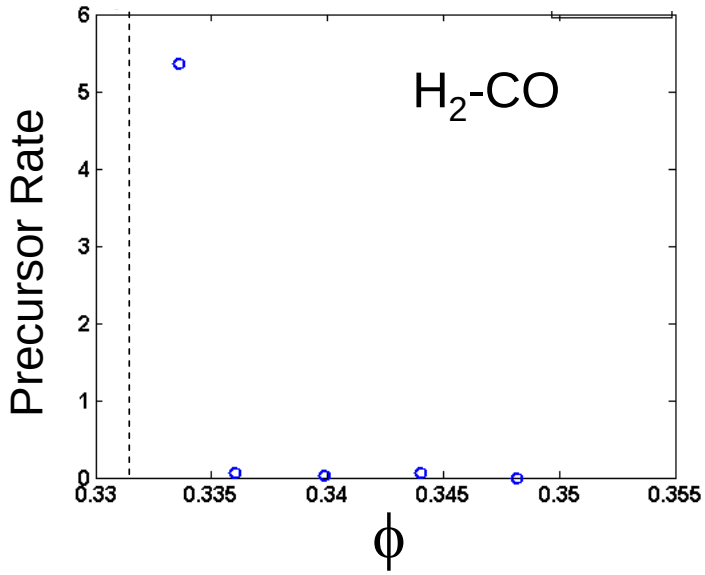

Figure 13. LBO sensor output as a function of operating fuel-air ratio for a syngas mixture. The combustor was run preheated at a pressure of 1.6 atm. LBO occurs just before an equivalence ratio of 0.33 (as indicated by the dashed line).

As part of this effort, we have worked with Alta Solutions, a turbine monitoring company, to code up and test an acoustic technique for monitoring blowout margin. We have shared our code with Alta and several test data sets. They are working to bring this technique to turbine field testing.

IV.B. Flame Zone Sensors

IV.B.1 Natural Gas Combustion

In the initial phase of this work, the flame zone sensing effort focused on examining the ratio of chemiluminescence from different species to monitor equivalence ratio (ϕ). We examined the chemiluminescence signals from the open tube burner (Figure 1), the confined, swirling combustor (Figure 2) and the high pressure, gas turbine combustor (Figure 3). Over most equivalence ratios of interest to modern gas turbines (ϕ<1.1) , CH and OH radiation are the dominant sources in natural gas combustion.

We examined the relative slope sensitivity, *S*, of the chemiluminescence signal, defined as,

$$S = \frac{d\left(CH^*/OH^*\right)}{d\phi}\frac{1}{\left(CH^*/OH^*\right)}$$

where CH^* is the chemiluminescence signal from the CH radical, and OH^* represents the OH chemiluminescence. Figure 14 shows results for methane (99.99% purity) and natural gas in the three combustor. Within the accuracy of the measurements, the difference between methane and natural gas is negligible. Thus small variations in the composition of natural gas should not effect this sensing approach. The good agreement in the various systems also shows that *S* is not a strong function of combustor geometry or overall flow velocity. This apparently universal behavior of the CH^*/OH^* signal was achieved only

when the data are properly corrected for broadband background emission due to CO_2^* chemiluminescence and blackbody (wall) radiation.

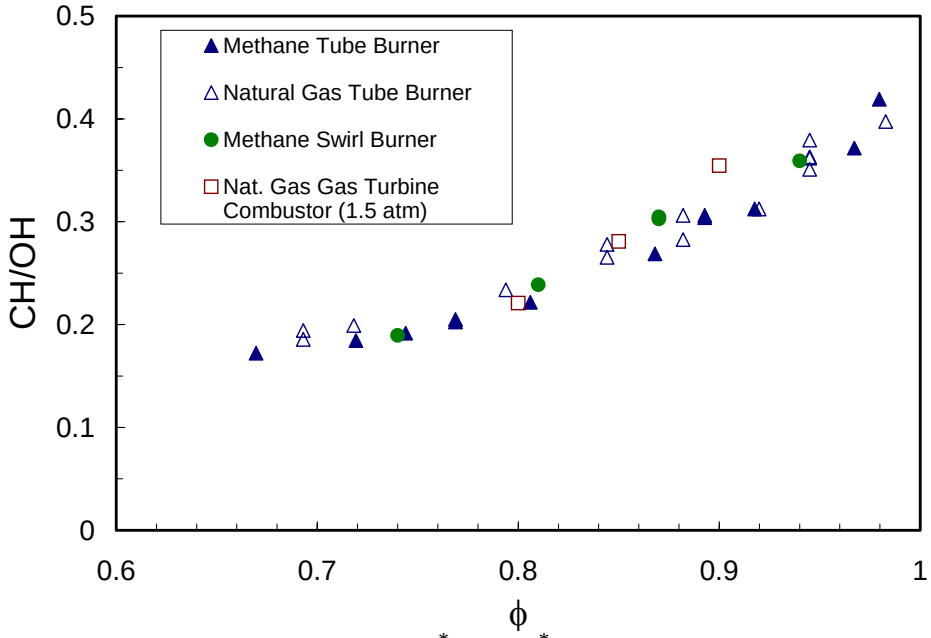

Figure 14. Comparison of the CH^* to OH^* chemiluminescence ratio in the three combustors studied.

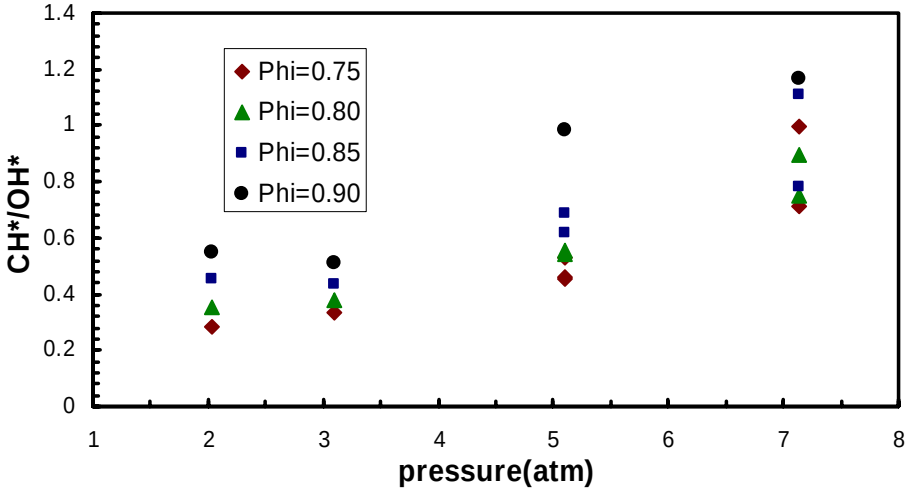

Figure 15. CH to OH chemiluminescence ratio measured in the high pressure, gas turbine combustor simulator at various pressures (absolute) for fixed mass flow rate (30g/s).

We also examined the effect of pressure on CH^*/OH^*. Results were obtained in the Georgia Tech high pressure gas turbine combustor simulator. As indicated in Figure 15, increases in fuel-air ratio still increase CH^*/OH^*. However, increasing the pressure at a fixed fuel/air ratio also generally increases CH^*/OH^*. Thus, use of this approach to monitor equivalence ratio (or fuel-air mixing variations) may also require measurement of the combustor pressure. This requirement is not severe, however, since combustor pressures are normally monitored, and because the sensitivity to pressure is not dramatic.

Figure 16 shows the separate OH^* and CH^* radiation. For lean cases, both signals increase with equivalence ratio (ϕ) and pressure. At higher ϕ, however, the signals drop with pressure. Part of this is likely due to the relative increase in the quenching collision rate of the excited state at high pressures, as compared to the production rates of OH and CH from chemical reactions. However, these results are also influenced by background radiation from the flameholder. At higher pressures, the flame sits on the flameholder, whose temperature therefore increases. This makes the background radiation underlying the (visible) CH* emission much greater than the CH^* signal (Figure 17). Thus, we conclude that some of the pressure dependence observed is due to difficulties in determining the true CH* signal at high pressures, where the flame in the current combustor sits close to the flameholder.

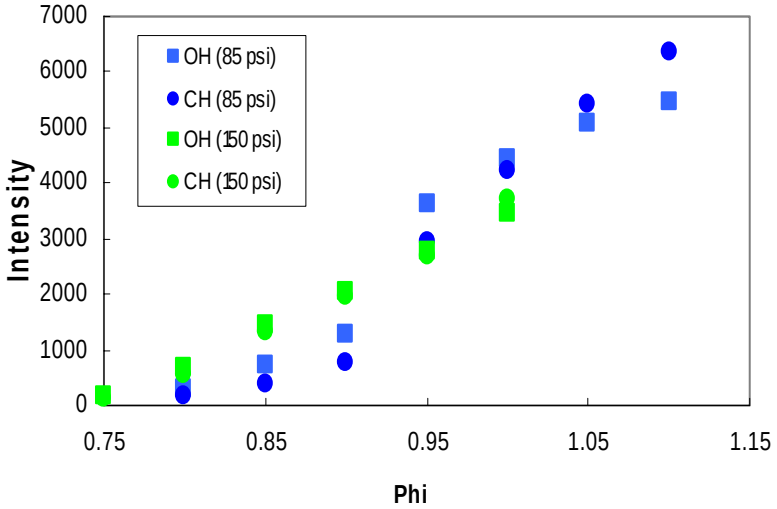

Figure 16. Chemiluminescence from OH* and CH* for a flowrate of 50 g/s at two pressures.

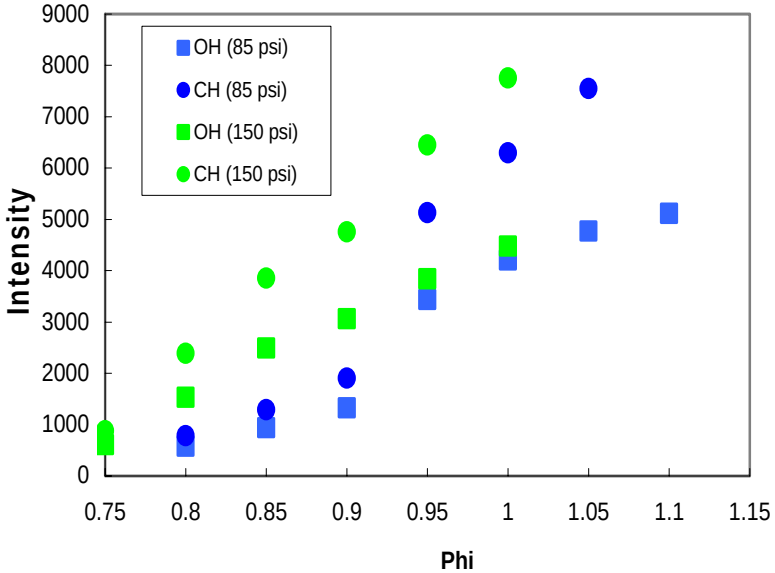

Figure 17. Background signals underlying the OH* and CH* for the same conditions of Figure 16.

IV.B.2 Syngas Combustion and Modeling

During the latter portion of this program, we focused on characterizing chemiluminescence from syngas fueled combustors. Such fuels are usually composed of varying amounts of H_2, CO, CO_2, H_2O and N_2, as well as other trace or minor species. The fuel species in these mixtures are H_2 and CO, while the other gases act primarily as diluents. The primary chemiluminescence species in these flames were found to be OH*, produced primarily through hydrogen oxidation reactions and CO_2*, produced primarily by the combination reaction of CO with O. The OH* emission is the narrow peak at ~310 nm, while CO_2* gives broadband emission centered in the blue part of the spectrum. For the results here, the CO_2^* emission is recorded at 375 nm.

It was found that the ratio, CO^*_2/OH^*, was only a weak function of equivalence ratio. In order to understand this better, we decided to attempt to model the chemiluminescence in this relatively simple chemical mixture. According to Ref. [21], chemiluminescence from CO_2^* can be modeled as a multistep mechanism, written in its simplest form as,

$CO + O + M \leftrightarrow CO_2^* + M$

$CO_2^* \rightarrow CO_2 + h\nu$

$CO_2^* + M \leftrightarrow CO_2 + M$

Assuming the first step proceeds slowly compared to the last step, the volumetric chemiluminescence rate can be modeled as

$$R_{CO_2^*} = k_{CO_2^*}[CO][O]$$

where $k_{CO_2^*}$ is 4.1×10^{29} $e^{-2300K/T}$ (photon/s)(cm^3/mol^2). Similarly, Petersen *et al.*[22] have proposed that OH* emission in hydrogen fueled systems is dominated by the reactions

$H + O + M \leftrightarrow OH^* + M$

$OH^* \rightarrow OH + h\nu$

$OH^* + Q \leftrightarrow OH + Q$

where Q is a third body quencher, e.g., water has a high efficiency as a quencher. Again making the assumption that the chemical formation step proceeds slowly, and the quenching is fast (typical rates would be 10^8-10^9 s), one can write the volumetric chemiluminescence rate as

$$R_{OH^*} = \frac{k_{OH*}}{\sum_i \eta_i T^n e^{-T_i/T}[Q_i]}[H][O]$$

where k_{OH*} is 2.5×10^{39} $e^{-3600K/T}$ (photon/s)(cm^3/mol^2) and η_i, n and T_i depend on the specific quenching species.

We used a laminar flame model (Chemkin PREMIX with GRIMech 3.0) to calculate the variation of T and composition across various syngas flames. Then the chemiluminescence was calculated from the two rate given above. Figure 18 shows results for a specific composition, with the reactants at room pressure and temperature. As expected, most of the chemiluminescence is produced in the reaction zone where most of the heat release occurs.

Figure 19 shows comparisons of our modeling and experiments (also in a laminar flame) for the OH^* and CO_2^* ratio for four fuel compositions and over a range of fuel-air

ratios. Similarly, Figure 20 shows results for preheated and diluted 50:50 CO:H_2 fuel compositions. The agreement between the modeling and experiments is quite remarkable, suggesting that the modeling can be used to better understand and predict the behavior of chemiluminescence sensors in syngas combustors. Both experiments and modeling show little dependence of the chemiluminescence ratio on equivalence ratio for ϕ>0.7. There is a more significant dependence for leaner mixtures, which may be important for undiluted H_2/CO syngas compositions, which would likely be burned in lean mixtures due to the high flame temperatures.

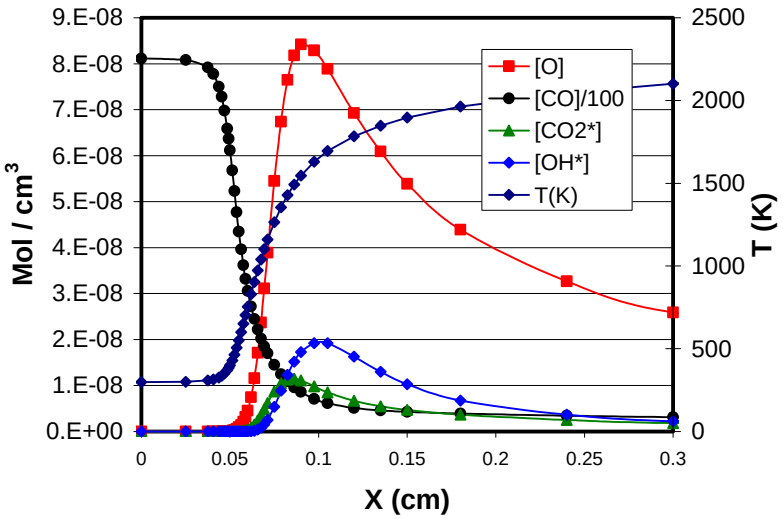

Figure 18. Laminar flame model results for composition, temperature and OH^* and CO_2^* variation across a syngas flame.

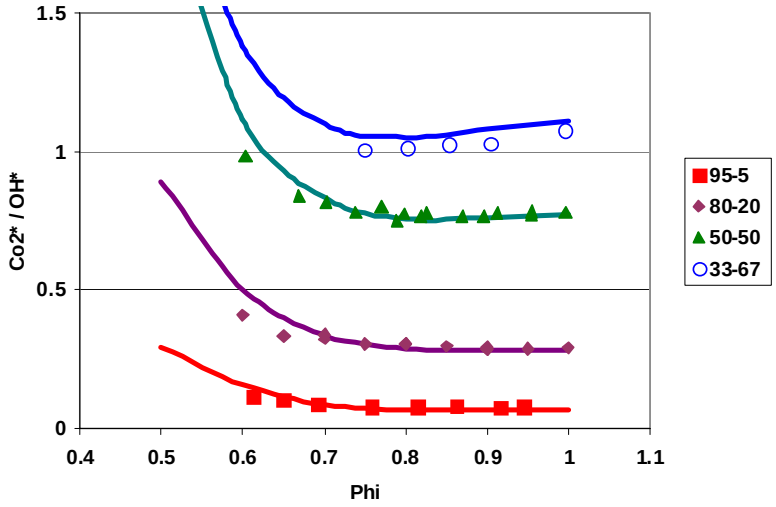

Figure 19. Comparison of model and experimental results for the chemiluminescence ratio CO_2*/OH* for various H_2:CO compositions and equivalence ratios (symbols=exper., lines=model).

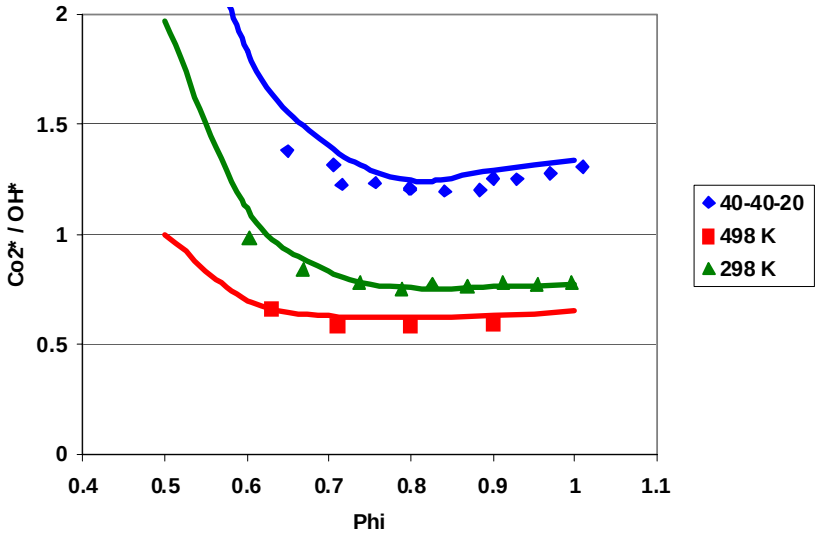

Figure 20. Comparison of model and experimental results for the chemiluminescence ratio CO_2^*/OH^* for a 50:50 H_2:CO composition at two initial temperatures (298 and 498 K), and for 298 K and 20% CO_2 dilution (symbols=exper., lines=model).

The results are also able to predict the absolute CO_2^* and OH^* signals. The results showed that both scale linearly with fuel flow rate for a fixed equivalence ratio, but both increase with increasing fuel-air ratio. Thus, the modeling is able to predict the response of the sensors to heat release rate variations.

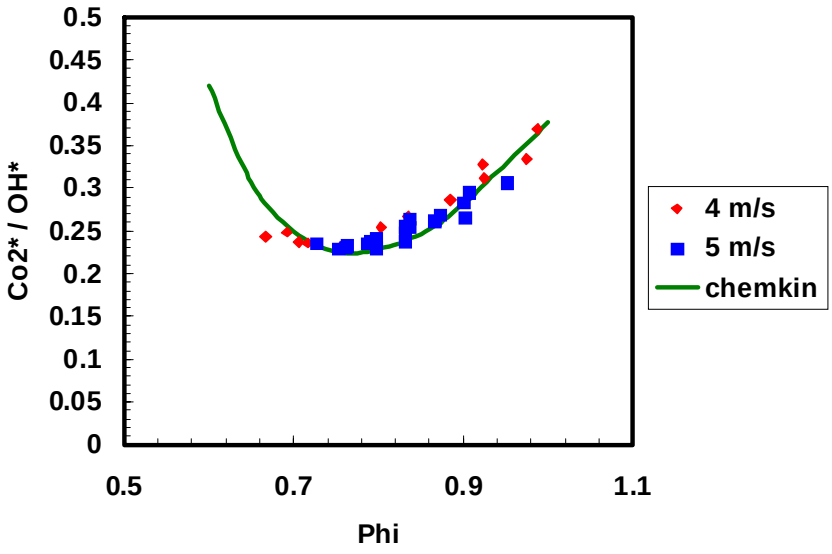

Figure 21. Comparison of model and experimental results for the chemiluminescence ratio CO_2^*/OH^* for methane-air combustion in the swirl-stabilized, atmospheric pressure combustor.

This ability to predict chemiluminescence signals via modeling is a new contribution of this work. The robustness of the method is indicated in Figure 21. We employed the

same modeling approach, except with one step added to the OH* mechanism due to a reaction with CH[23] to model CO_2^*/OH^* for the earlier methane/natural gas results. As in the syngas studies, the modeling results are able to accurately predict the measurements.

IV.C. Combustor Dynamics Stability Margin Sensors

Currently, when turbines are being commissioned or simply going through day to day operation, the operator has no idea how the stability of the system is affected by changes to fuel splits/operating conditions unless, of course, the system actually becomes unstable (which could result in, for example, flame blowoff and complete system shutdown). This point is illustrated in Figure 22 below, which plots combustor pressure amplitude data obtained from Georgia Tech's gas turbine combustor simulator. This figure shows that the combustor was stable and unstable at inlet velocities above and below, respectively, about 23.5 m/s. Suppose now that this system is operated under a stable condition, say at an inlet velocity of 22 m/s. Although the turbine operator will know that the system is stable, they will not, in general, know how close the system is to instability.

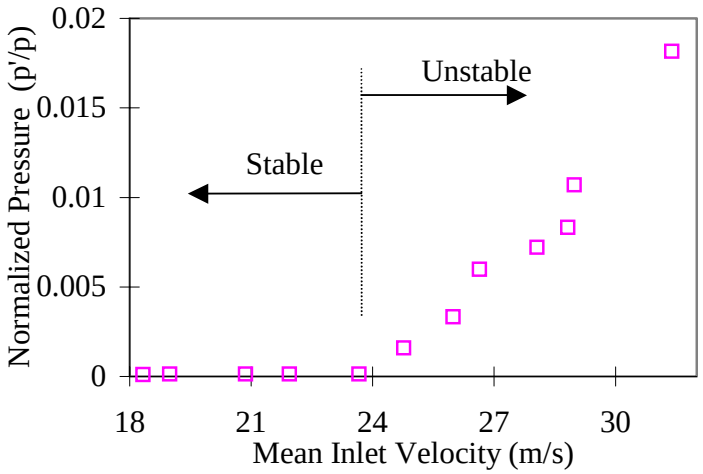

Figure 22. Variation of 630 Hz dynamic pressure amplitude in combustor with inlet velocity. Data obtained from Georgia Tech's gas turbine combustor simulator.

As part of the reported effort, we developed and tested an autocorrelation analysis of pressure data as a methodology for ascertaining stability margin. The autocorrelation of a signal is defined as:

$$C(\tau) = \frac{\int_0^T p'(t)p'(t+\tau)dt}{\int_0^T p'^2(t)dt} \qquad [2]$$

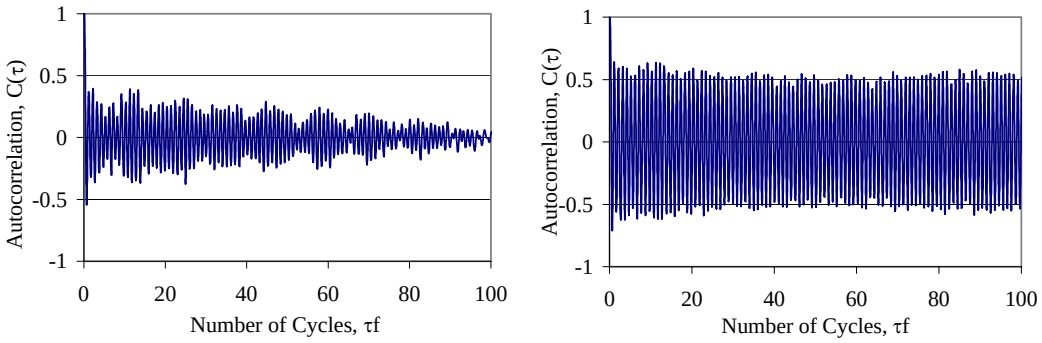

(a) (b)

Figure 23. Dependence of autocorrelation of acoustic pressure measured under stable (Figure 23-a, at inlet velocity of 21 m/s, see Figure 22) and unstable (Figure 23-b, at inlet velocity of 27 m/s) conditions.

IV.C.1 Stable Operation

Figure 23 plots two autocorrelations of the same data shown in Figure 22 measured under stable and unstable conditions. It is important to note the qualitatively different characteristics of these autocorrelations with increasing delay, τ. Under stable conditions, the amplitude of the autocorrelation steadily decays, while it remains relatively constant under unstable conditions. It is this behavior under stable conditions that is of interest here. Under these conditions the oscillations are driven by ambient background noise, but are damped. The decay in autocorrelation is physically due to the fact that this damping causes a loss of "memory" in the system, which causes oscillations at separate time instants to become increasingly uncorrelated. These points are illustrated by referring to the following equation:

$$\frac{d^2p'}{dt^2} + 2\varsigma\omega_o \frac{dp'}{dt} + \omega_o{}^2 p' = \xi(t) \qquad [3]$$

Such a second order oscillator equation resembles that typically used to model small amplitude oscillations in combustion chambers.[24] The variables p', ζ, ω_o, and ξ denote the unsteady pressure, damping, natural frequency, and background noise excitation, respectively. This is a linear equation and is suitable for describing combustor dynamics under *unstable* conditions, because inclusion of nonlinearities is necessary. The Fourier transform of the unsteady pressure described by this equation can be determined using standard techniques in spectral analysis. In turn, once the Fourier transform of the unsteady pressure is known, the autocorrelation, $C(\tau)$ can be determined from the inverse transform of the power spectrum using the Wiener-Khinchin theorem. It can be shown that the autocorrelation of Eq. [3] is given by:

$$C(\tau) = e^{-\omega_o \varsigma \tau}\left(\cos\left(\omega_o \tau\sqrt{1-\varsigma^2}\right) + \varsigma/\sqrt{1-\varsigma^2}\,\sin\left(\omega_o \tau\sqrt{1-\varsigma^2}\right)\right) \qquad [4]$$

The result is an *expression that relates the autocorrelation to the system damping*.

It was found that the autocorrelation decays at a rate that can be modeled as

$$C = e^{-cycles*a} \qquad [5]$$

where *C* is the autocorrelation coefficient, *cycles* is the instability frequency multiplied by time, and *a* is the **slope of the autocorrelation curve**. Because *C* is already calculated by the autocorrelation relationship [4], and the number of cycles is known (for a *known* instability frequency), *a* can be found using simple linear regression between cycles and the logarithm of *C*.

Figure 24 shows the slope trends for the entire range of inlet velocities. In order to see how well the autocorrelation predicts the onset of instabilities, the slope data (circles) is plotted with pressure amplitudes (crosses). It is readily apparent that as instability is approached, the slope data gradually decreases. The pressure data in conjunction with the slope data shows that the autocorrelation analysis not only determines whether or not a combustor is operating stably, it can be used as a method to determine the margin of that stability.

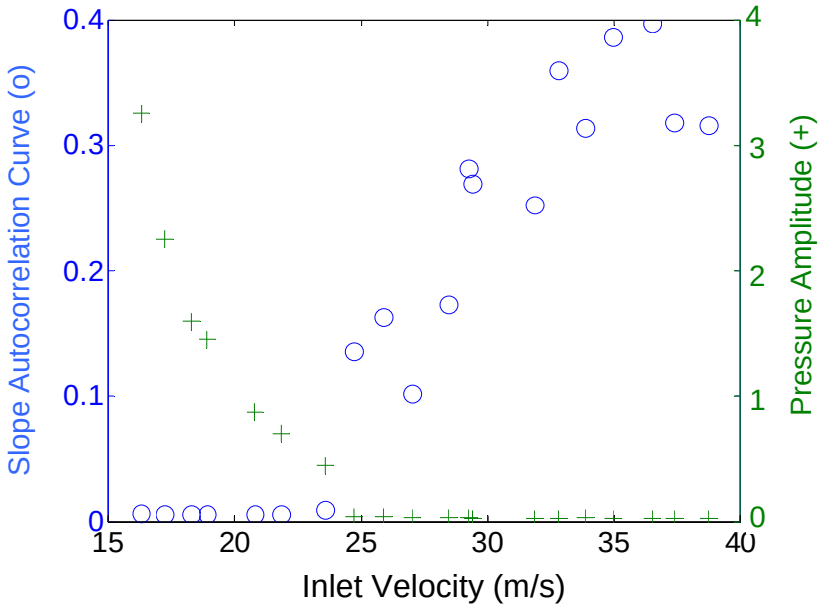

Figure 24. Slope of autocorrelation curve for varying inlet velocities, plotted with pressure amplitudes (Data filtered about 430 Hz)

IV.C.2 Field Testing of Stability Margin Algorithm

This algorithm was licensed to Alta Solutions, a well known turbine monitoring company whose software has been installed on a large number of Westinghouse and GE engines. Alta incorporated our algorithm into a software package compatible with their diagnostics, developed a graphical user interface that the turbine operator could use to adjust algorithm parameters, and implemented it at two beta sites, in cooperation with Calpine Corporation. A screen shot of this software module is illustrated in Figure 25.

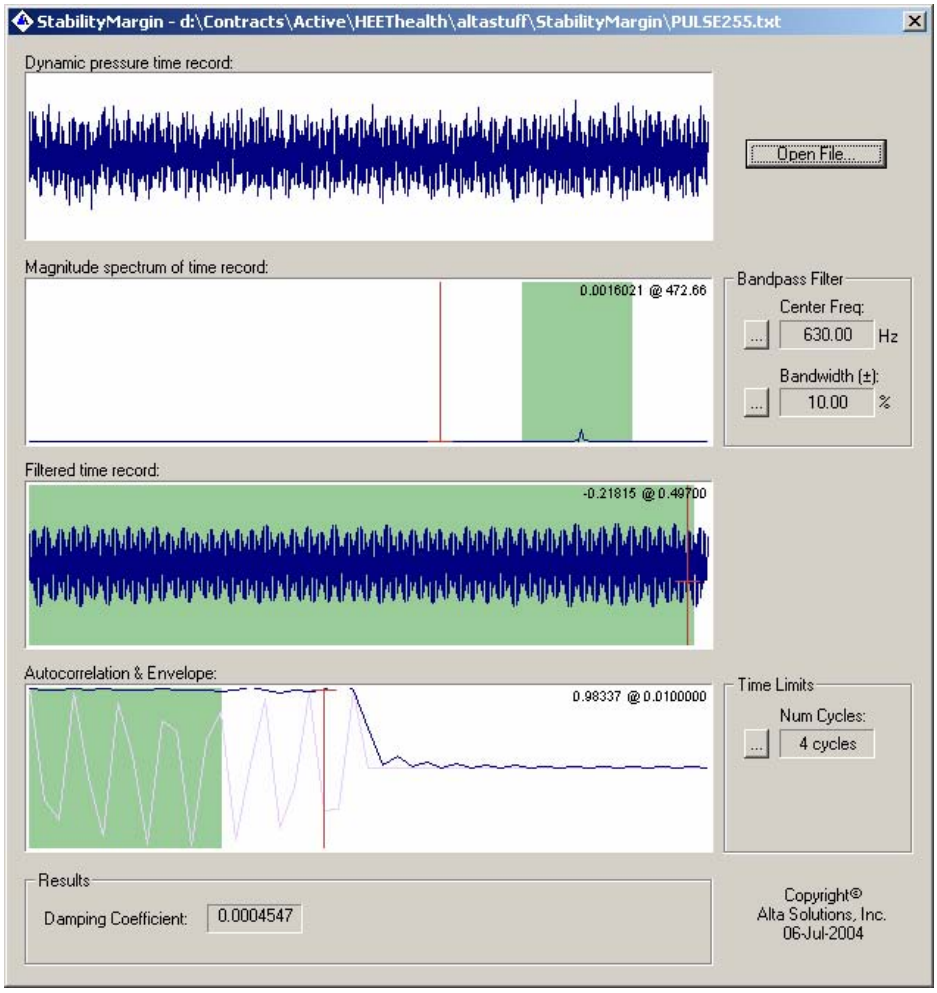

Figure 25. Relation between combustor damping parameter and observed pressure amplitude oscillations.

The Calpine installation data were evaluated, with a key question being the extent to which the algorithm could be used to discern relative differences in stability margin from one combustor can to another. Since combustor cans can acoustically interact, the measurements in each can are somewhat contaminated by others. To address this question, we determined the cross correlation between pressure oscillations measured in different combustor baskets, see Figure 26. This figure shows the correlation between one basket and another spaced a distance apart given by the number on the x axis. For example at a "Distance from Basket" of four, we evaluated the correlation between each combustor and the one 4 cans away from it. The data shows cross correlation values of about 0.35 between baskets next to each other, but that the value drops below 0.15 at larger separations. This data implies that the stability margin from each can is corrupted only by the baskets on either side; baskets farther away make a negligible contribution.

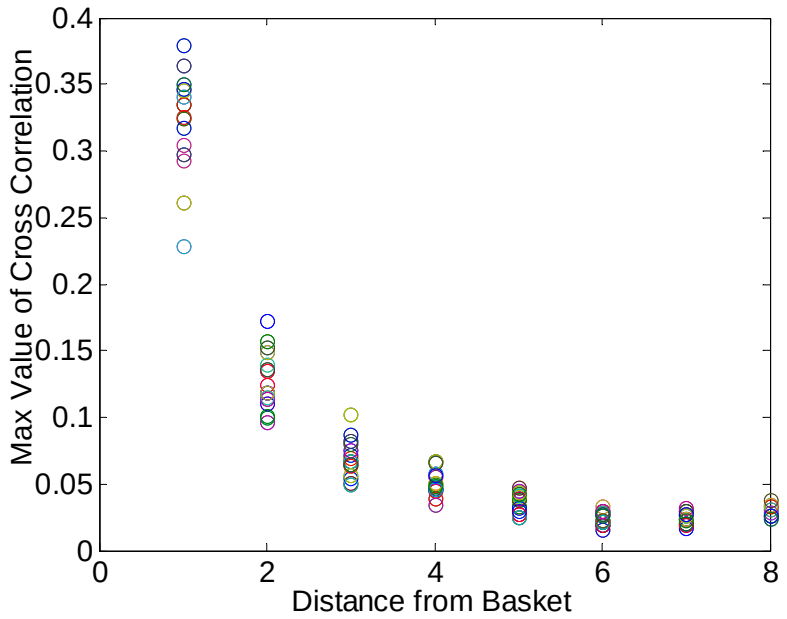

Figure 26. Dependence of cross correlation between oscillations in different combustor baskets.

In addition, data from Solar Turbines and KEMA show that the algorithm is effective over a wide range of conditions.

IV.C.3 Stability Margin in Unstable Operation

The stability margin technique described previously is applicable only to situations where the combustor is stable. The latter portion of this effort focused on developing techniques to evaluate stability margin when the combustor is unstable. This is a substantially more complicated problem as the analysis is no longer linear, but requires analysis of nonlinear, stochastic differential equations. However, the basic idea is similar – to determine the value of the instability growth or damping rate.

The basic analytical approach follows from prior work on statistically characterizing pressure oscillations in unstable combustors.[25] Acoustic oscillations in combustion chambers can be modeled as the superposition of nonlinearly interacting oscillators, where each oscillator typically represents a natural acoustic mode of the combustor. Accordingly, by retaining the contributions of the first *m* modes of oscillation, the pressure at a single point in the combustor can be written as:

$$p'(t) = \sum_{i=1}^{m} \eta_i(t) \qquad [6]$$

$$\frac{d^2\eta_i(t)}{dt^2} + \omega_i^2\eta_i(t) = \frac{\alpha_i}{\omega_i}\frac{d\eta_i(t)}{dt} + \theta_i\eta_i(t) - \hat{f}(\eta_j(t), \frac{d\eta_j(t)}{dt}, \ldots) \; i, j = 1, 2, \ldots m \qquad [7]$$

where the function $\hat{f}$ describes the nonlinearities in the system (specific expressions for $\hat{f}$ are introduced by gas dynamical or combustion processes). Here, we investigated a slightly modified form of Eq. (7) that incorporates the effects of temporal perturbations of

the system parameters and external forcing of the oscillators by "background noise" (e.g., by turbulent fluctuations) in the combustor:

$$\frac{d^2\eta_i(t)}{dt^2} + \omega_i^2\eta_i(t) = (\frac{\alpha_i + \tilde{\alpha}_i(t)}{\omega_i})\frac{d\eta_i(t)}{dt} + (\theta_i + \tilde{\theta}_i(t))\eta_i(t) - ((\hat{f} + \tilde{f})(\eta_j(t), \frac{d\eta_j(t)}{dt}, ...)) + \xi_i(t) \qquad i, j = 1, 2, \ldots m \qquad [8]$$

where $\tilde{\alpha}_i(t)$, $\tilde{\theta}_i(t)$, and $\tilde{f}$ denote parametric disturbances of the instability growth rate, frequency, and system nonlinearities, respectively, and $\xi_i(t)$ denotes an external excitation.

To reduce the complexity of this system of equations while retaining most of the important physical features of the investigated problem we assumed that: 1) the unsteady pressure is dominated by the oscillations of a single mode that interacts nonlinearly with itself, 2) the parametric excitation terms are negligible, 3) the correlation time of the external excitation is small relative to the other pertinent time scales of the problem and, thus, $\xi(t)$ is idealized as a random, white noise source, and 4) the terms on the right hand side of Eq. (3) are "small".

With these assumptions, Eqs. (6) and (8) are combined to yield:

$$\frac{d^2p'(t)}{dt^2} + \omega^2 p'(t) = \frac{\alpha}{\omega}\frac{dp'(t)}{dt} + \theta p'(t) - \hat{f}(p'(t), \frac{dp'(t)}{dt}) + \xi(t) = -f(p'(t), \frac{dp'(t)}{dt}) + \xi(t) \qquad [9]$$

Since the pressure oscillations are nearly harmonic, it is convenient to decompose $p'(t)$ and $dp'(t)/dt$ in the following manner:

$$p'(t) = A(t)\cos(\omega t + \sigma(t)) \qquad [10]$$

$$dp'(t)/dt = -A(t)\,\omega\sin(\omega t + \sigma(t)) \qquad [11]$$

where $A(t)$ and $\sigma(t)$ denote the fluctuating amplitude and phase of the oscillations. Using Eqs. (10-11), Eq. (9) can be rewritten as the following set of first order differential equations for the instability amplitude and phase:

$$\frac{dA(t)}{dt} = \frac{\sin\Phi}{\omega}(f(A\cos\Phi, -A\omega\sin\Phi) - \xi(t)) \qquad [12]$$

$$\frac{d\sigma(t)}{dt} = \frac{\cos\Phi}{A\omega}(f(A\cos\Phi, -A\omega\sin\Phi) - \xi(t)) \qquad [13]$$

where $\Phi = \omega t + \sigma(t)$.

Equations (12-13) describe the dynamics of the oscillatory amplitude, $A(t)$, and phase, $\sigma(t)$. Rather than analyzing the temporal evolution of $A(t)$ and $\sigma(t)$, however, the objective of this analysis is to determine their statistical characteristics. The Fokker-Planck equations for the PDF's of A and σ are:

$$W(A) = CAe^{-\frac{2\omega}{\pi S(\omega)}\int_0^A F(\psi)d\psi} \qquad [14]$$

$$W(\sigma) = 1/2\pi \qquad [15]$$

where C is a normalizing constant, S(ω) is the power spectral density of the noise ξ(t) at the frequency ω, and:

$$F(A) = -\frac{1}{2\pi}\int_0^{2\pi} f(A\cos\Phi, -A\omega\sin\Phi)\sin\Phi d\Phi \qquad [16]$$

No additional assumptions on the function f are required. Examination of these expressions shows that the amplitude PDF, W(A), depends upon the system nonlinearities and instability growth rate through the function F(A). The phase PDF, W(σ), is uniform; i.e., *there is equal probability that* σ(t) *will equal any value,* $-\pi<\sigma<\pi$ and, in contrast to the amplitude PDF, no value of σ(t) has maximum probability. Furthermore, this result is true regardless of the system parameters and nonlinearities. Thus, phase analysis provides no information for us on system parameters.

In order to complete the analytical description of W(A) in Eq. (14), it is necessary to derive an expression for the function F(A). This can be accomplished in a general fashion by expanding the function f(p', dp'/dt) in the following Taylor series:

$$\begin{aligned} f(p', dp'/dt) = -\theta p' - \frac{\alpha}{\omega}\frac{dp'}{dt} + b_{20}p'^2 + \frac{b_{02}}{\omega^2}(\frac{dp'}{dt})^2 + \frac{b_{11}}{\omega}p'\frac{dp'}{dt} + b_{30}p'^3 + \frac{b_{21}}{\omega}p'^2\frac{dp'}{dt} + \frac{b_{12}}{\omega^2}p'(\frac{dp'}{dt})^2 + \frac{b_{03}}{\omega^3}(\frac{dp'}{dt})^3 \\ + b_{40}p'^4 + \frac{b_{31}}{\omega}p'^3\frac{dp'}{dt} + \frac{b_{22}}{\omega^2}p'^2(\frac{dp'}{dt})^2 + \frac{b_{13}}{\omega^3}p'(\frac{dp'}{dt})^3 + \frac{b_{04}}{\omega^4}(\frac{dp'}{dt})^4 \end{aligned} \qquad [17]$$

where the b_{ij}'s are constants. Although f(p', dp'/dt) is truncated at fourth order in Eq. (17), it can be expanded to an arbitrary order in a straightforward manner. Substituting Eq. (17) into Eq. (16) yields:

$$F(A) = -\frac{\alpha A}{2} + (\frac{3b_{03}+b_{21}}{8})A^3 + \ldots = -\frac{\alpha A}{2} + \frac{k^2}{2}A^3 + \ldots \qquad [18]$$

Equation (13) shows that only three out of the fourteen terms in Eq. (12) contribute to F(A). Furthermore, two out of the three nonlinearities combine into a single cubic term. Inserting Eq. (13) into Eq. (9) yields the final result for the PDF of the mode's amplitude:

$$W(A) = \frac{4}{\sqrt{\pi}}\frac{\sqrt{\frac{k^2\omega}{\pi S(\omega)}}e^{-\frac{\alpha^2\omega}{4\pi k^2 S(\omega)}}}{1+\mathrm{erf}\sqrt{\frac{\alpha^2\omega}{4\pi k^2 S(\omega)}}}Ae^{\frac{\omega A^2}{\pi S(\omega)}(\alpha - k^2A^2)} \qquad [19]$$

Introducing the dimensionless amplitude $\tilde{A} = \sqrt[4]{\frac{\omega k^2}{\pi S(\omega)}}A$ yields:

$$W(\tilde{A}) = \frac{4}{\sqrt{\pi}}\frac{e^{-\Omega^2/4}}{1+\mathrm{erf}(\Omega/2)}\tilde{A}e^{\tilde{A}^2(\Omega-\tilde{A}^2)} \qquad [20]$$

where $\Omega = \frac{\alpha}{|k|}\sqrt{\frac{\omega}{\pi S(\omega)}}$. Significantly, Eq. (20) shows that $W(\tilde{A})$ only depends upon the parameter Ω, which in turn is directly proportional to the instability damping or growth rate, α. As opposed to our prior analysis, this result is applicable to situations where the combustor is either stable or unstable.

V. SUMMARY

Sensor methods were developed and tested for three specific applications: 1) sensing proximity static combustor stability loss (lean blow out); 2) determining local flame zone variables such as fuel-air ratio variations that can arise from unmixedness; and 3) sensing combustor dynamic stability margin, i.e., detecting how close the system is to the point where detrimental combustion instabilities would occur. Our work focused on physics-based analysis methods to extract relevant combustor performance and status information primarily from the light and sound naturally produced by the combustion processes. These optical and acoustic emissions can easily be monitored without requiring the placement of sensors directly into the most hostile regions of the combustor. Furthermore, acoustic and optical sensors are already employed to some extent in currently fielded industrial gas turbines. We also explored ion current sensing that could be added to combustor igniters.

Static stability sensing was successfully demonstrated for optical, acoustic and ion sensing in various combustors and for both natural gas and syngas fueled systems. The approach relies on capturing precursor events using a simple and robust thresholding method. Flame zone sensors for local fuel-air ratio monitoring were demonstrated for lean natural gas fueled combustors based on properly corrected ratios of CH and OH chemiluminescence. For lean ($\phi<0.7$) syngas systems, similar results can be obtained with the ratio of CO_2 and OH chemiluminescence. In addition, physics-based modeling of the combustion process was used to predict the chemiluminescence, which should allow further improvements in this sensing approach. Finally, dynamic stability margin sensing, based on dynamic pressure measurements, was demonstrated in various combustors by monitoring the decay of the autocorrelation at the known combustor instability frequencies. This method has been field tested in cooperation with industrial partners. The method was also extended to unstable operation conditions to help operators or control systems rapidly recover stable operation should instabilities occur.

These new sensing capabilities should enable the development of control systems that actively manage engine condition and compensate for changes in ambient conditions or system degradation. Used for monitoring purposes, they should help gas turbine operators more quickly identify potential system problems, before they become serious, and allow them to vary conditions to remove the problem. Used as long term monitors of system operation, they can be used to help schedule required maintenance.

VI. REFERENCES

[1]Gaydon, A.G. and Wolfhard, H.G., "Flames: Their Structure, Radiation, and Temperature", Fourth edition, Chapman and Hall, 1978.

[2]Keller, J.O. and Saito, K., "Measurements of the Combusting Flow in a Pulse Combustor", *Combustion Science and Technology*, Vol. 53, 1987, pp. 137-163.

[3]Lawn, C.J., "Distributions of Instantaneous Heat Release by the Cross-Correlation of Chemiluminescent Emissions," *Combustion and Flame*, Vol. 132, 2000, pp. 227-240.

[4]Roby, R.J., Hamer, A.J., Johnsson, E.L., Tilstra, S.A., and Burt, T.J., "Improved Method for Flame Detection in Combustion Turbines", *Transactions of the ASME*, Vol. 117, 1995, pp. 332 –340.

[5]Mehta, G.K., Ramachandra, M.K., and Strahle, W.C., "Correlations between Light Emission, Acoustic Emission and Ion Density in Premixed Turbulent Flames", *Eighteenth Symposium (International) on Combustion*, 1981, pp 1051-1059.

[6]Bragg, S., "Combustion Noise", *J. Inst. Fuel*, Vol. 36(1), 1963.

[7]Strahle, W.C., "On Combustion Generated Noise", *J. Fluid Mech.*, Vol. 49(2), 1971.

[8] Calcote, H. F., "Mechanism for the Formation of Ions in Flames", *Combustion and Flame*, Vo1.6, 1957,pp. 385-403.

[9] Fialkov, A.B., "Investigations on Ions in Flames", *Prog. Energy Comb. Sci*., Vol. 23, 1997, pp. 399-528.

[10] J.M. Goodings, D.K. Bohme and C.W. Ng., "Detailed ion chemistry in methane-oxygen flames", *Combustion and Flame*, Vol. *36*, 1979, pp. 27-43.

[11] Keller, J.O. and Saito, K., "Measurements of the Combusting Flow in a Pulse Combustor", *Combustion Science and Technology*, Vol. 53, 1987, pp. 137-163.

[12] Nicholson, H., Field, J., "Some Experimental Techniques for the Investigation of the Mechanism of Flame Stabilization in the Wake of Bluff Bodies", *Proc. Comb. Inst*., Vol.3, 1951, pp. 44-68.

[13] Chao, Y.C., Chang, Y.L., Wu, C.Y., Cheng, T.S., "An Experimental Investigation of the Blowout Process of a Jet Flame," *Proc. Comb. Inst*., Vol.28, 2000, pp. 335-342.

[14] Hedman, P.O., Fletcher, T.H., Graham, S.G., Timothy, G.W., Flores, D.V., and Haslam, J.K., "Observations of Flame Behavior in a Laboratory-Scale Pre-mixed Natural Gas/Air Gas Turbine Combustor from PLIF measurements of OH", *Proceedings of ASME Turbo Expo*, ASME Paper GT-2002-30052, Amsterdam, Netherlands, June, 2002.

[15] Wohl, K., Kapp, N.M., and Gazley, C., "Flame Stabilization and Quenching", *Proc. Comb. Inst.*, Vol.3, 1951, pp. 3-21.

[16] Longwell, J.P., Chenevey, J., Clark, W., and Frost, E., "Flame Stabilization by Baffles in a High Velocity Gas Stream", *Proc. Comb. Inst*., Vol.3, 1951, pp. 40-44.

[17] Williams, G., Hottel, H., Scurlock, A., "Flame Stabilization and Propagation in High Velocity Gas Streams", *Proc. Comb. Inst.*, Vol.3, 1951, pp. 21-40.

[18] Jensen, W.P., Shipman, C.W., "Stabilization of Flames in High Speed Flows By Pilot Flames", *Proc. Comb. Inst*., Vol.7, 1951, pp. 674-680.

[19] Williams, G.C., Shipman, C.W., "Some Properties of Rod Stabilized Flames of Homogeneous Gas Mixtures", *Proc. Comb. Inst*., Vol.4, 1953, pp. 733-742.

[20] Nair, S., Muruganandam, T. M, Meyers, A., Lieuwen, T.C., Seitzman, J.M., "Lean Blowout Detection in a Single Nozzle CFM56 Swirl Cup", *42nd AIAA Aerospace Sciences Meeting and Exhibit*, AIAA Paper 2003-5084, Reno, NV, January, 2004.

[21]Slack, M. and Grillo, A., "High-Temperature Rate Coefficient Measurements of CO + O Chemiluminescence," *Combustion and Flame*, 59 (2), 1985, pp. 189-196.

[22] Peterson, E, L., Kalitan, D, M. and Rickard, M. J. A., "Calibration and Chemical Kinetics Modeling of an OH Chemiluminescence Diagnostic," 39th AIAA/ASME/SAE/ASEE Joint Propulsion Conference and Exhibit, Huntsville, Alabama, July 20-23, 2003

[23] Petersen, E. Private Communication.

[24]Peracchio, A.A., Proscia, W.M., Nonlinear Heat Release/Acoustic Model for Thermo-Acoustic Instability in Lean Premixed ombustors, *ASME Paper # 98-GT-269*.

[25] Lieuwen, T., "Statistical Characteristics of Pressure Oscillations in a Premixed Combustor", *Journal of Sound and Vibration*, Vol. 260, 2003, pp. 3-17.

Assessment of Failure Mechanisms for Thermal Barrier Coatings by Photoluminescence, Electrochemical Impedance and Focused Ion Beam

Report Type:	Final Report
Reporting Period Start Date:	May 1, 2002
Reporting Period End Date:	November 1, 2005

Principal Investigators:	Y.H. Sohn and V.H. Desai
Affiliation:	Advanced Materials Processing & Analysis Center and Mechanical, Materials and Aerospace Engineering University of Central Florida Orlando, FL 32816-2455

Date Issued:	December 30, 2005
DOE Award Number:	DE-FC26-02NT41431
UTSR Project Number:	02-01-SR103

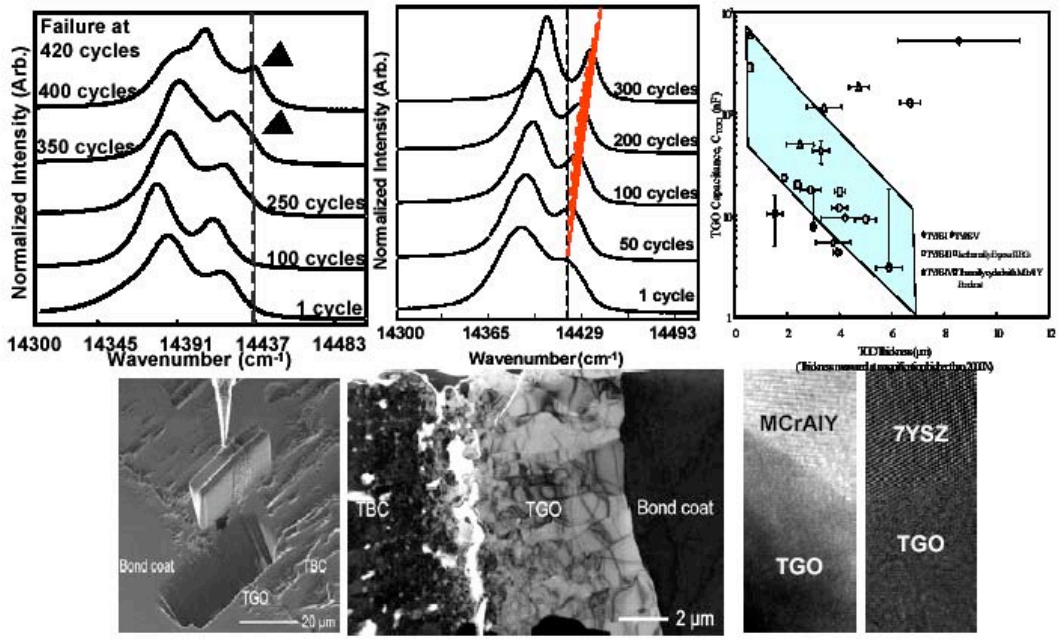

From upper left: TGO stress relief detected by photostimulated luminescence: TGO stress relaxation detected by photo luminescence: TGO thickness measurement by electrochemical impedance: From lower left: in-situ focused ion beam lift out: bright field image of thermally cycled TBC with 9mm-thick: lattice image of intact MCrAlY-TGO interface: and lattice image of intact TGO-YSZ interface.

DISCLAIMER

ABSTRACT

Development and applications of thermal barrier coatings (TBCs) based on a clearer understanding of failure mechanisms can help increase performance efficiency and reduce the emission of advanced gas turbine engines. In addition, development and refinement of robust non-destructive evaluation (NDE) techniques can enhance the reliability, availability and maintainability (RAM) of advanced gas turbines engines. Two complimentary non-destructive evaluation (NDE) techniques, namely photostimulated luminescence spectroscopy (PSLS) and electrochemical impedance spectroscopy (EIS) along with advanced characterization techniques, including focused ion beam (FIB) in-situ lift-out (INLO) and transmission electron microscopy (TEM) and scanning TEM (STEM), were employed in this investigation to provide a better understanding of TBC failure as well as to develop and refine PSLS and EIS. This report summarizes all results obtained from this study. Data acquisition and analysis of NDE was completed by PSLS and EIS for 1-, 10- and 50-hour thermal cycling. Relevant microstructural characterization for TBCs after 1-, 10- and 50-hour thermal cycling was carried out at specified lifetime using SEM and TEM/STEM via FIB-INLO. Results from PSLS and EIS as a function of thermal cycling demonstrated outstanding assessment of TBC degradation observed via microscopy, including sub-critical damage detection.

From PSLS NDE results for two types (III and IV) we can qualitative detect the damages in the TGO scale before the actual TBC failure. These sub-critical damages were related to stress relief/relaxation from the TGO scale. Also for type-IV TBCs, the damage detection was confirmed with another technique namely EIS, in which the TGO, represented as the capacitance (C_{TGO}), increased before the actual failure. These damages are further confirmed using microscopic techniques namely OM, SEM and TEM/STEM.

This report has been independently prepared by graduate and undergraduate students and has been approved by the principal investigators of this research program.

TABLE OF CONTENTS

LIST OF FIGURES

LIST OF FIGURES (Continued)

LIST OF FIGURES (Continued)

LIST OF FIGURES (Continued)

LIST OF FIGURES (Continued)

LIST OF FIGURES (Continued)

LIST OF FIGURES (Continued)

LIST OF FIGURES (Continued)

LIST OF FIGURES (Continued)

LIST OF FIGURES (Continued)

LIST OF FIGURES (Continued)

LIST OF FIGURES (Continued)

LIST OF FIGURES (Continued)

LIST OF FIGURES (Continued)

LIST OF FIGURES (Continued)

LIST OF TABLES

I. INTRODUCTION

Thermal barrier coatings (TBCs) are widely used for thermal protection of hot section components in turbines for power generations. TBCs, in general consist, of a thermally-insulating outer ceramic (ZrO_2-7wt.%Y_2O_3; YSZ) coating, a thermally grown oxide (TGO) scale, an oxidation resistant metallic bond coat, and a superalloy substrate. Commonly, YSZ coatings are deposited either by air plasma spray (APS) or electron beam physical vapor deposition (EB-PVD). Bond coats are deposited by low-pressure/vacuum plasma spray (LPPS/VPS) for a MCrAlY (M=Ni and/or Co) bond coat and a combination of plating and chemical vapor deposition (CVD) in the case of a (Ni,Pt)Al bond coat [1-5]. Reliable and durable TBCs can significantly improve the operating efficiency while reducing the harmful emission of turbine engines through an increased operating temperature and an increased durability of engine components. Figure 1 shows the typical microstructure of three types of commercial-production TBCs.

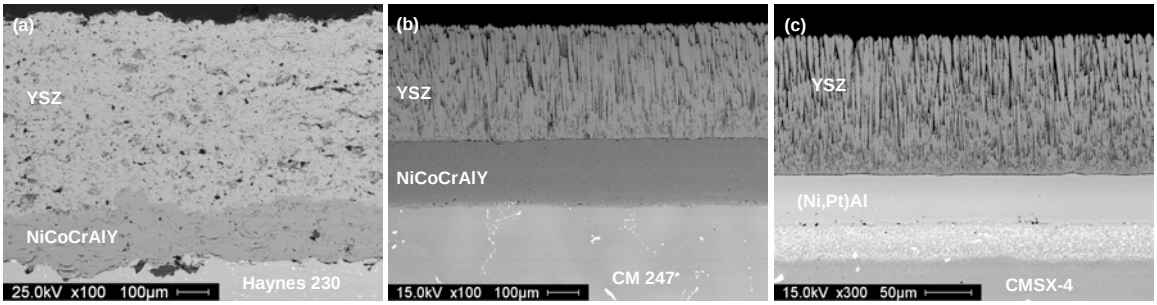

Figure 1. Backscatter electron micrographs of as-coated TBC: (a) APS YSZ on MCrAlY bond coat; (b) EB-PVD YSZ on MCrAlY bond coat; and (c) EB-PVD YSZ on (Ni,Pt)Al bond coat.

Generally, failure of TBCs occurs at the interface between bond coat and TGO, or TGO and YSZ, or within TGO [1-5]. Failure of TBCs can be attributed to time-dependent interplay between (1) chemical (i.e., thermo-kinetics) and (2) mechanical (i.e., thermo-mechanical) evolution associated with the growth of TGO via high temperature oxidation of metallic bond coat and thermal expansion mismatch between TGO and underlying metallic bond coat. Growth of TGO increases the strain energy stored within the TGO scale. Growth rate of TGO is essentially parabolic (i.e., diffusion-controlled) at high temperatures:

$$y^2 = 2k_p t \qquad \text{and} \qquad k_p = \tilde{D}_i \left(\delta_{YSZ/TGO} - \delta_{TGO/Bondcoat}\right) \qquad [1]$$

where y refers to the thickness of TGO, t, the time, k_p, the oxide growth constant, $\tilde{D}_i$, the interdiffusion coefficient of rate-controlling specie *i*, and δ, the stoichiometric deviation of TGO at the interfaces. In general, TGO primarily consists of α-Al_2O_3, whose growth rate is controlled by $\tilde{D}_i$ of oxygen (i.e., inward growth). Presence of metastable θ- and γ-Al_2O_3 can significantly alter the interfacial morphology and increase the TGO growth rate by altering the growth mechanism to outward, since $\tilde{D}_{Al} > \tilde{D}_O$ [6].

Compositional change and phase transformation in the metallic bond coat occur as a function of time due to high temperature oxidation and interdiffusion between bond coat and

the superalloy substrate. These changes and transformations are governed by the activity coefficient γ_i of component *i*, and other constituents *j*, which can be related by Gibbs-Duhem transformation:

$$\gamma_i = \frac{a_i}{X_i} \qquad \text{and} \qquad \log(\gamma_j) = -\int_1^{X_j} \left(\frac{X_i}{X_j}\right) d\log\gamma_i \Big|_{\gamma_{k..n-1}} \qquad [2]$$

where a_i is the activity of specie *i* and X_i is the mole fraction of *i* in the bond coat. The thermodynamic description of elemental constituents in the bond coat changes dynamically due to interdiffusion between the bond coat and the superalloy substrate and can be described by Onsager's formalism [7] of interdiffusion flux for component *i*, $\tilde{J}_i$:

$$\tilde{J}_i = -\sum_{j=1}^{n-1} \tilde{D}_{ij}^{n} \frac{\partial C_j}{\partial x} \quad (i = 1,2,3,...,n-1) \qquad [3]$$

where $\tilde{D}_{ij}^{n}$ refers to the interdiffusion coefficients and $\frac{\partial C_j}{\partial x}$ is the (n-1) independent concentration gradient. With compositional (or thermodynamic activity coefficient) changes, various types of oxidation can take place:

$$2(Al,Cr) + 3O = (Al,Cr)_2O_3 \qquad [4]$$
$$(Ni,Co)+O=(Ni,Co)O \qquad [5]$$
$$(Ni,Co)+2(Al,Cr)+4O=(Ni,Co)(Al,Cr)_2O_4 \qquad [6]$$
$$(Al,Cr)_2O_3+ (Ni,Co)O=(Ni,Co)(Al,Cr)_2O_4 \qquad [7]$$

In particular, formation of $(Ni,Co)(Al,Cr)_2O_4$ spinels after the depletion of Al in the bond coat has been documented to be detrimental to the integrity of TBCs due to their low fracture toughness [8]. Thus characterization of compositional change and phase transformation is critical in understanding the failure of TBCs.

Two main sources of stresses in the TGO exert additional influence on TBC failure: one from thermal expansion misfit upon cooling and the other from TGO growth [9]. Since TGO is thin, the stress in the TGO, denoted σ_{ij} from thermal expansion misfit is given by:

$$\frac{\sigma_{ij}}{\sigma_o} = H_{ij}\alpha_D \frac{A}{L} \text{ and } \sigma_o = \frac{E_o \Delta\alpha_o \Delta T}{1-\upsilon} \text{ and } \alpha_D = \frac{\bar{\varepsilon}_{TGO} - \bar{\varepsilon}_{bondcoat}}{\bar{\varepsilon}_{TGO} + \bar{\varepsilon}_{bondcoat}} \qquad [8]$$

where α_D is the Dundurs' parameter defined by plane strain $\bar{\varepsilon}_i$, Young's modulus of TGO, E_o, the temperature difference during thermal cycling, ΔT, Poisson ratio, υ, the thermal expansion coefficient difference, $\Delta\alpha_o$, and geometrical descriptors A and L. Also, oxidation (i.e., a process of converting metal to oxide) is accompanied by strain ε that is associated with growth stress σ^g:

$$\varepsilon = \varepsilon_{zz}\sigma_{xx}^{g} + 2\varepsilon_{xx}\sigma_{xx}^{g} \qquad [9]$$

where subscripts xx and zz refers to in-plane and out-of-plane (orthogonal to TGO/metal interface) directions, respectively. Additional factors that influence durability and reliability of TBCs include (1) creep of metallic bond coat and TGO, (2) imperfections and impurity segregation at the TGO/bond coat interface, and (3) phase transformation or sintering of YSZ coatings. Table I lists several critical materials phenomena associated with TBC failure.

Table I. Primary NDE and microstructural analysis techniques employed in this program to examine the critical materials phenomena associated with TBC failure.

Main factors Associated with TBC Failure	Potential NDE Technique	Microstructural Analysis
Thickness/Growth of TGO	EIS	SEM, TEM
Polymorphic Transformation of Al_2O_3 in TGO	PSLS	XRD, TEM
Residual Stress in α-Al_2O_3 TGO	PSLS	-
Formation of Ni/Co Rich TGO	PSLS (?)	SEM, TEM, n-EDS
Sintering of YSZ	EIS	SEM
Phase Transformation of YSZ	XRD, RS	
Adhesion Integrity of TGO/Bond Coat Interface	PSLS, EIS	SEM, TEM
Adhesion Integrity of YSZ/TGO Interface	EIS	SEM, TEM
Sulfur Segregation	AES, XPS, SIMS	

Given the wide applications and complexity of TBCs, detailed high resolution microstructural analysis via novel specimen preparation technique is essential to elucidate the failure mechanisms of TBCs. Concurrently, development of non-destructive evaluation (NDE) techniques for TBCs in commercial applications is needed for enhanced reliability, availability and maintainability (RAM) of advanced turbine engines. Development of NDE techniques must be based on a robust correlation to the mechanisms of TBC degradation and failure.

The overall objective of this program was to provide a clearer understanding of TBC failure by concurrently utilizing two NDE techniques, namely photostimulated luminescence spectroscopy (PSLS) and electrochemical impedance spectroscopy (EIS), and state-of-the-art characterization techniques including focused ion beam (FIB) in-situ lift out (INLO) [10], transmission electron microscopy (TEM) and scanning TEM (STEM). The PSLS and EIS were selected for this program since these two techniques can provide non-destructive methods to examine the critical materials phenomena associated with TBC failure as listed in Table I. Results of NDE were correlated with systematic microstructural analysis using FIB-INLO and TEM/STEM. Site-specific preparation of specimens that are thin enough for TEM/STEM analysis is now feasible through FIB-INLO for traditionally difficult-to-prepare specimens such as TBCs, especially after thermal cycling [11]. Upon FIB-INLO preparation, detailed microstructural analysis was carried out using TEM/STEM equipped with bright/dark field imaging, nano-spot energy dispersive spectroscopy (n-EDS), convergent beam electron diffraction (CBED), high angle annular dark field (HAADF) imaging, and electron energy loss spectroscopy (EELS). The main objective of this program was achieved by accomplishing the following goals:

1. Evaluate and examine five different types of commercial production TBCs during thermal cyclic oxidation concurrently by PSLS and EIS, the two complimentary NDE techniques.
2. Evaluate five types of commercial production TBCs after specified thermal cyclic oxidation and after failure by the state-of-the-art characterization techniques including SEM, EDS, FIB-INLO and TEM/STEM equipped with n-EDS, CBED, HAADF and EELS.
3. Define clearer failure mechanisms for five types of commercial production TBCs.
4. Demonstrate the relationship between the results of NDE techniques, microstructural analysis and failure mechanisms for five types of commercial production TBCs.
5. Transfer to industrial partners the attained knowledge on TBC failure, refinement of NDE techniques, feasible approaches to improve TBC durability and to develop/refine lifetime prediction models for TBCs.
6. Provide collaborative/competitive team-based research activities for student research teams with active interaction from industrial partners.

To achieve these goals, six tasks were defined, structured, and scheduled as presented in Figures 2 and 3. In this program, the University of Central Florida is privileged to have a strong and supportive partnership with four industrial gas turbine manufacturers and a coating manufacturer. The industrial partners will contribute to this program by supplying commercial production TBCs, providing non-proprietary experience to the program and interacting (technically, educationally and professionally) with student research teams.

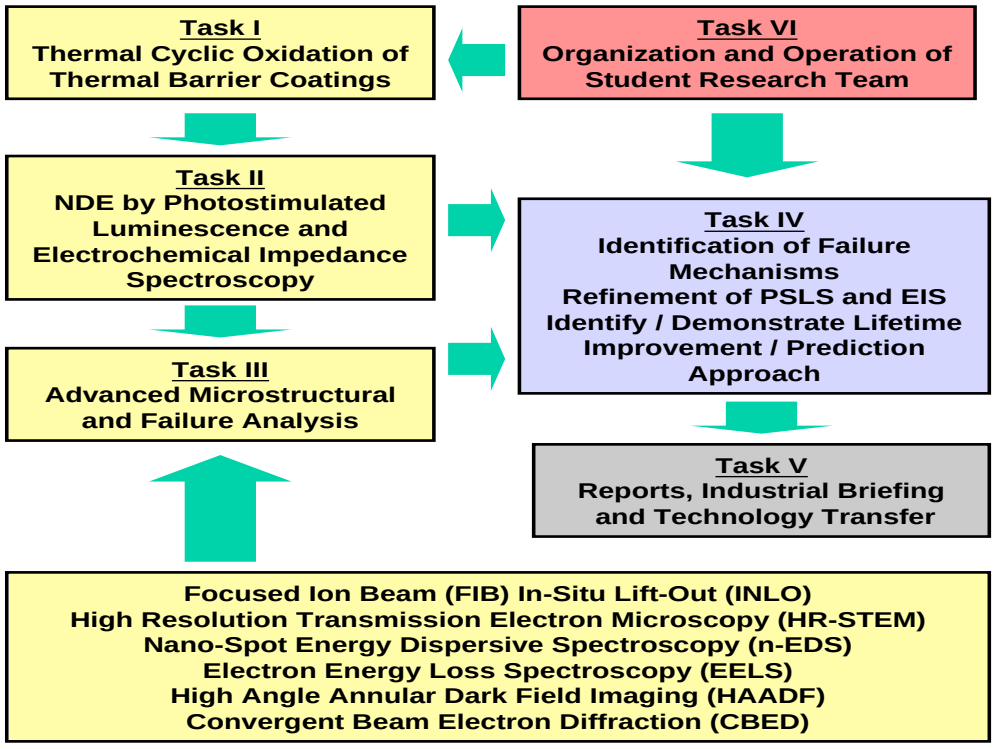

Figure 2. Task-based program flow chart.

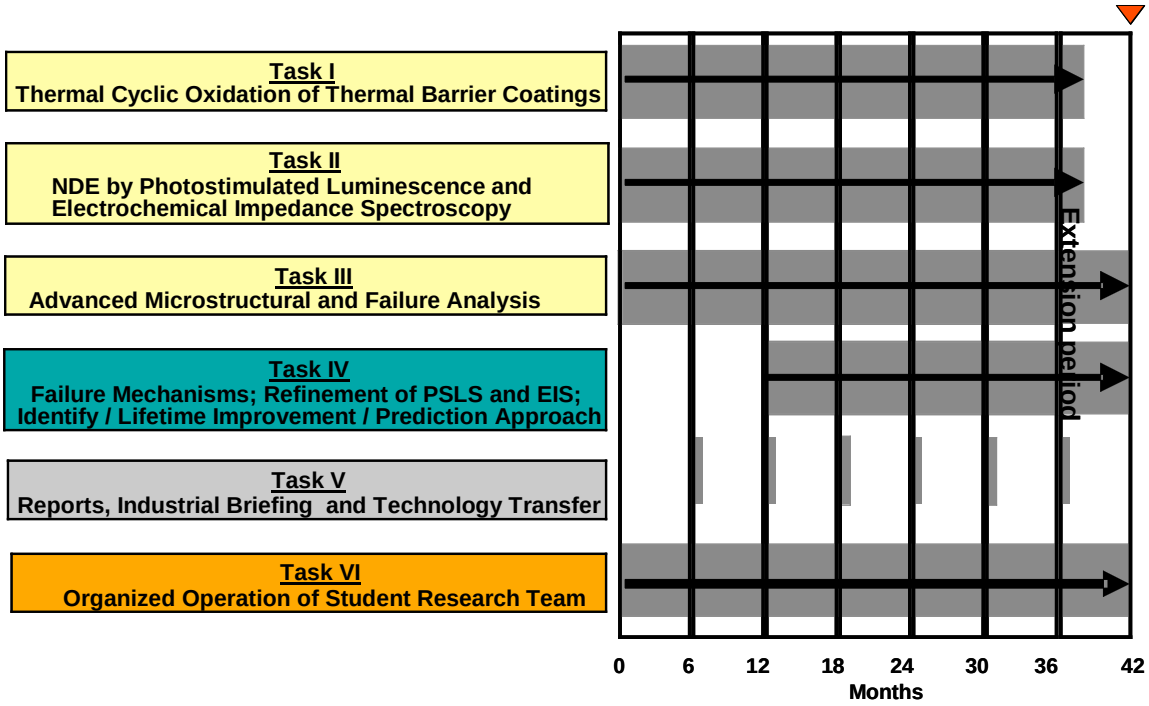

Figure 3. Program schedule according to specific tasks.

II. EXECUTIVE SUMMARY

Project Title: **Assessment of Failure Mechanisms for Thermal Barrier Coatings by Photoluminescence, Electrochemical Impedance and Focused Ion Beam**

Identifiers: **DOE DE-FC26-02NT41431 and UTSR No. 02-01-SR103**

PIs: **Yongho Sohn and Vimal H. Desai**
Affiliation: **Advanced Materials Processing and Analysis Center and Mechanical, Materials and Aerospace Engineering**
University of Central Florida
Orlando, FL 32816-2455

Reporting Period: **May 1, 2002 ~ January 30, 2006**
Date Issued: **December 30, 2005**

Durable and reliable service of thermal barrier coatings (TBCs) can increase the performance efficiency and reduce the harmful emission during the operation of advanced gas turbine engines. Enhanced reliability, availability and maintainability (RAM) of advanced turbine engines require robust non-destructive evaluation (NDE) techniques for TBCs. There is a need for a clearer scientific understanding for TBC failure mechanisms based on the fundamental foundation of thermo-kinetics and thermo-mechanics. There is even a greater need for NDE techniques that can monitor the degradation in TBCs, and can be correlated to the fundamental materials phenomena associated with mechanisms of TBC failure.

Faculty and students of Advanced Materials Processing and Analysis Center (AMPAC) at the University of Central Florida have elucidated the failure mechanisms for five types of commercial production TBCs during thermal cyclic oxidation under University Turbine Systems Research (UTSR) program. Failure characteristics and mechanisms have been examined by using two complimentary NDE techniques: photostimulated luminescence spectroscopy (PSLS) and electrochemical impedance spectroscopy (EIS). Concurrently, microstructural analysis of TBCs was carried out at atomic-micro-macro levels using a variety of characterization techniques including transmission electron microscopy (TEM) and scanning TEM (STEM). This program was specifically designed to correlate the results of NDE and microstructural analysis in order to better understand failure mechanisms of TBCs and to develop/refine NDE techniques.

During this study, the following tasks were successfully completed:

- **Completed lifetime evaluation of all five TBC types using 1, 10 and 50-hour thermal cycling at 1121°C (2050°F), and non-destructive evaluation of all TBCs as a function of thermal cycling by PSLS and EIS.**

- **Detected pre-spallation event by PSLS including TGO stress-relief (i.e., sub-critical cracking) and TGO stress-relaxation (i.e., racheting) for EB-PVD TBCs during 1- and 10-hour thermal cycling.**
- **Completed the microstructural analysis for each type of TBCs as a function of 1, 10 and 50- hour thermal cycling by SEM with EDS.**
- **Completed detailed site-specific microstructural analysis for TBCs with 1-hour thermal cycling using TEM/STEM via FIB-INLO with several analytical/imaging modes/detectors such as high angle annular dark field (HAADF), selected area diffraction (SAD), nano-spot energy dispersive spectroscopy (n-EDS) and electron energy loss spectroscopy (EELS).**

While this document reports the technical results and discussion of this program, some highlights can be found is refereed journal articles (complete list in Appendix A):

1. **B. Jayaraj et al., "Changes in Electrochemical Impedance with Microstructural Development in Thermal Barrier Coatings," *JOM*, vol. 57 (2006) pp. 61-64.**
2. **J. Byeon, et al., "Non-Destructive Evaluation of Degradation in Multi-Layered Thermal Barrier Coatings by Electrochemical Impedance Spectroscopy," *Mater. Sci. Eng. A*, Vol. 407 (2005) pp. 213-225.**
3. **J.W. Byeon, et al., "Transmission Electron Microscopy of Isothermally Oxidized EB-PVD Thermal Barrier Coatings on (Ni,Pt)Al Bondcoat," *Mater. Sci. Forum*, Vol. 486-487 (2005) pp. 149-152.**
4. **J.W. Byeon, et al., "Characterization of Isothermally Oxidized ZrO_2-8wt.%Y_2O_3 Thermal Barrier Coatings by Electrochemical Impedance Spectroscopy," *Mater. Sci. Forum*, Vol. 486-487 (2005) pp. 145-148.**
5. **Y.H. Sohn, et al., "Non-Destructive and Microstructural Characterization of Thermal Barrier Coatings," *JOM*, Vol. 56 (2004) 53-56.**
6. **B.W. Kempshall, et al., "An Observation of Nearly Failed Electron Beam Physical Vapor Deposited Thermal Barrier Coating with Grit Blasted (Ni,Pt)Al Bond Coat: Photostimulated Luminescence and Transmission Electron Microscopy," *Thin Solid Films*, Vol. 466 (2004) pp. 128-136.**
7. **B. Jayaraj, et al., "Electrochemical Impedance Spectroscopy of Porous ZrO_2 – 8 wt.% Y_2O_3 and Thermally Grown Oxide on Nickel Aluminide," *Mater. Sci. Eng. A*, Vol. A372 (2004) pp. 278-286.**
8. **B. Jayaraj, et al., "Electrochemical Impedance Spectroscopy of Thermal Barrier Coatings as a Function of Isothermal and Cyclic Thermal Exposure," *Surf. Coat. Technol.*, Vol. 177-178 (2004) pp. 140-151.**
9. **S. Laxman, et al., "Phase Transformation of Thermally Grown Oxide on (Ni,Pt)Al Bond Coat During Electron Beam Physical Vapor Deposition and Subsequent Oxidation," *Surf. Coat. Technol.*, Vol. 177-178 (2004) pp. 121-130.**
10. **Y.H. Sohn, B. Jayaraj, "Evolution in Photoluminescence and Electrochemical Impedance with Microstructural Changes in Thermal Barrier Coatings," *Surf. Coat. Technol.*, Submitted, March, 2006.**
11. **B. Jayaraj, Y.H. Sohn, "Thermal Cycling Lifetime and Microstructural Development of Thermal Barrier Coatings with Air Plasma Sprayed NiCoCrAlY Bond Coats," *Surf. Coat. Technol.*, Submitted, March, 2006.**

Findings and technical achievements of this program fertilized direct research interaction with UTSR-IRB members (Siemens, Solar and GE) with contract value of over $480,000, and formed a basis for a patent (U.S. Patent 6,979,991 B2, December 27, 2005) from one of the UTSR IRB members (P&W). Finally and most importantly, this program was carried out by two student research teams, each consisting of one graduate and one undergraduate student for collaborative and competitive development of PSLS and EIS. This program supported Mr. Balaji Jayaraj, who was a recipient of "UCF's Most Outstanding M.S. Thesis of 2003." Mr. Jayaraj expect to complete his doctoral dissertation in early 2005 and join Mitsubishi Power Systems, Orland, FL. Ms. Barbara Franke, now with Solar Turbines earned her M.S., and was a recipient of Recipient of Honeywell Leadership Scholarship, and 2003 and 2004 UTSR Fellow. Overall this program has support 1 Ph.D., 4 M.S. and 4 undergraduate students. A complete list of achievements and placement of students supported by this program are listed in Appendix B.

III. PROJECT DESCRIPTION

Development of durable and reliable thermal barrier coatings (TBCs) for blades and vanes can increase the performance efficiency and reduce the harmful emission during the operation of advanced turbine engines. In addition, development of robust non-destructive evaluation (NDE) techniques to detect a sub-critical, yet significant TBC damage prior to a complete failure can substantially enhance the reliability, availability and maintainability (RAM) of advanced turbine engines. To fulfill these industrial needs, a robust scientific foundation for TBC failure mechanisms must be established through understanding of materials thermo-kinetics and thermo-mechanics. In addition, novel NDE techniques must be developed on the premises that NDE data can monitor and be correlated to the fundamental materials phenomena related to TBC degradation and failure mechanisms.

Under the University Turbine Systems Research (UTSR) program, the University of Central Florida have elucidated the failure mechanisms for five types of commercial production TBCs during thermal cyclic oxidation. Failure characteristics and mechanisms were examined by using two complimentary NDE techniques, photostimulated luminescence spectroscopy (PSLS) and electrochemical impedance spectroscopy (EIS). Concurrent microstructural analysis of TBCs was carried out at atomic-micro-macro level. Site-specific and routine (<3 hours) preparation of TBC specimens for transmission electron microscopy (TEM) and scanning TEM (STEM) has been achieved through this program using focused ion beam (FIB) in-situ lift out (INLO) technique. This achievement now allows a systematic TEM/STEM investigation of TBCs as a function of thermal exposure, and will give a detailed understanding of microstructural evolution, and ultimately how TBCs fail when correlated with NDE.

IV. EXPERIMENTAL

IV.1. Description and Thermal Cycling of Thermal Barrier Coatings

Five TBC systems, identified in Table II as type I through V, were selected for this program. The industrial partners of this program have supplies 20 specimens of each TBC type with geometrical specification schematically illustrated in Figure 4 (25.4 mm in diameter and 3.2 mm in thickness).

Table II. Specifications for five types of commercial production thermal barrier coating systems employed in this program.

TBC System	7YSZ Deposition and Thickness	Bond Coat Type and Thickness	Superalloy Substrate	Notes
I	APS; 600 μm	NiCoCrAlY; 175 μm	Haynes 230	-
II	EB-PVD; 350 μm	NiCoCrAlY; 200 μm	CM247	-
III	EB-PVD; 145 μm	(Ni,Pt)Al; 50 μm	CMSX-4	As-Coated Bond Coat
IV	EB-PVD; 140 μm	(Ni,Pt)Al; 35 μm	Rene'N5	Grit-Blasted Bond Coat
V	APS; 200 μm	NiCoCrAlY; 100 μm	MAR-M-509	-

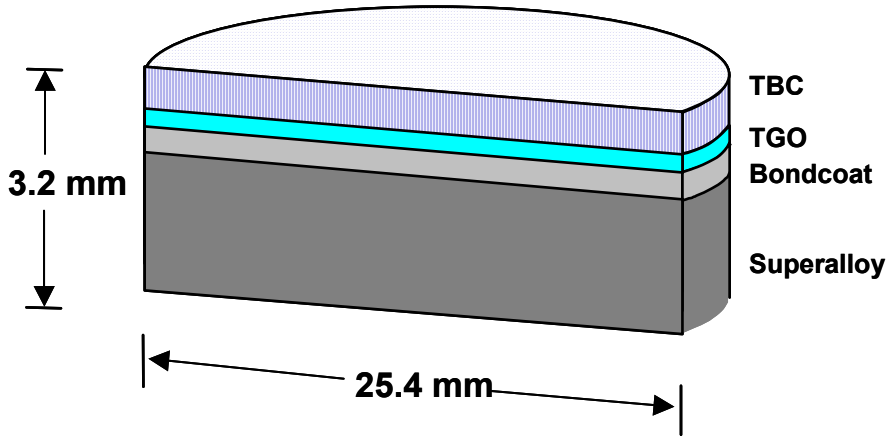

Figure 4. Specimen geometry for thermal barrier coatings employed in this program.

Thermal cyclic oxidation for each type of TBC has been carried out using CM™ Rapid Temperature furnace with vertical cycling package. Each cycle consists of 10-minute heat-up to 1121°C (2050°F), 0.67, 10 or 50-hour hold at 1121°C, and 10-minute forced-air quench. A schematic illustration of thermal cycling is presented in Figure 5. Temperature of the specimen stage (20 cm by 20 cm) has been monitored by S-type thermocouples attached to YSZ disk (25.4 mm in diameter and 3 mm in thickness). For 20 specimens of each TBC type, thermal cyclic oxidation testing has been carried out using the matrix given in Table III. At specified thermal cycles, TBCs have been visually inspected, photographed and examined by PSLS and EIS. Selected TBC specimens after specific thermal cycles have been also employed for microstructural analysis according to Table III.

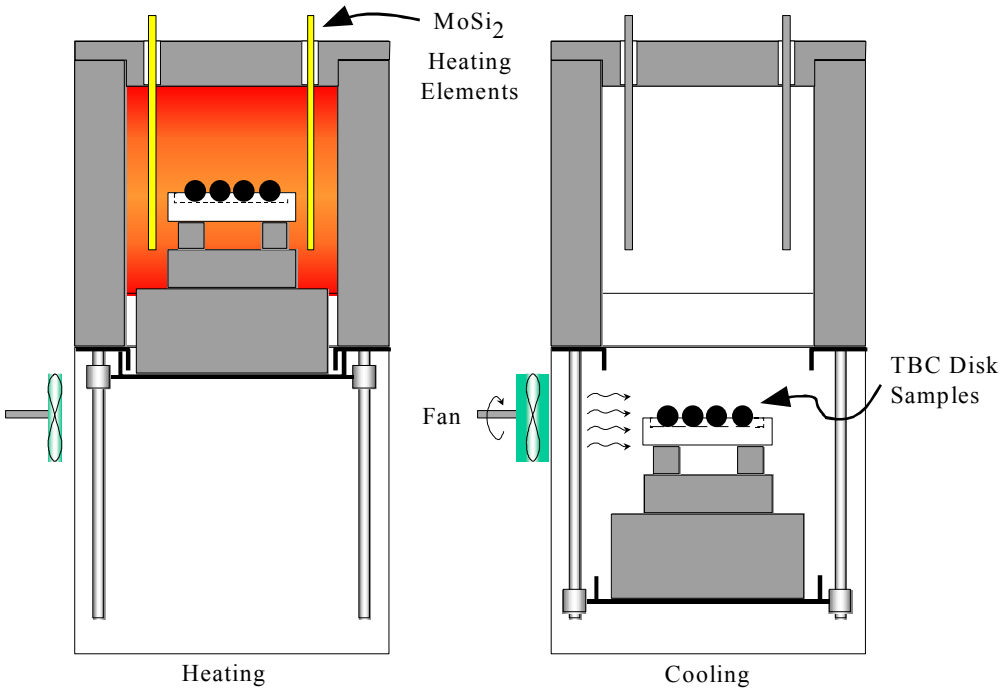

Figure 5. A schematic diagram of the CM™ Rapid Temperature cyclic oxidation furnace during (a) high temperature oxidation and (b) cooling.

Table III. Matrix of the thermal cyclic oxidation test for each TBC type.

Number of TBCs*	Type of Oxidation Test	NDE by PSLS and EIS (cycles)	Microstructural Analysis (% lifetime∇)
1	N.A.	0	0
9	1 hour	0,1,5,10-Failure#	10, 50, 80, 90, Failure (5 spc.)
5	10 hour	0,1,2,3,4,…Failure	30, 80, Failure (3 specimens)
5	50 hour	0,1,2,3,4,…Failure	30, 80, Failure (3 specimens)

* Total number of TBC specimens required for each type: 20.
# Every 10 cycles until failure.
∇ Approximate values; will be adjusted to equivalent time-at-1121°C.

IV.2. Photostimulated Luminescence Spectroscopy

Photo-Stimulated Luminescence Spectroscopy (PSLS), pioneered by Clarke et al. [12-16] and refined by Sohn, Gell, Jordan et al. [17-19] has demonstrated its capability as a NDE technique for TBCs. Specifically, PSLS can provide information regarding the following factors associated with TBC failures:

- Residual stress of α-Al_2O_3 (i.e., TGO structural integrity).
- Polymorphic transformation of Al_2O_3.
- Formation of other oxides (containing Ni, Co, Y, etc.) in TGO [20].

In PSLS technique, schematically illustrated in Figure 6, a systematic shift in the position of R_1 and R_2 luminescence doublets can be phenomenologically translated into residual stress in α-Al_2O_3, assuming that the TGO consists of randomly oriented polycrystals. The average biaxial residual stress $\overline{\sigma}$ in the α-Al_2O_3 scale is generally calculated from the average shift in the position of R_2 luminescence $\overline{\Delta\upsilon}$ using the relation [12-15]:

$$\overline{\Delta\upsilon} = \frac{2}{3}\Pi\overline{\sigma} \qquad [10]$$

where Π is the piezospectroscopic coefficients. Clarke et al. [15,16] as well as Sohn, Gell, Jordan et al. [17,18] have demonstrated that the damage of TGO by cracking during thermal cyclic oxidation results in relief of TGO residual stress. In addition, Figure 7 shows the N, Q and G-luminescences arising from, respectively, a significant Cr_2O_3 concentration in the TGO [21], the presence of metastable θ, and γ-Al_2O_3 in TGO. Intensity of these luminescence's can be determined relatively using the relation:

$$\frac{I_R}{I_T} + \frac{I_N}{I_T} + \frac{I_Q}{I_T} + \frac{I_G}{I_T} = 1 \qquad [11]$$

where I_R, I_N, I_Q, I_G and I_T refer to the integrated luminescence intensities of α-Al_2O_3, N-luminescence, θ-Al_2O_3, γ-Al_2O_3 and total luminescence, respectively. Formation of other constituents in TGO such as Y-rich oxide (e.g., YAl_5O_{12}, Y_2O_3), and Ni/Co-rich oxide (e.g., NiO, CoO, $(Ni,Co)(Cr,Al)_2O_4$-spinel) may be detected by the PSLS technique based on theory of photoluminescence [20]. Thus, NDE of these TGO characteristics by PSLS as a function of thermal cyclic oxidation can provide insight into the failure mechanisms of TBCs specifically associated with the factors listed in Table I.

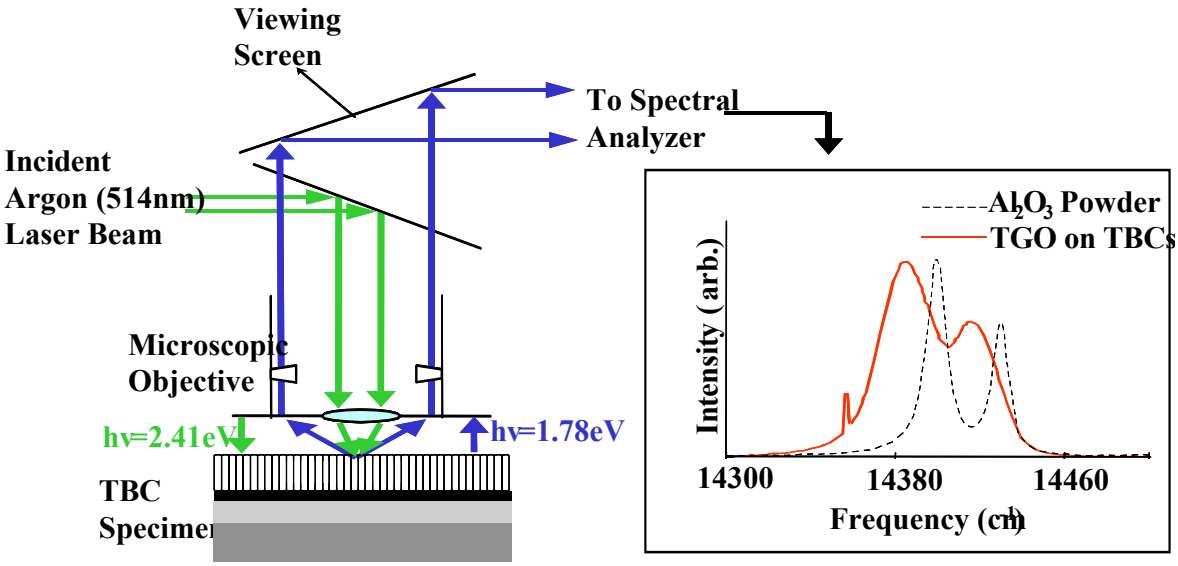

Figure 6. A schematic diagram of photostimulated luminescence spectroscopy, and R_1-R_2 luminescence doublets from stressed and stress-free α-Al_2O_3.

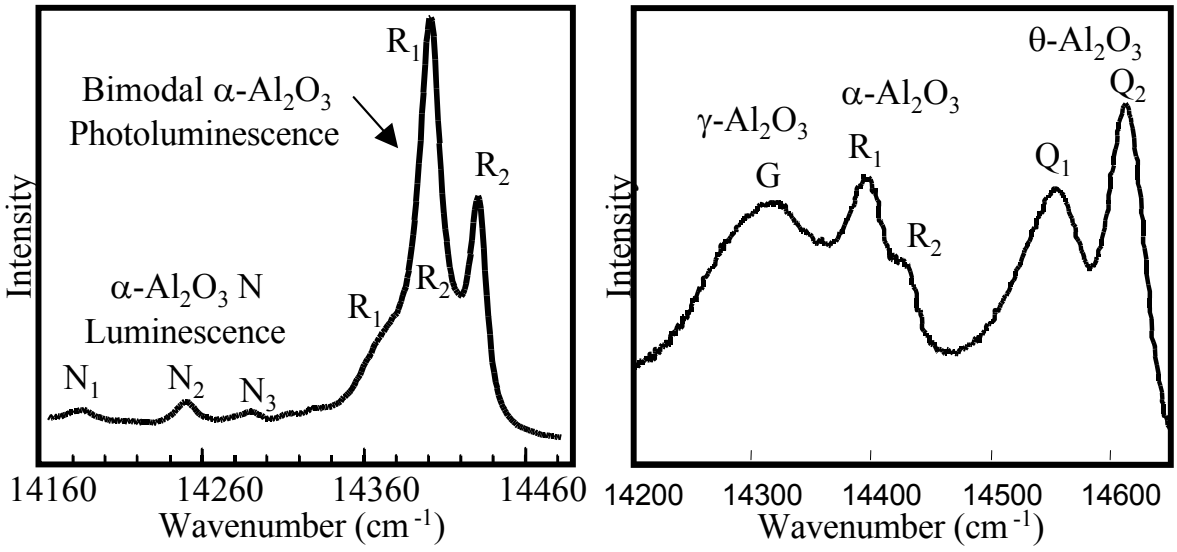

(a) (b)

Figure 7. (a) N-type luminescence arising from the presence of Cr_2O_3 in α-Al_2O_3 scale, (b) luminescence from γ, α and θ-Al_2O_3 labeled G, R_1-R_2 and Q_1-Q_2, respectively.

In this study, after specified thermal cycles reported in Table III, TBC specimens have been carefully removed from the CM furnace for NDE by PSLS. NDE by PSLS has been restricted to EB-PVD TBCs, since PSLS cannot be applied to APS TBCs without impregnating APS YSZ coatings with other medium [22] whose effect on TBC lifetime has not been investigated. TGO residual stress, polymorphic transformation of Al_2O_3, formation of Ni/Co rich TGO, and development of sub-critical TGO damage have been carefully monitored using PSLS. Minimum of 20 measurements, randomly over the surface of the specimen coupon are carried out for each specimen. Spectra are collected using Renishaw™ 1000B μ-Raman spectrometer and analyzed using GRAMS™ software.

IV.3. Electrochemical Impedance Spectroscopy

Electrochemical impedance spectroscopy (EIS) is a well-established technique in materials engineering related to corrosion. This technique was first employed to examine TBCs by V.H. Desai through a previous AGTSR program (No. 98-01-SR067) [23]. Results from this program indicated that the EIS technique has a good potential to provide information regarding the following factors associated with TBC failure [23,24]:

- Thickness of TGO.
- Adhesion integrity of TGO/bond coat and YSZ/TGO interfaces.
- Microstructure, thickness, sintering and cracking in YSZ.

EIS technique, schematically shown in Figure 8, involves measurement of the multi-layer system response subjected to a small ac signal at various frequencies, and representing it

with Nyquist and Bode plots, which represents the changes in impedance and phase angle. With concurrent simulation of equivalent ac circuits, various aspects of TBCs including YSZ microstructure, TGO thickness and TBC structural integrity can be evaluated non-destructively. An EIS ac equivalent circuit employed in this study is presented in Figure 9 for (a) as-coated APS TBCs without continuous/significant TGO scale and (b) as-coated EB-PVD TBCs with TGO and thermally cycled TBCs deposited either by APS or EB-PVD. For APS TBCs, constant phase elements are employed instead of pure capacitance to accommodate any non-uniform charge distribution that may arise due to surface/interface roughness. NDE of TBCs by EIS as a function of thermal cyclic oxidation can provide insight to the failure mechanisms, specifically associated with the factors listed in Table I.

Similar to PSLS, after specified thermal cycles reported in Table III, TBC specimens have been carefully removed from the CM furnace for NDE by EIS. TGO thickness, interfacial adhesion and damage, and microstructural evolution of YSZ coatings have been carefully monitored using EIS. Minimum of 3 measurements are carried out by applying 10mV over a frequency range of 1MHz to 10mHz. EIS set-up employed in this study consist of IM6E BAS Zahner frequency response analyzer and a three-electrode system, namely counter electrode (Pt-mesh), reference electrode (standard calomel) and working electrode (TBC) in contact with $K_3Fe(CN)_6/K_4Fe(CN)_6$-$3H_2O$ electrolyte solution. The center of the TBC coupons has been examined by EIS with a measurement diameter of 1 cm.

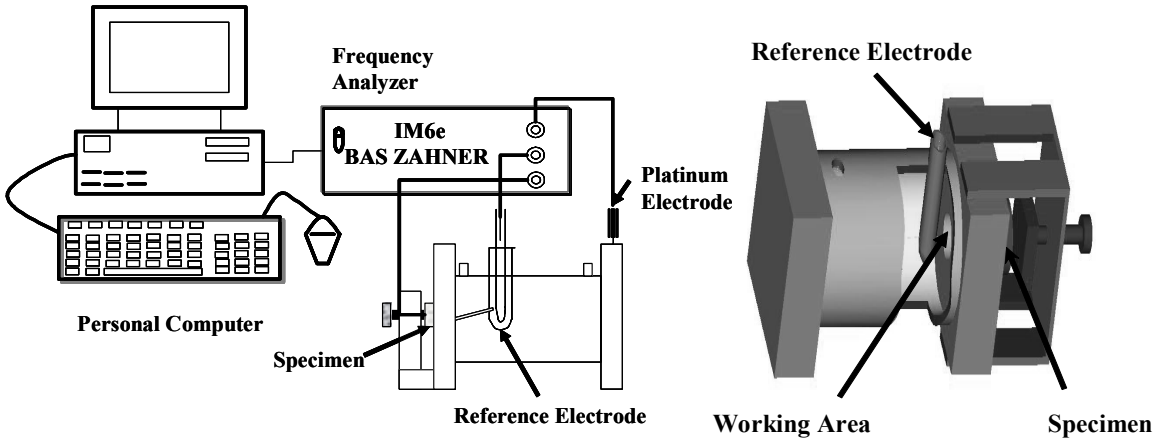

Figure 8. A schematic diagram of a typical set-up for electrochemical impedance spectroscopy.

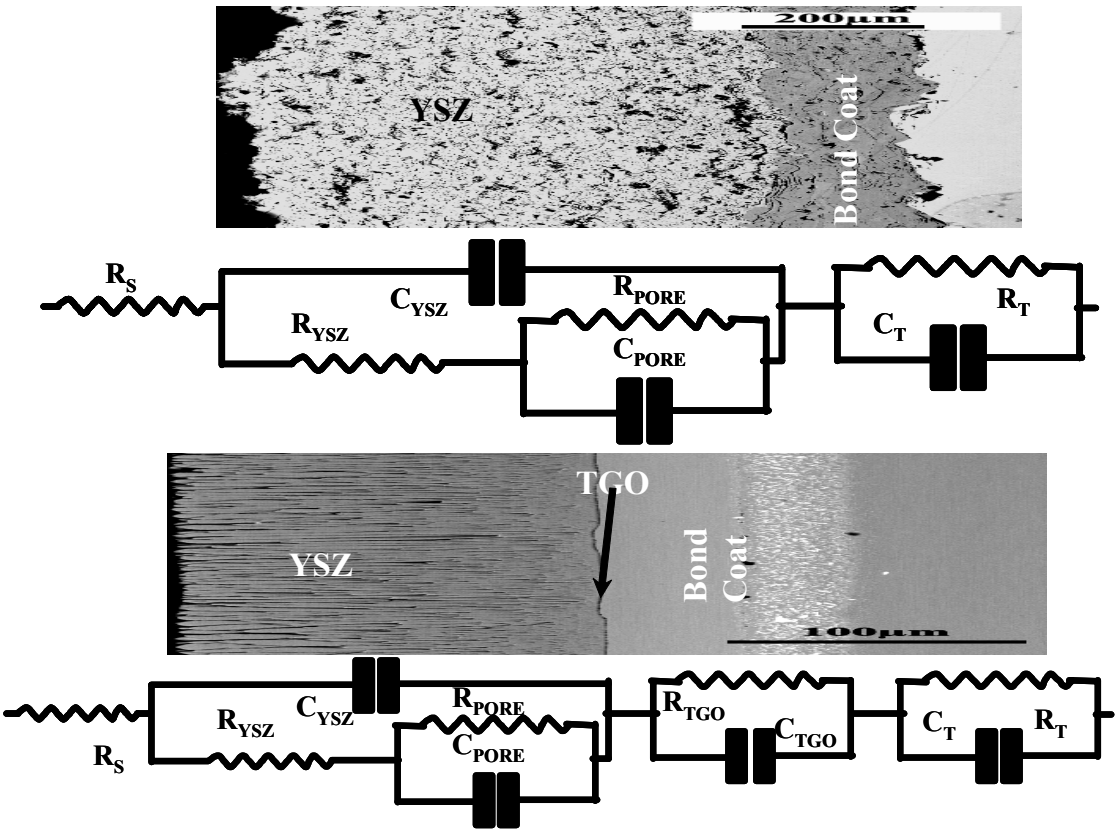

R_S: Solution Resistance
R_{YSZ}: Ceramic topcoat Resistance
R_{PORE}: Pore Resistance
R_{TGO}: Oxide Scale Resistance
R_T: Interface Transmission Resistance

C_{YSZ}: Ceramic topcoat Capacitance
C_{PORE}: Pore Capacitance
C_{TGO}: Oxide Scale Capacitance
C_T: Interface Transmission Capacitance

Figure 9. A model of an EIS ac-equivalent circuit for TBCs with and without TGO.

IV.4. Microstructural Characterization

During and after thermal cyclic oxidation testing as presented in Table III, selected specimens of TBCs have been employed for the microstructural and failure analysis as presented in Table III. Development of microstructural features and failure characteristics of TBCs have been examined as a function of thermal cycles. Aforementioned, this task employs state-of-the-art characterization techniques with emphasis on field emission scanning electron microscopy (FE-SEM), energy dispersive spectroscopy (EDS), focused ion beam (FIB) in-situ lift out (INLO), Philips™/Tecnai™ F30 300KeV transmission electron microscopy (TEM) and scanning TEM (STEM) equipped with nano-spot-EDS (n-EDS), convergent beam electron diffraction (CEBD), high angle annular dark field (HAADF) imaging and electron energy loss spectroscopy (EELS). In addition, facilities at the Advanced Materials Processing and Analysis Center (AMPAC) at UCF such as X-ray diffraction (XRD), auger electron spectroscopy (AES) with depth profiling, X-ray photoluminescence spectroscopy (XPS), Rutherford backscattering spectroscopy (RBS), and secondary ion mass spectroscopy (SIMS) with depth profiling can be employed if necessary.

V. RESULTS AND DISCUSSION

V.1. Lifetime Assessment and Visual Observation of TBC Spallation

V.1.1. Thermal Cycling Lifetime

The TBC lifetime for 1, 10 and 50- hour thermal cycling at 1121°C (2050°F) was determined with 5, 3 and 2 specimens, respectively. The furnace cycling consisted of 10-minute heat-up, 40-minute, 9.8 hours and 49.8 hours dwell at 1121°C and 10-minute forced air-quench. The TBC lifetimes are presented in Table IV and Figures 10 and 11. Independent of the dwell time at 1121°C (2050°F) the lifetime of type I TBCs remained the highest followed by types III, IV, II and V as shown in Figure 11. The cyclic dwell time life for the five different types of TBCs is also shown in Figure 12.

From the lifetime from all five types of TBCs, 10%, 50% and 70% lifetime was calculated as presented in Table V. Similar calculation of lifetime at 30% and 80% for the five types of TBCs was carried out for 10-hour and 50% for 50-hour thermal cycling as reported in Table V. Furnace thermal cycling was carried out up to these cycles to examine the microstructural evolution of TBC specimens as functions of thermal cycling.

Table IV. Specifications and thermal cycling lifetime for five types of commercial production TBCs employed in this program.

TBC System	7YSZ Deposition and Thickness	Bond Coat and Thickness	Superalloy Substrate	Dwell Time (Hrs) at 1121°C (2050°F)	Number of Specimens Tested	TBC Lifetime and Standard Deviation (#)
I	APS 600 μm	NiCoCrAlY 175 μm	Haynes 230	0.67 9.8 49.8	5 3 2	527 (20) 113 (1) 39 (0.7)
II	EB-PVD 350 μm	NiCoCrAlY 200 μm	CM247	0.67 9.8 49.8	5 3 2	280 (35) 25 (5) 3.5 (3.5)
III	EB-PVD 145 μm	As-Coated (Ni,Pt)Al 50 μm	CMSX-4	0.67 9.8 49.8	6 4 2	406 (22) 55 (3) 12 (1.5)
IV	EB-PVD 140 μm	Grit-Blasted (Ni,Pt)Al 35 μm	Rene'N5	0.67 9.8 49.8	6 3 2	360 (39) 42 (2) 9.5 (0.7)
V	APS 200 μm	NiCoCrAlY 100 μm	MAR-M-509	0.67 9.8 49.8	8 1 1	286 (76) 18 (0) 8 (0)

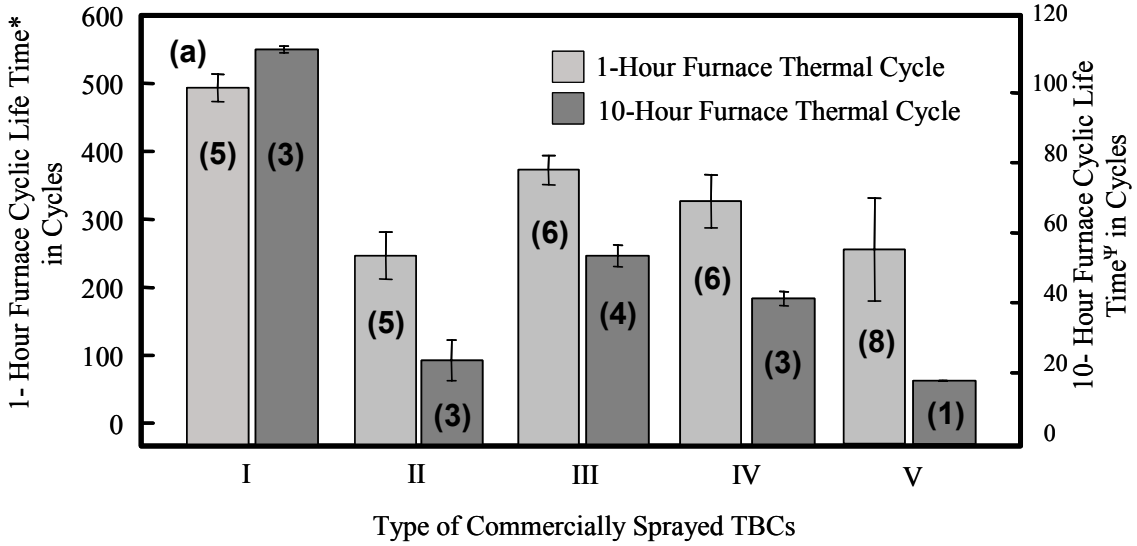

*1- Hour Cycle Consist of 10-minute ramp, 40- minute hold at 1121°C (2050 °F) and 10 –minute forced air quench

$^{\Psi}$10-Hour Cycle consist of 10-minute ramp, 9.8 hours hold at 1121°C (2050 °F) and 10 –minute forced air quench

Figure 10. Lifetime during thermal cycling at 1121°C for five-types of TBCs. Values in parenthesis represent the number of specimen employed to determine the lifetime (a) 1- and 10-hour thermal cycling.

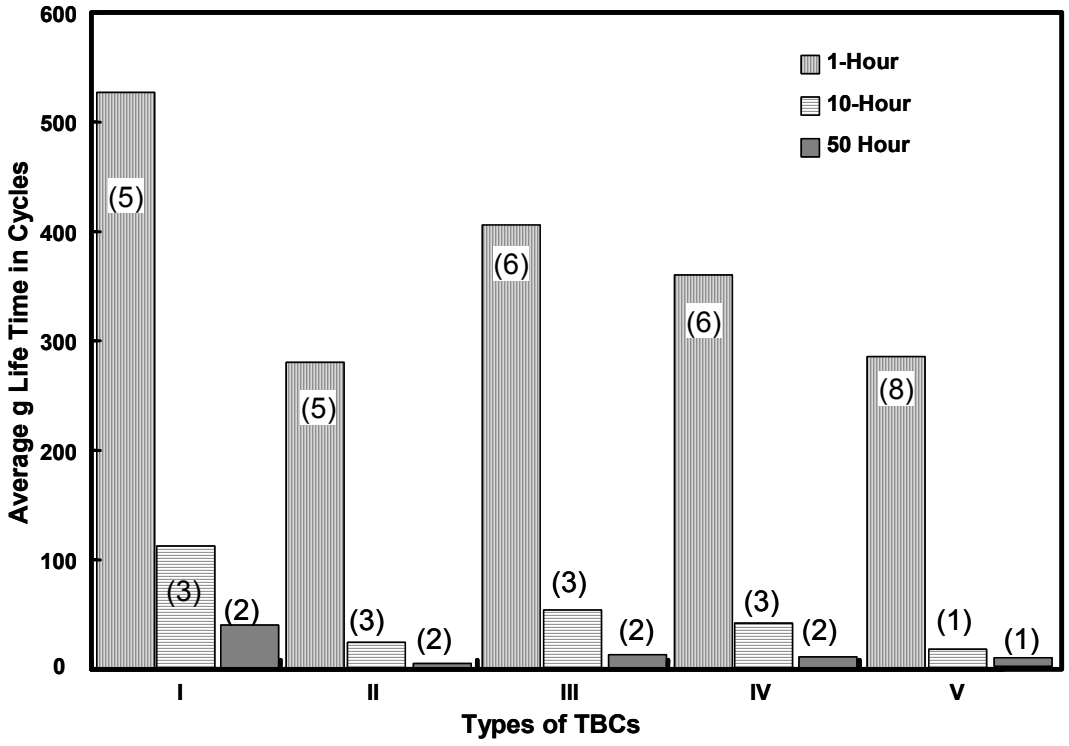

Figure 11. Lifetime during thermal cycling at 1121°C for five-types of TBCs. Values in parenthesis represent the number of specimen employed to determine the lifetime 1, 10 and 50 –hour thermal cycling.

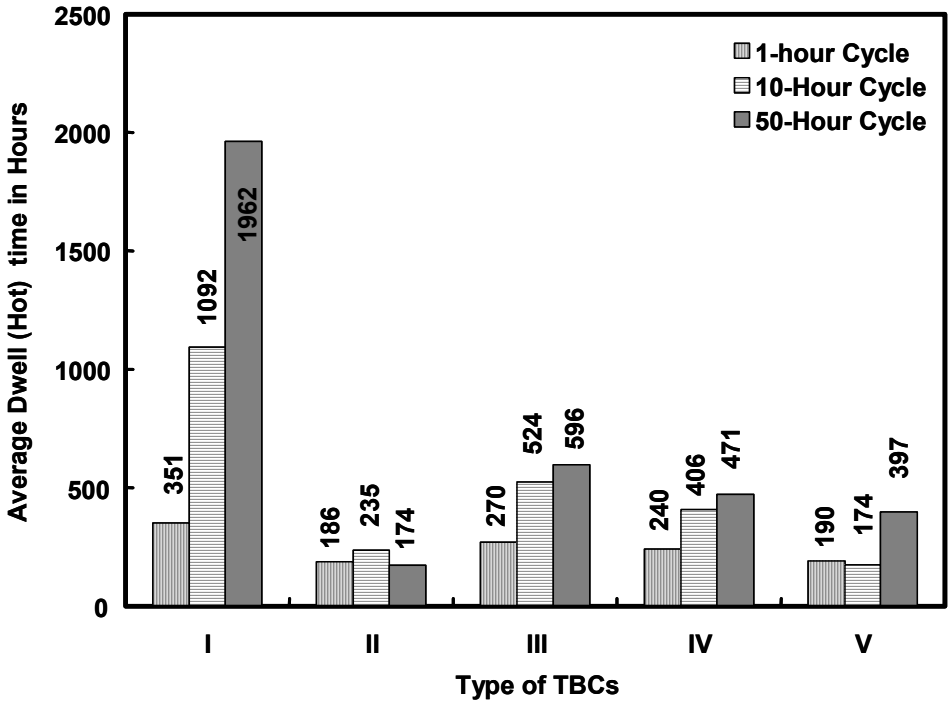

Figure 12. Dwell time life during thermal cycling at 1121°C for five-types of TBCs at 1, 10 and 50 –hour thermal cycling.

Table V. Thermal cyclic lifetime for commercial production TBCs and specimens employed for microstructural analysis.

TBC System	TBC Lifetime and Standard Deviation (#)	1-Hour Thermal Cycling			10-Hour Thermal Cycling		50-Hour Thermal Cycling
		10% Lifetime	50% Lifetime	70% Lifetime	30% Lifetime	80% Lifetime	50% Lifetime
I	527 (20) 113 (1) 39 (0.7)	50	260	360	35	90	20
II	280 (35) 25 (5) 3.5 (3.5)	30	140	200	8	20	2
III	406 (22) 55 (3) 12 (1.5)	45	200	280	20	45	6
IV	360 (39) 42 (2) 9.5 (0.7)	35	180	250	15	35	4
V	286 (76) 18 (0) 8 (0)	30	140	200	5	15	4

V.1.2. Visual Observation of TBC Spallation for 1-Hour Thermal Cycling-APS TBCs

Figure 13 shows the fractographic surface of the type-I APS TBCs with APS NiCoCrAlY bondcoat. Form the YSZ bottom surface we can observe two contrasts namely the black and the white. The black is supposedly the TGO and the white region is YSZ. A similar inference can be made on the bondcoat surface after spallation shown in Figure 11a. This leads to a conclusion that the fracture path was between the YSZ/TGO interfaces. A similar observation and explanation can be given to the type-V APS TBCs with VPS NiCoCrAlY bondcoat shown in Figure 14. A detailed analysis was carried out in section V.4.

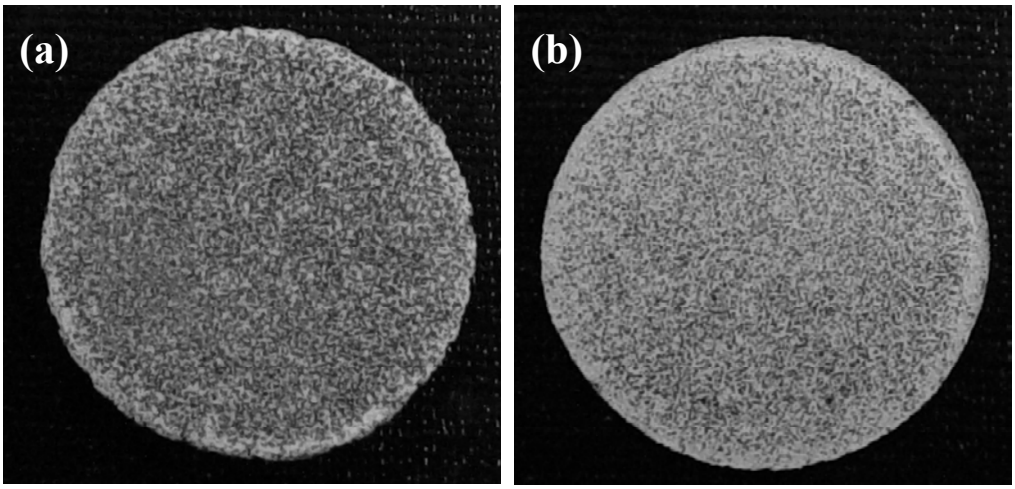

Figure 13. Macro photographs illustrating failure mode of type I APS TBCs with NiCoCrAlY bondcoat with average lifetime of 527 cycles: (a) bottom surface of spalled YSZ coating and (b) top surface of bondcoat after YSZ spallation.

Figure 14. Macro photographs illustrating failure mode of type V APS TBCs with NiCoCrAlY bondcoat with average lifetime of 286 cycles: (a) top surface of bondcoat after YSZ spallation that (b) occurred with initial damage at the edge of the button.

V.1.3. Visual Observation of TBC Spallation for 1-Hour Thermal Cycling-EB-PVD TBCs

Figure 15 shows the macro fractographic surface of the fractured type-II EB-PVD with NiCoCrAlY bondcoat. From these figures we can observe that the YSZ is cracked into pieces with cracks observed on the YSZ surface. This cracking of the YSZ may be due to the sintering and surface irregularities at the interface between the YSZ/TGO. This cracking of the YSZ may be related to the flat and large scale buckling failure of this particular type of TBCs. A detailed study was done this fracture surface and discussed in the section V.4.

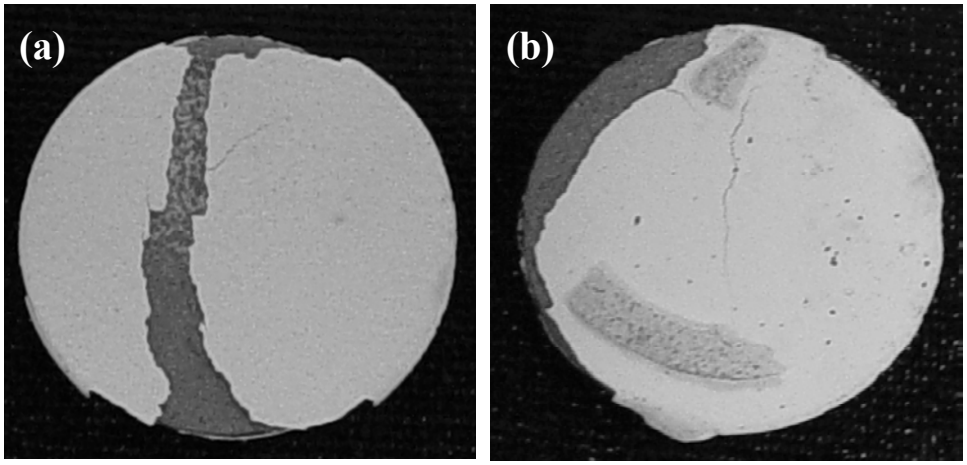

Figure 15. (a,b) Macro photographs illustrating failure mode of type II EB-PVD TBCs with NiCoCrALY bondcoat with average lifetime of 280 cycles.

Figure 16 shows the fracture surface of type-III EB-PVD TBCs with (Ni,Pt)Al bondcoat. This type showed the fracture of the entire YSZ coating. This type of fracture is related to the buckling of the YSZ coating due to the bondcoat ridges (discussed in section V.4). A similar observation type of observation is made for the type-IV coating with grit-blasted (Ni,Pt)Al bondcoat as shown in Figure 17. Here in this type the large scale buckling of the YSZ is due to another phenomena quiet frequently observed for this type of oxidation called racheting (see section V.4).

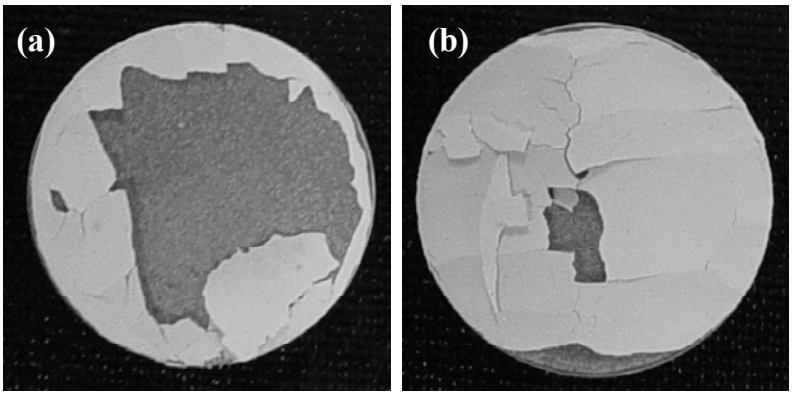

Figure 16. (a,b) Macro photographs illustrating failure mode of type III EB-PVD TBCs with as-coated (Ni,Pt)Al bondcoat with average lifetime of 418 cycles.

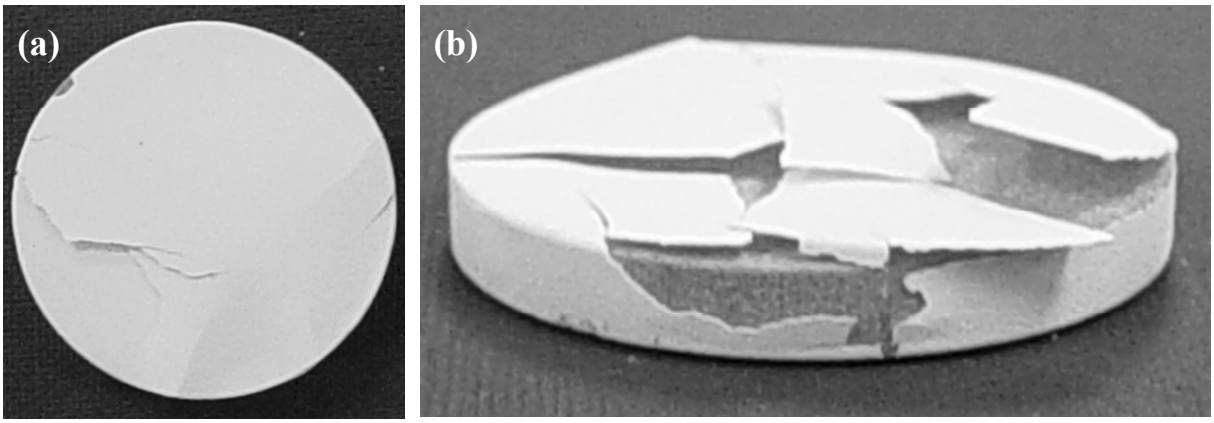

Figure 17. Macro photographs illustrating failure mode of type IV EB-PVD TBCs with grit-blasted bondcoat with average lifetime of 362 cycles: (a) top surface of buckled YSZ and (b) disintegration of the YSZ coating afterwards.

V.1.4. Visual Observation of TBC Spallation for 10-Hour Thermal Cycling for APS TBCs

Figures 18 and 19 show the fracture surface of type-I and type-V APS TBCs for 10-hour thermal cycling. The fracture surface remained the same macroscopically when compared to the 1-hour thermal cycling.

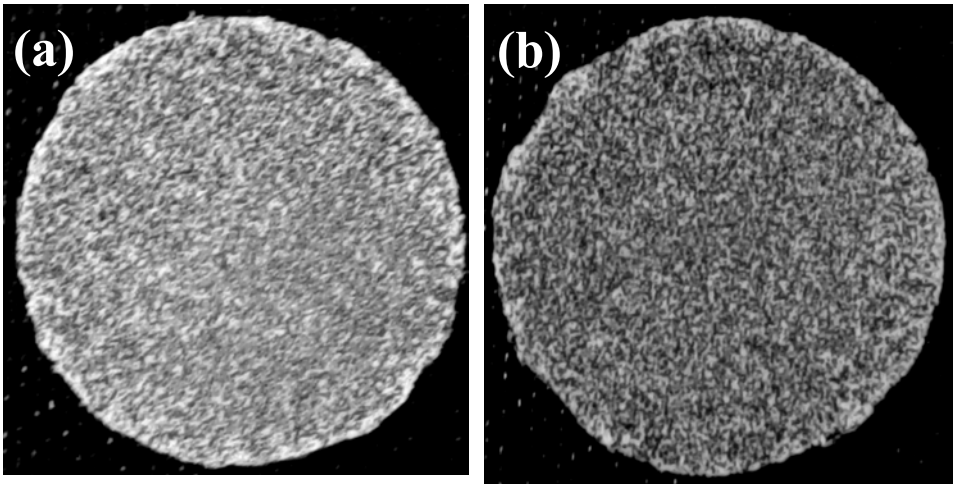

Figure 18. Macro photographs illustrating failure mode of type I APS TBCs with NiCoCrAlY bondcoat with average lifetime of 113 cycles: (a) bottom surface of spalled YSZ coating and (b) top surface of bondcoat after YSZ spallation.

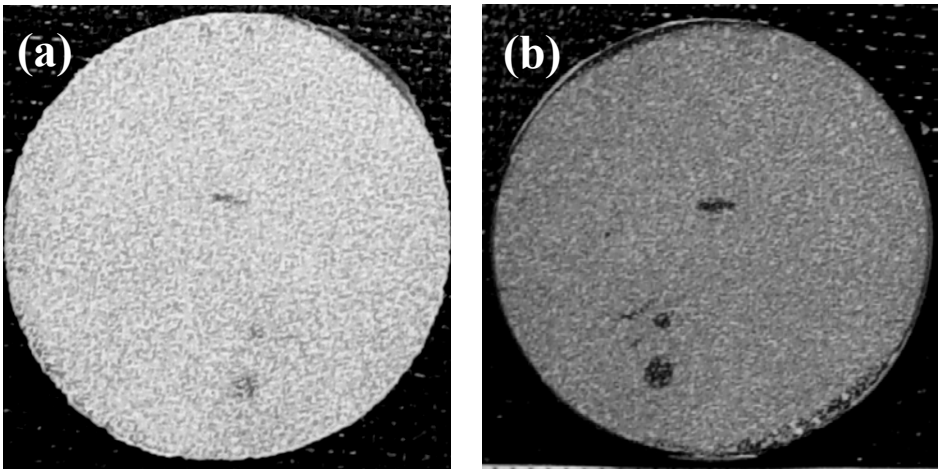

Figure 19. Macro photographs illustrating failure mode of type V APS TBCs with NiCoCrAlY bondcoat with average lifetime of 18 cycles: (a) bottom surface of the YSZ after spallation of the coating from the bondcoat (b) top surface of bondcoat after YSZ spallation.

V.1.5. Visual Observation of TBC Spallation for 10-Hour Thermal Cycling-EBPVD TBCs

Figure 20 shows the fracture of the type-II EB-PVD TBCs with NiCoCrAlY bondcoat. A similar fracture trend was observed when compared to 1-hour thermal cycling macroscopically. A detailed study was done and discussed comparing the 1-hour and 10-hour thermal cycling for this type in section V.4.

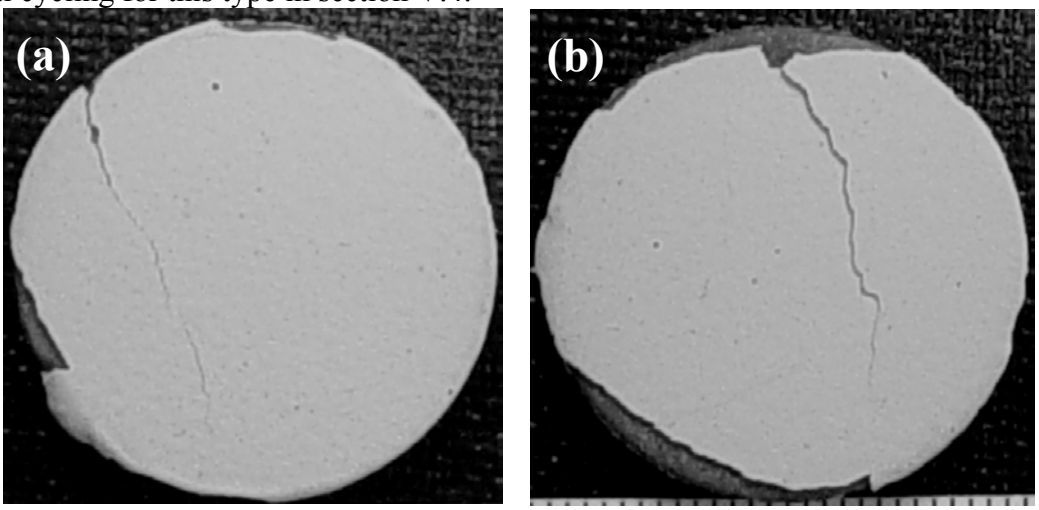

Figure 20. (a,b) Macro photographs illustrating failure mode of type II EB-PVD TBCs with NiCoCrALY bondcoat with average lifetime of 25 cycles.

Figure 21 shows the fractured surface type-III EB-PVD with as-coated (Ni,Pt)Al bondcoat. Macroscopically we can observe that this type of TBCs compared to the 1-hour thermal cycling did differ from 10-hour thermal cycling. This type of failure is related to the large scale buckling for this type of TBCs.

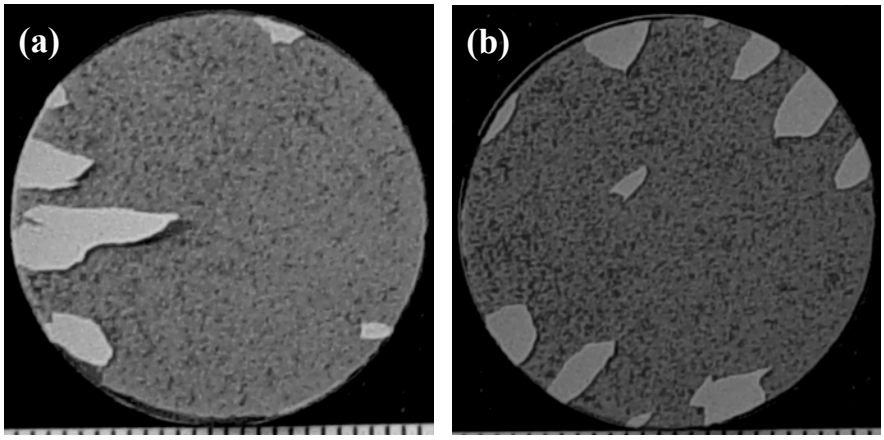

Figure 21. (a,b) Macro photographs illustrating failure mode of type III EB-PVD TBCs with as-coated (Ni,Pt)Al bondcoat with average lifetime of 55 cycles.

Figure 22 shows macroscopically the fracture surface of type-IV EB-PVD TBCs from 10-hour thermal cycling. Significantly this particular type did differ from 1-hour thermal cycling where we can observe that the buckling is localized to a particular region and also we can observe intact TBCs. A higher magnification on the buckled region shows cracks running through the YSZ. A detailed microstructural characterization was carried on this type and discussed in section V.4.

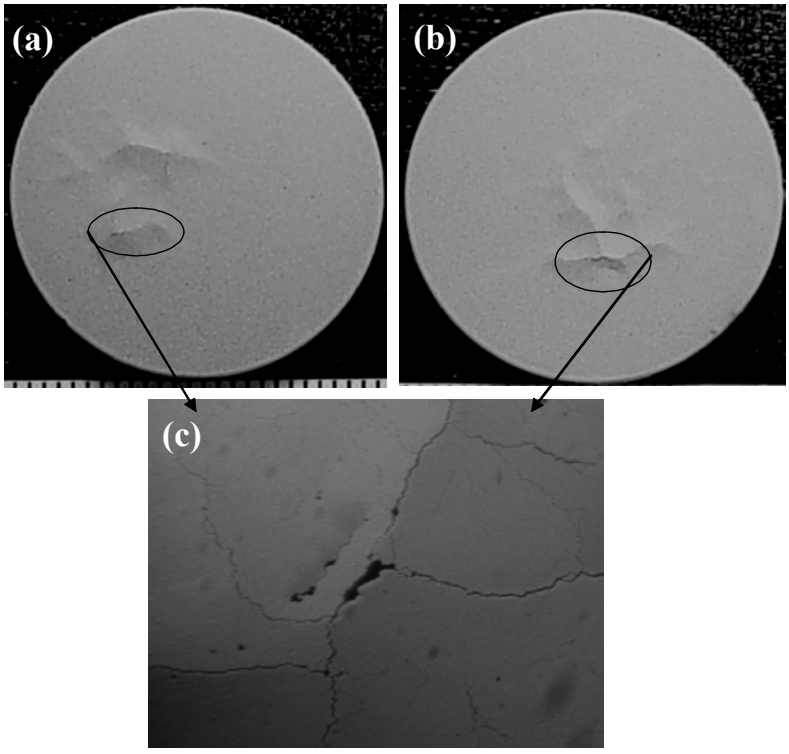

Figure 22. Macro photographs illustrating failure mode of type IV EB-PVD TBCs with grit-blasted bondcoat with average lifetime of 42 cycles: (a, b) top surface of buckled YSZ and (c) A magnified view of the buckling of YSZ coating.

V.1.6. Visual Observation of TBC Spallation for 50-Hour Thermal Cycling for APS TBCs

Figures 23 and 24 shows macroscopic fracture of type-I APS coatings for 50-hour thermal cycling. The fracture surfaces look similar to that of the 1 and 10- hour thermal cycling. The micro constituents of the fracture surface will be reported in the next report during the extension period.

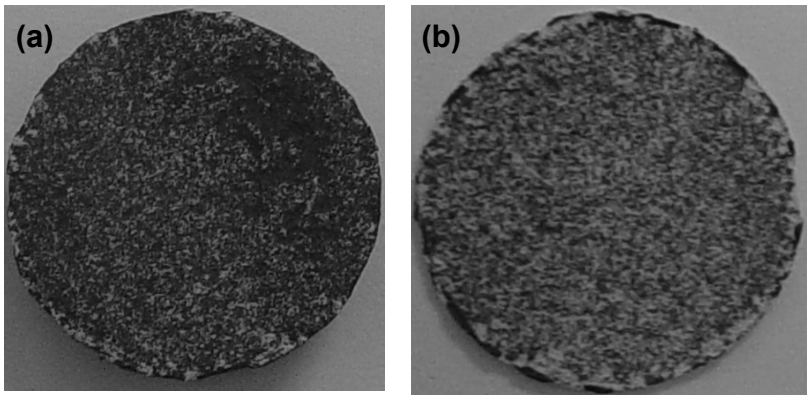

Figure 23. Macro photographs illustrating failure mode of type I APS TBCs with NiCoCrAlY bondcoat with average lifetime of 39 cycles: (a) top surface of bondcoat after YSZ spallation and (b) bottom surface of YSZ after spallation.

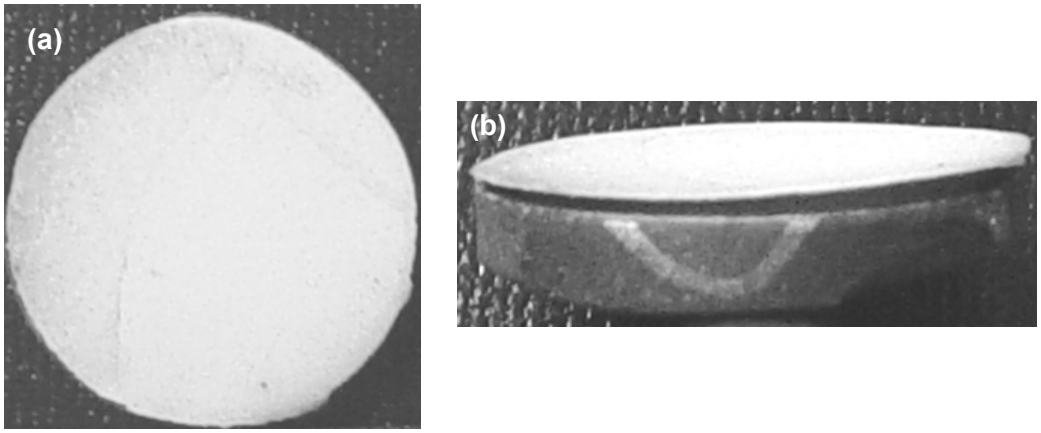

Figure 24. Macro photographs illustrating failure mode of type V APS TBCs with VPS NiCoCrAlY bondcoat with average lifetime of 8 cycles: (a, b) top surface of delaminated YSZ and (c) A front view of the delamination of YSZ coating.

V.1.7. Visual Observation of TBC Spallation for 50-Hour Thermal Cycling for EB-PVD TBCs

Figure 25 shows the fracture for type-II EB-PVD TBCs with shot-peened NiCoCrAlY bondcoat. The fracture was similar to that of the 1 and 10-hour thermal cycling. Both specimens shown in Figure 25 failed by buckling but one of the specimens shown in Figure 25 (b) failed after one cycle. A detailed microstructure analysis on these two types will be done in the following report.

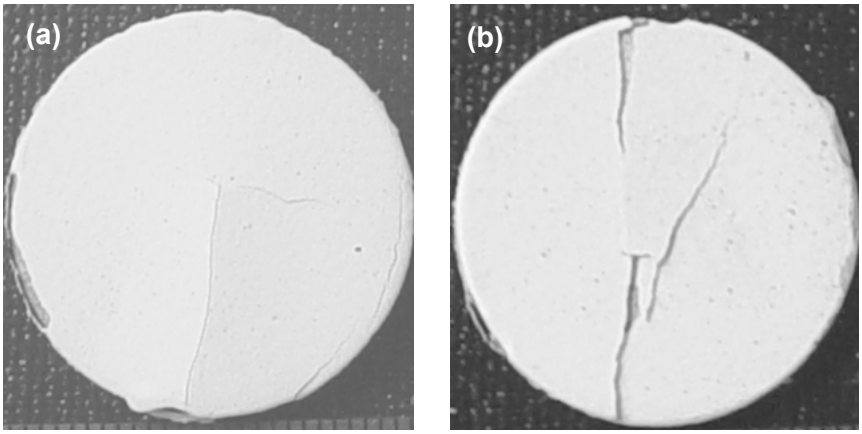

Figure 25. Macro photographs illustrating failure mode of type II EB-PVD TBCs with shot-peened NiCoCrAlY bondcoat with average lifetime of 3.5 cycles: (a) top surface of buckled YSZ after 6 cycles and (b) A top surface view of buckled YSZ after 1 cycle.

Figure 26 shows the macroscopic failure of type-III EB-PVD TBCs with as-coated (Ni,Pt)Al bondcoat after 50-hour thermal cycling. The fracture surface appeared different from those observed after 1 and 10-hour thermal cycling. A detailed investigation will be presented in the final report. This type of observation is related to large scale buckling that is observed for this type of TBCs.

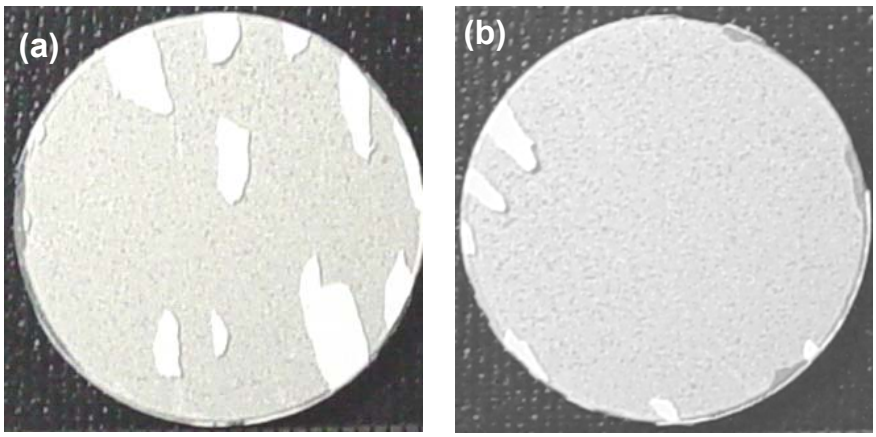

Figure 26. Macro photographs illustrating failure mode of type III EB-PVD TBCs with as-coated (Ni,Pt)Al bondcoat with average lifetime of 12cycles, Large scale buckling observed in both the samples after 50-hour thermal cycling.

Figure 27 shows the macrograph of type-IV EB-PVD TBCs with grit-blasted (Ni,Pt)Al bondcoat. From the macrograph it's observed that these samples did also fail by large scale buckling comparing to the 10-hour thermal cycling. The micro-constituents and any difference microscopically of the fracture surface will be presented in the final report.

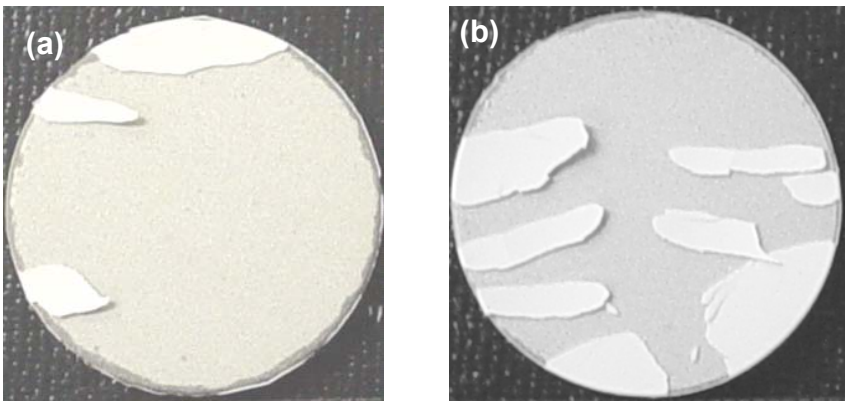

Figure 27. Macro photographs illustrating failure mode of type IV EB-PVD TBCs with grit-blasted (Ni,Pt)Al bondcoat with average lifetime of 9 cycles, Large scale buckling observed in both the samples after 50-hour thermal cycling.

V.2. Photostimulated Luminescence Spectroscopy of Thermal Barrier Coatings

V.2.1. As-Coated Electron Beam Physical Vapor Deposited Thermal Barrier Coatings

NDE by PSLS has been restricted to EB-PVD TBCs (type II, III and IV), since PSLS cannot be applied to APS TBCs (type I and V) without impregnating APS YSZ coatings with other medium [22], whose effect on TBC lifetime may be harmful.

For type II as-coated EB-PVD TBCs with NiCoCrAlY bond coat, PSLS was collected for all 20 specimens. For each specimen, 30 random-spot measurements were carried out. Typical luminescence observed from type II TBCs are presented in Figure 28. Due to the nature of the spectra, relative luminescence intensity and luminescence frequency for type II TBCs could not be analyzed properly in the as-received condition. This unclear and indistinguishable luminescence can be due to under-developed TGO scale, potentially consisting of θ-Al_2O_3. However, luminescence from type II TBCs has been carried out with ease after initial thermal cycling since a clearer and distinguishable luminescence from better-developed TGO was observed.

Luminescence from α-, γ- and θ-Al_2O_3 was observed in all spectra for all type III EB-PVD specimens with as-coated (Ni,Pt)Al bond coat in the as-received condition. Figure 29 represents typical luminescence observed from type III EB-PVD TBCs. Relative luminescence intensity from α-, γ- and θ-Al_2O_3 polymorphs is presented in Figure 30. In general, 70~80% of luminescence was from α-Al_2O_3 while 20~30% luminescence was from γ- and θ-Al_2O_3 for as-coated type III TBCs. These values *do not* correspond to the actual volume fraction of Al_2O_3 polymorphs.

Figures 31 and 32 present the shift in the position of R_2 luminescence $\overline{\Delta\upsilon}$ based on 30 random-spot measurements for type III TBCs. In all cases, bimodal (i.e., two sets of R_1 and R_2) luminescence corresponding to higher (~5 GPa) and lower (~3.5 GPa) compressive residual stress in α-Al_2O_3 was observed.

PSLS was collected for 20 specimens of type IV as-coated EB-PVD TBCs with grit-blasted (i.e., removal of grain boundary ridges) (Ni,Pt)Al bond coat. For all 20 specimens with luminescence, 30 random-spot measurements were carried out. Clear and distinguishable luminescence from α-, γ- and θ-Al_2O_3 was observed in all spectra for 16 specimens as presented in Figure 33(a). *Extremely weak luminescence with much noise was obtained from the remaining 4 specimens; possibly a result of under-developed TGO.* The remaining four specimens exhibited luminescence with low signal-to-noise ratio as presented in Figure 33(b). Relative luminescence intensity from α-, γ- and θ-Al_2O_3 polymorphs is presented in Figure 34. In general, 60~70% of luminescence was from α-Al_2O_3 while 30~40% luminescence was from γ- and θ-Al_2O_3 for as-coated type IV TBCs. These values *do not* correspond to the actual volume fraction of Al_2O_3 polymorphs. Relative to type III TBCs with as-coated (Ni,Pt)Al bond coat, a slightly stronger γ-Al_2O_3 luminescence than θ-Al_2O_3 was observed.

Figures 35 and 36 represent the shift in the position of R_2 luminescence $\overline{\Delta\upsilon}$ determined based on 30 random-spot measurements for type IV TBCs. In all cases, bimodal (i.e., two sets of R_1 and R_2) luminescence corresponding to higher (~6 GPa) and lower (~1 GPa) compressive residual stress in α-Al_2O_3 was observed.

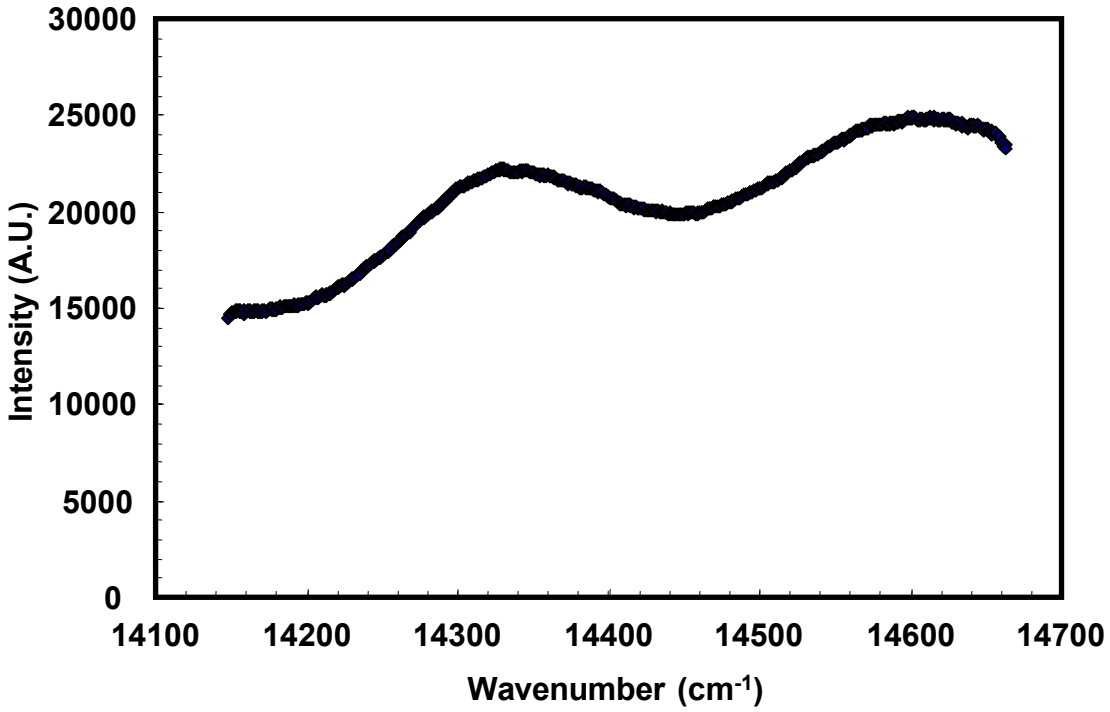

Figure 28. Typical photostimulated luminescence spectrum from as-received type II EB-PVD TBCs with NiCoCrAlY bond coat.

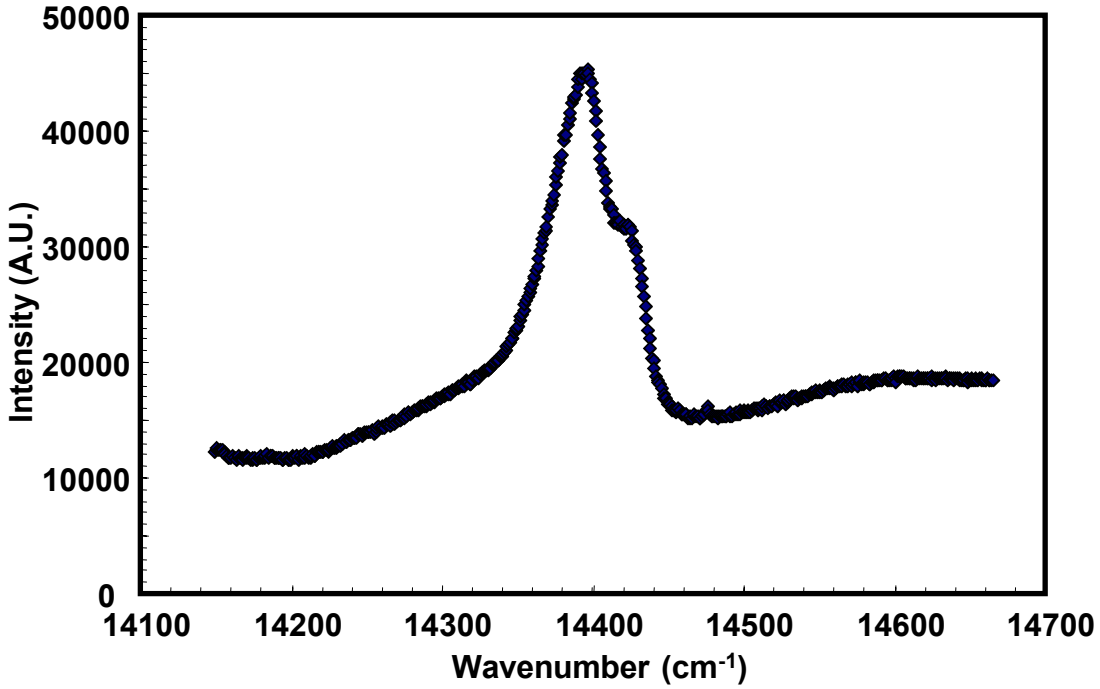

Figure 29. Typical photostimulated luminescence spectrum from as-received type III EB-PVD TBCs with as-coated (Ni,Pt)Al bond coat.

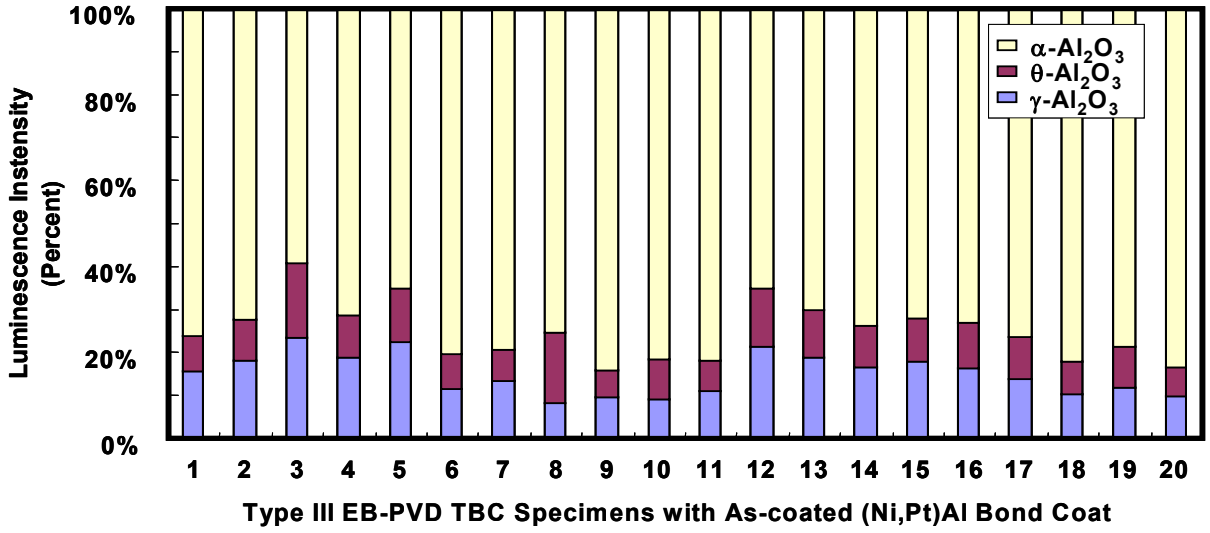

Figure 30. Relative luminescence intensity from α-, γ- and θ-Al_2O_3 in TGO for as-coated type III TBCs with as-coated (Ni,Pt)Al bond coat.

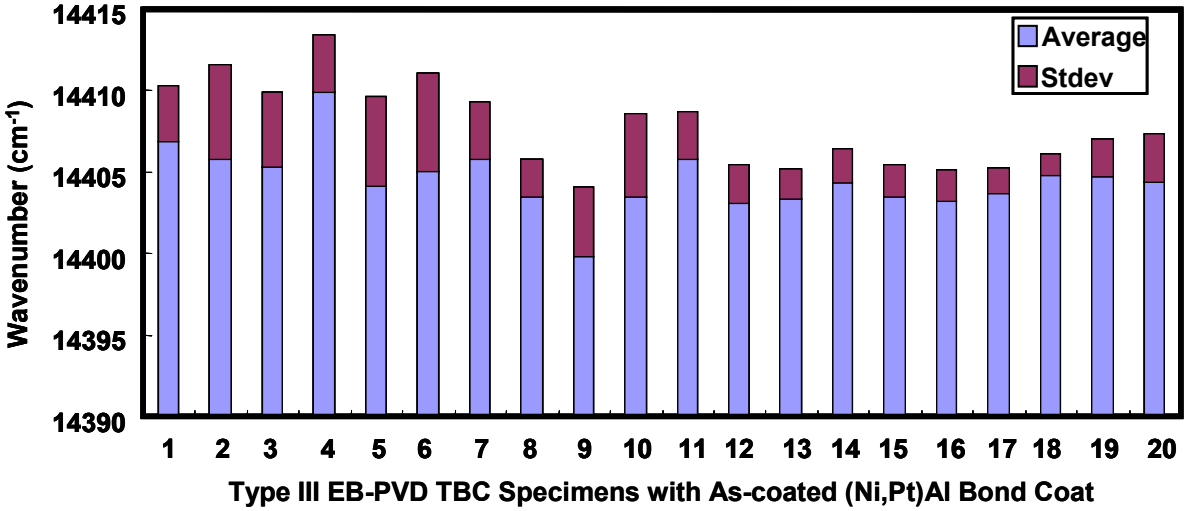

Figure 31. Higher average compressive residual stress of α-Al_2O_3 TGO determined from bimodal luminescence for as-coated type III TBCs.

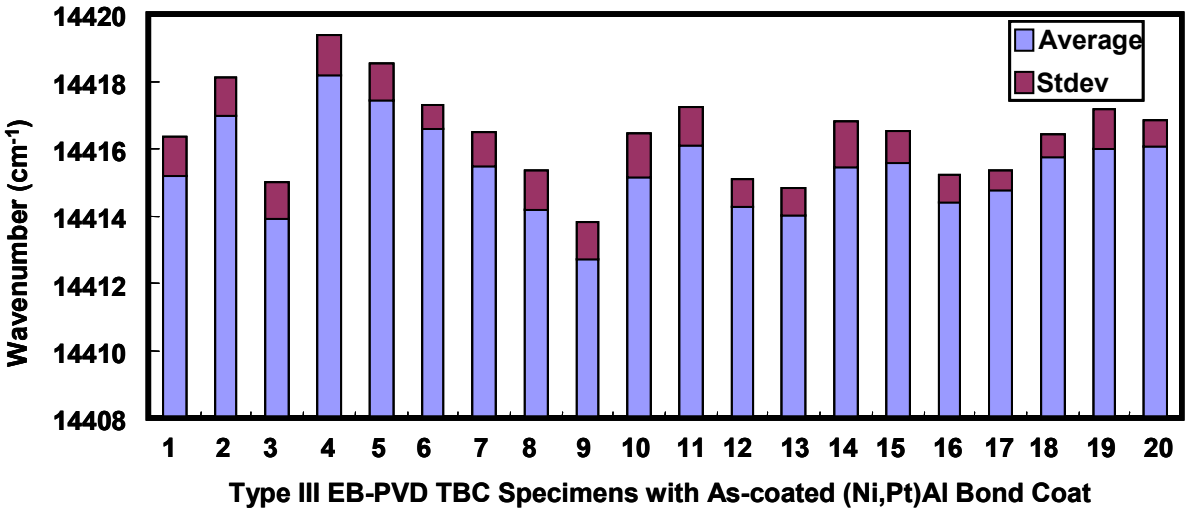

Figure 32. Lower average compressive residual stress of α-Al_2O_3 TGO determined from bimodal luminescence for as-coated type III TBCs.

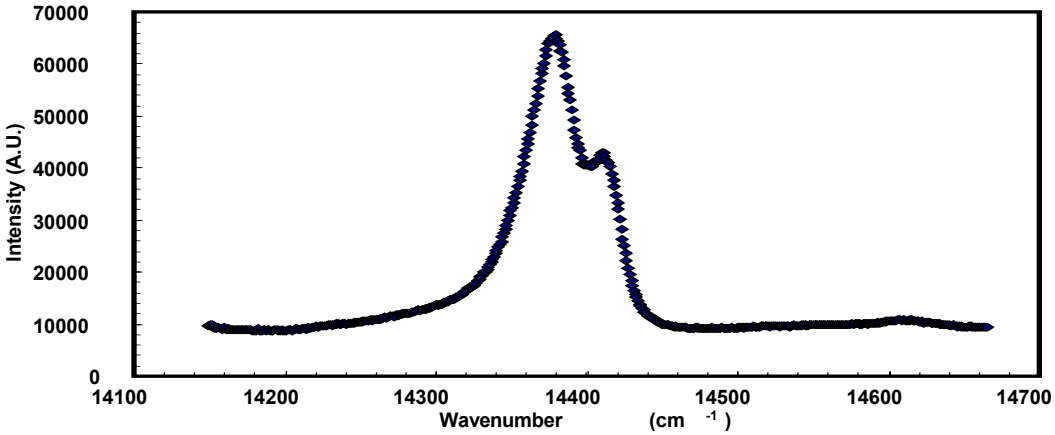

(a)

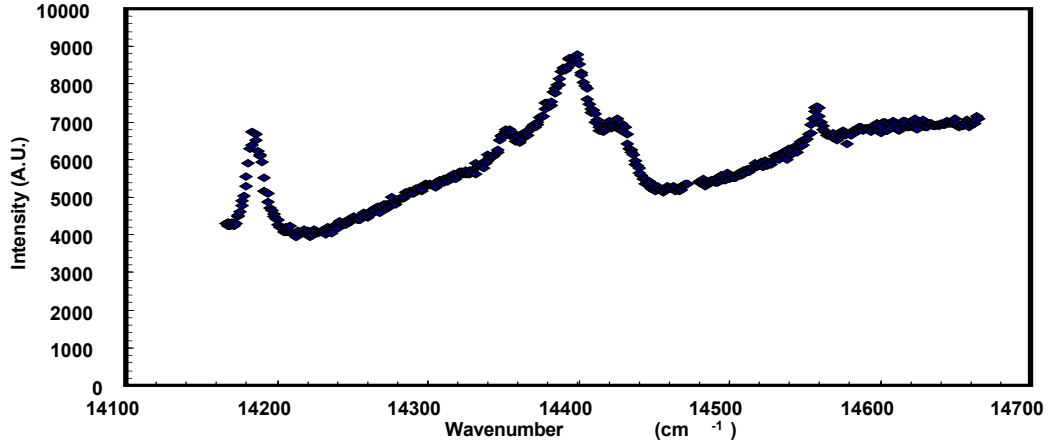

(b)

Figure 33. Typical photostimulated luminescence spectrum from as-received type IV EB-PVD TBCs with grit-blasted (Ni,Pt)Al bond coat: (a) 16 specimens with strong luminescence and (4) the remaining 4 specimens with low signal-to-noise ratio.

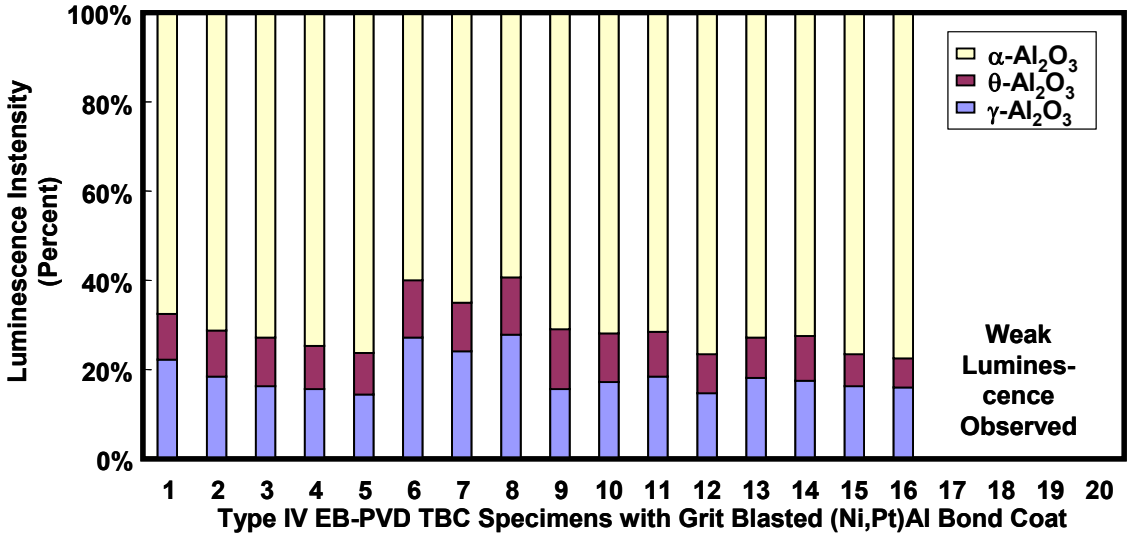

Figure 34. Relative luminescence intensity from α-, γ- and θ-Al_2O_3 in TGO for as-coated type IV TBCs with grit-blasted (Ni,Pt)Al bond coat.

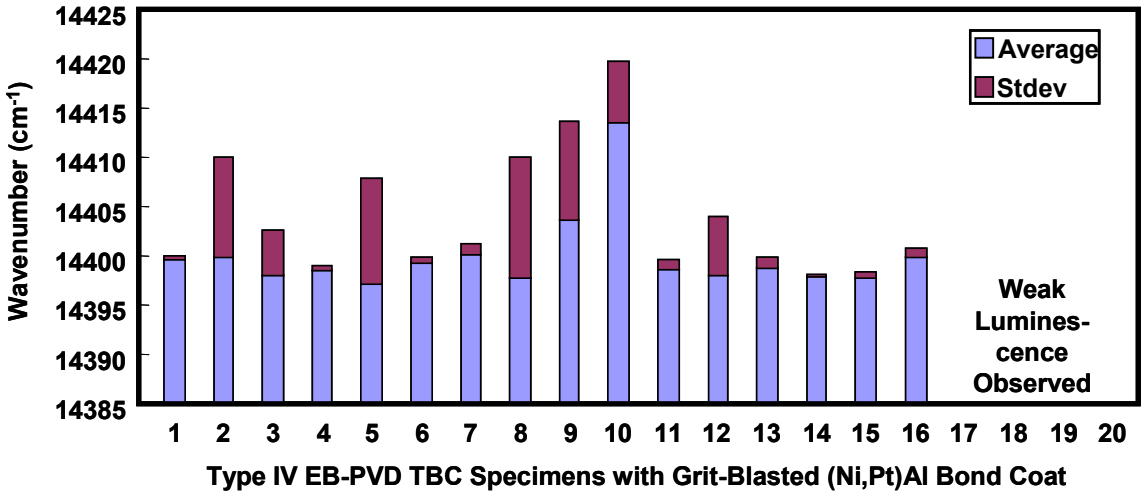

Figure 35. Higher average compressive residual stress of α-Al_2O_3 TGO determined from bimodal luminescence for as-coated type IV TBCs.

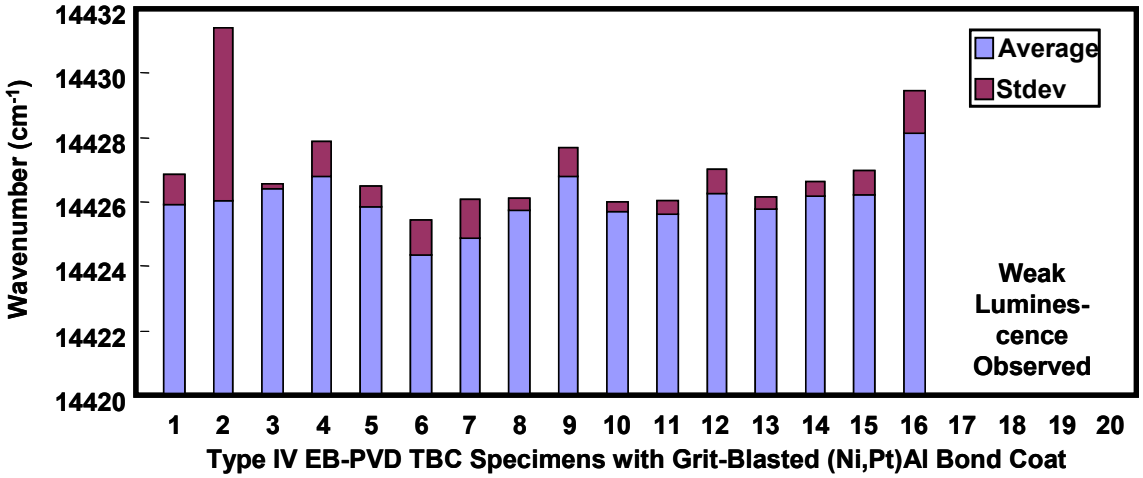

Figure 36. Lower average compressive residual stress of α-Al_2O_3 TGO determined from bimodal luminescence for as-coated type IV TBCs.

V.2.2. PSLS of EB-PVD TBCs as a Function of 1-Hour Thermal Cycling

The compressive residual stress within the TGO as a function of 1-hour thermal cycling for type II EB-PVD TBCs with NiCoCrAlY bond coats is presented in Figure 37. The value of stress is calculated based on shift of photostimulated luminescence via piezospectroscopic coefficients. Bimodal luminescence (i.e., two sets of R_1-R_2 luminescence) was observed for type II TBCs after thermal cycling. After the initial increase (i.e., starting 1st thermal cycle) in the compressive residual stress (for both higher and lower compressive residual stress arising from bimodal luminescence), the magnitude of the TGO stress remained quite constant throughout the entire thermal cycling (i.e., 5.5 and 3.5 GPa in compression). Luminescence from metastable Al_2O_3 phases disappeared after the 1st cycle.

No significant changes in the value of stress or standard deviation were observed prior to spallation as presented in Figure 37. While the initial increase may be due to development of the TGO scale, it is somewhat discouraging that no detectable changes in the luminescence was observed prior to failure of type II TBCs. Microstructural and failure investigation of type II TBCs indicate that the fracture primarily occurred at the YSZ/TGO interface and a significant internal oxidation of NiCoCrAlY bond coat has occurred (see section V.4.4). This is somewhat abnormal. Constant values of compressive residual stress can be correlated to lack of interfacial undulation at the NiCoCrAlY/TGO interface.

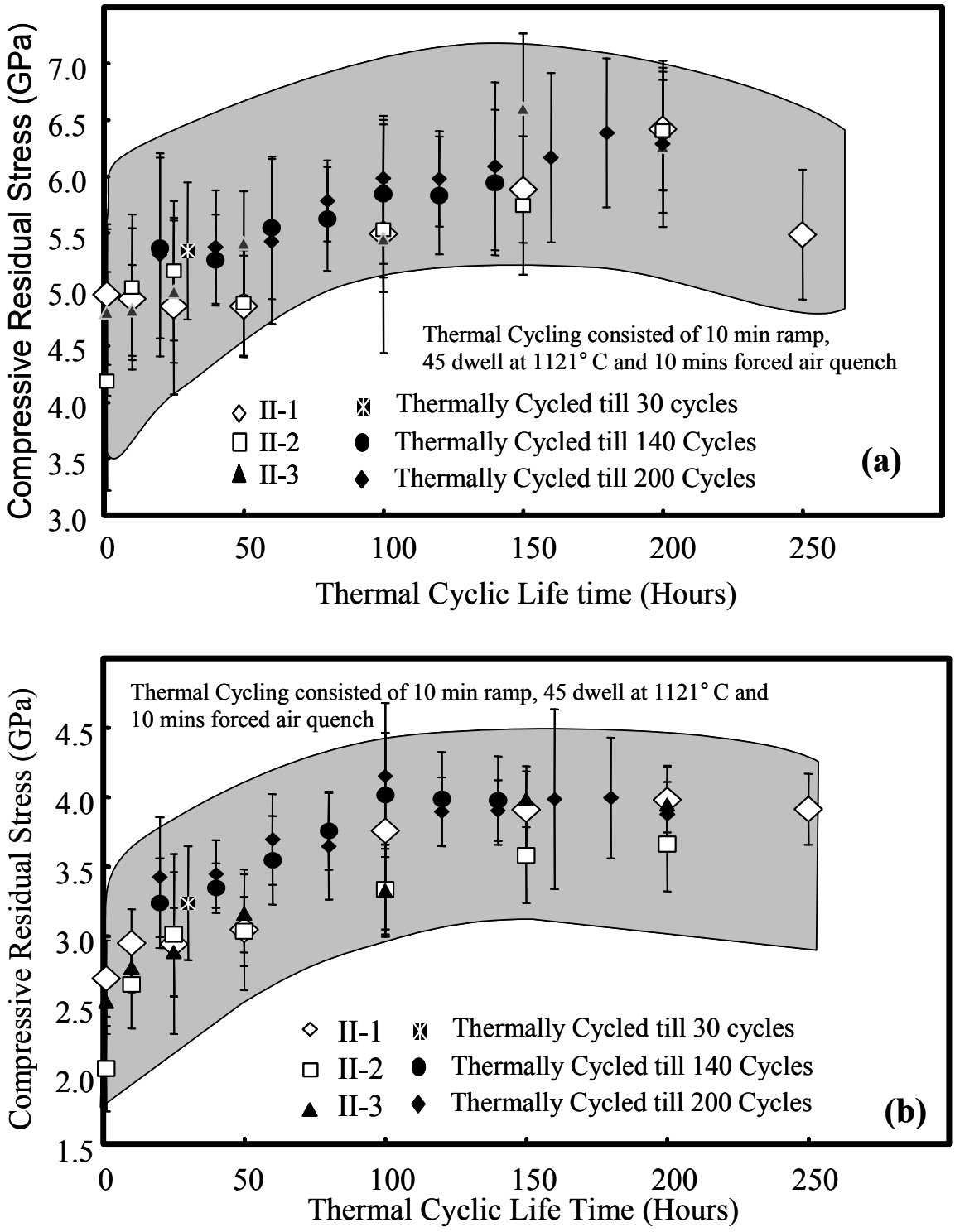

Figure 37. Compressive residual stress within TGO as a function of 1-hour thermal cycling for type II EB-PVD TBCs with NiCoCrAlY bondcoats. Values of compressive residual stress ere calculated from bimodal luminescence corresponding to (a) higher and (b) lower shifts in luminescence.

Figure 38 represents typical luminescence observed for type III TBCs as a function of 1-hour thermal cycling. While the failure of TBCs occurred at 420 1-hour cycles, detectable increase in the luminescence associated with stress-relief of the TGO emerged starting 350 cycles as shown in Figure 38. After 400 cycles, more than half of 20-randomly-selected measurement indicated localized stress-relief associated with damage in the TGO scale. The evolution and detection of stress-relief in the TGO for type III TBCs can be quantified by examining the first $(dc/d\upsilon)$ and second $(d^2c/d\upsilon^2)$ derivatives of luminescence spectrum associated with stress-relieved luminescence frequency at $\upsilon \cong 14432$ for R_2. As show in Figure 39(a), the luminescence spectrum with $(dc/d\upsilon) = 0$ at $\upsilon = 14432 \pm 3$ and $(d^2c/d\upsilon^2) = 0$ at $\upsilon = 14432 \pm 3$ was observed, starting 350 cycles, and thereafter gradually increased in terms of population out of 20 random-spot measurements with thermal cycling shown in Figure 39(b).

Similar to type II TBCs, bimodal luminescence (i.e., two sets of R_1-R_2 luminescence) was observed for type III TBCs throughout thermal cycling. However, for type III TBCs, a tri-mode luminescence emerged starting from approximately 50% lifetime, and the emerging third set of R_1-R_2 luminescence were clearly associated with stress-relief of the α-Al_2O_3 scale. The evolution of relative luminescence intensity obtained up to 50% and 70% of lifetime for the type III TBCs is presented in Figures 40 and 41, respectively. In these Figures, R_2, R_2', and R_2" refer to tri-mode luminescence of higher, lower and no shift, respectively, where the emergence of "no-shift" luminescence may be related to the stress-relief associated with damage within the TGO. The compressive residual stress within TGO as a function of 1-hour thermal cycling for type III EB-PVD TBCs with (Ni,Pt)Al bond coats is presented in Figures 42 and 46.

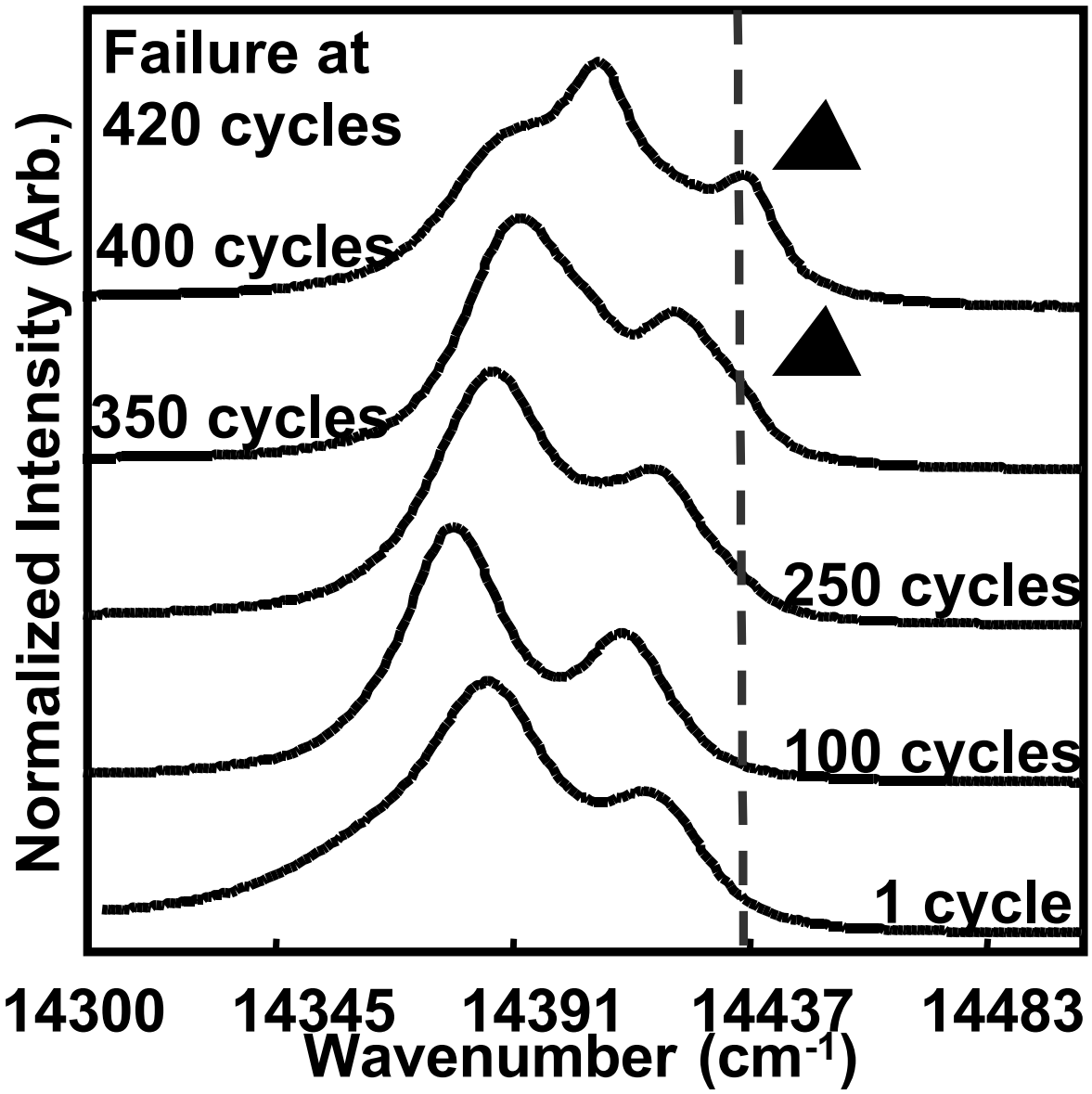

Figure 38. Typical photostimulated luminescence spectra as a function of 1-hour thermal cycling for type III EB-PVD TBCs with as-coated (Ni,Pt)Al bond coats. TBC spallation has occurred after 420 cycles and luminescence from stress-relieved TGO scale (marked by dotted vertical line and arrows) was observed starting 350 cycles by examining the derivatives of the spectra.

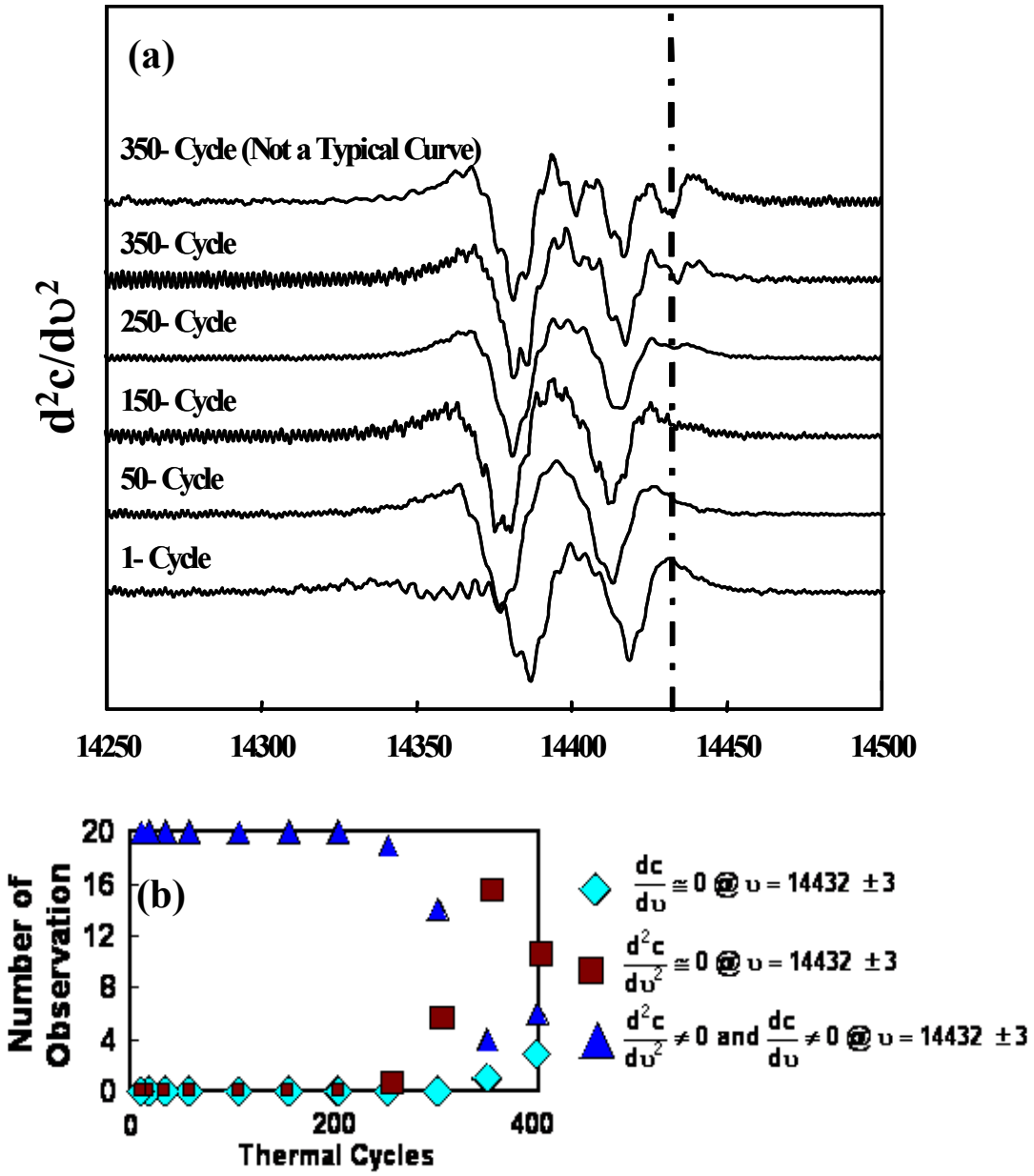

Figure 39. (a) Typical derivatives of luminescence spectrum associated with stress-relieved luminescence frequency at $\upsilon \cong 14432 \pm 3$ for R_2 for 1-hour thermal cycling. (b) Number of photostimulated luminescence spectra that exhibits variation in derivative at stress-relief luminescence as a function of 1-hour thermal cycling for type III EB-PVD TBCs with as-coated (Ni,Pt)Al bond coats.

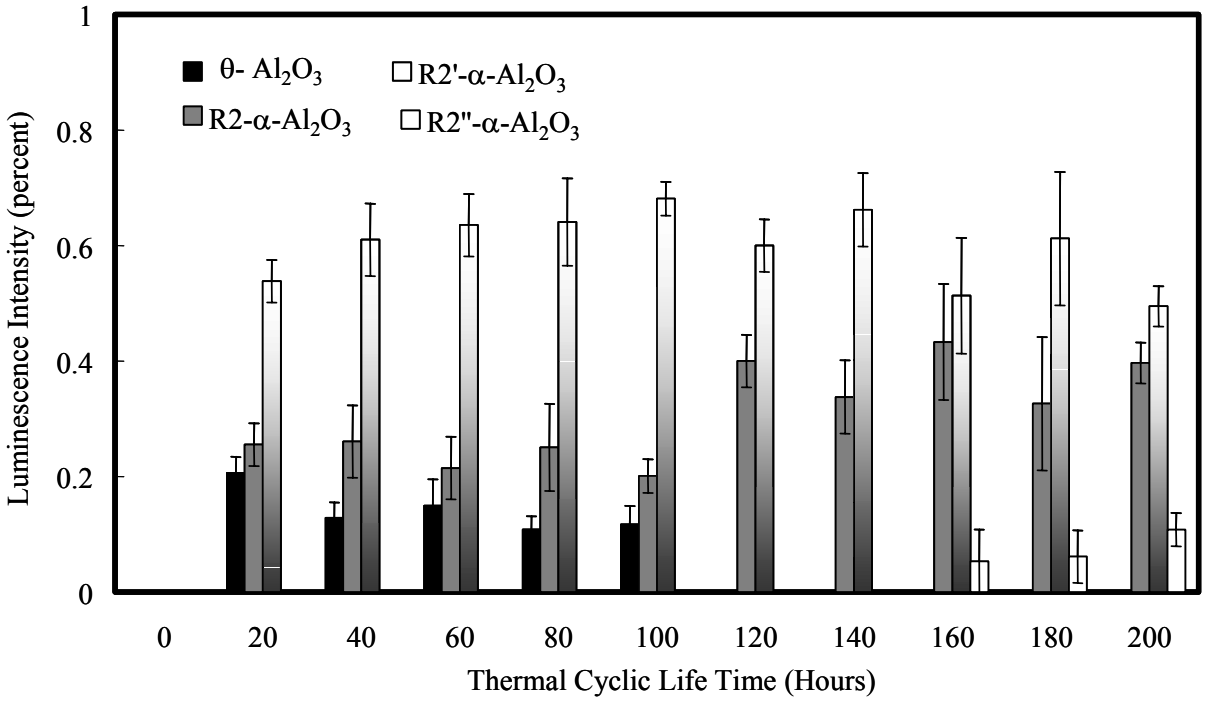

Figure 40. Type-III TBCs cycled until 50% thermal cyclic life time, Relative Luminescence Intensity from θ and α (R2, R'2 & R"2) in TGO with as-coated (Ni,Pt)Al bond coat.

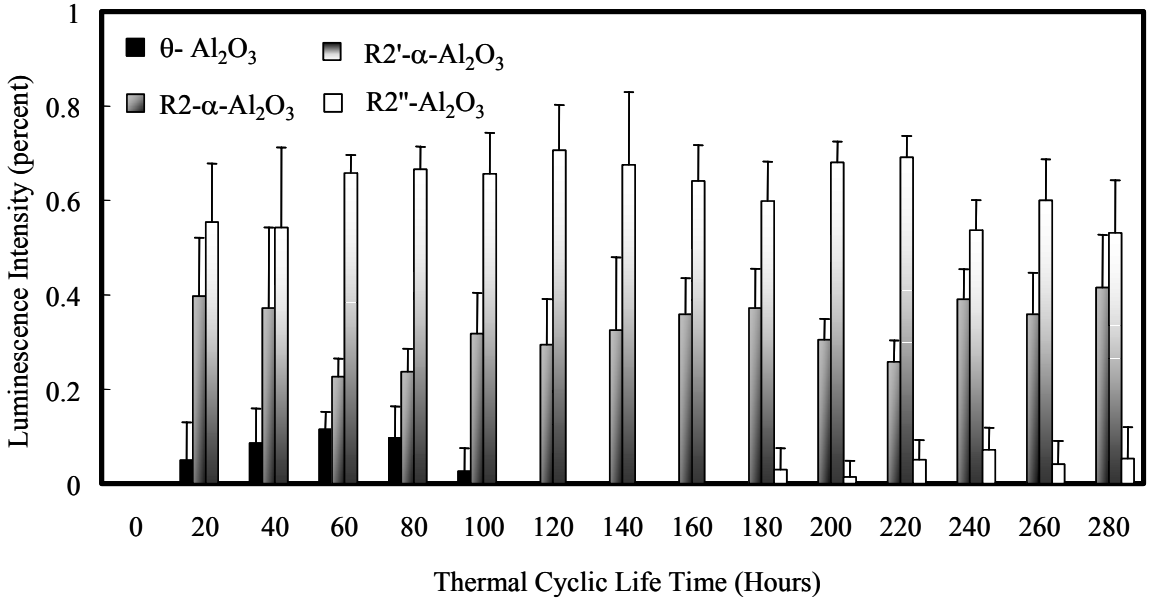

Figure 41. Type-III TBCs cycled until 70% thermal cyclic life time, Relative Luminescence Intensity from θ and α (R2, R'2 & R"2) in TGO with as-coated (Ni,Pt)Al bond coat.

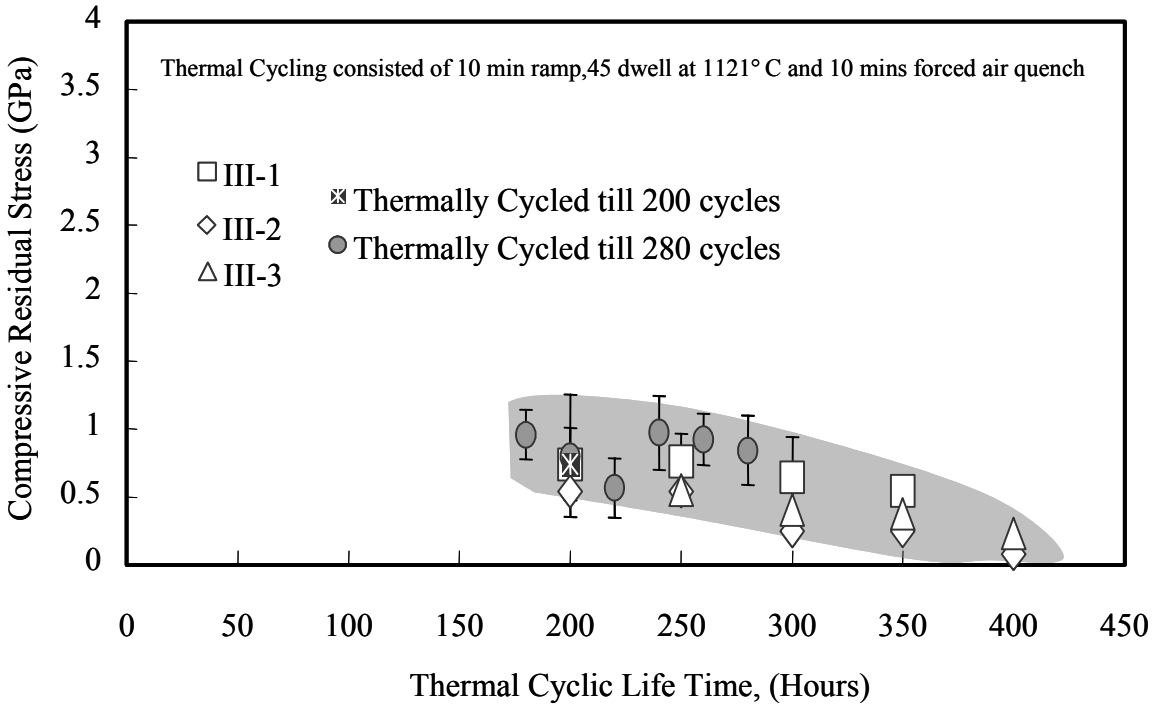

Figure 42. Compressive residual stress within TGO as a function of 1-hour thermal cycling for type III EB-PVD TBCs with (Ni,Pt)Al bondcoats. Values of compressive residual stress were calculated from the emerging luminescence with minimum shift in the tri-modal luminescence.

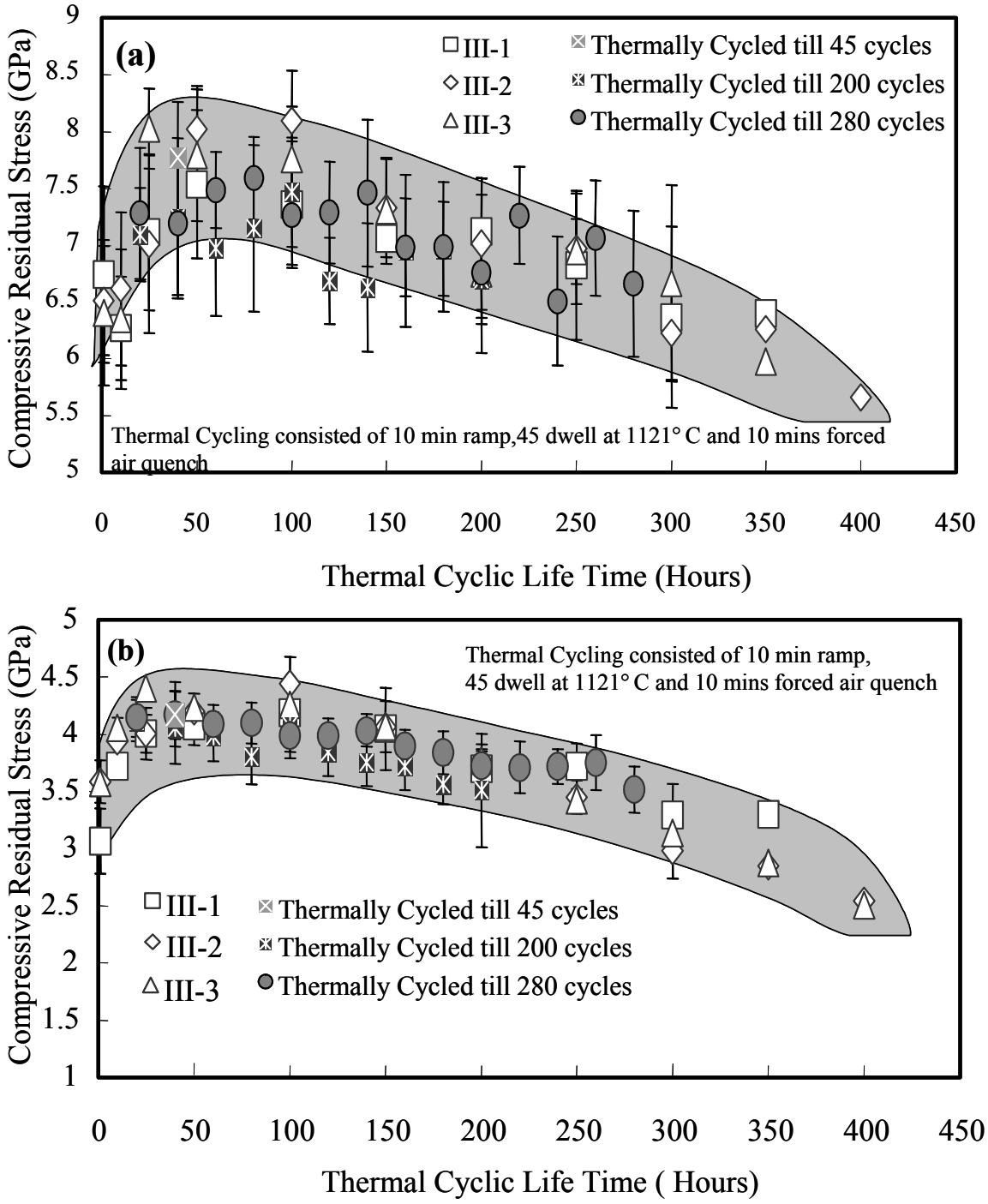

Figure 43. Compressive residual stress within TGO as a function of 1-hour thermal cycling for type III EB-PVD TBCs with as-coated (Ni,Pt)Al bond coats. Values of compressive residual stress were calculated from the (a) higher shift luminescence and (b) lower shift luminescence from the bimodal/trimodal luminescence.

Typical photostimulated luminescence spectra from type IV EB-PVD TBCs with grit-blasted bond coat are presented in Figure 44 as a function of 1-hour thermal cycling. Overall, a gradual decrease in the compressive residual stress was observed nearing complete stress-relief at 300 cycles as shown in Figure 45. This particular specimen failed after 350 cycles. Both higher and lower stressed luminescence arising from the bimodal luminescence exhibited an initial increase and a gradual and significant decrease before the final spallation. While the initial increase may be due to initially under-developed TGO scale, gradual changes in the luminescence frequency are significant and can serve to assess life-remain for type IV TBCs. This decrease may be related to undulation of TGO-bond coat interface and related damages (see section V.4.4) that occurred during the 1-hour thermal cycling.

The evolution in the magnitude of compressive residual stress within TGO, σ_{TGO} may be examined with respect to thermal cycling, c, quantitatively by using the relation:

$$\sigma_{TGO} = \sigma^{o}_{TGO} + K_1 c^{(l/n)} - K_2 c^{(l/m)} \qquad [10]$$

where σ^{o}_{TGO} is the initial value of the compressive residual stress, K_1 and n are the constants related to initial development of TGO scale and K_2 and m are the constants related to relaxation or relief of residual stress within the TGO scale. This type of quantitative analysis regarding life-remain assessment are being examined.

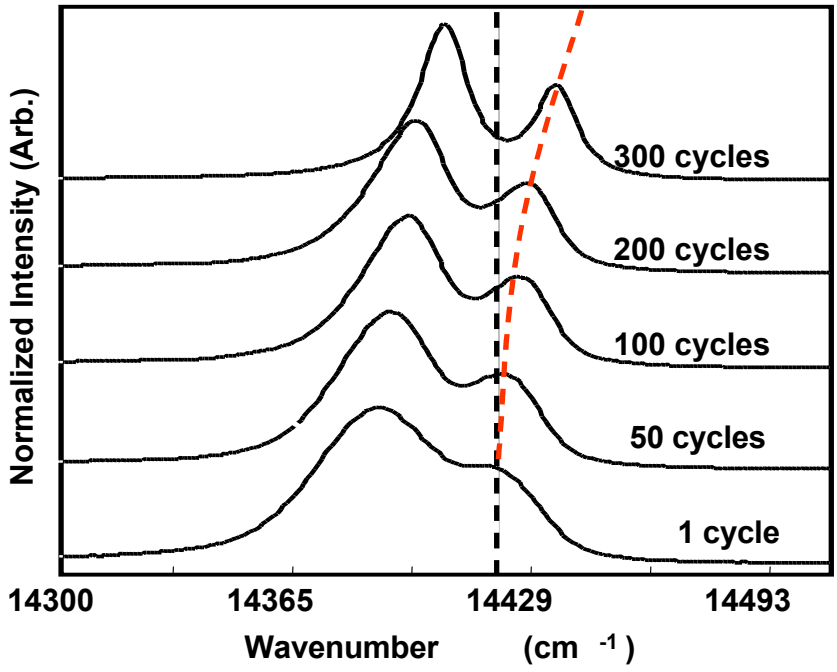

Figure 44. Typical photostimulated luminescence spectra as a function of 1-hour thermal cycling for type IV EB-PVD TBCs with grit blasted (Ni,Pt)Al bond coats. TBC spallation has occurred after 420 cycles and luminescence from stress-relieved TGO scale (marked by dotted vertical line) was observed starting 350 cycles by examining the derivatives of the spectra.

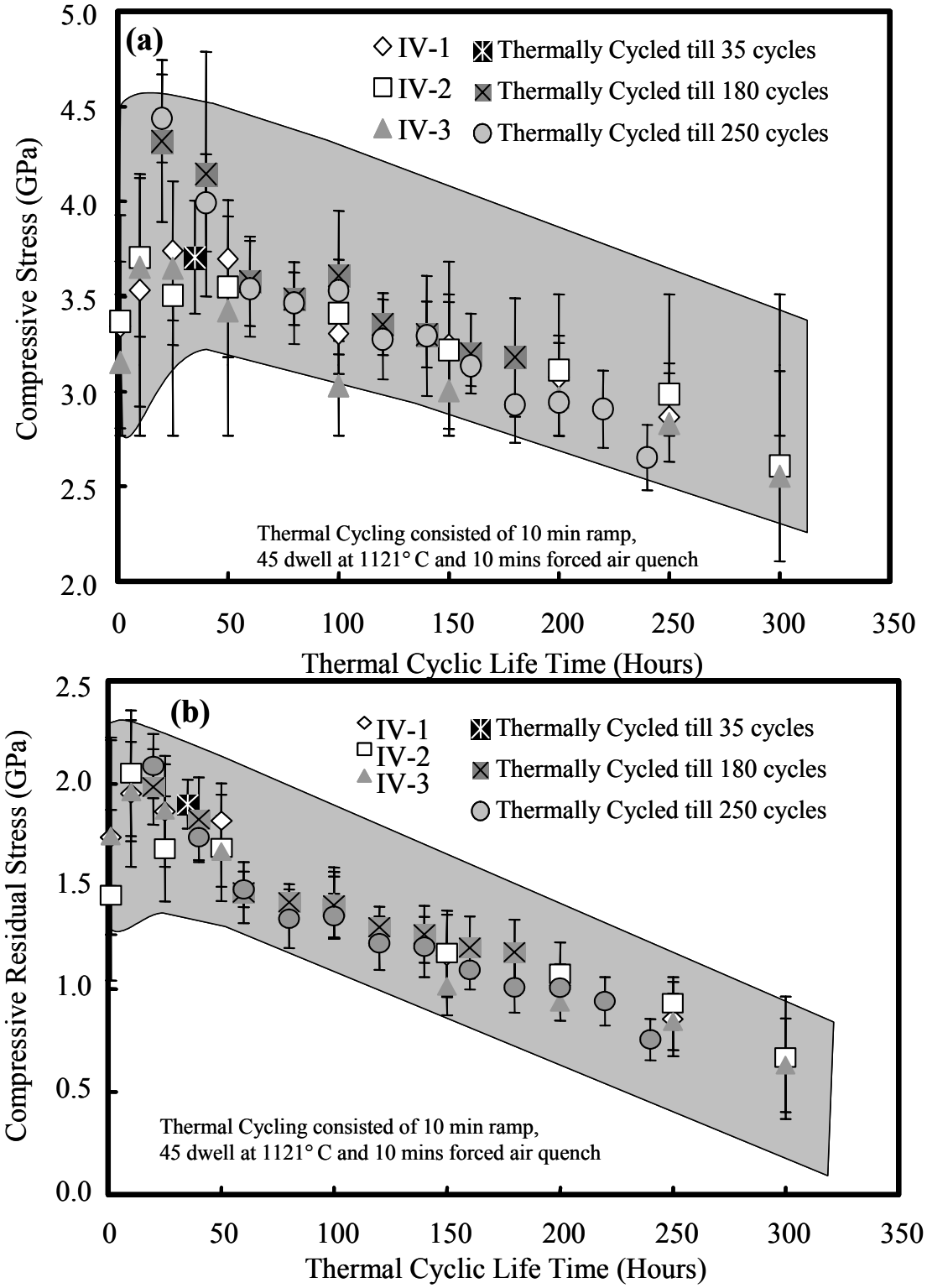

Figure 45. Compressive residual stress within TGO as a function of 1-hour thermal cycling for type IV EB-PVD TBCs with grit-blasted (Ni,Pt)Al bondcoats. Values of compressive residual stress were calculated from bimodal luminescence corresponding to (a) higher and (b) lower shifts in luminescence.

V.2.3. PSLS of EB-PVD TBCs as a Function of 10-Hour Thermal Cycling

The compressive residual stress within the TGO as function of 10-hour thermal cycling for type-II TBCs with NiCoCrAlY bondcoat is presented in the Figure 46. The value of the stress is calculated similar to the 1-hour thermal cycling based on shift of photostimulated luminescence via piezospectroscopic coefficients. The evolution of the compressive residual stress in the TGO scale was similar to that of TBCs with 1-hour thermal cycling: an initial increase (i.e., starting at 1st 10-hour thermal cycle) for both higher and lower compressive residual stress arising from bimodal luminescence. The magnitude of the compressive residual stress within the TGO remained constant throughout the entire thermal cycling as seen in Figure 46.

There was no significant or observable change in the magnitude and standard deviation of the TGO stress before the TBC spallation. Microstructural and failure investigation of type-II TBCs indicated that the failure occurred primarily at the YSZ/TGO interface and a significant internal oxidation of the NiCoCrAlY bondcoat occurred. This internal oxidation of the bondcoat was much more severe than type II TBCs tested with 1-hour thermal cycling.

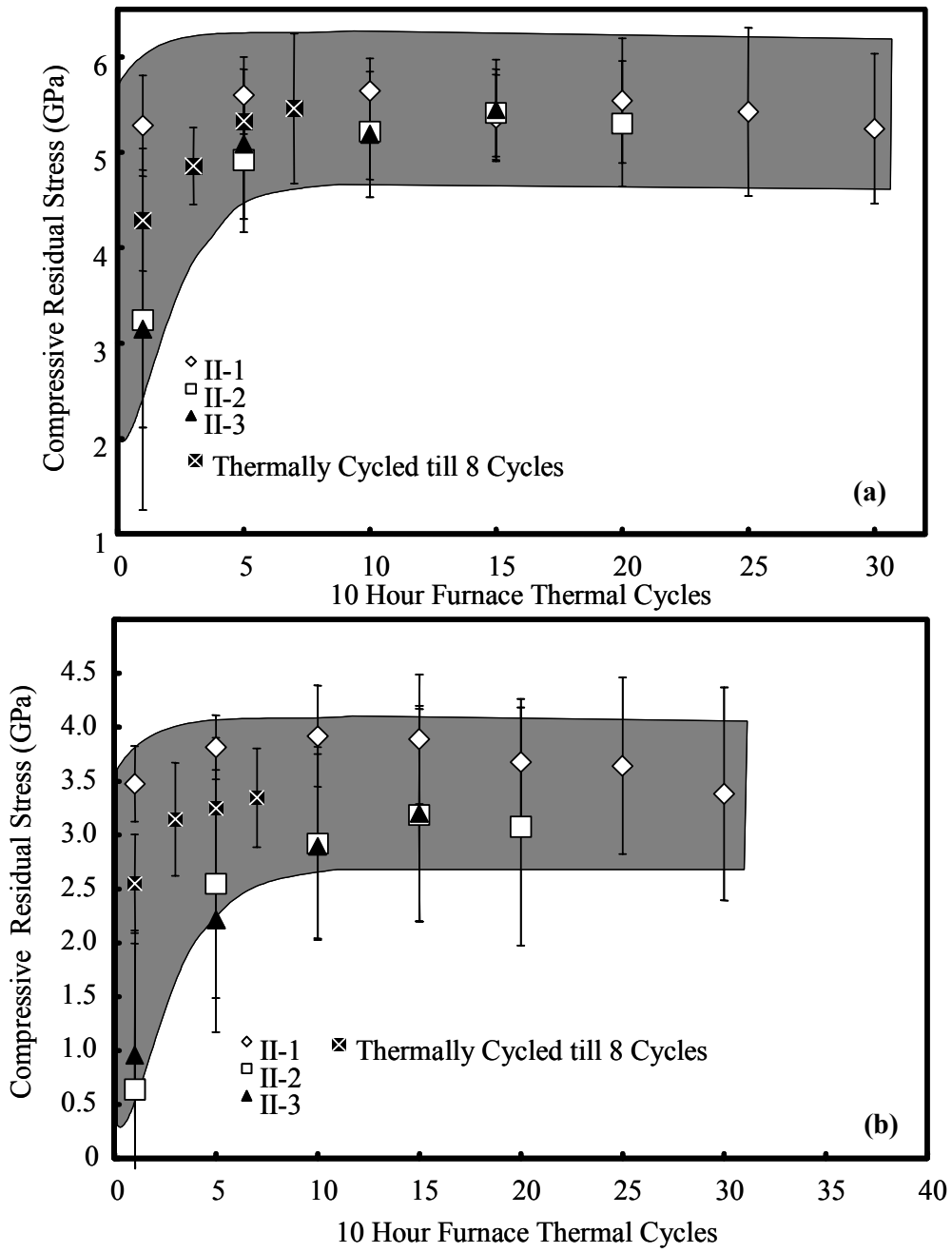

Figure 46. Compressive residual stress within TGO as a function of 10-hour thermal cycling for type II EB-PVD TBCs with NiCoCrAlY bondcoat. Values of compressive residual stress ere calculated from bimodal luminescence corresponding to (a) higher and (b) lower shifts in luminescence.

Figure 47 represents typical luminescence observed for type-III TBCs as a function of 10-hour thermal cycling. The TBC spallation occurred at 54 cycles. This trend is similar to type-III TBCs examined with 1-hour thermal cycling: stress relief associated with the damage in the TGO scale. The evolution and detection of stress-relief in the TGO scale for type-III TBCs can be quantified by taking the second derivatives ($d^2c/d\upsilon^2$) of luminescence spectrum at υ=14432 for R_2 luminescence. As shown in Figure 48, the luminescence spectrum with $d^2c/d\upsilon^2$ =0 at $\upsilon \cong 14432 \pm 3$ were observed.

For type-III TBCs with as-coated (Ni,Pt)Al bondcoat the luminescence shift associated with the stress relief of the TGO scale was observed even for 10-hour cycle as function of thermal cycling as shown in Figure 40. These spectrums were deconvoluted based on the bimodal luminescence (i.e., two sets of R_1-R_2 luminescence) until 60% lifetime. After 60% lifetime, a third set of R_1-R_2 luminescence emerged, which was clearly related to the stress free luminescence of α-Al_2O_3 that arises due to the stress-relief within the TGO scale. This stress-relief can be associated with the sub-critical damages within the TGO aforementioned. The compressive residual stress within the TGO scale for 10-hour thermal cycling and 30% lifetime of type-III TBCs is shown in Figure 49.

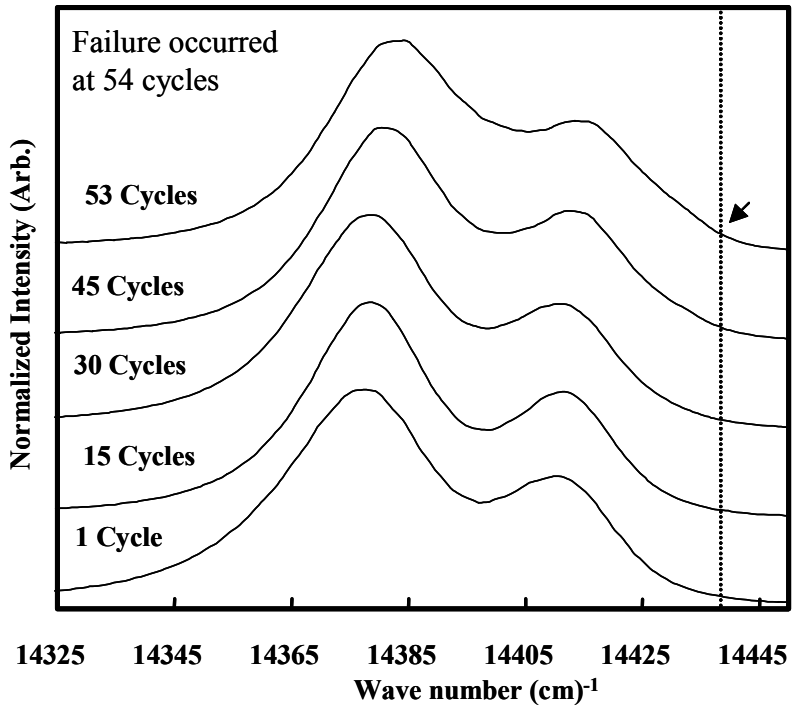

Figure 47. Typical photostimulated luminescence spectra from stress-relieved TGO scale (marked by dotted vertical line and arrows) was observed as a function of 10-hour thermal cycling for type III EB-PVD TBCs with as-coated (Ni,Pt)Al bond coats. TBC spallation has occurred at 54 cycles.

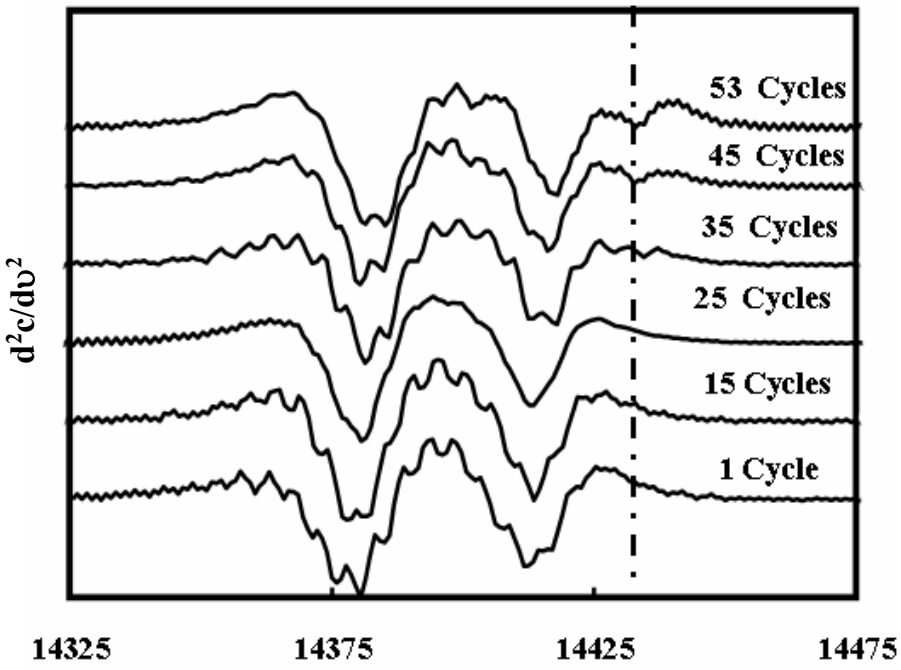

Figure 48. Typical derivatives of luminescence spectrum associated with stress-relieved luminescence frequency at $\upsilon \cong 14432 \pm 3$ for R_2 for 10-hour thermal cycling.

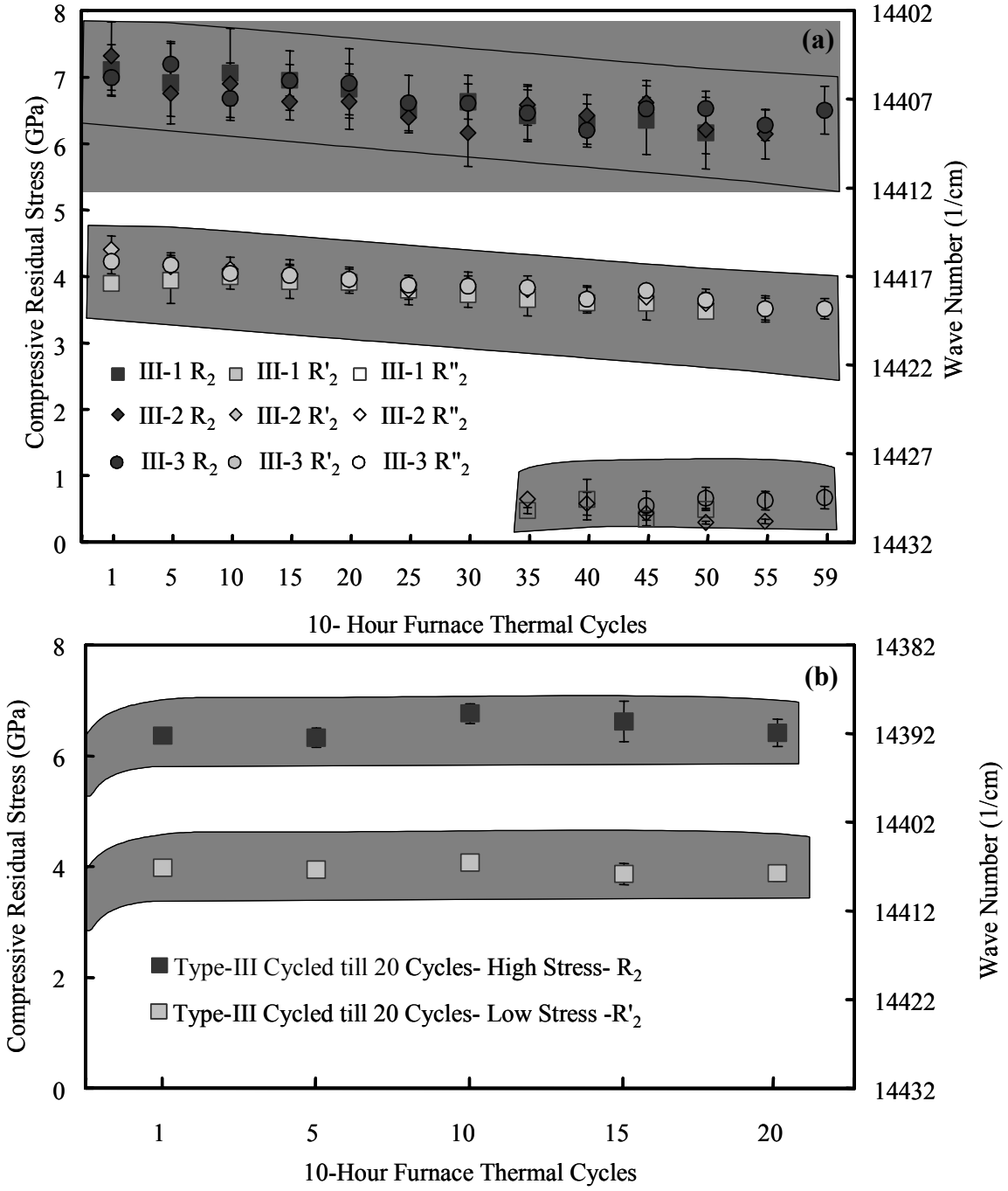

Figure 49. Compressive residual stress within TGO as a function of 10-hour thermal cycling for type-III TBCs with as-coated (Ni,Pt)Al bondcoat. Values of compressive residual stress were calculated from bimodal and tri-mode luminescence.

Typical luminescence spectra from type-IV TBCs with grit-blasted (Ni,Pt)Al bondcoat are presented in Figure 50. Unlike type-IV TBCs examined with 1-hour thermal cycling, a gradual shift towards stress free luminescence was not observed for these TBCs during 10-hour thermal cycling. The compressive residual stress within the TGO scale as a function of 10-hour thermal cycling, including up to 30% and 80% is presented in Figure 51. There was an initial increase in the magnitude of the compressive residual stress arising from under-developed TGO. However, the magnitude of the compressive residual stress in the TGO scale remained quite constant as a function of 10-hour thermal cycling. This type of behavior may be specific for TBC type, and in particular, type of thermal cycling (e.g., dwell time at high temperature).

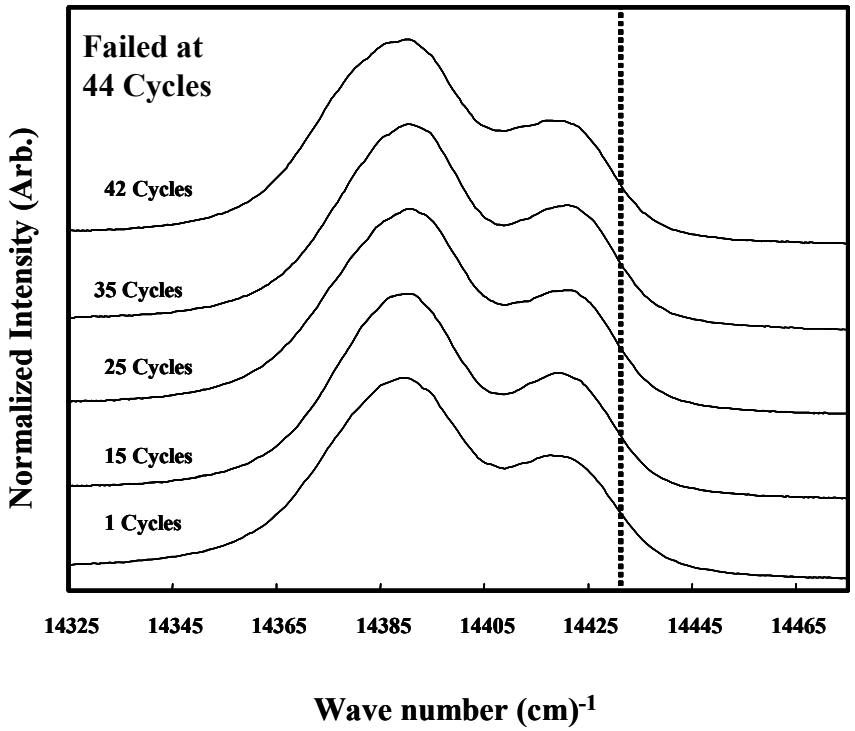

Figure 50. Typical luminescence spectrum observed as a function of 10-hour thermal cycling observed for type-IV TBCs with grit blasted (Ni, Pt)Al bondcoat. TBC spallation occurred at 44 cycles and there is no changes in the luminescence shifting towards stress free as observed in 1-hour thermal cycling.

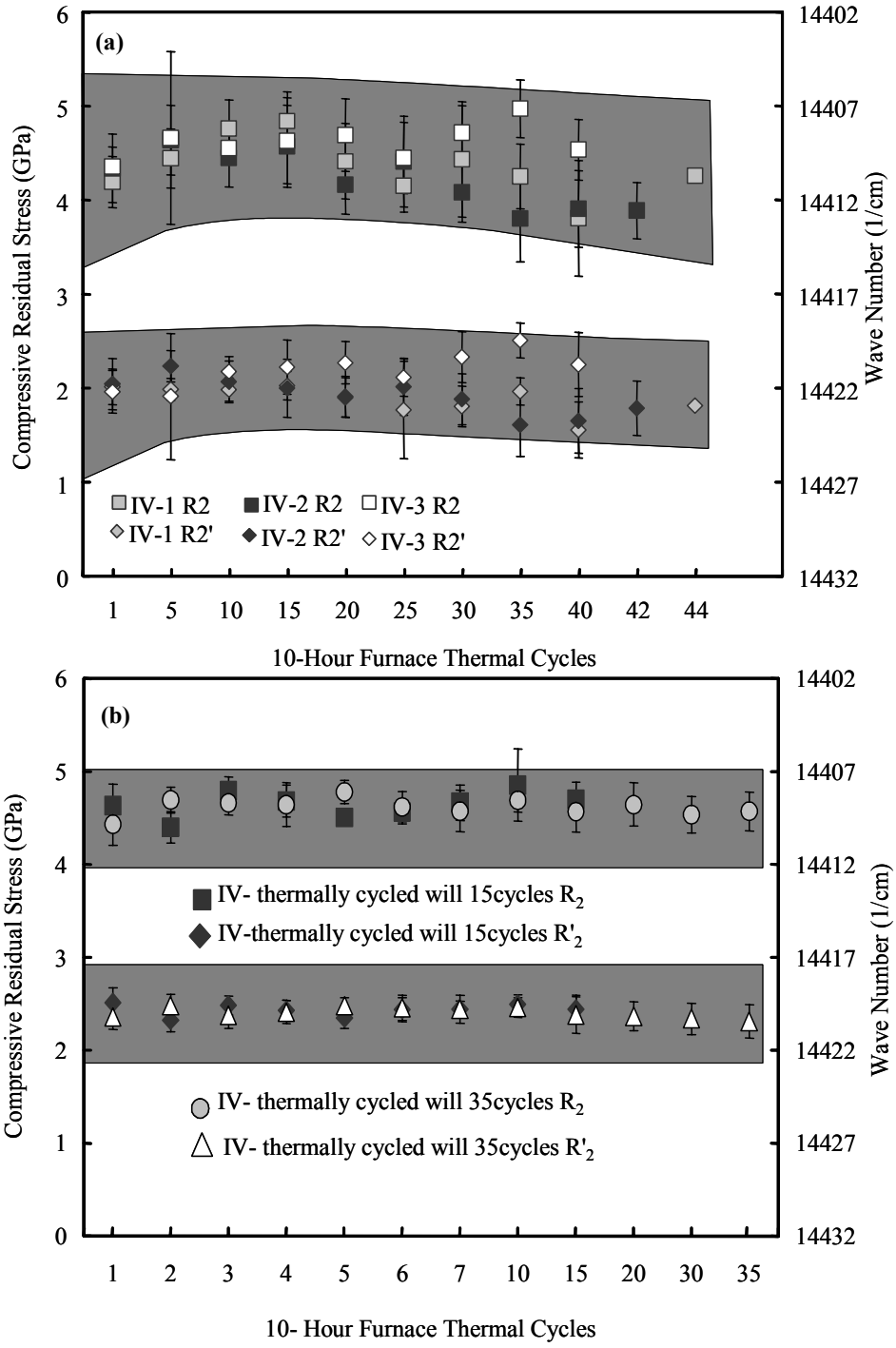

Figure 51. Compressive residual stress within TGO as a function of 10-hour thermal cycling for type-IV TBCs with grit-blasted (Ni, Pt)Al bondcoat. The values of compressive residual stress were calculated from bi-modal luminescence corresponding to higher and lower shift in luminescence (a) as a function of 10-hour thermal cycles (b) as a function of 10-hour thermal cyclic life time.

V.2.4. PSLS of EB-PVD TBCs as a Function of 50-Hour Thermal Cycling

The magnitude of compressive residual stresses within the TGO scale as a function of 50-hour thermal cycle is shown in Figure 52. The compressive residual stress magnitude calculated based on the systematic shift in PSLS luminescence via piezospectroscopic coefficient is quite similar to those observed previously for 1 and 10-hour cycles. The magnitude of stresses remained between 3-4.5 GPa on the higher side and around 2GPa from the lower shift in luminescence. The initial increase in the stress is because of the growth of TGO for both higher and lower compressive residual stresses arising from bimodal luminescence. There were no significant changes in the magnitude of the stress before the actual spallation of TBCs as reported earlier for this particular type.

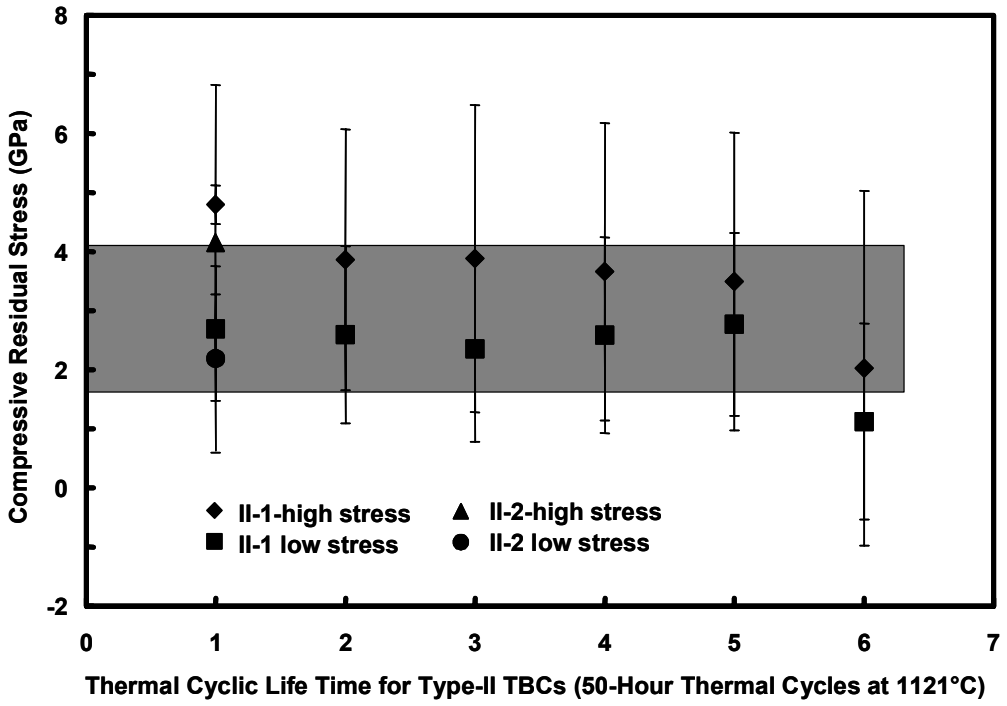

Figure 52. Compressive residual stress within TGO as a function of 50-hour thermal cycling for type II EB-PVD TBCs with NiCoCrAlY bondcoat. Values of compressive residual stress ere calculated from bimodal luminescence corresponding to higher and lower shifts in luminescence.

The value of compressive residual stress for type-III TBCs with as-coated (Ni,Pt)Al is shown in the Figure 53. The evolution of relative intensities obtained up to failure for type-III TBCs is presented in Figure 54. From the Figure R_2 and R_2' refer to bi-modal luminescence of the higher and lower shift in luminescence. In this particular type there was no emergence of stress free luminescence that was detected previously in 1 and 10 hour thermal cycles. The compressive residual stress reported in Figure 53 both high and low stresses continued to decrease till failure.

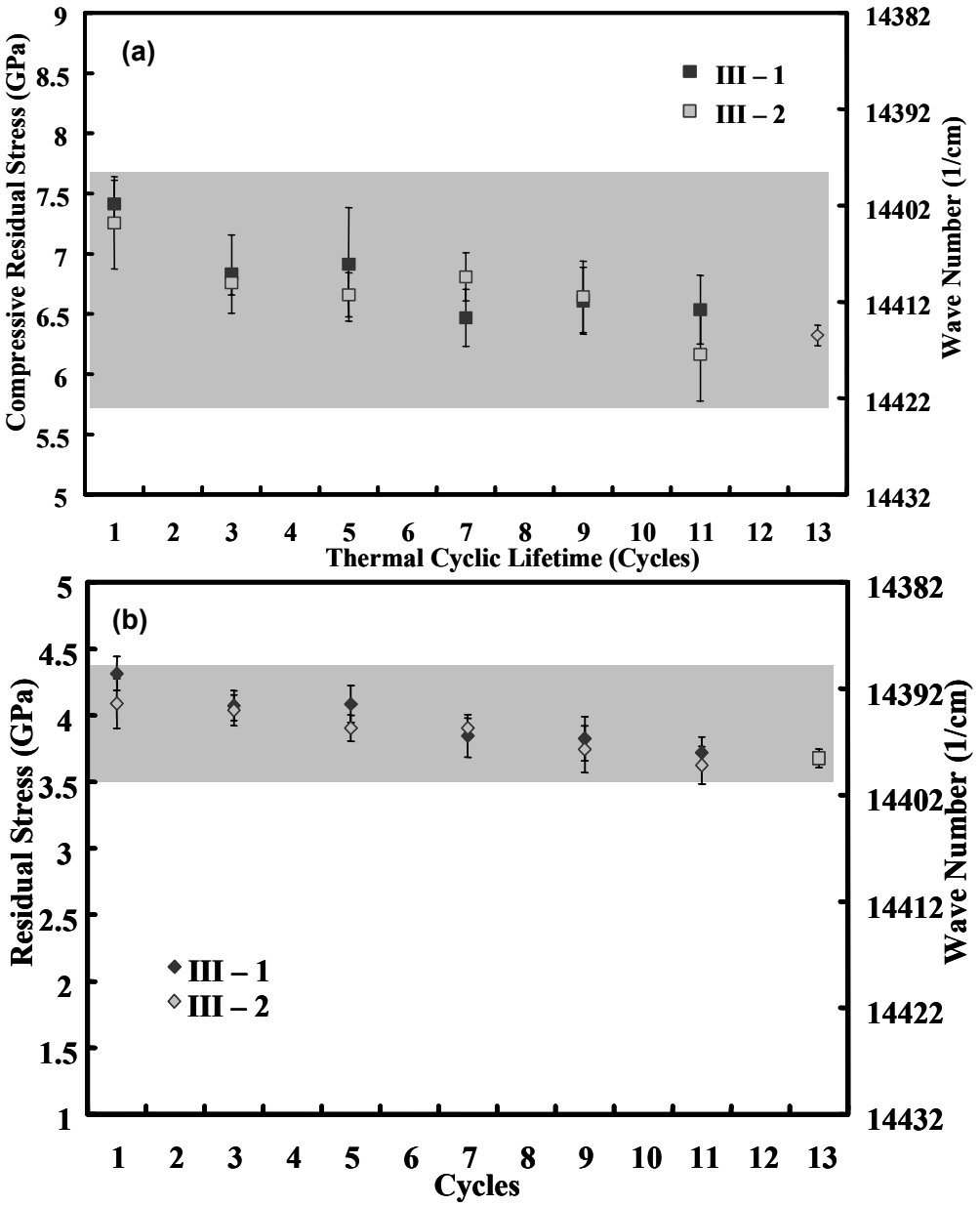

Figure 53. Compressive residual stress within TGO as a function of 50-hour thermal cycling for type-III TBCs with as-coated (Ni,Pt)Al bondcoat. Values of compressive residual stress were calculated from bimodal luminescence.

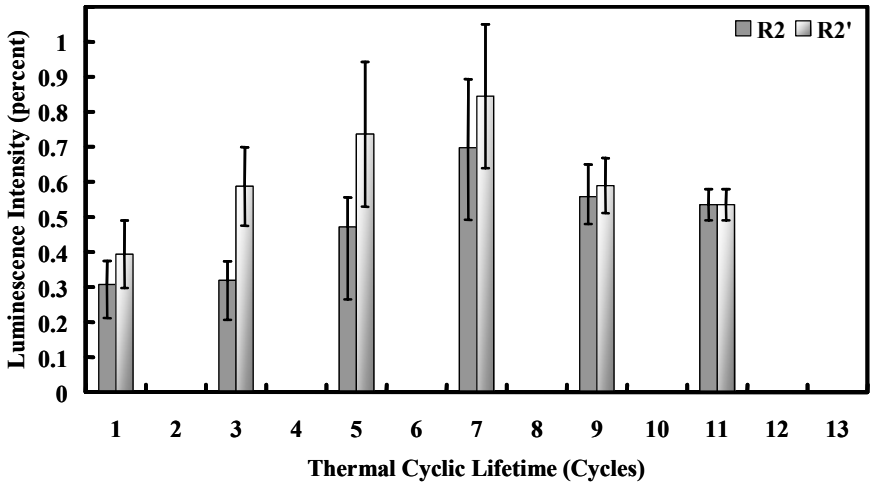

Figure 54. Type-III TBCs cycled until thermal cyclic life time, Relative Luminescence Intensity from R2, R'2 in TGO with as-coated (Ni,Pt)Al bond coat.

The values of compressive residual stress as function of 50-hour thermal cycles are shown in Figure 55. The compressive residual stress remained constant with an initial increase in the early stages due to the development of TGO. This trend was similar to 10-hour thermal cycles that were reported earlier for this particular type which is dependent on the type of thermal cycling.

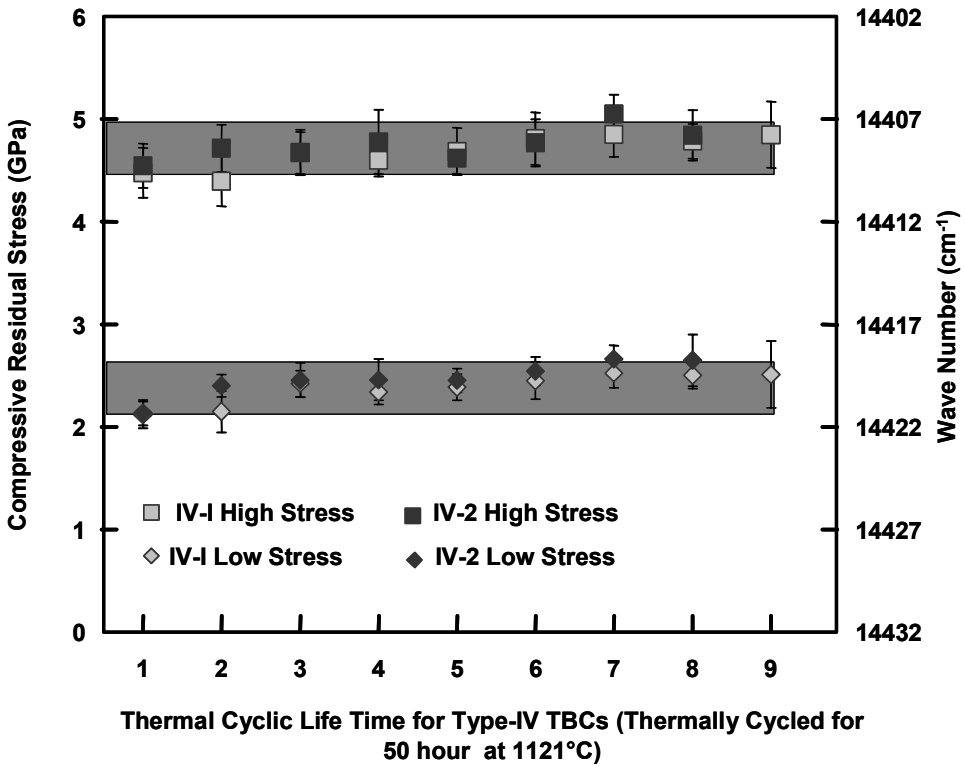

Figure 55. Compressive residual stress within TGO as a function of 50-hour thermal cycling for type-IV TBCs with Grit blasted (Ni,Pt)Al bondcoat. Values of compressive residual stress were calculated from bimodal luminescence.

V. 3. Electrochemical Impedance Spectroscopy of Thermal Barrier Coatings

V.3.1. NDE of Type I APS TBCs by EIS

For type I APS TBCs, EIS measurement was carried out 3 times on specimens before thermal cycling and after thermal cycling that corresponds to 10%, 50% and 70% of its lifetime. The variation in the impedance and phase angle plot with respect to the thermal cycling is presented in Figures 56 and 57, respectively. Table VI also reports the values of resistance and capacitance of the various TBC constituents, which were calculated based on the ac-equivalent circuit presented in Figure 9. For the as-coated APS TBCs, there is no significant presence of the TGO. Hence the TGO is not represented in terms of the electrical parameters. The ac equivalent circuit for APS TBCs, after exposure is different from that of the as-coated ones because of the bond coat oxidation and the formation of uniform and continuous TGO. The impedance of TGO cannot be neglected in the EIS measurement system. Thus, an ac equivalent circuit for the thermally cycled TBC consists of the electrical parameters that represent the TGO.

Resistance and capacitance of TBC constituents reported in Table VI is presented as a function of thermal cycles as presented in Figures 58 through 61. The impedance plot presented in Figure 45 shows that the impedance response of the TBCs increases initially during thermal cycling and then decreases after thermal cycling corresponding to 50% of its lifetime. This increase in the impedance response may be attributed to the sintering of the YSZ topcoat and growth of TGO with high temperature exposure. The decrease in the impedance response may correspond to the sub-critical damages that initiate in the topcoat and TGO with thermal cycling. These sub-critical damages prior to the final failure have been documented by microstructural analysis (see section V.4.1).

With an increase in the impedance, the resistance of the topcoat and the TGO increased. With further prolonged thermal cycling the resistance of the topcoat and the TGO decreased. The capacitance of the topcoat increased at failure because of the large scale damage in the topcoat. The capacitance of the TGO did not increase abruptly at failure because the fracture path of the APS TBCs observed for type-I TBCs primarily occur at the YSZ\TGO interface as shown in Figure 94 (see section V.4.4) and rarely exposes the conductive surface of the metallic bondcoat.

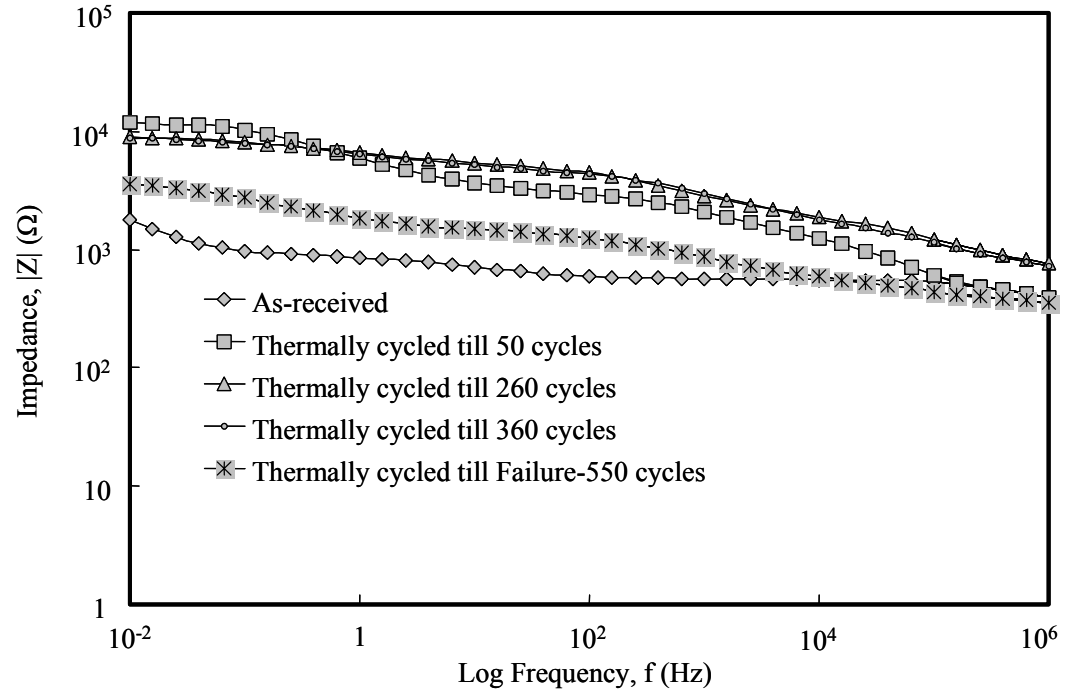

Figure 56. Typical Impedance plots from as-coated and as a function of thermal cyclic life time for type-I APS TBCs

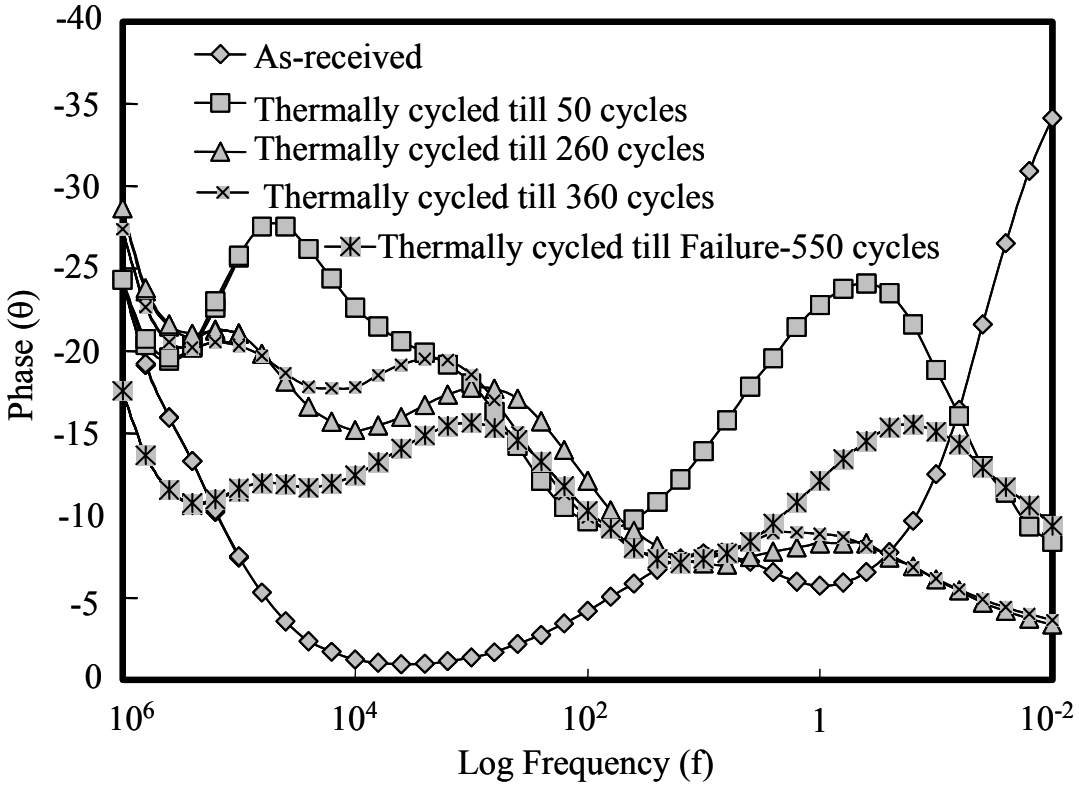

Figure 57. Typical Phase plots from as-coated and as a function of thermal cyclic life time for type-I APS TBCs.

Table VI. Resistance and capacitance of Type I APS TBC constituents as a function of thermal cycling.

Thermal cycles	R_C (kΩ)	C_C (nF)	R_P (kΩ)	C_P (νF)	R_O (kΩ)	C_O (nF)	R_T (kΩ)	C_T (νF)
As-received	0.50 ± 0.4	2.2 ± 0.4	10.6 ± 4.2	377700 ± 21959	0	0	0.3 ± 0.1	16486 ± 2747
50 (10% lifetime)	2.72 ± 0.7	60.7 ± 21.9	13.55 ± 1.38	1574.3 ± 502.3	0.58 ± 0.4	42.9 ± 10.9	1.22 ±0.86	1347.3 ±192
260 (50% lifetime)	3.31 ± 0.09	49.6 ± 0.8	4.40 ± 0.03	1505 ± 18	1.05 ± 0.02	5.38 ± 0.2	1.06 ±0.05	571.9 ±2.8
360 (70% lifetime)	3.25 ± 0.10	45.8 ± 0.4	4.64 ± 0.07	1449 ± 45.7	0.96 ± 0.03	4.32 ± 0.3	0.80 ±0.03	33.6.3 ±1.9
550 (Failure)	0.59 ± 0.03	191.4 ± 5.9	2.96 ± 0.18	10789 ± 983.2	0.40 ± 0.01	3.5 ± 0.3	0.35 ±0.02	1321.6 ±40.2

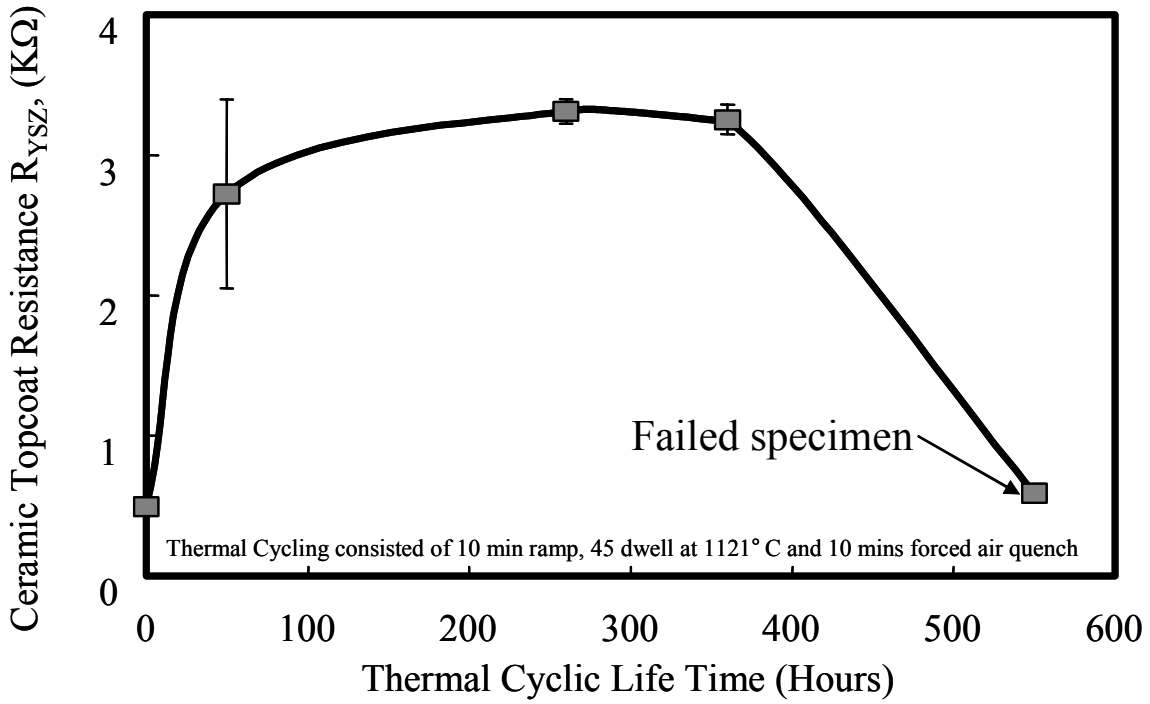

Figure 58.Evolution of ceramic topcoat resistance (R_{YSZ}) for type I APS TBCs as a function of thermal cycling at 1121°C.

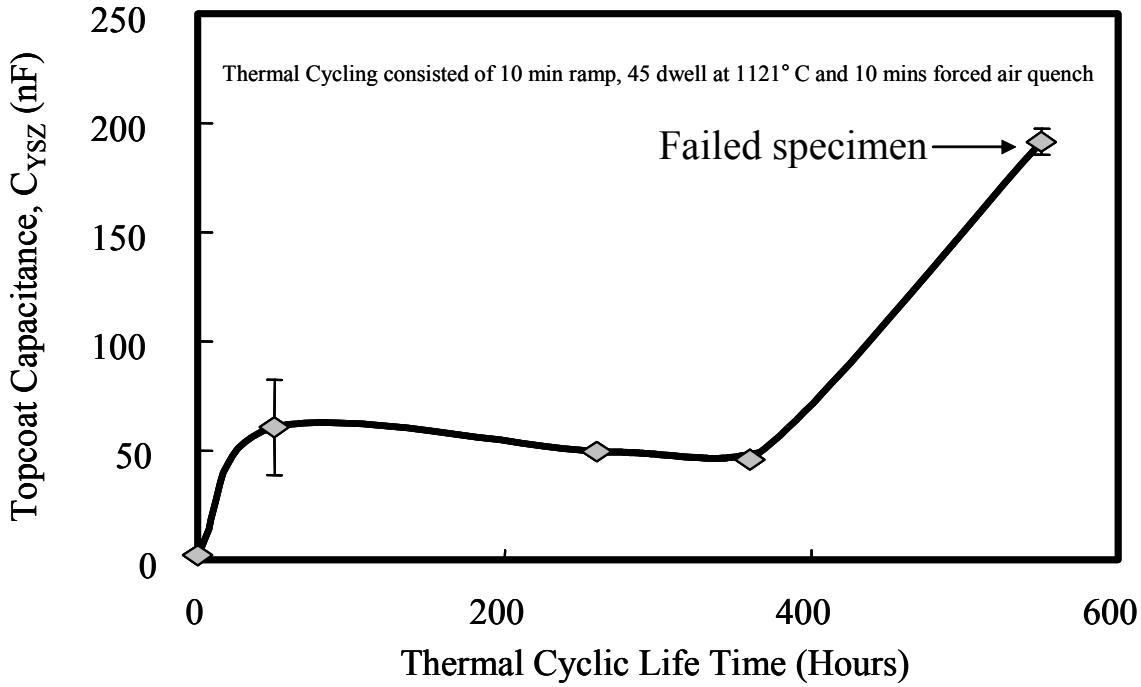

Figure 59.Evolution of ceramic topcoat capacitance (C_{YSZ}) for type I APS TBCs as a function of thermal cycling at 1121°C.

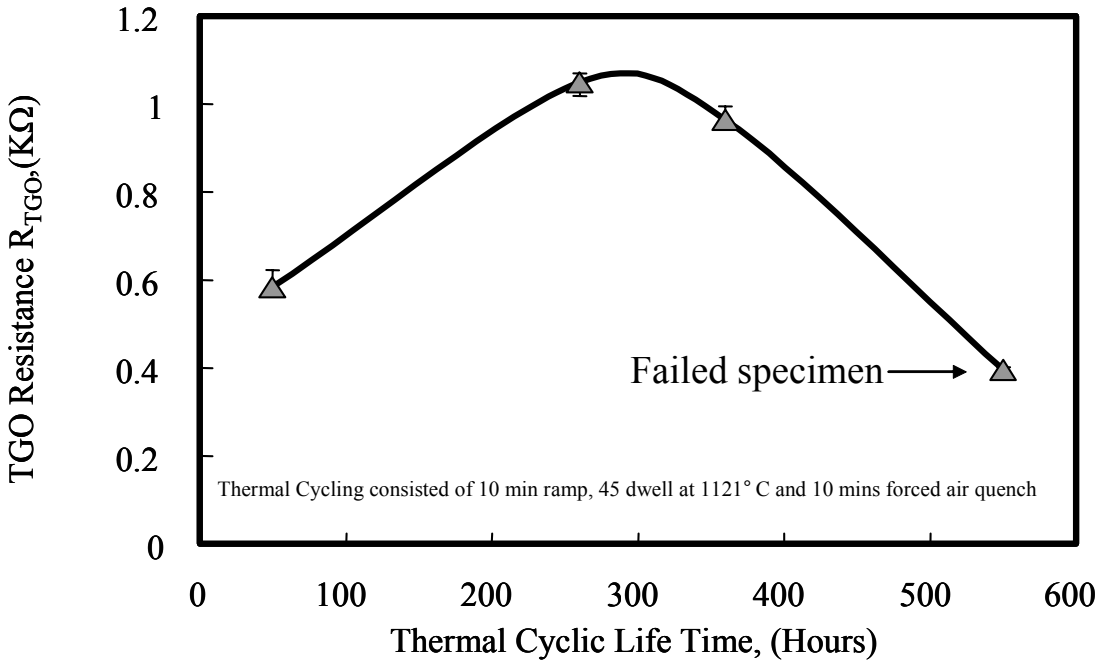

Figure 60. Evolution of TGO resistance R_{TGO} in type I APS TBCs as a function of thermal cycling at 1121°C.

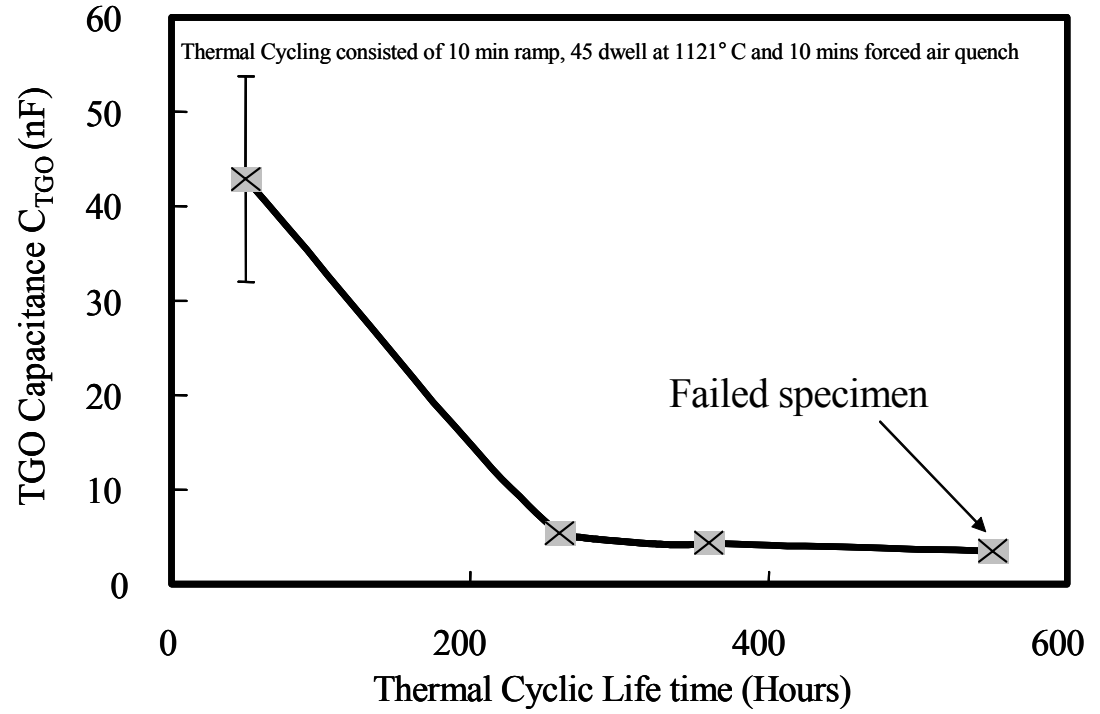

Figure 61. Evolution of TGO capacitance C_{TGO} in type I APS TBCs as a function of thermal cycling at 1121°C.

V.3.2. NDE of Type V APS TBCs by EIS

For type V APS TBCs, EIS measurement was carried out 3 times on specimens before thermal cycling and after thermal cycling that corresponds to 10%, 50% and 70% of its lifetime. The variation in the impedance and phase angle plot with respect to the thermal cycling is presented in Figures 62 and 63, respectively. Table VII also reports values of resistance and capacitance of the various TBC constituents, which were calculated based on the ac-equivalent circuit in Figure 9.

Resistance and capacitance of TBC constituents was determined as a function of thermal cycles as presented in Figures 64 through 67. Ceramic top coat resistance R_C initially increased then decreased and stabilized till failure with thermal cycling; this perhaps reflects two important microstructural changes, namely sintering and micro-cracking. While the growth of the TGO should intuitively increase the resistance and decrease the capacitance, the opposite results were observed for capacitance of the TGO as presented in Figures 66 and 67. As seen in Figure 66, the TGO resistance, R_{TGO} (not defined for as-coated condition) continuously decreases and the TGO capacitance, C_{TGO} continuously increases with thermal cycling. In addition, a sharp 2~5X increase in the C_{TGO} was observed as presented in Figure 67 for failed specimens. These trends have been consistently observed and may reflect early initiation and growth of sub-critical damage in the TGO through which electrolyte can penetrate. Similar trends were observed earlier for these types of TBCs and are reported in the Figures 68 through 70.

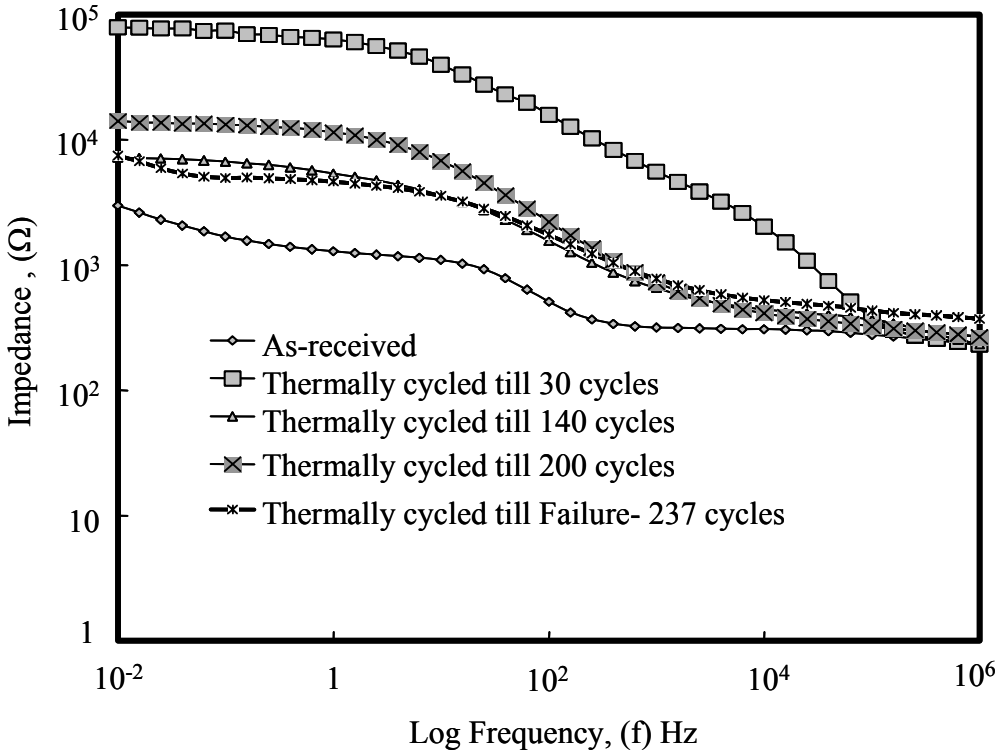

Figure 62. Typical Impedance plots from as-coated and as a function of thermal cyclic life time for type-VAPS TBCs.

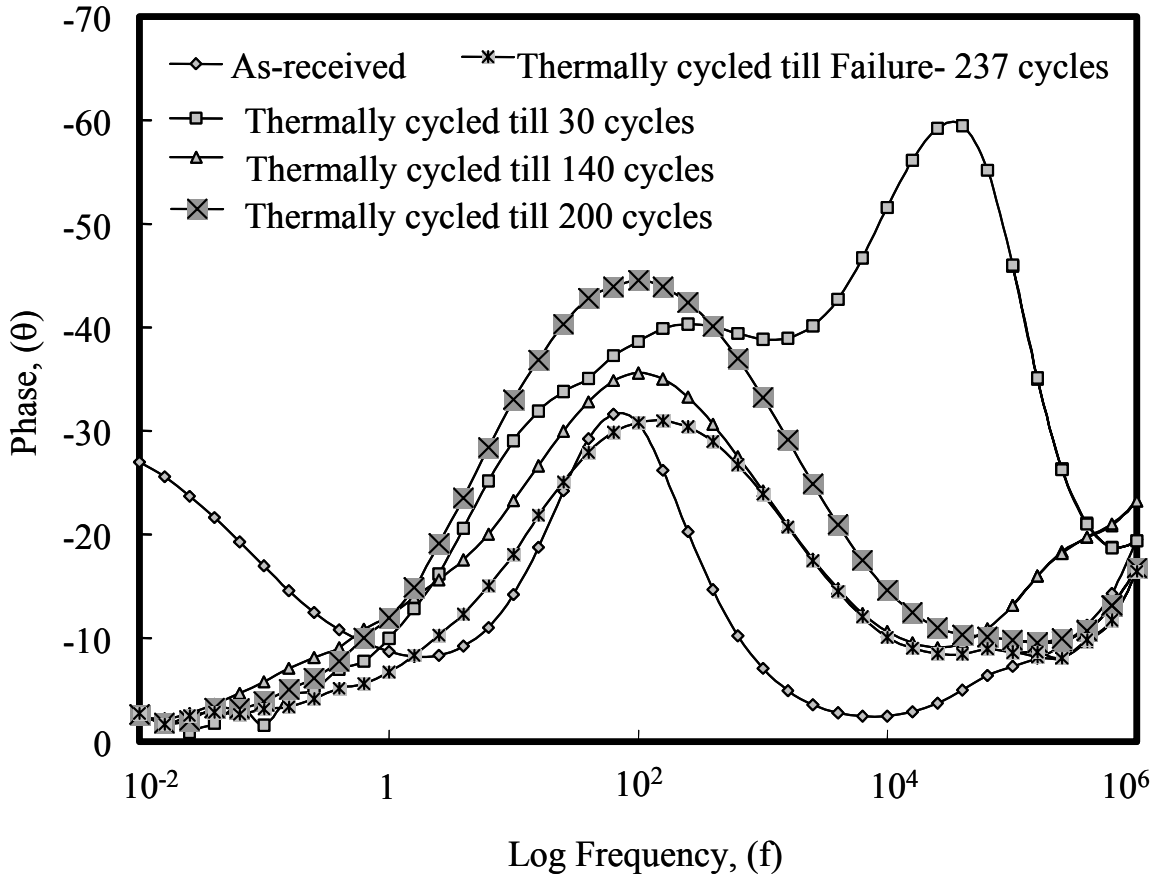

Figure 63.Typical Phase angle plots from as-coated and with respect to thermal cyclic life time for type-I APS TBCs

Table VII. Resistance and capacitance of type-V APS TBC constituents as a function of thermal cycling.

Thermal cycles	R_C (kΩ)	C_C (nF)	R_P (kΩ)	C_P (nF)	R_O (kΩ)	C_O (nF)	R_T (kΩ)	C_T (nF)
As-received	0.29 ± 0.02	4.8 ± 0.5	11.8 ± 1.4	38016.6 ± 9317	0	0	0.9 ± 0.1	3883 ± 219.2
35 (10% lifetime)	1 ± 0.06	13.9 ± 21.9	103.7 ± 3.3	33980 ± 1513	3.72 ± 0.2	9.42 ± 0.01	0.71 ±0.01	1228 ±39.6
140 (50% lifetime)	0.63 ± 0.03	4.6 ± 0.8	0.88 ± 0.8	351.3 ± 48.7	4.8 ± 0.1	517 ± 17.1	6.2 ±1.2	1534.7 ±131.4
200 (70% lifetime)	0.27 ± 0.01	3.3 ± 0.4	3.79 ± 0.3	941.1 ± 62.2	1.3 ± 0.07	32386.67 ± 644.7	9.7 ±0.6	454 ±3.3
Failure 237	0.37 ± 0.01	2.6 ± 5.9	1.04 ± 0.6	864.6 ± 182.1	1.3 ± 0.4	35635 ± 10981.4	5.2 ±1.8	623 ±164.1

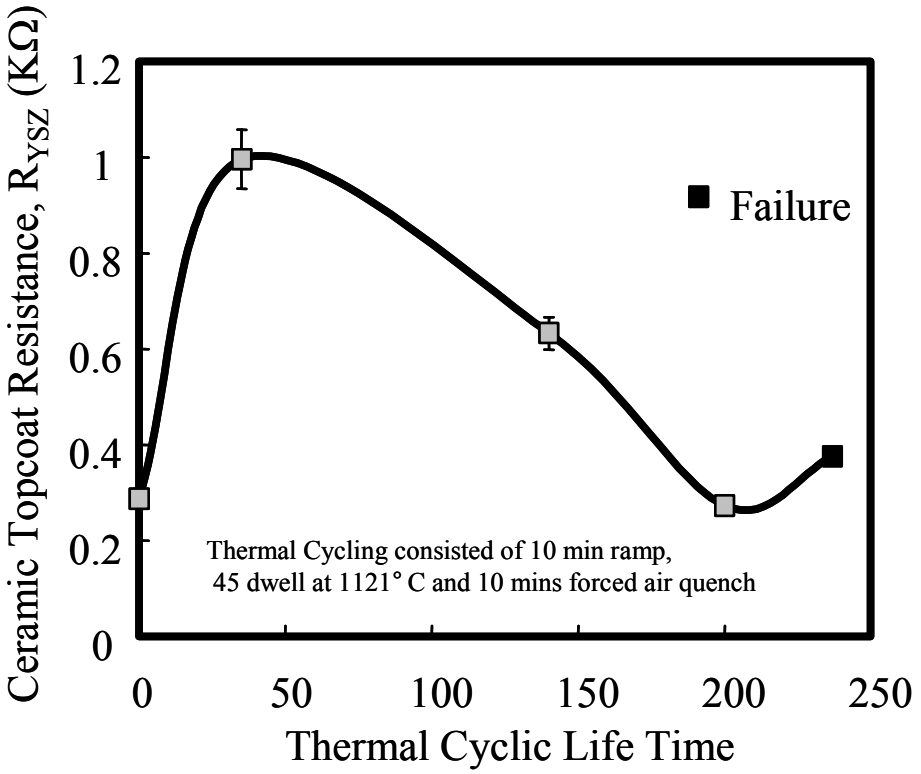

Figure 64. Evolution of ceramic top coat resistance (R_{YSZ}) for type V APS TBCs as a function of thermal cycling at 1121°C.

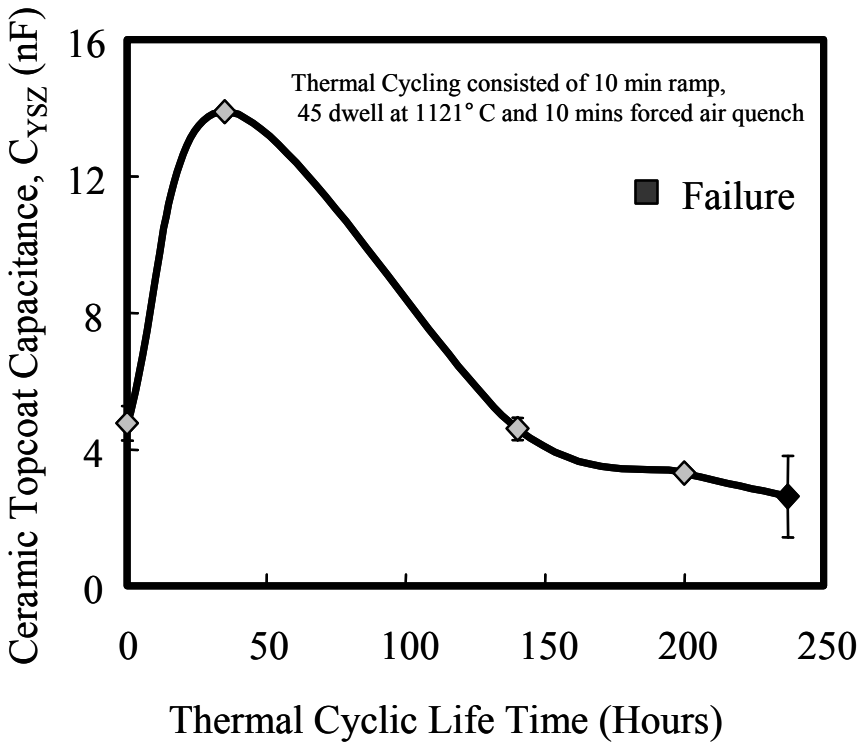

Figure 65.Evolution of ceramic top coat capacitance (C_{YSZ}) for type V APS TBCs as a function of thermal cycling at 1121°C.

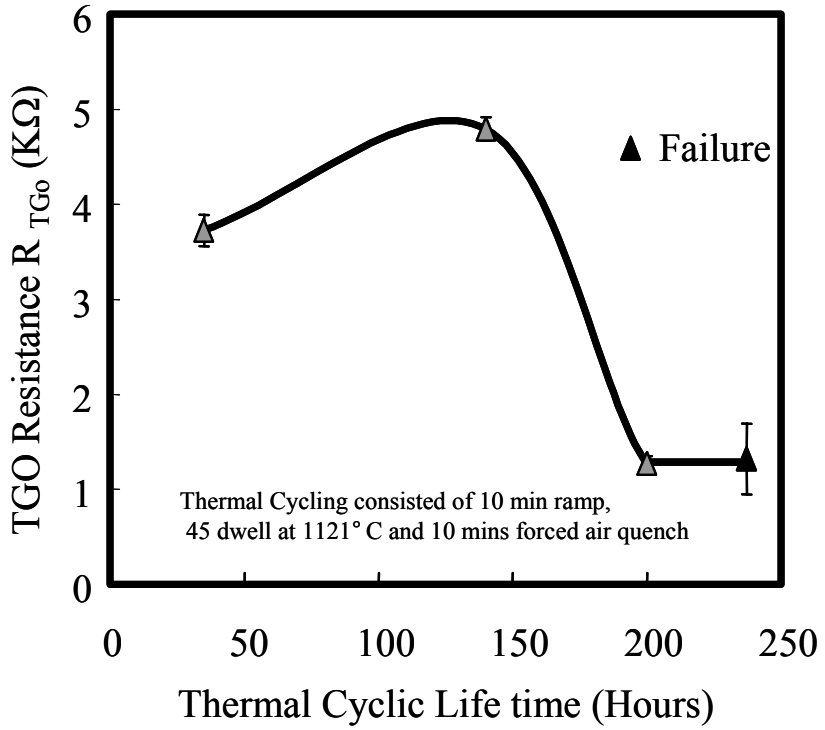

Figure 66.Evolution of TGO resistance (R_{TGO}) in type V APS TBCs as a function of thermal cycling at 1121°C.

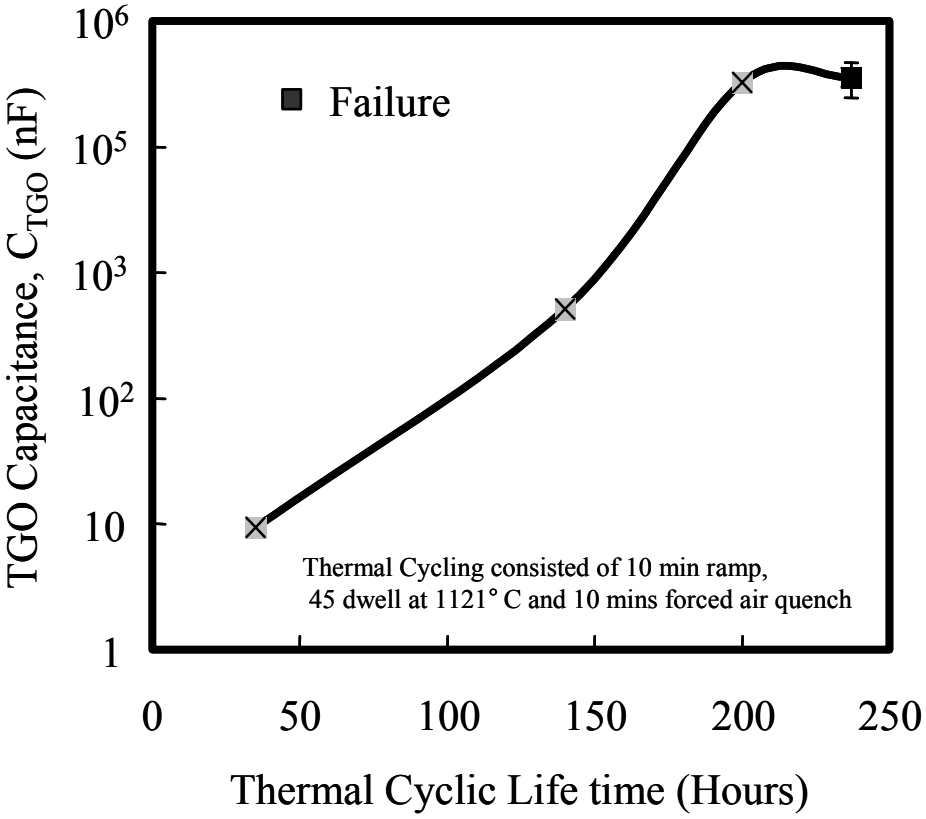

Figure 67. Evolution of TGO capacitance (C_{TGO}) in type V APS TBCs as a function of thermal cycling at 1121°C.

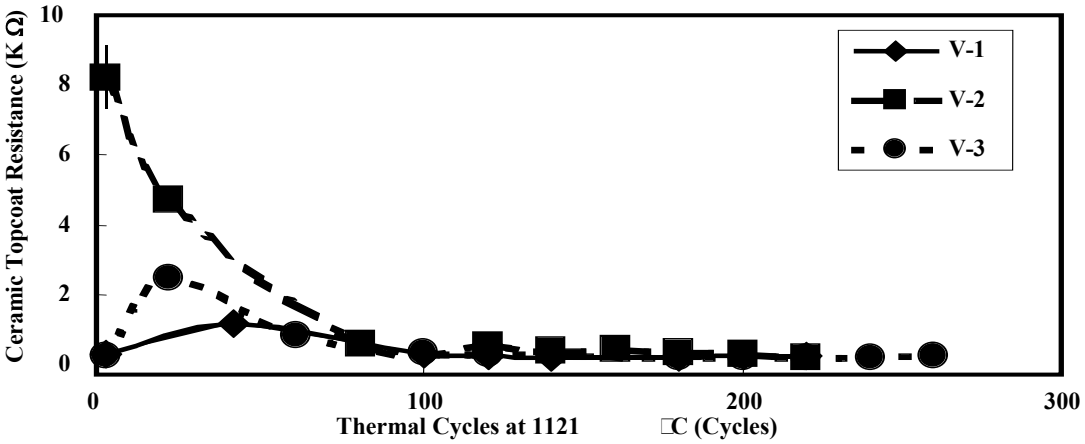

Figure 68. Evolution of ceramic top coat resistance (R_{YSZ}) in type V APS TBCs as a function of thermal cycling at 1121°C.

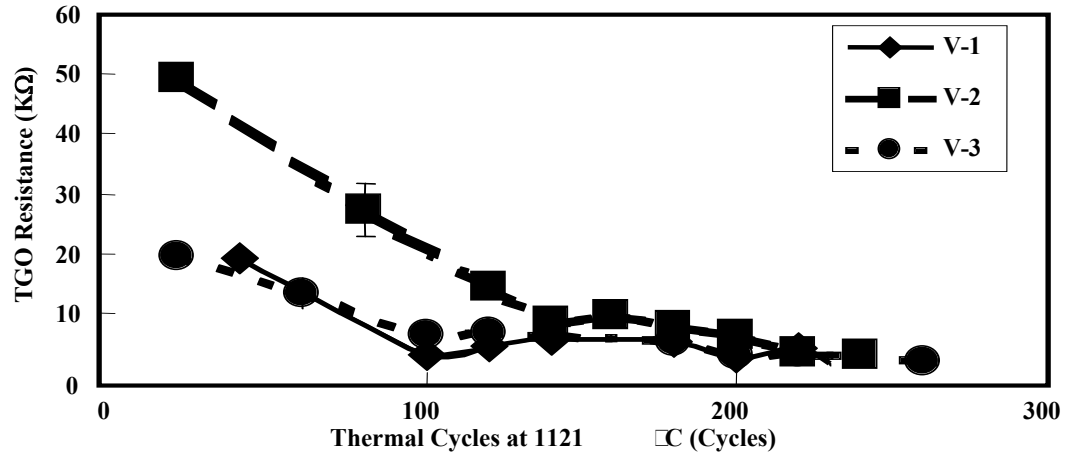

Figure 69. Evolution of TGO resistance (R_{TGO}) in type V APS TBCs as a function of thermal cycling at 1121°C.

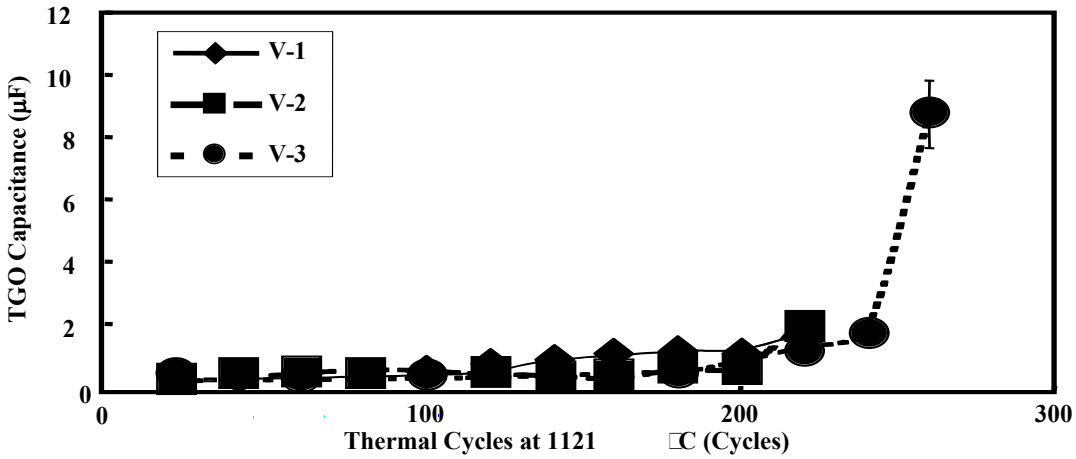

Figure 70. Evolution of TGO capacitance (C_{TGO}) in type V APS TBCs as a function of thermal cycling at 1121°C.

V.3.3. NDE of Thermally Cycled Type II, III and IV Thermal Barrier Coatings by EIS

For type II EB-PVD TBCs, frequent desktop failure was observed along the fragile interface between the YSZ/TGO. Early formation of non-protective spinels were observed for type II TBCs, and EIS could not be carried out.

For type III TBCs EIS measurement was carried out 3 times for as-received, thermally cycled and failed specimen. Typical impedance and phase angle plots for these specimens are presented in Figures 71 and 72, respectively. Table VIII reports values of resistance and capacitance of the various TBC constituents that were determined based on the ac-equivalent circuit presented in Figure 9. Evolution in the resistance and capacitance of TBC constituents as a function of thermal cycling is presented in Table VIII and Figures 73 through 76. The

initial increase in the resistance of the YSZ and the TGO, shown in Figures 73 and 75, may be due to the sintering of the YSZ and growth of the TGO with thermal exposure. After prolonged exposure corresponding to the 70% of thermal cyclic lifetime, the resistance of the YSZ and TGO started to decrease, indicating the penetration of electrolyte through damages (e.g., cracks and voids) in the YSZ and the TGO. At failure there is a sharp increase in the capacitance of the YSZ and the TGO, because of the large-scale cracks through which the electrolyte penetrates down to the exposed and conductive bond coat surface (see section V.4.4).

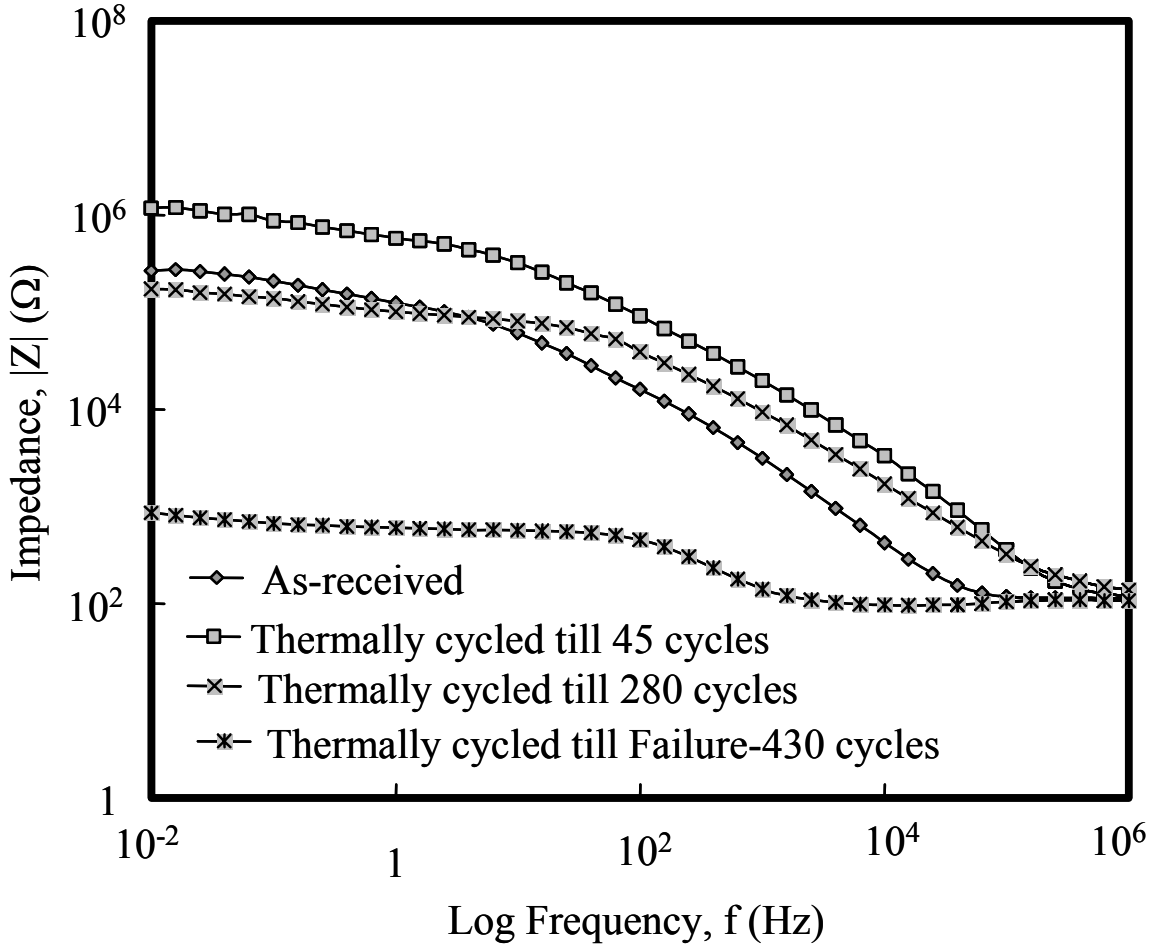

Figure 71.Typical Impedance plots from as-coated and as a function of thermal cyclic life time for type-III EB-PVD TBCs.

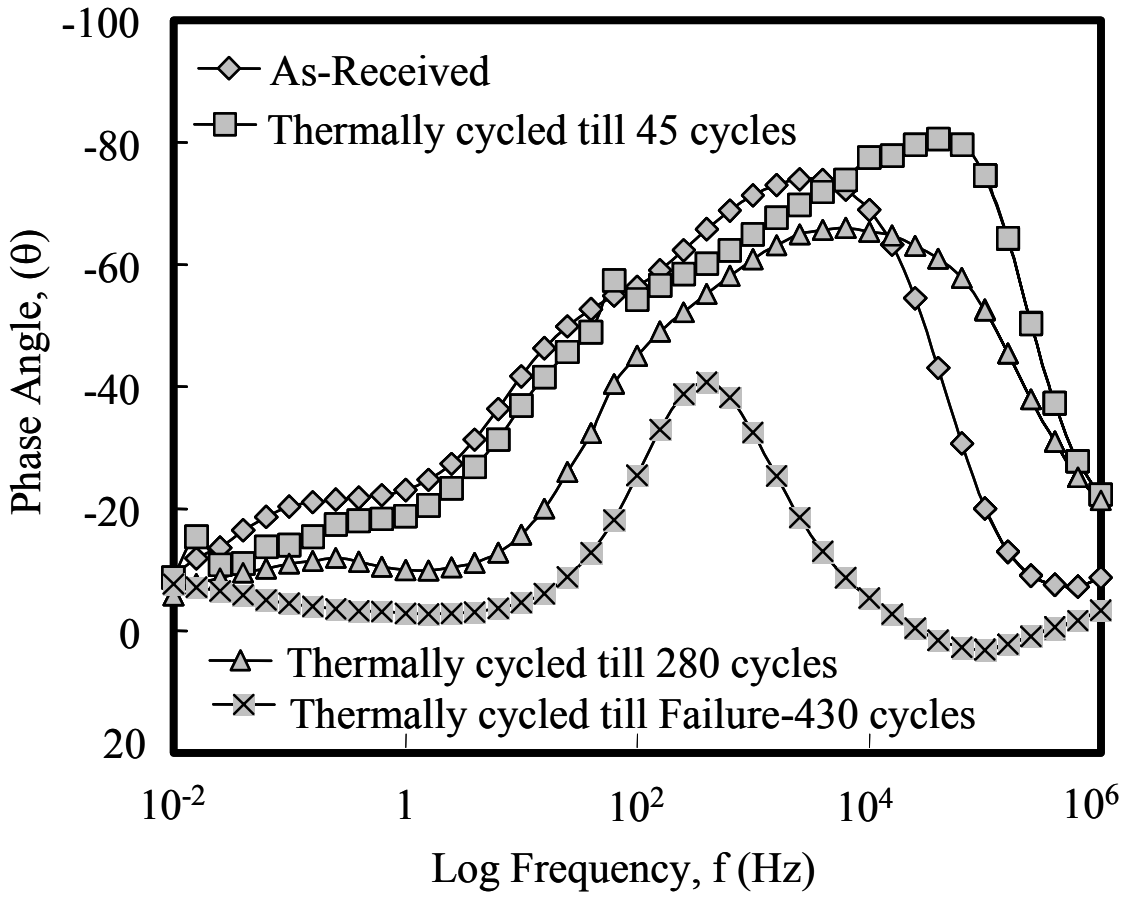

Figure 72.Typical Phase angle plots from as-coated and as a function of thermal cyclic life time for type-III EB-PVD TBCs

Table VIII. Resistance and capacitance of type-III EBPVD TBC constituents as a function of thermal cycling.

Thermal Cycles	R_C (kΩ)	C_C (nF)	R_P (kΩ)	C_P (nF)	R_O (kΩ)	C_O (nF)	R_T (kΩ)	C_T (μF)
As-received	1.90 ± 0.45	46.9 ±2.3	309.8 ±81.7	24.46 ±0.03	0.05 ±0.01	283 ±19.4	28.3 ±4.9	447 ±135
45 (10% lifetime)	38.0 ±1.3	9.8 ±0.3	163.7 ±5.2	7.4 ±0.8	7.5 ±4.7	20 ±1.5	1.6 ±0.02	14.7 ±0.1
280 (70% lifetime)	22.8 ±7.2	26.6 ±0.6	262.4 ±74.2	7 ±1.9	4.8 ±0.2	17.03 ±0.07	0.28 ±0.01	8.9 ±0.12
430 (After Failure)	0.25 ±0.01	5015 ±61.5	0.75 ±0.1	63813 ±6542	0.17 ±0.01	9999 ±70.3	0.07 ±0.01	4193 ±145.5

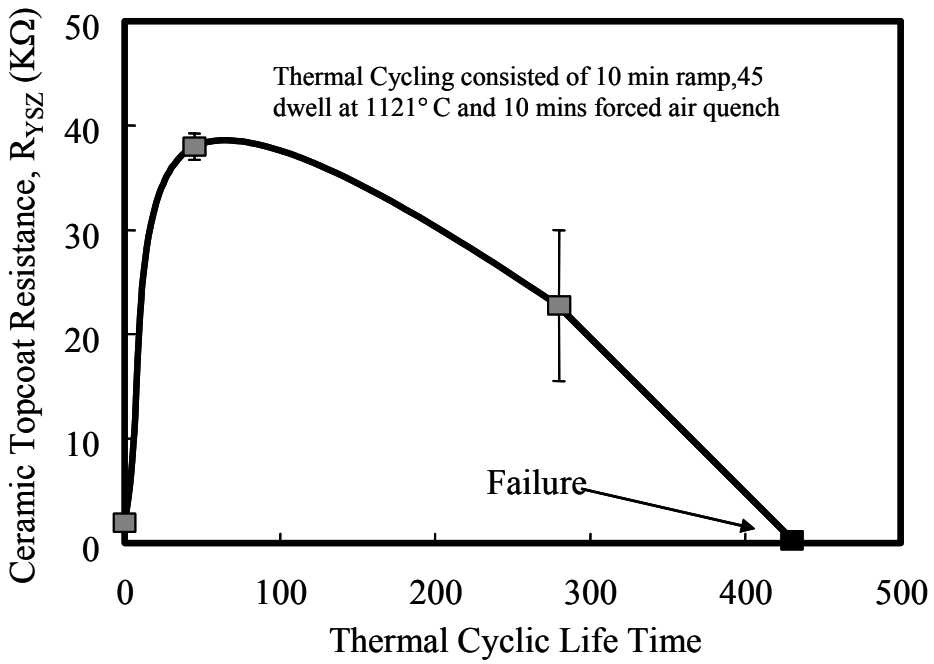

Figure 73.Evolution of Ceramic topcoat resistance (R_{YSZ}) for type III EB-PVD TBCs as a function of thermal cycling at 1121°C.

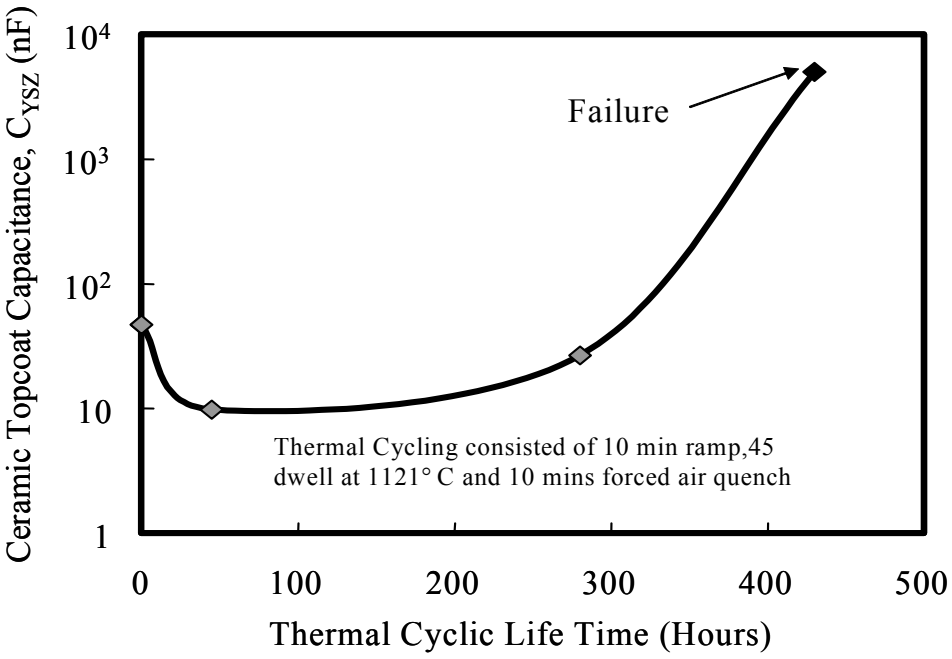

Figure 74.Evolution of Ceramic topcoat capacitance (C_{YSZ}) for type III EB-PVD TBCs as a function of thermal cycling at 1121°C.

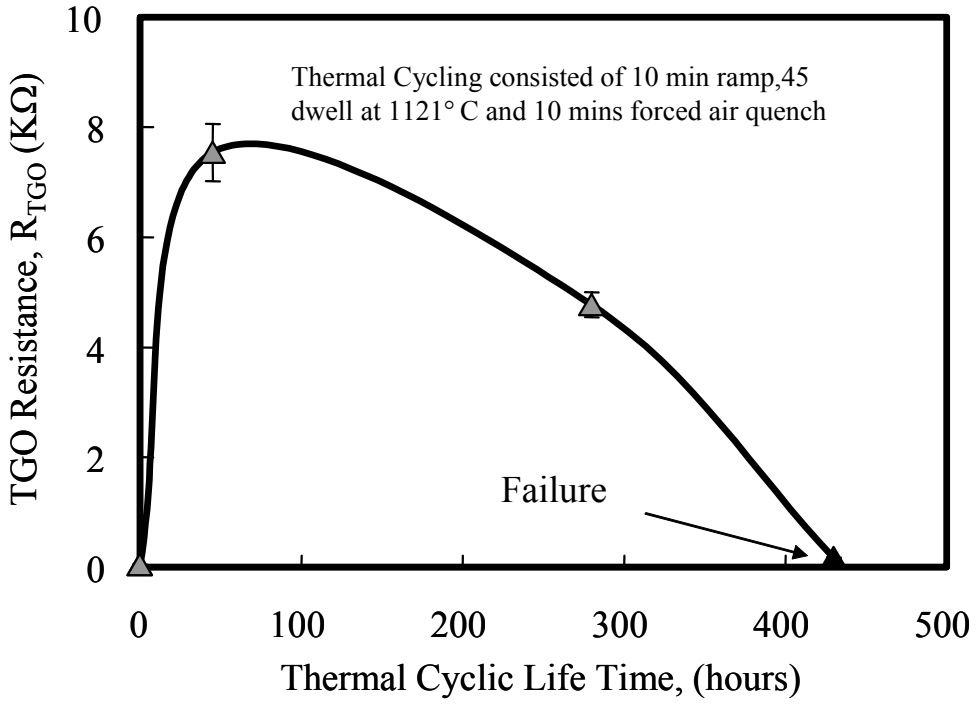

Figure 75.Evolution of TGO resistance (R_{TGO}) for type III EB-PVD TBCs as a function of thermal cycling at 1121°C.

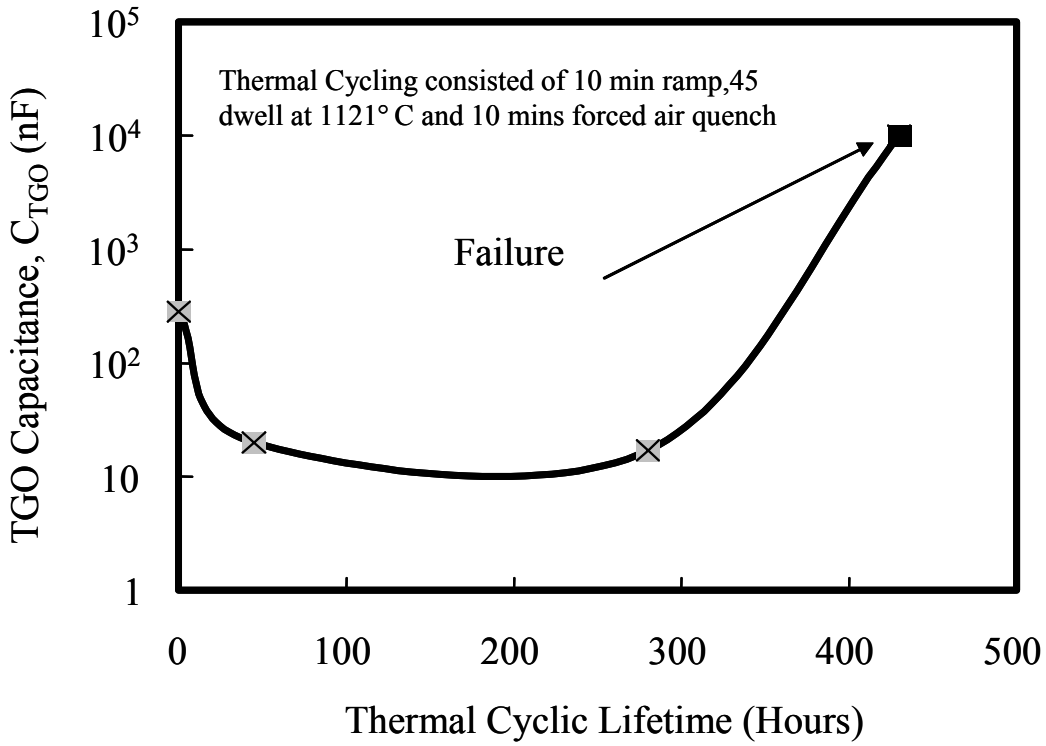

Figure 76.Evolution of TGO capacitance C_{TGO} for type III EB-PVD TBCs as a function of thermal cycling at 1121°C.

For type IV TBCs EIS measurement was carried out 3 times for as-received, thermally cycled and failed specimen. Typical impedance and phase angle plots for these specimens are presented in Figures 77 and 78, respectively. Table IX also reports the values of resistance and capacitance of the various TBC constituents that were calculated based on the ac-equivalent circuit in Figure 9. Evolution of resistance and capacitance of TBC constituents as a function of thermal cycling is presented in Table IX and Figures 79 through 82. Figure 77 shows that the impedance of the type-IV TBCs increased with thermal cycling and decreased after prolonged exposure. This increase in the impedance is attributed to the growth of the TGO and the high temperature sintering of the YSZ. Aforementioned, this microstructural changes can be related to the electrical parameters such as the resistance and capacitance of the YSZ and the TGO. The resistance of the YSZ and TGO increased initially and decreased after prolonged exposure as shown in Figures 79 and 80. Whereas the capacitance of the YSZ shown in the Figure 80, decreased initially and remained constant until failure when a sharp increase was observed. This is because the impedance of the failed specimen is lower than that of the as-received specimen due to the exposure of the bond coat surface observed on the fracture surface (see section V.4.4). On the other hand the capacitance of the TGO shown in Figure 71, decreased initially and increased with further thermal cycling.

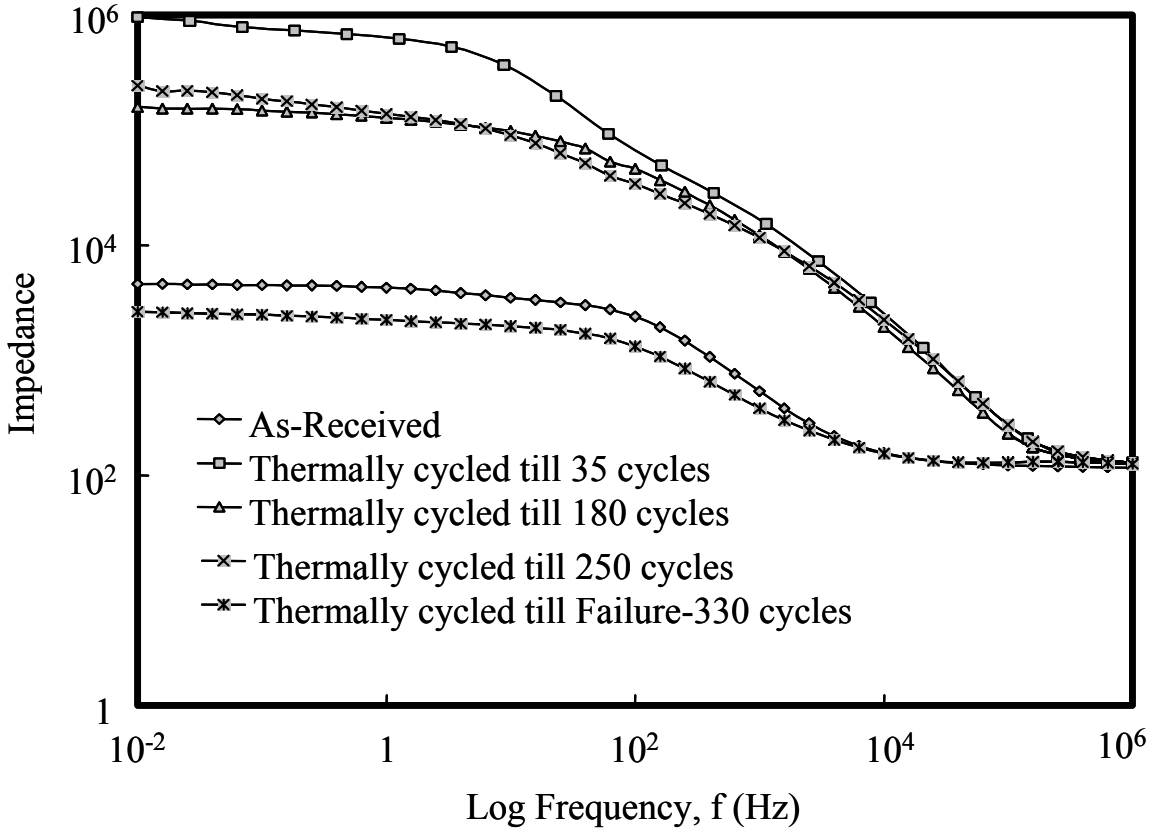

Figure 77. Typical Impedance plots from as-coated and as a function of thermal cyclic life time for type-IV EB-PVD TBCs

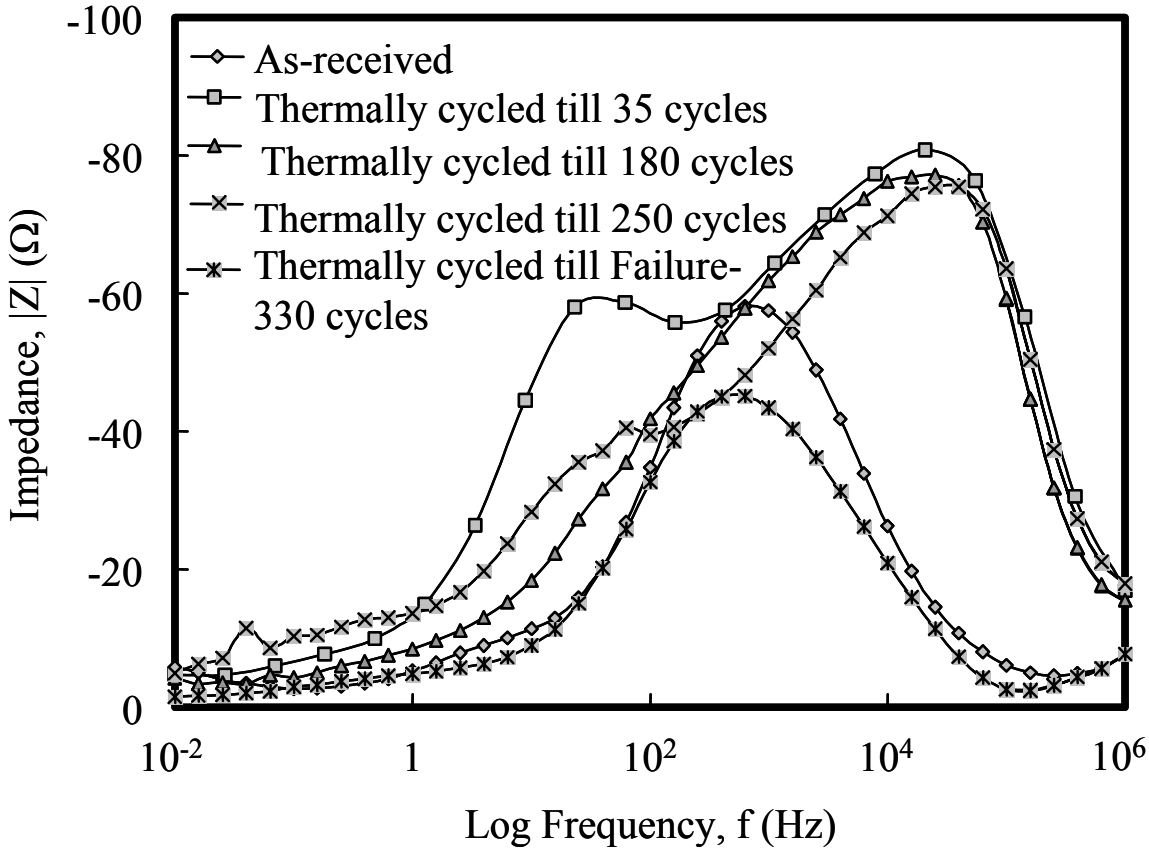

Figure 78. Typical phase angle plots from as-coated and as a function of thermal cyclic life time for type-IV EB-PVD TBCs

Table IX. Resistance and capacitance of type-IV EB-PVD TBC constituents as a function of thermal cycling.

Thermal Cycles	R_C (kΩ)	C_C (nF)	R_P (kΩ)	C_P (nF)	R_O (kΩ)	C_O (nF)	R_T (kΩ)	C_T (nF)
As-received	.01 ± 0	224 ±16.3	2.17 ±0.3	523.7 ±26.2	2.1 ±0.3	600 ±14.5	37.2 ±0.7	2 ±0.1
45 (10% lifetime)	6.2 ±2.2	6.8 ±0.2	735.5 ±175.6	8.6 ±0.8	431 ±6.6	50.1 ±2.3	23.8 ±0.9	2.4 ±0.3
180 (50% lifetime)	2.6 ±0.05	8.2 ±0.05	134.8 ±2.8	8.7 ±0.05	27.6 ±0.10	115 ±1.6	31.1 ±0.2	2.3 ±0.04
280 (70% lifetime)	0.44 ±0.05	6.5 ±0.04	140.2 ±26.8	9.72 ±0.15	31.43 ±0.8	182 ±15.8	35 ±0.3	1.9 ±0.01
330 (After) Failure	0.02 ±0	250 ±48.8	1.7 ±0.2	450.3 ±99.6	0.96 ±0.06	1203.2 ±365.4	40.8 ±0.9	1.7 ±0.1

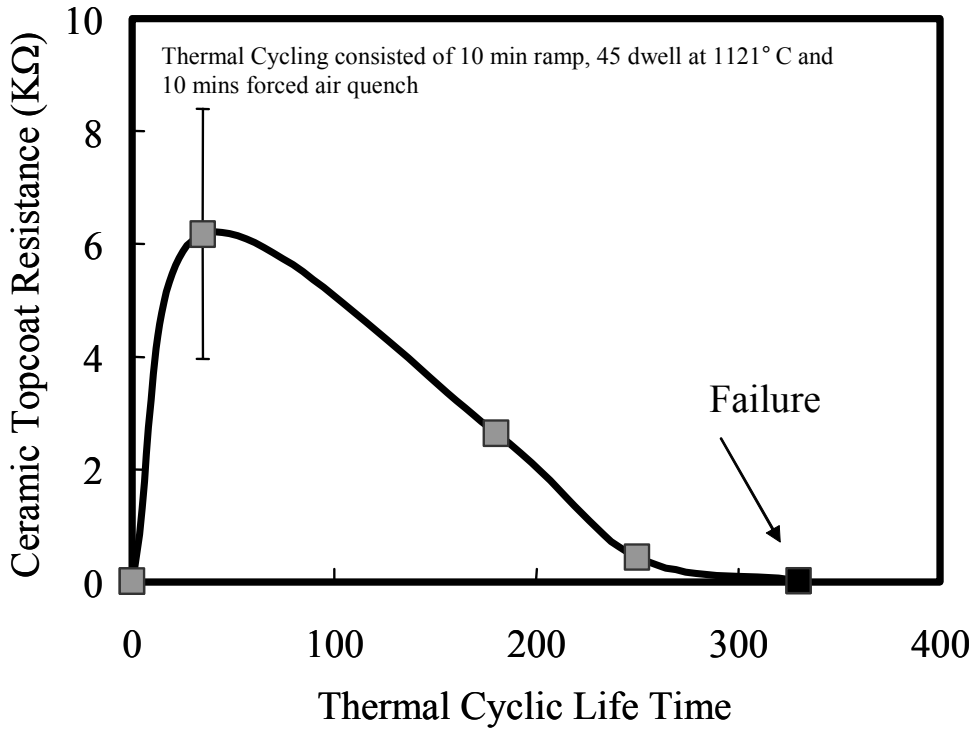

Figure 79. Evolution of Ceramic topcoat resistance (R_{YSZ}) for type IV EB-PVD TBCs as a function of thermal cycling at 1121°C.

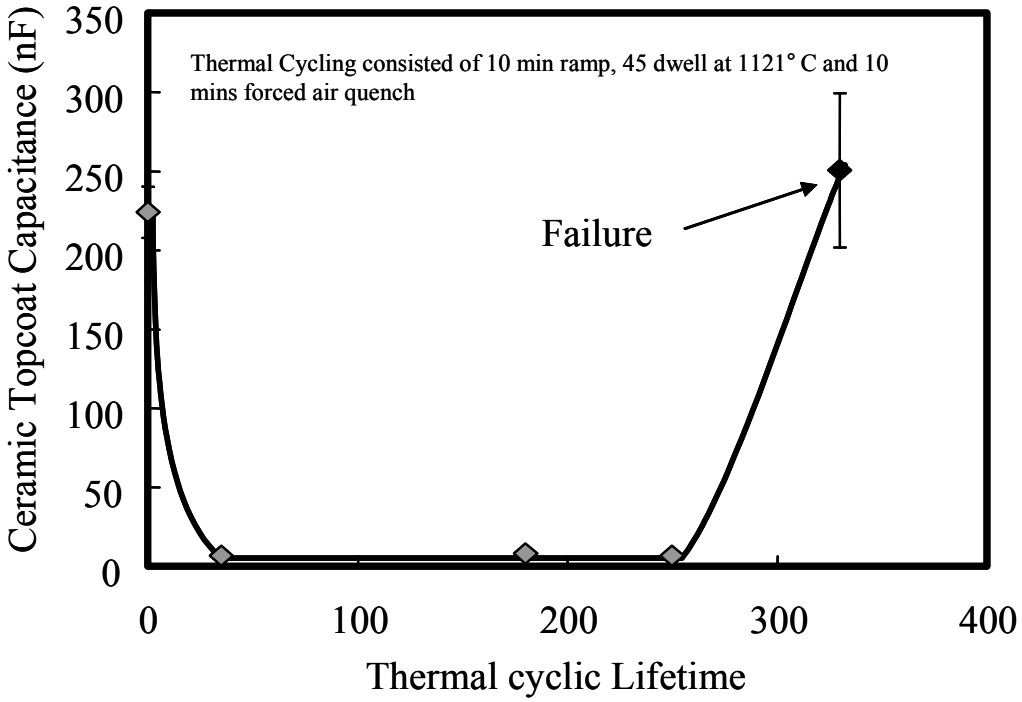

Figure 80. Evolution of Ceramic topcoat capacitance (C_{YSZ}) for type IV EB-PVD TBCs as a function of thermal cycling at 1121°C.

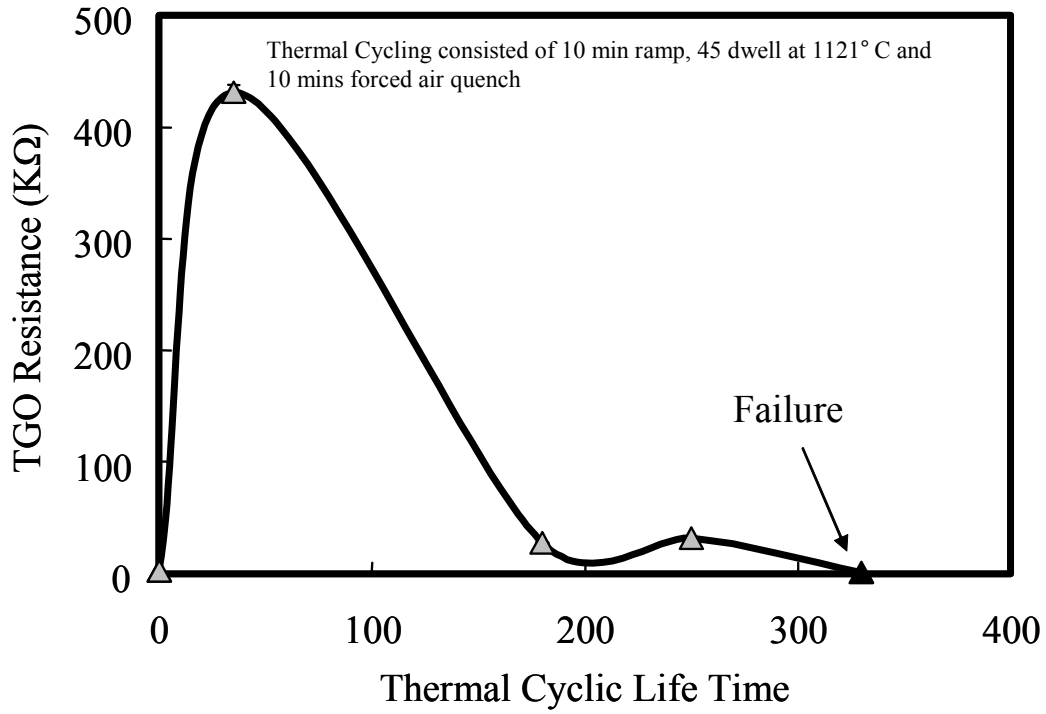

Figure 81. Evolution of TGO resistance (R_{TGO}) for type IV EB-PVD TBCs as a function of thermal cycling at 1121°C.

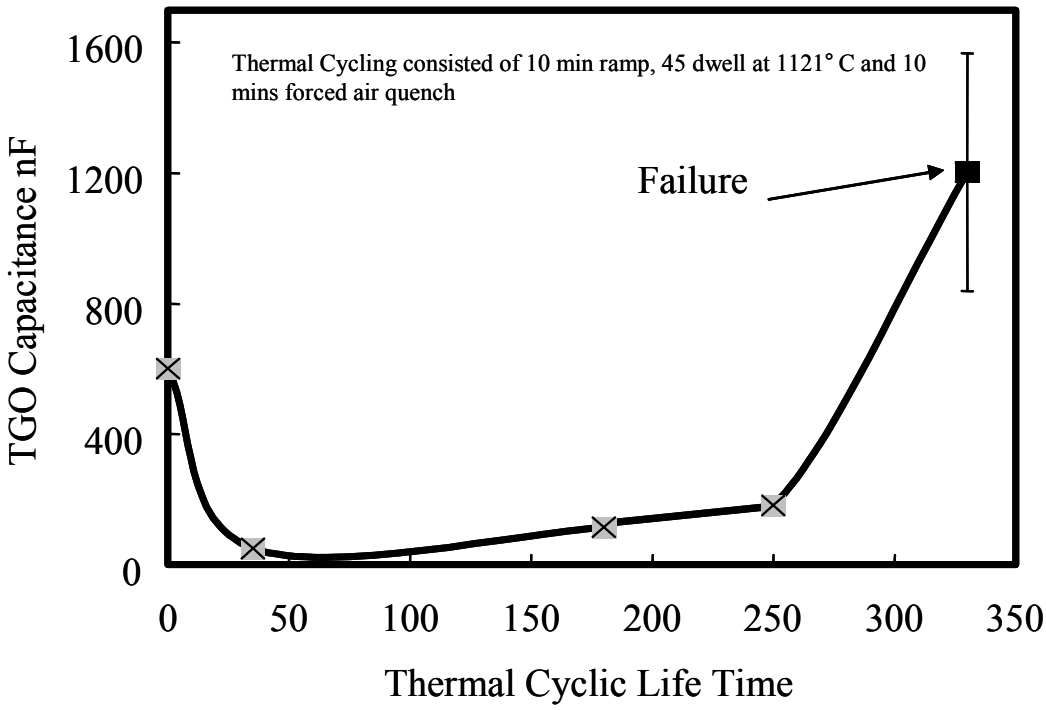

Figure 82. Evolution of TGO capacitance (C_{TGO}) for type IV EB-PVD TBCs as a function of thermal cycling at 1121°C.

V.3.4. Sub-critical damage detection before actual TBC failure

From the EIS results discussed in the previous section a master plot is generated for the C_{TGO} and thickness of the TGO and is shown in Figure 83. Without any damages there is an inverse linear trend between the C_{TGO} and the thickness of TGO. Since capacitance does vary inversely to the thickness [26]. A deviation from this trend was observed for one particular type-IV TBCs with grit-blasted (Ni, Pt)Al bondcoat. This may be due to the sub-critical damages in TGO that can expose the metallic surface or the effective thickness of the TGO scale reduces with this damage. These sub-critical damages are shown in the section v.4.

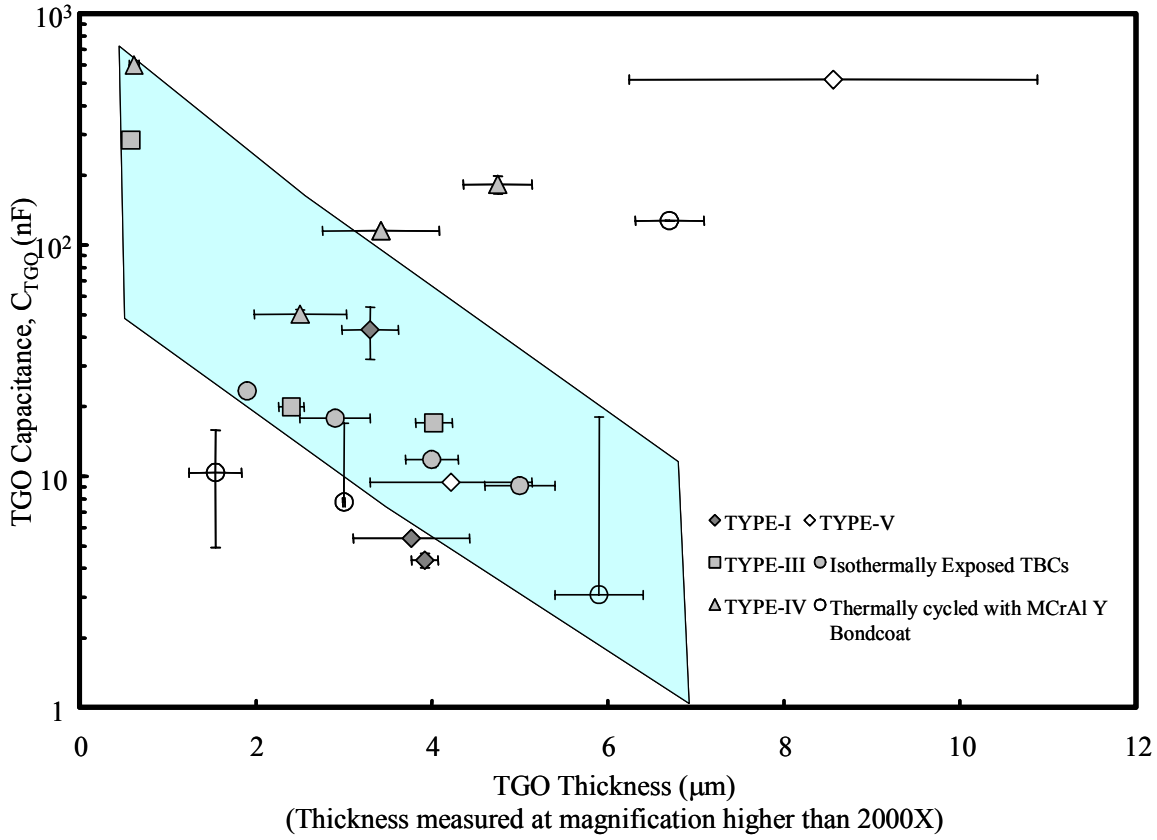

Figure 83. Master plot showing the linear relation between the CTGO and thickness of TGO prior to spallation and change in the linear relation with sub-critical damages.

V.3.5. NDE of Type I APS TBCs by EIS- 10 and 50- hour thermal cycling

For type I APS TBCs, EIS measurement was carried out 3 times on specimens before thermal cycling and after 10- hour thermal cycling that corresponds to 30% and 80% of its lifetime. The variation in impedance with respect to the 10 – hour thermal cycling is presented in Figures 56 and 57, respectively. Table X also reports the values of resistance and capacitance of the various TBC constituents, which were calculated based on the ac-equivalent circuit presented in Figure 9. For the as-coated APS TBCs, there is no significant presence of the TGO. Hence the TGO is not represented in terms of the electrical parameters. The ac equivalent circuit for APS TBCs, after exposure is different from that of the as-coated

ones because of the bond coat oxidation and the formation of uniform and continuous TGO. The impedance of TGO cannot be neglected in the EIS measurement system. Thus, an ac equivalent circuit for the thermally cycled TBC consists of the electrical parameters that represent the TGO.

The impedance plot presented in Figure 84 shows that the impedance response of the TBCs did not vary significantly with 10-hour thermal cycling however there are subtle changes in the values resistance and capacitance of YSZ and TGO these are reported in table X. This initial increase in the impedance response may be attributed to the sintering of the YSZ topcoat and growth of TGO with high temperature exposure from as received condition. After continuous 10-hour thermal cycling the impedance did not vary significantly this may be because of the micro-cracks that develop in the YSZ topcoat and also the sub-critical damages associated with topcoat sintering at the interface between YSZ/TGO. These sub-critical damages prior to the final failure have been documented by microstructural analysis (see section V.4.2, 4.7 and 4.9).

A further comparison of impedance response with 1-hour thermal cycling is shown in Figure 85. From Figure 85 we can see the increase in the impedance for 1-hour thermal cycling is because of prolonged exposure and formation of well developed TGO as well as topcoat sintering. Whereas in case of 10-hour and 50-hour thermal cycling the impedance response is lower in that frequency range which depends on TGO scale development and YSZ sintering this is because of the sub-critical damages that are seen in topcoat and YSZ/TGO interface (see section V.4.2, 4.7 and 4.9).

The resistance and capacitance of YSZ and TGO reported for type APS TBCs are presented as function of dwell time in Figures 86 through 89. With an increase in the impedance, the resistance of the topcoat and the TGO increased. With further prolonged dwell time the resistance of the topcoat and the TGO decreased. The capacitance of the topcoat increased at failure because of the large scale damage in the topcoat. The capacitance of the TGO did not increase abruptly at failure because the fracture path of the APS TBCs observed for type-I TBCs primarily occur at the YSZ\TGO interface as shown in Figures 146 and 159 (see section V.4.2, 4.7 and 4.9) and rarely exposes the conductive surface of the metallic bondcoat.

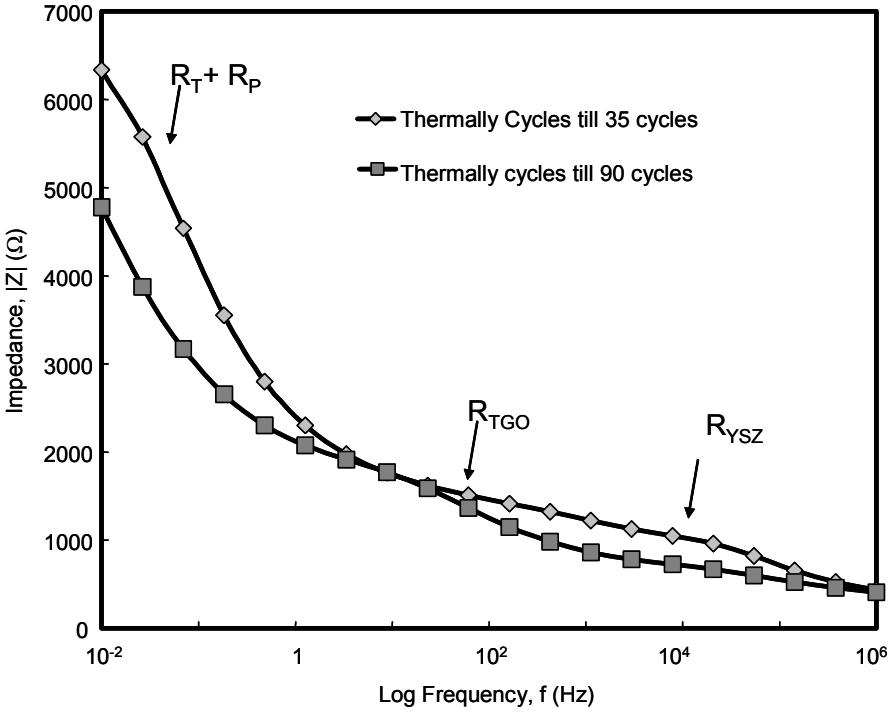

Figure 84. Typical Impedance plots from type-I APS TBCs as a function of 10-hour thermal cycling

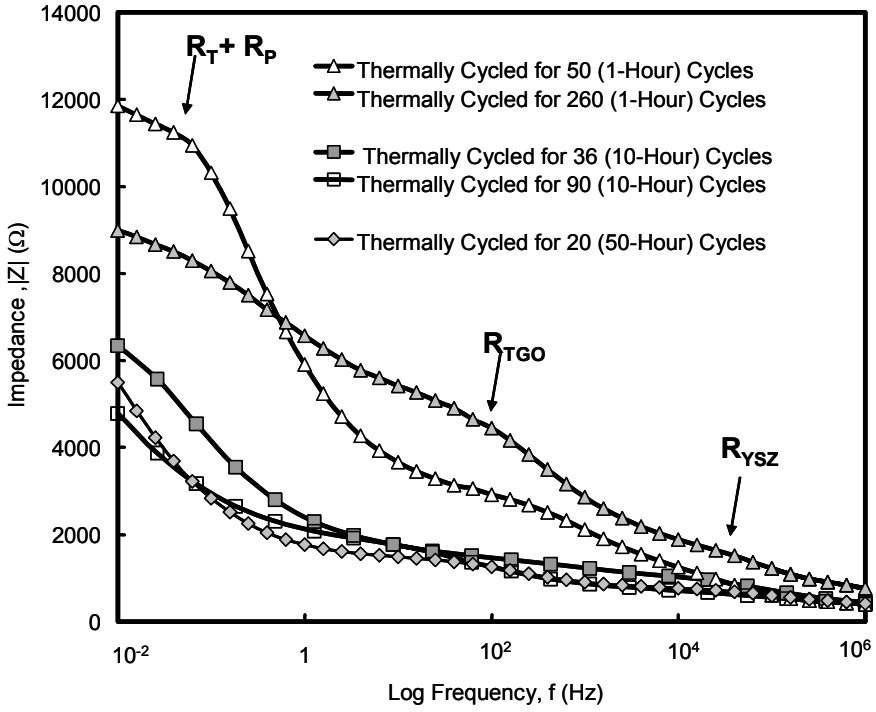

Figure 85. Typical Impedance plots from type-I APS TBCs as a function of 1, 10 and 50- hour thermal cycling

Table X. Resistance and capacitance of type- I APS TBCs constituents as a function of 10-hour thermal cycling.

Thermal Cycles	R_C (kΩ)	C_C (nF)	R_P (kΩ)	C_P (uF)	R_O (kΩ)	C_O (nF)	R_T (kΩ)	C_T (nF)
As-received	0.50 ± 0.4	2.2 ± 0.4	10.6 ± 4.2	377700 ± 21959	0	0	0.3 ± 0.1	16486 ± 2747
36 cycles (30% lifetime)	.64 ±0.002	374.6 ±82.1	5.6 ±0.18	18.48 ±0.22	0.98 ±0.02	9.94 ±0.72	0.55 ±0.02	10531 ±996
90 cycles (80% lifetime)	0.88 ±0.09	431.95 ±0.0	6.58 ±4.87	11.34 ±0.02	0.58 ±0.10	6.14 ±0.01	0.51 ±0.13	3262 ±15.5

Table XI. Resistance and capacitance of type- I APS TBCs constituents as a function of 50-hour thermal cycling.

Thermal Cycles	R_C (kΩ)	C_C (nF)	R_P (kΩ)	C_P (uF)	R_O (kΩ)	C_O (nF)	R_T (kΩ)	C_T (nF)
As-received	0.50 ± 0.4	2.2 ± 0.4	10.6 ± 4.2	377700 ± 21959	0	0	0.3 ± 0.1	16486 ± 2747
20 cycles (50% lifetime)	.60 ±0.01	892.3 ±21.7	4.03 ±0.08	7.3 ±0.32	0.78 ±0.02	8.5 ±0.16	9.6 ±0. 10	16085 ±148

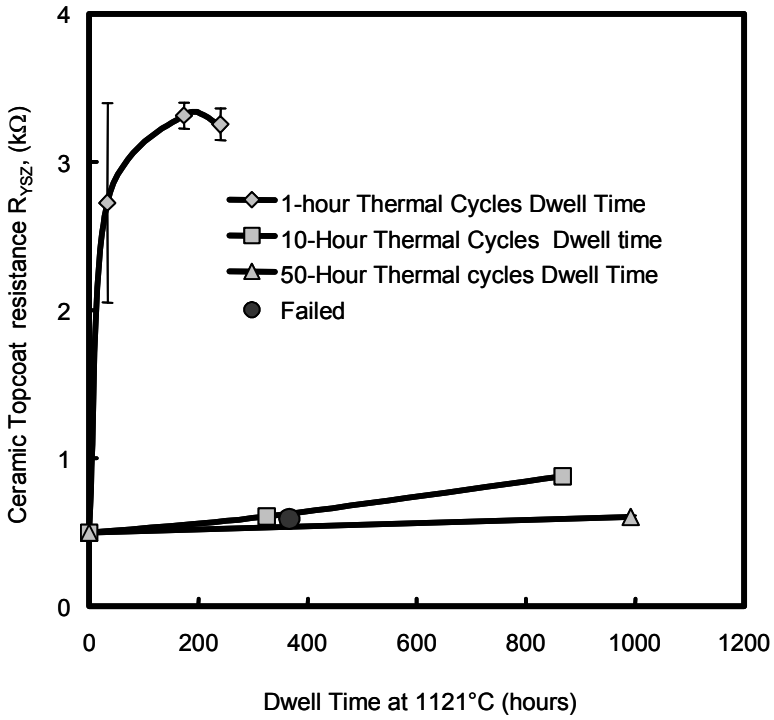

Figure 86. Evolution of ceramic topcoat resistance (R_{YSZ}) for type I APS TBCs as a function of dwell time at 1121°C.

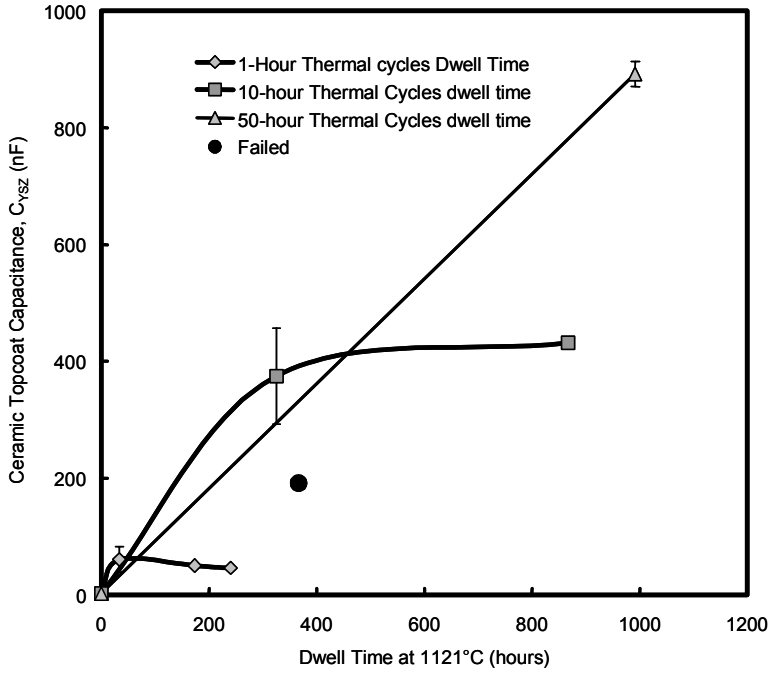

Figure 87. Evolution of ceramic topcoat capacitance (C_{YSZ}) for type I APS TBCs as a function of dwell time at 1121°C.

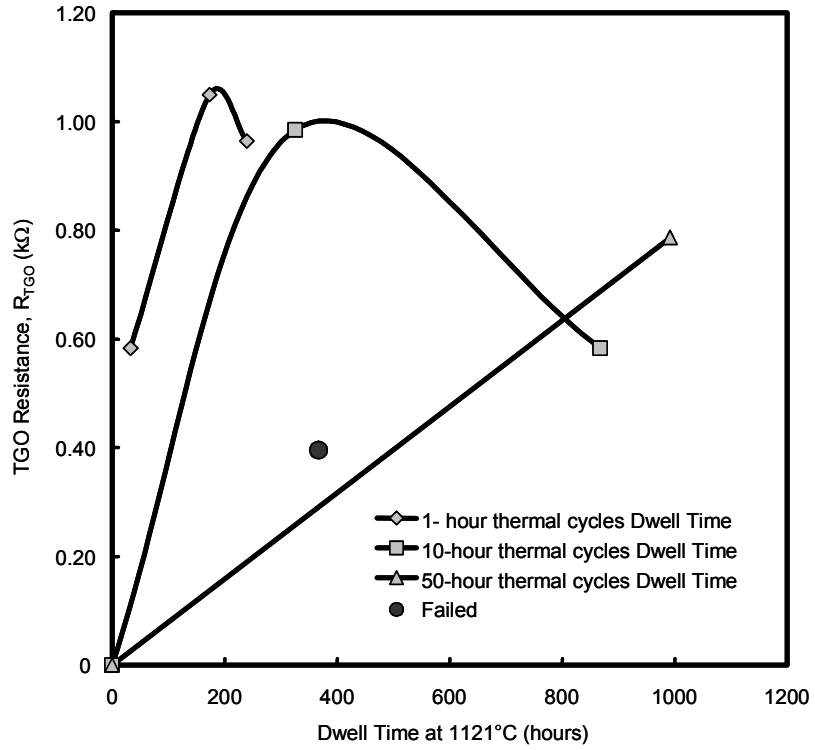

Figure 88. Evolution of TGO resistance (C_{YSZ}) for type I APS TBCs as a function of dwell time at 1121°C.

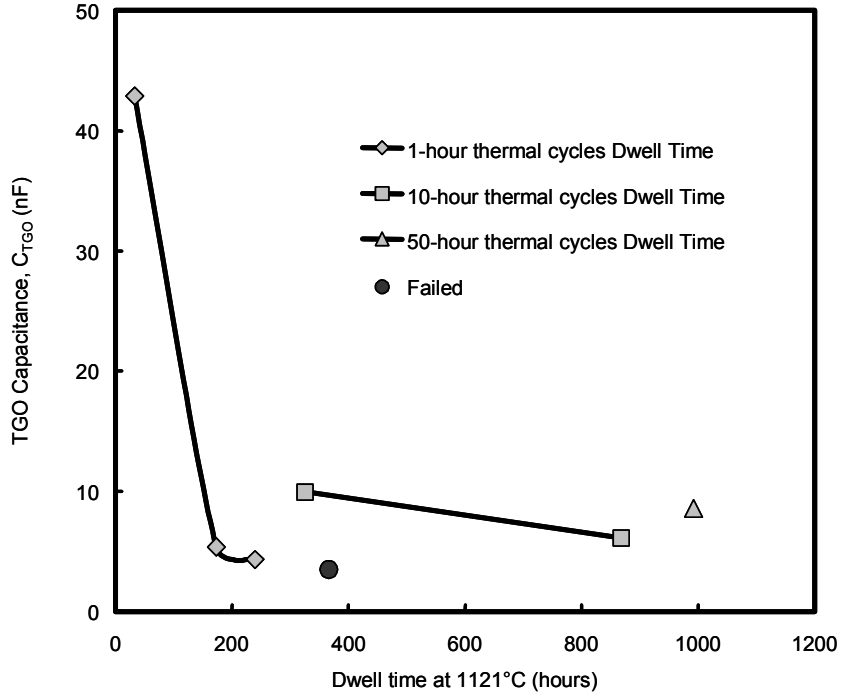

Figure 89. Evolution of TGO capacitance (C_{YSZ}) for type I APS TBCs as a function of dwell time at 1121°C.

V.3.6. Selected EIS Observations for TBC Applications

Along with NDE of five types of TBCs by EIS, selected experiments were carried out for EIS independently at UCF and in collaboration with industrial partners. The following summarizes the results from these additional specimens.

Monolithic 7YSZ with Varying Thickness and Density

Monolithic 7YSZ with varying thickness and density, received from Trans-Tech, Adamstown, PA, was examined by EIS. Figure 90 shows an increase in resistance (and a corresponding decrease in capacitance) with increasing thickness. In addition, lower resistance was observed for more porous 7YSZ as seen in Figure 90, reflecting greater conduction via electrolyte penetration through 7YSZ [25].

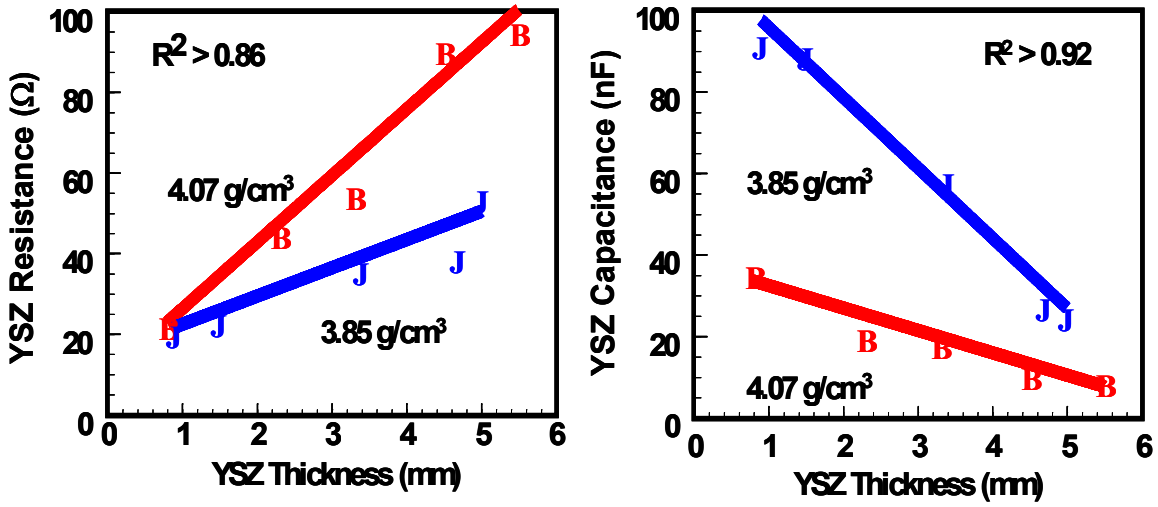

Figure 90. Ceramic resistance R_C and capacitance C_C of 7YSZ monoliths (open-pores) as a function of thickness and density non-destructively determined by EIS [25].

Electron Beam Physical Vapor Deposited 7YSZ with Varying Thickness

A series of as-coated EB-PVD 7YSZ TBCs with varying thickness, which is controlled by deposition time, was examined by EIS. Specimens were provided by one of the industrial partners. An increase in the ceramic resistance was observed with increasing thickness as presented in Figure 91 [25].

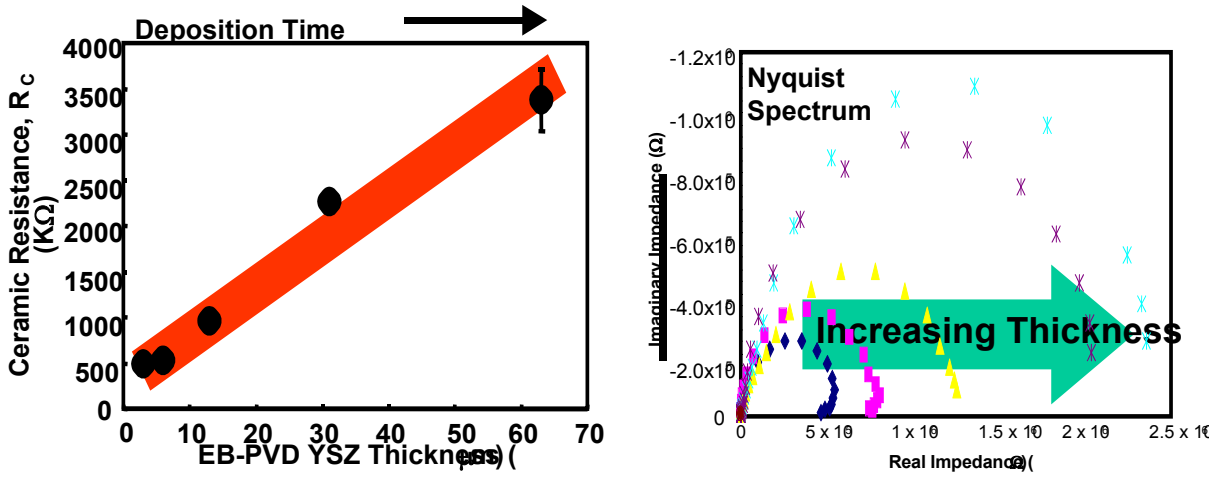

Figure 91. An increase in the ceramic top coat resistance R_C and the corresponding Nyquist plots as a function of thickness for as-coated EB-PVD TBCs.

NiAl Disk Specimens as a Function of Thermal Cycling

Hot-extruded NiAl disk specimens, received from NASA-GRC, were thermally cycled at 1121°C using a 10-minute heat-up, a 40-minute hot-time and a 10-minute forced-air-quench. Resistance and capacitance of TGO, R_O and C_O were monitored as a function of thermal cycles as presented in Figure 92. Initial increase and decrease, in the resistance and capacitance, respectively, of TGO correspond to the parabolic growth (thickening) of TGO scale [25]. This trend in the resistance and capacitance of the TGO, changes between 20 and 50 cycles, at which, the spallation of TGO was observed using optical microscopy [25]. Upon spallation of TGO, localized exposure of NiAl surface to the electrolyte will decrease the resistance, and increase the capacitance.

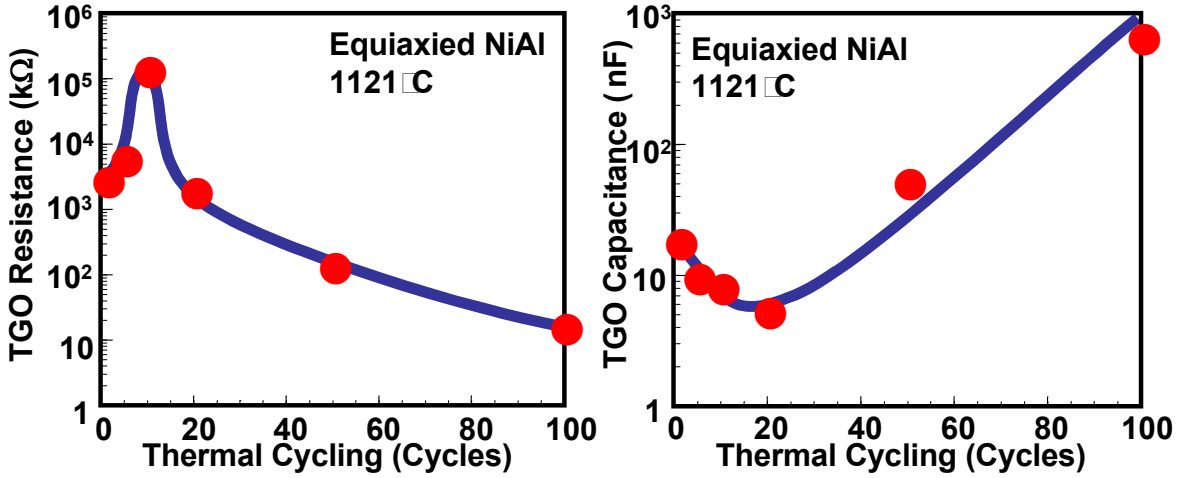

Figure 92. Evolution of TGO resistance and capacitance as a function of thermal cycling at 1121°C.

NiAl Disk Specimens as a Function of Isothermal Oxidation

Similar results were obtained for NiAl disk specimens, which were isothermally oxidized at various time (2, 5 and 10 hours) and temperature (1100°, 1200° and 1300°C). Figure 93 shows a decrease in capacitance (C_{TGO}) and corresponding increase in resistance (R_{TGO}) with increasing time and temperature. However, reverse trend was observed in resistance and capacitance for specimens oxidized at 1300°C with varying time. This trend is related to the spallation of the oxide scale on the NiAl substrate which leads to the contact of the electrolyte directly to the metal. Figure 94 shows the spallation of the oxide scale from the substrate. Upon spallation of TGO, localized exposure of NiAl surface to the electrolyte will decrease the resistance, and increase the capacitance.

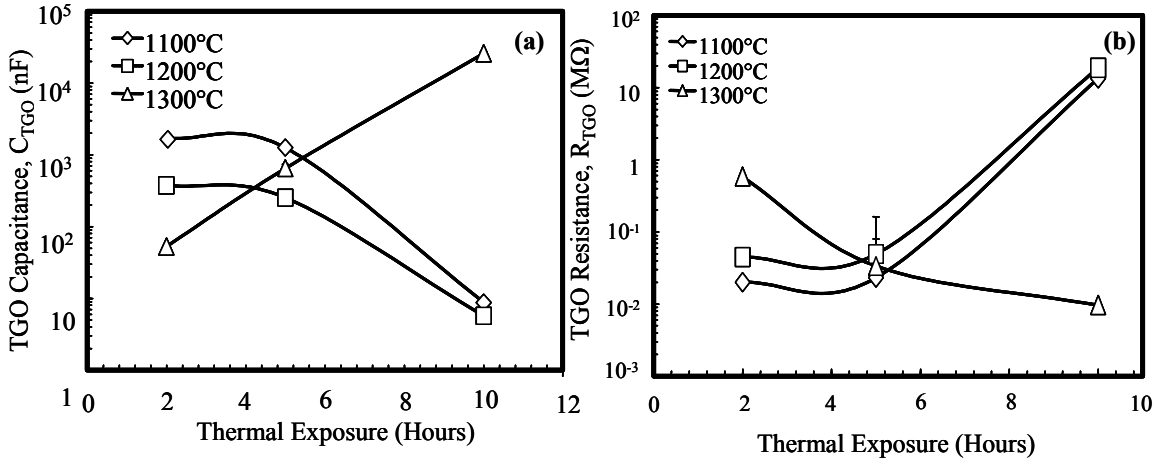

Figure 93. Evolution of TGO capacitance and resistance as a function of isothermal oxidation at various time and temperature.

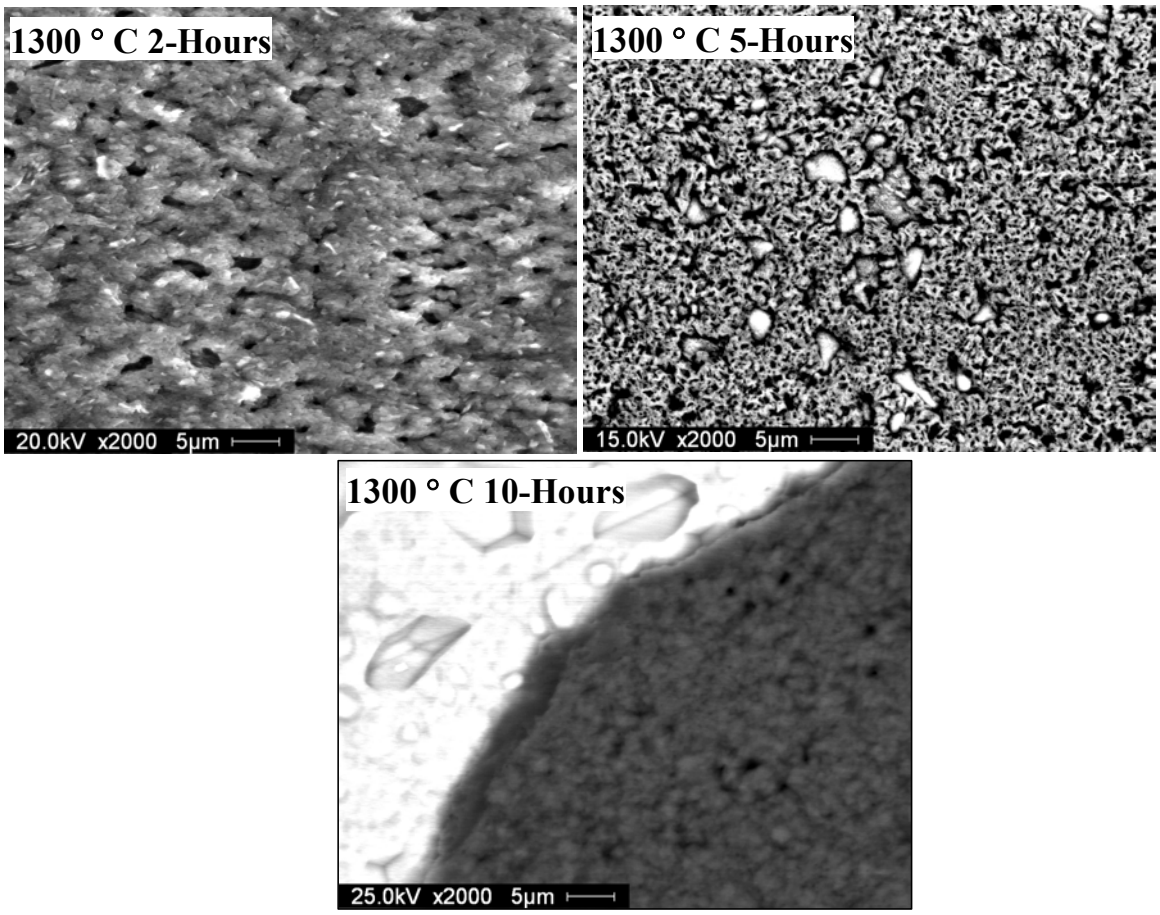

Figure 94.Spallation of TGO scale (Al_2O_3) from the NiAl surface after 5 and 10 hours of isothermal exposure at 1300° C.

Electron Beam Physical Vapor Deposited TBCs as a Function of Thermal Cycling

EB-PVD TBCs with various thermal cycling at 1121°C (40-minute hot-time) were examined by EIS with specimens provided by the University of Connecticut/industrial partner. Resistance and capacitance of YSZ and TGO were monitored as a function of thermal cycles as presented in Figure 95. After prolonged thermal cycling, a sharp decrease and an increase in the resistance and capacitance, respectively, of YSZ was observed [26]. Initial increase and decrease in the resistance and capacitance of TGO, respectively, correspond to the parabolic growth (thickening) of TGO scale [26]. Abrupt changes in the resistance and capacitance of TGO, by orders of magnitude, occurred with the failure [26]. A decrease in the resistance of TGO occurred prior to failure [26]. This observation is consistent with that from the oxidation of NiAl (Figures 92 & 93) and for the types of TBC specimens reported above.

A decrease in the resistance and the corresponding increase in the capacitance of insulating oxide (YSZ and TGO) reflect the conduction via penetration of electrolyte. This

penetration of electrolyte can occur through porosity, and more importantly, through damages/cracks that develop within YSZ and TGO during thermal cycling.

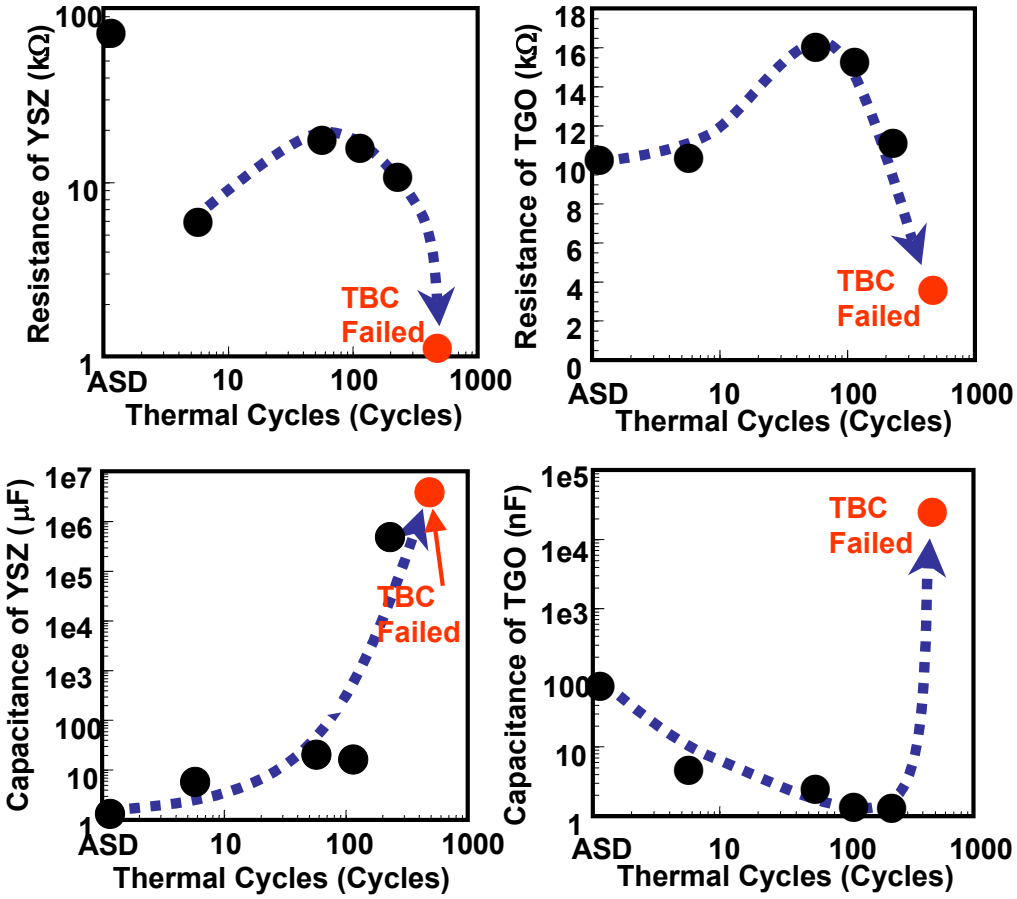

Figure 95. Evolution in (a,c) resistance and (b,d) capacitance of (a,b) EB-PVD 7YSZ and (c,d) TGO during thermal cycling at 1121C.

7YSZ and $CaTiO_3$ Air Plasma Sprayed Thermal Barrier Coatings

YSZ and $CaTiO_3$ TBCs with varying thickness, provided by one of the industrial partners, were examined by EIS. There is a decrease in the capacitance of ceramic top coat with increasing thickness as presented in Figure 96 [27]. A decrease in capacitance also corresponds to an increase in resistance as presented in Figure 96 [27]. Variation in thickness was measured on these specimens using scanning electron microscopy. The dielectric constant of $CaTiO_3$ is around 160 while that for YSZ is in the range of 40-60. The resistivity of $CaTiO_3$ is in the order of 10^{14} Ω-cm and that of YSZ is approximately 10^9 Ω-cm. From these values of dielectric constant and resistivity, the resistance and the capacitance of the $CaTiO_3$ must be higher than that of YSZ at similar thickness as presented in Figure 96.

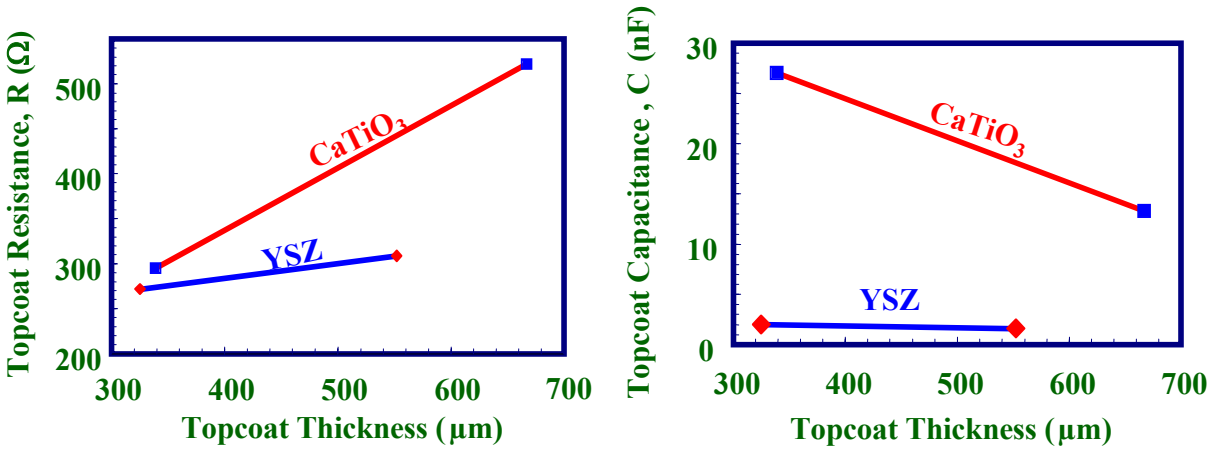

Figure 96. Ceramic top coat resistance R_C and capacitance C_C of APS 7YSZ and $CaTiO_3$ as a function of thickness.

Monolithic 7YSZ as a Function of Sintering

Monolithic 7YSZ with open pores, received from Trans-Tech, Adamstown, PA, was examined by EIS as a function of sintering time (2, 5 and 10 hours) and temperature (1100°, 1200° and 1300°C). Figure 97 shows a decrease in capacitance (and a corresponding increase in resistance) with increasing time and temperature of sintering after furnace cooling. However, air quenching after sintering at 1300°C for 5 and 10 hours produced a opposite trend in capacitance (i.e., an increase) and resistance (i.e., a decrease), which indicates that the penetration of electrolyte through sintered YSZ was easier for these specimens. In accordance with these EIS results, macro-scale cracks were observed for the specimens, which were air quenched after sintering at 1300°C for 5 and 10 hours as presented in Figure 98. The increase in capacitance and the decrease in the resistance due to electrolyte penetration through damage are consistent with observation made for TBCs presented in this report. Secondary electron micrographs of sintered specimens are presented in Figure 99.

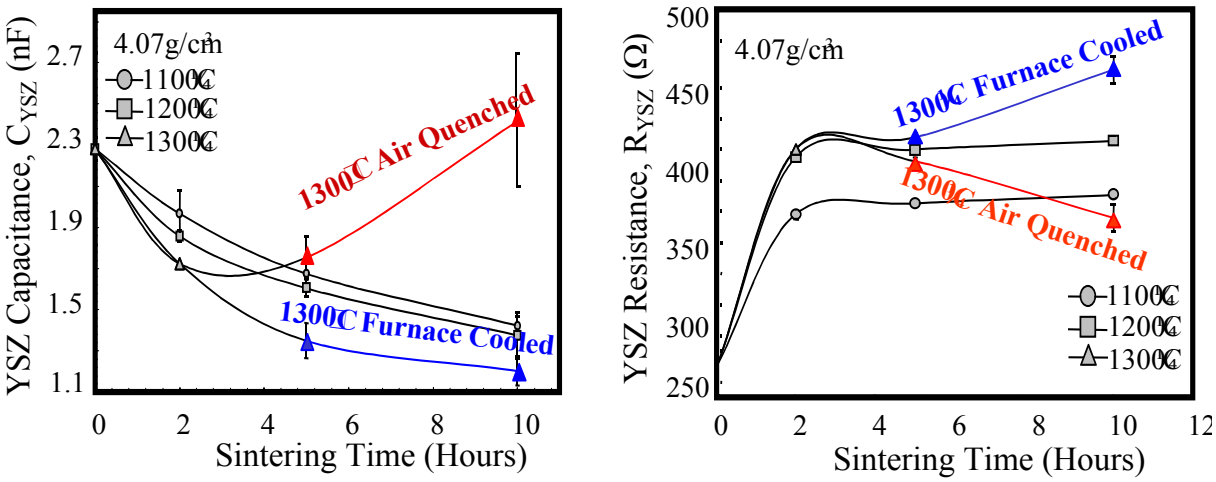

Figure 97. Evolution of YSZ capacitance and resistance as a function of time and temperature of isothermal sintering.

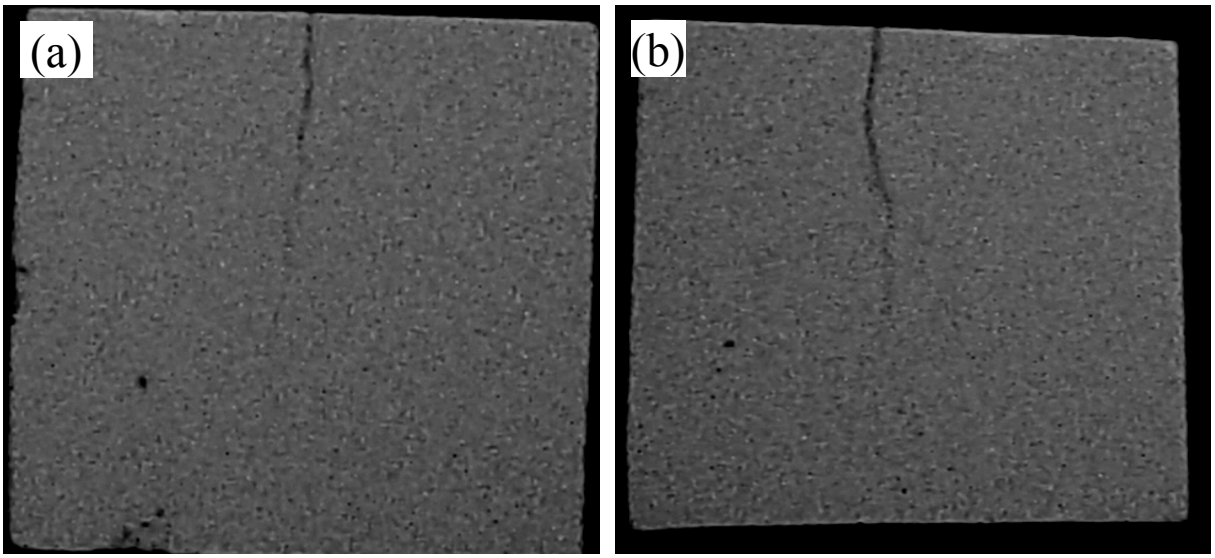

Figure 98. Macroscopic photographs of specimens after air-quenching from sintering at 1300°C for (a) 5 and (b) 10 hours. These specimens developed a large-scale crack upon air quenching to a room temperature.

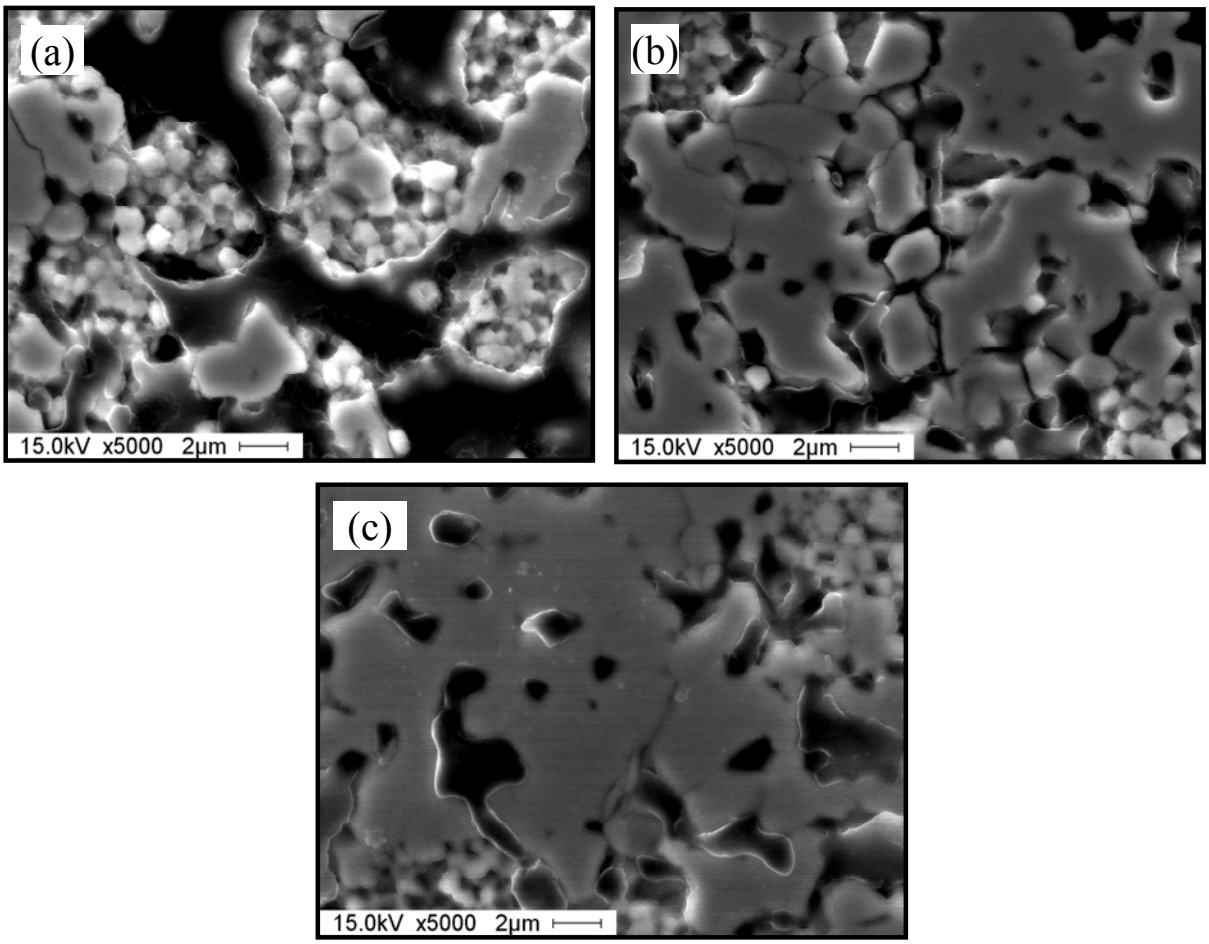

Figure 99. Secondary electron micrographs of YSZ monoliths with open pores: (a) as-received; (b) sintered at 1200°C for 5 hours, (c) sintered at 1300°C for 10 hours.

V.4. Microstructural Analysis of Thermal Barrier Coatings

V.4.1. As-coated Type I and V Air Plasma Sprayed Thermal Barrier Coatings

Figure 100 represents typical backscatter electron micrograph of as-received type I (600μm-thick) and type V (200μm-thick) APS TBCs. Specimens conformed to the specification described in Table II. Using SEM, no significant TGO scale was observed in the as-received APS TBCs as shown in Figure 100. However, a difference in the microstructure of APS YSZ was observed. Type I APS TBC did not exhibit splat morphology while type V TBC did as seen in Figure 100. This difference may be correlated to the NDE results by EIS (section V.3.1): a distinctive difference in pore capacitance C_P for these two specimens is reported in Table VI and Table VII. This difference in microstructure of the APS 7YSZ coatings is presented in Figure 101 with higher magnification backscatter electron micrographs. After OM and SEM, a site-specific specimen for TEM/STEM was prepared using FIB-INLO. Figure 102 shows an ion beam generated secondary electron images from the TEM specimen preparation of APS TBCs by FIB-INLO technique: the specimen has been welded to a micromanipulator and lifted out.

In the as-coated type I TBC specimen, extensive presence of voids between YSZ and MCrAlY bond coat was observed as presented in Figure 103(a). The TGO consisted of agglomerated α-Al_2O_3 particles ~100 nm in size. Figure 102 also shows that the microstructure of type I APS YSZ coating does not have the typical columnar grains within splats and splat boundaries. No other types of oxide (e.g., Ni, Cr, Co containing oxides) were found as presented by HAADF image in Figure 103(b). In general, APS 7YSZ coatings consisted of non-equilibrium tetragonal (t') phase as presented in Figure 103(c) by the SADP, however SADP from retained cubic (f') phase was also observed as presented in Figure 97(d). SADP from agglomerated α-Al_2O_3 particles is presented in Figure 103(e). At localized regions where TGO has fully developed, atomic level bonding was observed at YSZ/TGO and TGO/bond coat interfaces as presented in Figure 104. These microstructural observations indicate that the integrity of type I APS TBCs, at least in as-coated condition, may be maintained significantly by "mechanical interlocking" with some adhesion by "atomic bonding."

In the as-coated type V TBC sample, interfacial void between YSZ and MCrAlY bond coat was largely filled with carbon (presumably from mounting epoxy) as seen in Figure 105(a). Also, TGO was completely absent. Figures 105(a) and (b) also show that the microstructure of type V APS YSZ coating consists of typical columnar grains within splats, and splat boundaries. APS 7YSZ consisted of non-equilibrium tetragonal (t') and/or retained cubic (f') phase as presented by the SADP in Figure 105(c).

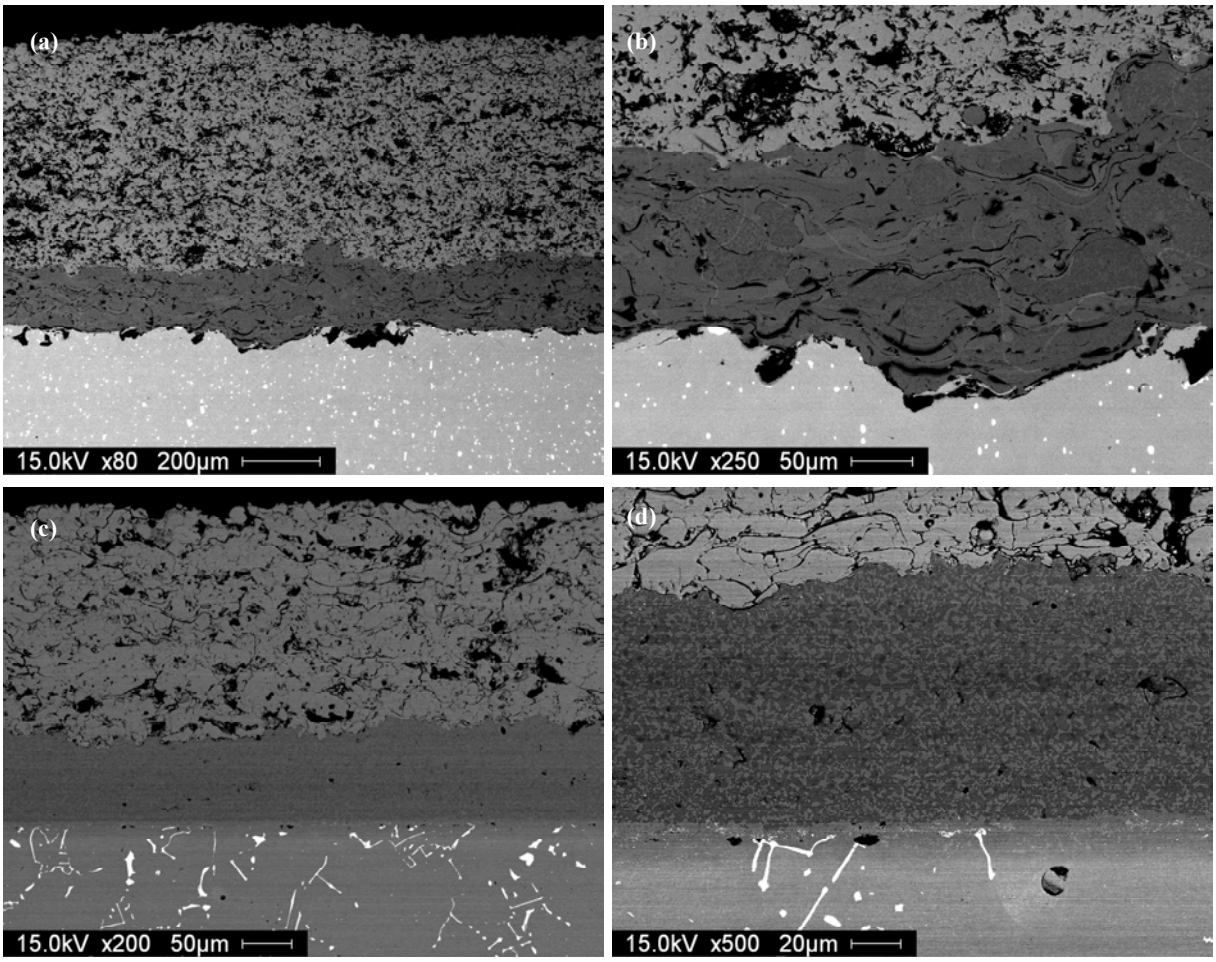

Figure 100. Typical backscatter electron micrographs of (a,b) type I and (c,d) type V APS TBCs specimens.

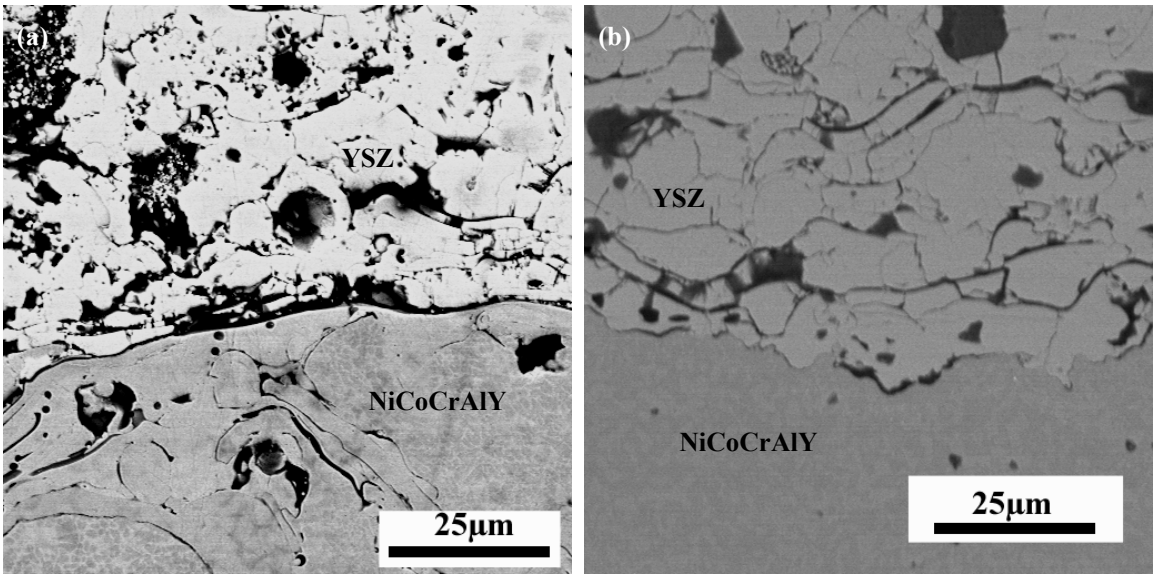

Figure 101. High magnification backscatter electron micrographs of (a) type I and (b) type V APS TBCs specimens.

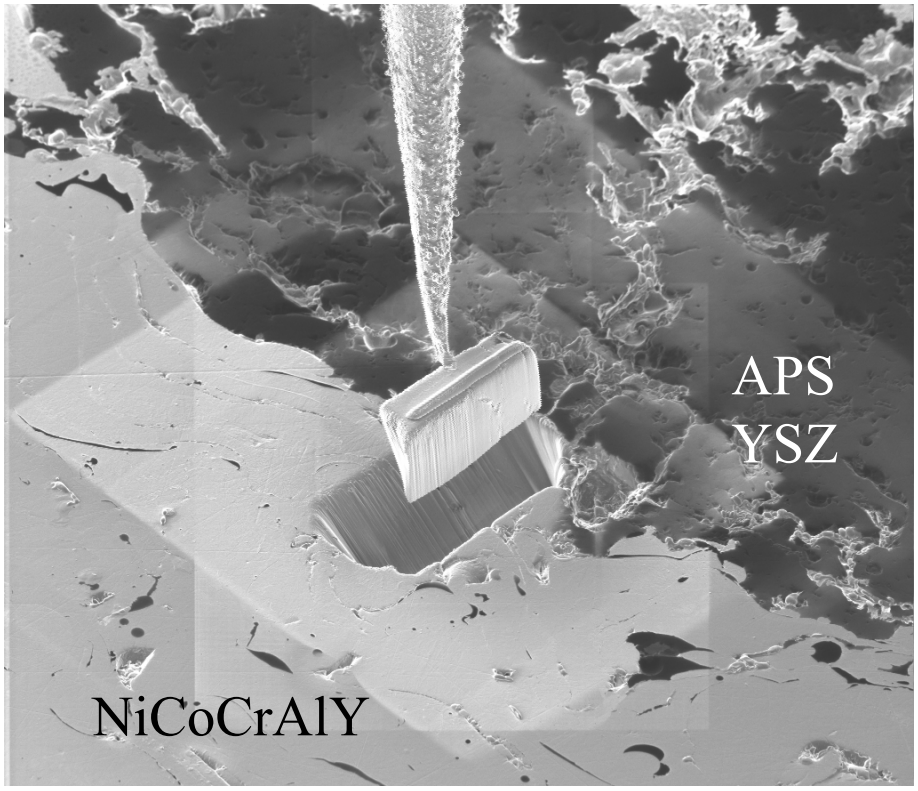

Figure 102. Secondary electron micrograph generated during FIB-INLO technique.

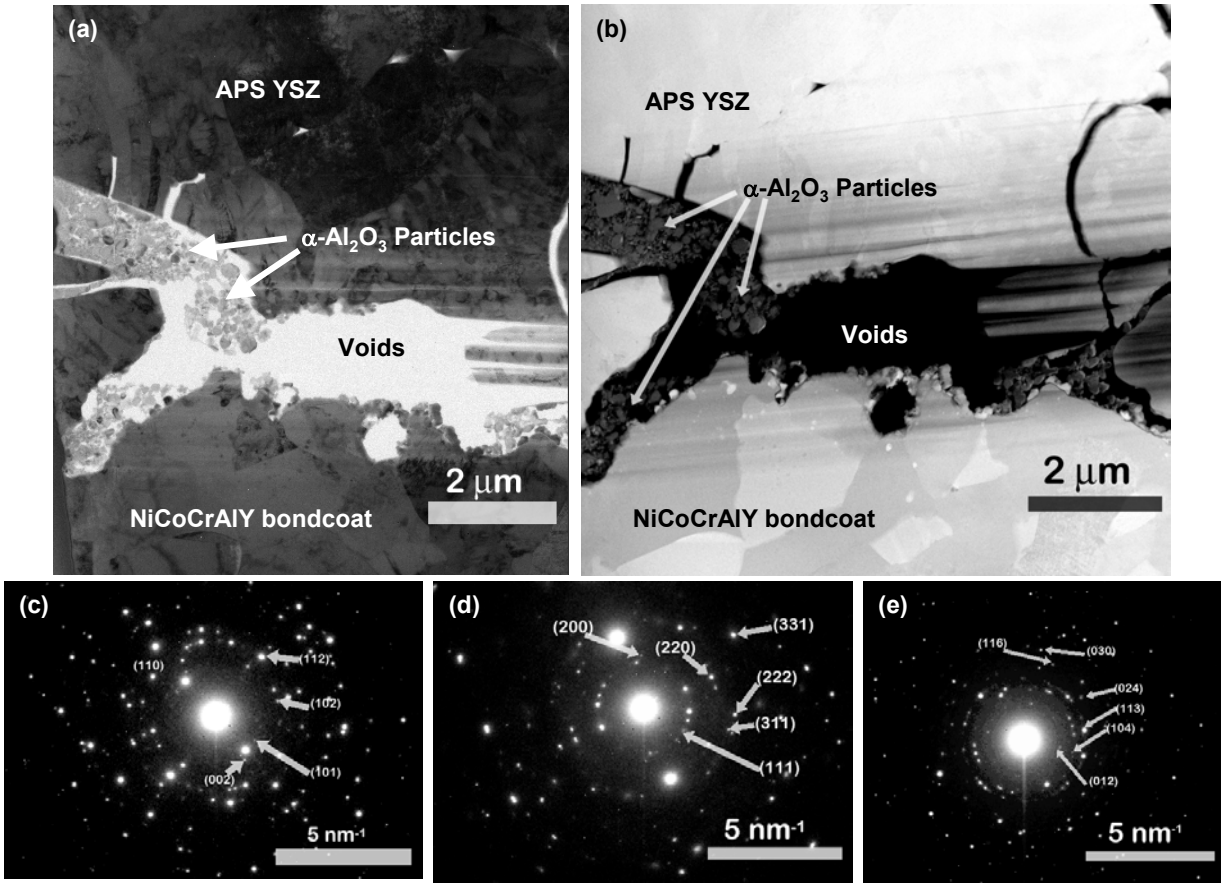

Figure 103.(a) Bright field and (b) HAADF micrograph of as-received type I APS TBC exhibiting extensive presence of voids, and TGO that consists of agglomerated α-Al_2O_3 particles (~100nm in size). (c,d) APS 7YSZ consisted of non-equilibrium tetragonal (t') and retained cubic (f') phase. (e) The agglomerated Al_2O_3 particles (~100nm in size) in TGO indexed to equilibrium α phase.

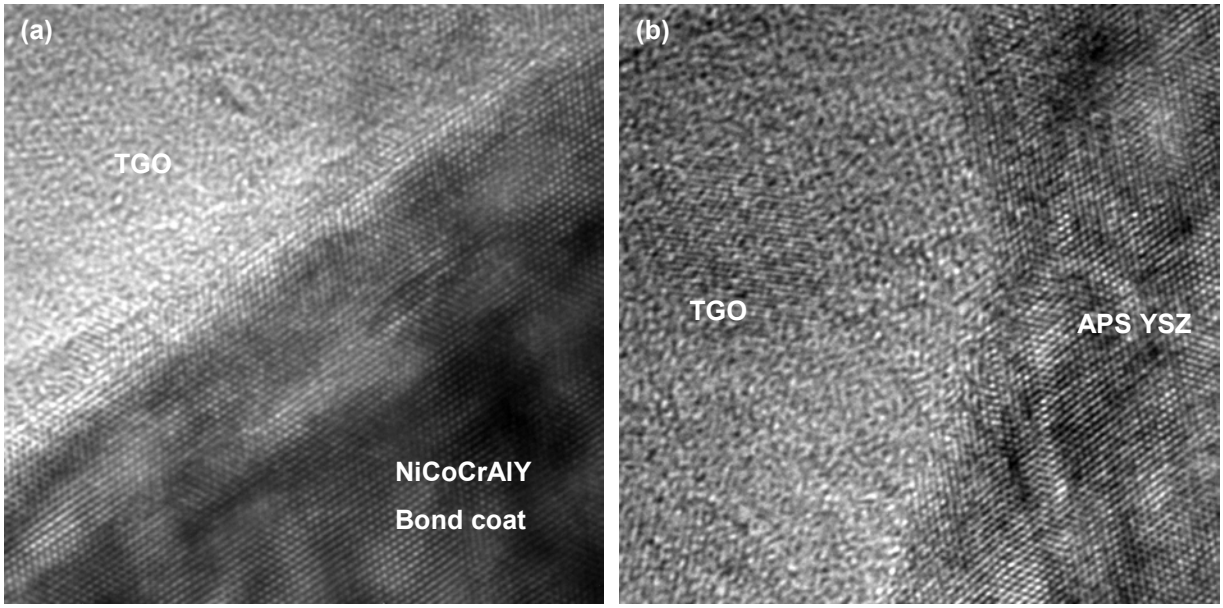

Figure 104. Bright-field lattice images showing intimate bonding at (a) TGO/bond coat and (b) YSZ/TGO interfaces. This atomic-level bonding was *not* frequently observed due to extensive presence of voids as presented in Figure 97(a).

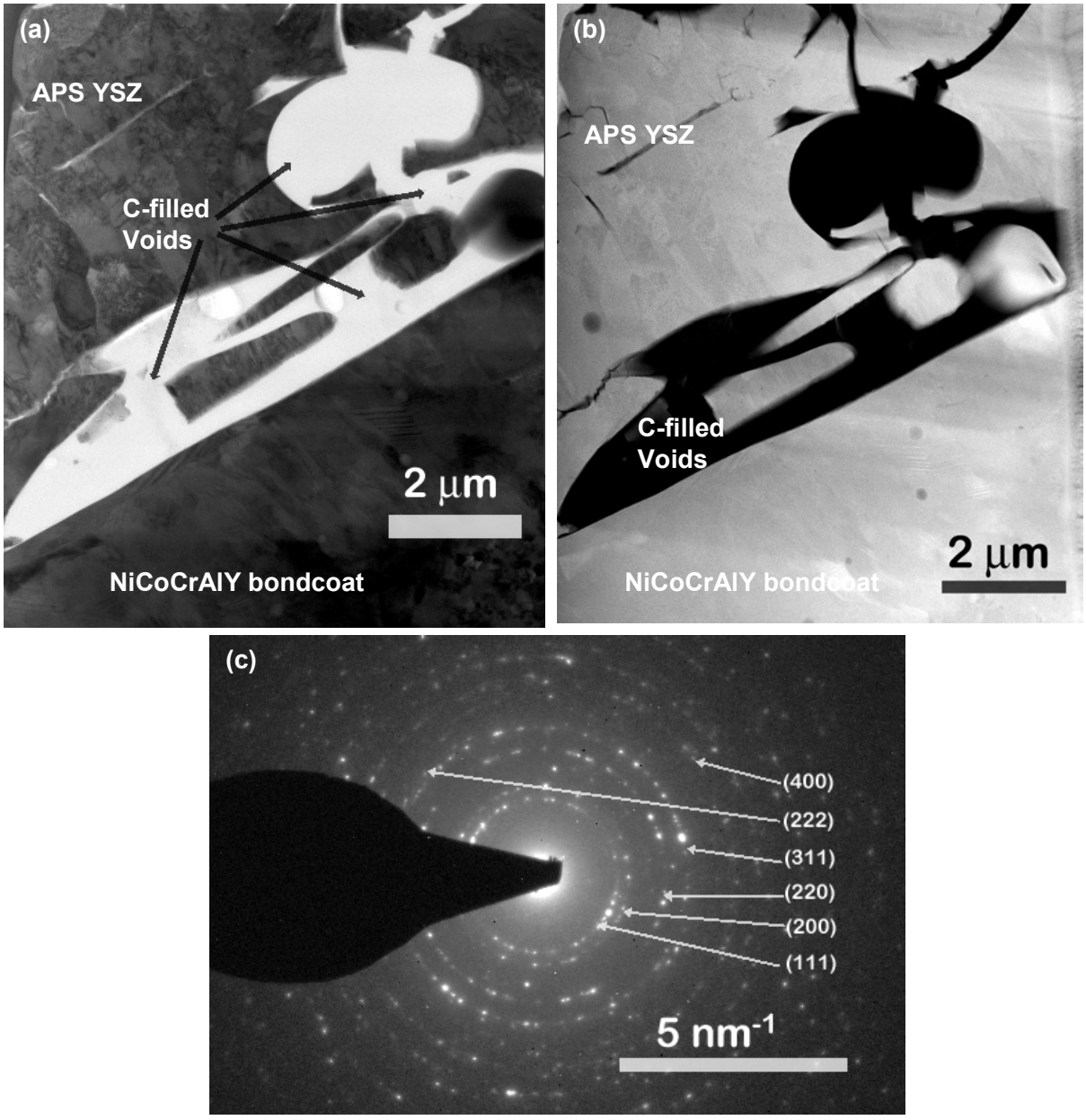

Figure 105. (a) Bright field and (b) HAADF image of as-coated type V APS TBC exhibiting extensive presence of carbon-filled voids, absence of TGO, and conventional columnar YSZ grains within splats. (c) SADP demonstrated that the APS 7YSZ consisted of non-equilibrium tetragonal (t') and/or retained cubic (f') phase.

V.4.2. Thermally Cycled Type I and V Air Plasma Sprayed Thermal Barrier Coatings

Figures 106, 107 and 108 represents typical backscatter electron images of type I APS TBCs as a function of 1-10 and 50-hours thermal cycling. Clearly there is a growth of the TGO scale with thermal cycling. In addition, there is an extensive internal oxidation of bond coats for this type I TBCs. The internal oxidation observed are parallel to the YSZ/bond coat interface, presumably following the splat boundaries of the NiCoCrAlY bondcoat, and mainly consists of Al-rich oxides (presumably α-Al_2O_3). A similar trend is also observed for 10 and 50 hour thermal cycles as reported in Tables X through XI. Abrupt changes [26] associated with C_{TGO} are not observed since the failure of type-I APS TBC occurs within the YSZ near the YSZ/TGO interface as shown in Figure 106(e) and 107(c). With progressive thermal cycling for various dwell the R_{YSZ} and C_{YSZ} increased and decreased as shown in Figures 86 and 89. This is because of YSZ sintering that take place at high temperature, and can be observed with progressive thermal cycling dwell time as shown in Figures 109 and 110. Also in Figure 86 the magnitude of R_{YSZ} for 1-hour thermal cycling is higher compared to that of 10 and 50-hour thermal cycles this is because of the effect of sub-critical damages that are seen as micro cracks in Figure 110 for 10 and 50-hour thermal cycles.

With the growth of TGO the R_{TGO} and C_{TGO} as shown in Figure 88 and 89 increased and decreased for 1, 10 and 50-hour thermal cycling. With progressive thermal cycling in case of 10 and 50-hour thermal cycles there is significant amount of damages at the YSZ/TGO interface as shown in Figures 107 and 108. These damages are observed around oxides rich in (Ni,Co)Cr commonly referred as spinals. Because of these damages the impedance response from 10-hour and 50-hour thermal cycles samples was less compared to that of 1-hour thermal cycles as shown in Figure 85.

Extensive presence of voids and cracks in the mixed oxide zone (MOZ) between the continuous TGO and the YSZ topcoat was observed for type I TBCs after 10% of its lifetime thermal cycling as shown in Figure 110 (a) and (b). In the BF and HAADF TEM images shown in Figure 110(a) and (b), the TGO on the type I TBC specimen contained Ni/Co-rich oxides at the interface between the YSZ/TGO. This Ni/Co rich oxides continued to grow with further thermal cycling which can be seen in Figure 110 (c) and (d). In general, the topcoat and the MOZ, and the MOZ within the TGO scale contained Y rich particles dispersed throughout the TGO. It is further observed at 70% thermal cycling life time there were extensive cracks/voids at YSZ/TGO interface, cracks within the TGO and voids at near the TGO/bondcoat interface.

As shown in Figure 111, extensive void formation in the interface between the TGO and Ni/Co oxides were observed. Further it is observed that Ca segregated in the phase interfaces and chromium oxide segregated in the regions near to the bondcoat in the TGO. In addition several Zr rich islands were observed dispersed on a Ti rich oxide matrix near to the carbon filled void in the type 1 APS TBC.

Figure 112 represents typical backscatter electron micrographs of thermally cycled type-V APS TBCs. Clearly there is a growth of TGO with thermal cycling. These

microstructural changes can related to the EIS NDE results presented in Figures 88 through 89.

EIS response for this type-V TBCs compared to the other types of TBCs was distinctively different. The R_{TGO} increased initially corresponding to the growth of the TGO that can be seen in Figure 112. However, the C_{TGO} increased continuously with thermal cycling. This can be related to the TGO scale cracking with thermal cycling that was observed as shown in Figure 113. The EIS results for R_{YSZ} and C_{YSZ} presented in Figures 64 and 65 can be related to the sintering behavior of the YSZ as shown in Figure 116. Figure 115 shows the microstructural evolution with respect to 10-hour thermal cycling. EIS measurements were not carried on these samples because of premature failure observed after thermal cycling.

In the thermally cycled type-V TBC specimen, development of a mixed oxide zone was observed after the thermal cycling that corresponds to the 10% of its lifetime as presented in Figure 117. It is further observed that the MOZ consisted of numerous voids and micro-cracks; however the TGO beneath the MOZ is dense, columnar and continuous as presented in BF TEM image in Figures 117(b) and (c). The MOZ consisted of Zr and Al oxide particles as observed in the HAADF image in Figure 113(b). Furthermore, large islands of oxides very rich in Y/Al were observed within the TGO scale as shown in Figure 117 (c). The diffraction phase analyses of these Y/Al rich oxides revealed that the lattice parameter is greater than 18 angstroms. The phase identification of these particles is currently in progress.

Development of microstructure for type V APS TBCs, after 50% thermal cycling lifetime is shown in Figure 118. This shows a splat YSZ morphology that is different from the YSZ morphology as discussed earlier with type-I APS TBCs.

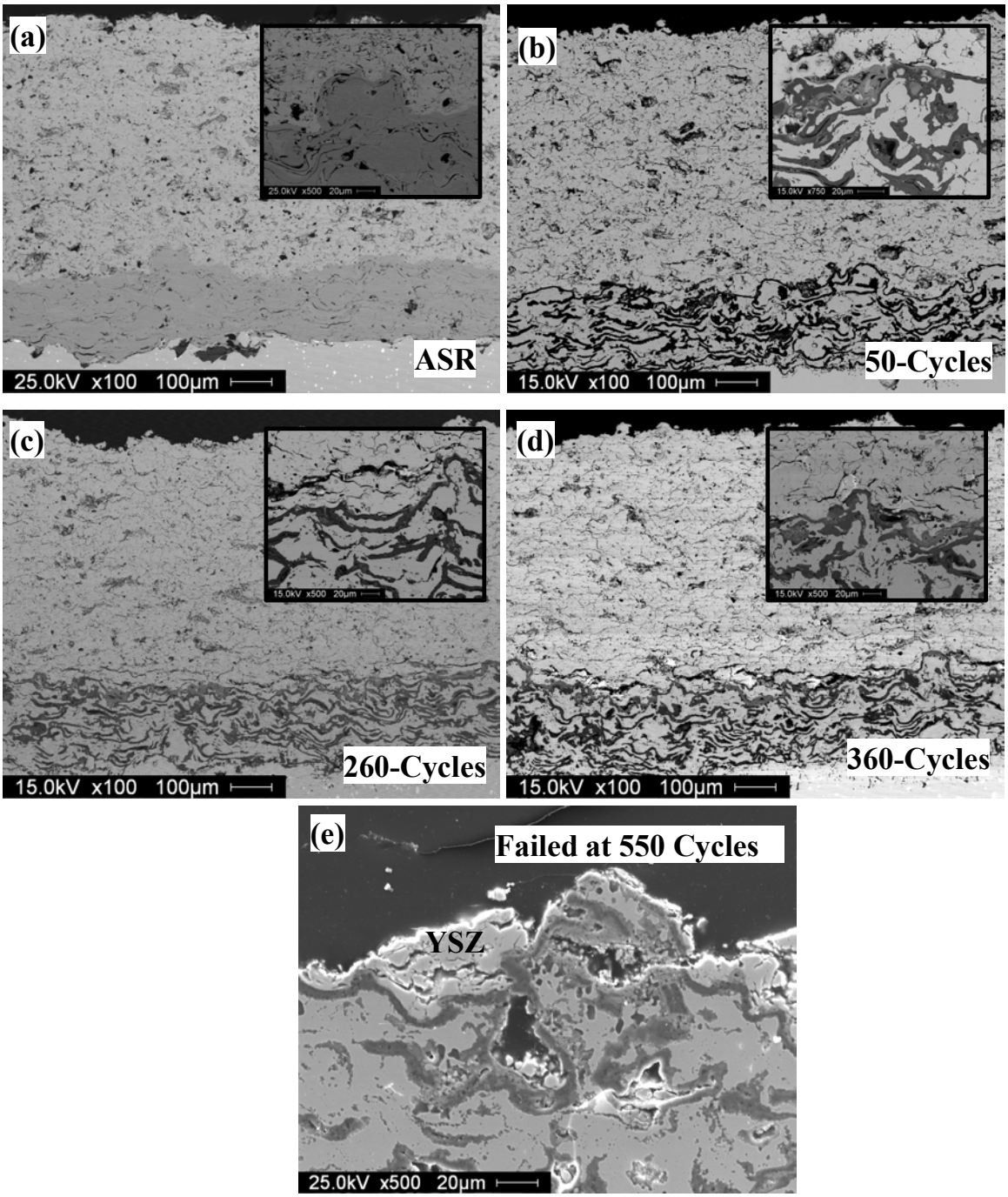

Figure 106. Typical backscatter electron micrographs of type I APS TBCs specimens with progressive 1-hour thermal cycles.

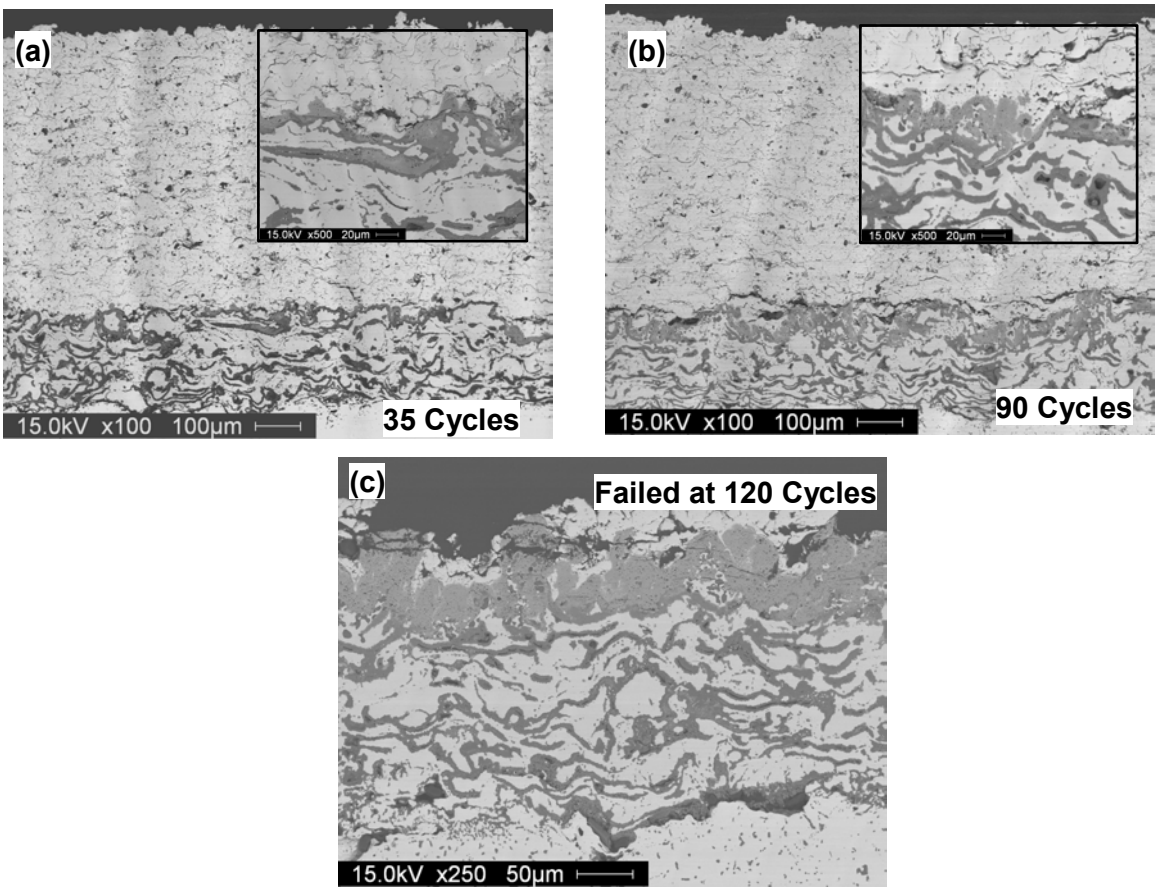

Figure 107. Typical backscatter electron micrographs of type I APS TBCs specimens with progressive 10-hour thermal cycles.

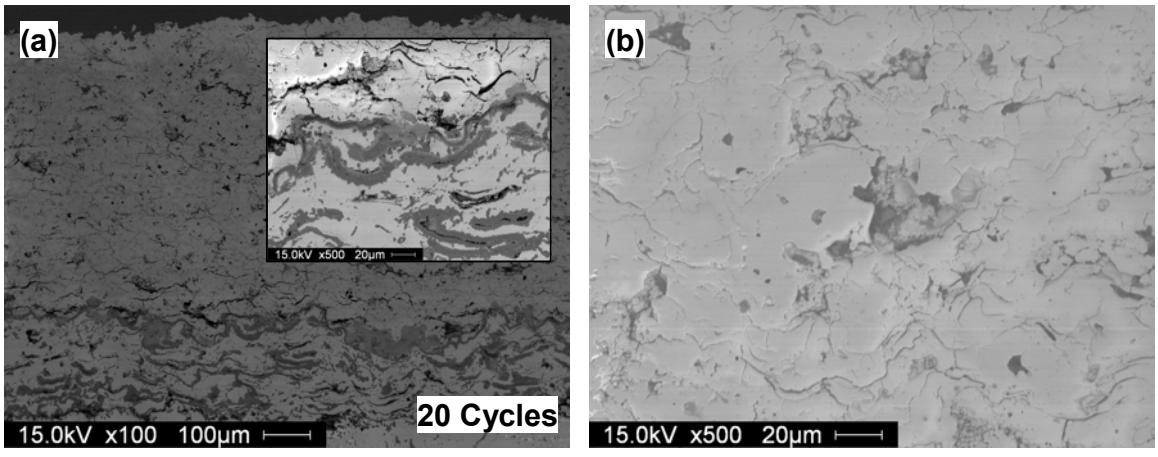

Figure 108. (a) Typical backscatter electron micrographs of type I APS TBCs specimens at 20 cycles (50-hour thermal Cycles) (b) BSE image of YSZ.

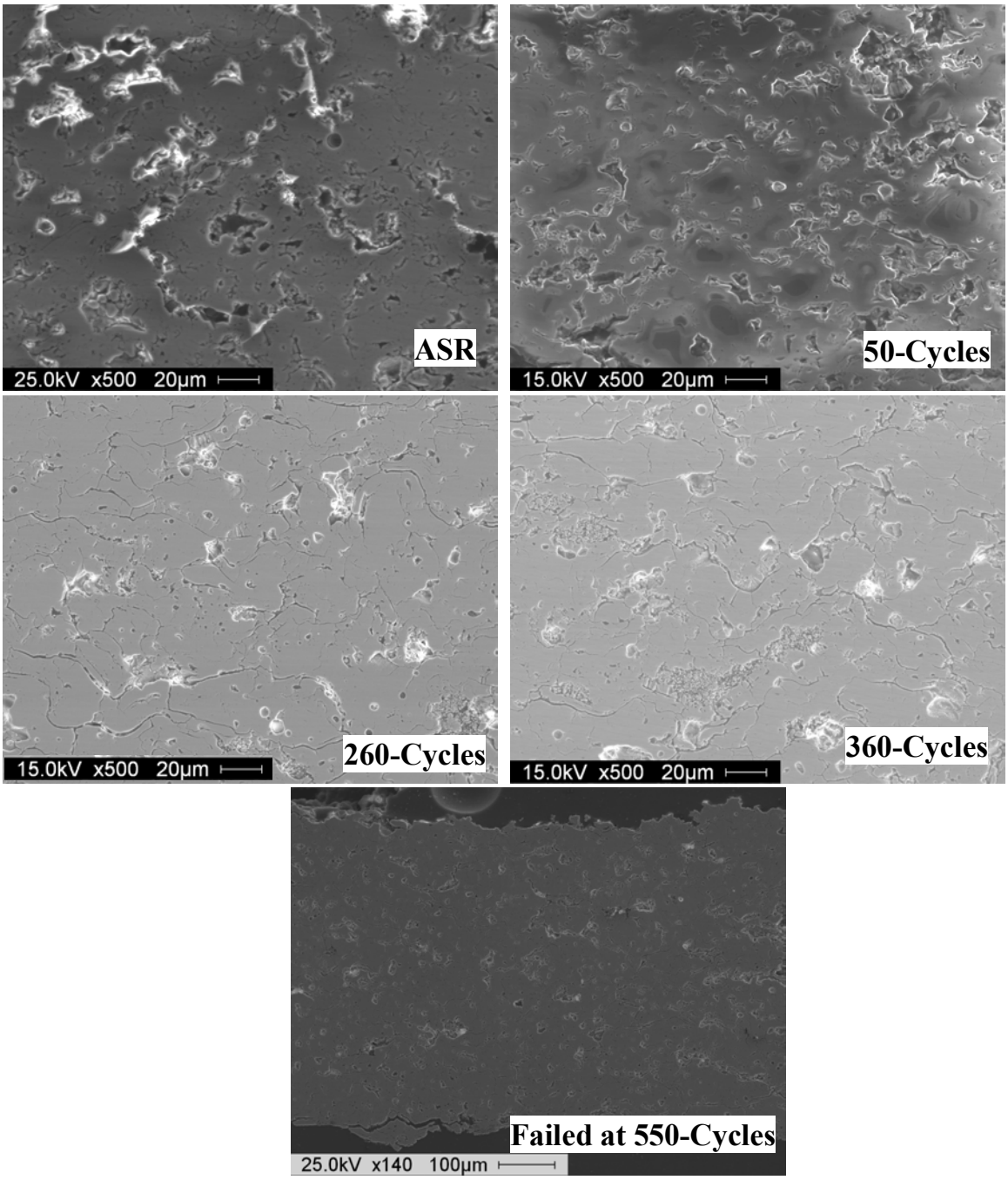

Figure 109. Secondary electron micrographs of type-I APS TBCs YSZ showing sintering/micro cracking behavior with progressive 1-hour thermal cycling.

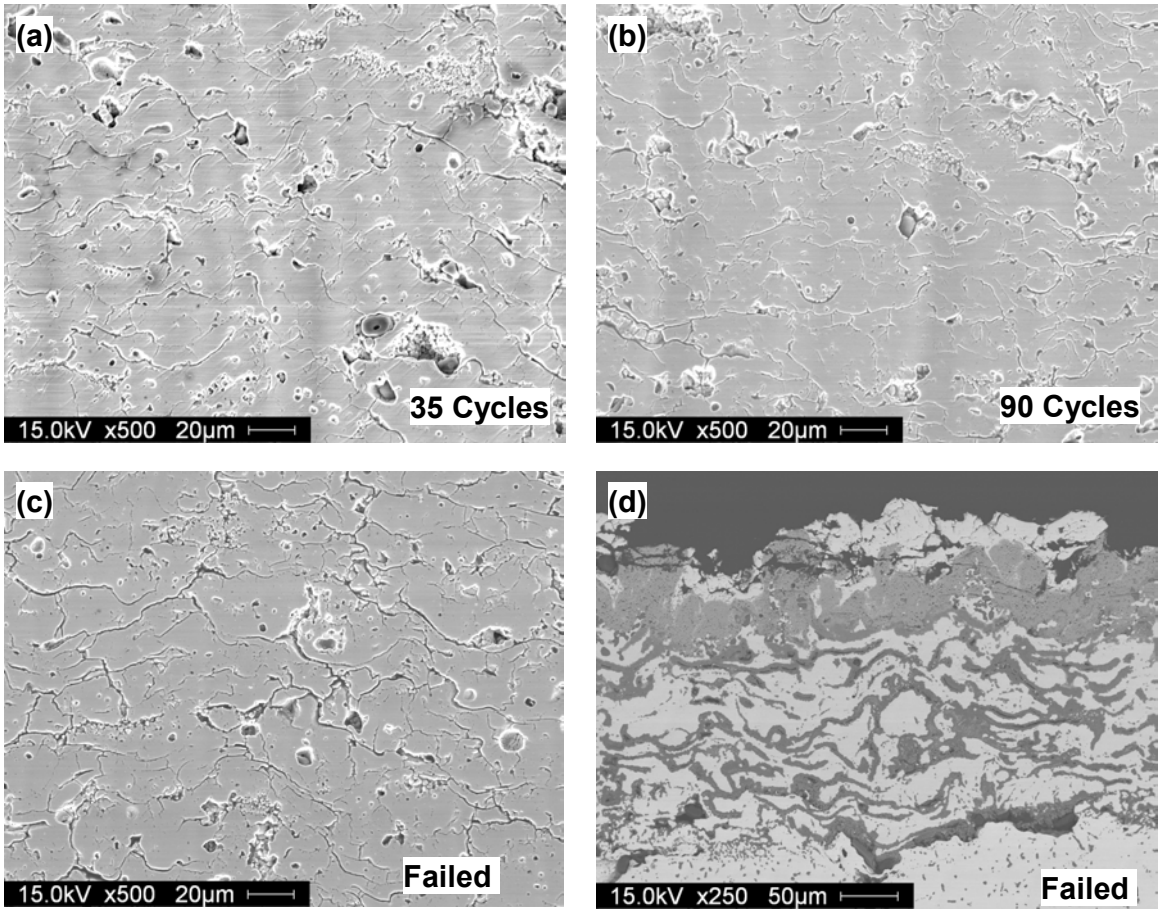

Figure 110. (a,b,c) Secondary electron micrographs of type-I APS TBCs YSZ showing sintering/micro cracking behavior with progressive 10-hour thermal cycling (d) back scatter electron micrograph of the cross section of bondcoat after YSZ spallation.

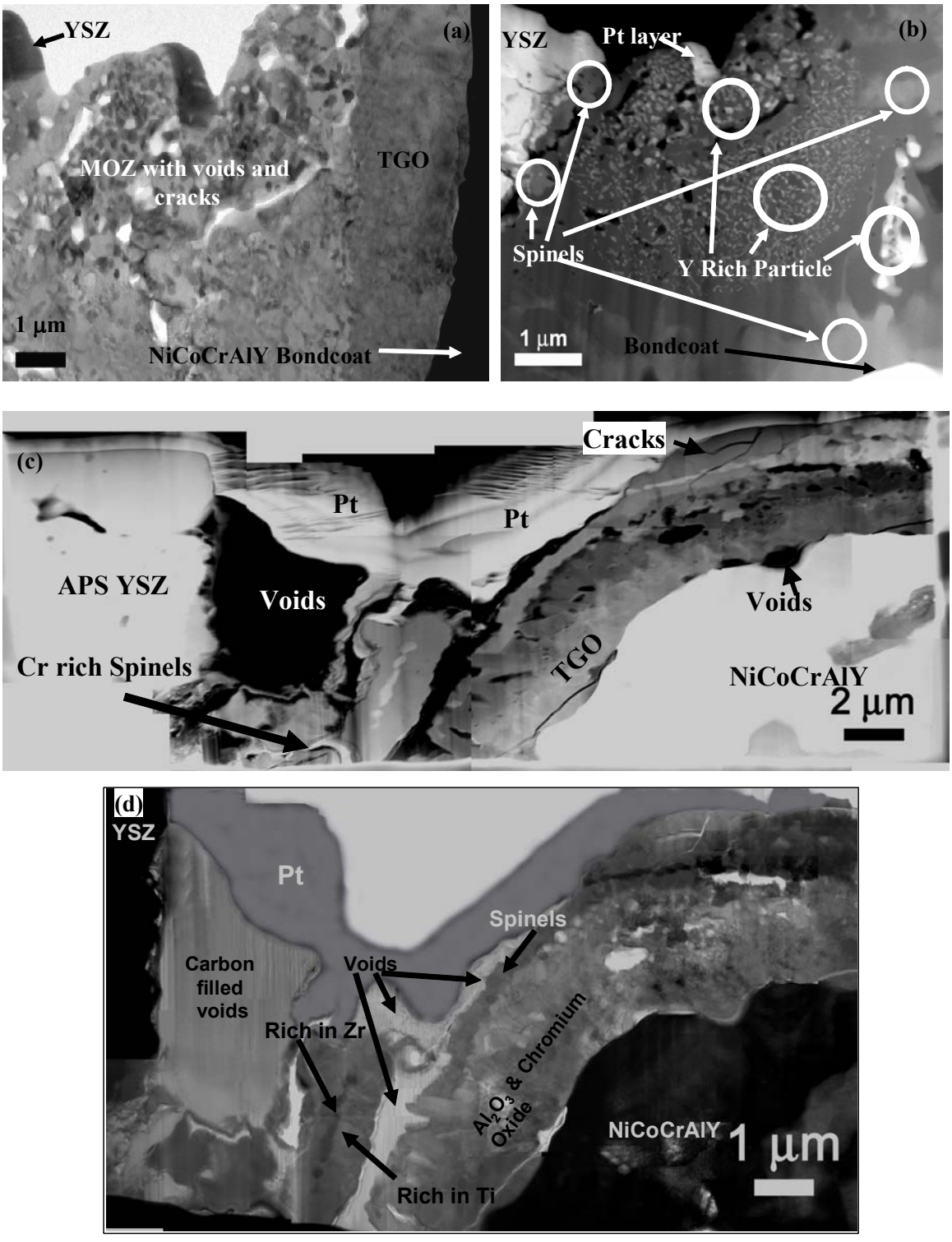

Figure 111. TBC specimen type I after thermal cycling (a) BF TEM and (b) HAADF STEM images after 10% lifetime (c) HAADF STEM images and (d) BF TEM after 70% lifetime.

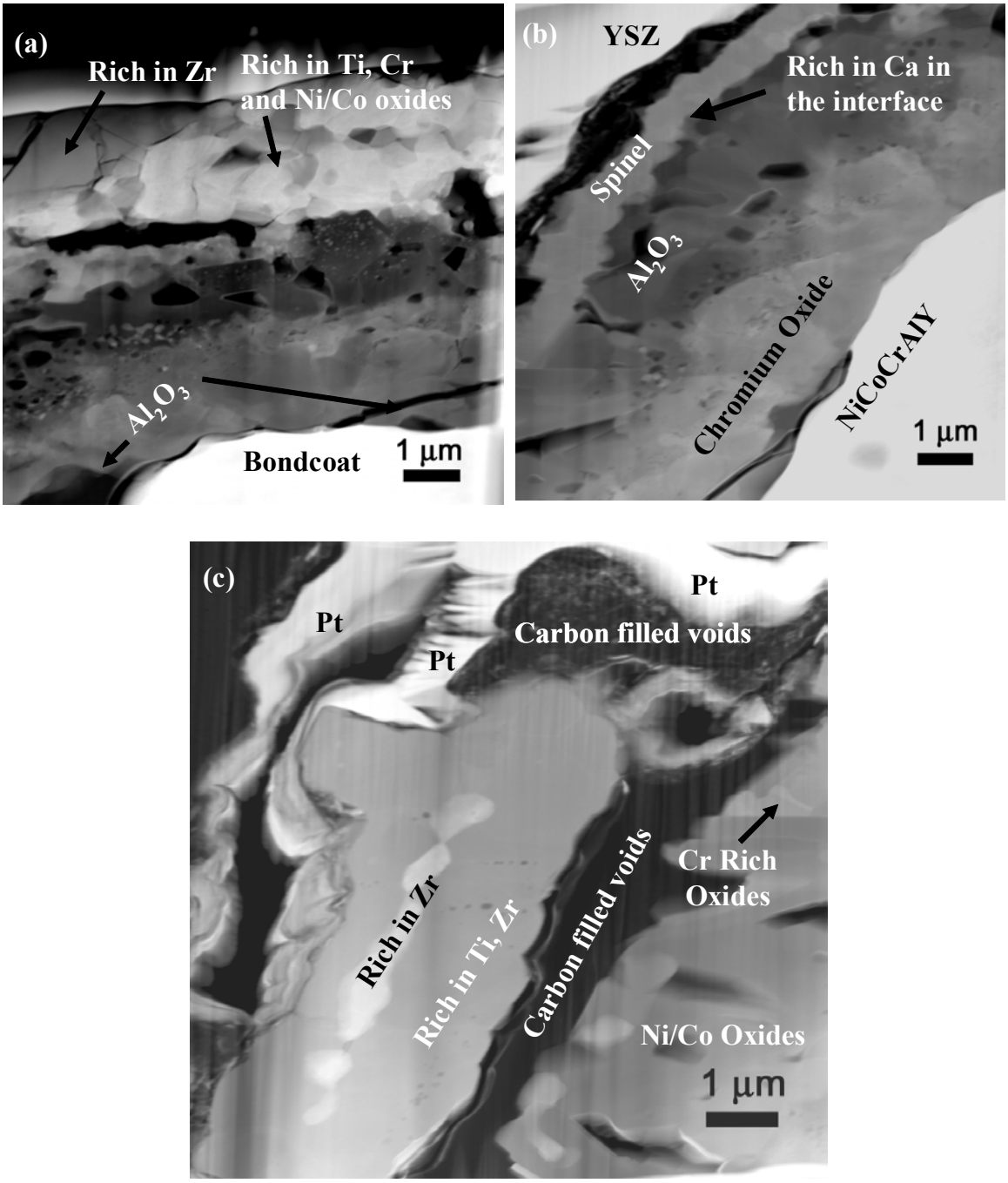

Figure 112. Higher magnification HAADF STEM images of type-I APS TBCs after 70% 1-hour thermal cyclic lifetime.

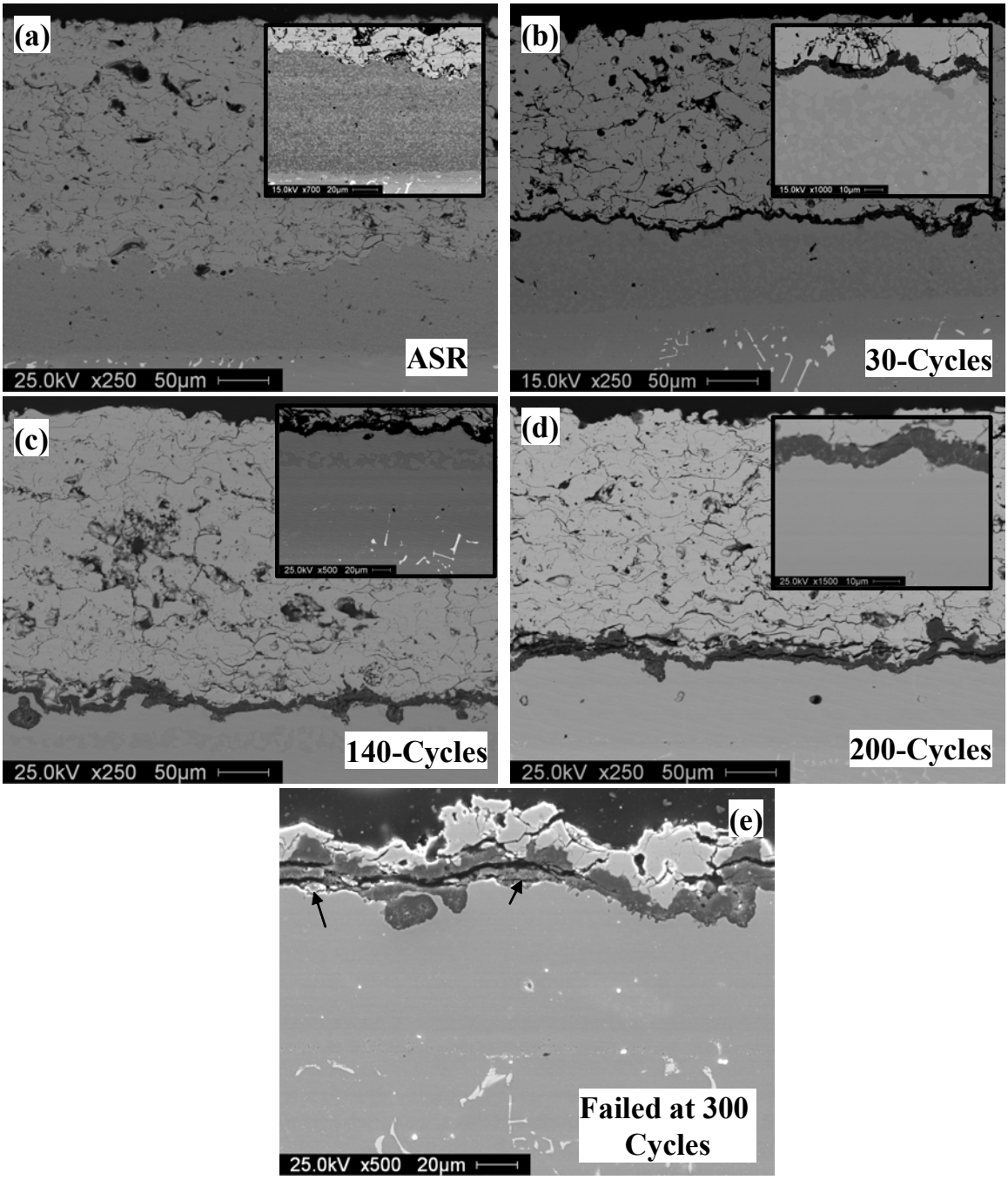

Figure 113. Typical backscatter electron micrograph of type-V APS TBCs with progressive thermal cycling.

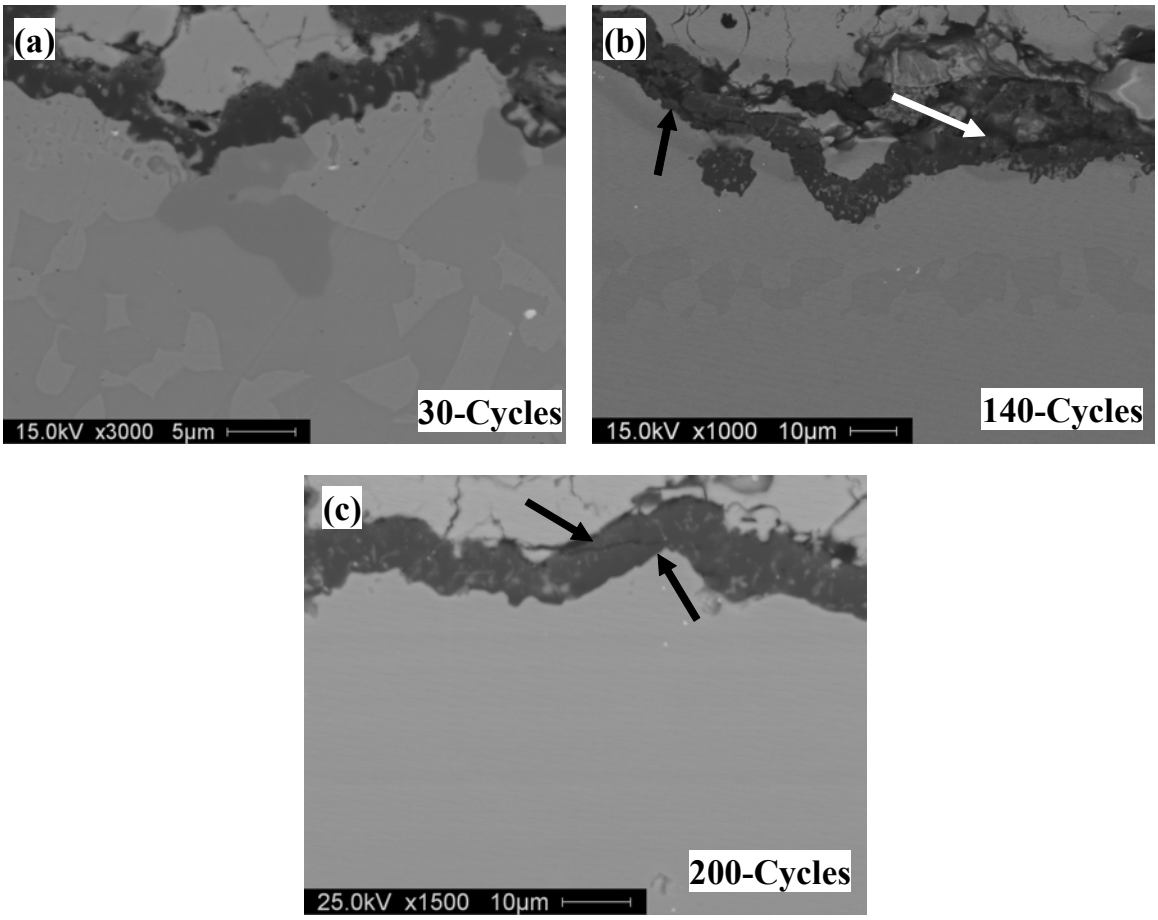

Figure 114. Typical backscatter electron micrographs for type-V showing the TGO scale cracking with 1-hour thermal cycling but the TBC remained intact.

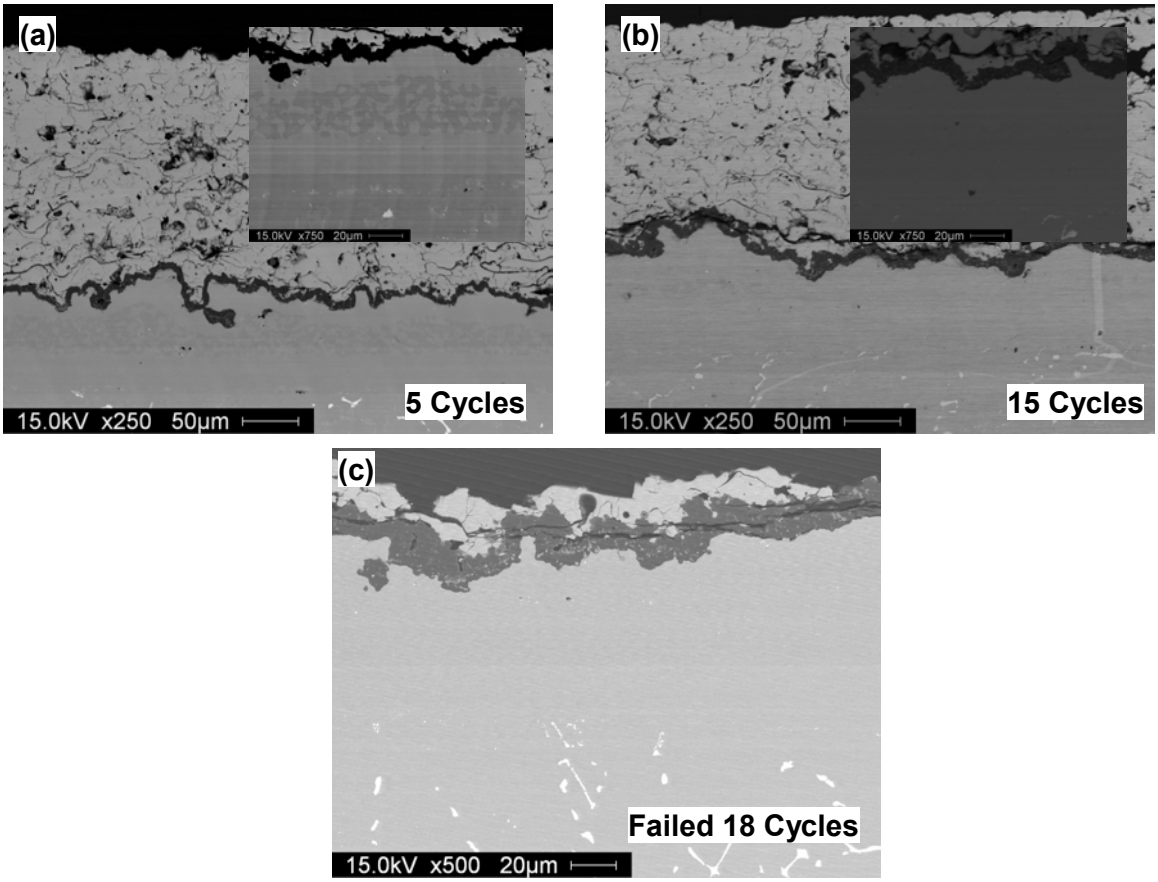

Figure 115. Typical backscatter electron micrograph of type-V APS TBCs with progressive 10-hour thermal cycling.

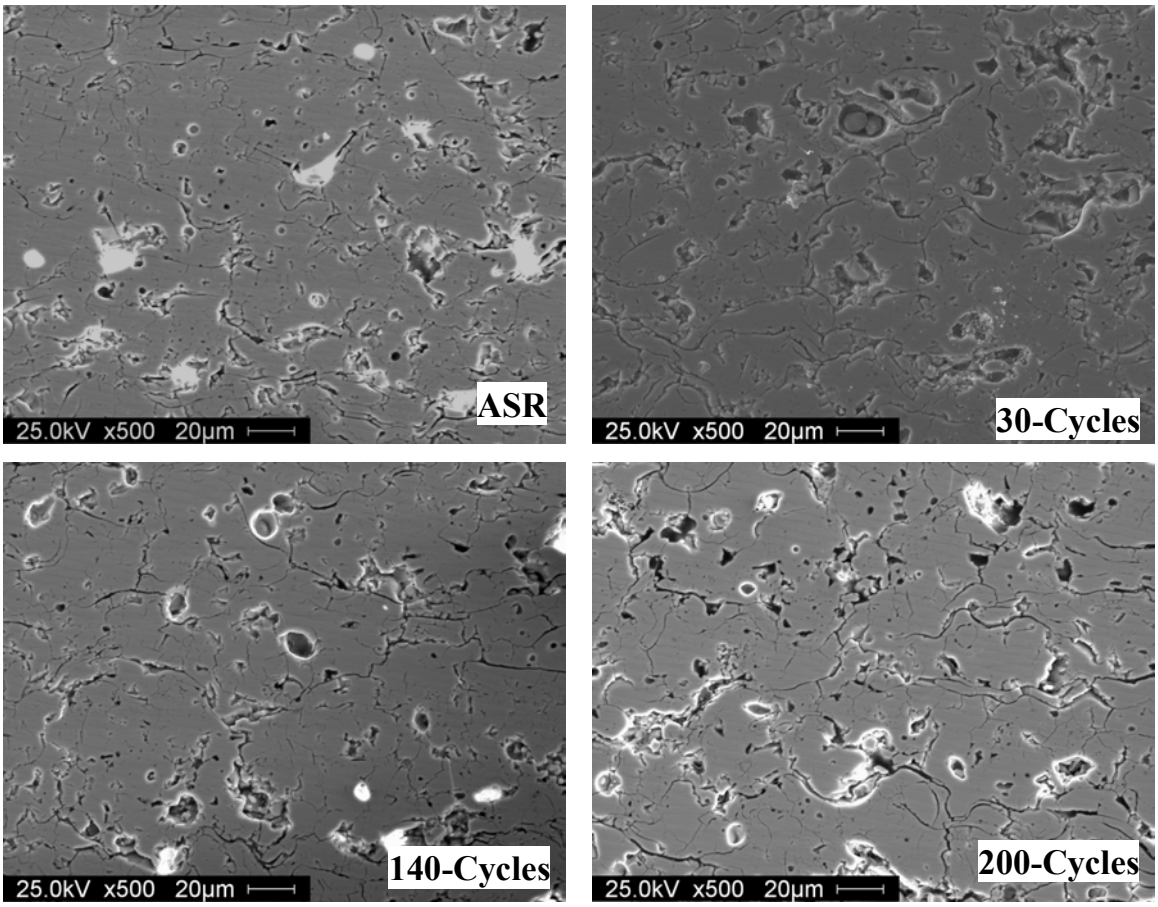

Figure 116. Secondary electron micrographs of type-V APS TBCs showing the sintering/micro cracking behavior within the YSZ with progressive 1-hour thermal cycling.

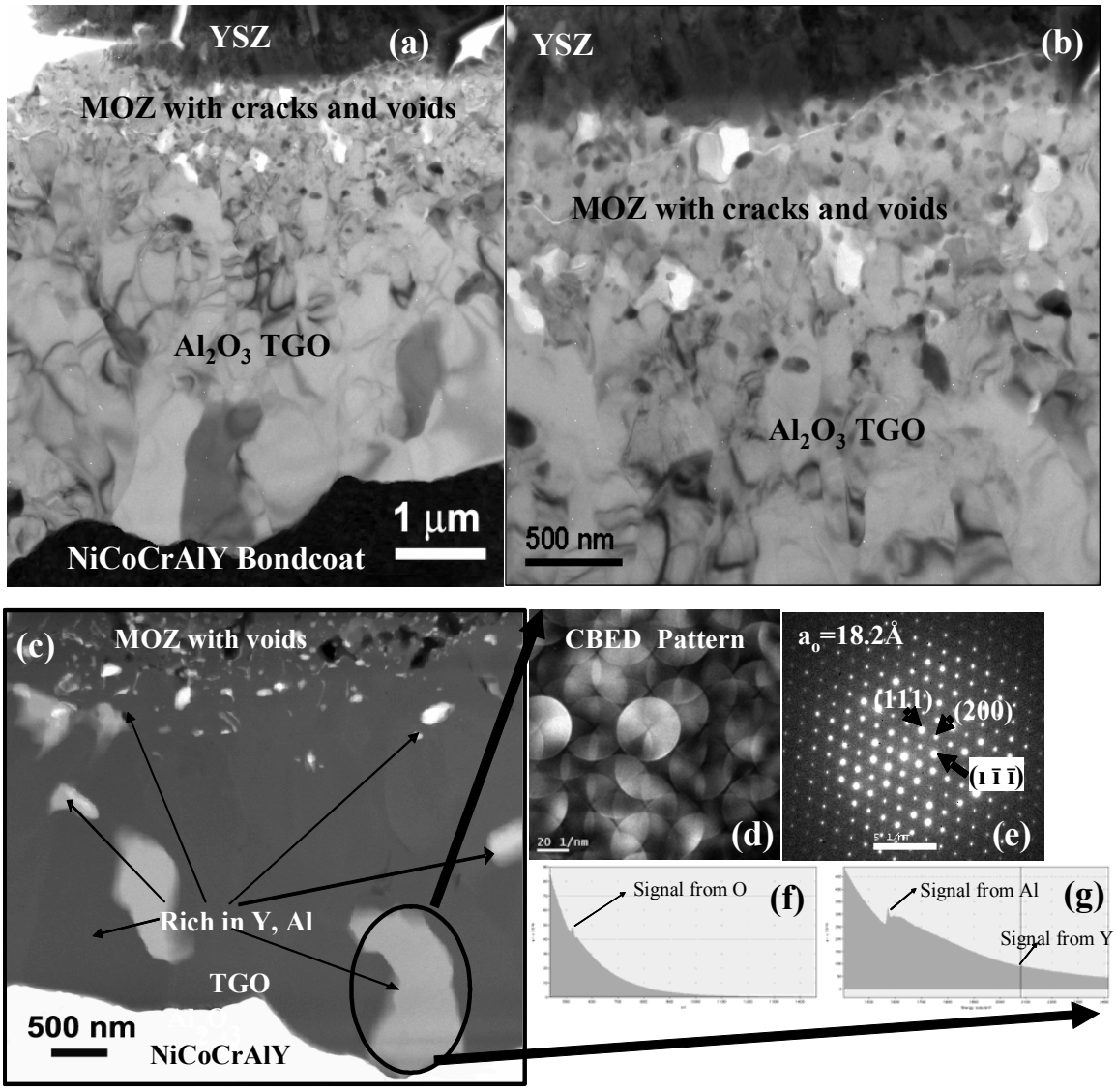

Figure 117. Bright field TEM image of type-V TBCs after 10% thermal cycling lifetime (a) presence of MOZ with cracks and voids near the YSZ/TGO interface and a dense-columnar-continuous Al_2O_3 TGO near the bond coat. (b) MOZ with cracks and voids near the YSZ/TGO interface, and (c) HAADF STEM image showing Y and Al rich oxides and a MOZ near to YSZ topcoat (d) Convergent Beam Electron Diffraction (CBED) pattern from the Y rich oxide (d) SAD pattern from the same Y rich oxide showing a lattice parameter > 18 Å and (f,g) EELS spectra from the same Y rich oxide.

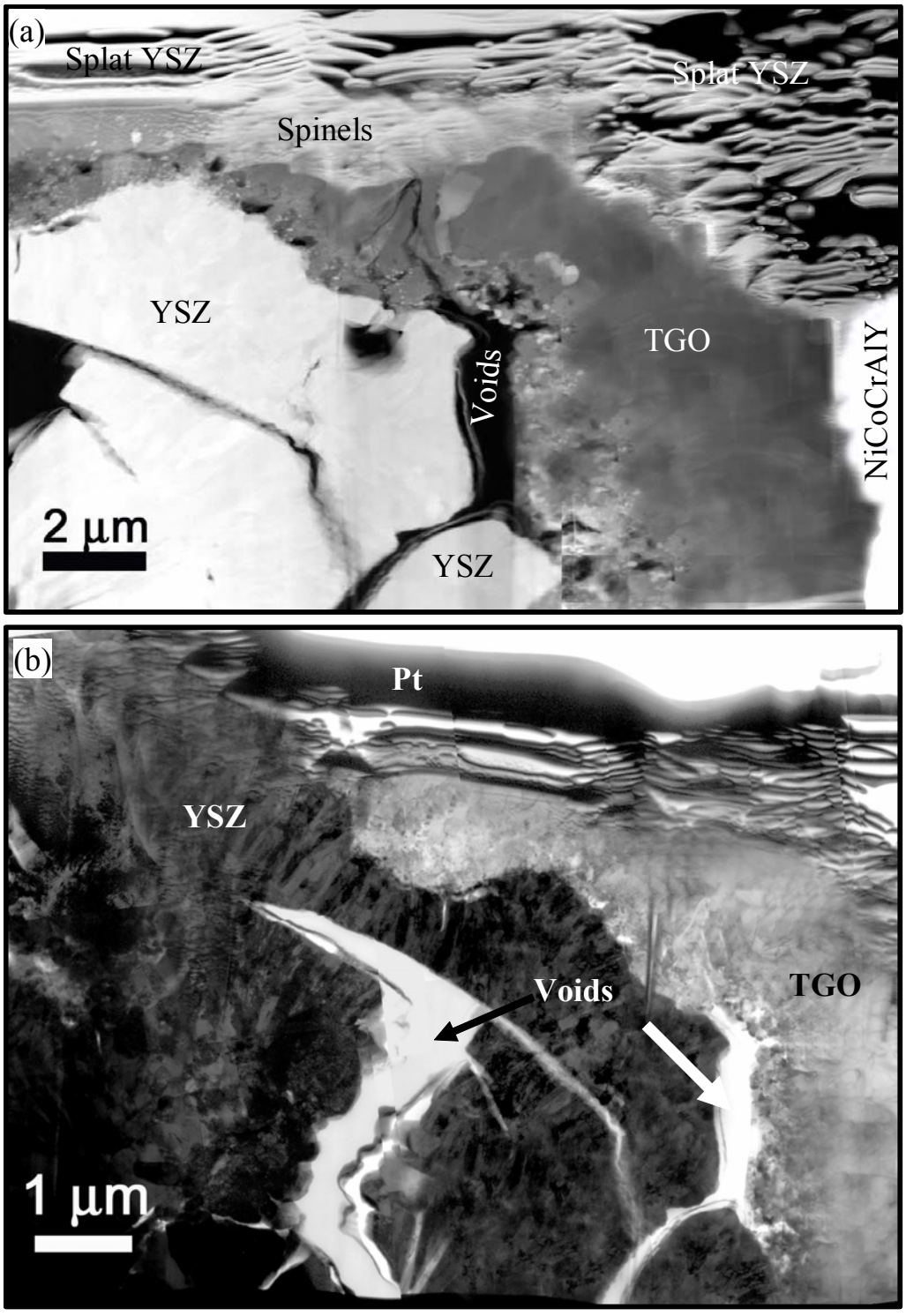

Figure 118. TEM images from type-V TBCs after 50% thermal cyclic lifetime (a) HAADF STEM image showing splat YSZ and voids at YSZ/TGO interface (b) Bright Field TEM image showing the same.

V.4.3. As-coated Electron Beam Physical Vapor Deposited Thermal Barrier Coatings

Figure 119 presents backscatter electron micrographs of the as-coated type II, III and IV EB-PVD TBCs. The specimens conformed to the specification described in Table II. All three types of EB-PVD YSZ coatings exhibited strain-tolerant columnar microstructure.

For all TBCs, a thin TGO layer was observed in the as-received condition as presented in Figures 119 and 120. Morphology of interface between YSZ and bond coat, where a thin TGO exists, was slightly different presumably due to the surface-finish treatment of bond coats. For type II TBC, a shot-peened NiCoCrAlY surface exhibited roughness and irregularity (ranging from ~5μm to less than 1μm) including sharp peaks and troughs as presented in Figures 120(a) and (b). The as-coated (Ni,Pt)Al bond coat for type III TBCs exhibited smooth interface except for the ridges associated with the bond coat grain boundaries as shown in Figure 120(c). The grit-blasted (Ni,Pt)Al bond coat for type IV TBCs exhibited rough and irregular interface where ridges associated with the bond coat grain boundaries have been removed as presented in Figure 120(d). For all TBCs, no significant amount of embedded oxide was observed.

After OM and SEM, the site-specific specimen was prepared for HR-STEM using FIB-INLO. In as-coated type II TBC, a continuous TGO layer was observed without a significant presence of "mixed-oxide" layer as seen in Figure 121. The SADP, inset of Figure 121(a) demonstrated that the EB-PVD 7YSZ consisted of non-equilibrium tetragonal (t') and/or retained cubic (f') phase.

In the as-coated type III TBC, a continuous TGO layer was observed along with patches of "mixed-oxide" layer as seen in Figure 112. Regions in the TGO with "mixed-oxide" were always thicker (~0.5μm) than those consisting of continuous α-Al_2O_3 layer (~0.1μm) as presented by Figure 122(b). Based on n-EDS and EELS, the "mixed-oxide" layer consisted of oxides containing primarily Al, Zr, Y and Ni with traces of Cr, Co and Mo. SADP presented in Figure 122(c) demonstrate that the EB-PVD 7YSZ consisted of non-equilibrium tetragonal (t') and/or retained cubic (f') phase. SADP in Figure 112(d) from TGO indexes to α-Al_2O_3. High magnification HAADF image of the "mixed oxide" layer is presented in Figure 123.

Relative to type III TBCs, the microstructure of type IV EB-PVD TBC specimen presented in Figure 124 exhibited many distinctive features including (1) larger intercolumnar voids, (2) more feathery YSZ columns, (3) thinner Al_2O_3 TGO without a "mixed-oxide" layer, (4) large residual α-Al_2O_3 particles from grit blasting, and (5) smaller β-(Ni,Pt)Al grains. The as-deposited YSZ consisted of non-equilibrium tetragonal (t') and/or retained cubic (f') phase as presented in Figure 124(c). The TGO scale primarily consisted of α-Al_2O_3 as presented by FFT diffractogram in Figure 125. A secondary and backscatter electron micrographs showing the residuals from grit-blasting are presented in Figure 126.

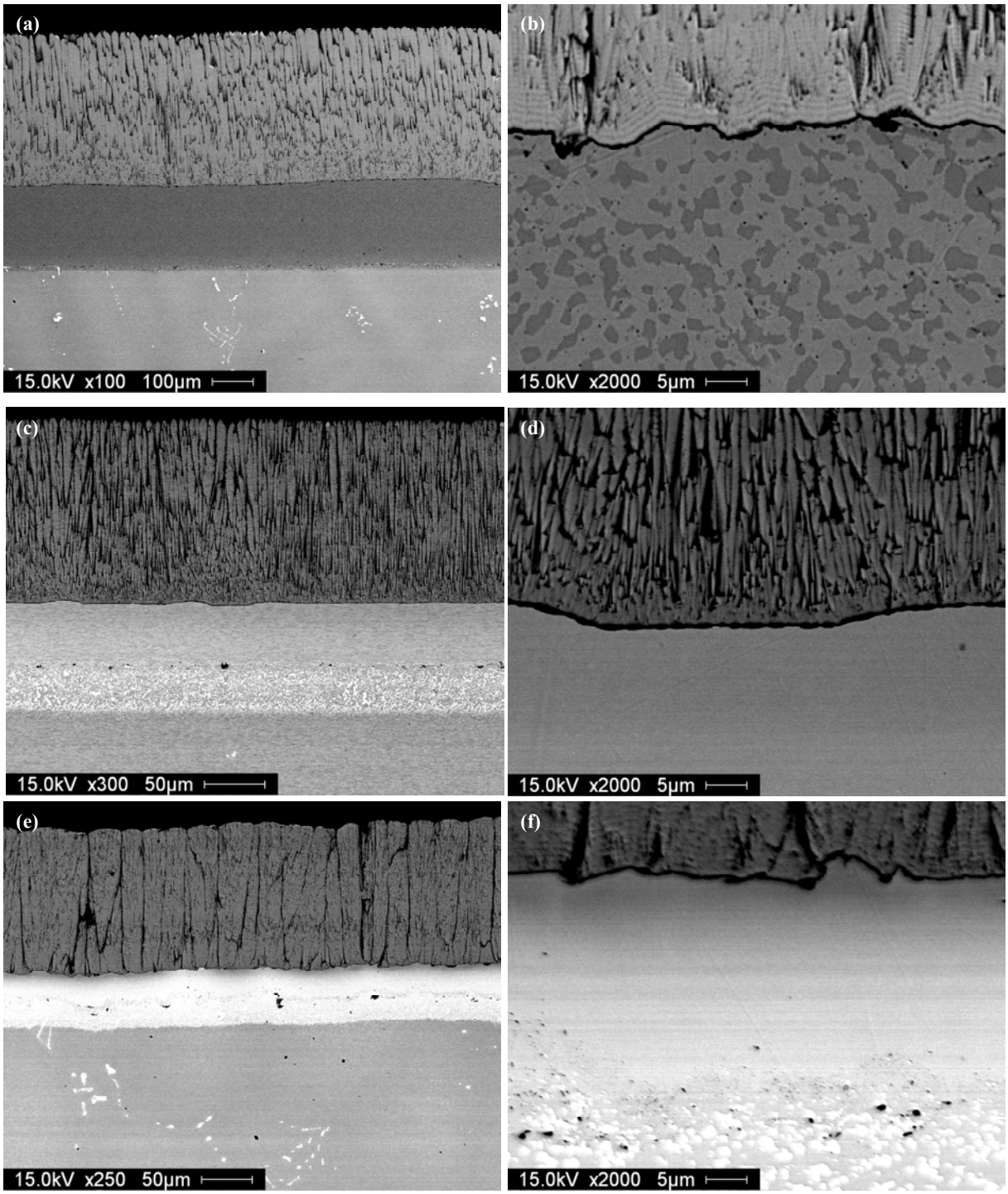

Figure 119. Typical backscatter electron micrographs of (a,b) type II, (c,d) type III, and (e,f) type IV EB-PVD TBCs specimens.

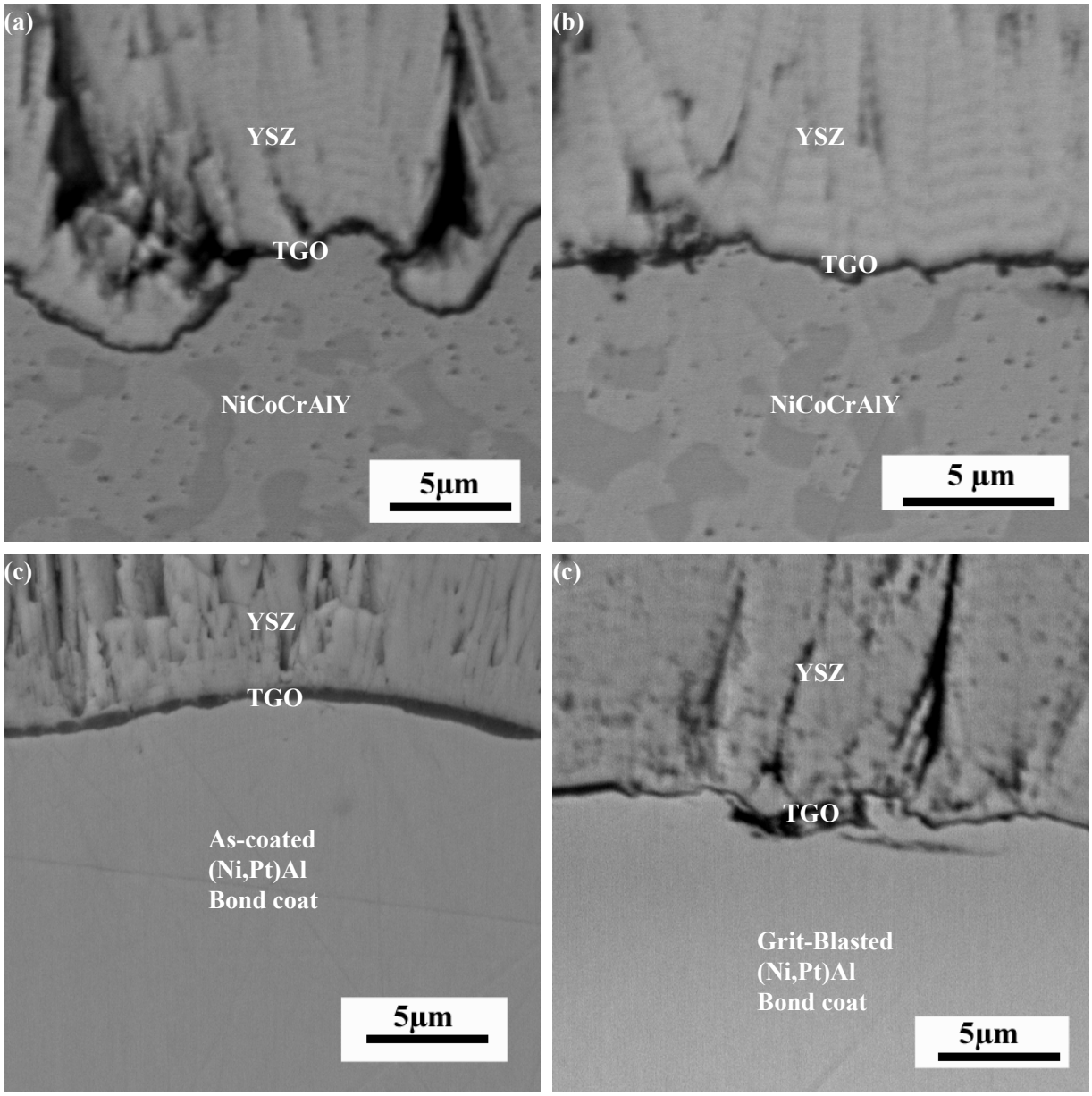

Figure 120. High magnification backscatter electron micrographs of (a,b) type II, (c) type III and (d) type IV EB-PVD TBCs specimens.

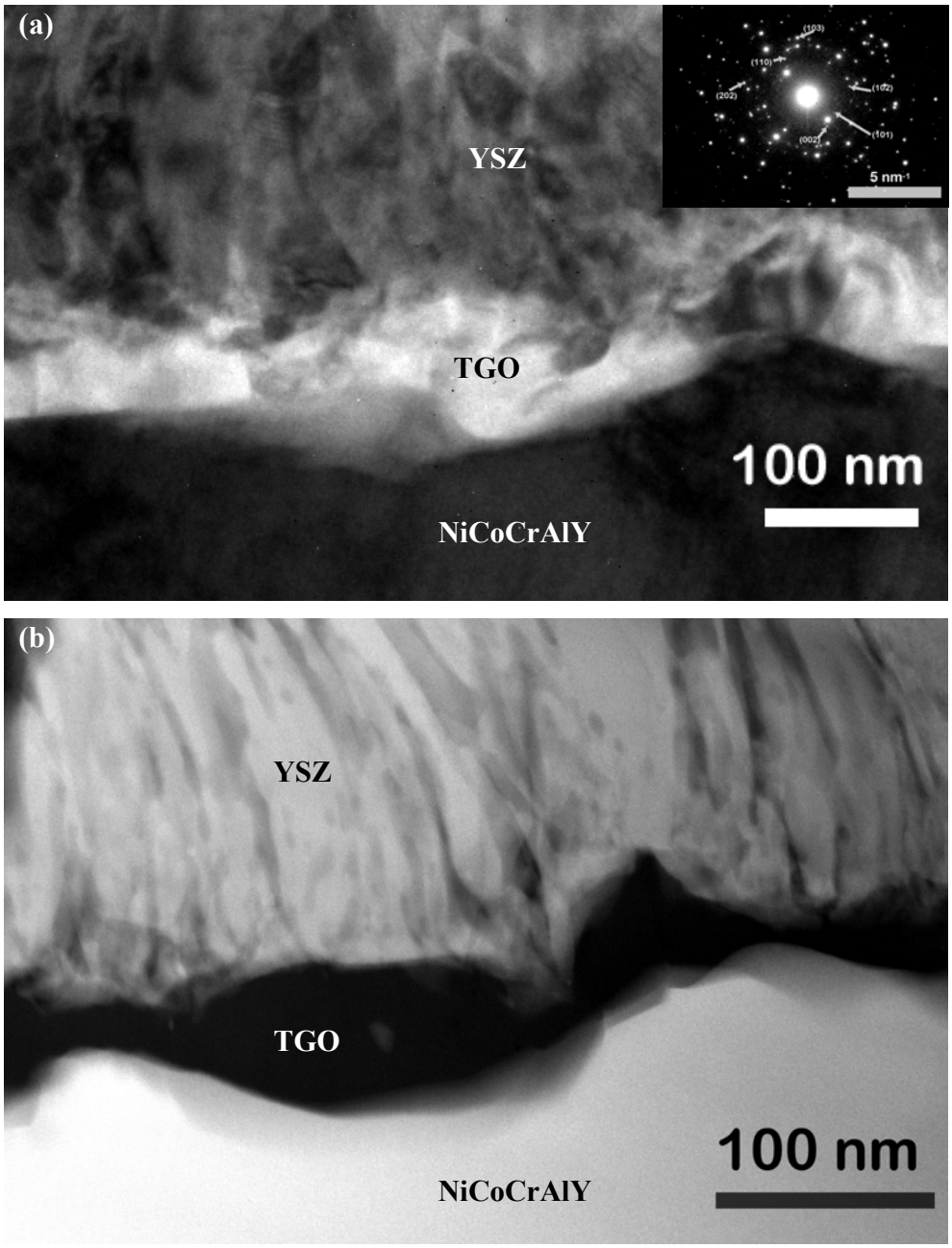

Figure 121.(a) Bright field and (b) HAADF image of as-coated type II EB-PVD TBC exhibiting columnar microstructure of 7YSZ coating and continuous TGO layer without presence of "mixed-oxide" layer. SADP (inset) demonstrated that the EB-PVD 7YSZ consisted of non-equilibrium tetragonal (t') and/or retained cubic (f') phase.

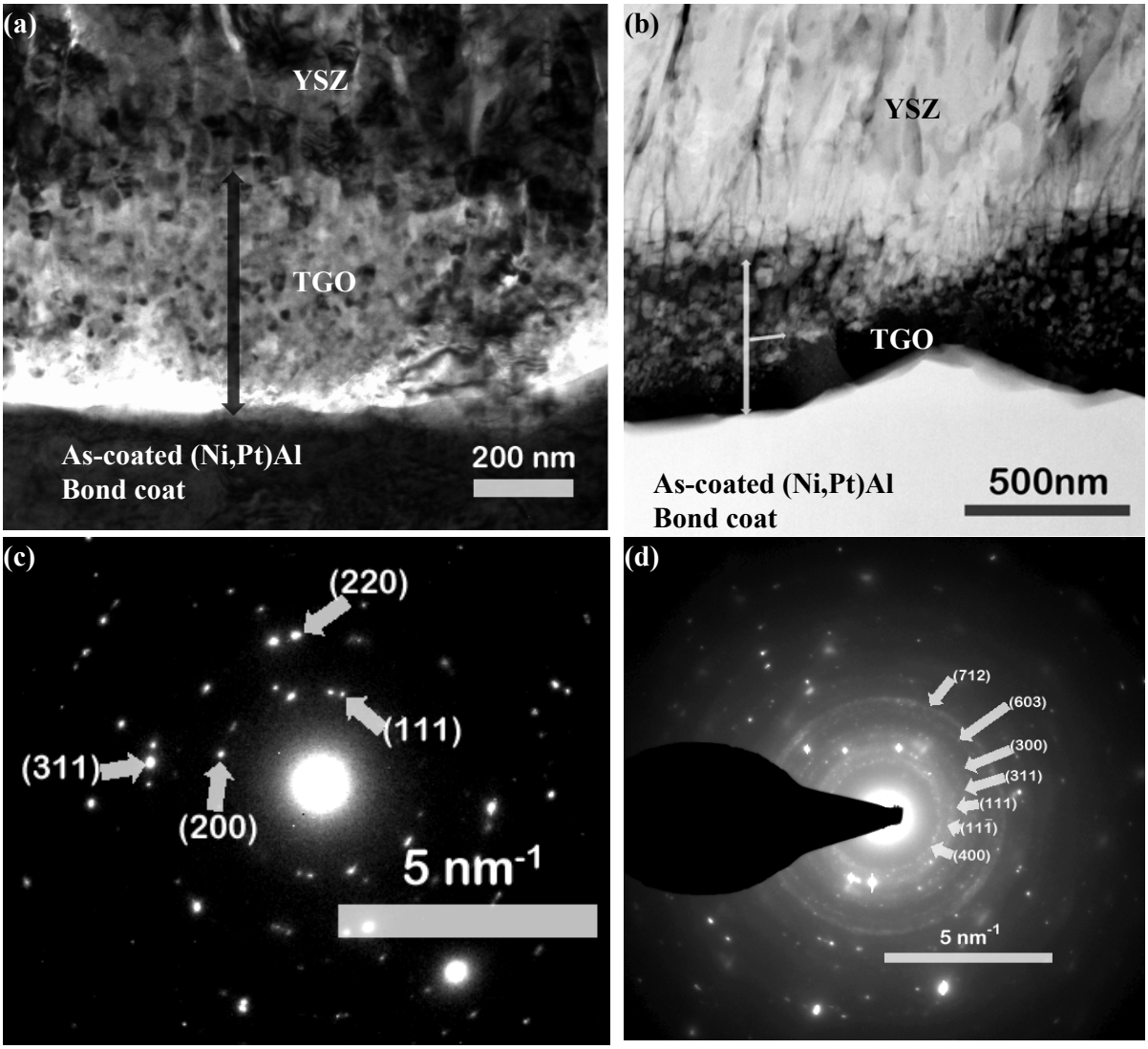

Figure 122.(a) Bright field and (b) HAADF image of as-coated type III EB-PVD TBC exhibiting columnar microstructure of 7YSZ coating and continuous TGO layer with a significant presence of "mixed-oxide" layer. (c) SADP demonstrated that the EB-PVD 7YSZ consisted of non-equilibrium tetragonal (t') and/or retained cubic (f') phase. (d) SADP of α-Al_2O_3 in TGO.

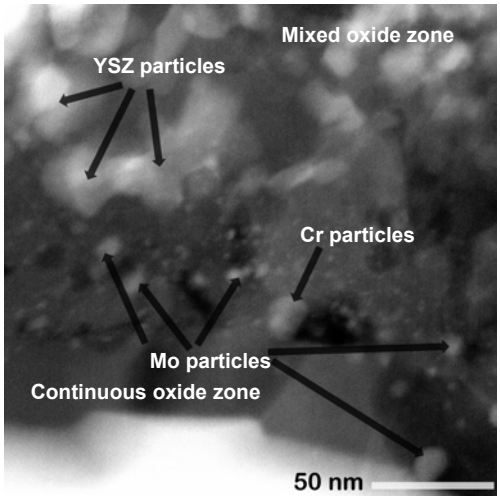

Figure 123. HAADF image of the "mixed-oxide" layer in TGO in as-coated type III EB-PVD TBC.

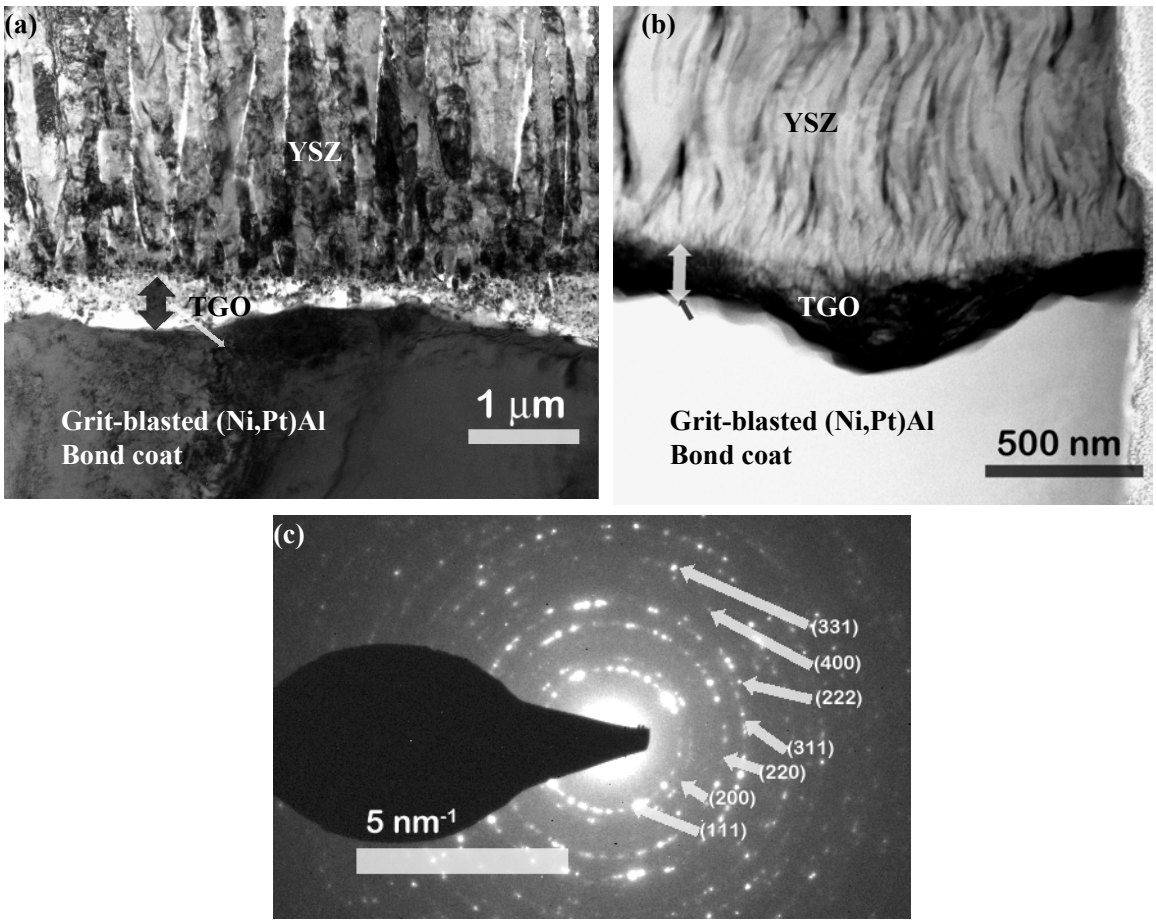

Figure 124. (a) Bright field and (b) HAADF images of as-received type IV EB-PVD TBCs with grit-blasted (Ni,Pt)Al bond coat. (c) SADP demonstrates that SADP demonstrated that the EB-PVD 7YSZ consisted of non-equilibrium tetragonal (t') and/or retained cubic (f') phase.

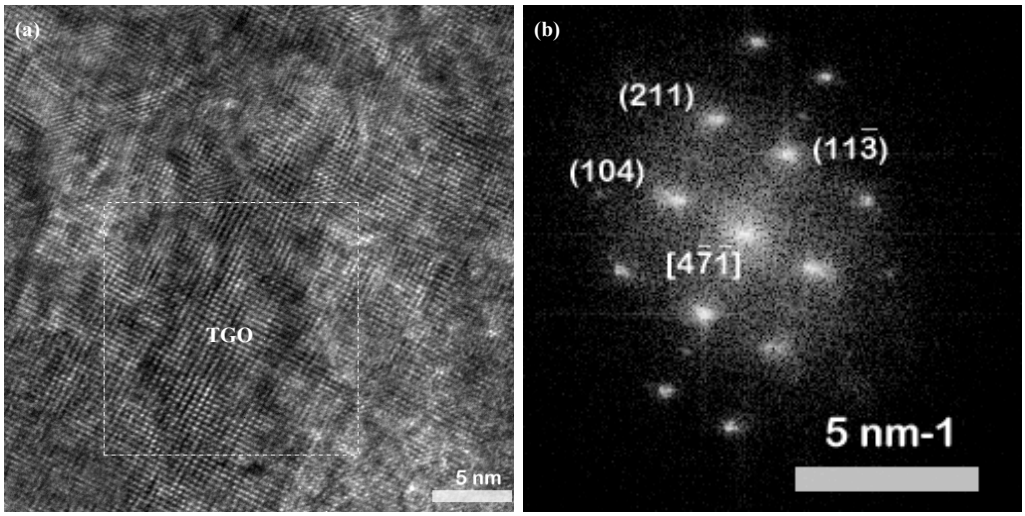

Figure 125. (a) High resolution image and (b) corresponding FFT diffractogram from TGO in re-received type IV EB-PVD TBCs with grit-blasted (Ni,Pt)Al bond coat.

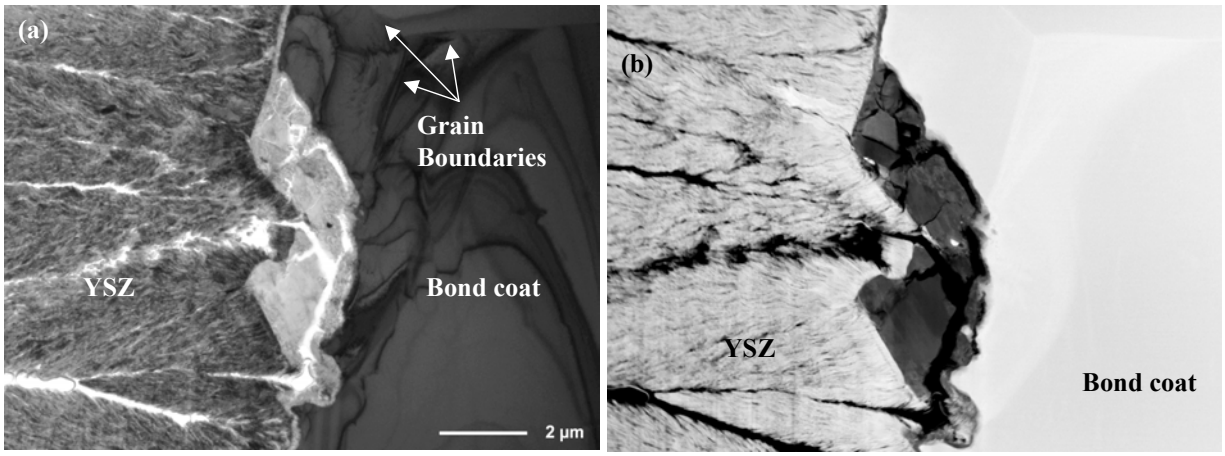

Figure 126. (a) Bright field and (b) HAADF images of as-received type IV EB-PVD TBCs with grit-blasted (Ni,Pt)Al bond coat. Presence of large residual α-Al_2O_3 particles from grit blasting was frequently observed.

V.4.4. Thermally Cycled Electron Beam Physical Vapor Deposited Thermal Barrier Coatings

Figure 127 represents backscatter electron micrographs of the type II EB-PVD TBCs as a function of 1-hour thermal cycling. From these figures we can observe the growth of the TGO with thermal cycles. For this type-II EBPVD TBCs we can clearly observe the depletion of the β-NiAl from the NiCoCrAlY bondcoat after the 10% thermal cyclic lifetime of the TBCs as shown in Figure 128. These TBCs had the lowest lifetime compared to the other EBPVD TBCs studied in this work. This may be due to the formation of the Ni/Co rich oxides that formed as early as 10% of its thermal cyclic lifetime of the TBCs with β-NiAl still present in the NiCoCrAlY bondcoat. Moreover with progressive thermal cycling, we observe damages within the TGO which is not detected by the NDE methods used in this study which is discouraging for this type of TBCs with NiCoCrAlY bondcoat.

Irrespective of the specification described in Table II for bond coat surface preparation, a "mixed-oxide" layer (MOZ) was observed for all types of EB-PVD TBCs. This MOZ consisted of spheroids of zirconia particles dispersed in the alumina matrix. With thermal cycling the growth of columnar $\propto$-Al_2O_3 was observed as shown in Figures 129 and 130 for type II TBCs. The interface between the YSZ and columnar TGO had a mixed oxide zone with voids and cracks. The yttrium rich particles that were dispersed in the TGO as shown in Figures 131(b) and 130(a) were identified as Y_2O_3 by diffraction analysis as seen in Figure 129(b). Another important observation that was made in 50% thermal cyclic life time is the identification of marternsitic structure (L_{10}) as shown in Figure 131(a). Further an ordered L_{12} super lattice structure was observed in 50% thermal cyclic life time as shown in Figure 131(b).

Figure 132 represents backscatter electron micrographs of type-III EBPVD TBCs with as-coated (Ni,Pt)Al bondcoat as a function of 1-hour thermal cycling from as-coated condition. With thermal cycling there is growth of TGO which can be correlated to the initial increase in the compressive residual stress within the TGO scale as shown in Figure 43. This growth in TGO is also correlated to the R_{TGO} and C_{TGO} as shown in Figures 75 and 76. With progressive 1-hour thermal cycles we observe damages in the TGO scale indicated by arrows in Figure 132. This sub-critical damage is manifested as stress-relief within the TGO, identified by PSLS as presented in Figure 39. Also these damages may be related to an increase in the C_{TGO} as shown in Figure 76.

Figure 133 represents backscatter electron micrographs of type-III EBPVD TBCs with as-coated (Ni,Pt)Al bondcoat as a function of 10-hour thermal cycling from as-coated condition. With thermal cycling damages were seen in TGO scale indicated by arrows in Figure 133 are related to the stress-relief within TGO scale as identified by PSLS and shown in Figure 47. These damages are not seen for 50-hour thermal cycling as shown in Figure 134.

For the type III TBC specimen with as-coated (Ni,Pt)Al bond coat, the TGO scale consisted of two distinctive microstructural zones as presented in the HAADF image in Figure 135: a mixed oxide zone containing Zr rich particles dispersed on a Al_2O_3 matrix near to the YSZ topcoat and a dense-continuous-columnar α-Al_2O_3 TGO near to the (Ni,Pt)Al bond coat. The thickness of the TGO, both the MOZ and the COZ (continuous oxide zone), grew with

thermal cycling. The MOZ consisted of numerous voids as observed in the BF TEM image in Figure 136 (a). The COZ near to the bond coat had a columnar structure as presented by the BF TEM image in Figure 136 (b). Fast Fourier Transformed diffractograms in Figure 137 indexes to γ-Al_2O_3 and t-ZrO_2 and demonstrate that the Al_2O_3 in the MOZ near the ZrO_2 particles is metastable. This observation explains the growth of the MOZ since the growth rate of metastable Al_2O_3 phases is much faster in comparison to the equilibrium α-Al_2O_3 phase. The volume contraction associated with the metastable-to-equilibrium Al_2O_3 transformation can be attributed to the formation of voids in the MOZ. The rate of phase transformations in the presence of γ-Al_2O_3 stabilizer such as ZrO_2 is being examined currently.

Figure 138 represents microstructure of the type-III EB-PVD TBCs with as-coated (Ni,Pt)Al bondcoat after 70% thermal cyclic lifetime. Aforementioned, the TGO was observed with two-zone microstructure consisting of the MOZ and COZ. With progressive thermal cycling the voids were more frequently observed. Further a diffraction analysis in the as-coated bondcoat near the TGO revealed B2 NiAl and martensitic twins as shown in Figure 138.

Typical backscatter electron micrographs of type IV TBCs with the grit-blasted (Ni,Pt)Al bond coat as a function of thermal cycling is shown in Figure 139. With thermal cycling there is a growth of TGO which can be related to NDE results of PSLS and EIS: an initial increase in the compressive residual stress as shown in Figure 45; an initial increase and a decrease in the R_{TGO} and C_{TGO} as shown in Figures 81 and 82. With progressive thermal cycles, "racheting" was observed during 1-hour thermal cycles as shown in Figure 139. Figure 139 also shows vertical cracks in the TGO scale due to "racheting" which is further confirmed by TEM micrographs in Figure 143. This "racheting" phenomena can lead to stress relaxation which was observed for type-IV EB-PVD TBCs with grit-blasted (Ni,Pt)Al bondcoat. For the type-IV TBCs, luminescence from PSLS shifted gradually towards stress-free luminescence with thermal cycling as presented in Figures 44 and 45. This type of sub-critical damages may be related to the evolution of the C_{TGO} that increased significantly before the final failure of TBCs as shown in Figures 82 and 83.

Figures 140 and 141 represents back scatter electron micrographs of type-IV TBCs with grit-blasted (Ni,Pt)Al bondcoat as a function of 10 and 50-hour thermal cycling. For this particular type of TBCs, racheting is dependent on thermal cyclic dwell time because in case of 10 and 50-hour thermal cycles "rumpling" of the bondcoat is observed more significantly than racheting. With rumpling of the bondcoat the damages are seen frequently at the TGO/bondcoat interface which is shown in Figures 165 and 170. Also there is no evidence of stress relaxation as observed for 1-hour thermal cycles.

Type IV TBC specimen with the grit-blasted (Ni, Pt)Al bondcoat had traces of mixed oxide zone even after progressive thermal cycling as shown in Figures 142 through 144. Further it is observed that the TGO near the YSZ topcoat had an equiaxed structure as seen in Figures 142 (b) and (c). After 50% thermal cyclic lifetime, cracks through the TGO near the ratcheted regions were observed as seen in Figure 143(b). This further confirms the stress-relaxation that was observed by PSLS. After 70% thermal cyclic lifetime, extensive voids

were present near to the ratcheted TGO as shown in Figure 144(a) and (b). A SAD pattern on the bondcoat confirmed that there is a L_{10} martensitic twin microstructure near to the TGO.

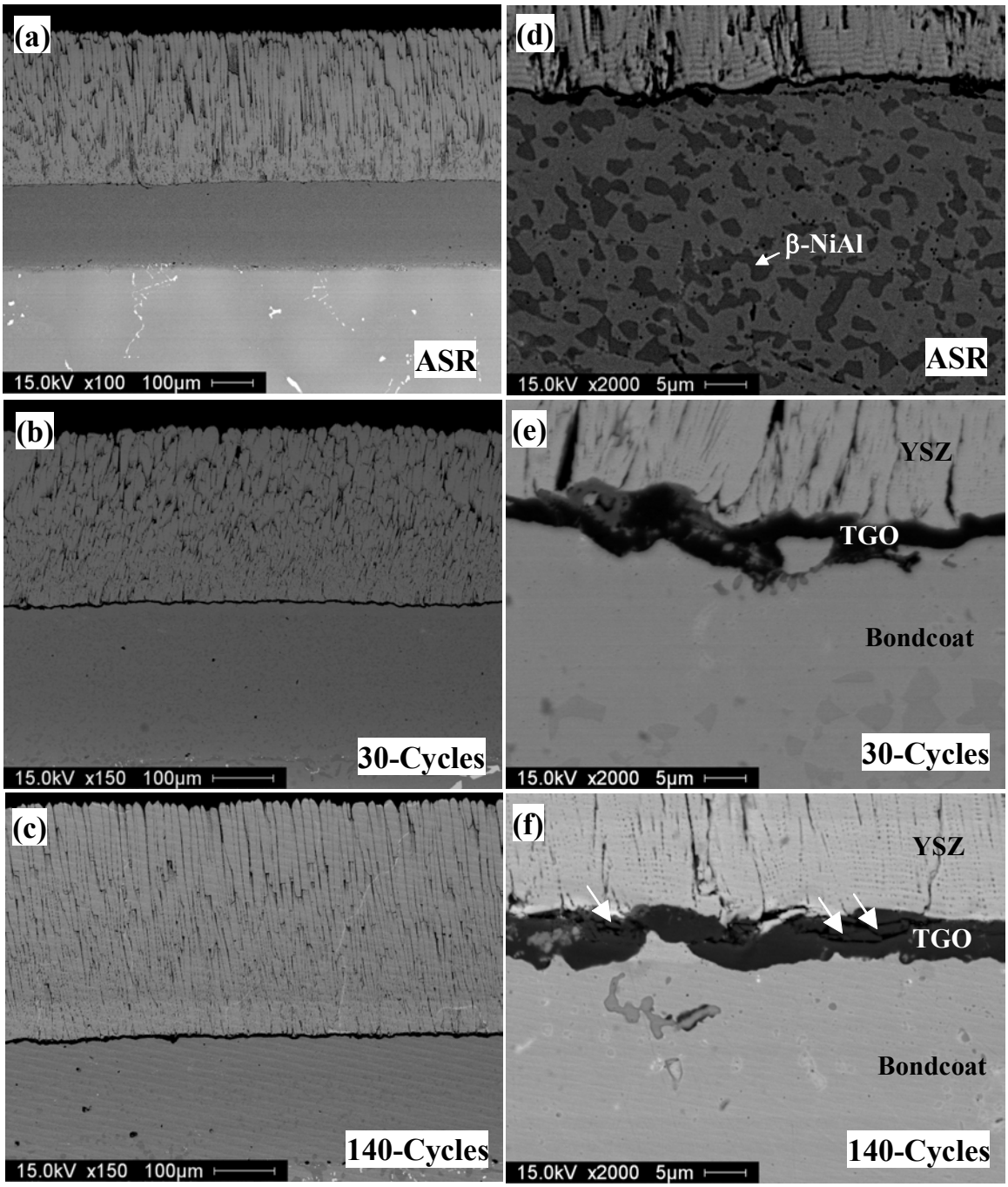

Figure 127. Typical backscatter electron micrographs of type II, EB-PVD TBCs specimens with NiCoCrAlY bondcoat after thermal cycling that corresponds to their lifetimes.

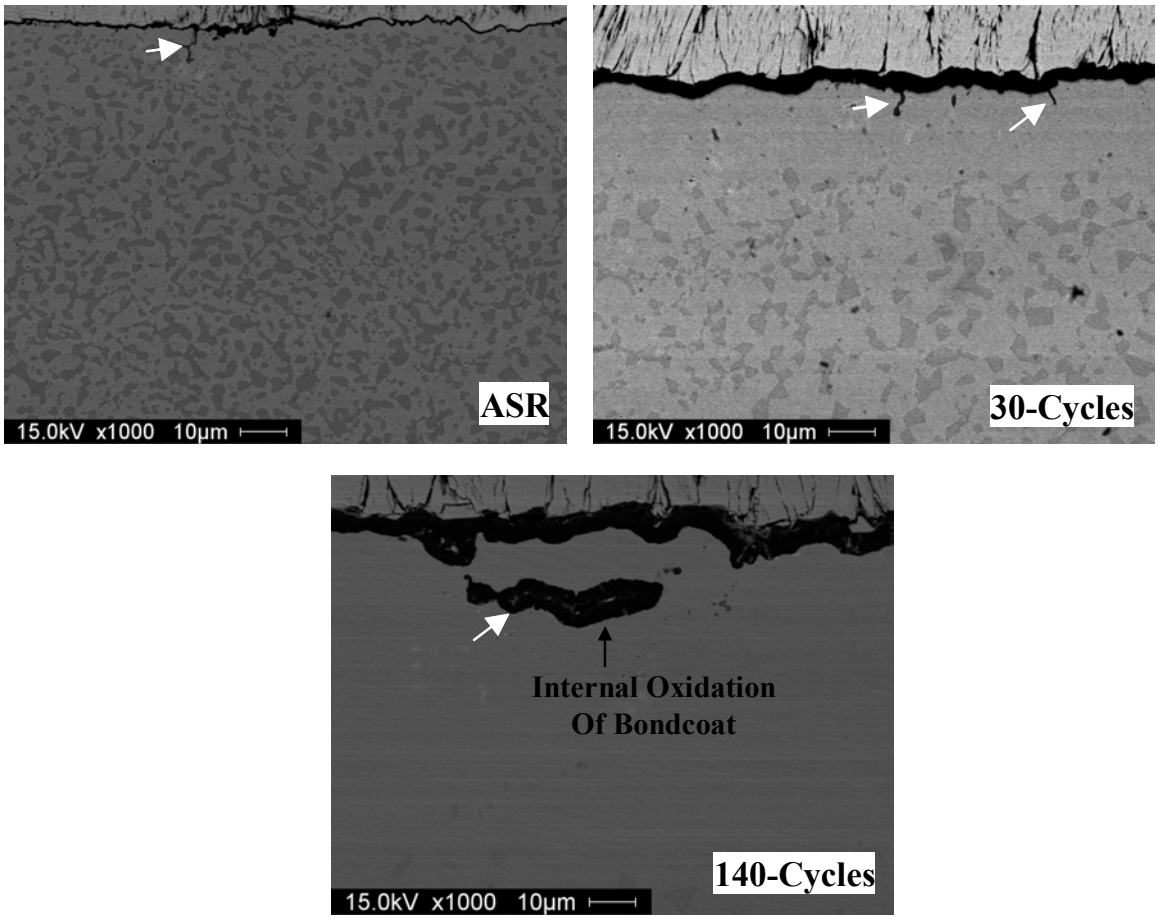

Figure 128. Typical back scatter electron micrographs of type-II TBCs showing the depletion of β-NiAl and also internal oxidation of the NiCoCrAlY bondcoat shown in arrows.

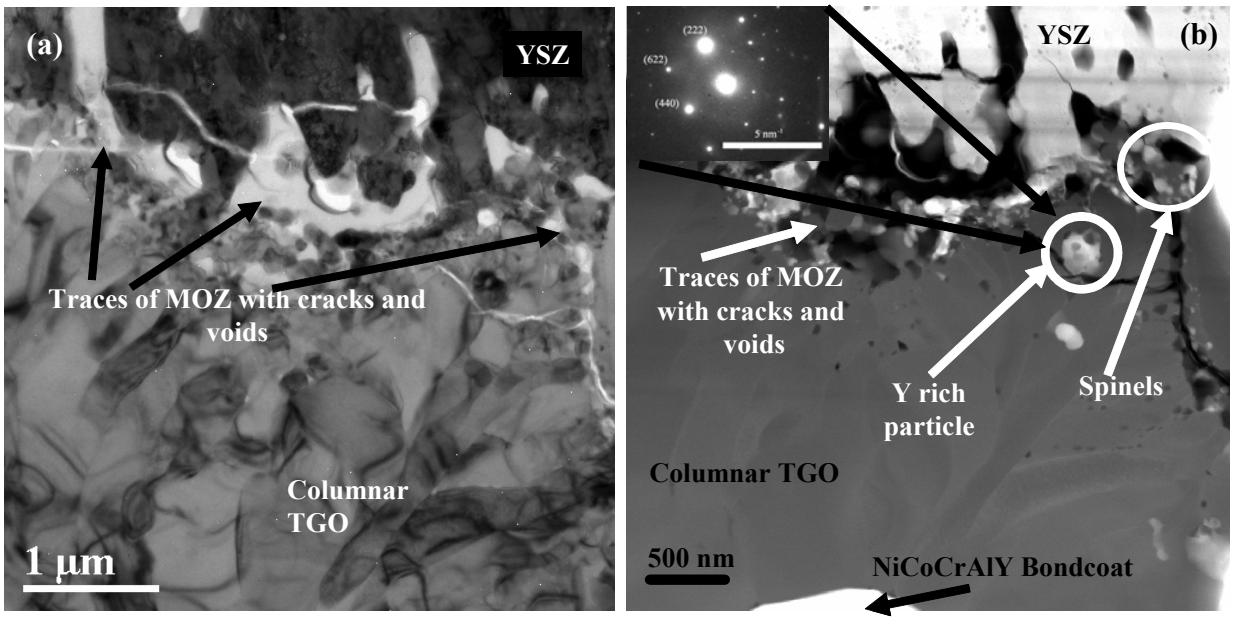

Figure 129. For type-II TBCs after thermal cycling (10% of lifetime): (a) BF TEM image showing presence of MOZ with cracks and voids near to the YSZ / TGO interface and a dense columnar Al_2O_3 TGO (b) HAADF STEM image showing presence of Ni/Co rich oxides near to the TGO/YSZ interface, MOZ with cracks and voids . The observed Y rich particle is identified as Y_2O_3 by diffraction analysis (SAD pattern as inset).

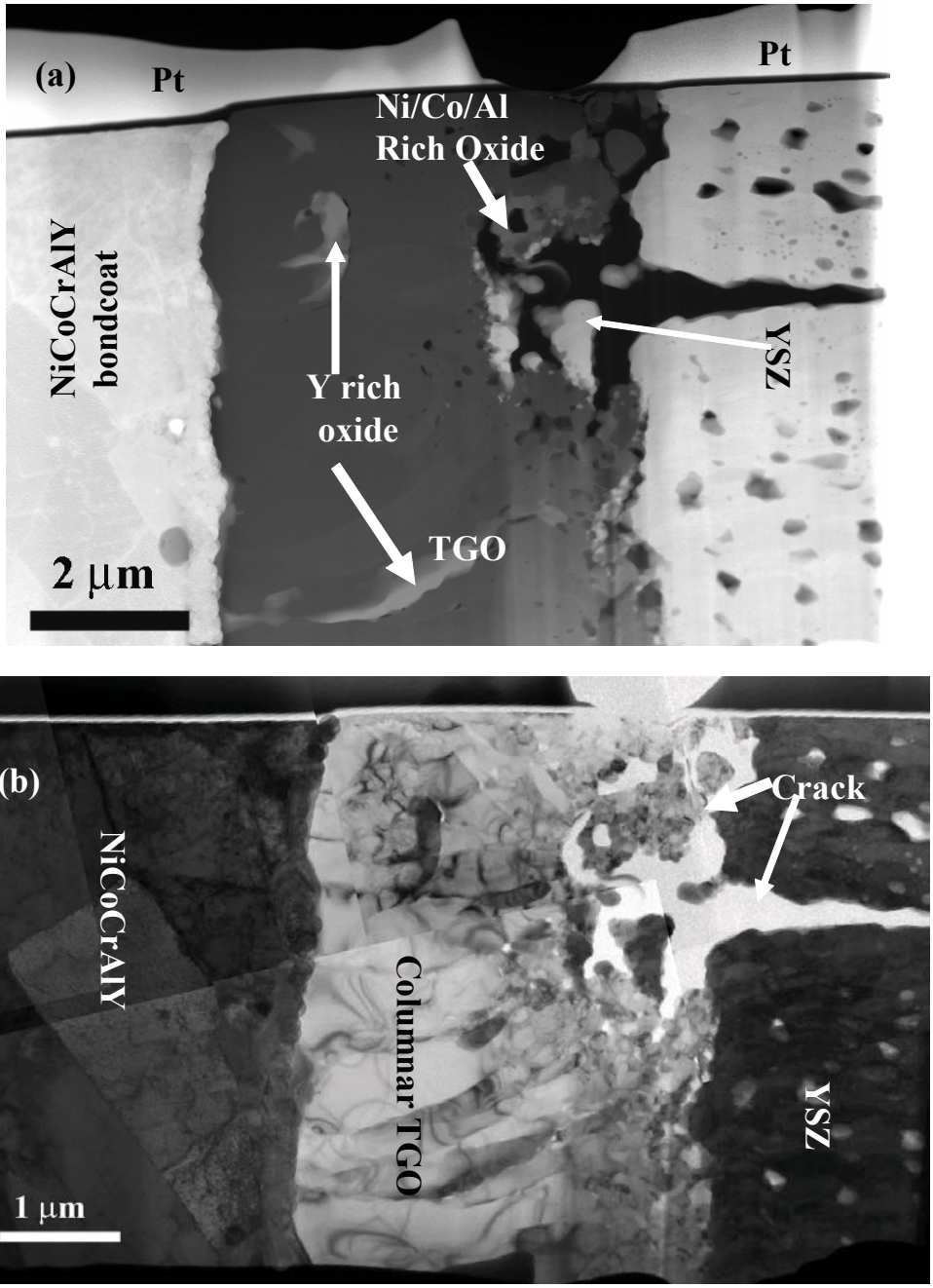

Figure 130. For type-II TBCs after thermal cycling (50% of lifetime): (a) HAADF STEM image showing presence of MOZ with cracks and voids near to the YSZ / TGO interface, a dense Al_2O_3 TGO and Ni/Co/Al rich oxides near the TGO/YSZ interface (b) BF TEM image showing MOZ with cracks and voids near to the YSZ / TGO interface and a dense columnar Al_2O_3 TGO near the TGO/bondcoat interface.

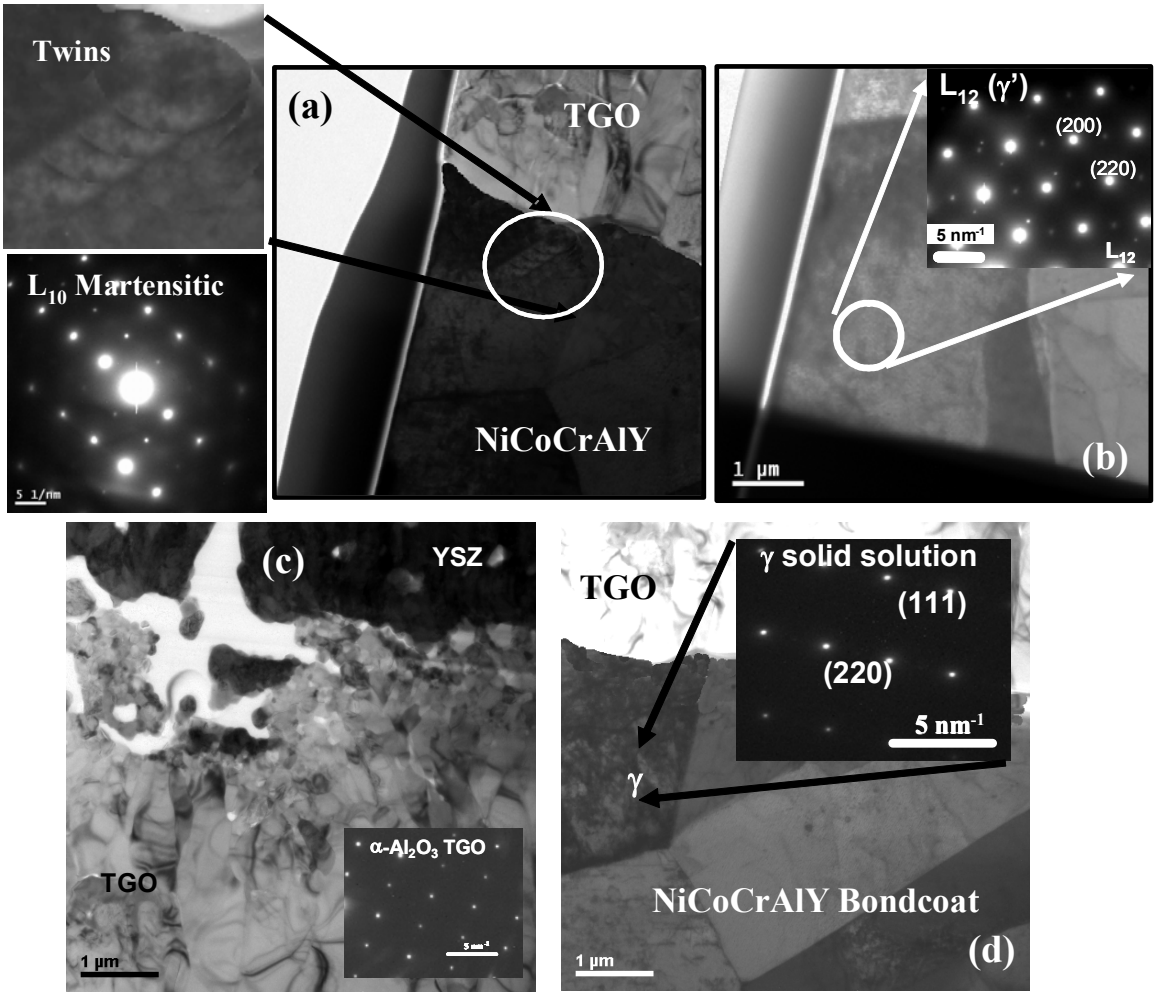

Figure 131. After 50% thermal cyclic lifetime for type-II TBCs (a) L_{10} martensitic twin structure (b) Ordered L_{12} super structure and (d) γ solid solution structure were observed in the (Ni,Pt)Al bondcoat and (c) the TGO identified was α-Al_2O_3.

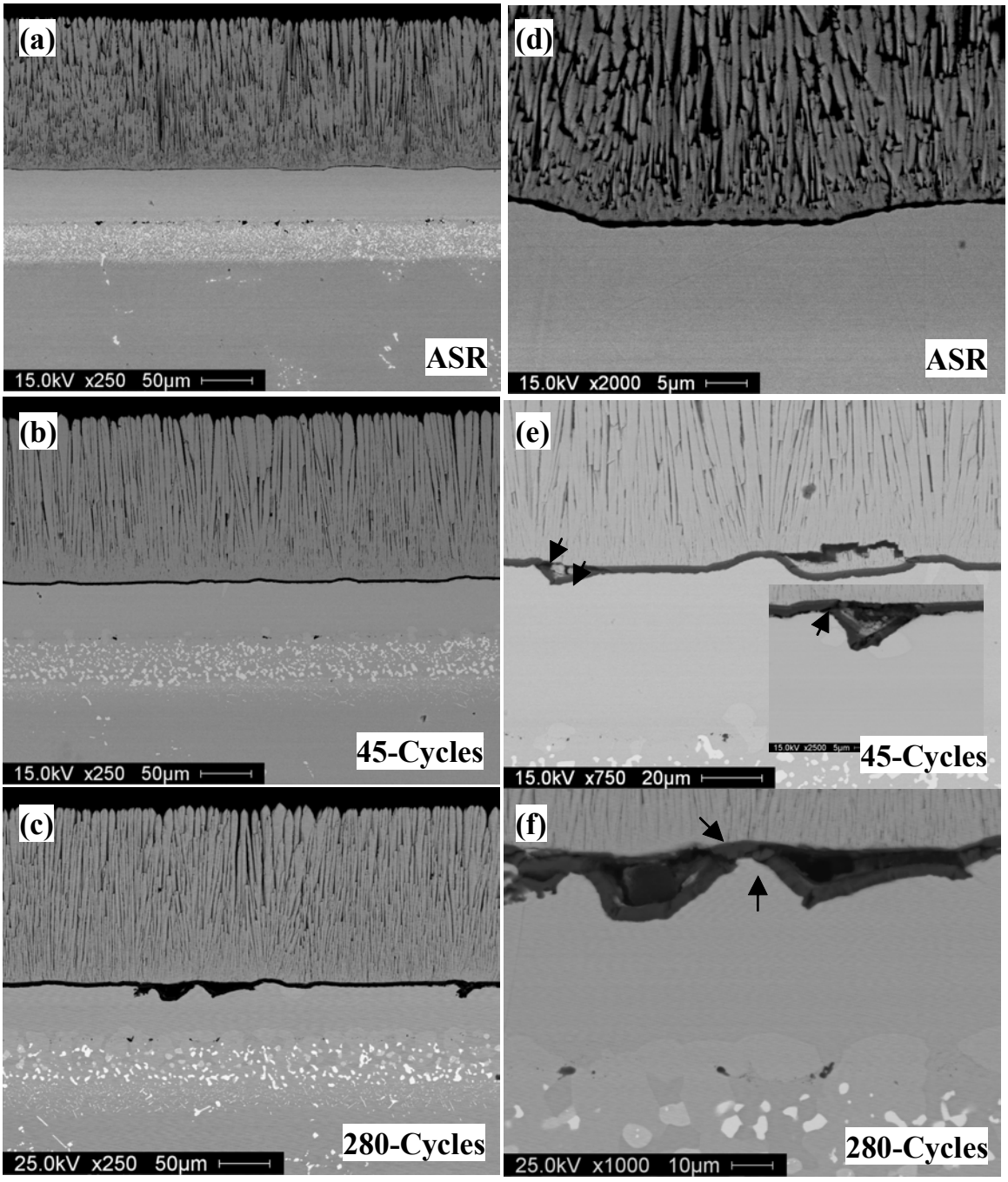

Figure 132. Typical back scatter electron micrograph of type-III EBPVD TBCs with as-coated (Ni,Pt)Al bondcoat with progressive 1-hour thermal cycling.

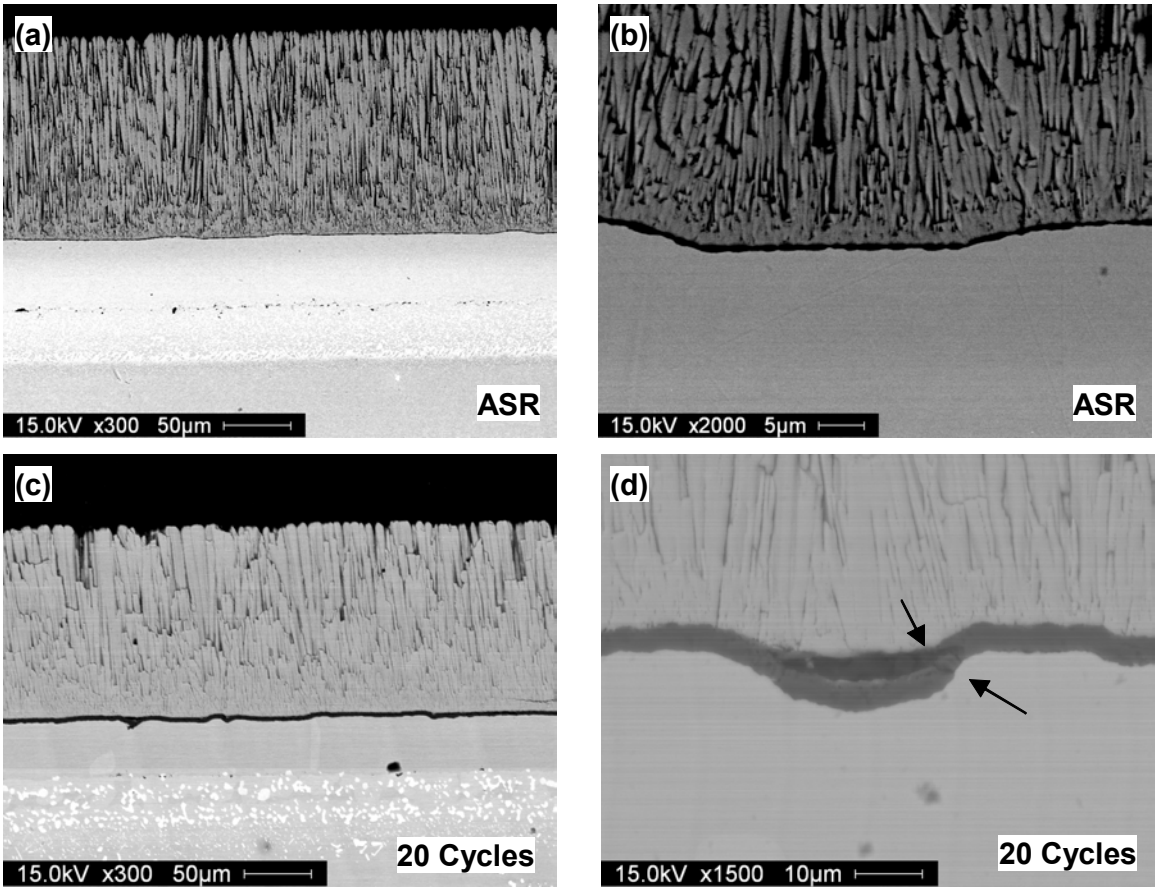

Figure 133. Typical back scatter electron micrograph of type-III EBPVD TBCs with as-coated (Ni,Pt)Al bondcoat with progressive 10-hour thermal cycling.

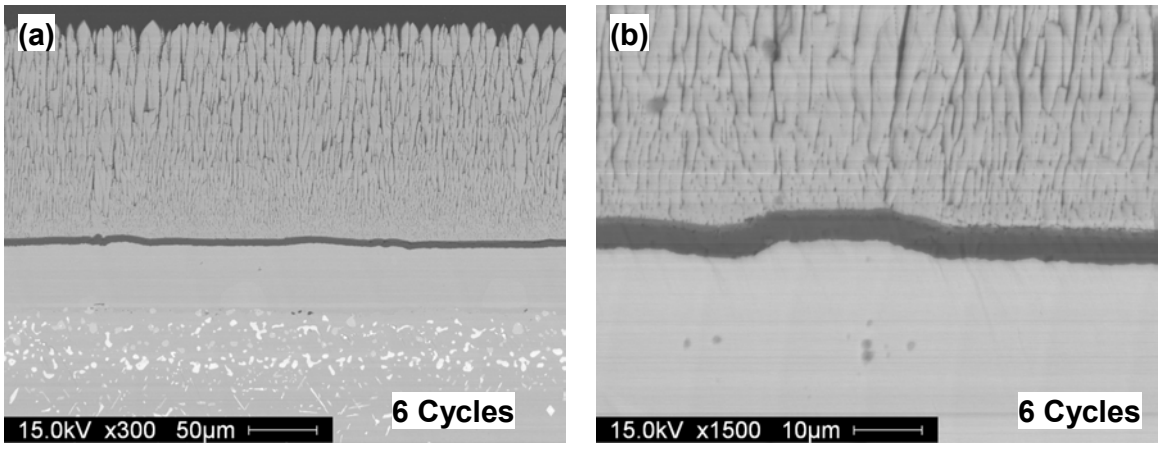

Figure 134. Typical back scatter electron micrograph of type-III EBPVD TBCs with as-coated (Ni,Pt)Al bondcoat after 6 cycles(50 hour thermal cycling).

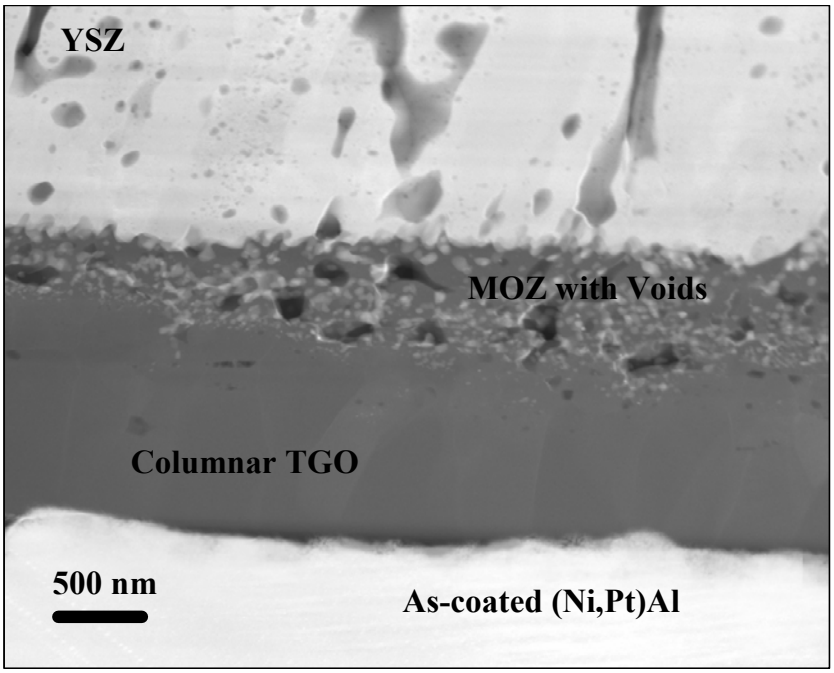

Figure 135. HAADF STEM image for type-III TBCs after thermal cycling (10% lifetime) showing distinct two zone TGO microstructure with presence of voids in the MOZ/Columnar TGO interface (MOZ: Mixed Oxide Zone).

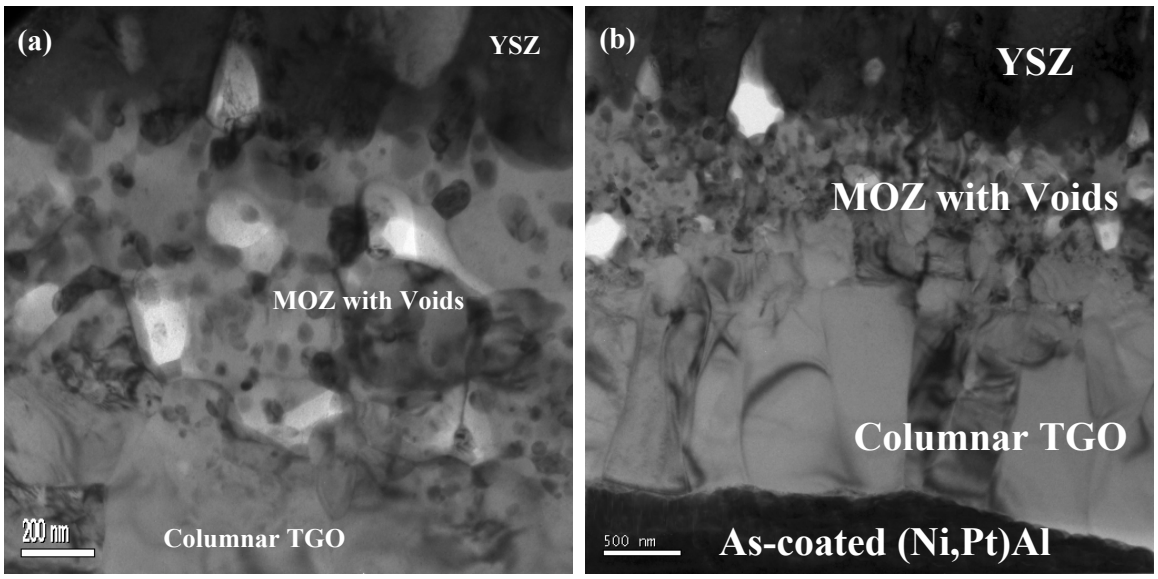

Figure 136. BF TEM images of type III EB-PVD TBCs after thermal cycling that corresponds to 10% of its lifetime: (a) presence of MOZ with voids near the YSZ/TGO interface and a dense-columnar-continuous Al_2O_3 TGO; (b) a distinctive two-zone TGO microstructure.

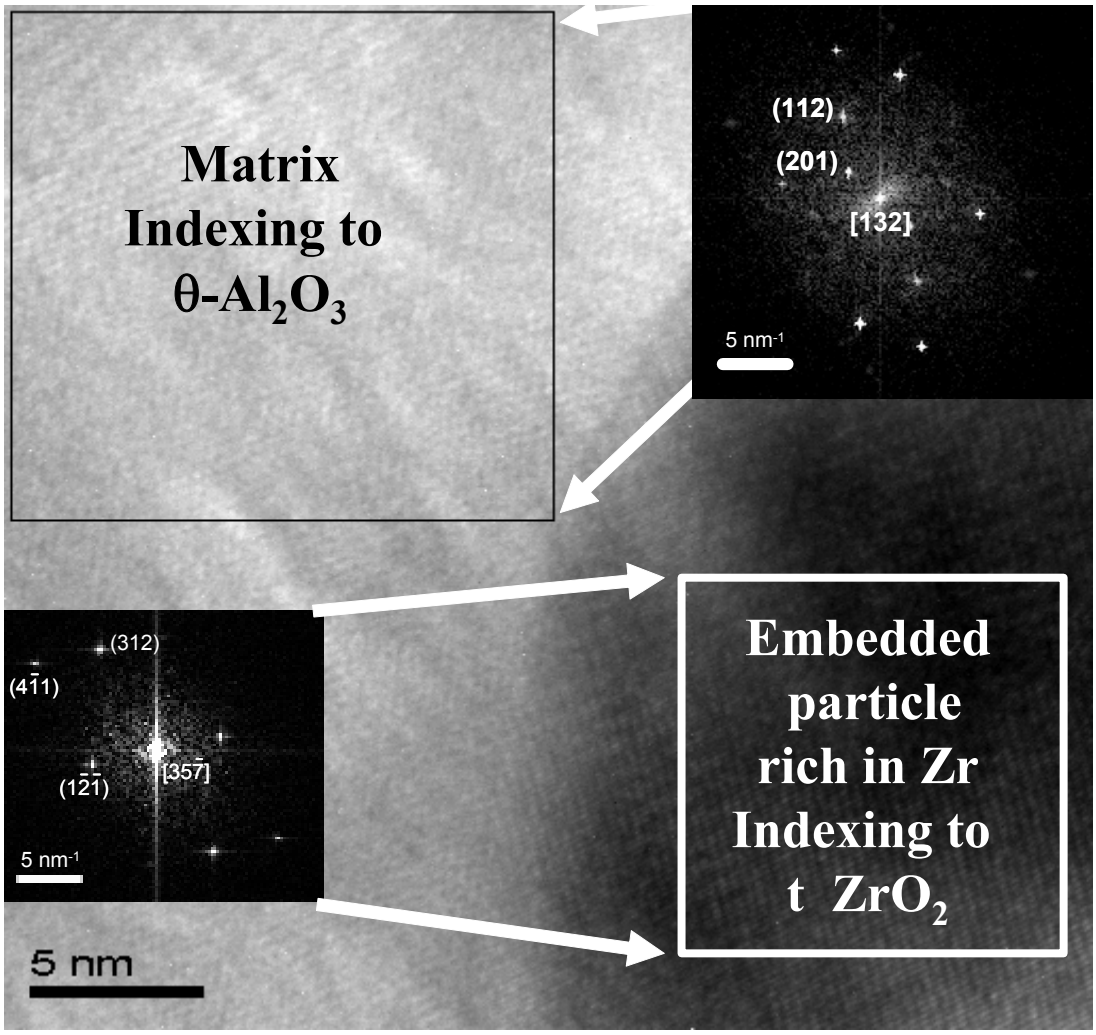

Figure 137. Type-III TBCs after thermal cycling (10% of lifetime): HRTEM image and the corresponding FFT diffractograms (inset) demonstrate MOZ matrix near the dispersed Zr-rich oxide consists of metastable θ-Al_2O_3, and the embedded Zr-rich oxide is t-ZrO_2.

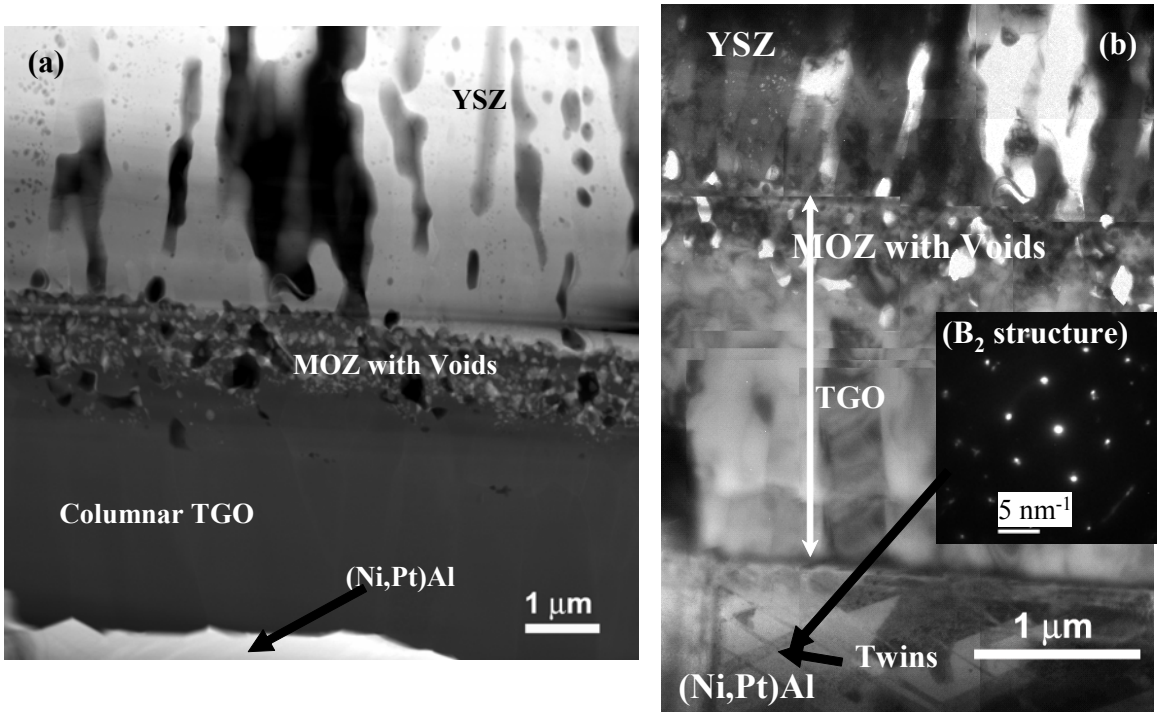

Figure 138. TEM image of type-III EBPVD with as-coated (Ni,Pt)Al bondcoat TBCs after 70% thermal cyclic life time (a) HAADF STEM image showing well defined two zone TGO microstructure (b) BF TEM image showing the as-coated (Ni,Pt)Al bondcoat having B_2 structure near to the TGO.

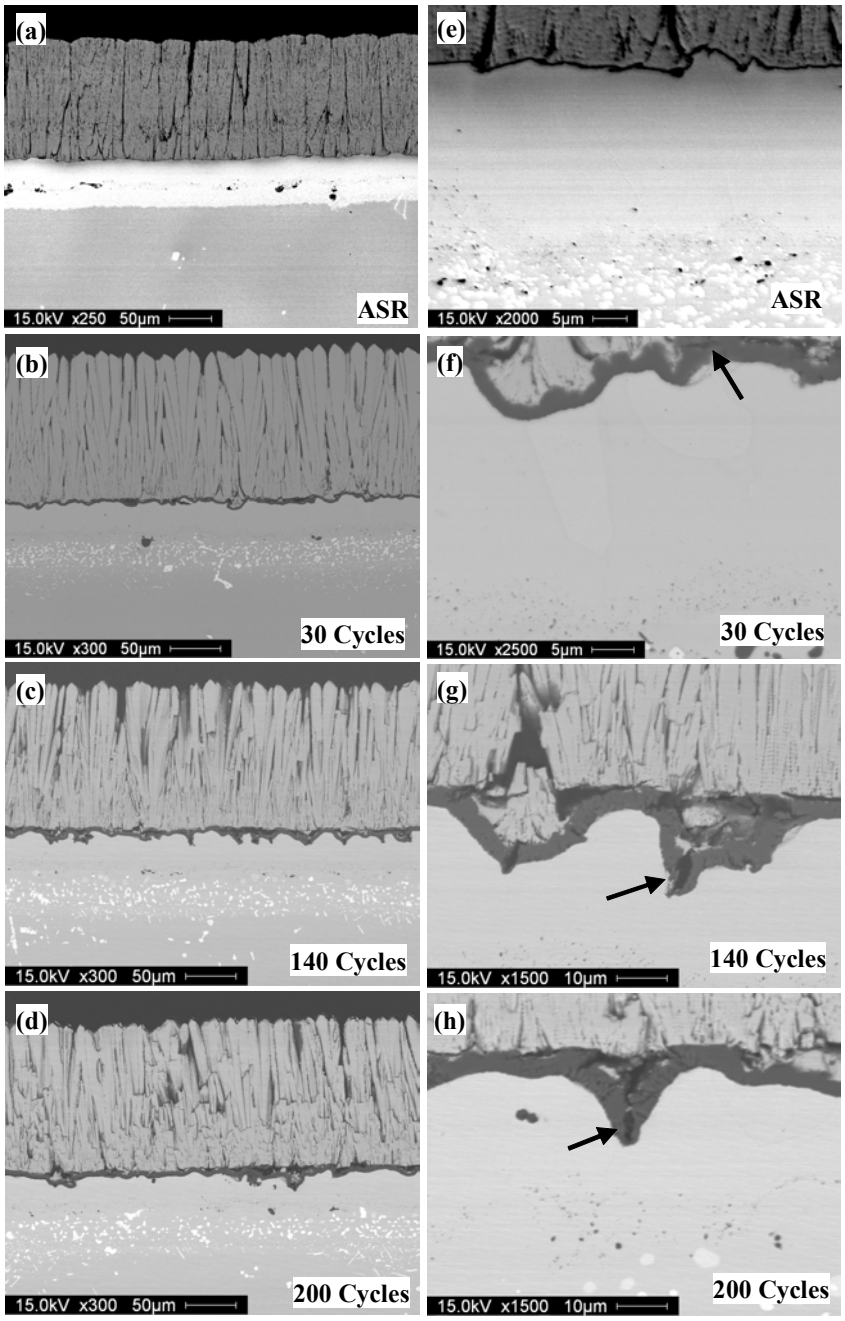

Figure 139. Typical back scatter electron micrograph of type-IV EB-PVD TBCs with grit blasted (Ni,Pt)Al bondcoat with progressive 1-hour thermal cycling.

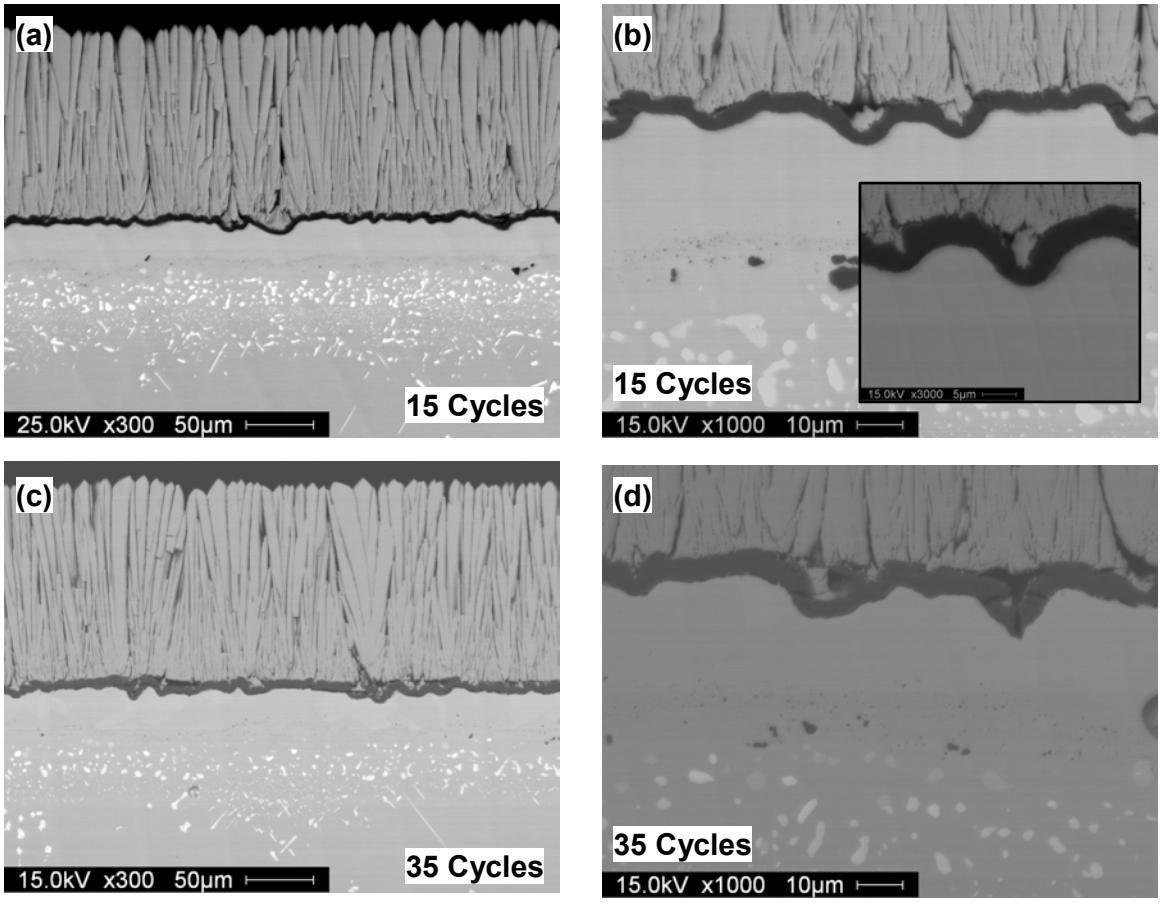

Figure 140. Typical back scatter electron micrograph of type-IV EB-PVD TBCs with grit blasted (Ni,Pt)Al bondcoat with progressive 10-hour thermal cycling.

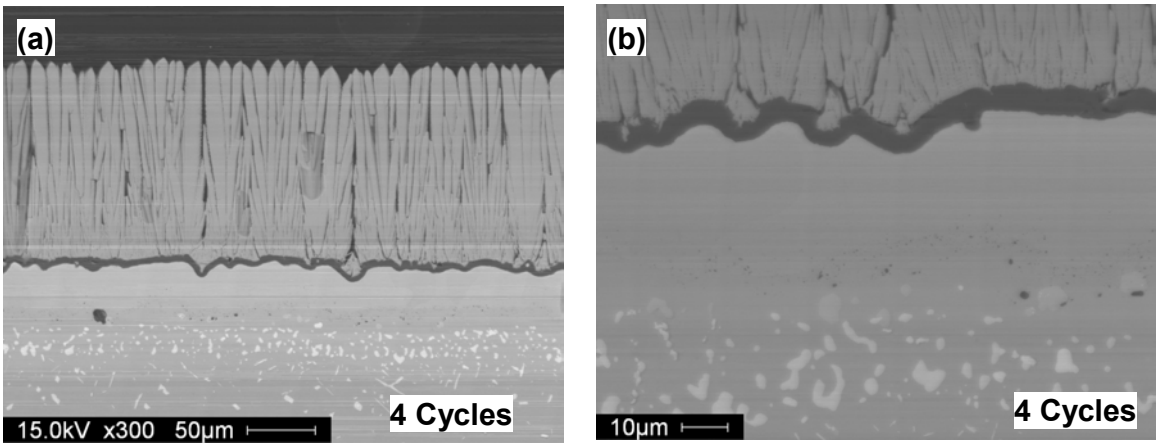

Figure 141. Typical back scatter electron micrograph of type-IV EB-PVD TBCs with grit blasted (Ni,Pt)Al bondcoat after 4 cycles (50-hour thermal cycling).

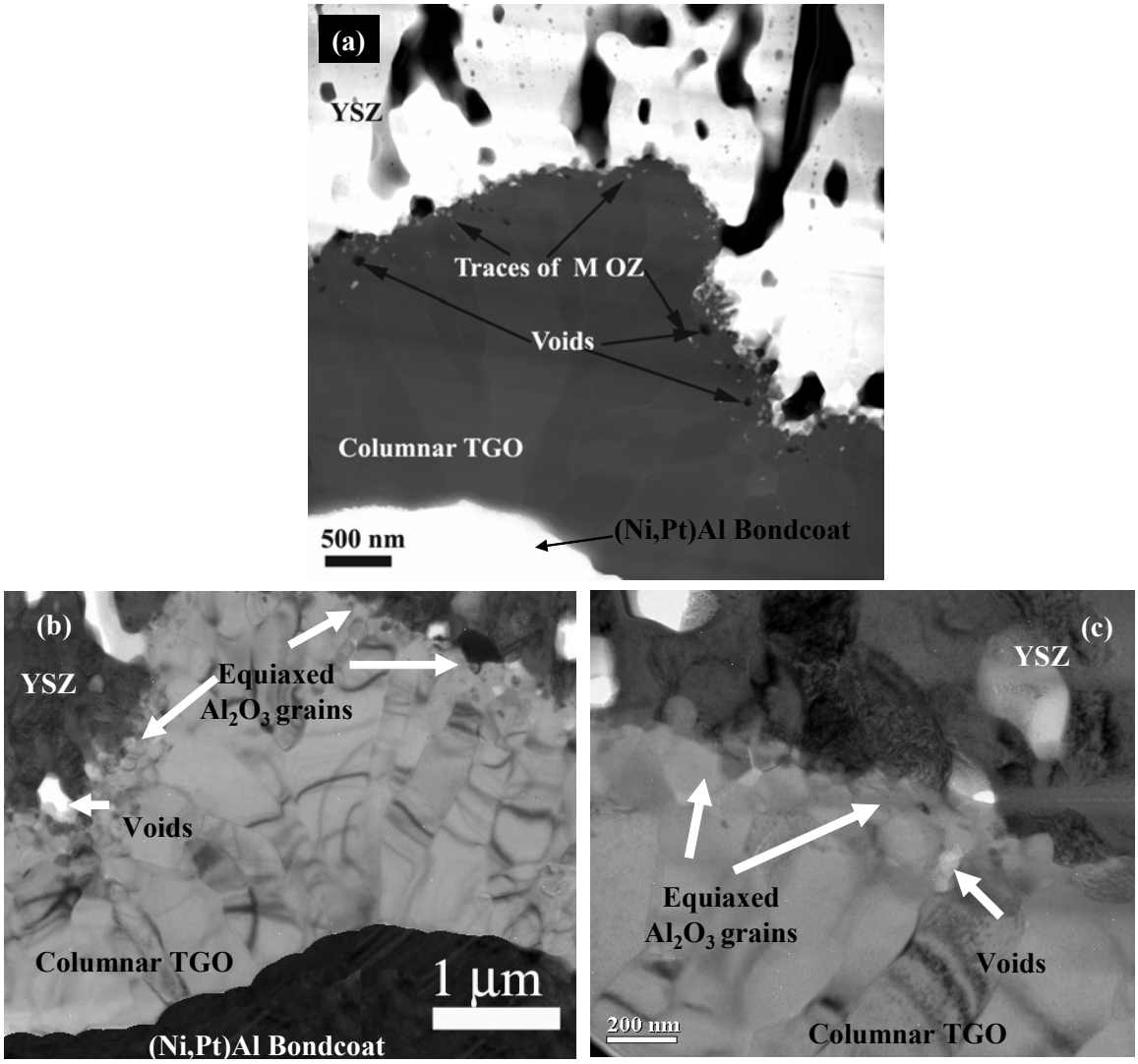

Figure 142. For type-IV TBCs after thermal cycling that corresponds to 10% of its lifetime: (a) HAADF STEM image showing the presence of MOZ traces near the YSZ/TGO interface and a dense Al_2O_3 TGO near the (Ni,Pt)Al bond coat; (b) BF TEM image showing presence of equiaxed Al_2O_3 grains near to the YSZ/TGO interface, and (c) a dense columnar continuous Al_2O_3 TGO.

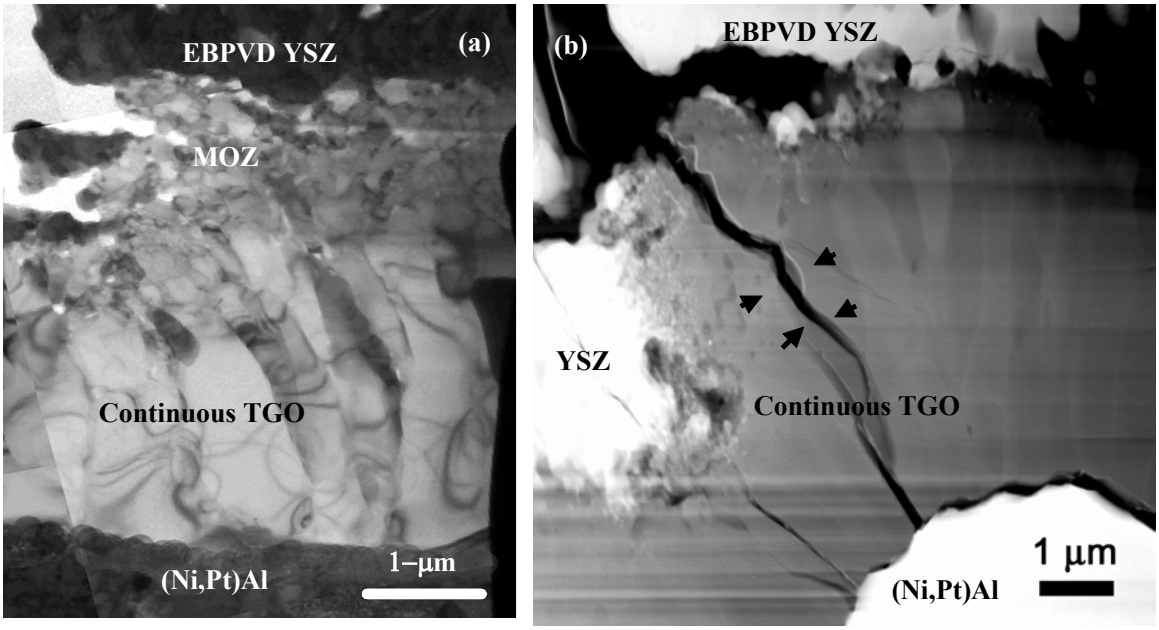

Figure 143. TEM images for type-IV EBPVD TBCs with grit blasted (Ni,Pt)Al bondcoat after 50% thermal cyclic lifetime (a) BF TEM image showing two zone microstructure in TGO and also voids present in the MOZ (b) HAADF STEM image showing through crack in the TGO scale with TBC still intact.

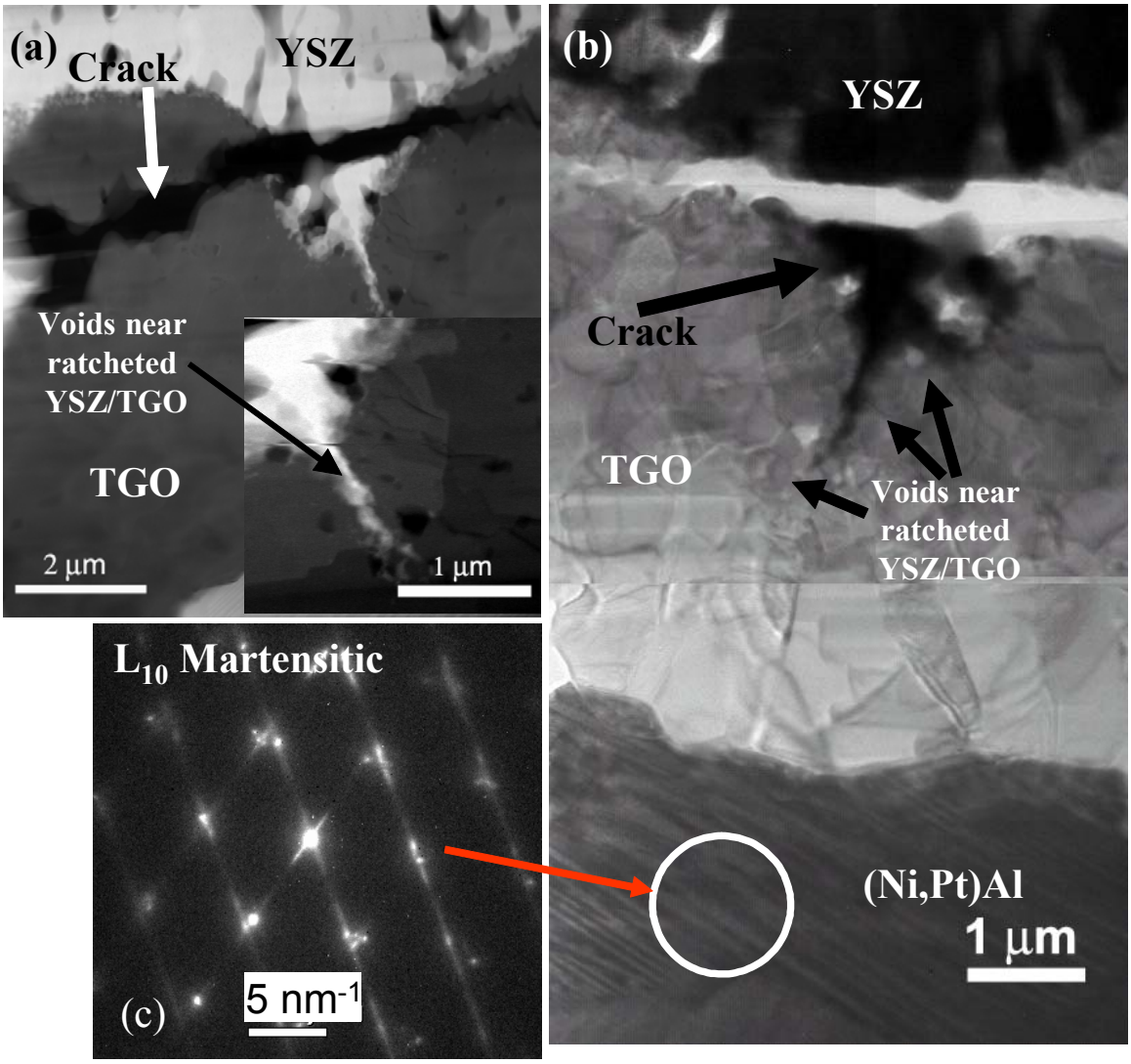

Figure 144. TEM images for type-IV EBPVD TBCs with grit blasted (Ni,Pt)Al bondcoat after 70% thermal cyclic lifetime (a) HAADF STEM image showing voids near the ratcheted TGO (b)BF TEM image showing the same (c) SAD pattern from the bondcoat showing L_{10} martensitic structure.

V.4.5. Characterization of Failure for Air Plasma Sprayed Thermal Barrier Coatings for 1-hour thermal cycling

Figure 145 represents backscatter electron micrograph of spallation surfaces in type I (600μm-thick) APS TBCs with NiCoCrAlY bond coat. This TBC type had an average lifetime of 527 1-hour cycles. Microscopic constituents of YSZ and TGO were observed on both bottom of the spalled-YSZ in Figure 145(a,b) and top of the bond coat surface where YSZ coating has spalled off in Figure 145(c,d). These micrographs indicate that the fracture for the spallation of type I TBCs occurred within the YSZ, within the TGO and at the YSZ/TGO interface. Most of the TGO were observed as islands, and contained Al, Ni, Co and Cr. The exposure of bond coat surface was extremely rare. Because of this kind of fracture the C_{TGO} does not change significantly as reported in the Figure 61.

Cross-sectional backscatter electron micrographs also demonstrated similar fracture paths as presented in Figure 146. A few residual TGO was observed on the spalled-YSZ as shown in Figure 146(b) while a few residual YSZ was observed on the top of the bond coat as shown in Figure 146(d). A significant internal oxidation of the bond coat was also observed as presented in Figure 146(c) following the splat boundaries of NiCoCrAlY bond coat. The TGO, both external and internal scale, primarily consisting of Al_2O_3 (dark gray) as well as those rich in Ni, Co and Cr (light gray) were also observed.

Similar fracture was observed for type V (200 μm-thick) APS TBCs with NiCoCrAlY bond coat as presented in Figures 147 and 148. This TBC type had an average lifetime of 286 1-hour cycles. Microscopic constituents of YSZ and TGO were observed on the bottom of the spalled-YSZ in Figure 147(a,b) and top of the bond coat surface where YSZ coating has spalled off in Figure 148(c,d). These micrographs indicate that the fracture for the spallation of type V TBCs occurred within the YSZ, within the TGO and at the YSZ/TGO interface. More of TGO on the fracture surface was observed for type V when compared to type I TBCs. Most of the TGO were observed as islands and contained Al only. The exposure of bond coat surface was extremely rare. But for one failed specimen, the C_{TGO} increased abruptly as reported in Figure 67, due to the bond coat surface exposure.

Cross-sectional secondary and backscatter electron micrographs also demonstrated similar fracture paths as presented in Figure 148. A few residual TGO was observed on the spalled-YSZ as shown in Figure 148(a) while a few residual YSZ was observed on the top of the bond coat as shown in Figure 148(d). No internal oxidation of the bond coat or TGO rich in Ni, Co, and Cr was observed for type V TBCs.

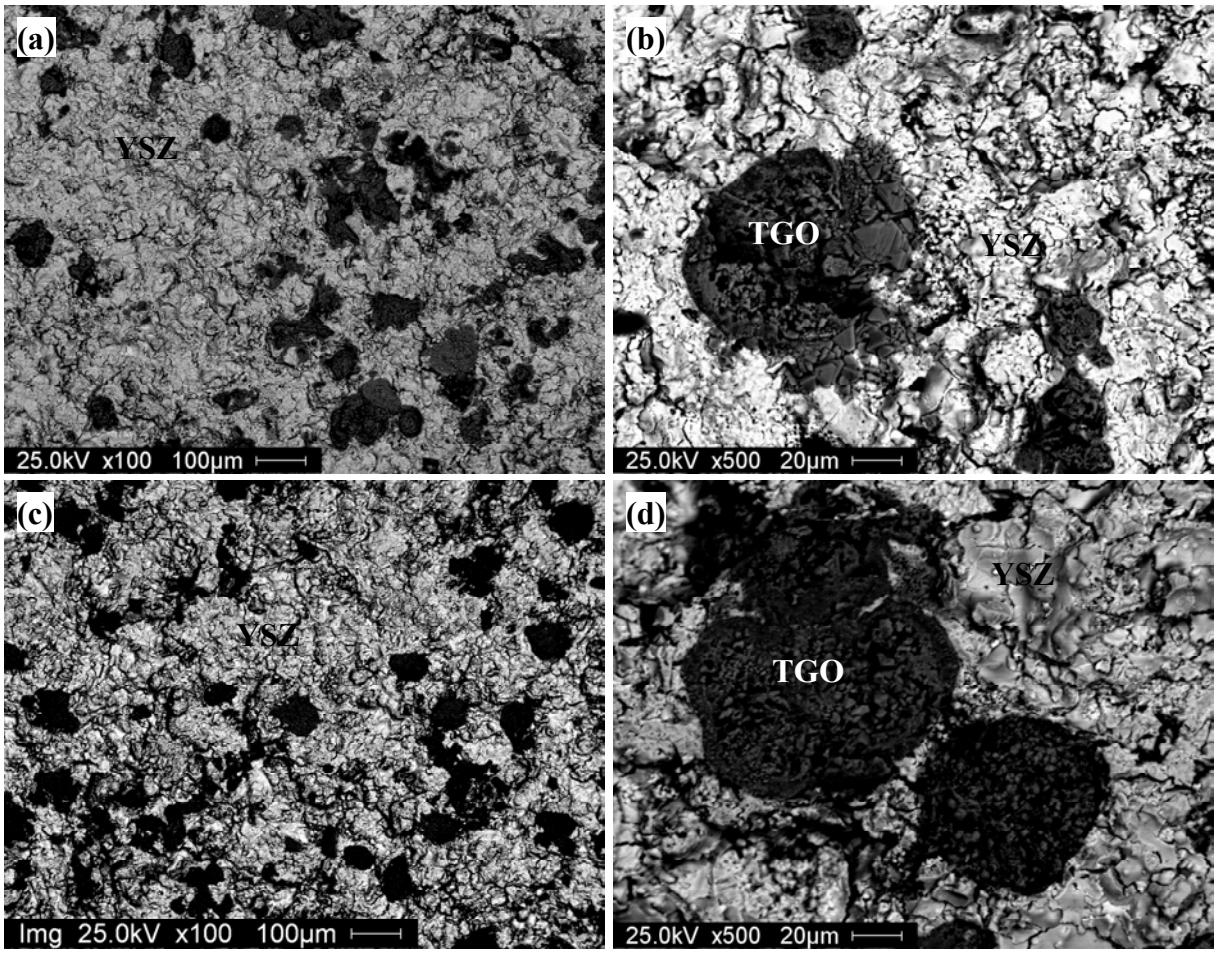

Figure 145. Backscatter electron micrographs of fracture surfaces in type I TBCs: (a,b) bottom of the spalled-YSZ coating and (c,d) top of the bond coat where YSZ coating has spalled off. Exposure of NiCoCrAlY surface was extremely rare.

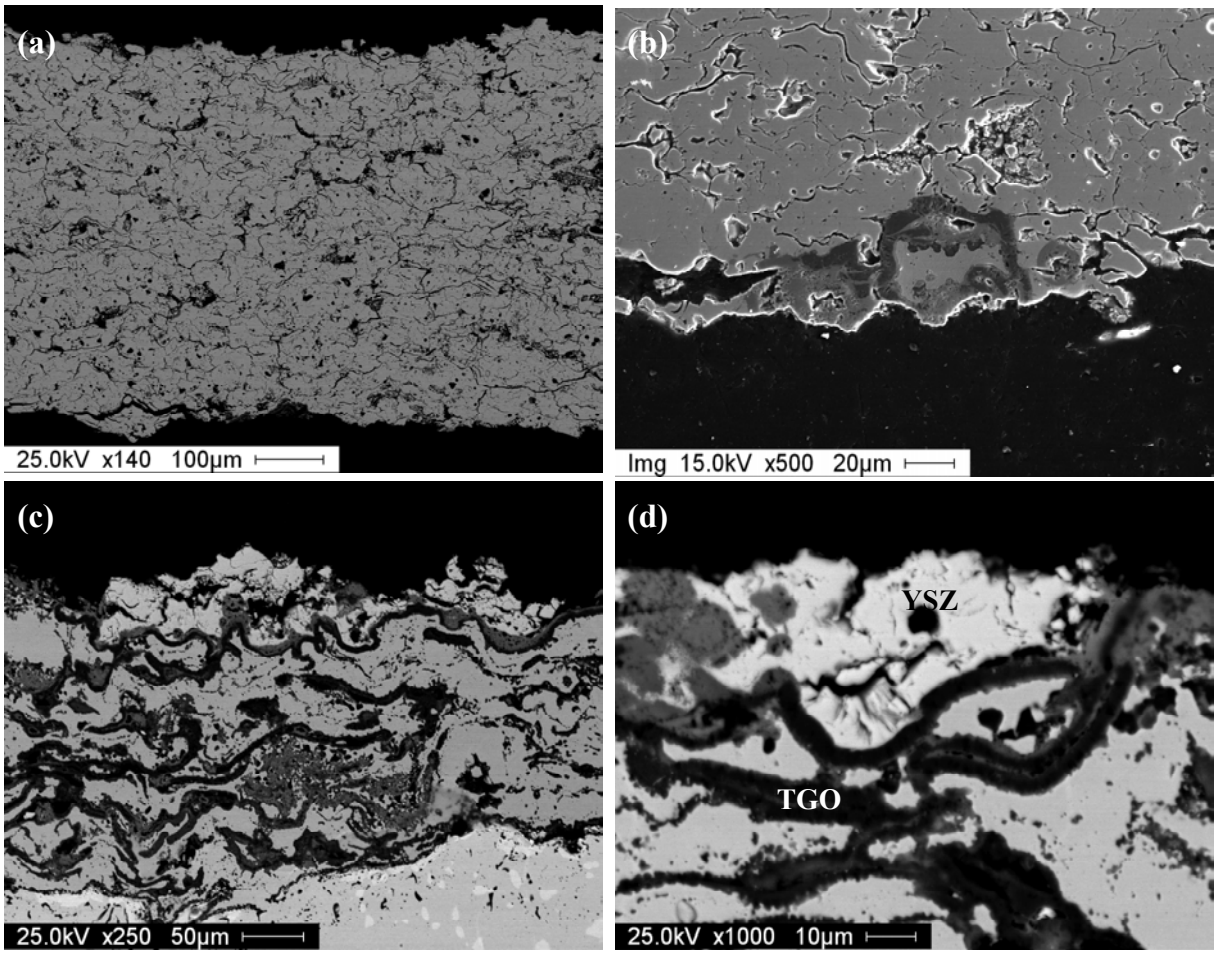

Figure 146. Cross-sectional backscatter electron micrographs of type I TBCs after spallation: (a,b) spalled-YSZ coating and (c,d) bond coat after YSZ spallation.

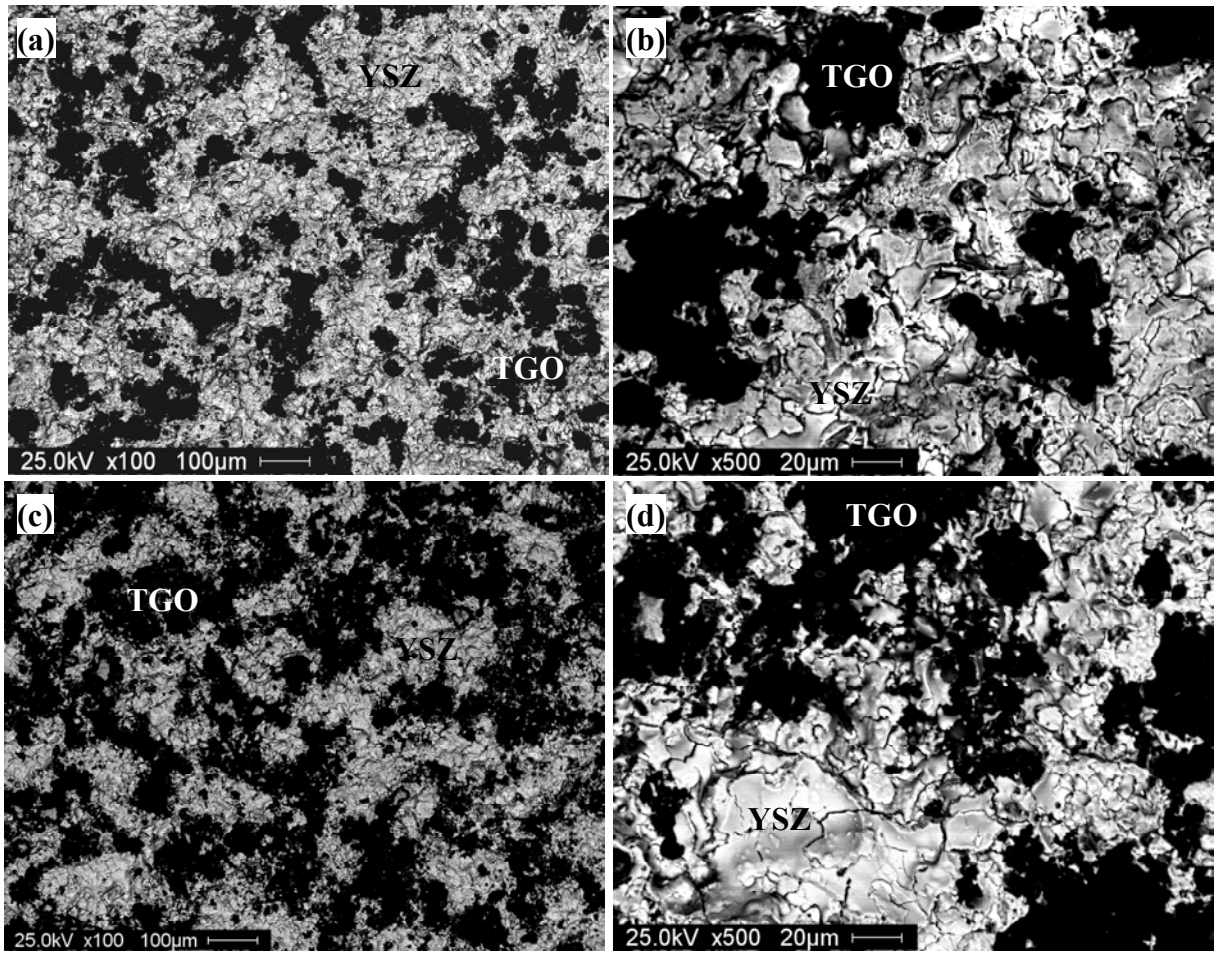

Figure 147. Backscatter electron micrographs of fracture surfaces in type V TBCs: (a,b) bottom of the spalled-YSZ coating and (c,d) top of the bond coat where YSZ coating has spalled off. Exposure of NiCoCrAlY surface was extremely rare.

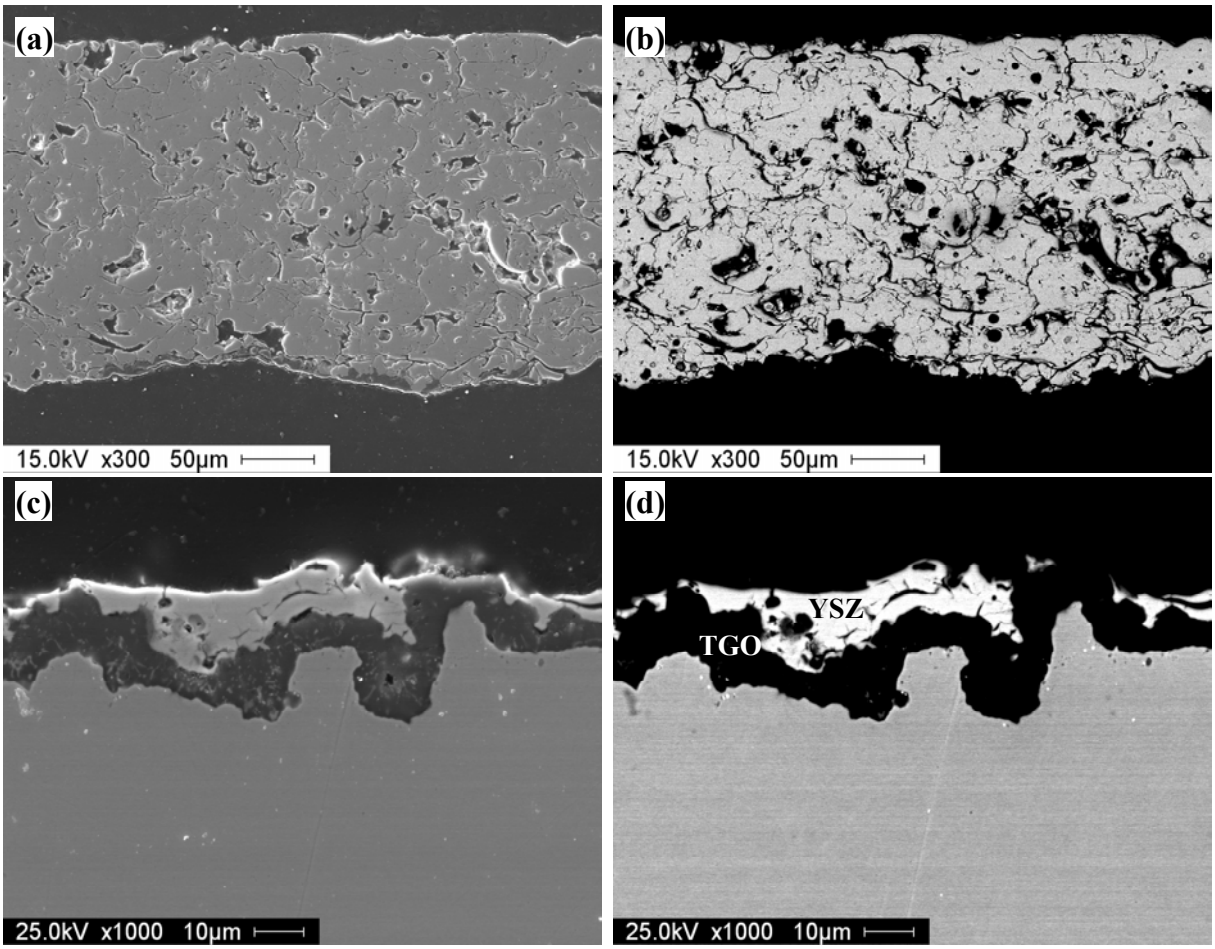

Figure 148. Cross-sectional secondary and backscatter electron micrographs of type V TBCs after spallation: (a,b) spalled-YSZ coating and (c,d) bond coat after YSZ spallation.

V.4.6. Characterization of Failure for Electron Beam Physical Vapor Deposited Thermal Barrier Coatings for 1-hour thermal cycling

Figure 149 represents backscatter electron micrographs of spallation surfaces for type II (350µm-thick) EB-PVD TBCs with NiCoCrAlY bond coat. This TBC type had an average lifetime of 280 1-hour cycles. Microscopic constituents of YSZ and TGO were observed on both bottom of the spalled-YSZ in Figure 149(a,b) and top of the bond coat surface where YSZ coating has spalled off in Figure 149(c,d). Small amount of metallic surface of NiCoCrAlY bond coats was observed. These micrographs indicate that the spallation of type II TBCs occurred within the YSZ, at the interface between YSZ and TGO, within the TGO and at the interface between TGO and bond coat. Most of the TGO were observed as islands and contained Al, Ni, Co and Cr. Cross-sectional secondary electron micrographs demonstrate that an internal oxidation of the bond coat occurred as presented in Figure 150. Cross-sectional bright-field images from TEM presented in Figure 151 also indicated that the TGO was still in-tact with NiCoCrAlY bond coat, and oxides containing Y_2O_3 were also observed.

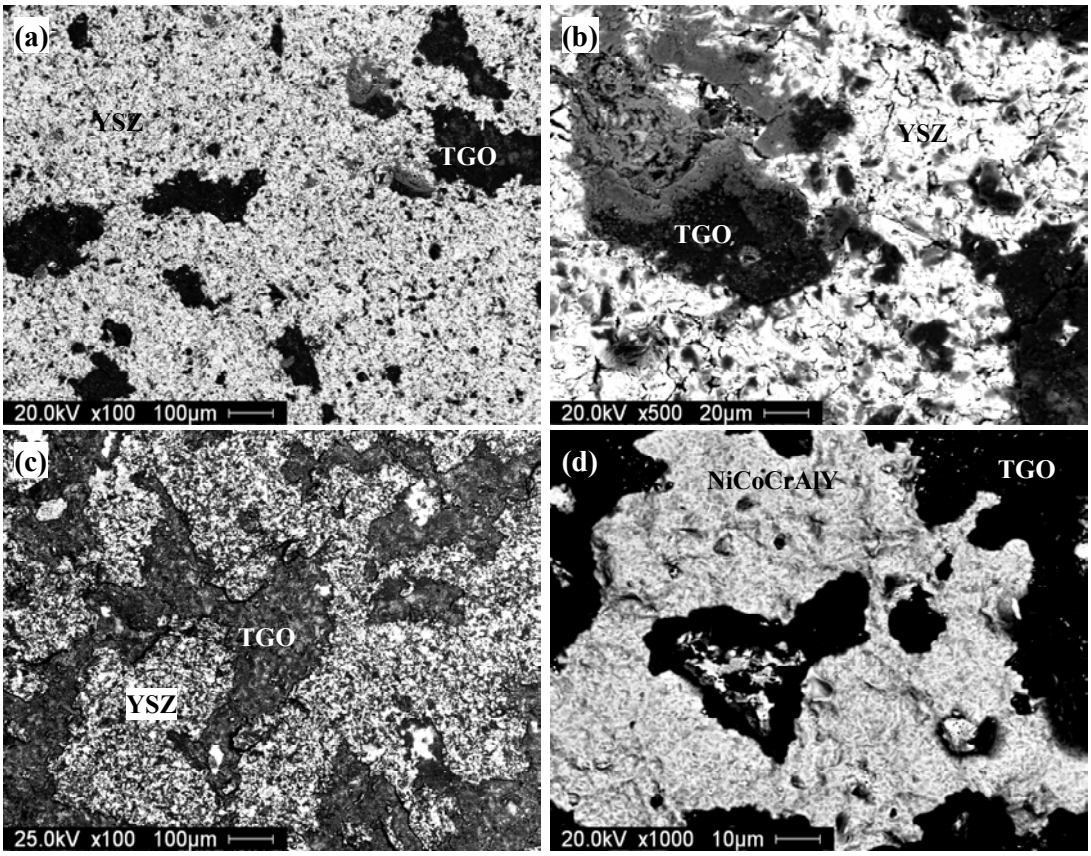

Figure 149. Backscatter electron micrographs of fracture surfaces in type II TBCs: (a,b) bottom of the spalled-YSZ coating and (c,d) top of the bond coat where YSZ coating has spalled off.

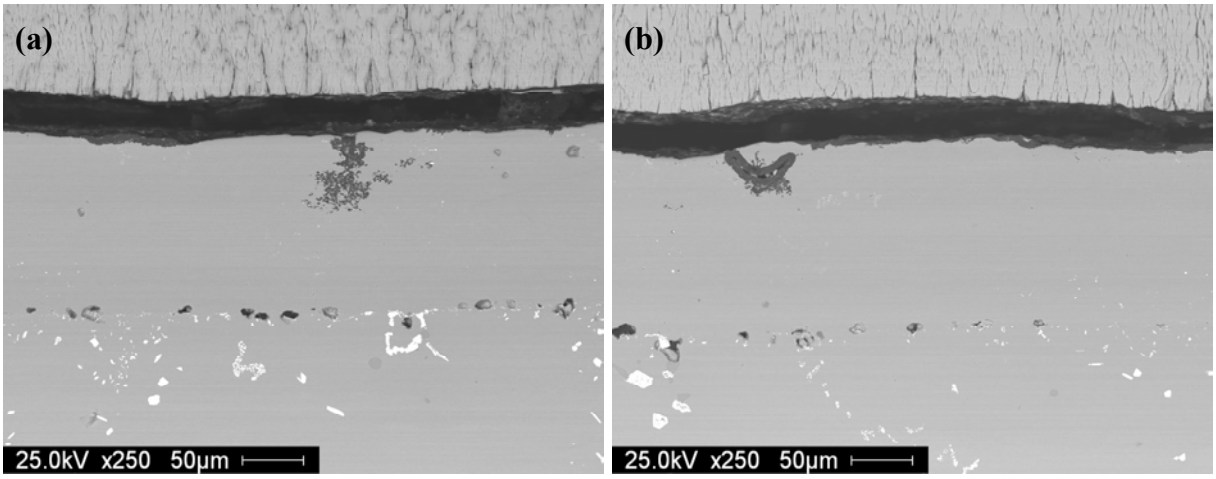

Figure 150. Cross-sectional secondary electron micrographs of type II TBCs after spallation showing the internal oxidation of NiCoCrAlY bond coat.

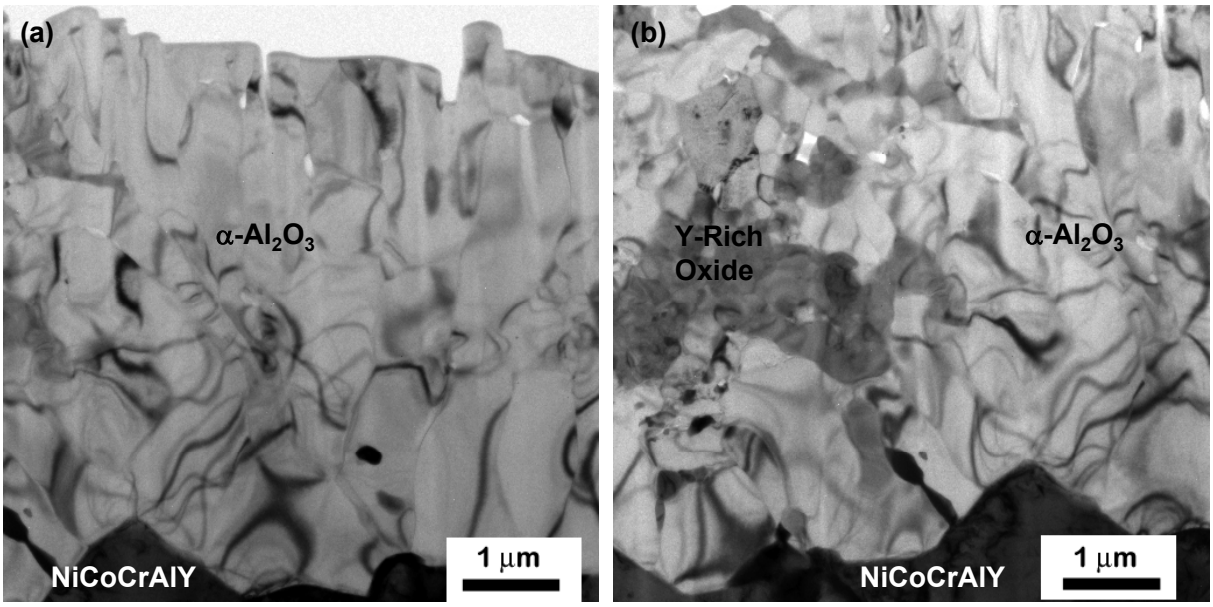

Figure 151. Cross-sectional bright field transmission electron micrographs of TGO scale on type II TBCs after failure.

Figure 152 represents backscatter electron micrograph of spallation surfaces in type III (145μm-thick) EB-PVD TBCs with as-coated (Ni,Pt)Al bond coat. This TBC type had an average lifetime of 418 1-hour cycles. Microscopic constituents of YSZ and TGO were observed on both bottom of the spalled-YSZ in Figure 152(a,b) and top of the bond coat surface where the YSZ coating has spalled off in Figure 152(c,d,e). Presence of mixed oxide zone (MOZ) and metallic surface of (Ni,Pt)Al bond coats were observed on the top surface of the bond coat. These micrographs indicate that the spallation of type III TBCs occurred within YSZ, at the interface between the YSZ and TGO including MOZ, within the TGO including MOZ and at the interface between the TGO and bond coat. With the exposure of the bond coat surface, the impedance response of the TBC specimen, shown in the Figure 60, decreased which in-turn is related to the decrease in the resistance (R_{TGO}) and a sharp increase in the capacitance (C_{TGO}) reported in Figure 75 and Figure 76. Most of the TGO observed on the fracture surface indicates the intimate relationship between grain boundary ridges of (Ni,Pt)Al bond coat.

Cross-sectional secondary electron micrographs demonstrate that a preferential oxidation of the bond coat below the ridges associated with the grain boundaries has occurred as presented in Figure 153. However, it should be noted that the crack at the asperity tip of the grain boundary ridges are not necessarily observed with the preferential oxidation of grain boundaries. Cross-sectional bright-field images from TEM presented in Figure 154 also indicated that TGO was still in-tact with (Ni,Pt)Al bond coat. Presence of MOZ was observed on the top of the TGO scale along with some voids.

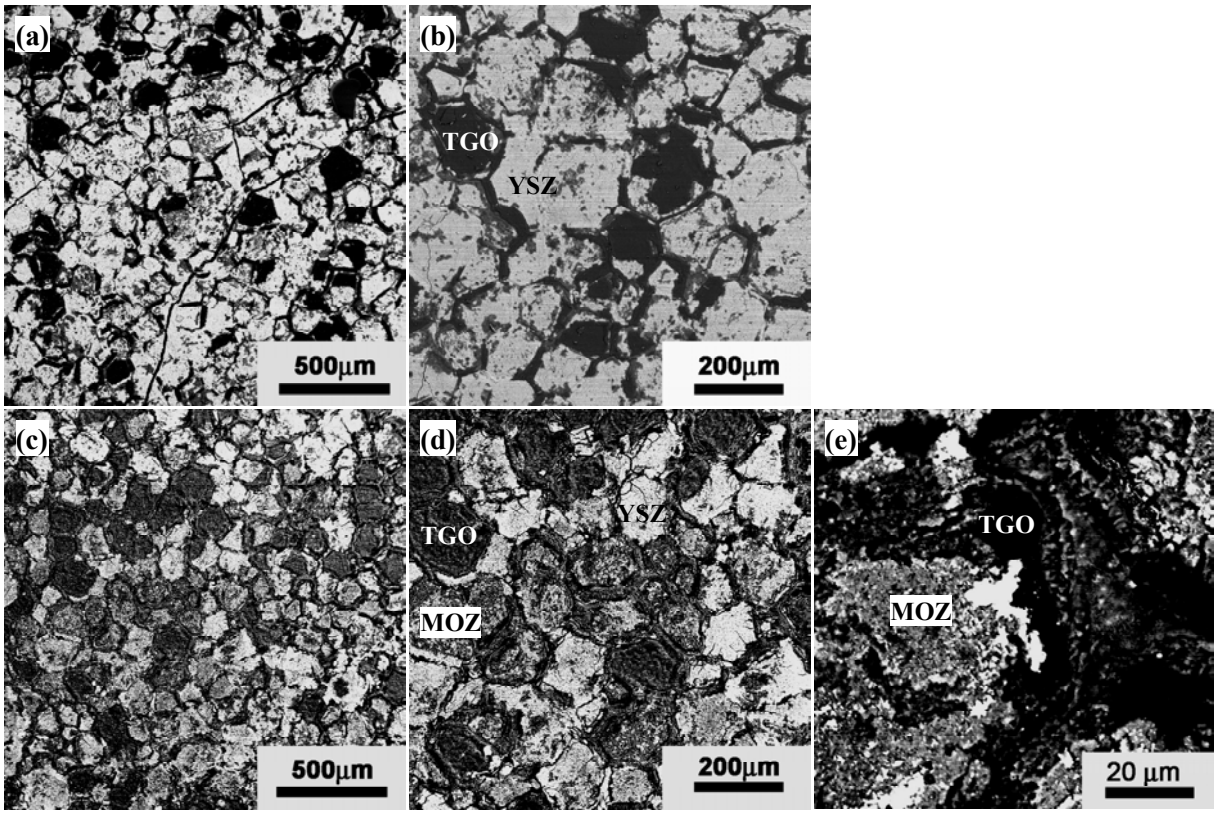

Figure 152. Backscatter electron micrographs of fracture surfaces in type III TBCs: (a,b) bottom of the spalled-YSZ coating and (c,d,e) top of the bond coat where YSZ coating has spalled off.

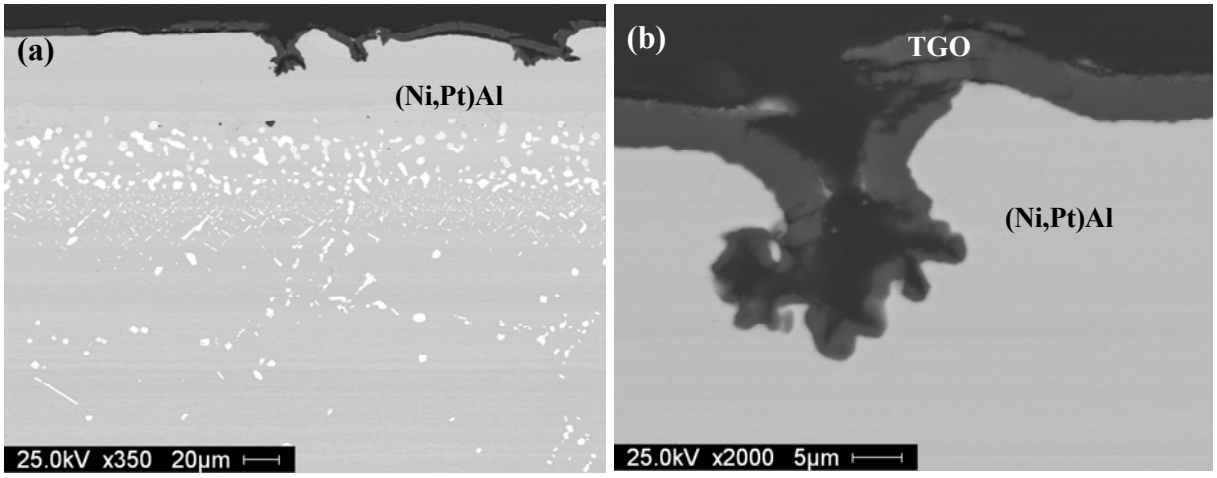

Figure 153. Cross-sectional backscatter electron micrographs of type III TBCs after spallation showing the preferential oxidation of (Ni,Pt)Al bond coat along the grain boundaries associated with ridges.

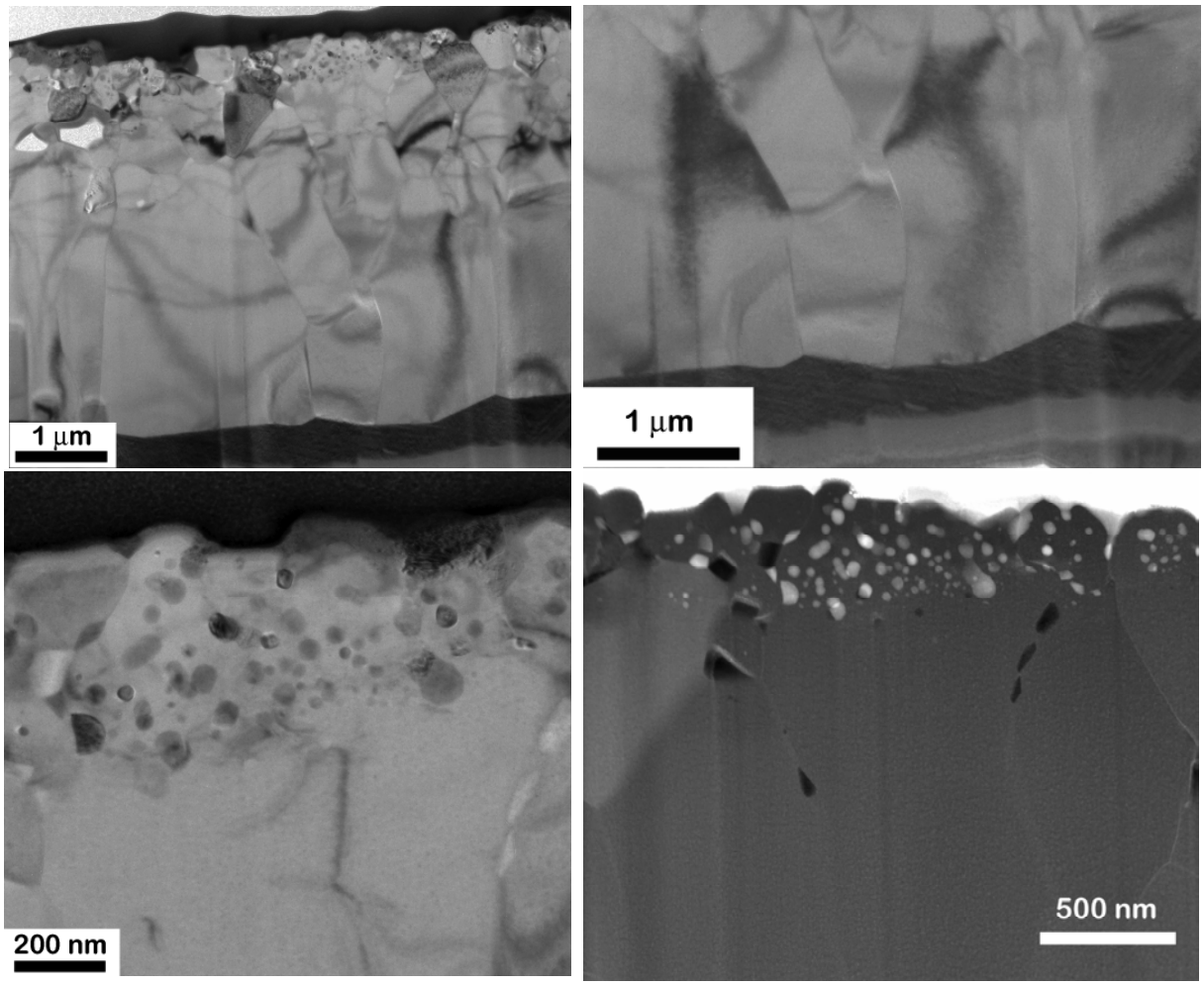

Figure 154. Cross-sectional bright field and high angle annular dark field transmission electron micrographs of TGO scale on type III TBCs after failure.

Figure 155 represents backscatter electron micrographs of spallation surfaces for type IV (140μm-thick) EB-PVD TBCs with grit-blasted (Ni,Pt)Al bond coat. This TBC type had an average lifetime of 362 1-hour cycles. Microscopic constituents of YSZ and TGO were observed on both bottom of the spalled-YSZ in Figure 155 (a,b) and top of the bond coat surface where YSZ coating has spalled off in Figure 155 (c,d). Presence of mixed oxide zone (MOZ) and metallic surface of (Ni,Pt)Al bond coats were also observed on the top surface of the bond coat. These micrographs indicate that the fracture for the spallation of type IV TBCs occurred within YSZ, at the interface between YSZ and TGO including MOZ, within TGO including MOZ and at the interface between TGO and bond coat. With the exposure of the metallic surface (bond coat) the impedance response as shown in the Figure 77 for failed specimen decreased compared to the as-coated condition. This decrease can be correlated to the electrical parameters representing the TGO namely, R_{TGO} and C_{TGO} reported in Figure 81 and 82. The resistance decreased and capacitance increased sharply at failure.

Cross-sectional secondary electron micrographs demonstrated a significant undulation of the TGO/bond coat interface (e.g., racheting) as presented in Figure 156. Cross-sectional bright-field images from TEM presented in Figure 157 also indicated that TGO was still intact with (Ni,Pt)Al bond coat. Presence of MOZ was observed on the top of the TGO scale along with some voids.

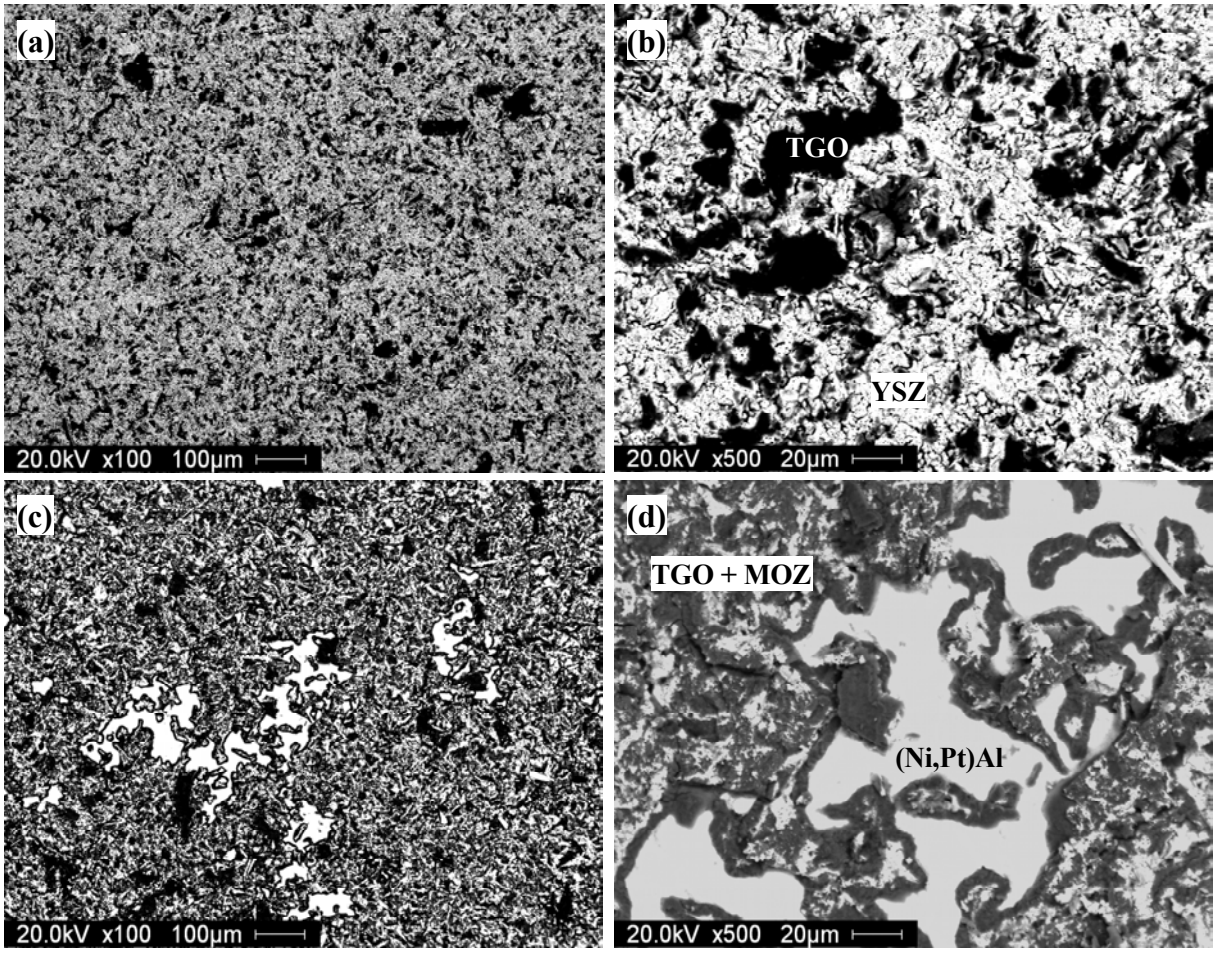

Figure 155. Backscatter electron micrographs of fracture surfaces in type IV TBCs: (a,b) bottom of the spalled-YSZ coating and (c,d) top of the bond coat where YSZ coating has spalled off.

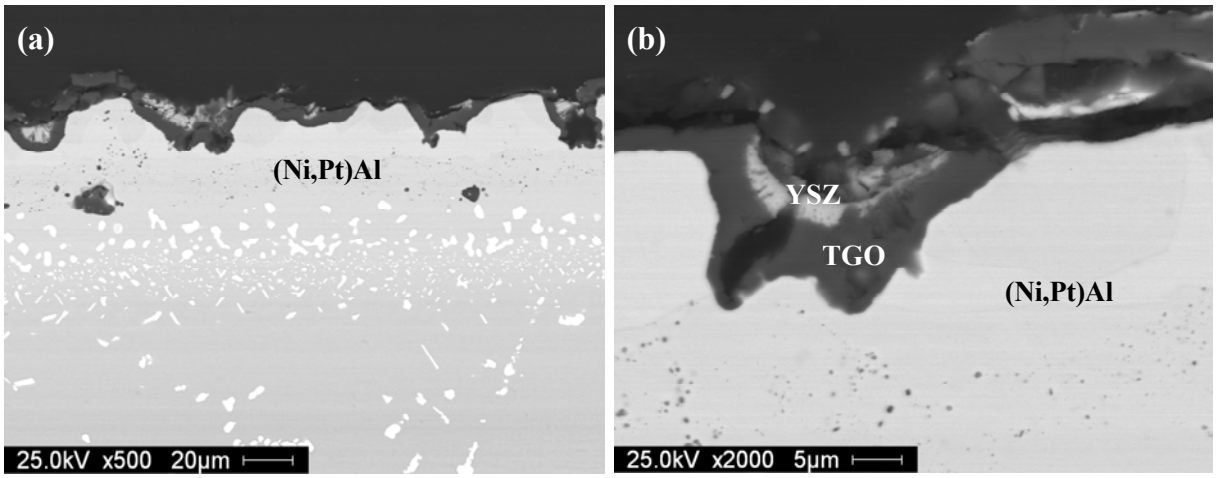

Figure 156. Cross-sectional backscatter electron micrographs of type IV TBCs after spallation showing the undulation of TGO/bond coat interface.

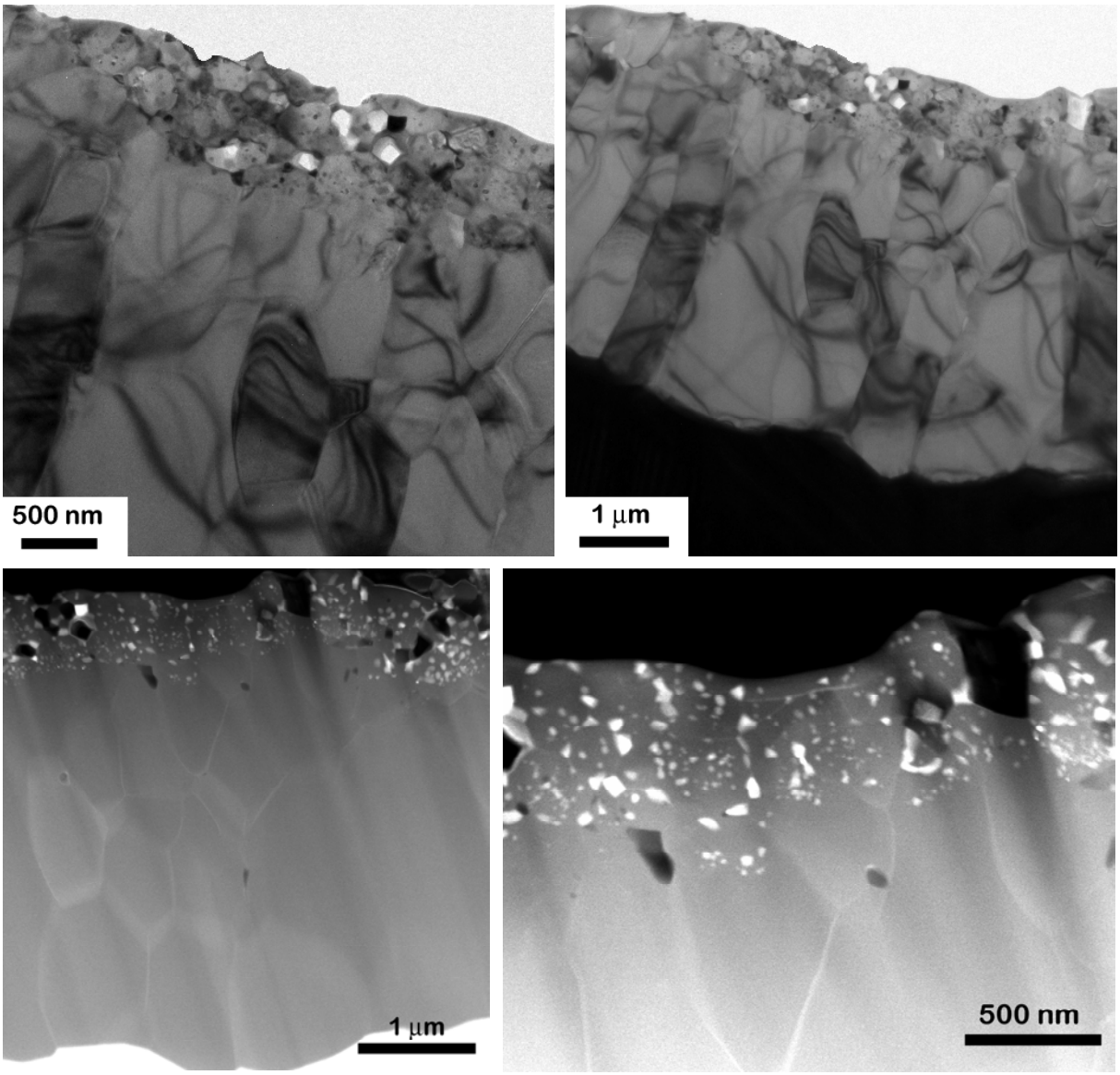

Figure 157. Cross-sectional bright field and HAADF transmission electron micrographs of TGO scale on type IV TBCs after failure.

V.4.7. Characterization of Failure for Air Plasma Sprayed Thermal Barrier Coatings for 10-hour thermal Cycling

Figure 158 represents backscatter electron micrographs of spallation of type-I APS TBCs with NiCoCrAlY bondcoat from 10-hour thermal cycling. This type of TBC had an average lifetime 113 10-hour cycles. The microscopic constituents were similar to the 1-hour thermal cycles as discussed earlier for this type of APS TBCs. Also the fracture path was similar to 1-hour thermal cycling and it occurred within YSZ near the YSZ/TGO interface. Further the cross-sectional micrographs from these coatings shown in Figure 159 showed that the micro constituents of the fracture are same as 1-hour thermal cycling.

Similar fracture was observed for type-V APS TBCs with 10-hour thermal cycling as shown in Figure 160. The average lifetime of these coatings is 18 10-hour thermal cycles. This fracture surface and path are similar to that observed for 1-hour thermal cycling as mentioned earlier in section V.4.5 and this is shown in Figure 161.

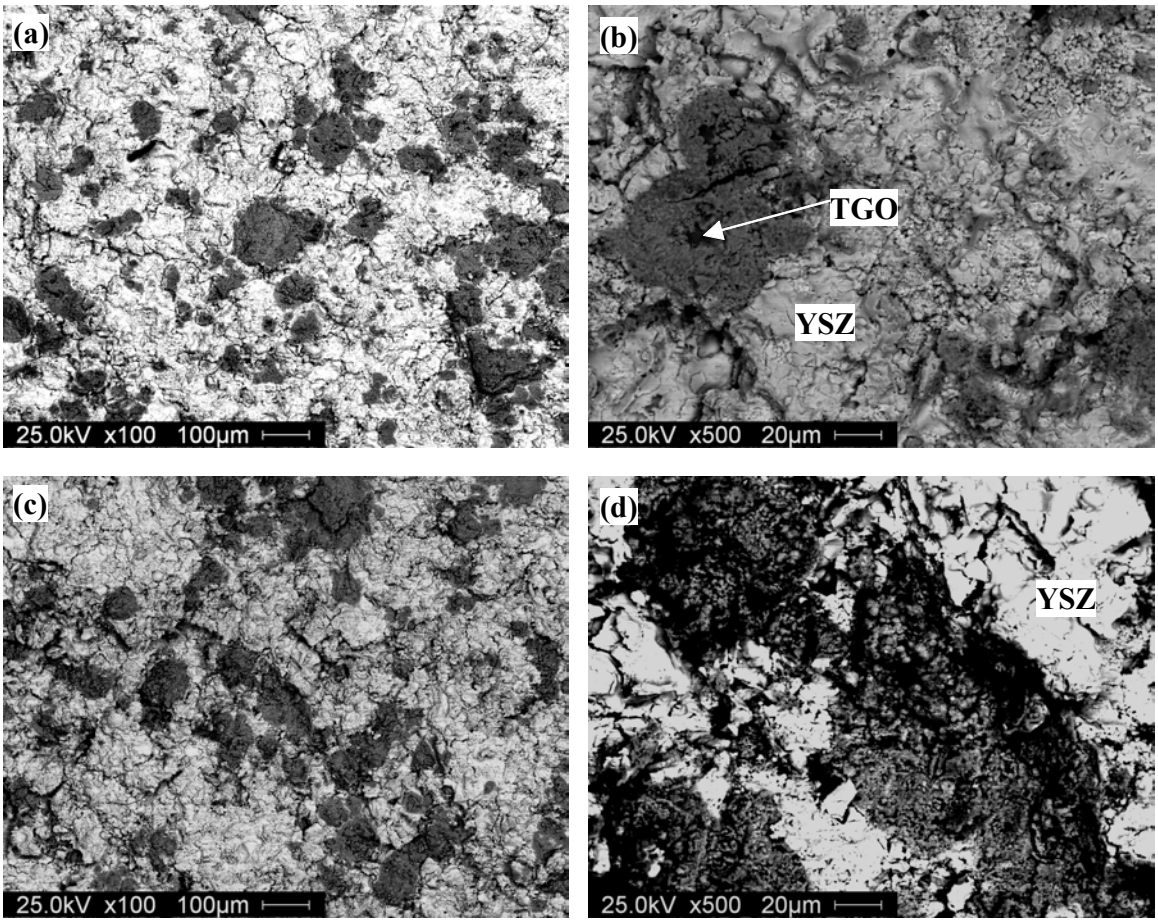

Figure 158. Backscatter electron micrographs of fracture surfaces in type-I TBCs from 10-hour thermal cycling (a,b) bottom of the spalled-YSZ coating and (c,d) top of the bondcoat where YSZ coating has spalled off. Exposure of NiCoCrAlY surface was extremely rare.

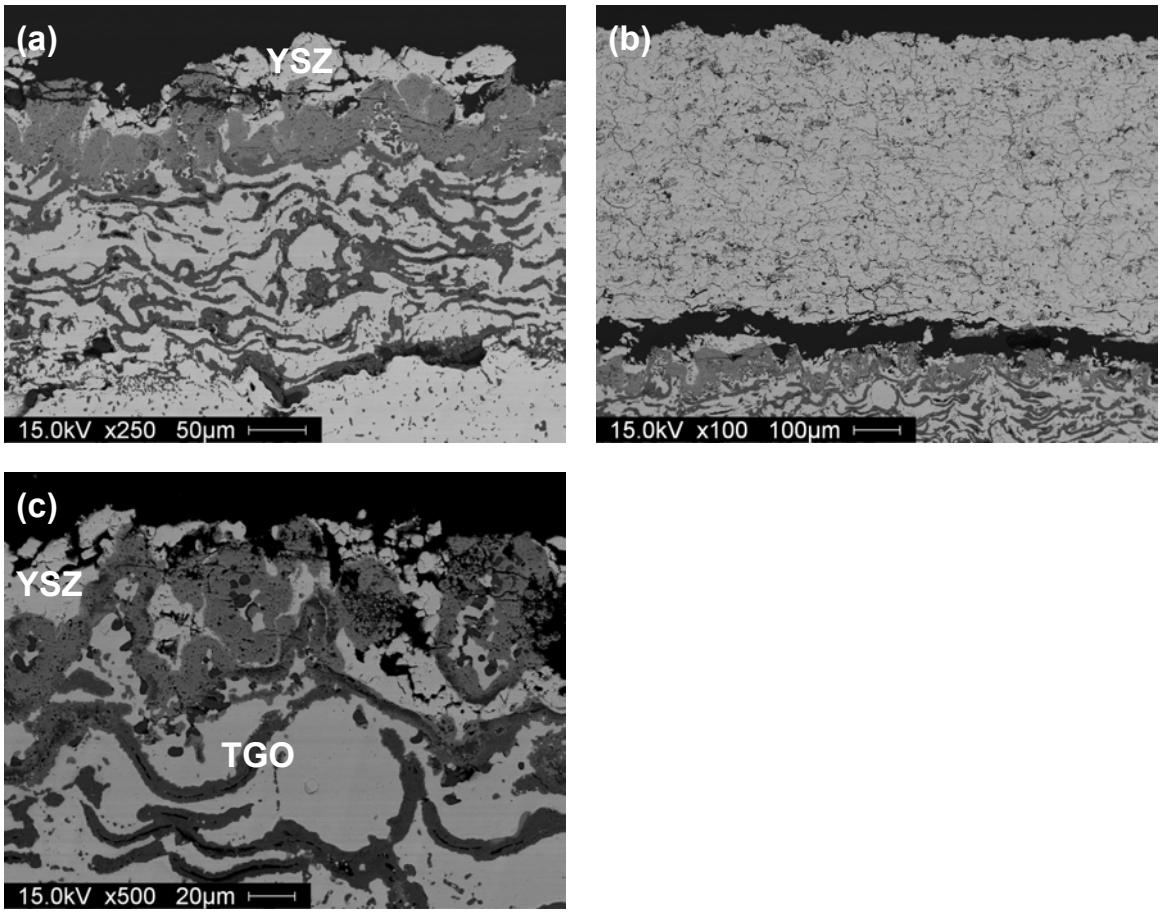

Figure 159. Cross-sectional backscatter electron micrograph of type I TBCs after spallation (a, c) bondcoat after YSZ spallation and (b) delamination at YSZ/TGO within the coating.

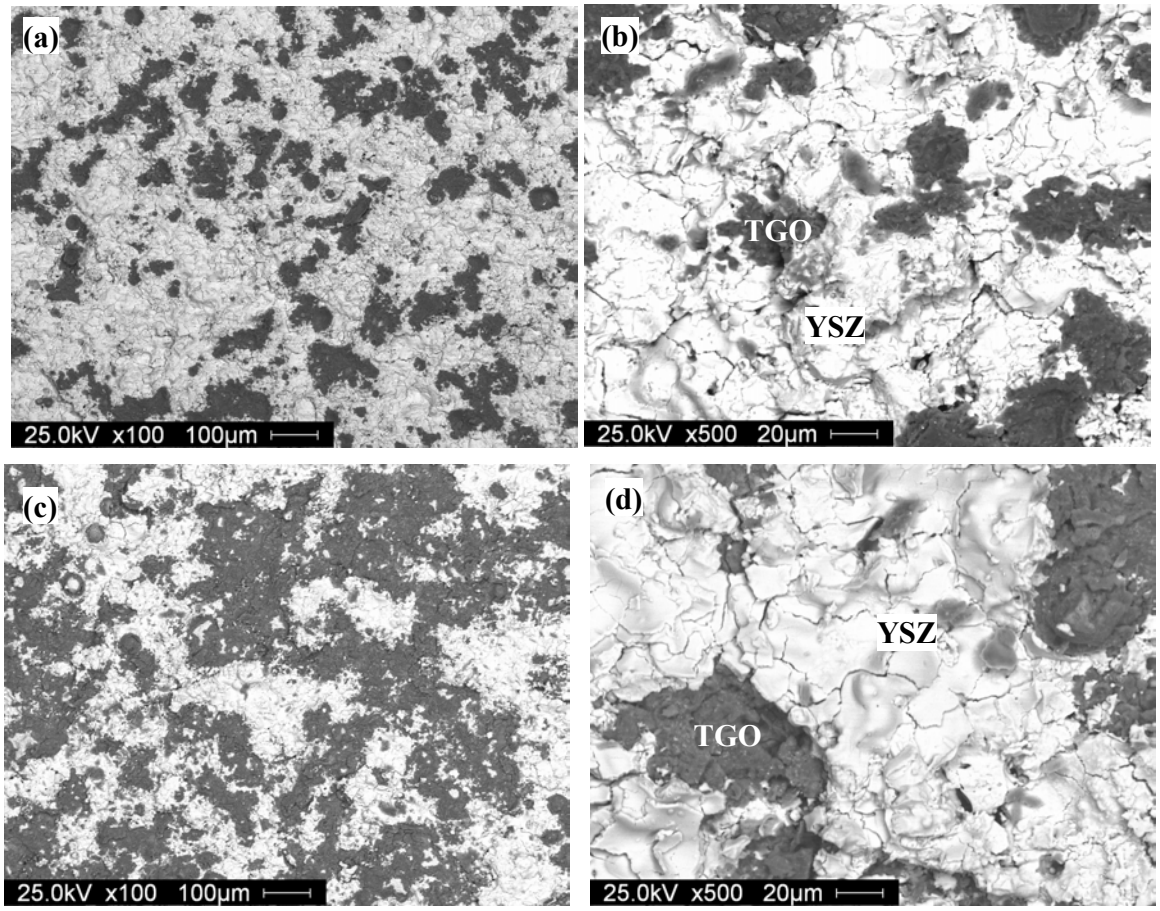

Figure 160. Backscatter electron micrographs of fracture surfaces in type-V APS TBCs from 10-hour thermal cycles (a,b) bottom of spalled YSZ coating and (c,d) top of the bondcoat where YSZ coating has spalled off. Exposure of NiCoCrAlY was extremely rare.

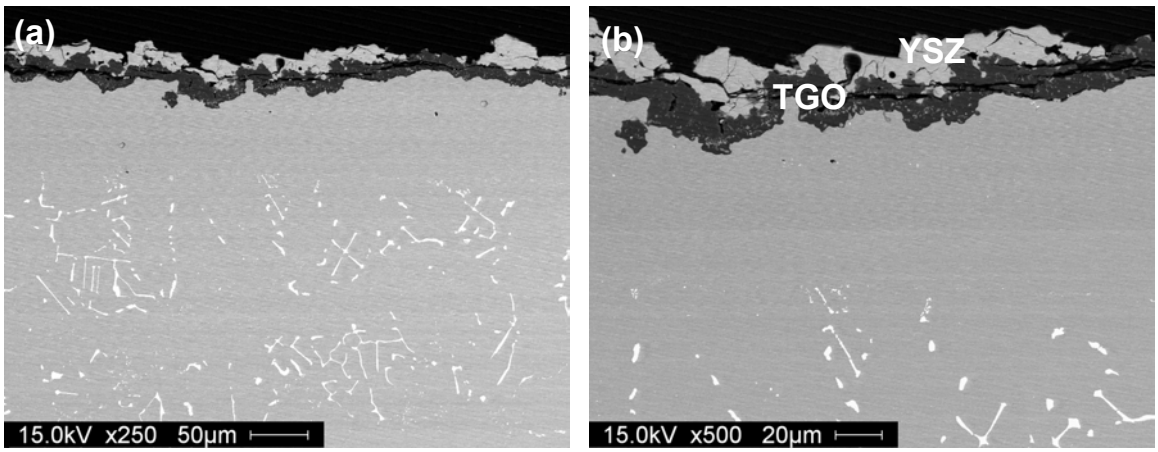

Figure 161 . Cross-sectional backscatter electron micrographs of type V TBCs after spallation: (a,b) bondcoat after YSZ spallation.

V.4.8. Characterization of Failure for EB-PVD Thermal Barrier Coatings for 10-hour thermal Cycling

Figure 162 represents backscatter electron micrographs of the spallation surfaces for type-II EB-PVD TBCs with NiCoCrAlY bondcoat from 10-hour thermal cycles. This TBC type had an average life time of 25 10-hour thermal cycles. Microscopic constituents of YSZ and TGO were observed on both bottom of the spalled-YSZ in Figure 162(a,b) and top of the bondcoat surface where YSZ coating has spalled off in Figure 162(c,d). One distinctive difference from that of TBCs failed by 1-hour thermal cycling shown in Figure 35 is that there was no exposure of the metallic NiCoCrAlY surface after spallation.

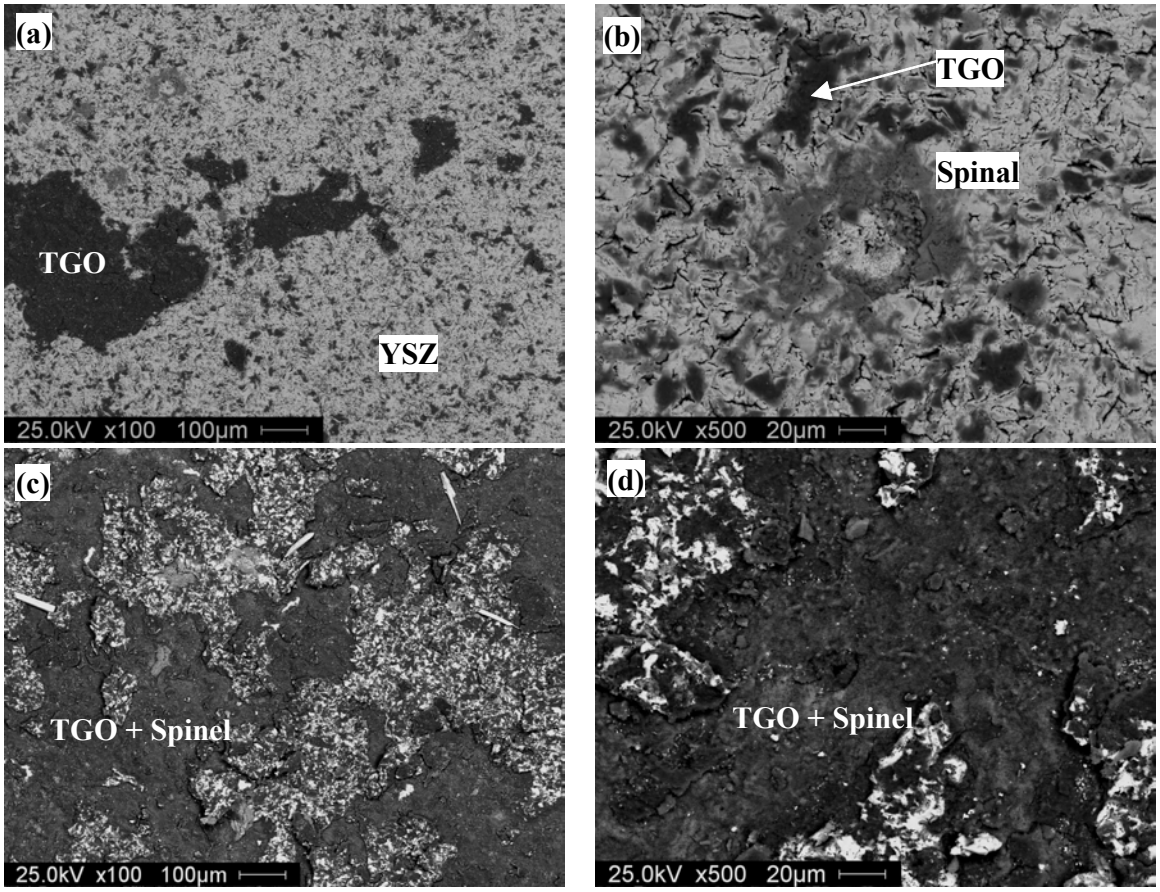

Figure 162. Backscatter electron micrographs of fracture surfaces in type II TBCs with NiCoCrAlY bondcoat (a,b) bottom of the spalled-YSZ coating and (c,d) top of the bondcoat where YSZ coating has spalled off.

Figure 163 represents backscatter electron micrographs of spallation surface of type-III EB-PVD TBCs with as-coated (Ni,Pt)Al bondcoat. This type of TBC had an average lifetime of 55 10-hour thermal cycles. Presence of extensive MOZ and metallic surface of (Ni,Pt)Al bondcoat were observed on the top surface of the bondcoat shown in 163(c,d). These micrographs indicate that the fracture for spallation of type-III TBCs occurred within

TGO including MOZ and also at the interface between TGO/bondcoat. This was different in case of 1-hour thermal cycles, were significant remains of YSZ was found on the top surface of the bondcoat. Also the cross-sectional images showed in Figure 164 shows less preferential oxidation along grain boundary associated ridges.

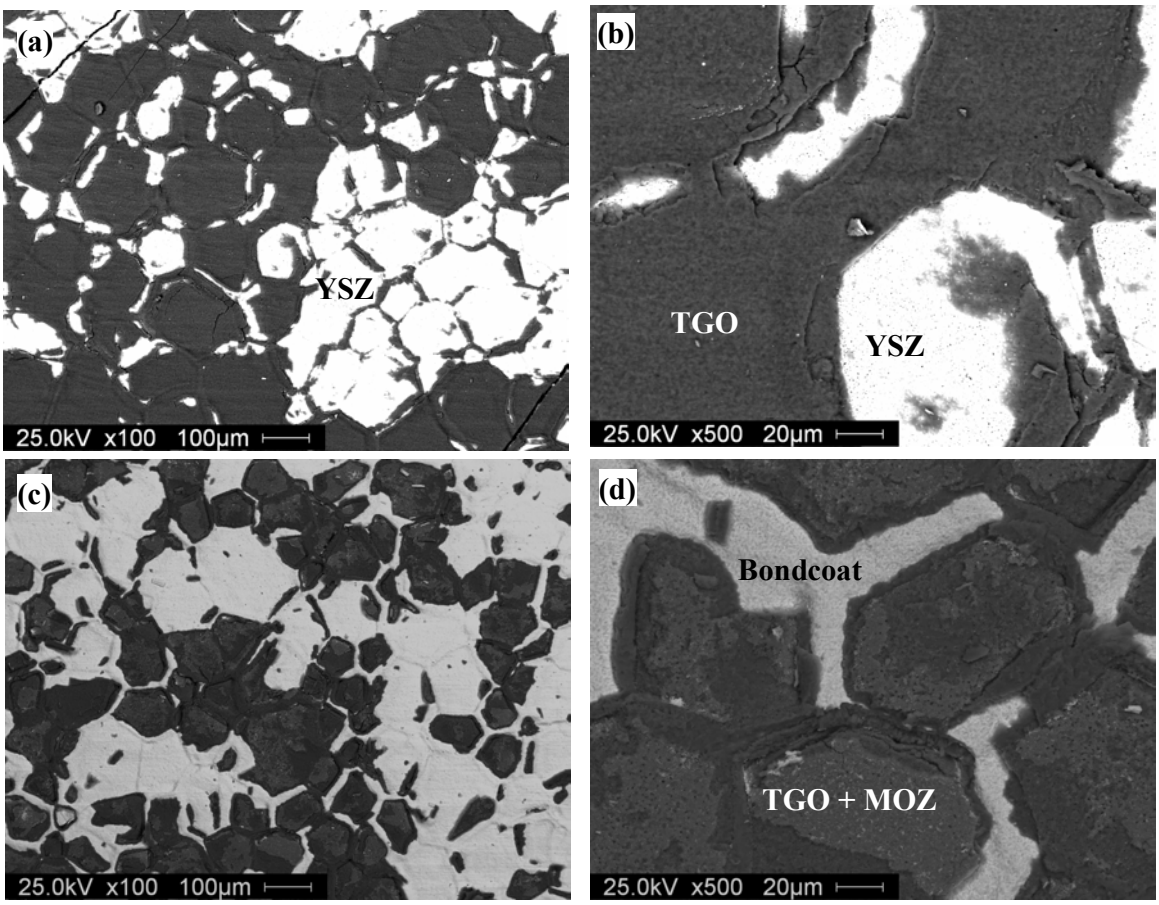

Figure 163. Backscatter electron micrographs of fracture surfaces in type III TBCs with (Ni,Pt)Al bondcoat (a,b) bottom of the spalled-YSZ coating and (c,d) top of the bondcoat where YSZ coating has spalled off.

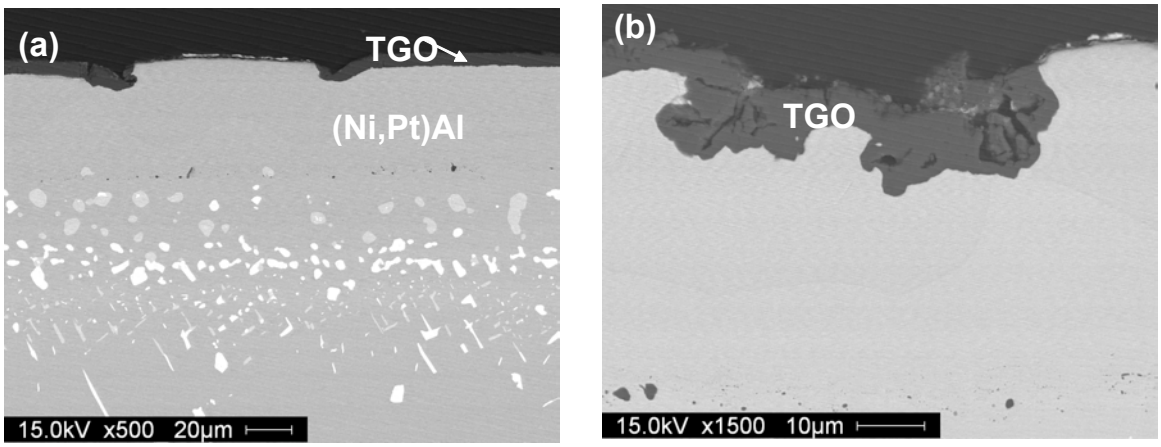

Figure 164. Cross-sectional backscatter electron micrographs of type-III TBCs after spallation showing less preferential oxidation of (Ni,Pt)Al bondcoat along grain boundaries associated with ridges.

Figure 165 represents backscatter electron micrographs of spallation surface of type-IV EB-PVD TBCs with grit-blasted (Ni,Pt)Al bondcoat. This type of TBC had an average lifetime of 42 10-hour thermal cycles. These micrographs indicate that the spallation of type IV EB-PVD TBCs with grit-blasted (Ni,Pt)Al bondcoat occurred predominantly at the TGO/bondcoat interface because the cross sectional backscatter micrograph of YSZ shown in Figure 165(c) shows that the TGO is still intact with the YSZ. Cross-sectional backscatter electron micrograph shown in Figure 165(d) demonstrates that there is minimum undulation of the TGO/bondcoat interface when compared to the racheting failure of TBCs after 1-hour thermal cycling. This mainly is due to the difference in dwell time for type IV TBCs.

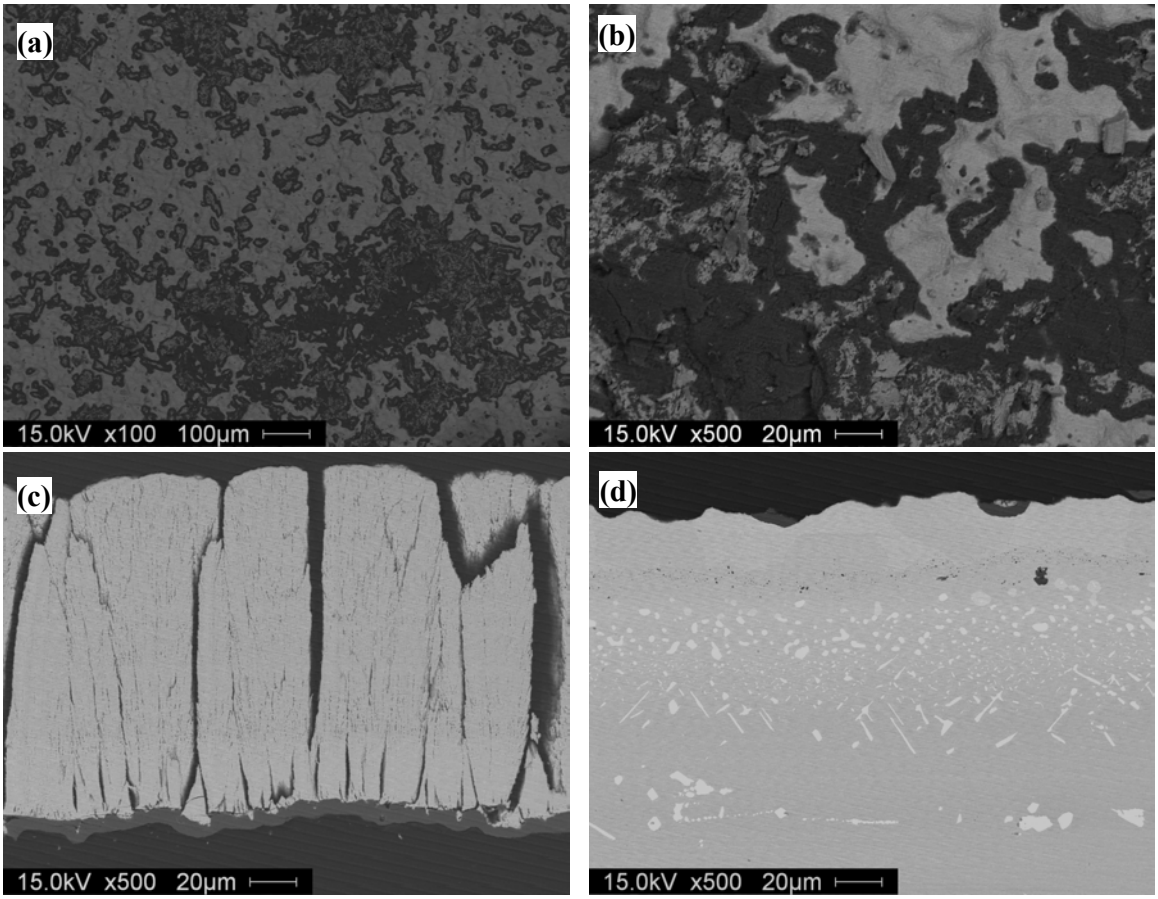

Figure 165. Backscatter electron micrographs of fracture surfaces in type IV TBCs with grit-blasted (Ni,Pt)Al bondcoat (a,b) top of the bondcoat where YSZ coating has spalled off (c) Cross section of the spalled-YSZ coating and (d) cross section of the bondcoat.

V.4.9. Characterization of Failure for APS Thermal Barrier Coatings for 50-hour thermal Cycling

Figure 166 represents backscatter electron micrographs of spallation of type-I APS TBCs with NiCoCrAlY bondcoat from 50-hour thermal cycling. This type of TBC had an average lifetime 39 50-hour cycles. The microscopic constituents were similar to the 1 and 10-hour thermal cycles as discussed earlier for this type of APS TBCs. Also the fracture path was similar to 1 and 10-hour thermal cycling and it occurred within YSZ near the YSZ/TGO interface.

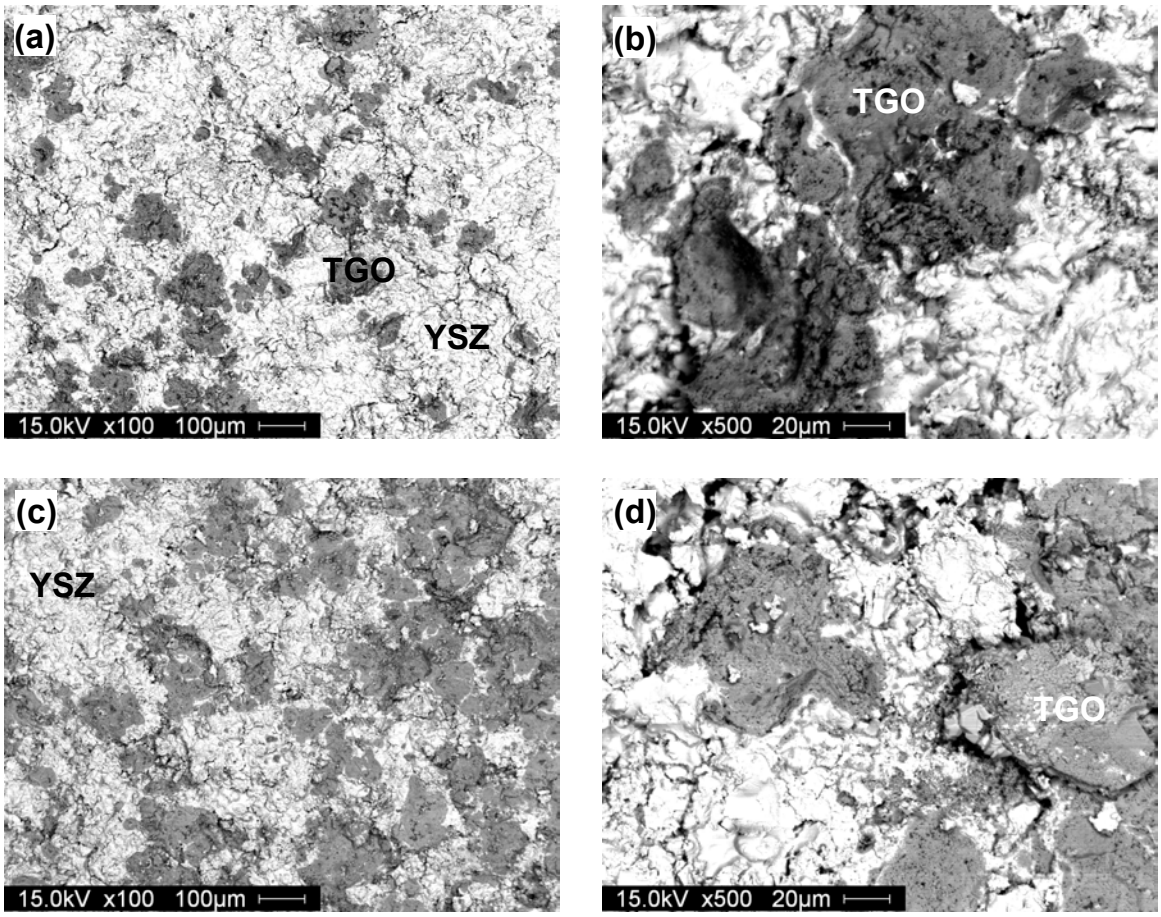

Figure 166. Backscatter electron micrographs of fracture surfaces in type-I TBCs from 50-hour thermal cycling (a,b) bottom of the spalled-YSZ coating and (c,d) top of the bondcoat where YSZ coating has spalled off. Exposure of NiCoCrAlY surface was extremely rare.

V.4.10. Characterization of Failure for EB-PVD Thermal Barrier Coatings for 50-hour thermal Cycling

Figure 167 represents backscatter electron micrographs of the spallation surfaces for type-II EB-PVD TBCs with NiCoCrAlY bondcoat from 50-hour thermal cycles. This TBC type had an average life time of 3.5 50-hour thermal cycles. Microscopic constituents of YSZ and TGO were observed on both bottom of the spalled-YSZ in Figure 167(a,b) and top of the bondcoat surface where YSZ coating has spalled off in Figure 167(c,d). One distinctive difference from that of TBCs failed from other thermal cycling is that exposure of the metallic NiCoCrAlY surface after spallation. The fracture predominantly occurred at the TGO/bondcoat interface.

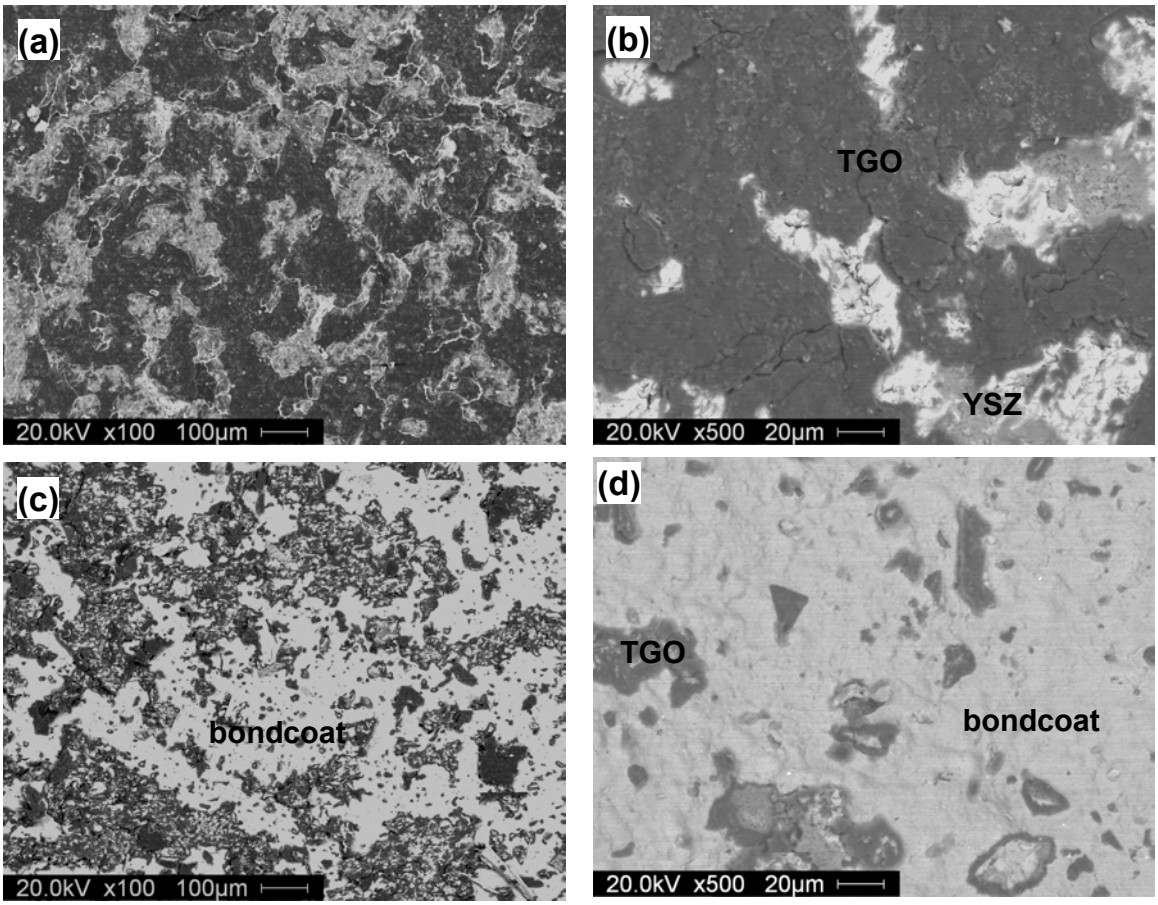

Figure 167. Backscatter electron micrographs of fracture surfaces in type-II TBCs from 50-hour thermal cycling (a,b) bottom of the spalled-YSZ coating and (c,d) top of the bondcoat where YSZ coating has spalled off.

Figure 168 represents backscatter electron micrographs of spallation surface of type-III EB-PVD TBCs with as-coated (Ni,Pt)Al bondcoat. This type of TBC had an average lifetime of 12 50-hour thermal cycles. Presence of MOZ and metallic surface of (Ni,Pt)Al bondcoat were observed on the top surface of the bondcoat shown in 168(a,b). These micrographs indicate that the fracture for spallation of type-III TBCs occurred at TGO/bondcoat interface including MOZ. This was different in case of 1-hour thermal cycles, were significant remains of YSZ was found on the top surface of the bondcoat. Also the cross-sectional images showed in Figure 169 shows less preferential oxidation along grain boundary associated ridges.

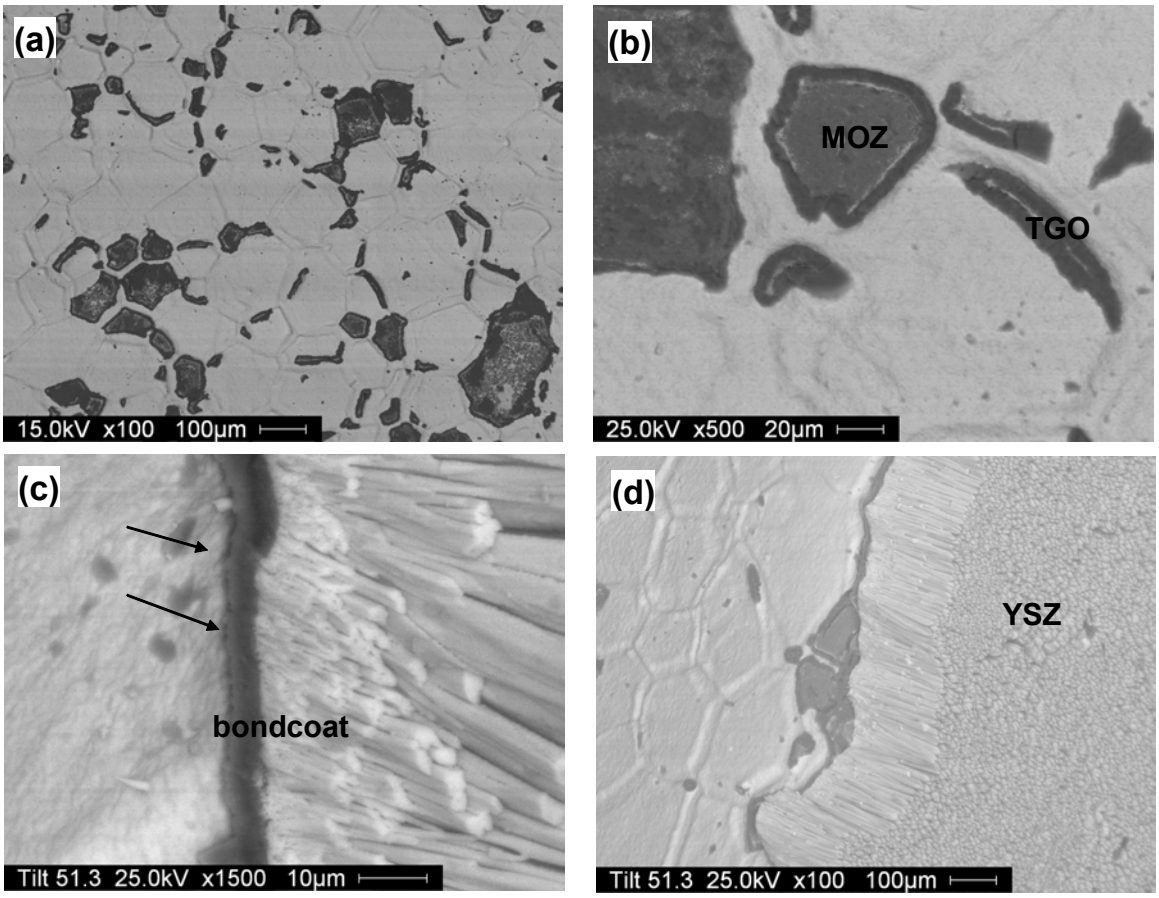

Figure 168. Backscatter electron micrographs of fracture surfaces in type III TBCs with (Ni,Pt)Al bondcoat (a,b) top of the bondcoat where YSZ coating has spalled off (c,d) delamination at TGO/bondcoat interface shown in arrows.

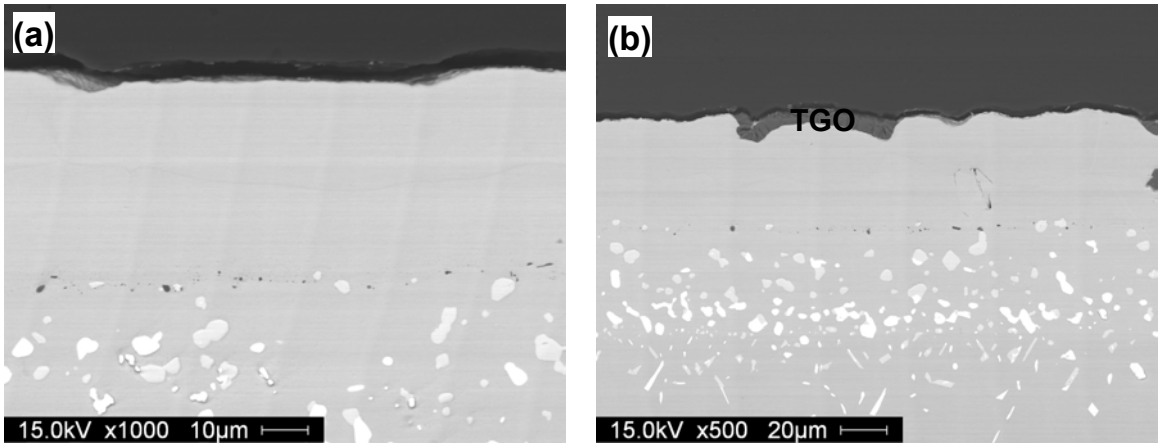

Figure 169. Cross-sectional backscatter electron micrographs of type-III TBCs after spallation showing less preferential oxidation of (Ni,Pt)Al bondcoat along grain boundaries associated with ridges.

Figure 170 represents backscatter electron micrographs of spallation surface of type-IV EB-PVD TBCs with grit-blasted (Ni,Pt)Al bondcoat. This type of TBC had an average lifetime of 9.5 50-hour thermal cycles. These micrographs indicate that the spallation of type IV EB-PVD TBCs with grit-blasted (Ni,Pt)Al bondcoat occurred predominantly at the TGO/bondcoat interface because the cross sectional backscatter micrograph of YSZ shown in Figure 170(b) shows that the TGO is still intact with the YSZ. Cross-sectional backscatter electron micrograph shown in Figure 170(c) demonstrates that there is minimum undulation of the TGO/bondcoat interface when compared to the racheting failure of TBCs after 1-hour thermal cycling. This mainly is due to the difference in dwell time for type IV TBCs.

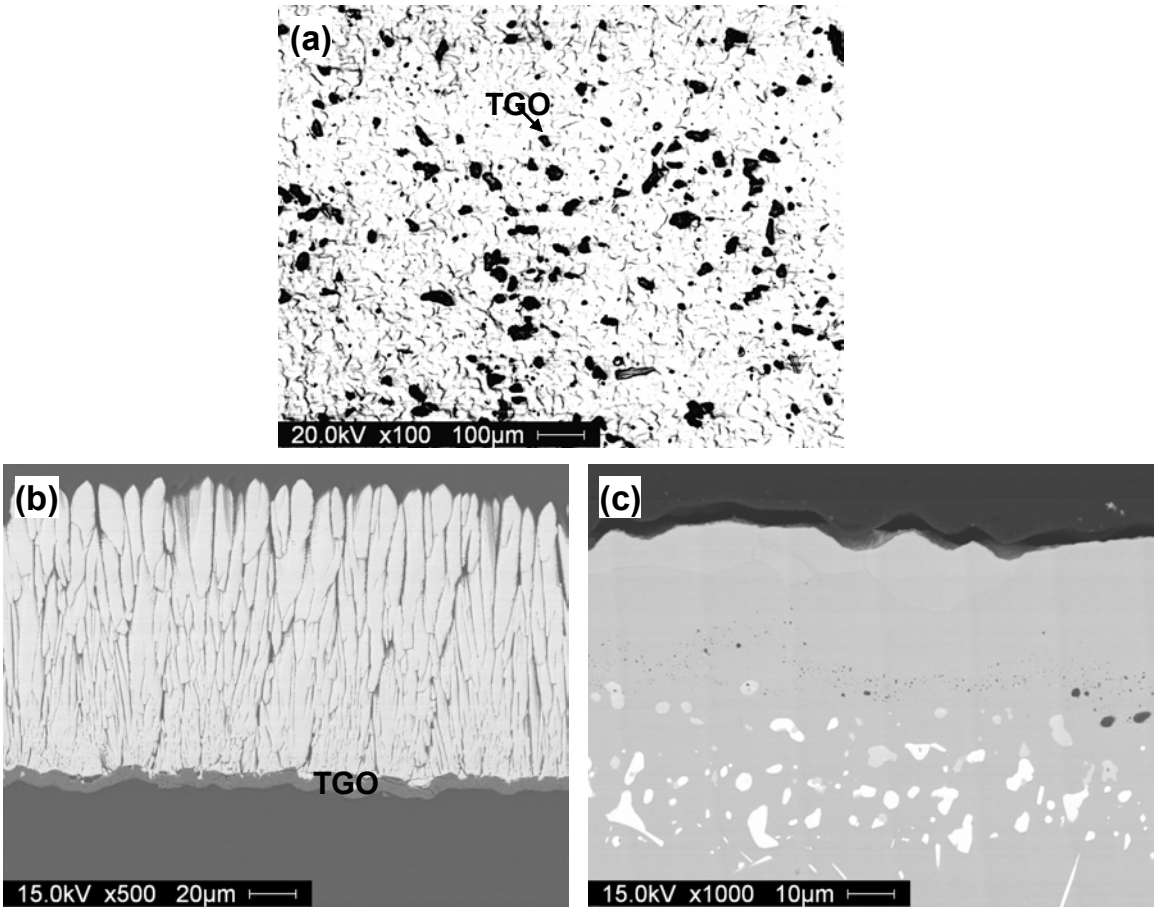

Figure 170. Backscatter electron micrographs of fracture surfaces in type IV TBCs with grit-blasted (Ni,Pt)Al bondcoat (a) top of the bondcoat where YSZ coating has spalled off (b) Cross section of the spalled-YSZ coating and (c) cross section of the bondcoat.

VI. CONCLUSION

Failure characteristics and mechanisms for five types of commercial production TBCs were investigated by using two complimentary NDE techniques PSLS and EIS. In addition, microstructural analysis of TBCs is carried out at atomic-micro-macro levels using a variety of characterization techniques including TEM/STEM with site-specific specimen preparation by FIB-INLO. The results of NDE and microstructural analysis were correlated to provide a clearer understanding of the failure mechanisms in TBCs, and further development/refinement of NDE techniques.

During thermal cycling, TBC specimens are being non-destructively examined by PSLS and EIS. For type III EB-PVD TBCs, a photostimulated luminescence associated with stress-relief of the TGO scale was observed prior to the final spallation. Correspondingly, micro-cracking associated with ridges on the (Ni,Pt)Al bond coat was observed via microscopy. For type IV TBCs, a stress-relaxation associated with racheting of the TGO/bondcoat interface towards complete relief was observed as a function of 1-hour thermal cycling. However, this observation related to racheting was not observed during 10- and 50-hour thermal cycling. Analyzing EIS results with TBCs and other selected experiments has demonstrated potentials to monitor several microstructural changes that occur in TBCs during thermal cycling. These include sintering of YSZ, growth of TGO scale, sub-critical damage in TBCs prior to failure.

Findings of this program have been published in 9 refereed journal publications (additional 3 in preparation/submitted) and 8 refereed conference proceedings, as well as 4 invited presentations (additional 3 invited), 25 presentations (additional 3 to be presented). This program fully and partially supported following graduate and undergraduate as research assistants. Mr. Balaji Jayaraj earned his M.S. and will be granted his Ph.D. in materials science and engineering. He is a recipient of UCF's Most Outstanding M.S. Thesis of 2003, and will be employeed at (March, 2006) Mitsubishi Power Systems, Orlando, FL. Ms. Barbara Franke, Now with Solar Turbines Incorporated, San Diego, CA, earned her B.S. and M.S. in materials science and engineering with honors such as Honeywell Leadership Scholarship, 2003 and 2004 UTSR Fellow, UTSR undergraduate research assistant prior to her graduate work. Through undergraduate research assitantship, Mr. Christopher Petorak earned his B.S. in mechanical engineering and is now at Purdue University for Ph.D. in materials science and engineering working on doctoral dissertation involving stress relaxation of APS TBCs. Mr. Travis Patterson was another undergraduate research assistant who just received his B.S. in mechanical engineering with 2005 UTSR Fellowship. Mr. Patterson will pursue his Ph.D. in materials science and engineering at University of Central Florida starting Fall, 2006.

REFERENCES

1. R.A. Miller, *J. Am. Ceram. Soc*., 67 (1984) 517.
2. A.G. Evans, D.R. Mumm, J.W. Hutchison, G.H. Meier, F.S. Pettit, *Prog. Mater. Sci.*, 46 (2000) 505.
3. N.P. Padture, E.H. Jordan, M. Gell, *Science*, 296 (2002) 280.
4. P.K. Wright, *Current Opinions in Solid State Mater. Sci*., 4 (1999) 255.
5. R.D. Sisson, Jr., E.Y. Lee and Y.H. Sohn, Proc. PRICM-II, (1995) 1203.
6. M.J. Graham, J.I. Eldridge, D.F. Mitchell, R.J. Hussey, *Mater. Sci. Forum*, 43 (1989) 207.
7. L. Onsager, *Ann. NY Acad. Sci*., 46 (1965) 241.
8. E.Y. Lee, R.R. Biederman, R.D. Sisson, Jr., *Micro. Sci*., 7 (1991) 505.
9. D.M. Lipkin, D.R. Clarke, *Oxi. Met*., 45 (1996) 267.
10. L.A. Giannuzzi, F.A. Stevie, *Micron*, 30 (1999) 197.
11. Y.H. Sohn, B.W. Kempshall, S.K. Jha, R.R. Vanfleet, J. Kimmel, *Thin Solid Films*., Submitted, 2003.
12. Q. Ma, D.R. Clarke, *J. Am. Ceram. Soc*., 76 (1993) 1433.
13. Q. Ma, D.R. Clarke, *J. Am. Ceram. Soc*., 77 (1994) 298.
14. J.R. Christensen, D.M. Lipkin, D.R. Clarke, K. Murphy, *Appl. Phys. Lett*., 69 (1996) 3745.
15. V. Sergo, D.R. Clarke, *J. Am. Ceram. Soc*., 81 (1998) 3237.
16. D.R. Clarke, J.R. Christensen, V. Tolpygo, *Surf. Coat. Technol*., 94/95 (1997) 89.
17. Y.H. Sohn, K. Vaidyanathan, M. Ronski, E.H. Jordan, M. Gell, *Surf. Coat. Technol.*, 146/147 (2001) 102.
18. Y.H. Sohn, K. Schlichting, K. Vaidyanathan, E.H. Jordan, M. Gell, *Metall. Mater. Trans. A*, 31A (2000) 2388.
19. M. Gell, E. Jordan, K. Vaidyanathan, *Surf. Coat. Technol*., 120/121 (1999) 53.
20. Q. Wen, D.M. Lipkin, D.R. Clarke, *J. Am. Ceram. Soc*., 81 (1998) 3345.
21. A.L. Schawlow, D.L. Wood, A.M. Clogston, *Phys. Rev. Lett*., 3 (1959) 271.
22. K.W. Schlitchting, K. Vaidyanathan, Y.H. Sohn, E.H. Jordan, M. Gell, N.P. Padture, *Mater. Sci. Eng. A*, A291 (2000) 68.
23. V.H. Desai, "Development of Electrochemical Impedance Spectroscopy for Non-Destructive Evaluation of Thermal Barrier Coatings," Final Report for AGTSR No. 98-01-SR067, 2001.
24. J. Zhang, "Development of Electrochemical Impedance Spectroscopy for Non-Destructive Evaluation of Thermal Barrier Coatings," Ph.D. Dissertation, The University of Central Florida, 2001.
25. B. Jayaraj, V.H. Desai, C.K. Lee, Y.H. Sohn, *Materi. Sci. Eng. A*., 372 (2004) 278.
26. B. Jayaraj, S. Vishweswaraiah, V.H. Desai, Y.H. Sohn, *Surf. Coat. Technol*., 177 (2004) 140.
27. S. Vishweswaraiah, B. Jayaraj, Y.H. Sohn, T. Du, V.H. Desai, Proc. 2003 International Thermal Spray Conferences, Proc. 2003 International Thermal Spray Conference and Exposition (2003) 1487.
28. L.A. Giannuzzi, J.L. Brown, S.R. Brown, R.B. Irwin, F.A. Stevie, *Mat. Res. Soc. Symp. Proc.*, 480 (1997) 19.
29. H.C. Chen, J. Heberlein, E. Pfender, *Thin Solid Films*, 301 (1997) 105.

30. A.H. Carim, T.A. Dobbins, L.A. Giannuzzi, D.R. Arenas, D.A. Koss, M.J. Mayo, *Mater. Sci. Eng. A*, A334 (2002) 65.
31. O. Unal, T.E. Mitchell, A.H. Heuer, *J. Am. Ceram. Soc*., 77 (1994) 984.
32. K.S. Murphy, K.L. More, M.J. Lance, *Surf. Coat. Technol*., 146/147 (2001) 152.
33. K. Fritscher, M. Schumuecker, C. Leyens, U. Schulz, *Mater. Sci. Forum*, 251/254 (1997) 965.
34. U. Schulz, M. Menzebach, C. Leyens, Y.Q. Yang, *Surf. Coat. Technol*., 146/147 (2001) 117.

LIST OF IMPORTANT ACRONYMS AND SYMBOLS

Acronyms	Description
(Ni,Pt)Al	Pt-modified nickel aluminide
7YSZ	7wt.% yttria stabilized zirconia
AES	Auger electron spectroscopy (or spectroscope)
AMPAC	Advanced materials processing and analysis center
APS	Air plasma spray (or sprayed)
CBED	Convergent beam electron diffraction
CVD	Chemical vapor deposition (or deposited)
CE	Counter electrode
EB-PVD	Electron beam physical vapor deposition (or deposited)
EDS	Energy dispersive spectroscopy (or spectroscope)
EELS	Electron energy loss spectroscopy (or spectroscope)
eFIB	Ex-situ focused ion beam
EIS	Electrochemical impedance spectroscopy (or spectroscope)
FE-EDS	Field emission scanning electron microscopy (or microscope)
FFT	Fast Fourier transformation (or transformed)
FIB	Focused ion beam
HAADF	High angle annular dark field
HEET	High efficiency engines and turbines
HR-STEM	High resolution scanning transmission electron microscopy (or microscope)
iFIB	In-situ focused ion beam
LPPS	Low pressure plasma spray (or sprayed)
NDE	Non-destructive evaluation
n-EDS	Nano-spot energy dispersive spectroscopy (or spectroscope)
NiAl	Nickel aluminide
OM	Optical microscopy (or microscope)
PSLS	Photostimulated luminescence spectroscopy (or spectroscope)
RAM	Reliability, availability and maintainability
RBS	Rutherford backscatter spectroscopy (or spectroscope)
SAD	Selected area diffraction
STEM	Scanning transmission electron microscopy (or microscope)
TBC	Thermal barrier coating
TGO	Thermally grown oxide
UCF	University of central Florida
UTSR	University turbine systems research
WE	Working electrode
XPS	X-ray photoluminescence spectroscopy (or spectroscope)
XRD	X-ray diffraction
YSZ	Yttria stabilized zirconia

LIST OF IMPORTANT ACRONYMS AND SYMBOLS (Continued)

Symbols	Description
α-Al_2O_3	Equilibrium Al_2O_3 with monoclinic structure
α_D	Dundur's parameter
a_i	Thermodynamic activity of component *i*
a_o	Linear thermal expansion coefficient
β	Nickel aluminde solid solution with B_2 crystal structure
C_{YSZ}	Electrochemical capacitance of ceramic top coat
C_{TGO}	Electrochemical capacitance of thermally grown oxide
C_{PORE}	Electrochemical pore capacitance
C_T	Electrochemical capacitance of interface transmittance
Δ	Change in; Difference in
$\widetilde{D}_i$	Interdiffusion coefficient in binary system
$\widetilde{D}_{ij}^{n}$	Multicomponent interdiffusion coefficient
$\partial C_i / \partial x$	Concentration gradient of component *i*
δ_i	Stoichiometric deviation at interface *i*
ε	strain
E_o	Young's modulus
G	Luminescence from γ-Al_2O_3
γ-Al_2O_3	Metastable Al_2O_3 with complex cubic structure
γ_i	Thermodynamic activity coefficient of component *i*
I_i	Integrated intensity of luminescence
$\widetilde{J}_i$	Interdiffusion flux of component *i*
k_p	Parabolic oxide growth constant
%LT	Percent thermal cyclic life time
N	Luminescence from α-Al_2O_3 with a significant amount of chromia
Π	Piezospectroscopic coefficients
Q	Luminescence from θ-Al_2O_3
θ-Al_2O_3	Equilibrium Al_2O_3 with hexagonal structure
R	Luminescence from α-Al_2O_3; Ruby fluorescence doublet
R_{YSZ}	Electrochemical resistance of ceramic top coat
R_{TGO}	Electrochemical resistance of thermally grown oxide
R_{PORE}	Electrochemical pore resistance
R_S	Electrolyte solution resistance
R_T	Electrochemical resistance of interface transmittance
σ	stress
σ^g	Growth stress of thermally grown oxide
t	Time
T	Temperature
υ	Luminescence frequency
X_i	Mole fraction of component *i*
y	Thickness of thermally grown oxide
$\|Z\|$	Modulus of electrochemical Impedance

Turbine Surface Degradation with Service and Its Effects on Performance

1 June2002 to 30 November 2005
Final Report

Principal Investigator: Dr. Jeffrey Bons
Report Issue Date: 15 November 2005
DOE Award Number: DE-FC26-02NT41431
UTSR Project Number: 02-01-SR104

Submitting Organization: Brigham Young University
435 CTB, PO Box 24201, Provo, UT 84602-4201

Co-Investigators
Drs. Richard Rivir and Rolf Sondergaard, Air Force Research Laboratory
Drs. Tom Shih and Z.J. Wang, Iowa State University
Drs. Awatef Hamed & Widen Tabakoff University of Cincinnati

ABSTRACT

This report summarizes work completed over the full three and a half year research effort into turbine roughness. In order to reduce the length of this report the activity from each of the entities represented has been summarized in brief. Thus, the reader is referred previous reports and conference/journal papers referenced in this document that will contain more details concerning this research effort. The objective of this effort is to document the service-related surface degradation of turbine hardware and evaluate the associated losses in performance. During the period of this grant, significant progress was achieved by all of the parties involved. BYU developed a facility capable of producing engine-like deposits in an accelerated format. This has allowed the evaluation of various material systems and synfuels with regard to their rate of deposition and degradation. It also permitted the study of evolving deposits which were then evaluated in a wind tunnel facility using scaled models of the evolved deposits. AFRL has analyzed aircraft engine components from several engine companies and from within the Air Force. A partial summary of their findings is included in this report. UC conducted a series of material system evaluations using a wind tunnel that simulates erosion in a gas turbine. They subsequently correlated erosion to roughness evolution and included this empirical model in their particle-tracking CFD simulations of erosion. Finally, ISU made significant progress with the use of 2D and 3D simulations over turbine roughness structures. The limitations of current 3-D time accurate simulations of roughness were evaluated and new roughness correlations were developed from a series of 2D simulations over rough surfaces.

TABLE OF CONTENTS

EXECUTIVE SUMMARY

The ultimate objective of this 3-year research effort is the development of a model that will allow the direct assessment of the effect of service time on turbine aerothermodynamics. To achieve this objective will require four essential building blocks: acquisition of relevant data from serviced hardware, experimental and computational modeling of deposition and erosion (the two primary degradation mechanisms), experimental measurement of performance degradation for surfaces with service-related roughness, and finally detailed computational modeling of these performance effects. The following is a brief summary for each task:

Roughness Measurement on Serviced Hardware: Measurements of serviced hardware were conducted at AFRL and BYU with blades from Oklahoma City (USAF engine maintenance facility), Pratt-Whitney, Siemens, Solar, GE, and Standard-Aero.

Deposition Laboratory Simulations: A new accelerated testing facility was developed at BYU for the study of foreign deposit layers typical to the operation of land-based gas turbines. This facility was designed to produce turbine deposits in a 4-hour test that would simulate 10,000 hours of turbine operation. This is accomplished by matching the net foreign particulate throughput of an actual gas turbine. Flow Mach number, temperature and particulate impingement angle are also matched. Validation tests were conducted to model the ingestion of foreign particulate typically found in the urban environment. The majority of this particulate is ceramic in nature and smaller than 10 microns in size, but varies up to 80 microns. Deposits were formed for flow Mach number and temperature of 0.4 and 1150degC respectively, using air plasma sprayed (APS) TBC material coupons donated from industry. Investigations over a range of impingement angles yielded samples with deposit thicknesses from 20 to 100 microns in 4-hour, accelerated-service simulations. Test validation was achieved using direct comparison with deposits from service hardware. Deposit characteristics affecting blade heat transfer via convection and conduction were assessed. Surface topography analysis indicated that the surface structure of the generated deposits were similar to those found on actual turbine blades. Scanning electron microscope (SEM) and x-ray spectroscopy analyses indicated that the deposit microstructures and chemical compositions were comparable to turbine blade deposit samples obtained from industry. Multiple tests were also conducted to study foreign deposit layers typical to the operation of land-based gas turbines. Tests were conducted to model the use of syngas fuels such as coal, petcoke, sawdust, and straw. Deposits were formed for flow Mach number and temperature of 0.4 and 1150degC respectively, using TBC-coated material coupons donated from Praxair. Experiments show substantial variations in deposition with fuel type. Finally, successive deposits were formed for flow Mach number and temperature of 0.4 and 1150degC respectively, using TBC-coated material coupons donated from Praxair. Each 2-hour test was conducted to simulate 3 months of gas turbine operation in typical atmospheric conditions. The evolved deposits were used in subsequent wind tunnel testing to measure heat transfer coefficient change over time.

Erosion Laboratory Simulations: Testing was completed in UC's erosion tunnels under the direction of Dr. Tabakoff. Coated and uncoated samples of typical turbine materials were subjected to hot and cold erosion simulations at various particulate loadings, impingement angles, and velocities. The eroded specimens were then evaluated at AFRL. The erosion

produced is fairly isotropic with scales depending primarily on particulate size and impingement angle. These data were helpful in characterizing particle restitution and rebound models for later study.

Experimental Measurement of Roughness Effects on Performance: Scaled models of evolved deposits were used for wind tunnel testing during this phase of the project. Heat transfer measurements were initiated at representative flow Reynolds numbers (750,000). Roughness measurements show an initial rapid growth of roughness followed by a lull in growth as valleys between deposit peaks are filled with subsequent deposits. Not surprisingly, St measurements showed a similar lull in their trend upwards with time.

Computational Modeling: Three parallel efforts were conducted in the computational arena.
i) Dr. Hamed (UC) made progress in erosion simulation using the GE E^3 first stage LP turbine as a test platform. Particle-tracking software was used to predict the trajectories of various sizes of particles released in the flowfield. Erosion and particle restitution data were then used to model the impact of the particles on the blade surface. This led to a prediction of the surface erosion for a given particle loading. These simulations provide insight into the variation of component erosion with various engine operating parameters.
ii) Dr. Shih (ISU) explored the use of 2D simulations over representative roughness panels. Parametric studies included the variation of the boundary layer thickness to roughness height ratio as well as stretching and compressing the roughness signature for a fixed boundary layer height. Dr. Shih has also initiated simulations of film cooling flows with and without roughness.
iii) Dr. Wang (ISU) pursued two parallel computational studies to model the effects of surface roughness on shear stress and heat transfer. He successfully integrated the industry standard Spalart-Allmaras turbulence model into his detached-eddy simulation (DES) solver for arbitrary unstructured grids (MUSIC). At the same time, a standard RANS solver with the Spalart-Allmaras turbulence model was used for comparison. Both solvers are being used with a dense 3D grid generated by Dr. Wang's adaptive griding routines. This unstructured adaptive grid generation method is very efficient in resolving disparate length scales. It is estimated that the number of cells generated is over an order of magnitude less than that with a structured grid. Results showed the RANS model to be accurate to within 3% on c_f and 13% on St. Due to convergence failure of the DES simulation, further investigations continued with the RANS solver for additional roughness panels, including one representative of TBC spallation.

Summary: In summary, results from this roughness study are very promising. Industrial participation was very strong. The study included both the measurement of actual hardware and the laboratory simulation of degradation mechanisms (erosion and deposition). By performing the two components in parallel, we hope to have insured the relevancy of the laboratory simulations. Because they are performed in a controlled environment, these erosion and deposition studies should provide the framework for semi-empirical roughness evolution models. As these models are incorporated into computational codes, this will in turn provide the engine community with powerful roughness predictive capabilities.

FULL PROGRESS REPORT

PROJECT DESCRIPTION:

Gas Turbine Research Need: Modern turbine airfoils operate in severe environments with high temperatures and near critical stresses. As design tools of ever increasing sophistication (CFD) are employed to reduce design uncertainty, manufacturing specifications and tolerances are tightened and factors of safety reduced. At the same time, it is well recognized that due to their harsh operating environment, turbine surfaces experience significant degradation with service. Measurements indicate an order of magnitude increase in rms roughness is typical (Bons et al., 2001). To allow user confidence in gas turbine reliability and maintainability, engine companies must be able to accurately predict the effect of such surface roughness on engine performance as a function of operational life. Traditional loss correlations based on the "equivalent sandgrain roughness" concept pioneered by Schlichting are becoming increasingly suspect as the true nature of surface degradation and its effects are uncovered (Bons, 2002).

Recent surveys of engine hardware (Bons et al., 2001) establish that turbine surface roughness is generally not uniform over the entire blade surface. In addition, different degradation mechanisms (erosion, deposition, and coating spallation) have distinctive roughness signatures. Laboratory measurements indicate that these distinctive features can have considerable influence on the Reynolds analogy, often used to relate skin friction to heat transfer effects. These recent insights into spatial and character variations of rough surfaces are helpful, but they don't directly address the real issue facing the turbine user. Specifically, the gas turbine user needs an accurate method to estimate the variation of turbine surface condition with service time so that the associated decreases in stage efficiency and increases in heat transfer can be accounted for. To our knowledge, there is no model or information available in the open literature that would provide this link between service life and performance loss due to surface condition. This research effort lays the groundwork for the development of such a complete model that will allow the direct assessment of the effect of service time on turbine aerothermodynamics.

Project Experimental and Analytical Approach: To meet the need stated above will require four essential tasks: the acquisition of surface data from serviced hardware as a function of service time, the experimental and computational modeling of the effects of deposition and erosion (the two primary degradation mechanisms) on surface roughness as a function of time, experimental measurement of performance degradation for surfaces at different times in their roughness evolution, and finally detailed computational modeling of these performance effects. To accomplish these tasks, we assembled a highly qualified research team with expertise in the required disciplines: BYU/AFRL in the surface measurement and wind tunnel testing of rough surfaces, Iowa State University in CFD and grid generation, and University of Cincinnati in erosion experimental and computational studies.

This effort began with the characterization of in-service turbine hardware arranged through industry contacts. 2D and 3D surface traces were taken on hardware from different engines and operating environments at various service intervals. These data provided the baseline surface trends for subsequent laboratory testing and computational modeling.

At the same time, UC researchers conducted experimental studies into the effects of erosion on typical turbine metals as part of Task 2. These experiments were accomplished in UC's erosion tunnels (with surface measurements made at AFRL) over a wide range of operating parameters.

In addition, experimental studies were conducted on particle rebound and restitution in order to develop adequate empirically-based models for numerical simulation of erosion and deposition. Also, deposition studies were conducted in a newly constructed combustor simulator at BYU. Evolution of deposits and surface character were measured for typical engine conditions. Following this, fundamental flat-plate measurements were made by BYU in a low speed wind tunnel. Heat transfer (Stanton number, St) was evaluated at appropriate Reynolds numbers and relative boundary layer dimensions.
The final step was the modeling and simulation of skin friction and heat transfer on rough surfaces. Both high accuracy/high resolution (DES) and lower-order modeling approaches (RANS) were pursued.

Expected Results/Benefits: This BYU-led roughness study will hopefully provide the power generation community with tools to aid in the predicting of surface degradation history of hot section components and their associated performance decrements. This critical information will eventually allow the engine user to establish more economical maintenance schedules and procedures. Operators will have a better idea of the cycle penalties associated with accumulated surface roughness and be able to make informed decisions about when to take power plants off line for maintenance. At the same time, engine designers will have the ability to estimate the expected performance history of their product for a given operating environment. The combination of these added capabilities will reduce operating costs for the energy producer and prevent possible emergency shut-downs due to unanticipated surface degradation or part failure.

EXPERIMENTAL METHOD

Airborne Deposit Simulation at BYU: A natural gas burner in the Advanced Combustion Engineering Research Center (ACERC) at BYU was used to conduct accelerated turbine deposition studies. Figure 1 shows a schematic of the facility. The combustor burns natural gas in a facility capable of mass flow rates up to 1000 slpm. With an exit contraction from 30.5cm to 1.6cm diameter, the exit flow from the combustor can exceed 350m/s at temperature. A number of tests were conducted with the following parametric ranges: exit Mach number from 0.3 – 0.4, exit temperature from 900°C to 1150°C, and impingement angles from 30° – 90° (stagnation). Sample turbine materials donated by General Electric, Siemens-Westinghouse, Praxair, and Solar Turbines were used as the target coupons in tests conducted to simulate 10,000hrs of 1st stage HP airfoil exposure to airborne particulate (particularly the stagnation zone).

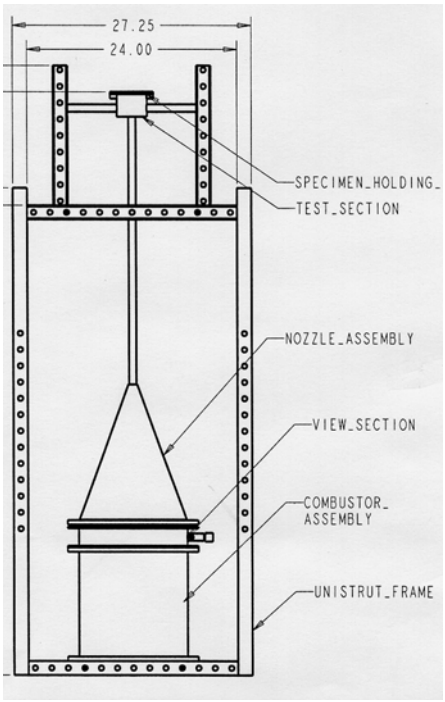

Figure 1: BYU Turbine Deposition Facility schematic.

Since the combustor fuel is methane mixed with filtered high pressure air, deposits are created by seeding with selected particulates using a particle feeder. The feeder allows controlled rates of fine, dry particulates (powders) to be added to the hot section and accelerated in the combustor exit. A 1.2m long exhaust pipe is provided to insure thermal and velocity equilibrium of the particulate with the gas stream. To study the effect of airborne particulates, experiments were conducted with varying concentrations (parts per million weight or ppmw)of a particle test mixture used in the characterization of GT inlet filter performance by the Air Filter Testing Laboratories, Inc. The dust selected conforms to the ASHRAE (American Society of Heating, Refrigeration, and Air Conditioning Engineers) test standards for size and is representative of real chemical compositions as it is collected from the atmosphere rather than artificially mixed. Tests with various synfuel ashes were also conducted with the following operating conditions: flow Mach number 0.3, gas temperature 1150°C, and 45° impingement angles. Turbine coupons donated by Siemens-Westinghouse and Praxair were used as the target coupons in these tests. Tests were also conducted to model deposit evolution. Specific test findings are presented in the Results section.

Turbine Component Measurements at AFRL and BYU: Turbine components donated from General Electric, Pratt-Whitney, Solar Turbines, Standard Aero Inc., Oklahoma City (USAF engine maintenance facility), and Siemens-Westinghouse were evaluated. The precise features of the various articles were not divulged in order to respect proprietary concerns of the industry participants. Surface measurements were made with a Taylor-Hobson Form Talysurf Series 2 contact stylus measurement system at AFRL and a Hommel contact stylus measurement system at BYU. Results from these measurement surveys are discussed in the Results section of this document.

Erosion Simulation at UC: The specific characteristics of the erosion tunnel employed in UC's testing are presented in Tabakoff and Wakeman (1979). A schematic of the facility is provided in Figure 2. The facility matches operating turbine temperatures and particle impact velocities over a full range of impingement angles with various target materials and particulates. Testing results are discussed in the Results section of this document.

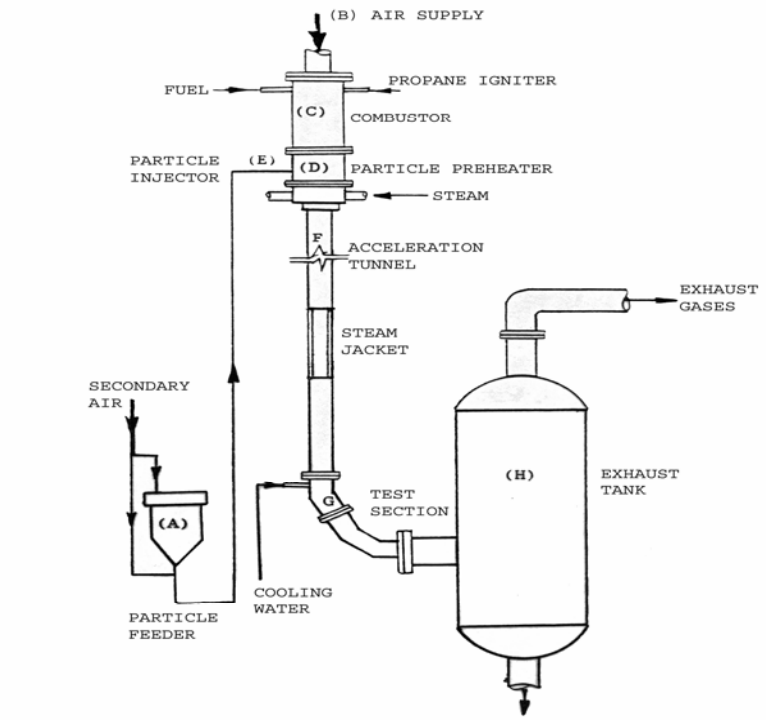

Figure 2: University of Cincinnati erosion tunnel schematic.

Computational Modeling at UC: Using erosion data from Dr. Tabakoff's experimental testing combined with particle trajectory predictions from CFD, erosion rate predictions were made for the GE E^3 first stage LP turbine. Details are summarized in the Results section.

Computational Modeling at ISU: At Iowa State University (ISU), two parallel computational efforts were conducted to study the effects of surface roughness on shear stress and heat transfer.
i) Direct numerical simulation (DNS) of real 3D rough surfaces by using detached-eddy simulation vs. RANS (Z.J. Wang): In this approach, every detail of the irregularities in surface geometry is simulated. With DES, the near wall region is simulated by using the Reynolds-averaged Navier-Stokes (RANS) approach. But, away from walls, large-eddy simulation is used, which enables the unsteady, three-dimensional flow structures induced by roughness to be captured by essentially first principles. This approach, though expensive, has the potential to reveal understanding that cannot be obtained by RANS. Also, DES results can be used to guide the modeling of more accurate RANS models.
ii) RANS computations over 2D surfaces taken from real 3D turbine surfaces using Spalart-Allmaras turbulence modeling (Tom Shih): In this approach, 2D traces are taken from 3D turbine roughness surfaces generated by Bons et al. Fluent calculations are performed over various profiles with particular attention given to flow structures and engineering properties. 2D

is used because it is considerably cheaper than 3D. The research plan is to use these simulations to guide further modeling of rough surfaces.
Results with these two complementary approaches are discussed in the Results section of this document.

RESULTS AND DISCUSSION - BYU

ORGANIZATION: This section is organized by school rather than by task.

Validation of Turbine Accelerated Deposition Facility: During the second year of this program a new deposition facility (TADF) was successful validated at BYU. A paper documenting the test facility validation was presented at the 2004 IGTI in Vienna, Austria (Paper # GT2004-53324: "Simulated Land-Based Turbine Deposits Generated In An Accelerated Deposition Facility" by Jensen, Squire, Bons, and Fletcher) in June, 2004. The paper has since been published in the ASME *Journal of Turbomachinery* (Vol. 127, pp. 462-470, July 2005) and was awarded the 2005 Heat Transfer Committee award for best paper.

Figures 3a&b show surface maps of two surfaces. Surface 3a is from a first stage turbine blade with 25,000 hrs of service. The topology map was taken at roughly 60% chord and 30% span on the blade suction surface, a region with obvious brownish deposits. Surface 3b is an accelerated deposition coupon that was tested for 4hrs at 60ppmw (T = 1150C and M = 0.4). The coupon was oriented for stagnation flow (impingement angle = 90), but the surface map shown was taken at the edge of the coupon where the flow was more tangential to the surface of the coupon as the impinging jet stream turned about the edges of the target. The strong similarities between the two images are reinforced by a review of their surface statistics.

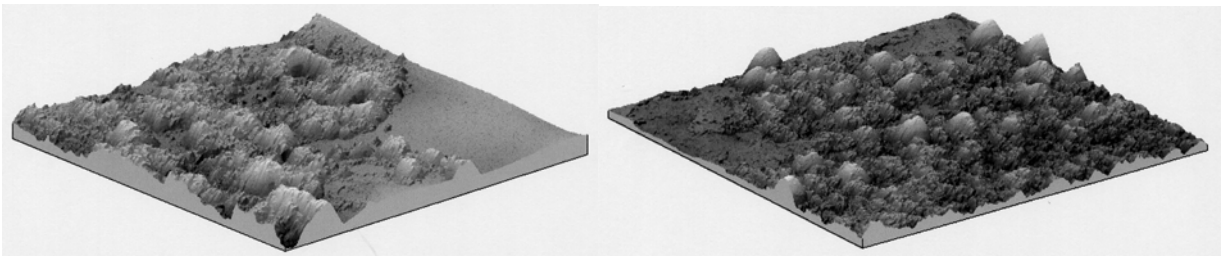

3(a) 3(b)

Figures 3: Surface map of deposits from (a) 1st stage turbine with 25,000 hours and (b) accelerated deposit surface after 4hrs at 60ppmw. Both maps are 4mm x 4mm with approximately the same vertical scale.

Table 1: Roughness statistics for surfaces in Figure 3a&b.

Surface	Ra [μm]	Rt [μm]	Surface Angle rms	Wetted Surface Fraction	Λ_s Form Parameter
Fig 3a	32	240	27	1.36	22
Fig 3b	28	257	29	1.43	13

Scanning electron microscopy (SEM) and x-ray spectroscopy were also used with both the deposits formed in this accelerated facility and actual turbine samples obtained from Standard Aero Inc. to evaluate the internal structure of the deposits. The deposit samples were potted in epoxy to prevent disruption of the structure during cross-section. Figure 4 shows SEM images of two different samples. Elongated structures oriented parallel to the blade surfaces are evident in

both images. Deposit chemistry evaluations also indicated similar types and concentrations of elemental constituents.

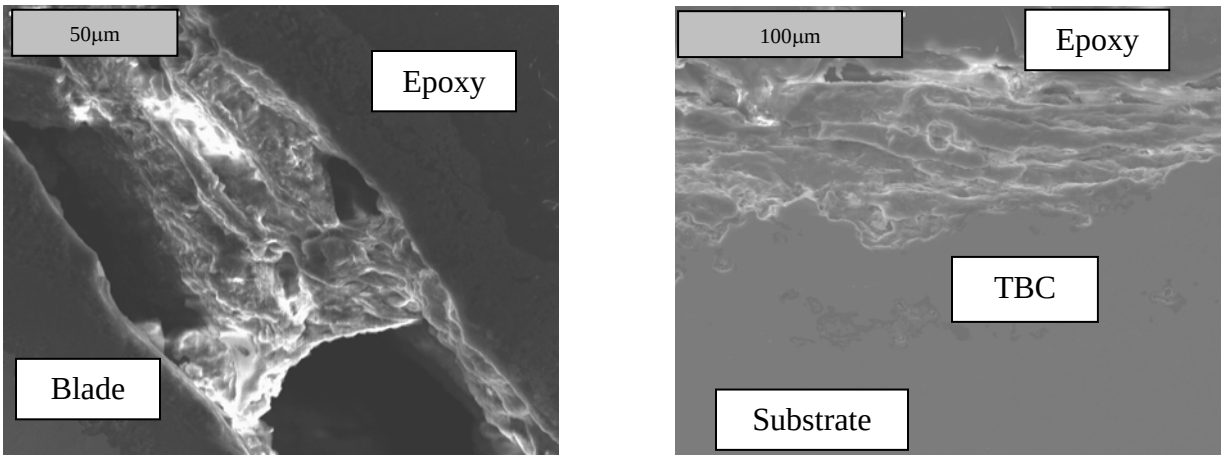

4(a) 4(b)

Figure 4: SEM cross-section of (a) a 16000-hour service blade with 50-μm metering bar at top left and (b) an accelerated deposit specimen with 100-μm metering bar at top left

Deposition Simulation with Synfuels at BYU: Subsequent to this, a study was conducted simulating syngas deposits with particulate from straw, sawdust, coal, and petroleum coke. These results were presented at the 2005 IGTI in Reno (Paper # GT2005-68479: "High Pressure Turbine Deposition in Land Based Gas Turbines from Various Synfuels" by Bons, Crosby, Wammack, Bentley, and Fletcher) in June, 2005. The paper has since been accepted for archival journal publication in the ASME *Journal of Turbomachinery*.

The combustor was seeded with finely-ground fuel ash particulate from four different fuels: straw, sawdust, coal, and petroleum coke. The four ash samples used in this study were collected from various sources. Coal and petcoke samples were obtained externally, while the biomass samples were prepared locally using facilities in BYU's Advanced Combustion Engineering Research Center (ACERC). Subbituminous coal fly ash was obtained from an operating power plant, while the petcoke ash is boiler slag obtained from a combined cycle gas turbine power plant operating with a blend of 55% petcoke and 45% coal. Straw ash was produced in a two-step process. First, raw material was partially burned to eliminate volatiles. Second, the partially burned ash was placed in a programmable furnace and cycled through a standard ashing process. This same two step process was repeated to generate sawdust ash. A standard kitchen wheat grinder set on the finest setting was used to grind the ash particles to the size needed for testing. Figure 5 show typical ESEM images from two of the ash samples. The coal ash particles appeared mostly spherical in shape while the straw ash particles were more uniform in size but more irregular in shape. A Coulter counter was used to measure particle size and spectroscopy yielded the elemental composition. Both of these are shown in Table 2.

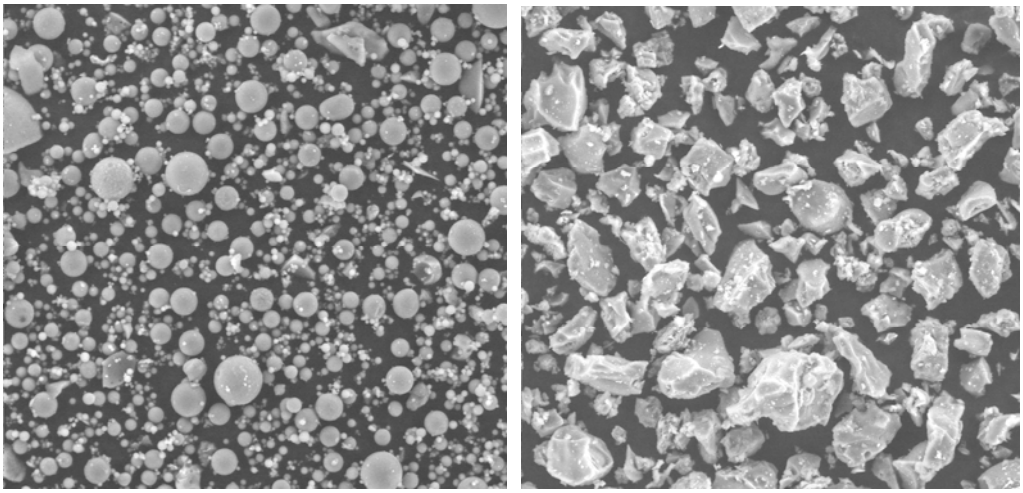

(a) Coal (b) Straw

Figure 5: ESEM images of (a) coal and (b) straw ash after processing. Images are approximately 150μm x 150μm.

Table 2: Ash particle summary statistics: size, density, and elemental composition.

	Coal	Petcoke	Straw	Sawdust
Mass mean diameter (μm)	13.3	33.0	17.6	19.7
Median diameter (μm)	10.6	28.5	15.1	11.8
Bulk density (g/cc)	0.99	1.45	0.84	0.48
Apparent density (g/cc)	1.98	2.90	1.68	0.96
Elements in order of atomic number	Weight %	Weigh t %	Weight %	Weigh t %
Na	6.9	4.3	1.7	5.9
Mg	3.6	2.2	2.54	12.4
Al	17.8	14.5	1.8	5.1
Si	47.4	38.3	48.4	11.6
P	1.6	0.0	3.4	2.2
S	1.8	1.0	3.0	1.3
Cl	0.0	0.0	2.8	0.0
K	2.6	2.5	23.4	10.7
Ca	8.7	7.5	7.8	42.9
Ti	1.6	0.8	0.0	1.3
V	0.0	3.4	0.0	0.0
Cr	0.0	0.0	0.0	0.0
Mn	0.0	0.0	0.0	4.5
Fe	6.4	22.9	5.0	1.0
Ni	0.0	0.9	0.0	0.0

The entrained ash particles were accelerated to a combustor exit flow Mach number of 0.31 before impinging on a thermal barrier coating (TBC) target coupon at 1150°C. Figure 6 shows typical post-test deposition patterns using coal and straw.

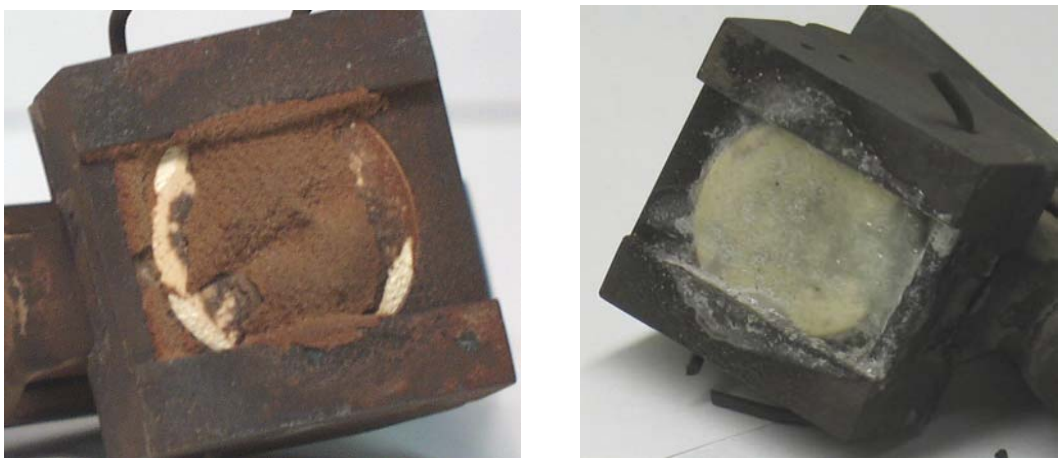

a) Coal b) Straw

Figure 6: Digital images of post-test coupons with deposit before removal from coupon holder. Coupon diameters are approximately 2.41cm.

Post exposure analyses included surface topography, scanning electron microscopy, and x-ray spectroscopy. After completing the tests each sample was weighed and compared to its pre-burn weight. The samples were then placed on a Hommel profilometer to measure the surface topography and roughness of the deposits. Multiple steps were required to prepare the sample for analysis in the ESEM. Each sample was potted in epoxy to preserve the deposit. Using a water-cooled, diamond tipped saw, each sample was cut in half perpendicular to the flow direction. The cut sample was then encased in bakelite and polished. Finally, because deposit layers and TBC are not electrically conductive, the sample was coated with a fine layer of carbon to prevent charge buildup from distorting the ESEM images.

Due to significant differences in the chemical composition of the various fuel ash samples, deposit thickness and structure vary considerably for each fuel. These data are summarized in Table 3. Using the pre-test and post-test weight measurements, the net specimen weight gain during exposure was assessed. Dividing this deposit weight by the exposed coupon surface area and the test duration yielded deposition rate measurements of 143 mg/cm^{2}hr and 76 mg/cm^{2}hr for the highest particle loading coal and petcoke cases, respectively (Table 3). This coal deposition rate is comparable to those witnessed in the coal water fuel study of Wenglarz and Fox [1990] where deposition rates from 200-400 mg/cm^{2}hr were recorded at comparable gas temperatures. The petcoke deposit is a factor of 4 less dense than the coal deposit. It has twice the average thickness but only half the weight. This is indicative of the porous nature of the petcoke deposit as will be seen in the ESEM images. This finding is particularly surprising since the petcoke ash apparent density is roughly 50% higher than that for coal ash (Table 2). One final deposition metric that is tabulated in Table 2 is the net particle capture efficiency (mg/hr of deposit divided by mg/hr of particulate in the flow). Coal has the highest capture efficiency (17%), which drops to 12% as particle loading (ppmw) is increased. The petcoke and biomass net capture efficiencies are less than half of the lowest value calculated for coal. Biomass products (e.g. sawdust and straw) are significantly less prone to deposition than coal and petcoke for the same particle loading conditions. In a test simulating one turbine operating year at a

moderate particulate loading of 0.02 parts per million by weight, deposit thickness from coal and petcoke ash exceeded 1 mm and 2 mm respectively. These large deposits from coal and petcoke were found to detach readily from the turbine material with thermal cycling and handling. The smaller biomass deposit samples showed greater tenacity in adhering to the TBC surface.

Table 3: Particle loading test conditions.

Ash Type	Test Duration [hrs]	Particle concentration [ppmw]	Net particle loading [ppmw-hr]	Net deposit weight [mg]	Deposition rate [mg/cm^{2}hr]	Net particle capture efficiency [%]
Coal	3	55	165	1.1	72	17%
Petcoke	2	70	140	Not measured	N/A	N/A
Straw	2	77	154	<0.1	N/A	N/A
Sawdust	3	37	111	0.2	13	5%
Coal	4	150	600	2.9	143	12%
Petcoke	3	165	495	1.15	76	6%

Scanning electron microscope (ESEM) cross-section images of the four different fuel deposits reveal significant differences in the deposit structure as well. The previous study with airborne dust particles showed layering in the deposit (Jensen et al.), with structures predominantly oriented parallel to the surface. By comparison, the fuel deposits in this study are fairly isotropic in structure and composition. Figure 7a is an ESEM cross-section image of the coal deposit. The coal deposit is riddled with 30-80 μm diameter inclusions. Further interrogation using x-ray spectroscopy indicated that while the majority are solid (metal) particles that were trapped in the molten deposit at temperature, some are porous cavities. The second coal ESEM image (Figure 7b) was taken at high magnification near the deposit/TBC interface. At this location, a crack in the TBC has been penetrated by the coal deposit. In all 4 cases, corrosive elements (e.g. Na, K, V, Cl, S) were found to penetrate the TBC layer during the accelerated deposition test.

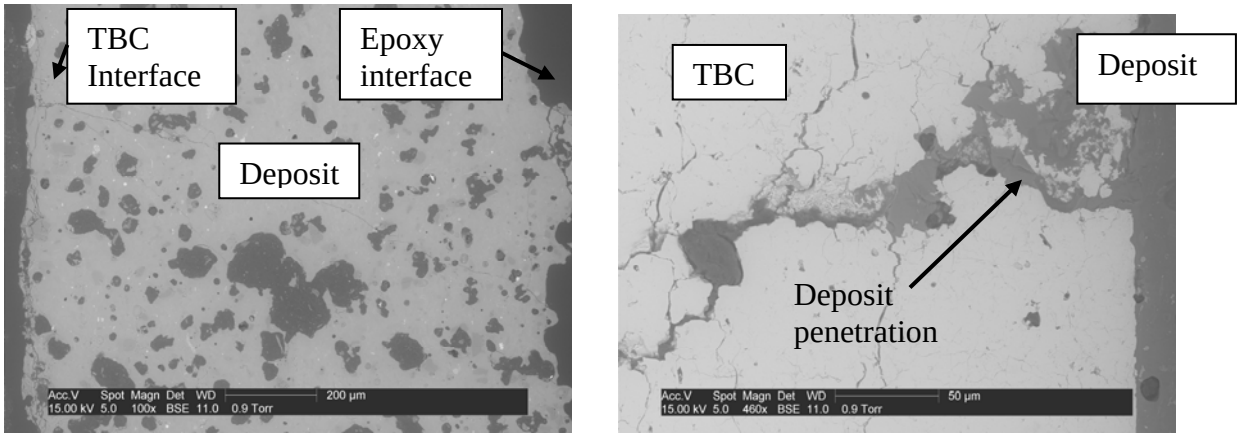

a) Coal surface deposit structure b) Coal deposit penetration into TBC

Figure 7: ESEM cross-section of coal surface deposit and coal/TBC interface.

While mounted in the ESEM, the deposits were interrogated using x-ray spectroscopy. The ESEM registers regions of different structure with distinctively different hues (e.g. the inclusions in Figures 7). Some of these regions exhibited significantly different elemental composition as well. In all cases, at least three measurements were made in each region of the deposit. The composition values are reported as area-weighted averages of the various measurements. In general, the relative concentration of elements detected in the deposits are similar to those detected in the ash. A side-by-side comparison of these data can be used to determine if there are specific preferences for deposition at the given operating conditions (Figure 8). For example, the petcoke and sawdust deposits show significant increases in the concentration of Si in the deposit (relative to the ash) at the expense of Fe (in the case of petcoke) and Ca, K, Mg (in the case of sawdust). Since silicon is non-corrosive and essentially insulates the TBC surface, this rend is favorable for blade life. On the other hand, sharp increases in Na, P, and Cl (e.g. the straw deposit) are undesirable for blade life.

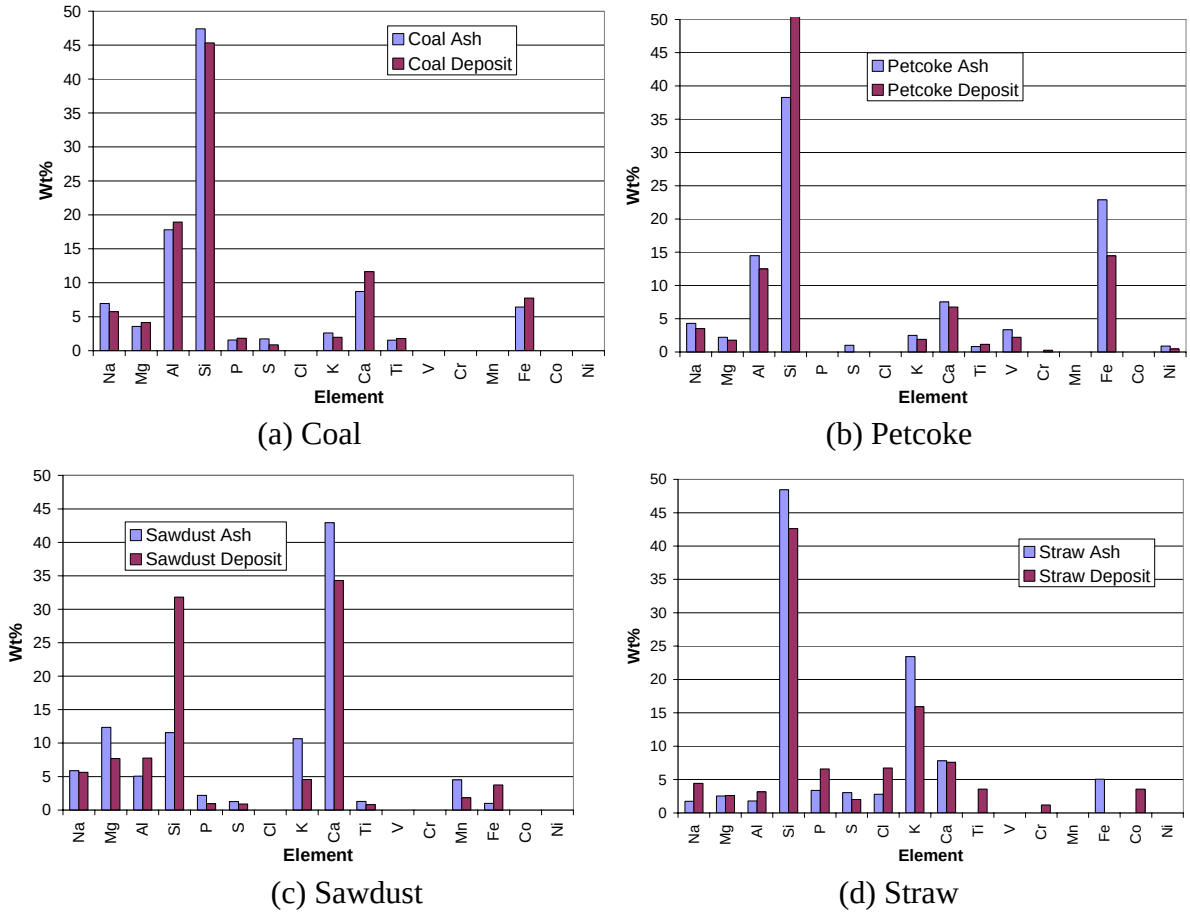

Figure 8: Comparison of element weight percent for fuel ash vs. deposit: (a) coal (b) petoke (c) sawdust (d) straw.

Perhaps even more worrisome for the health of the turbine blade material system is the observed penetration of deposit materials into cracks in the TBC (Figures 7). These vertical segmentation cracks are deliberately formed in the air plasma sprayed (APS) TBC to improve erosion and

thermal shock resistance. It is possible that these fissures present paths for premature contamination of the TBC. Further study is necessary to more rigorously examine these internal deposits and determine whether this deposit penetration leads to accelerated corrosion in the base metal alloy.

Evolutionary Deposits and Wind Tunnel Testing: During the third year, turbine blade coupons with three different surface treatments were exposed to deposition conditions in the accelerated deposition facility. Each of the coupons underwent four consecutive experiments in the TADF. Each burn was intended to simulate approximately one quarter of an operational cycle between maintenance periods. Following each test, the surface topography was measured with a Hommel profilometer. Scaled models were the placed in a low speed wind tunnel where St measurements were made using a transient IR technique. The results have been accepted for presentation at the 2006 IGTI in Barcelona, Spain in the form of two papers: "Evolution of Surface Deposits on a High Pressure Turbine Blade, Part 1: Physical Characteristics," by J.E. Wammack, J. Crosby, D.H. Fletcher, J.P. Bons, and T.H. Fletcher, and "Evolution of Surface Deposits on a High Pressure Turbine Blade, Part 2: Convective Heat Transfer," by J.P. Bons, J.E. Wammack, J. Crosby, D.H. Fletcher, and T.H. Fletcher. Both papers were also accepted for eventual publication in the *ASME Journal of Turbomachinery*.

In this experiment, the combustor exit flow was seeded with dust particulate that would typically be ingested by a large utility power plant. The particulate used in this study is identical to that used by Jensen et al. [2005], and is primarily composed of silicon and aluminum oxides (80%) with smaller concentrations of Na, K, Mg, Ca, and Fe. The mass mean diameter is 15 μm. The turbine blade coupons donated from the gas turbine industry for this study were flat, circular disks with a diameter of approximately 2.54 cm. Like actual turbine blades, the coupons consisted of a nickel-cobalt superalloy substrate with various surface treatments. Three types of surface treatment were studied: (1) bare polished metal, (2) polished thermal barrier coating with bondcoat, and (3) unpolished, 310 μm thick oxidation resistant bondcoat. The TBC was approximately 1 mm thick air plasma-sprayed (APS), yttria stabilized zirconia (YSZ). The polished bare metal and TBC coupons both had initial roughness levels (Ra) less than 0.6 μm, while the "as-applied" oxidation resistant bondcoat had a roughness level of 16 μm. This initial level of surface roughness had a significant effect on deposition evolution as will be shown.

Each of the coupons used in this study underwent four consecutive experiments (hereafter referred to as "Burns") in the TADF. Each burn was intended to simulate approximately one quarter of an operational cycle between maintenance periods. During a burn, each coupon experienced approximately 45 minutes of warm-up time, during which the TADF was brought to an operational freestream temperature of 1150ºC and a flow Mach number of approximately 0.31. Once steady state had been reached, particulate was introduced into the facility. This particulate flow was maintained for a period of two hours. During each two hour burn, an average of 25 ppmw of particulate was introduced into the TADF for a total of 50 ppmw-hrs. This is intended to simulate approximately 2500 hours of operation with a particulate concentration of 0.02 ppmw, for a total of 10,000 simulated hours during a standard series of four experiments per coupon. Figure 9 shows digital photographs of a coupon subjected to successive 2-hr periods of deposition (images are only shown at 0, 2, and 8 hrs). Uncertainty in the particle concentration measurement was <6 ppmw for typical flow conditions.

a) 0 hrs b) 2 hrs c) 8 hrs

Figure 9: Digital photographs of test coupons after successive deposition tests.

Following an experiment, the coupon was allowed to cool for several hours, after which it was removed from its fixture. Upon removal, the coupon was placed in a profilometer fixture while topological measurements were taken. Following this process, the coupon was stored until the subsequent burn. Three-dimensional maps of the deposit-roughened surfaces were created between each test, representing a total of four measurements evenly spaced through the lifecycle of a turbine blade surface. From these measurements the surface topology and roughness statistics were determined. Figure 10 shows the evolution of deposition on the bare metal coupon.

(a) Before

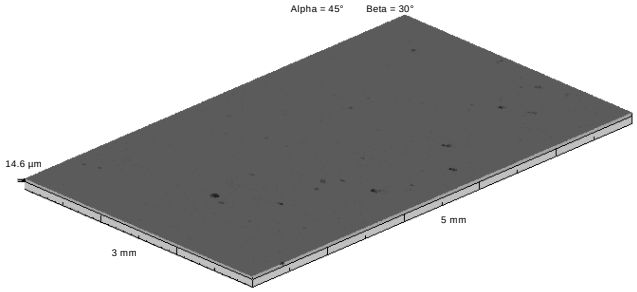

(b) After Burn 1

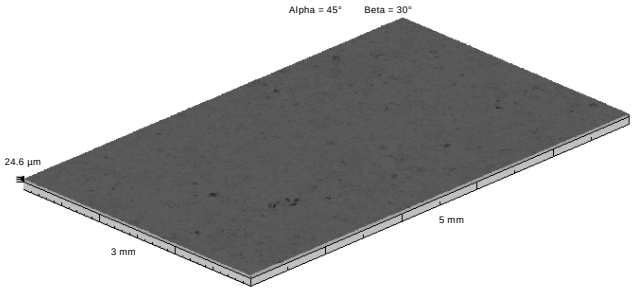

(c) After Burn 2

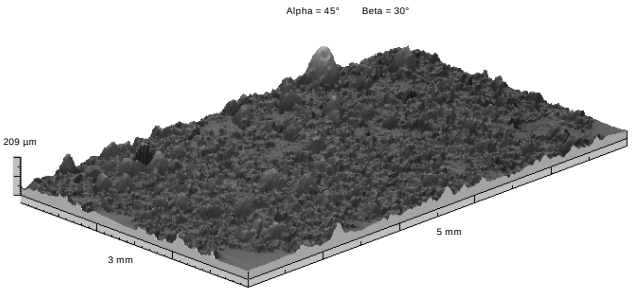

(d) After Burn 3

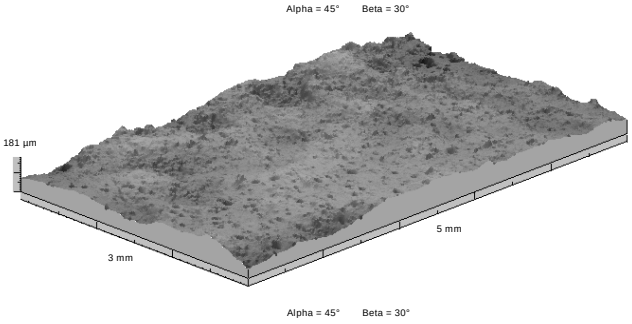

(e) After Burn 4

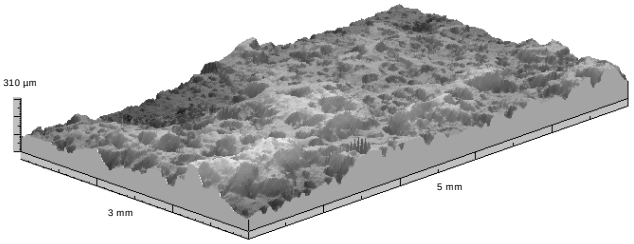

Figure 10: Surface topologies of 3 mm x 5 mm section of deposit on bare metal coupon after each burn.

The deposit structure changes substantially from Burn 2 to Burn 4. Figure 10 contains a series of 3D topologies showing the deposit evolution on a 3mm x 5mm area near the coupon center. The most dramatic changes occur during Burn 2, after the residue beneath the flaked off deposit from Burn 1 has altered the virgin surface by roughening it slightly (Ra = 0.5 µm after Burn 1). The deposit structures become noticeably less peaked after Burn 3, as the subsequent deposit fills in valleys in the irregular surface. Finally, Burn 4 again shows the reemergence of new deposit peaks.

This evolution can be summarized quantitatively by plotting the trend of roughness height (as represented by Ra and Rz) and the roughness shape (as represented by $\overline{\alpha_f}$). These data are plotted in Fig. 11 for the same 3 mm x 5 mm region of the coupon shown in Fig. 10. If the surface left behind after Burn 1—in which nearly all deposits had flaked off—were taken as a starting point for deposit evolution, then an interesting trend is revealed. Roughness height (Ra and Rz) initially increases substantially (Burn 1 to Burn 2). This is followed by a phase in which the rate of increase slows (Burn 2 to Burn 3). Finally, the roughness increases again (Burn 3 to Burn 4). At the same time, the peakedness of the deposit structures varies also, as shown both by a visual examination of the three-dimensional surface representations (Fig. 10) as well as by the average forward facing angle (Fig. 11). After Burn 1 and the subsequent flaking of the local deposits, the zoomed surface showed a relatively low value of $\overline{\alpha_f}$. This value increased

dramatically after Burn 2, resulting in the peak-dominated surface seen in Fig. 10c. With Burn 3, a 'wavier' surface was produced with an attendant 40% drop in average forward facing angle. Finally, Burn 4's surface returned to a more peaked state.

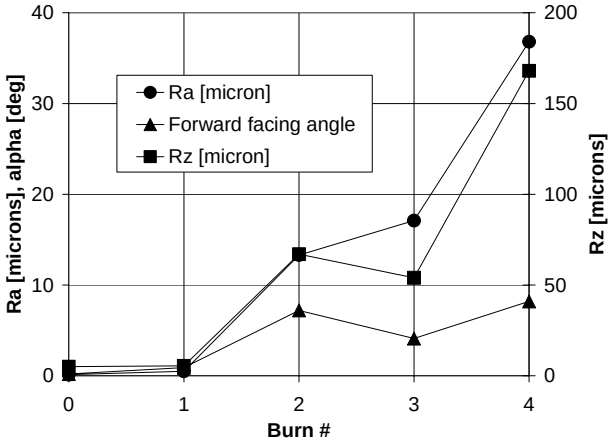

Figure 11: Roughness statistics for the bare metal coupon deposit.

Despite the different surface treatments, all three surfaces (bare metal, TBC, an unpolished coating) exhibited similar non-monotonic increases in roughness with repeated exposure. In each case, an initial build-up of isolated roughness peaks was followed by a period when valleys between peaks were filled with subsequent deposition. This trend is well documented using the average forward facing roughness angle in combination with the average roughness height as characteristic roughness metrics.

For the TBC coupons, there was also significant evidence of deposition-related mechanisms leading to spallation. Both TBC coupons began to show signs of spallation after the second burn. For the TBC1 coupon, this initially consisted of shallow 1-2mm patches of TBC that became dislocated from the surface leaving small 50-100 μm deep valleys in the TBC layer. This process came to a head after Burn 3 when a 6 mm long crack formed near the left edge of the coupon. The TBC on the side of the crack nearest the coupon edge was raised up 100 μm from the central portion of the coupon. This prevented the contact stylus of the Hommel profilometer from traversing this section of the coupon. Accordingly, the crack was manually enlarged until the entire edge of TBC spalled away from the coupon. The spalled piece of TBC was retained for later evaluation. The remaining coupon was then exposed to deposition in Burn 4. For the TBC2 coupon, the spallation process was much more rapid. Nearly 30% of the coupon surface showed TBC loss after Burn 2, increasing to over 60% after Burn 4. Some of the coupon edges experienced TBC loss down to the metal substrate.

To better understand the role of deposition in TBC spallation and crack development, the broken off piece from TBC1 as well as the entire coupon were prepared for cross-section analysis with the ESEM. Figures 12(a) and (b) show the cracked region and the spalled chip of TBC. Regions where deposit compounds were identified using x-ray spectroscopy are indicated on the figure. The top right corner of the chip shows significant penetration of deposit through cracks in the TBC. This is the portion of the chip nearest the exposed coupon surface that lifted away from the surface during Burn 3. The lower portions of the TBC chip show no signs of deposition penetration, which is understandable since this is the region where the crack was manually forced to propogate after Burn 3. The exposed TBC surface in the spalled crater does show signs of significant deposit, due to the subsequent burn (Burn 4) after the chip was

removed. Thus, it seems likely that spallation was initiated by the penetration of deposits into the upper corner of the TBC chip. Whether the crack would have naturally propogated to the coupon edge during the ensuing burn is difficult to speculate. It is clear, however, that deposition played a role in the development of the spalled region. To ascertain if the spallation was merely a result of thermal cycling, a third TBC coupon (TBC3) was subjected to the identical 4 x 2 hour testing sequence in the TADF, but without injecting particulate into the combustor. The surface showed no signs of spallation during the testing cycle, though the mean Rz roughness increased by a factor of three.

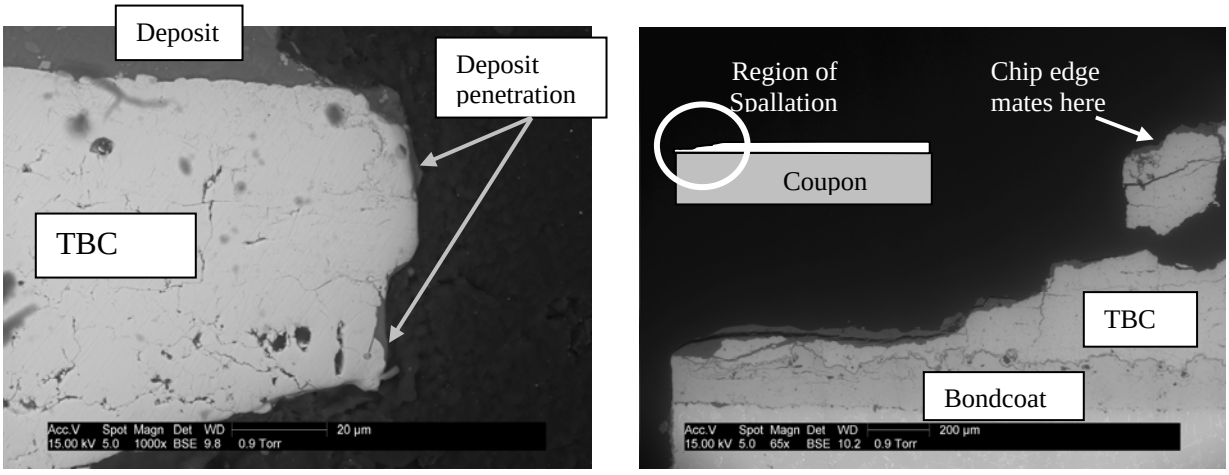

(a) enlarged view of TBC chip **(b) spalled corner of coupon**

Figure 12: ESEM cross-section of spalled region of the TBC1 coupon and spalled chip.

Three-dimensional maps of the deposit-roughened surfaces were created between each test, representing a total of four measurements evenly spaced through the lifecycle of a turbine blade surface. From these measurements, scaled models were produced for testing in a low-speed wind tunnel with a turbulent, zero pressure gradient boundary layer at Re = 750,000 (Fig. 13).

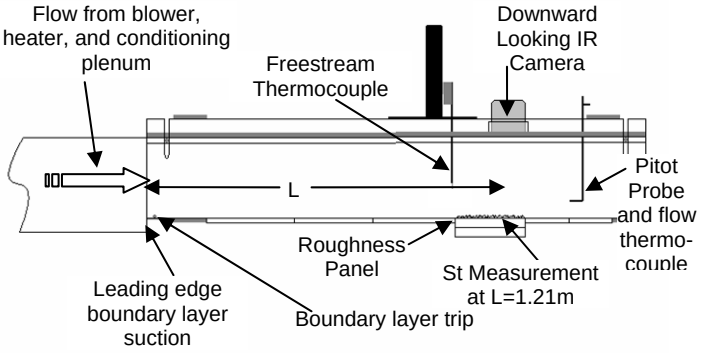

Figure 13: Wind Tunnel Facility

The average surface heat transfer coefficient was measured using a transient surface temperature measurement technique described in Bons [2002]. Heat transfer measurements were made at constant flow velocity for each of the four deposit models and a smooth baseline panel. Figure 14 shows the Stanton number computed using the area-averaged surface temperature as obtained from the IR camera measurement described above. Each data point in Fig. 14

represents the average of at least three separate transient tests, usually conducted on different days. Error bars show the range of measurements for each data point. The Stanton number values are presented as a percent difference between the rough surface value (St_R) and the smooth surface reference value (St_o).

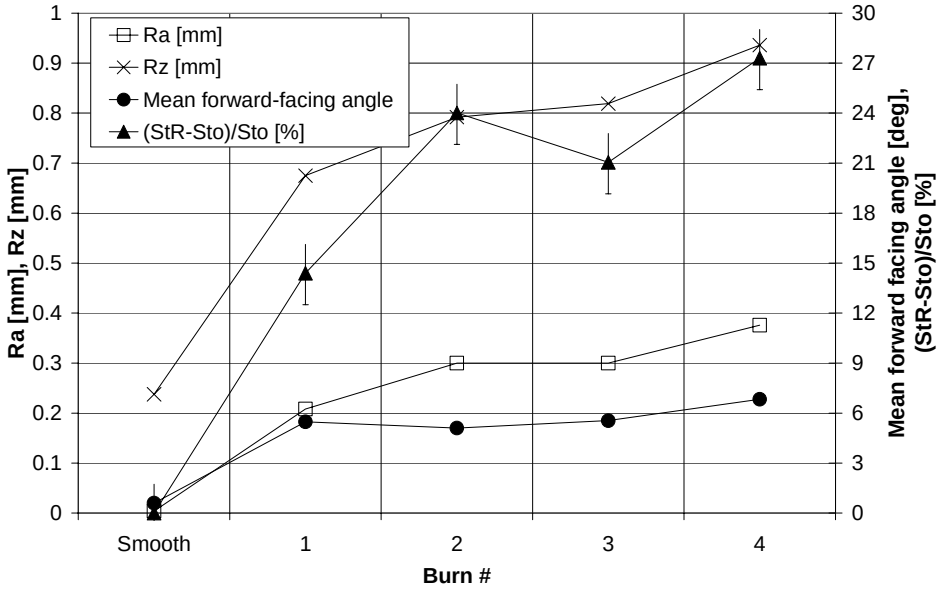

Figure 14: Stanton number augmentation and roughness statistics for the scaled roughness models

The trend in Stanton number follows closely the trend in roughness statistics. The St augmentation levels off between Burns 2 and 3 followed by a marked rise with Burn 4 as the roughness height and mean angle experience a resurgence. Data accumulated by Bons [2005] using roughness characterizations obtained from serviced turbine components indicate that the effect of roughness on c_f and St is reduced as the average forward facing angle decreases for the same mean roughness height (Rz). A comparison of Bons' correlation and that of Dipprey and Sabersky with the experimental data in Fig. 14 is shown in Fig. 15.

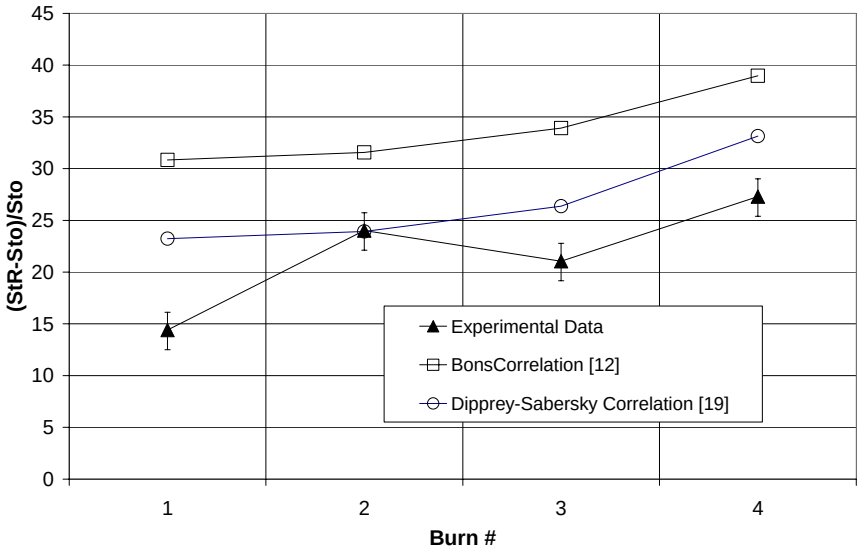

Figure 15: Comparison of experimental St augmentation with empirical prediction.

Both models capture the correct trend of increasing roughness with subsequent burns but appear to lack the sensitivity to capture the changes noted in the St data and the roughness statistics.

The spatial resolution of the infrared camera permits a detailed evaluation of the heat transfer around specific roughness features in addition to the area-averaged measurements presented above. Successive 240 x 320 pixel IR images were processed pixel by pixel using the same Eq. (3) methodology to obtain surface maps of Stanton number. This methodology makes no correction for lateral conduction within the three-dimensional roughness features on the scaled model. For instance, an isothermal roughness peak subjected to instantaneous heated flow will exhibit a more rapid temperature response partly because of the increased convective heat transfer of a roughened surface, but also partly due to its extremity from the base surface. Convection to the sides of the peak will increase the temperature in the 1-D path directly beneath the roughness crest. Thus, the assumption of 1-D transient thermal propogation into an isothermal, semi-infinite solid is jeopardized. Since this effect was not accounted for in the present analysis, the St values will be overestimates of the actual local convective heat transfer. Because the deposit roughness features studied are typically of relatively low aspect ratio (peak height to base diameter ratio ≤ 0.2), this is expected to have only a second order effect on the results presented. Table 4 contains the minimum, average, maximum, and standard deviation of St for each of the roughness surfaces.

Table 4: Spatial statistics for heat transfer coefficient.

	Min St	Avg St	Max St	Std Dev St
Burn 1	**0.00192**	**0.00264**	**0.00427**	**8.3%**
Burn 2	**0.00215**	**0.00284**	**0.00383**	**9.5%**
Burn 3	**0.00209**	**0.00282**	**0.00399**	**9.9%**
Burn 4	**0.00136**	**0.00291**	**0.00397**	**11.7%**

In all four cases, there is a substantial variation in heat transfer over the rough surfaces. In general, roughness peaks can experience nearly 100% higher heat transfer than adjacent valleys. This is partially due to the energetic interaction between the flow and the roughness peak as the flow accelerates to navigate around the obstruction. In addition, the peak reaches further from the wall into the thermal boundary layer where higher temperature fluid (on average) is present; thus, the elevated measurements in these regions. This is actually welcome news for turbine thermal load management. Since a substantial portion of the heat transfer augmentation occurs at these elevated peaks of the deposit, the path to the metal substrate (through the deposit peak) is longer, resulting in a greater thermal resistance. Thus, the increase in local metal temperature beneath the deposit (and TBC) will be less severe. Unfortunately, flow separation behind the deposit roughness peaks generates highly turbulent flow in the wake of the protuberances. This is shown in Fig. 6 which contains side-by-side surface height and St contour plots for the region near roughness peaks on the Burn 1 & 2 models. Though not as high as the heat transfer at the roughness peak, the wake regions [indicated by dashed circles in Fig. 16 (b)] still experience heat transfer augmentation that is 25% higher than the surrounding surface when compared to the smooth surface heat transfer. And if the deposit is thinner in this wake-affected region, the lack of added insulation from the deposit could result in a local hot spot penetrating deep into the TBC layer.

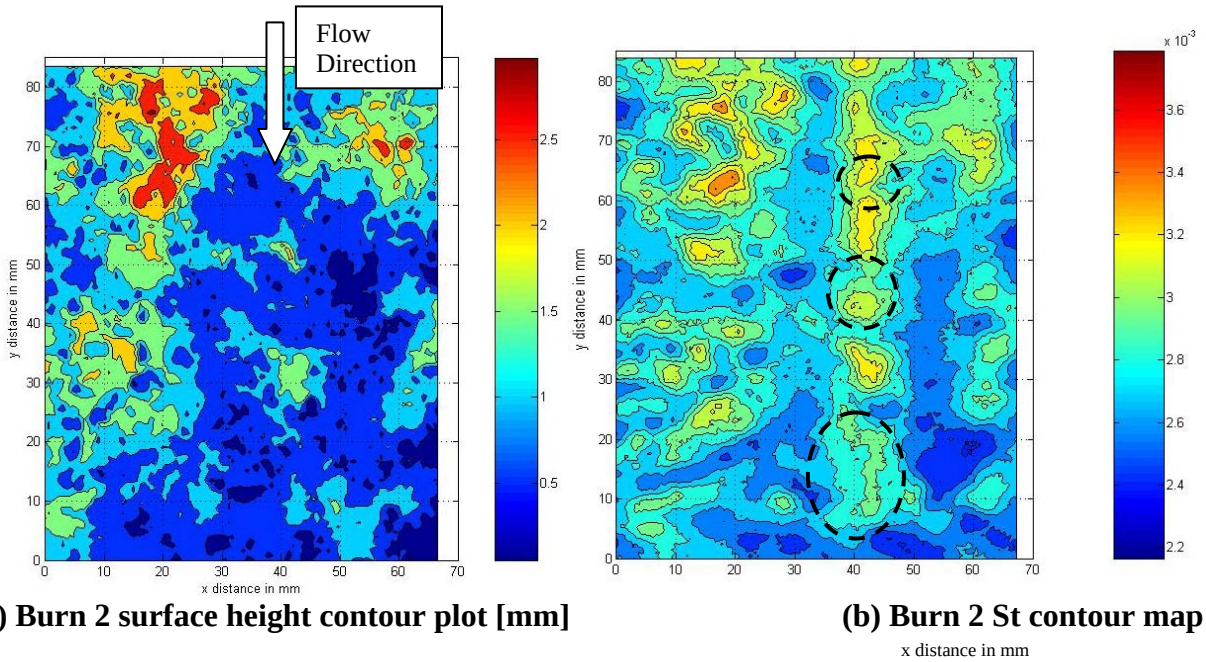

(a) Burn 2 surface height contour plot [mm] **(b) Burn 2 St contour map**

Figure 16: Heat transfer coefficient and surface height plots for a 67 mm x 83 mm region on the Burn 2 roughness model. (Flow direction is from top to bottom as indicated.) Wake regions with elevated St values are circled.

RESULTS AND DISCUSSION - AFRL

Turbine Component Measurements at AFRL: Sample blades and vanes were contributed from General Electric, Siemens-Westinghouse, and Pratt-Whitney. The majority of the test articles are from aircraft turbines with only a handful being from land-based turbines. The land-based articles generally have larger surface roughness, but are physically larger as well. Generally, the roughness appears to scale approximately with geometry. The aircraft vanes and rotor blades had operating times from 10,000 to 15,000 hours (3,000 to 9,000 cycles) while the land-based components were at 9,000 and 20,000 hours.

The aircraft turbine blades were film cooled and TBC coated. Nominally fourteen 2D traverses equally distributed on the stagnation, suction, pressure surfaces and two 3D traverses were taken on each blade. About 375 traverses were performed in all. Measurements were made using a Taylor Hobson profilometer. All relevant roughness parameters were calculated (e.g. Ra, Rq, Rz, correlation length, etc…). On the leading edge of each turbine blade, Ra ranged from 0.9 to 2.4 microns. There was no apparent correlation between Ra and service time in this region. A sample set of pressure surface data (near the leading edge) is illustrated in Figure 1 for 20 HPT blades. The centerline average roughness, Ra, is plotted vs. operating hours.

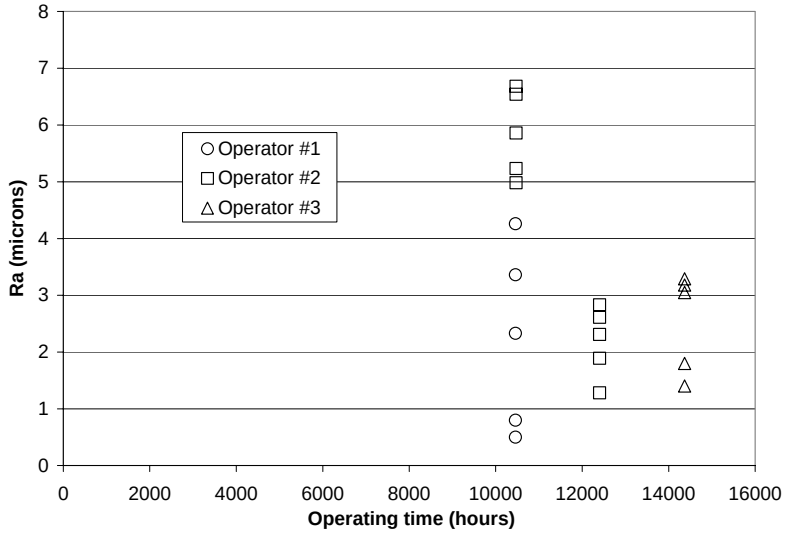

Figure 1: Ra vs. operating hours for sample of 20 HP turbine blades from 3 different operators. Data traces on pressure surface near leading edge.

The lack of correlation with service hours evidenced in Figure 5 is similar to data previously presented in Bons et al. (2001) and Tarada and Suzuki (1993). The same data plotted vs. number of cycles shows a similar lack of dependency. However, when the data is divided into blades originating from different aircraft operators, the results can be grouped as shown in the Figure. This correlation with operator suggests a dependency on operation and maintenance procedures that are specific to each engine operator. Data from the suction surfaces (not shown) evinces a similar trend - a correlation between roughness and operator rather than operating hours or cycles. This correlation appears on the suction and pressure surfaces but not on the leading edge, where values tend to remain consistent regardless of operator or cycles.

Measurements on a second set of LP and HP turbine hardware are still underway. Typical LPT roughness values are on the order of 6 to 9 microns and fairly uniform. The HPT

blades show signs of severe combustor exit temperature profiles with increases in roughness around the stagnation area near mid-span.

To supplement the data acquired from these industrial sources, contact was made with 2 engine service facilities: the Air Force's turbine maintenance facility at Oklahoma City (OC-ALC/LP) and Standard-Aero Inc. (an independent turbine overhaul facility located in Canada). Standard-Aero contributed over 20 small (3 cm chord) land-based turbine blades for the study. These test articles were taken from similar turbine designs which had operated for varying periods in different environments. A detailed analysis of the surface degradation exhibited from these specimens does indicate some evolution with time. Figure 2 shows pressure surface deposits from 3 different blades.

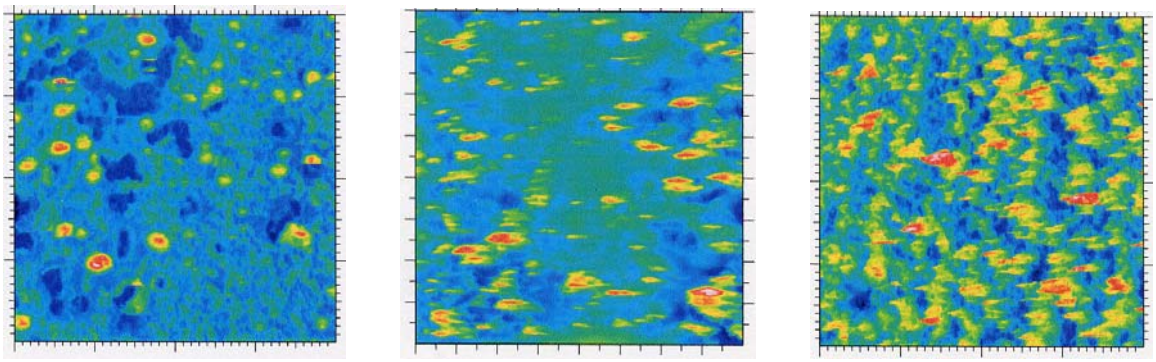

(a) (b) (c)

Figure 2: Pressure surface maps show increased deposition with service hours. Each map is 4mm x 4mm colored by height. Hours are: (a) 2,700 (b) 15,700 and (c) 25,200.

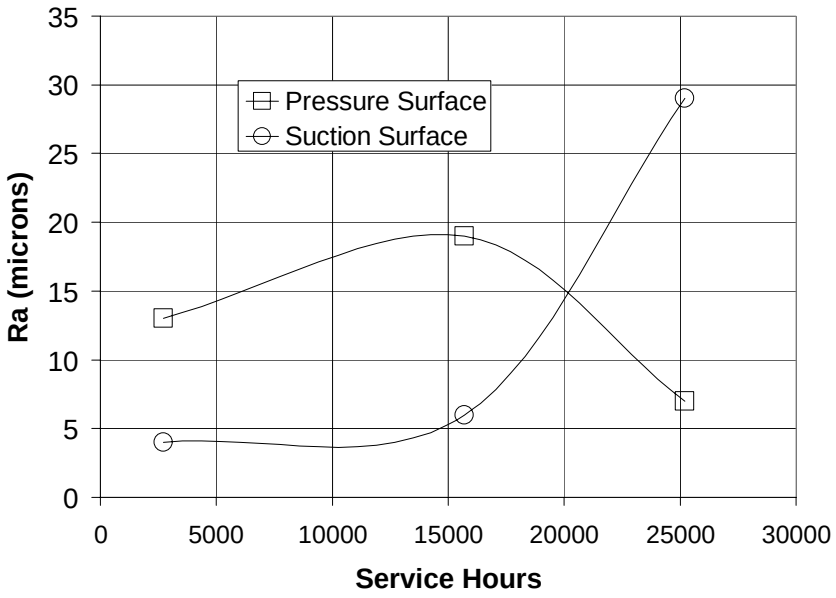

Figure 3: Trends in centerline averaged roughness (Ra) with service hours for Standard Aero turbine specimens.

Figure 3 quantifies the observed variation in Figure 2 by plotting the centerline averaged roughness (Ra) for the pressure surface measurements. The monotonic increase with service hours noted on the pressure surface is not repeated on the suction surface data. This is probably because the blades (though from similar turbines) were not operated in the same environment. As noted in the previous semi-annual report, operating conditions (including environment) appear to have a greater correlation with surface degradation than service hours alone. This explains the need for the laboratory simulation facilities being employed at BYU and UC.

Dr. Rivir also received 4 large boxes of serviced 119 blades from the Air Force's turbine maintenance facility at Oklahoma City (OC-ALC/LP).

Roughness measurements made by Dr. Rivir using eroded specimens from UC were instrumental in the development of a joint paper by UC and AFRL that was presented at the 2004 IGTI in Vienna, Austria (Paper # GT 2004-54328 "Turbine Blade Surface Deterioration by Erosion") in June, 2004. The paper has since been published in the ASME *Journal of Gas Turbines for Power and Propulsion* and was awarded the 2005 Aircraft Engine Committee award for best paper.

Previous surface roughness measurements in AFRL's 2D tunnel were extended with detailed surface static pressure measurements on one of the simulated turbine roughness surfaces. Results suggest the use of the ratio Ra/Rt (Ra, centerline-average, and Rt, peak to valley) to characterize the rough surface in the vicinity of the static pressure measurement, instead of just Ra or Rq. Data show a rate of increase in the local streamwise pressure gradient with roughness length and roughness height (Rt). Detailed BL measurements made with 2-component X wires show that all turbulence quantities increased, with normal stresses increased by factors of 2-3 over the smooth wall case. Figure 4 shows typical turbulent shear stress profiles over a scaled erosion roughness panel. Severe spanwise variations exist due to the highly irregular roughness character. Roughness was observed to cause a non-constant wall normal pressure gradient, invalidating the thin BL approximation, with wall pressures higher than free stream. It can be shown that this pressure variation is directly related to the generation of wall-normal velocity fluctuations. Inner layer recovery downstream of the roughness is slower than common sand paper roughness. The velocity profiles over these large roughness elements appear to scale with the pressure gradient velocity, u_p [$u_p^3 = (\nu/\rho)dP/dx$], rather than the traditional shear velocity, u_τ. These insights are critical to proper simulations of roughness in turbulence modeling. The paper "Effects of Strong Irregular Roughness on the Turbulent Boundary Layer" to Flow, Turbulence and Combustion Journal has been accepted for publication.

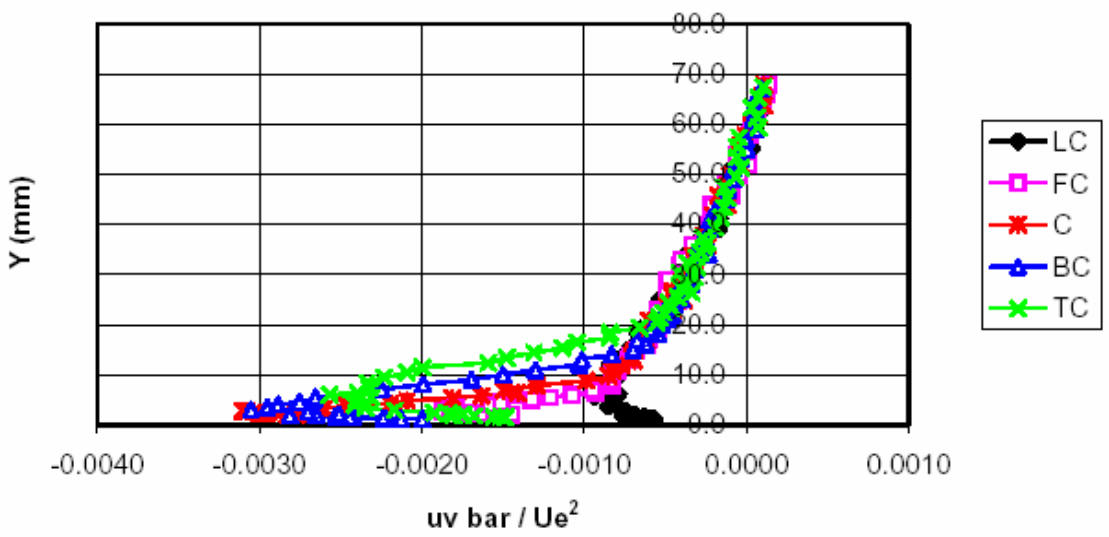

Figure 4: uv profiles vs. spanwise position for roughened surface from X-wire measurements near static pressure taps.

RESULTS AND DISCUSSION - UC

Erosion Simulation at UC: Dr. Tabakoff performed erosion testing of various coated and uncoated samples of typical turbine materials in his 2 erosion tunnels. Part of the focus during the 1st year was hot-erosion tests, conducted at 1000°F and 1500°F. Erosion rate data for 4 different materials are shown in Figure 1. Trends with impingement angle vary substantially with different coated and uncoated specimens. Though the particles used are more typical in size to those seen in aircraft turbine operation, land-based turbines can also see large particulate if operated with improper filtering.

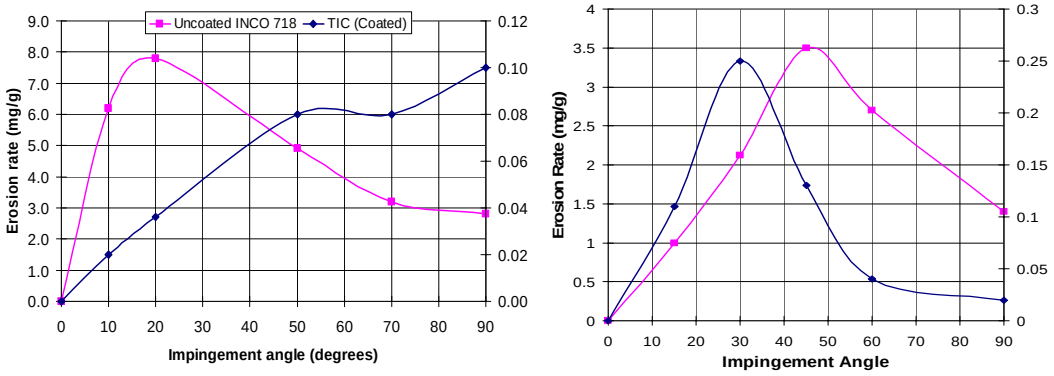

(a) (b)

Figure 1: Erosion rate data for (a) 1550 ft/sec, 1000°F with chromite particles and (b) 1850ft/sec, 1500°F, with fly ash particles.

Computational Modeling at UC: Dr. Hamed first completed a preliminary flow calculation validating 2D code accuracy for the 1st Stage GE E3 LP Turbine. The stage configuration is shown in Figure 2 with pertinent operating conditions.

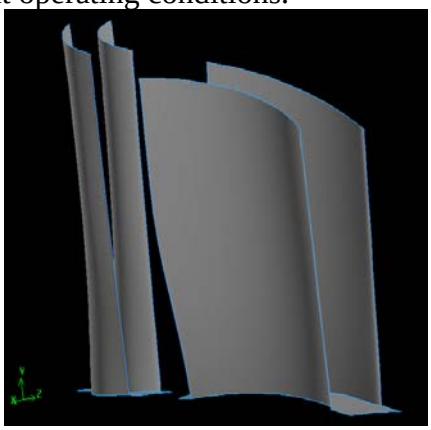

Figure 2: 1st Stage GE E3 LP Turbine configuration for UC flow simulation (Inlet stagnation temperature = 2000°R, inlet stagnation pressure=37 psia, stage pressure ratio = 1.3, at 3450 rpm).

Numerical simulations were next conducted to determine the three-dimensional flow field and the associated solid particle trajectories through the GE E3 first stage LP turbine. The compressible viscous flow simulations were based on the implicit solution of the Reynolds-

averaged Navier-Stokes equations in conservation law form, and the RNG κ–ε turbulence mode. The Lagrangian particle dynamics simulations were performed in the relative reference frame of each blade row and included models for the momentum exchanges with the flow field and blade passage surfaces. Particle-gas interaction models represent the momentum exchange between the two phases through the aerodynamic forces due to the motion of particles relative the gas flow field. Experimentally based particle-surface interaction models are used in the trajectory simulations to determine the particle restitution characteristics after they impact the vane and blade surfaces.

Figure 3 presents the discretizational grid used in the flow field, particle trajectories, and blade erosion rate computations. Sample results from the 3-D trajectory simulations for 30-micron particles through the vanes and rotor are presented in **Figure 4**. One can see that the particles impact the vane pressure surface and rebound with reduced absolute velocities. Because of their lower velocities relative to the gas they first impact the rotor blade suction surface and gain sufficient momentum to continue their trajectory and impact the rotor blade pressure surface. The experimentally measured erosion rate data previously acquired in Dr. Tabakoff's erosion tunnel testing was then used along with the vane surface impact data (e.g. Figure 4) to compute the vane erosion rate per unit surface area per unit mass of ingested particles in the turbine. **Figure 5** shows increasing erosion rates over the vane's pressure surface towards the trailing edge and a narrow high-erosion band at the vane's leading edge.

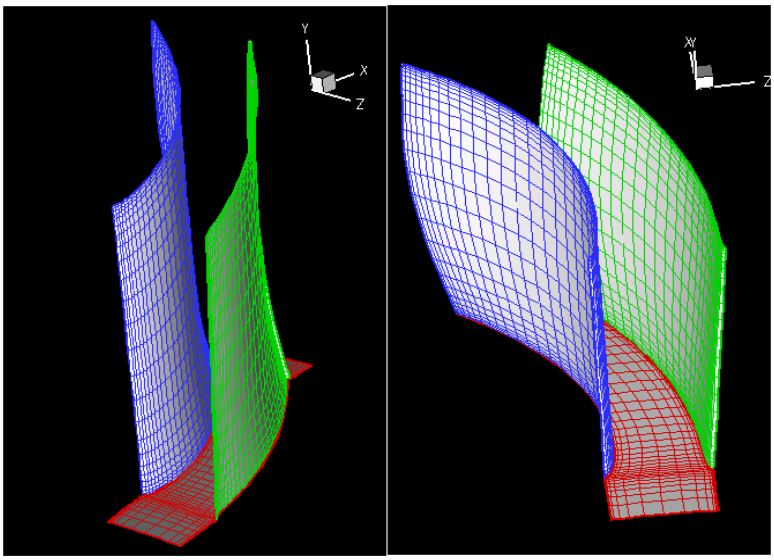

Figure 3. Computational grid for UC Erosion Simulation

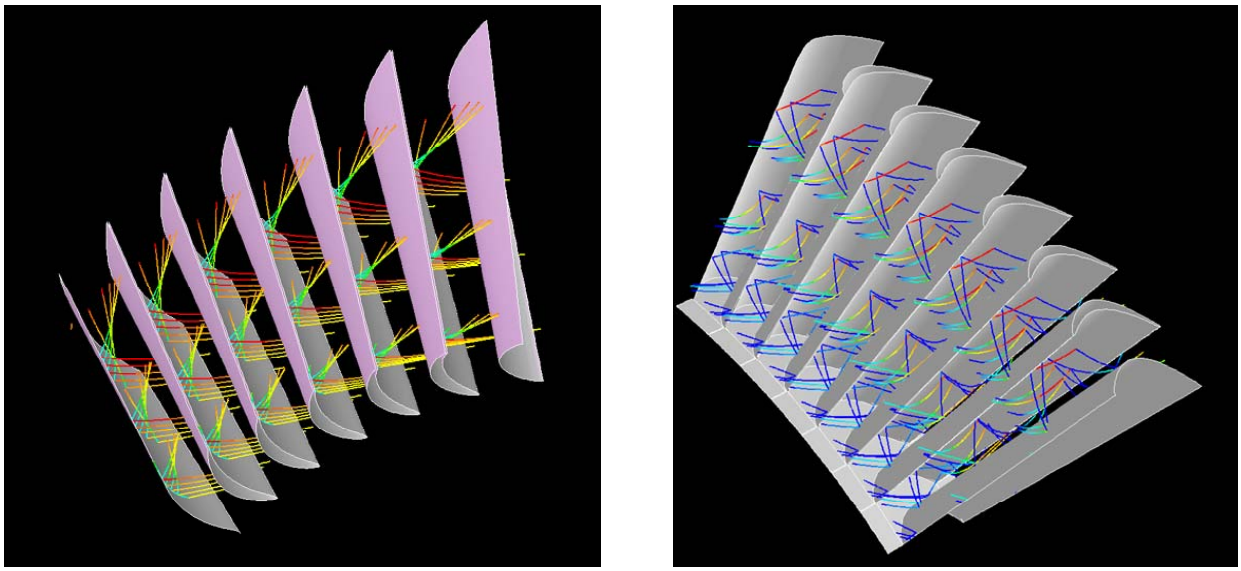

a. Rear view of the stator b. Front view of the rotor

Figure 4. Sample 30 micron particle trajectories

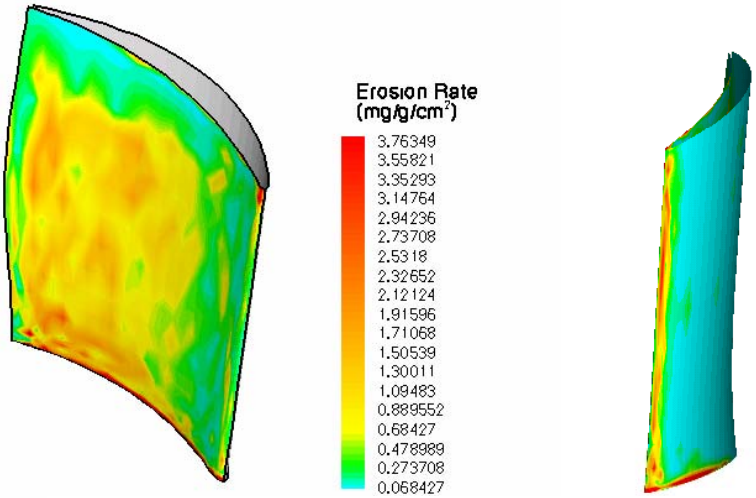

a: Vane pressure surface b: Vane leading edge

Figure 5. Vane Surface Erosion rate

These results were presented in a joint paper with AFRL at the 2004 IGTI in Vienna, Austria (Paper # GT 2004-54328 "Turbine Blade Surface Deterioration by Erosion") in June, 2004. The paper has since been published in the ASME *Journal of Gas Turbines for Power and Propulsion* and was awarded the 2005 Aircraft Engine Committee award for best paper.

RESULTS AND DISCUSSION - ISU

3D Computational Roughness Modeling at ISU: The following summarizes efforts conducted by Drs. Wang and Shih to produce accurate 3D roughness simulations.

Direct Simulation of Surface Roughness Effects with a RANS Approach on Viscous Adaptive Cartesian Grids

Z.J. Wang, X.K. Chi and Tom Shih
Department of Aerospace Engineering, Iowa State University, Ames, IA 50011-2271

Summary

The main objective of this research is to directly compute the skin friction (c_f) and heat transfer (St) coefficients on real rough surfaces using a state-of-the-art unstructured adaptive grid-based finite volume method. Recent experiments with real roughness panels by Bons are computationally simulated in this study. Computational results are compared with experimental data to assess the simulation accuracy. A RANS (Reynolds-Averaged Navier-Stokes) approach based on the Spalart-Allmaras turbulence model was employed for the computations, and grid refinement studies were conducted to assess the effects of grid resolution. In two cases with rough surfaces, the RANS approach is capable of accurately predicting c_f (within 3.5%) while under-predicting S_t by 13%.

Technical Approach and Results

Viscous Cartesian Grid Generation

The viscous Cartesian grid generation method is a recently developed automatic grid generation approach for very complex, and possibly "dirty" geometries. The three major steps in the method are described as follows.

Adaptive Cartesian Grid Generation: The grid generation method is initiated by specifying the minimum and maximum sizes of Cartesian grid cells to be generated. The adaptive Cartesian grid is generated by recursively subdividing a single coarse root Cartesian cell. Since the root grid cell must cover the entire computational domain, the surface geometry is contained in the root cell. The size of the Cartesian cells intersecting the geometry is controlled by constraining the cell size in the geometry normal and tangential directions. The recursive sub-division process stops when all the Cartesian cells intersecting the geometry satisfy the length scale requirements. To insure solution accuracy, the maximum cell aspect ratio and grid smoothness were also monitored. In the present study, the sizes of any two neighboring cells in any coordinate direction cannot differ by a factor exceeding two.

Cartesian Grid Front Generation and Smoothing: In order to "insert" a viscous layer grid between the Cartesian grid and the body surface, Cartesian cells intersected by the geometry must be removed, leaving an empty space between the Cartesian grid and the body surface. All the Cartesian cells intersected by the geometry are determined using a tree-based search algorithm. Once the Cartesian cells intersected by the geometry, and cells outside the computational domain are removed, a Cartesian grid "volume" remains. The boundary faces of this volume form the Cartesian front. Before this front is "projected" to the geometry, it is smoothed with a Laplacian smoother.

Projection of the Cartesian Front to the Body Surface: After the smoothed Cartesian front is obtained, each node in the front needs to be connected to the body surface to form the viscous grid needed to resolve the turbulent boundary layer. After the front is projected to the boundary geometric entities, a "water-tight" surface grid is generated on the boundary. The “foot prints” of the layer grids on the body surface have the same topology (or connectivity) as the Cartesian front. By connecting each point on the Cartesian front with the corresponding projected point on the boundary, a single layer of prism grids is obtained. This single layer can be sub-divided into multiple layers with proper grid clustering near the geometry to resolve a viscous boundary layer.

Example viscous adaptive Cartesian grids for both the fuel deposit and the erosion surface geometries are displayed in Fig. 1. The surface grid generated from the Cartesian front projection is displayed in Fig. 2 (for the erosion surface only). The grid cells near the roughness panels are adaptively refined to resolve the roughness elements.

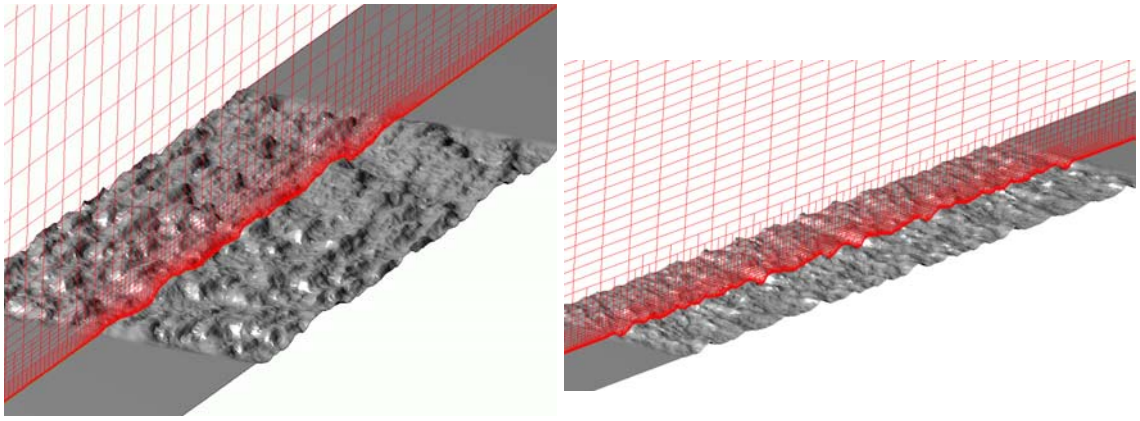

(a) (b)

Figure 1. Cutting planes showing the viscous adaptive Cartesian grids for the (a) fuel deposit and (b) erosion surfaces. Roughness regions are 240mm x 120mm and 240mm x 60mm respectively.

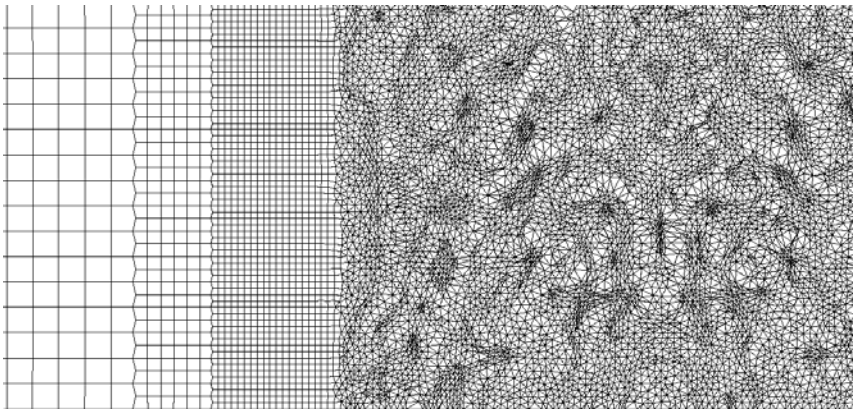

Figure 2. Surface grid on the erosion surface showing grid refinement near leading edge.

Numerical Method

A flow solver capable of handling arbitrary polyhedrons has been developed to uniformly handle the adaptive Cartesian and the viscous layer grids. The Reynolds-averaged Navier-Stokes equations can be written in the following integral form:

$$\int_V \frac{\partial Q}{\partial t} dV + \oint_S (F - F_v) dS = 0 \tag{1}$$

where Q is the vector of conserved variables, F and F_v are inviscid and viscous flux vectors, respectively. The integration of Eq. (2) in an arbitrary control volume, V_i, gives:

$$\frac{d\overline{Q_i}}{dt} V_i + \sum_f F_f S_f = \sum_f F_{v,f} S_f \tag{2}$$

where $\overline{Q_i}$ is the vector of cell-averaged conserved variables, F_f and $F_{v,f}$ are the numerical inviscid and viscous flux vectors through face f, and S_f is the face area. To compute the inviscid and viscous fluxes through any given face, the standard Godunov-type finite volume approach is employed. Using a linear least-squares reconstruction algorithm, a cell-wise linear distribution can be built for each solution variable (in the present study the primitive variables). To compute the inviscid flux, an approximate Riemann solver such as Roe flux difference splitting is used given the reconstructed solutions at both sides of a face. To handle steep gradients or discontinuities, a limiter due to Venkatakrishna is used. The viscous flux is computed using a simple and robust approach presented by Wang without a separate viscous reconstruction.

Although explicit schemes are easy to implement, and are often useful for steady-state, inviscid flow problems, implicit schemes are found to be much more effective for viscous flow problems with highly clustered computational grids. An efficient block LU-SGS (Lower-Upper Symmetric Gauss-Seidel) implicit scheme has been developed for time integration on arbitrary grids. This block LU-SGS (BLU-SGS) scheme takes much less memory than a fully (linearized) implicit scheme, while having essentially the same or better convergence rate. The BLU-SGS scheme can be used to integrate Eq. (2) with first or second order accuracy. For steady flow computations, the backward Euler approach is employed, i.e.,

$$\frac{Q_i^{n+1} - Q_i^n}{\Delta t} V_i + \sum_f F_f^{n+1} S_f = \sum_f F_{v,f}^{n+1} S_f . \tag{3}$$

To simulate flow turbulence, a RANS Spalart-Allmaras (S-A) model was employed without modifications. The computational domain extends from x = 0 to 2.04 m in the wind tunnel. To further reduce the computational cost, only 1/3 of the 0.36 m transverse span of the tunnel is included in the computational domain for the fuel deposit surface, while only 1/6 is included for the erosion surface. Symmetry or slip wall boundary conditions are used on the two end walls in the span-wise direction.

Two viscous adaptive Cartesian meshes were generated for each of three cases: smooth wall, fuel deposit surface, and erosion surface. The cell count and average y+ for the first layer grids next to the wall are shown in Table 1.

Table 1: Grid sizes for 3D RANS model.

	Number of Cells	Average y+
Smooth Wall – coarse	37,888	0.8
Smooth Wall – fine	58,368	0.3
Fuel Deposit Surface – coarse	1,260,051	~1
Fuel Deposit Surface – fine	3,999,040	~1
Erosion Surface – coarse	873,221	~1
Erosion Surface - fine	1,601,430	~1

For the rough surfaces, the fine grid essentially doubles the grid resolution near the roughness panels while maintaining an average y+ of 1 in the wall normal direction. The coarse mesh has about 64 cells in the span-wise direction with a grid resolution of about 1 mm along the tangential direction, while the fine mesh has a grid resolution of about 0.5 mm. The fine grids have about 50-80 layers in the tunnel height direction. If structured grids were used for this configuration, the fine grid would have about 10-25 million cells. Thus, by using the viscous adaptive Cartesian grid approach, the number of grid cells is reduced by over an order of magnitude.

To further speed convergence, local time steps are used in Eq. (3). The flow convergence is monitored by the history of the average c_f and St over the roughness panels, with the solution typically converging after a few thousands of iterations. Grid generation was executed on a Pentium 4 Linux workstation (2.8GHz), requiring 2-4 hrs per rough surface. Due to the size and complexity of the surfaces, even the finer computational grids required that the surface data matrix be sampled by every 4^{th} data point in the streamwise (x) and spanwise (z) directions. The surface resolution was thereby reduced from the printed experimental model, with approximately 14% less wetted surface area (i.e. $S_w/S = 1.06$ vs. 1.2). The RANS solver required 24 hrs to reach a converged solution on a Linux cluster with 8 processors.

To simulate the transient method used for the experimental St measurement, both models start the thermal and velocity boundary layers simultaneously at x=0 (without an unheated starting length). Also, since the thermal boundary condition at the wall is neither constant wall temperature nor constant wall heat flux, the models employed an exponential $T_w(x)$ boundary condition derived empirically, i.e… $[T_e-T_w(x)]/\Delta T_{TS} = (x/x_{TS})^{0.1}$. This distribution accounts for the increased thermal resistance of the thermal boundary layer from the leading edge to the measurement location. The experimental freestream velocity and temperature were used as inflow conditions.

Results and Discussion

Table 2 contains the predicted and experimental values of area-averaged c_f and St for the smooth and rough panels. The 3D RANS data are for the fine and coarse grid models. Also shown in the table are smooth and rough-wall correlation values which are provided as a reference. The various rough wall correlations were all derived using a sandgrain roughness height (k_s) based on the experimentally measured Sigal-Danberg (Λ_s) parameter from Table 1.

Table 2: Comparison of c_f and St data from experiment, computation, and correlations.

Skin Friction, c_f	Smooth	Fuel Deposit	Erosion Surface
Experimental	0.00349	0.00937	0.0103
3D RANS Model - fine	0.00345	0.00970	0.0100
3D RANS Model - coarse	0.00333	0.0128	0.0113
Empirical Correlations	0.00367	0.0083-0.0112	0.0087-0.0119
Stanton Number, St	Smooth	Fuel Deposit	Erosion 2
Experimental	0.00215	0.00308	0.00308
3D RANS Model - fine	0.00204	0.00274	0.00304
3D RANS Model - coarse	0.00199	0.00268	0.00268
Empirical Correlations	0.00219	0.0034-0.0037	0.00345-0.0038

The skin friction predictions for the 3D RANS fine-grid models are within 3.5% of the experimental values in all 3 cases. This is a marked improvement over the k_s-based empirical correlations for c_f which ranged from 16% below to 20% above the measured values. The agreement in St is not as good, with the RANS predictions falling within ±13% of the experimental data (compared to ±23% for the empirical correlations).

Conclusions

In the present study, the skin friction (c_f) and heat transfer (St) coefficient on real rough surfaces are directly computed using a state-of-the-art unstructured adaptive grid-based finite volume flow solver. Computational results are compared with experimental data to assess the simulation accuracy. Based on the present study, the following conclusions can be drawn:

1. The unstructured adaptive grid generation method is very efficient in resolving disparate length scales. It is estimated that the number of cells generated is over an order of magnitude less than that with a structured grid. The rough surfaces can be handled by the grid generator with minimum user interference;
2. On the flat panel case, the RANS approach is capable of predicting c_f and St, thus validating the implementation;
3. With proper grid resolution, the S-A model was able to accurately predict c_f for both rough surfaces (within 3.5% of experimental data). The computational predictions for St showed 13% differences from the experimental data.

This work has been presented in the following venues:

1) "A Comparison of Approximate vs. Exact Geometrical Representations of Roughness for CFD Calculations of cf and St," by J.P. Bons, S.T. McClain, Z.J. Wang, X. Chi, and T.I. Shih. Presented at IMECE 2005 in Orlando, FL, Nov. 2005. Submitted for publication in *ASME Journal of Turbomachinery* June 2005. Accepted for publication – Jan. 06.
2) "Direct Simulation of Surface Roughness Effects with a RANS and DES Approach on Viscous Adaptive Cartesian Grids," by Z. Wang, X. Chi, T. Shih, and J.P. Bons. Presented at the 2nd AIAA Flow Control Conference in Portland, OR, 28 June – 1 July (paper #AIAA 2004-2420)

2D Computational Modeling at ISU: Dr Tom Shih at Iowa State University is pursuing efficient models for roughness simulations. Since 3-D unsteady DNS calculations for a rough turbine blade are still prohibitive due to computational requirements, it is necessary to evaluate more efficient alternatives using 2D simulations and lower order turbulence models. During the past six months, Dr. Shih's team has focused on analyzing the statistical properties of the roughness surfaces provided by Jeffrey Bons. 2D slices were then selected from each 3D surface ensuring that they had similar statistics to the full 3D rough surface. Table 3 shows a typical result of this process.

	Ra	**Rq**	**Sk**	**Ku**	**Rt**	
3D surface	1.239274	1.503101	0.154	2.64	7.19	
2D sample	1.239954	1.507079	-0.0305	2.247641	6.16	X = **23.12782**

Table 3: 3D and 2D data for Ra, Rq, Rt, Sk, Ku

Using these 2D models, CFD simulations were performed of boundary-layer flow over the 2D slice. This was followed by a detailed parametric study of the effects of boundary-layer thickness and various roughness geometric parameters. Basically, Dr. Shih's team is doing a series of 2D CFD simulations in which the 2D slice is kept the same, but the approaching boundary layer has different thicknesses. The above is being repeated for several different 2D slices that represent typical and extreme roughness shapes. This study will be completed by the DOE workshop meeting in September 2004. In addition to the above, Dr. Shih is also performing 2D simulations of roughness after film cooling from a slot.

Some results from ISU's roughness study are shown below. Figure 3 shows a typical grid for a 2D slice of the 3D rough surface. Please note the high resolution of the roughness geometry. Figure 4 shows typical results for the velocity magnitude about the roughness. The predictions are made using Fluent with a Spallart-Almaras turbulence model. Figure 5 shows the separated region behind a roughness element via velocity vectors. Results from these studies can be compared to higher-order 3D calculations for validation. Also, c_f and St predictions from 2D simulations can be used to gage the relative importance of various roughness and boundary layer parameters.

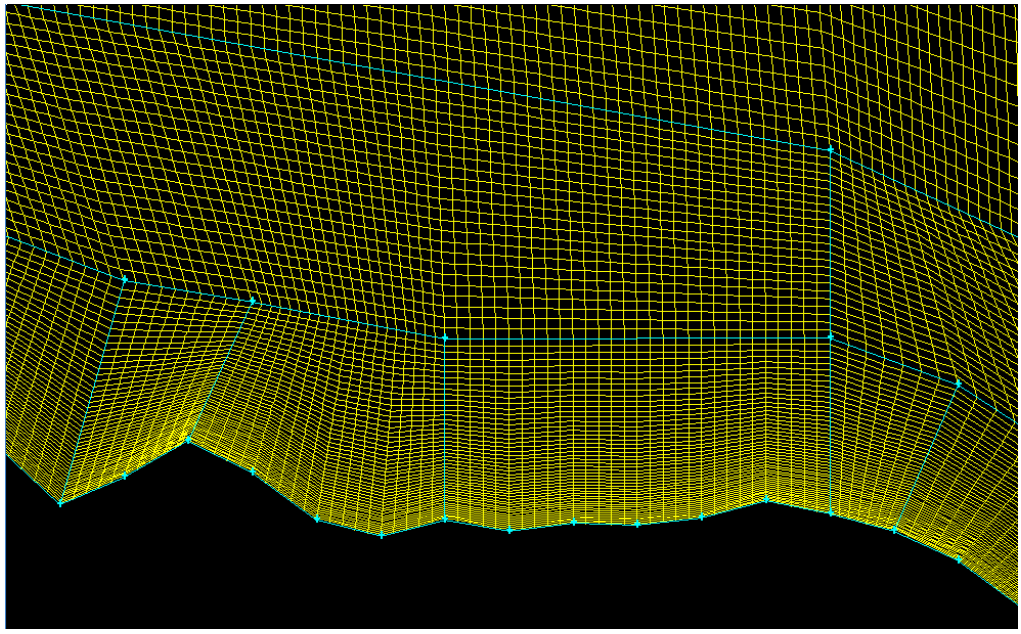

Fig. 3. Grid system for a 2D slice of the 3D rough surface.

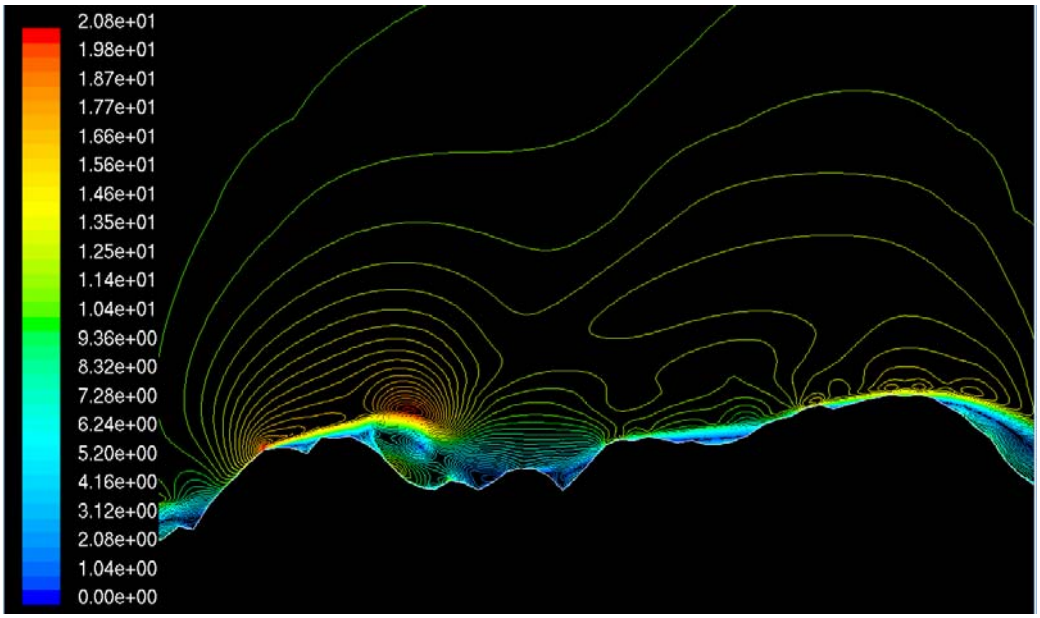

Fig. 4. CFD results for the velocity magnitude. Freestream velocity is 10 m/s.

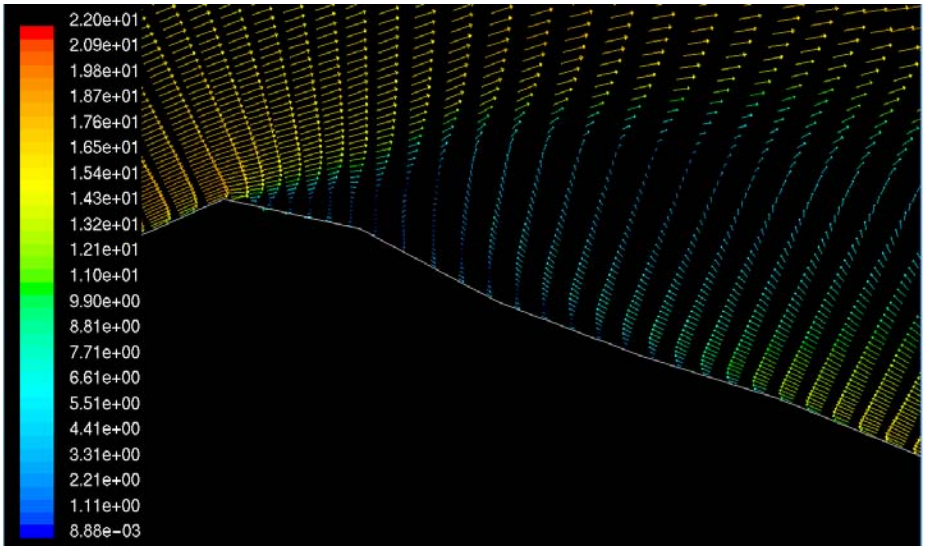

Fig, 5. Separated region downstream of a roughness element.

This work has been presented in "Flow and Heat Transfer over Rough Surfaces: Usefulness of 2-D Roughness-Resolved Simulations," by S. Yoon, S. Na, Z.J. Wang, J. P. Bons, and T.I-P. Shih. Presented at the AIAA 44th Aerospace Sciences Meeting and Exhibit in Reno, NV, 9-12 Jan 2006 (paper #AIAA 2006-0025).

CONCLUSIONS:

In conclusion, results from this three year roughness study are very promising. Industrial participation was excellent and synergy between the four groups on the team was healthy. The study included both the measurement of actual hardware and the laboratory simulation of degradation mechanisms (erosion and deposition). By performing the two components in parallel, we hope to have insured the relevancy of the laboratory simulations. Because they are performed in a controlled environment, these erosion and deposition studies should provide the framework for semi-empirical roughness evolution models. As these models are incorporated into computational codes, this will in turn provide the engine community with powerful roughness predictive capabilities.

REFERENCES:

Bons, J.P., Taylor, R., McClain, S., and Rivir, R.B., "The Many Faces of Turbine Surface Roughness," *Journal of Turbomachinery*, Vol. 123, No. 4, October 2001, pp. 739-748.

Bons, J.P., "St And c_f Augmentation For Real Turbine Roughness With Elevated Freestream Turbulence", *Transactions of the ASME J. Turbomachinery, Journal of Turbomachinery*, Vol. 124, No. 4, October 2002, pp. 632-644.

Bons, J.P, "A Critical Assessment of Reynolds Analogy for Turbine Flows," *ASME Journal of Heat Transfer – Special Issue on Gas Turbines* Vol. 127, May, 2005, pp. 472-485.

Borom, Marcus P., Johnson, Curtis A., and Peluso, Louis A., 1996, "Role of environmental deposits and operating surface temperature in spallation of air plasma sprayed thermal barrier coatings," Surface and Coatings Technology 86-87, pp116-126.

Hamed, A., Tabakoff, W., Rivir, R.B., Das, K., and Arora, P., "Turbine Blade Surface Deterioration by Erosion," presented at IGTI04 in Vienna, June 2004 and accepted for publication. Paper # GT-2004-54328.

Jensen, J.W., Squire, S.W., Bons, J.P., and Fletcher, T.H., "Simulated Land-Based Turbine Deposits Generated In An Accelerated Deposition Facility". To be presented at IGTI 2004 in Vienna, June 2004. Paper # GT2004-53324.

Kim, J., Dunn, M.G., and Baran, A.J. et al, 1993, "Deposition of Volcanic Materials in the Hot Sections of Two Gas Turbine Engines," J. Engr. Gas Turbines & Power vol. 115, Jul 1993, pp 641-651.

McClain, S.T., Hodge, H.T., and Bons, J.P., 2004, "Predicting Skin Friction and Heat Transfer for Turbulent Flow over Real Gas-Turbine Surface Roughness Using the Discrete-Element Method," *ASME Journal of Turbomachinery*. Vol. 126, pp. 259-267, Apr. 2004.

Subramanian, C.S., King, P.I., Reeder, M.F., Ou, S., and Rivir, R.B., "Effects of Strong Irregular Roughness on the Turbulent Boundary Layer," 2003, accepted for publication in the *International Journal of Flow, Turbulence and Combustion*.

Tabakoff, W., and Wakeman, T., 1979, "Test Facility for Material Erosion at High Temperature," ASTM Special Publication 664, pp. 123-135.

Tarada, F. and Suzuki, M., 1993, "External Heat Transfer Enhancement to Turbine Blading due to Surface Roughness," presented at ASME IGTI in Cincinnati OH, May 1993, ASME Paper 93-GT-74.

Wang, Z.J., Chi, X.K., Shih, T., and Bons, J., 2004, "Direct Simulation of Surface Roughness Effects with RANS and DES Approaches in Viscous Adaptive Cartesian Grids," presented at AIAA Flow Conference in Portland OR, June 2004, #AIAA-2004-2420.

Wenglarz, R. A., and Fox, R. G., "Physical Aspects of Deposition from Coal Water Fuels under Gas Turbine Conditions", ASME Journal of Engineering for Gas Turbines and Power, vol. 112, January, 1990, pp. 9-14.

Wenglarz, R.A., and Wright, I.G., "Alternate Fuels for Land-Based Turbines," published in proceedings of the "Workshop on Materials and Practices to Improve Resistance to Fuel Derived Environmental Damage in Land- and Sea-Based Turbines", October 22-24, 2002, Colorado School of Mines, Golden, Colorado.

Advanced optical sensor for monitoring and control of multiple gas and turbine-blade properties

Final report

Reporting period: 7/1/2003 – 6/30/2006

Principal investigator: Scott T. Sanders

Report date: March 13, 2007

DOE award number: DE-FC26-02NT41431

UTSR project number: 03-01-SR105

Submitted by:
Scott T. Sanders
University of Wisconsin-Madison
1500 Engineering Dr.
Madison, WI 53706

DISCLAIMER

ABSTRACT

Fiber-optic sensors for monitoring gas properties in turbine engines were developed in this project. The sensors are designed to measure information such as the temperature profile of combustion gases at the turbine inlet. We have also demonstrated the sensor's ability to monitor temperatures in the turbine blades themselves. This capability is not offered by thermocouples or similar instrumentation, which can only be used to monitor temperatures of stationary parts. We have regularly visited gas turbine test facilities to demonstrate our sensing technology and to remain abreast of challenges to practical optical sensors. We have also investigated the possibility of using the sensors for real-time control of gas turbine performance, with the goals of reduced emissions and increased efficiency.

TABLE OF CONTENTS

INTRODUCTION

We have demonstrated the capability to fiber-couple light to and from optically harsh turbine environments, such as the research mainburner test rig shown in Figure 1. This project aims to maximize the amount of useful information that can be obtained from such optical access. Key considerations include: tailoring fiber-optic access for gas turbine environments, using wavelength-tunable lasers to acquire spectral information from the test environment, and reducing measured optical data to quantitative properties. The "research-grade" sensors developed in this project are expected to be directly useful to gas turbine engine researchers; in addition, the sensing methodologies should ultimately contribute to the design of "production-grade" sensors.

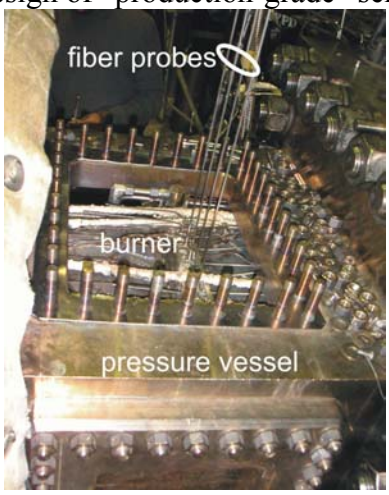

Figure 1. Gas turbine combustor test facility at Wright-Patterson Air Force Base with fiber-optic probes installed

EXECUTIVE SUMMARY

We are developing fiber-optic sensors for measuring gas and turbine blade properties in gas turbine engines. Toward that end, we have made many important accomplishments this reporting period. We categorize our accomplishments into four categories: fiber optic access, wavelength-agile lasers, optical data reduction, and technology transfer.

Fiber-optic access

Aided by discussions with Pratt & Whitney, General Electric, and Woodward Industrial Controls, we have refined our strategy for maintaining fiber-optic access to the mainburner/turbine area. We use a single fiber to deliver and receive laser light at each measurement station. This simplification is made possible by using a co-axial dual-clad fiber (DCF)[1]. Signal light is transmitted to the engine down the axis(core) of the DCF, and received from the engine in the cladding surrounding the core. Various reflective surface options are available to return light efficiently to the DCF; one candidate is a

thermal barrier coating (TBC) containing tailored voids or sapphire spheres. We have refined our strategy for distributing light to many dual-clad fiber locations (up to 64) using fiber-optic components; our design incorporates a single laser, a single detector, and no moving parts. We have carefully considered "beam steering", for example as discussed in [2]; "beam steering" refers to the non-ideal light propagation that occurs in materials of inhomogeneous refractive index, such as combustion gases. We have developed a computer code that optimizes optical designs in beam steering environments, and used it to make a three-fold improvement in collection efficiency. We have solved similar optical access problems relative to communicating optical signals with fiber Bragg gratings embedded in moving metal components[1].

Wavelength-agile lasers

A key to obtaining quantitative information in harsh environments is the ability to acquire optical spectra, rather than optical information at just one or two wavelengths. We have demonstrated the value of lasers that scan quickly through a broad range of wavelengths, such as 1374 nm – 1472 nm every 85 μs[3] and 1335 nm – 1375 nm every 5 μs (as described below). We continue to draw on our laser expertise in developing wavelength-agile lasers with high average power (> 10 mW), rapid tunability and low intensity noise. The lasers are based on robust moving parts such as laser printer scanners [4] or alternatively on supercontinuum generation[5,6]. We have also begun collaborating with Prof. James Fujimoto's group at the Massachusetts Institute of Technology to develop and apply next-generation wavelength-agile systems.

Data reduction

We have enhanced our computer algorithm used to infer gas properties from measured spectra. Our automated, LabVIEW-based system is now able to reduce H_2O vapor spectra recorded in gas turbine burners to temperature in near-real time, with an absolute accuracy of ± 2% or better. To accomplish this performance, we have used piston engines readily available to us in the UW Engine Research Center to record the spectra of hot, high-pressure gases in controlled experiments. These experiments are valuable not only for assessing the accuracy of our measurements but also as a preparation or "sensor check-out" that we routinely perform before visiting off-site gas turbine engine facilities.

Technology transfer

We have begun pursuing industrial partners to commercialize our wavelength-agile technology so that it can receive more widespread use in the gas turbine industry. We have begun discussions with Nufern, a company specializing in fiber optics and with Thermo Electron, a company with deep roots in commercialized spectroscopic sensors, predominantly Fourier transform infrared (FTIR) spectrometers. We have published an invited article in a prominent optics magazine in which we highlight the gas turbine application for wavelength-agile lasers[7]. This article has helped to capture the attention of additional industrial players that may prove important in helping to bring advanced fiber-optic sensing to the gas turbine community.

The accomplishments in each of these four categories bring our sensing strategy much closer to the goal of revealing temperature information in the mainburner and turbine. By providing this new information, the sensor will be useful in a number of ways, all of which ultimately increase efficiency, reduce emissions, and increase component lifetime. First, the sensor can be used in engine test facilities for optimization of the temperature profile entering the turbine. The most desirable operating conditions can be mapped out in this way. Second, the sensor can be used to diagnose new engine designs. By rapidly providing insight into the combustion process, new designs can be evaluated more effectively. The direct effects of operating an engine on syngas, for example, could be evaluated in this manner. Finally, once the sensor has established more widespread use as a testing aid in the turbine industry, the sensor could be integrated into production engines to enable active, real-time control of temperature distributions. This strategy would likely have the most dramatic effect on engine performance, by allowing robust optimization under dynamic conditions.

In addition to the uses listed above, the sensor could also have broader impacts in the turbine industry. The sensor is designed to measure gas temperature and water vapor mole fraction in combustion gases. However, the same strategy (and in some cases the exact same equipment) could also be used to measure temperature or other gas species concentrations at a variety of locations in turbine systems.

PROJECT DESCRIPTION

Gas turbine engine designers have expressed a desire to accurately monitor and / or control the temperature distribution of gases entering the turbine. This is because of the important role temperature plays in determining engine efficiency, emissions levels, and component lifetime. Careful optimization of the temperature distribution at the turbine inlet would enhance engine efficiency and reduce emissions. The optical sensor developed in this project will address this need by enabling measurements of gas temperature distributions at the turbine inlet as well as actual turbine blade temperatures. We envision laser light distributed by fiber-optics and pitched through the combustion gases as well as routed through turbine blade material to support these measurements. The primary goals of this project are demonstrations of the sensor in large-scale test facilities. These demonstrations will pave the way for more widespread sensor use in the gas turbine industry.

At the conclusion of the project, it is hoped that the sensor will become a ready tool for optimizing the gas temperature distribution entering the turbine, possibly by active closed-loop control. In addition, they can potentially be used for “plug-and-play” attachment to prototype engines under test, thus providing critical information at the design stage and thereby reducing the cost of evaluating engine designs.

EXPERIMENTAL

The enabling technology in this research program is "wavelength-agile" absorption spectroscopy; a technique developed by the principal investigator over the past 5 years. The details of the approach are available in the literature[8-11]. In brief, a laser is made to scan through a broad range of wavelengths (e.g., 1330-1670 nm) in a short time (e.g., once every microsecond). This wavelength-agile laser can then be used to continuously monitor the spectral characteristics of the test article. For example, the laser can be directed through combustion gases and its transmission recorded by a photodetector; as transmission spectra are acquired, gas temperature and composition information can be monitored. Note that the measured gas properties are an average along the line-of-sight through the gas. The temperature of fiber-optic components embedded in metals can be measured in a similar fashion; however, in that case the measurements are local rather than spatially averaged. In short, using wavelength-agile lasers, high-resolution spectra of just about anything can be measured rapidly and repeatedly, and we have identified ways to use such spectra for measuring temperatures of interest to gas turbine researchers.

The primary reason for scanning the laser through a broad range of wavelengths is to obtain a large amount of spectral information, which in turn yields accurate measurements of multiple parameters even when the measurement volume is cycled through a wide range of conditions. By scanning the laser quickly, factors such as vibrations, laser beam steering, and window fouling, which would normally impair a spectral measurement, are essentially frozen. Thus, high-quality spectra can be obtained even in very harsh environments. Another benefit of scanning the laser rapidly and repetitively is the ability to monitor properties continuously with fast time response, as required for tracking transient or unstable processes.

In conjunction with turbine engine testing, we have learned a tremendous amount by applying this same sensing strategy to piston engines running in homogeneous-charge compression ignition (HCCI) mode. Essentially, we treat the HCCI engine as a controlled gas charge and use the system to record gas spectra at combustion conditions. This approach helps our gas turbine measurement in two key ways: (1) by proving the sensors in a combustion environment prior to travel to off-site facilities and (2) by allowing us to develop a database of gas spectra at combustion conditions so that we can infer more accurate gas properties in the turbine environment. Results from recent measurements in the piston engine environment will be provided here, to familiarize the reader with the experimental procedures and the type of information provided by the optical sensors. More detail on HCCI engine measurements is available in the literature[3]. Also note that we have installed fiber Bragg gratings into pistons to measure the temperature of the moving piston. This application is likewise beneficial for refining turbine-blade temperature sensing strategies based on the same approach.

In Figure 2 we present our arrangement for gas temperature measurements in HCCI engines. The wavelength-agile laser generates light that rapidly scans through wavelengths where water vapor absorbs. This system scans from 1380 – 1470 nm in 43

μs with a power of approximately 100 μW. The wavelength-agile light is coupled to a single measurement path along a diameter of the engine. A straight-through coupling for transmission measurements, not always practical in turbine engines, is used here. The transmitted light is collected by a photodiode which is monitored by an oscilloscope.

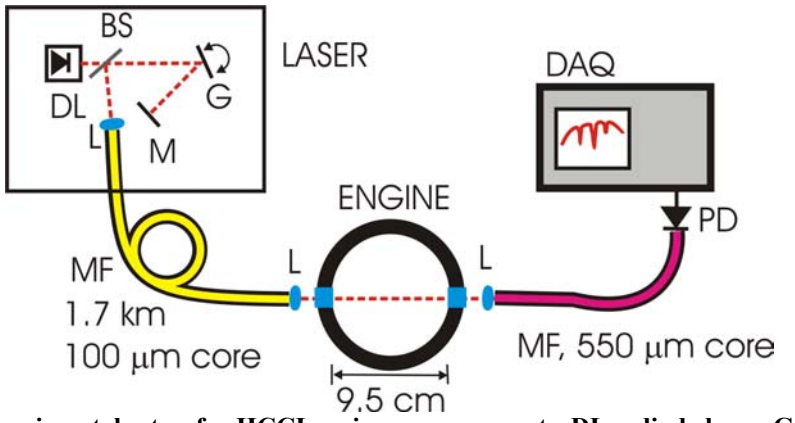

Figure 2. Experimental setup for HCCI engine measurements. DL = diode laser, G = vibrating diffraction grating, M = mirror, MF = multi-mode fiber, PD = photodiode.

In addition to optical data, a pressure trace was recorded with a piezoelectric transducer and is shown in Figure 3. The optical data we will present below are from the region between the two dotted vertical lines (-35 to 0 crank angle degrees, where 0 degrees is piston top-dead-center). The derivative of pressure is shown as a dashed curve in Figure 3, indicating two separate pressure jumps. These pressure jumps are indicative of a two-stage combustion process that is peculiar to low-temperature n-Heptane chemistry.

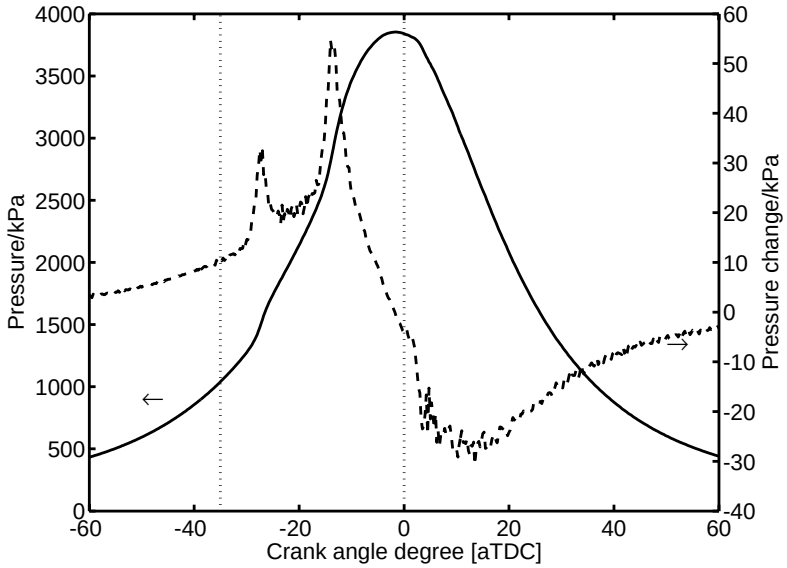

Figure 3. Pressure trace from the HCCI engine. Optical data was recorded between the two vertical dashed lines.

Raw optical data recorded in the experiment are shown in Figure 4. The incident intensity (before the light enters the engine) shows high-frequency noise due to an interference phenomena within the laser. This noise has been eliminated from our recent

wavelength-agile laser designs. After passing through the engine, the intensity has noticeable "dips" due to absorption by water vapor in the engine.

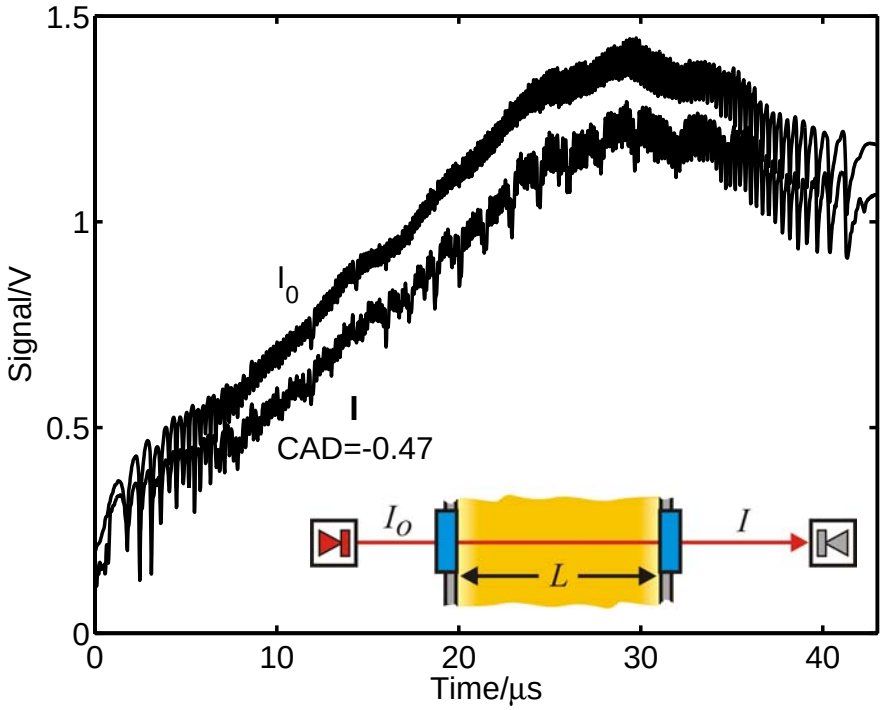

Figure 4. Sample raw optical signals recorded in the HCCI engine.

In accordance with Beer's law, $\frac{I}{I_O} = \exp(-absorbance)$, the ratio of the traces shown in Figure 4 provides water vapor absorption spectra. Several spectra recorded at various piston positions during a single compression stroke are shown in Figure 5. As the piston compresses the gas, the most noticeable change in the spectra is the increased overall absorption. This increased absorption is due to formation of water vapor in the engine. Although visually less noticeable, the spectra also change shape due to increasing gas temperature.

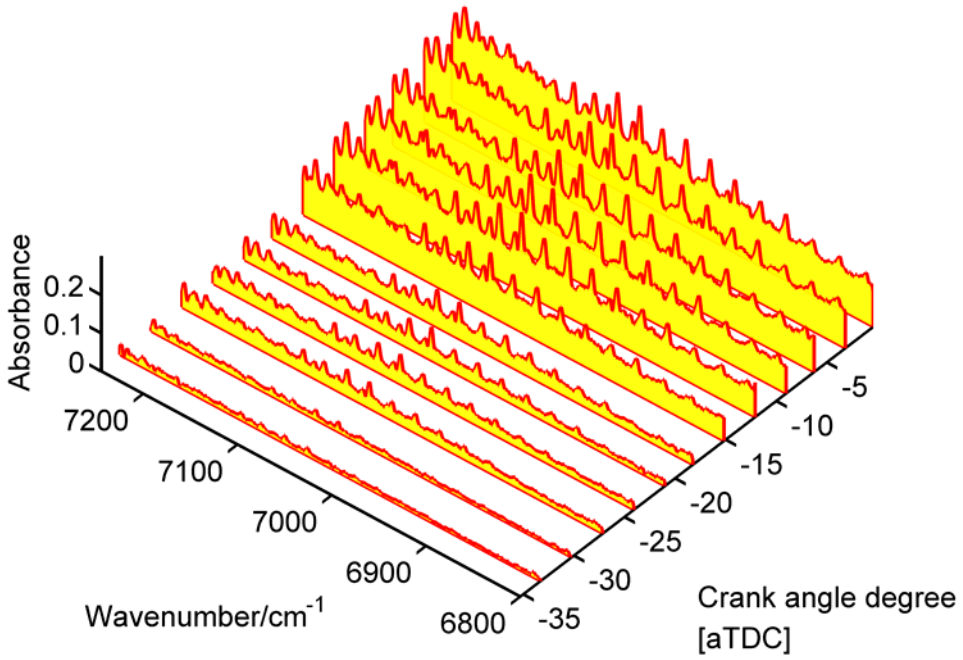

Figure 5. Sample water vapor absorption spectra recorded during a single compression stroke.

An instantaneous water vapor mole fraction and gas temperature can be inferred from each spectrum shown in Figure 5. This is accomplished by comparing each spectrum to a theoretical (HITEMP) spectrum. Results of these comparisons – running records of water mole fraction and temperature – are shown in Figure 6. Many details of the two-stage combustion are clearly visible.

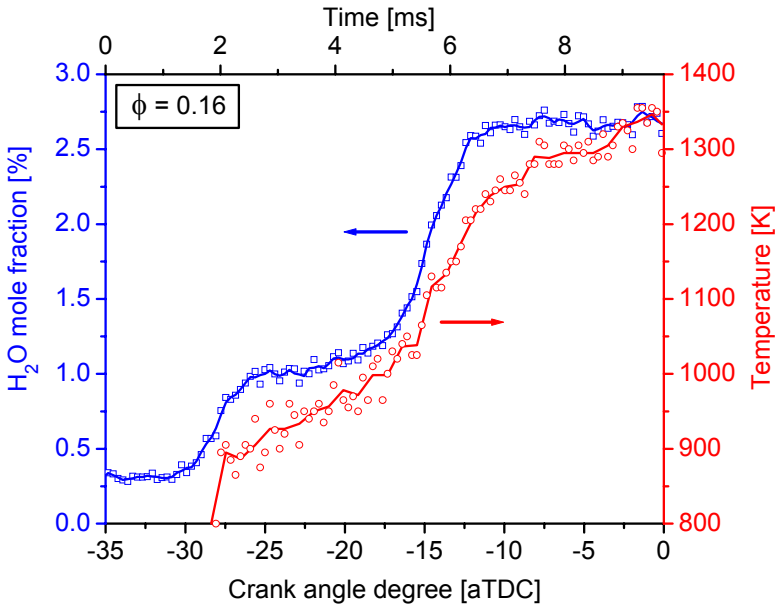

Figure 6. Gas properties measured during a single compression stroke of a piston engine operating in HCCI mode. The precision in the temperature measurements is best, approximately ±1%, between -17 and -5 CAD.

The data shown in Figure 6 is being used to better understand the combustion process occurring in the engine. Such detailed data also reveal practical engine performance information, such as the rate at which gas leaks past the piston seals in the engine.

RESULTS AND DISCUSSION

As in the executive summary, this section is arranged according to the four key areas of effort: fiber-optic access, wavelength-agile lasers, data reduction, and technology transfer.

Fiber-optic access

A major portion of our effort has been channeled into development of fiber-optic access for gas turbine engines. This is because existing fiber-optic access schemes, although useful for research, are not particularly well-suited to access of practical turbine environments. The discussion here is organized into three sub-tasks in the following topic areas: dual-clad fiber, beam steering, and fiber Bragg gratings.

Dual-clad fiber

We have developed an optical access approach that uses dual-clad fiber (DCF) to enable absorption spectroscopy measurements along a line-of-sight without complete line-of-sight access. A schematic of our approach is shown in Figure 7. Tunable source light is sent through a 50-50% beam splitter. Half of the light transmits through the splitter and is coupled into the core of the DCF. The remaining half of the light reflects at a ninety degree angle and is generally discarded.

Once the light has traveled through the single mode core and the measurement path, it is collected in the cladding. After returning through the cladding to the beam splitter, half of the light is transmitted through the splitter and does not participate in the measurement. The remaining light is reflected at a ninety degree angle and focused onto a photo detector. The "retroreflector" shown in Figure 7 could be any of several optics in practice; for example, we have successfully used a plane mirror, a corner-cube retroreflector (as shown), an array of corner cubes, and a diffuse scattering surface. A spherical mirror with a radius of curvature approximately equal to the length of the test section is expected to minimize sensitivity to beam steering, however it may be more cumbersome to implement in practice.

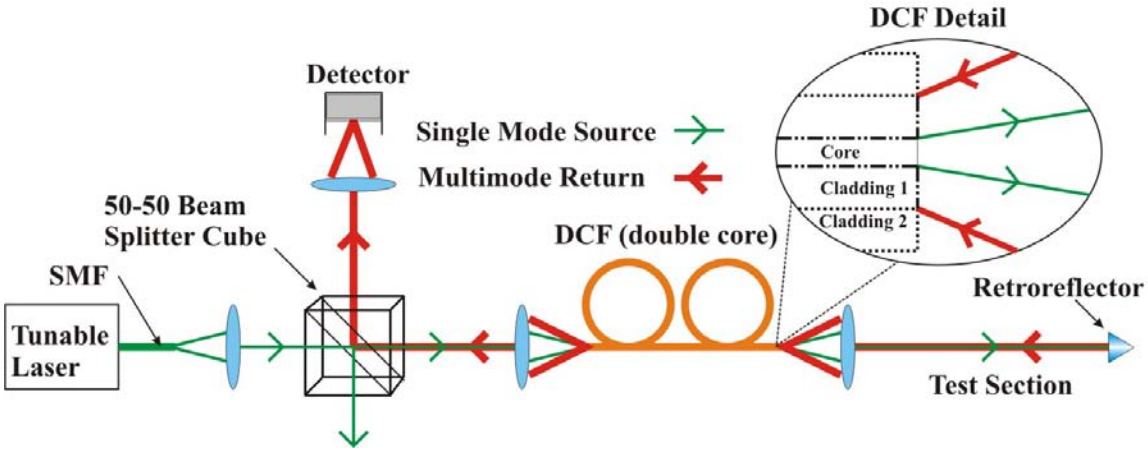

Figure 7. Schematic of dual-clad fiber approach for line-of-sight absorption measurements without complete line-of-sight access

The DCF approach to absorption spectroscopy shown in Figure 7 was used to measure H_2O vapor in a laboratory setting for which the "test section" was a mock-up of a gas turbine main burner. A tunable diode laser (New Focus 6327) with a scan range of 1380 – 1460 nm was used as the tunable laser, and the dual-clad fiber used had a length of 5m. Light was collected with a Thorlabs PDA 400 InGaAs detector and data was recorded by a 12 bit, 10 MS/s, PC based data acquisition system. The data was reduced to the absorption spectrum shown in Figure 8 using the Beer-Lambert law. We estimated the minimum detectable absorbance (MDA) for the data shown in Figure 8 to be 1% by comparing this spectrum with a spectrum measured in the absence of absorbing H_2O vapor. This MDA value is approximately 10x larger than we routinely achieve in a similar setup but without the DCF. The relatively large MDA is due to an insufficient polish angle on the end faces of the DCF, allowing unwanted back-reflections to be guided by the fiber. These back reflections have since been eliminated by improved DCF

design. However, even with an MDA of 1%, we expect to be able to measure gas temperatures accurate to within 1% in many applications.

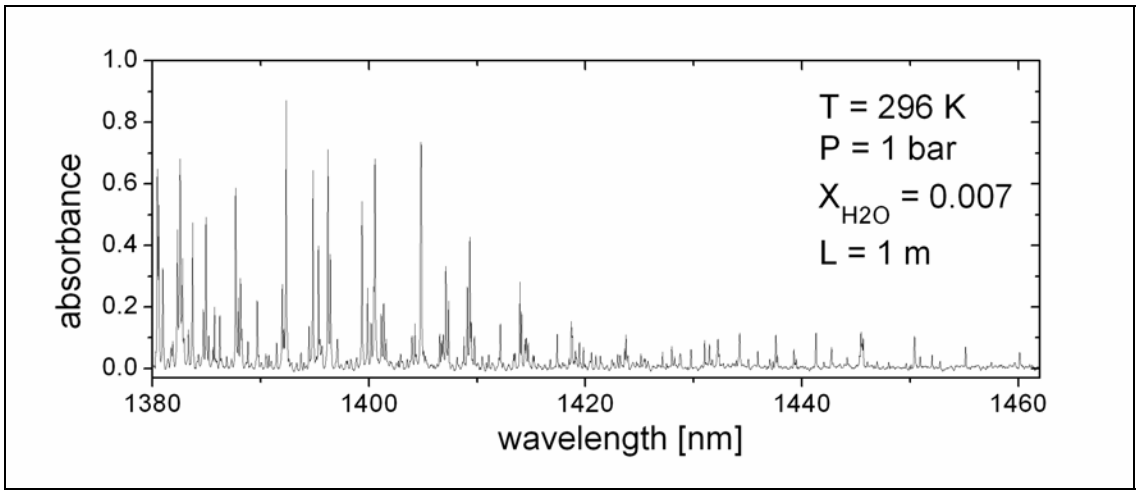

Figure 8. Sample H2O absorption spectrum measured in gas-turbine engine mock-up using dual-clad fiber access.

Beam steering

To couple laser light into and out of a gas turbine engine efficiently using the above dual-clad fiber approach, one must pay careful attention to the parameters of the lens that delivers fiber-coupled light to the engine environment (this is the lens facing the "test section" in Figure 7). In Figure 9 we demonstrate the motivation for careful lens design. We developed a simple analytical model for optimizing laser transmission performance in beam steering environments. Based on this model, we calculated an optimum lens focal length of 3.22 mm for a particular piston engine test case. In the measurements that followed, we verified that a lens with a focal length near this optimum outperformed other available lenses in dramatic fashion. Details on our optical design methodology, including a "lens selection map" are available in the literature[2].

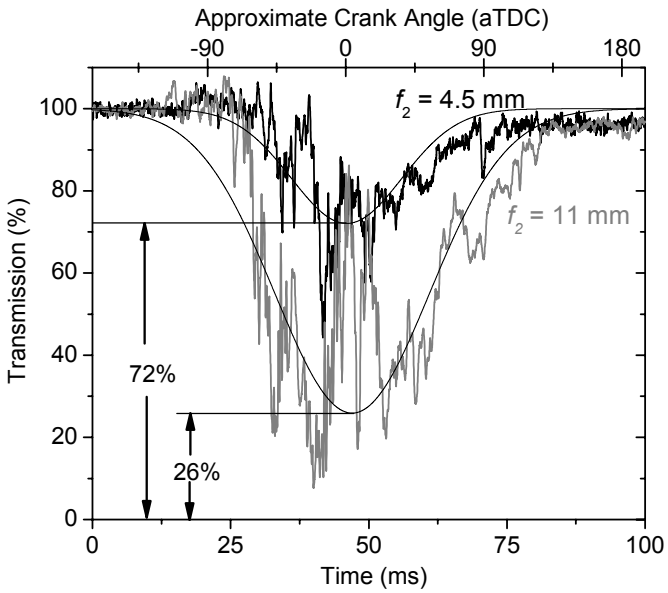

Figure 9. Improvement of transmission from ~26% to ~72% in a beam steering field generated in a piston engine, accomplished simply by changing a lens focal length from 11 mm to 4.5 mm. The 4.5 mm focal length lens is near the calculated optimumof 3mm.

Fiber Bragg gratings

One goal of this project has been to develop the capability to measure the temperature of moving metal parts (turbine blades) by embedding such parts with fiber optics. Typically a fiber Bragg grating (FBG) is embedded in the part at the location of interest. The reflection spectrum The FBG generally has a single reflection feature with a spectral width of 1 nm or less. The center wavelength of this reflection feature depends on FBG temperature and strain, as thoroughly discussed elsewhere[12]. In brief, a FBG is typically formed by exposing a portion of a single-mode fiber to ultraviolet light in such a way that the refractive index of the core varies along the fiber. Most light propagating in the fiber is unaffected by the FBG; however, wavelengths that are resonant with the periodicity of the index variations are partially reflected. The periodicity changes with strain and temperature, because the index of the fiber core and the physical size of the FBG depend on these parameters. The FBG can be made sensitive to only strain *or* temperature by clever design.

Traditional FBG sensors record either the reflected or the transmitted light. Both of these approaches are straightforward if the source light is coupled into a stationary FBG. Recent work has been done to explore the use of FBGs for non-contact measurements of moving metal parts. To enable temperature measurements in this case, a FBG is embedded in the part. Light coupled into the FBG only periodically as the part moves (e.g., briefly, once per rotation of a turbine blade). Until now, FBG measurements in moving parts had been performed in transmission mode only. This required two separate optical couplings (e.g., to and from the turbine blade). The application is simplified by monitoring the FBG reflection feature through a single conduit using dual-clad fiber (DCF). Use of only a single optical coupling to the moving fiber greatly simplifies the

setup. We demonstrated the enhanced performance of a FBG sensor based on DCF by performing measurements two ways in a piston engine. First we measure the light transmitted through the FBG and second we measured the reflected Bragg wavelength (λ_{Bragg}) with DCF. The experimental arrangement is shown in Figure 10 and results are shown in Figure 11. The cladding of the DCF (fiber A where λ_{Bragg} from the FBG is collected) is large enough to tolerate "slop" in the periodic optical coupling, just as the DCF tolerates some degree of beamsteering in the gas measurements. We have also begun testing large mode area fiber Bragg grating components. These larger fiber elements are still very small ~ 100 μm diameter "optical thermocouples" that can be embedded in moving metal parts, but the advantage of the larger size is the increased ease of coupling light into and out of the moving component under practical conditions.

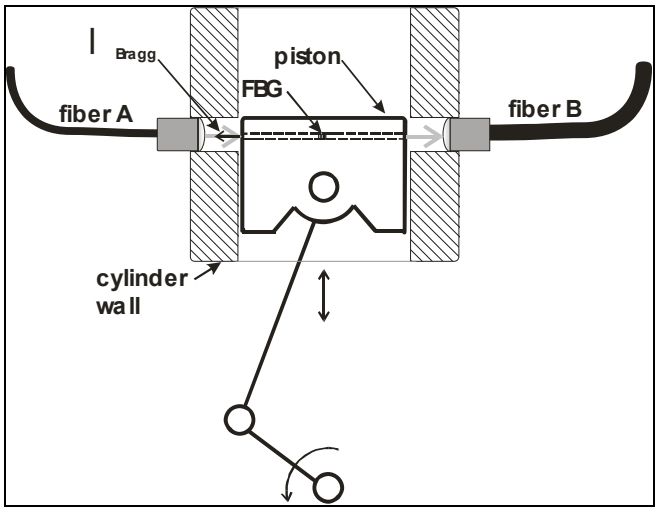

Figure 10 Schematic of the experimental setup for piston temperature measurements using an embedded fiber Bragg grating. Fiber A is DCF for both sending the scanned wavelength light and collecting the reflected Bragg wavelength (λ_{Bragg}) and fiber B is a multimode fiber for collecting transmitted light.

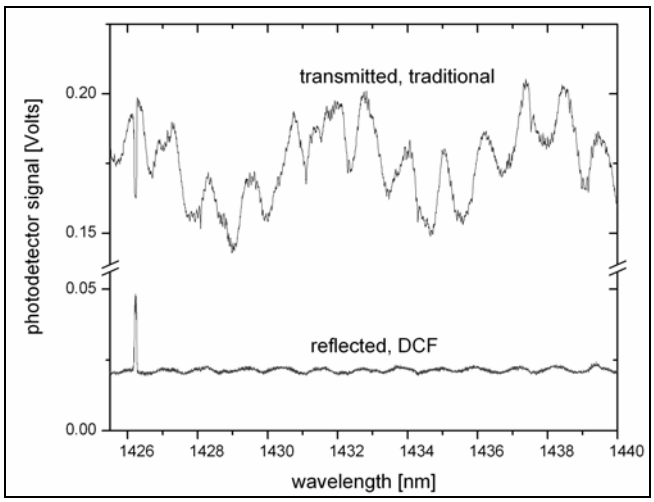

Figure 11. Demonstration of fiber Bragg grating measurements in a moving metal part (engine piston shown in Figure 10), showing superiority of DCF-based approach.

Figure 12 represents some possible approaches for routing fiber-coupled light to various measurement stations within an engine, given the aforementioned capabilities associated with dual-clad fiber. Shown are three arrangements for gas measurements represented by lines-of-sight (red) and one turbine blade measurement station enabled by an embedded fiber optic (green). For the turbine blade measurement, light would be periodically coupled into fiber optics embedded in the blade (once briefly per rotation).

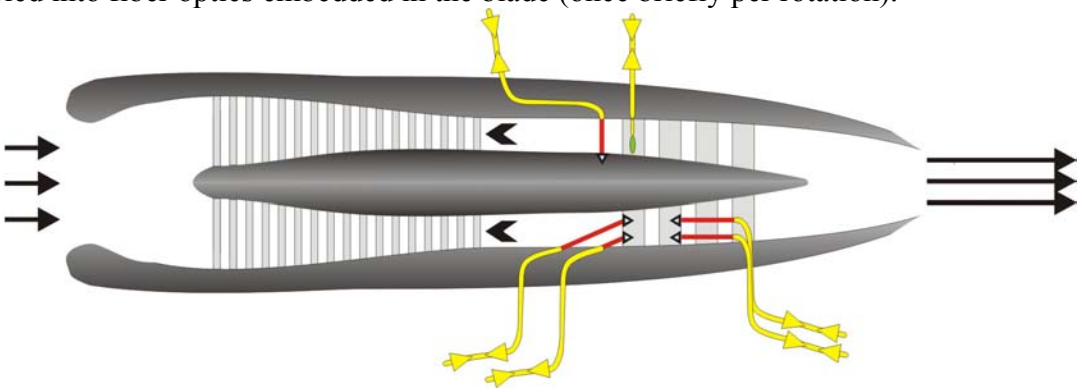

Figure 12. Possible schematic layout of optical access to combustion gases and to fiber optics embedded in turbine blades. Red lines represent gas measurement paths and green oval represents an embedded fiber Bragg grating.

Wavelength-agile lasers

We have developed numerous wavelength-agile lasers, most of which are enumerated in the literature[7]. A schematic of a wavelength-agile source based on supercontinuum generation that we developed for application in turbine engines is shown in Figure 13. This source is a modified version of sources previously developed at the University of Wisconsin[5,6]. Light originates from a diode-pumped solid state, passively Q-switched laser operating near 1064 nm. This laser has nearly ideal characteristics for wavelength-agile sensing. Furthermore, it offers high average power (500 mW) at low cost (~ 10,000 USD) because it is a standard laser with application in many other fields, including rapid prototyping and photopolymerization. The peak power (during each pulse) emitted by the laser is ~ 30 kW. These high-power pulses are coupled into a small-core-diameter (~ 5 μm) fiber known as a "photonic crystal fiber" or PCF. In the PCF, nonlinear processes generate wavelengths other than the 1064 nm input. The dispersion of the PCF is designed to be small so that as various colors are produced, they travel at similar speeds in the fiber and the pulse does not break up. When the process is optimized, a monochromatic input can produce broadband (white) output in ~ 6 m of PCF as illustrated in Figure 13. These white pulses are then coupled into a long spool (~20 km) of ordinary fiber that is tailored to have high dispersion. The length of the fiber causes it to be somewhat bulky and expensive (the size of a textbook and ~ 5,000 USD); however, in the future, the fiber could be replaced by a 40-m long fiber dispersion technology called a "chirped fiber Bragg grating". In the dispersive fiber shown in Figure 13, red wavelengths travel faster than blue wavelengths, so the white pulse is stretched in time as it travels through the fiber. Emerging at the output side of the dispersive fiber, then, is a wavelength scan from red to blue. This is the wavelength-agile light useful for sensing.

In this case, our goal is to generate wavelength scans from 1670 nm down to 1330 nm because water vapor in combustion gases absorb light in this range. Furthermore, temperature-sensitive fiber elements that can be embedded in turbine blades can be easily made to perform in this wavelength range.

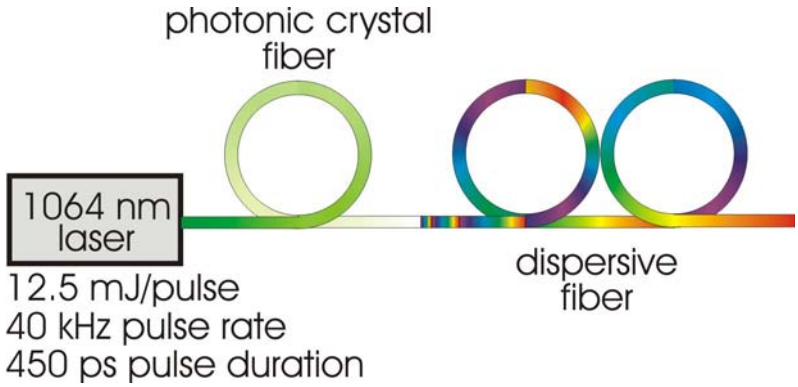

Figure 13. Wavelength-agile source appropriate for application in turbine engines.

The 1670-1330 nm wavelength scans emerging from the system shown in Figure 13 each last ~ 2 μs and exhibit ~ 100 mW of optical power. Since only ~ 1 mW is needed for the optical sensing end use, the light can be split as shown in Figure 14 to permit measurements at multiple locations. We plan to split into as many as $n = 64$ different optical fibers. Immediately following the splitter, each fiber is given a different length delay. This is because the n scans will ultimately be delivered to a single detector, and we desire each to arrive at a different time (time-division multiplexing). Next, the light passes through a fiber-optic circulator before reaching the measurement location, which can be a free-space path through combustion gases or a fiber optic embedded in a turbine blade. In the former case, light is pitched through the gas onto a retroreflector that returns the light back toward the source. In the case of the turbine blade measurement, an embedded fiber optic containing temperature-sensitive fiber Bragg gratings at various positions reflects a portion of the light back toward the source. The returning light does not feed-back all the way to the source, but is instead directed toward a photodiode using fiber-optic circulators. The signals are recombined before reaching the photodiode. The photodiode thus measures gas transmission spectra as well as reflection spectra from the fiber Bragg gratings. The gas transmission spectra can be reduced to gas temperature and water vapor concentration profiles by comparison with theoretical spectra (HITEMP[13]). We have recently refined this process and now possess a simple computer algorithm based on signal derivatives[3] for data reduction. The embedded fiber spectra are relatively easy to interpret; each fiber Bragg grating reflects a particular wavelength, and the reflected wavelength is a function of temperature. Note that 20 or more temperature measurement positions can be accommodated on *each* fiber that is routed into the turbine blade.

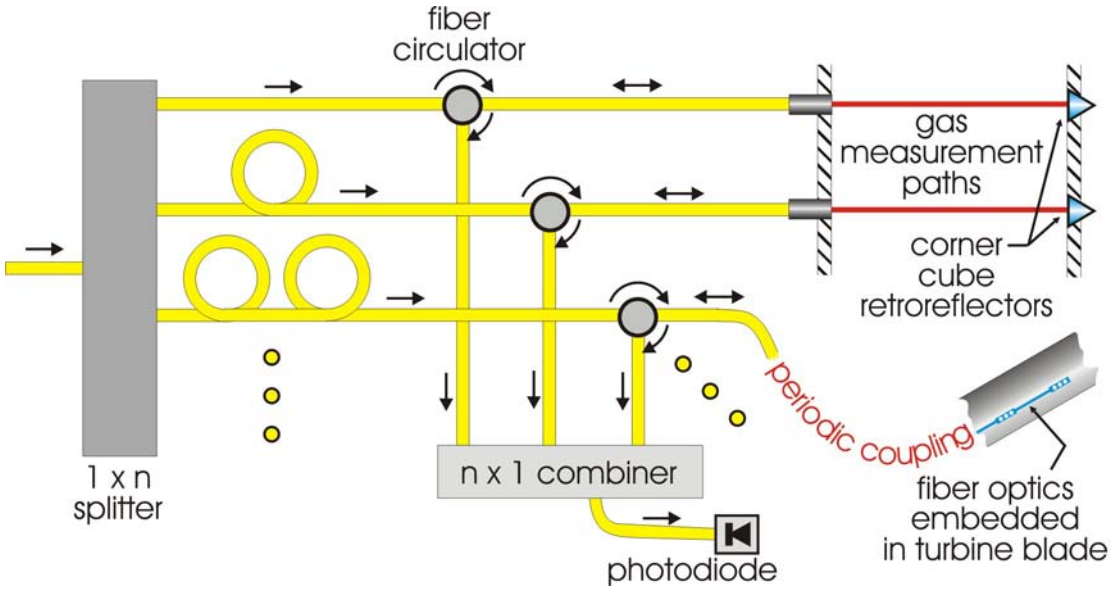

Figure 14. Schematic of distributed sensing system for wavelength-agile spectroscopy.

In this section we report recent measurements that demonstrate our wavelength-agile laser capabilities. Sample gas measurements are shown in Figure 15 and Figure 16. Figure 15 shows a representative signal that results when the free space path contains methane (CH_4) and acetylene (C_2H_2) gases. The wavelength axis on the right shows that the scan is from ~ 1700 nm to ~ 1500 nm over a time of 600 ns. The measurement shown in Figure 15 is a 10-shot average, so the cumulative time required is shown by the top axis to be ~ 6 μs.

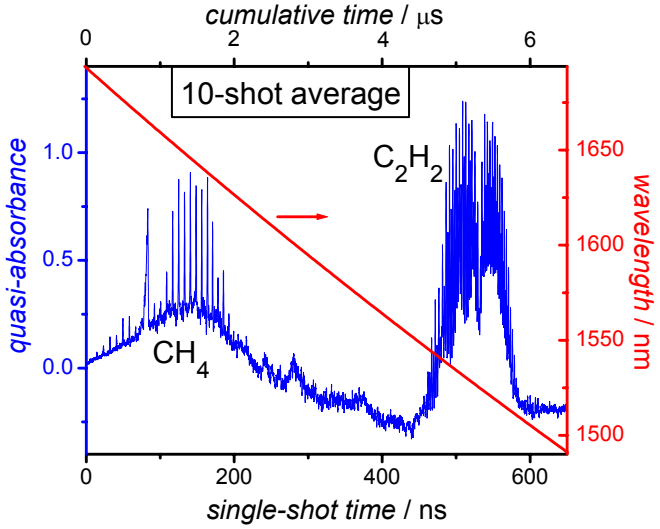

Figure 15. Sample multi-species measurement in 6 μs total time.

Figure 16 shows raw data for a similar case. However, data is displayed for only a 20 nm range (scanned by the laser in 80 ns) to highlight the details of the signal. In this case,

the free-space path contains carbon monoxide (CO), and its absorption features are visible. The strongest CO features visible correspond to an absorbance of approximately 20%. The noise level is ~ 3%, dominated by oscilloscope digitizer noise. We expect to reduce this to the shot noise limit of ~1% using an advanced photoreceiver unit that circumnavigates oscilloscope noise. This photoreceiver unit is currently under construction. The current 3% noise level can be improved if needed by averaging multiple scans as in Figure 4. Averaging, of course, reduces the overall time response, but this tradeoff can be attractive: for example, a noise level of 0.66% can be obtained by dropping the measurement update rate to 10 kHz, a rate still fast enough for most applications. Note, however, that the 3% noise level is already sufficient for measurements of H_2O vapor in a typical gas turbine engine.

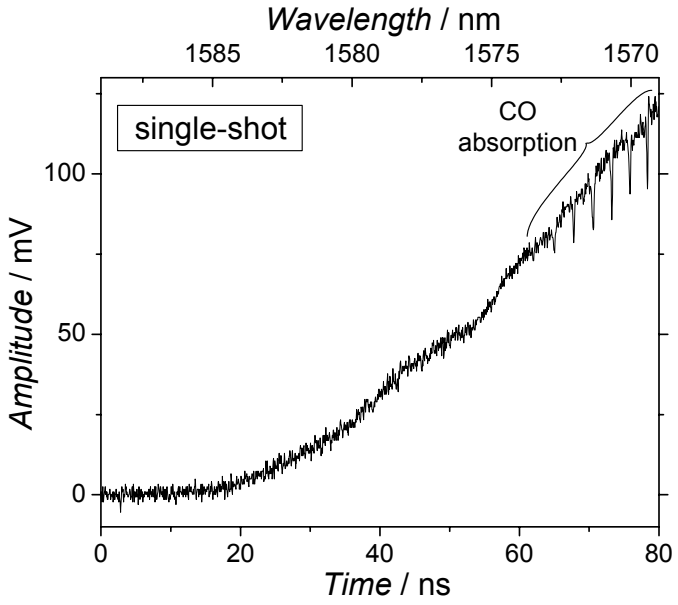

Figure 16. Raw data showing low noise level (~ 3%) in a single-shot, wavelength-agile measurement. The shot noise level is ~ 1% under these conditions, so these measurements are near the fundamental limit.

Data reduction

We have developed a LabVIEW-based code for converting spectra such as those shown in Figure 15 and Figure 16 to gas properties (particularly gas temperature but also species concentrations). The code is based on the HITEMP [13] spectral database and is enhanced by numerical differentiation and smoothing as described elsewhere [3,14]. The approach is believed to exhibit an absolute accuracy of 1.7% in temperature [3] up to temperatures of ~1500 K, but we are still working to prove this accuracy. We are working towards assessing the absolute accuracy of our inferred temperatures by performing controlled measurements in a heated, pressurized static cell. We have designed a cell that uses long sapphire rods (400 mm long x 3 mm diameter) as windows. The long rods sufficiently insulate the gas sample from the laboratory so that the sample can be maintained at a

uniform, high temperature (i.e., the long rods occupy the nonuniform-temperature region between the sample and the room, preventing laser absorption there). The cell design has been aided by finite-element analysis; Figure 17 represents results from an ANSYS model showing the excellent temperature uniformity in the test gas region. The cell is currently under construction. It will provide gas samples up to a temperature of ~ 1800 K and a pressure of ~ 30 bar. Water vapor (H_2O) and carbon dioxide (CO_2) will be our initial test gases in the heated sample volume. We will perform optical measurements in this cell and use the results to validate our data reduction techniques, in particular the temperature accuracy. Our validation experiments may require updates to the HITEMP database, particularly near and above 1500 K gas temperatures.

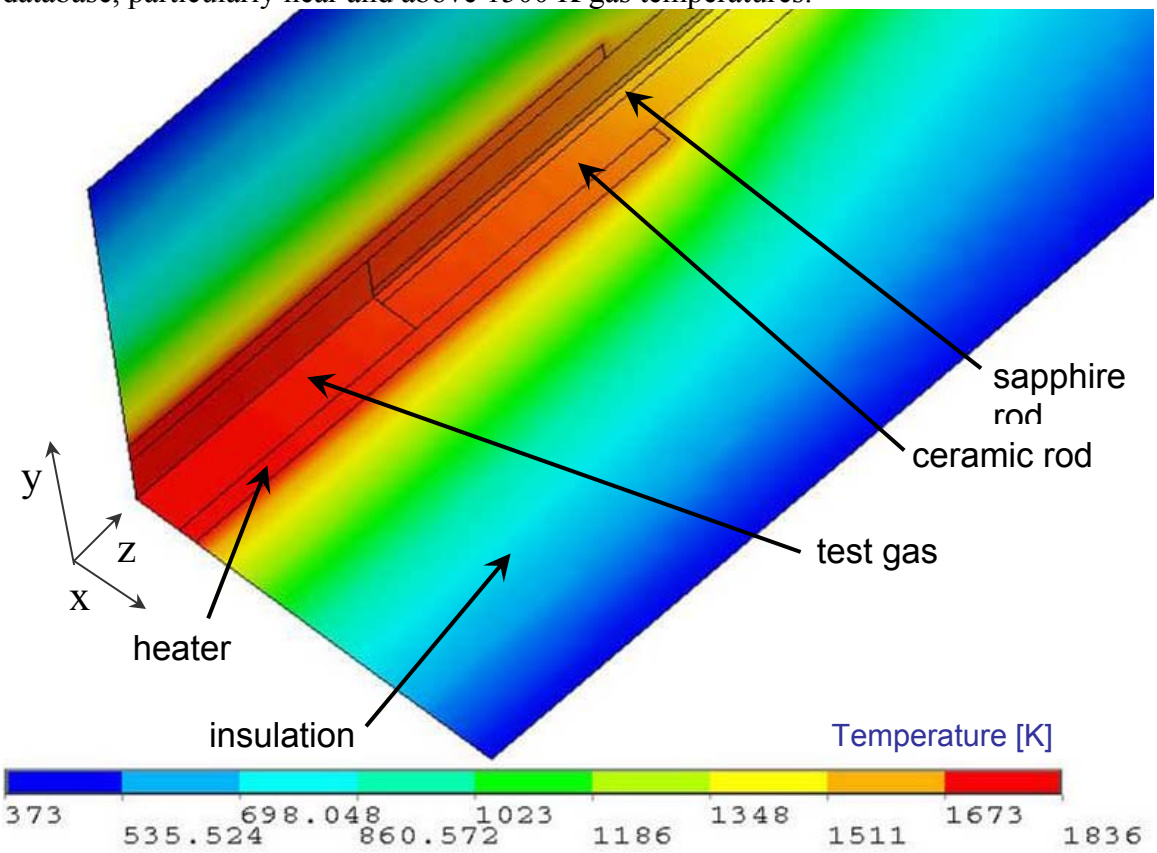

Figure 17. ANSYS model of heated static cell, showing exceptional uniformity of temperature in the test region. This cell is currently under construction.

In addition, we are using the piston engines available to us in the Engine Research Center to refine the sensing strategy and assess the accuracy of inferred gas temperatures. We use controlled charges in the engine to generate homogenous combustion gases and measure their spectra. A sample spectrogram is shown below in Figure 18. Such spectra measured under controlled conditions are critical for validating the spectral database used to infer gas temperature from spectra recorded in gas turbine environments. We are currently investigating the possibility of obtaining similar spectral validation data from shock tubes to further enhance the assessment of temperatures measured in gas turbine engines. Also, it should be reiterated that temperatures inferred from absorption spectra are in general average temperatures along the line-of-sight. Often, such average temperatures are insufficient information to the combustion researcher. The situation is

dramatically improved when multiple lines of sight are probed; then spatial information begins to be revealed. In addition, we are continuing to assess the possibility of measuring gas temperature distributions along a single line-of-sight in gas turbine engines using a spectral inversion process discussed in the literature[15].

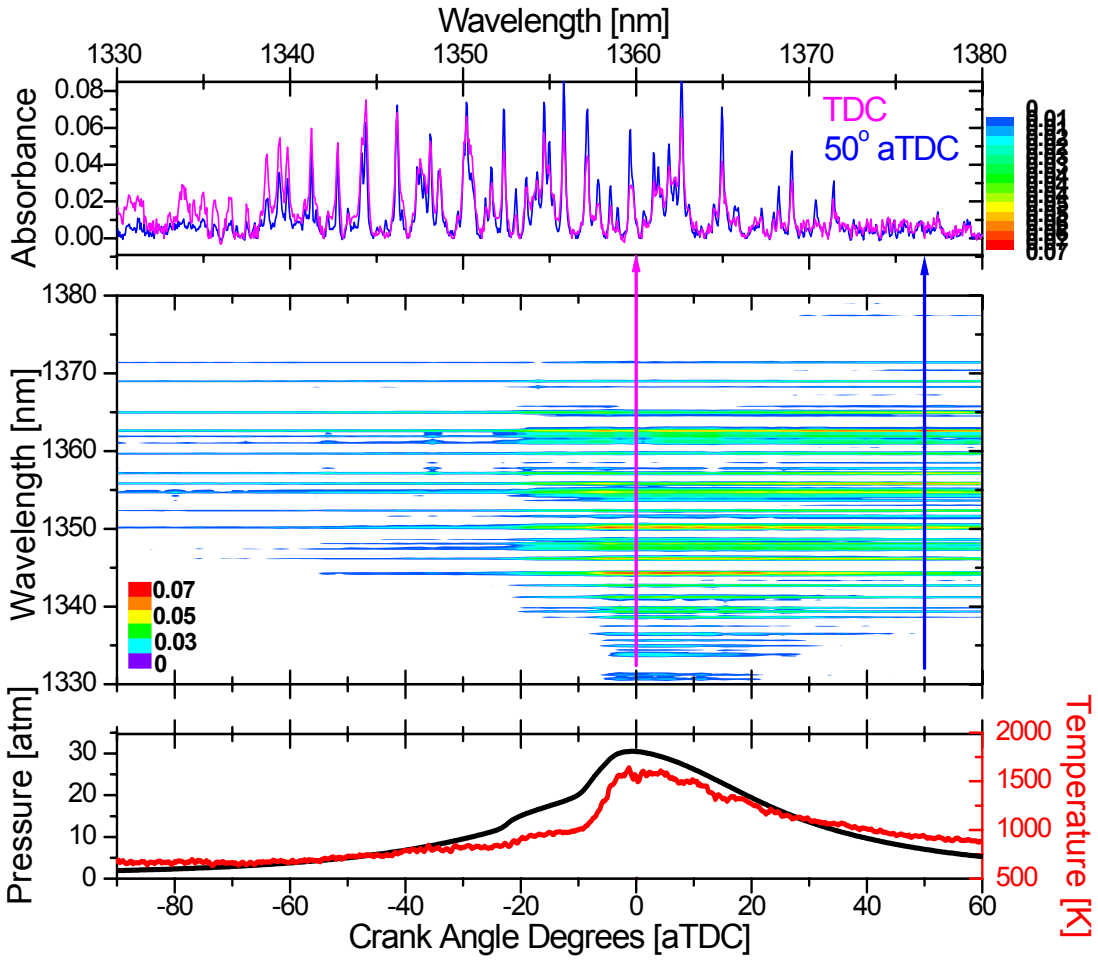

Figure 18. H_2O vapor absorption spectra recorded during combustion of a controlled charge in a piston engine operating in homogeneous charge compression ignition (HCCI) mode at an equivalence ratio of 0.35. The middle image maps all of the absorption spectra recorded over the entire engine cycle; sample spectra are given as vertical "cuts" through this image at TDC (30 bar, 1600 K) and 50 aTDC (7 bar, 950 K) in the top panel. Gas temperature is inferred from each spectrum and shown in the bottom panel. These data are particularly important for validating our H_2O vapor spectral database, thus allowing us to interpret temperatures recorded in gas turbine environments more reliably.

Technology transfer

The data shown in Figure 18 clearly demonstrates the ability to measure gas temperature over a wide range of combustion conditions using an optical sensor. Such an optical sensor has long been needed by the combustion community, and if the sensor could be made inexpensively (perhaps < $1000), it would receive widespread use. We are currently arranging to team up with industrial partners to commercialize an inexpensive

version of the sensor used to gather the data shown in Figure 18. Such partners include Nufern and Thermo Electron Corporation. We hope to test a prototype sensor in gas turbine environments in the coming year, so that by the conclusion of the project there is sufficient inertia to carry such sensing to many gas turbine research labs.

CONCLUSIONS

We have presented our designs for an optical system for monitoring gas and turbine-blade properties at multiple stations in turbine engine systems. By enabling measurements at many different locations, the spatial distribution of gas and turbine-blade properties will ultimately be revealed. The capability to measure such information will be invaluable to gas turbine engine researchers.

We have organized our effort into the categories of fiber-optic access, wavelength-agile lasers, data reduction, and technology transfer. These four components of the project are now coming together, and we have already begun testing our strategies at off-site facilities. A photograph from a recent visit to the Wright Patterson Air Force Base (WPAFB) in Dayton, OH is shown in Figure 19. We are scheduled to travel to WPAFB again this summer and also hope to visit other facilities, possibly including General Electric and Rolls-Royce. We look forward to these off-site measurement opportunities. If the reader has suggestions for other off-site measurement possibilities, please feel free to email Scott Sanders (ssanders@engr.wisc.edu) directly.

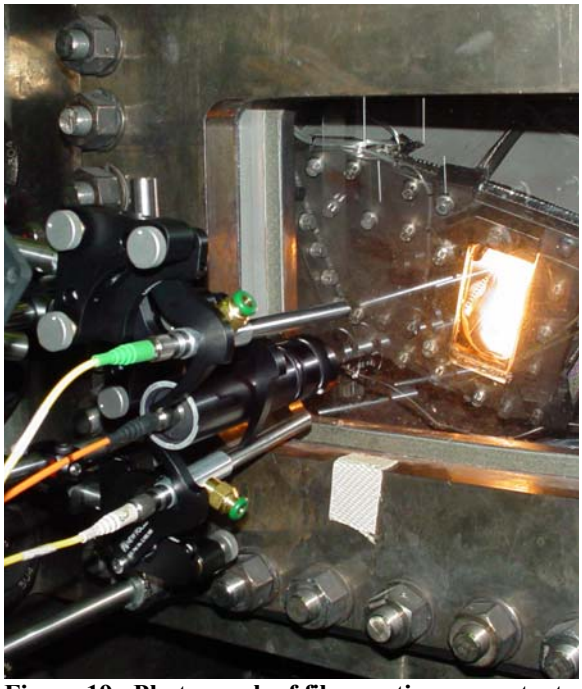

Figure 19. Photograph of fiber-optic sensor strategies under test at Wright-Patterson Air Force Base in Dayton, OH.

REFERENCES

[1] Hagen, C.L., Schmidt, J.R., and Sanders, S.T., "Spectroscopic Sensing via Dual-Clad Optical Fiber," *Sensors Journal, Institute of Electrical and Electronics Engineers,* **6**, 1227-1231, 2006.

[2] Kranendonk, L.A. and Sanders, S.T., "Optical design in beam steering environments with emphasis on laser transmission measurements," *Applied Optics,* **44**, 6762-6772, 2005.

[3] Kranendonk, L.A., Walewski, J.W., Kim, T., and Sanders, S.T., "Wavelength-agile sensor applied for HCCI engine measurements," *Proceedings of the Combustion Institute,* **30**, 1619-1627, 2005.

[4] Kranendonk, L.A., Bartula, R.J., and Sanders, S.T., "Modeless operation of a wavelength-agile laser by high-speed cavity length changes," *Optics Express,* **13**, 1498-1507, 2005.

[5] Sanders, S.T., "Wavelength-agile fiber laser using group-velocity dispersion of pulsed super-continua and application to broadband absorption spectroscopy," *Applied Physics B: Lasers and Optics,* **75**, 799-802, 2002.

[6] Walewski, J., Filipa, J., Hagen, C., and Sanders, S., "Standard single-mode fibers as convenient means for the generation of ultrafast high-pulse-energy super-continua," *Applied Physics B,* **83**, 75-79, 2006.

[7] Sanders, S., "Wavelength-agile lasers," *Optics and Photonics News,* **16**, 36-41, 2005.

[8] Sanders, S.T., "Diode-Laser Sensors for Harsh Environments with Application to Pulse Detonation Engines, " (Stanford University Editor, Stanford), , 2001.

[9] Sanders, S.T., Mattison, D.W., Jeffries, J.B., and Hanson, R.K., "Rapid temperature tuning of a 1.4-um diode laser with application to high-pressure H2O absorption spectroscopy," *Opt.Lett.,* **26**, 1568-1570, 2001.

[10] Sanders, S.T., Mattison, D.W., Ma, L., Jeffries, J.B., and Hanson, R.K., "Wavelength-agile diode-laser sensing strategies for monitoring gas properties in optically harsh flows: application in cesium-seeded pulse detonation engine," *Optics Express,* **10**, 505-514, 2002.

[11] Sanders, S.T., Mattison, D.W., Jeffries, J.B., and Hanson, R.K., "Sensors for high-pressure, harsh combustion environments using wavelength-agile diode lasers," *Proc.Comb.Symp,* **29**, 2661-2667, 2002.

[12] A. Othonos and K. Kalli, *Fiber Bragg Gratings : Fundamentals and Applications in Telecommunications and Sensing* (Artech House, Boston, 1999).

[13] Rothman, L.S., Barbe, A., Benner, D.C., Brown, L.R., Camy-Peyret, C., Carleer, M.R., Chance, K., Clerbaux, C., Dana, V., Devi, V.M., Fayt, A., Flaud, J.M., Gamache, R.R., Goldman, A., Jacquemart, D., Jucks, K.W., Lafferty, W.J., Mandin, J.Y., Massie, S.T., Nemtchinov, V., Newnham, D.A., Perrin, A., Rinsland, C.P., Schroeder, J., Smith, K.M., Smith, M.A.H., Tang, K., Toth, R.A., Auwera, J.V., Varanasi, P., and Yoshino, K., "The HITRAN molecular spectroscopic database: edition of 2000 including updates through 2001," *J. Quant. Spectrosc. Radiat. Transfer,* **82**, 5-44, 2003.

[14] Kosterev, A.A., Curl, R.F., Tittel, F.K., Gmachl, C., Capasso, F., Sivco, D.L., Baillargeon, J.N., Hutchinson, A.L., and Cho, A.Y., "Effective utilization of quantum-cascade distributed-feedback lasers in absorption spectroscopy," *Applied Optics,* **39**, 4425-4430, 2000.

[15] Sanders, S.T., Wang, J., Jeffries, J.B., and Hanson, R.K., "Diode-laser absorption sensor for line-of-sight gas temperature distributions," *Applied Optics,* **40**, 4405-4415, 2001.

Spectroscopic In-Situ Non Destructive Evaluation to monitor the Health of Thermal Barrier Coatings

Semi-Annual Report

1 January 2006 to 30 June 2006

Surendra Tewari, Principal Investigator
Kang Lee, Co-Principal Investigator
Guofeng Chen, Postdoctoral Fellow

July 6, 2006

DOE Award number: DE-FC26-02NT41431

UTSR Project Number: 03-01-SR106

Department of Chemical and Biomedical Engineering
Cleveland State University
Cleveland, OH 44115

DISCLAIMER:

ABSTRACT

During this period, spectral response of the plasma sprayed 1 wt% Li_2O doped TBCs was examined using flat-flame burner. Emission detection system was miniaturized so that it could be transported to the NASA-Glenn Research Center for gas turbine engine simulated testing using the burner-rig there. One hour thermal cycling response of the coating architecture for the 1100 ^oC as the hot temperature has now been completed. Tests have been conducted for the 1, 2 and 3 wt% Li_2O doped plasma sprayed TBC superalloy coupons with 1/9, 2/8 and 3/7 configurations (The values to the left of the slash correspond to thickness in mils of the inner Li_2O doped YSZ layer, and the values on the right indicate thickness of the outer YSZ layer). These thermal cycling tests show that in general, thinner doped layer is beneficial for TBC life. With 1/9 configuration 1 wt% Li_2O dopant concentration gave lives comparable with that of standard YSZ. The 1/9 configuration even with the high 3 wt% Li_2O content has good response. For the 2/8 configuration only the 1 wt% Li_2O dopant concentration gave thermal fatigue lives comparable with that of standard YSZ. CMX-4 superalloy cylindrical samples (1.2-cm diameter, 10-cm long) were coated at NASA-Glenn Research Center by plasma spraying with of 1~3 wt% Li_2O doped YSZ and YSZ ceramic powders. Preliminary testing of these samples in the burner rig at the NASA-Glenn Research Center has been completed. Initial purpose of the burner rig testing is twofold: 1) Evaluate the thermal cycling (spallation) resistance of the plasma spray coated superalloy samples with 1/9 and 3/7 configurations, and 2) to examine if detectable Li-emission signal can still be achieved in the extremely bright environment of the burner-exhaust stream in-spite of the very low Li_2O content of the coat. This report summarizes the observations from this research.

TABLE OF CONTENTS

LIST OF GRAPHICAL MATERIALS

1. INTRODUCTION

Due to the extreme environment it experiences, one gas turbine engine component most often associated with failure is the thermal barrier coating (TBC) on turbine blades. Early detection of TBC degradation and failure is critical to prevent catastrophic engine failure as more advanced gas turbine engines depend on TBCs for their high temperature operation. Thermal barrier coatings on turbine hot section components, therefore, require regular maintenance. A typical maintenance is a visual inspection of the TBC for cracks, erosion or other damages that will indicate the remaining TBC life. These visual inspections require the engine to be taken out of service and to be partially disassembled to provide access to the TBC by boroscope. This type of maintenance is costly because it requires skilled labor and the interruption of service. Substantial savings in engine maintenance could be obtained if the TBC materials could be made to emit signals that contain information about their deterioration (cracking/spalling) and instrumentation could be developed to detect these signals *in-situ* during engine operation.

An exciting development in rocket engine health monitoring shows great promise for application in in-situ, real-time TBC health monitoring. The technique consists of optical detection of species in the vapor phase inside the chemically reacting or expanding flow. Species originating from the deteriorating TBC would appear as atomic vapor, oxides, and/or hydroxide species in the engine flow path. During flow expansion through the turbine and nozzle, these species equilibrate, typically by collisional de-excitation or emission of radiation. This radiation can be monitored anywhere in the engine where optical access can be designed into the engine components. The use of fiber optics as light guides facilitates the optical access and could allow the design of low cost, in-situ TBC health monitoring equipment.

An ideal engine monitoring system would correctly identify the engine part before it fails. Our idea is to detect and track the TBC failure throughout the life of the component. We plan to dope the TBC with signature marker materials that can be monitored optically in the combustion gas or the exhaust. Marker materials can be incorporated in the area where the failure is generally initiated, which is the inner yittria-stabilized zirconia (YSZ) at the thermally grown oxide (TGO)/YSZ interface in the case of plasma-sprayed thermal barrier coatings. From the presence of the marker species in the combustion gas or the exhaust, determined by a spectroscopic interpretation of the observed optical emission, the mechanical condition and deterioration of TBC can be inferred.

Our preliminary research demonstrated the feasibility of spectroscopic in-situ NDE to monitor the deterioration of mullite/BSAS environment barrier coatings (EBC) on SiC/SiC composites. Lithium oxide (Li_2O) was identified as the most promising marker material for EBCs. A significant lithium emission spectra peak was detected when the mullite bond coat was doped with as low as 0.025 wt% Li_2O in the absence of BSAS topcoat, while no lithium peak was detected in the presence of the BSAS topcoat. The lithium peak was detected again when simulated cracks were machined through the BSAS topcoat, indicating that lithium vapors escaped through the cracks. The lithium spectral intensity increased linearly with the increasing number of cracks. These results

suggest that the lithium spectral intensity can be correlated with the extent of cracking and/or spallation of the EBC.

Literature survey indicates that Li_2O is also compatible with the key TBC components (ZrO_2, Y_2O_3, Al_2O_3), suggesting the feasibility of using emission spectroscopy of lithium as an NDE tool to monitor the cracking/spalling of Li_2O-doped TBC.

2. EXECUTIVE SUMMARY

In this period, thermal cycling tests were completed on the 1, 2 and 3 wt% Li_2O doped plasma sprayed TBC with two-layered ceramic top coat (1/9, 2/8 and 3/7) (The values to the left of the slash indicate inner Li_2O doped YSZ layer thickness in mils, and the values to the right indicate the thickness of the outer YSZ layer). Thermal cycling tests carried out on coated superalloy coupons indicate that in general, thinner doped layer is beneficial for TBC life. *The higher Li2O concentration and thicker inner doped layer are detrimental to the thermal fatigue response.* With 1/9 configuration 1 wt% Li_2O dopant concentration gave lives comparable with that of standard YSZ, whereas with 2/8 configuration only 1 wt% Li_2O dopant concentration gave lives comparable with that of standard YSZ.

Ten cylindrical superalloy samples have been coated by plasma spray with the varying TBC coating architecture: (a) the Li_2O layer varying from 1 to 3 mil while keeping the overall coating thickness as 10-mil, (b) Li_2O content varying from 1 to 3 wt% in the doped YSZ layer at the bond-coat. Some preliminary testing on these samples has been completed in a burner rig at NAA-Glenn Research Center. Preliminary results confirm the previous thermal fatigue observations made on the flat-plate shaped coupons that were coated on only one side of the plate using the flat-flame burner and also the oxy-acetylene flame: *1/9 coatings are extremely resistant to thermal cycling damage. But the 3/7 coats fail after just one thermal cycle in a burner rig.* It is *encouraging to note that despite the very brightly lit environment of the burner-rig exhaust stream the Li-emission signals are readily detected even for the lowest dopant level examined in this study, 1 wt% Li_2O and 99 wt% YSZ.*

3. PROJECT DESCRIPTION

Developing self-sensing smart high-temperature coating for critical gas turbine engine components that can allow in-situ monitoring of its own mechanical health during operation of the engine will result in significant cost saving, as compared with the present invasive inspection techniques that require the engine to be shut down and partially disassembled for inspection. This research will not only benefit the land based power turbines but will also be useful for aircraft engine applications

4. EXPERIMENTAL

A. Flat flame burner: A flat flame burner, shown in Figure 1, that uses an air and methane mixture set-up for this study is currently being used. It yields more stable flame temperatures between 1000-1500 K as compared with the welding torch used before. A Pt-Pt23%Rh thermocouple is located very close to the sample surface to record the gas temperature in the immediate vicinity of the sample.

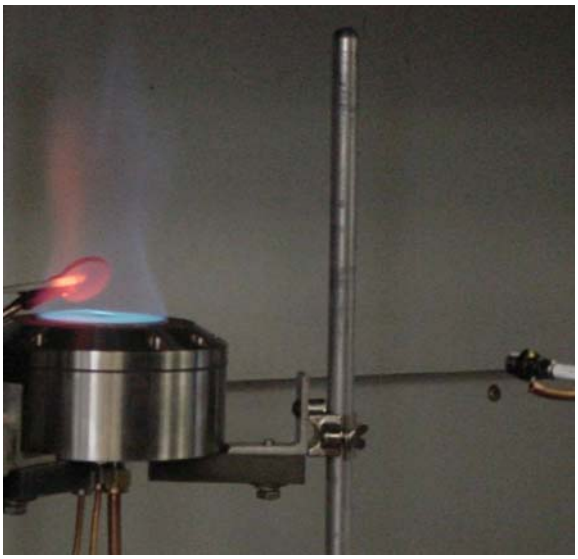

Figure 1 Flat-flame burner in use

B. Optical set-up: The miniature spectrometer (Model HR2000, Ocean Optics Inc., Dunedin, FL) centered at 670 nm is configured to cover the emission wavelengths from 320 to 800 nm. The light emitted from the Lithium emission source in the flame is collected by using a lense and fiber-optics cable that feeds the signal into the spectrometer. Spectrometer out-put is fed into a PC for data acquisition. This unit is mobile and was taken to NASA-Glenn Research Center for burner rig testing of some of the cylindrical samples.

C. Lithium oxide as a marker material in plasma sprayed YSZ coating: Yttria stabilized zirconia ($ZrO_2$8-wt% Y_2O_3) powders doped with Li_2O of 1, 2 and 3 wt % obtained from a commercial vendor (Praxair Specialty Ceramics, Woodinville, WA) were used. Plasma spraying was used to deposit the lithium oxide doped, and undoped YSZ ceramic layers on the CMSX-4 superalloy cylindrical samples having a NiCoCrAlY bond coat. The cylinders are 1.2 cm in diameter and 15-cm long. Following different types of configurations, presented in Table 1, have been prepared. Samples without Li_2O dopant were also prepared for comparison.

Table 1: Configuration of the plasma sprayed TBCs

Configuration	Li_2O concentration, wt%
Substrate / **B**ondcoat / Li_2O doped YSZ / YSZ (value indicating the thickness of YSZ in mil):	
S / B / 1 / 9	1
S / B / 2 / 8	1
S / B / 3 / 7	1
S/ B / 5/ 5	1
S / B / 1 / 9	3
S / B / 2 / 8	3
S / B / 3 / 7	3
S / 10	0
S /B / 1	1
S / B / 1	3

D. Thermal cycling of plasma-sprayed TBC coupons in air: All the as-processed samples (CMSX-4 superalloy substrate coupons, about 1-inch in diameter and 3-mm thick) were subjected to an annealing treatment at 1100^{o}C in Ar-5H_2 atmosphere for 4 hours before thermal cycling test. Thermal cycling test was performed at 1100-1150^{o}C in air. Each cycle includes heating up to the temperature, at a rate of 20^{o}C/min, 1 or 20 h at the temperature, cooling down to room temperature, at 20^{o}C/min.

E. Burner-rig testing: The plasma spray coated cylindrical samples were kept in a pedestal in front of the burner flame and rotated at about 50-rpm. A region about 2-cm long on the sample surface was heated by the flame. An optical pyrometer was used to record the sample surface temperature. The Li-emission detector was focused on the sample surface and was physically located at a distance of ~ 50-cm from the sample surface. Samples were thermally cycled by switching off the flame, and switching it back on. The typical arrangement is shown in Figure-2.

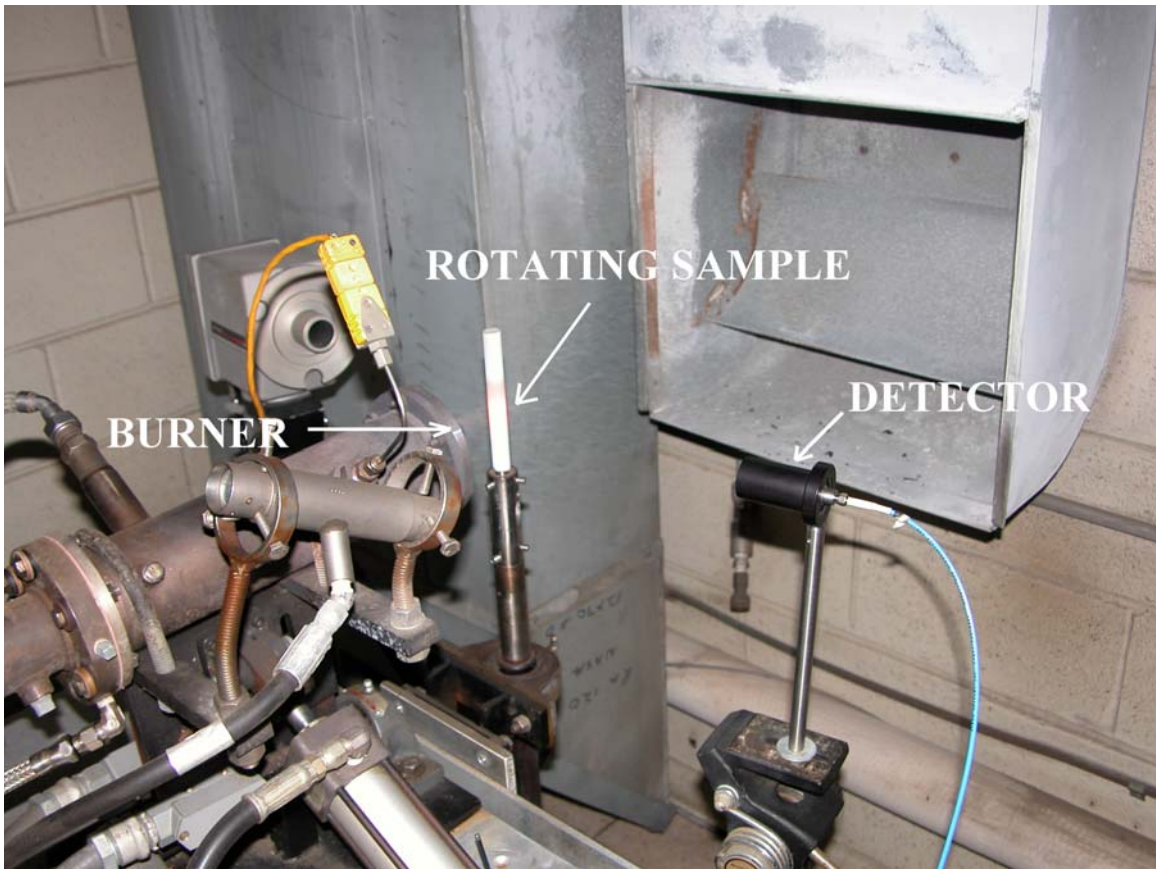

Figure-2 Plasma-spray coated CMX-4 superalloy cylindrical sample being tested in the burner rig. The Li-emission detector is shown on the right.

5. RESULTS AND DISCUSSION

A. Flat-flame burner set-up:

The flat flame burner yields a more stable flame compared to that from the welding torch. Figure-3 plots the typical in-situ measured temperature and luminescence intensity as a function of time for a sintered 1 wt% Li_2O doped YSZ pellet. The steps correspond to the times when adjustments in the gas-mixture were made to achieve higher temperatures.

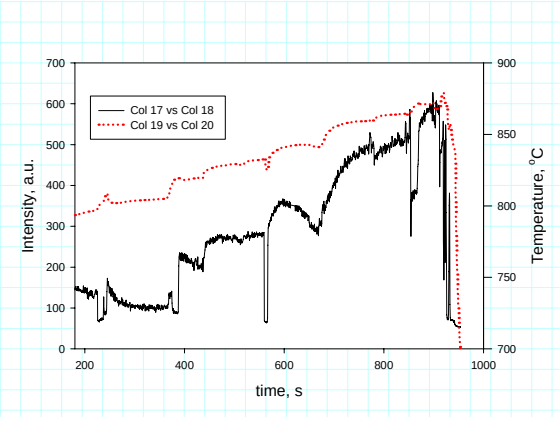

Figure 3. In-situ measured temperature and luminescence intensity for a 1 wt% Li_2O doped YSZ pellet by using flat burner arrangement.

It was earlier observed that for similar thermocouple out-puts the flat-flame burner arrangement yields higher emission intensity as compared with the welding torch. This difference is because of the more uniform flame-coverage of the sample when using the flat-flame burner and concentrated-localized heating of the sample surface in the case of welding torch. This temperature difference of about 260-270^{o}C to yield nearly identical emission intensities was observed to be constant in the temperature range examined, 800 to 1200^{o}C (Figure-4); the flat-flame arrangement consistently yields the same intensity at temperatures that are less than those with the welding-torch arrangement.

Figure 4. The flat-flame burner appears to yield the same emission intensity as the welding torch samples at 260-270 ^{o}C lower temperatures.

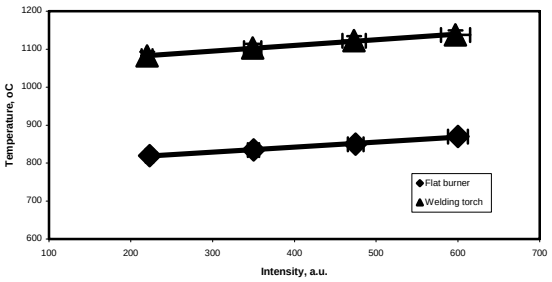

B. Thermal cycling

Tables 2, 3 and 4 show the thermal cycling life of doped and undoped (standard) YSZ TBCs on flat-superalloy coupons at various temperatures and cycling frequencies. In general, thinner doped layer is beneficial for TBC life. With 1/9 configuration 1 – 3 wt% Li_2O dopant concentration gave lives comparable with that of standard YSZ, whereas with 2/8 configuration only 1 wt% Li_2O dopant concentration gave lives comparable with that of standard YSZ. The higher temperature hold during thermal cycling is significantly more detrimental (compare the results from Table-2 and 3 below). The short duration cycles give large number of cycles. Considering all the data the 1/9 coating texture with 1-wt % Li_2O appears to be the optimum coating configuration.

Table 2. Thermal cycling life (20-h cycle test at 1150^{o}C)

Configuration	1 wt% Li_2O	3 wt% Li_2O
1/9	16, 22	24
2/8	18, 20	19
3/7	13, 20	3
Standard YSZ	22	

Table 3. Thermal cycling life (20-h cycle test at 1115°C)

Configuration	1 wt% Li_2O	2 wt% Li_2O	3 wt% Li_2O
1/9	25, 35	30	40, 103
Standard YSZ	25, 75		

Table 4. Thermal cycling life (1-h cycle test at 1100°C)

Configuration	1 wt% Li_2O	2 wt% Li_2O	3 wt% Li2O
1/9	790, 840	900	790, 910
2/8	900	-	20,15
3/7	-	2	1
Standard YSZ	483,750		

C. Burner-Rig Testing

Figure-4 shows a Lithium spectral record from the 1 wt% Li_2O-YSZ coated sample with the burner rig turned on. The Li peak at 673 nm is clearly evident despite the very bright environment of the burner-rig exhaust stream.

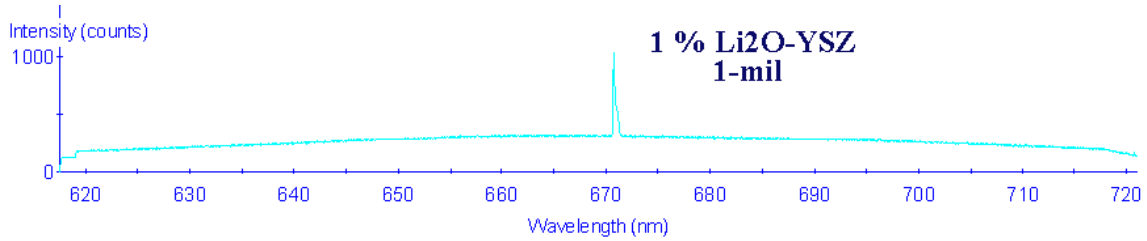

Figure-5. Li-emission specrum from a 1% Li_2O-YSZ sample.

Figure-6 shows the sample coated with S / B / 3 / 7 configuration (3-mil thick 3 wt% Li_2O-YSZ bond coat and 7-mil YSZ top coat) after one cycle in the burner rig. As seen before for the flat-coupon samples tested in a furnace the 3-wt% Li_2O samples fail readily by coating spallation. However, the 1-mil- 1 wt% Li2O samples were extremely resistant to thermal cycling in a burner rig environment. They did not fail even after 30 heating and cooling cycles.

Figure-6. Coating spallation for S / B / 3 / 7-coating configuration in burner rig testing.

6. CONCLUSION

The higher Li2O concentration and thicker inner doped layer are detrimental to the thermal fatigue response. For coupon shaped samples tested in a furnace with 1/9 configuration 1 wt% Li_2O dopant concentration shows lives comparable with that of standard YSZ, whereas with 2/8 configuration only 1 wt% Li_2O dopant concentration shows lives comparable with that of standard YSZ.

In burner rig environment also the 1/9 coatings are extremely resistant to thermal cycling damage. The 3/7 coats fail after just one thermal cycle in a burner rig. The1/9 coating did not fail for thirty burner-rig thermal cycles when the test was discontinued.

It is encouraging to note that despite the very brightly lit environment of the burner-rig exhaust stream the Li-emission signals are readily detected even for the lowest dopant level examined in this study, 1 wt% Li_2O and 99 wt% YSZ.

Other plasma-spray coated cylindrical superalloy samples will also have to be examined in the Burner rig for their thermal cycling resistance and lithium emission spectrum response. Samples coated with 1-wt% Li2O and then top coated with YSZ must be examined to investigate their spectral response and thermal cycling stability in the burner rig for longer time. Longer duration tests should be conducted on flat-disk shaped coated coupons in the flat flame burner set-up to examine the coating and its emission stability during long time high temperature exposure.

Superior Thermal Barrier Coatings for Industrial Gas-Turbine Engines Using a Novel Solution Plasma Spray Process

UTSR Final Report

July 1, 2003 to December 31, 2006

Principal Investigators:

Profs. Eric H. Jordan

Institute of Materials Science
University of Connecticut

Prof. Nitin P. Padture

Department of Materials Science and Engineering
The Ohio State University

Prime Agreement Contract No. DE-FC26-02NT41431
US Department of Energy

UTSR Subcontract No. 03-01-SR107

Principal Investigators: Eric H. Jordan, Professor
Department of Mechanical Engineering
The University of Connecticut
Storrs, CT 06269-3139
Phone: (860) 486-2371 Fax: (860) 486-5088
E-mail: jordan@engr.uconn.edu

Maurice Gell, Professor-in-Residence
Department of Materials Sci & Engr,
Institute of Materials Science
University of Connecticut
Storrs, CT 06269-3136
Phone: (860)486-3514 Fax: (860)486-4745
Email: mgell@mail.ims.uconn.edu

Research Students/Post-Doc: Mr. Amol Jadhav
Mr. Dianying Chen
Dr. Fang Wu
Dr. Alexander Vasiliev

Subcontractors: The Ohio State University (Prof. N.P. Padture)
2041 N. College Road
Columbus, OH 43210
Phone: (614)247-8114 Fax: (614)292-1537

Inframat Corporation (Dr. X. Ma)
74 Batterson Park Road, Farmington, CT 06032
Phone: (860)678-7561 Fax: (860)678-7569

DISCLAIMER

ABSTRACT

Thermal barrier coatings (TBCs) made of low thermal-conductivity zirconia ceramics (ZrO2-7 wt.% Y2O3 or 7YSZ) are routinely used to provide thermal insulation and protection to metallic turbine-engine components from the hot gas stream . The use of TBCs, along with internal cooling of the underlying metallic component, provides significant temperature reductions (100 to 200 °C) at the metal/ceramic interface. Application of thicker TBCs than the current state-of-art ones may result in increased thermal resistance, hence lower cooling requirements, or increased operating temperatures of gas turbine engines, and thus improved efficiency. Conventional air-plasma-sprayed (APS) coatings are limited to less than 0.6 mm thickness to prevent spontaneous premature spallation. Using the solution-precursor plasma-spray (SPPS) process, we have demonstrated the ability to produce durable ultra-thick (~4mm thick) TBCs. The large thickness of the coatings also allowed us to characterize the mechanical and thermal properties of the ceramic top-coat in some detail. Development of thermally grown oxide (TGO) at the thick TBC/substrate interface has been studied in details using interrupted thermal cycling experiments. Based on the experimental results and interface stress analysis, dramatic improvement in the thermal cycling life in the SPPS TBCs is attributed to superior mechanical properties of SPPS coatings. The presence of the strain tolerant vertical cracks in SPPS TBCs reduces the driving force for TBC spallation and the significantly higher in-plane fracture toughness (over fivefold) in the SPPS TBCs over APS TBCs creates more resistance to the TBC spallation. Finally, microstructural tailoring of these thick SPPS coatings has been shown to reduce their thermal conductivity significantly. Analytical and object-oriented finite element (OOF) models have been used to analyze the experimental thermal conductivity data.

TABLE OF CONTENTS

1. EXECUTIVE SUMMARY

In this 3-year project, we have focused on the following three tasks.

First, we have demonstrated feasibility of deposition of ultra-thick thermal barrier coatings (TBCs) (~4 mm thick) using solution precursor plasma spray (SPPS) process [1]. Thermal cyclic durability of the 4 mm thick TBCs deposited on bond-coated superalloy substrates has been determined and compared to reference air plasma spray (APS) TBCs deposited on the same bond-coated superalloy substrates. We have found that, while the APS TBCs lasted 40 thermal cycles (1-hour each cycle with peak temperature 1121 ˚C), the average life of SPPS TBCs is 819 cycles (average of 4 specimens).

Second, we have studied the fracture toughness behavior and compressive deformation behavior of thick YSZ SPPS and APS ceramic coatings [1]. Purpose of this study was to understand effect of mechanical and elastic properties of free-standing thick TBCs on their thermal cyclic performance. We have correlated the mechanical properties and failure mechanisms to the microstructures of these plasma-sprayed coatings. Also degradation of the TBC/substrate interface has been studied in details and a mechanism for "chemical failure" of the TBC is suggested.

Third, we measured the thermal conductivities of thick, free-standing SPPS and APS TBCs [2]. Additionally, SPPS process has been modified to deposit layered TBCs to reduce the overall thermal conductivity. We found that the thermal conductivity of layered TBCs is as low as 0.7 W/m/K. We have correlated these experimental results with results obtained by theoretical models expressed in terms of morphology and percentage of the porosity in the TBC material [2]. This approach along with parametric studies helps in advance to design thermal properties of a material. Also, finite element analysis based on the real microstructures of TBCs has been carried out to estimate their thermal conductivities. Good match between experimental and modeling results has been seen.

2. PROJECT DESCRIPTION

For the next generation of combustion engines used for aerospace applications and in energy production, higher operating temperatures (>1300 ^{o}C) are desirable. Thus, stricter environmental requirements can be fulfilled, and the efficiency of the gas turbine can be increased. Current state-of-art plasma-sprayed TBCs on NiCoCrAlY bond coats with top-coat thickness of about 0.35 mm permit a temperature of the inner air-cooled combustion chamber walls of about 900 ^{o}C [3]. The use of thicker TBCs allows for higher operating temperatures and lower temperatures at the bond coat. The latter reduces the oxidation of the bond coat.

One of the major hurdles with the development and application of thick TBCs on engine components is its reduced lifetime due to spallation under typical gas-turbine engine operating conditions. This is caused by faster degradation of the thick TBC due to higher volume under stresses, and steep thermal gradients present in the system [4]. These residual stresses in a TBC system can be reduced by introduction of through-thickness cracks in the ceramic top-coat [5]. Previously, it has been successfully

demonstrated that a novel process — Solution Precursor Plasma Spray (SPPS) — has the potential to satisfy all of these requirements [6, 7]. The SPPS process is ideally suited for the deposition of thick TBC, which is being explored in this project.

3. EXPERIMENTAL

3.1. Specimen Fabrication

The SPPS and APS coatings required for testing were fabricated by using the direct current (dc) plasma torch (Sulzer Metco, Westbury, NY), which was attached to a 6-axis robotic arm. For SPPS coatings the plasma precursor used was an aqueous solution containing zirconium and yttrium salts, to result in a solid solution of 93-wt % ZrO_2 and 7-wt % Y_2O_3 (7YSZ) in the coating. Coatings reported here were deposited under standard spray conditions [4] with the deposition rate of 3 μm/pass. For thermal cyclic testing as well as failure mechanisms studies, 7YSZ ceramic TBCs were deposited on plasma preheated (preheating temperature ~ 200°C) bond-coated superalloy circular substrates (diameter = 25.4 mm; thickness = 3.18mm). The APS coatings were deposited using (ZrO_2-8 wt % Y_2O_3) powder (Metco 204NS, 104 mesh+10 μm). The coatings thickness in each case was 4 mm. For mechanical testing, 3.5 mm thick APS and SPPS coatings were deposited on stainless steel substrate and then dipped in 40% HNO_3 solution for 2 hrs where to obtain free-standing coatings.

For thermal conductivity measurements, SPPS and APS coatings of ~1.3 mm thickness were deposited under standard deposition conditions. The SPPS process has also been used to deposit 7YSZ TBCs that contain alternate layers of low and high porosities (layered-SPPS). These coatings are referred as layered-SPPS coatings henceforth. The coatings were removed from the substrate by chemical etching.

3.2. Characterization

Carefully polished cross-sections (1 μm finish) of the coatings on the substrate were characterized using optical microscope, scanning electron microscope (SEM), focused ion beam (FIB) and transmission electron microscope (TEM). Quantative image analysis was done on the cross-section images of the coatings using Clemex Vision image analysis software (Clemex Technologies Inc., Canada).

3.3. Thermal Cycling

The usual practice for the thermal cycling experiments adopted as University of Connecticut is as follows: A specially designed bottom-loading box furnace is preheated to a temperature of 1121°C. The following steps constitute one thermal cycle: (i) the furnace is opened by lowering the floor of the furnace (using an elevator) and the samples are placed on the floor. The samples are leaned against a refractory holder such that the TBC coated circular face, which is almost normal to the floor, does not make contact with the refractory holder. (ii) The floor is raised and the furnace is closed; the time is set to zero. (iii) After 50 min, the floor is lowered and the samples are

convectionally cooled using a fan for 10 min. Steps (ii) and (iii) are repeated. Each red-hot sample was observed visually during the cooling cycle. The occurrence of spallation, where the TBC falls off the metal substrate, is easy to discern. Delamination, where a portion of the TBC is detached but is still hanging onto the substrate, results in a distinct change in contrast: the attached area appears dark whereas the detached area appears bright. A sample has been considered to fail when the TBC failure area (spallation plus delamination) reached 50% of the total TBC area. Note that in this test both the substrate and the coating are at the same temperature in the furnace. In an actual TBC application, the substrate is at a relatively lower temperature due to internal cooling, resulting in a thermal gradient across the TBC and relatively longer thermal cyclic lives. SPPS coatings were also thermally cycled for intermediate thermal cycling to study their failure mechanisms. The samples were taken out of the thermal cycling furnace after 1, 10, 40, 140, 400, 500 and 600 thermal cycles.

3.4. Mechanical Property Measurements

Indentation fracture toughness measurements were carried out on polished cross-sections of coatings using Vickers diamond pyramid with a contact load (P) of 49 N (5 indentations per material). Radial cracks, emanating from the indentation corners, running parallel to the deposition surface ("in-plane" direction) and perpendicular to that surface ("out-of-plane" direction) were measured using a scanning electron microscope or SEM (ESEM 2020, Philips Electron Optics, The Netherlands). The formulation due to Lawn and co-workers [8] was used to determine the in-plane and the out-of-plane toughness values: $K_{IC}=0.016(E/H)^{0.5}Pc^{-1.5}$ where H is the hardness and E is the elastic-modulus, which was measured using uniaxial compression testing.

The cube specimens (cube side ~ 3.3 mm) of free-standing SPPS and APS coatings were tested in uniaxial compression using a screw-driven mechanical testing machine (Model 5869, Instron Corp., Canton, MA), in two different orientations — in-plane and out-of-plane — as explained earlier. Monotonic loading tests were performed in order to determine compressive elastic moduli and the average ultimate compression strengths of the SPPS and the APS coatings. Additionally, cyclic loading tests were performed to study the mechanical hysteresis in both the types of coatings.

3.5. Thermal Conductivity

The thermal diffusivity (κ) for "regular" SPPS TBCs and SPPS TBCs containing IPBs, together with the reference APS TBC, was measured using the laser-flash method (Thermaflash 2200, Holometrix, Bedford, MA) as a function of specimen temperature (in the range 100 to 1000 ˚C) in Ar atmosphere. Prior to thermal diffusivity measurements, both the front and the back faces of each specimen were first coated with a thin layer of gold, followed by the deposition of a thin layer of carbon. This was done to prevent direct transmission of the laser beam through the translucent specimens. Appropriate corrections were made in the thermal diffusivity calculations to account for the presence of these layers. The accuracy of the thermal diffusivity measurements is ±5%. The specific heat capacities (c) as a function of temperature were measured using

differential scanning calorimetry (DSC-2, Perkin Elmer, Wilmington, DE). The thermal conductivity (k) for each materials was then calculated using the relation $k = \kappa\rho c$, where ρ is the density as measured using the Archimedes method.

4. RESULTS AND DISCUSSION

4.1. Microstructures

Fig. 1A shows the cross-section microstructure of a 4 mm SPPS TBC. These thick SPPS coatings are characterized by branched vertical cracks; this is in contrast with thin SPPS coatings (250-300 μm), where un-branched vertical cracks are observed [6]. The vertical cracks are a representation of separated columns running perpendicular to the substrate/coating interface. A higher magnification SEM micrograph of SPPS coating cross-section (Fig. 1B) shows uniformly spread mixture of elongated and circular porosity. The elongated pores in this case are oriented close to the horizontal direction. Fig. 1B also shows a lack of horizontal "splat" boundaries/cracks. Such horizontal "splat" boundaries/cracks are always present in APS coatings, as seen in the cross-sectional SEM micrograph of the free-standing APS coating, and they can be up to 100 μm long. The microstructures of APS ceramic coatings have been studied extensively, and the mechanisms by which they arise have been documented in the literature [9, 10]. Fig. 2 shows cross-sectional micrograph of a 1 mm thick SPPS coating with layered microstructure It can be observed that the microstructure consists of a layer of separated and elongated porosity (like flat spheroids) in between layers of denser material. The spheroidal porosity in the boundary region appears to be oriented with their major axis parallel to the coating-substrate interface. The denser region is found to posses pores of lower aspect ratio as compared to those of boundary layer pores.

The densities of the SPPS, layered-SPPS and the APS coatings are 4.73 $Mg.m^{-3}$, 4.13 $Mg.m^{-3}$, and 5.16 $Mg.m^{-3}$, respectively.

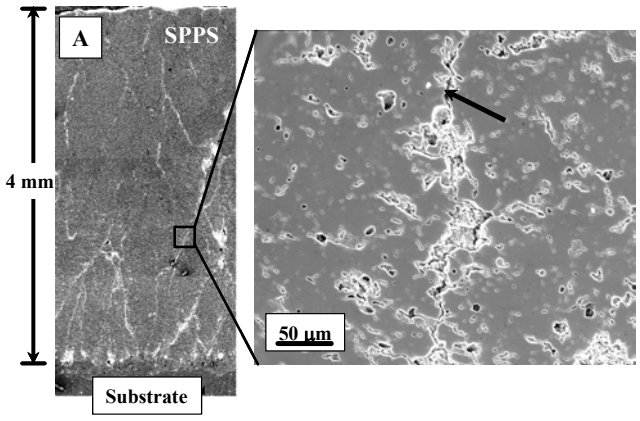

Fig. 1. (A) Cross-sectional optical micrograph showing vertical cracks in a SPPS TBC. (B) Higher magnification SEM micrograph showing mixture of elongated and spherical porosity.

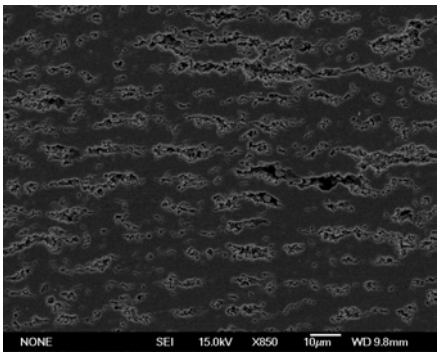

Fig. 2. Cross-section of a layerd-SPPS TBC shown by an SEM image.

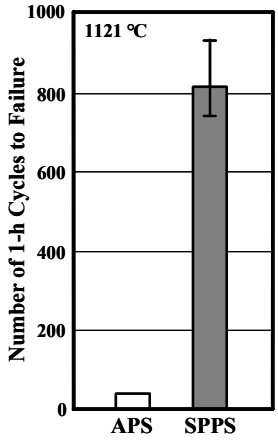

Fig. 3. Thermal cycling results for 4 mm thick APS and SPPS TBCs deposited on bond-coated superalloy substrate.

4.2. Thermal Cycling Performance

Fig. 3 shows a comparison of thermal-cycling lives of SPPS TBCs and reference APS TBCs. The 4 mm thick SPPS coatings subjected to the thermal cycling spalled after average 820 thermal cycles while APS coatings of the same thickness failed only after 40 thermal cycles. The dramatically high thermal-cycling in SPPS TBCs can be attributed to the lack of macro-splats in the SPPS, which are always present in APS coating. The strain-relieving vertical cracks present in the SPPS TBCs also contribute to their improved thermal-cycling lives. As noted earlier, the entire TBC specimen (substrate, bond-coat, top-coat) is at the same temperature in the thermal cycling test, therefore, the thermal conductivity differences in the SPPS and the APS coatings are not a factor.

4.3. Mechanical Properties

It can be seen in Fig. 4 that the in-plane indentation toughness of SPPS coating is over five times that of APS coating. The lower in-plane toughness in the APS

coatings can be attributed to the presence of weak, long "splat" boundaries and cracks in that orientation. Although "splat" boundaries exist in SPPS coatings, they are 50 to 100 times smaller than those found in APS coatings [11]. The toughness of the SPPS coating is isotropic within 30% (Fig. 4).

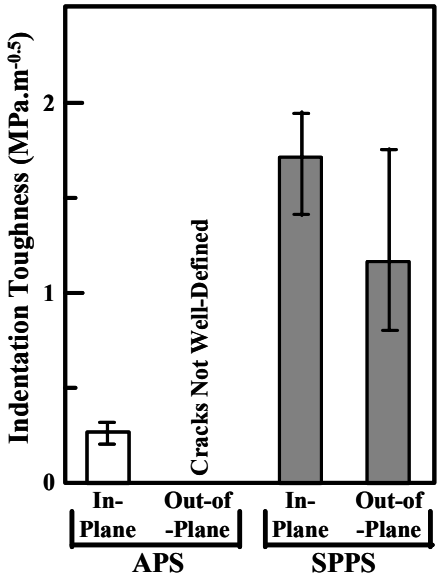

Fig. 4 Indentation fracture toughness for APS and SPPS samples.

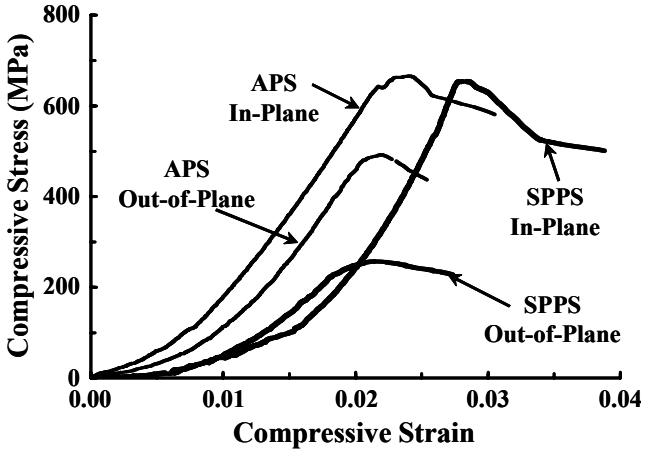

Fig. 5 Uniaxial compression stress-strain behavior for APS and SPPS Coatings.

The in-plane stress-strain curves for both materials are characterized by non-linear deformation behavior, followed by linear behavior prior to failure (Fig. 5). The in-plane ultimate compressive strengths and the elastic moduli for SPPS and APS coatings are reported in Table 1. Upon heat-treatment at 1100^{o}C for 2 hrs, the SPPS coatings become stiffer and stronger in both the in-plane and out-of-plane orientations

(Table 1). This is most likely due to the heat-treatment-induced complete pyrolysis of the unpyrolyzed material that is ubiquitously present in the as-sprayed SPPS coatings [11]. In cyclic loading specimens, the hysteresis is observed in the stress-strain behavior at low stresses for both the SPPS and the APS coatings. It is also found that secant elastic modulus increases with successive load/unload cycles. With increasing compressive stress micro-cracks close-up, resulting in elasticity, characterized by a linear stress-strain response. The more pronounced deformation (strain) in the SPPS coating at relatively lower stress values could be due to the higher porosity in the SPPS coating compared to the APS coating.

Table 1. Elastic modulus and compressive strength of SPPS and APS coatings.

Coating	Orientation	Ave. El. Mod. (Range) GPa	Ave. Comp. St. (Range) MPa
SPPS	In-Plane	49 (77-44)	540 (722-301)
	Out-of-Plane	22 (30-9)	258 (306-190)
SPPS (Heat-Treated)	In-Plane	100 (122-71)	629 (697-504)
	Out-of-Plane	67 (75-58)	368 (424-306)
APS	In-Plane	40 (47-35)	578 (648-423)
	Out-of-Plane	38(41-32)	476 (591-335)

4.4. Failure Analysis of Thick TBCs

Mechanical Failure:

Total stored elastic strain energy of a coating and the driving force for delamination (i.e. steady state strain energy release rate (G_{ss})) increases with thickness of the coating as given by the following relation.

$$G_{SS} = \frac{\sigma_{TBC}^2 H_{TBC}}{2E_{TBC}} \tag{1}$$

where σ_{TBC} gives in-plane compressive stresses within TBC developed during cooling from high temperatures due to differences in coefficient of thermal expansion of TBC and substrate. H_{TBC} denotes thickness and E_{TBC} elastic modulus of the TBC. From Fig. 6 it can be seen that due to higher in-plane elastic modulus, G_{ss} for APS coatings is much higher compared to the SPPS coatings of the same thicknesses. Also the G_{ss} values of APS coatings are higher than critical mode II energy release rates. Thus delamination of an APS coating can be expected either in as-sprayed conditions or during early thermal cycling. This confirms our experimental observation low thermal cyclic life of the thick APS TBC. In case of SPPS coatings, lack of sufficient mode II energy release rate, crack propagation will occur primarily under mode I loading conditions developed due to tensile stresses normal to the TBC/substrate interface. Development and modification of these tensile stresses occurs during thermal cycling

and TGO TBCs. Thus the failure mechanisms in thick SPPS TBCs can be expected to similar that of the thin TBCs.

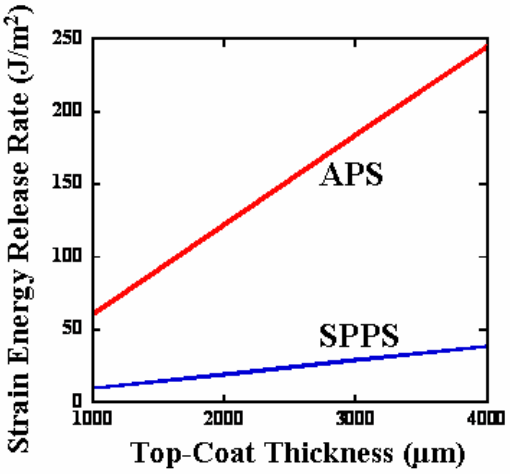

Fig. 6 Steady-state strain energy release rate with thickness variation in SPPS and APS coatings.

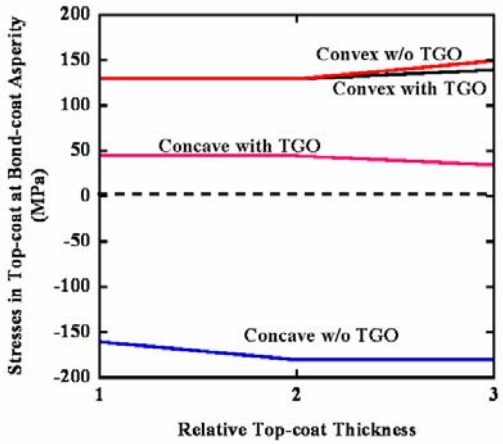

Fig. 7 Stresses normal to the interface within ceramic top-coat with varying TGO thicknesses and top-coat thicknesses.

By using 2 dimensional FEM analyses and introducing a crack in the concave asperity of bond-coat near the interface, strain energy release rate have been computed. Mode I energy release rate is found to be a strong function of elastic modulus of the TBCs and the out-of-plane tensile stresses. But these out-of-plane stresses in the interface region remain almost unchanged with the TBC thickness. Fig. 7 shows the maximum out-of-plane stresses in the interface region at various stages of TGO development. The stresses remain almost constant with increasing thickness. Thus contribution from mode I type pf loading to the crack propagation remains almost

unchanged with increasing thickness. This explains why thermal cyclic lives of thick SPPS TBCs are comparable to thin TBCs and much higher than thick APS TBCs.

Failure in the thick APS expected to occur along the path of the least resistance, i.e. within the ceramic top-coat in the interfacial vicinity. SEM image of the top side of the substrate of spalled ultra-thick APS TBC shown in Fig. 8. Only light phase (top-coat with porosity and cracks in it) can be observed. This indicates that total crack propagation inside the top-coat only. On the contrary, for SPPS coating failure path is seen to travel through both top-coat and TGO from Fig. 9, which shows both light (top-coat) and dark (TGO) phases. This is similar to failure of a thin TBC.

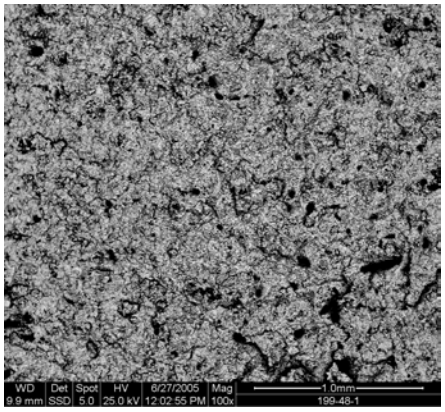

Fig, 7 Bond-coat surface of the failed thick APS coating showing remnant YSZ (light phase) and porosity (dark phase).

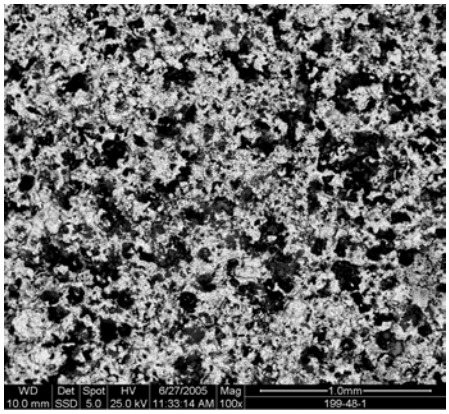

Fig. 8 Bond-coat surface of the failed thick SPPS coating showing remnant YSZ (light phase) and TGO (dark phase).

Chemical Failure:

Formation of non-alumina oxides is highly unexpected in the TGO of a TBC. Non-alumina oxides are associated with additional volume expansion as well as they have inferior mechanical properties compared to those of the alumina TGO [3]. Thus formation of mixed oxides/ spinels can be considered as 'chemical failure' of a TBC and is expected to deteriorate TBC durability [12]. Just after one thermal cycle, development of dark and grey phases of thermally grown oxide (TGO) was detected as shown in the Fig. 9. The dark phase is α-alumina whereas the grey phase is identified as mixture of oxides of Al, Ni and Cr. The thickness of both the TGO phases was observed to increase further with increase in thermal cycling of SPPS samples.

Low magnification TEM image of interface a SPPS TBC subjected one thermal cycle can be seen in Fig. 10. Five different layers of materials can be seen here. While alumina layer next to bond-coat contain equiaxed grains layer of $NiAl_2O_4$ spinel above that is much thicker (~1 μm) compared to alumina layer. Grains of Nickel oxide and chromia randomly have been found to spread randomly in the spinel layer. For a

sample subjected to 140 thermal cycle, TEM image (Fig. 11) shows thicker layer of columnar alumina. Thickness of non-alumina oxides remains almost unchanged.

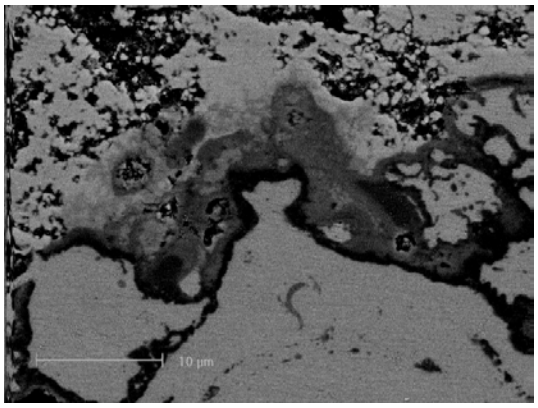

Fig. 9 Cross-section of a 1.5 mm thick SPPS TBC subjected to one thermal cycle. Dark phase (alumina) and grey phase (mixed non-alumina oxides) of TGO are evident.

In order to analyze the chemical failure of TBCs, we divide bond-coat asperity regions into two different types: 1. Flat bond-coat regions having total access to remainder of the bond-coat 2. Bond-coat material regions almost completely isolated from rest of the bond-coat by open porosity/oxide (Fig. 12). This could happen as this bond-coat has been prepared due to APS process.

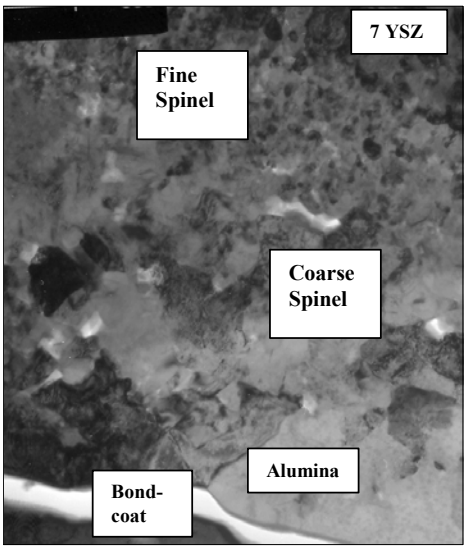

Fig. 10 TEM micrograph showing evolution of different phases at TBC interface after one thermal cycle.

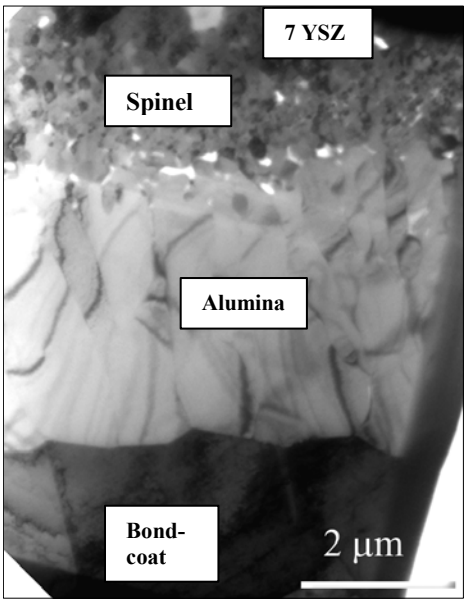

Fig. 11 TEM micrograph showing evolution of different phases at TBC interface after 140 thermal cycle.

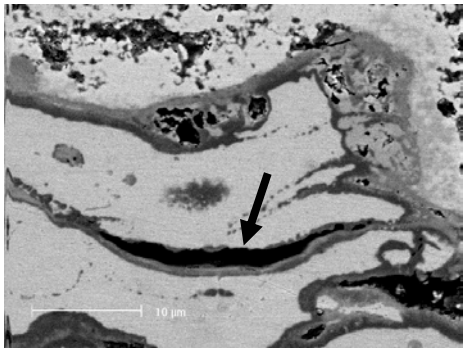

Fig. 12 SEM images of cross-section of interface of SPPS TBCs subjected to 10 thermal cycles. Region of bond-coat is separated from bulk by open porosity (shown by arrow).

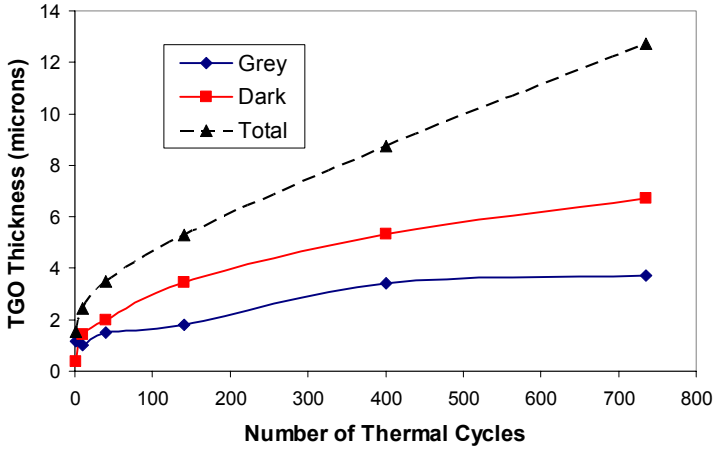

Fig. 13 TGO thickness as a function of thermal cycling in the asperity regions of interface.

Based on the observation of SEM micrographs and chemical analysis of the interrupted thermally cycled SPPS samples, following mechanism of chemical failure of SPPS coatings has been suggested. For the first types of regions, a 1-micron thick layer of mixed oxides forms due to transient oxidation and the layer thickness remains constant until sample failure. Beneath this layer columnar alumina grows parabolically.

Typically, aluminum consumed to form TGO is usually replenished by aluminum diffusion from interiors of the bond-coat. But for isolated bond-coat region (Fig. 12) layers of oxide or porosity effectively block the supply of Al from the bulk of BC. Amount of Al in the region falls below the certain critical value (~ 4-5 at %), which is required to form alumina [12]. Under such circumstances if the TGO cracks during continued thermal cycling, the cracks are healed with non-alumina oxides instead of alumina. Eventually, NiO and Alumina react with each other at the highest temperature. During later stages, mixed oxide layer offers partial protection and alumina layer grows under mixed oxide layer. Fig. 13 shows the relationship between

TGO thickness and thermal cycles for asperity (non-planer) region of the TBC/bond-coat interface.

4.5. Thermal Conductivity

Experimental Thermal Conductivity

The values of thermal conductivity of dense 7wt% YSZ (~4mol %) in the temperature range of 100°C – 1000°C have been obtained from linear interpolation method using data for dense 3mol% and 8mol% YSZ material [13]. These results along with results obtained for free standing SPPS and APS coatings have been plotted in Fig 14. It can be seen that thermal conductivity of the APS coating is much lower than that of the SPPS coating for the entire temperature range tested. The SPPS process has been used to deposit TBCs with modified microstructure that contains alternate layers of low and high porosities (layered-SPPS). The thermal conductivity of the layered-SPPS coating is found to be lower than those of both, the SPPS coating and the APS coating of the same composition, in the temperature range 100-1000 ˚C (Fig. 14).

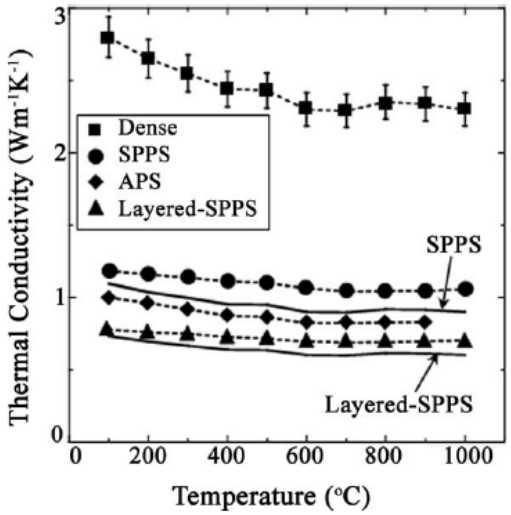

Fig. 14 Thermal conductivity of SPPS, APS and layered SPPS coatings plotted with temp. Symbols represent experimental data and solid lines are result of analytical modeling.

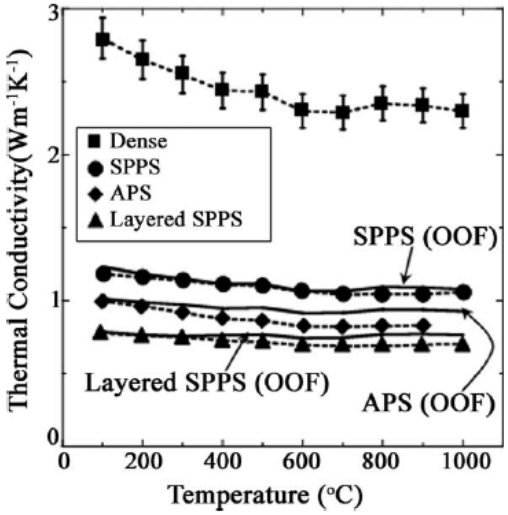

Fig. 15 Thermal conductivity of SPPS, APS and layered SPPS coatings plotted with temperature. Symbols represent experimental data and solid lines are result of OOF analysis.

Thermal Conductivity: Analytical Modeling

The porous coating can be treated as a composite of 7YSZ dielectric and air confined in the pore space. Following previous calculations [14, 15] thermal conductivity of air in pores, which is much smaller than thermal conductivity of YSZ,

contribution from pore-air conductivity is ignored in the ensuing calculations. Also the photon scattering by pores is also ignored in the following calculations.

Thus, the reduced thermal conductivity of the coatings relative to the dense 7YSZ is solely due to the missing dielectric medium in the form of pores. This is described by the Maxwell equation for materials with spherical, non-interacting pores of volume-fraction porosity ϕ_{Sphere} [16]:

$$\frac{k_{SphericalPores}}{k_{Dense}} = 1 - \frac{3}{2}\phi_{Sphere} \tag{2}$$

However, the coatings studied here contain non-spherical pores, and therefore we consider a model proposed by Kachanov and co-workers that takes into account non-spherical morphology of pores. For disk-shaped pores aligned normal to the heat flux the thermal conductivity reduction is given by [14, 17]:

$$\frac{k_{DiskPores}}{k_{Dense}} = 1 - \left(\frac{2\phi_{Disk}}{\pi}\right)\left(\frac{d}{t}\right) \tag{3}$$

Consider the SPPS coating which contains both spherical and disk-shaped pores. The combined effect of the two different types of porosities on the thermal conductivity SPPS is given by [18]:

$$k_{SPPS} = \frac{1}{2}\left\{ f_2\left(\frac{\phi_{Disk}}{1-\phi_{Sphere}}\right) f_1(\phi_{Sphere}) + f_1\left(\frac{\phi_{Sphere}}{1-\phi_{Disk}}\right) f_2(\phi_{Disk}) \right\} k_{Dense}, \tag{4}$$

where f_1 and f_2 are functions representing Eqns. 2 and 3, respectively. Using Eqns. 2-4 and the microstructural data from image analysis, the calculated thermal conductivity of the SPPS coating is plotted in Fig.14. The calculated thermal conductivities are within 12.7% of the experimental values, and they are consistently lower than the experimental values. This could be due to various reasons, including (i) overestimation of the porosities in the coatings and (ii) assumption of all disk-shaped pores being aligned normal to the heat flux, which may not be strictly valid.

Consider the layered-SPPS coating, which contains alternating layers of spherical pores (low porosity) and disk-shaped pores (high porosity) (Fig.14). Thus, the conductivity of the layered-SPPS coating is given by:

$$k_{LayeredSPPS} = \left(\frac{f_1(\phi_{Sphere}) f_2(\phi_{Disk})(L_{Sphere} + L_{Disk})}{f_1(\phi_{Sphere}) L_{Disk} + f_2(\phi_{Disk}) L_{Sphere}} \right) k_{Dense}. \tag{5}$$

Using Eqns.2, 3, and 5, and the microstructural data obtained by image analysis and corresponding stereological interpretations, the calculated thermal conductivities of the layered-SPPS coating are also plotted in Fig. 14. The agreement between the calculated and the experimental values is within 11.3%, which is better than that in the SPPS-coating case. Once again, the calculated values are consistently lower than the experimental values, which can be attributed also to the aforementioned reasons. Nevertheless, the agreement between the calculated and experimental thermal

conductivities is noteworthy considering that there are no adjustable parameters in the analytical model presented here.

Thermal Conductivity: Object-Oriented Finite Element (OOF)

In this study the inputs for two-dimensional object oriented finite element analysis software (OOF) were digitized SEM images of the APS, SPPS, and layered-SPPS coatings [19, 20]. The microstructures were converted into binary images consisting of only two distinct phases — 7YSZ and pores (air). The 7YSZ phase was assigned dense-7YSZ thermal conductivity. The binary images were then meshed using an adaptive meshing procedure. The top and the bottom of the meshed micrographs were assigned constant temperatures of T_1 and T_2, such that a thermal gradient of 10 ˚C (T_1-T_2) is set up across the meshed micrographs, in the direction of the expected heat flow in an actual TBC. The two vertical sides of the micrographs were kept adiabatic. The resultant heat flux was used to obtain the average thermal conductivity of the microstructure.

The thermal conductivity results from the OOF analysis for the APS, the SPPS, and the layered-SPPS coatings are plotted in Fig. 15. In the cases of the APS, SPPS, and layered-SPPS coatings the agreements between the experimental data and the OOF results are within 7.5%, 6.2%, and 10.9%, respectively. These agreements are better than those obtained using analytical modeling, despite that fact that OOF is a two-dimensional model. This can be attributed to fact that "real" microstructures are used as input in OOF, instead of the approximated, ideal microstructures used in the analytical modeling. This demonstrates the utility of OOF in capturing accurately the effect of real microstructures on the thermal conductivities of plasma-sprayed TBCs.

5. CONCLUSIONS

- We have demonstrated the ability of deposition of ultra-thick (~ 4 mm thick) SPPS TBCs, successfully. The microstructures of these coatings are characterized by vertical cracks, a lack of horizontal "splat" boundaries and cracks, and porosity of ~22%. The indentation-toughness of the SPPS coating was found to be over five times that of the reference 7YSZ APS coating in the most critical in-plane orientation. The improvement in the thermal cycling life in the SPPS TBCs can be attributed to: (i) the significantly higher in-plane local fracture toughness (over fivefold) in the SPPS TBCs over APS TBC and (ii) the presence of the vertical cracks in SPPS TBCs resulting in a high degree of strain tolerance.
- Due to higher in-plane elastic modulus driving force for delamination in 4 mm thick APS coatings is much higher compared to their SPPS counterparts. This leads to premature spallation of APS coatings. Chemical failure (formation of non-alumina mixed oxides) in both APS and SPPS TBCs is attributed to the bond-coat morphology and its chemical composition. Thus TGO growth is independent on the top-coat deposition method.

- The thermal conductivities of the 7YSZ layered-SPPS coating are found to be lower than those of both the SPPS coating and the APS coating of the same composition, in the temperature range 100-1000 ˚C. Analytical modeling and OOF analysis have been used to analyze the experimental thermal conductivity data, successfully.

6. **REFERENCES**

[1] A. Jadhav, N. P. Padture, F. Wu, E. H. Jordan, M. Gell, Materials Science and Engineering a-Structural Materials Properties Microstructure and Processing 405 (2005) 313-320.

[2] A. D. Jadhav, N. P. Padture, E. H. Jordan, M. Gell, P. Miranzo, E. R. Fuller, Acta Materialia 54 (2006) 3343-3349.

[3] N. P. Padture, M. Gell, E. H. Jordan, Science 296 (2002) 280-284.

[4] E. F. Rejda, D. F. Socie, B. Beardsley, Fatigue & Fracture of Engineering Materials & Structures 20 (1997) 1043-1050.

[5] H. D. Steffens, Z. Babiak, M. Gramlich, Journal of Thermal Spray Technology 8 (1999) 517-522.

[6] N. P. Padture, K. W. Schlichting, T. Bhatia, A. Ozturk, B. Cetegen, E. H. Jordan, M. Gell, S. Jiang, T. D. Xiao, P. R. Strutt, E. Garcia, P. Miranzo, M. I. Osendi, Acta Materialia 49 (2001) 2251-2257.

[7] T. Bhatia, A. Ozturk, L. Xie, E. H. Jordan, B. K. Cetegen, M. Gell, X. Ma, N. P. Padture, J. Mater. Res. 17 (2002) 2363-2372.

[8] B. R. Lawn, Fracture of Brittle Solids Cambridge University Press, Cambridge, U.K., 1993.

[9] H. Herman, S. Sampath, R. McCune, MRS BULLETIN (2000) 17.

[10] L. Pawlowski, The Science and Engineering of Thermal Spray Coatings, John Wiley & Sons Ltd, England, 1995.

[11] L. D. Xie, X. Q. Ma, E. H. Jordan, N. P. Padture, D. T. Xiao, M. Gell, Materials Science and Engineering a-Structural Materials Properties Microstructure and Processing 362 (2003) 204-212.

[12] H. E. Evans, M. P. Taylor, Oxidation of Metals 55 (2001) 17-34.

[13] J. Wu, X. Z. Wei, N. P. Padture, P. G. Klemens, M. Gell, E. Garcia, P. Miranzo, M. I. Osendi, Journal of the American Ceramic Society 85 (2002) 3031-3035.

[14] T. J. Lu, C. G. Levi, H. N. G. Wadley, A. G. Evans, Journal of the American Ceramic Society 84 (2001) 2937-2946.

[15] I. O. Golosnoy, S. A. Tsipas, T. W. Clyne, Journal of Thermal Spray Technology 14 (2005) 205-214.

[16] J. C. Maxwell, A Treatise on Electricity and Magnetism, Oxford, UK: Clarendon Press, 1904.

[17] I. Sevostianov, M. Kachanov, Materials Science & Engineering A 297 (2001) 235-243.

[18] F. Cernuschi, S. Ahmaniemi, P. Vuoristo, T. Mantyla, Journal of the European Ceramic Society 24 (2004) 2657-2667.

[19] S. A. Langer, E. R. Fuller Jr, W. C. Carter, Computing in Science & Engineering [see also IEEE Computational Science and Engineering] 3 (2001) 15-23.

[20] C. H. Hsueh, P. F. Becher, E. R. Fuller, S. A. Langer, W. C. Carter, Materials science forum 442-449.

An Advanced Diagnostic and Prognostic System for Gas Turbine Generator Sets with Experimental Validation

July 1, 2006 to December 31, 2006

John R. Wagner , Ph.D., P.E., Principal Investigator
J. Leo Gaddis, Ph.D., Co-Investigator
H. Bassily, Rajat Sekhon, Student Researchers
Department of Mechanical Engineering
Clemson University
Clemson, South Carolina 29634-0921

DOE Award Number: DE-FC26-02NT41431
UTSR Project Number: 03-01-SR108

DISCLAIMER

ABSTRACT

The demand for electric power continues to rise for both industrial and consumer needs throughout the world. Simple cycle gas turbines offer reliable power generation capabilities using multiple fuels such as natural gas and others. Gas turbines can experience short and long term transient operating conditions due to changing electrical loads, environmental effects, system disturbances, and component deteriorations which can lead to performance degradations. An effective health management strategy can enhance overall plant Reliability, Availability and Maintainability (RAM) through the continual monitoring of system operation using readily available sensor information. An efficient health management system is based on the integration of sensors and real-time diagnostic/prognostic monitoring strategies which can warn of impending problems within the gas turbine and its subsystems. Prognostic methods monitor the plant current and historical data to predict future behavior for enhanced maintenance scheduling. Similarly, diagnostic strategies review current operating data to detect the occurrence of degradation that are reflected in the sensory information. Once a failure has been detected, then the failure source and magnitude are identified so that it may be accommodated. This report presents the past six month effort by the Clemson University research team to develop a real-time diagnostic/prognostic algorithm for gas turbines. A series of empirical models have been proposed for Solar Mercury 50 and General Electric 7EA gas turbine systems. Experimental data acquisition has been performed for the Solar turbine' Mercury 50 4.5 MW gas turbine located at the Clemson University campus and other Off-site commercial turbines. Model-free diagnostic and prognostic strategies have been developed and results compared with experimental data. The report presents the past six months of research completed on the project.

TABLE OF CONTENTS

TABLE OF FIGURES

Page

1. INTRODUCTION

Gas turbine systems have become an integral part of the industrial and electric power generation sectors throughout the world. These systems operate under varying conditions which makes them susceptible to degradation and breakdowns. The objective for this research project is to develop a real-time monitoring and prediction program for stationary gas turbines to diagnose and predict short and long-term system health and readiness using behavior models, sensor fusion strategies, and extensive statistical analysis.

To monitor and control these machines as part of the desired health management system, the formulation and introduction of online diagnostics and prognostics modules is a necessity. The combination of these modules complements the plant sensors and controllers on a real time basis in a parallel manner. The implementation of these modules allows the detection and prediction of abnormal behavior. Diagnostic strategies utilize hardware and software to detect, isolate, and identify a deviation from the normal plant behavior. Prognostic algorithms focus on the estimation of the current health and prediction of the life of a critical component. A unified diagnostics and prognostics strategy has been investigated by the Clemson University research team for condition monitoring and fault diagnosis.

2. EXECUTIVE SUMMARY

This project developed a real-time health management system for stationary gas turbines to improve turbine reliability and allow higher availability levels. The formulation and implementation of real-time diagnostic and prognostic strategies, which detect and predict the onset of system degradation and maintenance needs, will constantly monitor the overall system performance to reduce operation and maintenance costs.

The project encompasses seven tasks. During the last six months, considerable gains have been made.

Task 1. Analytical Modeling of the Turbine System

A model based diagnostics approach requires the existence of a real time mathematical model that describes the turbine system using differential and algebraic equations. The model should depict the "normal" turbine system behavior. The Clemson research team has developed a transient gas turbine model. The major components have been modeled as subsystems and linked together to create a simulation tool. The model simulates a Mercury 50 gas turbine located at Clemson University. The model has undergone validation activities.

Task 2. Real-Time Turbine Sensor Data Streaming

Real-time experimental data has been collected and recorded from the Mercury 50 gas turbine located at the Clemson University main campus. Computer code initializes the recording of twenty eight different signals at the sampling rate of one second. This one way link permits data reading only to prevent interference with the plant operation. The data is stored in the form of arrays, using the MATLAB/SIMULINK software package on the Energy Systems Laboratory

computer workstation. The performance of the Mercury 50 can be evaluated using this streamed data. The benefit of such a data collection connection is that it can be used by turbine engineers to formulate a data base for turbine health management systems.

Task 3. Sensor Fusion for Data Analysis

The Clemson University research team has selected a set of twenty eight plant signals to be monitored and recorded. The total available number of signals is 180. This smaller subset of signals is being recorded in real time and can be fused to monitor the system. These signals include key temperature and pressure measurements which are used for model validation and in the diagnostic/prognostic module.

Task 4. Diagnostic Module Design

Model-free and model-based diagnostics are achieved. For the model-free diagnostic module, a statistical approach has been investigated in which time series methods have been used to analyze the plant signals to detect deviations. The model-based method compares the turbine behavior with the dynamic model outputs. The application of innovation (i.e., residual) generation algorithm has been accomplished. This algorithm includes an estimation technique for covariance matrices and an adaptation of the classical chi-squared technique to the case of non-white noise residuals resulting from slow system dynamics

Task 5. Prognostic Module Design

The prognostic system attach's to the diagnostic module and interprets the diagnostic information to predict three useful quantities: time to failure, time to component degradation for maintenance scheduling and remaining useful life. Two approaches have been investigated for gas turbine health prognostics: statistical and wavelet. The real-time statistical strategy uses the logged sensor data to identify trends. The second strategy is based on wavelet analysis. Which transform real-time data to compute the wavelet coefficients for a given turbine signal. A regression analysis of these coefficients can be performed to forecast these coefficients for the desired prediction time. The new set of coefficients obtained reconstructs the signal and hence, predict of the signal values for future times.

Task 6. Experimental Work

The periodic experimental data recorded from the Mercury 50 gas turbine runs, has been used by the Clemson University research team to initially validate the mathematical model, (described in Task 1) and explore the diagnostic/prognostic algorithms. In addition, supplemental data has been gathered for a General Electric 7EA simple cycle gas turbine for prognostic studies. The results from the mathematical model were compared with this experimental data and relevant model parameters were adjusted; the results are encouraging. The experimental data has also been used in diagnostic/prognostic algorithms to compare with the estimated results and validate the developed methodologies.

Task 7. Industry Interactions

Industrial interaction has been pursued with Solar Turbines (San Diego, California), through data sharing and technical conversations with field engineers. Other interactions were also established with power generating facilities (South Carolina and Louisiana) to validate the developed technology.

3. PROJECT DESCRIPTION

3.1 Gas Turbine Research Need

The Reliability, Availability, and Maintainability (RAM) technical area of the High Efficiency Engines and Turbines (HEET) program encompasses the design of gas turbine health management systems. The introduction of real-time diagnostic and prognostic capabilities on gas turbines can provide increased reliability, safety, and efficiency. The diagnostic module is responsible for the prompt detection of system degradations followed by the isolation, or classification, of the failure, and determination of the magnitude. Prognostic activities are focused on the prediction of anomalous plant behavior such that maintenance measures may be performed to permit continued operation.

3.2 Project Approach

The objective of the project is to develop an integrated diagnostic and prognostic health management system. The approach to achieve this objective is described in the following sections.

3.2.1 Analytic Model

The two primary monitoring approaches for dynamic systems (including stationary gas turbines) can be classified as model-free and model-based diagnostics. The Clemson University research team is investigating both methods. For the model based approach, a real time mathematical model must exist to estimate "normal" system operation. The reliability of a model based diagnostics strategy is dependent on the model's accuracy. The quantitative modeling of a physical system requires knowledge of the process, mathematical representation in the form of differential and algebraic equations, and availability of system parameters. However, system uncertainty, noise, and nonlinearities often introduce discrepancies and deviations from ideal behavior. Consequently, a mathematical model's estimates often differ from the experimental measurements. The various gas turbine subsystems have been modeled and analyzed with the explicit presentation of the governing differential and algebraic equations. The analytical model as described in previous reports has been used to simulate the behavior of a Mercury 50 gas turbine.

3.2.2 Diagnostic Module

Diagnostic strategies generally attempt to detect, isolate, and identify a deviation from "normal" behavior in dynamic systems through on-line health monitoring. Two methods were investigated: model-free (similarity of multivariate signal test) and model based (innovation testing). The Clemson University research team has successfully developed two methods to detect the occurrence of plant degradation with adjustable level of robustness.

A. Model Free Diagnostic

Model free techniques have the advantage of being independent from system analytical models. Since not all physical phenomenons in the dynamic system can be described by a closed form analytical equations, creating by this mean uncertainties often confused with possible malfunctions, signal analysis techniques are a practical alternative to represent the system behavior and detect deviations. Different approaches had been pursued in the literature. The research team has developed a unique statistical approach to analyze the gas turbine signals for diagnostics. The power of statistical methods in signal analysis (e.g., time series methods) emerges from the fact that they can represent the data in a well structured model capable to predict the system behavior and create the required analytical redundancy, if needed. In addition, they are capable to manipulate the data in both the time and frequency domains with equal ease.

A.1 Basic Concepts and Methodology

The strategy pursued for fault diagnosis is based on the comparison between the statistical properties of two multivariate (multi-channel) system signals. One signal may represent the system *healthy* or *faulty* conditions and referred as the reference signal, while the other pertains to the system condition to be assessed (test signal). First order (mean) and second order (auto-covariance matrix function) statistical properties are compared and similarity between them is considered as a similarity between the two system's statuses that generated the signals. Hypothesis tests (according to a pre-defined confidence limit to account for the false alarm) are used as the decision rule for the required similarity. In all tests, the system is considered to be in steady state mode with the same operating conditions of the reference signal. Consequently, all resulting signals are guaranteed to be statistically stationary with constant mean. The detailed derivation of this concept was presented in previous reports.

A.2 Implementation and Experimental Results

To assess the test, two experimental faults were introduced to a stationary Mercury 50 gas turbine generator set. The first fault was the blockage of oil cooler air passages. This fault, although performed manually during the experiment, represents a real condition that can occur in outdoor units due to ice formation in the early morning hours. During this experiment, the turbine normally ran for more than two hours (exactly 8000 seconds) to satisfy the peak shaving power demand and, hence a manual blockage of the oil cooler air passages was performed. The blockage was removed just before the oil temperature reaches the red line alarm value and initiates a turbine trip. The achieved fault duration was approximately 6500 seconds. Figure 1

demonstrates the oil header temperature during this experiment indicating the fault introduction and withdrawal timing.

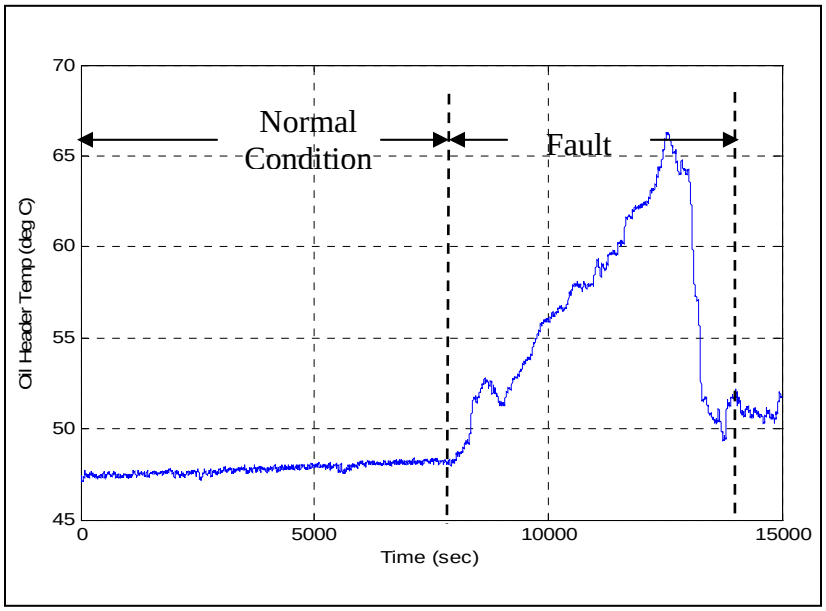

Figure 1. Lubrication oil header temperature response versus time for a cooler blockage on a Mercury 50 stationary gas turbine; fault introduced at t = 8,000 seconds.

The second experimental fault represents a real situation encountered in the Mercury 50 gas turbine. During normal operation, the compressor relief valve partially opens with no control command affecting by this mean the turbine foreseen power rating. To replicate this situation experimentally, after a certain period of normal operation, the calculation block of the Allen Bradley programmable logic controller was given a false feedback value indicating that the relief valve is fully closed while it was kept open by about 5.0%. The valve position sensor true feedback signal was overridden to mimic a relief valve leak situation. This experiment represented a severe test condition for the detection methodology as the fault magnitude in this case is small and the fault frequency is variable. It is important to mention that the experimentally introduced leak is very similar to the actual leak caused by an actuator malfunction. This experiment was performed three times with different fault introduction times and durations.

After signal pre-filtration and reference signal determination, signal sampling was performed. A sampling window L is defined according to the reference signal length and the multivariate signal dimension d. This window is partitioned into M samples of equal length W that satisfy the condition $M \geq d$. It is important to mention that the length of the partition M is directly proportional to the test resolution. Therefore, a long M will have higher resolution and more sensitivity to low frequency faults while for high frequency faults the partition length has no crucial effect on the test sensitivity. Furthermore, to guarantee the independence of the partitions, a buffer period κ should be present between each partition. For the first fault, values of 500 for W, 4 for M, and 20 for κ were selected for a multivariate dimension d of 3 corresponding to a multivariate signal having Turbine Rotor Inlet Temperature (TRIT), the

Pressure at Compressor Delivery (PCD), and the generated power as components. The reason for this selection is that the cluster represents the major thermofluidic properties of the gas turbine.

For the second fault (and due to the shortness of the available reference signal collected during a normal production operating period during the experimentation period), a two dimensional cluster including the PCD and the generated power was considered. Values of 790 for *W*, 2 for *M* and 15 for κ were chosen according to a total reference signal length of 1595 seconds. A value of $\alpha = 10\%$ was selected for all cases.

To compromise between the sample length requirement and the available data observations, recurrent sampling was executed on a sliding window basis. In this case, a recurrent step of arbitrary length (which is less than the total sample width) satisfies both the sampling requirements as well as an accurate test resolution. It is understood that the period of overlap between recurrent samples will exist, but experimental results showed that this situation does not represent any setback as the sampling independence is still valid. Figure 2 demonstrates the application of sliding sample concept. Useful to mention is the fact that for the first fault, a sampling step of 50 seconds was selected while steps of 5 seconds were applied in the second experiment to accommodate the observation length.

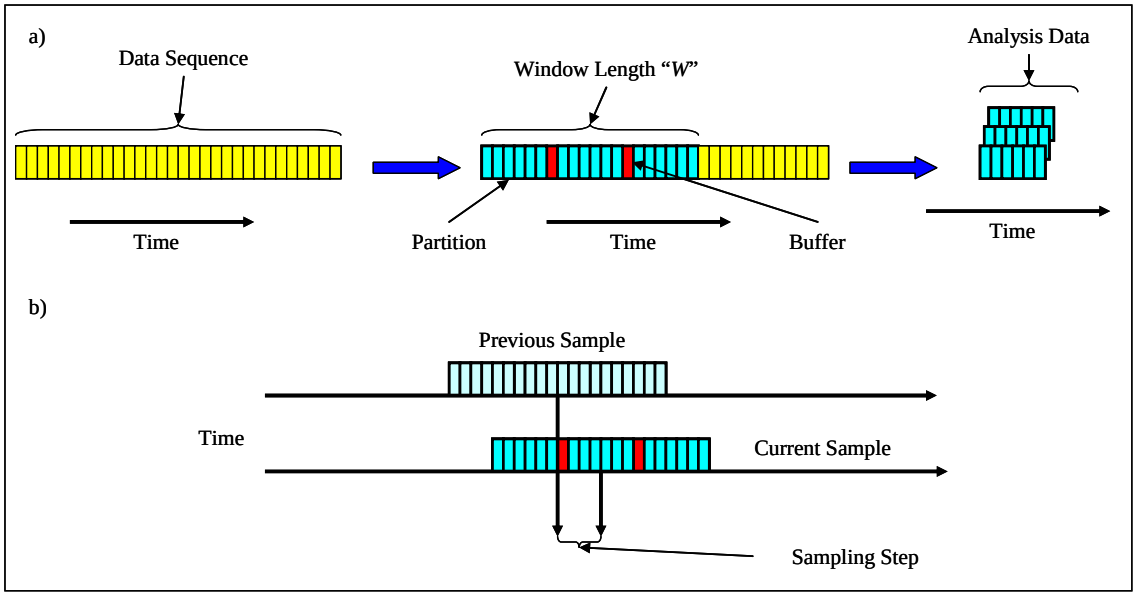

Figure 2. Data manipulation with (a) sample construction, and (b) step sampling for plant signals featuring the buffer zone between each partition and the overlap between consecutive samples

A.3 Results and Discussion

After implementing all the required test conditions and preprocessing of the selected signals to satisfy the stationarity condition (statistical time invariance), a violation probability was calculated and compared to the pre-defined 10% value. The violation probability was calculated using a counting procedure. The percentile probability is represented by the ratio between the total number of test statistics violating the confidence limit threshold to the total number of test statistics calculated for each Fourier frequency for the signal partition length *W*.

For each sampling step, the percentage of violation was calculated and plotted for all test experiments. Figures 3 and 4 illustrate the resulting plot of the fault detection test. It is clear from these graphs that the test was able to detect the introduced abnormality in all experiments. It is important to note that the apparent slopes in the graphs are a direct result of the correlation between the samples introduced by the overlapping period. This usefulness of this correlation is a further indication to the robustness of the test and its consistent sensitivity to fault occurrences. The abrupt deviation could be owed to instability in the detection procedure. The power of the test manifested by the maximum violation percentage in the graphs is a direct result to the frequency of the fault and the test resolution controlled by the sampling window length. Different powers can be achieved by changing the sampling width as a fine tuning left to the user to specify according to his specific application.

An important point can be induced from the presented results. For the first fault, although the multivariate signal cluster does not include any lubrication related property, the test was capable enough to detect this fault from observation of other signals that represent the general thermofluidic behavior of the gas turbine. In addition to proving the sensitivity of the test, this result is a direct indication of the fault propagation.

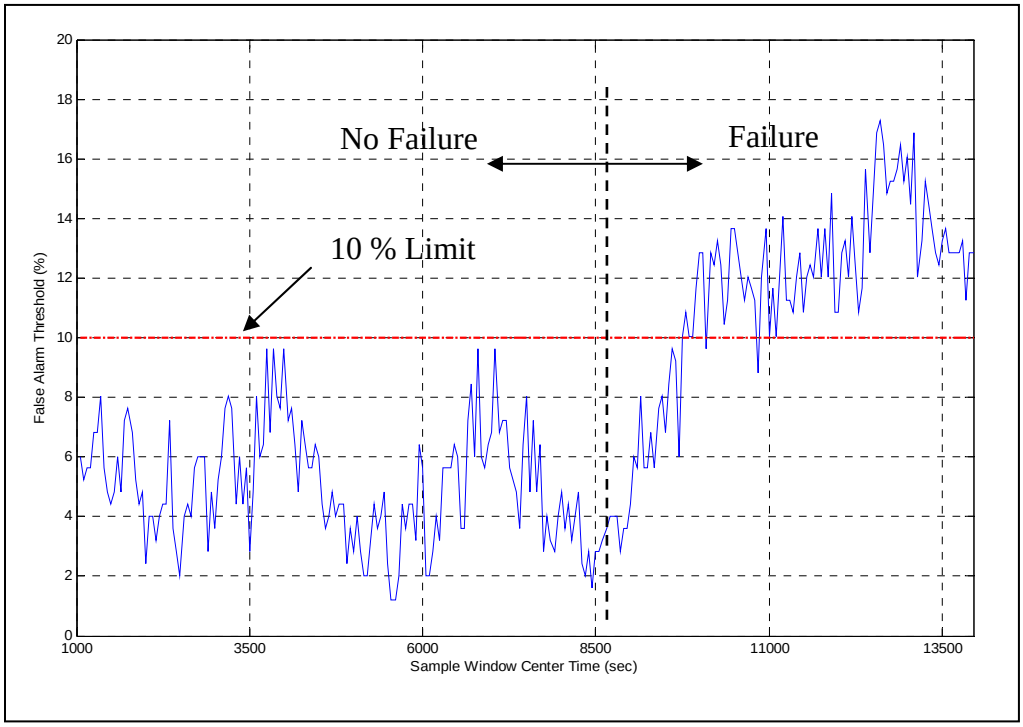

Figure 3. Test results for the first experimental fault showing high delectability using a multivariate cluster of TRIT, PCD and generated power

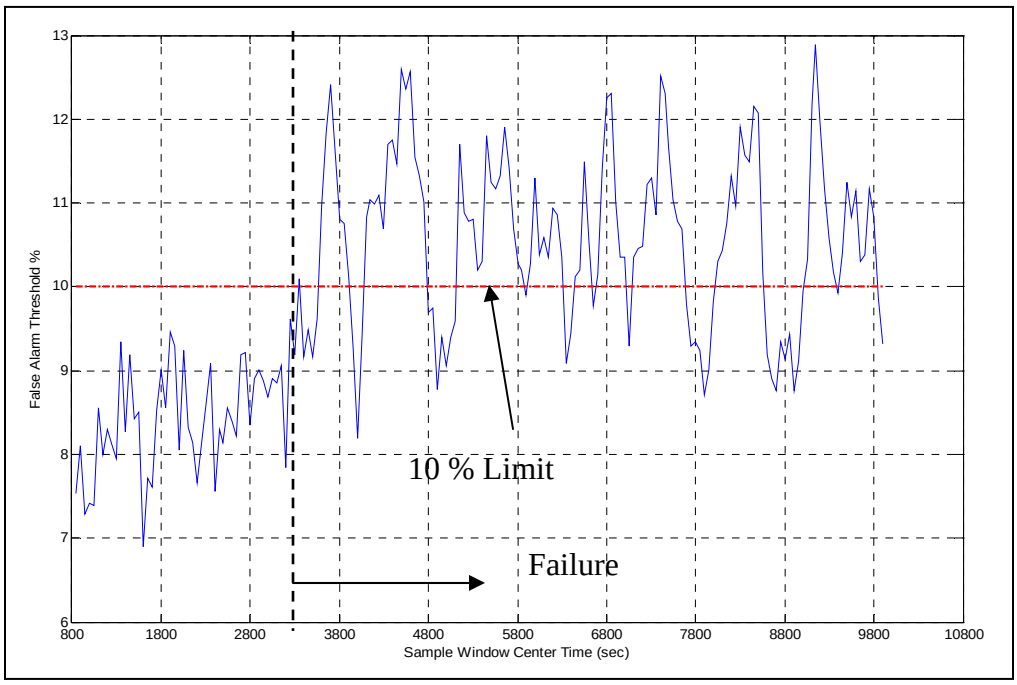

Figure 4. Test results for the second experimental fault using a multivariate cluster of PCD and generated power showing threshold violation

B. Model Based Diagnostics

The model based diagnostics strategies compare the actual behavior of the system versus the model estimates under the same operating conditions. A useful quantity for this comparison is the innovation (or residual) which is the difference between the actual model behavior and the model estimates. A deviation from the "normal" behavior of the residuals may be an indication of system departing from the normal or "no fault" condition. The main task is generating the residuals and setting the acceptable level of normal system operation. A full state Kalman observer is used to generate the model estimates. Since the analytical mathematical model state equations are nonlinear, a linearization of the system equations is first performed at a system operating point determined by the selected steady condition (e.g. load and speed). The developed algorithm includes two novel features which are: (i) an estimation technique of the disturbance covariance matrices from the actual observations leading to faster error decay, and (ii) an adaptation of the classical chi-squared technique to the case of non-white noise residuals resulting from slow system dynamics. Details of this strategy including the innovative features were presented in previous reports.

3.2.3 Prognostic Module

Prognostics predict the future health state of a system component from the present operating conditions and historical data. The health monitoring system can incorporate a prognostic algorithm to effectively interpret and determine the plant's healthy working span. The application of prognostics to a system can be based on different approaches, including physical/analytical models, "rules" databases, and statistical models. In the physical model based

approach, mathematical models which represent the system are used to predict the system behavior depending on the varying inputs. For the development of "rules" based on experience, experts from the field of design and maintenance are required to compare the past and present system behavior to estimate and predict the system health. Finally, statistical models use input/output data to analyze trends, it requires extensive data.

The Clemson University research team has formulated two prognostic approaches (statistical and wavelet) for gas turbine health management systems. The real-time statistical strategy uses the logged sensor data to identify trends. Short and long time trends are computed using regression analysis. This technique predicts the time to failure, or threshold violation, by forecasting system health at any desired future time. The second strategy is based on wavelet analysis. Wavelet transforms of real-time data are used to compute the wavelet coefficients for a given turbine signal. A regression analysis of these coefficients can be performed to forecast these coefficients for the desired prediction time. The new set of coefficients obtained can be used to reconstruct the signal and hence obtain the prediction of the signal values for future times.

A. Methodologies and Derivation

Dynamic systems may have a variety of input (e.g., force, heat, voltage) and output (e.g., acceleration, vibration, current) signals that can be measured using appropriate sensors. Let these input and output vectors be represented by $U(t) \in R^g$ and $Y(t) \in R^h$, respectively. It is likely that these signals may be discontinuous or arise from different operating modes. Hence, the system sensor data may need to be filtered, concatenated, and normalized such that the input and output vectors become $U^*(t) \in R^g$ and $Y^*(t) \in R^h$. A smaller set of input and output vectors, $u(t) \in R^n$ and $y(t) \in R^p$, may be selected to investigate the system health based on a correlation analysis. For this study, the correlation between the system inputs and outputs may be stated as

$$\Re_{jk} = \frac{\sum_{i=1}^{m} Y_j^*(t_i) U_k^*(t_i) - \left(\sum_{i=1}^{m} Y_j^*(t_i) \right) \left(\sum_{i=1}^{m} U_k^*(t_i) \right) / m}{\left(\sum_{i=1}^{m} \left(Y_j^*(t_i) \right)^2 - \left(\sum_{i=1}^{m} Y_j^*(t_i) \right)^2 / m \right)^{0.5} \left(\sum_{i=1}^{m} \left(U_k^*(t_i) \right)^2 - \left(\sum_{i=1}^{m} U_k^*(t_i) \right)^2 / m \right)^{0.5}} \quad (1)$$

As a general rule, the system outputs (i.e., the signals being forecasted) with a correlation $\left| \Re_{jk} \right| > 0.80$ for the given inputs were selected.

A.1 Model Free Regression Description

A multi-regression empirical model, based on the selected sensor signals, may be created to describe the system's behavior. Although these signals may be affected by noise, it has been assumed that the noise may be neglected. For degraded plant operation, the system's steady-state output should change so that time dependent trends may be observed while the system's inputs remain constant. Hence, time will be included in the prediction model. The derived regression curve, $\vec{Z}_{ji}$, for the j^{th} signal from the plant output vector y(t) may be expressed as

$$\left|\vec{Z}_{ji}\right| = \left(\sum_{k=1}^{n} \sum_{q=0}^{r} \left(a_{j_{qk}} t_i^{\,q} \right)^2 \right)^{0.5} \qquad \text{(i=1,2,…,m)} \tag{2}$$

where the parameters n and r denote the number of selected independent variables (input signals) and the regression order. The polynomial coefficients $a_{j0k}, a_{j1k}, ..., a_{jrk}$ correspond to of the r^{th} regression order for the k^{th} signal.

The sum of squares of the deviations, $\vec{D}_j$, between m time samples in the composite sample data, $V_{j_k}(t_i) = [y_j(t_i) \vdots u_k(t_i)]^T$, and the regression curve, $\vec{Z}_{ji}$, becomes

$$\left|\vec{D}_j\right| = \sum_{i=1}^{m} \left[\left(\sum_{k=1}^{n} \left(V_{j_k}(t_i) \right)^2 \right)^{0.5} - \left|\vec{Z}_{ji}\right| \right]^2 = \sum_{i=1}^{m} \left[\left(\sum_{k=1}^{n} \left(V_{j_k}(t_i) \right)^2 \right)^{0.5} - \left(\sum_{k=1}^{n} \sum_{q=0}^{r} \left(a_{j_{qk}} t_i^{\,q} \right)^2 \right)^{0.5} \right]^2 \tag{3}$$

The regression method is based on minimizing the error between the actual and the estimated data. To this end, equation (3) may be minimized, $\frac{\partial \vec{D}_j}{\partial a_{j_{qk}}} = 0$ for q = (0,1,…,r), to obtain the regression coefficients by solving the (r+1) equations numerically as

$$\frac{\partial}{\partial a_{j_{q\in[0,r]k}}} \left\{ \sum_{i=1}^{m} \left[\left(\sum_{k=1}^{n} \left(V_{j_k}(t_i) \right)^2 \right)^{0.5} - \left(\sum_{k=1}^{n} \sum_{q=0}^{r} \left(a_{j_{qk}} t_i^{\,q} \right)^2 \right)^{0.5} \right]^2 \right\} = 0 \tag{4}$$

A.2 Signal Forecasting

The regression model can predict a dependant variable's value both inside and outside the estimation time interval. The regression coefficients, $a_{j_{qk}}$, describe the signal trend so that the time extension of the regression curve may estimate the system's future behavior. In general, the meaningful prediction time for the regression curve depends on the estimation data. The larger the estimation data sample size, the better the forecast since the curve would be termed "well trained". The dependent variable trends represent the long term signal behavior, rather than fluctuations caused by plant disturbances and load changes. The forecast signal curve, $\vec{Z}_{ji}$, may be given as

$$\left|\vec{Z}_{ji}\right| = \left(\sum_{k=1}^{n} \sum_{q=0}^{r} \left(a_{j_{qk}} t_i^{\,q} \right)^2 \right)^{0.5} \qquad \text{(i=m+1, m+2,…,m+f)} \tag{5}$$

where m+f denotes the final time value. This forecast has an error of $\varepsilon_j = \left(\left| \sum_{i=m}^{m+f} \vec{Z}_{ji} \right| - \left| \sum_{i=m}^{m+f} y_j(t_i) \right| \right) / \left| \sum_{i=m}^{m+f} y_j(t_i) \right|$ which can be used for comparison purposes.

A.3 Health Evaluation

A prognostic strategy can estimate the system's future behavior to facilitate maintenance scheduling and component repair. An adjustable set of thresholds may be established for the

statistical estimates so that a violation results in appropriate action. Small variations in a system's output signal, without a change in the system inputs, may be due to extraneous noise, load fluctuations, and/or a slowly occurring degradation. In the proposed evaluation method, forecasted signals may be termed acceptable if they lie within established thresholds. For a normally distributed steady-state signal, 95% of the data should lie within two standard deviations, $\sigma_j = \left[\frac{1}{m} \sum_{i=1}^{m} (y_j(t_i) - \overline{y}_j)^2 \right]^{0.5}$, of the sample mean, $\overline{y}_j$. If the system forecast predicts a threshold violation, $\left|\vec{Z}_j\right| > 2\sigma_j$, then the remedial action should be dependent on the rate and severity of the threshold violation.

A.4 Wavelet Prognostic Strategy

In this study, the wavelet technique will predict dynamic system operation using a three step procedure. First, wavelet transforms of the real-time data will compute the given system signal wavelet coefficients. Second, a regression analysis of these coefficients will forecast the wavelet coefficients for the desired prediction time. Third, the new set of wavelet coefficients may then be used to reconstruct the signal, and hence, obtain a prediction.

A.5 Wavelet Description

Any waveform function, $\psi(t)$, can be selected for a wavelet transform if it satisfies the condition of finite energy and admissibility. The finite energy condition states that the energy, ϑ, of the wavelet function, $\psi(t)$, should be limited as

$$\vartheta = \int_{-\infty}^{\infty} |\psi(t)|^2 dt < \infty \qquad (\vartheta < \infty) \tag{6}$$

The admissibility condition states that the wavelet function has a zero mean, $E(\psi(t)) = 0$, and that the Fourier Transform of the wavelet function with frequency F cannot be zero, $\hat{\psi}(F) \neq 0$. The admissibility constant for the wavelet function has a finite value

$$\varsigma = \int_0^{\infty} \frac{|\hat{\psi}(F)|^2}{F} dF \qquad (\varsigma < \infty) \tag{7}$$

In this expression, $\hat{\psi}(F) = \int_{-\infty}^{\infty} \psi(t) e^{-i(2\pi F)t} dt$ represents the Fourier transform of $\psi(t)$. The value of the admissibility constant is dependent on the wavelet function. A discrete wavelet transform uses an orthonormal wavelet basis with the wavelet function, $\psi(t)$, to obtain the wavelet function, $\psi_{\chi,\eta}(t)$, at a given scale and time as

$$\psi_{\chi,\eta}(t) = \frac{1}{\sqrt{u_0^{\chi}}} \psi\left(\frac{t - \eta v_0 u_0^{\chi}}{u_0^{\chi}} \right) \tag{8}$$

The parameters $\chi \in R$ and $\eta \in R$ denote the dilation (scale) and translation (time) variables, respectively. The symbols u_0 and v_0 are wavelet control parameters.

The term "translation" refers to delaying or hastening the onset of a wavelet (i.e., a shift in time). The term "dilation" denotes wavelet scaling (i.e., stretching or compressing). Low and

high scales are associated with compressed and stretched wavelets. The scaling function, $\phi(t)$, is any waveform function that satisfies the condition $\int_{-\infty}^{\infty} \phi(t)dt = 1$. The orthonormal scaling function at a given scale and time becomes

$$\phi_{\chi,\eta}(t) = \frac{1}{\sqrt{u_0^{\chi}}}\phi\left(\frac{t - \eta v_0 u_0^{\chi}}{u_0^{\chi}}\right) \tag{9}$$

A.6 Wavelet Coefficient Signal Processing

In some instances, the plant output signals may be affected by disturbances, κ_d, and noise, κ_n. For example, consider $y_j(t) = s(t) + \kappa_d + \kappa_n$ which is composed of signal characteristics, s(t), and additive components κ_d and κ_n. A wavelet transform addresses signal noise by computing two sets of wavelet coefficients: detail and approximate. Signal details refer to the high frequency content of the signal which may be noise and disturbances. Signal approximations are the low frequency signal content. If the high frequency components of the signal are removed, then the signal still retains some characteristics which can be forecasted. However, if the signal approximations are removed, then the signal may loose its primary characteristic and the residual would likely be noise.

The detail and approximation coefficients, $\hat{\gamma}_{\chi,\eta_j}$ and $\hat{\xi}_{\chi,\eta_j}$, were generated on a dyadic scale (i.e., based on powers of two). The given discrete wavelet transform of the learning window may be computed to obtain the detail and the approximation coefficients as

$$\hat{\gamma}_{\chi,\eta} = \int_{-\infty}^{\infty} y_j(t)\frac{1}{\sqrt{u_0^{\chi}}}\psi\left(\frac{t-\eta v_0 u_0^{\chi}}{u_0^{\chi}}\right)dt = \left\langle y_j(t), \psi(t)\right\rangle \tag{10.a}$$

$$\hat{\xi}_{\chi,\eta} = \int_{-\infty}^{\infty} y_j(t)\frac{1}{\sqrt{u_0^{\chi}}}\phi\left(\frac{t-\eta v_0 u_0^{\chi}}{u_0^{\chi}}\right)dt = \left\langle y_j(t), \phi(t)\right\rangle \tag{10.b}$$

Note that the detail and approximation coefficients are obtained by the convolution of the system signal with the wavelet and scaling functions. The similar analysis of the input signal provides the corresponding detail, $\gamma_{\chi,\eta}$, and approximation, $\xi_{\chi,\eta}$, coefficients as

$$\gamma_{\chi,\eta} = \left\langle u_k(t), \psi(t)\right\rangle, \quad \xi_{\chi,\eta} = \left\langle u_k(t), \phi(t)\right\rangle \tag{11}$$

From a practical perspective, the signal vectors $y(t)$ and $u(t)$ may be filtered using the complementary filters in equations (10) and (11) to realize low and high frequency coefficients. The next step for the algorithm is a least square fit to obtain a regression model of the signal approximation coefficients.

A.7 Forecasting Methodology

The prognostic algorithm eliminates high frequency signal noise, through wavelet transforms, to predict system behavior. The wavelet coefficient regression model for the selected output variable may be derived from the approximation coefficients. This regression model forecasts the system's approximation coefficients by performing a one dimensional inverse wavelet transform on the coefficients so that

$$A_{\chi}(t) = \sum_{\eta=-\infty}^{\infty} \xi_{\chi,\eta}\phi_{\chi,\eta}(t) \tag{12}$$

The prognostic algorithm uses Daubechies wavelets with four scaling coefficients (Daubechies, 1992) for both the wavelet and inverse wavelet transforms. The corresponding wavelet and scaling function for these Daubechies wavelets become

$$\psi(t) = \sum_{e=1,3} d_e\phi[2t-(e-3)] - \sum_{e=0,2} d_e\phi[2t-(3-e)], \phi(t) = \sum_{e=0}^{3} d_e\phi(2t-e) \tag{13}$$

where the parameters d_e and e represent the scaling coefficient and the scaling coefficient index. The selected wavelet coefficient order depends on the data being analyzed. For instance, high and low frequency signals need higher and lower order wavelet coefficients, respectively. The coefficients in equation (13) can be obtained from the moment condition for compactly supported wavelets as

$$\sum_{e=0}^{3} d_e = 2, \sum_{e=0}^{3} d_e^2 = 2, \sum_{e=0,2} d_e - \sum_{e=1,2} d_e = 0 \tag{14}$$

B. Implementation Basics

A General Electric 7EA natural gas turbine served as the basis to evaluate the two prognostic methods. The turbine has a power production capacity of 85 MW with a nominal rotational speed of 3,600 RPM. The turbine features a single shaft, sixteen stage compressor with a 12.6:1 compression ratio. The heat rate is Q=10,991 kJ/kWh with an approximate mass flow rate of $\dot{m}_f = 292$ kg/s. The available turbine sensors were sampled at $\Delta t = 60$ s. The run time for the gas turbine was based on the power generation needs; operating data for two years was available. The GE 7EA input signals included power generated (PG), fuel flow rate (FF), and inlet guide vane angle (IGVA). The set of output signals selected to forecast system health consists of turbine inlet temperature (T_{TT}), generator temperature (T_G), exhaust temperature (T_{EX}), generator maximum vibration (A_{GV}), and gas turbine maximum vibration (A_{TV}). The output signals were selected based on their high correlations with the input signals.

A four step sequence was followed to analyze the turbine inlet temperature, T_{TT}. First, the steady-state signal was conditioned to obtain a concatenated and filtered signal. Second, the statistical prognostic methodology was applied to obtain the signal forecast. Third, the wavelet method was supplied the same signal to predict the system behavior. Finally, a comparison of the two methods was performed. Note that for real-time applications, the desired system operating mode must be present before signal filtering and analysis; signal concatenation will not occur.

B.1 Signal Conditioning

The turbine inlet temperature profile is shown in Figure 5a for a period of $t^* = 59{,}000$ minutes. The signal is somewhat oscillatory due to start ups, shut downs, and different operating loads. For a meaningful analysis of the turbine data, three operating ranges (or modes) were identified for the turbine inlet temperature (200-400$^\circ C$, 400-600$^\circ C$, and 600-800$^\circ C$). These operating ranges are user-defined and typically based on turbine operating modes (e.g., light, medium, and peak loads) per electrical power generating demands. The turbine inlet temperature range of $600 < T_{TT} < 800^\circ C$ was selected since this corresponds to the most common operating mode of nominal turbine load. Specifically, the turbine runs for t=32,200 minutes of the total $t^* = 59{,}000$ minutes in the peak load mode. In Figure 5b, the concatenated data for the turbine inlet temperature has been displayed. The next task was to normalize the concatenated data using a simple filter, $Y_j^* = Y_j(i+1) - Y_j(i)$, to further reduce fluctuations. The filtered turbine inlet temperature with a mean value of zero, refer to Figure 5c, shows variations about the actual signal mean, $\bar{y}_j$. The data has been divided into the learning (i.e., 0<t<22,200 minutes) and the validation (i.e., 22,200<t<32,200 minutes) windows, W_L and W_V. The prognostic algorithm used the learning window, W_L, as the training data for the regression curve to detect trends. The estimated system forecast was then compared with the experimental data in the validation window, W_V, to gauge the prognostic method accuracy

B.2 Statistical Forecasting

The filtered signal, Y_j^*, was analyzed using the statistical methodology to predict the system behavior. In Figure 6a, the regression curve for the initial turbine inlet temperature learning data has been graphed versus time with every 500 data point plotted to improve readability. The derived regression curve, $\vec{Z}_{ji}$, forecasts the system operation for a period of t=10,000 minutes (i.e., 22,200<t<32,200 minutes) as shown in Figure 6b. When comparing the predicted and actual data in the validation window, the forecast error is 11.47%. The system operation forecast for the turbine inlet temperature was mapped back into the operating domain, along with the forecast error bounds, $\pm\varepsilon$, as shown in Figure 6c. Note that the forecasted signal displays a non-fluctuating behavior which predicts the signal mean rather than the specific fluctuations which may be an advantage.

B.3 Wavelet Forecasting

The wavelet prognostic algorithm computes the fourth-order wavelet transform of the filtered data, Y_{ji}^*, in the learning window, W_L. This transform yields the low frequency (approximation) and the high frequency (detail) wavelet coefficients. The high frequency content is often the noise associated with the signal, while the low frequency content represents the signal trend that may be used for regression. A least squares fit was performed on the approximation coefficients (refer to Figure 7a) with the coefficients forecasted for t=10,000 minutes. The signal approximation was reconstructed from the coefficients by taking the inverse

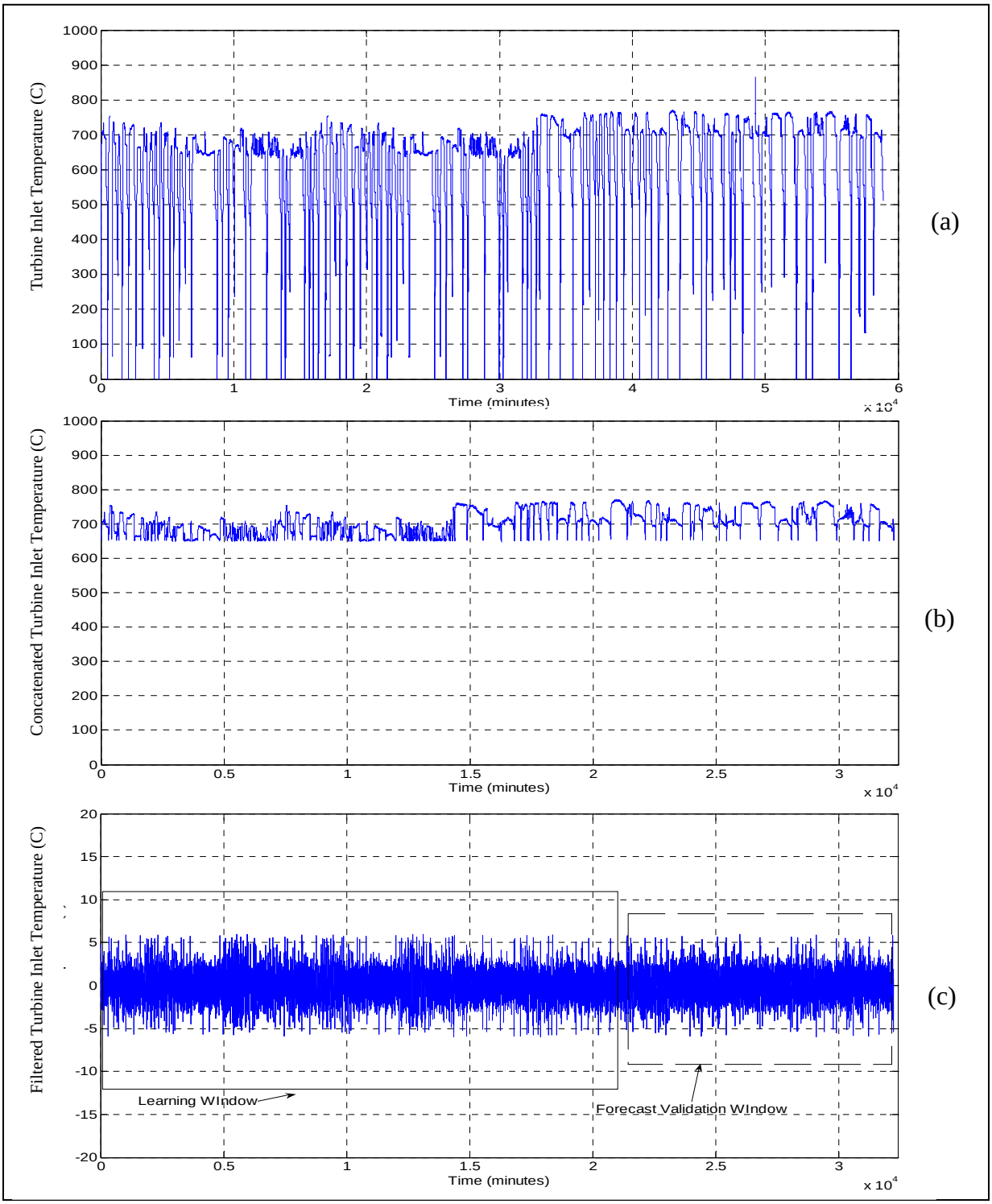

Figure 5. GE 7EA stationary gas turbine inlet temperature profile: (a) Raw data signal for $0<t^{*}<59{,}000$, (b) Restricted operating range of 600-800$^{\circ}C$ for 0<t<32,200 minutes, and (c) Filtered data showing the learning 0<t< 22,200 minutes and validation windows 22,200<t<32,200 minutes

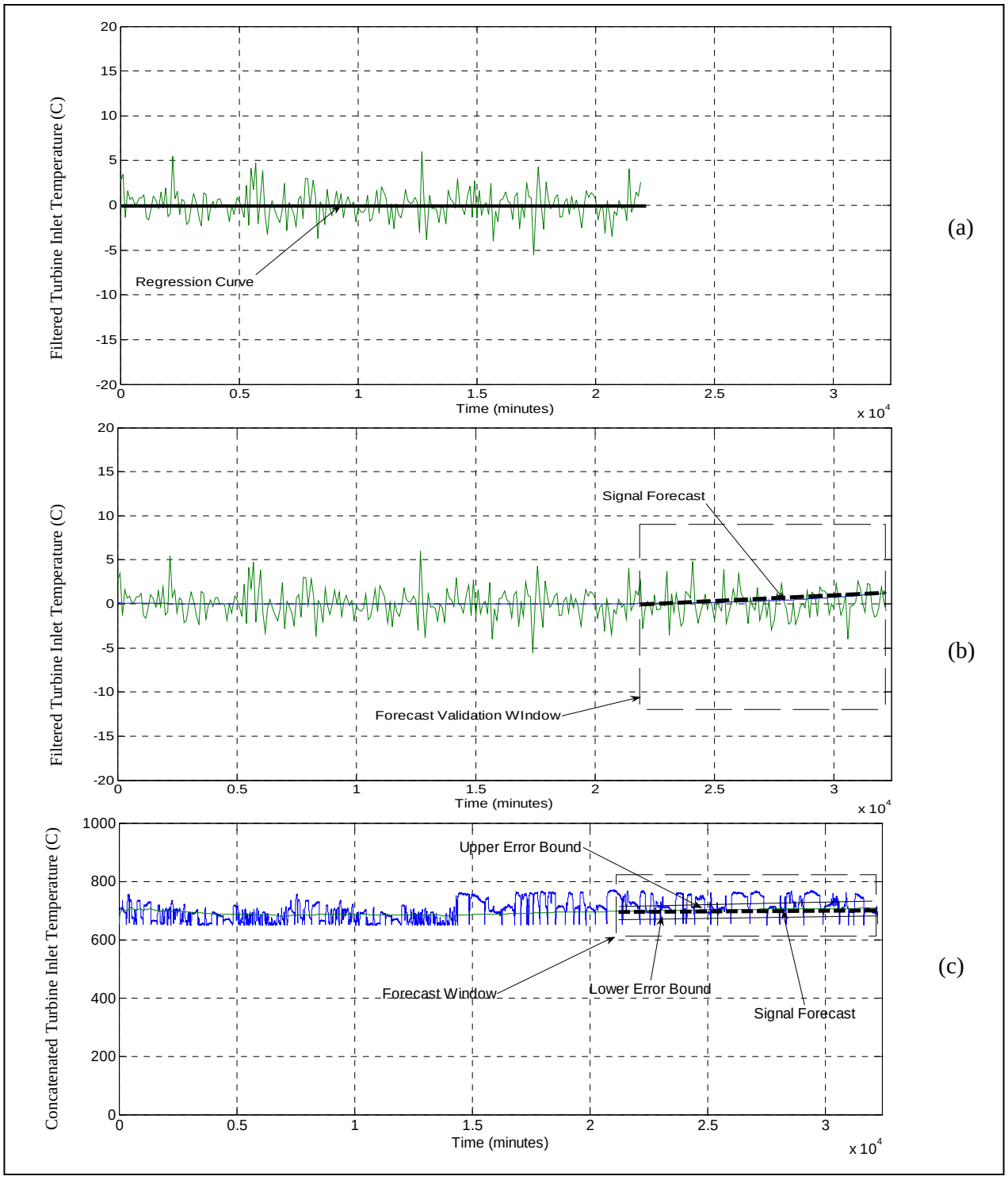

Figure 6. Statistical prognostic strategy: (a) Regression curve for turbine inlet temperature during learning window (0<t<22,200 minutes) minutes with reduced display intensity, (b) Statistical signal forecast (22,200<t<32,200 minutes) minutes with reduced display intensity, and (c) Signal and statistical forecast mapped back into the operating domain for 0<t<32,200 minutes

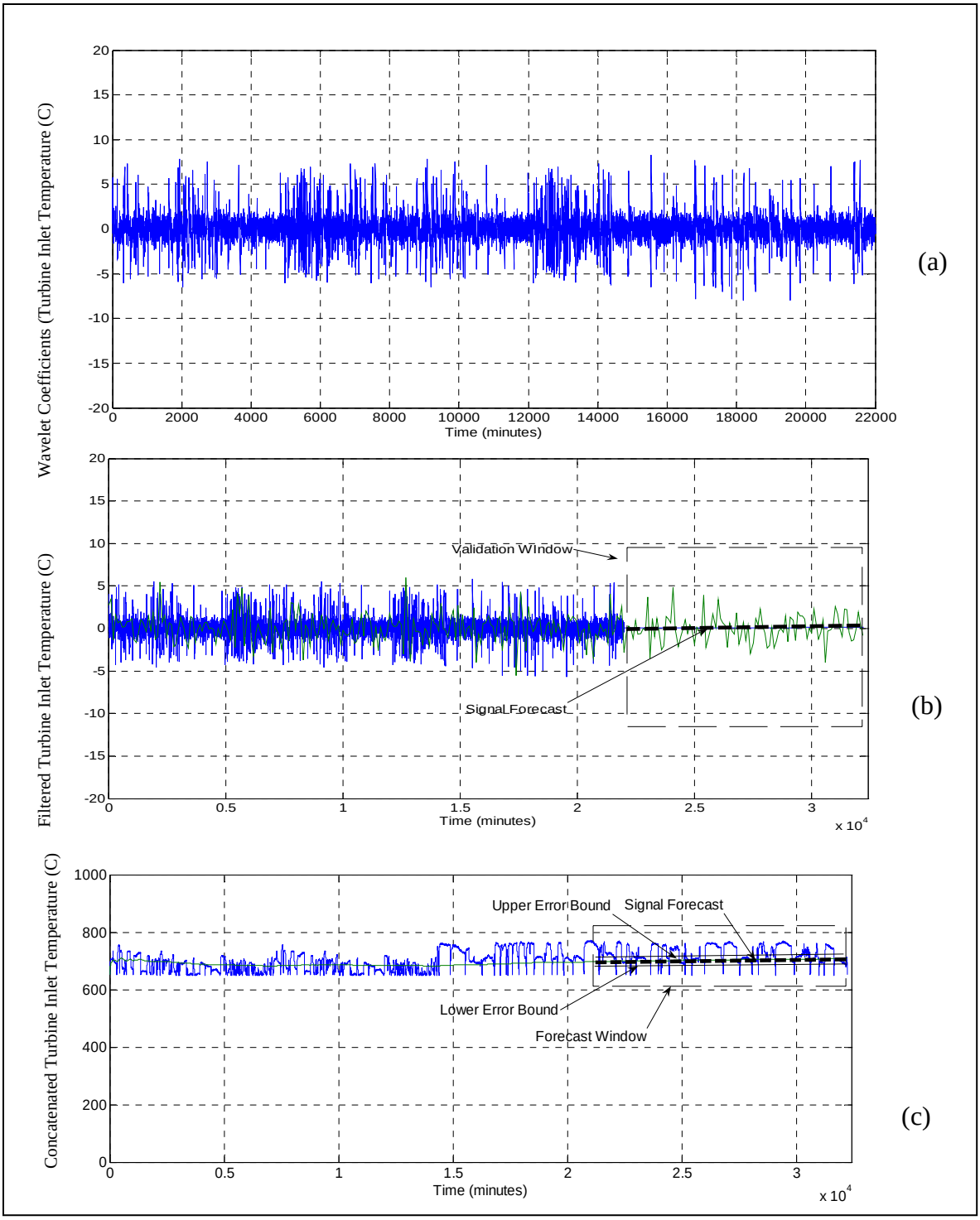

Figure 7. Wavelet prognostic strategy: (a) Approximation coefficients for turbine inlet temperature for learning window (0<t<22,200 minutes), (b) Wavelet signal forecast (22,200<t<32,200 minutes) with reduced display density, and (c) Signal and wavelet forecast mapped back into the operating domain for 0<t<32,200 minutes

wavelet transform. The length of the reconstructed signal approximation was equal to the sum of the desired forecasted signal and the learning window. A comparison between the turbine inlet temperature signal forecast and experimental data for 22,000<t<32,000 minutes is shown in Figure 7b. The thick line represents the wavelet forecast which has been superimposed on the experimental data; the forecast error estimation is 9.23%. For a better visual representation, the filtered data and the signal forecast are mapped back into the operating domain along with the error bounds, $\pm\varepsilon$, as shown in Figure 7c.

4. EXPERIMENTAL WORK

4.1 Gas Turbines

A Mercury 50 gas turbine is used by the Clemson University facilities to provide supplemental electrical power to the campus. It consists of a single shaft recuperated cycle turbine engine, a generator with accessories, and auxiliary systems. The Mercury 50 has a power production capacity of 4.5 MW with a maximum rotational speed of approximately 14,800 RPM. It contains a ten stage compressor and a two stage turbine. The Mercury50 turbine's operation can be recorded at the Clemson University research facility computer workstations to determine the status of the gas turbine's operation including system temperatures, pressures, vibration levels, and power output. This real time output data is available for observation and use with diagnostic and prognostic modules. In addition, data has been gathered from a General Electric MS7001EA gas turbine.

4.2 Data Acquistion

The experimental data from the Mercury 50 gas turbine is recorded using a RSLINX OPC server connection which links the Mercury 50 with the computer workstations in Energy Systems Laboratory at Clemson University. At present, twenty eight signals are recorded and transmitted to the MATLAB software in real time. This data is stored in the form of arrays. The data transmission from the Allen Bradley PLC is one way so that the turbine operation is not affected. The data acquisition is started by running the initializing code through the workstation at the Energy System Laboratory which includes specifying the signals to be recorded and the time for which the data has to be acquired. The present data acquisition rate is one second. Once initialized the algorithm records and stores the desired data signals. The data is acquired from a set of 180 sensors located at the various points in the Mercury 50 gas turbine. In Figure 19, the main sensor locations are displayed in addition to the signals detected at those points. The logged signals from the turbine sensors are compared to the model generated simulated values for the diagnostic strategy. These signals have been also used to validate and verify the current gas turbine model. Efforts are being made to install a flow meter for recording the air mass flow through the Mercury 50 gas turbine.

5. RESULTS AND DISCUSSIONS

A dynamic mathematical model has been formulated and validated. Both model-free and model-based strategies for diagnostics have been formulated and implemented. Two real-time prognostic methodologies have been developed. Developed algorithms were validated using recorded experimental data and showed strong sensitivity and robustness for both diagnostics and prognostics with capability of real-time application.

6. CONCLUSIONS

This report presents the work performed by the Clemson University research team during the past six months on stationary gas turbine diagnostic strategy. Model-free and model-based diagnostic strategies have been presented with accompanying discussion regarding its implementation. For the prognostic strategy two model-free real-time methods have been developed and implemented. Data from a Mercury 50 gas turbine and a General Electric MS7001EA gas turbine have been gathered for analysis and use in the modeling, diagnostic, and prognostic activities. Overall, the project results are promising and opportunities are present to implement the developed technology on an industrial scale.

REFERENCES

Ailer, P., Santa, I., Szederkenyi, G., and Hangos, K.M., "Non Linear Model-Building Of A Low-Power Gas Turbine", *Periodica Polytechnica Ser. Transp. Eng*., vol. 29, no. 1-2, pp. 117-135, October 2001.

Aboufadel, E., and Schlicker, S., *"Discovering Wavelets"*, Wiley Interscience: New York, 1999.

Barlas, I., Zhang, G., Propes, N., and Vachtsevanos, G., "Addressing Uncertainty and Confidence in Prognosis", proceedings of the ASNE Intelligent Ship Symposium, Philadelphia, PA, April 2003.

Boyce, M., "*Gas Turbine Engineering Handbook*", Gulf Publishing Company: Houston, 2005.

Brockwell, P. J. and Davis, R. A., "Time Series: Theory and Methods", Springer-Verlag: New York, 1991.

Brockwell, P. J. and Davis, R. A., "Introduction to Time Series and Forecasting", Springer-Verlag: New York, 2002.

Byington, C., Roemer, M., and Galie, T., "Prognostic Enhancements to Diagnostic Systems for Improved Condition-based Maintenance", proceedings of the IEEE Aerospace Conference, vol. 6, pp. 2815-2824, Big Sky, MT, March 2002.

Cooper, G., and McGillen, C., *"Probabilistic Methods of Signal and System Analysis"*, CBC College Publishing, 1986.

Daubechies, I., "*Ten Lectures on Wavelets*", Society for Industrial and Applied Mathematics: Philadelphia, 1992.

Frank, P. M., "Fault Diagnosis in Dynamic Systems Using Analytical and Knowledge Based Redundancy-A Survey and Some New Results", proceedings of IFAC Symposium on Advanced Information Processing in Automatic Control, pp. 457-459, Nancy, France, May 1990.

Greitzer, F., and Ferryman, T., "Predicting Remaining Life of Mechanical Systems", proceedings of the ASNE Intelligent Ship Symposium, Philadelphia, PA, April 2003.

Howell, J. R., and Buckius, R. O., *"Fundamentals of Engineering Thermodynamics"*, McGraw-Hill, 1987.

Jardim, R., Barata, M., Assis, L., Alavro, J., and Garcao, A., "Application of Stochastic Modelling to Support Predictive Maintenance for Industrial Environments", proceedings of the IEEE International Conference on Systems, Man and Cybernetics, vol. 1, 1996, pp. 117-122 , Beijing, China, October 1996.

Kim, D, and Mead, H., "Remaining Life Assessment of Refinery Heater Tubes" Proceedings of the ASME Pressure Vessels and Piping Conference, vol. 388, pp. 361-366, Boston, MA, August 1999.

Krikelis, J., and Papadakis, F., "Gas Turbine Modelling Using Pseudo-Bond Graphs", *International Journal of System Science*, vol. 19, no. 4, pp. 537-550, 1998.

Krishnaswami, V., Luh, G. C., and Rizzoni, G., "Nonlinear Parity Equation-Based Residual Generation for Diagnosis of Automotive Engine Faults", *Journal of Control Engineering Practice*, vol. 3, no. 10, pp. 1385-1392, October 1995.

Kwan, C., Zhang, X., Xu, R., and Haynes, L., "A Novel Approach to Fault Diagnostics and Prognostics", proceedings of IEEE International Conference on Robotics and Automation, vol. 1, pp. 604-609, Taipei, Taiwan, September 2003.

McAlpin, R., Tally, P., Bernstein, H., and Holm, R., "Failure Analysis of Inlet Guide Vanes", *Journal of Engineering for Gas Turbine and Power*, vol. 125, no. 1, pp. 236-240, 2003.

Orsagh, R., Roemer, M., Sheldon, J., and Klenke, C., "A Comprehensive Prognostics Approach for Predicting Gas Turbine Engine Bearing Life", proceedings of ASME Turbo Expo, vol. 7, pp. 777-785, Vienna, Austria, June 2004.

Pawlowski, R., and Greitzer, F., "Embedded Prognostics Health Monitoring", proceedings of the International Instrumentation Symposium, vol. 48, pp. 301-310, San Diego, CA, May 2002.

Roemer, M. J., and Kacprzynski, G. J., "Advanced Diagnostics and Prognostics for Gas Turbine Engine Risk Assessment", proceedings of the IEEE aerospace Conference, vol. 6, pp 345-354, Big Sky, MT, March 2000.

Roemer, M. J., Kacprzynski, G. J., and Orsagh, R. F., "Assessment of Data and Knowledge Fusion Strategies for Prognostics and Health management", proceedings of the IEEE Aerospace Conference, vol. 6, pp. 2979-2988, Big Sky, MT, March 2001.

Sarvanamuttoo, H. I. H., Rogers, G. F. C., and Cohen, H., *"Gas Turbine Theory"*, Pearson Education, 2001.

Tulino, A. and Verdu, S. "Random Matrix Theory and Wireless Communications", *Foundations and Trends in Communications and Information Theory*, vol. 1, no. 1, pp. 1 – 182, 2004.

Walsh, P., and Fletcher, P., *"Gas Turbine Performance"*, Blackwell Publishing, 2004.

Wang, P., and Vachtsevanos G., "Fault Prognosis Using Dynamic Wavelet Neural Networks", *Journal of Artificial Intelligence and Intelligent Design, Analysis and Manufacturing,* vol. 15, no. 4, pp. 349- 365, September 2001.

APPENDIX A: Nomenclature List

$A\chi$	Signal approximation
A_{GV}	Generator maximum vibration (g's)
A_{TV}	Gas turbine maximum vibration (g's)
a	Polynomial coefficient
d_e	Scaling coefficients
$\vec{D}$	Sum of squares of deviations
E	Statistical operator for mean
e	Scaling coefficients index
F	Function frequency (rad/s)
FF	Fuel flow (kg/sec)
f	Final forecast time
g	Input signal dimensions
h	Output signal dimensions
IGVA	Inlet guide vane angle (%)
i	Time index
j	Selected output signal number
k	Selected input signal number
m	Recorded time instances
$\dot{m}_f$	Mass flow rate (kg/s)
N	Shaft speed (R.P.M)
n	Input signals selected dimensions
PG	Power generated (MW)
p	Output signals selected dimensions
Q	Heat rate
q	Regression order index
r	Regression order
s	Signal component
$\hat{\xi}$	Output variable approx. coefficient
κ_d	Signal disturbance component
κ_n	Signal noise component
ϑ	Wavelet function energy
$\Re$	Correlation coefficient
ς	Admissibility constant
σ	Standard deviation
∞	Infinity
T_{EX}	Exhaust temperature ($^{\circ}C$)
T_G	Generator temperature ($^{\circ}C$)
T_{TT}	Turbine inlet temperature ($^{\circ}C$)
t	Time (minutes)
$\triangle t$	Sampling rate
t^*	Raw data time
U	Input signal
U^*	Conditioned input signal
u	Selected input signal
V	Composite data vector
u_0, v_0	Wavelet parameters
W_L	Learning window
W_S	Sampling window
W_V	Validation window
Y	Output signal
Y^*	Conditioned output signal
y	Selected Output signal
$\vec{z}$	Regression curve
χ	Dilation variable
ψ	Mother wavelet
$\hat{\psi}$	Fourier transform of mother wavelet
η	Translation variable
ε	Forecast error
ϕ	Scaling function
γ	Input variable detail coefficients
$\hat{\gamma}$	Output variable detail coefficients
ξ	Input variable approx. coefficient

All units used for this project are SI ("Le Systeme International d'Unites").

The Effects of Fuel Distribution, Velocity Distribution, and Fuel Composition on Static and Dynamic Instabilities and NO_x Emissions in Lean Premixed Combustors

Final Report

Project Period: July 1, 2003 to June 30, 2006

Prepared by:
Domenic A. Santavicca (Principal Investigator)

March 2007

DOE Award DE-FC26-02NT41431

UTSR Project No. 03-01-SR109

Submitted by:
The Pennsylvania State University
University Park, PA 16802

Disclaimer

"This report was prepared as an account of work sponsored by an agency of the United States Government. Neither the United States Government nor any agency thereof, nor any of their employees, makes any warranty, express or implied, or assumes any legal liability or responsibility for the accuracy, completeness, or usefulness of any information, apparatus, product, or process disclosed, or represents that its use would not infringe privately owned rights. Reference herein to any specific commercial product, process, or service by trade name, trademark, manufacturer, or otherwise does not necessarily constitute or imply its endorsement, recommendation, or favoring by the United States Government or any agency thereof. The views and opinions of authors expressed herein do not necessarily state or reflect those of the United States Government or any agency thereof."

Abstract

An experimental study has been conducted to determine of the effects of combustor operating conditions on the static and dynamic stability characteristics of lean premixed combustors operating on natural gas and coal-derived syngas fuels. The results of this study provide new insights and understanding of the mechanisms of unstable combustion which can be used to support the development of advanced numerical models and phenomenological-based models of unstable combustion.

The experiments were conducted in a laboratory-scale, lean-premixed, swirl-stabilized, dump combustor at atmospheric pressure over a range of inlet velocities, inlet temperatures, and natural gas/carbon monoxide/hydrogen fuel mixtures.

In the lean blowout study it was found that the lean blowout limit shifted to leaner conditions as increasing amounts of carbon monoxide and/or hydrogen were added to the natural gas. Using a stirred reactor analysis, the effect of fuel composition on the equivalence ratio at lean blowout was predicted within ±0.05 of the measured equivalence ratio.

In the instability study it was shown that a vortex time-lag model can be used to predict the preferred instability frequency as a function of operating conditions from measurements of the stable flame location. Furthermore, it was shown that the stable flame location, as defined by the flame's center of heat release, moved along a single path in the combustor as the operating conditions and fuel composition were varied; and that along that path there were regions of stable and unstable combustion. It is expected that the path of the flame's center of heat release is a characteristic of a given combustor design and that the determination of that path will be of significant value in the development of phenomenological models for predicting unstable combustion.

Table of Contents

Executive Summary

Static and dynamic instabilities continue to be limiting factors in the development and use of lean premixed gas turbine combustors for achieving the NO_x levels required by current and future emissions regulations. These issues assume even greater significance with current interest in the effects of fuel variability, which includes variations in the composition of natural gas, the use syngas fuels, and the use of 100% hydrogen fuel, as well as recent interest in the use of "oxygen-combustion". To date, the only successful strategy for addressing static and dynamic stability problems is through the application of passive and, in a few cases, active control systems after instabilities have been encountered. Such solutions are not always successful, can be expensive to implement and usually do not work over a broad range of operating conditions. What is needed is an understanding of the factors affecting static and dynamic stability, an ability to predict the occurrence of lean blowout and unstable combustion, and models that can be used as the basis of a methodology for designing stable lean premixed combustors. This research program is intended to provide detailed data and phenomenological understanding that is necessary for the development of such model-based design tools.

The goals of this research are (1) to determine the effect of combustor operating conditions on the static and dynamic stability characteristics of lean premixed combustors operating on natural gas and coal-derived syngas fuels, (2) to use this information to gain new insights and understanding of the causes of unstable combustion, and (3) to use this information to support the development of advanced numerical models and phenomenological models of unstable combustion.

Project Description

Gas Turbine Research Need: Static and dynamic instabilities continue to be limiting factors in the development and use of lean premixed gas turbine combustors for achieving the NO_x emission levels required by current and future emissions regulations. These issues assume even greater significance with current interest in the effects of fuel variability, which includes variations in the composition of natural gas, the use syngas fuels, and the use of 100% hydrogen fuel, as well as recent interest in the use of "oxygen-combustion". To date, the only successful strategy for addressing these problems is through the application of passive and, in a few cases, active control systems after instabilities have been encountered. Such solutions are not always successful, can be expensive to implement and usually do not work over a broad range of operating conditions. What is needed is an understanding of the factors affecting static and dynamic stability, an ability to predict the occurrence of lean blow-out and unstable combustion, and models that can be used as the basis of a methodology for designing stable lean premixed combustors. This research program is intended to provide the detailed data and phenomenological understanding that is necessary for the development of such model-based design tools.

Approach and Expected Benefits: The objective of this project is to conduct experiments in an optically-accessible, laboratory-scale combustor to determine the effect of combustor operating conditions on the static and dynamic stability characteristics of lean premixed combustors. Of interest are both natural gas and coal-derived syngas fuels. These experiments involve a number of measurements aimed at characterizing the overall and detailed behavior, and at identifying the instability mechanism(s), of any observed instabilities. These include simultaneous measurements of the pressure, overall heat release and equivalence ratio fluctuations, as well as, phase-synchronized measurements of the two-dimensional structure of the flame. A unique feature of the combustor which is used in this study is the capability of varying the length of the combustor while the combustor is operating. This allows for the identification of the preferred instability frequency as a function of operating conditions from which the relationship between the combustor's stability characteristics and operating conditions is revealed. It also allows for the study of stable and unstable operation at the same operating condition. Information obtained with this unique facility is expected to provide valuable new insights regarding the mechanisms of unstable combustion.

Description of the Experiment

The coaxial dump combustor used in this study consists of an annular mixing section (inner diameter of 19 mm, outer diameter of 37 mm, and length of 215 mm), an optically accessible air-cooled fused quartz combustion section (inner diameter of 108 mm and length of 337 mm), and an air-cooled exhaust section of variable length. A schematic drawing of the combustor is shown in Fig. 1.

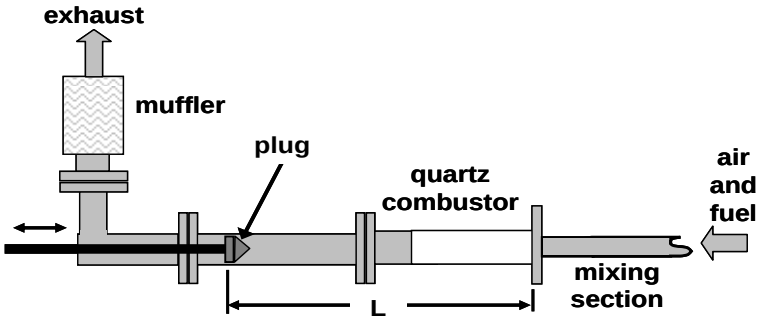

a. Schematic drawing of variable length combustor.

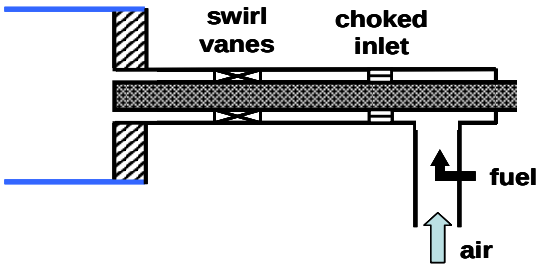

b. Schematic drawing of mixing section.

Figure 1. Schematic drawing of experimental set-up.

The air is heated to the desired inlet temperature by a 30 kW electric heater. The air-fuel mixture inlet temperature was monitored by a thermocouple located 105 mm upstream of the dump plane. A choked inlet at the entrance of the mixing section ensures that the flow is choked at all operating conditions. The fuel was injected well upstream the choked inlet, to ensure complete mixing of the fuel and air and to avoid the possibility of equivalence fluctuations during unstable combustion. The center-body is centered in the mixing section using a 30^o axial swirler located 51 mm upstream of the dump plane. The calculated swirl number is 0.45. The exhaust was partially restricted by a water-cooled plug that can continuously slide inside the exhaust section. The ratio of the exhaust section cross-sectional area and the annular open area

around the plug is 15. This partial restriction results in combustor pressures slightly above atmospheric. The exhaust gas temperature downstream of the exhaust plug was monitored with a thermocouple. In the first version of the variable length combustor, the combustor length could be varied from 23 to 51 inches. In a later version the combustor length could be varied from 30 to 60 inches. All the instability measurements were taken by increasing the length of the combustor to eliminate hysteresis effects.

The most basic measurement in unstable combustion studies is that of the dynamic pressure in the combustor. A water-cooled PCB high-frequency response piezoelectric pressure transducer was mounted in the dump plane to measure pressure oscillations in the combustor. The pressure signal was amplified, converted to a voltage signal, and saved in a PC. A sampling rate of 16384 Hz was used and the total of samples collected per experimental condition was 32768 (2 seconds of data). Later, the pressure time traces were analyzed using FFT algorithms. The uncertainty of the frequency measurements for the algorithms and data sampling parameters used was ±4 Hz. The spectra were used to determine the frequency and amplitude of the observed instabilities. The mean pressure inside the combustor, which was measured using a pressure gauge, was used to calculate the strength of the instabilities given by P_{rms}/P_{mean}.

Early studies found that in lean premixed flames the overall chemiluminescence emission from a variety of hydrocarbon flame radicals is proportional to the overall flame's heat release rate, where the proportionality constant is a function of the equivalence ratio. Based on this work, the intensity of the chemiluminescence emission has been widely used as a measure of the overall and local heat release rate in lean premixed flames. Such measurements, however, require that the equivalence ratio is spatially uniform and constant in time. In this study, because the fuel and air are well mixed upstream of the choked inlet to the missing section, this requirement is satisfied. Additional details on the use of chemiluminescence emission as a measure of the rate of heat release are given in the appendix.

Simultaneous dynamic combustor pressure and overall CH* chemiluminescence measurements were taken at selected unstable operating conditions. A UV grade fused silica collection lens was used to collect the chemiluminescence from the whole flame. The CH* chemiluminescence at 430 nm was isolated using a narrow band pass filter centered at 430.0 nm with a full width at half maximum of 10.3 nm and peak transmittance of 44 %, and then detected with a photomultiplier tube (PMT). The cross correlation of the heat release rate, i.e.,

chemiluminescence intensity, and combustor pressure signals was used to obtained the phase angle between the signals.

CH* chemiluminescence imaging was used to study the structure of stable and unstable flames. The value of chemiluminescence imaging relies on the qualitative information it can provide about the large scale details of the flame. For turbulent flames in the wrinkled-laminar flame regime, like the ones in the present work, two-dimensional chemiluminescence images are good representations of the two-dimensional flame brush.

A Princeton Instruments ICCD camera with a bandpass filter centered at 430 nm (±5 nm bandwidth) and a Nikon 60 mm 1:2.8 lens was used. The field of view was 178 x 120 mm. In order to capture the development of the flame structure during one period of the instability, the CH* images were phase synchronized with the pressure signal from the combustor. At each phase angle 40 individual images were taken and averaged to represent the heat release structure at that phase angle. A total of 12 average images, spaced at 30^o intervals, were taken during an instability cycle. In the case of stable flames, 30 images at equally spaced time intervals were averaged to represent the heat release structure. The resultant images are a record of the line-of-sight integrated chemiluminescence intensity and do not reveal the cross-sectional structure of the flame. The following procedure was used to reconstruct the two-dimensional flame structure. First, the background noise was subtracted from the images. The resultant images were found to be very nearly axisymmetric. Then, the upper and lower halves of the images were averaged to create an axisymmetric image. This is required for the next step. Finally, a 3-point Abel deconvolution procedure was used to deconvolute the images.

Results and Discussion

Lean Blowout Limits of Hydrogen/Carbon Monoxide/Natural Gas Fuel Mixtures

For the lean blow tests, the variable length section of the combustor was removed and the combustor was operated with the downstream end open. This was done to minimize the occurrence of combustion oscillations. In addition, to insure complete mixing, the fuel and air were mixed well upstream of the choked inlet to the combustor. Both the inlet temperature and fuel composition were varied. The 48 test conditions at which lean blowout measurements were made are given in Table 1. The yellow shaded cases are with 100% natural gas, the green shaded cases are with hydrogen/natural gas fuel mixtures, and the blue shaded cases are with

hydrogen/carbon monoxide/natural gas fuel mixtures. Note that the cases with 100% hydrogen, i.e., cases 10, 26 and 42, were not tested. (In the case of 100% hydrogen, the only chemiluminescence is that due to OH* which occurs at approximately 309 nm and therefore can not be seen by eye.)

The lean blowout results at an inlet temperature of 375°C for natural gas-hydrogen (cases 36-38) and natural gas-hydrogen-carbon monoxide (cases 44-48) fuel mixtures are shown in Fig. 2, where the velocity at lean blowout is plotted versus equivalence ratio. These results show, as expected, that as the equivalence ratio increases the velocity at lean blowout increases for a given fuel. It is also shows that as the hydrogen concentration increases, the lean blowout limit moves to lower equivalence ratios; and that for fixed hydrogen concentration, as the carbon monoxide concentration increases (cases 37 and 45; and cases 38 and 48) the lean blowout limit also shifts to lower equivalence ratios. Another important feature of these results is that the velocity at lean blowout for a given fuel mixture is very sensitive to the equivalence ratio, i.e., the velocity at lean blowout changes significantly with a very small change in equivalence ratio.

One explanation for lean blowout is that it occurs when the local gas velocity exceeds the flame speed at the location where the flame is anchored. This suggests that lean blowout results from a range of equivalence ratios, inlet temperatures and fuels, should collapse to a single line on a plot of the velocity at lean blowout versus the flame speed. Figure 3 shows the same lean blowout data presented in Fig. 2 plotted versus the laminar flame speed, which was calculated using Chemkin-III and GRIMECH 3.0. Figure 3 shows that the inlet velocity at lean blowout does increase with increasing laminar flame speed, however, the data do not collapse to a single line, i.e., lean blowout can not be predicted by the laminar flame speed alone. One possible explanation for this that is that the flame speed at the point of attachment is actually that of a stretched laminar flame and therefore an appropriate stretched laminar flame speed should be used to predict the velocity at lean blowout. Similar to the effect of equivalence ratio on the velocity at lean blowout, Fig. 3 shows that the velocity at lean blowout is extremely sensitive to the laminar flame speed.

Case	Swirl	Inlet Temp	% Nat Gas	% H_2	% CO
1	30°	200°C	100	0	0
2	30°	300°C	100	0	0
3	30°	400°C	100	0	0
4	30°	200°C	90	10	0
5	30°	200°C	75	25	0
6	30°	200°C	60	40	0
7	30°	200°C	45	55	0
8	30°	200°C	30	70	0
9	30°	200°C	15	85	0
10	30°	200°C	0	100	0
11	30°	200°C	45	45	10
12	30°	200°C	45	35	20
13	30°	200°C	45	25	30
14	30°	200°C	30	60	10
15	30°	200°C	30	50	20
16	30°	200°C	30	40	30
17	30°	200°C	15	75	10
18	30°	200°C	15	65	20
19	30°	200°C	15	55	30
20	30°	300°C	90	10	0
21	30°	300°C	75	25	0
22	30°	300°C	60	40	0
23	30°	300°C	45	55	0
24	30°	300°C	30	70	0
25	30°	300°C	15	85	0
26	30°	300°C	0	100	0
27	30°	300°C	45	45	10
28	30°	300°C	45	35	20
29	30°	300°C	45	25	30
30	30°	300°C	30	60	10
31	30°	300°C	30	50	20
32	30°	300°C	30	40	30
33	30°	300°C	15	75	10
34	30°	300°C	15	65	20
35	30°	300°C	15	55	30
36	30°	375°C	90	10	0
37	30°	375°C	75	25	0
38	30°	375°C	60	40	0
39	30°	375°C	45	55	0
40	30°	375°C	30	70	0
41	30°	375°C	15	85	0
42	30°	375°C	0	100	0
43	30°	375°C	45	45	10
44	30°	375°C	45	35	20
45	30°	375°C	45	25	30
46	30°	375°C	30	60	10
47	30°	375°C	30	50	20
48	30°	375°C	30	40	30
49	30°	375°C	15	75	10
50	30°	375°C	15	65	20
51	30°	375°C	15	55	30

Table 1. Test matrix for natural gas (yellow), hydrogen/natural gas (green), and hydrogen/natural gas/carbon monoxide (blue) lean blowout tests. [gray shaded cases were not tested]

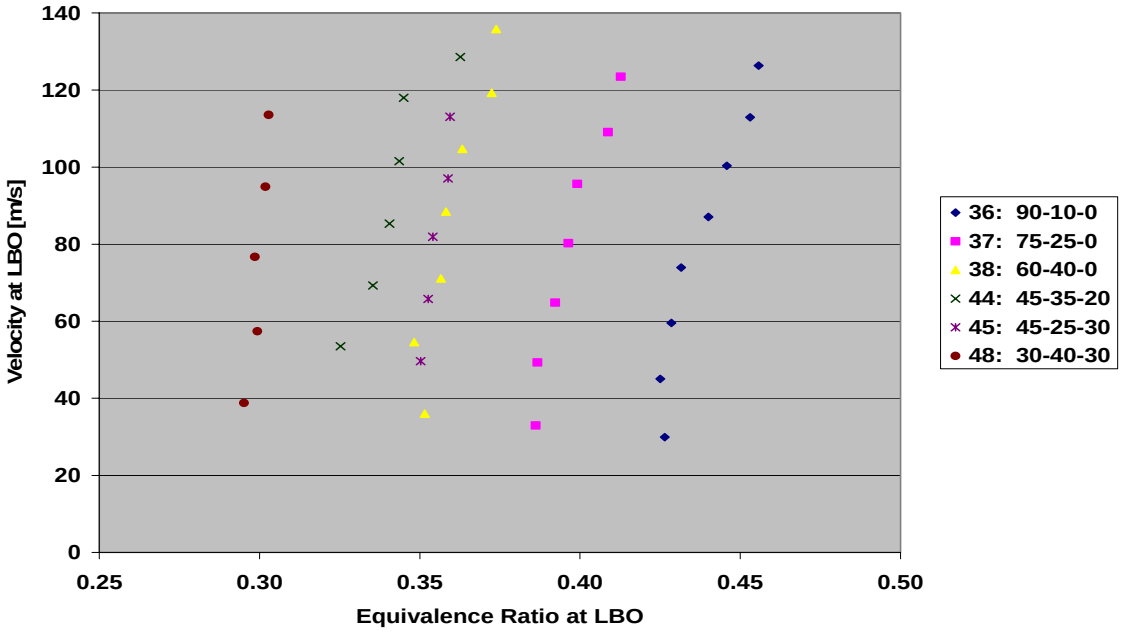

Figure 2. Velocity at lean blowout versus equivalence ratio at an inlet temperature of 375°C for various hydrogen-natural gas fuel-carbon monoxide fuel mixtures. (Legend Information - Case #: %NG - %H_2 - %CO

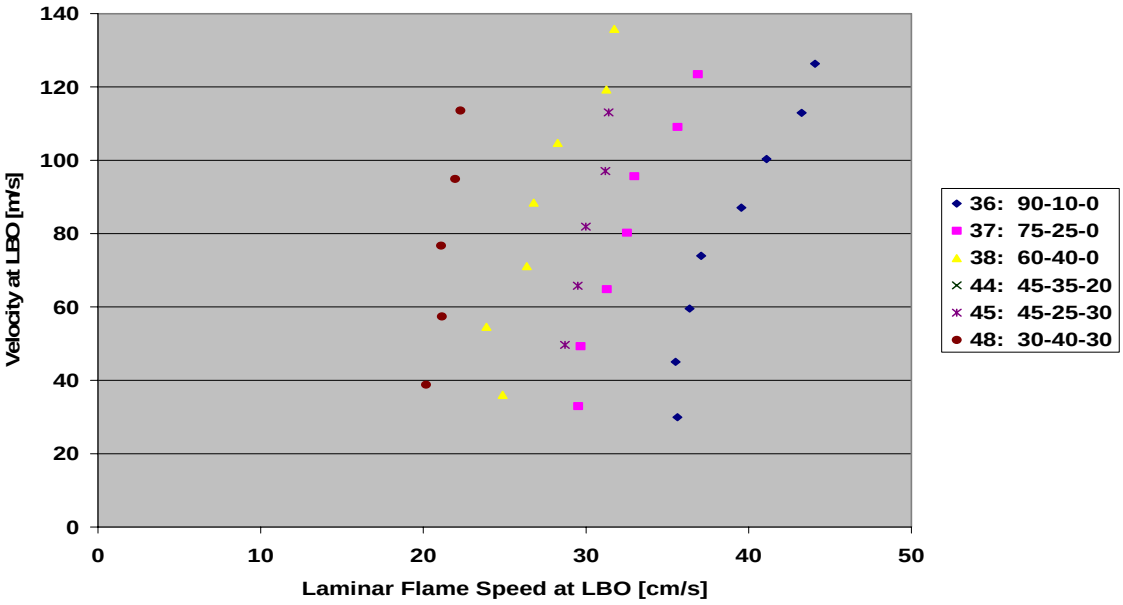

Figure 3. Velocity at lean blowout versus laminar flame speed for various hydrogen-natural gas-carbon monoxide fuel mixtures at an inlet temperature of 375°C. (Legend Information - Case #: %NG - %H_2 - %CO)

Another explanation for lean blowout is that the flame is stabilized by combustion in the dump plane recirculation zone and that blowout occurs when the residence time becomes less than the chemical reaction time of the reactants in the recirculation zone. This description is supported by the flame photographs shown in Fig. 4. (Note that the flow is from right to left.) This sequence of photographs corresponds to an actual lean blowout test where for a given air flow rate the equivalence ratio is initially set to a value that is above the lean blowout limit. At this condition the flame is clearly attached to the centerbody (photograph A) and there is no evidence of combustion in the dump plane recirculation zone. With fixed fuel flow rate the air flow rate is increased, causing the inlet velocity to increase and the equivalence ratio to decrease, until blowout occurs. The photographs in Fig. 4 show that as lean blowout is approached (photographs D – H) combustion moves up into the recirculation zone and stays there until the flame becomes detached from the dump plane (photograph I) and shortly thereafter blows out.

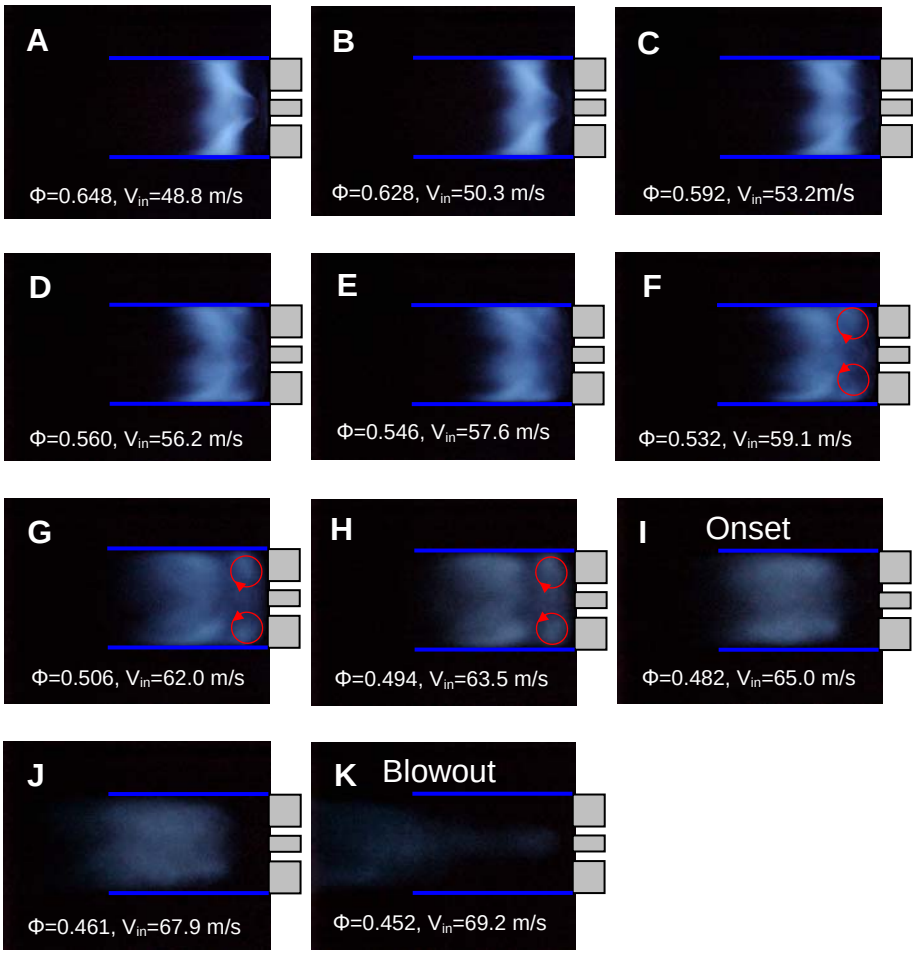

Figure 4. Flame image sequence approaching lean blowout. (Flow is from right to left.)

Combustion in the recirculation zone can be modeled as a stirred reactor, where lean blowout corresponds to the condition at which the stirred reactor blows out. Using the stirred reactor calculation in Chemkin-III and GRIMECH 3.0, the equivalence ratio at blowout was calculated for the lean blowout test conditions corresponding to cases 36 – 51 (except case 42) listed in Table 1. In the stirred reactor calculation it is necessary to specify a residence time, however, since the residence time in the dump plane recirculation zone is not known, the stirred reactor calculation was calibrated at one test condition, i.e., for a 45% natural gas, 45% hydrogen, 10% carbon monoxide fuel mixture, at an inlet temperature of 375°C and an inlet velocity of 80 m/s. At this operating condition the measured equivalence at lean blowout is 0.314. The stirred reactor calculation was performed for this fuel mixture and inlet temperature at different residence times until the calculated equivalence ratio at lean blowout was the same as the measured equivalence ratio at lean blowout. This was achieved with a residence time of 0.584 msec. Assuming that the residence time in the dump plane recirculation zone is the same for a given inlet velocity, The stirred reactor calculation was then repeated for the different fuel mixtures using the same 0.584 msec residence time to find the corresponding equivalence ratio at blowout for each fuel mixture. These results were then compared to the measured equivalence ratio at lean blowout for the different fuel mixtures at an inlet velocity of 80 m/s. This comparison is shown in Fig. 5. The agreement between the measured equivalence ratio at lean blowout and that calculated for a stirred reactor is very encouraging, especially given the fact that it covers a range of fuel composition from 90%NG/10%H_2 to 15%NG/85%H_2 to 15%NG/55%H_2/30% CO.

The occurrence of combustion in the dump plane recirculation zone as lean blowout is approached has also been observed in a number of prototype and production injectors supplied by the gas turbine manufacturers that have been tested in a similar optically-accessible combustor facility in our lab at Penn State.

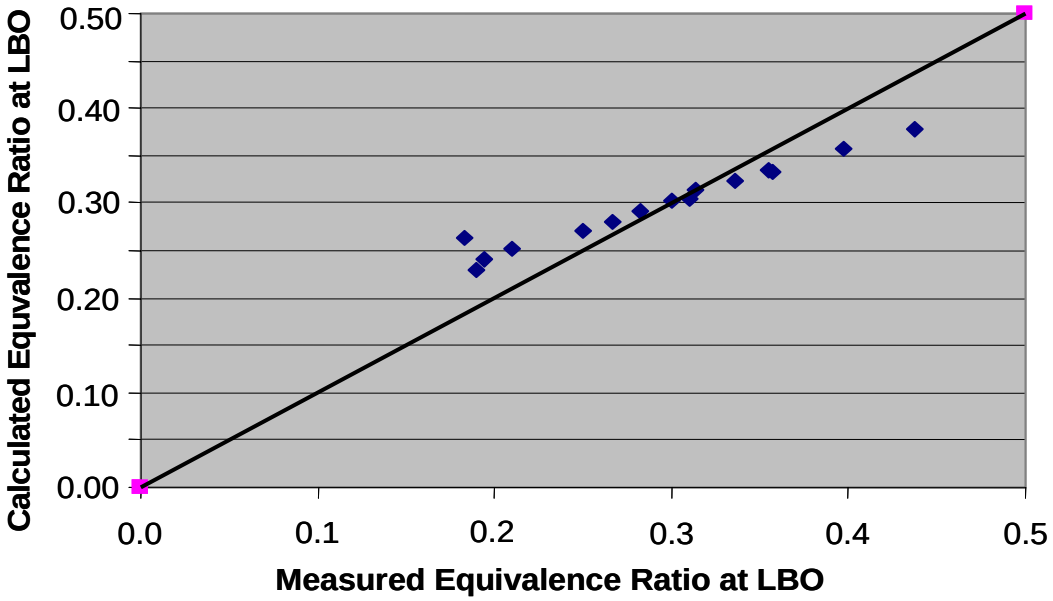

Figure 5. Measured equivalence ratio at lean blowout (V_{inlet} = 80 m/s) versus calculated equivalence ratio at lean blowout (τ_{res} = 0.584 ms) for cases 36-41 and 42-51.

Unstable Combustion with Natural Gas – Hydrogen Fuels

Abstract

The stability characteristics of a laboratory-scale lean premixed combustor operating on natural gas - hydrogen fuel mixtures have been studied in a variable length combustor facility. The fuel and air were mixed upstream of the choked inlet to the combustor to eliminate equivalence ratio fluctuations and thereby ensure that the dominant instability driving mechanism was flame-vortex interaction. The inlet velocity, inlet temperature, equivalence ratio and percent hydrogen in the fuel were systematically varied, and at each operating condition the combustor pressure fluctuations were measured as a function of the combustor length. The results are presented in the form of two-dimensional stability maps, which are plots of the normalized rms pressure fluctuation versus the equivalence ratio and the combustor length, for a given inlet temperature, inlet velocity, and fuel mixture. In order to understand the effects of operating conditions and fuel composition on the observed stability characteristics, two-dimensional chemiluminescence images of the flame structure were recorded at all operating conditions and for all fuel mixtures under stable conditions. Changes in the stable flame structure, as characterized by the location of the flame's "center of heat release", were found to be consistent with the observed instability characteristics. The location of the flame's "center of heat release" was found to lie along a single path for all operating conditions and fuel mixtures. It was also observed that there were regions of stable and unstable combustion as one moved along this path. Furthermore it was found that flames having the same "center of heat release" location, but different operating conditions and fuel composition, have very nearly the same flame shape. These results will be useful for developing phenomenological models for predicting unstable combustion.

Introduction

Driven by increasing demand for electrical power, environmental concerns, and the need for reduced dependence on non-domestic fuels, there is considerable interest in the development of advanced power generation systems based on integrated gasification combined cycle (IGCC) technology. In an IGCC power plant, coal is gasified to produce a synthetic fuel gas (syngas), which is typically a mixture of methane, hydrogen and carbon monoxide. The physical and chemical properties of such fuels vary significantly from those of natural gas and as a result, so can combustor operability, i.e., flashback, auto-ignition, lean blow out and combustion dynamics.

The operability issue of interest in this paper is combustion dynamics, which refers to the closed loop coupling between pressure oscillations and heat release oscillations. The underlying

process that enables this coupling is referred to as an instability driving mechanism. In lean premixed combustors the potential driving mechanisms include acoustic velocity fluctuations, flame-vortex interactions, periodic extinction and re-ignition, flame-wall interactions, and equivalence ratio fluctuations. Of these mechanisms, flame-vortex interactions and equivalence ratio fluctuations are generally considered to be the most important in lean premixed combustors.

The specific focus of the work presented in this report is flame-vortex driven combustion dynamics in lean premixed combustors operating on hydrogen – natural gas fuel mixtures. Experiments are conducted in an optically-accessible, variable-length, swirl-stabilized, dump combustor operating on hydrogen-natural gas fuel mixtures. Measurements are made of the pressure fluctuations over a range inlet temperatures, inlet velocities, equivalence ratios, natural gas – hydrogen fuel mixtures and combustor lengths; and the results are plotted in the form of two-dimensional stability maps. In addition, chemiluminescence imaging is used to obtain two-dimensional images of the flame structure under stable conditions for each operating condition and fuel mixture. The two-dimensional stable flame images and the corresponding stability maps are analyzed to obtain insights regarding the relationship between unstable combustion and the stable flame location. The possibility that the stability characteristics of the combustor can be determined from the location and structure of the stable flame would significantly simplify the prediction of unstable combustion.

Experiment

The optically-accessible, variable-length, swirl-stabilized, dump combustor used in this research was specifically designed for the study of combustion dynamics. The combustor consists of a stainless steel mixing section, an optically-accessible fused-quartz combustor section, and a variable length exhaust section. The combustor and mixing section were illustrated schematically in Fig. 1.

The mixing section is 215 mm long and has an annular cross section that is defined by a 19mm O.D. centerbody and a 37 mm I.D. mixing tube. The centerbody is centered in the mixing tube and is positioned such that its downstream end is flush with the combustor dump plane. A 30° flat vane swirler is mounted in the mixing tube, 50 mm upstream of the combustor dump plane. At the entrance to the mixing section the flow is choked. This provides a well defined acoustic boundary condition. In addition, the fuel is injected and mixed upstream of the choked inlet in order to eliminate the possibility of equivalence ratio fluctuations.

The combustor consists of a stainless steel dump plane, to which is attached (using high temperature silicon rubber) a 108 mm diameter by 337 mm long quartz tube combustor. The

downstream end of the quartz combustor is connected to a stainless steel variable-length, water cooled exhaust section. The length of the exhaust section is varied by moving a water-cooled plug along the length of the exhaust section. The combustor length (defined as the distance from the dump plane to the plug) can be varied continuously from a length of 30 inches to 60 inches.

The air supplied to the combustor is heated up a maximum temperature of 400°C by a 30 kW electric heater. The air temperature is monitored by a thermocouple located in the annular mixing section at a position 105 mm upstream of the combustor dump plane.

The primary measurements made in this study are of the pressure fluctuations in the combustor and two-dimensional chemiluminescence images of the stable flame structure. The combustor pressure fluctuations are measured using a water cooled piezoelectric pressure transducer mounted in the dump plane. These measurements are taken at a measurement rate of 10 kHz. The two-dimensional chemiluminescence flame structure images are obtained using an intensified CCD camera and a filter to isolate the CH* chemiluminescence emission. Fifty such images are recorded for each operating condition and fuel mixture and then averaged. The average image is then processed using an Abel deconvolution procedure to convert the original line-of-sight image to a two-dimensional image of the flame structure. Additional details on this technique can be found in reference.

The fact that the flame structure measurements are made under stable conditions and that this information is then used to understand the stability characteristics of the combustor is important. The rationale for this is that the stable flame location corresponds to the flame's location at the onset of unstable combustion. Therefore the stable flame location is of critical importance to the initiation of unstable combustion. Normally, i.e., in a fixed length combustor, the stable flame structure can not be determined at conditions where the flame is unstable. One of the advantages of the variable length combustor is that stable combustion can be achieved at all operating conditions by varying the combustor length.

Results

Measurements of the combustor pressure fluctuation were made over the range of operating conditions (T_{in}, V_{in}, ϕ), fuel mixtures and combustor lengths listed in Table 2. In addition, at each operating condition, for each of the three fuels, two-dimensional CH* chemiluminescence images of the flame were taken at a combustor length where the flame was stable.

Inlet Temperature	200°C, 300°C
Inlet Velocity	75, 90, 105 m/s
Equivalence Ratio	0.5, 0.55, 0.6, 0.65, 0.7,0.75
% Natural Gas/ % Hydrogen	100/0, 85/15, 75/25
Combustor Length	30" to 60" in 1" increments

Table 2. Test Conditions

The pressure fluctuation data are presented in the form of a two-dimensional stability map, which is a plot of the rms pressure fluctuation divided by the mean pressure versus the combustor length and the equivalence ratio. Figure 6 shows a stability map for 100% natural gas at an inlet temperature of 200°C and an inlet velocity of 75 m/s.

The stability map in Fig. 6 shows two distinct instability regimes, one at an equivalence ratio of 0.65 for combustor lengths near 55 inches and another at an equivalence ratio of 0.70 for combustor lengths near 38 inches. Figures 7a and 7b show the corresponding frequency spectra at the peak pressure fluctuation. In both cases the largest pressure fluctuation is at the fundamental frequency, and although the first harmonic is clearly evident it is much weaker than the fundamental. The fact that the fundamental frequency is higher for “case b” (354Hz) than for “case a” (250 Hz) is consistent with the fact that the “case b” instability occurs at a shorter combustor length (38”) than the “case a” instability (55”).

Figure 6 also shows two-dimensional chemiluminescence images of the stable flames for the two unstable operating conditions. From a time-lag analysis in can be argued that the flame-vortex interaction is most effective if the time required for the vortex to travel from the centerbody to the flame divided by the period of the instability is equal to a constant (~0.75). The vortex convection time, τ_{conv}, can be defined as $L_{flame}/\alpha\ V_{conv}$, where L_{flame} is the distance from the centerbody to the flame, α is a constant (~0.3), and V_{inlet} is the combustor inlet velocity. Because the flame is spatially distributed, there is some ambiguity in defining the distance from the centerbody to the flame. One approach is to define the flame as a point source that is located at the flame’s “center of heat release”, in which case $L_{flame} = L_{COHR}$, the distance from the centerbody to the flame’s “center of heat release”. The final result is then $L_{COHR}\ f_{instability}/\ V_{inlet}$ = constant, which in the case of constant inlet velocity becomes $L_{COHR}\ f_{instability}$ = constant. In other words, if the distance to the flame’s “center of heat release” decreases then the frequency of the corresponding instability must increase, which is consistent with the result shown in Fig. 6 where for the high frequency instability (364 Hz) L_{COHR} = 2.18" and for the low frequency instability L_{COHR} = 2.56"

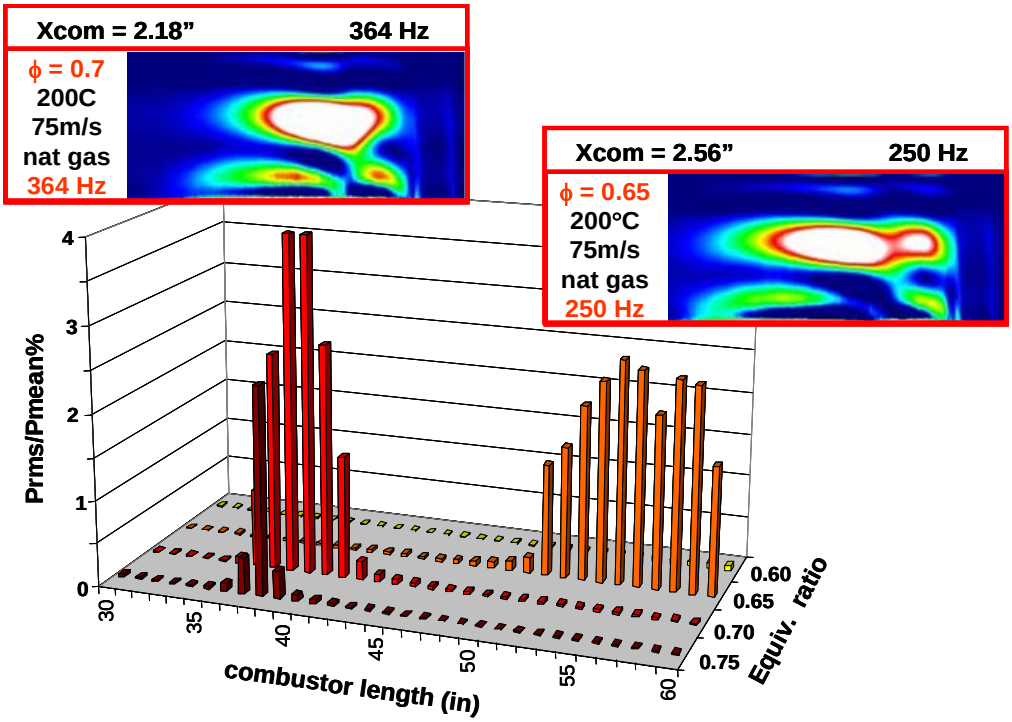

Figure 6. Two-dimensional stability map for 100% natural gas at an inlet temperature of 200°C and an inlet velocity of 75 m/s; and the corresponding stable flame images.

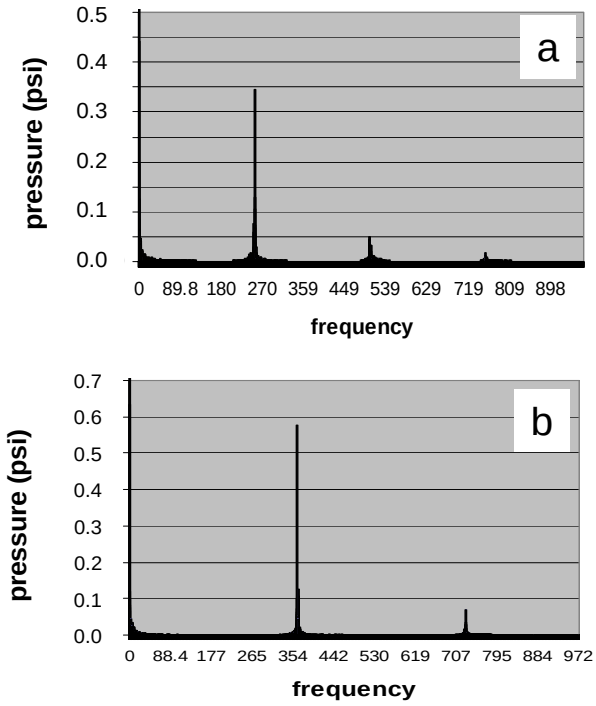

Figure 7. Frequency spectra for the two instabilities shown in Fig. 2. (a) ϕ = 0.65, L_{comb} = 55", (b) ϕ = 0.70, L_{comb} = 38 ".

Figure 8 shows the effect of inlet velocity on the stability characteristics for an inlet temperature of 200°C and for 15% hydrogen, at an inlet velocity of 75 m/s (Fig. 8a) and an inlet velocity of 105 m/s (Fig. 8b). (Note that in some of the stability maps data appears to be missing at certain equivalence ratios, for example at equivalence ratios of 0.50 and 0.75 in Fig. 8a. There are two reasons for this. In Fig. 8a, there are no data at an equivalence of 0.5 because this is below the lean blowout limit for these conditions. While there are no data at an equivalence ratio of 0.75 because the combustor was stable at all lengths for this equivalence ratio, hence the data was not plotted.) The results show that the equivalence ratio and combustor length values at which the combustor is unstable, as

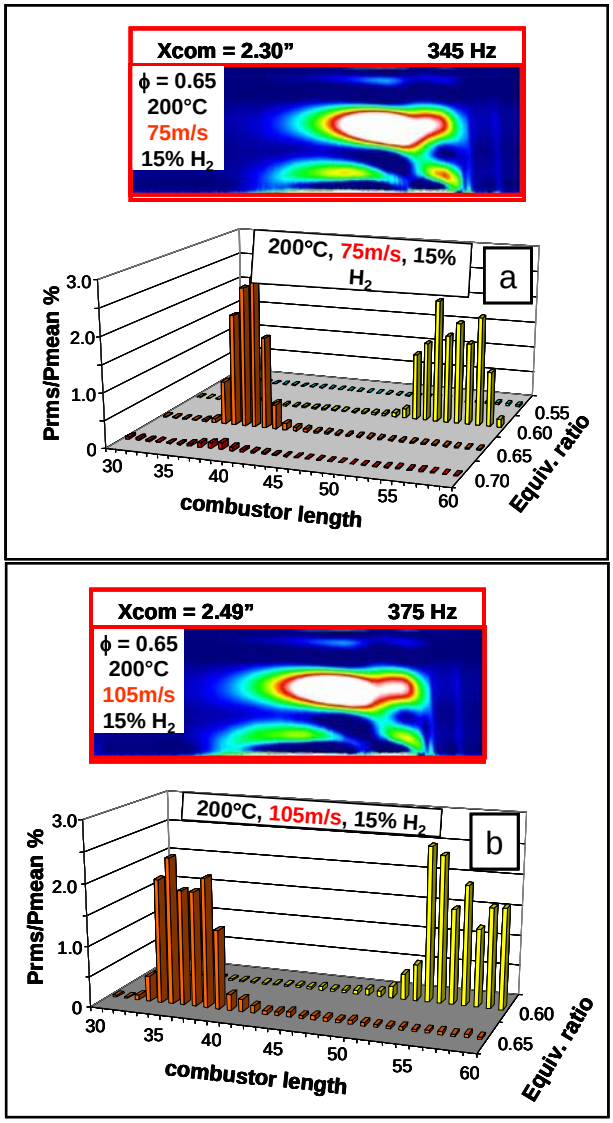

Figure 8. Two-dimensional stability maps for 200°C and 15% hydrogen for inlet velocities of (a) 75 m/s and (b) 105 m/s; and the corresponding stable flame images for ϕ = 0.65.

well as the magnitude of the pressure fluctuation, are similar at the two velocities. Also shown in Fig. 8 are the two-dimensional chemiluminescence images of the stable flames at an equivalence ratio of 0.65, which corresponds with the high frequency instability. The results show that the distance to the flame's "center of heat release" is slightly greater in the high velocity case (2.49") than in the low velocity case (2.30"), which is reasonable, however the corresponding increase in the instability frequency is the opposite of what was expected.

Figure 9 shows the effect of inlet temperature on the stability characteristics for an inlet velocity of 75 m/s and for 15% hydrogen. Figure 9a is for an inlet temperature of 200°C and Fig. 9b is for an inlet temperature of 300°C. These results show that as the temperature is increased from 200°C to 300°C, the high frequency instability shifts from an equivalence ratio of 0.65 to an equivalence ratio of 0.55. The other noticeable effect of increasing the inlet temperature is that the observed instabilities become considerably weaker. In fact the low frequency instability virtually disappears. This last observation can be attributed to the fact that heat release per unit volume decreases as the inlet temperature increases (density decreases) and as the equivalence ratio decreases

Figure 10 shows the effect of hydrogen on the stability characteristics at an inlet temperature of 200°C, and an inlet velocity of 75 m/s, with (a) 100% nat. gas and (b) 75% nat. gas/25% H_2. Again the bi-modal nature of the stability map is apparent with both fuels. The effect of hydrogen is to shift the instabilities to lower equivalence ratios and to weaken the instabilities. This latter effect can be attributed to the fact that heat release per unit volume decreases as the amount of hydrogen increases and as the equivalence ratio decreases. The fact that the instabilities shift to lower equivalence ratio as hydrogen is added to the flame is consistent with the stable flame images shown in Fig. 10 and the previously discussed time-lag concept, as represented by $L_{flame}\ f_{instability}/\ V_{inlet}$ = constant. In this case the instability frequency and the inlet velocity are the same for both fuels, therefore one would expect that the stable flame length should be the same for both cases, which is supported by the stable flame images shown in Fig. 10.

The results presented in Figures 6 and 8 through 10 demonstrate the importance of the location of the stable flame in determining whether or not a combustor is stable. Although the flame is spatially distributed, a simplified approach is to define the flame as a point source. As mentioned previously, one method for doing this is to define the flame location as the location of the flame's "center of heat release". Figure 11 is a plot of the location of the flame's "center of heat release" for all of the operating conditions and fuels used in this study (see Table 1), where X and Y refer to the x and y location of the flame's "center of heat release" relative to the shoulder of the

centerbody. Figure 11 shows that the location of the "center of heat release" moves along a relatively well-defined path as the operating conditions and the fuel composition change. It is also very interesting to note that flames having the same "center of heat release" location have very similar flame structure. This is also illustrated in Fig 11, which shows the stable flame images for the two adjacent data points indicated in the graph. This is true for any two adjacent data points on this graph.

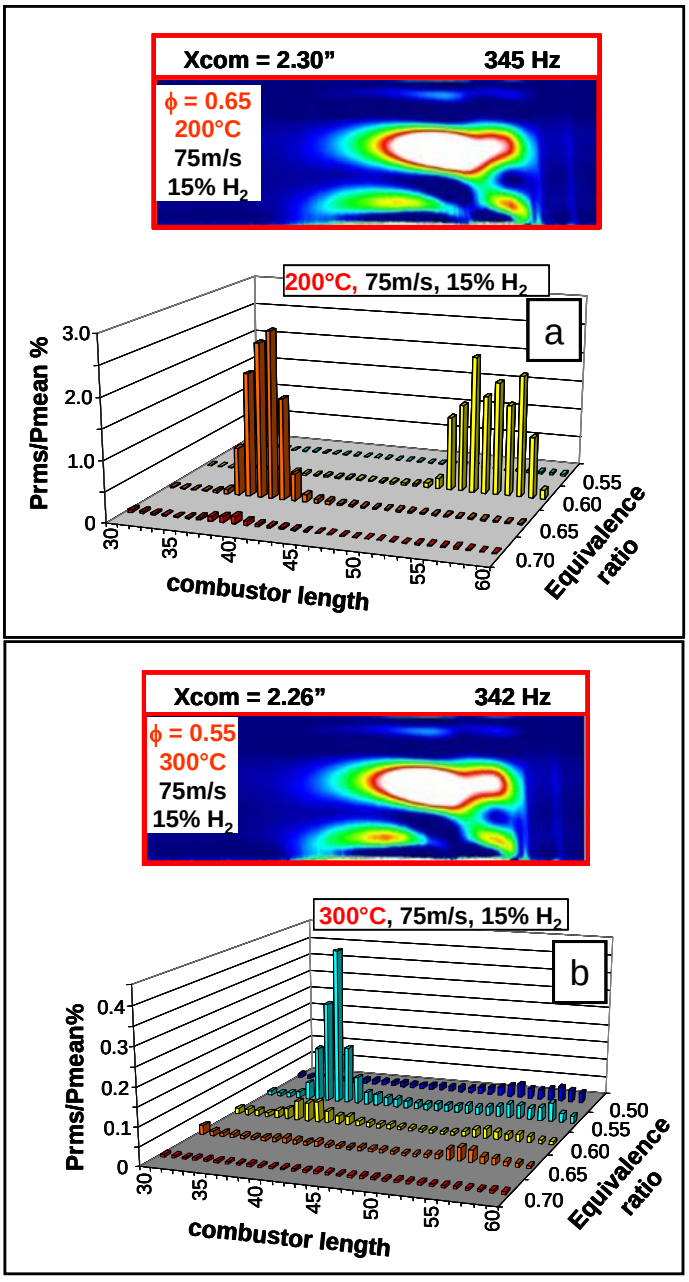

Figure 9. Two-dimensional stability maps for 75 m/s and 15% hydrogen for inlet temperatures of (a) 200°C and (b) 300°.

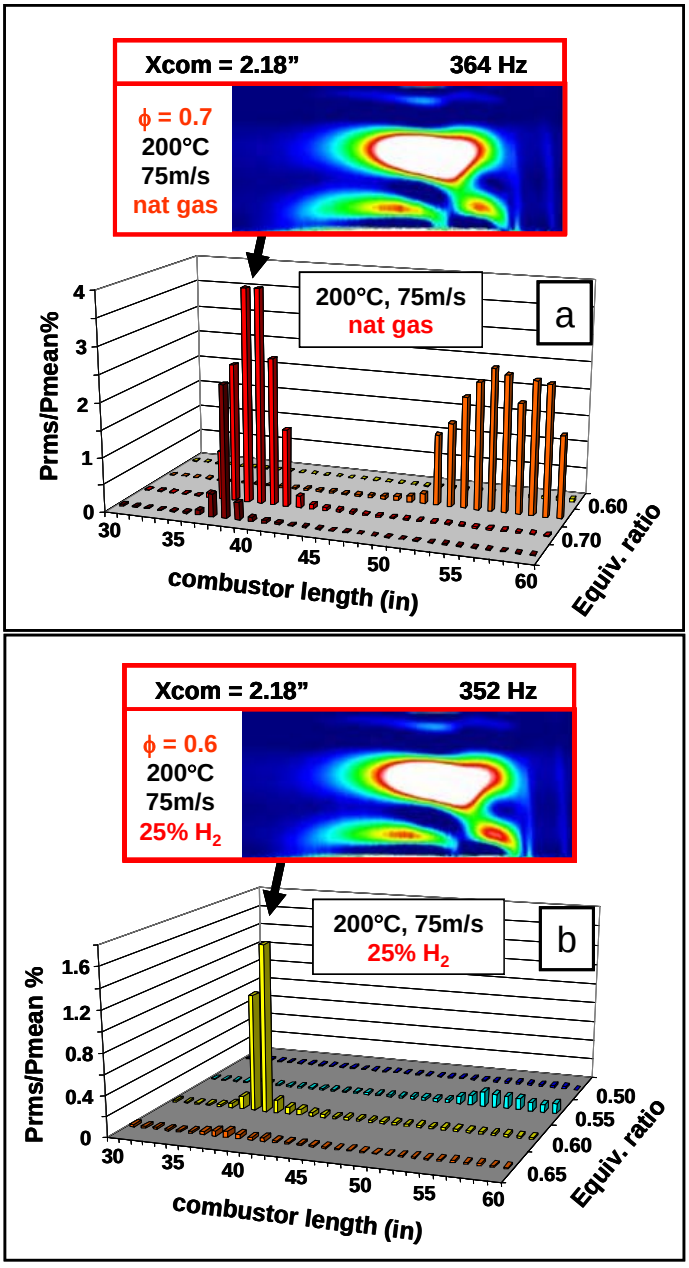

Figure 10. Two-dimensional stability maps for 200°C and 75 m/s for (a) 100% nat. gas and (b) 75% nat. gas/25% H_2; and the corresponding stable flame images at $\phi = 0.7$ and $\phi = 0.6$.

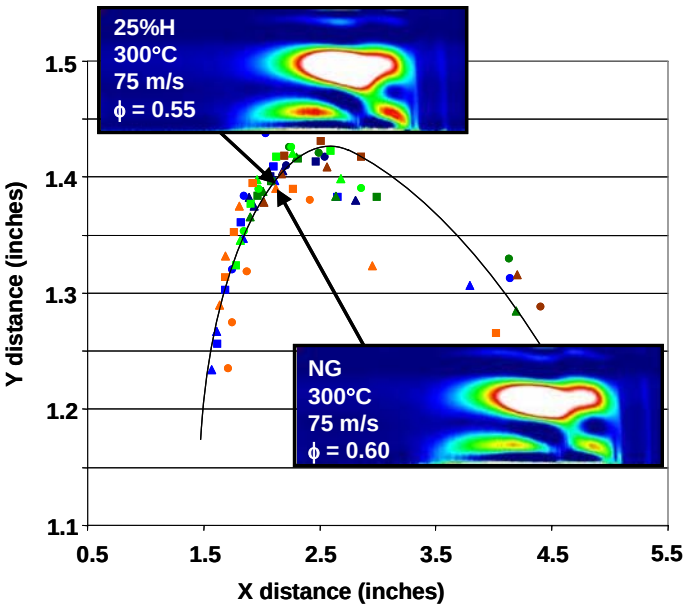

Figure 11. The location of the flame's "center of heat release" for all of the operating conditions and fuels tested.

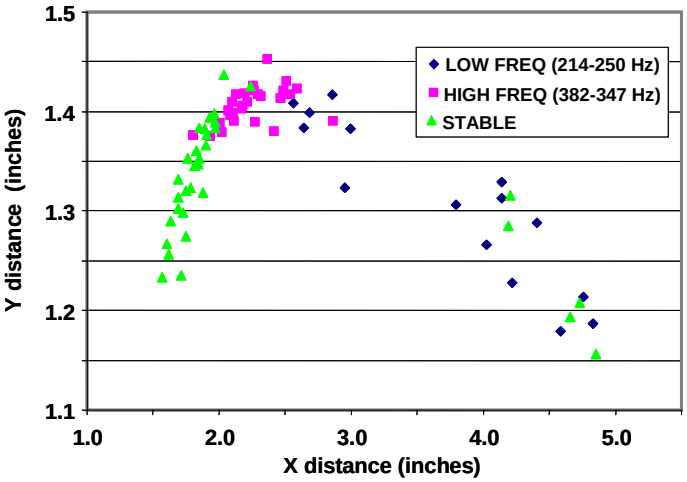

Figure 12. The stability characteristics along the path of the stable flame's "center of heat release".

Since the stability characteristics depend on flame location, it is interesting to look at how the stability characteristics vary along the path defined by the location of the flame's "center of heat release". This is shown in Fig. 12 where each data point is identified as exhibiting a high frequency instability (■), a low frequency instability (♦) or no instability (▲). It needs to be noted that the conditions that are identified as stable, are stable over the entire range of combustor lengths (30" to 60"). While the conditions that are identified as unstable exhibit unstable behavior over a small range of combustor lengths, i.e., the high frequency instabilities are observed at

combustor lengths of ~38", whereas the low frequency instabilities are observed at combustor lengths of ~55". Figure 12 shows that the combustor is stable when the stable flame location is closest to the centerbody, but that as the stable flame's "center of heat release" moves further away from the centerbody a region of high frequency instabilities is observed, then at greater distances a region of low frequency instabilities are observed, and finally at the greatest distances there appears to be a transition back to stable operation.

Conclusions

It was shown that the effect of operating conditions and fuel composition on the stability characteristics is to a significant extent determined by the flame's location under stable conditions. In other words, operating conditions and fuels that have the same stable flame location, have very similar stability characteristics.

It was shown that the stable flame's "center of heat release" is a good indicator of the overall stable flame shape and location. In other words, flames with the same "center of heat release" have very similar flame shapes.

It was shown that the "center of heat release" moves along a common path as the operating conditions and fuel composition change, and that along this path there are stable and unstable regimes.

It is expected that the "center of heat release" path is a characteristic of a given injector geometry and that a determination of this path can be used as part of a phenomenological model for predicting the effect of operating conditions and fuel composition on the stability characteristics of a given injector.

Appendix A: Chemiluminescence measurements of the rate of heat release.

Although chemiluminescence emission is widely used as a measure of local and overall heat release fluctuations in unstable lean premixed flames, the viability of this technique for such measurements has not been demonstrated. One concern is the possibility that the velocity and equivalence ratio fluctuations that occur during unstable combustion not only affect the rate of heat release, but also affect the relationship between the rate of heat release and the intensity of the chemiluminescence emission. Therefore it is necessary to understand the effects of equivalence ratio and velocity and to account for these effects when using chemiluminescence to measure heat release fluctuations. Another important issue is whether the effects of equivalence ratio and velocity on the relationship between chemiluminescence and heat release are the same in stable and unstable flames. In other words, can calibration data obtained in a stable flame be used when making measurements in unstable flames.

The effect of equivalence ratio on the relationship between overall chemiluminescence intensity and overall heat release rate in stable flames was discussed in a previous progress report. In summary, the overall chemiluminescence intensity has been shown to increase linearly with the rate of heat release, where the slope of the linear relationship increases with increasing equivalence ratio. Therefore, in order to measure the rate of heat release during unstable combustion when there are equivalence ratio fluctuations, an independent measurement of the time-varying equivalence ratio is required. In the last progress report, a measurement strategy was proposed wherein equivalence ratio is determined from a measurement the ratio of the CH* and OH* chemiluminescence. This measurement strategy, however, has yet to be demonstrated.

During this reporting period work has focused on the effect of velocity on the relationship between the overall chemiluminescence intensity and the overall rate of heat release in stable and unstable flames. Experiments were conducted in our lean premixed combustor over the range of operating conditions given in Table A1. For all of these tests the fuel and air were mixed upstream of the choked inlet to the mixing section in order to eliminate the possibility of equivalence fluctuations and thereby isolate the effect of velocity fluctuations. The variable length feature of the combustor made it possible to achieve stable and unstable operation at any operating condition.

Figures A1 and A2 show measurements, at stable operating conditions, of the overall CH* and CO_2* chemiluminescence intensities, respectively, divided by the fuel flow rate versus the combustor velocity at four different equivalence ratios. Both the CH* and CO_2* results show that the normalized chemiluminescence intensity increases with increasing velocity, indicating that when using chemiluminescence to measure heat release fluctuations during unstable combustion

Mean velocity in the mixing section, U_{mixer} (m/s)	36 – 120
Mean velocity in the combustor, U_{comb} (m/s)	3 - 10
Mixture inlet temperature, T_{inlet}(°C)	200 and 350
Equivalence ratio	0.50 - 0.70
Reynolds number	$10.8x10^3$ - $57.0x10^3$

Table A1. Test conditions for chemiluminescence measurements.

that it is necessary to make an independent measurement of the velocity fluctuations so this effect can be accounted for. It should be noted that the only reported measurements of the effect of velocity on chemiluminescence were in papers by John, R., and Summerfield, M. in 1957 and by Hurle, I.R. et al. in 1968 where it was observed that increasing velocity decreased the chemiluminescence intensity. It was argued that this was the result of increased turbulence intensity which through the effect of local flame stretch reduced the chemiluminescence emission. Another possible explanation for this result is that care was not taken to ensure that the chemiluminescence emission from the entire flame was detected so that as the velocity increased and the flame length increased, some of the flame fell outside of the field of view of the collection optics and thereby reduced the measured signal.

It is important to note that the CH* chemiluminescence measurements shown in Fig. A1, and those that have been reported in the literature, include a contribution due to the broadband CO_2* chemiluminescence spectrum, as shown in the chemiluminescence spectrum presented in Fig. A3. This suggests the possibility that the velocity dependence observed in the CH* chemiluminescence measurement is due to the velocity dependence of the background CO_2* chemiluminescence. The following procedure was developed whereby the CO_2* contribution to the CH* chemiluminescence measurement is subtracted from the CH* measurement. The CH* chemiluminescence is detected through a band pass filter centered on 430nm with a FWHM of 10 nm, while the CO_2* chemiluminescence is detected through a band pass filter centered on 470 nm with a FWHM of 10 nm. Using a curve fit to the broad band CO_2* chemiluminescence spectrum it was determined that the background CO_2* chemiluminescence intensity at 430 nm is equal to 1.2 times the CO_2* chemiluminescence intensity measured at 470 nm and that this is true over the range of inlet temperatures, inlet velocities and equivalence ratios used in this study. Therefore, the background subtracted CH* chemiluminescence intensity can be determined from simultaneous measurements of the chemiluminescence intensity at 430 nm and 470 nm. Using this

method gives the results shown in Fig. A4, which is a plot of the background subtracted CH* chemiluminescence intensity divided by the fuel flow rate versus combustor velocity for different equivalence ratios. Within the accuracy of the measurements, the relationship between the background subtracted CH* chemiluminescence and the fuel flow rate, i.e, the rate of heat release, is independent of velocity over the range of velocities tested. (The area ratio of the combustor is 12 to 1, therefore the corresponding range of inlet velocities in Fig. A4 is 36 to 96 m/s.)

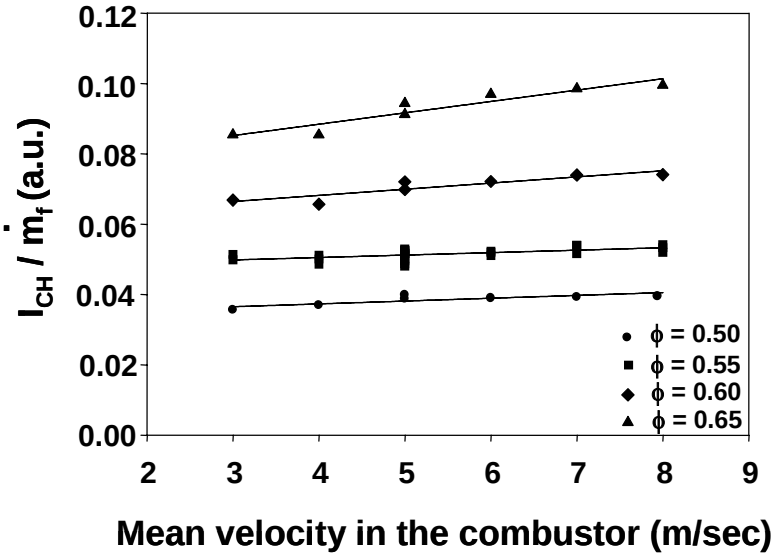

Figure A1. Overall CH* chemiluminescence divided by the fuel flow rate versus the mean velocity in the combustor for an inlet temperature of 350°C.

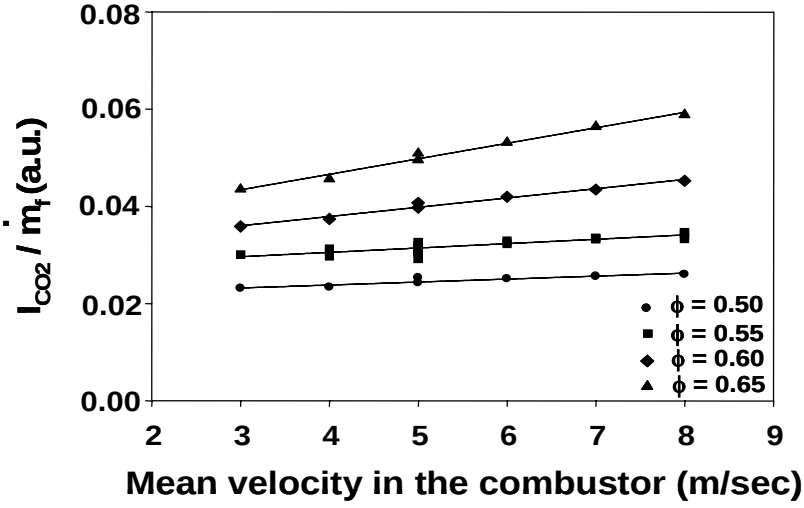

Figure A2. Overall CO_2* chemiluminescence divided by the fuel flow rate versus the mean velocity in the combustor for an inlet temperature of 350°C.

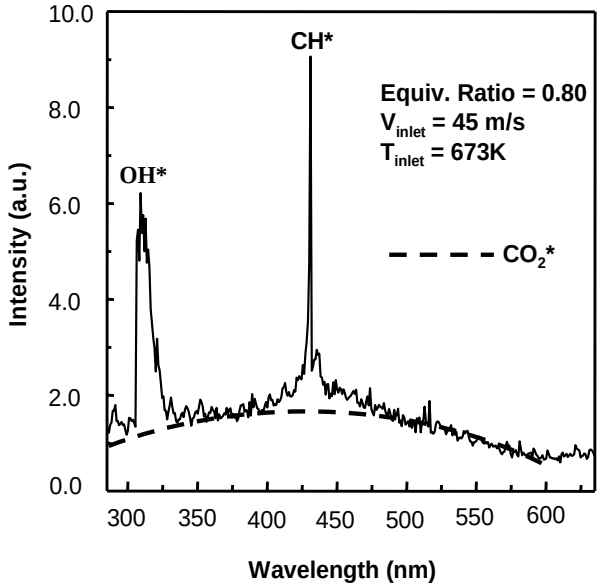

Figure A3. Chemiluminescence spectrum from premixed natural gas flame.

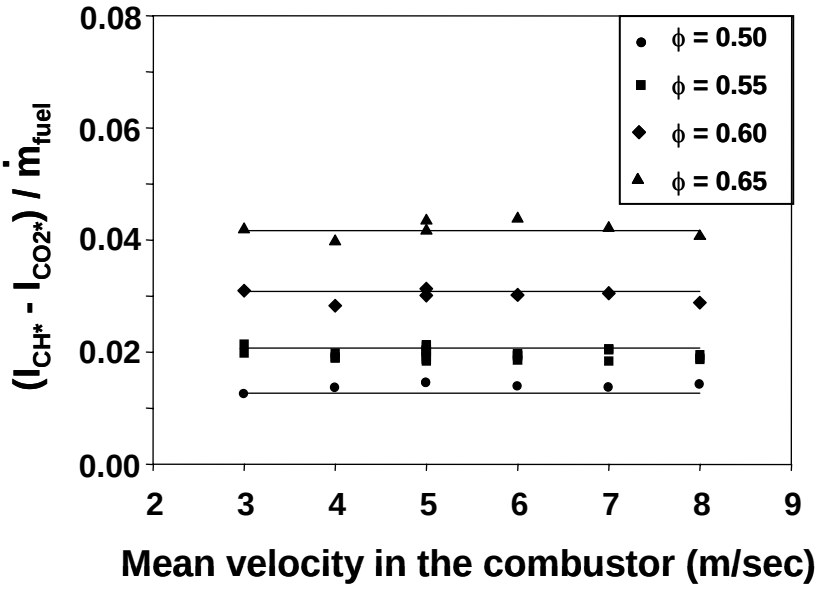

Figure A4. Overall CH* chemiluminescence intensity with background CO_2 chemiluminescence intensity subtracted divided by the fuel flow rate versus mean velocity.

In the case of stable flames, as discussed above, it has been shown that the overall background subtracted CH* chemiluminescence intensity is linearly proportional to the overall rate of heat release, where the slope of the relationship is a function of the equivalence ratio and the inlet temperature and is independent of the velocity. This is expressed by the following equation:

$$I_{CH^*\text{-}CO2^*\text{-}overall} = \kappa(\phi, T_{in})\, Q_{overall}$$

The important question is whether or not this relationship is also true during unstable combustion, in other words, is the following equation valid during unstable combustion?

$$I_{CH^*\text{-}CO2^*\text{-}overall}(t) = \kappa(\phi, T_{in})\, Q_{overall}(t)$$

There are two cases of interest, i.e., with and without equivalence fluctuations. In the following discussion, the equivalence ratio and inlet temperature are constant.

Consider the result shown in Fig. A5, which is a plot of the logarithm of the <u>average</u> background subtracted CH* chemiluminescence intensity divided by the <u>average</u> velocity of the reactants in the combustor versus the equivalence ratio for a fixed inlet velocity and a fixed inlet temperature. The combustor length was also fixed and the equivalence ratio was varied from 0.5 to 0.66. As shown, the combustor is initially stable and as the equivalence ratio is increased the combustor goes from stable to unstable and then back to stable again. These results show that there

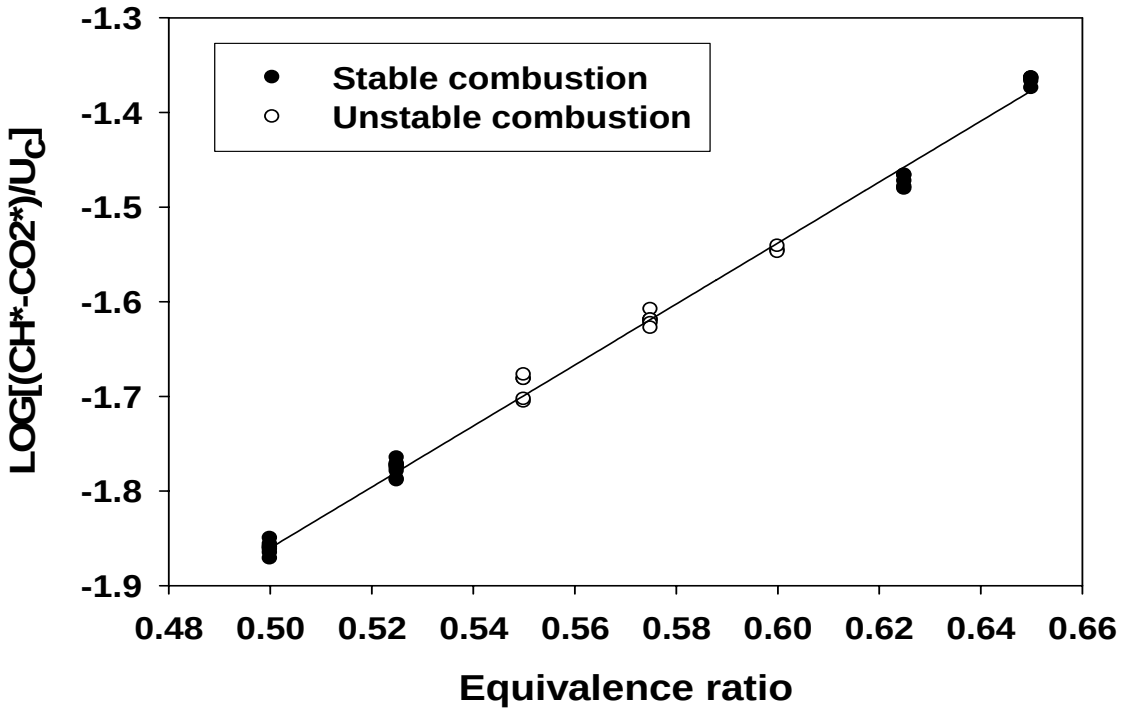

Figure A5. Typical simultaneous combustor pressure, overall CH* chemiluminescence and overall CO_2 chemiluminescence measurements during unstable combustion.

is a linear relationship between the logarithm of the average background subtracted CH* chemiluminescence intensity divided by the average velocity of the reactants in the combustor versus the equivalence ratio for both stable and unstable conditions. It can be shown, that the only way this can only be true is if the instantaneous background subtracted CH* chemiluminescence intensity is linearly proportional to the instantaneous rate of heat release, where the proportionality constant is a function of the inlet temperature and the equivalence ratio and is not affected by the fluctuating velocity. (This is not to say that the relationship between the local rate of heat release and the local chemiluminescence intensity is not a function of the local velocity, but that if there is such an effect it averages out when integrated over the entire flame.) Therefore it can be concluded that the instantaneous background subtracted CH* chemiluminescence intensity does provide a quantitative measure of the instantaneous rate of heat release during unstable combustion if there are no fluctuations in the equivalence ratio.

Another important issue regarding the rate of heat release during unstable combustion is illustrated in Fig. A6. This figure shows two separate sequences of CH* chemiluminescence flame images. In both cases the average inlet velocity is 84 m/s, the equivalence ratio is 0.75 and the inlet temperature is 200°C. The upper row of images is from an unstable flame and show how the flame structure changes over the half of the cycle when the pressure (velocity) is increasing (decreasing). Note that in this case the equivalence ratio and inlet temperature are constant in time. The lower row of images is from stable flames at conditions that approximately correspond to the same instantaneous inlet velocities as the different unstable flame images. Clearly there is a significant difference between the images from the unstable flame and the images from the stable flames, even though the inlet temperature, equivalence ratio and velocity are approximately the same in the two cases. This difference is the result of the flame-vortex interaction that occurs in the unstable case. As shown in this figure, the interaction between the flame and the vortex alters the flame structure and as a result also the rate of heat release. This is further evidenced by the measured pressure versus time and measured CH* chemiluminescence intensity versus time curves shown in Fig. A7. The positive and negative pressure fluctuations are very symmetric, whereas the positive and negative chemiluminescence fluctuations are noticeably different, i.e., the positive fluctuation has a sharp peak and the negative fluctuation has a rounded shape.

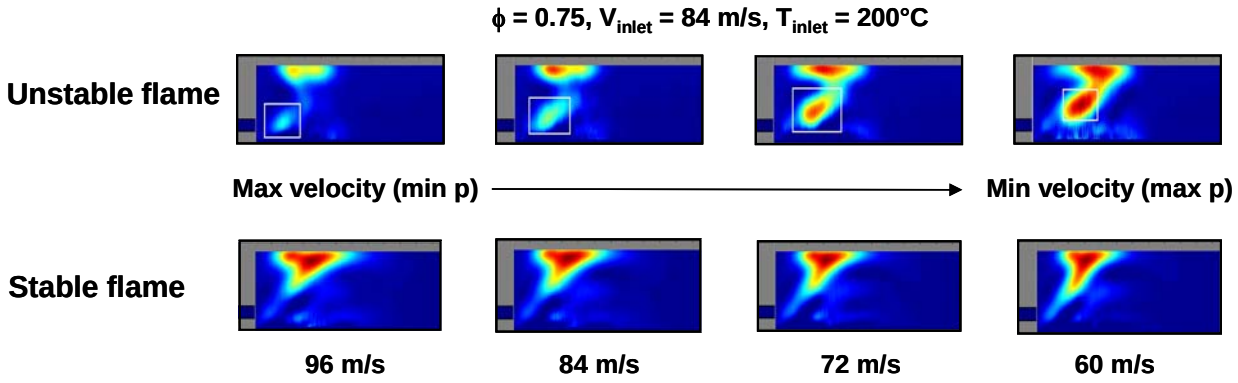

Figure A6. A comparison of stable and unstable flame images at similar conditions from a stable and an unstable flame.

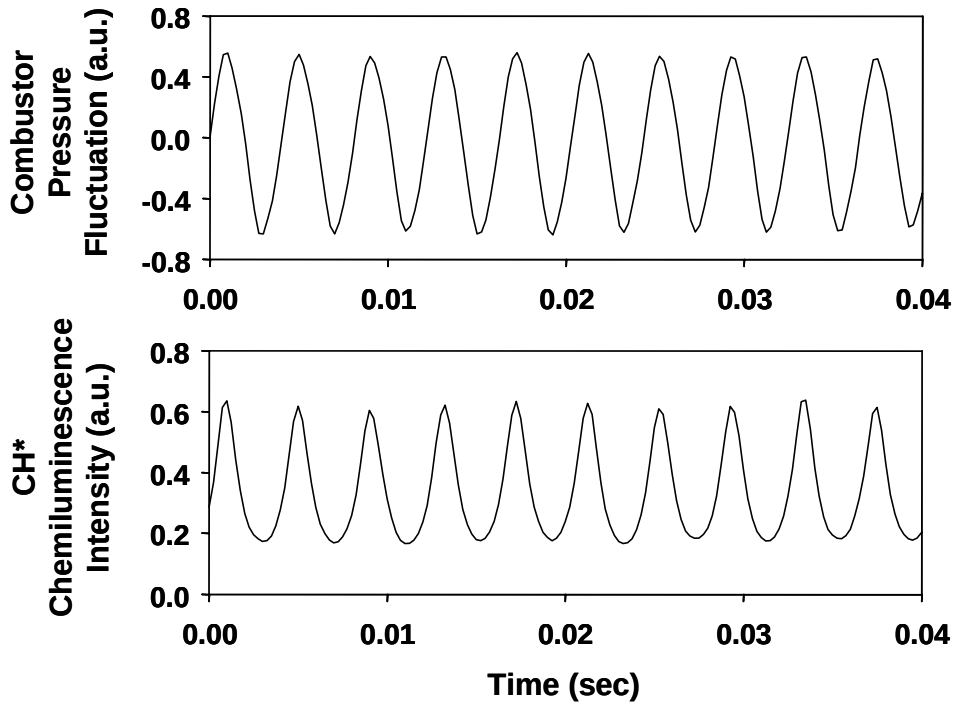

Figure A7. Simultaneous pressure fluctuation and CH* chemiluminescence intensity versus time during unstable combustion.

Report Title: Turbine Vanes and Endwalls with Realistic Surface Conditions

Type of Report: UTSR FINAL REPORT

Reporting Start Date: July 1, 2003

Reporting End Date: January 31, 2007

Principal Investigator: Karen A. Thole,
Virginia Polytechnic Institute and State University

Co-Principal Investigator: David G. Bogard, University of Texas-Austin

Report Issue Date: January 31, 2007

DOE Award Number: DE-FC26-02NT41431

UTSR Project Number: Contract Number 03-01-SR110

Submitting Organizations:

VT Experimental and Computational
Convection Lab (VTExCCL)
Mechanical Engineering Department
Virginia Tech
Blacksburg, VA 24060
Phone: (540)231-7192
Fax: (540)231-9100

Turbulence and Turbine
Cooling Research Lab (TTCRL)
Mechanical Engineering Department
University of Texas
Austin, TX 78712
(512)471-3128
(512)471-8727

Disclaimer

Abstract

Our research addressed issues relevant to gas turbine engine service that are directly linked to the part life for turbine airfoils. The focus of our study was to evaluate film cooling performance under realistic operating conditions including surface roughness, cooling hole blockage, particle deposition, erosion, and repeated applications of thermal barrier coatings (TBC). Deposits are formed on the endwall and vane surfaces when the molten contaminants in the mainstream gas are quenched and adhere to the surface. Although experiments were conducted using facilities incorporating simulated first vanes and endwalls, these results have general applicability in the turbine section. This work is particularly relevant for syngas operations, given the increased contaminants that occur with this fuel.

Studies were completed on a realistic endwall simulating surface roughness, combustor-turbine interface gap, and vane-to-vane interface gap. Results indicated that surface roughness has a degrading effect at higher blowing ratios and the coolant flow rate through the interface gaps greatly affect the endwall adiabatic effectiveness levels. Results indicated a uniform spread of coolant through a narrow combustor-turbine gap than a wider gap at a constant coolant flow rate. Effects of near hole deposition, cooling hole blockage and TBC spallation were also studied. Spallation and blockage showed a 10-40 % reduction in adiabatic effectiveness whereas deposition indicated an improvement in effectiveness levels at lower deposit heights. Different trench geometries were studied at the leading edge to enhance the adiabatic effectiveness levels. It was found that higher trench depths performed better at higher blowing ratios. An overall enhancement of 35-55% in the adiabatic effectiveness levels was achieved with the maximum enhancement occurring at a trench depth of 0.8D at a blowing ratio of 3.0.

Experiments completed with the simulated vane test facility included studies of effects of varying roughness levels on the suction and pressure sides of the vane, effects of obstructions near holes for two rows of holes on the suction side, and the viability of transverse, shallow trenches to mitigate roughness and obstruction degradation effects. Surface roughness and near hole obstructions were found to cause as much as 50% reduction in adiabatic effectiveness, and roughness was found to increase heat transfer coefficients as much as a factor of two. However, a major finding from this study was that a shallow, transverse trench with a sharp downstream edge will significantly increase adiabatic effectiveness and is relatively insensitive to the degradation effects of surface roughness and depositions near the trench.

Table of Contents

List of Tables

List of Figures

Executive Summary

Task 1 **Planning Meetings.**

Initial meetings took place between Virginia Tech (VT), University of Texas (UT), and our industrial partners (GE, P&W, & Rolls Royce) to decide on the type of surface distortions, their geometry and their location on the endwall and vane. In addition to this, bi-weekly meetings were held between VT and UT to discuss the progress of the work and the compatibility between the results obtained for the effects of roughness on the endwall and vane.

Task 2 **Determination of Appropriate Simulation of Hole Distortion.**

Based on the interactions with UT and our industrial partners a test matrix was designed to simulate endwall deposition, film-cooling hole blockage and TBC spallation. A test matrix was also devised to test geometries like placing film-cooling holes in trenches/slots to enhance the adiabatic effectiveness levels on the surface.

Summary of Results for Specific Tasks at Virginia Tech

Task 3 **Modify previous test configuration and conduct endwall cooling performance tests – with holes, upstream and passage gutter flows**

An important aspect of this work was to simulate realistic endwall geometries and surface conditions. After discussions with our industrial partners a realistic combustor-turbine interface gap and a vane-to-vane interface gap was designed and incorporated into the existing endwall with film-cooling holes. A detailed explanation of the geometries is given in this section of the report. Coolant was fed through separate plenums to film-cooling holes and the interface gaps. The purpose of this plenum is two fold: it is desired that the gutter flow be controlled independently of film-cooling and combustor/turbine interface leakage; and the gutter seal strip was modeled to ensure proper leakage flow distribution. Also, initial one-dimensional flow calculations using the inviscid pressure distribution on the endwall indicated that the passage gutter will be ingesting at the leading edge portion of the gutter. Given the modification, we also decided to make the testing more flexible by providing the capability of different platform heights on either side of the mid-passage gap (one suggestion given by industry).

Task 4 **Simulate a rough endwall and conduct cooling performance tests**

Based on our interaction with UT, surface roughness was simulated by installing 36 grit sandpaper on the existing foam endwall and comparisons were made with tests conducted on a smooth endwall. Results indicated that at higher flow rates, the film-cooling effectiveness is lowered due to the presence of roughness. This is most likely because at the higher coolant flow rates, the jets were separated from the endwall.

Task 5 **Simulate blocked film-cooling holes on a rough endwall and conduct cooling performance tests**

Tests were carried out to simulate a distorted endwall condition with: surface depositions at the leading edge and along the pressure side, film-cooling hole blockage at the leading edge, and TBC spallation. A total of 130 tests were carried out to study the effect of endwall distortion on film-cooling. Tests were carried out for three different deposition heights and three different flow rates through the upstream slot and film-cooling holes by keeping the mass flowrate through the mid-passage constant. Results indicated that these distortions dramatically decrease the film-cooling effectiveness, with hole blockage causing the most severe effect on cooling effectiveness. Results also indicated that depositions near the trailing edge of the endwall cause a greater degradation of film-cooling than deposits at the leading edge.

Task 6 **Measure cooling performance with a rough endwall and cooling holes placed in the upstream and passage gutter**

Under this task, tests were carried out to study the effect of thermal expansion and contraction of the combustor-turbine gap (upstream gap). Tests were carried out to quantify the effects of thermal expansion and contraction of the combustor-to-turbine gap. This task was completed by studying the effect of upstream slot width on the endwall cooling effectiveness. For this study comparisons were done between the nominal slot width, slot width expanded by 50%, and slot width contracted by 50%. Results indicated that with an increase in mass flux ratio between the combustor and turbine there was increased coolant coverage while increasing momentum flux ratio for the gap leakage dictated the coverage area for the cooling. With the mass flow held constant, decreasing the combustor-to-turbine gap width resulted in much improved coolant coverage while increasing the gap width resulted in reduced coolant coverage. These tests were carried out to understand the effect of upstream slot on endwall cooling. Given these baseline results tests are now being carried out for cooling holes placed in the upstream slot.

Tests were also carried out by placing film-cooling holes in a trench and in between bumps at the leading edge. These tests were carried out for a smooth and rough endwall surface. Film-cooling holes in a trench on a smooth surface performed the best and resulted in enhancing the effectiveness levels whereas trench on a rough surface degraded the effectiveness levels. Trench depths were also varied and it was found that a trench of depth 0.8D performed the best and it resulted in improved effectiveness levels with an increase in coolant blowing ratio.

Task 7 **Measure cooling performance with a rough endwall and partially blocked cooling holes placed on the endwall**

Previous results indicated that partially blocking film-cooling holes on the endwall resulted in severely degrading the cooling effectiveness levels. Based on those results it is speculated that partially blocking film-cooling holes placed in transverse

slots will lower the effectiveness levels and hence these tests will not be repeated for the transverse slot geometry.

Summary of Results for Specific Tasks at the University of Texas

Task 8 **Roughness effects on film cooling over full vane (UTexas)**

Film cooling experiments were carried out to determine the effects of surface roughness on film cooling performance on both the pressure and suction sides of the vane. Various levels of sandpaper were attached to the vane to simulate rough surfaces. Roughness caused as much as a 30% drop in film cooling effectiveness on both the pressure and suction sides of the vane at blowing ratios for which maximum performance was obtained.

Task 9 **Film cooling performance with distorted coolant holes (UTexas)**

The effects of distorted and obstructed film cooling holes on film cooling performance were examined. Obstruction size and shape were varied, as well as the location of the obstruction relative to the coolant hole. Obstructions upstream of the hole and inside the coolant hole were found to cause drastic reductions in film cooling effectiveness for both the first and second rows of suction side film cooling holes. In some cases, obstructions placed downstream of the coolant holes actually caused an increase in film cooling effectiveness.

Task 10 **Effect of a transverse slot on film cooling performance (UTexas)**

Nine different configurations for shallow, transverse trenches were tested to determine whether these trenches would improve film effectiveness. Three of the nine configurations were found to cause significant improvements in film effectiveness, particularly at high blowing ratios. The common characteristic of the high performance trenches was location of the downstream edge of the trench at the immediate edge of the coolant holes. The optimum narrow trench configuration was found to have performance similar to shaped holes.

Task 11 **Effect of a transverse slot on film cooling with distorted holes (UTexas)**

The optimum transverse trench was tested with obstructions upstream, downstream, and both upstream and downstream of the second row of holes on the suction side of the vane. These tests were conducted with smooth and rough surfaces and with low and high mainstream turbulence levels. The tests showed that although obstructions still degraded the film effectiveness, the level of degradation was much less with the trench installed. Furthermore, the worst performance with obstructions around a trench was still superior to the film cooling performance of clean holes on a smooth surface without a trench.

Industrial Contact

There was a continuous interaction between Virginia Tech and gas turbine manufacturers like Pratt & Whitney, Siemens and Rolls Royce. Dr. Karen Thole visited Pratt & Whitney and Siemens a number of times during the course of this project. Pratt & Whitney, Rolls Royce and Siemens also visited Virginia Tech. In addition to this Scott Walsh, Joe Scrittore, and Nick Cardwell received UTSR fellowships and Seth Lawson, Steve Lynch, and, Jason Ostanek did industrial internships at Pratt & Whitney.

Dr. David Bogard conducted multiple reviews of the study with representatives of General Electric Global Research, particularly the transverse trench results. Additionally, a UT student (Ruwan Somawardhana) worked at Precision Combustion, Inc on a UTSR Fellowship.

Project Description

Given the huge number of sustained operational hours required for industrial turbines, two important issues are part life and overall engine performance. Engine performance is highly dependent on the turbine and, in particular, airfoil life. Over time, airfoil roughness and film-cooling hole blockage on the airfoil and endwall, which are due to combinations of particle deposition and repeated TBC applications, can lead to reduced engine performance. While there have been numerous film-cooling and roughness studies in laboratory environments, there has been a lack of studies in which realistic coolant hole distortions have been simulated. Moreover, there have been no reported studies on a film-cooled endwall surface with roughness. These roughness and blockage effects are very important to understand, particularly when trying to assess film cooling performance for an extensive component life.

In the proposed research program, we are investigating the potential of using slots overlying the coolant holes to improve film cooling performance, or at least to alleviate the degradation of film cooling performance when the surface becomes contaminated with depositions of foreign material. For the realistic surface conditions that we are proposing to study here, the slots may have the additional benefit of alleviating the effects of hole contamination. Furthermore, for the endwall, inherent interface gaps in the endwall might be modified to operate as coolant-fed slots in the wall. These possibilities will be investigated in the proposed research program.

Experimental Facilities and Methods

Two existing large-scale, linear vane cascades were used for this research and have been described in detail in previous reports. Studies on the vane endwall are being conducted at Virginia Tech (VT), and studies on the vane itself are being conducted at the University of Texas (UT). Both facilities incorporate linear cascades with the same large scale (9x) vane geometry, and have the capability of generating high mainstream turbulence of varying levels and length scales. The spatial detail obtained with these large scale facilities is crucial for showing the physical characteristics of coolant jet interactions and dispersion, and for validation of CFD predictions. Numerous studies of film cooling performance on the turbine vane and secondary flow effects on the endwall heat transfer, which have been completed in these facilities over the

past several of years, serve as benchmark baselines for evaluating the changes in performance caused by the realistic surface conditions. Particular emphasis is placed on detailed velocity field and thermal field measurements. Infrared imaging of the surface temperatures is the primary means of quantifying effects on the surface heat load and film cooling performance on the vane and endwall.

Modifications to the endwall geometry were made for VT studies to include an interface gap, in the mid-passage between the two vanes, and the provision for a rough endwall. To simulate the effects of changing upstream slot areas, provisions were made to adjust the flow area of the upstream slot. To simulate roughness, large sheets of sandpaper were cut with the contour of the vane with provisions for the film-cooling holes. The sandpaper was attached to the endwall surface with double sided tape. To simulate the deposition, blockage, and spallation the endwall sandpaper was modified accordingly.

For heat transfer experiments at UT, a stainless steel heat flux plate was attached to the center airfoil in order to provide a uniform heat flux. The plate was attached downstream of the first row of coolant holes. For the conical roughness, the plate itself was stamped with the array of cones. When using sandpaper, the sandpaper was attached to a flat plate with double sided tape. Electrical power was provided from a DC power supply through bus bars that were soldered to the plates. An IR camera was used to take images of the heat flux plate for various levels of surface roughness. The temperatures from these thermocouples as well as the mainstream temperature, velocities, etc. were collected and processed with Labview. The voltage across the heat flux plate was recorded manually. The coolant temperature was maintained at ±0.2K of the mainstream temperature.

Results and Discussion

This section of the report discusses the results that have been achieved thus far in the project. This section is organized with respect to the various tasks that were initially proposed for the project.

Joint VT UT Tasks

Task 1. Planning Meetings.

Bi-weekly meetings took place between the research groups at VT and at UT to insure roughness simulations are being done consistently. Initial meetings were held to review papers in the literature as well as discuss on how to simulate the roughness on the component surfaces. VT performed an industrial survey on endwall designs from General Electric, Pratt & Whitney, Rolls-Royce, and Siemens-Westinghouse. These surveys helped us to better simulate the realistic endwall features, namely the combustor-turbine interface gap (upstream slot), the vane-to-vane interface gap (mid-passage gap) and endwall surface roughness.

After the first phase of tests were carried out, further meetings were held to design a test matrix to simulate various localized surface distortions like deposition, hole blockage, and spallation which greatly effects the adiabatic effectiveness levels and heat transfer coefficients. For the third and final phase, meetings were held to devise methods to enhance effectiveness levels on the endwall and vane surfaces.

Task 2. Determination of Appropriate Simulation of Hole Distortion.

This particular task proved to be very difficult given the relatively small or non-existent data available for IGCC airfoil components. Hole distortions were considered in a broader sense to incorporate deposition, hole blockage, and spallation. Deposition is of particular importance to the operation of an IGCC. Coal derived hydrogen (syngas) contains a higher amount of contaminates than natural gas, particularly ash. IGCC turbines also operate at much higher mass flow rates and turbine inlet temperatures. This section of the report discusses information provided by our industrial sponsors and the test matrix we derived through those interactions.

Surface distortion is relevant to IGCC gas turbines due to the varying amounts of contaminants present in coal derived synthetic gas. It is important to understand how these contaminants leading to endwall distortion can affect film-cooling adiabatic effectiveness levels. During engine operation, an endwall of a first stage vane is subjected to extreme conditions

resulting in the formation of deposits on the surface, blockage of film-cooling holes, and spallation of the TBC leading to oxidation of the metal surface. Deposits are formed on the endwall surface when the molten contaminants in the mainstream gas quenches and adhere to the endwall surface. Based on the information provided by our industrial partners on endwall hole distortions, depositions are more prone to occur in the vicinity of relatively colder locations like the film-cooling holes. Depositions could be upstream or downstream of the holes and are most likely never expected to be smooth. Since the region around the film-cooling holes are at a relatively lower temperature, which makes them locations of high thermal stresses, the deposits tend to adhere to these areas in and around the film-cooling holes. In some cases the deposits on the surface extend into the film-cooling holes and partially block the holes, thereby hindering the spread of coolant on to the surface.

Typically the edges of the base metal are manufactured with a radius to help TBC adhere better. The TBC is applied on an endwall and is either smoothened out or is applied with some small roughness level. Over the regular operation of a gas turbine TBC peels off from the base metal spalling in irregular arc-like pieces. Spallation occurs due to the detachment of TBC from the metal surface caused by varied temperature conditions on the endwall. Spallation is seldom constant along a line, but rather a more localized issue.

Derivation of the Endwall Film-Cooling Test Matrix

The test matrix was designed to be able to quantify the results in a better fashion and hence be more useful to study turbine durability. For all of the tests given in this report the endwall surface was covered with 36 grit sandpaper, as was discussed in our previous reports.

Figures 2.1a and b show the deviation from typical endwall deposition to that actually simulated. Note that the deposition heights were also varied as shown in Table 2.1. Tests were carried out for deposit locations *downstream* and *upstream* of the cooling rows located at the leading edge stagnation region (region A) and on the pressure side (region B). In addition to this, to see the combined effects of deposition as shown in Figure 2.1c, the deposits were also placed at the upstream and downstream location of a cooling row simultaneously. This simulated condition of placing the deposit on the upstream and downstream location simultaneously will be referred to as *both* in this report. This was primarily done to understand which deposit location, including upstream, downstream, or both, has a more detrimental effect on the endwall

effectiveness. This was also done to simulate the condition of deposit formation of deposit around an entire cooling hole, even though in this case it did not completely wrap around the circumference of the hole. The upstream and downstream conditions were defined relative to the mainstream flow and not relative to the coolant flow. Tables 2.1 and 2.2 show the test matrix for the deposition studies at each location (upstream, downstream, and both) along the leading edge stagnation region and along the pressure side, respectively.

Figure 2.2 illustrates the TBC spallation study carried out at the leading edge stagnation region and also along the mid-passage gap. When applied to the base metal, TBC usually has a rough surface, particularly after thousands of hours of turbine operation. Though spallation seldom occurs along the whole length of the mid-passage it was considered that simulating spallation in such a manner would give a better understanding of its effect on endwall effectiveness. For the leading edge study, the spallation width (in the streamwise direction) was set at 2D downstream of the film-cooling holes, very similar to leading edge deposition study. For spallation along the mid-passage gap the widths were set at G and 5G where, G was the mid-passage gap width. The testing matrix for spallation study is shown in Table 2.3 and 2.4.

Figure 2.3 illustrates the blockage study carried out at the leading edge near the stagnation location. Tests were carried out by sequentially blocking each one of the five holes in the stagnation region. Table 2.5 shows a complete listing of all the tests carried out for blocked hole study.

The above tests were carried out for three different film-cooling flow rates of 0.5%, 0.75%, and 0.9% of the main core flow, and three different upstream slot flow rates of 0.75%, 0.85%, and 1.0% of the engine core flow. The nominal case was set at 0.75% upstream slot flow and 0.5% film-cooling flow. For all the tests carried out, a constant coolant leakage flow of 0.2% was set for the mid-passage gap.

Construction and Geometry of Deposits, Hole Blockages and Spalled Endwall

Deposits

Even though deposits on an actual vane endwall do not have a characteristic shape and size, it was easier to simulate endwall realistic conditions by molding deposits of a definite shape and size. This was primarily done to quantify our results based on the total deposit area. The endwall deposits (shown in Figure 2.4a) were all semi-elliptical with varying minor radii (in the

wall-normal direction) of 0.5D, 0.8D and 1.2D. The streamwise length of all deposits was 2D, while the length of the deposit corresponded to the length of the cooling row.

These deposits were constructed using a mold made of aluminum, which corresponded to the shape of the deposit. The mold was filled with a Devcon S-210/21045 clear epoxy gel and black paint was used as a mold release. The epoxy was let to dry in the mold for about 5-10 minutes before it was peeled out of the mold and left to dry until it was rigid enough to be stuck on to the endwall. The dried epoxy was sprayed with adhesive (3M Super-77) and sprinkled with sand. The roughness created by the sand on the deposit was equivalent to the roughness on the endwall surface. As mentioned previously the endwall surface was covered with a 36 grit sand paper with an equivalent sand grain roughness value of 0.5 mm. Finally, the deposit was painted black and stuck on the endwall using a 1mm thick double sided tape.

Spallation

Surface roughness on the endwall (made of polyurethane) was simulated by covering it with a 36 grit sand paper. This sandpaper had an equivalent thickness of about 2 mm, which corresponded to a thickness of 220μm when scaled down to the engine size. In most gas turbine vanes and blades the TBC thickness is on the order of about 300μm and the 36 grit sand paper sufficiently simulated this thickness for our facility. To simulate a spalled endwall the sand paper was cut to the required width as shown in Figure 2.4b.

Blockage

Blockages were manufactured similar to the deposits conforming to the required dimensions. Figure 2.4c shows the cross-sectional view of a blocked film- cooling hole. The holes were blocked in such a manner as to reduce the exit hole area by 30%. The deposit extended one hole diameter into the hole and extended two hole diameters downstream of the cooling hole exit. Tests were also carried out to see the effect of extending the deposit two hole diameters into the film-cooling hole.

Specific Tasks at Virginia Tech

Task 3. Modify previous test configuration and conduct endwall cooling performance tests – with holes, upstream and passage gutter flows

The vane geometry chosen for this project is the same as that used in the 2001-2003 UTSR contract given to UT and VT. The vanes were ordered through General Plastics, a precision manufacturing high density foam company (FR-6700). The endwall film cooling pattern used is shown in Figure 3.1, which was designed through industry input as part of a 2001-2003 UTSR grant. The mid-passage gap (shown in red) was cut into the existing test section. The endwall is made of closed cell foam (thermal conductivity of 0.03 W/m-K), which allows for adiabatic wall temperature measurements.

Through responses from our industrial partners, a realistic mid-passage gap design was established and incorporated into the test setup. The results of this correspondence may be seen in Tables 3.1 and 3.2 and is illustrated in Figure 3.2. The addition of the mid-passage gap required a plenum that could be independently controlled from both the leading edge slot and film cooling feeds. Initial flow calculations suggested that the mid-passage gap ingests at the leading edge due to the higher static pressure than in the supply plenum. This ingestion is in part a reason that it was decided to feed the mid-passage gap independently. Figure 3.3 shows the schematic of the new plenum design. As seen in Figure 3.3, there will be a small channel supplying the coolant flow through the mid-passage gap with a seal strip.

Because of a need for structural integrity and ease of machining, Lexan was used as the primary material in building the plenum. A 0.125 inch aluminum plate that spans 60% of the plenum width was used to simulate the seal strip. Another feature built into the test setup is the ability to simulate a vane passage backward facing step (cascade) or forward facing step (dam), which results from an endwall misalignment. Endwall misalignments can be caused by both thermal expansion and mechanical stresses during engine operating conditions. Surveys of our industrial partners showed a large interest in the effects of this misalignment. Seventeen thermocouples were also placed along the mid-passage gap to obtain a temperature profile along the length of the gap.

A in depth calculation of the mid-passage gap flow was carried out using the inviscid pressure distribution on the endwall. This calculation utilized a known pressure coefficient map on the endwall. By knowing the Cp distribution and the free stream and plenum total pressures,

a relation was formed between these parameters and the total mass flow rate exiting the slot. However, solving for mid-passage gap mass flow rate in this manner did not take into account the seal strip region and its effect on the flow. It was decided that the significantly decreased metering area and viscous boundary layer effects would cause a discrepancy between the calculated and experimental slot flow rate/profile.

To insure the correct flow through the mid-passage gap, the mid-passage gap plenum supplied was isolated (sealed off) from the main film cooling plenum and given its own coolant supply. This separate coolant is supplied by a compressor. Volumetric flow rate of the coolant was calculated through the use of a Meriam laminar flow element (model 50MJ10-9). To ensure a constant mass flow rate through the passage mid-passage gap a ControlAir pressure regulator was also installed into the supply line. This regulator insured a constant downstream pressure despite variations in supply pressure due to compressor cycling.

Because we believed it was important to assess the effect of component misalignment, the left edge of the mid-passage gap was connected to a traversing mechanism. The placement and extent of this movable platform can be seen in Figure 3.4. Actuation of the platform is accomplished by four linear lead screw motivators. These motivators require 20 turns to move the endwall 1 inch, giving a high level of flexibility when setting a cascade/dam vane-to-vane junction. A flexible neoprene rubber was used to seal the platform, thus assuring that the air in the main plenum does not leak out through the endwall. The traversing platform's maximum extents of movement are 2% of span up and 2% down.

The aligned mode which is shown in Figure 3.5a, represents no disparity in height between adjacent vanes and the combustor, which is a flush endwall. The offset that was considered for the misaligned endwall was 1.2% of vane height or 0.65 cm for the 9X scale geometry. The dam endwall refers to a condition where the suction surface of vane 1 (V1) is raised relative to the pressure side of vane 2 (V2) which is flush with the combustor wall. This configuration is referred to as a dam because, as the secondary flows are driven from the pressure side of one vane towards the suction side of the adjacent vane, the flow faces an upward step. Figure 3.5b shows the dam configuration has a raised step for V1 at the upstream slot location.

The cascade endwall refers to a condition where the suction surface of V1 is lowered relative to the pressure side of the V2, which is flush with the combustor wall as shown in Figure

3.5c. This configuration is referred to as a cascade because the secondary flows from the pressure to the suction side experience a waterfall, or cascade, effect. For the cascade case, the upstream slot has a recessed step for the vane 1 portion of the platform.

Film-Cooling Effectiveness due to Endwall Misalignment

Figure 3.6 shows the nominal case of 0.75% upstream slot flow and 0.5% film-cooling flow for an endwall with and without mid-passage gap. It can be seen from Figure 3.6a that there is no coolant flow from the upstream slot crossing over the mid-passage gap location. This condition becomes apparent when comparing the contours of Figure 3.6a with those of Figure 3.6b where, in the absence of the gap, the coolant from the upstream slot convects towards the suction side of the vane sweeping over a large area of the endwall. In the presence of the mid-passage gap, Figure 3.6a shows no coolant exiting the upstream slot on the pressure side of the mid-passage gap. The reason for this lack of coolant is that the coolant from the upstream slot is ingested until the end of the vane passage where it then exits the gap. This effect will be discussed further in a later section of the report. As a result of this degradation of the coolant on the pressure side of the mid-passage gap, the hot streak through the center of the passage appears to be wider with the presence of a mid-passage gap relative to the no gap case.

In an actual engine the vane-to-vane interface is seldom perfectly aligned. The misalignment may be due to the thermal stresses which arise during operation and misalignment during assembly of the vanes. Hence, tests were carried out to understand which alignment mode results in a better overall endwall film-cooling and hence aid in a better turbine design.

As was discussed previously, there is a possibility for an aligned endwall configuration, a cascade endwall configuration, and a dam endwall configuration. The misalignment value was set to 1.2% of the vane span. For these comparisons, both the film-cooling and upstream slot flows remained constant at 0.5% and 0.75% of the core flow respectively. Figures 3.7a-c corresponds to aligned, dam, and cascade endwall configurations respectively. Indicated on the vanes on these figures is the portion of the endwall that is raised (U) and lowered (D). For explanatory purposes, the section of endwall closest to the top vane picture is referred to as the suction side section and the section of the endwall closest to the bottom vane will be referred to as the pressure side section.

In comparing the aligned case to the dam case, it can be seen that in the case of the dam

the overall platform cooling is much worse than in the case of the aligned endwall. It appears that because of the front slot misalignment, the leakage coolant from the upstream slot is directed into the hot gas path rather than along the endwall. It is also interesting to look at the end of the mid-passage gap. Figure 3.7a for the aligned endwall indicates that at the mid-passage gap exit, coolant exits the slot. This coolant was the upstream slot coolant and film-coolant that was ingested into the slot and then exited at the lowest external static pressure location. In the case of the dam endwall, Figure 3.7b indicates that there is no coolant exiting the end of the mid-passage slot. It is also quite interesting to see the diminished effectiveness levels in the vicinity of the mid-passage slot at about 20% of the slot length measured from the upstream slot shown in Figure 3.7b. This warmer region was also shown for aligned endwall in Figure 3.7a, but it is not as dramatic. At this location, there is no upstream slot flow, present, which was worsened for the dam configuration, nor is there any film- cooling flow present.

When the endwall surface is set to cascade configuration, coolant from the upstream slot can flow in an unobstructed manner onto the endwall. The effectiveness contours in Figure 3.7c indicate a much improved performance for the cascade case relative to both the aligned and the dam configurations. The lowered endwall in the case of the cascade acts like a trough in which the upstream slot flow does not mix out as quickly with the mainstream hot gas. As a result, higher effectiveness values occur on the suction side portion of the endwall. For the cascade configuration, the pressure side contours are very similar to the aligned endwall configuration, because there is no blockage for the secondary flows, as compared with the dam case. At 20% slot length downstream from the upstream slot the warm region previously discussed is diminished for the cascade condition relative to both the dam and aligned cases.

Figure 3.8a compares the pitchwise averaged effectiveness along the suction side of the endwall for the three endwall configurations and Figure 3.8b compares the effectiveness distribution along the suction and pressure sides for the aligned case. Figure 3.8a clearly substantiates the previous results that the cascade configuration results in better cooling along the suction side and Figures 3.8a-b strengthens the conclusion that there is better cooling on the suction side than on the pressure side for any kind of endwall configuration. It was also found that the pitch-wise averaged effectiveness on the pressure side for the three endwall settings remained the same. The area-averaged effectiveness was higher for the cascade configuration when compared to the aligned or dam. The area-averaged effectiveness levels, which include

both the pressure and suction side portions of the endwall, were 0.49 for cascade, 0.45 for the aligned and 0.42 for the dam respectively.

As discussed previously the air temperature inside the gap was measured by the thermocouples placed inside the gap. Recall that for the study reported in this paper there was no flow exiting the mid-passage gap such that the temperatures measured were those of any flow that might ingest into the mid-passage slot. The measured non-dimensional gap temperatures for the aligned and misaligned cases are shown in Figure 3.9. The non- dimensionalization was based on the coolant temperature and hot gas freestream temperatures. Also shown in Figure 3.9 are the inviscid gap velocities that were calculated based on the local static pressure at the gap exit. Note that this inviscid analysis assumed a constant total pressure difference between the mainstream and the gap plenum. An iterative procedure was used to calculate the pressure difference which resulted in zero net mass flow from the slot (ingested flow balanced with exiting flow).

Figure 3.9 shows that for the aligned and dam cases, a large amount of coolant is ingested into the leading edge of the mid- passage gap region relative to the cascade case. In the location $0<x/L<0.2$ there is coolant ingestion from the upstream slot resulting in higher θ, with the amount of coolant being ingested decreasing with an increase in x/L. There is also increased ingestion of the mainstream flow causing a rapid rise in the gap air temperature and hence a decrease in θ. The non-dimensional temperatures in the gap decrease dramatically as hot mainstream flow is ingested near $x/L = 0.2$. For the mid- passage gap location between $0.3 < x/L < 0.5$, all of the endwall cases show a decrease in the air temperature (increase in θ) along the mid-passage gap, which results from a fresh influx of coolant from the two rows of film-cooling holes directly upstream of this region (see Figure 3.7a-c). The dam case benefits less because of the step, in conjunction with the cross passage secondary flows that forces more hot flow into the gap. Figure 3.9 also shows that the temperatures inside the gap associated with the cascade endwall setting are cooler than that for the dam endwall setting, which is because of the cooler fluid from the upstream slot. Up to $x/L = 0.5$, the inviscid velocity is indicated to be into the slot (static endwall pressure is higher than the plenum pressure), which is consistent with the fact that flow is ingesting into the slot.

Beyond $x/L = 0.5$, Figure 3.9 shows that flow exits the mid-passage gap. Between $0.5 < x/L < 0.7$, there is an increase in the temperature within the mid-passage gap, which is followed

by a decrease beyond x/L = 0.9. The slight increase at the exit results from any coolant that was channeled through the mid- passage gap from the upstream slot.

Endwall Adiabatic Effectiveness with Varying Mid-Passage Gap Flow

The last comparison completed was for variation in the mid-passage gap with leakage. These experiments were conducted with a nominal slot width, 0.75% upstream slot mass flow rate (I = 0.08), and a film-cooling mass flow rate of 0.50%. Mid-passage gap mass flow rates were set to 0.1%, 0.2%, and 0.3%.

The contours of adiabatic effectiveness for the varying gap flows are shown in Figure 3.10. These contours are very similar with no large noticeable effect of varied mid-passage gap flow. As before, the contours were laterally averaged, and this is shown in Figure 3.11. No effect is observed in the leading edge region of the slot. At x/C_a = 0.2 values of averaged effectiveness rise slightly but not significantly. It appears that the mid-passage gap flows in this range has little to no effect on the endwall surface for the entire passage.

There is an effect of the coolant flow rate on the non-dimensional temperature distribution within the gap. Figure 3.12 shows the non-dimensional gap temperature profiles for the three cases as compared to the nominal no-flow case. As compared to the nominal (no gap flow) condition, the gap temperature is equally lower for all values of coolant mass flow between x/L = 0 to x/L = 0.4. The slot transitions from ingesting to ejecting at x/L = 0.4. This is where the effect of increasing gap flow rate was observed. Increasing the mid-passage gap flow rate reduces the temperature measured within the gap for $0.4 < x/L < 1$. In this region, decreased in gap temperature (higher θ‘s) were observed for increases is mid-passage gap flow.

Task 4. Simulate a rough endwall and conduct cooling performance tests

Simulation of a rough endwall was accomplished by installing belt sandpaper on the endwall. The sandpaper consists of a thick (1/16 inch) fibrous cloth backing, which is covered by high strength abrasive material on one side. The paper used to construct our rough endwall is manufactured by the 3M Company, model #240D. 36 grit sandpaper roughness was chosen based upon the meetings held between VT and UT (note actual roughness values are discussed later in this report).

Pictures of the sand paper used to simulate a rough endwall surface are shown in Figure 4.1. Slots were cut so that film-cooling hole inserts could be placed at each location as shown in Figure 4.1a. This was done to ensure that the rough surface did not block the film-cooling holes and the interaction between the rough surface and coolant jets is uniform for the entire endwall. Figure 4.1b shows the sand paper with film-cooling inserts. Once the hole pieces are in place no seam exists to disturb the cooling jets. Double sided tape was used to affix the roughness to the endwall. There was some concern over how well it would adhere to the painted foam endwall surface so several dummy pieces were made for testing purposes. Each piece was placed in the wind tunnel during operation and monitored for one hour. Once the pieces were allowed to cool, they were placed in the wind tunnel again for another hour. In each test piece the tape showed excellent adhesion to the endwall with no visible signs of damage to the foam surface once removed.

For this simulation, the study completed by Bons et al [2001]. was referenced to model realistic surface roughness on a first stage vane platform. Bons et al. [20011] measured values of endwall rms roughness height (R_a) as 28 μm. This rms value translates to a equivalent sand grain roughness of 227 microns for a 9X wind tunnel simulation scale (as described by Bogard et al.[1998]), which is the scaling factor for the test vane. At 9X scale, this resulted in equivalent sandgrain roughness (k_s) of 1.74 mm. On the endwall, which was made with a foam base, the roughness surface was simulated with a closed-coat 36 grit surface and grade Y cloth backing. The 36 grit sandpaper corresponds to sand grain roughness of 642 microns (www.sizes.com/tools/sandpaper.htm), which is slightly above the corresponding values in the engine. A closed-coat surface has roughness elements arranged in a random array over 100% of the surface. This ensured that the rough surface does not block the hole and that the interaction between the rough surface and coolant jets is uniform for the entire endwall.

Effect of Roughness on Endwall Film-Cooling

In determining the effect of roughness on the endwall film-cooling, comparisons can also be made between the contours shown in Figures 3.6a and 3.6b. Observing the coolant exiting from the leading edge holes upstream of the stagnation location on the suction side, one can see that the coolant is dispersed more rapidly for the case with the rough endwall relative to the smooth endwall. Along the pressure side, the jets merge more evenly in the case of the rough

endwall relative to the smooth endwall where in the case of the smooth endwall there are distinct jets.

To quantify the effects of roughness, a section of the endwall near the pressure side of the vane, as shown in Figure 4.2, was further analyzed. Figures 4.2a and 4.2b show the effect of roughness on the laterally averaged effectiveness for 0.5% and 0.75% film-cooling flows, respectively. Also indicated in Figure 4.2 are the row-averaged local blowing ratios for each row of holes along the pressure side. Note that CFD results were used to quantify the local coolant flows from each cooling hole and the local static pressure was used to calculate the local freestream velocity that was used in the blowing ratio definition. For the 0.5% case, where the local blowing ratios ranged from 0.58 and 0.78, the laterally averaged effectiveness values indicate that there is essentially no effect of roughness of the film-cooling performance.

For the higher coolant flow condition in Figure 4.2b, where the local blowing ratio ranges from 0.68 to 1.28, there is a dramatic decrease in the average effectiveness along the pressure side with roughness. The decrease in the laterally averaged effectiveness due to roughness is on the order of 30% mid-way between film-cooling rows. One plausible reason that there is a larger decrease at the higher blowing ratio relative to the lower blowing ratio is because for a rough wall the boundary layer is thicker thereby allowing the jets to separate from the endwall. As the front jet separates from the wall, this effect is compounded as one progresses downstream along the pressure side. This reduction in film-cooling effectiveness may also be attributed to increased interaction with hot mainstream. The rough surface greatly increases boundary layer thickness and turbulence levels, causing enhanced mixing between the coolant and mainstream and thereby lowering area averaged values of adiabatic effectiveness.

In comparing Figures 4.2a and 4.2b, it is seen that there is a benefit in cooling when increasing the coolant flow from 0.5% to 0.75% for the smooth wall case. In contrast, when increasing the coolant flow for the rough wall case, the average adiabatic effectiveness levels actually decrease with an increase in blowing ratio. As such, Figure 4.3 compares the laterally averaged effectiveness values for the rough endwall case along the pressure side holes for three different coolant flowrates: 0.35%, 0.5% and 0.75%. The corresponding contours for these lateral averages just along the pressure side are shown in Figures 4.4a-c. As is typically expected, by increasing the film-cooling flow from 0.35% to 0.5%, one sees that there is an increased gas performance in the film-cooling effectiveness levels. In comparing the contours

shown in Figures 4.4a and 4.4b, it is clear that the first row of holes in the averaging area defined in Figure 4.2 appears nearly the same between the two cases, but that cooling appears to be much better at the second row for the higher blowing ratio case.

By increasing the coolant flow to 0.75%, the laterally averaged effectiveness significantly decreases relative to the 0.5% coolant flow case but is better than the 0.35% coolant flow case, as shown in Figure 4.3. The contours in Figure 4.4c indicate better penetration towards the pressure side of the endwall for the 0.75% coolant flow case, but that the overall levels of effectiveness downstream of the film-cooling holes are significantly lower than for the 0.5% coolant flow case. These contours indicate that as the jets penetrate closer to the pressure side surface, they are also lifted off the surface. Knost and Thole [2004] observed a similar trend for the smooth wall case in that the pressure side film-cooling jets appeared to be lifted off the surface for the 0.75% coolant flow case, but as seen from Figure 4.2b this effect is worsened with roughness.

Outside of the averaging area, at the most upstream row of film-cooling holes, the contours in Figure 4.4a-4.4c indicate little change in effectiveness levels as a function of increased coolant levels. There was only slightly better performance for the 0.5% coolant flow condition relative to the 0.35% and 0.75% coolant flows. Just upstream of the stagnation location, the contours in Figures 4.4a-4.4c indicate that for the 0.5% and 0.75% coolant flow conditions, the leading edge film-cooling jets are impacting the vane and then being washed back down onto the surface indicating some coolant at the vane-endwall junction.

Task 5. Simulate blocked film-cooling holes on a rough endwall and conduct cooling performance tests

As mentioned earlier, endwall deposits and film-cooling hole blockages result from contaminants that are present in the main gas flow path. These contaminant particles are usually in molten form when they interact with the endwall or vane surface. In the regions of high endwall static pressure or low pressure ratio the dirt in the mainstream flow tends to adhere to the surface whereas in cases of high pressure ratios the contaminants flow into the passage and exit the engine. A total of 130 cases were tested with different coolant flowrates and endwall distortions.

Another region easily affected by deposition, is the pressure side surface. Heavy particles usually get pushed towards the pressure side and because of higher endwall static pressures in this region the particles tend to deposit on the surface. One of the primary aims of

this study was to determine which endwall distortion has the most detrimental effect on endwall film-cooling effectiveness and also how endwall deposition near vane pressure side affects film-cooling.

To compare these distortions a single cooling row at the leading edge stagnation region on the endwall was considered as shown in Figures 2.1 - 2.3. The cooling row at the leading edge stagnation region of the vane was considered for this comparison study due to the fact that at the leading edge the static pressure on the endwall is higher than at the trailing edge. Because of the lower pressure ratio at this location, ash and other contaminants in the mainstream flow tend to adhere to the surface.

In this study the effect of deposition, hole blockage, and spallation was studied for varying flow rates through film-cooling holes and the combustor turbine interface gap. For all the tests carried out, a constant flow rate was maintained through the mid-passage gap.

Results of Effect on Adiabatic Effectiveness due to Deposits, Hole Blockages and TBC Spallation on Leading Edge Stagnation region

First, the effect on effectiveness due to the formation of deposits in the leading edge stagnation region will be discussed. Second, the effect of film-cooling hole blockage on effectiveness will be presented with a discussion on the behavior of blocked holes at higher blowing ratios. Finally the results of spallation study in the same region will be discussed.

Adiabatic Effectiveness with Varying Deposit Height

One of the initial requirements in this study was to determine the appropriate deposit height. Based on the study by Bons et al. [2001] it was found that the centerline average roughness R_a was 28μm for the endwall of a turbine blade. This value corresponds to an equivalent sand grain roughness k_s of 196μm based on the criteria given by Forster [1967], which stated that an appropriate ratio of sand grain roughness to centerline average roughness should be $k_s / R_a = 7$. This would correspond to 1.76mm on our scaled up test section. Another study by Bons et al [2005] indicated that sometimes the deposits by coal and ash can be as high as 1mm. These studies were our basis for selecting the initial deposit heights. The three deposit heights tested were 0.5D, 0.6D, and 1.2D, where D is the diameter of the film-cooling hole. The scaled up heights of these deposits would correspond to 2.3mm, 3.6mm, and 5.5mm respectively.

On the engine scale the deposit height will correspond to 255 μm for 0.5D, 400 μm for 0.8D, and 610 μm for 1.2D.

The nominal/baseline coolant flow rate for all our tests was set at 0.75% of the engine core flow through the combustor turbine interface gap (referred to as the upstream slot), 0.5% of film-cooling flow and a constant mass flowrate of 0.2% through the vane-to-vane interface gap (referred to as the mid-passage gap). Figures 5.1a-d show the local adiabatic effectiveness for the different deposit heights at the leading edge region on the endwall for the nominal flow rate.

For the no-deposit nominal case the coolant from the leading edge holes was swept around the endwall junction from the stagnation region to the suction side. By placing a deposit of height 0.5D downstream of the cooling row, the coolant still tended to flow towards the endwall junction sweeping around from the stagnation side to the suction side. It can be seen from Figure 5.1b that at a deposit height of 0.5D the coolant tended to impact the roughness and effectively improve the cooling at the vane-endwall juncture. With the increase in deposit height to 0.8D the coolant failed to reach the junction between the endwall and the vane due to the lift off of the coolant jets. It can also be seen that due to this there is a higher temperature region at the junction which could cause component failures in this region. Comparing Figures 5.1c and 5.1d it can be seen that any increase in deposit height beyond 0.8D brought about the same effect on the cooling effectiveness. Because increasing the deposit height from 0.8D to 1.2D brought about a very marginal change in the effectiveness downstream of the cooling row, 0.8D was chosen as the nominal deposit height.

Adiabatic Effectiveness with Varying Upstream Slot flow

This study was done to understand the effect of varying the upstream slot flow on the effectiveness downstream of the cooling row at the stagnation region. These tests were conducted with a constant deposit height of 0.8D, a flow rate of 0.5% through the film-cooling holes, and 0.2% through the mid-passage gap. The upstream slot flows were set at 0.75%, 0.85%, and 1.0% of the engine core flow respectively.

Figures 5.2a-c show the contours with different upstream slot flow rates at the leading edge stagnation region. It can be seen that even though there was an effect upstream of the cooling holes due to the increase in slot flow, the downstream (boxed) region predominantly stayed the same with essentially no change in effectiveness. The study was done to substantiate

the fact that this region is cooled primarily by film-cooling and is very insensitive to the upstream slot flow. As mentioned before, due to the higher endwall static pressure at the leading edge region, dirt from the main gas path tends to deposit at this location.

Adiabatic Effectiveness due to Film-cooling Hole Blockage

In this study, in order to understand the effects of hole blockage, the upstream slot was closed (to remove that effect) and the endwall was cooled only by film-cooling. For results presented in this section all the tests were carried out at 0.5% film-cooling flow and 0.2% mid-passage flow.

Baseline tests with and without upstream slot flow with no hole blockages were done to observe the effectiveness from the leading edge holes near the stagnation region. Figures 5.3a and 5.3b compare the contours of both with and without upstream slot flow. Figure 5.3a shows that due to the interaction between the coolant from the upstream slot, there was better cooling effectiveness closer to the vane-endwall juncture as compared with the no upstream slot case.

Figures 5.4a-b compare the effectiveness contours of the all five leading edge film-cooling holes blocked (Figure 5.4b) with that where no blockages (Figure 5.4a) were present in the holes. It can be seen that there is a dramatic decrease in effectiveness level and the coolant from the holes cease to flow onto the endwall. The main reason for this is that when a hole is blocked the designed exit angle of the hole is changed, which causes the coolant to exit at a higher angle promoting separation. In this particular test the coolant from the blocked hole tended to flow directly into the mainstream resulting in lower adiabatic effectiveness on the endwall surfaces. With a decrease in adiabatic effectiveness levels the endwall surface is more prone to erosion and oxidation of the metal surface.

Figures 5.5a-c compare the adiabatic effectiveness of the blocked holes at higher blowing ratios. When the coolant mass flow rate through the film-cooling holes was increased from 0.5% to 0.9%, there was equally poor performance on the endwall cooling. Blockage intensifies jet separation making the jet flow into the mainstream thereby reducing the overall cooling effectiveness.

Adiabatic Effectiveness due to TBC Spallation

Spallation can be caused either by erosion of the thermal barrier coating or when a

deposit detaches itself from the endwall or vane surface. Figures 5.6a-b show the contours of adiabatic effectiveness of an unspalled endwall surface and spalled leading edge surface, respectively. In the case where the endwall surface was spalled just downstream of the cooling holes the forward facing step acted as a barrier and prevented the coolant from reaching the endwall junction. In Figure 5.6a where the surface was not spalled the coolant swept around the vane-endwall interface from the stagnation location to the suction side whereas in Figure 5.6b where the surface is spalled there is a hot band at the vane-endwall interface. Again, as with the effects of deposition and hole blockage, spallation at the leading edge stagnation region was seen to be detrimental to cooling performance.

Figures 5.7a and 5.7b compare the adiabatic effectiveness levels on the endwall with a spallation of width 5G and without spallation along the mid-passage gap respectively. As reported previously it was seen that the coolant from the upstream slot flows over a larger area and provides enhanced cooling on the suction side. Even though the surface was spalled along the mid-passage gap there seems to be no effect on the overall endwall effectiveness. It was found that as the mainstream flow enters the vane cascade and flows from the pressure side of the vane to the suction side it pushes the coolant flow from the upstream slot by the same amount even with spallation. It was concluded that spallation along the mid-passage gap had no or very little effect on endwall effectiveness.

The initial aim of this task was to ascertain which surface distortion causes the maximum amount of degradation on the endwall surface. As surface deposition caused the maximum amount of reduction in adiabatic effectiveness they were further investigated in detail to understand its effects on the whole endwall surface. A detailed study of deposition was carried out along the leading edge film-cooling rows and also along the pressure side cooling rows as shown in Figure 5.8a-b. Deposits of varying heights were placed downstream (previously reported), upstream and on both sides of the cooling rows (refer Table 5.1). Both sides refer to placing deposits both downstream and upstream of the cooling hole rows. Figure 5.8c shows the placement of deposits with respect to the cooling rows. All results were compared to a baseline case shown in Figure 5.9. The baseline test was carried out without any deposits for nominal coolant flowrates of 0.75 percent through the upstream slot, 0.5 percent through the film-cooling holes, and 0.2 percent through the mid-passage gap.

Effect on Adiabatic Effectiveness due to Deposition along the Leading Edge Cooling Rows

As mentioned previously, results were presented only for the effect on adiabatic effectiveness due to variation in deposit height downstream of a cooling row near the stagnation region. Deposit of heights 0.5D, 0.8D, and 1.2D were tested at three different locations along a cooling row: downstream, upstream, and both. For the leading edge study deposits were placed near the stagnation region of the vane and also along the cooling rows between the two stagnation location of the vanes (refer Figure 5.8). For the leading edge study only the upstream slot flow was varied from 0.75 percent to 1.0 percent while maintaining 0.5 percent mass flow through the film-cooling holes and 0.2 percent through the mid-passage gap region. First, results of varying deposit heights on adiabatic effectiveness levels at upstream and both locations will be presented and compared to downstream deposition. Second, the results for a 0.5D deposit at different slot flow rates and different locations will be presented. Finally, the results of placing the deposits at the leading edge cooling holes between the stagnation regions of the two vanes will be presented.

Figures 5.10a-c compare the contours of adiabatic effectiveness at the leading edge region with deposits placed upstream of the cooling row. It can be seen that with an increase in deposit height at the upstream location, the overall effectiveness downstream of the cooling row increases. These effects can be further quantified by looking at the lateral average plots shown in Figure 5.11. Effectiveness was laterally averaged across the pitch downstream of the leading edge film-cooling row as shown in Figure 5.10 (boxed region). Figure 5.11 shows the change in laterally averaged adiabatic effectiveness between the deposit cases, relative to the baseline case. Note that the values greater than one are enhancements in effectiveness levels and less than one are reductions in effectiveness levels. It can be seen that with an increase in deposit height from 0.5D to 0.8D there is a slight increase in overall effectiveness from X/C = -0.05 to X/C = 0.05. A further increase in deposit height to 1.2D increases the effectiveness levels by about 15 percent and adiabatic effectiveness ratio becomes greater than one showing an enhancement in that region. It can be seen that for all deposit heights effectiveness levels are higher between X/C = -.05 to X/C -0.025 and then decreases beyond X/C = -0.025. There is a gradual decrease from X/C > -0.025 due to jet separation caused by higher blowing ratios. A similar phenomenon was seen for higher slot mass flow rate of 0.85 percent. Later in the report it will be shown that increases in upstream slot flow rate have little to no effect on effectiveness levels in the

concerned region. An exact explanation for the increase in effectiveness levels with increase in upstream deposit height will become clearer after flowfield measurements are taken at this location.

Figures 5.12a-c compare the contours of adiabatic effectiveness at the leading edge region with deposits placed on both sides of the cooling row. Similar to the downstream deposits, at a deposit of height 0.5D (refer Figure 5.12a) the cooling effectiveness levels were much improved. The reason for this improved cooling is attributed to the fact that the coolant impacts the raised deposit downstream as the jet is slightly separated from the wall for the baseline case. Moreover, it is speculated that a Coanda effect further contributes to the improvement, causing the coolant to move towards the endwall surface. With the increase in deposit height to 0.8D and 1.2D (refer Figure 5.12b-c), the coolant flow stagnates and is then deflected from the surface thereby reducing the cooling effectiveness relative to that of the 0.5D case.

It can be seen from Figure 5.13 that at a deposit height of 0.5D there is an overall enhancement of cooling effectiveness. The initial peak near the exit of the cooling holes is due to the obstruction and collection of the coolant flow caused by the deposit. Though there is decay in the enhancement of cooling effectiveness as the flow proceeds towards the vane-endwall junction it can be clearly seen that a deposit of height 0.5D enhances the overall cooling effectiveness. Figure 5.13 also shows that for deposits of height 0.8D and 1.2D, there is an improvement in effectiveness in the near hole region, but due to jet lift off there is a sudden decrease with reduced cooling relative to the baseline case as the coolant flows towards the vane-endwall junction.

Figures 5.14a-c show the contours of adiabatic effectiveness at downstream, upstream and on both sides of the cooling row for 0.5D deposit. It can be seen that by placing deposits on both sides of the cooling row results in a combined effect of upstream and downstream deposition. This can be further quantified by looking at the lateral average plots shown in Figure 5.15, which shows that, the both configuration has higher adiabatic effectiveness levels than the downstream configuration till the stagnation region and then decreases similar to downstream deposition.

As previously reported for downstream deposition , increases in upstream slot flow rate had no effect on adiabatic effectiveness levels downstream of the leading edge cooling row near

the stagnation region. Figures 5.16a-c compare the contours of adiabatic effectiveness with 0.5D deposit placed upstream of the cooling row for different upstream slot flow rates. It can be seen that there is little to no effect on the adiabatic effectiveness levels. Figure 5.17 shows that the laterally averaged adiabatic effectiveness levels for the three slot flowrates are very similar. Figures 5.18-5.21 show similar results for deposits placed downstream and on both sides of the cooling row.

Figures 5.22-5.27 show the contours of adiabatic effectiveness for deposit of heights 0.8D and 1.2D respectively for different upstream slot flow rates and deposit locations. The trends with increase in flow rate and change in deposit location for these deposit heights were found similar to the 0.5D deposit.

Figures 5.28a-c compare the contour of adiabatic effectiveness for deposits placed along cooling rows between the stagnation regions of the vane, as indicated by the black lines. It can be seen that by placing deposits upstream of the cooling holes there is a localized reduction in effectiveness levels midway along the length of the mid-passage gap (see circled region in Figure 5.28). This effect intensifies with the increase in deposit height and there is higher reduction in effectiveness levels at 1.2D than at 0.8D or 0.5D.

This effect was seen irrespective of the location of the deposit, that is if the deposit was placed at downstream, upstream or on both sides of the cooling row. This can be seen by comparing the contours of adiabatic effectiveness levels in Figure 5.29a-c (see circled regions) for deposits placed on the upstream and downstream locations. It was also be observed that the effectiveness levels in this region increased with increase in upstream slot flowrate.

Results of Effect on Adiabatic Effectiveness due to Endwall Deposits on Vane Pressure Side Cooling Holes

In this section, the effects of individual and multiple row depositions (along the pressure side) on endwall adiabatic effectiveness will be presented. Similar to the leading edge study, on the pressure side deposits of height 0.8D and width 2D were placed upstream and downstream of the cooling row as well as at both locations simultaneously. First, the effect on multiple row deposition on effectiveness will be presented with a discussion on the behavior of multiple deposits at higher blowing ratios. Second, the results of effect of individual row deposits on cooling effectiveness will be discussed. Finally, the effect of sequentially increasing the number

of row deposits on adiabatic effectiveness will be discussed.

Adiabatic Effectiveness on Vane Pressure Side due to Multiple Row Deposits

As mentioned in the previous section, contaminants in the main flow convects towards the pressure side and adheres on to the endwall due to higher static pressure. The basis for this study was to understand whether deposits formed in the upstream or downstream locations of the cooling rows has a more detrimental effect on pressure side cooling effectiveness. Deposits were placed on the first four cooling rows in region B as shown in Figure 2.1a. The nominal flowrate was set at 0.75% through the upstream slot, 0.5% through the film-cooling holes, and 0.2% through the mid-passage gap.

Figures 5.30a-c compare the adiabatic effectiveness for a nominal flowrate on the pressure side with no deposits, deposits downstream of the cooling rows, and deposits upstream of the cooling rows respectively. Figure 5.30d shows the adiabatic effectiveness of the unique case with deposits at the upstream and downstream of the cooling rows. It was seen that by placing deposits either on the downstream or upstream of the cooling row reduces the overall effectiveness. The cooling effectiveness degradation caused by upstream deposit was much higher than the downstream deposit. Figure 5.31 compares the laterally averaged effectiveness along the pressure side cooling rows and it is shown that there is a dramatic decrease in average effectiveness due to deposition. With deposits, the laterally averaged effectiveness mid-way between film-cooling rows is of the order of 30 - 40% lower than the nominal case without any deposits.

In comparing the laterally averaged effectiveness for different deposit locations, it is seen from Figure 5.31 that with deposits on either side of the cooling row, the cooling effectiveness deteriorates the most along pressure side. Placing the deposit either at upstream or at both locations simultaneously brings about a similar degradation in cooling effectiveness and it is about 10 percent lower than the degradation caused by placing the deposit downstream. It is concluded that deposits placed upstream of the cooling rows were more instrumental in reducing cooling effectiveness than downstream. By placing the deposits on either side of the cooling row it was found that the coolant flow was channeled towards the endwall junction along the pressure side. Though cooling along the endwall junction improved, it degraded the cooling effectiveness at other regions on the pressure side.

Effect of Blowing Ratio on Pressure Side Cooling Effectiveness with Deposits

Figures 5.32a-c compare the contours of adiabatic effectiveness for flowrates of 0.5%, 0.75%, and 0.9% through the film-cooling holes for a constant upstream slot flow of 0.75% and a mid-passage gap flowrate of 0.2%. By placing the deposit on either side of the cooling row the coolant flow it was found that coolant flow gets channeled towards the pressure side endwall junction. With the increase in coolant flowrate from 0.5% to 0.75% there seemed to be an increase in coolant along the endwall junction on the pressure side there by improving effectiveness in this region. There seemed to be little or no improvement by further increasing the flowrate to 0.9% as shown in Figure 5.32c.

For any given mainstream flow through a passage and a mass flowrate through the film-cooling holes the local blowing ratio decreases towards the exit of the passage as the mainstream flow accelerates from the leading edge to the trailing edge. This was seen by increasing the film-cooling mass flowrate to 0.75% and 0.9%. The increase in mass flowrate caused jet liftoffs from the first two film-cooling rows on the pressure side, but towards the trailing edge seemed to effectively spread the coolant. Figures 5.33a and 5.33b compare the cooling effectiveness along the pressure side for with and without deposits at a film-cooling mass flowrate of 0.9%. It was seen that with deposits placed on either side of the cooling row, the coolant flow got channeled on to the endwall junction at the trailing edge. However, for the baseline case without deposits as shown in Figure 5.33b the coolant spread in the direction of the mainstream flow.

Also, another interesting effect was observed with an increase in mass flowrate through the film-cooling holes. As shown in Figures5.32a-c (see circled region) there is a formation of hot zone mid-way along the length of the mid-passage gap with an increase in film-cooling flowrate from 0.5% to 0.9%. The reason for this could be that the coolant from the upstream slot becomes obstructed by the high mass flowrate through the leading edge cooling holes and thus it fails to reach further downstream into the passage. The flow obstruction from the leading edge cooling holes can be further substantiated by the formation of ripples downstream of the leading edge cooling holes on the suction side. Another possible reason, which could be attributed to this effect, is that higher mass flow rate causes jet liftoff from the endwall surface thereby lowering the overall effectiveness in this region due to film-cooling holes.

As the coolant jets were directed towards the pressure-surface endwall junction, it was important to quantify the change in adiabatic effectiveness along flow streamlines passing

through the cooling holes and also along the pressure-surface endwall junction. Figures 5.34a-b show the variation of adiabatic effectiveness along the flow streamlines at different film-cooling flowrates with deposits placed on both sides of the cooling rows. Variation in adiabatic effectiveness was measured along two streamlines; S1 and S2 as shown in Figure 5.9. The flow streamlines were computationally predicted at 2 percent span from the endwall surface using FLUENT 6.1.2. Figure 5.34a shows that by placing deposits on both upstream and downstream locations the adiabatic effectiveness levels decreased by about 50 percent along S1 for 0.5 percent (M_{in}=1.5) film-cooling mass flowrate. A similar effect was seen for 0.75 and 0.9 percent flowrate through the film-cooling holes though there was a higher reduction at a mass flowrate of 0.9 percent. The 0.75 and 0.9 percent coolant flowrates corresponded to a global blowing ratio of M_{in}=2.2 and 2.7 respectively. The global blowing ratio M_{in} was calculated based on the inlet mainstream velocity U_{in}

Effect on Pressure Side Cooling Effectiveness due to Single Row Deposition along Pressure Side

As mentioned earlier, the variation in local blowing ratios through the flow passage plays an important role in effective film-cooling on the endwall. It is important to ascertain the region at which the formation of deposits would deteriorate film-cooling effectiveness along the pressure side. Tests were carried out by placing deposits from row 1 to row 4 (refer table 2.5) sequentially for film-cooling flowrates of 0.5%, 0.75%, and 0.9% for constant flowrates of 0.75% through the upstream slot and 0.2% through the mid-passage gap.

Figures 5.35a-d compare the adiabatic effectiveness for deposits placed on either side of the cooling row from row 1 to row 4 respectively. Comparisons were made for nominal flowrates of 0.75% through upstream slot, 0.5% through film-cooling hole, and 0.2% through mid-passage gap. It can be seen from Figure 5.35a that by placing the deposit on row 1, there was little or no effect on film-cooling downstream of the passage. But by placing the deposits on row 2 to row 4 there was significant degradation in film-cooling downstream as shown in Figures 5.35b-d. Figure 5.30a shows that without any endwall depositions coolant from row 3 gets attached row 4 and to each subsequent coolant row as it flows into the passage cascading downstream. But by placing deposits on row 3 the coolant flow separates from the endwall and does flow into row 4 and deteriorates film-cooling effectiveness.

A number of tests were carried out to study the effects on adiabatic effectiveness levels

caused by the increase in number of deposits along the pressure side cooling holes. This was done by sequentially increasing the number of row deposits from one (1R) to four rows (4R). Figures 5.36a-d compare the contours of adiabatic effectiveness with deposits placed on a single film-cooling row (Figure 5.36a) to four rows (Figure 5.36d). It can be seen that deposit at location 1R has very little effect on the pressure side effectiveness levels, whereas deposit configuration of 2R-4R have a substantial effect on lowering the effectiveness levels downstream of the film-cooling holes. In order to better quantify these effects the ratio of adiabatic effectiveness was plotted along streamlines S1 and S2 as shown in Figure 5.37a-b. Figure 5.37a shows that along S1 with the increase in the number of row deposits the amount of degradation downstream of the cooling rows increases. The 4R deposits cause the maximum degradation with the 1R deposit causing the least. Figure 5.37b shows that along S2 with the increase in the number of row deposits from 4R to 1R the overall enhancement in effectiveness increases. Also, from Figures 5.37a-b it can be seen that at the location of the deposit, there is a sudden dip in effectiveness levels along S1 showing the degradation and jump in effectiveness levels along S2 which shows an overall enhancement caused by the deposits.

It is important to ascertain the region at which the formation of deposits would deteriorate film-cooling effectiveness along the pressure side. To study these effects tests were carried out by placing individual row deposits from row 1 to row 4 for film-cooling flowrates of 0.5 percent, 0.75 percent, and 0.9 percent for constant flowrates of 0.75 percent through the upstream slot and 0.2 percent through the mid-passage gap.

Figures 5.38a-d compare the adiabatic effectiveness for deposits placed on either side of the film-cooling row from row 1 to row 4 respectively, all at the same cooling flow rates. Comparisons were made for nominal flowrates of 0.75 percent through upstream slot, 0.5 percent through film-cooling hole, and 0.2 percent through mid-passage gap. It can be seen from Figure 5.38a that by placing the deposit on row 1, there was little to no effect on film-cooling downstream of the passage. But by placing the deposits on row 2 to row 4 there was significant degradation in effectiveness levels downstream towards the trailing edge as shown in Figures 5.38b-d.

Similar to the previous tests the variation in adiabatic effectiveness was measured along streamlines S1 and S2. Figure 5.39a shows that along S1, maximum amount of degradation occurs at the location where the deposit is placed. Comparing location 1R1-1R4 it can be seen

that 1R1 causes the least amount of local degradation of about 20 percent whereas at locations 1R2-1R4 there is a local degradation of about 40 percent. The effectiveness ratio also increases downstream (s/C > 0.65) of the individual cooling row with 1R1 causing the least degradation and 1R4 causing the highest degradation. Figure 5.39b shows that along streamline S2 there is a gradual increase in effectiveness at the location where the deposit is placed. Though the effectiveness ratio levels drop at the downstream locations, there is still an overall enhancement in cooling effectiveness along streamline S2.

Figures 5.40a-d similar to Figures 38a-d compare the contours of adiabatic effectiveness for single row deposits placed from row 1 to row 4 at a higher film-cooling flow rate of 0.9 percent for the both configuration. Similar to 0.5 percent, deposit along row 4 showed a higher degradation than row 1. Also, for the same deposit configuration Figures 5.41-42 compare multiple row deposition along the pressure side holes for higher film-cooling flow rates of 0.75 and 0.9 percent respectively.

Figures 5.43-46 compare single row depositions along pressure side holes with deposits placed downstream of the film-cooling row for a higher film-cooling flow rate of 0.9 percent. Figures 47-49 compare the adiabatic effectiveness contours for downstream deposition for 0.5, 0.75 and 0.9 percent film-cooling flowrates. Similar to the both configuration (deposits on either side of the film-cooling row) it was found that with the increase in the number of row deposits, cooling effectiveness levels degraded downstream of the cooling rows.

Figures 5.50-53 compare the adiabatic effectiveness contours for single deposit placed upstream of the film-cooling row and Figures 5.54-56 compare upstream multiple row deposition. It should be noted that though the amount of degradation varied between the downstream, the upstream and the both configurations, the trends in variation of adiabatic effectiveness levels were similar.

Task 6. Measure cooling performance with a rough endwall and cooling holes placed in the upstream and passage gutter

In this task the effect of upstream slot on endwall adiabatic effectiveness levels was studied. The upstream slot width was varied to understand the overall effects caused on endwall cooling. For this task, cooling holes weren't placed in the upstream slot or in the mid-passage gap. Instead, film-cooling holes on the endwall surface were placed in a trenches/transverse slot. This change was carried out as results obtained by UT by placing film-cooling holes in trenches

(task 10) on the suction surface of the vane were very encouraging. Also, it was seen from results under task 3 that coolant flow through the mid-passage doesn't have any effect on the endwall adiabatic effectiveness levels.

The interface gap between the combustor and the first stage of the turbine is an important region of study to understand endwall cooling effectiveness. Since the combustor and turbine are not rigidly connected, this interface can leak coolant that is nominally 0.75% of engine core flow. The gap between adjacent vane sections is another area that allows leakage of high pressure coolant, typically on the order of 0.3% of core flow. This results in a significant loss in overall efficiency. Before understanding the effects of placing cooling holes in the interface gaps/slots, a more thorough understanding of gap expansion and its effect on leakage flow is needed so that ultimately it can be utilized for endwall cooling purposes. The first part of this task involved studying the effect of slot width variation on endwall adiabatic effectiveness levels. For this the metering slot width was expanded by 50% and then contracted by 50%, which will be referred to as double width and half width respectively. As with the nominal slot, both the double width and half width slots have a 45° surface injection angle. For these studies the upstream slot was expanded and contracted while keeping the slot centerline fixed relative to the vane. The second part of this task involved studying the effect of placing holes in between slots (trenches) and bumps (similar to deposits explained in task 5) on a smooth endwall surface.

Results of Upstream Slot Studies

Figure 6.1 shows the two dimensional slot which represents the mating interface of the turbine and combustor. This slot has a surface injection angle of 45° and is located 30% of the axial chord upstream of the vane stagnation location. This leakage interface will be referred to as the upstream slot. Table 6.1 provides a summary of parameters relevant to film-cooling and upstream slot geometries.

Similar to the previous studies, the endwall surface was covered with a uniform roughness level. To simulate a random array of a uniform roughness level a wide belt industrial sandpaper was used to cover the entire endwall. The sandpaper had a closed coat 36 grit surface and a grade Y cloth backing. A closed coat surface has roughness elements arranged in a random array over 100% of its surface. This technique ensured a uniform interaction between the rough surface and coolant jets for the entire endwall.

First, the effect of varying upstream slot width will be discussed for particular mass flux and momentum flux ratios. Second, the effect of a fixed slot width for varying upstream slot mass flux ratio will be discussed. A mid-passage gap comparison with and without flow for a given upstream slot flow and width will be discussed last.

Derivation of Testing Matrix

Significant consideration was given to the creation of a testing matrix (shown in Table 6.2), which would be of particular use to the turbine designer. A slot mass flow rate of 0.85% (relative to the main gas path flow) was matched for the double and half width slots. For this matched condition to be accomplished, the coolant to main gas pressure difference had to be changed accordingly. In the engine this would relate to a change in upstream slot plenum pressure, which is a realistic condition as the designer has some control of bypass coolant pressure within certain limits. Film-cooling was kept at the nominal value of 0.5% and no mid-passage gap leakage was simulated.

For a specific engine at standard operating conditions, the coolant pressure to main gas pressure is typically constant. Therefore the slot momentum flux ratio would be very similar if the slot metering width was contracted or expanded. To simulate this phenomenon, the upstream slot momentum ratio associated with 0.75% mass flow through a nominal slot width (I = 0.08) was matched for the double and half slot width. Film-cooling was kept at the nominal value of 0.5% and no mid-passage gap leakage was simulated.

Another set of tests that were completed involved varying slot mass flow ratios for the nominal slot width. Also analyzed was the effect of upstream slot mass flow rate for the double and half width slots. The values chosen for upstream slot mass flow rate were 0.75%, 0.85%, and 1.0%. Film-cooling and mid-passage gap leakages were kept at the nominal values of 0.5% and 0%, respectively.

The last set of tests to be conducted was to vary the mid-passage gap leakage flowrate. For a nominal slot width with 0.75% mass flow and a 0.5% film-cooling mass flow, the mid-passage gap mass flow varied between 0 and 0.3% of core passage flow.

Adiabatic Effectiveness with Varying Upstream Slot Width

The primary question raised for this work was how sensitive is endwall effectiveness to variation in the upstream slot width for a particular leakage flow. For a given upstream slot mass and momentum flux ratios, the slot width (and therefore flow area) was expanded and contracted by 50%. Film-cooling and mid-passage gap leakages were kept at their baseline values of 0.5%, and 0%, respectively.

As was stated in the derivation of the test matrix, two types of comparisons were made for the varying upstream slot width. One was a direct mass flow ratio comparison. For this, mass flow rate was kept constant by increasing or decreasing the plenum pressure accordingly, which resulted in a matched mass flow but varying momentum flux ratios.

For a nominal flow rate of 0.85%, Figure 6.2 compares contours of adiabatic effectiveness for different slot widths. The effect of contracting the slot, as shown in Figure 6.2c, is quite dramatic. Previously the upstream slot coolant had been primarily confined to the suction side surface by the pressure of the mid-passage gap. For the smaller gap width, the leakage flow is more evenly distributed over the entire slot pitch with a substantial increase in cooling on the pressure side of the mid-passage gap relative to the larger upstream gap widths. The pressure side hot ring, which is present for the larger gap widths around the vane, is no longer apparent. More even cooling is seen on the mid-passage gap suction side as well, but the very high values of effectiveness seen with the nominal upstream slot width (Figure 6.2b) are less apparent.

The effect of expanding the slot, shown in Figure 6.2a, is just as dramatic. No cooling is observed exiting the upstream slot on the pressure side of the mid-passage gap. The hot ring observed on the vanes pressure side is still apparent and effectiveness levels on the entire pressure side and suction side have decreased substantially.

Laterally averaged values of effectiveness for the varied slot width with matched mass flow rate are shown in Figure 6.3. Both expanding and contracting the slot show substantial decreases in averaged effectiveness. While the contracted slot shows overall better coverage than nominal slot, the resulting effectiveness levels are lower. The higher plenum pressure required to supply 0.85% from the contracted slot has resulted in a substantial increase in slot momentum flux ratio, which explains the increase in coolant coverage area. Since the coolant is exiting the upstream slot at a higher momentum, it is more likely to separate from the wall and

blow off into the passage, thereby decreasing the average effectiveness values on the endwall. For the expanded slot, less plenum pressure is required to supply the required 0.85% mass flow thereby resulting in a much lower exiting coolant momentum and thus allowing some ingestion that may occur in some regions of the slot.

For the matched momentum flux ratio cases, a nominal value of I = 0.08 was used, which corresponded to a nominal width upstream slot flow rate of 0.75%. As previously, the upstream slot width was contracted and expanded by 50%. There was no flow in the mid-passage gap and film-cooling flow rate was set to the nominal value of 0.50%.

Figures 6.4 and 6.5 shows the contours of adiabatic effectiveness and laterally averaged values of adiabatic effectiveness on the endwall for upstream slot I = 0.08. The coolant coverage area is very similar for all three slot widths, illustrating that the coverage area is a much stronger function of coolant momentum flux ratios rather than coolant mass flow ratios. By contracting the slot and keeping the plenum to main gas pressure difference the same, the mass flow of coolant exiting the upstream slot was reduced (see Table 6.2). This explains the observed reduction in effectiveness on the suction side platform and the lower values of averaged effectiveness. By the same logic mass flow would be higher for the expanded slot, thus explaining the increase in averaged coolant effectiveness on the suction side platform.

There is also an effect of slot width on the trailing edge of the mid-passage gap. In this region, the gap is ejecting a mixture of the coolant and main gas which was ingested in the leading edge region. A slight increase in effectiveness levels for the nominal slot (Figure 6.4b) was observed on the suction side of the mid-passage gap trailing edge. Effectiveness levels in this area were lower for the contracted slot (Figure 6.4c) and higher for the expanded slot (Figure 6.4a). Clearly different amounts of coolant were being ingested into the mid-passage gap. The momentum flux ratio for the upstream slot coolant was the same for all cases, but coolant mass flow was higher for the expanded slot and lower for the contracted slot. Therefore the amount of coolant being ingested into the leading edge portion of the mid-passage gap must be different. The laterally averaged effectiveness levels are shown in Figure 6.5.

Endwall Adiabatic Effectiveness with a Fixed Upstream Slot Width and Varied Mass Flow

For a constant upstream slot width and a varying pressure difference between the coolant and exit static pressure, the mass flow rate of coolant exiting the slot varies. These tests were

conducted, as before, with no mid-passage gap flow and upstream slot mass flow rates were set to 0.75%, 0.85%, and 1.0%. The effect was analyzed for a nominal slot width. Contours of adiabatic effectiveness for the above mentioned testing configuration is shown in Figure 6.6.

The primary result is that all three cases look nominally the same. For each case, there is very little coolant flow from the upstream slot crossing over the mid-passage gap as shown in previous reports. As the coolant comes in contact with the gap it is ingested until the end of the vane passage where it then exits the gap. The effect of film-cooling was also nominally the same for all upstream slot flows. As slot mass flow rate was increased, the amount of coolant observed on the pressure side of the slot increased. The suction side of the gap, which is well cooled for all flow rates, shows higher adiabatic effectiveness levels when slot flow rate is increased. Although coolant mass flow rate through the slot was increased substantially, much of the endwall still had low values of adiabatic effectiveness.

To quantify the effect of increasing slot flow at these levels, the endwall surface was laterally averaged for all flow rates, as shown in Figure 6.7. Increasing the upstream slot cooling shows increased values of laterally averaged adiabatic effectiveness levels.

Results of Placing Film Cooling Holes in Trenches and Bumps

In this task the effects of placing film-cooling holes in trenches and in between bumps were studied on a smooth endwall surface. As mentioned earlier the endwall of the vane was constructed of foam because of its low thermal conductivity (0.033 W/m.K). The endwall surface was covered with a thin layer of Balsa wood to simulate a smooth surface. These studies were carried along the film-cooling holes at the leading edge as shown in Figure 6.8. The endwall leading edge consisted of a single row of axial film-cooling holes with a hole spacing corresponding to P/D = 3. The cooling row was placed four cooling hole diameters (4D) upstream from the stagnation location and an upstream slot, representing the combustor-turbine gap, placed 17D from the stagnation location. Figures 6.9a-b show the geometries of the trench and bump modifications studied at this leading edge location. Figure 6.9a illustrates the trench geometry and Figure 6.9b illustrates the bump geometry previously described in tasks 2 and 5. Based on the above two concepts, four different cooling hole configurations were tested at varying blowing ratios on a rough and smooth surface as shown in Figures 6.10a-d. Figure 6.10a illustrates the baseline case which simulated a smooth endwall without any surface

modifications. It consisted of the axial film-cooling holes placed 30° to the endwall surface. Figure 6.10b simulates the individual hole trench configuration, where the trench surrounded each individual cooling hole. Figure 6.10c is the row trench configuration, similar to the one tested by Bunker [2002] on a flat plate, where the trench runs along the entire length of the cooling row. Figure 6.10d is the bump configuration, in which two semi-elliptical bumps were placed at the upstream and downstream locations of the film-cooling hole. The geometries shown in Figures 6.10b-d will be compared with the baseline case to see if these modifications result in any enhancement.

Effect of Varying Blowing Ratio at the Leading Edge

Before studying the effect of trenches and bumps at the leading edge it was important to understand the effect of varying the blowing ratio at the leading edge for the baseline case. It can be seen from the contours in Figure 6.11 that at low blowing ratios the adiabatic effectiveness levels are higher on the suction side of the endwall than on the pressure side. This is because of the lower static pressure on the suction side, which enables more coolant to exit the cooling holes near the suction side. With an increase in blowing ratio up to M = 2.0 there is a gradual increase in effectiveness levels along the pressure and suction sides. A further increase beyond M = 2.0 results in an increase in effectiveness levels on the pressure side with subsequent decrease on the suction side when compared to the lower blowing ratio. It can also be seen that at higher blowing ratios there is a reduction in effectiveness levels just downstream of the cooling holes. At high blowing ratios, the coolant jets are associated with high momentum resulting in jet lift off from the surface. It is also seen that at these high blowing ratios the adiabatic effectiveness levels increase near the vane-endwall junction. The adiabatic effectiveness levels also increase because of the horseshoe vortex formed at the leading edge, which pulls the coolant injected into the mainstream flow back to the surface. As a result, the adiabatic effectiveness levels increase at the vane-endwall junction along both the pressure and suction sides.

Figure 6.12 compares the lateral average effectiveness ($\overline{\eta}$) at varying blowing ratios for the baseline case. Adiabatic effectiveness values were laterally averaged in the streamwise (X-direction) direction as shown in Figure 6.8. Figure 6.8 also shows the stagnation location along the pitch where Y/D = 0. Lateral averaging was calculated for two areas on either side of the

stagnation location; suction side extending from Y/D= 0 to Y/D= -25 and pressure side extending from Y/D = 0 to Y/D = 10 (refer Figure 6.11). For calculating the lateral average, the area under consideration was divided into many small divisions starting at different pitch (Y/D) locations. The adiabatic effectiveness values were then averaged along each of these divisions to give the laterally averaged adiabatic effectiveness along the pitch. Note that lateral averaging was carried our for the same vane surface length of x/S = 0.15 along the suction and pressure sides from the vane stagnation.

From Figure 6.12 it can be seen that for blowing ratios from M = 0.5 to M = 2.0 the effectiveness levels increase on the suction side until Y/D = -10. Any subsequent increase in blowing ratio caused an increase on the pressure side and a decrease on the suction side. It is interesting to note that at a blowing ratio of M = 2.0 the effectiveness levels are the highest on the suction side as well on the pressure side when compared to other blowing ratios. The formation of peaks and valleys in the lateral average plot clearly show that at every blowing ratio, there is a variation in adiabatic effectiveness levels between the film-cooling holes. The variation in effectiveness levels is because of the formation of hot spots as a result of non-uniform coolant spread on the endwall surface.

The variation in adiabatic effectiveness levels on the suction and pressure sides can also be studied by comparing their area-averaged effectiveness ($\overline{\overline{\eta}}$). Figure 6.13 compares the area averaged effectiveness for the baseline cases at different blowing ratios. An overall area averaged effectiveness was calculated for the combined (SS+PS) region by averaging the adiabatic effectiveness values extending from the suction side to the pressure side (Y/D = -25 to Y/D = 10). Note that lateral averaging was carried our for the same vane surface length of x/S = 0.15 along the suction and pressure sides from the vane stagnation. The area averaged effectiveness of the combined region increases until a blowing ratio of M = 2.0 and then steadies out with any further increase. By looking at the individual effectiveness levels, on the suction side it peaks at M = 2.0 and then decreases and plateaus, whereas on the pressure side the effectiveness levels keep increasing with an increase in blowing ratio. So, for the baseline case with a smooth endwall surface, a blowing ratio of M = 2.0 was found to have the highest effectiveness levels.

Effect of Placing Trenches and Bumps at the Leading Edge on a Smooth Endwall Surface

An individual hole trench, a row trench, and a bump configuration upstream and downstream of the cooling row were tested on a smooth endwall surface. These modifications were carried out at a constant coolant flowrate through the upstream slot. Figure 6.14a-d compares the contours of adiabatic effectiveness of the three modified film-cooling hole exit configurations with the baseline case at a blowing ratio of M = 2.0. In this section the baseline is compared with the smallest trench depth and bump height. The smallest trench depth studied corresponded to 0.4D and the smallest bump height corresponded to 0.5D. Comparing the individual hole trench (Figure 6.14b) at M = 2.0 to the baseline case (Figure 6.14a), it is seen that due to a presence of a vertical wall at the cooling hole exit, the jets are detached from the surface but reattach further downstream of the holes. Hence, the adiabatic effectiveness levels are lower at the exit of the cooling holes. The row trench in Figure 6.14c showed the maximum enhancement in effectiveness levels on the leading edge. The trench walls upstream and downstream of the holes allow the coolant to spread laterally within the trench area resulting in enhancements in adiabatic effectiveness levels. It is speculated by Bunker [2002] that the trench walls reduce the typical vortex motion of the coolant jets and thereby preventing the hot gases from getting pulled underneath the coolant jets.

Placing bumps on the smooth surface caused varied results. From Figure 6.14d it can be seen that relative to the baseline case, it lowered the effectiveness levels on the suction side, whereas it increased the effectiveness levels on the pressure side. Bumps downstream of the cooling holes deflected the coolant jets off the surface thereby lowering the adiabatic effectiveness levels on the suction side, but caused an increase in effectiveness on the pressure side.

The effects of these modifications are quantified by calculating the laterally averaged effectiveness downstream of the film-cooling holes. From Figure 6.15 it can be seen that row trench performed the best on the suction and pressure sides. The individual hole trench and the bumps showed a reduction in adiabatic effectiveness levels from Y/D = -25 to Y/D = -5 and showed an improvement in effectiveness levels from Y/D > -5. The lateral averaged effectiveness curves for the baseline and individual trench seem to coexist with little variation. Their effects at varying blowing ratios can be seen in Figure 6.16 which compares the area averaged effectiveness for the three modifications. At a blowing ratio of M = 2.0 the area

averaged adiabatic effectiveness of the trenched hole, bumps, and the baseline coexist showing that their overall effectiveness levels downstream of the cooling holes are same. Trenches show an improvement over the whole range of blowing ratios tested with the maximum enhancement at a blowing ratio of M = 2.5.

Figures 6.17-6.19 show the contours for the different configurations at the leading edge for varying blowing ratios. These contours clearly show the variation along the pressure and suction sides of the vane for the individual trench (0.4D), row trench (0.4D) and the bump configurations (0.5D). It can clearly be seen that the row trench causes the maximum enhancement in adiabatic effectiveness.

Effect of Trench Depths on Adiabatic Effectiveness Levels

Three different row trench depths corresponding to 0.4D, 0.8D, and 1.2D were tested on a smooth endwall surface. This study was conducted to investigate the trench depth sensitivity to adiabatic effectiveness levels. Figure 6.20 compares the area averaged adiabatic effectiveness of the different trench depths. At the smallest trench depth of 0.4D, the enhancements in adiabatic effectiveness levels were seen for all blowing ratios. The adiabatic effectiveness levels for 0.4D trench increased with increasing blowing ratio up to a blowing ratio of M = 2.5. Upon a further increase in blowing ratio to M = 3.0, the effectiveness levels slightly dropped as a result of higher jet momentum associated with the coolant flow.

As the trench depth was further increased to 0.8D, higher enhancements in effectiveness levels were seen for all blowing ratios. Contrary to the 0.4D trench, the adiabatic effectiveness for the 0.8D trench depth increased until a blowing ratio of M = 2.5, and then stayed nearly the same with a further increase to M = 3.0. Compared to the baseline, the enhancement in effectiveness varied from $\eta = 0.24$ at M = 1.0 to a high value of almost $\eta = 0.48$ at M = 3.0.

An increase in trench depth to 1.2D also showed enhancements compared to the baseline case but the effectiveness levels were comparatively lower than the 0.8D trench as seen in Figure6.20. Also, the effectiveness levels at 1.2D depth were similar or lower than the 0.4D depth for blowing ratios less that M = 2.5 and showed higher levels only at M = 3.0. At a higher depth and low blowing ratio, the walls of the trench prevent the coolant from exiting uniformly resulting in lower effectiveness levels. As the blowing ratio is increased, the jets exit at a higher momentum making the trench more effective in the spreading of the coolant. From Figure 6.20

it can also be seen that the adiabatic effectiveness levels for the 1.2D trench follows a different pattern when compared to the 0.4D and 0.8D trench.

Figure 6.21 compares the adiabatic effectiveness levels for three blowing ratios at M = 1.0, M = 2.0, and M = 3.0 for different trench depths. The downstream edge of the trench forms a wall at the film hole exit, which forces the coolant to spread laterally within the trench before convecting over the endwall surface. At a smaller trench depth of 0.4D, it is seen that with an increase in blowing ratio the coolant spreads downstream of the cooling holes in a more uniform manner until the blowing ratio is high enough resulting in jet lift off. At a high blowing ratio of M = 3.0, there is less lateral spreading of coolant within the trench resulting in a deterioration in effectiveness levels.

An increase in trench depth to 0.8D results in a better lateral spread of coolant within the trench as there is less interaction between the mainstream gases and the coolant than when a set of axial holes are placed on a flat endwall surface. The contours of the 0.8D trench show that there are fewer hot spots between the cooling holes when compared to the 0.4D trench at the same blowing ratios. It is speculated that with an increase in trench depth the vortical nature of the flow leaving the cooling holes at the exit is less intense preventing the hot gases from getting pulled down to the surface resulting in a better lateral spread within the trench. Lateral spreading within the trench causes the coolant to exit the trench in a more uniform manner onto the endwall surface. When the trench depth is further increased to 1.2D it is seen that at low blowing ratios there is an increase in the coolant retention within the trench. A higher depth causes a recirculation of coolant within the trench preventing it from convecting over the surface. With an increase in blowing ratio the amount of coolant spreading onto the surface increases. As this study was done only until a maximum blowing ratio of M = 3.0, it is speculated that the 1.2D trench will perform better at a blowing ratio of M = 3.0 or higher.

The uniform spread of coolant as a result of trenches can also be seen by comparing the laterally averaged effectiveness at different blowing ratios for the 0.8D trench, as shown in Figure 6.22. For the baseline cases (refer to Figure 6.12) the laterally averaged adiabatic effectiveness levels showed definite peaks and valleys indicating regions of low effectiveness between the cooling holes. With the trench it is seen from Figure 6.22 that the height between the peaks and valleys are smaller and this height becomes smaller as the blowing ratio is increased, thus indicating a more uniform spread of coolant over the endwall surface. Also, the

0.8D trench was found to be the optimum depth from the three trench depths tested, and

Task 7. Measure cooling performance with a rough endwall and partially blocked cooling holes placed in the upstream and passage gutter

From task 5 it was found that blocked cooling holes greatly reduce the adiabatic effectiveness levels on a surface and hence blocked cooling holes in the upstream slot or in the mid-passage gap wasn't studied. Instead film-cooling holes in trenches and in between bumps were placed on a rough endwall surface and its effect on endwall effectiveness levels at the leading edge was studied. First, the effect of a row trench on a rough surface will be studied and compared to a trench on a smooth surface and then the effects of an individual trench on a rough surface will be studied and compared to a smooth surface.

Effect of Placing Film Cooling Holes in Row Trench on a Rough Surface

Placing film-cooling holes in a trench on a smooth endwall surface enhanced the adiabatic effectiveness levels. Figure 7.1 compares the laterally averaged adiabatic effectiveness levels at the leading edge for the baseline case, 0.4D trench on a smooth endwall surface, and 0.4D trench on a rough endwall surface at a blowing ratio of M = 2.0. It can be clearly seen that the trench on a smooth endwall performed better than the trench on a rough endwall. 0.4D-rough has similar and slightly lower effectiveness levels than the baseline on the suction side, but the effectiveness levels are higher on the pressure side and similar to 0.4D-smooth.

Figure 7.2 compares the contours of adiabatic effectiveness for 0.4D trench on a rough surface for varying blowing ratios. The trends shown by the 0.4D-rough trench at varying blowing ratios are similar to the baseline study. This is shown in Figure 7.3 which compares the laterally averaged effectiveness levels of the 0.4D-rough trench at varying blowing ratios. Similar to the baseline case the effectiveness improves till a blowing ratio of M = 2.0 on the suction side and then decreases on the pressure side. Whereas, for blowing ratios higher than 2, the effectiveness levels are lower on the suction side and higher on the pressure side. This is because the higher blowing ratio is associated with a higher momemtum flux causing the coolant jets to easily mix with the hot mainstream flow and lowering the effectiveness levels on the surface. The trench depths weren't varied on a rough surface as the overall effectiveness levels were lower than the trench on a smooth surface and also the baseline as shown in Figure 7.4 which compares the area-averaged effectiveness results. It can be clearly seen that beyond a

blowing ratio of 2.0, there is a overall decrease in the adiabatic effectiveness levels at the leading edge.

Effect of Placing Film Cooling Holes in Individual Trench on a Rough Surface

Similar to a row trench, film-cooling holes in an individual trench on a rough endwall surface resulted in lowering the adiabatic effectiveness. Figure 7.5 compares the laterally averaged adiabatic effectiveness levels for an individual trench on a rough surface with the baseline and a trench on a smooth surface. An individual trench on the rough surface decreases the adiabatic effectiveness by as much 40% and the decreasing effect is seen on both the pressure and suction sides.

By comparing the contours at different blowing ratios as shown in Figure 7.6 it can be seen that the effectiveness levels downstream of the cooling holes are lower at higher blowing ratios. Higher blowing ratio of the coolant results in the formation of localized hot spots between the cooling holes as a result of jet lift off. The trends shown by the individual trench on a rough surface are similar to the row trench though the effectiveness levels are lower and this is shown in Figure 7.7 and Figure 7.8 which compares the laterally averaged effectiveness and the area averaged effectiveness at all blowing ratios.

Specific Tasks at University of Texas

Task 8. Roughness effects on film cooling over full vane.

Adiabatic effectiveness measurements were conducted on the pressure side of the vane using four different roughness conditions: no roughness (smooth), 180 grit sandpaper, 50 grit sandpaper, and 30 grit sandpaper. The equivalent sandgrain roughness values for the sandpaper were k_s = 150 μm, 340 μm, and 630 μm, respectively. Relative to the coolant hole diameter of 4.1 mm, these roughness levels correspond to k_s/d = 0.04, 0.08, and 0.15. The sandpaper roughness extended from the stagnation region near the showerhead to a location of x/d ~ 70 downstream of the second row of cooling holes. For clarification, the location of the first row of coolant holes is at x/d = 25 and the second row is located at x/d = 46. Experiments were conducted with and without showerhead blowing and at high and low mainstream turbulence for the approach flow of Tu_0 = 20% and 3.5%, respectively. The showerhead blowing ratio was set

at M^* = 1.6 which was found to be the optimum by Cutbirth and Bogard (2002). Pressure side blowing ratios were varied from M = 0.5 to 1.4 in 0.1 increments. The density ratio of the showerhead and pressure side coolant was maintained at DR = 1.6 for all experiments.

Results of Studies of Surface Roughness Effects on Film Effectiveness on the Pressure Side of the Vane

For reference, laterally averaged film effectiveness, $\overline{\eta}$, distributions for the baseline conditions of smooth wall, Tu_0 = 3.5%, and no showerhead blowing are shown in Figure 8.1. These results show a maximum $\overline{\eta}$ occurs at the lower blowing ratios, and that there is a rapid decay in film effectiveness downstream of each row of holes. The variation of peak film effectiveness with blowing ratio M is better represented in Figure 8.2 which shows the peak $\overline{\eta}$ at two positions behind the first row of holes, x/d = 30 and 40, and at two positions behind to second row of holes, x/d = 50 and 60. From this figure it is clear that the maximum film effectiveness immediately downstream of the holes was at M = 0.5, but farther downstream of the holes the maximum occurred at a slightly higher blowing ratio of M = 0.6 to 0.7.

Roughness effects for low mainstream turbulence with no showerhead blowing

An example of the effect of surface roughness on film effectiveness is presented in Figure 8.3 which compares the performance for surfaces with 30 grit roughness (the largest roughness level tested) with a smooth surface. Clearly the rough surface generally has little effect on the film effectiveness. Downstream of the first row of holes the surface roughness actually causes a slight increase in adiabatic effectiveness for the higher blowing ratios. This may be due an effect that counteracts the reduction in adiabatic effectiveness which occurs for the higher blowing ratios when the coolant jet separates. The roughness may provide this counteracting effect due to the turbulence generated by the roughness causing the separated coolant jet to disperse towards the wall. Downstream of the second row of holes, at x/d = 45, the roughness caused as much as a 25% decrease in film effectiveness for the lowest blowing ratio of M = 0.6, about a 10% decrease for M = 1.0, but little effect for M = 1.4.

More insight into how surface roughness if affecting film effectiveness is gained from the spatial distributions of η shown in Figures 8.4 through 8.7. The η distributions for smooth and rough (30 grit) surfaces for the optimum blowing ratio of M = 0.6 are shown in Figures 8.4 and

8.5, respectively. Following the first row of holes it evident that the roughness has caused a broader distribution of coolant which accounts for the increased laterally averaged film effectiveness levels. This broader distribution is consistent with hypothesized greater dispersion of the coolant due to turbulence generated by the surface roughness. Downstream of the second row of holes the coolant jets for the smooth surface are broader than those from the first row. This may be due to the interaction of the coolant jets from the first row with the second row, i.e. turbulence generated by the first row jets may be causing the second row jets to be more dispersed. Another explanation may be that the superposition of the coolant from the first row of holes on the coolant jet from the second row of holes may cause a broader distribution. For the rough surface it is clear that the overall η distribution is significantly reduced. Similar results were seen for the intermediate blowing ratio of M = 1.0 shown in Figures 8.6 and 8.7 for the smooth and rough surfaces, respectively. In this case the roughness induces distinctly broader distributions of coolant downstream of the first and second row of holes. However, the decrease in peak level of η downstream of the second row of holes results in a decrease in the laterally average film effectiveness.

Roughness effects for high mainstream turbulence with no showerhead blowing

The effects of surface roughness was also studied with high mainstream turbulence conditions, i.e. Tu_0 = 20% for the flow approaching the vane. For reference, the effects of mainstream turbulence alone are shown in Figure 8.8 where $\overline{\eta}$ distributions for high and low (Tu_0 = 3.5%) mainstream turbulence levels are compared for blowing ratios of M = 0.6, 1.0, and 1.4. As is evident from this figure, the effect of mainstream turbulence on the pressure side cooling holes is minimal. The effect of roughness on film effectiveness with high mainstream turbulence is shown in Figure 8.9 for the case of the 30 grit roughness compared to a smooth surface. In contrast to the low turbulence case discussed previously, for high mainstream turbulence the roughness causes a significant ($\approx$ 30%) decrease in $\overline{\eta}$ downstream of the first row of holes for the optimum blowing ratio of M = 0.6. Downstream of the second row of holes there was again 30% decrease in $\overline{\eta}$ for M = 0.6 and 1.0, while for M = 1.4 there was negligible effect.

Contour plots of the η distributions for smooth and rough surfaces with high mainstream turbulence are shown in Figures 8.10 and 8.11, respectively. These contour plots are for the optimum blowing ratio of M = 0.6. These contour plots show that the high mainstream

turbulence caused a broadening of the coolant distribution for the smooth surface (compare to the low mainstream turbulence case shown in Figure 8.4). Consequently, there is little increase in the lateral spread of the coolant with the rough surface. But the roughness does decrease the film effectiveness throughout, presumably due to turbulence generated by the roughness.

Roughness effects for high mainstream turbulence with showerhead blowing

All surface configurations were also tested with the showerhead blowing at the nominal blowing ratio of $M^* = 1.6$. Representative results from these experiments are shown in Figure 8.12 in which $\overline{\eta}$ distributions for smooth and rough surfaces (30 grit) are compared for blowing ratios of $M = 0.6$, 1.0, and 1.4. The results in Figure 8.12 are for high mainstream turbulence which would be representative of engine conditions. Downstream of the first row of holes the surface roughness had negligible effect on film effectiveness. Downstream of the second row of holes roughness caused a 10% to 20% decrease in film effectiveness.

Effects of Surface Roughness on Film Cooling on Vane Suction Side

Experiments examining the effects of roughness on film cooling performance were conducted on the second row of holes on the suction side located at s/C = 0.367. The row tested had 30^o axial holes with a spacing of $p/d = 2.8$. Roughness simulation was provided by using 36-grit sand paper which simulates the level of roughness found on typical turbine vanes that have seen extended use (Demling, 2005). All rough surface experiments had rough surfaces both upstream and downstream of the second row of coolant holes on the suction side of the vane.

An important aspect of these tests was to understand how roughness performs on the second row of the suction side of the vane. Previous studies in this lab on the suction side were focused on the first row of holes. An overview of film cooling performance with smooth and rough surfaces is presented in terms of spatially averaged adiabatic effectiveness, $\overline{\overline{\eta}}$, in Figure 8.13. For the second row of holes, surface roughness degrades the effectiveness at lower M, reducing adiabatic effectiveness by as much as 30%. However, for $M > 0.9$ the effect is reversed and roughness begins to increase the adiabatic effectiveness. This occurs because the roughness mitigates the effects of coolant jet separation which occurs at higher blowing ratios.

More detail of the effect of roughness is evident in the laterally averaged effectiveness, $\overline{\eta}$, distributions presented in Figure 8.14. For M = 0.4 and 0.6, there was an approximate 30% degradation in film cooling effectiveness for all positions extending from the hole to 25d downstream of the hole. At M = 1.2 there was no significant change. These results are similar to the effects of surface roughness on the first row of holes on the suction side previously studied in this lab (Rutledge et al., 2006).

Heat Transfer Tests with Roughness on the Vane Suction Side

The sandpaper roughness and a regular roughness array (shown in Figure 8.15) were on the heat transfer coefficient on the suction side of the vane were examined. Boundary layer measurements were conducted at two locations for the conical roughness array, and 20, 36, 50, and 80 grit sandpapers, as well as a smooth tripped baseline. The measurement locations downstream of the second suction side row of film cooling holes were s/C=0.37 and s/C=0.57. The mean velocity profiles normalized to the smooth case boundary layer thickness for the s/C=0.37 and s/C=0.57 positions are shown in Figures 8.1 and 8.2, respectively. The appropriate roughness level was attached to the surface using double sided tape from the stagnation line to a position downstream of the s/C=0.57 position prior to testing.

For the s/C=0.37 position, all rough mean velocity profiles were seen to have a greater velocity defect when compared to the smooth tripped baseline case. Generally as the sandpaper grit size increased, the velocity defect was observed to increase. The 80 grit sandpaper case can be seen to have a slightly smaller boundary layer thickness than the smooth tripped condition, while all other roughness levels have slightly larger boundary layer thicknesses. Boundary layer thicknesses, momentum thicknesses, and shape parameters were found and are reported in Table 8.3. For the s/C=0.57 position, all rough boundary layer profiles can be seen once again to have noticeably larger velocity defects as compared to the smooth baseline case. The differences in boundary layer thickness between the rough surfaces and the smooth tripped baseline are more pronounced, with all rough surfaces showing larger boundary layer thicknesses than the smooth tripped baseline. The three roughest sandpapers and the conical roughness all have similar mean velocity profiles, with the 50 grit and 36 grit mean velocity profiles being nearly identical. Also, the difference between the tripped and untripped smooth cases can be seen at the s/C=0.57 position. The trip wire thickens the boundary layer for the smooth case by nearly a factor of two.

Using the data in Table 8.3, the momentum integral equation was used to determine the average skin friction coefficient value between the two positions where boundary layer measurements were taken. For the smooth tripped baseline, a standard Clauser plotting technique was also used to estimate C_f. The momentum integral returned a much lower value than the Clauser plotting technique for the smooth baseline case. For a boundary layer that is not fully turbulent, Clauser plotting will over predict the skin friction coefficient while the momentum integral relation should still yield accurate values. The discrepancy between the two methods suggests that the smooth tripped baseline may be in a transitional flow regime over the area tested. The skin friction coefficient was chosen to be the best way to directly compare the hydrodynamic effects of the different roughness levels. The skin friction coefficients for each test surface are shown in Figure 8.3. As shown in the figure, the 50, 36 and 20 grit sandpapers all closely matched the conical roughness in terms of the skin friction coefficient, with about a 65% augmentation relative to the smooth case as determined by the Clauser plotting method. The 80 grit sandpaper produced an augmentation of about 5% relative to the same smooth tripped baseline. In terms of the skin friction coefficient, the conical roughness accurately simulates the 50, 36, or 20 grit sandpaper, within the experimental uncertainty.

Heat transfer tests were also performed for each of the rough surfaces discussed above. For the heat transfer tests, a uniform heat flux plate was attached beneath the sandpaper between the s/C=0.37 and s/C=0.57 positions. Upstream heating was provided by a separate uniform heat flux plate (located between s/C=0.21 and s/C=0.36) connected in series in order to eliminate any unheated starting length effect. Surface Temperatures were measured with an IR camera. The IR camera was calibrated to two surface thermocouples that were not buried beneath the sandpaper, so that the true surface temperatures as seen by the IR camera were measured. Figure 8.4 shows the laterally averaged heat transfer coefficient values for all test surfaces. The laterally averaged h values for the 20, 36, and 50 grit sandpapers, whose C_f values all matched the skin friction coefficient value of the conical roughness array, are shown here to be substantially higher than the laterally averaged heat transfer coefficient for the regular cone array. The 80 grit sandpaper very closely matches the conical roughness array in terms of laterally averaged heat transfer coefficient.

The data presented shows that the conical roughness causes the same enhancement of the skin friction coefficient as the 50, 36, and 20 grit sandpapers, but does not cause the same enhancement in heat transfer. The heat transfer enhancement due to the conical roughness is about 30% lower than the sandpaper roughness levels with matching hydrodynamic effects. Bons (2002) reported a similar phenomenon except with the regular array in that study causing a larger heat transfer enhancement than a randomly rough surface with matching hydrodynamic effects. One potential reason for this discrepancy is that the current study focuses on a region where the flow is in transition from laminar to turbulent. Since the differences seen in the current study occur in a transitional zone, it is unclear if the differences between regular and random roughness are attributed solely to the differences in roughness type or if the transitional zone is a factor.

Task 9. Film cooling performance with distorted coolant holes

Effect of Obstructions on first row suction side cooling holes

The effects of obstructions near coolant holes on cooling performance were studied with a focus on the first row of holes on the suction side of the vane. The baseline condition used was rough surfaces and high mainstream turbulence levels. The surface roughness was provided by 36 grit sandpaper. The sandpaper was attached to the surface starting immediately downstream of the showerhead cooling holes and extending to 25*d* downstream of the first coolant row of holes on the suction side. The mainstream turbulence for these tests was Tu_0 = 20%. The effects of obstructions upstream, downstream, and in the coolant holes were investigated using obstructions that ranged from 1/8*d* to 1/2*d* in height. Since the upstream roughness was found to be most critical, the sensitivity to upstream position of the obstruction was investigated.

Schematics of the six basic obstruction shapes that were tested are shown in Figure 9.1. These shapes were selected to simulate possible obstruction shapes ranging from smooth, rounded obstructions to obstructions with sharp corners. For the experiments with rough surfaces, initial experiments showed that the obstructions located upstream of the coolant holes caused a greater degradation of film effectiveness than those located downstream of the coolant holes. Consequently a series of tests were done with Shapes #1, #2, and #3 located upstream of the coolant holes to determine the effect of obstruction shape. Laterally averaged film

effectiveness results from these experiments are presented in Figure 9.2. The obstructions were found to cause a significant reduction in $\overline{\eta}$ with shape #2 causing as much as a 60% decrease in $\overline{\eta}$ immediately downstream of the coolant hole. The strong effect of the upstream obstruction is due the obstructions inducing a separation of the coolant jet because the obstruction block the mainstream flow that would normally force the coolant jets to turn towards the wall. The separation of the coolant jets induced by the obstructions was verified by measurements of the temperature field above the wall (discussed later in this section). Interestingly, the smallest decrease was due to shape #3, which was a rectangular element that had more sharp edges than the other two shapes. Potentially this shape generated more turbulence which somewhat offset the separation of the coolant jet induced by all the shapes.

Based on these results, all subsequent testing was done using Shape #2 since it had the most significant effect on film effectiveness, except when testing very small obstructions, 1/8*d* in height, for which small cylindrical elements were used. Results of testing obstructions of various sizes and located upstream, downstream, and in the coolant holes are presented in the following sections.

Effects of obstructions downstream of the holes

The effects of an obstruction located downstream of the coolant hole was tested for varying size obstructions with blowing ratios of M = 0.4, 0.7, and 1.2. Representative results from these experiments are presented in Figure 9.3 showing $\overline{\eta}$ distributions for M = 0.7. Immediately downstream of the hole the obstructions had little effect, but caused a faster decay in film effectiveness resulting in a 20% decrease in $\overline{\eta}$ for x/d > 15. The degradation was essentially the same for all sizes, i.e. 1/4*d*, 1/2*d*, and 1*d*. The effects of the downstream obstructions for varying blowing ratios are presented in terms of area averaged film effectiveness, $\overline{\overline{\eta}}$, in Figure 9.4. This figure shows that the largest effect of the downstream obstruction occurs at the lowest blowing ratio of M = 0.4 where as much as a 30% reduction in film effectiveness occurs. At the highest blowing ratio of M = 1.2, the effect of the downstream obstruction was negligible. We speculate that the larger effect at the lowest blowing ratio may be due to the obstruction causing an increased static pressure over the hole and thereby reducing the coolant flow from the hole. This effect would be more noticeable at the low blowing ratio.

Effects of obstructions upstream of the holes

A schematic of the upstream position and dimensions of the shape #2 and cylindrical obstructions tested is shown in Figure 9.5. Note that the shape #2 obstruction was oriented so that the rounded side was at the leading edge of the obstruction. A cylindrically shaped obstruction was used for the smallest obstruction, 1/8*d* height, because of the difficulty of constructing a shape #2 obstruction this small. A special test was done to verify that, for a 1/4*d* height, the cylindrical obstruction and shape #2 obstructions had similar effects on film effectiveness. The $\overline{\eta}$ distributions for the upstream obstructions of varying size are shown in Figure 9.6. For obstruction heights greater than 1/4*d* the obstructions caused a decrease in film effectiveness with systematically greater decrease with increasing size of the obstruction. However, the $\overline{\eta}$ levels were essentially the same for 1*d* and 1/2*d* obstructions. The $\overline{\eta}$ levels for the 1/8*d* obstruction were the same as for the baseline showing that the obstruction needed to be at least 1/4*d* to affect the film cooling performance.

The effects of the upstream obstructions for varying blowing ratios are presented in terms of area averaged film effectiveness, $\overline{\overline{\eta}}$, in Figure 9.7. This figure shows that the 1/8*d* obstruction had no effect on film cooling performance for any blowing ratio. This result is understandable when taking into account that the height of the 1/8*d* obstruction is about the same as the height of the sandgrain roughness for the 36 grit sandpaper used for the rough surface. The largest effect of the upstream obstruction occurs at the highest blowing ratio of M = 1.2 where all obstruction elements greater than or equal to 1/4*d* in height caused about 75% reduction in film effectiveness. At all blowing ratios the 1/2*d* and 1*d* obstructions caused the same degradation of performance, while the 1/4*d* obstruction had no effect on performance at the lowest blowing ratio.

A series of experiments were done to establish the sensitivity to how far upstream of the coolant hole the obstruction was placed. Obstructions were placed at distances ranging from the edge of the hole to 2*d* upstream of the hole. For these experiments 1/2*d* Shape #2 obstructions were used. Results for M = 0.7 are shown in Figure 9.8. The degradation caused by the obstructions systematically decreased as the obstruction was moved farther from the hole. At 2*d* from the hole the obstruction had essentially no effect on the film effectiveness.

Effects of obstructions in the holes

Obstructions of 1/4*d* and 1/2*d* height and shape #2 were placed with coolant holes along the downstream side of the hole near the exit as shown in Figure 9.9. The effects on film effective for blowing ratios of M = 0.4, 0.7, and 1.2 are shown in terms of the area averaged $\bar{\bar{\eta}}$ in Figure 9.10. Not surprisingly these relatively large obstructions caused significant reductions in film effectiveness with the 1/2*d* obstruction generally reducing film effectiveness by more than 50%.

Comparisons of the effects of 1/2*d* height and shape #2 obstructions upstream, downstream, and within the hole are shown in Figure 9.11 in terms of area averaged $\bar{\bar{\eta}}$. This figure shows that the upstream position and the within hole position have essentially the same degradation effect on film effectiveness for all blowing ratios. The effect at the downstream position is similar to the other two positions at M = 0.4, but at the higher blowing ratios the downstream position had negligible effect on film effectiveness.

Thermal field measurements to determine jet separation

We speculated that the large degradation of film effectiveness induced by the upstream obstructions was caused by either jet separation or turbulent dispersion of the coolant jets. To gain greater insight into the physical mechanism causing degradation of the film effectiveness, measurements were made of the temperature field immediately downstream of the coolant holes with and without the upstream obstruction. Representative results from these experiments are presented in Figure 9.12 showing the temperature profiles for a coolant jet ejecting at a blowing ratio of M = 0.7. Temperature profiles are presented in terms of the normalized temperature parameter ϕ for three conditions: smooth surface with no obstruction, rough surface (36 grit) with no obstruction, and rough surface with an upstream 1/2*d* height and shape #2 obstruction. The profiles in Figure 9.12 were measured 1*d* downstream of the coolant holes so that separation of the coolant jet would be evident by observation of the peak ϕ being clearly displaced from the wall. The ϕ profiles for the smooth and rough surfaces with no obstructions show peak ϕ values very close to the wall, suggesting no or little jet separation. The significant decrease in ϕ values near the wall for the rough wall compared to the smooth wall can be attributed to the turbulence generated by the roughness. The thermal profile for case with an upstream obstruction shows a

peak ϕ value that is displaced 0.4*d* from the wall, indicating jet separation. In fact, the overall coolant distribution for the obstruction case is displaced much farther from the wall, which may be attributed to the wake region behind the obstruction allow a much greater penetration of the coolant jet.

Effect of Obstructions on second row of suction side cooling holes

In addition to the study on the first row of suction side film cooling holes, an additional study on the effects of obstructions were performed on the second row of suction side film cooling holes. The second row of holes on the suction side is located at *s/C* = 0.367 and had 30^o axial holes with a spacing of *p/d* = 2.775. Test to test uncertainty was determined to be $\bar{\eta} = \pm 0.007$ and $\bar{\bar{\eta}} = \pm 0.0056$, based on statistical analysis of 11 repeated experiments for the baseline hole configuration with 36-grit rough walls. These data are shown in Figures 9.13 and 9.14.

The first step was to determine what effects placing the #2 obstruction backwards (reversing which edge, round or square, is facing upstream) would produce. The nomenclature used in this study to relate the size of the obstruction is 'height x width x length', where width is spanwise based and length is streamwise based. Note that if the third dimension (length) is not specified, then it is the same as the second dimension (width). Figure 9.15 shows that changing the orientation of the #2 obstruction produces a negligible effect. With the values being nominally within uncertainty the conclusion can be drawn that a shape with a combination of sharp and round edges, representative of a random particle, will perform equally, regardless of orientation. To further test geometrical effects, fully rounded (#16) and fully square edged (#3) shapes were tested, the results shown in Figure 9.16. For the Upstream and Downstream cases, both the #16 and #3 performed the same. A determination from these results is with upstream obstructions, as long as there is an obstruction to deflect the mainstream and keep it from pushing down on the jets, degradation will occur due to separation. However, there is a small difference in performance, where the #16 and #3 performed better than the #2 shape in the Upstream position.

In the Downstream position, the coolant jets flow around the obstruction, thereby spreading the coolant over the surface in a similar fashion for #16 and #3 shapes. The Upstream+Downstream position was the only one where the #16 and #3 performed differently.

It is hypothesized that the #3 did better because the #16 obstruction allows for more separation due to the curved surface of the obstruction directing the mainstream away from the vane surface with the upstream obstructions and directing the coolant flow away from the vane as well from the downstream obstructions when there is no mainstream to keep the coolant at the surface level and thereby force it around the obstruction. The #3 square surface upstream would tend to block the mainstream but also cause more turbulence due to the sharp edges, which would disperse the coolant jets, thereby bringing some of the coolant back to the surface, and the downstream obstructions would force the coolant to spread around the obstruction more than over it, acting like a wall, also aiding in the spreading of the coolant. This overall larger spreading and uniform coverage by shape #3 over #16 can be observed from the contour plots of adiabatic effectiveness shown in Figure 9.17.

Effect of Overall Obstruction Size

Overall obstruction size was found to play a significant role in effects on adiabatic effectiveness. From Figure 9.18, it is clear that as the obstruction gets closer to the size of the sand grain size of the overall surface roughness, the degradation caused by an upstream obstruction becomes less. It is presumed this trend will continue, where a 1/8*d* x 1/8*d* obstruction will essentially perform the same as the baseline rough wall (36-grit rough surface, which has sand grains the size of 0.5mm or 1/8*d*) with no obstructions. The small 1/8*d* x 1/8*d* obstruction was tested on a less rough surface (60 grit, 0.27mm grain size or approximately 1/16*d*), shown in Figure 9.7. The 1/8*d* x 1/8*d* obstruction had little effect on the 60 grit surface, and it can be inferred that the assumption that the 1/8*d* x 1/8*d* obstruction would perform the same as the baseline 36-grit rough wall is valid. An interesting finding was that the baseline cases for the 36-grit and 60-grit rough walls performed the same. In addition, the use of 1/8*d* x 1/8*d* obstructions (the size of the 36-grit sand grains) on the 60-grit surface produced no difference. Finally, given that the baseline 60 and 36 grit surfaces had similar performance, the 1/4*d* x 1/4*d* obstruction performed similarly for the different surface roughness, again presented in Figure 9.19.

The similar effects of 60 grit and 36 grit sandpaper on film cooling performance warrants further explanation. Examining Figure 8.16, it is apparent that the boundary layer profiles for both the 60 grit and 36 grit rough surfaces are essentially the same compared to the smooth, un-

tripped case. The similarity of these profiles can be attributed to the effect on transition, i.e. both roughness levels are sufficient to force transition, and the changes due to transition dominate of the local effects of surface roughness. Our previous studies have shown the effect of upstream roughness on the approach flow has a dominating influence on film cooling performance. Consequently, the adiabatic effectiveness levels are the same for the 60 grit and 36 grit rough surfaces.

Effect of Obstruction Width and Length

Variation of width (spanwise dimension) and length (streamwise dimension) of obstructions were also tested to determine their effect. From Figure 9.20, it can be seen that width has little effect on adiabatic effectiveness with upstream obstructions present. As long as the obstruction is blocking directly in front of the core of the coolant jet, the core of the jet will not have the mainstream pushing down on it to keep it attached to the surface. Therefore, to a limited extent, as long as there is an obstruction directly upstream and centered on a coolant hole, width has little effect. However, when there are only downstream obstructions, the wider 1*d* case performs better than the 1/2*d* case with increasing M. Figure 9.21 shows that most of this improvement is in the near hole region, which can be attributed to better lateral spreading as the coolant has to spread out more to flow around the wider obstruction. This is confirmed in Figure 9.22 by the bulb shape of the coolant flow just downstream of the hole, indicating the coolant flowing around the obstruction. This spreading also keeps the coolant attached to the surface longer as observed with the higher effectiveness levels down stream up to $x/d = 18$.

Changes in length had slightly more of an effect than width and it tends to increase adiabatic effectiveness for all cases as the length goes up, with the most predominant differences with upstream obstructions at low-mid blowing ratios, shown in Figure 9.23. To try and understand the effects of length, we will examine the upstream conditions closer. For longer obstructions, Figure 9.24 shows that the coolant is both more spread out laterally, indicated by the better uniformity in effectiveness values between jets just downstream of the film holes, and the core of the jet is kept closer to the surface for longer, indicated by the longer distinct jets on the contour plots.

Effect of Location

Spanwise

The fact that naturally occurring obstructions are a random event, the odds of an obstruction depositing exactly on the centerline of a cooling hole are small. To determine whether a slight offset would have similar effects, upstream obstructions were offset by increments of 1/4*d* in the spanwise direction. As expected, moving the obstruction 1/4*d* off center decreased the degradation, as shown in Figure 9.25, which can be explained by recognizing that in this case, the mainstream is only partially deflected from pushing the coolant jets down. Furthermore, an interesting finding was that once the obstruction was offset by 1/2*d* and beyond, the performance was actually better than the baseline. This can be attributed to the flow acceleration around the obstruction helping to keep the coolant down on the surface. The importance of this finding is that unless an obstruction is directly blocking the mainstream, upstream of the center of a cooling hole, it will not degrade film cooling. Therefore, an obstruction would have to fall in a small region in order to have a significant negative effect.

Number of holes Blocked

All tests conducted in this study were done with three consecutive holes blocked. In order to see if there was any kind of interaction between the obstructed jets to get the given results, a test was run with only one obstructed hole. The data from the test with only one hole blocked was analyzed and compared against that same hole in the test with the three blocked holes, presented in Figure 9.26. Except for at high M, all data was within uncertainty, leading to the conclusion that there was no jet interaction.

Task 10. Effect of a transverse trench on film cooling performance

A shallow transverse slot was proposed as a configuration that potentially could mitigate the deleterious effects of obstructions around coolant holes, and as a means for protecting the edges of the holes from being blocked by obstructions. Use of a transverse had been proposed by Bunker (2002) as a means of improving film cooling performance by inducing a lateral spreading of the coolant. The concept of using a trench was also investigated earlier by Wang et al. (2000) who measured velocity distributions for various trench configurations.

For our study we modified the test vane to insert a shallow trench at the second row of holes on the suction side. The location of this row of holes is indicated on the schematic shown in Figure 10.1. The second row of holes is located at a position on the vane where the surface curvature was small and the pressure gradient was essentially zero. For these tests the row of holes was modified to have an injection of 30º and a spacing of p/d = 2.78, as shown in Figure 10.2. This hole injection angle and spacing between holes are more typical of the most film cooling configurations.

A shallow transverse trench was directly milled into the wall of the test model as shown in Figure 10.3. The trench depth was S/d = 0.5. As shown in Figure 10.3, the origin of the x coordinate for the trench configuration was set at trailing edge of the trench. The position is coincident with the origin at the downstream edge of the holes for baseline hole configuration with no trench. Nine trench configurations, designated as number 2-10, were created by using rectangular and triangular inserts as shown in Figure 10.4. Configuration 1 was the baseline axial hole case, i.e. with no trench.

Evaluation of Various Trench Configurations

Initially, the nine combinations of trench geometries were tested at one blowing ratio and one mainstream turbulence level (M = 1.0, Tu = 1.0%) in order to compare the configurations and decide which configurations warranted in depth testing. Full details of these tests are provided in the M.S. thesis by Scot Waye (2005). The blowing ratio of M = 1.0 because separation occurs for the baseline case at this blowing ratio, and it was hypothesized that the trench would mitigate this separation. The density ratio for this test was DR = 1.3. Results from these tests are shown in terms of laterally averaged adiabatic effectiveness, $\overline{\eta}$, in Figure 10.5. It is immediately obvious that configurations 2, 3, and 4 yields much higher $\overline{\eta}$ values than all the rest. The other configurations seem to be on par with the baseline case, providing little improvement to the adiabatic effectiveness levels. Configurations 2, 3, and 4 have one characteristic in common, each has the rectangular insert situated downstream of the hole. Also, only these configurations had the rectangular insert situated downstream of the hole. Consequently it is evident that edge of trench position right at the downstream edge of the coolant hole is critical for improved performance. Configurations 2, 3, and 4 had values for $\overline{\eta}$ that were 100% higher near the hole and 30% higher downstream for M = 1.0. Another

conclusion that can be made is that the downstream insert had much more of an effect on the total cooling of the surface than did the upstream insert. Configuration 2 gave the highest $\overline{\eta}$ values for all *x/d* locations compared to all the other configurations. This configuration was even 10% better than the other configurations with the rectangular insert downstream.

Spatial distributions of η are presented in Figures 10.6 (a)–(j) for baseline configuration and the nine trench configurations. For the baseline configuration, contours in Figure 10.6 (a) suggest jet separation and reattachment based on the higher peak effectiveness appearing downstream near x/d = 4 where the adiabatic effectiveness is lower immediately after the hole. The spatial distributions of η for configuration 2, shown in Figure 10.6 (b), shows that the trench greatly increased the lateral spread of the coolant resulting in a merging of the jets, although individual jet streaks were still evident. Both configurations 3 and 4 induced similar lateral spreading of the coolant as shown in Figures 10.6 (c) and (d).

Configurations 5, 6, and 7 each had a triangular insert in the downstream section of the trench, and each showed similar η patterns immediately downstream of the trench as shown in Figures 10.6 (e), (f), and (g). The most noticeable difference between these configurations and the baseline configuration was continuous high η levels immediately downstream of the holes which suggest that the coolant jets have not separated as they did for the baseline case. However, there was essentially no increased lateral spreading, and consequently there was no significant improvement in adiabatic effectiveness.

Configurations 8, 9, and 10 did not have an insert in the downstream section of the slot, so these essentially these were “wide” slots with varying upstream slot geometries. The spatial η distributions for these configurations, shown in Figures 10.6 (h), (i), and (j), show that these wide slot configuration did not induce a lateral spreading of the coolant, and this resulted in the wide slot not being effective for increasing adiabatic effectiveness.

Narrow Trench Configuration

Configuration 2 can also be defined as a narrow trench. The coolant, when ejected, was obstructed by the downstream lip. This helped fill the trench with coolant, before it was ejected out of the trench onto the vane surface. The highest levels of adiabatic effectiveness measured in this current study were those found for configuration 2, or the narrow trench configuration. The

dimensions of the trench were *s/d* = 0.5 and *w/d* = 2.0, or the length of the axial hole opening (due to the 30° injection angle, the opening was 2d long and 1d wide). This configuration had 10% higher $\overline{\eta}$ than the other configurations with rectangular inserts in the downstream part of the trench, and 30% to 100% higher than the other configurations including the baseline. These results were only for *M* = 1.0 and low mainstream turbulence, so further testing was carried out to test other blowing ratios as well as high mainstream turbulence. High and low mainstream turbulence levels were examined. Blowing ratios from *M* = 0.3 to 1.4 were tested for high mainstream turbulence, and *M* = 0.3 to 1.95 for low turbulence. All data was taken at *DR* = 1.3 plus a few points were additionally taken at *DR* =1.5.

Distributions of $\overline{\eta}$ for varying blowing ratios are presented in Figures 10.7 and 10.8 for high and low mainstream turbulence levels, respectively. Immediately apparent is that $\overline{\eta}$ monotonically increased with increasing M, even to blowing ratios of *M* = 1.95. The variation with blowing ratio is more clearly seen in Figure 10.9 where the spatially averaged adiabatic effectiveness, $\overline{\overline{\eta}}$, is presented as a function of *M*. This figure shows a strong increase in $\overline{\overline{\eta}}$ from *M* = 0.3 to 1.0, but essentially a constant level of $\overline{\overline{\eta}}$ for *M* > 1.0.

Also quite evident from Figure 10.9 is that the mainstream turbulence level had no noticeable effect on adiabatic effectiveness when using the narrow trench. Note that the high turbulence of *Tu* = 3.9% originated from a turbulence level in the mainstream approaching the vane of *Tu* = 20%, and the low turbulence of *Tu* = 1.0% originated from an approach mainstream turbulence level of *Tu* = 4%.

The spatial contour plots of η, presented in Figure 10.10 (a) and (b) for *M* = 0.4 and 1.95, show that the narrow trench significantly increases coverage at all blowing ratios. For *M* = 1.0 (Figure 10.6 (b)) and beyond, the spatial η distribution were essentially the same. All the previously presented experimental results were obtained using a coolant density ratio of *DR* = 1.3. This was done for practical reasons since it is much easier to maintain frost free conditions in the test section at this lower density ratio. To establish that this lower density ratio provided similar results to what would be obtained at higher density ratio, experiments were conducted with the narrow trench configuration using coolant density ratio of *DR* = 1.5. Comparisons of the results for *DR* = 1.3 and *DR* = 1.5 are shown in Figure 10.11. These results show that there was almost no effect of the density ratio on the $\overline{\eta}$ distributions.

Direct comparisons of the narrow trench and wide trench (Configuration 10) and baseline configuration are shown in Figure 10.12 in terms of $\overline{\overline{\eta}}$ vs M. This figure shows that the narrow trench produced greater average adiabatic effectiveness for all blowing ratios, ranging from a fairly low blowing ratio to very high blowing ratios. The most spectacular increase in adiabatic effectiveness occurred at high blowing ratios, i.e. $M > 1.0$, for which the adiabatic effectiveness for the baseline configuration essentially fell to zero, while the trench configuration still has large levels of adiabatic effectiveness. Since the low levels of adiabatic effectiveness for the baseline configuration at high blowing ratios is due to jet separation, the improvement induced by the trench clearly shows that the trench reduces jet separation. The wide trench configuration performed at much lower level than the narrow trench for all blowing ratios. But at high blowing ratios the wide trench was clearly superior to the baseline configuration, showing some effect on reducing jet separation.

A more detailed comparison between the narrow trench and the baseline configurations is presented in Figure 10.13 where the $\overline{\eta}$ distributions are presented for the $Tu = 3.9\%$ case. This figure shows that the greatest distinction between the two configurations is immediately downstream of the coolant hole exit, i.e. $x/d \geq 0$, where the narrow trench has greatly increased $\overline{\eta}$, presumably due to the greater lateral distribution of coolant.

Further insight into the influence of the trench on the film cooling flow was obtained by measurements of the thermal profiles above the surface. Thermal profiles at a location $2d$ downstream of the trailing edge of the hole are presented in Figure 10.14 for baseline "axial holes" configuration and the narrow trench configuration. The temperature measurements are presented in this figure in terms of the normalized parameter θ defined as follows:

$$\theta = \frac{T - T_\infty}{T_c - T_\infty} \tag{10.1}$$

These thermal profiles showed that the coolant jet was separating for the axial holes at $M = 1.0$, indicated by the peak θ region located off the wall, while the narrow trench thermal profile showed that the coolant was laterally spread and had not separated from the surface.

The narrow trench configuration performed very well compared to the baseline axial holes or the compound hole cases. In fact, it has been suggested that the holes embedded in a transverse trench may be on par with shaped holes (Bunker, 2005). Shaped holes have the

benefit of a diffused opening, thus diffusing the coolant along the surface. Adiabatic effectiveness levels for shaped holes are usually better than axial holes, although cost much more to manufacture.

Previous studies have produced data for shaped holes with similar parameters (Saumweber, 2003). Various shaped holes were tested, 14° laterally expanded holes, and full expansion holes (15° forward and 14° laterally expanded). The pitch of the shaped holes was p/d = 4, compared to p/d = 2.8 for the narrow trench configuration. It should also be noted that the shaped holes were tested on a flat plate. Therefore, the results from the comparison, although given quantitatively, should be viewed partially as qualitative. The two shaped holes are compared to the narrow trench configuration in Figure 10.15 with the round axial holes plotted as a reference. The performance of the axial holes embedded within a narrow transverse trench is clearly comparable to the shaped holes.

Performance of narrow trench configuration with a rough surface

The ideal trench configuration, the narrow trench, was tested with a rough surface to determine the performance of the trench under these conditions. Comparing the rough surface trench case to the smooth surface trench case, shown in Figure 10.16, showed that the trench makes the adiabatic effectiveness insensitive to roughness. In fact, at low M, there was no change in effectiveness with the rough surface. Moreover, at M = 1.2, there was actually a small increase of about 20% for the rough surface case. In this case the added turbulence from the roughness helps bring separated coolant jets back towards the surface.

Task 11 Effect of a transverse trench on film cooling with distorted holes

The goal of this task was to determine whether a shallow transverse trench would mitigate the degradation in film cooling performance due to obstructions around the holes. Experiments were conducted with the optimum narrow trench described in Task 10. The effects of the trench were tested with same Shape #2 obstruction described in Task 9, with a smooth and rough surface, and with low and high mainstream turbulence. All results presented in this section are for the high mainstream turbulence condition.

Effects of Obstructions on a Rough Wall with a Trench

Using a baseline of a rough surface with a narrow trench, the effects of the obstructions on film cooling performance were determined for obstructions positioned upstream alone, downstream alone, and upstream and downstream of the coolant holes. These results are presented in terms of $\overline{\overline{\eta}}$ vs M in Figure 11.1. From this plot it can be seen that at low M, the degradation is about 20% for all cases with obstructions and as M goes up, the degradation goes down. At high M, only the upstream case has a significant degradation relative to the rough surface, trench case, again around 20%.

In the worse case scenario, where the surface would exhibit both roughness and obstructions, the transverse trench is definitely beneficial. Figure 11.2 depicts a comparison of $\overline{\overline{\eta}}$ levels configurations with roughness and obstructions, and with and without a trench. For all cases shown, the narrow trench has increased performance over the baseline, and this improvement goes up with increasing M. In only one case, the downstream obstruction with M = 0.4 case, did the trench have no effect. Maximum improvement occurred for the highest blowing reaching as much as 250% improvement.

Effects of Obstructions on a Smooth Wall with a Trench

An examination of the effects of upstream obstructions on the smooth surface with a narrow trench case can be seen in Figure 11.3. There is a uniform degradation of about 40% across all blowing ratios, near the hole, but levels of adiabatic effectiveness are similar at x/d = 25. Performance with and without downstream obstructions, shown in Figure 11.4, indicate a significant degradation for the lowest blowing ratio of M = 0.4, but not for the higher blowing ratios. For both the combined downstream and upstream obstruction cases, shown in Figure 11.5, there was significant degradation for the M = 0.4 and 0.6 cases, but no degradation for the M = 1.2 case.

To determine if a shallow trench would mitigate the effects of obstructions, smooth test surfaces with obstructions and with and without a shallow trench were tested. These results are presented in Figures 11.6, 11.7, and 11.8, for the configurations with upstream obstructions alone, downstream obstructions alone, and combined upstream and downstream obstructions,

respectively. For all cases, at the highest blowing ratio of M = 1.2, the trench significantly improved the adiabatic effectiveness. At the lower blowing ratios of M = 0.4 and 0.6, the trench generally did had little effect on the performance.

Conclusions

The focus of this study was to evaluate the film cooling performance on a vane endwall and on the vane itself under realistic operating conditions-including surface roughness and cooling hole blockage, due to particle deposition and erosion. The experiments in this study were conducted using facilities incorporating simulated first vanes and endwalls and the results obtained have general applicability to gas turbines. This work is particularly relevant for IGCC operations which uses coal derived synthetic gases as the operating fuel.

This study used a large-scale turbine vane scaled 9X times to an actual gas turbine vane. The initial task was to investigate the effects of realistic endwall features like surface roughness, the vane-to-vane interface gap and the combustor-turbine interface gap on endwall adiabatic effectiveness levels. Roughness decreased the adiabatic effectiveness levels at high blowing ratios whereas it had very little effect at lower blowing ratios. A misaligned mid-passage gap indicated a severe reduction in the film-cooling effectiveness in the case where the pressure side endwall was below the endwall associated with the suction side of the adjacent vane. The combustor-turbine gap width was also varied to understand its effects of thermal expansion and contraction on endwall cooling. With the mass flow held constant, decreasing the combustor-turbine interface width caused an increase in uniformity of coolant exiting the slot, particularly across the pressure side endwall surface. Increasing the width of the interface had the opposite effect thereby reducing the coolant coverage on the endwall surface. These results also indicated that the upstream coolant coverage area was a function of momentum flux ratio, not mass flow rate.

The effect on endwall adiabatic effectiveness due to near-hole deposition, partial film-cooling hole blockage, and the spallation of a thermal barrier coating was also studied. The results indicated that deposits near the hole exit can sometimes improve the cooling effectiveness at the leading edge, but with increased deposition heights the cooling deteriorates. Partial hole blockage studies revealed that the cooling effectiveness deteriorated with the increases in the number of blocked holes. Spallation studies showed that for a spalled endwall surface downstream of the leading edge cooling row, cooling effectiveness worsened with an increase in blowing ratio. Studies were also carried out to enhance the effectiveness levels on the endwall. Film-cooling holes along the leading edge were placed in trenches along the leading edge of the vane endwall. Trenches improved the overall effectiveness levels and trenches at higher depth

performed better at high blowing ratios. Enhancements as high as 55% was achieved using a straight wall trench at a trench height of 0.8D.

Effects of increased surface roughness on film cooling performance was tested the suction and pressure sides of the vane. A roughness level of $k_s/d = 0.12$ was found to cause a significant degradation of adiabatic effectiveness on the suction side but not on the pressure side. The large effect on the suction side was found to be caused by a significant thickening of the boundary layer approaching the coolant holes. Consequently the coolant jets were not as effectively turned by the mainstream, and separated from the surface at lower blowing ratios. Of course, this decreased the maximum adiabatic effectiveness achievable. Significant increases in heat transfer due to roughness effects were verified. Both random surface roughness, simulated with sandpaper, and regular arrays of roughness elements were tested. These studies showed distinct differences between random and regular arrays of roughness in terms of the relative enhancements of skin friction and heat transfer.

Effects of depositions near holes were studied using two rows of holes on the suction side of the vane. Results from this study showed that depositions in the near vicinity of film cooling holes caused as much as 50% reduction in film cooling performance. These effects were relatively insensitive to the shape of the obstructing deposition, but were sensitive to the location of the obstruction. Large reductions in adiabatic effectiveness occurred only when the obstruction was within the coolant hole, or were upstream of the coolant hole, within one diameter of the edge of the hole and aligned with the centerline of the hole. Also, obstructions with a height as small as one half hole diameter caused significant reduction in adiabatic effectiveness.

A major finding in this study was a dramatically improved film cooling performance attained when imbedding the coolant hole exits in a shallow, transverse trench. Testing of nine shallow, transverse trench configurations on the vane showed that significantly improved performance was attained if the edge of the trench was flush with downstream exit of the hole. Furthermore, with a transverse trench installed, the vane film cooling performance was less susceptible to surface roughness and to effects of the obstructions near the coolant holes.

References

Bons, J.P., Taylor, R.P., McClain, S.T., and Rivir, R.B., 2001, "The Many Faces of Turbine Surface Roughness," 2001-GT-0163.

Bons, J. P., Corsby, J., Wammack, J. E., Bentley, B. I., and Fletcher, T. H., 2005, "High Pressure Turbine Deposition in Land Based Gas Turbines from Various Synfuels," GT2005-68479.

Bons, J. P., 2002, "St and c_f Augmentation for Real Turbine Roughness with Elevated Freestream Turbulence," ASME Paper No. GT-2002-30198.

Bogard, D. G., Schmidt, D. L., Tabbita, M., 1998, "Characterization and Laboratory Simulation of Turbine Airfoil Surface Roughness and Associated Heat Transfer," *J of Turbomachinery*, vol. 120, pp. 337-342.

Bunker, R. S., 2002, "Film-Cooling Effectiveness Due to Discrete Holes Within a Transverse Surface Slot," GT2002-30178.

Bunker, R.S., 2005, "A Review of Shaped Hole Turbine Film-Cooling Technology," *J. of Heat Transfer*, Vol. 127, pp. 441-453.

Cutbirth, J. M. and Bogard, D. G., "Thermal Field and Flow Visualization Within the Stagnation Region of a Film Cooled Turbine Vane," *ASME Journal of Turbomachinery*, Vol. 124, pp. 200-206, 2002.

Demling, T., 2005, "The Effects of Obstructions on Film Cooling Effectiveness on the Suction Side of a Gas Turbine Vane," M.S. Thesis, The University of Texas at Austin.

Forster, V. T., 1967 "Performance Loss of Modern Steam-Turbine Plant Due to Surface Roughness," *Proc. Instn. Mech. Engrs.*, 1966-67, Vol. 181, Pt. 1, pp. 391-405.

Knost, D. G., and Thole, K. A., 2004, "Adiabatic Effectiveness Measurements of Endwall Film-Cooling for a First Stage Vane," *Journal of Turbomachinery*, Vol. 127, pp. 297-305.

Rutledge, J.L., Robertson, D.R., and Bogard, D.G., 2005, "Degradation of Film Cooling Performance on a Turbine Vane Suction Side due to Surface Roughness," ASME Paper GT2005-69045.

Saumweber, C., Schulz, A., Wittig, S., 2003, "Free-Stream Turbulence Effects on film Cooling with Shaped Holes," J. of Turbomachinery, Vol. 125, pp. 65-73.

Waye, S.K., 2005, "Film Cooling Effectiveness of Suction Side Axial Holes, Compound Angle Holes, and Axial Holes Embedded within an Overlying Transverse Trench," M.S. Thesis, University of Texas at Austin.

Wang, T., Chintalapati, S., Bunker, R.S., and Lee, C.P., 2000, "Jet Mixing in a Trench," Experimental Thermal and Fluid Science, Vol. 22, pp. 1-17.

Nomenclature

C	true chord of stator vane
C_a	axial chord of stator vane
D, *d*	diameter of film-cooling hole
G	Mid-passage gap width
h	Heat transfer coefficient
I	momentum flux ratio, $I = \frac{\rho_s u_s^2}{\rho_\infty U_\infty^2} = \frac{\rho_s (\dot{m}/\rho_s A_s)^2}{\rho_\infty U_\infty^2}$
k	conical roughness element height
k_s	equivalent sand grain roughness height
L	length of mid-passage gap
$\dot{m}$	mass flowrate
M	Blowing ratio based on local freestream velocity, $\frac{\rho_j U_j}{\rho_\infty U_\infty}$
M_{in}	blowing ratio based on inlet mainstream velocity, $\frac{\rho_j U_j}{\rho_\infty U_{in}}$
M*	Blowing ratio based on approach velocity, $\frac{\rho_c U_c}{\rho_0 U_0}$
P	vane pitch; hole pitch
P_o or p	total and static pressures
Re_{in}	Reynolds number defined as $Re = CU_{in}/\nu$
R_a	centerline average roughness height
s	distance along vane from flow stagnation
S	span of stator vane
T	temperature
x,y,z	local coordinates
u,v,w	local velocity components
U	velocity global

Greek

ϕ	non-dimensionalized temperature, $\phi = (T_\infty - T)/(T_\infty - T_c)$
η	adiabatic effectiveness, $\eta = (T_\infty - T_{aw})/(T_\infty - T_c)$
$\overline{\eta}$	laterally averaged effectiveness
$\overline{\overline{\eta}}$	area averaged effectiveness
ρ	density
ν	kinematic viscosity
θ	non-dimensionalized gap effectiveness, $\theta = (T_\infty - T_G)/(T_\infty - T_c)$

Subscripts

aw	adiabatic wall
in	inlet conditions

j coolant flow through film-cooling holes
s flow through upstream slot
∞ local freestream conditions

Publications and Theses

Virginia Tech

List of publications from this work

Cardwell, N. D., Sundaram, N., and Thole, K. A., 2005 "Effects of Mid-Passage Gap, Endwall Misalignment, and Roughness on Endwall Film-Cooling", *Journal of Turbomachinery*, vol. 128, pp. 62-70, (ASME Turbo Expo, Reno, GT2005-68900) – Awarded the Heat Transfer Committee Best Paper Award for 2005.

Cardwell, N. D., Sundaram, N., and Thole, K. A., 2006, "The Effects of Varying the Combustor-Turbine Gap", accepted to the *Journal of Turbomachinery*, (ASME Turbo Expo, Barcelona, GT2006-90089).

Sundaram, N., and Thole, K. A., 2006, "Effects of Surface Deposition, Hole Blockage, and TBC Spallation on Vane Endwall Film Cooling", accepted to the *Journal of Turbomachinery***,** (ASME Turbo Expo, Barcelona, GT2006-90379).

Sundaram, N., and Thole, K. A., 2007, "Effects of Deposits on Film Cooling of a Vane Endwall along the Pressure Side", recommended to the *Journal of Turbomachinery***,** (ASME Turbo, Montreal, GT2007-27131).

Sundaram, N., and Thole, K. A., 2007, "Bump and Trench Modifications to Film Cooling Holes at the Vane Endwall Junction", recommended to the *Journal of Turbomachinery***,** (ASME Turbo Expo, Montreal, GT2007-27132).

Theses

Cardwell, N. D., 2005, "Effects of Realistic First-Stage Turbine Endwall Features," M.S. Thesis, Virginia Tech.

Sundaram, N., 2007, "Effects of Surface Conditions on Endwall Film-Cooling," PhD Dissertation, Virginia Tech (to be published).

University of Texas

List of publication from this work

Rutledge, J.L., Robertson, D.R., and Bogard, D.G., 2005, "Degradation of Film Cooling Performance on a Turbine Vane Suction Side Due to Surface Roughness," ASME Gas Turbine Expo, Reno, Nevada, ASME Paper GT2005-69045.

Demling, P. and Bogard, D. G., 2006, “The effects of obstructions on film cooling effectiveness on the suction side of a gas turbine vane,” ASME Turbo Expo, Barcelona, Spain, ASME Paper GT-2006-90577.

Waye, S.K. and Bogard, D. G., 2006, “High Resolution Film Cooling Effectiveness Measurements of Axial Holes Embedded in a Transverse Trench with Various Trench Configurations,” ASME Turbo Expo, Barcelona, Spain, ASME Paper GT-2006-90226.

Waye, S.K. and Bogard, D. G., 2006, “High Resolution Film Cooling Effectiveness Comparison of Axial and Compound Angle Holes on the Suction Side of a Turbine Vane,” ASME Turbo Expo, Barcelona, ASME Paper GT-2006-90225.

Rutledge, J.L., Robertson, D., and Bogard, 2006, “Degradation of Film Cooling Performance on a Turbine Vane Suction Side Due to Surface Roughness,” ASME J. of Turbomachinery, vol. 128, 2006, pp. 547-554.

Dees, J.E., and Bogard, D. G., 2007, “Effects of Regular and Random Roughness on the Heat Transfer and Skin friction Coefficient on the Suction side of a Gas Turbine vane,” ASME Turbo Expo, Montreal, Canada, ASME Paper GT-2007-27285.

Somawardhana, R.P. and Bogard, D.G., 2007, “Effects of Obstructions and Surface Roughness on Film Cooling Effectiveness With and Without a Transverse Trench,” ASME Gas Turbine Expo, Montreal, Canada, ASME Paper GT2007-28003.

Somawardhana, R.P. and Bogard, D.G., 2007, “Effects of Surface Roughness and Near Hole Obstructions on Film Cooling Effectiveness,” ASME Gas Turbine Expo, Montreal, Canada, ASME Paper GT2007-28004.

Waye, S.K. and Bogard, D.G., “High Resolution Film Cooling Effectiveness Comparison of Axial and Compound Angle Holes on the Suction Side of a Turbine Vane,” ASME J. of Turbomachinery, 2007. (accepted).

Waye, S.K. and Bogard, D.G., “High Resolution Film Cooling Effectiveness Measurements of Axial Holes Embedded in a Transverse Trench with Various Trench Configurations,” ASME J. of Turbomachinery, 2007. (accepted)

Theses

Robertson, D.R., 2004, “Roughness Impact on Turbine Vane Suction Side Film Cooling Effectiveness,” M.S. Thesis, University of Texas at Austin.

Rutledge, J.L., 2004, “Suction Side Roughness Effects on Film Cooling Heat Transfer on a First Stage Nozzle Guide Vane,” M.S. Thesis, University of Texas at Austin.

Demling, T., 2005, “The Effects of Obstructions on Film Cooling Effectiveness on the Suction Side of a Gas Turbine Vane,” M.S. Thesis, The University of Texas at Austin.

Warren, D. J., 2005, “Effects of Roughness on Film Effectiveness on the Pressure Side of a Turbine Vane,” M.S. Thesis, The University of Texas at Austin.

Waye, S.K., 2005, “Film Cooling Effectiveness of Suction Side Axial Holes, Compound Angle Holes, and Axial Holes Embedded within an Overlying Transverse Trench,” M.S. Thesis, University of Texas at Austin.

Dees, J.E., 2006, “Effects or Regular and Random Roughness on the Heat Transfer and Skin Friction Coefficient on the Suction Side of a Gas Turbine Vane,” M.S. Thesis, The University of Texas at Austin.

Somawardhana, R.P., 2006, “Rough Wall and Near-Hole Obstruction Effects on Film Cooling with and without a Transverse Trench,” M.S. Thesis, The University of Texas at Austin.

Tables and Figures

Table 2.1 Test Matrix for Deposition at the Leading Edge

Deposition Height	Endwall Roughness	Deposition Location	Film-Cooling flowrate	Upstream Slot flowrate	MP flowrate
0.5D	36 grit	Upstream, Downstream, & Both	0.50%	0.75%, 0.85%, 1.0%	0.20%
0.8D	36 grit	Upstream, Downstream, & Both	0.50%	0.75%, 0.85%, 1.0%	0.20%
1.2D	36 grit	Upstream, Downstream, & Both	0.50%	0.75%, 0.85%, 1.0%	0.20%

Table 2.2 Test Matrix for Deposition on Pressure Side

No of Rows	Film-cooling flowrate	Upstream Slot flowrate	MP flowrate	Cooling Row
4	0.5%,0.75%,0.9%	0.75%	0.2%	1 to 4
3	0.5%,0.75%,0.9%	0.75%	0.2%	1 to 3
2	0.5%,0.75%,0.9%	0.75%	0.2%	1 to 2
1	0.5%,0.75%,0.9%	0.75%	0.2%	1
1	0.5%,0.9%	0.75%	0.2%	2
1	0.5%,0.9%	0.75%	0.2%	3
1	0.5%,0.9%	0.75%	0.2%	4

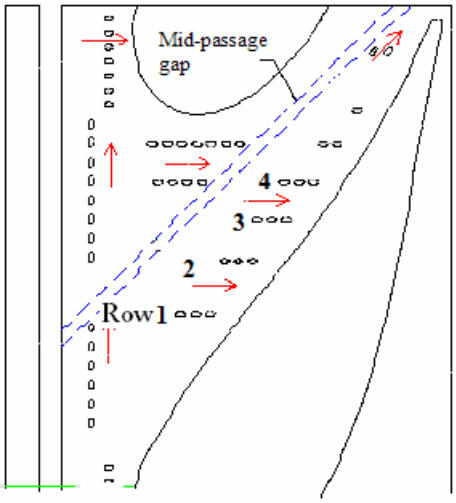

Table 2.3 Test Matrix for Spallation at the Leading Edge

Upstream Slot Flowrate	Spallation Width	Film-Cooling Flowrate	MP Flowrate
* 0.75 , 0.85, 1.0	2D	* 0.5	* 0.2
0.75	2D	0.5, 0.75, 0.90	0.2

Table 2.4 Test Matrix for Spallation along MP Gap

Upstream Slot Flowrate	Spallation Width	Film-Cooling Flowrate	MP Flowrate
* 0.75 , 0.85, 1.0	* G, & 5G	* 0.5	0.2
0.75	G, & 5G	0.5, 0.75, 0.90	0.2

Table 2.5 Test Matrix for Hole Blockage at Leading Edge

	Leading Edge row	No. of Holes	Film-cooling flowrate	Upstream Slot flowrate	MP flowrate
No Blockage	NA	NA	0.5, 0.75, 0.9	0	0.2
Blockage	a, b & c	1 in each	0.5,0.75,0.90	0	0.2
	c(25% blockage)	6	0.5,0.75,0.90	0	0.2
	c(25% blockage)	5	0.5, 0.75, 0.9	0	0.2
	c(25% blockage)	4	0.5,0.75,0.9	0	0.2
	c(25% blockage)	3	0.5,0.75,0.9	0	0.2
	c(25% blockage)	2	0.5,0.75,0.9	0	0.2
	c(25% blockage)	1	0.5,0.75,0.9	0	0.2

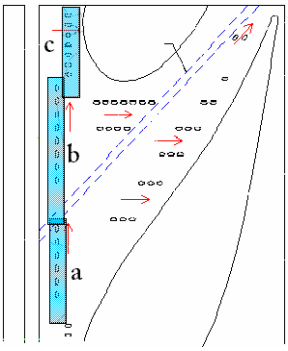

Table 3.1. Results of Passage Gutter Geometry Feedback Form

Passage Gutter	(Mike Blair) Pratt Whitney	(Ronald Bunker) General Electric	(John Weaver) Rolls-Royce
Gutter Width (in)	0.01-0.03	0.03-0.05	0.005-0.05
Extent	Leading edge to the trailing edge	Leading edge to the trailing edge	Leading edge to the trailing edge
Length/Width	10	10	----------
Breakout Angle	90^o	90^o	90^o
% Leakage Flow	0.5-1.0 %	0.5-1.0 %	0.002-0.006% per inch

Table 3.2. Results of Seal Strip Geometry Feedback Form (refer Figure 3.1)

Seal Strip Geometries	Pratt Whitney	General Electric	Rolls - Royce	Siemens - Westinghouse
A (in)	0.03	0.030-0.050	0.005-0.050	
B (in)	0.083	0.083	0.083	0.083
C (in)	0.150-0.250	0.150-0.250	0.150-0.250	0.150-0.250
D (in)	0.150-0.250	0.150-0.250	0.150-0.250	0.150-0.250
E (in)	0.23	0.4		
F (in)	0.4	0.402		
G (in)	0.06	0.150-0.200		
H (in)	0.01	0.050-0.100		

Table 5.1 Test Matrix for Deposition at the Leading Edge

Deposition Height	Endwall Roughness	Deposition Location	Film-Cooling flowrate	Upstream Slot flowrate	MP flowrate
0.5D	36 grit	Upstream, Downstream, & Both	0.50 %	0.75 %, 0.85 %, 1.0 %	0.20 %
0.8D	36 grit	Upstream, Downstream, & Both	0.50 %	0.75 %, 0.85 %, 1.0 %	0.20 %
1.2D	36 grit	Upstream, Downstream, & Both	0.50 %	0.75 %, 0.85 %, 1.0%	0.20 %

Table 5.2 Test Matrix for Deposition on Pressure Side

No of Rows	Film-cooling flowrate	Upstream Slot flowrate	MP flowrate	Cooling Row
4	0.5 %,0.75 %,0.9 %	0.75 %	0.2 %	1 to 4
3	0.5 %,0.75 %,0.9 %	0.75 %	0.2 %	1 to 3
2	0.5 %,0.75 %,0.9 %	0.75 %	0.2 %	1 to 2
1	0.5 %,0.75 %,0.9 %	0.75 %	0.2 %	1
1	0.5 %,0.9 %	0.75 %t	0.2 %	2
1	0.5 %t,0.9 %	0.75 %	0.2 %	3
1	0.5 %,0.9 %	0.75 %	0.2 %	4

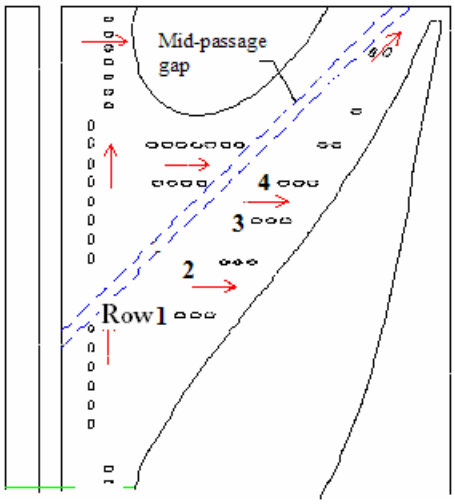

Table 6.1 Summary of Endwall Geometry

	Parameter	Experimental
Upstream Slot	Double slot flow length to width	0.94
	Nominal slot flow length to width	1.88
	Half slot flow length to width	3.76
	Upstream slot surface angle	45°
Film Cooling	FC hole diameter (cm)	0.46
	FC Hole L/D	8.3
	Film-cooling surface angle	30°

Table 6.2 Upstream Coolant Settings Summary

	% mass flow	M	I
Double Width Slot	0.75%	0.19	0.03
	0.85%	0.22	0.04
	1.00%	0.26	0.06
	1.13%	0.29	0.08
	1.25%	0.32	0.10
Nominal Slot Width	0.75%	0.29	0.08
	0.85%	0.33	0.10
	1.00%	0.39	0.13
Half Width Slot	0.38%	0.29	0.08
	0.42%	0.32	0.10
	0.75%	0.58	0.30
	0.85%	0.66	0.39
	1.00%	0.77	0.54

Table 8.1 Relevant boundary layer values for rough wall tests on the vane

	location	δ (mm)	θ (mm)	H
smooth w/o trip	s/C=0.57	2.08	0.19	1.68
smooth with trip	s/C=0.37	3.28	0.29	1.37
	s/C=0.57	4.02	0.39	1.44
80 grit	s/C=0.37	2.79	0.29	1.38
	s/C=0.57	3.17	0.49	1.48
50 grit	s/C=0.37	3.06	0.38	1.42
	s/C=0.57	5.27	0.68	1.49
36 grit	s/C=0.37	3.46	0.44	1.42
	s/C=0.57	5.36	0.77	1.56
20 grit	s/C=0.37	3.53	0.48	1.55
	s/C=0.57	5.48	0.76	1.56
Cones	s/C=0.37	3.43	0.45	1.46
	s/C=0.57	5.65	0.76	1.45

Table 9.1. Obstruction Geometry

Shape #16:
Shape #2:
Shape #2 (bkwd):
Shape #3:

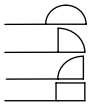

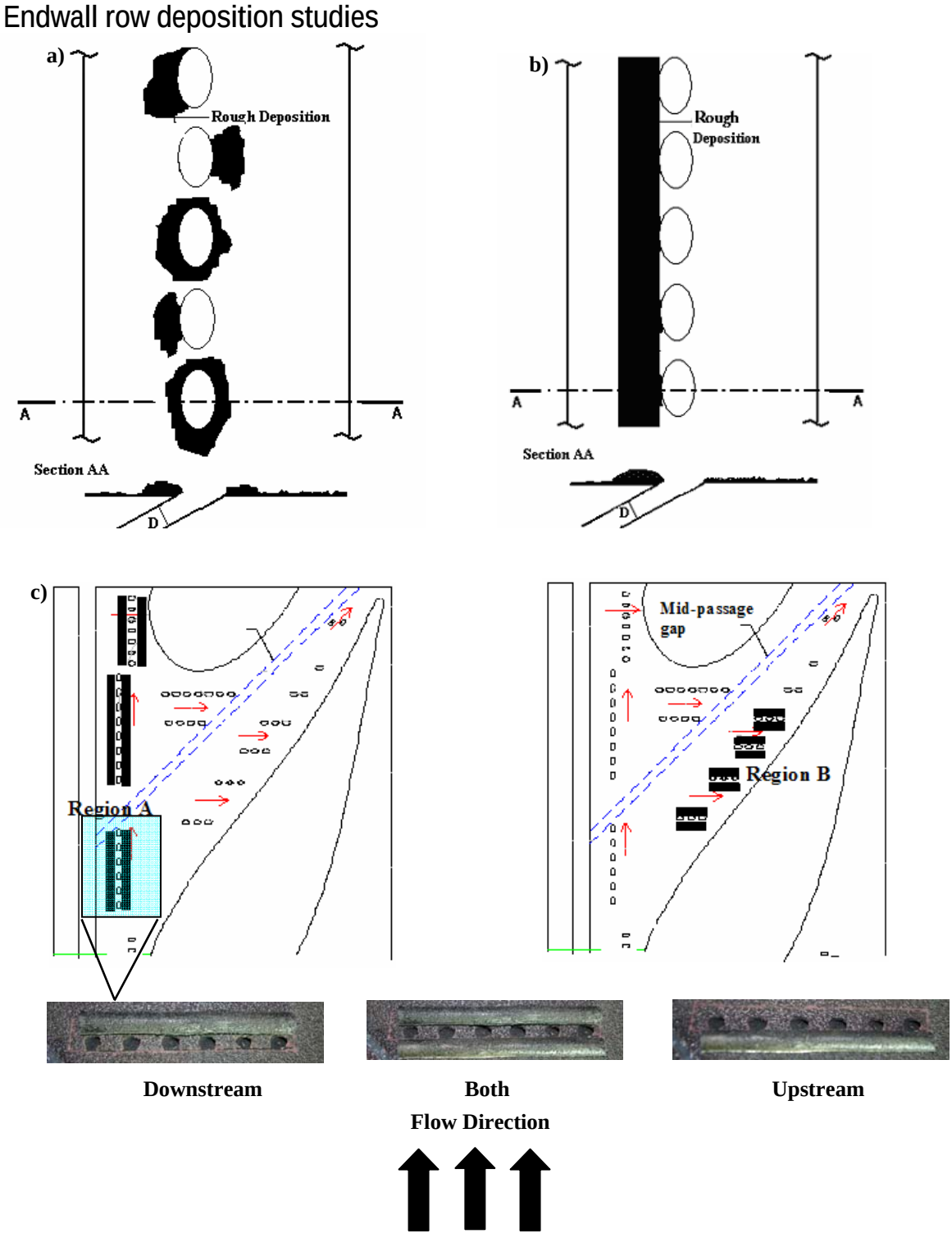

Figure 2.1 Illustration of the deposition effects to be studied on the leading edge and on the pressure side of the vane. Single row deposition will be studied in region A and multiple row deposition will be studied in region B. a) Typical engine deposition, b) Simulated Condition c) Illustrates the deposit location and the way the deposits were placed on the endwall.

Endwall erosion/spallation studies

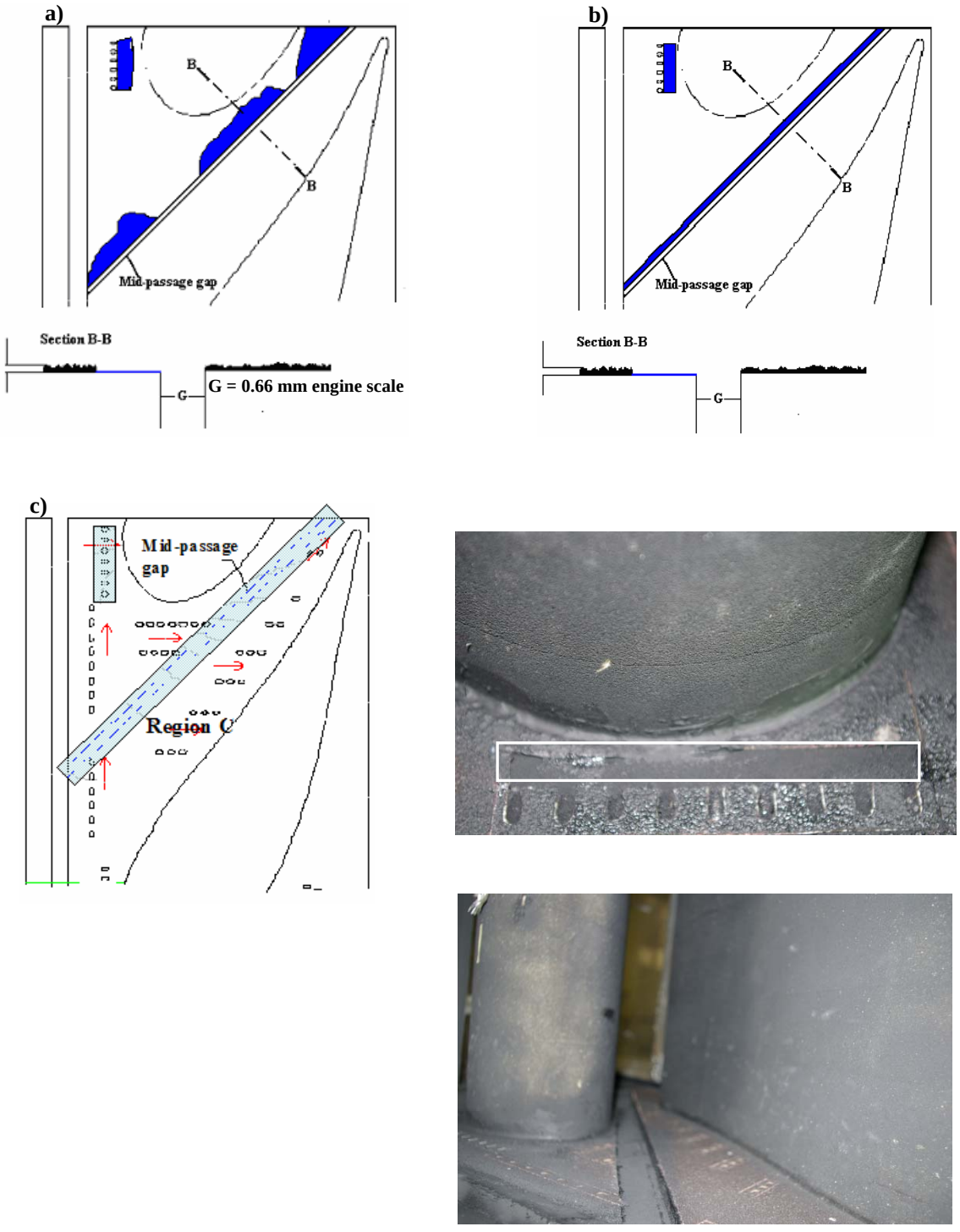

Figure 2.2 Illustration of the spallation studies that will be taking place on the surface downstream of the leading edge film-cooling row and along the mid-passage gap a) Typical vane endwall spallation, b) Simulated Condition.

Hole blockage studies

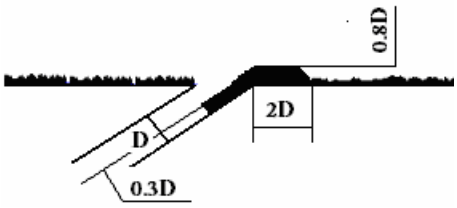

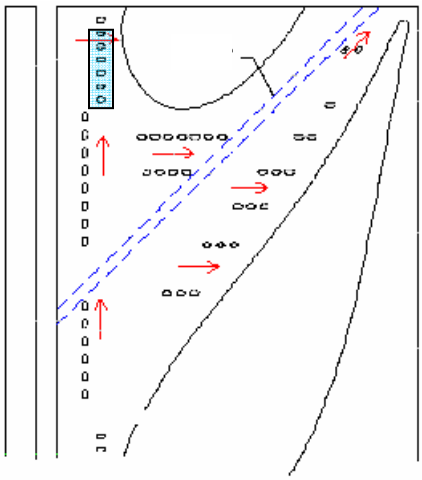

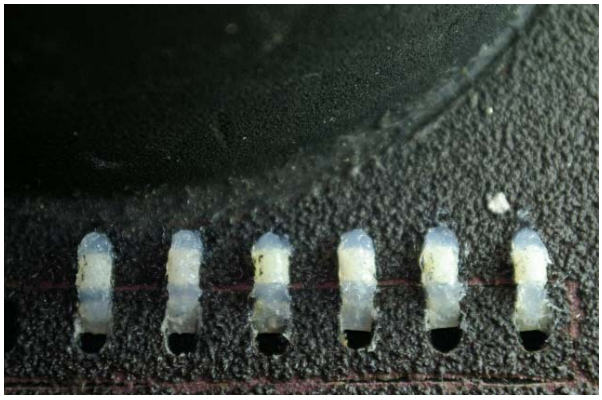

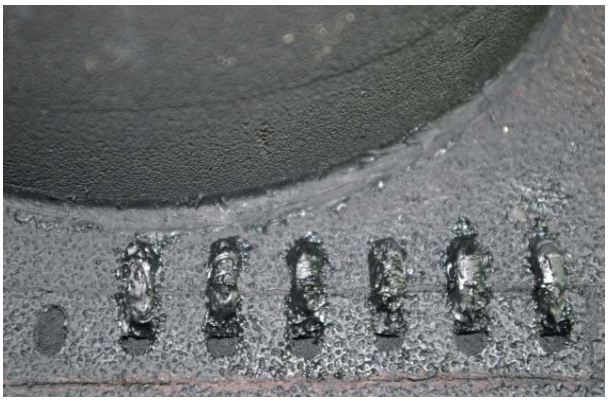

Figure 2.3 Hole blocked at the downstream of the film-cooling holes of the leading edge cooling row.

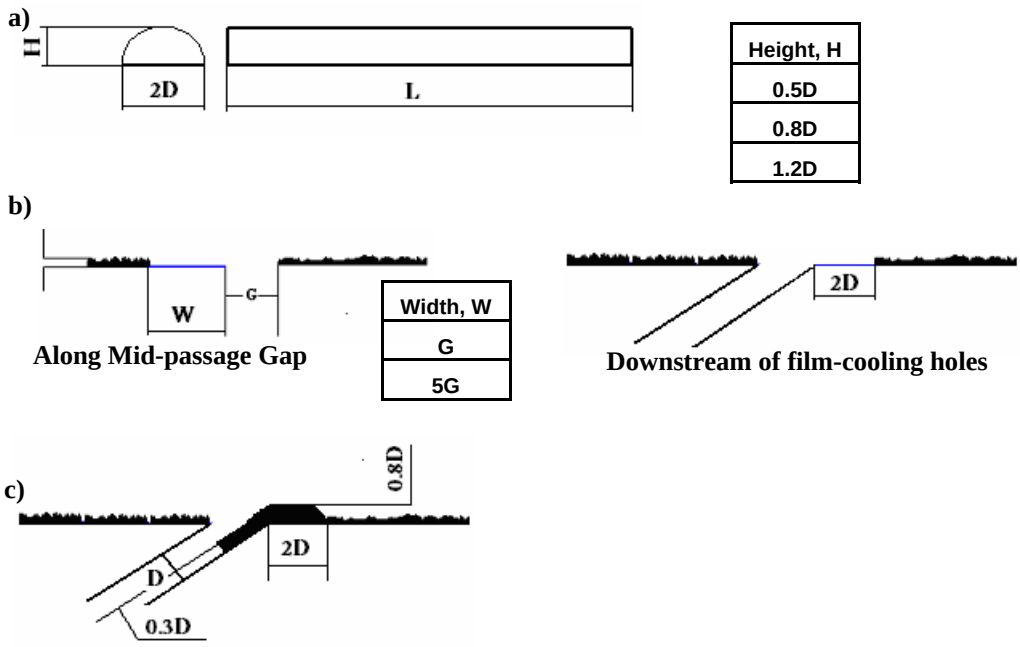

Figure 2.4 Illustrates the dimensions of the simulated distortions on the endwall a) Deposit of height H and length L corresponding to the length of the cooling row, b) Spallation widths along the MP gap and downstream of film-cooling holes and c) Hole blockage at downstream of film-cooling hole.

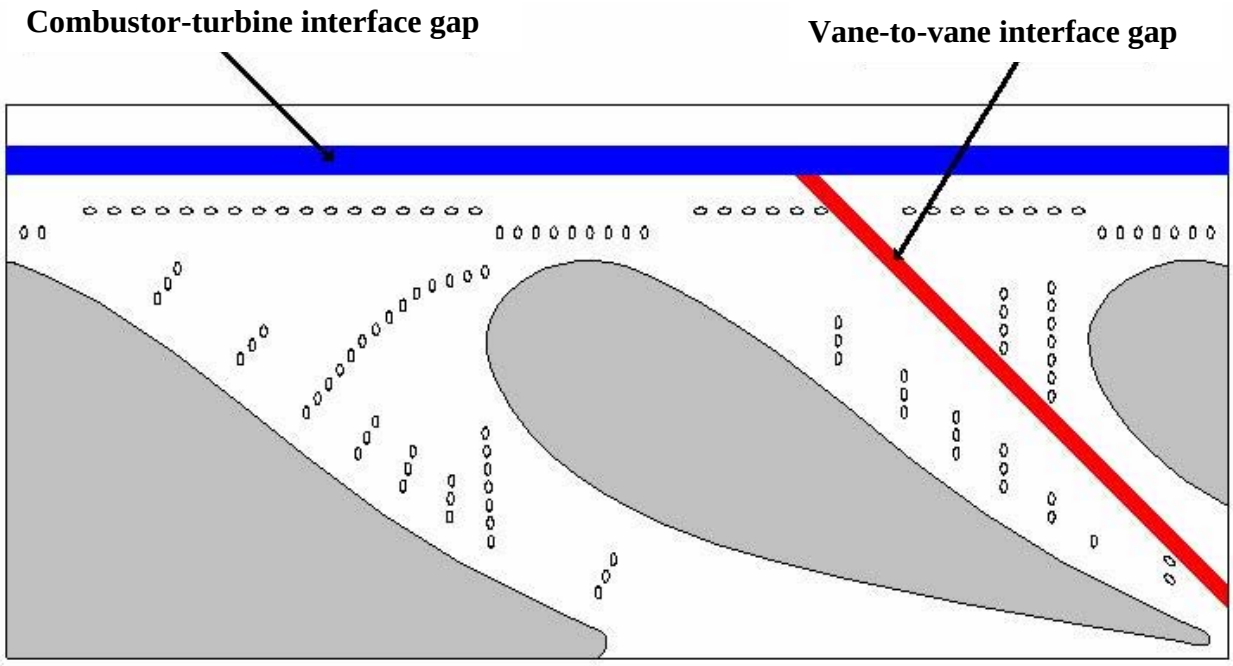

Figure 3.1. Mid-passage gap arrangement for the film-cooled endwall.

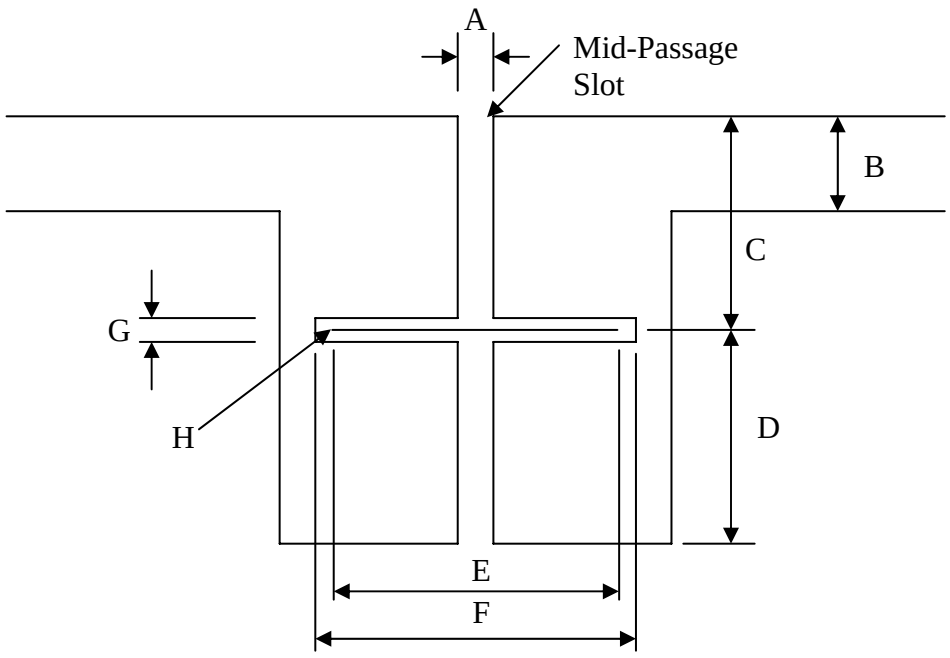

Figure 3.2. Seal strip geometry that will be simulated in the wind tunnel.

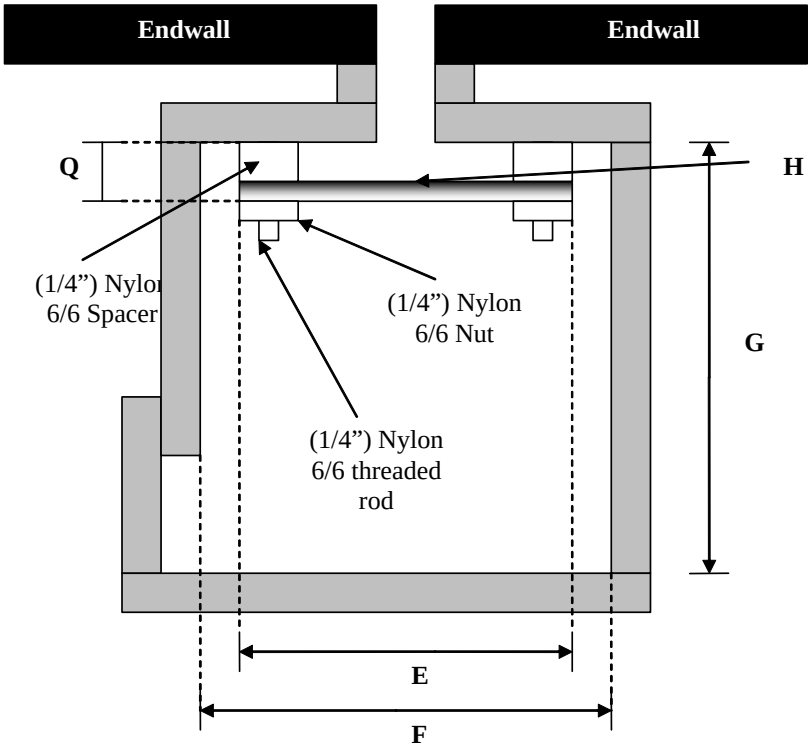

Figure 3.3. Schematic of the new plenum design for the mid-passage gap feed.

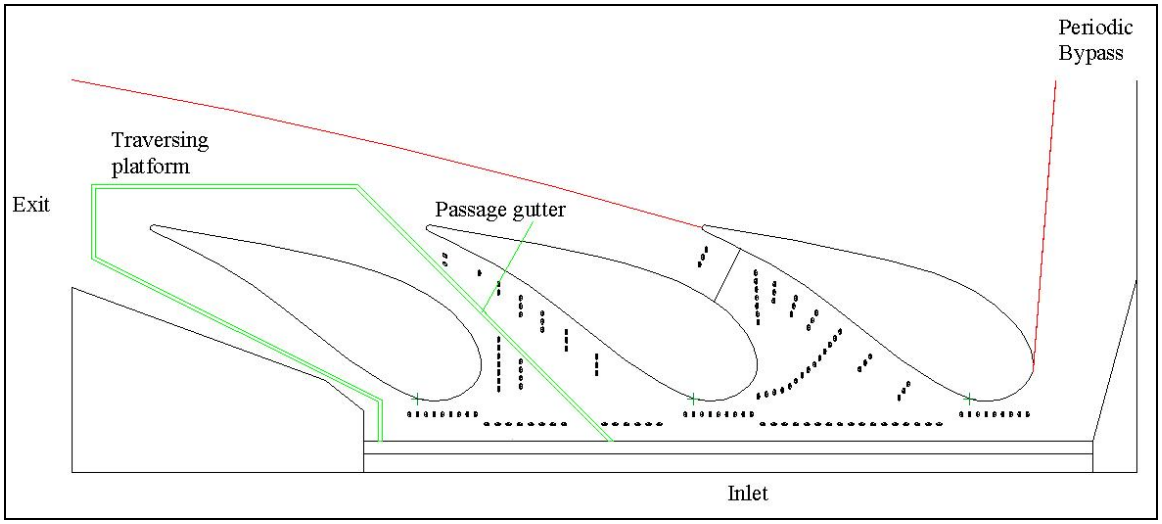

Figure 3.4. Placement of traversing platform to simulate component misalignment.

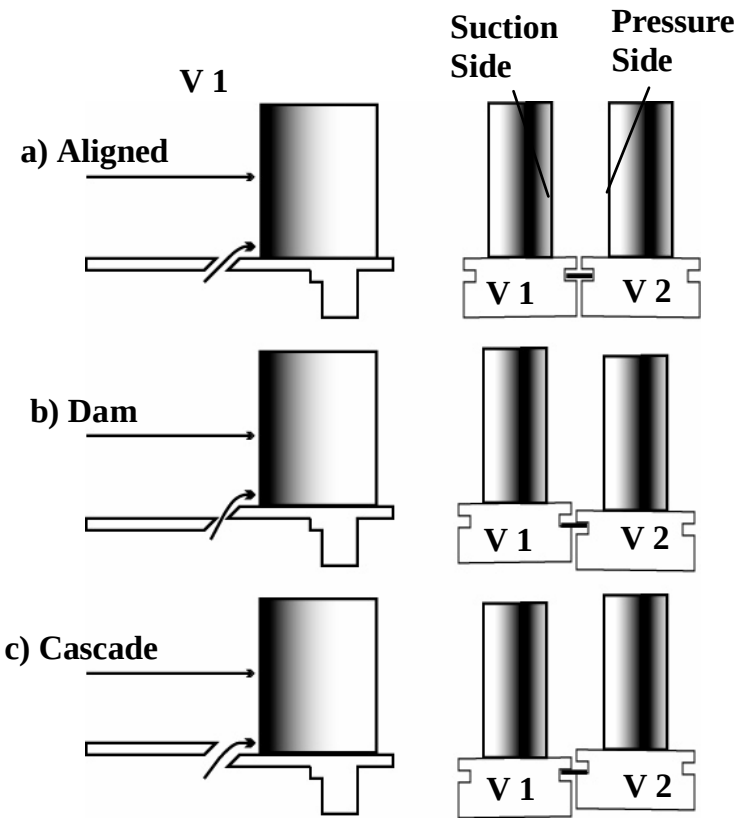

Figure 3.5. Side and upstream views of the three alignment modes for two adjacent vane platforms.

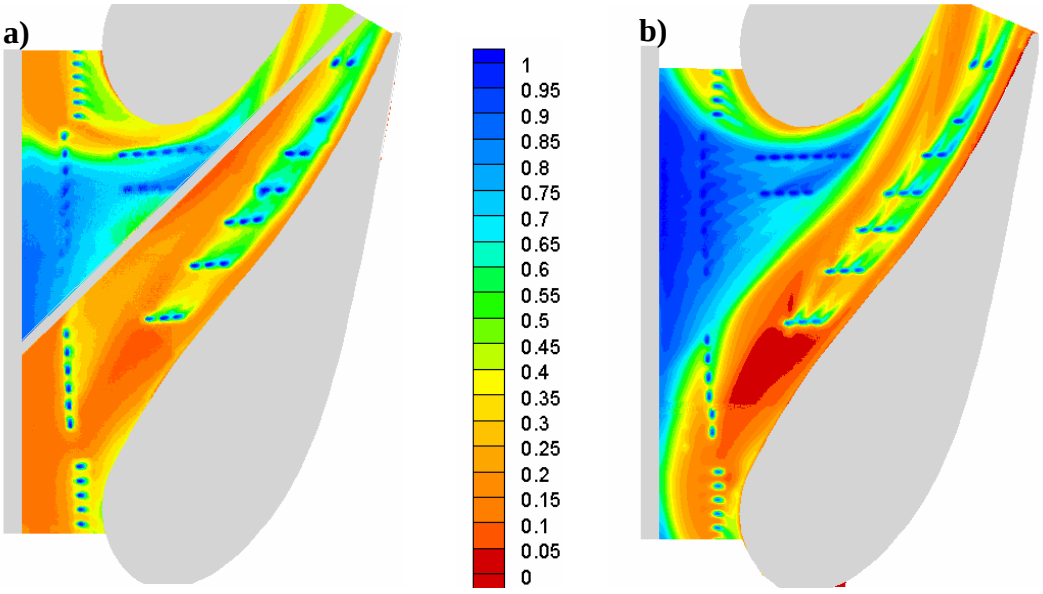

Figure 3.6. Contours of adiabatic effectiveness for film-cooling cases (a) rough endwall with mid-passage slot (b) smooth endwall with no mid-passage slot.

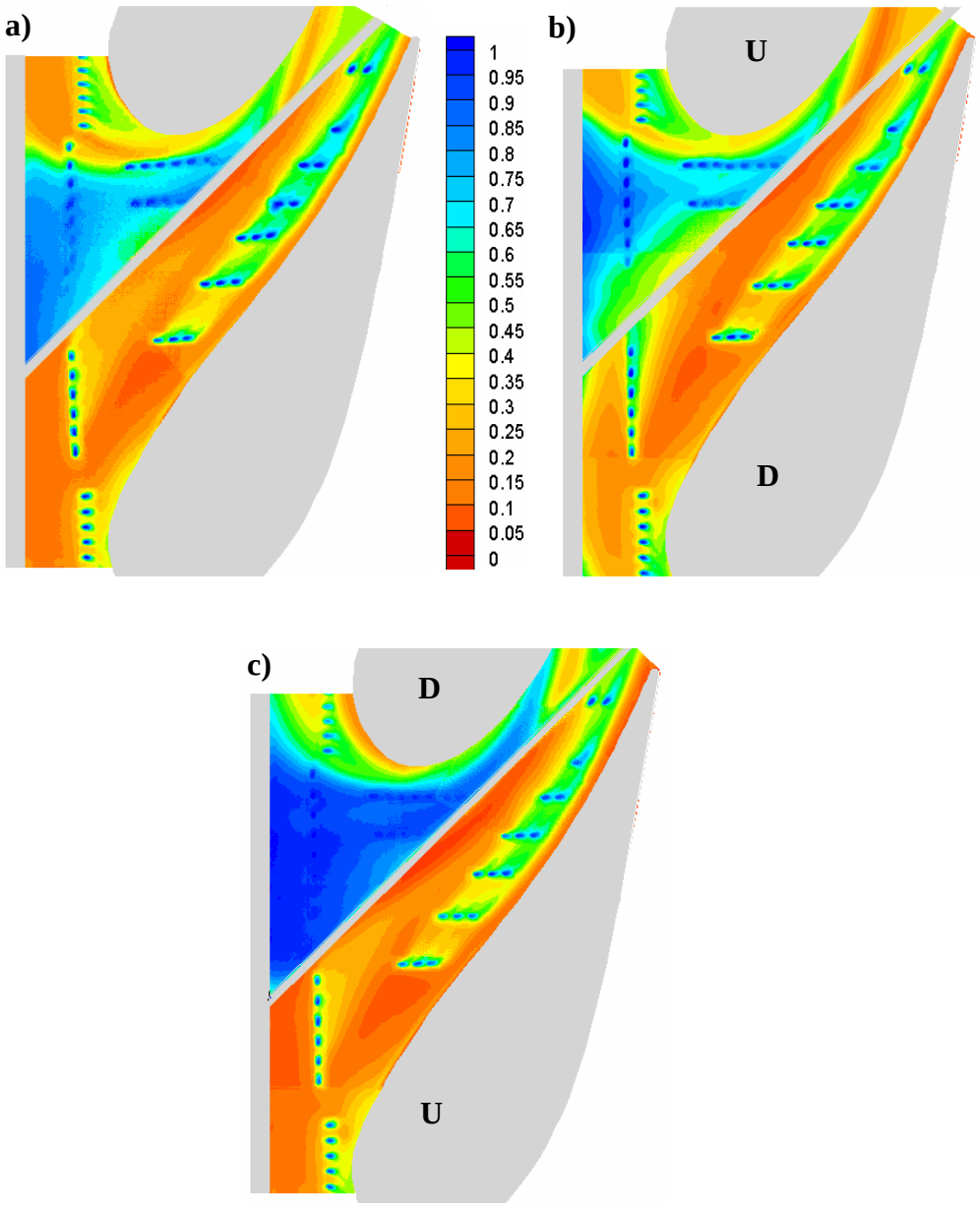

Figure 3.7. Contours of adiabatic effectiveness on a rough endwall for the baseline film and slot cooling cases: (a) aligned) (b) dam and (c) cascade endwall.

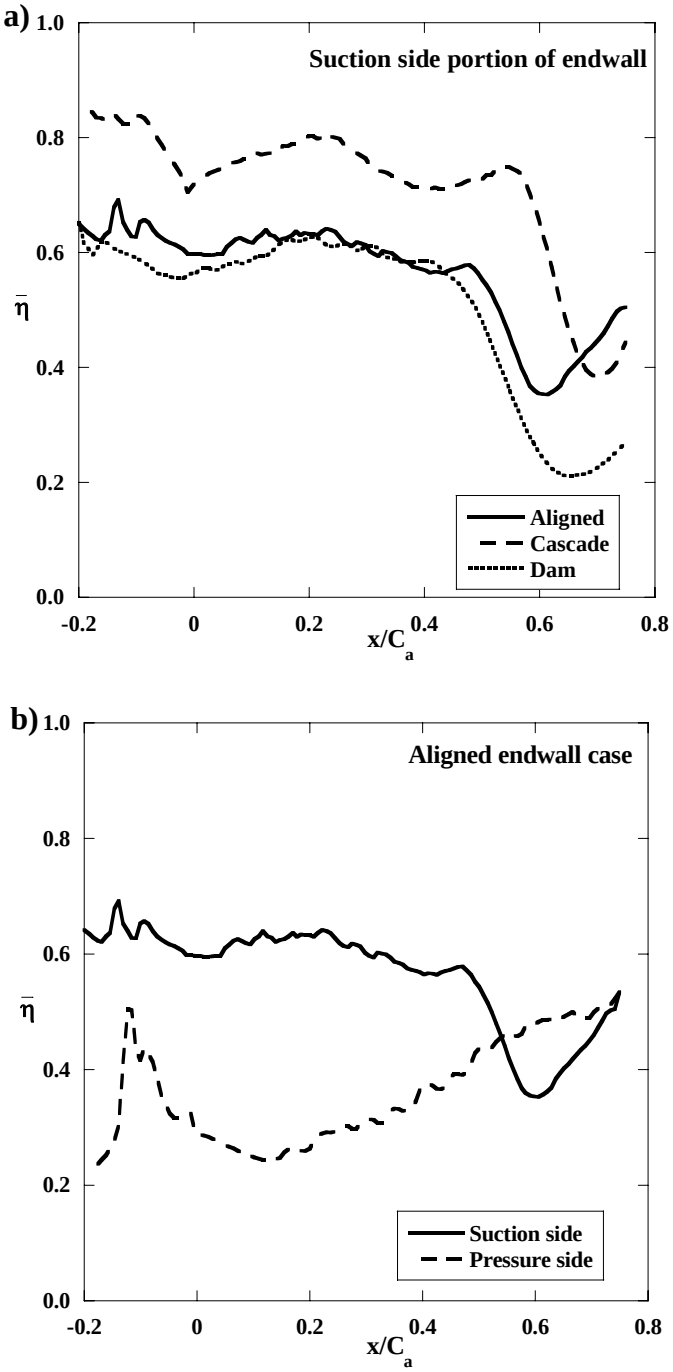

Figure 3.8. Pitch-wise averaged adiabatic effectiveness for the baseline film and slot cooling cases: a) along the suction side for the three endwall settings b) comparison between effectiveness on the suction and pressure side.

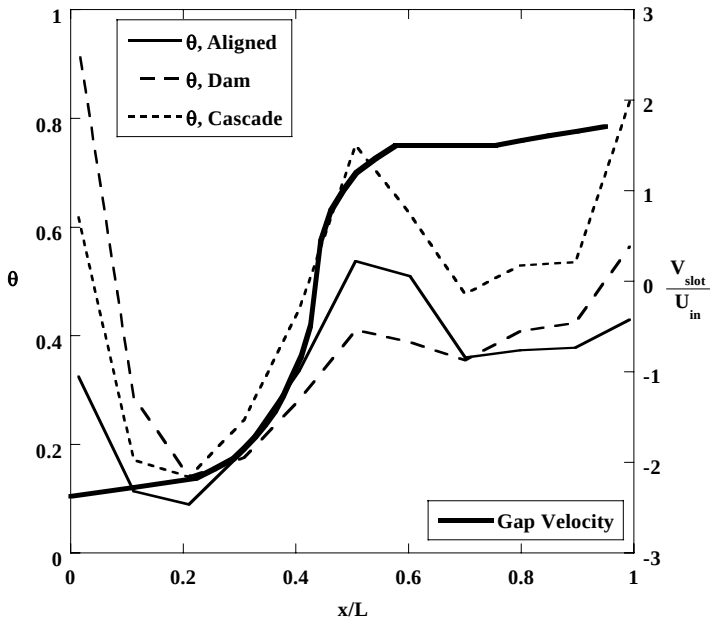

Figure 3.9. Non-dimensionalized gap temperature profiles for the three endwall alignment modes and the velocity profile for an aligned gap.

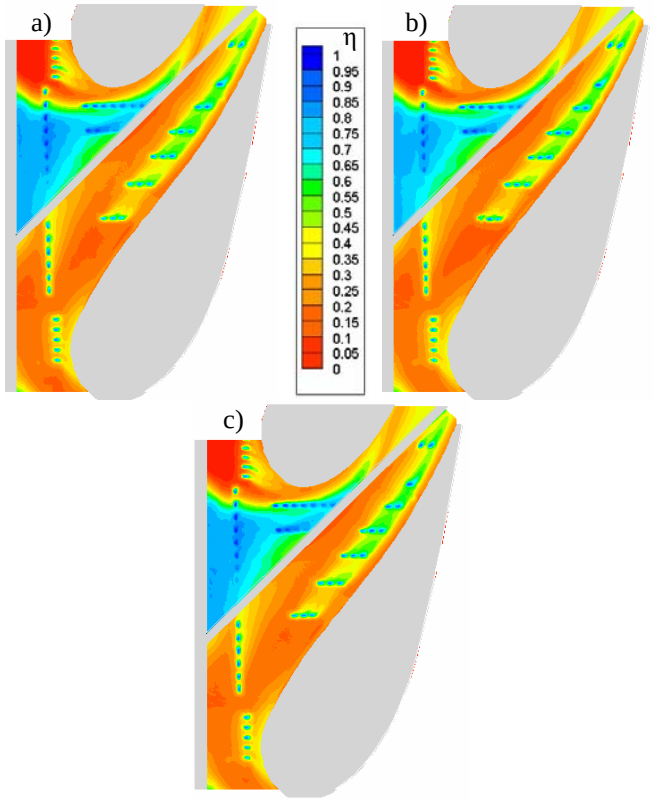

Figure 3.10. Contours of adiabatic effectiveness for a) 0.1%, b) 0.2%, and c) 0.3% mid-passage gap mass flow with nominal upstream slot width.

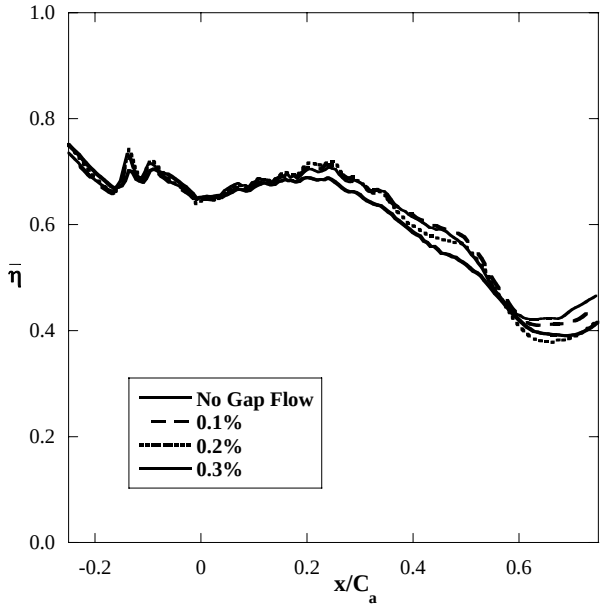

Figure 3.11. Laterally averaged adiabatic effectiveness with varied mid-passage gap flows

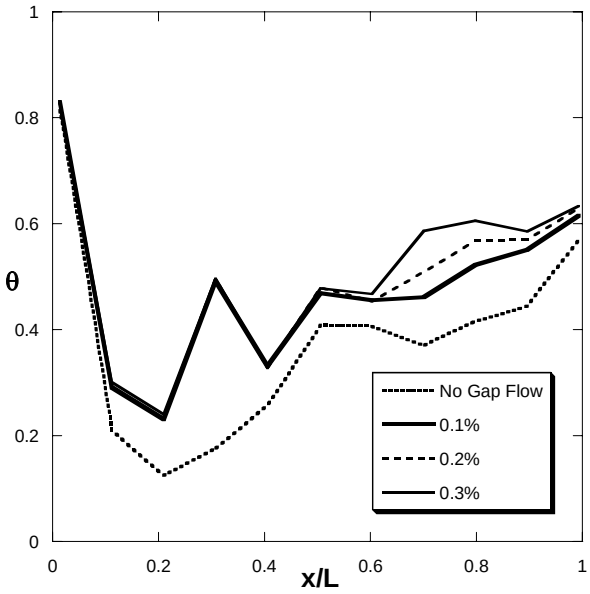

Figure 3.12 Mid-passage gap temperatures with varied mid-passage gap flows.

a)

b)

Figure 4.1 36 grit sand paper was used to simulate a rough endwall surface a)sand paper with slots at film-cooling hole locations and b)with film-cooling hole inserts.

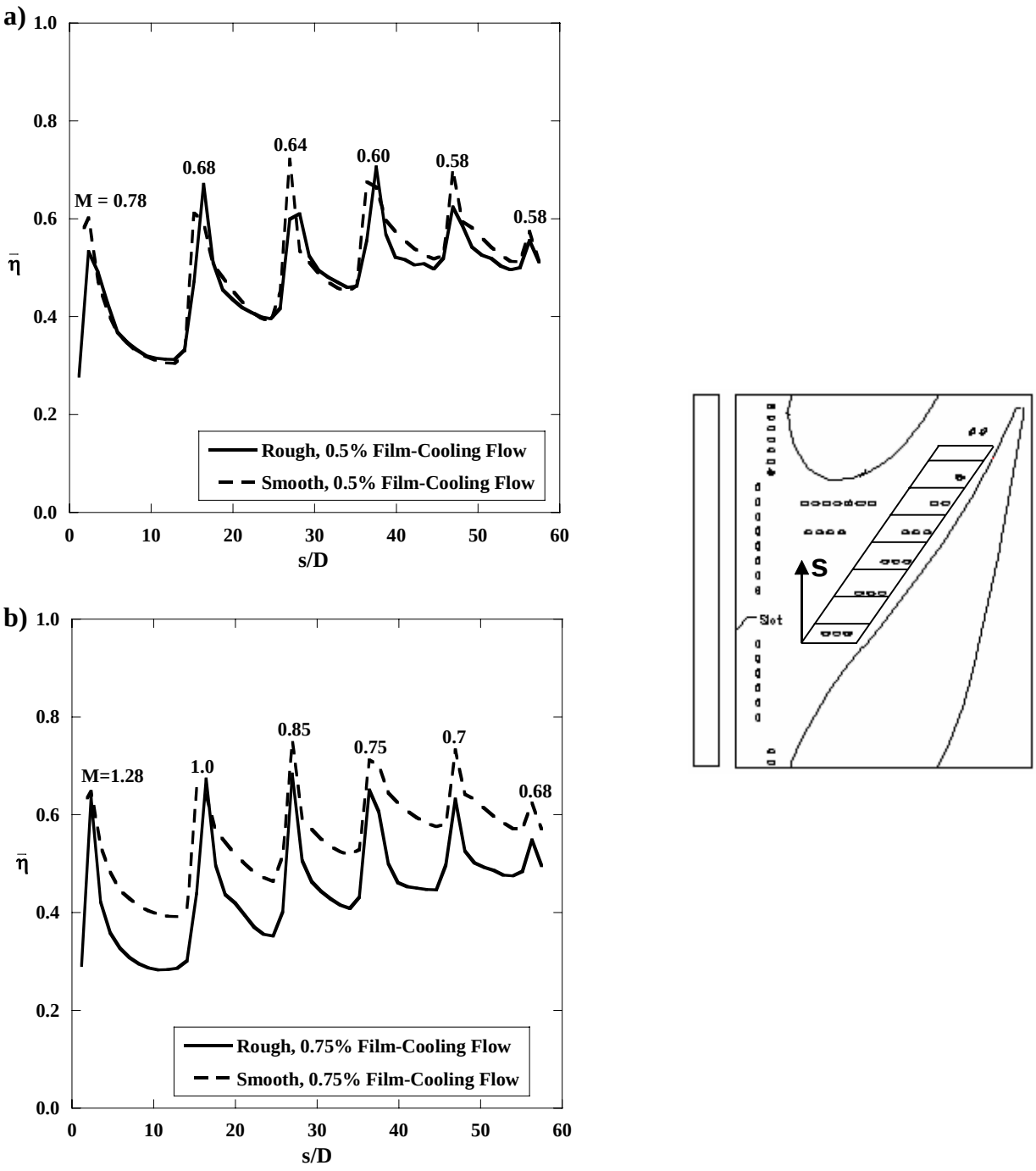

Figure 4.2a-b. Plots of laterally averaged adiabatic effectiveness on the film-cooling holes on the pressure side: (a) for 0.75% upstream slot flow and 0.5% film-cooling and (b) 0.75% upstream slot flow and 0.75% film-cooling.

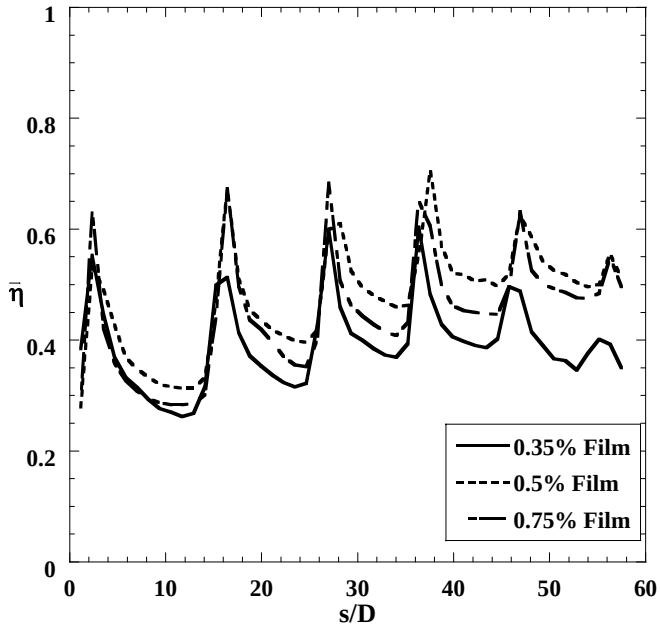

Figure 4.3. Laterally averaged adiabatic effectiveness for 0.35%, 0. 5% and 0.75% film-cooling flows for a rough endwall.

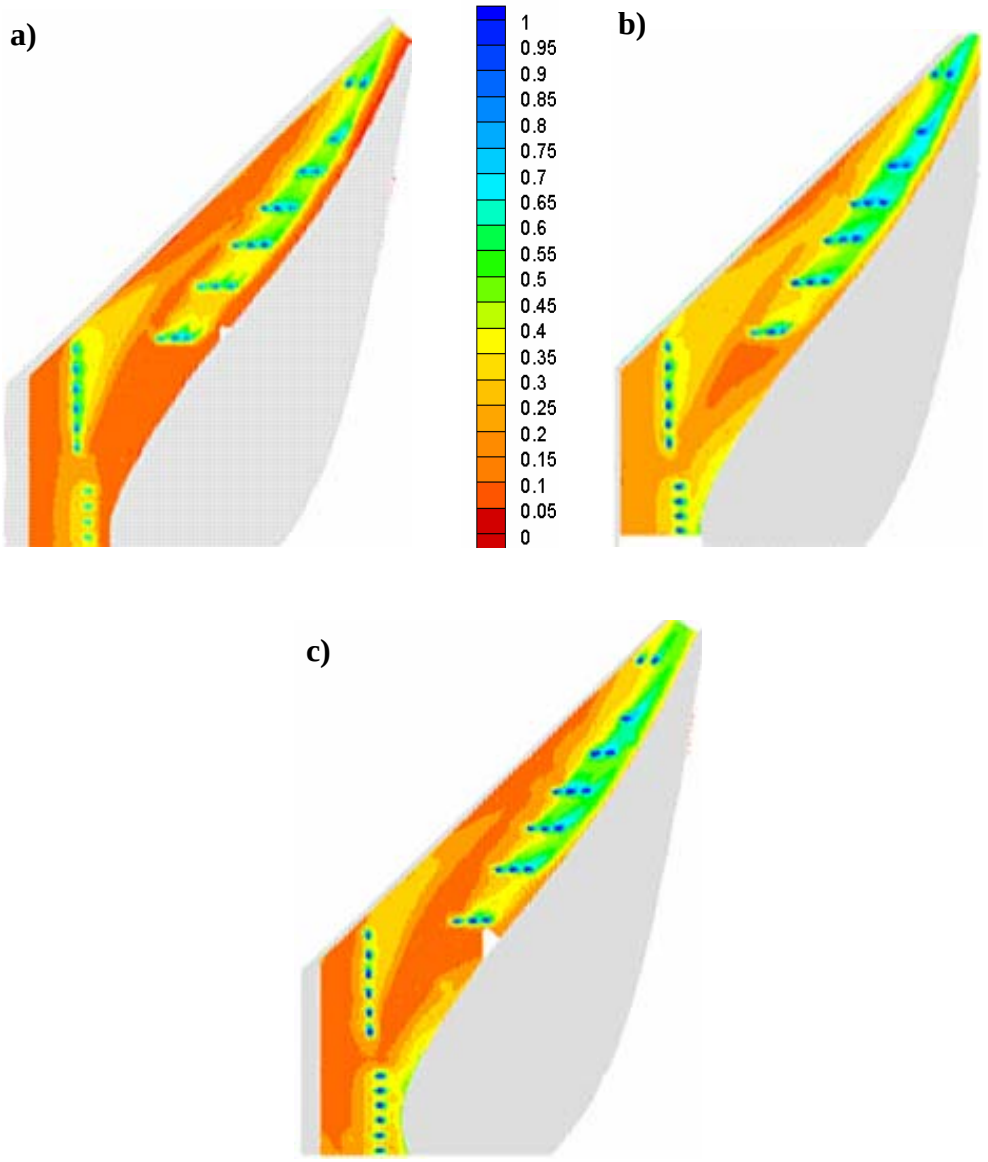

Figure 4.4a-c. Contours of adiabatic effectiveness with a rough endwall with 0.75% slot flow for (a) 0.35% film-cooling (b) 0.5% film-cooling (c) 0.75% film-cooling.

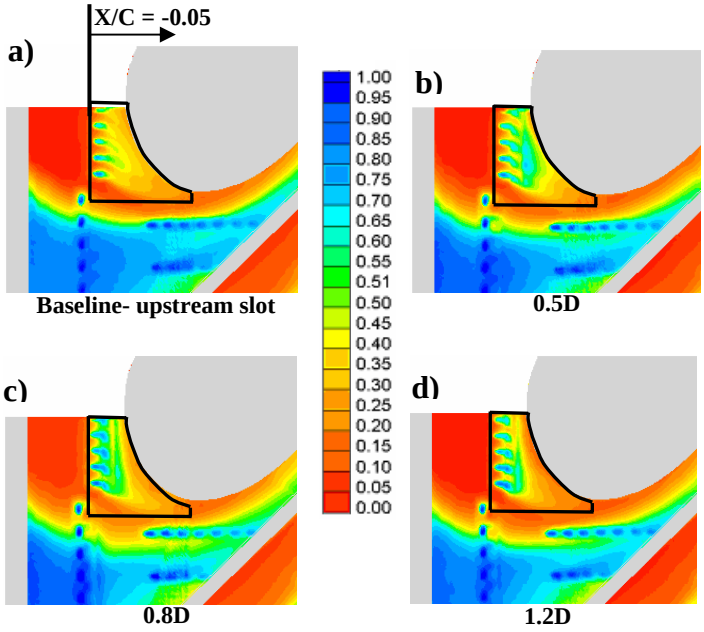

Coolant flowrates	
Upstream slot	0.75%
Film-cooling holes	0.5%
Mid-passage gap	0.2%

Figure 5.1 Comparisons of adiabatic effectiveness contours with varying deposit heights at the leading edge stagnation region with nominal flow rates.

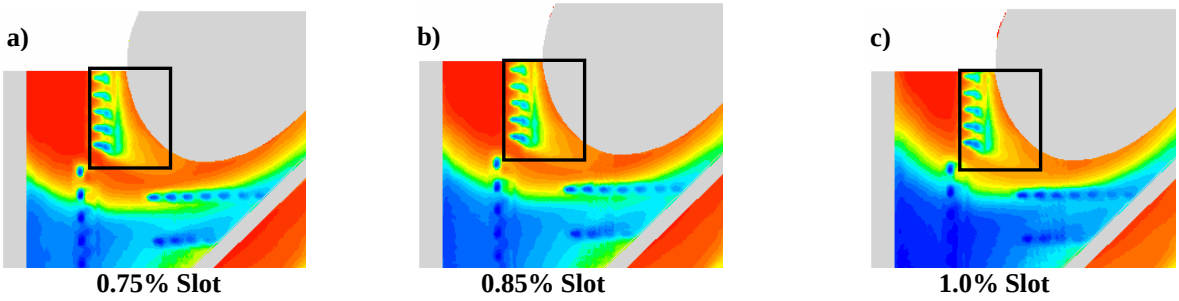

Figure 5.2 Comparisons of adiabatic effectiveness contours with varying slot flow and a constant film-cooling flowrate of 0.5% over a deposit height of 0.8D downstream of the cooling hole.

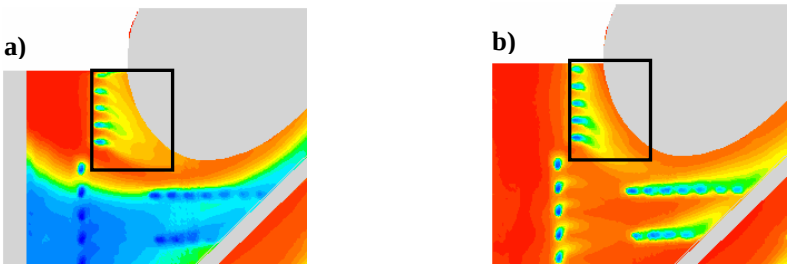

Figure 5.3 Comparisons of adiabatic effectiveness contours showing the effect of upstream slot flow on the leading edge cooling near the stagnation region.

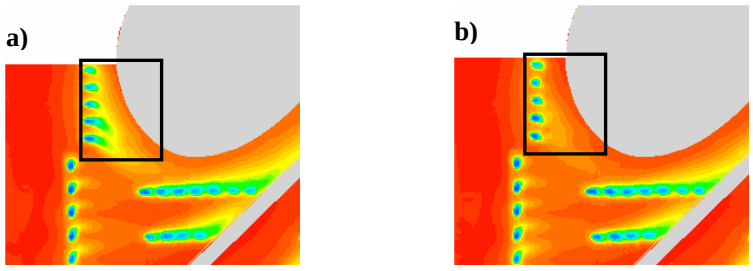

No holes blocked 5 Holes blocked 30%

Figure 5.4 Comparisons of adiabatic effectiveness contours showing the effect of blockage on film-cooling effectiveness.

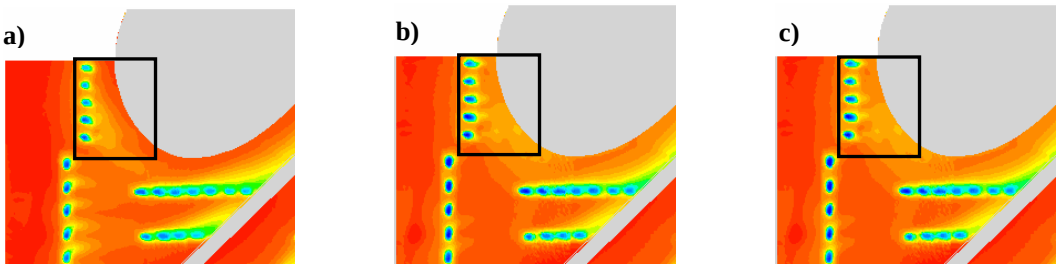

0.5% Film-Cooling 0.75% Film-Cooling 0.9% Film-Cooling

Figure 5.5 Contours of adiabatic effectiveness showing the effect of increase in blowing ratio with film-cooling holes blocked.

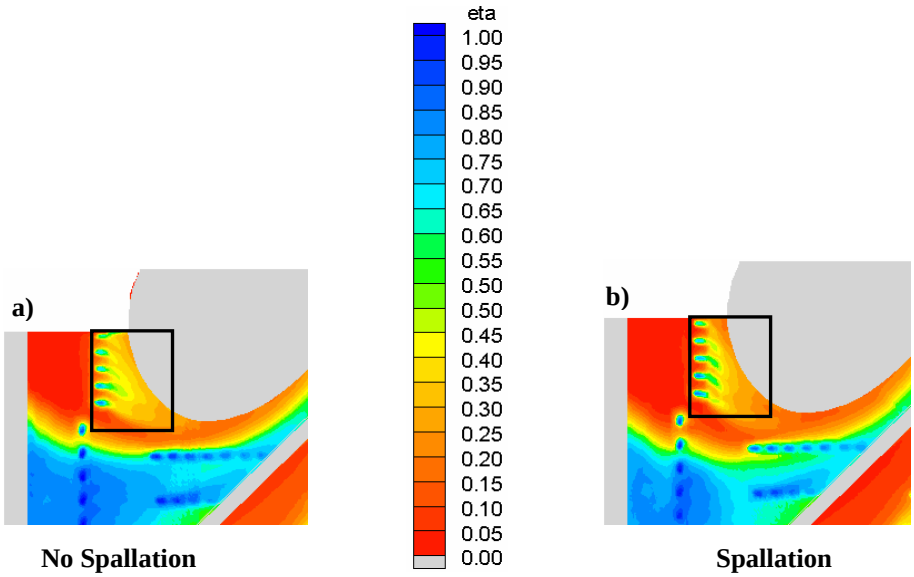

No Spallation Spallation

Figure 5.6 Contours of adiabatic effectiveness comparing the effect of spallation at the leading edge film-cooling row.

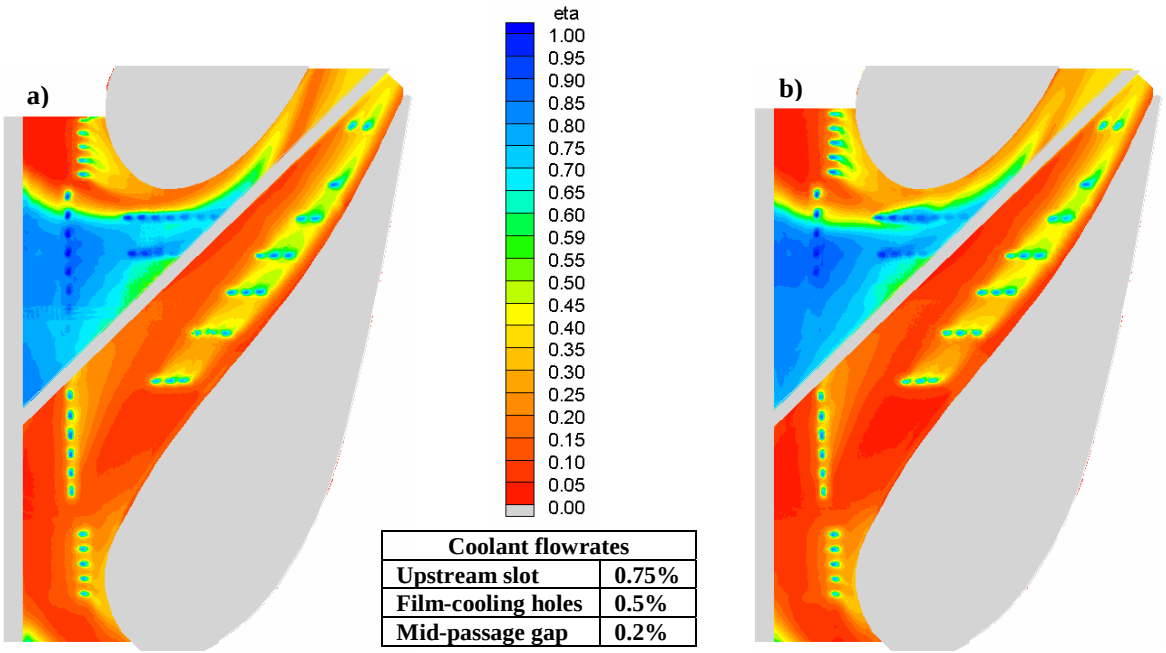

Coolant flowrates	
Upstream slot	0.75%
Film-cooling holes	0.5%
Mid-passage gap	0.2%

Figure 5.7 Comparison of contours of endwall adiabatic effectiveness for a) with spallation of width 5G and b) without spallation along the mid-passage gap.

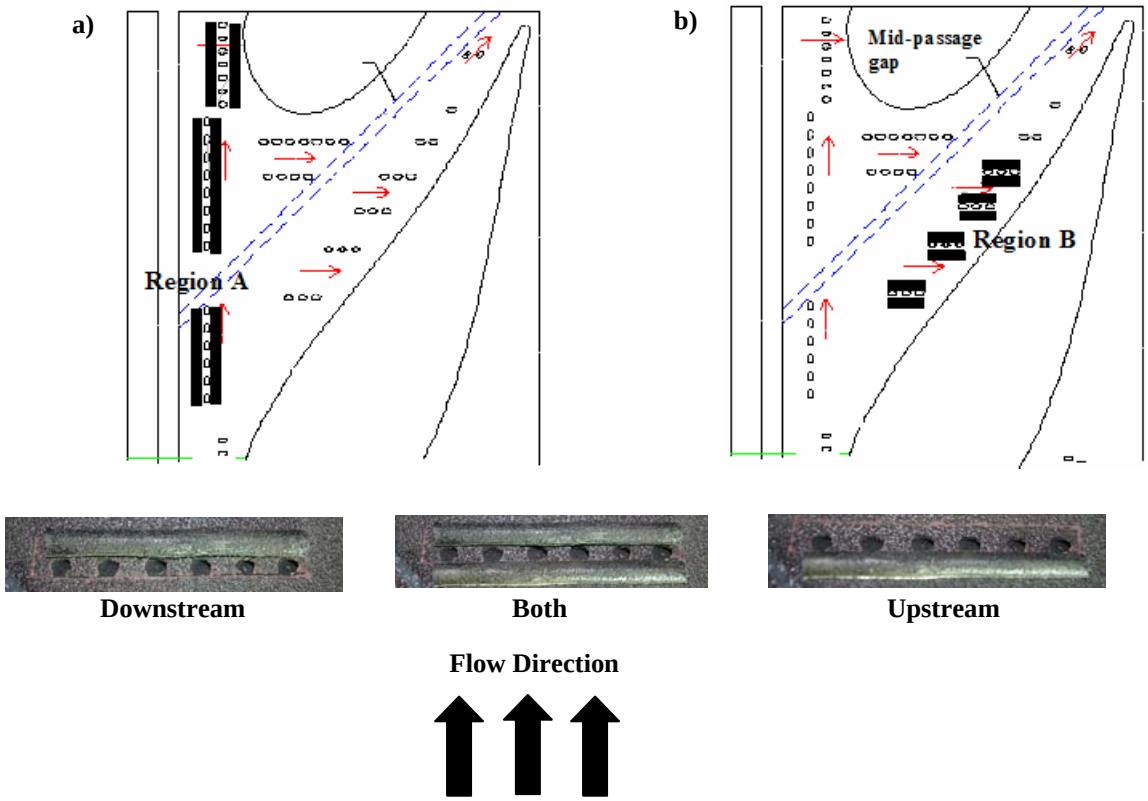

Figure 5.8. Illustrates a) leading edge deposition b) deposition along the pressure side of the vane and c) orientation of deposits with respect to the film-cooling row.

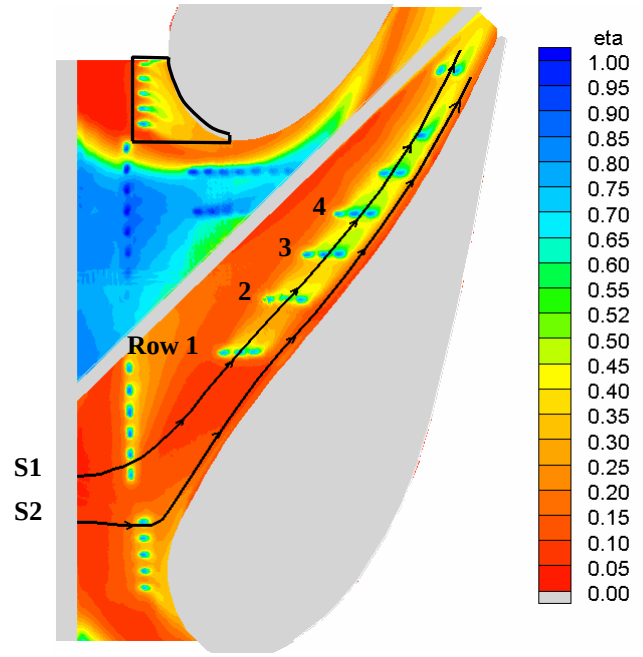

Figure 5.9. Contour of adiabatic effectiveness for the baseline case without any deposition with coolant mass flowrates of 0.75 percent through the upstream slot, 0.5 percent through the film-cooling holes, and 0.2 percent through the mid-passage gap.

Coolant flowrates	
Upstream slot	0.75%
Film-cooling holes	0.5%
Mid-passage gap	0.2%

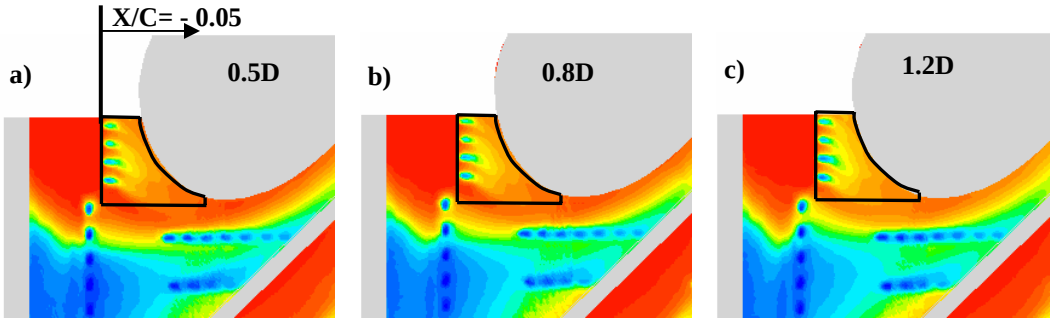

Figure 5.10. Effectiveness contours comparing the effects of different deposit heights at the leading edge stagnation region with deposit placed upstream of the cooling row.

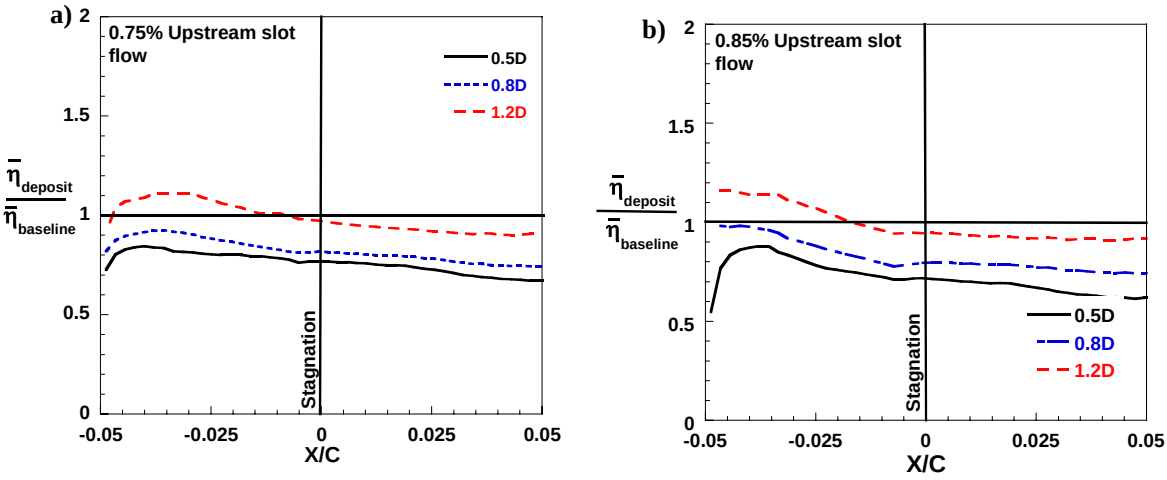

Figure 5.11. Ratio of laterally averaged effectiveness due to different deposit heights at the upstream location with upstream slot coolant mass flowrates of a) 0.75 percent and b) 0.85 percent.

Coolant flowrates	
Upstream slot	0.75%
Film-cooling holes	0.5%
Mid-passage gap	0.2%

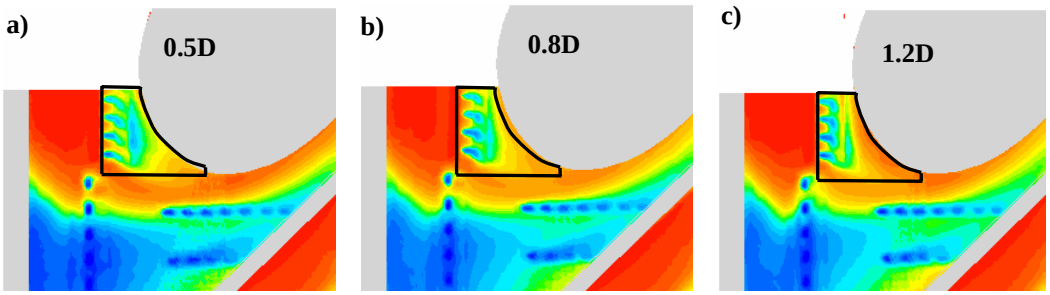

Figure 5.12. Effectiveness contours comparing the effects of different deposit heights at the leading edge stagnation region with deposit placed on either side of the film-cooling row.

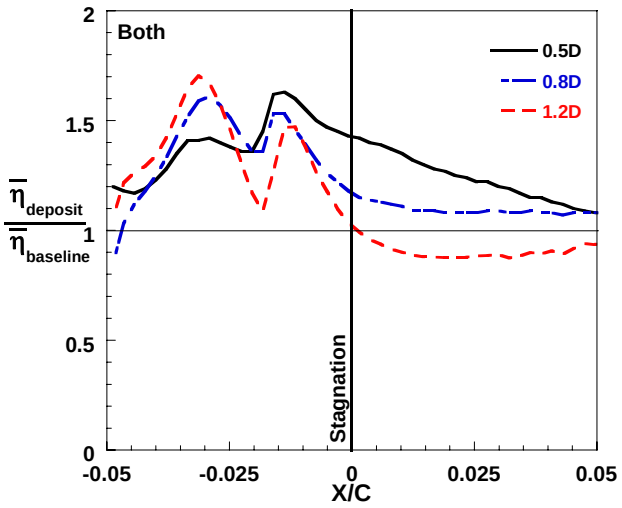

Figure 5.13. Augmentation of laterally averaged effectiveness downstream of the leading edge row (marked region in Figure 5.5) due to deposits of different heights placed on either side of the film-cooling row.

Coolant flowrates	
Film-cooling holes	0.5%
Mid-passage gap	0.2%

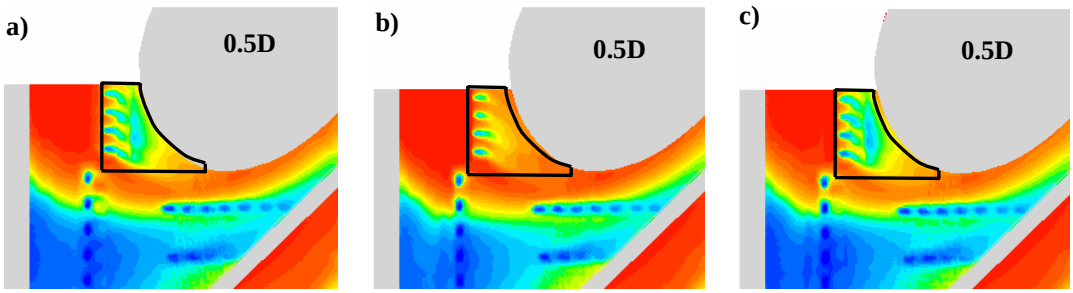

Figure 5.14. Effectiveness contours comparing the effect of placing a 0.5D deposit at a) downstream, b) upstream and c) on both sides of the film-cooling row.

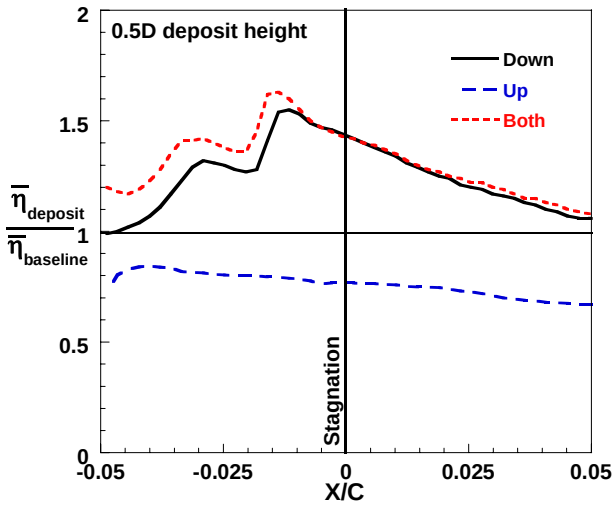

Figure 5.15. Augmentation of laterally averaged effectiveness downstream of the leading edge cooling row (marked region in figure 5.7) due to deposits placed at different locations along the cooling row.

Coolant flowrates	
Film-cooling holes	0.5%
Mid-passage gap	0.2%

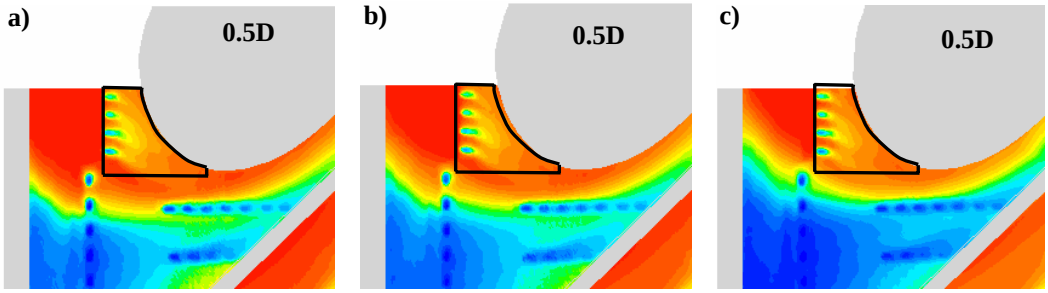

Figure 5.16. Effectiveness contours comparing the effect of upstream deposition at the leading edge with upstream slot coolant flow rate of a) 0.75 percent, b) 0.85 percent, and c) 1.0 percent.

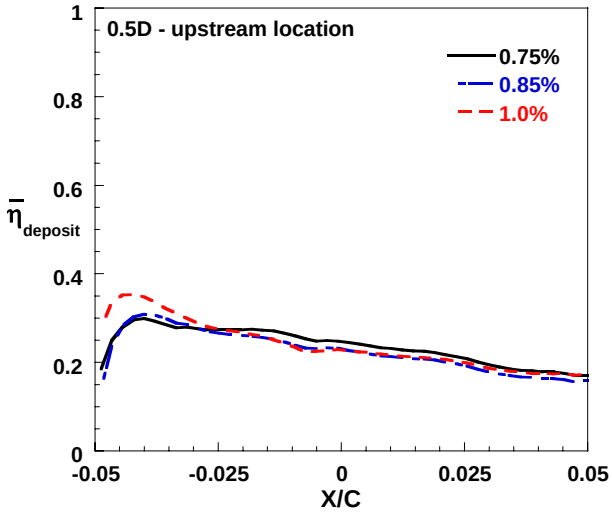

Figure 5.17. Adiabatic effectiveness laterally averaged pitchwise downstream of the leading edge cooling row (marked region in figure 5.9) with upstream deposition.

Coolant flowrates	
Film-cooling holes	0.5%
Mid-passage gap	0.2%

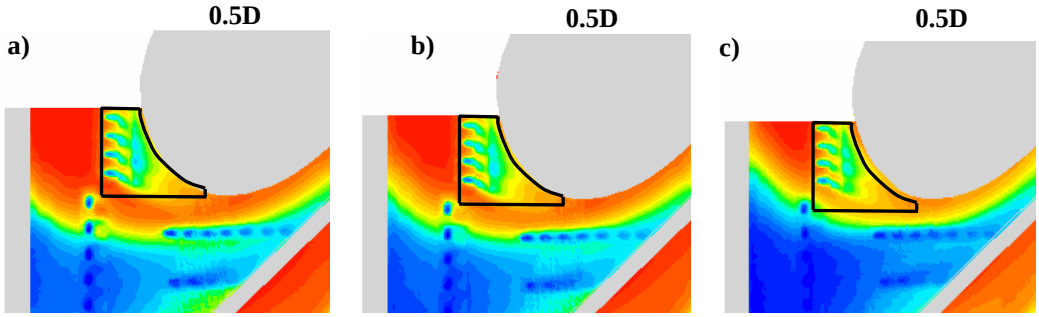

Figure 5.18. Effectiveness contours comparing the effect of downstream deposition at the leading edge with upstream slot coolant flow rate of a) 0.75 percent, b) 0.85 percent, and c) 1.0 percent.

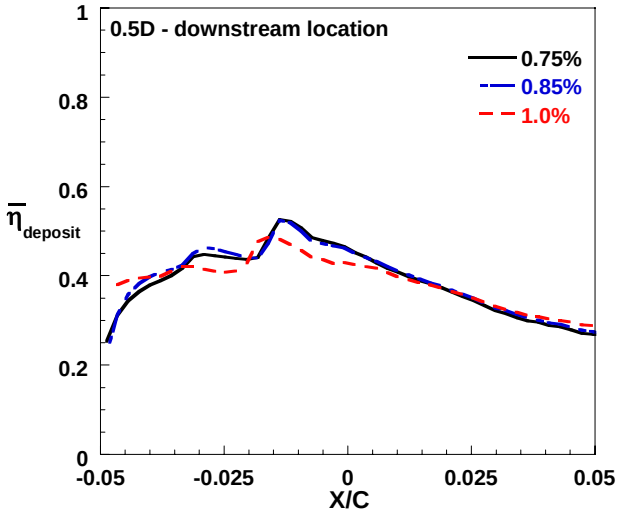

Figure 5.19. Adiabatic effectiveness laterally averaged pitchwise downstream of the leading edge cooling row (marked region in figure 5.11) with downstream deposition.

Coolant flowrates	
Film-cooling holes	0.5%
Mid-passage gap	0.2%

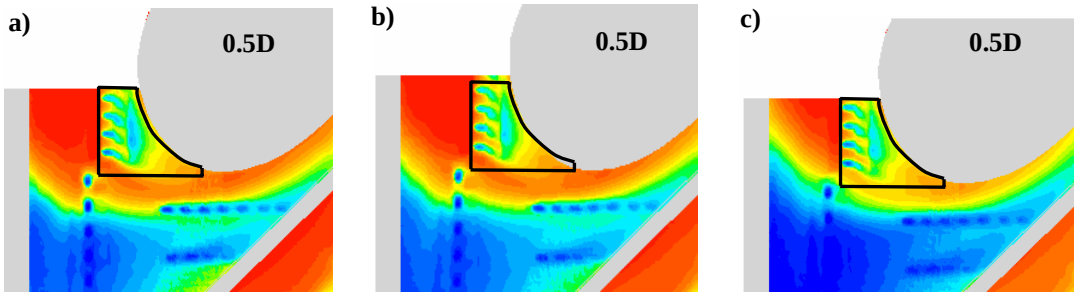

Figure 5.20. Effectiveness contours comparing the effect of deposition on either side of the cooling row at the leading edge with upstream slot coolant flow rate of a) 0.75 percent, b) 0.85 percent, and c) 1.0 percent.

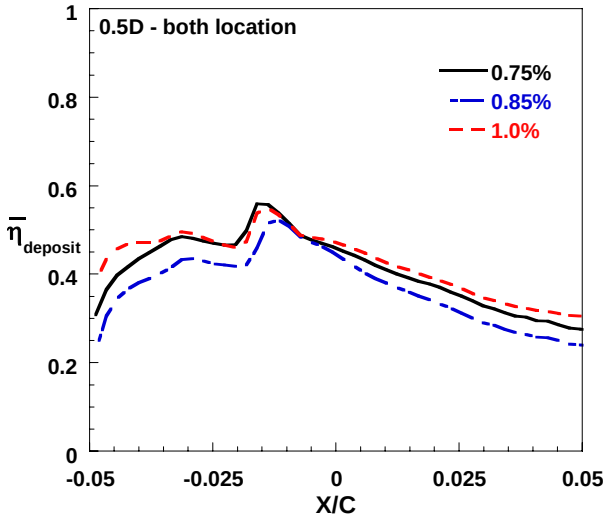

Figure 5.21. Adiabatic effectiveness laterally averaged pitchwise downstream of the leading edge cooling row (marked region in figure 5.13) with deposition on both sides of the cooling row.

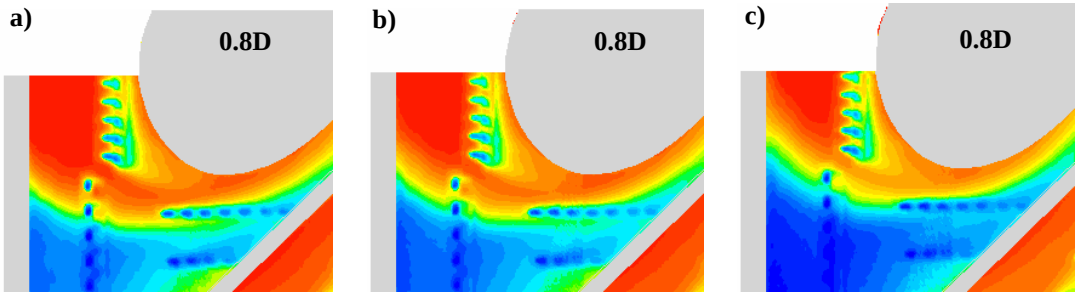

Figure 5.22. Effectiveness contours comparing the effect of downstream deposition at the leading edge with upstream slot coolant flow rate of a) 0.75 percent, b) 0.85 percent, and c) 1.0 percent.

Coolant flowrates	
Film-cooling holes	0.5%
Mid-passage gap	0.2%

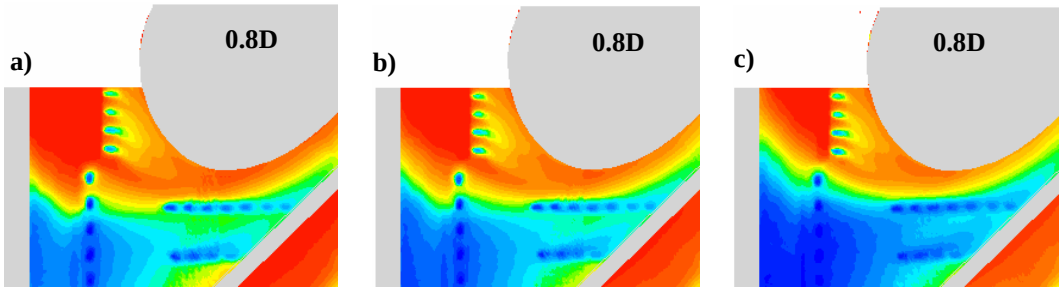

Figure 5.23. Effectiveness contours comparing the effect of upstream deposition at the leading edge with upstream slot coolant flow rate of a) 0.75 percent, b) 0.85 percent, and c) 1.0 percent.

Coolant flowrates	
Film-cooling holes	0.5%
Mid-passage gap	0.2%

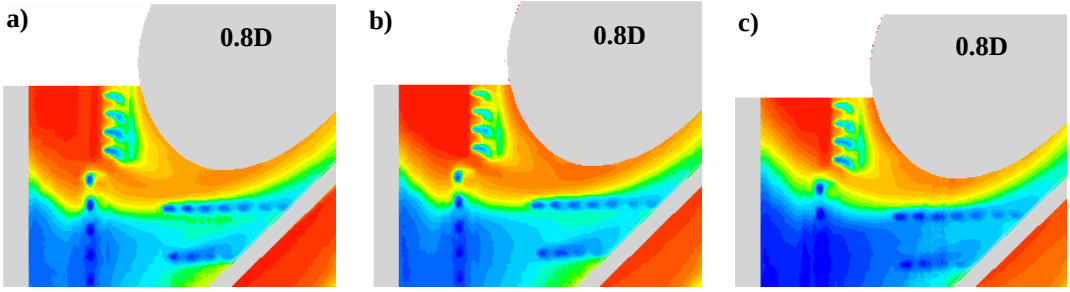

Figure 5.24. Effectiveness contours comparing the effect of deposition on either side of the cooling row at the leading edge with upstream slot coolant flow rate of a) 0.75 percent, b) 0.85 percent, and c) 1.0 percent.

Coolant flowrates	
Film-cooling holes	0.5%
Mid-passage gap	0.2%

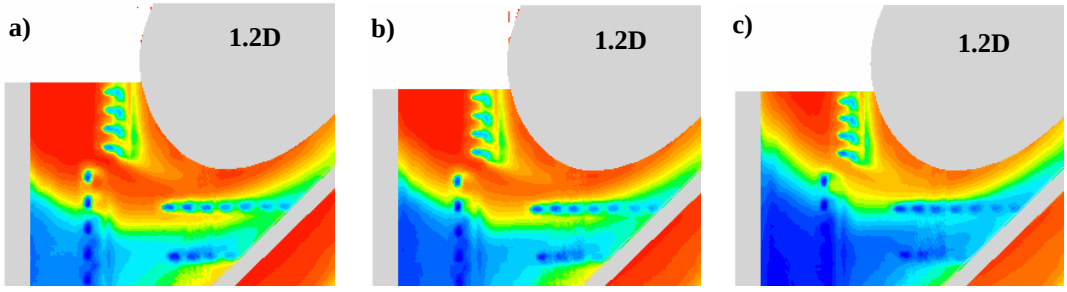

Figure 5.25. Effectiveness contours comparing the effect of downstream deposition at the leading edge with upstream slot coolant flow rate of a) 0.75 percent, b) 0.85 percent, and c) 1.0 percent.

Coolant flowrates	
Upstream slot	0.75%
Film-cooling holes	0.5%
Mid-passage gap	0.2%

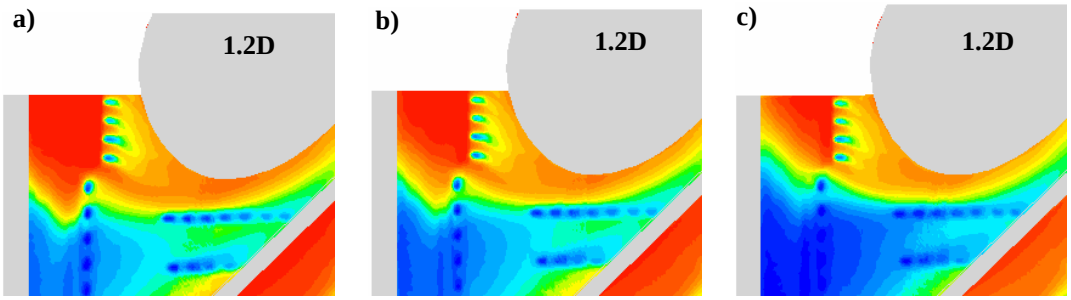

Figure 5.26. Effectiveness contours comparing the effect of upstream deposition at the leading edge with upstream slot coolant flow rate of a) 0.75 percent, b) 0.85 percent, and c) 1.0 percent.

Coolant flowrates	
Film-cooling holes	0.5%
Mid-passage gap	0.2%

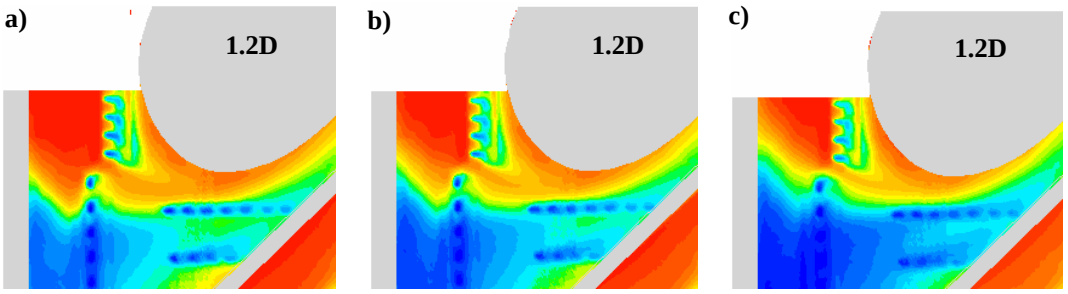

Figure 5.27. Effectiveness contours comparing the effect of deposition on either side of the cooling row at the leading edge with upstream slot coolant flow rate of a) 0.75 percent, b) 0.85 percent, and c) 1.0 percent.

Coolant flowrates	
Film-cooling holes	0.5%
Mid-passage gap	0.2%

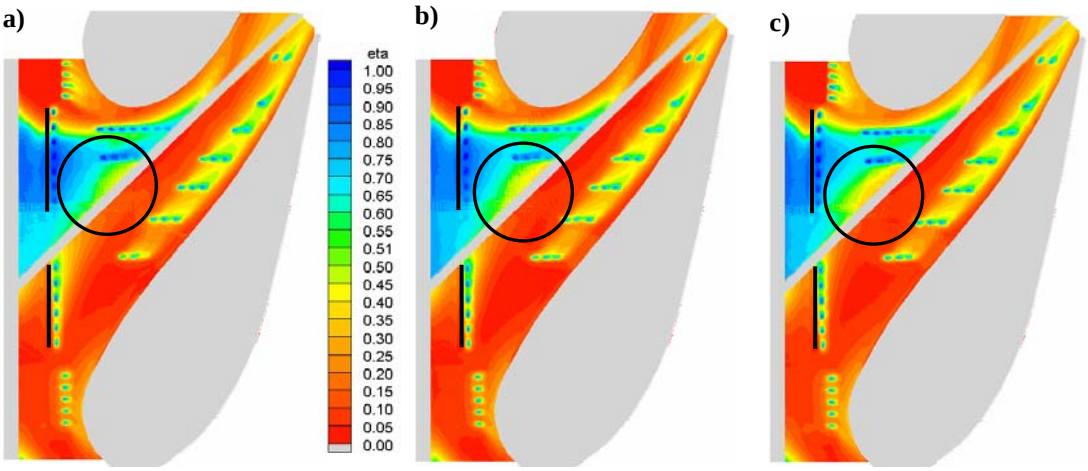

Figure 5.28. Effectiveness contours showing the effect of deposition at the leading edge between the stagnation regions of the two vanes for deposit heights of a) 0.5D, b) 0.8D, and c) 1.2D.

Coolant flowrates	
Upstream slot	0.75%
Film-cooling holes	0.5%
Mid-passage gap	0.2%

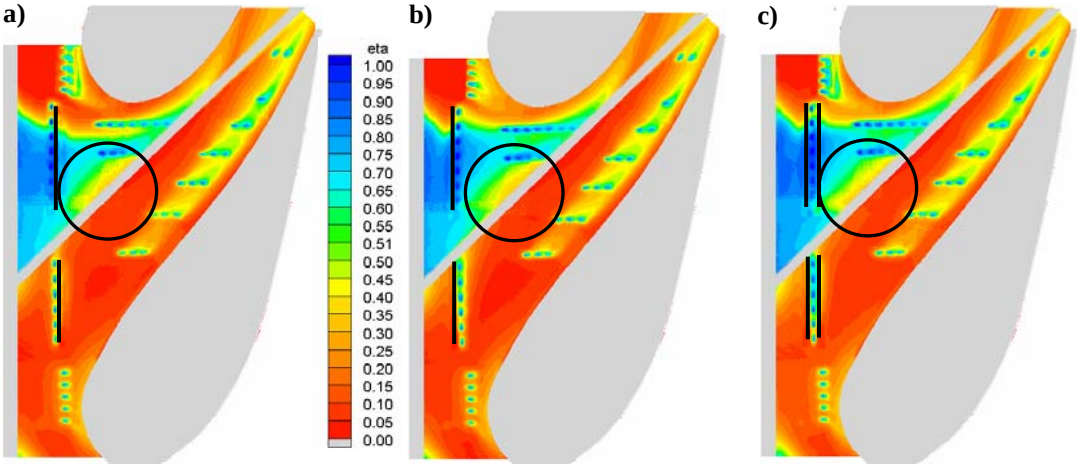

Figure 5.29. Effectiveness contours showing the effect of 1.2D deposition at the leading edge with deposit placed at a) downstream, b) upstream, and c) on both sides of the cooling row.

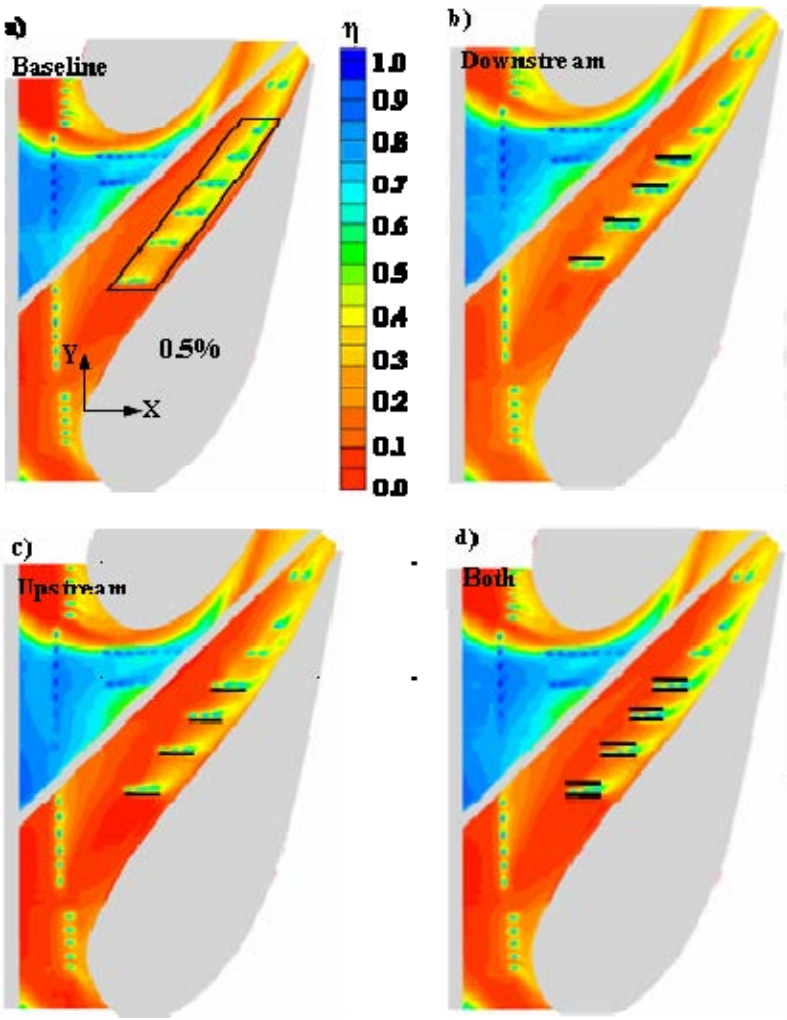

Figure 5.30 Contours of adiabatic effectiveness comparing the effect of deposit location for a) Nominal case without deposition, b) Deposit downstream of the cooling rows, c) Deposit upstream of the cooling rows, and d) Deposit at either side of the cooling rows.

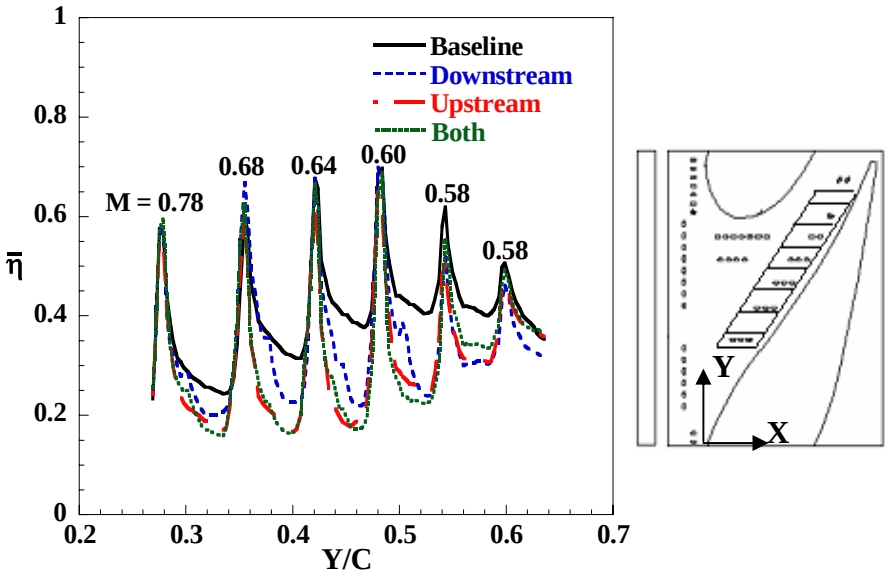

Figure 5.31 Compares the laterally averaged effectiveness along pressure side for different deposit locations.

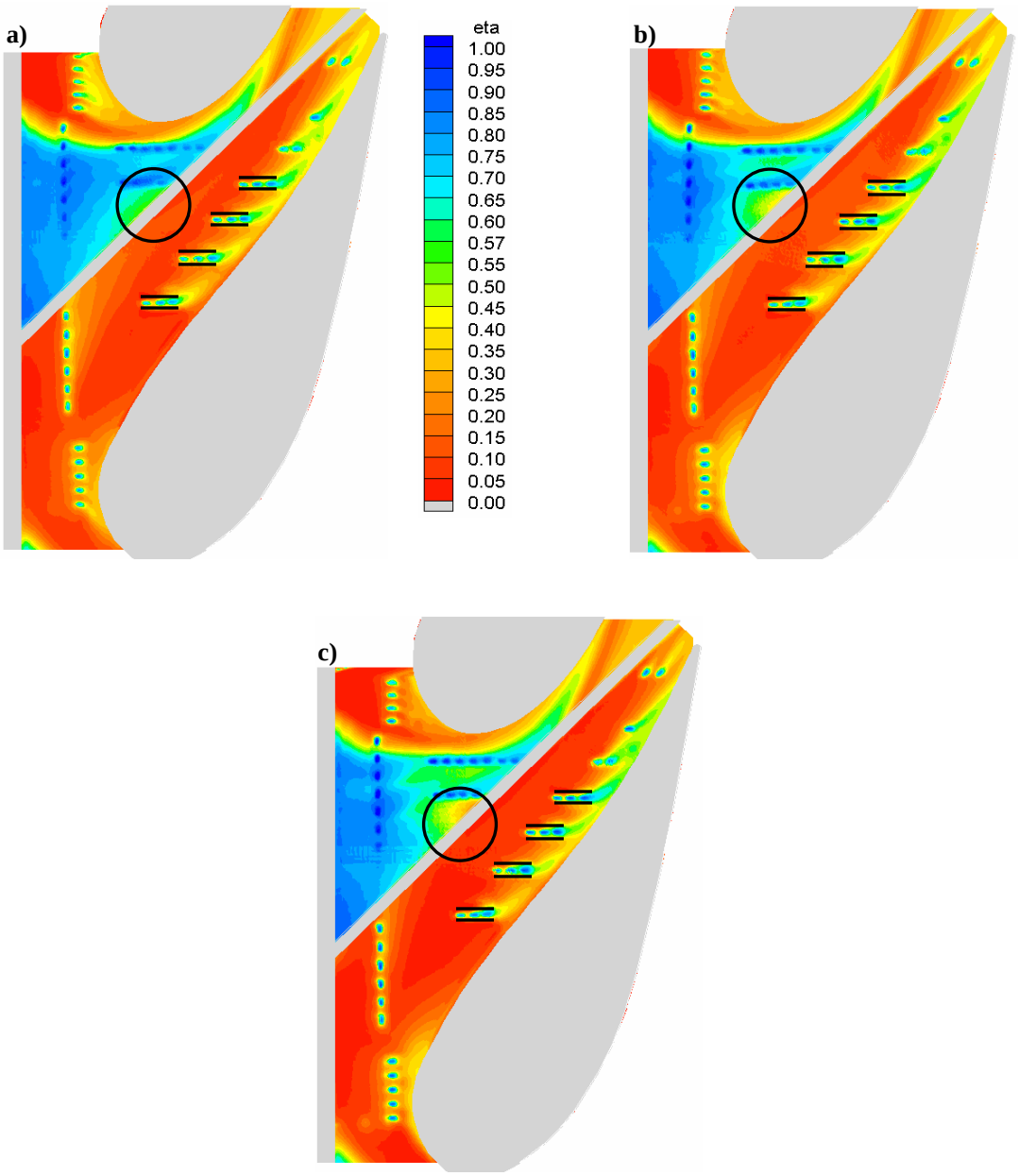

Figure 5.32 Compares the contours of adiabatic effectiveness for deposits placed on either side of the four cooling rows on the pressure side for a film-cooling mass flowrate of a) 0.5%, b) 0.75%, and c) 0.9% of the main core flow.

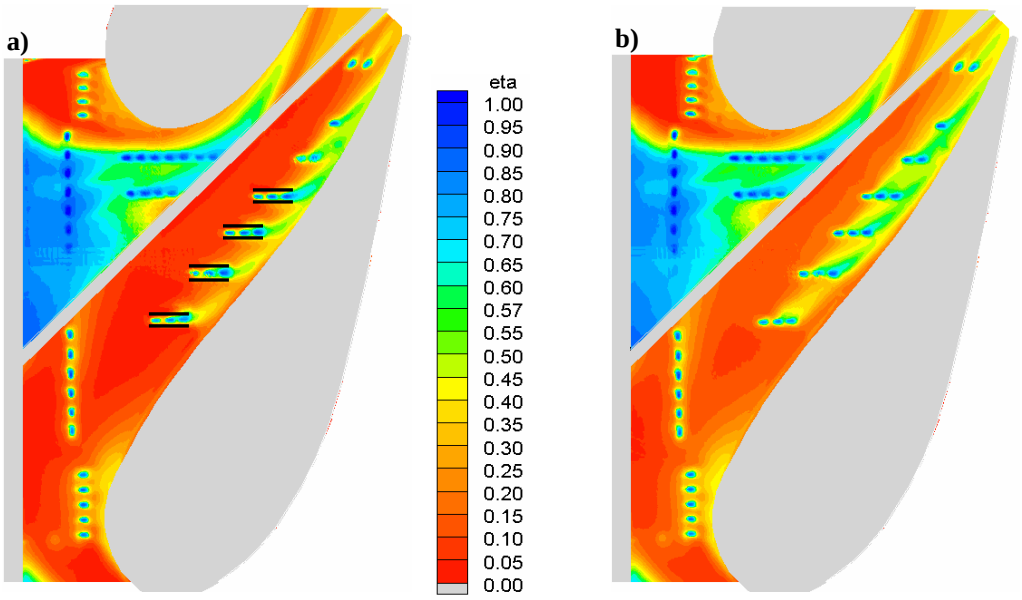

Figure 5.33 Contours of adiabatic effectiveness comparing the effect of deposition along pressure side at a high coolant mass flowrate of 0.9%.

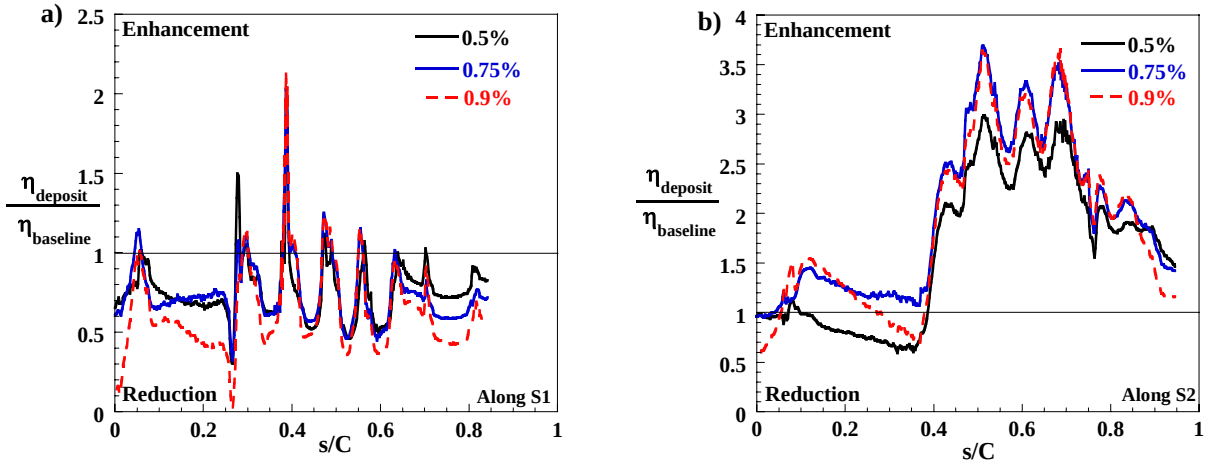

Figure 5.34. Change in adiabatic effectiveness levels along streamlines S1 and S2 (refer Figure 5.2) for deposits on both sides of the cooling rows.

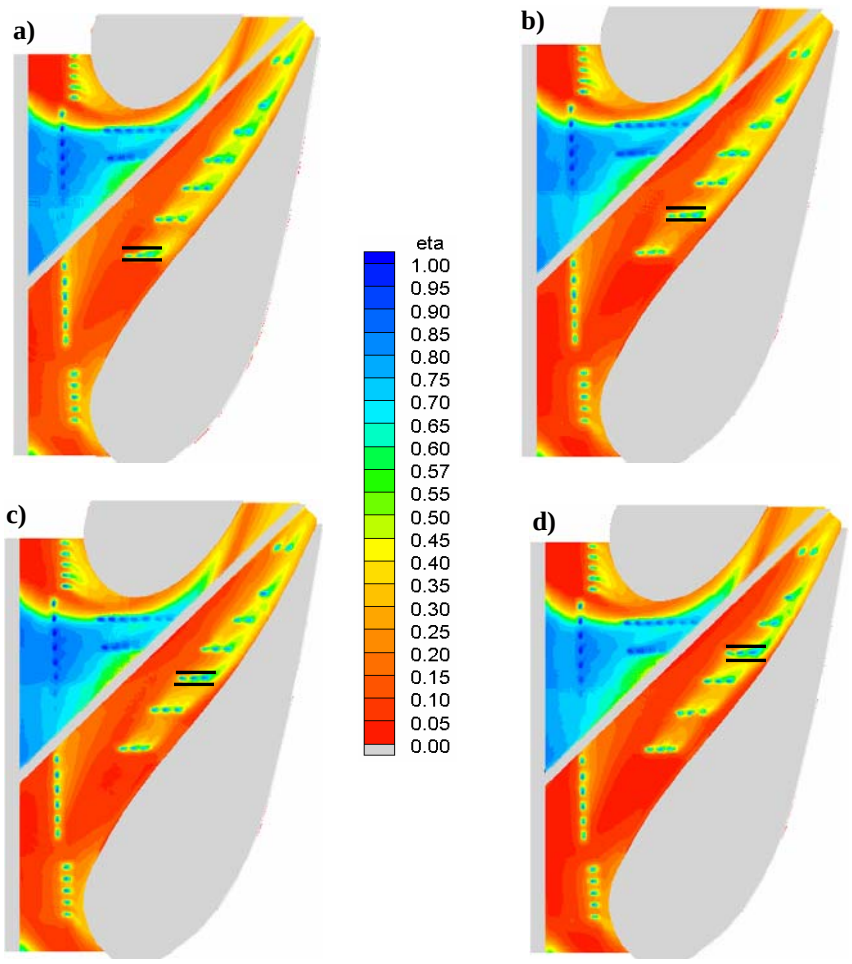

Figure 5.35 Contours of adiabatic effectiveness showing the effect of deposit at each individual row from a) Row 1, b) Row 2, c) Row 3, and d) Row 4 along the pressure side on the endwall for a film-cooling flow rate of 0.5%.

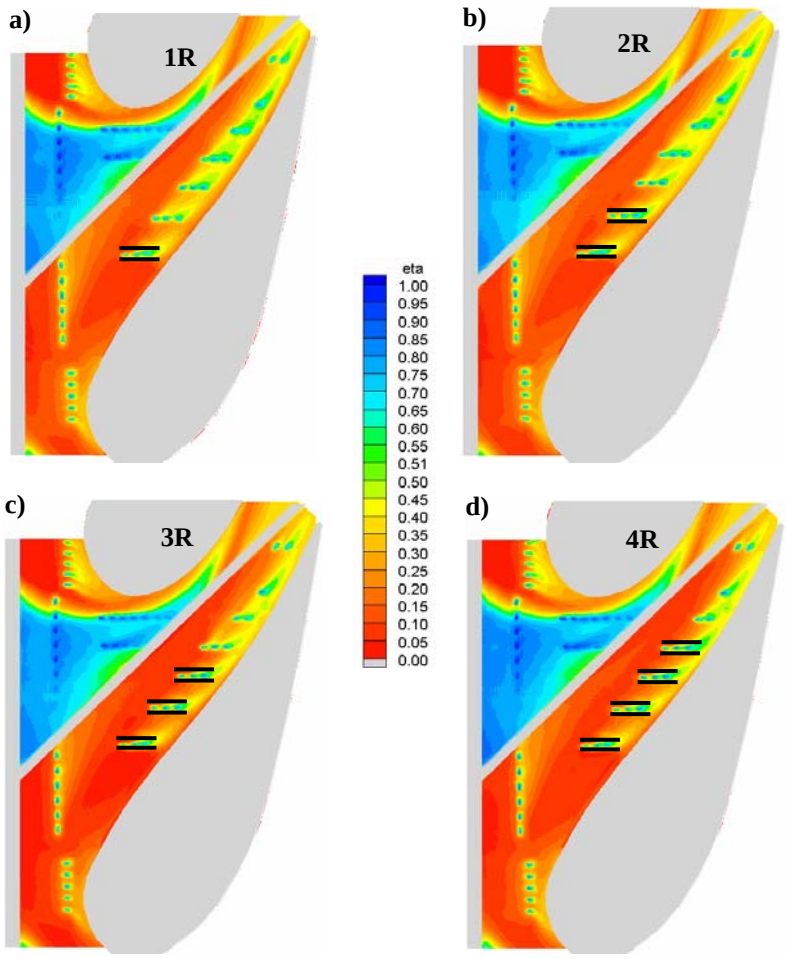

Figure 5.36. Adiabatic effectiveness contours showing the effect of sequentially increasing the number of row deposits from row 1 to row 4 along the pressure side film-cooling holes.

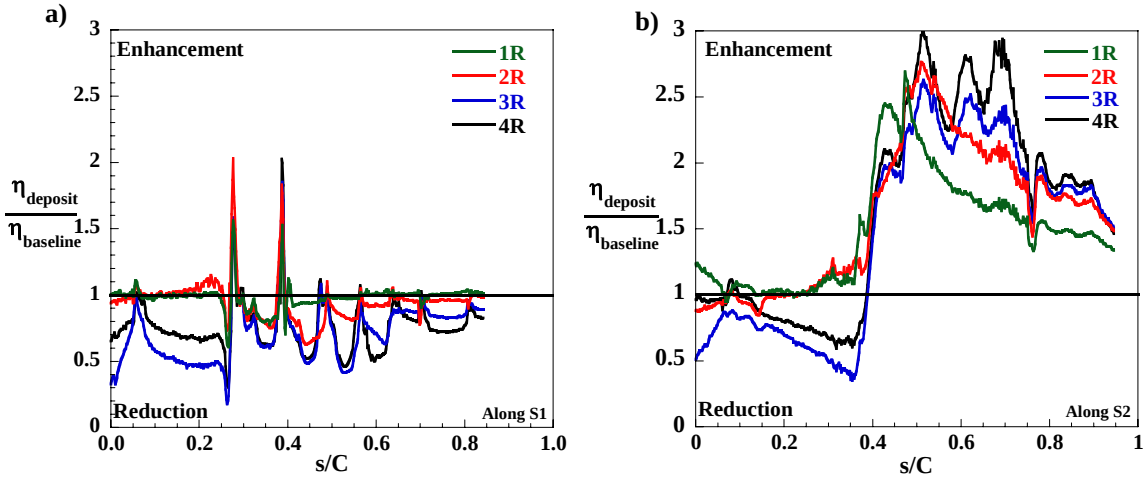

Figure 5.37. Change in adiabatic effectiveness levels along streamlines S1 and S2 (refer Figure 5.2) caused by sequential increment of deposits from row 1 to row 4.

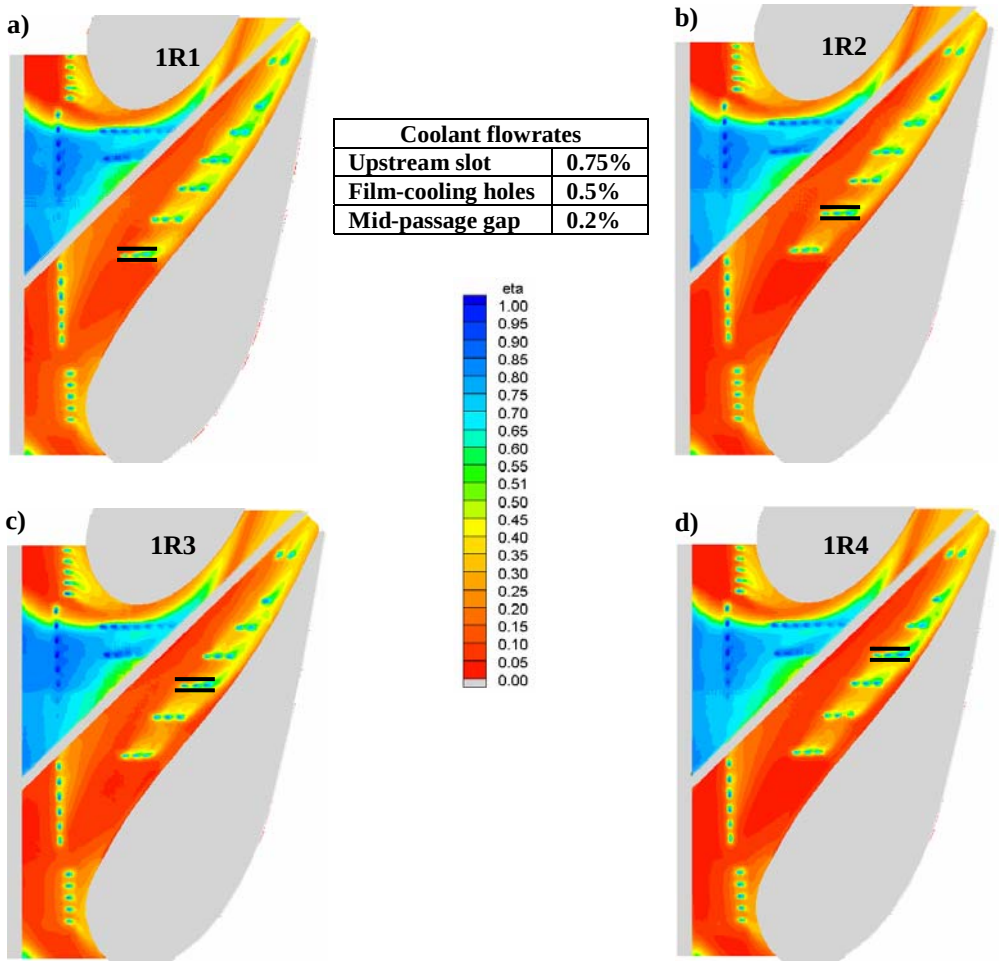

Figure 5.38. Adiabatic effectiveness contours showing the effect of single row deposits along the pressure side film-cooling holes.

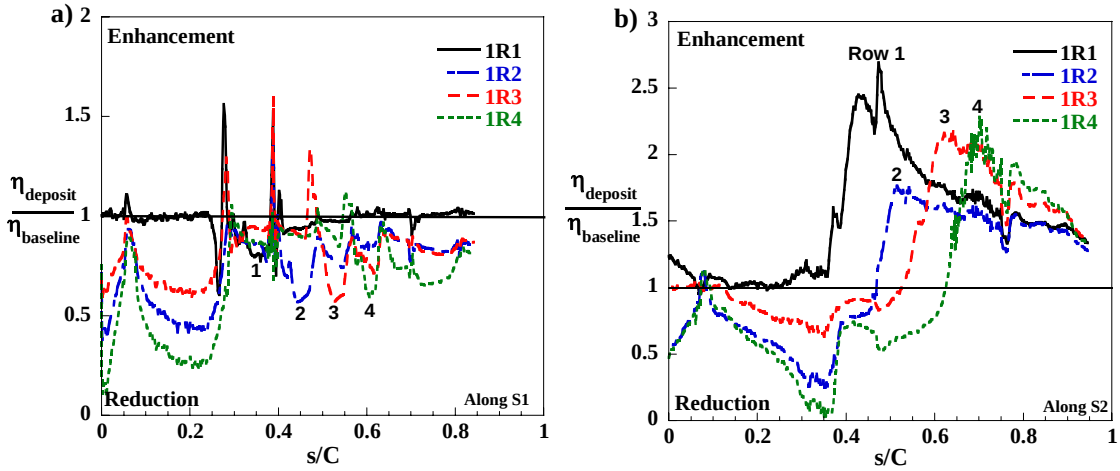

Figure 5.39. Change in adiabatic effectiveness levels along streamlines S1 and S2 (refer Figure 5.2) caused by single row deposition from row 1 to row4.

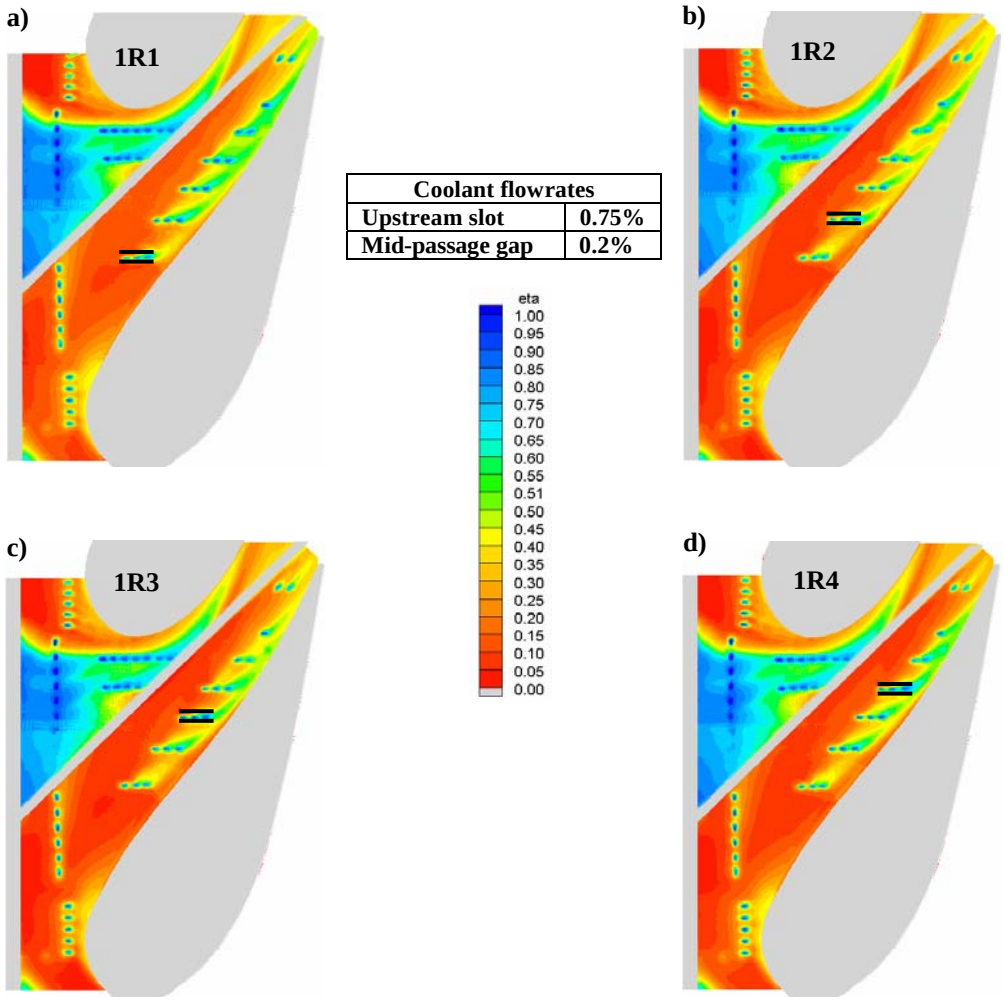

Figure 5.40. Adiabatic effectiveness contours showing the effect of single row deposits along the pressure side film-cooling holes for a film-cooling mass flowrate of 0.9 percent.

Coolant flowrates	
Upstream slot	0.75%
Mid-passage gap	0.2%

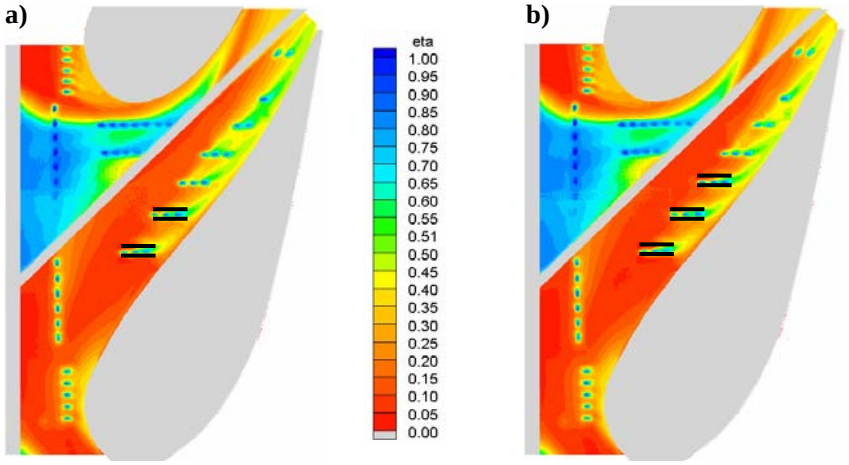

Figure 5.41. Adiabatic effectiveness contours showing the effect of multiple row deposits along the pressure side film-cooling holes for a film-cooling mass flowrate of 0.75 percent.

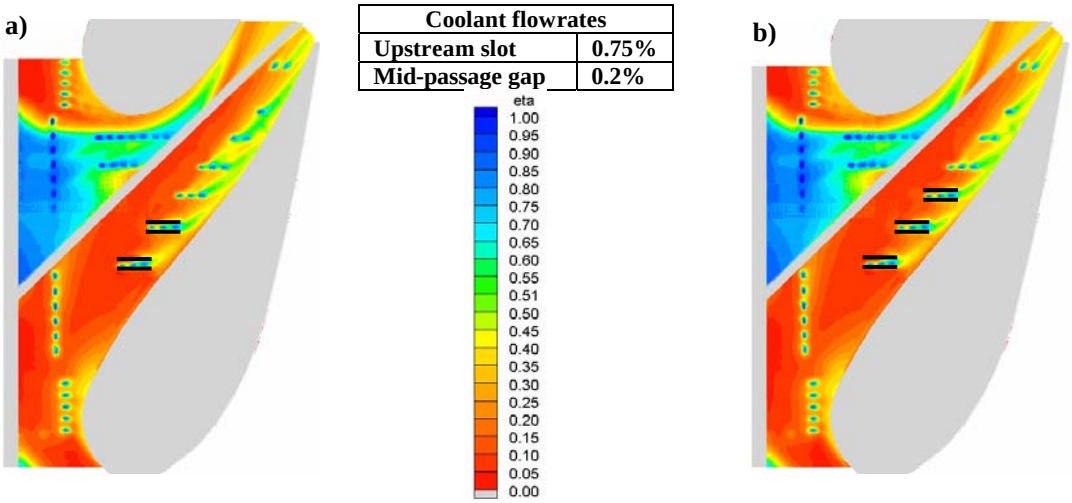

Figure 5.42. Adiabatic effectiveness contours showing the effect of multiple row deposits along the pressure side film-cooling holes for a film-cooling mass flowrate of 0.9 percent.

Coolant flowrates	
Upstream slot	0.75%
Mid-passage gap	0.2%

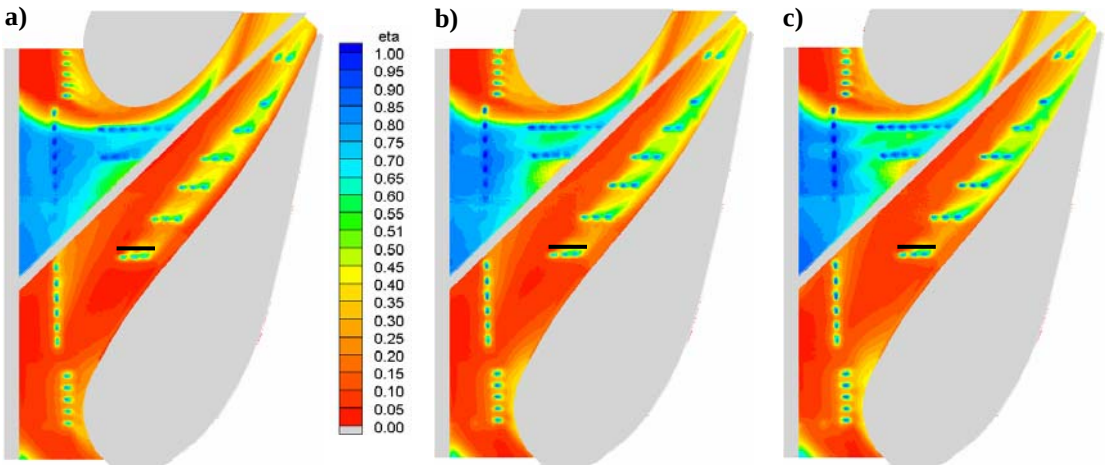

Figure 5.43. Adiabatic effectiveness contours with 0.8D deposition downstream of row 1 film-cooling holes with coolant mass flowrates of a) 0.5 percent, b) 0.75 percent, and c) 0.9 percent.

Coolant flowrates	
Upstream slot	0.75%
Mid-passage gap	0.2%

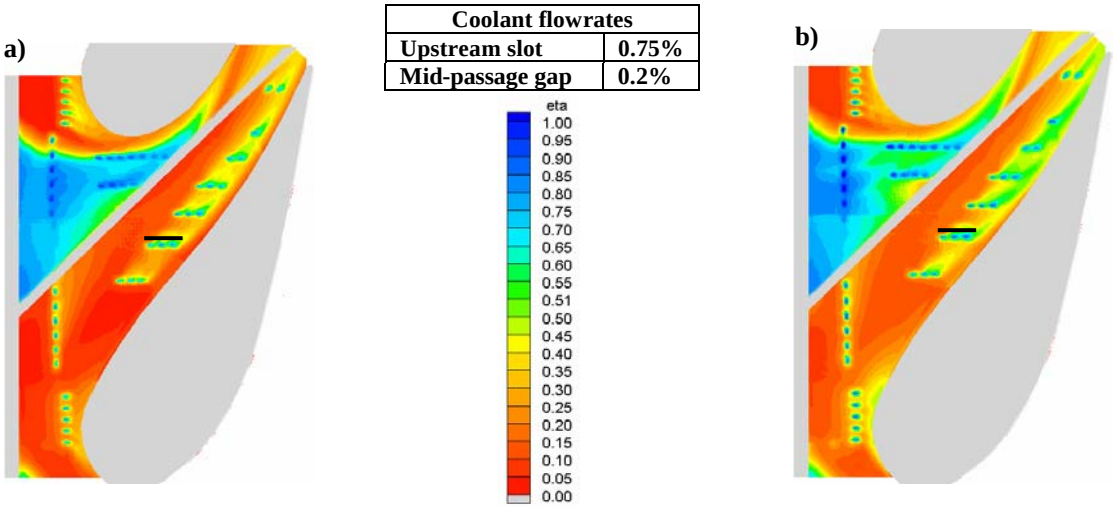

Figure 5.44. Adiabatic effectiveness contours with 0.8D deposition downstream of row 2 film-cooling holes with coolant mass flowrates of a) 0.5 percent and b) 0.9 percent.

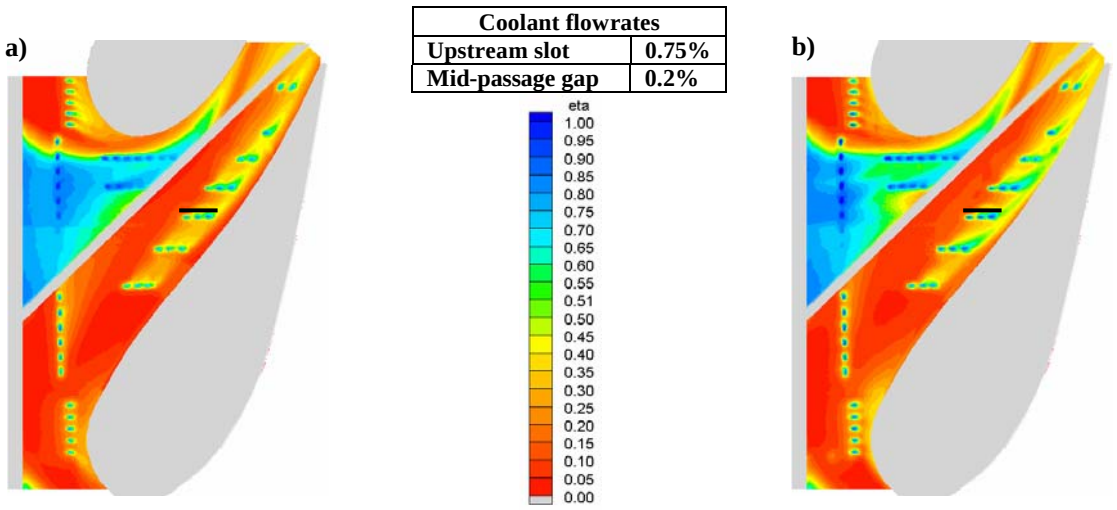

Figure 5.45. Adiabatic effectiveness contours with 0.8D deposition downstream of row 3 film-cooling holes with coolant mass flowrates of a) 0.5 percent and b) 0.9 percent.

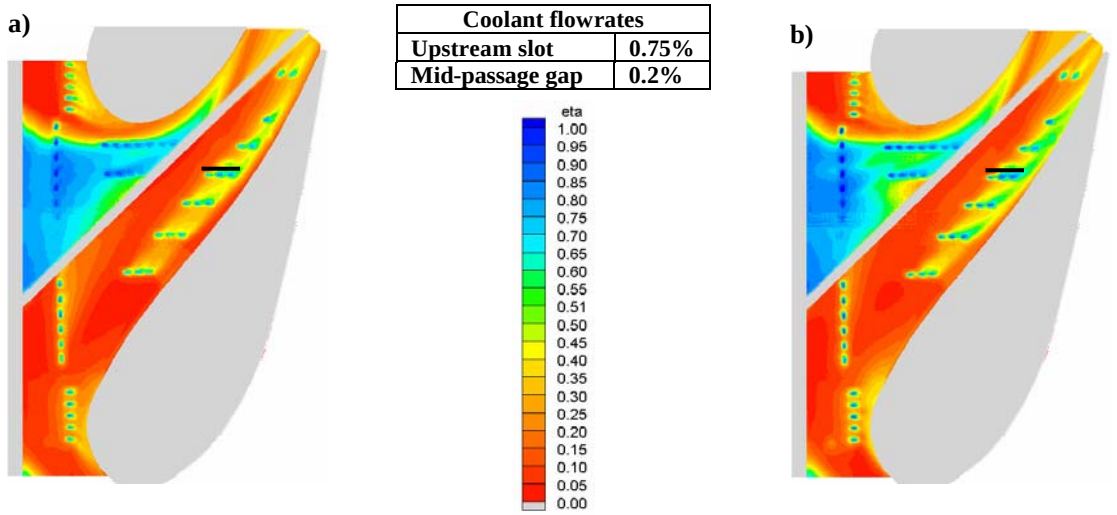

Figure 5.46. Adiabatic effectiveness contours with 0.8D deposition downstream of row 4 film-cooling holes with coolant mass flowrates of a) 0.5 percent and b) 0.9 percent.

Coolant flowrates	
Upstream slot	0.75%
Mid-passage gap	0.2%

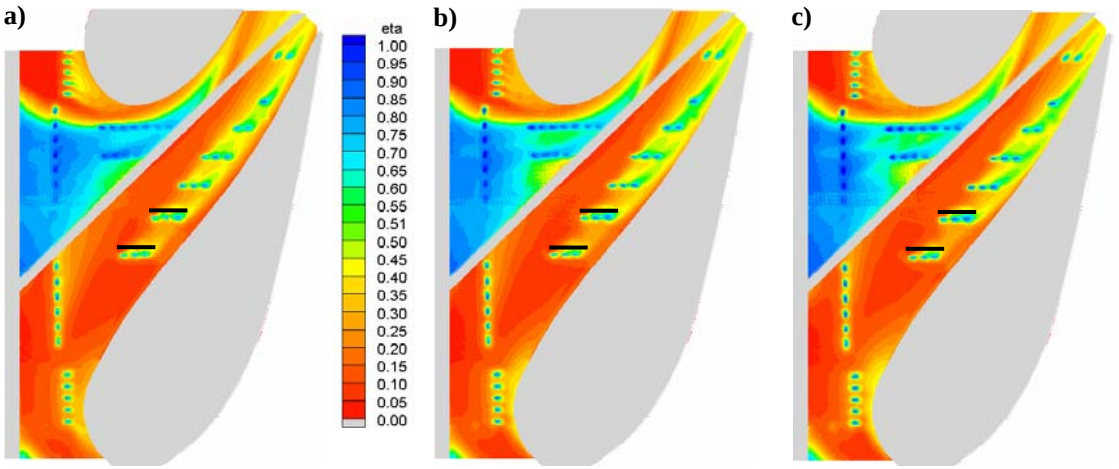

Figure 5.47. Adiabatic effectiveness contours with 0.8D deposition downstream of row 1 and 2 film-cooling holes with coolant mass flowrates of a) 0.5 percent, b) 0.75 percent and c) 0.9 percent.

Coolant flowrates	
Upstream slot	0.75%
Mid-passage gap	0.2%

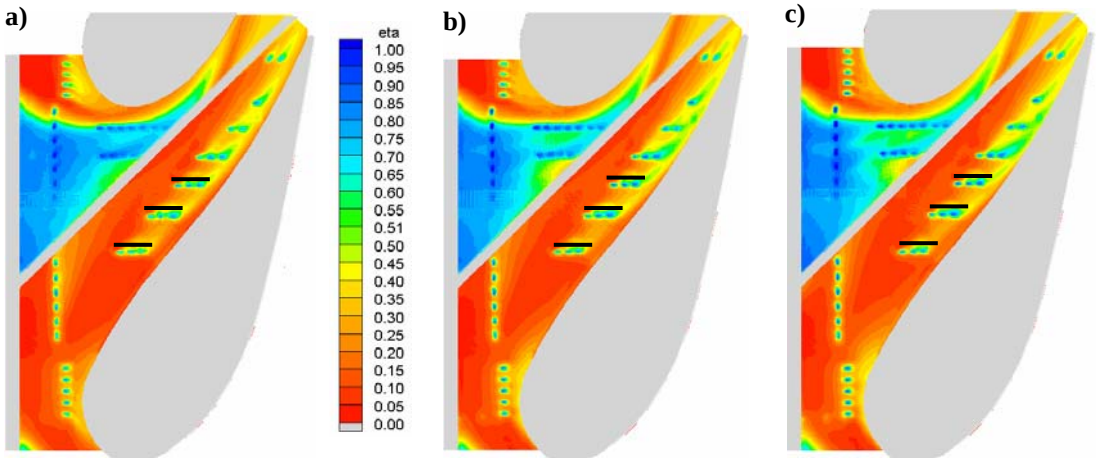

Figure 5.48. Adiabatic effectiveness contours with 0.8D deposition downstream of row 1, 2 and 3 film-cooling holes with coolant mass flowrates of a) 0.5 percent, b) 0.75 percent and c) 0.9 percent.

Coolant flowrates	
Upstream slot	0.75%
Mid-passage gap	0.2%

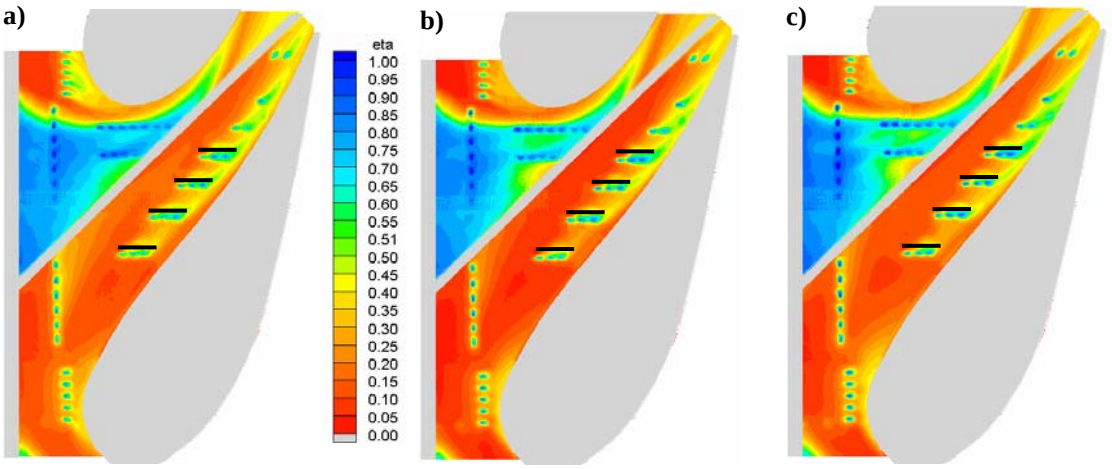

Figure 5.49. Adiabatic effectiveness contours with 0.8D deposition downstream of all four rows of film-cooling holes with coolant mass flowrates of a) 0.5 percent, b) 0.75 percent and c) 0.9 percent.

Coolant flowrates	
Upstream slot	0.75%
Mid-passage gap	0.2%

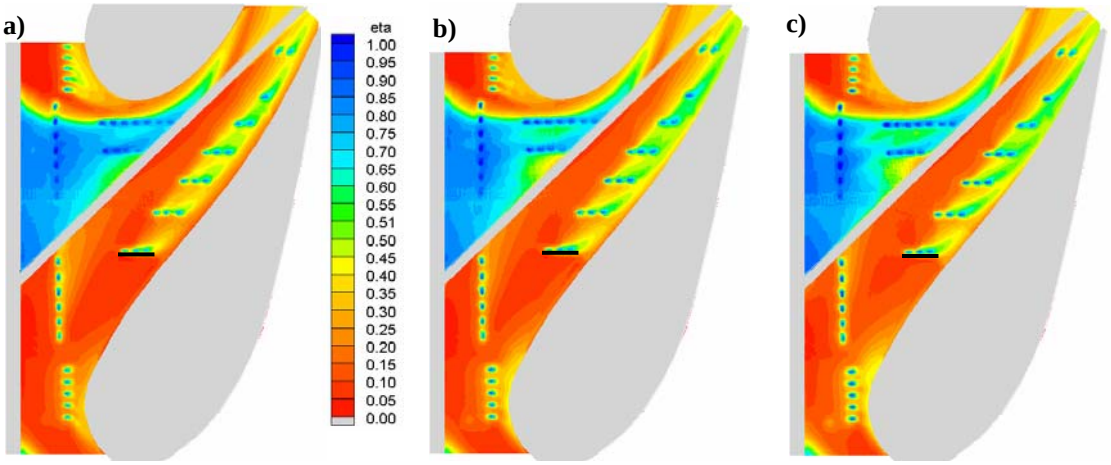

Figure 5.50. Adiabatic effectiveness contours with 0.8D deposition upstream of row 1 film-cooling holes with coolant mass flowrates of a) 0.5 percent, b) 0.75 percent, and c) 0.9 percent.

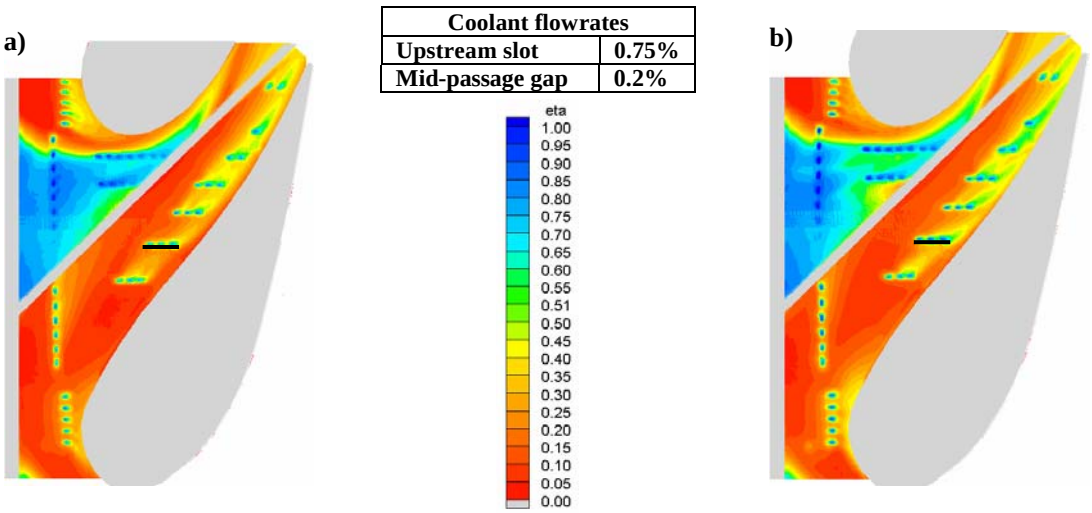

Figure 5.51. Adiabatic effectiveness contours with 0.8D deposition upstream of row 2 film-cooling holes with coolant mass flowrates of a) 0.5 percent and b) 0.9 percent.

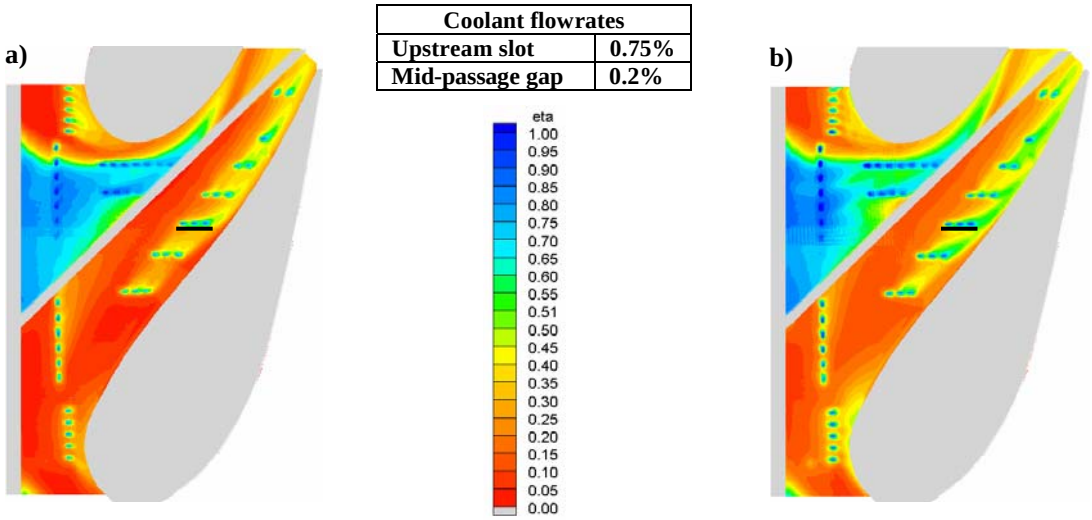

Figure 5.52. Adiabatic effectiveness contours with 0.8D deposition upstream of row 3 film-cooling holes with coolant mass flowrates of a) 0.5 percent and b) 0.9 percent.

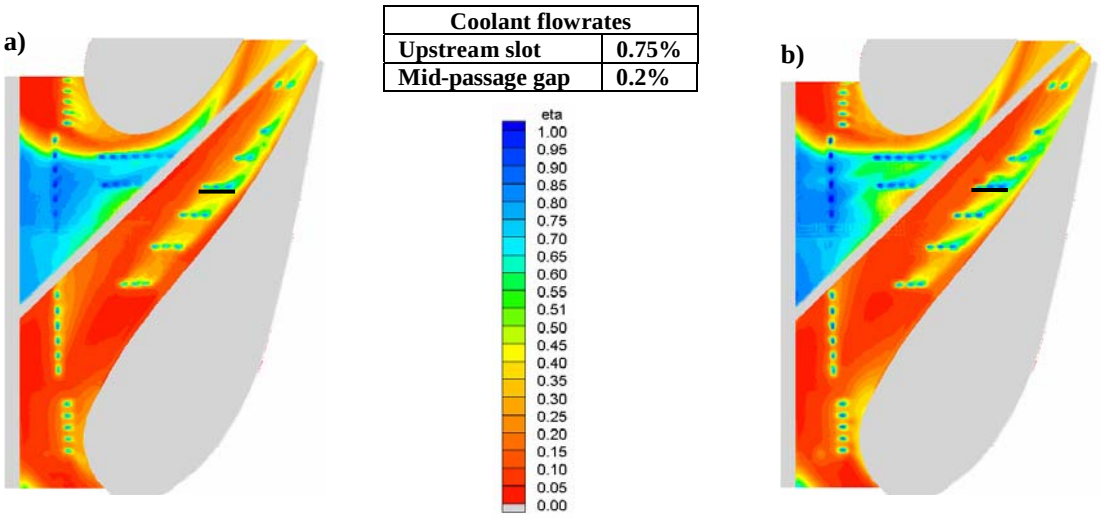

Figure 5.53. Adiabatic effectiveness contours with 0.8D deposition upstream of row 4 film-cooling holes with coolant mass flowrates of a) 0.5 percent and b) 0.9 percent.

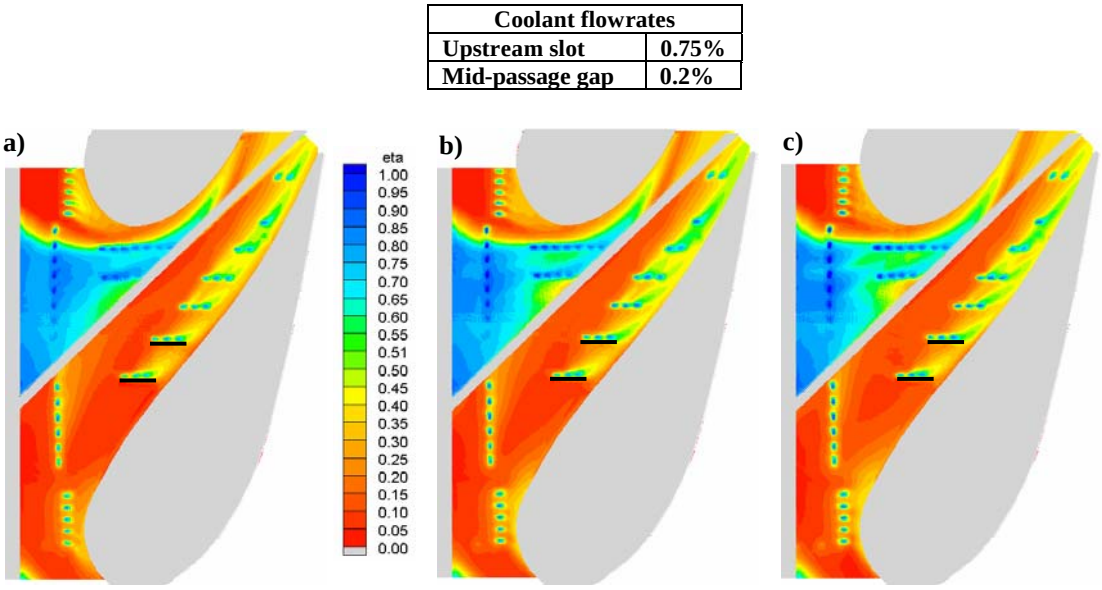

Figure 5.54. Adiabatic effectiveness contours with 0.8D deposition upstream of row 1 and 2 film-cooling holes with coolant mass flowrates of a) 0.5 percent, b) 0.75percent and c) 0.9 percent.

Coolant flowrates	
Upstream slot	0.75%
Mid-passage gap	0.2%

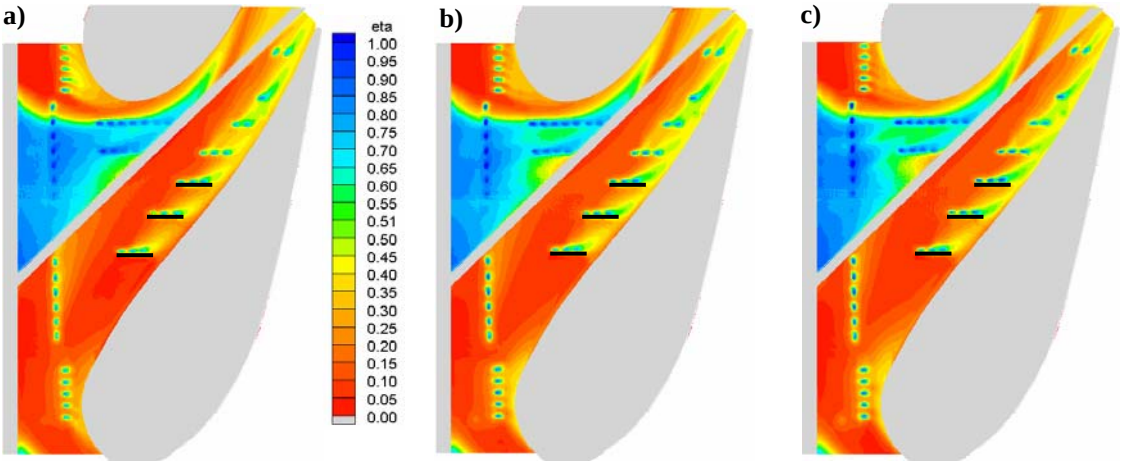

Figure 5.55. Adiabatic effectiveness contours with 0.8D deposition upstream of row 1, 2, and 3 film-cooling holes with coolant mass flowrates of a) 0.5 percent, b) 0.75 percent and c) 0.9 percent.

Coolant flowrates	
Upstream slot	0.75%
Mid-passage gap	0.2%

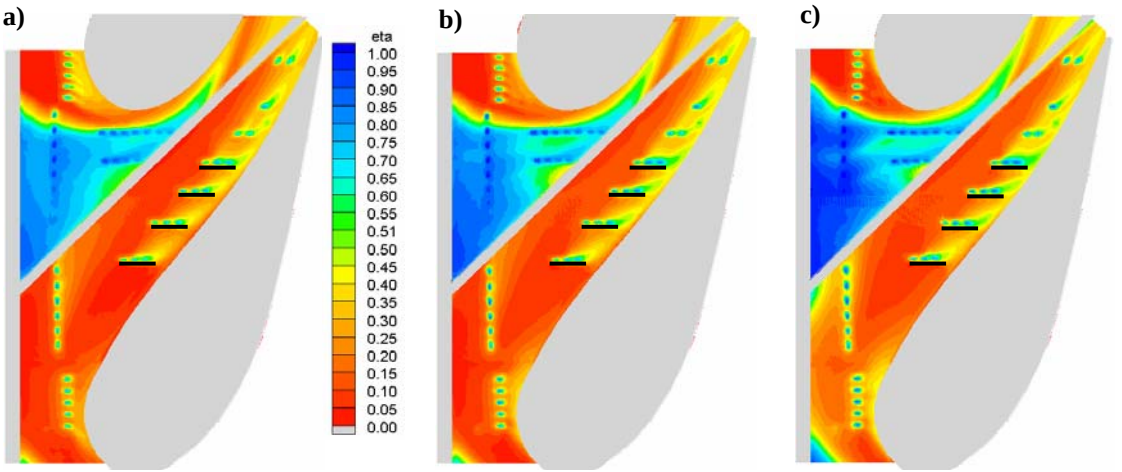

Figure 5.56. Adiabatic effectiveness contours with 0.8D deposition upstream of all four rows of film-cooling holes with coolant mass flowrates of a) 0.5 percent, b) 0.75 percent and c) 0.9 percent.

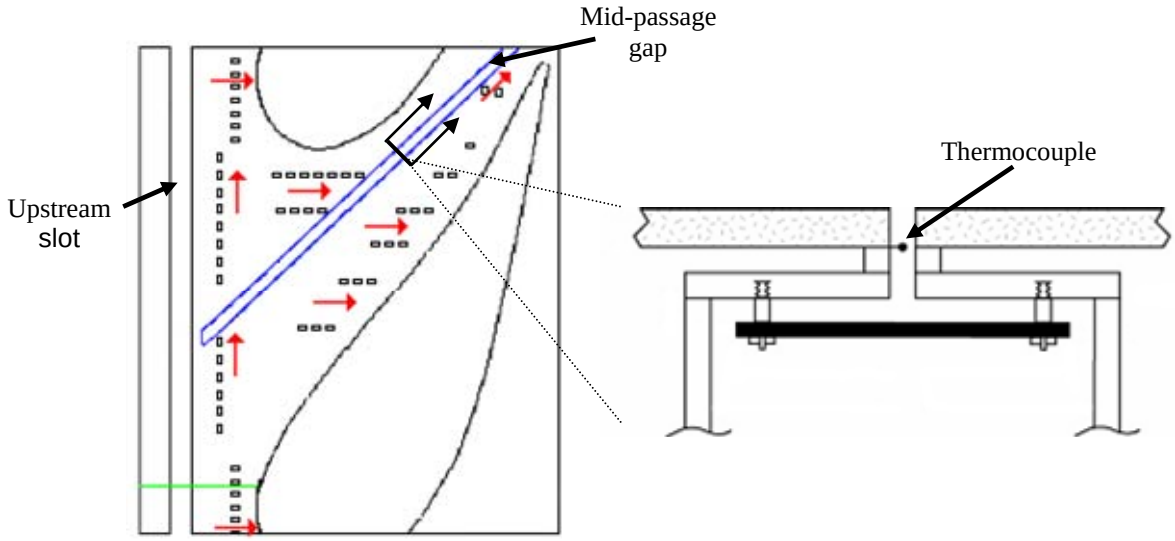

Figure 6.1 Endwall geometry with film-cooling holes, an upstream slot, and a mid-passage gap (with cross sectional view).

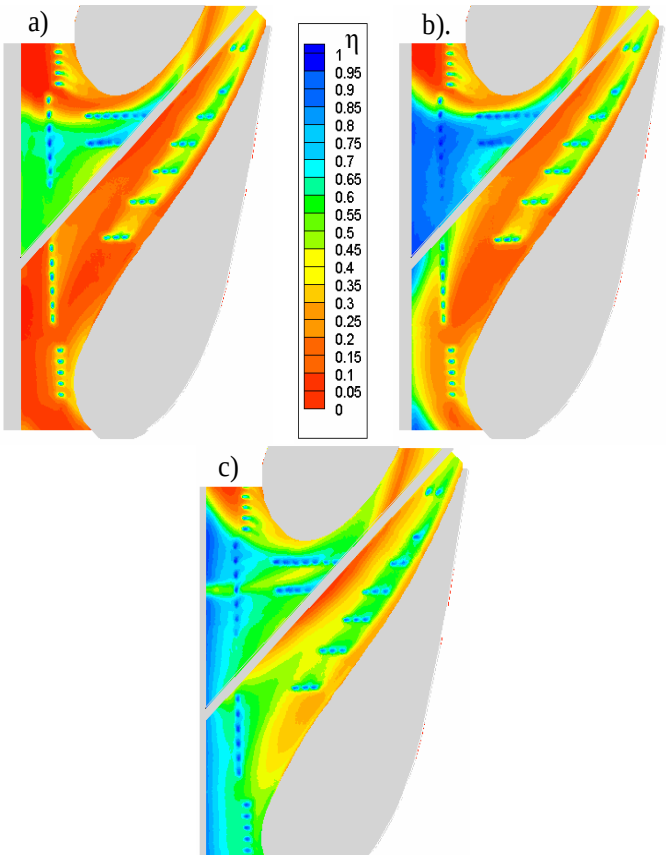

Figure 6.2. Contours of adiabatic effectiveness for a) double, b) nominal c) half width upstream slot with 0.85% slot mass flow ratio.

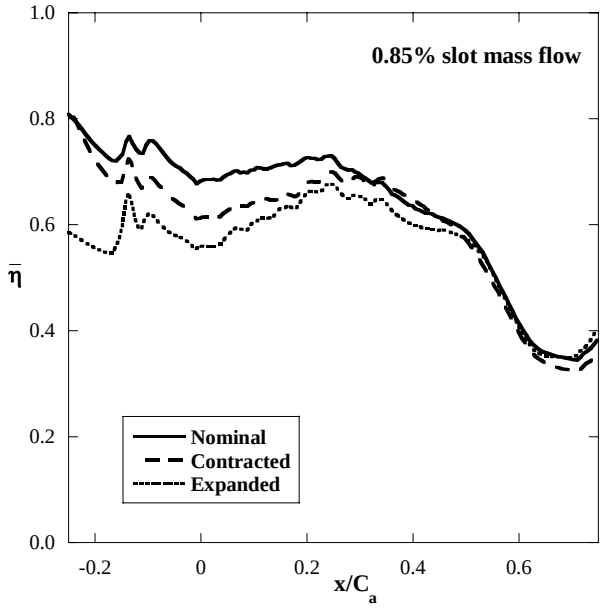

Figure 6.3 Laterally averaged adiabatic effectiveness for the entire passage with varied upstream slot width.

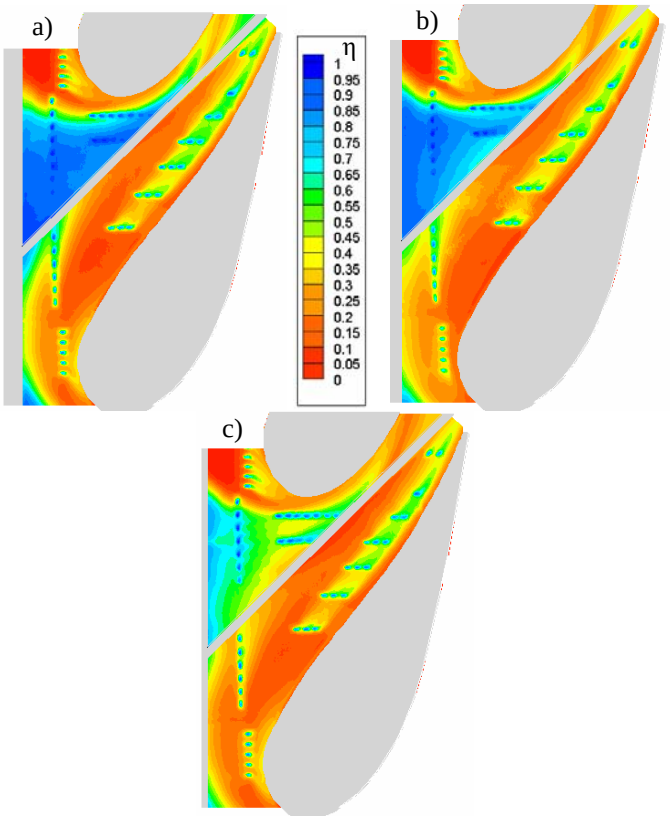

Figure 6.4. Contours of adiabatic effectiveness for a) double, b) nominal c) half-width upstream slot with I = 0.08 average slot momentum flux ratio.

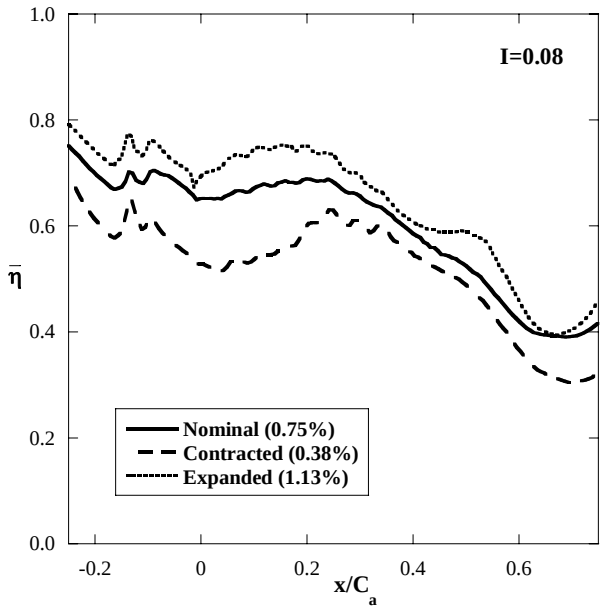

Figure 6.5 Plots of laterally averaged adiabatic effectiveness for the entire passage with varied upstream slot width given a nominal slot momentum given a nominal slot momentum flux ratio.

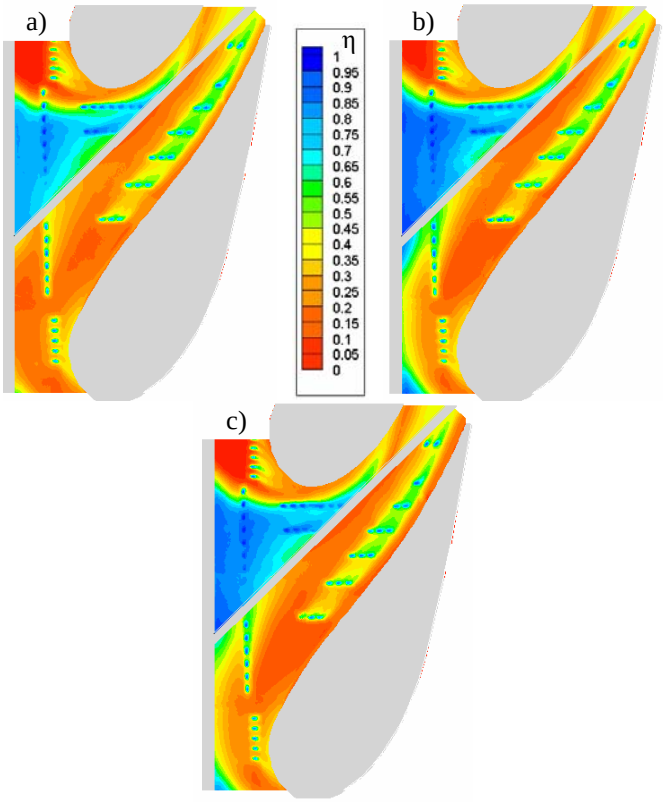

Figure 6.6. Contours of adiabatic effectiveness for a) 0.75%, b) 0.85% c) 1.0% upstream slot mass flow rate for a nominal slot width.

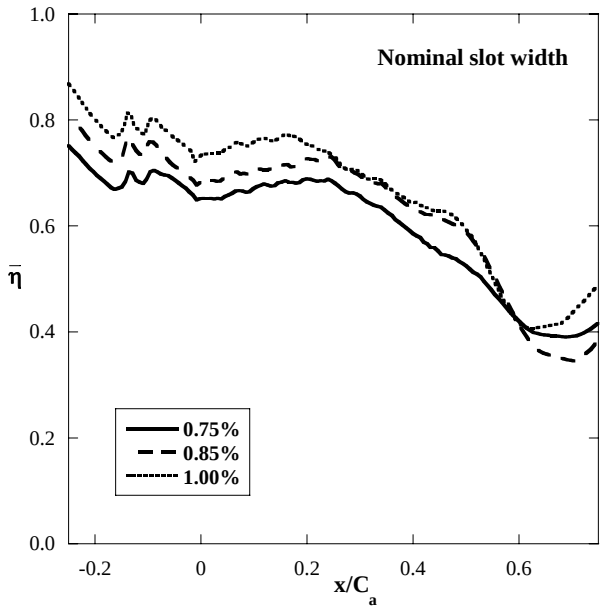

Figure 6.7 Plots of laterally averaged adiabatic effectiveness for the entire passage with varied upstream slot mass flow.

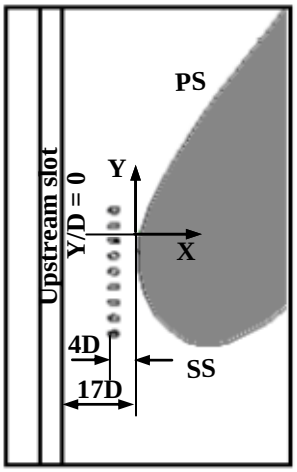

Figure 6.8. Illustrates the endwall design studied at the leading edge.

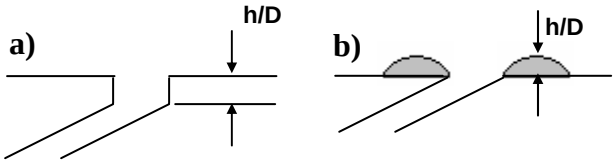

Figure 6.9. Illustrates the a) trench geometry and b) bump geometry studied at the leading edge.

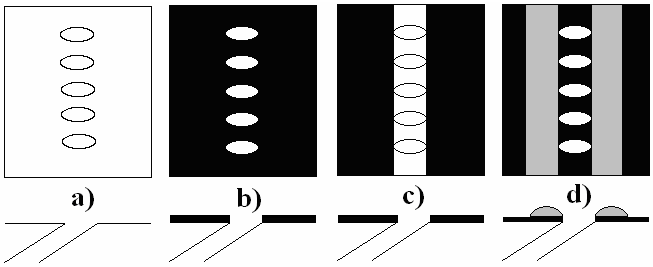

Figure 6.10. Schematic of the four configurations a) baseline, b) individual trench, c) row trench, and d) bumps tested at the leading edge.

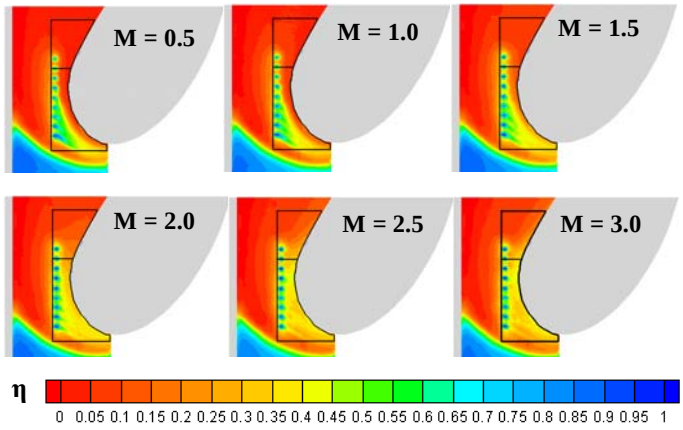

Figure 6.11. Contours of adiabatic effectiveness comparing the baseline case at different blowing ratios.

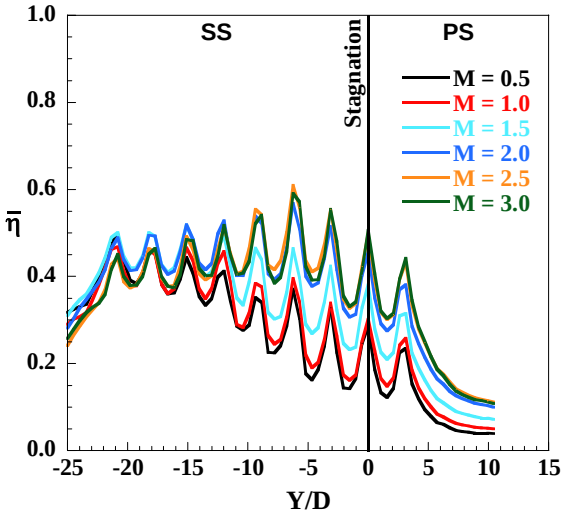

Figure 6.12. Lateral average effectiveness plots of the baseline case at different blowing ratios.

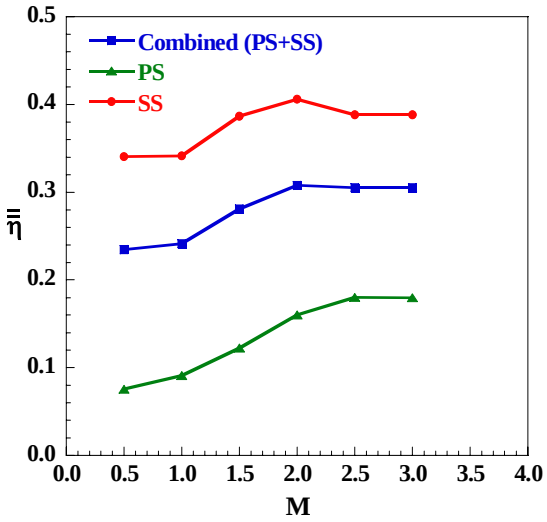

Figure 6.13. Area averaged effectiveness for the baseline geometry along suction, pressure and the whole leading edge region.

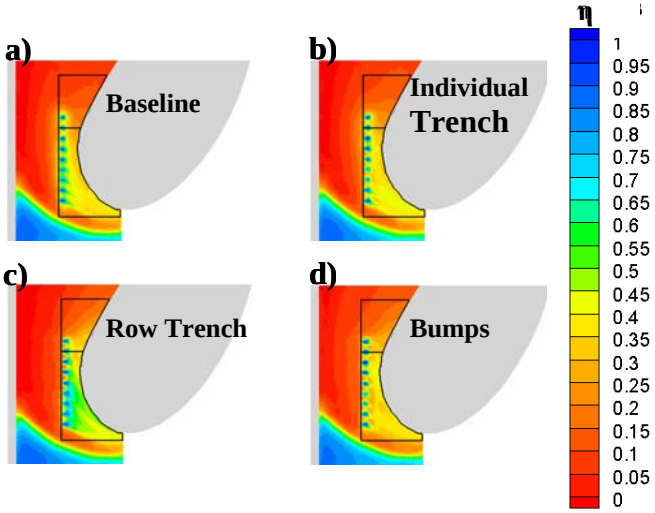

Figure 6.14. Contours of adiabatic effectiveness comparing the baseline case with the other configurations at a blowing ratio of M = 2.0.

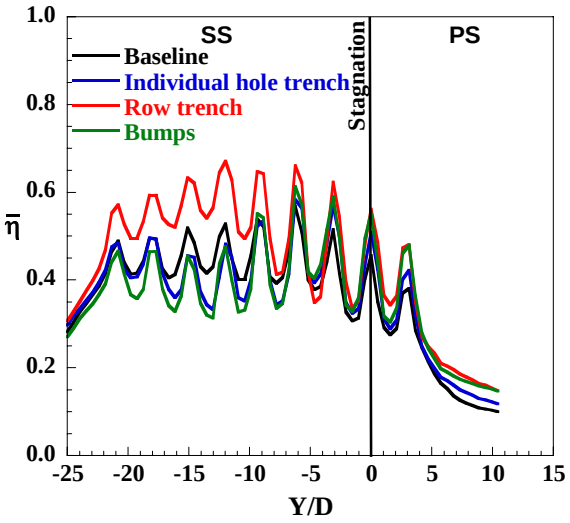

Figure 6.15. Laterally averaged adiabatic effectiveness comparing the effect of trenches and bumps at the leading edge.

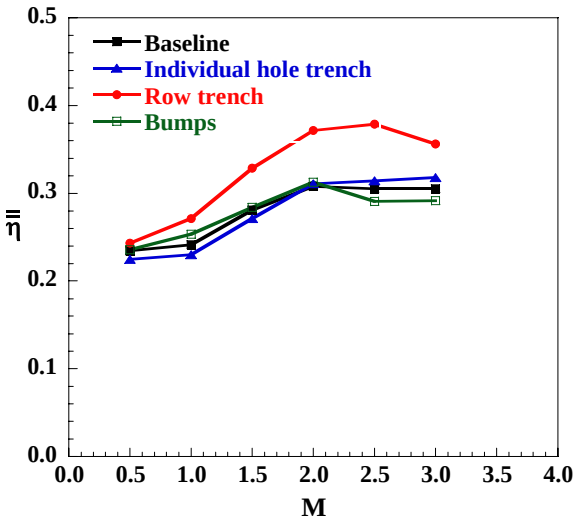

Figure 6.16. Area averaged effectiveness showing the effect of trenches and bumps on film-cooling effectiveness.

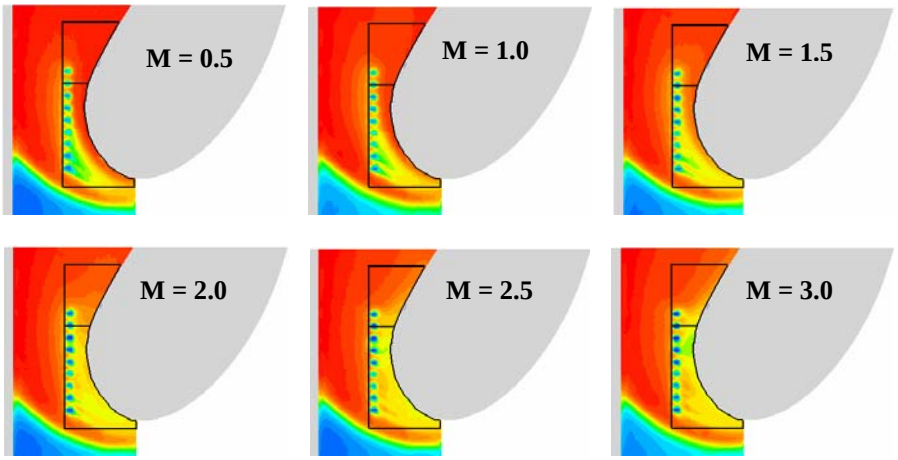

Figure 6.17. Contours of adiabatic effectiveness showing the effect of varying the blowing ratio from M = 0.5 to M = 3.0 for the individual trench configuration.

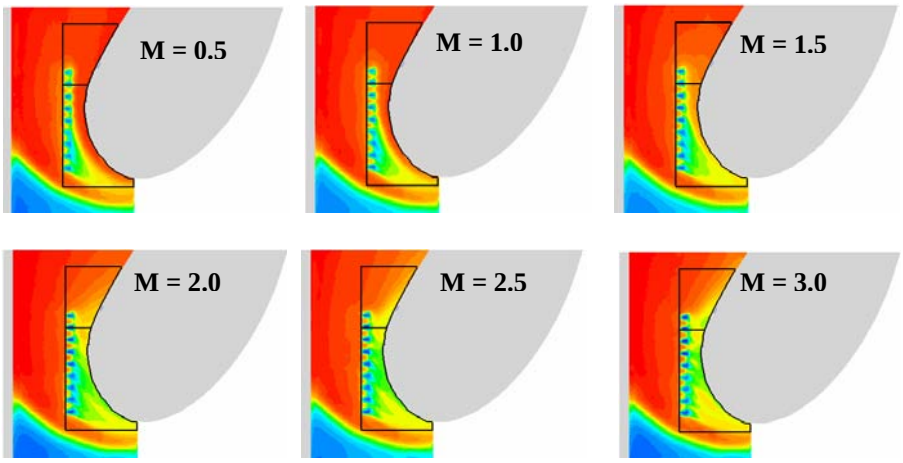

Figure 6.18. Contours of adiabatic effectiveness showing the effect of varying the blowing ratio from M = 0.5 to M = 3.0 for the row trench configuration.

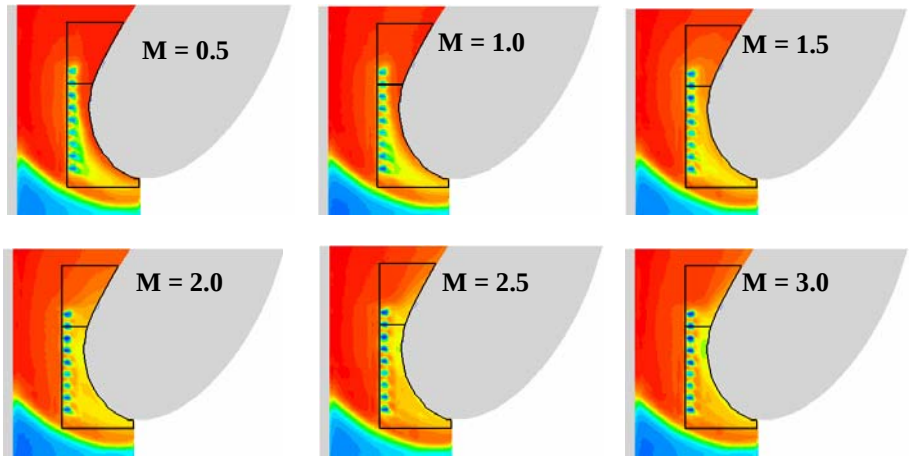

Figure 6.19. Contours of adiabatic effectiveness showing the effect of varying the blowing ratio from M = 0.5 to M = 3.0 for the bump configuration.

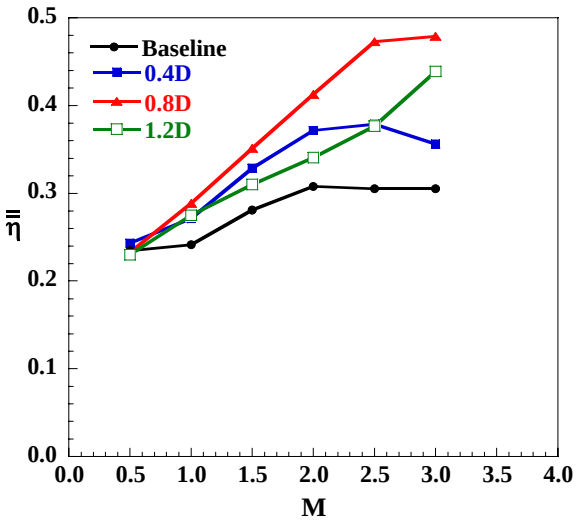

Figure 6.20. Area averaged effectiveness showing the effect of different trench depths for the row trench configuration at varying blowing ratios.

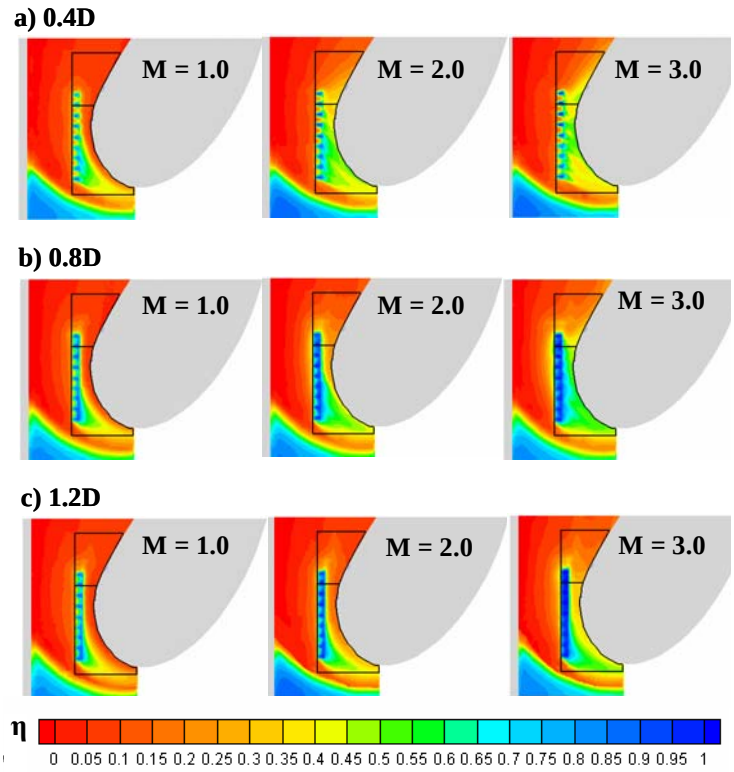

Figure 6.21. Contours of adiabatic effectiveness showing the effect of varying the trench depth for the row trench configuration at three different blowing ratios.

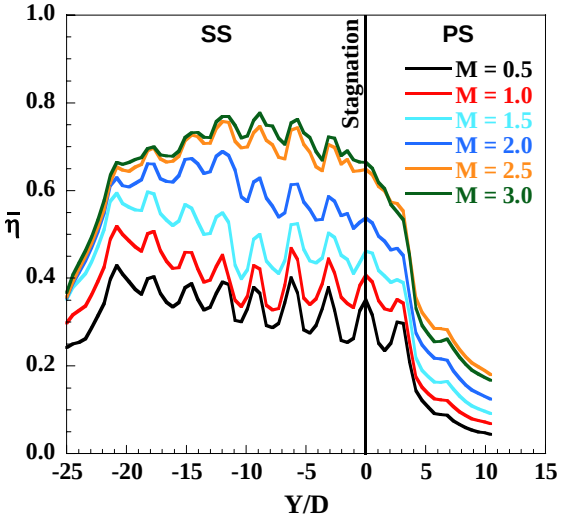

Figure 6.22. Lateral averaged effectiveness showing the effect of the 0.8D trench depth at different blowing ratios.

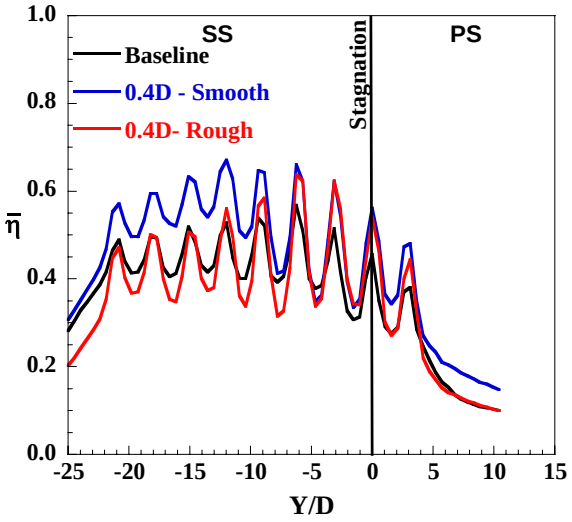

Figure 7.1. Lateral averaged effectiveness comparing the effect of the 0.4D row trench on the rough surface with the 0.4D on a smooth and the baseline at a blowing ratio of M = 2.0.

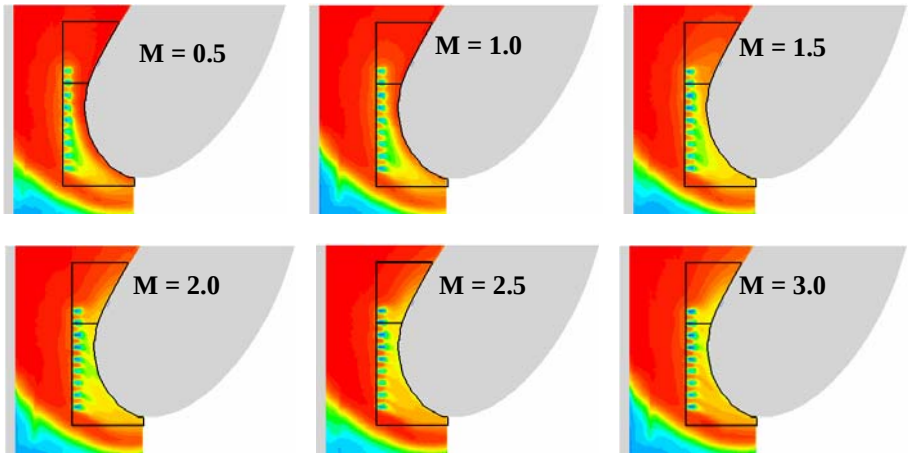

Figure 7.2. Contours of adiabatic effectiveness showing the effect a 0.4D row trench on a rough surface at different blowing ratios.

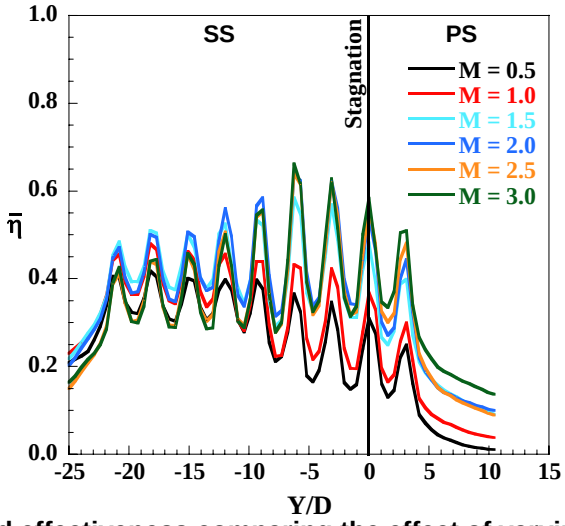

Figure 7.3. Lateral averaged effectiveness comparing the effect of varying the blowing ratio with a 0.4D row trench on a rough surface.

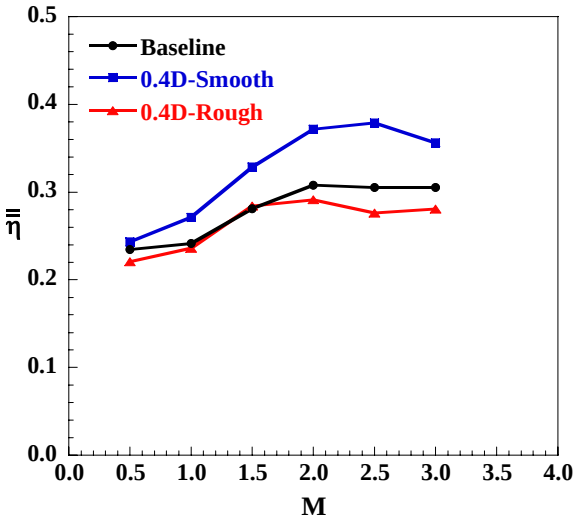

Figure 7.4. Area averaged effectiveness showing the effect of a rough and smooth endwall surface at a row trench depth 0.4D.

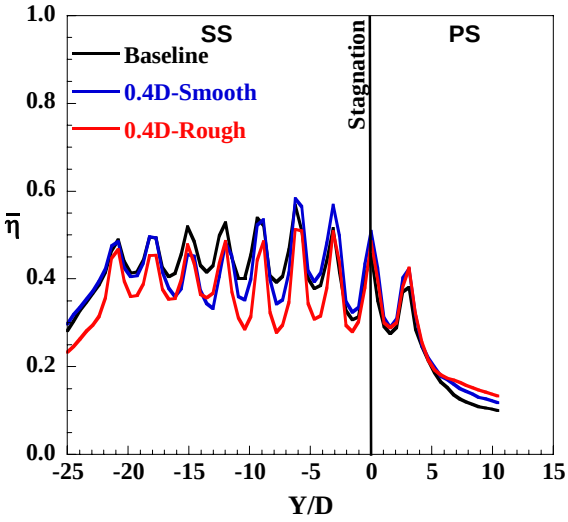

Figure 7.5. Lateral averaged effectiveness comparing the effect of the 0.4D individual trench on the rough surface with the 0.4D on a smooth and the baseline at a blowing ratio of M = 2.0.

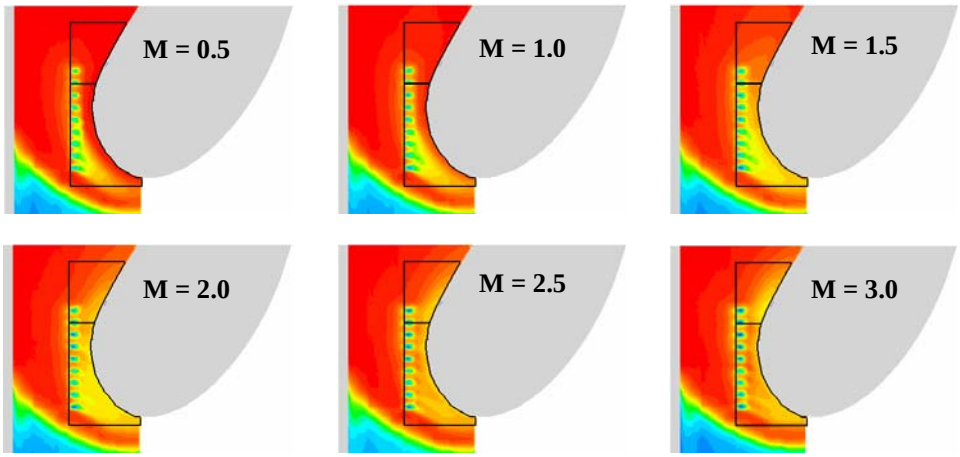

Figure 7.6. Contours of adiabatic effectiveness showing the effect a 0.4D individual trench on a rough surface at different blowing ratios.

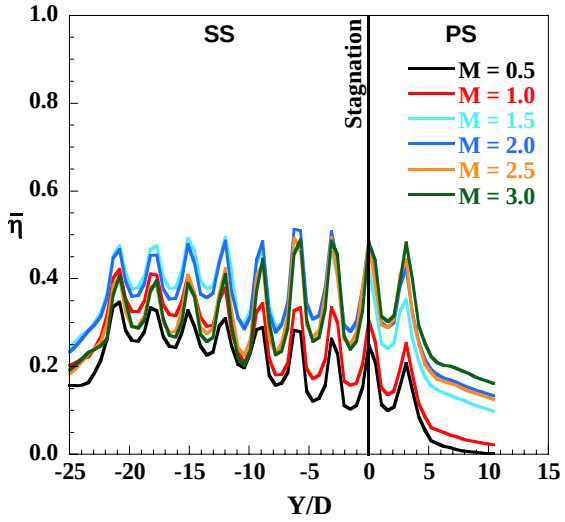

Figure 7.7. Lateral averaged effectiveness comparing the effect of varying the blowing ratio with a 0.4D individual trench on a rough surface.

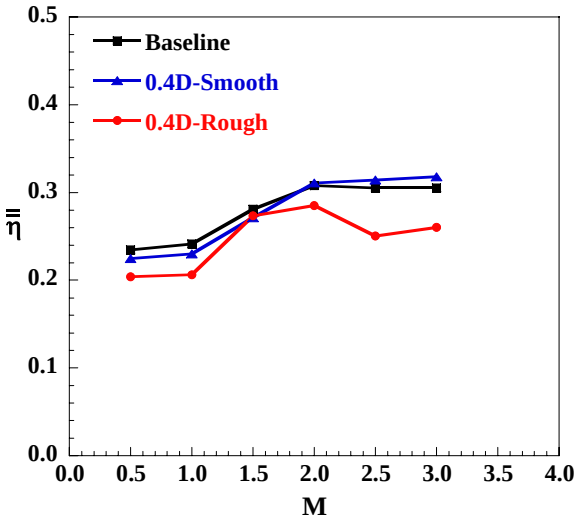

Figure 7.8. Area averaged effectiveness showing the effect of a rough and smooth endwall surface for an individual trench of depth 0.4D at all blowing ratios.

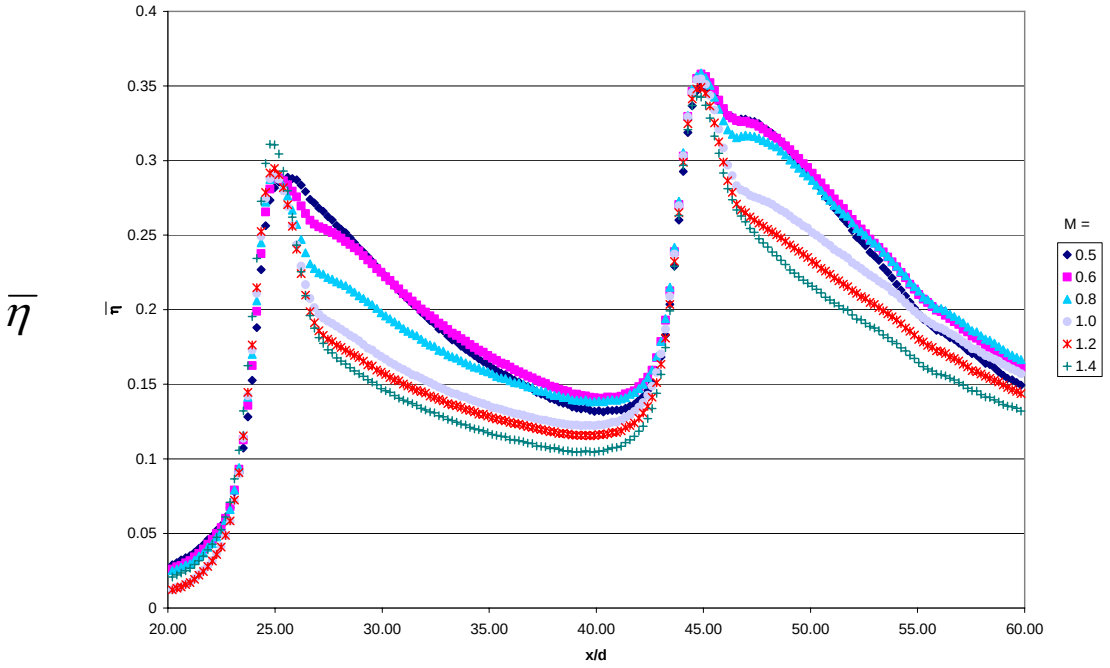

Figure 8.3. Laterally averaged effectiveness for various blowing ratios in the smooth configuration with low turbulence and no showerhead blowing.

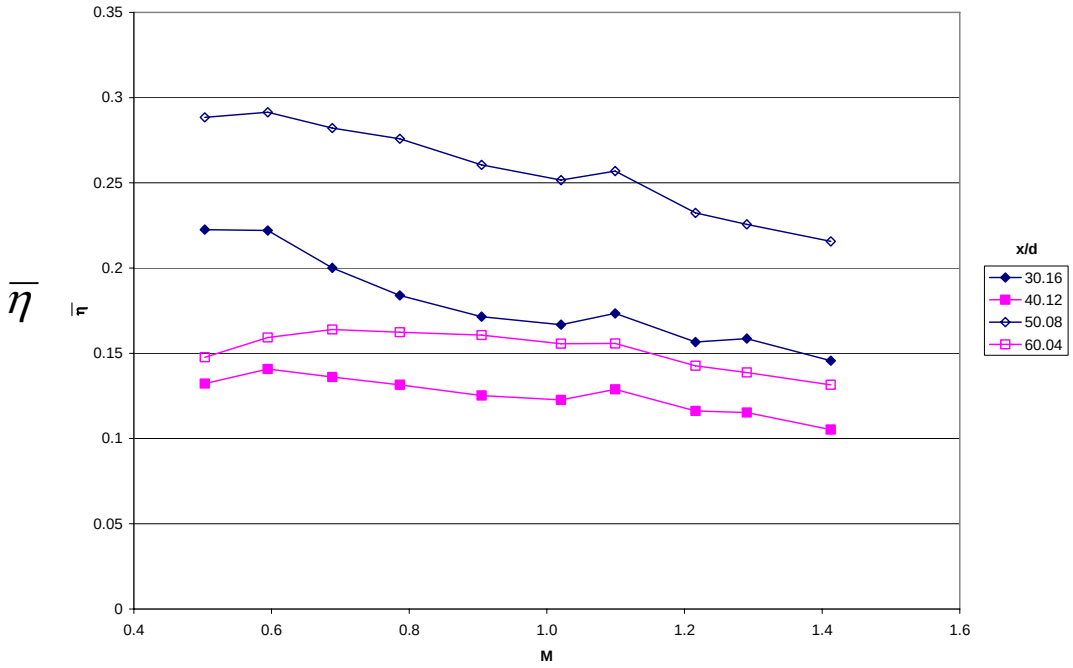

Figure 8.4. Peak effectiveness vs. blowing ratio for the smooth configuration at various *x/d* locations.

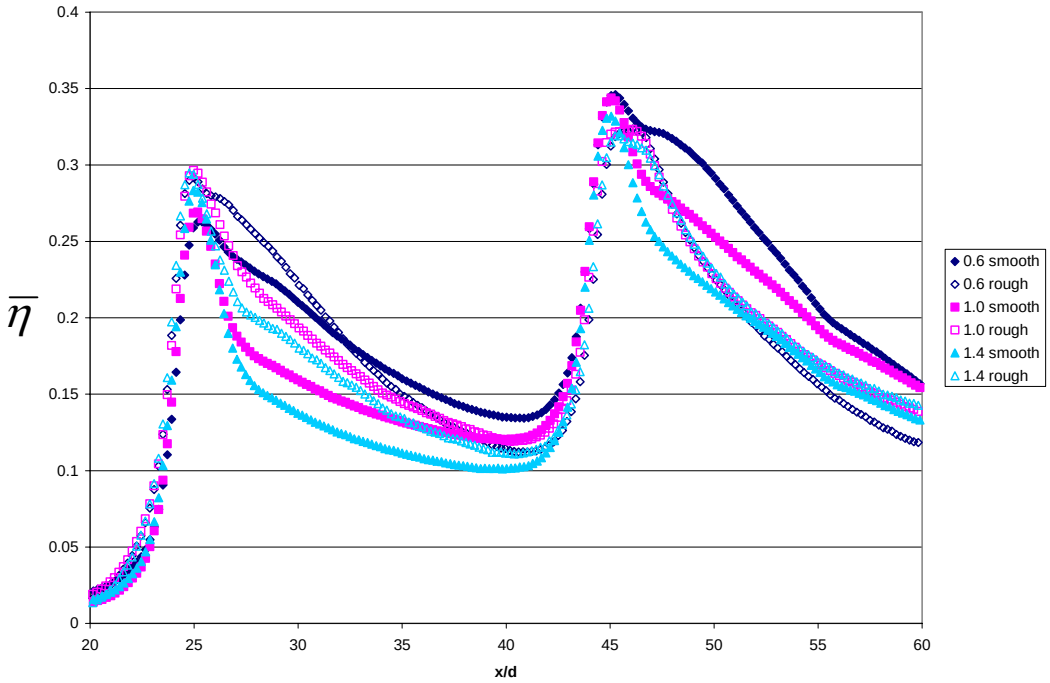

Figure 8.3. Effects of 30 grit roughness on the adiabatic effectiveness for a representative low, medium, and high blowing ratio with low mainstream turbulence with no showerhead blowing.

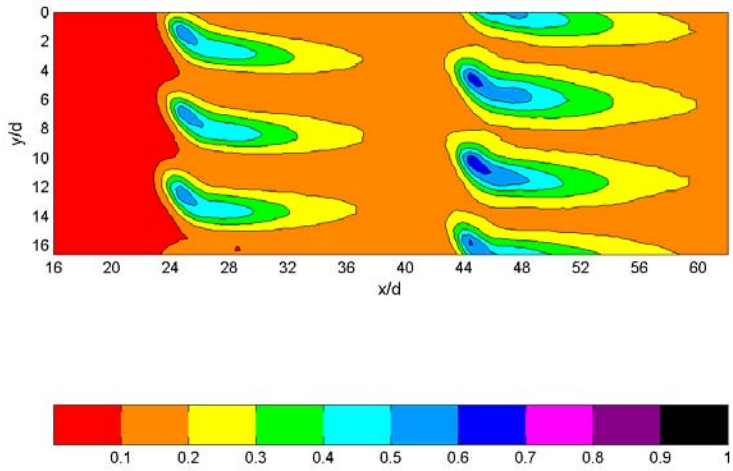

Figure 8.4. Film effectiveness contours for M = 0.6 with a smooth surface, low Tu_0, and no showerhead blow η

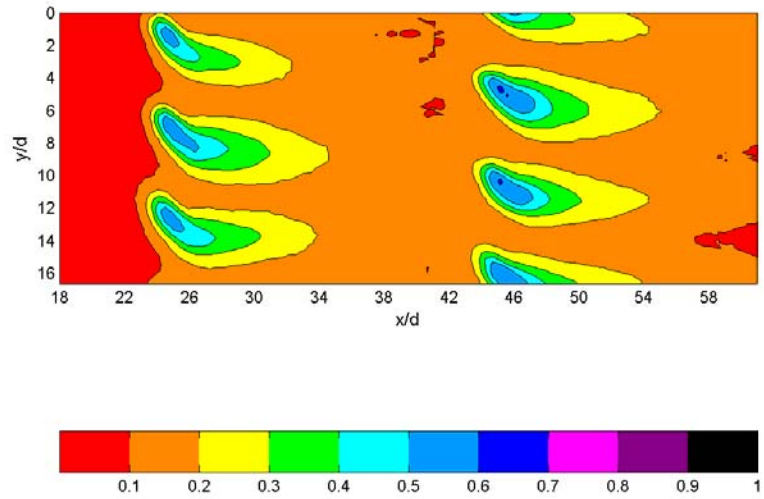

Figure 8.5. Film effectiveness contours for M = 0.6 with a 30 grit rough surface, low Tu_0, and no showerhead blow. η

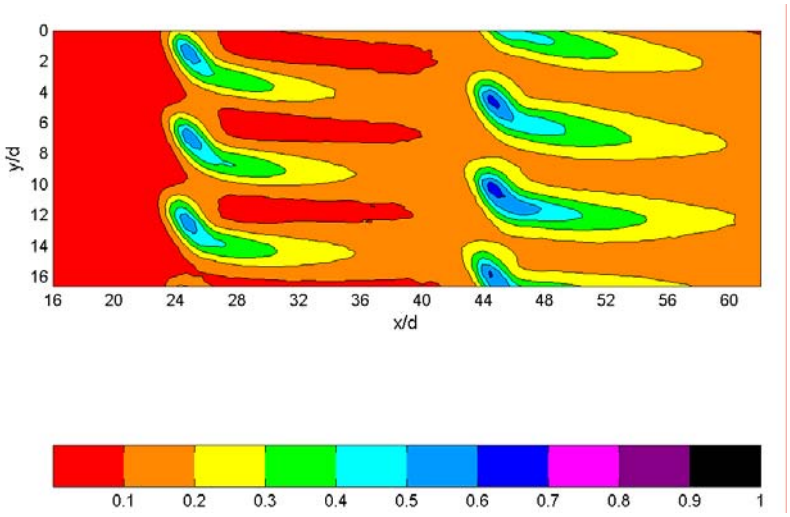

Figure 8.6. Film effectiveness contours for M = 1.0 with a smooth surface, low Tu_0, and no showerhead bl . η.

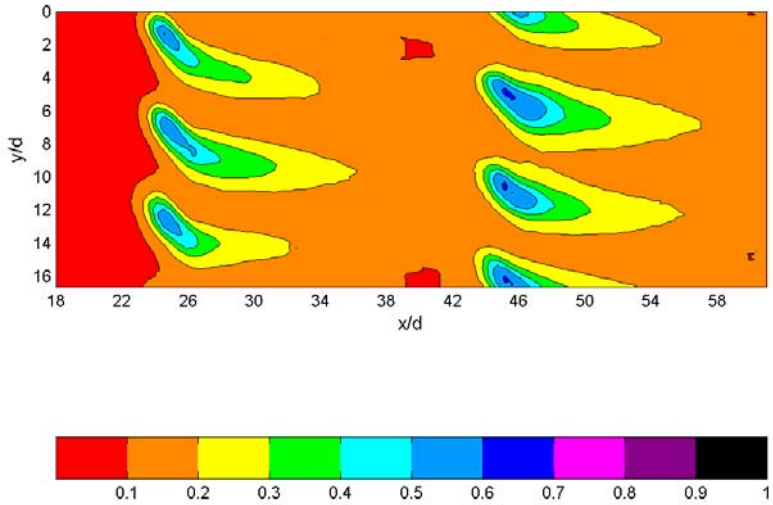

Figure 8.7. Film effectiveness contours for M = 1.0 with a 30 grit rough surface, low Tu_0, and no showerhead bl(. η

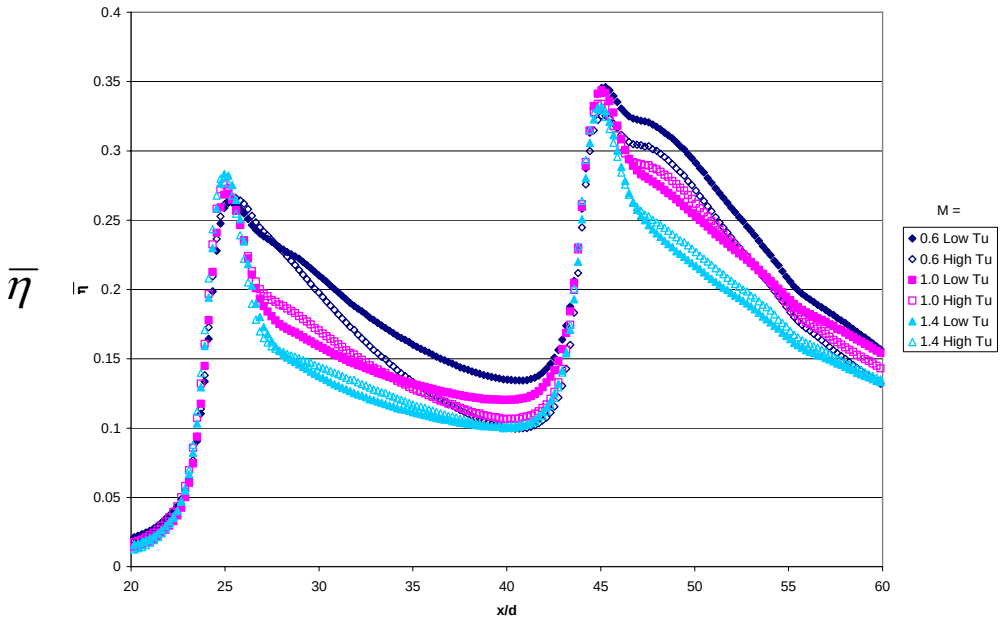

Figure 8.8. Effects of mainstream turbulence on the smooth configuration at a representative high, medium, and low blowing ratio.

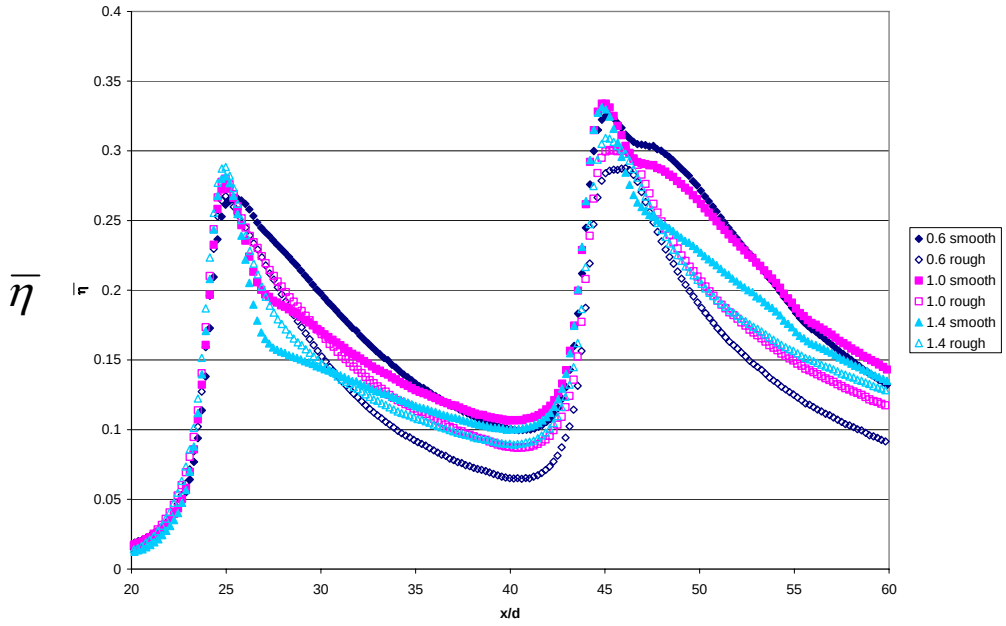

Figure 8.9. Effects of 30 grit roughness on the adiabatic effectiveness for a representative low, medium, and high blowing ratio with high mainstream turbulence with no showerhead blowing.

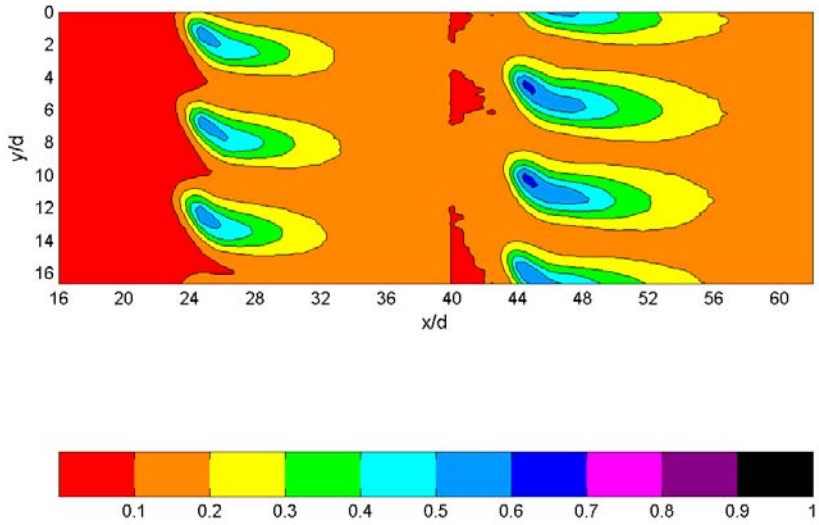

Figure 8.10. F η fectiveness contours for *M* = 0.6 with a smooth surface, high Tu_0, and no showerhead b g.

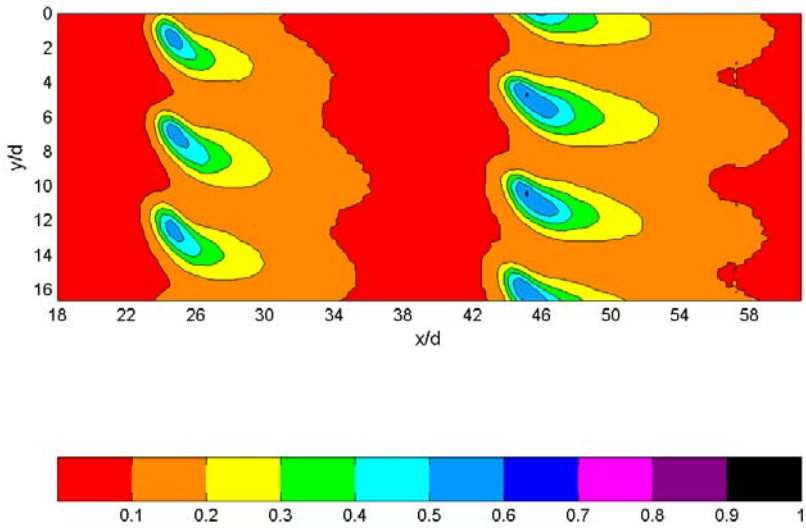

Figure 8.11. Film effectiveness contours for M = 0.6 with a 30 grit rough surface, high Tu_0, and no showerhead b g.

η

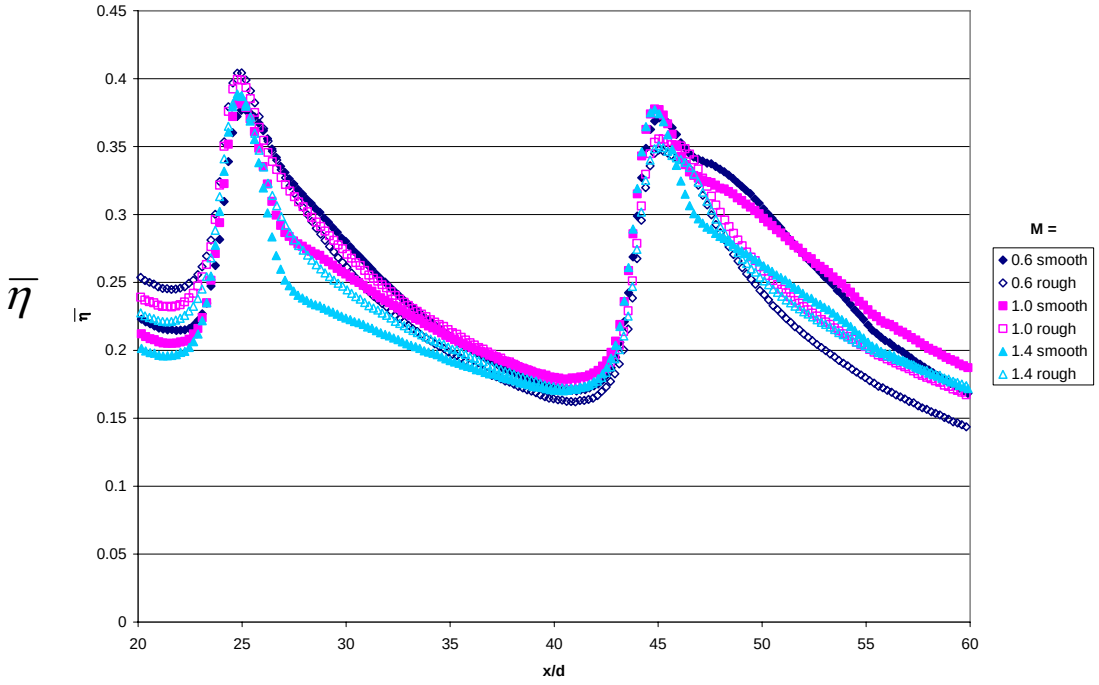

$\overline{\eta}$

Figure 8.12. Comparison of film effectiveness for smooth and 30 grit rough surfaces at low, medium, and high blowing ratios, with high mainstream turbulence and with showerhead blowing.

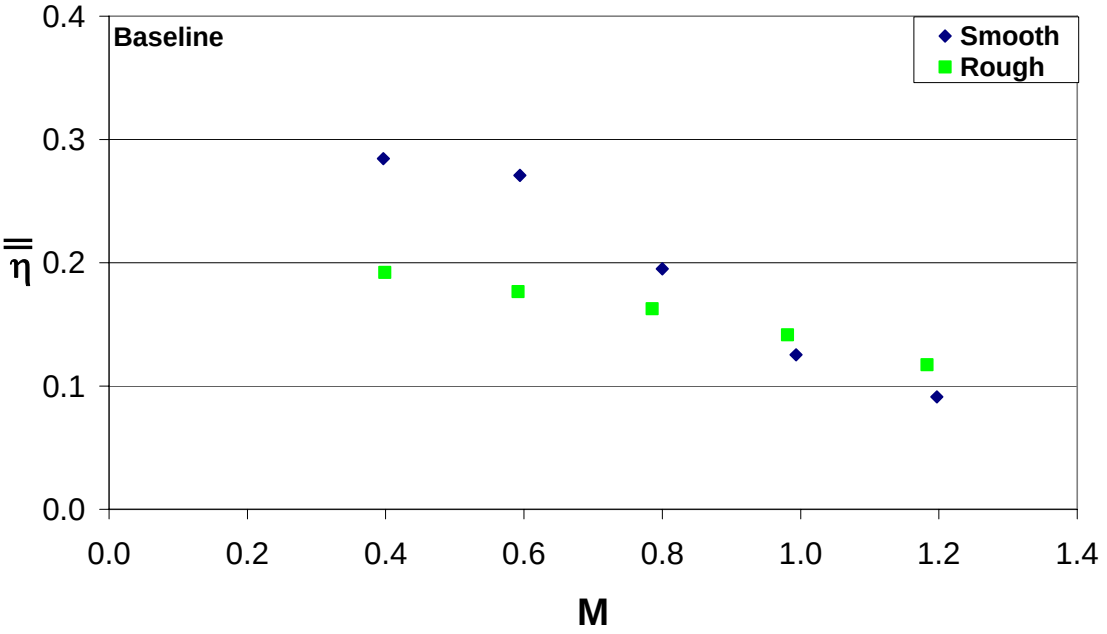

Figure 8.13. Spatially averaged effectiveness plot of the baseline case and the baseline case with the addition of roughness.

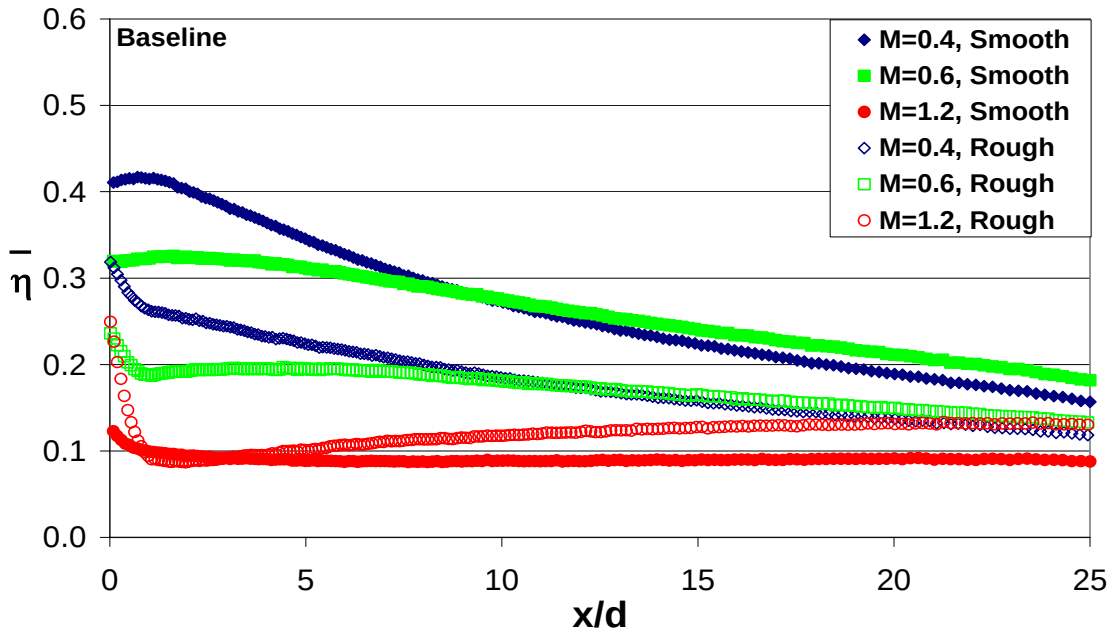

Figure 8.14. Laterally averaged effectiveness plot of the baseline case and the baseline case with a rough wall.

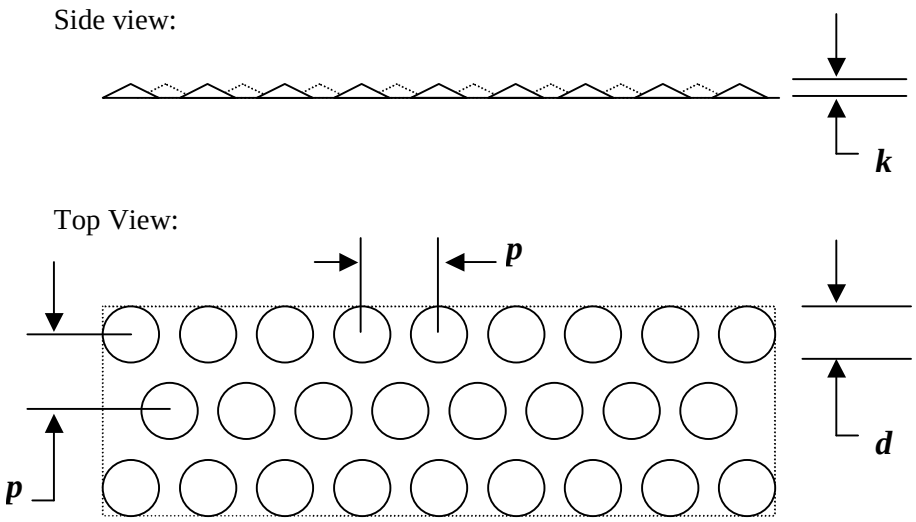

Figure 8.15 Schematic of Regular Roughness Array

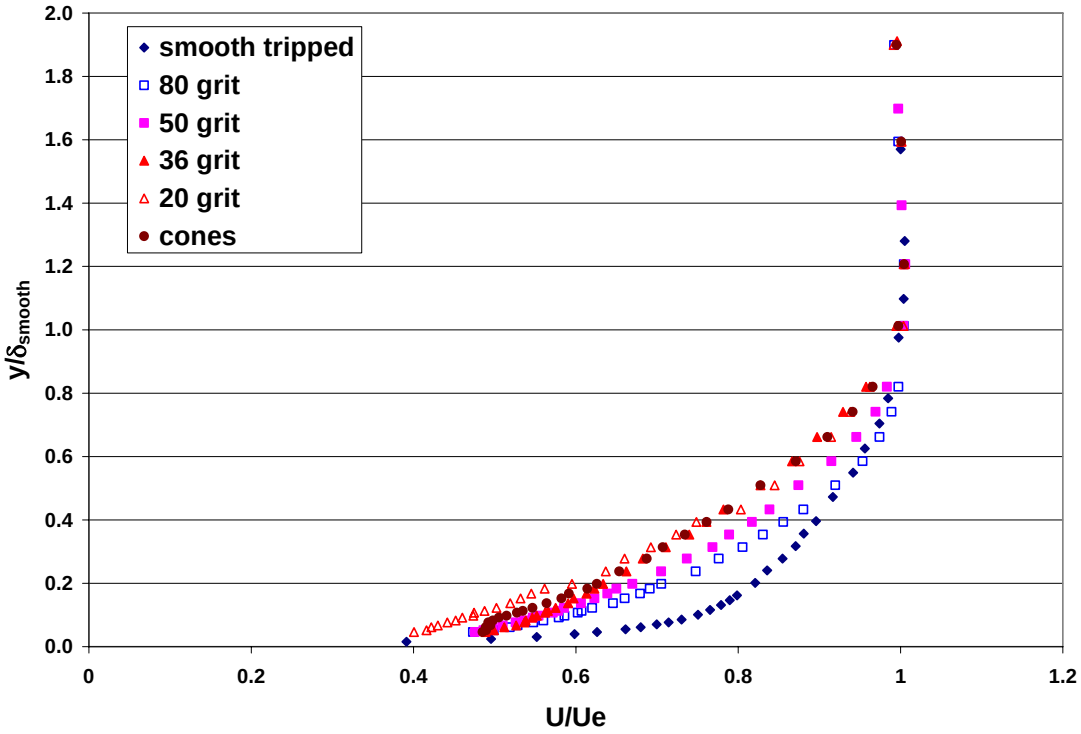

Figure 8.16 Mean velocity profiles for s/C=0.37

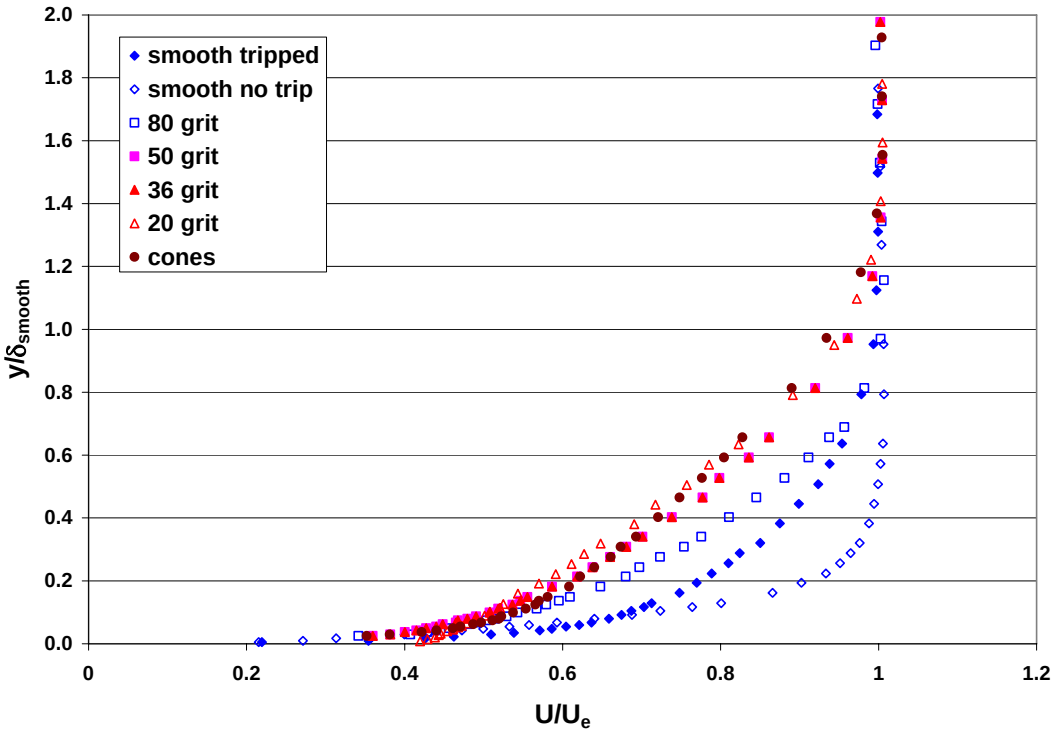

Figure 8.17 Mean velocity profiles for s/C=0.57

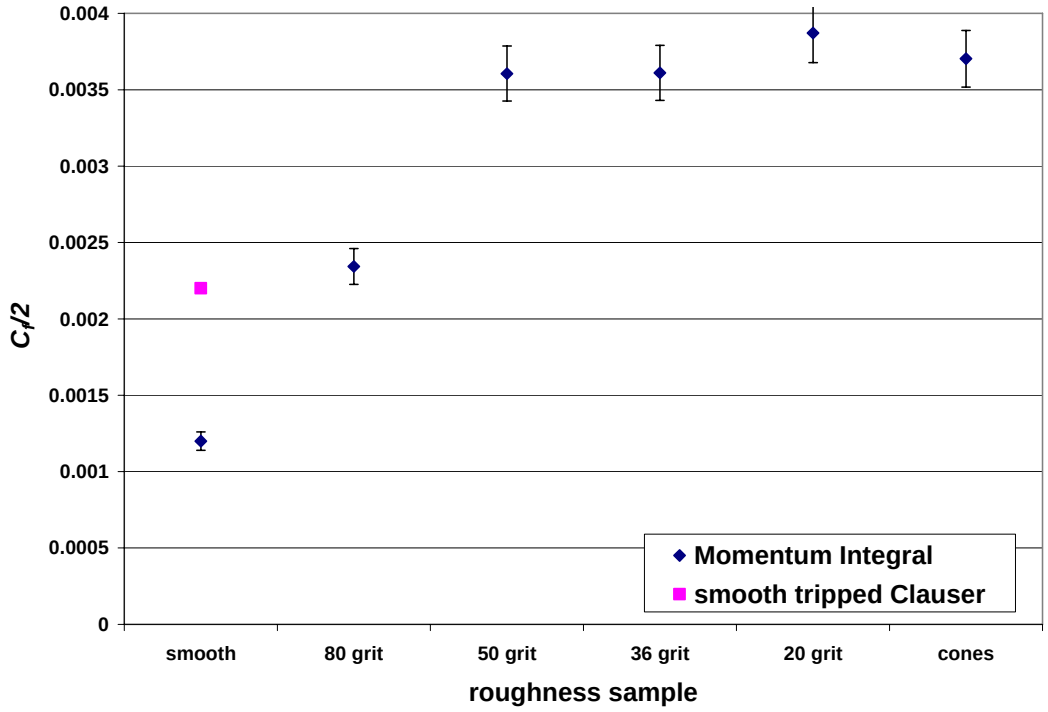

Figure 8.18 Skin friction coefficients for varying surface roughness.

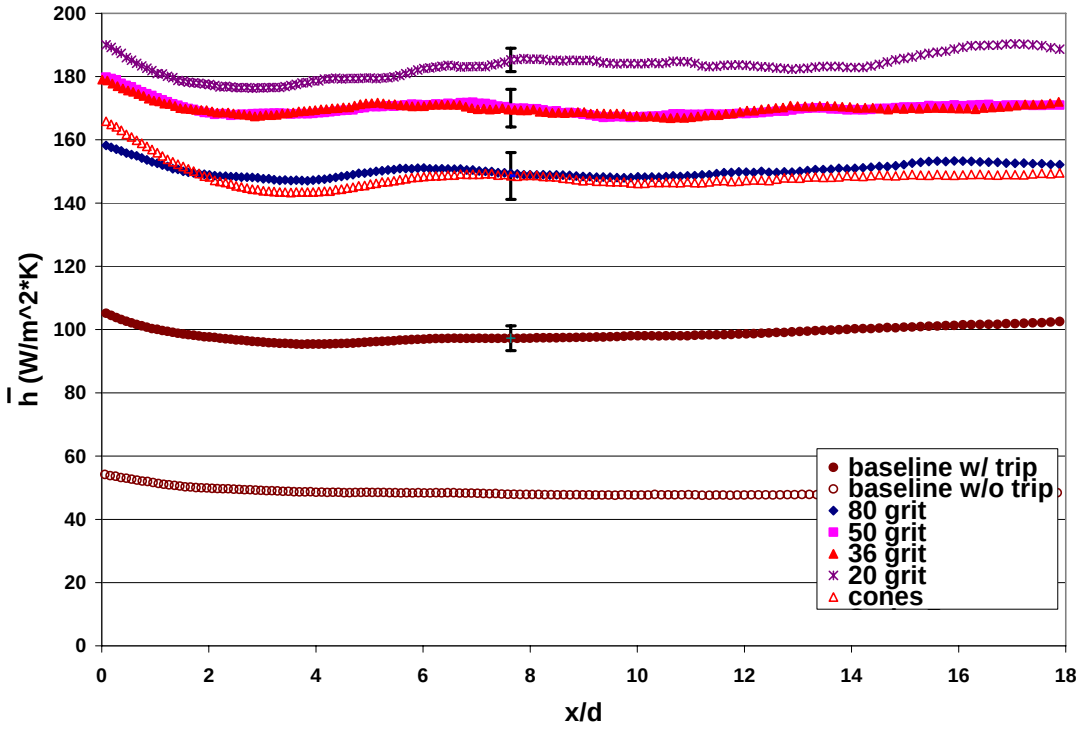

Figure 8.19 Laterally averaged heat transfer coefficient values for varying roughness.

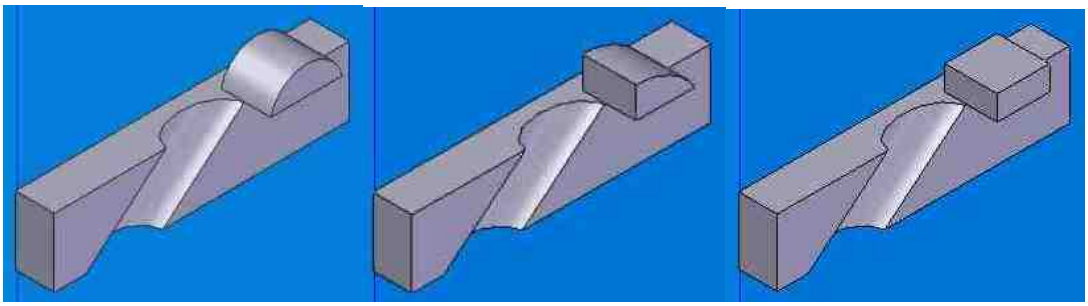

Shape #1 Shape #2 Shape #3

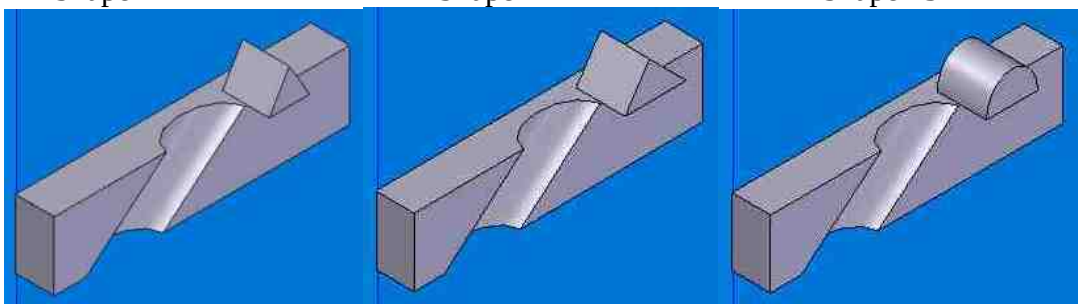

Shape #4 Shape #5 Shape #6

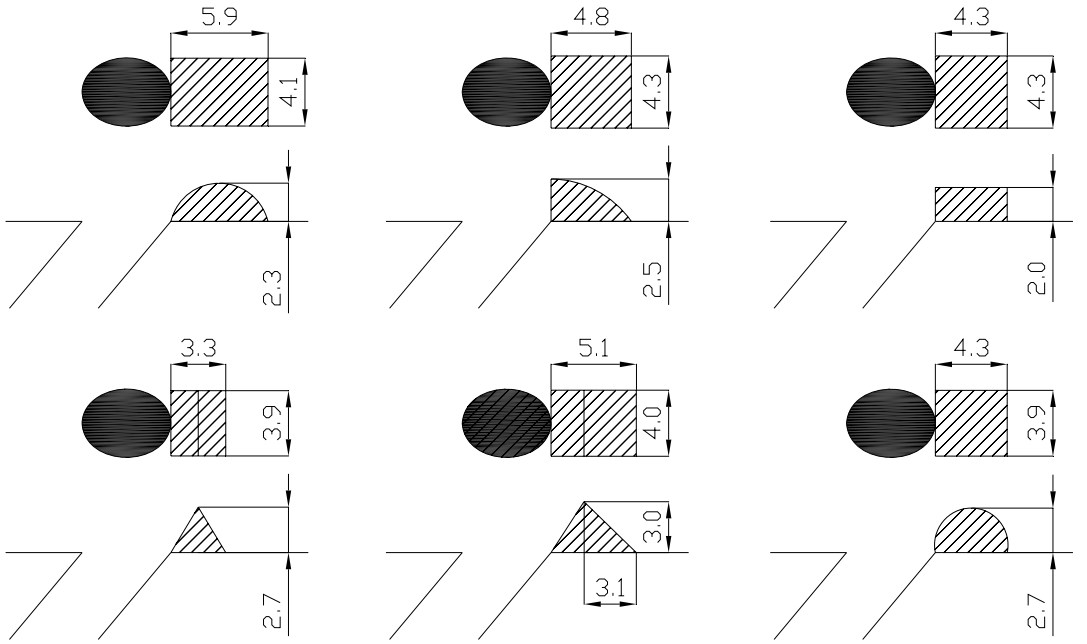

Figure 9.1. Six shapes tested (dimensions in mm). Shape #2 used for subsequent experiments.

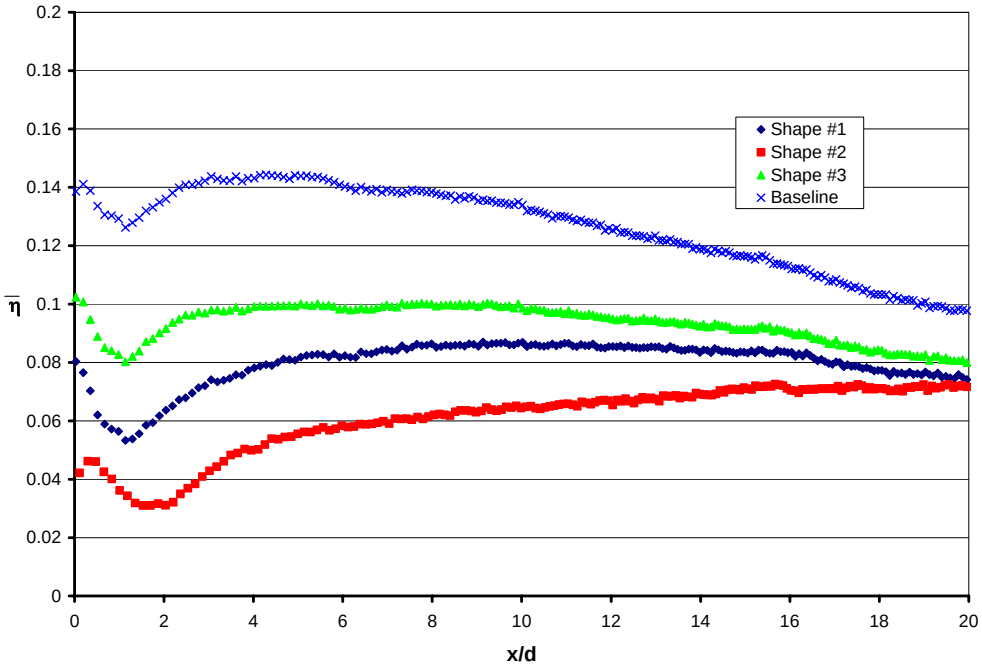

Figure 9.2. Laterally averaged adiabatic effectiveness with upstream obstructions of varying shapes each 1/2*d* in height. Conditions: rough surface, high Tu, M = 0.7.

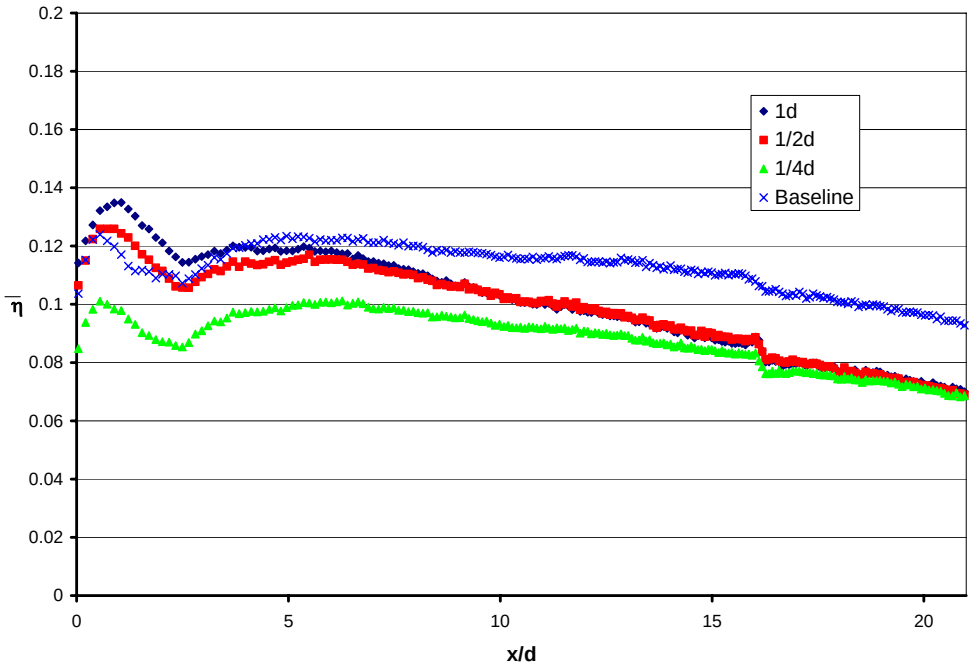

Figure 9.3. Laterally averaged adiabatic effectiveness with Shape #2 obstructions of varying size located immediately downstream of the coolant hole, M = 0.7.

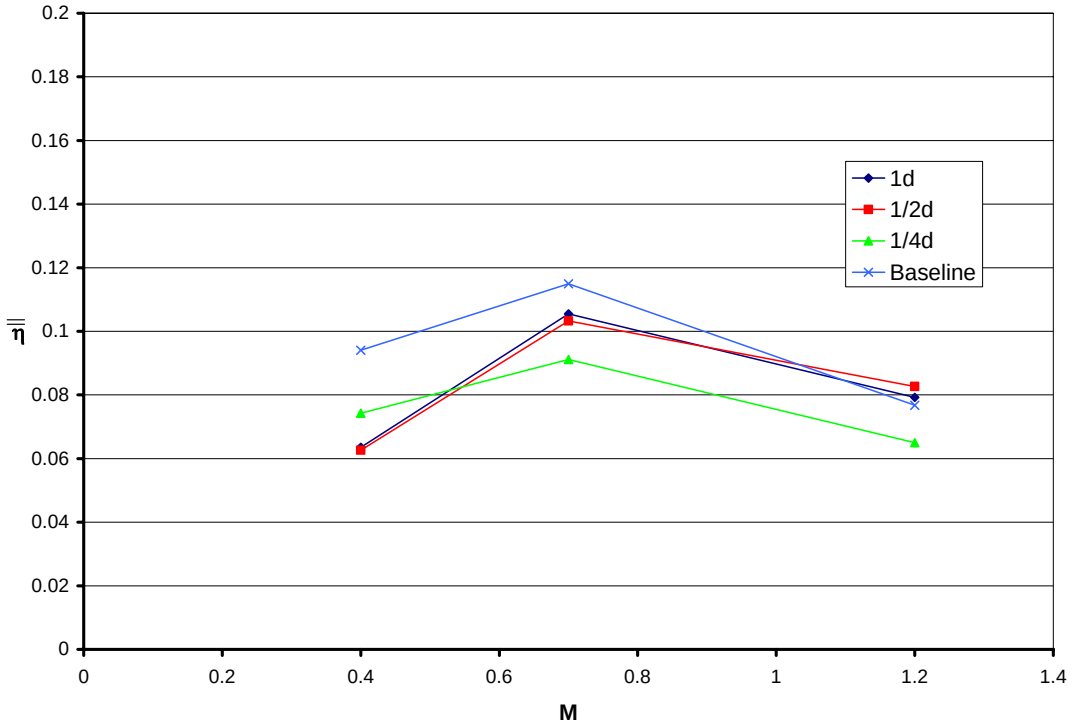

Figure 9.4. Area averaged adiabatic effectiveness with downstream, Shape #2 obstructions of varying size.

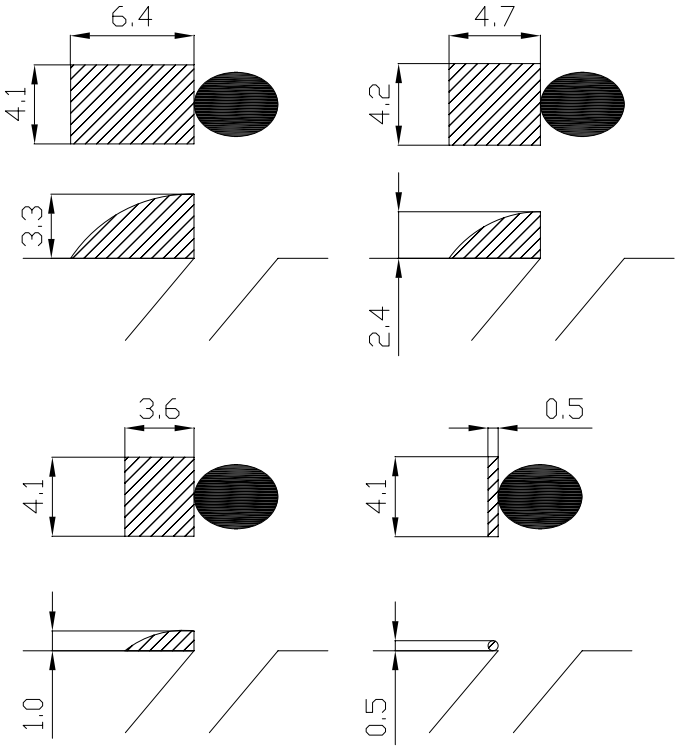

Figure 9.5. Positioning and dimensions (in mm) of the 1d, 1/2d, and 1/4d shape #2 and 1/8d cylindrical obstruction upstream of the coolant holes.

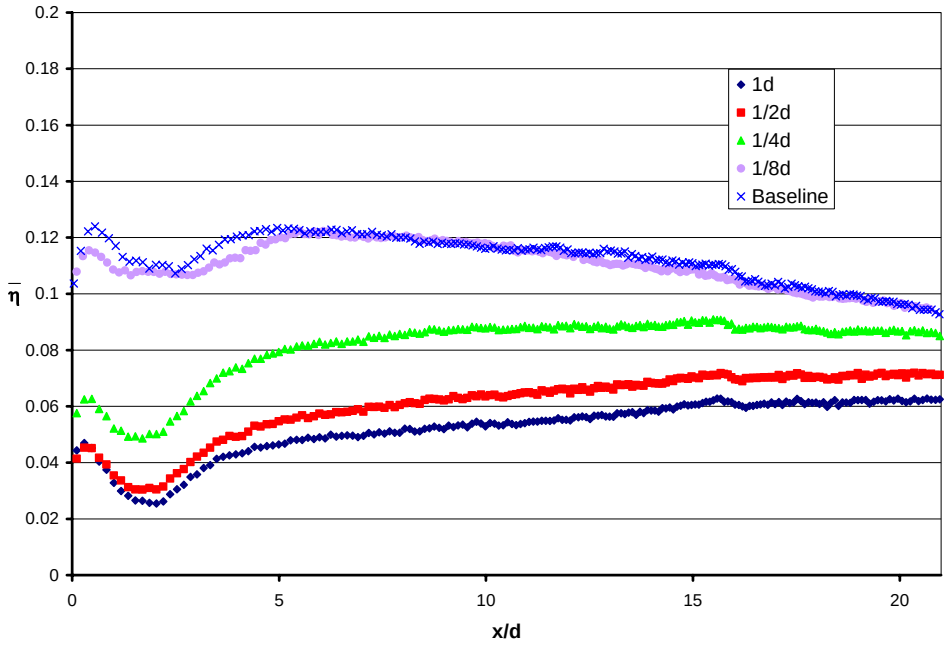

Figure 9.6. Laterally averaged adiabatic effectiveness with Shape #2 obstructions upstream of the coolant holes for M = 0.7.

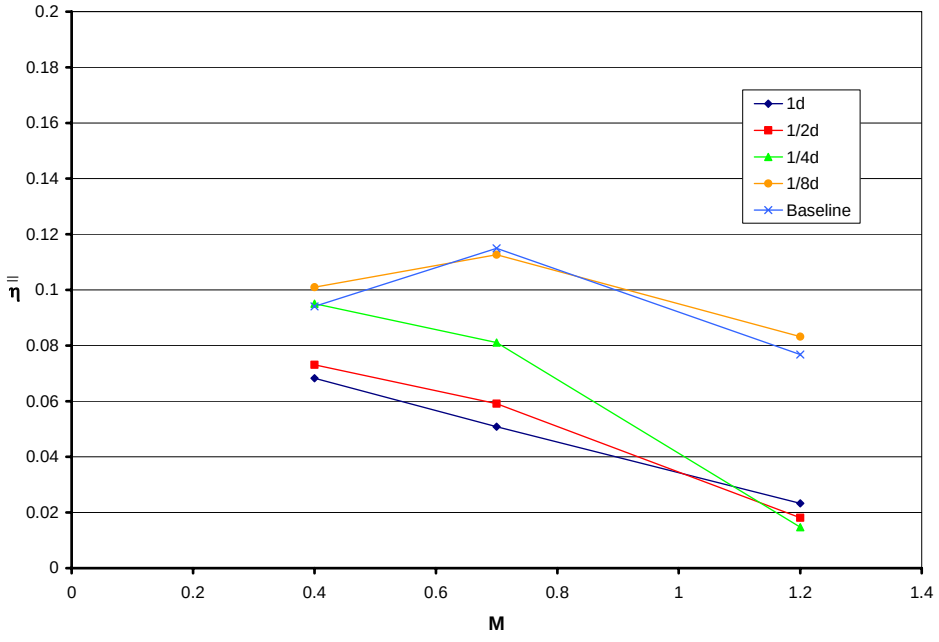

Figure 9.7. Area averaged adiabatic effectiveness with Shape #2 (1d, 1/2d, and 1/4d) and cylindrical (1/8*d*) obstructions of varying size upstream of the coolant holes.

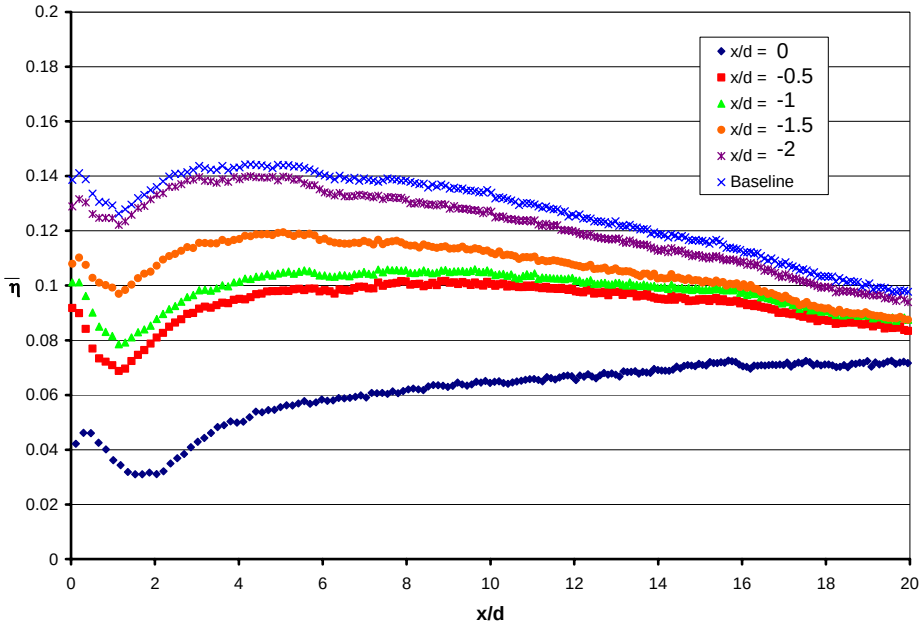

Figure 9.8. Effect of upstream position of the 1/2*d* shape #2 obstruction on laterally averaged adiabatic effectiveness with *M* = 0.7.

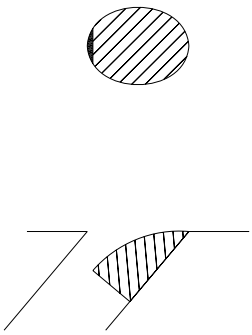

Figure 9.9. Schematic of the 1/2d size of shape #2 obstruction in the upstream position.

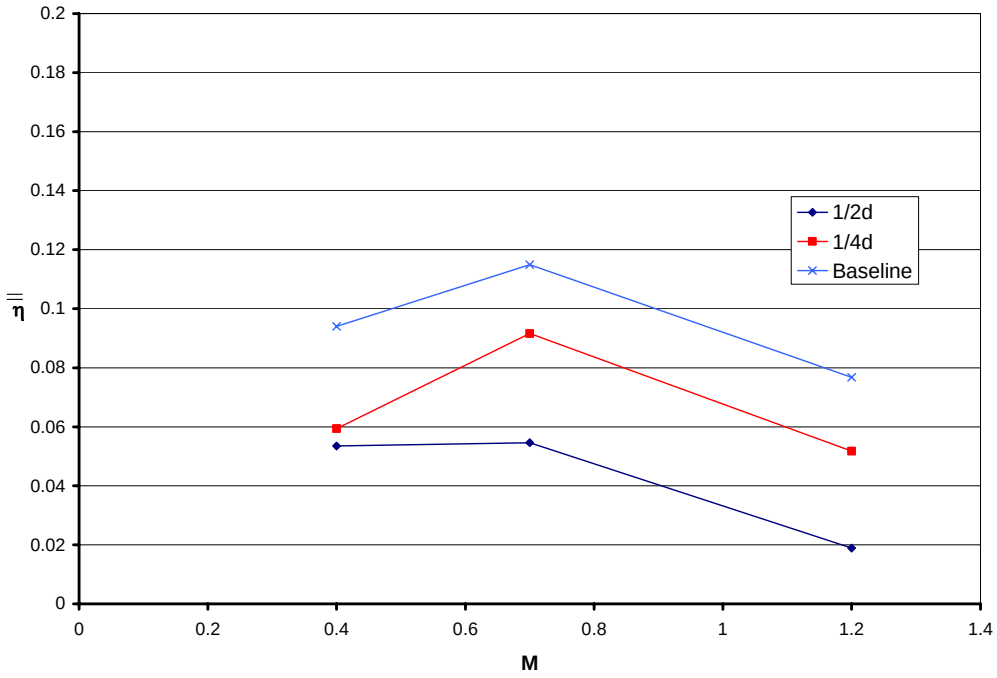

Figure 9.10. Area averaged adiabatic effectiveness with Shape #2 obstructions of varying size in and attached to the downstream side of the coolant holes.

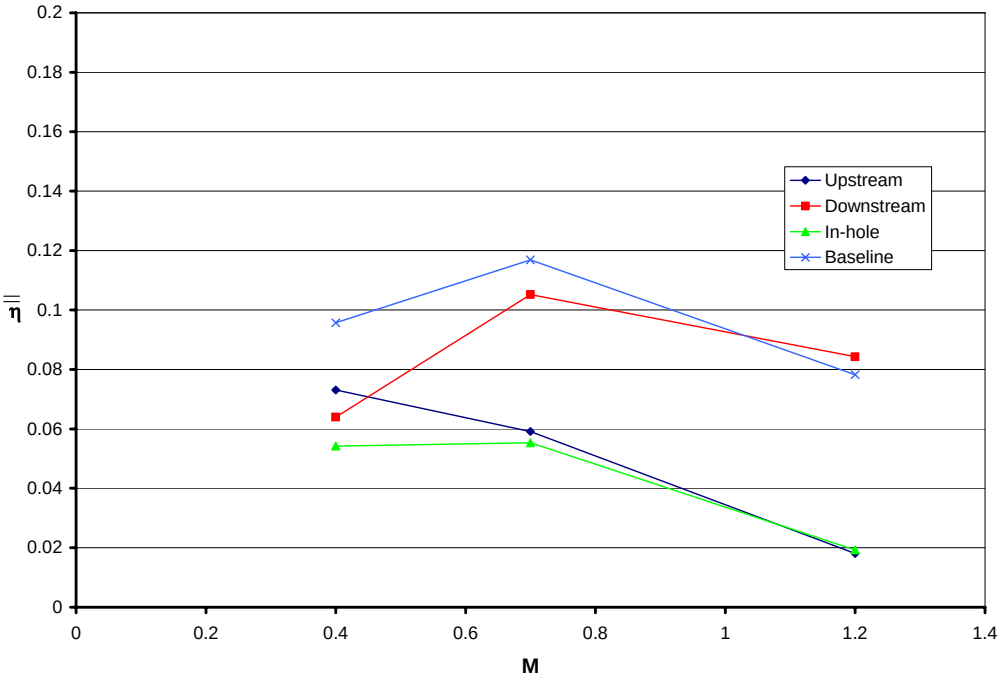

Figure 9.11. Area averaged adiabatic effectiveness for varying positions of 1/2*d* Shape #2 obstructions.

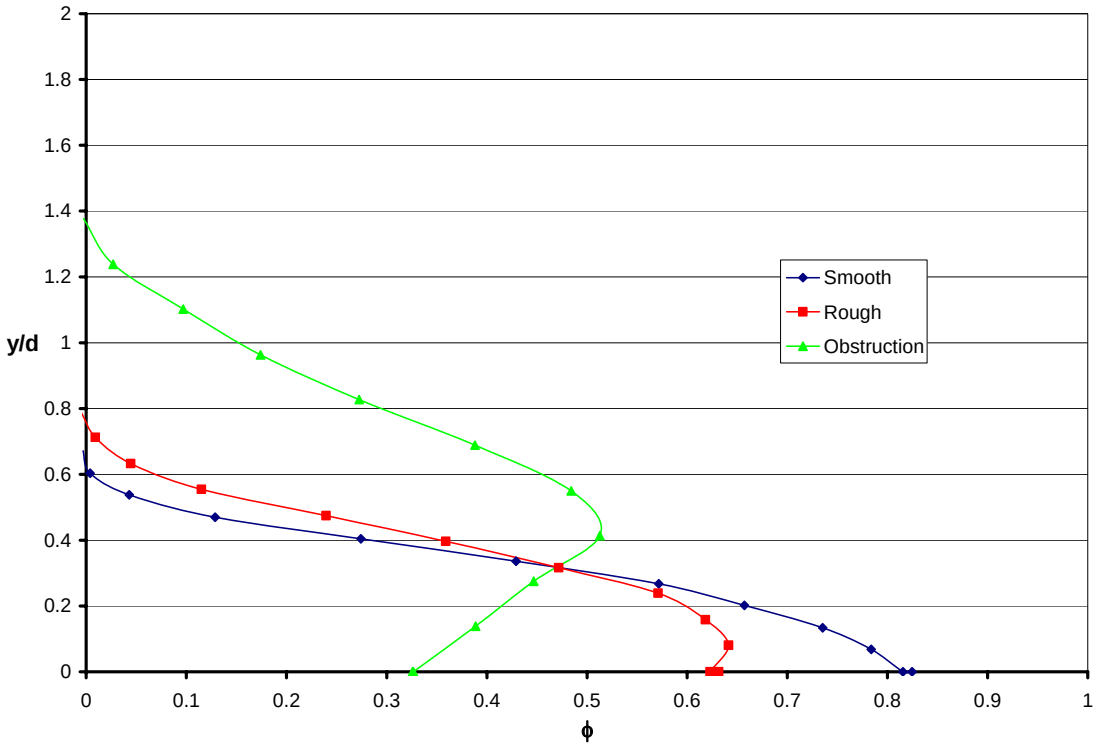

Figure 9.12. Temperature profiles at *x/d* = 1, *M* = 0.7 for smooth and rough surfaces with no obstruction, and for a rough surface with an upstream 1/2*d* Shape #2 obstruction.

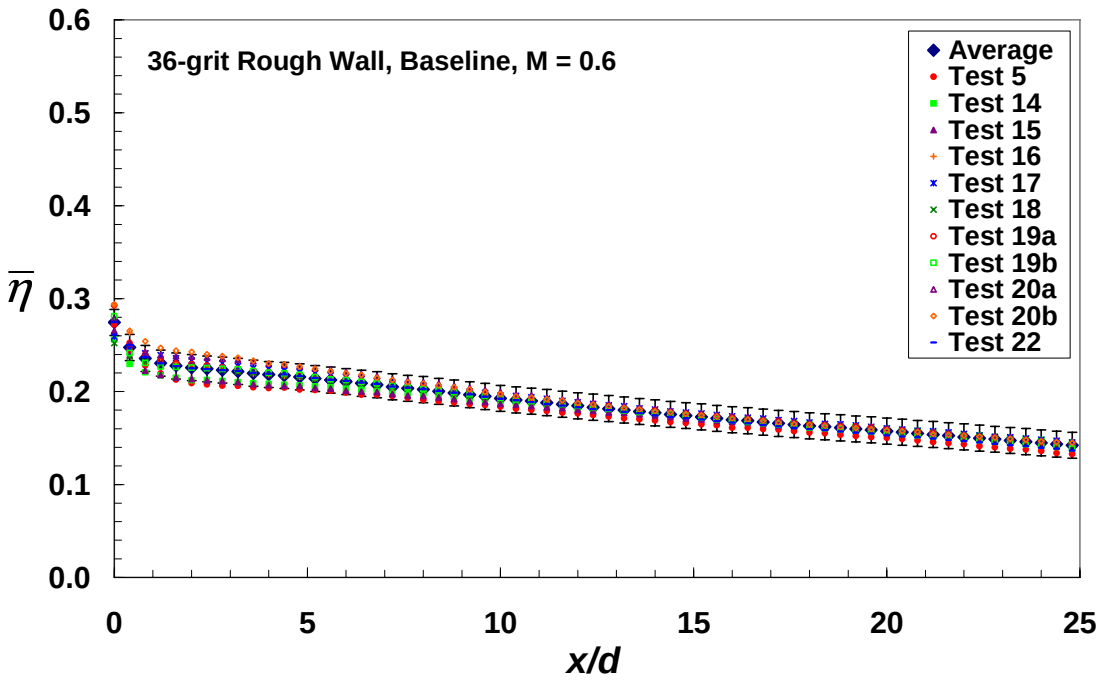

Figure 9.13. Laterally averaged effectiveness plot of the 36-grit rough wall baseline case at M = 0.6 with a 2σ uncertainty band for 11 repeated tests.

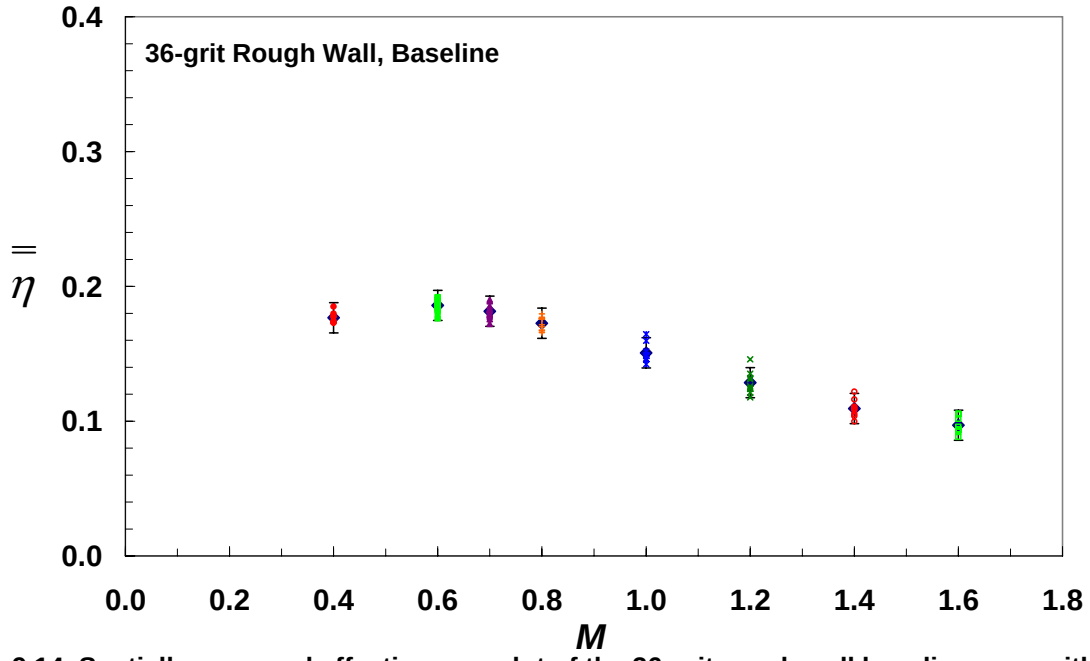

Figure 9.14. Spatially averaged effectiveness plot of the 36-grit rough wall baseline case with a 2σ uncertainty band for 11 repeated tests.

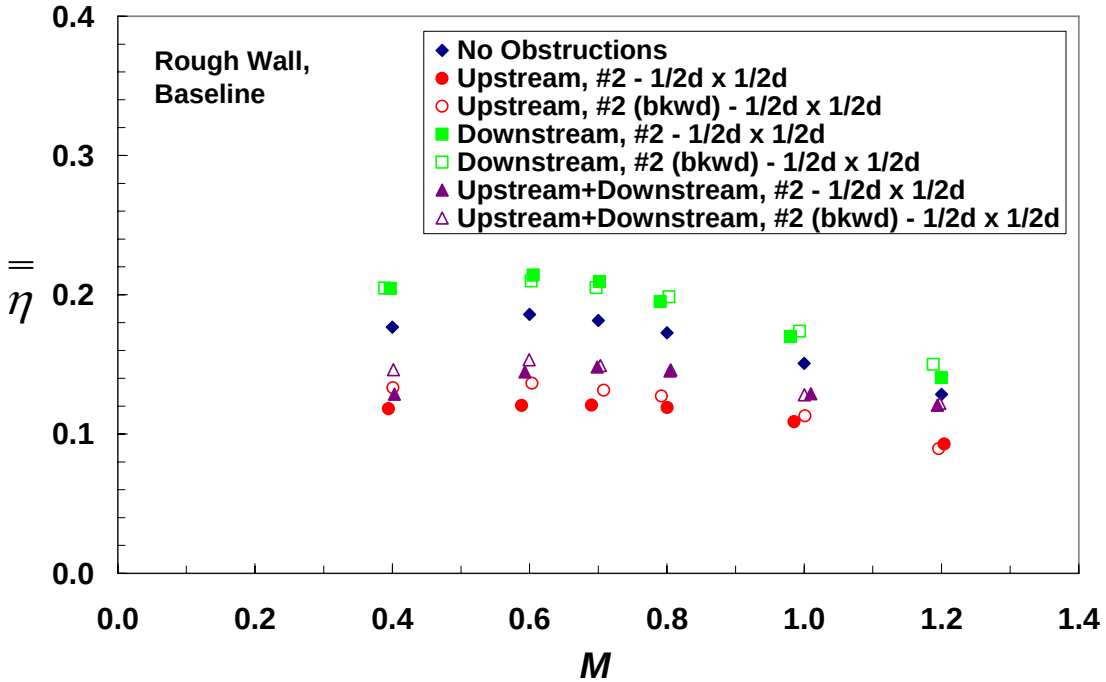

Figure 9.15. Spatially averaged effectiveness plot of the baseline case with a 36-grit rough wall comparing differing orientations of the #2 obstruction.

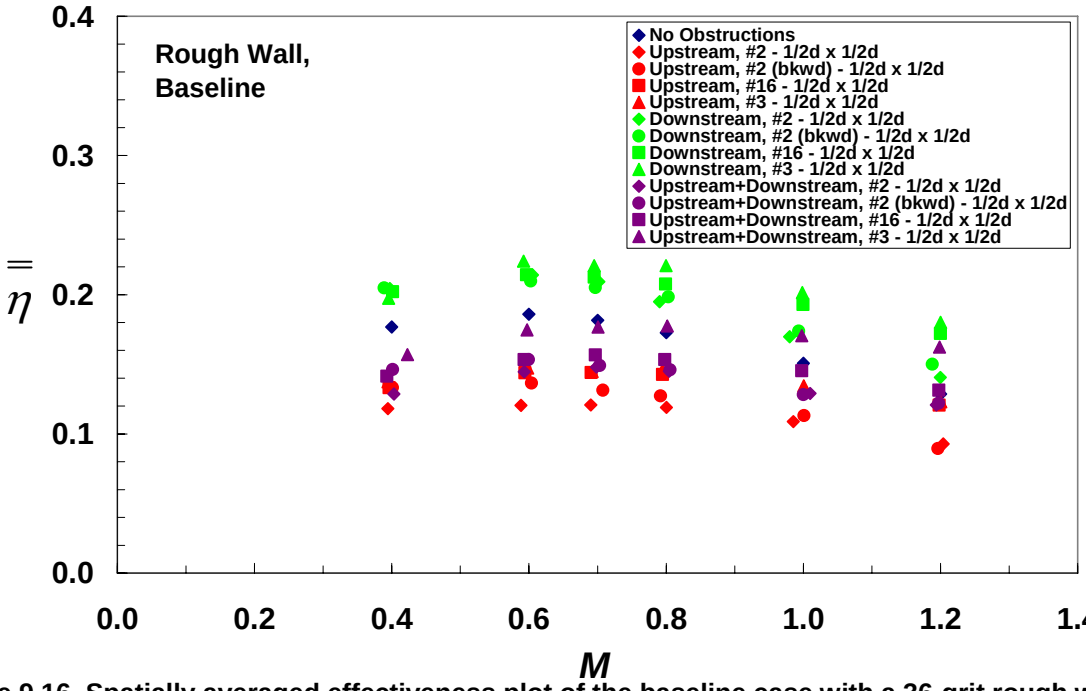

Figure 9.16. Spatially averaged effectiveness plot of the baseline case with a 36-grit rough wall with various obstruction configurations comparing shape effects.

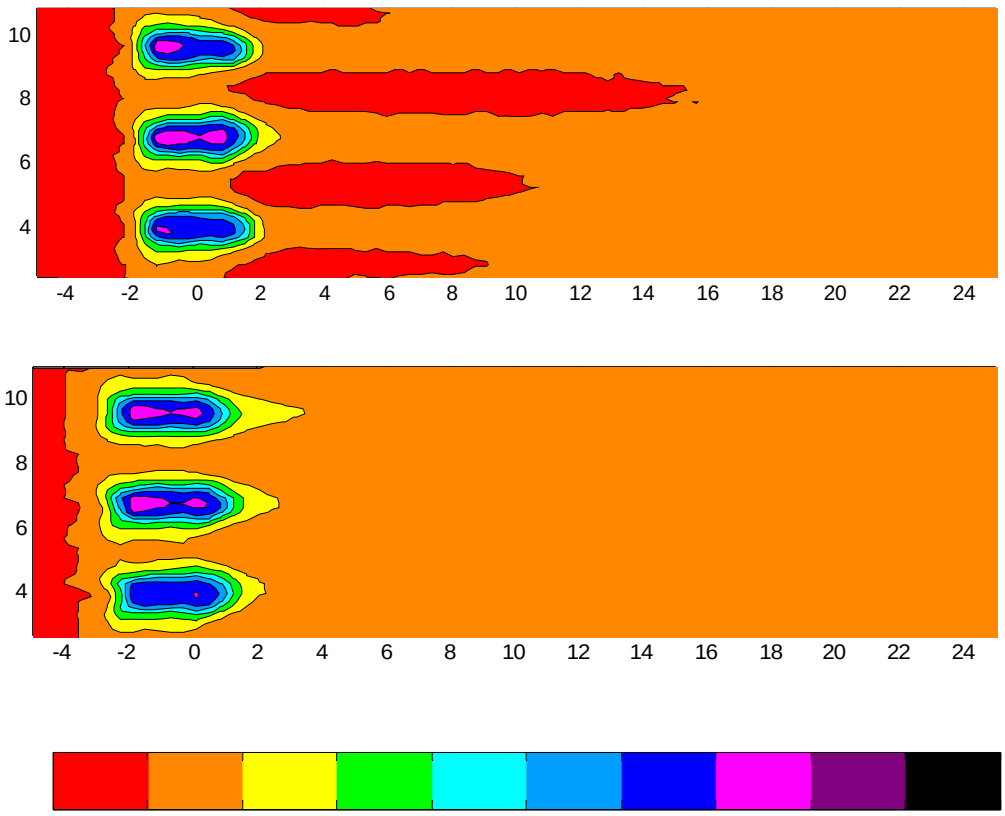

Figure 9.17. Local effectiveness plots of the baseline case with a 36-grit rough wall with #16 obstructions in the Upstream+Downstream configuration (top) and #3 obstructions in the Upstream+Downstream configuration (bottom) at M = 1.2.

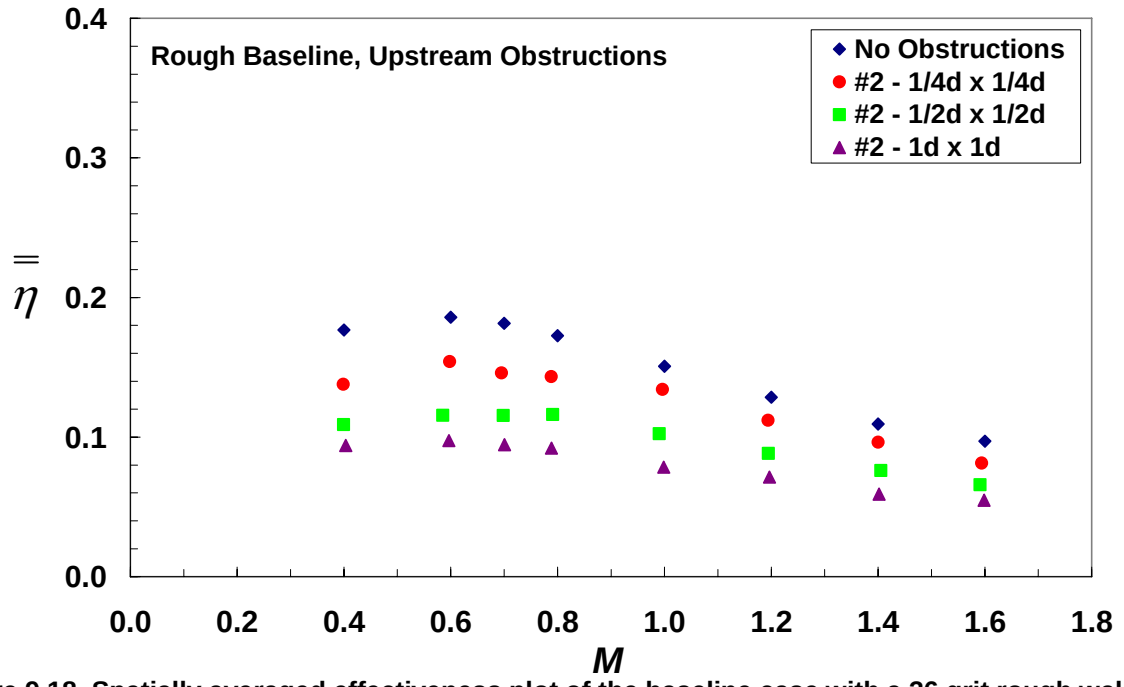

Figure 9.18. Spatially averaged effectiveness plot of the baseline case with a 36 grit rough wall comparing various obstruction sizes in the Upstream location.

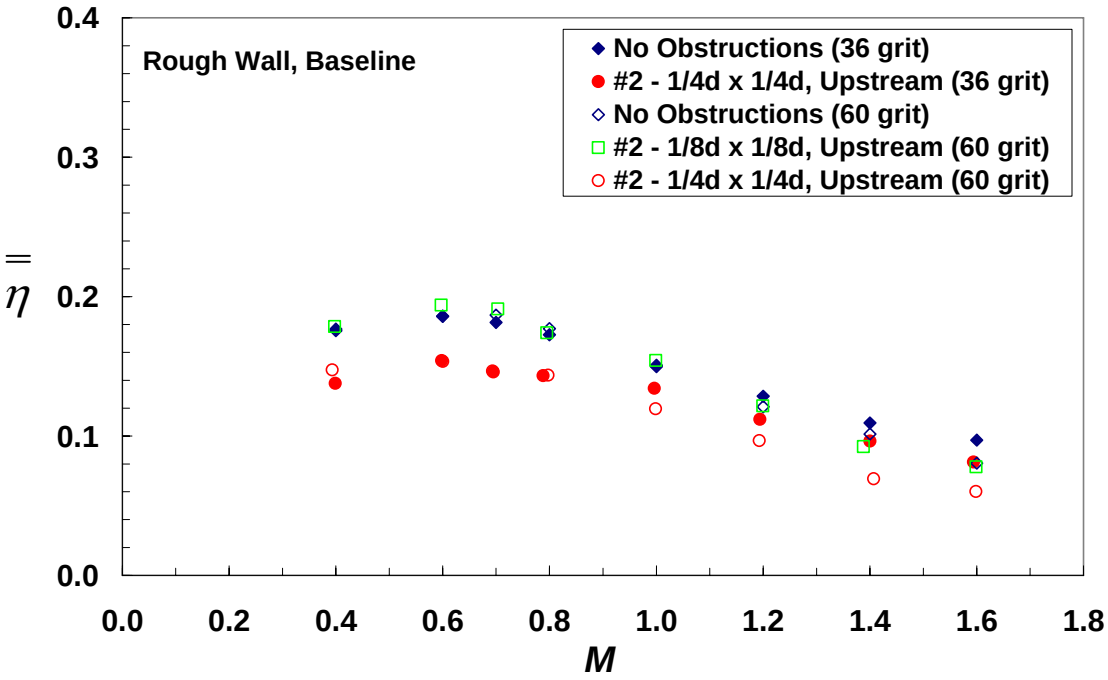

Figure 9.19 Spatially averaged effectiveness plot of the baseline case with a varying surface roughness and varying size of #2 obstructions in the Upstream location.

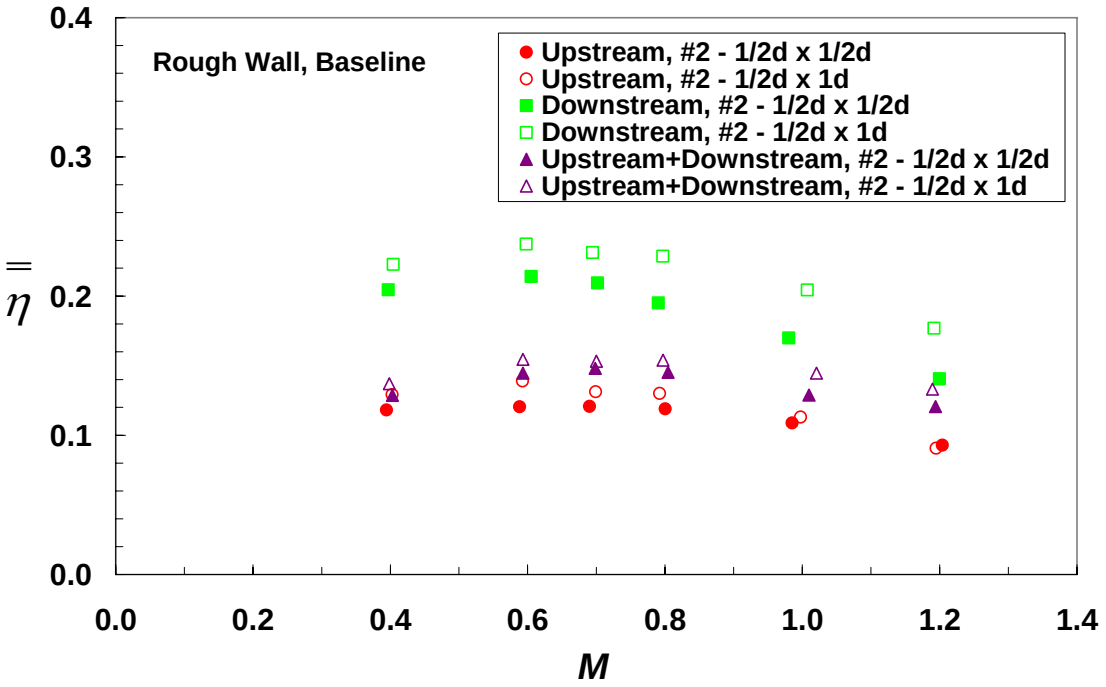

Figure 9.20 Spatially averaged effectiveness plot of the baseline case with a 36 grit rough wall comparing the #2 obstruction with varying widths in the Upstream location.

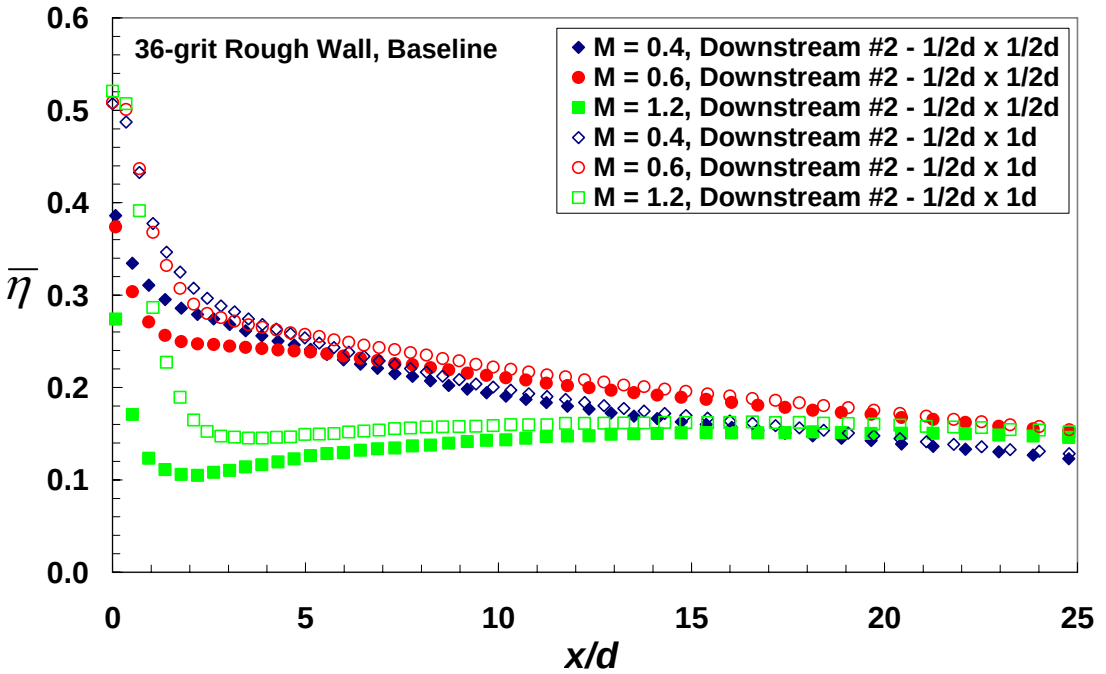

Figure 9.21. Laterally averaged effectiveness plot of the baseline case with a 36 grit rough wall comparing the #2 obstruction with varying widths in the Downstream location.

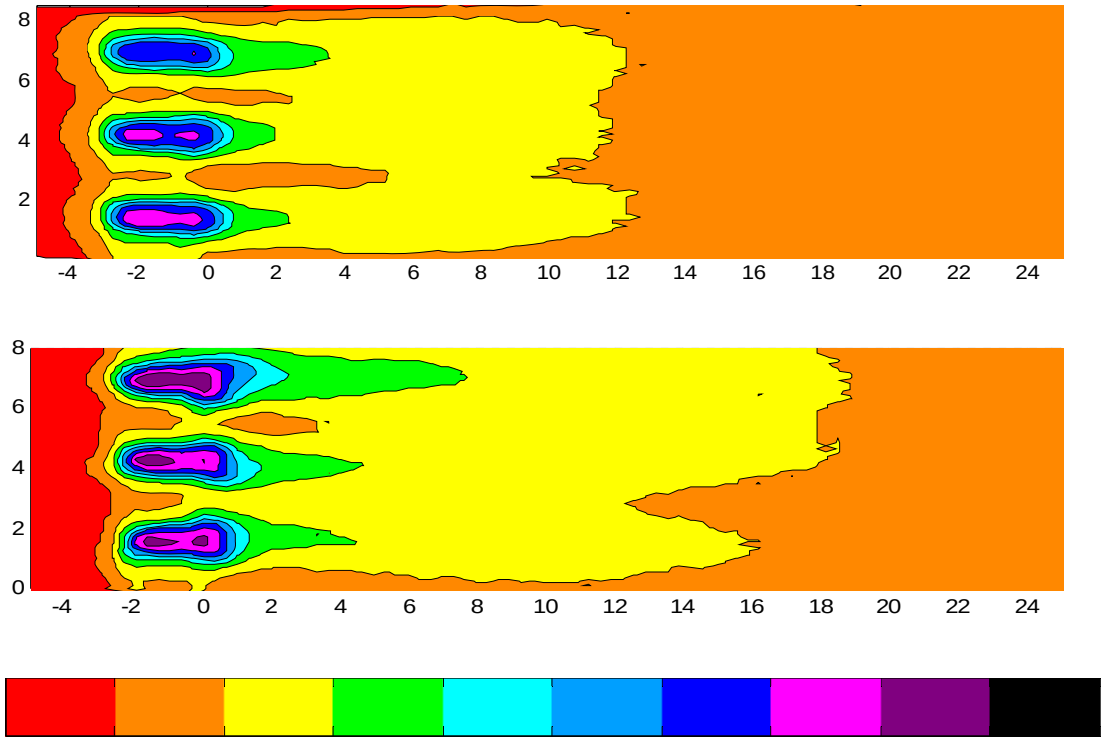

Figure 9.22. Local effectiveness plot of the baseline case with a 36 grit rough wall comparing the #3 obstruction with varying widths in the Downstream location.

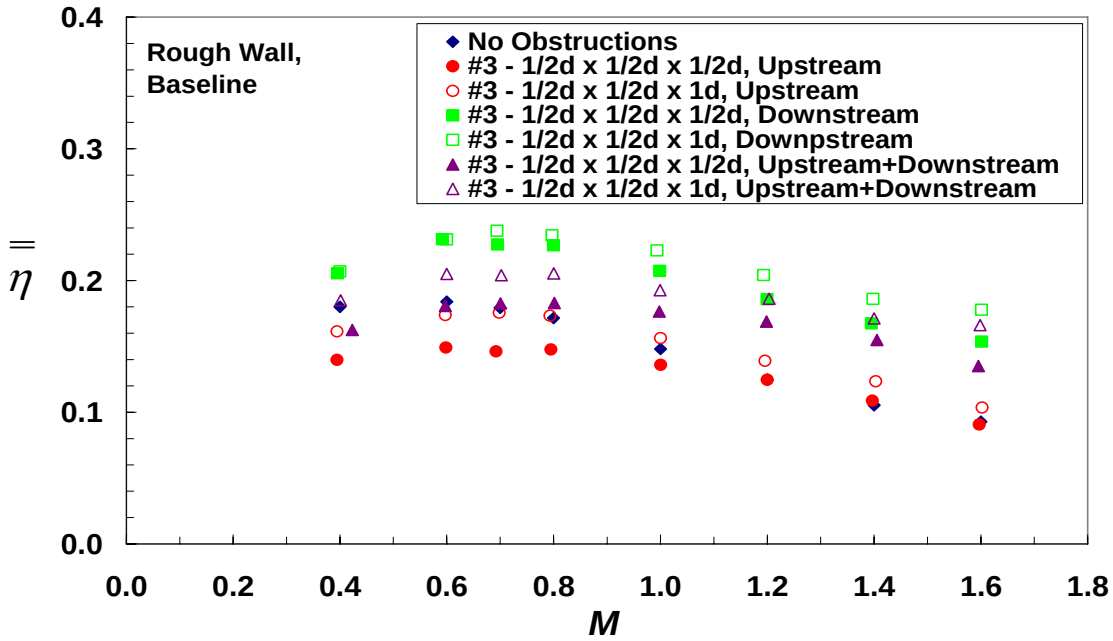

Figure 9.23. Spatially averaged effectiveness plot of the baseline case with a 36 grit rough wall comparing the #3 obstruction with varying lengths.

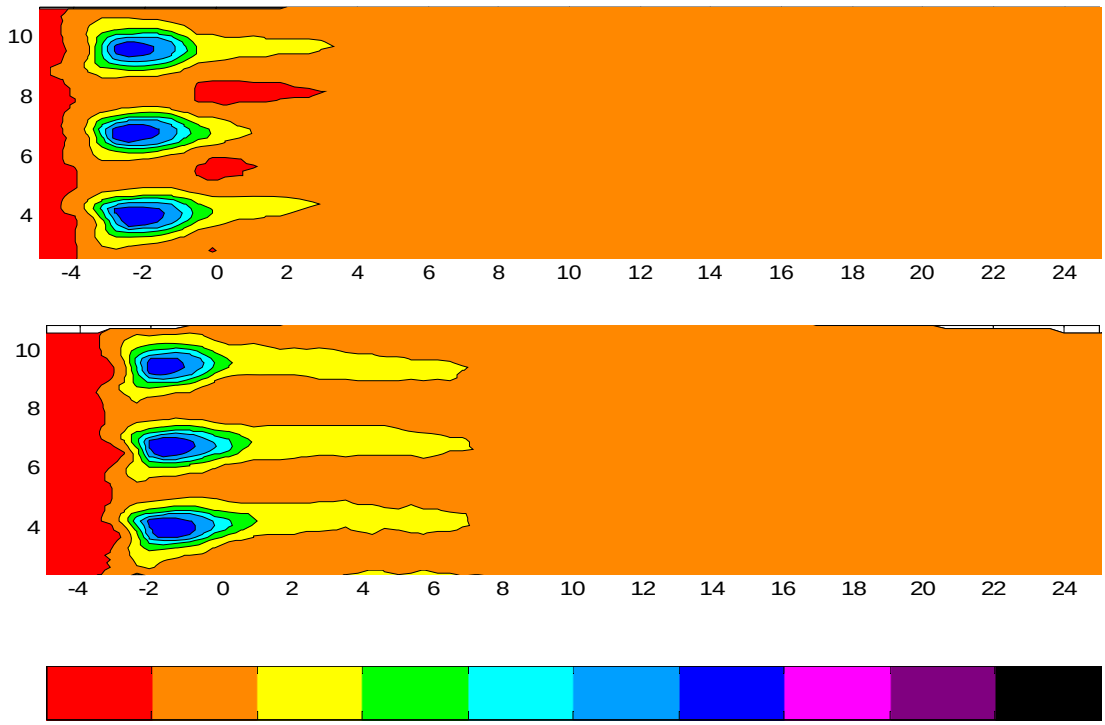

Figure 9.24. Local effectiveness plot of the baseline case with a 36 grit rough wall comparing the #3 obstruction with varying lengths.

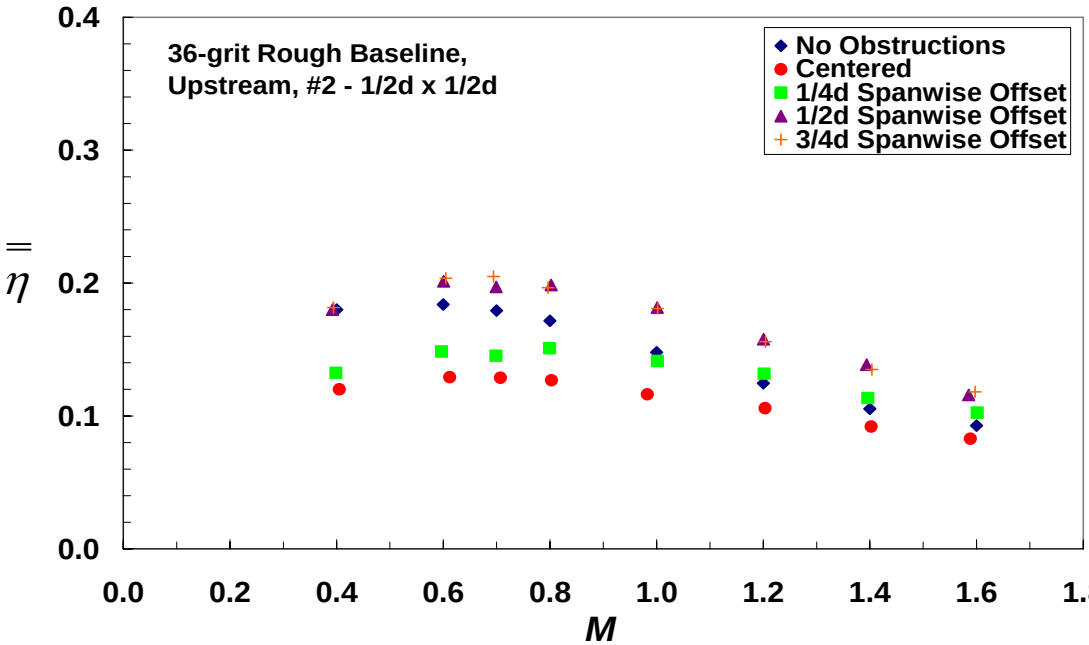

Figure 9.25. Spatially averaged effectiveness plot of the baseline case with a 36 grit rough wall comparing the spanwise positioning of #2 obstructions in the Upstream location.

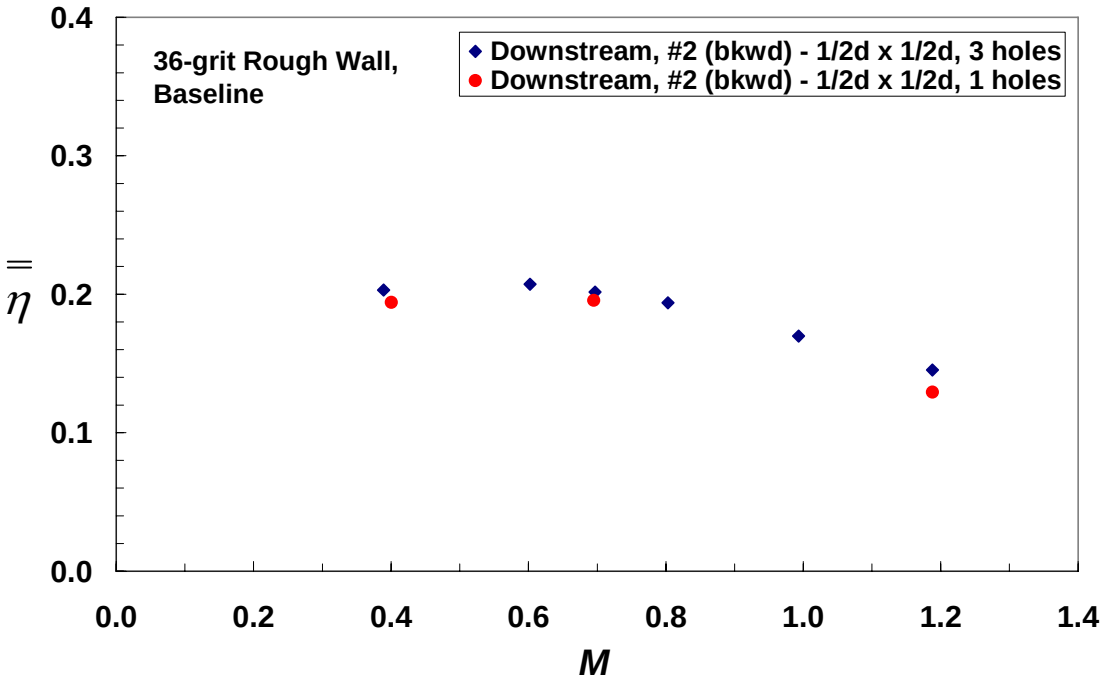

Figure 9.26. Spatially averaged effectiveness plot of the baseline case with a 36 grit rough wall comparing the effects of blocking consecutive holes (note that only one hole was analyzed for both cases).

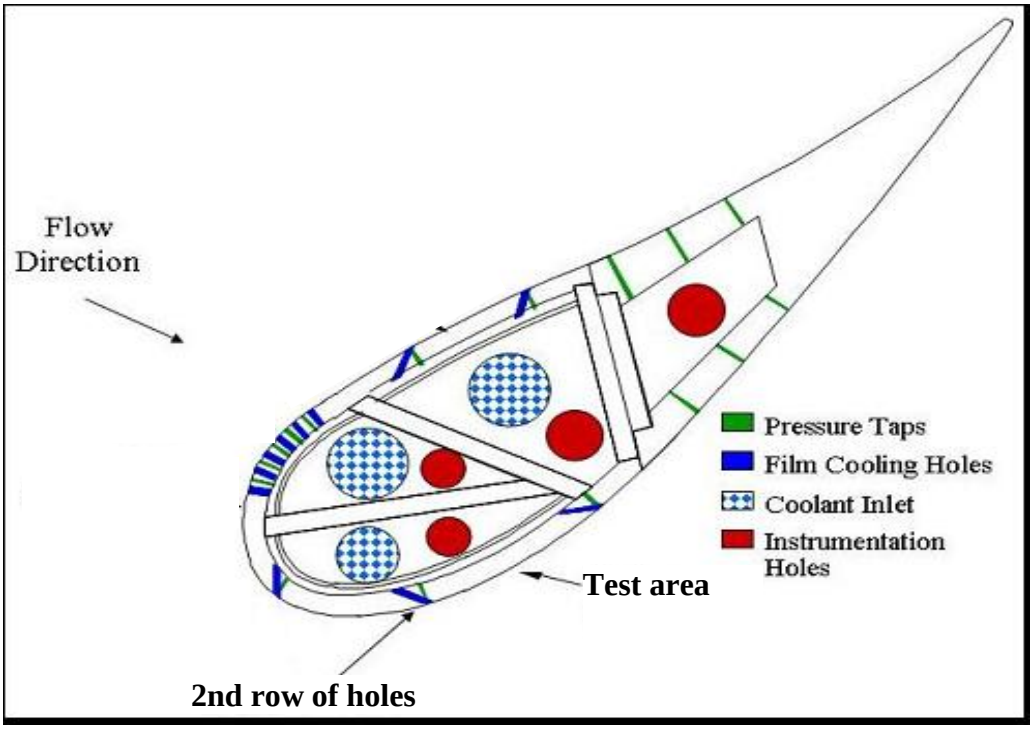

Figure 10.1. Schematic of test vane.

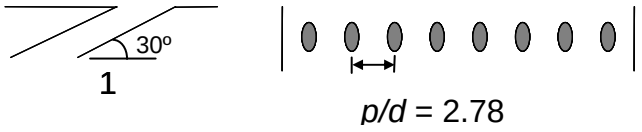

Figure 10.2. Baseline axial hole configuration.

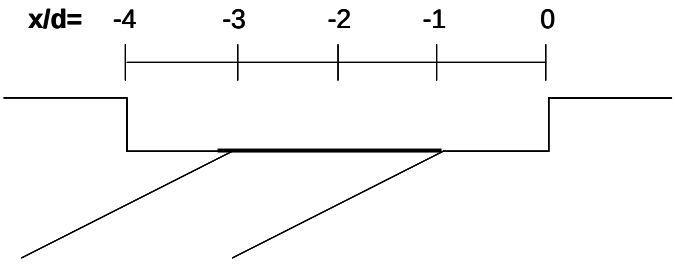

Figure 10.3. Coordinate origin for trench configurations.

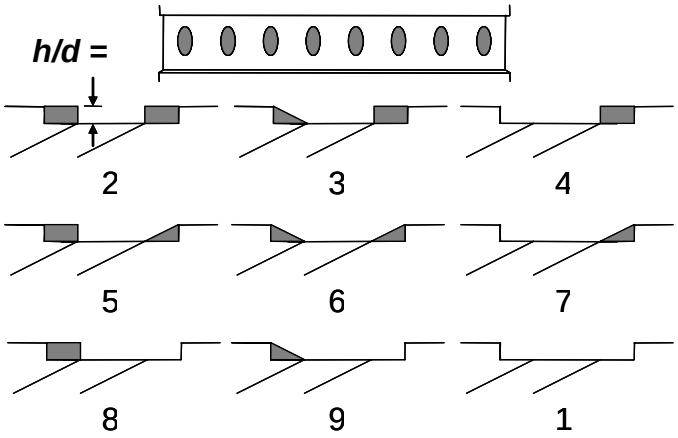

Figure 10.4. Schematic of shallow trench configurations.

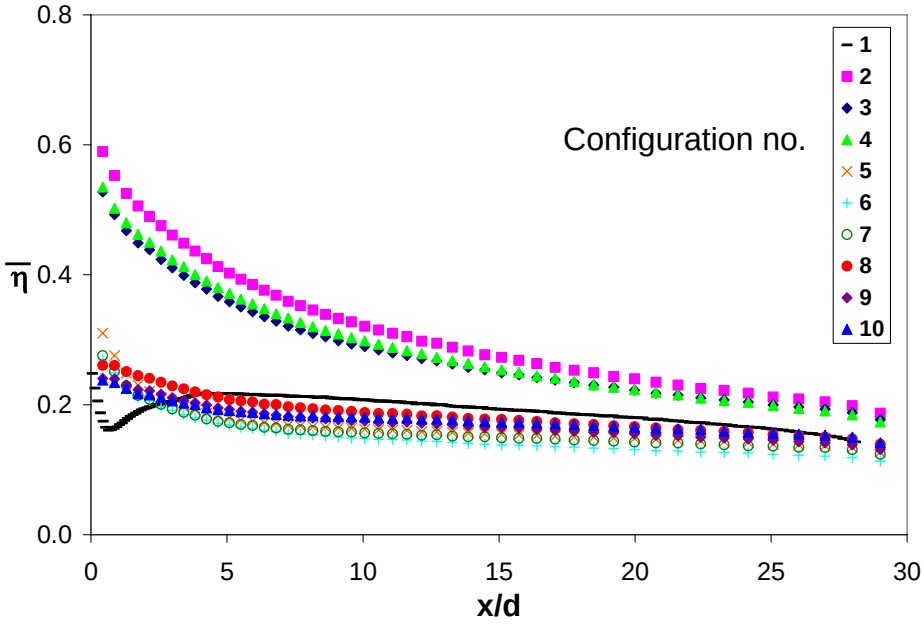

Figure 10.5. Comparison of laterally averaged adiabatic effectiveness for all trench configurations tested, M = 1.0, Tu_∞ = 1.0%

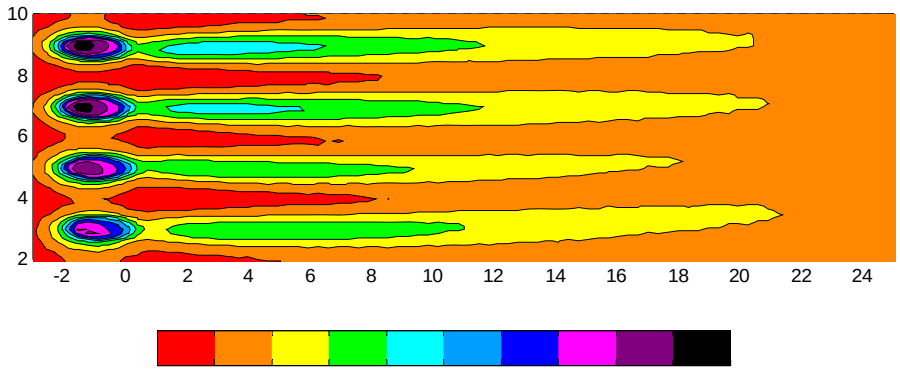

Figure 10.6 (a) Spatial adiabatic effectiveness distribution for baseline axial holes, *M* = 1.0, *Tu* = 1.0%

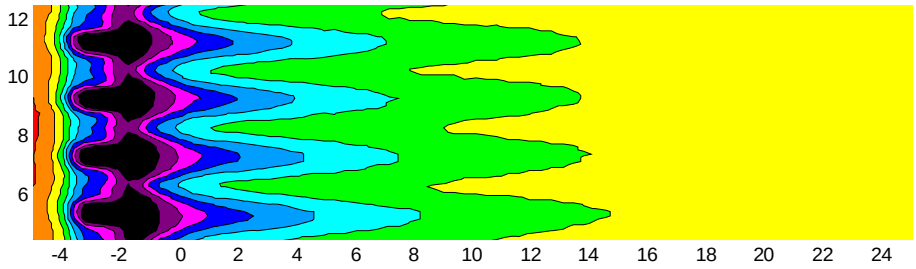

Figure 10.6 (b) Spatial adiabatic effectiveness distribution for configuration 2, *M* = 1.0, *Tu* = 1.0%

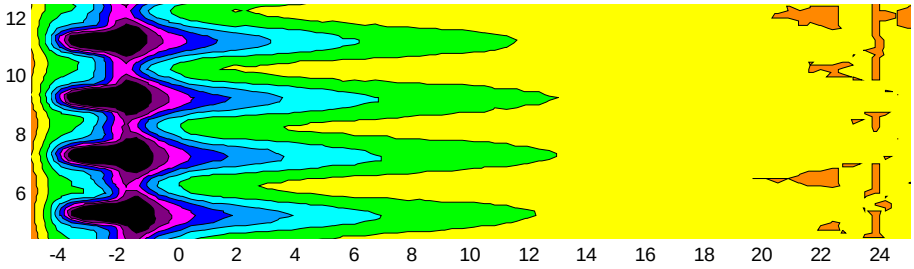

Figure 10.6 (c) Spatial adiabatic effectiveness distribution for configuration 3, *M* = 1.0, *Tu* = 1.0%

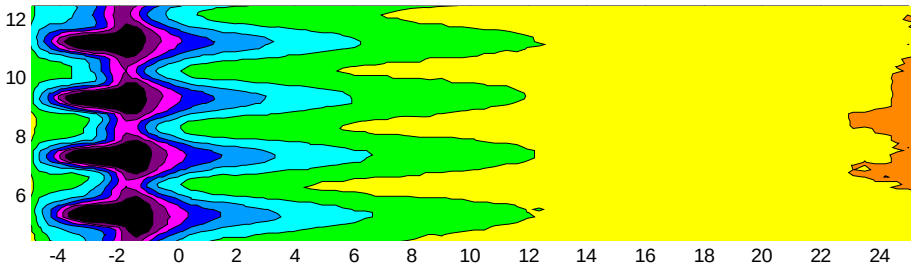

Figure 10.6 (d) Spatial adiabatic effectiveness distribution for configuration 4, *M* = 1.0, *Tu* = 1.0%

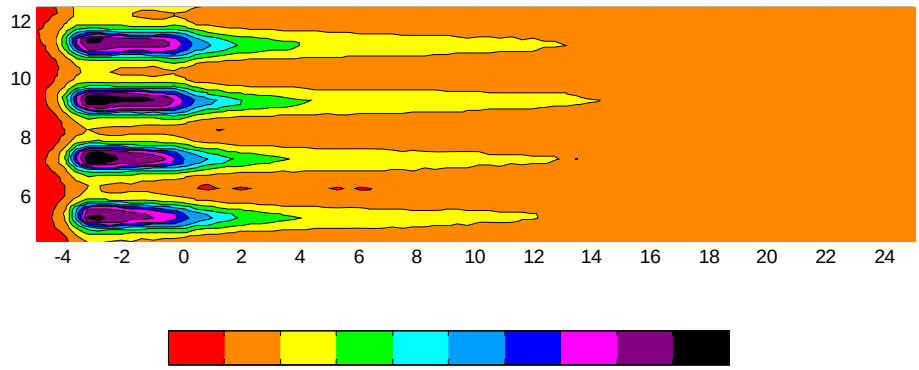

Figure 10.6 (e) Spatial adiabatic effectiveness distribution for configuration 5, *M* = 1.0, *Tu* = 1.0%

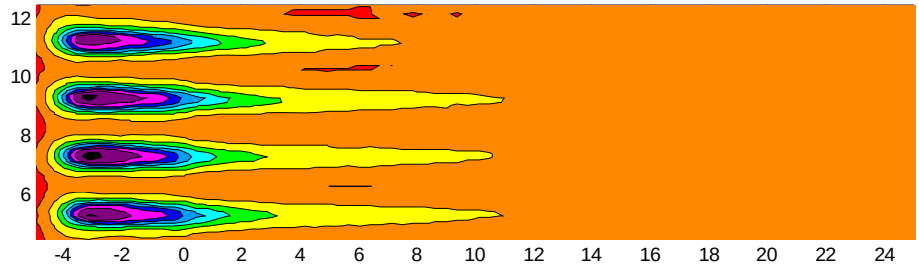

Figure 10.6 (f) Spatial adiabatic effectiveness distribution for configuration 6, *M* = 1.0, *Tu* = 1.0%

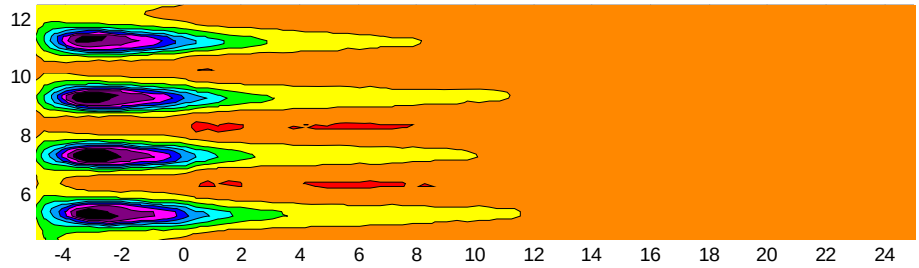

Figure 10.6 (g) Spatial adiabatic effectiveness distribution for configuration 7, *M* = 1.0, *Tu* = 1.0%

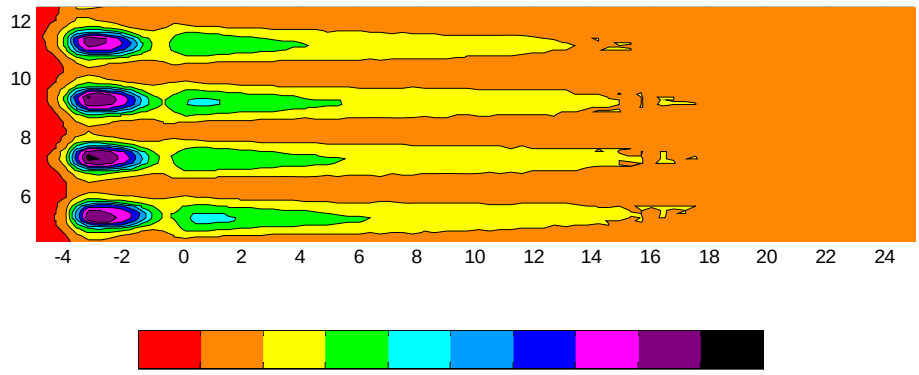

Figure 10.6 (h) Spatial adiabatic effectiveness distribution for configuration 8, *M* = 1.0, *Tu* = 1.0%

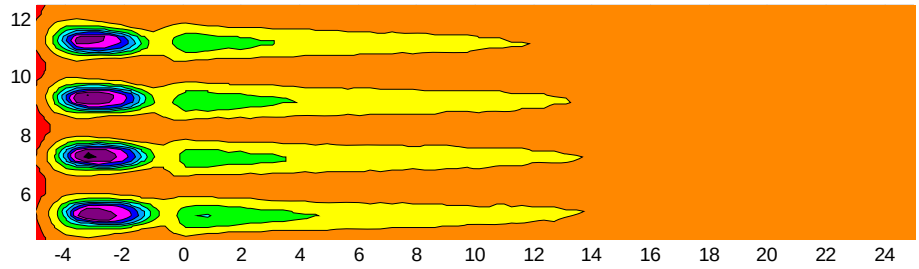

Figure 10.6 (i) Spatial adiabatic effectiveness distribution for configuration 9, *M* = 1.0, *Tu* = 1.0%

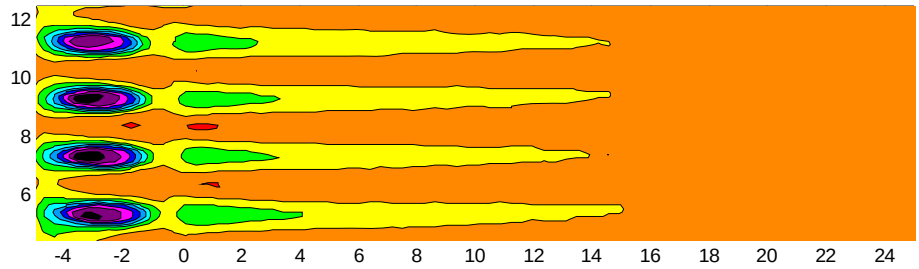

Figure 10.6 (j) Spatial adiabatic effectiveness distribution for configuration 2\10, *M* = 1.0, *Tu* = 1.0%

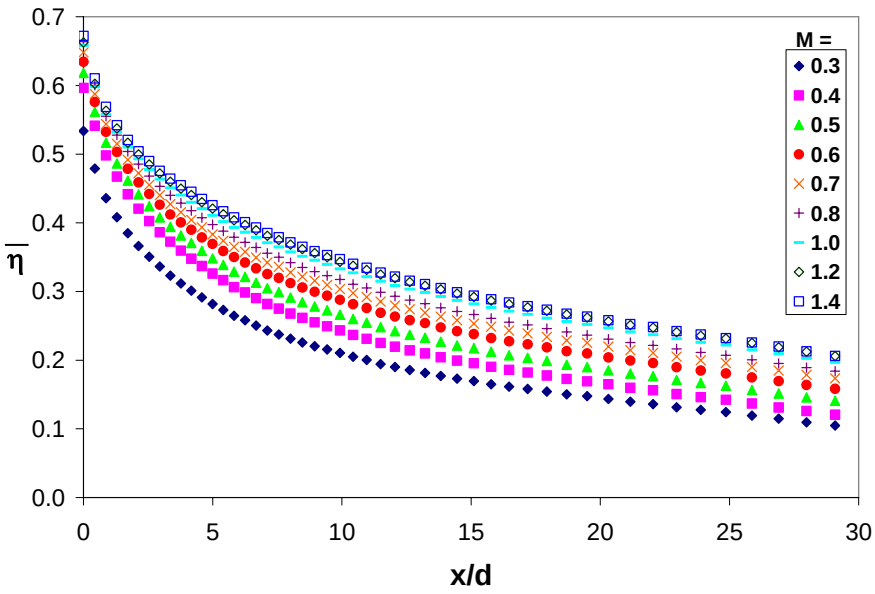

Figure 10.7. Laterally averaged adiabatic effectiveness for axial holes embedded in the narrow trench configuration, *p/d* = 2.8, and *Tu* = 3.9%

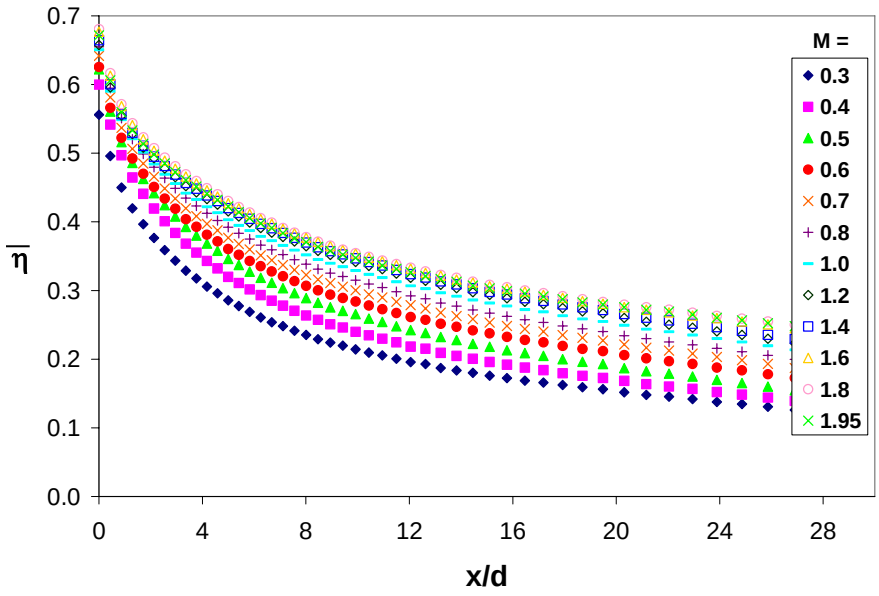

Figure 10.8. Laterally averaged adiabatic effectiveness for axial holes embedded in a narrow trench configuration, *p/d* = 8, *Tu* = 1.0%

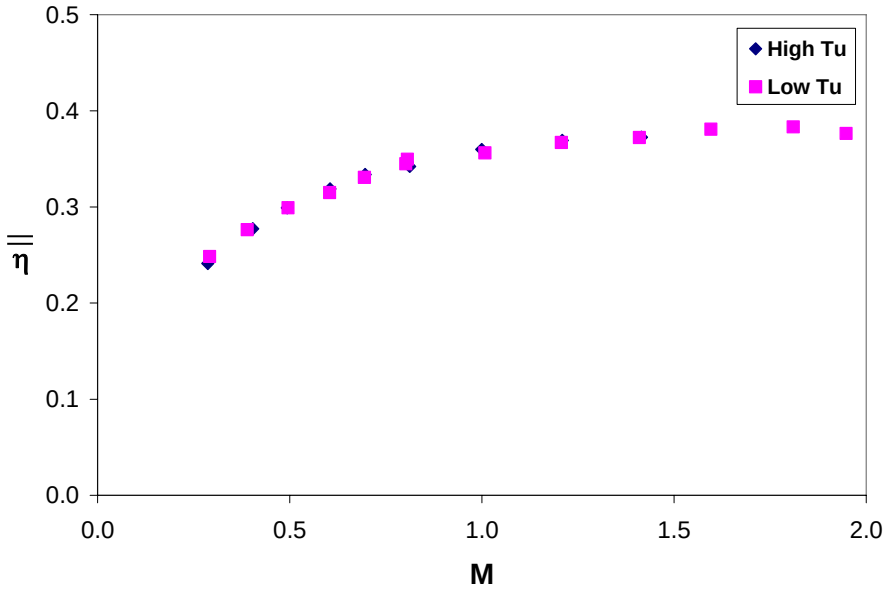

Figure 10.9. Spatially averaged adiabatic effectiveness (x/d = 0 to 25) for low and high mainstream turbulence levels.

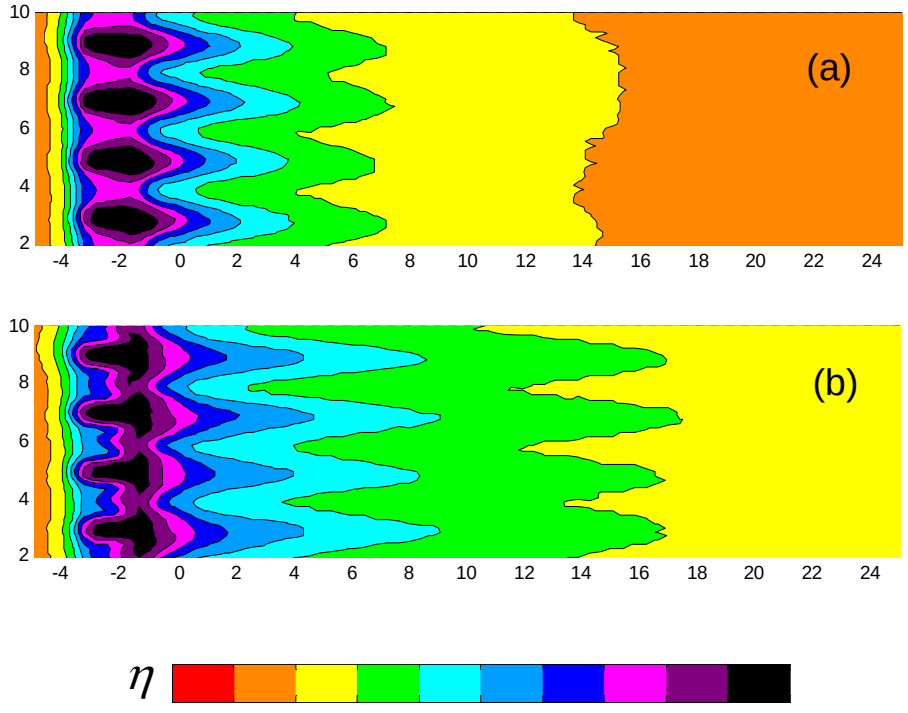

Figure 10.10. Spatial adiabatic effectiveness distribution for narrow trench configuration, (a) *M* = 0.4 and (b) *M* = 1.95.

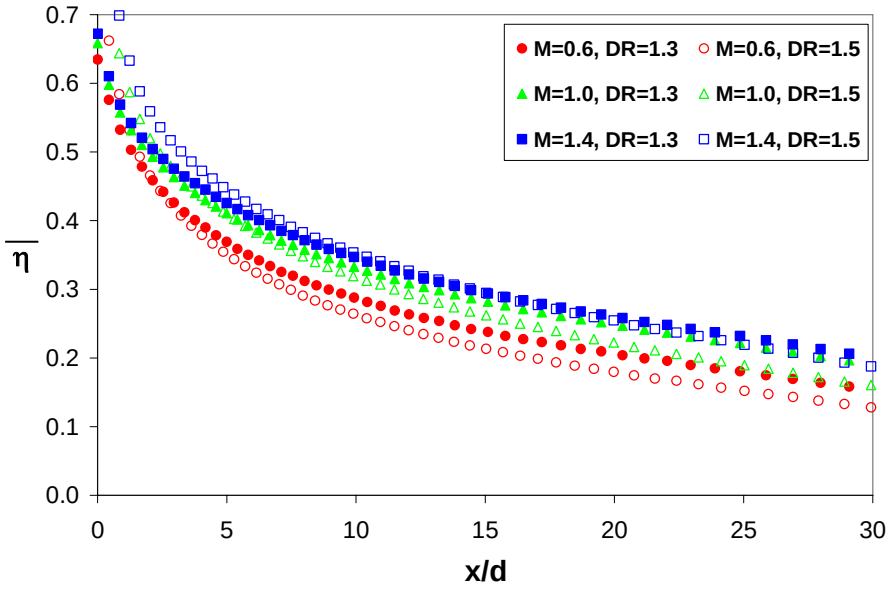

Figure 10.11. Comparison adiabatic effectiveness at density ratios of *DR* = 1.3 and 15 using the narrow trench configuration, *Tu* = 3.9%.

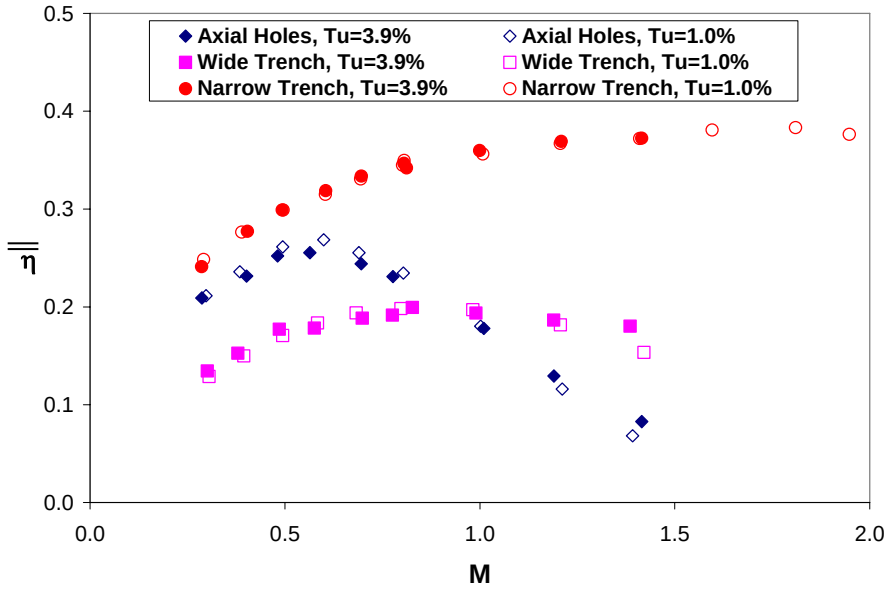

Figure 10.12. Comparison of spatially averaged adiabatic effectiveness for narrow and wide trench configurations (Configurations 2 and 10). For reference, the baseline axial hole configuration is also presented.

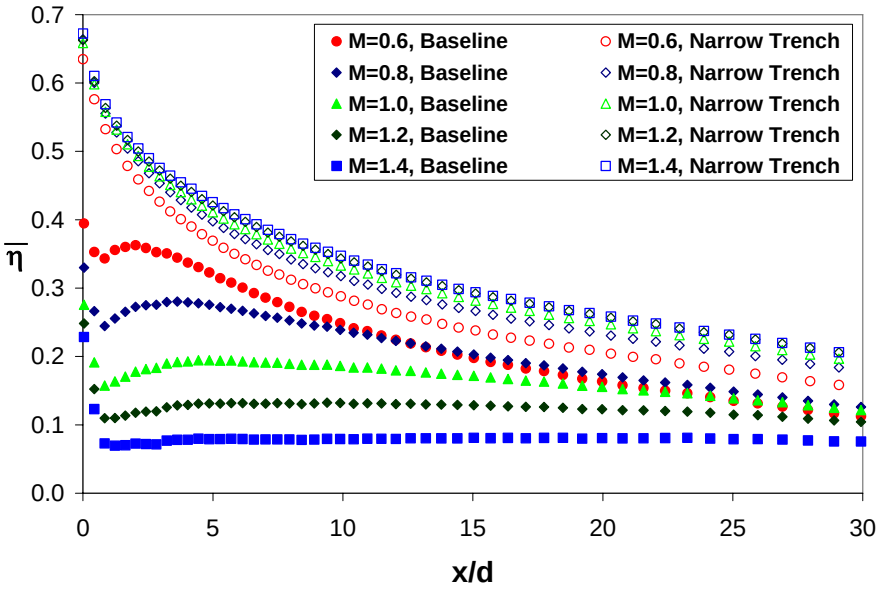

Figure 10.13. Comparison of baseline axial hole and narrow trench configurations, *Tu* = 3.9%

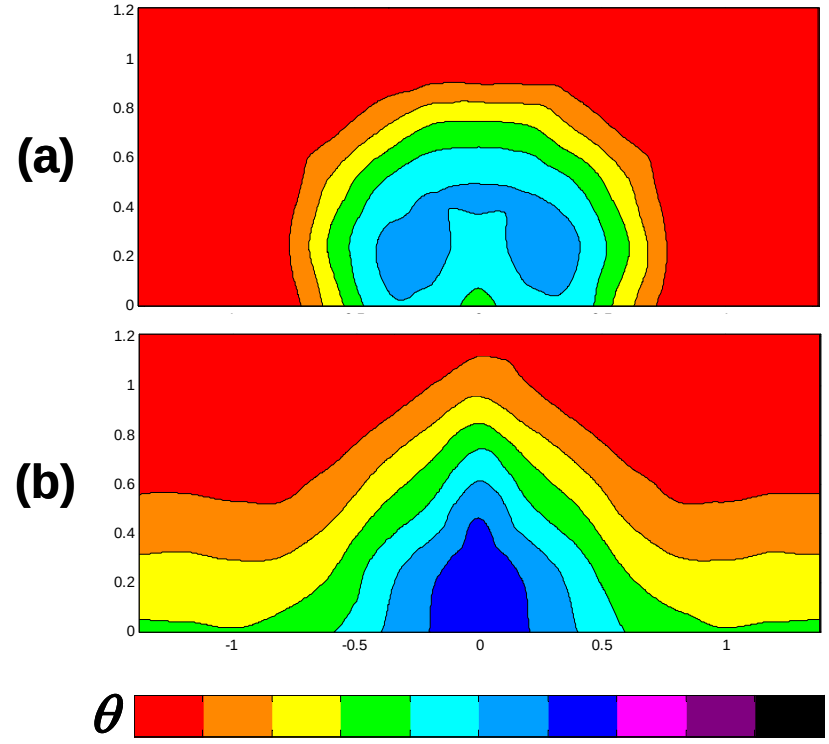

Figure 10.14. Lateral ˙ profiles at x/d = 2, with *M* = 1.0, *Tu* = 1.0% for (a) axial holes and (b) narrow trench configurations.

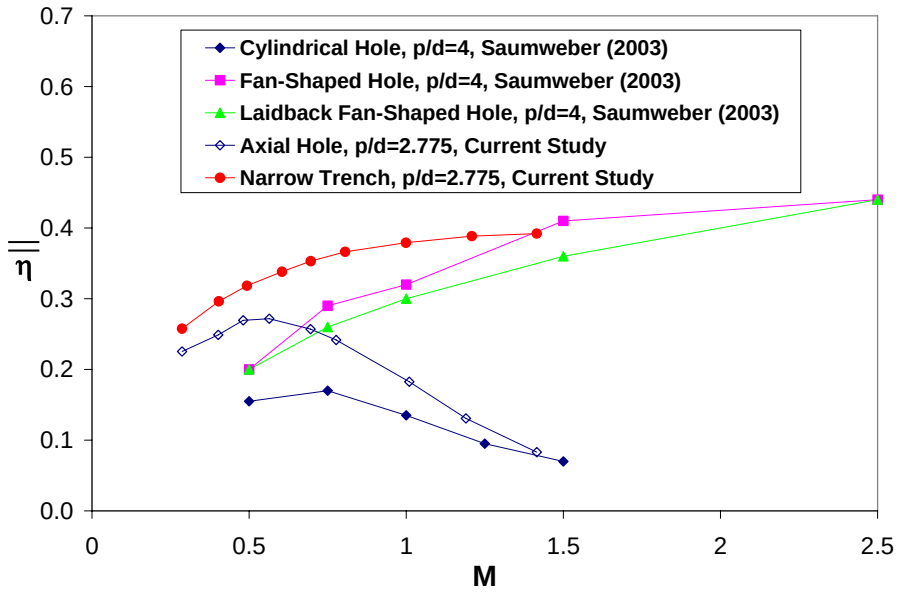

Figure 10.15. Comparison of the narrow trench configuration to shaped hole configurations.

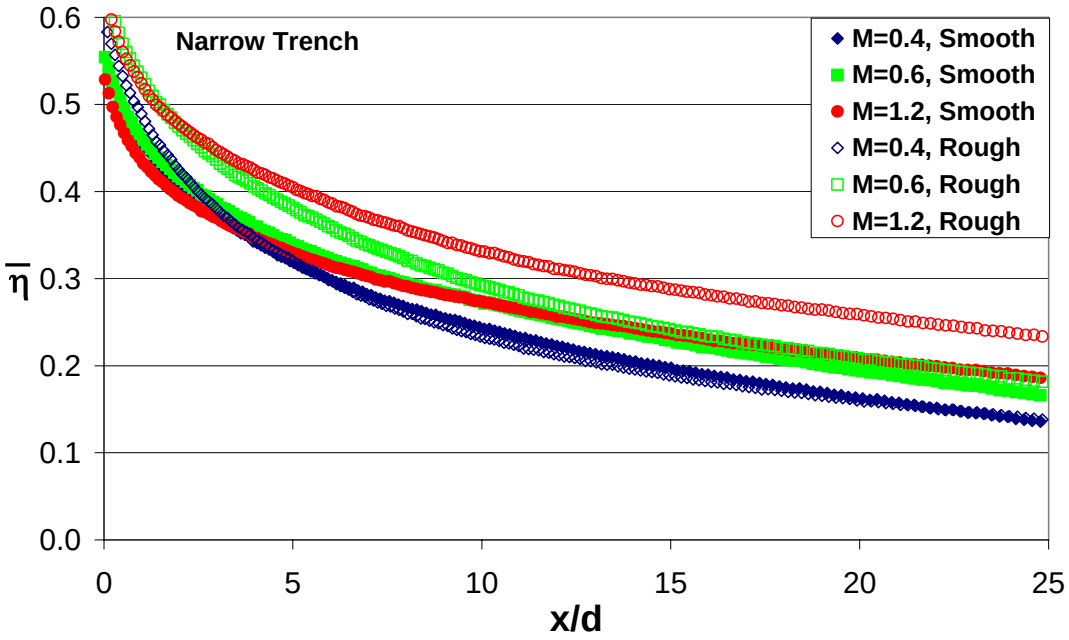

Figure 10.16. Laterally averaged effectiveness plot of the narrow transverse trench case and the narrow transverse trench case with a rough wall.

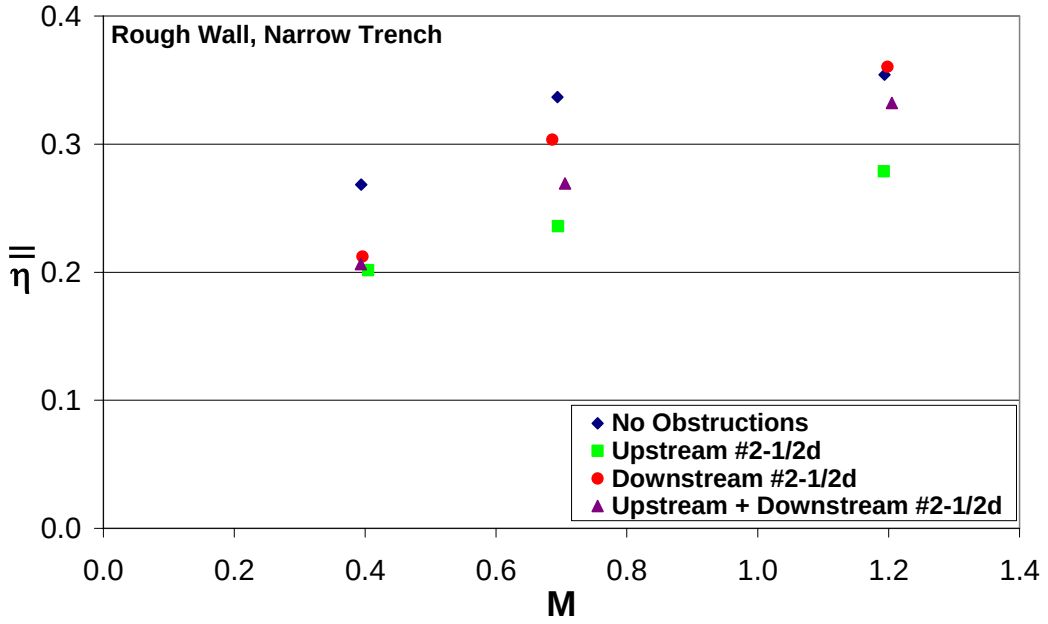

Figure 11.1. Spatially averaged effectiveness for a rough surface with a narrow transverse trench without and with obstructions.

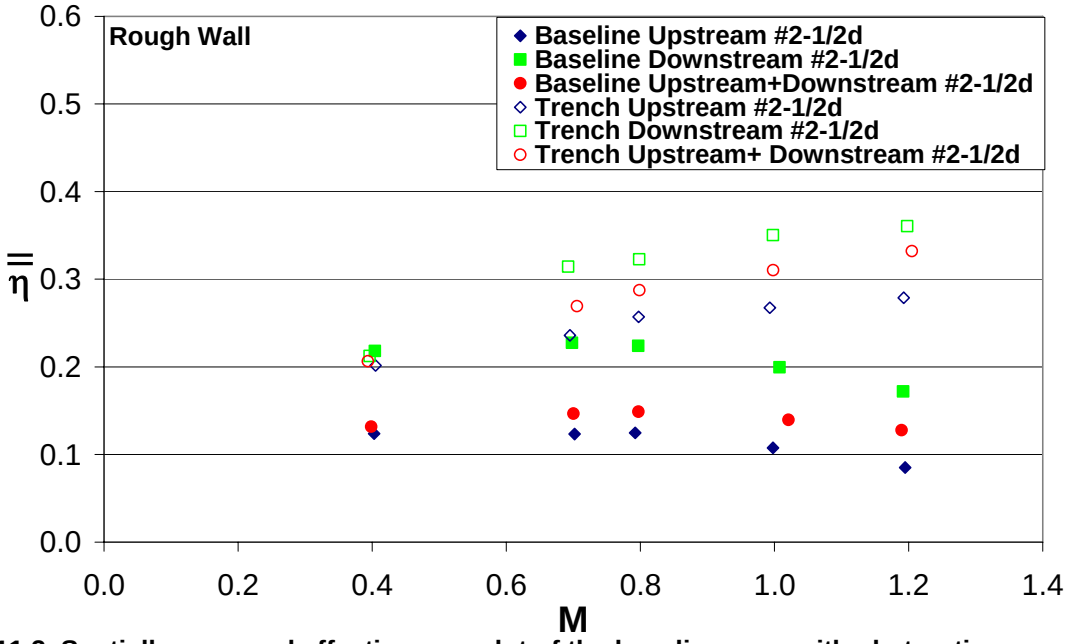

Figure 11.2. Spatially averaged effectiveness plot of the baseline case with obstructions on a rough wall and the narrow transverse trench case with obstructions on a rough wall.

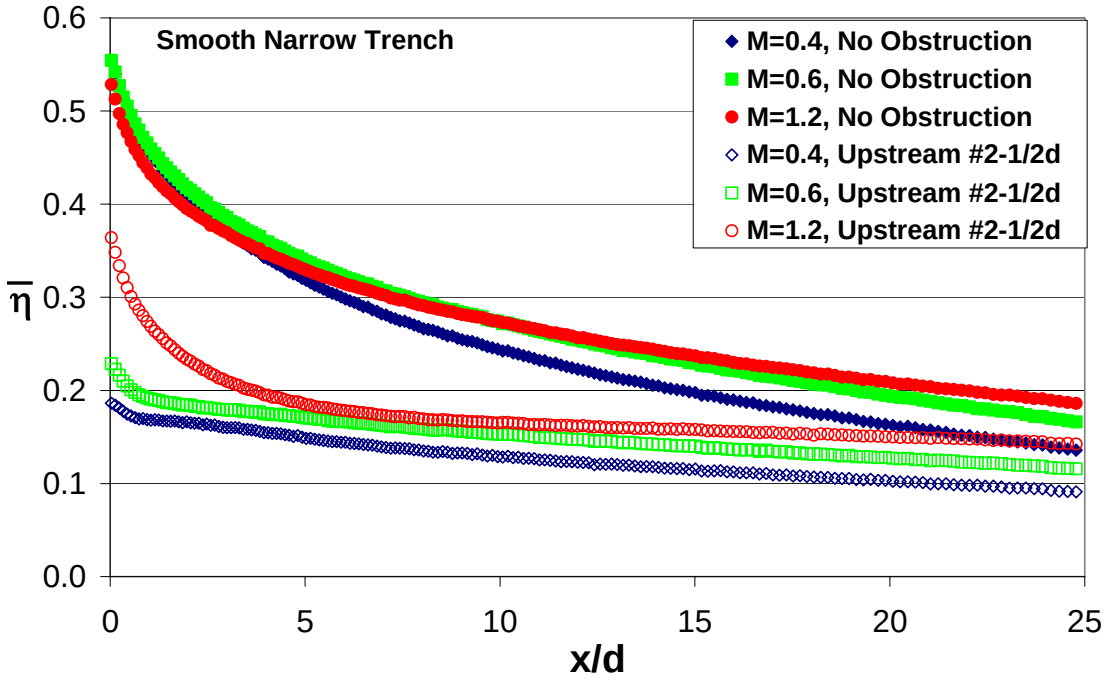

Figure 11.3. Laterally averaged effectiveness plot of the narrow transverse trench case and the narrow transverse trench case with the addition of upstream obstructions.

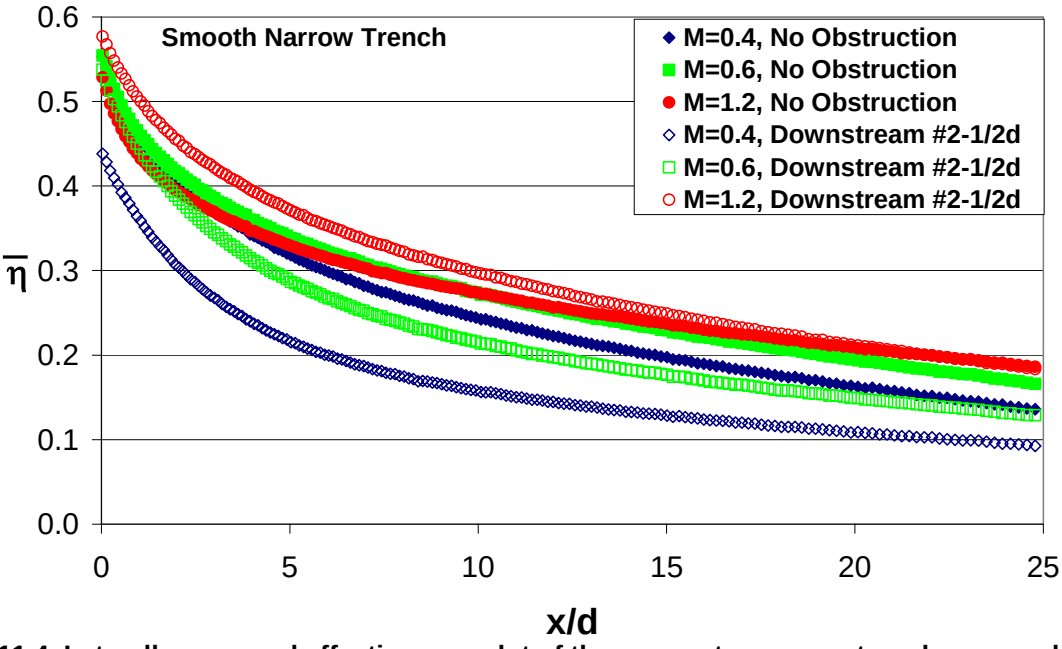

Figure 11.4. Laterally averaged effectiveness plot of the narrow transverse trench case and the narrow transverse trench case with the addition of downstream obstructions.

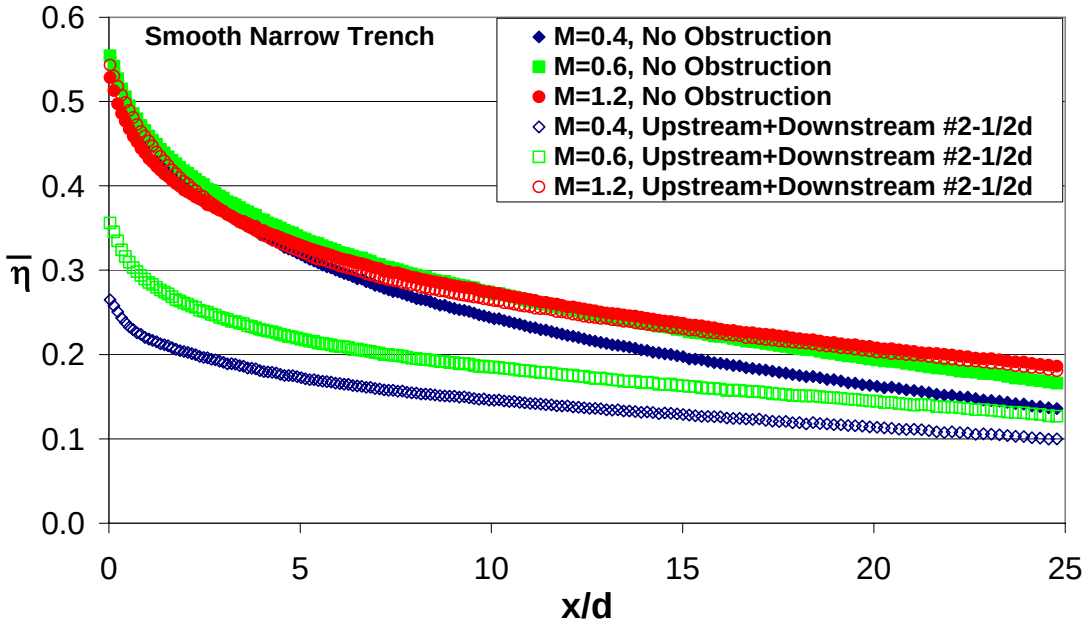

Figure 11.5. Laterally averaged effectiveness plot of the narrow transverse trench case and the narrow transverse trench case with the addition of upstream + downstream obstructions.

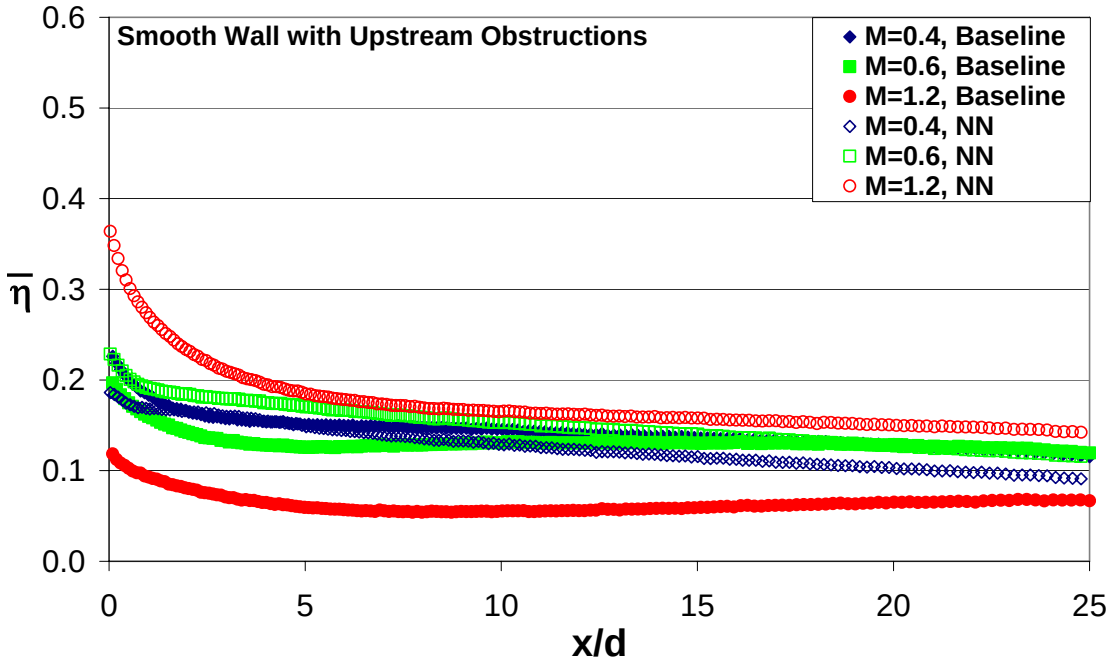

Figure 11.6. Laterally averaged effectiveness plot of the baseline case with upstream obstructions and the narrow transverse trench case with upstream obstructions.

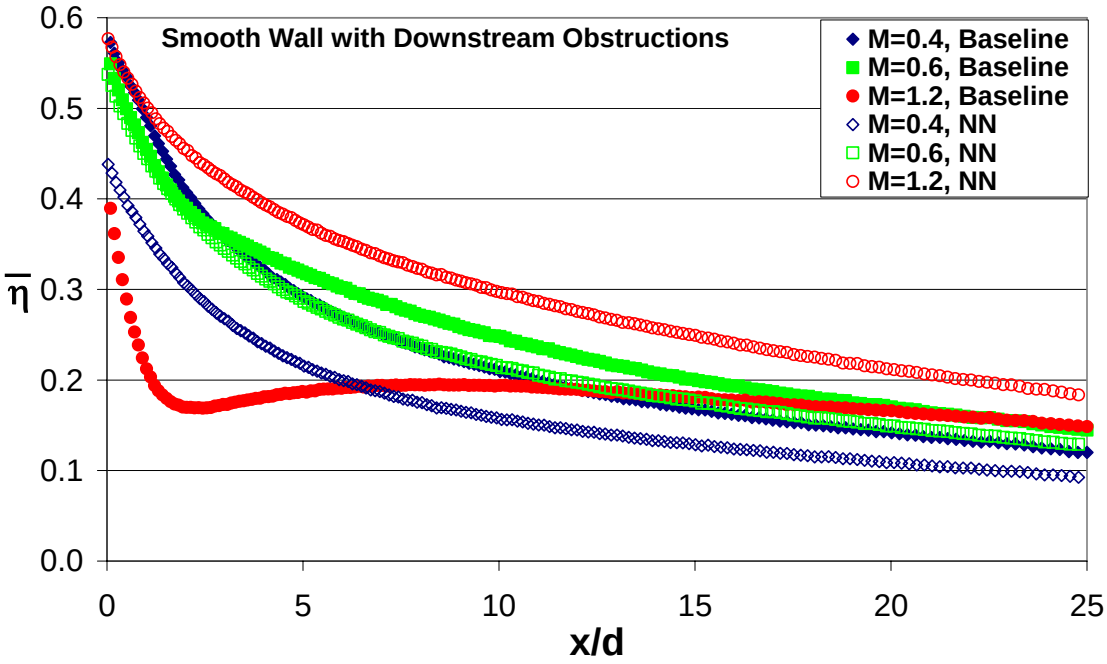

Figure 11.7. Laterally averaged effectiveness plot of the baseline case with downstream obstructions and the narrow transverse trench case with downstream obstructions.

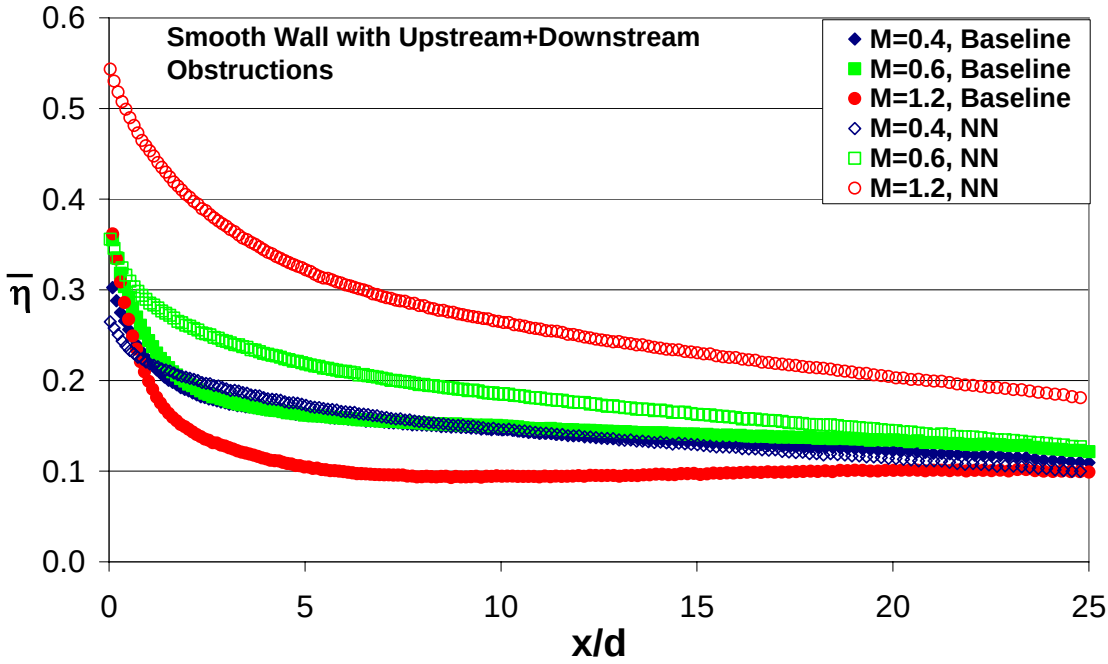

Figure 11.8. Laterally averaged effectiveness plot of the baseline case with upstream + downstream obstructions and the narrow transverse trench case with upstream + downstream obstructions.

Combustion Instability and Blowout Characteristics of Fuel Flexible Combustors

Final Report

Reporting Period Start Date: February 1, 2004

Reporting Period End Date: December 31, 2006

Principal Investigators: Tim Lieuwen and Ben Zinn

Date Report was issued January 31, 2007

DOE Award Number 03-01-SR111

School of Aerospace Engineering

Georgia Institute of Technology

Atlanta, GA 30332-0150

DISCLAIMER:

1. ABSTRACT

Under this program, Georgia Institute of Technology investigated the blowout characteristics of fuel-flexible combustors. Particular attention was given to coal-derived and high hydrogen gaseous fuels which are of interest to the DOE. The program consists of three main focuses.

Under the first research focus, we performed extensive chemical kinetic analyses of such quantities as flame speeds and stretch sensitivities of syngas fuels in order to develop the mixture characteristics information needed to correlate test data. In addition, we developed and distributed a software utility that utilizes these calculations, determines other basic mixture properties, and has such features as outputting all fuel mixture combinations with a given flame speed, adiabatic flame temperature, or heating value within some given tolerance.

Under the second research focus, we made extensive measurements of the combustor's blowout characteristics as a function of fuel composition. We designed and fabricated a gas-mixing facility to blend syngas-type fuels of arbitrary compositions of H_2, CO, CO_2, N_2, and CH_4. We then measured the equivalence ratios at lean blow off for a large number of H_2/CO/CH_4 mixtures at different inlet temperatures and combustion pressures. Consistent with prior studies, these results indicate that the percentage of H_2 in the fuel dominates the mixture blowout characteristics. It is shown that standard well stirred reactor based correlations, based upon a Damköhler number with a diffusivity ratio correction, can capture the effects of fuel composition variability on blowoff limits.

Under the third research focus, we performed more detailed diagnostics of near blowoff flames in order to characterize the blowoff phenomenology better and to provide further insight into how fuel composition (particularly H_2 levels in the fuel) alters this phenomenology. This was accomplished through high speed visualizations of the flame and velocity field measurements. Near blowoff, a variety of highly dynamic flow features are observed, which vary substantially with the H_2 levels in the fuel. These features involve complex interactions between the vortex breakdown bubble, outer recirculation zone of the rapid expansion, and flame extinction/reignition phenomenon.

2. TABLE OF CONTENTS

3. LIST OF FIGURES

4. EXECUTIVE SUMMARY

Under this program, Georgia Institute of Technology investigated the blowout characteristics of fuel-flexible combustors. Particular attention was given to coal-derived and high hydrogen gaseous fuels which are of interest to the DOE. This work is motivated by the fact that the inherent variability in composition and heating value of coal derived and other alternative fuels provides one of the largest barriers towards their usage. This fuel composition variability is of concern because low emissions combustion systems are generally optimized to operate with fuels that meet tight specifications. The successful completion of this project has benefited the nation by removing barriers toward the usage of coal derived gaseous fuels through improved understanding of their combustion characteristics. Ultimately, these benefits will increase the air quality and energy security of the USA, by allowing power plants to operate efficiently and with minimal pollution, using a variety of domestic fuel sources.

The program consists of three main focuses. Under the first research focus, we performed extensive chemical kinetic analyses of such quantities as flame speeds and stretch sensitivities of syngas fuels in order to develop the mixture characteristic information needed to correlate test data. In addition, we developed and distributed a software utility that utilizes these calculations, determines other basic mixture properties, and has such features as outputting all fuel mixture combinations with a given flame speed, adiabatic flame temperature, or heating value within some given tolerance.

Under the second research focus, we made extensive measurements of the combustor's blowout characteristics as a function of fuel composition. We designed and fabricated a gas-mixing facility to blend syngas-type fuels of arbitrary compositions of H_2, CO, CO_2, N_2, and CH_4. We then measured the equivalence ratios at lean blow off for a large number of H_2/CO/CH_4 mixtures at different inlet temperatures and combustion pressures. Consistent with prior studies, these results indicate that the percentage of H_2 in the fuel dominates the mixture blowout characteristics. It is shown that standard well stirred reactor based correlations, based upon a Damköhler number with a diffusivity ratio correction, can capture the effects of fuel composition variability on blowoff limits. In addition, visual observations indicate that the blowoff phenomenology qualitatively changes with hydrogen levels in the fuel, being very different for mixtures with H_2 levels above and below about 50%.

Under the third research focus, we performed more detailed diagnostics of near blowoff flames in order to characterize the blowoff phenomenology better and to provide further insight into how fuel composition (particularly H_2 levels in the fuel) alters this phenomenology. This was accomplished through high speed visualizations of the flame and velocity field measurements. Near blowoff, a variety of highly dynamic flow features are observed, which vary substantially with the H_2 levels in the fuel. These features involve complex interactions between the vortex breakdown bubble, outer recirculation zone of the rapid expansion, and flame extinction/reignition phenomenon.

5. PROJECT DESCRIPTION

Modern power turbines have the highest operating efficiencies and turn out fewer pollutants than other major combustion energy converting devices[1]. In addition, the low capital costs required to bring a new system online have made them attractive to investors. As a result, gas turbines have become the dominant technology for new power generating capacity in the U.S. and worldwide. These systems have met their aggressive emission targets by operating in a lean, premixed mode of combustion. This mode of burning has significant advantages over its nonpremixed counterpart in achieving low pollutant emissions, particularly in regards to NO_x and soot.[2]

Current low emissions technology primarily focuses on burning natural gas, a fuel that is mainly composed of methane. It seems clear, however, that natural gas cannot be relied upon as the exclusive source for fueling the clean power plants of the future. Rapidly increasing demand due to new installations has caused substantial price volatility and concerns about future supplies. In addition, interest in utilizing the United State's other energy resources, as well as concern about energy security have motivated interest in utilizing coal-derived syngas or fuels from other sources, such as biomass, landfill gas, process gas and others. The development of clean coal technologies is particularly compelling given the fact that coal is the United State's most abundant fuel source. Technologies such as integrated gasification combined cycle (IGCC) plants enable the combustion of coal and other solid or liquid fuels, while still maintaining aggressive emissions targets and high efficiency.

The inherent variability in composition and heating value of these fuels provides one of the largest barriers towards their usage, however. Syngas fuels are typically composed primarily of H_2, CO, and N_2, and may also contain smaller amounts of methane (CH_4), O_2, CO_2, and other higher order hydrocarbons.[3] The primary constituents of landfill or sewage gas are typically CH_4 and CO_2.[4] Depending upon the source and particular processing technique, these fuels can have significant ranges in relative composition of these constituents.

This variability is a significant problem because state-of-the-art low emission combustion systems are typically optimized to operate with fuels that meet tight fuels specifications. Specifications for gas fuels cover parameters such as heating value, hydrogen content, and solid

contaminant levels. Expensive test programs and hardware modifications are generally required if there are significant changes to gas fuel properties.

The objective of this program is to improve the state of the art in understanding and modeling lean blowout in low emissions, fuel-flexible gas turbines. Successful completion of this project benefits the gas turbine and energy industry in several ways. It will remove barriers toward the usage of coal derived gaseous fuels through improved understanding of their combustion characteristics. It will also improve the development of modeling tools needed by OEM's to design fuel-flexible combustion systems. Ultimately, these benefits will increase the air quality and energy security of the USA, by allowing power plants to operate efficiently and with minimal pollution, using a variety of domestic fuel sources.

6. KEY VARIAB LES AND MECHANISMS FOR LEAN BLOWOFF

BACKGROUND

Flame stabilization involves competition between the rates of the chemical reactions and the rates of turbulent diffusion of species and energy. While a significant amount of fundamental understanding of flame propagation and stability characteristics of lean, premixed systems has been gained in conventionally fueled, natural gas-air systems[5], little is known about these issues for alternate gaseous fuels, such as syngas or low BTU fuel mixtures. Furthermore, the majority of the fundamental investigations of the combustion characteristics of these synthetic gases are for nonpremixed flame configurations [6,7,8,9,10].

Consider syngas fuels which are composed primarily of H_2, CO and N_2. Both H_2 and CO act as fuels when oxidized. Individually, they produce higher adiabatic flame temperatures (at stoichiometric conditions in air) than CH_4, 2383 and 2385 K, as compared to 2220 K. H_2 and CO also have lower flammability limits (ϕ=0.14 and 0.34, respectively) than CH_4 (ϕ=0.46), and higher maximum adiabatic laminar flame speeds (320 and 55 cm/s versus 40 cm/s for methane)[11]. This would suggest that these fuels could have better flame holding characteristics than natural gas. The picture for the pure fuels becomes slightly more complicated at lean mixtures, however, because the flame speed of CO drops below that of CH_4. This comparison of pure fuels does not, however, paint a complete picture. The turbulent propagation and stability properties of premixed H_2/CO mixtures are not well documented, and performance characteristics of these mixtures cannot be simply inferred from knowledge of the global performance of the constituents. To begin, CO and H_2 have *significantly* different transport properties and flame speeds. Next, CO chemistry, which releases slightly more heat than the same amount of H_2 by mass, is highly coupled to H_2 oxidation through the reaction $CO+OH \rightarrow CO_2+H$, which dominates CO ignition (at least) at atmospheric pressure.

The coupling is also important in that, together, CO and H_2 oxidation can cover a wide range of time scales that may bridge the relevant fluid dynamic, turbulent time scales. As shown below, chemical time scales of CO/H_2 mixtures are quite different, and given the large spectrum of turbulent time scales in practical combustors, the combustion processes can cover several orders of magnitude of Damköhler number. For example, interactions between turbulent mixing

processes and, say, H_2 oxidation may occur in the "flamelet" regime, those associated with CO oxidation in a "torn flamelets" regime, and OH recombination (whose chemistry plays a key role in CO oxidation) in the distributed reaction regimes. Furthermore, the oxidation and, hence, rates of heat release of CO and H_2 display different or opposite sensitivities to mean pressure or flame strain/ stretch imposed by the turbulent flow field.

In addition, syngas fueled plants sometimes co-fire with a certain fraction of natural gas, so the additional interactions associated with H_2/CH_4 flame and CO/CH_4 flame also need to be considered. Several recent studies have focused on H_2/CH_4 flames [16,17] and shown that small additions of H_2 substantially enhances the mixture's resistance to extinction or blowoff. For example, fundamental studies in opposed flow burner geometries show that the extinction strain rate of methane flames is doubled with the addition of 10% H_2[12,13]. The acceleration of the CH_4 reaction rate by the radical pool created by the early breakdown of H_2 has been suggested as a key mechanism for this behavior.

CO/CH_4 flames also have interesting dynamics because of their coupled chemistry. The CO burning rate is highly dependent on the reaction $CO+OH \rightarrow CO_2+H$. Addition of CH_4 increases the radicals for this reaction. In addition, CO is also believed to be a significant intermediate during the low temperature reaction path of CH_4 [14].

The above discussion clearly indicates the need for more extensive systematic studies of the blowout characteristics of premixed flames using the fuels that will be encountered in fuel-flexible combustors. Several studies have been initiated relatively recently to investigate the characteristics of premixed, hydrogen-enriched methane fuels [15,16,17]. Additional studies are needed, however, to broaden the scope of fuels of interest.

Having briefly considered the kinetic characteristics of these fuels, we turn attention next to issues associated with blowoff. Developing physics-based correlations of blowout behavior is complicated by lack of understanding of the flame characteristics at the stabilization point. Currently, there is disagreement on whether premixed flames in high turbulent intensity gas turbine environments have flamelet, "thickened" flamelet, or well stirred reactor (WSR) – like properties.

Methods for developing blowout correlations in the latter case (i.e., using WSR scaling ideas) have been studied extensively. Several different theories or physical considerations have been used in past blowout correlation studies, such as those of Zukoski and Marble [18],

Spalding [19], or Longwell[20]. As noted by Glassman [11], however, they lead to essentially the same form of correlation. These correlations generally involve relating the blowoff limits to a ratio of a chemical kinetic time and residence time, τ_{chem}/τ_{res}. In well stirred reactor theory, this ratio is often referred to as a combustor loading parameter. It is possible that the recirculation regions that stabilize many high intensity flames, which may have flamelet properties at most other points along the flame, have distributed reactor-like properties; hence, the success in WSR models in correlating blowout behavior.

When applied to blowoff limits of premixed flames, this chemical time is typically estimated as:

$$\tau_{chem} = \alpha / S_L^2 \quad (1)$$

where S_L and α denote the laminar flame speed and thermal diffusivity, respectively[21,22]. Alternative methods of estimating a global chemical time are also possible, but generally lead to results qualitatively similar to Eq. (1). For example, **Figure 1** compares the blowoff residence time of a well stirred reactor model to the chemical time from Eq. (1) for several H_2/CO/CH_4 mixtures (the color of each point uniquely represents its composition, as will be explained below). The two time scales are closely related, except for cases with very high CO mixtures (not shown).

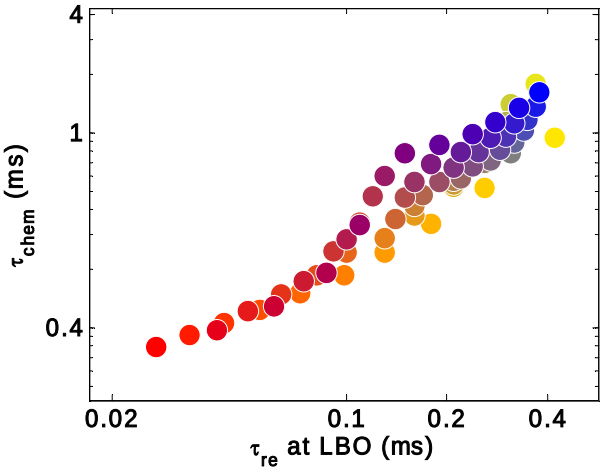

Figure 1: Relationship between chemical time calculated using Eq. (1) and blowout residence time for ϕ=0.6 H_2/CO/CH_4 mixtures. Results obtained using AURORA and TRAN in CHEMKIN with GRI 3.0 mechanism

Returning to WSR based methods for scaling blowoff limits, the residence time is generally scaled as d/U_{ref}, where d and U_{ref} denote a characteristic length scale (e.g., a recirculation zone length) and velocity scale, respectively. If this reactor based theory is correct, then blowoff limits should scale with the loading parameter:

$$L_1 = \frac{\tau_{chem}}{\tau_{res}} = \frac{\alpha U_{ref}}{S_L^2 d} \qquad (2)$$

This "loading parameter" correlation is equivalent to Peclet number correlations which are also used[23]. Defining Peclet numbers based upon flame and flow velocity: $Pe_u=U_{ref}d/\alpha$ and $Pe_{SL}=S_L d/\alpha$, note that:

$$L_1 = \frac{Pe_u}{Pe_{SL}^2} \qquad (3)$$

These purely combustion considerations are incomplete without consideration of the corresponding fluid mechanics, however. For example, note that U_{ref} need not directly scale with approach flow velocity, U_u, due to the acceleration of the burned gas[21]. Since the burned gas velocity scale is given by $U_b=(T_b/T_u)U_u$, then $U_{ref}=f(U_u, T_b/T_u)$. Similar considerations apply for the recirculation zone scale, d. For this reason, prior workers have often had to measure the recirculation zone length in order to use Eq. (2) (e.g., see Ref. 18).

The work of Hoffman *et al.*[24] is of special interest, as it found good success with the Peclet number correlation of Eq. (3) to capture the dependence of blowoff limits in swirling, premixed flames upon combustor diameter, flow velocity, and swirl number. They used the azimuthal velocity component, U_θ, as the reference velocity, $U_{ref}=U_\theta$, and combustor diameter, D, as the characteristic length, $D=d$.

Significantly less attention has been given to correlating premixed flame blowout limits assuming flamelet-like combustion properties, where the stabilization mechanism is related to front propagation, rather than reactor extinction. In this case, a flame would blow off when the turbulent flame speed is everywhere less than the flow velocity, $S_T<U_{ref}$, where S_T denotes the turbulent flame speed. If this propagation mechanism is controlling, then blowoff limits should scale with the parameter:

$$L_2 = \frac{S_T}{U_{ref}} \qquad (4)$$

Evaluating the turbulent flame speed introduces additional complications for mixtures with widely varying compositions. Correlations of the turbulent flame speed of the form: $S_T = S_L \cdot f(u', \text{geometry})$, where u' denotes turbulent intensity, have been used successfully in many prior studies across limited fuel ranges. However, recent studies across broader ranges of fuels clearly indicate the limitations of the above correlation; other fuel properties are also very important.

For example,

Figure 2 is reproduced from Kido *et al.*[25]and plots the dependence of the turbulent flame speed for a variety of H_2, CH_4, and C_3H_8 mixtures. These mixtures were carefully chosen to have identical laminar flame speeds, as indicated by the S_T curves converging at $u'=0$. Interestingly, however, the curves widely diverge as u' increases from zero. In particular, note the substantially higher turbulent flame speed of the H07-15N mixture, which is a hydrogen blend, relative to the methane fuels (MO7-15N, M09-15N, MO98-15N).

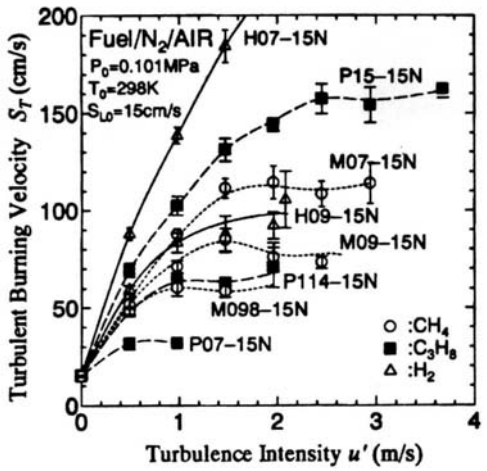

Mixture	Molar Fraction Fuel	O_2	N_2	ϕ	S_{L0} (cm/s)
H07-15N	H_2	0.71	7.14	0.7	15.26
H09-15N	H_2	0.56	6.94	0.9	15.88
M07-15N	CH_4	2.86	11.17	0.7	15.10
M09-15N	CH_4	2.22	10.82	0.9	14.91
M098-15N	CH_4	2.04	10.51	0.98	14.84
P07-15N	C_3H_8	7.14	29.05	0.7	14.94
P114-15N	C_3H_8	4.39	23.82	1.14	15.34
P15-15N	C_3H_8	3.33	13.70	1.5	14.99

Figure 2: Dependence of turbulent flame speed upon turbulence intensity for several fuel blends with the same laminar flame speed (reproduced from Kido *et al.*[25]).

This substantial increase in the turbulent flame speed of the hydrogen mixture my be due to thermal-diffusive instabilities of lean hydrogen mixtures; that is, these mixtures are unstable even in the absence of turbulence, resulting in the spontaneous wrinkling of the premixed flame[26]. This conclusion is supported by related studies that compare the turbulent flame speeds of thermo-diffusively stable/unstable mixtures with the same laminar flame speeds (e.g., by comparing rich and lean methane mixtures) that also show that the unstable mixtures have higher flame speeds [27].

These instabilities can be related to the stretch sensitivity of the flame speed. Recall that the flame speed of a stretched flame is given as [27]:

$$\frac{S_L}{S_{L,0}} = 1 - MaKa \qquad (5)$$

where $S_{L,0}$, Ma, and Ka, denote the unstretched laminar flame speed, $Ma=L/\delta$ (Markstein number), and $Ka=\tau_{chem}/\tau_k$ (Karlovitz number), respectively. L,δ and τ_k denote Markstein length, flame thickness, and Kolmogorov time scale. Thermo-diffusively unstable flames have negative Markstein numbers, which cause bulges in the flame to grow.

Some insight into the key parameters influencing *Ma* can be obtained from asymptotic results with single step kinetics[26]:

$$Ma = \frac{1}{\gamma}\ln\frac{1}{1-\gamma} + \frac{Ze(Le-1)}{2}\left(\frac{1-\gamma}{\gamma}\right)\int_0^{\gamma/1-\gamma}\frac{\ln(1+x)}{x}dx \qquad (6)$$

where $Ze = \frac{E}{RT_b^2}(T_b - T_u)$ and $\gamma = (T_b - T_u)/T_b$ denote the Zeldovich number and gas expansion parameter, respectively. This equation shows that *Ma* depends upon the gas expansion ratio, dimensionless activation energy and Lewis number. While the general relationship between these quantities is complex, for large *Ze* values. *Ma* has positive and negative values when *Le* > 1 and *Le* < 1, respectively.

EXPERIMENTAL SETUP

High Pressure Gas Turbine Simulator

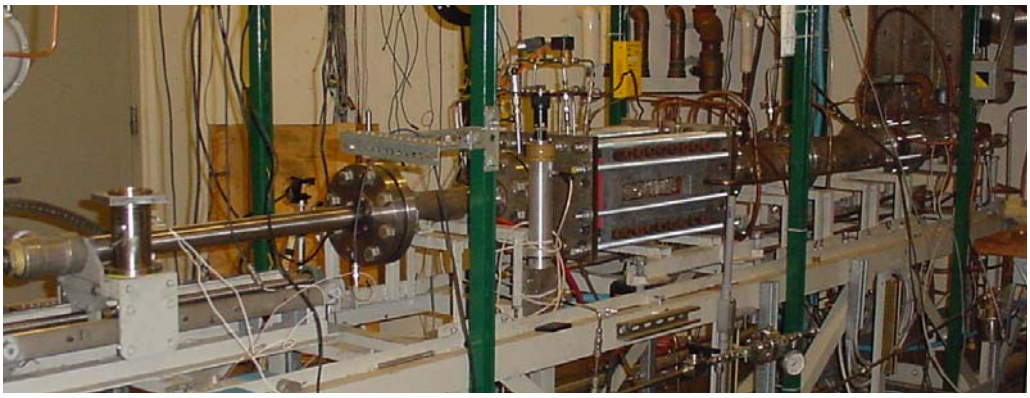

Figure 3: Photograph of lean, premixed combustor facility

Measurements were obtained in a lean, premixed gas turbine combustor simulator, shown in **Figure 3,** which has also been previously described in Ref. [28]. The facility consists of inlet/premixer, combustor, and exhaust sections. High-pressure natural gas and air are supplied

from building facilities. The air can be preheated up to 700 K. The hydrogen and carbon monoxide are supplied from bottles. The air and fuel flow rates are measured with a critical orifice and mass flow controllers (MFC's), respectively. Both the orifice and MFC's were calibrated using the specific gas with which they were to meter. This is necessary for H_2 in particular, as manufacturer supplied corrections that relate the flow of some other gas to the H_2 flow rate were found to be very inaccurate. The resultant uncertainty in the flow rate measurements is 2% of full scale. While only three fuels (H_2, CO, and CH_4) were used in this study, the system has capabilities to mix a total of six gases, in order to simulate a wide range of fuel blends of arbitrary compositions. In order to ensure that acoustic oscillations did not affect the fuel/air mixing processes, the fuel and air are mixed upstream of a second choke point. Thus, the equivalence ratio of the reactive mixture entering the flame is constant. The temperature of the reactants was measured with a thermocouple located just upstream of the swirler.

The fuel-air mixture entered the circular 4.75 cm diameter, 60 cm long inlet section and passed through a premixer with a swirler prior to entering the combustor, see **Figure 4**, (note that the word "premixer" is somewhat of a misnomer in this case as the fuel and air are already fully premixed). The premixer outer body slightly constricts along the axial flow direction. However, the overall flow area remains constant at 10.8 cm^2, as the center body diameter also decreases in the axial flow direction. This premixer is fully modular as the centerbody and swirler can be easily removed and replaced; however, these tests were performed with a single 12 vane, 35^o swirler. Moreover, a thermocouple is imbedded in the centerbody for flashback detection.

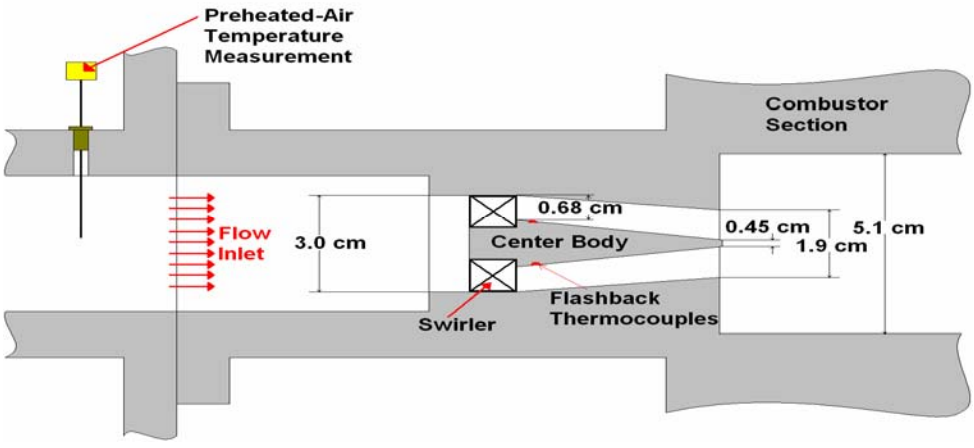

Figure 4: Cross section of premixer assembly

The premixer terminates into the 5x5 cm square combustor. The square part of the combustor is 51 cm long and optically accessible. It then transitions into a circular 7.6 cm diameter, 195 cm long exhaust section. The exhaust sections are water cooled[1]. The flow leaves the setup through an exhaust nozzle with an adjustable bypass valve. This adjustable bypass valve is controlled by LabVIEW in order to maintain the combustor pressure at some prescribed value.

Gas Mixing Facility

We designed and fabricated a Gas Mixing Facility. The development involved four main considerations and components: (i) bottle storage facility, (ii) bottle valving and controls, (iii) flow control and mixing, and (iv) safety.

Bottle Storage Facility

The bottle storage facility is an important aspect of the overall facility because of the safety and functional issues arising from the use of hydrogen and carbon monoxide. The special consideration involves the storage/use of the bottles not only during testing, but during non-operational periods. The final solution has been chosen because of concerns of safety and fire and building codes. The facility is comprised of two indoor storage cabinets, of which one will store three bottles of hydrogen and the other will store three bottles of carbon monoxide. Nitrogen and carbon dioxide bottles are stored in bottle racks in the test room. The gas cabinets are continuously vented by a negative pressure system. These cabinets are explosion proof with double doors and access windows on each door for safe valve/regulator adjustments. These cabinets are equipped with fire sprinklers.

[1] Note that the combustor top and bottom walls are water cooled and side walls are air cooled[28]. The combustor was only water cooled for these measurements, since we determined that some leakage of the sideflow cooling air impacted blowout limits.

Figure 5: Gas Storage Cabinets for Hydrogen and Carbon Monoxide Gas

Figure 6: Bottle Storage for Carbon Dioxide and Nitrogen

Bottle Valving and Controls

The bottle valving and controls are crucial to safely and efficiently transporting the syngas components to the combustor. Since the bottles are stored near the inlet of the combustor, the gases are piped overhead and brought down to the combustor. For the hydrogen and carbon monoxide bottles, the valving and controls are inside the cabinets so that if a leak occurred, the gas would be vented out. For these two gases, the three bottles of each gas were manifolded together. Each bottle has a flow limiter and check valve to prevent other bottles from leaking or a catastrophic venting of the gas. After the flow limiters and check valves, the gases are piped to a dual stage regulator for each gas so that the gases can be regulated between 0 and 500 psi. After the regulators, there is a pressure relief valve that releases to the exhaust vents in case a regulator failure occurs. Once the gases pass through the pressure relief valve, a block and bleed

valve combination is used. Both of these valves are electric, hazardous duty valves that can be controlled from the control room facility and automatically controlled by the safety system in case a leak occurs. The valving and controls are similar for the carbon dioxide and nitrogen, where the only difference is that the pressure relief valves and bleed valves are not included. Note that the block valves for the carbon dioxide and nitrogen are controllable by the user in the safe confines of the control room. The safety system does not block and bleed the nitrogen and carbon monoxide, because these gases will purge the fuel feed lines to the combustor. From the block and/or bleed valves, the gases are individually pipe overhead to the combustor.

Figure 7: Bottle Valving and Controls for Hydrogen and Carbon Monoxide

Figure 8: Bottle Valving and Controls for Carbon Dioxide (Left) and Nitrogen (Right)

Flow Control and Mixing

Once the gases are piped overhead, flow controls are necessary. The individual gases are plumbed to mass flow controllers that are remotely controlled by a LabView VI which linearly proportions an input voltage depending on the flow required. The input voltage is between 0 and 5VDC and is compared to a 5VDC reference signal to acquire the proper mass flow rate. These mass flow controllers are from AALBORG which are calibrated with nitrogen gas; thus a c_p correction must be made in the VI if another gas is used. After the mass flow controllers, the gases are combined into one line. This line is piped to a back pressure regulator which is necessary for the proper operation of the mass flow controllers. The back pressure regulator is remotely controlled by low pressure nitrogen gas, so that adjustments can be made without going into the test room. The mixed gas line is then connected with the natural gas line, which is then fed into the combustor.

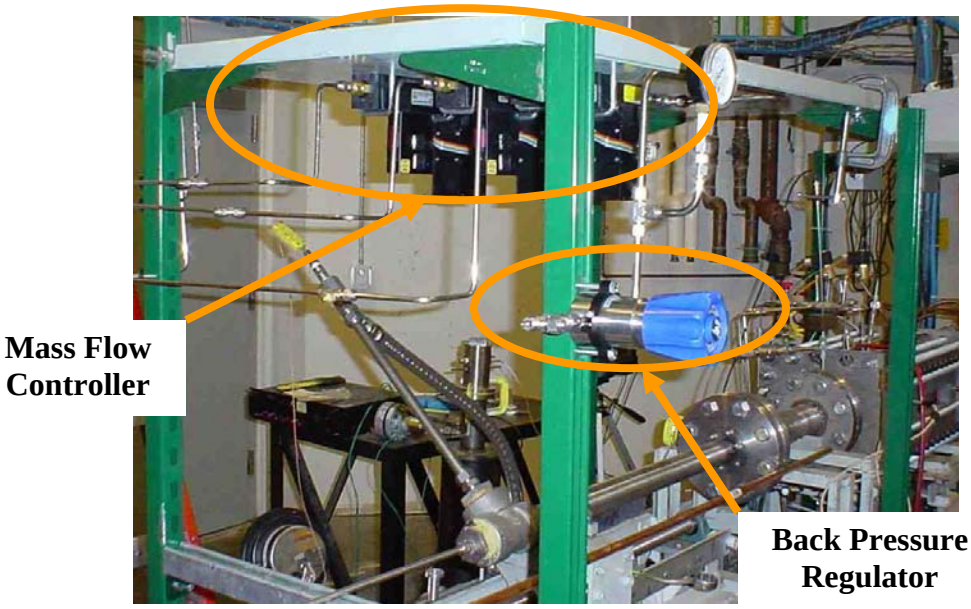

Figure 9: Mass Flow Controllers and Back Pressure Regulator

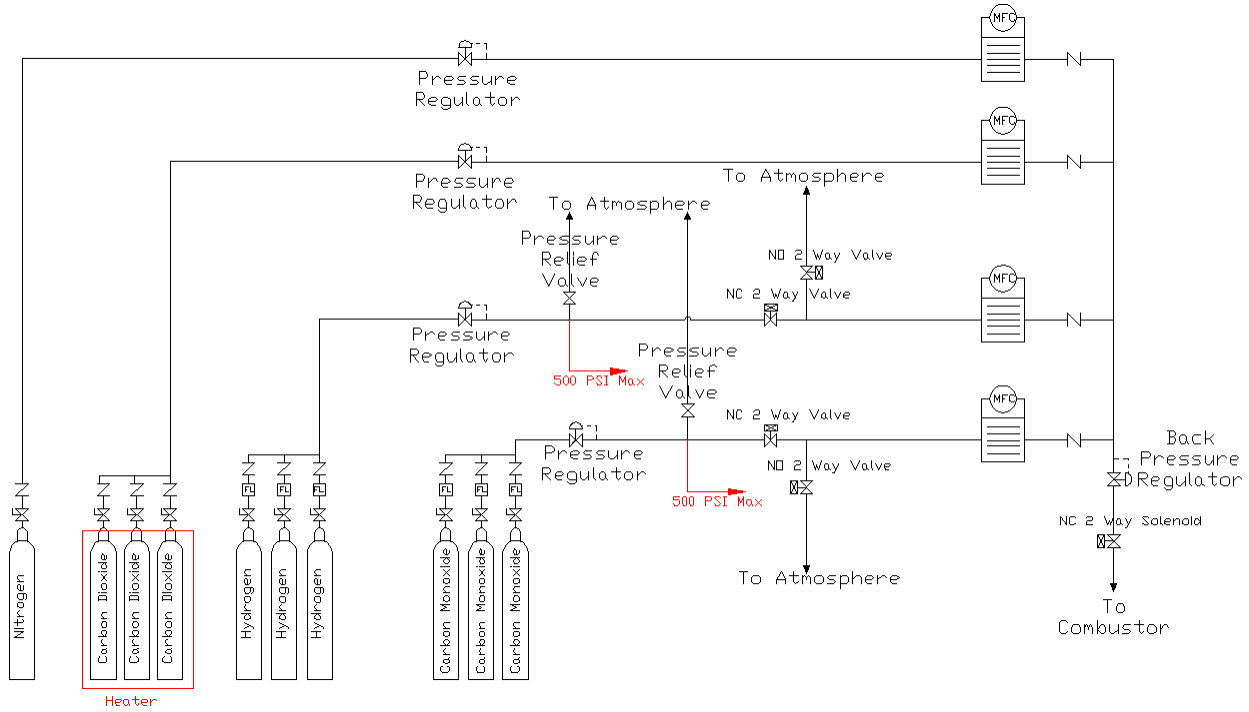

Figure 10: Full Piping Layout for Syngas System

Safety

Safety was a major focus during this project. An extensive plan was developed to monitor the cabinets and rooms affected by the hydrogen and carbon monoxide gases. This plan includes the active control integration of seven sensors: three hydrogen sensors, three carbon monoxide sensors, and one vacuum sensor. Hydrogen and carbon monoxide sensors are in the cabinets, the combustor room, and the associated control room. Also, there is a vacuum switch on the ventilation stack of the gas cabinets to ensure the system is working.

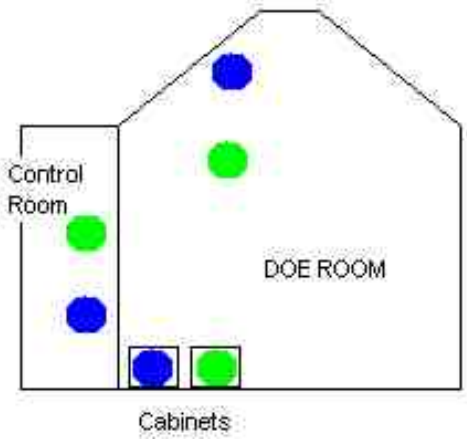

Figure 11: Laboratory Sensor Layout (Green--Hydrogen Sensor & Blue--Carbon Monoxide Sensor)

These sensors are integrated into an active control system. The system uses relays, sirens, strobe lights, and LED's to alert and safeguard the researchers operating in the control room and those near the high-pressure laboratory from gas leaks. If any of the sensors are tripped by a gas leak, a color coded LED and strobe light are illuminated alerting the location of the hazardous area. A tone-coded siren is alarmed, as well as a clear strobe and siren outside the high pressure room. As an added safety feature, the hydrogen and carbon monoxide gas lines block and bleed if a leak occurs. This action is delayed by 10 seconds to ensure that the alarm is not a false alert. Note that the delay does not occur for the low level alarm for the CO sensor in the gas cabinet because it has a dual stage alarm to eliminate false alerts. Moreover, the user can reset the siren for 30 seconds with a momentary push button on the control panel, as well as override the block/bleed action if the gas detection is known to be false. The override can only occur if the user holds down a momentary push button on the control panel. Moreover, the vacuum switch for the ventilation will alert the users that the ventilation fan is not working with a siren and strobe light. In addition to the alarms, the lack of ventilation in the cabinets blocks and bleeds the hydrogen and carbon monoxide from being distributed. Importantly, all of the block/bleed valves are connected into the E-stop button on the main control panel. Note that the power to the safety system can only be turned off by a key lock to ensure the safety system is not inadvertently disabled. There are also test buttons on the main safety control box to test all sensor relay systems for proper operation before each combustor startup.

Figure 12: Main Box for Relays/Controls for Safety System

Figure 13: Main Control Panel in Control Room

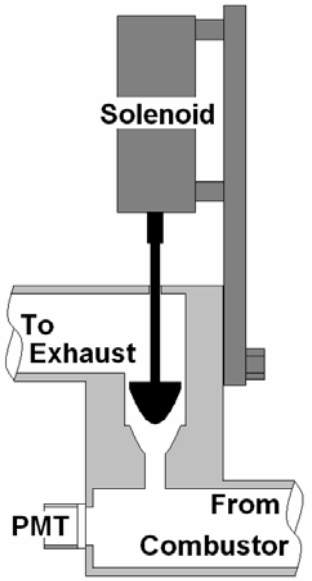

Figure 14 Back-pressure controller

Back-pressure controlling system

In order to ensure that the pressure in the combustor was held at a (approximately) constant pressure, a back-pressure controller was used. This controller used a pressure transducer located just upstream of the swirler and center body and proportions a plunger valve in the exhaust section to keep the right amount of pressure in the combustor. This plunger was controlled, up and down, by a computer through LabVIEW. Figure 14 is a cross-sectional view of the exhaust and shows how the plunger valve controls the back pressure of the combustor. The solenoid value shown is controlled from the computer.

ANALYSIS APPROACH

This section describes the methods used to post-process the data and correlate blowout limits with the adiabatic flame temperature, laminar flame speed, Lewis number, and chemical time, parameters identified in the background section.

An internally developed code, “Happy Temperature”, was developed to calculate temperature, heating value, and flame temperature. In addition, it can generate a matrix or list for syngas, which have the same heating value or adiabatic temperature, see **Figure 15.**

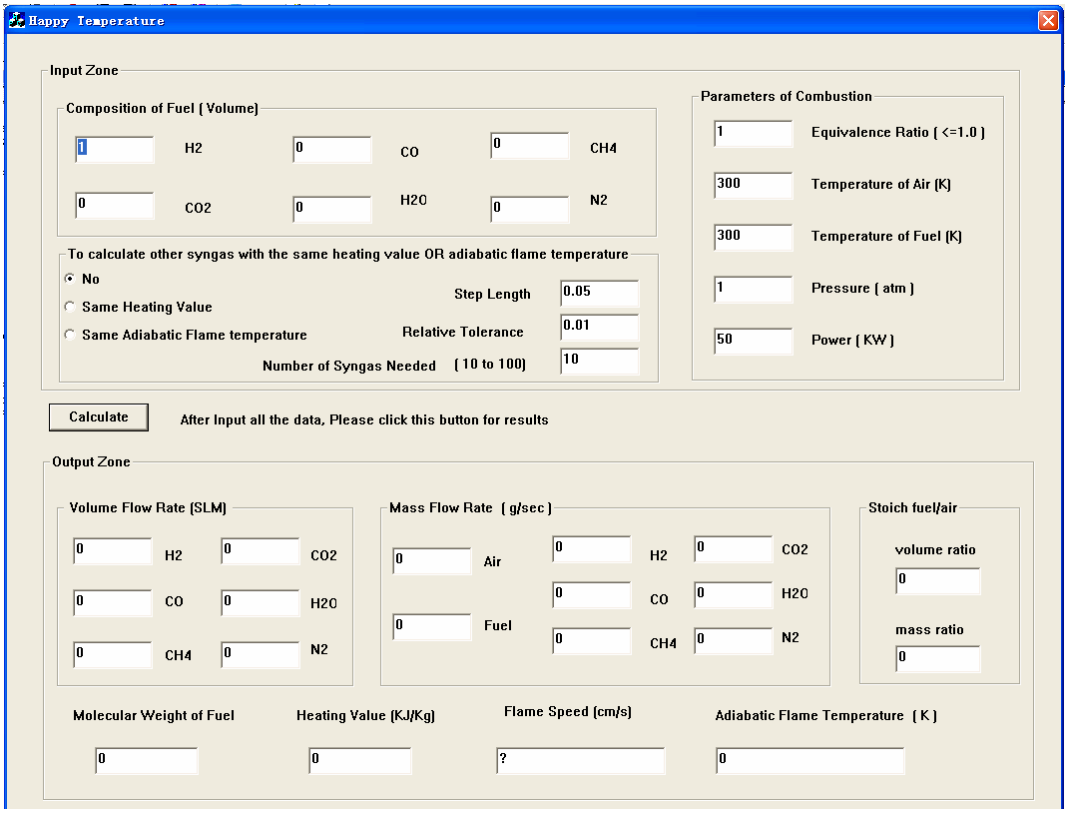

Figure 15: Snapshot of Happy Temperature

The mixture equivalence ratio is given by:

$$\phi = \frac{(Y_{Air}/Y_{Fuel})_{Stoic}}{Y_{Air}/Y_{Fuel}} \qquad (7)$$

where Y_i is the mass of the indicated specie.

Adiabatic flame temperatures were calculated for a given mixture using standard methods. Laminar flame speeds were calculated with the PREMIX application in CHEMKIN, using the GRI3.0 mechanism. While this mechanism was primarily optimized for methane/air mixtures, good comparisons between its results and measurements have been obtained for a range of H_2/CO mixtures as well [29]. Chemical times were estimated using Eq. (1), where the thermal conductivity of the reactive mixture was determined using transport properties from TRAN in CHEMKIN and the equation[30]:

$$\lambda = \frac{1}{2}\left(\sum_{k=1}^{K} X_k \lambda_k + \frac{1}{\sum_{k=1}^{K} X_k / \lambda_k}\right) \qquad (8)$$

Diffusivity coefficients of a given species in the mixture were determined from:

$$D_{km} = \frac{\sum_{j \neq k}^{K} X_j W_j}{\overline{W} \sum_{j \neq k}^{K} X_j / D_{jk}} \qquad (9)$$

These diffusivity coefficients, combined with the mixture thermal conductivity were used to determine the Lewis number of the *k*-th specie:

$$Le_k = \frac{\lambda}{\rho C_P D_{km}} \qquad (10)$$

Since the above Lewis number is defined for a given species, not the mixture, a mixture averaged Lewis number was also determined using the relation:

$$Le_{mix} = \frac{\lambda}{\rho C_p \sum_{k=fuel} A_k D_{km}} \qquad (11)$$

where A_k is the percentage of heat release due to fuel *k* relative to that of the entire mixture. We should emphasize that definition of the appropriate mixture averaged Lewis number is not trivial – analytical expressions derived using one-step kinetics and asympototics show that Lemix is not only a function of the Lewis number of the respective species, but also Zeldovich number[31].

In order to obtain the basic understanding of the properties of $CO/H_2/CH_4$ mixtures, a number of results showing the interdependence of these quantities are included below. Consider first the flame speed, S_L. Figure 16 illustrates the dependence of the flame speed upon fuel composition at two fixed adiabatic flame temperatures, 1500 and 2000 K. The fuel composition by volume is given by the location within the triangle, where the three vertices denote pure CO, H_2 or CH_4. At each point, the mixture equivalence ratio is adjusted such that the mixture has the given flame temperature. As expected, the high H_2 mixtures have the highest flame speeds. Note also the slightly higher flame speeds of the high CH_4 mixtures relative to those of CO mixtures.

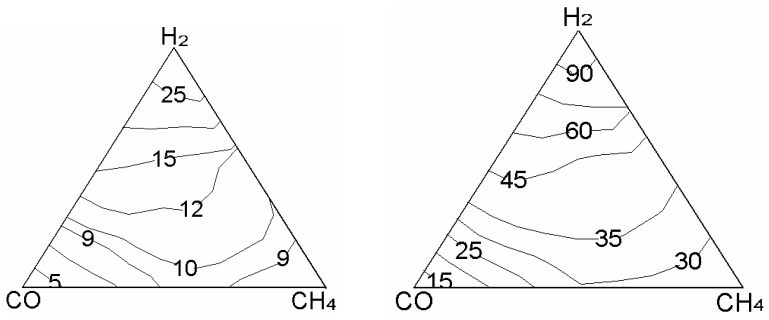

Figure 16: Dependence of flame speed (cm/s) upon fuel composition at fixed 1500 K (left) and 2000 K (right) adiabatic flame temperatures with 300K reactants temperature.

An alternative way to view these results is to plot adiabatic flame temperature at a fixed flame speed. This is done in Figure 17 for $S_{L,o}$=10 and 20 cm/s. Note the progression in flame temperatures from CO and H_2 mixtures being the highest and lowest, respectively.

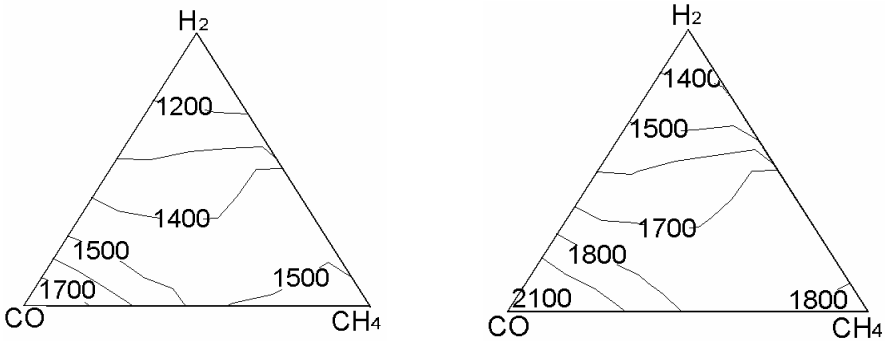

Figure 17: Dependence of adiabatic flame temperature (K) upon fuel composition at fixed laminar flame speed 10 cm/s (left) and 20 cm/s (right) with 300K reactants temperature.

Figure 18 plots the dependence of the mixture weighted Lewis number, Le_{mix}, upon fuel composition at a fixed flame temperature of 2000 K. As above, note that the mixture equivalence ratio is varying – it is the flame temperature that stays fixed. The figure shows that this Lewis number ranges from a low of 0.4 in the high H_2 mixtures to a high of slightly above one in the high CO mixtures.

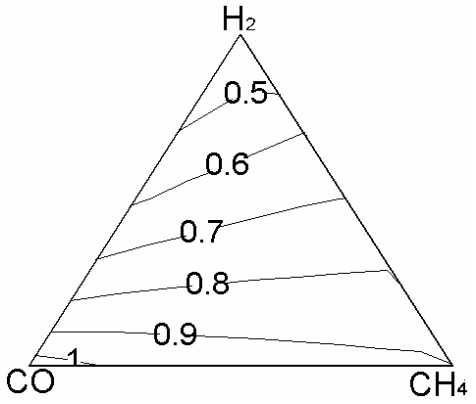

Figure 18: Dependence of mixture weighted Lewis number, Le_{mix}, upon fuel composition at fixed adiabatic flame temperatures, 2000 K with 300K reactants temperature.

Figure 19 plots the dependence of the chemical time, $\tau_{chem} = \alpha / S_L^2$, upon fuel composition at a fixed flame temperature 1500K. Note the order of magnitude variation in chemical time from the fast H_2 mixtures to the slow CO mixtures.

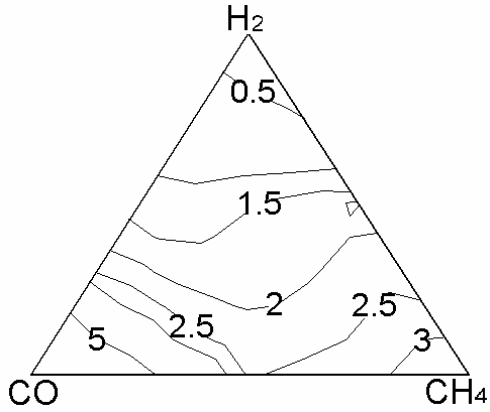

Figure 19: Dependence of chemical time (ms) upon fuel composition at fixed adiabatic flame temperature, 1500 K.

Kido and co-workers [32] have emphasized the significance of the relative mass diffusion rates of fuel and oxidizer, D_{fuel}/D_{ox}, over the Lewis number. However, there is nearly a one-to-one correspondence between these two dimensionless parameters for the mixtures considered here, as shown in Figure 20. This figure plots the dependence of D_{fuel}/D_{ox} upon Le_{mix} for a range of H_2/CO/ CH_4 mixtures. As such, in this report we only consider Le_{mix}, realizing that it is nearly

equivalent to mass diffusion ratios. D_{fuel} is defined as heat-release weighted fuel diffusivity in the air, $D_{fuel} = \sum_{k=fuel} A_k D_{k-Air}$, and D_{ox} is defined as oxygen diffusivity in the fuel and nitrogen.

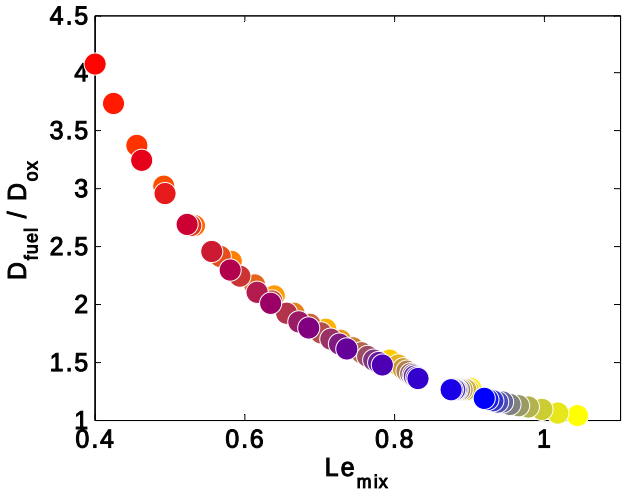

Figure 20: Dependence of D_{fuel}/ D_{ox} upon mixture Lewis number.

RESULTS AND DISCUSSION

This section presents blowout results obtained during this report at two constant nozzle exit velocities: 59 and 39 m/s. This corresponds to combustor velocities (cold flow) of 6.0 and 4.0 m/s. Tests were performed at two pressure/temperature conditions: combustor pressure of 1.7 atm and 300 K reactants, and combustor pressure of 4.4 atm and 460 K reactants. The mean equivalence ratios ranged from roughly 0.15 to 0.60.

In order to facilitate presentation of results, we represent the mixture composition of H_2/CO/CH_4 by its color. Primary colors at the three vertices are used to represent each fuel constituent, where red, yellow, and blue denote H_2, CO, and CH_4, respectively. This is illustrated in **Figure 21**.

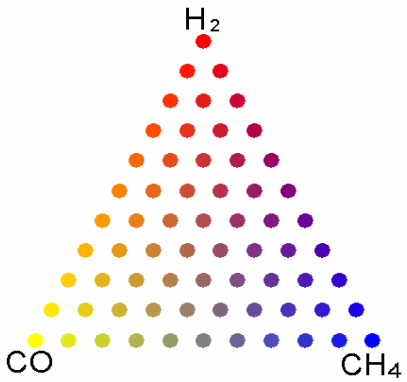

Figure 21: Primary color mixing scheme used to denote fuel blend composition

The basic test plan is to operate at uniformly spaced fuel compositions in $H_2/CO/CH_4$ space, such as is depicted in the figure above.

However, applying a uniform definition of blowoff is complicated by the fact that the manner in which the flame blew off varied with composition. In many cases, the blowoff event occurred abruptly with a small change in fuel composition, although sometimes preceded by slight liftoff of the flame from the burner. Defining the blowoff point was unambiguous in these instances; moreover, the point of blowoff and flame liftoff was nearly identical. This was the case for mixtures with mixtures with less than approximately 50% H_2 by volume. However, for high H_2 mixtures, the blowoff and liftoff events were quite distinct, see **Figure 22**. Usually, the flame became visibly weaker, lifted off from the holder, and moved progressively downstream with decreases in equivalence ratio before blowing off for good. As such, blowoff is defined in this report as the point where the flame is no longer visible in the 10.2 cm long optically accessible section of the combustor. Undoubtedly, this variation of liftoff/blowoff characteristics with fuel composition is responsible for some of the scatter in the experimental data. This point should be kept in mind when comparing 0-50% H_2 and 50-100% H_2 containing fuels.

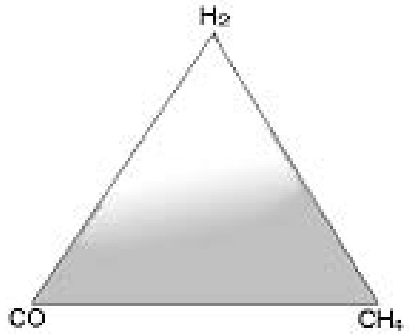

Figure 22: Composition map describing regions where sharply defined blowoff event occurs (gray) and blowoff preceded by significant flame liftoff (white)

These blowout limits were correlated with a variety of parameters. As noted in previous studies [17], the presence of H_2 has a strong impact on blowout limits of either H_2/CH_4 or H_2/CO flames. **Figure 23**, which plots the dependence of the blowoff equivalence ratio upon the mole fraction of H_2 in the fuel, shows that H_2 also strongly affects the lean blowout limits of syngas mixtures ($H_2/CO/CH_4$), in spite of the complicated coupling chemical mechanisms among these species. It shows the well known result that, in general, mixtures can be stabilized with lower equivalence ratios as the H_2 concentration increases. However, note that the addition of small amounts of H_2 has small impacts upon blowoff limits and that the sensitivity of the blowoff equivalence ratio to H_2 level variations remains essentially constant across the entire range of H_2 levels. In other words, no discontinuous or steep drop in blowoff equivalence ratio was observed with small amounts of H_2 addition.

Besides at constant premixer flow speed, blowoff limits were also obtained at constant combustor power level (Figure 24), and constant burned combustor flow speed (Figure 25). These data also show that H_2 strongly affects the lean blowout limits of syngas mixtures.

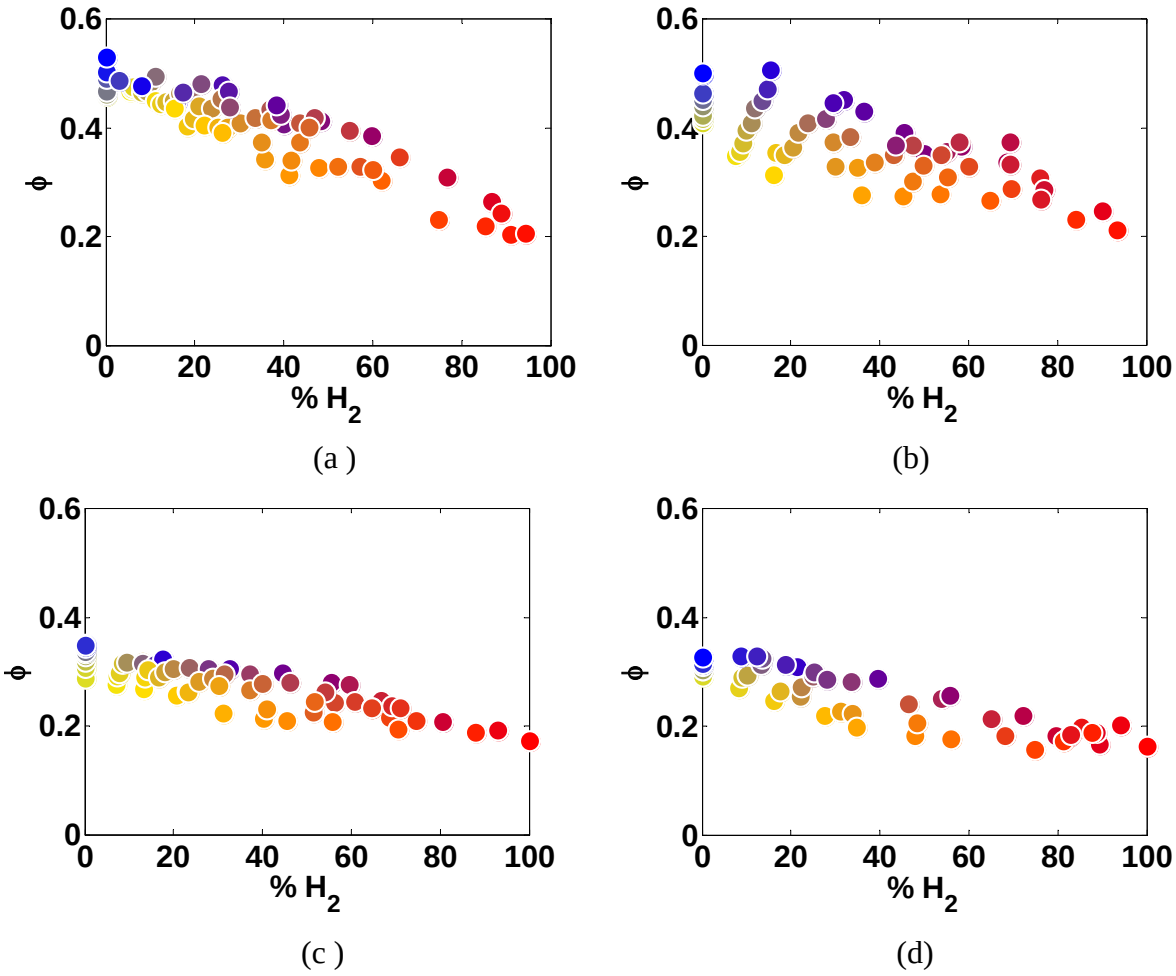

Figure 23: Dependence of LBO equivalence ratio upon H_2 mole fraction at premixer flow velocities of 59 m/s at 300K reactants temperature and 1.7 atmospheres combustor pressure (a), of 39 m/s at 300K and 1.7 atmospheres (b), of 59 m/s at 458K and 4.4 atmospheres (c), of 39 m/s at 458K and 4.4 atmospheres (d).

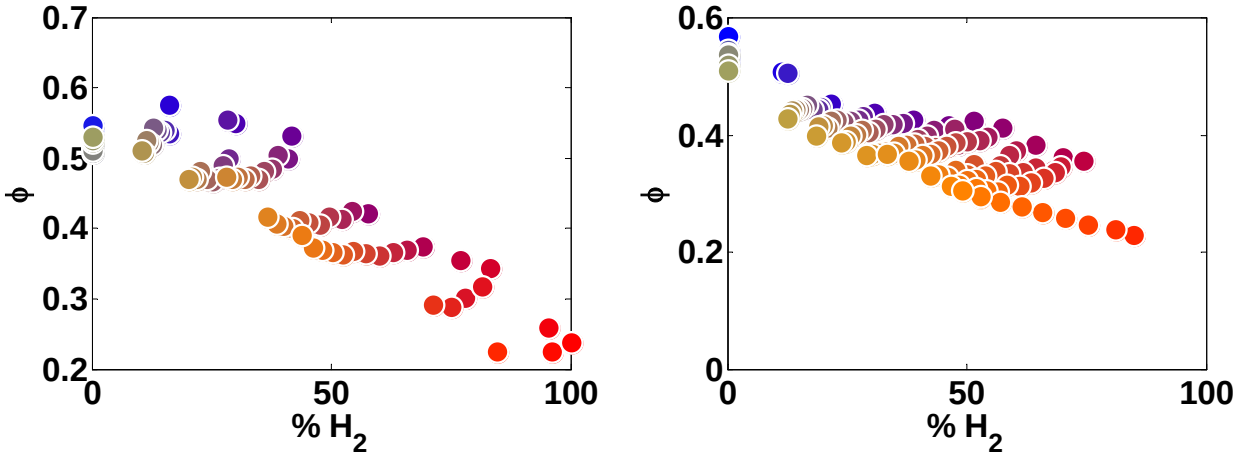

Figure 24: Dependence of LBO equivalence ratio upon H_2 mole fraction at constant combustor power of 80kw (left), of 120kw (right) at 300K reactants temperature and 1.7 atmospheres combustor pressure.

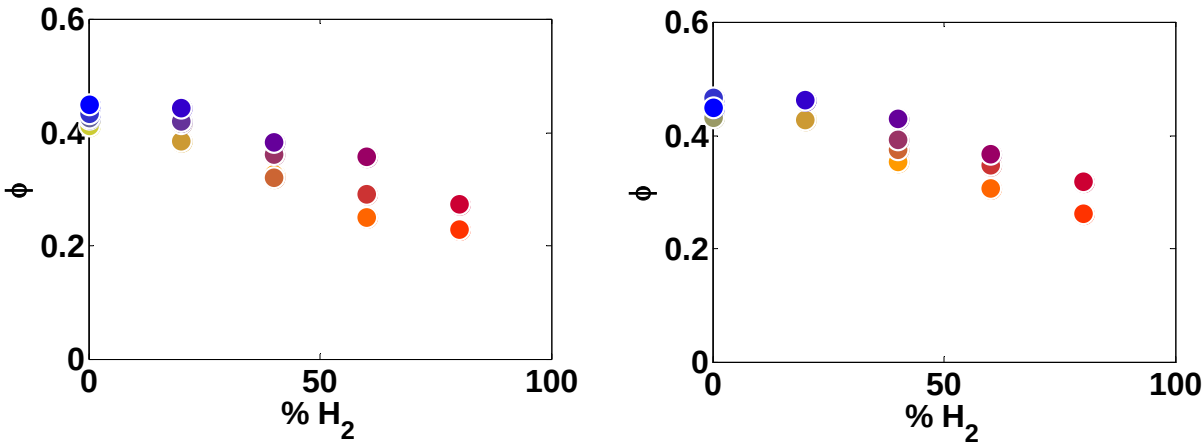

Figure 25: Dependence of LBO equivalence ratio upon H_2 mole fraction at burned combustor flow velocities of 10 m/s at 300K reactants temperature and 1.7 atmospheres combustor pressure (left), of 17 m/s at 300K and 1.7 atmospheres (right),

At one specific H_2 mole fraction, data scatters in a narrow band due to different ratios of CO and CH_4, and a higher ratio of CO/CH_4 makes the flames blowout in lower equivalence ratios,

although CO flame has a smaller flame speed or a large chemical time scale. It could be explained by the fact that H_2 has a stronger effect on CO than CH_4, or CO flame is much easier to be affected by the same amount of H_2 addition. **Figure 23** indicates that CO/H_2 flames are easier to blowout in a manner similar to H_2 flame than CH_4/H_2 flames. One possible reason is that H_2 supplies the OH radical pool, which plays a key role in CO oxidation, by the faster chain-branching reactions. Another possible reason is that CO has a higher adiabatic flame temperature which accelerates the overall reaction rate.

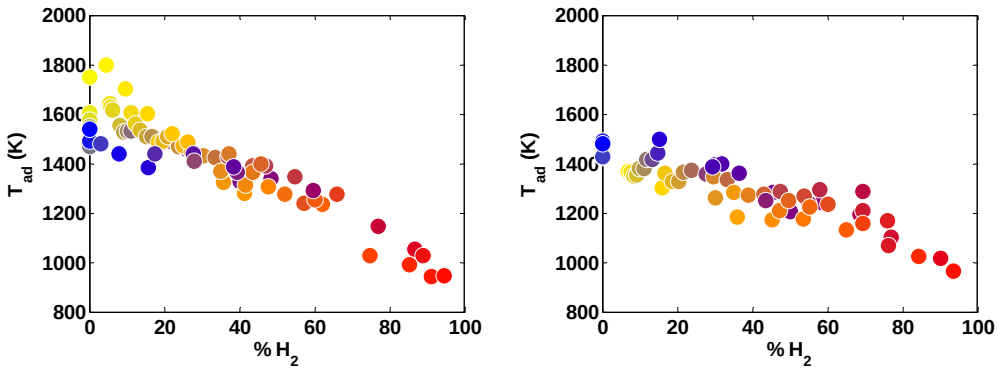

Figure 26: Dependence of adiabatic flame temperature at LBO upon percentage of H_2; 59 m/s (Left) 39 m/s (right), both at 1.7 atmospheres

Next, consider the dependence of adiabatic flame temperature at lean blowout upon the mole fraction of H_2. As shown in **Figure 26**, the data sets as a whole correlate well with these parameters. There is a nice trend between the percentage of H_2 and adiabatic flame temperature at lean blowout. That is, flames which have higher percentage of H_2 could stabilize at a lower adiabatic flame temperature. This could be partly explained by the chemical kinetics. The chain-branching reaction H+O2⇔ O+OH, which is very sensitive to flame temperature, plays an important role in such H_2 addition flames. For a given fuel composition, when the equivalence ratio decreases to some level where either flame zone temperature or the concentration of radicals is too low to maintain this chain-branching reaction, the local extinction or blowout happens. However, H_2 could provide more radicals for this chain-branching reaction, so that flames which have higher percentage of H_2 could stabilize at a lower adiabatic flame temperature. At one specific H_2 fraction, CO mixtures have a higher temperature level (more

obvious at low H_2 mole fractions in Figure 26 (a)). It is also noticeable that the adiabatic flame temperature is more sensitive to the percentage of H_2 for the higher flow speed case due to the overall higher stretch rate it has.

Similarly good correlations between the laminar flame speed, Lewis number, and a number of other combustion parameters at blowoff upon H_2 level were observed. This brings us to an important point that must be recognized in extracting an understanding of the blowoff physics from these correlations. First, blowoff limits are clearly a strong function of H_2 levels. Second, many other parameters, such as diffusivities, flame temperature, etc. are also strong functions of H_2 level. ***As such, it is important to not draw conclusions about blowoff physics only because one can correlate results with parameters that are simply functions of the H_2 percentage.*** For example, a very nice correlation between T_{ad} vs. *Le* at blowout exists, because both of them are functions of percentage of H_2. In other words, regardless of whether the mixture *Le* is a physically meaningful parameter, a good correlation will still be observed. In some sense, this is analogous to correlating T_{ad} vs $2*T_{ad}$ at blowoff – obviously, a perfect correlation is observed, regardless of whether this is a physically significant parameter.

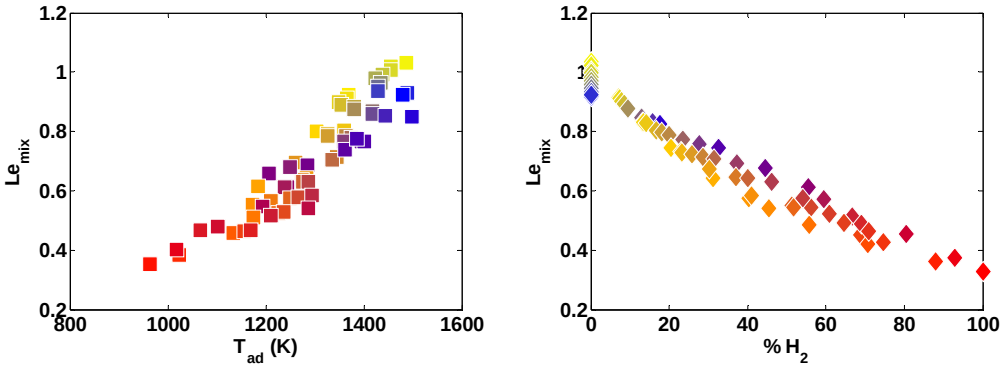

(a) (b)

Figure 27: Dependence of Lewis number (a) upon adiabatic flame temperature at LBO at 4 m/s 1.7 atm (b) upon percentage of H_2 at 59 m/s 4.4 atm

For example, Lewis number of the mixture, Le_{mix}, is a key parameter for the flame instability or flame propagation for stretched flame or turbulent flame, so using Le_{mix} to correlate the lean blowout data is reasonable and meaningful. Now, consider correlating these blowout results with

Lewis numbers, Le_{mix}, see Figure 27 (a). The correlation is quite good in all instances, although only one result is shown. However, in light of the comments in the last paragraphs of this section, some care must be taken in placing too much emphasis on this point, as the Lewis number is very closely related to the H_2 percentage, Figure 27 (b). A perfect linear relation exists between Le_{mix} and percentage of H_2. This is because the diffusivity of H_2 is much larger than that of CO or CH_4, so percentage of H_2 dominates the Le_{mix}.

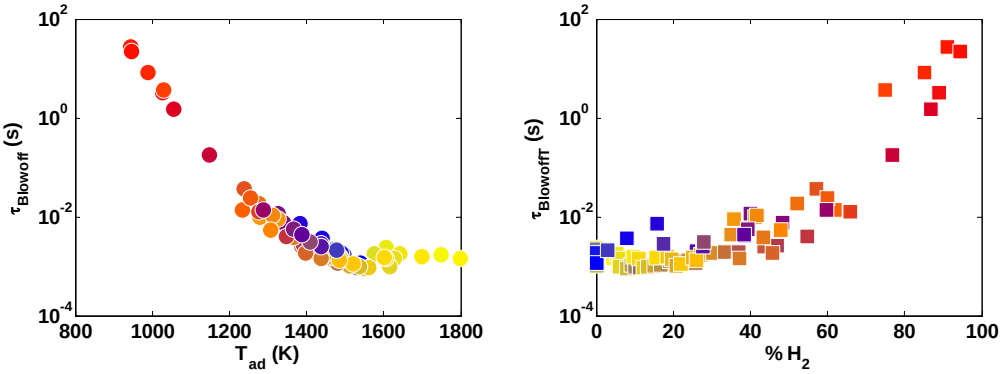

(a) (b)

Figure 28: Dependence of blowoff residence time (a) upon adiabatic flame temperature at LBO, 6 m/s (b) upon percentage of H_2 at 4 m/s , both at 1.7 atm

While chemical time based correlations, such as described in the Background section, have been used successfully in a number of prior studies for narrow fuel range variations, we have not found them very successful in correlating our data. Since these experiments were performed at fixed unburned gas temperature and velocity, the arguments in the context of Eq. (2) suggest that the "loading parameter" should then only be a function of burned gas temperature and chemical time. However, at some lean mixtures where stable flames were observed, we were unable to get PREMIX to converge, so blowoff residence time, $\tau_{Blowoff}$, is used here to scale chemical time. As shown in Figure 28 (a), it is noticeable that there are two parts of the correlation curve; one is that adiabatic flame temperature, $T_{ad,}$ greater than 1300K where $\tau_{Blowoff}$ changes slowly with T_{ad}, and the other part is that T_{ad} less than 1300K where $\tau_{Blowoff}$ changes greatly with T_{ad}. These two parts have the counterparts in Figure 28 (b), 0-50% H_2 and 50-100% H_2. Considering the different definitions of blowout for these two parts in the previous section, it is necessary to analyze these data separately.

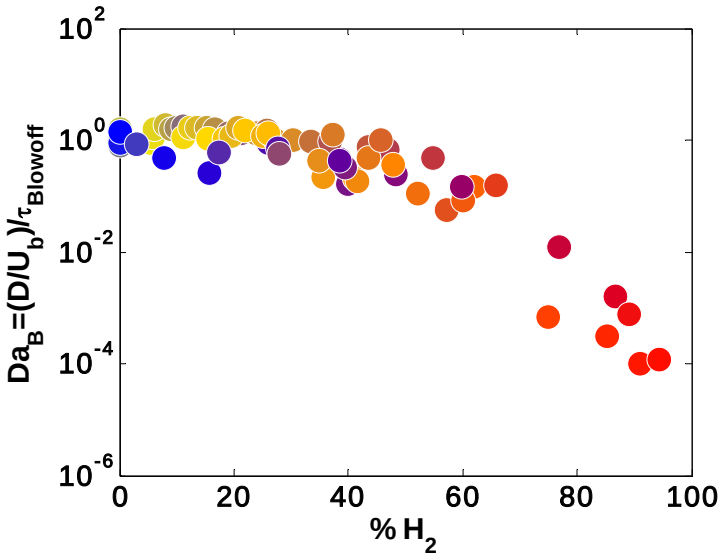

Figure 29: Damköhler numbers of mixtures at constant premixer flow speed of 59 m/s at 300K reactants temperature and 1.7 atm combustor pressure.

Damköhler (*Da*) number correlations were found to correlate the data over all flow velocities, pressures and temperatures for all mixtures with H_2 levels below 50%, as shown in **Figure 29**. In the plot, the reference length scale, *D*, was the combustor width, 5.1 cm. Damköhler numbers were evaluated using both the unburned, Da_U, and burned flow speed, Da_B, as reference velocity scales. Utilizing the burned gas speed resulted in slightly better ability to correlate the data, as reflected in slightly lower errors (about 10 %) in predicted blowoff equivalence ratio, $\delta\phi_{rms}$ (described below), and so is used for these results. **Figure 29** shows that blowout occurs at a nearly constant *Da* for these composition values (although

Figure 29 was plotted in *logarithm* scale, $\tau_{Blowoff}$ is an exponential function of equivalence ratio). At the same time,

Figure 29 also shows that a constant *Da* correlation is inadequate for describing blowout limits of higher H_2 level mixtures. It is possible that this is simply a reflection of the fact that the blowout process changes with H_2 levels and that our "blowoff definition" is not the most physically meaningful, see discussion of **Figure 22**. For example, perhaps identifying the point where the flame first lifted off the flame holder would have been more useful.

A second possibility for this change in blowoff *Da* value shown in **Figure 29** may be due to preferential diffusion effects, a consideration that has also been used to scale changes in turbulent flame speed of mixtures whose constituents have significant variations in diffusivity. One approach for incorporating these effects is to note that the local equivalence ratio changes along the wrinkled flame, being both higher and lower than the average at different spatial locations. Kido and co-workers [33] suggested correlating mixture turbulent flame speeds by utilizing mixture properties at an adjusted equivalence ratio, ϕ_{adj}; i.e., not at the average equivalence ratio, ϕ_{ave}, but the average value plus some $\Delta\phi$. As such, mixture properties are correlated at $\phi_{adj}=\phi_{ave}+\Delta\phi$. They suggest the following relation for $\Delta\phi$, based upon empirical fits of their data:

$$\Delta\phi = C * \ln(D_F / D_{OX}) \qquad (12)$$

where D_F and D_{OX} denote the mass diffusivity of fuel and oxygen, respectively, and C is an empirical constant whose value they suggest as 0.3.

We found that utilizing a value of C close to 0.1 gives a nearly constant blowoff Damköhler number for all of our data sets, **Figure 30**. This plot shows that blowoff occurs at a nearly constant value of local Damköhler number, where the $\tau_{Blowoff}$ is estimated at the equivalence ratio $\phi_{adj}=\phi_{ave}+\Delta\phi$. In this case, the best value for C=0.07 and the average value over all the test points of $\overline{Da_B}$, at blowoff is 0.2. **Table 1** summarizes the results from the other two tests by presenting the best fit value for C for each individual data set and the corresponding $\overline{Da_B}$ value. It can be seen that $\overline{Da_B}$ does vary somewhat with each data set, but is always an O(1) quantity.

In order to quantify the scatter in the correlations shown in the table and the capability for actually inverting the above procedure to be used as a blowoff prediction methodology, we employed the following procedure. Assume that the equivalence ratio at blowoff is now the unknown and must be predicted, $\phi_{LBO,pred}$. Assume also that the Damköhler number at blowoff is known and equal to the value $\overline{Da_B}$ compiled in the table. We then solve the following implicit equation for $\phi_{LBO,pred}$ for each fuel composition:

$$\overline{Da_B} = \frac{d}{U_b \tau_{Blowoff} (\phi_{LBO,pred} + C \ln(D_F / D_{ox}))} \qquad (13)$$

This procedure is repeated for each fuel composition. In general, $\phi_{LBO,meas}$ and $\phi_{LBO,pred}$ are not identical, and so the root mean square (rms) of their difference over all the data points is referred to as $\delta\phi_{rms}$. The table also compiles the values of $\delta\phi_{rms}$. As can be seen, assuming a constant Damköhler number at blowoff results in a capability for predicting the equivalence ratio value to within about 0.02 - 0.04.

Test group	Best Fit *C* Value		
	C	$\overline{Da_B}$ at ϕ_{adj}	$\delta\phi_{rms}$
T=300 K P=1.7 atm U_0=59 m/s	0.1	2.1	0.04
T=300 K P=1.7 atm U_0=39 m/s	0.08	1.1	0.03
T=458 K P=4.4 atm U_0=59 m/s	0.07	0.2	0.02

Table 1: Summary of optimum model constants for correlating blowoff data and resulting scatter in fitted data.

Moreover, due to the exponential dependence of $\tau_{Blowoff}$ upon equivalence ratio, varying the precise value of $\overline{Da_B}$ or C does not substantially impact the errors in $\phi_{LBO,pred}$. For example, in the first case above, assuming blowoff occurs at constant values of *Da*=1.0 or 3, instead of the best fit value of 2.1, results in $\delta\phi_{rms}$ =0.045 and 0.043, respectively.

Moreover, both T_{in}=300K, *P*= 1.7 atm data sets can be reasonably collapsed with a single $\Delta\phi$ equation or *C* value. To illustrate, **Figure 31** compares the predicted and actual blowoff equivalence ratios for all low temperature data taken in this study, assuming *C*=0.1 and $\overline{Da_B}$ =1.7. It can be seen that the error in $\phi_{LBO,pred}$ is generally less than 0.05, and $\delta\phi_{rms}$ = 0.045. Moreover, the highest errors are encountered with the very high CO mixtures, which may simply be a manifestation of the sensitivity of high CO mixtures to ambient humidity levels and other factors influencing H levels. If the P=4.4 atm, T=460 K data set were also plotted, they would also cluster along a line, but with a systematic difference from the grouping in this graph., In other words, the optimum model constants (particularly the C value) vary with operating conditions.

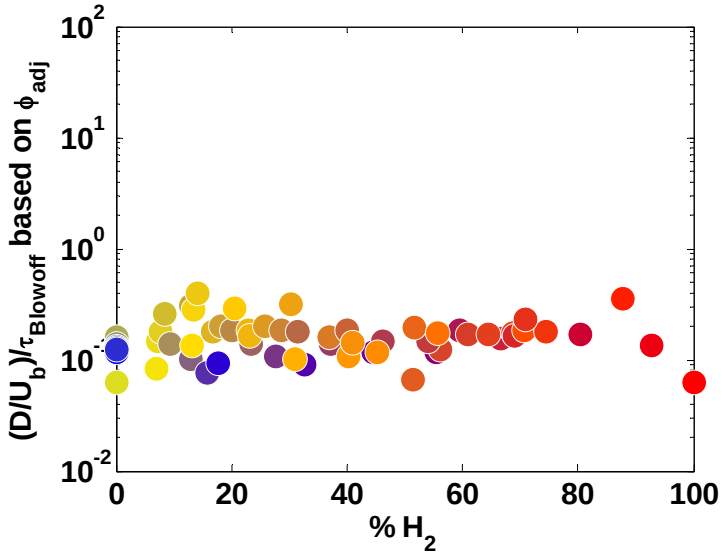

Figure 30: Damköhler numbers of mixtures based on local equivalence ratio at premixer flow velocities of 59 m/s at 458K reactants temperature and 4.4 atm combustor pressure.

There are a variety of reasons that the remaining scatter could be present, such as inherent noise in the blowoff equivalence ratio. In addition, other more subtle factors, such as reference length and reference flow velocity could easily change somewhat with approach flow velocity.

We should emphasize that the *C* value in the $\Delta\phi$ calculation was chosen *empirically* to give the best fit. Although the *Da* mechanism, considering preferential diffusion effects, could correlate and predict the lean blowout limits very well, the real physical meaning behind these correlations are still uncertain and require further study.

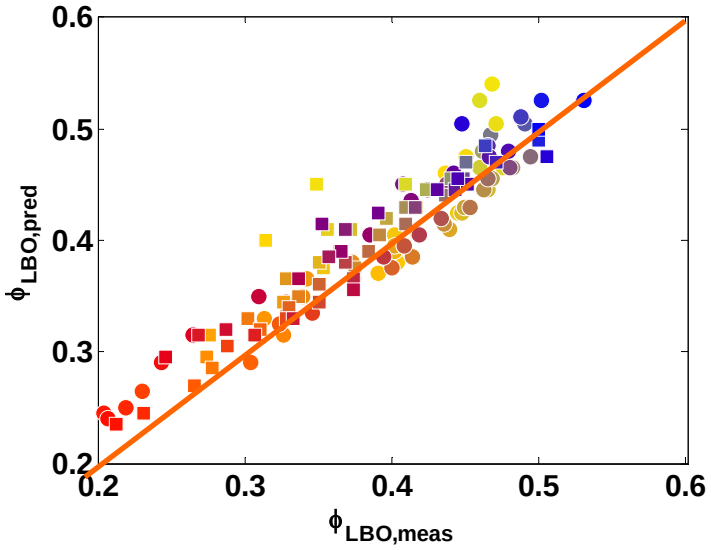

Figure 31: Comparison of predicted and measured blowoff equivalence ratio for all T=300 K, p = 1.7 atm data. circle: U_0= 59 m/s, square: U_0= 39 m/s.

7. DYNAMIC PHENOMENOLOGY OF LEAN BLOWOFF

BACKGROUND

In the previous section, it was noted that the phenomenology of blowoff changed markedly with H_2 levels in the fuel, see discussion of **Figure 22**. For lower H_2 mixtures (~<50% H_2 by volume), the blowoff event occurred abruptly and was precipitated by a small reduction in fuel/air ratio (although sometimes preceded by slight liftoff of the flame from the burner). However, for high H_2 mixtures, the flame liftoff and blowoff events were quite distinct. Furthermore, as the mixture approached blowoff, the flame becoming visibly weaker, lifted off from the holder and moved progressively downstream. Finally, it was noted that the definition of blowoff at these very high H_2 levels was somewhat arbitrary and very much a function of the definition of "blowoff".

The objective of this task was to follow up on these observations and systematically characterize the blowoff phenomenology as a function of the H_2 levels in the fuel. This was accomplished through high speed visualizations of the flame emission and velocity field measurements. The dynamic blowoff process of methane flames has been studied and characterized in different stabilization mechanisms, pilot, bluff body, and swirling flow[34,35,36,37]. In the swirling flame, it has been showed that the swirling flame tends to oscillate between extinction and reignition phases [36,37]. The flame is stabilized by the inner recirculation zone (the vortex breakdown bubble), and locally extinguishes/reignites under near blowoff conditions. The number of extinction/reignition events per unit time monotonically grows as blowoff is approached. These observations have formed the basis of an active control system that detects blowoff precursors and applies closed loop active control to prevent its occurrence [37]. Our objective in this task was to generalize the study of the dynamic blowoff process of a methane flame to flames with varying levels of H_2 dilution. It should be emphasized that this blowoff phenomenology is geometry dependent and is a function of, for example, the degree of constriction of the exhaust nozzle. As such, we took special effort to perform this study on a well characterized burner that is identical to studies performed at Sandia National Laboratory.

EXPERIMENTAL SETUP

Combustor and Flow System

For this task, we duplicated an experimental rig developed at Sandia National Laboratories by Dr. Bob Schefer and Joe Oefelein to capture chemiluminescence and visualize the flame front and flow field. This was done in order to have a similar test facility to facilitate comparisons of data and simulations. This gas turbine simulator is an atmospheric pressure, premixed, swirling stabilized dump combustor, which is the basic configuration of most gas turbine combustor. The combustor is shown in **Figure 32**.

The facility consists of a swirler/nozzle, combustor, and exhaust sections. Premixed gas, consisting of H_2/CH_4 mixtures and air flows through a swirler housed swirler/nozzle section. The nozzle is an annular tube with inner diameter of 28mm. The center body has an outer diameter of 19 mm. The overall flow area remains constant at 3.0 cm^2 inside the nozzle. Tests were performed with a six-vane, 45^o swirler, which is located in the annulus between the centerbody and nozzle wall, see **Figure 33**. The theoretical swirl number, which is 0.85, is calculated by [38],

$$S = \frac{2}{3}\left[\frac{1-(d_h/d)^3}{1-(d_h/d)^2}\right]\tan\theta \quad (14)$$

where d_h and d are the diameters of centerbody and swirler, respectively, and θ is the swirler vane angle. The fuel is injected 150 cm upstream of the combustor to achieve a premixed condition. The combustor consists of a 305 mm (12 inches) long quartz tube, which permits the detection of ultraviolet (UV) radiation and imaging. The quartz tube has an inner diameter of 115 mm and rests in a circular groove in a base plate. An adapter slides in four standing bars, sitting on the top of the quartz tube, and the exhaust nozzle is connected to the adapter. The exhaust nozzle has a 127mm contraction section with the area ratio 0.44, and a chimney section which is 102mm long with inner diameter of 51mm.

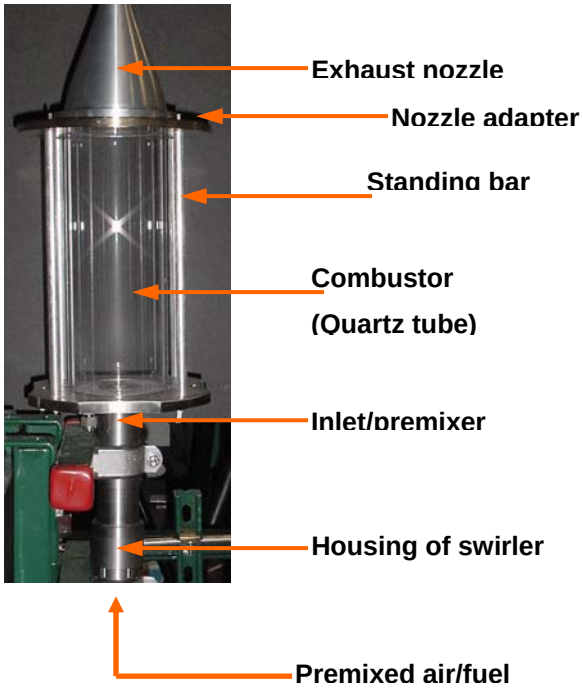

Figure 32: Photograph of the combustor facility

Figure 34 shows the schematic diagram of the flow control system. High-pressure natural gas and air are supplied from building facilities. The hydrogen is supplied from bottles. The air and fuel flow rates are measured with a flowmeter and mass flow controllers (MFC's), respectively. The same fuel mixing facility in the previous section was used to generate the syngas mixtures (H_2/CO/CH_4). Both the flowmeter and MFC's were calibrated using the specific gas with which they were to meter. The maximum resultant uncertainty in the flow rate measurements is 5% of full scale, and in blowoff equivalence ratios is 0.01-0.02 for most of the cases. The largest uncertainty in ϕ of 0.03 occurs with pure CH_4. The air is choked before the mixing section, and the premixed air/fuel is choked again inside the inlet tube of the combustor (not shown) upstream of the swirler to minimize the impact of perturbations in the combustor impacting the fuel/air mixing process.

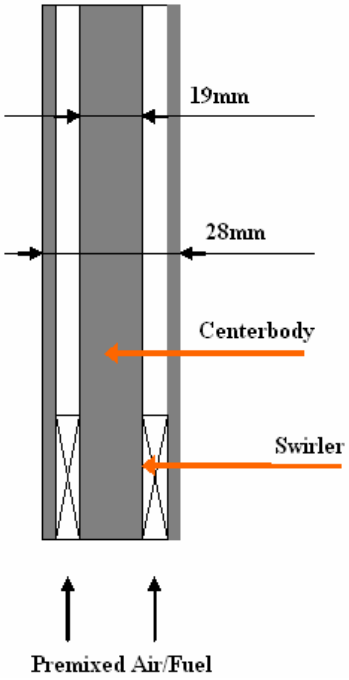

Figure 33: Cross section of inlet/premixer assembly

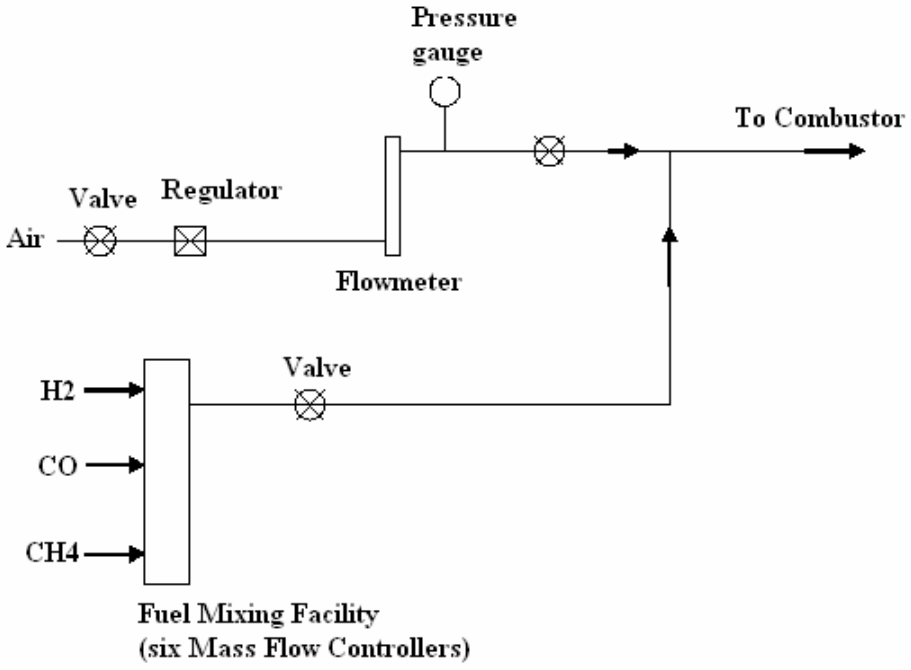

Figure 34: Schematic diagram of the flow control system

Diagnostic methods and Instrumentations

To help understand the dynamic processes of lean blowoff for syngas mixtures, several types of instrumentations and diagnostic methods were employed in this study.

High Speed Visualizations and OH chemiluminescence

High speed visualizations of the flame were obtained with an Ultracam3, Gen III intensified camera at 1000 frames/sec and 512 x 512 resolution. The photocathode is sensitive to light in the 400-900 nm spectral region and is, thus, unfortunately insensitive to the UV light that constitutes the primary chemiluminescence emission for high H_2 flames. As such, this variation of camera sensitivity should be kept in mind when comparing the images with varying H_2 levels in the images below.

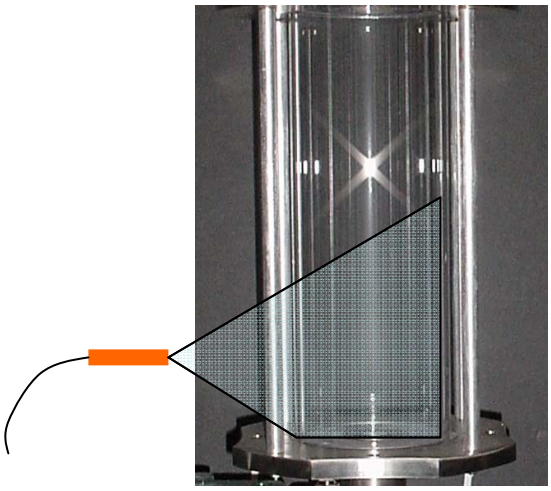

Figure 35: Location of the optical probe

In addition, UV radiation from the high H_2 flames was monitored with an optical fiber bundle (NA=0.44), with the head located 46 mm above the dump plate of the combustor and 171 mm radially from the combustor centerline, see **Figure 35.** This volume was placed such that light is collected from the IRZ (inner recirculation zone). The light passes through an interference filter centered at 308 nm and with a full-width-half-maximum (FWHM) of 10 nm, which corresponds to the primary spectral region of OH* emission. This radiation was detected

by a miniature, metal package PMT (Hamamatsu H5784-04). This PMT has a built-in amplifier (bandwidth of 20 kHz) to convert the current to voltage and operates from a 12 VDC source.

The signal output from the sensors was low pass filtered by a Krohn-Hite Model 3362 digital Butterworth filters and then fed into a National Instruments A/D board. The sampling frequency was 2 kHz. The low pass filter frequency (for anti-aliasing) was set at half the sampling frequency, 1 kHz.

PIV system

The velocity field in the combustor was measured using Particle Image Velocimetry (PIV) as explained by Raffel *et. al.* [39]. The system consists of a dual head Nd:YAG laser, a high resolution CCD camera, a mechanical shutter and a centralized timing generator orchestrating the activation of each component. In addition a cyclone seeder built in-house was used to supply anhydrous aluminum oxide (Al_2O_3) with an average particle size of 3μm.

Each laser head delivered a 120 mJ/pulse beam at a wavelength of 532 nm. The beams passed though sheet forming optics, consisting of a convex spherical (f = 1 m) and a convex cylindrical lens (f = 25.4 mm), resulting in a 500 μm thick light sheet at the center of the combustor. The CCD camera captured the images of the illuminated particles at a resolution of 1600 x 1200 pixels (corresponding to 76 mm x 102 mm) in frame straddling mode. This allowed for the duration between the laser shots to be at the desired level of 10 μs. In addition the camera was also fitted with a 532 nm laser line filter with a FWHM of 3 nm to restrict any background noise.

The images were processed using the DaVis software package, provided by LaVision Inc. This software uses an adaptive algorithm to obtain the velocity field. The grid size was 32 pixels x 32 pixels with a 50% overlap. The blue dashed line **in Figure 49** (a) illustrates the interrogation volume for the PIV measurements shown in this report.

One of the most significant errors present in PIV measurements in a swirling flow comes from out of plane motion of the flow which causes particles to exit and enter the interrogation volume between successive laser shots. The laser sheet thickness, the duration between laser shots, and the seed density have been carefully optimized to minimize this error. Assuming an overall 5 m/s tangential velocity, the distance traveling between two laser shots is 50μm, which

is 10 percent of the laser sheet thickness at the center of the combustor. We estimate that the velocity uncertainties to be on the order of 5% [17,**Error! Bookmark not defined.**].

RESULTS AND DISCUSSION

OH Chemiluminescence

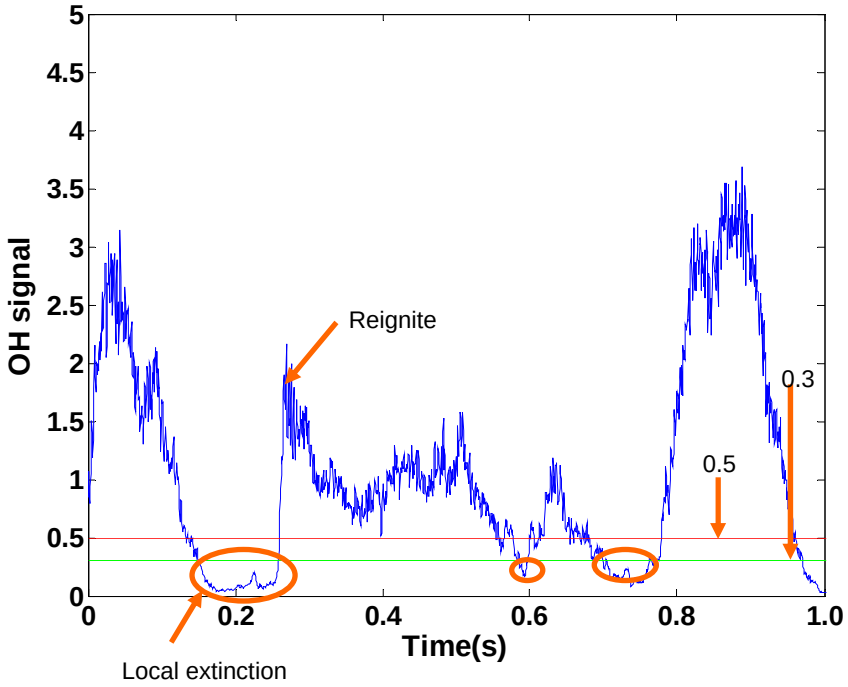

Figure 36: Time series data of OH signal of extinction-reignite events

Figure 36 shows the OH chemiluminescence signal from an optical probe which was focused at the inner recirculation zone, see **Figure 35**. Because the level of chemiluminescence signal is determined by the power of the flame, which is varying with equivalence ratio, the OH signal is normalized by its mean value. Local extinction is defined when the intensity of the signal drops lower than some threshold, and ends when the signal goes above this threshold. However, sometimes during a local extinction the signal oscillates above and below the threshold. As such, a second threshold was defined a little higher than the first threshold to make

sure that this is only counted as one event. For this example, 0.3 and 0.5 were used as the first and second thresholds for local extinction. Data in **Figure 36** was collected at an equivalence ratio of 0.50 for the CH_4/Air flame. It can be seen that unsteady events are characterized by an almost complete loss of chemiluminescence signal quickly followed by a strong signal spike. This corresponds to a local extinction of the flame followed by a strong reignition of the flame. The local extinction events were circled in this plot. These distinctive extinction and reignite span a period from O(1s) to O(0.001s), without any obvious periodicity or frequency prior to lean blowout. **Figure 37** shows the power spectral density of the signal for equivalence ratios of 0.6, 0.5, and 0.46(lean blowout occurred at an equivalence ratio of 0.45 in this set of experiments). There are no peaks arising in the low frequency range as LBO limit is approached. This indicates that there are no coherent, periodic oscillations occurring near the blowout limit. The only obvious peak is at 250 Hz, which is related to the natural frequency of the combustor.

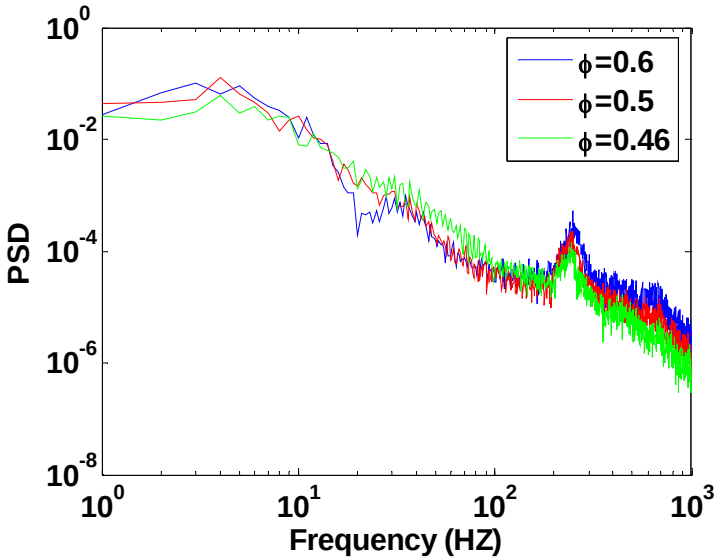

Figure 37: Power spectral density (PSD) of OH signal of CH_4 flame at different equivalence ratios

As the LBO limit is approached, more of these events occur in a given time period and thus the time between two such events decreases. **Figure 38** shows the dependence of the number of events per second on the equivalence ratio for five kinds of syngas. The data shows that flames can be stabilized at lower equivalence ratios with increasing H_2 percentage. When the flame is approaching the lean blowout, the number of events increased greatly. It shows that

more events are observed prior to blowout with higher percentages of H_2- this illustrates the enhanced robustness of these flames to blowout. More events means that the flame undergoes extinction events more frequently and undergoes a longer time in the extinction phase. As a consequence, the flame has a shorter and shorter time to reignite and sustain itself. This phenomenon may be explained by the difference of chemical time for these mixtures. The chemical time of H_2/CH_4 flame decreases with the increasing of H_2 percentage - so a higher level H_2 flame can stand a shorter time to reignite.

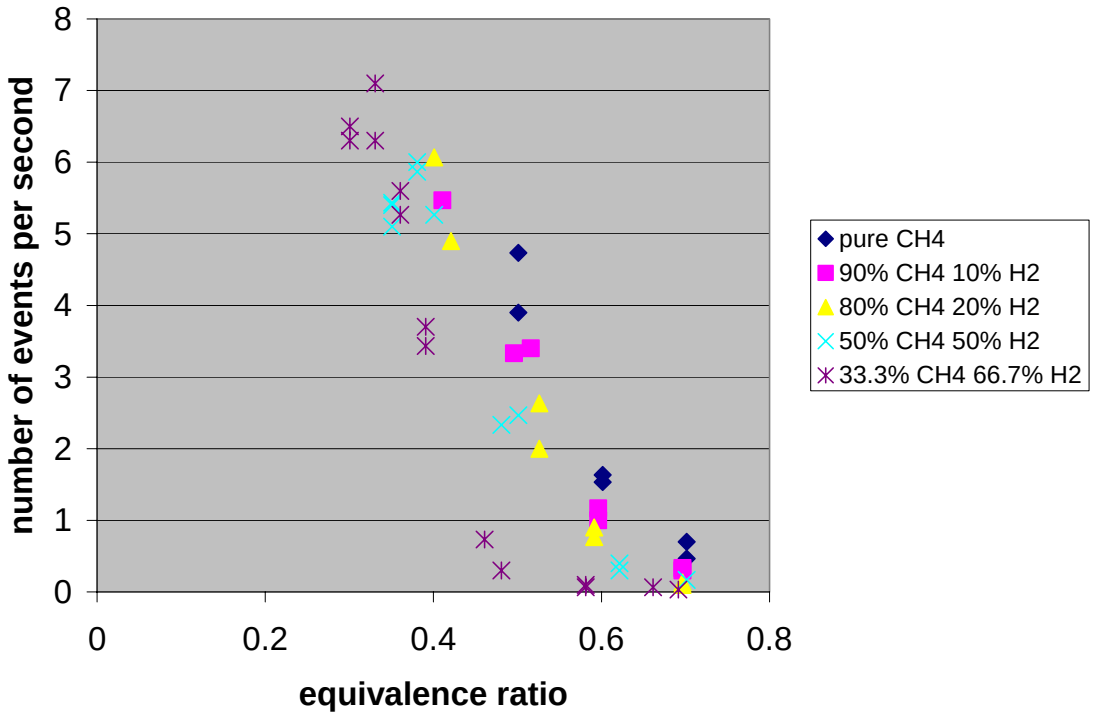

Figure 38: Dependence of events numbers upon equivalence ratio for different fuels

High Speed Images

This section describes the dynamics of near blowoff flames. Tests were performed at room temperature, atmosphere pressure, and constant nozzle exit velocity of 29m/s.

A qualitative stability diagram of H_2/CH_4 mixtures is shown in **Figure 39**. The regimes are differentiated by visual observation. For a given fuel composition, as we move vertically down the chart by reducing fuel/air ratio, at some point a certain level of "enhanced unsteadiness" becomes evident, indicated by the upper dashed line. For low levels of H_2, further

reductions in fuel/air ratio cause blowoff, indicated by the lower solid line. At higher levels of H_2, an additional flow regime, associated with a columnar flame zone is also present. This columnar region will be discussed later in this report. The four solid circle points represents the four cases studied in detail in this report. Note that there is a monotonic reduction in blowoff equivalence ratio with increasing H_2 levels, consistent with prior section (task 2).

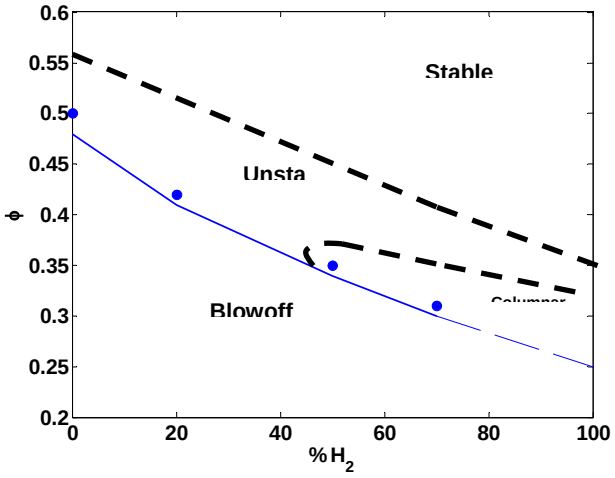

Figure 39: Diagram of flame stability with different H_2 addition levels.

To provide a baseline, a set of stable flame images are provided in **Figure 40**, which shows chemiluminescence gray scale image (intensity based coloring code) at an equivalence ratio of 0.56. The definition of equivalence ratio is based on the overall fuel mixture. We should note that these colorized images are difficult to interpret if viewed in grayscale. The boundary of the images corresponds to the combustor walls. A compact V shaped flame[2] stabilizes slightly downstream of the nozzle exit. There are minimal reactions at the two corners between the combustor wall and the dump plate, where the flow is recirculating (referred to here as the Corner Recirculation Zone, CRZ).

[2] This V-shape is not obvious from these images due to the integration of light intensity over the line of sight, but very obvious from direct visualizations.

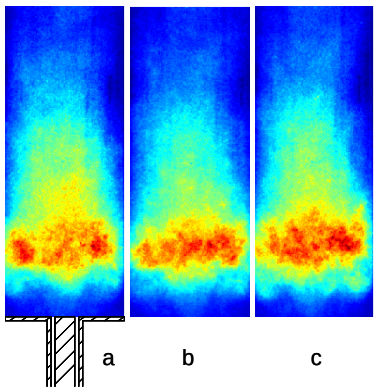

Figure 40: Consecutive images of stable CH_4/Air flame (ϕ =0.57; images separation =10ms)

A typical extinction/reignition process for a natural gas flame near blowoff is shown in **Figure 41**, at an equivalence ratio of 0.5. Moving from (a) to (g), the flame gradually weakens in intensity, particularly about half way up the image in the axial direction. In addition, it lengthens axially, reverting from a more compact region in (a) to an axially distributed region in (d) and (e). In images (f) and (g), the axially distributed flame appears to split into two sections, with hardly any radiation evident from the center. This region reignites in images (h)-(j) which leads to a more axially uniform, but axially compact intensity distribution in (k) and (l), similar to the image in (a). Although not obvious in these images except for (i), the "reconnection" of these two axial regimes appears to occur through a connecting helical tube. This process outlined above repeats itself more and more frequently as the flame approaches blow out.

Also evident in these figures are the dynamics of the flame zones near the premixer exit. In (a), no flame is visible in the corner recirculation zone (CRZ) or at the nozzle exit. Moving to (b) and (c), the flame intensities decreases, but combustion is present in the CRZ. These CRZ flames extinguish in (d) and (e), but are sometimes replaced by a sporadically appearing flame that goes almost to the nozzle exit in (d), (f) and several other images. The movement of the flame toward this very high velocity region suggests axial translation of the inner recirculation zone (IRZ), associated with the vortex breakdown bubble.

Measurements of OH chemiluminescence signal collected by an optical fiber directed at the IRZ also show the flame intensity oscillations. During the phase at which the flame intensity is decreasing, it is possible that unburned fuel is entering the combustor, mixing with the burned

hot products and active radicals. At some point a well-stirred reactor-like region is present which combusts and supplies a 'spark' to reignite the whole flame.

The extinction/reignition process is not periodic, but appears randomly with the average spacing between successive events decreasing as blowout is approached. Although not shown, measurements of OH chemiluminescence signal shows that the period of this extinction/reignition process varies between 10 – 200 ms for the case in **Figure 41**. Furthermore, each extinction/reignition event does not necessarily follow the identical sequence shown in **Figure 41**. For example, the flame can just move up and down axially, as in **Figure 41**(a-c).

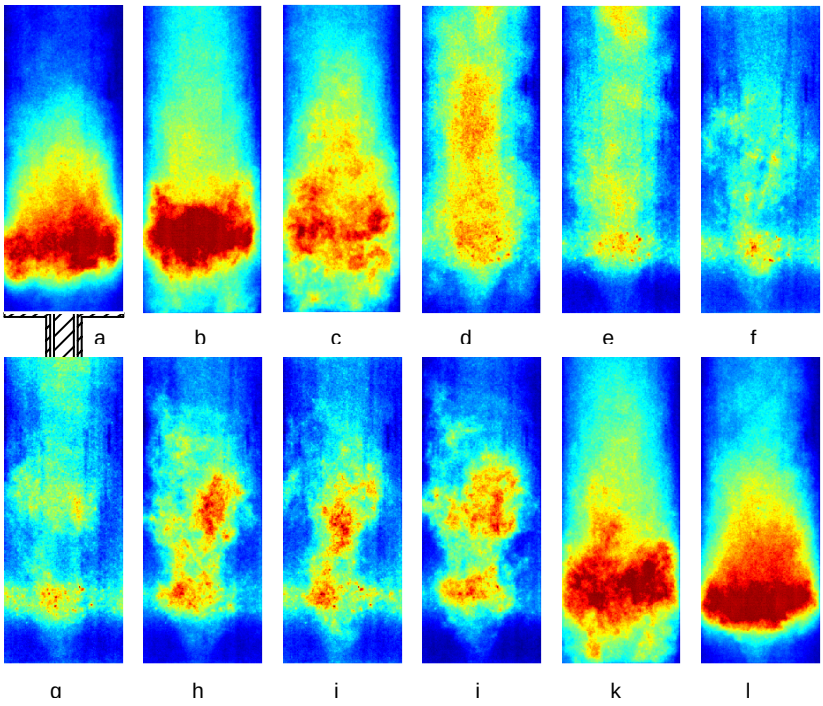

Figure 41: **Consecutive images of CH_4/Air flame under near blowoff conditions (ϕ =0.5; images separation ≈10ms)**

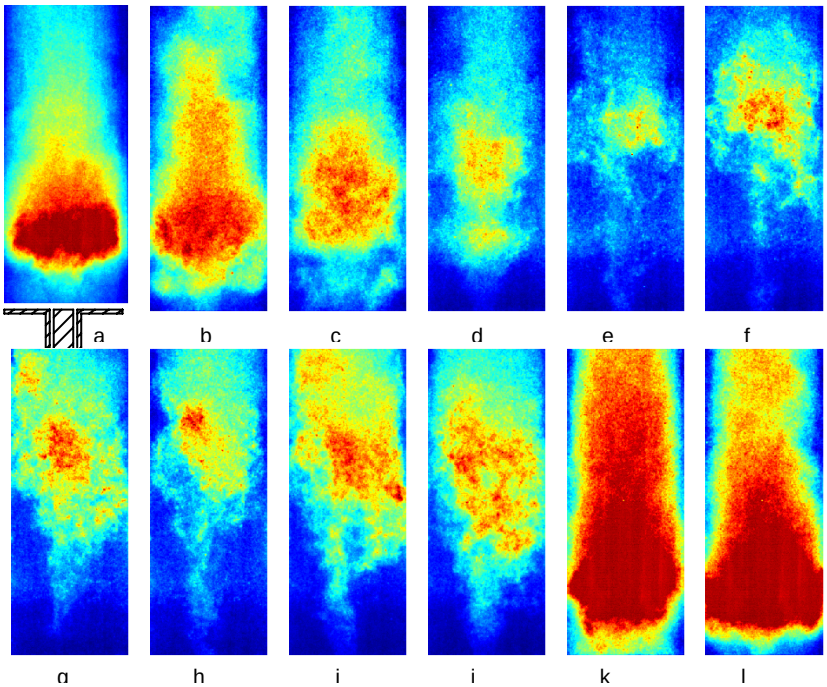

Figure 42: Consecutive images of 80%CH_4 --20% H_2 flame under near blowoff conditions (ϕ =0.42; images separation ≈10ms)

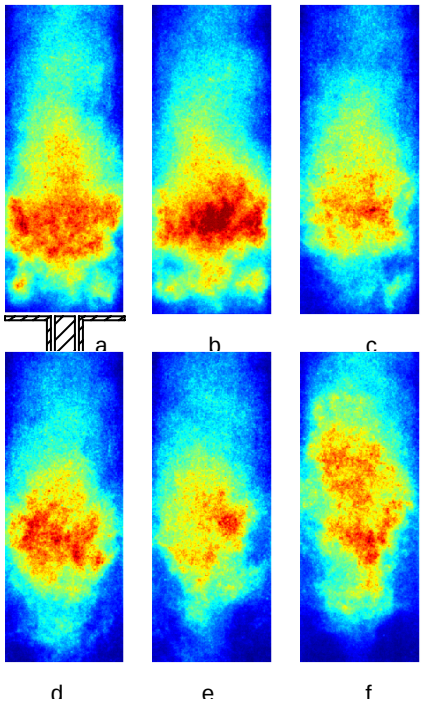

Figure 43: Consecutive images of 80%CH_4 --20% H_2 flame under near blowoff conditions (ϕ =0.42; images separation =2ms)

Next, consider the effects of H_2 addition to the CH_4 flame. **Figure 42** shows images for an 80%CH_4 -20%H_2 flame at ϕ=0.42. Many of the processes in **Figure 42** and **Figure 41** are very similar but there are some differences. Comparing the lowest intensity levels for CH_4 flame (f in **Figure 41**) and 20%H_2 addition flame **(**e in **Figure 42),** shows that the lower flame region is of lower intensity (c-d) or in some cases essentially gone (g-i), except for a helical tube that extends downward. Apparently, the strong reignition event in (k) and (l) is precipitated by flame propagation down this tube.

Although we do not fully understand the details, there are some interesting dynamics associated with flame stabilization in the IRZ and CRZ. We hypothesize that the CRZ is normally full of recirculating hot products, with minimal combustion there. As the flame moves downstream, it is anchored by the IRZ (see f-j). However, the CRZ is presumably also now filling with unburned reactants. This region extinguishes and reignites occasionally (see b, c, k), often times with different dynamics than that of the rest of the flame. This reignition can be prompted by flame flashback through the central core region or along the combustor wall by a fluctuation of temperature [40] or just the local turbulent vortex motion [41]. Once reignited, the flame in the CRZ supplies heat and active radicals to the V-flame, helping it reattach to the centerbody or stabilize as a lifted V-flame, see **Figure 43** (a,b). However, by doing so, it "starves" itself of reactants, extinguishes, and then becomes a region of recirculating hot products, such as shown in the sequence of **Figure 43** (a-d). Note also that because the CRZ is located between the combustor wall and the cold dump plate, the heat loss rate is very high, so that the flame in the CRZ quenches easily. Once the CRZ flame is gone, the V-flame loses some of its "pilot" and moves back downstream axially.

Once the mole fraction of H_2 is near or higher than 50% by volume, the blowoff phenomenology changes significantly. Like the 20% H_2 addition flame, 50% CH_4—50% H_2 flames still have the extinction/reignition process similar to that in **Figure 42**. Three different sequences of images are shown in **Figure 44, Figure 45, and Figure 46** for a 50%CH_4 -50% H_2 flame at equivalence ratio of 0.35. Starting with **Figure 44** (a) to (j), the flame intensity weakens gradually and the majority of the radiation intensity moves downstream. A flame is still evident within the helical tube (flame propagation is outward, the center is filled with hot products – evident from the seed density in PIV images), which through either reignition or propagation

downward, propagates back to the nozzle exit. However, in some cases, the flame is not present in this helical tube and is almost completely blown out, before abruptly propagating back upstream, see **Figure 45.**

Flame propagation outward from this columnar tube plays an important role in the re-ignition event, as is particularly evident in **Figure 46,** images (a-g)**.** The flame spreads out and fills the whole combustor, image (e)—(h)**.** However, the fuel/air ratio is apparently too low for the flame to remain stabilized in the entire combustor and the flame reverts back to tornado then columnar shape, image (j)—(l).

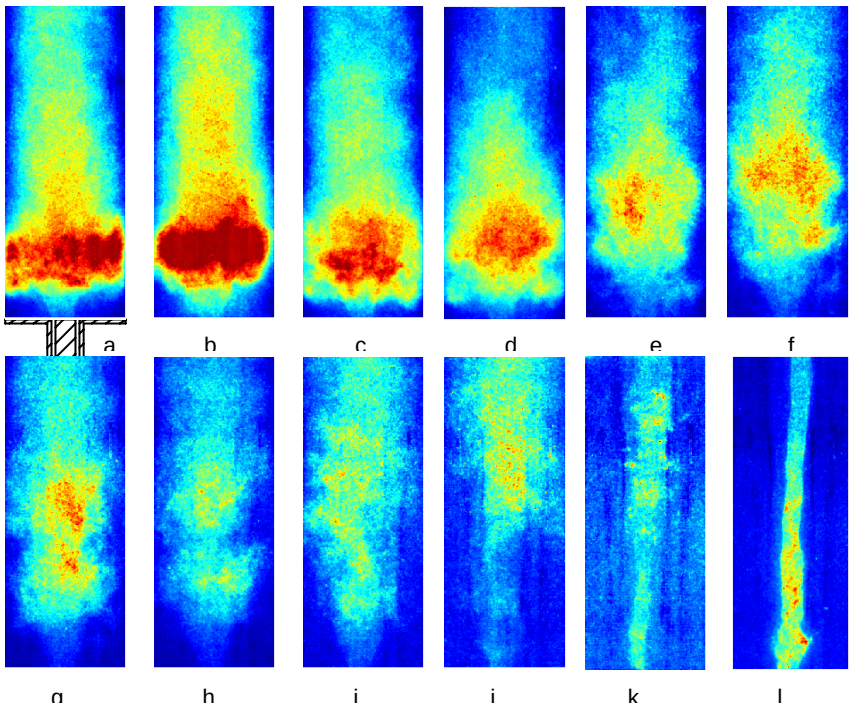

Figure 44: Consecutive images of 50%CH_4 --50% H_2 flame under near blowoff conditions (ϕ =0.35; images separation ≈10ms)

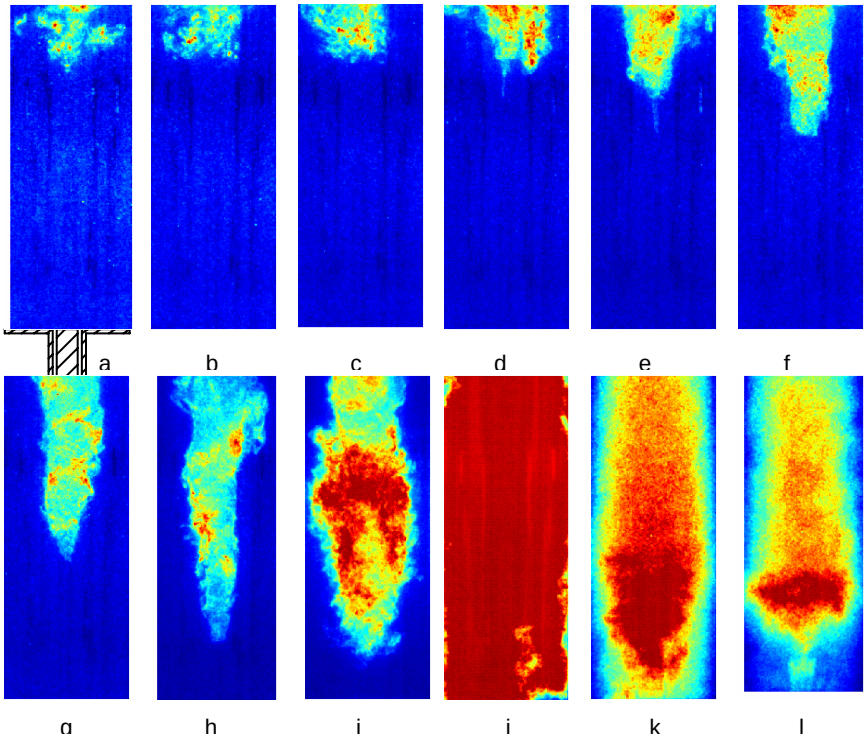

Figure 45: Consecutive images of 50%CH_4 --50% H_2 flame under near blowoff conditions (ϕ =0.35; images separation ≈10ms)

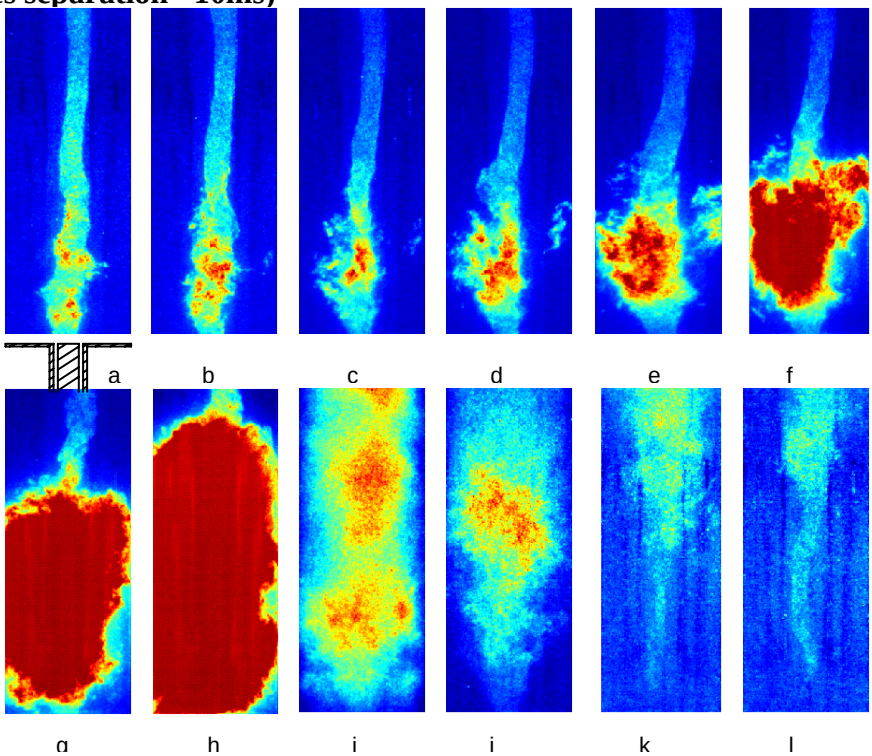

Figure 46: Consecutive images of 50%CH_4 --50% H_2 flame under near blowoff conditions (ϕ =0.35; images separation ≈10ms)

Further increases in the hydrogen content cause this columnar flame to more and more prominently dominate the flow physics. In fact, at very high H_2 levels, the flow prior to blowoff becomes much less unsteady than in the previously shown images, and consists simply of a nearly steady columnar flame (clearly, most of the reactants are exiting the combustor unburned in this situation), see **Figure 47**.

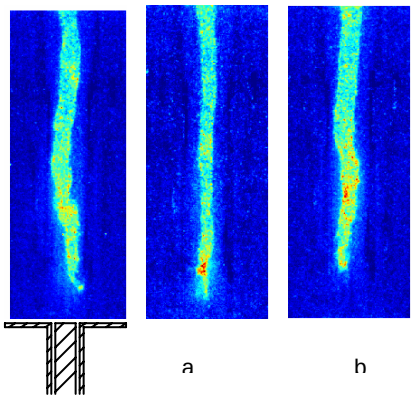

Figure 47: Consecutive images of 25%CH_4 --75% H_2 flame under near blowoff conditions (ϕ =0.31; images separation =10ms)

PIV Measurements

The measured blowoff limits of this system are shown by the black line in Figure 48. The details of test conditions are shown in Table 2.

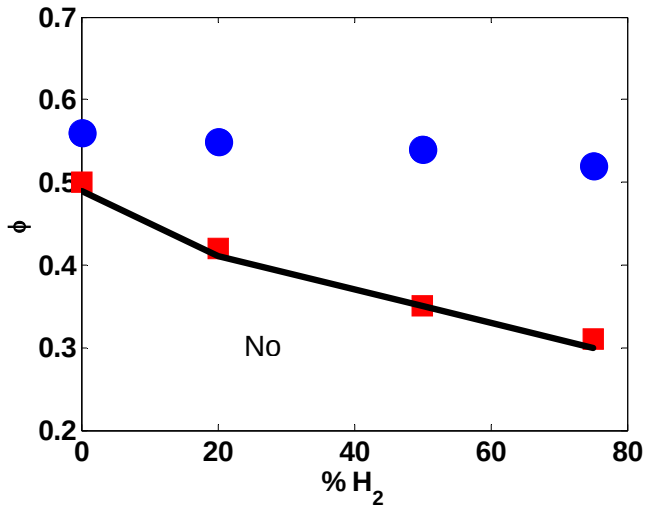

Figure 48: Dependence of blowoff limits upon percentage of Hygrogen. Constant flame temperature test points shown indicated by blue circles, near blowoff test points indicated by red squares.

Fuel Composition (volumetric)		Constant Temperature Test		Near Blowoff Tests	
H_2	CH_4	Φ	T_{ad} (K)	Φ	T_{ad} (K)
0	100	0.56	1595	0.5	1480
20	80	0.55	1587	0.42	1329
50	50	0.54	1594	0.35	1201
75	25	0.52	1595	0.31	1141

Table 2: Test conditions in PIV measurements

Averaged Flow Field

In order to obtain a feel for the basic structure of the swirling flow with or without combustion, time averaged measurements of the cold flow and stable CH_4 flame are shown in **Figure 49** (b). Some velocity vectors were removed in areas with significant number of spurious vectors at locations of window reflections. In addition, iso-vorticity lines are also indicated. The 2D vorticity was defined as,

$$\omega = \frac{\partial v}{\partial x} - \frac{\partial u}{\partial y} \qquad (2)$$

where x and y are the radial and axial coordinates, and u and v are the radial and axial velocities, respectively. For clarity, only high magnitude values, $|\omega|>4000\ s^{-1}$, are plotted.

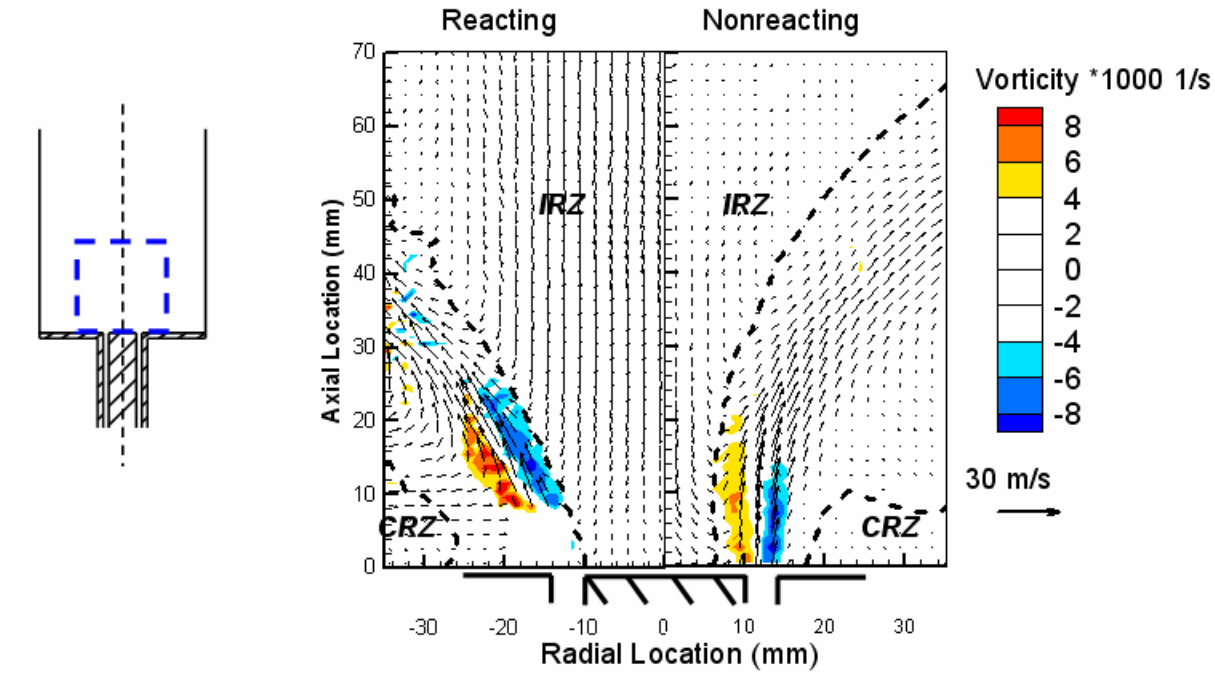

(a) (b)

Figure 49: PIV window arrangement (a) and averaged flow fields (b) of non-reacting flow (right) and reacting flow (stable methane flame, left)

The bottom boundary is the inlet plane of the combustor, and the centerline is the axis of the combustor. To compare the flow structures with and without combustions, half of each measurement volume is shown, with the nonreacting and reacting on the right and left sides, respectively. Each of the plots is the average of 128 images, sufficient for good convergence [17,43]. The inlet annulus is located between 10 and 14 mm radially.

In both the reacting and non-reacting flow situations, the same basic time averaged flow structure is observed, consisting of a corner recirculation zone (CRZ, due to the rapid expansion), inner recirculation zone (IRZ, due to the vortex breakdown bubble) and an annular jet. The annular jet flow is directed downstream and somewhat outward and separates the IRZ and ORZ. The IRZ and ORZ locations were quantified by the locus of points with zero vertical velocity. Note that the IRZ is merged with the small separation zone downstream of the centerbody [42]. These three flow regimes are separated by two layers of strong, oppositely signed shear, as can be seen from the overlaid vorticity iso-contours.

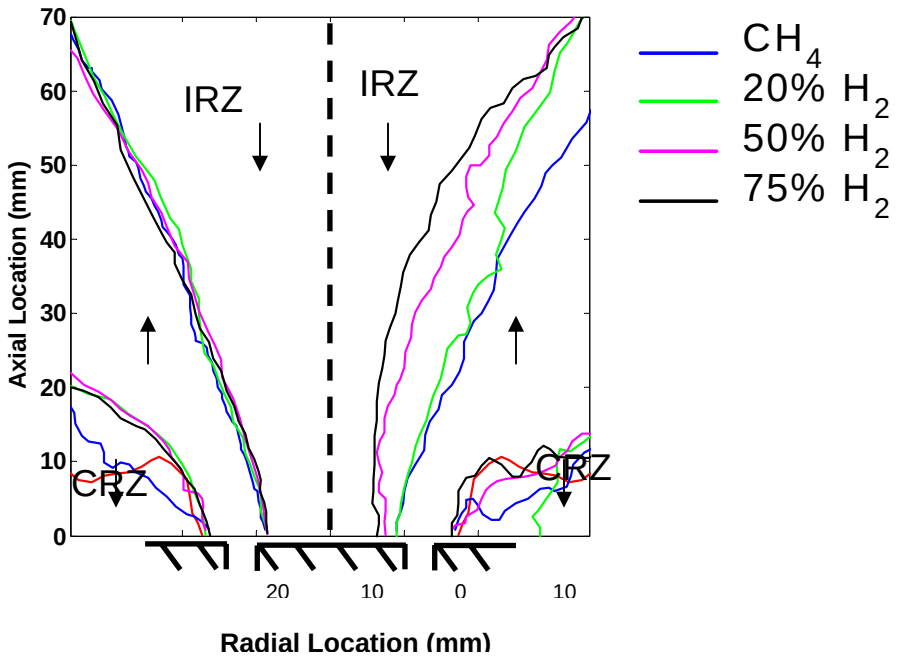

Figure 50: Contour lines of zero mean axial velocity for flames at the same adiabatic flame temperature (Left half) and near blowoff (Right half).

Although these three basic flow features are common to the nonreacting and reacting flows, their quantitative characteristics/locations vary significantly. The recirculation zones have much stronger velocity fields in the reacting case, and the IRZ zone is much wider. Therefore, the two shear layers are stronger, as manifested by the larger vorticity magnitudes. In addition, the annular jet region is somewhat narrower in the reacting case. These observations are consistent with others in these types of flows [43].

In order to better understand the relative role of chemical kinetics and fluid mechanics in this system, a set of data were obtained where the relative H_2/CH_4 mole fractions were varied, but by adjusting the overall mixture stoichiometry such that the gas expansion ratio across the flame and adiabatic flame temperature (calculated) remained nearly constant at 1590K. These test points are shown in **Figure 48**. Details of the stoichiometries and test conditions are shown in the Table 2. Results illustrating the time averaged location of the IRZ and CRZ boundaries are shown in the left half of **Figure 50.** These results show that all four reacting cases have essentially identical IRZ boundaries, regardless of the fuel H_2/CH_4 ratio. This result suggests that kinetic effects do not impact the average flow field structure of constant temperature flames– rather, that it is controlled by the thermal expansion ratio across the flame.

Because the flames with higher hydrogen levels blow out at lower fuel/air ratio's and flame temperatures, the thermal expansion ratio across the flame is different for the near blowoff flames we consider in this report; these test points are illustrated in **Figure 48**. Although the flame shows a strongly dynamic behavior when blowoff is approached, for completeness we plot the corresponding flow boundaries for the near blowoff cases in the right half of **Figure 50.** This figure shows that the size of the IRZ reduces as the percentage of H_2 increases, apparently corresponding to the decrease in expansion ratio across the flame. *As such, the fluid mechanic structure of the flow for the near blowoff flames considered in more detail below certainly varies with the fuel composition, not directly due to kinetic effects but due to the lower flame temperature near blowoff.*

Instantaneous Flow Field

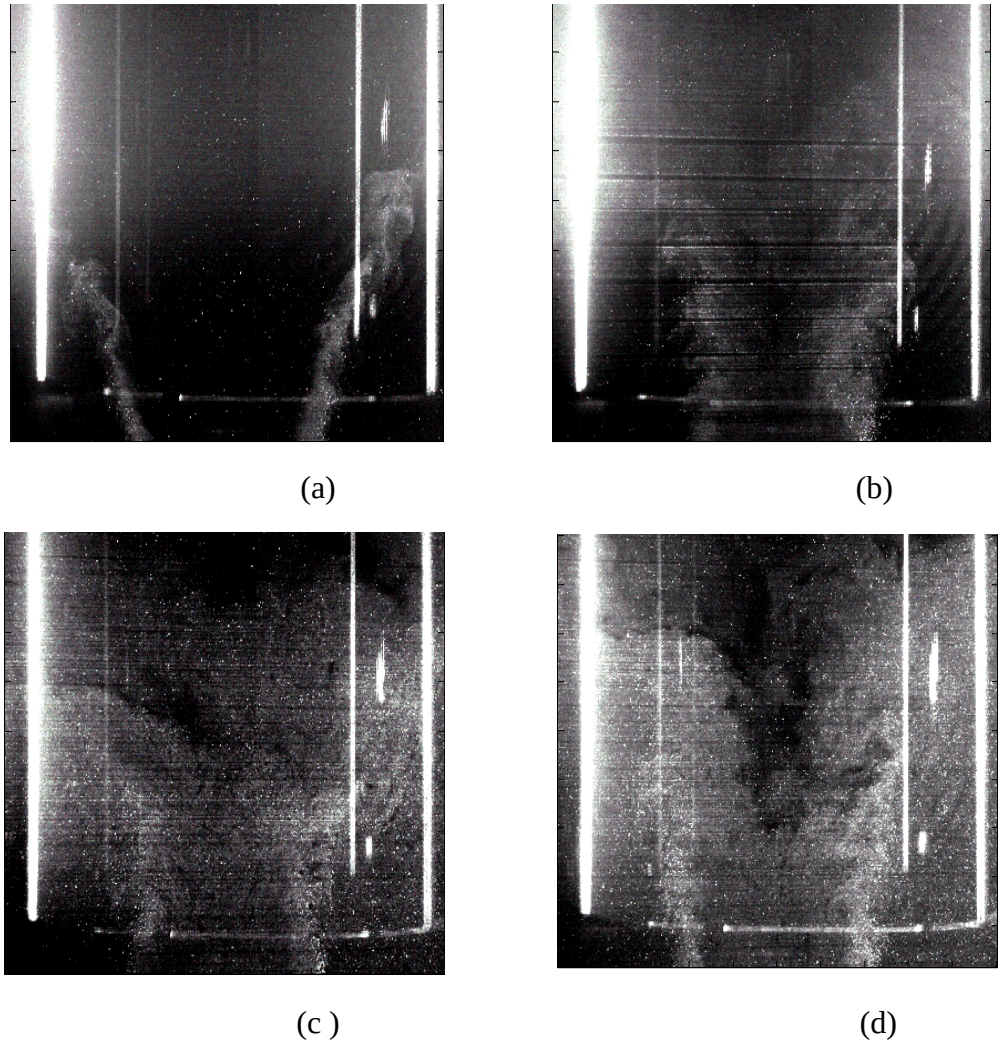

Figure 51: Typical raw PIV Mie scatting images for CH_4 flame near blowoff.

A group of typical raw Mie scatting images are shown in **Figure 51.** As discussed in our previous section, a flame near blowoff tends to exhibit substantial dynamics, including apparent extinction-ignition behavior. Unfortunately, it is difficult to discern the reaction zone location during these events because of local "holes" in the flame sheet and a highly disorganized field of reactant/product interfaces – in cases where the flame sheet is largely continuous, its location can be easily determined by simultaneous analysis of the seed density and its gradient. The latter situation is the case at points where the flame is stabilized on the centerbody or downstream,

such as shown in **Figure** 51 **(a).** However, the flame bounces between these two states for the majority of the time near blowoff (around 90% of the raw images for the low H_2 cases), and it is quite difficult to mark the reaction zone, see **Figure 51 (b,c,d)**. In such a phase, the flame surface has holes which cause the cold reactants to mix with the hot products. In the subsequent discussion, we focus on images where the flame front can be tracked along with the flow field. It should be recognized that this necessarily excludes the majority of images. It does, however, allow us to understand the two flame states that the system is oscillating between, which are separated by rather chaotic periods of disorganized product/reactant interfaces.

Figure 52 shows four typical instantaneous velocity fields for a CH_4 flame at equivalence ratio of 0.5, which is near blowoff. The solid black line represents the flame front near the nozzle exit, which is determined from the steep gradient in seed density. This approach for discerning the flame position only works well in the near nozzle region, however, and it is more difficult to discern the flame edge farther downstream. As such, although the lines indicating the flame front stop at some downstream/radial location, the flame persists farther beyond it. Many of the basic flow features described above are still discernable from these images. The annular jet extends downstream and radially outward, whose edges are demarcated by the regions of high shear and vorticity. At the center of the combustor, a strong backflow indicates the IRZ, and the CRZ is evident in the two corners. However, a number of fine scale vortex flow features are observed in these images which are averaged out in the images shown above. In particular, the jet and shear layers are distorted greatly by the small vortices (same order of the radius of the centerbody). In two of the images (a) and (d), the flame is attached to the centerbody, similar to prior observations [43]. The flame is stabilized in this high shear region and extends radially outward along the high shear, inner edge of the annular jet. Higher vorticity levels are observed instantaneously than on average; e.g., the instantaneous vorticity in the shear layers is around 16,000 s^{-1}, while it is 8,000 s^{-1} in the averaged field, see **Figure 49**.

In two of the images, (b) and (c), the flame is not attached to the centerbody and is situated downstream. It is stabilized in these cases by the recirculating flow in the IRZ. The centerbody wake flow is substantially altered in these two cases, as a much longer wake is evident. In contrast, when the flame is attached to the centerbody, the strong thermal expansion induced flow across the flame renders this wake region nearly unrecognizable. The CRZ region has multiple fine vortices. For example a pair of vortices, which have opposite senses, occupy the

corner region, see the right corner of **Figure** 52 **(c).** The sense of the rotation of the bottom vortex is counter-clockwise, which is opposite with the direction of high speed jet. It shows that the instantaneous fine vortices have different or even opposite properties than the averaged main flow structure. The bottom of the flame is inside the IRZ, and extends radially outward. In both images, however, the flame is clearly located downstream and inside the inner shear layer. This suggests that this image is only a snapshot of a dynamic phenomenon where the whole flame is for a few instances being blown downstream. Unfortunately, the sampling rate of the PIV system is not high enough to capture multiple images of a single one of these events

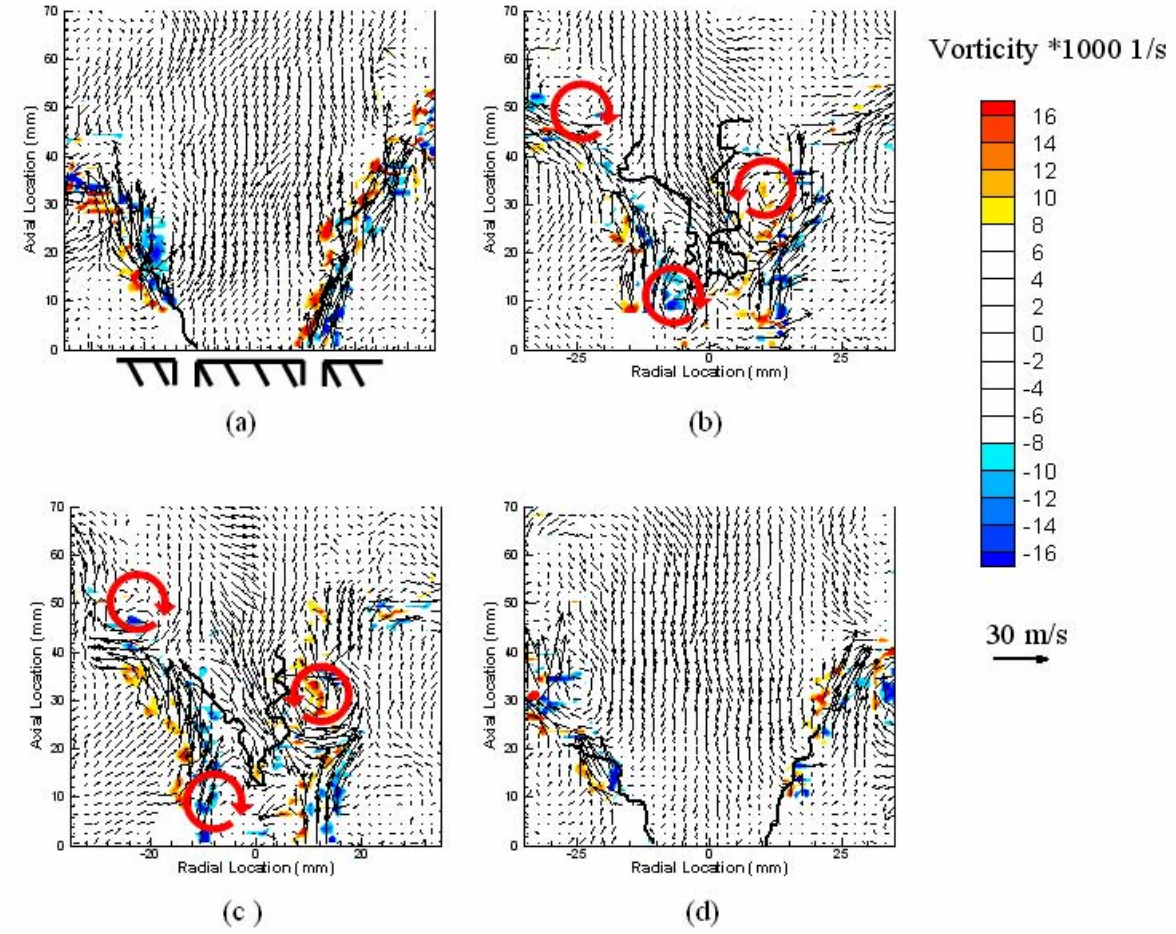

Figure 52: Instantaneous flow field and flame front for CH_4 flame near blowoff.

Notice also that the flame front is substantially more corrugated in these instances when it is located downstream, due to wrinkling from the fine scale vortices alluded to above. These vortices may be associated with a helical vortex tube that spirals downstream, see red circular

arrows in **Figure** 52 (b, c). Interestingly, these same vortices are not evident in images (a) and (d), where the flame is attached to the centerbody, **Figure** 52 (a, d). This suggests a complete restructuring of the dynamic flow field due to thermal expansion effects and fundamentally different flow features when the flame is and is not attached to the centerbody.

The previous section has consistently showed that near blowoff flames are quite unsteady and oscillate between "extinction" and "re-ignition" phases near blowoff. These images depict one of these unsteady phases, and show that, at least in this case, they are associated with an oscillation between two stabilization points, separated by local-extinction/reignition and product/reactant mixing. Presumably, the local strain rate at the flame attachment point becomes too high and the flame locally extinguishes, causing it to blow downstream. During this process, reactants can penetrate the wake region, causing substantial product-reactant mixing and making the reaction zone region unintelligible. Farther downstream, the two flame branches merge and, after some transient, the flow is again divided into regions of only high and low seed density – making it possible to determine flame location. This flame then moves back upstream. Notice that the velocity vectors in these cases are pointing upstream, showing that the flame is moving upstream. Interestingly, we have almost no images where the post flame velocity field is moving downstream. This shows that during these instances of downstream movement, substantial product-reactant mixing is present and the reaction location is not discernable.

Figure 53 shows the four typical instantaneous velocity fields for a near blowoff flame, consisting of 50%CH_4 /50% H_2 at an equivalence ratio of 0.35. Note that this corresponds to a lower flame temperature than the pure methane result. A similar flow structure and dynamical sequence of events is observed in **Figure** 53 as in **Figure** 52. The flame is also stabilized in the inner shear layer, when the flame is attached to the centerbody, see **Figure** 53 **(a,d)** and by the recirculating flow when it is lifted off, see **Figure** 53 **(b,c).**

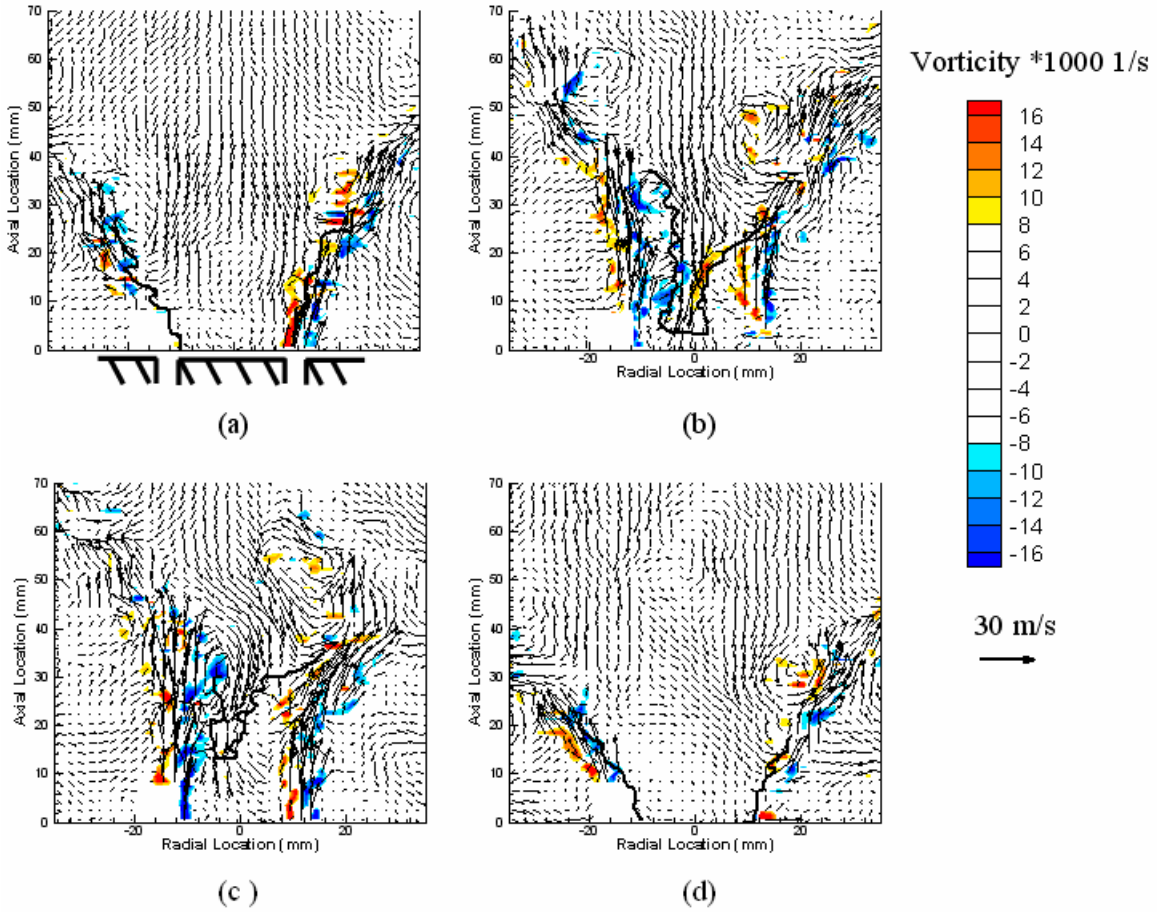

Figure 53: Instantaneous flow field and flame front for 50%CH_4 /50% H_2 flame near blowoff.

Higher hydrogen level flames near blowoff exhibit different dynamics because they never are stabilized on the inner centerbody shear layer, but only downstream. Furthermore, the flame exhibits a thin, columnar shape, evident in some cases in the 50%/50% case. Further increases in the hydrogen content cause this columnar flame to more and more prominently dominate the flow physics. In fact, at very high H_2 levels, the flow prior to blowoff becomes much less unstable, and consists simply of a nearly steady columnar flame (clearly, most of the reactants are exiting the combustor unburned in this situation). This is associated with a substantially higher percentage of the images having clear seed density interfaces corresponding to the flame – roughly 50%. Although these images closely resemble those shown above in cases where the flame is downstream, this point should be kept in mind as the more typical, larger number of events are not shown. **Figure** 54 shows four typical results for 25%CH_4 /75% H_2 flame at an equivalence ratio of 0.31, which is close to the blowoff limit. A columnar flame is not obvious

in this plot due to only a small part of the flame is plotted; however, it is very obvious from direct visualization. A columnar flame stabilized near the nozzle and extends to the exit of the combustor.

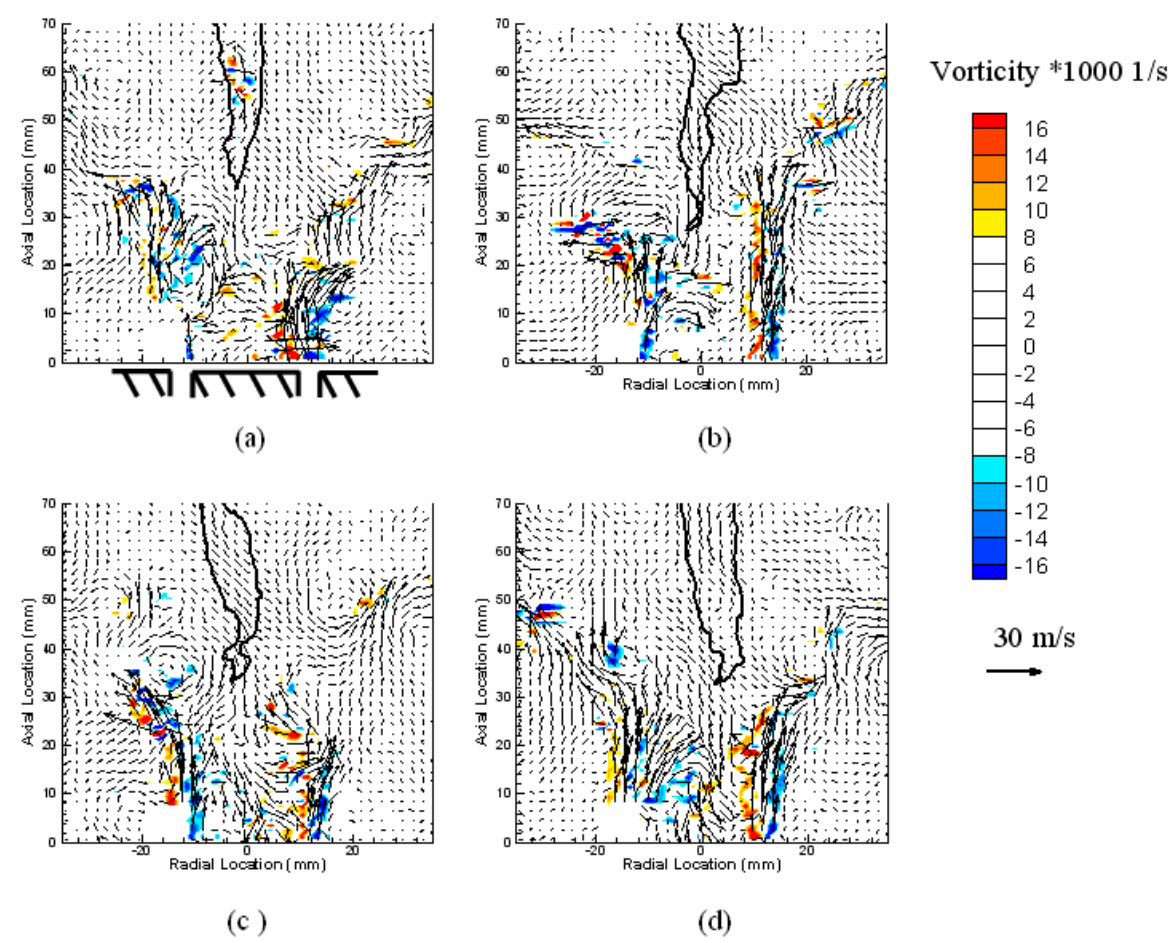

Figure 54: Instantaneous velocity field and flame front for 25%CH_4 /75% H_2 flame near blowoff.

This PIV image shows many of the same basic features as described in the earlier cases. There are some hot products between the bottom of the flame and the centerbody, which are determined by low seed density regions, see red circles in **Figure 55**. Normally, the hot products exist as small, unconnected wrinkled regions. Analysis of the seed density gradient suggests that these interfaces are not flame fronts.

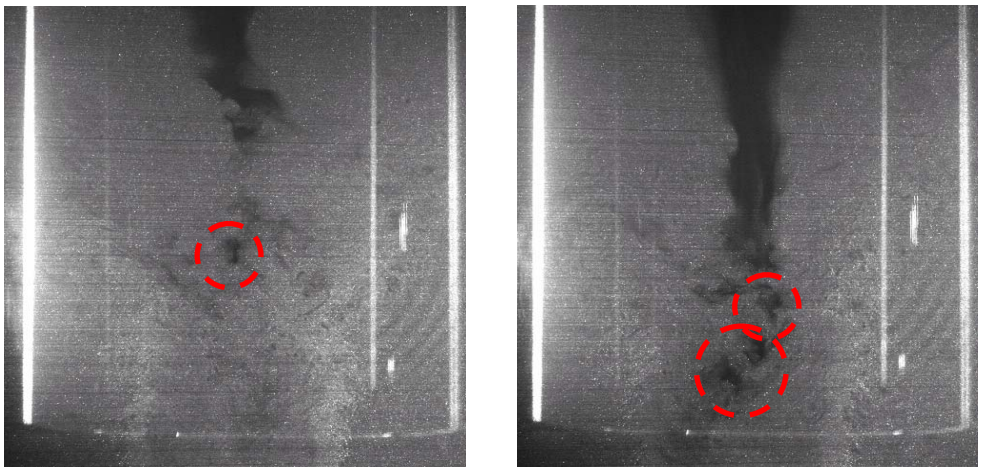

(a) (b)

Figure 55: Raw Mie scatting images in PIV measurements for 25%CH_4 /75% H_2 flame near blowoff.

An important question relates to the relative roles of fluid mechanics and chemical kinetics in causing the above described variation in near blowoff phenomenology. Fluid mechanics certainly exert some role as the average gas expansion ratio monotonically decreases as the H_2 levels increase, due to the lower flame temperatures these mixtures can sustain, see **Figure 50**. This variation in gas expansion ratio and flow velocity must cause some variations in the fluid mechanics of the flow.

Kinetics, particularly strain sensitivities, certainly exerts a role on the dynamic oscillation between the attached and unattached flames shown for the lower hydrogen level flames. These flames were never observed to persist downstream in the steady state, as was observed with higher hydrogen flames. It seems likely that the strain that the flame is subjected to is substantially lower downstream, so this is a puzzling result. In contrast, high H_2 flames under very near blowoff conditions are never observed to attach to the centerbody, suggesting that the local strain rate exceeds the extinction value. However, the flame can exist downstream. For example, many PIV images clearly show the flame interface right at the boundaries of high vorticity regions (this could also reflect the reduction in vorticity across the flame, however). Perhaps one of the reasons for the lack of a stable downstream configuration with low H_2 flames, in contrast to high H_2 flames, is the different flow field in the two situations because of the differing flame dilatation ratios.

It is well known that H_2 addition substantially increases the extinction strain rate of CH_4 flames. The situation is more complex when comparing near blowoff flames because the flame temperature and stoichiometry monotonically decreases with increasing H_2 levels – possibly the extinction strain rate of the high H_2 flames near blowoff is lower than the lower H_2 flames.

8. Concluding Remarks

Both expected and unexpected results were obtained from this study. First, the finding that blowoff limits were broadened with H_2 addition was expected and very consistent with other experience. However, the ability of the simple parameter, percentage of H_2, to correlate data over such a broad range of conditions and fuel compositions was surprising. Furthermore, the way in which the dynamics of the blowoff process changed in such a significant qualitative manner with H_2 levels was unexpected, but further demonstrated the rich character of the problem, involving complex interactions between kinetics and fluid mechanics.

Future studies are needed to further elucidate the subtle interactions between flame dilatation ratio and chemical kinetics on these blowoff dynamics. In addition, this study has highlighted the poor understanding of the dynamics of swirling flow dynamics, even for well stabilized flames. Continued study of swirling flow dynamics should be a key focus of the community, as these dynamics play such a prominent role in the observed flames.

9. REFERENCES

[1] Langston, Lee, "Gas Turbine Industry Overview", in 2001 IGTI Technology Report and Product Directory, ASME 2001.

[2]Correa, S.M., Power Generation and AeroPropulsion Gas Turbines: From Combustion Science to Combustion Technology, *Twenty Seventh Symposium (International) on Combustion*, The Combustion Institute, Pittsburgh, PA, 1998.

[3]Klimstra, Jacob, Interchangeability of Gaseous Fuels – The Importance of the Wobbe Index, *SAE paper # 861578*, 1986.

[4]King, Steve, The Impact of Natural Gas Composition on Fuel Metering and Engine Operating Characteristics, *SAE paper # 920593*, 1992.

[5]Durbin, M., Ballal, D., "Studies of Lean Blowout in a Step Swirl Combustor", *J. Engr. Gas Turbines and Power*, Vol. 118, 1996.

[6]Barlow, R.S., Fiechtner, G.J., Carter, C.D., Chen, J.Y., "Experiments on the Scalar Structure of Turbulent $CO/H_2/N2$ Jet Flames", *Comb. Flame*, Vol. 120, 2000.

[7]Correa, S.M., Gulati, A. "Non-premixed Turbulent CO/H2 flames at local extinction conditions", *Proc. Comb. Inst.* Vol. 22, 1988, pp. 599-606.

[8]Drake, M.C., "Stretched Laminar Flamelet Analysis of Turbulent H2 and $CO/H_2/N_2$ Diffusion Flames", *Proc. Comb. Inst*., Vol. 21, 1986, pp. 1579-1589.

[9]Correa, S.M., Gulati, A., Pope, S.B., "Assessment of a Partial Equilibrium/Monte Carlo Model for Turbulent Syngas Flames", *Comb. Flame*, Vol. 72, 1988, pp. 159-173.

[10] Masri, A. R., Dibble, R. W., "Spontaneous Raman Measurements in Turbulent CO/H2/N2 Flames Near Extinction", *Proc. Comb. Inst*. Vol. 22, 1988, pp. 607-618.

[11]Glassman, I., *Combustion*, Academic Press: New York, 1996.

[12] Sankaran, Ramanan, Im, Hong G, "Dynamic Flammability Limits of Methane/Air Premixed Flames with Mixture Composition Fluctuations", *Proc. Comb. Inst.*, Vol. 29, 2002, ,pp. 77-84

[13]Jackson, Gregory S., Sai, Roxanne, Plaia, Josephi M., Boggs, Christopher M., Kiger, Kenneth T., , "Influence of H_2 on the Response of Lean Premixed CH_4 Flames to High Strained Flows", *Comb. Flame*,, 132, 2003, pp. 503-511

[14]Vagelopoulos, C.M., Egolfopoulos, F.N., "Laminar Flame Speeds and Extinction Strains Rates of Mixtures of Carbon Monoxide with Hydrogen, Methane, and Air", *Proc. Comb. Inst.*, 1994, pp 1317

[15]Maloney, D., "The Simulation Validation Project at NETL", DOE Report, 2002.

[16]Schefer, R. W., "Hydrogen Enrichment for Improved Lean Flame Stability", *International Journal of Hydrogen Energy*, 28, 2003, pp. 1131-1141.

[17]Wicksall, D., Agrawal, A., "Effects of Fuel Composition on Flammability Limit of a Lean, Premixed Combustor", *ASME Paper #2001-GT-0007*

[18]Zukoski, E.E., "Afterburners", in Aerothermodynamics of Gas Turbine and Rocket Propulsion, G. Oates, Ed., 1997.

[19]Spaulding, D., "Some Fundamentals of Combustion", Ch. 5, Butterworth Press: London, 1955

[20]Longwell, J., Frost, E., Weiss, M., "Flame Stability in Bluff-Body Recirculation Zones", *Ind. Eng. Chem*., Vol. 45 (8), pp. 1629-1633.

[21]Plee, S.L, Mellor, A.M., "Characteristic Time Correlation for Lean Blowoff of Bluff Body Stabilized Flames", *Comb. Flame*,, 35, 1979, pp. 61-80.

[22]Radhakrishnan, K., Heywood, J., Tabaczynski, R., "Premixed Turbulent Flame Blowoff Velocity Correlation Based on Coherent Structures in Turbulent Flows", *Comb. Flame*,, 42, 1981, pp. 19-33.

[23] A.A. Putnam, R.A. Jensen, "Appplication of Dimensionless Numbers to Flash-back and Other Combustion Phenomena" , *Proc. Comb. Inst*., 3rd, 1949, ,pp 89-98

[24] S. Hoffmann, P. Habisreuther, B. Lenze, "Development and Assessment of Correlations for Predicting Stability Limits of Swirling Flames", *Chemical Engineering and Processing*, 33 (1994), pp 393-400

[25]Kido, Hiroyuki, Nakahara, Masaya, Nakashima, Kenshiro, Hashimoto, Jun, "Influence of local flame displacement velocity on turbulent burning velocity**",** *Proc. Comb. Inst*., Vol. 29, 2002, pp. 1855-1861

[26]Paul Clavin, "Dynamic Behavior of Premixed Flame Fronts in Laminar and Turbulent Flows", *Prog. Energy Comb. Sci.*,Vol.11,1985,pp.1-59

[27]Chen, Jacqueline H., Im, Hong G., "Stretch Effects on the Burning Velocity of Turbulent Premixed Hydrogen/Air Flames**",** *Proc. Comb. Inst*., Vol. 28, 2000, ,pp 211-218

[28]Lieuwen, T., Torres, H., Johnson, C., Daniel, B.R., Zinn, B.T., "A Mechanism for Combustion Instabilities in Lean Premixed Gas Turbine Combustors", *Journal of Engineering for Gas Turbines and Power*, 123(1), 2001, pp. 182-190

[29]J. Natarajan, S. Nandula, T. Lieuwen and J. Seitzman, "Laminar Flame Speeds of Synthetic Gas Fuel Mixtures", *ASME Paper # GT2005-68917.*

[30] Kee RJ, Warnatz J, Miller Ja. "A FORTRAN Computer Code Package for the Evaluation of Gas-Phase Viscosities, Conductivities, and Diffusion Coefficients." *Technical Report SAND89-8009*, Sandia National laboratories, 1983.

[31] G.Joulin, T.Mitani, " Linear Stability Analysis of Two-Reactant Flame", *Comb. Flame*,40,1981,pp.235-246

[32] Masaya Nakahara, Hiroyuki Kido, " A Study of the Premixed Turbulent Combustion Mechanism Taking the Preferential Diffusion Effect into Consideration", *Memoirs of the Faculty of Engineering*, Kyushu Univ., 58, 1998

[33] Kido, Hiroyuki, Nakahara, Masaya, "A Model of Turbulent Burning Velocity Taking the Preferential Diffusion Effect into Consideration," *JSME International Journal*, Vol. 41, No.3, 1998, pp. 666-673

[34] Nair, S., Lieuwen, T., "Acoustic Detection of Blowout in Premixed Flames" ", *J. Propulsion and Power*, Vol 21, No. 1, P32-39

[35] Nair, S., Rajaram, R., Meyers, A., Lieuwen, T., Tozzi, L., Beson, K., " Acoustic and Ion Sensing of Lean Blowout in an Aircraft Combustor Simulator", *43rd AIAA Meeting Papers*, 2005, p 3627-3634

[36] Muruganandam, T., Kim,B., Olsen, R., Patel, M., Romig, B., and Seitzman, J., "Chemiluminescence based sensors for Turbine Engines", *AIAA-2003-4490*, 2003

[37] Muruganandam, T.M., Nair, S., Scarborough, D., Neumeier, Y., Jagoda, J, Lieuwen, T., Seitzman, J., Zinn, B., " Active Control of Lean blowout for Turbine Engine Combustors", *J. Propulsion and Power*, Vol. 21, No. 5, pp. 807-814.

[38] Lilley, D. G., " Swirl Flows in Combustion: a Review", *AIAA J.* vol 15, No. 8, 1977

[39] Raffel, M., Willert, C. and Kompenhans, J. "Particle image Velocimetry: A Practical Guide", Springer, 1998 (3rd edition).

[40] Yang, V., Huang, Y., "Bifurcation of Flame Structure in a Lean-Premixed Swirl-Stabilized Combustor: Transition from Stable to Unstable Flame", *Comb. Flame*, 136, 2004, pp. 383-389

[41] Bradley, D., Gaskell, P. H., Gu, X. J., Lawes, M., Scott, M. J., "Premixed Turbulent Flame Instability and NO Formation in a Lean-Burn Swirl Burner", *Comb. Flame*, 115, 1998, pp. 515-538

[42] Huang, Ying, Yang, Vigor, " Swirling Flow Structures and Flame Characteristics in a Lean –Premixed Combustor", AIAA-2004-0978

[43] Ji, Jun, Gore P. Jay, " Flow Structure in lean Premixed Swirling Combustion", *Proc. Comb. Inst*., Vol. 29, 2002, pp. 861-867

FINAL REPORT

CORRELATION OF IGNITION DELAY WITH NATURAL GAS AND IGCC TYPE FUELS

07/01/03 – 08/30/06

Scott Samuelsen, Principal Investigator

Vince McDonell, Co-Investigator

Mayumi Greene, Graduate Student Researcher

David Beerer, Undergraduate Student Researcher

September 2006

DOE Award Number: DE-FC26-02NT41431
UTSR Project Number: 03-01-SR112

University of California, Irvine
Irvine, CA 92697-3550
www.ucicl.uci.edu

DISCLAIMER

ABSTRACT

Autoignition if of concern for advanced lean premixed combustion systems found on stationary gas turbines. The desire to reach higher efficiencies while at the same time operating on fuels containing significant quantities of hydrogen leads to a question of whether lean premixed strategies are viable for achieving low emissions. In order to address this question, the project described in this report was carried out. Given the increased interest and viability of IGCC as a strategy to meeting future energy needs in the United States, the emphasis of the project was directed at hydrogen containing fuels that would be used as a result of coal gasification. Numerical studies were carried out using a variety of recently developed detailed kinetic mechanisms for hydrogen or hydrogen/carbon monoxide mixtures. Two experimental studies were also identified and included in the analysis. The numerical predictions of ignition delay time were 2-3 order of magitude longer than the experimental results. A flow reactor was used to measure ignition delay times for both hydrogen and hydrogen/carbon monoxide mixtures at moderate pressures and temperatures from 850 to 1000F. The results obtained, when scaled for pressure, are virtually identical to the previous experimental results. As a result, (1) correlations developed in the previous studies have been reaffirmed for the lower temperature region for syngas type fuels and (2) the data suggest that some key deficiencies exist in all of the current kinetic mechanisms when applied at temperatures below 1000F.

TABLE OF CONTENTS

LIST OF FIGURES

LIST OF TABLES

1 EXECUTIVE SUMMARY

In lean premixed combustion, fuel is typically injected upstream of the desired reaction zone in an effort to thoroughly mix it with air prior to combustion. This has been commonly applied for natural gas fuel with good success. Given the increased interest and viability of IGCC as a strategy to meeting future energy needs in the United States, the emphasis of the project was directed at hydrogen containing fuels that would be used as a result of coal gasification. Little or no work was conducted with natural gas, although previous work on the same experiement established that autoignition of natural gas type fuels is not a major concern for typical gas turbine inlet temperatures. This observation is consistent with the large numbers of lean premixed natural gas fired turbines operating in the field today. However, the question of whether autoigntion is a concern when considering lean premixed combustion for IGCC type fuels has not been fully addressed, which is the motivation for this project.

The current project has resulted in the development of a continuous flow reactor that can be used to assess ignition delay time for fuels and fuel mixtures of interest. The facility developed is designed to reach inlet temperatures approaching 1400 deg F at pressures up to 18 atm. A schematic of the facility is shown in Figures ES-1. While the facility can accommodate a wide variety of fuels, the focus of the current study is on IGCC type fuels.

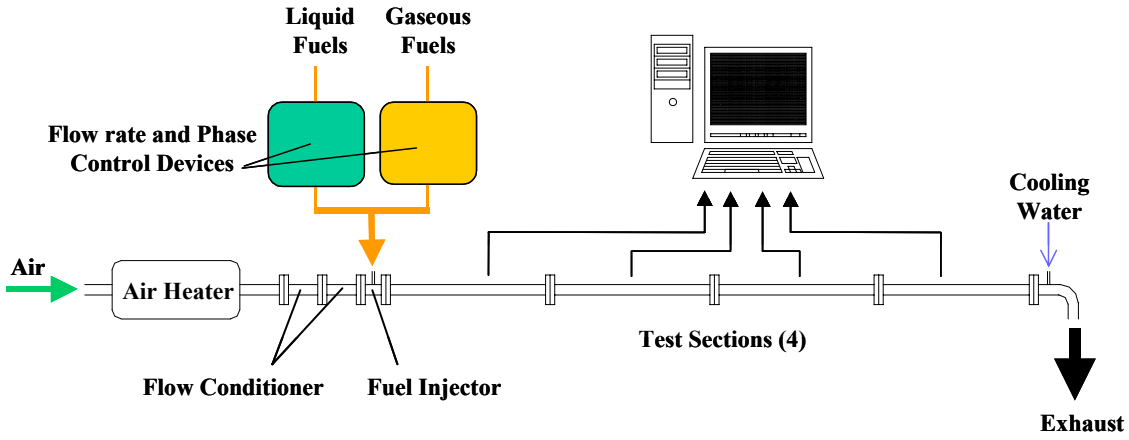

Figure ES-1. Facility.

As a first step in evaluating ignition delay times, existing results were compiled. The results include both experimental and numerical results. These results are shown in Figure ES-2. The results illustrate that all the existing kinetic mechanisms provide similar results for predicting ignition delay. However, none of the predictions are able to reproduce the measured ignition delay times in the one experimental dataset available. Since the experimental ignition delay times are on the same order as the residence times found in gas turbine premixers, concerns relative to applicability of lean premixed strategies for achieving low emissions when using syngas in gas turbines remain. As a result, it is clear that determining whether the calculated or measured values are accurate is a high priority. As discussed in the report, similar observations are made for pure hydrogen.

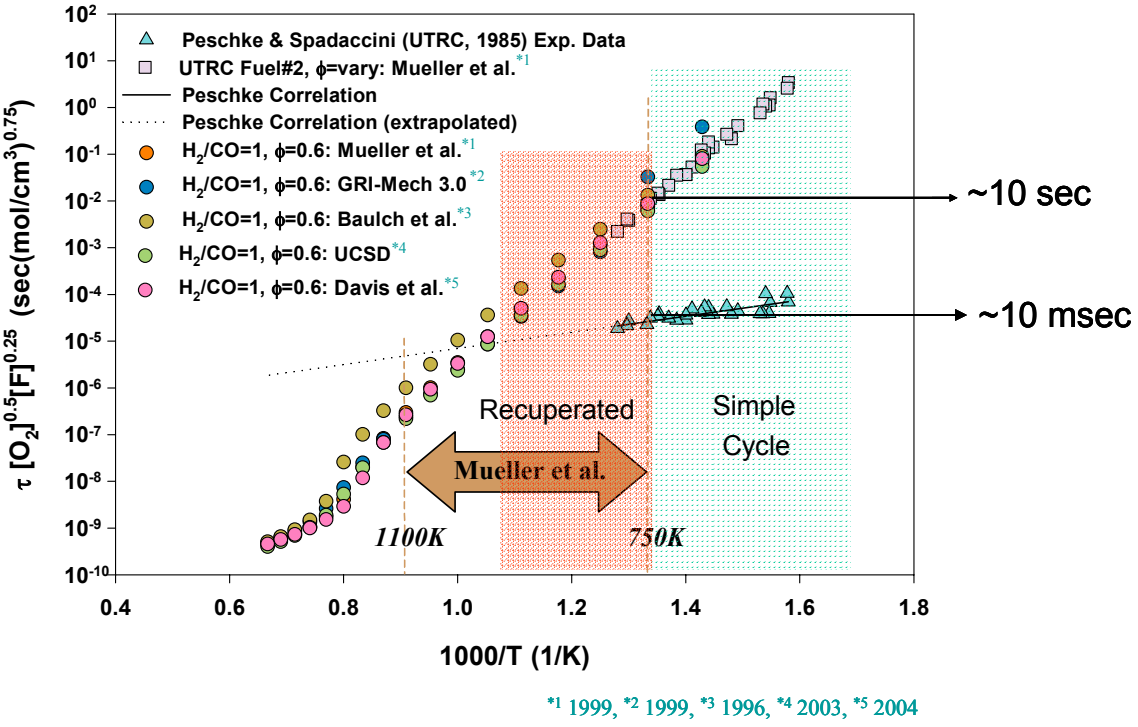

Figure ES-2. Comparison of Existing Results for IGCC type fuel.

Another objective of the current study was to establish empirical design tools for ignition delay for IGCC type fuels. As part of this, it was desired to capture fuel composition effects. However, after an assessment of the IGCC options that would likely be deployed in the United States, the variation in fuel composition was constrained to the ranges shown in Table ES-1.

Table ES-1. Range of IGCC Compositions found for oxygen blown gasifiers with coal or pet coke feedstock.

Mole Fraction / Constituent	Min	Max
H2	0.15	0.20
CO	0.20	0.25
CO2	0.05	0.10
N2	0.50	
H2/CO	0.5	1.0

A study was carried out to assess how much variation in ignition delay time would be observed with the range of conditions shown. The study suggested that for the extremes in composition, the ignition delay time would vary by only 5%. Even larger variations in CO concentrations (0 to 50%) were observed to result in only 10-15% differences in ignition delay time. As a result, the ability to physically measure the effect of CO/H2 composition was felt to be limited. Thus the study was focused on select compositions rather than carrying out tests for a large number of compositions because such as study would not have resulted in statistically significant results.

The results obtained in the current study and another previously unpublished study are shown in Figure ES-3 and corroborate the previous experimental results. As a result, the predicted ignition delay times are much longer than the actual delay time at gas turbine premixer inlet temperatures. The actual times observed range from 10-100 msec at the conditions studied (880-950F). These results suggest that premixing is viable for most simple cycle moderate pressure ratio engines, but that the margin available in residence time needs to be carefully considered. For recuperated cycles, the igntion delay times would be on the same order of the premixing time (1-10 ms) and therefore additional care must be taken if such a cycle were to be considered for use with hydrogen containing fuels.

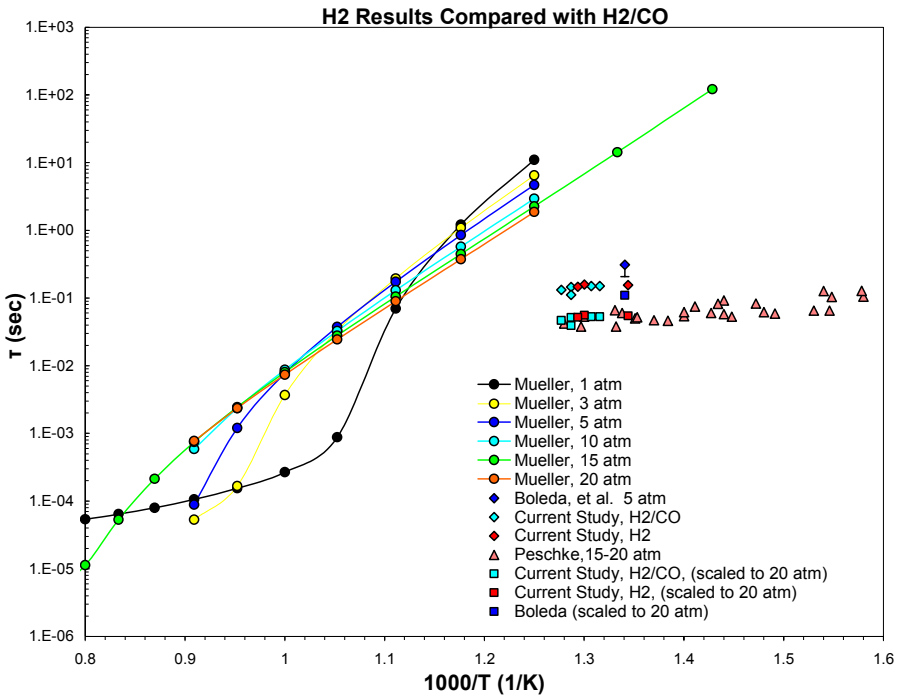

Figure ES-3. Comparison of Previous and Current Ignition Delay Results.

As a result of the current study, the following expression (from Peschke and Spadacinni) has been verified for estimating the ignition delay time for IGCC type fuels:

$$\tau \left[O_2\right]^{0.50}\left[F\right]^{0.25} = 1.29\times10^{-7}\exp\left(\frac{3985}{T}\right) \qquad \text{Equation ES-1}$$

Where

τ is an ignition delay time (sec),

$[O_2]$, $[H_2]$ and [F] are the molar concentration (moles/cm^3) of oxygen and fuel, T is a temperature (K).

As shown in Figure ES-3, the differences between H2/CO and pure H2 are not statistically significant. As a result, the following expression (from Peschke and Spadacinni) can be applied considering only the hydrogen concentration which may simplify its application for engineering purpose.

$$\tau \left[O_2\right]^{0.50}\left[H_2\right]^{0.25} = 1.02\times10^{-7}\exp\left(\frac{3985}{T}\right) \qquad \text{Equation ES-2}$$

2 PROJECT DESCRIPTION

2.1 Gas Turbine Research Need

The drive to achieve low emissions with the concomitant requirement to handle fuels of varying composition is requiring more consideration for issues associated with ignition delay. Of particular interest are fuels found in IGCC applications. In lean premixed combustion, fuel is typically injected upstream of the desired reaction zone in an effort to thoroughly mix it with air prior to combustion as illustrated in Figure 1. If this mixing can be accomplished, the equivalence ratio at which combustion occurs can be carefully controlled and set such that the resulting reaction temperatures are below the threshold at which the NOx formation rate rapidly increases (around 1850 K). Since this approach relies upon sufficient time to accomplish mixing, it also gives rise to the possibility of autoignition occurring within the premixing region which would be destructive to the hardware and/or will lead to high pollutant emissions. As a result, the question of whether or not ignition will occur in the premixing region for fuels and conditions of interest for gas turbine applications must be addressed.

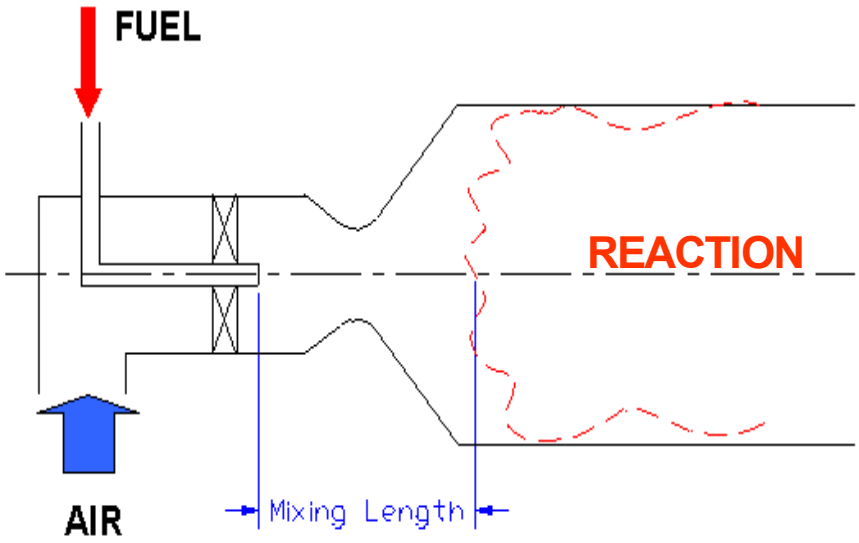

Figure 1. Basic Approach for Lean Premixed Combustion.

Fuels of interest for gas turbine applications include Natural Gas (NG) and the range of specific hydrocarbons present within NG, Liquefied Natural Gas (LNG), and fuels containing hydrogen and/or carbon monoxide. Synthetic gas (syngas) produced by the Integrated Gasification Combined Cycle (IGCC) technology, which contains H_2 and CO as main constituents, is emphasized in the work done in this project.

2.1.1 Lean Premixed Combustion

Lean premixed combustion is a proven strategy to reduce pollutant emissions. However, the reactive mixture in the premixed combustion system can spontaneously ignite without external ignition sources. This phenomenon, often called autoignition, is a critical safety and reliability issue for advanced low-emission gas turbines.

An example of a global expression for ignition delay (autoignition time) by Lefebvre et al. [**1**] is shown in Equation 1. Incorporating the inversely proportional relationship between the ignition delay and the global reaction rate with the Arrehenius expression of the reaction rate constant, Lefebvre et al. proposed that the ignition delay time τ at the temperature T and pressure P could be expressed as:

$$\tau \propto \frac{1}{A} \exp\left(\frac{E}{R_u T}\right) [O_2]^{-j} \, [Fuel]^{-m} \; P^{-n} \; T^{-0.5}$$

Equation 1

Where A is Arrehenius constant, E is the global activation energy, and R_u is the universal gas constant. Note that concentrations of oxygen and fuel are on volumetric bases to explicitly indicate the pressure effect.

Equation 1 indicates that ignition delay depends on operating conditions such as pressure, temperature, and equivalence ratio. The advanced gas turbines must be designed based on the autoignition characteristics relevant to their operating conditions.

In addition to the factors stated above, fuel composition is also recognized to have an impact on autoignition behavior. For example, Spadaccini and Colket [**2**] demonstrated that the presence of higher hydrocarbons in NG, a typical fuel of stationary gas turbines, decreases the ignition delay times comparing to that of pure methane. The proposed ignition delay, t is expressed by:

$$t = 1.77 \times 10^{-14} \exp(18693/T)\left[O_2\right]^{-1.05}\left[CH_4\right]^{0.66}\left[HC\right]^{-0.39}$$

Equation 2

where [HC] = total molar concentration of non-methane hydrocarbons.

Although the resulting expression (Equation 2) is significant in terms of accounting for the effect of non-methane hydrocarbons on ignition delay, data at lower-temperature and leaner condition are in need for this higher hydrocarbon effect to be fully applicable to the lean premixed gas turbines [3]. In general, studies of the effect of fuel composition are significantly lacking despite the knowledge that different fuel constituents play a role in ignition delay [4].

2.1.2 Fuel Flexibility

The use of alternative fuels has increasing interest in the energy industry and is being embraced by a society, which continues to have increased recognition of a need for clean energy and relieving the concentrated dependency on petroleum fuels. In the past two decades, stationary gas turbines have achieved significant emissions reductions especially when operated on NG. In light of this focus, it is inevitable that most of the previous autoignition studies for the gas turbine applications focused on methane, the main constituent of NG. In order to meet the increasing needs for alternative fuels, autoignition studies of the relevant fuels at gas turbine conditions are necessary to support the development of the fuel flexible gas turbines technology. In the current project, fuel gas as associated with IGCC plants is of particular interest. As seen in NG, IGCC syngas also varies widely in its compositions. Importance of fuel composition effect on ignition delay must be highlighted here again. This project is directed at the autoignition characteristics of IGCC syngas at gas turbine conditions. Currently, the work by Peschke & Spadaccini [**5**] is the only known experimental work for IGCC type fuels. As a result, additional data on ignition delay characteristics are needed.

2.2 Project Approach

The overall project consisted of four Tasks:

Task 1: Facility Modifications. The existing facility was upgraded to simulate various operating conditions (higher operating temperature and pressure) and fuel compositions and to also improve the detection schemes for ignition delay.

Task 2: Acquire Results. In Task 2, results were obtained both numerically and experimentally. To support the numerical results, available kinetic mechanisms for IGCC type fuels (i.e., H_2 and/or CO containing fuels) were collected and reviewed. The numerical and experimental results are also compared.

Task 3: Analyses. The results from Task 2 were then analyzed to explain the observations made.

Task 4: Correlation Development. Finally, recommendations regarding the appropriate empirical correlations are made as part of Task 4.

A summary of the experimental and analytical approaches is provided in sections **2.2.1** and Section **2.2.2**, respectively.

2.2.1 Experimental Approach

An existing continuous flow reactor is used to measure the ignition delay times for IGCC type fuels of various compositions and conditions. Under Task 1, facility upgrades were pursued to increase operating temperature from 922 K (1200 °F) to 1033 K (1400 °F) and pressure from 8 atm (103 psig) to 18 atm (250 psig) to provide a wider range of operating conditions. In order to study the fuel composition effect, various compositions of NG and IGCC syngas will be simulated utilizing the fuel composition control system, which is also being modified. Fuel, comprised of controlled mixtures of pure gases selected to simulate the compositions of interest, are injected into the separately preheated air stream. A carefully designed injector/venturi mixer system is used to ensure rapid and complete mixing of fuel and air with a few duct diameters. The subsequent mixture then flows through the reactor and, if the conditions are suitable, ignites. Operating temperatures are controlled and monitored throughout the flow path of the combustible fuel/air mixture. Autoignition is monitored using both temperature and light emission from the reaction.

2.2.2 Analytical Approach

A chemical kinetics codes collection, CHEMKIN, is utilized to provide guidance to the experiments and to also provide a basis for evaluation of existing analysis tools for prediction

auto-ignition. In the CHEMKIN collection, the AURORA application represents a well-mixed reactor model for both transient and steady state systems [**8**] and thus appropriate for the ignition delay analysis. Chemical reactions that contribute to the ignition delay can also be identified using the sensitivity analysis option in the AURORA application.

3 EXPERIMENTAL METHODS

3.1 Overview

An existing continuous flow reactor (Figure 2**)** was utilized for the experimental work [4]. The schematic of the experimental rig is shown in Figure 3. Under the current project, facility upgrades were undertaken. The upgrades were designed to enhance the ability of the facility to reach operating conditions outside of range found in other ignition delay projects using flow reactors and shock tubes. The upgrades were intended to allow maximum operating temperature and pressure to be increased from 922 K (1200°F) to ~1033K (1400°F) and 8 atm (103 psig) to 18 atm (250 psig), respectively.

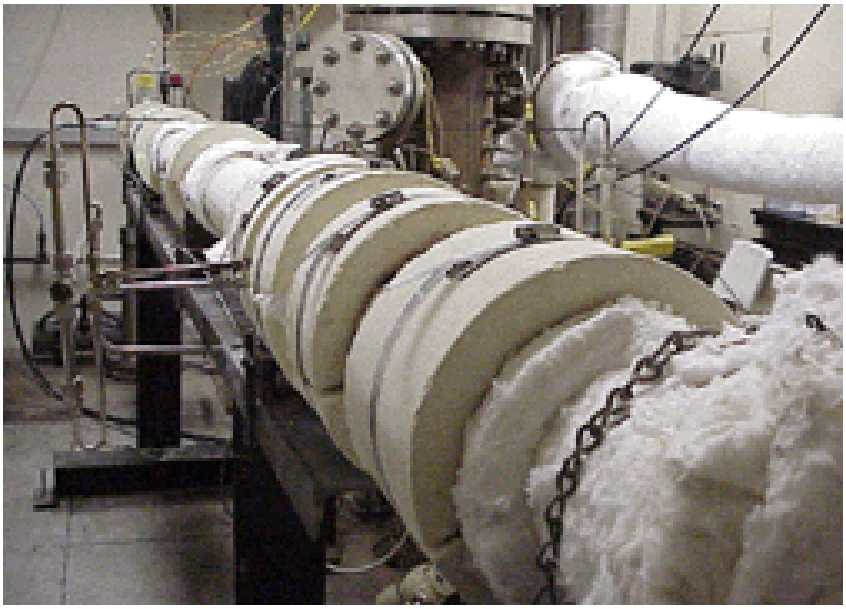

Figure 2: UCICL Continuous Flow Reactor with Clam Shell Heaters

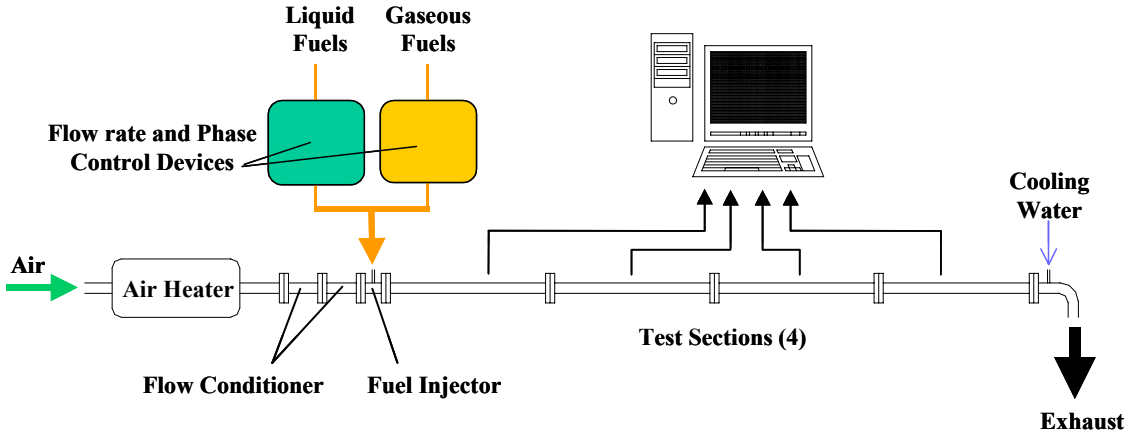

Figure 3: Schematic of the Experimental Rig

Because autoignition is a phenomenon that strongly depends on temperature, it is critical to have control of operating temperatures in any experiment carried out. As a result, a strategy involving a combination of active (clamshell type tube furnace) and passive (insulation) means to compensate the heat loss over the flow reactor length. For better handling and consistent application of insulation materials, 50.8 mm (2.0 in.) thick insulation blankets (Figure 4) were developed for this project. The insulation material is Aluminum Silica, synthetic fiber with the heat transfer coefficient of 5.68 W/m^2-K (1 BTU/hr-ft^2-^{o}F) per 25.4 mm (1.0 in.) thickness.

Figure 4: Insulation Blankets

Fuel is metered, optionally preheated, injected, and then rapidly mixed with the air stream using a venturi injector (Figure 5 (a)) designed under the previous project [4]. The injector is mounted onto the 600 lb 2" (nominal) flange. The best design in terms of mixing performance with no flow separation turned out to be a design with a central injector. The injection module

has two sets of fuel injection ports: one central injection port, just upstream of the venturi, and a set of eight side injection ports in the contraction part of the venturi. The diameter of each fuel injection port is 1/32 inch. A optimization of the split between side and center injection resulted in mixing profiles with less than 5% variation over the plane by the exit of the venturi expansion section.

a) Cross Section

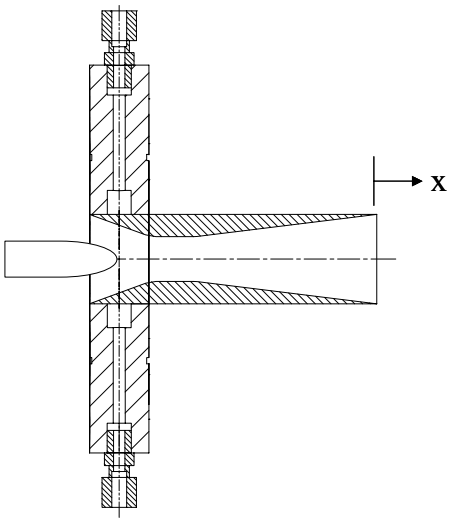

b) Photograph

Figure 5: Venturi Injector.

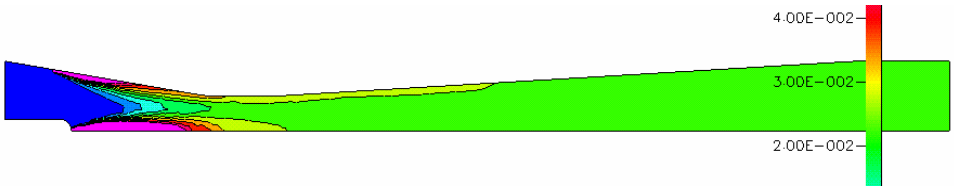

Figure 6. CFD Analyses of Fuel Mixing.

The 38.1 mm i.d. flow reactor is highly modular and features different sections shown in Figure 7 that serve various purposes. Three Test Sections C (0.91m (36") long each, plain duct) and a Test Section B (0.86m (34") long. with sensor ports) are illustrated. that is shown in Figure 5 (b). The inside diameter of the experimental rig is 38.1 mm (1.5"). Detailed descriptions of the experimental rig, hardware components, and heat loss compensation were provided in the final report of previous ignition delay study at UCICL [4].

a) Air Plenum

b) Flow Conditioner (2 pieces)

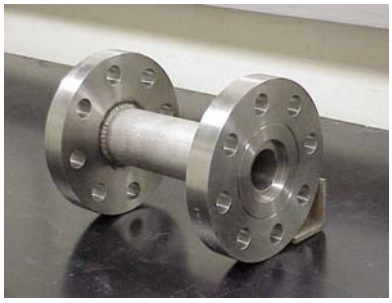

c) Fuel Injector (one example)

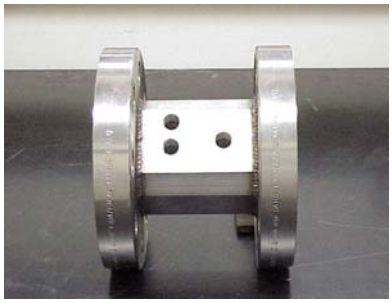

d) Test Section C (3 pieces)

e) Test Section B

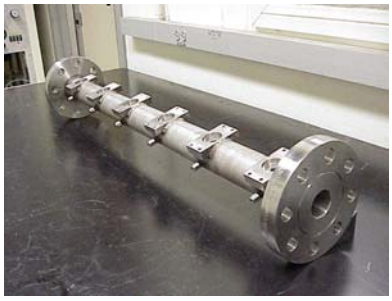

f) Water-Cooling Section

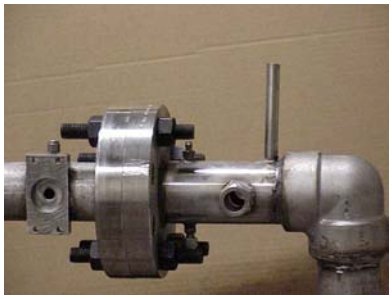

Figure 7. Test Rig Modules.

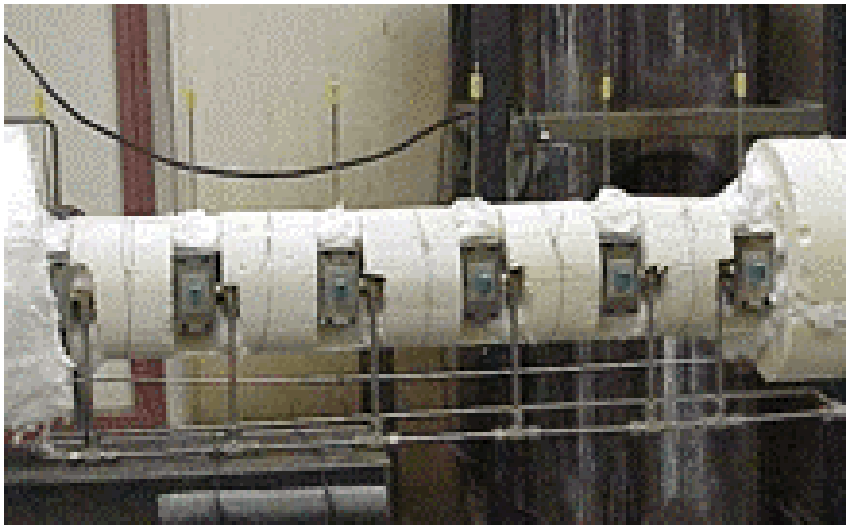

Figure 8. Insulated and Instrumented Test Section B.

3.2 Estimated Residence Time

In order to detect autoignition in the flow reactor, the residence time of a premixed combustible fuel/air mixture must be longer than its ignition delay time. Test Section B (Figure 5 (b)) is typically located at the most downstream of the four test sections. Because photodiodes

are mounted to the Test Section B, the clamshell heaters can be installed only to cover the non-sensor sections. As a result, a temperature drop in this sensor test section cannot be avoided despite the heat loss compensation efforts with insulation material. Thus, the valid flow reactor length was defined as the length from the venturi exit to the location of first sensor port in the Test Section B and calculated to be 2.73 m (107.42"). Locations of the components were summarized in Table 1.

Table 1: Actual Length of the Test Section

Components		Local Coordinates m (inch)	Components		Local Coordinates m (inch)	Effective Length m (inch)	X Coordinates m (inch)
Venturi Injector	Flange/Duct Inlet	0.00 (0.00)					
	Injection Face	0.01 (0.50)					
	Flange/Duct Exit	0.03 (1.00)					
	---	--- ---	**Test Section C** *[1]	Flange/Duct Inlet	0.00 (0.00)		
	Venturi Exit	0.12 (4.83)		Venturi Exit	0.10 (3.83)	--- ---	0.00 (0.00)
				Flange/Duct Exit	0.91 (36.00)	0.82 (32.17)	0.82 (32.17)
			Test Section C *[1]	Flange/Duct Inlet	0.00 (0.00)		
				Flange/Duct Exit	0.91 (36.00)	0.91 (36.00)	1.73 (68.17)
			Test Section C *[1]	Flange/Duct Inlet	0.00 (0.00)		
				Flange/Duct Exit	0.91 (36.00)	0.91 (36.00)	2.65 (104.17)
			Test Section B	Flange/Duct Inlet	0.00 (0.00)		
				Sensor Port 1	0.08 (3.25)	0.08 (3.25)	**2.73 (107.42)**
				Sensor Port 2	0.22 (8.75)		
				Sensor Port 3	0.36 (14.25)		
				Sensor Port 4	0.50 (19.75)		
				Sensor Port 5	0.64 (25.25)		
				Sensor Port 6	0.78 (30.75)		
				Flange/Duct Exit	0.86 (34.00)		

*[1] *Covered by the clam shell heater*

For an initial evaluation, residence times were calculated for air only at various operating conditions. Sample estimates at 21.4 atm (300 psig) are shown in Table 2.

Table 2: Residence Time (sec) of Air at P=21.4 atm (300 psig) for Various Temperatures

Vdot_air	Residence Time (sec)							
scfm	T=700K (800F)	T=755K (900F)	T=811K (1000F)	T=866K (1100F)	T=922K (1200F)	T=978K (1300F)	T=1033K (1400F)	T=1089K (1500F)
10	5.94	5.50	5.12	4.79	4.50	4.25	4.02	3.82
25	2.37	2.20	2.05	1.92	1.80	1.70	1.61	1.53
50	1.19	1.10	1.02	0.96	0.90	0.85	0.80	0.76
75	0.79	0.73	0.68	0.64	0.60	0.57	0.54	0.51
100	0.59	0.55	0.51	0.48	0.45	0.42	0.40	0.38
150	0.40	0.37	0.34	0.32	0.30	0.28	0.27	0.25

3.3 Fuel Handling

3.3.1 Fuel Preparation

The range of IGCC syngas composition produced at various facilities worldwide is shown in Table 3 (data source: [6]). IGCC syngas varies greatly in its composition due to differences in feedstocks (coal, petroleum coke, heavy oil, etc) and types of gasifiers (oxygen-blown or air-blown). In the current project, emphasis is placed on oxygen-blown gasification with coal and/or petroleum coke (Table 4). This reflects current U.S. implementation of IGCC.

Table 3: Range of IGCC Syngas Composition (Source: [6])

Vol% / Constituent	Min	Max	*Ave*
H2	8.6	61.9	*31*
CO	22.3	55.4	*37.17*
CH4	0	8.2	*2.16*
CO2	1.6	30	*11.96*
N2+AR	0.2	49.3	*12.21*
H2O	0.1	39.8	*7.83*
H2/CO	0.33	2.36	*0.86*

Table 4: Selected Facilities (Source: [6] and [7])

Facility / Constituent	Wabash River	Tampa	El Dorado	Motiva Delaware
H2	34.4	37.2	35.4	32
CO	45.3	46.6	45.0	49.5
CO2	15.8	13.3	17.1	15.8
H2/CO	0.76	0.80	0.79	0.65
Fuel	Coal / PC	Coal	PC*	PC
Technology**	CoP	CVX	CVX	CVX
Diluent	steam	N2	N2/steam	H2O/N

** PC = Petroleum Coke*
*** CoP = Conoco Phillips, CVX = Chevron Texaco*

Note that the data of the Wabash-River plant in Table 4, taken from [**7**], is for coal feedstaock. As shown, H_2, CO, and CO_2 are the three main constituents of the selected IGCC syngas and occupy approximately 96-98 % by volume. Although diluent type/amount differs among the facilities, nitrogen was selected as a baseline diluent for the current project at a diluent to fuel ratio of unity (D/F = 1). Table 5 shows the design range of the IGCC fuel composition based on the actual range (Table 4**)** and the constraint of D/F = 1. The amount and types of diluents will be continuously reviewed and adjusted.

Table 5: Fuel Composition for Mixture Modeling

Mole Fraction / Constituent	Min	Max
H2	0.15	0.20
CO	0.20	0.25
CO2	0.05	0.10
N2	0.50	
H2/CO	0.5	1.0

Given the variation exhibited in Table 5, it was decided to carry out a rough assessment of how sensitive the ignition delay time would be to fuel composition over these ranges. This exercise was, in effect, a sensitivity analysis to assess the viability of detecting the influence of specific fuel components. The rationale for this was, in part, due to the experience with the fuel blending system. Large numbers of fuel compositions, combined with the time required for the composition to stabilize, required fairly large quantities of gases. Due to limited budget for supplies of this nature, this shakedown evaluation indicated a need to be fairly efficient with gas usage. CO in particular is relatively expensive. Thusif it could be established, for example, that CO has a relatively small effect on ignition delay time, the quantity needed could be minimized.

Figure 9 shows examples of the ignition delay characteristics determined via a numerical experiment conducted following a statistical design for mixtures within the fuel composition range shown in Table 5. The ignition delay times were simulated using CHEMKIN. The results are shown here for D/F=1, ϕ = 0.5, P = 21 atm (300 psig) for two initial temperatures, (a) T = 850 K (1070 ^{o}F) and (b) 1000 K (1340 ^{o}F). The difference in operating temperatures results in different trends in terms of the role of fuel composition as well as the overall magnitude of the

ignition delay times. At 850 K (1070 ^{o}F, Figure 9 (a)), the contours are nearly parallel to the bottom side of the outer triangle, where the amount of H_2 is the lowest (= 0.15). In other words, H_2 concentration is the dominant factor determining autoignition at this particular condition with low to moderate impacts of CO and CO_2. Figure 9 (b), on the other hand, shows results at a higher temperature (1000K or 1340 ^{o}F). The contours of ignition delay time are now nearly perpendicular to the right side of the outer triangle (at the minimum CO concentration of 0.20). In this higher temperature case, the ignition delay depends upon all three components. Relating this result to chemical kinetics will be a next step to understand the effect of compositions on autoignition times.

a) T = 850 K

b) T = 1000 K

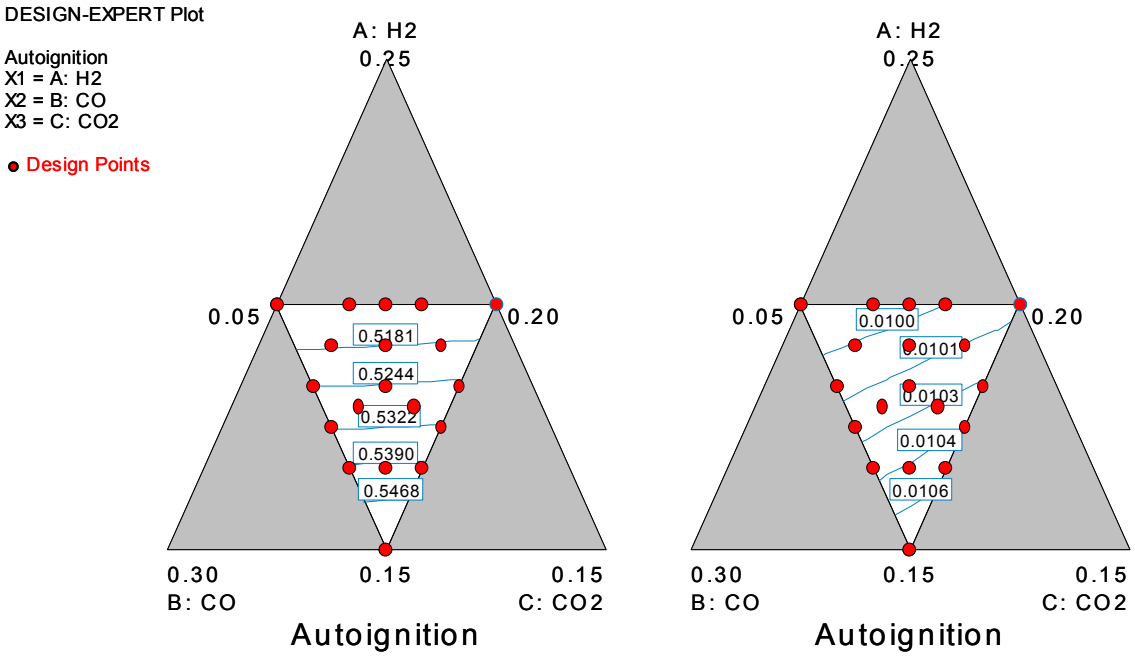

Figure 9: Mixture Modeling at ϕ = 0.5, P = 21atm: (a) T = 850 K and (b) T = 1000 K

The key point from the results shown in Figure 9 is that the fuel composition has a relatively small effect on ignition delay time. For example, the extremes in fuel composition that might be studied showed a change in ignition delay time of 5-10% at temperatures of 850 or 1000K. However, the ignition delay time due to this temperature difference was a factor of 50. Given the uncertainty in resolving delay times and temperatures in the flow reactor, it was thus concluded that conducting tests with widely varying fuel compositions may not be an effective

use of resources. As a result, it was decided to use bottled gases of fixed blends rather than trying to blend pure gases. 5 different gas blends were considered along with natural gas as as baseline. The compositions are summarized in Table 6.

Table 6. Fuel Compositions Studied

Fuel Blend	CH4	CO2	H2	CO	Comment
1	100% (Natural Gas)				Baseline
2	0	10.3	38.6	51.1	Peschke & Spadaccini baseline fuel
3	0	10	45	45	
4	0	10	30	60	
5	0	0	50	50	
6	0	0	100	0	Pure H_2

3.3.2 Fuel Injection

The fuel is injected through a venturi at the beginning of the test section. Fuel is supplied by tanks of compressed Hydrogen or H2/CO mix which are located in the control room away from the experimental test rig. The fuel flow is controlled and metered by needle valves and coriolis effect based mass flow meter (Micromotions). The mass flow is controlled by two knob valves placed in parallel which allows wide turndown and coarse and fine control.

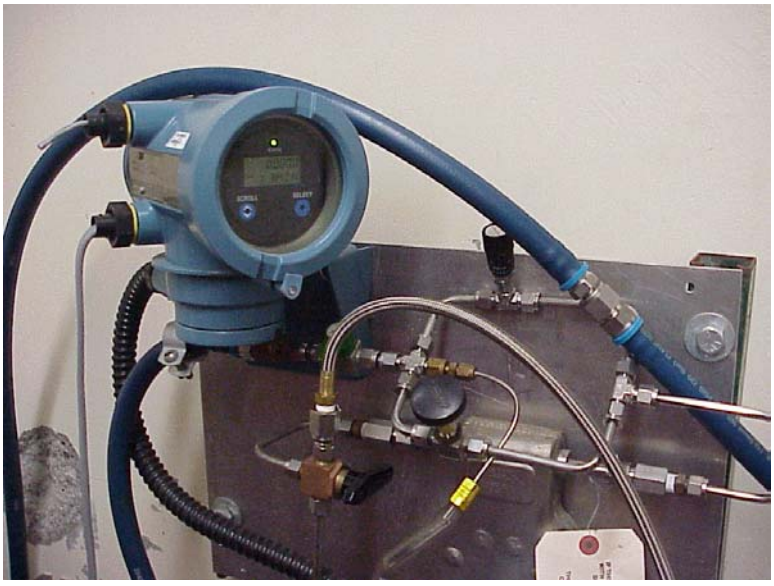

Figure 10. Fuel Flow Control and Metering.

The fuel is then conveyed to the experiment through a line that is connected to a four way solenoid valve as shown in Figure 11. This four way valve is used to help establish thermal and flow equilibrium in the system while allowing fuel to bypass the test rig when desired. To accomplish this, in addition to fuel, a nitrogen line is brought to the solenoid as well as fuel. The two in-flow ports at the four-way solenoid valve are for the fuel and nitrogen. The two out-flow ports of the valve lead to the venturi injector at the beginning of the test section, and the other to the rig after the test section and water dump.

a) 4-way solenoid

b) Downstream fuel/N2 dump

Figure 11. Four way valve setup for fuel control.

The default position for this set up is for the nitrogen to flow into the solenoid valve and be directed to the injectors, and the fuel to be injected after the dump. In this condition, there should not be a reaction. When the valve is turned (by actuating a "test start" control button), the fuel and nitrogen paths are switched allowing fuel to be injected into the test section. When the button is released, the valve switches back to its default position, purging the fuel line with nitrogen and mitigating any reactions.

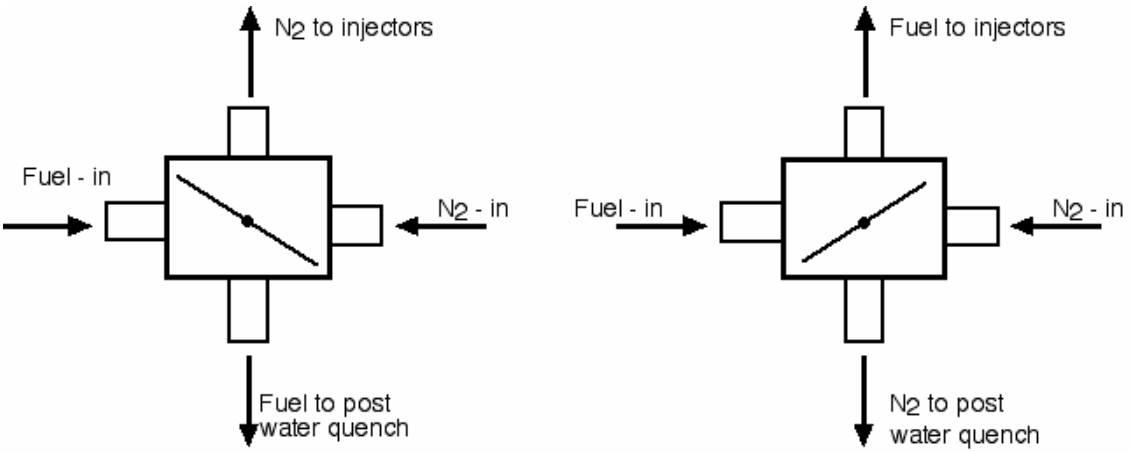

Figure 12. Operational Modes of Four-Way Fuel Control Switch.

3.3.3 Fuel/Air Mixture Residence Time

In order to determine the residence times in the fuel/air mixture inside the flow reactor, several approaches were considered. The first was that from earlier flow reactor work [1, 5]. In this approach, the condition were adjusted such that ignition was observed at a fixed downstream distance. The volumetric flow of air and fuel can then be used in conjunction with the flow reactor cross sectional area to determine a velocity. Hence the fixed downstream distance divided by the bulk velocity gives the residence time. This requires an accurate determination of the mixture temperature and pressure within the flow reactor in order to accurately determine the actual volumetric flow. This is frought with numerous uncertainties.

Alternatively, the residence time can be physically measured using fast time response sensors. In this approach, signals indicating “fuel flow on” and “ignition” can be used to measure the actual ignition delay time. In the current study, convenient signals are available from the fuel control switch and the optical sensors located in the test section. However, the residence time of the fuel within the fuel manifold between the four way valve and the fuel injectors must be accounted for.

This was accomplished by a study carried out to determine the volume in the manifold. Because the manifold is made of rigid pipe (stainless steel tubing and Swagelok), it is a constant volume (fixed) line. The Micromotions meter gives the mass flow rate of the fuel. Knowing the temperature and pressure of the fuel, the density is determined and from that the volumetric flow rate through the line. In this case, room temperature fuel was used. The pressure within the

manifold was determined using a pressure transducer. Knowing the volume of the fuel line allows the delay time from the 4-way valve to the point of fuel injection to be determined.

In order to find the volume of the line, the fuel injectors were plugged. At the front end where the 4-way valve normally connects into the line, a dry gas meter was connected instead. The line was then pressurized using air at room temperature. A pressure gauge (Ashcroft, accuracy ± 0.25%) and thermocouple allowed us to read the pressure and temperature at all times during the test.

Air was then allowed to bleed out of the line through the dry gas meter and out to normal atmospheric conditions. The dry gas measured the volume of air (at 1 atm) that left line during this time. In addition the dry gas meter measured the current room temperature and pressure. This allowed us to find the density of the air in the room. The fuel line pressure and temperature was written down before and after the air was bled out.

Knowing the initial line pressure, temperature, room air density, and volume of air bled out, the line's volume can be determined.

Tests were run multiple times at varying initial and final pressures to check for repeatability. In addition to this, an extension was attached to the fuel line (with a known volume) and the tests were repeated to see if the new volume equaled the old volume plus the extension's additional volume. Table 7 summarizes the test inputs and results.

Table 7. Summary of Fuel Manifold Volume Analysis.

V_out (L)	T_amb (K)	P_amb (kPa)	T1 (F)	T2 (F)	P1 (psig)	P2 (psig)	m_out (kg)	m2 (kg)	m1 (kg)	V_total (Litre)
7.46	293	101.3	67.9	68.3	133.5	23	0.006193	0.002111	0.008303	0.683632314
9.44	293	101.3	68.2	68.4	133	0	0.007836	0.000866	0.008702	0.719295493
8	293	101.3	68.3	68.3	133	20	0.006641	0.002039	0.00868	0.717627336
8	293	101.3	68.5	68.7	132.25	19	0.006641	0.001975	0.008616	0.716233739
6	293	101.3	68.3	68.6	133	47	0.004981	0.00357	0.008551	0.706908691
6	293	101.3	68.6	68.6	132.5	46.5	0.004981	0.003544	0.008525	0.707598546
6	293	101.3	68.5	68.5	132.5	44.5	0.004981	0.003351	0.008331	0.691385858
									Avg_1:	0.706097425
With extra teflon tube (.0658 L)										
6	292.9	101.3	68.2	69.6	135	60	0.004979	0.004932	0.009911	0.808267681
6	292.9	101.3	67.6	69.6	135	60.5	0.004979	0.004988	0.009967	0.81199641
6	292.9	101.3	67.6	69.6	134.5	60.5	0.004979	0.005022	0.010001	0.817462094
8	292.9	101.3	67.3	69.4	134.5	36.5	0.006639	0.003447	0.010086	0.823830707
8	292.9	101.3	67.2	69.4	134	35	0.006639	0.003311	0.009949	0.815159533
									Avg_2:	0.815343285
	Input from Dry Gas Meter									
	Input from Thermocouples				Avg_2- Avg_1 =		0.109246	L		
	Input from Pressure Guage									
	Output Volume									

The tests show good consistency between runs with the same volume. However, the method over estimated the increase in volume from the extra Teflon tube added. This is likely from measuring error for temperature, pressure or air out from the thermocouple, pressure gauge, and dry gas meter. The total error associated with this method is estimated to be 5%.

Average fuel flow rates for H2/CO during testing condition are between 1.5 to 2.7 cubic feet per minute, using the average line volume of .706 Liters, this equates out to 550 to 950 ms. This significant delay will effect results if not taken into account. Thus using the definition of ignition delay based on time differences between two signals, this time must be accounted for.

Our current tests measured ignition delay simply by raising or lowering residence time in the test section, eliminating the need for the knowledge of fuel line delay. However once the PMT is fully operational, which identifies delay time by measuring duration between injection and light from ignition, the above knowledge of the line volume will be vital.

3.4 Air Heating System

In order to achieve the wider range of operating temperatures (maximum temperature ~1033K or 1400°F), the air heating system has been upgraded with the support of an independent research project funded by the California Energy Commission (Contract 500-00-025). Previous experience with compact, resistive air heaters (e.g., Sylvania Osram, Convectronics) had proven very positive, therefore, this technology was selected for use in the current project. To achieve more heating, the three 6kW in-line heaters (total of 18kW) used in the previous ignition delay project [4] were replaced with three 24kW in-line heaters (total of 72kW, 54 kW actual due to use of 208V instead of 240 V). The newly fabricated and assembled air heating system is shown in Figure 13. The individual heaters can be staged on/off to accommodate the wide air flow turndown needed for the project. The heaters are protected by two fail-safe features. The venturi meter shown in Figure 13 will be utilized to monitor differential pressures as a safety measure to allow shutdown in the event of insufficient airflow through the heaters. Further description of these protective features is provided in Section 3.5.

The three in-line heaters are housed in a cylindrical pressure vessel (Figure 14), which has been fabricated utilizing a 12-inch schedule 80 carbon steel pipe. The pressure inside the vessel will be equalized to the pressure inside the air supply lines so that the heaters can be used exceeding their rated pressure limit of 11 atm (150 psig). Air supply lines consist of stainless

steel pipes and fittings of schedule 40 or 80. The three heaters merge at downstream in the vessel, which is subsequently mounted onto the flow reactor.

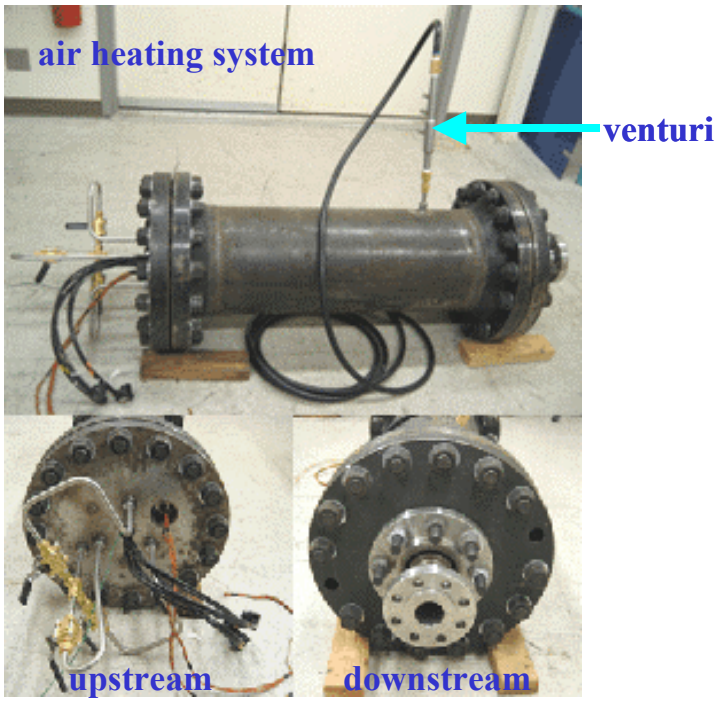

Figure 13: Air Heating System (Total of 72 kW Nominal, 54kW Actual).

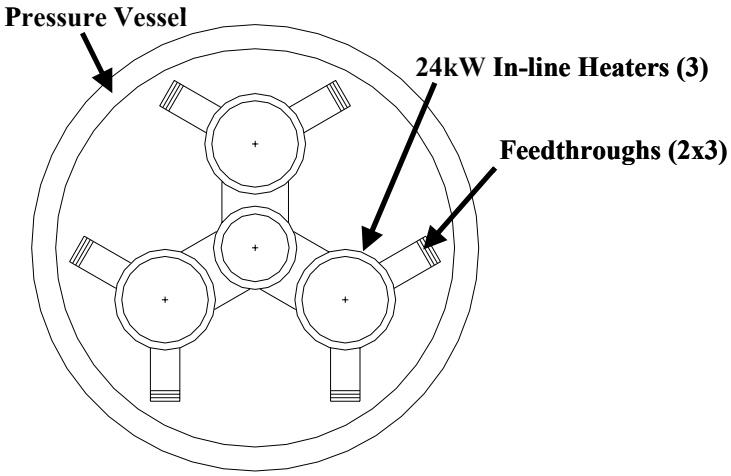

Figure 14: Cross-Sectional View of the Air Heating System

The assembly process of the air heating system is shown in Figure 15**.** Each heater consists of three elements, which are wired in a delta configuration utilizing power distribution blocks for a three-phase operation. Three thermocouples are also mounted near the heater exits to monitor air temperature to prevent overheating. Power supply lines for the heaters and thermocouple wirings are delivered through feedthroughs. The layout of air inlet/outlet and feedthroughs is shown in Figure 16**.**

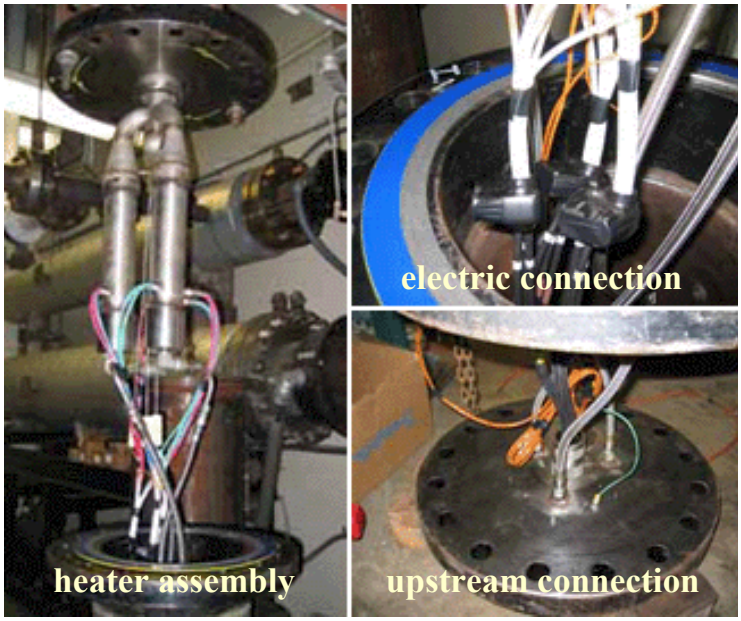

Figure 15: Heater Assembly Process

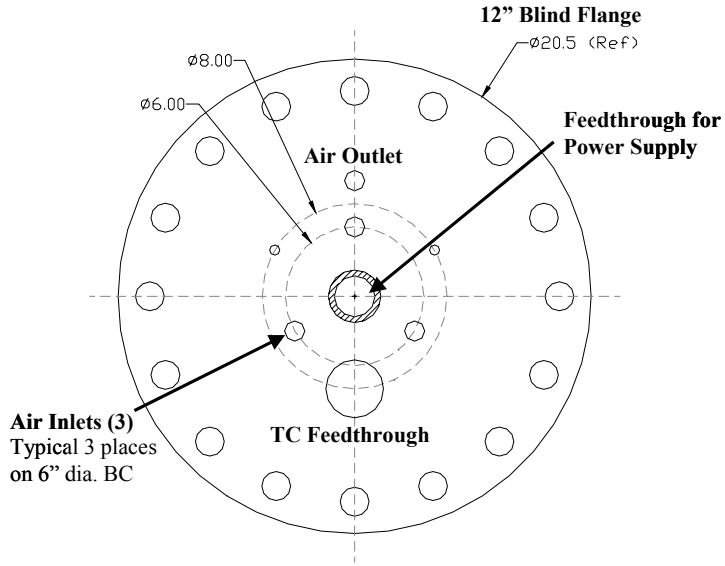

Figure 16: Upstream Flange Layout

3.5 Heater Protection

Air temperatures downstream of the heaters will be monitored utilizing multiple thermocouples and used to maintain the temperature at the set value by the power controller. In addition to this temperature control, air flow rates in the supply line will be monitored to ensure the minimum flow rate preventing overheat of the heaters. At upstream of the pressure vessel, a venturi is installed on the air supply line of 0.5" schedule 40 pipe to enable flow rate measurements. The design calls for $\beta = 0.45$ (Equation 3)

$$\beta = \frac{d}{D}$$

Equation 3

where d is the throat diameter of the venturi and D is the inside diameter of the line. In the present setup, D = 0.622". The discharge coefficient for an ASME conforming venturi, C, is calculated by:

$$C = 0.9975 - \frac{6.53\,\beta^{0.5}}{R_D{}^{0.5}}$$

Equation 4

where R_D is the pipe Reynolds number. Equation 4 can be also expressed as Equation 5:

$$C = 0.9975 - \frac{6.53}{\sqrt{R_d}}$$

Equation 5

where R_d is the Reynolds number at the throat. Thus, a pressure drop can be calculated from:

$$\Delta P = \frac{1}{2\rho}\left(\frac{\dot{m}_a}{K \cdot A_t}\right)^2 \qquad \text{where} \quad K = \frac{C}{\sqrt{1-\beta^4}}$$

Equation 6

In Equation 6, $\dot{m}_a$ is the actual mass flow rate, ρ is the density of air, and A_t is the throat area of the venturi. Calculating for the designed minimum volumetric flow rate of 10 SCFM, the pressure drop is: ΔP_{min} = 403.68 Pa (1.62 inH_2O). A 43000 series Capsu-Photohelic pressure switch/gage by Dwyer will be used to monitor the differential pressure and turn off the heaters when the pressure drop becomes below ΔP_{min} to protect the heaters from a low flow burnout.

3.6 Pressure System

During the project, a compressor system (Sullair) that had been sited at the UCICL, but not commissioned, was brought on line in a response to the desire to achieve results at higher pressures. The compressor is capable of the maximum pressure of 25 atm (350 psig) and mass flow rate of 0.29 kg/s (0.63 lb/sec). With this compressor, the attainable pressure will be approximately 18 atm (250 psig), which is a significant improvement from the 8 atm (103 psig) previously available for ignition delay studies at UCICL.

3.7 Data Acquisition (DAQ) System

The DAQ needs for this project include the control of air delivery and fuel composition as well as the sampling of the properties (temperature and pressure) of air and air/fuel mixture and sensor signals for ignitions. Sensors used to monitor ignitions are six Type-K thermocouples and six Si photodiodes (Hamamatsu, Type S2386-8K) that are mounted on Test Section B (Figure 5 (b)). Locations of the sensor ports are provided in Table 1. All the DAQ are performed using the code written in National Instruments LabVIEW. The specific data acquisition cards are summarized in Table 8.

Table 8: System Data Acquisition Cards (National Instruments).

DAQ Cards	AO (SE)	AI (SE)	Accessories	Sampling Rate
PCI-6024E	2	16	CD-68LP	200 kS/sec
PCI-MIO-16E-1	2	16	SCXI-1200, 1140, 1304	1.25 MS/sec
PCI-6071E	2	64	SCB-100	1.25 MS/sec
Total	6	96	---	---

The UCICL high-pressure facility is situated on two floors. Previously, this DAQ system was operated using; a flow control system located downstairs, and the experimental rig and fuel composition control system located upstairs. While this worked reasonably well, a lack of time resolution resulted from the LAN system throughput. As a result, a strategy to eliminate this bottleneck was implemented. In the current project, the DAQ system was upgraded to use a single computer downstairs to increase the frequency response of the overall system.

4 ANALYTICAL METHODS

To help guide the experimental work and to also aide in the understanding of the role played by various species in IGCC type fuels, analytical studied were carried out. In particular, detailed chemical kinetic simulations were carried out using various detailed mechanisms including those by Mueller et al. [9], GRI-Mech 3.0 [8], Baulch et al. [12], Davis et al. [14], and the San Diego Mechanism 2003/08/30 [15]. In this section, the methods followed and results obtained are described.

4.1 Kinetics Code

CHEMKIN 3.7 and 4.0 were used to carry out kinetic modeling of the ignition delay process [8]. In the CHEMKIN collection, the AURORA application represents a well-mixed reactor model for both transient and steady state systems and thus appropriate for the ignition delay analysis. Like for the experimental approaches, a definition of ignition delay needs to be applied in the interpretation of the results obtained. For the present study, the CHEMKIN default definition of the autoignition time, "the time at which the temperature reaches 400 K higher than the initial value," was employed. More accurate definitions (e.g., "at the maximum temperature gradient," and "at the maximum rate of production of OH radicals") were evaluated during the previous ignition delay project at UCICL [4]. However, for the purpose of the current project, comparison of results based on these various definitions indicated that the default definition provides representative results and is actually similar to times determined from the maximum temperature gradient. Regardless, the default definition is sufficient to address the trend of the autoignition characteristics for the relevant fuel (50% H_2 50% CO).

4.2 Mechanisms

A number of kinetic mechanisms were considered for the project:

1) The mechanism by Mueller et al. [9,10] that involves the H_2/O_2 and $CO/H_2O/O_2$ reactions,

2) The GRI-Mech 3.0 mechanism which is optimized for methane and natural gas [11]. Since this mechanism is widely used in the literature, it was selected as a baseline mechanism, even though it is not necessarily optimized for hydrogen.

3) The mechanism by Baluch et al. [12], compiled by Kaneshige [13] of the California Technology Institute Explosion Laboratory for their internal research.

4) The first version of the mechanism by Davis et al. [14], which is currently being developed and improved, and

5) San Diego Mechanism 2003/08/30 [15] developed at the Center for Energy Research of University of California, San Diego.

6) Hydrogen 2004 **[**16**]** Developed by the Lawrence Livermore Laboratory

The mechanisms are summarized in Table 9. Because establishment and improvement of mechanisms is an on-going efforts at many research facilities, evaluations of newly developed or "rediscovered" mechanisms for H_2/CO containing fuels is an important ongoing effort. In discussions with engine OEMs (Original Equipment Manufacturers) and the generally academic community, the reaction mechanism by Mueller et al.[9,10] appears to have gained some general acceptance and thus far, has been the primary mechanism utilized for the calculations in the current project.

Table 9: Chemical Reaction Mechanisms for Fuels Containing H_2 and/or CO.

Mechanism	# Species	# Reactions	Notes	Status
Mueller et al.	13	34	can include more elementary reactions	✓
GRI-Mech 3.0	53	325	designed for natural gas combustion	✓
Baulch et al.	42	167	compiled by Kaneshige (1996)	✓
San Diego 2003/08/30	39	173	Includes hydrocarbons for C#1-3	✓
Davis et al.	14	38	Version 1 of UD and USC	✓
Hydrogen 2004, LLNL	10	21	does not include CO reactions	✓

5 RESULTS AND DISCUSSION

In this section, the results regarding numerical simulation (CHEMKIN) and literature reviews are discussed along with the new experimental results obtained.

5.1 Analytical Results

Several investigations were carried out using numerical analyses. First, the various kinetic mechanisms outlined in Section 4.2 were compared relative to predicting ignition delay times for H_2/CO mixtures. Next, a sensitivity analysis was carried out to help isolate the key reactions that influence the ignition delay. Finally, a factorial study was carried out in an effort to generate a simplified model for ignition delay that could be used without the need for a complex kinetics code such as CHEMKIN. This result is directed to the deliverables associated with Task 4. The AURORA application of the CHEMKIN collection was used to simulate ignition delay times at various operating conditions.

5.1.1 Hydrogen vs. Natural Gas

As a first step, a comparison of expected ignition delay results for natural gas and hydrogen containing mixtures was carried out. Because of the familiarity of the gas turbine community with natural gas, an evaluation of how simply changing the fuel to hydrogen might affect ignition delay helps to place the issue into a familiar context.

For this assessment, simulations were carried out for H_2 and natural gas using appropriate mechanisms for each [9, 11]. The results are shown in Figure 17. The composition of NG used in the example is 80% CH_4, 10% C_2H_6, and 10% C_3H_8 on a volumetric basis. As predicted, ignition delay times for H_2 tend to be shorter than those of natural gas. Interestingly, the difference appears relatively small at temperatures below 1000 K (above 1000/T = 1.0). The differences are quite significant, however, as the temperature increases, especially above T = 1250K (below 1000/T = 0.8). For ignition delay in premixing ducts, the temperature ranges expected tend to be less than 1000K, thus for gas turbine applications, the result shown in Figure 17 appears promising in terms of required design changes because it suggests that ignition delay times for hydrogen are comparable to those for natural gas and that the delay times at gas turbine premixer conditions are 100 to 1000 msec.

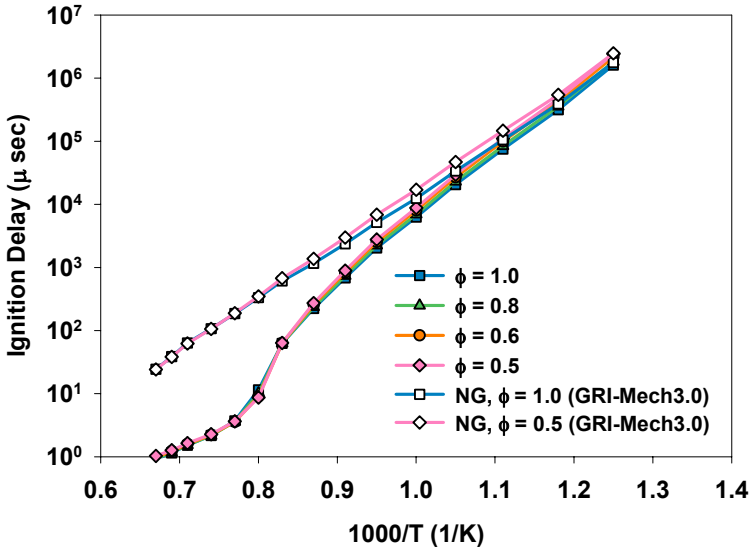

Figure 17: Ignition Delay Time – Pure Hydrogen vs. Natural Gas (NG) at various equivalence ratios and 15 atm.

5.1.2 Mechanism Comparison

Given the large number of mechanisms available for hydrogen containing fuels (Table 9), the question of which performs the best is apparent. As a starting point for this discussion, Figure 18 presents some example results and the general agreement between the resulted ignition delay times with the same mechanisms used to generate the results in Figure 17. In this case, the same two mechanisms are used for hydrogen and air mixtures. The differences can be quite large, however, in particular temperature windows. The simulation results also show a non-intuitive change in relative ignition delay in the low (T < 910 K, 1180 ^{o}F), medium, and high (T > 1250 K, 1790 ^{o}F) temperature regimes under different pressures: Ignition delay at the elevated pressure is shorter in the low and high temperature regimes, but longer at the medium temperature regime. To further illustrate the interesting pressure dependency, Figure 19 presents a more detailed evaluation of how pressure is predicted to affect ignition delay. As shown, a strong interdependency of ignition delay time with pressure is evident, supporting the notion that data at conditions that are as similar as possible to those expected in practice are needed to fully address concerns regarding ignition delay for IGCC type fuels.

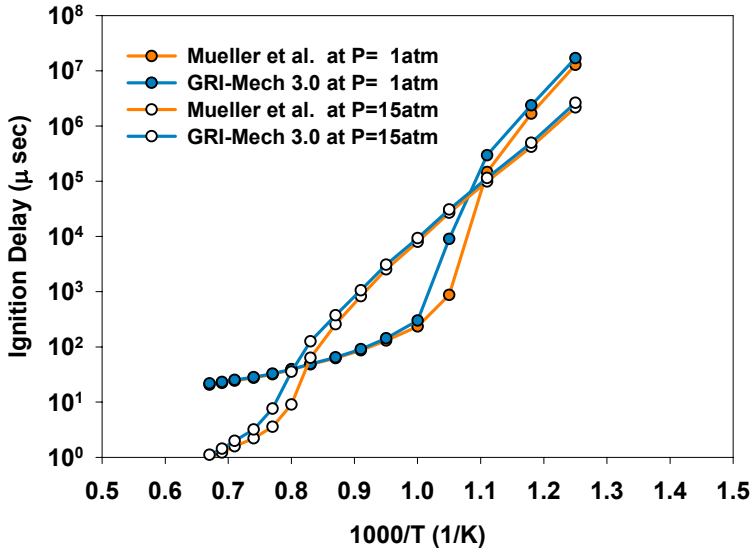

Figure 18: Mueller et al. vs. GRI-Mech3.0 (H2/CO/Air, $\phi = 0.6$)

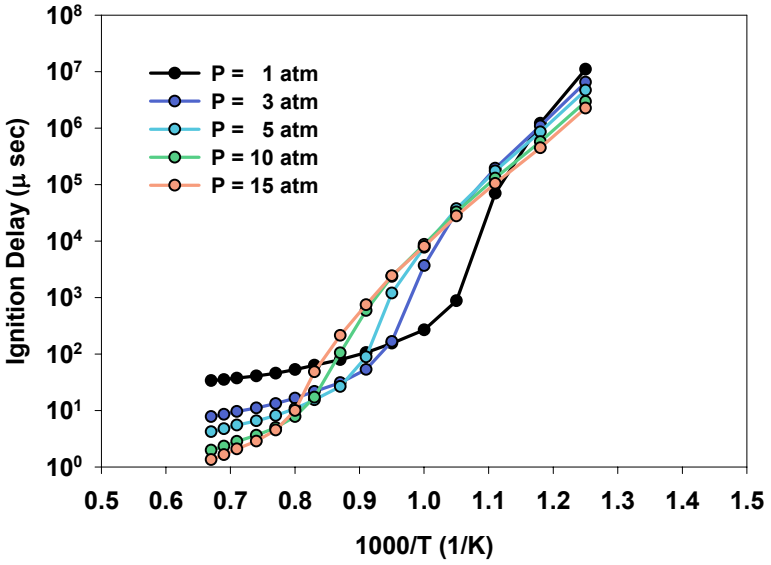

Figure 19. Effect of Pressure on Ignition Delay (50% H2/50% CO at equivalence ratio of 0.6).

With the previous results serving as a framework, a more in depth comparison among the mechanisms outlined in Table 9 is now presented. Figure 20 summarizes the simulation results for the 50% H_2 50% CO - air mixture at the pressure and equivalence ratio of 15atm and 0.6, respectively. Figure 20 shows general agreement in trends among the resulted ignition delay times with all the mechanisms. However, one mechanism (Baulch [12]) predicts ignition delay

significantly longer for the temperature range of 750 K (890 ^{o}F) to 1250 K (1790 ^{o}F) at the simulated condition. Below 750 K (890 ^{o}F), GRI-Mech 3.0 predicts far longer induction period than other mechanisms (Figure 21). Notice that pre-combustor temperatures of typical gas turbines fall in the range discussed above.

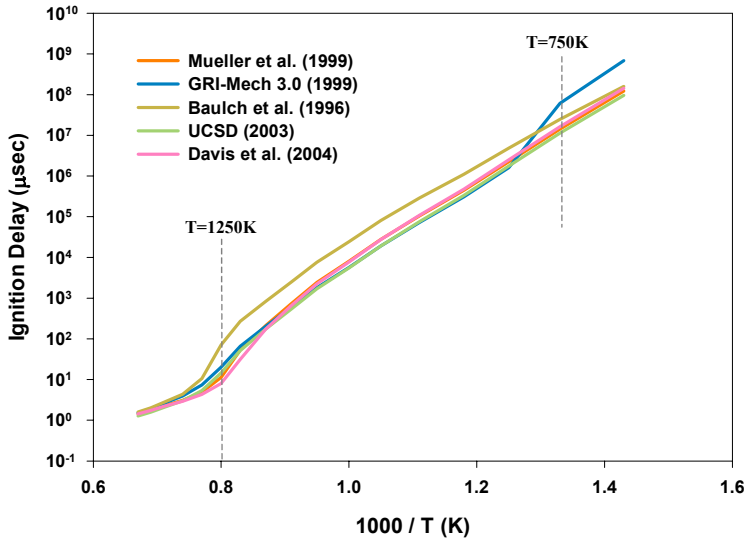

Figure 20: Comparison of Ignition Delay Predictions using Mueller et al., GRI-Mech3.0, Baulch et al., UCSD, and Davis et al. (H_2/CO/Air, 50% H_2 50% CO, ϕ = 0.6)

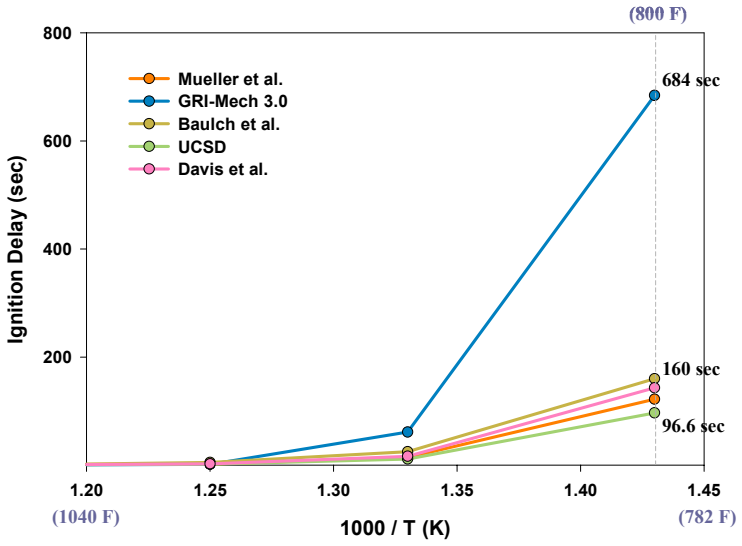

Figure 21: Range of Ignition Delay Predictions with Various Mechanisms

5.1.3 Mechanisms for Hydrogen

Two mechanisms were considered for use in comparison of H_2 ignition delay analysis [9,16]. As seen in Figure 22, the two mechanisms are quite similar at elevated pressures (15 atm) but start to diverge at lower temperatures and pressure. Because the two mechanisms are relatively close (especially in the pressure range we are interested in), simulations of only a single mechanism (Hydrogen 2004) were compared to Hydrogen –Air experimental data collected in literature in the next section.

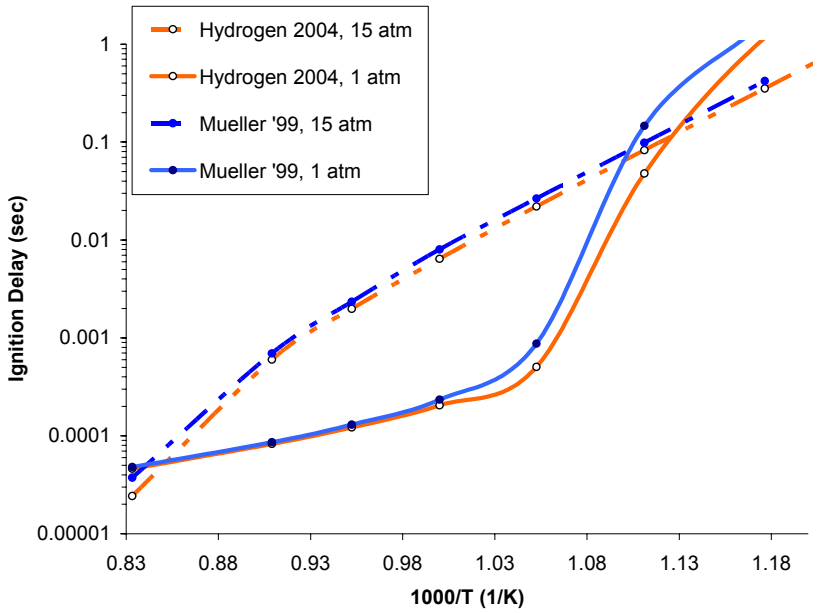

Figure 22**:** Comparison of Mueller and Hydrogen 2004 at 1 and 15 atm

5.1.4 Comparison with Existing Data

5.1.4.1 Pure Hydrogen

Figure 23 shows the comparison of Hydrogen 2004 with shock tube data at pressures of 1, 2, and 4 atmospheres [17,18,19,20]. As pointed out by Sabia [21], the curves for H_2 ignition delay in this temperature regime show three distinct slopes. For instance at 2 atm, the curve is shallow up to 1000/T of 1.0, after which it steepens from 1 to 1.03, and finally shallows off slightly after 1.03. The reason for the multiple slopes are generally associated with are different oxidation pathways that are associated with combinations of temperatures and pressure

conditions for the hydrogen oxygen system [21, 22]. This is discussed in more detail in Section 5.1.5.

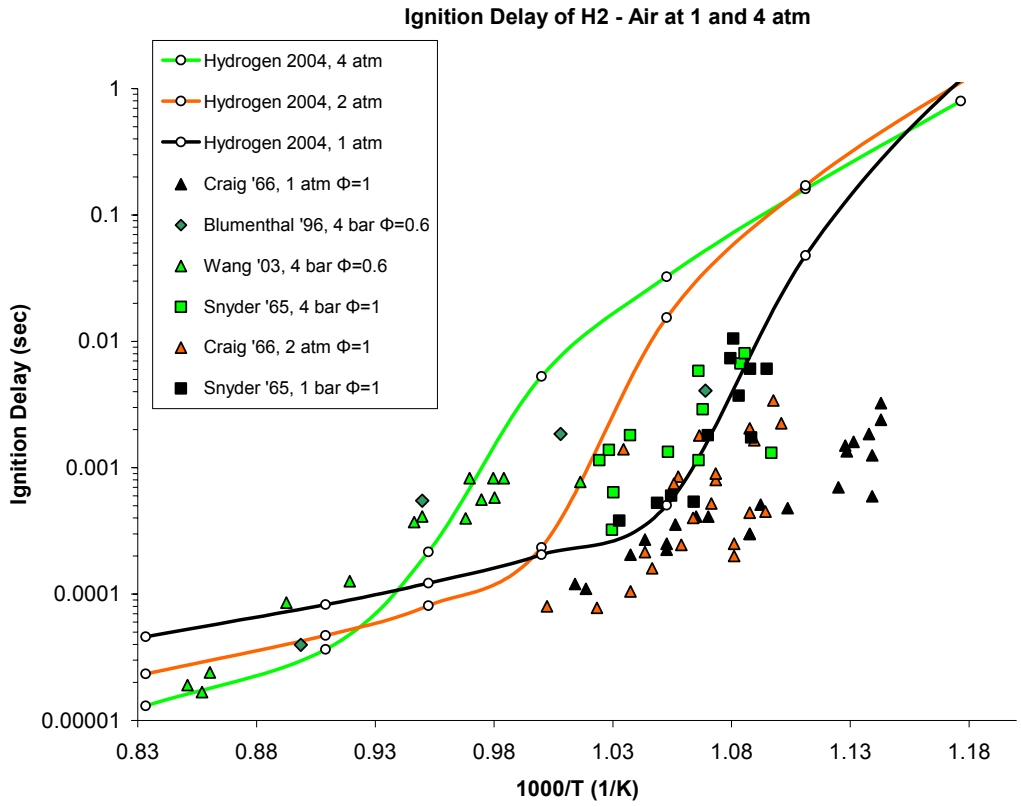

Figure 23: Ignition Delay of H2- Air for Calculated (using Hydrogen 2004 mechanism [16]) and Experimental Data [17, 18, 19, 20].

Two studies feature results for Φ = 0.6 at 4 bar [17, 18] while two studies were conducted back in the 1960's also with shock tube techniques. The experimental results for Φ = 0.6 at 4 bar compare closely to the simulated run for 1000/T from 0.83 up to 0.98 (for the first pathway). For temperatures lower than 1000/T of 0.98 (~1000 K) both the simulations and experiments curves show an increase their slopes, however the increase for the simulation is much larger than that of the experimental. Work done by Snyder [20] in 1965 for Φ = 1 at 1 bar exhibits a sharp slope change like the calculations for temperatures in the range of 900-1000K. The shock tube ignition delay times match the calculated values at higher temperatures, but once the slope begins to increase (at 0.90 for 4 atm, 1.0 for 2 atm, and 1.04 for 1 atm) discrepancies between

experimental and simulated times begin. The calculations always report a steeper slope than what the experimental results are showing.

The temperature range in the present study (~ 750K or 1000/T of 1.34), can be used to determine if the shallow trend seen from the shock tube study is only in the local range of 1000 K, or if it proceeds into the lower temperatures.

5.1.4.2 Hydrogen/CO Mixtures

In Figure 24, the CHEMKIN simulation results for 50% H2/50% CO are compared with experimental data [5] for a similar fuel ("UTRC Fuel #2--38.6% H_2, 51.1% CO, 10.3% CO_2). Although the simulations were conducted for 50% H2/50% CO rather than the actual fuel used in the experiments, the ignition delay times for both fuels were nearly identical based on simulation runs. The line shown through the data in Figure 24 is a least squares fit of the results. The expression corresponding to the line is shown in Equation 7:

$$\tau \left[O_2\right]^{0.50}\left[F\right]^{0.25} = 1.29\times10^{-7}\exp\left(\frac{3985}{T}\right)$$

Equation **7**

Where

τ is an ignition delay time (sec),

$[O_2]$ and [F] are the molar concentration (moles/cm^3) of oxygen and fuel,

T is a temperature (K).

In the report associated with this study [5], it was observed that the hydrogen content dominated the ignition delay behavior. In fact, it was proposed that ignition delay could be estimated closely using only the hydrogen content. In this case, Equation 8 presents a similar equation which can be used with only the hydrogen content.

$$\tau \left[O_2\right]^{0.50}\left[H_2\right]^{0.25} = 1.02\times10^{-7}\exp\left(\frac{3985}{T}\right)$$

Equation **8**

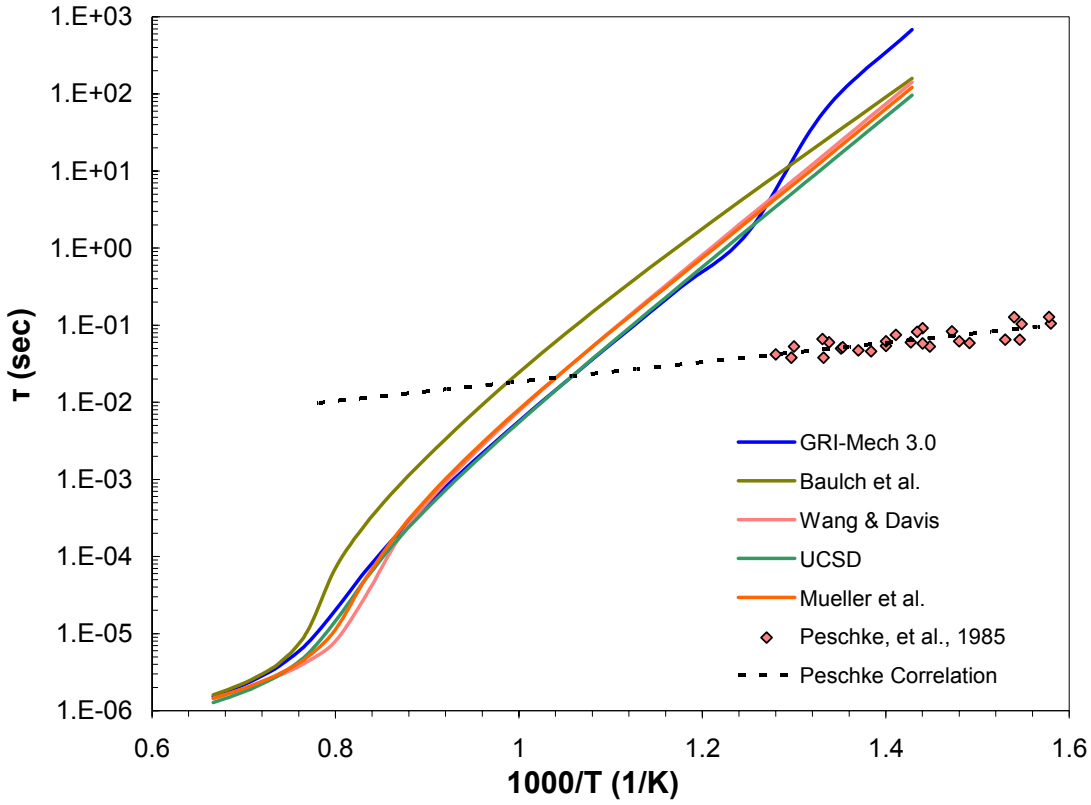

Figure 24: Comparison of CHEMKIN Ignition Delay Predictions with experimental data [5] Data: CHEMKIN Simulations Were Performed for 1) 50% H_2 50% CO – Air at $\phi = 0.6$ Using Mueller Mechanism at Various Pressures and 2) Peschke & Spadaccini Baseline Fuel (38.6% H_2 51.1% CO 10.3% CO_2)

The most striking feature of Figure 24 is that the calculated delay times are disturbingly far (by 2 – 5 orders of magnitude) from the experimental data. The simulated and measured results appear to be headed towards agreement at higher temperatures, but below 1000 K (which is of greatest interest for gas turbine applications), the agreement is poor. This result suggests a strong need for additional experimental data which is one of the motivations for the current project.

5.1.5 Temperature Sensitivity Analyses

Before turning to experimental results, in order to try and gain some understanding of why such discrepancies between the measured and predicted ignition delay times have been observed, the results from sensitivity analyses carried out for one of the mechanisms for H_2/CO mixtures are presented and discussed.

5.1.5.1 Overview

Temperature sensitivity analyses were conducted on results obtained using one mechanism [9, 10] for 50% H_2 50% CO – air mixture of the equivalence ratio 0.6 at T = 1000 – 1300 K (1340 – 1880 ^oF) and P = 1, 10, and 20 atm. NOx chemistry was not included in the mechanism. Among 34 elementary reactions contained in the mechanism, 18 reactions with significant sensitivities are listed in Table 10. Figure 25, Figure 26, and Figure 27 summarize the temperature sensitivity of each reaction at autoignition at the pressures of 1, 10, and 20 atm, respectively. In these results, the time at which autoignition occurs (i.e., the ignition delay time) is defined as the time where the maximum rate of change of the temperature ($(dT/dt)_{max}$) is observed. These times are summarized in Table 11. At atmospheric pressure (Figure 25), H_2-O_2 chain reactions and Reaction 11 (R11) are the only reactions with significant sensitivity whereas reactions involving HO_2, H_2O_2, and CO become important at elevated pressures (Figure 26 and Figure 27). Notice that sensitivity at 1 atm is significantly lower than that of 10 and 20 atm cases. Selected key reactions will be discussed in the following section.

Table 10: Elementary Reactions with Strong Temperature Sensitivities [10].

#	Reaction	Type
R1*	$H+O_2=O+OH$	H_2-O_2 Chain Reactions
R2	$O+H_2=H+OH$	
R3	$H_2+OH=H_2O+H$	
R11	$H+O_2(+M)=HO_2(+M)$	HO_2 Formation/Consumption
R14	$HO_2+H=OH+OH$	
R15	$HO_2+O=O_2+OH$	
R16	$HO_2+OH=H_2O+O_2$	
R17	$HO_2+HO_2=H_2O_2+O_2$ (duplicated)	H_2O_2 Formation/Consumption
R18	$HO_2+HO_2=H_2O_2+O_2$ (duplicated)	
R19	$H_2O_2(+M)=OH+OH(+M)$	
R21	$H_2O_2+H=H_2O+OH$	
R22	$H_2O_2+H=HO_2+H_2$	
R25	$H_2O_2+OH=HO_2+H_2O$ (duplicated)	
R26	$CO+O(+M)=CO_2(+M)$	CO Reactions
R27	$CO+O_2=CO_2+O$	
R28	$CO+OH=CO_2+H$	
R29	$CO+HO_2=CO_2+OH$	
R30	$HCO+M=H+CO+M$	

** Different rate coefficients are used for temperatures below and above 1200K*

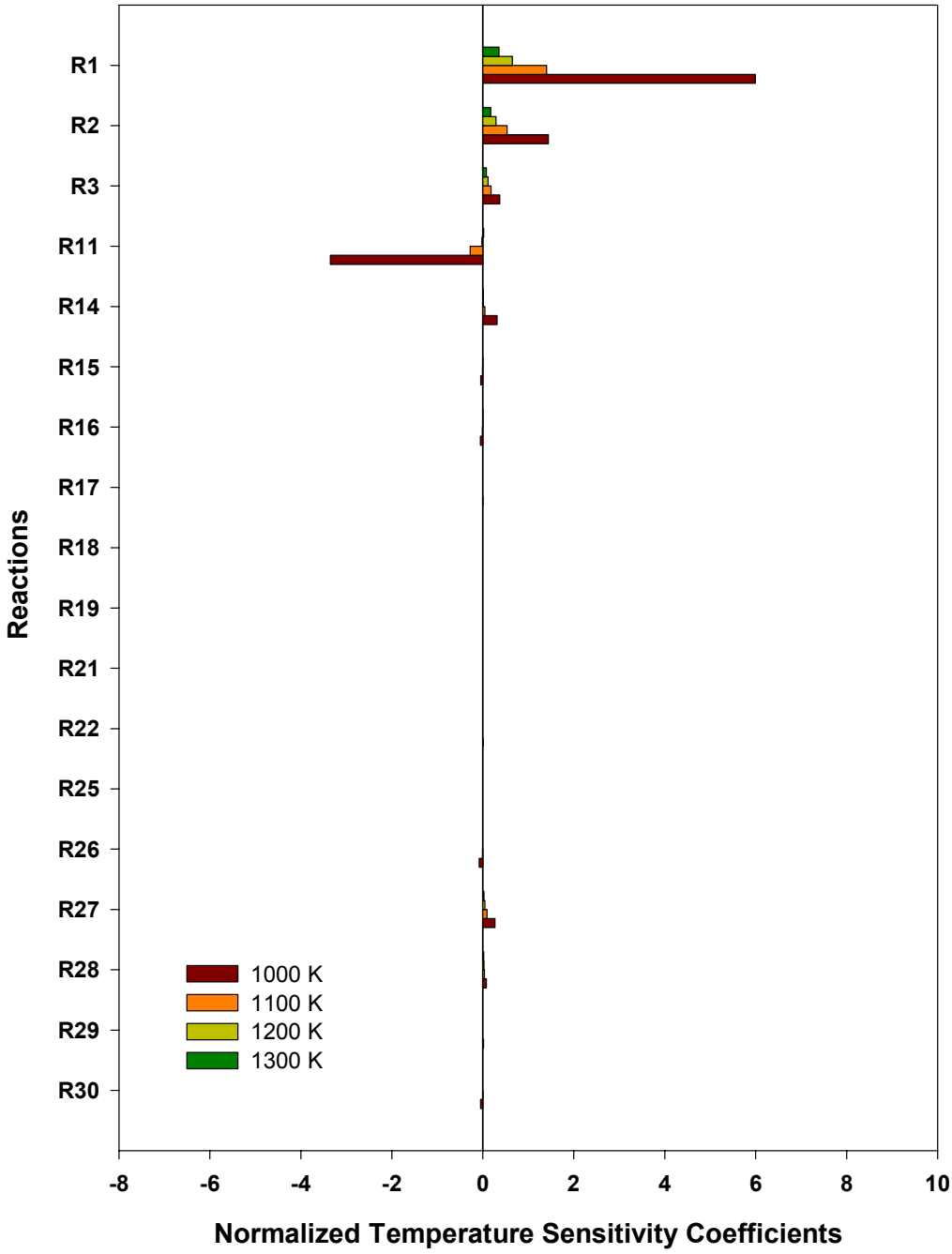

Figure 25: Temperature Sensitivity Analysis using Mueller et el. for 50% H_2 50% CO - Air at ϕ = 0.6, P = 1 atm, and T = 1000 – 1300 K

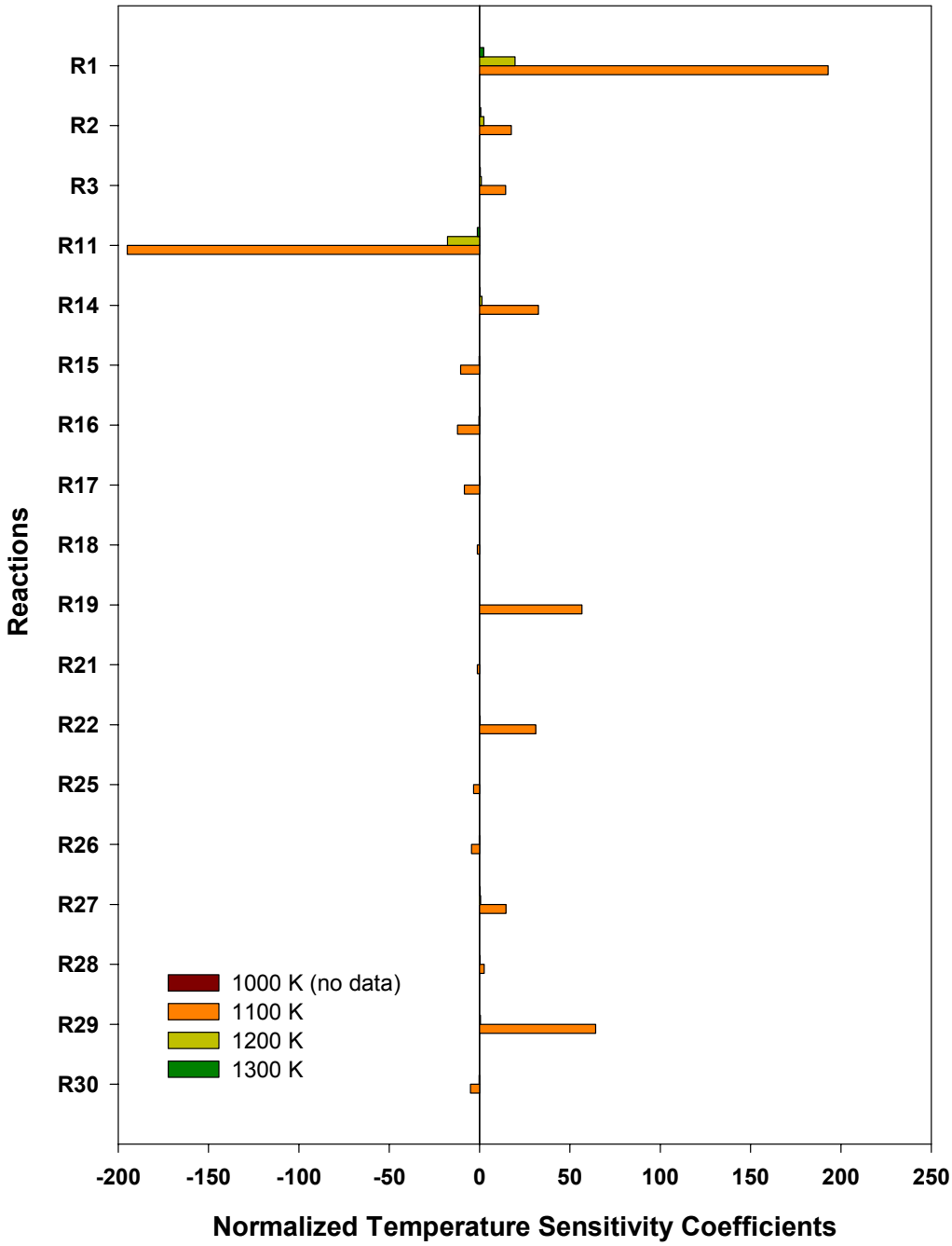

Figure 26: Temperature Sensitivity Analysis using Mueller et el. for 50% H_2 50% CO - Air at ϕ = 0.6, P = 10 atm, and T = 1100 – 1300 K (no convergence at 1000 K)

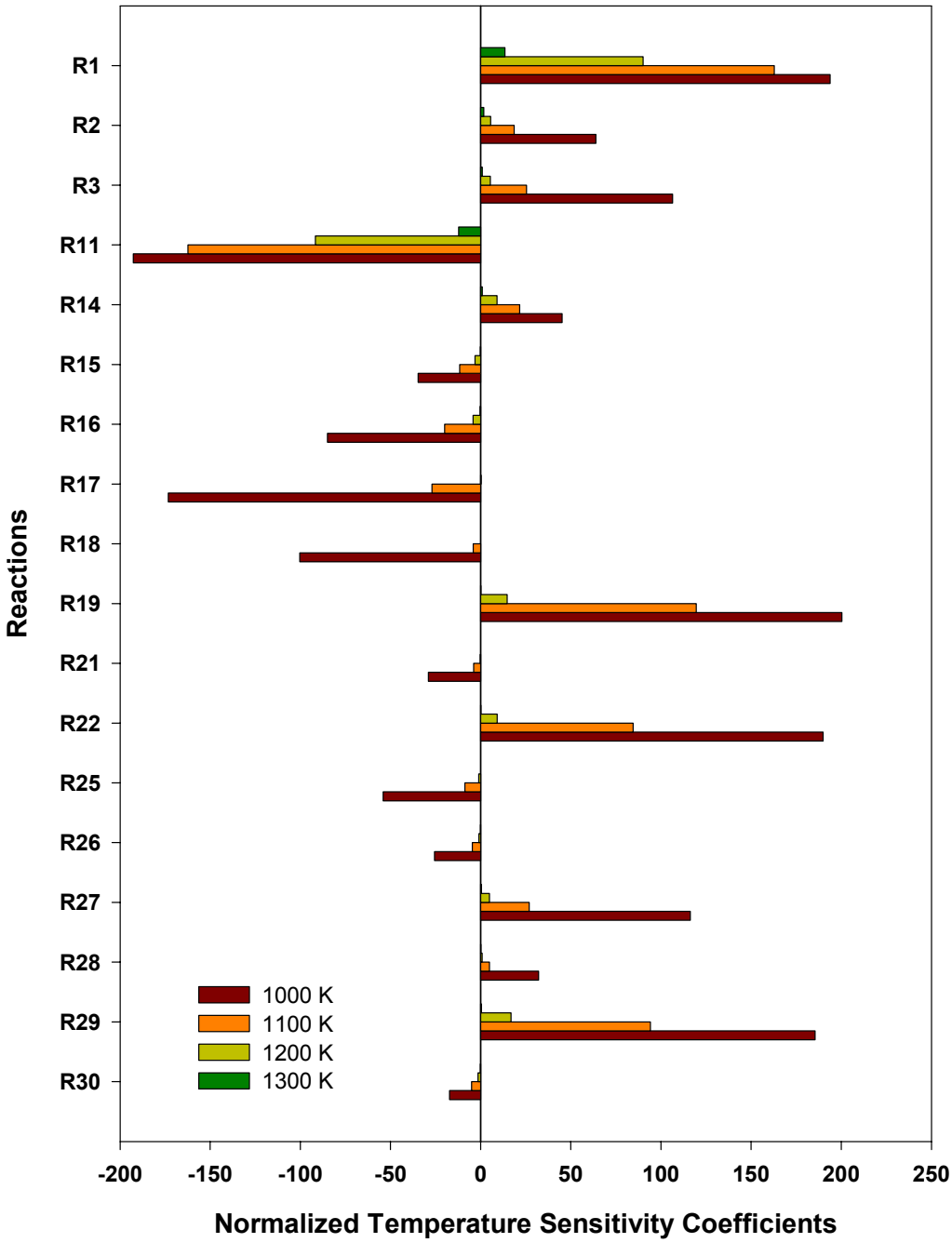

Figure 27: Temperature Sensitivity Analysis using Mueller et el. for 50% H_2 50% CO - Air at ϕ = 0.6, P = 20 atm, and T = 1000 – 1300 K

Table 11: Autoignition Times (msec) at Maximum Rate of Change of Temperature

		Pressure (atm)		
		1	10	20
Temperature (K)	900	---	---	---
	1000	0.265	---	7.346
	1100	0.100	0.589	0.776
	1200	0.055	0.019	0.083
	1300	0.035	0.005	0.006

5.1.5.2 Discussion of Key Reactions

R1 vs. R11

(R1) $H + O_2 = O + OH$

(R11) $H + O_2 (+ M) = HO_2 (+ M)$

Reactions 1 (R1) and 11 (R11) are of obvious importance at all pressures. Figure 28 shows the temperature sensitivities of R1 and R11 at autoignition. R1 is a bimolecular chain-branching reaction with positive temperature sensitivity, whereas R11 is a termolecular reaction with mostly (except for the 1300 K (1340 ^{o}F) case at 1 atm) negative sensitivity. At 1 atm, R1 is more dominant than R11 and occurs more frequently (relative to R11) as temperature increases. On the other hand, R11 becomes more competitive with R1 at elevated pressures for the simulated temperature range (1000 – 1300 K or 1340 – 1880 ^{o}F). This observation can be explained by the fact that R11 is a termolecular reaction: Interactions with third bodies can be more easily achieved at high pressures, and therefore ternary collisions become more common. R1 is a fast reaction relative to R11.

The changing role of R11 and HO_2 radical with pressure appears to explain the non-intuitive pressure effect on ignition delay shown in Section. In a H_2/O_2 system, R11 is considered a chain-terminating reaction up to second explosion limit because HO_2 is metastable and diffuses to the wall in that regime. However, at pressures above the second explosion limit, HO_2 participates to the chain propagations involving H_2O_2 decomposition [9, 10, 23]. In other words, the H_2/O_2 kinetics changes below and above the second explosion limit. Mueller et al. [9]

also point out that transition of the H_2/O_2 kinetics upon crossing the explosion limit becomes less obvious as pressure increases due to increasing rate of reaction above the limit. Ignition delay profiles in Figure 19 appear to fit to this kinetics change.

R14 vs. R16

(R14) $HO_2 + H = OH + OH$

(R16) $HO_2 + OH = H_2O + O_2$

Mueller et al. [9] identify the role of R16 (chain-terminating reaction) as inhibiting the overall reaction rate by competing with R14 (chain-propagating reaction). Because both reactions require HO_2, R14 and R16 become important at high temperatures (Figure 26 and Figure 27). The sensitivity of R14 decreases at 1100 K (1520 ^oF) as pressure increases from 10 atm to 20 atm, while the sensitivity of R16 increases at the same condition. At the initial temperature of 1100 K (1520 ^oF), ignition delay times are 0.589 msec at 10 atm, and 0.776 msec at 20 atm. Although the longer ignition delay at 20 atm may partly due to the R16 competition with R14, other reactions should be carefully analyzed since the sensitivity data are available only for limited conditions at this point.

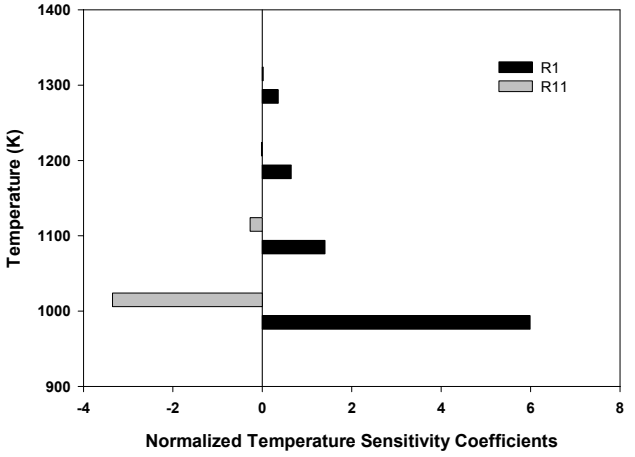

(a)

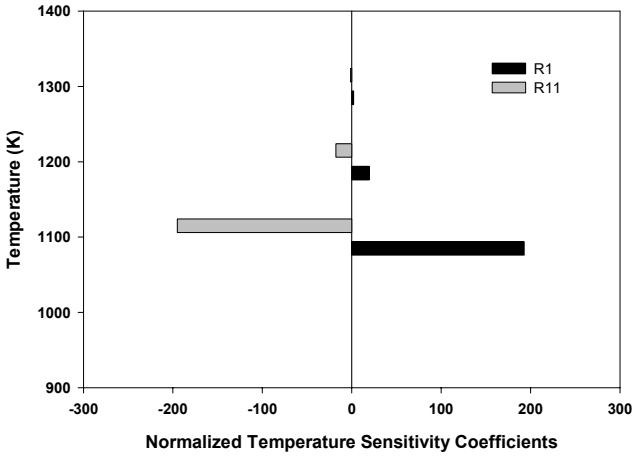

(b)

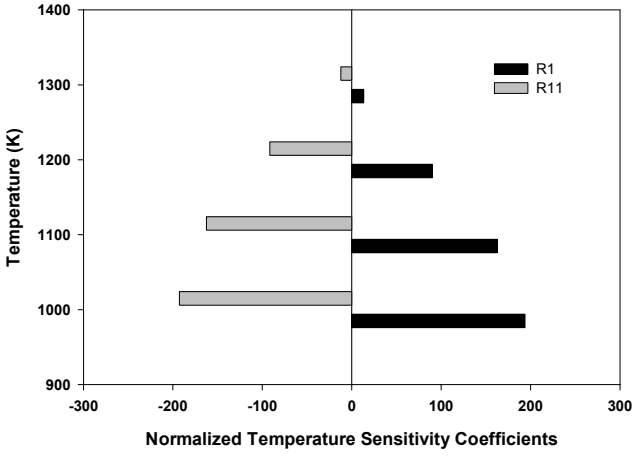

(c)

Figure 28: Temperature Sensitivities of R1 and R11 at Autoignition Time at (a) 1 atm, (b) 10 atm, and (c) 20 atm

R28 vs. R29

(R28) $CO + OH = CO_2 + H$

(R29) $CO + HO_2 = CO_2 + OH$

Figure 29 shows the time evolutions of the temperature sensitivities for the reactions involving CO at 1100 K, and pressures of 1, 10, and 20 atm. Notice that R27 and R29 in Figure 29 (c) are scaled by factors of 0.5 and 0.2, respectively. R28 is important at 1 atm, while R29 is far more important at higher pressures: Because HO_2 is a dominant radical at elevated pressures, R29 occurs more frequently. Mueller et al [9] identify R28 as a low pressure route, and R29 as a high pressure route of CO consumption.

The presence of CO was observed to increase or decrease the ignition delay time depending on the condition. This behavior is illustrated in Figure 30. The % change is calculated by Equation 9:

$$Change\ (\%) = \frac{\tau_{H_2+CO} - \tau_{H_2\ Only}}{\tau_{H_2\ Only}} \times 100$$

Equation 9

Thus, a negative value of "change (%)" in Figure 30 means that the presence of CO shortens the ignition delay time (i.e., autoignition happens more easily). As a general trend for all pressures, CO tends to enhance autoignition below a given critical temperature, i.e. the temperature at the "dip" of a curve, and impedes autoignition above this temperature. At higher operating pressures, higher temperatures are required for CO to shorten the ignition delay times with limited effects. Atri et al. [24] reported that R29 decreased induction time when they replaced N_2 in their $H_2/O_2/N_2$ system with CO at sub-atmospheric pressure. R29 may have the same effect in the present case. However, Mittal [25] observed at elevated pressures (15, 30, and 50 bar) increasing the fraction of CO in the mixture inhibits ignition. This observation contradicts, as he points out, the simulated results of GRI-Mech 3.0. Further simulations/analyses are recommended to clarify this.

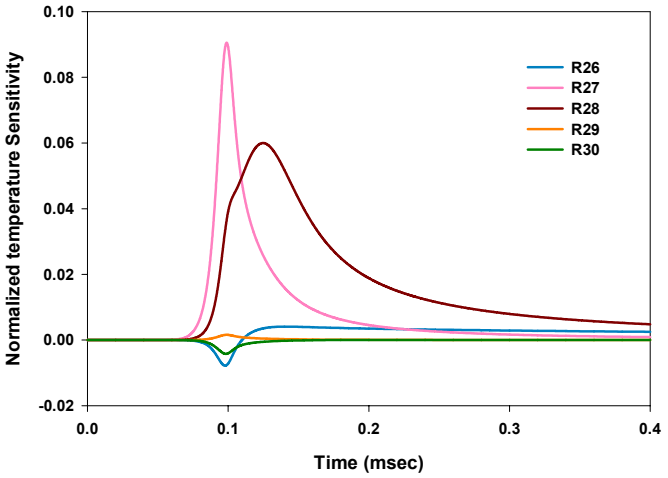

(a)

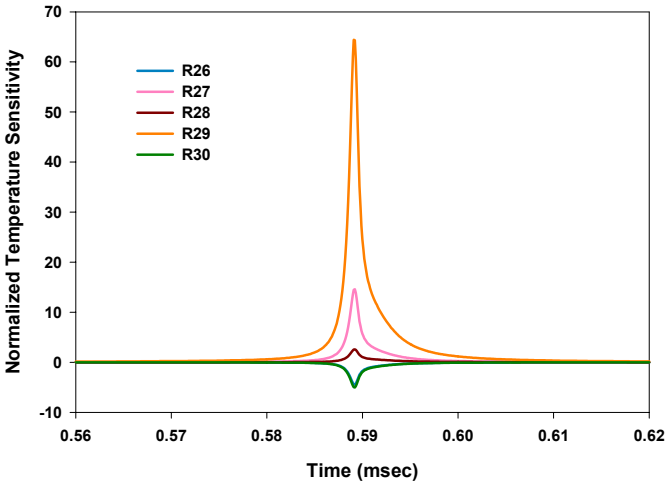

(b)

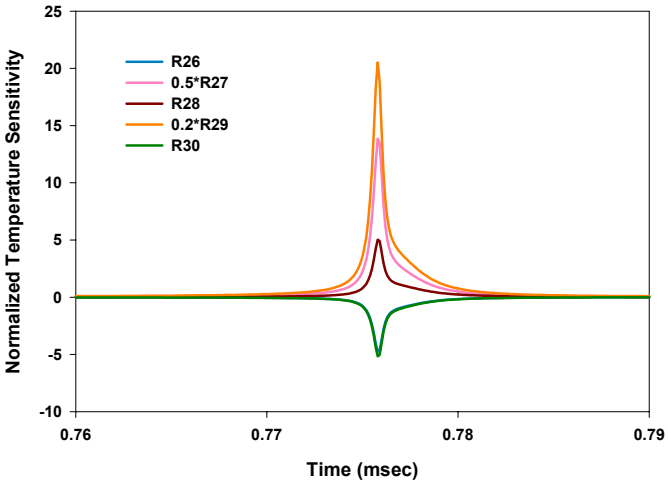

(c)

Figure 29: Sensitivity of CO reactions at 1100 K and (a) 1, (b) 10, and (c) 20 atm

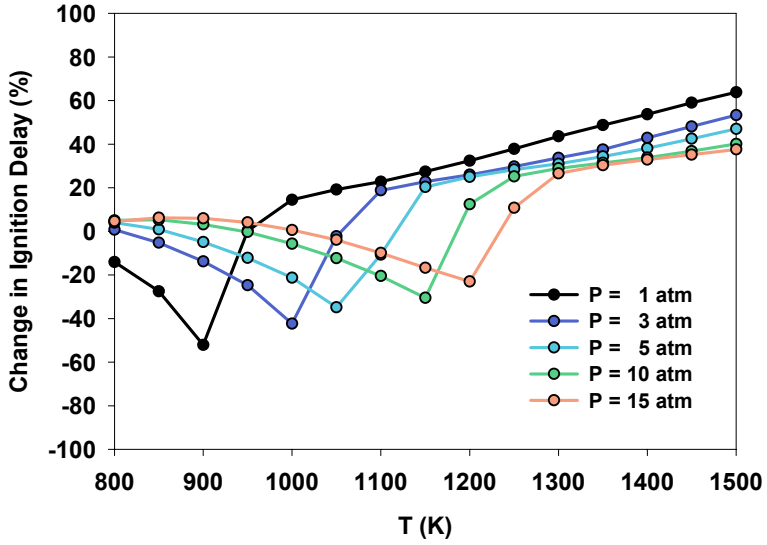

Figure 30: Effect of CO Presence

In summary, the results presented illustrate that all the existing kinetic mechanisms provide similar results for predicting ignition delay. However, none of the predictions are able to reproduce the measured ignition delay times in the one experimental dataset available. Since the experimental results are on the same order as the residence times found in gas turbine premixers, this gives rise to some serious concerns relative to applicability of lean premixed strategies for achieving low emissions when using syngas in gas turbines.

5.1.6 Ignition Delay Factorial Study - Design of Experiments

In order to develop a simplified tool for predicting ignition delay, a statistically designed test matrix was developed that could be carried out using either measurements or simulations. This approach could also potentially be used to gain some understanding of the discrepancy between the simulated and experimental data illustrated in Figure 24. Note that the randomness of the data entry was compromised to maintain the run order of original Peschke & Spadaccini [5] experiments. Two-level factorial models were created and analyzed using the Design-Expert software. The factors and their levels (i.e., minimum and maximum limits) are summarized in Table 12.

Table 12: Factors for Design of Experiment Approach

Factor	Name	Units	MIN	MAX
A	Pressure	atm	11.9	23
B	Temperature	K	632.9	781.2
C	Equivalence Ratio		0.23	0.72

Figure 31 shows half normal probability plots for (a) the CHEMKIN simulation results and (b) the experimental data. Note that the ignition delay times were transformed using base 10 log. Both simulated and measured ignition delay times are heavily dependent on temperature, which coincides with all the autoignition expressions proposed for various fuels. While no factor interactions are observed for the simulated results, the experimental data show apparent AC and AB interactions with the chances that an effect is due to noise are 0.34% and 1.61%, respectively based on ANOVA (Analysis of Variance, Figure 31(b)). ANOVAs also suggest that pressure (Factor A) and equivalence ratio (Factor C) have significant effects on the simulation (Figure 31 **(a)**), but are not significant for the experimental results (Figure 31 (b)).

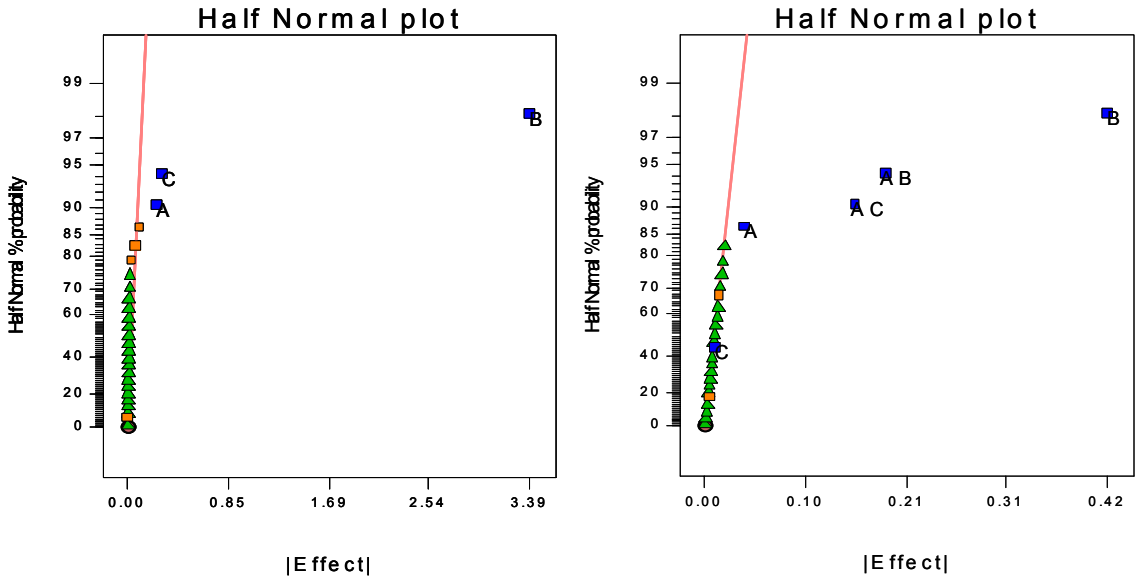

(a) (b)

Figure 31: Ignition Delay Times of UTRC Baseline Fuel: (a) Chemkin Simulation and (b) Experimental Data

Source	Sum of Squares	DF	Mean Square	F Value	Prob > F	
Model	20.39	3	6.80	1974.95	< 0.0001	significant
A	*0.089*	*1*	*0.089*	*25.97*	*< 0.0001*	
B	*18.62*	*1*	*18.62*	*5412.04*	*< 0.0001*	
C	*0.13*	*1*	*0.13*	*38.11*	*< 0.0001*	
Residual	0.079	23	3.441E-003			
Cor Total	20.47	26				

(a)

Source	Sum of Squares	DF	Mean Square	F Value	Prob > F	
Model	0.42	5	0.084	14.62	< 0.0001	significant
A	*3.546E-003*	*1*	*3.546E-003*	*0.62*	*0.4415*	
B	*0.27*	*1*	*0.27*	*46.32*	*< 0.0001*	
C	*7.907E-003*	*1*	*7.907E-003*	*1.37*	*0.2546*	
AB	*0.063*	*1*	*0.063*	*10.92*	*0.0034*	
AC	*0.039*	*1*	*0.039*	*6.85*	*0.0161*	
Residual	0.12	21	5.762E-003			
Cor Total	0.54	26				

(b)

Figure 32: Analysis of Variance (ANOVA) Summary for (a) CHEMKIN Simulation Results, and (b) Experimental Data

Interactions AB and AC for the factorial model of the experimental data are shown in Figure 33 and Figure 34, respectively. In both figures, a black line represents the lower limit of the corresponding factor while a red line represents the higher limit: T = 632.90 K (black) and T = 781.20 K (red) for Figure 33, and ϕ = 0.23 (black) and ϕ = 0.72 (red) for Figure 34. For example, at the lower temperature limit, pressure has a slight effect on the ignition delay at the very lean (ϕ = 0.23) condition while the pressure effect becomes more and more significant as the equivalence ratio increases within the experiment range. On the contrary, the pressure effect at the higher temperature limit shows the opposite trend.

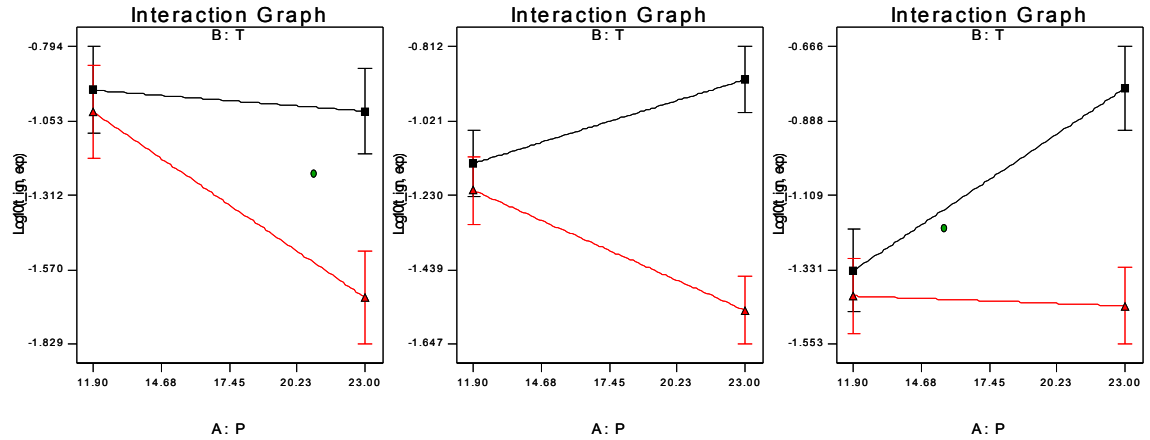

(a) $\phi = 0.23$ (b) $\phi = 0.47$ (c) $\phi = 0.72$

Figure 33: Pressure (Factor A) – Temperature (Factor B) Interaction at Various Equivalence Ratios. T = 632.90 K (black) and T = 781.20 K (red).

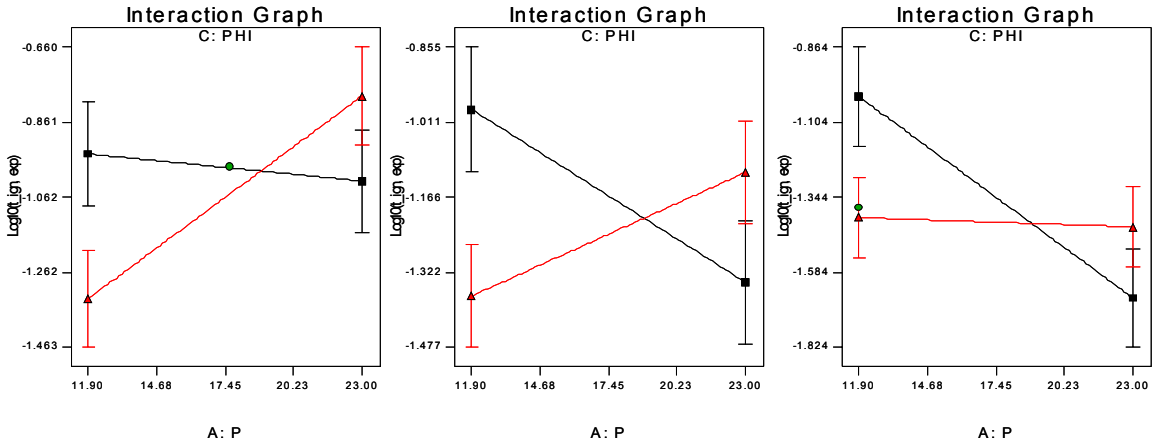

(a) T = 632.90 K (b) T = 709.05 K (c) T = 781.20 K

Figure 34: Pressure (Factor A) - Equivalence Ratio (Factor C) Interaction at Various Temperatures. $\phi = 0.23$ (black) and $\phi = 0.72$ (red).

Through the factorial numerical experiment, the expressions for the simulated (Equation 10) and measured (Equation 11) ignition delay can be obtained in terms of the selected effects (Figure 31). Figure 35 illustrates the variations of the actual data, (a) simulated and (b) measured), from the resulted Equation 10 and Equation 11, respectively.

$$\log_{10}(\tau_{ign,simulated}) = +16.98890 - 0.021154 \cdot \mathrm{P} - 0.020140 \cdot \mathrm{T} - 0.63959 \cdot \phi$$

Equation 10

$$\log_{10}(\tau_{ign,measured}) = -2.66723 + 0.18743 * P + 3.62066E-003 * T - 2.13800 * \phi - 3.47616E-004 * P * T + 0.11317 * P * \phi$$

Equation 11

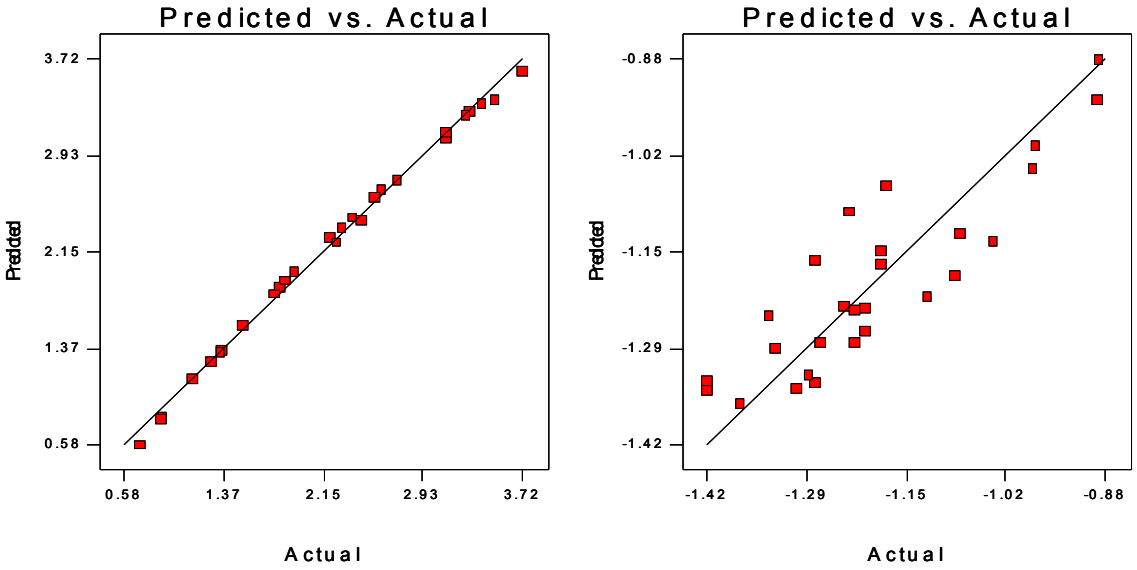

(a) (b)

Figure 35: Variation of the (a) Simulated and (b) Measured Ignition Delay Data from the Resulted Analytical Expressions.

The DoEx analyses shown are solely based on the results of Peschke & Spadaccini [**5**]. The results also raise some concerns in terms of the mechanism behind the observed P-T (AB) and P-ϕ (AC) interactions. If some physical interpretation of these interaction terms can be determined it could help establish the presence (or lack of) any systemic issues with the Peschke & Spadaccini dataset. Of course, the preferred approach is to simply carry out additional experiments, which are described in the next section.

5.2 Experimental Results

Despite the detailed assessment of the various simulation approaches and mechanisms, the lack of agreement shown in Figure 24 indicates a need for additional experimental results, hence the original motivation for the project. In this section, the experimental results obtained are described.

5.2.1 Experimental Procedures

Multiple tests were run on the UCICL continuous flow rig. The heater used for these tests was the 54 kW version shown in Figure 13. Unfortunately these heaters did not provide sufficient power to raise the air to the desired 1200 deg F. Instead maximum pre-mix air temperatures achieved were nominally around 1000 deg. F, (811 K). This has been a notorious challenge for electric preheating and despite efforts to maximize the heat rise, the current attempts were limited as mentioned. An air flow rate of 100 scfm (0.125 lb/m) at 60 psig (~ 5 atm) was used as a standard testing condition. As a first step, fuel was injected into the rig without any pre-heat since that more closely mimics the practical situation.

Initial facility check out tests revealed that the heat loss compensation (both active and passive) provided a relatively isothermal condition down the rig. With air from the main heaters at 1000 deg. F (811 K), the temperature of the cross flow measured down stream near the thermocouples read 930 deg. F. (772 K) Air temperature at the wall was normally 10 to 15 deg F (6 to 8 K) lower than at the pipe center. When the clamshell heaters were kept off, allowing only passive heat-loss resistance from the insulation blankets, temperatures remained surprisingly isothermal. The measured wall temperature half way through the rig (where the clamshells are located) measured within 2 deg. F (1.2 K) of the air temperature near the wall at the end of the rig near the PMTs. This would indicate that almost all the heat loss takes place in the initial half of the rig.

The test procedure followed to ensure consistency is summarized below:

- Initial air flow rate and pressure were set to 100 scfm (0.125 lb/min) and 60 psig. Temperatures were then set to 700 deg F. and raised by increments of 20 to 50 deg F. followed by fuel injection at varying rates to check for ignition at different concentrations.
- Once a desired temperature was achieved for the main flow, time was given until all thermocouple readings downstream remained steady. A manual 3-

way valve was turned to allow the correct fuel flow through which was monitored by a Micromotions Mass Rate measuring device. At this point the fuel was being inserted behind the water dump down into the exhaust line.

- Finally, the test initiator button as pushed which turned the solenoid valve and the fuel was injected into the test section. The four downstream thermocouples were then monitored to check for temperature difference. In cases of no ignition, temperature decreased as would be expected from adding a cold gas into the air stream. Whenever there was any increase in temperature, this was considered a sign of ignition, and a "Yes" data point given.
- At each temperature setting (700, 720, 740 etc..) , fuel was injected via the solenoid valve at flows varying from Phi = 0.05 to 0.7. According to past works, the greater fuel concentration results in faster ignition. However, because the fuels injected during these tests were at room temperature, the larger fuel flows resulted in lower mixture temperature, which extends ignition delay. From this we would be quite sure that at any temperature setting, the fuel concentration did not have a significant effect.
- If ignition (or a noticeable temperature rise) was observed for a specific residence time, the flow rate was increased to reduce residence time, and the tests were repeated. On the opposite end, if no reaction was observed, residence time was increased by reducing the flow rate. From this method it was hoped, that a temperature evolution could be plotted versus time, (similar to those seen in Mueller's Flow Reactor studies).

Table 13 and Table 14 shows one of the test runs completed. This specific test was run at 100 scfm, at a pressure of 61 psig, for H_2. As seen, at low temperatures no ignition was seen at all. But as temperatures increased in the 900 deg. F (755 K) range, the wall thermocouples (TC 1,2,3) registered small increase in temperature.

The residence time is determined by dividing the area of the test section by bulk flow rate of the mixture (air and fuel). The flow rates obviously change from increase in temperature and amount of fuel injected. However, typical residence times of remained between 150 to 200 ms

for most testing. While this does limit testing, the window can still be used to obtain data points that can be used to test existing correlations.

Once ignition was confirmed for a determined residence time, assigning a correct mixture temperature to this value was not a straight forward task either. As seen from Table 13, the temperature at different locations of the rig (even before injecting fuel) varied by as much as 70 deg F along the test section. Adding fuel with a different temperature adds an extra unknown to consider

Table 13 : Testing Conditions for run with H_2

Test	Phi	Fuel Rate	Main	Clamshell	Cross Flow	TC 1	TC 2	TC 3
		(lb/m)	(F)	(F)	(F)	(F)	(F)	(F)
1	0.30	0.05	700	498	505	483	506	505
2	0.25	0.05	745	600	570	547	573	569
3	0.30	0.06	800	-	648	625	649	649
4	0.28	0.05	847	751	700	677	700	700
5	0.28	0.05	885	763	730	-	-	-
6	0.28	0.05	900	772	750	-	-	-
7	0.28	0.05	935	738	771	-	-	-
8	0.16	0.03	970	800	769	798	799	-
9	0.28	0.06	970	800	769	798	799	-
10	0.37	0.07	970	800	769	798	799	-
11	0.26	0.05	988	822	828	-	-	-
12	0.26	0.05	990	835	846	816	844	843
13	0.26	0.05	1000	848	863	-	860	860
14	0.30	0.05	1000	880	885	-	-	-
15	0.30	0.05	1000	915	900	-	895	-
16	0.28	0.06	1000	938	912	-	910	-
17	0.30	0.06	1000	970	926	904	925	927
18	0.06	0.01	1000	970	926	904	925	927
19	0.37	0.07	1000	970	926	912	925	927

Table 14: Results of Test Run

Test	Mix T. (F)	Res. Time ms	Ign.	Temp Rise (F)	Temp Rise (K)	Comment
1	465	232	No	-	-	ClamShell off for now
2	533	221	No	-	-	
3	595	202	No	-	-	
4	645	195	No	-	-	
5	690	190	No	-	-	
6	717	186	No	-	-	
7	736	183	No	-	-	
8	760	191	No	-	-	No effect with diff. Fuel
9	736	184	No	-	-	flow rates
10	720	179	No	-	-	at this condition
11	757	178	No	-	-	
12	780	175	No	-	-	
13	795	173	No	-	-	
14	818	164	No	-	-	Clamshells are now on
15	818	161	No	-	-	
16	835	164	No	-	-	
17	846	162	Yes	61	34	TC1 Final: 907 F
18	907	175	Yes	22	12	TC3 Final : 929 F
19	831	158	Yes	86	48	TC1 Final: 917 F

Intuitively, one may consider that the temperature of the mixture to continuously decrease as it flowed down stream due to heat loss to walls and outside, however this is not the case in our tests. When the clamshells were kept off, the temperature of the wall was measured to be the same temperature as the air at the wall. This is not surprising considering the rig was left running at a set temperature conditions for a few minutes before injection to ensure steady state. When the cold fuel is injected, the new mixture temperature will be colder than the walls and heat transfer will be to the fluid, even more so when the clamshells are actually turned on. It was observed in all cases, the measured cross flow temperature at the end of the rig is lower than the main heater temperature, leading to the conclusion that in the end there must be a net heat loss to the surroundings. Therefore it is important to note, that temperature fluctuates in a less than predictable manner. Analysis of the results and evaluation of the sensitivities, a temperature uncertainty of +/- 30K was established.

5.2.2 H_2 ignition Measurements

Ignition or noticeable temperature increase occurred for H_2-air only 130-150 ms after injection. This was for the temperature range between 750-770 K and pressure at 5 atm. When the plot in Figure 23 for H2-air is extended out to much cooler regime where our current study was tested, it is obvious the simulation over predicts as was expected from the earlier work (Figure 36). These points suggest that true slope is much shallower than reported by Hydrogen 2004.

As discussed in Appendix A, even in the experimental cases where full auto-ignition was not observed, the rapid rise in temperature observed is much faster than that predicted by any of the models, leading to the conclusion that the models over predicts ignition time by the same factor as they are with predicting temperature rise.

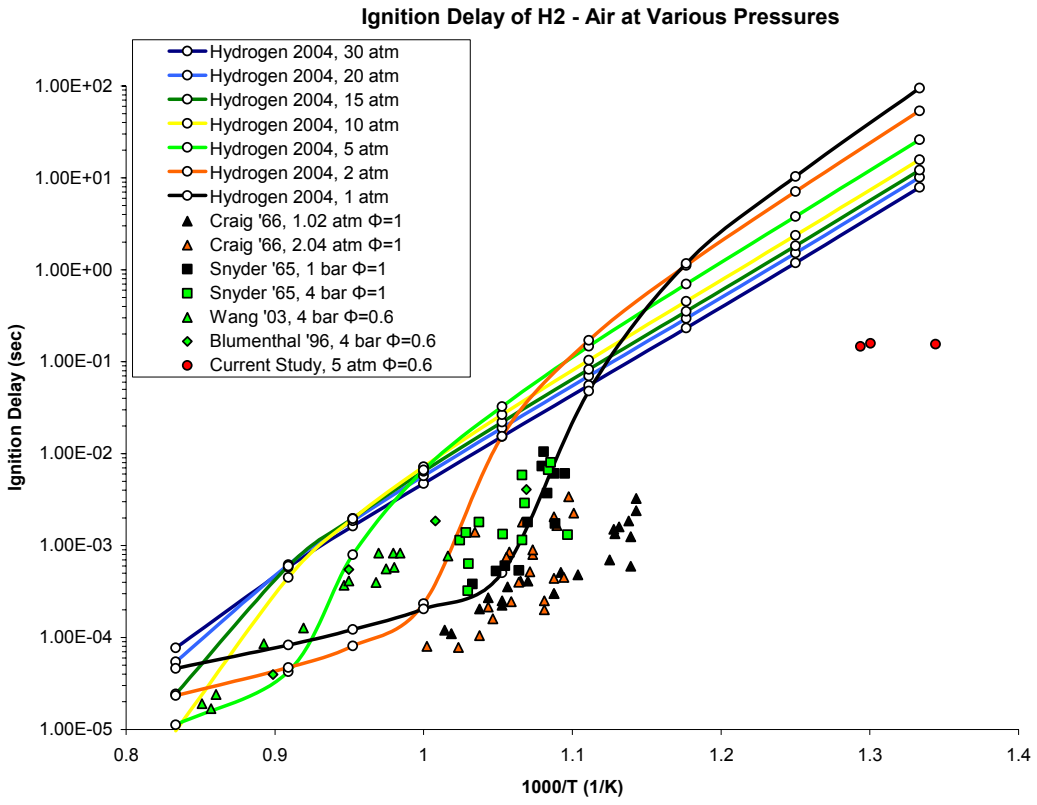

Figure 36: Comparison of Existing and Current Ignition Delay Results for Hydrogen.

5.2.3 H_2/CO Ignition Measurements

Results from the current study are plotted against the Mueller mechanism for various pressures in Figure 37. Because all the mechanisms are similar (recall Figure 24), comparing to only a single mechanism is sufficient to draw conclusions. Figure 37 shows the new data from this study along with a plot of predicted delay times, previous flow reactor data [5], and another previously unpublished study from carried out at the UCICL [26] using another H2/CO/CO2 mixture. Results from the current study coincide with the previous results [5, 26]. Peschke and Spadaccini [5] reported a pressure dependency of P^ (-0.75) for ignition time. When the current study's values are scaled using this relation, they lie directly on top of the previous results [5] which were obtained for pressures between 16-21 atm. The simulated delay times shows a shorter delay time for higher pressures in the lower temperature regions, but in all cases the predictions are 1-2 orders of magnitude longer than the measured values and diverge farther as temperature decreases. It is noted that, if the result from [26] were scaled for pressure, it would also fall nearly on top of the work from [5] as well as the pressure scaled results from the present work

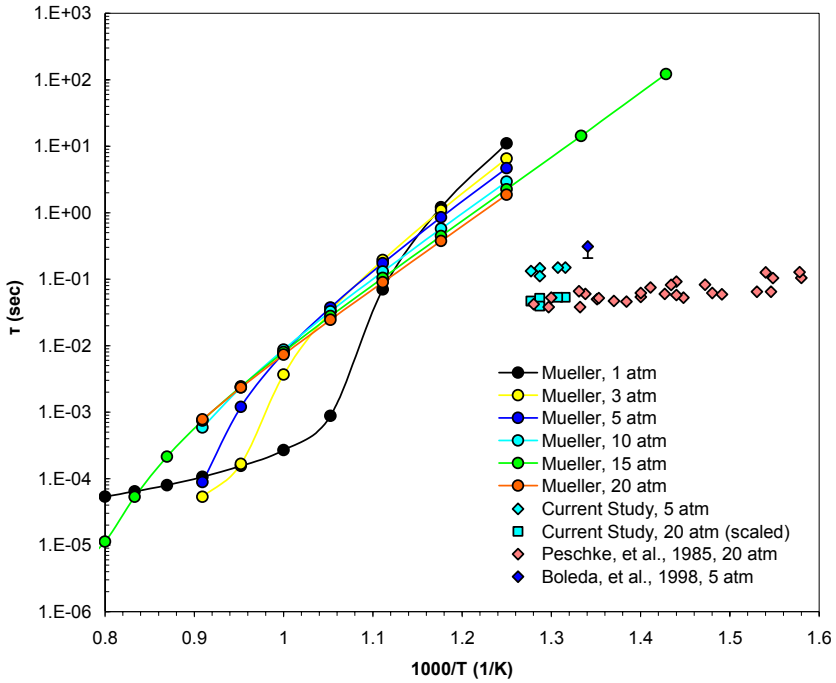

Figure 37. Comparison of Existing and Current Ignition Delay Results for Hydrogen/Carbon Monoxide Mixtures.

The measurement points shown in Figure 37 are tabulated in Table 15 for convenience.

Table 15: Current Study Ignition Points from Plots

Pressure	Fuel Type	Phi	Fuel Rate	Main	Clamshell	Avg. T mix	1000/T	T rise	Res. Time
(psig)			(lb/min)	(F)	(F)	(F)	(1/K)	(K)	(ms)
60	H2	0.30	0.500	998	977	880	1.344	64.4	155
61	H2	0.37	0.070	1000	970	925	1.300	53.3	158
63	H2	0.60	0.100	999	1013	933	1.294	77.8	147
63	H2/CO	0.40	0.709	1001	1015	950	1.277	65.6	132
63	H2/CO	0.33	0.709	944	1021	939	1.287	53.3	111
60	H2/CO	0.60	0.800	1000	968	939	1.287	79.4	146
60	H2/CO	0.60	0.540	-	995	910	1.314	75.0	150
60	H2/CO	0.54	0.709	995	974	921	1.304	67.8	150

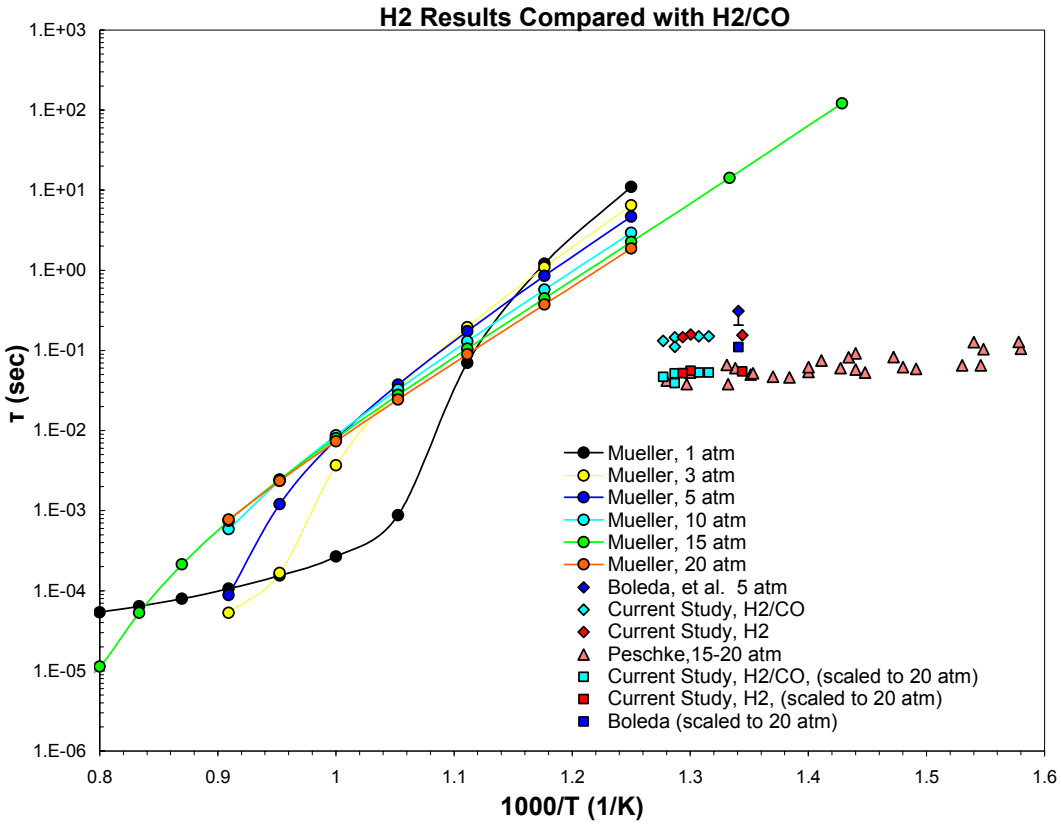

Figure 38: Comparison of H2 and H2/CO Results

6 CONCLUSIONS and RECOMMENDATIONS

A facility for measurement of ignition delay times for fuel/air mixtures at gas turbine combustor inlet temperatures and pressures has been developed. Enhancements to the facility carried out under the current project include additional temperature and pressure capability and improved ignition detection. Although the enhancements were implemented during the project, complete facility commissioning at the highest temperatures and pressures was not completed. Despite this, measurements of ignition delay times were conducted for Hydrogen and Hydrogen/Carbon Monoxide mixtures at moderate temperatures and pressures.

The results obtained have been compared to a number of simulated ignition delay times calculated using various detailed chemical kinetic mechanisms developed for syn-gas type fuels. Predicted ignition delay profiles calculated using mechanisms by Mueller et al. [910], GRI-Mech 3.0 [11], Baulch et al. [12], UCSD [15], Davis et al., [14] and Conaire, et al. [16], show general agreement. However, the Baulch et al. [12] mechanism and GRI-Mech 3.0 mechanisms [11] predicted systematically longer ignition delay for the temperature range of 750 – 1250 K (890 – 1790 ^{o}F) and below 750 K (890 ^{o}F), respectively.

Despite general agreement among the predicted delay times, significant discrepancy was observed between CHEMKIN simulation results, including simulations at the same conditions as Peschke & Spadaccini [5] for their baseline fuel (38.6% H_2, 51.1% CO, 10.3% CO_2). Measurements from the present work are consistent with the results observed previously from both Peschke and Spadaccini [5] as well as a previously unpublished study [26]. Results from the present study also indicate little effect of CO on the ignition delay time. Like the results from [5], the ignition delay of IGCC type fuels can apparently be well represented with ignition delay times of pure hydrogen.

The results for pure hydrogen obtained in the current project also matched closely the results for IGCC type fuels. Predictions using a recent mechanism developed for hydrogen were compared with the measurements from the present work and the trends were very similar to those for the hydrogen/carbon monoxide mixtures—namely that the predicted delay times were much longer than the measured times for the lower temperature regimes relevant to gas turbine premixers.

Efforts were initiated to explain the reason for the differences between the measured and predicted delay times. One approach taken involved execution of statistically designed matrices. The analysis of variance carried out indicated that temperature was predictably the biggest effect for both predicted and measured data. The results suggest pressure and equivalence ratio have a small, but significant effect on the simulated data, while their effects were insignificant for the experimental results. On the other hand, interactions between pressure and temperature, and pressure and equivalence ratio were found to be significant for the experimental data. No physical reason has been established for this interaction, but it may be a clue as to what is apparently missing the in the kinetic mechanisms developed thus far. Additional data are required to further investigate the auto-ignition profile of the IGCC type fuels.

In addition to the statistical assessment, sensitivity studies were conducted on the mechanisms and the key pathways identified. Additional analysis of these results may also lead to an explanation of the discrepancies between measured and predicted delay times.

In summary, the expressions developed previously for IGCC syngas from 1986 have been affirmed in the current work and it can be applied for gas turbine applications.

$$\tau \left[O_2\right]^{0.50}\left[F\right]^{0.25} = 1.29\times10^{-7}\exp\left(\frac{3985}{T}\right)$$

$$\tau \left[O_2\right]^{0.50}\left[H_2\right]^{0.25} = 1.02\times10^{-7}\exp\left(\frac{3985}{T}\right)$$

Where

τ is an ignition delay time (sec),

$[O_2]$, $[H_2]$ and [F] are the molar concentration (moles/cm^3) of oxygen and fuel, T is a temperature (K).

Regarding recommendations, while the current work has confirmed an existing expression, it would be helpful to operate the reactor at higher temperatures and pressures in order to bridge with previous data. The means for this have already been established it is just a matter of spending some additional time. Ideally, pressures up to 40 atm could be achieved. The present facility can reach 20 atm, although it was only operated at 5 atm for the current work. It is noteworthy that scaling the 5 atm results to 20 atm resulted in essentially identical results found previously. As a result, scaling up further may be reasonable. It would be helpful to study conditions that approach the region where the pressure and temperature coupling is seen in the

predicted ignition delay results. This would help elucidate some of the subtle effects that the predictions exhibit. In addition, while the thermocouples were effective in identifying ignition, the optical system developed and tried on a limited basis should be implemented formally. Finally, the sensitivity of the results to wall temperature details would be worth exploring. It would also be useful to explore the influence of water vapor on the results. Finally, it would be useful to ascertain why the existing predictions do not agree well with measured data.

7 REFERENCES

1. Lefebvre, A., Freeman, W., and Cowell, L., "Spontaneous Ignition Delay Characteristics of Hydrocarbon Fuel/Air Mixtures," NASA Contractor Report 175064, 1986.

2. Spadaccini, L. J., and Colket M. B., "Ignition Delay Characteristics of Methane Fuels," *Progress in Energy and Combustion Science*, Vol. 20, 1994, pp. 431-460.

3. Richards, G. A., McMillian, M. M., Gemmen, R. S., Rogers, W. A., and Cully, S. R., "Issues for Low-Emission, Fuel-Flexible Power Systems," *Progress in Energy and Combustion Science*, Vol. 27, 2001, pp. 141-169.

4. Chen, J., Jermakian, V., McDonell, V., Samuelsen, S., "Correlation of Ignition Delay with Fuel Composition and State for Application to Gas Turbine Combustion," Final Report for AGTSR Subcontract 00-01-SR084CS under DOE NETL Contract DE-FC21-92MC29061, University of California, Irvine Combustion Laboratory, January 2003.

5. Peschke, W. T., and Spadaccini, L. J., "Determination of Autoignition and Flame Speed Characteristics of Coal Gases Having Medium Heating Values," Final Report for AP-4291 Research Project 2357-1, November 1985.

6. Jones, R. M., Shilling, N. Z., "IGCC Gas Turbines for Refinery Applications," GE Power Systems, GER-4219, Schenectady, NY, May 2003.

7. Clean Coal Technology, "The Wabash River Coal Gasification Repowering Project – An Update," Topical Report No. 20, The U.S. Department of Energy and Wabash River Coal Gasification Project Joint Venture, September 2000.

8. Kee, R. J., Rupley, F. M., Miller, J. A., Coltrin, M. E., Grcar, J. F., Meeks, E., Moffat, H. K., Lutz, A. E., Dixon-Lewis, G., Smooke, M. D., Warnatz, J., Evans, G. H., Larson, R. S., Mitchell, R. E., Petzold, L. R., Reynolds, W. C., Caracotsios, M., Stewart, W. E., Glarborg, P., Wang, C., Adigun, O., Houf, W. G., Chou, C. P., and Miller, S. F., Chemkin Collection, Release 3.7.1, Reaction Design, Inc., San Diego, CA, 2004.

9. Mueller, M. A., Kim, T. J., Yetter, R. A., Dryer, F. L., "Flow Reactor Studies and Kinetic Modeling of the H_2/O_2 Reaction," *International Journal of Chemical Kinetics*, Vol. 31, 1999, pp. 113-125.

10. Mueller, M. A., Yetter, R. A., and Dryer, F. L., "Flow Reactor Studies and Kinetic Modeling of the $H_2/O_2/NO_X$ and $CO/H_2O/O_2/NO_X$ Reactions," *International Journal of Chemical Kinetics*, Vol. 31, 1999, pp. 705-724.

11. Smith, G. P., Golden, D. M., Frenklach, M., Moriarty, N. W., Eiteneer, B., Goldenberg, M., Bowman, C. T., Hanson, R. K., Song, S., Gardiner, W. C., Jr., Lissianski, V. V., and Qin, Z., http://www.me.berkeley.edu/gri_mech/

12. Baulch, D. L., Cobos, C. J., Cox, R. A., Frank, P., Hayman, G., Just, Th., Kerr, J. A., Murrells, T., Pilling, M. J., Troe, J., Walker, R. W., and Warnatz, J., "Summary Table of Evaluated Kinetic Data for Combustion Modeling: Supplement 1," *Combustion and Flame*, Vol. 98, 1994, pp. 59-79.

13. Akbar, R., Kaneshige, M., Schultz, E., Shepherd, J., "Detonations in H_2-N_2O-CH_4-NH_3-O_2-N_2 Mixtures," Explosion Dynamics Laboratory Report FM97-3, Graduate Aeronautical Laboratories California Institute of Technology (GALCIT), July 1997.

14. Davis, S. G., Joshi, A. V., Wang, H., and Egolfopoulos, F., "An Optimized Kinetic Model of H_2/CO Combustion," 30th International Symposium on Combustion, Chicago, IL, July 25-30, 2004.

15. Williams, F. A., et al., http://maeweb.ucsd.edu/combustion/cermech/

16. Conaire, M. Ó., Curran, H. J., Simmie, J. M., Pitz, W. J., and Westbrook, C. K., "A Comprehensive Modeling Study of Hydrogen Oxidation," International Journal of Chemical Kinetics, Vol. 36, 2004, pp. 603-622. (UCRL-JC-152569).

17. Blumenthal, R., "Experimentelle Untersuchung und numerische Simulation der Selbstzuendung von Kraftstoff/Luft-Gemischen im Stosswellenrohr unter Beruecksichtigung stroemungsmechanischer Einfluesse", Doctoral Thesis, Institut fuer Allgemeine Mechanik, RWTH Aachen, 1996

18. Wang, B.L., Olivier, H. and Groenig, H., "Ignition of Shock-Heated H_2-Air-Stream Mixtures", Comb. Flame, 133, 93-106, 2003

19. Craig, R.R., "A Shock Tube Study of the Ignition Delay of Hydrogen-Air Mixtures near the Second Explosion Limit", Report AFAPL-TR-66-74, 1966.

20. Snyder, A.D., Robertson, J. , Zanders, D.L. and Skinner, G.B., "Shock Tube Studies of Fuel/Air Ignition Characteristics", Report AFAPL-TR-65-93-1965

21. Sabia, P., Schiesswohl, E., de Joannon, M.R., Cavaliere, A., "Numerical Analysis of Hydrogen Mild Combustion," *Turkish Journal of Engineering Environmental Sciences* Vol. 30, 2006, 127-134

22. Glassman, I. *Combustion*, 3rd Edition, 2002.

23. Kuo, K. K., *Principles of Combustion*, John Wiley & Sons, Inc., New York, 1986.

24. Atri, G. M., Baldwin, R. R., Jackson, D., and Walker, R. W., "The Reaction of OH Radicals and HO_2 Radicals with Carbon Monoxide," *Combustion and Flame*, Vol. 30, 1997, pp. 1-12.

25. Mittal, G., Sung, C., Yetter, R., "Autoignition of H_2/CO at Elevated Pressures in a Rapid Comprssion Machine," *International Journal of Chemical Kinetics,* Vol. --- 2006

26. Boleda A., McDonell V., Samuelsen G.S., "Standalone Power Plant Running on Biomass Gas – Phase 1" Final Report. Prepared for Reflective Energies. UCI-ARTR-98-1

Appendix A - General Observations Regarding Ignition

Some of the general observations made during the tests warrant additional comment. In the present study, whenever the temperature readings on any of the thermocouples in the rig registered a sudden increase after injection of fuel, this was considered a sign of ignition and marked "Yes" in the data tables. While this apparently adds some uncertainty in the actual location of ignition within the flow reactor, the length of the test section and location of the thermocouples does not translate into a significant variation in time at least in the context of comparing with the orders of magnitude discrepancies observed in the comparison of the modeled and measured ignition delay times previously reported (Figure 24).

"Full auto-ignition" was not generally observed during the testing. The most commonly (and repeatable) experienced result observed were relatively small temperature rises up to 145 degrees F, (up to 80 K). These reactions occurred relatively soon after injection of the fuel. This was observed for both fuels tested, H_2 and the H_2/CO. Temperature rises under the same conditions were greater for H_2 than for H_2/CO.

Full auto-ignition was a very large increase in temperature (with final temperature in the range of 1600 + deg. F). At first this normally occurred within 2 or 5 seconds after fuel was injected. This type of ignition produced a noticeable pressure increase and acoustic emission from the test rig. The 'pop' preceded the temperature rise on the thermocouples by approximately one second due to their relatively long response time. The light emission from this type of event was clearly registered on with the chemiluminescence detection setup.

As discussed earlier, the residence time for the fuel line itself is in the 550- 950 ms. Therefore seeing ignition between 1 to 2 seconds after the test initiator switch is pushed is expected. However, when ignition is only observed after more than 5 seconds, it suggests a different type of ignition mechanism.

This was first experienced when the thermocouple measuring cross flow protruded into the flow stream perpendicular to the flow velocity. It was suspected that this protrusion was acting as a flame stabilizer. To test this, the thermocouple was replaced with one that did not protrude past the wall of the pipe. A second thermocouple replaced the chemiluminescence detection probe which was position along the axis of the pipe. It was hoped that a thermocouple in this position, rather than perpendicular to the flow would not cause a stabilizing point. This

new thermocouple had to be rigid, so a ¼" K Type which had a longer time constant than the smaller thermocouple measuring at the wall was used. Under this new set up only a single instance of "full auto ignition" was experienced. In this case it was with H_2 (.07 lb/min) and occurred with in 1.5 sec of triggering the fuel. It was concluded then, then that past ignition in the range of 5 + seconds were the result of the flame stabilizing on the tip of the thermocouple, where the one instance seen under the new set up was a desired full auto ignition without the enhancement of flame stabilization. The test run summarized in Table 13 was carried out with the thermocouple retracted, precluding the possibility of flame stabilization.

It is believed that the minor temperature rises are partial oxidation and that not all the reactants were consumed by the end of the testing section. However, this behavior always results in full autoignition shortly thereafter. Figure A-1 shows the temperature evolution of a reacting mixture of H2/CO with initial temperature and pressure of 800 K and 5 atm respectively according to GRI-Mech 3.0. The default setting for registering autoignition is a temperature increase of 400K. For this reaction, this occurs around 3.6s. All the plots in this report use this definition of autoignition unless stated otherwise. Figure A-1 registers a temperature rise of 5K in 1.5s, 10Kin 2.1s and 20K in 2.7s. If the default setting for autoignition is changed to a temperature rise of 10K, the perceived ignition delay time is reduced (compared to a 400 degree by a factor of 1.7. While significant, as shown in the following sections, it is small compared to differences observed.

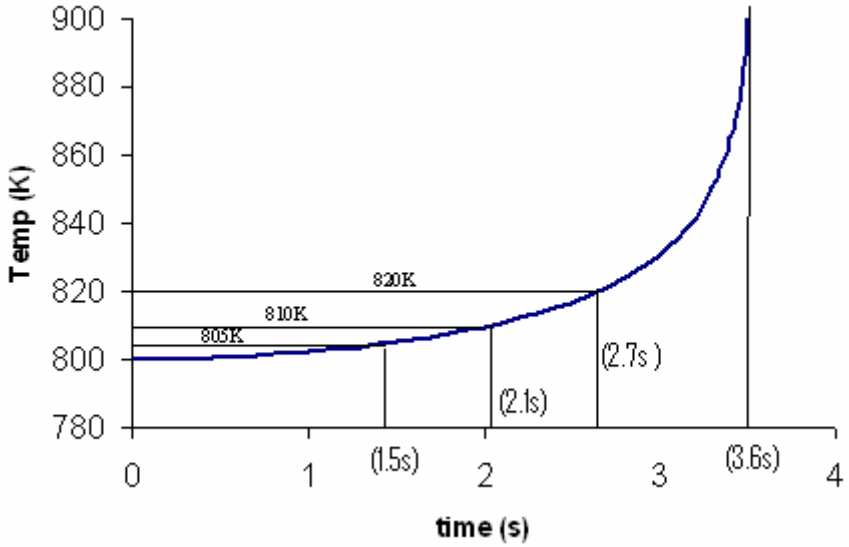

Figure A-1. Typcial Temperature Rise History.

Ideally, tests would have continued at even higher temperature ranges to confirm this. However, the 54 kW heaters were running at their maximum output and higher temperatures could not be reached. The points labeled under "Current Study" on the plots later in this report, show where maximum temperature rises occurred for each fuel tested. It is evident that if these points precede only slightly the occurrence of full auto-ignition, then experimental correlation of Peshke and others are correct.

Another interesting phenomena observed during testing conditions was the non-uniform temperature spike among the thermocouples in the end of the test section. Five of these thermocouples (positioned at the wall) are 1/32" exposed bead Type K's, while the thermocouple positioned axially down the rig is a 1/8" grounded Type K. The time constant of each are 1.8 and 11 seconds respectively.

During a full autoignition, all six measured a large spike (in the 1600 deg + F within a second of hearing the pressure increase). However, when the reaction resulted in the small temperature rises, the axially located thermocouple never read a temperature increase, while one or two of the wall thermocouples did. Typically the second thermocouple in the line of 5 measuring temperature at the wall was the only one to see increases. It was suspected that the thermocouple itself may be faulty, so it was switched with the first thermocouple in line, and tests were re-run. This had no effect on the system. However later tests did see increases in more than just thermocouple #2 along the wall, while the axial thermocouple typically did not measure any difference, while on a few occasions showed a drop in temperature. Two possible suggestions could explain this. First, the time constant and mass of the axial thermocouple (1/8" as opposed to 1/16") could mean that not enough time was allowed for it to measure an increase in temperature. Second would be that, ignition was starting at the walls and propagating toward the center. This could result from the slower velocity near the walls, resulting in a residence time slightly longer than that of the measured bulk time. In addition, the clam shells create a temperature gradient which is hotter near the walls than at the axis. To determine what is causing this, further tests will be run using propane. Propane's quenching distance should be larger than the boundary layer, diminishing the effect if the velocity profile. Tests with the walls at cooler temperatures (by removing insulation, keeping clamshells off) should be considered in the future.

Film Cooling Effectiveness and Heat Transfer on a Rotating Blade Platform

Annual Report

Reporting Period
March 1, 2006 – December 31, 2006

Principal Investigators
J.C. Han
M.T. Schobeiri

Report Submitted
February 2007

DOE Award Number
DE-FC26-02NT41431

UTSR Project Number
02-01-SR113

Texas A&M University
Department of Mechanical Engineering
College Station, Texas 77843-3123

DISCLAIMER

ABSTRACT

This project experimentally investigates the heat transfer phenomena on the rotor blade platform of gas turbine blades. Designers often rely on experimental data gathered from non-rotating models to provide cooling designs on rotating platforms. In many cases, the non-rotating models inadequately model the flow and heat transfer around the rotating blades. This might lead to insufficient protection of the hot gas path components leading to thermal failure. Also, over compensating for the non rotating model deficiencies by providing excessive coolant might lower the system efficiency. Hence, detailed film cooling effectiveness distributions were gathered on the rotating blade platforms using pressure sensitive paint to study the effects of rotation on platform film cooling and heat transfer. Film cooling experiments were conducted separately for upstream stator-rotor seal injection and downstream discrete hole injection at different rotational speeds for several blowing ratios. Film cooling effectiveness was measured for turbine rotor frequencies of 2400rpm, 2550rpm and 3000rpm. Coolant to mainstream mass flow ratio (MFR) of 0.5%, 1.00%, 1.50% and 2.00% were considered for the stator- rotor seal injection at the three rotational frequencies. For each of the turbine rotational frequencies, film cooling effectiveness is also determined for average film-hole blowing ratios of M_{holes}=0.5, 0.75, 1.0, 1.25, 1.5 and 2.0. To provide a complete picture of hub cooling under rotating conditions, simultaneous injection of coolant gas through upstream stator-rotor seal and downstream discrete film-hole was also studied. The combined tests were conducted for seal flow corresponding to coolant to mainstream mass flow ratio of MFR=1% with three downstream film-hole blowing ratios of M_{holes}=0.75, 1.0 and 1.25 for each of the three turbine speeds. Miniature five-hole pitot tubes are used to obtain profiles of the mainstream flow through the turbine stage. Rotation was found to significantly affect the distribution of coolant on the platform and the measured effectiveness magnitudes were lower than those observed for turbine cascades. This experimental data was used to

validate numerical simulations, and the numerical predictions will be extended to include a wide range of rotor platform configurations and film cooling flow conditions to better model actual engine conditions. The work in progress attempts to measure heat transfer coefficients on the rotating platform for the above stated experimental conditions

TABLE OF CONTENTS

LIST OF FIGURES

EXECUTIVE SUMMARY

This study investigates the flow behavior and heat transfer distributions on rotor blade platforms of gas turbine engines. The experimental and numerical results will provide turbine designers with new rotating blade platform heat transfer and film cooling data which will improve the cooling performances and thermal efficiency of power generation and industrial gas turbine engines. The three year project consists of three tasks in order to provide designers with applicable rotating blade platform cooling data. Task 1 of this project is to redesign and fabricate a new rotor platform to incorporate two coolant flows: stator-rotor ejection and film cooling flow. With Task 2, detailed pressure, heat transfer coefficient, and film cooling effectiveness distributions resulting from coolant ejection from the annular between the stator and rotor will be obtained on the rotating blade platform. In Task 3 of the project, detailed rotor blade platform pressure, heat transfer coefficient and film cooling effectiveness distributions with a typical film cooling hole geometry will be obtained. In addition a combined injection case with upstream stator-rotor seal and downstream discrete hole injection will also be studied. Equivalent numerical simulations will be performed to compare the experimental and predicted results.

The experimental results obtained thus far indicate the film cooling effectiveness on a rotating platform can be significantly lower than the film cooling effectiveness measured in non-rotating test facilities. The blade profile used in the present study is unlike the profile used in most non-rotating studies. The selected profile may alter the behavior of the horseshoe vortices formed at the leading edge of the blade and thus reduce the film cooling effectiveness. This profile, coupled with both the selected seal geometry (injection angle, seal width, coolant blowing ratio) and rotation, lead to reduced film cooling effectiveness on the rotating platform compared to previous non-rotating studies. It has also been observed that the film cooling

effectiveness increases as the rotational speed increases for upstream stator-rotor seal injection. Turbine platform with coolant holes provided sufficient cooling downstream of the throat region. The maximum effectiveness was found to be at the reference speed for the hole injection. A combination of the upstream stator-rotor seal and downstream hole injection covered most of the platform providing good coolant coverage. Turbine designers should need these new experimental results. If blade platforms are cooled using data developed from non-rotating facilities, the data can tremendously over predict the protection on the rotating platform. This can lead to blades that are not sufficiently protected and premature failure.

The film cooling effectiveness and heat transfer coefficients have also been predicted on the rotating blade platform. These predictions give additional insight of the flow around the rotating blades. Currently, the experimental results are being used to verify the numerical prediction, and then the simulations will be extended to consider the heat transfer and cooling on rotating platforms under more advanced conditions (which cannot be achieved in the laboratory).

The experimental results from this project will provide turbine designers with detailed heat transfer and film cooling data on the rotating turbine blade platforms. The experimental results will also validate the numerical predictions performed for the blade platforms. From this comprehensive detailed data, engineers will be able to design a more efficient platform geometry with film cooling holes which increase the durability and longevity of the blade platforms. The effective cooling schemes will also save cooling flow. By reducing the cooling flow while effectively cooling the rotating blades, the power output and efficiency of the engine will increase.

PROJECT DESCRIPTION

Introduction

As economies across the world continue to grow, the demand for power also continues to increase. Commercial, industrial, and residential customers have come to expect uninterrupted electrical service required to meet a variety of needs; however, the demand for power is growing faster than the power supply. Meanwhile, the commercial airline industry is facing numerous hurdles while the military is facing new challenges. The common bond between land based power generation and aircraft propulsion is gas turbine engines. With gas turbines also being used for marine propulsion and scores of other specific industrial applications, it is vital that these engines operate efficiently. The efficiency of a gas turbine engine can be increased by raising the temperature of the hot gases at the inlet of the turbine. However, increasing the temperature of the mainstream gas must be done cautiously, as additional problems can develop. The metallic turbine components must be protected in order to survive prolonged exposure to the hot gases. The life of the turbine airfoils can be increased by implementing any of a variety of cooling techniques, as shown in Figure 1. As presented by Han et al. [1], air is extracted from the compressor, and used to cool the airfoils. This coolant air is injected into the hollow airfoils, and circulates through internal cooling passage of the blades and vanes. The coolant is discharged through discrete holes, where it forms a protective film on the outer surface of the airfoil. Figure 2 shows the complex flow around a turbine blade, and this three-dimensional flow can have adverse effects on the film coverage across the airfoils. Many investigations have focused on increasing the heat transfer enhancement within the blades via rib turbulators, jet

impingement, and pin-fins. Also, film cooling has been studied for many years to determine the optimal hole configuration and flow conditions to maximize the protection of the coolant.

With the increasing temperature of the mainstream gases exiting the combustor, the stator vanes and rotor blades must be protected, so they can survive the extreme temperatures. Recently, the blade platform has received renewed attention for an adequate cooling scheme. The vane endwall and the blade platforms comprise a large percentage of the area exposed to the hot mainstream gases. There is a strong potential for "hot spots" to form on the endwalls and platforms. Over this large area it is vital to have accurate heat transfer distributions, so efficient cooling schemes can be developed. The cooling schemes should adequately protect the platforms while minimizing the amount of coolant.

Experimental investigations available in open literature on film cooling and heat transfer on rotating turbine blades and their components are few and far between, primarily due to the difficulty in instrumenting rotating parts. Dring et al. [2] investigated film cooling performance in a low speed rotating facility. A film cooling hole was located on both the pressure and suction sides. They used ammonia and Ozalid paper to qualitatively observe the coolant trace while the quantitative tests were conducted using thermocouples. Their results show that the film coolant had only a small radial displacement, similar to flat plate results, on the suction side. On the pressure side, the film coolant trace had a large radial displacement toward the blade tip. Effectiveness distributions on the blade span for a rotating turbine blade were also provided by Takeishi et al. [3] and Abhari and Epstein [4] using gas chromatography and thin film heat flux gages respectively.

Blair [5] studied the heat transfer on the pressure and suction sides as well as on the hub platform surface for a rotating turbine model. Enhanced heat transfer was observed on the

platform due to the secondary flow effects. Recently, Ahn et al. [6, 7] investigated the film cooling effectiveness on the leading edge of a rotating blade using the PSP technique. The same experimental facility has been used in this paper with a design modification to allow for stator-rotor cooling. They studied film cooling due to two row and three row coolant injection on the leading edge at design and off-design rotating conditions. Off-design conditions were found to significantly alter the film coolant traces on the leading edge.

A summary of film cooling effectiveness and heat transfer studies performed on the platforms of stationary cascades follows. Platform film cooling effectiveness investigations have been predominantly performed using cascade vanes. The secondary flow in a turbine passage is very complex and varies based on the blade profile being considered. Langston et al. [8, 9] performed flow measurements to gain insight into this complex secondary flow. They showed at the inlet of the passage, the boundary splits at the leading edge of the blade. A horseshoe vortex forms with one leg on the pressure side of the blade, and the other leg on the suction side of the blade (in the adjacent passage). The pressure side leg of the horseshoe vortex travels from the pressure side of the passage to the suction side; this pressure side leg of the horseshoe vortex becomes known as the passage vortex. This passage vortex will eventually meet the suction side leg of the horseshoe vortex that has remained near the junction of the suction surface and endwall. Goldstein and Spores [10] also studied the flow through a blade passage. They identified multiple "corner" vortices that developed throughout the passage. A pressure side corner vortex develops just downstream of the leading edge, and the vortex carries about one-third of the chord length. Two suction side corner vortices develop along the suction surface in the latter half of the passage. After the passage vortex carries to the suction side of the passage, it lifts from the endwall surface. Below the passage vortex, along the junction where the suction surface meets the endwall, suction side, counter rotating, corner vortices form.

The highly complex, three-dimensional flow has a strong influence on the heat transferred from the mainstream flow to the blade platform. Blair [11] pioneered the study of endwall heat transfer. He found significant variation of the heat transfer coefficient across the passage and downstream to the trailing edge of the vane due to the secondary flow along the endwall. Graziani et al. [12] also reported large variations in the endwall heat transfer coefficients. They showed the heat transfer coefficients on the suction surface of the blade are also influenced by the secondary flow through the passage; however, the heat transfer coefficients on the pressure surface are not affected by the strong secondary flows. Using a mass transfer technique, Goldstein and Spores [10] showed as the boundary layer splits to form the two legs of the horseshoe vortex near the leading edge of the blades, the heat transfer coefficients increase, and the greatest heat transfer enhancement on the endwall occurs near the leading edge. Other variations are present on the endwall due to the path of the passage and corner vortices. In addition near the trailing edge of the blade, the heat transfer coefficients are elevated as the two flows from the two passages meet at the trailing edge. The heat transfer coefficients were also measured on the endwall of a vane passage [13 – 15]. Similar variations were found, as the heat transfer continues to be dominated by the secondary flow. When the effect of freestream turbulence was considered [14, 15], it was found that increasing the turbulence intensity increases the heat transfer coefficients on the passage endwall. However, the effect of the freestream turbulence intensity was minimal near the leading edge and the near the suction surface, where the horseshoe and passage vortices dominate the heat transfer behavior.

With the local areas of high heat transfer identified, film cooling can be implemented on the blade platform to reduce the heat load in these areas. Takieshi et al. [16] obtained heat transfer and film effectiveness distributions on a vane endwall with discrete film cooling holes

placed at three locations in the passage. They found that the effectiveness is very low near the leading edge on the suction side; with the rollup of the horseshoe vortex, the film coolant lifted from the surface, and offered little or no protection. The path of the coolant was also influenced by the passage vortex transporting the coolant from the pressure to the suction side of the passage. Harasgama and Burton [17] used film cooling near the leading edge, just inside the passage, with the film cooling holes located along an iso-Mach line. Although the row of film cooling holes was evenly distributed to span the passage, no coolant reached the pressure side of the passage. The film cooling configuration used by Jabbari et al. [18] consisted of discrete holes placed on the downstream half of the passage. Similar to the upstream design [17], the film cooling effectiveness varied significantly through the passage, with the coolant moving to the suction side of the passage.

Friedrichs et al. [19 – 21] studied the film cooling effectiveness using the ammonia and diazo technique. They found that a simple layout of the film cooling holes throughout the passage can result in areas being over cooled (or under cooled) due to the secondary flow. With their proposed "improved design," the film holes were placed, so the strong secondary flow could be used advantageously. Using the same amount of coolant, they were able to provide improved coolant coverage. Recently, Barizozzi et al. [22] compared the film cooling effectiveness on a passage endwall with cylindrical or fan-shaped film cooling holes. With their cooling designs, they showed that by increasing the blowing ratios, the passage vortex is weakened and the passage cross flow is reduced; therefore, coolant coverage is more uniform across the passage. Similar to flat plate film cooling, shaped film cooling holes offer better protection than cylindrical holes.

A similarity between the vane endwall and the blade platform is the existence of slot (or) upstream of the airfoil leading edge. A is commonly in place in the transition from the combustion chamber to the turbine vane (stator). Similarly, a exists between the stator and rotor, so the turbine disk can rotate freely. To prevent ingestion of the hot mainstream gases, it is a common practice to inject coolant air through these slots. If this preventive measure is utilized properly, unnecessary discrete film holes can be eliminated, so coolant is not wasted by overcooling areas on the rotating platform. Blair [11] also measured the film cooling effectiveness with upstream injection in his pioneering study; he showed large variations in the film cooling effectiveness over the entire passage due to the strong secondary flow. Roy et al. [23] placed coolant slots upstream of their vane. They showed the heat transfer near the leading edge was reduced due to the secondary air injection. Because the slots were placed directly upstream of the blades, a large area in the center of the passage did not receive adequate film cooling coverage. Slot injection has been the focus of many studies performed at the University of Minnesota [24 – 26]. They found using slots, which span the majority of the passage upstream of their vanes, can provide film coverage over most of the passage to the trailing edge of the vane [24, 25]. They also found that increasing the amount of coolant through the slot can reduce the effect of the secondary flow. In addition, strategically blocking the slot, so the coolant does not exit the slot uniformly provides thermal advantages (and disadvantages) [26].

The heat transfer coefficients and the film cooling effectiveness was measured on endwall of a vane passage with film cooling combined with upstream slot injection by Nicklas [27]. They found that in the upstream region, the film cooling effectiveness was elevated due to the large amount of cooling flow from the slot. However, the effectiveness near the discrete holes located near the center of the passages suffered due to the passage vortex. Liu et al. [28]

used a high volume of discrete holes upstream of their vanes to emulate the effect of upstream slot injection. They determined the film cooling effectiveness was primarily affected by the blowing ratio of the injection; in addition, as the blowing ratio increases, the uniformity of the coverage increases.

The film cooling effectiveness has been measured using pressure sensitive paint by Zhang and Jaiswal [29] and Zhang and Moon [30]. They first measured the effectiveness with two upstream injection geometries: two rows of discrete holes and a single row slot. The effect of a backward facing step was also considered with the discrete hole configuration. They confirmed that increasing the coolant flow can significantly increase the effectiveness, and they reported that the use of a backward step significantly decreases the effectiveness within the passage. Knost and Thole [31] showed that with increased slot flow, the critical areas of the leading edge and pressure side junction can be adequately cooled. Cardwell et al. [32] extended this work to include mid-passage misalignment. With the misalignment that may occur between two adjacent vanes, the film cooling effectiveness is dramatically reduced.

With the secondary flow strongly influencing both the heat transfer coefficients and the film cooling effectiveness on the platform surface, recently, efforts have been directed at mitigating this destructive secondary flow. One method that is gaining popularity is endwall contouring. Han and Goldstein [33] observed that with a fillet around the leading edge of the blade, the horseshoe vortex disappears, and the passage vortex is delayed with elevated turbulence intensity. However, with low freestream turbulence, the strength of the passage vortex is comparable to that in a passage without the fillet. The drawback of the fillet is the increased heat transfer near the leading edge on the pressure side due to the intensified corner vortices.

Gas Turbine Needs and Project Objectives

Most of the turbine blade cooling designs are based on the non-rotating blade and very limited rotating blade data. Based on this type of idealized film cooling heat transfer data, the blade metal temperature prediction can be off by up to 100 to 200°F in certain critical regions of the blade. It is known that blade life can be reduced by half if the blade temperature prediction is off by around 50°F. To overcome the hot spots, the turbine cooling designs need to consume extra amounts of cooling air from the compressor, hurting efficiency and power output. It is clearly an urgent need to have heat transfer and film-cooling data applicable to rotating blades with a generic film-hole geometry at the critical region of the airfoil under realistic engine flow conditions.

Another important issue is the flow parameter in the rotating blade film cooling heat transfer design. The Reynolds number, rotating speed, and Mach number for today's gas turbine engines are much higher than those published in the literature. This creates a challenge for researchers to provide rotating film cooling and heat transfer data for realistic blade film-hole geometry at higher Reynolds number, rotating speed, and Mach number conditions. Few facilities can provide such data. To solve this problem, the computational prediction of flow and heat transfer in rotating film-cooled blades is necessary. It is known that the Fluent commercial code has been validated and used by many researchers through technical publications for turbine blade heat transfer and film cooling predictions. The Fluent commercial code can be used to predict the proposed rotating blade surface heat transfer with film cooling at engine representative flow conditions. The predicted results can be compared with measured data at similar geometric and flow conditions. The prediction can be extended beyond the experimental

conditions. The upgraded CFD-based tool will be the new design trend and will greatly improve the current film cooling heat transfer design.

As mentioned above, there is very limited experimental data available for rotating blade heat transfer and film cooling in the literature. Moreover, there is very limited information available dealing with the turbine platform heat transfer and film cooling under rotating conditions. Therefore, there is a need to study the detailed turbine platform heat transfer and film cooling under engine representative flow and rotating conditions. This investigation provides the designers with new rotating blade platform heat transfer and film cooling data and numerical predictions for improving the cooling performance and thermal efficiency of land-based gas turbines. The objective of the rotating blade platform heat transfer and film-cooling experimental program is to obtain reliable detailed data under land-based gas turbine representative Reynolds and Mach numbers and rotation conditions. In addition, detailed measurements of the mainstream flow will be gathered to show how the mainstream flow is affected by the coolant flows. As a secondary effort, numerical simulations will be preformed to model engines under realistic operating conditions to further understand the heat transfer behavior on the rotating platform. With a better understanding of the flow physics and heat transfer distributions on the rotating blade platforms, it will be possible to reduce the amount of air extracted from the compressor for the purpose of turbine blade cooling. The more effective cooling designs could also result in increased turbine inlet temperatures. The increased temperatures will further enhance the thermal efficiency and power output of the engine. This will dramatically impact the rotor blade cooling design and greatly benefit to the entire land-based gas turbine industry.

Project Tasks

The current project investigates the heat transfer on rotor blade platforms. An existing turbine research facility is used to investigate the rotating blades. The current research turbine facility can be seen in Figure 3. The project consists of three tasks to meet the stated objectives. Detailed pressure distributions, heat transfer coefficient distributions, and film effectiveness distributions will be obtained on the rotor blade platforms with generic cooling geometries as described by the following tasks.

Task 1 – Rotor Platform Modification and Measurement Technique Development

To study cooling techniques commonly employed in gas turbine engines, the existing research facility required modification. The existing facility is incapable of studying the effect of coolant leakage in the seal between the stator and rotor. Therefore, a new rotor platform must be designed and fabricated. This new rotor platform not only incorporates stator-rotor seal ejection, but also has discrete holes for platform film cooling. Figure 4 shows the overall design of the research facility with the two separate coolant flows, and Fig. 5 shows the detailed schematics of the coolant flows to the rotor platform. While the new rotor platform is fabricated, the experimental techniques which are used for the heat transfer and flow measurements are developed. This includes the design and calibration of several miniature five-hole probes that are used for detailed mainstream flow measurements. In addition, the pressure sensitive paint (PSP) and temperature sensitive paint (TSP) techniques are developed. The surface pressure distribution and film cooling effectiveness are measured with PSP; while the surface heat transfer coefficient distributions are determined using the TSP. Also, as a secondary effort, preliminary numerical predictions of pressure, heat transfer coefficient, and film effectiveness distributions are performed.

Task 2 – Rotor Platforms with Stator-Rotor Seal Ejection

The effect of coolant ejection from the annular between the stator and rotor on the detailed film cooling effectiveness distributions will be experimented as the second task (see Fig. 6). A typical stator-rotor seal geometry is selected based on the suggestions of industrial experts. The detailed film cooling effectiveness distributions on the rotating platform will be measured using the PSP technique for several upstream blowing ratios at different rotor frequencies. The film cooling effectiveness predictions will be compared to the measured results at similar rotating speeds and coolant ejection rates.

Task 3 – Rotor Platforms with Stator-Rotor Seal Ejection and Film Cooling Holes

The detailed rotor blade platform film cooling effectiveness distributions with a typical film cooling hole geometry will be performed as the final task (see Fig. 7). Cooling hole geometry and location along the passage is selected based on the advice of industrial experts. Detailed film cooling effectiveness distributions of the film-cooled rotating platform will be measured using PSP technique for different blowing ratios at different rotor frequencies. As with Task 2, the detailed film cooling effectiveness of the film-cooled rotating blade platform will be calculated and these numerical predictions will be compared to the measured results at the above-mentioned rotational conditions and blowing. To obtain a complete picture of film cooling on the rotor platform, combined upstream stator-rotor coolant injection and downstream hole injection will be considered and film cooling effectiveness will be measured for different blowing ratios and rotor frequencies. The results will once again be compared with the numerical predictions using Fluent.

EXPERIMENTAL PROCEDURE

Turbine Research Facility

The experimental investigations have been carried out in a three-stage turbine research facility at the Turbomachinery Performance and Flow Research Laboratory of Texas A&M University. The turbine is the core component of the *TPFL*-research facility designed by Schobeiri [34] in 1997 to address aerodynamics, efficiency, performance and heat transfer issues of high pressure (HP), intermediate pressure (IP), and low pressure (LP) turbine components. Detailed aerodynamic, efficiency, loss and performance measurements were carried out to verify and document the efficiency and performance of a high efficiency 3-D, bowed blade. To compare the results of the investigations reported in [34] with those for 2-D cylindrical blades, detailed measurement were conducted and summarized in the subsequent reports [35] and [36].

To determine the film cooling effectiveness under rotating conditions for leading edge film cooling (Ahn et al. [6, 7]), the turbine rotor was modified to integrate the coolant loop into the downstream section of the hollow turbine shaft and into the cylindrical hub cavity. The same rotor was not compatible with the new geometry which included the circumferential stator-rotor which provides for platform cooling. Hence, to perform the research reported in this paper, a further modification of the existing rotor unit did not seem to be feasible. A new rotor incorporating the stator-rotor was designed and manufactured.

The overall layout of the test facility is shown in Fig. 3. It consists of a 300HP electric motor connected to a frequency controller which drives the compressor component. A three-stage centrifugal compressor supplies air with a maximum pressure difference of 55kPa and a volume flow rate of $4m^3/s$. The compressor operates in suction mode and its pressure and volume flow rate can be varied by a frequency controller operating between 0 to 66Hz. A pipe with a

transition piece connects the compressor to a Venturi mass flow meter used to measure the mass flow through the turbine component. The exit diffuser serves as a smooth transition piece between the turbine component and the Venturi, which is used for mass flow measurement. The three-stage turbine has an automated data acquisition system for detailed flow measurement at each blade row location. The turbine inlet has an integrated heater that prevents condensation of water from humid air expanding through the turbine during the test. The turbine shaft is connected through a flexible coupling with one end of a high precision torque meter that has a maximum rotational speed of 8500 rpm and a maximum torque rating of 677.9N-m. The other end of the torque meter is coupled via a second flexible coupling with an eddy current low inertia dynamometer with a maximum power capacity of 150kW and a maximum torque of 500Nm.

New Turbine Component Design

A completely new advanced three-stage turbine component as shown in Figs. 4, 5, and 8 was designed to replace the one discussed in [34 – 36] and [6, 7]. In addition to the tasks performed by the old rotor, the new one was designed to operate at high speeds of 8500 rpm close to the transonic range. The first critical speed for vibration for the new rotor at its natural frequency occurs at 6500 rpm. The details of the turbine geometry and operating conditions are as shown in Table 1. Two independently controlled, concentric coolant loops provide the necessary mass flow for film cooling experiments. The outer loop supplies coolant for film cooling experiments for the discrete film cooling holes on the platform in the blade passage section. Nine discrete compound angled coolant holes of 1mm diameter are machined on the 1st stage rotor platform as per the angles shown in Table 2. The holes are located about 50% downstream of the blade passageway. The approximate pitch to diameter ratio for the holes is 5 in the axial and tangential

directions. The inner loop coolant jet ejecting from a circumferential between the 1st stator and rotor provides for hub platform cooling.

A concentric jet exits this circumferential at an angle of 25° into the mainstream (Fig. 5). The maximum normal width is designed to be 3mm. However, it can be decreased to up to 0.5mm by translating the entire rotor towards the front bearing. For the current study it was set to 2.3mm. The axial stator-rotor for the 1st stage was measured at 5mm. Similar to the optimization of the trailing edge slot ejection, the reduction of slot width is instrumental in establishing an optimum ejection ratio while keeping the cooling mass flow constant.

The blades attached to the new rotor were taken from the rotor described in [34 – 36] and also used in [6, 7]. They are typical HP-turbine blades used in steam turbines characterized by a relatively thick leading edge portion. This particular blade design allows reducing the total pressure losses due to the adverse off-design incidence changes caused by part-load operation. Thus, these blades are not typical of power generation or aircraft gas turbines. Given the considerable amount of manufacturing expenses that a new set of rotor and stator blades require and the lack of sufficient research funds, it was decided to use the same existing blades to carryout the current research. Although the blade geometry does not represent a typical gas turbine blade geometry, it provides the basic features to extract information relevant to gas turbine design community. These features are (a) stator-rotor unsteady interaction, (b) blade and platform rotation including the relative blade circulation and the exposure of the platform boundary layer to centrifugal and coriolis forces, and (c) the flow acceleration. Except for the last feature (c), none of the above features can be simulated in a cascade investigation.

To ensure that no coolant escapes through the rotary-stationary interfaces, the internal and external loops were sealed with labyrinths. A 24-channel slip-ring is mounted to the rear shaft as

shown in Fig. 8 to transfer temperature data from thermocouples from the rotating frame to the data acquisition system.

Pressure Sensitive Paint (PSP) Technique

Data for film cooling effectiveness was obtained by using the PSP technique. PSP is a photo-luminescent material which emits light when excited, with emitted light intensity inversely proportional to the partial pressure of oxygen. This light intensity can be recorded using a CCD camera and can then be calibrated against the partial pressure of oxygen. Details of using PSP for pressure measurement are given in McLachlan and Bell [37]. The image intensity obtained from PSP by the camera during data acquisition is normalized with a reference image intensity taken under no-flow conditions. Background noise in the optical setup is removed by subtracting the image intensities with the image intensity obtained under no-flow conditions without excitation. The resulting intensity ratio can be converted to pressure ratio using the previously determined calibration curve and can be expressed as:

$$\frac{I_{ref} - I_{blk}}{I - I_{blk}} = f\left(\frac{\left(P_{O_2}\right)_{air}}{\left(P_{O_2}\right)_{ref}}\right) = f\left(P_{ratio}\right) \tag{1}$$

where I denotes the intensity obtained for each pixel and $f(P_{ratio})$ is the relation between intensity ratio and pressure ratio obtained after calibrating the PSP.

Calibration for PSP was performed using a vacuum chamber at several known pressures varying from 0 to 1atm with intensity recorded for each pressure setting. The same optical setup was chosen for calibration as well as for data acquisition during the experiments. A schematic of the calibration setup is shown in Fig. 9. PSP is sensitive to temperature with higher temperatures resulting in lower emitted light intensities. Hence, the paint was also calibrated for temperature. It was observed that if the emitted light intensity at a certain temperature was normalized with

the reference image intensity taken at the same temperature, the temperature sensitivity can be removed. Hence, during data acquisition, the reference image was acquired immediately after the experiment was completed to avoid errors related to temperature variation. Reference images were acquired after the rotor came to a halt and the temperature change from loaded to stationary condition was small enough to disregard its effect on PSP measurement. Flow and surface temperatures were monitored by a thermocouple placed 2mm above the surface close to the suction side and by another thermocouple placed underneath the platform surface respectively. The thermocouples were wired through a slip-ring and connected to a microprocessor thermometer with a digital readout.

To obtain film cooling effectiveness, air and nitrogen were used alternately as coolant. Nitrogen which can be assumed to have the same molecular weight as that of air displaces the oxygen molecules on the surface causing a change in the emitted light intensity from PSP. By noting the difference in partial pressure between the air and nitrogen injection cases, the film cooling effectiveness can be determined using the following equation.

$$\eta = \frac{C_{mix} - C_{air}}{C_{N_2} - C_{air}} = \frac{C_{air} - C_{mix}}{C_{air}} = \frac{\left(P_{O_2}\right)_{air} - \left(P_{O_2}\right)_{mix}}{\left(P_{O_2}\right)_{air}} \tag{2}$$

where C_{air}, C_{mix} and C_{N2} are the oxygen concentrations of mainstream air, air/nitrogen mixture and nitrogen on the test surface respectively. The definition of adiabatic film cooling effectiveness is

$$\eta = \frac{T_f - T_m}{T_c - T_m} \tag{3}$$

The accuracy of the PSP technique for measuring film-cooling effectiveness has been compared by Wright et al. [38] on a flat plate with compound angled ejection holes using several measurement techniques such as steady and transient liquid crystal, IR camera and using a foil

heater with thermocouples. Results were obtained for a range of blowing ratios and show consistency with each other. Wright et al. [38] found that IR, TSP as well as PSP gave effectiveness results within 15% of each other. Larger uncertainties for heat transfer techniques such as IR and TSP methods were observed due to lateral conduction in the flat plate.

The platform passage under investigation was layered with PSP using an air brush. This coated surface was excited using a strobe light fitted with a narrow bandpass interference filter with an optical wavelength of 520nm. Upon excitation from this green light, the PSP coated surface emitted red light with a wavelength higher than 600nm. A 12-bit scientific grade CCD camera (High speed Sensicam with CCD temperature maintained at -15^{o}C using 2-stage peltier cooler) was used to record images and was fitted with a 35mm lens and a 600nm longpass filter. The filters were chosen to prevent overlap between the wavelength ranges such that the camera blocked the reflected light from the illumination source. A schematic of the optical components setup is depicted in Figs. 10 and 11. The camera and the strobe light were triggered simultaneously from an angular position optical sensor offset to the shaft. By detecting the same angular position, the camera was able to view the same region of interest at every rotation, making it possible to average the image intensities without blurring the information. A minimum exposure time of 18μs was used for image capture from the camera. Estimated rotor movement during image capture at 2550 rpm, for an 18μs exposure time was 1.2mm. A total of 150 TIF images were captured for each experiment with air and nitrogen injection and the pixel intensity for all images was averaged. The image resolution obtained from the camera was 1.5 mm/pixel with each image containing about 500 data points. The relatively low pixel resolution is a consequence of a binning of 8 used on the camera, as the emitted light intensity captured by the camera CCD in such a short exposure time was very low. A computer program was used to

convert these pixel intensities into pressure using the calibration curve and then into film cooling effectiveness. The coolant flow rate was set using a rotameter based on prior calculation for the desired mass flow ratio. The coolant was heated to the same temperature as mainstream air (45^{o}C) before injection through the .

Uncertainty calculations were performed based on a confidence level of 95% and are based on the uncertainty analysis method of Coleman and Steele [39]. Lower effectiveness magnitudes have higher uncertainties. For an effectiveness magnitude of 0.3, uncertainty was around ±2% while for effectiveness magnitude of 0.07, uncertainty was as high as ±10.3%. This uncertainty is the result of uncertainties in calibration (4%) and image capture (1%). The absolute uncertainty for effectiveness varied from 0.01 to 0.02 units. Thus, relative uncertainties for very low effectiveness magnitudes can be very high (>100% at effectiveness magnitude of 0.01). However, it must be noted that very few data points exist with such high relative uncertainty magnitudes. Uncertainties for the blowing ratios are estimated to be 4%.

Temperature Sensitive Paint (TSP) Technique

Like PSP, temperature sensitive paint (TSP) is also comprised of luminescent molecules suspended in a polymer binder. However, the photophysical process associated with TSP is thermal quenching, rather than oxygen quenching. Unlike with PSP, the polymer binder is not oxygen permeable. Therefore, the luminescence intensity of the TSP is related only to temperature, and is not a function of pressure (unlike the reverse relationship observed with PSP). Like PSP, the luminescent molecules in the TSP must be excited with the absorption of a photon. The molecules return to their ground state with the emission of the photon at a longer wavelength. Increasing the temperature of the luminescent molecules makes the molecules more

likely to return to their ground state (releasing the photon through a radiationless process) [38]. Therefore, the emission intensity from molecules at elevated temperatures is lower than the emission of molecules at relatively lower temperatures. This photophysical process is known as thermal quenching.

Similar to the use of PSP, a reference condition is used for the TSP measurements. Typically, the reference condition is set at the room temperature in which the experiments are performed. However, for cryogenic applications, the reference temperature maybe much lower. With the reference condition, and the black image used to eliminate the background intensity from the optical components, the emission intensity is related to the surface temperature as shown in Equation 4.

$$\frac{I(T)-I_b}{I(T)_{ref}-I_b} = f(T) \tag{4}$$

A calibration must be completed to determine the relationship between the emission intensity and the surface temperature. The calibration is completed by attaching a thermocouple to the surface of a copper block. The copper block is coated with the TSP, and positioned between the excitation light and CCD camera. UniCoat TSP from ISSI is sprayed on the copper plate; the same strobe light for excitation and camera used with PSP are now used with TSP. The copper block is heated from room temperature up to 145°F (24 - 63°C). At specific temperatures, the emission intensity is recorded (coupled with black images), so a relationship between the intensity and temperature can be determined.

After completion of the TSP calibration, the TSP can be applied to the rotating blade platform. The experimental setup is identical to the PSP. As the name implies, TSP detects changes in temperature; therefore, this method requires a temperature difference. For this study, TSP is used to measure the steady state surface temperature. The heater fixed to the platform,

heats the surface by supplying the surface with uniform heat flux. The unheated film coolant mixes of the mainstream and temperature variations are present on the platform. From the measured surface temperature, mainstream temperature, and power input to the heater, the heat transfer coefficient on the platform can be determined from Equation 5.

$$h = \frac{q''_{in} - q''_{loss}}{T_{wall} - T_{\infty}} \tag{5}$$

During the actual film cooling experiment, only three images are required: black image (no flow, no excitation light), reference image (no flow, with excitation light), and air image (mainstream and coolant flows, with excitation light). With these images, and the calibration data, the adiabatic wall temperature can be determined. If the reference image corresponds to a different temperature than the reference image from the calibration, this must be taken into account. With a temperature being recorded at every pixel in the viewing window, detailed distributions of the film cooling effectiveness can be obtained on the film cooling plate.

RESULTS AND DISCUSSION

Experimental Film Cooling Effectiveness Measurements

Task one of this project has been completed. Significant modifications were required to the existing turbine research facility. The existing facility was incapable of studying the effect of coolant ejection through the stator-rotor seal and platform film cooling. Therefore, the project began with the design of a new rotor platform. As shown in Fig. 4, modifications of the facility allow two coolant flows to be controlled independently: ejection flow and film cooling flow. Figure 5 shows detailed views of the modified rotor platform. Not only are modifications required for the platform, the rotor shaft required modification for a slip ring. The slip ring will transmit thermocouple and signals to and from the rotating blades. Finally, the housing of the research facility must be modified, so a window can be included. The window will allow the camera to view of the platforms and record images of the PSP and TSP coated surfaces. Design, fabrication, installation, and instrumentation of the modified rotor platform have been completed. Figure 8 shows the newly fabricated rotor platform installed in the existing research facility.

With the fabrication of the new rotor platform, the housing of the existing facility has also been modified. This is due to the required optical access of the instrumented platforms. Figure 9 shows a model of the turbine housing with a window for the required optical components. As described previously, both an excitation light and camera are needed to capture images of the pressure and temperature sensitive paints, and Figure 12 shows the viewing window with the rotor at two different positions to capture images of the rotor platforms with either PSP or TSP.

Data acquisition begins with Task two of this project. Thus far, film cooling effectiveness measurements were performed for four coolant-to-mainstream mass flow ratios of 0.5%, 1.0%,

1.5% and 2.0%. Film cooling data was also obtained for four rotational speeds, 2550 rpm (reference condition), 3000rpm, 2000 rpm and 1500 rpm (off-reference conditions). Total mass flow in the engine was 3.728 kg/s and was ensured to be the same for all three rpm's by adjusting the blower frequency through the frequency controller. Blowing ratios for each rotating speed differ slightly as the relative mainstream velocity at the rotor inlet changes with the rotating speed.

Film Cooling Effectiveness from Upstream Slot Cooling

Upstream Injection At Reference Rotating Condition

Film cooling effectiveness measurements were performed for four coolant-to-mainstream mass flow ratios of 0.5%, 1.0%, 1.5% and 2.0%. Film cooling data was also obtained for four rotational speeds, 2550 rpm (reference condition), 3000, 2000 rpm and 1500 rpm. Total mass flow in the engine was 3.73 kg/s and was ensured to be the same for all three rpm's by adjusting the blower frequency through the frequency controller. The four coolant-to-mainstream mass flow ratios approximately correspond to blowing ratios of 0.12, 0.24, 0.36 and 0.48 respectively after assuming that the coolant exits the axially. Blowing ratios for each rotating speed differ slightly as the relative mainstream velocity at the rotor inlet changes with the rotating speed.

Variation of rotational speed performed in the [6, 7] showed that the location of the leading edge stagnation line, which yielded symmetric spreading of coolant on the suction and pressure surfaces of the leading edge was at an rpm of 2550. This rotational speed was chosen as the reference rotating condition for the current investigation. The effectiveness results obtained from using PSP for the reference rotating condition of 2550 rpm are plotted in Fig. 13. The

figure shows the contour plots for all four mass flow ratios tested. The contour plots also show the location of the stator-rotor upstream of the passage and the path of the mainstream and coolant flow. The effectiveness in the , as the coolant escapes through it, could not be recorded as the plexiglass window through which the rotor platform was viewed was not wide enough.

Higher mass flow ratios result in coolant injection with higher momentum. As this momentum increases, it can be observed that the spread of the coolant as well as the effectiveness magnitudes are higher. The injected coolant is at the same density as the mainstream i.e. the coolant to mainstream density ratio is 1. Hence, the injected coolant velocity is higher for higher mass flow ratios. This affects the secondary flow structure in the passage. At lower blowing ratios, the low momentum coolant is not capable of penetrating into the highly vortical secondary flow region on hub platform. It mixes with the main flow where its kinetic energy dissipates, making only a marginal contribution to effectiveness improvement. For the lowest mass flow ratio (MFR = 0.5%), the maximum effectiveness magnitude is less than 0.2

As the mass flow ratio increases, the coolant injection velocity increases due to which the coolant can penetrate the complex secondary flows in the passage resulting in higher effectiveness on the platform. For the highest mass flow ratio of 2%, a region of high effectiveness can be observed near the entrance of the blade passage. The effectiveness from the to the beginning of this high effectiveness region is slightly lower. This indicates that the coolant probably detaches itself from the surface as it exits from the and then reattaches as it is pushed by the mainstream towards the surface which is marked by the high effectiveness spot (at around 15% of axial chord). Effectiveness magnitudes as high as 0.6 can be observed at this reattachment spot. Smaller reattachment spots can be observed for MFR = 1.5% too. Thus, as the mass flow ratio increases, the effectiveness magnitude and its spread become larger. The

same phenomenon has been recorded by several researchers mentioned earlier with studies for slot film cooling on stationary, flat as well as curved platforms. Common to all blowing ratios investigated is that the suction surface is the location of inception of the effectiveness. Major parameters instrumental in making the suction surface the inception location are: (a) the platform secondary flow, (b) the Coanda effect that helps the injected coolant attach on the suction surface and (c) the coolant injection angle.

The coolant distribution on the platform is predominantly governed by its flow characteristics. A strong pressure gradient exists within the passage from the pressure to the suction side with the static pressure near the pressure side being much higher due to lower mainstream velocities and blade curvature. The coolant traces show slightly higher effectiveness magnitudes towards the suction side near the leading edge. More coolant gets diverted away from the higher pressure stagnation region on the leading edge of the blade and finds its way towards the suction side. Effectiveness magnitudes on the pressure side begin to fade away rapidly as the coolant travels along the axial chord. As the passage vortex moves towards the suction side while gaining strength, it entrains the mainstream on the platform surface damaging the coolant film which results in a sharp drop in effectiveness magnitudes. This sudden drop gives a good indication of the path traced by the passage vortex. Similar coolant spread profiles affected by secondary flows can be observed for stationary platform cooling through slots akin to the current design in turbine as well as vane cascades in the tests conducted by Blair [11].

Upstream Injection At Off-Reference Rotating Conditions

At rotational speeds lower than the reference speed, the blade flow deflection becomes larger leading to higher specific stage load coefficient and the stagnation region moves towards the

pressure side as the flow incidence angle increases as sketched in Fig. 14. At progressively lower rotating speeds, the stagnation line will further move towards the blade pressure side resulting in a higher pressure zone owing to higher flow deflection. The pressure gradient on the platform from the pressure to the suction side gets affected by this shift in the stagnation region due to larger flow incidence angles. Fig. 15 shows the numerical predictions of local static pressures on the platform surface with flow pathlines for 2550 rpm and 2100 rpm. These numerical predictions were performed using the CFD code, FLUENT for the same geometry and flow conditions. About 1.1 million cells were used to grid 1.5 stages of the turbine. A sliding mesh was used to simulate rotation. A Reynolds stress model with a non-equilibrium wall function was used to solve the Reynolds Averaged Navier-Stokes equations. From the figure, the movement of the stagnation region towards the pressure side for lower rpm can be easily discerned. Lower pressure at lower rotating speeds can be observed near the suction side. Fig. 15 also shows the mainstream pathlines near the platform surface. The pathlines for 2100 rpm appear to converge together as the flow gets pushed to the suction side.

The larger gradients in the platform static pressure distribution for lower rotating speeds cause significant movement of the coolant film on the platform surface when it comes from the stator-rotor . The local mass flow of coolant from stator-rotor depends on the pressure difference between the plenum and the mainstream static pressure. A higher pressure region near the blade pressure side close to the leading edge at lower rotating speeds will result in a smaller pressure difference across the as compared to reference condition. This will promote non-uniform coolant distribution from the stator-rotor with the coolant traces re-orienting themselves towards the suction side of the platform. This phenomenon can be clearly observed from data taken for 2000rpm and 1500rpm as shown in Figs. 16 and 17. Both figures include

contour plots for 4 different mass flow ratios. More coolant appears to come out from near the suction side of the platform where the pressure difference across the from inlet to outlet is larger with the lowest rotational speed of 1500 rpm showing the largest non-uniformity. Thus, the coolant film distribution and hence film cooling effectiveness strongly depends on the pressure distribution on the platform surface. As the blowing ratio increases, the traces get stronger due to the increase in the coolant momentum similar to that observed in Fig. 15.

After comparing Figs. 16 & 17 for lower rotating speeds with Fig. 13 at 2550 rpm (reference speed), it can be observed that the effectiveness magnitudes progressively decrease with lower rpm for the same mass flow ratio. This may be a result of stronger horseshoe vortices close to the suction side owing to the shift in the flow incidence angle at lower rpm. Very low effectiveness levels can be discerned for the lowest blowing ratio, MFR = 0.5% for 1500 rpm as compared to other rpm's. Coolant traces can only be observed locally near the suction side of the blade. The coolant spread for MFR = 2.0% is appreciably larger and some reattachment of coolant can also be observed for 2000 rpm similar to that observed for 2550 rpm. Effectiveness traces on the suction side though are more visible than that for 2550 rpm. Some coolant traces can even be observed close to the trailing edge near the suction side for higher mass flow ratios. For both reference and lower rotating speeds, the region downstream of the throat remains uncooled. Weak traces can be observed in this region for 2550 rpm for MFR = 2.0% near the throat. This region experiences much higher velocities from the accelerating mainstream flow resulting in high local heat transfer coefficients. The secondary flow vortices in the passage erode the coolant film before it reaches the throat.

Figure 18 shows the measured film cooling effectiveness on the rotating platform operating at 3000 rpm. Although the measured film cooling effectiveness measured at 3000 rpm varies

from that measured at 2550 rpm, the variation is less for the higher rotational speed than the lower rotational speeds. Increasing the coolant flowrate increases the coolant coverage area on the rotating platform. As the flowrate increases to 2%, the coolant covers the entire passage; whereas at the other rotational speeds, the pressure side of the passage and the trailing edge region were left unprotected.

In addition to the effect on static pressure distribution and film cooling due to inlet flow incidence angle change with rotational speed, rotation may also affect the coolant flow as it exits the stator-rotor . The and the disk cavity are bounded by two walls, stator endwall and the rotor platform. The enclosed coolant mass in the disk cavity will rotate with a certain frequency due to the cavity wall shear stress. High shear stresses, caused by relative motion in the circumferential , may introduce some swirl in the coolant flow as it exits. Hence, a tangential component may exist in the coolant flow as it exits the stator-rotor . This may cause some additional spreading of the coolant which cannot be achieved for film cooling studies in stationary cascades. This might also explain the larger coolant spread with increasing rotational speeds due to a larger tangential velocity component in the coolant as it exits the . The determination of the swirl angle as well as the measurement of this tangential velocity component was not the subject of the current paper. However, these are items of high importance along with the inter-stage measurements.

Pitchwise Averaged Film Cooling Effectiveness with Upstream Injection

The film cooling effectiveness results were averaged along the pitchwise direction and the averaged data for all coolant-to-mainstream mass flow ratios and rotational speeds are presented in Fig. 19 along the axial chord. The increase in effectiveness magnitudes with increasing mass flow ratio can be clearly observed from this figure. The averaged plots show a sharp decrease in

effectiveness magnitude along the axial chord as indicated earlier with the region beyond x/C_x = 0.6 remaining mostly uncooled with average effectiveness magnitudes below 0.1. The spikes occurring as a result of coolant jet reattachment at MFR = 2.0% for 2550 rpm, 2000 rpm, and 3000 rpm can also be observed. The decrease in effectiveness with lower rotational speeds can also be discerned. Figure 20 shows the same pitchwise averaged film cooling effectiveness results plotted for the four different coolant-to-mainstream mass flow ratios. The impact of turbine rotational speeds on film cooling effectiveness can be clearly perceived from this plot. As rpm increases, the effectiveness magnitudes increase for the same mass flow ratio. Figure 21 shows the average film cooling effectiveness plotted with *x/MS* as the abscissa. The figure compares the data with a correlation from Goldstein [40] for an equivalent two-dimensional slot on a flat stationary surface as given in Eq. 6.

$$\overline{\eta} = \left(1 + 0.249 \cdot \left(x/M_{gap}S\right)^{0.8}\right)^{-1} \tag{6}$$

This correlation works well for $x/MS > 10$, where the flow regime is more two-dimensional. For $x/MS < 10$, the 3-dimensional flow regime due to mixing of the coolant jet with mainstream results in lower effectiveness than that predicted by the correlation. When compared to current data, for reference rotating condition, it shows relatively good comparison with the correlation at $x/MS = 10$ but decays rapidly due to the destructive action of the passage vortex on the coolant film. For lower rotating speeds than reference, more non-uniform pitchwise effectiveness distribution lowers the average effectiveness value with the data for 1500 rpm showing the largest deviation from the correlation.

Film Cooling Effectiveness from Discrete Film Cooling Holes

As shown in the previous figures, the gas from the stator-rotor seal can adequately protect the upstream half of the blade platform. However, much of the pressure side of the passage, as

well as the downstream half of the platform, is not covered by the coolant, and thus left exposed to the hot mainstream gas. To protect these areas of the blade platform, it is necessary to add discrete film cooling holes. The discrete film holes can be used sparingly, as additional coolant is not needed on the upstream half of the blade platform. Taking this into account, nine discrete holes have been added to the rotating platform, as shown in Fig. 7. The film cooling effectiveness can be measured on the rotating platform with PSP. The blowing ratio for the coolant through the discrete film hole is varied from M_{holes} = 0.5 – 2.0 at intervals of 0.25, based on the relative velocity of the mainstream flow at the rotor exit (station 3). In addition, the rotational speed of the turbine is varied to investigate the effect of rotation at reference and off-reference conditions over a range of blowing ratios. Before combining the upstream slot injection with the discrete film cooling, it is necessary to isolate each flow. Therefore, effectiveness is measured on the platform with only the discrete film cooling holes.

This section presents the results obtained from the film cooling experiments performed on the 1st stage rotor platform for downstream discrete hole coolant injection. Experiments were conducted at three rotational speeds, 2400rpm, 2550rpm and 3000rpm, with the average film hole blowing ratios of M_{holes}=0.5, 0.75, 1.00, 1.25, 1.50, 1.75 and 2.00. The Reynolds number based on the rotor axial chord length and the exit velocity was around 200,000 and the pressure ratio was 1.12 for the first stage. The rotation numbers corresponding to 3000 rpm, 2550 rpm and 2400 rpm are 0.23, 0.19 and 0.18 respectively. Film cooling effectiveness was calculated by applying the calibration curves to the intensity fluctuation captured by the camera between air and nitrogen injection. Overall it is found that film cooling effectiveness is maximum as we approach an approximate average blowing ratio of M_{holes}=1.00 for all three rotational speeds. The reference rotational speed of 2550rpm has the maximum effectiveness amongst all rotational

speeds for all blowing ratios. Platform cooling using simultaneous upstream slot and downstream discrete hole injection yielded results similar to the individual blowing cases with little to no effects due to synchronized coolant ejection for MFR=1% and M_{holes}=.0.75, 1.00 and 1.25.

Reference Rotating Case

Film cooling results on the effects of rotational speed performed Ahn (6, 7) showed that the location of the leading edge stagnation line, which yielded symmetric spreading of coolant on the suction and pressure surfaces of the leading edge was at a rotational speed of 2550. This rotational speed was chosen as the reference rotating condition for the current investigation. Fig. 22 shows film cooling effectiveness on the rotor platform for downstream hole film cooling for the reference speed, 2550 rpm, and all the blowing ratios. As expected film cooling effectiveness is maximum near the coolant hole exit. As we proceed downstream of the holes, effectiveness magnitude diminishes as the coolant mixes with the mainstream flow. Peak effectiveness values occur as we approach M_{holes}=1 and is approximately equal to η=0.70 exactly where the coolant ejects out of the holes. Effectiveness values and film distribution begin to decrease below and above M_{holes}=0.75 and 1.25 respectively. M_{holes} in this range provide good film cooling protection on the platform covering most of the downstream passage surface. The contribution of each hole towards effective film coverage also varies depending on its location on the platform surface.

Since coolant density is assumed to be the same as that of the mainstream, M_{holes} is dependent only on the exit velocity of the coolant gas. For M_{holes}=1.00, the velocity of the coolant ejecting out of the individual holes is approximately the same as that of the mainstream relative velocity at the 1st stage rotor exit. As the coolant flow velocity approaches the

mainstream relative velocity, it appears that the ejected coolant has just the right momentum to adhere to the platform surface displacing the mainstream boundary layer and minimizing the effects of the secondary flows. This allows the coolant to provide better film coverage and higher effectiveness magnitudes as minimal coolant is dissipated into the mainstream flow before providing any protection. At M_{holes} lower than 0.75, the coolant quantity for film cooling is small and is incapable of providing any effective protection on the platform surface. The lower momentum prevents the coolant from penetrating the boundary layer on the platform surface, hindering the development of an effective thermal barrier. The low momentum coolant tends to get carried away by the higher momentum mainstream flow decreasing the effectiveness. On the contrary, the ejected coolant for M_{holes} higher than 1.25, possess larger momentum and have a tendency to lift-off as they leave the coolant holes. The high velocity coolant merges with the mainstream immediately having little time to shield the platform surface. This effect of coolant mass on film effectiveness is similar to that seen by Zhang and Jaiswal (29) with their experiments on a linear cascade.

The coolant distribution on the platform is predominantly governed by the mainstream and secondary flow characteristics. The secondary flow generated by the pressure differential between neighboring blades influence the behavior of coolant gas in their path and significantly affects the capability of the coolant to offer uniform thermal protection. The coolant under the effects of the secondary flow is drawn towards the suction surface leading to better protection near the suction surface. This movement of the coolant to the suction side under the influence of the platform secondary flow has also been documented by researchers experimenting with cascades. The higher tangential velocity of the coolant jet under rotation also increases the migration of the coolant from the pressure side to the suction side on the platform. Interestingly,

the holes 1 and 4 (Fig .7) show lower effectiveness and coolant coverage compared to the other holes. It is believed that these two holes lie in the path of the passage vortex and hence the coolant ejected through them is immediately dissipated into the mainstream. It can be deduced that providing protection closer to the suction surface is relatively easier due to the tendency of the coolant to flow towards the suction surface.

Effect of Rotation on Film Cooling

At rotational speeds lower than the reference speed, the blade flow deflection becomes larger leading to higher specific stage load coefficient and the stagnation region moves towards the pressure side as the flow incidence angle increases as sketched in Fig. 14. Similarly, higher rotational speeds lead to negative incidence angle and cause the stagnation region to move towards the suction side. The pressure gradient on the platform across the pressure and suction side is affected by the change of the incidence angle based on the rotational speed change. This will alter the location of formation and the strength of the passage vortex and other secondary vortice which affect platform film cooling. Figs. 23 and 24 show the film cooling effectiveness distribution for off-reference rotational speeds of 2400 rpm and 3000 rpm. The figures contain contour plots for all the blowing ratios with the arrows depicting the geometric orientation of the coolant holes on the platform. Under no mainstream flow, the coolant exiting the holes is assumed to follow the arrow direction. Overall, it is seen that the effectiveness values for off-reference speeds are lower when compared to the reference speed. Reference speed of 2550 rpm has larger areas of the platform with higher film cooling effectiveness though the peak effectiveness lies in the same range as the off-reference speeds. Blowing ratios below 0.75 and above 1.25 provide minimal protection to the platform surface irrespective of the rotational

speeds. The coolant traces once again follow the cross flow from the pressure side to the suction side.

Maximum effectiveness for 2400 rpm occurs between M_{holes}=1.00 and 1.25 and for 3000 rpm it is between M_{holes}=0.75 and 1.00. The effectiveness magnitudes for both cases show a peak value of approximately η=0.70 close to the coolant hole exit. Varying the rotational speed over or under the reference speed affects the coolant distribution on the platform surface with the higher rotational speed showing the lowest coolant coverage. At rotational speeds lower than the reference speed and for same blowing ratio, the coolant mass ejected through the holes is smaller and hence has a lower relative velocity than the reference case. Similarly at higher rotational speeds the coolant ejecting out of the holes has a higher relative velocity due to the higher coolant mass necessary to maintain the same blowing ratio. This causes the M_{holes} =1.00 and 1.25 (higher coolant flow mass) to have a better effectiveness at 2400 rpm than the lower blowing ratios while at 2550 rpm and 3000 rpm, the best film protection is between M_{holes} =0.75 and 1.00 which has the ejected coolant mass comparable to M_{holes} =1.00 and 1.25 at 2400 rpm.

Pitchwise Average Film Cooling Effectiveness

The film cooling effectiveness data obtained for the three rotational speeds and all the blowing ratios are averaged pitchwise and plotted along the axial chord (Fig. 25) to study the effects of individual blowing ratios. The peaks on the plot represent the location of the holes on the platform in the axial direction. The holes are positioned to provide cooling to approximately 50% of the passageway. It is clearly seen that the effectiveness values are maximum for M_{holes}=0.75 to 1.25 for all three rotational speeds. For 2400 rpm, M_{holes}= 1.00 and 1.25 have higher effectiveness as the coolant velocity and in turn the ejected coolant quantity is higher at

these blowing ratios. Similarly, 2550 rpm and 3000 rpm have higher effectiveness magnitudes between M_{holes}= 0.75 and 1.00. At these blowing ratios the coolant velocity and hence the coolant mass effectively suppress the effects of the secondary flow leading to better coolant distribution on the platform surface. Increase in rotational speed causes the coolant exit velocity to increase for the same blowing ratio. To quantify the effects of rotation on film cooling effectiveness, the pitchwise averaged film cooling effectiveness was plotted along the axial chord for different rotational speeds but same blowing ratio (Fig. 26). It is obvious from the plot that for the same blowing ratio, film cooling effectiveness is maximum for the reference speed of 2550 rpm. The effectiveness magnitudes decrease on either side of the reference speed with 2400 rpm having slightly higher values as 3000 rpm as the flow conditions prevailing on the platform for 2400 rpm is much closer to the reference speed.

Combined Upstream Stator-Rotor Purge Flow cooling and Downstream Discrete Hole Cooling

A combined platform cooling case involving coolant ejection through upstream stator-rotor annular slot presented in a recent study by Suryanarayanan et al. (42) and downstream discrete holes was examined for 2400 rpm, 2550 rpm and 3000 rpm to understand the interaction between the two methods of cooling under rotation. It is expected that the coolant ejected out of the slot will cover the platform front portion while the holes will provide protection in the downstream region. For the upstream blowing a coolant to mainstream mass flow ratio of 1% was considered as it was found to cover most of the upstream platform surface at all rotational speeds by Suryanarayanan et al. (42). For the downstream hole blowing, M_{holes}= 0.75, 1.00 and 1.25 were chosen as they provided the maximum film cooling benefits. Film cooling effectiveness data

was acquired using PSP technique with coolant supplied simultaneously through both the loops. Temperatures of both the coolant loops were maintained the same as the mainstream flow to eliminate any temperature effects.

Figs. 27, 28 and 29 show the film cooling effectiveness for the combined coolant ejection case for all three turbine rotational speeds. Red and blue arrows depict the mainstream and stator-rotor coolant flow respectively. The figures also show the relative location of the stator-rotor upstream with respect to the blade leading edge. The coolant supplied through the stator-rotor as expected provides fairly good coverage in the upstream region though the distribution in the pitchwise direction is not uniform near the blade leading edge. Coolant concentration near the suction side (SS) is greater than near the pressure side (PS) for all rotational speeds. The pressure gradient that persists between the pressure and suction surface of the blade tends to draw most of the coolant towards the suction side. At 2400 rpm, a strong vortex on the platform near the leading edge pressure side depletes any coolant supplied in this region and leads to lower effectiveness magnitudes. As the rotational speed is increased, the position of stagnation point on the leading edge changes. This movement of the stagnation point from the pressure surface leading edge for the lower rotational speed to the suction surface for the higher rpm's causes the pressure gradient (□P/□S) across the platform between the suction side and the pressure side to decrease leading to a much more uniform static pressure distribution on the platform surface. This reduction in the spanwise pressure gradient reduces the strength of the horse shoe vortex and allows for the spreading of the purge flow coolant on the platform surface leading to higher effectiveness.

Also, the coolant exiting the , as it travels from the disk cavity into the rotating frame, undergoes a swirl due to the high shear associated with relative motion in the circumferential .

This might cause some further spreading of the coolant on the platform surface for the higher rotor speeds. A little downstream of the leading edge near the pressure surface on the platform, the effect of upstream coolant ejection is drastically reduced as the passage vortex detaches from the pressure side and travels across the platform to merge with the suction side horse shoe vortex, diminishing the coolant coverage on the platform surface closer to the blade pressure side. These results are comparable to that seen in Fig. 30 which shows the film cooling effectiveness distribution with just stator-rotor ejection for MFR=1.00% at all three rotational frequencies under consideration. The downstream hole blowing follows the trend seen in individual hole blowing cases discussed earlier. Reference rotation speed has the best spread and effectiveness magnitudes. Pitchwise averaged film cooling effectiveness for the combined case is as shown in Fig. 31. The results for the combined case reflects data for the individual blowing cases put together and gives a comprehensive view of the appropriate upstream slot blowing MFR, average hole blowing ratio and location of the coolant holes to provide appropriate coolant coverage for each rotational speed.

Flow Measurements and Numerical Predictions

Interstage Instrumentation

To achieve a high degree of versatility, the turbine facility has provision for radial aerodynamic measurements at inlet and exit of each blade row and circumferential measurements at 1st stage rotor exit, 2nd stage stator and rotor exit. The turbine was designed with a casing that incorporated stator rings. It also incorporated three T-rings for sealing the three 90^{o} circumferential traversing slots. The sealed T-rings can move circumferentially inside these slots

and effectively prevent the leakage of mass flow through them. Five-hole probes can be mounted on each of the three traversing systems with decoder and encoder for accurate probe positioning. Each of the three circumferential traversing systems has seven axes: 3 axes for radial traverse, 1 axis for circumferential traverse and 3 axes for turning the probes, whenever the flow angle is out of the calibration range. This is particularly true, when the probe is close to the hub or tip. The traverse in the radial direction spans from 1mm below the hub diameter to 1mm above the blade tip.

Aerodynamic Flow Measurement

Aerodynamic flow measurements were performed along the exit of the 1st stage stator to quantify the nature of the mainstream flow ahead of the stator-rotor platform . A five-hole probe calibrated for ±20° in pitch and yaw was traversed radially from hub to tip at an interval of 1mm up to 5% of the blade near the hub and tip and 2mm in the central region to obtain accurate pressure, velocity and flow-angle distributions at the stator exit. The precise alignment of the five-hole probe with the direction of flow ensures the accuracy of the data acquired. To enable accurate probe alignment, a stepper motor along with a worm-gear arrangement was used to actively rotate and adjust the five-hole probe inside the turbine. Figures 32 and 33 show the radial distribution of total pressures and absolute velocities for varying turbine speeds. The total pressure distribution for all the three rotor speeds is similar with magnitudes increasing with operating speeds. The effects of the secondary flow at the hub and near the casing are distinctly seen in the radial velocity distributions for all three rotor speeds. Up to 5% of the flow in the radial direction near the hub and blade tip is affected by the secondary flow.

The absolute velocity (Fig. 34) at the 1st stage stator exit decreases by 3-4m/s as the shaft speed is increased for 1500rpm to 2550rpm. The overall average absolute and relative velocities for all speeds at the exit of the 1st stage stator were measured to be 69.3m/s and 38.8m/s respectively resulting in Mach numbers of 0.2 and 0.11 respectively. The Reynolds number based on the rotor axial chord length and the exit velocity was around 200,000 and the pressure ratio was 1.12 for the first stage. The rotation number corresponding to 2550 rpm, 2000 rpm and 1500 rpm is 0.19, 0.15 and 0.11 respectively. The flow incidence angle change, *i*, relative to the incidence angle at the design operating condition (3000 rpm) shown in Fig. 14, for 2550 rpm, 2000rpm and 1500rpm was determined as 23.2^o, 43.4^o and 54.8^o respectively. This change in incidence angle causes the stagnation line on the blade leading edge to shift towards the pressure side affecting the static pressure distribution on the blade as well as the platform. Consequently, the coolant spread on the platform gets affected with changing rotational speed. The inlet flow conditions thus help to better explain the film cooling effectiveness distributions on the blade platform.

Numerical Prediction of the Heat Transfer Coefficients and Film Cooling Effectiveness

Computational Details

The present three-dimensional calculations were carried out for a 1-½ turbine stage, which includes the first-stage stator (stator 1), the first-stage rotor (rotor), and the second-stage stator (stator 2), as shown in Figure 35.

The film coolant enters the disk cavity of the first stage stator and purges through the angled slot in the hub junction between the first-stage stator and the rotor to form a film cooling

sheet to protect the rotating platform as shown in Figure 35(a). The portion outlined by blue color is non-rotating, including stator 1, disk cavity of stator 1 and stator 2; while the red color denotes the rotating domain, such as the rotor and its disk cavity. The horizontal width of the slot is 7 mm with 25 degree inclined angle to the rotor platform. The slot length is 16.5 mm and the slot bottom is connected to both the stator 1 and the rotor disk cavity. The length of the disk cavity for stator 1 is 25.4 mm (1 inch), and 12.7 mm (0.5 inch) for the rotor. The height of the disk cavity is 144.8 mm (5.7 inch). Only the rotor platform is film cooled in the present study. The blade height is 63.5 mm (2.5 inch), the root diameter is 558.8 mm (22 inch), and the shroud diameter is 685.8 mm (27 inch). Both the stator and rotor blades are two-dimensional with the same blade profiles in the spanwise direction. To simulate the experimental conditions exactly, it is necessary to use 29 first-stage stator blades, 23 rotor blades and 26 second-stage stator blades with periodic boundary conditions along the circumferential direction. In order to significantly reduce the computer memory and CPU time requirements, it is desirable to use the same number of blades for both the rotor and stators in the 1- ½ turbine stage. This enables us to simulate only one flow passage with periodic boundary conditions in the circumferential direction. Since this paper focuses on the film cooling on the rotor platform, it is reasonable to simplify the turbine stage by using 46 blades for both the first- and second-stage stators while maintaining the correct number of rotor blades as shown in Figure 35(b).

The simulations were performed using the CFD software package Fluent (version 6). The solutions are obtained by solving the compressible Reynolds-Averaged Navier-Stokes (RANS) equations together with a Reynolds stress model (RSM) using a finite volume method to discretize the continuity, momentum and energy equations. The GAMBIT software with Turbo function was employed to generate the unstructured grids. The computational domain consists of

fluid around the stator 1 and its disk cavity, film cooled rotor platform and its disk cavity, and stator 2 with periodic boundary conditions imposed in the circumferential direction as shown in Figure 35. The computational domain is composed entirely of the hexahedral cells, which are more accurate with less numerical diffusion. An interface technique was applied to handle the information exchanged between stators and rotor since the sliding meshes were used for the rotor domain. Relatively coarse grids are used for the majority of the 1-½ turbine stage, while the angled film (purge) slot, the platform of rotor, and the boundary layer of the stator and rotor blades consist of much finer grids for accurate resolution of the film cooling effectiveness and heat transfer. The $y^* = \rho C_\mu^{1/4} k_p^{1/2} y_p / \mu$ value for the non-equilibrium wall function falls between 30 and 100 for most of the regions, where k is the turbulent kinetic energy and the subscript p denotes the near-wall grid point. The geometry and detailed numerical grids around the coolant slot and rotor platform are shown in Figure 36.

Calculations were performed for four different rotating speeds of 2000, 2550, 3000 and 4000 rpm, where the 3000 rpm is the best performance point for the highest turbine efficiency. The inlet total and exit static pressures of the turbine stage are P_{in} = 101,356 Pa and P_{ex} = 85 kPa, respectively, with a pressure ratio of 1.19. At the inlet of the first stage stator, the total temperature (323 K) and turbulence intensity (5%) are specified with an inlet flow angle of 0 degree.

The absolute velocity at the stator 1 inlet is about 30 m/s. A fixed mass flow rate boundary condition is specified at the inlet of the coolant cavity, with temperature 300K and overall mass flow ratios MFR = 0.5%, 1%, and 1.5%, which correspond to blowing ratios of M = 0.12, 0.24 and 0.36, respectively.

Three sets of calculations with different thermal boundary conditions were performed to evaluate the adiabatic film cooling effectiveness (η_{aw}) and the heat transfer coefficient (h). For the calculation of adiabatic film cooling effectiveness $\eta_{aw} = (T_{aw,0}-T_{aw,f})/(T_{aw,0}-T_{tc})$, the turbine inlet total temperature is specified at $T_{t\infty} = 323$ K and the coolant total temperature is $T_{tc} = 300$ K. The adiabatic wall boundary condition is used for the platform and blades to obtain $T_{aw,f}$. It should be noted that $T_{aw,f}$ includes not only the effects of film cooling, but also the temperature change due to turbine work process. In order to determine the true film cooling effectiveness without the complication caused by turbine work process, it is necessary to calculate another adiabatic wall temperature $T_{aw,0}$ for the same blade configurations in the absence film coolant injection. This enables us to isolate the true effect of coolant protection by comparing the temperature differences with and without the presence of purged coolant. For the simulation of heat transfer coefficient, the coolant total temperature is the same as the turbine inlet total temperature 323 K, while the wall temperature is fixed as 300 K to calculate the wall heat flux q_w. The overall heat transfer coefficient is calculated from this formula: $h= q_w/(T_w-T_{t\infty})$, while the adiabatic heat transfer coefficient: $h_{aw}= q_w/(T_w-T_{aw,0})$. It should be noted that the overall coefficient includes the effect of both turbine passage flow and turbine work process, while adiabatic one only includes the passage flow effect, which will be further discussed in the later section.

All calculations were converged to residual levels of the order of 10^{-5}, and to less than 0.1% error in the mass flow rate between the turbine mainstream and coolant inlet and outlet of the computational domain. The selection of the time step in calculating one passing period of the rotor blade is critical for accurate time-dependent flow predictions. Our previous study shows that the difference between 100 and 200 time steps is below 3%. Therefore, 200 time steps reach

the time-step independency, and are used in these simulations. The passing period, T, is defined as the time it takes for the rotor blade to move from one stator to another. The computed results are recorded and analyzed once every 50 time steps (i.e., every 1/4 passing period). To achieve good periodic results, simulations were performed for 10 passing periods and the numerical results were presented at four different time phases with t/T = 9¼, 9½, 9¾, and 10, respectively. The present simulations are computationally intensive since they involve unsteady three-dimensional flow with a sliding rotor mesh. Each simulation was performed using the parallel version of Fluent on two processors, and requires about two weeks of CPU time on the SGI Altix 3700 supercomputer at Texas A&M University. A total of seven simulations were performed to determine the film cooling effectiveness and heat transfer coefficients for the 2000, 2550, 3000 and 4000 rpm, respectively.

Figure 37 shows the predicted laterally averaged $T_{aw,f}$ for the rotating blade platform using two different numerical grids. The coarse grid consists of about 1.1 million elements with 0.3 million cells for the stator-1 domain, 0.5 million cells for the rotor domain, and 0.3 million cells for the stator-2 domain. For the fine grid case, the number of numerical elements for the rotor domain was doubled to about 1 million cells. It is seen from Figure 36 that the maximum change in the laterally averaged $T_{aw,f}$ is less than 0.83 K. In addition to the grid independency study, comparison of 1st order upstream scheme and 2nd order QUICK scheme has been made in Figure 38. The laterally averaged cooling effectiveness shows a small difference between these two schemes in figure 38(a), while unsteady intensity demonstrates a huge difference in Figure 38(b). Because the 1st order upwind scheme inherently has numerical diffusion, and dilutes the unsteady characters. All the numerical results presented in this paper were obtained based on the find grid with QUICK scheme solutions.

Flow Structure Study

Figure 39 shows a vertical cross section plane and the corresponding streamlines and dimensionless temperature (φ) contours for the film cooled platform with the purged coolant slot. Note that the domain in Figure 39(b) on the right hand side of the white vertical line is rotating, while the left hand side solution domain is non-rotating. Due to the rotating centrifugal force, the fluid in the right hand side of the disk cavity is rotating in counter-clockwise direction and driven radically outward. The centrifugal force pushed (purged) the coolant out of the disk cavity through the inclined coolant slot into the rotor blade passage. It is interesting to note that there is a small circulation region near the slot entrance due to the sharp turn between the disk cavity and the coolant slot. In addition, some mainstream flow was entrained into the coolant slot as seen from the relatively low temperature fluid near the slot exit. It should also be noted that the coolant flow in the slot is highly three-dimensional with significant variations in the circumferential directions.

Besides the flow pattern in the vertical cross plane in Figure 39, an annular (constant radius) cross plane is also shown in Figure 40 to provide a better understanding of the pressure and flow fields for various working conditions. This annular plane is located at 2% of the blade span away from the hub and parallel to the platform. As mentioned earlier, the increasing rotating speed slightly shifts the stagnation point from the pressure side to the suction side direction with a dramatic change in inflow angle. Figure 40(a) compares the pressure ratio ($P_{static,\ local}/P_{\infty,t}$) on the annular cross plane. For the 2000 rpm condition, the high pressure region was observed on the leading portion of the pressure side due to the flow impingement in that region. The stagnation point gradually shifts from the pressure side to the leading edge direction

with increasing rpm to 2550. When the rotating speed was further increased to the 3000 rpm conditions, the high pressure stagnation region was moved to the leading edge of the best performance point. However, the 4000 rpm shifts the stagnation point to the suction side. Figure 40(b) compares the streamlines and dimensionless temperature contours for various rotating speeds. For the 2000 and 2550 rpm condition, the dividing streamline impinges on the pressure side with a positive inflow angle. The coolant from the inclined slot can be clearly detected by the high value dimensionless temperature (φ) near the leading portion. The coolant is pushed away from the blade leading portion suction side by the positive incidence angle flow. For the 3000 rpm condition, the stagnation point shifts to the leading edge of best performance and the coolant is converged near to the blade suction side. However, the coolant does not adhere to the suction side due to the presence of horseshoe vortex along the blade-hub junction. For the 4000 rpm condition, the rotor inlet flow angle switches to negative and the stagnation point is shifted to the suction side. Generally, the streamlines move parallel to the blade pressure side, but converged on the suction side due to the passage vortex. The high value of φ on the rotor trailing portion is not due to the coolant protection. It is, in fact, due to the turbine work process since the adiabatic total temperature decreases significantly along the flow direction.

Figure 41 shows a comparison of the static pressure contours around the rotor blade suction side hub region with and without film cooling. For the non-film-cooled blade shown in Figure 41(a), a low static pressure region is seen on the suction side rotor region. On the other hand, a higher pressure region was observed on the suction side root region for the film-cooled blade shown in Figure 41(b) since the purged coolant from the angled slot was pushed towards the suction side of the rotor blade. It is also worthwhile to note that the effect of the purged coolant is confined to the root region.

Adiabatic Film Cooling Effectiveness Study for Stator – Rotor Injection

Figure 42 compares the adiabatic total wall temperature on the rotating blade platform with and without film coolant to facilitate a direct evaluation of the true film cooling effectiveness. It is quite clear that the adiabatic wall temperature around the leading edge region is significantly lower for the film cooling case shown in Figure 42(a) as a result of purged coolant protection. In the trailing edge section of the blade passage, however, both blade configurations show a significant decrease in the adiabatic wall temperatures either with or without film coolant protection. As noted earlier, the reduction of the adiabatic total temperature in the trailing edge region is due to the turbine work process rather than the coolant protection.

Figure 43 compares the instantaneous adiabatic cooling effectiveness for various rotating speeds. Generally speaking, the cooling effectiveness decreases along the turbine passage flow due to the mixture with the mainstream flow, and keeps away from the blade suction side because of the horseshoe vortex developing at the leading edge root junction. For the low rpm cases (2000 and 2550 rpm cases), the coolant is pushed away from the suction side due to the positive inlet flow angle of rotor. The difference of effectiveness for the various time phases is not significant, because the rotor-stator interaction is weak for such low rotating speeds; and the wake and turbulence intensity is not strong enough to affect the purged coolant flow distribution on the rotor platform. For the high rpm case (3000 rpm), however, the coolant is pushed towards the blade suction side because of decreasing inlet flow angle. The cooling effectiveness shows a significant difference among various time phases. This maybe attributed to: 1) the high rpm increases the rotor-stator interaction affect; 2) high turbulence and high wake are introduced by the increasing rpm; and 3) more chaos is produced by the high rotating speed.

Figure 44 compares the laterally averaged cooling effectiveness and unsteady intensity on the rotating platform. The laterally averaged adiabatic cooling effectiveness has been compared

in Figure 44(a) for various rotating speeds with MFR=1% (M=0.24). As discussion before, the film cooling decreases along the passage flow direction. Also the effectiveness increases with increasing rpm from 2000, 2550 to 3000, since 3000 rpm is the best performance point. The instantaneous and time averaged adiabatic cooling effectiveness has been plotted in Figure 44(b) for 2500 rpm condition with MFR=1%. Clearly to see that the fluctuation of cooling effectiveness increase from the leading edge to the middle part of the blade, then decreases on the trailing portion. Therefore, it is desirable to quantitatively study the unsteady characteristics of the film cooling effectiveness by defining a cooling effectiveness unsteady intensity $\sqrt{\frac{\Sigma(\eta_i-\bar{\eta})^2}{N}}/\bar{\eta}$ based on a similar concept of root mean square (RMS) of turbulence intensity. Figure 44(c) shows the comparison of cooling effectiveness unsteady intensity for various rotating speeds. Generally, the off-design conditions increase the unsteady intensity. For the 2000 rpm case, the unsteady intensity increases from the leading edge to the peak value of 22% at the location x/Cx of 0.6. With rpm increasing to 2550 rpm, which is more close to the best performance condition, the maxim intensity decreases with the peak value of 15% and locates at the x/Cx of 0.38. When the rpm is further increased to the best performance condition of 3000, the unsteady intensity is further reduced, and the peak value is about 12% with location at x/Cx 0.22. Because the best performance working condition streamlined the passage flow, and thus damped the unsteady fluctuation. The shifting of the intensity peak to the leading portion with increasing rpm is attributed to the changing of inlet flow angle of rotor as shown in figure 40(b).

Figure 45 shows the calculated adiabatic cooling effectiveness for various mass flow ratios (MFRs) for the 2550 rpm condition. The simulation indicates that the film cooling effectiveness, as well as the area of coolant protection, increase with increasing mass flow ratio. All simulations show that the film cooling covers a wide area when existing from the slot, but

contracts gradually downstream and adheres to the blade suction side to form a curved triangle region of high effectiveness. In the leading edge portion of the blade passage, the coolant was pushed away from the blade root region by the horseshoe vortex. The experimental results (Fig. 13), however, shows that the film cooling is more uniform in the passage and adheres to the platform leading edge region. In addition, the reattachment of film coolant near the platform leading edge region was also observed in the experiment for the high mass flow ratio (MFR = 1.5%) case.

Figure 46 shows a comparison of the calculated and measured laterally average adiabatic film cooling effectiveness for various mass flow ratios. Except for the leading edge portion, the predictions are in good agreement with the experiment data for the middle and high mass flow ratio cases. The experiment, however, shows some coolant reattachments in the leading edge portion with high film cooling effectiveness, which was not predicted in the present simulations. In addition, the simulation under-predicts the film cooling effectiveness for the MFR=0.5% case.

Figure 47 compares the simulated and measured laterally averaged adiabatic film cooling effectiveness on the rotating blade platform for various rotating speeds. Both the experiment and simulations indicated that the film cooling effectiveness increases with increasing rotating speed. For the 2550 rpm case, the predicted adiabatic film cooling effectiveness is in good agreement with the corresponding measurement except for the leading edge region. However, the film cooling effectiveness is significantly overpredicted for the 2000 rpm case in the leading portion.

Figure 48 shows a comparison of the adiabatic film cooling effectiveness on the blade suction side for various rotating speeds with MFR = 1%. The experimental data on the suction side is not available for comparison at this moment. In general, the coolant jet from the slot not only protects the rotating platform, but also benefits the root region of the rotor blade suction

side. A high effectiveness strip, extending from the leading edge to the trailing edge, is observed on the suction side. The cooling effectiveness increases with increasing rpm until the 3000 rpm of the best performance condition, then drops significantly for the 4000 rpm of over-design condition.

Heat Transfer Study for Stator – Rotor Injection

Figure 49 compares the overall and adiabatic heat transfer coefficient on the rotating blade platform at various time phases for the 2550 rpm condition with MFR = 0.5%. As mentioned before, the overall heat transfer coefficient is based on the turbine stage inlet total temperature, which is widely used in the industry due to the simple; while the adiabatic heat transfer coefficient is referred to the local adiabatic total temperature, which can isolate the effect of turbine work process. For the both kinds of heat transfer coefficient, a high heat transfer coefficient exists at the rotor leading edge due to the horseshoe vortex. A high heat transfer strip develops on the trailing passage portion because of the passage vortex. In addition, there is a low heat transfer region downstream of the rotor trailing edge due to the low velocity in the wake. The unsteady characteristic of both heat transfer coefficient is explicitly, especially for the overall one. The adiabatic heat transfer coefficient shows a higher value than the overall one, especially on the trailing passage portion. Because the adiabatic total temperature decreases along the passage flow direction due to the turbine work process, the driving temperature difference of adiabatic heat transfer coefficient decreases too.

Figure 50 compares the overall and adiabatic heat transfer coefficient for the whole turbine stage. As discussed before, the adiabatic heat transfer coefficient demonstrates a higher value than the overall one because of the turbine work process, especially for the downstream

location of the turbine stage, such as rotor and stator 2. Since in that location, the dramatically dropping of the adiabatic total temperature happens, which will be further discussed in the later section. Also for each stator and rotor blade endwalls, the overall and adiabatic heat transfer coefficient increases from the leading edge to the trailing edge, which is confirmed by experiment measurement of Harasgama and Burton [17].

Turbine Work Process Impact on Film Cooling Effectiveness for Stator – Rotor Injection

Figure 51 shows the area averaged total and static temperature at various stations in the 1-1/2 turbine stage. The four station positions have been denoted in Figure 35(a). Turbine is a rotating machine, which extracts the total energy from the hot gas and transfers it into the mechanical energy by the rotating blades. Due to the turbine work process, it is seen that the total energy decreases significantly from station 2 to station 3, where the rotor converts the thermal energy into the mechanical energy. On the other hand, the total energy remains the same across the stators, such as from station 1 to station 2 (position of stator 1), and from station 3 to the station 4 (position of start 2). The static temperature, however, changed significantly for each station, even for the stators. Because the flow is accelerated through the blades to achieve better performance, the difference between the total and static temperature of each station reflects the gas kinetic energy. By comparing the total and static temperatures in Figure 51, it is desirable to use the total temperature rather than the static temperature as the reference temperature for the study of film cooling effectiveness and heat transfer coefficient since the total temperature is constant across the stators. In view of this, it is useful to define an overall film cooling effectiveness $\eta = (T_{t\infty}-T_{aw,f})/(T_{t\infty}-T_{tc})$ based on the turbine inlet total temperature $T_{t\infty}$ (= 323 K). As noted earlier, the adiabatic wall temperature $T_{aw,f}$ includes not only the

temperature change due to film cooling but also the turbine work process. For the overall film cooling effectiveness in the turbine stage shown in Figures 51 and 52, the high cooling effectiveness in the leading portion is due to the coolant protection, while the high value in the trailing portion can be attributed to the low mainstream temperature caused by the turbine work process.

Figure 52 compares the three-dimensional coolant images in the rotor passage for various working conditions. Note that the overall film cooling effectiveness is used for the contour plots in this figure, and the 4000 rpm case is not plotted here due to the small value. For the 2000 rpm condition, the coolant is pushed to the middle of the rotor passage by the positive inflow angle, and looks more concentrated and higher film cooling effectiveness values in comparison with the other working conditions. As the coolant moves downstream, it lifts off the platform and diffuses gradually toward the trailing portion. For the 2550 rpm condition, the coolant trajectory moves to the blade suction side due to the low pressure near the suction side surface. The coolant, however, is not adhered to the leading portion suction side due to the presence of horseshoe vortex along the blade-hub junction. It is also noted that the coolant is pushed away from the pressure side because of the high pressure near the pressure side. For the 3000 rpm condition, the coolant is pushed to the suction side by the increasing inflow angle. Also, the coolant is more dilute with lower overall cooling effectiveness than those observed at the lower rpm conditions. As noted earlier, the high cooling effectiveness near the trailing edge of the blade passage is attributed to the turbine work extraction.

Figure 53 compares the overall film cooling effectiveness on the rotor blade platform at four time phases for 2550 rpm condition with MFR = 1%. Generally, the difference of cooling effectiveness among the various time phases is not significant in the leading edge portion for this

case. The high cooling effectiveness stays outside of the blade leading edge due to the horseshoe vortex, and exists near the suction side due to coolant streamline convergence in the low pressure region. Also as indicated before, the high cooling effectiveness on the trailing portion is not due to the coolant protection. This is because of the turbine work process decreasing the mainstream temperature in the trailing portion, which is strongly influenced by the stator-rotor interaction for various time phases, especially in the rotor wake region.]

Combined Stator – Rotor and Discrete Hole Injection

The present three-dimensional calculations were carried out for a 1-½ turbine stage, which includes the first-stage stator (stator 1), the first-stage rotor (rotor), and the second-stage stator (stator 2), as shown in Figure 54. There are two different film cooling configurations on the rotating platform; one is the purge slot on the rotor leading edge and the other consists of nine discrete film holes on the platform trailing portion. For the purge slot cooling, the film coolant enters the disk cavity of the first stage stator and purges through the inclined slot in the hub junction between the first-stage stator and the rotor as shown in Figure 54(a). For discrete holes film cooling, the coolant flows into a plenum, and discharges though nine tubes with compound angle to the platform trailing portion. In Figure 54(a), the portions outlined in blue color are non-rotating domains which include stator 1, disk cavity of stator 1 and stator 2; while the red color represents the rotating domains such as the rotor and its disk cavity, coolant plenum and nine connecting tubes for discharge of coolant jets. All other geometries are similar to that used for just the stator-rotor purge flow explained earlier. A matrix of nine discrete compound angled coolant holes of 1mm diameter are placed on the rotor platform at about 50% downstream of the blade passage. The approximate pitch to diameter ratio for the discrete holes is 5 and the

compound angles for all nine holes are given in Suryanarayanan et al. [17]. Figure 54(b) shows the surface grids for stators, rotor, platform, and disk cavity. Calculations were performed for one row of stators and rotor passages with periodic boundary conditions in the circumferential direction as shown in Figure 54(a), but the numerical grids were repeated in Figure 54(b) to provide a clear view of the blade passage. The geometry and detailed numerical grids around the purge slot, nine discrete film holes, and rotor platform are shown in Figure 55.

Figure 6 shows a comparison of the static pressure contours around the rotor blade hub region with and without platform purge flow. For the blade without purge flow shown in Figure 56(a), high pressure is confined to pressure side while a low static pressure region exists on the suction side rotor region. For the rotor blade with platform purge flow shown in Figure 56(b), the high pressure region extends from the pressure side to the suction side due to the impingement of purged coolant flow on the blade leading edge. It can also be clearly seen that the effect of the purged coolant is confined to the root region of the rotor blade.

For completeness, the three-dimensional coolant flow structures and the associated adiabatic film cooling effectiveness contours in the rotor blade passage were also plotted in Figure 57 to provide a more detailed understanding of the coolant flow and heat transfer characteristics at various rotating speeds. It should be noted that the streamlines in the rotor inlet region shown in Figure 57(a) were plotted in rotating reference frame using the relative velocity, while the absolute velocity was used for streamlines in the outlet sections shown in Figure 57(b). For the purge slot coolant flow structure in Figure 57(a), the coolant accumulates on the blade suction side with very little protection of the pressure side of the rotor platform except in the leading edge region. The coolant traces diminishes gradually downstream of the purge slot and vanishes completely towards to the trailing portion after mixing with the mainstream flow. In the mid-

chord region (i.e., third cross section from the blade leading edge), the purged coolant flow is driven by the blade passage vortex from the pressure side towards the suction side, leaving the pressure side of the platform unprotected. For the 2000 rpm condition, a pair of horseshoe vortices is clearly visible in the blade root region and the suction side vortex is much stronger than that on the pressure side. With increasing rotation speed, the strength of the suction horseshoe vortex reduces quickly and the pressure side vortex disappeared completely. For the design condition at 2550 rpm, the mainstream flow impinges directly on the rotor leading edge. Consequently, the coolant from the purge slot accumulates around the blade leading edge region. When the rotating speed is further increased to the best performance point at 3000 rpm, the horseshoe vortex is very weak and the coolant is pushed away from the suction side root region into the middle section of the rotor blade passage.

Figure 57(b) shows the downstream coolant flow structures and the corresponding adiabatic film cooling effectiveness distributions. The streamlines were plotted using the tangential components of the absolute velocity at each cross section. It is interested to note that there are two distinctive coolant strips on the rotor suction side. The upper coolant strip is produced by the platform purge slot, while the bottom one along the blade-platform junction is produced by the discrete-hole coolant jets. The coolant from the platform purge slot covers a fairly wide section of the blade suction side up to about 25% of the blade span, but provides very limited coverage for the pressure side of the platform as noted earlier in Figure 57(a). On the other hand, the discrete-hole coolant jets protect a wide region of the platform passage but provide very limited protection of the blade suction along the blade-platform junction. It is worthwhile to note that the passage vortex develops from the mid-chord portion to the trailing portion with increasing rpm.

Adiabatic Film Cooling Effectiveness Study for Combined Stator – Rotor and Discrete Hole Injection

Figure 58 shows detailed comparisons of the instantaneous adiabatic film cooling effectiveness at four time phases for various rotating speeds. In general, the film cooling effectiveness decreases along the flow direction due to the mixing of coolant with the mainstream flow in turbine blade passage. The purge slot film cooling is strongly affected by the stator-rotor interactions in the leading edge region, while the discrete-hole film cooling is not significantly influenced by the unsteady intensity of the stator wake flow. As mentioned earlier in Figure 58, the coolant from purge slot is driven by the blade passage vortex away from the pressure side and accumulates on the suction side. Consequently, most of the coolant coverage is confined to a curved triangular region adjacent to the blade suction side with diminishing protection for the blade pressure side in the mid-chord and downstream areas.

For the low rpm case at 2000 rpm, the slot coolant is pushed away from the suction side by the positive incident flow angle. The film cooling effectiveness fluctuates significantly among four different time phases in the leading edge region due to strong stator-rotor interactions. The effects of stator-rotor interaction reduce rapidly in the mid-chord and downstream regions. Therefore, the discrete-hole film cooling tends to be more stable with relatively small fluctuations. For the intermediate rotating speed of 2550 rpm, the purge slot coolant impinges directly on the rotor leading edge and produced a high level of adiabatic film cooling effectiveness around the leading edge and spread out over a fairly wide area. In addition, the film cooling effectiveness is highly unsteady around the blade leading edge region due to strong stator-rotor interactions. However, the film cooling effectiveness and unsteady intensity of the purge flow diminishes rather quickly in the rotor blade passage. Therefore, it is desirable to

place the discrete holes in the mid-chord region in order to provide necessary protection of the platform surface in the mid-chord and trailing edge regions. For the high rotating condition at 3000 rpm, the purge slot coolant spreads more uniformly across the blade passage but the adiabatic film cooling effectiveness level is somewhat lower comparing to the design condition. The reduction of platform purge flow cooling effectiveness may be attributed to (1) shift of the stagnation point to suction side, and (2) stronger wake effect of the first-stage stator.

Figure 59 shows the laterally averaged cooling effectiveness and unsteady intensity on the rotating platform for various rotating speeds with a purge flow rate MFR = 1% and discrete holes blowing ratio M = 1. In the upstream section of the blade passage ($0 < X/Cx < 0.5$), the film cooling effectiveness decreases along the turbine passage due to the mixing of purged coolant with mainstream flow. With increasing rotating speed, the purge slot cooling effectiveness increases slightly because high rpm decreases the rotor relative velocity and reduce the strength of the horseshoe vortex. At the trailing portion ($0.5 < X/Cx < 1$), the cooling effectiveness varies in a saw-tooth pattern due to the superposition of staggered coolant jets from the nine discrete holes. It is further noted that the laterally averaged film cooling effectiveness at the design condition is somewhat lower than those observed for the 2000 and 3000 rpm conditions. This can be attributed to the rapid decay of the film cooling effectiveness for purge slot flow at 2550 rpm as noted earlier in Figure 58.

Figure 59(b) shows the instantaneous and time-averaged adiabatic cooling effectiveness for the design condition with slot mass flow ratio MFR=1%, and discrete-hole blowing ratio M=1. It is clearly seen that the fluctuation of cooling effectiveness increases from the leading edge and reaches the peak value at 20% of the blade axial chord length (i.e., $X/Cx = 0.2$), then decreases towards the trailing edge since the effect of stator-rotor interaction diminishes rapidly after the

mid-chord section. The film cooling effectiveness pattern due to the discrete-hole coolant jets is fairly steady with relatively small fluctuations. In order to quantify the level of unsteady fluctuations, we evaluate the unsteady intensity of the film cooling effectiveness using the following definition:

$$Tu_\eta = \sqrt{\frac{1}{N}\sum_{i=1}^{N}(\eta_i - \bar{\eta})^2} \Big/ \bar{\eta}$$

where η_i is the cooling effectiveness for time step *i* and $\bar{\eta}$ is the averaged cooling effectiveness over *N* time steps. Figure 59(c) shows the comparison of cooling effectiveness unsteady intensity for various rotating speeds. In general, the purge slot film cooling shows a high level of unsteady intensity for all the rotating speeds over the first half of the rotor blade passage due to strong rotor-stator interactions at the rotor inlet. In the mid-chord and trailing edge regions, the discrete-hole coolant jets produced high film cooling effectiveness but the corresponding unsteady intensity is relatively low since the influence of stator-rotor interactions diminishes rapidly downstream of the mid-chord section.

Figure 60 shows a comparison of the measured (Suryanarayanan et al. [17]) and calculated adiabatic cooling effectiveness for 2550 and 3000 rpm, respectively, with a purge flow rate MFR = 1% and discrete holes blowing ratio M = 1. The predicted film cooling effectiveness patterns are in reasonably good agreement with the corresponding measurement, but the discrete-hole film cooling effectiveness is somewhat over predicted. Both the simulation and experiment indicate that the purge slot cooling covers the leading portion of the rotor platform and the purged coolant tends to accumulate on the suction side with diminishing coverage of the pressure side beyond 25% of the axial chord length. Both the measured and predicted cooling traces from discrete holes were driven by the passage vortex from the pressure side to the suction

side. Although the purge slot film cooling mass flow rate (MFR) is 1%, the corresponding local blowing ratio (M) is only 0.24, which is far below the blowing ratio for discrete holes film cooling of M = 1. Consequently, the simulation predicted a high local cooling effectiveness downstream of the discrete holes than that of the purge slot which is confirmed by the experimental data. However, the predicted discrete-hole film cooling effectiveness levels are considerably higher than the corresponding measurements. The measured film cooling effectiveness reduces slightly when the rotating speed was increased from 2550 rpm to 3000 rpm. The simulation also shows a reduction of purge slot cooling effectiveness at the rotor inlet at 3000 rpm, but the laterally averaged effectiveness increases significantly in the mid-chord and downstream regions as shown earlier in Figure 59(a).

Adiabatic Heat Transfer Study for Combined Stator – Rotor and Discrete Hole Injection

Figure 61 shows the heat transfer coefficient based on the adiabatic wall temperature, $h_{aw} = q_w/(T_w-T_{aw,0})$, on the rotor platform at four time phases for three rotating speeds. The high heat transfer coefficient region develops from the leading portion pressure side and increases along the mainstream flow direction towards the trailing edge due to flow acceleration in the rotor passage, which is confirmed by the experiment studies of Harasgama and Burton [2-3]. Downstream of the rotor trailing edge, the heat transfer coefficient decreases due to the deceleration of mainstream flow in the rotor wake region. The heat transfer coefficient is also low in the leading edge region because purge slot coolant is slower than the mainstream flow and acts as a blockage to reduce the heat transfer coefficient. Similarly, the heat transfer coefficient also decreases downstream of the discrete-hole coolant jets since the blowing ratio (M = 1) for

the coolant jets is defined based on the rotor exit velocity which is lower than the mainstream velocity in the mid-chord region where the discrete holes are located.

As noted earlier, the rotor relative velocities decreases with increasing rotating speed for the fixed inlet/outlet pressure ratio considered in the present study. It is clearly seen that the heat transfer coefficient is quite high for 2000 rpm case due to high rotor relative velocity. When the rotating speed was increased to 2550 rpm and then to 3000 rpm, the heat transfer coefficients decrease sharply since the rotor relative velocities are significantly lower for high rpm conditions. Similar to the adiabatic film cooling effectiveness, the heat transfer coefficients also fluctuate significantly among four different time phases. In general, the unsteady intensity of heat transfer coefficient is high in the platform leading portion but diminishes in the mid-chord and downstream regions where the discrete film holes are located.

Overall heat transfer coefficients and film cooling effectiveness

In order to evaluate h_{aw} as shown earlier in Figure 61, it is necessary to determine the adiabatic wall temperature $T_{aw,0}$ separately with additional measurements or calculations. On the other hand, the overall heat transfer coefficient $h = q''_w/(T_w-T_{t\infty})$ can be easily evaluated since the turbine inlet total temperature $T_{t\infty}$ can be measured directly. However, the overall heat transfer coefficient h involves not only the effects of the velocity field but also the turbine work process while h_{aw} depends only on the flow field. In general, the turbine work process reduces the mainstream temperature since a portion of the thermal energy is converted to mechanical energy to turn the rotor blades. Therefore, the local adiabatic wall temperature $T_{aw,0}$ in the rotor passage is lower than the inlet total temperature $T_{t\infty}$ for the turbine stage and closer to the wall

temperature T_w on rotor blade surface. It is clearly seen from Figure 62 that the overall heat transfer coefficient h is significantly lower than the h_{aw} based on adiabatic wall temperature (note for different color bar ranges in Figures 61 and 62) since the denominator T_w-$T_{t\infty}$ is larger than T_w-$T_{aw,0}$ for the same wall heat flux q_w.

To study the impact of turbine work process on the film cooling effectiveness, the overall film cooling effectiveness $\eta = (T_{t\infty}-T_{aw,\,f})/(T_{t\infty}-T_{tc})$ is also presented in Figure 13 using the same color bar range as the adiabatic cooling effectiveness $\eta_{aw} =(T_{aw,\,0}-T_{aw,\,f})/(T_{aw,\,0}-T_{tc})$ shown earlier in Figure 8. As noted earlier, the turbine work reduces the mainstream temperature and produced an overall film cooling effectiveness even without the presence of coolant in platform purge slot or discrete film holes. This resulted in a high overall cooling effectiveness η near the trailing edge as shown in Figure 63 since the mainstream temperature reduces along the rotor blade passage as a result of the turbine work. Comparing to the adiabatic film cooling effectiveness η_{aw} in Figure 58, it is clearly seen that the overall film cooling effectiveness η is much higher than the corresponding true cooling effectiveness η_{aw} for all three rotating speeds. Furthermore, the overall film cooling effectiveness tends to increase with increasing rotating speed since more turbine work is produced at higher rpm for the range of rotating speeds considered in the present study.

CURRENT INVESTIGATION

Rotating Heat Transfer

Using the pressure sensitive paint technique, the film cooling effectiveness has been measured on the rotating platform with coolant flow from the stator-rotor seal. The effectiveness has also been measured with coolant from discrete film cooling holes. A combined case with stator-rotor and hole injection was also experimented with to determine the interaction between the two methods and to best provide for platform cooling. This will provide engineers with detailed film cooling effectiveness distributions under more realistic coolant flow conditions. Following the final film effectiveness measurements, detailed heat transfer coefficient distributions will be obtained on the rotating platform using temperature sensitive paint for the different cooling methods used earlier. The effect of rotation on the heat transfer coefficient will be quantified for several blowing ratios. A uniform flux heater was designed and incorporated into the rotor platform to enable heat transfer measurements (figure 64).

In addition to the experimental work, numerical simulations are also continuing for equivalent test conditions. The experimental results will be used to validate the numerical simulations, and the predictions will be extended to a wider range of flow conditions. The film cooling effectiveness and heat transfer coefficients will be predicted on the rotating platform with separate coolant flow from the stator-rotor seal and discrete film holes, as well as when the coolant flows are combined.

CONCLUSIONS

Both the experimental and numerical data are vital for engineers to develop more effective platform cooling schemes which will increase platform durability and longevity. The effective cooling schemes will also reduce coolant flow, and ultimately increase power output and thermal efficiency of the engine. To aid designers in developing more effective cooling schemes, detailed film cooling effectiveness distributions have been obtained on turbine platforms and compared with numerical simulations to verify the prediction capabilities of CFD. From the data obtained on the rotating blade platform, it was shown that the film cooling effectiveness due to coolant injection from the stator-rotor increases with increasing coolant-to-mainstream mass flow ratio. Unlike results that have been obtained in non-rotating facilities, complete coverage of the passage platform cannot be obtained by using coolant injection from the stator-rotor unless a very large mass flow ratio is injected. The passage vortex over the platform has an adverse impact on film adherence. If the engine deviates from its design condition the film coolant traces get reoriented more toward the suction side for off-design rotating conditions due to the shifting of the stagnation zone on the blade leading edge.

Additional film cooling holes are needed to adequately protect the downstream half of the rotating platform. The level of protection offered by these holes is dependant on the rotational speed of the blades, the blowing ratio of the coolant and their location on the platform. Film cooling effectiveness was quantified for downstream discrete hole film cooling for M_{holes}=0.5, 0.75, 1.00, 1.25, 1.50, 1.75 and 2.00. Further, combined film cooling tests were performed for an upstream stator-rotor purge flow ejection and downstream discrete hole coolant ejection at MFR=1.00% and M_{holes}=0.75, 1.00 and 1.25. The results of the above research are summarized below:

1. Film cooling effectiveness and coolant coverage on the rotor platform due to coolant ejection through downstream holes is maximum for the reference speed of 2550 rpm.
2. M_{holes} between 0.75 and 1.25 provided the best protection on the rotor platform for all three rotational speeds. Coolant coverage and effectiveness magnitudes were highest at these blowing ratios than the others tested. This result confirms that the blowing ratio of unity not only provides the best film coverage, but it also minimizes the aerodynamic losses due to mixing of the cooling jets with the main flow.
3. Two downstream film cooling holes (1 and 4 in Fig. 7) were affected more by the passage vortex than the other cooling holes owing to their position on the rotor platform.
4. Secondary flow from the blade pressure surface to the suction surface strongly affected by the rotational motion caused the coolant traces from the holes to clearly flow towards the suction surface.
5. Complete film cooling protection on a rotating platform can be provided with combined upstream stator-rotor ejection and discrete hole ejection. Positioning the holes with angles oriented more towards the pressure surface will help reduce the effects of passage vortex and cross flow.
6. To optimize coolant usage, maintaining the stator-rotor injection close to MFR=1% and increasing the number of holes on the platform without compromising the structural integrity is the way forward in providing proper film protection on the platform.

Numerical simulations were performed for the three-dimensional 1-½ turbine stage to determine the effect of stator-rotor interaction on platform purge slot and discrete holes film cooling and heat transfer. The platform purge slot with overall coolant mass flow rate MFR =

1% of mainstream flow and discrete film holes with local blowing ratio M = 1 were investigated for low, intermediate and high rotating speeds. Both the adiabatic film cooling effectiveness and heat transfer coefficient based on adiabatic wall temperature were evaluated to determine the true effect of film cooling. The overall film cooling effectiveness and heat transfer coefficient were also calculated to determine the influence of turbine work process. The primary findings from this study are summarized as follows:

1) The stator-rotor interaction produced high unsteady intensities for platform purge slot film cooling and heat transfer, while the discrete holes film cooling is only slightly affected.

2) With increasing rotating speed, the flow incidence angle changed significantly and the stagnation point shifts gradually from the pressure side to the suction side on the rotor leading edge. Higher rotating speed also reduces the rotor relative velocity and increases the local blowing ratio for platform purge flow.

3) At the design condition of 2550 rpm, the film cooling effectiveness is very high in the upstream section of rotor passage since the platform purge coolant impinges directly on the rotor leading edge. For lower rotating speed of 2000 rpm, the purge flow cooling effectiveness reduces due to lower blowing ratio (higher rotor relative inlet velocity) and the shift of stagnation point to the blade pressure side. At 3000 rpm, the film cooling effectiveness is also lower due to stronger wake effect from the first-stage stator blades and the shift of stagnation point to the blade suction side. The trend is reversed in the mid-chord and downstream sections with the lowest discrete holes film cooling effectiveness for the design condition.

4) The turbine work process reduces the mainstream temperature in the rotor blade passage. This results in a significant increase of the overall film cooling effectiveness and a reduction of the overall heat transfer coefficients.

5) The predicted adiabatic film cooling effectiveness is in reasonably good agreement with the corresponding experiment data, but the effectiveness of the discrete film holes was over predicted.

The present study provides detailed film cooling data on rotating platforms, which is not openly available for designers. By utilizing these results for film cooling, turbine researchers and designers will be better equipped to implement cooling schemes that adequately protect the turbine components while minimizing coolant consumption. Extending the life of vital components while reducing the amount of cooling air will lead to more efficient and reliable engines.

REFERENCES

[1] Han, J.C., Dutta, S., and Ekkad, S.V., 2000, *Gas Turbine Heat Transfer and Cooling Technology*, Taylor and Francis, New York ,646 pages.

[2] Dring, R. P., Blair, M. F., and Hoslyn, H. D., 1980, "An Experimental Investigation of Film Cooling on a Turbine Rotor Blade," ASME J. of Engineering for Power, 102, pp. 81-87.

[3] Takeishi, M., Aoki, S., Sato, T., and Tsukagoshi, K., 1992, "Film Cooling on a Gas Turbine Rotor Blade," ASME J. of Turbomachinery, 114, pp. 828-834.

[4] Abhari, R.S., and Epstein, A.H., 1994, "An Experimental Study of Film Cooling in a Rotating Transonic Turbine," ASME J. of Turbomachinery, 116, pp. 63-70.

[5] Blair, M.F., 1994, "An Experimental Study of Heat Transfer in a Large-Scale Turbine Rotor Passage," ASME J. of Turbomachinery, 116, pp. 1-13.

[6] Ahn, J., Schobeiri, M.T., Han, J.C., and Moon, H.K., 2004, "Film Cooling Effectiveness on the Leading Edge of a Rotating Turbine Blade," ASME Paper No. IMECE 2004-59852.

[7] Ahn, J., Schobeiri, M.T., Han, J.C., and Moon, H.K., 2004, "Film cooling effectiveness on the leading edge of a rotating Film-Cooled Blade Using Pressure Sensitive Paint," ASME Paper No. GT-2005-68344.

[8] Langston, L.S., Nice, L.M., and Hooper, R.M., 1976, "Three-Dimensional Flow within a Turbine Cascade Passage," ASME Paper No. 76-GT-50.

[9] Langston, L.S., 1980, "Crossflows in a Turbine Cascade Passage," *ASME J. Engineering for Power*, Vol. 102, pp. 866-874.

[10] Goldstein, R.J. and Spores, R.A., 1988, "Turbulent Transport on the Endwall in the Region between Adjacent Turbine Blades." *ASME J. Heat Transfer*, Vol. 110, pp. 862-869.

[11] Blair, M.F., 1974, "An Experimental Study of Heat Transfer and Film Cooling on Large-Scale Turbine Endwall," *ASME J. Heat Transfer*, Vol. 96, pp. 524-529.

[12] Graziani, R.A., Blair, M.F., Taylor, J.R., and Mayle, R.E., 1980, "An Experimental Study of Endwall and Airfoil Surface Heat Transfer in a Large Scale Turbine Blade Cascade," *ASME J. Engineering for Power*, Vol. 102, pp. 257-267.

[13] York, R.E., Hylton, L.D., and Mihelc, M.S., 1984, "An Experimental Investigation of Endwall Heat Transfer and Aerodynamics in a Linear Vane Cascade," *ASME J. Engineering for Gas Turbines and Power*," Vol. 106, pp. 159-167.

[14] Radomsky, R.W. and Thole, K.A., 2000, "High Free-Stream Turbulence Effects on Endwall Heat Transfer for a Gas Turbine Stator Vane," *ASME J. Turbomachinery*, Vol. 122, pp. 299-708.

[15] Kwak, J.S., Lee, J.H., and Han, J.C., 2002, "Heat Transfer and Pressure Distributions on a Gas Turbine Vane End-Wall," Proceedings of the Twelfth International Heat Transfer Conference, pp. 693-698.

[16] Takeishi, K., Matsuura, M., Aoki, S., and Sato, T., 1990, "An Experimental Study of Heat Transfer and Film Cooling on Low Aspect Ratio Turbine Nozzles," *ASME J. Turbomachinery*, Vol. 112, pp. 488-496.

[17] Harasgama, S.P. and Burton, C.S., 1992, "Film Cooling Research on the Endwall of a Turbine Nozzle Guide Vane in a Short Duration Annular Cascade: Part 1 – Experimental Technique and Results," *ASME J. Turbomachinery*, Vol. 114, pp. 734-740.

[18] Jabbari, M.Y., Marston, K.C., Eckert, E.R.G., and Goldstein, R.J., 1996, "Film Cooling of the Gas Turbine Endwall by Discrete-Hole Injection," *ASME J. Turbomachinery*, Vol. 118, pp. 278-284.

[19] Friedrichs, S., Hodson, H.P., and Dawes, W.N., 1996, "Distribution of Film-Cooling Effectiveness on a Turbine Endwall Measured Using the Ammonia and Diazo Technique," *ASME J. Turbomachinery*, Vol. 118, pp. 613-621.

[20] Friedrichs, S., Hodson, H.P., and Dawes, W.N., 1997, "Aerodynamic Aspects of Endwall Film Cooling," *ASME J. Turbomachinery*, Vol. 119, pp. 786-793.

[21] Friedrichs, S., Hodson, H.P., and Dawes, W.N., 1998, "The Design of an Improved Endwall Film Cooling Configuration," ASME Paper No. 98-GT-483.

[22] Barigozzi, G., Benzoni, G., Franchini, G., and Derdichizzi, A., 2005, "Fan-Shaped Hole Effects on the Aero-Thermal Performance of a Film Cooled Endwall," ASME Paper No. GT2005-68544.

[23] Roy, R.P., Squires, K.D., Gerendas, M., Song, S., Howe, W.J., and Ansari, A., 2000, "Flow and Heat Transfer at the Hub Endwall of Inlet Vane Passages – Experiments and Simulations," ASME Paper No. 2000-GT-198.

[24] Burd, S.W., Satterness, C.J., and Simon, T.J., 2000, "Effects of Slot Bleed Injection Over a Contoured End Wall on Nozzle Guide Vane Cooling Performance: Part II – Thermal Measurements," ASME Paper No. 2000-GT-200.

[25] Oke, R., Simon, T., Shih, T., Zhu, B., Lin, Y.L., and Chyu, M., 2001, "Measurements over a Film-Cooled Contoured Endwall with Various Coolant Injection Rates," ASME Paper No. 2001-GT-0140.

[26] Oke, R.A. and Simon, T.W., 2002, "Film Cooling Experiments with Flow Introduced Upstream of a First Stage Nozzle Guide Vane through Slots of Various Geometries," ASME Paper No. GT-2002-30169.

[27] Nicklas, M., 2001, "Film-Cooled Turbine Endwall in a Transonic Flow Filed: Part II – Heat Transfer and Film Cooling Effectiveness," *ASME J. Turbomachinery*, Vol. 123, pp. 720-729.

[28] Liu, G., Liu, S., Zhu, H., Lapworth, B.C., and Forest, A.E., 2004, "Endwall Heat Transfer and Film Cooling Measurements in a Turbine Cascade with Injection Upstream of Leading Edge," *Heat Transfer – Asian Research*, Vol. 33, pp. 141-152.

[29] Zhang, L.J. and Jaiswal, R.S., 2001, "Turbine Nozzle Endwall Film Cooling Study Using Pressure-Sensitive Paint," *ASME J. Turbomachinery*, Vol. 123, pp. 730-735.

[30] Zhang, L.J. and Moon, H.K., 2003, "Turbine Nozzle Endwall Inlet Film Cooling – The Effect of a Backward Facing Step," ASME Paper No. GT2003-38319.

[31] Knost, D.G. and Thole, K.A., 2004, "Adiabatic Effectiveness Measurements of Endwall Film Cooling for a First Stage Vane," ASME Paper No. GT2004-53326.

[32] Cardwell, N.D., Sundaram, N., and Thole, K.A., 2005, "Effects of Mid-Passage , Endwall Misalignment and Roughness on Endwall Film-Cooling," ASME Paper No. GT2005-68900.

[33] Han, S. and Goldstein, R.J., 2005, "Influence of Blade Leading Edge Geometry on Turbine Endwall Heat (Mass) Transfer," ASME Paper No. GT2005-68590.

[34] Schobeiri, M. T., 1999, "Efficiency, Performance and Flow Measurement of Siemens-Westinghouse HP-Turbine Blades, Series 9600 and 5600, Final Report.

[35] Schobeiri, M. T., Gilarranz, J.L, Johansen, E.S., 2000, "Aerodynamic and Performance Studies of a Three Stage High Pressure Research Turbine with 3-D Blades, Design Points and Off-Design Experimental Investigations," 2000-GT-484.

[36] Schobeiri, M.T., Suryanarayanan A., Jermann, C., and Neuenschwander, T., 2004,"A Comparative Aerodynamic and Performance Study of a Three-Stage High Pressure Turbine with 3-D Bowed Blades and Cylindrical Blades," GT-2004-53650.

[37] McLachlan, B., and Bell, J., 1995, "Pressure-Sensitive Paint in Aerodynamic Testing," Exp. Therm. Fluid Sci., 10, pp. 470–485.

[38] Wright, L.M., Gao, Z., Varvel, T.A., and Han, J.C., 2005, "Assessment of Steady State PSP, TSP and IR Measurement Techniques for Flat Plate Film Cooling," ASME Paper No. HT-2005-72363.

[39] Coleman, H.W., and Steele, W.G., 1989, *Experimentation and Uncertainty Analysis for Engineers*, John Wiley & Sons, New York.

[40] Goldstein, R.G., 1971, "Film Cooling," *Advances in Heat Transfer*, Vol. 7, pp. 321 – 379.

[41] Zhang, L. and Han, J.C., 1994, "Influence of Mainstream Turbulence on Heat Transfer Coefficients from a Gas Turbine Blade," *ASME J. Heat Transfer*, Vol. 116, pp. 896-903.

[42] Suryanarayanan, A., Mhetras, S.P., Schobeiri, M.T. and Han, J.C., 2006, "Film-Cooling Effectiveness on a Rotating Blade Platform," ASME paper, GT-2006-90034.

Stage no., N	3	Mass flow	3.728 kg/s
D_t	685.8mm	D_h	558.8mm
Reference speed	2550 rpm	Speed range	2400 to 3000 rpm
Inlet pressure	101.356 kPa	Exit pressure	71.708 kPa
Blade height	63.5 mm	Power	80.0-110.0 kW
Blade no.	Stator 1 = 56	Stator 2 = 52	Stator 3 = 48
Blade no.	Rotor 1 = 46	Rotor 2 = 40	Rotor 3 = 44
$_2$	19^o		0.353
$_3$	161^o		1.0
$_3$	110^o	r	0.5

Table 1 Turbine dimensions and operating conditions

	D, mm	γ º	θ º
Hole 1	1.00	35º	47.39º
Hole 2	1.00	35º	34.50º
Hole 3	1.00	35º	25.31º
Hole 4	1.00	35º	49.58º
Hole 5	1.00	35º	42.29º
Hole 6	1.00	35º	32.62º
Hole 7	1.00	37º	57.46º
Hole 8	1.00	37º	40.25º
Hole 9	1.00	37º	33.83º

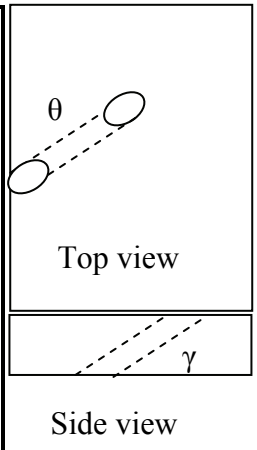

Table 2 Film Cooling Hole Orientation

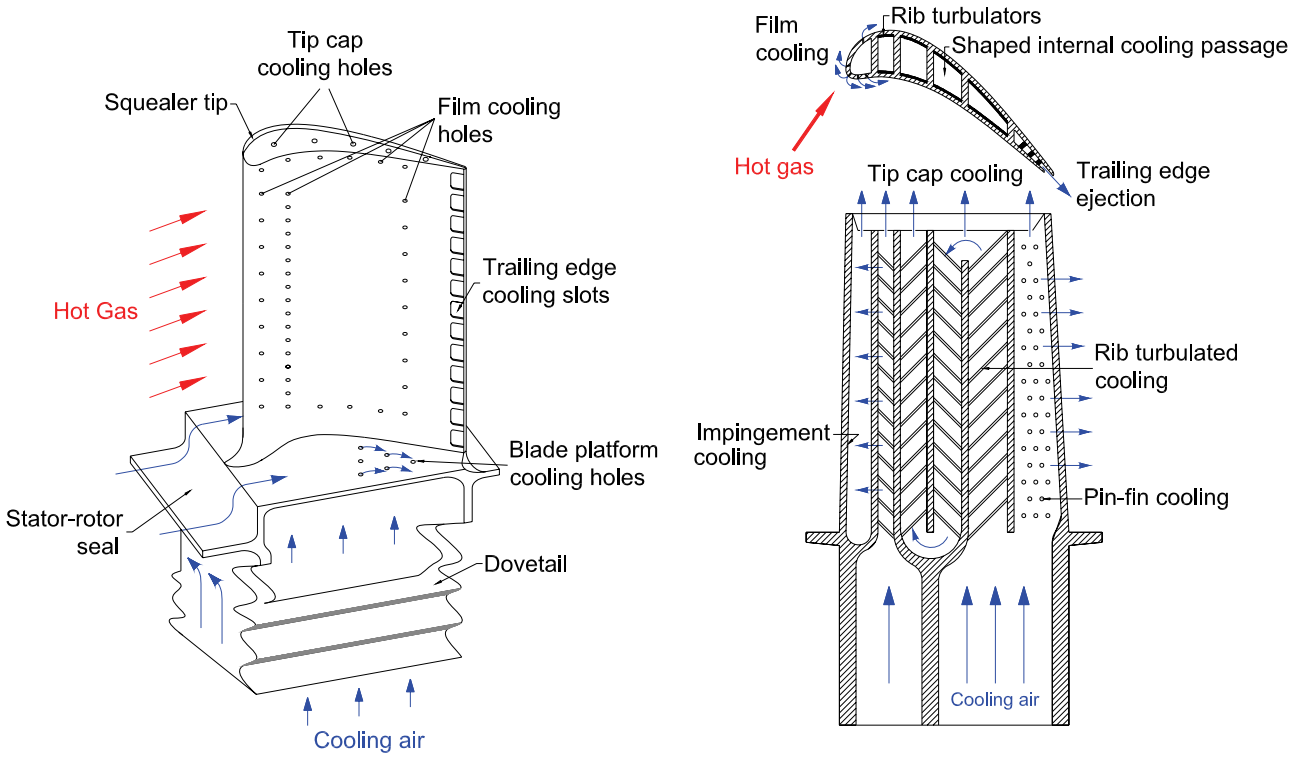

Figure 1: Modern Cooled Gas Turbine Blade

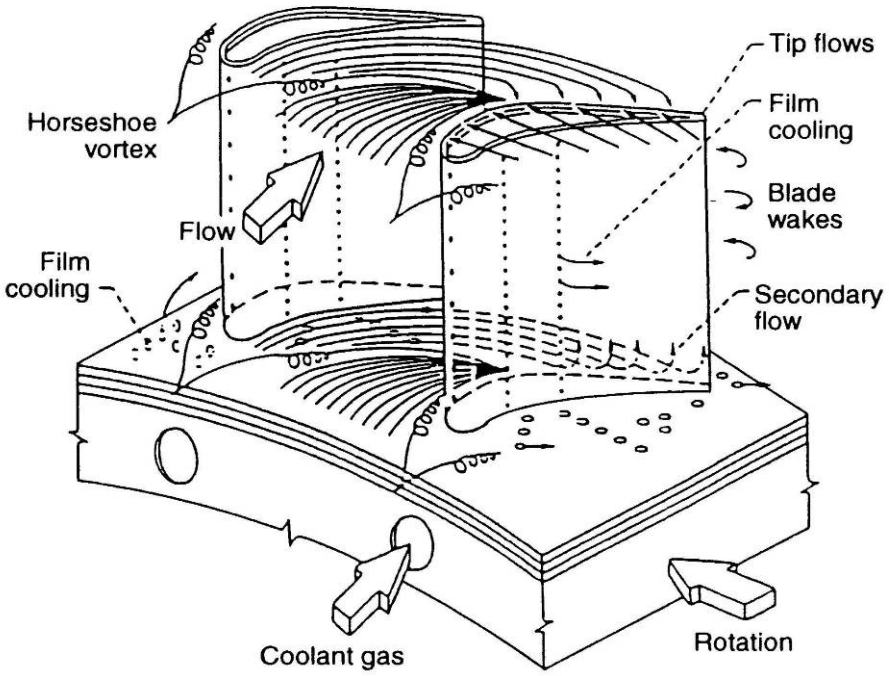

Figure 2: Secondary Flow through a Blade Passage (from Han et al. [1])

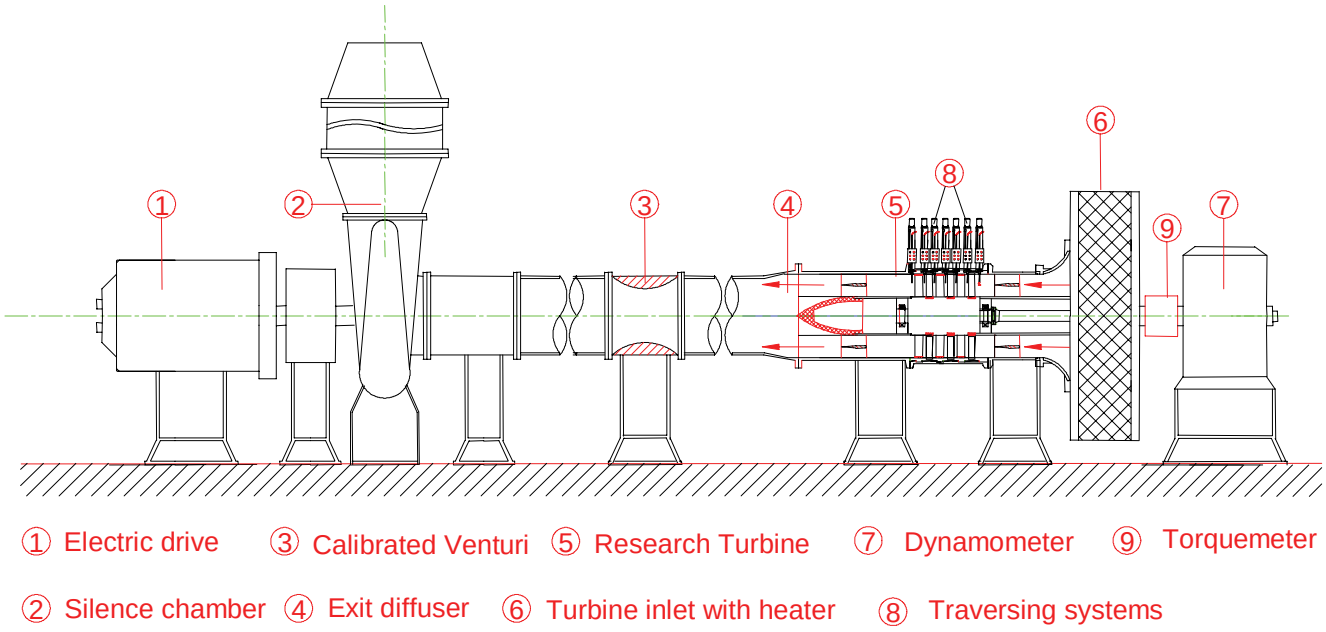

Figure 3: Existing Turbine Research Facility

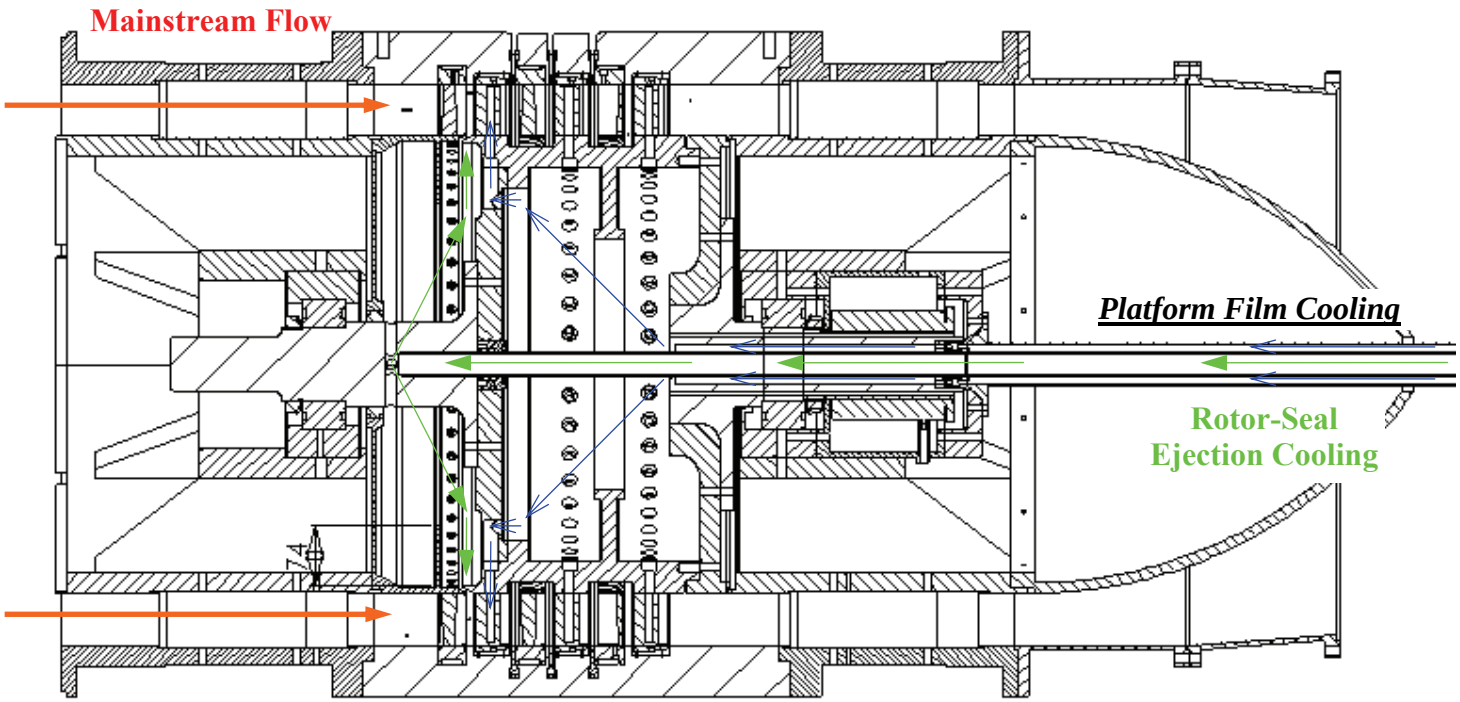

Figure 4: Coolant Flow for Film Cooling and Coolant Ejection

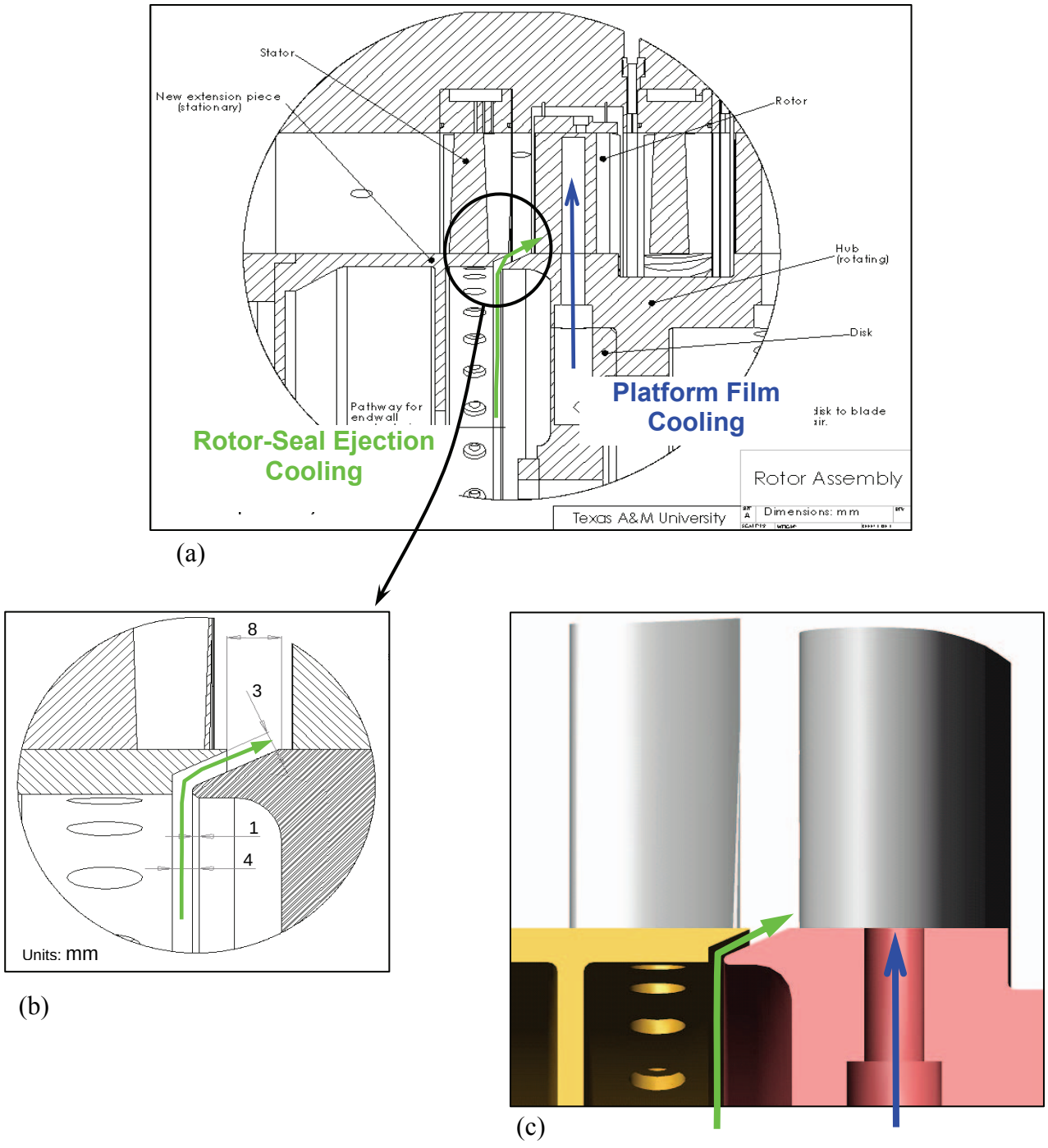

Figure 5: Detailed Views of Coolant Ejection and Film Coolant Flow Paths

(a) Enlarged View of First Stage with Coolant Flows
(b) Detailed View of Stator-Rotor Seal
(c) Solid Model of Stator-Rotor Seal Ejection and Film Coolant Paths

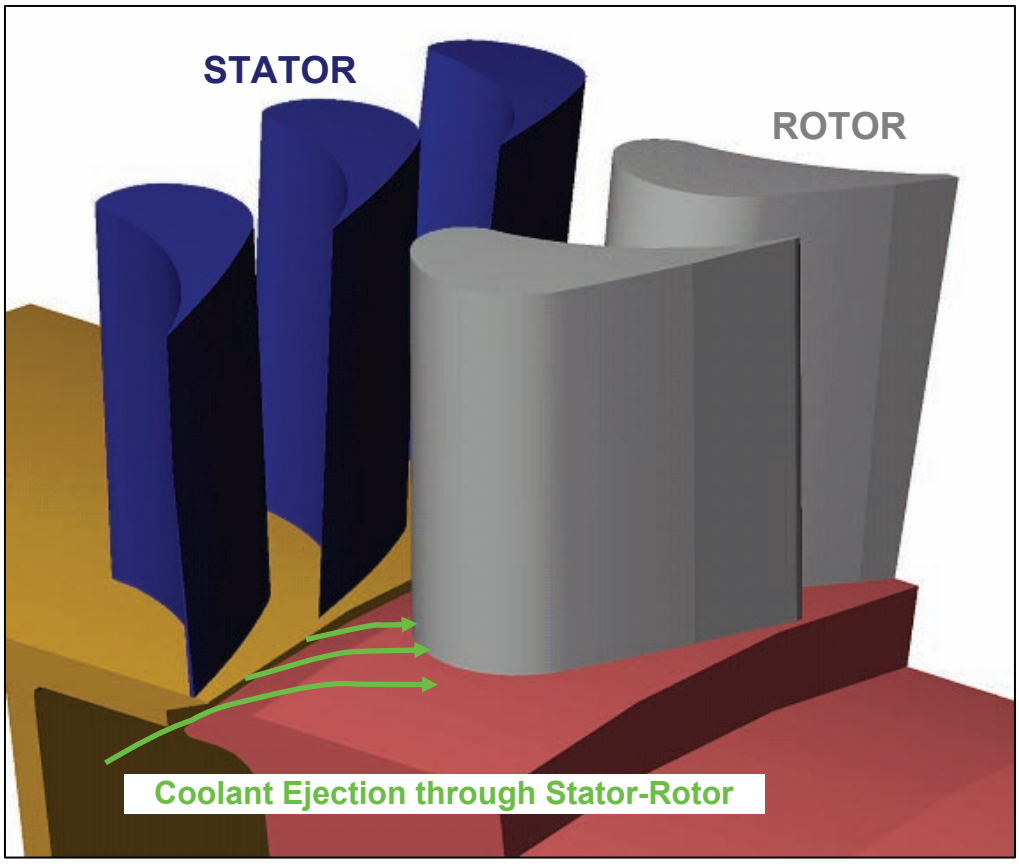

(a)

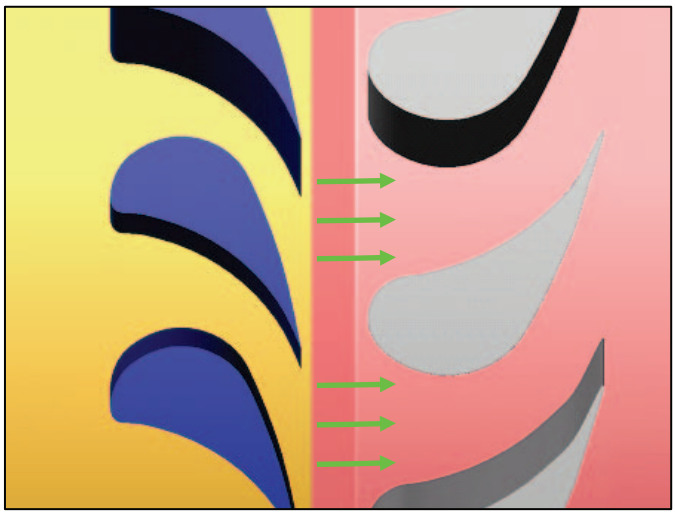

(b)

Figure 6: Coolant Ejection on the Rotor Blade Platform

(a) Three-Dimensional View (One Rotor Blade Removed)
(b) Top View

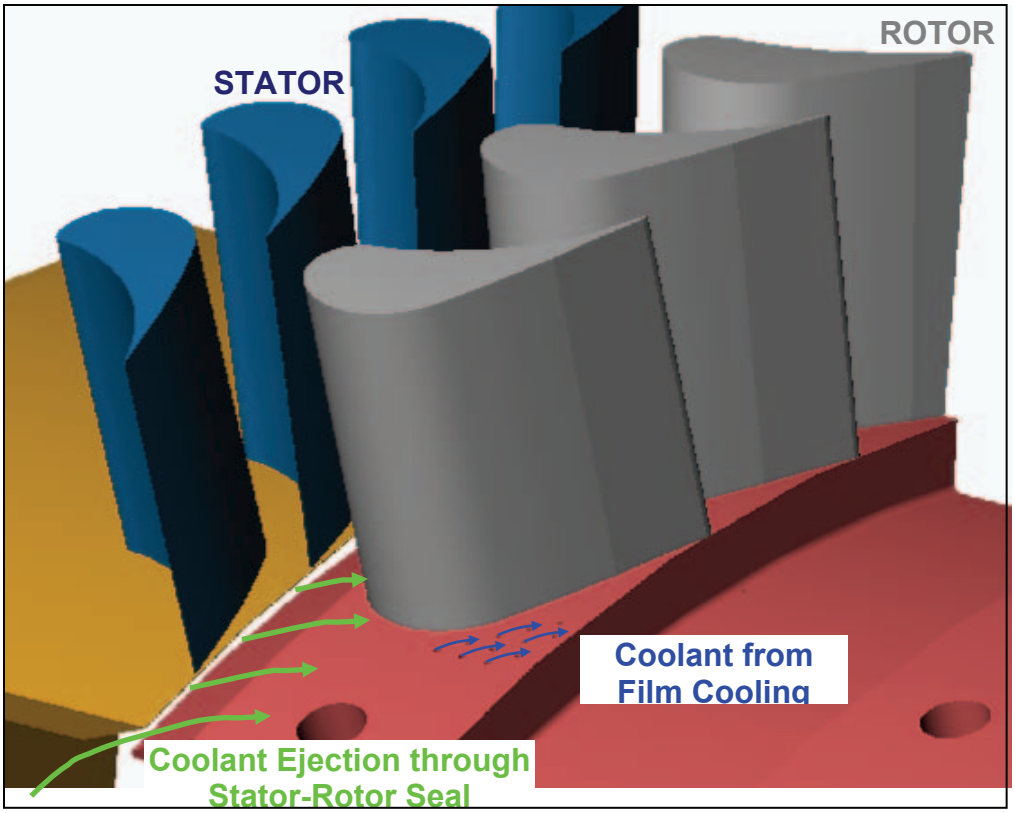

(a)

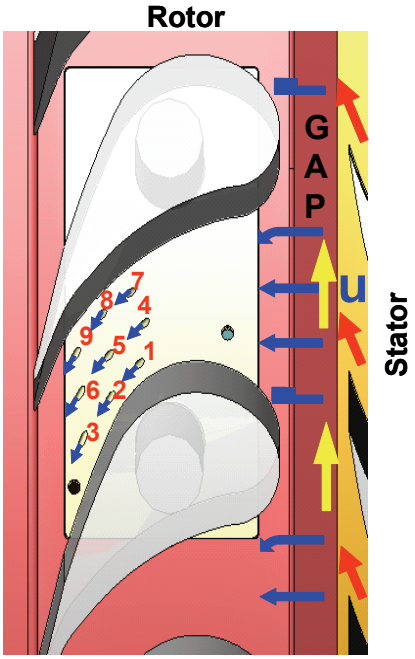

(b)

Figure 7: Coolant Ejection and Film Cooling on the Rotor Blade Platform

(a) Three-Dimensional View (One Rotor Blade Removed to Expose Film Cooling Holes)
(b) Top View

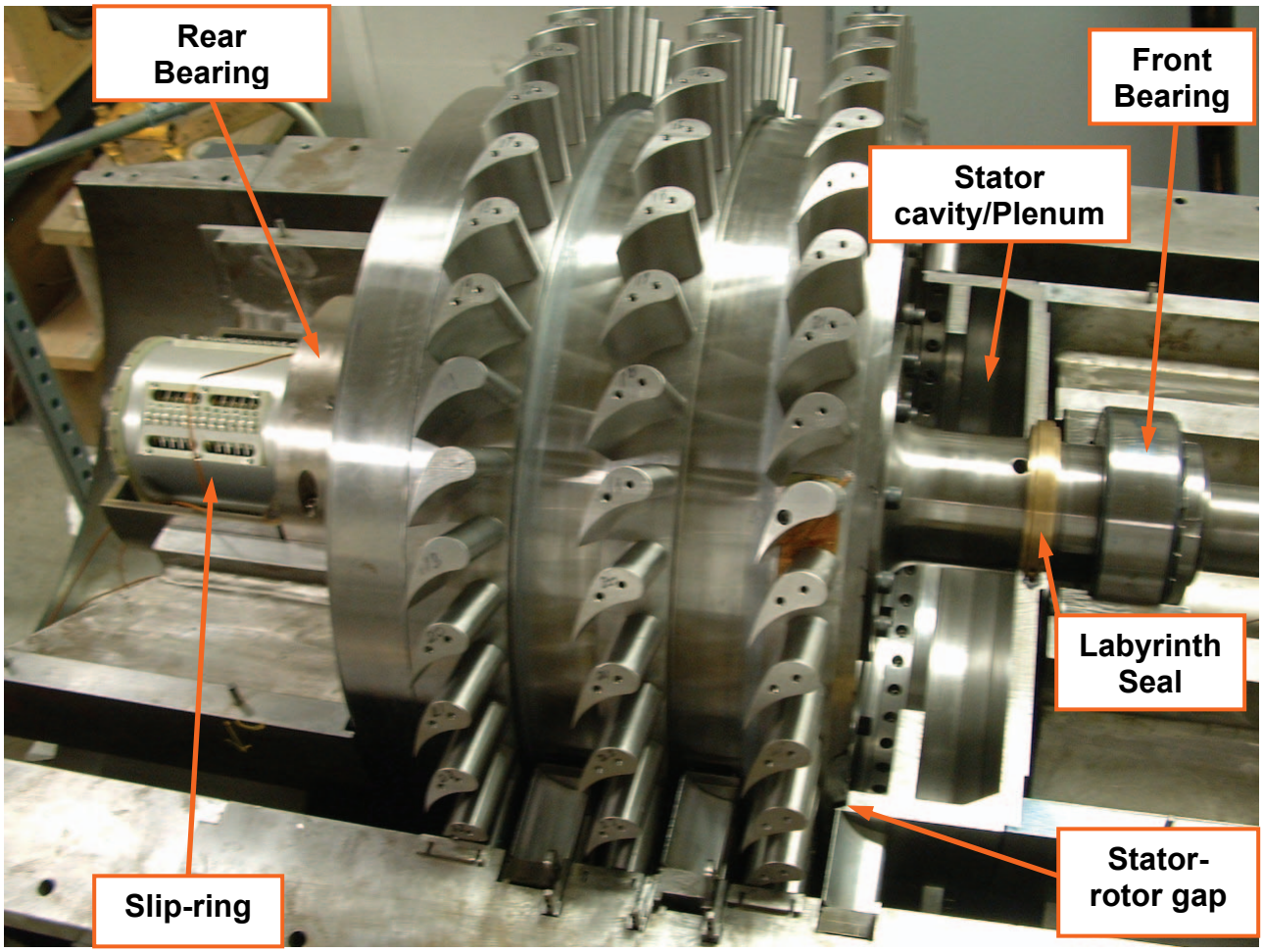

Figure 8: Newly Fabricated Rotor Platform with Stator-Rotor Seal Ejection and Platform Film Cooling Holes

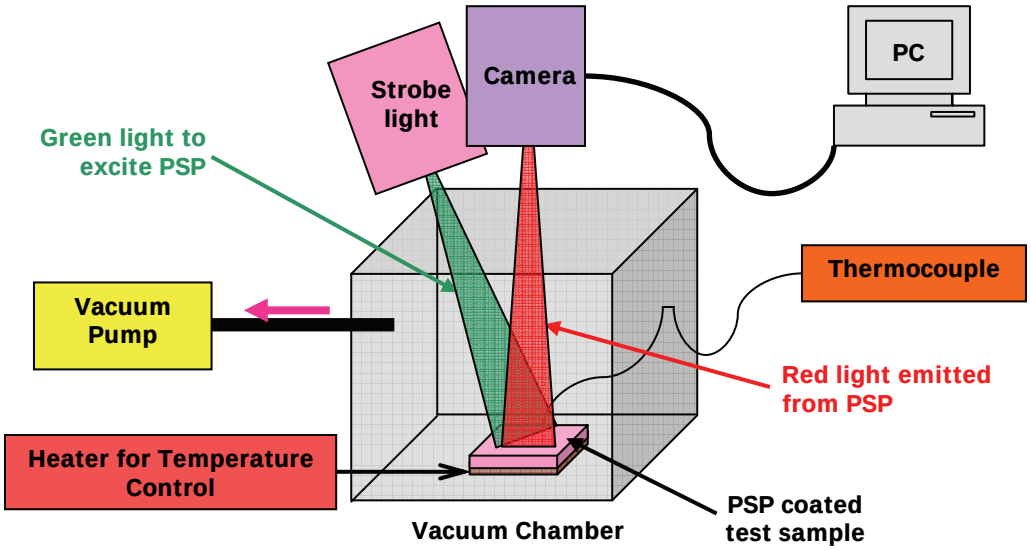

(a)

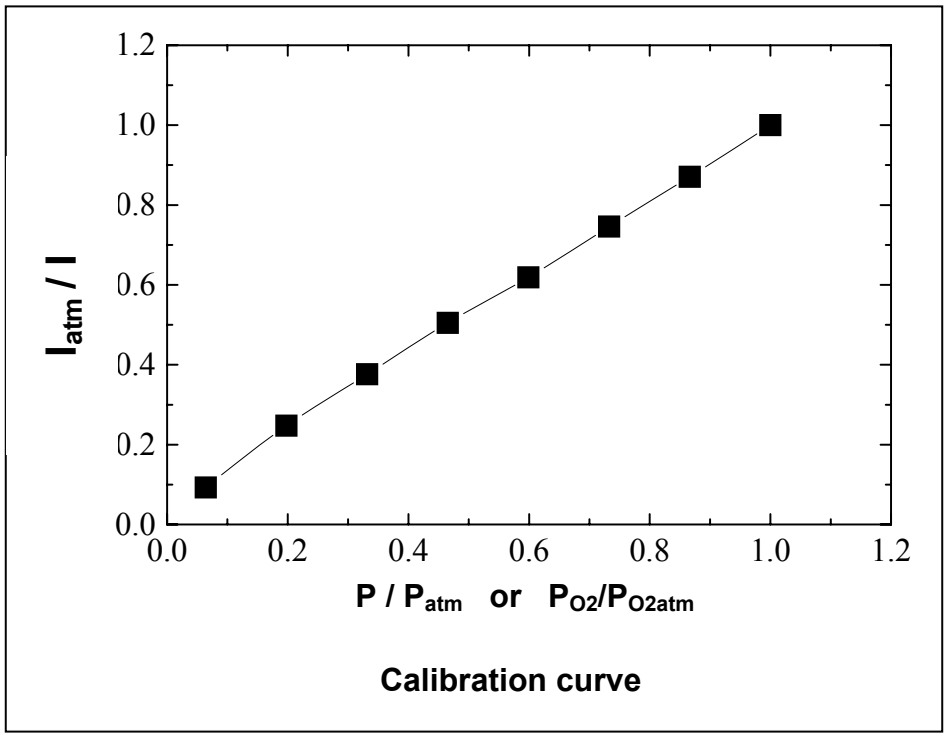

(b)

Figure 9: Typical Pressure Sensitive Paint Calibration Setup and Calibration Curve

(a) PSP Calibration Setup
(b) PSP Calibration Curve

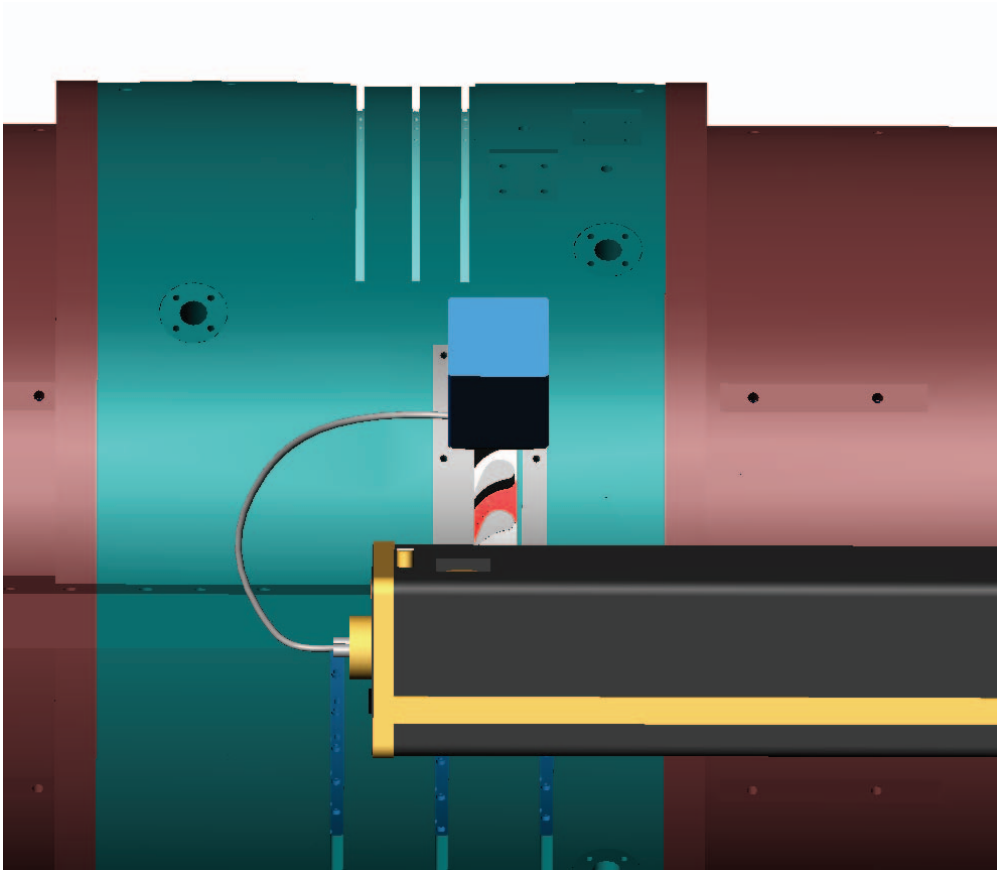

Figure 10: Modified Engine Housing to Accommodate Viewing of the Rotor Blade Platform with the Required Optical Componenets for PSP and TSP Measurements

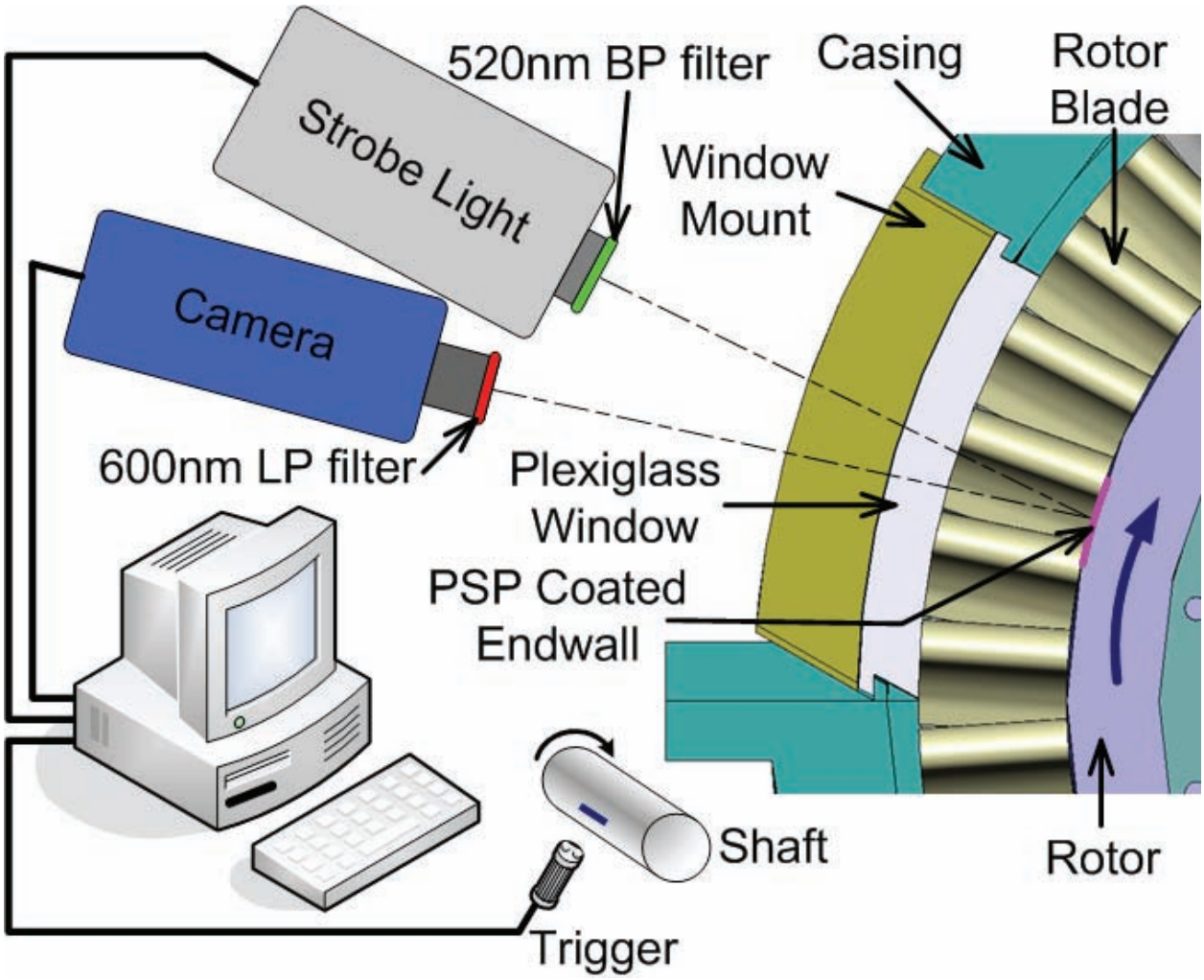

Figure 11: Optical Components Setup for the Model Turbine and PSP

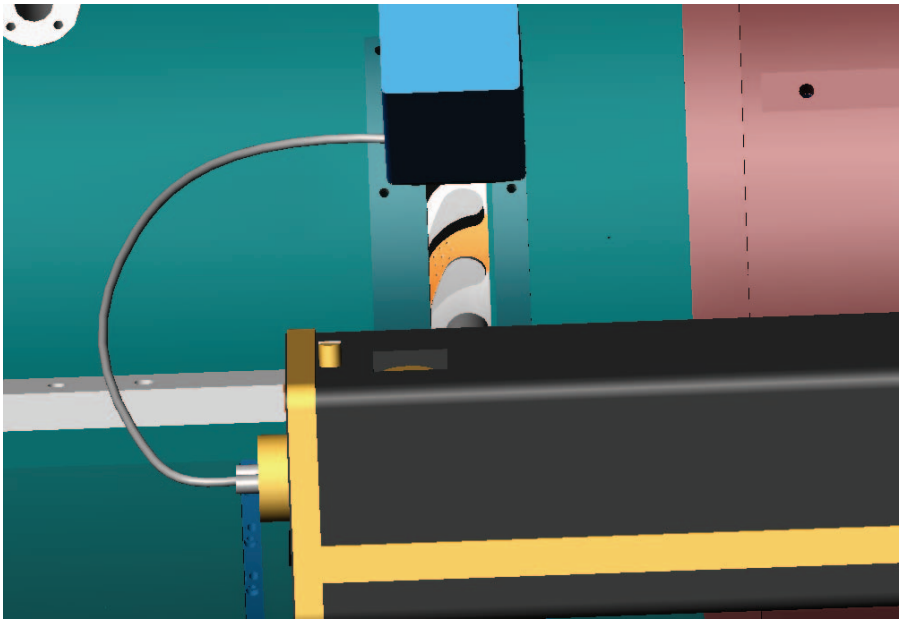

(a)

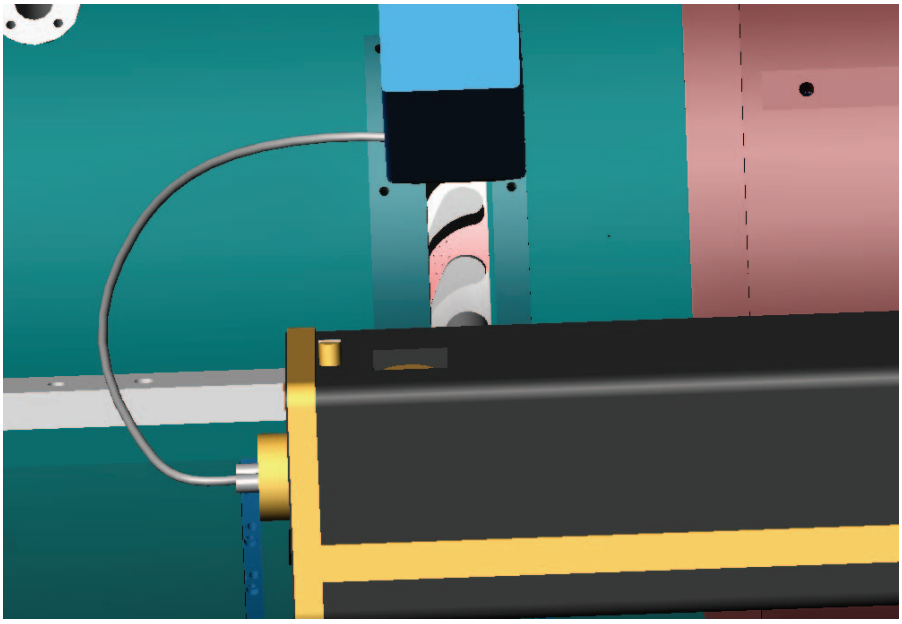

(b)

Figure 12: Viewing Windows for Rotor Platform Measurements

(a) Pressure Sensitive Paint (PSP) Coated Surface
(b) Temperature Sensitive Paint (TSP) Coated Surface

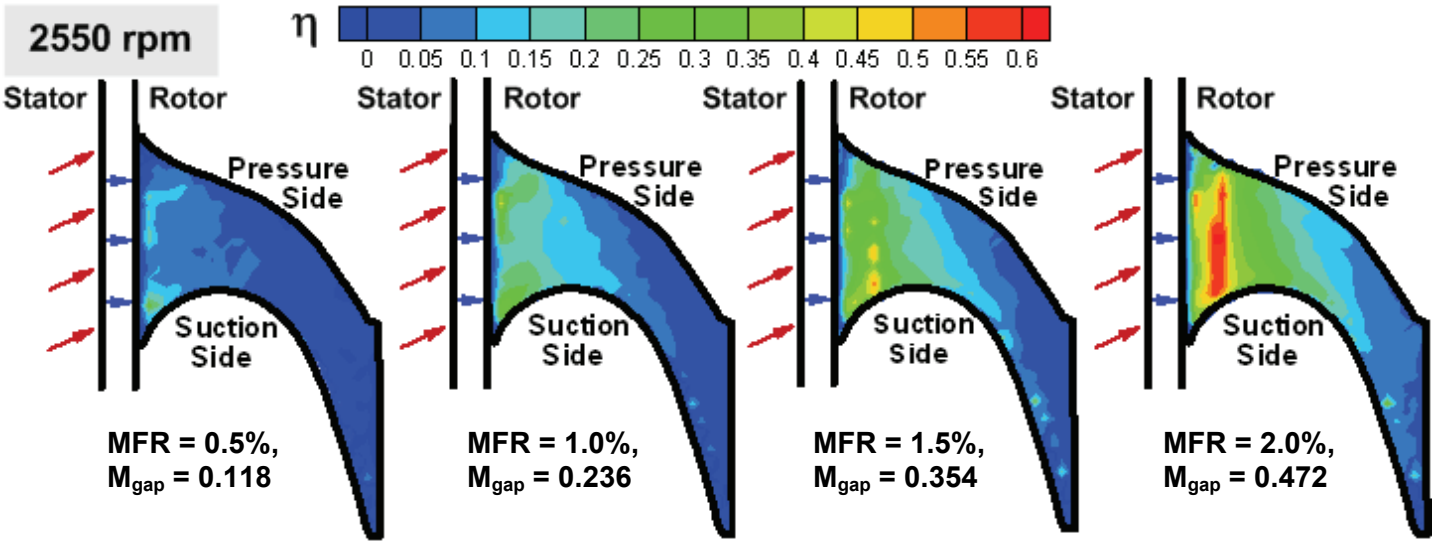

Figure 13: Film Cooling Effectiveness Distribution on the Rotating Endwall for 2550 rpm

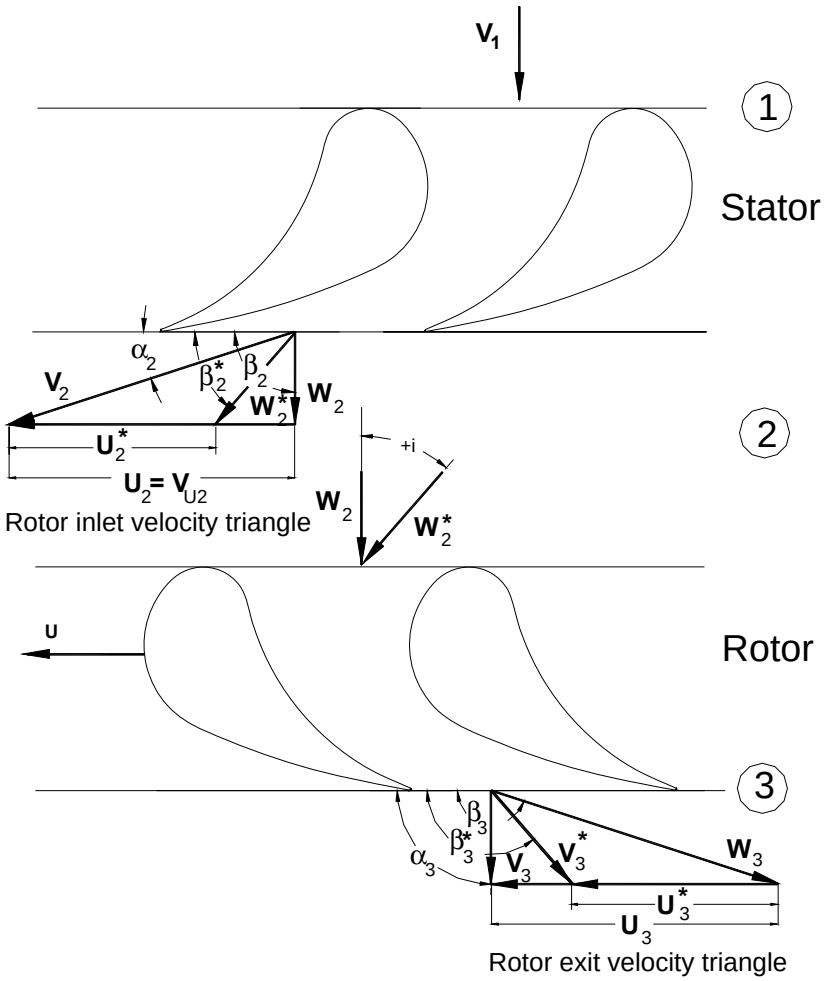

Figure 14: Velocity Triangles and Relative Inlet and Exit Flow Angles for Design and Off-Design Rotating Speeds

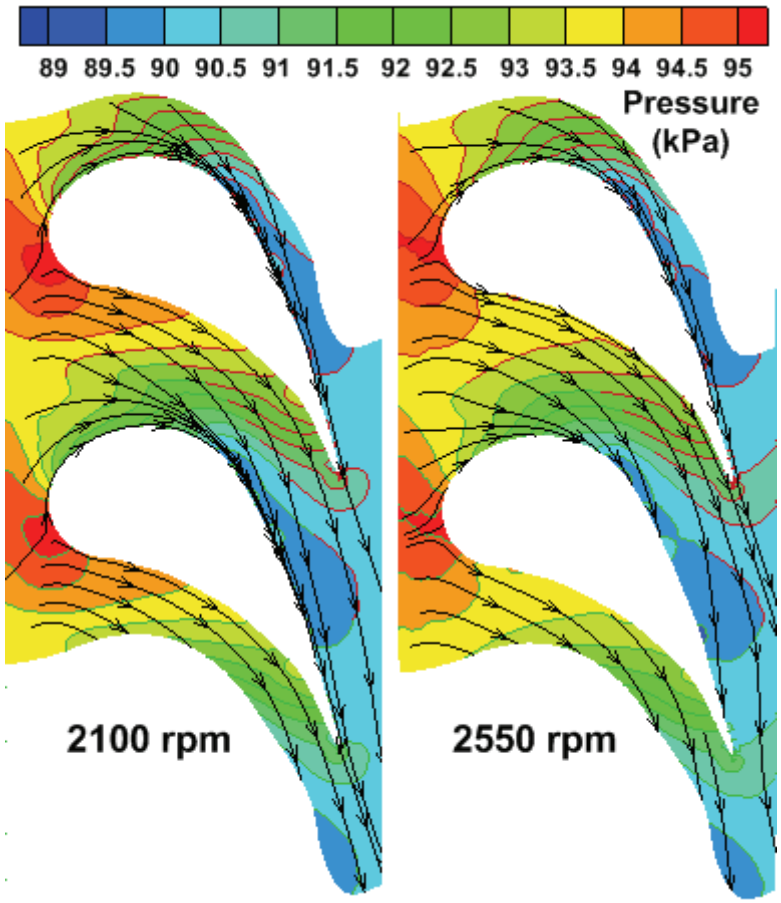

Figure 15: Numerical Prediction of Endwall Static Pressure Distribution (kPa) along with Flow Pathlines

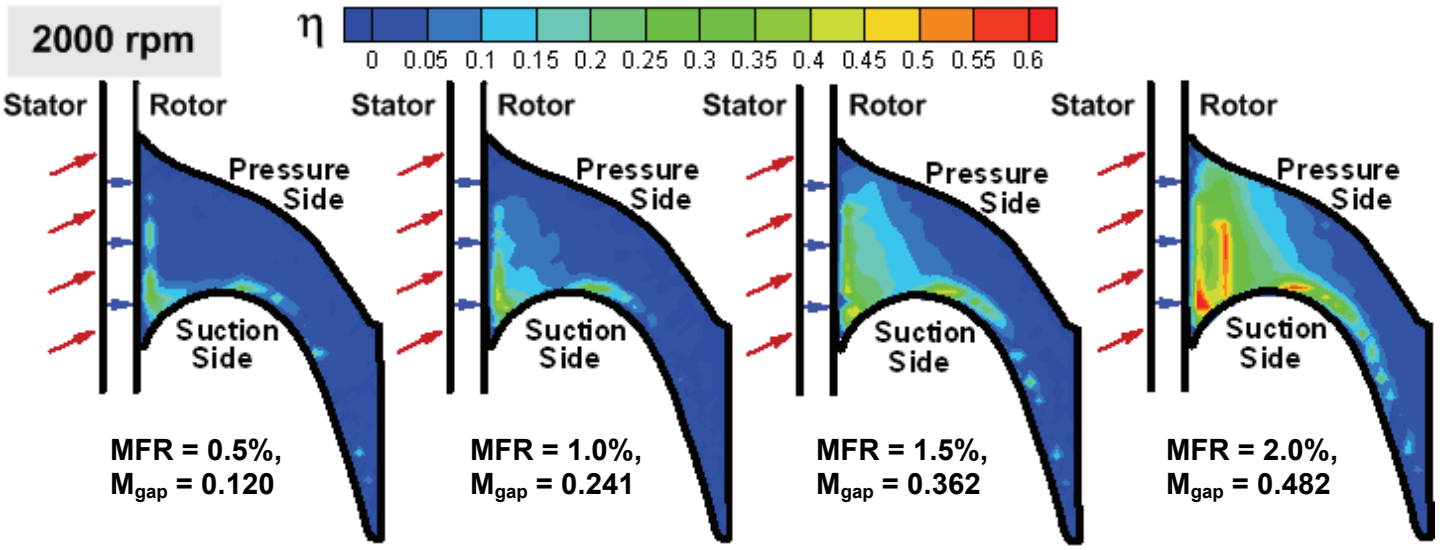

Figure 16: Film Cooling Effectiveness Distribution on the Rotating Endwall for 2000 rpm

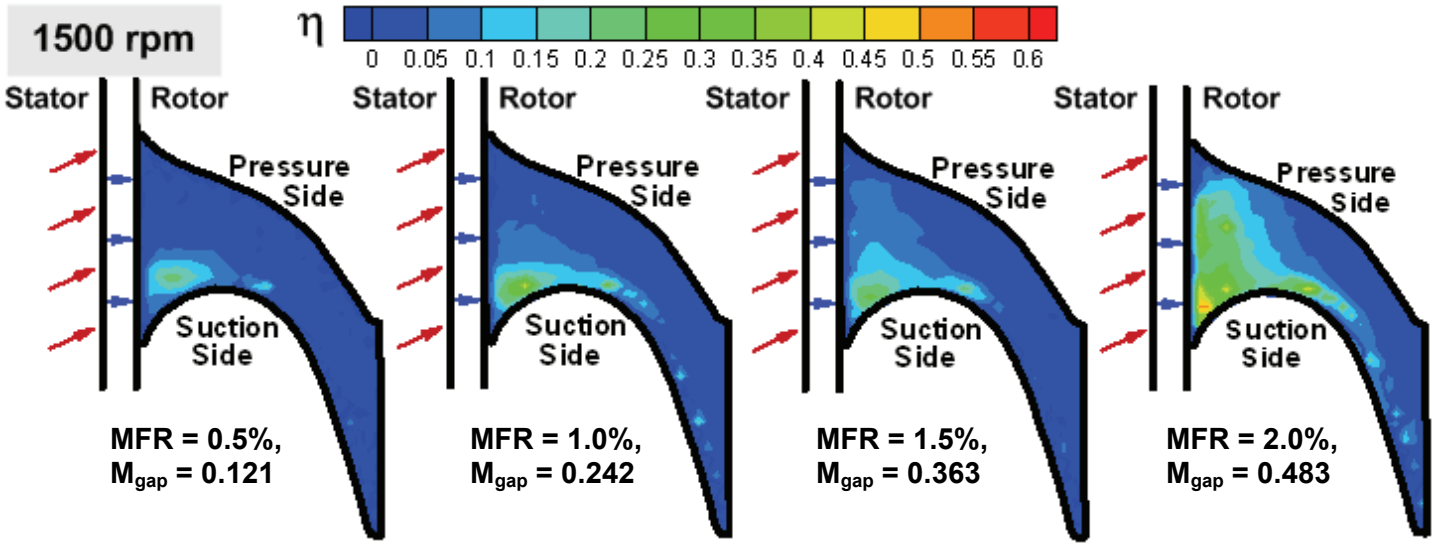

Figure 17: Film Cooling Effectiveness Distribution on the Rotating Endwall for 1500 rpm

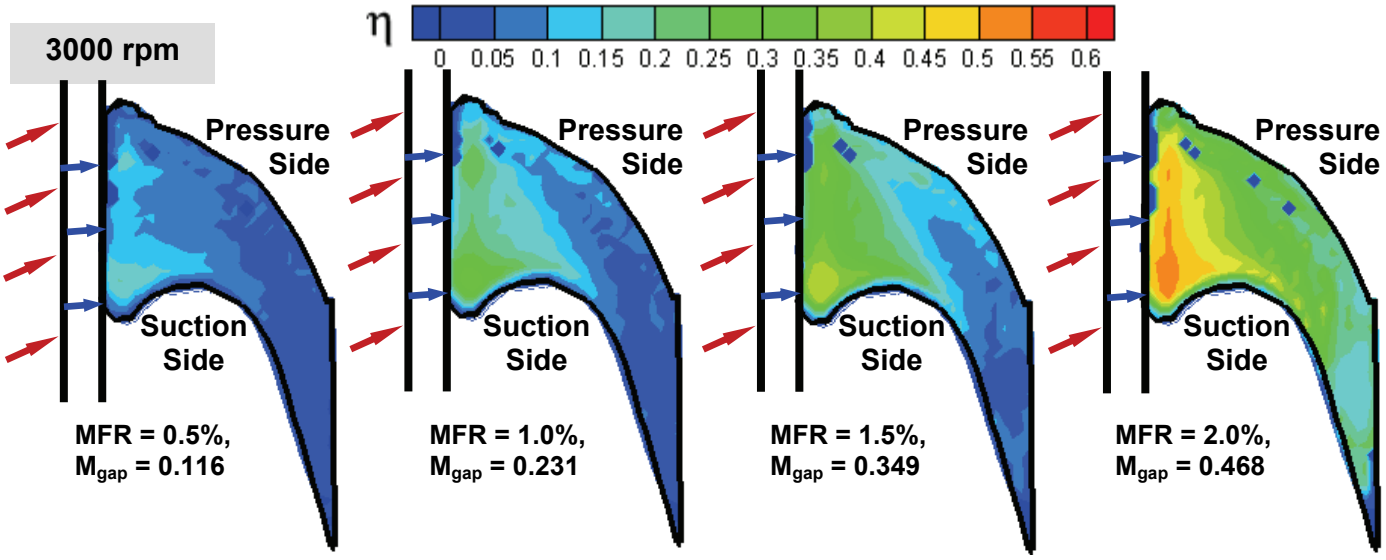

Figure 18: Film Cooling Effectiveness Distribution on the Rotating Endwall for 3000 rpm

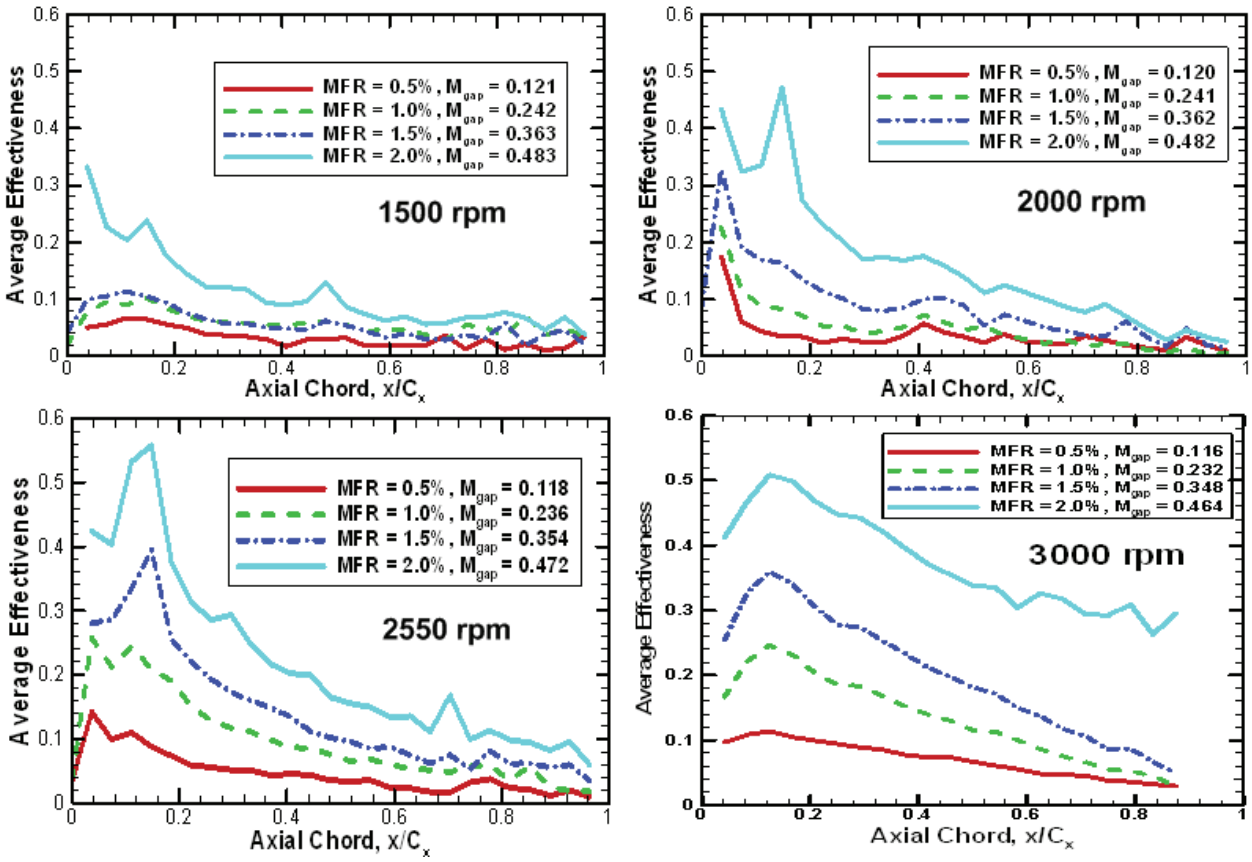

Figure 19: Pitchwise Averaged Film Cooling Effectiveness Distribution along Axial Chord for Different Turbine Rotating Speeds (Mass Flow Ratio Effect)

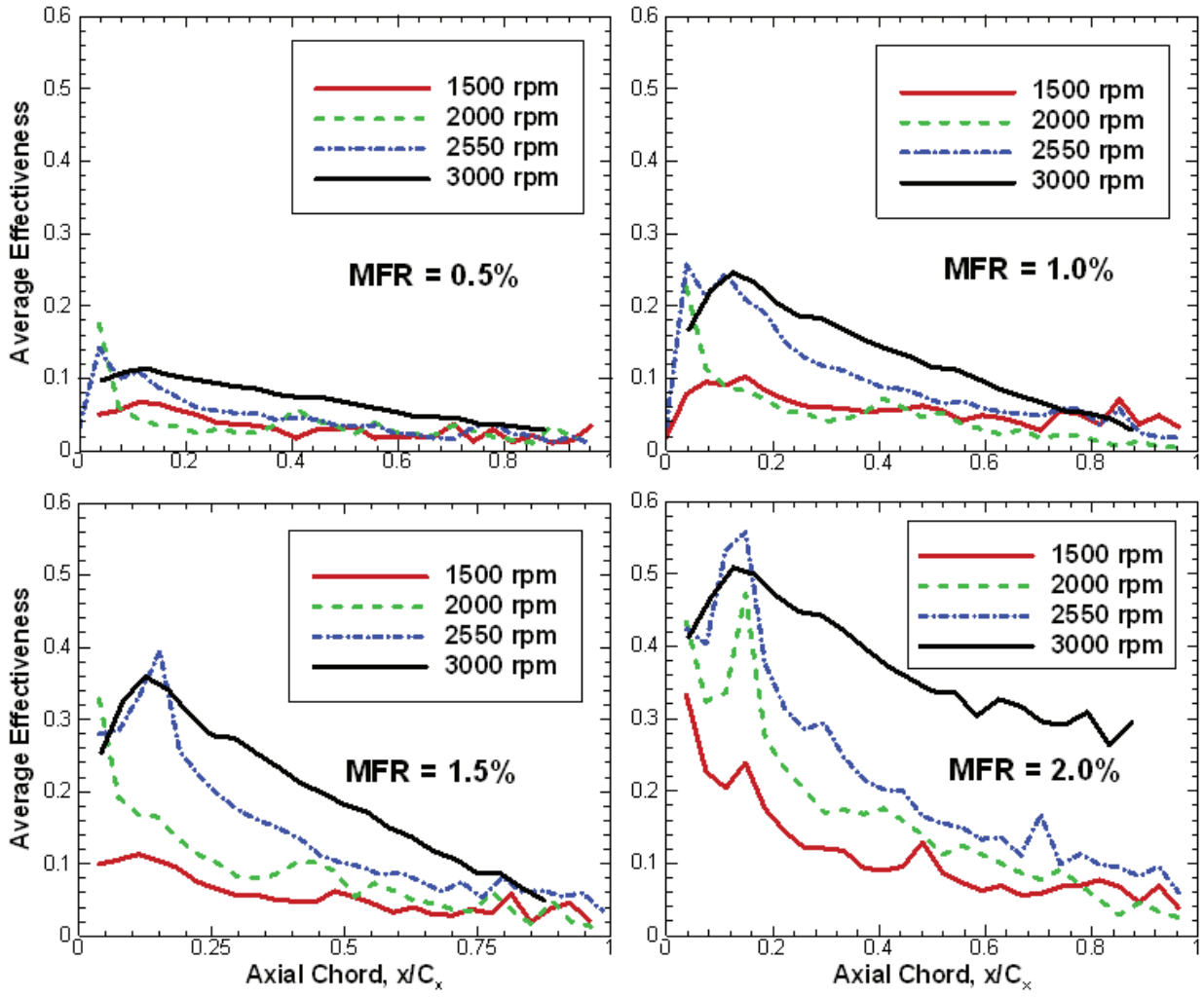

Figure 20: Pitchwise Averaged Film Cooling Effectiveness Distribution along Axial Chord for Different Mass Flow Ratios (Turbine Rotation Speed Effect)

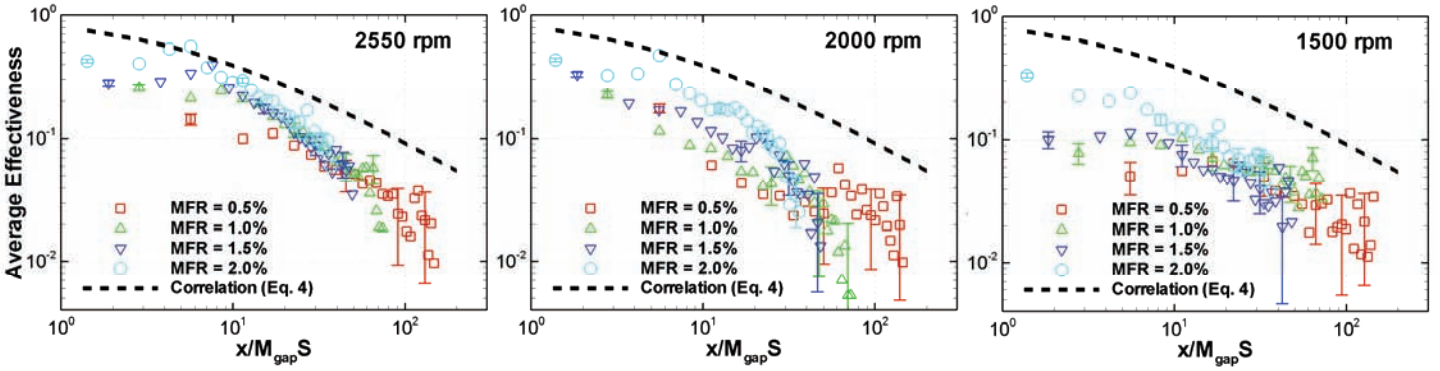

Figure 21: Comparison of Pitchwise Average Effectiveness with a Correlation from Goldstein [40] for Different Speeds

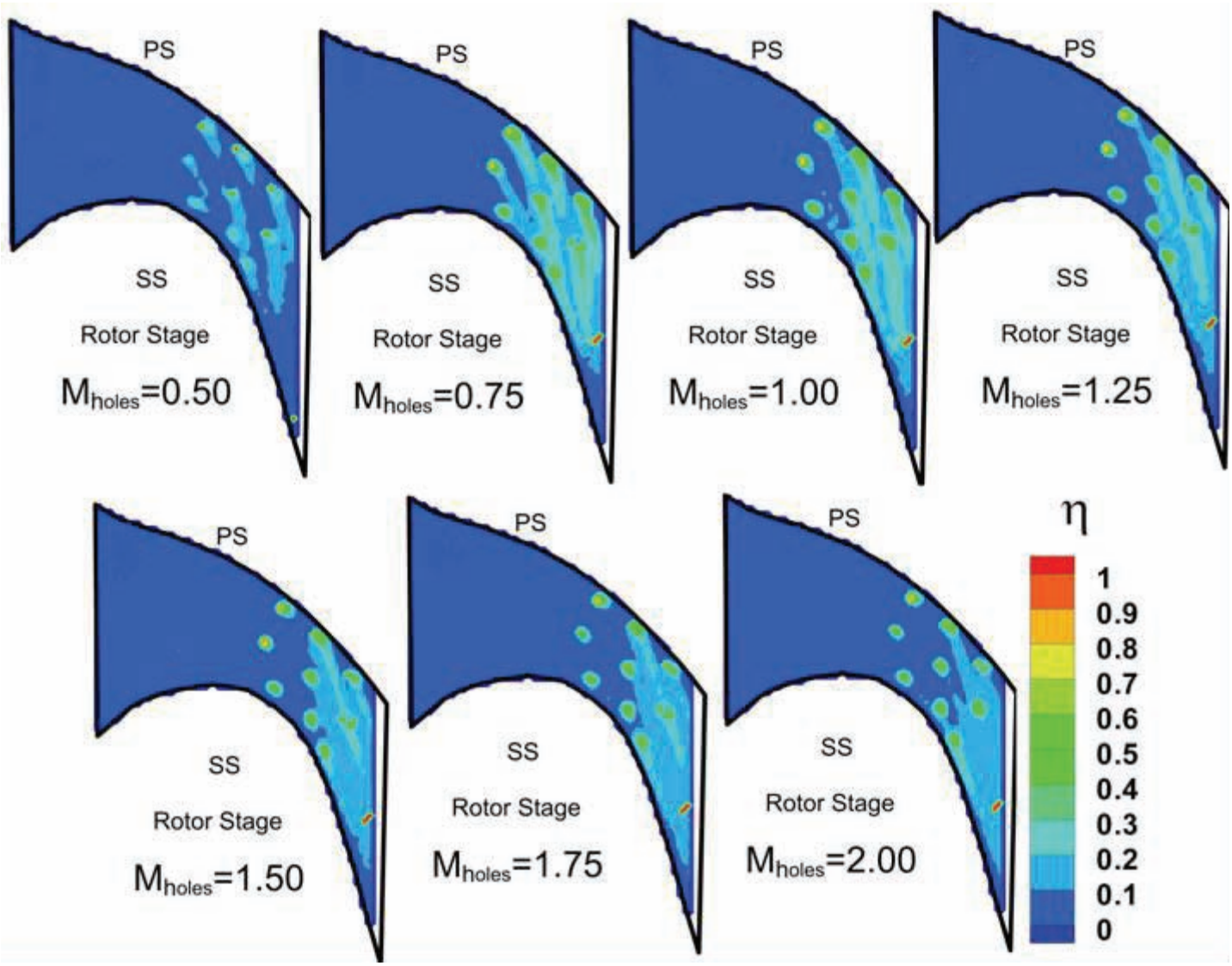

Figure 22: Film Cooling Effectiveness Distribution From Downstream, Discrete Film Cooling Holes on the Rotating Endwall for 2550 rpm

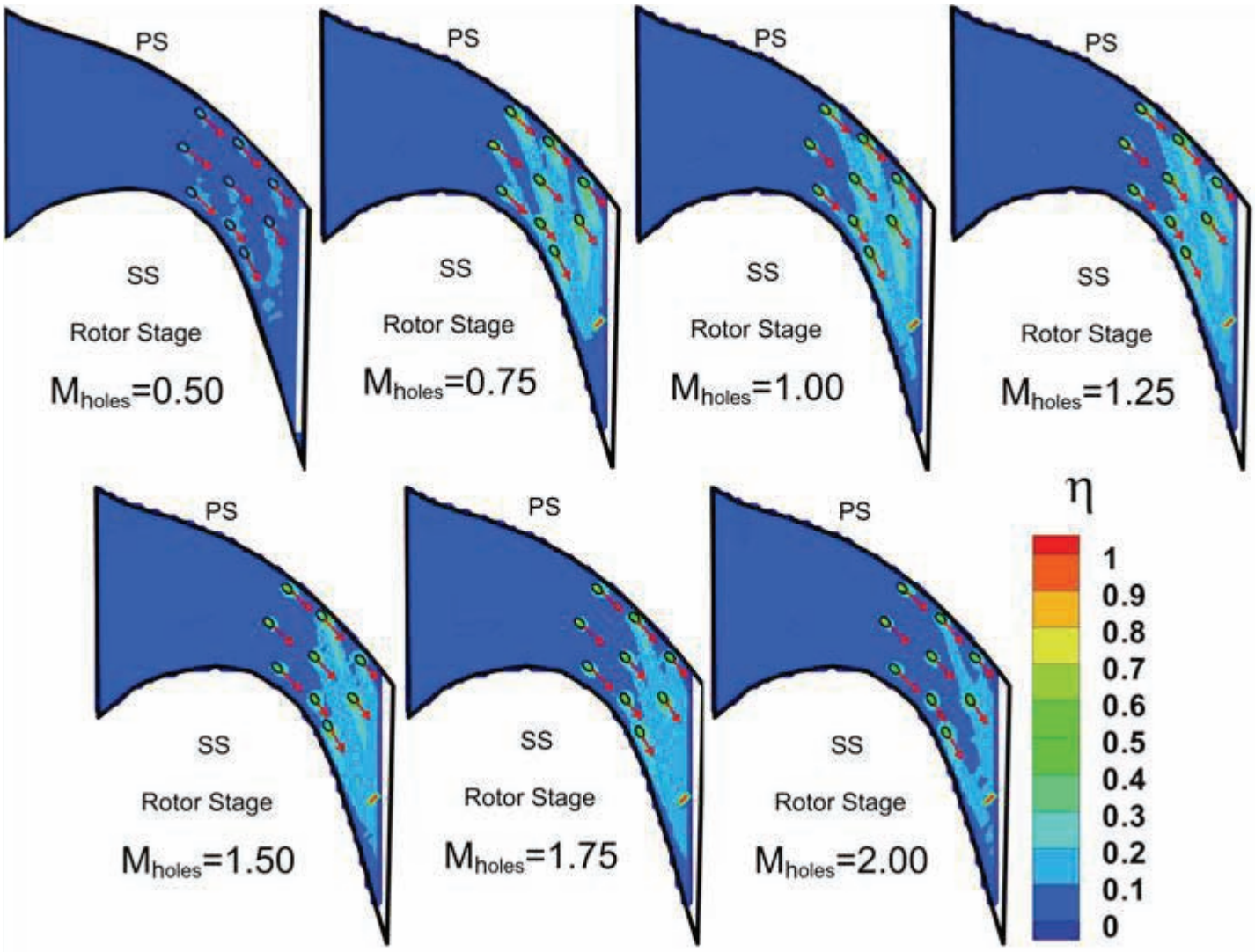

Figure 23: Film Cooling Effectiveness Distribution From Downstream, Discrete Film Cooling Holes on the Rotating Endwall for 2400 rpm

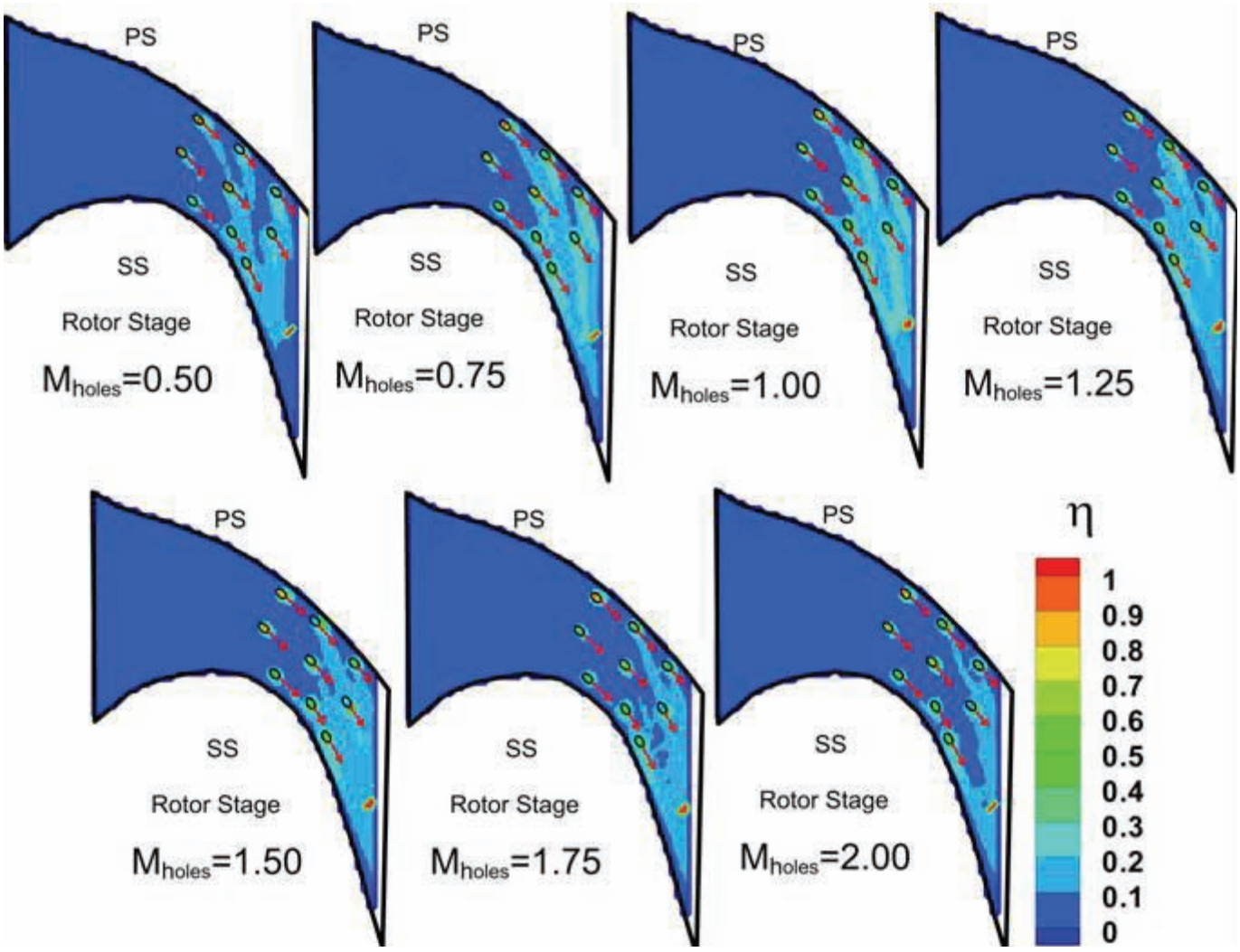

Figure 24: Film Cooling Effectiveness Distribution From Downstream, Discrete Film Cooling Holes on the Rotating Endwall for 3000 rpm

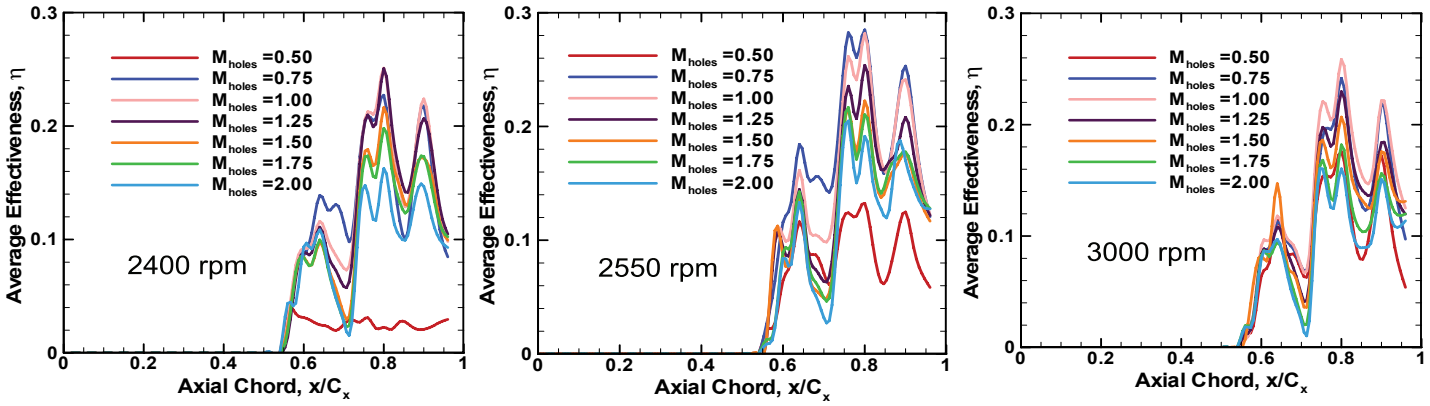

Figure 25: Pitchwise Averaged Film Cooling Effectiveness Distribution along Axial Chord for Different Turbine Rotating Speeds (Mass Flow Ratio Effect)

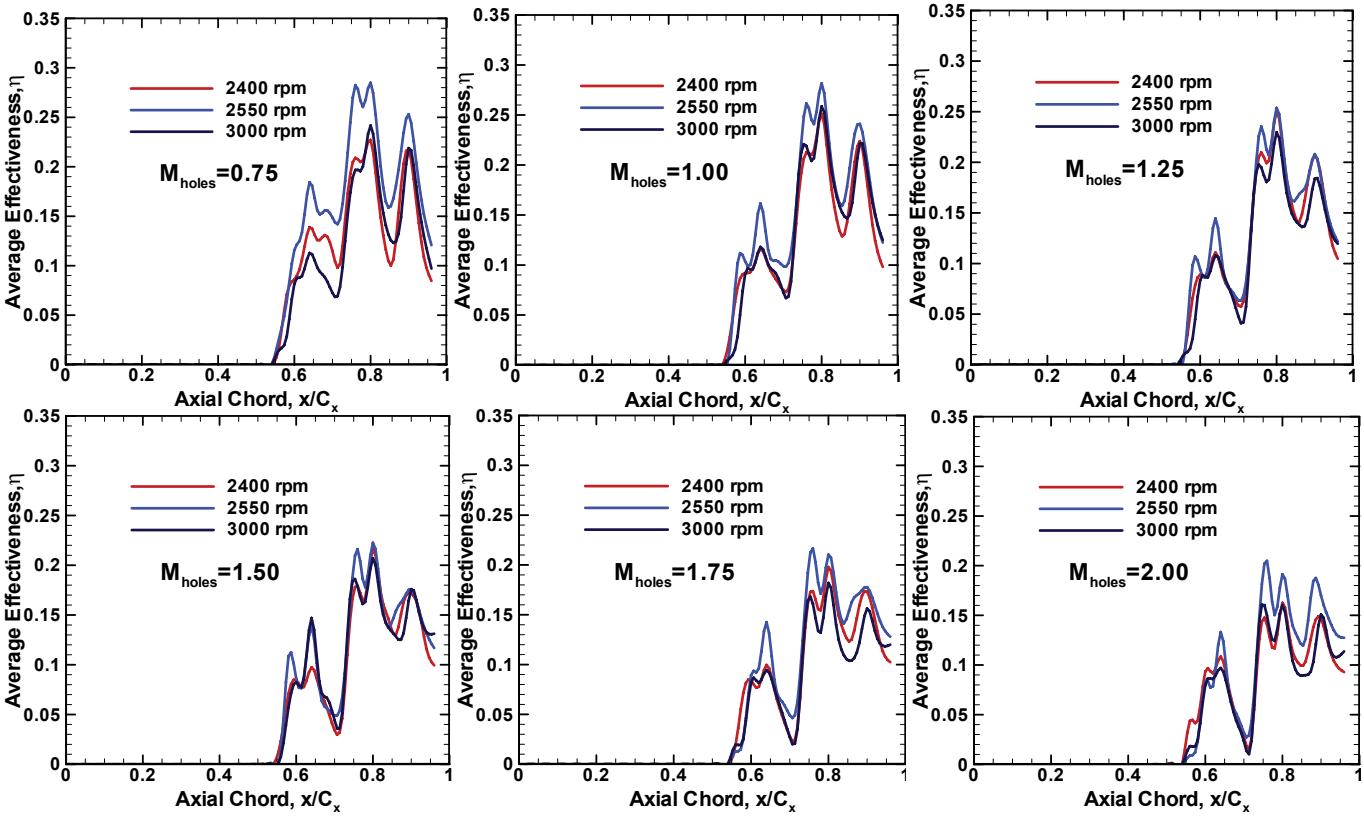

Figure 26: Pitchwise Averaged Film Cooling Effectiveness Distribution along Axial Chord for different Hole Blowing Ratios (Rotation Effect)

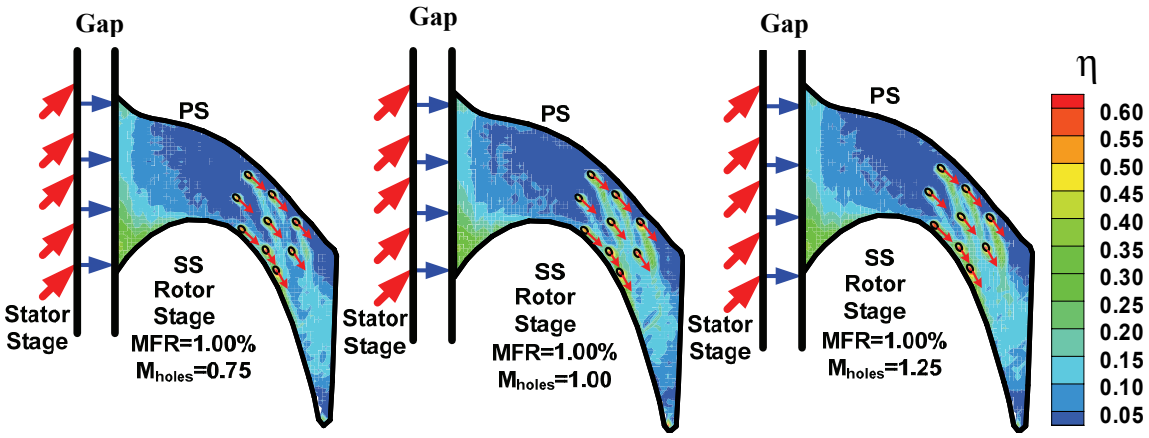

Figure 27: Film cooling effectiveness for combined stator-rotor and hole coolant injection, 2400rpm

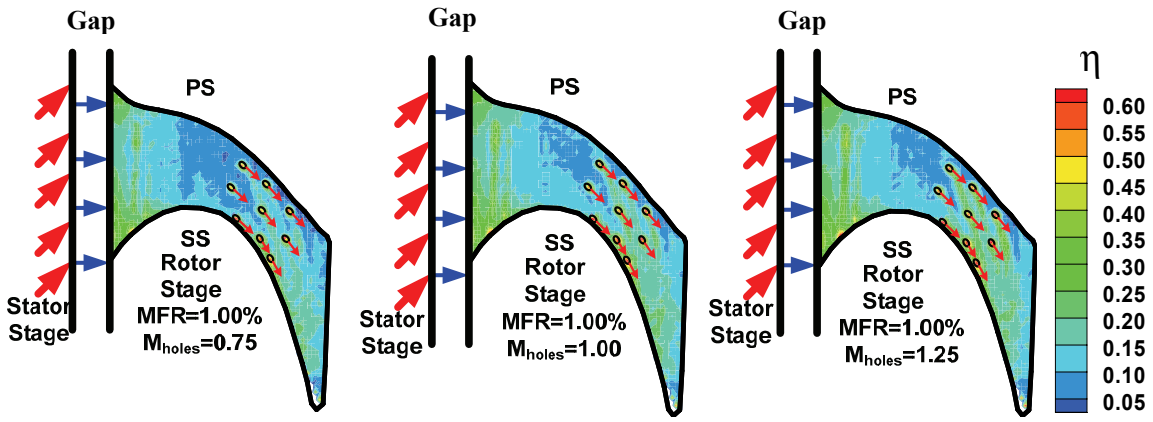

Figure 28: Film cooling effectiveness for combined stator-rotor and hole coolant injection, 2550rpm

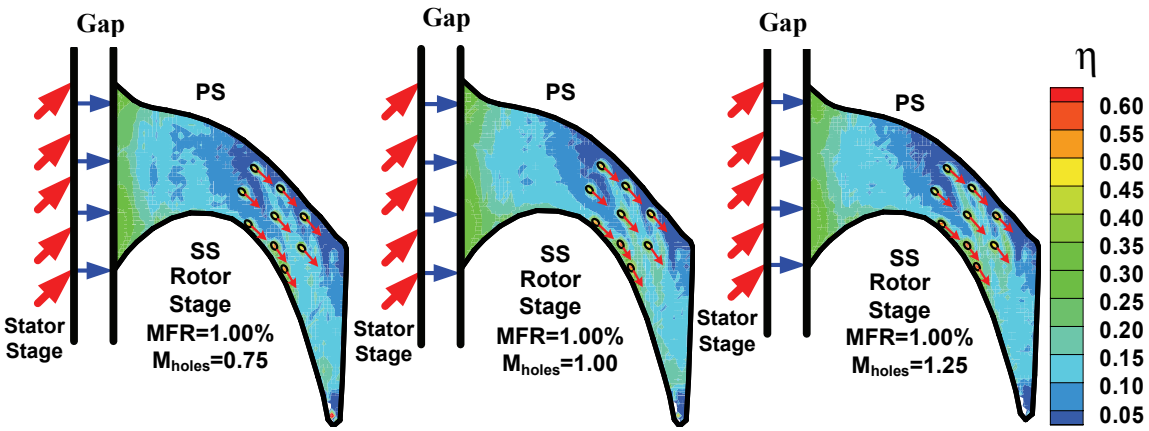

Figure 29: Film cooling effectiveness for combined stator-rotor and hole coolant injection, 3000rpm

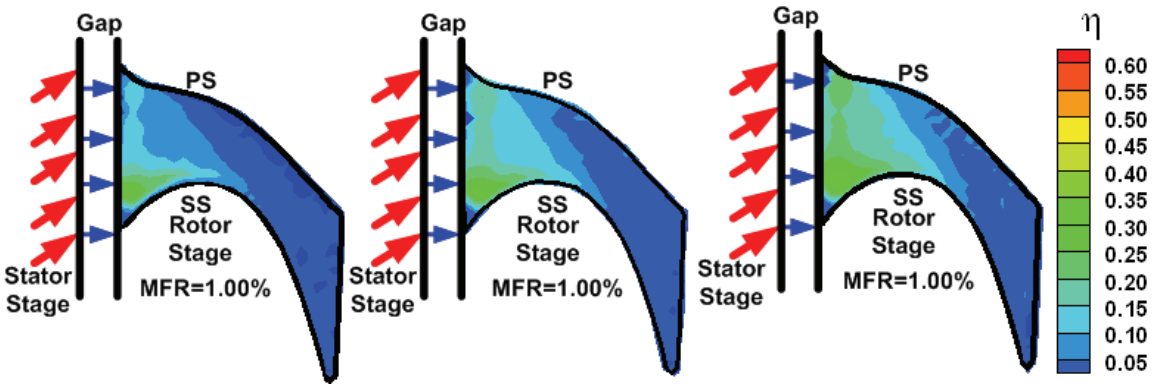

Figure 30: Film cooling effectiveness for stator-rotor injection for 2400rpm, 2550rpm and 3000rpm

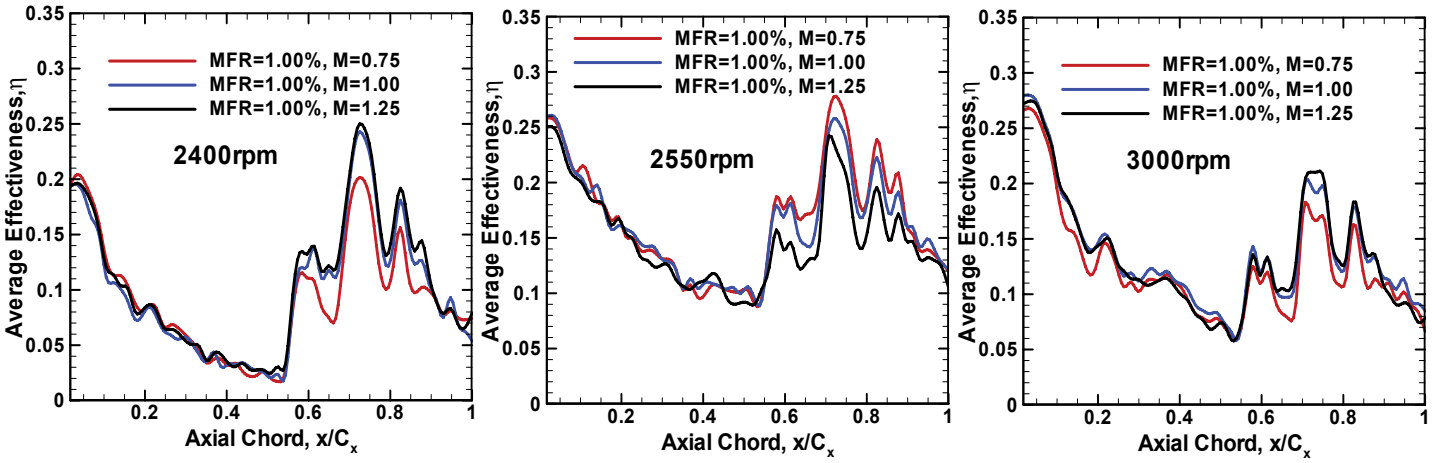

Figure 31: Pitchwise averaged film cooling effectiveness for combined upstream slot and downstream discrete hole injection

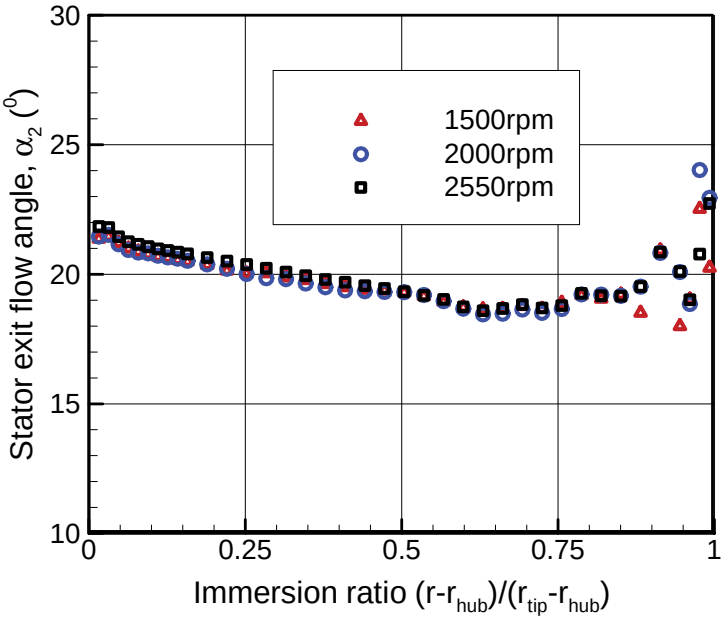

Figure 32: Radial Distribution of Stator Exit Flow Angle for Varying Rotor Speeds

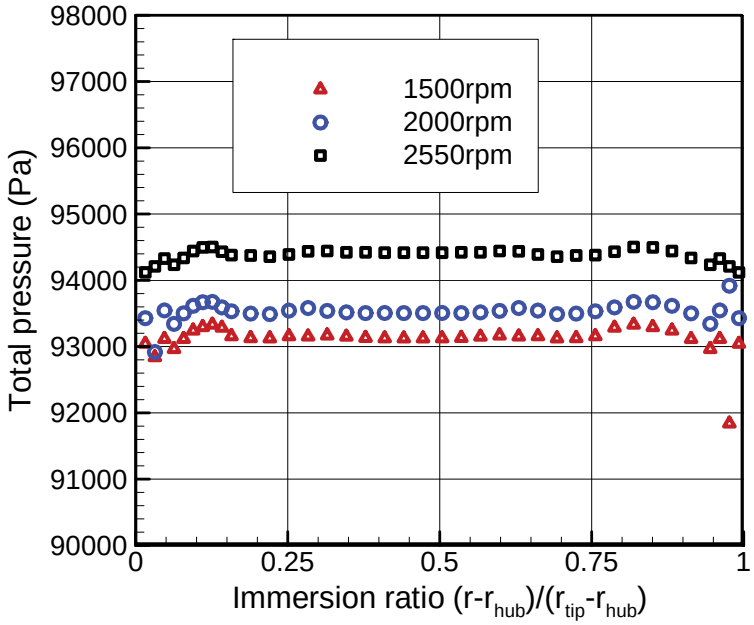

Figure 33: Radial Distribution of Total Pressure Distribution for Varying Rotor Speeds

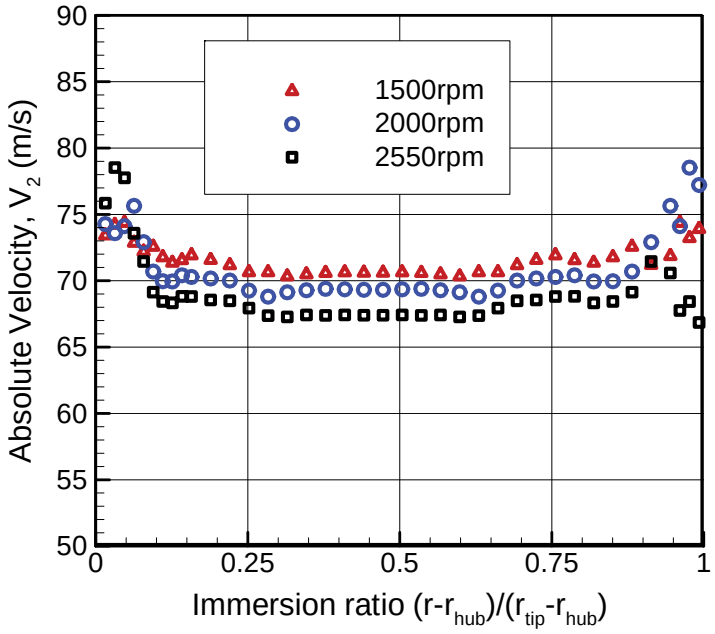

Figure 34: Radial Distribution of Absolute Velocity for Varying Rotor Speeds

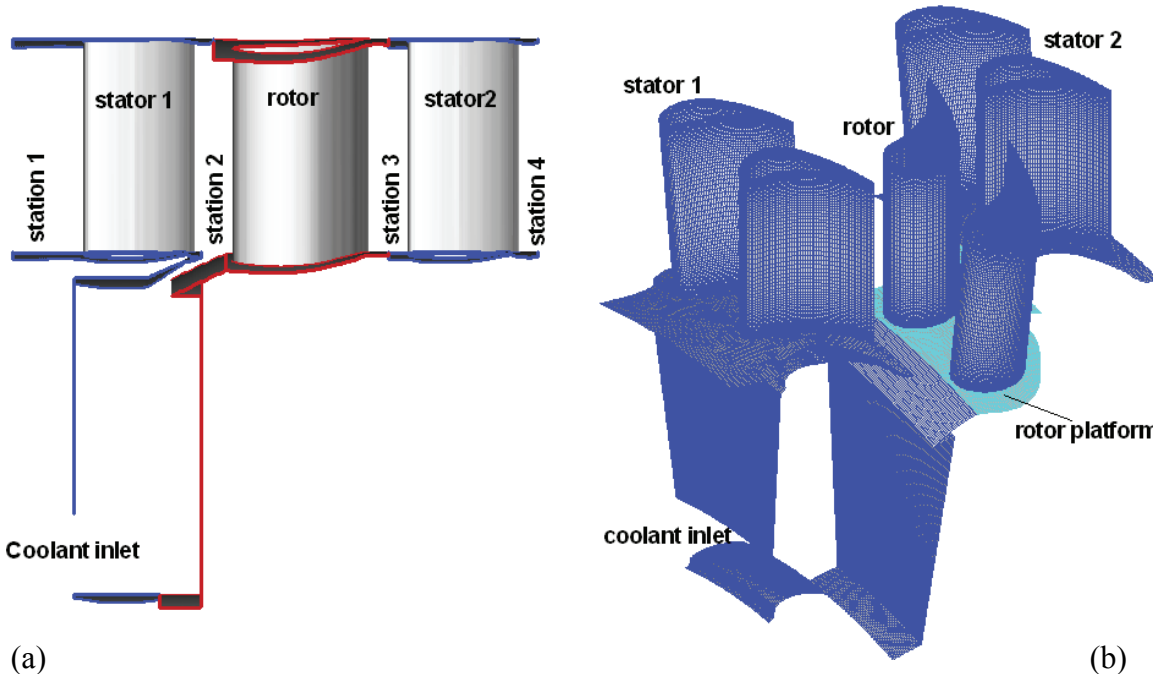

Figure 35: Prediction of Film Cooling Effectiveness and Heat Transfer Coefficients on Rotating Blade Platform

(a) Computational Domain of Platform with Upstream Slot Injection
(b) Numerical Grid

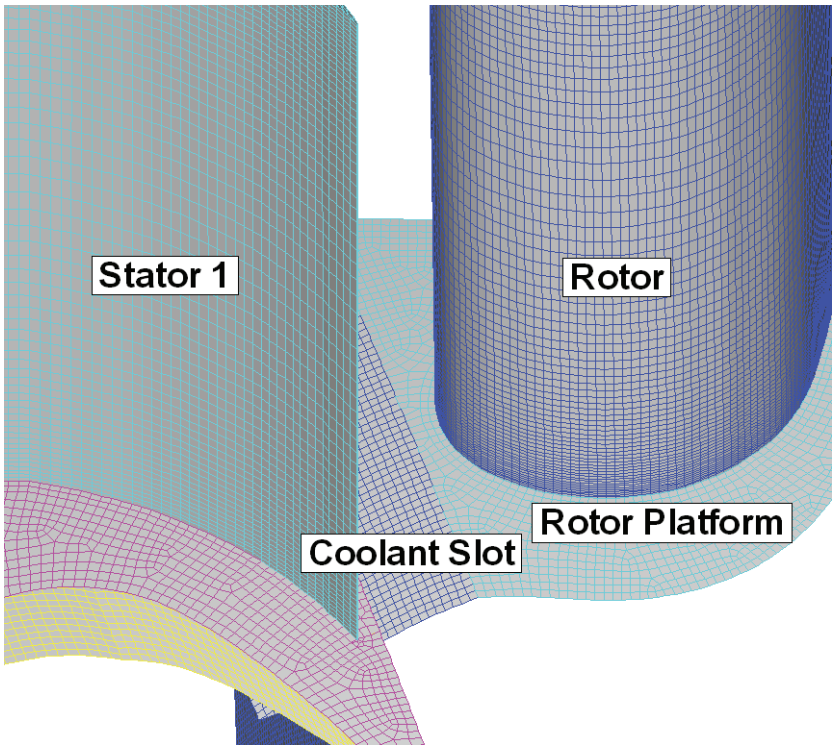

Figure 36: Detailed Grid Distributions Near the Angled Coolant Slot

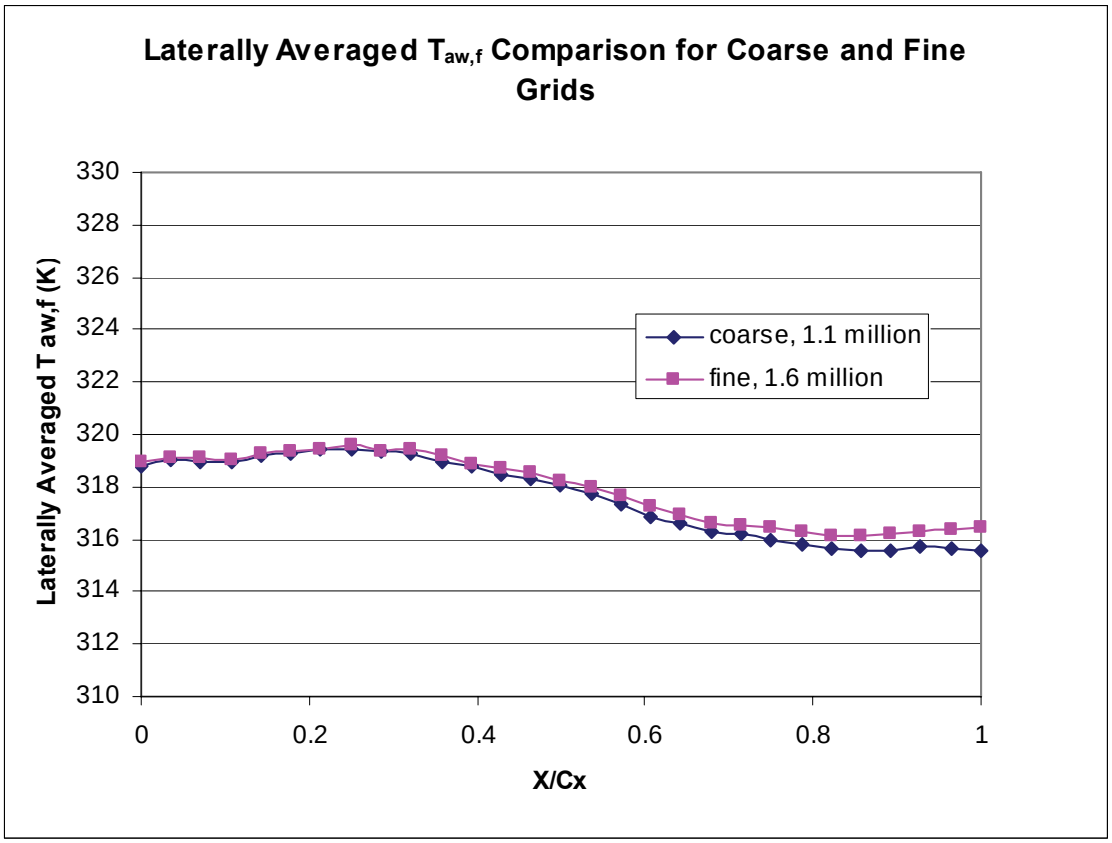

Figure 37: Grid Refinement Sutdy for Laterally Averaged Adiabatic Temperature on Rotating Blade Platform

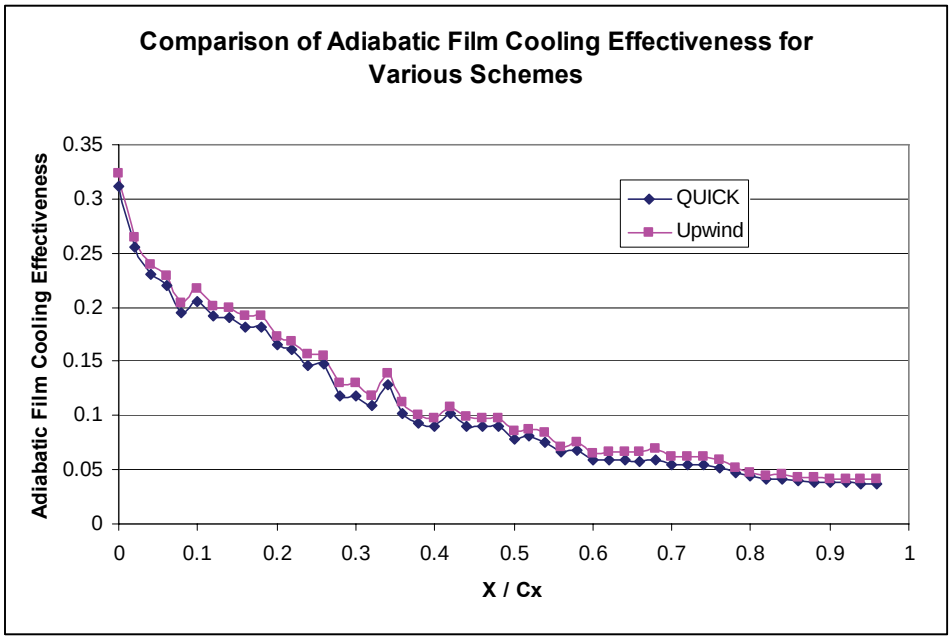

(a)

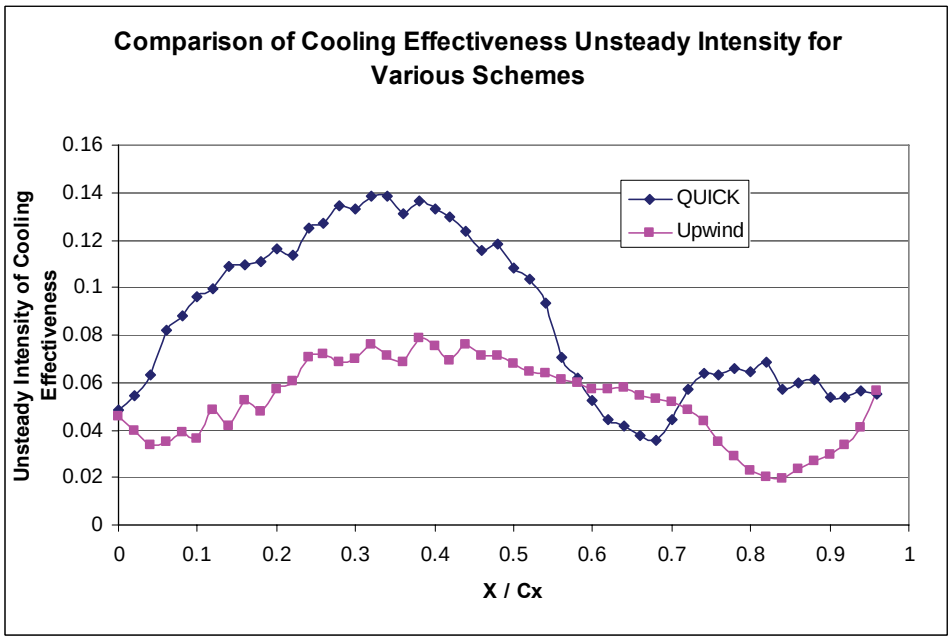

(b)

Figure 38: Scheme Comparison for Predicted Film Cooling Effectiveness (2550 RPM, MFR = 1.0%)

(a) Laterally Averaged Adiabatic Film Cooling Effectiveness
(b) Cooling Effectiveness Unsteady Intensity

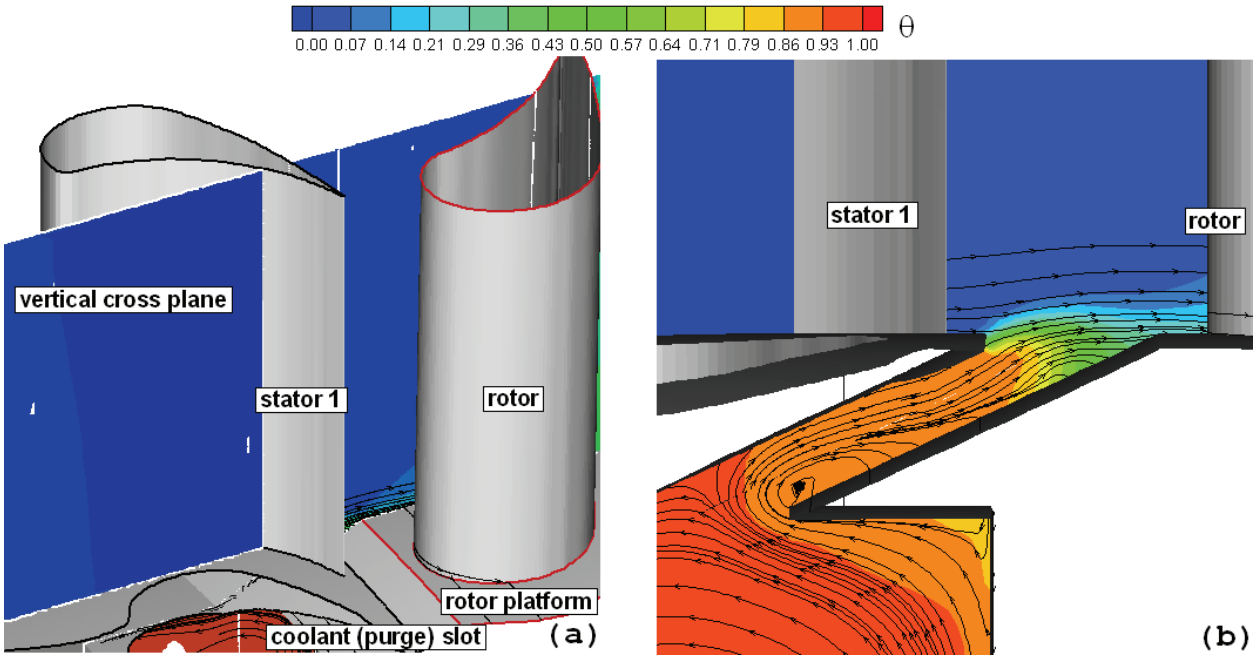

Figure 39: Predicted Path of the Coolant From the Rotating Disk onto the Rotating Platform (2550 RPM, MFR = 1.0%)

(a) Location of Vertical Plane
(b) Dimensionless Temperature Contours and Streamlines

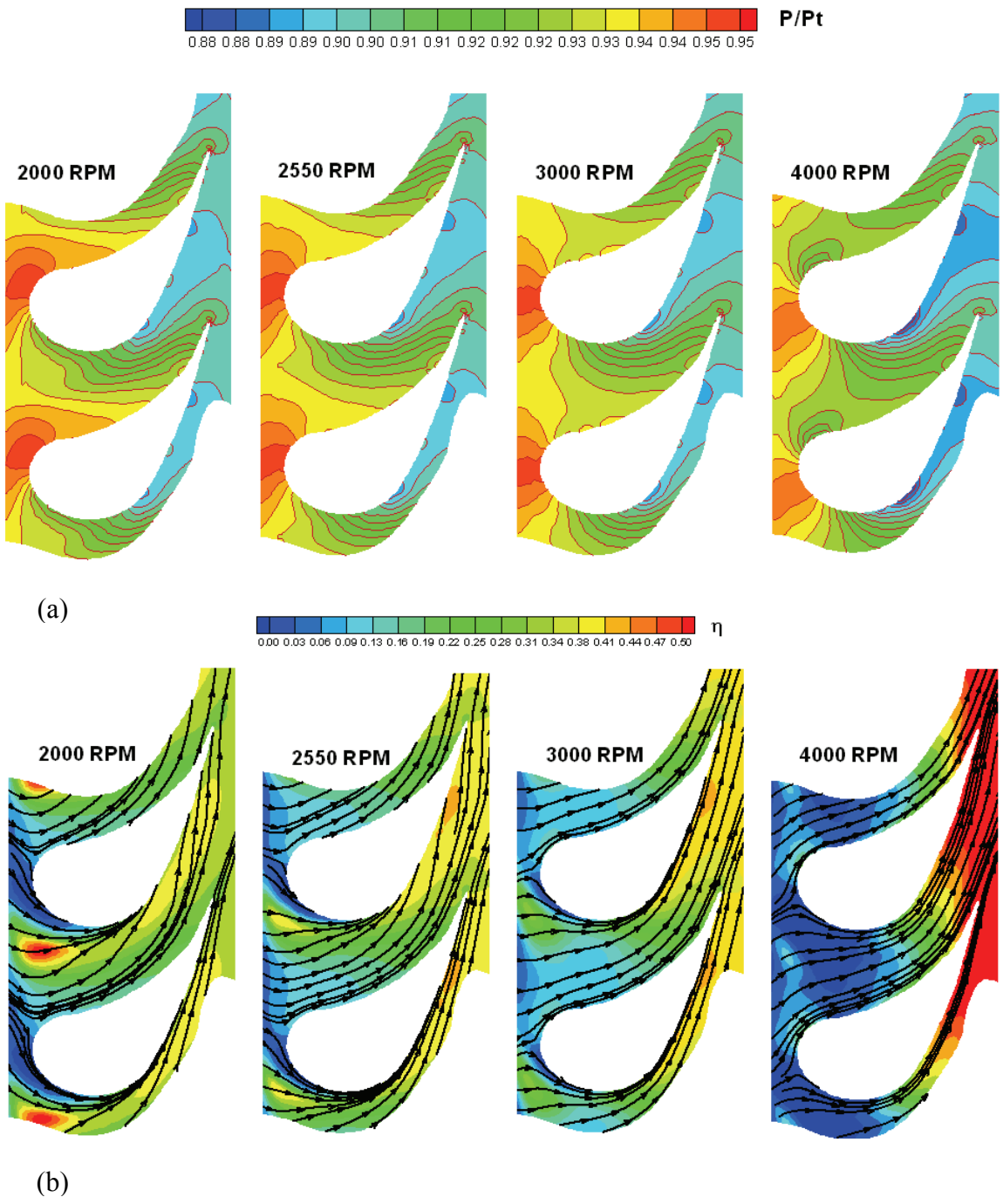

Figure 40: Predicted Pressure Ratio, Streamlines, and Dimensionless Temperature on the Annular Cross-Plane

(a) Pressure Ratio
(b) Streamlines and Dimensionless Temperature Contours

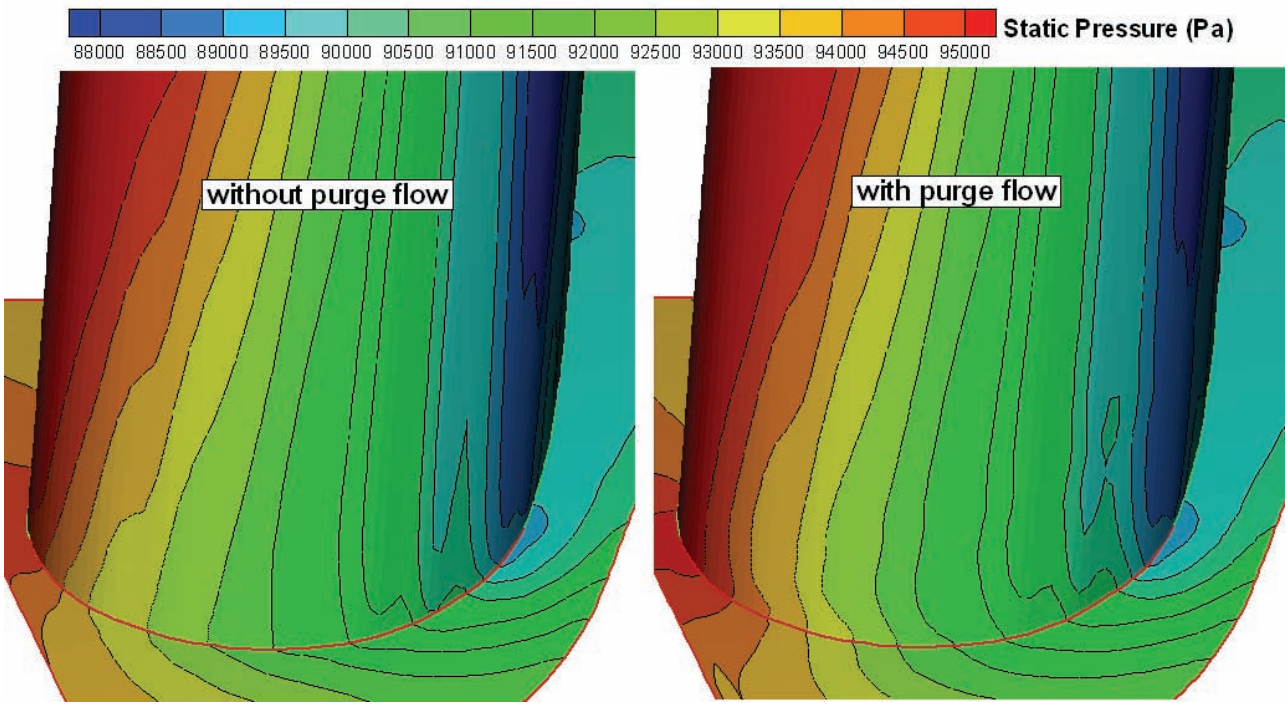

Figure 41: Comparison of the Static Pressure Contours on the Suction Side of the Rotor Blade with and without Purge Flow (2550 rpm, MFR = 1%)

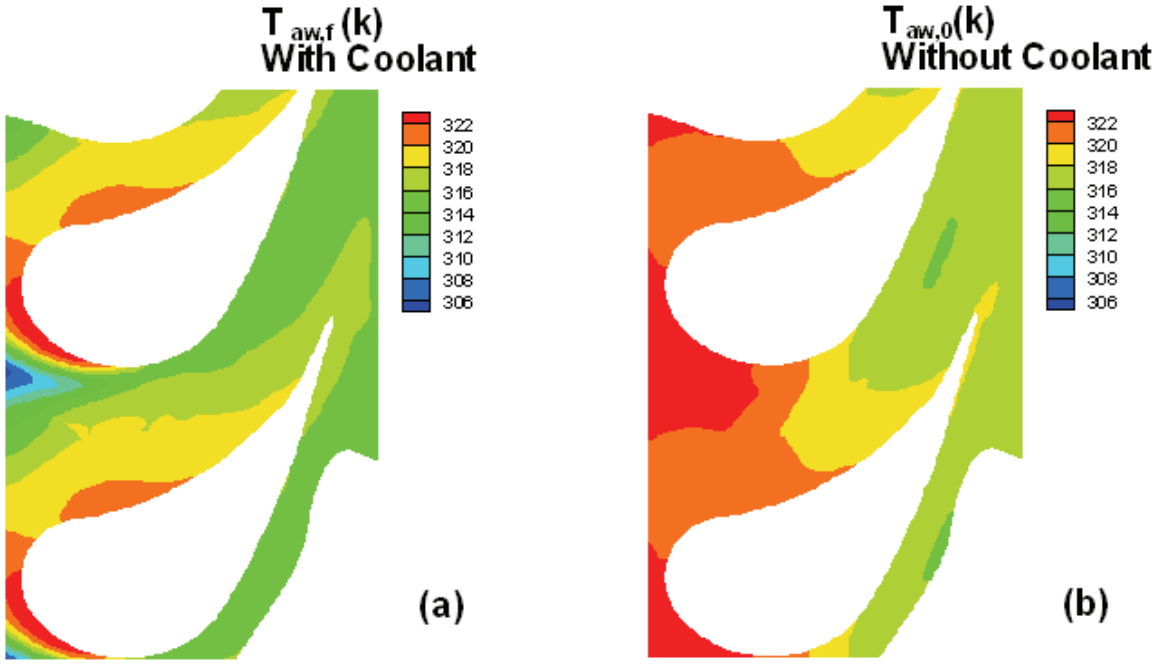

Figure 42: Comparison of the Total Wall Temperature on the Rotor Platform with and without Purge Flow (2550 rpm, MFR = 1%)

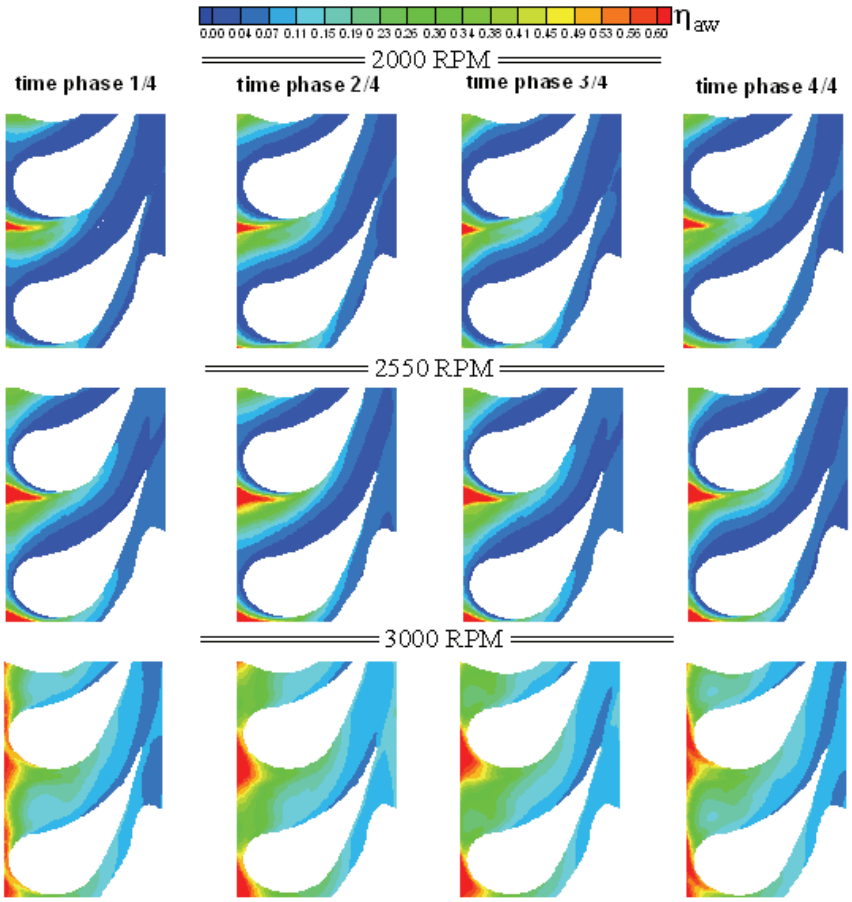

Figure 43: Comparison of the Adiabatic Film Cooling Effectiveness on the Rotor Platform with Various Rotational Speeds (MFR = 1%)

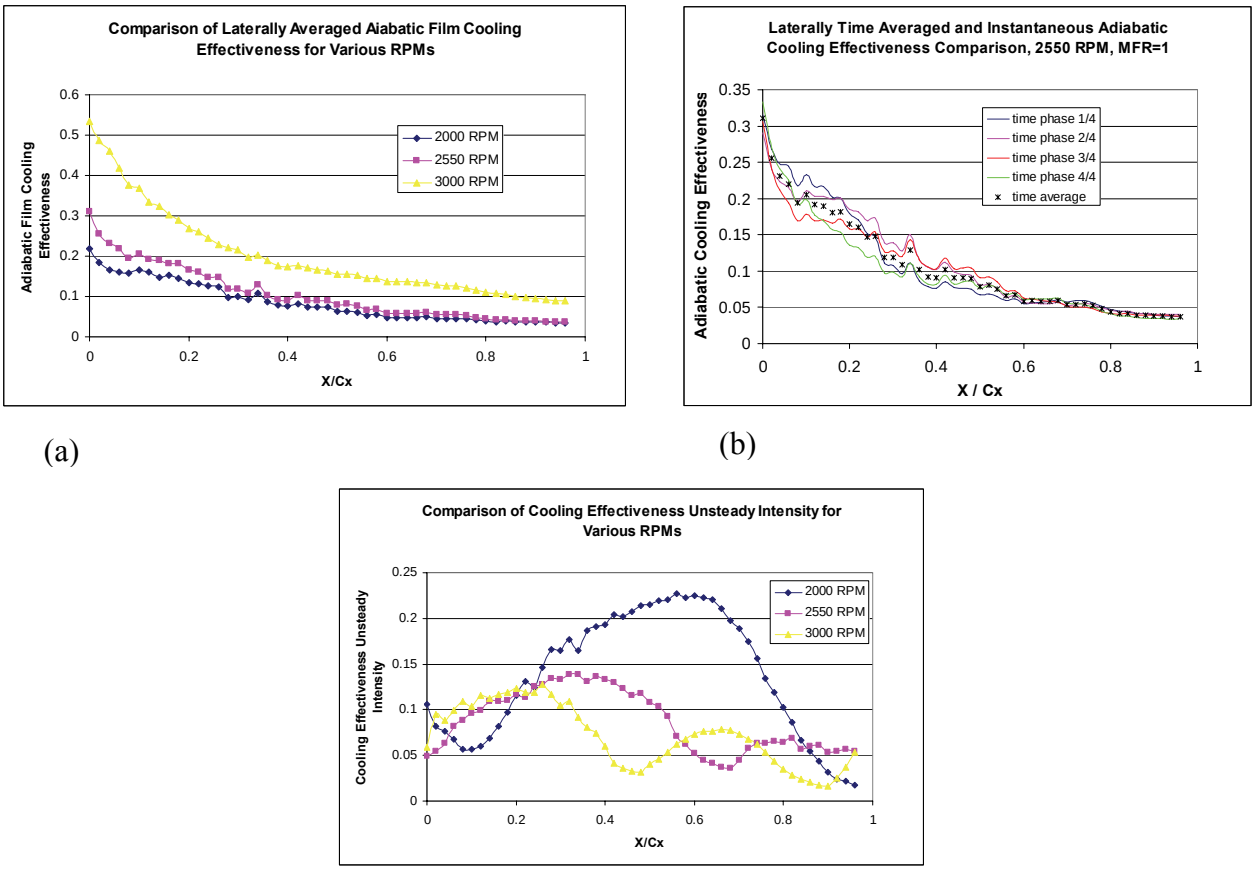

Figure 44: Effect of Rotational Speed on Laterally Averaged Film Cooling Effectiveness (MFR = 1%)

(a) Laterally Averaged Adiabatic Cooling Effectiveness Comparison at Various Rotational Speeds
(b) Instantaneous and Time Averaged Adiabatic Film Cooling Effectiveness (MFR = 1%, 2550 RPM)
(c) Laterally Averaged Unsteady Intensity at Various Rotational Speeds

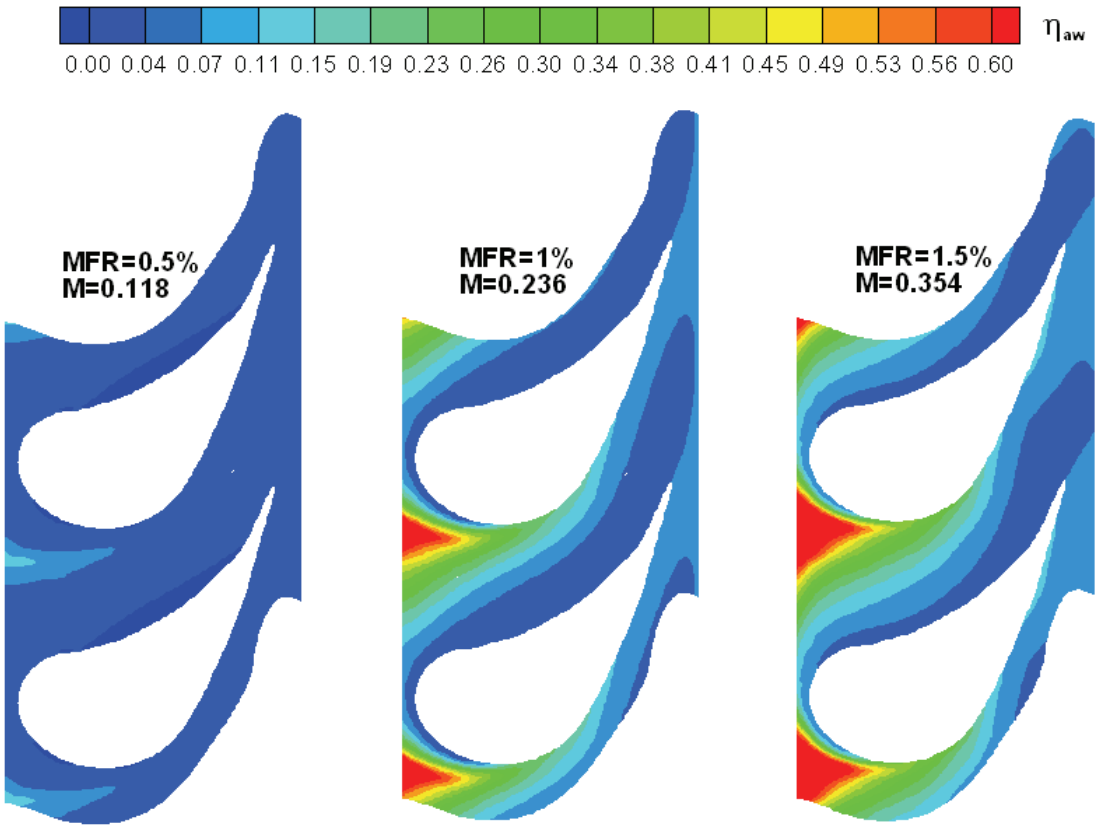

Figure 45: Predicted Adiabatic Film Cooing Effectiveness on the Rotating Blade Platform with Various Coolant Flow Rates

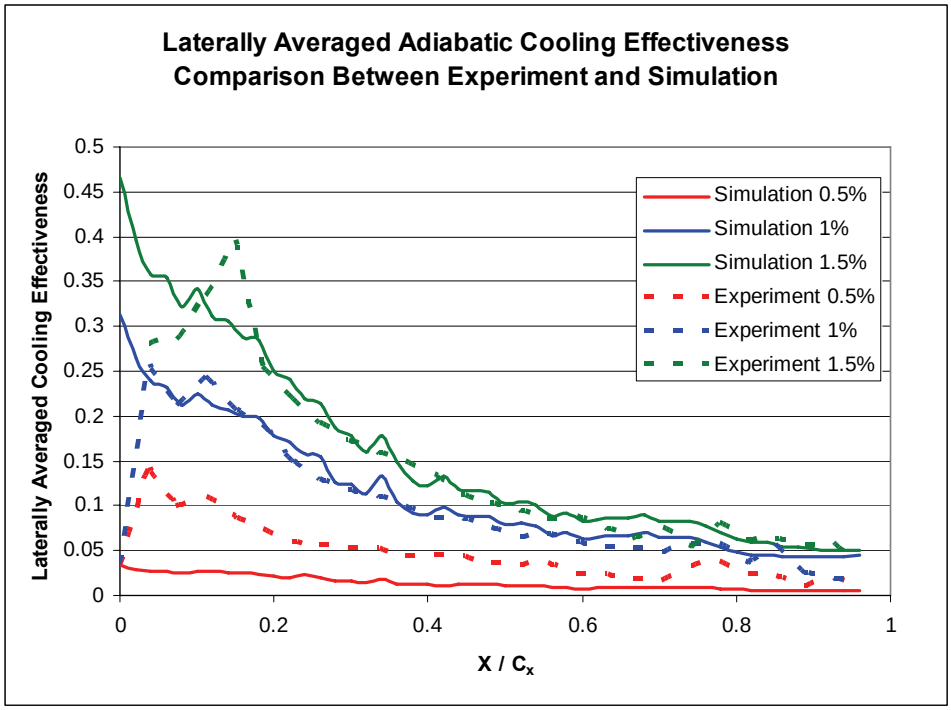

Figure 46: Laterally Averaged Adiabatic Cooling Effectiveness Comparison for Various Coolant Flow Rates (2550 RPM)

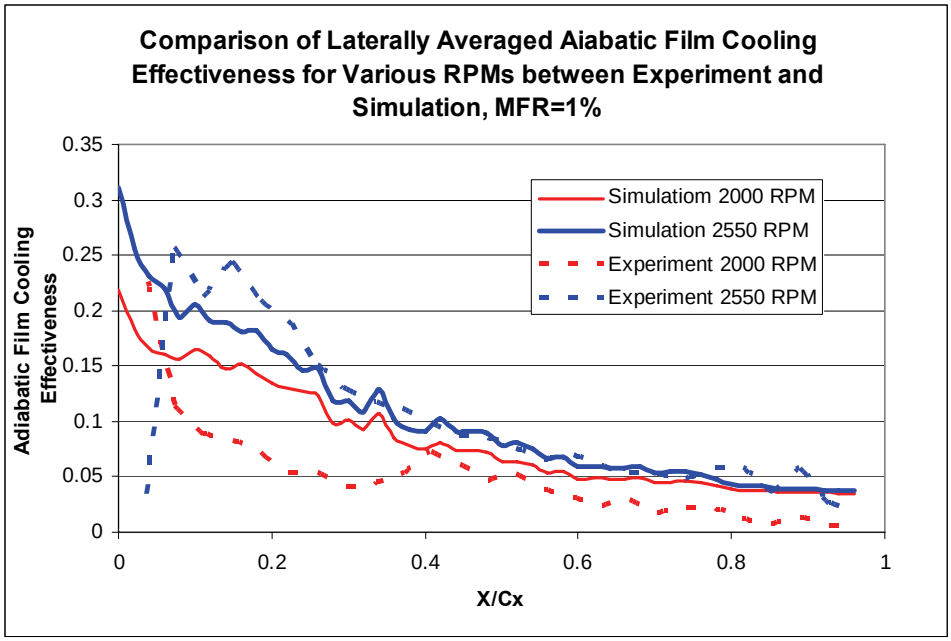

Figure 47: Laterally Averaged Adiabatic Cooling Effectiveness Comparison for Various Rotational Speeds (MFR = 1%)

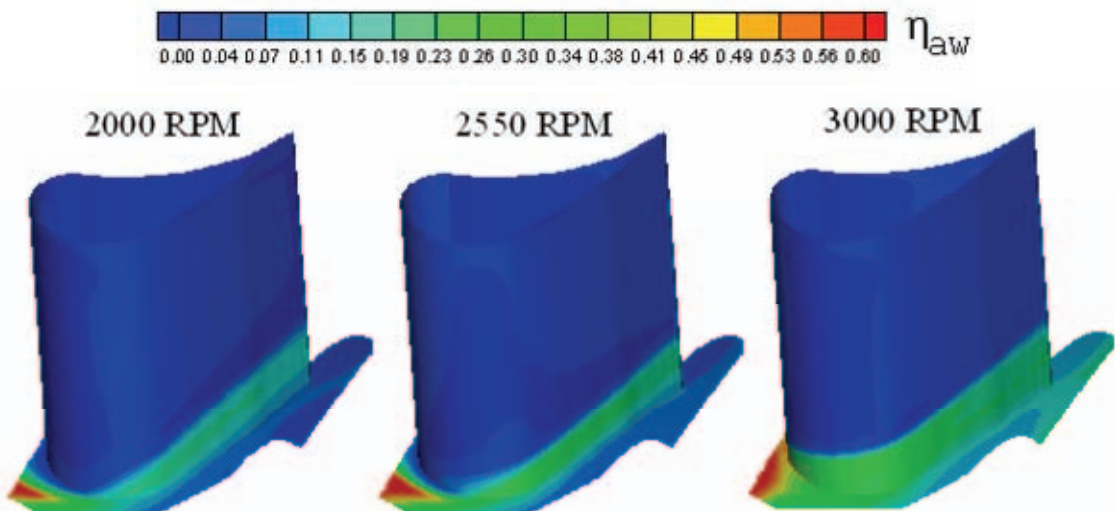

Figure 48: Predicted Adiabatic Film Cooling Effectiveness on the Suction Side of the Rotor Blade at Various Rotational Speeds (MFR = 1%)

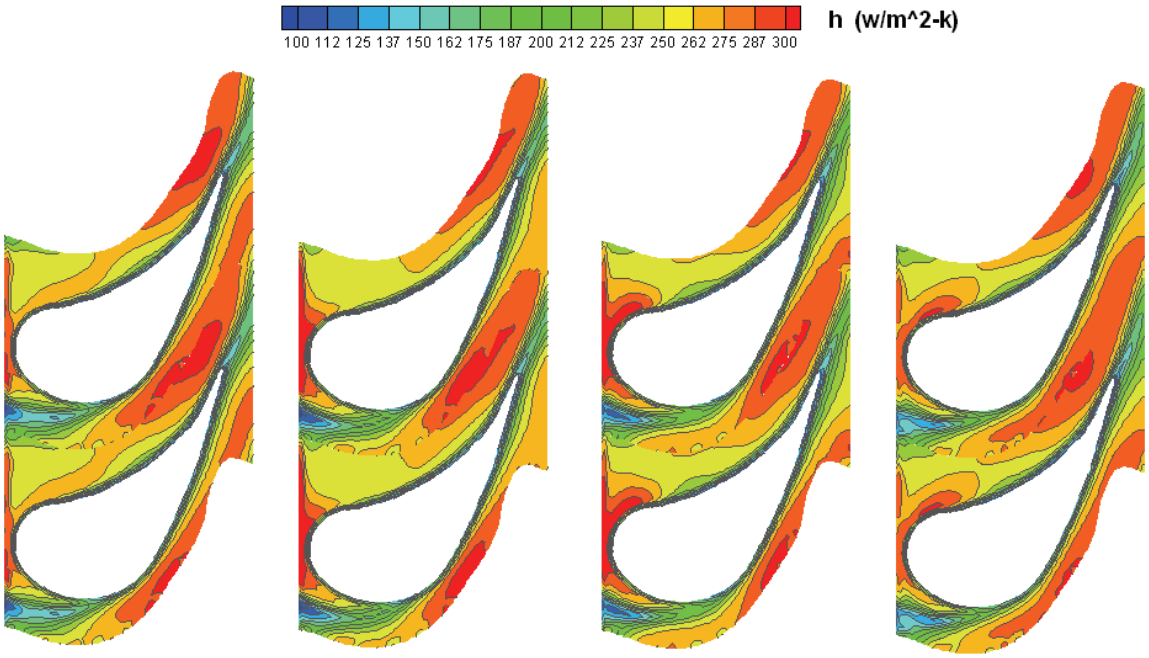

(a)

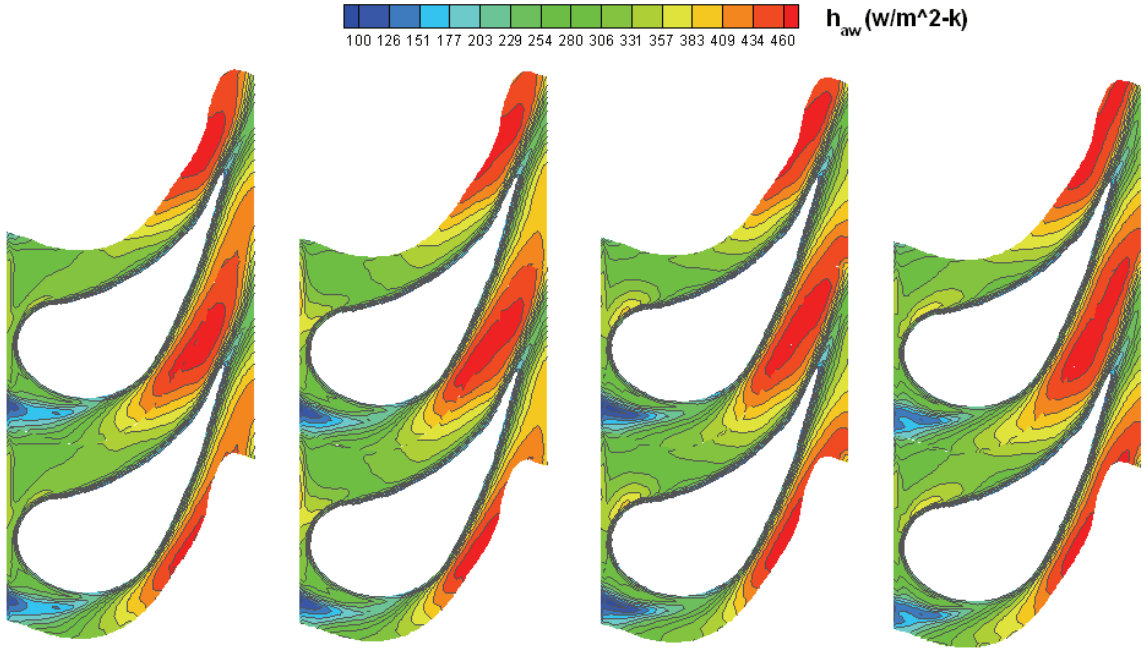

(b)

Figure 49: Predicted Overall and Adiabatic Heat Transfer Coefficients on the Rotating Platform at Various Time Phases (2550 RPM, MFR = 0.5%)

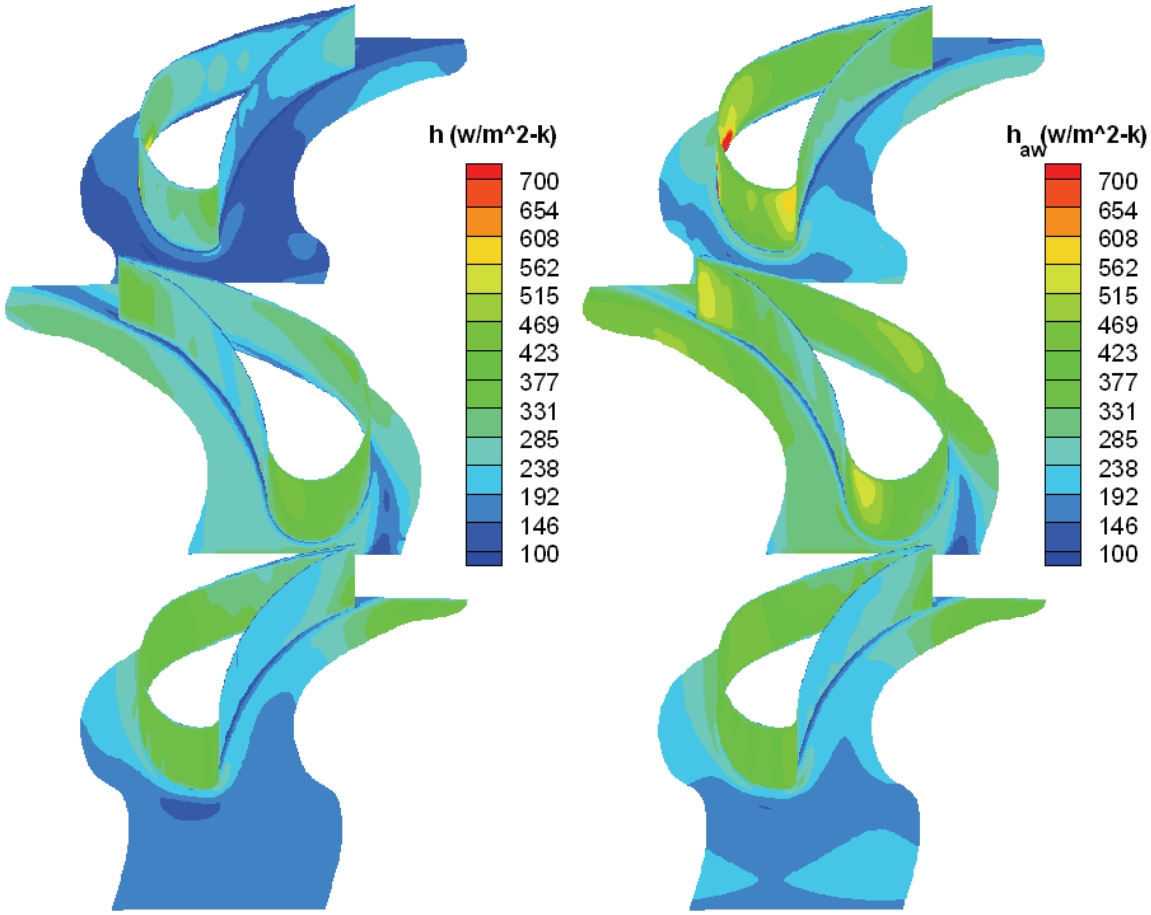

Figure 50: Predicted Overall and Adiabatic Heat Transfer for the Turbine Stage (2550 RPM, MFR = 0.5%)

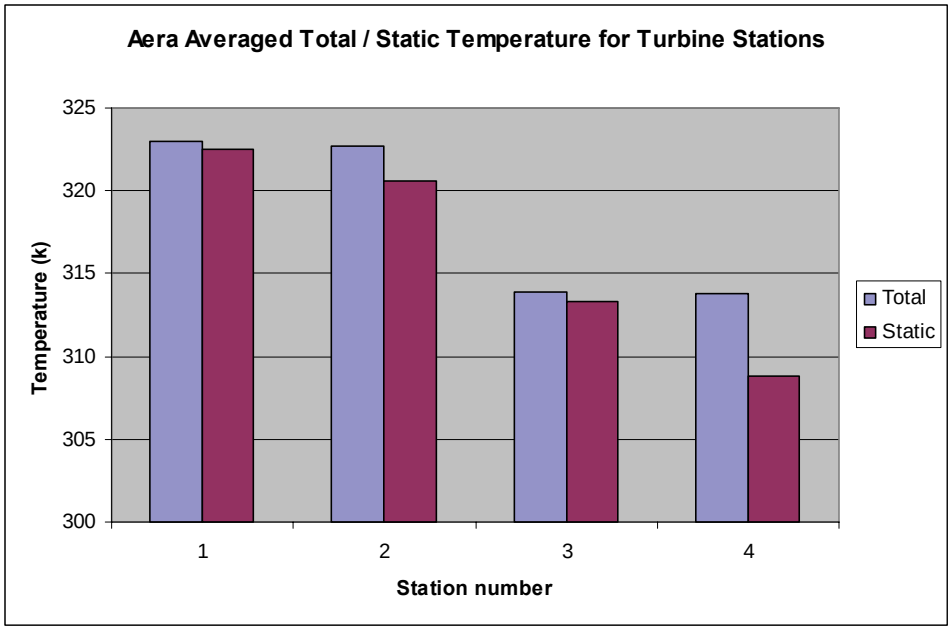

Figure 51: Area Averaged Total / Static Tempeature for Various Stations in the Turbine Stage (2550 RPM)

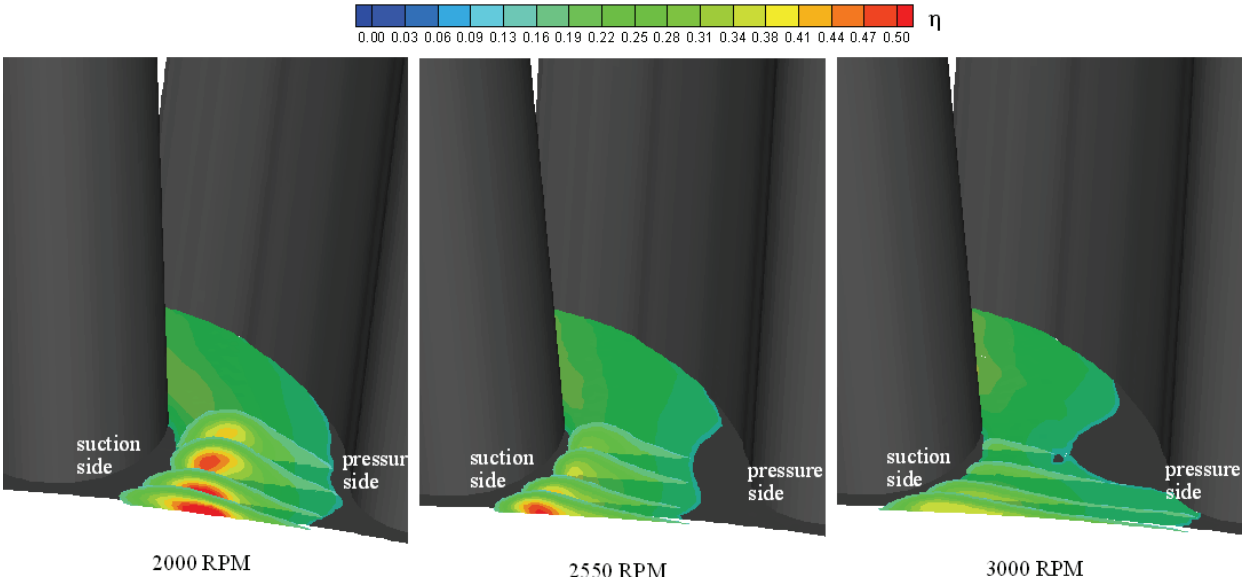

Figure 52: Coolant Path Inside the Rotor Passage for Various Rotational Speeds (MFR = 0.5%, Colored by the Overall Film Cooling Effectiveness)

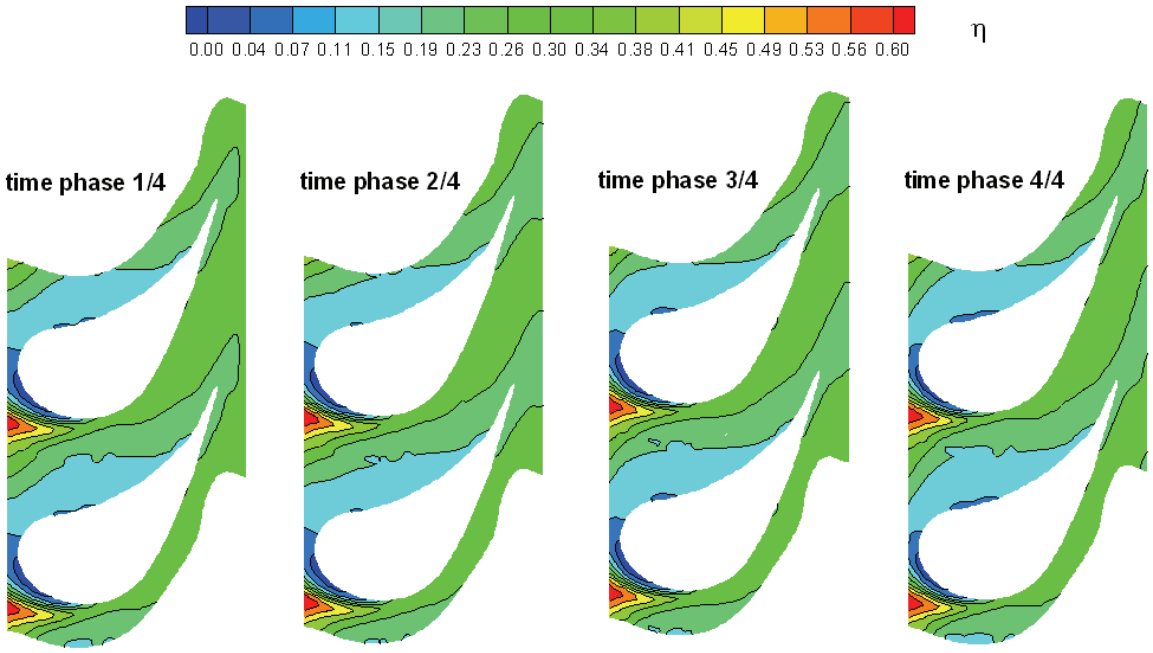

Figure 53: Overall Film Cooling Effectiveness Comparions on the Rotating Blade Platform for Various Time Phases (2550 RPM, MFR = 1.0%)

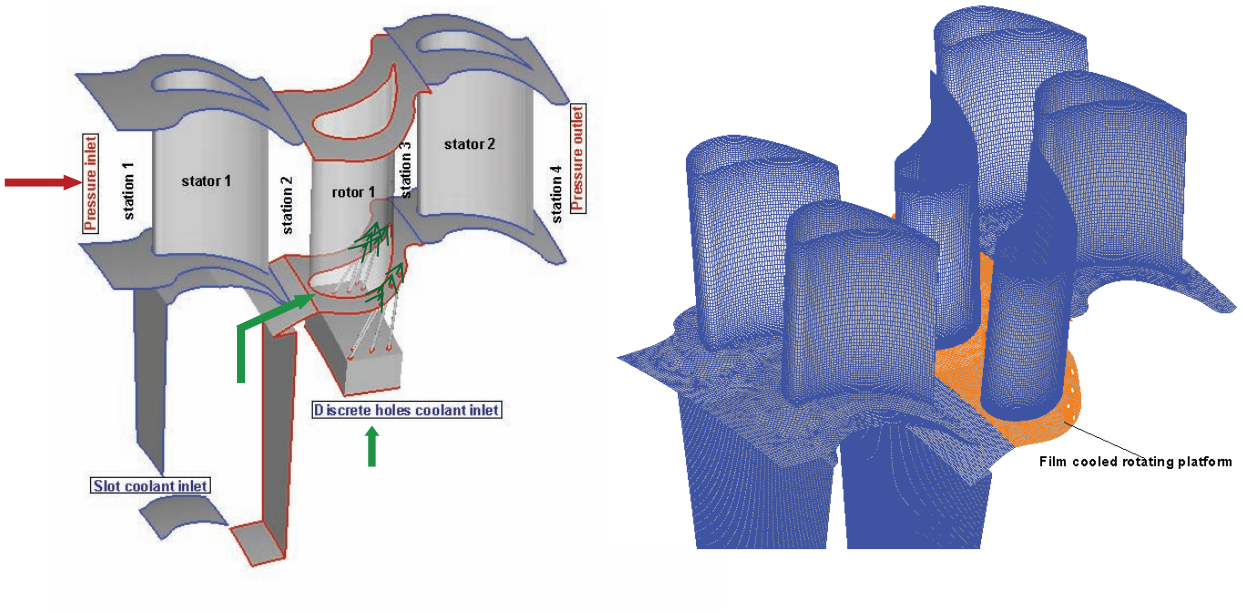

Figure 54: (a) Computational domain of purge slot and discrete holes film cooled platform in a 1-1/2 turbine stage, and (b) numerical grids (repeated two times and the orange color is the cooled platform).

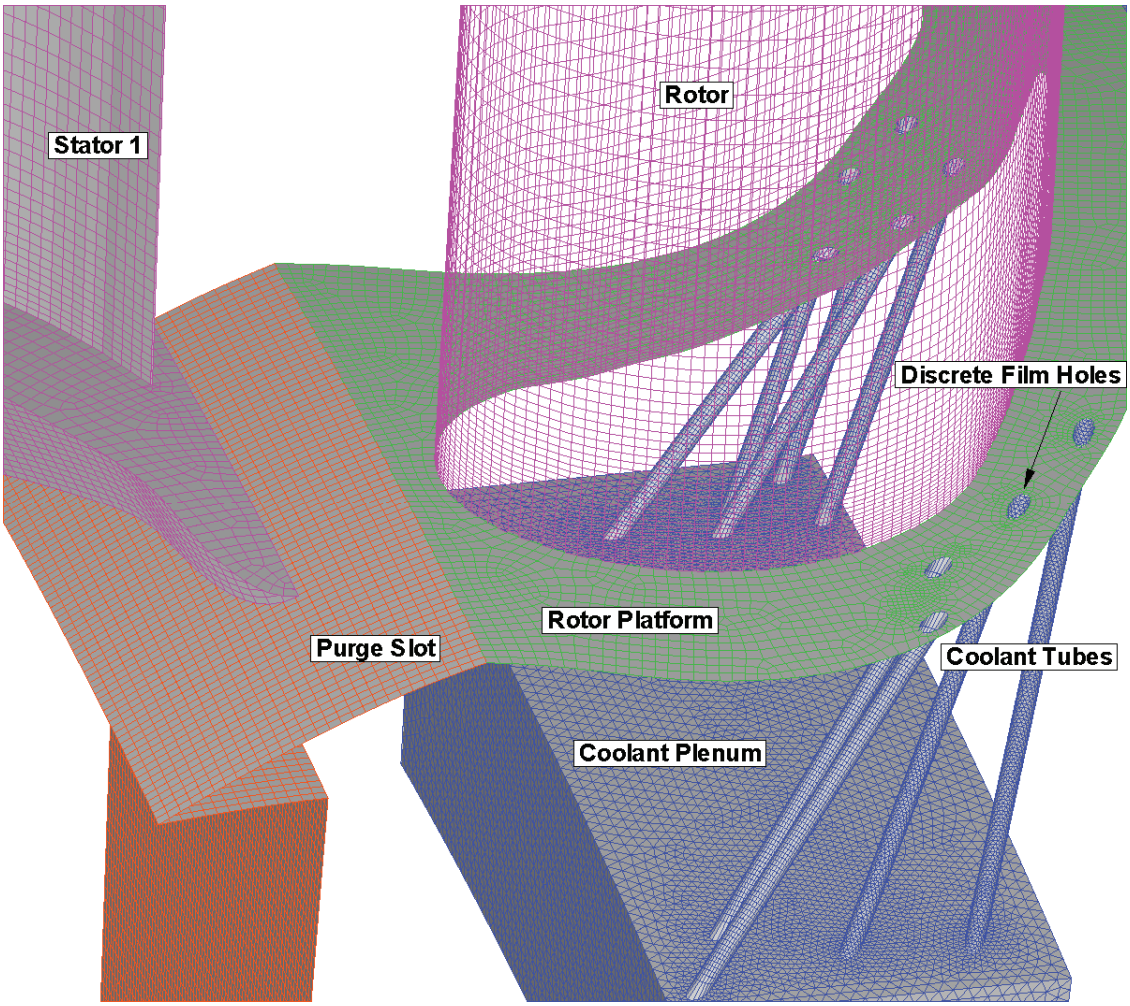

Figure 55: Detailed grid distributions of the platform purge slot and discrete film holes on the rotating platform.

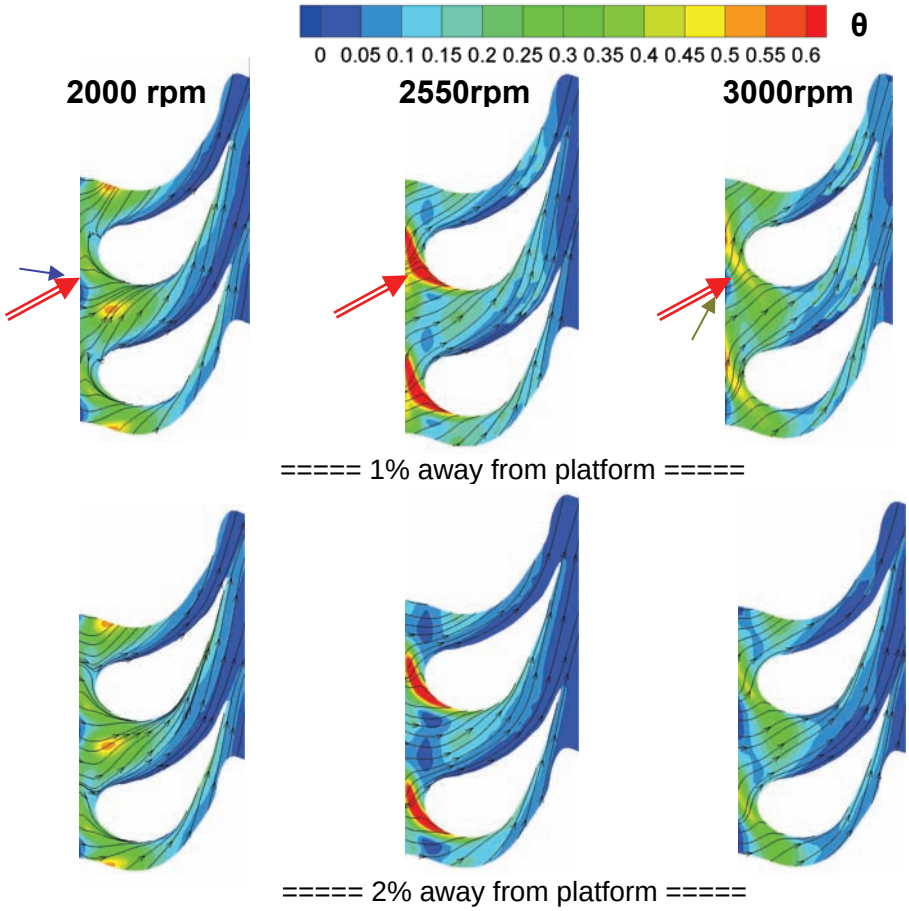

Figure 56: Comparison of streamlines and dimensionless temperature (θ) contours on the annular cross sections for various rotating speeds, time phase ¼.

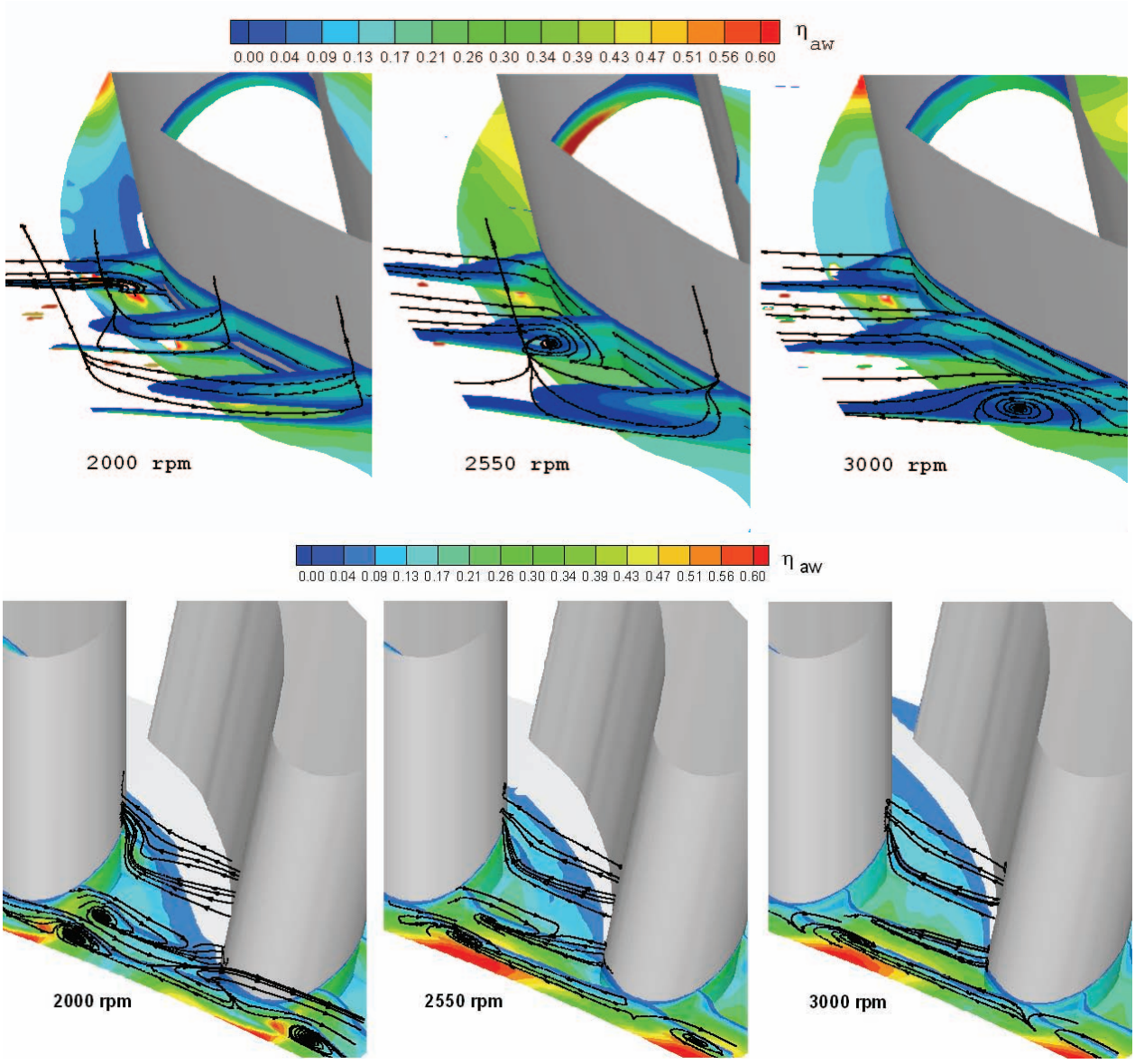

Figure 57: Coolant flow structures for (a) purge slot at leading portion based on the rotor relative velocity, and (b) discrete holes at trailing portion based on the rotor absolute velocity.

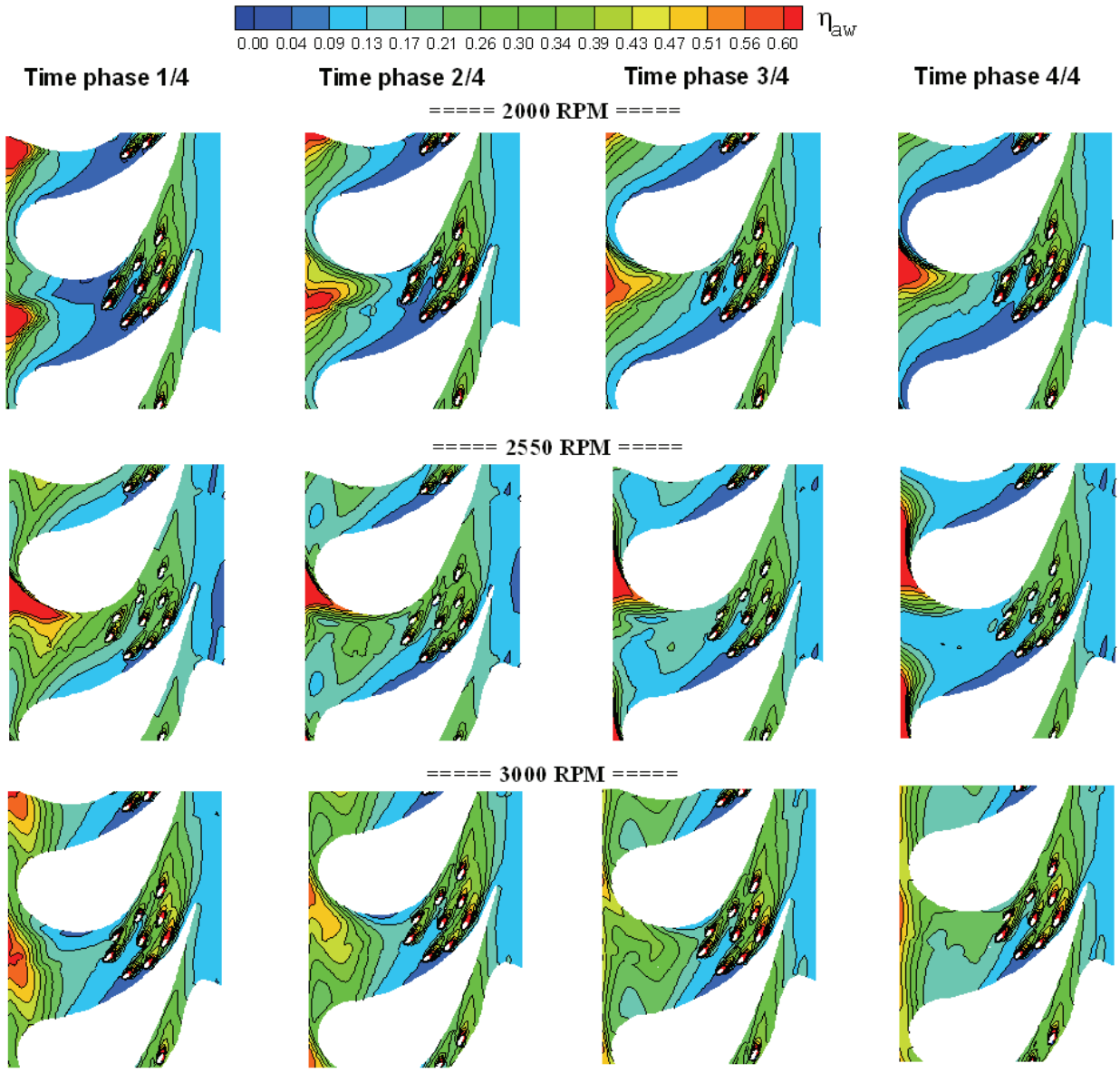

Figure 58: Adiabatic film cooling effectiveness comparison on the rotating blade platform for various rotating speeds, platform purge slot MFR = 1%, discrete film holes M = 1.

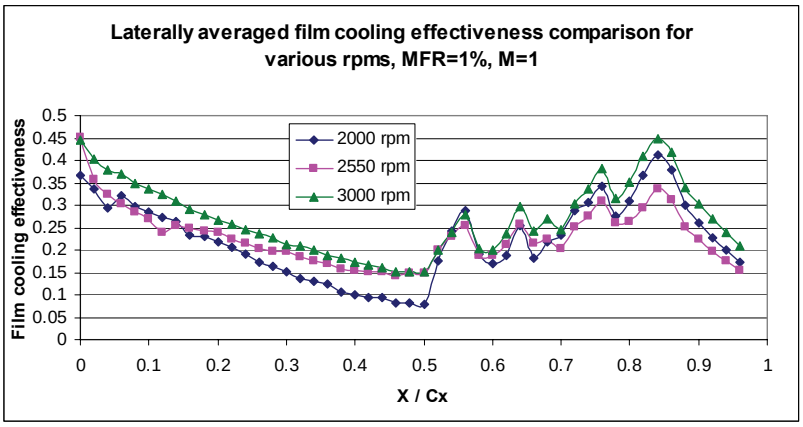

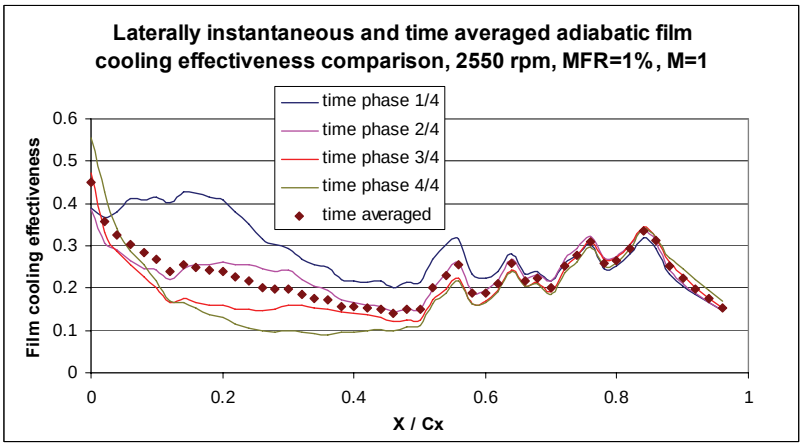

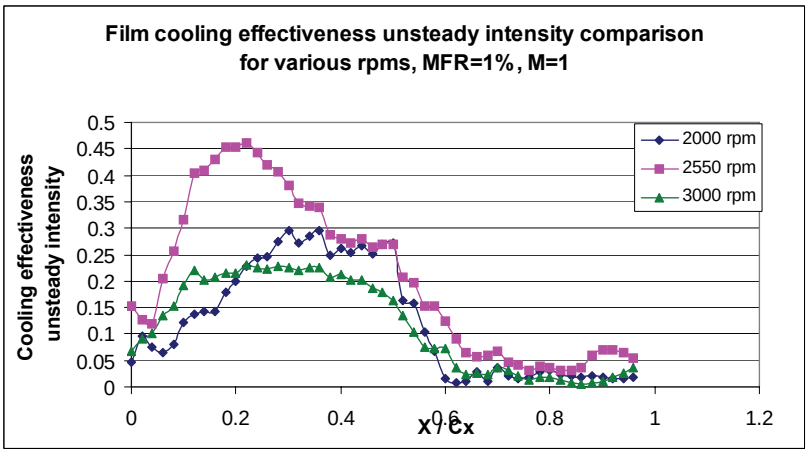

Figure 59: (a) Laterally averaged adiabatic cooling effectiveness for various rotating speeds (b) Instantaneous and time averaged adiabatic film cooling effectiveness for 2550 rpm, and (c) Laterally averaged unsteady intensity of adiabatic cooling effectiveness for various rotating speeds, with platform purge slot MFR=1%, discrete film holes M=1.

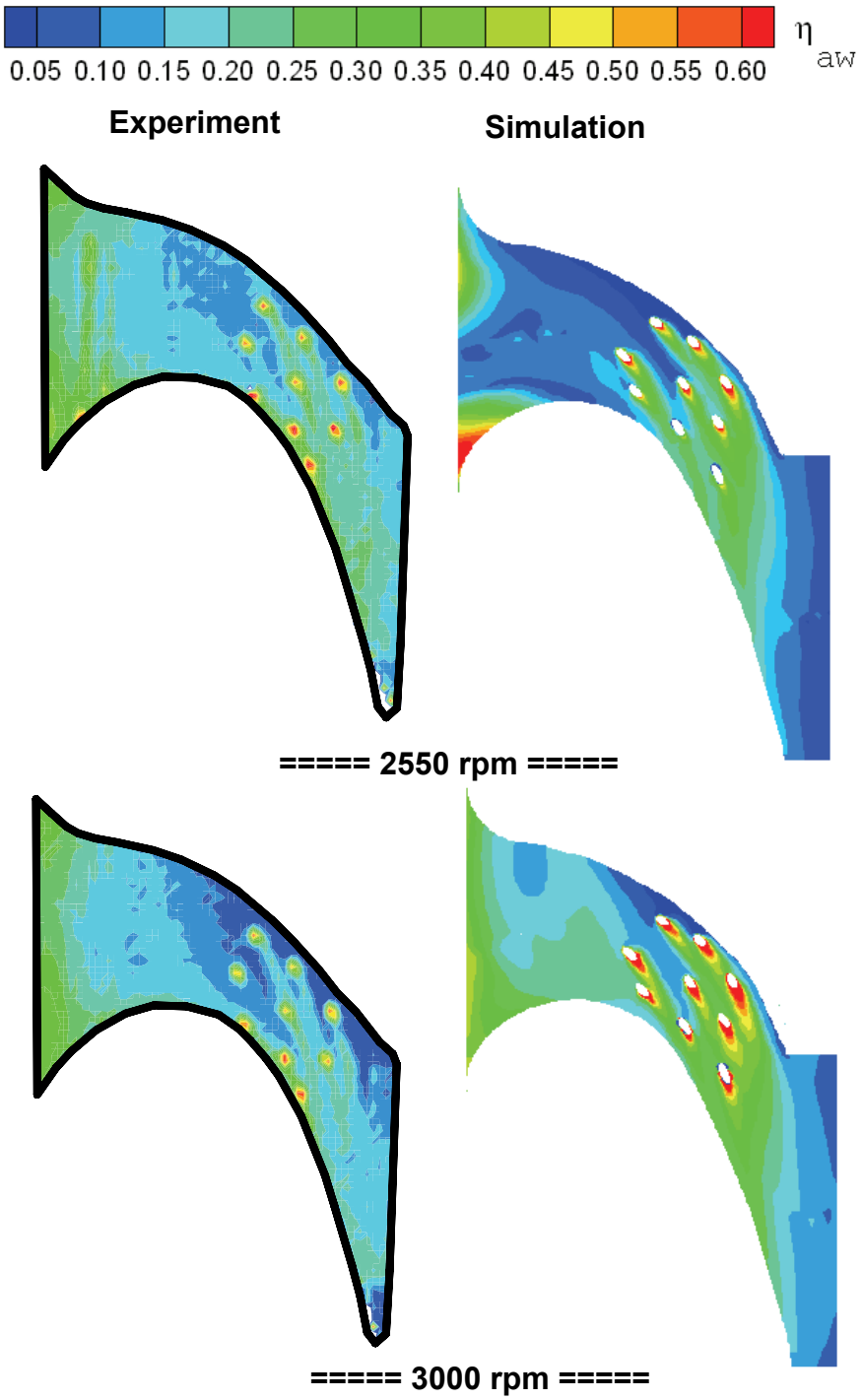

Figure 60: Comparison of adiabatic film cooling effectiveness on the rotating blade platform between experiment (Suryanarayanan et al. [17]) and simulation for 2550 and 3000 rpm, purge slot MFR=1%, discrete holes M=1.

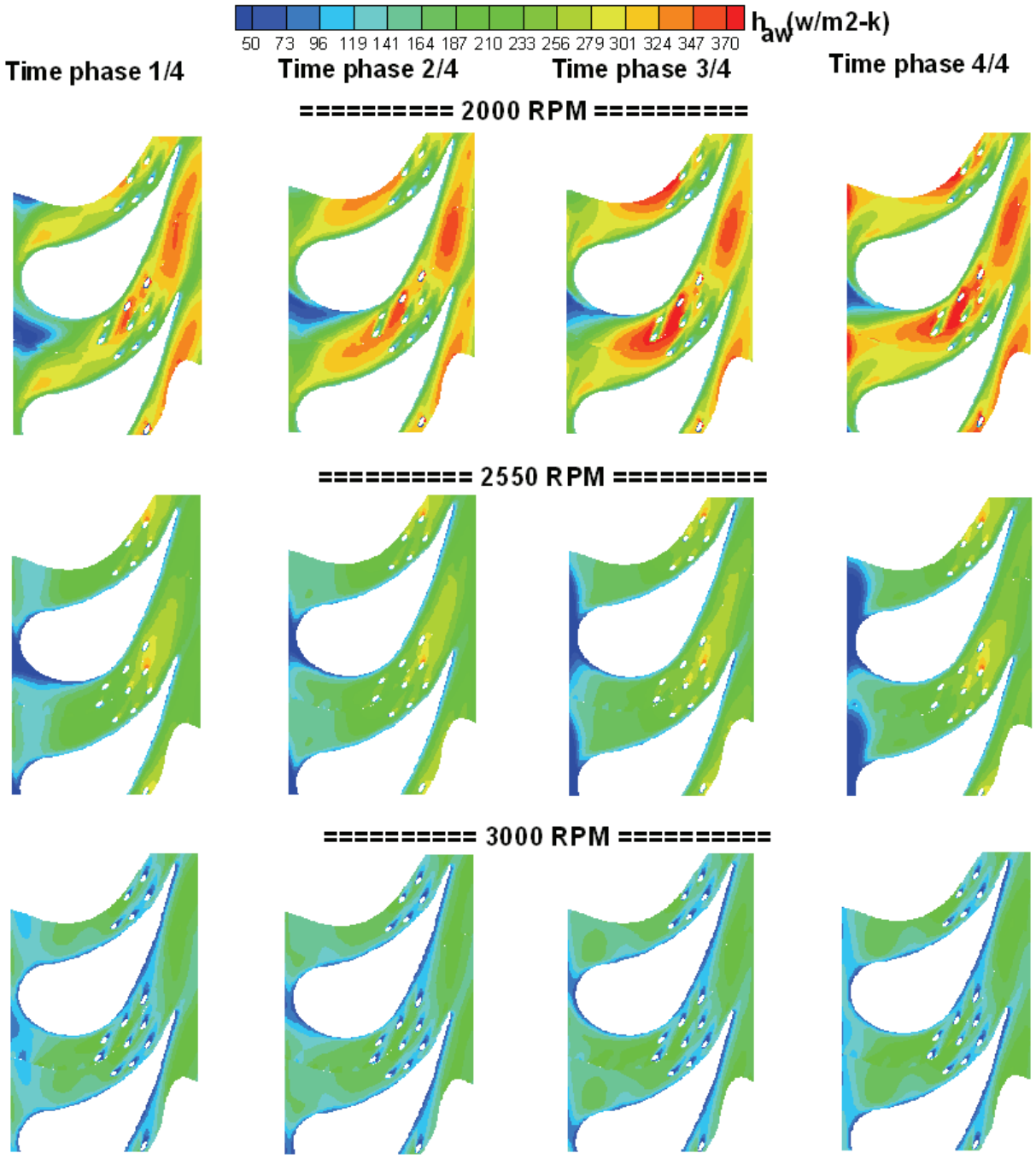

Figure 61: Heat transfer coefficients (based on the adiabatic wall temperature) on the rotating platform for various rotating speeds, purge slot MFR=1%, discrete holes M=1.

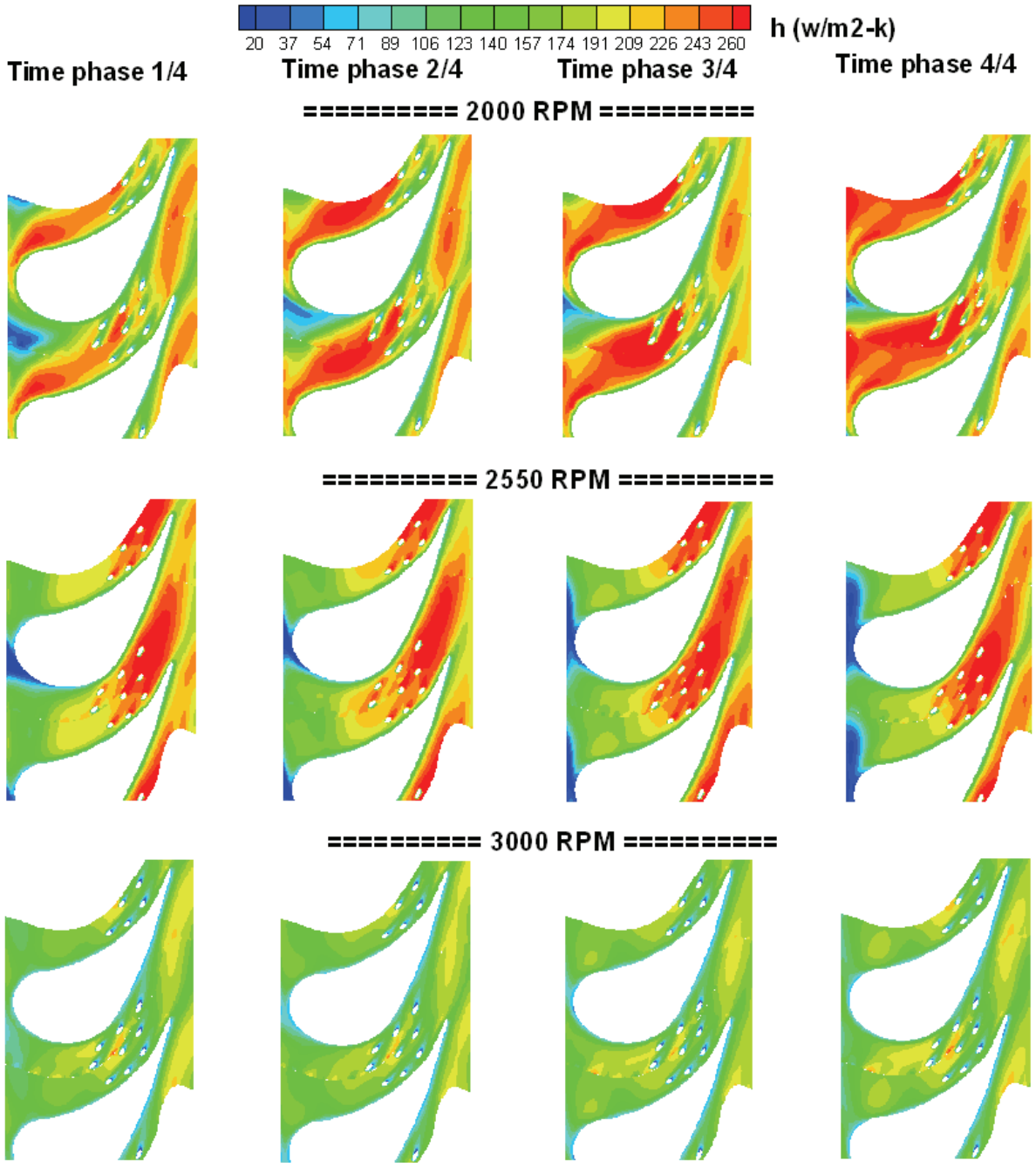

Figure 62: Overall heat transfer coefficients on the rotating platform for various rotating speeds, purge slot MFR=1%, discrete holes M=1.

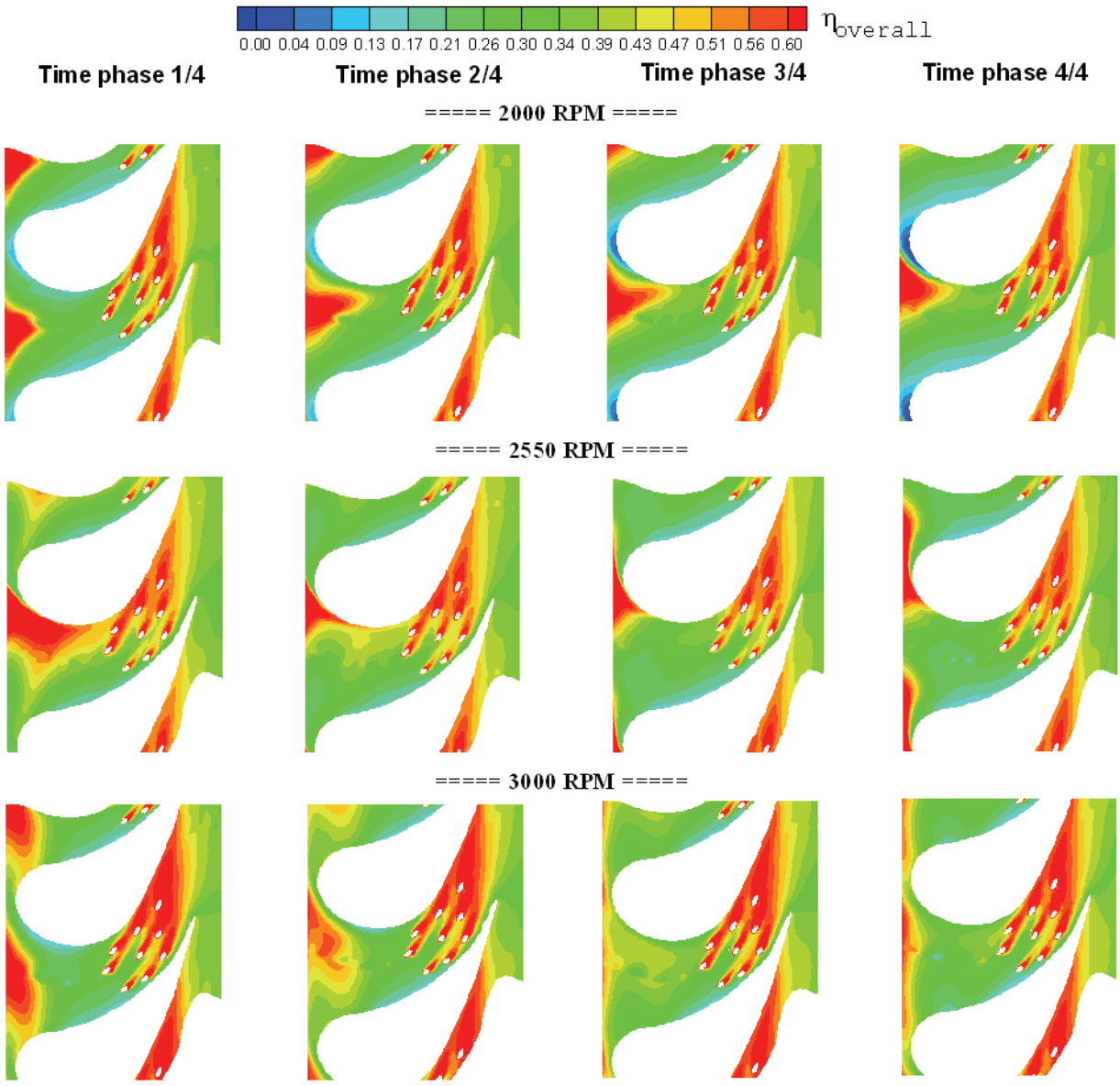

Figure 63: Overall film cooling effectiveness on the rotating blade platform for various rotating speeds at four time phases, purge slot MFR=1%, discrete holes M=1.

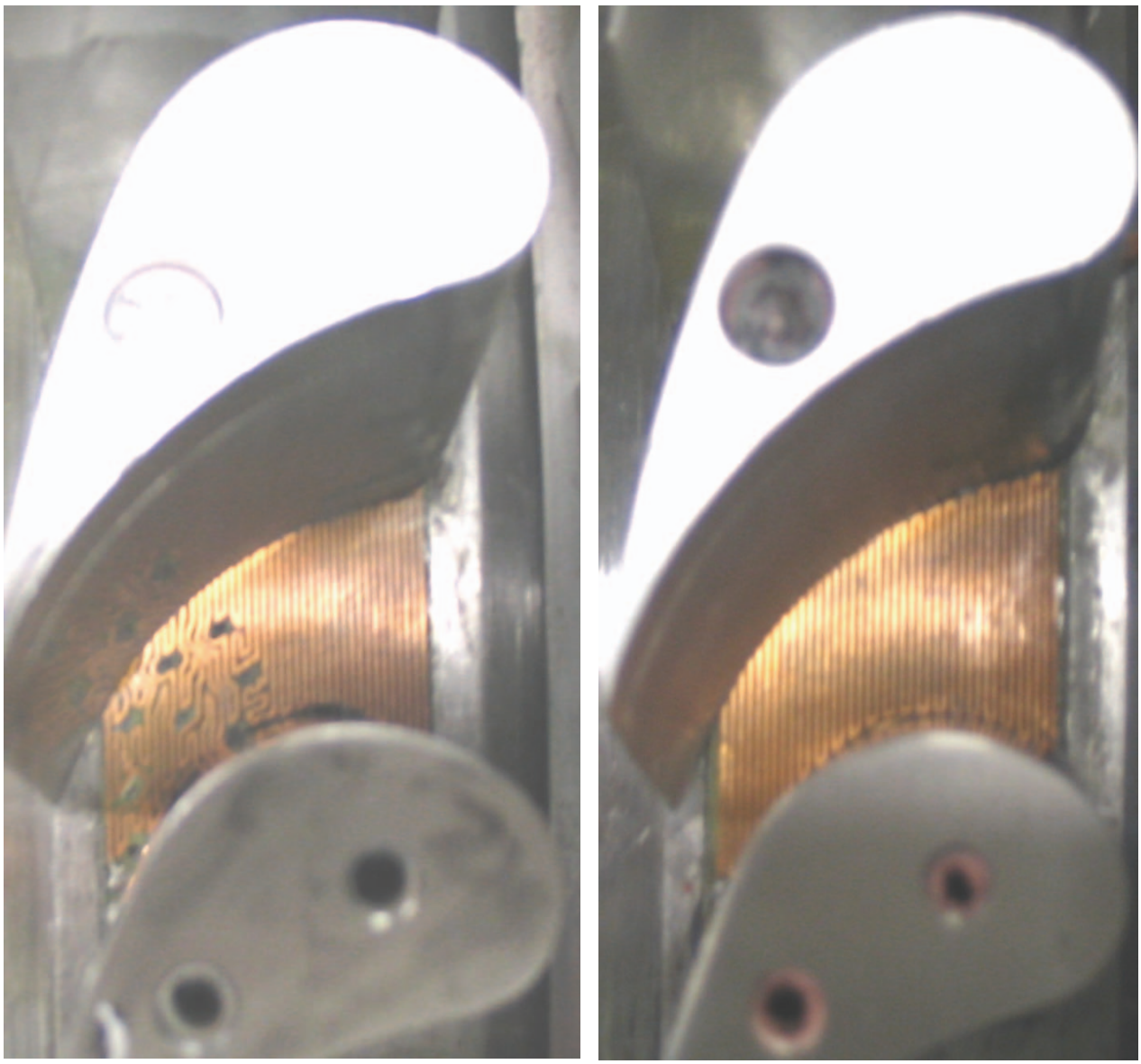

Figure 64: Heater coils mounted on rotor platform for discrete hole and stator-rotor upstream injection respectively.

Combustion Characterization and Modeling of Fuel Blends for Power Generation Gas Turbines

Semi-Annual Report

Start Date: May 1, 2006
End Date: October 31, 2006

Eric L. Petersen (PI)

Issue Date: March 5, 2007

DOE Award Number DE-FC26-02NT41431

UTSR Project Number 04-01-SR114

Mechanical, Materials & Aerospace Engineering
University of Central Florida
PO Box 162450
Orlando, FL 32816

ABSTRACT

In this report, we present new data for synthesis gas ignition at practical conditions that, when used in conjunction with an earlier set of data from UTRC, show considerable disagreement with what is predicted by state-of-the-art chemical kinetics models. This result is significant because coal-derived synthesis gas (i.e., syngas) is comprised primarily of H_2 and CO along with varying levels of CO_2 and other gases, and the CO/H_2 kinetics are often considered to be reasonably well known, even at elevated pressures and lower temperatures. The reason for this discrepancy is not known at this time.

Computational fluid dynamics modeling of the complex processes that occur within the burner of a gas turbine engine has become a critical step in the design process. However, due to computer limitations, it is very difficult to completely couple the fluid mechanics solver with the full combustion chemistry. Therefore, simplified chemistry models are required, and one topic of this research was to provide reduced chemistry models for CH_4/O_2 gas turbine flow fields to be integrated into CFD codes for the simulation of flow fields of natural gas-fueled burners. The reduction procedure for the CH_4/O_2 model utilized a response modeling technique wherein the full mechanism was solved over a range of temperatures, pressures, and mixture ratios to establish the response of a particular variable such as chemical reaction time. The conditions covered were between 1000 and 2500K for temperature, 0.1 and 2 for equivalence ratio, and 0.1 and 50 for pressure. The kinetic times include the time to ignition, the time to equilibrium H_2O formation, the time to equilibrium CO formation, and the time to equilibrium NO formation. The kinetic time models are given in Arrhenius type formulas as functions of equivalence ratio, temperature, and pressure; or fuel-to-air ratio, temperature and pressure. A single, global kinetics model was obtained for the entire range of conditions, and separate models for the low-temperature and high-temperature regions as well as for fuel-lean and rich cases were also derived. Predictions using the reduced model were verified using results from the full mechanism and empirical correlations from experiments. The models are intended for (but not limited to) use in CFD codes for flow field simulations of gas turbine combustors in which initial conditions and degree of mixedness of the fuel and air are key factors in achieving stable and robust combustion processes and acceptable emissions levels. The new model was applied to CFD simulations of a typical gas turbine burner with premixer with good results.

A constant-pressure cylindrical flame speed vessel (30-cm ID, 36.2-cm length) has been built for the study of constant-pressure, freely propagating, spherical flames. A Z-type schlieren setup, using either a vertical or a circular knife edge, in combination with a high-speed camera is used to capture the progression of the flame. Flame speed data were analyzed using special image tracking software. A linear regression of flame speed versus stretch was obtained, giving the Markstein length and the unstretched flame speed. A high-speed, piezo-resistive pressure transducer is used to obtain pressure data during the experiment and guarantees constant-pressure conditions. The vessel was designed for initial pressures up to 30 atm, where full use of the 12.7-cm aperture can be utilized within 3.5% of the pressure rise. Several methane-air mixtures have been tested around 1 atm and show good agreement with published data.

TABLE OF CONTENTS

LIST OF GRAPHICAL MATERIALS

TABLES

FIGURES

INTRODUCTION

With the necessity for clean, efficient electric power generation in all parts of the world, the need to manufacture stationary gas turbine engines with the ability to operate on a wide range of fuel compositions is crucial. Hence, fuel flexibility as a goal for gas turbine combustors is very important and is the topic of the current project. A good example is syngas, which contains significant but often varying levels of H_2, CO, and H_2O. Mixtures of natural gas containing significant levels of hydrocarbons and H_2 will also have significantly varied compositions, depending on the location and application of the blend. Such wide variations in fuel composition often produce wide variations in the chemical behavior of the fuels, not only in terms of their overall energy content but also in important design and performance parameters such as reactivity and flame speed.

Of primary concern, ultimately, is how fuel variability impacts the operation of a stationary gas turbine. For example, the flame speed of the fuel-oxidizer mixture in the combustor relates to its flashback or blowoff tendencies. Likewise, the fuel reactivity, often expressed in terms of its autoignition delay time, has a direct impact on the performance and stability of a given combustor design. Assuming a gas turbine designer or field engineer is aware of the flashback and ignition limitations of a given combustor, a determination as to whether or not a certain fuel will behave adequately in that particular combustor can be made if that fuel's flame speed and ignition characteristics were known *a priori*. However, very little if any fundamental flame speed and ignition data are available for uncommon fuel mixtures such as those mentioned above, much less at realistic engine pressures and concentrations.

A three-year project is underway in which UCF and its collaborators, Flow Parametrics and The Aerospace Corporation, are generating data and models on the combustion characteristics of various fuel blends at gas turbine operating conditions. Presented in this report are the results of the fourth 6 months of the project, covering the time frame from Nov. 1, 2005 through April 30, 2006. Following the Executive Summary is an overview of the project and the seven specific tasks to be performed. Details on the progress made during this second semi-annual reporting period are provided in the bulk of this report and are divided according to the research topic.

EXECUTIVE SUMMARY

Several results of particular interest to the gas turbine community have been obtained. These results are listed as follows.

1) New syngas data were obtained from our shock tube for a mixture that overlaps with flow reactor data from UTRC and UC Irvine that show significant disagreement with current kinetics models (faster ignition in the experiment than in the model) at lower temperatures and higher pressures. This result is significant in that either the ignition in this regime is not purely kinetic, or the well-known CO/H_2 kinetics models need improvement.

2) A reduced chemistry model for methane combustion was derived for use in CFD models. The reduced model takes the form of correlations for chemical times; these correlations are comprehensive in that they take the place of the detailed methane kinetics mechanism, but without having to couple the full mechanism with the CFD. The full mechanism was chosen from a methane-based mechanism that takes into account higher-pressure data that have recently become available under this program (see earlier quarterly reports). Some sample CFD simulations using the updated model are provided.

3) A new facility has been completed and demonstrated for the measurement of laminar flame speeds at elevated initial pressures (up to 30 atm). Some sample experiments for methane-air mixtures are shown. The facility incorporates large windows and a schlieren diagnostic in addition to pressure so that detailed flame speed measurements can be taken under constant-pressure, wrinkle-free conditions.

PROJECT DESCRIPTION

GAS TURBINE RESEARCH NEED

For several years now, natural gas has been widely used as a fuel for stationary power generation gas turbine engines [1]. Although composed primarily of methane, natural gases can contain from a few percent up to as much as 18% of other gases, depending on the international source [2]. These natural gas impurities are usually higher-order hydrocarbons such as ethane and propane. Composition variations in native and foreign natural gases can cause changes in the combustion chemistry, emissions formation, and stability, among other concerns [3-5].

However, in the near future, power generation gas turbines may be required to burn ever more exotic gaseous fuel blends in addition to indigenous natural gas. Typical fuel blends can include potentially high concentrations (> 10%) of hydrogen and even larger concentrations of hydrocarbons than what are common in natural gases. In addition to changes in the heating value of the fuel blends, significant changes in the ignition chemistry occur when gases such as H_2 and C_2H_6 are added to methane. According to previous studies, even a few percent of higher-order hydrocarbons can greatly accelerate the ignition process of a methane-based fuel [2]. Even larger changes in the combustion chemistry may then occur if the methane-based fuel were to contain significant levels of hydrogen or hydrocarbons. Such chemical effects can have dramatic impacts on existing gas turbine combustors designed to operate on natural gases typical of those found, for example, in the United States. These concerns are complicated by the fact that few data exist on the fundamental effects of fuel composition variation at the fuel/air mixture ratios, temperatures, and pressures of interest to the designers of power generation gas turbines.

With these issues and concerns in mind, the authors are conducting a research program to study ignition delay times, flame speeds, and related chemical kinetics over a wide range of fuel composition, mixture stoichiometry, temperature, and pressure. ***This program will provide data related to fuel flexibility issues, allowing gas turbine designers and field engineers to predict the effects of fuel flexibility on the likelihood of autoignition in premixed regions, flashback, combustor efficiency, emissions, and combustion instability.*** Provided in the next section is an outline of the research effort.

PROJECT EXPERIMENTAL AND ANALYTICAL APPROACH

This 3-year effort is divided into seven experimental and analytical tasks, outlined as follows.

<u>Task 1 – Test Matrix and Literature Search</u>

Since the objective of the experiments is to provide critical flame speed and ignition data as quickly as possible to impact gas turbine designers and field engineers, a Design of Experiments (DOE) approach will be taken. In a DOE test matrix, specific ranges of multiple test variables are chosen using readily available statistical procedures to devise a test matrix that covers the entire breadth of the variables without testing every possible combination of variable levels. Matrices will be developed for the various fuel-blend experiments, with emphasis on the autoignition experiments and the flame speed experiments. In parallel with the DOE selection phase, a comprehensive literature search will be conducted covering the main facets of the program.

Task 2 – Autoignition Measurements

Ignition delay times for the range of mixtures and conditions defined in Task 1 will be measured in Task 2. These experiments involve primarily the shock-tube facilities and related diagnostics. The early focus of this task will be on conditions of most interest to the gas turbine community: fuel lean fuel/air mixtures at elevated pressures. These tests will form the bulk of the experiments during the first two years of the effort. Both methane-based fuel blends and syngas (CO/H_2) fuel blends will be studied.

Task 3 – Flame Speed Measurements

A new flame speed apparatus is being built at UCF to measure the flame speed of gas turbine fuel blends at elevated pressures. The test apparatus includes a spherical (or large cylindrical), stainless steel chamber with two quartz windows to provide optical access. The combustible mixture is ignited at the center of the vessel using electrodes. Measurements involve observing the flames using schlieren motion picture photography in conjunction with a high-speed digital camera to yield an exposure time less than 1 millisecond. The key parameter to be measured is the one dimensional radial propagation velocity of the spherical flame front relative to the unburned mixture, or dr/dt.

Task 4 – Chemical Kinetics Modeling

This task supports and is conducted in parallel with each of the other tasks and forms a critical link between the experimental efforts (Tasks 2,3,6 and 7) and the CFD modeling effort (Task 5). In addition, Task 4 will produce combustion chemistry models that can be used for calculations beyond those that can be performed using empirical correlations obtained in Tasks 2 and 3. This effort will produce two types of models: 1) a full mechanism (or mechanisms) containing hundreds of possible reactions between dozens of molecules in the reaction zone, and 2) reduced mechanisms containing perhaps only dozens of reactions for use in the CFD models. Both types of mechanisms will rely heavily on both existing hydrocarbon-based kinetics models and the data obtained in the proposed effort.

Task 5 – CFD Modeling Effort

This task is being performed by Flow Parametrics and consists of three stages, leading towards the use of finite-rate kinetics for simulations of combustors with emphasis on fuel flexibility. During Year 1, computations of model combustors using established heat release models for synthetic fuels will be performed and compared with available data or design system results. The dynamics of a propagating flame will be emphasized (as in the flame speed experiments). During Year 2, new and improved finite-rate kinetics models for the selected fuel blends will be implemented and compared to the model combustor results. During Year 3, final calibration of the reduced chemical kinetics models within the combustion CFD flow solver will be completed, and demonstration simulations on production or research hardware will be performed. These simulations will be compared with available experimental data and/or design system performance predictions.

Task 6 – NOx Measurements

This task involves a series of quantitative measurements of NOx species such as NO_2 and NO as well as CO for a representative range of syngas and other gas turbine fuel mixtures. Following

an approach similar to that used in Tasks 2 and 3, fuel and parameter combinations from the fuel-blend matrices determined in Task 1 will be explored at realistic temperatures and pressures in the Aerospace and UCF facilities. From the proposed NOx measurements, we will be able to compare the NOx-producing tendencies of the complete range of fuels and conditions defined in Task 1. Likely fuel combinations that are more or less likely to produce NOx will be identified, and empirical correlations will be determined if possible. This task also involves the use of the CFD model under Task 5 to explore the effects of fuel flexibility on NOx production in typical gas turbine configurations using realistic flow rates.

Task 7 – Mechanism Validation Measurements

True validation of any chemical kinetics mechanism for use in gas turbine-related calculations cannot come from comparisons with ignition and flame speed data alone, but from a combination of these and other fundamental data such as species concentration measurements. This task therefore is concerned with acquiring the necessary data from shock-tube experiments. Most of the measurements in Task 7 will be performed using a combination of emission and laser absorption diagnostics. Although the species targeted will depend somewhat on the diagnostics set up in the laboratory from other projects, we anticipate that OH, CO, CH, CH_4, and H_2O can be studied. Typically, such measurements are performed in a chemically well-behaved environment, namely in mixtures with a higher level of dilution. The resulting data will be used to validate the chemical kinetics mechanism(s) over a wider range of ϕ, temperature, and pressure than the initial ignition experiments in Task 2.

SYNGAS IGNITION AND COMPARISON TO MODERN MODELS (Tasks 2, 7)

As shown by Peschke and Spadaccini [6], Lieuwen et al. [7] and Richards et al. [8] among others, syngas is important as an alternative fuel for gas turbines and other power applications. Variations in its composition can have considerable impact on an engine's performance and operability, and autoignition times of premixed fuel-air mixtures at compressor discharge temperatures and pressures on the order of 600 – 950 K and 10 – 30 atm are important design constraints. In addition, ignition delay time is traditionally an important parameter for benchmarking the validity of combustion chemistry models. Unfortunately, few data exist at engine pressures and for undiluted fuel-air mixtures. Therefore, ignition delay time measurements of CO/H_2 mixtures at practical conditions have been the subject of recent study [9-12].

One relatively obscure work by Peschke and Spadaccini [6] covered pressures as high as 26 atm and temperatures of 633 – 781 K in a continuous flow reactor (hereafter referred to as the UTRC data); as pointed out by McDonell et al. [7], the UTRC ignition data are considerably faster than what is predicted by current kinetics models. Recently, an identical mixture to the baseline fuel composition studied at UTRC (38.6% H_2 + 51.1% CO + 10.3% CO_2, by volume) was shock heated by the authors behind reflected shock waves using the facility and procedures described by Kalitan et al. [9,10]. This syngas fuel blend was mixed with air (O_2 + 3.76 N_2) at a fuel-to-air equivalence ratio (ϕ) of 0.5, as in the UTRC experiment. The new shock-tube data have an average pressure of 22.5 atm and are presented in Table 1. Ignition delay time was defined at the onset of the strong ignition pressure rise as seen from a pressure transducer mounted in the endwall, as in Kalitan et al. [9]. The uncertainty in the shock-tube data are on the order of the size of the data symbols in Fig. 1 with respect to the ignition time and less than 15 K for the temperature. The UTRC data for the same mixture are also included in Table 1 for completeness, taken directly from the original report [6] and have an average pressure of 18 atm.

Figure 1 presents the results of the new shock-tube data in comparison with the UTRC flow reactor data. Although the lowest-temperature shock-tube data point is for a temperature of 943 K, the ignition-time versus inverse temperature trend agrees with that of the earlier flow reactor data. Uncertainty in the shock-tube temperature is less than 15 K, and the ignition times are known to within 10% of the listed values.

New, elevated-pressure flow reactor data were also taken by Vince McDonell and coworkers at the University of California, Irvine using the facility and procedure described in Chen et al. [13] and Beerer et al. [14] (under a separate UTSR contract, 03-01-SR112). Their flow reactor is similar to that used by Peschke and Spadaccini [6] but uses active heating of the tube walls to maintain the test temperature throughout the length of the apparatus. The syngas mixture in this case was a 50/50 blend of CO/H_2 and was burned in air at equivalence ratios between 0.33 and 0.6 at a pressure of approximately 5 atm. When ignition occurred, a temperature rise of at least 50 K was observed, and this temperature rise was taken as the definition of the ignition delay time. The temperature uncertainty for the measurements is ±30 K, and the uncertainty in ignition time is ±15%. These new data are also presented in Table 1 and on the ignition plot in Fig. 1 where they noticeably agree with the data of UTRC and the new shock-tube data. Note that the data in Fig. 1 were adjusted to a pressure of 20 atm to allow direct comparison to the shock-tube and UTRC data. This correction assumes that the syngas ignition delay time is roughly

proportional to P^{-1} as commonly seen in fuel ignition studies (although the exact pressure dependence cannot be determined until more data are available in this regime).

Table 1 Ignition delay time data. Shock-tube data are from the present study (7.33% H_2 + 9.71% CO + 1.98% CO_2 + 17.01% O_2 + 63.97% N_2). UTRC data are from Peschke and Spadaccini, Fuel No. 2 in air (same as shock-tube mixture) [6]. UCI flow reactor data are from McDonell et al. and are for a 50/50 blend of CO/H_2.

Source	T (K)	P (atm)	τ (ms)	ϕ
Shock Tube	943	22.3	3.34	0.50
	947	20.9	3.52	0.50
	962	28.9	2.46	0.50
	987	23.8	2.01	0.50
	990	20.9	1.97	0.50
	1001	20.9	1.88	0.50
	1013	21.6	2.03	0.50
	1019	32.7	1.57	0.50
	1024	16.5	2.38	0.50
	1033	23.7	2.15	0.50
	1053	18.7	1.56	0.50
	1059	20.1	1.25	0.50
	1148	21.4	0.38	0.50
UTRC	646	17.7	104	0.50
	633	17.6	105	0.50
	634	22.6	128	0.50
	649	23.0	127	0.50
	694	16.4	92	0.50
	698	19.3	82	0.50
	709	18.5	75	0.50
	679	18.8	83	0.50
	747	15.0	60	0.50
	651	15.5	66	0.50
	714	13.7	54	0.50
	714	15.8	62	0.50
	676	15.6	62	0.50
	781	11.9	42	0.50
	654	14.9	65	0.50
	769	14.5	53	0.50
	647	15.0	65	0.50
	730	19.7	47	0.50
	771	16.8	38	0.50
	740	21.0	50	0.50
	739	22.6	52	0.50
	751	17.1	38	0.50
	671	22.3	59	0.50
	691	21.0	53	0.50
	723	18.2	46	0.50
	694	20.9	58	0.50
	701	22.3	60	0.50
UCI	783	5.3	132	0.40
	760	5.0	150	0.54
	765	5.0	150	0.54
	777	5.1	146	0.60
	777	5.1	111	0.33

Other data on syngas ignition have become available over a similar temperature and pressure regime using rapid compression machines (RCM), namely the data of Walton et al. [11]. Selected data from their study for CO/H_2/air mixtures with roughly a 50/50 split by volume have been added to Fig. 1; these data are the closest in condition to those herein and cover a range of equivalence ratios from 0.3 to 0.7 and pressures from 12 to 23.5 atm (adjusted to 20 atm as discussed above). Although the Walton et al. data encompass a wider range of ϕ and composition, their results seem to agree with the new results herein and those of Peschke and Spadaccini.

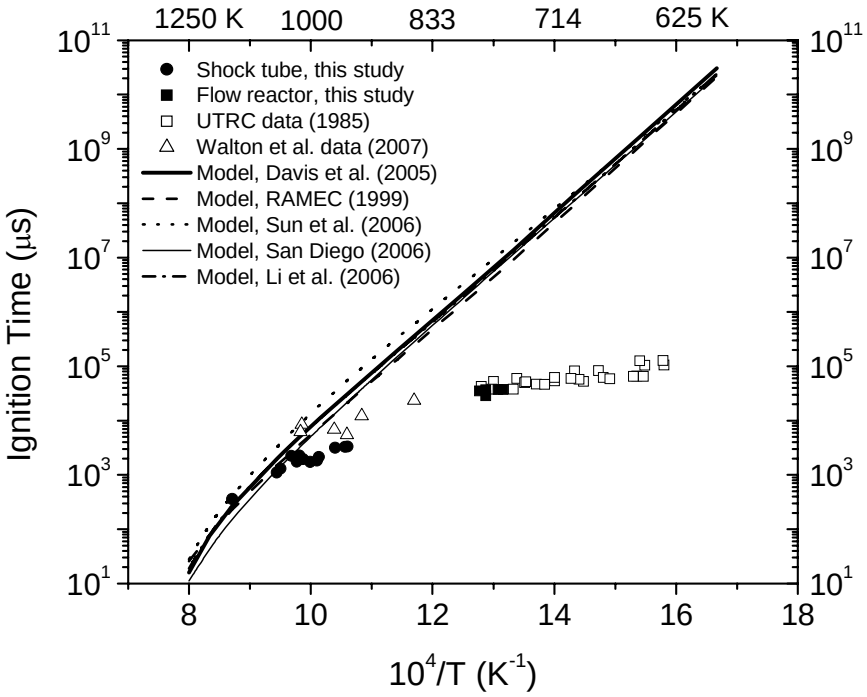

Figure 1 Ignition delay time data and comparison to chemical kinetics mechanisms of Davis et al. [15], RAMEC [16], San Diego Mechanism [17], Sun et al. [18], and Li et al. [19]. All calculations were performed for the shock-tube mixture (Table 1) at 20 atm. The new flow reactor data were adjusted on the plot to a pressure of 20 atm (see text).

Calculations were performed using four chemical kinetics models containing full CO/H_2 chemistry, three of which were published within the past year. These models include Davis et al. [15], RAMEC (based on GRI-Mech) [16], Saxena and Williams (San Diego Mechanism) [17], Sun et al. [18], and Li et al. [19]. All calculations were performed using Chemkin at zero-dimensional conditions and under constant-internal energy, constant-volume constraints for the UTRC mixture at 20 atm. Figure 1 presents the results of the calculations in comparison with the new experimental data.

From the results presented in Fig. 1, there exists a clear and disturbing disagreement between experiment and model at conditions of direct interest to power generation gas turbines operating on syngas. At temperatures near 700-800 K, the measured autoignition times are as much as two-to-three orders of magnitude lower than what is predicted by current kinetics models. Even at the shock-tube conditions near 950 K, the model predicts ignition delay times an order of magnitude higher than the data. Note that the experimental data presented in Fig. 1 come from three different research groups using three different techniques (shock tube, flow reactor, and RCM). Comparing the model to the new flow reactor experiments at the experimental pressure of 5 atm shows just as much of a discrepancy as it does when adjusting the data to a common 20 atm, and running the model using a constant enthalpy-constant pressure assumption (more applicable to flow reactors) also shows the same discrepancy between model and experiment.

Nonetheless, the disagreement between experiment and model may not be surprising since few data have existed at the temperature and pressure ranges of the present study to which the models could be calibrated. Resolution of the disagreement is beyond the scope of this brief communication, although calculations by the authors clearly indicate that uncertainties in the rates of elementary reactions commonly found to be important between and above the second and third explosion limits of hydrogen/CO oxidation will not entirely explain the discrepancy. For example, although the present authors [9,10] and others [20] have pointed out the importance of the reaction $CO + HO_2 = CO_2 + OH$ at the conditions of interest herein, reasonable adjustments in its rate do not resolve the disagreement. Recent shock-tube kinetics experiments by Sivaramakrishnan et al. [21] for CO/H_2 mixtures at pressures up to 450 atm and temperatures between 1000 – 1500 K show reasonable agreement with current models, suggesting that the differences observed herein may be due more to the lower temperatures than the elevated pressures. The authors will provide more detailed summaries of their experiments and results when the presently ongoing studies are completed.

CHEMICAL TIME MODEL AND SIMULATIONS FOR METHANE-BASED FUEL BLENDS (Tasks 4, 5)

Modeling the interaction between flow fields and chemical reactions is a complicated process due to the excessive computational resources required to couple the full chemistry with a full-scale numerical flow solver. Combustion modeling using detailed chemistry is important to accurately predict certain combustion phenomena in a gas turbine design phase. However, detailed chemistry contains many reactions and species, and since the computational cost and time associated with a given reaction mechanism are directly affected by the number of species, the process becomes very computationally expensive. Hence, there is a demand for reliable models that use less computational time yet still accurately reproduce some of the important aspects of the combustion phenomena. This awareness of the importance of accurate chemical kinetics models that require minimal computational time for combustion simulations has led to the development of reduced mechanisms.

One-, two-, and multi-step reduced mechanisms for methane oxidation were developed by Westbrook and Dryer [22]. Similarly, Bilger [23] developed a four-step reduced mechanism, as did Seshadri and Peters [24]. Five-, six-, seven-, and nine-step mechanisms were developed by Mallampalli et al. [25] Several other reduced mechanisms have been developed for methane [26,27] as summarized by Smooke [28]. The accuracy of these mechanisms has been investigated by Cao and Pope [29] and Volchkov et al. [30] In general, the fewer-step mechanisms have been used more extensively in combustion modeling due to their simplicity. For instance, one-step methane combustion has been modeled with good results [31-32]. Although these mechanisms, like Westbrook and Dryer's [33] provide good agreement with experimental data for flame speed results, they fail to reproduce some of the important aspects of combustion phenomena over the range of operating conditions for gas turbines. This lack of accuracy is primarily due to the development of reduced mechanisms from experimental results and the many unrealistic assumptions made to fit data. In cases where the reduced mechanisms are accurate, they either have too many species leading to an increased computational time, or fail to predict results for a wider range of gas turbine operating conditions.

One could even argue that the only way to accurately model the combustion phenomena is through using a detailed reaction mechanism which means requiring more computational time, and therefore research should be concentrated on developing computer models with greater computational capabilities rather than coming up with chemistry models with fewer species. The purpose of this study was to derive a chemistry model that is computationally efficient when used in CFD codes, yet is able to predict the combustor flow fields with high accuracy. One way to achieve this is to develop a model that is derived from the full mechanism but is based on chemical time scales rather than solving multiple simultaneous reactions. The model developed in this paper was derived from the detailed reaction mechanism GRI 3.0 [34] modified by Petersen et al. [35] to agree with high-pressure ignition data. First, background information on the different processes of mechanism reduction and combustion modeling are provided. Details and predictive capabilities of the new CH_4/O_2 chemistry model are presented and compared with the full mechanism and the results of experiments.

MECHANISM REDUCTION PROCEDURE

There are three different types of reduction techniques of a large chemical kinetics mechanism as summarized by Tomlin et al. [36]: 1) mechanism reduction without time scale analysis, 2) reduction based on the investigation of time-scales, and 3) fitted kinetics models. Each is summarized briefly as follows.

Mechanism reduction without time scale analysis. This technique is based on the identification of redundant species by analyzing the sensitivity of the reaction to its production rate or by inspecting sensitivities of temperature rates. The unimportant species and reaction rates are then eliminated, resulting in what is referred to as a skeletal mechanism or quasi-global model. This technique can be found in the works of Warnatz [37], Turanyi [38], Wang and Frenklach [39], and Yungster and Rabinowitz [40].

Reduction based on the investigation of time-scales. This technique includes the quasi steady state approximation [22,41,42] (QSSA), the computational singular perturbation method [43] (CSP), and the intrinsic low-dimension manifold method [44,45] (ILDM). The skeletal mechanism can be reduced further based on the quasi steady state approximation through what is called the systematical reduction of the detailed mechanism to few global steps. This method was initiated by Peters [41] and Peters and Williams [42]. The computational singular perturbation method [40] (CSP) through which the selection of QSSA species can be automated, and the intrinsic low-dimensional manifold approach, as the ILDM technique proposed by Maas and Pope [44,45], result in look-up tables with coordinates associated with the mixture fraction and the reaction progress variables. The *in situ* Adaptive Tabulation method (ISAT) [46] is another technique for the purpose of reducing mechanisms.

Fitted kinetic models. The fitted kinetic models technique is also referred to as empirical kinetic models where parameters of one-, two-, or multiple-step reactions are fitted to experimental data or to detailed kinetics simulations. The mathematical models in most of the times are given in Arrhenius-type expressions. The technique of fitting reactions to experimental data with the assumptions of quasi-global approximation and steady state is referred to as the global modeling technique. Examples of this technique can be found in Westbrook and Dryer [22], Hautman et al. [47] and the compilation edited by Peters and Rogg [26]. Examples of fitting algebraic expressions to detailed kinetic simulations can be found in the works of Oran et al. [48], Clifford et al. [49], and Molnar and Marek [50,51]. They developed a global parameterized model of the induction time as a function of pressure, species concentration, and temperature. This technique is also referred to as IPM, or induction parameter modeling, and the response modeling technique. This reduction method proved to be very effective in terms of its accuracy in predicting the induction times and heat release and also its simulation speed; when compared to a reduced model with elementary reactions, it was 20 times faster [49].

Combustion simulation would be much easier using such models knowing that more effort could be spent on simulating the complex behavior of flow fields rather than on the chemical kinetics calculations (but without losing the accuracy of a detailed mechanism). The response modeling technique has been validated in a study done by Clifford et al. [49], where the model was used in a 2-D simulation of complex behavior of a shock passing over a rectangular obstacle in a reacting mixture. The model reproduced all the main features of the experiments using less than

5% of the computational time of the full chemical kinetics model. Moreover, the model has proven that it can be used with confidence in reactive flow models. Brankovic et al. [52] used a time-dependent CFD code and combustion modeling to predict burning velocity of fuel-air mixtures in a closed vessel and swirl-stabilized reacting flow in a representative turbine engine fuel nozzle. They used a combustion chemistry approach developed at NASA Glenn Research Center by Molnar and Marek [51]. The chemistry model is based on the response modeling approach. The time accuracy of the model has been confirmed through accurate prediction of flame speed for a methane-air reactant mixture.

In the present study, a fitted kinetic/response modeling technique was adopted. Ignition delay times were utilized as the selection criteria for a wide range of input parameters: temperatures between 1000 and 2500 K, pressures between 0.1 and 50 atm, and equivalence ratios (ϕ) between 0.1 and 2. Although reduced mechanisms through traditional reduction techniques, such as the ones listed above for hydrocarbons (specifically methane) widely exist, the response modeling technique to the authors' knowledge has only been developed for Hydrogen based on shock-tube studies with high argon dilutions [48] and for ethylene oxidation [49] with the exception of a recent study done by Molnar and Marek [50,51] for methane and Jet-A fuels.

REACTING FLOW MODELING

When a chemistry model is coupled with the governing equations for viscous flows, a reacting flow model results. The means of modeling the combustion process are chosen based on the combustion conditions. When infinitely fast chemistry and a premixed homogeneous mixture are assumed, the Bray-Moss-Libby, turbulent flame speed, or Eddy Break-up models are used. The Eddy Break-up model is the typical example of a "mixed is burnt" combustion model and is popular for its simplicity, steady convergence, and implementation. The first attempt to develop the model is due to Spalding [53], whose idea was to replace the chemical time scale of a one-step reaction by the turbulent time scale, eliminating the influence of chemical kinetics. The model was then improved by Magnussen and Hjertager [54], who called it the eddy-dissipation model. It simply relates the rate of combustion to the rate of dissipation of eddies and expresses the rate of reaction by the mean concentration of a reacting species, the turbulent kinetic energy, and the rate of dissipation of this energy. Combustion could then be described by a single-step global reaction:

$$F + \nu O \rightarrow (1+\nu)P \tag{1}$$

In which F stands for fuel, O for oxidizer, P for products of the reaction, and ν is the stoichiometric oxygen-to-fuel mass ratio. Alternatively, a multi-step scheme can be used, where each reaction has it own mean reaction rate. The mean reaction rate is given by:

$$\omega_F = A_{EB}\frac{\varepsilon}{\kappa}\min\left[C_F, \frac{Co}{\nu}, B_{EB}\cdot\frac{C_P}{(1+\nu)}\right] \tag{2}$$

Where C_F, C_O, and C_P are the mean concentration of fuel, oxidizer, and products, respectively. A and B are model constants, k is the kinetic energy, ε is the dissipation of the kinetic energy, and EB stands for Eddy Breakup. Examples of simulations that employed the eddy break

up/dissipation model in conjunction with one-, two-, or multiple- step reactions can be found in the works of Brankovic et al. [52,55] and Lee and Yeh [56].

For the case of infinitely fast chemistry with a heterogeneous mixture, the conserved scalar equilibrium approach is considered. When finite-rate chemistry is assumed, the flamelet based on G-equation [55], the coherent flame, or the flame surface density model is used for homogeneous mixtures. In the case of heterogeneous mixtures, the flamelet based on conserved scalar [57] or the conditional moment closure (CMC) model is considered [58].

CHEMISTRY MODEL

The combustion model used to model the chemical kinetics herein is the Eddy Dissipation (ED) Model. When infinitely fast chemistry is assumed, the Eddy Dissipation Model of Magnussen and Hjertager [54] is used as shown in Eq. (2). The model takes the minimum of three rates: the mean fuel mass fraction, the mean oxidizer mass fraction, and the product mass fraction, in order to calculate the chemical source term. And combustion would be described by a single step global reaction:

$$CH_4 + \frac{2}{21} Air \xrightarrow{\tau_c} CO_2 + 2H_2O + 7.52N_2 \tag{3}$$

The eddy dissipation model assumes that the reaction is limited by micro-mixing, meaning that the chemical kinetic times are fast compared to the mixing times. However, when the chemical time τ_c becomes greater than the mixing time τ_{mix}, then the reaction is limited by chemical kinetics. In this case, chemical kinetics become more important, and finite-rate chemistry should be assumed.

Several attempts have been made for finite-rate chemistry correction of the ED combustion model [59,60], and now, the eddy dissipation model is used in a form that allows for finite-rate chemistry. This new form of the ED model has been used in combustion simulations with encouraging results [51,60,61,62]. The chemical source term is given by:

$$\dot{\omega}_i = \min\left(\frac{A\varepsilon}{k} y_{fuel}, \frac{A\varepsilon}{k} \frac{y_{oxygen}}{r_i}, \dot{\omega}_{kinetic,i} \right) \tag{4}$$

where y is the mass fraction and r is the overall reaction stoichiometric coefficient on a mass basis. The subscript i indicates the number of the reaction considered. In this form, it is possible to take multi-step reaction kinetics into account. At equilibrium conditions, the model automatically reduces to the Magnussen –Hjertager [54] model. The rate expression in Eq. (4) can be rewritten in terms of the times, such that,

$$\frac{k}{A\varepsilon} = \tau_{mix} \text{ and } \frac{y_{fuel}}{\dot{\omega}_{kinetic}} = \tau_c \tag{5}$$

Equation (4) then becomes:

$$\dot{\omega} = \min\left(\frac{y_{fuel}}{\tau_{mix}}, \frac{1}{r}\frac{y_{oxygen}}{\tau_{mix}}, \frac{y_{fuel}}{\tau_c}\right) \tag{6}$$

where $\frac{y_{fuel}}{\tau_{mix}}$ is the mixing rate and $\frac{y_{fuel}}{\tau_c}$ is the chemical rate.

The chemical source term $\dot{\omega}$ is then determined by taking the minimum of the chemical kinetic rate and the mixing as shown in Eq. (7) .

$$\dot{\omega} = \min\left(\frac{1}{\tau_{mix}}, \frac{y_{oxygen}}{r y_{fuel}}\frac{1}{\tau_{mix}}, \frac{1}{\tau_c}\right) \tag{7}$$

Based on this approach, chemical kinetic time models are generated for incorporation into Eq. (7).

It is now crucial to come up with a definition of the kinetic times. First, it is important to understand how the ED model works in terms of the limiting times. Let us assume a linear approximation of the Arrhenius reaction with three time regions; non-mixed, mixed, and reactive/mixed. Figure 2 illustrates the process. This approach is similar to the PASR model (Partially Stirred Reactor) [59]. The rate of fuel consumption is then determined from Fig. 2.

$$\frac{d[CH_4]}{dt} = -\frac{C}{\tau_3}, \frac{C - C_1}{\tau_2}, \frac{C_1 - C_0}{\tau_1} \tag{8}$$

If τ_3 is the chemical time and τ_2 is the mixing time, then the reaction is mixing-controlled and the chemical source term is determined from the mixing rate. However, when finite chemistry is more important, the kinetic time becomes the limiting time, and the reaction is chemically controlled. In this case, $\tau_c > \tau_{mix}$ where $\tau_{mix} = \tau_1 + \tau_2$ and $\tau_c = \tau_1 + \tau_2 + \tau_3$. The rate of fuel consumption becomes,

$$\frac{d[CH_4]}{dt} = -\frac{[CH_4]}{\tau_c} \tag{9}$$

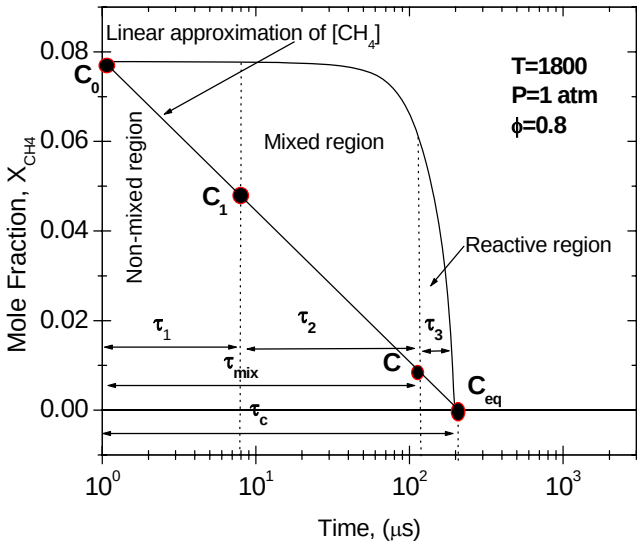

Figure 2. CH_4 mole fraction change over time.

The reaction zone (Fig. 3) is where the reaction takes place and the products form. The chemical time is defined by the time it takes for the fuel to react or ignite, so therefore the kinetic time could be modeled as the ignition delay time such that $\tau_c = \tau_{ign}$.

Three additional kinetic times for CO, NO, and H_2O can be defined and determined from plots as in Fig. 3.

$$\tau_c = \left\{\tau_{ign}, \tau_{CO}, \tau_{NO}, \tau_{H_2O}\right\} \tag{10}$$

Another method to determine the kinetic time is based on the assumption of an exponential decay in $[CH_4]$, from first-order response theory, which turns out to be a good approximation for ignition delay time determination for methane-air mixtures as is shown in Fig. 4. The chemical time from first-order theory is therefore given by: τ_c = time @0.37 $[CH_4]$, where $[CH_4]_0$ is the initial methane concentration. To elaborate, this expression is achieved from the well-known solution of the first-order equation, such that:

$$\frac{d[CH_4]}{dt} = -\frac{[CH_4]}{\tau_c} \tag{11}$$

$$[CH_4] = [CH_4]_0 \exp\left(\frac{-t}{\tau_c}\right) \tag{12}$$

$t = \tau_c = \tau_{ign}$ when:

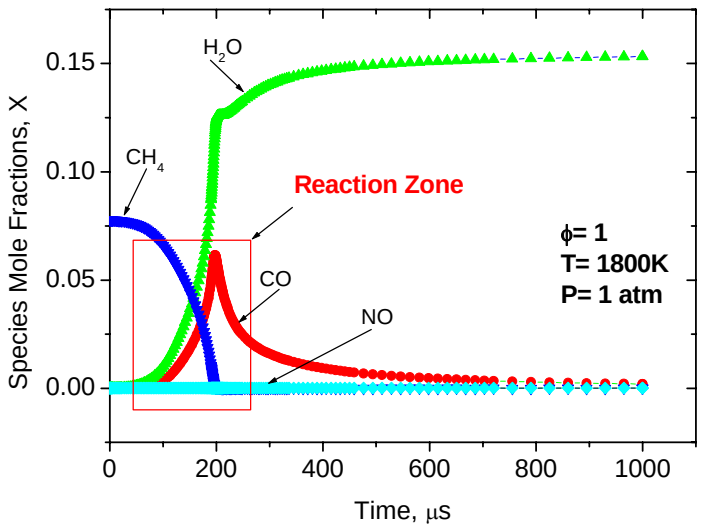

Figure 3. CH_4, CO, NO, and H_2O concentration change over time

$$\frac{[CH_4]-[CH_4]_\infty}{[CH_4]_o-[CH_4]_\infty}=63\% \tag{13}$$

Figure 4 shows the methane fuel concentration (mole fraction) as a function of time for a methane/air mixture with ϕ = 0.8 at 1800 K and 1 atm as calculated by the detailed kinetics model described in more detail below. The ignition delay time is 189 μs for this result. Also shown in Fig. 4 is the result of Eqn. (12) (plotted in terms of mole fraction rather than $[CH_4]$) assuming the 63% time constant, τ_c, is equal to the ignition delay time of 189 μs. The general shape of the CH_4 mole fraction time history agrees qualitatively with the assumption of a first-order fuel depletion.

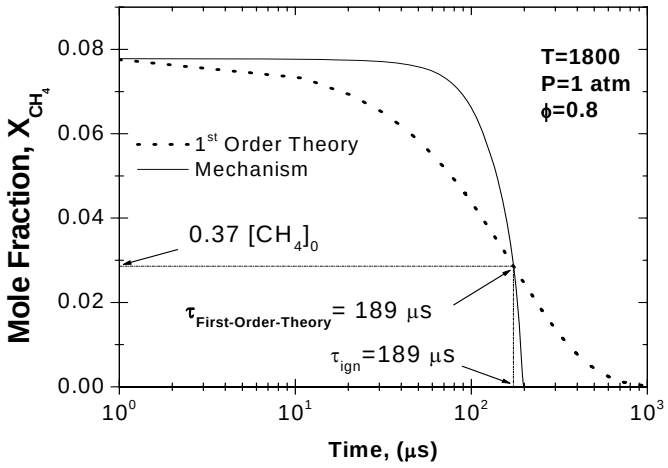

Figure 4. The kinetic time could be determined from the well-known first order theory.

KINETIC TIME DEFINITIONS

The Petersen et al. [35] chemical kinetics mechanism was employed for the kinetic time computations. It is based on GRI-Mech 3.0 [34] and is intended for ignition times only, taking into account lower temperatures and higher pressures from ignition experiments, making the mechanism a good candidate for this study. Further details behind the development of the chemical kinetics mechanism can be found in Petersen et al. [35], and a thorough description of the shock-tube facility used to acquire the data for the Petersen et al. [35] mechanism validation can be seen in Petersen et al. [63] Numerical simulations were conducted using the CHEMKIN SHOCK application found in the Chemkin collection software package [64] that predicts the chemical changes occurring after reactive gas mixture shock heating. For the calculations herein, constant pressures and enthalpies were assumed as this is the case most representative of gas turbine combustion. For modeling a premixed fuel and oxidizer at constant h, P conditions, the solution from the SHOCK module for an initial temperature corresponding to the post-shock conditions is the same as treating the mixture as if it were in a well-stirred reactor at the same initial temperature.

It can be shown that modeling the kinetic times based on an isothermal process (as in Molnar and Marek [50,51]) does not affect the results appreciably. An example is provided in Fig. 5, where CO and NO concentrations are plotted against time for the two processes, the first process being that of constant enthalpy and pressure, and the second process being that of constant temperature. The latter calculation was achieved through simulation with the CHEMKIN SENKIN application that can also be found in the Chemkin software package [64]. It can be shown from Fig. 5 that by assuming either one of the processes, the times corresponding to the maximum concentration levels are nearly the same in both cases. A similar conclusion can be drawn by comparing

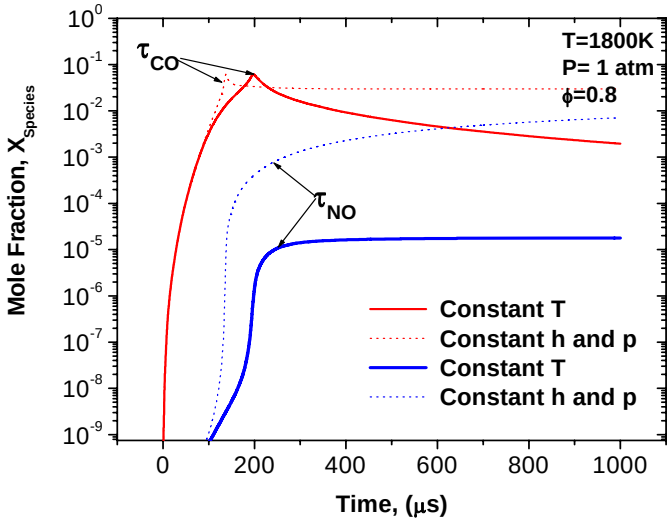

Figure 5. Modeling the reaction as an isothermal process does not have a big influence on the kinetic times.

ignition times between the two process assumptions.

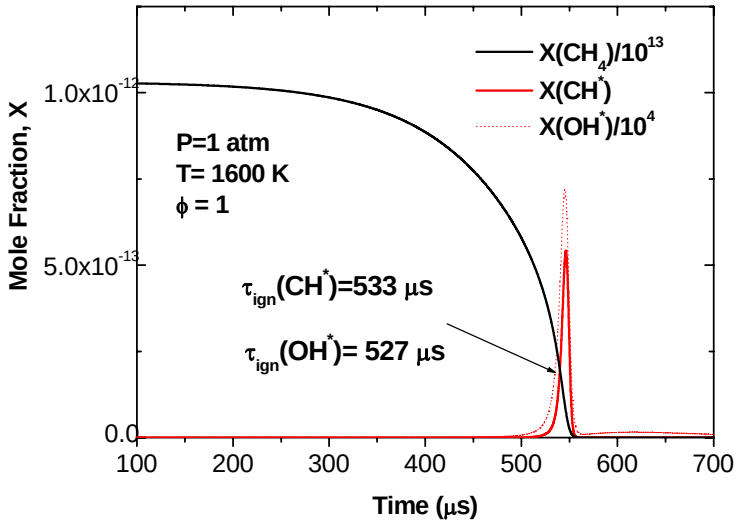

Figure 6. The ignition delay time (τ_{ign}) is defined as the sudden rise in CH* or OH^* concentrations.

For the calculations herein, the ignition delay time is defined as the sudden increase in CH* (Fig. 6) since CH* chemiluminescence has been shown to be a good representation of hydrocarbon ignition in shock-tube experiments [65]. Ignition times can also be determined from OH^* concentration rise as is shown in Fig. 6. Both species yield similar ignition times. In fact, for the real fuel-air mixtures of interest herein (i.e., undiluted), there is little difference between ignition delay times defined using OH, CH, or even the abrupt change in temperature or other key species.

Similarly, CO, NO, and H_2O kinetic times are determined from the concentration time histories and can be defined as the times corresponding to the maximum concentration when the reaction starts reaching equilibrium (Fig. 7).

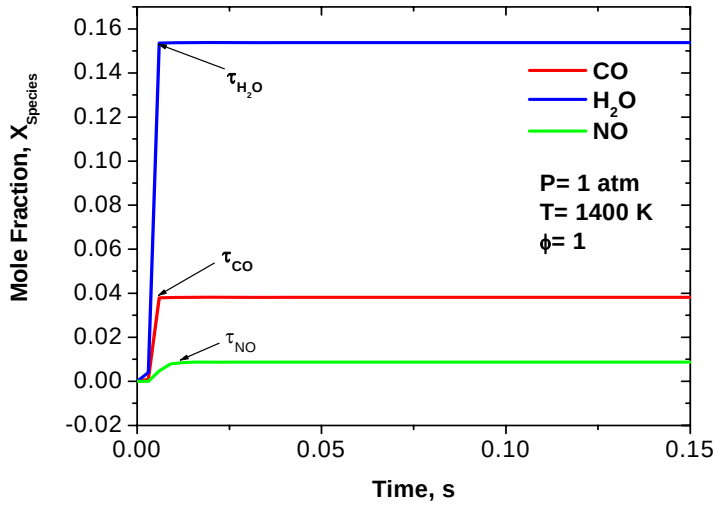

Figure 7. CO, NO, and H_2O kinetic time determinations

METHODOLOGY

Since the goal of the present effort was to develop chemical time expressions at temperatures and pressures of interest to gas turbines, a matrix of conditions was formulated. Table 2 shows the different CH_4/Air mixtures used in this experiment and their corresponding mole fractions and equivalence ratios, which ranged from 0.1 to 2.0. Table 3 shows the range of conditions over which the kinetic times were computed with Chemkin using the Petersen et al. [35] mechanism. These included temperatures from 1000 to 2500 K and pressures from 0.1 to 50 atm. Over 900 computer runs were performed, and the ignition delay time and times for NO, CO, and H_2O were recorded for each.

Table 2. Experimental mixtures and mole fractions (%).

Mix No.	$\%CH_4$	$\%O_2$	$\%N_2$	Φ
1	1.04	20.80	78.20	0.1
2	2.06	20.60	77.40	0.2
3	4.04	20.20	75.80	0.4
4	5.90	19.80	74.30	0.6
5	7.70	19.30	72.80	0.8
6	9.50	19.01	71.50	1.0
7	11.20	18.70	70.20	1.2
8	12.80	18.30	68.90	1.4
9	14.40	18.00	67.60	1.6
10	15.90	17.70	66.40	1.8
11	17.40	17.40	65.30	2.0

Table 3. Input conditions

Input Parameters	Range	Increment
Temperature, K	1000-2500	100
Pressure, Atm	0.1-50	≈10
Equivalence Ratio Φ	0.1-2	0.2

KINETIC TIME MODEL

Once the kinetic times were generated for the conditions given in Tables 2 and 3, analytical fits were performed for the behavior of the ignition time as a function of the pressure, temperature, and equivalence ratio. The generated kinetic times were plotted on Arrhenius-type plots, and their behavior was monitored as the different parameters changed. The results are shown in Fig.

8 for pressures of 0.1, 1, 5, 20, and 50 atm. It can be observed that at about a temperature below 1400 K, the model starts showing non-linearity on a logτ versus 1/T plot, and the slope of the ignition delay curve starts decreasing. In addition to the effect temperature has on the shape of the curve, the mixture concentration contributes to the shift of the data vertically. Mixtures with the highest equivalence ratios resulted in the shortest ignition delay times.

Furthermore, Fig. 9 shows the significant effect pressure has on the ignition delay time. The highest ignition delay time corresponds to the lowest pressure, and vice versa. Once the dependence on temperature, pressure and equivalence ratio was determined, the kinetic times were fitted to equations of the form:

$$\tau_{ign} = \tau_c = A X^{x}_{CH_4} X^{y}_{O_2} P^{z} \exp\left[\frac{E}{RT}\right] \tag{14}$$

and,

$$\tau_{ign} = \tau_c = A\left(\frac{f}{a}\right)^{x} P^{z} \exp\left[\frac{E}{RT}\right] \tag{15}$$

where τ_{ign} is the ignition delay time or general chemical (or kinetic) time; X_{CH4}, X_{O2}, are the element mole fractions; P is the system pressure; (f/a) is the fuel-to-air ratio by mass, and, E, A, x, y, and z are constants. The Linest function on Microsoft Excel was employed for this operation. The function uses the multiple linear regression analysis to estimate the value of some function Y based on some independent variables x_1, x_2, etc. Taking the natural log of Eq. (14) yields Eq. (16).

$$\ln(\tau_c) = \ln(A) + x\ln(X_{CH_4}) + y\ln(X_{O_2}) + z\ln(P) + \left[\frac{E}{RT}\right] \tag{16}$$

which is a multi-parameter linear equation suitable for use with the Linest function in Excel.

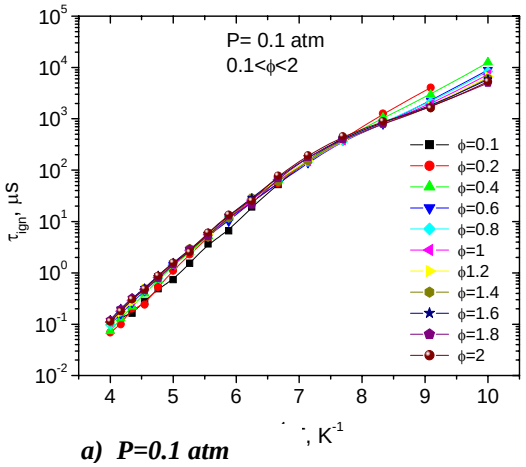

a) P=0.1 atm

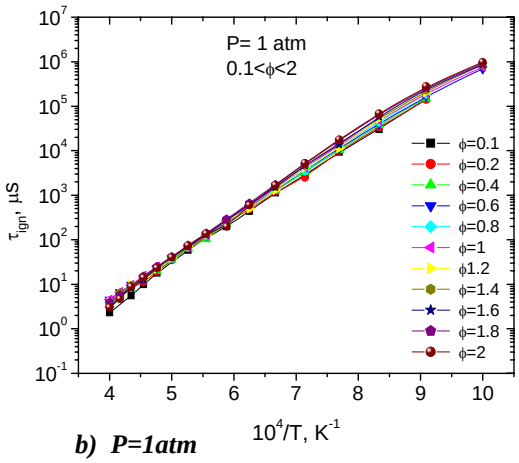

b) P=1atm

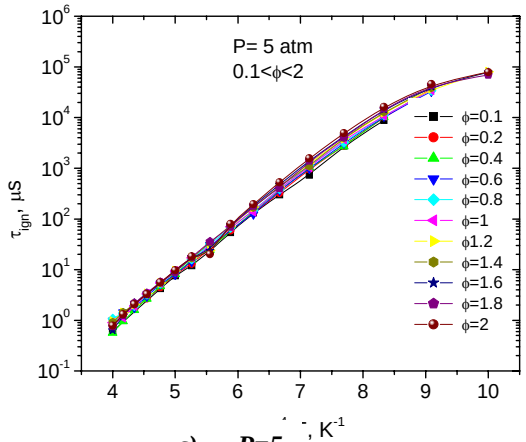

c) P=5

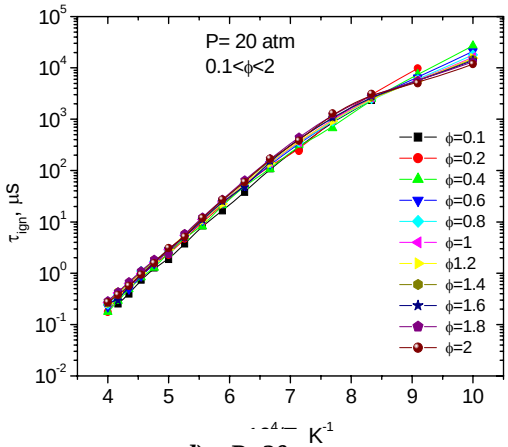

d) P=20

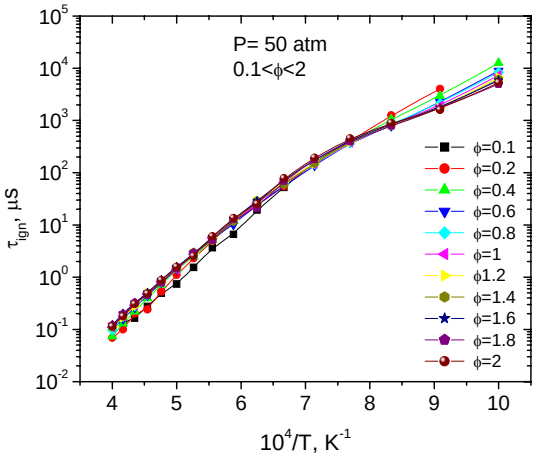

e) P=50

Figure 8. Results for CH_4/Air mixture ignition delay times as a function of temperature and equivalence ratios.

Fitting Kinetic Time Data to Equations using Mole Fractions. Figure 10 shows ignition delay time (i.e., chemical time) correlations for three temperature regions: 1000<T<2500 K (a,b), 1400<T<2500 K (c,d), and 1000<T<1400 K (e,f). It is seen from Fig. 10a that the correlation does not fit the data as well for temperatures less than 1400 K as it does for higher temperatures. On the other hand, Fig. 10b shows a minimal amount of scatter for ignition times less than 10^2 μs. The amount of scatter starts increasing for ignition delay times greater than about 10^2 μs, indicating the need for a separate correlation in the low-temperature region. To this end, a correlation for the high-temperature region was performed. This does not by any means mitigate the validity of the first correlation, as its r^2 value is 0.96. It is to the user's discretion to decide on which correlation to use. The high-temperature correlation is represented in Figs. 10c and 10d. As expected, the amount of scatter has greatly lessened when the data are correlated for high temperatures only. As previously stated, the r-squared value for the overall correlation is very high and can still be used for temperatures below 1400 K, but a separate correlation for T<1400 K was developed for even greater accuracy.

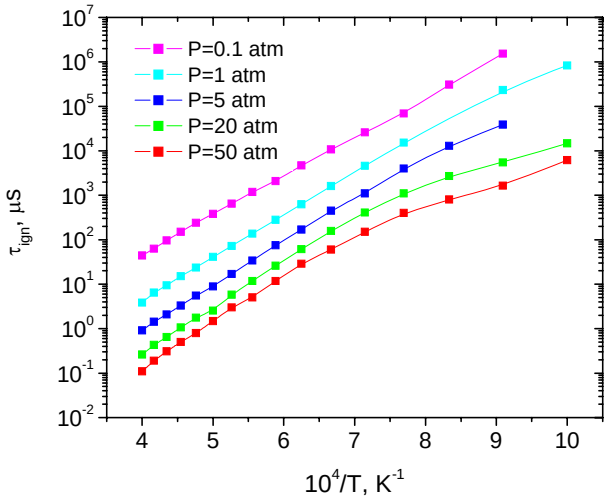

Figure 9. Results for CH_4/Air mixture ignition delay times as a function of temperature and pressure for a mixture with $\phi = 1$.

Table 4. Summary of CH_4/Air mixture ignition delay time correlations with respect to temperature. τ is in seconds, P in atm, and T and (E/R) in K.

	$\tau_{ign} = A \times X^x_{CH4} \times X^y_{O2} \times P^z \times \exp[E/RT]$					
Temperature(K)	A	x	y	z	E/R (K)	r^2
1000<T<1400	2.90×10^{-7}	0.087	-0.004	-0.960	14472	0.965
1400<T<2500	1.94×10^{-9}	0.177	0.541	-0.894	22595	0.993
1000<T<1402	2.37×10^{-9}	0.104	0.030	-0.915	20264	0.987

Contrary to Fig. 7a, data for temperatures below about 1400 K are well aligned with the correlation line, and the scatter is greatly reduced (Fig. 10e) compared to Fig. 10b. To better demonstrate the non-linearity effect discussed above, it would be beneficial to show the last two correlations on one plot (Fig. 11). Plotting two different correlations on one plot would be impossible since constants and magnitudes are not the same, but after modifying the y-axis scale to account for both cases, the result is shown in Fig. 11. The ignition activation energy (E) for the low-T, high-T, and overall-T correlations are 28.7 kcal/mol, 44.9 kcal/mol, and 40.2 kcal/mol, respectively. The correlation results for methane oxidation ignition delay times are presented in Table 4.

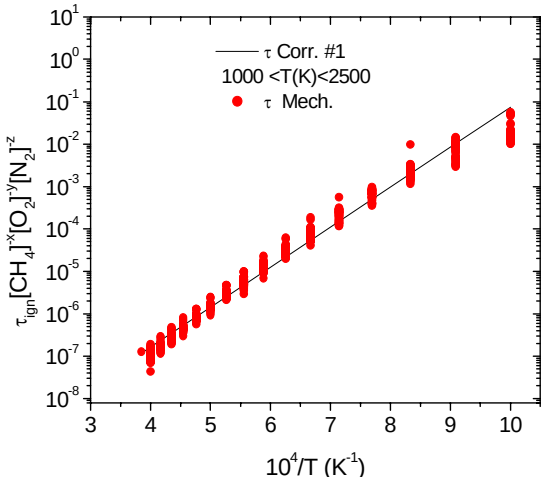

a) *Methane/Air ignition delay times. Comparison is with overall correlation of current data.*

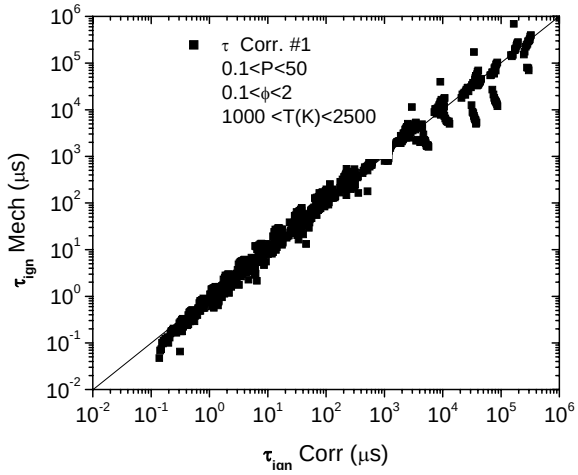

b) *Ignition data from mechanism. Comparison is with data from overall-T region correlation.*

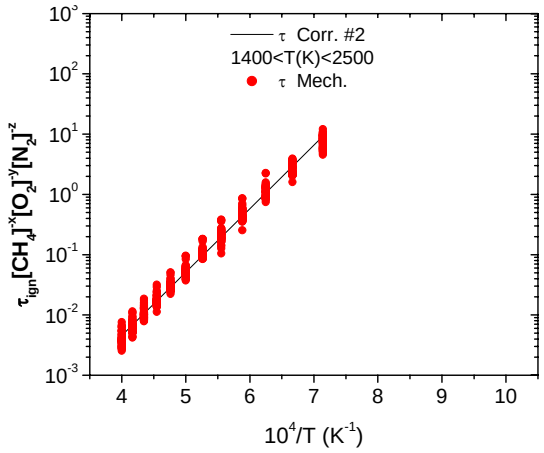

c) *Ignition delay time data at high T. Comparison is with high-T correlation of current data*

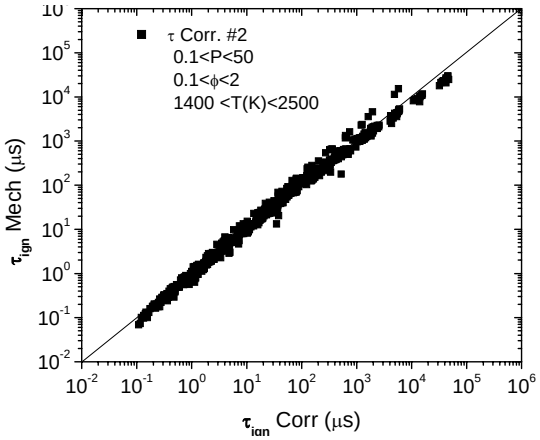

d) *Ignition data from mechanism and comparison with data from high-T region correlation*

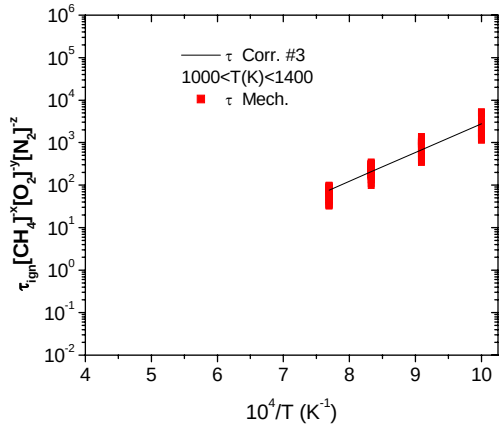

e) *Methane/Air ignition delay times at low T Comparison is with low- T correlation of current data*

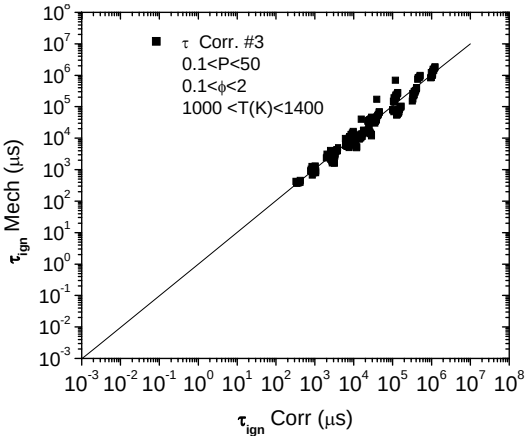

f) *Ignition data from mechanism and comparison with data from low-T region correlation.*

Figure 10. Methane/Air mixture ignition delay times at low and high temperatures. Comparison is with high- and low –T correlations of ignition data.

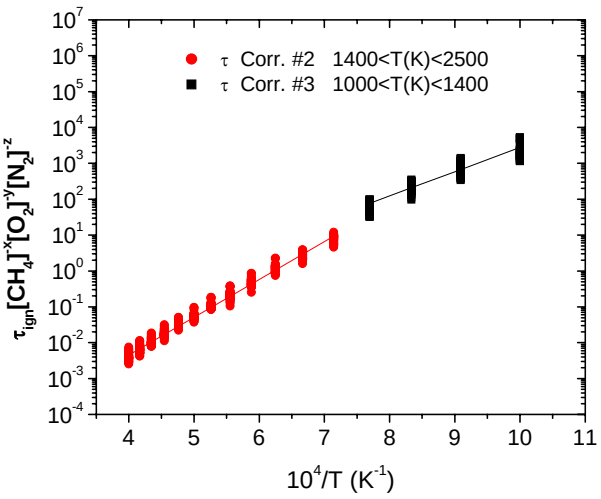

Figure 11. Methane/Air ignition delay times. Comparison is with high-T and low-T correlations.

Fitting Kinetic Time Data to Equations using f/a. Due to the influence of fuel-lean and-rich mixtures on the reaction rates, the ignition delay times are also expressed as a function of fuel-to-air ratio, pressure and temperature. Comparison of the fitted data to the full mechanism data shows a strong agreement as seen in Fig. 12. Some scatter is noticeable at lower temperatures but that does not lessen the correlation's validity, as the r^2 value is high (0.99). The correlation results expressed in the fuel-to-air ratio form are summarized in Table 5.

Table 5. CH_4/Air mixture ignition delay time correlations expressed in the fuel-to-air ratio form. τ is in seconds, P in atm, T and (E/R) in K.

	$\tau_{ign} = A \times (f/a)^x \times P^z \times \exp[E/RT]$				
	A	x	z	E/R (K)	r^2
Lean	1.90×10^{-9}	0.093	-0.900	20535	0.990
Rich	4.19×10^{-9}	0.238	-0.931	19899	0.984
Overall	2.30×10^{-9}	0.096	-0.915	20264	0.987

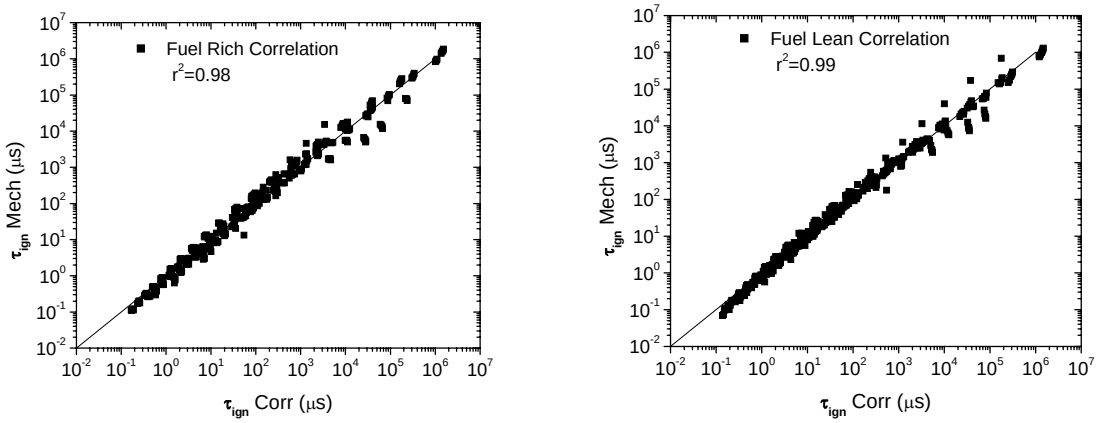

Figure 12. Fuel rich and fuel lean methane ignition delay time correlations.

Table 6. CH_4/Air mixture ignition delay time correlations expressed as functions of the fuel-lean and rich cases in the mole fraction form. τ is in seconds, P in atm, T and (E/R) in K.

$\tau_{ign} = A \times X^{x}_{CH4} \times X^{y}_{O2} \times P^{z} \times \exp[E/RT]$						
	A	x	y	z	E/R (K)	r^2
Lean	2.27×10^{-8}	0.155	1.434	-0.901	20536	0.990
Rich	4.13×10^{-11}	-0.187	-2.099	-0.931	20006	0.985
Overall	2.37×10^{-9}	0.104	0.030	-0.915	20264	0.987

Additional correlations for methane ignition delay times are given in Table 6 as a function of mole fraction, temperature, and pressure for fuel-lean and rich cases as in Molnar and Marek [50,51]. When this correlation is applied, the results achieved are similar to the results obtained from the correlations in Table 4. It is for the user to decide which of the two forms to use based on the conditions given. Note that the results of the correlations expressed in fuel-to-air ratio form and in the mole fraction form for fuel lean and rich cases are the same. The correlations expressed in the mole fraction form for fuel-lean and -rich cases are summarized in Table 6.

CO, NO, and H_2O Kinetic Time Modeling. CO and NO kinetic times were determined from CHEMKIN for the conditions specified in Tables 2 and 3. Kinetic times were defined as the time the species first reaches equilibrium, as in Fig. 5. Figure 13 shows the kinetic times for CO and NO species as a function of temperature. For a pressure of 1 atm and equivalence ratio of 0.2, kinetic times range between 5μs and 10^4μs. The kinetics follow a linear trend when plotted on an Arrhenius plot, as shown in Fig. 13.

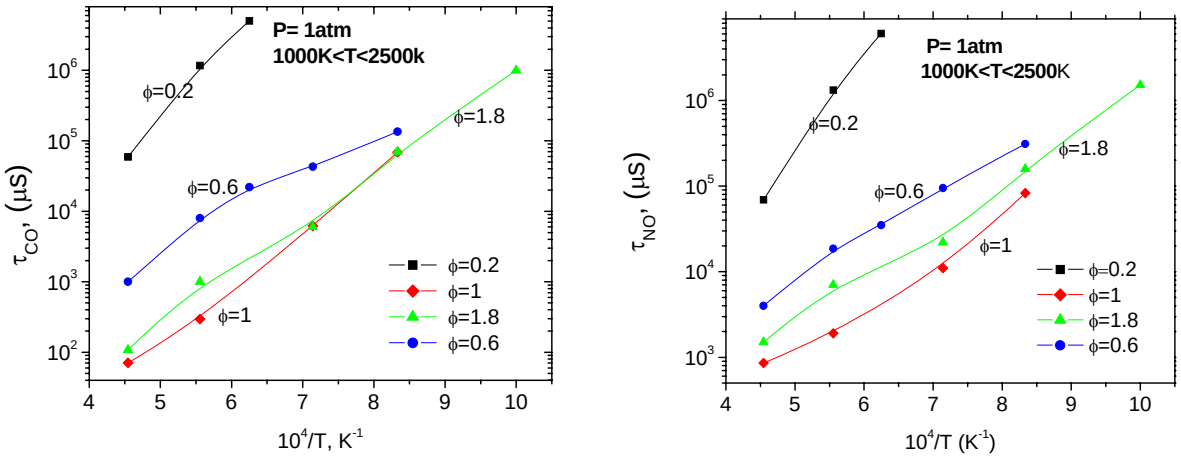

a) *CO kinetic times as a function of temperature and equivalence ratio*

b) *NO kinetic times as a function of temperature and equivalence ratio*

Figure 13. CO and NO kinetic times as a function of temperature and equivalence ratio. Kinetic times decrease with increasing ϕ for ϕ's up to 1 and decrease for ϕ's greater than 1.

From Fig. 13, the kinetic times decrease as the equivalence ratio increases until ϕ =1 is reached, then kinetic times do not show a big variation as the mixture becomes richer. In Fig. 13a, the CO kinetic time increases as the mixture content changes from an equivalence ratio of 1 to 1.8. Therefore, it cannot be concluded necessarily that CO and NO kinetic times decrease with increasing ϕ. This observation is true for ϕ's up to 1.

CO, NO, and H_2O kinetic times were fitted to equation (18) as functions of fuel-to-air ratio (f/a), pressure, and temperature. Figure 14 compares CO and NO kinetic times obtained from the detailed mechanism to those obtained from the model. Overall, the data sets exhibit good agreement with a minimum r^2 value of 0.94. It is observed that CO and NO data for fuel-rich conditions (Figs. 14 b and d) correlate better than those from fuel-lean data (Figs. 14a and c). This observation is mainly due to the NO and CO behavior at low ϕ's. Table 7 summarizes the CO, NO, and H_2O kinetic time models.

Table 7. CO, NO, and H_2O kinetic time correlations.

		$\tau_{kinetic} = A \times (f/a)^x \times P^z \times \exp[E/RT]$				
		A	x	z	E/R (K)	r^2
CO	Lean	2.80×10^{-14}	-4.710	-0.629	17894	0.943
	Rich	4.67×10^{-8}	-0.244	-0.763	15668	0.965
NO	Lean	5.24×10^{-12}	-4.100	-0.775	14179	0.974
	Rich	7.84×10^{-5}	1.241	-0.874	12351	0.987
H_2O	Lean	7.64×10^{-13}	-3.491	-0.830	17965	0.972
	Rich	5.18×10^{-7}	0.648	-0.987	15748	0.981

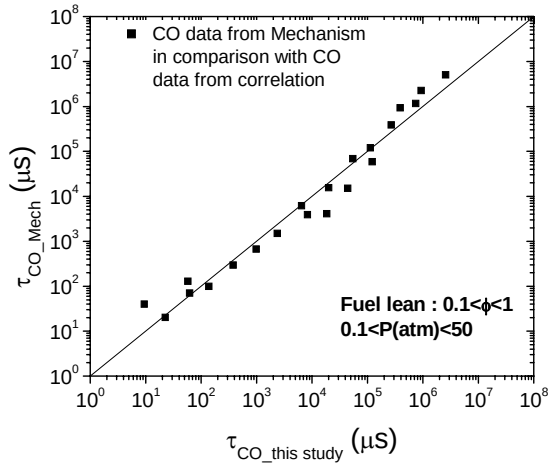

a) *CO kinetic times and comparison with fuel-lean correlation of current data*

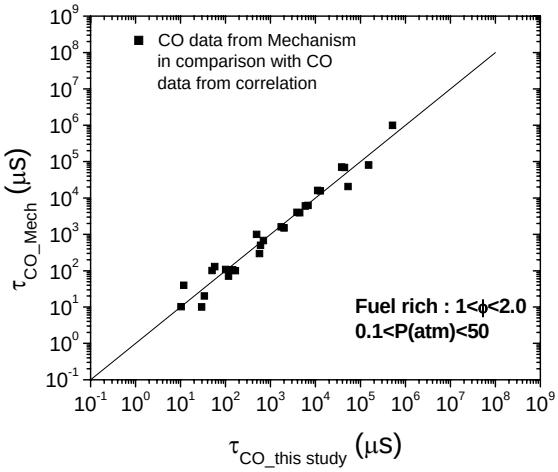

b) *CO kinetic times. Comparison is with fuel-rich correlations of current data.*

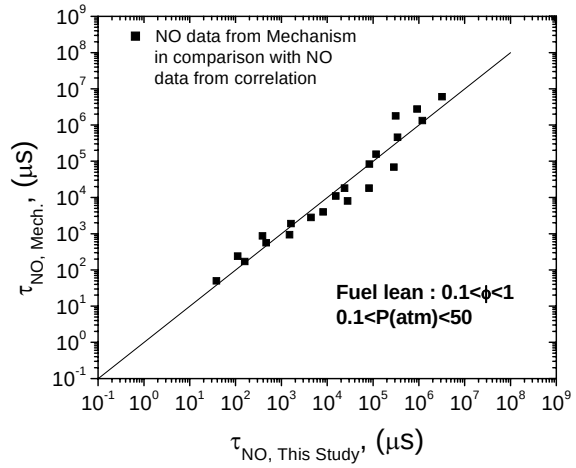

c) *NO kinetic times and comparison with fuel-lean correlation of current data*

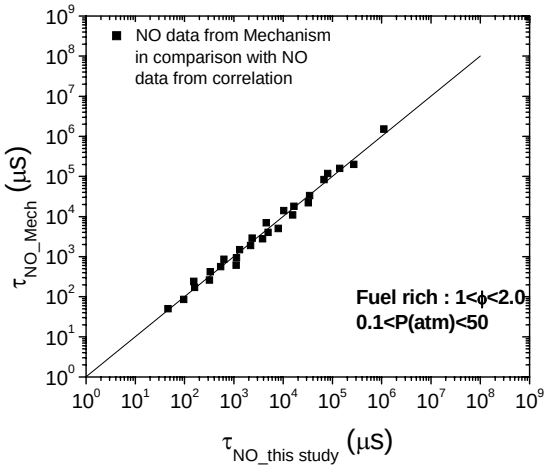

d) *NO kinetic times. Comparison is with fuel-rich correlation of current data.*

Figure 14. NO and CO kinetic times from mechanism. Comparison is with fuel lean and rich correlations of current data.

Validation of Results. To investigate the validity and accuracy of the models presented herein, comparison to previous efforts would be beneficial. Petersen et al. [66] presented a comprehensive correlation of ignition delay time data for similar conditions studied herein: temperatures (1400 to 2050 K), pressures (1 to 480 atm), ϕ (0.5 to 2.0), and concentrations up to $[CH_4] = 3.6\times10^{-5}$ mol/cm^3, $[O_2] = 3.6\times10^{-5}$ mol/cm^3, and $[M] = 3.6\times10^{-3}$ mol/cm^3. The correlation is given in the following expression:

$$\tau_{ign} = 4.05e^{-15}\,[CH_4]^{0.33}[O_2]^{-1.05}\exp[51.8/RT] \qquad (17)$$

where τ_{ign} is the ignition delay time in seconds, the activation energy is in kcal/mol, and R is the universal gas constant. The overall pressure dependence is $P^{-0.72}$. The Petersen et al. [66] correlation was based on shock-tube mixture ignition data. Figure 15 presents this study's overall correlation in comparison to the Petersen et al. [66] correlation (17). Note that the Petersen et al. correlation is only valid for temperatures between 1400 and 2050 K, so the comparison is performed over that range only. The agreement between the two correlations is quite good leading to the conclusion that the model developed herein is able to accurately predict real experimental data such as shock tube experiment data. This result is not unexpected since the detailed mechanism and its inherent kinetics rates were validated rather thoroughly over a similar range of temperature and stoichiometry.

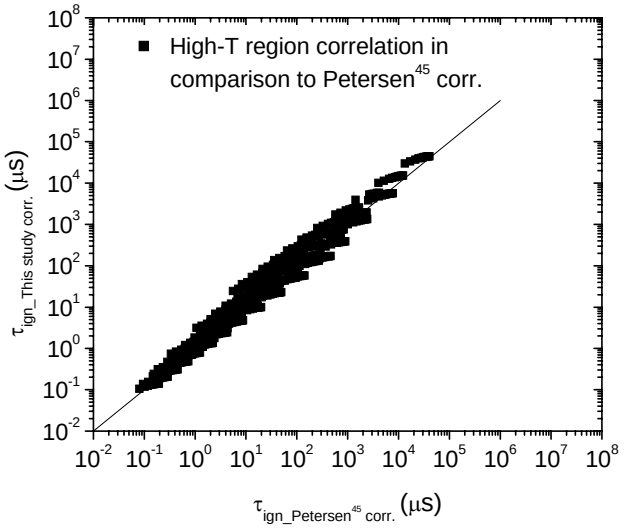

Figure 15. This study's high-T region correlation in comparison with Petersen et al. correlation [66].

COMPUTATIONAL FLUID DYNAMICS MODELING

The validation and accuracy investigations of the kinetic time models have led to improved correlations for ignition delay time that enable prediction of the combustion of fuel-air mixtures using computational fluid dynamics (CFD) design tools. These tools combine full three-dimensional, time-dependent Navier-Stokes representation of the flow aerodynamics and time-dependent chemical reaction models for the incoming reactants. In application to practical combustion systems, the simulations capture complete details of boundary layers, recirculation zones and turbulent mixing processes between fuel and air. The simulations are therefore especially capable of predicting non-uniformities in the fuel-air profile entering the combustor, which can lead to combustion instabilities and operational problems in practical systems. Careful application of the tool, together with accurate modeling of the ignition delay and heat release, can potentially enable the prediction of important design factors such as combustion instability, flashback, and flame holding, which can then be addressed by more detailed design application of the tool.

In this study, attention has been directed to the prediction of four separate flows to investigate the performance of the new kinetic time model for the case of methane-air combustion, at operating conditions representative of power generation gas turbine combustors. Incoming flow into power generation turbine combustors falls into a wide range of operating conditions, depending on the output power level and type of machine. Mass flow rates of air for the largest machines can range up to several hundred kg/sec at the fan inlet. Typical values for the air at the fan inlet are static pressure = 20 atm, and static temperature = 800 K, with various levels of turbulence and swirl imparted to the flow as it enters the combustor.

A representative cylindrical, annular dump combustor, with a long pre-mixer section is used here to investigate the different flame shapes and temperature contours determined using a combination of inlet mixing conditions and fuel/air temperatures. The computational domain used here is shown in Fig. 16. The length of the pre-mixer was selected to be 1.6 m, so that residence times using typical fuel and air gas velocities would be approximately 40 msec. Following the pre-mixer is a cylindrical dump combustor featuring a central, cylindrical bluff body. The dump combustor is 2.0 m long, and is configured with a small diameter, central exit port to eliminate or minimize combustion oscillations. The area ratio of the pre-mixer to dump

Figure 16. Schematic of premixer section of the computational domain used in CFD simulations for improved kinetic time model.

zone is 20:1. The (overall) ignition delay equation used in the flow simulation is that shown in

Table 6. The baseline chemistry model utilized is that developed by Molnar and Marek [50,51], and previously investigated by Brankovic et al. [52] for model problems featuring time-dependent flame phenomena.

Four test cases have been simulated using CFD, each at $\phi = 0.5$ which is representative of the overall combustor equivalence ratio for low-NOx power generation turbines. The specific test cases are listed as follows: **Case 1**: Co-annular, air swirled at 45º, fuel non-swirled at 300 K. **Case 2**: Co-annular shear-layer mixing with air (non-swirled), fuel non-swirled at 300 K. **Case 3**: Co-annular, non-swirling perfect pre-mix of fuel and air at 800 K. **Case 4**: Co-annular, non-swirling un-mixed of fuel and air at 800 K. In Cases 1 and 2, iterative studies of the cold flow mixing were performed to ensure that average (or fully mixed) temperature at the pre-mixer exit plane was 800 K. The four conditions investigated, therefore, cover a range of mixing and temperature effects common in gaseous fueled combustion systems.

Computational results, in the form of graphic contours of axial velocity and static temperature are shown in Figs. 17, 18 and 19. The pre-mixer and upstream component of the combustor is shown in Fig. 17, where axial velocity contours display little variation across the four types of inlet conditions. Early mixing of the two streams (i.e., before the dump plane of the combustor) leads to relatively similar velocity and temperature contours within the combustor. Closer inspection of the flows, as shown in Figs. 18 and 19, indicates that the new kinetic time ignition delay model results in only minor differences in the thermal field when temperature scales reflect the local values better. This is because the particular ignition time delay in this model, using typical input values for the inlet of the premixer, suggests ignition delay times of approximately 9.5 seconds. Based on the geometry and inlet velocities of the fuel-air stream, the 9.5 second residence time occurs well within the dump combustor, and therefore, peak burning temperatures

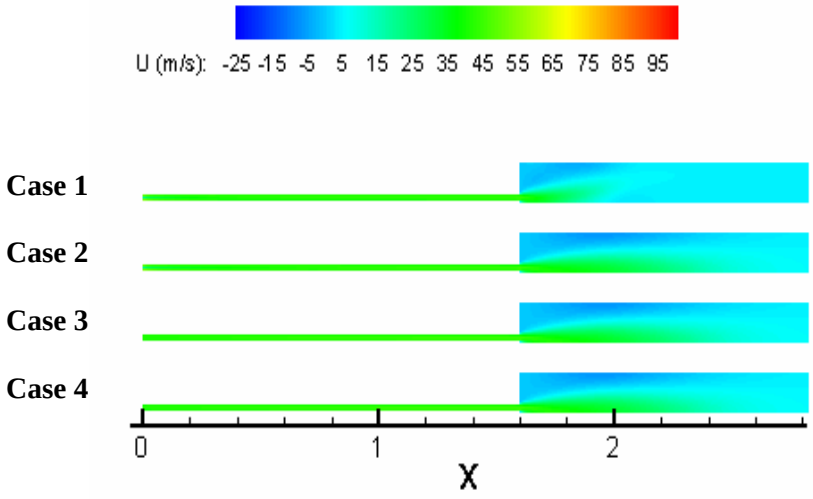

Figure 17. CFD simulation results for four test cases (see Section V for description of cases). Axial velocity contours, with emphasis on flow in the pre-mixer and near-field of the dump combustor.

occur only far downstream into the combustor. This indicates that the ignition time delay model

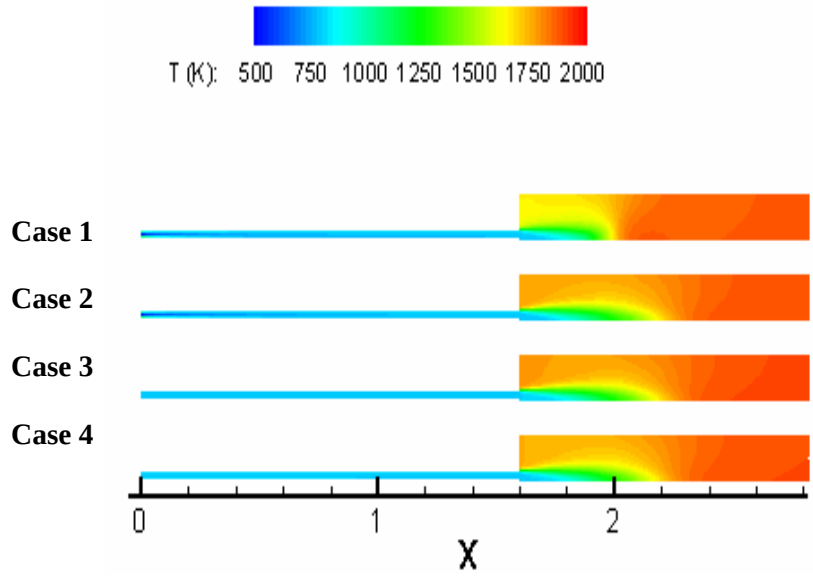

Figure 18. CFD simulation results for four test cases (see Section V for description of cases). Static temperature contours, with emphasis on flow in the pre-mixer and near-field of the dump combustor.

is producing expected results, but also that the model requires anchoring to flames that are characteristic of practical combustors.

CFD simulations based on combustion chemistry that do not include ignition delay models explicitly, e.g., those by Spalding [53], and Magnussen and Hjertager [54], typically produce results with little variation in these cases. Comparison of CFD results with experimental data for simple combustors is in progress, in an effort to validate the ignition delay models using performance data such as combustion flame shape, combustor exit temperature, and emissions values for NO and CO species.

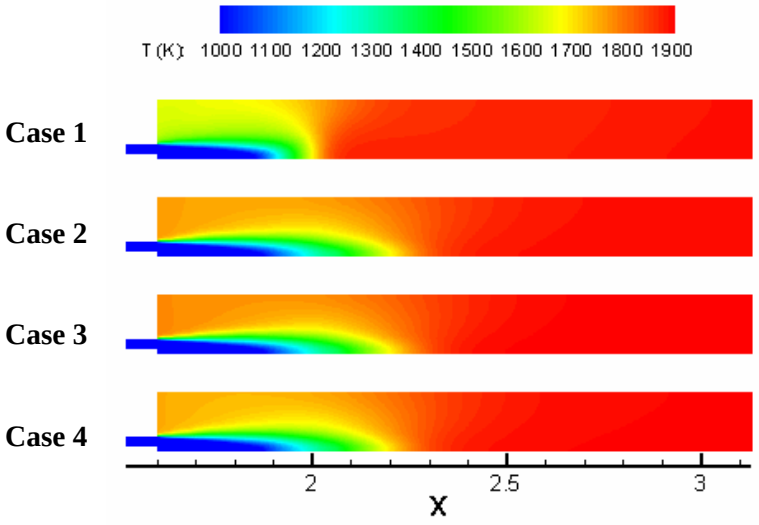

Figure 19. Temperature contours for the four test cases, at expanded temperature scale.

FLAME SPEED FACILITY DEMONSTRATION (Task 3)

It is evident that the increasing demand for fuel flexible gas turbine engines raises many questions about their ignition and flame characteristics [67-69]. Of particular concern are issues such as flashback, blow-off, autoignition, and stability. The two main, fundamental combustion properties studied are laminar flame speed and ignition delay time. Ignition delay time is an important parameter for premixed fuel/air mixtures and is usually studied using shock tubes [70] or rapid compression machines [71-73]. Laminar flame speed can be obtained using freely propagating spherical expanding flames (both constant volume and constant pressure), Bunsen flames, counterflow flames and stabilized flat flames [74,75]. Both experimentally obtained flame speed as well as ignition delay time can be used for validation of chemical kinetics mechanisms. Laminar flame speed data could be used for modeling turbulent combustion, pollutant formation and for general understanding of the flame physics relevant for the automotive [76], power generation and even aerospace industries [77]. Two main methods have been used to obtain spherical flame speed; one where the flame radius is relatively large compared to the characteristic dimension of the vessel causing a pressure rise that can be converted into flame speed by doing an energy balance; the other method is to use an 'overdesigned' explosion vessel where the flame radius remains relatively small compared to the vessel's dimension, keeping the pressure constant during the flame expansion.

In this section of the report, background information is given describing studies using both of the aforementioned techniques. Then, the experimental apparatus used herein is described, followed by a preliminary uncertainty analysis. Finally, some experimental results are presented using methane/air mixtures.

BACKGROUND

The importance of spherically expanding flames has been recognized for over half a century, and early experiments have been conducted by Manton et al. [78], Smith and Agnew [79], Agnew and Graiff [80], and Nair and Gupta [81], among others [82,83]. These experiments utilized rotating drum camaras, ionization gaps or a combination of both. Mathematical solutions for the determination of flame speed in spherical vessels during these early experiments were given by Rallis and Tremeer, Bradley and Mitcheson, and Garforth and Rallis [84-86]. Metghalchi and Keck also used ionization probes in combination with a heated vessel to extend experiments for fuels with lower vapor pressures [87]. Groff used both a camera as well as the pressure history to obtain the flame speed over a large range of radii [88]. Several studies employed in the 1980's used a combination of ionization probes and pressure histories [89,90] as well as laser shadowgraphs [91,92]. In 1984, Wu and Law investigated the effect of flame stretch on the laminar burning velocity using a Bunsen flame and a stagnation flame [93]. It became evident that the positive flame stretch in spherically expanding flames needed to be taken into account. A simple linear relationship between laminar burning velocity and flame stretch was proposed [94-96]:

$$S_b = S_b^0 - L_b\alpha \tag{18}$$

Table 8: Spherical flame speed research in the last 15 years (add '66' to each of the reference citations).

Researchers	P (atm)	T (K)	Fuel	Year	Refs
Dowdy et al.	1	296	H_2	1990	[29]
Tseng et al.	1	298	CH_4-C_3H_8, $C2H_4$	1993	[31]
McLean et al.	1	298	H_2/CO	1994	[30,33]
Aung et al.	1	298	H_2	1997	[34]
Daly et al.	1	295	DME+CH_4	2001	[35]
Huang et al.	1	300	NG + H_2	2006	[36]
Chen et al.	1	298	DME+CH_4	2007	[37]
kwon et al.	3	298	H_2, C_3H_8	1992	[38]
Kwon and Faeth	3	298	H_2	2001	[39]
Johnston and Farrell	3	450	Aromatics	2005	[40]
Aung et al.	4	298	H_2	1998	[41]
Hassan et al.	4	298	CH_4	1998	[42]
Halter et al.	5	298	CH_4/H_2	2004	[43]
Bradley et al.	10	450	i-Octane, Heptane	1998	[32]
Gu et al.	10	400	CH_4	2000	[44]
Haq	10	450	CH_4 + i-Octane	2005	[45]
Tse et al.	60	298	H_2	2000	[46]
Rozenchan et al.	60	298	CH_4	2002	[47]
Qin et al.	30	298	DME	2004	[48]
Sun et al.	60	298	CO/H_2	2006	[49]

where S_b is the stretched burning velocity, S_b^0 is the unstretched burning velocity, and α is the instantaneous stretch rate. For a spherically expanding flame, α is defined as the rate of increase of surface area of the flame, normalized by the area at that moment [94]. The effect of flame stretch and Markstein number was investigated by Brown et al. [96], Tjeng et al. [97], and Bradley et al. [98] among others.

There are numerous studies using high-speed photography under constant-pressure conditions. However, most of those were conducted at low pressures, not representative of gas turbine conditions. A summary of constant-pressure, spherical flame speed experiments over the past 15 years is given in Table 8. The high initial pressure created by Law et al. is accomplished by a double cylindrical vessel allowing the products of the inner cylinder to expand into inert gas inside the outer cylinder [112-115]. To achieve flame speeds using higher initial pressures, usually windowless flame speed vessels are used. The flame speed in a windowless vessel is derived by combining the measured pressure rise with numerical differentiation of the mass fraction burned [116-122]. The main disadvantage of this 'blind' technique is that potential cellularity, or other types of flame front discrepancies cannot be detected. This method is not used by the authors and will not be investigated in depth herein.

Several studies have been conducted into modeling laminar flame speed. Introducing realistic reaction mechanisms for simple hydrocarbons was investigated by Warnatz [122]. Spherical laminar flame propagation was modeled by Bradley et al. as well as Saeed and Stone [123,124]. The effect of simplified transport models on the burning velocity of premixed flames was investigated by Bongers and de Goey [125].

The cylindrical flame speed vessel described herein was designed to target the conditions representative of a gas turbine engine, with initial pressures P_i up to 30 atm. Data from this facility will cover future fuel flexibility issues and can be used for model verification. The goal was a simple yet robust and safe design capable of covering a wide range of pressures and temperatures.

FLAME SPEED EXPERIMENTAL SETUP

The cylindrical vessel has an inner diameter of 30 cm (11.75 in) and an internal length of 36.2 cm (14.25 in), with 3.18 cm (1.25 in) thick walls. The material used is 7075 Aero-grade Aluminum, for strength, ease of machining and its high thermal conductivity. Both ends are capped with 9.89 cm (3.5 in) thick threaded inserts. Two fused quartz windows, 20.3 cm OD, 6.3 cm thick (8 in, 2.5 in) are clamped between the insert and 5.1 cm thick endplates leaving a 12.7 cm (5 in) clear aperture. Vacuum up to 50 mTorr is provided by an Edwards E2M8 Rotary Vane Pump and is read with a Varian 0531 TC pressure transducer. Pressure during the experiment is provided by an Endevco 8511A piezo-resistive pressure transducer (0-10,000 psi), with a direct feed to a GageScope PCI (5 MHz, 16 bit resolution) computer data acquisition system, see Fig. 20 and 21. Temperature is read using a K-type fast response thermocouple inserted into the vessel. All plumbing is done using stainless steel Swagelok components. Four Swagelok pneumatic ball valves allow for remote operation behind a blast wall partition designed for safety. The total system pressure rating P_{max} is set by the Swagelok connecters at 5,000 psi (345 bar). Rupture disks are included in the system and can be set at a pressure < 5000 psi to never exceed P_{max}.

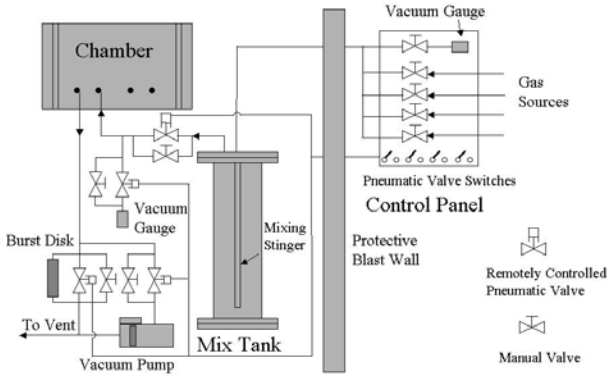

Figure 20. Plumbing for the flame speed vessel.

A Z-type Schlieren setup is used as described by G.S. Settles [126]. Two 15.2-cm Diameter f/8 parabolic mirrors are used in combination with a mercury arc lamp and an Oriel constant current DC power supply. Both a vertical knife edge and a pinhole aperture were used as can be seen in Figs. 22a and 22b. When using a vertical knife edge, it is clear from Fig. 22a that one side is saturated while the other is underexposed. It is better to capture an axisymetric phenomenon using a circular knife edge, showing a clear discrete flame front propagating radially outward (Fig. 22b). The flame propagation is captured using a high-speed digital camera (Cooke Corp. PCO 1200-hs) with a frame rate around 3000 fps (see Fig. 23).

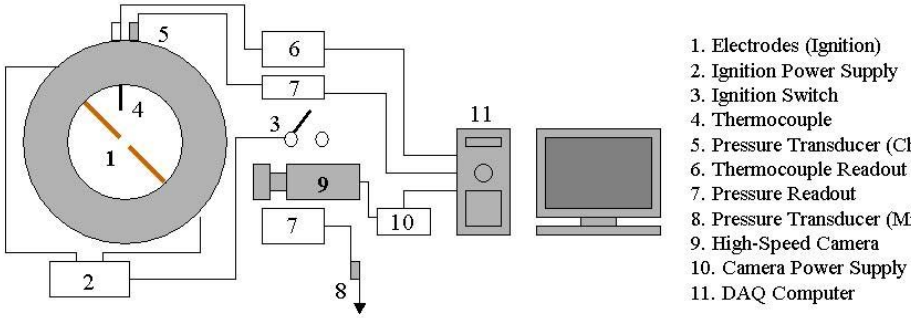

Figure 21. Electrical circuit.

The ignition is provided by an automotive coil with a 10-μF condenser between the points. Power for the coil is provided by a constant-current power supply (GwInstek GPR-1810HD)

which allows for simple, non-discrete adjustment of the ignition energy by setting the input current to a known value before saturating the coil. Using this method, the ignition energy can be adjusted to the minimal value the stoichiometry of the mixture demands. Two copper electrodes are positioned opposite leaving a spark gap of less then 1 mm.

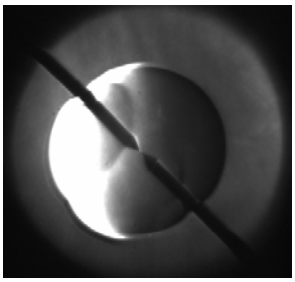

(a)

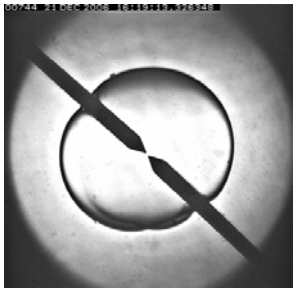

(b)

Figure 22. Vertical (a) versus circular (b) knife edge for stoichiometric methane-air, 1 atm, 298 K.

For low-pressure experiments (P_i < 10 atm), the mixtures are created in a separate mixing tank using the partial pressure method. The mixture is then introduced to the evacuated flame speed vessel up to the desired initial pressure. Time is given for the mixture to come to rest and the temperature to readjust to the surroundings (usually 10 minutes). The mixture is then ignited while simultaneously sending a signal to trigger the pressure reading and the camera. After completion of the experiment, the vessel is evacuated through a vent system.

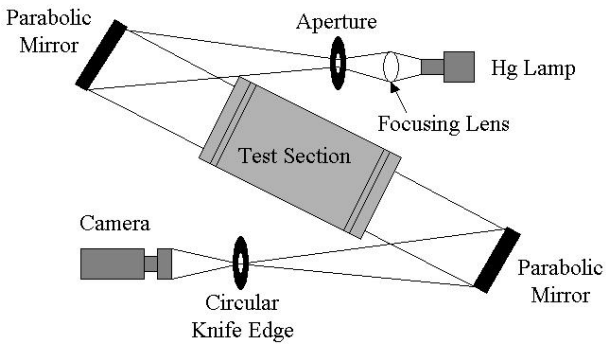

Figure 23. Z-Type schlieren setup.

DATA INTERPRETATION

For flames with a radius up to 6 cm, it can be shown that the compression is around 4% using an isentropic assumption. For a radius of 5 cm, the pressure rise would be less than 2%. It has been shown by Chen and Ju that for these conditions the compression-induced flow velocity behind the flame front is less than 2% [127] (see Fig. 24). All flame-front propagation is processed through Spotlight-8 Image Analysis Software, developed by Klimek and Wright [128].

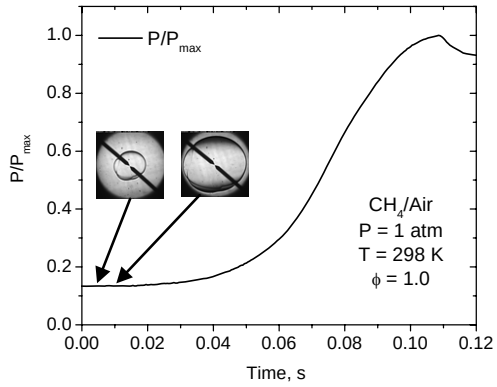

Figure 24. Pressure profile for stoich-iometric methane/air.

To test the apparatus, several methane/air mixtures were tested under atmospheric conditions. The spherically expanding flames create a photo-array such as shown in Fig. 25, which is converted in a radius versus time array. The flame stretch is given as:

$$\alpha = \frac{1}{A}\frac{dA}{dt} = \frac{1}{4\pi R^2}\frac{d\left(4\pi R^2\right)}{dt} = \frac{2}{R}\frac{dR}{dt} \qquad (19)$$

The unburned-stretched flame speed S_b is dR/dt. Equations (18) and (19) can be combined to form:

$$\frac{dR}{dt} = S_b^0 - L_b\frac{2}{R}\frac{dR}{dt}$$

Separating variables and integrating gives:

$$\int\left(dR + L_b\frac{2}{R}dR\right) = \int S_b^0 dt$$

$$R = S_b^0 t - 2L_b\ln(R) + const \qquad (20)$$

Equation (20) can be recognized to be in the form;

$$Y = m_1 X_1 + m_2 X_2 + b$$

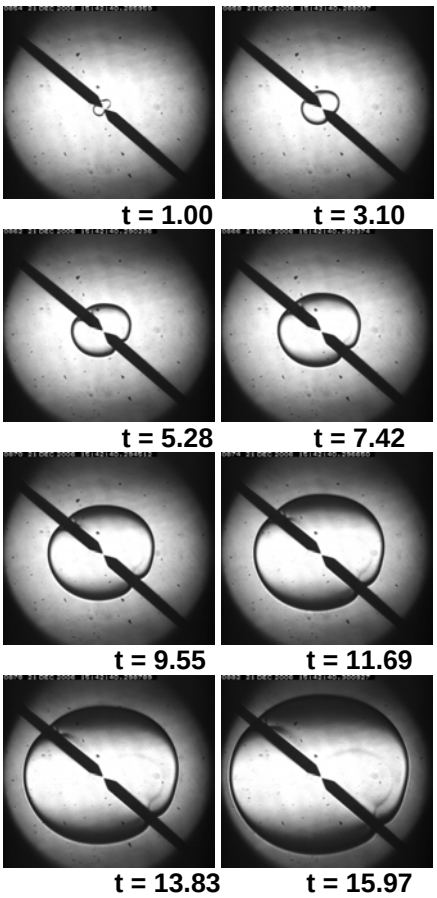

Figure 25. CH_4/Air, 1 atm, ϕ = 0.8, time in ms.

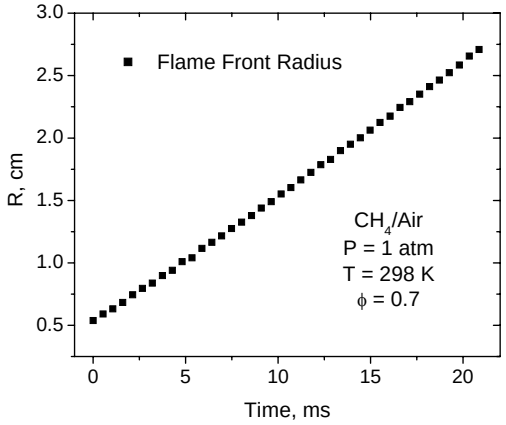

Figure 26. Growth of flame radius.

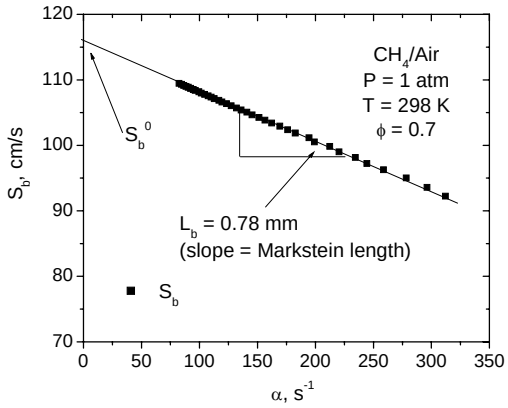

Figure 27. Calculation of Markstein length for a fuel-lean methane/air mixture.

This allows for a linear least squares fit through Eqn. (21). It was found by the authors that this method is preferred over using finite difference to obtain the stretched flame speed directly, since even small (< 1%) random scatter can cause a large variance in the slope taken over small time intervals. The radius for a fuel-lean methane/air mixture is plotted in Fig. 26 versus time, and the flame speed versus stretch is plotted in Fig. 27. From continuity, the relation between the burned and unburned flame speeds is given by the density ration between the two.

$$\rho_u S_u = \rho_b S_b \tag{21}$$

The density for both the reactants and the products is obtained using the STANJAN equilibrium code [129]. Results to date with methane-air mixtures at 1 atm compare favorably with established data and kinetics models. Further details will be published in the final report, including experiments with synthesis gas mixtures.

CONCLUSIONS

Syngas experiments from four different groups and three different experimental techniques (shock tube, flow reactor, rapid compression machine) were shown and were compared with modern kinetics models. The data, including recent shock-tube experiments that duplicated earlier work at UTRC done in a flow reactor, showed faster ignition at lower temperatures and higher pressures than what is predicted by the kinetics model. ***The results of these experiments indicate potential weaknesses in the CO/H_2 mechanism at higher pressures and lower temperatures and/or the fact that the experiments are producing ignition times that are not purely chemical kinetic based..***

A reduced mechanism for methane oxidation kinetic times has been developed. The models presented herein are valid over a wide range of gas turbine conditions. The temperatures ranged from 1000 to 2500 K, and pressures were varied from 0.1 to 50 atm. The mixture compositions covered equivalence ratios between 0.1 and 2. Kinetic times for CH_4, CO, and NO species were obtained from a detailed mechanism based on GRI-Mech 3.0. The data were fitted into reduced models as functions of temperature, pressure and mixture composition. An overall model for ignition delay times was also provided. Since ignition delay times vary strongly with temperature, pressure, and the mixture concentrations, multiple models were developed for low and high-temperature regions, as well as fuel rich and lean cases. **The accuracy and high predictive capability of the model makes it an excellent candidate to be incorporated in CFD codes for gas turbine flow field simulations, and some representative CFD calculations using the new model were provided.**

There is an increase in demand for reliable, high-pressure flame speed data to cover the fuel flexibility issues in the gas turbine industry. Few studies have been conducted where high initial pressures were combined with optical access for high-speed schlieren photography. **A high-pressure combustion vessel was built at the University of Central Florida's Gas Dynamics Laboratory to measure flame speeds at gas turbine conditions.** When analyzing flame speed data, it was found that linear regression is preferred to obtain the unstretched flame speed and the Markstein length. Several methane/air mixtures at atmospheric conditions were measured to validate the flame speed data, and some sample data were presented.

REFERENCES

[1] Lefebvre, A. H., 1999, *Gas Turbine Combustion*, 2nd Ed, Taylor & Francis, Philadelphia PA.

[2] Spadaccini, L. J. and Colket, M. B. III, 1994, "Ignition Delay Characteristics of Methane Fuels," Progress in Energy and Combustion Science, **20**, pp. 431-460.

[3] Naber, J. D., Siebers, D. L., Di Julio, S. S., and Westbrook, C. K., 1994, "Effects of Natural Gas Composition on Ignition Delay under Diesel Conditions," Combustion and Flame, **99**, pp. 192-200.

[4] Flores, R. M., Miyasato, M. M., McDonell, V. G., and Samuelsen, G. S., 2001, "Response of a Model Gas Turbine Combustor to Variation in Gaseous Fuel Composition," Journal of Engineering for Gas Turbines and Power, **123**, pp. 824-831.

[5] Flores, R. M., McDonell, V. G., and Samuelsen, G. S., 2003, "Impact of Ethane and Propane Variation in Natural Gas on Performance of a Model Gas Turbine Combustor," Journal of Engineering for Gas Turbines and Power, **125**, pp. 701-708.

[6] W.T. Peschke, L.J. Spadaccini, Determination of Autoignition and Flame Speed Characteristics of Coal Gases Having Medium Heating Values, Report No. EPRI AP-4291, Electric Power Research Institute, 1985.

[7] T. Lieuwen, V. McDonell, E. Petersen, D. Santavicca, ASME Paper GT2006-90770 (2006); also, *J. Eng. Gas Turb. Power*, in press.

[8] G.A. Richards, M.M. McMillian, R.S. Gemmens, W.A. Rogers, S.R. Cully, *Prog. Energy Combust. Sci.* 27 (2001) 141-169.

[9] D.M. Kalitan, E.L. Petersen, AIAA Paper 2005-3767, 2005; also, *J. Prop. Power*, submitted.

[10] D.M. Kalitan, E.L. Petersen, J.D. Mertens, M.W. Crofton, ASME Paper GT2006-90488, 2006.

[11] S.M. Walton, X. He, B.T. Zigler, M.H. Wooldridge, *Proc. Combust. Inst.* 31 (2007) in press.

[12] G. Mittal, C.-J. Sung, R.A. Yetter, *Int. J. Chem. Kinet.* (2006) 516-529.

[13] J.H. Chen, V.J. Jermakian, V.G. McDonell, G.S. Sameulsen, (2003). Correlation of Ignition Delay with Fuel Composition and State for Application to Gas Turbine Combustion, Final Report, Contract 00-01-SR084CS, Prepared for South Carolina Institute for Energy Studies.

[14] D.J. Beerer, M.U. Greene, V.G. McDonell, G.S. Samuelsen (2006). Correlation of Ignition Delay with IGCC and Natural Gas Fuels, Final Report, Contract 03-01-SR112, Prepared for South Carolina Institute for Energy Studies.

[15] S.G. Davis, A.V. Joshi, H. Wang, F. Egolfopoulos, *Proc. Combust. Inst.* 30 (2005) 1283-1292.

[16] E.L. Petersen, D.F. Davidson, R.K. Hanson, *Combust. Flame* 117 (1999) 272-290.

[17] P. Saxena, F.A. Williams, *Combust. Flame* 145 (2006) 316-323.

[18] H.Y. Sun, S.I. Yang, G. Jomaas, C.K. Law, *Proc. Combust. Inst.* 31 (2007) in press.

[19] J. Li, Z. Zhao, A. Kazakov, M. Chaos, F.L. Dryer, J.J. Scire *Int. J. Chem. Kin.*, in press.

[20] G. Mittal, C.J. Sung, M. Fairweather, A.S. Tomlin, J.F. Griffiths, K.J. Hughes, *Proc. Combust. Inst.* 31 (2007) in press.

[21] R. Sivaramakrishnan, A. Comandini, R. S. Tranter, K. Brezinsky, S.G. Davis, H. Wang, *Proc. Combust. Inst.* 31 (2007) in press.

[22] Westbrook, C. K., and Dryer, F. L., "Simplified Reaction Mechanisms for the Oxidation of Hydrocarbon Fuels in Flames," *Combustion Science and Technology*, Vol. 27, 1981, pp. 31–43.

[23] Bilger, R. W., S. H. Starner and R. J. Kee, "On Reduced Mechanisms for Methane-Air Combustion in Nonpremixed Flames," *Combustion and Flame,* Vol. 80, 1990, pp 135-149.

[24] Seshadri, K., and Peters, N., "Asymptotic Structure and Extinction of Methane-Air Diffusion Flames," *Combustion and Flame,* Vol. 73, 1988, pp. 23–44.

[25] Mallampalli, H., Fletcher, T. H., and Chen, J. Y., "Evaluation of CH_4/Nox Reduced Mechanisms Used for Modeling Lean Premixed Turbulent Combustion of Natural Gas," *Journal of Engineering for Gas Turbines and Power*, Vol. 120, 1998, pp. 703-712.

[26] Peters, N., and Rogg, B., editors, *Reduced Kinetic Mechanisms for Applications in Combustion Systems*, Springer-Verlag, Berlin-Heidelberg, 1993.

[27] Rogg, B., "Flamelet Models and Reduced Mechanisms," Technical Report CUED/A-THERMO/TR57, Cambridge University, Engineering Department, September 1992.

[28] Smooke, M. D., "Reduced Kinetic Mechanisms and Asymptotic Approximations for Methane-Air Flames," *Lecture Notes in Physics*, Vol. 384, Springer-Verlag, pp. 1-28.

[29] Cao, R. R., and Pope, S. B., "The Influence of Chemical Mechanisms on PDF Calculations of Nonpremixed Piloted Jet Flames," *Combustion and Flame,* Vol. 143, No. 4, 2005, pp. 450-470.

[30] Volchkov, E. P., Dvornikov, N. A., and Perepechko, L. N., "Comparison of Different Methods of Modeling Turbulent Combustion in a Boundary Layer," *Combustion, Explosion, and Shock Waves*, Vol. 32, No. 4, 1996, pp. 390-394.

[31] Zhu, M., Bray, K. N. C., and Rogg, B., "PDF Modeling of Spray Autoignition in High Pressure Turbulent Flows," Combustion Science and Technology, Vol. 120, 1996, pp.357-319.

[32] Bruel, P., Rogg, B. and Bray, K. N. C., "On Auto-Ignition in Laminar and Turbulent Non-premixed Systems," *Proceedings of the Combustion Institute*, Vol. 23, 1990, pp. 759-766.

[33] Westbrook, C. K., and Dryer, F. L., "Chemical Kinetic Modeling of Hydrocarbon Combustion," *Progress in Energy Combustion Science*, Vol. 10, 1986, pp. 1-57.

[34] Smith, G. P., Golden, D. M., Frenklach, M., Moriarty, N. W., Eiteneer, B., Goldenberg, M., Bowman, C. T., Hanson, R. K., Song, S., Gardiner, W. C., Lissianski, V. V., and Qin,, Z., GRI-Mech 3.0, http://www.me.berkeley.edu/gri-mech/

[35] Petersen, E. L., Hall, J. M., Smith, S. D., and De Vries, J., "Ignition of Lean Methane-Based Fuel Blends at Gas Turbine Pressures," ASME Turbo Expo, GT68517, ASME, Nevada, Reno-Tahoe, June 6-9, 2005.

[36] Tomlin, A. S., Turanyi, T., Pilling, M. J., "Mathematical Tools for The Construction, Investigation, and Reduction of Combustion Mechanisms," *Comprehensive Chemical Kinetics, Low-Temperature Combustion and Autoignition*, M.J. Pilling editor, Vol. 35, Chapter 4, 1997.

[37] Warnatz, J., "Hydrocarbon Oxidation at High-Temperatures," *Journal of Physical Chemistry*, Vol. 87, 1983, pp. 1008-1022.

[38] Turanyi, T., Beres, T., and Vajda, S., "Reaction Rates Analysis of Complex Kinetics Systems," *International Journal Chemical Kinetics*, Vol. 21, 1989, pp. 83-99.

[39] Warng, H., and Frenklach, M., "Detailed Reduction of Reaction Mechanisms for Flame Modeling," *Combustion and Flame*, Vol. 87, No. 3, 4, 1991, pp. 365-370.

[40] Yungster, S., and Rabinowitz, M. J., "Computation of Shock Induced Combustion Using Detailed Methane-Air Mechanism," *Journal of Propulsion and Power*, Vol. 10, No. 5, pp. 609-617, 1994.

[41] Peters, N., "Numerical and Asymptotic Analysis of Systematically Reduced Reaction Schemes for Hydrocarbon Flames," In Numerical Simulation of Combustion Phenomena, Golwinski, R. et al., Eds., *Lecture Notes in Physics*, p. 90, 1985.

[42] Peters, N. and Williams, F. A., "The asymptotic Structure of Stoichiometric Methane Air Flames," Combustion and Flame, Vol. 68, 1987, pp. 185.

[43] Lam, S. H., and Goussis, D. A., "The CSP Method for Simplifying Kinetics," *International Journal of Chemical Kinetics*, Vol. 26, 1994, pp. 461-486.

[44] Maas, U. and Pope, S. B., "Simplified Chemical kinetics: Intrinsic Low-Dimentional Manifolds in Composition Space," *Combustion and Flame*, Vol. 88, pp. 239-264, 1992.

[45] Maas, U. and Pope, S. B., "Implementation of Simplified Chemical Kinetics Based on Intrinsic Low-Dimensional Manifolds," *Proceedings of the Combustion Institute*, Vol. 24, 1992, pp. 103.

[46] Pope, S. B., "Computationally Efficient Implementation of Combustion Chemistry Using In Situ Adaptive Tabulation," *Combustion Theory and Modeling*, Vol. 1, 1997, pp. 41-64.

[47] Hautman, D. J., Dryer, F. L., Schug, K. P., and Glassman, I., "A Multiple Step Overall Kinetic Mechanism for the Oxidation of Hydrocarbons," *Combustion Science and Technology*, Vol. 25, No. 5, 6, 1981, pp. 219-235.

[48] Oran, E. S., Boris, J. P., Young, T. R., Flanigan, M., and Picone, M., "Numerical Simulations of Detonations in Hydrogen-Air and Methane-Air Mixtures," *Proceedings of the Combustion Institute*, Vol. 18, 1981, pp. 1641-1649.

[49] Clifford, L. J., Milne, A. M, and Murray, B. A., "Numerical Modeling of Chemistry and Gas Dynamics During Shock-Induced Ethylene Combustion," *Combustion and Flame*, Vol. 104, No. 3, 1996, pp. 311-327..

[50] Molnar, M., and Marek, C. J., "Reduced Equations for Calculating the Combustion Rates of Jet-A and Methane Fuel," NASA TM-212702, 2003.

[51] Molnar, M., and Marek, C. J., "Simplified Two-Time Step Method for Calculating Combustion and Emission Rates of Jet-A and Methane Fuel With and Without Water Injection," AIAA Paper 2005-0549, 43rd Aerospace Sciences Meeting and Exhibit, January 2005.

[52] Brankovic, A., Ryder, R. C., and Petersen, E. L., "Time-Dependent Simulation of Fuel-Flexible Gas-Turbine Burners," AIAA Paper 2006-806, 44th Aerospace Sciences Meeting and Exhibit, January 2006.

[53] Spalding, D. B., "Development of The Eddy-Break-Up Model of Turbulent Combustion," *Proceedings of the Combustion Institute*, Vo. 16, 1976, pp. 1657-1663.

[54] Magnussen, B. F. and Hjertager, B. H., "On Mathematical Models of Turbulent Combustion with Special Emphasis on Soot Formation and Combustion," *Proceedings of the Combustion Institute*, Vol. 16,1976, pp. 719-729.

[55] Eggenspieler, G., and Menon, S., "Large Eddy Simulation of Pollutant Emission in a DOE-HAT Combustor," *Journal of Propulsion and Power*, Vol. 20, No. 6, 2004, pp. 1076.

[56] Lee, D., and Yeh, C. L., "Numerical Simulations of Gas Turbine Combustor Flows," *Journal of Propulsion and Power*, Vol. 9, No. 2, 1993, pp. 322-328.

[57] Blanquart, G. and Pitsch, H., "Modeling Autoignition in Non-Premixed Turbulent Combustion Using a Stochastic Flamelet Approach," *Proceedings of the Combustion Institute*, Vol. 30, 2005, pp. 2745-2753.

[58] Bilger, R.W., "Conditional Moment Closure for Turbulent Reacting Flow", *Physics of Fluids A*, Vol. 5, No. 2, 1993, pp. 436-444.

[59] Golovitchev, V.I. and Chomiak J., "Analysis of Main Assumptions Underlying Extended Eddy Dissipation Model of Turbulent Combustion," Scandinavian-Nordic Section of the Combustion Institute, September 10-11, Trondheim, Norway.

[60] Peters, A. A. F., and Weber, R., "Mathematical Modeling of a 2.25 MW_t Swirling Natural Gas Flame. Part 1: Eddy Break-up Concept for Turbulent Combustion; Probability Density Function Approach for Nitric Oxide Formation," Combustion Science and Technology, Vol. 110, 1995, pp. 67–101.

[61] Magel, H. C., Schneider, R., Risio, B., Schnell, U., and Hein, K. R. G., "Numerical Simulation of Utility Boilers with Advanced Combustion Technologies," 8th International Symposium on Transport Phenomena in Combustion, San Fransisco, CA, 1995.

[62] Brink, A., Mueller, C., Kilpinen, P., and Hupa, M.,"Possibilities and Limitations of The Eddy Break-Up Model," Combustion and Flame, Vol. 123, No. 1, 2000, pp. 275-279.

[63] Petersen, E. L., Rickard, M. J. A, Crofton, M. W, Abbey, E. D., Traum, M. J., and Kalitan, D. M., "A Facility for Gas-and Condensed-Phased Measurements Behind Shock Waves," *Measurement Science and Technology*, Vol. 16, 2005, pp. 1716-1729.

[64] Kee, R. J., Rupley, F. M., Miller, J. A., Coltrin, M. E., Grcar, J. F., Meeks, E., Moffat, H. K., Lutz, A. E., Dixon-Lewis, G., Smooke, M. D., Warnatz, J., Evans, G. H., Larson, R. S., Mitchell, R. E., Petzold, L. R., Reynolds, W. C., Caracotsios, M., Stewart, W. E., Glarborg, P., Wang, C., Adigun, O., *Chemkin Collection*, Release 3.6, Reaction Design, Inc., San Diego, CA, 2000.

[65] Hall, J. M., Rickard, M. J. A., and Petersen, E. L., "Comparison of Characteristic Time Diagnostics for Ignition and Oxidation of Fuel/Oxidizer Mixtures behind Reflected Shock Waves," *Combustion Science and Technology*, 2005, 455-483.

[66] Petersen, E. L., Röhrig, M., Davidson, D. F., Hanson, R. K., and Bowman, C. T., "High-Pressure Methane Oxidation Behind Reflected Shock Waves," *Proceedings of the Combustion Institute*, Vol. 26, 1996, pp. 799-806.

[67] G.A. Richards, M.M. McMillan, R.S. Gemmen, W.A. Rogers, S.R. Cully, *Progress in Energy and Combustion Science* 27 (2001) 141-169.

[68] T. Lieuwen, V.G. McDonell, E.L. Petersen, D. Santavicca, *ASME Paper* (2006) GT2006-90770.

[69] R.M. Flores, V.G. McDonell, G.S. Samuelsen, *Journal of Engineering for Gas Turbines and Power* 125 (2003) 701-708.

[70] J. de Vries, E.L. Petersen, *Proceedings of the Combustion Institute* 31 (2007) 3163-3171.

[71] W.S. Affleck, A. Thomas, *Proceedings of the Institution of Mechanical Engineers* 183 (1969) 365-385.

[72] L. Brett, J. MacNamara, P. Musch, J.M. Simmie, *Combustion and Flame* 124 (2001) 326-329.

[73] J. Würmel, J.M. Simmie, *Combustion and Flame* 141 (2005) 417-430.

[74] C. Zheng, Ju. Yiguang, AIAA Paper 2007-378 (2007).

[75] F.N. Egolfopoulos, P. Cho, C.K. Law, *Combustion and Flame* 76 (1989) 375-391

[76] Y. Huang, C.J. Sung, J.A. Eng, *Combustion and Flame* 139 (2004) 239-251.

[77] F. Parsinejad, C. Arcari, H. Metghalghi, *Combustion Science and Technology* 178 (2006) 975-1000.

[78] J. Manton, G. Von Elbe, B. Lewis, *Proceedings of the Combustion Institute* 4 (1953) 358-363.

[79] D. Smith, J.T. Agnew, *Proceedings of the Combustion Institute* 6 (1956) 83-88.

[80] J.T. Agnew, L.B. Graiff, *Combustion and Flame* 5 (1961) 209-219.

[81] M.R.S. Nair, M.C. Gupta, *Combustion and Flame* 22 (1974) 219-221.

[82] D.D. Agrawal, *Combustion and Flame* 42 (1981) 243-252.

[83] S.P. Sharma, D.D. Agrawal, C.P. Gupta, *Proceedings of the Combustion Institute* 18 (1981) 493-501.

[84] C.J. Rallis, G.E.B. Tremeer, *Combustion and Flame* 7 (1963) 51-61.

[85] D. Bradley, A. Mitcheson, *Combustion and Flame* 26 (1976) 201-217.

[86] A.M. Garforth, C.J. Rallis, *Combustion and Flame* 31 (1978) 53-68.

[87] M. Metghalchi, J.C. Keck, *Combustion and Flame* 38 (1980) 143-154.

[88] E.G. Groff, *Combustion and Flame* 48 (1982) 51-62.

[89] Ö.L. Gülder, *Proceedings of the Combustion Institute* 19 (1982) 275-281.

[90] T. Iijima, T. Takeno, *Combustion and Flame* 65 (1986) 35-43.

[91] M. Metghalchi, J.C. Keck, *Combustion and Flame* 48 (1982) 191-210.

[92] B.E. Milton, J.C. Keck, *Combustion and Flame* 58 (1984) 13-22.

[93] C.K. Wu, C.K. Law, *Proceedings of the Combustion Institute* 20 (1984) 1941-1949.

[94] G.H. Markstein, *Non-Steady Flame Propagation,* Pergamon, New York, 1964.

[95] D.R. Dowdy, D.B. Smith, S.C. Taylor, A. Williams, *Proceedings of the Combustion Institute* 23 (1990) 325-332.

[96] J.M. Brown, I.C. McLean, D.B. Smith, S.C. Taylor, *Proceedings of the Combustion Institute* 26 (1996) 875-881.

[97] L.K. Tseng, M.A. Ismail, G.M. Faeth, *Combustion and Flame* 95 (1993) 410-426.

[98] D. Bradley, R.A. Hicks, M. Lawes, C.G.W. Sheppard, R. Woolley, *Combustion and Flame* 115 (1998) 126-144.

[99] I.C McLean, D.B. Smith, S.C. Taylor, *Proceedings of the Combustion Institute* 25 (1994) 749-757.

[100] K.T. Aung, M.I. Hassan, G.M. Smith, *Combustion and Flame* 109 (1997) 1-24.

[101] C.A. Daly, J.M. Simmie, J. Würmel, N. Djebaïli, C. Paillard, *Combustion and Flame* 125 (2001) 1329-1340.

[102] Z. Huang, Y. Zhang, K. Zeng, B. Liu, Q. Wang, D. Jiang, *Combustion and Flame* 146 (2006) 302-311.

[103] Z. Chen, X. Qin, Y. Ju, Z. Zhao, M. Chaos, F.L. Dryer, *Proceedings of the Combustion Institute* 31 (2007) 1215-1222.

[104] S. Kwon, L.K. Tjeng, G.M. Faeth, *Combustion and Flame* 90 (1992) 230-246.

[105] O.C. Kwon, G.M. Faeth, *Combustion and Flame* 124 (2001) 590-610.

[106] R.J. Johnston, J.T. Farrell, *Proceedings of the Combustion Institute* 30 (2005) 217-224.

[107] K.T. Aung, M.I. Hassan, G.M. Faeth, *Combustion and Flame* 112 (1998) 1-15.

[108] M.I. Hassan, K.T. Aung, G.M. Faeth, *Combustion and Flame*, 115 (1998) 539-550.

[109] F. Halter, C. Chauveau, N. Djebaïli-Chaumeix, I. Gökalp, *Proceedings of the Combustion Institute* 30 (2005) 201-208.

[110] X.J. Gu, M.Z. Haq, M. Lawes, R. Woolly, *Combustion and Flame* 121 (2000) 41-58.

[111] M.Z. Haq, *Transaction of the ASME* 127 (2005) 1410-1415.

[112] S.D. Tse, D.L. Zhu, C.K. Law, *Proceedings of the Combustion Institute* 28 (2000) 1793-1800.

[113] G. Rozenchan, D.L. Zhu, C.K. Law, S.D. Tse, *Proceedings of the Combustion Institute* 29 (2002) 1461-1469.

[114] X. Qin, Y. Ju, C.K. Law, AIAA Paper 2004-3708 (2004).

[115] H. Sun, S.I. Yang, G. Jomaas, C.K. Law, *Proceedings of the Combustion Institute* 31 (2007) 439-446.

[116] M. Elia, M. Ulinski, M. Metghalchi, *Transaction of the ASME* 123 (2001) 190-196.

[117] M. Radwan, M. Ismail, M.Y. Selim, H. Saleh, *Energy Sources* 23 (2001) 345-361.

[118] F. Rahim, M. Elia, M. Ulinski, M. Metghalchi, *International Journal of Engine Research* 3 (2002) 81-92.

[119] K. Saeed, C.R. Stone, *Combustion and Flame* 139 (2004) 152-166.

[120] A.E. Dahoe, *Journal of Loss Prevention in the Process Industry* 18 (2005) 152-166.

[121] F. Parsinejad, C. Arcari, H. Metghalchi, *Combustion Science and Technology* 178 (2006) 975-1000.

[122] Jürgen Warnatz, *Twenty-Fourth Symposium (International) on Combustion* (1992) 553-579.

[123] D. Bradley, P.H. Gaskell, X.J. Gu, *Combustion and Flame* 104 (1996) 176-198.

[124] K. Saeed, C.R. Stone, *Combustion Theory and Modeling* 8 (2004) 721-743.

[125] H. Bongers, L.P.H. de Goey, *Combustion Science and Technology* 175 (2003) 1915-1928.

[126] G.S. Settles, *Schlieren and Shadowgraph Techniques*, 1st edition, Springer Heidelberg New York, Germany 2006.

[127] Z. Cheng, Y. Ju, AIAA Paper 2007-378 (2007).

[128] R. Klimek, T. Wright, NASA/TM-2006-214084 (2006).

[129] W.C. Reynolds, *The Element Potential Method for Chemical Equilibrium Analysis: Implementation in the Interactive Program STANJAN*, Department of Mechanical Engineering, Stanford University, Stanford, CA, 1986.

EFFECTS OF COATING BLOCKAGE AND DEPOSITS ON FILM COOLING EFFECTIVENESS AND HEAT TRANSFER

Semi-Annual Report
August 1 2006 - January 31, 2007

Minking K. Chyu
Department of Mechanical Engineering
University of Pittsburgh
Pittsburgh, PA 15261
(412) 624-9784
mkchyu@engr.pitt.edu

Tom I-P. Shih
Department of Aerospace Engineering
Iowa State University
2271 Howe Hall, Rm 1200
Ames, IA 50011-2271
(515) 294-6241
tomshih@iastate.edu

January 31, 2007

DOE Award Number - DE-FC21-02NT41431
UTSR Project Number - 04-01-SR115

Department of Mechanical Engineering
University of Pittsburgh
Pittsburgh, PA 15261

Department of Aerospace Engineering
Iowa State University
2271 Howe Hall, Rm 1200
Ames, IA 50011-2271

ABSTRACT

This report describes the progress over the first six months of year 3 of this three-year UTSR research project. The project is concerned with the effects of coating partial blockage and surface deposits on film cooling performance. The research is a joint pursuit of experiment and computational simulation. Progress has been made during this second phase of the program in exploring new film cooling design concepts for better performance. On the computational front, FLUENT code is being used to develop and study three new design concepts for film cooling to increase adiabatic effectiveness. Experimentally, progress has been made on two fronts. First, a new test system that is capable of accommodating a wider test range for hole-blockage study is established. Second, the experiment to explore the effects of surface deposits near film cooling holes is being developed. Key focus of this aspect of research is to potentially control TBC deposit profile for better film cooling performance. All tasks are on schedule and consistent with the original proposal. Both computational and experimental results will be reported in the annual report and presented in the UTSR workshop.

TABLE OF CONTENTS

EXECUTIVE SUMMARY

The main objective of this DOE UTSR project is to use a coordinated experimental and computational approach to systematically explore the transport processes associated with film-hole partial blockage and surface deposits on the film cooling performance for both round (unshaped) and shaped film holes. Spatially-resolved film effectiveness and heat transfer coefficient for all the test cases will be acquired using an IR transient technique. The objective on the computational front is to develop optimal practice guidelines for CFD simulations of film cooling affected by partial blockage and realistic surface roughness. The experimental database will serve as a reference for validating the CFD simulation. The CFD efforts will complementarily provide important transport insight that is otherwise unattainable by experiments. During the first period of the third year program, experimental effort has been directed to explore the effects of modeled deposits on the film cooling characteristics. Computationally, continuing effort is given to identify innovative shaped-hole designs. Experimental exploration on certain down-selected configurations based on the current computational efforts will be pursued in the later part of the year. The collective information gained from this research could further provide guidelines for advanced film cooling strategies, which includes modifying and optimizing hole shapes, better fuel filtration, and improved maintenance scheduling as well as specific clean-up procedures for future turbine engines.

PROJECT DESCRIPTION

This University Turbine System Research program is a combined effort of experiment and numerical computation for studying the transport phenomena related to the effects of blockage and surface deposits around film cooling holes. The primary goal of this research is to provide the turbine manufacturers with fundamental insight that can impact the future design of film cooling. The research team consists of participants from two universities: University of Pittsburgh (Pitt) and Iowa State University (ISU). The Pitt portion of the combined program is an experimental investigation of the film cooling performance affected by blockage and surface deposits. The specific tasks are to perform detailed measurements of surface heat transfer coefficient and film effectiveness. The experimental work at Pitt is coordinated with the computational effort at ISU. The research focus at ISU is to perform CFD simulation of transport phenomena and providing guidelines for improved designs in film cooling. Validation of computational models will use the heat transfer and flow data obtained from the experimental aspect of the program. On the other hand, information gained from the computation will provide the experiment with more detailed insight in data interpretation. This will eventually aid the selection of optimal test geometry and parameters.

RESULTS AND DISCUSSION

Experimental

The experimental effort during the first part of the third year program is to explore the effects of surface roughness or deposits on the film cooling performance. To initiate this study, film cooling characteristics around a generic, cylindrical protruding element (a pin) are being investigated. The particular effects of interest include the relative position and geometry between the pin and film injection hole, the film cooling blowing ratio, and the mainstream flow conditions. Described below is the test set up and sample results.

The experimental setup is shown in Figure 1. The test section was made of Plexiglas with the thickness of 0.5 inch. The width and height of the test section is 7 and 0.5 inch, respectively. 0.25 inch diameter pin was used in this experiment. The film cooling hole is located at 1.25D in front of the pin. The diameter of the film cooling hole is 0.125 inch. The test section is connected by a two inches pipe supplying air to the test section from the in house compressed air. An orifice plate located at the upstream of the heater is used to measure flow rate of the main flow. The flow rate of the film cooling flow is determined by using a rotameter. A transformer connected to the heater is regulated to heat up the main flow to the desired temperature, about 45-50 C. During the heating period, the flow is diverted away from the test section through the three way valve. When the temperature of the main flow reached steady state condition, the three way is switched, diverting the main flow to the test section.

The temperature distribution of the specified domain at the test section throughout the experiment is recorded using the Infrared camera. The infrared thermography used is a FLIR system ThermaCAM S40. The camera offers a high quality, non-intrusive method for obtaining thermal data through a commercially available software package for data analysis. The accuracy of the camera is ± 2% of the chosen measurement range or ± 2°C whichever is larger. The

camera is set to capture the images at the sampling rate of 7.5Hz. The IR camera was positioned at a perpendicular position, 0.3m above the test section.

Six thermocouples are used to record the temperature profile throughout the experiment through a data acquisition set from National Instruments, SCXI Chassis modeled, SC 1000 coupled with the digitizer SC1600, and two modules, SC1202 and SC1303. Two thermocouples located at 40mm after the inlet and the other two are located at 40mm before the outlet of the test section. The fifth thermocouple is used to monitor the temperature of the film cooling flow. The last thermocouple was used to measure the ambient temperature in the laboratory. The Data Acquisition was set to record the data at the sampling rate of 5 Hz.

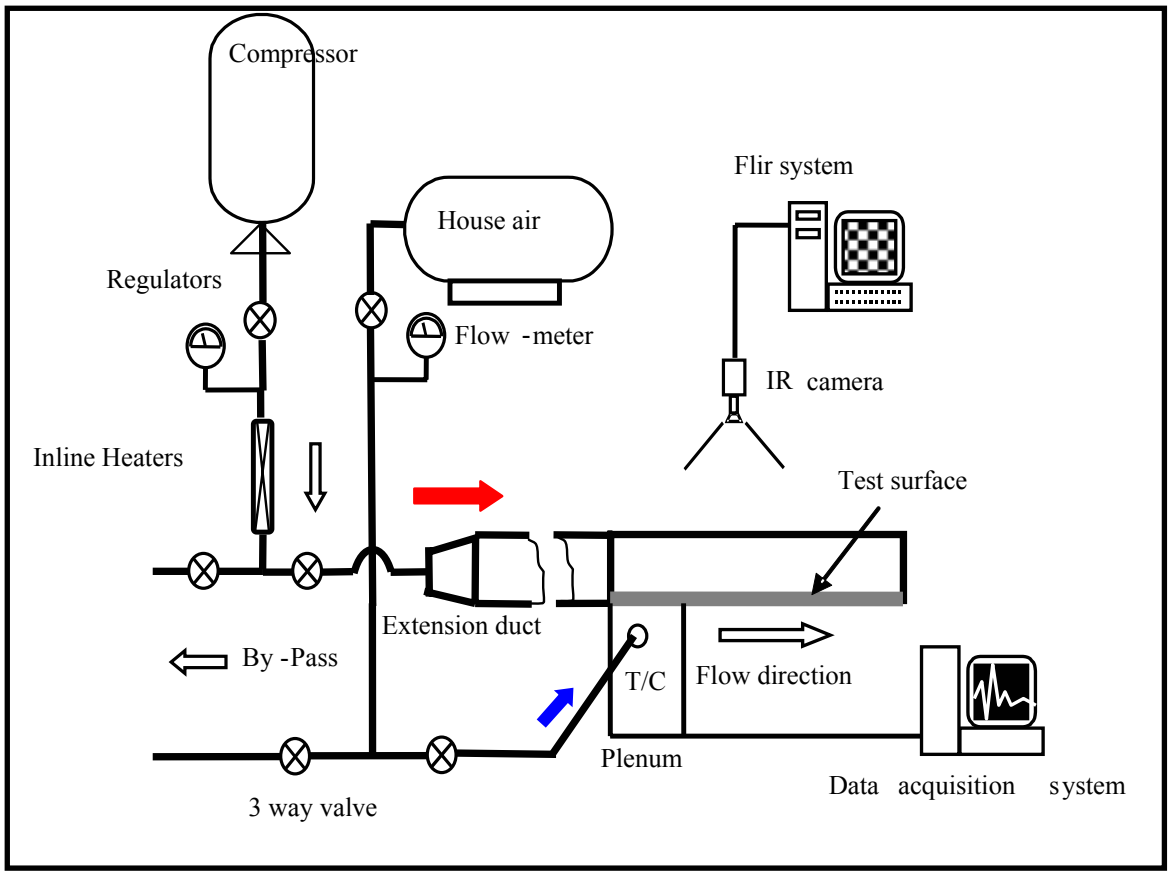

Layout of the Test Facilities

Shown below are the distributions of local heat transfer coefficients for cases with different blowing ratios and relative positions between the injection hole (dark blue) and pin (black). The Reynolds number based on the freestream velocity and pin diameter is about 11,000 for all the cases. Evidently, the heat transfer characteristics are strongly affected by all the parameters aforementioned. Upon completion of this phase of study, the focus of experiment will be

directed to complementarily study the new film hole concepts currently being explored computationally.

Local Heat Transfer Distribution: Jet Located Directly Ahead of a Pin

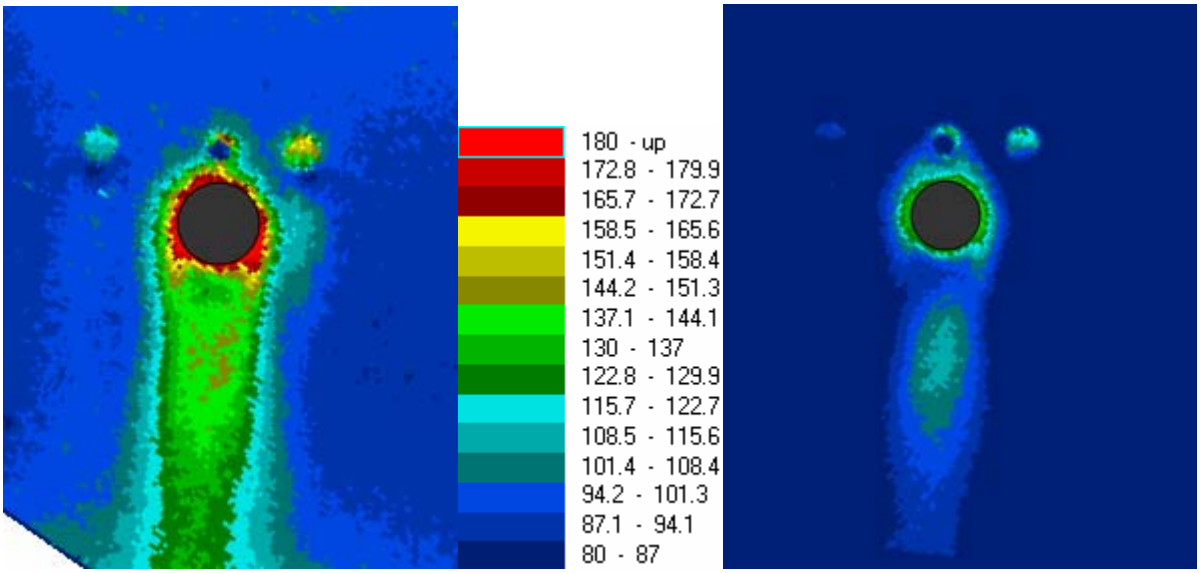

Blowing Ratio = 1.0 Blowing Ratio = 0.5

Local Heat Transfer Distribution: Jet Located 1.25D off the Centerline

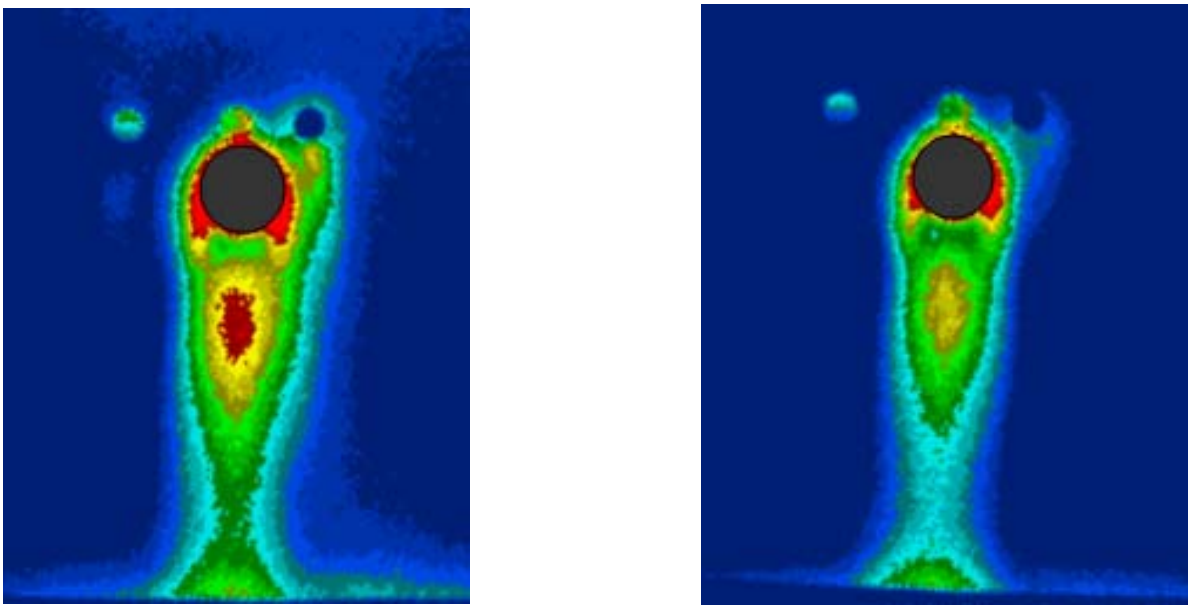

Blowing Ratio = 1.0 Blowing Ratio = 0.5

Computational

During the third year of this project, the computational effort focused on exploring new shaped-hole designs. Shaped holes increase film-cooling effectiveness by using the Coanda effect to make the cooling jet stay attached to the surface and an expanding flow cross-sectional area about the hole exit to make the cooling jet spread out laterally so that more surface can be cooled. Though shaped holes increase lateral spreading, downstream penetration of the coolant is reduced because the expanding cross-sectional area decreased the momentum of the cooling flow. Under this study, a new shaped-hole design concept was developed to enable increased lateral spreading as well as greater downstream penetration. The new shaped-hole design concept involves a W-shaped cross-sectional area in which the middle part of the W-shape protrudes and widens as the W-shaped hole widens. The goal is to keep the film-cooling flow cross-sectional area nearly constant as the shaped hole widens so that momentum can be preserved to increase both lateral and streamwise coverage of the film-cooling jet. To examine the usefulness of this design concept, CFD analyses were performed for two W-shaped holes. In one design, the W-shaped hole is similar to traditional shaped holes except that the middle part of the shaped hole is protruded to form the W shape. In the other design, the W-shaped hole continues as a shallow trench that is aligned with the main flow direction to minimize the entrainment of hot gases and to reduce pressure drag and aerodynamic interference. Computed results show the W-shaped-hole design concept to be promising in enhancing surface adiabatic effectiveness.

New W-Shaped Hole Geometry 1:

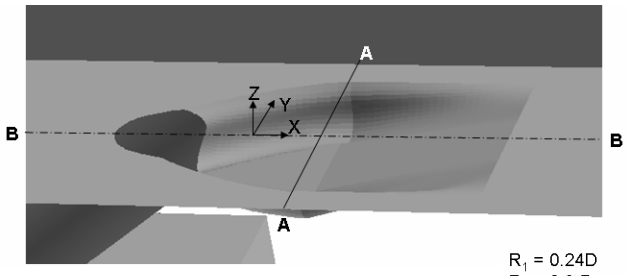

$R_1 = 0.24D$
$R_2 = 0.3\ D$
$H_1 = 0.2D$
$H_2 = 0.23D$
$H_3 = 0$ or $0.4D$
$S_1 = 0.26D$
$S_2 = 0.24D$
$S_3 = 0.3D$
$S_4 = 0.7D$
$S_5 = 1.14D$

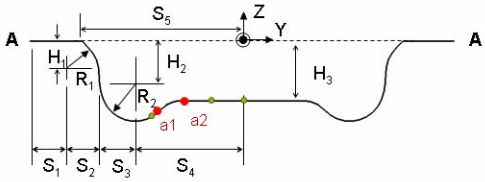

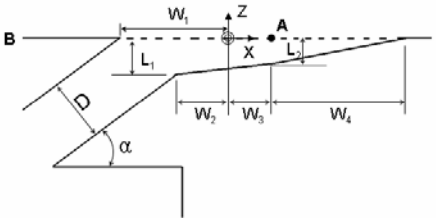

$W_1 = D/\cos\alpha$
$W_2 = 0.81D$
$W_3 = 0.79D$
$W_4 = 2D$

$L_1 = 0.57D$
$L_2 = 0.40D$

$\alpha = 35^\circ$, $D = 12.7$ mm

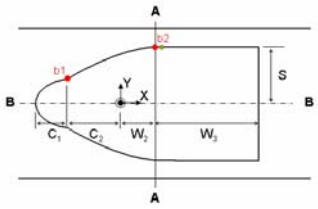

$S = 1.14D$
$C_1 = 0.79D$
$C_2 = 0.95D$
$W_2 = 0.79D$
$W_3 = 2D$

New W-Shaped Hole Geometry 2:

Same as Geometry 1
Except add trench.

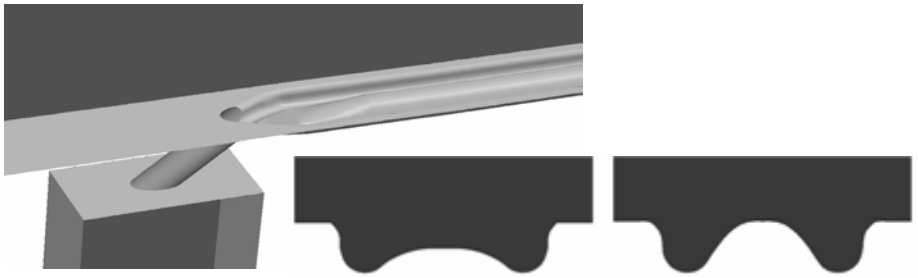

Sample Grid Systems Used:

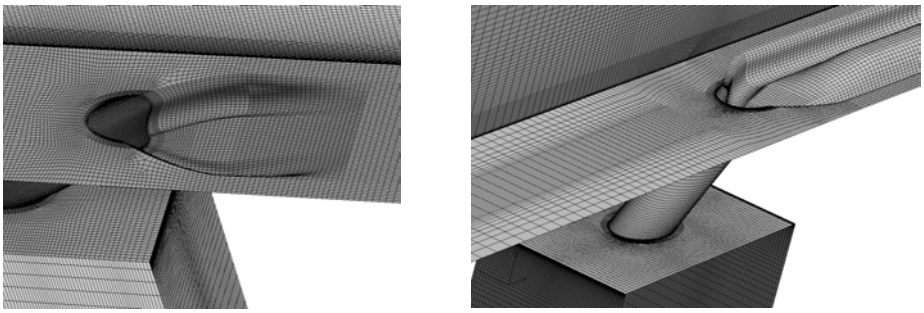

Sample Results:

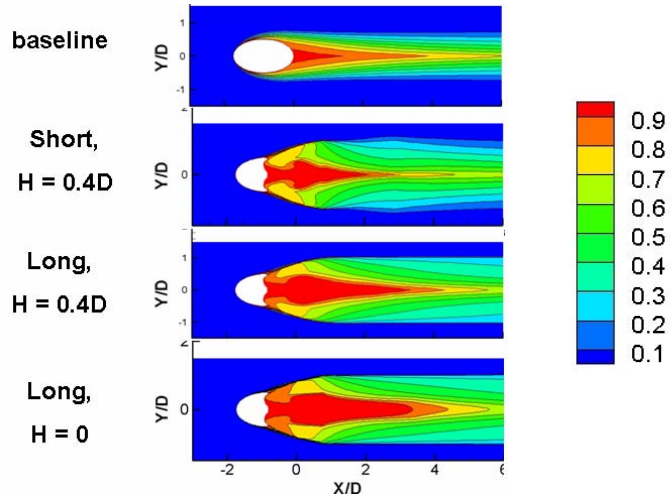

Adiabatic effectiveness (η) on the plate and the film-cooling hole surface as viewed from the –Z direction: circular hole (baseline) vs. W-shaped hole (short) and W-shaped hole with trench (long).

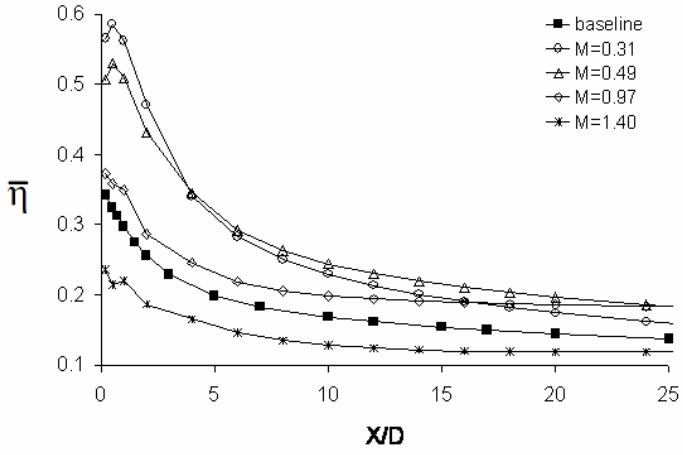

Laterally averaged adiabatic effectiveness: baseline vs. W-shaped hole with trench (H_3 = 0.0). Baseline is unshaped hole with M = 0.5.

CONCLUSIONS

Built on the accomplishments made in the first two years, reasonable progress in both experimental and computational fronts has been made during the first reporting period of Year 3. A new film-cooling-shape-hole concept was developed and evaluated. The computational results not only reveal significant promises for improved film cooling performance but also provide the experiment with important design guidelines. On the other hand, design and fabrication of the test rigs for experimental investigation of these innovations are completed. New experimental data will be obtained during the second half of the Year 3. Both detailed computational and experimental results will be presented in the year-end annual report and next UTSR workshop.

INVESTIGATION OF MATERIALS PERFORMANCES IN HIGH MOISTURE ENVIRONMENTS INCLUDING CORROSIVE CONTAMINANTS TYPICAL OF THOSE ARISING BY USING ALTERNATE FUELS IN GAS TURBINES

Semiannual Report
1 August 2006-31 January 2007

Principal Investigators
Gerald H. Meier (ghmeier@engr.pitt.edu)
Frederick S. Pettit (pettit@engr.pitt.edu)

Report Date: January 31, 2007

DOE Award: DE-FC26 02NT41431
UTSR Project: 04 01 SR 116

Submitted by:
Department of Mechanical Engineering and Materials Science
848 Benedum Hall
University of Pittsburgh
Pittsburgh, PA 15261

DISCLAIMER

ABSTRACT

This report covers the period 1 August, 2006 through 31 January, 2007. This project is concerned with the degradation of alloys and coatings on alloys due to the presence of deposits that may form on gas turbine hardware using syngas derived from coal as a fuel. The alloys being examined in this project are René N5, GTD 111, and IN 738. In addition to the uncoated alloys, three coatings on these three superalloys are also being investigated. These coatings are a platinum aluminide, a CoNiCrAlY and a NiCrAlY coating. In previous reports for this project it was shown that CaO deposits, in wet and dry air at 950^{o}C, represented reasonable test conditions to examine the influence of typical deposits arising from the use of syngas.

In this current report, it is shown that CaO deposits at 950^{o}C cause severe degradation of all three superalloys as well as all three coatings on these alloys. In the case of the uncoated superalloys, René N5 is attacked more severely than IN738 and GTD 111. This attack appears to be more severe in the case of wet air compared to dry air, however the increase due to wet air is small compared to the attack caused by the presence of the CaO deposit. In the case of the coatings on the superalloys, all three coatings were significantly degraded by the CaO deposit. More work is necessary to determine if one coating is more resistant to this attack compared to the others.

The amount of attack of the uncoated alloys was found to increase as the amount of the CaO deposit was increased. Work is in progress to determine the effects of water vapor pressure on this CaO induced degradation.

TABLE OF CONTENTS

LISTS OF GRAPHICAL MATERIALS

List of Figures

Figure 15. Weight change versus time measurements for platinum aluminide (GP), CoNiCrAlY (GC), and NiCrAlY (GN) coatings on GTD 111 without any deposit exposed at 950^{o}C in dry air.

Figure 16. Weight change versus time measurements for platinum aluminide coatings on René N5 (NP), GTD 111 (GP), and IN 738 (IP) without any deposit exposed at 950^{o}C in dry air.

Figure 17. Weight change versus time measurements for CoNiCrAlY coatings on René N5 (NC) and GTD 111 (GC) without any deposit exposed at 950^{o}C in dry air.

Figure 18. Weight change versus time measurements for NiCrAlY coatings on René N5 (NN) and GTD 111 (GN) without any deposit exposed at 950^{o}C in dry air.

Figure 19. Micrograph showing cross-section of platinum aluminide coating on René N5 without any deposit at 950^{o}C in dry air after 200 hours exposure.

Figure 20. Micrograph showing cross-section of platinum aluminide coating on GTD 111 without any deposit at 950^{o}C in dry air after 200 hours exposure.

Figure 21. Micrograph showing CoNiCrAlY coating on GTD 111 without any deposit at 950^{o}C in dry air after 20 hours exposure.

Figure 22. Weight change versus time measurements for platinum aluminide (NP), CoNiCrAlY (NC), and NiCrAlY (NN) coatings on René N5 without any deposit exposed at 950^{o}C in wet air.

Figure 23. Weight change versus time measurements for platinum aluminide (GP), CoNiCrAlY (GC), and NiCrAlY (GN) coatings on GTD 111 without any deposit exposed at 950^{o}C in wet air.

Figure 24. Weight change versus time measurements for platinum aluminide coatings on René N5 (NP), GTD 111 (GP), and IN 738 (IP) without any deposit exposed at 950^{o}C in wet air.

Figure 25. Micrograph showing cross-section of the platinum aluminide coating on René N5 without any deposit at 950^{o}C in wet air after 200 hours exposure.

Figure 26. Micrographs showing cross-section of the platinum aluminide coating on GTD 111 without any deposit at 950^{o}C in wet air after 200 hours exposure.

Figure 27. Micrographs showing the platinum aluminide coating on GTD 111 without any deposit at 950^{o}C in wet air after 80 hours exposure.

Figure 28. Weight change versus time measurements for platinum aluminide (NP), CoNiCrAlY (NC), and NiCrAlY (NN) coatings on René N5 with CaO deposits exposed at 950^{o}C in dry air.

List of Tables

1.0 INTRODUCTION

1.1 Background

When gas turbines use alternate fuels, such as syngas derived from coal, ash from the fuels can deposit on turbine hardware. This deposited ash can cause substantial corrosion of turbine hardware which may have significantly different characteristics than Type I and Type II hot corrosion. This program is directed at investigating and understanding the corrosion of materials induced by ash deposits typical of that from use of alternate fuels. The added complication of high moisture environments is also considered.

1.1.1 Ash Deposits

The accumulation of airborne contaminants which deposit on hot surfaces in gas turbines has always been a point of concern due to degradation of engine performance resulting from blockage of flow paths and cooling holes, as well as due to accelerate corrosion of alloys and coatings induced by the deposits. This program is concerned with the latter problem, namely, the deposit-induced accelerated corrosion of alloys and coatings. Over the past three quarters of a century a number of examples of deposit induced accelerated corrosion of alloys have been documented[1-3]. The nature of the deposit that is formed depends upon the operating conditions of the gas turbine, in particular, the turbine inlet temperature, the quality of the fuel and the characteristics of the intake air. Whenever fuels with high impurity contents such as S, Na, and V are used in gas turbines, deposits of Na_2SO_4 or $NaVO_3$ may be formed on turbine blades and vanes. Also, in the case of gas turbines used for propulsion of marine vehicles, sea salt can be present in the ingested air. As discussed in previous reports for this program, there have been numerous studies on the corrosion induced by deposits of Na_2SO_4, $NaVO_3$, and NaCl[4-8]. For example, Na_2SO_4-induced attack can occur over the temperature range 600^o to 950^{o}C and includes Type I and Type II hot corrosion.

As the turbine inlet temperatures have been increased, due to the use of thermal barrier coatings (TBCs), deposits of calcium-magnesium-aluminum-silicate (CMAS) with melting points around 1100^{o}C have been observed to develop on turbine hardware[9]. Such deposits form due to material in the intake air and can cause degradation of the TBCs. Upon cooling to ambient temperatures, the CMAS on the surface of the TBC solidifies with an effective modulus significantly larger than that of the porous TBC structure. This stiffer layer can have enough stored energy in it to debond from the rest of the TBC layer. Once debonding occurs, the newly exposed surface of the TBC can be infiltrated by subsequent CMAS deposits, with the process repeating itself until unacceptable amounts or all of the TBC is removed. There is not much data in the literature describing the effect of CMAS on the corrosion of alloys and metallic coatings but research is in progress[10].

When fuels are used in gas turbines that have been derived from coal, or other practicable sources, ash can be formed on turbine hardware which can cause corrosion[11]. It is the inorganic matter in fuels that leads to problems with corrosion and deposits[12]. The composition of the ash is difficult to describe precisely. In most coals about 95% of

all the mineral matter is made up of kaolinite ($Al_2O_3 \cdot 2SiO_2 \cdot 2H_2O$), pyrites ($FeS_2$) and calcite ($CaCO_3$)[12]. In tests performed using 2 to 3 ppmw ash particulate in the combustion stream, more deposition and corrosion was observed at a gas temperature of 1260°C compared to 1093°C[11]. This corrosion differed from Type I hot corrosion and involved calcium.

Both physical and chemical factors play roles in the formation of deposits. Deposits accumulate on surfaces by at least four physical processes[12] : molecular diffusion, Brownian motion, turbulent diffusion and inertial impact. Although particles of ash may arrive at a surface by physical transport, the accumulation of the ash to form substantial deposits will depend upon the adherence of particle to particle. When the particle to particle adherence is strong ash will continue to build up into thick layers. The sintering characteristics of the ash are affected by many factors, but the composition, temperature, and the time the particles are in contact with each other on a heat receiving surface are the most important factors. Depending upon such factors a transition temperature can exist above which increased deposition occurs.

In considering the deposits that may develop when using fuel derived from coal, it is reasonable to consider CaO and $CaSO_4$, and to compare the attack to that induced by Na_2SO_4 deposits. The influence of deposits of CaO, $CaSO_4$, and MgO on the oxidation behavior of a number of Cr_2O_3-forming and Al_2O_3-forming alloys has been investigated over the temperature range 850° to 1050°C[13]. Deposits of CaO were observed to accelerate the degradation of Cr_2O_3-forming alloys in oxygen or air by two mechanisms, namely; accelerated CrO_3 evaporation over the entire range studied, and liquid formation by reaction between CaO and Cr_2O_3 at temperatures above 1000°C which resulted in catastrophic corrosion. The corrosion of Al_2O_3-forming alloys that developed transient Cr_2O_3 was also substantially increased by the CaO deposit. Deposits of $CaSO_4$ did not cause any accelerated corrosion. Deposits of MgO caused increased evaporation of CrO_3, but not any corrosion due to the formation of liquid phases containing MgO.

In examining the effect of deposits upon the corrosion of alloys and coatings, it is also necessary to consider the effect of water vapor on such corrosion processes. The effect of water vapor on the oxidation of a number of Cr_2O_3-forming and Al_2O_3-forming alloys has been investigated in a previous program funded by the South Carolina Energy Research and Development Center[14]. The results from this investigation showed that water vapor caused the oxidation resistance of Cr_2O_3-forming and Al_2O_3-forming alloys to be decreased. Water vapor affected the oxidation resistances of these alloys by causing the oxide scales to crack and spall more severely. This increase in spalling of the oxide scales occurred because water vapor decreased the interfacial toughness of aluminum oxide-alloy interface. Water vapor also adversely affected the selective oxidation in the alloys that were Al_2O_3 formers. This adverse effect on selective oxidation was observed in nickel base superalloys rather than coatings on such superalloys. The selective oxidation of aluminum in the nickel base superalloy was adversely affected by water vapor since it caused more transient oxidation during the development of Al_2O_3 scales on these alloys.

1.1.2 Objectives

The objectives of this program are to conduct experiments, whereby the oxidation degradation of selected materials are documented in high moisture gas environments and in such environments but with corrosive contaminants on specimens typical of deposits that are encountered in use of alternate fuels in gas turbines, more specifically, the goals are to perform laboratory cyclic and isothermal oxidation tests in a gas environment of air with water vapor and in the same gas environment but with deposits of Na_2SO_4, CaO, and $CaSO_4$ to achieve the following:

1. Develop a fundamental understating of the degradation processes in moisture environments and in such environments where the specimens have deposits which are typical of deposits that will be encountered from alternate fuels, namely, CaO and $CaSO_4$.
2. Attempt to describe how moisture/contaminant levels and temperature affect the corrosion processes.
3. Determine the alloy compositions and coatings that are most resistant to corrosion induced by deposits from alternate fuels.
4. Compare and describe the failure mechanisms of state-of-the-art TBCs operating with conventional fuels and with alternate fuels.
5. Compare the degradation of a ceramic matrix composite (CMC) under conditions typical of gas turbines using conventional fuels and environments containing water vapor and contaminants representative of turbines using alternate fuels.

2.0 EXECUTIVE SUMMARY

Much of the previous materials development for power generating gas turbines has been performed with natural gas as the fuel of choice. More recently, the need for fuel flexibility has caused alternate fuels such as syngas to be considered for use in gas turbines. Preliminary testing with a variety of alternative fuels has shown increased deposition of ash as well as highly aggressive corrosion of turbine materials that was more severe in the presence of moisture[11]. This program is directed at investigating the corrosion induced by ash deposition and moisture from use of alternative fuels. The alloys and coatings to be studied are typical of those used in current power generating gas turbines, as well as those that may be used in advanced systems. This project has the following five objectives:

- Develop a fundamental understanding of the degradation processes in moisture environments and in such environments where the specimens have deposits which are typical of deposits that will be encountered from the use of alternate fuels.
- Attempt to describe how moisture/contaminant levels and temperature affect the corrosion processes.
- Determine the alloy compositions and coatings that are most resistant to corrosion induced by deposits from alternate fuels.
- Compare and describe the failure mechanisms of state-of-the-art TBCs and one ceramic matrix composite (CMC) operating with conventional fuels and with alternate fuels.

To achieve these objectives, the alloys GTD 111, IN 738, and René N5 as well as these alloys coated with CoNiCrAlY, NiCrAlY, and platinum aluminide, have been exposed to conditions relevant to corrosion induced using alternative fuels. The initial test conditions involved a number of deposits including Na_2SO_4, CaO, and $CaSO_4$ in dry and wet air at temperatures from 750^o to 1150^oC. Based upon these results, in order to compare these alloys and coatings in a manageable number of experiments, it was decided to perform subsequent experiments at 950^oC using CaO deposits (0.5–1.0 mg/cm^2) in dry and wet (p_{H20}=0.1 atm) air, since these conditions were considered to be representative of those that may be encountered when using syngas.

Specimens of René N5, GTD 111, and IN 738 have been exposed to cyclic oxidation conditions at 950^oC with deposits of CaO in dry and wet air. It has been found that all three of these alloys were attacked more severely when CaO deposits were present and this attack became even more severe in wet compared to dry air. However, the increase in attack due to the presence of water vapor was small compared to the attack caused by the CaO deposit. It was also found that the degradation induced via CaO deposits caused more severe degradation of René N5 compared to GTD 111 and IN 738. The attack induced by CaO caused similar amounts of degradation of GTD 111 and IN 738.

Tests using CaO deposits and cyclic oxidation conditions at 950^oC in dry and wet air have also been performed for the three coatings on the three alloy substrates. All three coatings were significantly degraded by attack induced by the CaO deposits. No

effect of the alloy substrates on coatings performances was apparent. More work is required to compare the attack between the different coatings as well as to the uncoated superalloys.

It was also determined that the amount of attack of the uncoated superalloys increased as the amount of the CaO deposit was increased. Work is in progress to determine the effects of water vapor pressure on the CaO induced degradation.

This project is scheduled to end on January 31, 2007. At present it may not be possible to complete all the work that is required by this end date. It is planned to request a 6 month no cost increase extension.

3.0 PROJECT DESCRIPTION

There is a need to determine the effects of deposits, that may form on gas turbine hardware when using alternate fuels, on the high temperature corrosion of this hardware. In this program the approach to determine the effects of deposits consists of exposing coupon specimens to cyclic oxidation conditions in controlled gas environments. The results from this program will provide information on the degradation caused by specific deposits and identify the alloys and coatings which are most resistant to the degradation. The deposits being used in the program are CaO, $CaSO_4$, and Na_2SO_4. CaO and $CaSO_4$ were selected because they are expected to be present in synthetic gas derived from coal. Na_2SO_4 was selected since a wealth of data is available for the effects of this deposit on alloy and coating degradation.

More specifically, this program is directed at achieving the goals that were described in the previous section. This program consists of six tasks which are schematically presented in Figure 1. The timeline for these tasks is presented in Figure 2. Task I is concerned with the selection and preparation of alloys and coatings to be investigated in this program. Task II is concerned with identifying the test conditions that are most realistic for examining the degradation of alloys and coatings in moist-contaminant environments. Task III involves testing a number of alloys and coatings at one temperature and deposit conditions in moist air. The resistance of these materials to the moisture-contaminant induced corrosion will be described and compared. Task IV is directed at determining moisture-contaminant limits for the attack of the alloys and coatings used in this program. Task V is directed at comparing the degradation of state-of-the-art TBCs under the conditions selected in Task II. Finally, Task VI will examine the degradation of a CMC using conditions determined in Task II.

This program involves the University of Pittsburgh, Praxair Surface Technologies, Howmet, Inc., and GE Power Systems. The oxidation and deposit-induced corrosion experiments are being performed at the University of Pittsburgh. The alloys, some of the coated alloys, the TBCs and the CMC are being provided by GE Energy.

4.0 EXPERIMENTAL

In this program, the cyclic oxidation exposures are performed in furnaces with controlled gas environments, as shown in Figure 3. The specimens (coupons 15×10×3 mm) are cycled into and from the furnace automatically; 45 minutes in the hot zone, 15 minutes in the cold zone. Weight change versus time measurements are performed and the exposed specimens are characterized using optical metallography (OM), x-ray diffraction (XRD) and scanning electron microscopy (SEM). Deposits of CaO, Na_2SO_4, and $CaSO_4$ (0.5-1.0 mg/cm^2) are applied to the coupon specimens by spraying an aqueous solution containing the deposit onto the specimen. These deposits are removed using warm water in an ultrasonic bath prior to weight change measurements. In order to have a controlled surface condition for all test specimens, all specimens are grit blasted at 30 psi for 45 minutes using 20 μm α-Al_2O_3 particles. This provides a surface roughness (R_a) of 2 μm. After grit blasting, the specimens are rinsed with water in an ultrasonic bath.

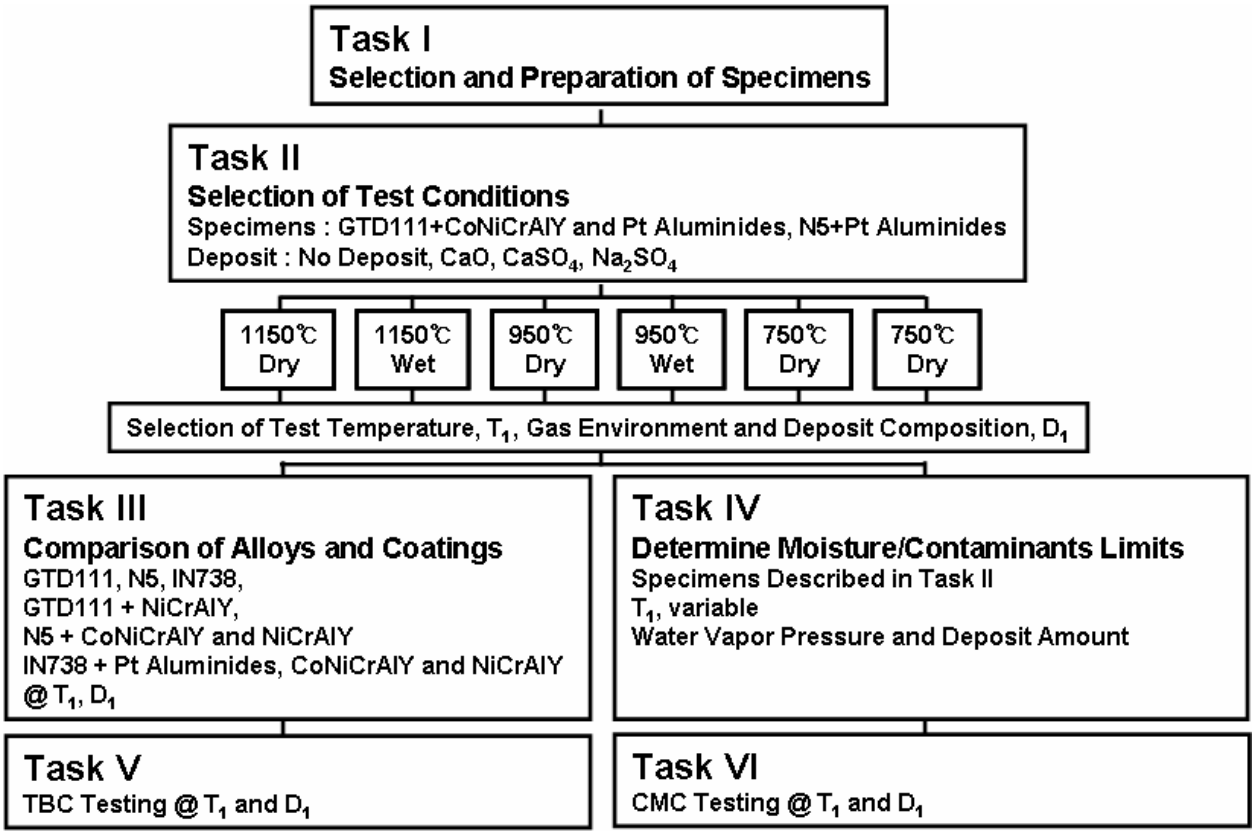

Figure 1. Schematic flow diagram for the present program.

	Year1		Year2		Year3	
Task I Selection and Preparation of Specimens	→					
Task II Selection of Test Conditions		→				
Task III Comparison of Alloys and Coatings			→	→	→	
Task IV Determine Moisture and Contaminant Limits			→	→	→	
Task V TBC Testing					→	→
Task VI CMC Testing					→	→

Figure 2. Time line of tasks.

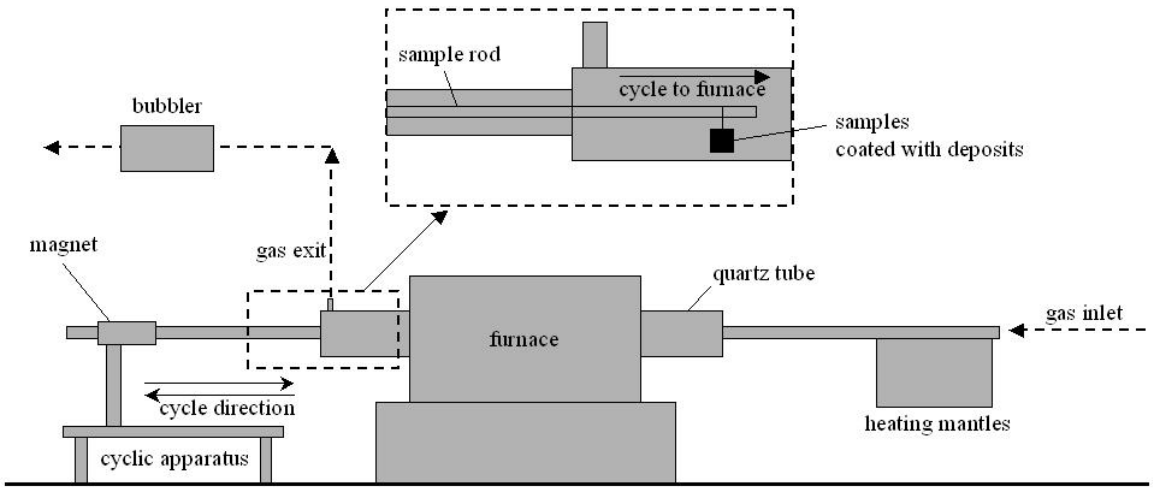

Figure 3. Schematic diagram showing the apparatus to cyclically oxidize coupon specimens in gases with defined and controlled amounts of water vapor in air at a total pressure of 1 atm.

5.0 RESULTS AND DISCUSSION

The results obtained and progress made in this program will be presented in terms of the six tasks that have been described in Section 3.0

5.1 Task I: Selection and Preparation of Alloys and Coatings to be Studied in This Program

The alloys being studied in this program are GTD 111, René N5, and IN 738. The alloy GTD 111 was selected because it is used in current industrial gas turbines. The alloy René N5 is to be used in advanced gas turbines. The alloy IN 738 is looked upon as an alloy that has some resistance to Na_2SO_4-induced hot corrosion attack. René N5 is a single crystal alloy and an α-Al_2O_3 former. IN 738 is a polycrystalline alloy and a chromia-former. GTD 111 is a directionally solidified alloy and is also a chromia-former. The compositions of these alloys are presented in the following table.

Table 1. Alloy Compositions*

Alloy	Ni	Cr	Al	Co	Ta	W	Mo	Ti	B	Hf	Re
IN738	Bal.	16	3.4	8.5	1.7	2.6	1.7	3.4	.01	---	---
Rene′ N5 (SC)	Bal.	7	6.2	7.5	6.5	6.0	0.2	---	---	0.1	3.0
GTD111 (DS)	Bal.	14	3.0	9.5	2.8	3.8	1.5	4.9	.01	---	---

The results obtained from the prior oxidation studies in wet and dry air[14] definitely show that coatings should be investigated in the current program. In this program, CoNiCrAlY (Co-32Ni-22Cr-10Al-0.3Y), NiCrAlY (Ni-22Cr-10Al-0.3Y) and a platinum-modified aluminide are being investigated. All three of these coatings should provide resistance to cyclic oxidation in wet environments. CoNiCrAlY and NiCrAlY coatings are used in some current power generating gas turbines. Platinum aluminides are mainly used in aircraft gas turbines, however a substantial amount of data is available for the degradation of these coatings in moist and dry air. In this program the platinum modified aluminide coating is included because it is believed to be necessary to have an aluminide coating for comparison with the MCrAlY coatings.

As can be seen in Figure 1, the coating-alloy systems being investigated in Task II are GTD 111 with a CoNiCrAlY coating, GTD 111 with a platinum-modified aluminide coating, and René N5 with a platinum-modified aluminide coating. Ingots of GTD111 and René N5 have been obtained from GE Power Systems. Coupon specimens (15×10×3mm) of GTD 111 and René N5 have been cut from these specimens. Platinum-modified aluminide coatings (MDC-150L) have been applied to the GTD 111 and René N5 specimens, Figures 4 and 5. Some of the GTD111 specimens have had the aluminide coating removed from one side by polishing. A CoNiCrAlY coating (Co-32Ni-22Cr-10Al-0.3Y) has been applied to these GTD 111 specimens using HVOF (polished side only) at GE Power Systems, Figure 6. This coating consists of two metallic phases. It also contains alumina inclusions.

* Unless indicated otherwise all compositions are presented in weight percent.

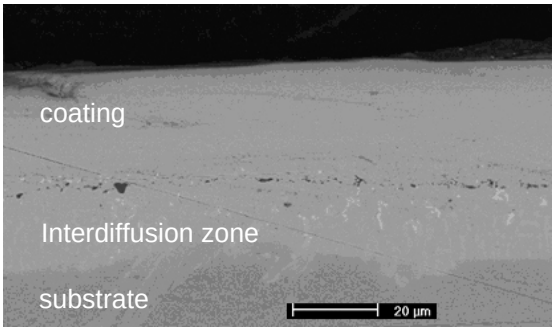

Figure 4. Scanning electron micrograph showing the platinum modified aluminide coating on GTD 111.

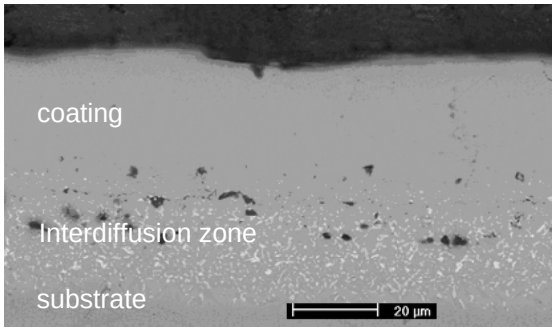

Figure 5. Scanning electron micrograph showing the platinum modified aluminide coating on Rene′ N5.

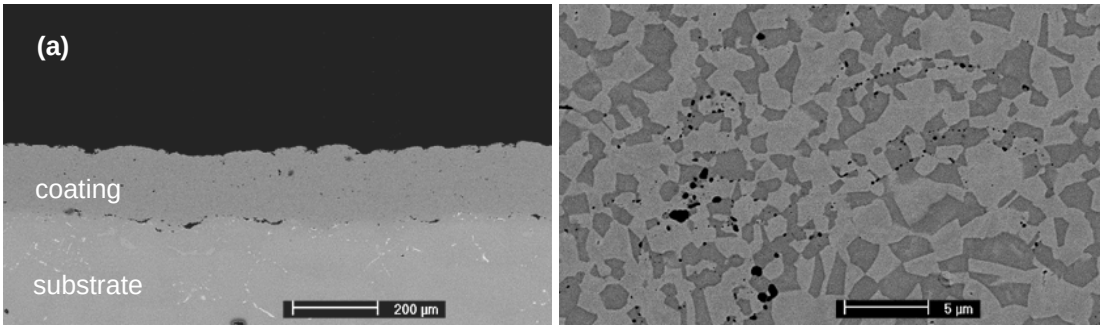

Figure 6. (a) Scanning electron micrograph showing the CoNiCrAlY coating on GTD111. (b) The bright and dark regions represent αβ phase (aluminum depleted CoNiCrAlY) and β phase (aluminum rich CoNiCrAlY), respectively. Black particles are Aluminum oxides.

5.2 Task II: Selection of Test Conditions

The objective of Task II was to determine the test conditions to be used for evaluating materials in the remainder of this program, as shown in Figure 1. In this task three temperatures have been examined, namely 750°, 950°, and 1150°C. Three deposits were considered, in particular Na_2SO_4, CaO, and $CaSO_4$. The gas environments were dry air and air with water vapor (p_{H2O} = 0.1 atm). At 750°C, the air contained 1000 ppm SO_2 to establish an SO_3 pressure of about 10^{-5} atm. These conditions were selected based upon the best available information for gas turbines operating with syngas as a fuel. The

systems studied were: GTD111 with a CoNiCrAlY coating and a platinum-modified aluminide coating, and René N5 with a platinum-modified aluminide coating.

As discussed in the previous report for this program[15], based upon the results that have been obtained from the cyclic oxidation tests performed at 1150°C, 950°C, and 750°C using deposits of CaO, Na_2SO_4, and $CaSO_4$, it was clear that coating degradation had occurred with all of the deposits at 950°C and 1150°C. At 750°C, the attack was induced by Na_2SO_4 only. The results obtained at 750°C show that the attack is that of low temperature hot corrosion and such conditions should not be used for the testing to be performed in Task III where the resistance of alloys and coatings on alloys are to be compared.

The testing that was performed at 1150°C showed that CaO deposits caused more attack than deposits of Na_2SO_4 or $CaSO_4$. However, the amount of degradation was severe due to the high temperature and it is believed that the testing in Task III should not be at this temperature.

The testing at 950°C showed that all of the deposits caused increased degradation compared to the coatings with no deposits, but the CaO deposits caused the most severe degradation. CaO deposits will be used to compare the behavior of the alloys and coatings in Task III. In most cases, the degradation induced by deposits was usually more severe in wet air compared to dry air, but in a few cases the specimens exposed in dry air showed comparable attack to that in wet air. The tests to be performed in Task III will consist of CaO deposits in dry and wet air at 950°C. The effects of water vapor on the degradation process are to be examined in detail in Task IV where moisture-CaO contaminant limits are being investigated.

5.3 Tasks III: Comparison of Alloys and Coatings

Task III is an important task in this program. After the appropriate test conditions have been selected as described in Task II, the alloys and coated alloys described in Figure 1 are now being exposed under these conditions. In particular, the degradation of GTD 111, René N5, IN 738, and these alloys with platinum-modified aluminide, CoNiCrAlY, and NiCrAlY coatings is being compared upon exposure to CaO deposits at 950°C in dry and wet air.

Task III examines the degradation of the alloys and coatings used in Task II, namely, GTD111 with CoNiCrAlY and platinum aluminide coatings and René N5 with a platinum aluminide coating. This Task also examines additional alloys and coatings. The as processed microstructures of the coatings to be used in Task III are compared in Figures 7 through 9. The platinum aluminide coatings are about 40 μm thick, whereas the CoNiCrAlY and NiCrAlY coatings are over 200 μm thick. Both of the MCrAlY coatings contain some oxide inclusions. Such inclusions are extremely numerous in the NiCrAlY coatings. These inclusions are predominantly alumina.

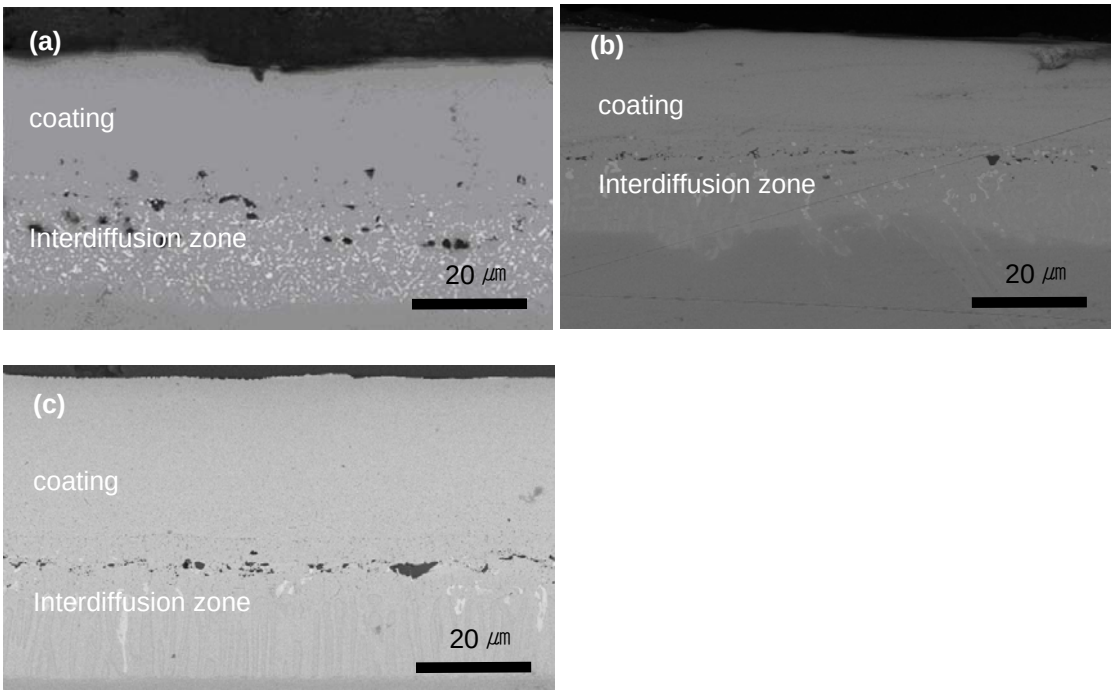

Figure 7. Platinum modified aluminide coatings on (a) Rene′ N5, (b) GTD 111, and (c) IN 738.

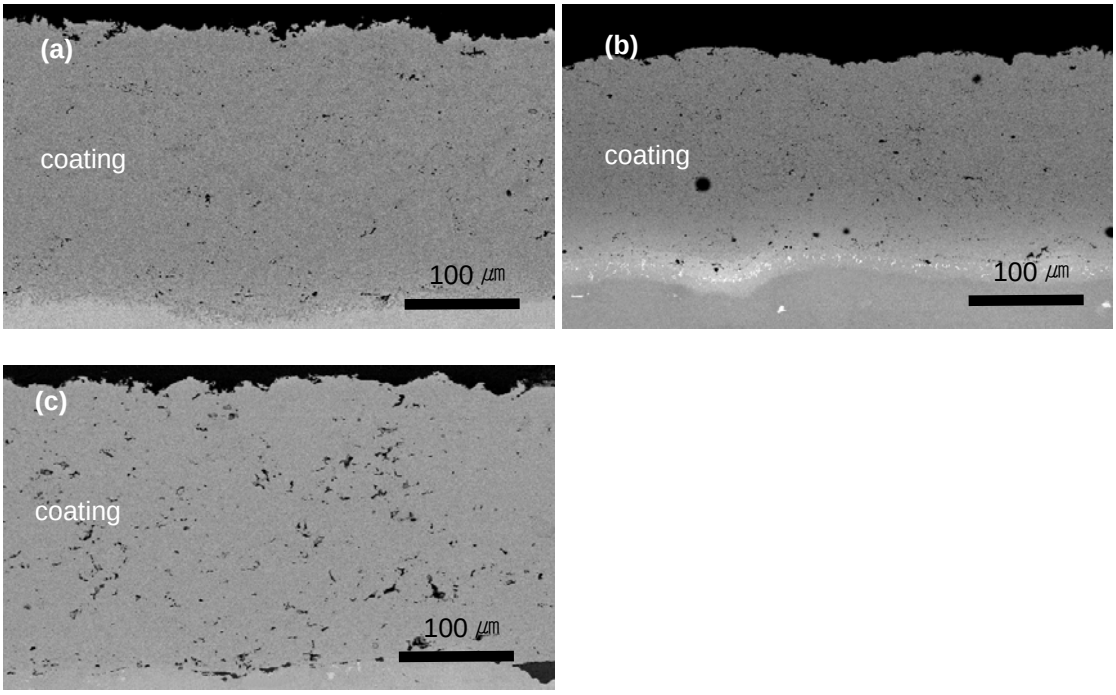

Figure 8. CoNiCrAlY coatings on (a) Rene′ N5, (b) GTD 111, and (c) IN 738.

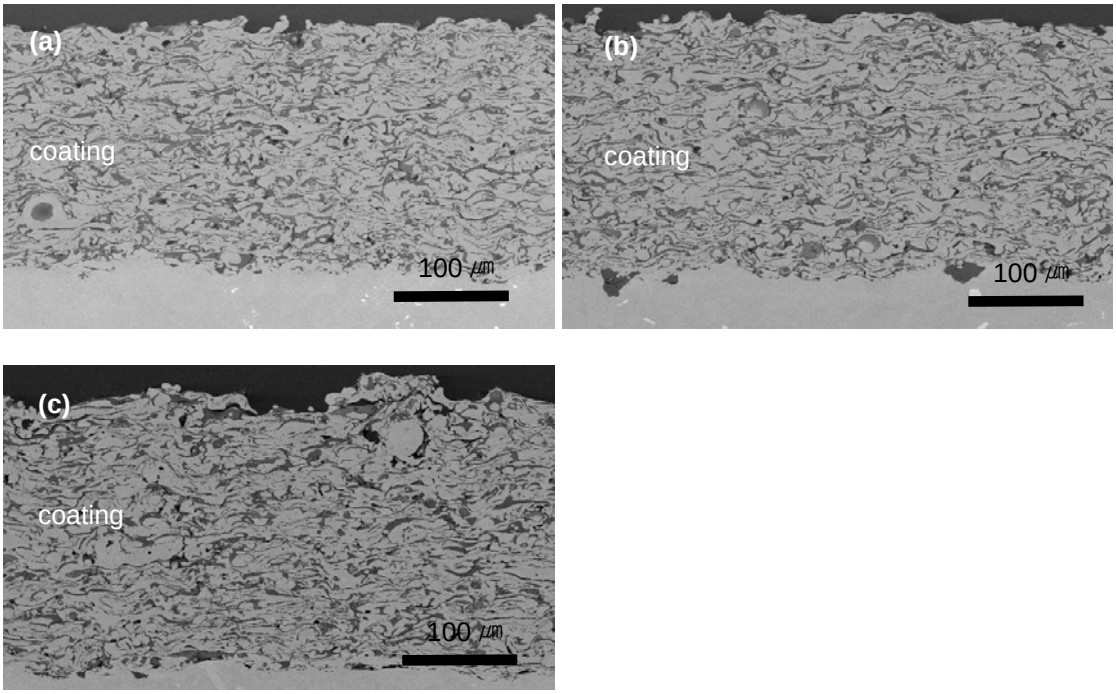

Figure 9. NiCrAlY coatings on (a) Rene′ N5, (b) GTD 111, and (c) IN 738.

5.3.1 Comparison of the Attack of René N5, IN738, and GTD111 Induced by CaO Deposits at 950°C in Dry and Wet Air

In a previous report[16], the results obtained with uncoated René N5, IN 738, and GTD 111 exposed to CaO deposits in dry and wet air were presented. The results obtainted in the cyclic oxidation of the three alloys show some important features. When CaO deposits are not present, René N5 oxidizes significantly slower than GTD 111 and IN 738. This occurs because René N5 is an Al_2O_3-former whereas GTD 111 and IN 738 are Cr_2O_3-formers, Figure 10. When water vapor is present in the gas environment the oxidation is not too much different than in dry air, but the internal oxidation appears to occur along alloy grain boundaries in the two polycrystalline alloys, Figure 11. More importantly, the internal oxidation of aluminum in GTD 111 and IN 738 is more pronounced in wet air. Such results show that the movement of oxygen in these two alloys is more rapid in wet compared to dry air. CaO deposits in dry air cause all three alloys to exhibit more degradation but this attack is more severe on René N5 compared to GTD 111 and IN 738, Figure 12. The addition of water vapor to the gases causes the attack induced by CaO deposits to be more severe for all three alloys because there is more cracking and spalling of oxide in wet air. However, the attack does not appear to be substantially more severe in wet air. Again the degradation of René N5 is more severe than that of GTD 111 and IN 738, Figure 13.

The mechanism by which CaO causes increased degradation of these alloys is still in the process of being developed. It has been found that CaO deposits react with Al_2O_3 and Cr_2O_3 scales to form calcium aluminates and calcium chromates. At 950°C these phases appear to be solid. At present it appears that the phases that form on the surfaces of these alloys are less protective and more prone to spalling compared to the unreacted Al_2O_3 and Cr_2O_3 oxide scales. Consequently, the degradation is more severe.

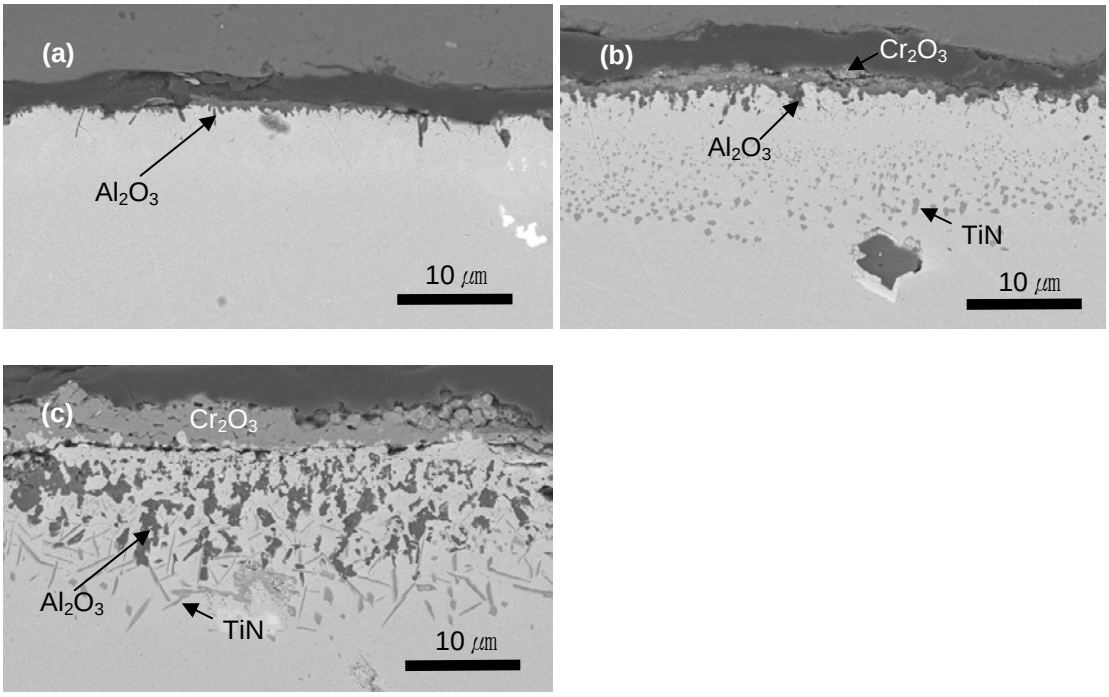

Figure 10. Scanning electron micrographs comparing the oxidation products formed on (a) René N5, (b) GTD 111, and (c) IN 738 after 140 hours of cyclic oxidation at 950°C in dry air.

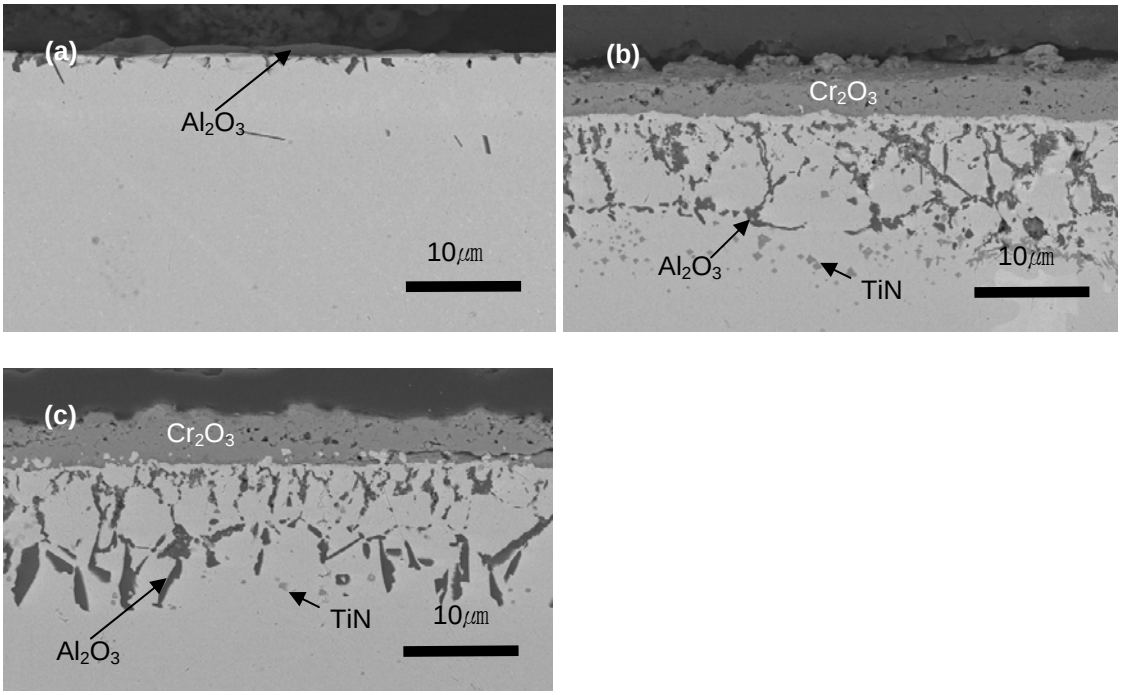

Figure 11. Scanning electron micrographs comparing the oxidation products formed on of (a) René N5, (b) GTD 111, and (c) IN 738 after 140 hours of cyclic oxidation at 950°C in wet air.

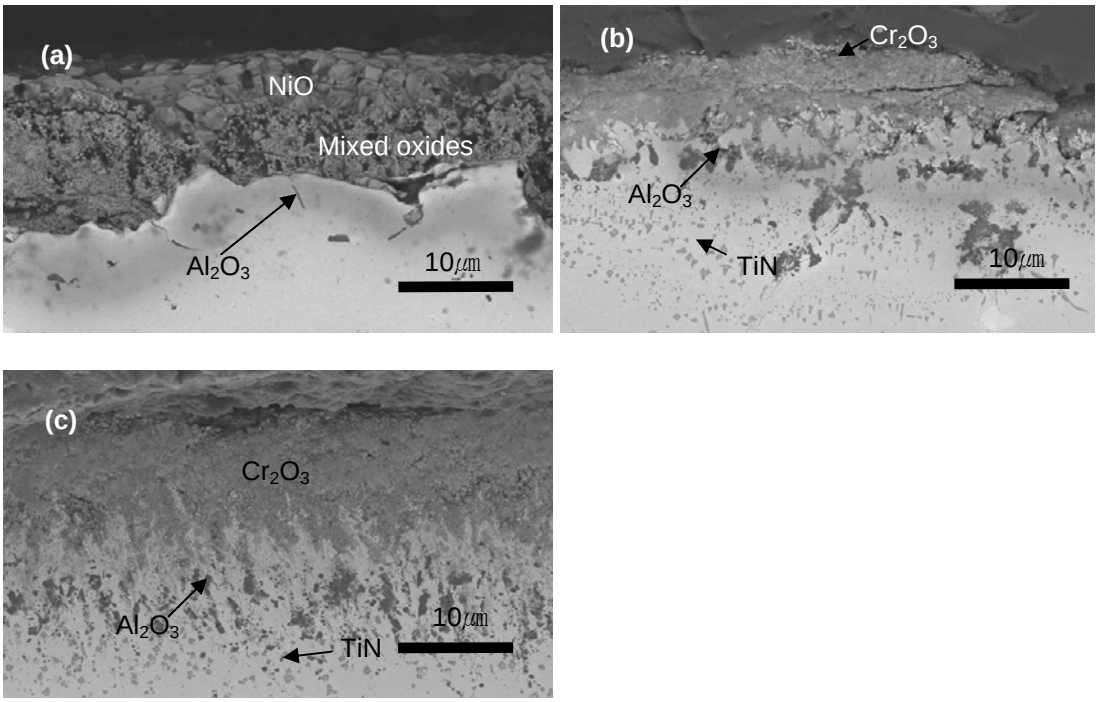

Figure 12. Scanning electron micrographs of cross-sections through René N5, GTD 111, and IN 738 after 80 hours at 950°C in dry air with CaO deposits on their surfaces.

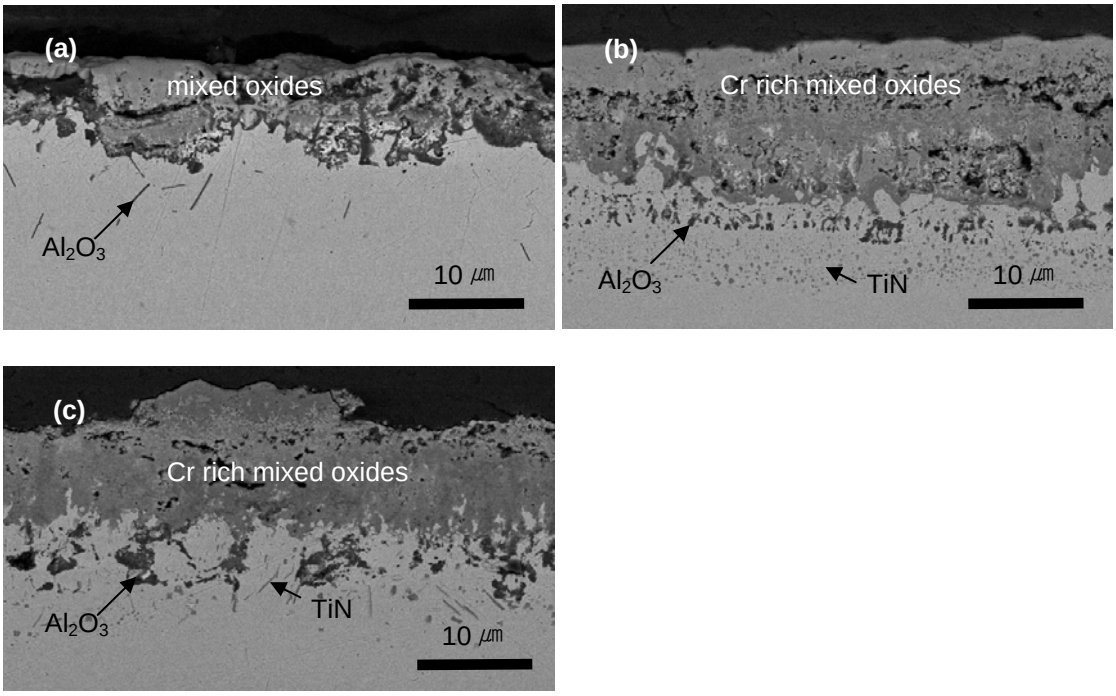

Figure 13. Micrographs showing cross-sections of René N5, GTD 111, and IN 738 with CaO deposits at 950^{o}C in wet air after 80 hours exposure.

5.3.2 Comparison of the Degradation of the Coated Alloys at 950°C

In this project, there are three superalloy substrates with three different coatings exposed at 950°C in dry and wet air with and without CaO deposits. In order to discuss the results in an orderly manner, the degradation of the coatings on the three alloys will be considered first in dry air, then wet, followed by CaO deposits in dry air, and finally with CaO deposits in wet air.

5.3.2.1 Dry Air at 950°C

Weight change versus time measurements for René N5 with the platinum aluminide, CoNiCrAlY and NiCrAlY coatings during exposure to dry air at 950°C are presented in Figure 14. The platinum aluminide coating exhibits smaller weight changes than the CoNiCrAlY and NiCrAlY coatings but none of these systems show indications of excessive degradation. Such measurements for these coatings on GTD 111 are presented in Figure 15. The results presented in this Figure are similar to those obtained for the René N5 substrate, Figure 14. The coatings on the different substrates are compared in Figures 16, 17, and 18 for the platinum aluminide, CoNiCrAlY and NiCrAlY, respectively. As in the previous results there is not any apparent effect of the substrate on the oxidation behaviors of the three coatings. Metallographic cross sections of some of the exposed specimens are presented in Figures 19, 20, and 21 for the platinum aluminide coating on René N5 and on GTD111, and for the CoNiCrAlY coating on GTD111, respectively. The oxide scales that are evident in these micrographs are predominantly alumina with some transient oxides in the case of the CoNiCrAlY coating.

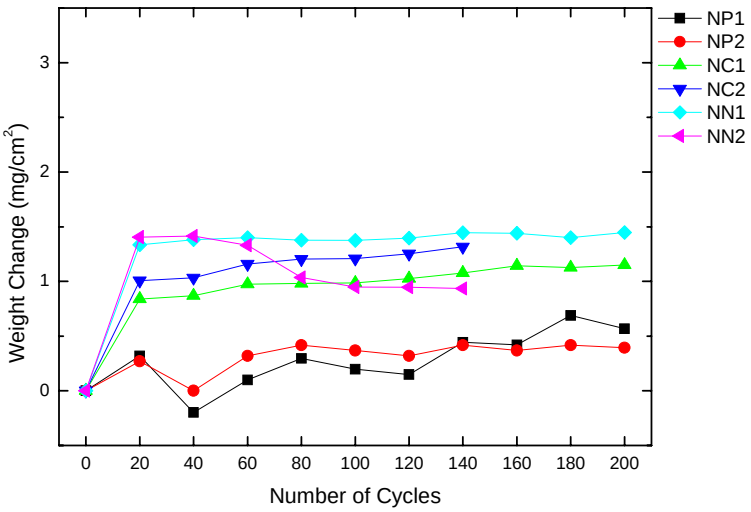

Figure 14. Weight change versus time measurements for platinum aluminide (NP), CoNiCrAlY (NC), and NiCrAlY (NN) coatings on René N5 without any deposit exposed at 950°C in dry air.

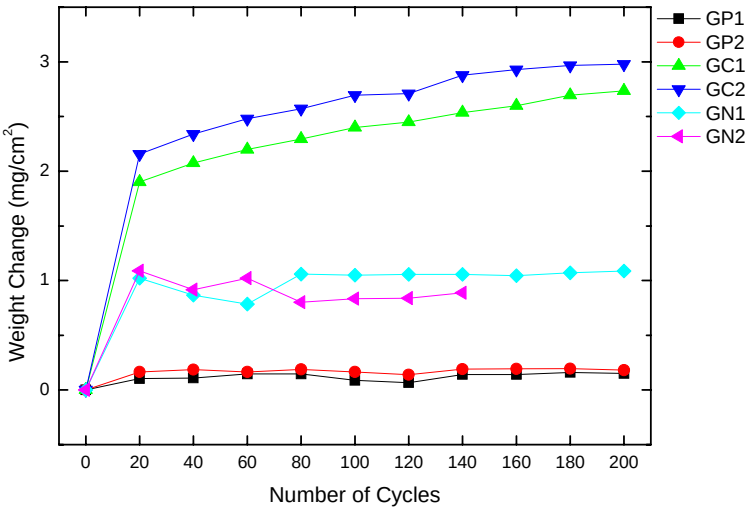

Figure 15. Weight change versus time measurements for platinum aluminide (GP), CoNiCrAlY (GC), and NiCrAlY (GN) coatings on GTD 111 without any deposit exposed at 950^{o}C in dry air.

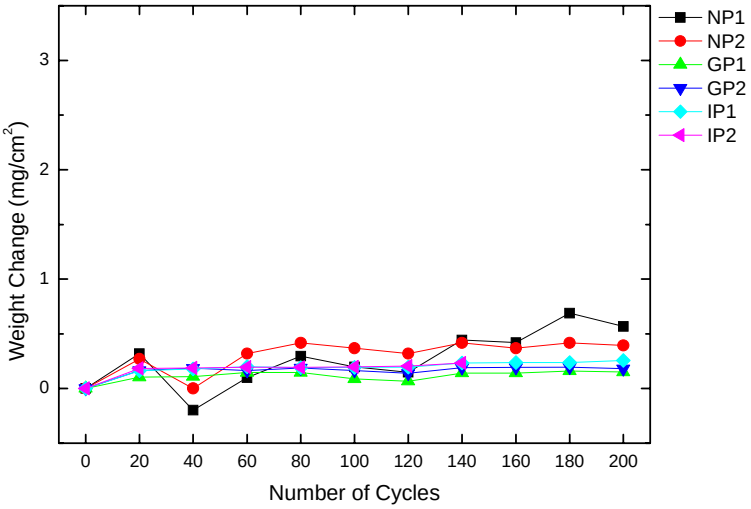

Figure 16. Weight change versus time measurements for platinum aluminide coatings on René N5 (NP), GTD 111 (GP), and IN 738 (IP) without any deposit exposed at 950^{o}C in dry air.

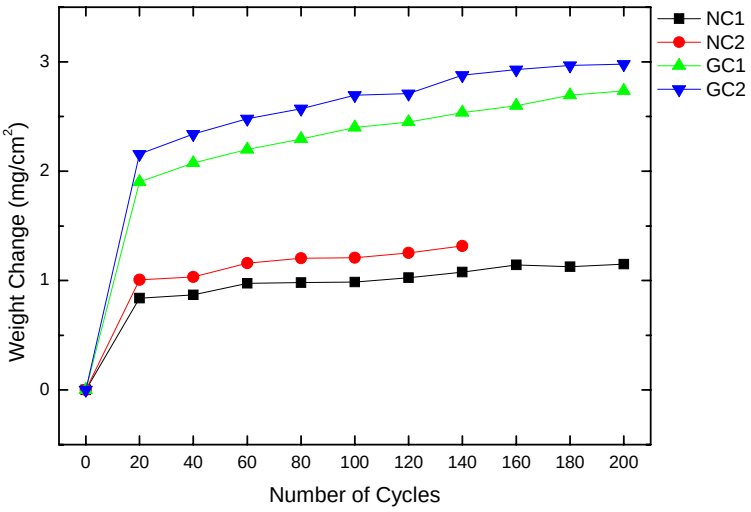

Figure 17. Weight change versus time measurements for CoNiCrAlY coatings on René N5 (NC) and GTD 111 (GC) without any deposit exposed at 950^{o}C in dry air.

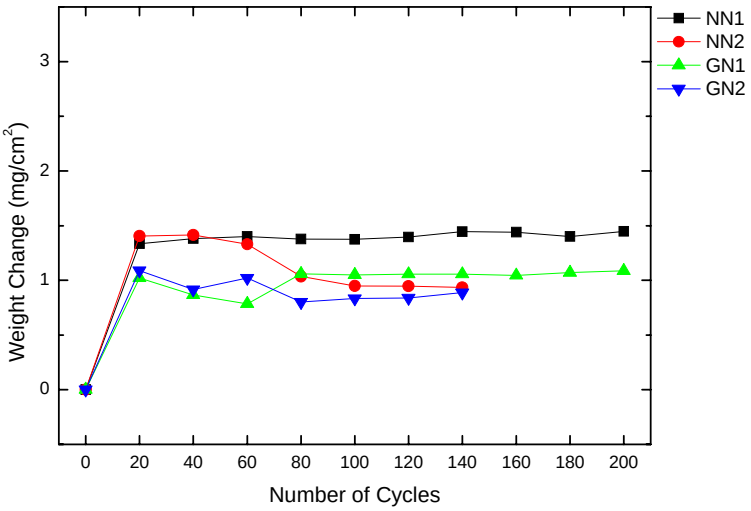

Figure 18. Weight change versus time measurements for NiCrAlY coatings on René N5 (NN) and GTD 111 (GN) without any deposit exposed at 950^{o}C in dry air.

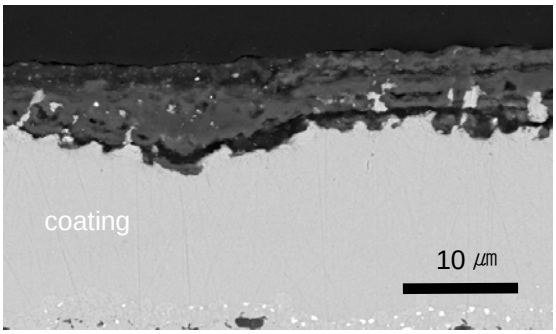

Figure 19. Micrograph showing cross-section of the platinum aluminide coating on René N5 without any deposit at 950^{o}C in dry air after 200 hours exposure.

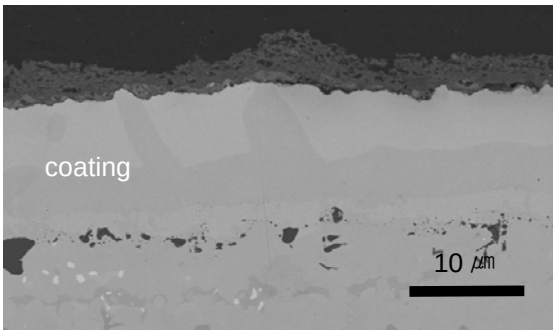

Figure 20. Micrograph showing cross-section of the platinum aluminide coating on GTD 111 without any deposit at 950^{o}C in dry air after 200 hours exposure.

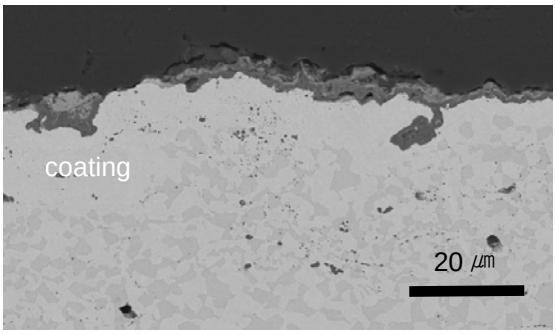

Figure 21. Micrograph showing CoNiCrAlY coating on GTD 111 without any deposit at 950^{o}C in dry air after 20 hours exposure.

5.3.2.2 Wet Air at 950^{o}C

Weight change versus time measurements for the cyclic oxidation of the three coatings on René N5 and GTD 111 are presented in Figures 22 and 23, respectively. No effect of the two different substrates on the oxidation behavior is evident. Also, comparison of Figure 14 and 15 with Figures 22 and 23 shows that the presence of water vapor has not caused the oxidation to become substantially more severe, although more spalling of oxide scales may have occurred in the water vapor environment. Data obtained for the cyclic oxidation of the platinum aluminide coating on the three different substrates is presented in Figure 24. These results show no pronounced effect of the substrate on the oxidation performance of this coating. Also, comparison of the data

presented in Figure 16 and 24 show no larger difference between specimens tested in dry and wet air.

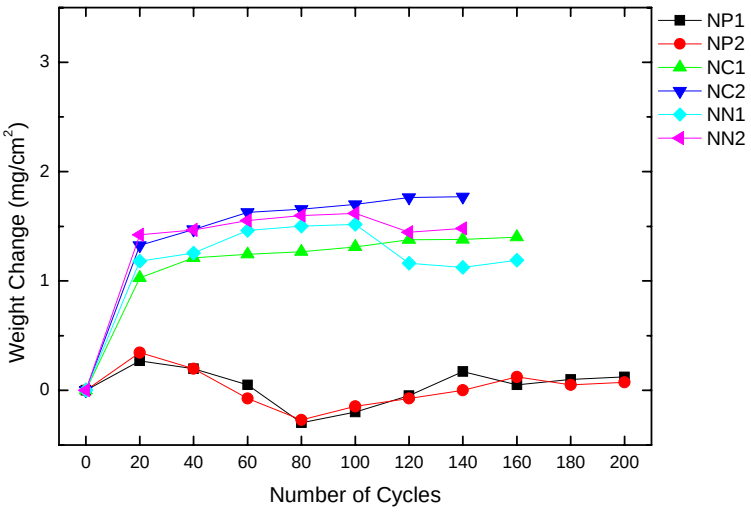

Figure 22. Weight change versus time measurements for platinum aluminide (NP), CoNiCrAlY (NC), and NiCrAlY (NN) coatings on René N5 without any deposit exposed at 950^{o}C in wet air.

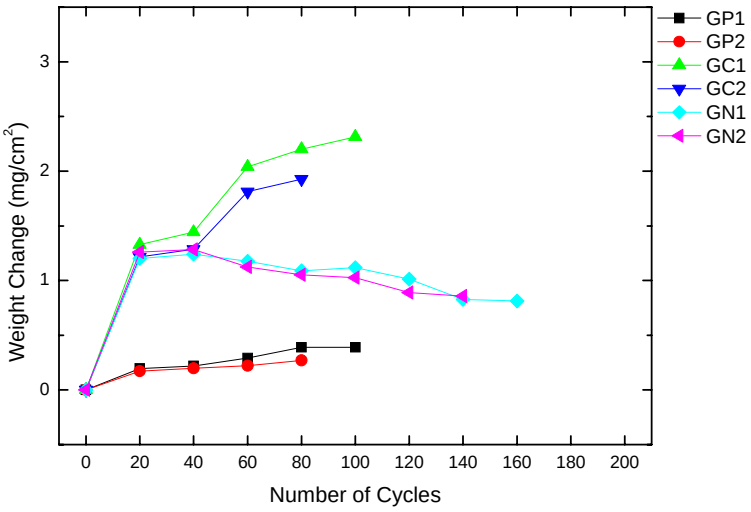

Figure 23. Weight change versus time measurements for platinum aluminide (GP), CoNiCrAlY (GC), and NiCrAlY (GN) coatings on GTD 111 without any deposit exposed at 950^{o}C in wet air.

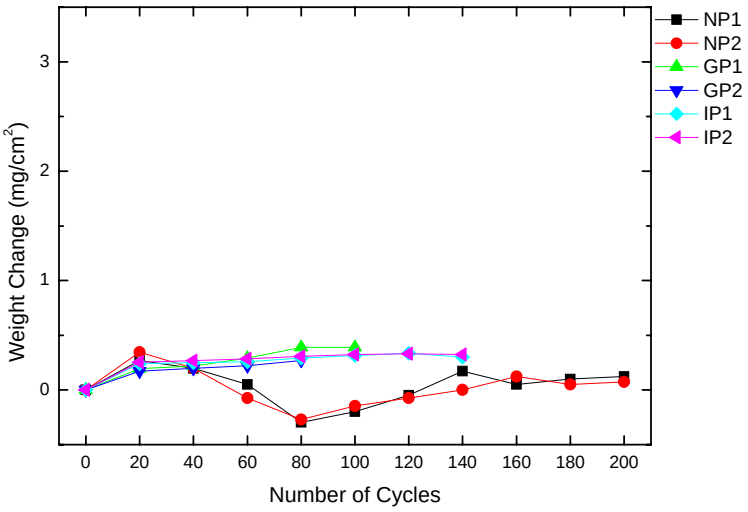

Figure 24. Weight change versus time measurements for platinum aluminide coatings on René N5 (NP), GTD 111 (GP), and IN 738 (IP) without any deposit exposed at 950°C in wet air.

Metallography is still in progress on some of the exposed specimens. Figures 25, 26, and 27 show micrographs of the platinum aluminide coating on René N5, GTD 111, and the CoNiCrAlY coating on GTD 111, respectively. The oxide scales are predominantly alumina, but some transient oxides are apparent on the CoNiCrAlY coating.

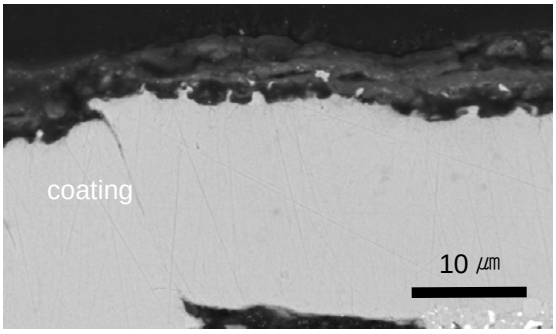

Figure 25. Micrograph showing cross-section of the platinum aluminide coating on René N5 without any deposit at 950°C in wet air after 200 hours exposure.

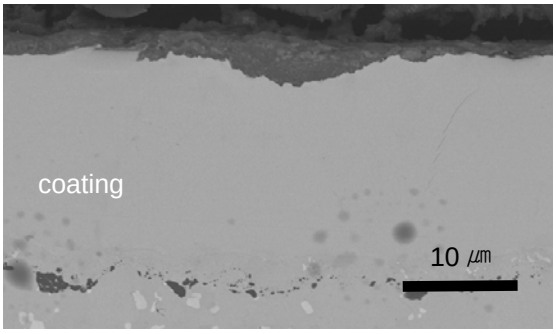

Figure 26. Micrographs showing cross-section of the platinum aluminide coating on GTD 111 without any deposit at 950°C in wet air after 200 hours exposure.

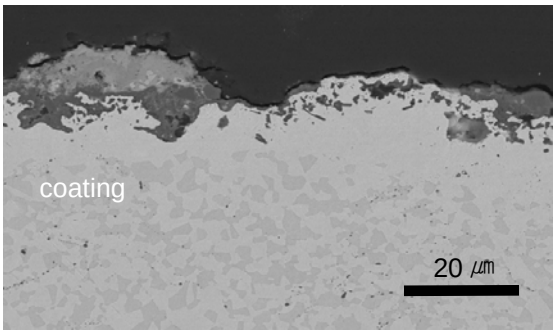

Figure 27. Micrographs showing cross-section of the platinum aluminide coating on GTD 111 without any deposit at 950°C in wet air after 80 hours exposure.

5.3.2.3 With CaO Deposits in Dry Air at 950°C

Weight change versus time measurements for the cyclic oxidation of the three coatings on René N5 and GTD 111 are presented in Figure 28 and 29, respectively. Significant weight losses are evident on most of the samples. It is clear that the CaO deposit is causing significant attack on all of the coatings. Data obtained for cyclic oxidation of the platinum aluminide coating on all three substrates are presented in Figure 30. More testing with this coating on IN 738 is required, but it appears substantial attack is occurring on all three substrates. The larger weight losses evident for the René N5 substrate must be compared with metallography of the exposed specimens. In Figures 31 and 32, the platinum aluminide coating on René N5 and on GTD 111 are shown after cyclic oxidation with CaO deposits in dry air. Substantial attack of this coating on both substrates is evident.

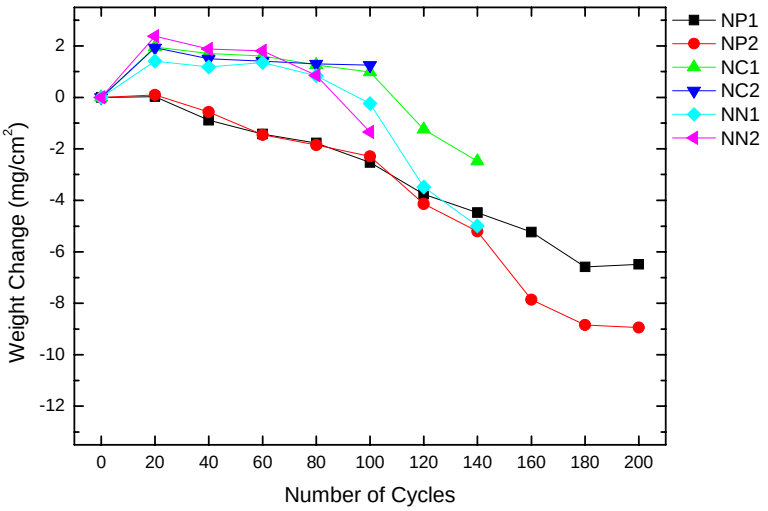

Figure 28. Weight change versus time measurements for platinum aluminide (NP), CoNiCrAlY (NC), and NiCrAlY (NN) coatings on René N5 with CaO deposits exposed at 950°C in dry air.

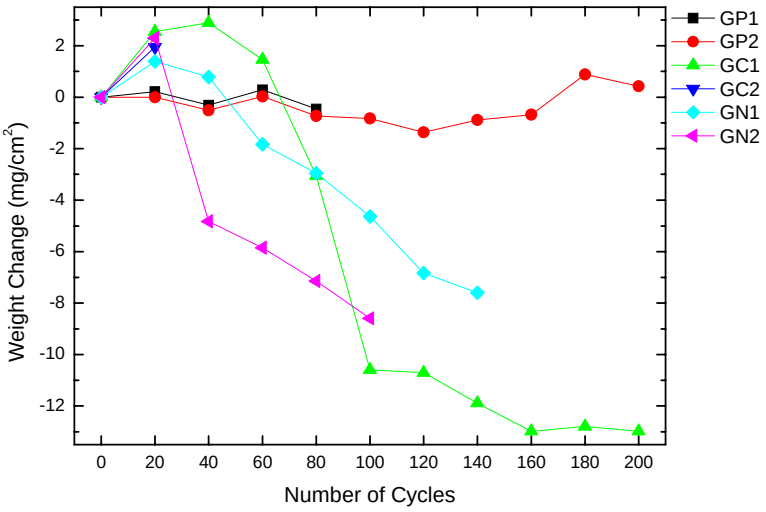

Figure 29. Weight change versus time measurements for platinum aluminide (GP), CoNiCrAlY (GC), and NiCrAlY (GN), coatings on GTD 111 with CaO deposits exposed at 950^{o}C in dry air.

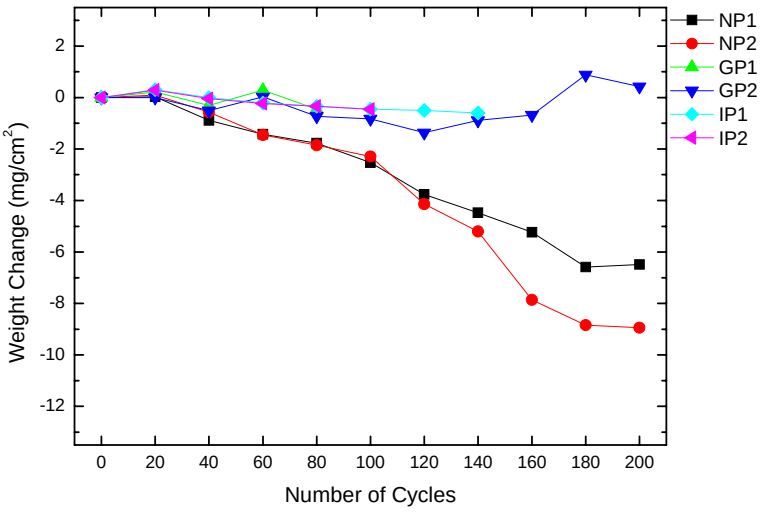

Figure 30. Weight change versus time measurements for platinum aluminide coatings on René N5 (NP), GTD 111 (GP), and IN 738 (IP) with CaO deposits exposed at 950^{O}C in dry air.

5.3.2.4 With CaO Deposits in Wet Air at 950^{o}C

The Cyclic oxidation tests of the three coatings with CaO deposits in wet air are still in progress. A few tests have been completed. All of the results for these conditions will be presented in the next semiannual report. The results that are available show that

the attack of the coatings with CaO deposits in wet air is substantial, but more work is required to determine if the attack with CaO is more severe in wet compared to dry air.

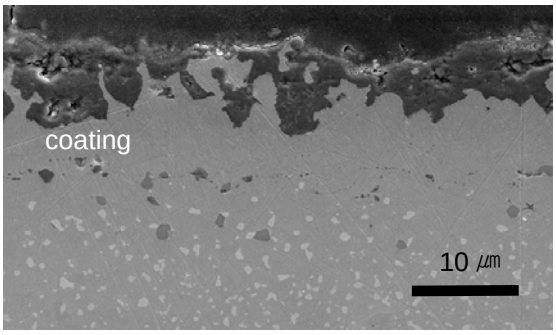

Figure 31. Micrograph showing a cross-section of the platinum aluminide coating on René N5 with CaO deposits at 950°C in dry air after 200 hours exposure.

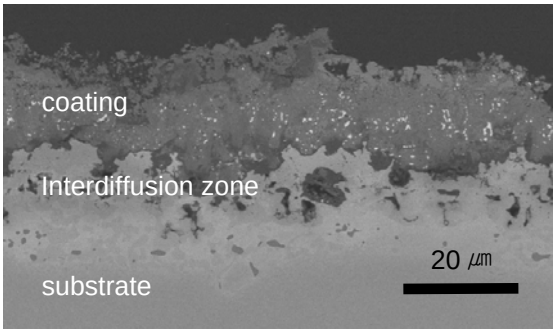

Figure 32. Micrograph showing a cross-section of the platinum aluminide coating on GTD 111 with CaO deposits at 950°C in dry air after 80 hours exposure.

5.3.2.5 Summary of Results Obtained from Testing with CaO Deposits in Dry and Wet Air at 950°C

The results obtained for the uncoated alloys, namely René N5, GTD 111, and IN 738, show that René N5 is more resistant to attack compared to GTD 111 and IN 738 when CaO deposits are not present. The presence of water vapor caused increased degradation of all three alloys, but this increase was not large. In the presence of CaO deposits, René N5 was attacked more severely than the other two alloys, but substantial attack of all three alloys was observed. When water vapor was present, substantial attack occurred for all three alloys, but this attack was more severe in the case of René N5. The attack of all three alloys was substantially increased when CaO deposits were present. This attack was so severe that it was not possible to determine if water vapor increased this severity. In the case of the coatings, the CaO deposit caused substantial attack of all three coatings, but this attack did not appear to be as severe as that observed for the uncoated superalloys. More work is required to determine the added effects of water vapor on the CaO-induced degradation of the coatings.

5.4 Tasks IV: Determine Moisture/Contaminants Limits

The purpose of this task is to determine the effects of contaminant amount and water vapor partial pressure on the deposit-induced degradation. The results presented in this report show that CaO deposits cause increased attack of all the systems studied in dry air. It is, therefore, apparent that water vapor is not required to have contaminant-induced degradation. In order to examine the effects of the amount of deposit, as well as water vapor content, experiments are being performed where the amount of the CaO deposit, and water vapor content, are being varied. In Figure 33, weight change versus time measurements are presented for GTD 111 specimens with different amounts of CaO deposits. In these experiments, 1mg/cm^2 of CaO was applied to four coupons and the specimens were exposed for 20 hours at 950^{o}C. After examination of the exposed specimens, 1mg/cm^2 of CaO was applied to three of the specimens, and all four specimens were exposed and additional 20 hours at 950^{o}C. This procedure was repeated until all specimens had been exposed 80 hours and specimen four had four times as much CaO as specimen one. These experiments were performed in dry air and in air with water vapor at 0.1atm. The data in Figure 33 are presented where the weight of the deposits are included in the measurements as well as where the weight of the deposits are subtracted from the weight change measurements. Both approaches show that the amount of attack, Figure 33, increases as the amount of deposit is increased. Surface photographs of the exposed specimens are presented in Figure 34.

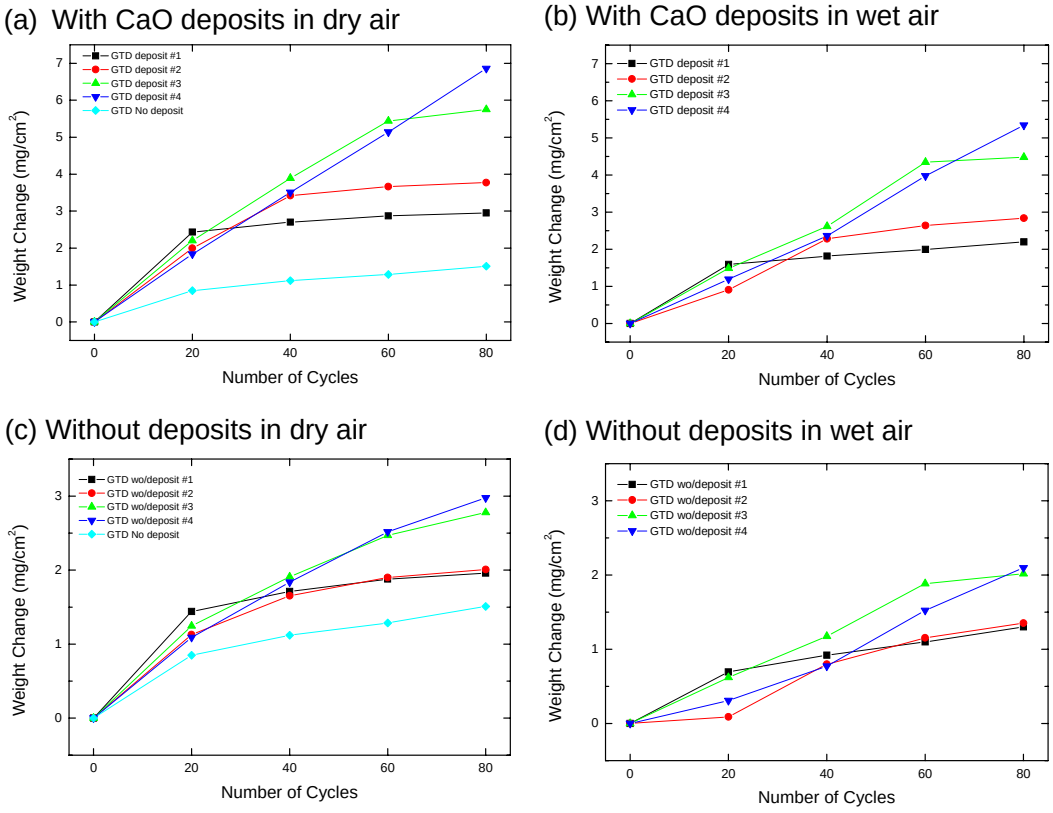

Figure 33. Weight change versus time measurements for GTD 111 exposed at 950^{o}C (a) and (c) in dry, (b) and (d) in wet air with different amounts of CaO deposits.

It is evident that the degradation increases as the amount of CaO is increased, but it is not clear if there is more attack in water vapor compared to dry air. Sections through exposed specimens are presented in Figure 35 and 36 for dry and wet air conditions. It is clear that the amount of attack increases with the amount of CaO deposit. However, it is not clear if the attack is more severe in water vapor. Work is now in progress to examine the effect of higher water vapor pressures.

(a) in dry air

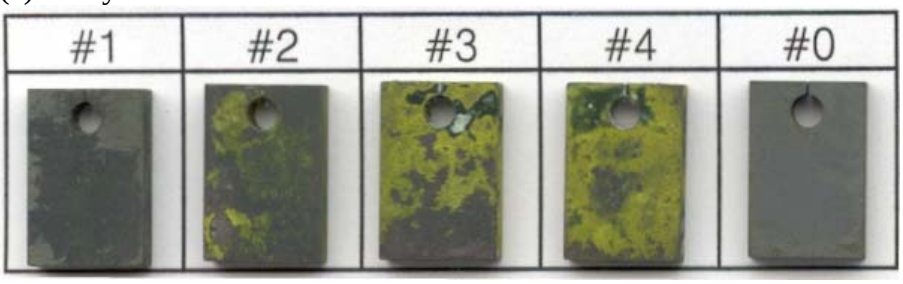

(b) in wet air

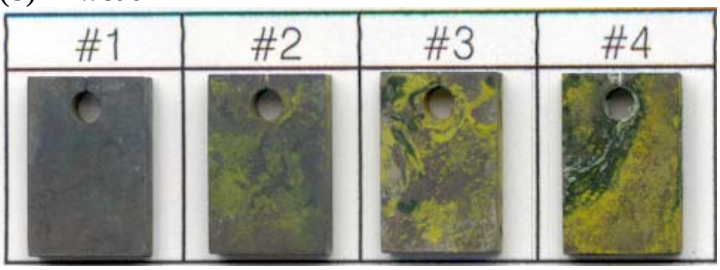

Figure 34. Surface photographs of specimens described in Figure 33 after 80 hours exposure (a) in dry and (b) wet air. Note that the specimen #0 is the one that no CaO was deposited.

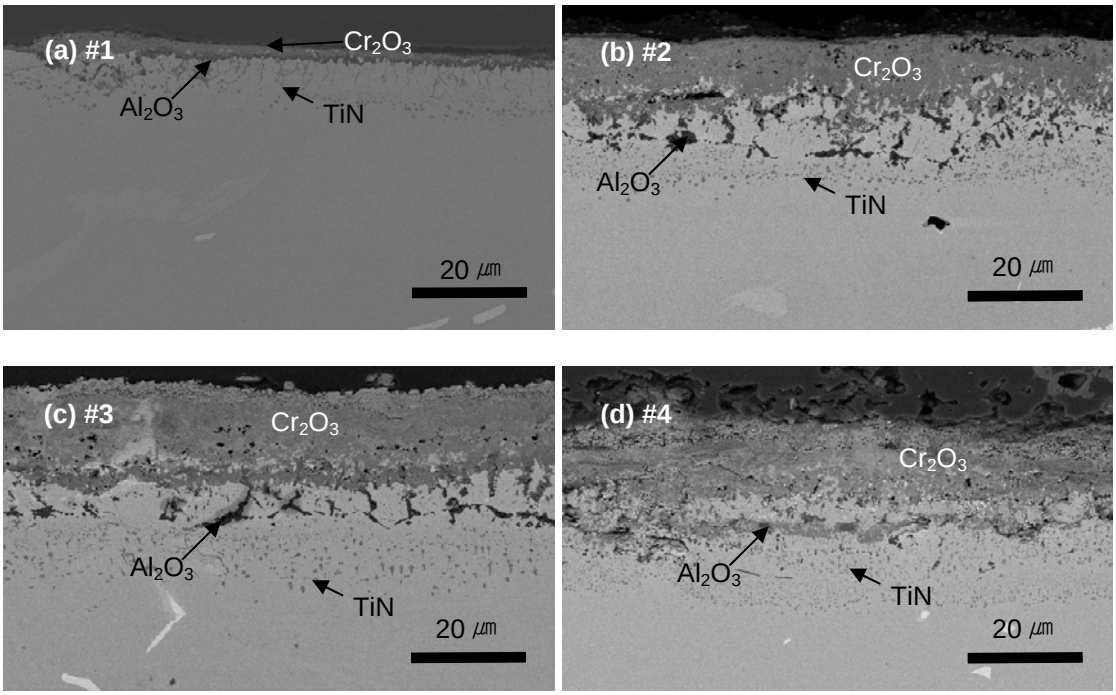

Figure 35. Cross-sections of GTD 111 with different amounts of CaO deposits exposed at 950^{o}C after 80 hours in dry air.

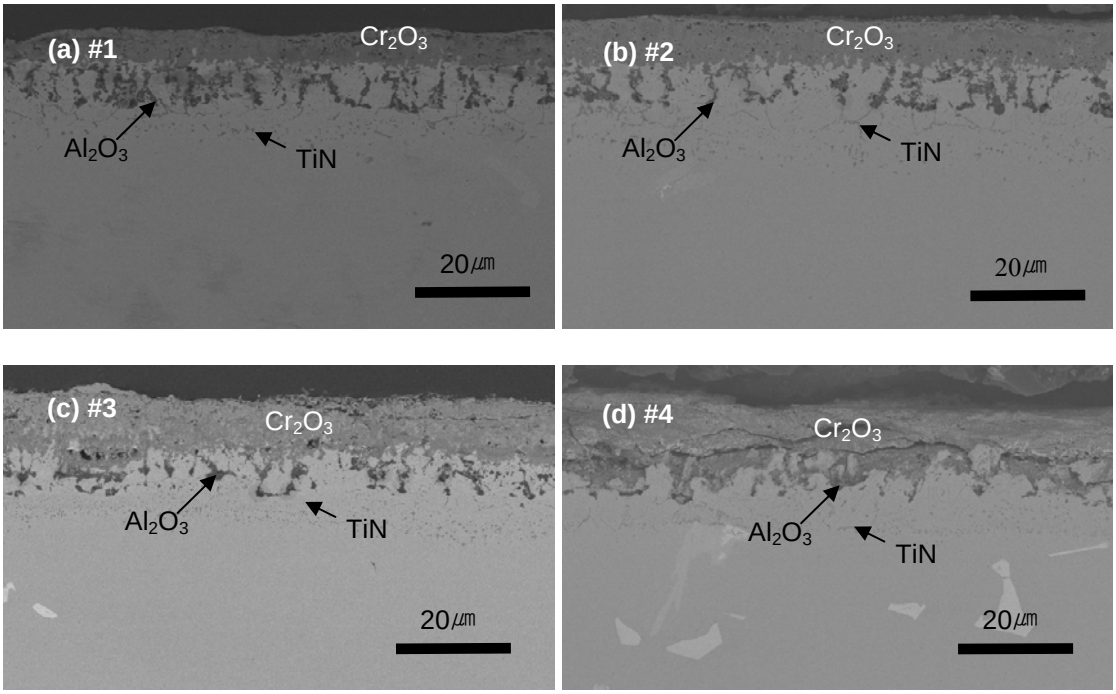

Figure 36. Cross-sections of GTD 111 with different amounts of CaO deposits exposed at 950^{o}C after 80 hours in wet air.

5.5 Task V and VI

These two tasks involve tests using TBCs (Task V) and a CMC (TaskVI). To investigate the effect of CaO-induced attack on such systems in dry and wet air at 950^{o}C, procurement of specimens is now in progress.

6.0 CONCLUSIONS

Uncoated specimens of René N5, GTD 111, and IN 738 have been exposed to CaO deposits at 950^{o}C. All three alloys were severely attacked and the degradation of René N5 was more severe than that of GTD 111 and IN 738. This attack appeared to be more severe in water vapor compared to that in dry air. However, since the attack was severe in dry air, it was difficult to determine how much more attack occurred in the presence of water vapor.

Tests have been performed using CaO deposits on the following coatings, platinum aluminide, CoNiCrAlY, and NiCrAlY. These coatings were deposited upon the three substrates, René N5, GTD 111, and IN 738. Severe attack of all three coatings was observed in the case of CaO deposits

It has been determined the larger the amount of the CaO deposit, the more the degradation of GTD 111. Additional work is planned with the coatings on the influence of the amount of the CaO deposit, as well as any added complication due to the presence of water vapor.

7.0 REFERENCES

1. N. Birks, G. H. Meier, and F. S. Pettit, Introduction to High Temperature Oxidation of Metals, 2nd Edition, Cambridge University Press, Cambridge, 2006.
2. F.S. Pettit and C.S. Giggins, Hot Corrosion, Chapter 12, Superalloys II, C.T. Sims, N.S.Stoloff and W.C. Hagel, eds; John Wiley & Sons, New York (1987).
3. J. Stringer, Ann. Rev. Mat. Sci. 7, 477 (1976).
4. R.A. Rapp, Hot Corrosion of Materials, pp. 291-329, in Selected Topics in High Temperatures Chemistry, O. Johnannesen and A. Anderson, eds; Elsevier, New York (1989).
5. N.S. Bornstein and M.A. DeCrescente, Met. Trans., 2, 2875 (1971).
6. B.M. Warnes, The Influence of Vanadium on the Sodium Sulfate Induced Hot Corrosion of Thermal Barrier Coating Materials, PhD Dissertation, University of Pittsburgh (1990).
7. K.L. Luthra, Met. Trans., 13A, 1647, 1843 (1982).
8. R.H. Barkalow and G.W. Goward, in High Temperature Corrosion, R.A. Rapp, ed; NACE 6, Houston, TX (1983).
9. M.P. Borom, C.A. Johnson and L.A. Peluso, Surface and Coatings Technology, 86-87, 116 (1996).
10. S. Krämer, J. Yang, C. A. Johnson, and C. G. Levi, "Thermochemical Interaction of Thermal Barrier Coatings with Molten CaO-MgO-Al_2O_3-SiO_2 Deposits", J. Amer. Ceram. Soc., 89, 3167-3175 (2006)
11. R.R. Wenglarz, "Turbine Flow Path Issues for Syngas and Other Alternate Fuels", Impact of Alternative Fuels on Turbine Materials, Materials Workshop III, DOE, University of Connecticut, October 14-16, 2002.
12. W.T. Reed, External Corrosion and Deposits, American Elsevier Publishing Co., Inc., New York, NY (1971).
13. K.T. Chiang, G.H. Meier and R.R. Perkins, J. Materials for Energy Systems, 6, 71-86 (1984).
14. G.H. Meier and F.S. Pettit, "Interaction of Steam/Air Mixtures with Turbine Airfoil Alloys and Coatings", Subcontract No. 99-01-SR077, South Carolina Energy Research and Development Center, Clemson, SC.
15. G.H. Meier and F.S. Pettit, Investigation of Materials Performances in High Moisture Environments Including Corrosive Contaminants Typical of Those Arising by Using Alternate Fuels in Gas Turbines, Semiannual Report, February 21, 2006, UTSR Project 04 01 SR 116.
16. G.H. Meier and F.S. Pettit, Investigation of Materials Performances in High Moisture Environments Including Corrosive Contaminants Typical of Those Arising by Using Alternate Fuels in Gas Turbines, Second Annual Report, July 31, 2006, UTSR Project 04 01 SR 116.

Autoignition Studies of Syngas and Hydrogen (SGH) Fuels

Semi-Annual Report
For
August 1, 2006 to January 31, 2007

R. J. Santoro, Principal Investigator

March 2007

DOE Award No. DE-FC26-02NT41431
UTSR Project No. 05-01-SR117
Clemson University Research Foundation
South Carolina Institute for Energy Studies
Clemson, South Carolina 29634-5181

Department of Mechanical and Nuclear Engineering
The Pennsylvania State University
University Park, PA 16802

DISCLAIMER

ABSTRACT

During this six-month reporting period, which covers the period August 1, 2006 to January 31, 2007, work has focused on fabrication of the redesigned high-pressure high-temperature flow reactor to be used in the autoignition studies of syngas. Fabrication of the major components of the high-pressure high-temperature flow reactor has been completed. Assembly of the flow reactor has also been completed and testing will begin in the next reporting period. The redesigned high-pressure high temperature flow reactor can achieve a maximum temperature of 950 K (1710 R) as compared to 800 K for the original design. At this maximum operating temperature, there is a sufficient overlap with shock tube data to allow a meaningful comparison with flow reactor data obtained in the current project. Comparison with the shock tube data, also being conducted under the University Turbine Systems Research (UTSR) program, is critical as shock tubes can not achieve the lower temperatures available in flow reactor studies. Thus, data from both shock tube and flow reactor techniques is required to fully characterize the autoignition process relevant to gas turbine systems. The unique capabilities of this flow reactor allow measurements of autoignition time for syngas and hydrogen syngas mixtures under conditions relevant to gas turbine operating conditions in terms of pressure and temperature. These measurements are required if syngas produced by coal gasification is to be utilized in land-based gas turbine systems to generate electric power. Interactions with leading gas turbine manufacturers such as Pratt and Whitney, General Electric and Siemens have established the need for autoignition data for syngas as well as providing the foundation for the rapid transition of the results of our studies to the user community.

TABLE OF CONTENTS

LIST OF FIGURES

INTRODUCTION

The renewed interest in coal-based integrated gasification combined cycle (IGCC) plants is due to the desire for greater fuel supply flexibility and the large known resources of coal in the United States. Current Department of Energy plans strive for efficient, environmentally clean IGCC technologies that can provide both electrical generation and hydrogen production capabilities. Combustion of syngas produced from the coal gasification process, as well as a broader range of syngas and hydrogen (SGH) fuels, has been identified as a key technology area. From an operations standpoint, to meet gas turbine fuel demand requirements, the fuel composition will vary as a function of the gasifier operating levels. Clearly, this introduces new challenges to gas turbine technology since fundamental characteristics of SGH fuels related to autoignition, flashback and blowout are presently not available. The current three year effort will systematically examine autoignition phenomena related to SGH fuels at the high pressure, temperature and flow velocity conditions representative of actual gas turbine operating conditions.

The autoignition phenomenon involves a series of spontaneous physical and chemical processes that usually overlap and eventually lead to the ignition of the mixture within a time period referred to as the ignition delay time. For unmixed gaseous fuel and air, the autoignition process involves mixing along with concurrent combustion occurring that lead to a rapid release of energy. The characteristic times for mixing and chemical reaction processes can vary widely for different combustion devices due to differences in initial equivalence ratio, pressure, temperature and flow velocity. Thus, care must be exercised as one utilizes autoignition data obtained under different experimental conditions. Ignition delay is usually characterized using either shock tubes or high-temperature and high-pressure flow reactors. For shock tube studies, the reactants are usually premixed and the near-instantaneous arrival of the shock wave imposes the high-temperature, high-pressure test conditions. Here, mixing effects are absent and the ignition delay time is dominated by energy release processes due to chemical kinetics. In contrast, for flow reactor studies, the fuel and oxidizer are typically introduced separately and mixing times can be a significant fraction of the overall ignition delay time. Consequently, measurements made in these different devices can lead to differing ignition delay times.

The objective of the current work is to experimentally characterize autoignition of syngas and SGH fuels at high pressures and high temperatures typical of lean premixed gas turbine engine conditions. For gas turbine engines, the temperature and pressure regime of interest usually extends to pressures and temperatures up to nominally 3 MPa (~450 psia) and 1000 K (1800°R), respectively. Since these conditions can readily be matched by flow reactors but not by shock tubes, the experimental research effort on characterizing autoignition for SGH fuels is planned to be carried out in a constant-diameter, variable-length flow reactor.

EXECUTIVE SUMMARY

Project Title: Autoignition Studies of Syngas and Hydrogen (SGH) Fuels

DOE Award Number: DOE Award No. DE-FC26-02NT41431

UTSR Project Number: UTSR Project No. 05-01-SR117

Principal Investigator: Robert J. Santoro

Telephone: (814)863-1285 Fax: (814)865-3389 E-mail rjs2@psu.edu

Summary of Progress

The objective of the current research effort is to parametrically determine the autoignition delay time for CO/H_2 (SGH fuels) as a function of CO concentration, equivalence ratio, pressure and temperature. In addition, the effect of water concentration on autoignition will be determined using mixtures of $CO/H_2/H_2O$ subject to the availability of funding. Measurements will be obtained for operating pressures up to 3.0 MPa (435 psia) and typical air mass flow rates of 0.45 kg/s (1.0 lbm/s).

During the period from August 1, 2006 to January 30, 2007, major progress has been in the fabrication and assembly of the high-pressure high-temperature flow reactor to be used in these studies. As reported in the previous Semi-Annual Report (February 1, 2006 to July 31, 2006), a complete redesign of this flow reactor was completed in order to allow a wider range of high temperatures to be achieved. The need for this increased temperature range is to provide an overlap of the test conditions studied in the present work with studies conducted with shock tubes. In the material presented below, further details of the high-pressure, high-temperature flow reactor will be briefly presented. A more detailed discussion will follow in the *Results and Discussion Section* of this report.

Task 1 – Experimental Effort

With the completion of the redesign of the high-pressure, high-temperature flow reactor reported during the previous reporting period (February 1, 2006 to July 31, 2006), work during the current reporting period has focused on the fabrication of the individual components of the flow reactor, which has been completed. As described in our semi-annual report of August 1, 2005 to January 31, 2006, modeling studies indicated that the temperature of the mixture of air and syngas may need to be in excess of 800 K, which was the maximum temperature for the original design for the flow reactor, for the mixtures to autoignite within the length of the reactor (approximately 1.8 m (6 ft)). Furthermore, the

existing 280 kW electric heater can heat the air flow to approximately 800 K (1440°R), however, due to the relatively high heat capacity of the fuel (mainly due to hydrogen), the air/fuel mixture temperature will be reduced significantly if the fuel is introduced at ambient temperature. The redesigned flow reactor will allow a maximum temperature of 950 K (1710°R) to be achieved. A customized clam shell heater system was fabricated by a commercial source to heat the test section, which will significantly reduce heat loss as the air/fuel mixture flows through the test section. This redesign also incorporates heat exchangers to heat the both fuel and air prior to the mixing section of the flow reactor. With the completion of the fabrication of the flow reactor components, assembly of the high-pressure high-temperature flow reactor has been substantially completed. During the next reporting period, the mixing uniformity of the injector and temperature field in the flow reactor will be characterized. Measurements of the autoignition time for H_2 and CO/H_2 mixtures will also be initiated.

Task 2 – Analytical Effort

During this six-month reporting period, work on analytical and chemical kinetic modeling studies related to the existing H_2/O_2 and $H_2/CO/O_2$ mechanisms to predict the autoignition times has been limited. The next significant phase of the chemical kinetic modeling effort will require data on autoignition of syngas mixtures obtained from the flow reactor that will be made in the next reporting period (February 1, 2007 to July 31, 2007). In the mean time, a separate study to determine the laminar flame speed for a variety of $H_2/CO/Air$ mixtures has been completed and comparison with current model prediction is underway.

Industrial Interactions

The principal investigator has interacted with Dr. Med Colket III of United Technologies Research Center to draw on his experience in autoignition and analysis of detailed chemical kinetic models for a wide variety of combustion systems. Additionally, several discussions have occurred with General Electric involving engineers at their Greenville, SC facility who are interested in this syngas project. Interactions with Siemens involving Dr. Anil Gulati have also commenced during the present reporting period.

PROJECT DESCRIPTION

For the experimental phase of the research effort, autoignition of SGH fuels will be systematically investigated over a range of CO concentrations in a high-pressure (up to 3.04 MPa (441 psia)) high-temperature (800-900 K (1440-1620°R)) flow reactor. Using the extensive data base developed during the study, the ignition delay time will be modeled using both a global ignition delay time approach as well as a detailed chemical kinetic reaction rate mechanism appropriate for the $CO/H_2/Air$ and $CO/H_2/H_2O/Air$ systems. These systems represent two of the most thoroughly studied in combustion in terms of detailed chemical kinetic results with much of the existing data incorporated into regularly utilized models such as GRIMECH using the CHEMKIN^{TM} solver [1]. However, there is little data available for the pressure and temperature range to be studied in the current effort. Thus, the current research will provide a critical test for these models regarding their applicability to syngas, SGH and even pure hydrogen at operating conditions for gas turbine systems.

RESULTS AND DISCUSSION

Experimental Effort

The SGH fuels autoignition characterization experiments will be conducted at the Cryogenic Combustion Laboratory at Penn State where high pressure and high temperature experiments utilizing hydrogen fuel are routinely carried out in a safe manner. The high-pressure high-temperature flow reactor to be used for these studies is shown in Fig. 1. Three features in general should be noted as identified on the figure. A custom designed clamshell heater (feature 1 in Fig. 1) was added to the original design to heat the test section to reduce heat loss from the hot air/fuel mixture as it flows through the test section. A preburner/heat exchanger (feature 2 in Fig 1) is incorporated into the fuel delivery system to provide heated fuel to the flow reactor. Heating of the fuel will reduce the temperature drop that results if ambient temperature fuel is mixed with the heated air. Calculations have shown that depending on the equivalence ratio, mixing ambient temperature fuel with the heated air decreases the temperature of the mixed air/fuel mixture by 50 to 100 K (90 to 180°R). Such a large reduction in the temperature of the air/fuel mixture would restrict the upper temperature over which experiments could be conducted. Finally, a second heat exchanger (feature 3 in Fig. 1) that is also connected to the preburner allows for the heated air from the electric air heater to be raised to temperatures as high as 950 K (1710°R). Chemical kinetic modeling studies reported on in a previous semi-annual report (August 1, 2005 to January 31, 2006), indicated that this maximum temperature will allow the present flow reactor studies to overlap experiments conducted in shock tubes.

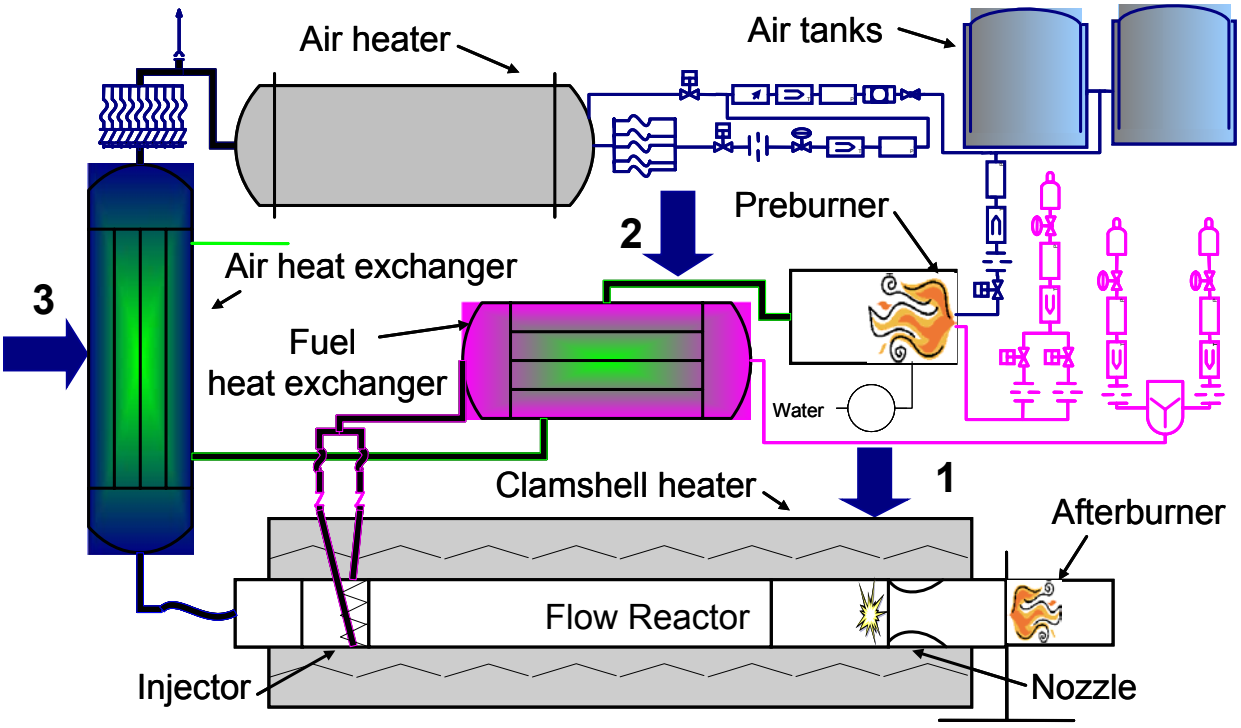

Fig. 1. Schematic of High-Pressure High-Temperature Flow Reactor Facility that specifically highlights are (1) the clam shell heater used to reduce heat loss, (2) Preburnr/heat exchanger for heating the fuel and (3) the heat exchanger for increasing the air temperature to 950 K (1710°R) from the 800 K temperature provided by the air heater.

Figure 2 shows a photograph of the assembled flow reactor with the upper half of the clam shell heater removed. The variable-length test section (maximum length of 1.83 m (6 ft)) has a circular cross section (diameter of 43 mm (1.7 in.)) and limited optical access for laser diode line-of-sight CO absorption measurements as well as flame and chemiluminescence detection at the downstream location. The optical access ports are designed such that the internal geometry is smooth. The test section is instrumented with pressure transducers and an axial array of thermocouples. Such measurements are necessary to document the conditions at which autoignition occurs.

With respect to the air flow conditions, a maximum flowrate of 2.5 kg/s (5.5 lbm/s) is supplied from two blowdown tanks to an electric resistance-type air heater that can heat approximately 0.45 kg/s (1 lbm/s) of air to a maximum temperature of 800 K (1440 R). Air flow then passes through the heat exchanger discussed above. The heated air flows through a flow straightener section and subsequently mixes with the fuel in the mixer section. The mixed air/fuel mixture then flows through a constant-diameter variable-length instrumented test section followed by a flow nozzle.

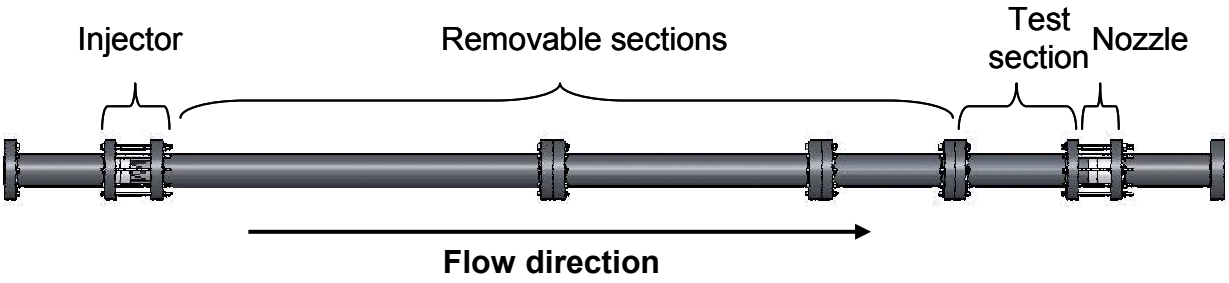

(a)

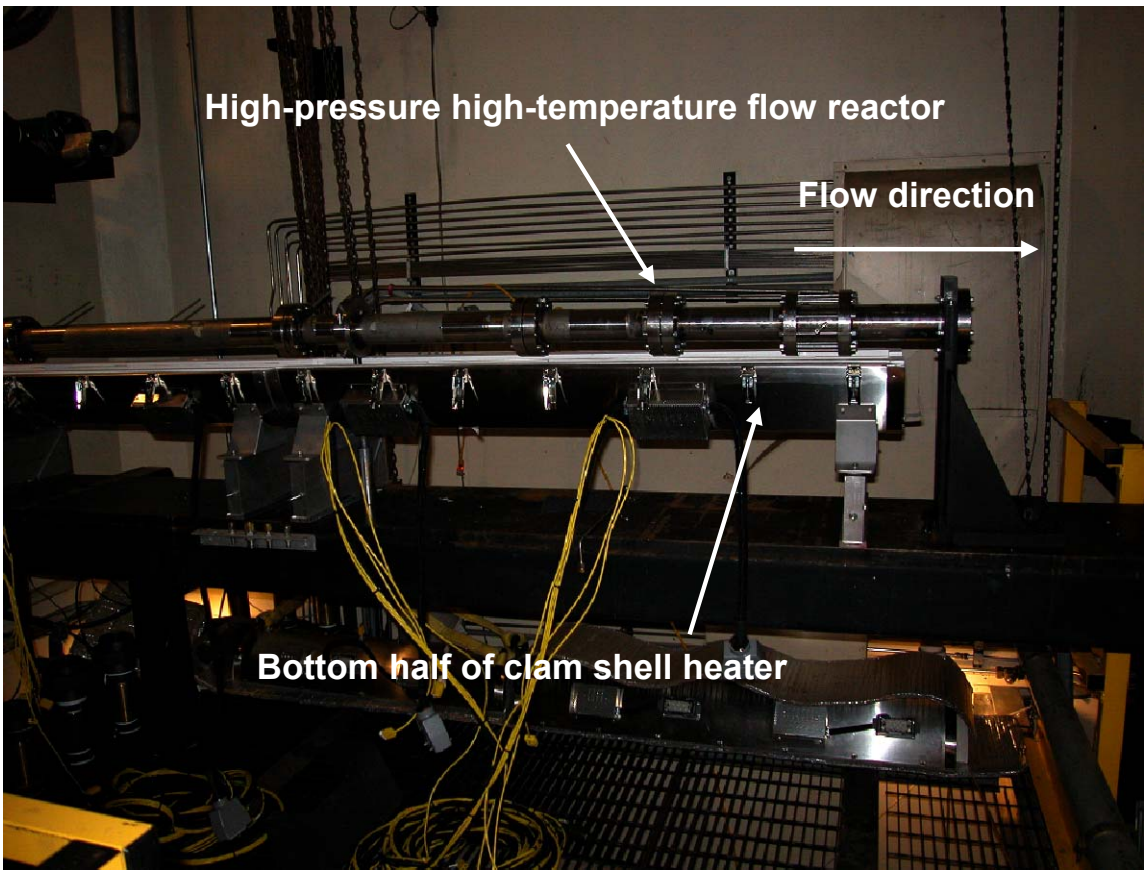

(b)

Fig. 2. Schematic (a) and photograph (b) of the assembled high-pressure high-temperature flow reactor with the upper half of the clam shell heaters removed.

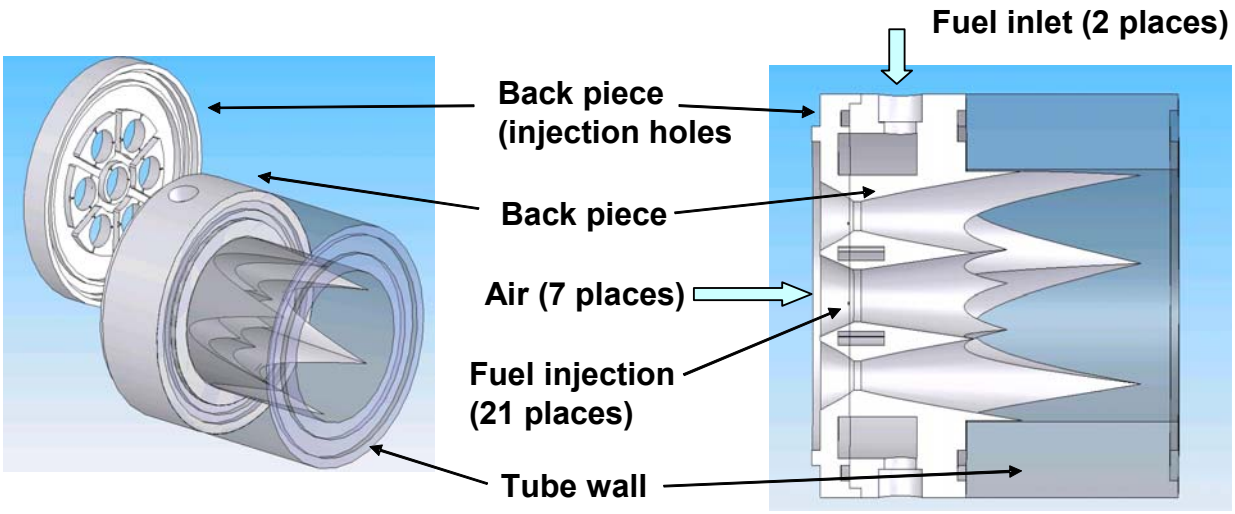

(a)

(b)

Fig. 3. A schematic (a) and photograph (b) of injector that rapidly mixes fuel and air. Two fuel injector plates along with the converging-diverging nozzle where fuel is injected are shown in the photograph.

The flowpath including the fuel injector is designed to minimize the possibility of recirculation zones since the presence of any recirculation can cloud the interpretation of data [2]. For autoignition studies, the gaseous fuel injector also needs to be designed to provide rapid mixing without creating wakes and recirculation zones. The injector design, which is shown in Fig. 3, involves introducing the gaseous fuel radially inward into the upstream converging sections of seven converging-diverging (C-D) nozzles through which the air flows. The gaseous fuel is introduced through three radial passages for each C-D air nozzle. This design improvises on the injection scheme for rapid mixing used by Spadaccini and TeVelde [2], and provides for a mixed flow without the presence of any local recirculation zones or wakes. In order to assure good mixing conditions over the entire range of flow rates and pressures, four fuel injector plates have been fabricated with appropriate fuel injector to diameters to maintain the

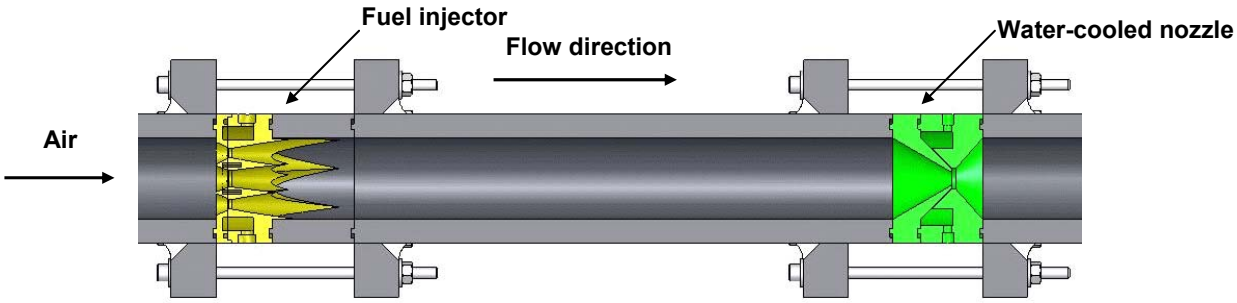

(a)

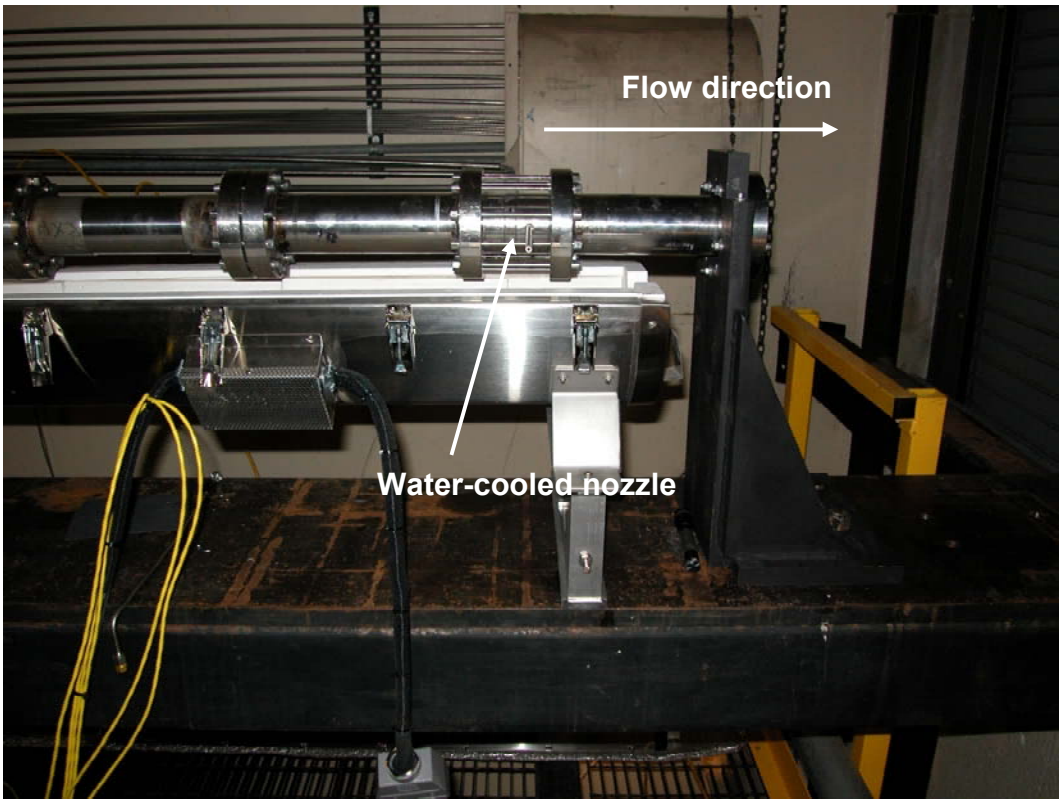

(b)

Fig. 4. (a) Schematic of the high-pressure high-temperature flow reactor showing the injector and nozzle sections, and (b) close up photograph showing the nozzle of the reactor.

required jet momentum to penetrate the air flow and result in the desired mixing uniformity. Two of the fuel injector plates are shown in Fig. 3.

Figure 4 shows a schematic of the test section of the flow reactor and a photograph of the nozzle end of the flow reactor. On the left hand side of Fig. 4(a), the injector can be seen with the right hand side showing the water cooled sonic nozzle and water quenching to isolate the test section from the afterburner. The water-cooled nozzle is also seen in the photograph shown in Fig. 4(b).

This combination of a sonic nozzle and water quenching assures that no ignition event occurring downstream of the test section can propagate back up into the test section. Currently, planar laser-induced fluorescence studies are being conducted to document the mixing uniformity. Concurrently, characterization of the radial and axial temperature profiles achieved in the test section of the flow reactor will be conducted.

Analytical Effort

During this six-month reporting period, work on analytical and chemical kinetic modeling studies related to the existing H_2/O_2 and $H_2/CO/O_2$ mechanisms to predict the autoignition times has been limited. The next significant phase of the chemical kinetic modeling effort will require data on autoignition of syngas mixtures obtained from the flow reactor that will be made in the next reporting period (February 1, 2007 to July 31, 2007). In the mean time, a separate study to determine the laminar flame speed for a variety of $H_2/CO/Air$ mixtures has been completed and comparison with current model prediction is underway.

CONCLUSIONS

During the present reporting period, the most significant accomplishment has been fabrication and assembly of the high-pressure high-temperature flow reactor that will be utilized in the syngas autoignition studies. There can be no question given the current energy crisis and the reemergence of coal as a primary fuel for meeting U.S energy that understanding the combustion properties of syngas is critical to practical utilization of this fuel in lean-premixed gas turbine systems used for electrical power generation. The challenges that gas turbine manufacturers and operators face as syngas fuels emerge for practical use are daunting, but solvable if the fundamental engineering research base is in existence that characterize these fuels. Without such an engineering data base, implementation of coal-based approaches, such coal gasification, will not be able to meet the demand for energy in the U.S. The present study has established a unique experimental capability to measure syngas autoignition properties over the required pressure, temperature and composition range required for industry to incorporate the needed changes in their existing gas turbine technology. However, more than just data is required to impact the future utilization of syngas in land-based gas turbines. Models, both of an analytical and detailed chemical mechanistic form, are required to update design and operational methodologies that will enable the use of syngas. Cleary, the present work reported on here has taken the approach to concurrently develop both the required hardware and modeling tools to study autoignition of syngas and hydrogen (SGH). Integrating both experiments and modeling into our project has already shown benefits in the design of the experimental hardware that will allow us to achieve the necessary

conditions to provide relevant data. By also working with leading gas turbine manufacturers such as Pratt and Whitney, General Electric and Siemens, the foundation for the rapid transition of the results of our studies to the user community has been established.

REFERENCES

[1] Kee, R. J., Rupley, F. M., Meeks, E., and Miller, J. A.,"CHEMKIN-III: A FORTRAN Chemical Kinetics Package for the Analysis of Gas-Phase Chemical and Plasma Kinetics," Sandia National Laboratories Report No. SAND-96-8216, Livermore, CA, 1996.

[2] Spadaccini, L. J. and TeVelde, J. A., "Autoignition Characteristics of Aircraft-Type Fuels," *Comb. and Flame*, Vol. 46, 1982, pp. 283-300.

Degradation of Thermal Barrier Coatings with Syngas Combustion: Testing by Hyperbaric Advanced Development Environmental Simulator and Characterization by Advanced Electron Microscopy

Report Type:	Semi-Annual No. 3
Reporting Period Start Date:	August 1, 2006
Reporting Period End Date:	January 31, 2007

Principal Investigators:	Yongho Sohn
Affiliation:	Advanced Materials Processing and Analysis Center and Mechanical, Materials and Aerospace Engineering University of Central Florida Orlando, FL 32816-2455

Date Issued:	March 12, 2007
DOE Award Number:	DE-FC26-02NT41431
UTSR Project Number:	02-01-SR118

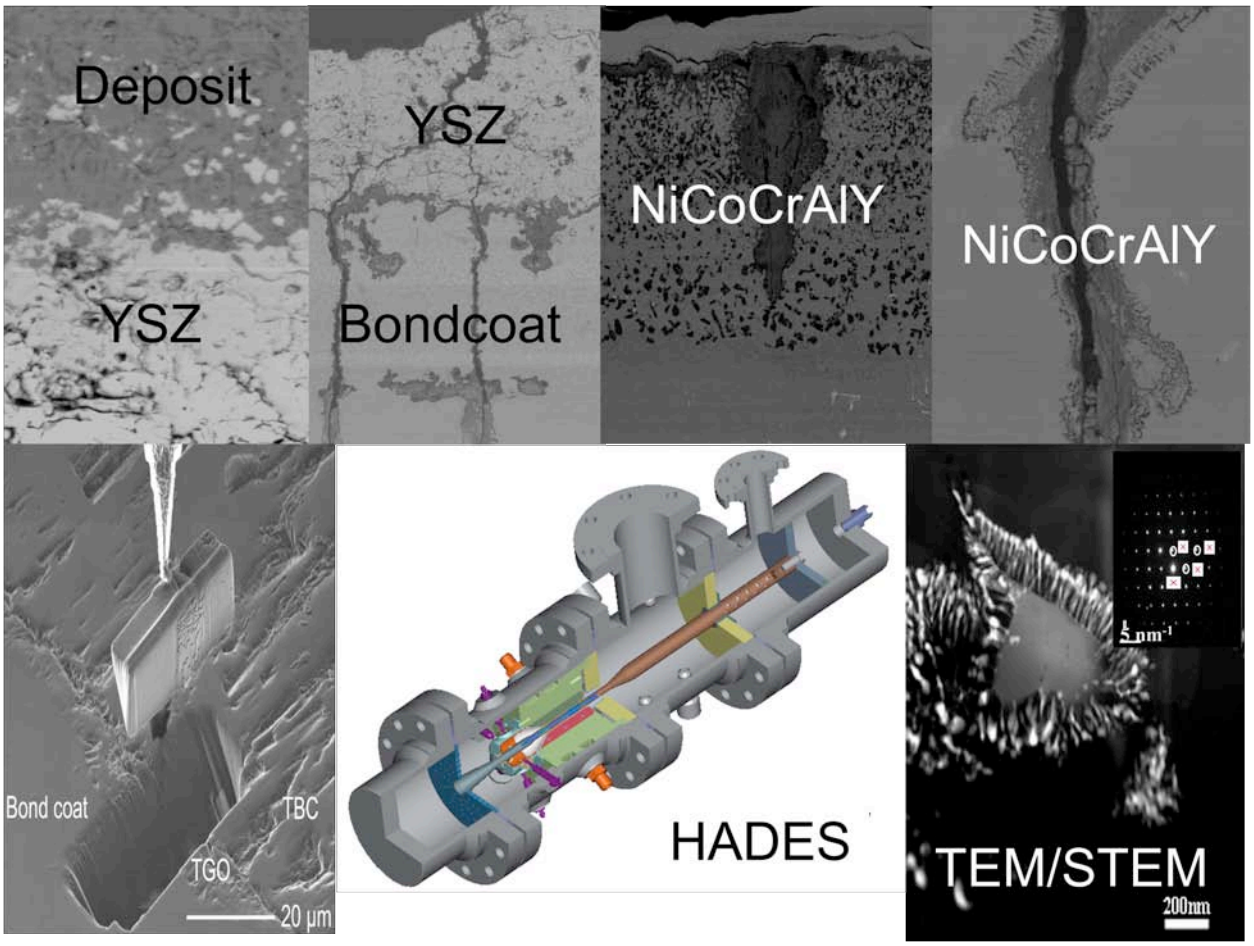

DISCLAIMER

ABSTRACT

An understanding in materials science and engineering that will allow turbine power plant fuel flexibility, and increase the efficiency as well as reliability, availability, and maintainability, with low emissions and life cycle costs is the primary objective of this study. This program is designed to examine the degradation mechanisms of TBCs in a realistic syngas combustion environment using Hyperbaric Advanced Development Environmental Simulator (HADES) built by Florida Turbine Technologies (FTT), Inc., and advanced microstructural analysis techniques including field-emission scanning electron microscope (FESEM), x-ray diffraction (XRD), focused ion beam (FIB) with in-situ lift-out (INLO), transmission electron microscope (TEM), and scanning TEM (STEM). Emphasis is given to the phase identification (i.e., crystallography and compositions) of deposits and their penetration/reaction products as well as reaction products from gaseous contaminations, related to TBC degradation. Critical materials information, such as deposit solubility, eutectic composition, and reaction/hot corrosion rates in the light of TBC constituents will be provided from the selected in-laboratory thermodynamic/kinetics experiment/modeling in addition to HADES testing.

This third semiannual report summarizes results from the third six-month period during which microstructural characterization of TBC degradation was carried out using TBC- and MCrAlY-coated blades that were employed in turbines with syngas combustion. Observations made provided first look at mechanisms of degradations. TBC button specimens on various Ni-base superalloys exposed to Syngas and Sulfur-poisoned Syngas were characterized. A detailed reaction mechanism of degradation by V_2O_5 and P_2O_5 was identified for a broad range of temperature through in-laboratory experiments using free-standing APS YSZ coatings. PI at UCF is consulting Siemens Power Generation who has purchased HADES for access.

TABLE OF CONTENTS

LIST OF FIGURES

LIST OF FIGURES (Continued)

LIST OF FIGURES (Continued)

LIST OF TABLES

I. INTRODUCTION

The main driver of technology development in modern turbines for energy generation is to increase turbine power plant fuel flexibility and efficiency as well as reliability, availability, and maintainability, with low emissions and life cycle costs. Critical tasks to achieve this objective include the development of turbine technologies that enable low-cost and environmentally acceptable use of its large reserves of coal and operation at high turbine inlet temperature for efficient energy production with reduced emissions. Inevitably, turbines need advanced hot section components and coatings that can tolerate higher operating temperature while being significantly more resistant to the contaminations that erode, corrode, and deposits. The development of advanced TBCs that can tolerate the more aggressive combustion byproducts, while still enable high turbine inlet temperatures, increased power output, and power plant efficiency is highly warranted [1,2].

This program is designed to provide, for the first time, investigation on the mechanism of TBC degradation in syngas combustion environment by using Hyperbaric Advanced Development Environmental Simulator (HADES) that will be build by Florida Turbine Technologies (FTT) Inc. The use of HADES provides realistic test conditions and real time monitoring/controlling of high temperature, high pressure, temperature gradient, erosion, and turbine operation from real syngas combustion. These offer a significant advantage over furnace or burner-rig testing, which requires several assumptions (e.g., effects of total and partial pressures, deposit constituents, gas or oxide constituents, etc.). State-of-the-art characterization techniques such as FIB INLO and TEM/STEM will be employed to identify deposit constituents and hot corrosion reactions to understand the mode and mechanisms of TBC degradation in realistic syngas combustion environment. Use of FIB-INLO and TEM/STEM will enable detailed identification of phase constituents of deposits, penetrants and reaction products, thus providing the exact mechanisms for degradation of TBCs in syngas combustion environment. Critical materials information, such as deposit solubility and eutectic composition, reaction/hot corrosion rates in the light of TBC constituents will be provided from the selected in-laboratory thermodynamic/kinetics experiment/modeling in addition to HADES testing.

Hot Corrosion in Thermal Barrier Coatings

Application of TBCs in syngas combustion environment presents a unique challenge to understand the mode and mechanisms of degradation. It is generally known that the degradation via hot corrosion of ZrO_2-based TBCs becomes a problem when low quality fuels containing appreciable levels of Sulfur, and especially Vanadium, are used [1-5]. The contaminants containing Sulfur, Vanadium and Chlorine such as H_2S, SO_3, V, and HCl have been documented by a recent analysis of syngas [6]. These contaminants, in gaseous form and/or oxidized form (i.e., oxide deposition) are expected to react with ceramic topcoat, destabilize the phase constituents and degrade the integrity of TBCs. For example, for Y_2O_3 stabilized ZrO_2 (YSZ) TBCs in Vanadium-containing environment at high temperature, Kvernes [7], Hamilton and Nagelbert [8] as well as Hertl [9] have reported the tetragonal to (monoclinic+cubic) destabilization of YSZ as:

$$ZrO_2(Y_2O_3) + V_2O_5 \rightarrow ZrO_2 \text{ (monoclinic+cubic)} + 2YVO_4$$

The same reaction leading to degradation of YSZ TBCs has been reported in the presence of phosphorous (i.e., reaction with oxidized P_2O_5) [10]. Based on the argument of thermodynamics, Jones [11] has reported the additional reaction of:

$$ZrO_2(Y_2O_3) + P_2O_5 \rightarrow ZrP_2O_7 + Y_2O_3$$

Although not reported, similar reactions with oxidized Arsenic (As_2O_5) from ArH_3, and Antimony (Sn_2O_5) based on their electronic structure and acidity.

While the effects of Berylium, Chromium, Mercury, Selenium have not been reported, a significant levels of these contaminants would lead to reaction with YSZ that would lead to phase destabilization and formation of deleterious reaction products.

Although YSZ tends to resist sulfur degradation in the presence of SO_3, reaction of Y_2O_3 with SO_3 in the presence of Na_2SO_4 can give a rise to destabilization of YSZ as reported by Pettit and Barkalow [12]:

$$ZrO_2(Y_2O_3) + 3SO_3\ (+Na_2SO_4) \rightarrow ZrO_2\ (\text{monoclinic}) + Y_2(SO_4)_3\ (\text{in } Na_2SO_4 \text{ solution})$$

It should be noted that most of the previous investigations for TBC hot corrosion employed furnace or burner-rig testings that lack realistic high pressure. The effects of pressure in the case of hot corrosion may significantly influence the reaction of gaseous species (e.g., oxidation, hot corrosion and reaction with YSZ) and hence the degradation mechanisms of TBCs.

In addition, other condensed phases including molten salts that pass through the syngas cleanup system have not been identified and the degradation mechanism associated with these unknown condensed phases is an unexplored area of study for materials scientists and engineers. Strangman [13,14] have reported that the deposition of molten sulfate salts and glassy CMAS (calcia magnesia alumina silicate) dust onto porous TBCs can significantly reduce the durability. In an recent review, Bose and Strangman [15] discussed that the reaction to destabilize YSZ was usually not the life-limiting effect. The more immediate effect has been reported as the penetration of these deposits into the porous YSZ and subsequent thermo-mechanical damage. Considering that the identity of deposits has not been studied in the syngas combustion environment, the use of syngas combustion in HADES with realistic turbine environment will provide valuable information to understand the degradation mechanisms of TBCs and to develop TBCs with superior environmental resistance.

Hyperbaric Advanced Development Environmental Simulator (HADES)

HADES is a test rig, being built by FTT, to examine materials and coatings degradation in syngas combustion environment. As presented in Figure 1, FTT HADES consists of high pressure compressor, syngas combustor, 6-inch long hot zone for specimen testing, exhaust chamber with cooler and silencer. Test section of HADES accommodates tubular specimens (0.5” in diameter with a 0.0375” wall thickness and 6” long) of TBCs, metallurgical coatings and

superalloys. During testing, specimens are exposed to realistic engine conditions as presented in Table I, using the approximate gas composition presented in Table II for combustion.

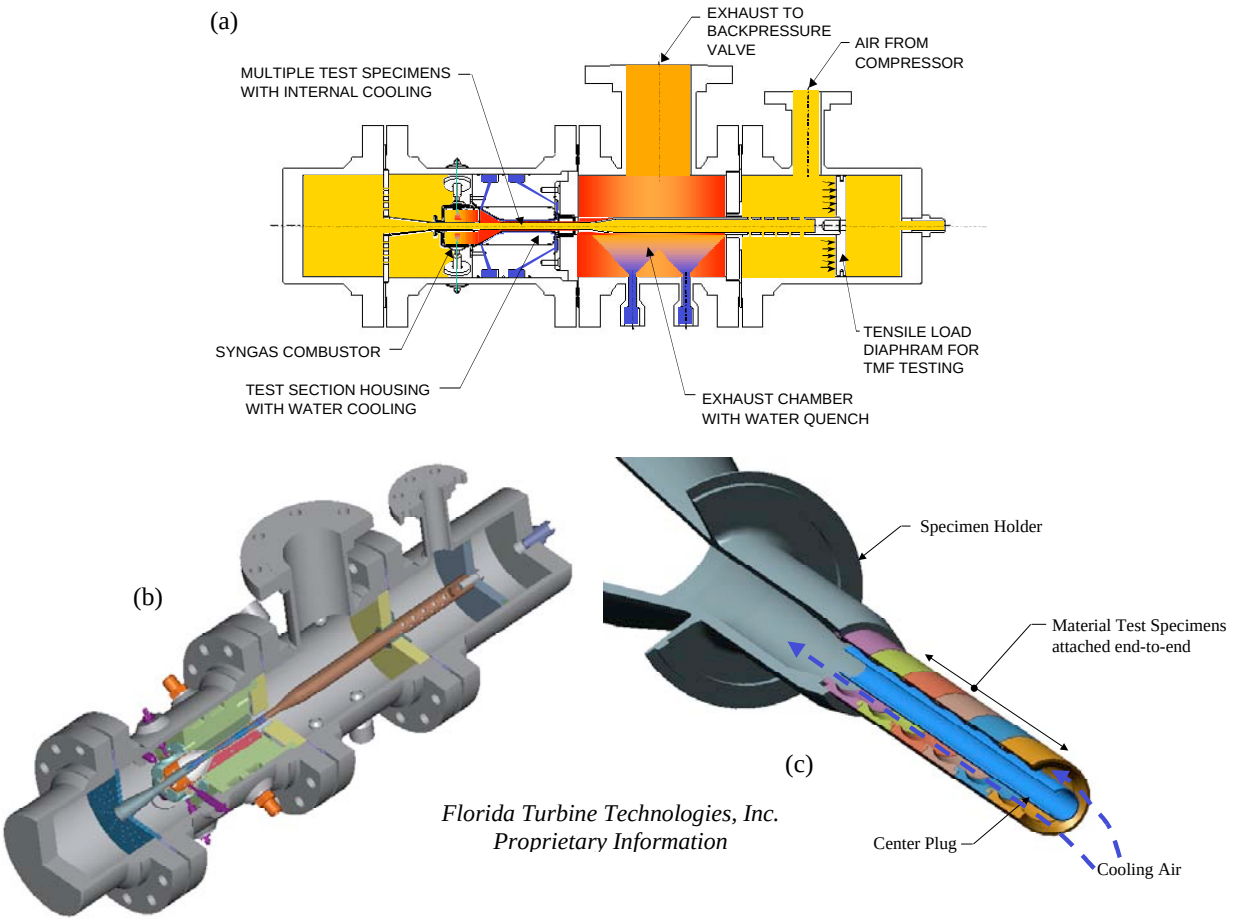

Figure 1. Schematics of FFT HADES: (a) conceptual configuration of the rig; (b) isometric cutaway of the rig; and (c) isometric cutaway of the test specimen section.

Table I. Comparison of testing conditions for TBC degradation.

Factors Related to TBC Failure	Engine Test	FTT HADES	Burner Rig	WaltzMills Plasma Rig	NASA Laser Rig
High Pressure	Yes	Yes	No	No	No
High Temperature	Yes	Yes	Yes	Yes	Yes
Temperature Gradient	Yes	Yes	Partial	Yes	Yes
Thermal Cycling	Yes	Yes	Yes	Yes	Yes
High Velocity Flow Erosion	Yes	Yes	Partial	No	No
Syngas Contaminants	Yes	Yes	Yes	No	No
Axial Fatigue Loading	Yes	Yes	No	No	Unknown

Table II. Typical bulk gas compositions (mole% - dry basis) of syngas to be employed for TBC testing at Dakota Gasification Company site [16].

Bulk Gas Compound	Raw Gas	Shifted Gas	Rectisol Syngas	Product Syngas
Hydrogen	38.60	42.75	62.16	3.1
CO_2	32.4	36.7	0.37	1.4
H_2S	0.72	0.47	ND	ND
O_2/Ar	0.16	0.17	0.20	0.5
Nitrogen	0.02	0.02	0.02	0.1
Methane	11.9	10.9	16.7	94.9
CO	15.4	8.2	20.5	0.01
C_2 + Hydrocarbons	0.81	0.79	0.05	ND
Specific Gravity	0.7546	0.7457	0.3432	0.5562
Compressibility	0.9990	0.9990	0.9999	-
Dry BTU	315	295	438	970
Molecular Weight	21.92	21.66	10.02	16.3
Organic Nitrogen Compound	~100 ppm	~10 ppm	< 1 ppm	ND
Organic Sulfur Compound	200~300 ppm	100~150 ppm	24 ppb	ND

Note: ND refers to Non-Detectable. Does not include trace contaminants analysis.

Current estimates of operating conditions and testing capabilities of FTT HADES satisfy the design point set forth by U.S. DoE and includes TBC surface temperature of 1250°C (2282°F), combustor exit temperature of 1650°C (3000°F), gas pressure of 370 psi, and coolant temperature of 412°C (775°F). The rig will also be equipped with real time monitoring/controlling capabilities including TBC spallation detection through heat flux sensoring.

Microstructural Analysis of TBC Degradation in Syngas Combustion Environment

In addition to pioneering TBC test with syngas combustion in realistic engine conditions, advanced microstructural analysis to understand degradation mechanisms will be carried out using state-of-the-art characterization techniques in this program. This is a step over any previous investigation that relied solely, at best, on qualitative, correlation based on resolution limited XRD and SEM with EDS. Advances in understanding of TBC degradation/hot corrosion in syngas environment require advanced characterization techniques that will exactly identify the phase constituents (both crystallography and composition) at atomic-scale and their microstructural evolution in contact with TBCs. To that end, this program offers, in addition to conventional tools such as XRD, FESEM/EDS, an advantage of microstructural analysis by TEM/STEM with specimen preparation by FIB-INLO. Using these advanced techniques, a site-specific observation of microstructure and identification of phase constituents can be carried out easily for identification of deposits and hot corrosion reaction products that arise from trace contaminants of syngas environment using analytical techniques of TEM/STEM.

FIB prepares a large (20 μm x 20 μm) and uniformly thin (<100 nm) TEM specimens for TEM microstructural analysis. In FIB, gallium (Ga) ions, wetted at a sharp tungsten tip are accelerated through a vacuum column, and section (i.e., mill) materials at lateral resolutions up to 5 nm. The milled specimen is lifted out after being welded to an in-situ probe (INLO). The process of FIB INLO technique is illustrated in Figure 2 with ion beam generated secondary electron images collected during the actual TEM specimen preparation of TBCs. The use of FIB-INLO has been successful in preparing delicate specimens such as heavily oxidized/damaged TBCs as shown in Figure 3. Although the current preparation has been focused on YSZ/TGO/bond coat interfaces [17-19], FIB-INLO process for syngas degradation of TBCs, including near YSZ surface will not pose any difficulties, if not easier. Details of the TEM specimen preparation process by FIB-INLO have been published elsewhere [17-19].

Upon successful completion of TEM specimen preparation by FIB-INLO, syngas degradation of TBCs will be carefully characterized by TEM/STEM. An FEI/Tecnai F30 TEM/STEM system operating at 300 KeV with analytical techniques such as high angle annular dark field (HAADF), STEM imaging that gives compositional contrast (i.e., analogous to backscatter electron images), selected area diffraction (SAD), convergent beam electron diffraction (CBED), fast-Fourier transformed (FFT) diffractograms, nano-spot EDS (n-EDS), and electron energy loss spectroscopy (EELS) will be employed to identify the phase constituents of deposits and reaction products that are critical in understanding the mechanisms of TBC degradation in syngas combustion environment. Identification of the phase constituents would involve accurate determination of crystal structures, compositions, and electron-state. The advanced microstructural analysis using TEM/STEM via FIB-INLO is a progress over any previous investigation that relied solely, at best, on qualitative correlation based on resolution limited XRD, SEM with EDS. Figure 4 represents a typical example illustrating the advantage of TEM/STEM investigation made possible by FIB-INLO [19]. Recently, research effort at UCF, made possible through UTSR No. 02-01-SR103 identified the exact phase constituents of so-called “oxide stringers” in the thermally grown oxide (TGO) from NiCoCrAlY bond coat, including those at the interface, leading to a conclusion that Y_2O_3 oxide stringers grow by eutectoid reaction through grain boundary diffusion of Y^{3+} ions in the Al_2O_3 matrix [20].

Anticipated Public Benefits

The evaluation of TBCs in syngas combustion environment using HADES proposed in this program will help develop IGCC power generation technologies; leading to less expensive and more reliable energy sources, and reduce U.S. dependence on foreign resources. Development of reliable and durable TBCs for IGCC based on decrease fuel cost will increase the performance efficiency of turbines by 2.2%, equivalent to CO_2 emission reduction by 300 million tons per year per unit and operational savings of 6.3% (assuming 40/60 split in fuel/capital cost).

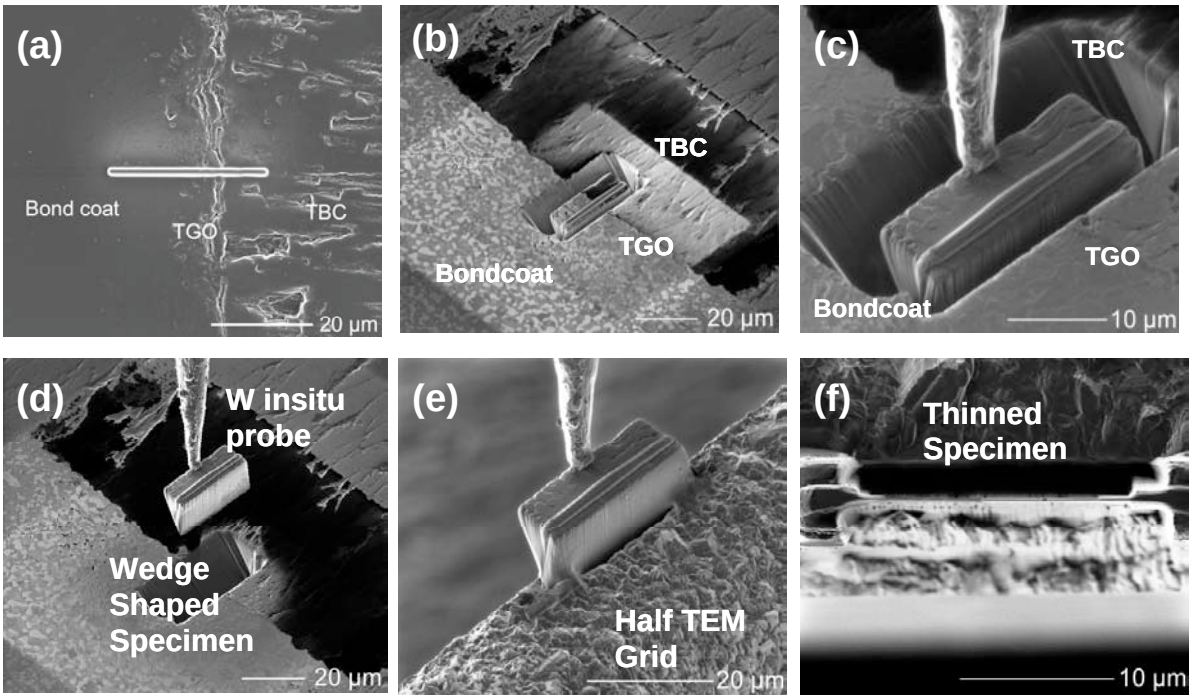

Figure 2. Sequential ion beam images from TEM specimen preparation of TBCs by focused ion beam (FIB) in-situ lift out (INLO) technique: (a) Pt wire is deposited at a site of specific interest; (b) focused ion milling is carried out to create a wedge-shaped specimen, (c) specimen is welded to a micromanipulator, and (d) lifted out, (e) specimen is welded to a TEM grid, and (f) thinned further for TEM analysis.

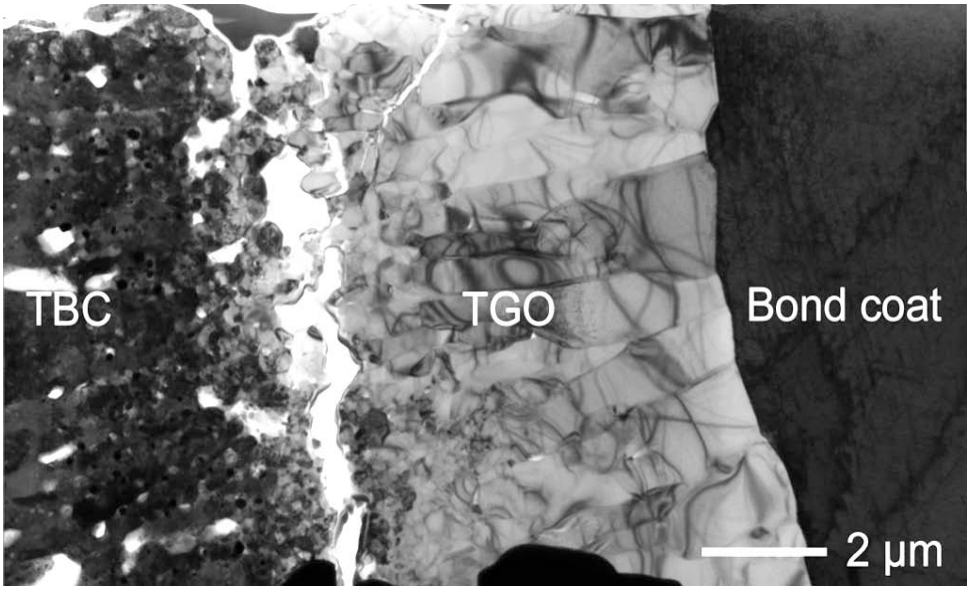

Figure 3. Bright field TEM micrograph of intact EB-PVD TBC specimen after 645, 10-hour thermal cycles at 1038°C (1900°F). Extensive decohesion at or near the YSZ/TGO interface was observed [19].

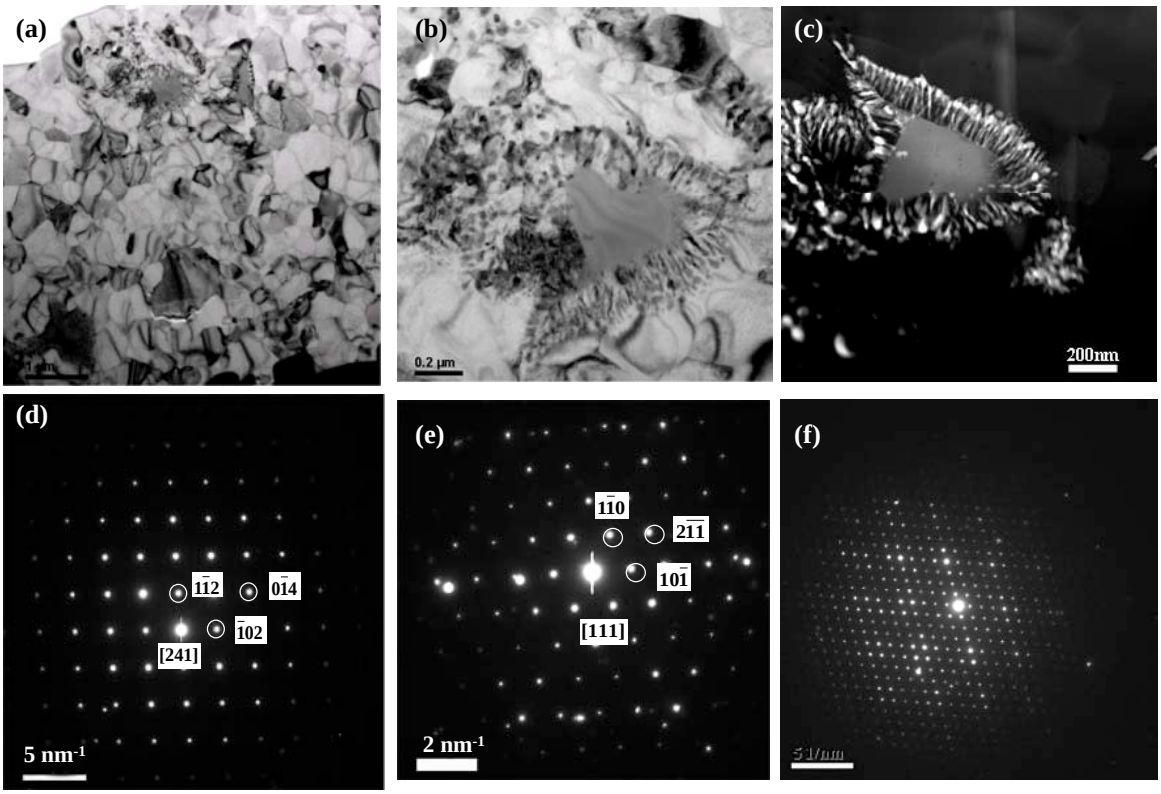

Figure 4. Transverse TEM/STEM analysis of "oxide-stringers" within the TGO of NiCoCrAlY bond coat: (a) Bright field TEM micrograph of TGO; (b) Bright field TEM micrograph of the Y-rich "oxide-stringer"; (c) HAADF micrograph of the Y-rich "oxide-stringer" indicating eutectoid reaction microstructure; (d) SAD pattern of Y-rich "oxide-stringer" indexed to Y_2O_3; (e) SAD pattern of TGO indexed to Al_2O_3; (f) SAD pattern (unidentified yet) of the white regions in (c).

Objectives

The overall objective of the proposed research program is to understand the degradation mechanisms of thermal barrier coatings in syngas combustion environment using advanced microstructural analytical techniques. The findings of the program will provide, for the first time, degradation modes and mechanisms of TBCs that lead to failure, with realistic syngas turbine conditions. TBC tests will be carried out in high pressure, high temperature, temperature gradient and syngas combustion environment using HADES rig designed and built by FTT. APS, DVC and EB-PVD TBC specimens, according to the required specification need of HADES, will be provided by industrial partners. Materials characterization will be carried out using state-of-the-art electron microscopy that includes FESEM, FIB-INLO, TEM/STEM. In order to achieve the overall objective of this program, the following goals have been set forth:

- Degradation testing of APS, EB-PVD and DVC TBCs in air and in syngas combustion environment:
  - Baseline furnace isothermal testing in air.
  - HADES testing with syngas combustion.
- Identification and characterization of the degradation using advanced characterization techniques such as FESEM, FIB-INLO, TEM and STEM:

  - Deposits identification.
  - Penetration/reaction/degradation characterization
- Development of fundamental understanding of the difference in degradation behavior of TBCs in air and syngas:
  - Identify degradation (e.g., hot corrosion) mechanisms (e.g., YSZ destabilization, deposit penetration and reaction, etc.).
  - Generate critical materials data (e.g., solubility, eutectic compositions and degradation kinetics for realistic turbine environment).
  - Provide feasible approaches to improve resistance against TBC degradation in syngas combustion environment.
- Transfer to industrial partners, the attained knowledge on TBC degradation in syngas combustion environment.
- Provide two pairs of student research teams, with interdisciplinary team-based research activities in collaboration with industrial partners.

To achieve specific goals and the overall objective of this program, six tasks have been defined with corresponding schedule as presented in Figure 5. Task I involves furnace isothermal testing of six types of commercial production TBCs at 1150°C (2100°F) and 1050°C (1920°F) for 10, 100 and 400 hours. The results of this simple task serve as a baseline to be compared to the syngas testing. Task II involves testing of the six types of TBCs using HADES rig in syngas combustion with the same TBC surface temperature and test duration. All tested TBC specimens will be characterized with respect to degradation and microstructural development using advanced characterization techniques as task III. Coupled with extensive literature review and selected in-laboratory experiments, characterization and modeling, detailed mechanisms of TBC degradation in syngas combustion environment will be determined as task IV. In addition, feasible approaches (e.g., chemistry, processing, overlay coating, etc.) for improving the resistance of TBCs in syngas combustion environment will be recommended based on conclusions of this program. Findings and understanding from this program will be frequently communicated with industrial partners for efficient technology/knowledge transfer as task V. A flow chart associated with specific tasks is presented in Figure 5.

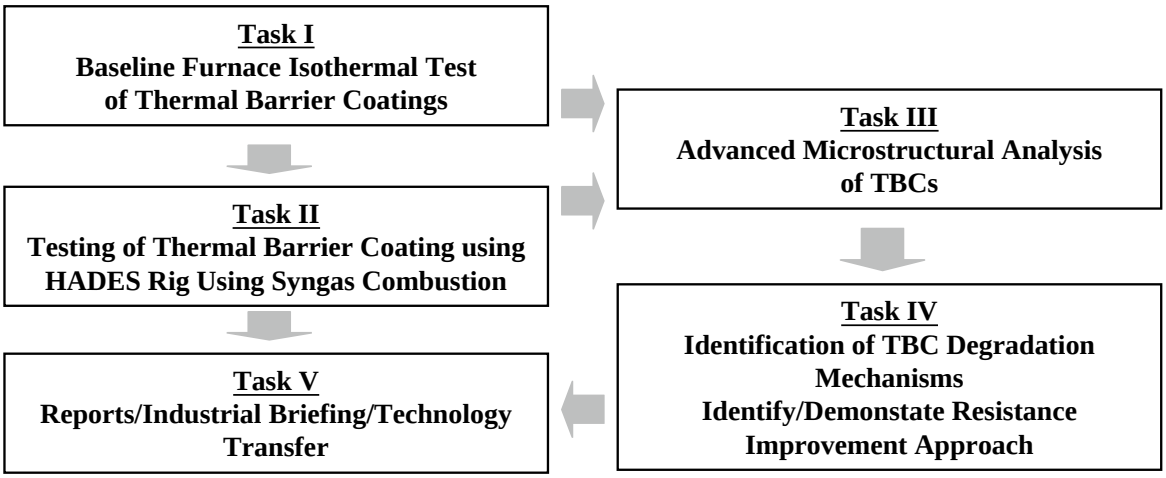

Figure 5. Flowchart of the tasks proposed in this program.

In achieving the overall objective of this program and specific deliverables, the individual tasks, previously described will be carried out according to the schedule shown in Figure 6.

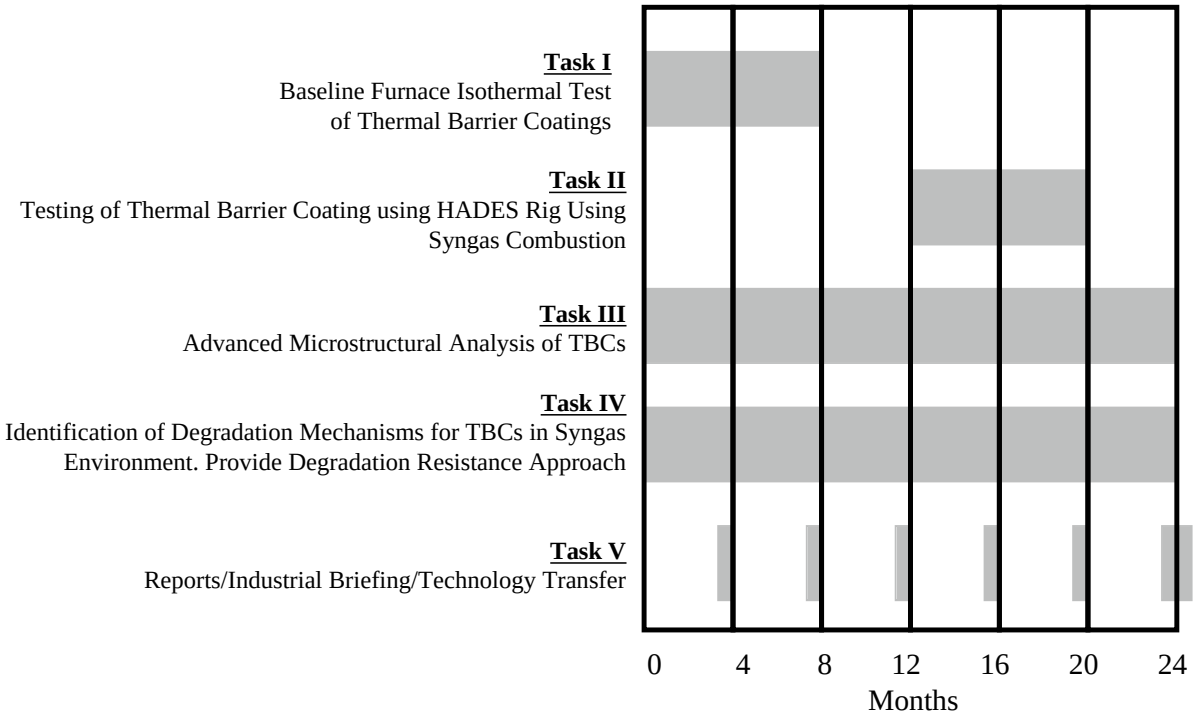

Figure 6. Program schedule according to the specified tasks.

II. EXECUTIVE SUMMARY

Project Title:	**Degradation of Thermal Barrier Coatings with Syngas Combustion: Testing by Hyperbaric Advanced Development Environmental Simulator and Characterization by Advanced Electron Microscopy**
Identifiers:	**DOE DE-FC26-02NT41431 and UTSR No. 02-01-SR118**
PIs:	**Yongho Sohn**
Affiliation:	**Advanced Materials Processing and Analysis Center and Mechanical, Materials and Aerospace Engineering University of Central Florida Orlando, FL 32816-2455**
Reporting Period:	**August 1, 2006 ~ January 31, 2007**
Date Issued:	**March 12, 2007**

This program examines the degradation mechanisms of TBCs in a realistic syngas combustion environment using advanced microstructural analysis techniques. The findings of the program will provide degradation modes and mechanisms of TBCs that lead to failure in realistic syngas turbine conditions that includes high pressure, high temperature, temperature gradient, syngas combustion contaminants, and high velocity flow erosion using Hyperbaric Advanced Development Environmental Simulator (HADES). Materials characterization will be carried out using state-of-the-art electron microscopy that includes field-emission scanning electron microscope (FESEM), x-ray diffraction (XRD), focused ion beam (FIB) with in-situ lift-out (INLO), transmission electron microscope (TEM), and scanning TEM (STEM). Emphasis will be given to the phase identification (i.e., crystallography and compositions) of deposits and their penetration/reaction products as well as reaction products from gaseous contaminations. Critical materials information, such as deposit solubility, eutectic composition, and reaction/hot corrosion rates in the light of TBC constituents will be provided from the selected in-laboratory thermodynamic/kinetics experiment/modeling in addition to HADES testing.

Including the third reporting period, the following tasks were successfully carried out according to the proposed schedule:

- **Completed characterization of TBC degradation using TBC-coated blades that were employed in turbines with syngas combustion.**
  - **Deposits consisting of cubic Fe_3O_4 with a large solubility and monoclinic Fe_2O_3 with minimal solubility.**
  - **TGO scale consisting of α-Al_2O_3 and tetragonal spinel-$(Ni,Co)(Al,Cr)_2O_4$.**
  - **Internal oxidation in NiCoCrAlY bond coats consisted of α-Al_2O_3 and cubic NiO.**

- **Characterization of TBCs and Ni-base superalloys degradation in Syngas and Sulfur-poisoned Syngas using button specimens (through independent contract with Siemens Power Generation).**

- **Successful production of free-standing APS YSZ coatings (t' phase) at UCF's Thermal Spray Facility (UCF-TSF).**

- **Degradation of free-standing APS YSZ coatings by V_2O_5:**
  - **Formation of YVO_4 and ZrV_2O_7 above and below 750°C, respectively.**
  - **YSZ destabilization with the formation of YVO_4.**

- **Degradation of free-standing APS YSZ coatings by P_2O_5:**
  - **Formation of ZrP_2O_7 at all temperature.**
  - **No destabilization of YSZ with the formation of ZrP_2O_7.**

- **Further consultation regarding HADES among PIs at UCF and FTT for a discussion on status of HADES and specification of TBC.**
  - **Delay in development of HADES was reported by FTT, and hence specification of TBC samples has not been finalized.**

In the fourth reporting period (February 1, 2007 ~ July 31, 2007), we will complete all characterization of engine-tested and laboratory-tested TBCs and superalloys. We will also examine TBC degradation in $SO_{x(g)}$ with free-standing APS YSZ coatings and NiCoCrAlY powders. PI will continue to work with Siemens Power Generation for access to HADES.

III. PROJECT DESCRIPTION

This University Turbine Systems Research (UTSR) program is designed to examine the degradation mechanisms of TBCs in a realistic syngas combustion environment using Hyperbaric Advanced Development Environmental Simulator (HADES) and advanced microstructural analysis techniques including field-emission scanning electron microscope (FESEM), x-ray diffraction (XRD), focused ion beam (FIB) with in-situ lift-out (INLO), transmission electron microscope (TEM), and scanning TEM (STEM). Emphasis is given to the phase identification (i.e., crystallography and compositions) of deposits and their penetration/reaction products as well as reaction products from gaseous contaminations. Critical materials information, such as deposit solubility, eutectic composition, and reaction/hot corrosion rates in the light of TBC constituents will be provided from the selected in-laboratory thermodynamic/kinetics experiment/modeling in addition to HADES testing.

In addition, this program is designed to harvest two graduate and two undergraduate students with strong background in TBCs and other engineering issues related to goals and challenges defined by U.S. DOE. This program is primarily carried out by two graduate students, Mr. Biao Yuan and Mr. Prabakar Mohan, and two undergraduate students, Miss Ananda Leon and Mr. Nathan Hotaling. Additional assistance and collaboration for FIB-INLO and TEM/STEM are provided by Miss Jing Liu, a Ph.D. candidate and an Amelia Earhart Fellow.

IV. EXPERIMENTAL

IV.1. Characterization of Syngas Degraded Coatings

TBC- and NiCoCrAlY-coated blades from turbines operated under syngas combustion were supplied by industrial partners for preliminary microstructural characterization. Based on characterization techniques described in section IV.4, these blades were characterized.

In addition, TBC-coated button specimens thermally treated in Syngas and Sulfur-poisoned Syngas environment were supplied by Siemens Power Generation. While this work was carried out as an independent research contract, Siemens Power Generation has agreed to publish the outcome of the results (approval pending for documentation). Details of the testing parameters will be provided upon approval by Siemens Power Generation. Characterization techniques described in section IV.4 were employed.

IV.2. Furnace Isothermal Test of Thermal Barrier Coatings

Tubular specimens (0.5" diameter, 0.0375" wall thickness and 6" long) coated with TBCs will be supplied by industrial partners of this program. TBCs will be fabricated with current commercial processing practices. Details of the specimen specifications are presented in Table III. These TBC specimens will be subjected to furnace isothermal test using Blue/Lindberg 3-zone high temperature tube furnace at 1150°C (2100°F) and 1050°C (1920°F) for 10, 100 and 400 hours. The results of the microstructural analysis (task III) of the oxidized specimens will serve as a baseline and be compared to the results of syngas testing of TBCs (task II). This task will also introduce and train graduate students about benefits, failure mechanisms, and characterization techniques of TBCs.

Table III. Types of commercial production TBCs employed in this program.

TBC Type	**Topcoat Chemistry and Processing**	**Bond coat Chemistry and Processing**	**Superalloy Substrate**
I	YSZ; APS	MCrAlY; APS	Ni/Co-base Superalloys
II	YSZ; DVC	MCrAlY; VPS	
III	YSZ; EB-PVD	(Ni,Pt)Al; CVD	

IV.3. Testing of Thermal Barrier Coating using HADES Rig Using Syngas Combustion

Tubular specimens (0.5" diameter, 0.0375" wall thickness and 6" long) coated with TBCs according to Table III will be supplied by industrial partners of this program. TBC specimens will be subjected to HADES rig testing of syngas combustion using the operating parameters presented in Table IV. The degradation of TBCs as a function of microstructural variation, including the size, shape and amount of porosity would be examined.

Table IV. Operating parameter of HADES rig testing of TBCs using syngas combustion.

Parameter	**High Temperature Testing**	**Low Temperature Testing**
TBC Surface Temperature	1150°C (2100°F)	1050°C (1920°F)
Combustor Exit Temperature	Up to 1650°C (3000°F)	Up to 1650°C (3000°F)
Gas Pressure	Up to 350 psi	Up to 350 psi
Coolant Temperature	~ 412°C (775°F)	~ 412°C (775°F)
Mechanical Loading	None	None
Test Duration	10, 100 and 400 hours	10, 100 and 400 hours

IV.4. Microstructural Characterization

All air- and syngas-tested TBC specimens will be characterized using advanced microstructural analysis techniques. Aforementioned, this task will employ state-of-the-art characterization techniques including FESEM with EDS, XRD, XPS, AES, EPMA, FIB-INLO, and TEM/STEM equipped with nano-EDS, SAD, HAADF, FFTD, EELS, PEELS. During the characterization, emphasis will be given to the identification of surface deposits and understanding of contaminant-induced reaction/degradation mechanisms in syngas combustion environment. Environment-induced reaction of YSZ (e.g., destabilization) and penetration of deposits will be quantitatively understood in terms of fundamentals of thermodynamics and kinetics.

IV.5. Identification of Degradation Mechanisms for TBCs in Syngas Environment

Results from microstructural analysis coupled with extensive literature review and selected in-laboratory experiments/modeling will be compiled to provide degradation mechanisms of TBCs in syngas combustion environment. Based on results of HADES tests and microstructural analysis, selected experimental investigation will be designed and carried out to quantitatively examine and understand the materials thermodynamics (e.g., phase stability/equilibrium) and kinetics (e.g., rates of reaction/diffusion/penetration) related to TBC degradation in syngas environment. Additional modeling effort (e.g., ThermoCalc) can be carried out to refine the understanding of these fundamentals of TBC degradation. Results and correlation observed will be reported to industrial partners for suggestions and criticisms. Conclusions drawn from this collaborative effort will elucidate degradation mechanisms for TBCs and form a sound basis for identifying feasible approaches (e.g., chemistry, processing, overlay coating, etc.) for improving the resistance of TBCs in syngas combustion environment.

V. RESULTS AND DISCUSSION

V.1. Characterization of Syngas Degradation

V.1.1. Air Plasma Sprayed Thermal Barrier Coatings on Turbine Blade

A turbine blade coated with TBC was supplied by an industrial partner to assist the effort to understand the syngas degradation of TBCs. While the specification of TBC, turbine blade and operating condition remains proprietary, this specimen provide the first look at syngas degraded TBC. Visually, localized damage and spallation of TBCs was observed along with "red" iron oxides on the remaining TBC surface. The blade was sectioned with slow speed Isomet Buehler using diamond wafering blade, mounted in Epo-Thin™ low viscosity epoxy, and metallographically polished down to 0.25 μm.

In regions where TBCs had spalled, a significant local-internal oxidation was observed as presented in Figure 7. This penetration attack through the length of the bond coat extended into the superalloy substrate as shown in Figures 7(a) and 7(c). The interface between internal oxidation and bond coat revealed a distinctive microstructure as seen in Figure 7(b). Additional deposits on top of the TGO scale were observed without any indication of TGO/deposit interaction as shown in Figure 7(d).

In regions where TBC is still adherent, several distinctive degradation modes were observed as shown in Figure 8. Clearly, deposits arising from fuel contaminates (a) spalled, (b) penetrated, (c) deposited, and (d) dissolved the YSZ topcoat. While the observed spallation in Figure 8(a) and penetration in Figure 8(b) may be a result (rather than the cause) of other types of damage (such as nearby spallation, foreign object damage, and erosion), microstructural features observed in Figures 7(b), 8(c) and 8(d) warrants a further examination by TEM/STEM in order to understand reaction mechanism between the YSZ and deposits. Figure 9 summarizes locations where FIB-INLO technique was applied to examine the degradation of YSZ (and subsequently NiCoCrAlY bond coats) by TEM/STEM.

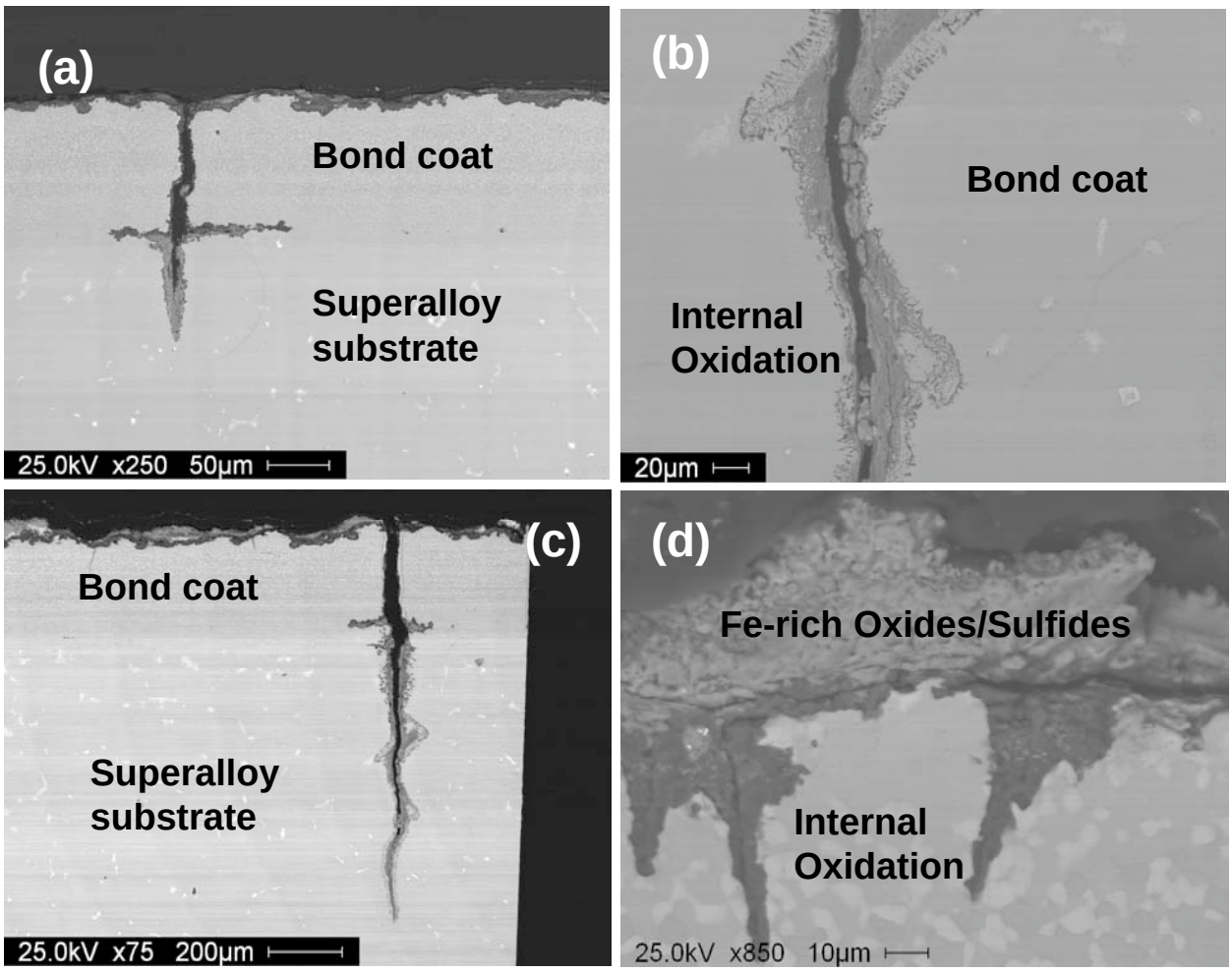

Figure 7. Internal oxidation damage after TBC spallation: (a,b) internal oxidation through the bond coat; (c) penetration into the superalloy substrate; (d) Fe-rich deposits on the TGO scale after TBC spallation.

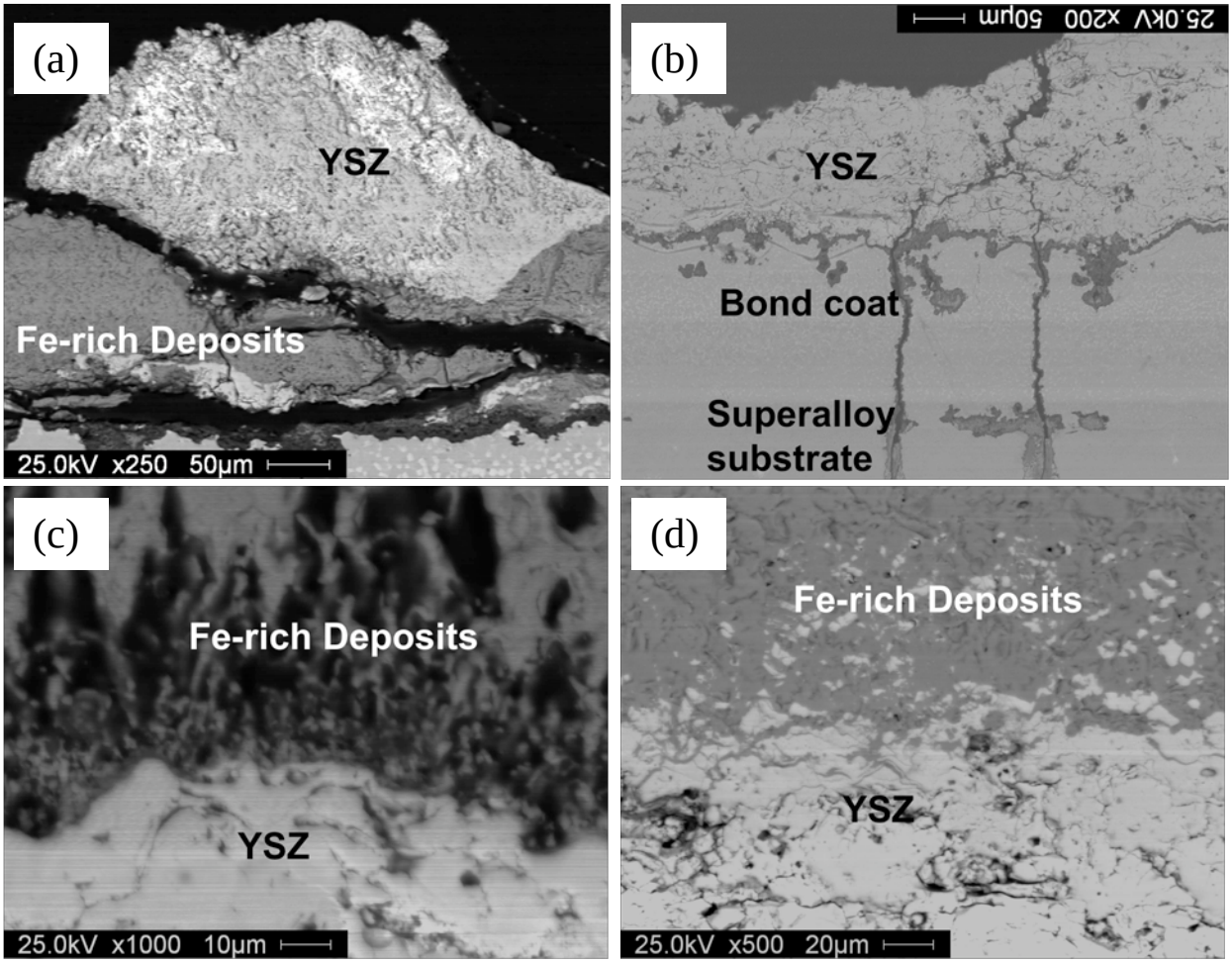

Figure 8. Degradation of the YSZ top coat in the form of: (a) YSZ spallation; (b) deposit penetration through YSZ; (c) deposit; (d) YSZ dissolution.

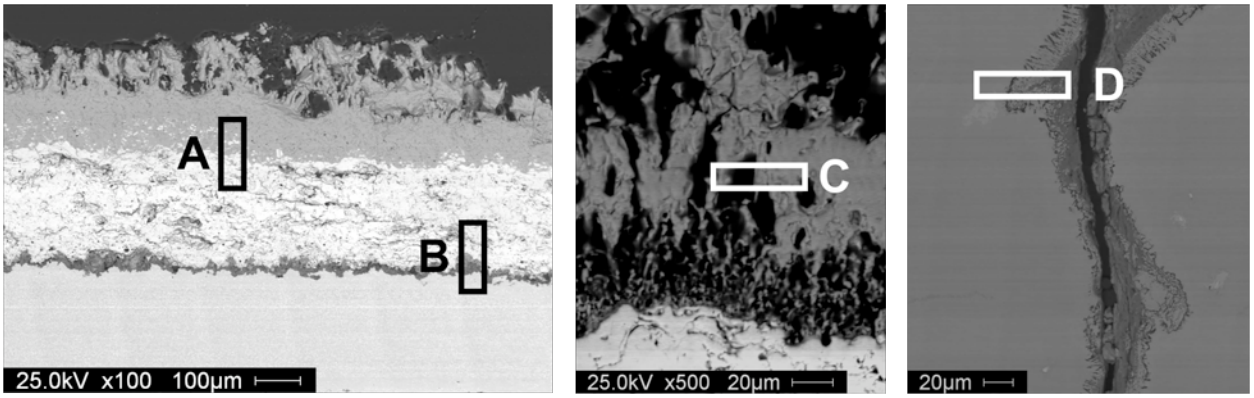

Figure 9. Microstructural locations where FIB-INLO was employed to prepare TEM/STEM specimens. Figures 7 and 8 describe the details.

Location A: Fe-Rich Deposits

Deposits in specimen prepared from location A in Figure 9 was Rich in Fe and Ni, and identified as cubic Fe_3O_4. Typical microstructure in bright-field and electron diffraction patterns from this specimen are presented in Figure 10. The YSZ coatings in contact with deposits were tetragonal and showed no reaction with the deposits. However, localized and detached particles of the YSZ coatings were observed as shown in Figure 8(d).

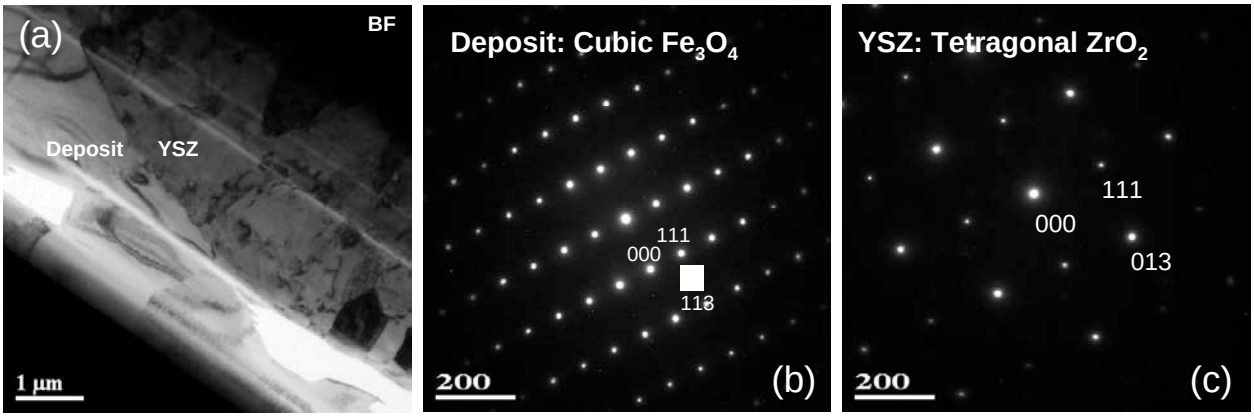

Figure 10. (a) Bright-field TEM micrograph of Fe-rich deposits on top of the YSZ coating; (b) selected area electron diffraction from the Fe-rich deposit indexed as cubic Fe_3O_4; (c) selected area electron diffraction from the YSZ coating indexed as tetragonal YSZ.

Location B: TGO Scale

The TGO Scale in location B in Figure 9 consisted of α-Al_2O_3 and spinel-$(Ni,Co)(Al,Cr)_2O_4$ as presented by HAADF, BF, and electron diffraction patterns in Figure 11. The tetragonal spinel oxide had lattice parameters of a = 0.5835 nm and c = 0.8412 nm. Aside from the fact that the scale was porous, no other abnormality was observed for the TGO scale.

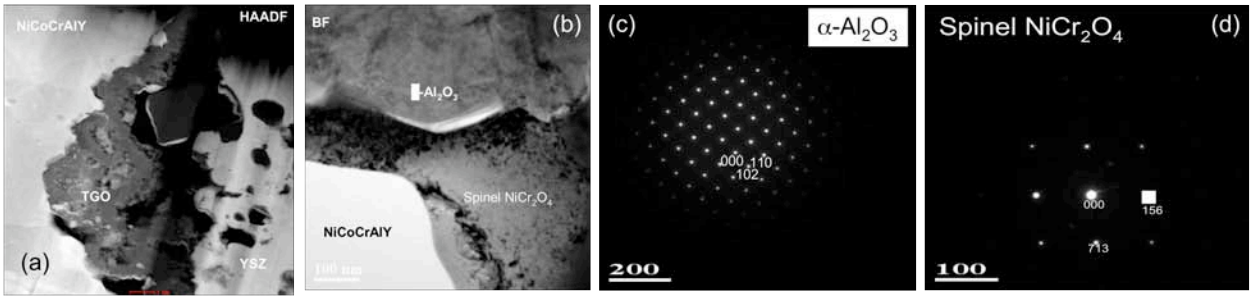

Figure 11. (a) HAADF and (b) BF TEM micrograph of the TGO scale in the TBCs; selected area electron diffraction from the TGO scale along with the HAADF contrast identified the presence of α-Al_2O_3 and (d) tetragonal spinel-$(Ni,Co)(Al,Cr)_2O_4$.

Location C: Two-Phase Fe-Rich Deposits

The deposits observed, in general, contained two different phases of Fe-oxide: cubic Fe_3O_4 with a large solubility (e.g., Ni) and monoclinic Fe_2O_3 with minimal solubility. As shown in Figure 9(b), backscatter electron micrograph shows distinctive compositional contrast, and Figure 12 shows distinctive electron diffraction patterns and composition spectra between these two phases. A controlled laboratory study on how these two different phases react, if any, with the YSZ coating is currently being carried out.

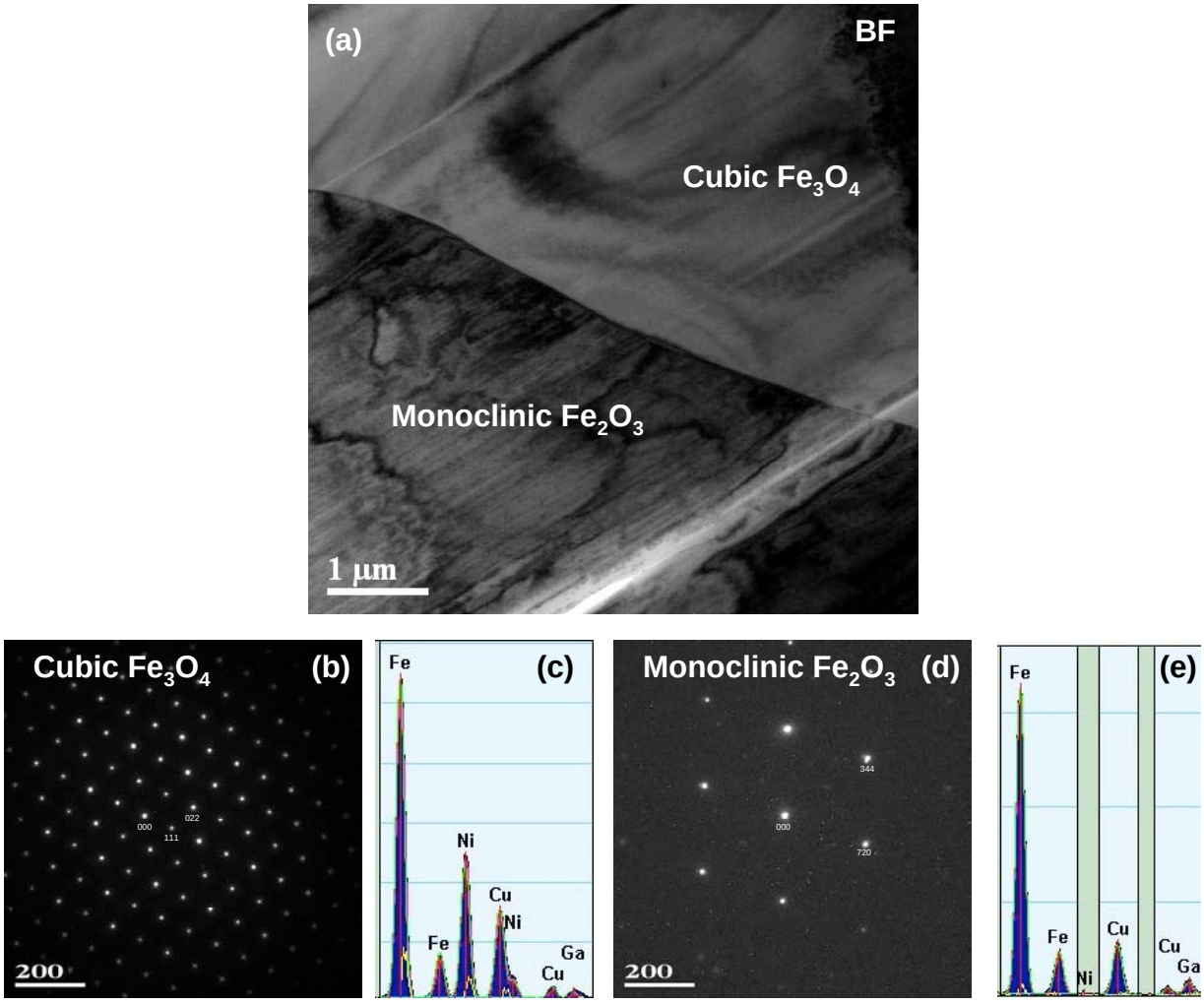

Figure 12. (a) Bright-field TEM micrograph of two-phase deposit identified as (b) cubic Fe_3O_4 with (c) a large solubility of Ni and (d) monoclinic Fe_2O_3 with (d) minimal solubility.

Location D: Internal Oxidation in NiCoCrAlY Bond Coat

Internal oxidation of NiCoCrAlY bond coats was observed to occur by oxidation of Al and Ni, and formation of α-Al_2O_3 and cubic NiO as presented in Figure 13.

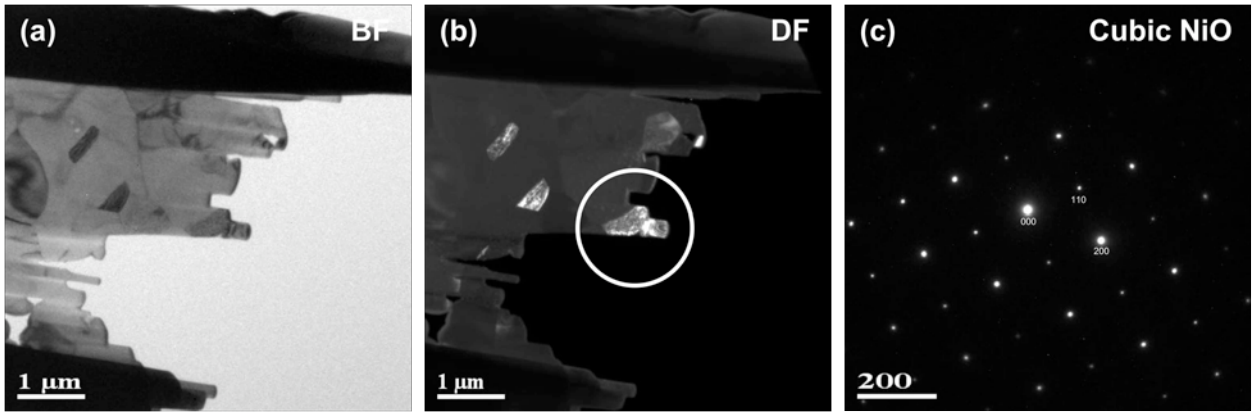

Figure 13. (a) BF and (b) DF TEM micrographs showing the internally oxidized NiCoCrAlY bond coat where (c) cubic NiO formation was observed.

In summary, characterization of a turbine blade coated with TBC after syngas degradation identified deposits on top of the YSZ coatings as cubic Fe_3O_4 and monoclinic Fe_2O_3. The cubic Fe_3O_4 exhibits solubility (e.g., Ni). However, the YSZ coating in contact with cubic Fe_3O_4 and monoclinic Fe_2O_3 deposits was tetragonal and showed no reaction with the deposits. However, isolated and detached particles of the YSZ coatings were observed where cubic Fe_3O_4 was identified. The TGO scale mainly consisted of α-Al_2O_3 with dispersed oxides of $(Ni,Co)(Al,Cr)_2O_4$ spinels (tetragonal). Internal oxidation in NiCoCrAlY bond coats consisted of α-Al_2O_3 and cubic NiO.

V.1.2. Stand-Alone NiCoCrAlY Coatings

Another turbine blade coated with stand-alone NiCoCrAlY was supplied by an industrial partner to assist the effort to understand the syngas degradation of NiCoCrAlY coatings. While the specification of coatings, turbine blade and operating condition remains proprietary, this specimen provided the first look at syngas degraded stand-alone NiCoCrAlY coatings. Visually, localized damage was observed as "roughened" surface. The blade was sectioned with slow speed Isomet Buehler using diamond wafering blade, mounted in Epo-Thin™ low viscosity epoxy, and metallographically polished down to 0.25 μm.

On the top surface that appeared "roughened," abnormality in TGO scale was observed as presented in Figure 14. This abnormality was determined to be predominantly NiS based on preliminary EDS analysis. While this protruding sulfide feature was not captured on the cross-section, a significant internal oxidation in the form of pitting and selective internal oxidation of β-NiAl solid solution phase was observed as shown in Figure 15. This selective internal oxidation indicates the oxygen solubility in the NiCoCrAlY has changed drastically due to its interaction with fuel-contaminants, and β-phase with higher Al activity has oxidized selectively. Presence of mechanical damage such as craze-crack may accelerate this damage process.

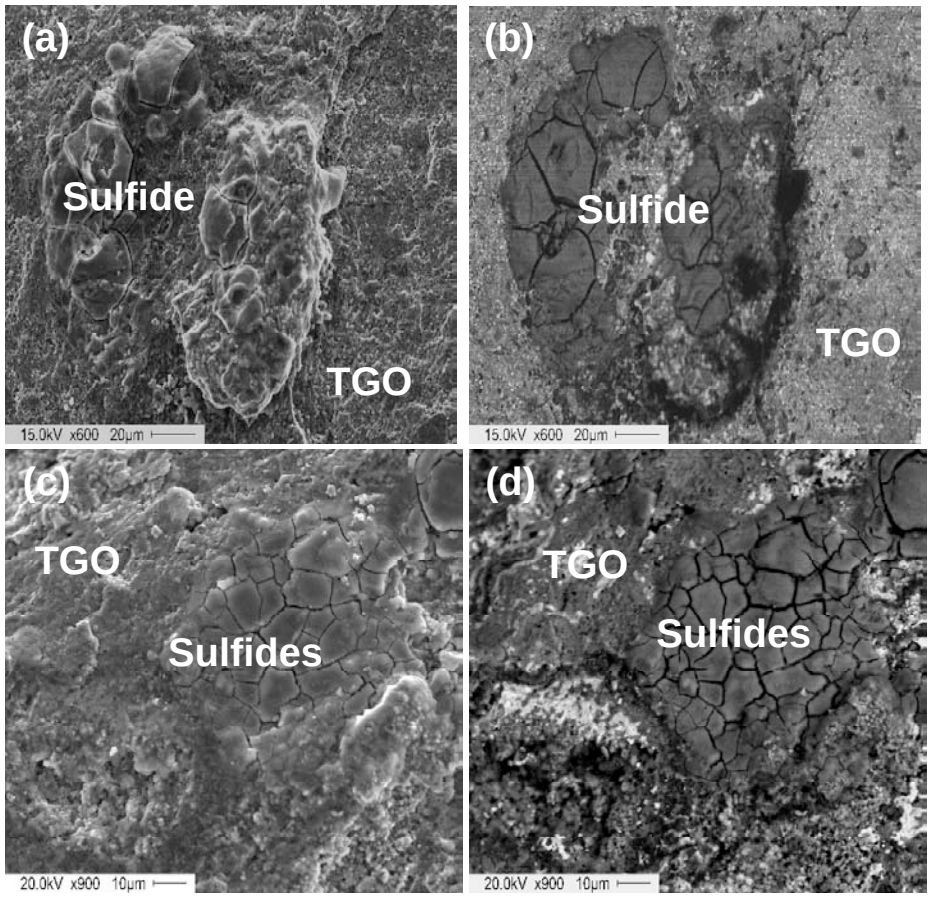

Figure 14. (a,c) Secondary and (b,d) backscatter electron micrographs of sulfides and TGO scale observed from the top surface of the stand-alone NiCoCrAlY coatings.

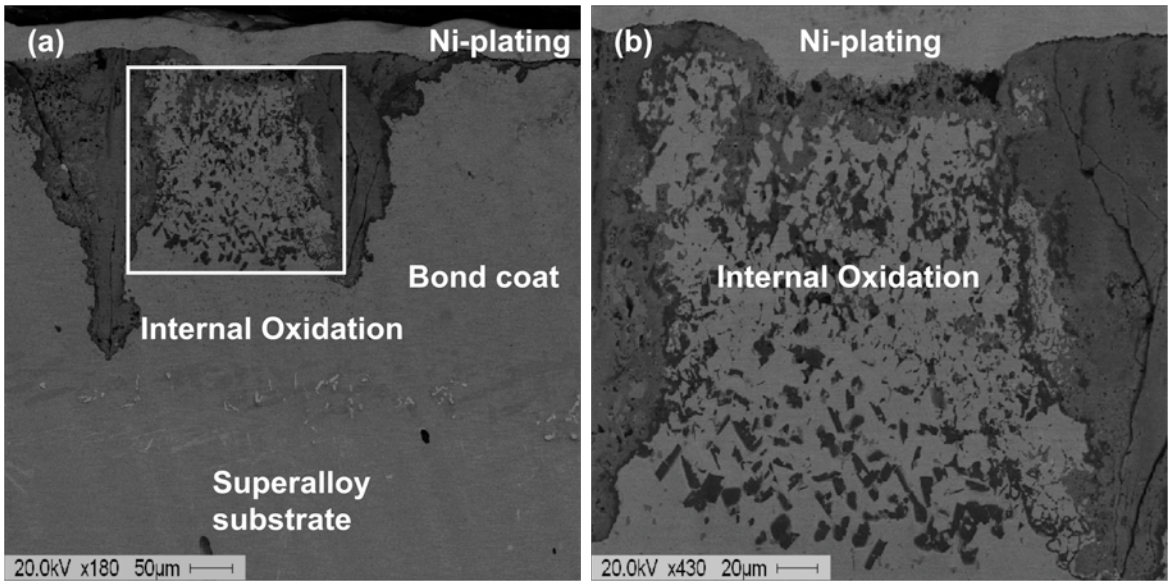

Figure 15. Internal oxidation of stand-alone NiCoCrAlY coatings in the form of pitting and selective oxidation of Al-rich β-NiAl solid solution.

V.1.3 TBC Specimens Tested with Syngas and Sulfur-Poisoned Syngas

TBC-coated button specimens thermally treated in Syngas and Sulfur-poisoned Syngas environment were supplied by Siemens Power Generation. While this work was carried out as an independent research contract, Siemens Power Generation has agreed to publish the outcome of the results (approval pending for documentation). Details of the testing parameters, results and discussion will be provided upon approval by Siemens Power Generation.

V.2. HADES Experiments

V.2.1. Current Status of HADES at Siemens Power Generation

Siemens Power Generation has acquired HADES from FTT, and HADES is going through installation and testing. PI will work with Siemens Power Generation to access HADES for this program.

V.3. In-Laboratory Investigation of TBCs and NiCoCrAlY Degradation

In addition to characterization of syngas degraded TBCs and NiCoCrAlY coatings, the following experimental plan was devised to provide a fundamental understanding of degradation mechanisms and kinetics. This laboratory testing employs free-standing APS YSZ coatings produced at UCF's Thermal Spray Facility (UCF-TSF) and NiCoCrAlY powders.

- Contaminants in the form of Na_2SO_4, V_2O_5, P_2O_5 and their combination
- Concentration of 0.5, 1, and 10 mM.
- Isothermal reaction at temperature ranging from 650° to 1000°C.
- Isothermal reaction duration of 5 minutes to 10 hours.

The APS TBCs produced on dissolvable Cu-substrates are presented in Figure 16(a). By dissolving the substrate, free standing APS YSZ coatings were obtained as shown in Figure 16(b) along with the corresponding microstructure shown in Figure 16(c). They consisted of non-equilibrium tetragonal (t') phase as shown in Figure 17. For NiCoCrAlY coatings, powders will be mixed in with contaminants and reacted as described above. These specimens are being examined before and after hot-corrosion experiments using XRD, SEM/EDS and TEM/STEM using FIB-INLO.

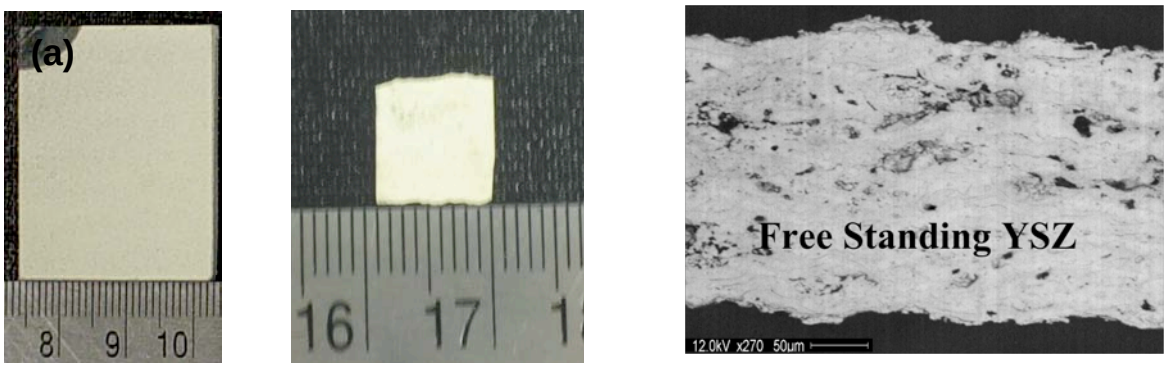

(a) (b) (c)

Figure 16. (a) APS YSZ coatings deposited on dissolvable Cu-substrate. (b) Free standing YSZ coatings, and (c) corresponding microstructure.

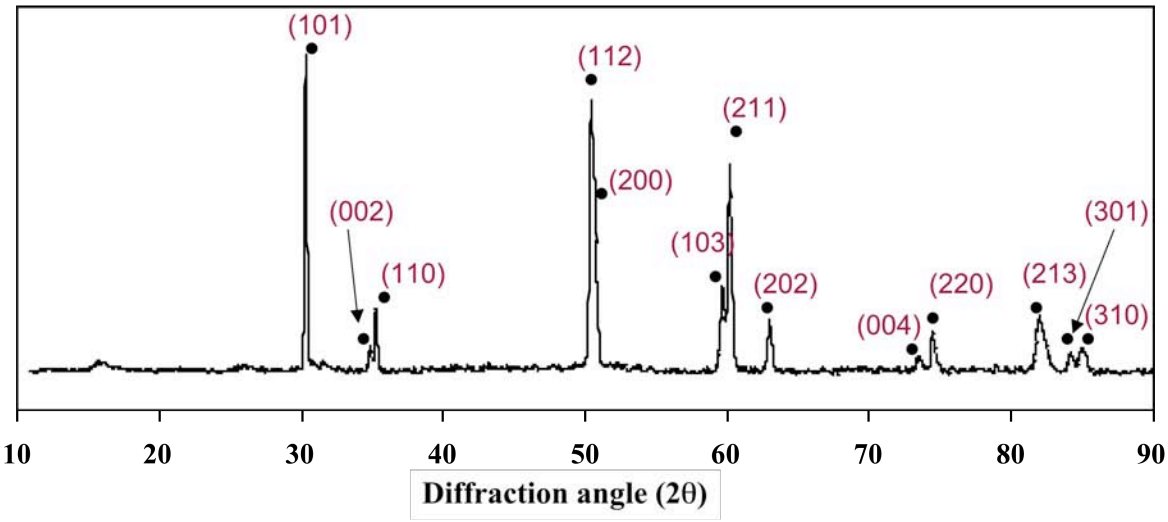

Figure 17. XRD pattern from an as-sprayed non-equilibrium tetragonal (t') YSZ coating after the dissolution of Cu-substrate.

V.3.1 Degradation of Free-Standing YSZ Coatings by V_2O_5

The V_2O_5 (applied as 20 mg/cm^2 on YSZ) melts at 690°C, and thus penetrates quickly through the porous YSZ regardless of its thickness. Molten V_2O_5 reacted with ZrO_2 as well as Y_2O_3 at high temperatures resulting in different reaction products; specifically below and above 747°C. Between 690° and 747°C, ZrO_2 in YSZ reacted with molten V_2O_5 to form **ZrV_2O_7 (zirconium pyrovanadate)** as shown in Figures 18 and 19. This reaction mechanism enriches YSZ with Y_2O_3 by leaching out ZrO_2 from the YSZ. However within the experimental duration, no significant phase transformation was observed by XRD, and t'-YSZ is the only phase observed in addition to the reaction product ZrV_2O_7. Figure 20 shows cross-sectional backscatter electron micrographs with EDS on reaction products. Figure 21 shows the bright-field TEM micrograph of cubic ZrV_2O_7 and tetragonal YSZ along with appropriate selected area diffraction patterns.

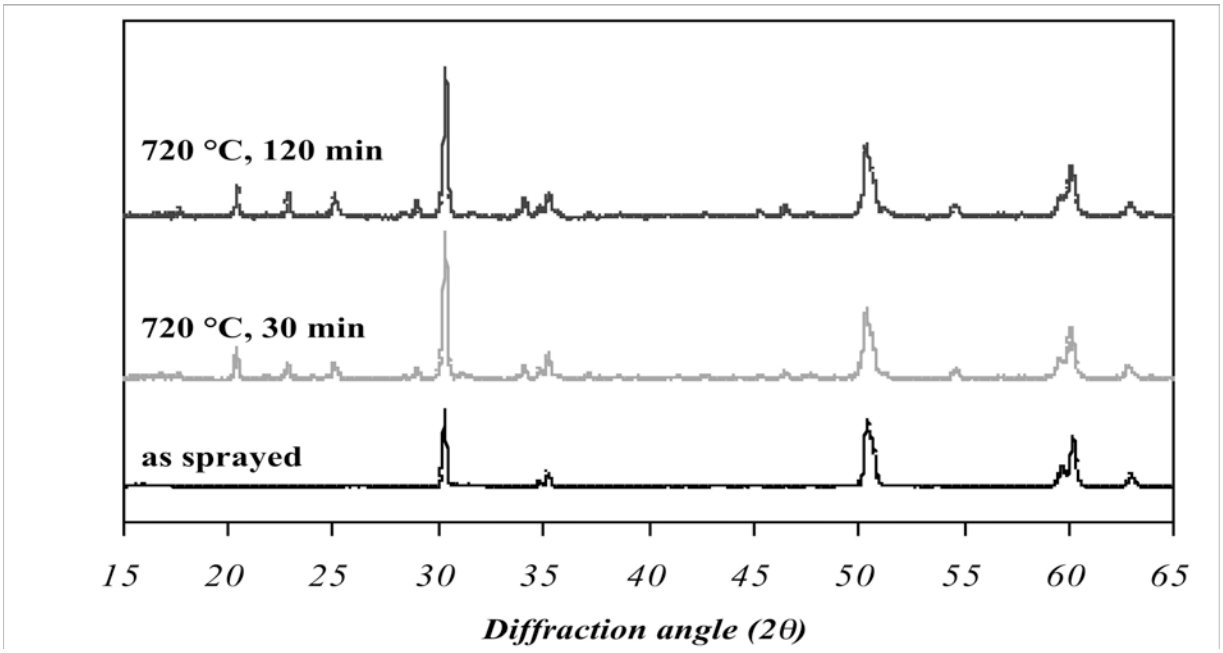

Figure 18. XRD patterns from as-sprayed and V_2O_5 reacted (720°C for 30 and 120 minutes) YSZ coatings.

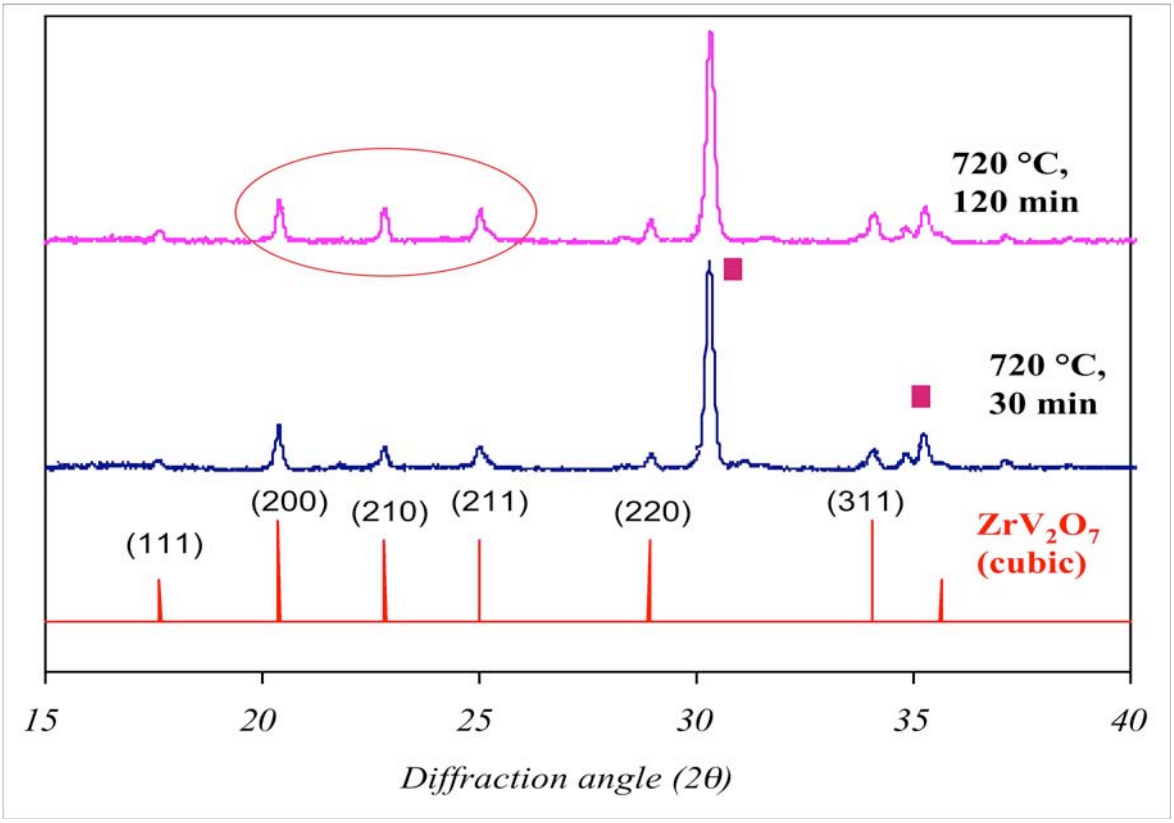

Figure 19. XRD patterns showing V_2O_5 reaction (720°C for 30 and 120 minutes) with the YSZ coatings demonstrating the formation of cubic ZrV_2O_7 (zirconium pyrovanadate).

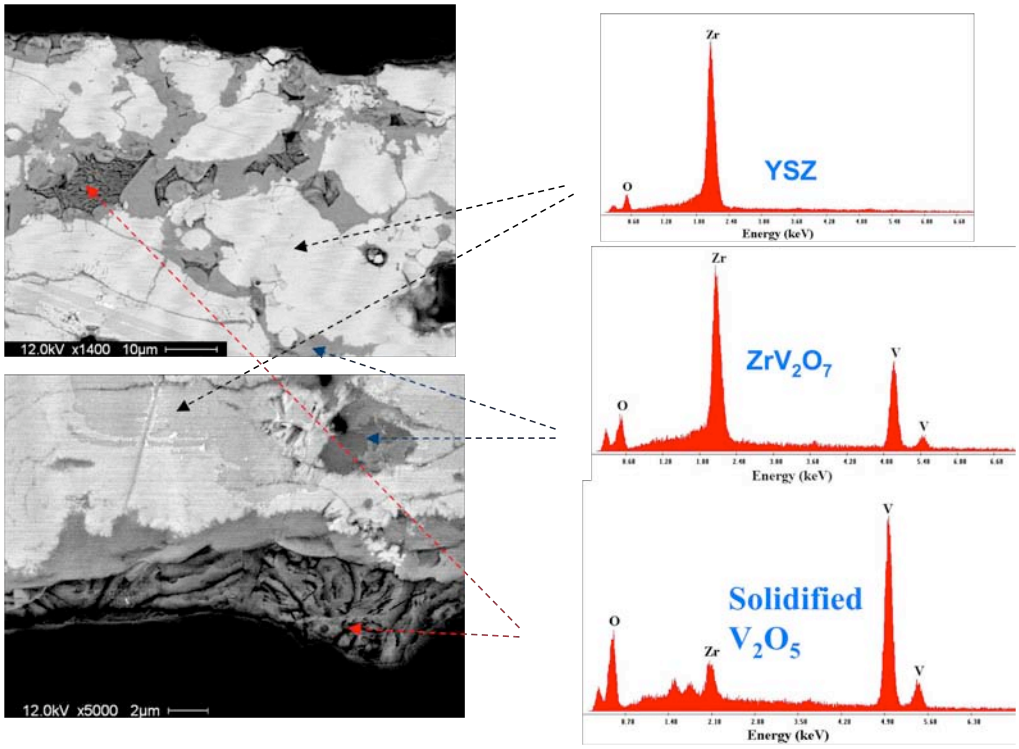

Figure 20. Cross-sectional backscatter electron micrographs with EDS on YSZ, cubic ZrV_2O_7 (zirconium pyrovanadate) and solidified V_2O_5 (residual).

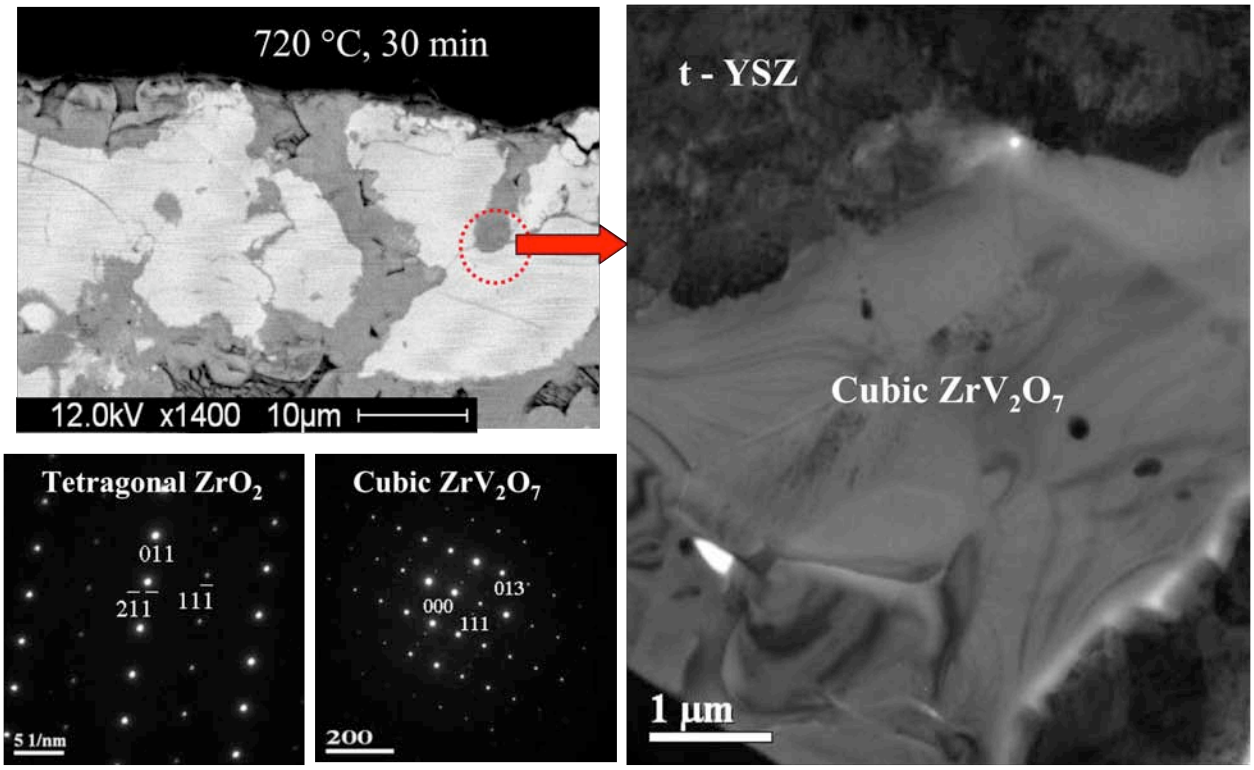

Figure 21. Bright-field TEM micrograph illustrating phase transformations t'-YSZ into cubic cubic ZrV_2O_7 with appropriate selected area diffraction patterns (indexed).

Above 747°C, molten V_2O_5 reacted with Y_2O_3 in YSZ, produced **YVO_4 (yttrium vanadate),** and destabilized YSZ as shown in Figure 22. YVO_4 (yttrium vanadate) is a very stable compound up to 1810°C. YVO_4 (yttrium vanadate) forms by leaching out Y_2O_3 from YSZ solid solution, and yielded formation of monoclinic and cubic ZrO_2, which is clearly observed in XRD patterns in Figures 22 and 23. In fact, a complete destabilization of t'-YSZ into equilbrium (f+m) phases occurred within 120 minutes at 750°C.

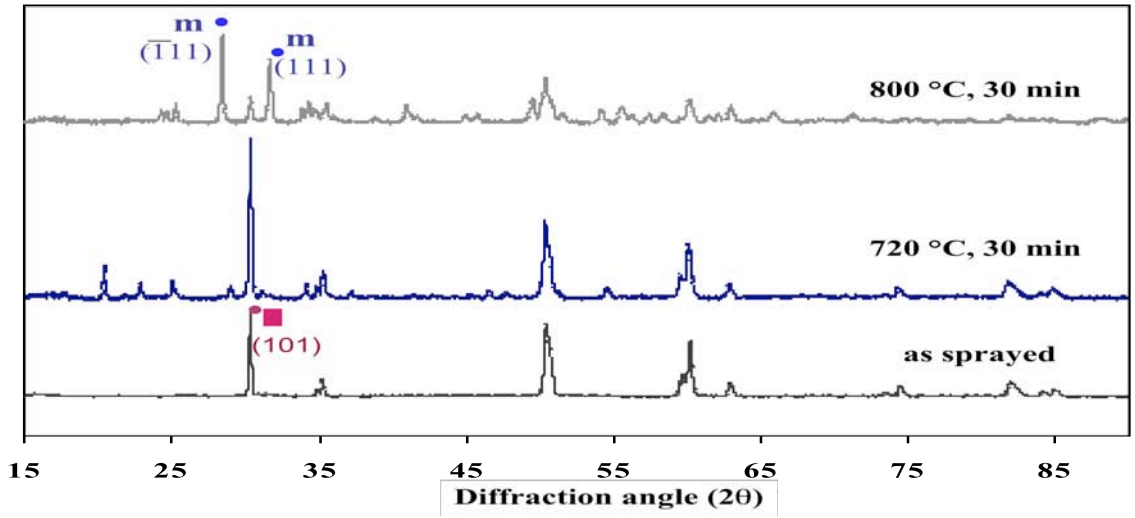

Figure 22. XRD patterns from the free-standing as-sprayed YSZ, V_2O_5 reaction (720°C for 30 minutes) with the YSZ coatings and formation of cubic ZrV_2O_7 (zirconium pyrovanadate), (c) V_2O_5 reaction (800°C for 30 minutes) with the YSZ coatings and formation of cubic YVO_4 (yttrium vanadate). The formation of cubic YVO_4 (yttrium vanadate) destabilized the YSZ coatings and produced t'-to-(f+m) phase transformation.

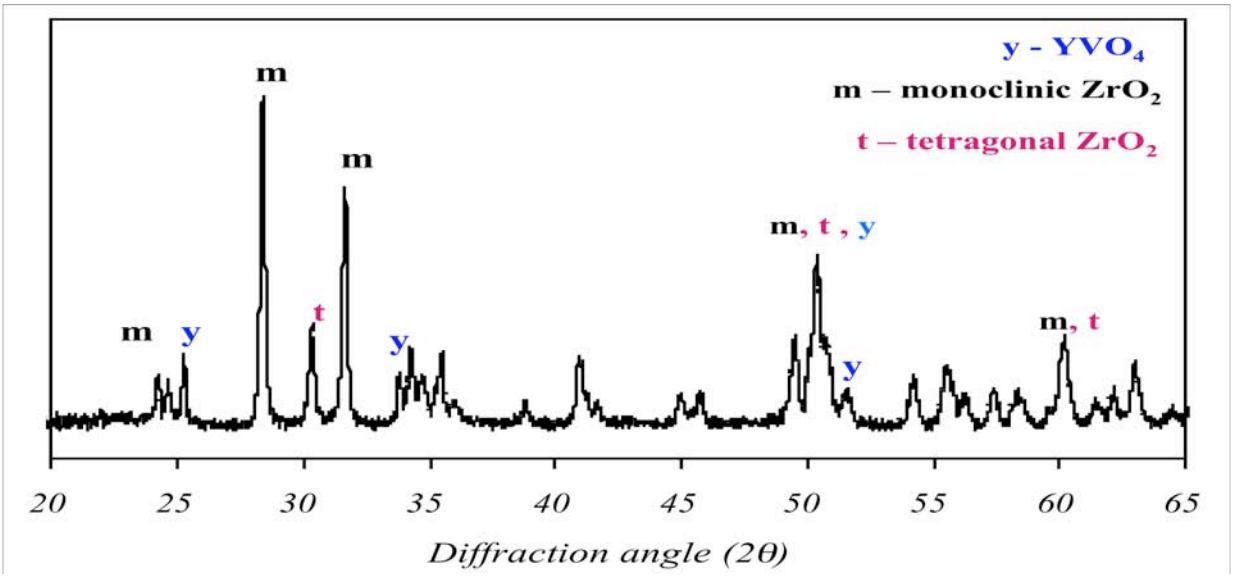

Figure 23. XRD patterns from V_2O_5 reaction (800°C for 30 minutes) with the YSZ coatings and formation of cubic YVO_4 (yttrium vanadate). The formation of cubic YVO_4 (yttrium vanadate) destabilized the YSZ coatings and produced t'-to-(f+m) phase transformation.

Formation of YVO_4 was observed to occur predominantly above 747°C, and the formation of ZrV_2O_7 (zirconium pyrovanadate) was observed to be the predominant reaction below 747°C. The formation of ZrV_2O_7 (zirconium pyrovanadate) did not destablize t'-YSZ. According to the phase diagrams, ZrV_2O_7 (zirconium pyrovanadate) melts incongruently at 747°C to ZrO_2 plus a liquid of composition 64% V_2O_5 - 36% ZrO_2. Thus, above 747°C, the liquid V_2O_5 from incongruent melting of ZrV_2O_7 leaches out with Y_2O_3, and the formation of YVO_4 is observed as the dominant YSZ – V_2O_5 reaction mechanism. Formation of YVO_4 depletes Y_2O_3 from the YSZ, and produces the deleterious transformation of the metastable tetragonal phase to the monoclinic and cubic phases, and destabilizes the t'-YSZ. The solidified ZrV_2O_7 (zirconium pyrovanadate) for this case is presented in Figure 24 by backscatter electron micrograph with EDS. Using TEM, presence of YVO_4 and monoclinic ZrO_2 was clearly observed as presented in Figure 25.

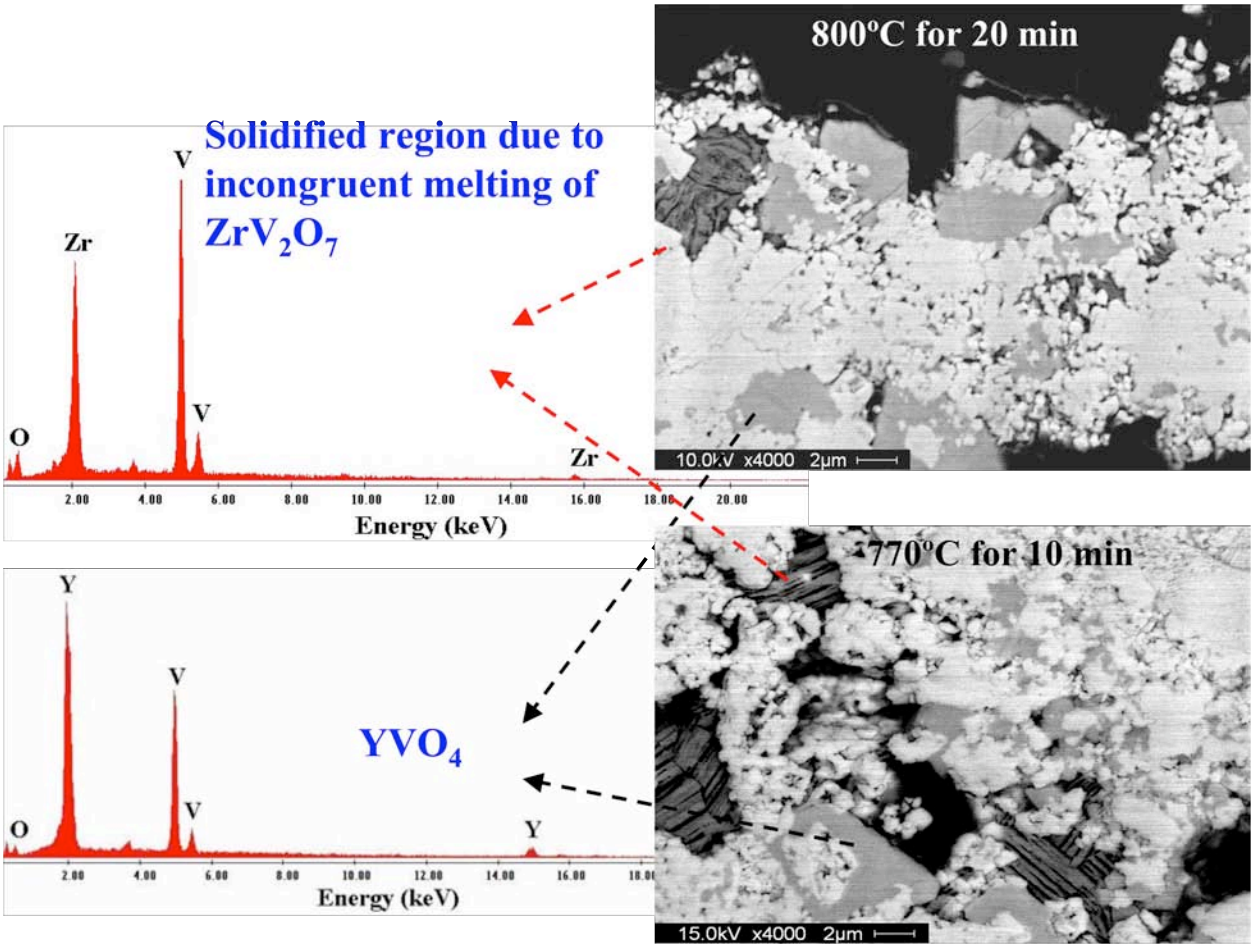

Figure 24. Cross-sectional backscatter electron micrographs with EDS on solidified ZrV_2O_7 (residual) and YVO_4.

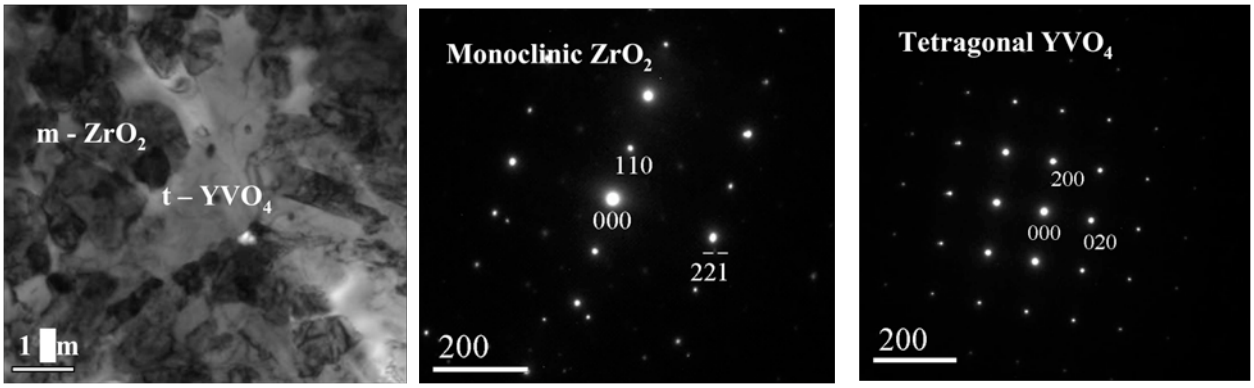

Figure 25. Bright-field TEM micrograph of destabilized monoclinic ZrO_2 and reaction product YVO_4 and the corresponding electron diffraction patterns (indexed).

V.3.2 Degradation of Free-Standing YSZ Coatings by Na_2SO_4, and Mixture of Na_2SO_4 and V_2O_5

Na_2SO_4 (sodium sulfate) itself had no effect on high temperature degradation of the free-standing APS YSZ coatings since no evidence of phase transformation and/or reaction product was observed up to 1000°C for 5 hours as shown in Figure 26. It is well known that Na_2SO_4 (sodium sulfate) at high temperature melts and dissociates into $Na_2O_{(l)}$ and $SO_{3(g)}$. The by-product Na_2O tends to form $NaVO_3$ in the presence of V_2O_5, which has a lower melting point (610°C), including a eutectic of 500°C, and S in SO_3 may leach out Y_2O_3 to destabilize t'-YSZ. In order to examine the degradation of YSZ under mixture of Na_2SO_4 and V_2O_5, $NaVO_3$ was synthesized using 50 mol% mixture. This mixture destabilized YSZ into monoclinc ZrO_2 by forming YVO_4 at very low temperature (e.g., 610°C based on phase diagram) as presented in Figure 27.

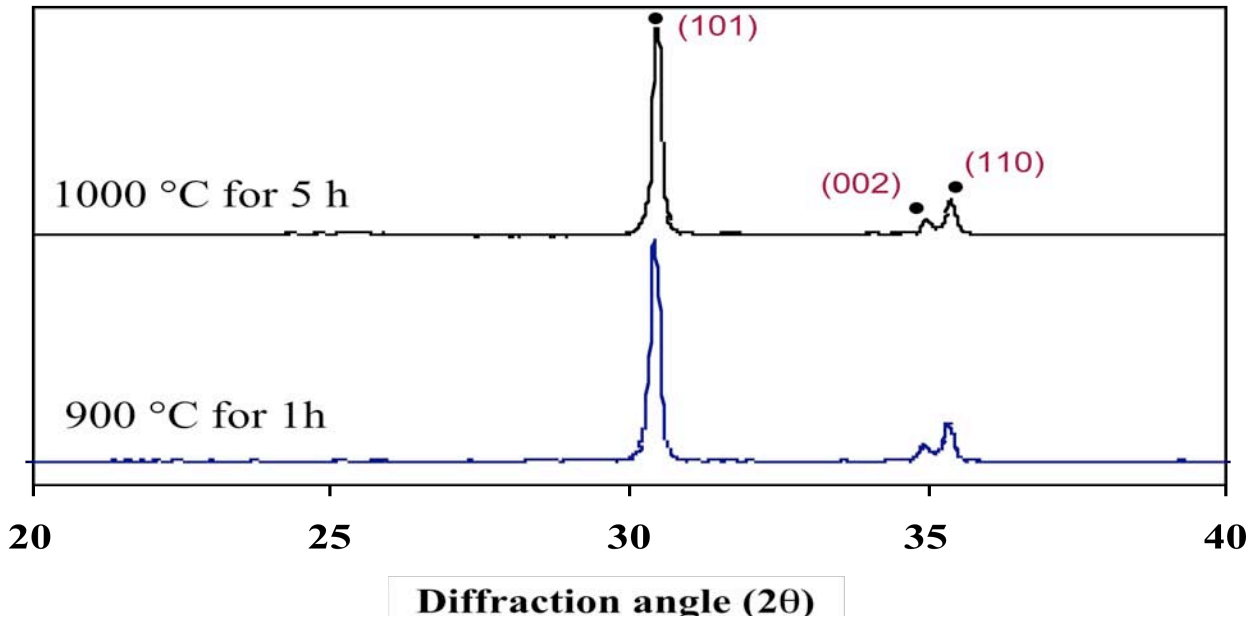

Figure 26. XRD patterns from YSZ in contact with Na_2SO_4 for 900° for 1 hour and 1000°C for 5 hours.

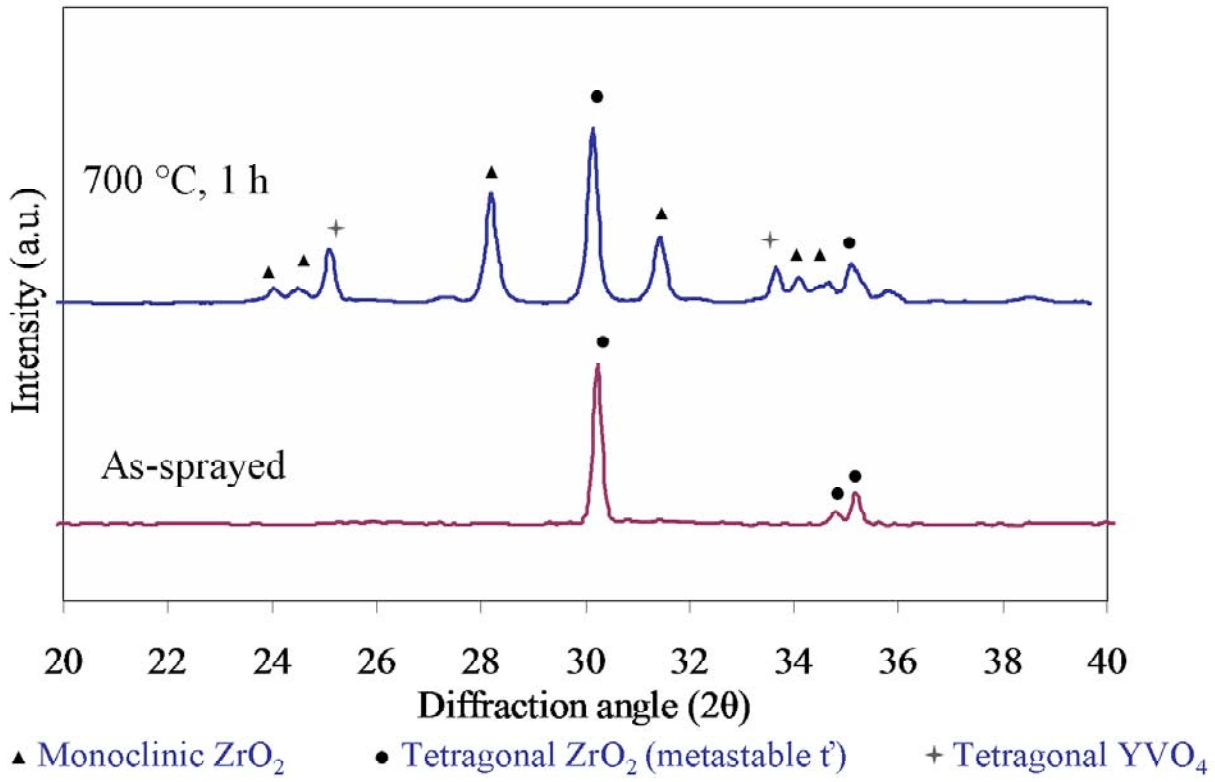

Figure 27. XRD patterns from YSZ in contact with 50 mol% mixture of Na_2SO_4 and V_2O_5 for 1 hour at 700°C.

Since presence of $SO_{x(g)}$ in gaseous form along with contaminant deposit may play a critical role in understanding Syngas degradation of TBCs, experimental set-up to examine degradation of YSZ by mixture of Na_2SO_4 and $SO_{x(g)}$ as well as gaseous $SO_{x(g)}$ has been devised and is under development.

V.3.3 Degradation of Free-Standing YSZ Coatings by P_2O_5

A similar study using P_2O_5 (instead of V_2O_5) was carried out to examine the degradation characteristics of YSZ from very low (200°C) to very high temperature (1000°C). A reaction between ZrO_2 (in YSZ) and P_2O_5 results in the formation of ZrP_2O_7 at temperature as low as 200°C even though P_2O_5 Melts at 340 °C and sublimes at 360°C. This reaction at low temperature occurs due to polymorphic transformation of P_2O_5 prior to melting at 200°C. Formation of ZrP_2O_7 enriched YSZ with Y_2O_3 and formation of fluorite cubic YSZ phase was observed as presented in Figure 28.

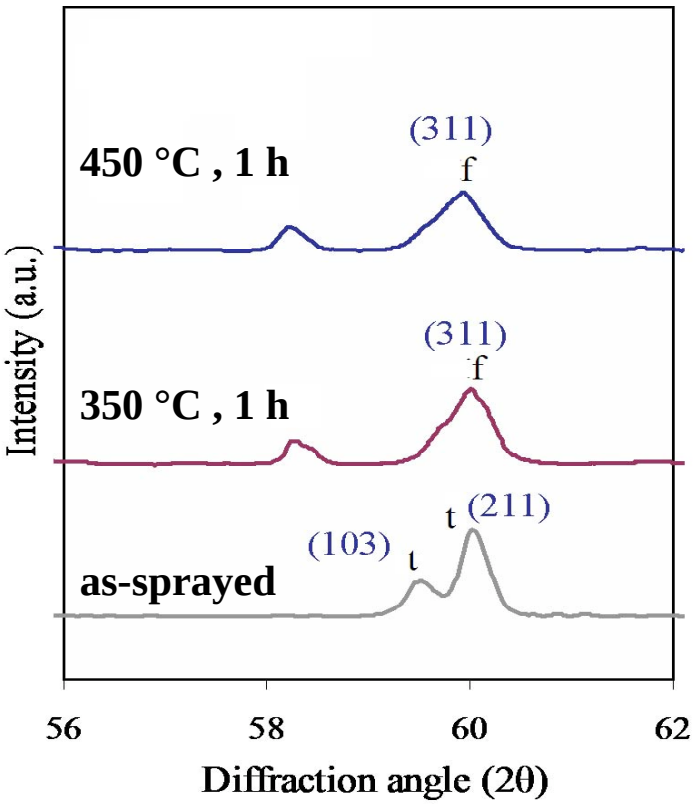

Figure 28. Formation of fluorite cubic YSZ phase due to enriching of YSZ with Y_2O_3 and formation of ZrP_2O_7 during reaction of YSZ and P_2O_5.

VI. CONCLUSION

This program seeks to provide an understanding for the mechanism of TBC degradation in syngas combustion environment by using in-laboratory experiments and Hyperbaric Advanced Development Environmental Simulator (HADES). The use of HADES provides realistic test conditions and real time monitoring/controlling of high temperature, high pressure, temperature gradient, erosion, and turbine operation from real syngas combustion. These offer a significant advantage over furnace or burner-rig testing, which requires several assumptions (e.g., effects of total and partial pressures, deposit constituents, gas or oxide constituents, etc.). State-of-the-art characterization techniques such as FIB INLO and TEM/STEM will be employed to identify deposit constituents and hot corrosion reactions to understand the mode and mechanisms of TBC degradation in realistic syngas combustion environment. Use of FIB-INLO and TEM/STEM will enable detailed identification of phase constituents of deposits, penetrants and reaction products, thus providing the exact mechanisms for degradation of TBCs in syngas combustion environment. Critical materials information, such as deposits, reaction/hot corrosion rates in the light of TBC constituents will be provided from the selected in-laboratory thermodynamic/kinetics experiment/modeling in addition to HADES testing.

Including third reporting period, microstructural characterizations were carried out on syngas degradation using TBC- and MCrAlY-coated blades that were employed in turbines with syngas combustion. Localized failure of TBCs and NiCoCrAlY coatings were observed visually. Microscopically, deposits containing Fe, Si, Al, Ca, Mg, Na, K, S were identified. These deposits arising from fuel contaminants penetrated and/or dissolved the YSZ coatings. Internal oxidation of NiCoCrAlY either in bond coats and stand-alone coating was observed along with selective internal oxidation of Al-rich β-NiAl solid solution.

The deposits observed, in general, contained two different phases of Fe-oxide: cubic Fe_3O_4 with a large solubility (e.g., Ni) and monoclinic Fe_2O_3 with minimal solubility. Detached particles of YSZ coatings were observed within cubic Fe_3O_4 deposits. The TGO scale consisted of α-Al_2O_3 and tetragonal spinel-$(Ni,Co)(Al,Cr)_2O_4$. Aside from the fact that the scale was porous, no other abnormality was observed for the TGO scale. Internal oxidation in NiCoCrAlY bond coats consisted of α-Al_2O_3 and cubic NiO. TEM/STEM characterization of degradation in stand-alone NiCoCrAlY coatings is in progress.

In addition, TBC-coated button specimens thermally treated in Syngas and Sulfur-poisoned Syngas environment were supplied by Siemens Power Generation. While this work was carried out as an independent research contract, Siemens Power Generation has agreed to publish the outcome of the results (approval pending for documentation). Details of the testing parameters, results and discussion will be provided upon approval by Siemens Power Generation.

In the presence of V_2O_5, formation of YVO_4 and ZrV_2O_7 was observed to occur above and below 747°C, respectively. The formation of ZrV_2O_7 (zirconium pyrovanadate) did not destablize t'-YSZ. According to the phase diagrams, ZrV_2O_7 (zirconium pyrovanadate) melts incongruently at 747°C to ZrO_2 plus a liquid of composition 64% V_2O_5 - 36% ZrO_2. Thus, above 747°C, the liquid V_2O_5 from incongruent melting of ZrV_2O_7 leaches out Y_2O_3, and this formation of YVO_4 is observed as the dominant YSZ – V_2O_5 reaction mechanism. This results in the depletion of Y_2O_3 from the YSZ, and the deleterious transformation of the metastable tetragonal phase to the monoclinic and cubic phases (i.e., destabilization of the YSZ).

Na_2SO_4 (sodium sulfate) itself has no effect on high temperature degradation of the free-standing APS YSZ coatings. However, a mixture of Na_2SO_4 and V_2O_5 (e.g., $NaVO_3$) quickly destabilized YSZ with the formation of YVO_4. Reaction between ZrO_2 (in YSZ) and P_2O_5 results in the formation of ZrP_2O_7 at temperature as low as 200°C resulting in phase transformation (t' ➔ f).

Siemens Power Generation has acquired HADES from FTT, and HADES is going through installation and testing. PI will work with Siemens Power Generation to access HADES for this program.

VII. RESEARCH PLAN FOR THE NEXT REPORTING PERIOD

In the fourth reporting period (February 1, 2007 ~ July 31, 2007), we will complete in-laboratory experiments involving degradation of free standing APS YSZ and NiCoCrAlY powders by V_2O_5, P_2O_5, Na_2SO_4 and their by-products at high temperature. Due to delayed allocation of second year funding, the following tasks will now be initiated during the fourth reporting period and we will request no-cost extension of this program.

- Environmental testing with Na_2VO_4 and $SO_{x(g)}$ in laboratory set-up.
- HADES testing through access granted by Siemens Power Generation.

REFERENCES

1. Materials and Practices to Improve Resistance to Fuel Derived Environmental Damage in Land- and Sea-Based Turbines, ed. D. Olson, G. Edwards, P. Bollinger, A. Lasseigne, G. Atkins, EPRI, Palo Alto, CA, CSM, Golden, CO, ONR, Arlington, VA, DOE, Oak Ridge, TN, 2003.
2. University Turbine Systems Research Request for Proposal No. UTSR 04-01, South Carolina Institute for Energy Studies, Clemson University, Clemson, SC, 2004.
3. R.L. Jones, in Metallurgical and Ceramic Protective Coatings, ed. K.H. Stern, Chapman and Hall, London, p. 194.
4. R.L. Jones, C.E. Williams, S.R. Jones, *J. Electrochem. Soc.*, 133 (1986) 227.
5. R.L. Jones, *High Temp. Mater.*, 6 (1988) 187.
6. A. Wang, Poison Resistant Catalyst Development and Testing: A Report Prepared for U.S. DoE by Air Products and Chemicals, Inc., 1997.
7. I. Kvernes, J.K. Solberg, K.E. Lillerud, in Procd. First Conf. Adv. Mater. Altern. Fuel Capab. Dir. Fired Heat Engines, ed. J.W. Fairbanks, J. Stringer, U.S. DoE, 1979, p. 367.
8. J.C. Hamilton, A.S. Nagelberg, *J. Amer. Ceram. Soc.*, 67 (1984) 686.
9. W. Hertl, *J. Appl. Phys.*, 63 (1988) 5514.
10. S.C. Singhal, R.J. Bratton, *Trans. ASME J. Engng. Power*, 102 (1980) 770.
11. R.L. Jones, *Mater. High Temp.*, 9 (1991) 228.
12. R.H. Barkalow, F.S. Pettit, in Procd. in Procd. First Conf. Adv. Mater. Altern. Fuel Capab. Dir. Fired Heat Engines, ed. J.W. Fairbanks, J. Stringer, U.S. DoE, 1979, p. 704.
13. T.E. Strangman, J.L. Schienle, Trans. AIME *J. Engng. Power*, 112 (1990) 531.
14. T.E. Strangman, J. Neumann, A. Liu, Thermal Barrier Coatings Life-Prediction Model Development – Final Report, NASA CR-179648, 1987.
15. S. Bose, T.E. Strangman, in Materials and Practices to Improve Resistance to Fuel Derived Environmental Damage in Land- and Sea-Based Turbines, ed. D. Olson, G. Edwards, P. Bollinger, A. Lasseigne, G. Atkins, EPRI, Palo Alto, CA, CSM, Golden, CO, ONR, Arlington, VA, DOE, Oak Ridge, TN, 2003.
16. Prepared by Dakota Gasification Company, 2003.
17. S. Laxman, B. Franke, B.W. Kempshall, Y.H. Sohn, L.A. Giannuzzi, K.S. Murphy, Surf. Coat. Technol., 177-8 (2004) 121.
18. A.J. Burns, R. Subramanian, B.W. Kempshall, Y.H. Sohn, Surf. Coat. Technol., 177-8 (2004) 89.
19. B.W. Kempshall, S.K. Jha, Y.H. Sohn, R.R. Vanfleet, J. Kimmel, Thin Solid Films, 466 (2004) 128.
20. J. Liu, J.W. Byeon, Y.H. Sohn, Surface and Coatings Technology, 200 (2006) 5869.

Semi-Annual Report – UTSR Project SR-119

Titled

Aero Losses, Heat Transfer, Discharge Coefficients for Different Vane Trailing Edge Cooling Technologies for Syngas Fired Turbines

Period of Performance

1 August 2006 through 31 January 2007

Prepared by:

Dr. Forrest Ames, Principal Investigator, Mr. Nathan Fiala, Mr. Indrajit Jaswal

Mechanical Engineering Department, University of North Dakota
P O Box 8359, Grand Forks, North Dakota 58202-8359
Phone: (701) 777-2095, Fax: (701) 777-2271
Email: forrestames@ und.nodak.edu

12 March 2007

DOE Award Number: DE-FC26-02NT41431

DISCLAIMER* -- The Disclaimer must follow the title page, and must contain the following paragraph:

"This report was prepared as an account of work sponsored by an agency of the United States Government. Neither the United States Government nor any agency thereof, nor any of their employees, makes any warranty, express or implied, or assumes any legal liability or responsibility for the accuracy, completeness, or usefulness of any information, apparatus, product, or process disclosed, or represents that its use would not infringe privately owned rights. Reference herein to any specific commercial product, process, or service by trade name, trademark, manufacturer, or otherwise does not necessarily constitute or imply its endorsement, recommendation, or favoring by the United States Government or any agency thereof. The views and opinions of authors expressed herein do not necessarily state or reflect those of the United States Government or any agency thereof."

ABSTRACT

This third semi-annual report documents the research progress by the University of North Dakota (UND) during the third six months of UTSR Project 04-01 SR-119, "Aero Losses, Heat Transfer, Discharge Coefficients for Different Vane Trailing Edge Cooling Technologies for Syngas Fired Turbines." The present project has been structured to acquire technology, which will provide gas turbine designers the means to assess competing trailing edge cooling configurations for a syngas environment. In this third semi-annual report, the progress made over this period of performance is presented. The focus at the University of North Dakota has been to acquire the aerodynamic and heat transfer measurements for the letter box geometry and to begin to build up the high solidity pin fin array. Both aerodynamic exit survey measurements and trailing edge heat transfer and film cooling measurements have been completed for the letterbox geometry. The high solidity pin fin arrays have been fabricated (and instrumented) in both a constant height channel (to provide a baseline geometry) and in a converging array geometry. Preparations are nearly complete to begin testing the high solidity pin fin array

Work on the project was stopped at the University of Utah after the first year of effort on July 31, 2006 because Dr. Ligrani, project co-investigator, changed his professional affiliation during the Summer of 2006 from the University of Utah to Oxford University in the United Kingdom. Note that the present project could not be transferred to Oxford University because DoE/SCIES will not provide support for a non-U.S. institution.

The planned work for the University of North Dakota is expected to continue. In the next six months, UND plans to complete aero-loss, heat transfer, and discharge coefficient measurements for the pressure-side hole geometry. Additionally, UND plans to complete internal heat transfer and pressure drop measurements for the high solidity pin fin array. At the same time, efforts will be made to develop the low pressure drop internal cooling geometry for covered vane trailing edge cooling and to develop a simulated syngas roughened surface for vane geometries. Currently, the project milestones have been met or exceeded by the research team at the University of North Dakota.

TABLE OF CONTENTS

LIST OF FIGURES AND TABLES

Introduction

Gas turbine engineers who develop designs for turbine airfoils must balance the competing tradeoffs between cooling performance and efficiency, aerodynamic performance, and manufacturability. Designers rarely have complete information on heat transfer boundary conditions and aerodynamic performance for a new design. They often must rely on the useful but imprecise data determined from engine tests to gage the reliability and performance of a given design. The use of syngas derived fuels produces added complexity. Particulates from these fuels are expected to deposit onto or erode turbine airfoil surfaces. The deposition and erosion can be expected roughen airfoil surface above levels typical of more conventional fuels. This increased surface roughness can be expected to have an adverse effect on turbine aerodynamics and heat transfer. Surface roughness is known to cause early transition and increase heat transfer rates across the turbulent boundary layer when the roughness features are larger than the sublayer. Roughness has been found to have an even larger impact on aerodynamic losses. Additionally, designers need to account for the potential of particulate deposition to clog cooling exit flow paths and the influence this clogging could have on cooling scheme effectiveness. Consequently, designers have these added variables to consider in their designs.

Executive Summary

This semiannual report presents the experimental progress for the third semi-annual period of this project to characterize the aerodynamic and heat transfer performance for competing vane trailing edge designs for a syngas fueled gas turbine. In the initial six month period, the trailing edge geometries for the gill slot and letterbox configurations were specified based on feedback from our industrial heat transfer points of contact. At the University of North Dakota, aerodynamic loss measurements were made on both the base vane and the gill slot geometry. During the second semi-annual period the University of North Dakota acquired internal heat transfer results and pressure drop for the converging pin fin array and on external heat transfer and film cooling results for the gill slot vane. The pin fin array was tested over a wide range in Reynolds numbers documenting both row average heat transfer levels and row to row pressure drop. Vane surface heat transfer and adiabatic effectiveness measurements were acquired on the gill slot vane for low (< 1%), grid (8.5%), and aero-combustor (13.5%) turbulence levels, at exit chord Reynolds numbers ranging from 500,000 to 2,000,00 for a range of internal flow rates.

The present project has been designed to provide accurate external and internal heat transfer and aerodynamic loss data on each of the cooling configurations so designers can objectively compare the tradeoffs in life and performance for each competing design. During the third semi-annual period we have completed external heat transfer and aerodynamic testing for the letterbox vane. These heat transfer and adiabatic effectiveness measurements include values acquired on the inner suction surface as well as the partition. Heat transfer and effectiveness measurements have been taken at exit Reynolds numbers ranging from 500,000 to 2,000,000 for the low, grid, and aero-combustor turbulence conditions. Aerodynamic measurements have been acquired at these same conditions and for each turbulence and Reynolds number condition we have varied the ejection rate to document its influence on vane and partition surface heat transfer, adiabatic effectiveness, and aerodynamic loss. Comparisons are made for letterbox aerodynamic losses showing difference between base vane and gill slot geometries with blowing. Together, these heat transfer and aerodynamic loss data provide designers with objective information on the aerodynamic trade-offs for these cooling designs.

The letterbox external heat transfer and adiabatic effectiveness measurements should provide a useful database for designers. Additionally, the measured pressure drop from the array inlet to the letter box discharge outlet will provide a method to gage pressure drop for a given flow rate. Also, our

aerodynamic loss surveys have demonstrated that the letterbox design provides a marginally significant reduction (0.20%) in losses compared to the gill slot for the design flow. The present data provide heat transfer and adiabatic effectiveness results over a range of Reynolds numbers, blowing ratios, and external turbulence conditions and these results should prove to be useful to designers.

Work on the project at the University of Utah was stopped after the first year of effort because Phil Ligrani, project co-investigator, changed his professional affiliation during the summer of 2006 from the University of Utah to Oxford University in the United Kingdom. Note that the present project could not be transferred to Oxford University because DoE/SCIES will not provide support for non-U.S. institutions.

The University of North Dakota has elected to apply a simulated syngas roughened surface to its vanes using a surface generated by Brigham Young University's accelerated roughness rig. This program change has resulted from discussions with a UTSR heat transfer point of contact (task 1). Currently, the external geometries for the base vanes and the vanes with the four external cooling schemes have been specified after discussion with industry (task 2). Also, construction of the base vanes, gill slot vanes and letterbox vanes is complete and construction has begun on the other externally cooled vanes (task 2). Aerodynamic loss and pressure distributions have been completed on the base vane, gill slot vane, and letterbox vane (task 3 and 4). Activities to assess internal heat transfer as well as external heat transfer and adiabatic effectiveness are also underway. The converging pin fin array used on the gill slot and letterbox designs has been constructed and tested in a bench scale heat transfer rig. The high solidity pin fin array has also been designed and built (task 6). External heat transfer and adiabatic effectiveness measurements have also been acquired on the gill slot and letterbox vanes and work is currently underway to prepare the pressure side holes vane (tasks 5 and 7).

Broader Impacts. In addition to the experimental results that have been generated during this project, this project has been producing publications and has been supporting graduate students. Thus far this project has also produced two IGTI papers, provided support and served as a thesis project for three graduate students. Jake Johnson defended his thesis in June of 2006 and received his MSME in August of 2006. He is currently serving as a 2nd Lt. in the USAF and he is presently undergoing flight training. Nathan Fiala has finished acquiring data for the letterbox design and is currently working on his master's thesis. He recently accepted a full time position at UND's Energy and Environmental Research Center as a research engineer. He is expecting to graduate in May of 2007. Indrajit Jaswal has been working on the project since October of 2006 and is currently involved in testing related to the pressure-side holes vane. Prior to returning to school at UND Indrajit worked for Alstom for about ten years.

Project Description

The overall objective of the three year study is to experimentally investigate heat transfer and aerodynamic tradeoffs of four competing trailing edge cooling designs: the gill slot, the letterbox, pressure side holes, and the covered trailing edge. This experimental assessment will include an evaluation of the aerodynamic performance, external heat transfer performance, internal cooling performance, and cooling configuration discharge coefficients. Each test will be run with a smooth external surface as well as with the simulated roughness of a syngas fueled turbine. The vane aerodynamics of each design will be compared with the aerodynamics of the base vane design without any cooling discharge features. Full passage exit surveys will be acquired at two axial spacings and at two coolant flow rates to assess both profile and endwall losses of each cooling configuration in the low speed cascade and the University of North Dakota (UND). The UND cascade will be run over a relevant range of chord exit Reynolds numbers (500,000 to 2,000,000). In addition, the UND cascade will be run at, low, grid, and aero-combustor turbulence conditions. ***Recently, with the move of Co-PI, Dr. Phil Ligrani, from the University of Utah (UoU) to Oxford University, the contract statement of work (SOW) has be changed to eliminate the remainder of the tasks originally scheduled to be accomplished by the UoU.***

External heat transfer levels will also be documented experimentally for the base vane and the four trailing edge cooling configurations. Additionally, internal heat transfer levels and flow discharge coefficients will be acquired for three separate internal cooling configurations. External heat transfer measurements will include both external heat transfer rates and an experimental assessment of any film cooling effectiveness on the external surface due to the coolant discharge. External measurements will be made for both surface conditions (smooth and syngas roughened), for all three turbulence conditions, over the full range of Reynolds numbers, and for design and reduced cooling flows. Internal heat transfer levels will be acquired over a full range of the expected Reynolds numbers for the vane tests. This resulting comprehensive database is expected to supply trailing edge cooling scheme designers with the information needed to assess the tradeoffs of the different trailing edge configurations.

Experimental Approach

The measurements for this study will be conducted using a "fully" or conventionally loaded vane. The large-scale, low-speed cascade facility at the University of North Dakota is being engaged to conduct these experiments. The UND cascade runs at low Mach numbers (0.05 – 0.2) and requires a special vane geometry to achieve a fully loaded pressure profile similar to the midspan pressure distribution of the engine nozzle guide vane. The large scale low speed cascade can be run at steady state allowing for detailed full passage exit surveys and good detail in internal and external heat transfer and pressure distribution investigations. A comparison of engine midspan and the low Mach number geometries is shown in Figure 1. (These two geometries were graciously provided by the turbine aerodynamics and heat transfer group at Rolls Royce.) The resulting calculated compressible (Mach = 0.8) and incompressible (Mach = 0.2) pressure profiles are compared in Figure 2 showing closely agreeing loading distributions. Figure 3 shows a comparison between the measured and predicted pressure distributions for the incompressible vane, both are presented at a Mach number close to 0.2. The comparison shows the very close agreement between the experimental base vane pressure distribution and the Fluent calculation. This close agreement provides confidence that the midline aerodynamics developed by the linear cascade are consistent with the 2-D blade to blade aerodynamics.

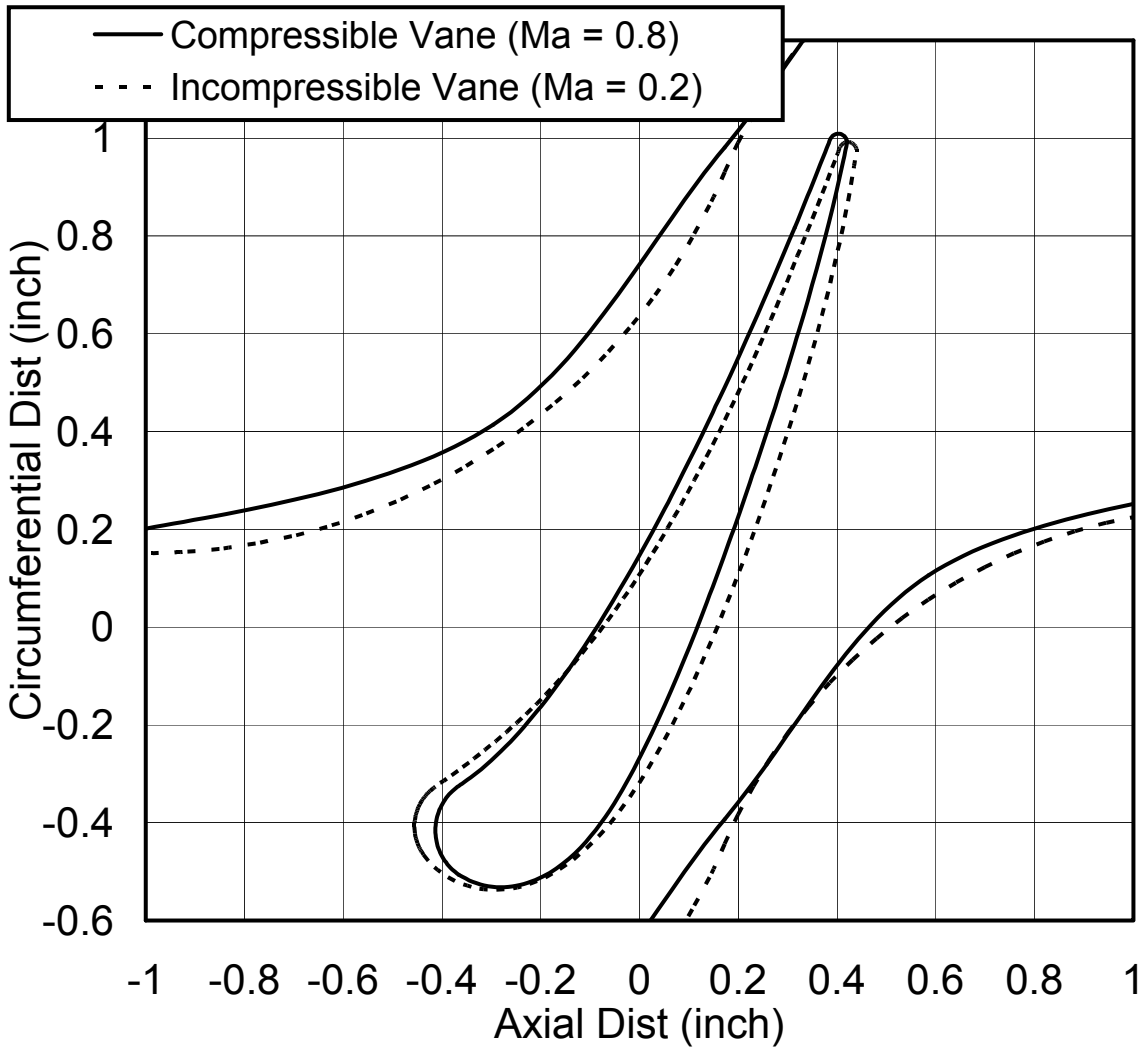

Figure 1. Comparison of compressible and incompressible vane geometries showing periodic boundaries of the calculation domain.

Aerodynamic loss, surface pressure distributions, external heat transfer, adiabatic effectiveness, and trailing edge discharge coefficients will be in acquired UND's cascade facility. The facility will be run over a four to one range of chord exit Reynolds numbers, at low and at two elevated turbulence levels, and at design and partial coolant discharge flow rates. The large scale of the University of North Dakota cascade will allow acquiring a high level of detail. An example of the aerodynamic detail developed by exit surveys is shown in Figures 4 and 5 which present contours of total pressure loss coefficients for the base vane at low turbulence (0.7%) and aero-combustor (13.5%) turbulence.

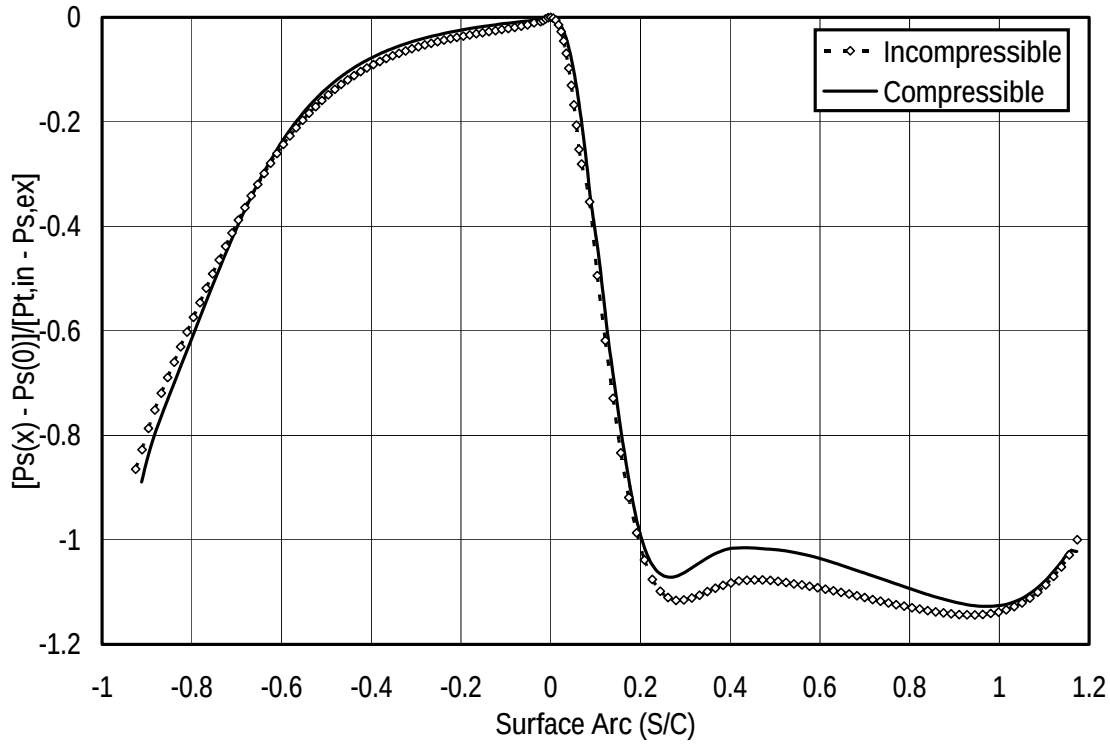

Figure 2. Comparison of calculated compressible and incompressible pressure distributions.

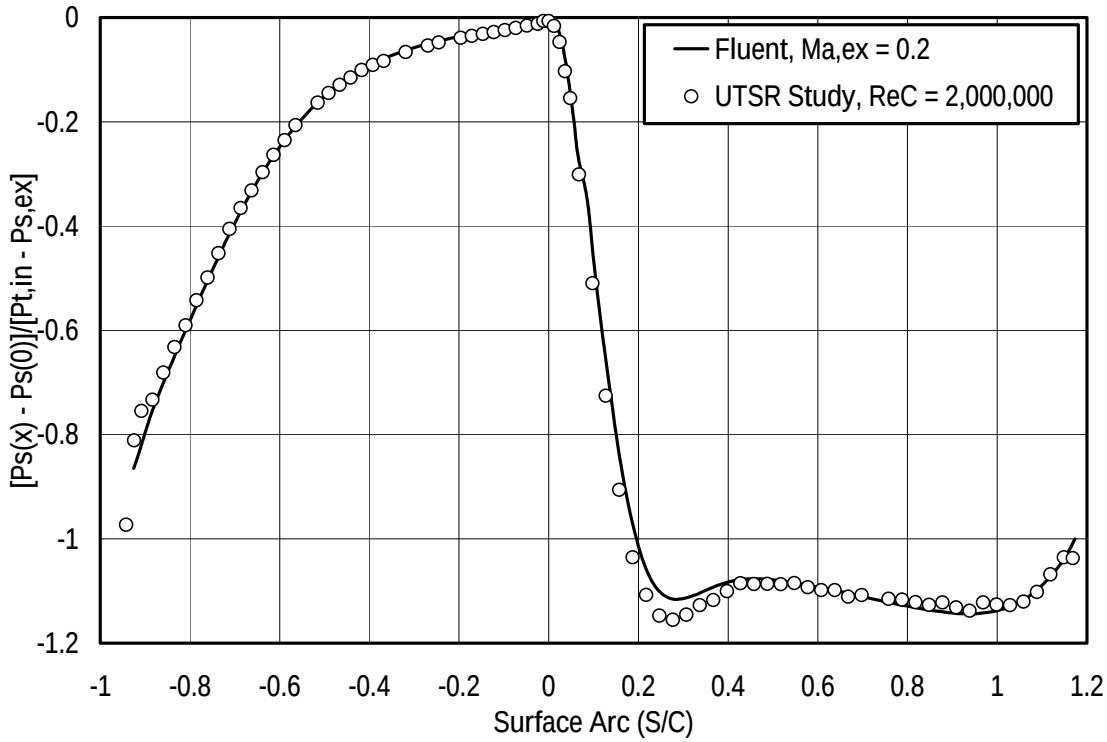

Figure 3. Comparison between calculated and measured pressure distributions for incompressible vane.

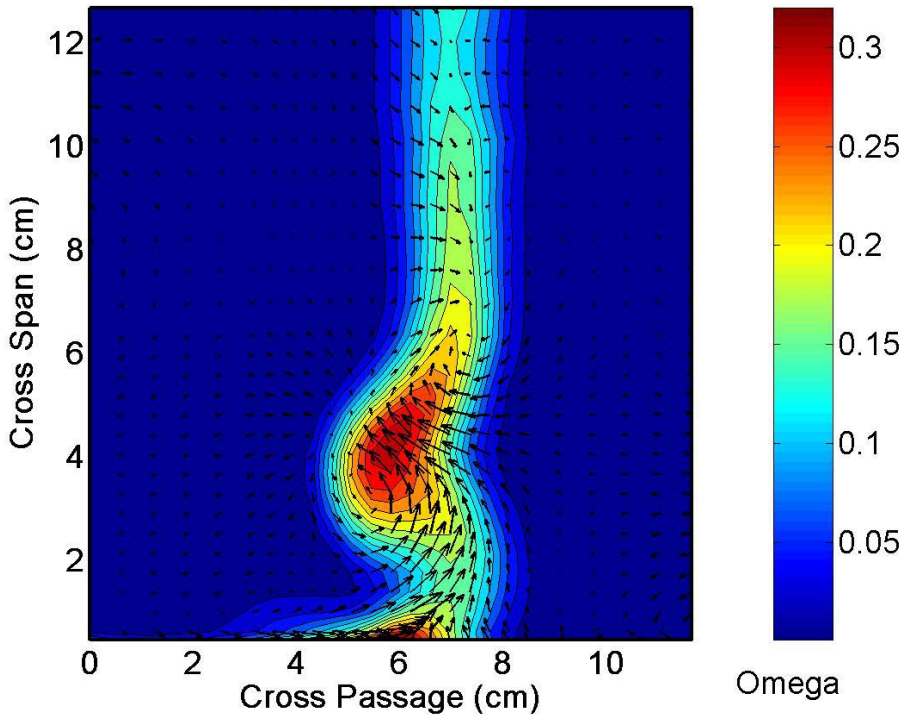

Figure 4. Total pressure loss contours (Omega) and secondary velocities, base vane, Re_C = 2,000,000, low turbulence, taken at ¼ axial chord downstream.

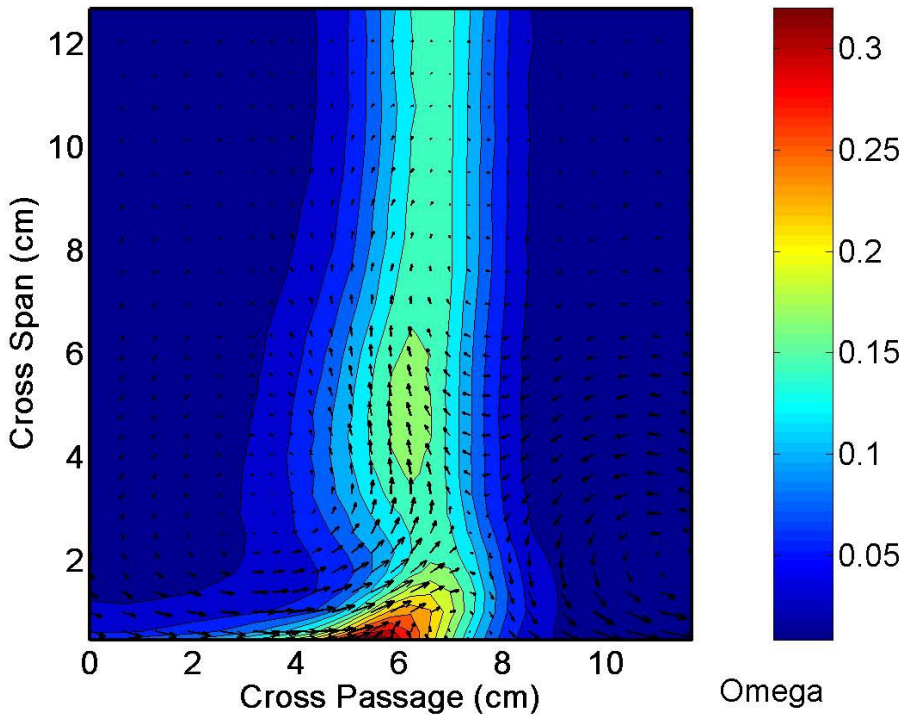

Figure 5. Total pressure loss contours (Omega) and secondary velocities, base vane, Re_C = 2,000,000, aero-combustor turbulence, taken at ¼ axial chord downstream.

The initial geometry investigated was the gill slot. This geometry has been developed in the envelope of the base vane configuration. The letter box geometry is similar to the gill slot geometry but has the addition of partitions at the exit of the gill slot vane. The letterbox geometry for UND's incompressible base vane is shown in Figure 6 along with the static pressure instrumentation. The scaling for UND's base vane and gill slot vane is 11 times. The dimensions of the large-scale cascade vane are shown below. The locations of the pressure taps are displayed in the figure along with the locations of the five row pin fin array and the letterbox patricians which engage the gill slot and extent to the trailing edge. The locations of the pressure taps and thermocouples on the letterbox vane are consistent with the gill slot vane.

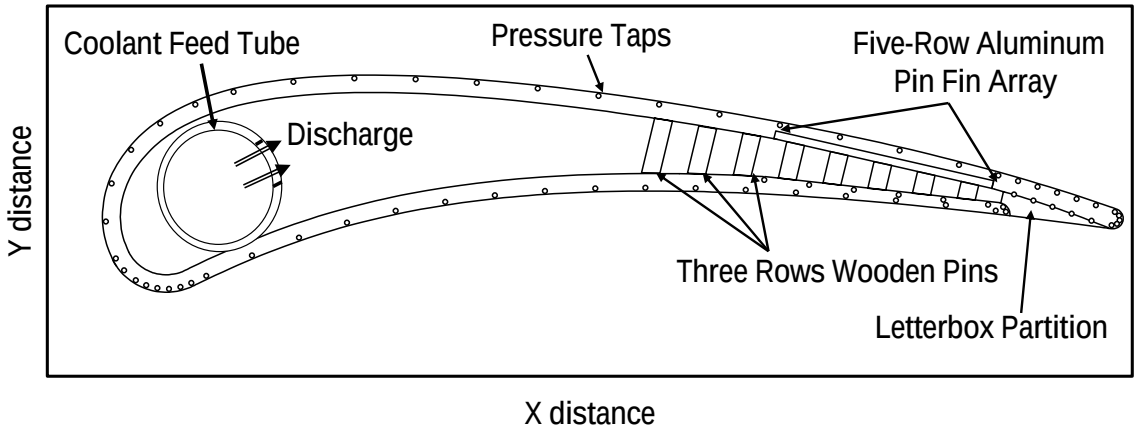

Figure 6. Letterbox geometry for UND's incompressible base vane showing pressure taps, pin fin array and partition locations.

A cross-sectional view of the 5-row aluminum pin fin array and letterbox partitions are shown in Figure 7. The aluminum pin fin array has been machined from a solid piece of aluminum. The diameter of the pins is 0.838 cm and the pin spacings are 2.5 diameters in both the X and Z (spanwise) directions. The leading edge diameter and width of the letterbox partitions are 0.635 cm. The leading edge plane of the partitions is 1.5 diameters downstream from the trailing edge plane of the last row of pins in the array. The leading edge plane is also located at the minimum slot height as the gill slot lip radiuses (0.559 cm) around to intersect with the pressure side surface. The partitions follow the shape of the solid vane pressure side profile on the exposed surface of the patrician. Surface static pressure taps at the exit of the slot and on the inside of the suction surface wall had to be moved 1.25 pin diameters in the spanwise direction to avoid being covered by a partition.

Heat transfer and adiabatic film cooling measurements were acquired using an aluminum patrician and an aluminum top surface. The aluminum heat transfer partition, shown schematically in Figure 8, was instrumented with a heater and a thermocouple and insulated on top, bottom and the lip radius using balsa wood. The aluminum heat transfer partition was reduced in thickness on the top (exposed surface), radius, and bottom by 1 mm to accommodate the balsa wood insulation. A balsa wood partition, shown schematically in Figure 9, was fabricated to accommodate a 0.794 mm thick aluminum top surface to acquire heat transfer and adiabatic effectiveness measurements on this exposed top surface. The partition heater consisted of a small resistor cemented into a hole with high conductivity epoxy. The heater had fine wire

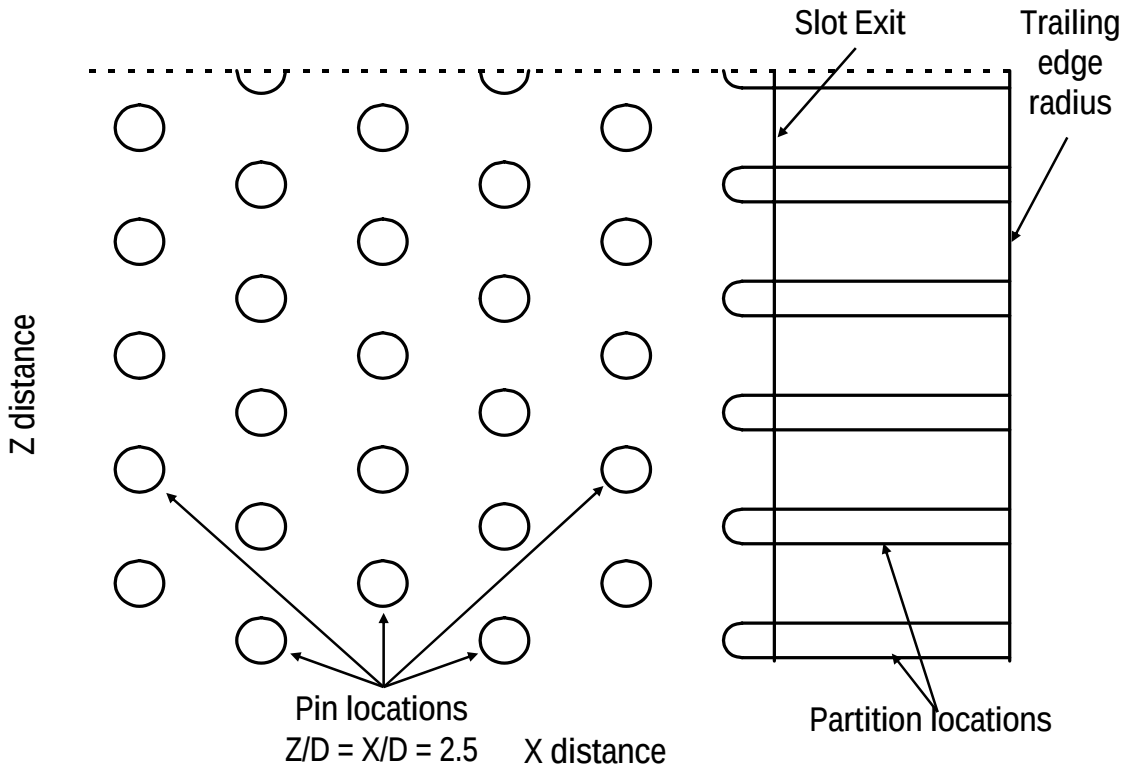

Figure 7. Cross-sectional view of 5-row aluminum pin fin array showing location of letterbox partitions.

copper leads and fine wire voltage sense leads. Additionally, a fine wire thermocouple was cemented into the partition to sense its temperature. The leads were routed into a small brass tube, which was cast into the slot lip at the slot exit. The instrumentation and heater for the top surface was similarly made, except that the heater consisted of a fine wire resistance heater fabricated from chromel thermocouple lead. Here the heater and leads were embedded into a shallow slot in the balsa wood partition.

Heat transfer measurements have been made by heating the partition, measuring the energy dissipated in the heater, estimating the losses, and measuring the partition temperature and coolant outlet temperature. The energy dissipated in the heater was calculated by determining the current through the heater with a calibrated shunt resister and the voltage across using the separate voltage leads attached at the resistor. The coolant outlet temperature was determined using fine wire type K thermocouples located at the exit of the slot. The conduction losses were determined using a 2-D representation of the losses from the partition to the inner suction surface and the lip accounting for convection on the sides. A 2-D representation was also made to determine the heat loss out the top through the balsa wood strip by conduction and convection. Heat transfer measurements for the aluminum top surface were acquired in a similar manner. However, the top surface of the partition is located directly downstream from the pressure surface and as a consequence there is an unheated starting length affect. As a result, measurements were acquired both with and without vane surface foil heating. Adiabatic effectiveness measurements were taken for both surfaces and corrections are needed to be made due to losses from the heated surfaces through the balsa wood. Recently, we received a complete set of roughness measurements for a coupon from Dr. Jeffrey Bons and Dr. Tom Fletcher [1] of

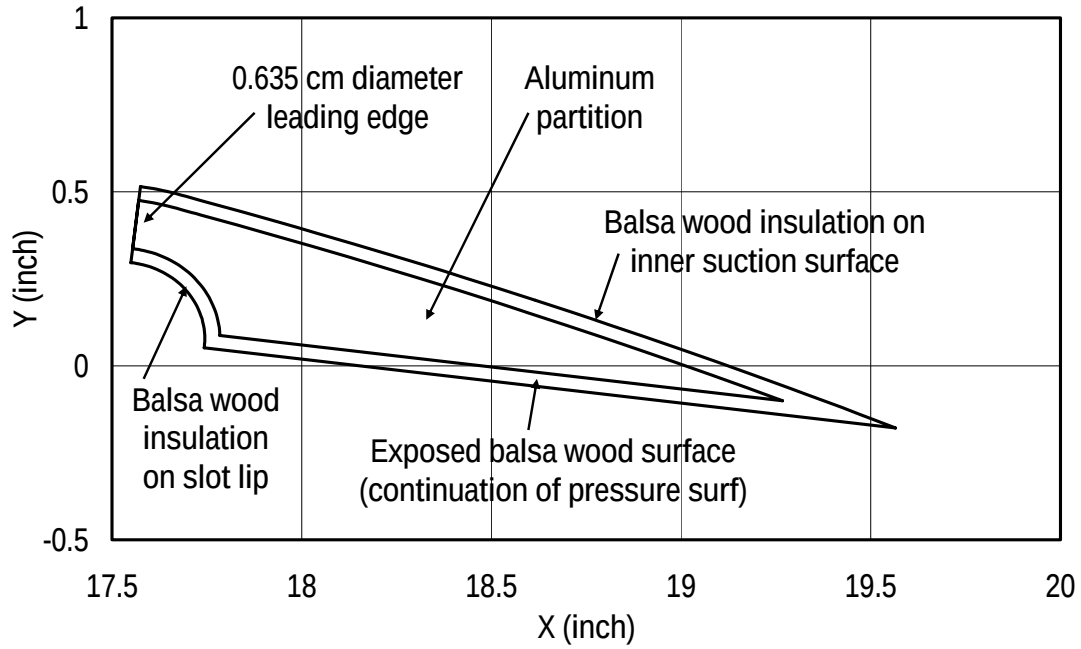

Figure 8. Aluminum heat transfer partition used to acquire partition side heat transfer coefficients and adiabatic effectiveness.

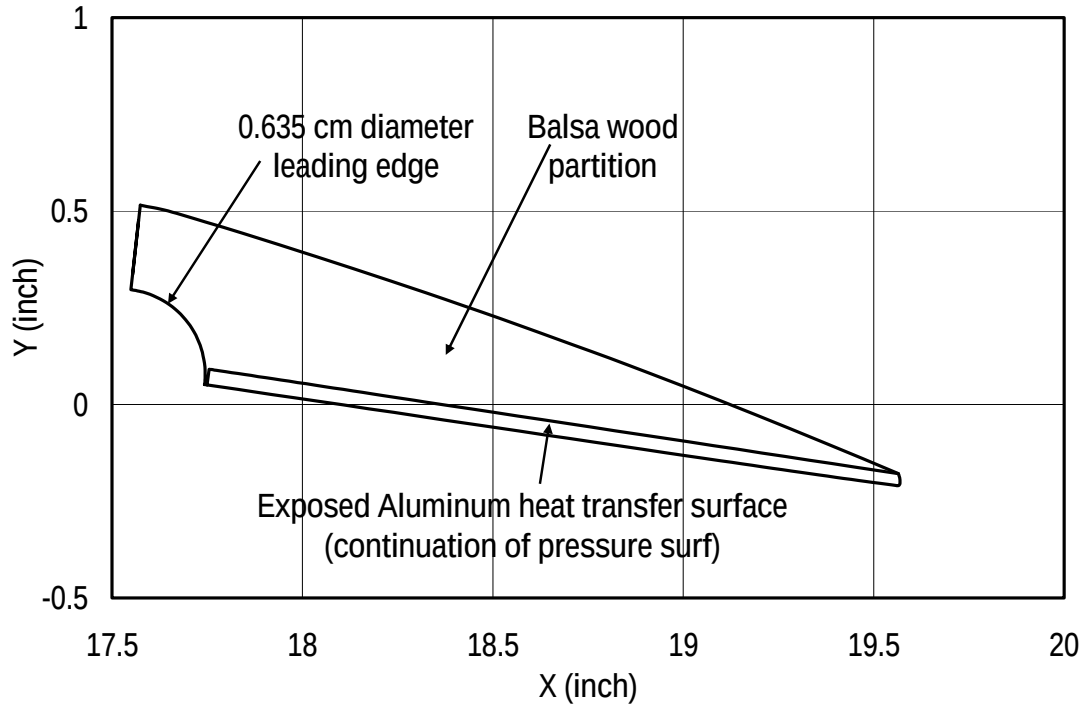

Figure 9. Balsa wood partition with active aluminum heat transfer surface used to acquire partition top heat transfer coefficients and adiabatic effectiveness measurements.

Brigham Young University. They developed this roughened surface using their accelerated deposition rig. At this time we expect to fabricate a scaled inverse mold of the surface in order to cast the roughness pattern onto sections of UND's scaled vanes. Additionally, we are currently preparing to acquire heat transfer measurements on the high solidity pin fin array both for a constant height channel and for a converging channel. Subsequently, the converging array will be installed into vane with the pressure side holes to enable testing for heat transfer and aerodynamic losses.

Experimental Results

During the period covered by this semi-annual report we conducted and finished aerodynamic and heat transfer testing on the letterbox vane. The high solidity pin fin array was fabricated both in a converging arrangement and in a constant height arrangement. We are currently making preparations to conduct heat transfer testing for the constant height and converging high solidity pin fin arrays. The gill slot vane has been tested for aerodynamic losses as well as external heat transfer and adiabatic effectiveness at exit chord Reynolds numbers of 500,000, 1,000,000, and 2,000,000 for the low, grid, and aero-combustor turbulence conditions. The vane tests include changing the slot discharge flow over a range of relevant flow rates for the condition.

Exit survey measurements were conducted for the letterbox vane over true chord exit Reynolds numbers of 500,000, 1,000,000, and 2,000,000. Measurements were made for the low, grid, and aero-combustor turbulence conditions at the full design discharge flow rate. Additionally, for the 1,000,000 Reynolds number case for the low and aero-combustor turbulence, the slot discharge flow was varied from half design flow to double design flow in half design flow increments. These measurements are summarized in Tables 1 and 2.

Exit survey total pressure loss contours with secondary flows are shown in Figures 10, 11, and 12 for the letterbox vane for the low, grid, and aero-combustor turbulence conditions, respectively. All surveys shown were taken at an exit chord Reynolds number of 1,000,000 for full design flow at ¼ axial chord downstream. Qualitatively, these results are very much like the gill slot exit survey measurements. The letterbox vane shows an intense secondary loss core about 4.5 cm or about 18% of span (25.4 cm) off the endwall for the low turbulence condition in Figure 10. Based on the secondary velocities, the passage vortex is convecting this loss core off the endwall and away from the turning angle. In this region, we see that the local cross passage averaged turning angle is reduced. The secondary velocities are in the direction of the turning angle along the endwall due to the cross passage pressure gradient acting on the low momentum fluid near the endwall. This action produces the characteristic over turning near the endwall. There are also some intense secondary velocity vectors in the region of the corner vortex, which also is a local area of high losses. Away from the endwall and above the secondary loss core we observe a nearly two-dimensional region midspan.

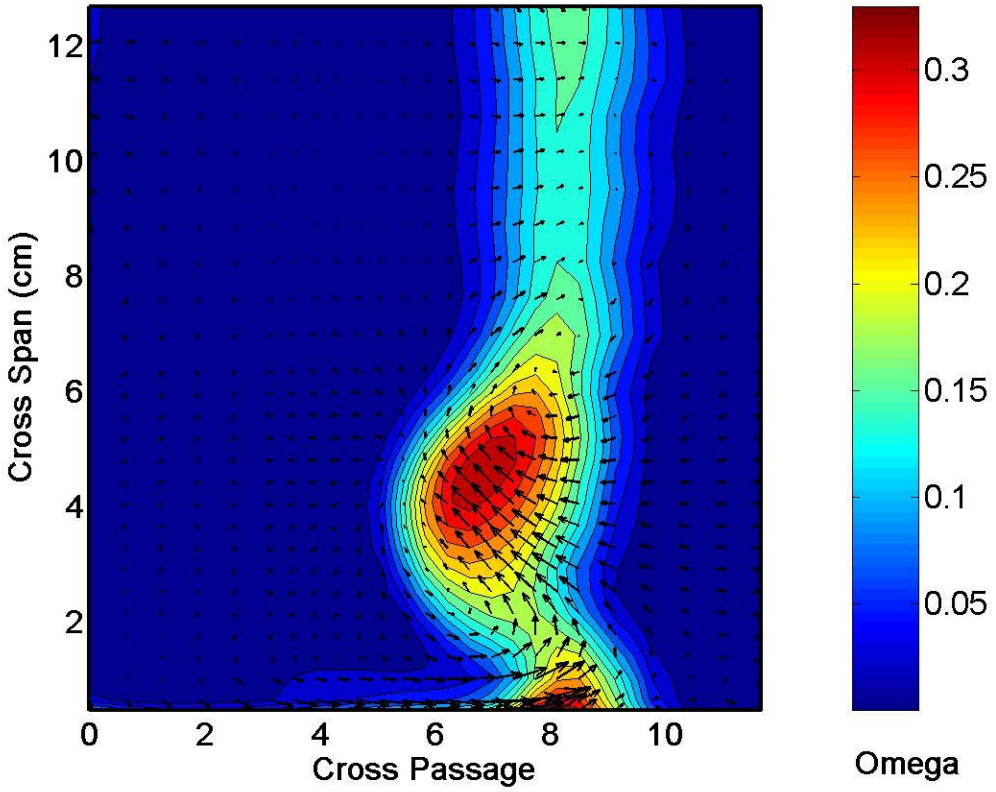

Figure 10. Letterbox vane total pressure loss contours, Ω, with secondary velocity vectors, Re_C = 1,000,000, design flow, low turbulence condition.

The letterbox vane produces an intense secondary loss core about 5 cm or about 20% of span (25.4 cm) off the endwall for the grid turbulence condition as shown in Figure 11. Here also the secondary velocities from the passage vortex are convecting this loss core off the endwall and away from the turning angle. Again, in this region the local cross passage averaged turning angle is reduced. The secondary velocities are again seen in the direction of the turning angle along the endwall producing the characteristic over turning near the endwall. There are also some intense secondary velocity vectors in the region of the corner vortex, which also is locally associated with high losses. Again in the region near midspan it can be observed that the profile losses are close to two-dimensional in nature. In comparison with the low turbulence condition, the losses for the grid turbulence are both broader and deeper. The grid turbulence condition produces a turbulent boundary on the suction surface of the vane. However, the low turbulence condition produces a laminar boundary layer over nearly the entire suction surface. The difference in suction surface boundary layer losses is the biggest driver for the differences in the mid-span profile losses. Additionally, the loss core for the grid turbulence is less intense than the loss core for the low turbulence condition.

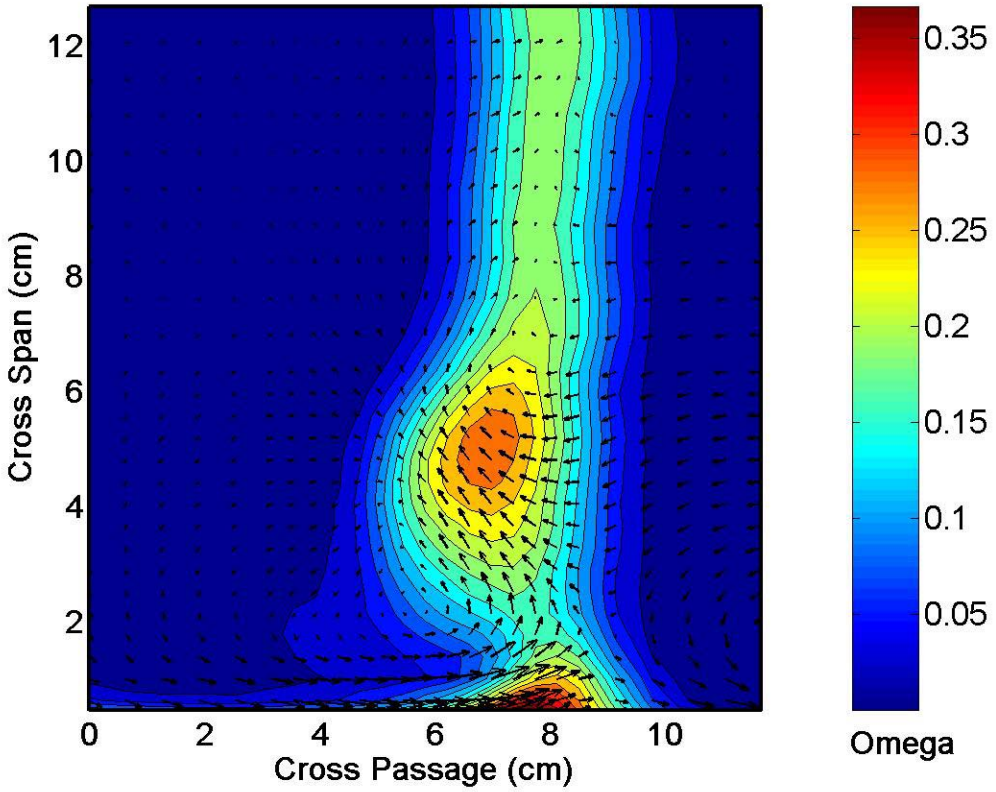

Figure 11. Letterbox vane total pressure loss contours, Ω, with secondary velocity vectors, Re_C = 1,000,000, design flow, grid turbulence condition.

The letterbox vane produces no distinct secondary loss core for the aero combustor turbulence as shown in Figure 12 in contrast to the loss cores shown for the low and grid turbulence conditions. We also see little in the way of secondary velocities from the passage vortex. However, secondary velocities are again seen in the direction of the turning angle along the endwall producing the characteristic over turning in that region. Secondary velocity vectors are also observed in the region of the corner vortex, along with its high losses. In general, the loss contours for the aero-combustor turbulence condition are closer to two-dimensional in nature than the low and grid turbulence conditions. In comparison with the low and grid turbulence conditions, the losses for the aero-combustor turbulence are much broader and any sign of the passage vortex has been eliminated by the random transport of the aero-combustor turbulence. The aero-combustor turbulence condition produces a turbulent boundary on the suction surface and earlier transition along the endwall through the passage. High turbulence can also produce losses due to mixing across inertial velocity gradients. In addition, the cascade inlet velocity profile also contained a higher level of losses than the other turbulence conditions. In general, the action of the aero-combustor turbulence is seen to spread out the total pressure losses more rapidly than observed for the low and grid turbulence conditions.

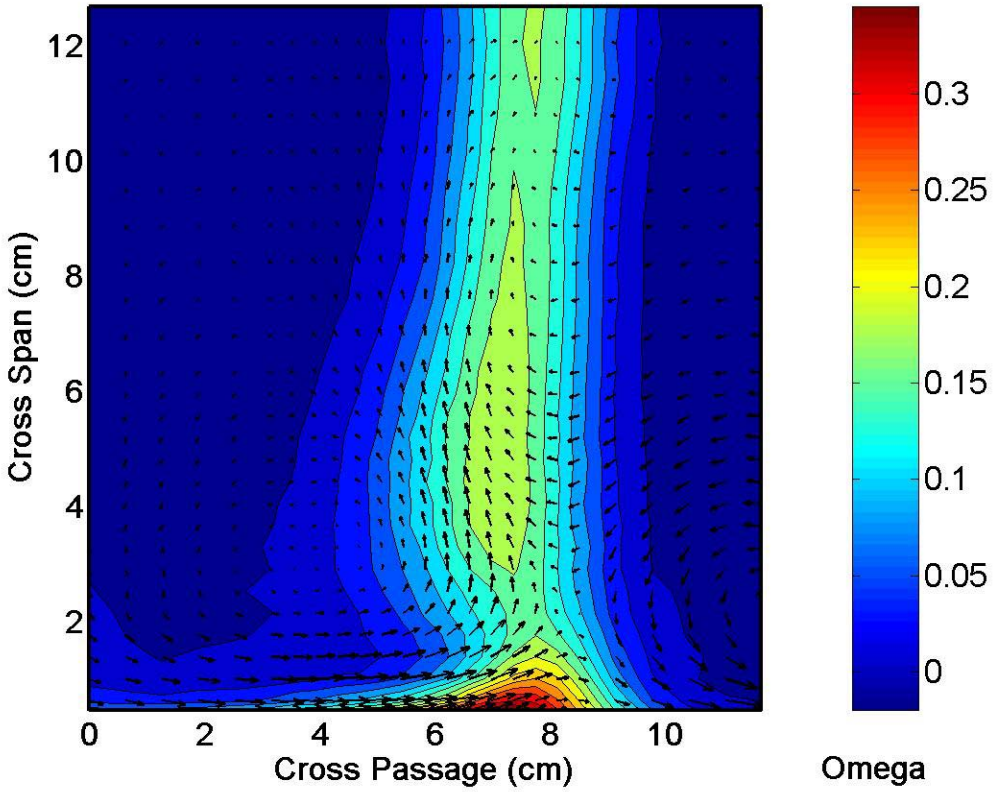

Figure 12. Letterbox vane total pressure loss contours, Ω, with secondary velocity vectors, Re_C = 1,000,000, design flow, aero-combustor turbulence condition.

The mass averaged full passage total pressure losses, **Ω**, are summarized below in Figure 13 comparing letterbox vane with gill slot vane results across the range of Reynolds numbers. The results show a decreasing loss with increasing Reynolds number and an increasing loss with increasing turbulence level. Part of the difference in exit losses is due to the cascade inlet velocity profile losses which are largest for the aero-combustor turbulence condition. Additionally, there is an incremental increase between the low turbulence condition with a laminar suction surface boundary layer and the higher turbulence conditions, which have turbulent boundary layers growing on their suction surfaces. A comparison between the letterbox and gill slot condition show a small and marginally significant reduction in losses. This small reduction in losses is due to the higher slot exit velocity of the letterbox for the same flow rate due to the reduced exit flow area as a result of the partitions. However, based on 28% reduction in exit flow area of the letterbox scheme, a larger reduction in losses would be expected. The letterbox has an addition mechanism for loss generation over the gill slot with the separation of coolant flow off the top of the partitions. The combination of the higher velocity exit flow with the separation off the partition combines to produce a marginally significant 0.2% average reduction with the letterbox for the nine full design flow cases. Note that the 500,000 Reynolds number case shows an increased uncertainty in the massed average total pressure loss. This condition uses the same pressure sensor array as the 1,000,000 Reynolds number case. Consequently, the uncertainty in the sensors zero pressures are significantly reduced due to the four to one reduction in the dynamic pressure.

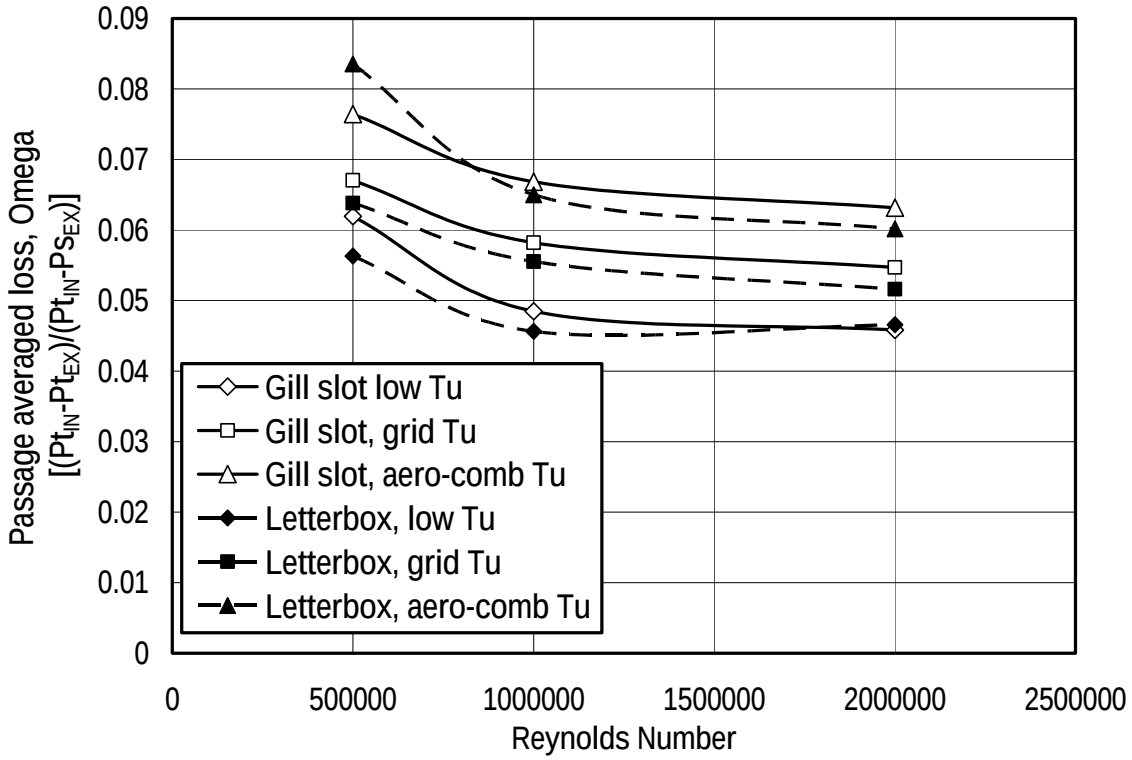

Figure 13. Variation of mass averaged passage total pressure loss, **Ω**, with Reynolds number comparing gill slot vane with letterbox vane at the design flow rate.

Coolant flow rate does have an impact on passage averaged total pressure losses as shown in Figure 14. In this figure, mass averaged total pressure loss is compared as a function of the coolant flow rate relative to the design flow rate. As shown in the figure below half and full design flow rates have little impact on the mass average total pressure losses. This similarity in losses between the half and full design flow rates suggests that the increased momentum of the higher coolant flow counters the losses due increased mass injection. At higher flow rates we see that there is actually a reduction in the losses due to the increased momentum of the coolant injection. The calculated loss is based on the cascade inlet total pressure, not the total pressure required to drive the flow. The design flow rate for the letterbox has been taken to be the same as the gill slot. The rationale for the gill slot design flow is stated below:

Design Flow Rate. Gill slot coolant flow rates have been presented in terms of half, full, 1 ½ times, and 2 times the design flow rate. First stage vanes are fed from compressor discharge air which bypasses the combustor. Consequently, the feed pressure available for the vane is related to the pressure drop across the combustor as well as the exit Mach number of the nozzle guide vane. A typical pressure drop credited to the combustor is 4%, while at an exit Mach number of 0.8 $P_{T,IN}/P_{S,EX}$ is about 1.5. The present experiment had a ratio $(P_{T,IN}-P_{S,CO})/(P_{T,IN}-P_{S,EX})$ of 0.55 at the gill slot. These ratios were used to estimate a pressure drop for the experiment which was consistent with the pressure drop for a first stage vane in an engine. Consequently, the "design flow rate" pressure drop was set at approximately two-thirds of this available pressure drop assuming that roughly one-third is typically taken across the

impingement tube. Our "design flow rate" velocity ratio was approximately 50% of the exit velocity and approximately 66% of the external velocity at the gill slot.

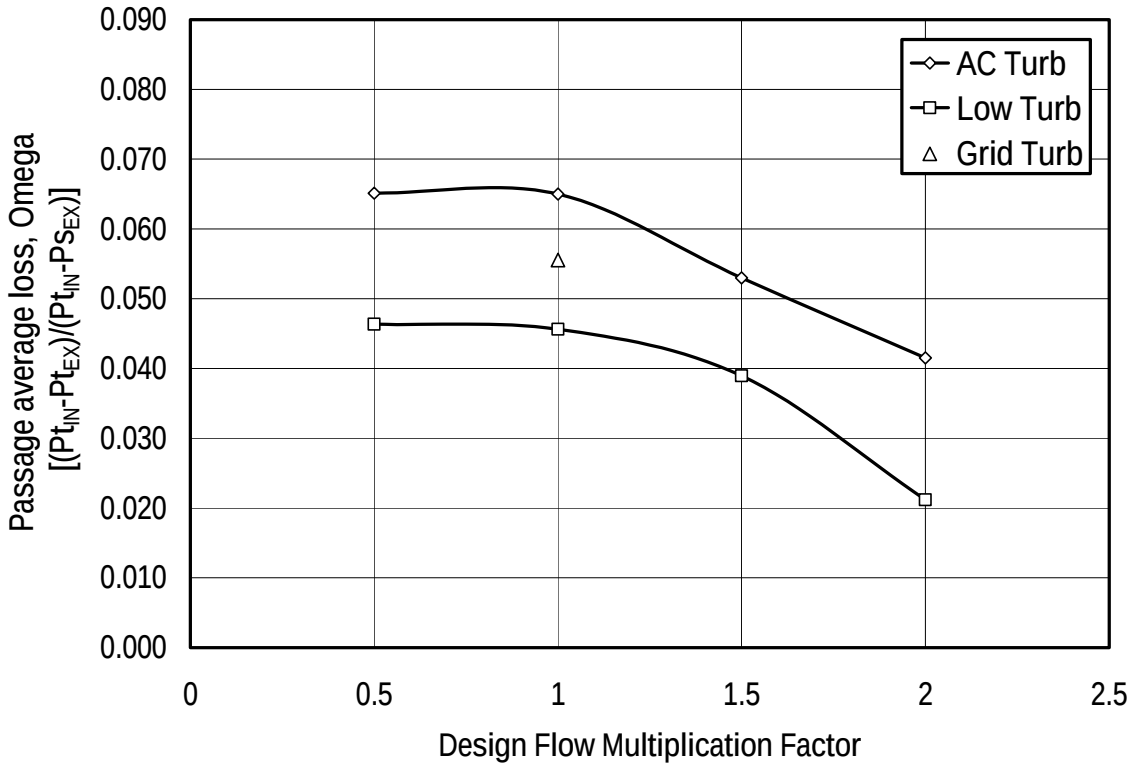

Figure 14. Total pressure loss for letterbox design as a function of design mass flow rate and turbulence condition, Re_C = 1,000,000, ¼ C_{AX}.

First stage vanes would not normally have enough input coolant pressure to drive flow rates much past the design flow rate. However, higher relative mass injection rates are possible in downstream vanes and blades depending on the coolant source and the losses in the flow circuit. Figure 15 presents total pressure loss contours for the letterbox vane at double the design flow rate. Qualitatively, the total pressure loss contours and secondary velocity vectors look similar to the design flow case presented in Figure 12. However, to the right of wake, Figure 15, actually shows a negative Omega due to the high injection flow velocity. While this figure shows how an exit loss distribution would look with high momentum injection, the expectation would be that this condition is not a typical design situation for an engine.

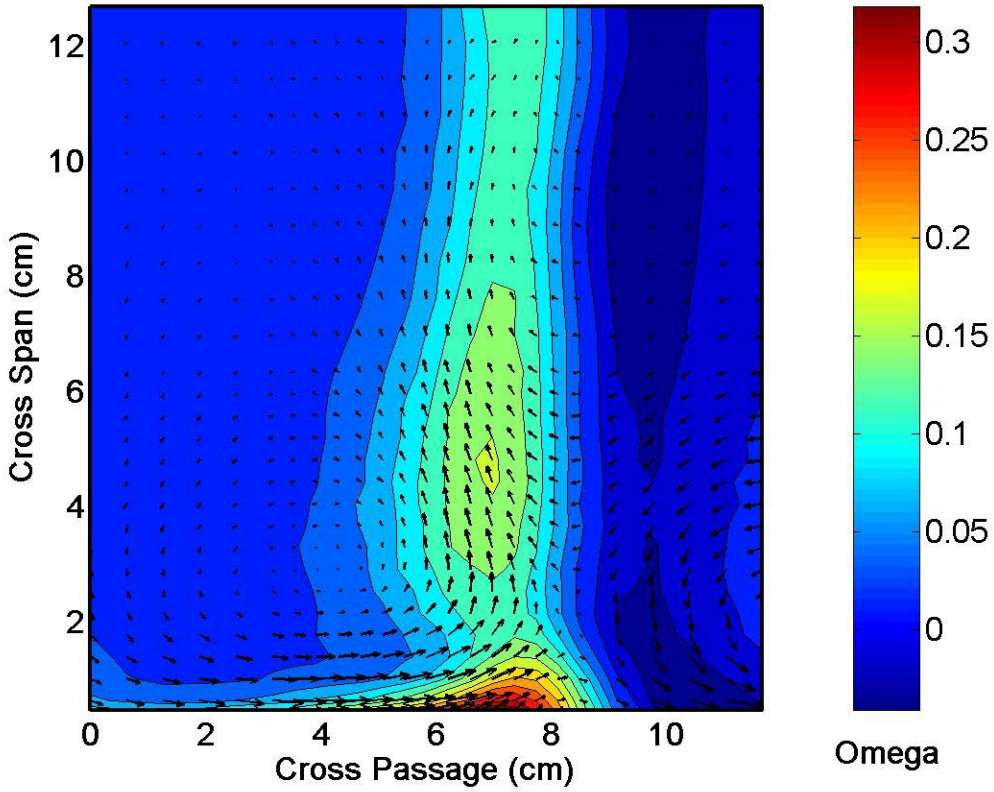

Figure 15. Letterbox vane total pressure loss contours, Ω, with secondary velocity vectors, Re_C = 1,000,000, double design flow, aero-combustor turbulence condition.

The letterbox vane geometry is identical with the gill slot vane except the addition of the partitions. As shown in Figure 6 and 7 the partitions funnel the flow downstream from the pin fin array into separate channels and in the process restrict the flow area at the exit of the gill slot. The flow area at the gill slot exit is about 72% of the minimum area of the last row of the pin fin array. Consequently, the pressure drop between the inlet of the five row converging array and the outlet of the slot, in between the partitions is expected to be different than the simple gill slot. The pressure drop between the inlet of the converging 5-row pin fin array and the exit of the slot was determined using the first pressure tap downstream of the slot on the inner surface of the suction surface wall. This same pressure difference was measured for the letterbox vane. A comparison of the results is shown in Figure 16 below. Generally, the pressure drop through the converging pin fin array and the letterbox exit is about 0.57 $\rho Vmax^2/2$ greater than the loss for the gill slot arrangement. However, if we base this pressure drop on the last pressure tap on the pressure surface, which is less sensitive to discharge flow, the difference is about 0.39 $\rho Vmax^2/2$. Here in both the gill slot and letterbox cases, Vmax is based on the minimum area of the last row of the converging pin fin array.

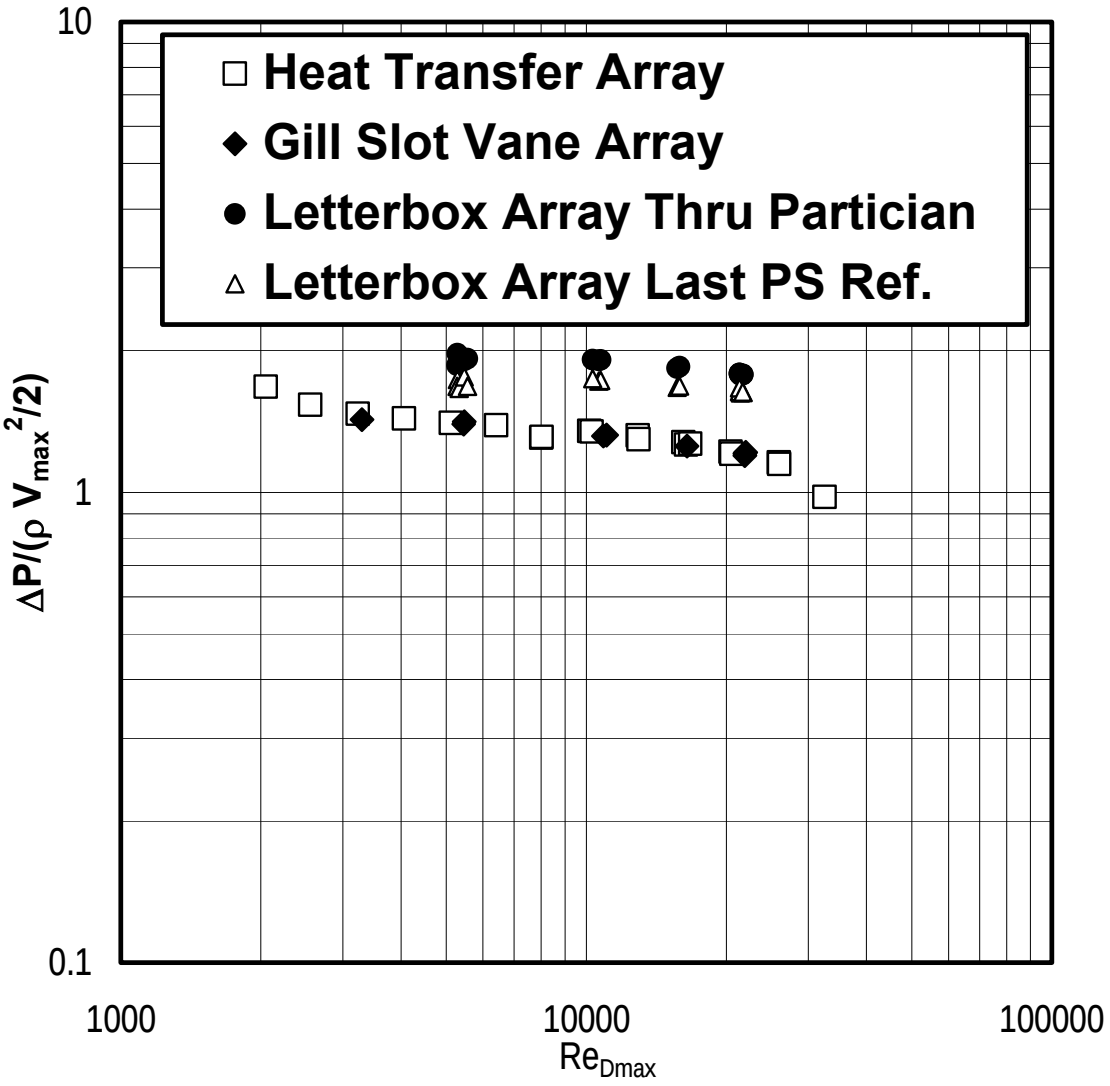

Figure 16. Comparison of normalized pressure drop across the pin fin array to the vane exit for the gill slot and letterbox vanes with Vmax defined for the last row in the converging pin fin array.

The letterbox partitions have an influence on the coolant flow pressure drop and ejection velocity and also on the surface static pressure distribution. Figure 17 compares the surface pressure distributions for the letterbox and gill slot vanes at the design flow rate along with the calculated surface pressure distribution by Fluent. On the suction surface and on the pressure surface before the gill slot lip, the letterbox and gill slot pressure distributions are quite consistent with the calculated surface pressure distribution. However, downstream from the lip the pressure distributions vary from the prediction. Initially the pressure distributions recover and then they show strong acceleration. However, the letterbox pressure distribution varies from the gill slot distribution.

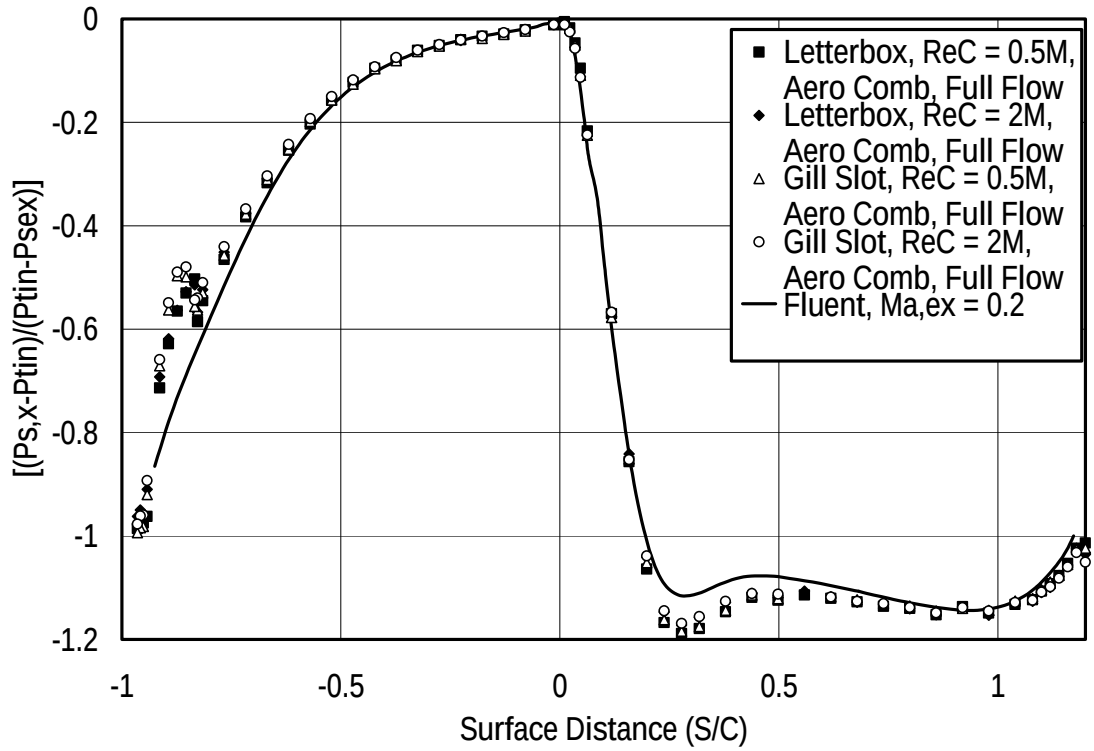

Figure 17. Vane surface pressure distribution comparison between letterbox vane and gill slot vane, base vane Fluent calculation shown for comparison.

The pressure distribution downstream from the slot exit as shown in Figure 18 is noticeably different for the letterbox compared with the gill slot. The gill slot shows a consistent static pressure level between the last static pressure tap on the pressure surface to the first static pressure tap on the inside wall of the suction surface. However, the letterbox geometry shows a pressure recovery at the first tap on the inside wall of the suction surface. On the gill slot a pressure recovery occurs on the inside wall of the suction surface downstream from the first tap but the pressure distribution on the letterbox only shows a favorable pressure gradient for this flow rate.

The pressure distribution downstream from the letterbox slot ejection also varies with flow rate as shown in Figure 19. The trend shows an increasing pressure recovery with increased blowing immediately downstream from the exit slot. Since the pressure drop correlation shown in Figure 16 was initially referenced to the first pressure tap downstream from the slot ejection on the inner suction surface wall, this pressure recovery had a noticeable influence on the correlation in Figure 16. A more stable location to base the correlation appears to be the last static pressure tap on the pressure surface. This pressure loss using this reference is also shown in Figure 16. We will reconsider this issue before this work is published in the open literature.

Preliminary aluminum partition heat transfer data are presented in Figure 20 for the low and aero-combustor turbulence conditions at a chord Reynolds number of 1,000,000. Partition heat transfer level appears to be a function of array flow rate. Thermal losses account for up to 1/3 of the power dissipated in the partition and FEA conduction models are in the process of being developed and assessed. The preliminary data shown below suggests the Reynolds number dependence produces an exponent of around 0.606.

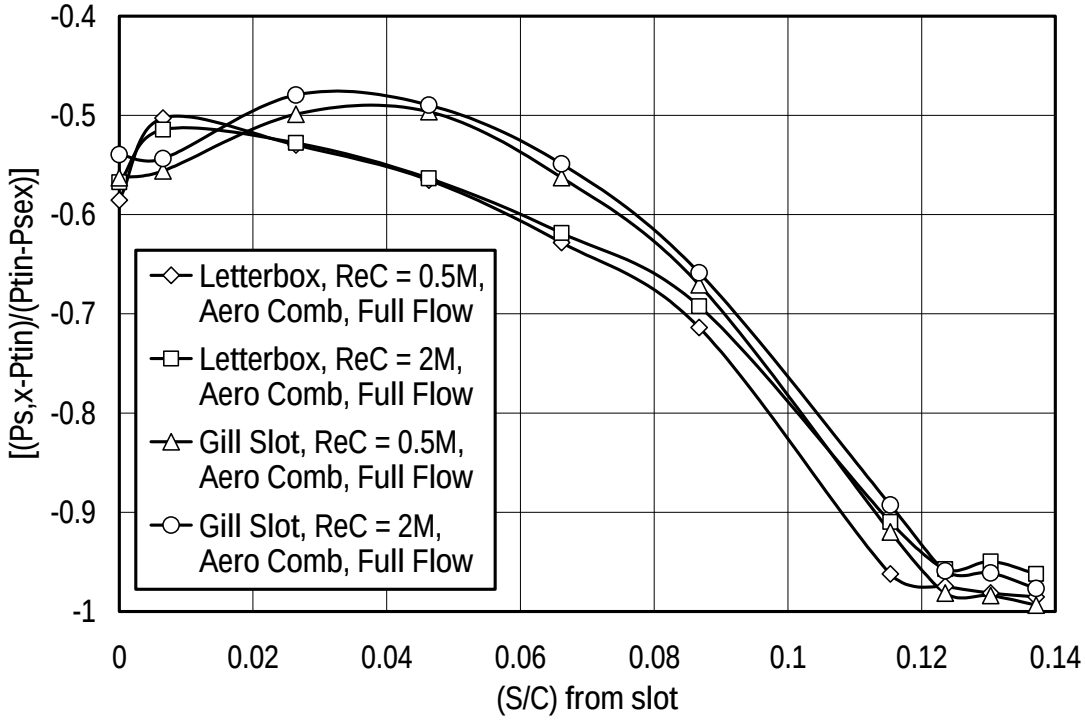

Figure 18. Comparison between pressure distribution downstream from gill slot ejection with distribution downstream from letterbox ejection.

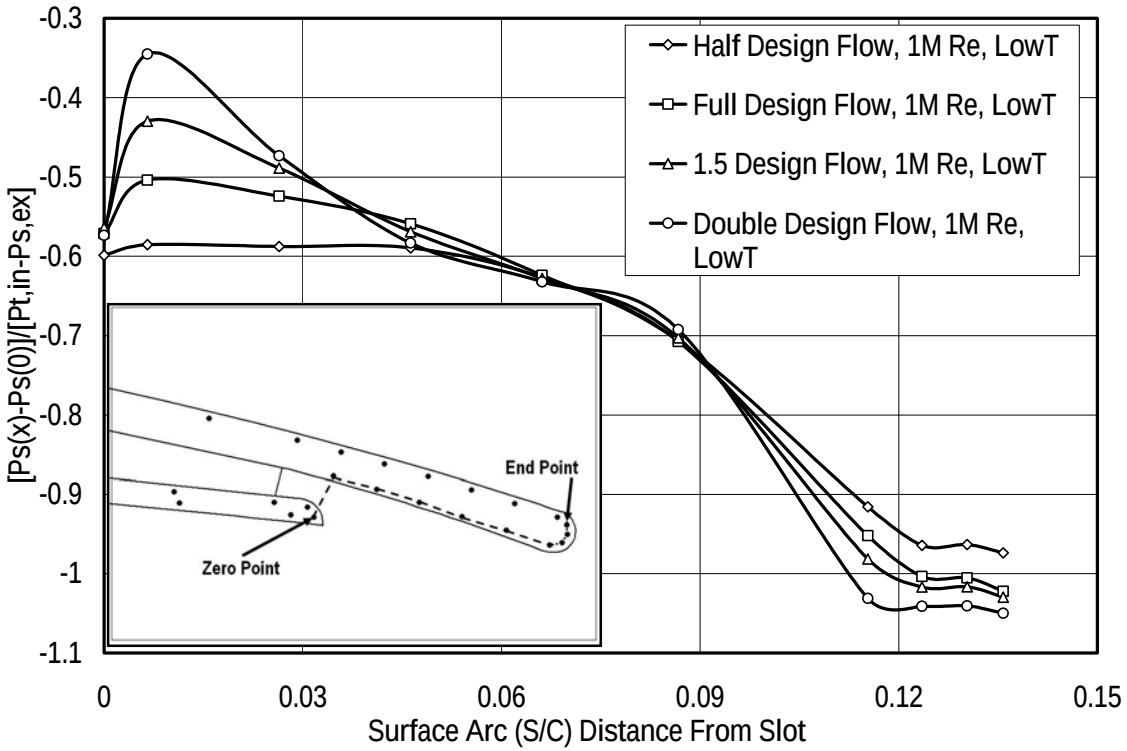

Figure 19. Comparison of pressure distribution downstream from letterbox ejection for various flow rates, Re_C = 1,000,000.

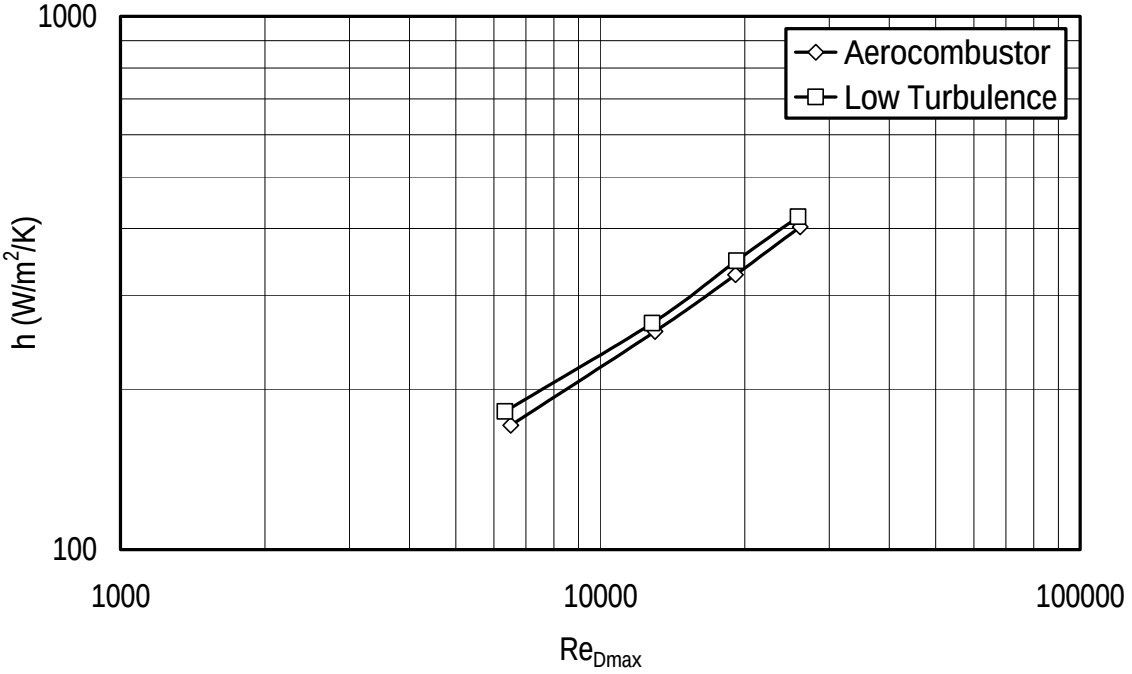

Figure 20. Preliminary letterbox partition heat transfer levels with Re_{Dmax} based on last row of pin fin array.

Expected Results for the Next Six Months

The results expected in the next six months will include some very useful measurements for heat transfer designers. Under task 1, we have recently obtained a surface generated in Brigham Young University's accelerated roughness rig relating to syngas fired gas turbines. In addition, we expect to be developing strategies to produce this representative surface roughness on aerodynamic and heat transfer airfoils. Under task 2, all facility modifications are expected to be complete and work will continue with the fabrication of aerodynamic and heat transfer vanes for the pressure side holes geometry and the other trailing edge geometries. Under task 3, we expect to acquire pressure distributions and discharge Cd's for the pressure side holes geometry. At the University of North Dakota we have recently completed pressure distributions and discharge coefficient measurements for the letterbox geometry. Under task 4, aerodynamic measurements, we are expecting to complete the exit surveys for the pressure side holes geometry (smooth surface) and expect to be progressing on the other geometry. Under task 5, we will acquire heat transfer measurements for the pressure side holes vane geometry to compile part of a cohesive set of heat transfer measurements. Under task 6 we expect to complete internal heat transfer measurements for the high solidity pin fin array and begin preparations for fabricating and acquiring heat transfer and pressure drop measurements for the low pressure drop high solidity pedestal array. Under task 7 we are currently planning to acquire adiabatic film cooling effectiveness measurements for the pressure side holes geometry in the next six months. We are

currently progressing very well with the planned research and fully expect to stay on schedule over the next six months.

Conclusions and Summary

(UND) UTSR Project SR-119, **"**Aero Losses, Heat Transfer, Discharge Coefficients for Different Vane Trailing Edge Cooling Technologies for Syngas Fired Turbines," is currently on track to meet planned goals. In the third six months of this project the University of North Dakota made good progress and has generated results that are consistent with the original GANT timeline. The team at the University of North Dakota has recently completed aerodynamic, heat transfer and adiabatic effectiveness testing for the letterbox configuration and has nearly completed preparations for internal heat transfer measurements for the high solidity pin fin configurations in both constant channel height and converging arrangements. Additionally, we have obtained a relevant roughness surface from Brigham Young University from their accelerated deposition rig.

Recent results have shown that aerodynamic loss measurements for the letterbox configuration are very similar with the gill slot configuration. When results taken at the design flow rate were compared, the letterbox vane produced losses which were an average of 0.2% less than the gill slot vane. This incremental decrease is only marginally significant. At the design flow rate the velocity leaving the reduced slot exit area of the letterbox design is higher than the gill slot vane. The flow exiting from the slots between the letterbox partitions also eventually separates from those partitions. This separation produces another loss mechanism that apparently reduces the impact of the higher velocity slot flow.

The normalized pressure drop across the converging pin fin array and through the letterbox exit slots is also higher than the gill slot pressure drop due to the reduced exit area. However, the choice of a reference pressure has a significant influence on the pressure drop correlation for the letterbox. The static pressure immediately downstream from the exit slot is strongly influenced by the discharge flow rate in the letterbox configuration.

Heat transfer and adiabatic effectiveness data for the top (balsa) and sidewall (Al) partitions are currently in the process of being analyzed.

1/4 Cax	Aero-Combustor			Low Turbulence			Grid Turbulence		
File:	exsvlbac53	exsvlbac13	exsvlbac23	exsvlblt53	exsvlblt13	exsvlblt23	exsvlbgt53	exsvlbgt13	exsvlbgt23
ReCex	510231	1014509	2002773	500344	1003353	2006766	502455	1000178	1998762
Tt,in (K)	291.6	293.0	298.6	294.2	294.9	300.9	288.0	298.7	297.6
Pt,in (Pa)	98532	100156	100216	100533	99358	100116	99852	100320	100239
Vex (m/s)	16.42	32.61	68.68	16.02	32.88	69.87	15.60	33.22	68.06
Maex	0.0479	0.0950	0.1975	0.0466	0.0954	0.2002	0.0458	0.0958	0.1961
Ω (Full)	0.0836	0.0650	0.0602	0.0563	0.0456	0.0466	0.0638	0.0555	0.0516
Ω (Midline)	0.0717	0.0561	0.0515	0.0599	0.0360	0.0363	0.0501	0.0446	0.0407
B (Full)	73.18	73.70	73.76	73.28	73.53	73.62	73.25	73.66	73.57
B (Midline)	72.91	73.39	73.67	73.22	73.96	74.07	73.60	73.87	74.16
M,dot (kg/s)	0.0135	0.0272	0.0542	0.0133	0.0270	0.0555	0.0142	0.0261	0.0548
Torf (K)	288.5	293.7	300.0	292.8	294.6	298.1	290.4	296.1	296.3
ΔPorf (Pa)	72.9	298.4	1201.0	70.6	296.8	1265.6	80.5	277.0	1211.0
P,atm (Pa)	99310.7	99750.8	98498.0	100428.0	98938.2	97550.0	100224.9	99886.3	98531.9

Table 1. Mass averaged exit survey losses and turning angle for full design flow at 500,000, 1,000,000 and 2,000,000 Reynolds number and low, grid, and aero-combustor turbulence condition.

1/4 Cax	Aero-Combustor			Low Turbulence		
File:	exsvlbac513	exsblbac313	exsvlbac213	exsvlblt513	exsvlblt313	exsvlblt213
Re_{Cex}	1002227	1017136	997004	1004601	1028110	1005902
Tt,in (K)	297.2	296.9	296.8	295.3	294.5	299.3
Pt,in (Pa)	99499	99495	99278	100137	100892	98662
V_{ex} (m/s)	33.26	33.71	33.08	32.75	33.12	34.12
Ma_{ex}	0.0962	0.0975	0.0957	0.0950	0.0962	0.0983
Ω (Full)	0.0651	0.0530	0.0415	0.0463	0.0390	0.0212
Ω (Midline)	0.0558	0.0439	0.0311	0.0372	0.0306	0.0083
B (Full)	73.61	73.68	73.71	73.52	73.54	73.70
B (Midline)	73.35	73.48	73.50	73.97	74.05	73.94
M,dot (kg/s)	0.0132	0.0415	0.0539	0.0137	0.0399	0.0543
T_{orf} (K)	296.8	291.3	294.3	293.1	296.2	297.3
ΔP_{orf} (Pa)	71.1	690.4	1164.1	75.9	640.7	1199.2
P,atm (Pa)	99073.7	99073.7	98870.5	99717.0	100461.9	98227.2

Table 2. Mass averaged exit survey losses and turning angle for off design flow at 1,000,000 Reynolds number with low and aero-combustor turbulence condition.

References

1. J.M. Crosby, S. Lewis, J.P. Bons, W. Ai, and T.H. Fletcher, 2007, "Effects of Particle Size, Gas Temperature, and Metal Temperature on High Pressure Turbine Deposition in Land Based Gas Turbines from Various Synfuels," ASME Paper No. GT2007-27531 (accepted for presentation at the 2007 IGTI conference in Montreal, 14-17 May 2007).

Deposition of Alternative (Syngas) Fuels on Turbine Blades with Film Cooling

1 Aug 2006 to 31 Jan 2007
Annual Report

Principal Investigator: Dr. Jeffrey Bons
Report Issue Date: 13 Mar 2007
DOE Award Number: DE-FC26-02NT41431
UTSR Project Number: 05-01-SR120

Submitting Organization: Brigham Young University
435 CTB, PO Box 24201, Provo, UT 84602-4201

Co-Investigators
Dr. Thomas Fletcher, Brigham Young University

ABSTRACT

This report documents work completed during the first 6 months of the second year of a three year research effort into turbine deposition from synfuels. The objective of this effort is to document deposition on turbine hardware from the combustion of synfuels that are or could be used in the power generation industry and evaluate the influence of these deposits on turbine cooling. Four series of tests were performed in the accelerated deposition test facility to study the independent effects of particle size, gas temperature, and metal temperature on ash deposits from two candidate power turbine synfuels. In the first series of tests, four different size particles were studied by seeding a natural-gas combustor with finely-ground subbituminous coal ash particles. The entrained coal ash particles were accelerated to a combustor exit flow Mach number of 0.25 before impinging on a thermal barrier coated (TBC) target coupon at 1183°C. Particle size was found to have a significant effect on capture efficiency, with larger particles causing significant TBC spallation during a 4-hour accelerated test. In the second series of tests, different gas temperatures were studied while the facility maintained a constant exit velocity of 170m/s (Mach=0.23-0.26). A subbituminous coal ash with a mass mean diameter of 3μm was used. The particle deposition rate was found to decrease with decreasing gas temperature. The threshold gas temperature for deposition was approximately 960°C for this coal. In the third and fourth test series impingement cooling was applied to the backside of the target coupon to simulate internal vane cooling. Ground subbituminous coal and petcoke ash particles were used for the two tests respectively. Capture efficiency was reduced with increasing mass flow of coolant air, however at low levels of cooling the deposits attached more tenaciously to the TBC layer. Post exposure analyses of the third test series (scanning electron microscopy and x-ray spectroscopy) show decreasing TBC damage with increased cooling levels. Implications for the power generation goal of fuel flexibility are discussed.

TABLE OF CONTENTS

EXECUTIVE SUMMARY

Turbine inlet temperatures for large power generation gas turbines have been steadily increasing over the last several decades due to significant advances in materials and cooling technologies. By incorporating these critical advancements, the H-class combined cycle machines are expected to operate at up to 1425°C. While this higher combustor exit temperature translates directly to higher cycle efficiency, it does not bode well for the severe operating environment of turbine materials. At the same time, political and economic pressures are pushing utilities to consider fuel flexibility. Limited natural gas resources necessitate the integration of more plentiful sources of coal and biomass into the fuel reserve for gas turbines. Compared to "clean" burning natural gas, these alternative fuels have higher concentrations of trace elements and ash that present significant corrosion challenges to turbine operation.

Coal utilization introduces S, Al, Fe, Ca, and various alkali metals (e.g. Na, K) to the gas turbine, while biomass has lower sulfur content than coal, but has higher concentrations of Ca, Mg, Cl, and K. The concentrations and sizes of these compounds that actually reach the turbine surfaces depend on the combustion and gas-cleanup processes. If combustion products arrive at the turbine blade surface in the liquid (or vapor) phase, it is likely that they will deposit (or condense) there and accelerate material corrosion. A number of studies conducted in the 1970's and 1980's (before the dominant use of natural gas in gas turbines) showed that corrosive deposition is strongly dependent on temperature. Depending on the syngas fuel employed, the threshold temperature for deposition varied from 900C – 1100°C. Above this threshold, studies showed up to an order of magnitude increase in deposition rates. Since those tests were conducted, several key technologies (e.g. thermal barrier coatings, advanced cooling schemes, and single crystal blades) have permitted substantial increases in firing temperatures. The compatibility of these advances with ash-bearing syngas fuels has yet to be assessed. Clearly, there is a critical need for fundamental experimental studies to determine the magnitude of deposition, erosion, and corrosion for the application of alternative fuels in modern gas turbines.

In addition, limited experimental evidence suggests that by sub-cooling turbine components, deposition may be mitigated. Additional studies are necessary to determine necessary cooling levels for adequate protection from syngas deposits. Finally, film cooling flows provide a cool air stream at the turbine surface that may influence local deposition as molten combustion products cool and harden near the film cooling hole. Such deposition in and around the film cooling hole could significantly impede the flow of critical coolant to the blade surface. These effects must be adequately evaluated and modeled to provide turbine operators with the tools they need to assess the in-service health of cooled turbine components.

This proposal addresses all three of these critical turbine operability and maintainability issues in three phases. In Phase 1, deposition studies will be conducted in an accelerated turbine deposition facility at Brigham Young University to document the influence of temperature on deposition, erosion, and corrosion from syngas fuels. This facility is part of BYU's Advanced Combustion Engineering Research Center (ACERC), a laboratory founded in 1987 by the National Science Foundation. With active contracts totaling approximately $1.5 million/year, the center encompasses research on combustion, mineral matter transformation, deposition, and corrosion in power systems fired by coal, biomass, black liquor, oil shale, petroleum coke, and natural gas. Rather than simulate the syngas gasification and cleanup process, this research will be conducted by seeding a natural gas combustor with coal and biomass products of combustion and accelerating them onto target turbine materials. Combustion byproducts from two of the

reactors within ACERC (one for coal and one for biomass) will be collected, analyzed, and ground down to a mass-mean 10μm solid particulate for use in the accelerated turbine deposition facility. By performing experiments in this controlled laboratory environment the individual effects of corrosive elements can be properly evaluated. BYU's accelerated turbine deposition facility is capable of matching both the impact velocity and gas temperature of modern industrial turbines. Arrangements are in place with industrial contacts at GE, Solar, Praxair, and Siemens to make available modern turbine materials and coatings as targets for this study. Once syngas deposits are formed on the target, various analyses will be conducted, including: surface mapping, roughness assessment, deposit thermal conductivity measurement, and elemental decomposition with corrosion assessment. Elemental analyses will employ existing ACERC diagnostic equipment including: scanning electron microscopy, inductively-coupled plasma with atomic absorption, and x-ray analysis for quantitative analysis of deposits.

Phase 1 of the proposed research will also explore the possibility of sub-cooling the turbine surface to mitigate deposition. This will be accomplished by cooling the backside of the target coupon, similar to internal convection cooling in a turbine blade. Similar post-exposure analyses will be conducted to evaluate both the extent of turbine damage and changes in depositing constituents with surface temperature.

The 2nd phase will evaluate the influence of deposit formation on film cooling flows. This study will be accomplished in the same turbine deposition facility by injecting coolant from film holes in the target coupon. Sections of turbine blades with cooling holes will be solicited for this effort so that the coolant hole geometry is representative of current practice. Deposits in and around cooling holes will be measured and analyzed as before.

During the optional 3rd year of the research program, scaled models of the deposit-laden film holes will be installed in a low-speed wind tunnel at BYU for flow and heat transfer assessments. A 3-D PIV system and IR camera will be used to gather 3-dimensional velocity data as well as surface heat transfer and film effectiveness. The data density available from these sophisticated diagnostics will provide an important database for CFD validation. This phase will also consider the effects of TBC residue left in film holes during the plasma-spray application process since it is likely that this residue bears resemblance to deposits formed during turbine operation.

With this aggressive research program, DOE and industry will gain valuable insights into factors affecting the safe, efficient operation of modern industrial turbines with alternative fuels. Findings will also be used to help establish maintenance guidelines and gas cleanup specifications for IGCC plants. Ultimately, this will reduce the time and cost to certify and commercialize modern gas turbines operating with syngas fuels.

A no-cost 6-month extension of the first-year funds ended January 31, 2007. No second-year funds have been received as yet, although plans for this funding are underway.

FULL PROGRESS REPORT

PROJECT DESCRIPTION

Gas Turbine Research Need

Turbine inlet temperatures for large power generation gas turbines have been steadily increasing over the last several decades due to significant advances in materials and cooling technologies. By incorporating these critical advancements, the H-class combined cycle machines are expected to operate at up to 1425°C. While this higher combustor exit temperature translates directly to higher cycle efficiency, it does not bode well for the severe operating environment of turbine materials. At the same time, political and economic pressures are pushing utilities to consider fuel flexibility. Limited natural gas resources necessitate the integration of more plentiful sources of coal and biomass into the fuel reserve for gas turbines. Compared to "clean" burning natural gas, these alternative fuels have higher concentrations of trace elements and ash that present significant corrosion challenges to turbine operation.

Coal utilization introduces S, Al, Fe, Ca, and various alkali metals (e.g. Na, K) to the gas turbine, while biomass has lower sulfur content than coal, but has higher concentrations of Ca, Mg, Cl, and K. The concentrations and sizes of these compounds that actually reach the turbine surfaces depend on the combustion and gas-cleanup processes. If combustion products arrive at the turbine blade surface in the liquid (or vapor) phase, it is likely that they will deposit (or condense) there and accelerate material corrosion. A number of studies conducted in the 1970's and 1980's (before the dominant use of natural gas in gas turbines) showed that corrosive deposition is strongly dependent on temperature. Depending on the syngas fuel employed, the threshold temperature for deposition varied from 900C – 1100°C. Above this threshold, studies showed up to an order of magnitude increase in deposition rates. Since those tests were conducted, several key technologies (e.g. thermal barrier coatings, advanced cooling schemes, and single crystal blades) have permitted substantial increases in firing temperatures. The compatibility of these advances with ash-bearing syngas fuels has yet to be assessed. Clearly, there is a critical need for fundamental experimental studies to determine the magnitude of deposition, erosion, and corrosion for the application of alternative fuels in modern gas turbines.

In addition, limited experimental evidence suggests that by sub-cooling turbine components, deposition may be mitigated. Additional studies are necessary to determine necessary cooling levels for adequate protection from syngas deposits. Finally, film cooling flows provide a cool air stream at the turbine surface that may influence local deposition as molten combustion products cool and harden near the film cooling hole. Such deposition in and around the film cooling hole could significantly impede the flow of critical coolant to the blade surface. These effects must be adequately evaluated and modeled to provide turbine operators with the tools they need to assess the in-service health of cooled turbine components.

Project Experimental and Analytical Approach

This proposal addresses all three of these critical turbine operability and maintainability issues in three phases. In Phase 1, deposition studies will be conducted in an accelerated turbine deposition facility at Brigham Young University to document the influence of temperature on deposition, erosion, and corrosion from syngas fuels. This facility is part of BYU's Advanced Combustion Engineering Research Center (ACERC), a laboratory founded in 1987 by the National Science Foundation. With active contracts totaling approximately $1.5 million/year,

the center encompasses research on combustion, mineral matter transformation, deposition, and corrosion in power systems fired by coal, biomass, black liquor, oil shale, petroleum coke, and natural gas. Rather than simulate the syngas gasification and cleanup process, this research will be conducted by seeding a natural gas combustor with coal and biomass products of combustion and accelerating them onto target turbine materials. Combustion byproducts from two of the reactors within ACERC (one for coal and one for biomass) will be collected, analyzed, and ground down to a mass-mean 10μm solid particulate for use in the accelerated turbine deposition facility. By performing experiments in this controlled laboratory environment the individual effects of corrosive elements can be properly evaluated. BYU's accelerated turbine deposition facility is capable of matching both the impact velocity and gas temperature of modern industrial turbines. Arrangements are in place with industrial contacts at GE, Solar, Praxair, and Siemens to make available modern turbine materials and coatings as targets for this study. Once syngas deposits are formed on the target, various analyses will be conducted, including: surface mapping, roughness assessment, deposit thermal conductivity measurement, and elemental decomposition with corrosion assessment. Elemental analyses will employ existing ACERC diagnostic equipment including: scanning electron microscopy, inductively-coupled plasma with atomic absorption, and x-ray analysis for quantitative analysis of deposits.

Phase 1 of the proposed research will also explore the possibility of sub-cooling the turbine surface to mitigate deposition. This will be accomplished by cooling the backside of the target coupon, similar to internal convection cooling in a turbine blade. Similar post-exposure analyses will be conducted to evaluate both the extent of turbine damage and changes in depositing constituents with surface temperature.

The 2nd phase will evaluate the influence of deposit formation on film cooling flows. This study will be accomplished in the same turbine deposition facility by injecting coolant from film holes in the target coupon. Sections of turbine blades with cooling holes will be solicited for this effort so that the coolant hole geometry is representative of current practice. Deposits in and around cooling holes will be measured and analyzed as before.

During the optional 3rd year of the research program, scaled models of the deposit-laden film holes will be installed in a low-speed wind tunnel at BYU for flow and heat transfer assessments. A 3-D PIV system and IR camera will be used to gather 3-dimensional velocity data as well as surface heat transfer and film effectiveness. The data density available from these sophisticated diagnostics will provide an important database for CFD validation. This phase will also consider the effects of TBC residue left in film holes during the plasma-spray application process since it is likely that this residue bears resemblance to deposits formed during turbine operation.

Expected Results/Benefits

With this aggressive research program, DOE and industry will gain valuable insights into factors affecting the safe, efficient operation of modern industrial turbines with alternative fuels. Findings will also be used to help establish maintenance guidelines and gas cleanup specifications for IGCC plants. Ultimately, this will reduce the time and cost to certify and commercialize modern gas turbines operating with syngas fuels.

A no-cost 6-month extension of the first-year funds ended January 31, 2007. No second-year funds have been received as yet, although plans for this funding are underway.

EXPERIMENTAL METHOD

Turbine Accelerated Deposition Facility (TADF)

A natural gas burner has recently been commissioned for accelerated turbine deposition studies in the Advanced Combustion Engineering Research Center (ACERC) at BYU (Figure 1). The combustor burns natural gas in a facility capable of mass flow rates up to 1500 slpm. With an exit contraction from 30.5 cm to 2.4 cm diameter, the exit flow from the combustor can exceed 250 m/s. A target holder positioned at the combustor exit is used to expose turbine material coupons to the hot exhaust gases at various impingement angles. The entire hot section of the combustor facility is manufactured from Inconel 601, capable of steady state operation up to 1250°C. Though the pressure at the target coupon is not that of a gas turbine (it is atmospheric pressure), by matching both the velocity and temperature of the exhaust gases, deposition mechanisms similar to those found in an actual engine can be simulated.

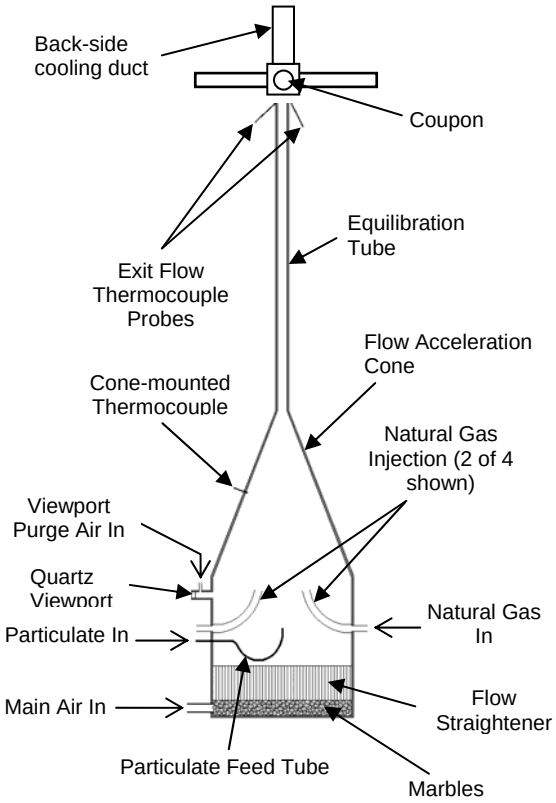

Figure 1. BYU Accelerated Turbine Deposition Facility: schematic and photograph. Photo taken while operating at 1150°C (note glowing Inconel test coupon).

Since the fuel is methane mixed with filtered high pressure air, deposits are created by seeding the combustor with selected particulates using an automated particle feed system. The feeder allows controlled rates of fine, dry particulates (powders) to be added to the hot section and accelerated in the combustor exit. A 1.2 m long exhaust pipe is provided to insure thermal and velocity equilibrium of the particulate with the gas stream.

Wenglarz and Wright (2002) describe various experiments where particulate concentration and service time seemed to tradeoff between each other. Turbines exhibited large deposits or could even be driven to failure either by high particle loading at low service time or low particle loading for long periods. This suggests that the net particulate throughput is a key parameter for proper deposit simulation. Therefore, the time to produce a surface deposit can be reduced considerably by increasing the concentration of particulate. Since operating a university research facility for a typical 8,000 hour plant operating year is impractical, deposits are instead generated during short one to eight hour tests. Particle feed rates are selected to match the net throughput of particulate.

Tests conducted using airborne particulates serve as a validation of this accelerated testing procedure (Jensen et al., 2005). Seed particles from Air Filter Testing Laboratories, Inc. were selected to match the typical particulate size (mass mean particle size of 15μm with half of the particles less than 5μm) and chemistry found in the urban atmosphere. Tests with this particulate were conducted for a combustor exit temperature of 1150°C and a Mach number of 0.3. Several 4-hour tests were completed at loadings from 60 to 280 ppmw. This is the same net particulate as 10,000 hrs of operation at 0.024 to 0.061 ppmw, which are typical values for filtered intake air. The test coupons were standard Ni-based alloy with various coating treatments donated from industry. The conclusion of Jensen et al.'s study was that deposits generated in the TADF were similar in deposit structure, surface topography, and thickness to those found on in-service turbine hardware. Since all of these features have a direct influence on heat transfer, deposits generated in this accelerated facility are suitable for assessing the impact of deposition on turbine performance.

Deposition tests were conducted to explore the influence of gas temperature and particle size on deposition rates of coal ash; these results are shown again in this report to compare with additional test series.

TADF Redesign for Backside Cooling

During the last 6-month period of the first year, the TADF specimen holder was modified to allow coupon backside cooling and eventually film cooling to the front of the test coupon. The objective of the specimen holder redesign was to be able to simulate the appropriate thermal gradient through the turbine sample during deposition testing. In all previous deposition studies, the backside of the specimen was flush mounted against a solid metal support that was itself immersed in the exiting jet flow. This created a nearly isothermal environment for the TBC-coated test coupon. Due to their low thermal conductivity (~1 W/m·K), TBCs typically experience front to backside temperature differences of 50-150ºC, depending on coating composition and thickness. During the first six months of this research program, several conceptual designs for the proposed redesign were discussed with UTSR technical point contacts within industry, including a visit by Dr. Bons to Siemens' facility in Orlando, FL in January 2006.

Based on this valuable industry feedback, the test specimen holder was redesigned as shown in Figure 2. The coolant chamber design is intended to simulate impingement cooling

that is typically used in the leading edge region of a modern vane or rotor. The design allows for backside coupon temperature measurement using welded thermocouples. Also, the mass flow of coolant is measured during testing using an in-line mass flowmeter. A cylindrical heat shield positioned around the test coupon limits radiative heat loss but also obstructs the view somewhat (see Fig. 1).

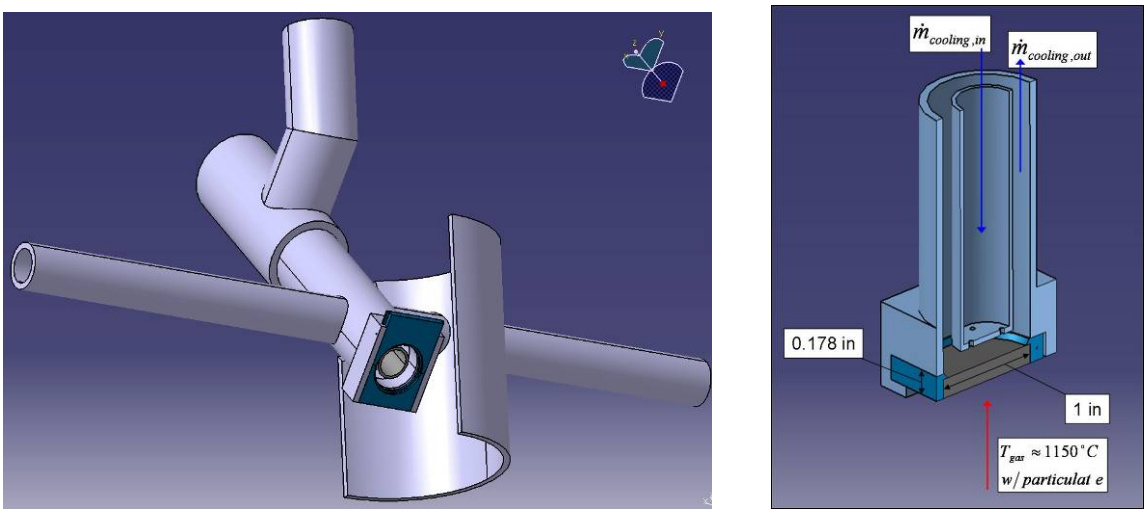

(a) Redesigned coupon holder **(b) Impingement Cooling**

Figure 2. TADF test coupon holder redesign with backside cooling.

RESULTS AND DISCUSSION

Minor modifications to the combustor included: increasing the equilibration tube diameter to 2.54 cm to allow for a more uniform temperature profile and increasing the number of flame holders from 4 to 8 to maintain flame stability. The increase in tube diameter resulted in a slight decrease in exit velocity with the Mach number reduced to 0.25 for the operating temperature of 1183°C. Primary air flow was measured with a choked flow orifice to an uncertainty of ±3%. Figure 3 shows the temperature profile at standard test operating conditions (gas exit temperature = 1183°C, Mach = 0.25). The profile was measured by traversing a high temperature thermocouple probe across the lip of the tube exit. The thermocouple was not shielded and a radiation correction of 33°C at 1150°C was estimated using an emissivity of 0.5 for the oxidized Omegaclad^{TM} probe surface. The thermocouple uncertainty was less than 15°C and the uncertainty in calculated Mach number was ±0.021.

The NASA Lewis chemical equilibrium code (McBride and Gordon, 2006) was used to determine the composition of the combusted gas stream at 1183°C, based on the composition and flow rates of natural gas and air. For base condition in the TADF (1183°C, 0.0214 kg/s of inlet air, 0.000471 kg/s of inlet natural gas), the composition of the combusted gas (in mole%) was 12.9% O_2, 3.8% CO_2, 7.2% steam, and the balance N_2.

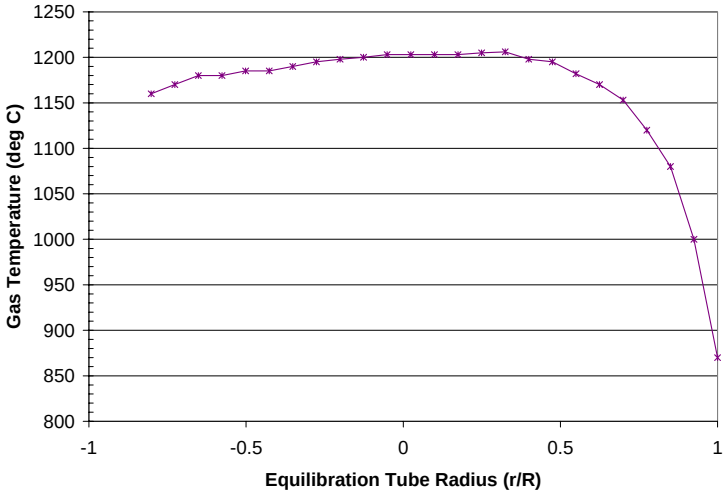

Figure 3. Equilibration tube exit temperature profile for standard testing conditions of Mach=.25 and gas temperature=1183°C.

Three sets of circular turbine blade samples, all approximately 2.54 cm in diameter, were obtained from multiple industry sources for this study. In order to respect proprietary concerns of the manufacturers, strict source anonymity has been maintained for all data presented in this report. The samples are representative of a high performance turbine material system: a nickel based super alloy substrate approximately 0.3 cm thick was common to all three sets, an MCrAlY bond coating approximately 225μm thick for the first set, 200μm for the second, and 175μm for the third, and an air plasma sprayed (APS) yttrium stabilized zirconium (YSZ) thermal barrier coating (TBC) layer approximately 0.45 mm thick for the first set, 0.40 mm for the second, and .17 mm for the third. The samples were polished to a centerline-averaged roughness (Ra) value of 1-1.5μm. Each of the three sets of coupons was used for a different test series as will be explained in later sections therefore consistency for each test series was maintained. A small groove was machined around the circumference of each sample to allow it to be held in the cooling fixture with adequate sealing to contain the coolant. For all tests pre and post-test masses were measured as well as digital images taken. Uncertainty in the mass measurement is ±5mg. Scanning electron microscopy (ESEM) was employed as a post-test diagnostic to determine the extent of deposition and material system degradation. To prepare the samples for the ESEM the samples were placed in epoxy, to preserve the deposit, cross sectioned, placed in Bakelite, and then polished.

Frontside Temperature Measurement Technique

The temperature of the coupon surface exposed to the jet at 1183°C (i.e., the frontside temperature) was measured with two different methods. An Ultimax infrared one-color thermometer was used, but the emissivity of the hot coupon surface was unknown. A two-color technique was therefore employed in order to avoid the uncertainty in surface emissivity. The technique used in the experiment was taken from Lu (2006), and uses the blue and green signals from the RGB ports on a SVS285CLCS Sony Exview HAD CCD camera. The measured spectral response (S_λ) of each color from the RGB camera is shown in Fig. 4 as a function of wavelength (λ).

As explained by Lu (2006), the signal from the detector (DN) is defined by:

$$DN = C_{\exp} \cdot \int_{\lambda_1}^{\lambda_2} \varepsilon_\lambda S_\lambda \cdot \frac{C_1 \cdot \lambda^{-5}}{e^{C_2/\lambda \cdot T} - 1} d\lambda \tag{1}$$

where ε_λ is the surface emissivity, C_1 and C_2 are the two Planck's law constants, and C_{exp} is a constant that depends on the experimental geometry, exposure time, and gain factor.

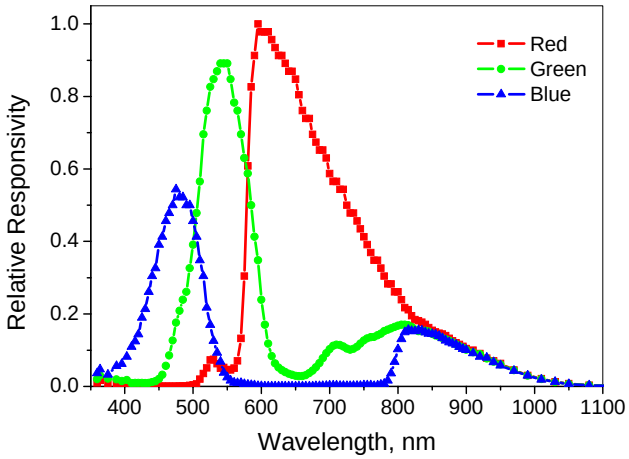

Figure 4. Measured relative spectral response of the SVS285CSCL camera.

The value of C_{exp} was calibrated for each color using a blackbody source at temperatures from 530°C to 1130°C. The temperature of the surface can then be measured using the ratio of detector signals from two colors, as shown in Eq. 2.

$$\frac{DN_{Blue}}{DN_{Green}} = \frac{C_{Blue} \int_{\lambda_1}^{\lambda_2} S_{\lambda,Blue} \cdot \frac{C_1 \cdot \lambda^{-5}}{e^{C_2/\lambda \cdot T} - 1} d\lambda}{C_{Green} \int_{\lambda_1}^{\lambda_2} S_{\lambda,Green} \cdot \frac{C_1 \cdot \lambda^{-5}}{e^{C_2/\lambda \cdot T} - 1} d\lambda} \tag{2}$$

This technique is very similar to other two-color pyrometry experiments, except that broadband wavelengths are used instead of narrow wavelengths. Lu (2006) studied the sensitivity of the different color combinations as a function of temperature and recommended the blue-green combination for the intermediate temperatures studied here. The red-blue combination would be better for higher temperature (~ 1700°C) applications. Over the range of 950-1150°C, the uncertainty in temperature was estimated at 15.4°C.

A set of experiments was performed to determine the difference between the frontside and backside temperature of the coupon as a function of the flow rate of backside cooling air. Frontside temperatures were measured for the standard experimental conditions in the TADF (i.e., 1183°C, Mach 0.25) as a function of the backside cooling air flow rate. No particles were injected into the combustor while these data were obtained. Backside temperatures were measured using thermocouples welded to the back surface of the coupon. The experiment was performed in the morning, followed by a period where the reactor cooled down, and then repeated in the afternoon. The camera and thermometer were not moved in between these experiments to reduce errors due to focal length and location of the focal spot on the coupon.

The frontside temperatures were determined from the image of a rectangular area in the center of the coupon in order to avoid edge reflections and hot spots. The measured temperature data are shown in Fig. 5. Both the frontside temperature and the backside temperature decrease with increased cooling. The temperature difference between the frontside and the backside increases as the cooling flow rate increases, as expected, with temperature differences ranging from 200°C to 400°C. There is a slight discrepancy in the a.m. and p.m. frontside temperature measurements using the BG method at the higher coolant flow rates.

The IR thermometer results are plotted in Fig. 5 as well. A surface emissivity of 0.2 was used to match the 2-color temperature at the lowest cooling rate. The IR temperature measurements seem to follow the average of the two 2-color measurements at the higher cooling rates with this constant emissivity value.

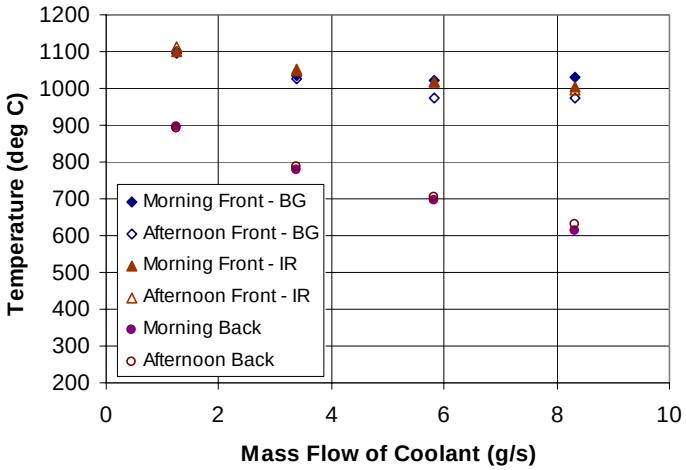

Figure 5. Measured frontside and backside temperatures as a function of cooling

The temperatures of the inlet and outlet air streams used to cool the backside of the coupon were measured with thermocouples for each cooling flow rate. Since the heat capacity of air is known, the heat removed by the cooling stream can be calculated as follows:

$$Q = \dot{m} C_p \left(T_{out} - T_{in} \right) \tag{3}$$

The heat removed was divided by the area exposed on the backside of the coupon in order to obtain an area-averaged heat flux. In addition, the conductive flux through the coupon under each condition was computed from the average frontside and backside temperatures using estimates for the thermal conductivities of the coupon substrate and the thermal barrier coating. The comparison of the computed fluxes is shown in Fig. 6. The agreement is reasonable considering the simple 1-D analysis employed in the computation. Both heat flux estimates increase with increased cooling, matching the expected trend. Also, the absolute magnitude of heat flux is comparable to estimates for 1st stage vanes in a modern gas turbine (800-1200 kW/m^2, denoted by the gray band in Fig. 6). The conductive flux is generally lower than the backside cooling flux estimate. This result is consistent with insufficient insulation surrounding the cooling apparatus to prevent three-dimensional heat flows around the coupon. Such peripheral heat flows would not register with the backside thermocouple measurement but would eventually make their way into the coolant flow. At the lowest coolant flow rate, the single thermocouple measurement in the coolant exit flow may not be registering a representative

"mixed-out" temperature. A more sophisticated analysis is underway to more accurately measure the surface heat flux for future studies.

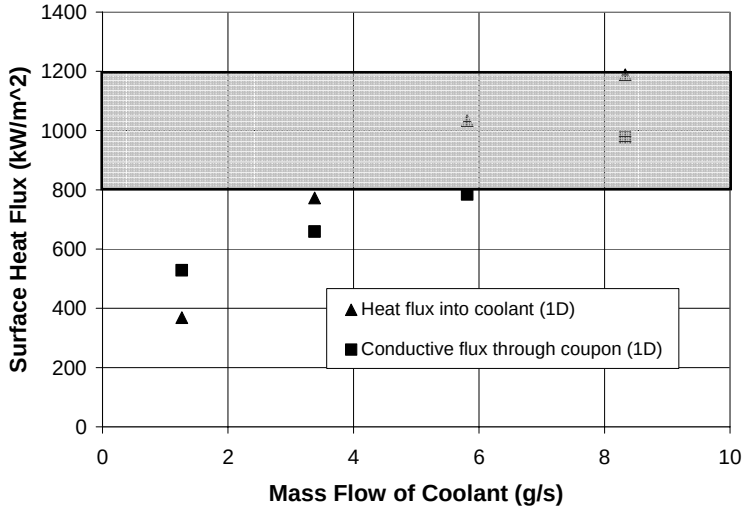

Figure 6. Calculated heat fluxes due to conduction through the coupon and due to backside cooling for a coupon in the TADF at 1183°C at Mach 0.25. The gray band represents the absolute magnitude of heat flux is comparable to estimates for 1st stage vanes in a modern gas turbine.

Particulate Preparation

The coal and petcoke samples used in this study are the same as those described in Bons et al (2005), with the exception that the particle sizes have been substantially reduced. This was accomplished using a mechanical grinder with a collector to trap the particles exhausted out of the air filter. Subbituminous coal fly ash was obtained from an operating power plant, while the petcoke ash is boiler slag obtained from a combined cycle gas turbine power plant operating with a blend of 55% petcoke and 45% coal. The ash was characterized using an environmental scanning electron microscope (ESEM) to perform x-ray spectroscopy which can identify the elemental composition down to the atomic number of carbon. An independent elemental analysis was also conducted on the ash samples by ALS Chemex using inductively coupled plasma atomic emission spectroscopy (ICP-AES). The results were similar with only slight variation in the weight percentages of silicon which were attributed to the ESEM measurements being spot measurements while the ICP-AES were bulk measurements.

To simulate ash that could be entrained by the flow leading to the turbine, the particles must be small enough to pass through the various gas cleanup systems. Filtration systems in modern gas turbine power plants are designed to remove all particles with diameters greater than 10μm and a majority of particles larger than 1 μm. With inadequate or degraded filtration, these levels can be exceeded. This study focuses only on contamination from the fuel gas system. In addition to particles from the fuel stream, sand and dirt from the inlet air and rust from the gas turbine flow path can also form deposits resulting in spallation and TBC loss. This study is intended to supplement other studies performed by the authors in which sand, biomass, and other synfuels have been used (Jensen et al., 2005; Bons et al., 2005; Wammack et al., 2006; Bons et al., 2006).

Table 1. Ash particle summary statistics: size, density, and average elemental composition.

	Subbituminous Coal	Petcoke
Mass mean diameter (μm)	3.1-16	6.3
Bulk density (g/cc)	0.99	1.45
Apparent density (g/cc)	1.98	2.90
Element	Weight %	Weight %
Na	6.9	4.3
Mg	3.6	2.2
Al	17.8	14.5
Si	47.4	38.3
P	1.6	0.0
S	1.8	1.0
K	2.6	2.5
Ca	8.7	7.5
Ti	1.6	0.8
V	0.0	3.4
Fe	6.4	22.9
Ni	0.0	0.9

After grinding, the size of the ash samples was determined using a laser-based Coulter Counter. The Coulter Counter operates using a laser beam to illuminate the particles contained in a water slurry which scatter light according to their size. Photodetectors convert the scattered light to particle size distributions. A more detailed explanation of the Coulter Counter is given in Bons et al (2005). Table 1 shows the particle size and elemental composition of the particulate used in the majority of the tests conducted in this study. The bulk density of each ash sample was measured in a graduated cylinder, and the apparent density (mass per particle exterior volume) was calculated using an estimated packing factor of 0.5.

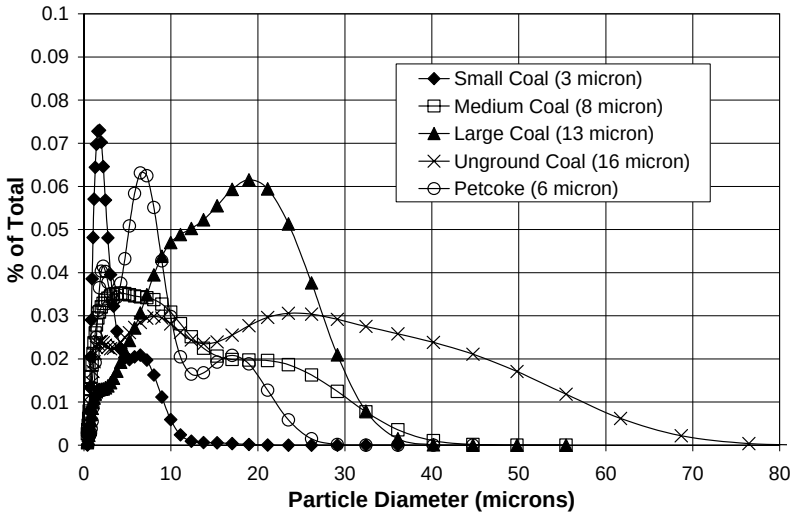

Figure 7. Particle size distributions for the four subbituminous coal ashes and the petcoke ash tested.

Deposition Test Series

Four series of tests were performed in the accelerated deposition test facility to study the independent effects of particle size, gas temperature, and metal temperature on ash deposits from two candidate power turbine synfuels:

Series 1 (Particle Size).

Four different size particles were studied by seeding a natural-gas combustor with finely-ground subbituminous coal ash particles. The entrained coal ash particles were accelerated to a combustor exit flow Mach number of 0.25 before impinging on a thermal barrier coated (TBC) target coupon at 1183°C.

Series 2 (Gas Temperature).

Gas temperature was varied while the facility maintained a constant exit velocity of 170m/s (Mach=0.23-0.26). A subbituminous coal ash with a mass mean diameter of 3μm was used.

Series 3 (Impingement Cooling-Subbituminous coal ash).

Impingement cooling was applied to the backside of the target coupon to simulate internal vane cooling using subbituminous coal ash particles.

Series 4 (Impingement Cooling-Petcoke ash).

Impingement cooling was applied to the backside of the target coupon to simulate internal vane cooling using petcoke ash particles.

Particle Size Series

Three series of tests were conducted to study the effects of particle size, gas exit temperature, and metal temperature on deposition. The first test series looked at the effects of particle size on deposition. For the case of erosion, Hamed et al. (2004) calculated the trajectories of various sizes of particles (10-50μm) in a modern LPT stage using a semi-empirical particle rebound model. They found that larger particles actually have multiple rebounds between neighboring blades while smaller particles primarily impact the pressure surface only. To explore the effect of particle size on deposition, the present study used standard combustor operating conditions (gas exit temperature = 1183°C, Mach = 0.25) with the first set of 1" diameter turbine samples. The tests were run with no cooling air and the interior passage of the cooling fixture was insulated with blanket insulation material. The backside temperature was measured with two welded K-type thermocouples and found to be approximately 990°C, which is roughly 200°C below the combustor exit temperature.

Recently, Wammack et al (2006) conducted a deposition study using polished TBC turbine samples where the specimens were subjected to four consecutive testing cycles, returning the sample to room temperature between each test. They measured a significant increase in TBC surface roughness following the first thermal cycling. As a result, this roughened surface was much more susceptible to deposit accumulation compared to the highly polished surface prior to the first test cycle. To account for this effect in the current test series, an initial one hour "burn-in" test was conducted with particulate injection, following which the combustor was shut down. The sample was allowed to cool without removing it from the fixture. Following this, the combustor was again brought to steady state and a standard four hour test was conducted. Coal ash particulate was used in this test series, with four different sizes, each obtained from different locations in the mechanical grinder. The four particle size distributions (shown in Fig. 7) were obtained using the Coulter Counter. The data shown in the figure are weight percent, so in all

samples there are a majority of particles (by number) in the range below the mass mean diameter. ESEM images of the largest and smallest samples show a representative distribution of particle sizes (Fig. 8).

Table 2. Deposition results from particle size test series.

Particle Size [μm]	Preburn Button Mass [g]	Button Mass Change [mg]	Separated Deposit Mass [mg]	Separated Deposit %	Net Deposit Mass [mg]	Deposition Rate [mg/cm^{2}hr]	Net Particulate Mass added to flow [mg]	Net Capture Efficiency [%]
3	14.73	70	300	81	370	14.6	10050	3.68
8	14.88	60	450	88	510	20.13	10350	4.93
13	14.12	-10	880	101	870	34.34	12720	6.84
16	14.99	-140	1220	113	1080	42.63	13390	8.07

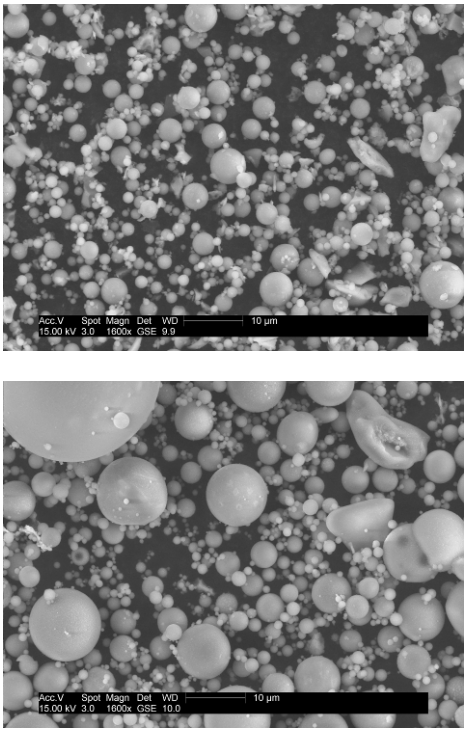

Figure 8. ESEM images of smallest (top) and largest (bottom) size subbituminous coal ash particles.

Using the pre-test and post-test mass measurements, the net specimen mass gain during exposure was assessed (Table 2). In some cases the deposit was very fragile and much of it flaked off following the test as it cooled. The separated deposit percentage, defined as the amount of deposit that separated after the test ended divided by the net specimen mass gain, is also shown in the table. Percentages greater than 100% are indicative of significant spallation of the TBC layer where the mass of the separated deposit (plus TBC) weighed more than the net specimen mass gain. The increasing percentage of separated deposit with increasing particle size indicates that TBC is more prone to spall with larger deposit formations.

Figure 9. Post test images of coupon subjected to 13 μm particle size.

Figure 9 shows two post-test images of the 13 μm particle test coupon. The first image was taken immediately after combustor shut-down while the second image was taken after the sample had cooled to room temperature. Streamwise aligned deposit structures are evident in the hot deposit image (Fig. 9a). These structures are similar to fuel deposit structures previously measured on a serviced turbine blade pressure surface by Bons et al. (2001) (Fig. 10). The deposits in Fig. 10 were considerably more tenacious than the accelerated coal deposits in this case, since they were still intact on the blade surface after cool down. With rapid cooling, the mismatch in thermal expansion coefficients between the metal, the TBC, and the deposit results in the removal of most of the deposit with some of the TBC as well. Just last month, the TADF was operated with a significantly slower cool-down sequence (2 hrs vs. 5 minutes) to assess the impact of thermal transient on the tenacity of the deposit. It was found that flaking was substantially reduced if not eliminated with slower cooldown. Since the slower cool down sequence more closely models the shut down procedure for an operating turbine, the intact deposits in Fig. 10 are understandable. Future TADF testing will employ this slower cooldown procedure.

TBC spallation is evident primarily along the leading edge of the circular specimen (Fig. 9b), even though the deposit thickness is approximately uniform over the entire coupon (Fig. 9a). Wammack et al. observed similar behavior in their deposition tests and attributed this to the impingement of deposit-laden gas at the exposed metal/TBC interface (Bons et al., 2005). Thus, material system degradation (e.g. TBC spallation) was always most significant at the leading edge of the turbine specimen. In a gas turbine, similarly exposed TBC/metal interfaces are evident at each of the film cooling holes in the stagnation region of the blade. This explains the common occurrence of TBC spallation adjacent to stagnation film holes as described by Bons et al. (2001). The extent of spallation and material system degradation will be discussed further using ESEM images.

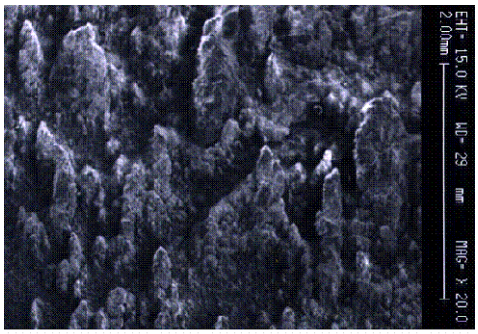

Figure 10. Micrograph image taken of deposits found on a turbine blade pressure surface (flow direction is from bottom to top).

Dividing the net deposit mass by the exposed coupon surface area and the test duration yielded deposition rate measurements from 14 mg/cm^{2}hr to 43 mg/cm^{2}hr for the smallest and largest size particles (Table 2). Figure 11 shows the effect of particle size on net capture efficiency (mg/hr of deposit divided by mg/hr of particulate added to the flow). Capture efficiency increases asymptotically with particle size with a more than 50% increase from 3μm to 16μm. These results suggest that with filter degradation, deposition problems as well as turbine hardware damage are likely to increase considerably. Additionally, it is important to note that even the smallest size particles tested showed significant deposition. This would indicate that even with properly functioning filtration systems the problems associated with deposition and spallation cannot be entirely eliminated. These deposition rates are lower than previous measurements in the same facility reported by Bons et al. (2005) (70-140 mg/cm^{2}hr) and those reported by Wenglarz and Fox (1990) (200-400 mg/cm^{2}hr). This may be due to the lower particulate loadings used in the present study compared to Bons et al. (2005) (less than 100 ppmw-hr vs. 150-600 ppmw-hr respectively).

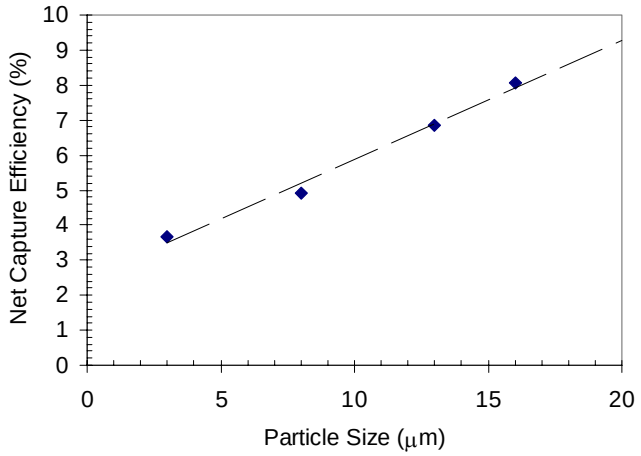

Figure 11. Effect of particle size on net capture efficiency

Gas Temperature Series

The second test series was performed using coal ash with a mass mean diameter (MMD) of 3μm with no cooling air and the interior of the coolant passage still insulated. Six tests were performed at five different gas exit temperatures using the second set of samples. Two of the tests were performed at a gas exit temperature of 1183°C which is typical in many modern first stage gas turbine engines while the other tests were at lower temperatures. All of the tests experienced a nominal particulate loading of 96 +/- 12 ppmw-hrs. This loading is intended to simulate an engine operating for one year (8,000 hrs) at a low particulate concentration of 0.01 ppmw. This standardization of ppmw-hrs has been used previously (Jensen et al., 2005; Bons et al., 2005; Wammack et al., 2006) to simulate long duration turbine operation. A similar metric was used by Caguiat (2002) in which accelerated compressor fouling caused by salt water ingestion was studied. By using this metric, the results can be interpreted to a wide range of applications. Airflow was adjusted to maintain an exit velocity of 170 m/s for each test, which at the gas temperatures tested yielded Mach numbers ranging from 0.23-0.26. Since the mode of deposition for particles on the order of 3μm is inertial impaction, this constant jet velocity

condition maintains the same kinetic energy at particle impact. Accordingly, the only relevant variable in this test series is the particle temperature, which was calculated to be in thermal equilibrium with the gas at the exit of the 1m long equilibration tube. Once the facility reached steady state, particle seeding commenced and lasted for four hours after which the facility was immediately shut down. The initial one hour "burn-in" test was not performed for this test series.

Deposits were very similar to the 3μm test from the particle size series. The same flaking was observed for the tests run at 1183°C, but very little flaking was noticed at lower temperatures. Deposition results are summarized in Table 3. Repeated tests were run at an exit temperature of 1183°C to show the repeatability of the facility. The deposition rate decreased by approximately 58% with the first 100°C drop in gas temperature. This was followed by another 50% decrease with an additional 50°C drop. An additional 50°C drop in gas temperature to 966°C resulted in a 67% decrease in deposition rate. At 860°C no deposit formed indicating a gas temperature threshold for deposition around 960°C for this study. This compares well with studies performed previously by Wenglarz and Fox using coal-derived fuel, Kim et al. using volcanic ash, Jensen et al. using airborne dust. Since these gas temperatures are all lower than the melting temperature of the ash compounds, the rising deposition rate with gas temperature is likely due to the increased tendency for deposit sintering at elevated temperatures. Sintering creates large deposit masses that are less susceptible to removal by erosion from subsequent particle impacts.

Table 3. Deposition results from gas temperature test series

Gas Temperature [°C]	Preburn Button Mass [g]	Button Mass Change [mg]	Separated Deposit Mass [mg]	Separated Deposit %	Net Deposit Mass [mg]	Deposition Rate [mg/cm^{2}hr]	Net Particulate Mass [mg]	Net Capture Efficiency [%]
1183	13.66	40	100	71	140	6.91	7880	1.78
1183	13.66	40	110	73	150	7.4	8220	1.82
1074	13.64	60	0	0	60	2.96	7590	0.79
1020	13.64	30	0	0	30	1.48	7820	0.38
966	13.69	10	0	0	10	0.49	7360	0.14
860	13.62	0	0	0	0	0	7860	0

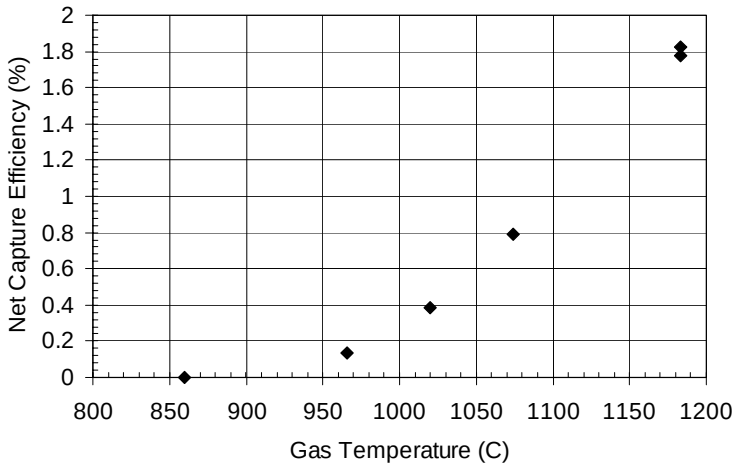

Figure 12. Effect of gas temperature on net capture efficiency.

Figure 12 shows the corresponding decrease in net capture efficiency with gas temperature. It is noted that the capture efficiency at 1183°C in Fig. 12 is approximately 50% of that shown in Fig. 11 for the same 3μm particle size. This is due to the effect of the "burn-in", which was not performed for this test series. Figure 13 (a)-(c) show digital images of specimens at 1183°C, 1074°C, and 966°C. Note the large amount of separated deposit for the high temperature case and the lack of substantial deposits at low temperature (though the coupon is still discolored at the lower edge near jet impact). Based on the trend in Figure 12 we would expect deposition rates to increase for G and H-class engines which operate above 1500°C. However, some of the constituents may be in a vapor phase at these temperatures so the degree to which deposition would increase might not be exponential as indicated in Figure 12. The authors are unaware of any deposition tests in the open literature that operate at higher temperatures than those in this study.

Figure 13. Digital images of post burn coupons at (from left to right) 1183, 1074, and 966°C.

The strong dependency of deposition rate on gas (and particle) temperature has important implications for modern turbine blade rows where the gas temperature can drop by 150-250ºC per stage. If the turbine inlet temperature is high enough so that particles are molten or sinter readily, they may collect primarily near the leading edge – since with falling temperatures through the vane passage, sintering may no longer be possible. If however, the gas temperature at the vane inlet is so high that corrosive elements are in the vapor phase, then they may not deposit on the vane. Rather, they may wait until the temperature drops and then begin to condense on the surface – perhaps in the subsequent blade row. Another factor affecting deposit buildup is of course the flow angle relative to the local surface. The flow is directly impinging at the leading edge, whereas it is mostly parallel to the wall at mid-span. Finally, this temperature study was conducted with subbituminous coal and the results should not be applied too broadly. A single test was recently conducted using Illinois #6 coal particulate (a bituminous coal) and no deposition was generated for the standard TADF test conditions of 1183ºC. The ash elements in this bituminous coal are bound up in a glass matrix that prevents deposit buildup until the glass melting temperature is reached. That said, previous TADF testing with other particulate types (including petcoke, sawdust ash, straw ash, and airborne particulate) produced significant deposit at 1183ºC.

Impingement Cooling Series (subbituminous coal ash)

The third test series was performed to study the effects of impingement cooling on deposition. The insulation was removed from the interior of the cooling fixture and two K-type thermocouples were welded to the backside of each sample to measure the backside temperature. This test series used the same set of samples as in the particle size series. The RGB camera was used to measure the sample frontside temperature and two K-type thermocouples were used to

measure the incoming and outgoing coolant temperature. Four tests were run at varying mass flows of coolant. The same coal ash was used as in the gas temperature series (3 μm diameter) and the standard combustor operating conditions, as used in the particle size series, were used including the initial one hour "burn-in" test. All of the tests experienced a nominal particulate loading of 110 +/- 7 ppmw-hrs, only slightly higher than the gas temperature series due to the additional one hour "burn-in" test.

The deposits formed in this test series were much more tenacious than the previous ones. Appreciable deposit flaking was only observed for the 1.26 g/s cooling case and it was minimal. This result is consistent with the behavior of the gas temperature series in which the lower gas temperatures showed a more tenacious deposit. The applied coolant lowers the temperature of the TBC surface producing a thinner deposit layer. Thin deposit layers are not as susceptible to flaking induced by thermal contraction during cool down. Table 4 provides a summary of the deposition results. The deposition rate was reduced by approximately 40% with the initial level of cooling.

Table 4. Deposition results from impingement cooling test series using coal

Mass flow of Coolant [g/s]	Heat Flux [kW/m^2]	Preburn Button Mass [gr]	Button Mass Change [mg]	Separated Deposit Mass [mg]	Separated Deposit %	Net Deposit Mass [mg]	Deposition Rate [mg/cm^{2}hr]	Net Particulate Mass [mg]	Net Capture Efficiency [%]
0	0	14.73	70	300	81	370	14.6	10050	3.68
1.26	500.68	30.56	130	90	41	220	8.68	8480	2.59
3.38	1049.21	30.69	120	20	14	140	5.53	9270	1.51
5.81	1404.35	30.53	100	0	0	100	3.95	8120	1.23
8.33	1614.26	30.93	0	0	0	0	0	9540	0

This was followed by further reductions as the amount of cooling was increased. Corresponding trends in net capture efficiency are shown in Fig. 14. For this series, spallation occurred, but was limited to very small portions of the edge at the base of the sample. The amount of visible spallation decreased slightly with increased coolant mass flow. The drop in capture efficiency noted in Fig. 14 is similar to the result of Wenglarz and Fox (1990) who observed a factor of 2.5 reduction in deposits for a 200°C drop in metal surface temperature produced by sub-cooling. The present results show a factor of 4 reduction in deposits for a 360°C drop in backside temperature (100°C drop in frontside temperature – see Fig. 5) with cooling. These results clearly show the benefits of cooling in reducing deposition. However, in G and H class engines the amount of cooling needed to obtain the necessary drop in frontside temperature could be prohibitive. These results also suggest that film cooling could provide an additional reduction in deposition and spallation. However, Bons et al. (2001) noted that film cooling holes introduce exposed TBC/metal interfaces that are actually more prone to spallation.

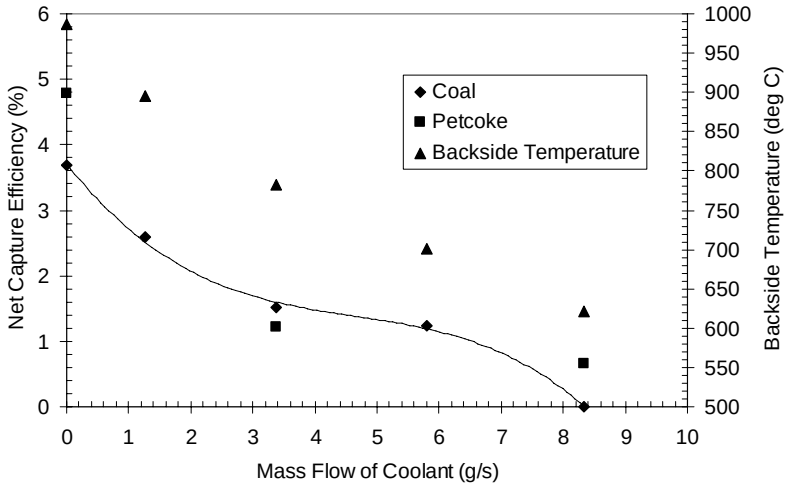

Figure 14. Effect of impingement cooling on net capture efficiency.

To further assess the level of TBC degradation, the test articles from this test series were analyzed using the ESEM. The cross sectioned samples were first used to measure the thickness of deposit remaining on the surface (Fig. 15). Three images were taken of the cross sectioned sample: one at the bottom of the sample (closest to the combustor exit), one near the middle, and one at the top. Figure 16 shows a typical series of images taken from the 5.81 g/s cooling level sample. As seen in Fig. 15, residual deposit thickness is fairly uniform for the no cooling and lowest level of cooling cases. This is indicative of the large percentage of separated deposit for these two cases as noted in Table 4. To estimate the deposit thickness before shutdown, the thickness of deposit flakes from the lowest coolant level tests was measured using calipers. For the no cooling case, the average flake thickness was 0.42mm and for the 1.3 g/s coolant case the average flake thickness was 0.25mm. This thickness was added to the residual thickness and the sum is presented in Fig. 15 as well. The dashed curves exhibit the expected monotonic decrease in deposit thickness with increasing coolant level. The residual deposit thickness at the top of the coupon drops off considerably with initial coolant compared to the middle and bottom which experience more tenacious deposit formation near the leading edge. Since the top of the coupon was furthest from the jet it experienced the lower temperatures and thus less deposition. Further increases in the amount of coolant result in decreasing deposit thicknesses at all locations. This spatial variation in deposit thickness is similar to what occurs in an actual turbine with deposition buildup at the hottest spots near the leading edge (Bons et al., 2001).

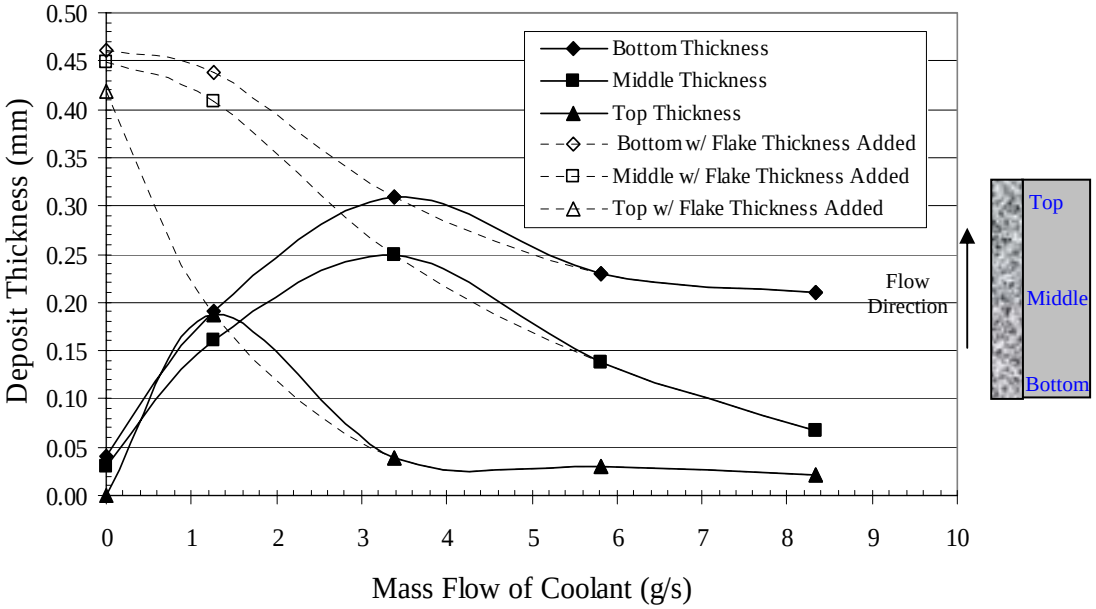

Figure 15. Deposit thickness as a function of cooling level.

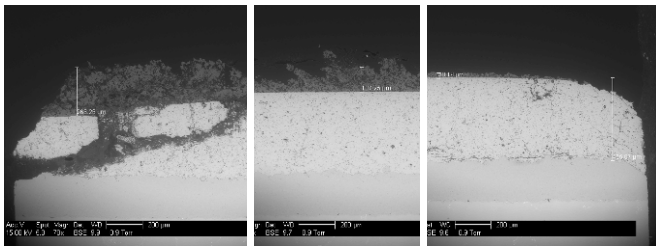

Figure 16. Typical image series of bottom (left), middle, and top (right) portions of 5.81 g/s coolant test sample.

Figure 16 shows the level of spallation which occurred at the leading edge as a result of deposit penetration. Similar spallation was seen in the particle size test series. Wammack et al [8] observed a similar deposit penetration effect although with a different TBC material system. With the exception of the highest cooling case all other tests in this series had varying amounts of spallation damage caused by penetration of the deposit along the cross section. X-ray spectroscopy was conducted to determine the elemental constituents in the surface deposit, as well as the penetrating deposits. Figure 17 shows the elemental composition in weight percent compared with the ash. The surface deposits showed a similar makeup as the ash, however there was a significant increase in Ca while Na and Si showed large decreases. The figure also clearly shows that the TBC studied is penetrated by Si, Ca, and Al from the ash. The spallation appears to be the result of the difference in coefficients of thermal expansion between the TBC and the penetrating ash elements. Upon shutdown of the facility, this mismatch in contraction rates causes significant thermal stresses in the TBC, resulting in separation of the TBC layer particularly near the edges of the coupon.

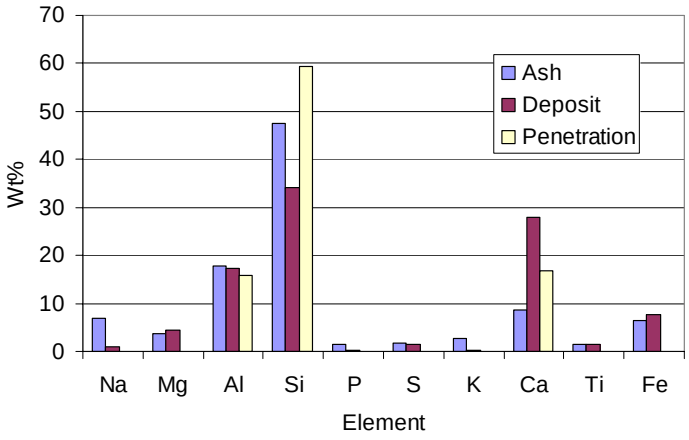

Figure 17. Elemental comparison of ash, deposit, and penetration for subbituminous coal impingement cooling series.

Impingement Cooling Series (petcoke ash)

A final series of tests were performed using the petcoke/coal blend particulate. Three tests were conducted using particles with a MMD of 6 μm. The third set of samples described earlier were used in this test series. First, a no cooling test was performed with the interior of the coolant fixture insulated as in the gas temperature and particle size test series. Following this, two impingement cooling levels were tested in the same configuration as the coal series. The same standard operating conditions were used, namely T = 1183°C, Mach = 0.25. The deposits looked similar to those of the coal impingement cooling series. The same large amount of flaking occurred on the no cooling case, however there was more flaking on the cooling cases compared to the coal series perhaps due to the larger particle size. There was slightly more spallation of the TBC in the no cooling case compared to the coal, however the different MMD makes a direct comparison difficult. A summary of the deposition results is shown in Table 5. Trends in net capture efficiency are included in Figure 14 with the coal.

Table 5. Deposition results from impingement cooling test series using petcoke

Mass flow of Coolant [g/s]	Heat Flux [kW/m^2]	Preburn Button Mass [gr]	Button Mass Change [mg]	Separated Deposit Mass [mg]	Separated Deposit %	Net Deposit Mass [mg]	Deposition Rate [mg/cm^{2}hr]	Net Particulate Mass [mg]	Net Capture Efficiency [%]
0	0	13.8	10	360	97	370	14.60	7720	4.79
3.38	1049.20	29.4	40	60	60	100	3.95	7680	1.22
8.33	1614.26	29.42	20	30	60	50	1.97	8200	0.65

FUTURE RESEARCH

Current research efforts are underway in several areas; results from these research efforts will be presented in the next contract report.

Further Analysis of Deposits

The deposits from the four test series discussed in this report are being analyzed by ESEM, both for composition and for physical morphology. A complete set of these ESEM images and results will be included in the MS thesis by Crosby (2007), and will be discussed in the next contract report. Roughness characteristics of these deposits are also being measured using a profilometer. This analysis has been complicated by the flaking seen in many of the deposits.

Film Cooling

Coupons with no TBC are being prepared that have several cooling holes in order to study the effects of deposition in areas where film cooling is present. One coupon has been made with cylindrical holes, and a coupon with shaped holes is being fabricated. The completed coupon has three cylindrical holes with dimensions shown in Fig. 18. The film cooling holes are typical of those seen in industry and have centerline angles of 30 deg relative to the surface tangent. The shaped hole has the same sized holes as the cylindrical holed coupon, but also has a divergence angle of 10 deg on each lateral side and on the side into the surface. The pitch to diameter ratio is 3.0 and the length to diameter ratio is 5.7 for each of the coupons. Arrangements are also being made to obtain TBC coupons with film holes from industry.

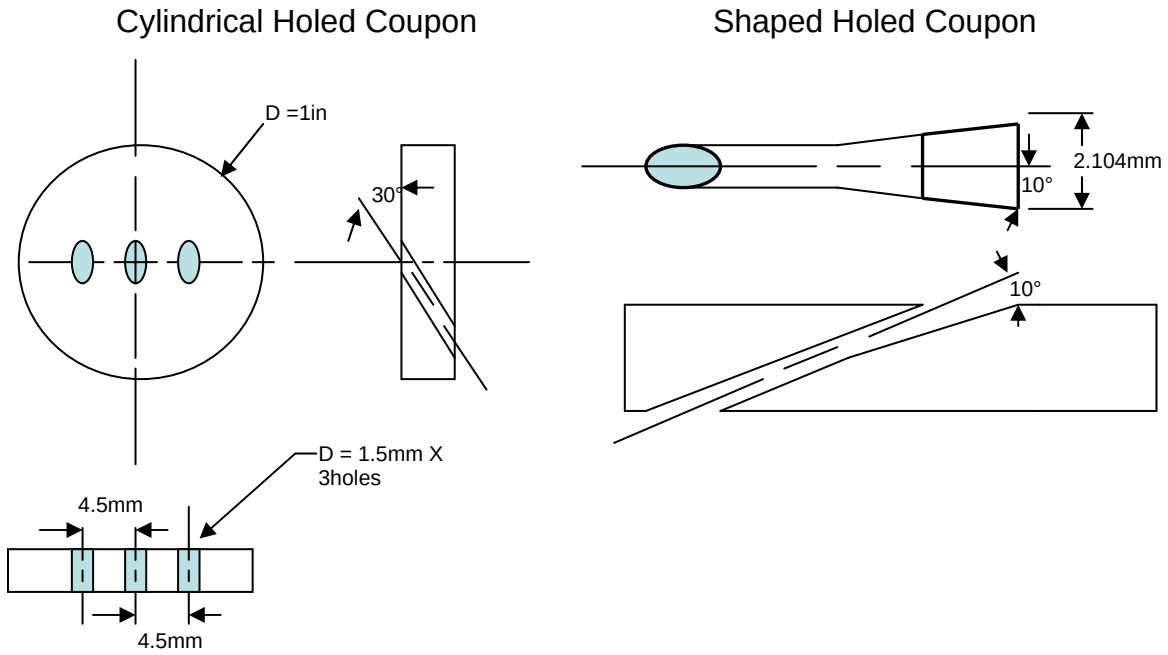

Figure 18: Relative dimensions of cylindrical and shaped hole coupons to be used for film cooling tests.

The TADF is being modified to replicate the flow rates and blowing ratios that occur on actual film cooling holes in typical land-based gas turbines. A rotometer has been added to the coolant flow to measure the coolant level and heat exchanger has been constructed which uses the hot combustor air to heat up the coolant air in order to get the correct density ratios out of the coupon holes. The facility is almost completely transitioned to allow film cooling/deposition tests, and these tests will be conducted during the next six month period.

Deposition tests will be conducted for the cylindrical holed coupon and the shape holed coupon at different film cooling levels. The net capture efficiency, coupon roughness, and temperature profile will be measured. The coupon roughness will be measured with a high precision contact profilometer and the temperature profile will be measured with a two-color infrared camera. This data will allow us to better understand the relationship of deposition with respect to different film cooling levels. The 3rd year option for this effort will involve the testing of scale models of these film hole roughness patterns in a low-speed wind tunnel.

Backside Temperature Measurement

The measurement of the frontside coupon surface temperature using the 2-color technique and the RGB camera, as discussed earlier in this report, has proven fairly successful. Preliminary temperature measurements have been taken of the backside of the coupon using the same camera system, viewing through the impingement cooling tube. This technique will be explored in more detail in the coming 6 months, along with the possibility of using two cameras simultaneously. In addition, the software will be modified to determine the temperature at each pixel or group of pixels, allowing measurement of spatial temperature distributions. This should prove fruitful in combination with the film cooling experiments.

CFD Modeling

The flow and heat transfer around the coupon in the TADF are being studied using conjugate flow and heat transfer calculations using the FLUENT™ computational fluid dynamics (CFD) code. These calculations will include coupons with and without the cooling holes. Preliminary results of the CFD calculations look promising, and have shown the need for sufficient grid cells in the boundary layer to calculate a convective heat transfer coefficient.

CONCLUSIONS

Four series of tests were performed in an accelerated deposition test facility to study the independent effects of particle size, gas temperature, and metal temperature on ash deposits from two candidate power turbine synfuels. Testing was conducted in the TADF by matching gas temperature, velocity, and net throughput of particulate out of the combustor with that experienced by a modern power turbine. Nominal combustor exit flow conditions are: Mach number of 0.25 and gas temperature of 1183°C. Testing with four different sizes of coal ash particles showed greater than double the deposition rate as particle mass mean diameter was increased from 3 to 16 μm. In the second series of tests, different gas temperatures were studied while the facility maintained a constant exit velocity of 170 m/s (Mach = 0.23-0.26). Particle deposition rate was found to decrease with decreasing gas temperature. The threshold gas temperature for deposition was approximately 960°C. Ground coal and petcoke ash particulates were used in the third and fourth test series with impingement cooling on the backside of the target coupon. Deposition rates decreased with increasing mass flow of coolant air, as expected.

Post exposure analyses of the third test series (scanning electron microscopy and x-ray spectroscopy) show decreasing TBC damage with increased cooling levels. Work is currently under way to study the effects of different TBC application techniques on deposition.

REFERENCES

Bons, J.P., Taylor, R., McClain, S., and Rivir, R.B.. "The Many Faces of Turbine Surface Roughness," *ASME Journal of Turbomachinery*, Vol. 123, Oct. 2001, pp. 739-748.

Bons, J.P., Crosby, J., Wammack, J.E., Bentley, B.I., and Fletcher, T.H., "High Pressure Turbine Deposition in Land-Based Gas Turbines with Various Synfuels," presented at IGTI 2005 in Reno, NV, June 2005. Paper # GT2005-68479. Accepted for publication in *ASME Journal of Engineering for Gas Turbines and Power*.

Bons, J.P., Wammack, J.E., Crosby, J., Fletcher, D., and Fletcher, T.H., 2006, "Evolution of Surface Deposits on a High Pressure Turbine Blade, Part II: Convective Heat Transfer," presented at IGTI 2006 in Barcelona, Spain, May 2006, #GT2006-91257.

Caguiat, D., 2002, "Rolls Royce/Allison 501-K Gas Turbine Anti-Fouling Compressor Coatings Evaluation," presented at IGTI 2002 in Amsterdam, The Netherlands, June 2002, #GT2002-30261.

Crosby, J.M., "Particle Size, Gas Temperature, and Impingement Cooling Effects on High Pressure Turbine Deposition in Land Based Gas Turbines from Various Synfuels," M.S. Thesis, Mechanical Engineering Department, Brigham Young University, Provo, Utah (April, 2007).

Hamed, A., Tabakoff, W., Rivir, R.B., Das, K., and Arora, P., "Turbine Blade Surface Deterioration by Erosion," Paper No. ASME-IGTI 2004-54328, June 2004.

Jensen, J.W., Squire, S.W., Bons, J.P., and Fletcher, T.H., "Simulated Land-Based Turbine Deposits Generated In An Accelerated Deposition Facility". *ASME Journal of Turbomachinery*. Vol. 127, pp. 462-470, July 2005.

Kim, J., Dunn, M.G., and Baran, A.J. et al, 1993, "Deposition of Volcanic Materials in the Hot Sections of Two Gas Turbine Engines," J. Engr. Gas Turbines & Power vol. 115, Jul 1993, pp 641-651.

Lu, H., "Experimental and Modeling Investigations of Biomass Particle Combustion," PhD Dissertation, Chemical Engineering Department, Brigham Young University, Provo, UT (2006).

McBride, B. J. and Gordon, S., "Computer Program for Calculation of Complex Chemical Equilibrium Compositions and Applications II. User's Manual and Program Description," http://www.grc.nasa.gov/WWW/CEAWeb/RP-1311P2.htm (2006).

Wammack, J.E., Crosby, J., Fletcher, D., Bons, J.P., and Fletcher, T.H., 2006, "Evolution of Surface Deposits on a High Pressure Turbine Blade, Part I: Physical Characteristics," presented at IGTI 2006 in Barcelona, Spain, May 2006, #GT2006-91246.

Wenglarz, R. A., and Fox, R. G., "Physical Aspects of Deposition from Coal Water Fuels under Gas Turbine Conditions", ASME Journal of Engineering for Gas Turbines and Power, vol. 112, January, 1990, pp. 9-14.

Wenglarz, R.A., and Wright, I.G., "Alternate Fuels for Land-Based Turbines," published in proceedings of the "Workshop on Materials and Practices to Improve Resistance to Fuel Derived Environmental Damage in Land-and Sea-Based Turbines", October 22-24, 2002, Colorado School of Mines, Golden, Colorado.

Fundamental Studies in Syngas Premixed Combustion Dynamics

Semi-annual Report

Reporting Period:
August 2006 through February 2007

Principal Investigator:
Ahmed F. Ghoniem

Co-PI:
Anuradha Annaswamy

Students:
Raymond Speth, graduate student, lead researcher
Murat Altay, graduate student, modeling
Duane Hudgins, graduate student, instrumentation

Report Date:
February, 2007

DOE Award Number:
DE-FC26-02NT41431

UTSR Project Number:
05-01-SR121

Submitting Organization:
Massachusetts Institute of Technology
77 Massachusetts Ave
Cambridge, MA 02139

Disclaimer:

Abstract

The objective of our project is to develop a fundamental understanding of syngas combustion dynamics in two generic configurations: a wake stabilized flame downstream a backward-facing step in a tunnel with a rectangular cross section, and a swirl stabilized flame in a circular tunnel with sudden expansion. During the past six months, we have accomplished all of the objectives for this reporting period, which were defined in our proposal, including construction and assembly of the swirl-stabilized flame experimental facility, rebuilding the test stand to accommodate both combustion tunnels with the available range of the diagnostics, and conducting a range of tests in the new facility. These tests were conducted to determine the stability limits of lean premixed syngas combustion over a range of conditions defined by the hydrogen-carbon monoxide ratio in the fuel, the equivalence ratio, the inlet temperature and the Reynolds number. Pressure spectra, spatial and temporal heat release rate and spatially resolved flame videos are captured and used to determine the dynamic characteristics and define the underlying mechanisms leading to changes in the flame response to its environment. Several regimes were identified, including a stable operating regime, a quasi-stable regime, and an unstable regime. Comparing the results obtained in the new swirl stabilized flame tunnel, with those obtained during our previous work in a planar combustor reveals many similarities, confirming the fundamental nature of the phenomena that we have observed. We used one set of radially-fired microjets located near the sudden expansion to suppress the instability. Measurements show the effectiveness of this instability mitigation approach, and define the conditions under which one achieves optimal operation. During the next six months, we will expand the range of test cases to help define the conditions which lead to combustion instability or blowout, and to define the underlying mechanisms that lead to combustion oscillations. We also plan to introduce different swirl centerbodies to examine the dependence of the stability conditions on the flowfield in the immediate downstream on the swirl section.

Table of Contents

List of Figures

Executive Summary

The objectives of this effort are to develop a fundamental understanding of syngas combustion dynamics in cases when flames are stabilized in recirculating flows established in the wake behind sudden expansions or in swirl stabilized flows. For this purpose, syngas with different hydrogen-carbon monoxide ratios, premixed with air at different equivalence ratios, and at different inlet combustor temperature and Reynolds numbers will be used in two types of combustors, a planar combustor and an axisymmetric combustor. Stability maps, optical diagnostics of the time dependent flame shape and heat release profiles, and other mechanistic characteristics will be recorded. The insight gained from these experiments will be used to suggest different variations on the flame stabilizations environments aimed at passively stabilizing the flames. Other more advanced probing techniques that may be necessary for this purpose, such as PIV, are currently being investigated. In the past six months of the project, we have:

(i) Installed the newly built swirl stabilized combustion rig;
(ii) Conducted initial tests in the swirl combustor by changing the equivalence ratio, Reynolds number and syngas composition;
(iii) Experimented with microjet stabilization in the swirl-stabilized combustor

During the next six months, we plan to:

(i) Develop complete stability maps for the swirl-stabilized combustor by varying the inlet temperature and swirl number and measuring the pressure oscillations, in addition to variations in equivalence ratio, fuel composition and Reynolds number;
(ii) Change the swirl section and the swirl vane centerbody to study the impact of the flowfield established immediately downstream of the swirl section on flame attachment and stability.
(iii) Measure the products composition and define the relation between the burning conditions and the concentration of NO_x and CO in the products.
(iv) Adapt optical system to axisymmetric geometry and determine spatial heat release rate distribution in space and time under different conditions.
(v) Use these data to construct reduced models for the response of lean premixed syngas combustion to external perturbation.

Project Description

Syngas, produced by the partial oxidation of coal in pure oxygen and steam inside high pressure gasifiers, has been proposed as the fuel of choice for modern high efficiency low emission combined cycle power plants. In these IGCC plants, gas turbine engines are used as topping cycles that take advantage of high temperature combustion products of syngas to improve the overall energy conversion efficiency. Incorporating technologies to filter out turbine-corroding gases from the gasifier products, and delivering clean syngas

to the gas turbine combustor enables the use of syngas in gas turbines. The sequestration of carbon dioxide, e.g., following the production of steam for the bottoming cycle, makes this plant environmentally ideal.

Combustion of syngas differs fundamentally from that of other complex hydrocarbon for a number of reasons, including the high hydrogen content, the short ignition delay, and the high flame speed. The latter endows syngas combustion with extra resistance to extinction under highly turbulent conditions, which can lead to interesting opportunities in terms of ultra lean burning, but may also exasperate the dynamics. The objective of this study is to investigate experimentally the fundamental properties of syngas combustion over a wide range of conditions. Data and models necessary for the design of stable, efficient and clean combustors for gas turbine engines running on syngas are being collected and assembled, and insight into the mechanisms governing the stability limits and the ensuing dynamics is being acquired, with the goal of proposing solutions that lead to efficient, clean and stable burning at high temperatures and high efficiency. Innovative solutions for stabilizing combustion at lean and ultra lean conditions will be demonstrated in the laboratory, as well as abstracted in design guidelines.

We plan to construct stability maps of premixed syngas combustion, whose coordinates are the fuel composition, that is the ratio of hydrogen to carbon monoxide, the equivalence ratio, the Reynolds number, the inlet temperature, for a step-stabilized combustor and a swirl stabilized combustor. The focus of the experiments are the lean and ultra lean limits and the associated dynamics observed as the equivalence ratio is reduced and the flow velocity is increased, and how the gas composition and other factors affect the blowout limits of the combustor. Mechanisms and precursors of dynamics, and the relationship between the dynamics and the blowout limits will be investigated using extensive, spatially resolved non-intrusive measurements, and modeling analysis. Besides the static stability limits measured in the experiments, dynamics associated with unstable operation are being categorized under different operating conditions. The experimental measurements will be used to suggest means of modifying the stabilization zone so as to improve the stability limits, passively, and without impacting other performance metrics such as emission and efficiency. Modeling of flame propagation in syngas mixtures will be used to support the analysis of the experimental data.

Experimental Work

Over the past six months, we conducted additional tests in the planar step stabilized combustor, installed the new swirl stabilized combustor, and conducted a series of preliminary tests in the swirl stabilized combustor.

Planar Combustor

We have expanded on our previously reported results in the planar step combustor by exploring the effect of different Reynolds numbers on the combustor's behavior. A paper based on our analysis of syngas combustion in the step stabilized paper, "Dynamics and

Stability Limits of Syngas Combustion in a Backward-facing Step Combustor," has been accepted for publication in the proceedings of the 2007 ASME Turbo Expo. A copy of the paper is included with this report.

Swirl Combustor

Since completing construction of the swirl stabilized combustion rig, shown in Figures 4 and 5, we have conducted a range tests which show the effect of varying several operating parameters, including the Reynolds number, the syngas composition and the equivalence ratio. Additionally, we have conducted a series of tests to assess the use of microjet air injection to enhance the combustor's stability. For each case, sound pressure data was collected from 3 pressure sensors mounted in the combustor, and video and still images were captured to visualize the flame structure and dynamics.

Discussion

In this section, we show some of the results obtained for varying Reynolds numbers in the step combustor, as well as the results of a range of tests performed in the swirl combustor which demonstrate the effects of varying Reynolds number, the syngas composition and the equivalence ratio.

Step Combustor

Figures 3, 4 and 5 show the overall sound pressure level (OASPL) for syngas mixtures with compositions varying from 20% CO and 80% H_2 to 80% CO and 20% H2 over a range of equivalence ratios at Reynolds numbers of 5000, 6500 and 8500, respectively. Three distinct operating modes may be distinguished as the equivalence ratio is varied for each syngas composition and equivalence ratio:

1. A stable region near the lean flammability limit, characterized by the shedding of small-scale vortices in the shear layer.

2. A quasi-stable region at intermediate equivalence ratios. Video images show that the flame remains attached to the step, but responds to shedding of large scale vortices in the wake.

3. At high equivalence ratios, an unstable operating mode characterized by a detached flame that exhibits periodic interaction between a large vortex and the flame.

As the amount of hydrogen in the fuel is increased, the lean flammability limit is extended and transitions between operating regimes shifts to lower equivalence ratios. Increasing the Reynolds number causes the stable region to become narrower and the unstable region to become broader. The transition to flashback at high equivalence ratio becomes more abrupt at high Reynolds numbers.

Swirl Combustor

Now we show the results from a set of tests conducted in the swirl-stabilized combustor at a Reynolds number of 25,000, defined by the average inlet velocity and the inlet diameter. The syngas composition was varied from 70% CO and 30% H_2 to 30% CO and 70% H_2, in 10% increments. The overall sound pressure levels in the combustor for these cases are shown in Figures 6 and 7. At each syngas composition, we collected data over the range of equivalence ratios at which a flame could be established in the test section, in increments of 0.02. The bars in the figures show the range over which the OASPL varied for each case. The cases with the longer bars were conditions where the combustion was more likely to switch between different operating modes, at the same operating condition. The lower limit in each case is the lean flammability limit, below which flame blowout is observed. The upper limit is reached when the flame anchors upstream of the test section.

For each syngas composition, we observe a similar set of behaviors. At low equivalence ratios, the flame is stable, with overall sound pressure levels in the range of 135 to 145 dB. As the equivalence ratio is increased, there is an abrupt transition to a "quasi-stable" operating mode, with sound pressure levels near 160 dB. Further increasing the equivalence ratio forces the combustor into an unstable operating regime with overall sound pressure levels in the range of 165 to 170 dB. As the hydrogen concentration in the syngas is increased, the transition points between operating modes shifts to leaner equivalence ratios. It is worth noting the striking similarity between these results and those previously shown for syngas mixtures in the step-stabilized combustor. Despite substantial changes in the combustor geometry, a significant increase in Reynolds number and the addition of swirl, the same sequence of operating regimes is still present.

In Figure 8, the pressure frequency spectra for representative stable and unstable cases are shown. In the unstable case, the spectrum exhibits its strongest peak at 160 Hz, corresponding to the full-wave mode of the combustor. Harmonics of diminishing amplitude are visible at 320 Hz, 480 Hz and 640 Hz. In the stable case, these peaks are not present, and instead the spectrum is dominated by a broad peak centered around 40 Hz, corresponding to the quarter-wave mode of the combustor.

A sequence of images extracted from high-speed videos taken of representative unstable and stable flames is shown in Figure 9. The final image in each sequence shows the average flame structure. In the stable case, the flame is shaped like a funnel, with the majority of the burning occurring in the vortex break-down region downstream of the swirler. The base of the flame extends upstream of the expansion plane, where it is anchored on the swirler centerbody. The flame burns steadily, and the intensity in the burning zone varies only slightly with time. In the unstable case, the fuel burns in pulses, with a frequency corresponding to the 160 Hz frequency observed in the pressure spectrum. The rapidly-burning flame is convoluted around a vortex which is periodically shed at the expansion plane. The enhanced mixing of the vortical interaction produces the rapid burning and produces a flame which is much more compact than the stable case.

To determine the effects of equivalence ratio and flow velocity on the flame, we conducted tests by varying equivalence ratio and Reynolds number while holding the syngas composition fixed at 50% CO and 50% hydrogen. The overall sound pressure levels for tests with Reynolds numbers ranging from 15,000 to 30,000 are shown in Figure 10. As the Reynolds number is increased, the sound pressure level in the stable region tends to increase. In the unstable region, however, the effect of Reynolds number is much weaker, with the exception of the Re = 15,000 case. For this case, the low flow speed permits the flame to anchor further upstream than it would otherwise, resulting in different dynamic behavior and flashback at the highest equivalence ratios, apparent here from the large variability in sound pressure level at equivalence ratios above 0.35.

As a method of suppressing combustion instability, we have installed a system where air is injected through a ring of 0.5 mm diameter holes just upstream of the expansion plane. By adjusting the air flow rate through these microjets, we can affect the combustor dynamics and in some cases, we can suppress the combustion instability. We conducted a series of tests in which we vary the microjet flow rate while holding the Reynolds constant at 25,000 and the fuel composition at 50% CO and 50% H_2. The tests were repeated for three equivalence ratios ranging from 0.32 to 0.40. The overall sound pressure level in the combustor as a function of microjet flow rate for each equivalence ratio is shown in Figure 11. For all three cases, sufficient microjet flow rate can reduce the OASPL in the combustor by 10 dB or more. High speed images of the flames before and after microjet air injection are shown in Figure 12. The microjets appear to introduce small scale turbulence and create a barrier which prevents the flame from traveling upstream of the expansion plane.

A clue to the combustion dynamics in the swirl stabilized flames is found in Figure 13, which shows the frequencies of the dominant SPL mode for the cases shown in Figure 11. For each equivalence ratio, the peak frequency shifts to a lower mode at about the same time there is a significant reduction in the OASPL. This describes how the unstable modes operate at a different frequency than the stable modes, corresponding to the large change in flame geometry observed in Figure 12. Since the microjets completely change the shape of the flame, the combustion is now taking place in a different region of the combustor. In the unstable case, the flame pulsates about the expansion plane at its dominant frequency. This pulsating is not present with the microjet injection.

Conclusions

In the past six months of this effort, and as stated in our proposal, we have assembled a new swirl-stabilized combustor and used it to study premixed combustion of lean and ultra-lean syngas mixtures over a range of conditions as defined by the fuel composition, equivalence ratio and Reynolds number. Additionally, we have explored the effectiveness of microjet air injection as a method for controlling combustion instability. We used simultaneous video recoding and pressure measurements to correlate the changes in the flame dynamics to the response of the acoustic field. We will continue our work by expanding the range of test conditions to include inlet temperature variations, different

swirl numbers, and different microjet injector geometries.

The results of our tests in the swirl combustor show that while the stability characteristics of syngas, as defined by the dependence of the overall sound pressure level on the equivalence ratio, is rather similar for all fuel compositions, the entire curve shifts to lower equivalence ratios, and lower pressure amplitudes, as the hydrogen percentage in the fuel increases. Thus, higher hydrogen concentration in the fuel enables leaner operation at lower pressure amplitudes. The trends observed in the swirl combustor correspond closely with those previously noted in the step-stabilized combustor, indicating that these phenomena are robust and that similar trends may be expected in a range of combustor designs.

During the next six months, we plan to develop complete stability maps for swirl-stabilized combustion of syngas, including installing different swirl vanes and different center bodies that change the flowfield downstream of the vane-centerbody section. Our current measurements and visualizations indicate that the flame, under most conditions, is partly anchored on the centerbody, even under unstable condition.

Figures

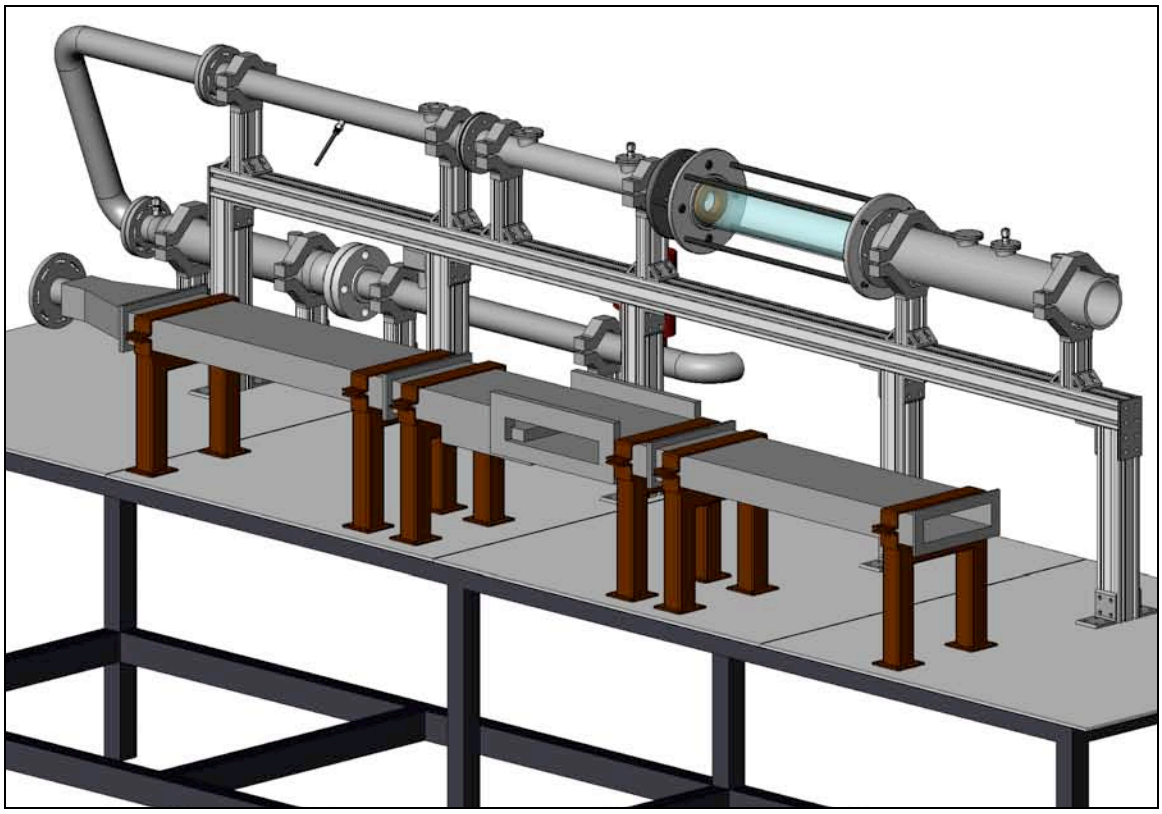

Figure 1: Solid model of combined lab setup with swirl stabilized and planar combustors.

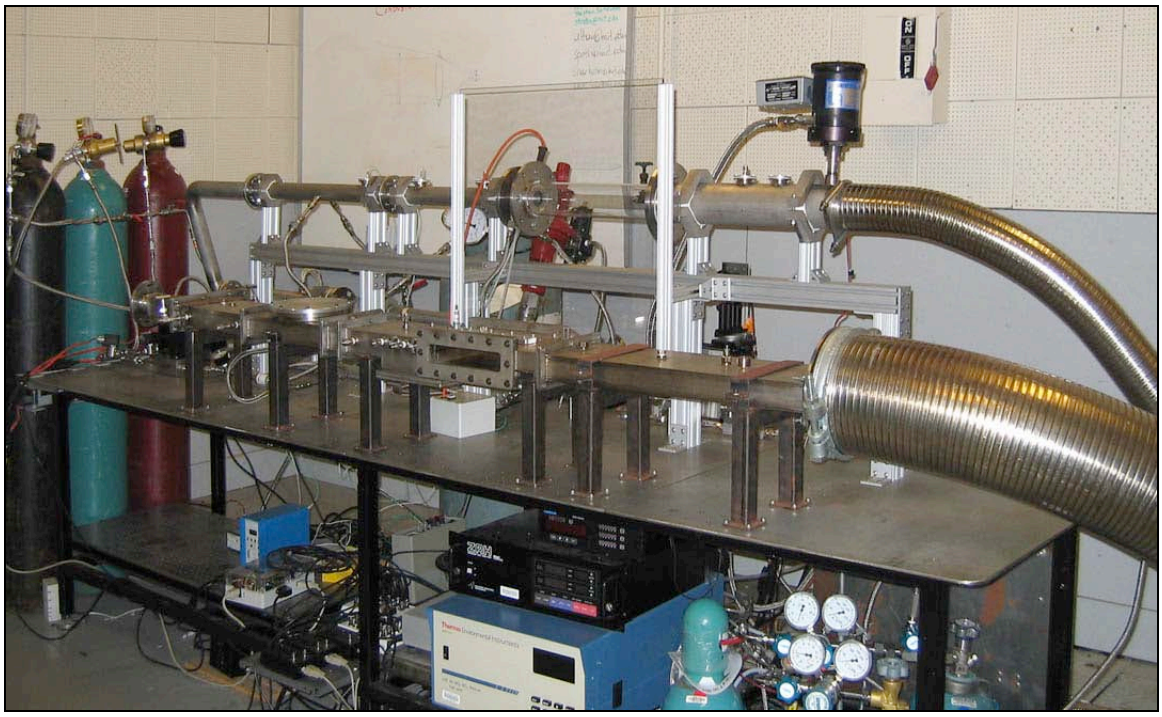

Figure 2: Swirl stabilized and planar combustors installed in the lab.

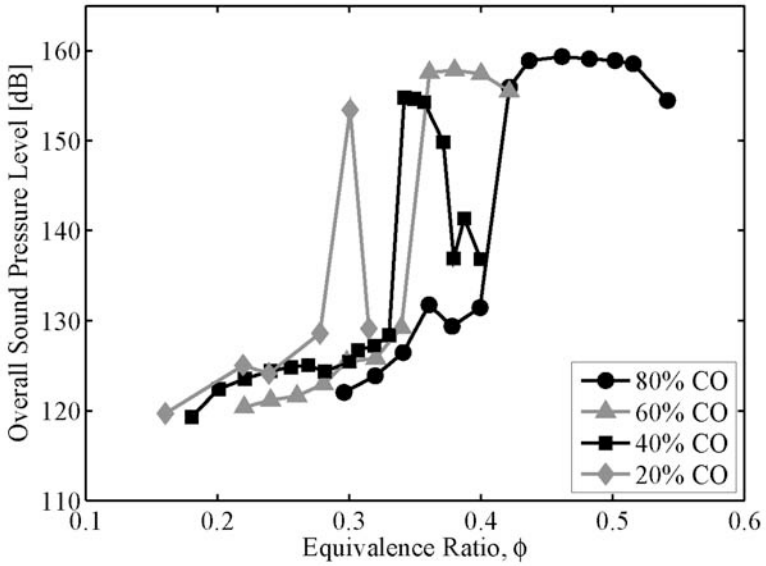

Figure 3: Dependence of overall sound pressure level on equivalence and syngas composition in the planar combustor at a Reynolds number of 5000.

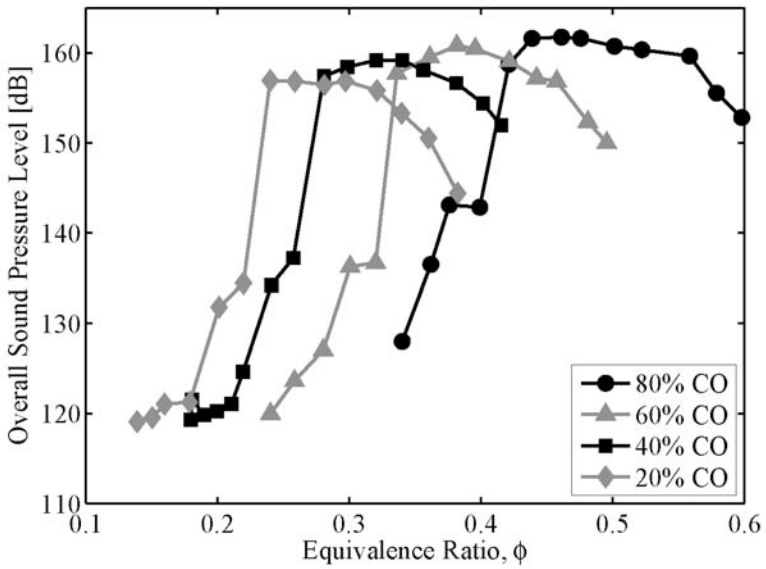

Figure 4: Dependence of overall sound pressure level on equivalence and syngas composition in the planar combustor at a Reynolds number of 6500.

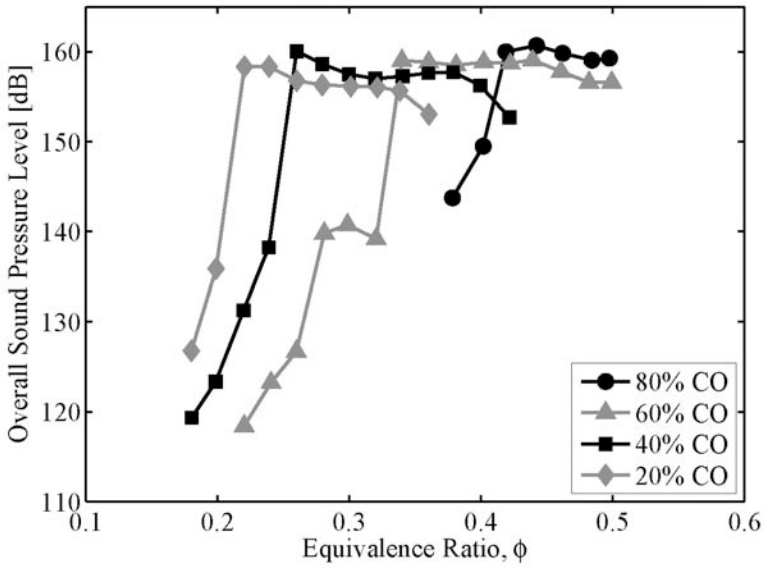

Figure 5: Dependence of overall sound pressure level on equivalence and syngas composition in the planar combustor at a Reynolds number of 8500.

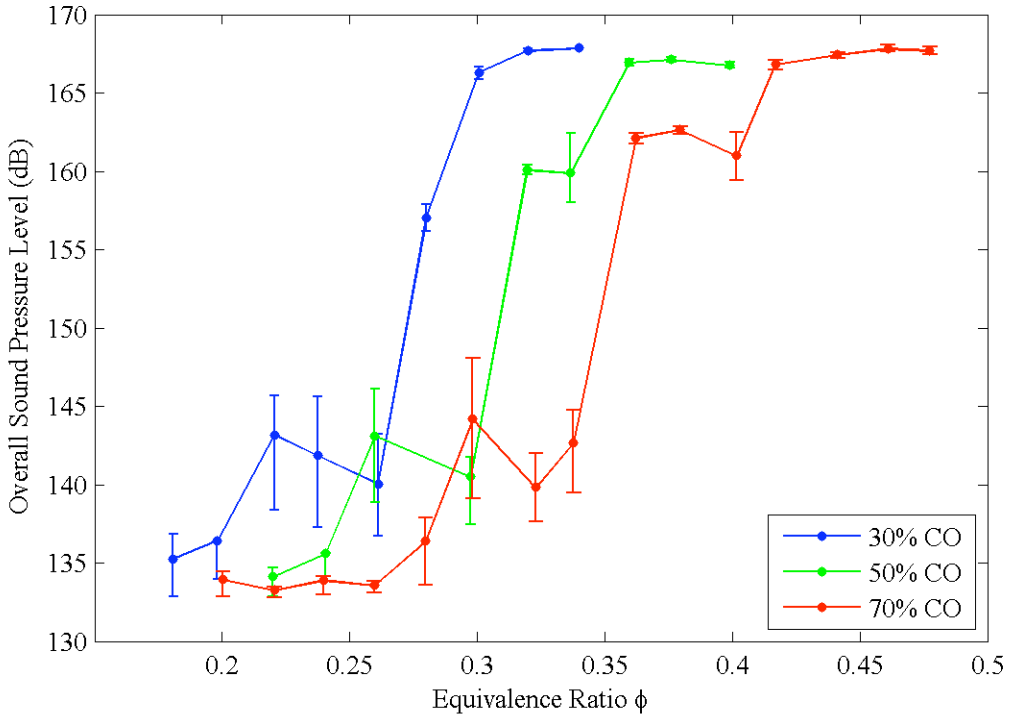

Figure 6: Overall sound pressure level in the swirl-stabilized combustor over a range of equivalence ratios and syngas compositions, with Reynolds number fixed at 25,000.

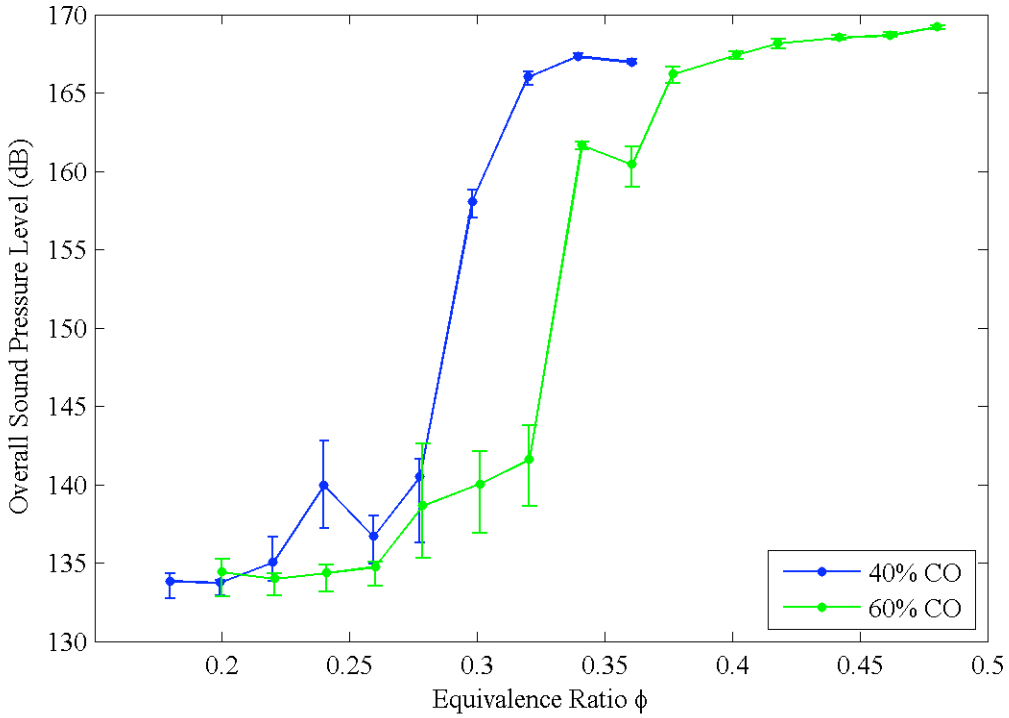

Figure 7: Overall sound pressure level in the swirl-stabilized combustor over a range of equivalence ratios and syngas compositions, with Reynolds number fixed at 25,000.

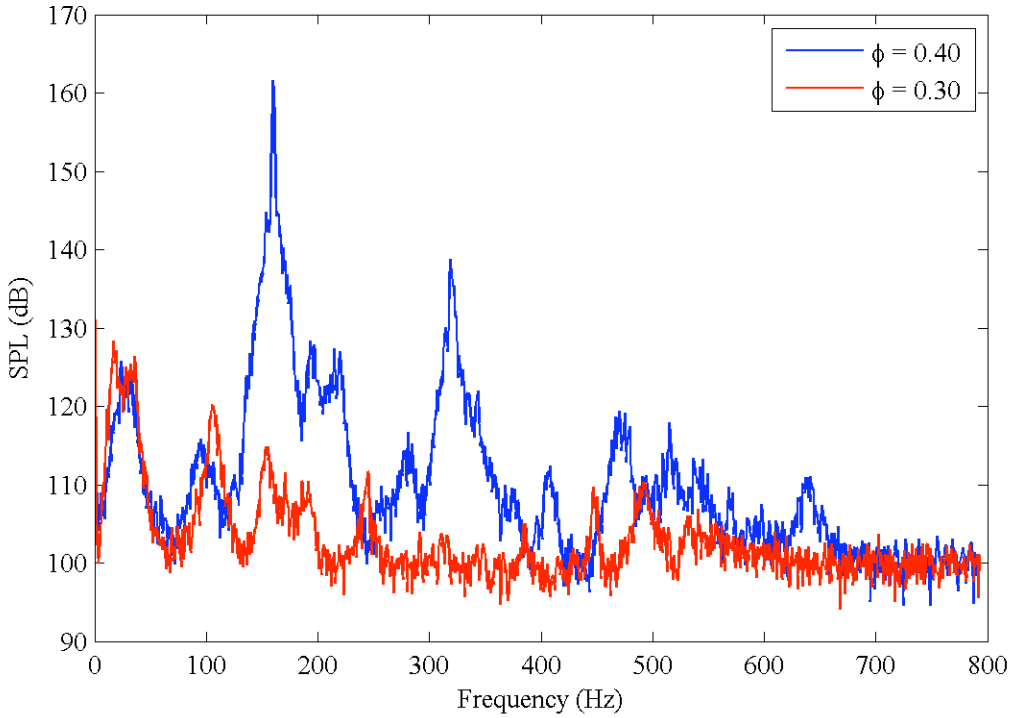

Figure 8: Sound Pressure Level frequency spectra for stable (Φ=0.30) and unstable (Φ=0.40) modes with 50% CO and 50% H_2 with a Reynolds Number of 25,000.

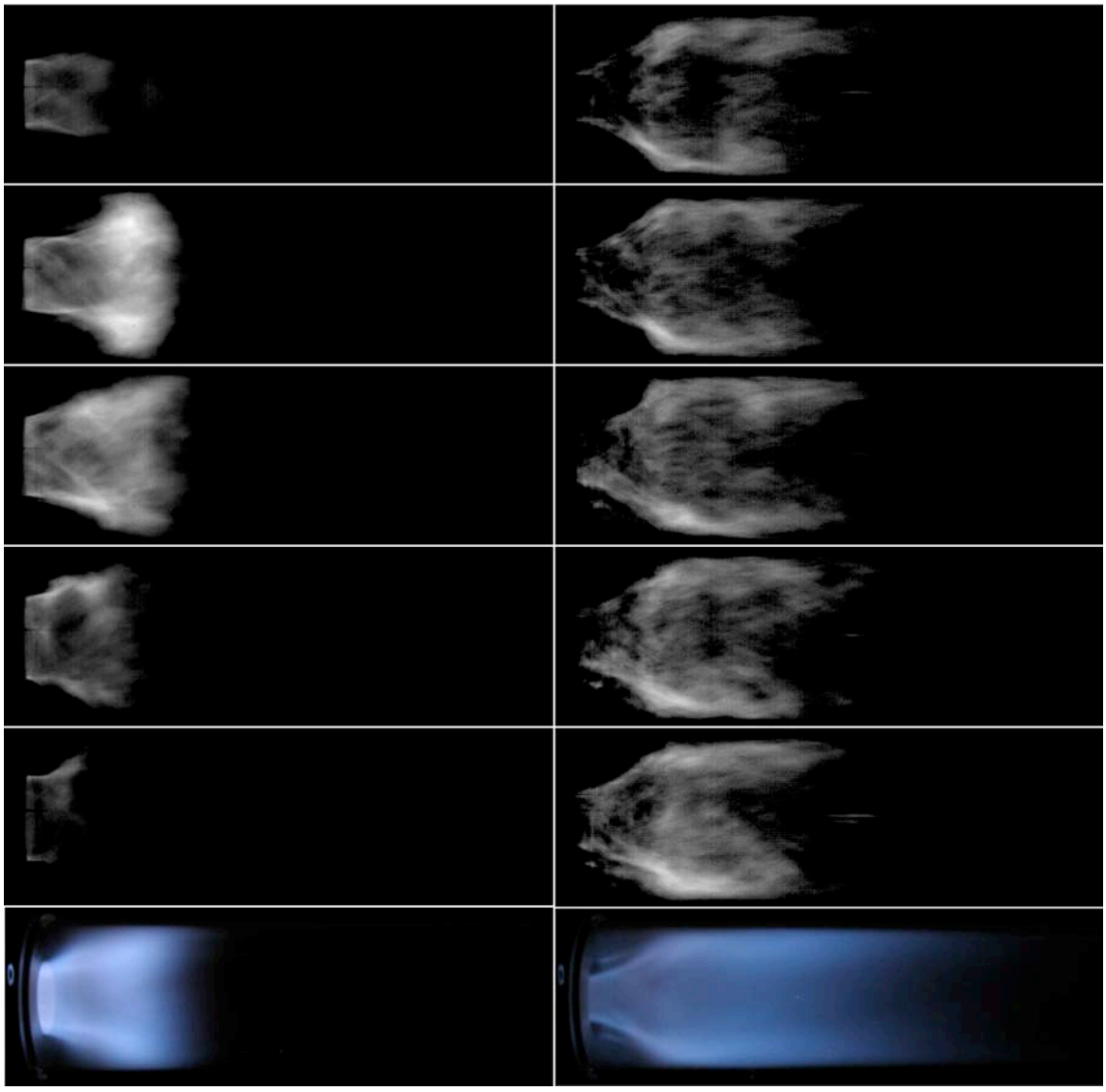

Figure 9: Image Sequence of unstable (left, Φ=0.44) and stable (right, Φ=0.32) flames with 60% CO fuel composition. The Reynolds number is 25,000. The inter-frame timing is approximately 2 ms. The exposure time is 1 ms. The final frame in each is a 500 ms exposure showing the average flame structure.

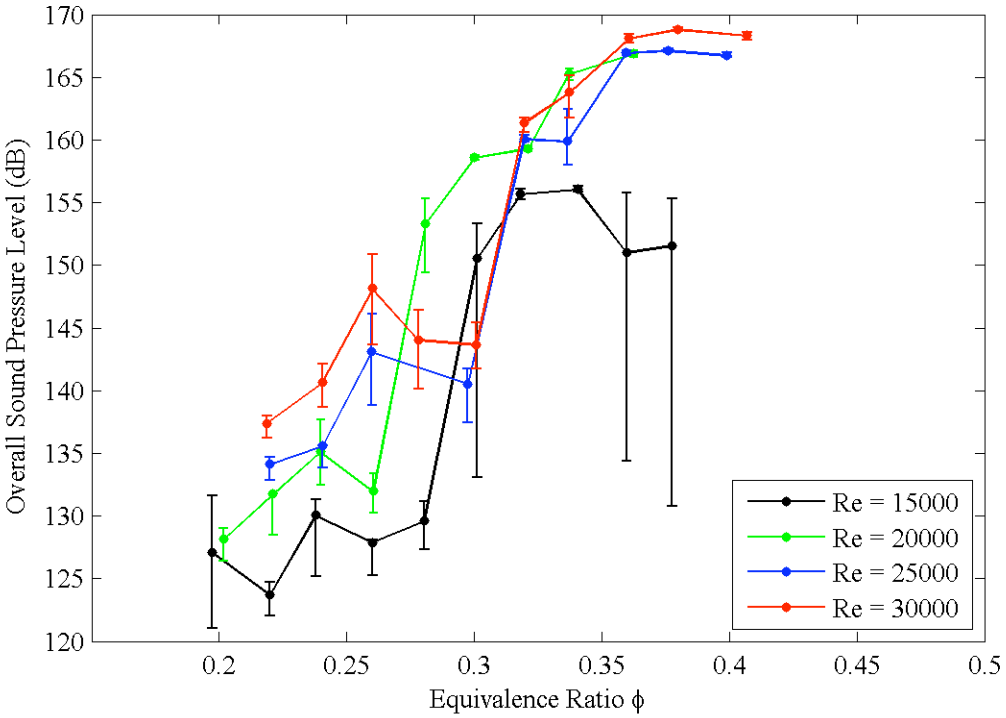

Figure 10: Overall sound pressure level in the swirl-stabilized combustor over a range of equivalence ratios and Reynolds numbers, with fuel composition fixed at 50% CO and 50% H_2.

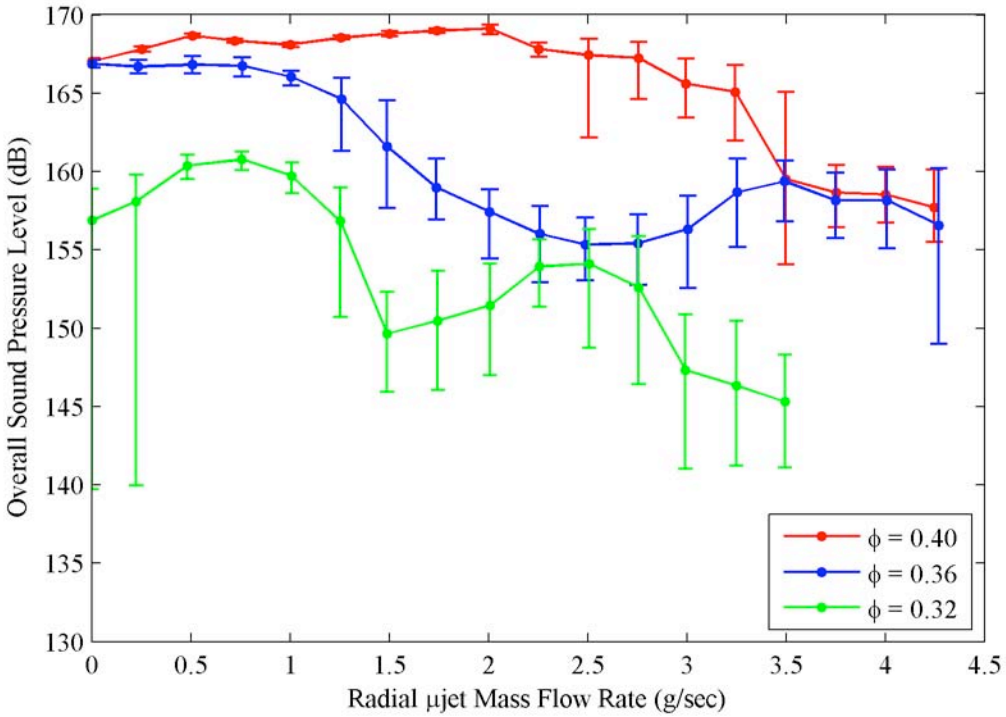

Figure 11: Overall Sound Pressure Level for swirl-stabilized combustion at varying equivalence ratios and microjet flow rate. The Reynolds number is 25,000 and the syngas composition is 50% CO and 50% H_2.

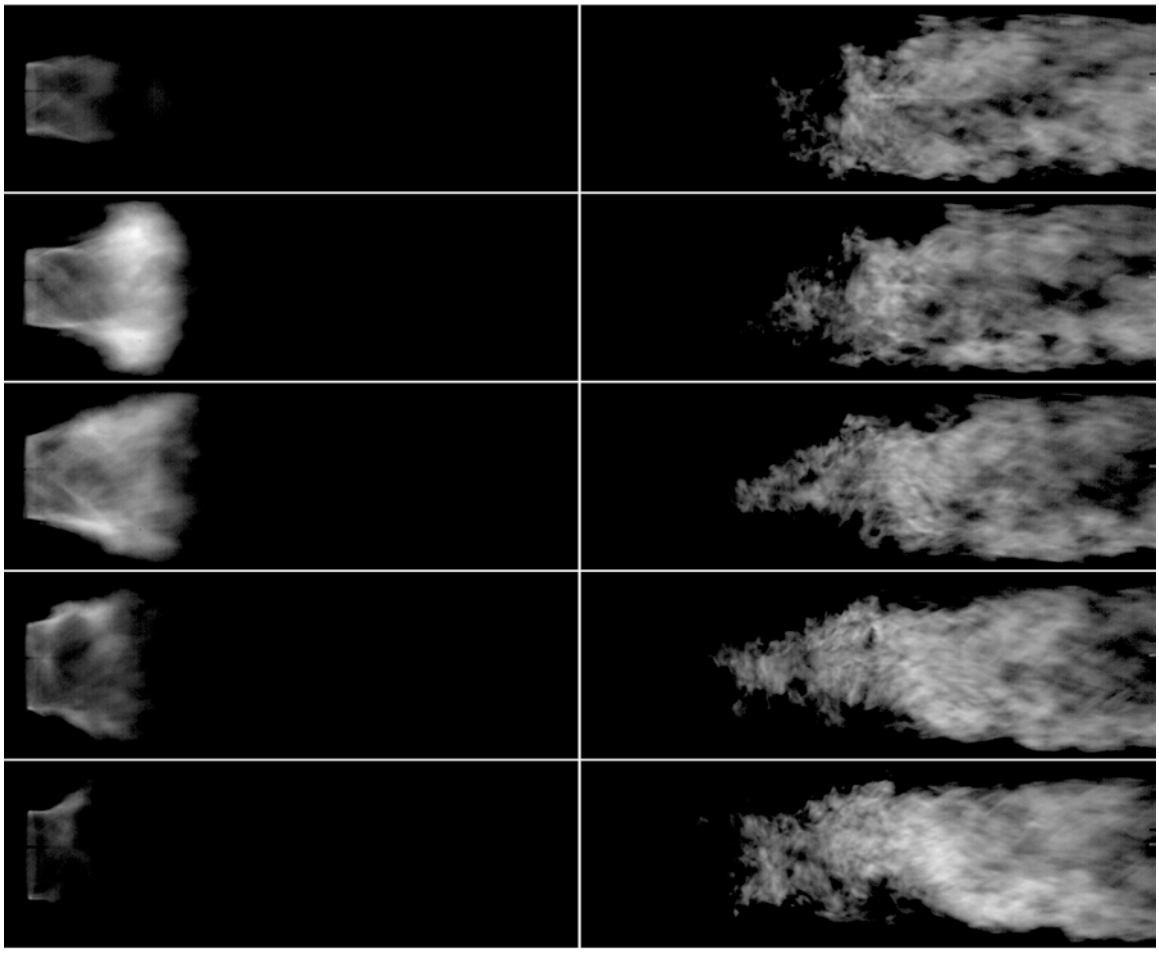

Figure 12: Image sequences of an unstable flame (left, Φ=0.40, flow rate = 0.0 g/sec) and a microjet stabilized (right, Φ=0.40, flow rate = 2.0 g/sec) flame with 80% CO fuel composition. The Reynolds number is 25,000. The inter-frame timing is approximately 2 ms. The exposure time is 1 ms.

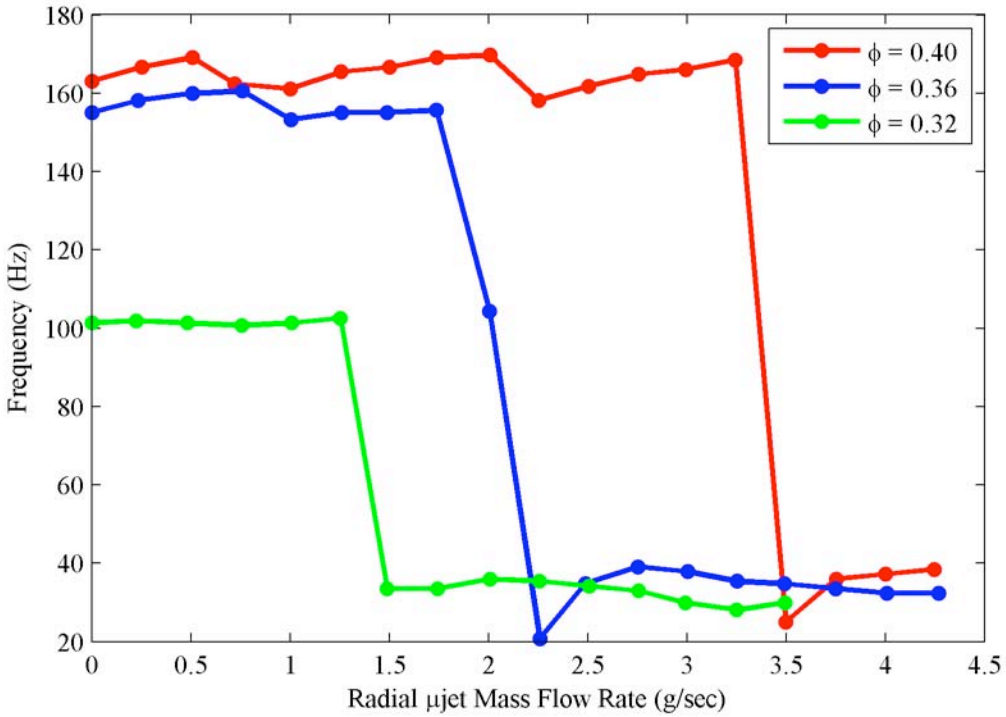

Figure 13: Peak SPL frequencies for swirl-stabilized combustion as a function of microjet flow rate at varying equivalence ratios. The Reynolds number is 25,000 and the fuel composition is 50% CO and 50% H_2.

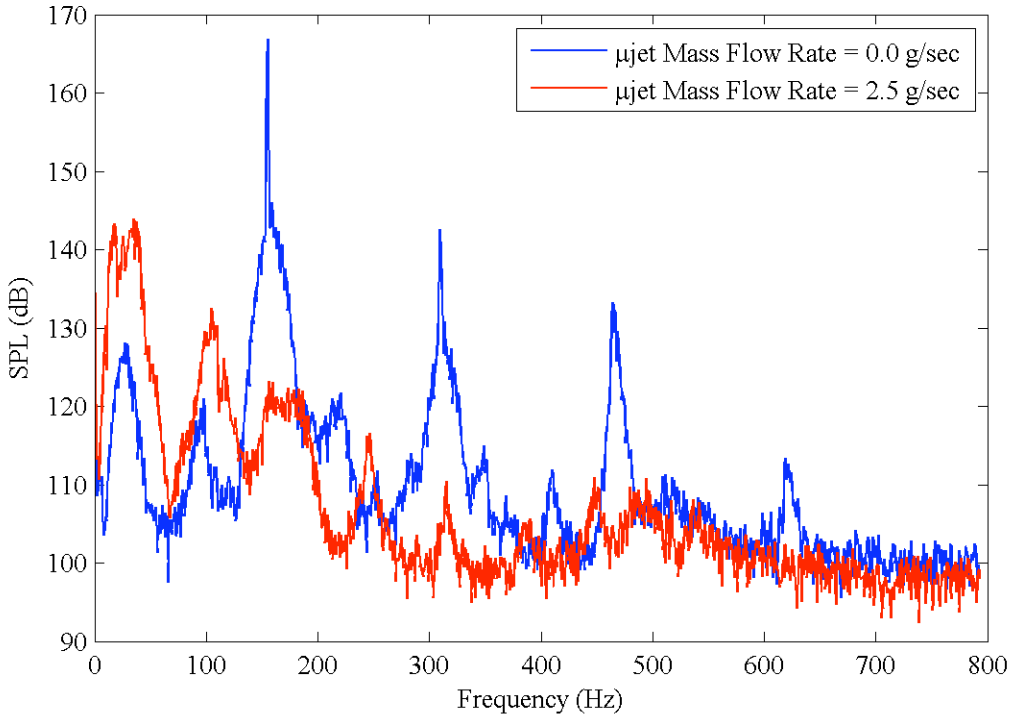

Figure 14: Sound pressure level spectra comparing noise levels without microjets and for a radial microjet flow rate of 2.5 g/sec. The fuel composition is 50% CO and 50% H_2 at an equivalence ratio of 0.36 with a Reynolds number of 25,000.